



**PROCEEDINGS OF
THE TWELFTH
INTERNATIONAL SYMPOSIUM ON
ARTIFICIAL LIFE AND ROBOTICS
(AROB 12th'07)**

Jan.25 - Jan.27, 2007
B-Con Plaza, Beppu, Oita, JAPAN

Supported by Japan Society for the Promotion of Science (JSPS)
International Meeting Series

Editors: Masanori Sugisaka and Hiroshi Tamaka
ISBN 978-4-9902880-1-3

The Twelfth International Symposium on Artificial Life and Robotics 2007(AROB 12th '07),
B-Con Plaza, Beppu, Oita, Japan, January 25-27, 2007

**Program of The Twelfth International Symposium on
ARTIFICIAL LIFE AND ROBOTICS**

(AROB 12th '07)

**January 25-27, 2007
B-Con Plaza, Beppu, Oita, Japan,**

Editors: Masanori Sugisaka and Hiroshi Tanaka

**THE TWELFTH INTERNATIONAL SYMPOSIUM
ON
ARTIFICIAL LIFE AND ROBOTICS**

(AROB 12th '07)

ORGANIZED BY

Organizing Committee of International Symposium on Artificial Life and Robotics
(Department of Electrical and Electronic Engineering, Oita University, Japan)

OPERATED BY

Santa Fe Institute (SFI, USA)
The Robotics Society of Japan (RSJ, Japan)
The Institute of Electrical Engineers of Japan (IEEJ, Japan)
Institute of Control, Automation and Systems Engineers (ICASE, Korea)
Chinese Association for Artificial Intelligence (CAAI, P. R. China)

CO-OPERATED BY

The Institute of Systems, Control and Information Engineers (ISCIE)
The Institute of Electronics, Information and Communication Engineers (IEICE)
The Institute of Electrical and Electronics Engineers, Inc.(IEEE Japan Council)
Japan Robot Association (JARA)
The Society of Instrument and Control Engineers (SICE, Japan)

SPONSORED BY

Japan Society for the Promotion of Science (JSPS)
Mitsubishi Electric Corporation Advanced Technology R&D Center
Oita Gas Co., Ltd.
ME System Co., Ltd.
Sanwa Shurui Co., Ltd.

SUPPORTED BY

Kyushu Bureau of Economy, Trade and Industry, Ministry of Economy, Trade and Industry
Oita Prefecture
Oita City
Beppu City
The Federation of Oita Prefecture Chambers of Commerce and Industry
The Oita Prefectural Organization of the Industrial Groups
Kyodo News
JIJI PRESS
Oita Godo Shimbunsha
The Asahi shimbun Co.
The Mainichi Newspapers Co.
The Yomiuri Shimbun Seibuhonsya
The Nishinippon Newspaper Co.
The NIKKAN KOGYO SHIMBUN. LTD.
NHK Oita Station
Oita Broadcasting System

Television Oita System corporation
Oita Asahi Broadcasting Co., Ltd.

ADVISORY COMMITTEE CHAIRMAN

F. Harashima (Tokyo Denki University, Japan)

GENERAL CHAIRMAN

M. Sugisaka (Oita University, Japan)

PROGRAM CHAIRMAN

H. Tanaka (Tokyo Medical & Dental University, Japan)

VICE-CHAIRMAN

J. J. Lee (KAIST, Korea)

J. L. Casti (Technical University of Vienna, Austria)

Y. G. Zhang (Academia Sinica, P. R. China)

ADVISORY COMMITTEE

T. Fukuda (Nagoya University, Japan)

F. Harashima (Tokyo Denki University, Japan)

H. Kimura (RIKEN, Japan)

M. Tomizuka (University of California Berkeley, USA)

INTERNATIONAL ORGANIZING COMMITTEE

K. Aihara (The University of Tokyo, Japan)

C. Barrett (Los Alamos National Laboratory, USA)

M. Bedau (Reed College, USA)

J. L. Casti (Technical University of Vienna, Austria)

M. Eaton (University of Limerick, Ireland)

J. M. Epstein (The Brookings Institution, USA)

T. Fukuda (Nagoya University, Japan)

H. Hashimoto (The University of Tokyo, Japan)

D. J. G. James (Coventry University, UK)

K. Kyuma (Mitsubishi Electric Corporation, Advanced Technology
R&D Center, Japan)

C. G. Langton (Santa Fe Institute, USA)

M. H. Lee (Pusan National University, Korea)

J. J. Lee (KAIST, Korea)

S. Rasmussen (Santa Fe Institute, USA)

T. S. Ray (University of Oklahoma, USA)

M. Sugisaka (Oita University, Japan) (Chairman)

C. Taylor (University of California-Los Angeles, USA)

W. R. Wells (University of Nevada-Las Vegas, USA)

Y. G. Zhang (Academia Sinica, P. R. China)

INTERNATIONAL PROGRAM COMMITTEE

- K. Abe (Nihon University, Japan)
- K. Aihara (The University of Tokyo, Japan) (Co-chairman)
- T. Arita (Nagoya University, Japan)
- M. Bedau (Reed College, USA)
- R. Belew (University of California-San Diego, USA)
- S- M. Chen (National Taiwan University of Science and Technology, Taiwan)
- Y. Y. Fan (University of California-Davis, USA)
- S. H. Han (Kyungnam University, Korea)
- H. Hashimoto (The University of Tokyo, Japan)(Co-chairman)
- N. Homma (Tohoku University, Japan)
- H. Inooka (Tohoku University, Japan)
- S. Ishikawa (Kyushu Institute of Technology, Japan)
- T. Ishimatsu (Nagasaki University, Japan)
- T. Iwamoto (Mitsubishi Electric Corporation, Advanced
Technology R&D Center, Japan)
- J. Johnson (The Open University, UK)
- O. Katai (Kyoto University, Japan)
- M. Kono (University of Miyazaki, Japan)
- H. Kawamura (Hokkaido University, Japan)
- S. Kumagai (Osaka University, Japan)
- J. M. Lee (Pusan National University, Korea)
- H. H. Lund (University of Southern Denmark, Denmark)
- M. Minami (Fukui University, Japan)
- T. Nagashima (Muroran Institute of Technology, Japan)
- M. Nakamura (Saga University, Japan)
- K. Nakano (The University of Electro-Communications, Japan)
- K. Naitoh (Wasada University, Japan)
- J. Nishii (Yamaguchi University, Japan)
- W. Nistico (University of Dortmund, Germany)
- S. Omatu (Osaka Prefecture University, Japan)
- K. Onishi (Niigata University, Japan)
- M. Okamoto (Kyushu University, Japan)
- M. Osano (Aizu University, Japan)
- M. Oswald (Vienna University of Technology, Austria)
- R. Pfeifer (University of Zurich-Irchel, Switzerland)
- T. S. Ray (University of Oklahoma, USA) (Co-chairman)
- S. Sagara (Kyushu Institute of Technology, Japan)
- P. Sapaty (National Academy of Sciences of Ukraine, Ukraine)
- T. Sawaragi (Kyoto University, Japan)
- T. Shibata (AIST, Japan)
- K. Shimohara (Doshisha University, Japan)
- K- B. Sim (Chung-Ang University, Korea)
- K. Sugawara (Tohoku Gakuin University, Japan)
- M. Sugisaka (Oita University, Japan)
- H. Suzuki (The University of Tokyo, Japan)
- H. Tanaka (Tokyo Medical & Dental University, Japan) (Chairman)
- M. Tanaka-Yamawaki (Tottori University, Japan)
- K. Tsuchiya (Kyoto University, Japan)
- K. Uosaki (Osaka University, Japan)
- H. Umeo (Osaka Electro-Communication University, Japan)
- K. Watanabe (Saga University, Japan)
- T. Yamamoto (University of Ryukyus, Japan)

H. Yanagimoto (Osaka Prefecture University, Japan)
M. Yano (Tohoku University, Japan)
Y. Yin (The Beijing University of Science and Technology, P. R. China)
M. Yokota (Fukuoka Institute of Technology, Japan)

LOCAL ARRANGEMENT COMMITTEE

S. Sagara (Kyushu Institute of Technology, Japan)
M. Rizon (Northern Malaysia University College of Engineering, Malaysia)
M. Sugisaka (Oita University, Japan) (Chairman)
J. Wang (Oita University, Japan)
X. Wang (Niihama National College of Technology Japan)
F. Dai (Matsue National College of Technology, Japan)
M. Ito (Konan University, Japan)
R. Mamat (Terengganu Advanced Technical Institute, Malaysia)

HISTORY

This symposium was founded in 1996 by the support of Science and International Affairs Bureau, Ministry of Education, Culture, Sports, Science and Technology, Japanese Government. Since then, this symposium has been held every year at B-Con Plaza, Beppu, Oita, Japan except in Oita, Japan (AROB 5th '00) and in Tokyo, Japan (AROB 6th '01). The twelfth symposium will be held on 25-27 January, 2007, at B-Con Plaza, Beppu, Oita, Japan. This symposium invites you all to discuss development of new technologies concerning Artificial Life and Robotics based on simulation and hardware in the twenty first century.

OBJECTIVE

The objective of this symposium is the development of new technologies for artificial life and robotics which have been recently born in Japan and are expected to be applied in various fields. This symposium will discuss new results in the field of artificial life and robotics.

TOPICS

Artificial brain research
Artificial intelligence
Artificial life
Artificial living
Artificial mind research
Bioinformatics
Brain science
Chaos
Cognitive science
Complexity
Computer graphics
Evolutionary computations
DNA computing
Fuzzy control
Genetic algorithms
Human-machine cooperative systems
Human-welfare robotics
Innovative computations
Intelligent control and modeling

Micromachines
Micro-robot world cup soccer tournament
Mobile vehicles
Molecular biology
Multi-agent systems
Nano-biology
Nano-robotics
Neural networks
Neurocomputers
Neurocomputing technologies and its application for hardware
Pattern recognition
Robotics
Robust virtual engineering
Virtual reality
Others

COPYRIGHTS

Accepted papers will be published in the proceeding of AROB and some of high quality papers in the proceeding will be requested to re-submit their papers for the consideration of publication in an international journal ARTIFICIAL LIFE AND ROBOTICS and APPLIED MATHEMATICS AND COMPUTATION. All correspondence related to the symposium should be addressed to AROB Secretariat.

**Dept. of Electrical and Electronic Engineering,
Oita University
700 Dannoharu, Oita 870-1192, JAPAN
TEL: +81-97-554-7841, FAX: +81-97-554-7818
E-MAIL arobsecr@cc.oita-u.ac.jp
Home Page <http://arob.cc.oita-u.ac.jp>**

MESSAGES



Fumio Harashima
Advisory Committee Chairman
(President, Tokyo Denki
University)

A handwritten signature in black ink that reads "Fumio Harashima".

Fumio Harashima
Advisory Committee Chairman of AROB

The science and technology (S&T) on Artificial Life and Robotics is newly born recently. This new S&T provides human being with happiness. Research is heart and desire of human being and the S&T is going toward clarifying human mind and heart. Artificial Life and Robotics provides us with a strong tool to achieve our objective.

I would like to congratulate researchers who work in the fields on Artificial Life and Robotics.



Masanori Sugisaka
General Chairman
(Professor, Oita University)

A handwritten signature in black ink that reads "Masanori Sugisaka".

Masanori Sugisaka
General Chairman of AROB

It is my great honor to invite you all to the Twelfth International Symposium on Artificial Life and Robotics (AROB 12th '07).

The symposiums from the first (1996) to the Eleventh (2006) were organized by Oita University under the sponsorship of the Science and Technology Policy Bureau, the Ministry of Education, Science, Sports, and Culture (Monbusho), presently, the Ministry of Education, Culture, Sports, Science, and Technology (Monkasho), Japanese Government, The Commemorative Organization for the Japan World Exposition ('70), Air Force Office of Scientific Research, Asian Office of Aerospace Research and Development (AFOSR/AOARD), USA and co-operated by Santa Fe Institute (USA), RSJ, IEEJ, ICASE (Korea), CAAI (P. R. China), ISCIE, IEICE, IEEE (Japan Council), JARA , and SICE.

I would like to express my sincere thanks to Monkasho, The Commemorative Organization for the Japan World Exposition ('70) and scientific societies for their repeated support.

This Twelfth symposium is sponsored by Japan Society for the Promotion of Science (JSPS) and Japanese companies (Mitsubishi Electric Corporation Advanced Technology R&D Center, Oita Gas Co., Ltd., ME System Co.,Ltd., Sanwa Shurui Co., Ltd.). I would like to express special thanks for JSPS and the companies stated above.

The symposium invites you to discuss the development of new technologies in the 21st century concerning Artificial Life and Robotics, based on simulation and hardware.

We hope that AROB 12th '07 will facilitate the establishment of an international joint research institute on Artificial Life and Robotics in future. I hope that you will obtain fruitful results from exchange of ideas between researchers during the symposium.

Hiroshi Tanaka
Program Chairman of AROB



Hiroshi Tanaka
Program Chairman
(Professor, Tokyo Medical
and Dental University)



On behalf of the program committee, it is my great pleasure and honor to invite you all to the Twelfth International Symposium on Artificial Life and Robotics (AROB 12th '07). This symposium is made possible owing to the cooperation of Oita University and Santa Fe Institute. We are also debt to Japanese academic associations such as SICE, RSJ, and several private companies. I would like to express my sincere thanks to all of those who make this symposium possible.

As is needless to say, the Alife and biologically-inspired Robotics approach now attracts wide interests as a new paradigm of science and engineering. Take an example in the field of bioscience, the accomplishment of HGP (Human Genome Project) and subsequent post-genomic comprehensive "Omics data" such as transcriptome, proteome and metabolome, bring about vast amount of bio-information. However, as a plenty of omics data becomes available, it becomes sincerely recognized that the framework by which these omics data can be understood to make a whole picture of life is critically necessary. Thus, in the post-genomic era, Alife approach is expected to give one of new alternative ideas to integrate this vast amount of bio-data.

This example shows the Alife approach is very promising and becomes widely accepted as a paradigm of next generation of life science. We hope this symposium becomes a forum for exchange of the ideas of the attendants from various fields who are interested in the future possibility of complex systems approach.

I am looking forward to meeting you in Beppu, Oita.



Y. G. Zhang
Vice Chairman
(Professor, Academia Sinica)

A handwritten signature in black ink that reads "Yongguang Zhang". The signature is written in a cursive, flowing style.

Y. G. Zhang
Vice Chairman of AROB

Dear all friends and all participants,

Here I would like to show my warm welcome to you all attending the Twelfth International Symposium on Artificial Life and Robotics (AROB '07). As you know, this annual symposium was founded in 1996 by the support of Science and International Affairs Bureau, Ministry of Education, Science, Sports, and Culture (presently, Ministry of Education, Culture, Sports, Science and Technology) of Japan. Since then AROB is gradually become worldwide famous international symposium. Now AROB is already not an "academic baby", but "academic teenage", and AROB also owns an international journal, named the "Journal of Artificial Life and Robotics" published by Springer in last nine years.

The objective of AROB is aimed to develop new technologies for Artificial Life and Robotics which have been born recently. The important devotion of AROB is not only to pay attention to the development of theory on Artificial Life, but also expected to apply the principle to various fields, especially, the combination of both the Artificial Life and Robotics together. So far there are only few international symposiums or conference on artificial life, however, AROB is the only one that to explore the new generation of Robotics in far-sight with artificial life principle. This is a very great and difficult career, and need continuous and consistent efforts of more and more scientists and engineers. All participants to AROB are the part of team and we are devoting to the same target.

Beppu, the place of held most AROB symposium, is very charming city in Japan, she has variety of hot spring (jigoku), beautiful bay and colorful mountains. Her phantasmagoric visual change in various season attract many tourists. I hope all of you enjoy and appreciate her.

Finally, I would like to show my great thanks to all people who are working for this AROB'07, including all staffs of AROB Lab, secretariat, and students, the successful holding of AROB symposium is dependent on the contributions of you all.



Ju-Jang Lee
Vice Chairman
(Professor, KAIST)

A handwritten signature in black ink, appearing to read 'J. Lee'.

Ju-Jang Lee
Vice Chairman of AROB

The Twelfth International Symposium on Artificial Life and Robotics (AROB) will be held in Beppu, Oita, JAPAN from Jan. 25th to 27th, 2007. This year's Symposium will be held amidst the high expectations of the increasingly important role of the new interdisciplinary paradigm of science and engineering represented by the field of artificial life and robotics that continuously attracts wide interests among scientist, researchers, and engineers around the globe.

Since the time of the very first AROB meeting in 1996, each year, distinguished researchers and technologists from around the world are looking forward to attending and to meeting at AROB. AROB is becoming the annual excellent forum that represents a unique opportunity for the academic and industrial communities to meet and assess the latest developments in this fast growing artificial life and robotics field. AROB enables them to address new challenges and share solutions, discuss research directions for the future, exchange views and ideas, view the results of applied research, present and discuss the latest development of new technologies and relevant applications.

In addition, AROB offers the opportunity of hearing the opinions of well known leading experts in the field through the keynote sessions, provides the bases for regional and international collaborative research, and enables to foresee the future evolution of new scientific paradigms and theories contributed by the field of artificial life and robotics and associated research area. The twenty-first century will become the century of artificial life and intelligent machines in support of humankind and AROB is contributing through wide technical topics of interest that support this direction.

It is a great for me as the Vice Chairman of the 12th AROB 2007 to welcome everyone to this important event. Also, I would like to extend my special thanks to all the authors and speakers for contributing their research works, the participants, and the organizing team of the 12th AROB. Looking forward to meeting you at the 12th AROB in Beppu-Oita and wishing you all the best.

TIME TABLE

	RoomA	RoomB	RoomC	RoomD
1/24 13:00 (Wed) 17:00	Registration (Registration Desk)			
	Welcome Party (at Hanabishi Hotel)			
1/25 8:00 (Thur) 8:40	Registration (Registration Desk)			
	GS 22 (6) Chair M. Zhao	OS 2 (6) Chair M. Kono	OS 14 (6) Chair S-H. Han	
10:10 10:30	Coffee Break			
				Ceremony
				Plenary Talk PT1 Y. G. Zhang Chair M. Nakamura
11:40	Lunch			
12:40	GS 23 (5) Chair M. Eaton	OS 6 (4) Chair S. Omatu will end at 13:40	GS4 (3) Chair G. Cui will end at 13:25	
13:55 14:05	Coffee Break			
	GS 24 (4) Chair I. H. Suh	GS 2 (4) Chair M. Nakamura	GS5 (5) Chair V. Trifa will end at 15:20	
15:05	GS 20 (4) Chair D. Ai	GS 3 (4) Chair P. Sapaty	GS 15 (4) Chair S. Yaacob will end at 16:20	
16:05	GS 21 (5) Chair K. Ikeda	OS 1 (5) Chair O. Sato	GS 16 (4) Chair D. H. Kim	
17:20				

GS: General Session

OS: Organized Session

GS1 Artificial Brain Research & Brain Science
GS2 Artificial Intelligence- I
GS3 Artificial Intelligence- II
GS4 Artificial Life- I
GS5 Artificial Life- II & Artificial Living
GS6 Bioinformatics & Chaos
GS7 Cognitive Science & Evolutionary Computations
GS8 Complexity
GS9 Computer Graphics- I
GS10 Computer Graphics- II
GS11 Fuzzy Control
GS12 Genetic Algorithms
GS13 Innovative Computations- I
GS14 Innovative Computations- II & Human- Machine Cooperative Systems
GS15 Intelligent Control and Modeling-I
GS16 Intelligent Control and Modeling- II
GS17 Intelligent Control and Modeling-III
GS18 Mobile Vehicles- I
GS19 Mobile Vehicles- II
GS20 Neural Networks- I

GS21 Neural Networks- II & Neurocomputers
GS22 Robotics-I
GS23 Robotics- II
GS24 Robotics-III
GS25 Robotics-IV
GS26 Robotics-V & Micro-Robot World Cup Soccer Tournament
GS27 Robust Virtual Engineering & Virtual Reality
OS1 Intelligent Systems and Robotics
OS2 Automata and Control
OS3 Models for Neural Networks and Brains
OS4 Methods for Complex Systems: Feature Identification and Control
OS5 Fundamental Research on Recognition and Control
OS6 Intelligent Networks
OS7 Financial Market and Related Topics
OS8 Intuitive Human-System Interaction
OS9 Biomimetic Machines and Robots
OS10 Soft Robotics
OS11 Intelligent Robot Control and Sensors
OS12 Bio-inspired Approach and Application
OS13 Membrane Computing. From Calls to Computers and Back
OS14 Robot Control and Application

The Twelfth International Symposium on Artificial Life and Robotics 2007(AROB 12th '07),
B-Con Plaza, Beppu, Oita, Japan, January 25-27, 2007

	RoomA	RoomB	RoomC	RoomD
1/26 8:00	Registration (Registration Desk)			
(Fri) 8:40	OS 10 (4) Chair H. Kinjo	GS 11 (4) Chair S. Sagara	GS 12 (7) Chair K. B. Sim	
9:40		Poster Session PS1, PS2, PS3, PS4		
10:25	Coffee Break			
10:40				Plenary Talk PT2 H. Tsumura Chair M. Sugisaka
11:30	Lunch			
12:30	GS 25 (5) Chair Y. Wang will end at 13:45	GS 18 (6) Chair H. Hashimoto	OS 3 (6) Chair H. Suzuki	
14:00	GS 26 (6) Chair K. Uosaki will end at 15:15	GS 19 (6) Chair J. Wang	GS 17 (6) Chair A. Kanasugi	
15:30	Coffee Break			
15:40	GS 9 (3) Chair S. Ishikawa will end at 16:25	OS13 (4) Chair M. Oswald	OS 4 (6) Chair T. Kohno	
16:40	GS 10 (4) Chair H. Furutani will end at 17:25	Invited Talks session IT1 H. H. Lund IT2 L. Pagliarini Chair M. Rizon will end at 17:30	will end at 17:10 GS 6 (3) Chair K. Naitoh will end at 17:55	
18:10	AROB Award Ceremony (Chair K. Watanabe)			
20:10	Banquet – Hotel Shiragiku (Chair S. Sagara)..... Welcome Address T. Fukuda / J. J. Lee			

GS: General Session OS: Organized Session

GS1 Artificial Brain Research & Brain Science
GS2 Artificial Intelligence- I
GS3 Artificial Intelligence- II
GS4 Artificial Life- I
GS5 Artificial Life- II & Artificial Living
GS6 Bioinformatics & Chaos
GS7 Cognitive Science & Evolutionary Computations
GS8 Complexity
GS9 Computer Graphics- I
GS10 Computer Graphics- II
GS11 Fuzzy Control
GS12 Genetic Algorithms
GS13 Innovative Computations- I
GS14 Innovative Computations- II & Human- Machine Cooperative Systems
GS15 Intelligent Control and Modeling-I
GS16 Intelligent Control and Modeling- II
GS17 Intelligent Control and Modeling-III
GS18 Mobile Vehicles- I
GS19 Mobile Vehicles- II
GS20 Neural Networks- I

GS21 Neural Networks- II & Neurocomputers
GS22 Robotics-I
GS23 Robotics- II
GS24 Robotics-III
GS25 Robotics-IV
GS26 Robotics- V & Micro-Robot World Cup Soccer Tournament
GS27 Robust Virtual Engineering & Virtual Reality
OS1 Intelligent Systems and Robotics
OS2 Automata and Control
OS3 Models for Neural Networks and Brains
OS4 Methods for Complex Systems: Feature Identification and Control
OS5 Fundamental Research on Recognition and Control
OS6 Intelligent Networks
OS7 Financial Market and Related Topics
OS8 Intuitive Human-System Interaction
OS9 Biomimetic Machines and Robots
OS10 Soft Robotics
OS11 Intelligent Robot Control and Sensors
OS12 Bio-inspired Approach and Application
OS13 Membrane Computing. From Calls to Computers and Back
OS14 Robot Control and Application

The Twelfth International Symposium on Artificial Life and Robotics 2007(AROB 12th '07),
B-Con Plaza, Beppu, Oita, Japan, January 25-27, 2007

		RoomA	RoomB	RoomC	RoomD
1/27	8:00	Registration (Registration Desk)			
(Sat)	8:40	OS 5 (3) Chair F. Dai	Invited Talks session IT3 B. Pillai Chair J. J. Lee	GS 8 (3) Chair Y. Ishida	
	9:25	OS 12 (5) Chair I. Yoshihara	GS 1 (5) Chair X. Wang	OS 8 (5) Chair M. Yokota	
	10:40				
	10:50	Coffee Break			
	11:40				Plenary Talk PT3 Y. I. Cho Chair Y. G. Zhang
	12:40	Lunch			
	13:40	GS 13 (4) Chair T. Arita	GS 7 (4) Chair T. Kondo	GS 27 (3) Chair J. Du will end at 13:25	
	15:10	GS 14 (3) Chair K. Yamasaki will end at 14:25	OS 9 (6) Chair K. Watanabe	OS 11 (6) Chair Y. I. Cho will end at 14:55	
	16:10	OS 7 (3) Chair M. Tanaka- Y			
		Farewell Party (Room B)			

GS: General Session OS: Organized Session

GS1 Artificial Brain Research & Brain Science
GS2 Artificial Intelligence- I
GS3 Artificial Intelligence- II
GS4 Artificial Life- I
GS5 Artificial Life- II & Artificial Living
GS6 Bioinformatics & Chaos
GS7 Cognitive Science & Evolutionary Computations
GS8 Complexity
GS9 Computer Graphics- I
GS10 Computer Graphics- II
GS11 Fuzzy Control
GS12 Genetic Algorithms
GS13 Innovative Computations- I
GS14 Innovative Computations- II & Human -Machine Cooperative Systems
GS15 Intelligent Control and Modeling-I
GS16 Intelligent Control and Modeling- II
GS17 Intelligent Control and Modeling-III
GS18 Mobile Vehicles- I
GS19 Mobile Vehicles- II
GS20 Neural Networks- I

GS21 Neural Networks- II & Neurocomputers
GS22 Robotics-I
GS23 Robotics- II
GS24 Robotics-III
GS25 Robotics-IV
GS26 Robotics-V & Micro-Robot World Cup Soccer Tournament
GS27 Robust Virtual Engineering & Virtual Reality
OS1 Intelligent Systems and Robotics
OS2 Automata and Control
OS3 Models for Neural Networks and Brains
OS4 Methods for Complex Systems: Feature Identification and Control
OS5 Fundamental Research on Recognition and Control
OS6 Intelligent Networks
OS7 Financial Market and Related Topics
OS8 Intuitive Human-System Interaction
OS9 Biomimetic Machines and Robots
OS10 Soft Robotics
OS11 Intelligent Robot Control and Sensors
OS12 Bio-inspired Approach and Application
OS13 Membrane Computing. From Calls to Computers and Back
OS14 Robot Control and Application

TECHNICAL PAPER INDEX

January 25 (Thursday)

Room D

10:50~11:40 Plenary Talk

Chair **M. Nakamura (Saga University, Japan)**

- PT1 *K(Knowledge)-Net: Building up and its dynamics*
Y. G. Zhang (Academia Sinica, P. R. China)

January 26 (Friday)

Room B

16:40~17:30 Invited Talks Session

Chair **M. Rizon (Northern Malaysia University College of Engineering
(KUKUM), Malaysia)**

- IT1 *Robomusic*
H. H. Lund (University of Southern Denmark, Denmark)
- IT2 *Polymorphic intelligence*
L. Pagliarini (University of Southern Denmark, Denmark)

Room D

10:40~11:30 Plenary Talk

Chair **M. Sugisaka (Oita University, Japan)**

- PT2 *A computer simulation in surgery for human hip joint*
H. Tsumura (Oita University, Japan)

January 27 (Saturday)

Room B

8:40~9:25 Invited Talks Session

Chair **J. J. Lee (Korea Advanced Institute of Science and the Technology, Korea)**

- IT3 *Artificial intelligent inserts in healthcare systems*
B. Pillai (Helsinki University of Technology, Finland)

Room D

10:50~11:40 Plenary Talk

Chair **Y. G. Zhang (Academic Sinica, P. R. China)**

- PT3 *Intelligent multi agent application system in AI system*
Y. I. Cho (The University of Suwon, Korea)

January 25 (Thursday)

8:00~Registration

Room A

8:40~10:10 GS22 Robotics- I

Chair: M. Zhao (Tsinghua University, P. R. China)

GS22-1 *Hybrid tracking control of eye-in-hand robotic manipulators*

W- C. Chang, C- W. Cho (National Taipei University of Technology, Taiwan)

GS22-2 *Robust adaptive sliding-mode fuzzy-neural-network model-following position control of PMSM servo drives for robotic applications*

F. F. M. El-Sousy (Electronics Research Institute, Egypt)

GS22-3 *Multi-agent robotics: towards energy autonomy*

T. D. Ngo, H. Raposo, H. Schioler (Aalborg University, Denmark)

GS22-4 *Realization of a visuo-motor system based on multiple self-organizing maps in a 3D space*

R. Uehara, N. Okada, E. Kondo (Kyushu University, Japan)

M. Han (TOYOTA AUTO BODY Co., LTD., Japan)

GS22-5 *Development of an autonomous mobile system for an autonomous robot in an indoor environment*

T. Uewaki, E. Hayashi (Kyushu Institute of technology, Japan)

GS22-6 *A study on improvement of the surveillance system of an indoor robot*

T. Takaya (Richo Software Inc., Japan)

H. Kawamura, Y. Minagawa M. Yamamoto, A. Ohuchi (Hokkaido University, Japan)

12:40~13:55 GS23 Robotics- II

Chair: M. Eaton (University of Limerich, Ireland)

GS23-1 *Human face detection with neural networks and the direct algorithm*

Y. Z. Chang, G. T. Hung (Chang Gung University, Taiwan)

S. T. Lee (Chang Gung Memorial Hospital, Taiwan)

GS23-2 *High shock disturbance rejection of single-link robot arm with a disturbance observer*

S. H. Kang, C. S. Kim, M. H. Lee (Pusan National University, Korea)

GS23-3 *Learning landing control of indoor blimp robot for autonomous energy recharging*

Y. Minagawa, H. Kawamura, M. Yamamoto (Hokkaido University, Japan)

T. Takaya (Richo Software Inc., Japan)

A. Ohuchi (Hokkaido University, Japan)

GS23-4 *User-recognition system for an autonomous robot in human living environments*

Y. Hane, E. Hayashi (Kyushu Institute of technology, Japan)

GS23-5 *Development of a robot following human using color information*

K. Tsugimura, J. K. Tan, S. Ishikawa (Kyushu Institute of Technology, Japan)

14:05~15:05 GS24 Robotics-III

Chair: I. H. Suh (Hanyang University, Korea)

GS24-1 *Development of a self-care robot*

H. Henta, E. Hayashi (Kyushu Institute of Technology, Japan)

GS24-2 *Adaptive control of a looper-like robot based on the CPG-Actor-Critic method*

K. Makino (Nara Institute of Science and Technology, Japan)

Y. Nakamura (Osaka university, Japan)

T. Shibata, S. Ishii (Nara Institute of Science and Technology, Japan)

GS24-3 *Explorations in evolutionary humanoid robotics*

M. Eaton (University of Limerick, Ireland)

GS24-4 *Vision based control for line following blimp robot*

R. Nishioka, H. Kawamura, M. Yamamoto (Hokkaido University, Japan)

T. Takaya (Richo Software Inc., Japan)

A. Ohuchi (Hokkaido University, Japan)

15:05~16:05 GS20 Neural Networks- I

Chair: D. Ai (University of Science and Technology Beijing, P. R. China)

GS20-1 *Learning properties of recurrent neural network with parametric biases*

K. Ikeda, K. Narita (Kyoto University, Japan)

GS20-2 *Three dimensional medical image recognition of the brain by the feedback*

GMDH-type neural network self-selecting optimum neural network architecture

T. Kondo, J. Ueno (The University of Tokushima, Japan)

GS20-3 *Applying neural networks for diagnosis of cancer relapse*

K. J. Mackin (Tokyo University of Information Sciences, Japan)

GS20-4 *Learning how, what, and whether to communicate: emergence of protocommunication in reinforcement learning agents*

T. Sato, E. Uchida, K. Doya (IRP OIST, Japan)

16:05~17:20 GS21 Neural Networks- II & Neurocomputers

Chair: K. Ikeda (Kyoto University, Japan)

GS21-1 *A neural network model of the olfactory system of mice: computer simulation of an attention behavior of mice for some components in an odor*

Z. Soh, T. Tsuji, N. Takiguchi (Hiroshima University, Japan)

H. Ohtake (Osaka University, Japan)

GS21-2 *Graphical analysis of time-series data from waste incinerator using self-organizing map*

T. Yamaguchi, K. J. Mackin (Tokyo University of information Sciences, Japan)

GS21-3 *Design of a real time evaluation system for multiple neuro-biological signals*

T. Zhang (Tsinghua University, P. R. China)
M. Nakamura, T. Sugi (Saga University, Japan)
H. Shibasaki (National Institutes of Health, USA)

GS21-4 *Feedback GMDH-type neural network algorithm self-selecting optimum neural network architecture*

T. Kondo, J. Ueno (The University of Tokushima, Japan)

GS21-5 *Remarks on adaptive type neural network direct controller with separate learning rule of each layer*

T. Yamada (Ibaraki University, Japan)

Room B

8:40~10:10 OS2 Automata and Control

Chair: M. Kono (University of Miyazaki, Japan)

Co-Chair: M. Yokomichi (University of Miyazaki, Japan)

OS2-1 *Three-dimensional parallel turing machines*

T. Ito, M. Sakamoto, Y. Nagamizu, K. Iihoshi, N. Tomozoe,
H. Furutani, M. Kono, S. Ikeda (University of Miyazaki, Japan)
T. Tamaki (Ube National College of Technology, Japan)
K. Inoue (Yamaguchi University, Japan)

OS2-2 *Remarks on recognizability of topological components by three-dimensional automata*

Y. Nagamizu, M. Sakamoto, T. Ito, K. Iihoshi, N. Tomozoe, H. Furutani,
M. Kono, S. Ikeda (University of Miyazaki, Japan)
T. Tamaki (Ube National College of Technology, Japan)
K. Inoue (Yamaguchi University, Japan)

OS2-3 *Leaf-size hierarchy of four-dimensional alternating turing machines*

K. Iihoshi, M. Sakamoto, T. Ito, N. Tomozoe, Y. Nagamizu, H. Furutani,
M. Kono, S. Ikeda (University of Miyazaki, Japan)
T. Tamaki (Ube National College of Technology, Japan)
K. Inoue (Yamaguchi University, Japan)

OS2-4 *A relationship between the accepting powers of alternating finite automata and nondeterministic on-line tessellation acceptors on four-dimensional input tapes*

N. Tomozoe, M. Sakamoto, K. Iihoshi, Y. Nagamizu, T. Ito, H. Furutani,
M. Kono, S. Ikeda (University of Miyazaki, Japan)
T. Tamaki (Ube National College of Technology, Japan)
K. Inoue (Yamaguchi University, Japan)

OS2-5 *Guaranteed cost control of discrete time system with performance index including cross term*

N. Takahashi, M. Kono, O. Sato (University of Miyazaki, Japan)
K. Hiranuma (Tokyo University of Mercantile Marine, Japan)

OS2-6 *An LMI approach to observer-based guaranteed cost control*

M. Miyachi, M. Ishitobi (Kumamoto University, Japan)
N. Takahashi, M. Kono (University of Miyazaki, Japan)

12:40~13:40 OS6 Intelligent Networks

Chair: S. Omatu (Osaka Prefecture University, Japan)

Co-Chair: H. Ido (Niihama National College of Technology, Japan)

OS6-1 *Isomorphic structure of graphs with the maximum number of trees*

H. Ido, Y. Ohama (Niihama National College of Technology, Japan)
S. Omatu (Osaka Prefecture University, Japan)

OS6-2 *Relations between network reliability and number of trees of graph*

H. Ido (Niihama National College of Technology, Japan)
S. Omatu (Osaka Prefecture University, Japan)

OS6-3 *Acoustic signals separation of mechanical devices using the ICA with band-pass filters*

S. Omatu (Osaka Prefecture University, Japan)

OS6-4 *Reliability of bank note classifier by neural networks*

S. Omatu (Osaka Prefecture University, Japan)

14:05~15:05 GS2 Artificial Intelligence- I

Chair: M. Nakamura (Saga University, Japan)

GS2-1 *A new concept of flexible organization for distributed robotized systems*

P. Sapaty, A. Morozov (National Academy of Sciences, Ukraine)
M. Sugisaka (Oita University, Japan)
R. Finkelstein (Robotic Technology Inc., USA)
D. Lambert (Defence Science and Technology Organisation, Australia)

GS2-2 *Information display system using active projector in intelligent space
-Integration of distributed devices based on RT-middleware*

Y. Toshima (The University of Tokyo, Japan)
N. Ando (National Institute of Advanced Industrial Science and Technology (AIST),
Japan)
H. Hashimoto (The University of Tokyo, Japan)

GS2-3 *Elementary developmental process of intentional agency:*

Artificial construction of gaze alternation in communicative eye gaze by infants
T. Konno, T. Hashimoto (Japan Advanced Institute of Science and Technology, Japan)

GS2-4 *The research of data mining for quantitative association rules and algorithm for
numerical attribute*

J. Du (Beijing University of Posts and Telecommunications, P. R. China)
W. R. Jie (University of Science and Technology, P. R. China)

(Paper Only)

GS2-5 *Skill-based manipulation and error recovery in maintenance tasks*

A. Nakamura, K. Kitagaki (National Institute of Advanced Industrial Science and
Technology (AIST), Japan)

15:20~16:20 GS3 Artificial Intelligence- II

Chair: P. Sapaty (National Academy of Science, Ukraine)

GS3-1 *TV program recommender using user's preference*

J. Kim, S. Cheon, J. Kim, S. Kim (Pusan National University, Korea)

GS3-2 *A multi-labeled classification method based on error-correcting output coding*

T. Yamashita, T. Takenouchi, S. Ishii (Nara Institute of Science and Technology, Japan)

GS3-3 *A control method of an electric vehicle*

M. Sugisaka, H. Tanaka, M. Hara (Oita University, Japan)

GS3-4 *The influence for human boredom in interaction by mutual prediction*

M. Shimamoto, T. Shiose, H. Kawakami, O. Katai (Kyoto University, Japan)

16:20~17:35 OS1 Intelligent Systems and Robotics

Chair: O. Sato (University of Miyazaki, Japan)

Co-Chair: A. Date (University of Miyazaki, Japan)

OS1-1 *A property of associative memory model with replacing units*

A. Date (University of Miyazaki, Japan)

K. Kurata (University of the Ryukyus, Japan)

OS1-2 *Force control of 6-DOF pneumatic joystick*

T. Moriki (Kyushu Institute of Technology, Japan)

Y. Tanaka (Kitakyushu National College of Technology, Japan)

Y. Tanaka (Hosei University, Japan)

I. Yokomichi, Y. Hitaka, J. Ishii, (Kitakyushu National College of Technology, Japan)

C. Wada (Kyushu Institute of Technology, Japan)

OS1-3 *Force analysis of the 6DOF parallel manipulators*

Y. Hitaka, Y. Tanaka, J. Ishii (Kitakyushu National College of Technology, Japan)

OS1-4 *Braille block recognition for an autonomous wheelchair*

M. Tabuse (Kyoto Prefectural University, Japan)

Y. Takehara (NTT Date Sanyo System Corp., Japan)

OS1-5 *Throwing motion of manipulator with passive revolute joint*

A. Sato (Miyakonojo National College of Technology, Japan)

O. Sato, N. Takahashi, M. Kono (University of Miyazaki, Japan)

Room C

8:40~10:10 OS14 Robot Control and Application

Chair: S-H. Han (Kyungnam University, Korea)

OS14-1 *A study on real time intelligent control of a three fingers hand system*

X- T. Le, S- B. Oh, W- S. Lee, W- I. Kim, S- H. Han (Kyungnam University, Korea)

OS14-2 *A Study on design of multifingered robot hand with 15 D.O.F and applications*
X- T. Le, S- B. Oh, H. B. Shin, Y. K. Kim, S- H. Han (Kyungnam University, Korea)

OS14-3 *Accuracy improvement of a 5-axis hybrid machine tool*
J- W. Kim, H- Y. Kim, H- S. Kim (Kyungnam University, Korea)

OS14-4 *The design of automatic grease lubricator type of the cylindrical cam piston pump*
W. Choi, J. Yang, H. S. Koo, D. H. Wang, S- H. Lee (Kyungnam University, Korea)

OS14-5 *Non-contact 3-D surface profiler using optical fiber*
Y. K. Kwon, S. H. Kim, E. C. Heo, B. C. Kim (Kyungnam University, Korea)

OS14-6 *Fault tolerant control of magnetic actuators*
U. J. Na, J. S. Won, D. D. Lee, C. W. Ju (Kyungnam University, Korea)

12:40~13:25 GS4 Artificial Life- I

Chair: G. Cui (Zhengzhou University of Light Industry, P. R. China)

GS4-1 *Automated wildlife monitoring using self-configuring sensor networks deployed in natural habitats*

V. Trifa (ATR HRCN, Japan)

L. Girod (MIT, USA)

T. Collier, D. Blumstein, C. Taylor (UCLA, USA)

GS4-2 *Analysis of circuit breakers using artificial stock market*

S. Kobayashi, T. Hashimoto (Japan Advanced Institute of Science and Technology, Japan)

GS4-3 *Interactive musical editing system to support human errors and offer personal preferences for an automatic piano : Method of searching for similar phrases with DP matching and inferring performance expression*

Y. HIKISAKA, E. HAYASHI (Kyushu Institute of Technology, Japan)

14:05~15:20 GS5 Artificial Life- II & Artificial Living

Chair: V. Trifa (ATR HRCN, Japan)

GS5-1 *Self-reproduction on 1-bit communication cellular automata*

R. Takebayashi, H. Umeo (University of Osaka Electro-Communication, Japan)

GS5-2 *On the abundance of energy sources and evolution of collective swarm in auto-constructive artificial life*

A. R. Adzni, J. Teo, A. Saudi (Universiti Malaysia Sabah, Malaysia)

GS5-3 *Interactive musical editing system to support human errors and offer personal preferences for an automatic piano –information system about a musical sign-*

Y. Chigoi, E. Hayashi (Kyushu Institute of Technology, Japan)

GS5-4 *Cognitive modeling of artificial fish learning and memory*

D. Ai, X. Ban (University of Science and Technology Beijing, P. R. China)

S. Zhang (Ocean University of China, P. R. China)

W. Wang (Shandong Agriculture Mechanism Administration, P. R. China)

GS5-5 *Design of robotic behavior that imitates animal consciousness*
N. Goto, E. Hayashi (Kyushu Institute of Technology, Japan)

15:20~16:20 GS15 Intelligent Control and Modeling-I

**Chair: S. Yaacob (Northern Malaysia University college of Engineering,
Malaysia)**

GS15-1 *Design and implementation of a use friendly JAVA based GUI software for
maneuvering mobile robot*
T. C. Manjunath (Indian Institute of Technology Bombay, India)

GS15-2 *The effect of occasional rational decision on the cooperative relationship between
groups*
T. Ohdaira, H. Ohashi (University of Tokyo, Japan)

GS15-3 *Intelligent motor control using advanced bacterial foraging combined with immune
algorithm*
Y. D. Kim, D. H. Kim (Hanbat National University, Korea)

GS15-4 *Unmanned navigation of container transporter using U-SAT (Ultrasonic satellite
system)*
K. S. Lee, S. Y. Kim, T. Y. Shin, J. M. Lee, M. H. Lee (Pusan National University,
Korea)

16:20~17:20 GS16 Intelligent Control and Modeling- II

Chair: D. H. Kim (Hanbat National University, Korea)

GS16-1 *Spreader pose control using dual-electric compasses*
S. Han, H. Jeong, J. Lee (Pusan National University, Korea)

GS16-2 *P2P sensor data mining system for school temperature measurement system*
A. Niimi, H. Shimada, R. Goto, M. Wada, K. Ito, O. Konishi (Future University
-Hakodate, Japan)

GS16-3 *A probabilistic modeling of MOSAIC learning*
S. Osaga, J. Hirayama, T. Takenouchi, S. Ishii (Nara Institute of Science and
Technology, Japan)

GS16-4 *Iterative learning control for linear time-variant continuous systems based on
two-dimensional system theory*
D. Meng, Y. Jia (Beihang University, P. R. China)

January 26 (Friday)

8:00~ Registration

Room A

8:40~9:40 OS10 Soft Robotics

Chair: H. Kinjo (University of the Ryukyus, Japan)

Co-Chair: K. Kurata (University of the Ryukyus, Japan)

OS10-1 *Solution searching for multi-variable optimization problems by GA with momentum offspring*

H. Kinjo, S. D. Chau, M. Maeshiro, K. Nakazono, T. Yamamoto (University of the Ryukyus, Japan)

OS10-2 *Improvement of training method for dynamic neural network*

K. Nakazono (University of the Ryukyus, Japan)

K. Ohnishi (Keio University, Japan)

H. Kinjo, T. Yamamoto (University of the Ryukyus, Japan)

OS10-3 *A learning model of head-direction cells and grid cells by VQ layers connected via anti-Hebbian synapses*

N. Oshiro, K. Kurata, T. Yamamoto (University of the Ryukyus, Japan)

OS10-4 *Color system for skin color extraction*

N. Toma (University of the Ryukyus, Japan)

E. Tamaki (University of Tsukuba, Japan)

12:30~13:45 GS25 Robotics -IV

Chair: Y. Wang (Hunan University, P. R. China)

GS25-1 *Cooperative manipulation of a floating object by some space robots -Application of a tracking control method using transpose of generalized jacobian matrix-*

S. Sagara (Kyushu Institute of Technology, Japan)

Y. Taira (National Fisheries University, Japan)

GS25-2 *Improvement of the algorithm for the search of periodic gaits of a passive dynamic walker*

X. Su, M. Zhao, M. Wang (Tsinghua University, P. R. China)

GS25-3 *Clothes manipulation by inchworm robot grippers*

K. Salleh, H. Seki, Y. Kamiya, M. Hikizu (Kanazawa University, Japan)

GS25-4 *Development of an obstacle recognition system for autonomous robots in indoor environments*

H. Mizoguchi, E. Hayashi (Kyushu Institute of Technology, Japan)

GS25-5 *The autonomous control of a robot arm based on contact with an object*

M. Shimono, E. Hayashi (Kyushu Institute of Technology, Japan)

13:45~15:15 GS26 Robotics - V & Micro- Robot World Cup Soccer Tournament

Chair : K. Uosaki (Fukui University of Technology, Japan)

GS26-1 *Real-time target detection using infrared camera*

M. Sugisaka, E. R. M. Faizal (Oita University, Japan)

GS26-2 *Digital type disturbance compensation control of a floating underwater robot with 2 link manipulator*

T. Yatoh, S. Sagara, M. Tamura (Kyushu Institute of Technology, Japan)

GS26-3 *Simulating crowd motion with shape preference and fuzzy rules*

J- Y. Chang, T- Y. Li (National Chengchi University, Taiwan)

GS26-4 *Development of an autonomous driving personal robot "Development of arm's mechanism and control program"*

M. Tone, E. Hayashi (Kyushu Institute of Technology, Japan)

GS26-5 *Knowledge evolution in a dynamic environment of robocup simulation*

T. Nakashima, H. Ishibuchi (Osaka Prefecture University, Japan)

M. Mii (University of Hyogo, Japan)

GS26-6 *Control of autonomous mobile robot through environment recognition with photoelectric Sensor*

T. Kurita, N. Abe, K. Tanaka (Kyushu Institute of Technology, Japan),

H. Taki (Wakayama University, Japan)

S. He (Eastman Kodak Company, USA)

15:40~16:25 GS9 Computer Graphics- I

Chair: S. Ishikawa (Kyushu Institute of technology, Japan)

GS9-1 *An interactive system for creating a 3-D graphical road map*

K. Tou (Kyushu Institute of technology, Japan)

T. Irie (GEO Technical Laboratory, Japan)

J. K. Tan, S. Ishikawa (Kyushu Institute of technology, Japan)

GS9-2 *Interactive denoising using non linear filter in wavelet domain*

M. Hariharan, Paulraj MP, S. Yaacob, M. Rizon (Northern Malaysia University College of Engineering (KUKUM), Malaysia)

M. Sugisaka, D. Hazry (Oita University, Japan)

GS9-3 *Computer aided diagnosis system for pulmonary nodules using hierarchical feature extraction*

K. Takei, N. Homma, T. Ishibashi, M. Sakai, M. Yoshizawa (Tohoku University, Japan)

K. Abe (Nihon University, Japan)

(Paper only)

GS9-4 *Segmentation and tracking of cells in the image sequences*

T. Kubik (Wroclaw University of Technology, Poland)

M. Sugisaka (Oita University, Japan)

16:25~17:25 GS10 Computer Graphics- II

Chair: H. Furutani (University of Miyazaki, Japan)

GS10-1 *Level set methods and auto-relation for detection of objects*

X. Wang (Niihama National College of Technology, Oita University, Japan)

M. Sugisaka (Oita University, Japan)

GS10-2 *Motion trace in real-time processing*

E. Gobaru, M. Hara, M. Sugisaka (Oita University, Japan)

GS10-3 *On the application of lip features in classifying human emotions*

M. Karthigayan (Northern Malaysia University College of Engineering (KUKUM),
Malaysia)

M. Rizon (Northern Malaysia University College of Engineering (KUKUM),
Malaysia, Oita University, Japan)

S. Yaacob, R. Nagarajan (Northern Malaysia University College of Engineering
(KUKUM), Malaysia)

M. Sugisaka (Oita University, Waseda University, Japan)

M. Rozalian (TATI, Malaysia)

D. Hazry (Oita University, Japan)

GS10-4 *Face localization for facial features extraction using symmetrical filter and linear
hough transform*

H. Arof (University Malaya, Malaysia)

F. Ahmad (International University College of Technology Twintech, Malaysia)

N. M. Shah (University Malaya, Malaysia)

Room B

8:40~9:40 GS11 Fuzzy Control

Chair: S. Sagara (Kyushu Institute of Technology, Japan)

GS11-1 *Imitation of human action intelligence for the environment of desktop teleoperation*

T. Shang (Shenyang University of Technology, P. R. China)

S. Wang (Kochi University of Technology, Japan)

GS11-2 *A modified K-means clustering method for microarray data classification*

D. Park, Y. Kim, S. Kim, C-H. Lee (Pusan National University, Korea)

GS11-3 *A cost-based fuzzy system for pattern classification with class importance*

T. Nakashima, Y. Yokota, H. Ishibuchi (Osaka Prefecture University, Japan)

G. Schaefer (Aston University, UK)

GS11-4 *A verification of normalization results using variable clustering methods in cDNA
microarray data*

G. Beak, Y. Kim, J-Y. Kim, S. Kim, C-H. Lee (Pusan National University, Korea)

9:40~10:40 Poster Session & Coffee Break

PS1 *Improvement of color images halftoning with simulated annealing*

K. Tanaka, R. Isoi (Meiji University, Japan)

PS2 *Optimization of area traffic control parameter using a GA*

H. Sasaki, M. Shinohara, K. Shoji, F. Toyama, J. Miyamichi (Utsunomiya University,
Japan)

PS3 *Three dimensional medical image recognition of the lungs using artificial neural network*
T. Matsuki, T. Kondo, J. Ueno (University of Tokushima, Japan)

PS4 *A design of rough set processor for knowledge discovery*
M. Matsumoto, A. Kanasugi (Tokyo Denki University, Japan)

12:30~14:00 GS18 Mobile Vehicles - I

Chair: H. Hashimoto (The University of Tokyo, Japan)

GS18-1 *An outdoor autonomously moving robot using a distributed image processing system*
H. Goto, N. Abe (Kyushu Institute of Technology, Japan)
H. Taki (Wakayama University, Japan)
S. He (Eastman Kodak Company, USA)

GS18-2 *Lateral control design of an autonomous land vehicle using RTK-DGPS*
H. G. Park, J. H. Ryu, S. T. Hwang, M. H. Lee (Pusan National University, Korea)

GS18-3 *Navigation system for a mobile robot using an omni-directional camera*
T. Mochizuki, E. Hayashi (Kyushu Institute of Technology, Japan)

GS18-4 *Adaptation of a distributed controller depending on morphology*
N. Labhart, S. Miyashita (University of Zurich, Switzerland)

GS18-5 *On-line variational PCA for adaptive visual tracking*
T. Date, T. Bando, T. Shibata, S. Ishii (Nara Institute of Science and Technology,
Japan)

GS18-6 *The development of an indoor positioning system using incident angle detection of infrared emitters*
S. T. Hwang, J. H. Ryu, C. H. Lee, M. H. Lee (Pusan National University, Korea)

14:00~15:30 GS19 Mobile Vehicles - II

Chair: J. Wang (Oita University, Japan)

GS19-1 *An efficient localization algorithm in the RFID sensor space for mobile robot localization*
H. Lim, J. M. Lee (Pusan National University, Korea)

GS19-2 *Development of an autonomous mobile robot*
K. Niimoto, E. Hayashi (Kyushu Institute of Technology, Japan)

GS19-3 *Linux-based real time monitoring system of mobile robots*
S. Cho (Pusan National University, Korea)
I. O. Lee (Ninety system, Korea)
J. M. Lee (Pusan National University, Korea)

GS19-4 *Ontological representation of vision-based 3D spatio-temporal context for mobile robot application*
G. H. Lim, J. Chung, G. G. Ryu, J. B. Kim, S. H. Lee, S. Lee, I. H. Suh (Hanyang University, Korea)
J. H. Choi, Y. T. Park (Soongsil University, Korea)

GS19-5 *Cortical current sources for processing visual target motion revealed by MEG and fMRI*

D. Kawawaki, T. Shibata, Y. Fujiwara (Nara Institute of Science and Technology, Japan)

O. Yamashita, M. Sato, M. Kawato (ATR Computational NeuroScience Laboratories, Japan)

GS19-6 *Robust tracking control based on neural network for nonholonomic mobile robot*

Y. Wang, J. Peng (Hunan University, P. R. China)

15:40~16:40 OS13 Membrane Computing. From Calls to Computers and Back

Chair: M. Oswald (Vienna University of Technology, Austria)

Co-Chair: Y. Suzuki (Nagoya University, Japan)

OS13-1 *Parallel software architectures analysis for implementing P systems*

L. Fernandez, F. Arroyo, I. Garcia, A. Gutierrez (Universidad Politecnica de Madrid, Spain)

OS13-2 *An architecture for attacking the bottleneck communication in P systems*

A. Tejedor, L. Fernandez, F. Arroyo, G. Bravo (Universidad Politecnica de Madrid, Spain)

OS13-3 *Dynamics of an abstract chemical system with few molecular*

Y. Suzuki (Nagoya University, Japan)

OS13-4 *Spiking neural P systems with inhibitory axons*

R. Freund, M. Oswald (Vienna University of Technology, Austria)

Room C

8:40~10:25 GS12 Genetic Algorithms

Chair : K. B. Sim (Chung-Ang University, Korea)

GS12-1 *Genetic algorithms for buffer size and work stations capacity in serial-parallel production lines*

A. Q. Jaber, R. Ramli, H. Yamamoto (Gifu University, Japan)

GS12-2 *Implementation of a GA driven programming training support system*

E. Nunohiro, K. Matsushita, K. J. Mackin, M. Ohshiro, K. Yamasaki (Tokyo University of Information Sciences, Japan)

GS12-3 *Computer simulation of an augmented automatic choosing control designed by Hamiltonian and absolute anti-windup measure*

T. Nawata (Kumamoto National College of Technology, Japan)

H. Takata (Kagoshima University, Japan)

GS12-4 *Estimation of the source-filter model via GA-like algorithm for acoustical feature extraction*

M. Ihara, S. Maeda, S. Ishii (Nara Institute of Science and Technology, Japan)

GS12-5 *A network analysis of simple genetic algorithms*
H. Funaya, K. Ikeda (Kyoto University, Japan)

GS12-6 *Function-discovery-system by the evolutionary strategy using the search-accumulation*
M. Saito, S. Serikawa (Kyushu Institute of Technology, Japan)

GS12-7 *Development of satellite image searching using distributed genetic algorithm with normalized correlation*
K. Matsushita, K. Katayama, K. Mackin, E. Nunohiro (Tokyo University of Information Sciences, Japan)

(Paper only)

GS12-8 *Job-shop scheduling problems based on immune ant colony optimization*
M- L. Sui, Y- I. Zhang (PLA University of Science and Technology, P. R. China)

12:30~14:00 OS3 Models for Neural Networks and Brains

Chair: H. Suzuki (The University of Tokyo, Japan)

Co-Chair: Y. Hirata (The University of Tokyo, Japan)

OS3-1 *Features of action potential initiation in cortical neurons with multiple internal states*
M. Matsuo (Aihara Complexity Modelling Project, ERATO, JST, Japan)
K. Aihara (Aihara Complexity Modelling Project, ERATO, JST, The University of Tokyo, Japan)

OS3-2 *Signal processing with spikes*
M. Gutmann (The University of Tokyo, Japan)
K. Aihara (Aihara Complexity Modelling Project, ERATO, JST, The University of Tokyo, Japan)

OS3-3 *A mathematical model of planning in the prefrontal cortex*
M. Oku (The University of Tokyo, Japan)
K. Aihara (Aihara Complexity Modelling Project, ERATO, JST, The University of Tokyo, Japan)

OS3-4 *Pattern recognition in chaotic neural networks*
G. He (Aihara Complexity Modelling Project, ERATO, JST, The University of Tokyo, Japan, Zhejiang University, P. R. China)
L. Chen (Aihara Complexity Modelling Project, ERATO, JST, The University of Tokyo, Osaka Sangyo University, Japan)
K. Aihara (Aihara Complexity Modelling Project, ERATO, JST, The University of Tokyo, Japan)

OS3-5 *Bistability of synchronous and desynchronous dynamics in a network with gap junctions*
Y. Katori, Y. Hirata (Aihara Complexity Modelling Project, ERATO, JST, Japan)
H. Suzuki (The University of Tokyo, Japan)
K. Aihara (Aihara Complexity Modelling Project, ERATO, JST, The University of Tokyo, Japan)

OS3-6 *Digital spiking silicon neuron: concept and behaviors in GJ-coupled network*
T. Kohno, K. Aihara (Aihara Complexity Modelling Project, ERATO, JST, The University of Tokyo, Japan)

14:00 ~15:30 GS17 Intelligent Control and Modeling-III
Chair: A. Kanasugi (Tokyo Denki University, Japan)

GS17-1 *Hexagon-based Q-learning for object search with multiple robots*
H- C. Yang, H- D. Kim, K- B. Sim (Chung-Ang University, Korea)

GS17-2 *Motion generation of pneumatic artificial muscle*
S. Ichikawa, M. Hara, M. Sugisaka (Oita University, Japan)

GS17-3 *An antibody-based computing: An application to stable marriage problem*
Y. Ishida (Toyohashi University of Technology, Japan)

GS17-4 *Network route design of public transport system with network evolution*
T. Majima (National Maritime Research Inst., Japan)
K. Takadama (University of Electro-Communications, Japan)
D. Watanabe (National Maritime Research Inst., Japan)
M. Katuhara (Hokkaido Intellect Tank, Japan)

GS17-5 *Robot multiple tasks performance and neural complexity*
G. Capi (Fukuoka Institute of Technology, Japan)
K. Bode (Polytechnic University of Tirana, Albania)

GS17-6 *Motion control of biped robot by using simulation*
K. Kabata, M. Hara, M. Sugisaka (Oita University, Japan)

15:40~17:10 OS4 Methods for Complex Systems: Feature Identification and Control

Chair: T. Kohno (The University of Tokyo, Japan)
Co-Chair: S. Horai (Aihara Complexity Modelling Project, ERATO, JST, Japan)

OS4-1 *A new technique for adjusting the learning rate of RPEM algorithm automatically*
X. Zhao (Aihara Complexity Modelling Project, ERATO, JST, The University of Tokyo, Japan)
Y. Cheung (Hong Kong Baptist University, P. R. China)
L. Chen (Aihara Complexity Modelling Project, ERATO, JST, The University of Tokyo, Osaka Sangyo University, Japan)
K. Aihara (Aihara Complexity Modelling Project, ERATO, JST, The University of Tokyo, Japan)

OS4-2 *Fitting a predictive model with a priori information*
Application in intermittent androgen suppression for prostate cancer
Y. Hirata (Aihara Complexity Modelling Project, ERATO, JST, The University of Tokyo, Japan)
K. Aihara (Aihara Complexity Modelling Project, ERATO, JST, The University of Tokyo, Japan)

OS4-3 *Effect of facility closure in the SEIR epidemic model*

H. Maeda (The University of Tokyo, Japan)

Y. Ohkusa (Infectious Disease Surveillance Center, National Institute of Infectious Diseases, Japan)

K. Aihara (Aihara Complexity Modelling Project, ERATO, JST, The University of Tokyo, Japan)

OS4-4 *A systematic approach to analysis of robustness in oscillatory networks*

R. Wang (Aihara Complexity Modelling Project, ERATO, JST, Japan)

L. Chen (Osaka Sangyo University, Japan)

K. Aihara (Aihara Complexity Modelling Project, ERATO, JST, The University of Tokyo, Japan)

OS4-5 *Phase synchronization of limit cycle oscillators in a fluctuating environment*

K. Hashimoto (Aihara Complexity Modelling Project, ERATO, JST, Japan)

K. Aihara (Aihara Complexity Modelling Project, ERATO, JST, The University of Tokyo, Japan)

OS4-6 *Mathematical modeling of frog's calling behaviors and its possible application to artificial life and robotics*

I. Aihara, H. Kitahata, K. Yoshikawa (Kyoto University, Japan)

K. Aihara (Aihara Complexity Modelling Project, ERATO, JST, The University of Tokyo, Japan)

17:10~17:55 GS6 Bioinformatics & Chaos

Chair: K. Naitoh (Waseda University, Japan)

GS6-1 *Local cause of coherence in Boolean networks*

C. Oosawa (Kyushu Institute of Technology, Japan)

K. Takemoto (Kyoto University, Japan)

S. Matsumoto (Kyushu Institute of Technology, Japan)

M. A. Savageau (University of California, USA)

GS6-2 *Continuous modeling of biomolecular systems based on process calculus*

Y. Pu, X. Dong (Shanghai Jiao Tong University, P. R. China)

GS6-3 *Modeling chaos neural networks for classification of EEG signals*

T. Q. D. Khoa, M. Nakagawa (Nagaoka University of Technology, Japan)

January 27 (Saturday)

8:00~ Registration

Room A

8:40~9:25 OS5 Fundamental Research on Recognition and Control

Chair: F. Dai (Matsue National College of Technology, Japan)

OS5-1 *Fundamental research on polymer material as artificial muscle*

T. Hanamoto, Y. Neba, Y. Fujihara, J. Hayashida (Matsue National College of

Technology, Japan)

OS5-2 *Fundamental research on face recognition by genetic algorithm*

F. Dai, T. Adachi, Y. Fujihara (Matsue National College of Technology, Japan)
H. Zhao (Zhengzhou University, P. R. China)

OS5-3 *The characteristics of Mckibben muscle based on the pneumatic experiment system*

H. Zhao, M. Sugisaka (Oita University, Japan)
F. Dai (Matue National College of Technology, Japan)

9:25~10:40 OS12 Bio-inspired Approach and Application

Chair: I. Yoshihara (University of Miyazaki, Japan)

Co-Chair: M. Yasunaga (University of Tsukuba, Japan)

OS12-1 *Effect of using partial solutions in creating new candidate solutions with EDA and ACO schemes*

S. Tsutsui (Hannan University, Japan)

OS12-2 *Stochastic analysis of schema distribution in OneMax problem*

H. Furutani, S. Katayama, M. Sakamoto (University of Miyazaki, Japan)

OS12-3 *Identification of exon-intron boundaries by Integration of base-oriented genetic programming and statistical heuristics*

K. Yamamori (University of Miyazaki, Japan)
Y. Fujita (Mitsubishi Space Software, Co., Japan)
I. Yoshihara, M. Aikawa (University of Miyazaki, Japan)

OS12-4 *Variable-length-segmental-transmission-line and its design guidelines*

N. Koizumi (University of Miyazaki, Japan)
K. Hayashi, M. Yasunaga (University of Tsukuba, Japan)
K. Yamamori, I. Yoshihara (University of Miyazaki, Japan)

OS12-5 *A reconfigurable-VLSI-based double-lens tracking-camera*

M. Yasunaga, N. Aibe, N. Y. Yamaguchi (University of Tsukuba, Japan)
Y. Yamamoto (Yamamoto System Design Inc, Japan)
T. Awano (Bethel inc., Japan)
I. Yoshihara (University of Miyazaki, Japan)

12:40~13:40 GS13 Innovative Computations- I

Chair: T. Arita (Nagoya University, Japan)

GS13-1 *Fault detection by evolution strategies based particle filters*

K. Uosaki (Fukui University of Technology, Japan)
T. Hatanaka (Osaka University, Japan)

GS13-2 *A synergetic particle swarm optimization algorithm-DHPSO*

J. Guo (Huazhong University of Science and Technology, P. R. China)
G. Cui (Zhengzhou University of Light Industry, P. R. China)

GS13-3 *Inevitability of bio-molecules*
K. Naitoh (Waseda University, Japan)

GS13-4 *Calculation of 3-D nonnegative outer product expansion by the power method and its application to digital signal processing*
C. Okuma, J. Murakami, N. Yamamoto (Kumamoto National College of Technology, Japan)

13:40~14:25 GS14 Innovative Computations- II & Human- Machine Cooperative Systems

Chair: K. Yamasaki (Tokyo University of Information Science, Japan)

GS14-1 *Adaptive knowledge base for Japanese-to-Braille translation*
S. Ono, T. Yamasaki, S. Nakayama (Kagoshima University, Japan)

GS14-2 *Language evolution and the baldwin effect*
Y. Watanabe, R. Suzuki, T. Arita (Nagoya University, Japan)

GS14-3 *A distributed algorithm of group robots applied to maze searching*
T. Onitsuka, O. Araki (Tokyo University of Science, Japan)
T. Tamura (TOSHIBA Corporation, Japan)

14:25~15:10 OS7 Financial Market and Related Topics

Chair: M. Tanaka- Yamawaki (Tottori University, Japan)

Co-Chair: A. Sato (Kyoto University, Japan)

OS7-1 *Interaction of agents in financial markets and informational method to quantify it*
A. Sato (Kyoto University, Japan)

OS7-2 *Trend predictions of tick-wise stock prices by means of technical indices selected by genetic Algorithm*
S. Tokuoka, M. Tanaka-Yamawaki (Tottori University, Japan)

OS7-3 *Effective indices to characterize short sequences of human random generations*
M. Mishima, M. Tanaka-Yamawaki (Tottori University, Japan)

Room B

9:25~10:40 GS1 Artificial Brain Research & Brain Science

Chair: X. Wang (East China University of Science and Technology, P. R. China)

GS1-1 *Intelligent management of distributed dynamic sensor networks*
P. Sapaty (National Academy of Sciences, Ukraine)
M. Sugisaka (Oita University, Japan)
J. Delgado-Frias (WSU, USA)
J. Filipe (INSTICC, Portugal)
N. Mirenkov (Aizu University, Japan)

GS1-2 *Brain enhancement attempt based on visual recognition*
Y. Jiang, S. Wang (Kochi University of Technology, Japan)

GS1-3 *Designing brain machine interfaces for rehabilitation: a study*
C. R. Hema, Y. Sazali, A. Hamid Adom, R. Nagarajan, M. P. Paulraj, M. Rizon
(Northern Malaysia University College of Engineering (KUKUM), Malaysia)

GS1-4 *Soft-hard memory structure for cognitive systems*
L. Xiong, N. Zhao, C. Zhang (Tsinghua University, P. R. China)

GS1-5 *Artificial realization of decision making for sleep stage of EEG contaminated with artifacts: conditional probability of knowledge-base of expert visual inspection*
B. Wang (Saga University, Japan)
X. Wang (East China University of Science and Technology, P. R. China)

12:40~13:40 GS7 Cognitive Science & Evolutionary Computations
Chair: T. Kondo (The University of Tokushima, Japan)

GS7-1 *A study on quantum-inspired evolutionary algorithm based on pair swap*
T. Imabeppu, S. Nakayama, S. Ono (Kagoshima University, Japan)

GS7-2 *Epidemic models and a self-repairing network with a simple lattice*
Y. Aoki, Y. Ishida (Toyohashi University of Technology, Japan)

GS7-3 *The novel feature selection algorithm for emotion recognition*
H. D. Kim, K. B. Sim (Chung-Ang University, Korea)
Y. I. Cho (The University of Suwon, Korea)

GS7-4 *A trial to improve the intelligibility of spontaneous concatenative speech synthesis*
K. Fujii (Kumamoto National College of Technology, Japan)

13:40~15:10 OS9 Biomimetic Machines and Robots
Chair: K. Watanabe (Saga University, Japan)
Co-Chair: K. Izumi (Saga University, Japan)

OS9-1 *Feature based estimation for mapping robot environments using fuzzy kalman filter*
C. D. Pathirana, K. Watanabe, K. Izumi (Saga University, Japan)

OS9-2 *Kansei with behavioral patterns for human-robot interaction in ubiquitous environments*
J. C. Balasuriya, K. Kamohara (Saga University, Japan)
C. A. Marasinghe (University of Aizu, Japan)
K. Watanabe, K. Izumi (Saga University, Japan)

OS9-3 *Improvement of group performance of job distributed mobile robots by emotionally biased control system*
S. C. Banik, K. Watanabe, K. Izumi (Saga University, Japan)

OS9-4 *Feed rate control using fuzzy reasoning for NC machine tools*
F. Nagata, K. Kuribayashi (Tokyo University of Science, Yamaguchi, Japan)
Y. Kusumoto (Fukuoka Industrial Technology Center, Japan)
K. Watanabe (Saga University, Japan)

OS9-5 *Control of three-link underactuated manipulators using a switching method of fuzzy energy regions*

K. Ichida, K. Izumi, K. Watanabe, N. Uchida (Saga University, Japan)

OS9-6 *Central pattern generators based on Matsuoka Oscillators for the locomotion of biped robots*

G. L. Liu, M. K. Habib, K. Watanabe, K. Izumi (Saga University, Japan)

Room C

8:40~9:25 GS8 Complexity

Chair: Y. Ishida (Toyohashi University of Technology, Japan)

GS8-1 *Networks on earth from the climate data*

K. Yamasaki, K. J. Mackin, M. Ohshiro, K. Matusita, E. Nunohiro (Tokyo University of Information Sciences, Japan)

GS8-2 *An approach to the learning curves of an incremental SVM*

T. Yamasaki, K. Ikeda (Kyoto University, Japan)

GS8-3 *An experimental study on geometric support vector machines*

Y. Nomura, T. Yamasaki, K. Ikeda (Kyoto University, Japan)

9:25~10:40 OS8 Intuitive Human-System Interaction

Chair: M. Yokota (Fukuoka Institute of Technology, Japan)

Co-Chair: T. Oka (Fukuoka Institute of Technology, Japan)

OS8-1 *Towards integrated multimedia understanding for intuitive human-system interaction*

M. Yokota (Fukuoka Institute of Technology, Japan)

OS8-2 *Designing a multi-modal language for directing multipurpose home robots*

T. Oka, M. Yokota (Fukuoka Institute of Technology, Japan)

OS8-3 *Tele-immersive collaborative virtual environment for intuitive interpretation*

N. Kukimoto (Tohwa University, Japan)

Y. Ebara, K. Koyamada (Kyoto University, Japan)

OS8-4 *A next generation video streaming system for intuitive remote interaction*

K. Sugita, N. Nakamura, S. Baba, M. Yokota (Fukuoka Institute of Technology, Japan)

OS8-5 *Face recognition across illumination*

S. Aly, A. Sagheer (Kyushu University, Japan)

N. Tsuruta (Fukuoka University, Japan)

R. Taniguchi (Kyushu University, Japan)

12:40~13:25 GS27 Robust Virtual Engineering & Virtual Reality

Chair: J. Du (Beijing University of Posts and Telecommunications, P. R. China)

GS27-1 *Construction of super-micro sense of force feedback and visual for elastic body*

T. Sonoda, E. Hayashi (Kyushu Institute of Technology, Japan)

GS27-2 *A system allowing concurrent design and implementation of both virtual and real robots*

T. Oomori, N. Abe, K. Tanaka (Kyushu Institute of Technology, Japan)

GS27-3 *Real-time interactive dialog system between human and virtual agent*

S. Uchino, N. Abe (Kyushu Institute of Technology, Japan)

H. Taki (Wakayama University, Japan)

S. He (Eastman Kodak Company, USA)

13:25~14:55 OS11 Intelligent Robot Control and Sensors

Chair: Y. I. Cho (The University of Suwon, Korea)

Co-Chair: J. J. Lee (Korea Advanced Institute of Science and Technology, Korea)

OS11-1 *Design of the tactile sensor element using microbending optical fiber sensors*

J- S. Heo, C- H. Han, J. J. Lee (Korea Advanced Institute of Science and Technology, Korea)

OS11-2 *A localization of mobile robot based on ultra-sonic sensor using dynamic obstacles*

B- S. Choi, J. J. Lee (Korea Advanced Institute of Science and Technology, Korea)

OS11-3 *On the periodic sequence of a discrete sliding mode control system for a single-link robot arm*

S- H. Son (Agency for Defense Development, Korea)

K- B. Park (Korea University, Korea)

OS11-4 *Stable adaptive neural control for a nonlinear robot system in the presence of actuator failures and uncertainties*

J- H. Shin (Dong-eui University, Korea)

K- H. Seo, M- S. Kim, J. J. Lee (Korea Advanced Institute of Science and Technology, Korea)

W- H. Kim, M- N. Lee (Dong-eui University, Korea)

OS11-5 *Intelligent automatic community grouping system by multiagents*

Y. I. Cho (The University of Suwon, Korea)

OS11-6 *PID controller design using double helix structured DNA algorithms with recovery function*

J. J. Kim, J. J. Lee (EE&CS Korea Advanced Institute of Science and Technology, Korea)

K(Knowledge)-net: Building up and its dynamics

Y. G. Zhang

(Institute of Systems Science, Academia Sinica, Beijing, China, 100080, yzhang@iss.ac.cn)

Masanori Sugisaka

(Dept. of Electronic and Electric Engineering, Oita University, Japan, msugi@cc.oita-u.edu.jp)

Lu Tang

(Institute of Systems, Academia Sinica, Beijing, China, 100080)

Abstract: The essence of intelligence is to possess certain abilities that to obtain knowledge, to use knowledge and to operate knowledge. So, the knowledge in our brain exists in isolated and accumulated form, but it has certain dynamic structure to ensure the emergence of this kind of abilities. Based on the understanding to real process of learning knowledge by human being, in this paper we discussed how to make a model to describe the dynamic structure of knowledge. The most knowledge of ours is leaned by using of natural language, we introduce the notion of semantic knowledge and model its growing up process by a network, we named it as K-net. It is a dynamic network with two main dynamics: one is added new knowledge, the other is to aggregate knowledge existed in the network with some probability. Under these very natural conditions we found that originally the network is a random simple net and then some characteristics of complex network appeared gradually when more new knowledge s be added and aggregated. More interesting phenomena is the appearance of random hierarchical structure, is that means emergence?

Keyword: semantic knowledge; complex networks; small-world; scale-free; hierarchical organization

1. Introduction

Human brain has two main functions:

- 1) Control Body's movement;
- 2) Learn knowledge and to form intelligence

Artificial Brain research has similar purposes:

- 1) To control the complex movements of robots;
- 2) To learn knowledge and make emergence of intelligence in a computer or some other machines which can. Then human tries to equip complex robots by this kind of artificial brain finally.

So-called "intelligence" means the abilities:

- To learn knowledge;
- To use knowledge; and
- To operate knowledge.

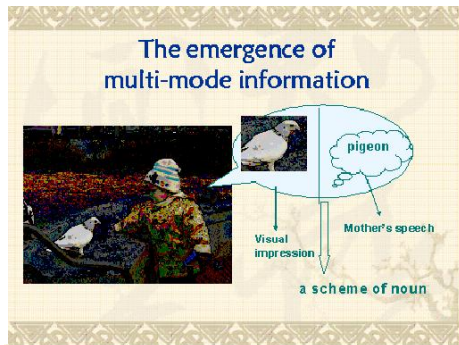
Obviously, "intelligence" depends on the expression of knowledge and its structure in brain.

Our research aims to discuss the principle to design an artificial brain. Observing the relation of knowledge it is easy to understand that knowledge has a network form. This network is a dynamic network. Depending on the Piagent's theory we proposed two main dynamics: one is a new knowledge is added into this network; the other is that knowledge are combined based on the similarity. In our research we have found that the knowledge in human brain formed a complex network, we call it "K-net", in which small word characteristic and almost hierarchical structure appeared. The model of knowledge we proposed in this paper is a kind of design of artificial brain.

2. Structure of semantic knowledge

2.1 The elements of semantic knowledge

At beginning child learn knowledge from “mother” and their perception, we say it is presentative knowledge, or semantic knowledge. Baby learned more and more. However, the sort of



knowledge is very limited, so the number of knowledge in some sort become more dense.

Comparing with the abstract thinking, semantic (presentative) knowledge is concrete, perceptual, primitive, elementary, and evolable. Abstract knowledge is evolved knowledge from semantic (presentative) knowledge, it is usually not perceptual, it is complex and logic.

Semantic knowledge can be expressed in several level layers. For example, “apple” is only a noun, but it is a real presentative knowledge. “eat” is only a verb, but it is still a real presentative knowledge. We say it is semantic knowledge in the “fragment” level. The basic semantic knowledge are grouped as several layers, such that

- “fragment” ,
- “very simple” ,
- “simple” ,
- “usual” ,
- “complex” ,
- “very complex” , etc.

Any relation in those groups will combine some schemes, this combination is very similar to the structure of a sentence but it is not a sentence.

We say an element of Semantic Knowledge
 = “sentence” + mapping

2.2 To form simple network

At beginning, baby learned only few words, for example he/she learns some nouns, verbs and some adjectives, because the classes of knowledge is very limited, so when he/she learned more and more the knowledge in the same class become denser and denser, not only the amount of knowledge arise, but also links between the knowledge appeared, this time this kind of links made the all knowledge formed a simple network. Maybe there are several small simple networks. These small networks are the original seeds for evolution later.

2.3 The dynamic process of semantic knowledge evolution



Jean Piaget (1896 - 1980)

The famous psychologist Jean Piaget had done research on the process of knowledge evolution, he pointed out that the change of knowledge has several ways, two of which are more important, they are Accommodation (顺化) and Assimilation (同化). Assimilation of knowledge means new knowledge is added into the existed structure, or that means one learned a new knowledge and it is adapted into the semantic knowledge network. Accommodation of knowledge means that certain knowledge in the semantic knowledge network has been absorbed or combined with others, usually a new concept appeared and is incorporated. These two processes presented and appeared continually in our brain. In fact, he/she learn new knowledge continually and put them into adequate position of semantic network, it make the network enlarged; also he/she work. Due to these dynamics the network become a dynamic network and presents some complexities.

3. Some Concepts of Complex Networks

The most interesting features of complex networks are the small-world and scale-free. The

statistical quantities characterizing small-world networks are clustering coefficient C and the average length of shortest path L .

Regular networks have high clustering coefficient and large average length of shortest path, opposite to random networks which have low clustering coefficient and small average length of shortest path. Between these two extremes somewhere, the clustering coefficient is almost as high as that of a regular network while the average length of shortest path is almost as small as that of a random network with the same number of nodes and edges. This type of networks is called as "small-world" for it is similar to the small world phenomenon. The average length of shortest path of small world networks increase slowly with the total number of its nodes: $\bar{L} \propto \ln(N)$

The study of scale-free networks concerns behavior in the probability distribution of degree, the possible number of links at a random chosen node in the networks. Unlike the Poisson degree distribution for random networks, in a scale-free network, the distribution of degree follows a power law,

$P(k) \propto k^{-\gamma}$, where k is the degree of nodes and $P(k)$ is the probability of the degree of an arbitrary node equals k . In such a network most nodes have only a few connections and few nodes have very large number of neighbors [9].

It has been discovered recently that aggregation and regeneration of nodes can also leads to the power law distribution of degree [11-12]. Kim and his cooperators propose a network model in which nodes can merge with one of their neighbors and new nodes been added to the network to maintain the number of nodes [11]. Another model proposed by Alava and Dorogovtsev permit to aggregate nodes which are selected at random [12]. Those mechanisms give us new suggestions on how could scale-free networks emerge.

Different from BA model networks, some real scale-free networks have hierarchical structures. A model with network duplication mechanism could

cause such a structure [13]. It displays a hierarchical and coarse-grained similarity. This intrinsic hierarchy can be characterized in a quantitative manner. The clustering coefficient of a node with k links follows the scaling law $C(k) \propto k^{-1}$. This type of structure could give an explanation to the feature of small-world in many scale-free networks.

Degree correlation coefficient r could distinguish assortative and disassortative networks. In assortative networks, nodes with many connections tend to be connected to other nodes with many connections. It was found that social networks are often assortative while biological networks are often disassortative [14]. r could be measured by

$$r = \frac{M^{-1} \sum_i j_i k_i - [M^{-1} \sum_i \frac{1}{2} (j_i + k_i)]^2}{M^{-1} \sum_i \frac{1}{2} (j_i^2 + k_i^2) - [M^{-1} \sum_i \frac{1}{2} (j_i + k_i)]^2}$$

where j_i, k_i are the degrees of the vertices at the ends of the i th edge, with $i = 1 \dots M$.

4. The dynamics 1 of K-net (K-net growing model)

We consider the first dynamic that to add a new knowledge (a new node) to the existed K-net. The principle to add a new node is to choose a node J in the K-net which has the best conditional probability proportional to the connection degree

$$P_i(t) = \frac{k_i(t)}{\sum_{j \in N} k_j(t)}$$

Our connection is not to link the node J directly, but to the m ($m < M$) neighbors of node J randomly. This means the new node has metaphor relation with node J . see the Fig.1a and 1b. The new one is green one and node J is the red one, the 5 neighbors of J is blue.

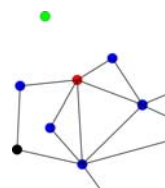


Fig. 1a

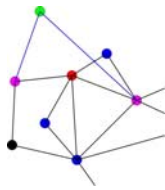
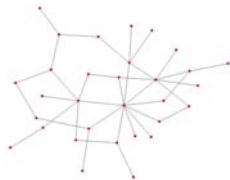


Fig. 2b

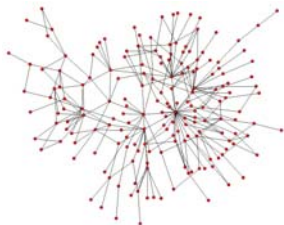
where $m=2$.

The evolution process is in Fig.2a and 2b.



$n=30$

Fig. 2a



$n=180$

Fig. 2b

The result shows us that K-net presents the feature of small word.

5. The dynamics 2 of K-net (K-net aggregation model)

We consider another dynamics of K-net now, aggregation of nodes, that means two nodes are combined as one node, or two very related knowledge are aggregate a concept. This is very important process to knowledge evolution, either for the emergence of intelligence. The criterion of aggregation depends on the similarity between the two knowledge (nodes). It is defined as

$$P_{e_i}(t) = \frac{\lambda_{e_i}(t)}{\sum_{e_j \in E(t)} \lambda_{e_j}(t)}$$

where

$$\lambda_{e_i} = S(a, b) = \frac{1}{1 + |k_a - k_b|}$$

The two nodes which has the highest similarity will be combined as one node. See Fig. 3a and 3b. This single process cannot go through to the end, it has to be run with the growing process.

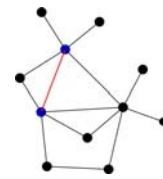


Fig. 3a

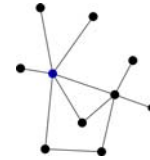


Fig. 3b

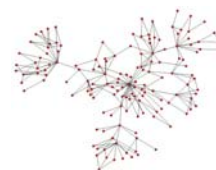
6. The meta-process when these two dynamics together

Based on the theory of J. Piagent The two dynamics of semantic knowledge will appear randomly and continuously, he say that is the equilibrium. We design the K-net has these two dynamics together with certain probability. We found the result still lead to a small word feature in K-net. The evolutionary process is shown in the following simulation. There we assume $M=2$, without loss of generality, and probability $P=0.5$. The evolutionary process shows in Fig.4



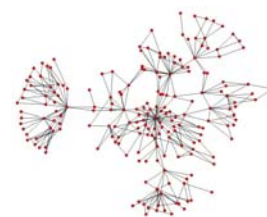
$n=100$

Fig. 4a



$n=150,$

Fig. 4b



$n=200$

Fig. 4c

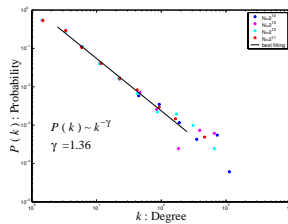


Fig. 4d The link degree presents power law

More interested things is this evolution appears the almost hierarchical structure, maybe we could explain it as a emergence of intelligence.

Summary

In this paper we introduce the semantic knowledge, defined the elements of semantic knowledge, the building up K-net. Also, we have introduce two kind of dynamics for K-net and some simulations have been done, the results presented K-net evolutionarily become a complex network and possess the feature of scale-free and small word. The almost hierarchical structure could be explained as the emergence of intelligence. This model could be a constructive model for artificial brain.

References

- [1] A.M. Collins, E.F. Loftus, "A Spreading-activation Theory of Semantic Processing", *Psych. Rev.*, 1975, 82(6): pp. 407-428.
- [2] C. Fellbaum, *WordNet, an electronic lexical database*, MIT Press, Cambridge, 1998.
- [3] Z-D. Dong, *HowNet2000*, <http://www.keenage.com>, 2000.
- [4] R. Ferrer, R.V. Solé, "The Small World of Human Language", *Proc. Roy. Soc. London B*, 2001, 268(1482): pp. 2261-2265.
- [5] S.N. Dorogovtsev, J.F.F. Mendes, "Language as an Evolving Word Web", *Proc. Roy. Soc. London B*, 2001, 268(1485): pp. 2603-2606.
- [6] M. Sigman, G.A. Cecchi, "Global Organization of the Wordnet Lexicon", *Proc. Natl. Acad. Sci.*, 2002,99(3): pp. 1742-1747.
- [7] M. Steyvers, J.B. Tenenbaum, "The Large-scale Structure of Semantic Networks: Statistical Analyses and a Model of Semantic Growth", *Cognitive Science*, 2005, 29(1): pp.41-78.
- [8] A.E. Motter, A.P.S. de Moura, Y-C. Lai, P. Dasgupta, "Topology of the Conceptual Network of Language", *Phy. Rev. E*, 2002, 65: 065102.
- [9] A-L. Barabási, R. Albert, "Emergence of Scaling in Random Networks", *Science*, 1999, 286: pp. 509-512.
- [10] D.J. Watts, S.H. Strogatz, "Collective Dynamics of Small-world Networks", *Nature*, 1998, 393: pp. 440-442.
- [11] E. Ravasz, A-L. Barabási, "Hierarchical Organization in Complex Networks", *Phys. Rev. E*, 2003, 67: 026112.
- [12] M.E.J. Newman, "Assortative mixing in networks", *Phys. Rev. Lett.*, 2002, 89: 208701.
- [13] P. Érdi, J. Szentagothai, "Neural connectivities: between determinism and randomness", In *Dynamics of Macrosystems*, J.P.Aubin, D. Saari & K. Sigmund (eds.), pp. 21-29. Springer, 1985.
- [14] J.M.J. Murre, D.P.F. Sturdy, "The connectivity of the brain: multi-level quantitative analysis", *Biol. Cybernet.*, 1995, 73, pp. 529-545.
- [15] V.M. Eguíluz, D.R. Chialvo, G. Cecchi, M. Baliki, A.V. Apkarian, "Scale-free brain functional networks", *Phys. Rev. Lett.*, 2005, 94, 018102.
- [16] B.J. Kim, "Geographical Coarsegraining of Complex Networks", *Phys. Rev. Lett.*, 2004, 93, 168701.
- [17] J.M. Beggs, D.J. Plenz, "Neuronal avalanches in neocortical circuits", *J. Neurosci.*, 2003, 23, 11167.
- [18] D.R. Chialvo, "Critical brain networks", *Physica A*, 2004, 340, pp. 756-765.
- [19] O. Sporns, "Network analysis, complexity, and brain function", *Complexity*, 2002, 8 (1), pp. 56-60.
- [20] R. Quiñan Quiroga, L. Reddy, G. Kreiman, C. Koch, I. Fried, "Invariant visual representation by single neurons in the human brain", *Nature*, 2005, 435, pp. 1102-1107.

RoboMusic

Henrik Hautop Lund Martin Ottesen

Maersk Mc-Kinney Moller Institute
University of Southern Denmark, Campusvej 55, 5230 Odense M., Denmark

hhl@mip.sdu.dk funkstardeluxe@funkstardeluxe.com
www.adaptronics.dk www.funkstardeluxe.com

Abstract

Based on principles from modern artificial intelligence and robotics, we developed the RoboMusic concept. In RoboMusic we use a number of robotic devices as instruments, and the tunes are composed as a behaviour-based system. The music artist composes a baseline behaviour of the robotic instruments and composes the behavioural response to interaction by human musicians. The music artist is transformed from a composer of static music tunes to a developer of robot behaviours – behaviours that are expressed by the robotic system as music pieces. Music compositions are transformed to become robotic behaviours as in a behaviour-based system. A RoboMusic concert is performed with robotic instruments, and changes the concept of live concerts by inviting the audience to interact with the band's instruments themselves and thereby guide the live performance of the music themselves.

Introduction

Where robotic technology was used mainly in heavy industries in the past, the last decade has shown a widening of the use of robotic technology into the professional and private service sector, including the entertainment sector. For instance, inspired by Brooks' early development of behaviour-based systems, iRobot has developed vacuum cleaning and floor washing robots for the home market, and Wow-Wee has developed toy robots based upon Tilden's bio-inspired bottom up approach to robotics. We have ourselves developed the behaviour-based approach for interactive robot entertainment such as RoboCup Junior [7], I-BLOCKS play in hospitals and developing countries [5], and interactive playgrounds [4].

Here, we will be looking at the possibility of using the behaviour-based robotic approach to develop a new genre of music that we term *RoboMusic*. In this and the above-mentioned robot service and entertainment applications, the robot technology is merging with other developments

in artificial intelligence such as ambient intelligence and ubiquitous and pervasive computing. In many cases, however, we observe that developments in such sub-fields seems to build upon (parts of) the general definition of robotics. We use the following definition of a robot:

A robot is defined to be a programmable machine that by its interaction with the surrounding environment autonomously can perform a variety of tasks, and its behaviour is different from a computer program by the interaction with the environment through sensors and actuators.

According to the definition, we may develop robotic instruments being programmable instruments that by their interaction with the surrounding through sensors and actuators can be used for playing a variety of tunes.

Related work

Robotics and AI has been used previously to develop music by other researchers and musicians. Most notably, Gil Weinberg [11] and his research group at Georgia Tech have developed a number of robot instruments, such as the Haile drumming robot and other instruments like the beat bugs and squeezables. The robotic drummer Haile is an impressive robotic design made to listen to two live percussionists, analyze their drumming in real-time, and use the product of this analysis to play back in an improvisational manner [11], e.g. as shown at live performances at the Robots at Play Festival in Odense, Denmark in September 2006.

Also, a number of researchers have worked with multimodal interactive environments, including musical environment. Antonio Camurri [2] developed a multimodal environment, in which users were allowed to communicate by means of full-body movement, singing

or playing. In the multimodal environment, the users could get feedback from the environment in real time in terms of sound, music, visual media, and actuators, i.e. movement of semi-autonomous mobile systems including mobile scenography, on-stage robots behaving as actors or players, possibly equipped with music and multimedia output.

Other interactive environments were developed with focus on musical composition with novel interactive instruments, such as the Bubble Bumble and Musical Desk by Zhou et al. [12].

Also, interactive computer music researchers and artists such as Wayne Siegel have explored the possibility of creating real-time interaction with music pieces, as exemplified with Wayne Siegel's "Music for Wind" and "Movement Study" performances in which wind speed and direction control the music and dancer movement control the music [10].

Other artists and researchers have explored similar concepts, developments and performances with interactive computer music and movement control of sound. The work that we present here on RoboMusic distinguishes itself from such related work in the inspiration from and exploitation of different strands of robotics to create intuitive interaction with robotic instruments for both audience and composer, and to create musical compositions as *robotic behaviours* as known from the behaviour-based robotics.

In many cases of related work, a well instructed professional dancer or musician has to control the interactive devices, and the professional musician or dancer has to do so in a precise way in order to create a musical response which is pleasant for the audience. On the other hand, the RoboMusic is taking advantage of the work in human-robot interaction to create a seamless interface for any non-expert human user to make pleasant run-time manipulations of musical pieces.

RoboMusic

RoboMusic defines a novel genre of music. In RoboMusic, music is composed using robotic instruments, music is recorded based on playing robotic instruments, and concerts are performed with robotic instruments.

According to the definition above, a robot is defined to be a programmable machine that by its interaction with

the surrounding environment autonomously can perform a variety of tasks, and its behaviour is different from a computer program by the interaction with the environment through sensors and actuators. Hence, a robotic instrument is programmable instrument that by its interaction with the surrounding through sensors and actuators can be used for playing a variety of tunes. Through communication, robotic instruments can be used together to orchestra an ensemble. If left untouched by human (or environmental) interaction, the robotic instrument will behave with its own performance composed by the music artist. When a human or other environmental subject interacts with a robotic instrument, the instrument may change performance from its normal autonomous behaviour.

The artistic and technological challenge of the music artist is to compose baseline behaviour of the robotic instruments and compose the behavioural response to interaction by human musicians. The music artist is transformed from a composer of static music tunes to a developer of robot behaviours – behaviours that are expressed by the robotic system as music pieces. Music compositions are transformed from being static to become dynamic; music compositions are transformed from being static nodes to become robotic behaviours.

A RoboMusic concert is performed with robotic instruments, and changes the concept of live concerts by inviting the audience to interact with the band's instruments themselves and thereby guide the live performance of the music themselves. The audience is actively engaged in the performance of the music of their concert, and their interaction with the robotic instruments guide the robotic behaviour and thereby creates a unique live concert performance that change from concert to concert depending on the behaviour of the audience. Each RoboMusic concert is a unique live performance. The music artist has composed the baseline, and the audience is manipulating the robotic instruments to allow the robotic behaviour to change, and thereby the music tune to diverge. For the audience, the concert form has changed from passive listening to active participation in playing the concert.

Behaviour-based RoboMusic composition

Behaviour-based robotics [1] can be used to create easy access and manipulation of complex technology by non-expert users, and therefore becomes an appealing technology for creating RoboMusic, in which both musicians and audience with no robotics/technology

knowledge should be able to manipulate the robotic instruments in an easy and straightforward manner.

Interaction between human and traditional robotic systems can be problematic, as the traditional robotic systems often perform repetitive actions in a restricted environment, whereas human interaction often is characterised by novel ways of interactions, which creates an ever changing environment (which should be the case with RoboMusic live concerts). Therefore, traditional robotic system methods and technologies are often difficult to apply in situations and applications where the interaction plays a major role. So we developed a new kind of *user-guided behaviour-based robotics* (e.g. [3]) and applied this method to many robotic systems, such as manipulative robotic technologies, mobile and humanoid robots, etc. in order to investigate how non-expert users could develop their own complex robot behaviours within very short time (e.g. 30-60 minutes) with no prior knowledge to the robot technology. For instance, the robotic building block concept allows us to develop 'programming by building', which, for instance, allow African school children and African hospitalised children with no a prior knowledge whatsoever about IT, robotics and technology to develop their own electronic artefacts [5].

The behaviour-based robotics approach (and in general the embodied artificial intelligence approach [8]) puts emphasis on placing the robot/system in the real, physical environment and utilise the characteristics of the real world in the development of the intelligent system. The resulting control systems provide a close loop between environmental stimuli and actuation in the environment through the use of primitive behaviours executed in *parallel* and coordinated to provide the overall behaviour of the system. So, the overall behaviour of the system becomes the *emergent effect* of the interaction with the environment and the coordination of the primitive behaviours. The task of the system designer becomes to design the correct primitive behaviours and to set up the primitive behaviours in the right manner to allow the desired, overall behaviour to emerge as the interplay between the primitive behaviours. With the same primitive behaviours, the designer may be given the opportunity to design many different overall behaviours of the system, depending on the designer's selection and set up of the primitive behaviours [4].

Therefore, in RoboMusic, the design challenge becomes to create primitive robotic behaviours and to coordinate these primitive behaviours in order for the music piece to emerge as the coordination of primitive behaviours. Thereby, a music composition emerge from the way the

composer, musicians or audience interact with the robotic instruments that provide the primitive behaviours.

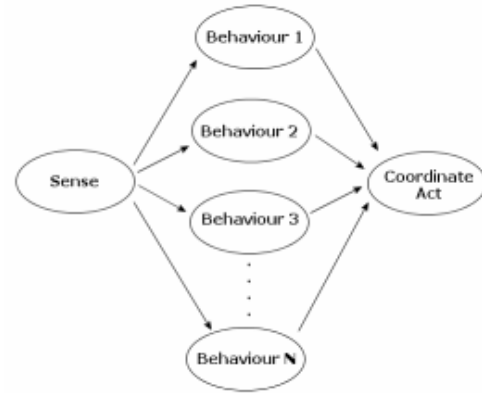


Figure 1. The behaviour based robotics approach.

Each robotic instrument is used to trigger a particular primitive behaviour (Behaviour 1, Behaviour 2, ... , Behaviour N on Fig. 1) dependent on the interaction (Sense on Fig. 1) with the instrument(s). In RoboMusic, the primitive behaviours can be anything from a volume or a cut-off to a small sequence of tones. The music composer designs the way in which the primitive behaviours that are triggered should interact with each other (Coordinate Act on Fig. 1).

Hence, as is the case when designing behaviour based robots such as mobile robots, the robot designer (in this case the music composer) designs the primitive behaviours and the coordination scheme. And, as is the case with user-guided behaviour based robotics, if non-expert users (e.g. live concert audience) are supposed to manipulate and become creative with the systems, it is crucial that the designer (music composer) creates primitives on a fairly high abstraction level that allows the non-expert user to understand and have positive feedback from the human-robot interaction within a very short time frame (seconds in the case of live music concerts).

Therefore, we initially created understandable robotic instruments and primitives. The instruments used to play the music include interactive mats that measure touch, rolling pins that measure rotational acceleration, and light&sound cylinders that measure distance (of a person/hand). Such features as pressure, rotational acceleration and distance are used to trigger primitive behaviours which include variations in resonance, cut-off, volume and pan of musical tracks in the musical composition.

Experimental set-up and test

For the first RoboMusic concert (Robo[rave] in Odense, Denmark on 15/9/2006) and for the recording of the Funkstar De Luxe album “No Man’s Planet”, we developed three kinds of robotic instruments, primitive behaviours and coordination.



Figure 2. Two Rehab Tiles and a RollingPin used as robotic instruments.

The system we made for this purpose is composed by three elements:

1. Device with MIDI in/out features (E.g. PC with Cubase or Keyboard)
2. MIDI controller box (MCB)
3. Robotic instruments

The robotic instruments communicate with radio communication (Xbee) to the “base station” where the coordination is taking place (see Fig. 3 and Fig. 4).

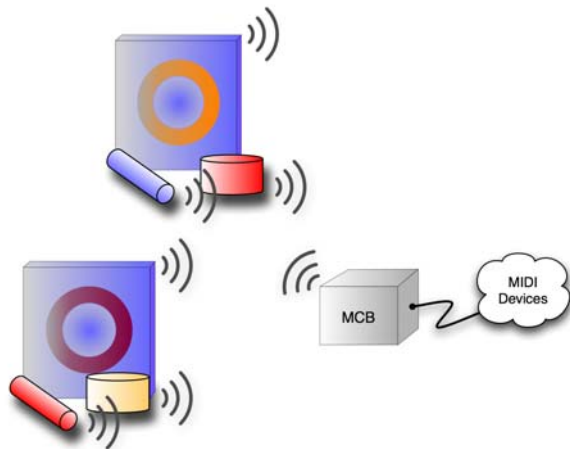


Figure 3. Concert set-up.

For the particular concert, 10 robotic instruments were used: 2 RollingPins, 2 Light&Sound cylinders and 6 Rehab Tiles. The Rehab Tiles were divided into two main groups with the same ID number. This implies that 3 tiles mimic each other. This is mainly done for robustness of the system. There is not implemented any additional transmission reliability or robustness other than the default mechanisms in the Xbee protocol (which may be necessary in future concert environments). The setup used for the Funkstar De Luxe concert is illustrated in Figure 3. The instruments can be activated or deactivated by MIDI control commands. This can be done from any MIDI device connected to the MCB that respects the implemented protocol.

The command control sequence is illustrated in Fig. 4 where a MIDI device¹ activates an instrument by sending a command on a MIDI channel. Furthermore, the MIDI Controller Box defines control numbers for input and output (e.g. 24 and 54 respectively).

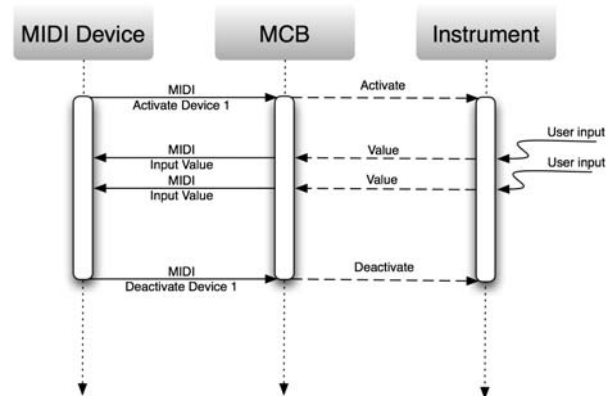


Figure 4. Control flow diagram.

The robotic instruments were developed by modifying modular robotic tools designed specifically for the purpose of supporting dynamic configurations of the environment, initially utilized in physiotherapy with cardiac patients and in dementia treatment [6]. We used inspiration from modular robotics to develop three different kinds of tools, namely the Rehab Tiles, the Light&Sound Cylinders and the RollingPins. According to the robotic building block concept used in some modular robotic work [4, 5, 6], a building block needs to have a physical expression and should be able to process and communicate with its surrounding environment, where the communication with the surrounding

¹ In this particular case the MIDI device is a Laptop running Cubase

environment can be through communication to neighbouring building blocks and/or through sensing or actuation.

The Light&Sound Cylinders and RollingPins were initially developed for the non pharmacological therapeutic treatment and were designed to allow very easy and understandable physical operation by dementia affected patients and therapists (see [6] for details), and likewise the Rehab Tiles were initially developed for physiotherapeutic rehabilitation, e.g. of cardiac patients, with an easy interface for both therapists and patients.

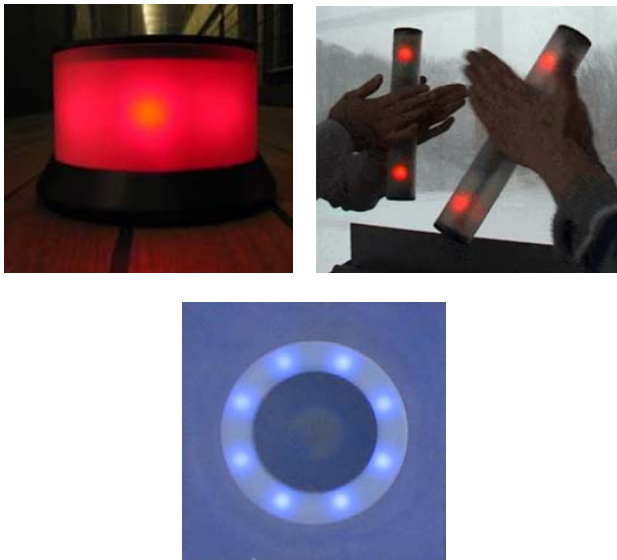


Figure 5. Light&Sound Cylinder, RollingPins and Rehab Tile.

In all cases, the modular robotic units were modified to become robotic instruments by allowing them to use Xbee radio communication to the MIDI Controller Box, see figure 3,4. Hence, the musical composition can radio communicate with the robotic instruments and for instance control the robotic instruments to light up in different colours, patterns and intensities according to the kind of human interaction which may be possible or desirable at a given point in time during the music composition. For instance, the musical composition (or the composer) may send a signal to a robotic instrument to blink in red, which may be understood by a human player as the signal that it is possible to increase a volume by interacting with the instrument.

When a robotic instrument receives an input from a human player, it will trigger a primitive behaviour. The three kinds of robotic instruments developed here have

the following possibilities for receiving input from a human player:

1. Light&Sound Cylinders contain an ultrasound sensor that measures the distance to a reflection, e.g. from a hand moving up and down over the Light&Sound Cylinder
2. RollingPins contain an accelerometer and a gyroscope to measure angle and rotational speed, e.g. when a human player is rolling the pin
3. Rehab Tiles contain a force sensitive resistor to measure the force of pressure, e.g. when a human player puts a hand or foot on the tile

And all three kinds of instruments produce output in the form of coloured light in different patterns and radio communication of primitive behaviours to the MIDI controller box for further coordination (see fig. 3).

In general, it is possible to view the standard musical composition as a baseline robotic behaviour, and the interaction with the robotic instruments as triggering deviations from the baseline behaviour. Therefore, the task of the music composer is to create the “standard” behaviour when there is no interaction with the robotic instruments (i.e. the normal “static” music piece), the primitive behaviours of the individual robotic instruments and the coordination that defines the influence of the human players on the “standard” behaviour.

In the case of the first RoboMusic live concert with presentation of the Funkstar De Luxe album “No Man’s Planet”, we (i.e. the artist Funkstar De Luxe) designed when and how the audience could interact with the robotic instruments, the form and limits of primitive behaviours, and how they would be coordinated.

To keep things simple for the first live concert, the robotic instruments would trigger primitive behaviours being volume control, cut-off, pan, and resonance – but only when the robotic instruments were active, as signalled in the standard musical composition with different MIDI signals that would actuate the robotic instruments to turn on and off their lights in different colours and patterns. In those intervals, the audience were allowed to interact with robotic instruments, and the interaction pattern would define parameters in the primitive behaviours, e.g. the volume of a particular channel in the musical composition.



Figure 6. The RoboMusic live concert set-up, with Funkstar De Luxe and his control station in the center, and the robotic instruments on the left and right side of the stage.

The art of the music composer is to design the primitive behaviours and their limits (in time and form), so that the human player (e.g. audience) interactions with the robotic instruments provide deviations from the standard music piece in a manner that is at the same time improvisational and controllable – i.e. *improvisational* in the sense that the human player (audience) should be able to create a unique version of the music piece, and *controllable* in the sense that the deviations provided by the coordination of the primitive behaviours should in all cases manipulate the standard music piece in a manner that it is guaranteed to provide a pleasant music piece according to the art of the composer.

The first RoboMusic live concert was played as part of the Robo[rave] concert during the Robots at Play Festival (www.robotsatplay.dk) in Odense, Denmark on 15/9/2006 – a concert that also featured percussion music by Gil Weinberg, Scott Driscoll and their Haile drumming robot. The RoboMusic performance was the inauguration live concert of the Funkstar De Luxe “No Man’s Planet” album, and audience were allowed to enter on both the left side and right side of the stage where the robotic instruments in the form of RollingPins, Light&Sound Cylinders, and Rehab Tiles were placed (see figure 6). Documentation of the effect of the audience interaction with the robotic instruments and the music can be seen and heard on the concert video available on [9].

The same RoboMusic system was used to record several tracks on the Funkstar De Luxe album “No Man’s Planet”.

Conclusion

We developed the concept of RoboMusic based upon the use of modern artificial intelligence and behaviour-based robotics to allow live music to emerge as the coordination of primitive behaviours. We thereby transform the role of the music composer to become a composer of robotic/music behaviours. In order to test the concept, we developed three kinds of simple robotic instruments, and tested the system with the development of the Funkstar De Luxe album “No Man’s Planet” and the inaugural live concert when the audience was invited on stage to perform together with Funkstar De Luxe by interacting with the robotic instruments.

Acknowledgements

R. Beck, A. Derakhshan, F. Hammer, C. Isaksen, T. Klitbo, J. Nielsen, L. Pagliarini and Entertainment Robotics (www.e-robot.dk) collaborated on developing the concept and technology.

References

- [1] R. A. Brooks. A robust layered control system for a mobile robot. *IEEE Journal of Robotics and Automation*, 2(1):14--23, 1986.
- [2] A. Camurri, P. Ferrentino. Interactive environments for music and multimedia. *Multimedia Systems*, 7:1, 32-47, 1999.
- [3] H. H. Lund. Modern Artificial Intelligence for Human-Robot Interaction. *Proceedings of the IEEE journal*, 92:11, 1821-1838, 2004
- [4] H. H. Lund, T. Klitbo, and C. Jessen. Playware Technology for Physically Activating Play, *Artificial Life and Robotics Journal*, 9:4, 165-174, 2005
- [5] H. H. Lund and P. Marti. Designing Manipulative Technologies for Children with Different Abilities. *Artificial Life and Robotics Journal*, 9:4, 175-187, 2005
- [6] H. H. Lund, P. Marti, A. Derakhshan, R. Beck, T. Klitbo, and J. Nielsen. Modular Robotics for Novel Tools in Dementia Treatment. *Proceedings of the 15th IEEE Int. Symposium on Robot and Human Interactive Communication (RO-MAN 2006)*, IEEE Press, ISBN: 1-4244-0565-3, 2006.
- [7] H. H. Lund and L. Pagliarini. RoboCup Jr. with LEGO Mindstorms. In *Proceedings of Int. Conf. On Robotics and Automation (ICRA2000)*, IEEE Press, NJ, 2000.
- [8] R. Pfeifer and C. Scheier. *Understanding Intelligence*. MIT Press, Cambridge, MA, 1999.
- [9] RoboMusic web-site (checked 17/12/2006):

<http://www.e-robot.dk/robomusic.html>

[10] W. Siegel. The Challenges of Interactive Dance - an overview and case study. *Computer Music Journal*, vol. 22, no. 4, 1998.

[11] G. Weinberg, S. Driscoll, T. Thatcher. Jam'aa – A Percussion Ensemble for Human and Robotic Players. *ACM International Conference on Computer Graphics and Interactive Techniques (SIGGRAPH 2006)*, Boston, MA, 2006.

[12] Z. Zhou, A. D. Cheok, W. Liu, X. Chen, F. Farbiz, X. Yang, M. Haller. Multisensory Musical Entertainment Systems. *IEEE MultiMedia*, 11:3, 88-101, 2004.

Professor Henrik Hautop Lund is known for his work in robotics and modern artificial intelligence. His team developed the ATRON shape-shifting robots, which he presented to the emperor of Japan, HM Queen of Denmark, etc. His team has developed playware with the novel intelligent playgrounds, and has won the RoboCup Humanoids Free Style World Championship 2002. Professor Henrik Hautop Lund is engaged also in the development of intelligent artefacts, I-BLOCKS, for the teaching of creativity in Africa, where his team were one of the driving forces behind the first science park in East Africa in Iringa, Tanzania. He is member of the Danish national research council, and numerous international committees. He has produced more than 100 scientific publications in robotics and modern artificial intelligence.

Funkstar De Luxe (Martin Ottesen) became world famous for his remix of Bob Marley's Sun Is Shining. The remix sold more than one million copies and won several awards including a World Music Award for the best-selling reggae single of 2000. Besides releasing two albums resulting in several gold plates Funkstar De Luxe has been touring most of the world performing as a DJ and musician. The list of artists remixed is long and includes Grace Jones, Bob Dylan, Mary J Blige and Barry White to name a few. With a characteristic touch in his remixes and original songs Funkstar De Luxe's influence on electronic dance music is significant. With his new album No Man's Planet he continues to push back boundaries of creating and performing electronic music.

Polymorphic Intelligence

Luigi Pagliarini

Maersk Mc-Kinney Moller Institute
University of Southern Denmark, Campusvej 55, 5230 Odense M., Denmark

luigi@mip.sdu.dk
www.adaptronics.dk

Abstract

The need of defining a multiple, multifaceted and *Polymorphic Intelligence* concept comes up as a possible answer to many 'false' paradigms and philosophical and conceptual orientations that, recently, pervade many research fields, as psychology, pedagogy, literature, art, and, of course, science, technology and A.I.

Indeed, in this exact moment of human history, it becomes necessary to clarify with a strong theoretical construct in which relationships are machines and humans, without compromises. We need to free our thoughts from ambiguities and face a new definition of mind and intelligence.

The first step to take consists in burring the idea of *human-machine interaction* or *interaction design* – basically these two terms are out of times – to move on and start thinking of a *human-machine interrelation*. It has become necessary to abandon the scheme that the *constructive* (and, symmetrically, *destructive*) intelligence is an exclusive prerogative of the humans (or, more in general, biological), to fully recognize, admit, and capacitate ourselves that artefacts are able to create, to express a real collaborative and/or competitive force and to produce ideation, inspiration and to contribute to the wealth of ideas that are about to take part of our own world, and our own existences.

Introduction

Being conscious of our own final goals is one of the most important rule to follow to achieve good results while conceiving and implementing ideas. On the opposite, it is our feeling that for much too long A.I. researchers and experts when focusing on 'how to make a machine intelligent' or 'intelligent as humans and other life forms are' have been keeping in their mind the "wrong" target. It is not a case, indeed, that the word *intelligence*, itself, has gained dozens additional meanings and has had to incorporate so many extra aspects (either in psychology, literature and science) that today one could almost

rename it as "*everything*". Of course, this overall tendency is not as good as we would expect since it is leading to a neutral and senseless portrait of what, on the opposite, should be the core-business of our philosophical and technological research.

Further, and more specifically, in the robotics and AI fields the inheritance of *old* paradigms, ideas and approaches seems to be strangling the upcoming needs for a new definition of human-machine *interaction* based at the moment on a sort of human-machine *extraneity*.

Unfortunately, these ideas originated from few, but very popular, scientific, philosophic and artistic theoretical constructs has been simply prejudicing and polluting the entire domain of human thought and the way we've been thinking about intelligent artefacts in the last century.

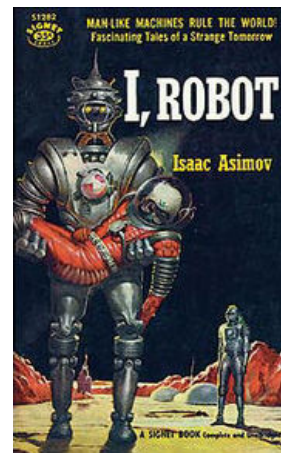


Figure 1. One of the first editions of the famous Isaac Asimov's *I, Robot* [2].

Amongst all, the most *dangerous and mining* were those theories popping out of the Turing's [1], Asimov's [2], Orwell's [3] manuscripts where, paradoxically, the distance between humans and machines is thought as absolute. Their notion of machines (and therefore *machine-intelligence*) is of a somehow isolated *external*

device, while the relationship they thought we could build is extrinsic, either physically and mentally. In our opinion, such an idea is to be demolished because generates a conceptual and structural approach to machine-thinking *disintegrated* to what is to be considered the human specie evolution. Indeed, since years now, humans and machines share the same spaces either physical and geographical, or cerebral and virtual and, in other words, machines are an integrated part of our *Ego* or, at least, part of our own world and everyday life.

To overcome the old way of thinking modern artifacts it seems to be necessary to step back to old schemata typical of Oriental, Indian or Native American cultures and integrate them with most recent western psychological and philosophical theories like those postulated by G. Bateson [4] in "*Steps to an Ecology of Mind*", or by J. Gibson [5] in "*The ecological approach to visual perception*", theories that can be seen as the bases for "Ecological Psychology" [6] or "Environmental Psychology" [7]. In short, the idea that lays behind these theories is that the whole world takes part in our own computational brain, and intellectual potentialities, and is an important component of our motor and sensory systems. If so, it would become essential for those who deal with AI and Robotics to inherit the Bateson's [4] principle for which the "blind man stick is part of his sensory-motor system of his brain associative areas, and of his mind", and facing the idea that artefacts might be integral part of our abilities of elaboration, besides perception and action. Of course, this has been true for centuries but, recently, also thanks to the IT sophistications and worldwide information digitalization, is becoming unequivocal.

Indeed, while modern *Psychotechnologies* [8] differentiate from the traditional ones - motor (e.g. bicycle) and sensory (e.g. telescope) - and accordingly with the famous De Kerckhove [9] classification, include radio, television (i.e. connectivity) and, overall, computers and Internet (i.e. interconnectivity) it is to be noticed that nowadays many automations, more than an integrative processes, are pervasive ones or, even further, are substituting human cognitive process, even at high-level, like for example creativity and problem solving.

Now, although all of that has become truth it seems that we are not fully conscious of the changes that are taking place, and while we easily understand that the mobile phones agenda are replacing part of our long-term memory functionality we find it harder to catch how the famous "cut&paste" or "undo" or "T9text input" are

changing the way we write and, therefore, think and communicate. In short, the symbolic system we are inheriting by the electronic culture is affecting our minds and is likely to engrave up to the revolution of our entire semeiotic system.

In addition, elements like hypertexts, global searches, internet maps, GPS, wearable computers, autonomous robotics, and so on represent an increasing number of functions the biological brain is enriched with and, in parallel, delegating to machines. In other words, these artifacts are the witnesses of the idea of restructuring to which the same brain is pushed to, while they also represent the increasing level of "*dependency*" the human intelligence is destining to machine themselves. One practical example might be seen in the recent growth of such disciplines as *Psychogeography* [10] (i.e.: how to create geographical maps linked to humans emotional experiences) or tools like *Brain Training* [11].

Essentially, intelligence as doubled its evolution speed and hugely enlarged its domains. That's happening because, besides the natural genetic evolution, intelligence is evolving as definition as well. This is due to both the power the new technological achievements to improve our ability of self observation (and self-consciousness), and to the fact that our minds are themselves influenced by the advent of "intelligent" artifacts. Indeed, as G. Rizzolatti pointed out with his *Mirror Neurons* [13] theory humans mostly learn by imitation. Of course, we all - computer scientists, AI and Robotics experts - use that knowledge to apply it to machine learning, but we must notice that by doing so we have initiated a never ending loop in which learning and teaching is somehow simultaneous (in terms of a society extended to intelligent machines). These facts, are taking us straight to the first forms of hybridized intelligences. Last but not the least, intelligence evolves in a new dimension since the latest artificial apparatuses have started creating intelligence, thinking and metacognition, themselves.

To summarize, if on one side it is very easy to predict that - as affirmed by the lucid Alexander Chislenko's analysis [12] - "the ability of future machines to directly share experiences and knowledge with each other will lead to evolution of intelligence from relatively isolated individual minds to highly interconnected structural entities" and that "the development of a network of communicating mobile and stationary devices may be seen as a natural continuation of biological and technological processes leading to a community of intentionally designed and globally interconnected structures", on the other hand, what is much harder to

comprehend to us is that the human brain is not extraneous to all of that but, on the contrary, it gets deeply influenced by A.I. in action. Part of that is what we can call the Polymorphic Intelligence.

Polymorphic Intelligence

As far as we know, humans are the most “intelligent” organisms since their brain functions are complex and sophisticated at the very same time. Indeed, when in *Frames of Mind* [14] the psychologist and neurologist Howard Gardner tried to define intelligence he came out with seven different substructures:

1. *Linguistic intelligence* (sensitivity to spoken and written language);
2. *Logical-mathematical intelligence* (the capacity to analyze problems logically, carry out mathematical operations, and investigate issues scientifically);
3. *Musical intelligence* (encompasses the capacity to recognize and compose and perform music);
4. *Bodily-kinesthetic intelligence* (the potential of using one's whole body or parts of the body to solve problems);
5. *Spatial intelligence* (the potential to recognize and use the patterns of wide space and more confined areas);
6. *Interpersonal intelligence* (the capacity to understand the intentions, motivations and desires of other people);
7. *Intrapersonal intelligence* (the capacity to understand oneself, to appreciate one's feelings, fears and motivations).

Certainly, also thanks to such a refined biological evolution of their computational functions it has become possible to human beings to reach an high level of social and technological evolution that, only recently, is flowing to such a stage that might be defined as the *intelligent machines age*. Amongst us few great artists (e.g. W. Shelley [15]; G. Orwell [16]; P.K. Dick [17]) , many years ago, envisioned we were about to get to this point and consequently depicted a possible scenario to try to prevent the moral and the ethical decay of our societies and specie. In particular, Asimov [2] who tried to define the three famous A.I. constrains:

1. A robot may not injure a human being or, through inaction, allow a human being to come to harm.

2. A robot must obey orders given it by human beings except where such orders would conflict with the First Law.
3. A robot must protect its own existence as long as such protection does not conflict with the First or Second Law.

So, while artists were anticipating crucial philosophical goals for the future human-machine relationship, on the other side, many different scientists were defining practical objectives. Amongst them a special mention goes to A. Turing who tried to define through the famous *Turing Test* [1] the meaning of A.I.

1. A human judge engages in a natural language conversation with two other parties, one a human and the other a machine; if the judge cannot reliably tell which is which, then the machine is said to pass the test.

For what came later all these conceptual paradigms were very significant for any further theoretical development and worked as lighthouses for thinking about AI.

Despite that, as it often happens in the history of ideas, what was a fundamental and inspiring landmark in the past might represent an obstacle for further evolutions, and, most likely, either Asimov's and Turing's (and other authors) principles today are still being followed too much and believed, while they actually seem to be fully out of time.



Figure 2. The Atron modules [20].

Things have changed because, since then, the definition of AI itself has changed. Indeed, it is clear how the Turing Test has been surmounted and AI is moving towards the idea of *Collective Intelligence* - e.g. Swarm

[18], Boids [19] – as well as that robotics is moving away from the basic concept of mono-shaped body structure and the ‘prison’ of its canonical aspect – e.g. *Atron* [20], *RoboMusic* [26].

Even more, A.I. has started opening to such problems like interfacing humans, hence taking us to a *Polymorphic Intelligence* state where Artificial Intelligences deeply interacts with biological ones. This is occurring at all levels. In virtual worlds (SecondLife [21], Gazira Babeli [22] and Marco Cadioli [23]) in real world (MipTiles [24], I-BLOCKS [25], RoboMusic [26]), and in mixed realities (Stelarc [27]; Talkers [28]; Ambient Addition [29]).



Figure 3. Stelarc [27]. *ExoSkeleton*

In other words, what is happening is that we cannot point at A.I. as the result of a single, linear artificial process but, on the opposite, the new picture tells us of a multidimensional non-linear process which is difficult to handle and, more or less, impossible to fully control. Things get even more complex when, instead of the old fashioned interactivity (i.e. the switch on activate/deactivate rule) we insatiate a run-time multi interactive dynamic (i.e. interrelation) with a single ‘specie’ of AI artefacts or even “worse” a multitude of them, simultaneously. Obvious enough, the outcome is a scenario where the Asimov’s laws largely loses sense since machines themselves are loosely controllable (i.e. often dealing with non-linear maths and non-complete problems) and largely interconnected and therefore non directly responsible of the general system outputs. In this perspective, we both need to renew our methods and move from the idea of *Human-Machine Interaction* (or *Interaction Design*) to the concept of *Human-Machine Interrelation* where the basic principles of interactivity

are a bit more aleatory or, at least, less predictable and, even more important, are completely different from what we have been dealing with in the past, since the interactive procedure moves from a one way to a bidirectional intelligence flow.

Indeed, what we will call here the *Imitational Intelligence*, a factor, neglected by the Howard theory [14] but indirectly consecrated by the Rizzolati’s recent discovery, seems to be a crucial issue that must be taken into consideration and that will play a large role in future human-machine theories. Theories that, inevitably so, will lead us towards a new conceptualization of the meaning of Intelligence as a domain hybridized by machine and therefore Polymorphic.

Conclusion

When looking at all ideas and definitions of AI and Robotics of the last centuries it becomes evident that there is something wrong regarding the philosophical approach that has been developed in the so called *machine* (or android, or cyborg, or robot) *thinking*. What seems to be missing is the idea of feedback that machine intelligence impose to biological intelligence therefore creating brand new forms of intelligence (either natural and artificial) that we define as *Polymorphic Intelligence* and that might be leading the way we will approach AI in the next future.

Acknowledgements

All the Adaptronics Group and, in particular, Prof. Henrik H. Lund and Vibeke Nielsen for the great support given in my Danish research activities. Sergio Lombardo for the precious conversations and the support of my researches in Art Psychology. Salvatore Iaconesi for the feedbacks and the English revision of the manuscript. All the Artificialia staff for the valuable research made along the years on the topic.

References

- [1] S. Harnad (2004) *The Annotation Game: On Turing (1950) on Computing, Machinery, and Intelligence*, in Epstein, Robert and Peters, Grace, Eds. *The Turing Test Sourcebook: Philosophical and Methodological Issues in the Quest for the Thinking Computer*. Kluwer
- [2] I. Asimov, (1950). *I, Robot*. New York: Doubleday & Company
- [3] G. Orwell (1949). *Nineteen-Eighty-Four*. London: Secker & Warburg. (later ed. ISBN 0-451-52493-4)

- [4] G. Bateson, (2000), *Steps to an Ecology of Mind*, Chicago: University of Chicago Press
- [5] J. J. Gibson (1979), *The Ecological Approach to Visual Perception*, Boston: Houghton-Mifflin.
- [6] R. G. Barker, (1968), *Ecological Psychology: Concepts and methods for studying the environment of human behavior*, Stanford University Press, Palo Alto, CA.
- [7] P. Bell, T. Greene, J. Fisher, & A. Baum (1996). *Environmental Psychology*. Ft Worth: Harcourt Brace.
- [8] M. Cardaci (2004) *Psicotecnologie e cognizione*. In: Immagini della emergente società in Rete. S.Martelli e S. Gaglio (a cura di) Franco Angeli (pp.169-171).
- [9] D. de Kerckhove (1991), *Leonardo*, Vol. 24, No.2, Connectivity: Art and Interactive Telecommunications, pp. 131-135.
- [10] M. Coverley (2006). *Psychogeography*. Pocket Essentials.
- [11] Dr. Kawashima (2006) *Brain Training: How Old Is Your Brain?* Nintendo DS.
- [12] A. Chislenko (1996) *Networking in the Mind Age* <http://www.lucifer.com/~sasha/mindage.html>
- [13] G. Rizzolati (2005), *The mirror neuron system and its function in humans*. *Anat. Embryol.*, 210(5-6):419-21.
- [14] H. Gardner (1993) *Frames Of Mind. The Theory Of Multiple Intelligences*.
- [15] M. W. Shelley (1918), *Frankenstein*.
- [16] G. Orwell (1948), *1984*.
- [17] P.K. Dick (1968), *Do Androids Dream of Electric Sheep?*
- [18] V. Grimm, (1999). *Swarm* <http://www.swarm.org>
- [19] C. W. Reynolds (1987) *Flocks, Herds, and Schools: A Distributed Behavioral Model*, in *Computer Graphics*, 21(4) SIGGRAPH '87 Conference Proceedings. p. 25-34.
- [20] H. H. Lund, R. Beck, L. Dalgaard, (2005). "Self-Reconfigurable Robots with ATRON Modules" In Proceedings of 3rd International Symposium on Autonomous Minirobots for Research and Edutainment (AMiRE 2005), Springer-Verlag, Fukui, 2005.
- [21] *SecondLife*, <http://www.secondlife.com>;
- [22] *Gazira Babeli*, <http://www.gazirababeli.com>;
- [23] *Marco Cadioli*, <http://www.internetlandscape.it/>
- [24] H. H. Lund, C. Jessen, K. Moeller, T. Klitbo, (2005) "Playware - Intelligent technology for children's play", short position paper to appear in Workshop on Metapolis and Urban Life, UbiComp 2005.
- [25] Nielsen, J., and Lund, H. H. (2004) "Building Blocks with Spiking Neural Networks", Submitted to *European Symposium on Artificial Neural Networks (ESANN'2004)*, 2004.
- [26] H.H. Lund, M. Ottesen, (2006). *RoboMusic*, <http://www.e-robot.dk/robomusic.html>

- [27] *Stelarc*. <http://www.stelarc.va.com.au/>
- [28] *Talkers*. <http://www.artisopensource.net/talkers/>
- [29] N. Vawter (2006), *Ambient Addition* <http://web.media.mit.edu/~nvawter/thesis/>

Professor Luigi Pagliarini is psychologist, multimedia and software designer, expert in robotics, AI and Artificial Life, and artist. He is currently Associate Professor at Maersk Institute, University of Southern Denmark; Professor of Perception Theory and Psychology of Shape at the Academy of Fine Arts of Bari, Italy; Director of the Pescara Electronic Artists Meeting; President of the Cultural Association Artificialia; Art Director of Ecoteca Café; Member of the International Committee RoboCup Junior; Board Committee of "Rivista di Psicologia dell'Arte" (Journal of Psychology of Art); Member of EvoNet and Executive Member of EvoMusArt; Partner Consultant of Entertainment Robotics; Partner Consultant of the Visual Emotion - Video Productions. He has published in different international books, journals, congresses and conferences proceedings and has been rewarded with international prizes more than once. He has exhibited his work in different museums and institutions all over the world. Luigi Pagliarini has worked for many different institutes and universities as teacher or researcher and, as consultant, with many enterprises and multinational factories. His work has often been reported on many international newspapers, magazines and televisions.

A Computer Simulation in Surgery for Human Hip Joint

H. Tsumura

Department of Orthopaedic Surgery, Faculty of Medicine
Oita University

1-1 Idaigaoka Hasama-machi Yufu-shi Oita 879-5593, Japan

Abstract

For patients who have early signs of hip joint disease resulting from structural abnormality, various surgeries for correcting abnormal stress distribution can be useful to prevent the progression of the disease. However, it is difficult to confirm the optimal procedure of surgeries. To deal with this problem, we devised a computer program to support preoperative planning. Hip images obtained by computed tomography were loaded into our program, and a three-dimensional voxel model was created. Then the pressure distribution of hip joint was analyzed with a rigid-body spring analysis (computational non-linear mechanical analysis). This system has a module for performing virtual surgeries. This program allows the hip joint mechanics to be evaluated easily, so that the advantages and disadvantages of various surgical methods could be examined biomechanically prior to surgery. However, this system has several problems that should be solved in the near future.

1 Introduction

For patients who have early signs of hip joint disease resulting from structural abnormality, various surgeries for correcting abnormal stress distribution can be useful to prevent the progression of the disease. To correct this condition, periacetabular osteotomy is frequently performed [1, 2]. This osteotomy involves cutting of the bone around the circumference of the acetabulum and moving the osteotomized acetabular fragment to increase the coverage of the femoral head. It is believed that these procedures have a sound theoretical basis, but it is difficult to confirm the optimal transposition of the osteotomized acetabular fragment. Conventionally, plain X-ray films have been used for preoperative planning. Recently, three-dimensional computed tomography has become available for assessment of the hip joint preoperatively [3]. As mentioned previously, the aim of acetabular osteotomy is to improve mechanical condition of the hip joint. Therefore, it is desirable to include mechanical assessment of the hip joint in the preoperative planning. To deal with this problem, we

devised a computer simulator to support preoperative planning.

2 Methods

This computer simulator is composed of two parts (with three programs): Data Preparation part and Mechanical Analysis /Virtual Osteotomy part. All of these programs were written by one of the authors with Visual C++ (Microsoft, Redmond, WA).

Images of the hip joint were obtained with computed tomography. Image data from each slice were stored as a 320 x 320 or 512 x 512 matrix and then were loaded into our program. A threshold was set to distinguish the bones from the other tissues. The program reconstructed automatically the pelvis and the femur as a voxel model (Fig. 1). The joint surface could not be determined automatically by this system, so joint lines were delineated using a mouse and the joint surface was reconstructed as a polygonal model. Figure 2 shows views of the femoral head and the joint surface.

Fig. 1

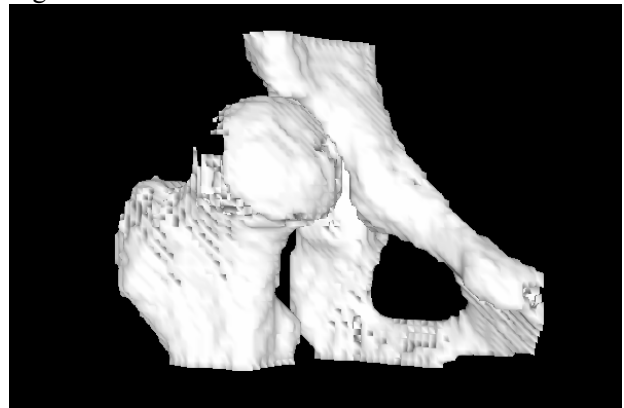
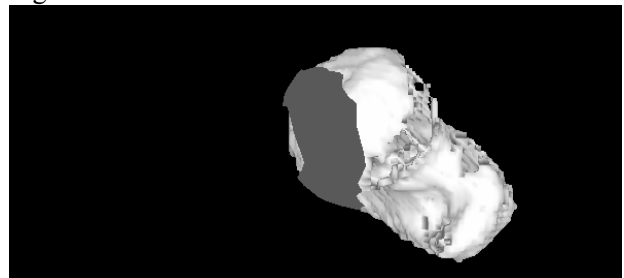


Fig. 2



For mechanical analysis, the joint contact pressure distribution was calculated using the rigid-body spring method of Kawai (computational non-linear mechanical analysis) [4]. The articular surface is assumed to consist of numerous small triangular planes. Each plane has one normal spring and two shear springs. These springs connect components of the joint articulation system that are assumed to be rigid elements.

Formulation of a rigid-body spring model

In addition to the global coordinate system (X, Y, Z), a local coordinate system (x, y, z) was also considered on every contact triangle (Fig. 3). Two rigid elements (G_1, G_2) contact at triangle ABC. An arbitrary point P (X_p, Y_p, Z_p) on triangle ABC moves to P_1 and P_2 after loading (Fig. 4). Because of the rigid body assumption, the displacement vector, \mathbf{U}_p , of point P on the contact surface of bodies 1 and 2 moving to P_1 and P_2 can be expressed as a function of the displacement of the selected reference point \mathbf{U}_G :

$$\mathbf{U}_p = [\mathbf{Q}]\mathbf{U}_G \quad (1)$$

where

$$\mathbf{U}_p = [U_{p1}, V_{p1}, W_{p1}; U_{p2}, V_{p2}, W_{p2}]^t$$

$$\mathbf{U}_G =$$

$$[U_{G1}, V_{G1}, W_{G1}, \theta_{G1}, \phi_{G1}, \chi_{G1}; U_{G2}, V_{G2}, W_{G2}, \theta_{G2}, \phi_{G2}, \chi_{G2}]^t$$

and the transformation matrix

$$[\mathbf{Q}] = \begin{bmatrix} 1 & 0 & 0 & 0 & (Z_p - Z_{G1}) & -(Y_p - Y_{G1}) \\ 0 & 1 & 0 & -(Z_p - Z_{G1}) & 0 & (X_p - X_{G1}) \\ 0 & 0 & 1 & (Y_p - Y_{G1}) & -(X_p - X_{G1}) & 0 \\ 1 & 0 & 0 & 0 & (Z_p - Z_{G2}) & -(Y_p - Y_{G2}) \\ 0 & 1 & 0 & -(Z_p - Z_{G2}) & 0 & (X_p - X_{G2}) \\ 0 & 0 & 1 & (Y_p - Y_{G2}) & -(X_p - X_{G2}) & 0 \end{bmatrix}$$

where (X_p, Y_p, Z_p), (X_{G1}, Y_{G1}, Z_{G1}) and (X_{G2}, Y_{G2}, Z_{G2}) are the coordinates of point P, reference point G_1 and reference point G_2 , respectively, based on the global coordinate system before deformation.

For each contact area, transformation from the global coordinate, \mathbf{U}_p , to the local coordinate, \mathbf{u}_p , was achieved through the transformation matrix \mathbf{R} :

$$\mathbf{u}_p = [\mathbf{R}]\mathbf{U}_p \quad (2)$$

where

$$[\mathbf{R}] = \begin{bmatrix} l_1 & m_1 & n_1 & 0 & 0 & 0 \\ l_2 & m_2 & n_2 & 0 & 0 & 0 \\ l_3 & m_3 & n_3 & 0 & 0 & 0 \\ 0 & 0 & 0 & l_1 & m_1 & n_1 \\ 0 & 0 & 0 & l_2 & m_2 & n_2 \\ 0 & 0 & 0 & l_3 & m_3 & n_3 \end{bmatrix}$$

and $l_1, m_1, n_1, l_2, m_2, n_2, l_3, m_3$ and n_3 are directional cosines between (x, X), (x, Y), (x, Z), (y, X), (y, Y), (y, Z), (z, X), (z, Y) and (z, Z), respectively.

The relative displacement between the matched points P_1 and P_2 was :

$$\delta = [\delta_{sx}, \delta_{sy}, \delta_n]^t = [\mathbf{M}]\mathbf{u}_p \quad (3)$$

where

$$[\mathbf{M}] = \begin{bmatrix} -1 & 0 & 0 & 1 & 0 & 0 \\ 0 & -1 & 0 & 0 & 1 & 0 \\ 0 & 0 & -1 & 0 & 0 & 0 \end{bmatrix}$$

and δ_{sx}, δ_{sy} and δ_n represent the components tangential and normal to the contact surface.

Combining equations (1), (2), and (3), the relative displacement vector δ is expressed as follows :

$$\delta = [\mathbf{M}][\mathbf{R}][\mathbf{Q}]\mathbf{U}_G = [\mathbf{B}]\mathbf{U}_G$$

Denoting the stiffness constants of normal and shear springs by k_{sx}, k_{sy} and k_n , the stored strain energy, W , is :

$$W = \frac{1}{2} \int_A {}^t[\mathbf{D}] dA = \frac{1}{2} \mathbf{U}_G^t \int_A [\mathbf{B}]^t [\mathbf{D}] [\mathbf{B}] dA \mathbf{U}_G$$

where

$$[\mathbf{D}] = \begin{bmatrix} k_{sx} & 0 & 0 \\ 0 & k_{sy} & 0 \\ 0 & 0 & k_n \end{bmatrix}$$

and integration is performed on the contact area.

According to the principle of minimum potential energy, the external force, \mathbf{F} , which is related to the member stiffness matrix, $[\mathbf{K}]$, was calculated as follows :

$$\mathbf{F} = \frac{\partial W}{\partial \mathbf{U}_G} = \int_A [\mathbf{B}]^t [\mathbf{D}] [\mathbf{B}] dA \mathbf{U}_G = [\mathbf{K}]\mathbf{U}_G$$

Fig. 3

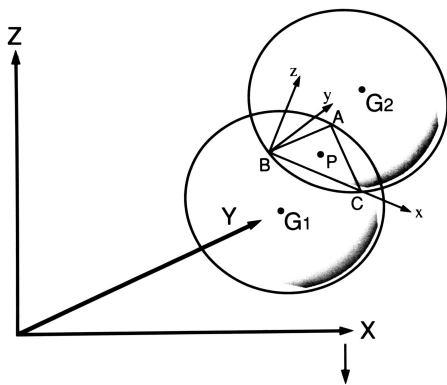
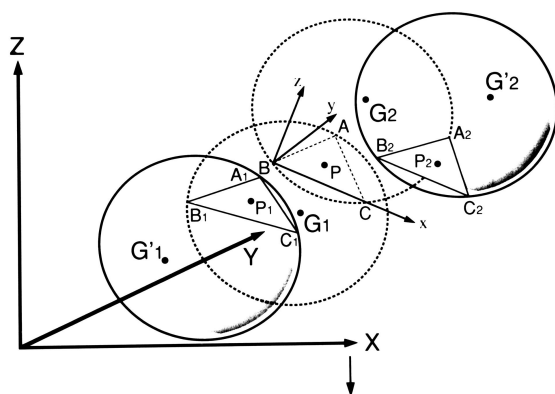


Fig. 4



Algorithm

At the joint contact surface, tensile stress cannot be transmitted. If tensile force is applied to the hip joint, the acetabulum and femur easily become separated. The rigid-body spring model can easily simulate these mechanical characteristics. After the initial stiffness equation was solved to determine the stress distribution, inadmissible solutions for the spring, such as tension on the joint surface, were removed from the model by subtracting their member stiffness matrices from the global stiffness matrix and then repeating the process until no inadmissible stresses were detected.

Modeling of Hip Joint

The reference point for the pelvis was set as the center of the body, and the reference point for the femur was the center of the femoral head. All displacements of the femur were constrained and the load was applied to the acetabulum. The applied load was based on the hip contact force reported by Bergmann [5] during the one-legged stance phase of the normal walking cycle at 3km/h walking velocity. Amount of force was 3.3 times the body weight and the components of loading vector are backward: 0.11, inward: 0.44, downward: 0.89.

Osteotomy simulation

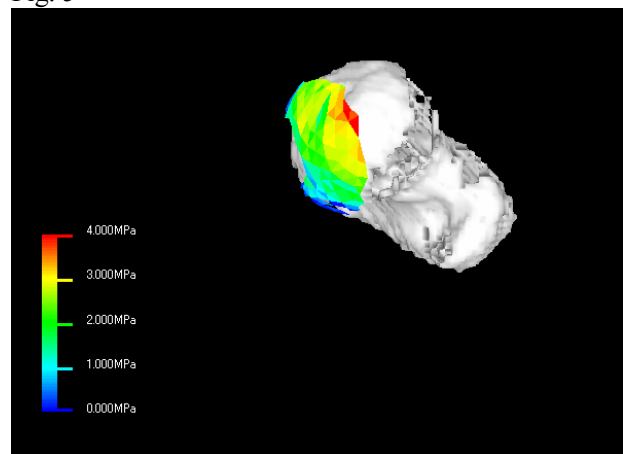
Osteotomy simulation is conducted by cutting the bone and by moving the acetabular fragment on the computer. In this software, the cut surface can be chosen among the flat plane, cylindrical surface and spherical surface. The osteotomized fragment of the bone can be rotated and/or translated as needed.

In the simulation of the rotational osteotomy of acetabulum, the first step is to choose the acetabulum as a target bone, and the second step is to choose the spherical surface as a cut plane. The third step is to set the cut plane at the osteotomy site and cut the acetabulum (Fig. 3), while the final step is to move the osteotomized acetabular fragment and the articular surface. In this study, the diameter of the cut plane was 40mm and the center of the cut plane was set at the center of the inscribed sphere to the acetabulum. To determine the optimal transposition of the acetabular fragment, a peak pressure was calculated for every 5 degrees of rotation of the acetabular fragment.

3. Results

Figure 5 shows an original contact pressure distribution of the example case that was shown in Fig. 1 and 2.

Fig. 5



Virtual osteotomy was performed in this patient. The osteotomy is shown in Figure 6. The osteotomy plane for the pelvic bone was spherical with a 40-mm radius. The acetabular fragment was rotated 25 degrees anteriorly and 15 degrees laterally. This increased coverage of the femoral head caused decrease in the peak pressure and the pressure distribution became less unequal (Fig. 7).

The peak pressure was predicted to decrease to 2.28 MPa from a peak pressure before operation of 4.03 MPa.

Fig. 6

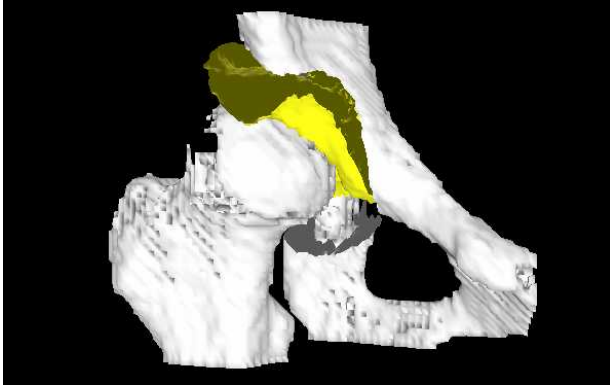


Fig. 7

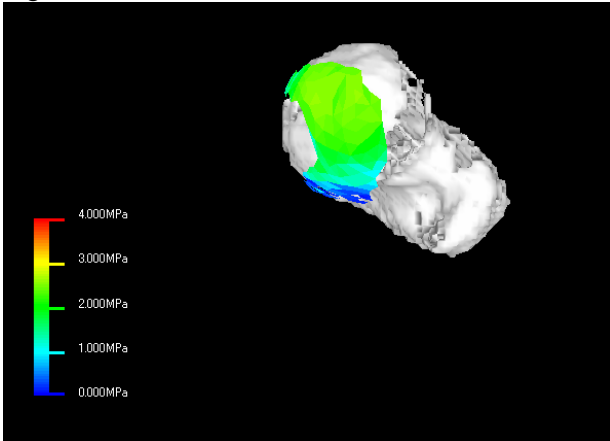
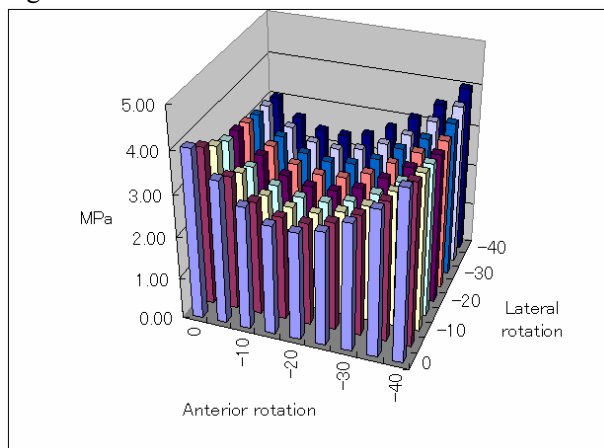


Figure 8 shows the peak pressures that were calculated for every 5 degrees of rotation of the acetabular fragment. The peak pressure was lowest with 25 degrees of anterior and 15 degrees of lateral rotation. However, low peak pressure zone spread from 15 to 25 degrees anterior and from 15 to 20 degrees of lateral rotation.

Fig. 8



4. Discussions

Klaue et al. reported a computer program that could simulate the coverage and the congruency of pelvic

osteotomy for preoperative planning [3]. Their program could only show the relationship between the articular surface of the acetabulum and the femoral head three-dimensionally. Our simulator program is more advanced and also incorporates a mechanical analysis module to predict the results of osteotomy [6, 7].

In the actual operation, osteotomy cannot be performed exactly as planned at the present time. However, computer navigation systems and robotics are continuously improving. If this program will be linked to computer navigation system, it will become more useful to determine the most appropriate treatment method for coxarthrosis with acetabular dysplasia.

References

1. Ninomiya S, Tagawa H. Rotational acetabular osteotomy for the dysplastic hip. *J Bone Joint Surg Am* 1984; 66:430-6.
2. Nozawa M, Shitoto K, Matsuda K, et al. Rotational acetabular osteotomy for acetabular dysplasia. A follow-up for more than ten years. *J Bone Joint Surg Br* 2002; 84: 59-65.
3. Klaue K, Wallin A, Ganz R. CT evaluation of coverage and congruency of the hip prior osteotomy. *Clin Orthop* 1988; 232: 15-25.
4. Kawai T, Toi Y. A new element in discrete analysis of plane strain problems. *Seisan Kenkyu* 1977; 29: 204-7.
5. Bergmann G, Graichen F, Rohlmann A. Hip joint loading during walking and running, measured in two patients. *J Biomech* 1993; 26: 969-90.
6. Tsumura H, Miura H, Iwamoto Y. Three-dimensional pressure distribution of the human hip joint: comparison between normal hips and dysplastic hips. *Fukuoka Acta Med* 1998; 89: 109-18.
7. Tsumura H, Kaku N, Ikeda S, Torisu T. A computer simulation of rotational acetabular osteotomy for dysplastic hip joint: does the optimal transposition of the acetabular fragment exist? *J Orthop Sci.* 2005;10:145-51.

ARTIFICIAL INTELLIGENT INSERTS IN HEALTHCARE SYSTEMS

BALAN PILLAI

PROFESSOR, D.Sc. (TECHNOLOGY)

KISBED ORG, Teknillinen korkeakoulu [Helsinki University of Technology], Espoo, Finland

Abstract

The presentation is here to make a technical walk through to the most recent initiatives in healthcare technology INSERTS predominantly in European Union Countries. We may penetrate on bio-materials and Implants.

Early adopters of new technologies require both innovative product partners and clinical teams. With this in mind, a group of leading-edge researchers, forward-thinking clinical experts, and innovative product partners have formed the Healthy Aims Consortium. They have chosen a range of implants and diagnostic equipment to demonstrate how key Micro- and nano-systems technology components and processes can be developed and integrated into new products. To rapidly demonstrate technology integration, some products have been chosen which can be designed, fabricated and prepared for clinical trials within few years. We reveal here the Functional Electrical Stimulation (FES) implant, an implant intracranial pressure sensor system, retina and cochlear implants, and glaucoma, sphincter, and inertial sensors.

Within this short speech, we could merely walk through the state-of-the-art; confirm technically the emerging need of engineering and human-body science-fusion; into the next-level of cross-cultural scientific body that could achieve the future "connected" smart systems, and or are rolling at the bit stream technology trajectory and the "free-sky".

1 INTRODUCTION

The health care is a local and at the same time global conspiracy subject to handle. Mr. Bill Clinton, last

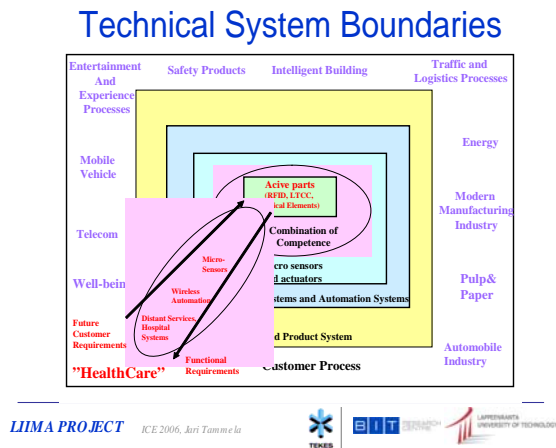
President of the United States of America [2000], introduced the Medicare Bill that could not successfully passed as final Law enforcement at the Senate in the Capital Hill, at Washington, D.C.,US, and still it is hanging with Mr. George W. Bush's cabinet, who lives his Offices as President at 2008. It is obviously a never-ending process on healthcare; now and tomorrow and no one wants to make any compromises to decision! Demand for nanotechnology in health care products will jump 48% annually through 2009, led by improved cancer and central nervous system therapies; based on solubilization technologies. Diagnostic tests focused on nanoarrays and quantum dots, and imaging agents conducted on superparamagnetic iron oxide nanoparticles; would also see strong growth.

1.1 A study [1] analyzes the \$ 906 million US market for nanotechnology in health care products. It presents historical demand data for 1999 and 2004, and forecasts to 2009, 2014 and 2020 by material and product (e.g., nanoparticles, nanoarrays, nanotubes, dendrimers); by application (e.g., pharmaceuticals, diagnostic products, medical supplies and devices); and by indication (e.g., cancer, central nervous system conditions, infectious and viral conditions). The study also considers market environment trends and indicators, details industry structure and profiles 73 industry participants including Elan Drug Delivery, NUCRYST Pharmaceuticals, Quantum Dots, Bristol-Myers Squibb, Dow Chemical, and GlaxoSmithKline¹.

1.2 This speech is not anticipated to be a large sum of paper supplies; except to show that a great number of studies that are not made any efforts to get there a road map on medical technology or policy; not to mention about the drivers and trend in medically used chemicals to human-body systems. The "Committee for Future," consistently offered the plot with a sundry scenario on political-cum-financial prospective. A paper [Elina Savola, *et.al.* (2005)] produced last year in Finland; showing the global evaluation methods in medical practices and its footings. To land a real-touch-roadmap of the future; one needs much more time and ground-to-earth studies, which, of course, is not expected due to either of the both or available monies.

¹ Notes extracted from the publication Source of NIST, Gaithersburg, MD, USA. [2005].

1.3 The Finnish government funding agency, [TEKES], beside the other European Union Countries; have conducted a “map-out project” on competitiveness and Healthcare. See figure below:



The figure [Salminen, V, 2005] shows above the broad boundaries that interleaving with several emerging technologies; and endless entities.

2 ARTIFICIAL INTELLIGENTS IN HUMAN-BODY-SYSTEMS

2.1 The present era of Internet, people around the globe are searching ways to be happy and long living healthily. The legal instrument in some extent preventing or doing so; this is due to rejection of embryonic inserts or use. This is also a moral issue; to use or insert artificial intelligent into the human-body-system [Pillai, B (2006). The implants; we now consider mainly for the teeth-based levels. While ago, we revolutionized with immense success; the Internet, wireless connectivity, handheld devices, and cell phones. Now “the-time” to-go; for the human health issues with; smart systems implants that could help an extended comfortable life to the elderly, chronic or otherwise sick and handicapped human-beings. We owe many thanks to our elderly citizens of the world who dedicated their expensive life to us now to flourish. We should now consider helping them to survive in guiding again to an extended success in healthy-life.

2.2 Apparently we bump into several challenging obstacles; they are the following:

- Microfabrication technology
- Range of electrode and sensor capability for current and future applications
- Challenge is to work with suitably biocompatible materials
- Dense arrays that require microfabrication
 - New markets / devices (e.g. retinal)

- Automation of processing which is very difficult / expensive by “conventional” means
 - Offers a key to substantially larger, valuable market (e.g. Cochlear)
- Enables novel sensors (e.g. glaucoma, sphincter-closure)

3 ELECTRODES AND SENSORS

3.1 In a generic thinking, electrodes and sensors are very sensitive in their surveillance due to the following reasons: Electrodes are; key to active implants –

- They provide the interface to the body tissue
- Applications range from short term <1 day to entire life implants
- Active electrodes are being developed to allow dense arrays with minimal wiring
- Electrode is integrated to multiplex component

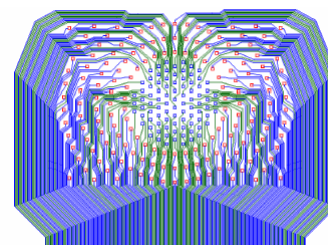
3.2 The lifecycle is downscaled to meet eminent processes at the body system; and electrodes and sensors are therefore needed to be (see table) -

	Long term (electrodes)	Short term (sensors)
Macro		Sphincter closure
Micro	Muscle stimulation	Glaucoma
(array)	Cochlear Retina	

Table: Shows the long-term and short term applications.

3.2 Let us take a quick at another smart device, that is; Retinal stimulator -

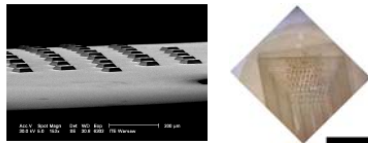
- This requires a dense array of electrodes
- This can only be made by microfabrication techniques. See the image –



3.3 This is a fantastic stimulator. It has proven working perfectly though the microfabrication techniques are extremely high. In this application the electrode structure is very thin (10µm) and;

- The electrode tips are formed as truncated pyramids,
- This improves the contact to the tissue.

3.4 See also a couple of other images below –

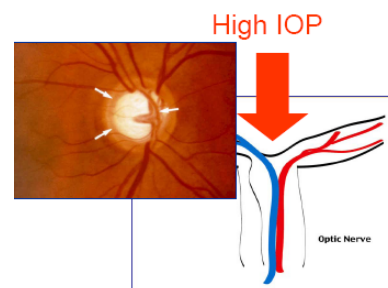


4 BIOMATERIALS & FUNCTIONAL INTERFACES

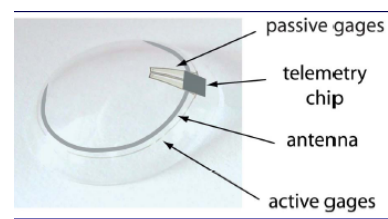
4.1 Biomaterials and Functional Interfaces - exists to address the need for achieving optimal interface between implanted devices and the host tissues. The active implants being developed within the Healthy Aims² project present considerable additional challenges over current devices owing to the integration of active electronics and multi-electrode arrays on flexible substrates. One partner, QMUL, is developing biocompatible, flexible, and impermeable device coating materials to the product partners' specifications and evaluating their performance using cell-culture and other models of biocompatibility. The other partner, INEX, is developing physical and biological surface treatments for electrodes that improve coupling with the target cells (primarily nerve cells) to eliminate much of the loss of efficiency with time currently seen in many implanted electrodes. This is particularly important for the very small electrodes making up the complex stimulation arrays being developed within the project. A development roadmap has been produced and tasks allocated in consultation with others. Activity is now being focused on three materials developments at QMUL; polyurethane, primarily for the urethral device, modified silicones for the other devices and the application of diamond-like carbon to impart an impermeable yet biocompatible coating. QMUL have also established detailed biocompatibility test strategies in partnership with the product partners. Test methodologies have been developed and initial tests have been completed on key materials. At INEX studies have focused on topographic surface modifications in relation to the behavior of mixed populations of cells. In addition a sophisticated and systematic approach to chemical and biomolecular surface fictionalization has highlighted the importance of specific chemical groups in the adhesion of cells to surfaces.

² European Union Initiative, funded by the FP 6 Framework Program, and is being continued unto 2010 and beyond.

4.2 It is mentioned earlier that the artificial intelligent inserts; are no longer an imaginary thinking; virtually they are already here. Ubiquitous and ambient system integration needs more accurate performance in experimenting; though it is a time-consuming effort that could yield the next generation healthcare technology for sure. At the beginning this presentation started in saying that the technical walk includes the glaucoma sensor development. This disease is affecting more than seventy million human-being around the globe. Leonard, et al [2006] reported in Dissemination Day at EPF de Lausanne, Switzerland that glaucoma sensor develops story and its successes. Human-being lost their retina cells due to excessive intraocular pressure (IOP) and also natural phenomenon that causes a gradual and irreversible losing their vision leading to complete blindness, when not treated properly and timely. An image presented below the vision problem -



4.3 The future wireless contact lens would be like the one shown below. This implant would create a new generation technology to sustain the health and sight.



5 THE IMLANTS

5.1 Latest implantable telemetric pressure measurements are aiming to monitor quality and functionality of therapeutic implants inserted; by simply invasive procedures. In order to reduce, the hospital stay of patients to a minimum number of days; implantable sensors for therapy control, integrated into commercial Tele-healthcare applications; provide cost-saving option in monitoring, and allowing the patient to carry on participating their everyday life normally. In a wireless hybrid sensor system approach (Fig below) as described by T Eggers et al (5), the basic components are –

- a long-term stable absolute capacitive pressure sensor,
- an ultra-low power interface circuitry,
- a radio-frequency transponder for bi-directional communication to an outside body area network unit, and
- a micro coil for inductive data and energy transmission to the implant.

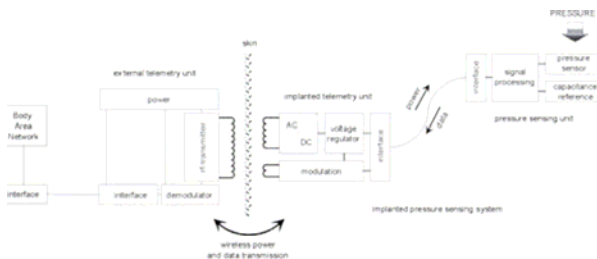


Fig: Block diagram of an implantable telemetric pressure measurement system.

5.2 To avoid the lifetime of the system being limited to the capacity of a battery; contemporary systems use a passive, inductively coupling method; to provide the implant with power from outside. However, at the same time transfer the data over a sufficiently long transmission distance; to an external reader unit. Consequently ultra low power consumption on part of the implant is essential. The encapsulation of the implant has to provide hermetically sealing in order to assure a driftfree and highly reliable system; over the entire lifetime of the implant. An additional nanotype coating ensures highly biocompatible performance of the implant. The latest three-dimensional micro packaging technologies facilitate the development of flexible devices; like integrated pressure sensor systems that meet the elevated demands of modern surgical insertion procedures; and could stay stable and reliable inside the human body over a long period of time.

6 Summary

6.1 The next generation technology scenarios are already set; for connecting into human-body-science, and information technology. This is not a trap but value-added well-being technology and permanent approach to better and happy life; the life time available or provided by the nature.

6.2 Let me conclude this presentation here with thanks to you all.

Acknowledgement

At this point, my personal greetings and thanks go to two eminent professors, who got dirtied their hands in arranging this Conference successful here. They are namely Professor Masanori Sugisaka, Department of Electrical Engineering of Oita University, Japan, and Professor Ju-Jang Lee, Korea Advanced Institute of Science and Technology, Daejeon, South Korea.

References

[1] National Institute of Sciences and Technology, *NIST*, Gaithersburg, Maryland, USA

[2005]: *Nanotechnology Trends and Markets* – Source search unpublished documents.

[2] Vesa Salminen (2005): *LIIMA Project*, published by TEKES, Finland

[3] Savola, E, et.al [2005]: *Evaluation Methods of Medical Practices*, Published by the Finnish Parliament, *Suomen Eduskunta*, Helsinki, Finland

[4] Pillai, B [2006]: A squat scenario on healthcare technology globally: Roadmap for Finland, *A proprietary document presented to LIIMA Project for TEKES*, Finland.

[5] Eggers, T, et.al [2000]: MEMS2000.

Intelligent Multi Agent Application System in AI System

Young Im Cho

Dept. of Computer Science, The Suwon University

San 2-2, Wau-ri, Bongdam-eup, Hwaseong, Gyeonggi-do, KOREA, 445-743

e-mail : ycho@suwon.ac.kr

Abstract

In this paper, I will present about the intelligent multi agent application system in AI. The research trend of multi agent is changed from centralized computing environment to distributed computing environment. Also, the research of multi agent can be changed to mobile environment. Initially, the study of multi agent is from the research of the human modeling.

Therefore, I will present a brief the concept of mobile multiagent, and present some application areas of mobile multi agents, especially in bioinformatics, control, and information retrieval etc. And finally I will present the research theme of multiagent in AI.

I. Introduction

Artificial Intelligence Artificial Intelligence (AI) is the area of computer science focusing on creating machines that can engage on behaviors that humans consider intelligent. The ability to create intelligent machines has intrigued humans since ancient times, and today with the advent of the computer and 50 years of research into AI programming techniques, the dream of smart machines is becoming a reality. Researchers are creating systems which can mimic human thought, understand speech, beat the best human chess player, and countless other feats never before possible.

Recent developments of the internet and network technologies evoke the technical change of the data processing from a conventional centralized and local processing system to the distributed processing system. The research about this network and the various approaches have been studied in order to efficiently manage mutual operations in such a network environment.

Many studies have been actively carried out in a distributed processing environment by using agent systems for efficient network management. An agent system has the following characteristics: multi agents in the distributed environments promote efficiency by solving one problem through any cooperation. Each agent manages the problem by dividing a common work into the number of agents, or each agent manages it independently, and then they solve the problems by analyzing the results. In addition, it has some

advantages such that intelligent agents reflecting the tendency of users make no limitation of movement in a network, and it remarkably decreases the network traffic [1].

The study of multiagent systems focuses on systems in which many intelligent agents interact with each other in distributed environment. The agents are considered to be autonomous entities, such as software programs or robots. Their interactions can be either cooperative or selfish. That is, the agents can share a common goal (e.g. an ant colony), or they can pursue their own interests (as in the free market economy).

Multiagent system researchers develop communications languages, interaction protocols, and agent architectures that facilitate the development of multiagent systems. For example, a multiagent system researcher can tell you how to program each ant in a colony in order to get them all to bring food to the nest in the most efficient manner, or how to set up rules so that a group of selfish agents will work together to accomplish a given task. Multiagent system researchers draw on ideas from many disciplines outside of AI, including biology, sociology, economics, organization and management science, complex systems, and philosophy.

In this paper, I will explain the distributed multiagent system which is a modern AI approach and their applications as an example case.

This paper is composed of the followings. Multiagent digital library is explained in chapter 2, and the application areas in multiagent are explained in chapter 3, and finally I will conclude this research in chapter 4.

2. Multiagent Digital Library

2.1 Distributed Agent Framework

There are so many application areas of agents in the real world. One of these areas is a digital library system. The digital library is called an *electronic library* or a *virtual library*. This is a library developed to replace the conventional library, in order to serve information from databases on the web to users, according to the development of computers and the related fields.

However, there are several problems in the searching of data of the existing digital libraries.

First, as the searching method is one dimensional and distinguishes the existence of the searching keyword from the database, the result is very simple. Second, the results may contain unnecessary information under a condition that was not given the prior information about the user. Thirdly, whenever a client connects to the servers, he has to receive the certification and be under the dominant power of the influence of network.

To overcome such problems, a new platform of mobile multi agents for a personal digital library is necessary.

For the user's preference, some modular clients are applied to a neural network. A multi agent platform and a mobile agent platform are combined to develop a new mobile multi agent platform so as to decrease a network burden. Also, a new negotiation algorithm and a scheduling algorithm are activated for the effectiveness of PDLs.

DECAF is a kind of operating system including agent communication, planning, scheduling, monitoring, coordination, diagnosis, and learning among agents[2]. DECAF makes a socket program by itself, and presents some building blocks which makes messages and communicates between agents. Therefore, users or programmers can produce agents without having some knowledge about API approaches. Also, users or programmers do not need to make the communication codes directly to communicate among agents. Agent systems have been developed using various languages and platforms, and they are classified into so many types by purpose. In DECAF, many agents' tasks are divided by both GPGP (Generalized Partial Global Planning) and TAEMS (Task Analysis Environment Modeling and Simulation) algorithms.

GPGP is for improving of PGP which acts as a coordination algorithm of multiagents [3]. The first advantage of GPGP is that it reduces the system overhead which occurs by overlapping interaction among agents. And the second advantage of GPGP is that it is independent from some specific domain areas. Therefore, GPGP can make heterogeneous multi agents system having different functions. User's requirements can be decomposed by GPGP, and be structured by TAEMS [4]. User's requirements can be decomposed by GPGP, and be structured by TAEMS [4]. The root task can be decomposed into subtasks, and the subtasks can be decomposed into methods. The leaf node acts as a method which means actually acted elements.

Voyager [5] is a distributed mobile agent's framework for developing agent's applications,

whereas DECAF is a non-mobile agent's framework. Voyager is an interactive framework with Java programming. Also, Voyager can activate any Java class in remote sites, and it makes use of network bandwidths effectively.

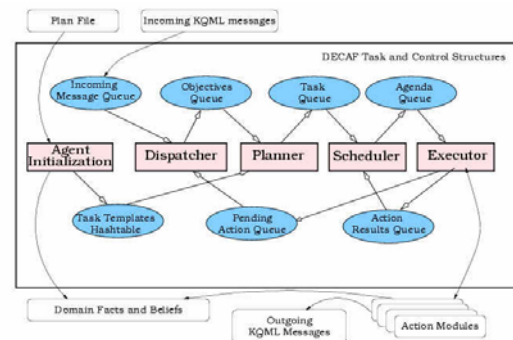


Figure 1. DECAF

2.2 The Concept of Agent-based Digital Library

A digital library serves a lot of information on-line [6,7]. The advantages of digital libraries are user friendly, on-site service and accessibility. However, in case of not having standardized platform, the search of heterogeneous information from digital libraries may be hard, as well as impossible. If it does not have or learn about the user's information, unnecessary or useless information will appear in the searched results from the digital library. Each agent can access DBMS and search documents according to the user profile. And then each agent categorizes the searched results.

The proposed system PDLs based on a new multi mobile agent platform. The system combines a mobile system and a distributed processing system to make an optimization of behaviors in a distributed environment. To establish a distributed environment, DECAF is used, and to activate a mobile framework, Voyager is used here.

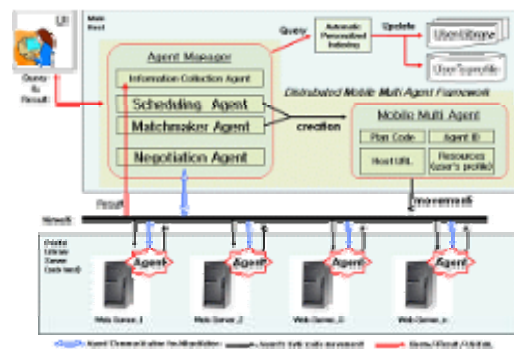


Figure 2. PDLs Structure

As shown in Figure 2, PDLs has two modules and two databases. The monitoring agent module is composed of Voyager and DECAF, and it monitors the agents' movements and controls their executions. When the user's requirements are transferred to the PDLs, the monitoring agent module checks whether the servers are available or not. After that, it makes some agents, and passes them to the servers. The searched results are saved in a temporary repository. They are filtered by negotiation agents, and the final results are saved in the result repository.

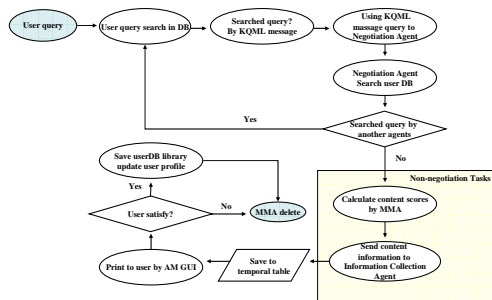


Figure 3. Negotiation Algorithm among Multiagent

The construction of the initial user's profile is constructed by the user's first input information. According to the user's searched results, PDLs endows the user's keywords to weight values, and updates user's profile information by SOM (self organizing map) network in real time [8]. SOM is an unsupervised neural network. In this paper, 2-layered SOM network is used here.

2.3 Simulation Results

The scenario is the followings. User can login by user interface. The monitoring agent(MA) is activated, and MA check the current connected remote digital library. At the same time, a user profile is read from database. The queries according to users are sent to PDLs. MA makes a search agent 1 and registers it in ANS. The search agent 1 is sent to the remote library. The agent 1 is activated by receive the parameters from PDLs. The results from the agent 1 with information such as name and index and abstract of the remote library are sent to PDLs. And then they are sent to the negotiation agent(NA) for negotiation. At the same time, they inform to the MA and ANS. MA is clustered using SOM network according to the received results. The results by the user profile can be shown in the remote plane. user can move to his local library after receiving his necessary results. The user profile's update is activated.

As time passed, the searching times between the proposed PDLs and the traditional client-server model PDLs showed a faster search time as well as a much safer search than the client-server model. The result showed that as the numbers of servers were increased, the searching time was decreased in PDLs.

3. Multiagent Health System

3.1 TMA(Tissue Mineral Analysis)

TMA[9] is a very popular method in hair mineral analysis for health care professionals in medical centers in over 48 countries[10,11]. The assessment of the relative relationship between nutritional minerals and toxic elements in hair is very important for determining adequacy, deficiencies, or the unbalance of nutritional minerals in the body.

There are some problems in the TMA method. The TMA method, which uses a TMA database, applies a pattern matching method in producing outputs when the mineral ratios and the properties of a patient are entered into the database for requesting. This pattern matching method may be effective if the database of TMA has a large-scale data, but it may produce inaccurate results if the database of TMA consists of a small number of data. Secondly, because there are insufficient health information databases for TMA in KOREA, it could not get the effective medical information. Also, it can cause some problems in the reliability of the TMA results, since the TMA results are based on the database of western health and mineral standards.

For these reasons, I propose the first Intelligent Medical Health Information System (IHIS). The IHIS uses a new TMA method. In the TMA method, a new multiple fuzzy rule base is proposed for intelligent inference. A multi-level statistical analysis is used to reduce some errors in statistical analysis, so that a new TMA database is developed and some medical data inferred from the TMA database. Also, this system can produce Korean reports about both patients' reports and doctors' reports as well. The effectiveness of the proposed method is verified through a series of simulation using some real clinical data.

3.2 IHIS Overview

The proposed Intelligent Health Information System(IHIS) is composed of 3 modules as shown in Figure 4: TMA statistical analysis module, TMA health information system module, and the

intelligent inference system module. After finishing the statistical analysis module, TMA database can be developed and it can receive feedback with real medical data for verification.

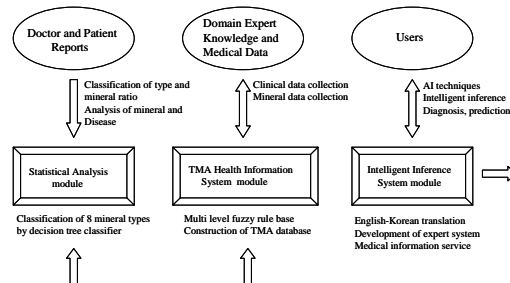


Figure 4. System Overview

In the Statistical Analysis module, the 8 type of metabolic types such as 4 slow metabolic types and 4 fast metabolic types, and mineral ratios are classified by a decision tree classifier[12,13]. The decision tree classifier can be adopted for the following reasons. The first step of the classifier makes use of the combination of the characteristics that is a maximum mean value among classes. However, the combination of characteristics does not represent an optimal classification among classes. Therefore, several repeating classifications between two types of decisions should be adopted so that it can be decided into input patterns correctly.

In the classification process of input patterns by a decision tree classifier, four types of slow metabolic types $\{S_1, S_2, S_3, S_4\}$ and four types of fast metabolic types $\{F_1, F_2, F_3, F_4\}$ are classified in root node on the basis of a mineral ratio of $Ca/P(=2.63)$. And in the second step, the sub slow metabolic types $\{S_1, S_2\}$ and $\{S_3, S_4\}$ are classified on the basis of a mineral ratio $Ca/K(=4.2)$, and the sub fast types $\{F_1, F_2\}$ and $\{F_3, F_4\}$ are classified on the basis of a mineral ratio $Na/Mg(=4.0)$. And in the final step, $\{S_1\}$ $\{S_2\}$ $\{S_3\}$ $\{S_4\}$ are finally classified on the basis of a mineral ratio $Na/Mg(=4.0)$.

Likewise, $\{F_1\}$ $\{F_2\}$ $\{F_3\}$ $\{F_4\}$ are finally classified on the basis of a mineral ratio of $Ca/K(=4.2)$, too. In this paper, I have classified the basic metabolic types and the correlation of nutritional minerals and toxic minerals by correlation analysis among minerals over coefficient of correlation 3.0.

The metabolic type classification shows the same results when using class type distributions

about characteristics variables such as Ca/P , too. Figure 5 show the classifications of metabolic type using class distributions by adopting some characteristics variables.

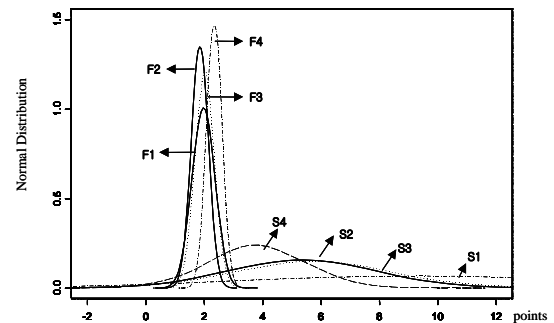


Figure 5. Metabolic Type Classification by Mineral Ratio of Ca/P

3.3 TMA IHIS Development Steps

I propose a new multiple fuzzy rule base system based on a statistical analysis method, which is designed for an intelligent inference from a lot of uncertain health information data. The purpose of the multiple fuzzy rule base system is following. In case that the complicated decisions by a lot of minerals are necessary, a rule base may be complicated in the conventional fuzzy rule base system. Therefore the rule base should be distributed so that it can be found, searched, and inferred by some multi-level relations among rules in the multiple fuzzy rule base.

Due to this, IHIS is composed of multi level tree structures which represent relations between the conclusion parts of a rule and the conditional parts of other rules, so that IHIS is appropriate for representing more complicated fuzzy rules.

The reason why the fuzzy theory is adopted as an uncertain handling method in IHIS, is that a fuzzy theory is appropriate for inference as well as representing the clinical minerals than any other uncertain handling techniques [9, 10]. The implemental steps of the multiple fuzzy rule base are the followings.

<Step 1> Classification of Metabolic Types and Development of a Fuzzy Rule base

The <Step 1> is an initial implementation step of a multiple fuzzy rule base on the basis of the correlation analysis of minerals by which defines fast metabolic types and slow metabolic types. To implement the multiple fuzzy rule base in this paper, I analyzed the following mineral types: nutritional mineral 30 types, toxic mineral 8 types, the relations between nutritional minerals and

toxic minerals, the ratios of nutritional minerals, the ratios of toxic minerals, the tendencies between all types of diseases and minerals.

The linguistic values which are in the mineral ratio's analysis, such as 'high', 'low', and 'acceptable', can be represented by fuzzy membership functions as shown in Figure 8. In Figure 8, X axis represents mineral ratios and Y axis represents fuzzy membership function values. These values are obtained by a statistical analysis method using a decision tree classifier.

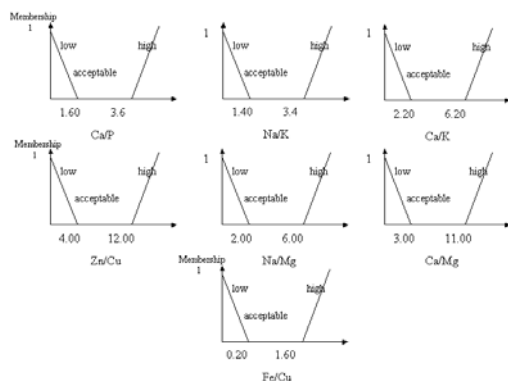


Figure 6. Fuzzy Membership Functions of Mineral Ratios

Not only those above minerals ratios but also all of the minerals such as 15 types of nutrient minerals (Ca, Na, Mg) and 8 types of toxic minerals (Hg, Pb) and other 15 types of minerals can be represented by fuzzy membership functions as shown in Figure 4.

<Step 2> Development of relations between endocrine glands and minerals by measuring the amounts and ratios of minerals

The <Step 2> is a refinement step of the multiple fuzzy rule base that implemented by <Step 1>. And also it implements a database about correlations between endocrine glands and minerals. The results of this analysis, shown in Figure 5, are used in designing the multiple fuzzy rule base. For example, if some mineral ratios are increased, such as $Ca/P, Ca/Mg$

$Ca/Na, Ca/K, Ca/Fe$, then parathyroid is increased. However, if Fe/Cu is increased, then parathyroid is decreased. If $Na/Mg, Fe/Cu$ are increased, then thyroid is increased. If $Zn/Mg, Fe/Cu$ are increased, then progesterone is increased. If $Ca/P, Ca/K$ are increased, then thyroid is decreased. If $Na/K, Ca/K$ are increased, then progesterone is decreased. If $Ca/P, Ca/Mg, Ca/K, Ca/Fe, Ca/Na$ are increased,

then pancreas is increased. However, if $Zn/Mg, Fe/Cu$ are increased, then pancreas is decreased.

If $Ca/Mg, Ca/P, Ca/K, Ca/Na, Ca/Fe, Na/K$ are increased, then Estrogen is increased. However, if $Zn/Cu, Fe/Cu$ are increased, then estrogen is decreased. If $Zn/Cu, Fe/Cu$ are increased, then progesterone is increased. However, if $Na/K, Ca/K$ are increased, then progesterone is decreased. The other results of statistical analysis are used to implement the multiple fuzzy rule base.

<Step 3> Paragraph Analysis by Mineral Distribution

Patient and doctor's report have so many paragraphs explaining a patient's examination by TMA. Since a doctor's report contains extra information plus the contents of a patient's report, the doctor can explain the patient's examination to the patient very effectively. Patient and doctor's report have so many paragraphs explaining a patient's examination by TMA. Since a doctor's report contains extra information plus the contents of a patient's report, the doctor can explain the results of the patient's examination to the patient very effectively.

For the implementation of the refined fuzzy rule base, I analyzed the paragraphs explaining a patient's examination according to mineral distribution.

The rule type of the proposed multiple fuzzy rule base and the rule type of conventional simple fuzzy rule base are very different. In the multiple fuzzy rule base, only 3 propositions (fuzzy membership functions) are in antecedent part of a rule to make a multilevel inference effectiveness. Also, because of a hierarchical structure in the multiple fuzzy rule base, the system can infer the next relative rules from the multiple fuzzy rule base. However, in a conventional simple fuzzy rule base, there are so many propositions being represented by fuzzy membership functions in antecedent part of a rule. Even though it can be represented by small sized propositions, it is necessary to have some intelligent techniques, such as time scheduling or optimality, as well as some intelligent fuzzy inference techniques, because the medical minerals are very huge as well as complex, and they have so many relations among them.

3.4 Implementation Step

The format of the multiple fuzzy rule base is as

follows. The antecedent part of a rule is composed of mineral ratios, and the conclusion part of a rule is composed of both metabolic types and mineral ratios entering antecedent of the rules. In this paper, rules in a fuzzy rule base which has been implemented so far are more than 1000 cases.

<Format of Fuzzy Rule base>

- Rule 1: IF X_1 is A_1 and Y_1 is B_1 and
..... Z_1 is C_1 THEN K_1 is R_1
- Rule 2: IF X_2 is A_2 and Y_2 is B_2 and
..... Z_2 is C_2 THEN K_2 is R_2
-
- Rule n: IF X_n is A_n and Y_n is B_n and
..... Z_n is C_n THEN K_n is R_n

Where, X_1, Y_1, Z_1, K_1 : mineral, mineral ratios, endocrine gland etc. A_1, B_1, C_1, R_1 : fuzzy sets (*high, low, medium* etc.)

In this paper, the multiple fuzzy rule base makes use of TAEMS in order to be an effective fuzzy inference using data gained from multi-level statistical analysis.

Each rule in the fuzzy rule base has an interrelationship like Figure 7. The fuzzy implications that are composed of fuzzy antecedent and conclusion parts of a rule have some interrelationships which send to other antecedent parts of rules in the fuzzy rule base. The reason is that TMA mineral data is classified by the complicated interrelationship and not simple mineral data.

To infer the ID paragraph, the three rules should be interconnected as shown in Figure 7. The conclusion part of 'THEN' such as ' S_1 ', ' Ca/K is low', ' Na/Mg is high', are entered to the antecedent part of a Rule #2. And the relative ID paragraphs are inferred by multilevel scheduling process using TAEMS. In the IHIS system, each conclusion part of rules is repeatedly finding the antecedent parts of the upper level rules, and finally it finds the appropriate ID paragraphs of the conclusion part of rules. The inferred relative ID paragraphs are as follows.

Therefore, according to the inferred ID paragraphs by mineral amounts and ratios, the translated paragraphs in Korean are inferred from the TMA database, and they finally served to patients and doctors as a format of reports.

Since USA-TMA consists of simple structured RDB with approximately 0.35 million cases, it could be carried out by the inference of some required data via just pattern matching. Even

though the IHIS has small-sized database with about 2000 cases, it could successfully find out the desired results by using the statistical classification and the intelligent multiple fuzzy rule bases. If it is compared with the simple fuzzy rule basis method, the proposed multiple fuzzy rule basis method has increased the effectiveness of the IHIS where the size of the sample is about 2000 cases.

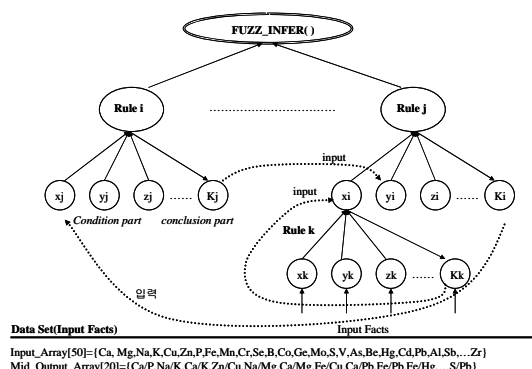


Figure 7. Interrelationship of Rules in Multiple Fuzzy Rule Base

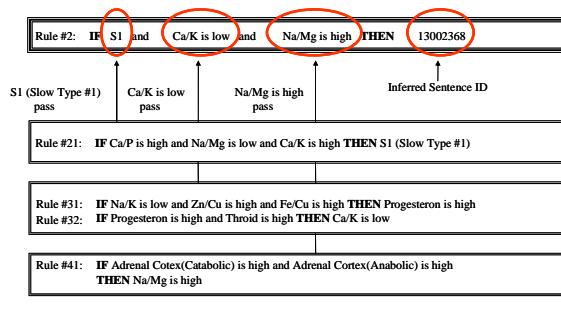


Figure 8. Inference Process in Multiple Fuzzy Rule Base

<ID: 13002312 English Paragraph>

“Magnesium deficiency has been shown to be associated with decreased antibody production. Published studies have revealed that the lymphocytes, which are the body’s defence against foreign invaders, are inhibited when there is a deficiency of Magnesium”

The average processing speed of the proposed system means, the rate of searching the literal sentence matching with the mineral data of TMA, at which must be inserted in the initial menu of the IHIS. While the processing speed of the simple fuzzy rule basis method is considerably slow due to frequent comparison between input data of rules, the proposed multiple fuzzy rule basis method has been increased 5 times by

decreasing the number of comparison of input data of rules and reinserting the resulting data.

In order to measure the accuracy of output in the IHIS, I inspected the matching sentences between the resultant documents (set of paragraphs) from the proposed IHIS system and those from TMA in the US for about 2000 cases of domestic patients' clinical data occurred from July 2001 to February 2002. For 50 sentences of a result document per patient, the simple fuzzy rule base's method resulted in 30 matched sentences in average, but the multiple fuzzy rule base's method resulted in 46 matched sentences. The accuracy of the proposed multiple fuzzy rule base's method has been increased by 32% than that of the simple fuzzy rule base's method. Presently, the total number of result sentence saved in the database of the IHIS is approximately 700 per each metabolism and mineral. Consequently, the performance of the inference by the proposed multiple fuzzy rule basis method, having only 2000 cases, is exceedingly better than that of the conventional method with 0.35 million data.

I have analyzed the degree of satisfaction, which means the ratio of the degree of the application and the efficiency of the IHIS. Usually, the proper time required for a patient is three minutes. Here, I set the basic processing time to 3 minutes and counted the over time for evaluating the degree of the customer's satisfaction.

4. Conclusions

In this paper, I will present about the intelligent multi agent application system in AI. The research trend of multi agent is changed from centralized computing environment to distributed computing environment. Also, the research of multi agent can be changed to mobile environment. Initially, the study of multi agent is from the research of the human modeling.

Therefore, I will present a brief the concept of mobile multiagent, and present some application areas of mobile multi agents, especially in bioinformatics, control, and information retrieval etc.

In this paper, I proposed a Personal Digital Library System. PDL is designed based on a new mobile multi agent platform using Voyager and DECAF agent framework. The new platform is a hybrid system of a mobile and a distributed system in order to achieve an optimality in distributed. Also, I have developed the new TMA System, named IHIS.

In the future, PDL needs to be compensated in order to be activated in the real world. Also, IHIS

will be constructed the eastern style medical database not western style database as time passed. Also, I anticipate the system could be served on the World Wide Web very soon.

Acknowledgements

This paper is carried out by supporting of KOSEF(KOrea Science and Engineering Foundation) during 2003 to 2005 as an Eminent Woman Science Program.

References

- [1] David C., Colin H., Aaron Kershenbaum, Mobile Agents: Are They a Good Idea?, 1995
- [2] John R. Graham, Keith S. Decker, Towards Distributed, Environment Centered Agent Framework. Appearing in *Intelligent Agents IV, Agent Theories, Architectures, and Languages* Springer-Verlag, 2000, Nicholas Jennings, Yves Lesperance, Editors
- [3] Keith S. Decker, Victor R. Lesser Generalizing the partial global algorithm. *Intelligent Cooperative Information Systems*, vol.2, no.2, pp.319~346. 1992
- [4] Keith S. Decker, Task Environment Centered Simulation, 1996
- [5] ObjectSpace, Voyager Core Technology 2.0 User Guide, ObjectSpace, 1998
- [6] Sánchez, AGS: Introducing Agents as Services Provided by Digital Libraries, 1997
- [7] Jonas Holmstrom, A framework for Personalized Library Services, October 2002
- [8] Kohonen, Self Organizing Feature Map, 1995
- [9] Watts, D.L., *Trace Elements and Other Essential Nutrients-Clinical Application of Tissue Mineral Analysis*, 2nd Writer's BLOCK edition, 1997.
- [10] Baumgartner, W.A., and Hill, V.A., and Blahd, W.H., "Hair Analysis for Drugs of Abuse", *Journal of Forensic Science*, vol.34, no.6, 1989.
- [11] Vir et al, "Serum and hair concentrations of Copper During Pregnancy", *American Journal of Clinical Nutrition*, vol.34, 1981.
- [12] Jang, S.I. et al., "Research of hair minerals in a diabetic", *Medical news*, .vol.45, no.5, 2002.
- [13] Safavian, S.R., and Landgrebe, D., "A survey of decision tree classifier methodology", *IEEE Transactions on System, Man, and Cybernetics*, vol.21, no.3, pp. 660-674, 2001.

Hybrid Tracking Control of Eye-in-Hand Robotic Manipulators

Wen-Chung Chang and Chih-Wei Cho
 Department of Electrical Engineering
 National Taipei University of Technology
 Taipei 106, Taiwan, R.O.C.

Abstract

Classical force and vision-based tracking control approaches typically require expensive six-axis force sensors in addition to vision sensors. In this article, a new approach is presented which only requires a single-axis force sensor together with a laser cross projector in addition to a vision sensor. The key idea is to estimate the direction normal to an unknown 3-D surface by projecting and reconstructing a laser cross on it. The proposed autonomous task is to drive the end-effector of a 6-DOF manipulator to a visually determined trajectory and continue tracking the trajectory in desired pose, contact force, and speed. The proposed hybrid force and vision-based control approach is successfully validated in a real task environment by performing experiments with an industrial robotic manipulator on an arbitrary-shaped acrylic fiber 3-D object.

1 Introduction

Vision is becoming a popular sensor in robot control since it can extract extensive information without contacting with the environment. Based on available visual information, appropriate feedback laws can be synthesized for variety of control applications [1, 2]. Xiao *et al.* [3], proposed force and position control of a robotic manipulator in Cartesian space with an expensive 6-axis force sensor and a CCD video camera. In [4], an autonomous dexterous planar robotic system capable of tracking unknown contours has been presented and validated in experiments. This system can guarantee task precision employing only a single-axis force sensor and an imprecisely calibrated CCD camera. In this research, force and pose tracking control can be further performed on 3-D unknown surfaces by a low-cost single-axis force sensor, a CCD camera, and a laser cross projector. In order to control the pose of the end-effector with respect to an unknown 3-D surface, the direction normal to the tangential plane at the contacting point, a normal vector, must be esti-

mated. This normal vector is computed based on the reconstruction of the projected laser cross onto the unknown surface provided that the fixed transformation between the coordinate systems of the camera and the laser projector is known a priori.

The configuration of the proposed autonomous system is shown in Figure 1, where the system includes a robot arm, an unknown surface, a laser cross projector, a PC, and a CCD camera. The problem of in-

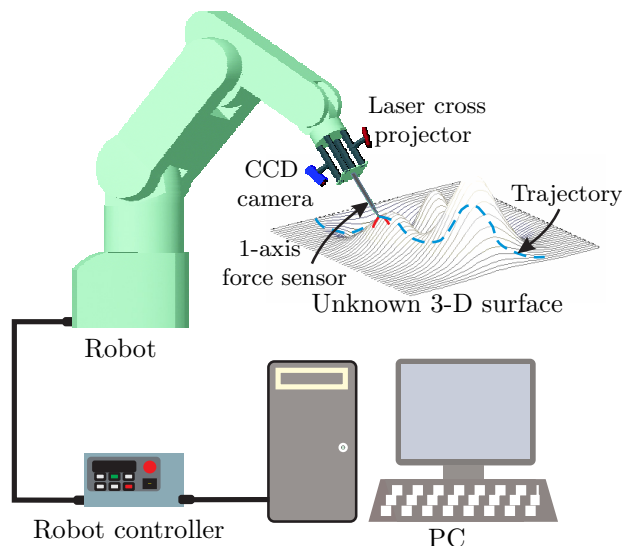


Figure 1: System configuration.

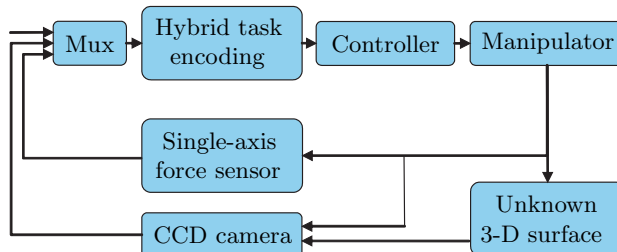


Figure 2: Hybrid control structure.

terest is to simultaneously control the normal contact force and the pose of a six-degree-of-freedom robotic manipulator on the unknown 3-D surface. The goal of the autonomous task is to drive the end-effector to the trajectory and continue tracking the trajectory in desired pose and contact force. The proposed hybrid control structure is illustrated in Figure 2.

2 Normal vectors on 3-D surface

2.1 Detection of laser cross

As the color of the laser cross is different from the surrounding environment, the laser cross could be detected by color filtering and connected components labelling [5]. A typical observed image from a CCD camera and the corresponding image processing results can be seen in Figure 3. In order to locate the two curves

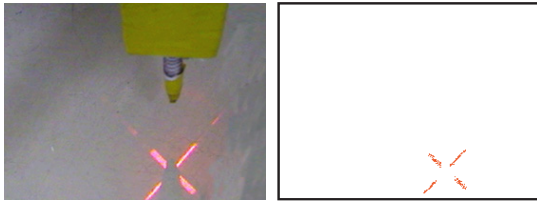


Figure 3: Laser cross on image plane.

that the laser cross is composed of, one could first identify the corresponding two sets of pixels and apply least square algorithm to determine their equations in image space. An effective way of computing the center of the cross for correctly allocating sets of pixels to the two curves is as follows. Let $[u \ v]^T$ be the 2-D coordinates in the image plane, α denote the distance between the edges of laser cross at fixed u , and β denote the distance between the edges of laser cross at fixed v as illustrated in Figure 4. By determining the

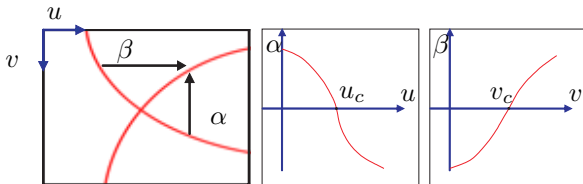


Figure 4: Laser cross curves on image plane{left}, $u\alpha$ -plane{middle}, and $v\beta$ -plane{right}.

equation of the curves

$$\alpha = g_1(u) \text{ and } \beta = g_2(v) \quad (1)$$

on the $u\alpha$ -plane and the $v\beta$ -plane as illustrated in Figure 4, the image coordinate of the laser cross center $[u_c \ v_c]^T$ are calculated by setting $\alpha = 0$ and $\beta = 0$ in (1). To determine the two curves and the precise center of laser cross, four regions are partitioned by the previously detected laser cross center $[u_c \ v_c]^T$. The curve in quadrant I and quadrant III can be estimated by least square algorithm. Similarly, the other curve in quadrant II and quadrant IV can also be estimated.

2.2 Reconstruction of normal vectors

To determine the directional vector normal to the 3D unknown surface, the image projection of laser cross onto the unknown surface is used to estimate the normal vector. Firstly, calculate the transformation matrix between the camera and the laser projector, and then the transformation matrix between the laser projector and the robot. Finally, reconstruct the projected laser cross on the surface in laser projector frame by the known transformation between the camera and the laser projector as shown in Figure 5. Specifically, when projecting a laser line to form the yz -plane in the laser projector frame, one can reconstruct a 3-D laser point \bar{m} with ${}^I\bar{m}$ as the 3-D coordinate of its projection on the image space by setting the x -component of \bar{m} to be zero in the following equality.

$$\bar{m} - c = k({}^I\bar{m} - c) \quad (2)$$

Similarly, one can reconstruct a 3-D laser point by setting the y -component of \bar{m} to be zero in (2) if a laser line is projected to form the xz -plane. Based on

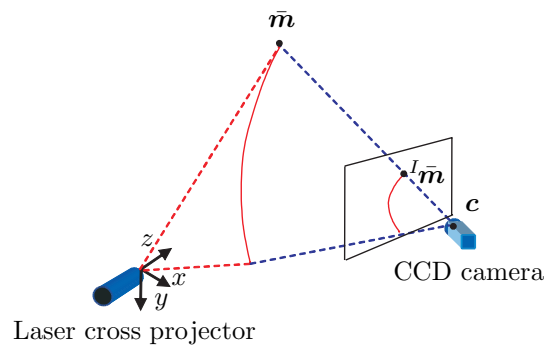


Figure 5: Reconstruction of laser cross curves.

the reconstructed laser cross in Cartesian space, one can compute the normal vector n at the laser cross center, which is the cross product of the two tangential lines at the laser cross center.

3 Hybrid control design

There are three subtasks for the hybrid task including position, orientation, and force control tasks.

3.1 Position control

The purpose of this subtask is to control the robot to reach the desired target position. The task can be divided into two parts. The first part is an image-based set-point control task. The second part is a contacting control task. Based on the perspective projective model G of the camera, the image coordinate ${}^I\mathbf{r}$ of a point feature $\mathbf{r} \in \mathbb{R}^3$ can be computed as

$${}^I\mathbf{r} = G(\mathbf{r}) = \begin{bmatrix} \gamma \frac{\mathbf{i}^T(\mathbf{r}-\mathbf{c})}{\mathbf{k}^T(\mathbf{r}-\mathbf{c})} \\ \gamma \frac{\mathbf{j}^T(\mathbf{r}-\mathbf{c})}{\mathbf{k}^T(\mathbf{r}-\mathbf{c})} \end{bmatrix} \quad (3)$$

where γ is the focal length and \mathbf{c} is the optical center of the camera, and \mathbf{i}^T , \mathbf{j}^T , and \mathbf{k}^T are the row vectors of the rotation matrix from the base frame to the camera frame. The encoded error for this task can be defined as

$$\mathbf{e}_1 = {}^I\mathbf{r} - {}^I\mathbf{r}^* \quad (4)$$

where \mathbf{r} and \mathbf{r}^* are the positions of the end-effector tip and the laser cross center respectively. Differentiate (4) with respect to time, it follows that

$$\dot{\mathbf{e}}_1 = \mathbf{J}_1(\mathbf{r})\dot{\mathbf{r}} \quad (5)$$

where

$$\mathbf{J}_1(\mathbf{r}) = \begin{bmatrix} \frac{f}{\mathbf{k}^T(\mathbf{r}-\mathbf{c})} \left(\mathbf{i}^T - \frac{\mathbf{i}^T(\mathbf{r}-\mathbf{c})}{\mathbf{k}^T(\mathbf{r}-\mathbf{c})} \mathbf{k}^T \right) \\ \frac{f}{\mathbf{k}^T(\mathbf{r}-\mathbf{c})} \left(\mathbf{j}^T - \frac{\mathbf{j}^T(\mathbf{r}-\mathbf{c})}{\mathbf{k}^T(\mathbf{r}-\mathbf{c})} \mathbf{k}^T \right) \end{bmatrix} \quad (6)$$

The image-based position control law capable of driving \mathbf{e}_1 to zero can be chosen as follows.

$$\dot{\mathbf{r}} = -(\mathbf{J}_1 \circ \mathbf{L}(\boldsymbol{\theta}))^+ \mathbf{e}_1 \quad (7)$$

where \mathbf{L} denotes the forward kinematic function and the superscript $+$ denotes the pseudo-inverse. Since one cannot perform 3D positioning task with only single-camera vision, a contacting control law is considered which together with the image-based feedback law can guarantee precise positioning at the target point \mathbf{r}^* on the 3-D trajectory. Let $\mathbf{P} \in \mathbb{R}^{3 \times 3}$, the projector onto the null space of \mathbf{J}_1 , be defined as

$$\mathbf{P} = \mathbf{I} - \mathbf{J}_1^+ \mathbf{J}_1. \quad (8)$$

Consider the feedback connection $\dot{\mathbf{r}} = \dot{\mathbf{r}}_p$, where

$$\dot{\mathbf{r}}_p = -(\mathbf{J}_1 \circ \mathbf{L}(\boldsymbol{\theta}))^+ \mathbf{e}_1 + k_1(f)\mathbf{P}\mathbf{l} \quad (9)$$

$\mathbf{l} = {}^I\mathbf{r}^* - \mathbf{c}$, f denotes the contact force, and with suitably defined positive numbers k_1 and δ

$$k_1(f) = \begin{cases} 0 & f > \delta; \text{if contacting} \\ k_1 & f \leq \delta; \text{otherwise} \end{cases}. \quad (10)$$

In the light of (5) and (9), it follows that

$$\dot{\mathbf{e}}_1 = -\mathbf{e}_1. \quad (11)$$

Therefore, the end-effector tip continues reaching the laser cross center while $\mathbf{e}_1 \rightarrow 0$ exponentially.

3.2 Orientation control

Based on the reconstructed normal vector \mathbf{n} and the orientation of the end-effector, denoted by \mathbf{z} , one can define the encoded error for the orientation control subtask as

$$\mathbf{e}_2 = \mathbf{z}(\boldsymbol{\theta}) \times \mathbf{n} = \mathbf{h}(\boldsymbol{\theta}) \quad (12)$$

where $\boldsymbol{\theta}$ denotes the joint position vector and \mathbf{z} can be computed based the forward kinematics of the manipulator. Differentiate (12) with respect to time, it follows that

$$\dot{\mathbf{e}}_2 = \frac{\partial \mathbf{h}(\boldsymbol{\theta})}{\partial \boldsymbol{\theta}} \dot{\boldsymbol{\theta}} = \mathbf{J}_2(\boldsymbol{\theta})\dot{\boldsymbol{\theta}} \quad (13)$$

The following joint control law when placed in the feedback loop, $\dot{\boldsymbol{\theta}} = \dot{\boldsymbol{\theta}}_o$, is capable of driving \mathbf{z} to align with \mathbf{n} .

$$\dot{\boldsymbol{\theta}}_o = -\mathbf{J}_2(\boldsymbol{\theta})^+ \mathbf{e}_2 \quad (14)$$

3.3 Force control

This subtask is to maintain the required contact force along the normal direction to the unknown surface. Let f_d denote the desired contact force and the force encoded error be defined as

$$\mathbf{e}_f = f - f_d. \quad (15)$$

Consider the feedback connection $\dot{\mathbf{r}} = \dot{\mathbf{r}}_f$, where

$$\dot{\mathbf{r}}_f = k_f e_f \mathbf{n}, \quad k_f > 0. \quad (16)$$

Then, the joint velocity command for the force control task can be synthesized as follows.

$$\dot{\boldsymbol{\theta}}_f = \mathbf{J}_m(\boldsymbol{\theta})^{-1} \begin{bmatrix} \dot{\mathbf{r}}_f \\ \mathbf{0}_{3 \times 1} \end{bmatrix} \quad (17)$$

where $\mathbf{J}_m(\boldsymbol{\theta}) \in \mathbb{R}^{6 \times 6}$ is the mechanical Jacobian of the manipulator.

3.4 Hybrid control

The encoded error for the pose control task can thus be defined as

$$e = \begin{bmatrix} e_1 \\ e_2 \end{bmatrix} \quad (18)$$

Differentiate (18) with respect to time, it follow that

$$\dot{e} = M(\theta)\dot{\theta} \quad (19)$$

where

$$M(\theta) = \begin{bmatrix} (J_1 \circ L(\theta)) J_{m1}(\theta) \\ J_2(\theta) \end{bmatrix}; J_{m1}(\theta) = \frac{\partial L(\theta)}{\partial \theta}.$$

With the understanding that the force control law does not disturb the pose control law, the hybrid control law in the joint space capable of driving e and e_f to zero exponentially can thus be defined as follows.

$$\dot{\theta} = -M^+(\theta)e + \dot{\theta}_f \quad (20)$$

4 Experiments

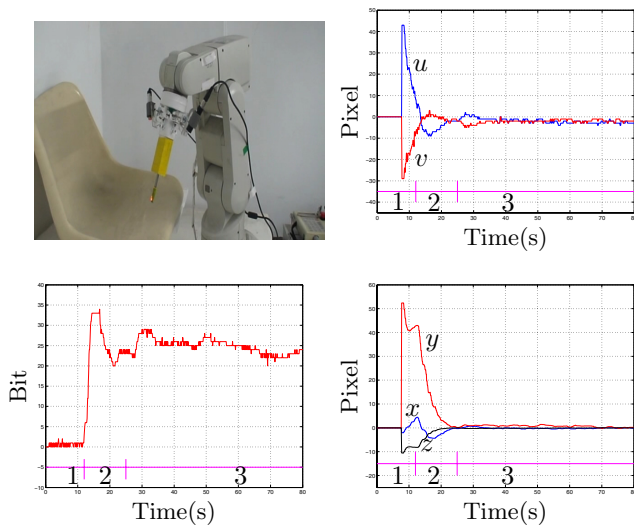


Figure 6: Experimental setup{top left}, position tracking error{top right}, force tracking error{bottom left}, and orientation tracking error{bottom right} .

The experimental system is composed of a 6-DOF Mitsubishi robot RV-1A, a JAI CV-S3200 camera, a laser cross projector, a P4-2.4G computer, and an arbitrary-shaped acrylic fiber 3-D object as illustrated in Figure 6. Successive stages in the autonomous hybrid tracking control are as follows. In Stage 1, the tool tip is driven to the laser cross center with orientation normal to the unknown surface by employing the

proposed pose control law. In Stage 2, force control is applied while maintaining the desired pose. In Stage 3, the tool is controlled to follow the moving laser cross in desired pose and contact force. The tracking errors for position, orientation, and force in these stages are shown in Figure 6. In these experiments, the proposed hybrid control approach has demonstrated satisfactory performance on tracking control.

5 Conclusion

This paper presents a seemingly novel approach to autonomously control the pose of a robotic manipulator with respect to an unknown 3-D surface. In particular, the end-effector can be driven to a set-point and trajectory on the surface while kept normal to the surface. A low-cost single-axis force sensor together with a CCD camera and a laser cross projector are required to perform such control tasks. Compared with existing approaches, the proposed system is not only effective but also less expensive.

Acknowledgements

This research is supported by the National Science Council of Taiwan, R.O.C. under grants NSC 94-2213-E-027-006 and NSC 95-2221-E-027-049.

References

- [1] Gregory D. Hager and Wen-Chung Chang and A. Stephen Morse, "Robot hand-eye coordination based on stereo vision," *IEEE Control Syst. Mag.*, Vol. 15, pp. 30-39, 1995.
- [2] Seth A. Hutchinson and Gregory D. Hager and Peter I. Corke, "A Tutorial on Visual Servo Control," *IEEE Trans. Robot. Automat.*, Vol. 12, pp. 651-670, 1996.
- [3] Di Xiao and B.K. Ghosh and Ning Xi and T. J. Tarn, "Sensor-Based Hybrid Position/Force Control of a Robot Manipulator in an Uncalibrated Environment," *IEEE Transactions on Control Systems Technology*, Vol. 8, pp. 635-645, 2000.
- [4] Wen-Chung Chang, "Hybrid Force and Vision-Based Contour Following of Planar Robots," *Journal of Intelligent and Robotic Systems*, Vol. 47, pp. 215-237, 2006.
- [5] I. Pitas, *Digital Image Processing Algorithms and Applications*, Wiley, 2000.

Robust Adaptive Sliding-Mode Fuzzy-Neural-Network Model-Following Position Control of PMSM Servo Drives for Robotic Applications

Fayez F. M. El-Sousy

Electronics Research Institute (ERI), Power Electronics & Energy Conversion Department
Al-Tahrir Street, Dokki, Cairo, Egypt

fayez@eri.sci.eg

Abstract

In this paper, an intelligent sliding-mode controller (SMC) for achieving favorable decoupling control and high precision position tracking performance of permanent-magnet synchronous motor (PMSM) servo drives is proposed. The intelligent position controller consists of a SMC in the position feed-back loop in addition to an on-line trained fuzzy-neural-network model-following controller (FNNMFC) in the feed-forward loop. The intelligent position controller combines the merits of the SMC with robust characteristics and the FNNMFC with on-line learning ability for periodic command tracking of a PMSM servo drive. The theoretical analyses of the SMC are described with a second order switching surface which is insensitive to parameters uncertainties and external load disturbances. The FNNMFC generates an adaptive control signal which is added to the SMC output to attain robust model-following characteristics under different operating conditions regardless of parameter uncertainties and load disturbances. The results of simulations confirm that the proposed SMC with FNNMFC grants robust performance and precise response to the reference model regardless of load disturbances and PMSM parameter uncertainties.

Keywords: PMSM Servo Drives, Sliding-Mode Control, Fuzzy-Neural-Network, Model Following Control

1 Introduction

The permanent-magnet synchronous motor (PMSM) servo drives play a vitally important role in high-performance motion-control applications such as industrial robots and machine tools. Utilizing the field-oriented control (FOC) technique simplifies the dynamic model of the PMSM and control scheme [1–10]. In recent years, the variable structure control (VSC) with sliding-mode or sliding-mode control (SMC) has received much attention to control PMSM servo drives because it can offer good properties such as insensitivity to parameter variations, external load disturbance and fast dynamic response. The first step of SMC design is to select a sliding surface that models the desired closed-loop performance in state variable space. Then, the controller is designed such that the system state trajectories are forced toward the sliding surface. The sensitivity of the controlled system to

uncertainties exists only in the reaching phase. Thus, the system dynamic in the reaching phase is still influenced by uncertainties. To keep robustness in the whole sliding-mode control system, several researchers have focused on eliminating the effects of uncertainties [3–6]. Intelligent control techniques in many researches have been developed to improve the performance of the PMSM servo drives. The concept of incorporating fuzzy logic into a neural network has grown into a popular research topic. The fuzzy neural network (FNN) possesses both their advantages; it combines the capability of fuzzy reasoning in handling uncertain information and the capability of artificial neural networks in learning from process. However, the adaptive control schemes of PMSM servo drives that incorporate the techniques of FNNs have also grown rapidly [7–10].

The aim of this paper is to design a proposed intelligent SMC for PMSM servo drive system. The intelligent position controller consists of a SMC in the position feed-back loop in addition to an on-line trained FNNMFC in the feed-forward loop. First, the SMC is designed and applied to the control of the rotor position of the PMSM servo drive. In the sliding-mode control system, when the sliding mode occurs, the servo drive system dynamic behaves as a robust state feedback control system. Then, a proposed on-line trained FNNMFC system is designed in addition to the SMC to improve the dynamic performance and to preserve a favorable model-following characteristics under various operating conditions of the servo drive system. In the proposed FNNMFC, the error between the reference model and the PMSM servo drive system output is used to train the connective weights and membership functions of the FNN. The output of the FNNMFC is added to the SMC output to compensate the error between the reference model and the PMSM servo drive system output under parameter uncertainties and external load disturbances. The dynamic performance of the PMSM servo drive system has been studied under load changes and parameter uncertainties. The simulation results are given to demonstrate the effectiveness of the proposed robust non-linear intelligent sliding-mode controller.

2 Robust Intelligent Sliding-Mode Control

2.1. Problem Formulation

To solve the problems of uncertainties, an intelligent SMC is proposed to increase the robustness of the FOC-

PMSM servo drive system. The proposed intelligent robust position controller combining the SMC and the FNNMFC. Utilizing FOC, the proposed intelligent PMSM servo drive can be simplified to the control system block diagram as shown in Fig. 1. The adaptive control law is designed as:

$$i_{qs}^{rc}(t) = U_{SMC}(t) + U_{FNNMFC}(t) = i_{qs}^{r*}(t) + \delta i_{qs}^{r*}(t) \quad (1)$$

The q -axis current command, i_{qs}^{r*} , is generated from the SMC and δi_{qs}^{r*} is the adaptive control signal generated from the proposed FNNMFC to automatically compensate the performance degradation due to load disturbances and PMSM parameter uncertainties. The inputs to the SMC are the position error, e_θ , and the rotor speed ω_r to construct the sliding surface $S(t)$ and the sliding-mode control law to get the q -axis current command, $U_{SMC} = i_{qs}^{r*}$. While the inputs to the FNNMFC are the error between the reference model and actual rotor position, e_θ^{mf} , and the rate of change of the rotor position (speed), $K_\theta \dot{\theta}_r$. Those signals are used to train the connective weights and membership functions of FNNMFC. The output of the FNNMFC is the adaptive control signal, $U_{FNNMFC} = \delta i_{qs}^{r*}$.

$$e_\theta^{mf} = (\theta_r^{mf} - \theta_r), \quad \dot{\theta}_r = k_\theta d\theta_r / dt \quad (2)$$

2.2 Sliding-Mode Position Controller

The sliding-mode control of the PMSM servo drive system is shown in Fig. 1. By considering the dynamics with parameter variations, disturbance load and unpredictable uncertainties will give:

$$\ddot{\theta}_r(t) = A_{mn} \dot{\theta}_r(t) + B_{mn} U(t) + L(t) \quad (3)$$

$$L(t) = \Delta A_m \dot{\theta}_r(t) + \Delta B_m U(t) + (D_{mn} + \Delta D_m) T_L \quad (4)$$

where ΔA_m , ΔB_m and ΔD_m are the uncertainties due to mechanical parameters J_m and β_m and $L(t)$ is called the lumped parameter uncertainty and is defined as:

The bound of the lumped parameter uncertainty is assumed to be $|L(t)| \leq K_f$. The objective is to design a control law so that the rotor position of the PMSM can track any desired command. To achieve this control objective, we can define the error function $e_\theta(t) = (\theta_r(t) - \theta_r^*(t))$. The sliding surface can be defined as a PID performance measure with the positive constants K_1 , K_2 and K_3 that are chosen based on the desired system response.

$$S(t) = K_1 e_\theta(t) + K_2 \dot{e}_\theta(t) + K_3 \int_0^t e_\theta(\tau) d\tau \quad (5)$$

In (5), with $K_2=1$, differentiating $S(t)$ with respect to time and using the error position function $e_\theta(t)$, the tracking control law can be derived from (3-5), $U_{SMC}(t)$, so that the rotor position, θ_r , remaining on the sliding surface, $S(t)$, for

all $t > 0$. The sliding-mode control objective is given by (6). The first term in (6) describes the desired system performance, the second term is a torque estimator which is able to compensate for the nonlinear effect in the PMSM model, while the third term keeps the PMSM servo drive system dynamics on the sliding surface, $S(t)=0$ for all the time. To keep the trajectory in the sliding surface, the selection of the control gain, K_f , is very important due to its significant effect on the magnitude of the lumped parameter uncertainties of the PMSM servo drive system and hence its performance. The incorrect selection of this control gain will yield to the deviation from the sliding surface and causing chattering phenomena. To solve this problem an adaptive control signal, $U_{FNNMFC} = \delta i_{qs}^{r*}$, is generated from the proposed on-line trained FNNMFC to compensate for the error in the control effort of the sliding-mode position controller, $U_{SMC} = i_{qs}^{r*}$.

$$U_{SMC}(t) = i_{qs}^{r*} = B_m^{-1} [(\ddot{\theta}_r^*(t) - K_1 \dot{e}_\theta(t) - K_3 e_\theta(t)) - A_m \dot{\theta}_r(t) - K_f \text{sgn}(S(t))] \quad (6)$$

2.3 Fuzzy-Neural-Network Position Controller

The online trained FNNMFC for a high-performance PMSM servo drive system integrates the ideas of the fuzzy logic controller and neural network structure into an intelligent control system.

(A) Architecture of the FNNMFC: The architecture details of the proposed four-layers FNNMFC, the signal propagation and the basic function in each layer are given in [7]. Nodes in the input layer represent input linguistic variables. Nodes in the membership layer act as the membership functions. All the nodes in the rule layer for a fuzzy rule base. In the proposed FNNMFC, an input layer (the i layer), a membership layer (the j layer), a rule layer (the k layer) and an output layer (the o layer) are two, six, nine and one respectively [8-9]. The nodes in layer 1 transmit the input signals to the next layer. Each node corresponds to one input variable. The input variables are the error signal, e_θ^{mf} , and the rate of change of the rotor position (speed), $K_\theta \dot{\theta}_r = K_\theta \omega_r$. The output of the FNNMFC is given by the following adaptive control signal.

$$U_{FNNMFC}(t) = \delta i_{qs}^{r*}(t) \quad (7)$$

(B) On-Line Training Signal Analysis for FNNMFC: The details of the on-line training signal analysis for FNNMFC will be given in the full paper. The selection of parameters for the weights and membership functions has a considerable effect on the network performance. The connecting weights between rule layer and output layer are adjusted on-line in addition to the weights and the membership functions. To describe the on-line learning algorithm of the FNNMFC using the supervised gradient descent method, the energy function is chosen as in (8).

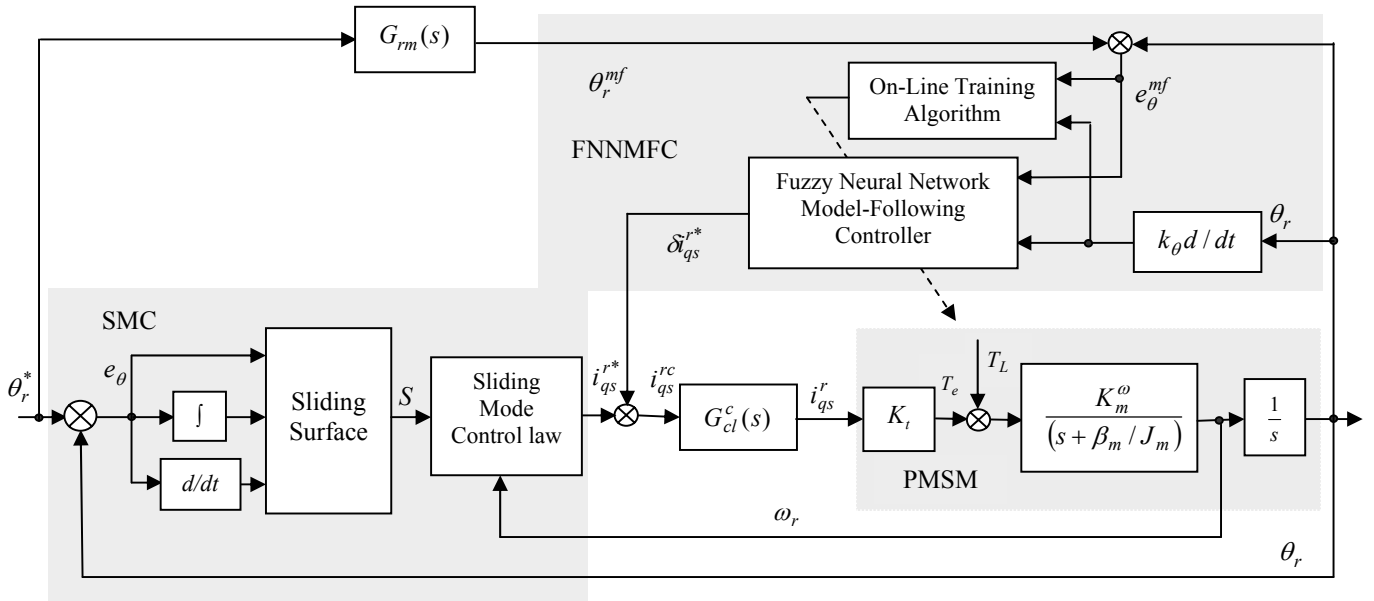


Fig. 1. Configuration of the proposed intelligent sliding-mode FNNMFC for a vector controlled PMSM servo drive system

The learning algorithm based on the backpropagation method is described in [10]. To overcome the problem of uncertainties of the PMSM due to parameter variations and to increase the on-line learning rate of the network parameters, a control law is proposed as in (9).

$$E_\theta = \frac{1}{2}(\theta_r^{mf} - \theta_r)^2 = \frac{1}{2}(e_\theta^{mf})^2 \quad (8)$$

$$\delta_o^4 = e_\theta^{mf} + K_\theta \dot{\theta}_r \quad (9)$$

3 Simulation Results

To investigate the effectiveness of the proposed intelligent sliding-mode position controller, five cases with parameter uncertainties are considered. The PMSM used in this drive system is a three-phase type, 1 hp, four poles, 208 V, 60 Hz, 1800 rpm and has the parameters, voltage constant= 0.314 V.s/rad, $R_s=1.5 \Omega$, $L_{ss}=L_d=L_q=0.05 \text{ H}$, $J_m=0.003 \text{ kg.m}^2$, $\beta_m=0.0009 \text{ N.m/rad/sec}$.

Case 1: $1.0 \times (R_s \text{ and } L_s)$, $1.0 \times (J_m \text{ and } \beta_m)$, $1.00 \times \lambda_m$,

Case 2: $0.5 \times (R_s \text{ and } L_s)$, $0.5 \times (J_m \text{ and } \beta_m)$, $1.00 \times \lambda_m$

Case 3: $1.5 \times (R_s \text{ and } L_s)$, $3.0 \times (J_m \text{ and } \beta_m)$, $1.00 \times \lambda_m$

Case 4: $1.0 \times (R_s \text{ and } L_s)$, $1.0 \times (J_m \text{ and } \beta_m)$, $0.85 \times \lambda_m$

Case 5: $1.0 \times (R_s \text{ and } L_s)$, $1.0 \times (J_m \text{ and } \beta_m)$, $1.25 \times \lambda_m$

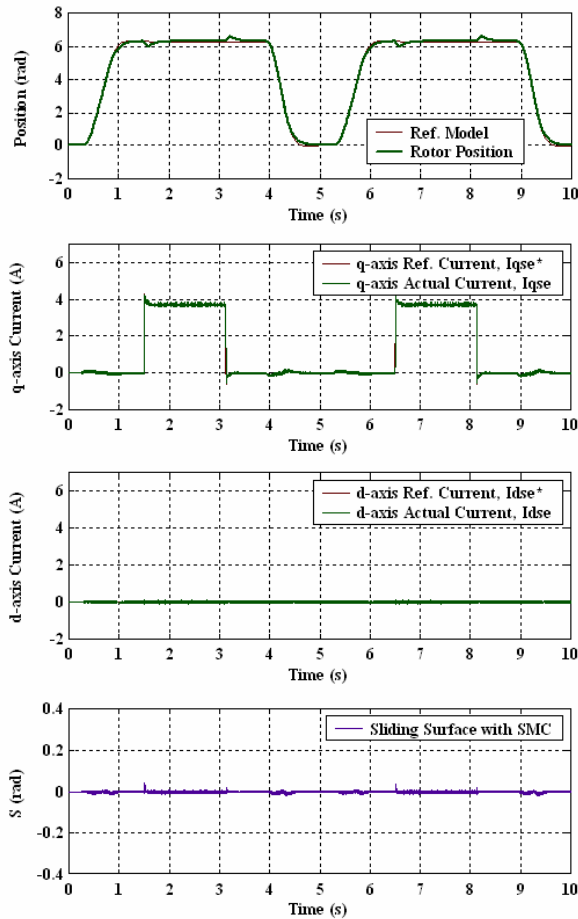
The dynamic performance of the drive system due to reference model of 2π rad under subsequent loading of 0-3.6 N.m is predicted as illustrated in Fig. 2 at Case 1. The disturbance rejection capabilities have been checked when a load of 3.6 N.m is applied to the shaft at $t = 1.5 \text{ s}$ and removed after a period of 1.625 s. These Figures clearly illustrate favorable tracking responses and robust characteristics in command tracking and load regulation performance are realized for both controllers. The sliding

motion characteristics without reaching phase are obvious by determining the sliding-surface shown in Fig. 2.

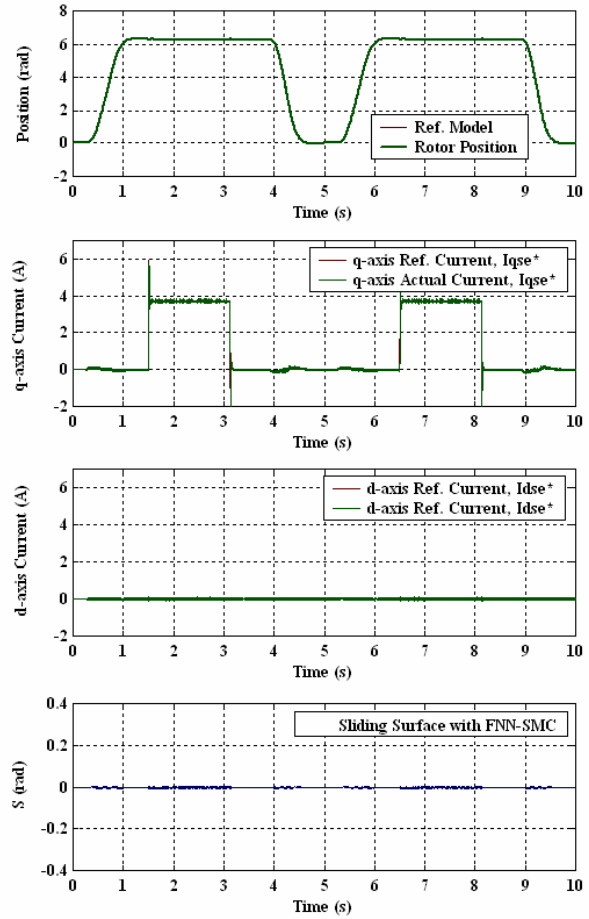
Improvement of the control performance by augmenting the proposed FNNMFC to the SMC shown in Fig. 1 can be observed from the obtained results in command tracking and load regulation characteristics. The simulation results of the dynamic response for both position controllers under parameter variations are plotted in Figs. 3-4. The position response, speed response and the load regulation performance of the servo drive system with the SMC and SMC with FNNMFC are shown in Figs. 3-4 under the cases of PMSM parameter uncertainties. Fig. 3 illustrates the position and speed tracking responses for both position controllers. At the same conditions, the load regulation performance and torque current responses are given in Fig. 4. The results shown in these Figures clearly indicate that as the uncertainties of the PMSM parameters occurred, the responses deviate insignificantly from the nominal case for both SMC and SMC with FNNMFC but the SMC with FNNMFC confirms the correct operation and slightly influenced by full load conditions under the five cases of PMSM uncertainties. The proposed intelligent controller quickly returns the rotor position to the reference model under full load condition with a recovery time of 0.05s and a maximum dip of 0.053 rad while the SMC provides a slow response for the reference model under full load condition with a long recovery time of about 0.5s and a large dipping in the rotor position of about 0.28 rad under the five cases of PMSM uncertainties. Therefore, robust control characteristics under occurrence of uncertainties can be clearly observed utilizing both the proposed position controllers. An obvious model-following error (MFE) due to the SMC reaches to 0.15 rad while the MFE due to SMC with FNNMFC is about 0.05 rad. Also, good model-following and tracking responses using SMC with FNNMFC at all cases of parameters uncertainties are

observed from these results, and the resulting regulation performances are also much better, in both position dip and recovery time, than those obtained by the SMC. Therefore,

the SMC and SMC with FNNMFC are more suitable to control the rotor position of the PMSM servo drives considering the existence of parameters uncertainties.

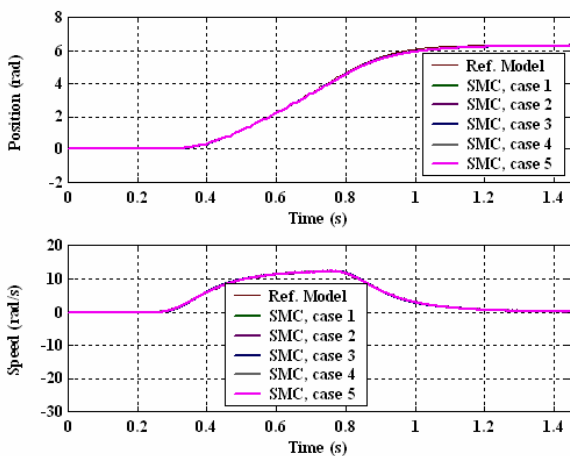


(a) Dynamic response using SMC

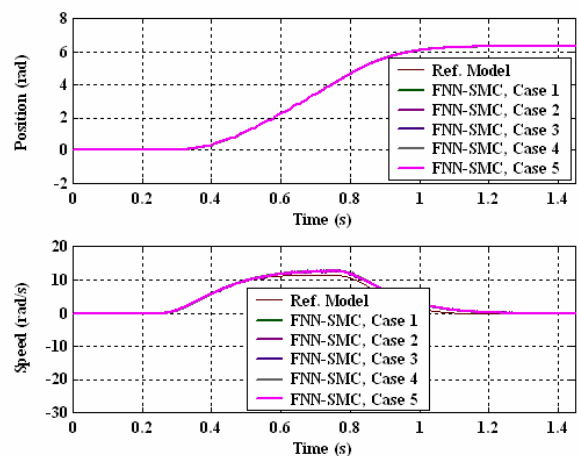


(b) Dynamic response using SMC with FNNMFC

Fig. 2. Dynamic response for a reference model of 2π rad and loading of 3.6 N.m of the servo drive system for both position controllers

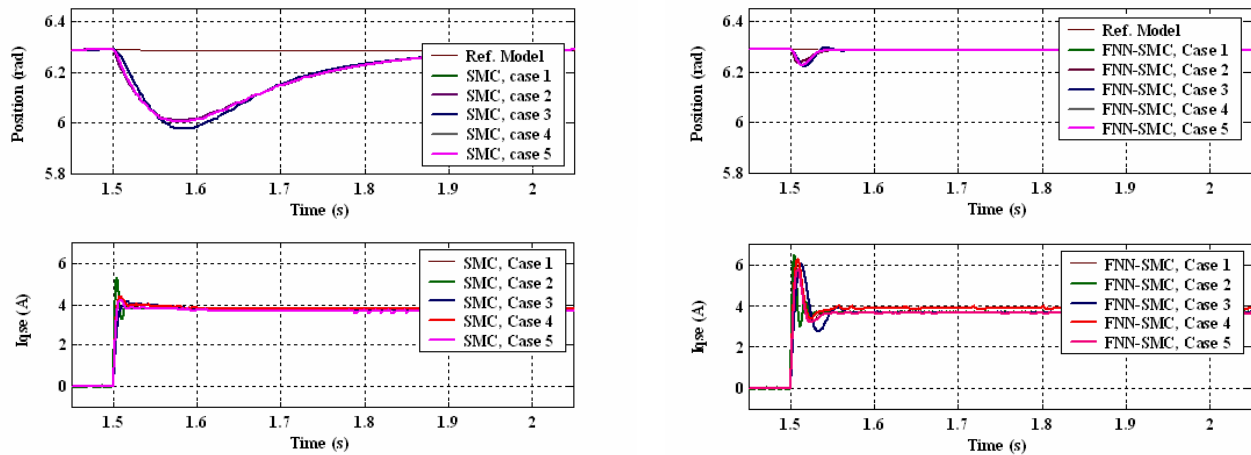


(a) Model-following response using SMC



(b) Model-following response using SMC with FNNMFC

Fig. 3. The model-following position and speed responses of the servo drive system under parameter variations for both position controllers



(a) Load regulation performance using SMC

(b) Load regulation performance using SMC with FNNMFC

Fig. 4. The load regulation performance of the servo drive system under parameter variations for both position controllers

4 Summary

This paper proposed a robust intelligent and adaptive position controller for PMSM servo drive system under field orientation control which guarantees the robustness in the presence of parameter uncertainties. The proposed robust position controllers (SMC and SMC with FNNMFC) consists of a feed-back SMC in addition to an on-line trained FNNMFC. The theoretical bases and the stability analyses of the proposed SMC and SMC with FNNMFC control systems were described in details. An adaptive control signal is generated from the proposed FNNMFC and was added to the SMC output to preserve good model-following response under various operating conditions. Simulation results have shown that the proposed SMC and SMC with FNNMFC grant robust model-following tracking response and good regulation characteristics in the presence of PMSM parameter uncertainties and external load disturbance. Finally, the major contributions of this paper are the successful development of the intelligent SMC system, in which a FNNMFC is utilized to compensate the uncertainty bound in the SMC system on-line and the successful application of the proposed SMC with FNNMFC system methodology to control the rotor position of the PMSM with the existence of parameters uncertainties.

References

- [1] Ned Mohan, *Advanced Electric Drives: Analysis, control, and Modeling using Simulink*, MNPRESS Press, USA, 2001.
- [2] V. I. Utkin, "Sliding mode control design principles and applications to electric drives," *IEEE Trans. Ind. Electron.*, Vol. 40, pp. 23-36, Feb. 1993.
- [3] I. C. Baik, K. H. Kim, and M. J. Youn, "Robust nonlinear speed control of PM synchronous motor using adaptive and sliding mode control techniques," *Proc. IEE—Elect. Power Applicat.*, Vol. 145, No. 4, pp. 369-376, 1998.
- [4] Z. H. Akpolat, G. M. Asher, and J. C. Clare, "A practical approach to the design of robust speed controllers for machine drives," *IEEE Trans. Ind. Electron.*, Vol. 47, pp. 315-324, April 2000.
- [5] S. K. Chung, J. H. Lee, J. S. Ko, and M. J. Youn, "Robust speed control of brushless direct drive motor using integral variable structure control," *Proc. Inst. Elect. Eng.*, Vol. 142, No. 6, pp. 361-370, 1995.
- [6] Franck Betin, Daniel Pinchon, and Gérard-André Capolino, "A Time-Varying Sliding Surface for Robust Position Control of a DC Motor Drive," *IEEE Transactions on Industrial Electronics*, Vol. 49, No. 2, pp. 462-472, April 2002.
- [7] Faye F. M. El-Sousy, "A Vector-Controlled PMSM Drive with a Continually On-Line Learning Hybrid Neural-Network Model-Following Speed Controller," *The Korean Institute of Power Electronics (KIPE), Journal of Power Electronics (JPE)*, Vol. 5, No. 2, pp. 197-210, April 2005.
- [8] Faye F. M. El-Sousy, "Intelligent Model-Following Position Control for PMSM Servo Drives," *6th WSEAS International Conference on Neural Networks, Lisbon, Portugal*, pp. 230-238, June 16-18, 2005.
- [9] Faa-Jeng Lin, and Chih-Hong Lin, "A Permanent-Magnet Synchronous Motor Servo Drive Using Self-Constructing Fuzzy Neural Network Controller," *IEEE Trans. on Energy Conversion*, Vol. 19, No. 1, pp. 66-72, March 2004.
- [10] F. J. Lin, W. J. Huang, and R. J. Wai, "A supervisory fuzzy neural network control system for tracking periodic inputs," *IEEE Trans. Fuzzy Syst.*, Vol. 7, pp. 41-52, Feb. 1999.

Multi-Agent Robotics: Towards Energy Autonomy

Trung Dung Ngo

Center for Embedded Software Systems (CISS)
Aalborg University
Fr. Bajersvej 7B, 9220 Aalborg East, Denmark
dungnt@cs.aau.dk

Hector Raposo, Henrik Schiøler

Control & Automation Department
Aalborg University
Fr. Bajersvej 7C, 9220 Aalborg East, Denmark
{hrve05, henrik}@control.aau.dk

Abstract

In this paper, we aim to propose a novel trend in multi-agent robotics: energy autonomy. A definition of energy autonomy is developed from an original concept “potential energy” that is under constraints of remaining energy capacity and related distance among robotic agents. Towards energy autonomy, we initially present a simulation of multi-agent robotic system in which each robot is capable of exchanging energy cells to other robots. Our simulation points out that: (1) each robot is able to not only act as an autonomous agent but also interact with the others to be beyond the individual capabilities; (2) To adapt change of the environment, each robot is situated as an adaptive agent in a network or a cluster of the neighboring robots to lead to a state of energy autonomy. Finally, based on discovery of the simulation we adjust rules for our real multirobot system.

1. Introduction

A multi-agent system (MAS) is a system composed of a number of agents that are collectively capable of reaching goals that are difficult to achieve by an individual agent or monolithic system [6]. In a MAS there is no centralized control, information is distributed, computation is asynchronous, therefore each agent is incompletely capable of solving a problem [8], it needs assistant from other agents to solve its own problem or helps other agents with their problem appropriately. Adaptiveness of an agent is depending on the characteristic of such an agent, its surrounding environment, its capabilities of interaction with other agents or environment and capabilities of organization in a network or a cluster. Therefore, mapping MAS to multirobot system, an autonomous robot is able to exhibit as an autonomous agent in the MAS - robotic agent. However, a robotic agent is aware of as a physical robot in fact, thus the robot exists if it is capable of solving energy resource.

In the paper, we propose a multi-agent robotic system in which each robotic agent is a mobile agent and is equipped with a special mechanism of energy exchange, so that it is capable of fairly collecting and carrying energy cells, rechargeable batteries to share with others. The paper is organized as: we briefly describe our models of single robotic agent and their cooperation in section 2. In section 3 we perform our simulation of robotic agent behaviors under

constraints of remaining energy and related distances. We implement the simulation in accordance with agent characteristics, interaction, organization and change of environment in order to suggest course of our real multirobot implementation. Finally, the paper is concluded in section 4.

2. Model of Multi-Agent Robotic System

Because Matlab software supports a lot of graphical libraries to easily execute mathematical computation, or generate graphs and charts, we are using the tool to implement our multirobot system.

2.1 Model of Single Robotic Agent Robot

We focus on the energetic autonomy of a multi-agent robotic system so we are going to simplify robotic agent as points moving on scanlines in the Euclidean space. Therefore, distance relation among robotic agents is based on Manhattan space. Because of difficulty of modeling a general equation of power consumption in robotics we are temporally using the Peurket's discharging function $C = I^k t$ where k is supported by the battery manufacturer.

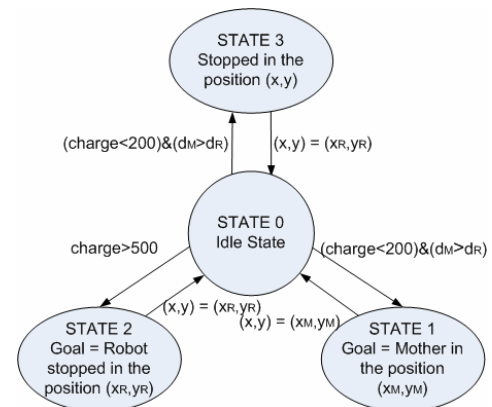


Fig1: Model of single robot

In the simulation, a robotic agent is initialized with 800 energy unit (eu) and it consumes a specific amount of energy using Peurket's equation for each step so we propose 4 states of a robotic agent: (State 1): a robotic agent has to go to mother to take full energy if its energy is less than 200 eu and by default, it has higher priority to go to the mother station;

(State 2): a robotic agent is able to exchange 100 eu to other robotic agent if its energy amount is more than 500 eu; (State 3): a robotic agent will stop to wait for other robot coming to charge 100 eu if its energy is less than 100 eu and it is impossible to go to the mother charging station; and (State 0): otherwise, a robotic agent is autonomously free to go anywhere to consume energy.

2.2 Model of Robot Coordination

To facilitate our approaching to battery exchange, we implement a coordination algorithm for the multi-agent robotic system based on two phases: path planning and battery exchange. Briefly, each robotic agent has a own battery

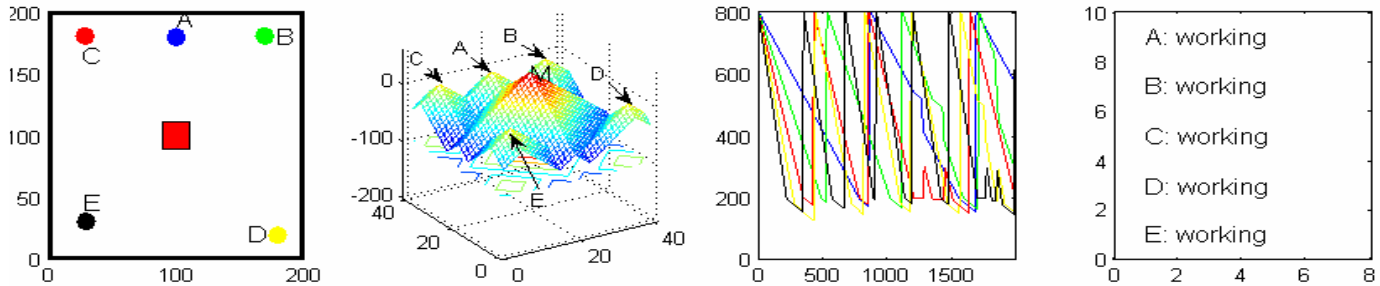


Fig 3: Graphical simulation setup

exchange supervisor. The supervisor collects input data of the robots: current coordinate (X,Y) and current state of energy STATE; deals with such updating data; issue output commands: NEXT STATE of energy, goal coordinate (Xgoal, Ygoal). To be more detailed, algorithm of the battery exchange executes infinite loops of comparison of energy states and current positions among the robotic agents as well as the robotic agent with the mother to issue commands what the robotic agent should do (goal of the robot). Meanwhile path planner is to guide the robotic agent to reach the directed goal and updating the next position of the robotic agents, which is used as a feedback for the battery exchange algorithm to compute the next states of the robotic agents.

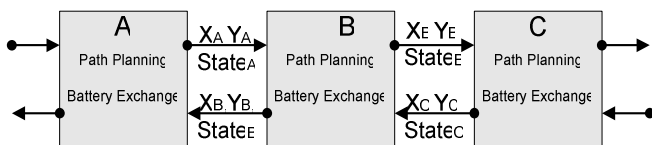


Fig 2: Model of multi-agent robotic system

3. Simulation

We present early simulation results of our objectives. First, we emphasize potential energy and its constraints among robotic agents, and the robotic agent with the mother agent. Second, we examine how interaction and environment can

effect to behavior of robotic agents in the entire network. Third, we demonstrate that an robotic agent is able to be energetically autonomous if it is able to exchange energy with other robotic agents or the mother agent.

In the simulation setup shown in figure 3, we present significant information of the system. It shows four graphical windows (left to right): animation of robotic motion, potential energy of the mother agent and the robotic agent, the energy state of the robotic agents, and the task of the robotic agents. That is, the animation window shows us the motion planning of the robotic agents; the potential energy window presents the remaining energy of the robotic agents (height of the pyramids) and their capability to share energy with the others (projected contour of the pyramids); the window of the state of

energy realizes the energy chart of the robotic agents according to the instant; and the task window reports operating tasks of the robotic agents. We also generate a register of the states of the robotic agents in every experiment:

Time	A	B	C	D	E
221	'A: working'	'B: working'	'C: working'	'D: working'	E -> Mother *
281	'A: working'	'B: working'	'C: working'	D -> Mother *	'E: working'
351	'A: working'	'B: working'	C -> Mother *	'D: working'	'E: working'
491	'A: working'	B -> Mother *	'C: working'	'D: working'	'E: working'
571	'A: working'	'B: working'	'C: working'	'D: working'	E -> Mother *
721	'A: working'	'B: working'	'C: working'	D -> Mother *	'E: working'
781	A -> Mother *	'B: working'	'C: working'	'D: working'	'E: working'
781	'A: working'	'B: working'	C -> Mother *	'D: working'	'E: working'
891	'A: working'	'B: working'	'C: working'	'D: working'	E -> Mother *
1021	'A: working'	B -> Mother *	'C: working'	'D: working'	'E: working'
1101	'A: working'	'B: working'	'C: working'	D -> Mother *	'E: working'
1131	'A: working'	'B: working'	'C: working'	'D: working'	E -> Mother *
1201	A -> C *	'B: working'	C <- A *	'D: working'	'E: working'
1341	'A: working'	B -> C *	C <- B *	'D: working'	'E: working'
1411	'A: working'	'B: working'	'C: working'	'D: working'	E -> Mother *
1461	'A: working'	'B: working'	'C: working'	D -> Mother *	'E: working'
1501	'A: working'	'B: working'	C -> Mother *	'D: working'	'E: working'
1551	A -> Mother *	'B: working'	'C: working'	'D: working'	'E: working'
1581	'A: working'	B -> Mother *	'C: working'	'D: working'	'E: working'
1691	'A: working'	'B: working'	'C: working'	D -> E *	E <- D *
1801	'A: working'	B -> E *	'C: working'	'D: working'	E <- B *
1841	'A: working'	B -> D *	'C: working'	D <- B *	'E: working'
1881	'A: working'	'B: working'	'C: working'	'D: working'	E -> Mother *
1901	'A: working'	'B: working'	'C: working'	D -> Mother *	'E: working'
1981	'A: working'	'B: working'	C -> Mother *	'D: working'	'E: working'

Fig 4: An example of a register of 5 robotic agents in 2000 running steps

3.1 Potential Energy

In this section we emphasize the potential energy of robotic agents under constraints of remaining energy and related distance. As described in figure 5, the potential energy can be divided into two meanings: **Height of the pyramids (H)** is to imply the remaining capacity of an agent while **Contour of the pyramids (C)** is to determine how wide the robotic agent is capable of distributing energy to the others. Actually, considering a robotic agent in state of low energy, if its pyramid peak, **H** is fully covered by the another pyramid, it means it is now in the space where the other robotic agent is able to share energy, also we can say *the agent is inside the potential energy of other agents*, and it will be in rechargeable state. Otherwise, the robotic agent must be waiting until the other robotic agents are moving close to it. Further, interfering wave of Contour of the pyramids also tells us more about the distance and the energy relationship among the robotic agent, and these with the mother agent.

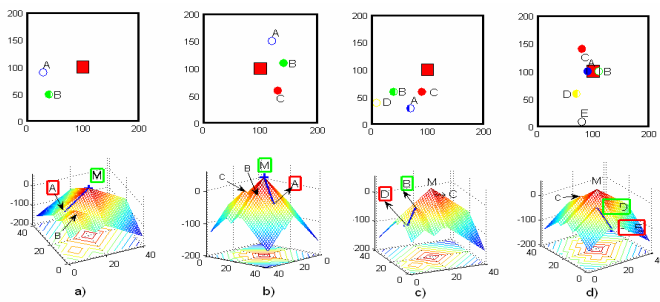


Fig 5: Potential Energy of robotic agents

The blue lines in figure 6 show the energy and related distance constraints between the robotic agents, or between the robotic agents and the mother agent. Moreover, creating the blue line is based on the gradient of the potential energy between the robotic agents, or the mother agent. The slope of the blue lines shows us the reciprocal energy effects and the length of the projected blue lines to the corresponding distance.

Indeed, figure 5 is to perform that density of the potential energy is stronger when the number of agents is increasing (a): 2 agents, b): 3 agents, c): 4 agents, d) 5 agents) in the same field. We discuss that a robotic agent in need of energy has more opportunity to be recharged if the density of the potential energy in the field raises up, but it is more hard to reach other robotic agents since the number of physical interaction increases. Thereby, we have to estimate the balance of the number of robots and the mother location to deploy such a multi-agent robotic system.

3.2 Effective Elements in Multi-Agent Robotic System

The section is to present effectiveness to energy in a multi-agent robotic system. First we experiment with increasing the number of agents in the same field. Figure 6 shows that if the number of agents increases (left to right) from 2 to 5, the number of battery exchange between robots also raises from 0 to 4. It is indispensable that the battery exchange between agents is proportional to the number of agents and the robotic agent being far away from the mother agent need more assistance than the closer ones. Thereby, we have to take a number of robotic agents into account when we deploy them in a specific environment.

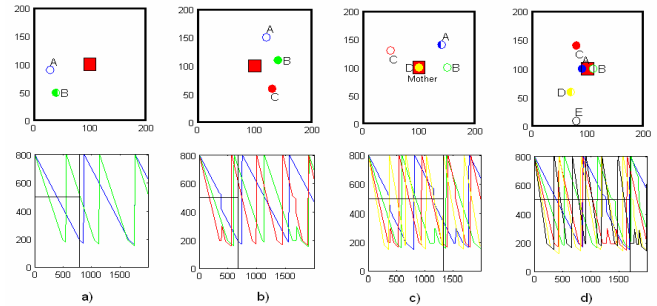


Fig 6: A comparison of the increasing number of robotic agents

Consequently, keeping a number of 5 robotic agents, we try to change the location of the mother agent in the same field. First, we locate the mother agent in the center of field. The result of 100 experiments shows that the total number of the battery exchange is almost the same. That is, the overall energy consumption is only depending on the size of the field. However, in the distribution seen in figure 7, since we move the mother to one corner of the field, robotic agents must come back at a more narrow area thereby, they are preferable to be charged by the other agents than the mother agent (red-line).

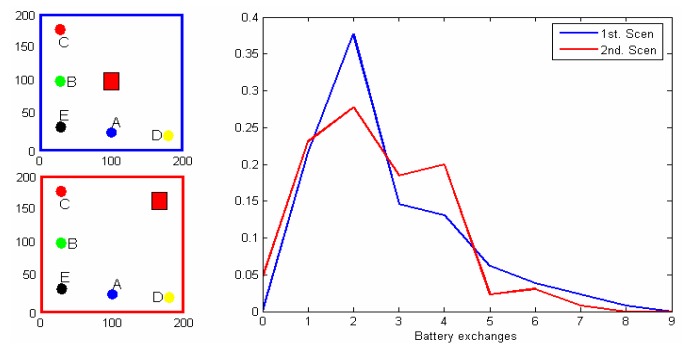


Fig 7: A comparison of the different location of the mother agent

3.3 Energy Autonomy

In fact, if a mobile agent wants to act, it will face the problem of providing food as animals. Most of mobile robots are using rechargeable batteries as a power source. Thereby, it has only autonomous behavior in the duration of the battery-life, e.g. free moving around to explore, free searching a way

to carry heavy objects, or searching to rescue humans after earthquake. A robot is able to be absolutely autonomous if it achieves state of energy autonomy.

The section shows that the robotic agents are able to self-organize in order to achieve complete autonomy, without human intervention if they are able to coordinate energy sharing with the other robotic agents. The objective also means that each robotic agent is able to be energetically autonomous or assist others to be completely autonomous.

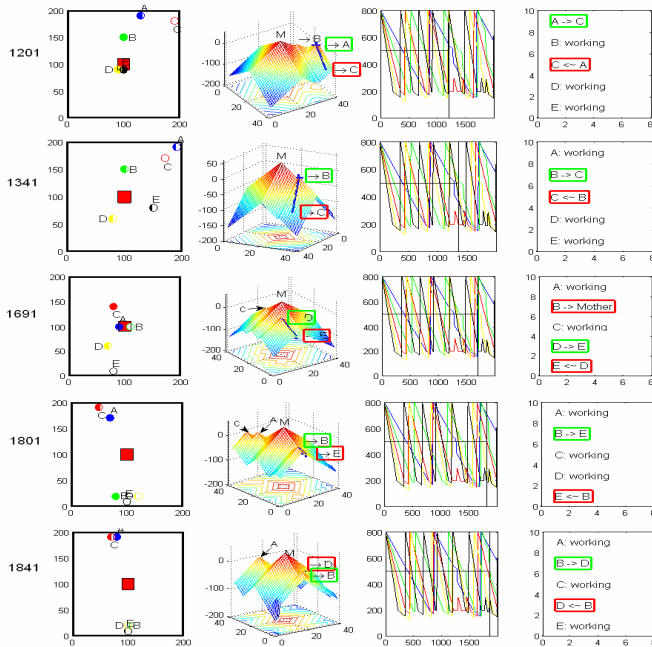


Fig 8: Energy autonomy of 5 robotic agent in time scale

Figure 8 shows an experiment of 5 robotic agents executing in 2000 steps. On the second column, we see that the potential energy of the mother agent can always cover the field. That is, every robotic agent can be globally covered by the mother agent (M) so it can be refilled if it is able to come to the mother agent. However, the potential energy of the robotic agents (A, B, C, D, E) is much lower so it is capable of covering a local vicinity. Because the robotic agent is a moving agent, it can be sub-mother agent for the other agents in its local vicinity. Therefore, every agent can be a first-aid unit in the case of emergency in which other agents have not enough energy to go back to M, or desire to finish their duty in a short time before coming back to M. Additionally, referring to the fourth column, we see that at the instant 1201, A is going to (->) share 100 eu with C, and C stops working to save energy and waiting (<-) for A. At the instant 1341, C still needs energy again since C has already consumed 100 eu, B is indicated to give battery for C. Therefore, at the instant 1691, we can easily be aware that C has already come back to M in order to be fully replenished and is now working with an amount of 700 eu approximately. Due to the assistance of A and B, C can survive to continue its duty, instead of being stuck on the field. As a result, robotic agents can have

complete autonomy if they are able to achieve energy autonomy.

4. Conclusion & Future Works

This paper issues the concept of the potential energy in multi-agent robotic system and how to make the system to be complete autonomy. In a multi-agent robotic system, each robotic agent is a mobile agent, so it has own potential energy. This is the reason why it is able to be self-sustained with energy if it is capable of sharing energy. To deploy robotic agents in a specific environment, we have to solve the problem under constraint of effective elements as mentioned in section 2. However, to facilitate the process, we proposed the concept Potential Energy and its elements in order to analysis and setup a multi-agent robotic system in section 1.

Next, based on initial results of the simulation, we are going to experiment with our testbed of the real multirobot system. First, to simplify high requirements of localization and approaching, our mobile robots are also following the lines in a grid so the robot is able to know its current location. In this way it is rather easy to approach to contact to the mother station, or the other robot in order to exchange batteries. We will improve the techniques of sensor fusion for such robots to remove the grid, so our robots can be more sociable. They can be applied for home, office or manufacturer environments.

References

- [1] Chris Melhuish and Masao Kubo (2004). Collective Energy Distribution: Maintaining the Energy balance in Distributed Autonomous Robots, in the proceedings of 7th International Symposium on Distributed Autonomous Robotic Systems, June 23-25, 2004 Toulouse, France, p261-70,2004.
- [2] Gregory Dudek, Michael Jenkin, Evangelos Milioes, and David Wilkes. A Taxonomy for Multi-agent Robotics, Autonomous Robots, vol. 3. pp. 375-397,1996
- [3] Yongguo Mei, Yung-Hsiang Lu, C.S. George Lee and Y. Charlie Hu Energy-Efficient Motion Planning for Mobile Robots, International Conference on Robotics and Automation 2004.
- [4] Ngo. T.D, Schioler. H, An Approach to Sociable Robots through Self-distributed Energy, in proceedings of IEEE/R SJ International Conference on Intelligent Robots and Systems, Beijing, China, Oct 2006.
- [5] N.R. Jennings, K. Sycara, and M.Wooldridge. A Roadmap of Agent Research and Development. Journal of Autonomous Agents and Multi-Agents Systems, 1:7-38, 1998.
- [6] E.H. Durfee, and V.R.Lesser, Negotiating Task Decomposition and Allocation using Partial Global Planning. In Distributed Artificial Intelligence, vol.2, pages 229-244, 1989.

Realization of a visuo-motor system based on multiple self-organizing maps in a 3D space

Ryunosuke UEHARA[†]

Min HAN[‡]

Nobuhiro OKADA[†]

Eiji KONDO[†]

[†]*Department of Intelligent Machinery and System
Graduate School of Engineering, Kyushu University
744 Motoooka, Nishi-ku, Fukuoka 819-0395, Japan*

[‡]*TOYOTA AUTO BODY CO., LTD.
100, Kanayama Ichiriyama-cho
Kariya, Aichi 448-8666, Japan*

Abstract

This paper describes a visuo-motor system which realizes a feasible collision avoidance of a manipulator in an unknown environment. In order to handle spaces occluded by obstacles, we adapt the plural cameras system and multiple self-organizing maps (SOMs). Each self-organizing map is directly connected to the camera system and trained to perform motion control, by which the joint angle of the manipulator are determined. In our visuo-motor system, neither any priori knowledge about the manipulator nor the camera parameters are required. In addition, the system is robust to change in its geometry. Simulation result shows that the proposed learning method ensures that the manipulator moves smoothly and consistently in whole workspace even using multiple maps. In this paper, we validated the proposed approach by an experiment and confirmed that proposed method realizes collision avoidance for the visuo-motor system in a 3D space. Thus, we presented simulation result that the system overcomes the collision problem in cluttered environments and variety of obstacle shapes by increasing the number of cameras and self-organizing maps.

1 introduction

Collision avoidance is a basic problem that a robot handles its end-effector avoiding obstacles cluttered in an environment performing the primary task for autonomous or industrial robots. To plan a path avoiding collision in an intricate environment, two contrasting approaches have been studied.

First, the high-level path planning is to find globally a collision avoidance path in the configuration space. One example of a global method is PRM (Probabilistic Roadmap Method) that computes a cell decomposition of the free space and uses a search graph based on this decomposition [1]. RRT (Rapidly-exploring

Random Trees) is a roadmap method where a set of canonical paths is used to cover the components of the free space, and the planning task is reduced to determine a connection to the canonical paths [2, 3]. However, in these approaches, an exact, known and static environment model is required. In addition, the calculation time grows exponentially with the geometry complexity and the number of degree of freedom (DOF).

Therefore, local path planning techniques are potentially more efficient in robot motion planning when the environment is unknown or only partially known. An efficient local path planning method is the potential field method which has been widely used in collision avoidance [4]. In this method, a potential function is defined in the free space, based on an attraction component from the goal point and a repulsion component from the obstacle boundaries, and the planning process becomes to a determination of the global minimum of the potential function using a greedy and local search.

Alternatively, obstacle avoidance can be solved online by a robot controller at the low-level, which is focused on the problem of controlling a redundant robot so that the end-effector tracks a given path in the workspace as closely as possible and simultaneously ensures that the links avoid obstacles. Reasoned as above, such techniques naturally depend on the use of different control frameworks [5, 6].

On the other hand, some methods tried to integrate a task planning and a motion control, motivated by Khatib's work [7]. This work and a few other integrated architectures [8] have utilized methods based on potential fields in their reactive control algorithms, while their planning and interface techniques differ [9]. The SOMs also can be used for path-planning or trajectory formation tasks [10]. After the mapping has been established, a path is generated from any initial position to a given target, e.g., to guide an end-effector of a robot manipulator in the presence of obstacles

within the workspace. Using the TRN model [11], showed that a locally optimized path can be determined by minimizing the Euclidean distance from the current position to a given target position. However, a collision check was necessary in the path planning, and the proposed method was only investigated by using a non-redundant manipulator.

In our studies, we integrate the path planning of the end-effector and SOMs to achieve collision avoidance. The SOMs are learned to perform motion control, by which joint angles of the manipulator are determined. The learning promises to make the manipulator reach targets precisely with obstacle-free poses. The path planning system plans a collision-free path for the end-effector from an initial point to a target point in the image spaces. The proposed collision avoidance approach differs from others in: (1) The system only needs to plan a collision-free path for the end-effector; the computational cost of the path planning does not increase exponentially even for a high dimensional redundant manipulator. (2) The obstacle-free poses of the manipulator are achieved in the learning of the SOMs, so collision checking is not necessary in whole path planning process.

2 visuo-motor system

Visuo-motor system which we propose is illustrated in Fig.1. The system contains:

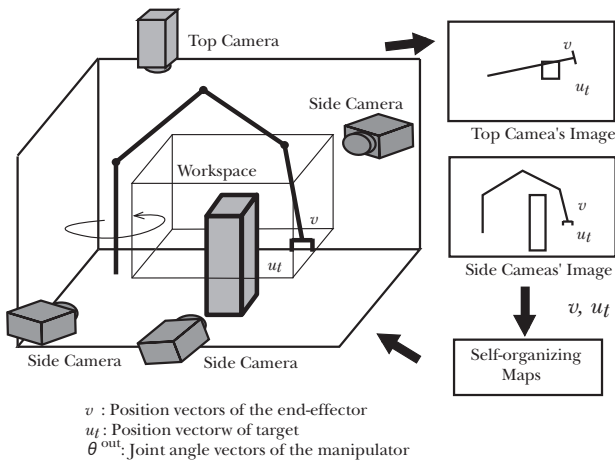


Fig. 1: Simulation model

1. A 4-degree of freedom redundant manipulator moving in a 3D space.
2. The plural CCD cameras.
3. Multiple related self-organizing maps.

CCD cameras are used to acquire information about obstacles and to recognize the position of the target, the location of the end-effector and the pose of the manipulator while learning. Based on visual information provided by cameras, each SOM learns projections that convert the image vectors of targets in the image spaces into joint angles vectors of the manipulator. The manipulator is ordered by a set of joint angle commands θ_{out} which are outputs of SOMs.

In our previous works, the system could not deal with spaces occluded by obstacles. In this paper, a redundant camera system is introduced to overcome the occlusion problem [13]. One camera observes the workspace from the top and other cameras are arranged from the sides. Because the valid workspace is increased obviously by adding the redundant camera, multiple related SOMs are employed in our system. As shown in Fig.1, the projections of a target point u_t in side cameras and top camera are (u_i, v_i) and (u_t, v_t) respectively. A pair of image coordinates of side camera (u_i, v_i) and top camera (u_t, v_t) is combined into a 4 dimensional vector (u_i, v_i, u_t, v_t) which is used as the point of one. In the same way, a pair of the other side camera and top camera is combined into the input of another map. Since the valid workspaces of each map and camera are different, maps are used alternately. Besides the number of joint, no further information about the manipulator and cameras will be used in our visuo-motor system.

2.1 The self-organizing maps

As shown in Fig.2, each self-organizing map is consisted of neurons, which are distributed in the image spaces of the camera. Each neuron N_i has 4-parameters.

For ξ_i , refer to our previous study.

W_i : position of the neuron in two image spaces.

J_i : Jacobi matrix from the joint space to the image spaces.

θ_i : Joint angle of the manipulator at W_i .

ξ_i : The gradient vector.

When a target u_t is given in the workspace, an appropriate map is chosen based on which cameras can see the target. In the chosen map, the neuron which w_i is the nearest to the projection of the target is chosen. The joint angles θ_{out} , which conduct end-effector to the target, are calculated obeying following linear equation. Although the transformation from the image spaces to the joint angle spaces is not a linear projection for a redundant manipulator, the domain of a neuron is small enough to use the linear projection as

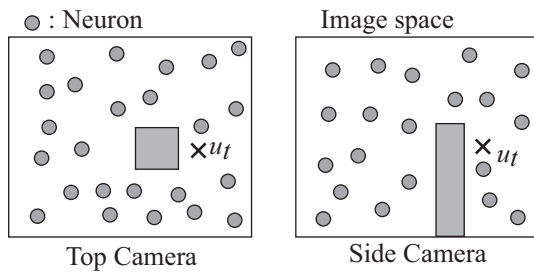


Fig. 2: Self-Organizing Map

an approximation of the non-linear projection. In the actual system, weighted sum of outputs from plural neurons around the target is used instead of the linear equation.

$$\theta_{out} = \frac{\sum g_n(\theta + J^\dagger(u_t - W))}{\sum g_n} \quad (1)$$

Where, J^\dagger is a pseudoinverse matrix of J . g_n is the weight defined by the following equation.

$$g_n = \begin{cases} \exp(-n/\lambda) & \text{for } \exp(-n/\lambda) > \epsilon \\ 0 & \text{for } \exp(-n/\lambda) \leq \epsilon \end{cases} \quad (2)$$

Where, n is the order of the neuron determined according to the distance between the neuron and the target. It has a large value for the neuron that is near to the target, and has a small value for the neuron that is far from the target. The symbol λ and ϵ are value to define neuron numbers that can affect θ_{out} .

3 Process

3.1 Learning procedure of the Self-Organizing Map

In our system, plural SOMs are employed. If they are learned separately, their outputs are different even for the same target. This will result in that the manipulator moves inconsistently when it is driven from valid workspace of one map to another. In the learning algorithm, the problem has to be solved effectively. The problem also can be described as: the algorithm should guarantee that the manipulator moves smoothly and consistently in whole workspace no matter which SOM outputs joint angles for it.

The learning procedures illustrated in Fig.3. When a target position u_t is presented randomly in the workspace, each camera sees the target. If a camera can see the target, the SOM which is connected to the camera will learn. While more than two SOMs learn

for a common visible target, they learn with influence each other. In this case, one of SOMs is chosen to determine the joint angles θ_{out} of the manipulator for the target. The manipulator is driven by the θ_{out} , and each camera obtains end-effector position v in each SOM respectively. Then, each SOM corrects its parameters by using u_t, θ_{out} and v . This learning procedure results in that in the end of learning the neurons of plural SOMs possess the similar value if θ_{out}, ξ and different W, J for the target given in the common visible space.

Thus, the outputs from either SOMs will ensure the manipulator has the same pose. This means: while a target is given in common visible parts, the outputs from either SOMs do not result in a change of the manipulator pose. In addition, the assignment of similar joint angles to adjacent target point is, in fact, one of the main features of the learning algorithm of the SOM. By the construction of a map between inputs in the image space and the neural net, learning algorithm makes sure that adjacent target points always activate adjacent neuron in the network. The learning forces adjacent neurons to adapt their output towards similar values.

Therefore, at the end of the learning phase the output values will very smoothly from a neuron to another neuron. Both features bring about a continuous and smooth transformation from the input image spaces of target points to the out put space of joint angle sets. According to such a learning algorithm, SOMs guarantee smooth and consistent movements of the manipulator in whole workspace. For details about evaluation function, learning algorithm and update of the parameter, refer to our previous paper [13].

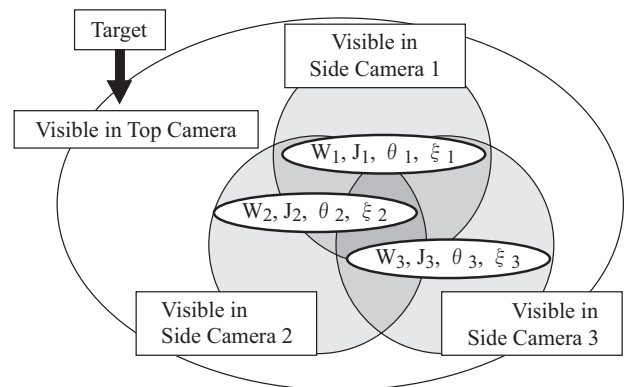


Fig. 3: Relation of Plural Self-Organizing Maps

3.2 Path planning

In our system, collision avoidance is based on the idea, While projected path does not interfere with pro-

jected obstacle, the path in 3 dimensional space can avoid the obstacle. Here collision avoidance is realized in the image spaces. It is not required to reconstruct a 3D model. Consequently collision avoidance in the image spaces by combining a SOM and a path planning system. The SOM determine joint angles of manipulator so that the end-effector of the manipulator reaches a target position given in the image spaces arbitrarily, and also ensures the manipulator taking obstacle-free poses. Here, the path planning system adapts Laplaces potential method to plan a collusion-free path for the end-effector from an initial to a goal position without plagued into local minima.

Since the manipulator can drive the end-effector to a target point given in the image spaces with obstacle-free poses under control of the SOMs, the path planning system only needs to plan a path for the end-effector of the manipulator. Accordingly, it is not necessary to pay attention to the collision between obstacles and links in the process of driving the end-effector along the planed path. It is different from most of existing algorithm, which are intended to work in configuration space. Our system always plans paths in 2D spaces, so the computational cost of planning does not increase exponentially for a high dimensional redundant manipulator. For procedure of the path planning and path planning by Laplaces potential method, refer to our previous study [12].

4 Simulation and experimental result

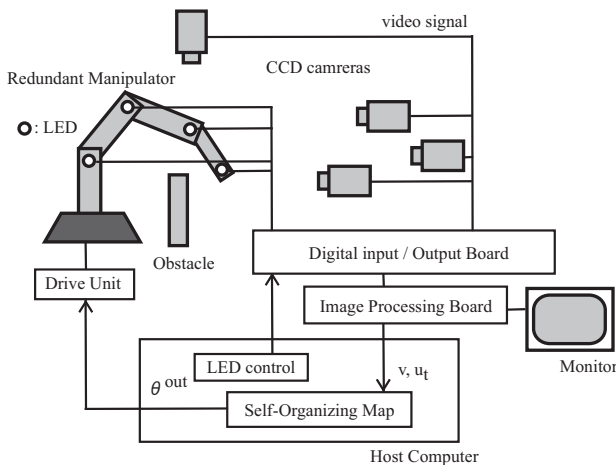


Fig. 4: Outline of experimental system

A photograph and the outline of our system are respectively shown in Fig.4 and Fig.5. The manipulator is Mitsubishi Manipulator RV-1A. It is driven by using the operating signal θ_{out} which is received through



Fig. 5: Our experimental system

a Drive unit. The CCD cameras see the manipulator and the outputs from cameras are lead to a frame memory in the host computer. The size of the frame memory is 640[pixel] \times 480[pixel]. The SOMs are composed in a host computer. LEDs, which are lighted by the host computer, are set on joints so that the system can find the position of the end-effector and links of the manipulator in camera images. Cameras are also used to get shapes of obstacles.

At first, by simulation, we will show that our system can output joint angles using 3 CCD cameras and 2 related SOMs so that the end-effector of the manipulator reaches to the target with obstacle-free poses, and that the system accomplish collision avoidance using proposed approach. Then, we will confirm reproductivity of the system to experiment in actual environment.

Secondly, we will expend the system to increase CCD cameras and SOMs and show that the system makes the manipulator take obstacle-free poses and accomplish collision avoidance.

Simulation results were shown in Fig.6 and Fig.7. In the simulation, a SOM consisted 240 neurons was used, and 15000 targets were given for learning. There was one obstacle. Fig.6 shows the target positions and the poses of the manipulator, when all cameras can see the target after learning. In the figure, we can see that the manipulator takes obstacle-free poses and the end-effector reaches targets correctly. The average error of the end-effector position was 1.57[pixel]. Fig.7 illustrates planed path from initial to goal point and manipulator poses driven by the SOMs without stopping at local minima. The average error along planed path was 3.06 [pixel].

An experimental result is shown in Fig.8 and Fig.9. To shorten the learning time and confirm robustness of the system, the SOMs of above simulation were

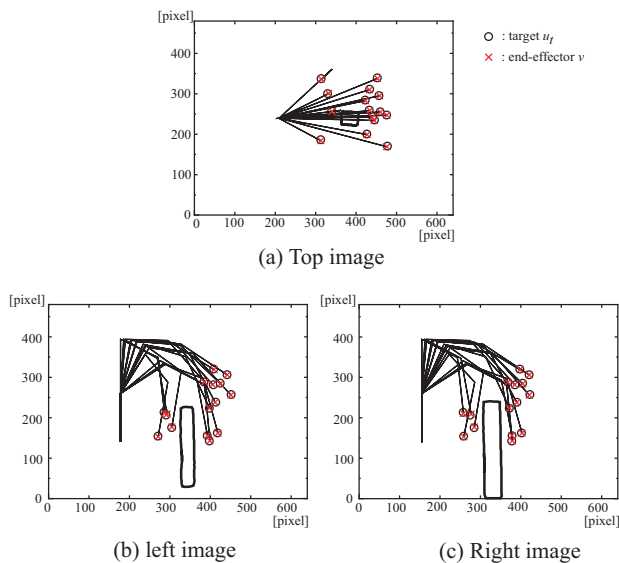


Fig. 6: Output for manipulator by simulation

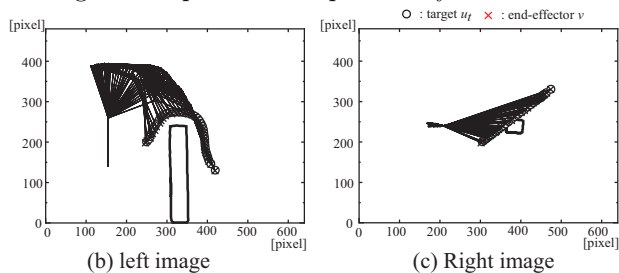


Fig. 7: Output of collision avoidance by simulation

used as initial state by experiment. The number of re-learning time was 1500 and the time required process was about 16,500[sec]. Similarly with Fig.6, Fig.8 shows target positions and poses of the manipulator after re-learning. The average error of the end-effector position was 1.57[pixel], and it was about 2[mm] in the real environment. Also, Fig.9 illustrates the planned path and the manipulator poses. The average of error along planned path was 2.75[pixel].

By the simulation and experiments, we have verified that the system can make the manipulator take obstacle-free poses and practice collision avoidance.

Next, simulation results, which are led from the extended system, are shown in Fig.10 and Fig.11. In the simulation, a SOM consisted 240 neurons was used, and 30000 targets were given for learning. There was one obstacle. Fig.10 shows the target positions and the poses of manipulator, when all camera can see the target after learning. In the figure, we can see that manipulator takes obstacle-free poses and the end-effector reaches the targets correctly. The average error of the end-effector was 1.74[pixel]. Fig.11 illustrates planned

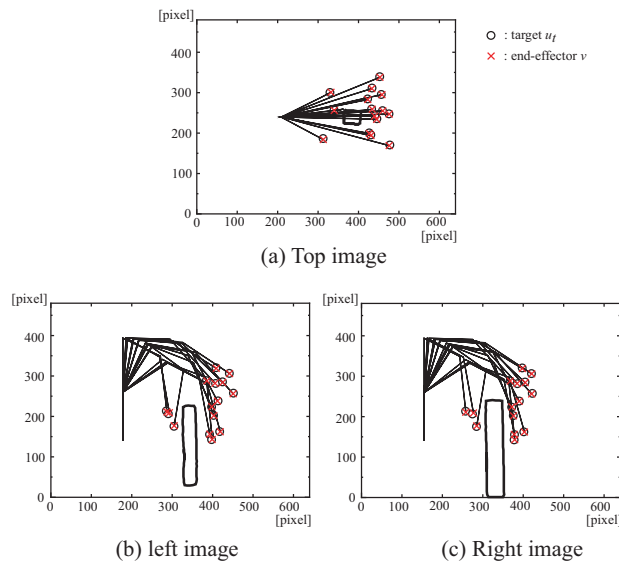


Fig. 8: Output for manipulator by experiment

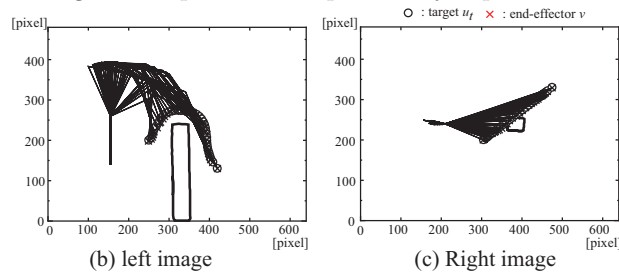


Fig. 9: Output of collision avoidance by experiment

path from an initial to a goal point and the manipulator poses driven by SOMs without stopping at local minima. The average of error along planned path was 2.56 [pixel].

5 Conclusion

In this paper, we validated the proposed method approach by real experiment and confirm the efficiency of the proposed method and robustness of the system. Then, we extended the system by increasing number of camera and SOM and showed the efficiency of the system. Advantages of this approach are (1) By employing multiple SOMs alternately, the system overcomes the occlusion problems in cluttered environment, (2) In our visuo-motor system, neither any priori knowledge about the manipulator nor the camera parameters are required.

In the present system, when a target point is put under obstacles and the top camera can not see it, SOMs can not learn joint angles because of dependence

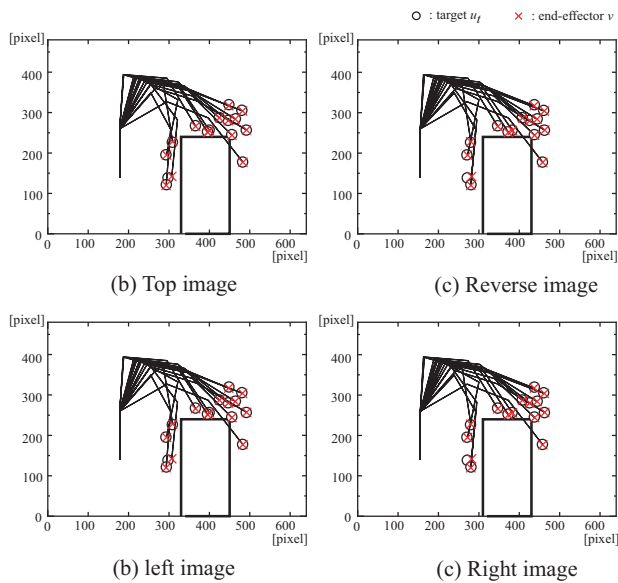


Fig. 10: Output for manipulator in extended system by simulation

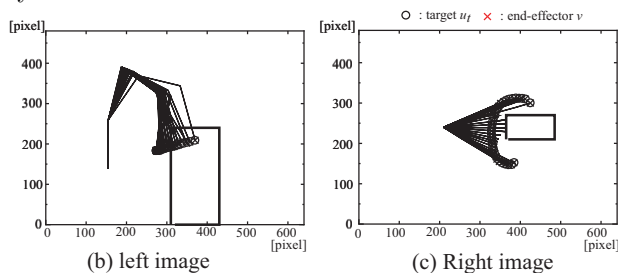


Fig. 11: Output of collision avoidance in extended system by simulation

on the top camera. Therefore, we have to extend the system and make each camera independent.

A part of this study is financially supported by Electro-Mechanic Technology Advancing Foundation, Japan.

References

[1] S.M LaValle, "Rapidly-exploring random trees: A new tool for path planning," *Technical Report 98-11*, Computer Science Dept., Iowa State University, 1998

[2] J.F. Canny, "The complexity of robot motion planning," *MIT Press*, 1988

[3] R. Bohlin and L.E. Kavraki, "Path Planning using lazy PRM," *In Proc. ICRA*, pp. 521-538, 2000.

[4] O. Khatib, "Real-time obstacle avoidance for manipulators and mobile robots," *Int. J. of Robotics Reseach*, 5(1): 90-98, 1986

[5] K. Glass, R. Colbaugh, D. Lim and H. Seraji, "Real-time collision avoidance for redundant manipulators," *IEEE Trans. On Robot. and Automat.*, vol.11, no.3, pp-. 448-457, June, 1995

[6] H. Seraji and R. Colbaugh, "Improved configuration control for redundant robots," *J. of Robot. Syst.*, vol.7, no.6, pp-. 897-928, 1990

[7] O.Khatib, S. Quinlan and D. Williams, "Robot planning and control," *Robotics and Autonomous System*, 21: 249-261, 1997

[8] O.Brock and L.E. Kavraki, "Decomposition-nased motion planning: A framework for real-time motion planning in high-dimensional configuration spaces," *In Proc. ICRA*, vol.2, pp. 1469-1474, 2001

[9] K.H. Low, W.K. Leow and M.H. Ang, Jr., "Integrated planning and cotrol of mobile robot with self-organizing neural network," *In Proc. ICRA*, 2002

[10] S.X. Yang and M. Meng, "Neural network approaches to dynaic collision-free trajectory generation," *IEEE Trans. Systems Man Cybernet*, B 31(3), pp. 302-318, 2001

[11] M. Zeller, R. Sharma and K. Schulten, "Motion planning of a pneumatic robot using a neural network," *IEEE Control System Mag*, 17, pp. 89-98, 1997

[12] N. Okada, K. Minamoto and E, Kondo, "Collision avoidance for a visuo-motor system with a redundant manipulator using a self-organizing map," *ISATP*, pp. 104-109, 2001

[13] M. Han, N. Okada and E. Kondo, "Coorination of an Uncalibrated 3-D Visuo-Motor System Based on Multiple Self-Organizing Maps," *JSME International Journal*, Series C, vol.49, No.1, pp. 230-239, 2006

Development of an autonomous mobile system for an autonomous robot in an indoor environment

Toshifumi Uewaki

Eiji Hayashi

Department of Mechanical Information Science and Technology

Faculty of Computer Science and Systems Engineering, Kyushu Institute of Technology

680-4, Kawazu, Iizuka-City, Fukuoka Prefecture, Japan

Key Words: Personal robot, Autonomous driving, Image Processing

Abstract

We are developing an autonomous robot that can perform work in a human living environment. To move safely in a human environment, a robot should be able to recognize changes in the environment. Thus, we have developed a mobile system for autonomous robots with an obstacle-detection function and a human-following function. This system uses image information from a CCD camera and image processing. The obstacle-detection function, which is one of the functions of this system, detects obstacles for safe move, while the human-following function allows the robot to follow a person using information from images.

In this paper, we explain in detail the image-processing algorithm used with both the obstacle-detection function and the human-following function. Furthermore, we experimentally evaluate the system and discuss its problems based on the results.

1. Introduction

Autonomous robots are expected to provide various services in human living environments in the future. It is important that such robots can move safely in an environment with human activity and can communicate with humans. Therefore, we are developing an autonomous robot that can perform work in a human living environment and possesses these abilities.

Our robot has a drive mechanism of two front wheels and one back wheel. The front wheels are attached to the motor, which operates the wheels on either side independently, while the back wheel is a castor wheel. This method has the advantage of being able to negotiate a far smaller turn than that of a passenger car's steering system, for instance. DC servo motors are used for the robot's drive mechanism, and position control and speed control are achieved by the control system of the drive mechanism. The robot also has two arms and hands and sensors; these devices

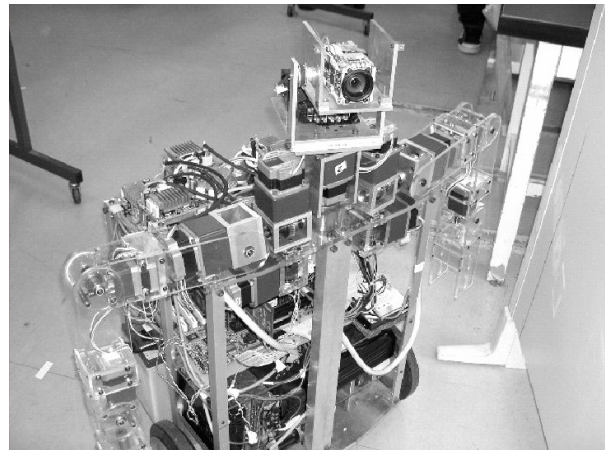


Fig. 1 Robot appearance

enable the robot to respond to various demands. An installed wireless LAN provides remote control for humans. All devices are controlled by a PC, and lead batteries supply electric power. [1], [2], [3]

In order to acquire a distance perspective for the autonomous driving robot, we developed an autonomous mobile system. This system creatively uses two functions based on the presence of an obstacle or human in the first image. The obstacle-detection system is used when there are no humans in the image; the human-following function is used when there are. The obstacle-detection function uses image differences found during the robot's motion, by which obstacles can be quickly detected. After detection, the position of the obstacle is calculated using the principle of triangulation. From this result, the suitable operation of the robot is decided. In the human-following function, the location of the human user is first determined from the location information acquired before the robot runs. After acquisition, this function uses the color distribution of the area specified as a human image as a model to match. A similar area of the present image is sought using this model color distribution. Thus, if the robot can recognize a human, it can be made to follow the human.

2. Obstacle-detection function

2.1 Outline

The robot being developed in this laboratory moves by using the finite-space map stored in the database. If an unknown obstacle not existing on the map appears during this motion, the robot cannot avoid this obstacle without an obstacle-detecting function, such as the one we developed. In section 2, we explain and experiment on this function.

2.2 Method for obstacle detection

In this section 2.2, we explain the method for the obstacle detection. The flow for obstacle detection is shown in Fig 2.

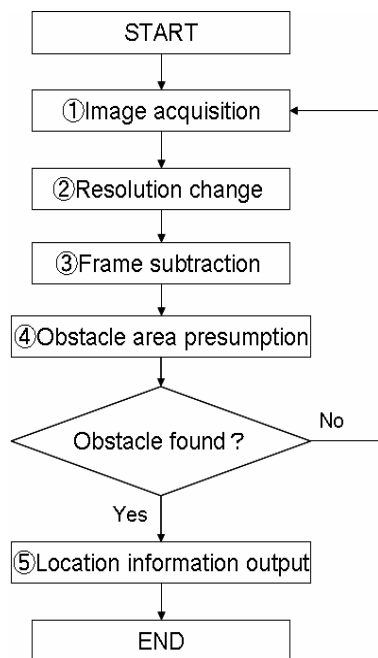


Fig.2 Flow for obstacle detection

Step1. Image capture

The PC in the robot captures two CCD camera images at short intervals of time for the post-processing algorithm.

Step2. Image resolution change

The mean value of an arbitrary block in the image is found, and the pixels in the block are replaced by the mean value.

Step3. Image differences

The wall and an obstacle in the image that doesn't actually move seem to have moved due to the movement of the robot. Thus, a moving obstacle and a static obstacle cannot be distinguished by simple image differences. Thus, we subtract each pixel of the

two images of low resolution. As a result, the change in the appearance of the background is removed. The surrounding area of the moving obstacle appears as an output image.

Step4. Obstacle area presumption

A histogram of the image differences value is made for the vertical and horizontal axes of the image. The moving obstacle area is presumed based on this histogram.

Step5. Output of position information

The distance from the moving obstacle area specified in the image to the bottom of the obstacle in real space is calculated by the following equation:

$$L = \frac{hf}{f \sin \theta + y_i \cos \theta},$$

where f is the focal length, θ is the depression angle, and y_i is the y-coordinate in the image.

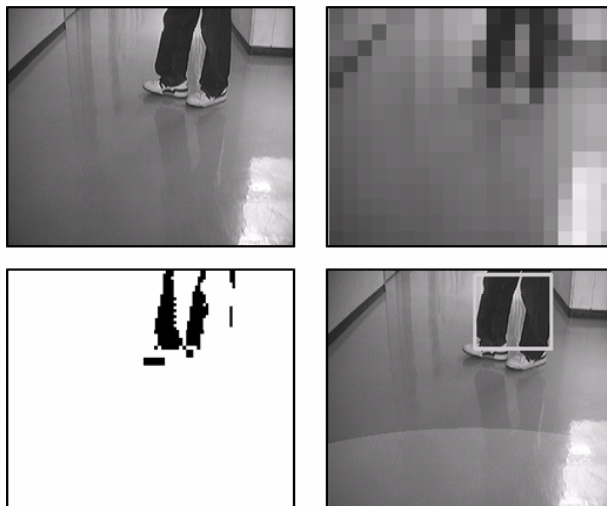


Fig.3 Result of obstacle detection

2.3 Experiment

We performed an experiment to evaluate the performance of the function. The robot was made to run on an indoor flat passage at the speed of 0.5m/s. The function detected when an obstacle approached and when an obstacle appeared suddenly from the side. Moreover, the angle of depression of the camera was set to 30 degrees. Fig. 4 shows the result of the obstacle's approach. Fig. 5 shows the result of the obstacle's sudden appearance from the side.

As a result of the experiment in the two situations, the obstacle was almost exactly detected using the function. Thus, the effectiveness of the system at the speeds used in this experiment was shown.

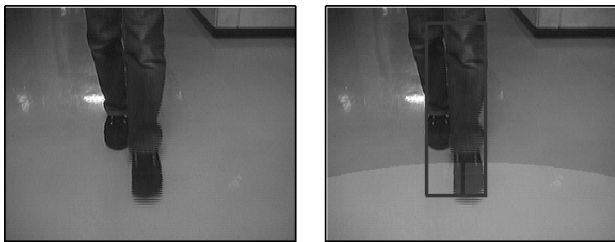


Fig.4 Approach of an obstacle

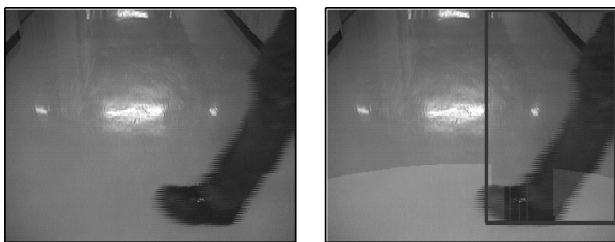


Fig.5 Sudden appearance of an obstacle from the side

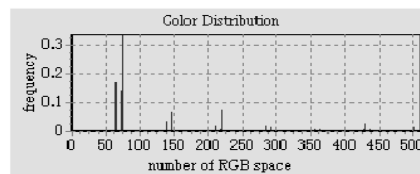


Fig.6 Creating a histogram

3. Human-following function

3.1 Outline

To move safely in a human environment, a robot should be able to recognize the external environment. This environment recognition must combine self-positional presumption, obstacle recognition, route selection, etc. It is difficult for the robot to correctly recognize the environment given the limitations in its memory and calculation capacities. Therefore, when a person is walking forward, the robot can be made to follow the human. The amounts of memory and calculation required decrease because the robot simply has to recognize the human. In addition, it is possible to move safely because the robot can follow the route of the human, who recognizes and understands the environment. In section 3, we explain this human-following function.

3.2 Method for human following

The human who is the target of tracking is not a constant shape, but rather, the change in shape is great. Thus, the tracking of a human using the shape feature is difficult. Consequently, in order to acquire the human feature, this function uses color distribution. First, the area where the human exists in the image is selected. After the area is selected, a histogram in RGB space is created for this area. Fig. 6 shows the appearance of the image by which the histogram is created. The RGB space is divided into $8 \times 8 \times 8$. The memory required for a more detailed RGB space, for instance, $256 \times 256 \times 256$, is huge.

Next, in order to seek a similar area in image we analyze correlation between created histogram of human feature and histogram of arbitrary area of present image. Two normalized histograms are overlapped, and the minimum value of the pair of the value is taken. The value in which all these minimum values were added is set as a similarity. If this similarity is high overlapping of two histograms increase as shown upper in upper of fig.6. In contrast, if this similarity is low overlapping of two histograms decrease as shown in bottom of fig.7. The area where this similarity is the highest in the image is judged to be an area where the human exists.

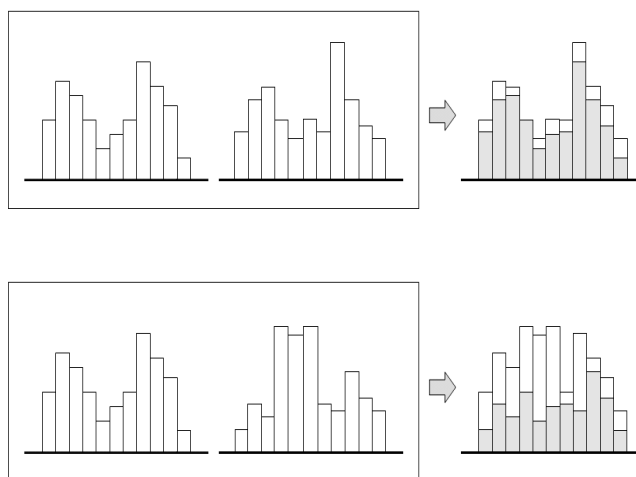


Fig.7 Comparing histograms

After seeking the similar area, the distance is calculated using the y-coordinate at the bottom of the area specified as a human. The speed of the robot is changed in proportion to this distance, and the human is followed.

3.3 Experiment

We experimented of human tracking in the image for the evaluation of the function.



Fig. 8 Tracking images

The tracking image for every fifth frame is shown in Fig. 8. The human was tracked over 30 frames. The similarity of the histogram during the pursuit of the person was maintained at 70% or more. As a result, the area where the human existed was able to be presumed with considerable accuracy. Furthermore, the distance to the bottom of the obstacle was able to be calculated with considerable accuracy.

4. Conclusions

We have proposed a mobile system for autonomous robots with an obstacle-detection function and a human-following function. We were able to show the effectiveness of both the obstacle-detection function and the human-following functions.

The problem of the obstacle-detection system is to reflect the obstacle data detected in a finite space map so that the robot can select a safe route that avoids an unknown moving obstacle. However, changes in the speed of the robot or increases in the background's complexity impairs this detection. Thus, we want to improve the accuracy of the obstacle-detection by combination with other method.

In order to acquire a human-following function, we used color distribution. However, this function has not been mounted on the robot yet. Thus, we mount on the robot this function and we want to test in real space the performance of the human-following function.

Our next subject of study is to develop a system for action planning.

References

- [1] Toru Azuma, Yoshihiro Takenaga, Eiji Hayashi, Development of a self-driven personal robot, Artificial Life and Robotics (AROB 8th '03), pp.1-3, Oita, Japan, 2003
- [2] Eiji Hayashi, Keisuke Ikeda, Development of a system for self-driving by an autonomous robot, proceeding of 10th international symposium on artificial life and robotics, Vol.10th, pp.4, Beppu, Oita, Japan, 2005
- [3] Takuma Umeno, Eiji Hayashi, Navigation system for an autonomous robot using an ocellus camera in indoor environment, proceedings of the 11th international symposium on artificial life and robotics, Vol.11th, pp.229, Beppu, Oita, Japan, 2006

A study on improvement of the surveillance system of an Indoor blimp robot

T.Takaya

Business Strategy Group
Business Strategy & Control Office
Sapporo, Hokkaido.
060-0807

Y.Minagawa

Graduate School of Information
Science and Technology
Hokkaido University
Sapporo, Hokkaido,060-0814

A.Ouhi

Graduate School of Information
Science and Technology
Hokkaido University
Sapporo, Hokkaido,060-0814

H.Kawamura

Graduate School of Information
Science and Technology
Hokkaido University
Sapporo, Hokkaido,060-0814

M.Yamamoto

Graduate School of Information
Science and Technology
Hokkaido University
Sapporo, Hokkaido,060-0814

Abstract

Blimp robots are attractive as indoor flying robots because it can float in the air, land safely with low energy, and stay in motion for a long time compared with other flying robots. However, controlling of blimp robots for surveillance is difficult, because it has nonlinear characteristics, is influenced by air streams and is easy to be influenced of inertia. Therefore, it is not easy to control blimp robot only by PID control and to carry out position control.

However, since PID control can change the control characteristic easily by adjustment of a parameter, it is thought possible to use for rough control of operation. Therefore, when performing control of blimp robot of operation, PID control performs rough operation. And application of blimp robot is considered to round and surveillance by using the more precise control method for detailed control of operation near the surveillance point.

By this research, in order that the control instructions from the outside may make operation there is nothing independently possible, having

improved the certainty of round surveillance is shown by developing blimp robot which carried all the parts for control and in which autonomous control is possible. Using learning control near the surveillance point and using PID control between surveillance points.

1 introduction

As compared with other flight move objects, floating and movement are possible for Blimp robot with low energy. Therefore, it is observed as a flight robot for indoor. Recently, researches have studied ways to make the best use of the features of blimp robot and how to apply it to indoor applications, such as situation, the area and house that received the calamity survey [1], indoor security [2].

Blimp robot will be wanted direct motion when flying, example through narrow spaces for security and round an indoor surveillance. The thrust unit of an indoor blimp robot must be designed high mobility. And, blimp robot has to operate in the limited range. the entire blimp robot must be kept small. Buoyancy decreases by miniaturizing the airframe. In designing

a blimp robot, one must considering the weight of the controller unit, thruster unit, and the sensor unit on the airframe. Characteristic of blimp robots is influenced of inertia; establishing original control architecture compares the other robots.

Based on the flight navigation of insects [5], by position detection using beacons [6], and based on camera pictures [8] are researched about the method of controlling Blimp robot. In addition, investigation in outdoor environment has been conducted using cooperative operation with ground robots [4], an original method is proposed by each research. The research on the round system that uses the PID control is performed. [10]

2 Experiment

This chapter explains the experimental environment and the experiment blimp robot to show that blimp robot accurately reaches the target surveillance point.

2.1 Experimental environment

Experiment environment is an inside of a building. And the blue and red circle are arranged with a diameter of 0.50m at intervals of 0.75m to the floor at the space for an experiment. As experiment space, it is referred to as over 3m at width, depth, and height for experiments in Blimp robot.

2.2 Experiment operation

"S" was made a starting point, and the operation of Blimp robot in the actual experiment was set for the straight line to move in order of P1~P7. In this experiment, P1~P7 is made a relay point, and it makes it to surveillance point.

1. When the camera installation part of blimp robot enters the space of 50cm in the radius for the point where P1~P7 is observed, it switches to the learning control[11].
2. It rotates when is in the space of 30cm in the radius for five seconds for each surveillance points of P1~P7.
3. After rotations are made, it moves to the next point.

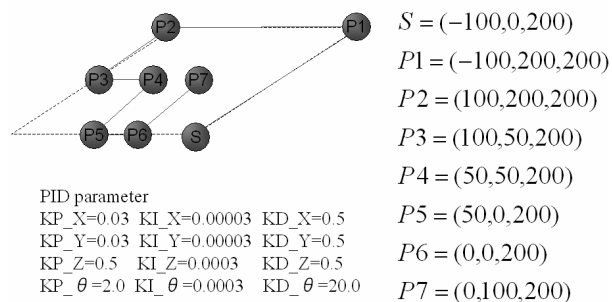


Fig.1 Round condition and PID parameters

2.3 Blimp robot and PID controller

Figure 2 showed appearance of blimp robot. The balloon is a column type, and the diameter is 0.94m, and 0.80m in height for enough to obtain buoyancy [8]. And, it has a controller and driving part under the balloon.

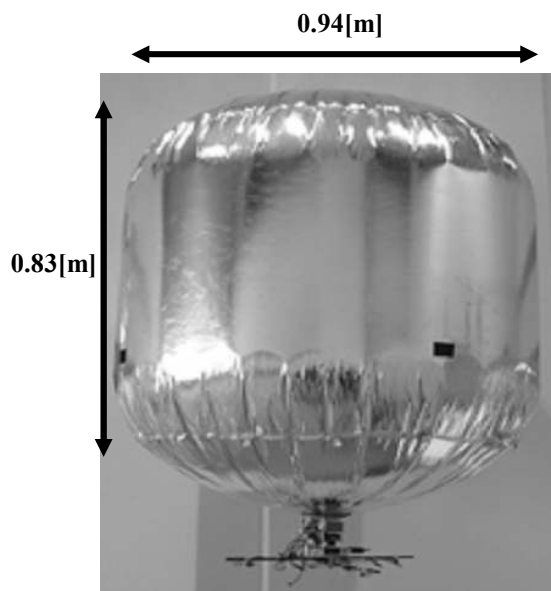


Fig.2 Appearance of developed Balloon Robot

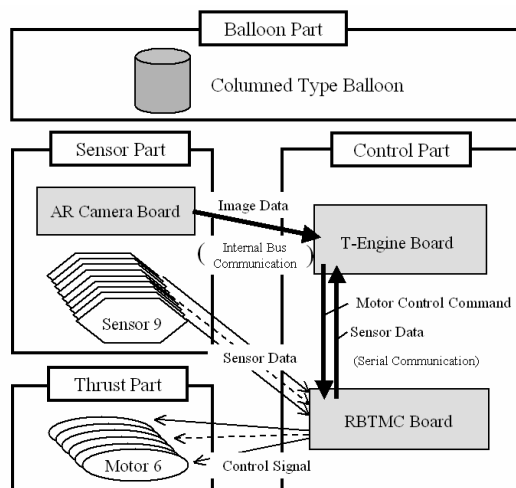


Fig.3 Abstraction of the Developed Blimp Robot

In this research, the camera of the resolution of 160×144pixel is installed and the RGB 16bit color image to be able to acquire the location information by recognizing the landmark in the experimental environment is position acquired. μ T-Engine calculates information and the image data processing from the sensor, and taken image and sensor value are processed $\Delta T=0.3$ sec or less of the sampling duration of the propeller motor control.

Fig.3 shows the block diagram of developed blimp

robot, μ T-Engine board (M32104) controls the DC motor driver of the RBTMC one-board microcomputer board by the serial port after doing the processing of sensor information and the calculation concerning the decision of the control output, and six propellers (ch0~ch5) are driven. Thrust was able to be generated axially each for a direct movement in the direction of the desire and the propeller was arranged. Propeller motor ch4 and ch5 that intersected, united the midair carbon pipe, arranged the propeller motor of ch0~ch3 that generated thrust x axis and y axis, and generated thrust z axis were arranged.

The variables manipulated for translation and rotational motion in our PID controller were decided by deviations based on the relative distance from the x, y, and z axes and the relative yaw angle. The relative distances e_x , e_y , and e_z [cm] are from the blimp to the target. The relative angle e_θ [rad] is the angle from the yaw angle of the blimp to that of the target. The manipulated variables $m_x(t)$, $m_y(t)$, and $m_z(t)$ [g] for translational motion, and $m_\theta(t)$ [g] for rotational motion at time t, are calculated as

$$m_x(t) = K_{px}e_x(t) + K_{ix}\sum e_x(t)\Delta T + K_{Dx}\frac{e_x(t) - e_x(t - \Delta T)}{\Delta T} \quad (1)$$

$$m_y(t) = K_{py}e_y(t) + K_{iy}\sum e_y(t)\Delta T + K_{Dy}\frac{e_y(t) - e_y(t - \Delta T)}{\Delta T} \quad (2)$$

$$m_z(t) = K_{pz}e_z(t) + K_{iz}\sum e_z(t)\Delta T + K_{Dz}\frac{e_z(t) - e_z(t - \Delta T)}{\Delta T} \quad (3)$$

$$m_\theta(t) = K_{p\theta}e_\theta(t) + K_{i\theta}\sum e_\theta(t)\Delta T + K_{D\theta}\frac{e_\theta(t) - e_\theta(t - \Delta T)}{\Delta T} \quad (4)$$

where KP is the proportional gain, KI, is the integral gain, and KD is the derivative gain. The parameters are adjusted for each basic motion.

$m_x(t)$ – $m_\theta(t)$ generated for propellers ch0–ch5 are determined by using m , m_y , m_x , and m_θ as follows:

$$m_0(t) = m_y(t) + m_\theta(t) \quad (5)$$

$$m_1(t) = m_x(t) + m_\theta(t) \quad (6)$$

$$m_2(t) = m_y(t) - m_\theta(t) \quad (7)$$

$$m_3(t) = m_x(t) - m_\theta(t) \quad (8)$$

$$m_4(t) = m_z(t) \quad (9)$$

$$m_5(t) = m_z(t) \quad (10)$$

$m_0(t)$ – $m_5(t)$ are continuation values that are calculated by equations (5) through (10). However, the motor drive developed by this research cannot control a continuous rotational speed. As for the drive of the motor, only a binary control of ON-OFF is possible. The drive of the motor is adjusted and thrust is adjusted according to the time width for that. As for the motor, a

positive rotation and the reverse rotation are individually possible. By these devices, controlling such a propeller motor, it becomes possible to generate an independent thrust and blimp robot is freely movable to x, y, and z axis.

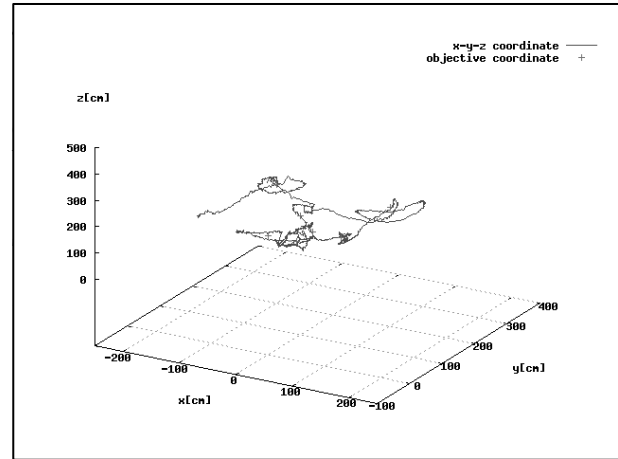


Fig.4 Three-dimensional orbit result of blimp

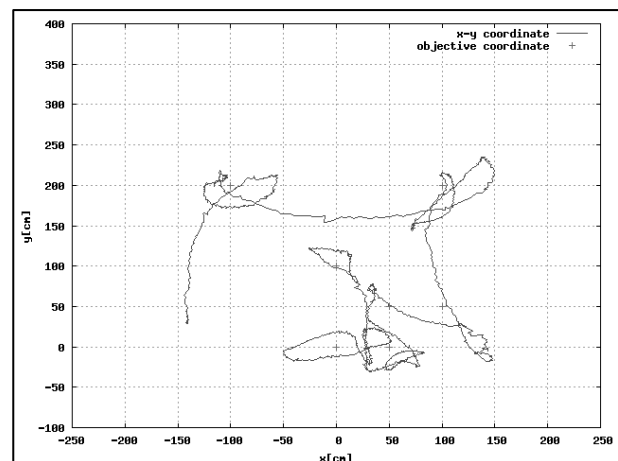


Fig.5 The orbit of X-Y plane of blimp

Figure 4 showed three dimension orbit of blimp robot. The orbit of X-Y plane was shown for Figure 5.

A straight line orbit lacks stability because it has received the influence of inertia. The control that moves between the target points is done by the PID control now. However, the appearance in which the orbit is corrected is shown toward the target point. Especially, it is shown that it is operation to which adjacent to the target point is done as it is a setting.

Figure 6.7.8 showed the transition of the time of the orbit in x, y, and z each axis. In each axis, blimp independently corrects the orbit, and does the movement operation to the target point. And, an individual axis and the orbit result shows, it is understood that the influence of inertia is large.

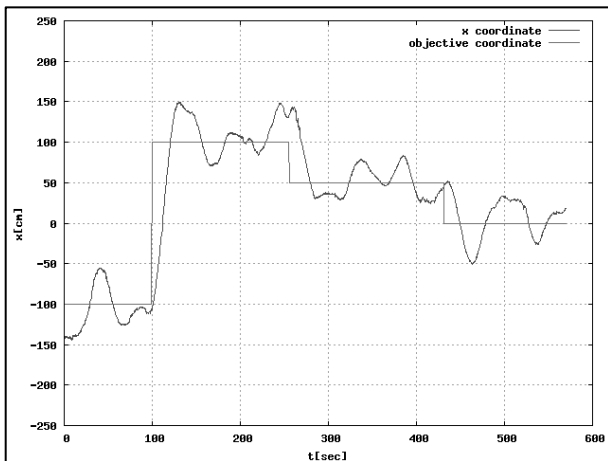


Fig.6 Transition at time in x axis

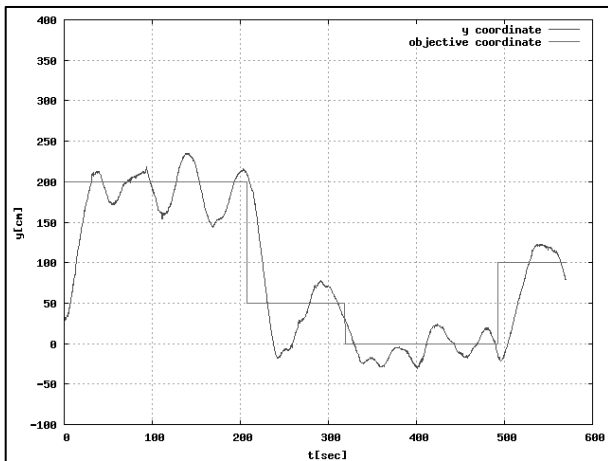


Fig.7 Transition at time in y axis

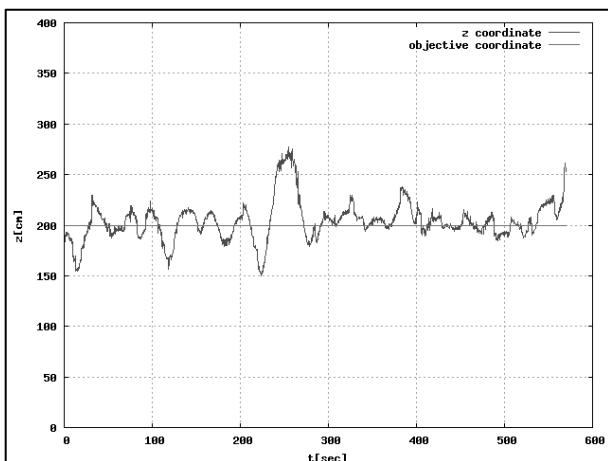


Fig.8 Transition at time in z axis

4 Conclusion

The rotation operation in the PID control and the surveillance point (each target point) was able to be achieved. However, there is a problem that the disorder of the orbit by the influence of inertia is caused in other side. And, the error margin of keeping position in the surveillance point is large.

The orbit is stabilized and it will be necessary to improve keeping position with surveillance point in the future. It is scheduled to change the PID control from a positional control to the speed control and to try to this improvement.

References

- [1]T.Yabuuchi,M.Onosato, "Development of A Small Airship for Surveying Damaged Buildings", SICE SI 2002 Kobe, Vol. 3, pp. 17-18,2002(in Japanese)
- [2]A.Hosoi, Masanori Sugimoto, "An Autonomous Security System Using Multi-Flying Robots", The 18th Annual Conference of the Japanese Society for Artificial Intelligence, 2C1-04,2004(in Japanese)
- [3]Hidenori Kawamura et al., "Development of Entertainment Indoor Blimp Robot based on Hovering Control", Entertainment Computing 2004, pp. 69-74, 2004 (in Japanese)
- [4]A. Elfes et al., "Air-Ground Robotics Ensembles for Cooperative Applications, Concepts and Preliminary Results", Proceedings of the International Conference on Field and Service Robotics, pp. 75-80,1999
- [5]F. Iida, "Biologically inspired visual odometer for navigation of a flying robot", Robotics and Autonomous Systems 44, pp. 201-208, 2003
- [6]C. Melhuish, J. Welsby, "Gradient Ascent with a group of Minimalist Real Robots: Implementing Secondary Swarming", Proceedings of 2002 IEEE International Conference on Systems, Man and Cybernetics, pp. 509-514,2002
- [7]J. Kobayashi et al., "Flight Control of Blimp based on CCD Camera Images", Proceedings of International Symposium on Advanced Control of Industrial Processes, pp. 269-274 ,2002
- [8]H.Kawamura et al., "Motion design for Indoor Blimp Robot with PID Controller", Journal of Robotics and Mechatronics, Vol. 17,No. 5, pp. 500-508, 2005
- [9]S. Zwaan et al., Visual Station Keeping for Floating Robots in Unstructured Environments, Robotics and Autonomous Systems 39, pp. 145-155,2002
- [10]T. Takaya et al, "Motion Control in Three Dimensional Round System of Blimp Robot", SICE- I CASE 2006(CD-ROM) ,2006
- [11]Y.Minagawa et al, "Learning Docking Control of Autonomous Recharging for Indoor Blimp Robot", Fuzzy System Symposium,pp689-692, 2006

Human Face Detection with Neural Networks and the DIRECT Algorithm

Yau-Zen Chang

Kao-Ting Hung

Shih-Tseng Lee

Medical Augmented Reality Research and Development center

Department of Mechanical Engineering

Chang Gung University, Tao-Yuan 33302, Taiwan

zen@mail.cgu.edu.tw

kattin@st.cgu.edu.tw

joe1181o@adm.cgmh.org.tw

ABSTRACT

Based on Rowley's approach [2], this paper aims at proposing a new architecture that uses a specific optimization technique, the DIRECT (Dliding RECTangle) algorithm, to improve the efficiency of face detection in images. The system consists of two main parts: a neural network-based face detection arbitrator and a search strategy based on an integer-handling DIRECT algorithm. By the architecture, the number of arbitration is dramatically reduced, and human faces, if they are present in an image, are not restricted to predetermined resolutions and aspect ratios. Experimental results show that the proposed architecture is efficient in terms of both speed and robustness.

INDEX TERMS: face detection, neural network, image processing, Image pattern recognition, DIRECT algorithm

1. INTRODUCTION

Human face detection from complex background and in different positions of an image is an important step for surveillance and intelligent human-machine interface.

Rowley's approaches [2] [3] are typical image-based face detection methods in which upright and frontal views of human face are detected using artificial neural networks (ANN). Owing to its conceptual simplicity, the approach of [2] has been followed by many researchers, such as [4]-[6] which use ANNs. In our previous work [11], we adopted both the image and feature-based techniques to design two ANNs to estimate the position as well as planar orientation of faces.

However, the approach of [2] is restricted to a fixed training and classification template, which is of 20×20 pixels. And the original image must be re-sampled at several preset resolutions due to the so-called image

pyramid arrangement. Furthermore, the ANN must check all the extracted windows in all the sampled images for the potential existence of human face. These restrictions can lead to prolonged processing time and overlook of faces that are difficult to identify in these resolutions and aspect ratios.

With these shortages of [2] in mind, this paper aims at proposing a new architecture that uses a specific optimization technique, the DIRECT (Dliding RECTangle) algorithm, to improve the efficiency of face detection in images.

2. THE INTEGER DIRECT ALGORITHM

We propose to apply the DIRECT algorithm [13] to improve the face detection architecture described in Section 2. The name of the optimization algorithm is an abbreviation of Dliding RECTangles, describing a specific manipulation procedure. Developed by Jones et al. in 1993, the procedure is deterministic, guaranteed to converge, and has a very fast convergence rate without trapping in local extremes [14]-[16].

In this work, the images are of finite resolution, and we need an integer version of the DIRECT algorithm. There are two parts to be considered: center definition and trisecting manipulation. The center point between two integers, say a to b , is defined as $\text{floor}((a+b)/2)$, where output of the floor function is the greatest possible integer.

In order to divide boxes into 3 parts, the trisected widths are calculated according to the following equation:

$$\Delta = \text{floor}\left(\frac{(b-a+1)}{3}\right)$$

The above equation would lead to two specific conditions of Δ :

$$\text{If } \Delta \geq 1, \begin{cases} \text{Child}_L : [a, a + \Delta - 1] \\ \text{Child}_C : [a + \Delta, b - \Delta] \\ \text{Child}_R : [b - \Delta + 1, b] \end{cases}$$

$$\text{If } \Delta = 0, \begin{cases} Child_C = a \\ Child_R = b \end{cases}$$

where $Child_C$, $Child_L$ and $Child_R$ denote the center, left, and right decedents after participation, respectively. That is, when $\Delta \geq 1$, the box will be divided into 3 parts: $Child_L$ ranges from a to $a + \Delta - 1$ with width Δ , $Child_C$ ranges from $a + \Delta$ to $b - \Delta$ with width $b - a - 2\Delta + 1$, and $Child_R$ ranges from $b - \Delta + 1$ to b with width Δ . When $\Delta = 0$, the box is divided into 2 parts: $Child_C$ and $Child_R$, each is of unit length.

3. PROPOSED FACE DETECTION METHOD

Our system consists of two main parts: a neural network-based face detection arbitrator and a search strategy based on an integer-handling DIRECT algorithm. As shown in Fig. 1, the position, size, and aspect ratio of the windows to crop sub-images for face detection are based on the DIRECT algorithm. After cropping and preprocessing, the feature is extracted at predetermined 49 locations. The feature values are then sent to the ANN to decide how close they represent a human face.

In other words, the face detection problem is converted into an optimization problem to find out the best position and size of the cropping window that contains a human face.

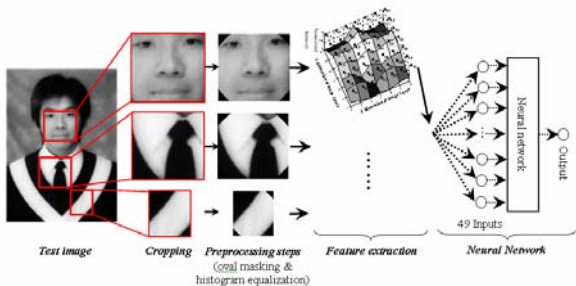


Fig. 1 The proposed face detection architecture

4.1. Neural network-based face arbitrator

The training and testing images for ANN in [2] are based on a fixed window (20×20 pixels). This approach not only restricts its applicability to face images with different aspect ratios, but also requires the computationally intensive resizing operation.

Based on these observations, we propose a moment-based feature extraction strategy that can alleviate the restrictions on aspect ratio and resolution.

The strategy takes the symmetrical property of human face into consideration. As Fig. 2 (a) illustrates, we segment the face image into 8 by 8 grids, this would result in 64 nodes from $N_{0,0}$ to $N_{8,8}$. Note that only the intensities at the node are used, thus no resize operation is required, and the template images are not required to be square.

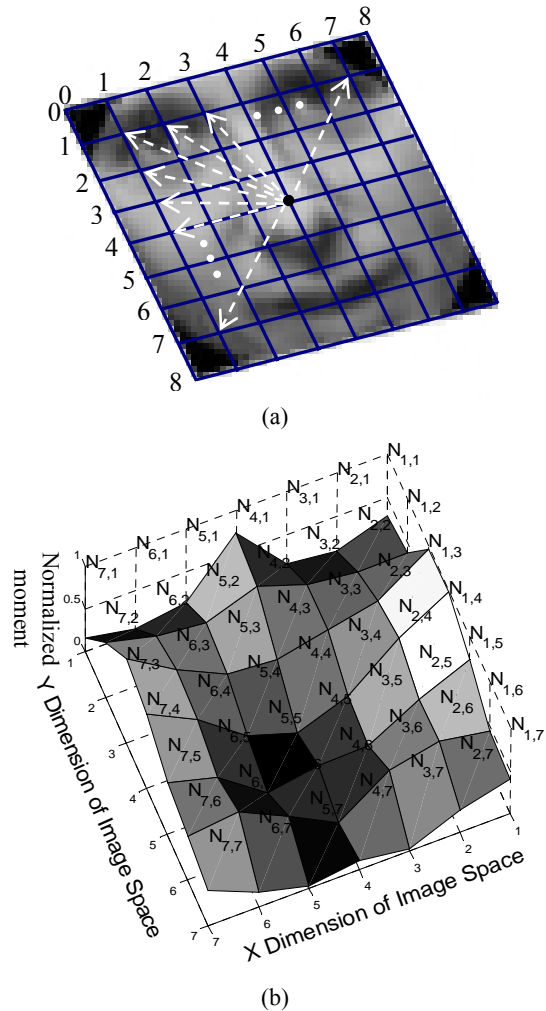


Fig. 2 (a) Location of the 49 nodes. (b) Distribution of these 49 normalized values.

Based on the first moment values of these nodes, 49 quantities are obtained:

$$M_{i,j} = I(p_{i,j}) \times \|p_{i,j} - p_C\|, i = 1 \sim 7, j = 1 \sim 7$$

where $p_{i,j}$ denotes the position of node $N_{i,j}$, p_C are the position of central node of this grid map, i.e., $N_{4,4}$, and $I(p_{i,j})$ represents the intensity of node $N_{i,j}$. Fig. 9 (b) shows distribution of these 49 normalized values corresponding to the example image. Obviously, the central moment would be smallest, and the distribution has a symmetrical characteristic along horizontal axis.

The ANN uses these 49 values as inputs to judge for the existence of human face. There are two output neurons, and the ANN is trained such that the output is [1, 0] when a human face is present, and [0, 1] when none.

There are at least four variables to be decided in the face detection problem: the X and Y coordinates, x and y , width, w , and height, h . These variables are summarized in to an unknown vector:

$$\theta = \{x, y, w, h\}.$$

The ranges of these variables are defined within the following boundaries:

- $1 \leq x \leq \text{width of the image}$
- $1 \leq y \leq \text{height of the image}.$
- $24 \leq w \leq 90$
- $24 \leq h \leq 90$

The problem is then formulated as finding the parameter vector, θ , by the DIRECT algorithm, such that the corresponding output of the ANN approximates the output of the arbitrator when a human face is present, which is the value [1, 0] in our current design. Fig. 3 shows the flow chart of the face detection architecture using the integer-handling DIRECT algorithm

In general, DIRECT algorithm proposes a searching strategy to obtain all possible solution. We extract all solution according to a specific threshold, i.e. if the values of objective function less than the predefined threshold, the corresponding solution would be considered.

5. EXPERIMENTAL RESULTS

We randomly selected 340 frontal-view face images and 306 non-face images from the MIT-CBCL face recognition database, CMU face database, and our own database to train the ANN. Besides, we prepare 138 images contains no face in order to improve the robustness of the ANN using the so-called “bootstrap” method [12].

The network is of the two-layered Multi-layered Perceptron (MLP) architecture with 20 neurons in the first hidden layer and 15 neurons in the second hidden layer. A standard back-propagation algorithm [17] was used to train this 49-20-10-2 network for 500 cycles. Fig. 4 shows the positions in the search space visited by the integer-handling DIRECT algorithm. Note that, for a 3-dimensional illustration, only the X and Y coordinates, x and y , and width, w are shown.

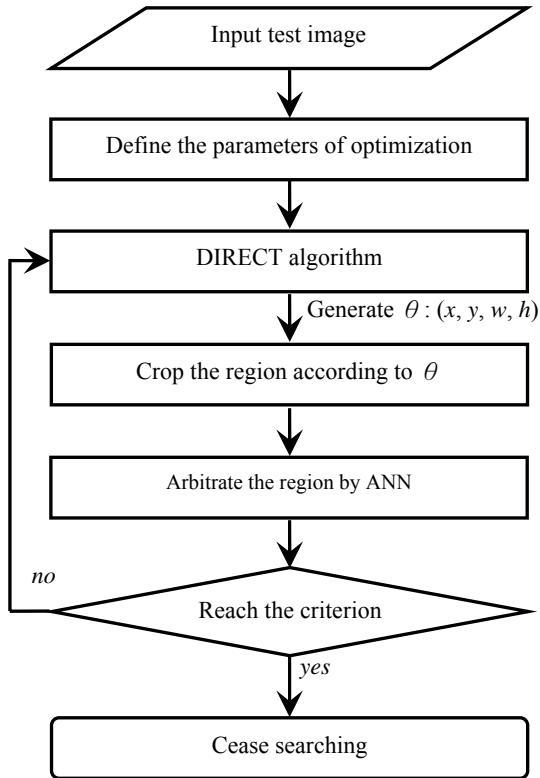


Fig. 3 Flow chart of the face detection architecture using the integer-handling DIRECT algorithm

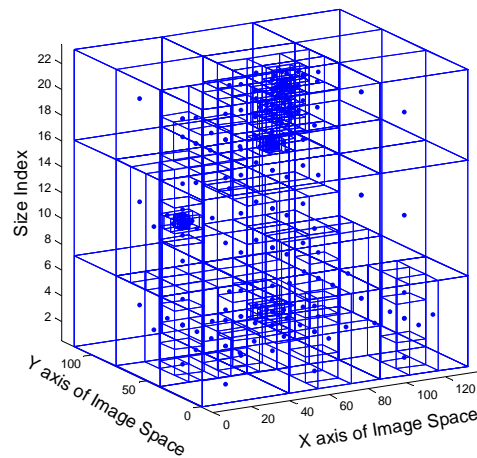


Fig. 4 Positions in the search space visited by the integer-handling DIRECT algorithm

Based on 50 detection results, the system based on the DIRECT algorithm can efficiently locate the human face within 1000 arbitrations using the ANN. As a comparison, when a typical 600 by 400 image is encountered, the number of arbitration in the approach of [2] can easily exceed the amount of 300,000.

Also found in the experiments, the DIRECT algorithm could cause repetitive detection. This problem can be easily solved by integrating all the neighboring positions into one by, for instance, the fuzzy c-mean method. Furthermore, we can integrate other image processing techniques, such as the skin color segmentation, to reduce the search area to further reduce the computing effort.

6. CONCLUSION

Based on the architecture of [2], we proposed a new human face detection architecture using the integer-handling DIRECT algorithm. The newly designed face classifier is computationally efficient and invariant to image size. Furthermore, the architecture is robust in terms of correctness, since the aspect ratio of face images is not fixed.

As for future work, we will address the issues of rotated faces and side-view faces. Skin color segmentation may also be included to provide further acceleration.

ACKNOWLEDGEMENT

This study is supported by Technology Development Program for Academia (TDPA) of the Ministry of Economic Affairs, R.O.C., under contract no. 94-EC-17-A-19-S1-035.

REFERENCES

[1] E. Hjelmås and B. K. Low, "Face Detection: A Survey," *Computer Vision and Image Understanding*, Vol. 83, pp. 236-274, 2001.
[2] H. A. Rowley, S. Baluja and T. Kanade, "Neural Network-based Face Detection," *IEEE Transaction Pattern Analysis and Machine Intelligence*, Vol. 20, pp. 23-38, January, 1998.
[3] H. A. Rowley, S. Baluja and T. Kanade, "Rotation Invariant Neural Network-based Face Detection," *Proceedings of Computer Vision and Pattern Recognition*, pp. 38-44, 1998.

[4] C. Garcia, M. Delakis, "Convolutional Face Finder: A Neural Architecture for Fast and Robust Face Detection", *IEEE Transaction Pattern Analysis and Machine Intelligence*, Vol. 26, No. 11, pp. 1408-1423, 2004.
[5] K. Curran, X. Li, and N. M. Caughley, "The Use of Neural Networks in Real-time Face Detection," *Journal of Computer Science*, Vol. 1(1), pp. 47-62, 2005.
[6] P. Hartono, S. Hashimoto, "A Robust Face Detector Algorithm Utilizing Neural Networks and Partial Template Matching," *Proceedings of the SPIE*, Vol. 5603, pp. 119-127, 2004.
[7] S. Birchfield, "Elliptical head tracking using intensity gradients and color histograms," *Proceedings of the IEEE Computer Society Conference on Computer Vision and Pattern Recognition*, pp.232-237, 1998.
[8] C.C. Han, H.Y. Liao, G.J. Yu, and L.H. Chen, "Fast face detection via morphology-based pre-processing," *Pattern Recognition*, Vol.33, pp. 1701-1712, 2000.
[9] C.H. Lin and K.C. Fan, "Triangle -based approach to the detection of human face," *Pattern Recognition*, Vol.34, pp.1271-1284, 2001.
[10] R.L. Hsu, "Face detection in color images," *IEEE Transaction on Pattern Analysis and Machine Intelligence*, Vol.24, pp.696-706, 2002.
[11] Y. Z. Chang and G. T. Hung, "Detection of Face Pose with Neural Networks," *International Symposium on Artificial Life and Robotics*, B-Con Plaza, Beppu, Oita, Japan, January 23-25, 2006.
[12] K. K. Sung, "Learning and Example Selection for Object and Pattern Detection," PhD Thesis, *MIT AI Lab*, January 1996.
[13] D. R. Jones, C. D. Perttunen, and B. E. Stuckman, "Lipschitzian optimization without the Lipschitz constant," *Journal of Optimization Theory and Application*, Vol. 79(1), pp. 157-181, 1993.
[14] C. A. Floudas, and P. M. Pardalos, *Encyclopedia of Optimization*, Kluwer Academic Publishers, London, 2001.
[15] H. Zhu and D. B. Bogy, "DIRECT Algorithm, and Its Application to Slider Air-Bearing Surface Optimization," *IEEE Transactions on Magnetics*, Vol. 38, No. 5, September, 2002.
[16] H. Zhu and D. B. Bogy, "Hard disc drive air bearing design: modified DIRECT algorithm and its application to slider air bearing surface optimization," *Tribology International*, Vol. 37, pp. 193-201, 2004.
[17] F. M. Ham, I. Kostanic, *Principles of Neurocomputing for Science & Engineering*, McGraw-Hill, 2001.

High Shock Disturbance Rejection of Single-Link Robot Arm with a Disturbance Observer

Seong Ho Kang and Chang Sup Kim

Department of Mechanical and
Intelligent Systems Engineering
Pusan National University,
Busan, 609-735, KOREA

Man Hyung Lee

School of Mechanical Engineering,
Pusan National University,
Busan, 609-735, KOREA

Abstract

In this paper, we propose a disturbance observer system for an instrument that is affected by regular shock. The disturbance observer uses the position error signal and a nominal model of the plant to create an estimation of the disturbance. The disturbance observer algorithm is designed to enforce robust input/output behavior by canceling the effects of disturbances and modeling errors. We apply to the filter using the binomial filter design method. The design of disturbance observer using the methods improves the performance of disturbance rejection. The effectiveness of the disturbance observer in rejecting high shock disturbances is demonstrated in simulation.

1 Introduction

Recently, robot motion control has been the important technology. It has been expected that robots help us, human beings, or that robots work in various fields instead of us. Especially, robots have been expected to work in the heavy environment where human beings can not stand, or to be active in the medical and welfare fields. In order to respond to the above expectations, teleoperation has been researched as one of the robot motion control methods[1].

Position controller is one of the important parts in robot motion control system. It mainly functions to accept command signals from the process control computer and feed-back signals from load, and output control signals to motor velocity control system so as to drive the mechanical transmission to ensure that the load tracks its target timely and precisely. It remains as a hard nut many people are trying to crack that restrict requirements are placed on input signal smoothing, motional disturbance, and system precision, stability and quick response, as well the parameters are difficult to mach with each other. The currently available position controls

mostly adopt PID control mode. PID control is effective for simple process control but limited for the targets whose parameters vary in large range or are remarkably non-linear[3]. To meet these advanced requirements, various kinds of controllers have been proposed. Disturbance observer is adaptive robust controller.

In this paper, we propose a disturbance observer system for an instrument that is affected by regular shock. The regular disturbances cause a position error of the machine. Research about reducing the position error by the disturbance has been made progress. But, it is insensibility to high shock regular vibration. So we research possible to implement a disturbance observer (DOB) in the systems that has high shock regular vibration.

This research suggest a disturbance observer for position control of a BLDC motor that is used to position control of a single-link robot arm. The system model of the motor is calculated using ADAMS. And, the parameters of the disturbance signals are 9000N of high shock and 11Hz of regular shock. Fig. 1 show disturbance signal.

2 Selection of Disturbance Observer

Among these kinds of robust motion control methods with two-loop structure, it can be said that the most popular method is the disturbance-observer (DOB)-based control. The disturbance observer uses

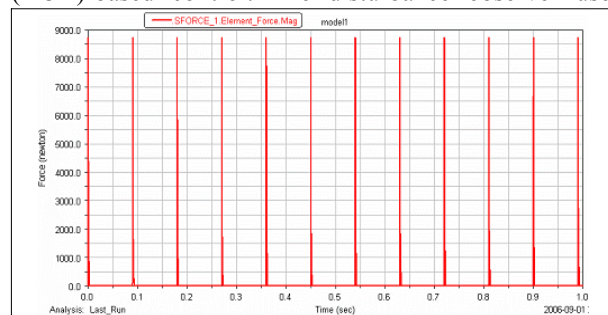


Fig.1 Disturbance

the position error signal and a nominal model of the plant to create an estimation of the disturbance. The estimation is then used to compensate for the disturbance effects.

Using the low-pass filter $Q(s)$ and the inverse of a nominal model, the DOB estimates the disturbance and the estimate signal is utilized as a disturbance cancellation input. Hence, the DOB makes the system's behavior between control input and plant output robust in the presence of uncertainties and disturbances. Fig. 2 shows the structure of the DOB. From the block diagram in Fig. 2, the plant $P(s)$ output y can be expressed in terms of the reference control input u_r , the external disturbance d_{ex} , and the measurement noise ξ

$$y = [P_n(s)u_r + P_n(s)1 - Q(s)d_{ex} - Q(s)\xi] \frac{P(s)}{X(s)} \quad (1)$$

where, $X(s) = P_n(s) + [P(s) - P_n(s)]Q(s)$, nominal model $P_n(s)$ of DOB. Below the cutoff frequency of $Q(s)$, $|Q(jw)| \approx 1$ is achieved. Hence, low-frequency disturbances are attenuated and the mismatch between the plant $P(s)$ and the nominal model $P_n(s)$ is compensated. Thus, the behavior of the real plant is to be the same as the given nominal model. On the other hand, $|Q(jw)| = 0$ is achieved above the cutoff frequency of $Q(s)$. Hence, high-frequency measurement noise is attenuated. As a result, the following observations come to light. Firstly, the most important design parameter in the DOB design is the low-pass filter Q , and secondly, the main concern is the tradeoff between making $|Q(jw)|$ small and $|1 - Q(jw)|$ small.

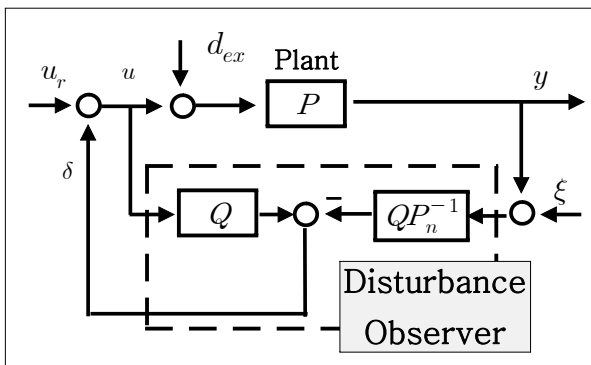


Fig.2 Disturbance Observer (DOB)

order	condition	performance
denominator m	↑	robustness ↑
numerator n	↑	disturbance rejection rate ↑
relative r	↑	robustness ↓ sensor noise ↓
time constant τ	↑	sensor noise ↓

Table.1 Factors of Q Filter

$$\sigma_{max} \triangleq \left\| \begin{bmatrix} (1-Q(s)) & (1-Q(s))P_n(s) \\ -Q(s)P_n(s)^{-1} & -Q(s) \end{bmatrix} \right\| < \gamma \quad (2)$$

DOB is made to disappear the effect of perturbation, but it doesn't mean to remove perfectly. Therefore, we need to be concerned about robustness. Since Eq(2) implies the degree of robustness of DOB system against the perturbation, we define it as “robustness measure of a DOB system” denoted by σ_{max} . Actually, there are three important factors in designing a Q filter: the filter time constant, numerator order and denominator order (or relative degree) of Q filter. Studies in [4] and [5] papers show condition and performance of each factors at Table.1.

We apply to the filter using the Binomial filter design method. The method can consider to important facts. Now, we are to use the robustness measure Eq(2) as the design method of a Q filter for second-order systems. First, we assume the Q filter of the following form:

$$Q_{mn}(s) = \frac{\sum_{i=0}^n a_{mi}(\tau s)^i}{(\tau s + 1)^m} \quad (3)$$

where τ is the filter time constant, $a_{mi} = \frac{m!}{(m-i)!i!}$ the binomial coefficient, m the denominator order and n the numerator order. Hence, $m \geq n + 2$. Second, since our system can be described by the second order transfer function, we assume that the nominal plant is given as follows:

$$P_n = \frac{k}{s^2 + 2(\zeta w_n s + w_n^2)} \quad (4)$$

where, ζ is a damping ratio, w_n the undamped natural frequency and k a constant.

In short, this technique considers the numerator order, the denominator order and relative order of the nominal plant. The disturbance rejection performance

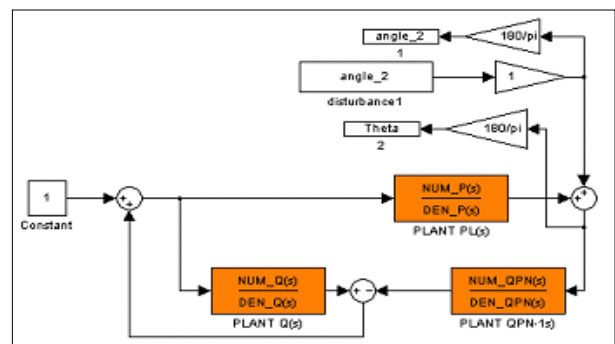


Fig.3 Structure of the simulink

of the filter depends on the numerator order and time constant. And robustness is decided by the denominator and relative order. Also, the relative order decides measurement noise reduction performance.

3 Design of DOB

Fig. 3 shows simulink at MATLAB based Fig.2 DOB. Where, Theta(2) is the Plant output and angle_2(disturbance) disturbance signal, and the system uses unit step input.

3.1 Initial environment of Q Filter

Fig. 4 depicts maximum singular values of (2) according to frequencies. The robustness measure corresponds to the maximum among maximum singular values for each Q_{mn} filter. As we suggested in Table.1, the robustness becomes better

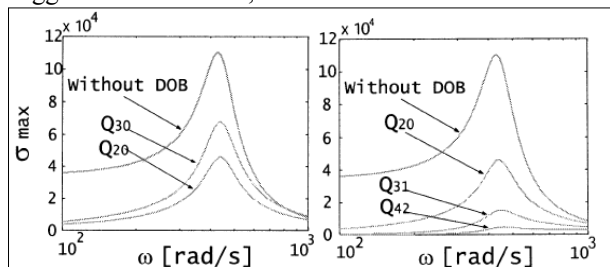
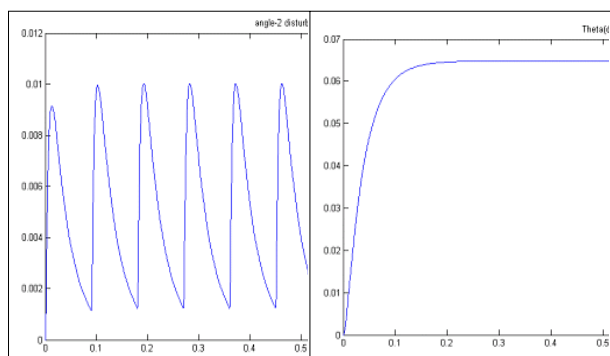


Fig. 4 Robustness comparison according to Q_{mn} filters



(a) Disturbance (b) Response without disturbance

Fig. 5 Disturbance & Response without disturbance (deg)

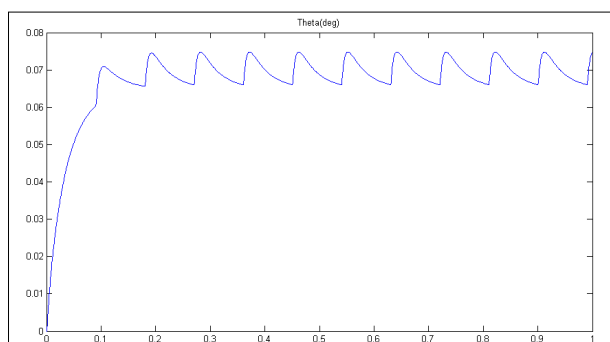


Fig. 6 Response with disturbance

as the relative degree decreases and as the denominator order increases with the same relative degree[4]. Where, the Q_{mn} filter selects Q_{42} (relative degree is two) And it proved through simulation. Fig.7 shows effect of disturbance in response without disturbance in Fig.5.

3.2 Design of Important Parameter

The system model is defined as

$$P(s) = \frac{6.19s^2 + 44.13s + 0.00006265}{s^4 + 226s^3 + 0.00001092s^2 + 0.000000219} \quad (5)$$

To decide optimum parameters of DOB, is referred Table.1 about factors effect. In order to prove performance of disturbance rejection, is used the simulink of MATLAB. It fix Q_{20} because of second-order system, find a optimum time constant τ . Fig. 7 shows results of simulation when τ change 0.0005 to 1. Where, a optimum time constant is 0.0005. And, Fig. 8 is results of simulation to decide denominate order. And optimum denominate order confirm forth-order. Finally, Fig. 9 shows results about numerator order change (τ is 0.0005, denominate order is forth-order). We can estimate optimum nominal order of second-order.

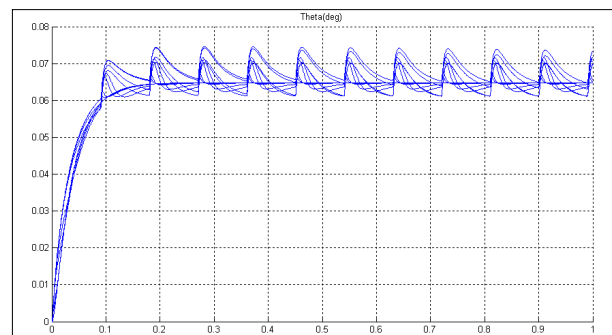


Fig.7 Response according to τ (Q_{20})
 $\tau=1, 0.5, 0.1, 0.05, 0.01, 0.005, 0.001, 0.0005$

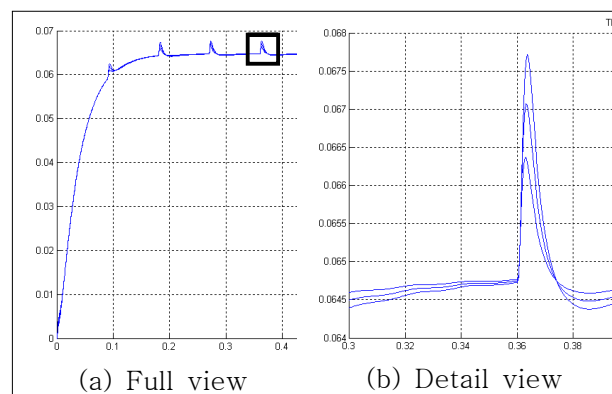


Fig. 8 Response according to d ($\tau=0.0005, n=0$)
 Rejection performance : $Q_{20} < Q_{30} < Q_{40}$

Q filter can design to simulation. In short, a time constant is 0.0005, relative order second-order, denominator order forth-order, and numerator order second-order.

3.4 Stabilization

Also, Fig. 9 shows performance of disturbance rejection. Where, output angle is changed 0.01° to 0.0005° degrees after Q_{42} filter design. Namely, disturbance rejection rate is over 95%. In order to consider degree of stability, is used to five times of disturbance. The effectiveness of the disturbance observer in rejecting high shock disturbances is demonstrated in simulation. In the Fig. 10, the simulation shows disturbance rejection performance over 95%.

4 Conclusions

This paper presents improving performance of high shock disturbance rejection. We propose a disturbance observer (DOB) system for an instrument that is affected by regular shock. To consider to important facts, apply to the filter using the Binominal filter design method. Optimum value of the Q filter parameters is found through simulation using simulink of MATLAB. In order to consider degree of stability, is used to five times of disturbance. Then demonstrates disturbance rejection

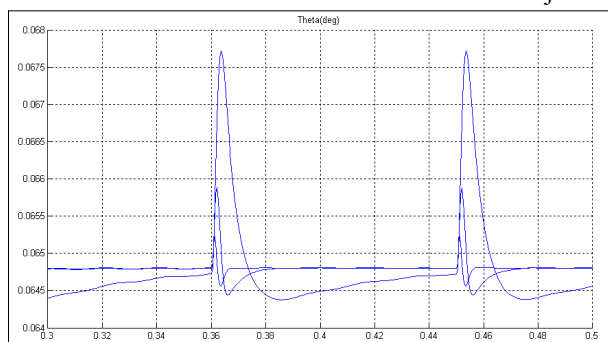


Fig. 9 Response according to numerator ($\tau=0.0005$, $d=4$)
Rejection performance : $Q_{40} < Q_{41} < Q_{42}$

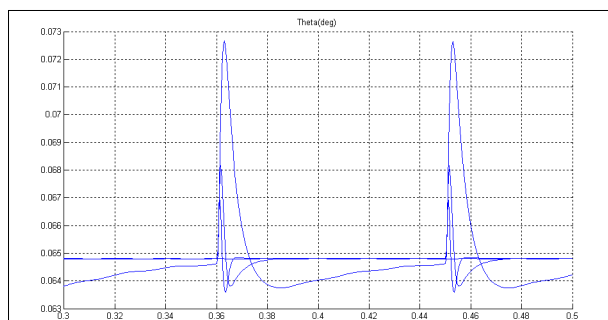


Fig. 10 Five times of disturbance
Rejection performance : $Q_{20} < Q_{31} < Q_{42}$

performance over 95%.

Acknowledgment

This work was supported by the Brain Korea 21 Project.

References

- [1] T Shimono, S Katsura, K Ohnishi, "Improvement of Operationality for Bilateral Control based on Nominal Mass Design in Disturbance Observer," *IEEE on Industrial Electronics Society*, pp. 6, 6-10 Nov. 2005 .
- [2] Seong-Ho Song, Yoon-Tae Im, Baek-Sop Kim', and Seoyong Shin, "Robust Control of Linear Systems with Nonlinear Uncertainties via Disturbance Observer Techniques," in *Proceedings IEEE Conference on Emerging Technologies and Factory Automation*, vol. 1, pp. 241-244, 16-19 Sept. 2003
- [3] Ying Zhang, Ling Cai, Qingde Meng,, Ming, Dong, "A Novel Active Disturbances Rejection Fuzzy Servo System Position Controller," *ISSCAA on Systems and Control in Aerospace and Astronautics*, pp. 5, 1st International Symposium on 19-21 Jan. 2006
- [4] Youngjin Choi, Kwangjin Yang, Wan Kyun Chung, Hong Rok Kim, Il Hong Suh, "On the robustness and performance of disturbance observers for second-order systems," *IEEE Transactions on Robotics and Automation*, vol 48, pp. 315-320, Feb. 2003.
- [5] Bong Keun Kim; Wan Kyun Chung; "Advanced Disturbance Observer Design for Mechanical Positioning Systems," *IEEE Transactions on Industrial Electronics*, vol 50, pp. 1207-1216, Dec. 2003.
- [6] H. S. Lee and M. Tomizuka, "Robust motion controller design for high accuracy positioning systems," *IEEE Transactions on Industrial Electronics*, vol. 43, pp. 48-55, Feb. 1996.

Learning landing control of indoor blimp robot for autonomous energy recharging

Yoshihiro Minagawa¹, Hidenori Kawamura¹, Masahito Yamamoto¹
Toshihiko Takaya², and Azuma Ohuchi¹

¹ Graduate School of Information Science and Technology, Hokkaido University
North 14, West 8, Kita-ku, Sapporo, Hokkaido 060-8628, Japan

E-mail : {mina, kawamura, masahito, ohuchi}@complex.eng.hokudai.ac.jp

² Ricoh Software Inc.

North 7, West 4, Kita-ku, Sapporo, Hokkaido 060-0807, Japan

E-mail : toshihiko.takaya@rsi.ricoh.co.jp

URL : <http://harmo.complex.eng.hokudai.ac.jp/>

Abstract

We report on learning landing control of autonomous energy recharging for indoor blimp robots. Indoor blimp robots have potential applications in monitoring, surveillance, and entertainment. It might be necessary for long term flight to achieve these applications,. Since blimp robots cannot load a heavy battery, it is difficult for long time flight. We focused on autonomous energy recharging to solve this problem, especially moving to the charging station, we call it landing control. We make use of learning control for landing control because of its satisfactory accuracy. The results of experiments demonstrated that learning control is effective for landing control.

key words - indoor blimp robot, autonomous energy recharging, landing, controller

1 introduction

Indoor blimp robots have the features of using buoyancy to move three dimensional movements, moving less energy, and safety in crashed compared to small air-crafts or helicopters. For these features, indoor blimp robots have enormous potential for applications such as entertainment movement, monitoring activity at high attitudes.

However they have difficulties to control because of nonlinear thrust, balloon imbalance, and air resistance, so many researches focus on control design for indoor blimp robots, such as maintaing a fixed position[1], and circular or triangle motion[3]. These control design are based on achieving applications of ahead, also it might be necessary for long periods movement. Because of payload restrict, indoor blimp robots cannot load batteries for long periods move-

ment. For long periods movement, we describe autonomous energy recharging system, especially landing control to charge battery.

2 Indoor Blimp Robot

We use columned blimp robot. Compared to ellipsoidal typed balloon, columned type balloon have the advantages of uniform air resistance for directions, moving precisely in the desired direction directly without rotation. These features might be necessary to achieve the applications for indoor blimp robots.

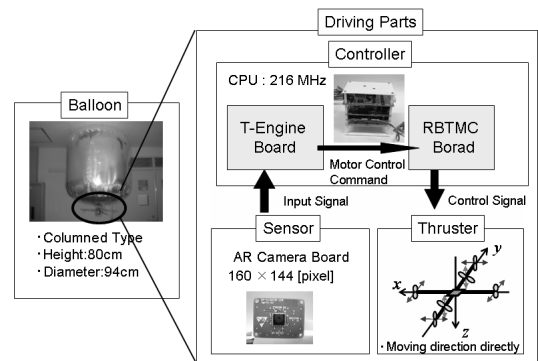


Figure 1: Overview of indoor blimp robot: balloon and control system.

Figure 1 shows a columned blimp robot and control system overview. Blimp robot consists of a balloon for enabling to float and a driving parts for moving. Driving parts consist of the controller, thrusters, and sensor.

In design of balloon, we decided on diameter as $0.94[m]$ and height as $0.8[m]$ to enable the blimp to

float by buoyancy.

The controller consists of a T-Engine board and *RBTMC* board. Image processing calculations and decisions on outputs to control the blimp are run on the T-Engine board and sent to the *RBTMC* board as control commands for propellers on thrusters. Based on control commands, the *RBTMC* board controls motors that drive propellers at a sampling time $\Delta T = 0.3[s]$, which is based on consumption time for image process and control decision.

The blimp recognizes positional information and environmental conditions through camera sensor, AR camera, which sends image data to the controller via an internal bus and is fitted on the T-Engine board. The image resolution is 160 × 144 pixels, and color information is composed of 16bit data in RGB color space.

The blimp robot has six propellers, *ch0* and *ch2* for *x*-axial movement, *ch1* and *ch3* for *y*-axial movement, and *ch4* and *ch5* for *z*-axial movement. Propeller thrust is adjusted by controlling motor rotation due to hardware constraints. We attempt to adjust thrust by switching On/Off signals controlling motor rotation.

3 Autonomous energy recharging

Autonomous recharging is the key of long periods movement and activities for mobile robots. In the research activity of 2D mobile robots, autonomous recharging are proposed [4],[5]. Many researches focus on 1)making the charging station including environment, and 2)control design to the station. In the field of 3D mobile robots, indoor or outdoor robots, these functions are required.

3.1 Environment

The left figure of Figure 2 shows the environment and charging station for indoor blimp robots. The blimp recognizes its position information from landmarks placed on ground and moves based on position information, see as [3]. The blimp moves to the two 130[cm] height poles, which set 75[cm] apart, for autonomous energy recharging, which movement called as landing control for indoor blimp robots.

The right figure of Figure 2 shows landing overview. Indoor blimp robot must move to the two-poles from the upper space. Landing control is necessary to descend straight. As landing control accurately, 1)putting plane coordinates, 2)slowing horizontal velocity, and 3)retrying docking to the station apart from

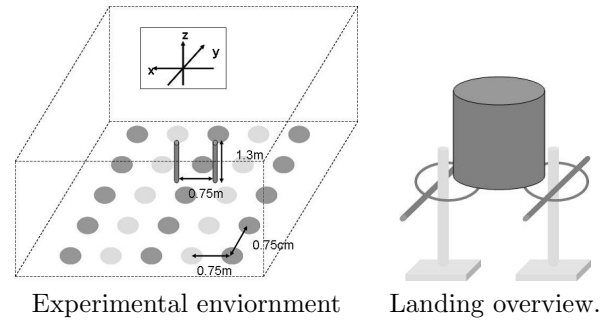


Figure 2: Experimental environment and charging station

the station, are required. The control design of the blimp robots satisfies these requirements.

3.2 Control design

It is difficult to design an analytical controller based on a dynamic model because a blimp has such nonlinear characteristics as air resistance, and inertia during movement.

Researchers have experimented with PID [3],fuzzy [6],and learning [2] controllers for blimp robots because they do not need the complex analysis required for dynamic model. We use a PID controller for movements, such as circular and triangle, and learning controller for landing control. PID controller for the blimp robot might be difficult for landing control with satisfactory accuracy in the related work [3]. Learning control has the advantages compared with PID control, such as parameters are a little and it reflects on an inertia, air resistance and temperature.

3.2.1 PID control

In our PID controller, the manipulated variable $m(t)$ is given as the ratio of the rotation time for each propeller in sampling time ΔT . The manipulated variables $m_x(t)$, $m_y(t)$, $m_z(t)$ are decided by the relative velocity from the blimp robot to the target point. The manipulated variable $m(t)$ is calculated by the relative angular. These manipulated variables are defined as follows.

$$m_x(t) = K_{Px}e_x(t) + K_{Ix}\Sigma e_x(t)\Delta T + K_{Dx}\frac{De_x}{\Delta T}$$

$$m_y(t) = K_{Py}e_y(t) + K_{Iy}\Sigma e_y(t)\Delta T + K_{Dy}\frac{De_y}{\Delta T}$$

$$m_z(t) = K_{Pz}e_z(t) + K_{Iz}\Sigma e_z(t)\Delta T + K_{Dz}\frac{De_z}{\Delta T}$$

$$m(t) = K_P e(t) + K_I \int e(t) \Delta T + K_D \frac{De(t)}{\Delta T}$$

where K_P is proportional gain, K_I is integral gain and K_D is derivative gain, and $De(t) = e(t) - e(t - \Delta T)$. Thrusts $M_0(t), \dots, M_5(t)$ generated for propellers ch_0, \dots, ch_5 are determined by using $m_x(t), m_y(t), m_z(t), m(t)$ as follows.

$$\begin{aligned} M_0(t) &= m_y(t) + m(t), & M_1(t) &= m_x(t) + m(t), \\ M_2(t) &= m_y(t) - m(t), & M_3(t) &= m_x(t) - m(t), \\ M_4(t), M_5(t) &= m_z(t). \end{aligned}$$

3.2.2 Learning control

Learning control is realized by updating the learning table, its horizontal axis is the relative distance and vertical axis is the relative velocity. The blimp robot becomes the preferable condition using learning control after updating the learning table. Figure 3 shows the overview of the learning control, where 0 is the positive rotation and 1 is the negative rotation. When the relative distance do not reach to the zero of the horizontal axis and the relative velocity gets across the zero of the vertical axis, the learning table is updated with inversion of each element. There is the possibility to update the learning table in movements to adjust the environment condition.

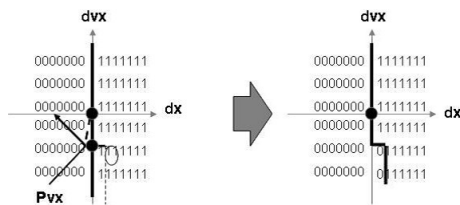


Figure 3: Overview of learning control

3.2.3 Landing area

We divide the movement area of the blimp robot into three for landing achieving with satisfactory accuracy. We consider that it is possible to land by this area division even if the blimp robot misses the desired orbit to the station. First area is that the blimp robot get near to the charging station. In this area, we make use of PID control. Second area is near the charging station, but the precision cannot be satisfied. In the second area, the blimp robot move to the upper space of the charging station by learning control to satisfy the accuracy of the landing. Third area is that the blimp robot descend to the charging station. In this area, the blimp robot is controlled by its velocity with

learning control not to break the charging station and blimp itself. If the blimp robot moves from the third area to the second area, the blimp robot moves up and retries landing.

4 Experiment

4.1 Experimental setup

In the experiment, we confirm the achievement of the landing control using learning control and the complicated motion for applications. The blimp robot moves for the square and rotational motion. After the square and rotation, the blimp robot tries the landing motion. The square motion includes basic motions for straight-line and twisting a corner. These motion can be applied to various movements for indoor blimp robot. In the square motion, the blimp robot is controlled to pass apexes on the square, 200[cm] on a side in XY -plane. The blimp robot is controlled to move 150[cm] and 250[cm] high for Z coordinate alternately on each apex. Before the rotational motion, the blimp robot moves to the target point for the landing motion. In the rotational motion, the blimp robot rotate from $\pi/2[rad]$ to $\pi/2[rad]$. The rotational motion can be applied to the autopilot and monitoring. In the landing motion, the blimp robot tries to descend to the target point its 3D coordinate $P_s = (0, 150, 120)$. Landing to the station is required accuracy, X and Y coordinate within 10[cm] from the center of the station, and yaw angular within $\pi/16[rad]$.

The blimp robot change its control from PID control to learning control after rotational motion. The experimental environment is the space in the building of University as shown Figure 2. The controllable parameters are manually set by repeated trial and error in preliminary experiments.

4.2 Result

Figure 4, 5, and 6 shows the whole motion of the blimp robot. In the square motion, the blimp robot has moved approximately along the objective orbit in XY -plane. Z coordinate movement of the blimp robot has also moved approximately, a little unstable because of the difficulty of the neutral buoyancy. In the rotational motion, the blimp robot has rotated approximately to the objective angular. In the landing motion, the blimp robot has descended to the target point P_s instantly. Also, X, Y coordinates and yaw angular are within the required precision. In another experiment, the blimp robot cannot descend to the

target point P_s instantly because of unsatisfying precision to the station. In this case, the learning control is more effective compared to instant movement because of updating its table repeatedly. We conclude that learning control is effective for landing motion from the experimental result.

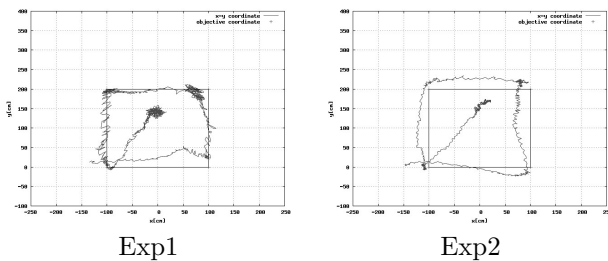


Figure 4: X-Y coordinate trajectory of the blimp robot

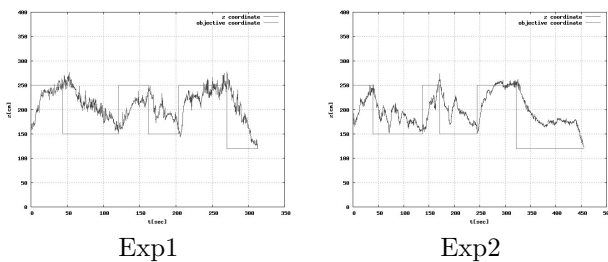


Figure 5: Z coordinate transition of the blimp robot

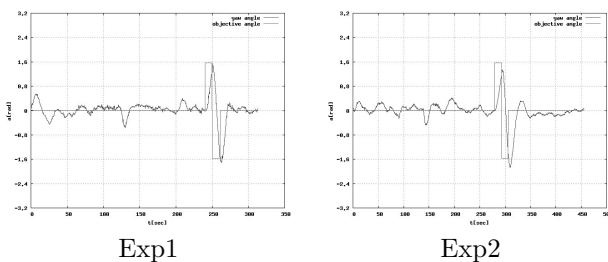


Figure 6: Yaw angle transition of the blimp robot

5 Conclusion

In this paper, we reported the learning landing control of autonomous energy recharging for indoor blimp

robot. In the experiment, we showed the motion combination of the square, rotational and landing motion. We could achieve the reliable accuracy for the landing with learning control.

In the future works, we need to configure the electrical device to charge the battery. Also, we need to achieve a less time consumption for movements to save the battery. In these functions, the blimp robot act the performances, entertainment movements, and monitoring for the long time.

Acknowledgements

We thanks Yoshikatsu Henmi, Hiroshi Murakami and Yoshihiro Uchimi of Hitachi East Japan Solutions,Ltd., and Dr Dun Wu of North Technology Co., Ltd. We also thank Masashi Yamaguchi of Cyber.Domain and Dr.Keiji Suzuki of Hakodate Future University.

References

- [1] S.Zwaan, A.Bernardino, J.Santos-Vitrol, "Visual station keeping for floating robots in unstructured environments", *Robotics and Autonomous Systems*, Vol. 39, pp. 145-155, 2002.
- [2] K.Motoyama et.al. , "Development of Autonomous Blimp Robot with Intelligent Control", *Entertainment Computing - Technologies and Applications*, pp. 191-198, Kluwer Academic Publishers, 2003.
- [3] H.Kawamura et.al., "Motion Design for Indoor Blimp Robot with PID Controller", *Journal of Robotics and Mechatronics*, Vol.17, No5, pp. 500-508, 2005.
- [4] S.Oh, A.Zenlinsky, K.Taylor, "Autonomous Battery Recharging for Indoor Mobile Robot", *Proceedings of Austrlian Conference on Robotics and Automation*, 2000.
- [5] M.C.Silverman et.al., "Staying Alive: A Docking Station for Autonomous Robot Recharging", *IEEE International Conference on Robotics and Automation*, 2002.
- [6] M.Sugisaka et.al., "Development of the Fuzzy Control for a GPS-located Airship", *Proceedings of the Tenth International Symposium on Artificial Life and Robotics*, 2005.

User-recognition system for an autonomous robot in human living environments

Yoshitaka Hane

*Graduate School of Computer Science
and System Engineering
Kyushu Institute of Technology
680-4, Iizuka City, Fukuoka, Japan, 820-8502
hane@mmcs.mse.kyutech.ac.jp*

Eiji Hayashi

*Department of Mechanical Information
Science and Technology
Kyushu Institute of Technology
680-4, Iizuka City, Fukuoka, Japan, 820-8502
haya@mse.kyutech.ac.jp*

Abstract

In this report, we describe a user-recognition system for an autonomous robot. The proposed method enables the robot to recognize the person who instructs it without placing any markers in human living environments. The system is based on differences information between some camera's images, matches the template, and recognizes color based on HSV information. The threshold can be lowered by combining features of these in formations. This system enables recognition under various environments.

A moving object is initially extracted by using the difference between frames. Next, to reduce the load, the image is narrowed to the area on which the difference is concentrated. The system matches the template and forecasts the user's position. In addition, it determines a flesh-colored area by using HSV information. When two or more people are present in the field of view, the system determines that the person with the largest-width silhouette is closest to the robot. After confirming that the person is standing still in its presence, the robot waits for the potential user to identify his or her intention to use the robot; this is signaled by the user raising his or her right hand. This process is repeated every 100 milliseconds.

1 Introduction

Due to the insufficient number of workers in Japan's low-birthrate society, autonomous self-driving robots will be called upon to provide various services within human living environments. Robots are currently used in industry, where they simply perform a given motion previously made by humans. However, such robots are less useful for tasks in the home. We are developing an autonomous personal robot with the ability to perform practical tasks in a human living environment using information derived from sensors and a knowledge database.

Our robot has a drive mechanism composed of two front wheels and two back wheels. The two front wheels are attached to the motor, which operates them independently, while the back wheels are castor wheels. DC servo motors are used for the robot's drive mechanism, and position control and speed control are achieved by means of the control system of the drive mechanism. One CCD camera is installed on the head of the

robot. It can be rotated to some sides (90 degrees to top direction, 65 degrees to lower degrees, 90 degrees to right direction, and 90 degrees to left direction) by two DC motors. This camera contains approximately 300,000 pixels. All devices are controlled by a personal computer, and electric power is supplied by lead batteries.

To work, the robot needs to receive a command from the user. The robot can be easily sent instructions from devices such as remote controls, personal computers and so on. However, this step is inconvenient. We consider that the robot should recognize human activity via its visual and auditory sensors, and thereby understand a command so that it may allow human users to act more naturally in their living environments. In light of this, we have developed a system based on images taken by the CCD camera installed in the robot aimed at determining the face of the human who has made a command. The information is passed on to the human instruction recognition system and the human tracing system.

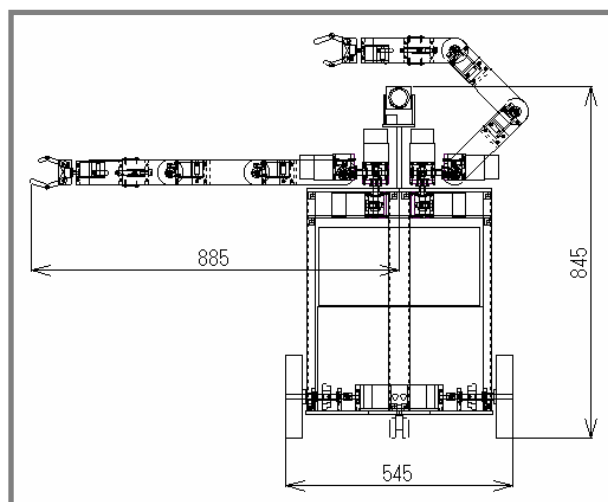


Fig.1 our developed robot

2 User-position recognition system

2.1 Outline of the system

To communicate with people, the robot must confirm the

position of people within its field of view. We have thus developed a system that can achieve position recognition. The system is informed by the fact that people move slightly even after they stop, unlike a static object. It certain moving objects from the camera image, and selects one prospective area from them. It determines whether the image is that of a human being by comparing the image with certain human characteristics. When it is judged that the image is that of a human being, this system outputs the position information.

2.2 Method for estimating distance error

By this system, we consider that this system is able to operate in real time and that it is not affected by changes in background

I. Image Acquisition

The image obtained by the CCD camera is read into a PC in the robot.

II. Processing using the difference between frames

We use the difference between frames to extract certain objects moving within the camera's view. It is hard to be affected by a change of a background. This allows this system to resist being affected by changes in background. First, our robot acquires an image via the camera and saves it. Next, it acquires a succession of images. They are compared with the first image until differences of more than a total of 2% appear. When differences of RGB color model exceed the threshold, the system determines that a difference appears. When a moving object is not detected, even if the system performs ten comparisons, it photographs the first image again. In this way, our robot acquires a binary image including a human outline (Fig.2).

III. Determining one object for range processing

The purpose of this system is to determine the position of a human face. The view does not have to be obtained unless a human being is present in the image. Therefore this system can treat an image in less view in other processes. At first, our system creates a histogram of the binary image in the lengthwise direction, the image having been acquired in the previous process, and calculates the average value of the histogram. Some smaller-than-average values are taken as noise, and they are removed. The value of the histogram at a near position is considered one block. (Fig. 3) The widest of the blocks is judged the range of the human being. By doing so, the robot recognizes the nearest human being as a user. (Fig. 4) From this point on, only the range of this image is determined.

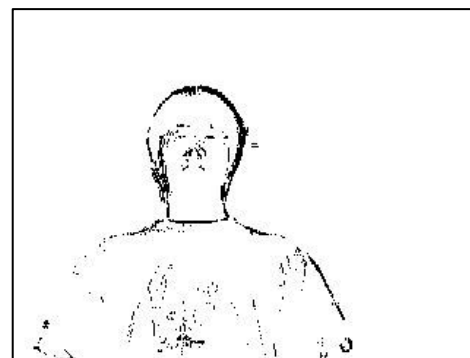


Fig.2 Difference between frames

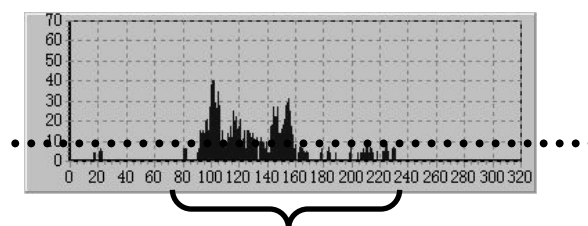


Fig.3 Lengthwise histogram of Fig2

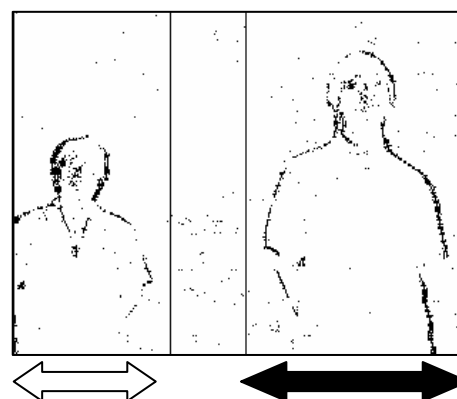


Fig.4 two human beings in view

IV. Template matching processing

When this system begins its operation, it reads the template imitating the head of a person. The outline acquired by the previous process is compared with the template. The size of the template changes according to size of the search range. Generally, this process requires a great deal of calculation time. Thus, real time operation is achieved by reducing the number of comparisons. When the matching rate is higher than the threshold and reaches its maximum, the position is output as the position of a human face.

V. Confirmation by using color information

An image is difficult to identify using only conventional processing. The system has to finally confirm that the image is that of a human being. Thus, skin color is used to ultimately determine, using the template matching process, the identity and position of the human image. In this case, color information processing uses the HSV color model.(Fig.5)

When our system performs these processes, and it is determined that the head of a person is in view, it outputs the position information. The flow of this system is shown in Figure 6.



Fig.5 Check with HSV information

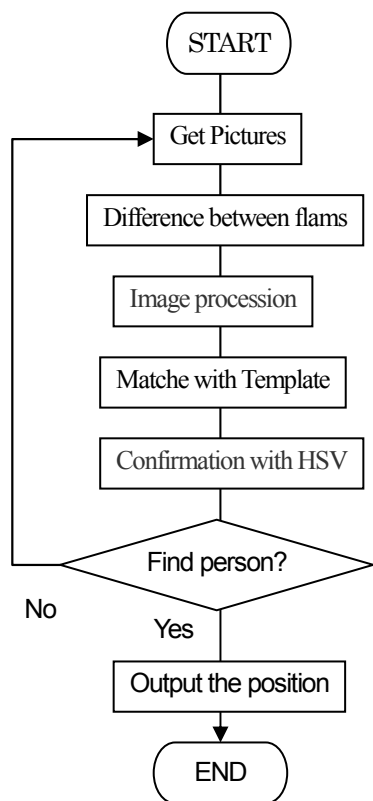


Fig.6 System flow

2.3 Experiment

The system's performance was evaluated under three conditions.

- A: One person under normal lighting
- B: Two person s under normal lighting
- C: One person under strong lighting

The strong lighting condition in case C was a fluorescent light placed above the robot's head, coming into view when the robot turns its head upward. The experiments were conducted in a conventional human living environment.

In case A, this system was seen to operate effectively. In case B, it was able to identify a person and follow him or her throughout the field of view, but could not continue following the particular person and irregularly shifts its focus from object to object. In case C, the system has a slight difficulty in identifying the person's color, so the robot's ability to follow the person under this condition deteriorates. (Fig.7)

We consider that these results demonstrate that the system can detect a person and follow him or her in a human living environment.



(A)



(B)



(C)

Fig.7 Experiment

3. Sign recognition system

3.1 Outline of the system

The user-position recognition system outputs the position of a person within the robot's field of view. However, the robot has to determine whether the person requests it. We created a rule in which the human operator, after the robot's face (camera) turns in a person's direction, must raise his or her right arm to the side of the face. After confirming the signal, the system recognizes the human being as the user.

3.2 Method of sign recognition

The robot recognizes a humans' position by repeatedly using the user-position recognition system. When these outputs show values close to one another's, it is determined that the person is a generally fixed position. The robot then initiates the sign recognition system. First, the system establishes a recognition range beside a human face and saves the image. The system photographs the range in succession again. The image is compared with an image obtained at the beginning of the process. In the range, when differences exist within the range and the user's skin color is detected, the system identifies the user's signal.

3.3 Method for the first position of the arm recognition

As soon as this robot recognizes the sign from the user, this system gets the first position of the hand. The difference image between before and after raising the user's right hand in prior process is cleared away the small noise by the Closing and Opening methods. Next, this system puts labels on left pixel blocks, judges the biggest blocks as the palm of hand, and erases the other small blocks. The slope of the palm is calculated with the next model. (Fig.8, 9, 10, Formula (1), (2))

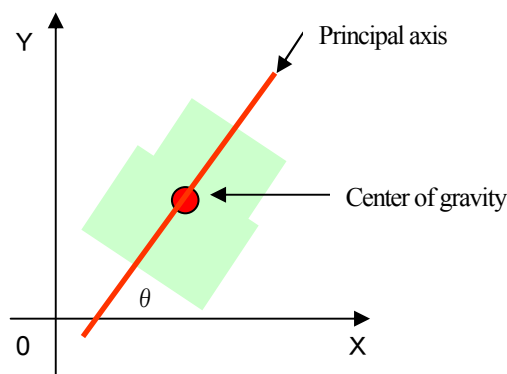


Fig.8 Principal axis

$$(1) M(p, q) = \sum_{i, j} i^p j^q$$

Formula (1) is for calculating "moment feature". The "i" and "j" are each position on the x-axis and the y-axis.

$$(2) \tan^2 \theta + \frac{M(2,0) - M(0,2)}{M(1,1)} \tan \theta - 1 = 0$$

Formula (2) is for calculating the slope of the principal axis. When this formula is used, the center of gravity has to move to the origin of the coordinates.



Fig.9 Recognition a signal from user

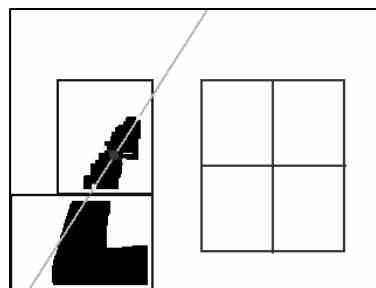


Fig.10 Different image of the right hand

4. Conclusions

We have proposed a system, composed of an ocellus camera and for use in a indoor environment, that extracts a human's position from a field of view and determines whether the human requires use of the robot. This system constitutes an opening of communication between a robot and a human being.

Our next subject of study is the development of a system for tracking the movement of a human arm using an initial value as the position of the right arm which the sign recognition system outputted. The robot will communicate with people effectively by identifying the direction of the human arm and acting upon it.

References

- [1] Toru Azuma, Yoshihiro Takenaga, Eiji Hayashi, Development of a self-driven personal robot, Artificial Life and Robotics (AROB 8th '03), pp.1-3, Oita, Japan, 2003

Development of a Robot Following a Human Using Color Information

Kouichi Tsugimura, Joo Kooi Tan, Seiji Ishikawa
Department of Control Engineering,
Kyushu Institute of Technology, Sensuicho 1-1,
Tobata, Kitakyushu 804-8550, Japan
{tugimura, etheltan, ishikawa}@ss10.cntl.kyutech.ac.jp

Abstract

Carrying luggage is one of the daily tasks done in our life. It is tight work to carry heavy luggage especially for senior people. This research pays attention to helping those senior people carrying luggage by a mobile robot. The robot developed in this research aims at carrying luggage and following the possessor. Therefore, the person whose luggage is carried by the robot does not need to tell the destination to the robot. The person is also possible to stop on the way freely. The extraction method of a person that the user specifies, the following method of the person, and the control method of a mobile robot using captured images are described in this paper. The effectiveness of the developed robot is examined by the experiment performed on the corridor in the building. Some results are shown and discussion is given.

Keywords: Mobile robots, human support, color tracking, robot vision

1. INTRODUCTION

When a person becomes aged, assistance in a daily life is needed because the body becomes weak. However, vivid life can be achieved as long as there is assistance to him/her. Recently, senior citizen's ratio has increased in Japan. Therefore, the number of those who need assistance is increasing, whereas the number of those who can provide assistance is decreasing. Then, the development of a robot which assists the function of a human body becomes more and more important. Operation of carrying luggage is one of popular tasks done in our daily life. This research pays attention to helping senior people by carrying their luggage.

A robot system is proposed in this paper which finds a person who has luggage, approaches to the person, and carries the luggage in place of him/her, if he/she hopes to do so. The robot follows the person to his/her destination. Therefore, the person does not need to tell the robot his/her destination. He/she is also possible to stop on the way freely. The system structure is explained along with the algorithms and experimental results are shown.

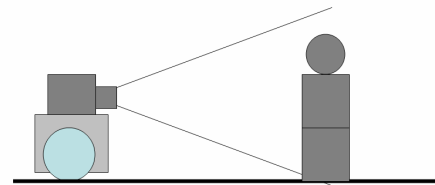


Fig. 1 A robot system

2. ALGORITHM

2.1 A luggage carrying robot system

First of all, the size of the luggage carrying robot is explained. The robot is unsuitable for carrying luggage if it is small. On the other hand, the user may feel the pressure if it is too big. Therefore, a robot of the height almost equal to the chest of an adult is introduced in this research. (Fig. 1)

2.2 Particle filter

The particle filter [1] is used in this research to track a particular person. The particle filter is an approximated probability distribution by a weighted sample set

$$S = \left\{ \left(s^{(n)}, \pi^{(n)} \mid n = 1 \dots N \right) \right\} \quad (1)$$

s : hypothetical state

π : probability

n : particle number

Particle filter has many advantages for tracking objects as they are robust to partial occlusion and change in shape.

2.3 Setting of the center position of an object

A method is explained for the reduction of the influence of occlusion by the change in the distance of the object interested.

When the distance between the robot and the object is farther as shown in Fig. 2(a), the camera view is given by Fig. 3(a), whereas, when the distance is nearer as in Fig. 2(b), the view becomes the one depicted in Fig. 3(b). Therefore occlusion occurs when the object is nearer.

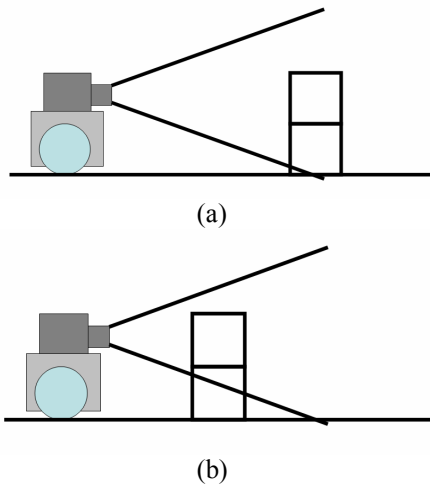


Fig. 2 Robot and an object

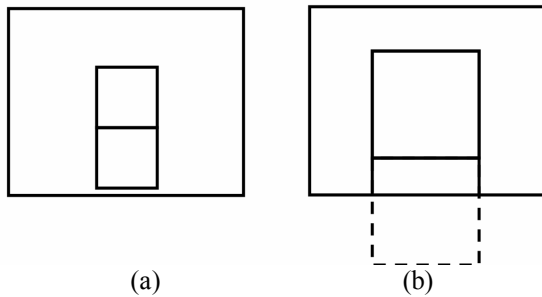


Fig. 3 Camera view

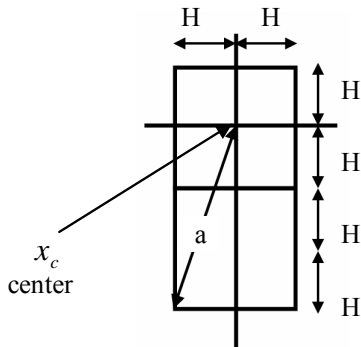


Fig.4 Shape of an object

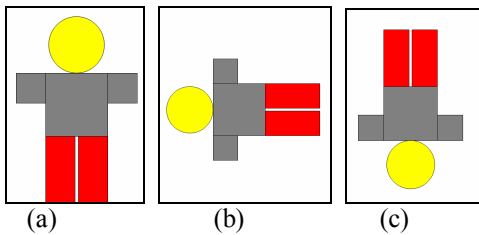


Fig.5 Walking posture

To solve this difficulty, emphasis is placed on the upper part of a human body, which is realized by using a kernel centered at the center of the upper body (See Fig.4).

In this particular study, Epanechnikov Kernel [2] defined as follows is used as a kernel.

$$k(r) = \begin{cases} \frac{1}{2} c_d^{-1} (d+2)(1-r) & \text{if } r < 1 \\ 0 & \text{otherwise} \end{cases} \quad (2)$$

d : dimension

c_d : volume of the unit d -dimensional sphere

2.4 Division of a histogram

The robot follows a walking person. The walking posture is given in Fig. 5(a). It does not become those postures given in Fig. 5(b) or (c). Therefore the top and the bottom information of a person can be used.

The region of a person is divided into an upper part and a lower part as shown in Fig. 6. The upper half of the body is given a label 0, and the lower half of the body is given a label 1. With each part, position $x \equiv (x, y)$ has the HSV values and the label, which makes a quadruple. If H, S and V are digitized into H, S and V levels, respectively, they make $H \times S \times V \times 2 \equiv M$ bins. These bins are numbered and denoted by $h(x)$.

The influence of light is reduced by using the HSV color model. Therefore, M bins considering the two positions labeled 0 and 1 and the HSV color space is employed in this research.

The distribution model $p(x_c) = \{p(x_c)^{(u)}\}_{u=1 \dots M}$ at the center x_c is defined with each part as follows;

$$p(x_c)^{(u)} = f \sum_{i=1}^I k\left(\frac{\|x_c - x_i\|}{a}\right) \delta[h(x_i) - u] \quad (3)$$

δ : Kronecker delta function

u : the bin number

$$f = \frac{1}{\sum_{i=1}^I k\left(\frac{\|x_c - x_i\|}{a}\right)} \quad (4)$$

The parameter I is the number of all the coordinates in the squared region.

The Bhattacharyya coefficient ρ is used for the calculation of the agreement between two distributions $p(x)$ and $q(x)$, which is defined by

$$\rho[p, q] = \sum_{u=1}^M \sqrt{p^{(u)} q^{(u)}} \quad (5)$$

q : the target model

The coefficient ρ approaches 1 when the difference is small.

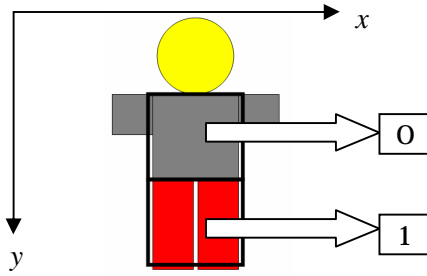


Fig. 6 Histogram division

2.5 Observation model

The shape of an object is expressed in two squares in this research. The hypothetical state is expressed by the expression given in the form of

$$\mathbf{s} = \{x, y, \dot{x}, \dot{y}, H\}. \quad (6)$$

x, y : location of the center

\dot{x}, \dot{y} : motion

H : length

The transition of the object at time t is expressed by the state.

$$\mathbf{s}_t = \mathbf{A}\mathbf{s}_{t-1} + \mathbf{w}_{t-1}. \quad (7)$$

\mathbf{A} : deterministic component

\mathbf{w}_{t-1} : stochastic component

A present state is inferred from the previous state by matrix \mathbf{A} , and the noise is added by vector \mathbf{w} .

Parameter a used in the kernel of Eq.(3) is computed by

$$a = \sqrt{H^2 + (3H)^2} \quad (8)$$

The weight which uses the Bhattacharyya coefficient is converted into the probability by Eq.(9).

$$\pi^{(n)} = \frac{1}{\sqrt{2\pi}} e^{-\frac{(1-\rho[p(s^{(n)}), q])}{2\sigma^2}} \quad (9)$$

Finally the position of the object is decided by taking the average of the state as follows;

$$E(S) = \sum_{n=1}^N \pi^{(n)} \mathbf{s}^{(n)} \quad (10)$$

S : hypothetical state

π : probability

n : particle number

2.6 Mobile robot control

A camera has been installed in the developed mobile robot. We need two control strategies; one for the camera and the other for the mobile robot.

2.6.1 Camera control

The camera moves right to left to track an object. Speed of the camera is changed by the proportional control so that it captures the object at the center of the visual plane. The strategy is formulated as follows;

$$\dot{d}_c = p_c (x_t - x_c) \quad (11)$$

\dot{d}_c : speed of camera

p_c : proportion constant

x_t : object position

x_c : image center

2.6.2 Mobile robot control

The control of the mobile robot consists of the speed control and the control of the steering wheel. The speed is controlled so that the width of the object may become constant in the captured image. The view angle of the object is calculated from its position in the image and the angle of the camera.

The speed of the robot is controlled by the following formula;

$$s_r = p_{r1}(H_p - 2H) + i_{r1} \sum (H_p - 2H) \quad (12)$$

s_r : speed of robot

H_p : width of target

p_{r1} : proportion constant

i_{r1} : integration constant

On the other hand, the steering wheel is controlled by the following formula;

$$d_r = p_{r2}\theta + i_{r2} \sum \theta. \quad (13)$$

d_r : steering wheel angle

θ : angle of object

p_{r2} : proportion constant

i_{r2} : integration constant

3. COMPOSITION of THE SYSTEM

A person following robot system developed in this research is composed of a single camera, a video capture device, a note PC (Pentium M, 1.6GHz), and a mobile robot. The entire equipment is built on the mobile robot using a single frame of approximately 0.85 meter high. Overview of the system is given in Fig.7.

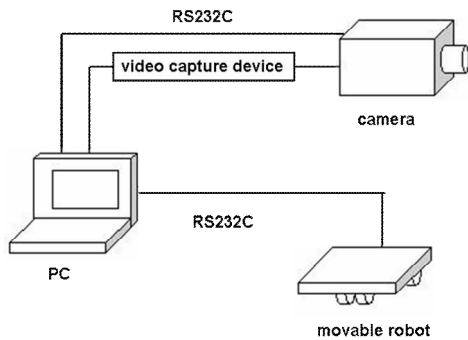


Fig. 7 Composition of the system

4. EXPERIMENTAL RESULTS

4.1 Performance of human tracking

A person wearing a light jacket with dark blue check pattern and a black pair of trousers is captured in a double green square window and the region is tracked as the person moves. The experimental result of the tracking is shown in Fig. 8.

4.2 Person following

We performed the experiment on person following indoors using the developed robot system. An image containing a target person was taken initially and his clothes were registered manually to the system. Then, according to the target person walking away on the corridor, the robot followed him capturing his images. The performance is shown in Fig. 9. The robot followed just behind a person keeping the distance constant.

5. CONCLUSIONS

In this research, a robot system was developed for following a person and carrying luggage. A satisfactory result was obtained by the experiment. However, there are some problems that the illumination and the background sometimes give negative influence to the person following because the proposed technique only uses color information. Uemura et al. [3] proposed a color region tracking technique robust to illumination change. The technique may be employed in the present system. The interactive nature of the robot system is also going to be improved to realize various robot activities.

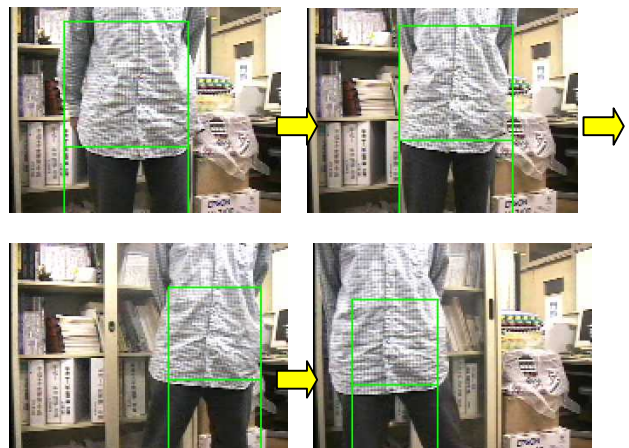


Fig. 8 Result on human tracking



Fig. 9 The robot following a specified person

REFERENCES

- [1] K. Nummiaro, E. Koller-Meier, L. V. Gool: "A color-based particle filter", *Proc. First Int. Work. on Generative-Model-Based Vision*, vol.1, pp.53-60(2002).
- [2] D. Comaniciu, V. Ramesh, P. Meer: "Real-time tracking of non-rigid objects using mean shift", *IEE E Conf. on Comput. Vision and Pattern Recogn.*, vol. 2, pp.142-149 (2000).
- [3] H.Uemura, J.K. Tan, S.Ishikawa:"A color tracker employing a two-dimensional color histogram under unstable illumination", *Proc. SICE-ICASE Int. Joint Conf. 2006*, pp.2725-2728 (Oct., 2006).

Development of a self-care robot -Study of automatic holding of object using Robotic arm-

Hisatoshi Henta

Graduate School of Computer Science
and System Engineering
Kyushu Institute of Technology
680-4, Kawazu, Iizuka City, Fukuoka, Japan, 820-8502
henta@greenall.i.ccr.kyutech.ac.jp

Eiji Hayashi

Department of Mechanical Information
Science and Technology
Kyushu Institute of Technology
680-4, Kawazu, Iizuka City, Fukuoka, Japan, 820-8502
haya@mse.kyutech.ac.jp

Abstract

This paper describes the development of a self-care support robot, developed to support elderly people with mobility problems. The Kitasap2 consists of a host computer and the physical body of a robot equipped with a robotic arm. The two are connected by a wireless LAN. The robotic arm has six degrees of freedom and is equipped with a robotic hand having three fingers. This paper describes the development of the ability of the robotic arm to hold and transport an object so as to reduce the user's operational load. It is necessary that such an operation be based on easily given instructions from the user. Therefore, we have developed systems in which selection and the recognition of the object are carried out using images provided by an omni-directional camera and a CCD camera.

1 . Introduction

Currently, the birthrate in Japan continues to decline, while the proportion of elderly people increases. As the population of older people increases, so does the number of elderly with mobility problems. In the near future, we will see an increased burden placed on attendants of the elderly as a result of the falling birthrate. The quality of life of the immobile elderly could be improved by assistance from a robot capable of doing housework. The development of a "self-care support robot" that supports an elderly person's independence can help to decrease a helper's workload.

We have developed the self-care support robot Kitasap2 and exhibited it in the "Prototype Robot Exhibition" at

Aichi Expo 2005. Kitasap2 was developed through a commission from NEDO (New Energy and Industrial Technology Development Organization).

This paper describes the development of the ability of the robotic arm to hold and transport an object so as to reduce the user's operational load.

It is necessary that such an operation be based on easily given instructions from the user. Therefore, we have developed systems in which selection and the recognition of the object are carried out using images provided by an omni-directional camera and a CCD camera.

2 . System Architecture

The Kitasap2 consists of a host computer and the physical body of a robot equipped with a robotic arm. The two are connected through a wireless LAN. The robotic arm has six degrees of freedom and is equipped with a robotic hand having three fingers. The robot also has various sensors, including an omni-directional camera (at the top of the robot), a small CCD camera (inside the robotic hand), a laser range sensor, and some encoders.

All of the robot's devices are controlled by the computer. Lithium-ion batteries supply the robot's electric power.

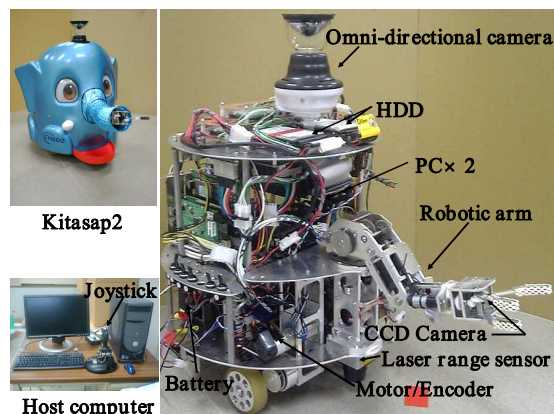


Fig. 1 Overview of the Robot system

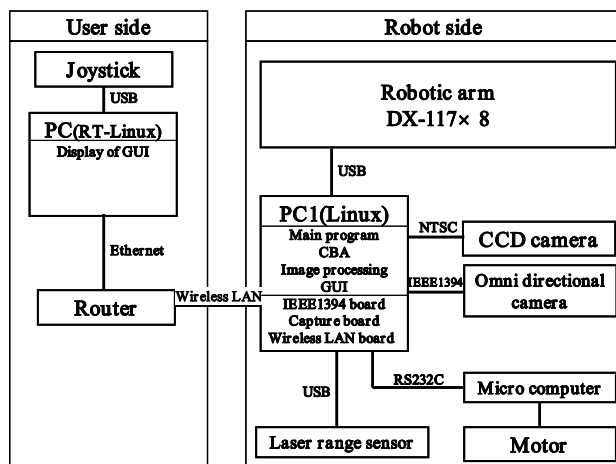


Fig. 2 System Structure of the robot

3 . Robotic arm

3.1 Structure of the Robotic arm

Many degrees of freedom are required for the robotic arm to hold an object automatically. So far, it has been necessary to move the physical body of the robot in order to hold an object because its degree of freedom was not sufficient.

Recently, we produced a robot arm that has six degrees of freedom and a total length of 450 millimeters, and we mounted it on Kitasap2. Fig. 1 shows a comparison between the old and new robotic arms.

The robotic arm is equipped with a robotic hand having three fingers. Each finger has two joints and can grab objects like a human finger. Moreover, a CCD camera that is used to recognize an object is mounted inside the robotic hand.

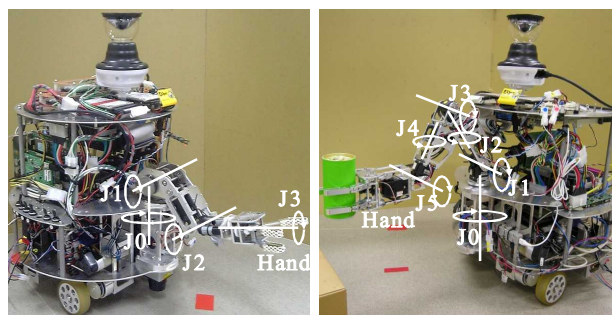


Fig. 3 Comparison between old and new robotic arm

3.2 The Actuator

We adopted the actuator "Dynamixel DX-117," made by ROBOTIS, to provide the power for each joint of the robotic arm. The DX-117 is an actuator composed of a microcomputer, motor, gears and an angle sensor.

Moreover, because this actuator uses RS485 for the communication method, the actuator for each joint is connected as a multidrop link. For this reason, the actuator's wiring can be simple. Specifically, this is because the control calculation for the angle of each joint can be done on the actuator side by using the DX-117. Previously, this calculation had been done on the PC side, requiring that the load of the calculation be large.

3.3 Kinematics

To perform the calculation processing easily, the calculation of the inverse kinematics of the robotic arm was carried out according to the following method.

The wrist of the robotic arm moves up and down in a vertical direction and extends and retracts horizontally while the position of the wrist remains horizontal. Moreover, the robotic arm rotates around the J0 axis.

The calculation involves, first, subtracting the length of the wrist from the point of the fingers (X_e, Z_e), to give the point of the wrist joint (X_6, Z_6). Next, we draw a circle whose center is located at point2 (X_2, Z_2), with its radius being equal to the length of link A. Next, we draw a circle whose center is located at point 6 (X_6, Z_6) with its radius being equal to the length of link B.

Finally, we decide on the point of the elbow joint (X_4, Z_4) and the angle of each joint of the arm.

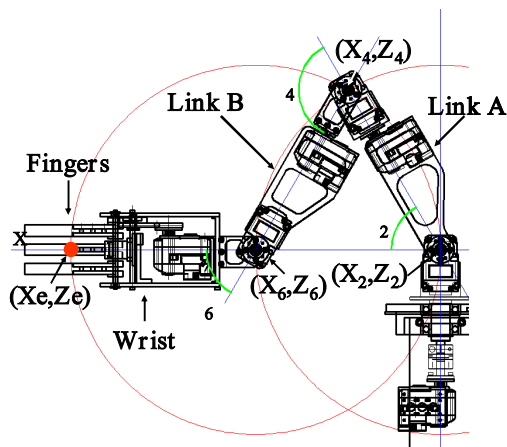


Fig. 4 Kinematics

4 . The automatic holding system

In this system, we first select the object whose image is obtained by the omni-directional camera. Next, the object is recognized based on the CCD image. This allows the robotic arm to be adjusted automatically and to automatically grasp the object.

4.1 System for selecting the object

This system uses the image obtained from a perspective projection conversion from the omni-directional image obtained by the omni-directional camera.

First, the object is displayed like the image shown in Fig. 5(L) when it is put front of the robot. The user selects the object he wants to hold by clicking its image. Then, the system gets pixel information (RGB data) from the clicked point and memorizes the color information about the object. Finally, this color information is converted into HSV data.

4.2 System for recognizing the object

This system uses the image obtained by the CCD camera and the color information about the object. First, the object is displayed like the image shown in Fig. 5(C). Next, all pixel data about the image is converted into HSV data and compared with the color information about the object. Then, a group of pixels similar to the color of the object is recognized as the object. Next, the center

position of the recognized object and image are displayed on the image, as shown in Fig. 5(R).

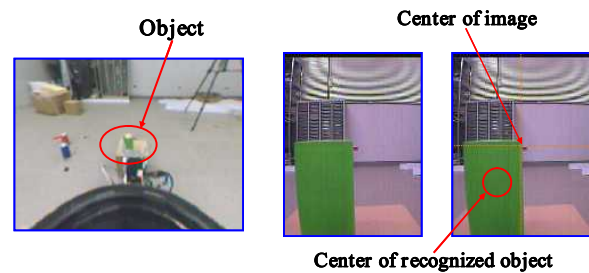


Fig. 5 The image obtained by the omni-directional camera (L) and the image obtained by CCD camera (C),(R).

4.3 Automatic holding

When the object is selected and recognized, the angles of the robotic arm's joints are adjusted automatically.

First, when the object is put in front of the robot, the robotic arm's position is as shown in Fig. 6. Then, the robotic arm is adjusted to the center position of the recognized object, corresponding to the center of the image supplied by the CCD camera. (Fig. 6) Next, the hand is extended horizontally, and the object is grasped by the robot. Finally, the fingers close tightly, and the holding operation is completed (Fig. 6).

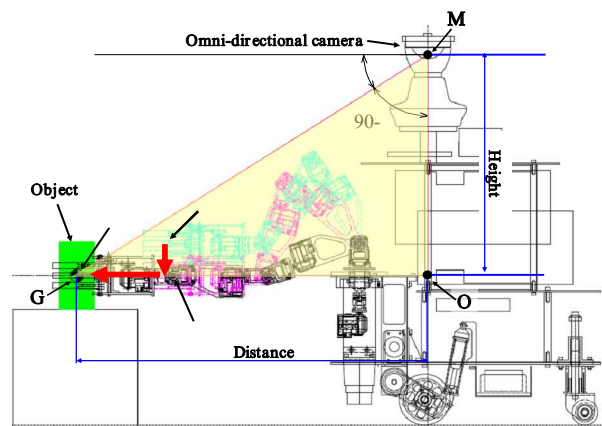


Fig. 6 Automatic holding

5 . Experiment

The experimental environment is shown in Fig. 7(a). The object is put in front of the robot, where is displayed like the images shown in Fig. 7(b),(c). We directed the

arm to hold the green object that was put in front of the robot.

First, the robotic arm was adjusted to the center position of the recognized object, corresponding to the center of the image supplied by the CCD camera. The wrist of the robotic arm moved up and down in a vertical direction while its position remained horizontal. Next, the robotic arm rotated around the J0 axis. Fig. 8 shows the change in the image when the robotic arm automatically adjusted.

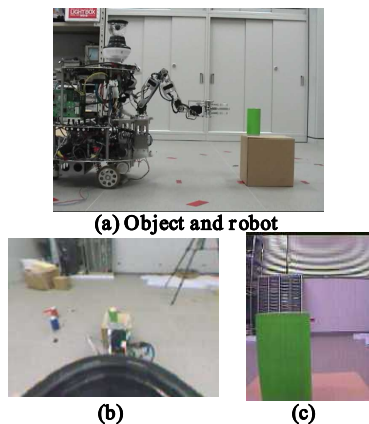


Fig. 7 Experimental environment

Fig. 9 shows the appearance of the experiment while the object was being held. The robotic arm as it adjusted to the center position of the recognized object is shown in images (1) to (3). Next, the arm's appearance when the wrist was extended and held the object is shown in images (4) to (6). Finally, the arm's appearance when the fingers are closed tightly and the robotic arm returns to its original position is shown in images (7) to (9).

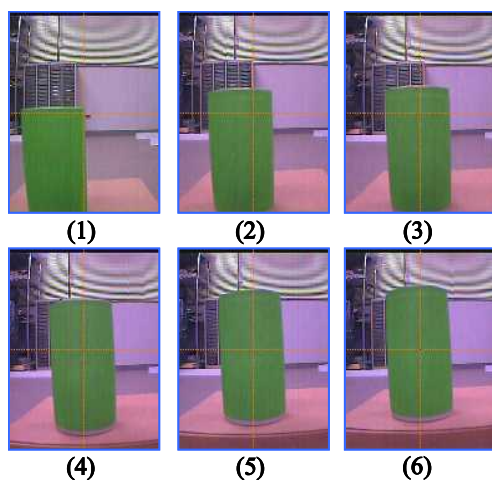


Fig. 8 Center correction

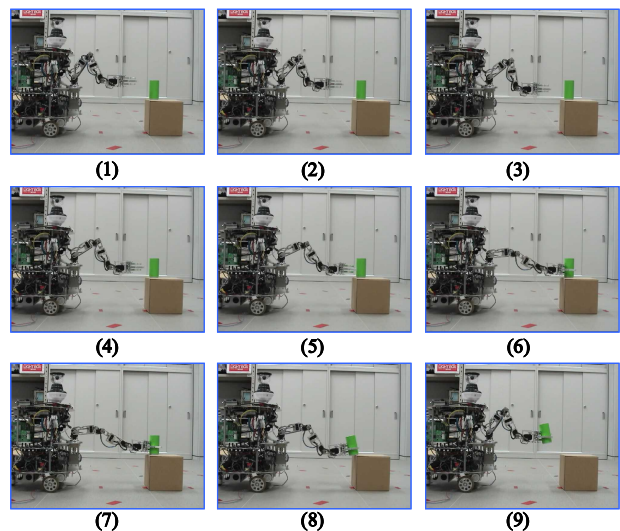


Fig. 9 Experiment of automatic holding of the object

6 . Conclusion

We have developed a system for a robotic arm that automatically holds an object in order to reduce a user's operational load.

The developed system is able to select and recognize an object in an image obtained by an omni-directional camera and a CCD camera. In addition, the robotic arm can be adjusted automatically to grasp the object.

Our next subject of study will be to develop another method for the recognition of the object.

Acknowledgment

The authors would like to acknowledge the advice and assistance of Professor Tadashi Kitamura of Kyushu Institute of Technology who died in 2006.

References

- [1] Kazumasa Yamazawa, Yoshio Onoe, Naokazu Yokoya, and Haruo Takemura: "Telepresence by Real-Time View-Dependent Image Generation from Omnidirectional Images", Systems and Computers in Japan, Vol.31, No.6, pp.56-64 (2000.6).

Adaptive Control of a Looper-like Robot based on the CPG-Actor-Critic Method

Kenji Makino* Yutaka Nakamura† Tomohiro Shibata* Shin Ishii*

* Graduate School of Information Science
Nara Institute of Science and Technology (NAIST)
8916-5 Takayama-cho, Ikoma, Nara 630-0192, Japan
† Graduate School of Engineering, Osaka University
Yamadaoka 2-1, Suita, Osaka, 565-0871, Japan

Abstract

Adaptability to the environment is crucial for mobile robots, because the circumstance, including the body of the robot, may change. A robot with a large number of degrees of freedom possesses potential to adapt to such circumstances, but it is difficult to design a good controller for such a robot. We previously proposed a reinforcement learning (RL) method called the CPG-actor-critic method, and applied it to automatic acquisition of vermicular locomotion of a looper-like robot through computer simulations. In this study, we developed a looper-like robot and apply our RL method to the control of this robot. Experimental results demonstrate fast acquisition of a vermicular forward motion, supporting the real applicability of our method.

1 introduction

To realize a mobile robot that acts in a real environment, adaptability to changes in the environment due to its dynamic nature and various disturbances is necessary. Reinforcement Learning (RL) is a framework for autonomous acquisition of control rules and has been successfully applied to various automatic control problems [1]. Because real robots often have a large number of degrees of freedom (DOF), RL methods to control them need some devices to avoid the problem of "curse of dimensionality".

Motivated by the animal's control mechanism for rhythmic locomotion, which is induced by neural circuits in the spinal cord of vertebrates called central pattern generators (CPGs), robot control schemes using a CPG controller have been studied mainly in the field of robotics [2][3]. Because the parameter of the CPG controller is designed such that the CPG controller and the robot interact with each other and are

eventually entrained into a stable limit-cycle attractor, the robot controlled by a CPG controller is robust against possible disturbances from the environment.

Although there have been some studies of designing a CPG controller, autonomous learning framework for a CPG controller is necessary to realize the adaptability to dynamic nature of the environment including its own body. We formerly proposed an RL framework called the CPG-actor-critic model for designing a CPG controller [4]. Since control signals are restricted to be rhythmic in favor of the CPG, this RL method would be able to avoid "curse of dimensionality". In this method, the parameter of the CPG controller is updated according to the gradient of the performance indicator, the average reward per step for example, with respect to the parameter (policy gradient) and this gradient can be obtained by interaction with the environment. After learning, the CPG controller becomes to generate stable locomotion suited to the environment surrounding the robot.

In the current study, we configure a real looper-like robot and its CPG controller. Because a looper has an ability to move by many of simple and rhythmic telescopic motions, a looper-like robot would have an adaptability to various environments. In our previous study, we showed through computer simulations that a good CPG controller can be obtained by the CPG-actor-critic method [5]. In real environments, however, there may arise much difficulty; e.g., it is difficult to approximate contact between the robot and ground, outputs of sensors generally include unknown noise and time delays. In this study, we apply the CPG-actor-critic method to the real looper-like robot we have developed, for achieving automatic acquisition of "vermicular" locomotion.

2 Robot System

Looper-like robot

The looper-like robot we have developed is depicted in Fig.1. This robot is composed by three links, eight actuators and six passive wheels. The first to fourth actuators are linear actuators which are each located between two links, and used to expand-and-contract the body of the robot. We call these actuators **body actuators**. The length of these actuators is about 13cm at minimum and about 18cm at maximum. Black semicircles in Fig.1 denote the ball joint, so that the body of the robot bends when lengths of these actuators are different from one another. The fifth to eighth actuators are also linear actuators which are located to the head or tail link. They move vertically to clamp corresponding links to the ground. We call these actuators **leg actuators**.

In order to make the robot move forward, it is required to repeat expand-and-contract motions, by clamping the head link and the tail link in an appropriate but different timing.

CPG controller

Because a looper-like robot has a substantial potential to move by a rhythmic locomotion, we employ a CPG controller [5] which outputs rhythmic control signals. As shown in Fig. 2, the CPG controller comprises three neural oscillators each of which consists of two neurons, and each actuator is controlled by a single neural oscillator. The $(2i - 1)$ -th and the $2i$ -th neuron's dynamics are defined as

$$\begin{aligned} \frac{1}{c} \dot{y}_{2i-1} &= -y_{2i-1} + \tanh(W^S y_{2i-1} + W^I y_{2i} + u_i) \\ \frac{1}{c} \dot{y}_{2i} &= -y_{2i} + \tanh(-W^I y_{2i-1} + W^S y_{2i}) \end{aligned}, \quad (1)$$

where y_{2i-1} and y_{2i} denote the $(2i - 1)$ -th and the $2i$ -th neuron's states, respectively. W^S , W^I and c are the self-excitatory connection weight, the mutual inhibitory connection weight and the time constant, respectively. u_i is an input to the i -th neural oscillator, in this study, calculated as the weighted sum of the robot's state variable x and the output of the CPG controller y : as $u_i = \theta_j y_0 + \dots + \theta_k x_0 + \dots$. Each neural oscillator outputs sinusoidal control wave whose amplitude and frequency are mainly determined by W^S and W^I , and c , respectively. The phase relation between the neural oscillators and the robot are determined by the input to the CPG neurons \mathbf{u} , i.e., the phase can be tuned by changing the weight parameter θ of the CPG. In this study, this weight parameter θ is trained by the CPG-actor-critic method (see below).

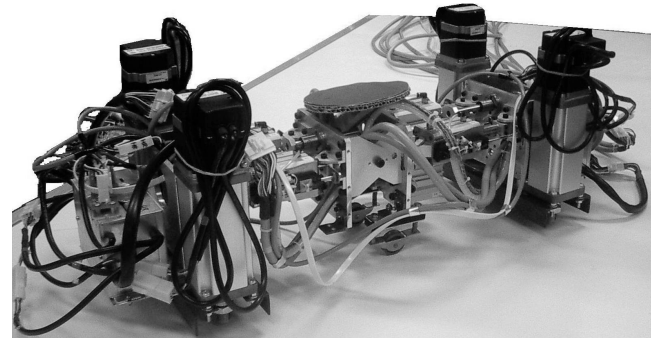
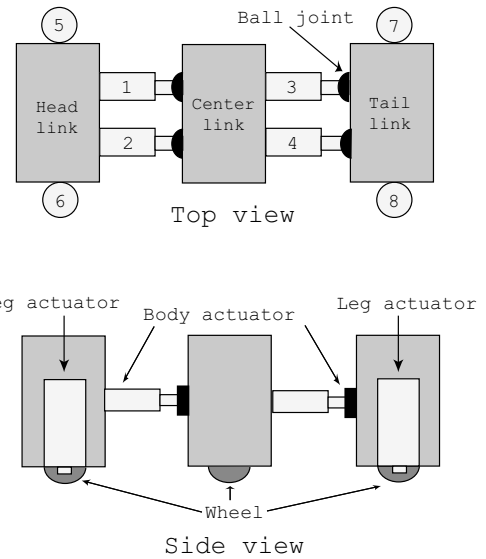


Figure 1: Looper-like robot

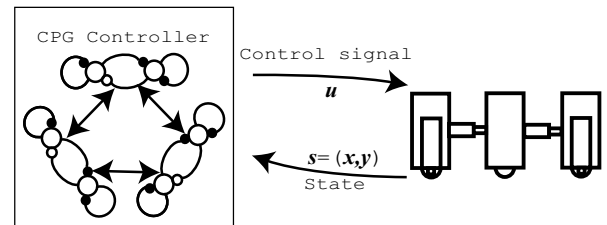


Figure 2: Control scheme using a CPG controller

3 Learning method

Here, we describe our RL algorithm for the CPG controller, which we formerly proposed and called the CPG-actor-critic model [5]. In this controlling by a CPG controller, the control signal depends not only on the state of the target system, but also its own state, because the CPG controller has its own dynamics. This is problematic because most RL algorithms assume the target policy is stationary (time-

independent), and furthermore, heavy computation would be required for training recurrent neural networks like the naive CPG controller. In order to overcome these difficulties, the CPG controller is divided into two parts, the basic CPG and the actor [4]. The basic CPG is a part of the CPG controller with fixed connection parameters, i.e., W^I , W^S , and c are fixed. We treat the physical system and the basic CPG as a single dynamical system to control, and we call this system a CPG-coupled system.

Since the actor turns out to be a feed-forward neural network having no its own dynamics in the CPG-coupled system, we can easily apply usual RL algorithms. The control signal \mathbf{u} for the CPG-coupled system is conceptually represented as

$$\mathbf{u} \sim \pi(\mathbf{u}, \mathbf{s}), \quad (2)$$

where π denotes the control policy of the actor and $\mathbf{s} \equiv (\mathbf{x}, \mathbf{y})$ is a state of the CPG-coupled system. For the sake of simplicity, we assume that Eqs. (1) and (2) are discretized in time by an appropriate method, and the learning system receives an immediate reward $r(\mathbf{s}(t), \mathbf{u}(t))$ at a discrete time step t . The policy $\pi_{\theta}(\mathbf{s}, \mathbf{u})$ is defined by a parametric stochastic policy, i.e., the probability of a control signal \mathbf{u} at a state \mathbf{s} is given by $p(\mathbf{u}|\mathbf{s}; \theta)$, where θ is a parameter vector of the policy. The objective of RL here is to obtain the policy parameter that maximizes the expected reward accumulation defined by $\rho(\theta) \equiv \mathbf{E}_{\theta}[\sum_t \gamma^{t-1} r(\mathbf{s}(t), \mathbf{u}(t))]$, where $\gamma \in (0, 1]$ is a discount factor. The partial differential of $\rho(\theta)$ with respect to the policy parameter θ_i is calculated [6][7] as

$$\frac{\partial \rho(\theta)}{\partial \theta_i} = \langle \psi_i(\mathbf{s}, \mathbf{u}) Q_{\theta}(\mathbf{s}, \mathbf{u}) \rangle, \quad (3)$$

where $\psi_i(\mathbf{s}, \mathbf{u}) \equiv \frac{\partial}{\partial \theta_i} \ln \pi_{\theta}$ and $Q_{\theta}(\mathbf{s}, \mathbf{u})$ denotes the action-value function (Q -function). $\langle \cdot \rangle$ stands for the expectation with respect to the stationary distribution of the state-action pair (\mathbf{s}, \mathbf{u}) . When the Q -function is approximated by a weighted sum of base functions $\psi : Q_{\theta}^w(\mathbf{s}, \mathbf{u}) \equiv \sum_i w_i \psi_i(\mathbf{s}, \mathbf{u})$, where \mathbf{w} is the weight vector of the approximate Q -function, the optimal weight in the least square sense, $\tilde{\mathbf{w}} = \arg \min_{\mathbf{w}} \langle (Q_{\theta}(\mathbf{s}, \mathbf{u}) - Q_{\theta}^w(\mathbf{s}, \mathbf{u}))^2 \rangle$, provides the natural policy gradient with no estimation bias for the gradient, so that the policy parameter can be updated [1] as

$$\theta_i := \theta_i + \eta \tilde{w}_i, \quad (4)$$

where η is the learning rate. the optimal weight $\tilde{\mathbf{w}}$ is thus estimated simultaneously based on the least square method [4][1].

4 Experiment

Setup

The aim of the experiment have is to examine if our RL can be applied to a real looper-like robot, we then conducted an experiment attempt to obtain a controller which allows the looper-like robot to move in the forward direction. For the simplicity of the experiment setting, all **body actuators** were controlled by a single neural oscillator, and front **leg actuators** (5-th and 6-th actuators) and hinder **leg actuators** (7-th and 8-th actuators) were controlled by a single neural oscillators, respectively. The output signal τ to these actuators is defined by

$$\tau_i = \begin{cases} 1, & y_{2i-1} > 0 \\ 0, & \text{otherwise} \end{cases}.$$

When $\tau_i = 1(0)$, the corresponding actuator expands (contracts). The control signal \mathbf{u} to the CPG-coupled system is defined by

$$\begin{aligned} u_1 &= \theta_1 X_1 + \theta_2 X_2 + \epsilon_1 \\ u_2 &= \theta_3 y_1 + \theta_4 y_2 + \epsilon_2, \\ u_3 &= \theta_5 y_1 + \theta_6 y_2 + \epsilon_3 \end{aligned} \quad (5)$$

where $\mathbf{X} = \{x_2 - x_3 - l, \dot{x}_2 - \dot{x}_3\}$, x_2 and x_3 denote the position of the head link and that of the tail link, respectively. $\epsilon_i (i = 1, 2, 3)$ is a small random noise obeying a normal distribution. l denotes the mean length between the head link and the tail link. The policy parameter θ determines phase relations among the robot and the neural oscillators and was adjusted by RL. W^S , W^I , and c which are CPG system parameters were fixed at 1.1, 0.7, and 4.0, respectively.

The immediate reward $r(\mathbf{s}(t))$ was given by

$$r(\mathbf{s}(t)) = \dot{x}_1,$$

where x_1 denote the position of the center link. Because the robot currently possesses no sensors to measure its position, an USB camera is placed above the experimental field.

We chose the state representation for RL as follows. Because the phase portrait between two neurons presents a circle whose center is the origin, the angle $\omega_1 = \arctan(y_2/y_1)$ carries the essential feature of the first neural oscillator. Similarly, $\omega_2 = \arctan(y_4/y_3)$ and $\omega_3 = \arctan(y_6/y_5)$ should be useful features of the second and the third neural oscillators, respectively. Furthermore, when the looper-like robot repeats expansion and contraction, $\omega_4 = \arctan((\dot{x}_3 - \dot{x}_2)/(x_3 - x_2))$ is also an important feature of the robot's movements. Because the phase difference seemed to be more important than the phase

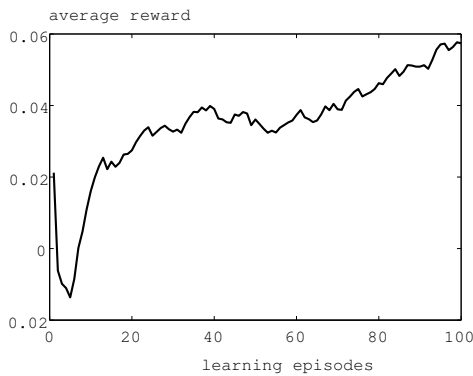


Figure 3: Learning curve. The horizontal axis denotes the number of learning episodes, and the vertical axis denotes the average reward in one episode. The line shows the moving average over 30 episodes.

in this experiment, we employed 49 basis functions for the approximate state-value function: $\phi_{16(i-2)+j}(\mathbf{s}) = \exp(-3 \cos(\omega_i - \omega_1 + \pi/16j) - 1)$ for $i = 2, 3, 4$ and $j = 1, 2, \dots, 16$ and $\phi_{49} = 1$. At the beginning of an episode, the learning parameter was initialized at random: $\theta = \{0.0006, 0.0001, 0.0012, -0.0005, -0.0004, 0.0011\}$. In each episode during the training, the robot was controlled by the current actor for 45 sec.

Result

Fig.4 shows the learning curve, indicating that appropriate control was achieved after about 10 training episodes. Fig.5 shows actual movements of the looper-like robot before learning and after learning(after 100 learning episodes). Before learning, the robot accidentally moved backward first, and then started to move forward slowly. After learning in contrast, the robot became to move forward much faster. After the learning 100 episodes, the CPG parameters grew as: $\theta = \{0.0007, -0.0064, -0.0027, -0.0011, -0.0102, 0.0017\}$.

5 Conclusion

In this study, we have configured a CPG-based control architecture for a real looper-like robot, and applied RL to obtain a controller for the robot to move in the forward direction. The experiments showed that a good CPG controller for this robot can be efficiently obtained by our RL method. Applying our RL method to many other situations including changes in the ground condition and changes in its body, for example, is our future work.

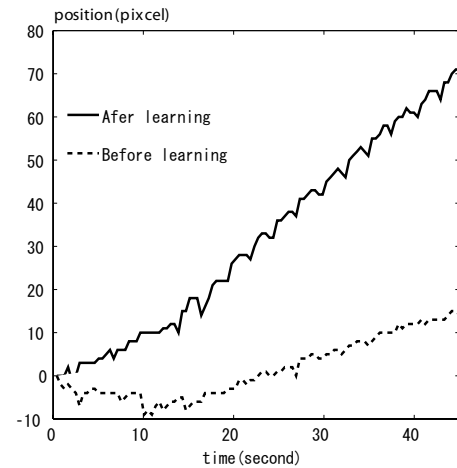


Figure 4: Control result, showing the location of the position of the robot's center.

References

- [1] J. Peters, S. Vijayakumar and S. Schaal: "Reinforcement learning for humanoid robotics", Third IEEE International Conference on Humanoid Robotics 2003, Germany (2003).
- [2] G. Taga, Y. Yamaguchi and H. Shimizu: "Self-organized control of bipedal locomotion by neural oscillators in unpredictable environment", *Biological Cybernetics*, 65, pp. 147.159 (1991).
- [3] Y. Fukuoka, H. Kimura and A. H. Cohen: "Adaptive dynamic walking of a quadruped robot on irregular terrain based on biological concepts", *International Journal of Robotics Research*, 22, 3.4, pp. 187.202 (2003).
- [4] Y. Nakamura, T. Mori and S. Ishii: *International conference on parallel problem solving from nature (PPSN VIII)*, pp. 972.981 (2004).
- [5] Y. Nakamura, T. Mori, S. Ishii: "Natural policy gradient reinforcement learning method for a looper-like robot", *International Symposium on Artificial Life and Robotics (AROB 11th '06)*, GS3-3. (2006)
- [6] V. R. Konda and J. N. Tsitsiklis: "Actor-critic algorithms", *SIAM Journal on Control and Optimization*, 42, 4, pp. 1143.1146 (2003).
- [7] R. S. Sutton, D. McAllester, S. Singh and Y. Manour: "Policy gradient method for reinforcement learning with function approximation", *Advances in Neural Information Processing Systems*, Vol. 12, pp. 1057.1063 (2000).

Explorations in evolutionary humanoid robotics.

Malachy Eaton

Department of Computer Science and Information Systems,
College of Informatics, University of Limerick, Ireland
email: malachy.eaton@ul.ie

Keywords: *Evolutionary computation, Humanoid robotics*

Abstract:

The field of evolutionary humanoid robotics is a branch of evolutionary robotics specifically dealing with the application of evolutionary principles to humanoid robot design. Previous studies [1,2] demonstrated the possible future potential of this approach by evolving walking behaviours for simulated humanoid robots with up to 20 degrees of freedom. In this paper we extend the work presented in the previous publications in several ways. We present preliminary results in the analysis of the behaviour of specific high-fitness evolved controllers and of the evolutionary process itself by examining the changes in diversity over time in the evolutionary process.

We then investigate the effect of minor alterations in robot morphology in walking ability. These include an alteration of the surface area of the robot in contact with the ground (foot size) and the effect of the immobilization of individual joint or joints in the robot. The latter study may be of potential future use in prosthetic design.

We explore also the possibility of the evolution of humanoid robots which can cope with different environmental conditions. These include reduced ground friction (ice) and modified gravitation (moon walking).

Finally we present initial results in the implementation of our simulated humanoid robots in hardware using the Bioloid robotic platform.

Introduction

The humanoid robot is simulated using the Webots mobile robot simulation package [3,4,5]. This system allows for the creation and modification of a large variety of robot types and robot worlds and it also allows for the creation of controllers for these robots. It also employs an accurate physics simulator allowing for the potential transfer of evolved

robots from simulation to real embodied robots with little or no modification.

A number of keyframe values are defined and then passed to a separate existing utility; the sequence manager. These keyframes are values that must be reached at a specific point in the movement. An interpolation function in the sequence manager then fills in the motor values between individual keyframes. Every keyframe must be passed through in turn; once the final frame is reached the cycle repeats. A genetic algorithm is used to provide the values for the individual keyframes. The initial fitness function employed was a simple function mainly based on the robot remaining standing together with the distance traveled by the robot in a forward direction. Different varieties of walking behaviours were developed by the evolved robots and many observers commented of the lifelike nature of some of the walks developed.

Nolfi and Floreano provide a good introduction to the general topic of evolutionary robotics [6]. For a discussion on the general topic of the performance evaluation of bio-inspired embodied and simulated artifacts Eaton et al [7]. See references [8-11] for other work in this general area.

Experimental setup

In previous experiments it was found that the proportion of the maximum range of movement allowed to the robot for each joint was an important factor in evolving successful Initial experiments placed no restriction on the range of movement allowed and walks did not evolve unless the robot was restricted to a stooped posture and a symmetrical gait, even then results were not impressive. In these experiments we include a value in the genome that specifies the fraction of the maximum movement range that is allowed for each joint. The genome length is 336 bits comprising 4 bits determining the position of the 20 motors for each of 4 keyframes; 80 strings are used

per generation. 16 bits define the fraction of the maximum movement range allowed. The maximum range allowed for a particular genome is the value specified in the corresponding to each motor divided by the number of bits set in this 16-bit field, plus 1, divided by 2. The genetic algorithm uses roulette wheel selection with elitism; the top string being guaranteed safe passage to the next generation, together with standard crossover and mutation. Two-point crossover is applied with a probability of 0.5 and the probability of a bit being mutated is 0.04. These values were arrived at after some experimentation.

In order to gain some insight into the evolutionary process we use a slightly modified version of the degree of population diversity described in by Leung et al [12]. This measure provides an easy to calculate and useful measure of population diversity: i.e. how alike the different strings in a population. We subtract this value from the genome bit length to produce our inverse degree of population diversity measure (IDOPD). This value will vary from 0 (no similarity in the strings) to a value corresponding to the genome length (all genomes have the same value at every bit location).

Evolution of walking in a robot with full functionality

Figure 1 shows the maximum and average fitness values together with the diversity measure described above, for a 20 degree of freedom robot with full functionality, and with 16 bits defining the maximum joint range. The 20 degrees of freedom comprise three for each leg (knee and two ankle joints), three for each hip, two for the back (twist and bend), two for each shoulder, and two elbow joints. The graph shows results as averaged over three runs and the fitness function is as described previously [2]. Diversity value is given on the right-hand vertical axis. The diversity value starts very low initially (corresponding to low similarity) as we would expect, as all strings are initially created at random. Sharp increases in the diversity measure correspond then to increases in maximum fitness as highly fit individuals attempt to make many copies of themselves. This is followed by a reduction thereafter as the genetic operators of mutation and crossover strive to maintain diversity in the population.

A fitness above about 800 should correspond to a reasonable walk in the forward direction, 1200 or above corresponding to stable walks in the forward direction. We see that the average

maximum value peaks at around the value 3000, corresponding to a fast forward walk, with the knees kept fairly straight.

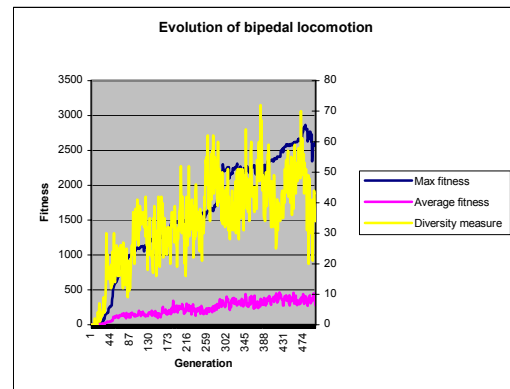


Figure 1. Evolution of walking in a fully functional robot

Effect of alterations in robot morphology

We now investigate the effect of restraining motion in part of the robot. We do this by immobilising the robots right knee joint, and both ankle joints. This might correspond to a situation of a person walking with a prosthetic leg. Figure 3 shows the results of this experiment again averaged over 3 runs

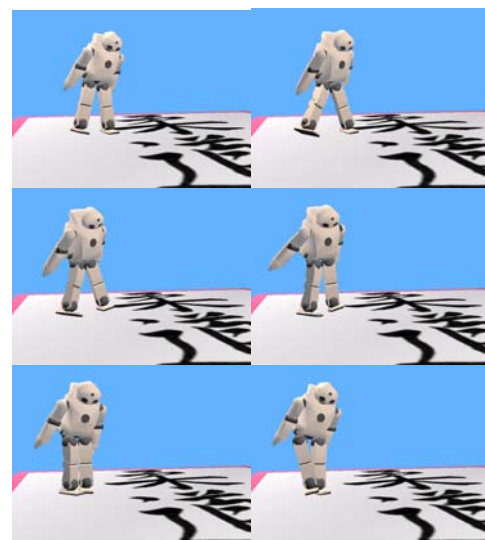


Figure 2. Walking with right leg restrained

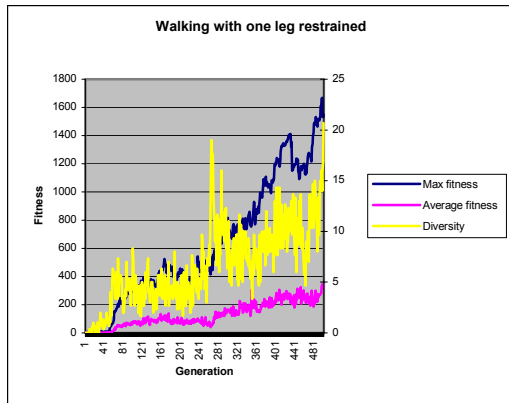


Figure 3. Average of three runs with right leg restrained

The robot learns to walk albeit with a reduced maximum fitness compared to the robot with no constraints. Figure 2 illustrates a typical walk which develops. The right (constrained) leg moves sideways and forwards, coming well off the ground, as the right arm moves backwards in a steady motion. The left leg follows in a shuffling motion, and the cycle repeats. This pattern of motion proved surprisingly effective. We have also experimented with the alteration in foot size successfully producing walking with much reduced foot size but space precludes a detailed discussion of these results.

Effect of different environmental conditions

We are currently investigating the effect that different environmental conditions have on the evolution of walking (skating) behaviour; specifically walking on a surface with reduced friction, simulating icy conditions, and walking under conditions of reduced gravity. Fig. 4 shows the effect of reducing coulomb friction to 0.01, simulating the effect of very icy conditions. This is for a single run so the variation of diversity with fitness can be clearly seen. A quite effective sideways skating motion develops around generation 150. Further investigations are continuing to see what different patterns of skating develop. We have also started experiments in moon-like gravity producing walking, but far slower than in earth-like gravity; these results will be discussed in more detail in a later article.

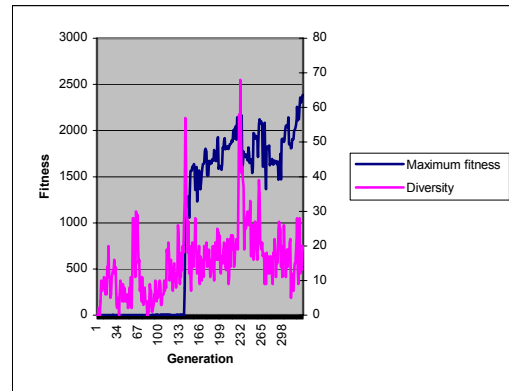


Figure 4. Results for reduced friction run

From simulation to reality

We are now beginning work to implement our simulated robots in the real world using the Bioloid robot platform. This platform is produced by Robotis Inc. Korea and consists of a CPU (CM-5), a number of senso-motoric actuators (Dynamixel AX12+) and a large number of universal frame construction pieces. Using this platform it is possible to construct a wide variety of robots, from simple wheeled robots to complex humanoid robots with many degrees of freedom. To gain initial experience with this kit we constructed a “puppy-bot” (Fig. 5) which can walk on four legs, avoid obstacles and perform several cute tricks. With this experience we then constructed the Bioloid humanoid robot (Fig. 6), which has 18 degrees of freedom in total. A modified version of this humanoid robot was used for Humanoid Team Humboldt in the RoboCup competitions in Bremen 2006. [13]

The Bioloid system has two pieces of software provided; the behaviour control programmer, and the motion editor. The behaviour control programmer programs the humanoids response to different environmental stimuli, while the motion editor describes individual motions based on the keyframe concept described in our work. We are currently building an accurate model of the Bioloid humanoid in Webots, and working on translating the information in our sequence control file into a format understandable by the Bioloid motion editor. Once this work is completed we hope to evolve walking, and other behaviours, in Webots using our accurate model, and then transfer the evolved behaviour directly to the Bioloid humanoid robot.

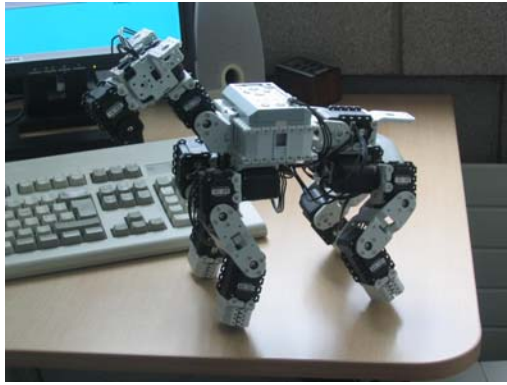


Figure 5. The “puppy-bot”



Figure 6. The Bioloid humanoid robot

Summary and future work

Using an accurate physics simulator a humanoid robot has evolved bipedal locomotion under a variety of different morphological constraints and under different environmental conditions. We have looked at the changes in diversity over the evolutionary process and at the behaviour of evolved robots. Finally we introduced the Bioloid robotic platform, which because of its modular and extensible nature is well suited to research in evolutionary robotics, and the 18 DOF Bioloid humanoid robot. Work is continuing in all of the areas described above, and particularly in moving our simulated humanoid robots into the real world using an enhanced (20 DOF) version of the Bioloid humanoid robot.

References:

[1] Eaton M, Davitt T.J. (2006) “Automatic evolution of bipedal locomotion in a simulated humanoid robot with many degrees of freedom” in *Proceedings of the 11th International Symposium on Artificial Life and*

Robotics”, Jan 23-25,2006, Japan, pp. 448-451.

[2] Eaton M. (2006) “Evolutionary humanoid robotics: first steps towards autonomy?” in *50th Anniversary Summit of Artificial Intelligence: Summit Proceedings*, Monte Verita, Switzerland, July 9-14 2006.

[3] Michel O. (2004), “Webots: Professional Mobile Robot Simulation”, *International Journal of Advanced Robotic Systems*, Vol. 1, No. 1, pages 39-42.

[4] Webots. <http://www.cyberbotics.com>. Commercial Mobile Robot Simulation Software.

[5] Mojon S (2003) “Realization of a Physics Simulation for a Biped Robot” Semester project, School of Computer and Communication Sciences EPFL, Switzerland 2003.

[6] Nolfi S, Floreano D.(2000) “Evolutionary Robotics: The Biology, Intelligence, and Technology of Self-Organizing Machines”. MIT press, 2000.

[7] Eaton M, Collins JJ, Sheehan L (2001), “Towards a benchmarking framework for research into bio-inspired hardware-software artefacts”, in *Artificial Life and Robotics*, Vol. 5 No. 1, 2001 pp. 40-46.

[8] Sellers W, Dennis L, Wang W et al(2004) “Evaluating alternative gait strategies using evolutionary robotics” *J. Anat* (2004) Vol 204, pp343-351.

[9] Collins S, Ruina A, Tedrake R et al(2005) “Efficient bipedal robots based on passive-dynamic walkers” *Science* Vol. 307, Feb. 2005, pp. 1082-1085.

[10] Zykov V, Bongard J, Lipson H (2004) “Evolving Dynamic Gaits on a Physical Robot” *Proceedings of Genetic and Evolutionary Computation Conference*, Late Breaking Paper, GECCO'04, 2004

[11] Boeing A, Hanham S, Braunl T (2004) “Evolving autonomous biped control from simulation to reality” in *Proc. 2nd International Conference on Autonomous Robots and Agents* December 13-15, 2004, pp. 440-445.

[12] Leung Y, Gao Y, Xu Zong-Ben (1997) “Degree of population diversity – a perspective on premature convergence in genetic algorithms and its Markov chain analysis”, *IEEE Transactions on Neural Networks*, Vol.8, No.5 pp.1165-1176.

[13] Hild M, Jungel M, Spranger M(2006) “Humanoid team Humboldt team description 2006” in *Proceedings CD Robocup 2006*, Springer-Verlag, Bremen, Germany, June 2006.

Vision based control for line following blimp robot

Ryouta Nishioka*, Hidenori Kawamura*, Masahito Yamamoto*
Toshihiko Takaya**, Azuma Ohuchi*

* Graduate School of Information Science and Technology, Hokkaido University
North 14, West 8, Kita-ku, Sapporo, Hokkaido 060-8628, Japan
E-mail : {nishioka, kawamura, masahito, ohuchi}@complex.eng.hokudai.ac.jp

** Ricoh Software Inc.
North 7, West 4, Kita-ku, Sapporo, Hokkaido 060-0807, Japan
E-mail : toshihiko.takaya@rsi.ricoh.co.jp
URL : <http://harmo.complex.eng.hokudai.ac.jp/>

Abstract

We report on following the line based on camera image for indoor blimp robot. Indoor blimp robot can be moved to the altitude and the place with differences in the building. There are applications of the guide and the round in the building by using those features. It is generable target orbit to put the one that becomes a landmark on the moved place. Therefore, we put the line as a landmark. The line is showing flat information in the target orbit, and information on height can be obtained according to the width of the line. In this paper, we report the extraction method of the line, and how to follow the line.

key words - indoor blimp robot, following line, autonomous robot

1 Introduction

The blimp robot can be moved to the altitude and the place with differences in the building, it is an advantage for blimp robot that the place to which the robot of a humanoid type is not moved easily can be moved. Moreover, it is possible to move safely in the building compared with a small airplane and the helicopter, etc. and use to the applications like the guide in the building, the round and the watch are thought by using of such a feature.[1] There is a problem of enlarging the balloon to obtain big buoyancy, so it is difficult to use a lot of sensors. Moreover, the control is difficult because the influence of inertia is large, and it sensitively reacts to turbulence by movement of air-conditioning and the person on an environmental inside.

It is needed to make it follow to the generation of the target orbit and the orbit to achieve such an ap-

plication. It is moved to the target point recognizing a three-dimensional position of an environmental inside by using the landmark in a research up to now. However, the target orbits on the plane can be given by closely arranging the landmark in the moving place in the application that moves only a specific indoor place. Then, it aims to move to the target point to assume the landmark to be a line, to give the target orbits, and to make on the orbits follow in research. The line is an easy landmark that expresses the target orbits, and the height of the target orbits is recognized from the width of the line. Because the calculation cost of this is lower than the method such as putting the sign on the line, it is thought the control way is effective in the place where the turbulence that rotates by 180 degrees momentarily does not occur.

In this paper, the composition of the balloon robot used, the extraction method of the line, and how to decide to thrust are described as follows.

2 Blimp robot

Blimp robot has an elliptical body to reduce air resistance. These airships are generated by high-speed movement. However, it is not necessary important for indoor blimp robots to generate high-speed movement. So we designed a columned blimp robot.[1][2][3] This design can make air resistance in the direction of movement equal. And the column type can greatly take the volume. And, it is preferable the airframe's without turning when thinking a narrow indoor space is moved to be able to move directly. This blimp robot has three propulsion units.Ch4 is enabled vertical movement, and ch0, ch1, ch2 and ch3 are enabled dimensional horizontal plane movement.

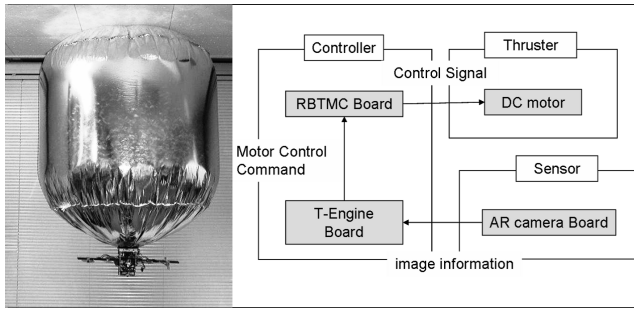


Figure 1: blimp robot and overview

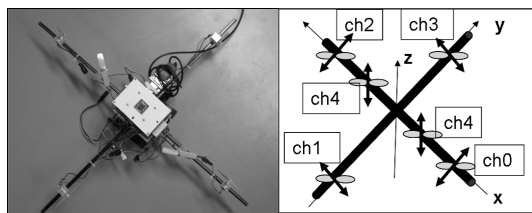


Figure 2: propeller unit

We decided on diameter D [m] and height H [m] to determine balloon size. Total weight of blimp robot W [g] is calculated as follow calculation.

$$W = \pi \rho_{he} H \left(\frac{D}{2}\right)^2 + \pi c D \left(H + \frac{D}{2}\right) + U \quad (1)$$

$\rho_{he} = 178.5$ [g/m³] is helium density and, c [g/m²] is the unit weight of balloon material. Balloon material is aluminum film, whose unit weight c is 30.0[g/m²]. U is the weight of the propeller unit consisted of the six propellers, the camera sensor, and the controller. Weight U is about 480[g]. And, B_u is the buoyant force.

$$B_u = \pi \rho_{air} H \left(\frac{D}{2}\right)^2 \quad (2)$$

$\rho_{air} = 1226.0$ [g/m³] at 0.1atm. B_u must be larger than W . We set diameter D to 0.94[m], and height H to 0.8[m].

The propellers are positioned independently axial direction fixed to the blimp. Because the motors for propellers are driven by ON/OFF signal, it is difficult to generate certain amount of thrust. So 10 switching points set at sampling time $\Delta T = 0.3$ [s]. Blimp robot is equipped AR camera as a sensor. The image resolution is 160 144 pixels. And, Color information is sent

by 16 bits RGB color space. The image information obtained with the camera is sent to T-Engine board, and thrust that processes the image there is decided. The motor control command is sent from T-Engine board to RBTMC board and the motor is rotated.

3 Line extraction

To follow the line, width and the centerline of the line are acquired from the image. The purpose of the width of the line is to request the height of the blimp robot, and it is followed to the centerline of the line to take both sides of the line in the image. To calculate them, the edge point of the line is searched out. The edge point is a verge of the color of the line and the color of the floor. The distinction of the color of the color of the line or the floor is judged from a color near the threshold by the YUV space. It is difficult in

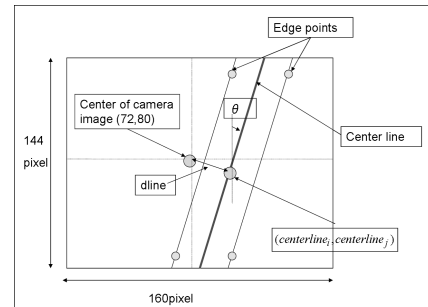


Figure 3: Information on line in camera image

the point of the calculation time to judge whether it is an edge point of all pixels of the camera image. So, we search edge points from the pixel of the image of a round. And, it searches for the pixel of the image in putting several points and it looks for an internal point of the seeing line. An internal point is a point judged that four pixels in surroundings are the colors of the line. When every one point, it is searched for to the edge of the image from the internal point, and it is judged an internal point, the edge point, and the color of floor, the edge point is judged as an edge point of the line.

When the line is taken in the camera image, it might have the edge point in four points. Two straight lines of the edge line are calculated from the edge point in four points. The centerline of the line is calculated by averaging expressions two straight lines.

The method of calculating the width of the line calculates the distance with another edge line from one

edge point.

$$linewidth = \frac{|j \quad Ai \quad B|}{\sqrt{1 + A^2}} \quad (3)$$

J and i are shown the pixel position in the camera image of one edge point. A and B are shown the gradient and the cut in the camera image of another edge line from the edge point. And, the value of the width of the line changes by the position of the calculated point because the edge lines are not parallel when calculating only in one point. Therefore, the width of the line is calculated with each edge point in two points on the same edge line, and the average value is used as width of the line at that time.

Next, the distance of the blimp and the line is calculated. The standard of the distance is a centerline of the line. The distance of the center of the camera image and the centerline of the line are calculated because it is made in the composition of this balloon robot so that the position of the camera may come to the center of the airframe. Because the size of the camera is 160 × 144 now, a center pixel of the camera becomes point (72, 80). The point that distances shorten most in the centerline of the line for this point is calculated. These points are $centerline_i$ and $centerline_j$. Because the distance of these points is a unit of the pixel, the number of pixels for the actual width of a line and the width of the line acquired from the image is used for an actual distance to change.

$$dline = \frac{\sqrt{(centerline_i \quad 72)^2 + (centerline_j \quad 80)^2}}{\frac{line}{linewidth}} \quad (4)$$

The line is actual width of the line, and linewidth is calculated width of line. And, the angle to the line with centerline is calculated. This angle is calculated by trigonometric function as follows.

$$\theta = Cos^{-1}\left(\frac{1}{\sqrt{1 + A_{center}^2}}\right) \quad (5)$$

A_{center} is gradient of centerline.

4 Control method

It is described how to decide to thrust in this section. Because it is possible to be thought about the direction of Z of the propeller independently, we think about the control by the X-Y plane. It is necessary

to control to approach the centerline in X-Y plane. The blimp robot is made to follow to the line by keeping producing thrust in the direction and adjusting the angle hand like the robot of the car type[4] and the mouse type. Then, it keeps putting out constant thrust in two of four propellers of the X-Y plane, and the angle is adjusted by other two. Constant thrust is generated with ch0 and ch2 of Figure 2, and the angle is ch1 and ch3 of Figure 2. To adjust the angle to be suitable for the direction of the centerline of the line, the angle of the target is set. The angle of the target makes it can be influenced by deflection with the line though it grows and set greatly.

$$\theta_{target} = Cos^{-1}\left(\frac{dline}{\sqrt{FORWARD^2 + dline^2}}\right) \quad (6)$$

θ_{target} is the angle of target, and FORWARD is a constant number to decide the angle of the target. Blimp robot is difficult to decide the analytical controller.[3] Because the parameter can be decided by the trial and error, the PID control is used for the control of the direction of height. However, it is made to control by the PD control because it is thought that the influence of the paragraph of I effective after time passes doesn't come out in the adjustment of the angle.

$$m_z(t) = K_{zP}e_z(t) + K_{zI} \int e_z(t)dt + K_{zD} \frac{de_z(t)}{dt} \quad (7)$$

$$m(t) = K_{Pe}(t) + K_{D} \frac{de(t)}{dt} \quad (8)$$

K_{zP} and K_P are proportional gain, K_{zI} is integral gain, and K_{zD} and K_D are derivative gain. $e(t)$ is deflection with velocity of target, and $de(t) = (e(t) \quad e(t \quad \Delta T))$. m_z is thrust in propeller ch4, and m is thrust in propeller ch1 and ch3. And, number of propellers ch0 and ch2 are propeller for generating constant thrust.

5 Experiment

5.1 Experimental setting

In this experiment, the line is drawn at the straight line and blimp robot moves on that. The line puts red paper with length of 5[m] on the floor. And, the width of the line is set by 0.1[m]. If the width of the line is 0.1m, it sees it by 32 pixels when the position of the camera of the blimp is 0.5[m], and 16 pixel when 1[m]. The interval that searches for the edge point is made four pixels. And, the constant to decide the angle of

the target to control the angle is set as 100. Moreover, the target position of height is assumed to be 1[m]. This is because of thinking the blimp robot moves in the building. The camera has equipped the under the airframe of the robot and the top part of the robot is about 2.3[m] at 1[m] in the height of camera.

5.2 Result

Fig.4, Fig.5 and Fig.6 show with the target value when blimp robot is made to follow the line. Even if each graph is seen, the part where the value changes greatly is seen. This is caused from the large difference from the previous value when the width of the line is calculated. Fig7 is the one that the number of extracted edge points was shown. It is showed when it is a number of edge points less than it though the width of the edge calculates correctly if the edge point is gotten by four points. Moreover, because height and the distance with the line are calculated based on the value of the width of the line, this value is personally effective in the control. And, power toward direction that came off might be larger than power to face the line by the turbulence such as the winds. It is not possible to control by disappearing the line in the camera image. The angle is an error margin of about 0.1[rad] against the angle of the target.

In this experiment, it mostly went off from the line around 3[m] of the line, and it was possible to move by 5m because it advances straight when the influence of the deflection of the angle and the wind is little. Every experiment, the erratic value was seen in the graph of height.

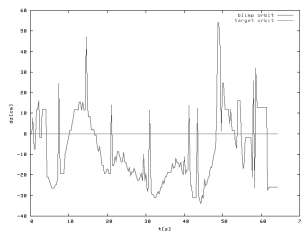
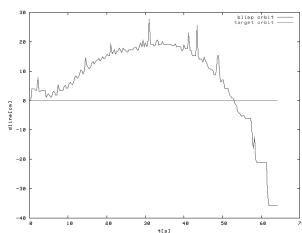


Figure 4: Deflection with line Figure 5: Deflection with height of target

6 Conclusion

In this paper, we reported the following to the line for indoor blimp robot. It needs to be improved in the extraction accuracy of the line because graph of height actual has resulted greatly the vibration. Moreover, it

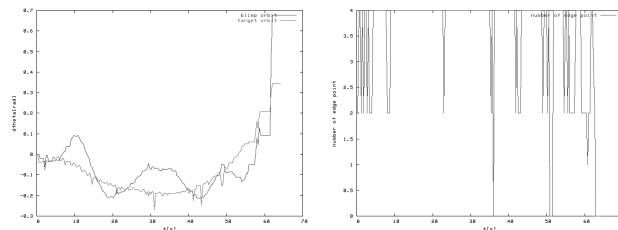


Figure 6: Deflection with Figure 7: Number of the angle of target edge points

was often thrown away from the line by the power of the disturbance such as the winds.

In the future work, it is necessary that blimp robot is moved by guessing actual height whether to improve the extraction accuracy of the width of the line. In addition, the line is not made easy to lose sight by installing the fish-eye lens in the camera to get wider view. We want to move blimp robot in not only the straight line but also the curve.

References

- [1] Keiko Motoyama, et.al., "Design of Action-value Function in Motion Planning for Autonomous Blimp Robot", *IEEJ Transactions on Electronics, Vol. 10*, 2004.
- [2] Hidenori Kawamura, et.al., "Motion Design for Indoor Blimp Robot with PID Controller", *Journal of Robotics and Mechatronics, Vol.17*, 2005.
- [3] Hisao Kadota, et.al., "Vision-Based Motion Control of Indoor Blimp Robot", *Proceedings of The 4th International Conference on Advanced Mechatronics*, 2004.
- [4] David Collins, Gordon Wyeth, "Cerebellar Control of a Line Following Robot", *In Proceedings Australian Conference on Robotics and Automation*, 1999.

Learning Properties of Recurrent Neural Network with Parametric Biases

Kazushi Ikeda
Department of Systems Science
Kyoto University
Kyoto 606-8501 Japan

Kentaro Narita
Department of Systems Science
Kyoto University
Kyoto 606-8501 Japan

Abstract

Some properties of the recurrent neural network with parametric biases (RNNPB) are discussed here. The RNNPB is applied to a humanoid robot and is a candidate model of the mirror system in neuroscience. A recent experimental study reported that the RNNPB encodes given periodical patterns into the PB vector in a smart manner. This study is the first step to reveal how the RNNPB works. More concretely, some conditions are given for the transition matrix of the RNNPB to produce the stored dynamical patterns and how the learning algorithm of the RNNPB works is shown.

1 Introduction

One of the applications of neural networks is the central pattern generator of a robot or others since a recurrent neural network can store periodical patterns as attractors (limit-cycles) by learning them [1]. The recurrent neural network with parametric biases (RNNPB) is one of such robot controllers [2] and has recently attracted attentions as a humanoid controller [3] as well as a model of mirror neurons in neuroscience [4-6].

The RNNPB consists of a multi-layer perceptron, feedback connections and the PB neurons, where the multi-layer perceptron receives two types of input. One is the vector of the current internal states via the feedback connections some components of which are observed as the output of the RNNPB, and the other is the vector of parameter biases (PBs) which externally controls the output.

The RNNPB has the following three phases: The learning phase where the RNNPB learns the given dynamical patterns using the back-propagation through time (BPTT) algorithm [1] as well as the PBs are updated in a self-organizing manner, the generation phase where the RNNPB outputs a dynamical pattern according to the PB vector given externally, and

the interaction phase where the PB vector is updated so that the output of the RNNPB coincides with the desired one.

In general, the number of PBs is much less than that of internal states. This means that high-dimensional dynamical patterns are encoded into the PB space in the learning phase. In the generation phase, on the other hand, the RNNPB decodes a PB vector and retrieves the corresponding dynamical pattern. Hence, the relationship between the dynamical patterns and the PB vectors is essential in analyzing what the RNNPB does in the learning and generation phases. However, it has little been clarified so far due to its complicated structure and update equations.

Recently, Yamada and Suyari showed by exhaustive experiments that the three parameters of a sinusoidal, the frequency, the amplitude and the offset, are smoothly mapped into the PB space so that the topology of the parameter space is kept [7]. This result suggests that the RNNPB would have an elegant theory in encoding dynamical patterns. The purpose of this study is to give a theoretical background to the useful neural model, taking the experimental results into account.

2 Problem Formulation

In order to understand the RNNPB, we try to give a theoretical background to the results by Yamada and Suyari. Since sinusoids are a basis-set of the space of periodical patterns, we substitute a linear system for a multi-layer perceptron and see how the RNNPB learns periodical patterns as limit-cycles and codes their properties into the PB vector.

The problem we treat in this study is formulated as follows. The one-dimensional output, the $(N - 1)$ -dimensional unobservable internal state vector and the M -dimensional PB vector at time t are denoted by s_t , \mathbf{c}_t and \mathbf{b}_t , respectively, where $M < N$ as we consider how the dynamical patterns are encoded into the PB

vector. In this study, we assume that the PB vector is constant, that is, the self-organization of the PB vector is finished. Then, the N -dimensional vector $(s_t, \mathbf{c}_t^T)^T$ is the state vector and is updated as

$$\begin{pmatrix} s_{t+1} \\ \mathbf{c}_{t+1} \end{pmatrix} = A \begin{pmatrix} s_t \\ \mathbf{c}_t \end{pmatrix} + \mathbf{b}, \quad (1)$$

where A is the state transition matrix.

It is obvious that an arbitrary time-series with period N is reproduced if A equals to the shift matrix

$$S \equiv \begin{pmatrix} \mathbf{0}_{N-1} & I_{N-1} \\ 1 & \mathbf{0}_{N-1}^T \end{pmatrix} \quad (2)$$

and \mathbf{b} is null, where I_n and $\mathbf{0}_n$ are the n -dimensional identity matrix and the n -dimensional null vector, respectively, and T denotes the transposition of a matrix or a vector.

3 Transition Matrix for Periodical Patterns

We first introduce the conditions on the transition matrix A under which the RNNPB can produce the stored dynamical patterns with period N , assuming $\mathbf{b} = \mathbf{0}_M$. This problem is not easy since it includes an essential ambiguity in A and the internal state \mathbf{c}_t . In fact, the RNNPB produces the same output when the internal state is

$$\mathbf{c}'_t \equiv \begin{pmatrix} 1 & \mathbf{0}_{N-1}^T \\ \mathbf{0}_{N-1} & Q \end{pmatrix} \begin{pmatrix} s_t \\ \mathbf{c}_t \end{pmatrix} \quad (3)$$

instead of $(s_t, \mathbf{c}_t^T)^T$ and

$$A' \equiv \begin{pmatrix} 1 & \mathbf{0}_{N-1}^T \\ \mathbf{0}_{N-1} & Q \end{pmatrix} A \begin{pmatrix} 1 & \mathbf{0}_{N-1}^T \\ \mathbf{0}_{N-1} & Q^{-1} \end{pmatrix} \quad (4)$$

instead of A , where Q is an arbitrary regular matrix.

To remove this ambiguity, we rewrite (1) to a form without \mathbf{c}_t , that is, an update equation of

$$\mathbf{s}_t^T \equiv (s_t \quad s_{t+1} \quad \cdots \quad s_{t+N-1}). \quad (5)$$

In fact,

$$\mathbf{s}_t = C \begin{pmatrix} s_t \\ \mathbf{c}_t \end{pmatrix} \quad (6)$$

holds true from (1) where

$$C \equiv \begin{pmatrix} (A^0)_1 \\ (A^1)_1 \\ \vdots \\ (A^{N-1})_1 \end{pmatrix} = \begin{pmatrix} 1 & \mathbf{0}_{N-1}^T \\ \mathbf{a}' & A'' \end{pmatrix}, \quad (7)$$

$(A^k)_1$ is the first row of A^k , and \mathbf{a}' and A'' are a certain vector and a certain matrix. Using the ambiguity of \mathbf{c}_t and A , we set $Q = A''^{-1}$ in (3) and get

$$C = \begin{pmatrix} 1 & \mathbf{0}_{N-1}^T \\ \mathbf{a}' & I_{N-1} \end{pmatrix} \quad (8)$$

$$C^{-1} = \begin{pmatrix} 1 & \mathbf{0}_{N-1}^T \\ -\mathbf{a}' & I_{N-1} \end{pmatrix}. \quad (9)$$

From (6), (1) is rewritten as

$$\mathbf{s}_{t+1} = CAC^{-1}\mathbf{s}_t \quad (10)$$

and then

$$S^{t+1}\mathbf{f}_{t+1} = CAC^{-1}S^t\mathbf{f}_t \quad (11)$$

where

$$\mathbf{f}_t \equiv S^{-t}\mathbf{s}_t. \quad (12)$$

Since \mathbf{s}_t being periodical is equivalent to \mathbf{f}_t being constant, its condition is described as $CAC^{-1} = S$, that is, $A = C^{-1}SC$ or

$$A = \begin{pmatrix} a_1 & 1 & 0 & 0 & \cdots & 0 \\ -a_1^2 + a_2 & -a_1 & 1 & 0 & \cdots & 0 \\ -a_1a_2 + a_3 & -a_2 & 0 & 1 & \ddots & 0 \\ -a_1a_3 + a_4 & -a_3 & 0 & 0 & \ddots & 0 \\ \vdots & \vdots & \vdots & \ddots & \ddots & \vdots \\ -a_1a_{N-1} + 1 & -a_{N-1} & 0 & 0 & \cdots & 0 \end{pmatrix} \quad (13)$$

from (8), where a_k is the k th element of \mathbf{a} .

Substituting this for (1), we get

$$s_{t+1} = a_1s_t + c_t \quad (14)$$

$$c_{t+1} = (-a_1^2 + a_2)s_t - a_1c_t + c_{t+1} \quad (15)$$

$$c_{t+2} = (-a_1a_2 + a_3)s_t - a_2c_t + c_{t+2} \quad (16)$$

$$\vdots \quad (17)$$

$$c_{t+N-1} = (-a_1a_{N-1} + a_3)s_t - a_{N-1}c_t + c_{t+N-1} \quad (18)$$

and can show $a_k = 0$ for $k = 1, \dots, N$ from the periodicity of \mathbf{s}_t . This means $C = I$ and hence $A = S$. From the ambiguity in (3),

$$A = \begin{pmatrix} 1 & \mathbf{0}_{N-1}^T \\ \mathbf{0}_{N-1} & Q^{-1} \end{pmatrix} S \begin{pmatrix} 1 & \mathbf{0}_{N-1}^T \\ \mathbf{0}_{N-1} & Q \end{pmatrix} \quad (19)$$

is the condition under which the RNNPB produces arbitrary periodical patterns, where Q is an arbitrary regular matrix.

Although (19) is derived under the assumption that the RNNPB produces arbitrary patterns with period N , we can easily show that the result above still stands if $\mathbf{s}_t, \mathbf{s}_{t+1}, \dots, \mathbf{s}_{t+N-1}$ are linearly independent, that is,

$$\sum_{\tau=t}^{t+N-1} \mathbf{s}_\tau \mathbf{s}_\tau^T \quad (20)$$

has full rank, which we assume in the following.

4 PB Vector and Corresponding Pattern

In this section, we see how the PB vector \mathbf{b} affects the dynamical pattern the RNNPB produces. When \mathbf{b} is constant, the state vector is updated as

$$\begin{pmatrix} s_{t+1} \\ \mathbf{c}_{t+1} \end{pmatrix} = A \begin{pmatrix} s_t \\ \mathbf{c}_t \end{pmatrix} + \mathbf{b} \quad (21)$$

$$\begin{pmatrix} s_{t+2} \\ \mathbf{c}_{t+2} \end{pmatrix} = A^2 \begin{pmatrix} s_t \\ \mathbf{c}_t \end{pmatrix} + A\mathbf{b} + \mathbf{b} \quad (22)$$

$$\vdots \quad (23)$$

$$\begin{pmatrix} s_{t+N} \\ \mathbf{c}_{t+N} \end{pmatrix} = A^N \begin{pmatrix} s_t \\ \mathbf{c}_t \end{pmatrix} + \sum_{j=0}^{N-1} A^j \mathbf{b} = \begin{pmatrix} s_t \\ \mathbf{c}_t \end{pmatrix}. \quad (24)$$

Letting the first element of

$$\sum_{j=0}^{k-1} A^j \mathbf{b} \quad (25)$$

be the $(k-1)$ st element of \mathbf{b}' , that is, $\mathbf{b}' = LC\mathbf{b}$ where

$$L \equiv \begin{pmatrix} 0 & 0 & \cdots & 0 & 0 \\ 1 & 0 & \ddots & 0 & 0 \\ 1 & 1 & \ddots & 0 & 0 \\ \vdots & \ddots & \ddots & \ddots & \vdots \\ 1 & 1 & \cdots & 1 & 0 \end{pmatrix} \quad (26)$$

and C is defined in (7), then

$$\mathbf{s}_t = C \begin{pmatrix} s_t \\ \mathbf{c}_t \end{pmatrix} + LC\mathbf{b} \quad (27)$$

holds true, which leads to

$$\mathbf{s}_t - LC\mathbf{b} = C \begin{pmatrix} s_t \\ \mathbf{c}_t \end{pmatrix}. \quad (28)$$

Hence, (21) is rewritten using (12) as

$$\mathbf{f}_{t+1} = S^{-t-1}CAC^{-1}S^t\mathbf{f}_t + (L - CAC^{-1}L + I)C\mathbf{b}. \quad (29)$$

This means

$$\mathbf{f}_t = \frac{1}{1-c}(L - CAC^{-1}L + I)C\mathbf{b} \quad (30)$$

is constant when $CAC^{-1} = cS$ for $|c| < 1$.

When \mathbf{f}_t is a constant vector \mathbf{f} , conversely,

$$(I - S^{-t-1}CAC^{-1}S^t)\mathbf{f} = (L - CAC^{-1}L + I)C\mathbf{b} \quad (31)$$

holds and

$$B \equiv I - S^{-t-1}CAC^{-1}S^t \quad (32)$$

does not depend on t , where all the eigenvalues of B must be in $(0, 2)$. Substituting $t = 0$, we get $S(I - B) = CAC^{-1}$ and hence

$$I - B = S^{-t-1}CAC^{-1}S^t \quad (33)$$

$$= S^{-t}(I - B)S^t \quad (34)$$

is a constant matrix. This means that $I - B$ (and also B) is a cyclic Toeplitz matrix.

5 Learning Properties of BPTT

The RNNPB employs the BPTT algorithm to learn given dynamical patterns, which approximates a recurrent network to a layered one of finite length and applies the error back-propagation algorithm [1]. In this section, we discuss how the linearized RNNPB learns the patterns with the BPTT algorithm.

Let the transition matrix A be divided to four components as

$$A = \begin{pmatrix} a_{11} & \mathbf{a}_{12}^T \\ \mathbf{a}_{21} & A_{22} \end{pmatrix}, \quad (35)$$

where we assume that A satisfies (19), that is, this is the goal. The transition matrix in the learning phase at time t is denoted by \hat{A} and their components by

$$\hat{A} = \begin{pmatrix} \hat{a}_{11} & \hat{\mathbf{a}}_{12}^T \\ \hat{\mathbf{a}}_{21} & \hat{A}_{22} \end{pmatrix}. \quad (36)$$

Note that we omit the subscript t for simplicity.

The BPTT algorithm in the RNNPB approximate the recurrent network to the three-layered network, that is,

$$s_{t+1} = a_{11}s_t + \mathbf{a}_{12}^T \mathbf{c}_t \quad (37)$$

$$= a_{11}s_t + \mathbf{a}_{12}^T \mathbf{a}_{21}s_{t-1} + \mathbf{a}_{12}^T A_{22} \mathbf{c}_{t-1}, \quad (38)$$

$$\hat{s}_{t+1} = \hat{a}_{11}s_t + \hat{\mathbf{a}}_{12}^T \mathbf{c}_t \quad (39)$$

$$= \hat{a}_{11}s_t + \hat{\mathbf{a}}_{12}^T \hat{\mathbf{a}}_{21}s_{t-1} + \hat{\mathbf{a}}_{12}^T \hat{A}_{22} \mathbf{c}_{t-1}. \quad (40)$$

and applies the steepest descent method to the squared error $\varepsilon(\hat{A}) = (\hat{s}_{t+1} - s_{t+1})^2/2$.

Since (38) has terms of the second order with respect to \hat{A} , a direct analysis is difficult. Therefore, we divide it two parts: One is a_{11} and \mathbf{a}_{12} and the other is \mathbf{a}_{21} , A_{22} , since the latter appears via \mathbf{c}_t .

From (37) and (39), the BPTT algorithm for a_{11} and \mathbf{a}_{12} is expressed as

$$\Delta \begin{pmatrix} \hat{a}_{11} \\ \hat{\mathbf{a}}_{12} \end{pmatrix} = -\eta \begin{pmatrix} s_t \\ \mathbf{c}_t \end{pmatrix} (s_t \quad \mathbf{c}_t^T) \begin{pmatrix} \hat{a}_{11} - a_{11} \\ \hat{\mathbf{a}}_{12} - \mathbf{a}_{12} \end{pmatrix} \quad (41)$$

and can be shown to make $(\hat{a}_{11}, \hat{\mathbf{a}}_{12}^T)$ converge to $(a_{11}, \mathbf{a}_{12}^T)$ when the assumption (20) is satisfied and η is appropriately small.

In the analysis of $(\hat{\mathbf{a}}_{21}, \hat{A}_{22})$ based on (38), we assume that $(\hat{a}_{11}, \hat{\mathbf{a}}_{12}^T)$ already converges to $(a_{11}, \mathbf{a}_{12}^T)$, that is,

$$\hat{s}_{t+1} - s_{t+1} = \mathbf{a}_{12}^T (\hat{\mathbf{a}}_{21} - \mathbf{a}_{21}) s_{t-1} + \mathbf{a}_{12}^T (\hat{A}_{22} - A_{22}) \mathbf{c}_{t-1}. \quad (42)$$

Then, the BPTT algorithm for $\hat{\mathbf{a}}_{21}$ and \hat{A}_{22} is expressed as

$$\Delta \begin{pmatrix} \hat{\mathbf{a}}_{21} & \hat{A}_{22} \end{pmatrix} = -\eta \mathbf{a}_{12} \mathbf{a}_{12}^T \cdot \begin{pmatrix} \hat{\mathbf{a}}_{21} - \mathbf{a}_{21} & \hat{A}_{22} - A_{22} \end{pmatrix} \begin{pmatrix} s_{t-1} \\ \mathbf{c}_{t-1} \end{pmatrix} (s_{t-1} \quad \mathbf{c}_{t-1}^T). \quad (43)$$

Therefore, under the assumption (20) $(\hat{\mathbf{a}}_{21}, \hat{A}_{22})$ stops when it satisfies

$$\mathbf{a}_{12}^T (\hat{\mathbf{a}}_{21} \quad \hat{A}_{22}) = \mathbf{a}_{12}^T (\mathbf{a}_{21} \quad A_{22}), \quad (44)$$

which means that $(\hat{\mathbf{a}}_{21} \quad \hat{A}_{22})$ does not converge to $(\mathbf{a}_{21} \quad A_{22})$.

6 Conclusions and Discussions

The analysis so far reveals that the essence of the RNNPB may be the shift operator, which explains the

result by Yamada and Suyari very well. However, the analysis based on the linear approximation is limited, as shown in the previous section, since the RNNPB cannot learn the dynamics by the BPTT algorithm. More extensive analysis is our future work.

Acknowledgments

This study is supported in part by a Grant-in-Aid for Scientific Research (15700130, 18300078) from the Japanese Government.

References

- [1] P. Werbos, "Backpropagation through time: What does it mean and how to do it," *Proc. IEEE*, vol. 78, pp. 1550–1560, 1990.
- [2] J. Tani, "Learning to generate articulated behavior through the bottom-up and the top-down interaction processes," *Neural Networks*, vol. 16, no. 1, pp. 11–23, 2003.
- [3] M. Ito, K. Noda, Y. Hoshino, and J. Tani, "Dynamic and interactive generation of object handling behaviors by a small humanoid robot using a dynamic neural network model," *Neural Networks*, vol. 19, no. 3, pp. 323–337, 2006.
- [4] J. Tani, M. Ito, and Y. Sugita, "Self-organization of distributedly represented multiple behavior schemata in a mirror systems: Reviews of robot experiments using RNNPB," *Neural Networks*, vol. 17, no. 8–9, pp. 1273–1289, 2004.
- [5] M. Ito and J. Tani, "On-line imitative interaction with a humanoid robot using a dynamic neural network model of a mirror system," *Adaptive Behavior*, vol. 12, no. 2, pp. 93–115, 2004.
- [6] E. Oztop, M. Kawato, and M. Arbib, "Mirror neurons and imitation: A computationally guided review," *Neural Networks*, vol. 19, no. 3, pp. 254–271, 2006.
- [7] K. Yamada and H. Suyari, "The properties of the PB space self-organized by RNNPB learning," IE-ICE, Tech. Rep. NC2004-183, 2005.

Three dimensional medical image recognition of the brain by feedback GMDH-type neural network self-selecting optimum neural network architecture

Tadashi Kondo
School of Health Sciences,
the University of Tokushima,
Tokushima, 770-8509, Japan

Junji Ueno
School of Health Sciences,
the University of Tokushima,
Tokushima, 770-8509, Japan

Abstract

The feedback Group Method of Data Handling (GMDH)-type neural network algorithm proposed in this paper is applied to 3-dimensional medical image recognition of the blood vessels in the brain. The neural network architecture fitting the complexity of the medical images is automatically organized by the feedback GMDH-type neural network algorithm so as to minimize the prediction error criterion defined as Akaike's Information Criterion (AIC). In this feedback GMDH-type neural network algorithm, the optimum neural network architecture is automatically selected from three types of neural network architectures such as the sigmoid function type neural network, the radial basis function (RBF) type neural network and the polynomial type neural network. The recognition results show that the feedback GMDH-type neural network algorithm is useful for the 3-dimensional medical image recognition of the blood vessels in the brain and is very easy to apply the practical complex problem because the optimum neural network architecture is automatically organized.

Keywords: GMDH, Neural network, Medical image recognition

1 Introduction

The Group Method of Data Handling (GMDH)-type neural networks and their applications have been proposed in our early works [1],[2]. The GMDH-type neural networks can automatically organize the neural network architecture by using the heuristic self-organization method [3],[4]. In this study, a feedback GMDH-type neural network algorithm self-selecting the optimum neural network architecture is proposed. In the feedback GMDH-type neural network algorithm, the optimum neural network architecture is automatically selected from three types of neural network architectures such as the sigmoid function type neural network, the radial basis function (RBF) type neural network and the polynomial type neural network. Furthermore, the structural parameters such as the number of layers, the number of neurons in the hidden layers and the useful input variables are automatically selected so as to minimize the prediction error criterion defined as Akaike's Information Criterion (AIC) [5] or Prediction Sum of Squares (PSS) [6]. The feedback GMDH-type neural

network has a feedback loop and the complexity of the neural network increases gradually using feedback loop calculations so as to fit the complexity of the nonlinear system.

The feedback GMDH-type neural network algorithm proposed in this paper is applied to 3-dimensional medical image recognition of the blood vessels in the brain. The neural network architecture fitting the complexity of the medical images is automatically organized by the feedback GMDH-type neural network algorithm so as to minimize the prediction error criterion defined as AIC.

2 Feedback GMDH-type neural network

The architecture of the feedback GMDH-type neural network proposed in this paper has a feedback loop as shown in Fig.1. The feedback GMDH-type neural network algorithm can select the optimum neural network architecture from three types of neural network architectures such as the sigmoid function type neural network, the RBF type neural network and the polynomial type neural network. The feedback GMDH-type neural network algorithm uses three types of neuron architectures which are the sigmoid function type neuron, the RBF type neuron and the polynomial type neuron. In the feedback GMDH-type neural network, optimum neuron architectures fitting the characteristics of the nonlinear system are automatically selected by using AIC.

The feedback GMDH-type neural network is shown as follows.

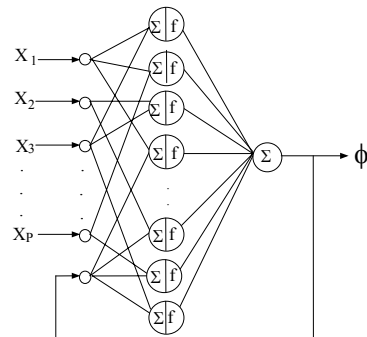


Fig.1 Architecture of the feedback GMDH-type neural network

2.1 First loop calculation

First, all data are set to the training data. In this algorithm, it is not necessary to separate the original data into the training and test data because AIC can be used for organizing the network architectures. Then the architecture of the input layer is organized.

1) Input layer

$$u_j = x_j \quad (j=1,2,\dots,p) \quad (1)$$

where $x_j (j=1,2,\dots,p)$ are the input variables of the system, and p is the number of input variables. In the first layer, input variables are set to the output variables.

2) Hidden layer

All combinations of the r input variables are generated. For each combination, three types of neuron architectures which are the sigmoid function type neuron, the RBF type neuron and the polynomial type neuron, are generated and L neurons which minimize AIC value are selected for each type of neuron architectures.

Furthermore, for each combination, optimum neuron architectures fitting the characteristics of the nonlinear system are automatically selected by using AIC.

a) Sigmoid function type neuron:

i) The first type neuron

Σ : (Nonlinear function)

$$z_k = w_1u_i + w_2u_j + w_3u_iu_j + w_4u_i^2 + w_5u_j^2 + w_6u_i^3 + w_7u_i^2u_j + w_8u_iu_j^2 + w_9u_j^3 - w_0\theta_i \quad (2)$$

f : (Nonlinear function)

$$y_k = \frac{1}{1 + e^{(-z_k)}} \quad (3)$$

ii) The second type neuron

Σ : (Linear function)

$$z_k = w_1u_1 + w_2u_2 + w_3u_3 + \dots + w_ru_r - w_0\theta_i \quad (r < p) \quad (4)$$

f : (Nonlinear function)

$$y_k = \frac{1}{1 + e^{(-z_k)}} \quad (5)$$

b) RBF type neuron:

i) The first type neuron

Σ : (Nonlinear function)

$$z_k = w_1u_i + w_2u_j + w_3u_iu_j + w_4u_i^2 + w_5u_j^2 + w_6u_i^3 + w_7u_i^2u_j + w_8u_iu_j^2 + w_9u_j^3 - w_0\theta_i \quad (6)$$

f : (Nonlinear function)

$$y_k = e^{(-z_k^2)} \quad (7)$$

ii) The second type neuron

Σ : (Linear function)

$$z_k = w_1u_1 + w_2u_2 + w_3u_3 + \dots + w_ru_r - w_0\theta_i \quad (r < p) \quad (8)$$

f : (Nonlinear function)

$$y_k = e^{(-z_k^2)} \quad (9)$$

c) Polynomial type neuron:

i) The first type neuron

Σ : (Nonlinear function)

$$z_k = w_1u_i + w_2u_j + w_3u_iu_j + w_4u_i^2 + w_5u_j^2 + w_6u_i^3 + w_7u_i^2u_j + w_8u_iu_j^2 + w_9u_j^3 - w_0\theta_i \quad (10)$$

f : (Linear function)

$$y_k = z_k \quad (11)$$

ii) The second type neuron

Σ : (Linear function)

$$z_k = w_1u_1 + w_2u_2 + w_3u_3 + \dots + w_ru_r - w_0\theta_i \quad (r < p) \quad (12)$$

f : (Linear function)

$$y_k = z_k \quad (13)$$

Here, $\theta_i = 1$ and $w_i (i=0,1,2,\dots)$ are the weights between the first and second layer and estimated by applying the stepwise regression analysis [7] to the training data. Only useful input variables $u_i (i=1,2,\dots)$ are selected by using AIC. In the first type neuron, the value of r , which is the number of input variables u in each neuron, is set to two. In the second type neuron, the value of r , which is the number of input variables u in each neuron, is set to be greater than two and smaller than p . p is the number of input variables $x_i (i=1,2,\dots,p)$. The output variables y_k of the neurons are called as the intermediate variables.

L neurons having the smallest AIC values are selected for three types of neuron architectures which are the sigmoid function type neuron, the RBF type neuron and the polynomial type neuron. The output variables y_k of L selected neurons for three types of neuron architectures are set to the input variables of the neurons in the output layer.

3) Output layer

For three types of neural network, the outputs y_k of the neurons in the hidden layer are combined by the following linear function.

$$\phi^* = a_0 + \sum_{k=1}^L a_k y_k \quad (14)$$

Here, L is the number of combinations of the input variables and y_k is the intermediate variables. The useful intermediate variables y_k are selected by using the stepwise regression analysis in which AIC is used as the variable selection criterion.

Equation (14) is calculated for three types of neural network architectures which are the sigmoid function type neural network, the RBF type neural network and the polynomial type neural network. Then, the neural network architecture which has smallest AIC value is selected as the GMDH-type neural network architecture from three types of neural network architectures

Then, the estimated output values ϕ^* which is selected in the output layer is used as the feedback value and it is combined with the input variables in the next loop calculation.

2.2 Second and successive loop calculations

The optimum neural network architecture is selected from three types of neural network architectures in the output layer. Therefore, in the second and successive loop calculations, only one type of neuron architecture, which is the sigmoid function type neuron or the RBF type neuron or the polynomial type neuron, is used for the calculation.

First, the estimated output value ϕ^* is combined with the

input variables and all combinations between the estimated output value ϕ^* and the input variables are generated. The same calculation as the first feedback loop is carried out for each combination. Here, only one type of neuron architecture, which is selected in the first loop calculation, is used in the calculation. When AIC value of the linear function in (14) is increased, the loop calculation is terminated and the complete neural network architecture is organized by the L selected neurons in each feedback loop.

3 Application to 3-dimensional medical image recognition of the blood vessels in the brain

In this study, regions of the blood vessels in the brain is recognized automatically using the following two recognition procedures. Multidetector row computed tomography (MDCT) images of the brain are used in this study. In the first recognition procedure, the feedback GMDH-type neural network is organized to recognize the brain regions and then these regions are extracted using organized neural network. In the second recognition procedure, another new feedback GMDH-type neural network is organized to recognize the blood vessel regions and then these regions are extracted using organized new neural network. Using these recognition procedures, the blood vessel regions are recognized and extracted.

3.1 Recognition of brain regions

In this study, an original MDCT image shown in Fig. 2 is used for organizing the feedback GMDH-type neural network. Then, image features are extracted and used as input variables of neural network. Statistics of image densities in neighboring regions, $N \times N$ pixel regions, are used as image features. The following statistics are used as input variables. 1) mean, 2) standard deviation, 3) variance, 4) median, 5) minimum, 6) maximum, 7) range. Out of these statistics, only three parameters namely, mean, standard deviation and variance are selected as useful input variables. Output value of neural network is zero or one. When $N \times N$ pixel region is contained in regions of the brain, neural network sets pixel value at the center of $N \times N$ pixel region to one and this pixel is shown as white point. Neural network was organized when values of N are 5, 10 and 15. When N equals 5, output image is most accurate. Calculation of the feedback GMDH-type neural network was terminated at the fourth layer. Three useful neurons were selected in each hidden layer. RBF neural network architecture was selected as the feedback GMDH-type neural network in the first feedback loop calculation. Feedback GMDH-type neural network output brain image and post-processing analysis of brain image was carried out, based on which regions of the brain were extracted. In

post-processing of output image of the neural network, small isolated regions outside or inside of the brain regions are eliminated by the image processing such as the dilatation and the erosion. Then, outlines of regions of the brain were expanded outside by $N/2$ pixels and outline of the brain were extracted. Fig.3 shows output image after this processing. In order to check matching between original image and output image of the neural network, the output image was overlapped on original image after post-processing. Overlapped image is shown in Fig.4. From Fig.4, we can see that extracted regions are very accurate.

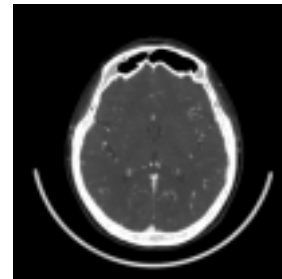


Fig.2 Original image(1)



Fig.3 Output image after post-processing (1)

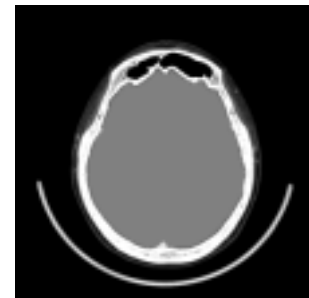


Fig.4 Overlapped image (1)

3.2 Recognition of blood vessel regions in the brain

The blood vessel regions are recognized by the feedback GMDH-type neural network and extracted. First, gray scale image of the brain (Fig.5) was subtracted from the original image (Fig.2) by using the output image of the feedback GMDH-type neural network (Fig.3). This gray scale image is used as a new original image to organize new feedback GMDH-type neural network. The new feedback GMDH-type neural network was organized and recognized the blood vessel regions. The organization procedures of the new feedback GMDH-type neural network are the same as those of the brain regions. Image features are extracted and used as input variables of neural network. Statistics of image densities in neighboring regions, $N \times N$ pixel regions, are used as image features. Only three parameters namely, mean, standard deviation and variance are selected as useful input variables. Neural network was organized when values of N are 5, 10 and 15. When N equals 5, output image is

most accurate. RBF neural network architecture was selected as the feedback GMDH-type neural network architecture in the first feedback loop calculation. Feedback GMDH-type neural network output blood vessel image and post-processing analysis was carried out, based on which regions of the blood vessels were extracted. Fig.6 shows output image after the post-processing. Then, gray scale image of the blood vessel was subtracted from the original image by using the output image of the feedback GMDH-type neural network (Fig.6). Figure 7 shows overlapped image of blood vessel regions. These subtraction processing were carried out for the all slices of MDCT. Then, 3-dimensional images of the blood vessels were generated using gray scale images for all slices of MDCT by the rendering software. Figure 8 are 3-dimensional blood vessel images.

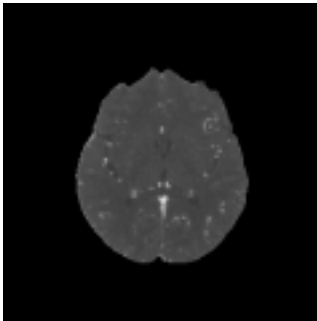


Fig.5 Subtraction image of the brain (1)

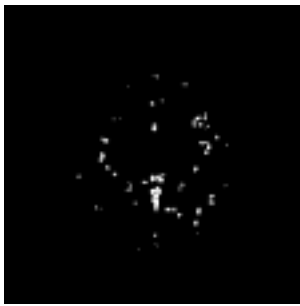


Fig.6 Output image of blood vessel regions (1)

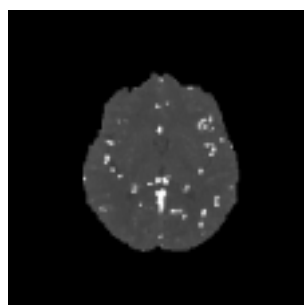
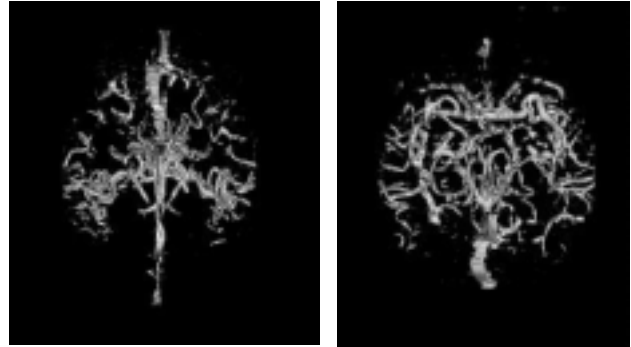


Fig.7 Overlapped image of blood vessel regions (1)

4 Conclusion

In this paper, the feedback GMDH-type neural network algorithm self-selecting optimum neural network architecture was proposed. In this algorithm, optimum neural network architecture is automatically selected from three neural network architectures such as sigmoid function neural network, RBF neural network and polynomial neural network. Furthermore, structural parameters such as the number of layers, the number of neurons in hidden layers and useful input variables are automatically selected to minimize prediction error criterion defined as AIC.

In this paper, this algorithm was applied to 3-dimensional medical image recognition of the blood vessels in the brain and it was shown that feedback GMDH-type neural network algorithm was a useful method for 3-dimensional medical image recognition of the blood vessels in the brain because the neural network architecture is automatically organized by the feedback GMDH-type neural network algorithm.



(a) (b)
Fig.8 3-dimensional images of the blood vessels

References

- [1] T.Kondo, "GMDH neural network algorithm using the heuristic self-organization method and its application to the pattern identification problem", *Proc. of the 37th SICE Annual Conference*, pp.1143-1148, 1998.
- [2] T.Kondo, "Revised GMDH-type neural networks using prediction error criterions AIC and PSS", *Proc. of SCIS & ISIS 2004, WP-6-4*, pp.1-6, 2004.
- [3] S.J.Farlow ed., *Self-organizing methods in modeling, GMDH-type algorithm*, Marcel Dekker, Inc., New York, 1984.
- [4] A.G.Ivakhnenko, "Heuristic self-organization in problems of engineering cybernetics", *Automatica*, Vo.6, No.2, pp.207-219, 1970.
- [5] H.Akaike, "A new look at the statistical model identification", *IEEE Trans. Automatic Control*, Vol.AC-19, No.6, pp.716-723, 1974.
- [6] H.Tamura and T.Kondo, "Heuristics free group method of data handling algorithm of generating optimum partial polynomials with application to air pollution prediction", *Int. J. System Sci.*, Vol.11, No.9, pp.1095-1111, 1980.
- [7] N.R.Draper and H.Smith, *Applied Regression Analysis*, John Wiley and Sons, New York, 1981.

Applying Neural Networks for Diagnosis of Cancer Relapse

Kenneth J. Mackin

Department of Information Systems

Tokyo University of Information Sciences

1200-2 Yatoh-cho, Wakaba-ku, Chiba 265-8501, Japan

mackin@rsch.tuis.ac.jp

Abstract

Early detection of cancer relapse is very important for cancer patients, but prevention or early diagnosis of cancer relapse can be very difficult, depending on the type of cancer involved. In this research, we use real data for cancer operation patients, and investigate the possibility of applying artificial neural networks to predict early relapse. Artificial neural networks (ANN) can be characterized by its "black box" approach to learn and classify complex data patterns.

For this research, we propose applying 3 layer network structure (1 input layer, 1 hidden layer, 1 output layer) for the training of early cancer relapse classification, using the neural network to learn the complex relationship between risky and safe patient data. The input will include all the provided patient data including blood test results and the diagnosis of the cancer, and the single output of the neural network will be the risk factor or possibility of cancer relapse.

We analyze the data by using artificial neural networks using back propagation training, and compare the validity of predicting early relapse from the provided cancer patient data. We conclude with a discussion of the results and the validity of applying neural networks to assist physicians in predicting early cancer relapse.

1 Introduction

Recently, there is increased interest in applying data analysis methods to medical data, in order to find useful information from patient data which can be applied to medical diagnosis. On the other hand, medical data is complex and often contain error or noise in each data, and is therefore difficult to analyze using simple statistical methods. For example, early detection of cancer relapse is very important for cancer patients, but prevention or early diagnosis of cancer relapse can be very difficult, depending on the type of cancer involved. In this research, we use real data for cancer operation patients, and investigate the possibility of applying artificial neural networks to predict early relapse.

Artificial neural networks (ANN) can be characterized by its "black box" approach to learn and classify complex data patterns. For this research, we propose applying 3 layer neural network structure (1 input layer, 1 hidden layer, 1 output layer) for the training of early cancer relapse classification, using the neural network to learn the complex relationship between risky and safe patient data. We use actual medical data of kidney cancer (renal cell carcinoma) patients provided by Kitasato University Hospital, and aim at predicting the occurrence of cancer relapse in kidney cancer patients within 5 years.

2 Kidney (renal cell) cancer data

For the experiment data, we used actual kidney cancer (renal cell carcinoma) cancer patient data provided by Kitasato University Hospital.

Surgery to remove part or all of the kidney (nephrectomy) is the most popular treatment for kidney cancer, and in general 80% of the patients do not have cancer relapse, or recurrence of kidney cancer. The provided patient medical records also show the same ratio, and approximately 20% of the data record relapse within 5 years. The patient medical records show no strong 'markers' for patients with high relapse risks, and there is no simple correlation between medical test results and occurrence of relapse within 5 years. Therefore, we propose applying artificial neural networks which can learn non-linear patterns in data, for categorizing high risk and low risk patients from the medical test data.

3 Artificial Neural Network

Artificial neural networks (ANN) can be characterized by its "black box" approach to learn and classify complex data patterns. For this research, we propose applying 3 layer network structure (1 input layer, 1 hidden layer, 1 output layer) for the training of kidney cancer relapse risk classification, using the neural network to learn the complex relationship between medical test data of kidney cancer patients.

First we describe the basic artificial neural network for land cover classification. We considered the 3 layer artificial neural network (1 input layer, 1 hidden layer, 1 output layer) as the basic training classifier. We use a sigmoid function for the synapse function of the neuron, with back propagation (BP) training of the medical test data. The number of hidden neurons was

decided by results of preliminary experiments of the neural network.

For the network training we used the database of collected MODIS sensor data, and applied BP training based on the difference between classified land cover and land-truth data provided by the Japanese Ministry of the Environment.

The constructed ANN structure took 12 medical test and diagnosis data for input, and output 1 value for the categorizing the risk of cancer relapse. The medical database contained 162 patient data, of which 2/3 were used for training, and the remaining 1/3 were used for untrained testing data.

4 Conclusion

Figure 1 shows the training curve of trained and untrained data using the artificial neural network. The results showed that for the untrained data the error rate was 0.2. The error rate was still quite high, showing that the medical data was indeed difficult to learn from.

For future works, we will consider processing the input data prior to applying to neural network training, in order to improve the categorization accuracy.

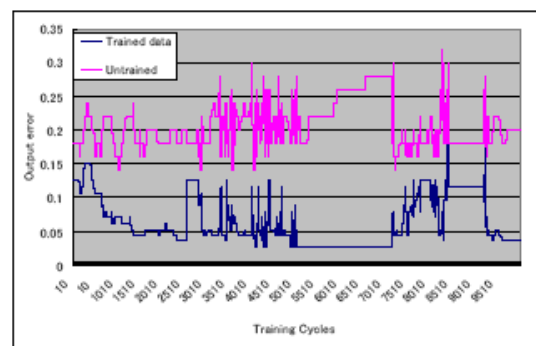


Figure 1. Training curve results

Learning how, what, and whether to communicate: emergence of protocommunication in reinforcement learning agents

Takashi Sato
stakashi@oist.jp

Eiji Uchibe
uchibe@oist.jp

Kenji Doya
doya@oist.jp

Initial Research Project (IRP), Okinawa Institute of Science and Technology (OIST)
12-22, Suzaki, Uruma, Okinawa, Japan, 904-2234

Abstract

This paper examines whether and how a primitive form of communication emerges between adaptive agents by using their excess degrees of freedom in action and perception. As a case study, we consider a game in which two reinforcement learning agents learn to earn rewards by intruding into the other's territory. Our simulation showed that the agents with lights and light sensors could learn turn-taking behaviors by avoiding collisions using visual communication. Further analysis revealed that there was a variety in what message is mapped to what signal, and in some cases there was role differentiation into a sender and a receiver.

Keywords: Reinforcement Learning, Intrusion Game, Emergence of Protocommunication, Role Differentiation

1 Introduction

The prototype of communication, or protocommunication, would have emerged to help individuals to earn rewards and to improve fitness. Then how did protocommunication emerge based on what capacity of individuals? These questions have been discussed in various fields for a long time, but unlike other questions in archeology, these questions are hard to answer as there is no fossil of communication until written languages emerged recently. Thus, we address this question by "understanding by construction" using mathematical modeling and computer simulations [1].

The studies on emergence of communication can be classified into two broad categories: one adopting evolutionary optimization [2, 3] and the other employing learning agents [4, 5]. However, a major limitation in most previous studies is that they assumed the pre-existence of the basic frameworks for communication, such as signals and meanings or a speaker and a hearer, and just verified the evolution or learning of mappings between signals and meanings by taking the success of

communication itself as the objective function. Therefore, it is difficult for those studies to answer how communication emerged from a world where concepts like signals, words, and speaking did not exist.

The purpose of this study is to test if communication can emerge between individuals who have basic behavior learning functions but do not have dedicated mechanisms or absolute needs for communication. Specifically, we run a case study of an "intrusion game" in which two agents move on a linear track and earn rewards by intruding into the other's territory while avoiding collisions. We consider what action, sensation and memory capacities are necessary for learning of cooperative behaviors, and when it is learned, what meanings agents assign to their excess degrees of action and sensation. Further, we investigate the developmental process of cooperative behaviors by communication and the cases of role differentiation into a speaker and a hearer.

2 Intrusion Game

We consider an "intrusion game (IG)," which simplifies situations like a turf war between foraging animals. Two players can move back and forth on a one dimensional space with four slots. Players are bounded by walls on the "west" and "east" ends of the track and cannot jump over or stay together in the same slot with another agent. Figure 1 depicts six possible sets of positions that the players can take. We denote the six position patterns by 0 to 5. The "west" player can get a reward by entering the east half of the track (i.e., position pattern 5) and the "east" player by entering in the west half (i.e., position pattern 2) without a collision. A punishment (negative reward) is given when a player collides with a wall or another player.

A crucial problem in this game is how the players resolve the conflict at the position pattern 4. If the players act selfishly, i.e., to maximize its own reward,

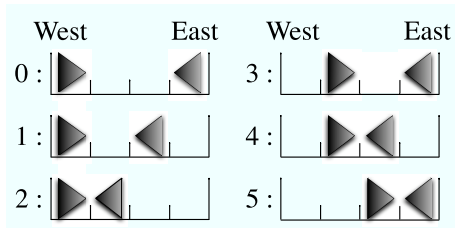


Figure 1: Six possible position patterns of the players, denoted by 0 to 5.

both would take an action to move forward, but it will cause a collision with negative rewards to both players.

3 Reinforcement Learning Agents

In order to test whether agents with general action learning capability can also learn to communicate, we adopt reinforcement learning agents [6] which can learn various behaviors based on rewards and punishment. We use the Q-learning method [6] which is standard for discrete tasks like IG. Q-values are updated by the following equation.

$$Q(s_t, a_t) := Q(s_t, a_t) + \left[r_{t+1} + \max_a Q(s_{t+1}, a) - Q(s_t, a_t) \right],$$

where α is a learning rate ($0 < \alpha < 1$), γ is a discount rate ($0 < \gamma < 1$), and $r(t)$ is the reward given after action $a(t)$ was taken at state $s(t)$. We used the ϵ -greedy policy in which an actions is randomly selected with probability ϵ and otherwise an action that maximize Q-value for a given state is selected.

In order to investigate how the agents' sensory, action, and memory capabilities affect the learned behaviors, we tested four types of agents. A null or N-type agent simply has two moving actions (backward or forward) and can sense the position pattern (0 to 5) of the two agents. In addition, a light-capable, or L-type agent has actions of turning on or off its headlight and also a light sensor to see if the other agent's light is on or off. A memory-based, or M-type agent keeps the memory of its previous action (backward or forward) to augment its state space. A light-and-memory, or LM-type agent has both light signaling and memory capabilities.

4 Simulation Results

We performed 10 simulation runs each for the four types of agents with the following setups: positive reward +1 for successful intrusion, negative rewards -1 each for collision with the wall and the other agent, $\epsilon = 0.01$, $\gamma = 0.01$, and $\alpha = 0.9$.

4.1 Agents' Behaviors

First, we present examples of typical behavioral patterns obtained from the analysis of the change of each agent's position pattern (Fig. 2).

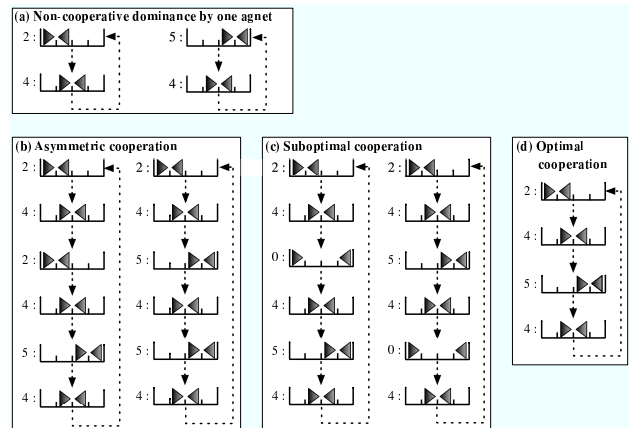


Figure 2: Four examples of typical behavioral patterns. (a) Non-cooperative dominance by one agent. (b) Asymmetric cooperation. (c) Suboptimal cooperation. (d) Optimal cooperation.

Figure 2(a) shows a non-cooperative dominance by one agent. In this pattern, only one agent can earn a positive reward every two steps. The other can get no reward, but can receive negative reward if it changes its behavior. Figure 2(b) presents an asymmetric cooperation which can be seen only in LM-type agents. In this case, one agent can get two positive rewards during a six step cycle, the other can obtain while only once. Figure 2(c) depicts a suboptimal cooperation leading to one reward every six steps. Figure 2(d) shows an optimal cooperation in which both agents earn a reward every four steps.

We analyze the occurrence frequency of four typical behavioral patterns for the four types of agents. As can be seen in Fig. 4, the agents without light (N- and M-type) can learn only the non-cooperative dominance. In contrast, the agents with light (L- and LM-type) can show various cooperation. Further, LM-type agents can achieve the optimal cooperation more frequently than L-type agents without action history.

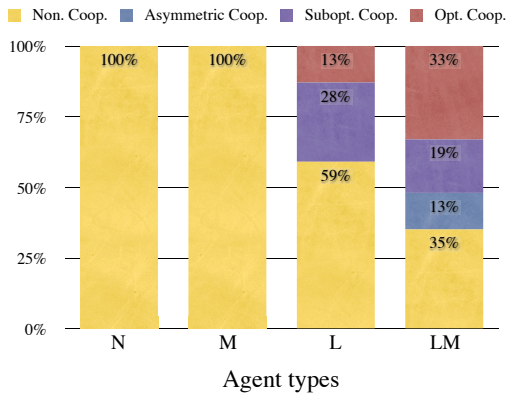


Figure 3: Occurrence frequency of four typical behavioral patterns for four types of agents.

4.2 Developmental Process

Next we examined how the behaviors changed by learning before converging to one of four typical patterns. Figure 4 shows the developmental history of four LM-type agents who acquired one of four typical behavioral patterns at final episode. We recorded the Q-values of the agents every 1,000 steps and let the agents play the IG (with $\epsilon = 0$) from all possible initial states¹.

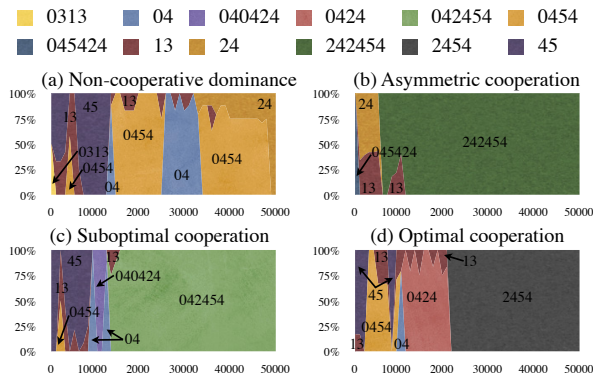


Figure 4: History of occurrence frequency of behavioral patterns. The x -axis and the y -axis of each figure are the steps and the occurrence frequency of converged behavioral patterns, respectively. Each numerical string represents a sequence of position patterns in a cyclic behavior.

Figure 4(a) shows an example of the history of a pair that converged to non-cooperative dominance by

¹For example, the number of states of the L-type agents is 24, where initial positions and light states are 6 and 4, respectively.

the east agent. The other diagrams in Fig. 4 indicate (b) asymmetric, (c) suboptimal and (d) optimal cooperation. A common feature in these cooperative cases that the agents experienced took both position pattern sequences 4 to 2 and 4 to 5 in the early stage before becoming able to switch between the two.

4.3 Variety of Signaling

We observed emergence of various types of communication emergence. Figure 5 exemplifies four typical types of communication that realizes the optimal cooperation.

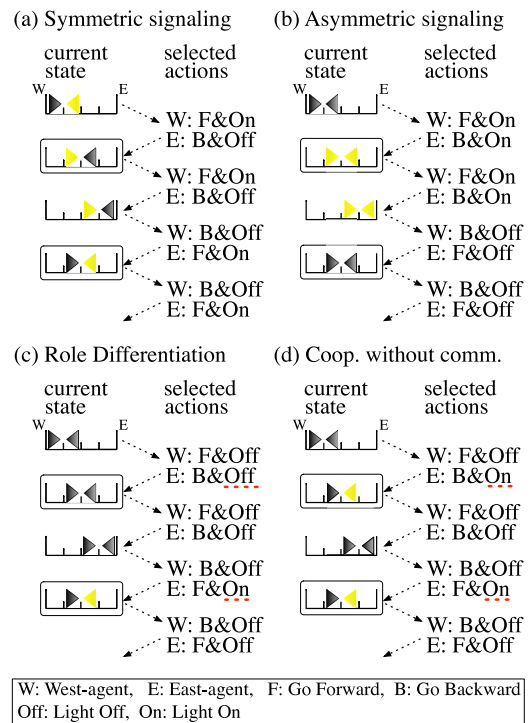


Figure 5: Typical examples of emerged communication. (a) Symmetric signaling. (b) Asymmetric signaling. (c) One-way communication between a sender and a receiver after a role differentiation. (d) Cooperation without communication.

Figure 5(a) shows an example of symmetric signaling in which agents can resolve the conflict at the position pattern 4 by alternately turning on the light while stepping forward. This means that the agents can convey their next actions as messages by their lights. An asymmetric signaling can also be observed, in Fig. 5(b), in which one agent turns the light on to step forward, while another agent turns the light on to step back.

Unlike the symmetric and asymmetric signaling, communication examples shown in Fig. 5(c) and (d) can be seen only in LM-type agents. Figure 5(c) depicts a one-way communication between a sender (the east agent) and a receiver (the west agent) after a role differentiation. In this case, only the east agent uses its light source, and the west agent behaves according to the east agent's light signal. The east agent, who cannot rely on the light signal of the west agent, determines its actions based on memory of its own past action in order to solve the conflict on the position pattern 4. Figure 5(d) is a case of optimal cooperation without communication. As can be seen, the east agent always turns on its light when entering the position pattern 4 from 2 or 5. Therefore, the west agent cannot solve the conflict on the position pattern 4 by using the east agent's light signal. Both agents behave based only on the memory of their past actions.

5 Discussion

Our simulation study showed that simple communication can emerge from iteration of searching for roles of redundant actions through a generic reinforcement learning process and interaction with the others.

Animal communication is defined as a transmission of signals that senders can profit by reactions of receivers [7]. Our simulation confirms that this type of communication can be emerged from repeated interactions between reinforcement learning agents with enough physical capacity. Tomasello claims that communicative signals can be created by forming each other's behaviors between two individuals through iteration of social interaction [8]. Our simulation results also support his claim.

Tomasello furthermore advocates that the following is important for acquisition of habitual use of linguistic symbol [8]. An individual 1) understands that the others are individuals with some intents, 2) participates in a joint attention situation, 3) comprehends the other's intent in such situation, and 4) can use a symbol that others used toward the individual. Although our reinforcement learning agents did not explicitly have such functions, the simple two-person setup of the game probably made it unnecessary to use attentive mechanisms.

6 Conclusion

We have proposed an intrusion game (IG) for investigating the emergence of protocommunication from a

world where a teacher of communication or even any dedicated mechanisms for communication do not exist.

Using computer simulations of IG, we have shown that agents who can turn on/off their lights as redundant actions became able to spontaneously acquire meanings of light signals and cooperate with the other agent. We have also found that agents with working memories can differentiate their roles as a sender and a receiver. Further, our simulation demonstrated that a cooperation without communication can emerge from interaction between the agents having both signaling and memory capabilities.

Our simulation results suggest that repeated interaction between individuals with a reinforcement learning function can play an important role in establishing protocommunication, even if individuals do not have dedicated mechanism for communication.

References

- [1] T. Hashimoto, *Knowledge Science* (in Japanese), K. Sugiyama, *et al.* (Eds.), Kinokuniya shoten, pp.126–131, 2002.
- [2] A. Cangelosi, D. Parisi, "The emergence of a language in an evolving population of neural networks," *Connection Science*, 10(2), pp.83–97, 1998.
- [3] D. Marocco, S. Nolfi, "Emergence of communication in embodied agents: co-adapting communicative and non-communicative behaviours," A. Cangelosi, *et al.* (Eds.), *Modeling language, cognition and action: Proceedings of the 9th Neural Computation and Psychology Workshop*, 2004.
- [4] L. Steels, P. Vogt, "Grounding adaptive language games in robotic agents," C. Husbands, I. Harvey, (Eds.), *Proceedings of the Fourth European Conference on Artificial Life*, MIT Press, 1997.
- [5] S. Tensho, *et al.*, "Gradual emergence of communication in a multi-agent environment" (in Japanese), *IPSSJ SIG-ICS*, 139, pp.73–78, 2005.
- [6] R. S. Sutton, A. G. Barto, *Reinforcement Learning*, MIT Press, 1998.
- [7] T. R. Halliday, P. J. B. Slater, (Eds.), *Animal Behavior*, Blackwell Scientific Publications, 1983.
- [8] M. Tomasello, *The Cultural Origins of Human Cognition*, Harvard Univ. Press, 1999.

A neural network model of the olfactory system of mice: Computer simulation of an attention behavior of mice for some components in an odor

Zu Soh[†], Toshio Tsuji[†], Noboru Takiguchi^{††}, and Hisao Ohtake^{†††}

[†]Graduate School of Engineering, Hiroshima Univ., Hiroshima 739-8527, Japan

^{††}Graduate School of Advanced Sciences of Matter, Hiroshima Univ., Hiroshima 739-8530, Japan

^{†††}Graduate School of Engineering, Osaka Univ., Osaka 565-0871, Japan

Abstract

Recently, it was observed that mice could identify an odor by paying attention to only a few components comprising the odor. It was also reported by Nakamura *et al.* [1] that each individual is attracted to different components. This mechanism is called “attention;” however, it has not been completely elucidated.

In this paper, first, we propose a novel artificial neural network model based on the biological structure of an olfactory system. Then, a series of computer simulations of odorant discrimination are performed to confirm the ability of attention of the proposed model. Finally, we changed the connective weights between the neurons to simulate individual differences. The simulation results lead us to believe that the inhibitory connections from piriform cortex to olfactory bulb may contribute to the individual differences that are observed in the behavioral experiment.

1 Introduction

In recent years, the demand for odor processing apparatuses has been increasing in fragrance and entertainment industries. Odorant information is one that is difficult to handle because it is composed of a combination of 200 to 400 thousands of molecules [2], thereby forming high-dimensional information. Therefore, it requires vast amounts of computation to discriminate or classify odors. Thus far, to reduce the dimension of odorant information, the ability of most odor discriminating apparatuses, for example, an electronic nose for banana ripeness developed by Llobet *et al.* [3] has been specialized for particular odors; further, it is not comparable to that of a living nose. Therefore, learning from the olfactory system of a living nose would be one of the most efficient and prospective approaches.

A number of studies have been reported on the olfactory system of mice. It can be considered to have

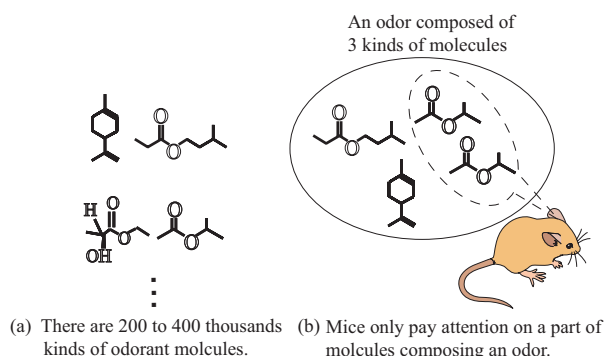


Figure 1: The concept of attention behavior

three parts: olfactory receptors (ORs), which respond to odorant molecules; an olfactory bulb (OB), which performs the integrated process of the response of the ORs; and a piriform cortex (PC), which discriminates the odorants based on the information provided by the OB [2] (Fig.2). Haberly *et al.* [4] have revealed more detailed structure of the olfactory system anatomically. Through a series of behavioral experiments on odor discrimination, Nakamura *et al.* [1] reported that mice could identify an odor focussing on only a part of components composing the odors. It was also observed that each individual focuses on different components. This behavior is termed as “attention.” The mechanism of attention was researched by Li *et al.* [5] using their computer model of the OB; they referred to attention as “adaptation”. Li *et al.* suggested that an inhibitory signal to the OB might be one of the causes of attention. However, the origin of the inhibitory signal and its control mechanism is still unknown; thus, the mechanism of attention has not been completely elucidated.

In this research, we first construct a novel artificial neural network model of the olfactory system that consists of OR, OB, and PC based on biological insights [4]. In the proposed model, the inhibitory connection from the PC to the OB reported by Heimer [6] are also taken into account. Then, a series of computer

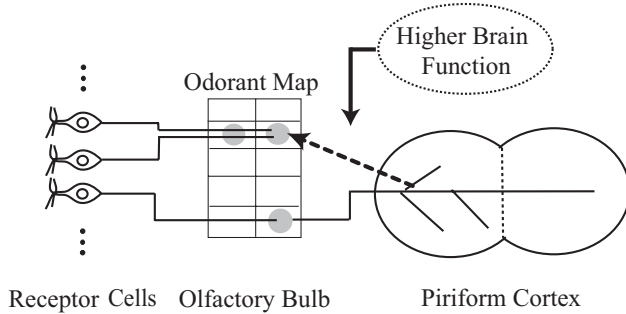


Figure 2: Schematic figure of the olfactory system.

simulations of the model is carried out with changes in the inhibitory connections. The simulation results are compared to the result of the behavioral experiment performed by Nakamura *et al.* to elucidate the mechanism of attention. In this paper, we report that the inhibitory connections from the PC to the OB can cause attention, and differences in the inhibitory connections can cause the individual differences among mice.

2 Behavioral experiments for odor discrimination of mice

Nakamura *et al.* implemented a series of behavioral experiments on odor discrimination by mice to reveal the behavior of attention. This section describes the experiments and its results.

2.1 Methods

The behavioral experiments on odor discrimination by mice were carried out by Nakamura *et al.* [1] using a Y-shaped passage (Y-maze), as shown in Fig.3. First, a mouse that is deprived of water is placed at the start point (point C). The mouse was allowed to drink water as a reward only if it chose the correct point-A or B-from where the odor emanated. Then, one trial was defined as the duration from the mice starting at point C to its arrival at either point A or B. Twenty-four trials, which were defined as one session, were performed in a day for each mouse. The accuracy rate at which the mice chose the rewarded odor was recorded. When the correct rate surpassed eighty percent, it was considered that the mice have learnt the rewarded odor. Because the experiments required discriminating between two kinds of odors, an accuracy rate of fifty percent indicates that the mice could not discriminate between the odors at all. In the experiments, the mice were to learn an rewarded odor [Ci:EB:IA] that composed of three types of molecules-isoamyl acetate (IA), ethyl butyl (EB), and citral (Ci). Then,

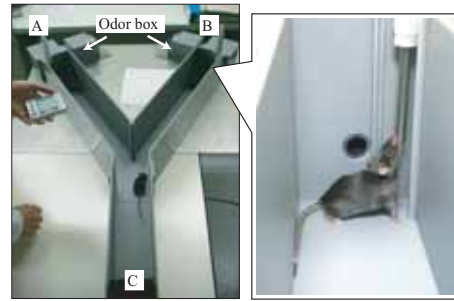


Figure 3: Structure of Y-maze and drinking behavior of mouse (revised from the figure in the literature 1.)

the mice were made to discriminate the rewarded odor from the odors containing the same types of molecules as the rewarded odor ([Ci], [EB], [IA], and [EB:IA]) [1].

2.2 Results

Fig.4 shows the experimental results of two out of the eight individuals on whom the experiment was performed. In Fig.4, the vertical and horizontal axes show the accuracy rate and the odors for discrimination, respectively.

In the case of individual A, we observe that the accuracy rates for odors containing the EB molecule ([EB], [EB:IA]) are approximately fifty percent. This result implies that individual A paid attention only on the EB molecules to discriminate between the odors; therefore, it could not discriminate between the odors of [EB] and [EB:IA] from the rewarded odor containing the EB molecules. Two out of eight individuals paid attention on the EB molecules.

Now, in the case of individual B, we observed that the accuracy rate for odor [EB:IA] is approximately fifty percent. This result implies that individual B paid attention to the combination of molecules EB and IA. It was observed that five out of eight individuals paid attention to the combination of EB and IA.

From these results, Nakamura *et al.* suggested that the mice pay attention to a part of the molecules that is contained in the odors to perform the odor discrimination task; further, there are individual differences between the mice with respect to the molecules that they would pay attention to.

3 A model of the olfactory system of mice

In this section, we propose a model of the olfactory system constructed based on biological insights. An overview of the proposed model is shown in Fig.5. In

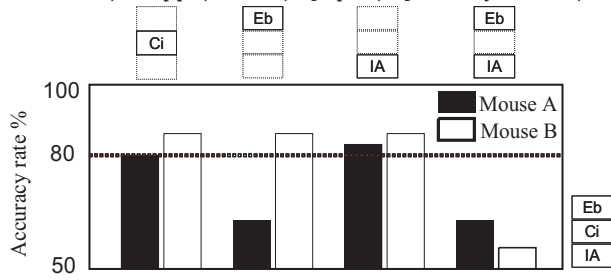


Figure 4: Results of odor discrimination experiment. (unpublished data)

Fig. 5, the R layer comprises olfactory receptors (ORs) that respond to odorant molecules; B layer, the olfactory bulb (OB); P layer, the anterior piriform cortex; and Z layer, the post piriform cortex that outputs the discrimination results. Each layer consists of a neuron model, and the neuron models are connected based on the biological insights [4], [6]. The connective weights are subject to change by Hebbian learning rule. The details of each layer are given below.

3.1 Receptor layer

There are about 1000 types of ORs in the nasal passage of mice, and each type of OR responds to different types of molecules [7]. The proposed model is designed to discriminate odors that consist of N types of molecules S_1, S_2, \dots, S_N ; thus, the R layer is composed of N types of receptors. The density of each molecule is expressed as a value in the interval $[0, 1]$. The receptor model is defined by using the following equation according to the general neuron model, which is expressed as the sigmoid function [8]:

$$U_{R(i,j)}(t) = \frac{1}{1 + \exp\{-\epsilon_{R(i,j)}(u_{R(i,j)}(t) - \theta_{R(i,j)})\}}, \quad (1)$$

where ϵ is the gradient of sigmoid function; $u(t)$, the internal state of a neuron at time step t ; and θ , the firing threshold of the neuron. Each receptor of the j column in the R layer, which is shown in Fig. 5, responds to the same molecule S_j with a different firing threshold θ . The internal state of each receptor in the R layer is defined as $u_{l(i,j)}(t) = s_i(t)$. The output of the receptors calculated by equation (1) are inputted to the OB layer (B layer).

3.2 Olfactory bulb layer

The olfactory bulb consists of glomeruli, excitatory neurons known as mitral cells, and inhibitory neurons

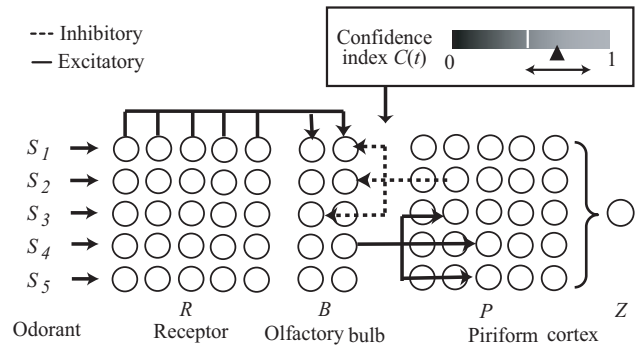


Figure 5: A model of the olfactory system in mouse.

known as granule cells. Glomeruli are a convergence of the nerve terminal extending from the olfactory receptors, and they map the responded molecules. There are around 1000 pairs of glomeruli on the olfactory bulb surface. The response pattern of the glomeruli is called odorant map [9]. The outputs of the glomeruli are transmitted to the mitral cells. Further, the mitral cells receive an inhibitory input from the PC via the granule cells [6].

In the proposed model, the glomeruli is omitted for simplification, and the receptor $R_{i,j}$ that responds to the same molecule S_j is directly connected to the same mitral cell $B_{i,j}$. Mitral cell $B_{i,j}$ maps molecule S_j , and the firing pattern of the B layer represents the odorant map-mediated mitral cells. The neurons in the B layer receive excitatory input from the R layer and inhibitory input from the P layer; thus, the internal states $u_{B(i,j)}(t)$ are as follows:

$$u(t)_{B(i,j)} = \sum_{R(m,n)} w(t)_{R(m,n),B(i,j)} U_{R(m,n)}(t) - \sum_{P(x,y)} w_{P(x,y),B(i,j)}(t) U(t)_{P(x,y)}, \quad (2)$$

where $w_{R(m,n),B(i,j)}$, $w_{P(m,n),B(i,j)}$ are the connective weights from the B and P layers, respectively. The output of each neuron, $U_{B(i,j)}(t)$, is expressed as a sigmoid function in equation (1). The outputs of mitral cells are transmitted to neurons in the PC.

3.3 Piriform cortex layer

The PC can be divided into anterior piriform cortex (APC) and posterior piriform cortex (PPC). It is considered that the APC processes the input from the OB, while the PPC discriminates the odor [4]. Therefore, in the proposed model, the PC layer was divided into the P and Z layers. Further, it was found by Heimer *et al.* that inhibitory connections exist from

the PC to the OB [6]. However, these connections are very complex and consist of individual difference, and hence, the connections between the B and P layers are randomly connected in the proposed model. The internal state $u_{P(i,j)}(t)$ of each neuron in the P layer is given by the following equation:

$$u_{P(i,j)}(t) = \sum_{B(m,n)} w_{B(m,n),P(i,j)}(t) U_{B(m,n)}(t), \quad (3)$$

where $w_{B(m,n),P(i,j)}(t)$ are the connective weights from the B layer to the P layer. On the other hand, the internal state $u_Z(t)$ of the neuron in the Z layer is given by the following equation:

$$u_Z(t) = \sum_{P(m,n)} w_{P(m,n),Z}(t) U_{P(m,n)}(t), \quad (4)$$

where $w_{P(m,n),Z}(t)$ are the connective weights from the P layer to the Z layer. Similar to the R and B layers, the output of each neuron in the P and Z layers is defined as a sigmoid function of equation (1).

The discrimination result was obtained according to the output of the Z layer. Output $U_Z < 0.5$ indicates that the model has discriminated the odor as unrewarded odor, while output $U_Z \geq 0.5$ indicates rewarded odor. In this way, the Z layer discriminates odor based on the output of the P layer.

3.4 Learning algorithm

The connective weights between the neurons in each layer are initialized by a uniform random value of interval $[0, 1]$ and are updated by the Hebbian learning rule [10]:

$$w_{l(m,n),k(i,j)}(t+1) = w_{l(m,n),k(i,j)}(t) + \delta w(t)_{l(m,n),k(i,j)},$$

$$\delta w_{l(m,n),k(i,j)}(t) = \alpha \{U(t)_{k(i,j)} - b_k\} \{U(t)_{l(m,n)} - b_l\},$$

where α is the learning rate; b_l and b_k are the thresholds of the change in the sign of $\delta w_{l(m,n),k(i,j)}(t)$. The connective weights between the B, P and P, Z layers are updated by the Hebbian rule. The connection between the R, B layer are considered to be genetically determined [9] and as a result the connective weights remained unchanged.

Learning is assumed to be controlled by a higher brain function. For simplification, the higher brain function is modeled as confidence index $C(t)$ ($0 \leq C(t) \leq 1$). When the discrimination result is correct, the confidence index increases by $1/n$, while for an incorrect result, the confidence index decreases by $1/n$. Here, n is defined as a constant number representing the volatility of the confidence index. When

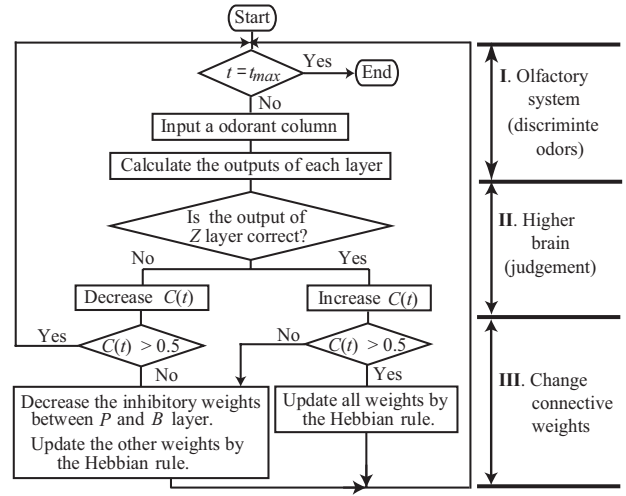


Figure 6: The flowchart of weight training.

the confidence index $C(t) \geq \theta_c$, the inhibitory connection, from the P layer to the B layer, is updated by the Hebbian learning rule, while when $C(t) < \theta_c$, the inhibitory connection is decreased by a constant rate β ($0 \leq \beta \leq 1$). The learning algorithm can be summarized in Fig.6.

4 Simulation

In this section, a series of simulations is performed to confirm if the proposed model can simulate attention behavior and individual differences.

4.1 Simulation of learning and attention

First, the connection between the B and P layers was initialized to a random value in the interval $[0, 1]$. For this initial state, the model was labeled as a neural network model M1. One step was defined as from inputting molecules to R layer to output of Z layer. The rewarded odor A ($N = 5, s_1 = s_2 = s_3 = 1, s_4 = s_5 = 0$) was repeatedly inputted to the model for 15 steps. While these steps were carried out, the weights were subject to be updated toward the neuron in Z layer fires stronger by the algorithm shown in Fig.6.

The changes in the outputs of the neural network model M1 is shown in Fig.7; where (a) and (b) show the firing patterns of each layer when $t = 1$ and $t = 15$, respectively. The output of each neuron is represented by a square. The larger the output of the neuron is, the whiter the corresponding square is. The changes in the inhibitory weights from the P layer to the B layer and the confidence indices are also shown in Fig.9 and Fig.10, respectively. From Fig.7(a), it can be observed that the neuron in the Z layer fires weakly when

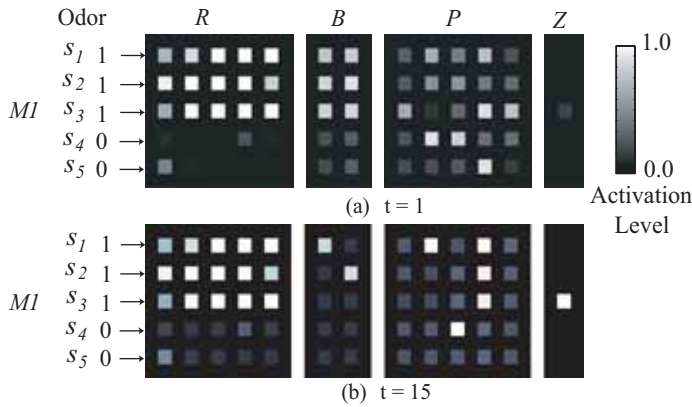


Figure 7: Changes in output states of M1.

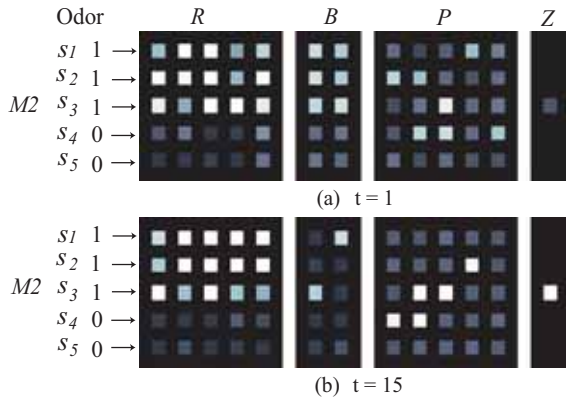


Figure 8: Changes in output states of M2.

$t = 1$. This means that the model discriminated the odor as unrewarded odor, which is incorrect discrimination. After the rewarded odor A was repeatedly inputted, connective weights were updated by the algorithm shown in Fig.6; thus, the model M1 learnt odor A as the rewarded odor. This result can be observed in Fig.7(b) in which the neuron in the Z layer fires strongly when $t = 15$.

At the same time, the inhibitory connective weights from the P layer to the B layer increases, for example, the inhibitory weights from $P_{4,3}$ to $B_{3,2}$ increase, as shown in Fig.9. Hence, the neurons mapping molecule S_3 were inhibited. As the result, the model M1 discriminates odors only by molecules S_1 and S_2 , for which the attention ability of the model M1 has been confirmed.

Next, the same simulation, which was described above, was carried out for another neural network model M2, which is initialized with different connective weights of inhibitory connections from the P layer to the B layer. This simulation result is shown in Fig.11; (a) and (b) show the firing pattern when $t = 1$ and $t = 15$, respectively. When $t = 15$, the model learnt odor A as a rewarded odor because the neuron

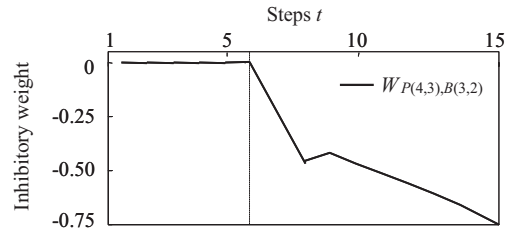


Figure 9: Changes in inhibitory weight from the P to the B layers.

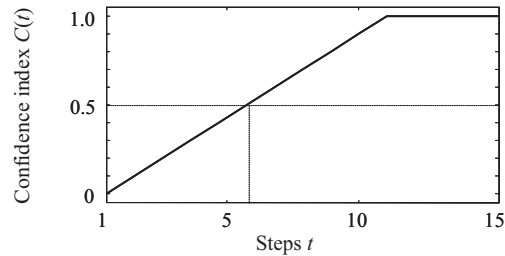


Figure 10: Changes in the confidence index.

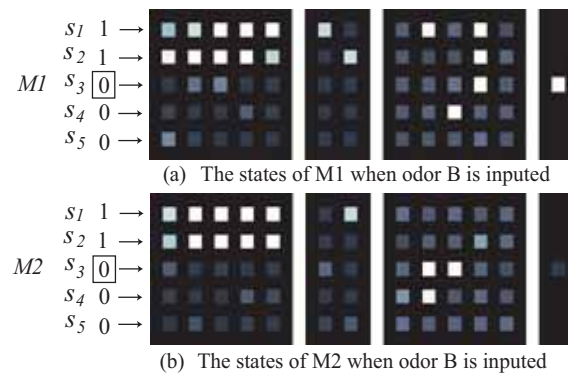


Figure 11: The states of M1 and M2 when odor B is inputted.

in the Z layer fired strongly. It can be also observed that M2 has paid attention to molecules S_1 and S_3 , while M1 has paid attention on S_1 and S_2 . These results suggest that the difference in the initial weights of inhibitory connections from the P layer to the B layer can make the proposed model pay attention to different molecules.

4.2 Individual differences in attention

In section 4.1, the neural network models M1 and M2 have learnt to discriminate the rewarded odor A by paying attention to the different molecules. Here, to determine the discrimination ability of both the models, an unrewarded odor B, which contained some of the common molecules from the rewarded odor A, is inputted to M1 and M2.

The result is shown in Fig.11. Fig.11(a) and (b) show the outputs of M1 and M2 respectively when the

unrewarded odor B is inputted. It can be observed from Fig.11(b) that the neuron in Z layer fired weakly, thus M2 has successfully discriminated the odor B as the unrewarded one. However, M1 has discriminated it as the rewarded odor A, because the neuron in Z layer fired strongly as the same way when the odor A was inputted. In the simulation described in the previous section, M1 has paid attention to molecules S_1 and S_2 . Therefore, whenever the inputted odor contains both molecules S_1 and S_2 , M1 would discriminate it as the rewarded odor A.

These simulation results correspond to the behavioral experiment carried out by Nakamura *et al.* [1], which was described in section 2. Further, the results lead us to believe that the individual differences in odor discrimination could be caused by differences in inhibitory connections from the anterior piriform cortex (P layer) to the olfactory bulb (B layer). As mentioned in section 1, Li *et al.* [5] have suggested that the attention is caused by inhibitory signal. Our simulation results support their hypothesis and imply that the unspecified origin of the inhibitory connection might be the anterior piriform cortex.

5 Conclusion

In this paper, we focused on the attention behavior of mice observed from behavioral experiments, and proposed a neural network model of their olfactory system based on biological insights. A series of simulations of the proposed model was carried out so that the attention behavior was observed. Also, by changing the inhibitory connection from piriform cortex to olfactory bulb, a possible cause of the individual differences in attention was discussed.

Although the proposed model is a macroscopic model, the simulation results showed that it captured the feature observed in the odorant discrimination experiment of mice. Further works have to be carried out to enable the model to deal with more complicated odorant information like odors that exist in the real world. Therefore, for next step, we are planning to improve the receptor model and olfactory bulb model.

Acknowledgements

This work is partially supported by the 21st Century COE Program of JSPS (Japan Society for the Promotion of Science) on *Hyper Human Technology toward the 21st Century Industrial Revolution*.

The authors would like to thank Dr.Okuhara Keisuke for his biological advise, Dr.Suzuki Michiyo and Mr.Hirano Akira for thier editing skill and having always been supportive.

References

- [1] T. Nakamura, K. Okuhara, and N. Takiguchi, "Explore algorithms in olfactory system of mice," *Software Biology*, Vol.4, pp.45-50, 2005. (in Japanese)
- [2] T. Kurahashi, "Olfactory physiology, from nose to brain, the mechanism of sensing odors," *fragrance journal*, 2004. (in Japanese)
- [3] E.Llobet, E. L Hines, J. W. Gardner, and S. Franco, "Non-destructive banana ripeness determination using a neural network-based electronic nose," *Measurement science and technology*, Vol.10 pp. 538-548, 1999.
- [4] L. B. Haberly, "Parallel-distributed Processing in Olfactory Cortex, New Insights from Morphological and Physiological Analysis of Neuronal Circuitry," *Chem. Senses*, vol.26, No.5, pp.551-576, 2001.
- [5] Z. Li, "A Model of Olfactory Adaptation and Sensitivity Enhancement in the Olfactory Bulb," *Biological Cybernetics*, vol.62, pp.349-361, 1990
- [6] L. Heimer, "Synaptic distributions of centripetal and centrifugal nerve fibres in the olfactory system of the rat. An experimental anatomical study," *Journal of Anatomy* Vol.103, pp. 413-432 1968.
- [7] L. Buck and R. Axel, "A novel multigene family may encode odorant receptors: a molecular basis for odor recognition," *Cell*, Vol. 65, pp.175-187, 1991.
- [8] P. Smolensky, "Neural and conceptual interpretation on PDP Models," *Parallel distributed processing: explorations in the microstructure*, vol. 2, The MIT Press, pp.390-431, 1986.
- [9] K. Mori and Y. Yoshihara, "Molecular recognition and olfactory processing in the mammalian olfactory system," *Progress in Neurobiology*, Vol.45, p.p.585-619, 1995.
- [10] D.O. Hebb, "The organization of behavior," John Wiley, New York., 1949.

Graphical Analysis of Time-series Data from Waste Incinerator Using Self-organizing map

Takashi Yamaguchi

Kenneth J. Mackin

Department of Information Systems,

Tokyo University of Information Sciences

265-8501 1200-2 Taniate, Wakaba-ku, Chiba, Tokyo University of Information Sciences

Abstract

The emission of dioxins from waste incinerators is one of the most important environmental problems today. It is known that optimization of waste incinerator controllers is a very difficult problem due to the complex nature of the dynamic environment within the incinerator.

In this paper, we propose applying self-organizing map (SOM) for visualizing topological information of waste incinerator data for time-series data, and aimed at finding correlation in real waste incinerator data to predict high dioxin emission.

1. Introduction

The emission of dioxins from waste incinerators is one of the most important environmental problems today. It is known that optimization of waste incinerator controllers is a very difficult problem due to the complex nature of the dynamic environment within the incinerator. This is because the environment in the incinerator is a complex dynamic environment in which the different items are dependent on each other, and is not a simple dependency relationship.

There has been past research in intelligent estimation of dioxins emission from waste incinerators. Fujiyoshi et al [1] has proposed applying fuzzy control to incinerator control to decrease the dioxins emission. Ichihashi et. al [2] has applied statistical analysis to calculate the correlation of various input signals with dioxins emissions. Fukushima [3] has proposed applying fractal fuzzy control in order to estimate and control dioxins emission.

For this research we investigate methods applying SOM to classify time-series data for complex environments, and propose applying self-organizing map (SOM) for visualizing topological information of waste incinerator data for time-series data. Our aim is to find correlation in real waste incinerator data to predict high dioxin emission.

2. Training Requirements for Waste Incinerators

For this experiment, we used sensor data from a waste incinerator plant as the time-series data, and aimed at visually classifying instances of high dioxin emission. We used real waste incinerator data provided by Hitachi Zosen Corporation. Figure 1 shows the schematic diagram of the fluidized bed waste incinerator.

The data consists of the following 12 sensor values measuring various conditions of the incinerator. Flapper angle (0 - 100.00%), oxygen concentration in incinerator exit (0 - 25.000%), garbage rate (t/H), incinerator temperature (0 - 1200.0 °C), carbon monoxide concentration (0 - 500.0ppm), incinerator pressure (-2000.0 - 1000.0ppm), cooling liquid rate (0-1.0000m³/h), conveyer belt speed (0 - 7.000rpm), primary air supply(0 - 7.500KNm³/h), secondary air supply base (0 - 7.500Nm³/h), secondary air supply modification (0 - 7.500KNm³/h).

It is known that CO (carbon monoxide) concentration over 100ppm show strong correlation with dioxins

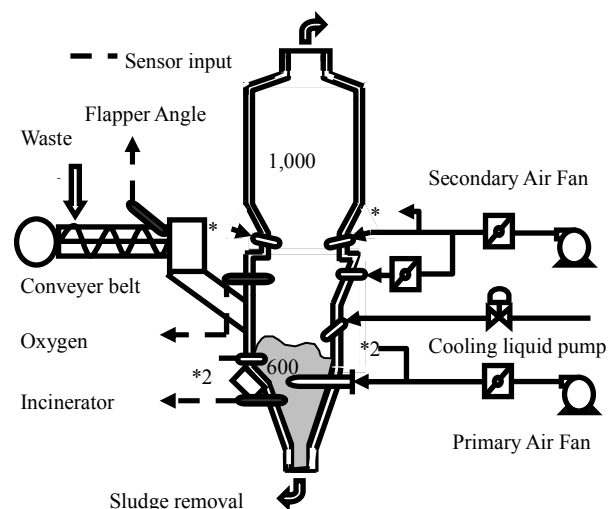


Figure 1. Schematic diagram of Fluidized Bed

concentration. For this research, we use the CO concentration as the target output, and aim to reduce the average CO concentration as well as to reduce the number of CO concentration peaks over 100ppm.

3. Learning Time-series Data using Self-organizing map

Self-organizing map (SOM) is a type of artificial neural networks proposed by Kohonen[5]. It is trained using unsupervised learning to produce low dimensional representation of the training samples while preserving the topological information of the input space. SOM applies neighborhood learning to enable the creation of close output for similar input. This feature is effective for classification and visualizing in complex problems.

On the other hand, standard SOM cannot directly handle time-series data. Several approaches to allow SOM to learn patterns in time-series data have been previously proposed, such as adding a feedback loop[7] to create a multi-layer SOM, and adding delayed time units to SOM[6].

For this research, we used delayed-time units in order to map time-series data into the input pattern space. Figure 2 shows the model of time-series data that consists of two elements (A, B) is input to SOM using delayed-time unit. Its approach to learn patterns in time-series data does not require change in the SOM method, because it is possible to implement the additional input by preprocessing.

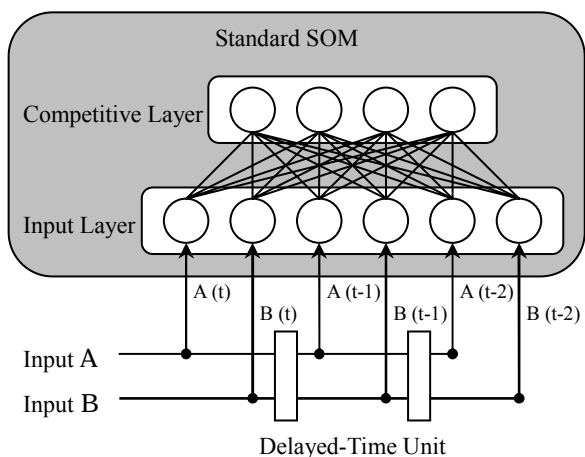


Figure 2. Model of SOM using Delayed-Time Unit

4. Method for Visualizing Information of Time-series Data

For this research we use delayed-time units to learn time-series pattern on SOM. For the output we construct the map using the weight values of the competitive layer.

For this experiment we construct the following two

patterns of maps. The first pattern of maps is visualized from difference between predicted values and the actual values of each sensor recorded for the same time frame. For the values of predicted sensor values, the weight values of winner node at each time frame were used. In this map, the purpose is to display the state of the sensor value in each time frame.

The second pattern of maps is visualized from weight values of each element of the time-series data. For example, using time-series data that consists of three elements (A, B, C), three maps are constructed for each elements. These maps can be displayed by using AND operation (ex. [A AND B,] [A AND B], and [B AND C]). This function has the aim of displaying correlation from each element of data.

Additionally, for this experiment we draw the tracks of the winner node for each time frame over the above two maps. Figure 3 shows the method for drawing tracks of the winner node. Tracks of winner nodes are drawn in a line such that newer data are emphasized. Drawing tracks of winner node have the aim of presenting the change in the temporal pattern in the visually.

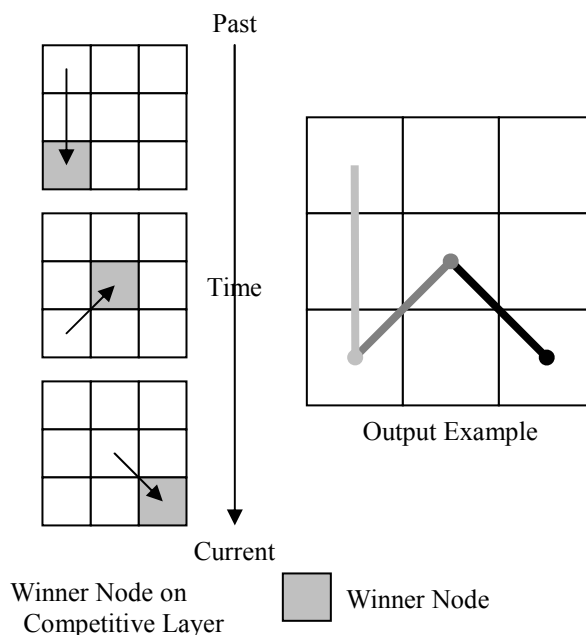


Figure 3. Visualizing Tracks of Winner Node

5. Experiment Result

For the SOM input data, we use all of the 12 sensor types, and 20 continuous time-series data (each data at 30 seconds delay for 10 minutes) per each sensor type as 1 time-series sequence. The input data used for learning was selected from a day high frequency of abnormal range of CO (>100ppm) from the incinerator sensor data base. 15000 time-series sequences were used for the input data set.

For this experiment we used following SOM. The

competitive layer of size the 100x100, and the weights for the competitive layer was initialized by random. For neighborhood function we use the Gaussian type. For the decision of winner node we use Euclidian distance.

Figure 4 and Figure 5 is the maps that constricted by proposed method at the same time frame. Figure 6 shows

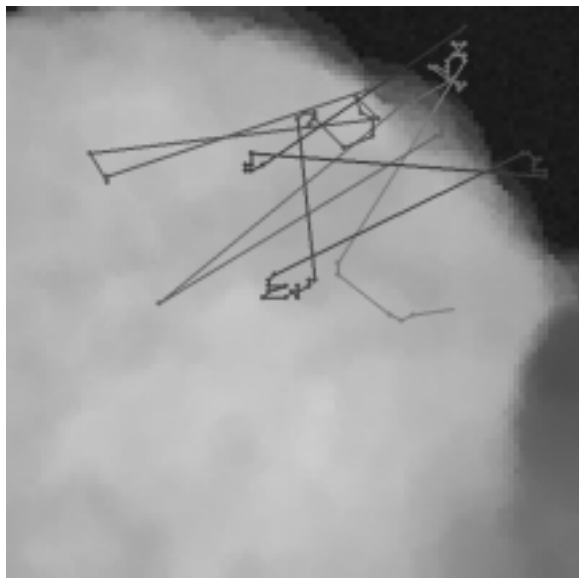


Figure 4. Map of difference between predicted values and the actual values

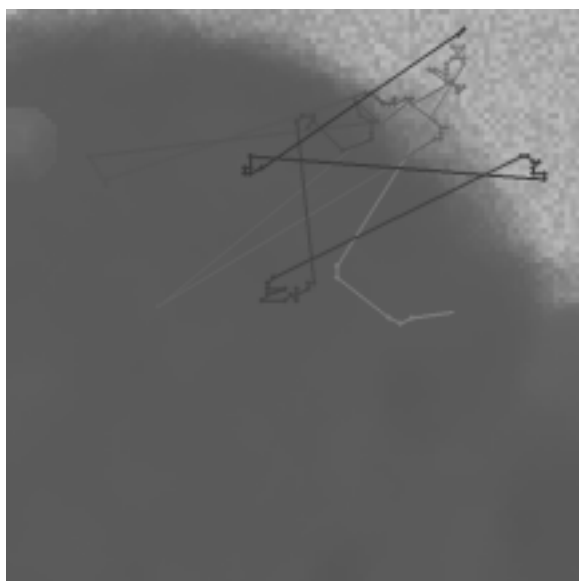


Figure 5. Map of an Elements Weight Values (CO concentration)

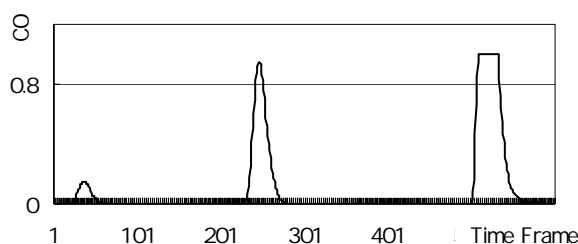


Figure 6. CO Concentration

the change of the time series of CO concentration corresponding to tracks of the winner node. Figure 4 shows that the map that consists of difference between predicted values and the actual values was able to visually represent low and high dioxin emission combustion states. Similarly, Figure 5 shows that the map that consists of an element of sensor data was able to visually classify abnormal range.

6. Conclusion

Through computer simulation, we showed that the proposed SOM method was able to visually represent low and high dioxin emission combustion states. The change in state of the waste incinerator was able to be confirmed by drawing tracks of the winner node visually. Further, we felt that the tracks of the winner node contain important information on the time-series pattern.

For future works, we will consider methods to visualize time-series patterns, as well as reevaluate learning method for time-series data using SOM. Specially, we plan to divide the learning of time-series data in two stages. We hope that by separately training the time-series pattern and state at a time frame will enable visualizing these information more directly.

References

- [1] Makoto Fujiyoshi, Ryutaro Fukushima, Mitiharu Masuya, "Intelligent Control System for Fluidized Bed Incinerator", *Proceedings of 18th Fuzzy System Symposium*, pp.25-28, 2002 (in Japanese)
- [2] H. Ichihashi, et. al, "Fuzzy Bi-plot of Correlation Analysis for Waste Incinerator", *Proceedings of 19th Fuzzy System Symposium*, 2003 (in Japanese)
- [3] R. Fukushima, "Fractal Fuzzy Intelligent Control System", *Proceedings of 20th Fuzzy System Symposium*, 2004 (in Japanese)
- [4] Kenneth J. Mackin, Ryutaro Fukushima Makoto Fujiyoshi, "Waste Incinerator Emission Prediction using Recurrent Neural Networks", *Proceedings of the 2nd International Conference on Soft Computing and Intelligent Systems*, 2004 (in Japanese)
- [5] Teuvo Kohonen, *Self-Organizing Maps*, Springer-Verlag, 1984
- [6] Takashi Yamaguchi, Kenneth J. Mackin, "Architecture of Self-Organizing Map for Time Series Data", *Proceedings of 21th Fuzzy System Symposium*, 2005 (in Japanese)
- [7] Takashi Yamaguchi, Kenneth J. Mackin, "Architecture of feedback SOM for learning time-series data ", *Proceedings of 20th Annual Conference of the Japanese Society for Artificial Intelligence*, 2006 (in Japanese)

Design of a Real Time Evaluation System for Multiple Neuro-Biological Signals

T. Zhang^{*}, M. Nakamura^{**}, T. Sugi^{**} and H. Shibasaki^{***}

^{*}Dept. of Automation, Tsinghua University, Beijing 100084, China

^{**}Dept. of Advanced Systems Control Engineering, Saga University, Saga 840-8502, Japan

^{***}National Institutes of Health, Bethesda, MD 20892-1428, USA

Abstract

This paper introduces the design of a real time evaluation system for multiple neuro-biological signals. In this system, multiple types of neuro-biological signals can be automatically processed in a single system in real time, including EEG, EMG, EOG, ECG, etc. It not only can display the wave shapes of these signals both in online and offline, calculate the feature parameters, but also can evaluate these signals based on different criteria. Therefore, it is possible to provide information about multiple types of neuro-biological signals simultaneously, which will provide great assistance for doctors to interpret neuro-biological signals for judging the diseases and for engineers to define the control signals for BCI device using different types of neuro-biological signals. This system will be an open system that can integrate more kinds of neuro-biological signals. New functions can be easily added into this system according to different requests.

1. Introduction

At present, there already have plenty of researches on the processing and evaluation of neuro-biological signals and the applications of these signals for the interpretation of these signals and control of Brain-Computer Interface (BCI) devices. The main methods include Fourier analysis, brain mapping, feature extraction and pattern recognition [1-3]. However, it is lack of an effective system which can process and evaluate multiple types of neuro-biological signals in a single system in real time, so that it is possible to provide information about several types of neuro-biological signals simultaneously. Therefore, it can be adopted to assist doctors to interpret neuro-biological signals for judging the diseases and assist engineers to define the control signals for BCI devices. In this research we want to develop a new real time evaluation system for multiple neuro-biological signals, such as electroencephalogram (EEG), electromyogram (EMG), electrooculogram (EOG), electrocardiogram (ECG), and so on.

So far, we have already carried out a lot of works for developing this system, such as summarizing the

methods of processing and evaluating neuro-biological signals, developing a prototype of this system for EEG [4], designing some types of BCI devices [5][6], and so on. In this research, we design a real time evaluation system for multiple neuro-biological signals based on our previous works. In the paper, we will introduce the structure, main functions, operation of this system. In the discussion part of this paper we will introduce the possible applications of this system and the future research on this system.

2. System Structure

In the real time evaluation system for multiple neuro-biological signals, as illustrated in Fig.1, it mainly has the following modules: (1) human-friendly interface module; (2) real time pre-processing module; (3) evaluation module; (4) output module for the interpretation of neuro-biological signals and the design of controlling signals for BCI device.

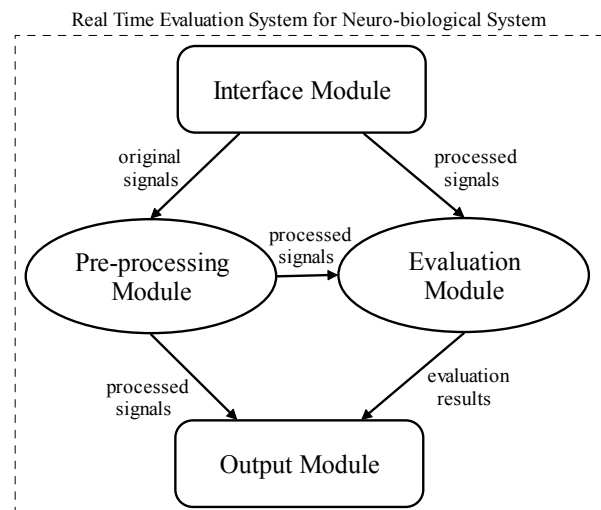


Fig.1 System structure of real time evaluation system for multiple neuro-biological signals

Each module contains the following parts.

(1)Interface module: a human-friendly windows-type menu, displaying wave shape region, displaying processing and evaluation results region, etc.

(2) Pre-processing module: judgement of types of

neuro-biological signals, segmentation of signals, elimination of noise in the signals, selection of qualified signals, etc.

(3) Evaluation module: calculation parts for different types of signals, comparison parts among segmentations of multiple signals, generating evaluation reports, etc.

(4) Output module: output control signals through I/O interface of computer, printing signals as well as evaluation reports, etc.

The system structure is designed for implementing the functions introduced in the following section. Actually, it can be extended according to the requests on this real time evaluation system for multiple neuro-biological signals.

3. System Functions

The real time evaluation system for multiple neuro-biological signals mainly has the following three functions: (1) real time pre-processing; (2) evaluation of multiple neuro-biological signals; (3) output for interpretation of signals and controlling BCI devices using information from multiple neuro-biological signals. In the following parts, these three functions are explained in detail.

3.1 Pre-processing of multiple neuro-biological signals

The purpose of pre-processing of multiple neuro-biological signals is to obtain qualified signals. First of all, it needs to automatically judge which type of signals will be processed. Since the basic features of various neuro-biological signals are quite different, it will be easy to judge the type of signals. For example, for each type of neuro-biological signal, one specific frequency region is defined as the judgement criterion. In the system, to determine the type of signals, it is only needed to check the specific frequency region.

Secondly, there always have a large amount of neuro-biological signals. According to the request, they can be divided into each segment. For example, a continuous signal can be divided into a set of segments and each segment may have 5 second long. Therefore, it will be helpful to make the further processing. This segmentation work can be automatically made by the system in online or offline.

Thirdly, in the pre-processing of signals, one of the important jobs is to obtain qualified signals. The so-called qualified signal is based on the requirement. For example, Fig.2 (a) illustrates the qualified EEG signals and Fig.2 (b) the qualified EMG signals. The selection of qualified signals is based on the calculation of feature parameters. In addition, the noise contaminated in the signals should be eliminated. There are two ways to eliminate the noise. One is to eliminate them when recording the signals in real-time. Another is to pick up the segments contaminated with noises

offline from the existed signals. Any ways are both important to obtain the qualified signals..

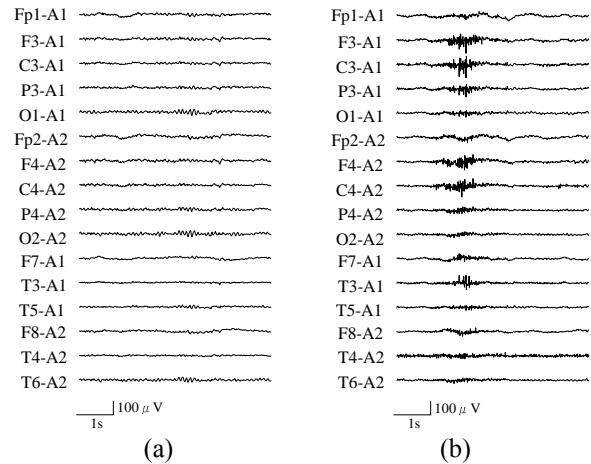


Fig.2 Example of wave shape displaying on the screen, (a) A qualified EEG signal, (b) A qualified EMG signal.

When selecting the qualified signals and eliminating the noise, feature parameters are quite important. For example, the features of EEG records in each channel can be expressed by the periodogram parameters, including:

- Amplitude: $A_z(x) = 6\sqrt{S_z(x)}$
- Symmetry: $P_z(x, y) = 6\sqrt{S_z(x-y)} / 6\sqrt{S_z(x+y)} \times 100$
- Asymmetry: $G_z(x, y) = 6\sqrt{S_z(x+y)} / 6\sqrt{S_z(x-y)} \times 100$
- Extension: $E_z(x, y) = 6\sqrt{S_z(y)} / 6\sqrt{S_z(x)} \times 100$
- Duration: $D_z(x) = S_z(x) / S_T(x) \times 100$
- Central frequency: $f_z(x) = f_z^c(x) |_{P_{\max}} \cdot P_{\max} = \max_{f_{\text{lower}} \leq f_z(x) \leq f_{\text{upper}}} P(f_z(x))$
- Normalization of parameter: $\Phi_z^Q(i) = (Q_z(i) - \min Q_z(i)) / (\max Q_z(i) - \min Q_z(i))$

where x, y both represent each electrode of Fp1, F3, C3, P3, O1, Fp2, F4, C4, P4, O2, F7, T3, T5, F8, T4, T6; z denotes the respective EEG components: L(0-0.5 Hz), δ (0.5-4 Hz), θ (4-8 Hz), α (8-13 Hz), β (13-25 Hz), T(0.5-25 Hz), H(35-50 Hz); $f_z(x)$ is the frequency within the frequency band of z in channel x ; $f_z^c(x)$ is the central frequency within the frequency band of z in channel x and corresponding to the maximal power spectrum; f_{lower} is the lower limit of the frequency band; f_{upper} is the upper limit of the frequency band; and i is the segment number.

The following items are employed in the parameters definition:

- $S_z(x)$ is the amount of EEG components calculated by the summation of periodogram with the frequency band of z in channel x ;

- $S_T(x)$ is the amount of EEG components calculated by the summation of periodogram with the frequency band of 0.5-25 Hz in channel t ;
- $S_z(x-y)$ is the amount of EEG components calculated by the summation of periodogram with the frequency band of z in channels x and y , in which the EEG time series of channel y is subtracted from that of the channel x ;
- $S_z(x+y)$ is the amount of EEG components calculated by the summation of periodogram with the frequency band of z in channels x and y , in which the EEG time series of channel x adds that of the channel y .

Based on the above parameters and relative criteria of judgement, the qualified EEG records can be selected. Due to the limitation of space, we will not introduce the criteria of judgement.

3.2 Evaluation of multiple neuro-biological signals

One of most important functions of the real time evaluation system for multiple neuro-biological signals is to evaluate various types of neuro-biological signals. Therefore, for this purpose the system should be able to carry out calculation, comparison and making report.

The evaluation of neuro-biological signals is also based on the feature parameters of neuro-biological signals. For different types of neuro-biological signals, the evaluation items and equations are quite different. For example, based on the following criteria, the technical artifacts in EEG can be evaluated.

- Electrode:
 - $A_\delta(x) \geq 25\mu V$, (x : respective electrodes on one side)
 - $\sum P_\delta(x,y)/11 \leq 30\%$, (x, y : respective neighborhood electrode on one side of the scale)
 - $\sum P_\delta(x,y)/8 \leq 50\%$, (x, y : a pair of homologous electrodes on both sides)
- Base-line drift:
 - $A_L(x) \geq 60\mu V$, (x : respective electrodes)

With the same way, various types of neuro-biological signals can be evaluated for different items.

3.3 Output of the system

The output is an important function of the real time evaluation system for multiple neuro-biological signals because it is related with the application of the system. In this system, it has two types of output ways. Some information will be displayed on the screen of the computer. Some information can be directly output through I/O interface of computer so that it can be adopted to control the BCI devices.

Concerning the output of information by displaying on the screen, as illustrated by Fig.3, it could be the signal recordings, control signals, evaluation reports, etc., for multiple neuro-biological signals.

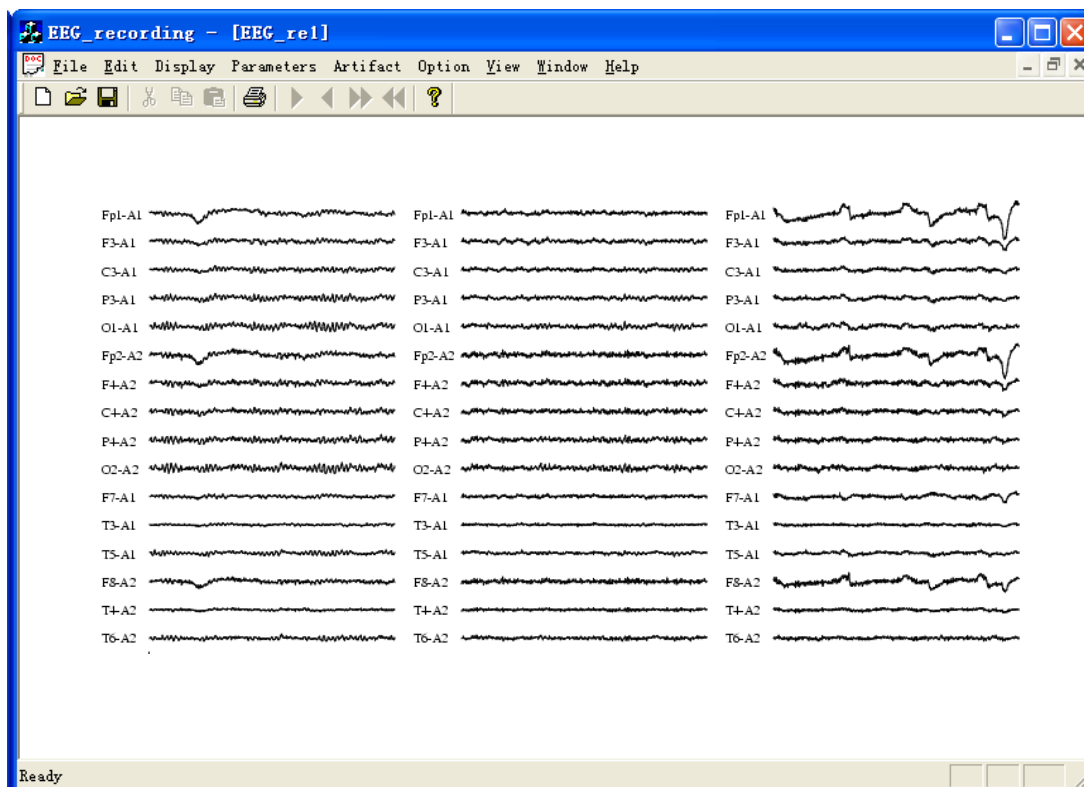


Fig.3 Output of information by displaying on the screen of computer

Concerning the output of information through I/O interface of computer, it can be directly adopted to control BCI devices. For example, a developed meal assistance robot has been directly controlled by the signals generated by EOG [5]. Besides, considering the requirement from users, based on the above system, multiple neuro-biological signals can be processed and adopted simultaneously to control BCI devices.

4. System Operation

Since the real time evaluation system for multiple neuro-biological signals has a human-friendly interface, the operation of the system is easy by use of its menu. Based on its different functions, its operation has three stages.

Stage 1: Pre-processing:

For pre-processing, the operation procedure is as below:

Step 1: Input data;

Step 2: Select pre-processing mode: online or offline;

Step 3: Start pre-processing program;

Step 4: Display the pre-processing results.

Stage 2: Evaluation

For this stage, the operation procedure is as below:

Step 1: Input the processed data;

Step 2: Select the evaluation items;

Step 3: Start the evaluation program;

Step 4: Display the evaluation reports.

Stage 3: Output

For this stage, the operation procedure is as below:

Step 1: Input the processed data;

Step 2: Select the output mode: displaying or outputting control signals;

Step 3: Start the output program;

Actually, in the system there also have many other items, which can be executed by use of menu of the system. In the near future, we will also extend the functions of the system.

5. Discussion

The proposed real time evaluation system for multiple neuro-biological signals has many attractive applications. Basically, it can be adopted for doctors to interpret the neuro-biological signals and therefore diagnose the diseases. Particularly, it can provide enough information from multiple neuro-biological signals. In addition, the output of the system can be directly used to design the control signals to control the BCI devices. Besides, the proposed system can be used for other situation. For example, when using the online processing of neuro-biological signals, engineers can assist doctors to obtain qualified signals during the

course of getting the neuro-biological signals. In addition, with this system we can create a neuro-biological signals database for each specific subject. This system not only can be regarded as a tool to process the multiple neuro-biological signals, but also can be regarded as a platform for interpretation of neuro-biological signals and controlling BCI devices.

6. Conclusions

This paper introduces the design of a real time evaluation system for multiple neuro-biological signals. This system not only can pre-process various types of neuro-biological signals online or offline, but also can evaluate the signals based on the user's requirement. The output of the system can be possibly adopted to assist doctors to interpret neuro-biological signals for judging the diseases and define the control signals for BCI devices. In the near future, we will continue to develop this system and extend its functions.

References

- [1] E. R. John, L. Prichep, J. Fridman and P. Easton, "Neurometrics: computer-assisted differential diagnosis of brain dysfunctions", *Science*, vol. 239, pp.162-169, 1988.
- [2] J. Hasan, K. Hirvonen and A. Varri, "Validation of computer analyzed polygraphic patterns during drowsiness and sleep onset", *Electroenceph Clin Neurophysiol*, vol 87:, pp.117-127, 1993.
- [3] M. Nakamura, H. Shibasaki, K. Imajoh, S. Nishida, R. Neshige and A. Ikeda, "Automatic EEG interpretation: a new computer-assisted system for the automatic integrative interpretation of awake background EEG.", *Electroenceph Clin Neurophysiol*, vol. 82, pp. 423-431, 1992.
- [4] M. Nakamura, Q. Chen, T. Sugi, A. Ikeda and H. Shibasaki, "Technical quality evaluation of EEG recording based on electroencephalographers' knowledge", *Medical Engineering and Physics*, Vol. 27, No. 1, pp.93-100, 2005.
- [5] T. Zhang and M. Nakamura, "Neural network-based hybrid human-in-the-loop control for meal assistance orthosis", *IEEE Trans. on Neural Systems and Rehabilitation*, Vol.14, No.1, 2006.
- [6] M. Nakamura and T. Zhang, "Human assistance robot following the human intention extracted from neuro-biological signals", *Proceedings of the 16th International Conference on Systems Engineering (ICSE 2003)*, pp.506-511, Coventry University, UK, Sept. 2003.

Feedback GMDH-type neural network algorithm self-selecting optimum neural network architecture

Tadashi Kondo
 School of Health Sciences,
 the University of Tokushima,
 Tokushima, 770-8509, Japan

Junji Ueno
 School of Health Sciences,
 the University of Tokushima,
 Tokushima, 770-8509, Japan

Abstract

In this study, a feedback Group Method of Data Handling (GMDH)-type neural network algorithm self-selecting the optimum neural network architecture is proposed. In this algorithm, the optimum neural network architecture is automatically selected from three types of neural network architectures such as the sigmoid function type neural network, the radial basis function (RBF) type neural network and the polynomial type neural network. Furthermore, the structural parameters such as the number of layers, the number of neurons in the hidden layers and the useful input variables are automatically selected so as to minimize the prediction error criterion defined as Akaike's Information Criterion (AIC). The feedback GMDH-type neural network has a feedback loop and the complexity of the neural network increases gradually using feedback loop calculations so as to fit the complexity of the nonlinear system. This algorithm is applied to the identification problem of the complex nonlinear system.

Keywords: GMDH, Neural network, Identification

1 Introduction

The Group Method of Data Handling (GMDH)-type neural networks and their applications have been proposed in our early works [1],[2]. The GMDH-type neural networks can automatically organize the neural network architecture by using the heuristic self-organization method [3],[4]. The GMDH-type neural networks can also determine such structural parameters as the number of layers, the number of neurons in the hidden layers and the useful input variables. In the GMDH-type neural networks, the neural network architecture is organized so as to minimize the prediction error criterion defined as Akaike's Information Criterion (AIC) [5] or Prediction Sum of Squares (PSS) [6].

In this study, the feedback GMDH-type neural network algorithm self-selecting the optimum neural network architecture is proposed. In this algorithm, the optimum neural network architecture is automatically selected from three types of neural network architectures such as the sigmoid function type neural network, the radial basis function (RBF) type neural network and the polynomial type neural network. The feedback GMDH-type neural network has a feedback loop and the complexity of the neural network increases gradually using feedback loop

calculations so as to fit the complexity of the nonlinear system.

The feedback GMDH-type neural network algorithm proposed in this paper is applied to the identification problem of the complex nonlinear system. The optimum neural network architecture fitting the complexity of the nonlinear system is selected from three types of the neural network architectures. The identification results of the feedback GMDH-type neural network are compared with those of the GMDH algorithm and the conventional multi-layered neural network trained using the back propagation algorithm. It is shown that the feedback GMDH-type neural network is a very useful identification method of the complex nonlinear system because the optimum neural network architecture is automatically organized so as to minimize AIC.

2 Feedback GMDH-type neural network

The architecture of the feedback GMDH-type neural network proposed in this paper has a feedback loop as shown in Fig.1. The feedback GMDH-type neural network algorithm can select the optimum neural network architecture from three types of neural network architectures such as the sigmoid function type neural network, the RBF type neural network and the polynomial type neural network. The feedback GMDH-type neural network algorithm uses three types of neuron architectures which are the sigmoid function type neuron, the RBF type neuron and the polynomial type neuron.

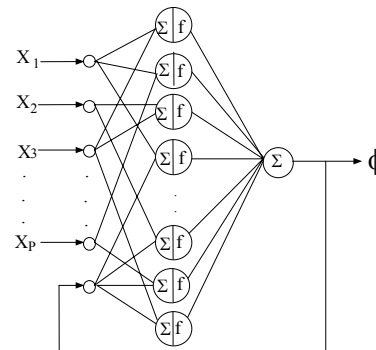


Fig.1 Architecture of the feedback GMDH-type neural network

2.1 First loop calculation

First, all data are set to the training data. In this algorithm, it is not necessary to separate the original data into the training and test data because AIC can be used for organizing the network architectures. Then the architecture of the input layer is organized.

1) Input layer

$$u_j = x_j \quad (j=1, 2, \dots, p) \quad (1)$$

where x_j ($j=1, 2, \dots, p$) are the input variables of the system, and p is the number of input variables. In the first layer, input variables are set to the output variables.

2) Hidden layer

All combinations of the r input variables are generated. For each combination, three types of neuron architectures which are the sigmoid function type neuron, the RBF type neuron and the polynomial type neuron, are generated and L neurons which minimize AIC value are selected for each type of neuron architectures.

Furthermore, for each combination, optimum neuron architectures fitting the characteristics of the nonlinear system are automatically selected by using AIC.

a) Sigmoid function type neuron:

i) The first type neuron

Σ : (Nonlinear function)

$$z_k = w_1u_i + w_2u_j + w_3u_iu_j + w_4u_i^2 + w_5u_j^2 + w_6u_i^3 + w_7u_i^2u_j + w_8u_iu_j^2 + w_9u_j^3 - w_0\theta_i \quad (2)$$

f: (Nonlinear function)

$$y_k = \frac{1}{1 + e^{(-z_k)}} \quad (3)$$

ii) The second type neuron

Σ : (Linear function)

$$z_k = w_1u_1 + w_2u_2 + w_3u_3 + \dots + w_ru_r - w_0\theta_i \quad (r < p) \quad (4)$$

f: (Nonlinear function)

$$y_k = \frac{1}{1 + e^{(-z_k)}} \quad (5)$$

b) RBF type neuron:

i) The first type neuron

Σ : (Nonlinear function)

$$z_k = w_1u_i + w_2u_j + w_3u_iu_j + w_4u_i^2 + w_5u_j^2 + w_6u_i^3 + w_7u_i^2u_j + w_8u_iu_j^2 + w_9u_j^3 - w_0\theta_i \quad (6)$$

f: (Nonlinear function)

$$y_k = e^{(-z_k^2)} \quad (7)$$

ii) The second type neuron

Σ : (Linear function)

$$z_k = w_1u_1 + w_2u_2 + w_3u_3 + \dots + w_ru_r - w_0\theta_i \quad (r < p) \quad (8)$$

f: (Nonlinear function)

$$y_k = e^{(-z_k^2)} \quad (9)$$

c) Polynomial type neuron:

i) The first type neuron

Σ : (Nonlinear function)

$$z_k = w_1u_i + w_2u_j + w_3u_iu_j + w_4u_i^2 + w_5u_j^2 + w_6u_i^3 + w_7u_i^2u_j + w_8u_iu_j^2$$

$$+ w_9u_j^3 - w_0\theta_i \quad (10)$$

f: (Linear function)

$$y_k = z_k \quad (11)$$

ii) The second type neuron

Σ : (Linear function)

$$z_k = w_1u_1 + w_2u_2 + w_3u_3 + \dots + w_ru_r - w_0\theta_i \quad (r < p) \quad (12)$$

f: (Linear function)

$$y_k = z_k \quad (13)$$

Here, $\theta_i = 1$ and w_i ($i=0, 1, 2, \dots$) are the weights between the first and second layer and estimated by applying the stepwise regression analysis [7] to the training data. Only useful input variables u_i ($i=1, 2, \dots$) are selected by using AIC. In the first type neuron, the value of r , which is the number of input variables u in each neuron, is set to two. In the second type neuron, the value of r , which is the number of input variables u in each neuron, is set to be greater than two and smaller than p . p is the number of input variables x_i ($i=1, 2, \dots, p$). The output variables y_k of the neurons are called as the intermediate variables.

L neurons having the smallest AIC values are selected for three types of neuron architectures which are the sigmoid function type neuron, the RBF type neuron and the polynomial type neuron. The output variables y_k of L selected neurons for three types of neuron architectures are set to the input variables of the neurons in the output layer.

3) Output layer

For three types of neural network, the outputs y_k of the neurons in the hidden layer are combined by the following linear function.

$$\phi^* = a_0 + \sum_{k=1}^L a_k y_k \quad (14)$$

Here, L is the number of combinations of the input variables and y_k is the intermediate variables. The useful intermediate variables y_k are selected by using the stepwise regression analysis in which AIC is used as the variable selection criterion.

Equation (14) is calculated for three types of neural network architectures which are the sigmoid function type neural network, the RBF type neural network and the polynomial type neural network. Then, the neural network architecture which has smallest AIC value is selected as the GMDH-type neural network architecture from three types of neural network architectures

Then, the estimated output values ϕ^* which is selected in the output layer is used as the feedback value and it is combined with the input variables in the next loop calculation.

2.2 Second and successive loop calculations

The optimum neural network architecture is selected from three types of neural network architectures in the output layer. Therefore, in the second and successive loop calculations, only one type of neuron architecture, which is the sigmoid function type neuron or the RBF type neuron or

the polynomial type neuron, is used for the calculation.

First, the estimated output value ϕ^* is combined with the input variables and all combinations between the estimated output value ϕ^* and the input variables are generated. The same calculation as the first feedback loop is carried out for each combination. Here, only one type of neuron architecture, which is selected in the first loop calculation, is used in the calculation. When AIC value of the linear function in (14) is increased, the loop calculation is terminated and the complete neural network architecture is organized by the L selected neurons in each feedback loop.

3 An application to nonlinear system identification

To verify the performance of the feedback GMDH-type neural network, it is applied to the nonlinear system identification problem.

3.1 Nonlinear system identification problem

The nonlinear system is assumed to be described by the following equations:

$$\phi_1 = (1.0 + 1.1x_1 + 1.2x_2 + 1.3x_3)^4 + \varepsilon_1 \quad (15)$$

$$\phi_2 = (1.0 + 1.4x_1 + 1.5x_2 + 1.6x_3)^4 + \varepsilon_2 \quad (16)$$

$$\phi_3 = (1.0 + 1.7x_1 + 1.8x_2 + 1.9x_3)^4 + \varepsilon_3 \quad (17)$$

$$\phi_4 = (1.0 + 2.0x_1 + 2.1x_2 + 2.2x_3)^4 + \varepsilon_4 \quad (18)$$

Here, $\phi_1 \sim \phi_4$ show output variables and $x_1 \sim x_3$ show input variables. $\varepsilon_1 \sim \varepsilon_4$ show noises. Furthermore, x_4 is added as the input variable of the neural network in order to check that the feedback GMDH-type neural network can eliminate the useless input variables. The neural network is organized by using twenty training data. The prediction is carried out by using twenty testing data so as to check the generalization ability.

3.2 Identification results obtained by using the GMDH-type neural network

(1) Input variables

Four input variables were used but the useless input variables x_4 was automatically eliminated.

(2) Number of selected neurons

Four neurons were selected in the hidden layer.

(3) Selection of the neural network architecture

Polynomial type neural network architecture was selected as the GMDH-type neural network architecture in the first feedback loop calculation.

(4) Structure of the neural network

The calculation of the GMDH-type neural network was terminated at the seventh feedback loop calculation.

(5) Estimation accuracy

The estimation accuracy was evaluated by using the following equation:

$$J_1 = \frac{\sum_{i=1}^{20} |\phi_i - \phi_i^*|}{\sum_{i=1}^{20} |\phi_i|} \quad (19)$$

where ϕ_i ($i=1,2,\dots,20$) were the actual values and ϕ_i^* ($i=1,2,\dots,20$) were the estimated values by the feedback GMDH-type neural network. The values of J_1 for four output variables are shown in Table 1.

(6) The prediction accuracy

The prediction accuracy was evaluated by using the following equation:

$$J_2 = \frac{\sum_{i=21}^{40} |\phi_i - \phi_i^*|}{\sum_{i=21}^{40} |\phi_i|} \quad (20)$$

where ϕ_i ($i=21,22,\dots,40$) were the actual values and ϕ_i^* ($i=21,22,\dots,40$) were the predicted values by the feedback GMDH-type neural network. The values of J_2 for four output variables are shown in Table 1.

Table 1 Prediction and estimation accuracy

Models	J	$\Phi 1$	$\Phi 2$	$\Phi 3$	$\Phi 4$
GMDH-NN	J1	0.013	0.022	0.023	0.024
	J2	0.025	0.028	0.029	0.029
GMDH	J1	0.056	0.058	0.038	0.039
	J2	0.055	0.058	0.044	0.044
NN	J1	0.119	0.133	0.108	0.11
	J2	0.114	0.133	0.102	0.109

(7) Variation of AIC and estimated values

The variation of AIC in Eq.(14) of the output variables ϕ_i is shown in Fig.2. It decreased gradually by the feedback loop calculations and converged at the seventh feedback loop calculation. The estimated values of ϕ_i by the feedback GMDH-type neural network is shown in Fig.3. We can see that the estimated values are very accurate.

3.3 Comparison of the feedback GMDH-type neural network and other models

The identification results were compared with those of the GMDH algorithm and the conventional multilayered neural network trained using the back propagation algorithm.

(1) The GMDH algorithm

The identification results were referred from [8]. Four input variables were used but the useless input variable x_4 was automatically eliminated. Four intermediate variables were selected. The calculation was terminated at the fourth layer.

The values of J_1 and J_2 are shown in Table 1.

(2) The conventional multilayered neural network

The neural network had three layered structures. Four input variables were used in the input layer and eight neurons were used in the hidden layer. The neurons in the output layer were described by the linear function. The values of J_1 and J_2 are shown in Table 1.

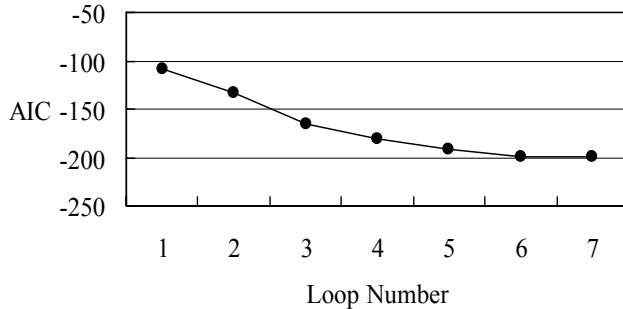


Fig.2 AIC variation

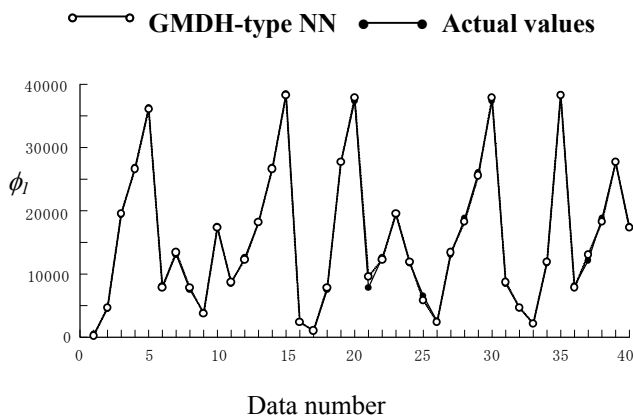


Fig.3 Estimated values of ϕ_1 by feedback GMDH-type neural network

4 Discussion

From the identification results, we can say the following:

- (1) Both estimation and prediction errors of the feedback GMDH-type neural network were smallest in the three identified models. We can see that the feedback GMDH-type neural network was a very accurate identification method for the nonlinear system.
- (2) In the feedback GMDH-type neural network, AIC value at the first loop calculation was not small but it was gradually decreased by the feedback loop calculations. So we can see that the feedback loop calculation plays a very important role in the feedback GMDH-type neural network.
- (3) In the conventional neural network, the effects of high order terms of the input variables are not considered. Furthermore, it does not have the ability of self-selecting useful input variables and the optimum neural network

architecture. So the accuracy of the neural network was not good.

The feedback GMDH-type neural network can organize the conventional neural network architecture (sigmoid function type architecture) and the GMDH architecture (polynomial type architecture). This algorithm contains the characteristics of the conventional neural network and the GMDH algorithm and it is a very flexible method for the identification problem of the complex nonlinear system.

5 Conclusion

In this study, the feedback GMDH-type neural network self-selecting optimum neural network architecture was proposed. This algorithm can automatically organize a multilayered neural network architecture fitting the complexity of the nonlinear system by using the heuristic self-organization method. It is very easy to apply this algorithm to the identification problem of the practical complex system because the optimum neural network architecture fitting the complexity of the nonlinear system is automatically organized. This algorithm was applied to the nonlinear system identification problem and it was shown that this algorithm was a very useful method.

References

- [1] T.Kondo, "GMDH neural network algorithm using the heuristic self-organization method and its application to the pattern identification problem", *Proc. of the 37th SICE Annual Conference*, pp.1143-1148, 1998.
- [2] T.Kondo, "Revised GMDH-type neural networks using prediction error criterions AIC and PSS", *Proc. of SCIS & ISIS 2004, WP-6-4*, pp.1-6, 2004.
- [3] S.J.Farlow ed, *Self-organizing methods in modeling, GMDH-type algorithm*, Marcel Dekker, Inc., New York, 1984.
- [4] A.G.Ivakhnenko, "Heuristic self-organization in problems of engineering cybernetics", *Automatica*, Vo.6, No.2, pp.207-219, 1970.
- [5] H.Akaike, "A new look at the statistical model identification", *IEEE Trans. Automatic Control*, Vol.AC-19, No.6, pp.716-723, 1974.
- [6] H.Tamura and T.Kondo, "Heuristics free group method of data handling algorithm of generating optimum partial polynomials with application to air pollution prediction", *Int. J. System Sci.*, Vol.11, No.9, pp.1095-1111, 1980.
- [7] N.R.Draper and H.Smith, *Applied Regression Analysis*, John Wiley and Sons, New York, 1981.
- [8] T.Kondo, "GMDH type Neural Network Algorithm Identifying a Network Structure with the Heuristic Self-Organization Method", *Trans. ISCIE*, Vol.11, No.4, pp.198-207, 1998.

Remarks on adaptive type neural network direct controller with separate learning rule of each layer

Takayuki Yamada

Department of Computer and Information Sciences

Faculty of Engineering

Ibaraki University

4-12-1 Nakanarusawa, Hitachi, Ibaraki, 316-8511, Japan

Abstract

This paper proposes a new learning rule of multi-layer neural network controllers in order to eliminate an inference of neural network weights of each layer and to discuss stability condition of nonlinear three layer neural network controllers. This learning rule is that the neural network weights between one layer and next layer are only changed at same time and other neural network weights are not changed, and after some sampling numbers, the neural network weights between other layer and next layer are changed. The proposed learning rule is applied to an adaptive type neural network direct controller and a simulation result shows it performed well.

1. Introduction

Many studies have been undertaken in order to apply both the flexibility and the learning capability of neural networks to control systems.[1]-[3] However, there are few attempts to clear the stability conditions of neural network control systems. Among these attempts, we proved local stability condition of a three layer neural network direct controller whose neurons have a linear input output relation.[1][2] We also confirmed that the interference between neural network weight learning of each layer causes more difficulty to analyze the stability condition in comparison with the stability analysis of conventional adaptive controllers in this study. This interference is caused by an usual neural network learning rule so as to change whole neural network weights at same time. In other words, the usual neural network learning rule has good efficiency of the neural network weight convergence, but it causes difficult stability analysis of the neural network controllers. One of simple methods to avoid this interference is to use a two layer neural network as a controller. However, the nonlinear mapping capability of such neural network is limited because it was proved that a nonlinear three layer neural network was able to approximate any continuous nonlinear functions. That

is, this method means that such neural network controllers have less nonlinear mapping capability in comparison with the nonlinear three layer neural network. Another method to avoid above problem is to use a linear three layer neural network. However, the linear three layer neural network can not realize sufficient approximation for nonlinear functions. This also means that such neural network controllers have less nonlinear mapping capability.

Thus, we propose a new neural network learning rule for three layer nonlinear neural network controllers in this paper. It is called separate learning rule of each layer in this paper. This learning rule is that the neural network weights between one layer and next layer are only changed at same time and other neural network weights are not changed, and after some sampling numbers, the neural network weights between other layer and next layer are changed. That is, we can eliminate the interference between layers and realize easier discussion about the nonlinear neural network controller stability although the separate learning rule has slow convergence in comparison with the usual neural network learning rule. We can realize the same nonlinear mapping capability because the neural network has the nonlinear three layer structure. The proposed learning rule is applied for an adaptive type neural network direct controller and the discussion about its stability condition is presented. A simulation result of the adaptive type neural network direct controller with the separate learning rule shows that the proposed learning rule can be realized.

2. Interference between neural network weights

This section explains the structure of the adaptive type neural network direct controller briefly.[1][2] The interference between neural network weight learning of each layer is focused and it is discussed why the stability analysis of the nonlinear neural network controllers with the three layer structure is difficult in comparison with that

of controllers with linear two layer structure such as conventional adaptive controllers. Based on this discussion, necessity of the separate learning rule of each layer is confirmed.

The following object plant is selected in this paper.

$$Y(k) = f(Y(k-d) \dots Y(k-d-n), U(k-d) \dots U(k-d-m)) \quad (1)$$

Where $Y(k)$ is the plant output, $U(k)$ is the plant input, k is the sampling number, d is the dead time, n & m are the plant orders and f is the nonlinear function which expresses a nonlinear characteristic of the plant. The output error $\epsilon(k)$ is defined by the following equation.

$$\epsilon(k) = Y_d(k) - Y(k) \quad (2)$$

Where Y_d is the desired value. Figure 1 shows the scheme of the direct controller. As shown here, the plant input is only composed of the neural network output in the direct controller. From eqs.(1) and (2), the neural network input vector I is selected as follows;

$$I^T(k) = [Y_d(k+d), Y(k) \dots Y(k-n), U(k-1) \dots U(k-m)] \quad (3)$$

To simplify, the following discussion selects that the neural network has three layers, its output neuron is one and both the number of neurons in the input and hidden layers are the same as the order of the input vector I . When the adaptive type learning is selected, the usual neural network learning rule is expressed as the following equation through the use of the δ rule.

$$\begin{aligned} W(k+1) &= W(k-d) - \eta' \frac{\partial J(k)}{\partial W(k-d)} & J(k) &= \frac{1}{2} \epsilon^2(k) \\ \omega(k+1) &= \omega(k-d) - \eta' \frac{\partial J(k)}{\partial \omega(k-d)} \end{aligned} \quad (4)$$

Where W is the weight matrix composed of the neural network weights between the input and hidden layers, ω is the weight vector composed of the neural network weights between the hidden and output layers, J is the cost function and η' is the parameter determining convergence speed. When the neural network is linear, we derive the following learning rule from eq.(4).

$$\begin{aligned} W(k+1) &= W(k-d) - \eta \epsilon(k) \omega(k-d) I^T(k-d) \\ \omega(k+1) &= \omega(k-d) - \eta \epsilon(k) W(k-d) I(k-d) \\ \eta &= \eta' \left(\frac{\partial Y(k)}{\partial U(k-d)} \right) \end{aligned} \quad (5)$$

As shown in eq.(5), the learning of the weight matrix W uses the weight vector ω and the learning of the weight vector ω uses the weight matrix W . This fact causes the interference between the neural network weight learning of each layer and the difficulty of the stability analysis in comparison with that of the linear two layer structure controllers such as the conventional adaptive controller. The separate learning rule is proposed as one solution of above problem in the next section.



Fig.1 Scheme of direct controller.

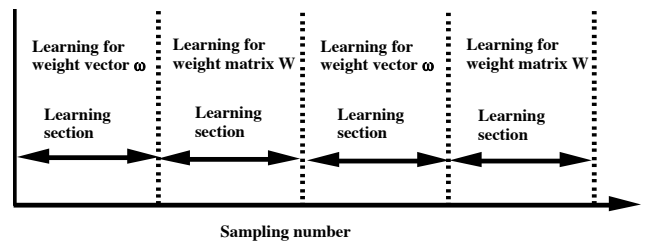


Fig.2 Scheme of separate learning of each layer.

3. Separate learning rule of each layer

This section proposes the separate learning rule of each layer as a solution to overcome the interference between the neural network weights. Figure 2 shows its scheme. This learning rule is that the neural network weights between one layer and next layer are only changed and other neural network weights are not changed within some sampling numbers which is called learning section. For this example, the weight vector ω is selected in the first learning section. That is, the learning rule for the weight ω of eq.(4) is only used. In the second learning section, the neural network weights between other layer and the next layer are changed. For this example, the weight matrix W is selected and the learning rule for the weight matrix W of eq.(4) is only used. As mention above, the neural network weights of each layer are independently changed. That is, we can eliminate the interference of the neural network weights. The nonlinear mapping capability is not reduced because our neural network has the three layer structure.

The stability condition of the weight vector ω is briefly discussed in the neighborhood of the converged vector. The following equation is obtained from the separate learning rule and eq.(4).

$$\omega_0 - \omega(k+1) = \omega_0 - \omega(k-d) - \eta' \frac{\partial Y(k)}{\partial U(k-d)} \text{Sg}(WcI(k-d)) \quad (6)$$

Where ω_0 is the converged vector within one learning section and Sg is the sigmoid function. When the weight vector ω is changed, the weight matrix W is the constant matrix Wc. Form eq.(6), the following stability condition of the weight vector ω is obtained when the Taylor expansion of the output error with regard to the weight vector ω is used. (Details are mentioned in the Appendix)

$$0 \leq \eta \left(\frac{\partial Y(k)}{\partial U(k-d)} \right) \lambda_0 \leq 2 \quad \eta = \eta' \left(\frac{\partial Y(k)}{\partial U(k-d)} \right) \quad (7)$$

Where λ_0 is the maximum eigen value of the following matrix P.

$$P = \text{Sg}(WcI(k-d)) \{ \text{Sg}(WcI(k-d)) \}^T \quad (8)$$

The stability condition of the weight matrix W can be obtained in the similar method if we can use some assumptions. (Details are mentioned in the Appendix)

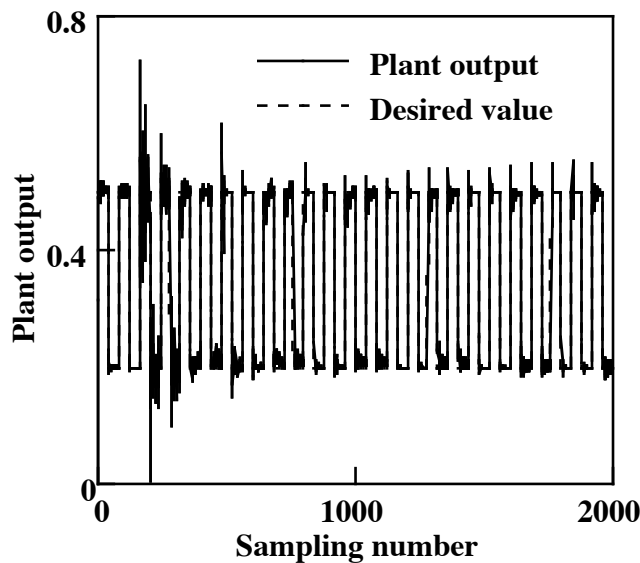


Fig.3 Simulation result.

4. Simulation

This section shows a simulation result of the adaptive type direct controller with the proposed separate learning rule of each layer. The simulated plant is follows: A simulated plant is selected as follows;

$$Y(k) = -a_1 Y(k-1) - a_2 Y(k-2) + U(k-1) + bU(k-2) - a_3 Y(k-3) + C_{non} Y^2(k-1) \quad (9)$$

Where a_1, a_2 & b are the plant parameters, a_3 is the parasite term and C_{non} is the nonlinear term. For this simulation, $a_1=-1.3, a_2=0.3, b=0.7, a_3=-0.03$ and $C_{non}=0.2$ are selected. The rectangular wave is also selected as the desired value Yd. We select the following sigmoid function $f(x)$ as the input output relation of the hidden layer neuron.

$$f(x) = \frac{X_g \{1 - \exp(-4x/X_g)\}}{2\{1 + \exp(-4x/X_g)\}} \quad (10)$$

Where X_g is the parameter determining the sigmoid function shape. $X_g=0.5$ is selected in this simulation.

Figure 3 shows the simulation result where $\eta=1.5$ and the learning section is 2 cycle of the desired value. The solid line is the plant output Y and the broken line is the desired value Yd. As shown here, the output error suddenly increases after 2 cycle of the desire value, but after that, the plant output converges with the desired value as learning progresses. This result shows that the proposed learning rule performs well.

4. Conclusion

This paper proposed the new learning rule of the multi-layer neural network controller in order to eliminate the inference of the neural network weights of each layer. We can discuss the stability condition of the nonlinear three layer neural network controller through the use of this learning rule. It was applied to the adaptive type neural network direct controller and the simulation result showed that it performed well.

Acknowledgment

The author wishes to express his thanks to Mr.Masaki Kobayashi, graduated student, Ibaraki University, for his programming and simulation.

References

- [1]T.Yamada and T.Yabuta, "Some Remarks on Characteristics of Direct Neuro-Controller with Regard to Adaptive Control", Transactions of the Society of Instrument and Control Engineers, Vol.27, No.7, pp.784-791,1991 (in Japanese)
- [2]T.Yamada and T.Yabuta, "Adaptive Neural Network Controllers for Dynamics Systems", Journal of Robotics and Mechatronics Vol.2, No.4, pp.29-41, 1989
- [3]K.S.Narendra and K.Parthictsarathy, "Identification and Control of Dynamics System Using Neural Networks",

IEEE Transaction on Neural Networks, Vol.1, No.1,
pp.4-27, 1990

Appendix

First, this appendix discusses the stability condition of the weight vector ω . The following parameter error vector ζ is defined.

$$\zeta(k) = \omega_0 - \omega(k) \quad (a-1)$$

It is assumed that $\epsilon(k)=0$, when $\omega(k)=\omega_0$. From eq.(6) and the first order Taylor expansion of the output error $\epsilon(k)$ with regard to the weight vector $\omega(k-d)$, Following equations are obtained.

$$\begin{aligned} \zeta^T(k+1) &= \zeta^T(k-d)[E - \eta'g^2(k)Sg(WcI(k-d))\{Sg(WcI(k-d))\}^T] \\ \epsilon(k) &= g(k) Sg(I^T(k-d)Wc^T) \quad g(k) = \frac{\partial Y(k)}{\partial U(k-d)} \end{aligned} \quad (a-2)$$

Where E is the identity matrix. When $\varphi(k)=\zeta^T(k)\zeta(k)$ is selected as a candidate of the Lyapunov function, we can obtain the following equation.

$$\begin{aligned} \Delta\varphi &= \varphi(k+1) - \varphi(k-d) \\ &= \zeta^T(k-d)Q\zeta(k-d) \\ Q &= -2\eta'g^2(k)P + \eta'^2g^4(k)P^2 \end{aligned} \quad (a-3)$$

Since P defined by eq.(8) is the real symmetric matrix whose eigen values are not negative, there is a real orthogonal matrix V so as to $P=V^{-1}\beta V$ where β is a diagonal matrix whose diagonal elements are the eigen values of P . From eq.(a-3), the following equation is derived.

$$Q = V^{-1}(\eta'^2g^4(k)\beta^2 - 2\eta'g^2(k)\beta)V \quad (a-4)$$

When λ_i is defined by the eigen value of β , λ_i is not negative and the rank of β is 1. That is, the positive λ_i is 1 and this is the maximum eigen value λ_0 . From eqs.(3)(4), when the following equation is satisfied, $\Delta\varphi$ is not positive and the neural network controller is stable with regard to the weight vector ω learning.

$$0 \leq \eta \left(\frac{\partial Y(k)}{\partial U(k-d)} \right) \lambda_0 \leq 2 \quad \eta = \eta' \left(\frac{\partial Y(k)}{\partial U(k-d)} \right) \quad (7)$$

Next, the stability condition of the weight matrix W is discussed. When the weight matrix W is changed,

the weight vector $\omega(k)$ is constant vector whose symbol is ωc . When the chain rule is use, the following equation is obtained from eqs.(2) and (4).

$$\frac{\partial J(k)}{\partial W(k-d)} = -\epsilon(k) \frac{\partial Y(k)}{\partial U(k-d)} \frac{\partial U(k-d)}{\partial W(k-d)} \quad (a-5)$$

From the neural network structure, the following equation is obtained.

$$\frac{\partial U(k)}{\partial W_{ij}(k)} = \omega c_i Sg' \left\{ \sum_{j=1}^n W_{ij}(k) I_j(k) \right\} I_j(k) \quad (a-6)$$

Where Sg' is the derivative of the sigmoid function Sg with regard to its input and n is the number of the input and hidden layers. We can define the diagonal matrix Γ whose i th diagonal element is follows;

$$Sg' \left\{ \sum_{j=1}^n W_{ij}(k) I_j(k) \right\} \quad (a-7)$$

From eqs.(4) and (a-5)-(a-7), the learning rule of the weight matrix W is expressed as the following equation.

$$W(k+1) = W(k-d) + \eta' \epsilon(k) g(k) \Gamma(k-d) \omega c I^T(k-d) \quad (a-8)$$

Here, when the input vector I is continuous, we can derive the following equation from eq.(8).

$$\begin{aligned} W(k+1)I(k+1) &\equiv W(k-d)I(k-d) \\ &= W(k-d)I(k-d) + \eta' \epsilon(k) g(k) \Gamma(k-d) \omega c I^T(k-d) I(k-d) \end{aligned} \quad (a-9)$$

The following equation is the definition of the parameter error vector ζ for the weight matrix W .

$$\zeta(k) = W_0 I(k) - W(k) I(k) \quad (a-10)$$

Where W_0 is the converged weight matrix W within one learning section. From eqs.(4)(a-9)(a-10) and the first order Taylor expansion of output error $\epsilon(k)$ with regard to $W(k-d)I(k-d)$, we can obtain the following equation.

$$\zeta^T(k+1) = \zeta^T(k-d) \{ E - \eta'g^2(k)\Gamma(k-d) \times \omega c \omega c^T \Gamma(k-d) I^T(k-d) I(k-d) \} \quad (a-11)$$

From eq.(a-11), we can obtain the stability condition of the weight matrix W in the same way.

Three-Dimensional Parallel Turing Machines

Takao ITO¹, Makoto SAKAMOTO¹, Yuusuke NAGAMIZU¹, Kouichi IHOSHI¹,
Naoko TOMOZOE¹, Hiroshi FURUTANI¹, Michio KONO¹, Satoshi IKEDA¹,
Tatsuhiko TAMAKI², and Katsushi INOUE³

¹ Dept. of Computer Science and Systems Engineering, University of Miyazaki, Miyazaki 889-2192, JAPAN

² Dept. of Business Administration, Ube National College of Technology, Ube 755-8555, JAPAN

³ Dept. of Computer Science and Systems Engineering, Yamaguchi University, Ube 755-8611, JAPAN

Abstract

Informally, a parallel Turing machine (PTM) proposed by Wiedermann is a set of identical usual sequential Turing machines (STM's) cooperating on two common tapes – storage tape and input tape. Moreover, STM's which represent the individual processors of the parallel computer can multiply themselves in the course of computation. On the other hand, during the past about twenty-five years, automata on a three-dimensional tape have been proposed as computational models of three-dimensional pattern processing and several properties of such automata have been obtained. In this paper, we propose a three-dimensional parallel Turing machine (3-PTM), and investigate its some properties. Especially, we deal with a hardware-bounded 3-PTM, whose inputs are restricted to cubic ones. We believe that this machine is useful in measuring the parallel computational complexity of three-dimensional images.

Key Words: computational complexity, hardware-bounded computation, nondeterminism, parallel Turing machine, three-dimensional automaton

1 Introduction

A parallel Turing machine (PTM) is a set of identical sequential Turing machines (STM's) cooperating on two common tapes – storage tape and input tape [5]. Moreover, STM's which represent the individual processors of the parallel computer can multiply themselves in the course of computation. In [5] it is shown, for example, that every PTM can be simulated by an STM in polynomial time, and that the PTM cannot be simulated by any sequential Turing machine in linear space.

In [1], two-dimensional version of PTM was investigated. On the other hand, due to the advances in many application areas such as computer vision, robotics,

and so forth, it has become increasingly apparent that the study of three-dimensional pattern processing has been of crucial importance. Thus, we think that the research of three-dimensional automata as a computational model of three-dimensional pattern processing has also been meaningful. During the past about twenty-five years, automata on a three-dimensional tape have been proposed and several properties of such automata have been obtained. In this paper, we propose a three-dimensional parallel Turing machine (3-PTM), and investigate its some properties. Especially, we deal with a hardware-bounded 3-PTM, a variant of the 3-PTM, whose inputs are restricted to cubic ones. The hardware-bounded 3-PTM is a 3-PTM, the number of whose processors is bounded by a constant or variable depending on the size of inputs. The investigation of hardware-bounded 3-PTM's is more useful than that of 3-PTM's from the practical point of view.

2 Preliminaries

Definition 2.1. Let Σ be a finite set of symbols, a *three-dimensional tape* over Σ is a three-dimensional rectangular array of elements of Σ . The set of all three-dimensional tapes over Σ is denoted by $\Sigma^{(3)}$. Given a tape $x \in \Sigma^{(3)}$, for each integer j ($1 \leq j \leq 3$), we let $l_j(x)$ be the length of x along the j th axis. The set of all $x \in \Sigma^{(3)}$ with $l_1(x) = n_1, l_2(x) = n_2$ and $l_3(x) = n_3$ is denoted by $\Sigma^{(n_1, n_2, n_3)}$. When $1 \leq i_j \leq l_j(x)$ for each j ($1 \leq j \leq 3$), let $x(i_1, i_2, i_3)$ denote the symbol in x with coordinates (i_1, i_2, i_3) . Furthermore, we define

$$x[(i_1, i_2, i_3), (i'_1, i'_2, i'_3)],$$

only when $1 \leq i_j \leq i'_j \leq l_j(x)$ for each integer j ($1 \leq j \leq 3$), as the three-dimensional input tape y satisfying the following conditions:

- (1) for each j ($1 \leq j \leq 3$), $l_j(y) = i'_j - i_j + 1$;

(2) for each r_1, r_2, r_3 ($1 \leq r_1 \leq l_1(y), 1 \leq r_2 \leq l_2(y), 1 \leq r_3 \leq l_3(y)$), $y(r_1, r_2, r_3) = x(r_1+i_1-1, r_2+i_2-1, r_3+i_3-1)$. (We call $x[(i_1, i_2, i_3), (i'_1, i'_2, i'_3)]$ the $[(i_1, i_2, i_3), (i'_1, i'_2, i'_3)]$ -segment of x .)

For each $x \in \Sigma^{(n_1, n_2, n_3)}$ and for each $1 \leq i_1 \leq n_1, 1 \leq i_2 \leq n_2, 1 \leq i_3 \leq n_3$, $x[(i_1, 1, 1), (i_1, n_2, n_3)]$, $x[(1, i_2, 1), (n_1, i_2, n_3)]$, $x[(1, 1, i_3), (n_1, n_2, i_3)]$, $x[(i_1, 1, i_3), (i_1, n_2, i_3)]$, and $x[(1, i_2, i_3), (n_1, i_2, i_3)]$ are called the i_1 th (2-3) plane of x , the i_2 th (1-3) plane of x , the i_3 th (1-2) plane of x , the i_1 th row on the i_3 th (1-2) plane of x , and the i_2 th column on the i_3 th (1-2) plane of x , and are denoted by $x(2-3)i_1$, $x(1-3)i_2$, $x(1-2)i_3$, $x[i_1, *, i_3]$, and $x[* , i_2, i_3]$, respectively.

Definition 2.2. *Three-dimensional parallel Turing machine* (denoted by 4-PTM) is a 10-tuple $M = (Q, E, U, q_s, q_0, \Sigma, \Gamma, F, \delta_n, \delta_f)$, where

- (1) $Q = E \cup U \cup \{q_0\}$ is a finite set of states;
- (2) E is a finite set of nondeterministic states;
- (3) U is a finite set of fork states;
- (4) q_s is the quiescent state;
- (5) $q_0 \in Q - \{q_s\}$ is the initial state;
- (6) Σ is a finite input alphabet ($\# \notin \Sigma$ is the boundary symbol);
- (7) Γ is a finite storage tape alphabet containing the special blank symbol B ;
- (8) $F \subseteq Q - \{q_s\}$ is the set of accepting states;
- (9) $\delta_n : E \times (\Sigma \cup \{\#\}) \times \Gamma \rightarrow 2^{(Q - \{q_s\}) \times (\Gamma - \{B\}) \times D_{in} \times D_s}$ (where $D_{in} = \{\text{east, west, south, north, up, down, no more}\}$ and $D_s = \{\text{left, right, no more}\}$) is a next nondeterministic move function; and
- (10) $\delta_f : U \times (\Sigma \cup \{\#\}) \times \Gamma \rightarrow U_{1 \leq k \leq \infty} ((Q - \{q_s\}) \times (\Gamma - \{B\}) \times D_{in} \times D_s)$ is a next fork move function with the restriction that for each $q \in U$, each $a \in \Sigma \cup \{\#\}$, and each $A \in \Gamma$, if $\delta(q, a, A) = ((p_1, c_1, d_{11}, d_{21}), (p_2, c_2, d_{12}, d_{22}), \dots, (p_k, c_k, d_{1k}, d_{2k}))$, then $c_1 = c_2 = \dots = c_k$.

As shown in Figure.1, M has a read-only three-dimensional rectangular input tape with boundary symbols “#’s”, and one semi-infinite storage tape (extended to the right), initially filled with the blank symbols. Furthermore, M has infinite processors, P_1, P_2, \dots , each of which has its input head and storage-tape head. M starts in the situation that (1) the processors P_1 is in the initial state q_0 with its input head on the upper north-westmost corner of the input tape and with its storage-tape head on the leftmost cell of the storage tape, and (2) each of other processors is in the quiescent state q_s with its input head on the upper northwestmost corner

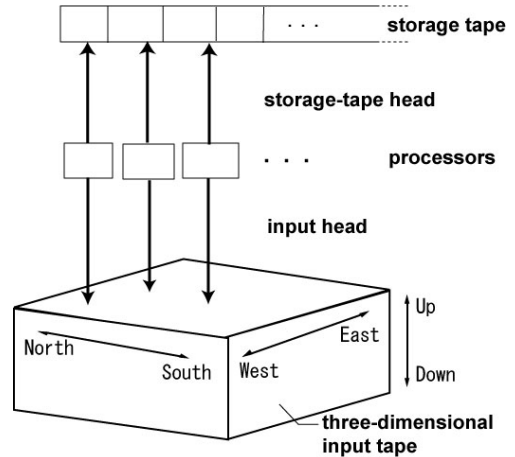


Figure 1: Three-dimensional parallel Turing machine.

of the input tape and with its storage-tape head on the leftmost cell of the storage tape.

Five-way three-dimensional parallel Turing machine (denoted by FV3-PTM) is a 3-PTM, input heads of whose processors cannot move up. In this paper, we are concerned with three-dimensional parallel Turing machines whose input tapes are restricted to cubic ones. Let $L : \mathbf{N} \rightarrow \mathbf{N}$ and $H : \mathbf{N} \rightarrow \mathbf{N}$ be functions. A 3-PTM (FV3-PTM) M is called $L(n)$ space-bounded if for any $n \geq 1$ and for any input tape x with $l_1(x) = l_2(x) = l_3(x) = n$, M on x uses at most $L(n)$ cells of the storage tape, and M is $H(n)$ hardware-bounded if for any $n \geq 1$ and for any input tape x with $l_1(x) = l_2(x) = l_3(x) = n$, M on x activates at most $H(n)$ processors. We use the following notations:

- D3-PTM($L(n), H(n)$): the class of sets of cubic tapes accepted by $L(n)$ space-bounded and $H(n)$ hardware-bounded deterministic 3-PTM's
- N3-PTM($L(n), H(n)$): the class of sets of cubic tapes accepted by $L(n)$ space-bounded and $H(n)$ hardware-bounded nondeterministic 3-PTM's
- DFV3-PTM($L(n), H(n)$): the class of sets of cubic tapes accepted by $L(n)$ space-bounded and $H(n)$ hardware-bounded deterministic FV3-PTM's
- NFV3-PTM($L(n), H(n)$): the class of sets of cubic tapes accepted by $L(n)$ space-bounded and $H(n)$ hardware-bounded nondeterministic FV3-PTM's

3 Main Results

This section mainly investigates accepting powers of FV3-PTM's, based on hardware complexity.

A function $L : \mathbf{N} \rightarrow \mathbf{N}$ is *fully space constructible* by a k head one-dimensional deterministic Turing machine if there is a k head one-dimensional deterministic Turing machine [4] M such that for any $n \geq 1$ and any input word x of length n , M on x marks off exactly $L(n)$ cells of the storage tape and halts. (In this case, we say that M *constructs* the function L .)

Theorem 3.1. Let $H : \mathbf{N} \rightarrow \mathbf{N}$ be a function which satisfies the following (1), (2), and (3), where $k \geq 1$ is an integer:

- (1) H is fully space constructible by a k head one-dimensional deterministic Turing machine;
- (2) $\exists n_0 \in \mathbf{N}, \forall n \geq n_0 [H(n) \geq k]$;
- (3) $\binom{H(n)}{2} \leq \frac{n}{2} (n \leq 2)$.

Furthermore, let $H' : \mathbf{N} \rightarrow \mathbf{N}$ and $L : \mathbf{N} \rightarrow \mathbf{N}$ be functions which satisfy the following (4) and (5):

- (4) $\exists n_0 \in \mathbf{N}, \forall n \geq n_0 [\binom{H'(n)}{2} \leq \binom{H(n)}{2}]$;
- (5) $\max \{ H'(n)^2 \binom{H(n)}{2} \log n, H'(n)^2 \binom{H(n)}{2} \log L(n), L(n)H'(n) \binom{H(n)}{2} \} = o(n)$.

Then,

$$DFV3\text{-}PTM(H(n), H(n)) - NFV3\text{-}PTM(L(n), H'(n)) \neq \phi.$$

Proof: Let $T(H)$ be the following set depending on the function H in the theorem:

$$T(H) = \{ x \in \{0, 1\}^{(3)} \mid \exists n \geq 2 \binom{H(n)}{2} [l_1(x)=l_2(x)=l_3(x)=l_4(x)=n \ \& \ \forall_i (1 \leq i \leq \binom{H(n)}{2}) \text{ [the } i\text{th plane of } x \text{ is identical with the } (2 \binom{H(n)}{2} + 1 - i)\text{th plane of } x]] \}.$$

To prove the theorem, we show that $T(H) \in DFV3\text{-}PTM(H(n), H(n)) - NFV3\text{-}PTM(L(n), H(n))$. $T(H)$ is accepted by an $H(n)$ space-bounded and $H(n)$ hardware-bounded $DFV3\text{-}PTM$ M which acts as follows. Suppose that an input tape x with $l_1(x) = l_2(x) = l_3(x) = n$ is presented to M . Let M_1 be a k head one-dimensional deterministic Turing machine which constructs the function H . By simulating the action of M_1 on the first plane of x , the first k processors P_1, P_2, \dots, P_k of M mark off exactly $H(n)$ cells of the storage tape.

After this, each processor $P_i (2 \leq i \leq k)$ positions its storage-tape head on the i th cell (from the left) of the storage tape, and processor P activates processors $P_{k+1}, P_{k+2}, \dots, P_{H(n)}$ in such a way that for each $j (k+1 \leq j \leq H(n))$, the storage-tape head of P_j is positioned on the j th cell (from the left) of the storage tape. Then P_1 positions the input head at the northwestmost corner of the $(2 \binom{H(n)}{2} + 2 - H(n))$ th plane of x , which for each $i (2 \leq i \leq H(n))$, P_i po-

sitions the input head on the northwestmost corner of the $(H(n) - i + 1)$ th plane of x . And P_1 systematically traverses the $(2 \binom{H(n)}{2} + 2 - H(n))$ th plane, \dots , the $2 \binom{H(n)}{2}$ th plane (from the first column to the last column in each plane, and from the first row to the last row in each column), and compares these planes with the $(H(n) - 1)$ th plane, \dots , the first plane, respectively, by using the information from $P_2, P_3, \dots, P_{H(n)}$.

These input heads are then positioned at the northwestmost end of the $H(n)$ th plane of x . The same procedure is used inductively to verify that $H(n)$ th plane through the $(2 \binom{H(n)}{2} + 1 - H(n))$ th plane has a desired form.

Next, we show that $T(H) \notin NFV3\text{-}PTM(L(n), H'(n))$. Suppose to the contrary that there is an $NFV3\text{-}PTM(L(n), H'(n))$ M' accepting $T(H)$. Let s and t be the numbers of states of the finite control of each processor and storage tape symbols of M' , respectively. For large $n \geq 2 \binom{H(n)}{2}$, let

$$V(n) = \{ x \in \{0, 1\}^{(3)} \mid l_1(x) = l_2(x) = l_3(x) = n \ \& \ \forall_i (1 \leq i \leq \binom{H(n)}{2}) \text{ [the } i\text{th plane of } x \text{ is identical with the } (2 \binom{H(n)}{2} + 1 - i)\text{th plane of } x] \ \& \ [(1, 1, 2 \binom{H(n)}{2} + 1), (n, n, n)] \in \{0\}^{(3)} \}.$$

Below, we consider the computation of M' on input tapes in $V(n)$. Clearly, each tape x in $V(n)$ is in $T(H)$, and so x is accepted by M' .

A configuration of M' is an infinite-tuple $(\alpha, ((i_1, j_1, k_1), q_1, h_1), ((i_2, j_2, k_2), q_2, h_2), \dots, ((i_m, j_m, k_m), q_m, h_m), \dots)$ where α is the non-blank contents of the storage tape of M' , and for each $m \geq 1$, (i_m, j_m, k_m) , q_m and h_m are the input head position, the state of the finite control and the position of storage-tape head of the m th processor of M' , respectively. The type of a configuration $C = (\alpha, ((i_1, j_1, k_1), q_1, h_1), ((i_2, j_2, k_2), q_2, h_2), \dots, ((i_m, j_m, k_m), q_m, h_m), \dots)$, denoted by $Type(C)$, is an infinite-tuple $([i_1], \dots, [i_m], \dots)$, where for each $m \geq 1$,

$$[i_m] = \begin{cases} i_m & \text{if } i_m \leq \binom{H(n)}{2} \\ 2 \binom{H(n)}{2} & \text{otherwise.} \end{cases}$$

Let $c_1(x), c_2(x), \dots, c_{l_x}(x)$ be the sequence of configurations of M' during an (arbitrary selected) accepting computation of M' on a tape x in $V(n)$. Here l_x is the length of this computation. Let $d_1(x), d_2(x), \dots, d_{l'_x}(x)$ be the subsequence obtained by selecting $c_1(x)$ and all subsequent $c_i(x)$'s such that $Type(c_i(x)) \neq Type(c_{i+1}(x))$. We call $d_1(x), d_2(x), \dots, d_{l'_x}(x)$ the pattern of x . Let $p(n)$ be the number of possible pattern of M' on x in $V(n)$. Since $L'_x \leq H'(n)(2 \binom{H(n)}{2} - 1) + 1 \equiv Q(x)$ (note that M' uses at most $H'(n)$ processors when it reads tapes in $V(n)$), we get the following inequality:

$$p(x) \leq ((s(n+1)(n+1)(n+1)L(n))^{H'(n)t^{L(n)}})^{Q(n)}.$$

Now we classify the tapes in $V(n)$ according to their patterns. There must exist a pattern $\hat{d}_1, \hat{d}_2, \dots, \hat{d}_l$ which corresponds to a set $S(n)$ of at least $2^{n \times n \times \binom{H(n)}{2}} / p(n)$ tapes in $V(n)$. Since $\binom{H'(n)}{2} \leq \binom{H(n)}{2}$ (from condition (4) in the theorem), the same observation as in the proof of Theorem 3 in [2] reveals that for any computation of M' on an $x \in V(n)$, there exists an index i such that the i th plane of x and the $(2^{\binom{H(n)}{2}} + 1 - i)$ th plane of x are never being read simultaneously.

Let i_0 be such a value for the pattern $\hat{d}_1, \hat{d}_2, \dots, \hat{d}_l$. we now define a binary relation E on tapes in $S(n)$ as follows: For each u and v in $S(n)$, let

${}_u E_v \Leftrightarrow \forall_i (\notin \{i_0, i_0, 2^{\binom{H(n)}{2}} + 1 - i_0\})$ [i th planes of u and v are identical].

Obviously the relation E is an equivalence relation, and there are $q(n) = 2^{n^2 \binom{H(n)}{2}}$ E-equivalence classes of tapes in $S(n)$. From condition (5) in the theorem, we can easily show that $|S(n)| > q(n)$ for large n . Therefore, there exist two different tapes in $S(n)$ which belong to the same equivalence class. Let x and y be such two different tapes in $S(n)$. And let z be the tape obtained from x by replacing the $(2^{\binom{H(n)}{2}} + 1 - i_0)$ th plane with the $(2^{\binom{H(n)}{2}} + 1 - i_0)$ th plane of y . By an argument similar to that in the proof of theorem 1 in [6], it can be shown that there is an accepting computation of M' on z . Consequently, z must be accepted by M' . This contradicts the fact z is not in $T(H)$. \square

We consider the following functions:

$$\cdot \log^{(1)} n = \begin{cases} 0 & (n = 0) \\ \lceil \log n \rceil & (n \geq 1), \end{cases}$$

and for each $r \geq 1$,

$$\cdot \log^{(r+1)} n = \log^{(1)}(\log^{(r)} n).$$

It is shown in [3] that the function $\log^{(k)} n$ ($k \geq 1$) are fully space-constructible by three head one-dimensional deterministic Turing machines. From this fact and Theorem 3.1, we have:

Corollary 3.1. For each $k \geq 3$,

$$DFV3-PTM(\log^{(k)} n, \log^{(k)} n) - NFV3-PTM(\log^{(k)} n, \log^{(k+1)} n) \neq \phi.$$

Corollary 3.2. For each $X \in \{D, N\}$ and each $k \geq 3$,
 $XFV3-PTM(\log^{(k)} n, \log^{(k+1)} n) \subseteq XFV3-PTM(\log^{(k)} n, \log^{(k)} n)$.

Letting $H(n) = k + 1$ (where k is a positive integer), $H'(n) = k$, and $L(n) = o(n)$ in Theorem 3.1, we have :

$$DFV3-PTM(k + 1, k + 1) - NFV3-PTM(o(n), k) \neq \phi.$$

From this and from the obvious fact that

$$DFV3-PTM(k + 1, k + 1) = DFV3-PTM(1, k + 1),$$

we have the following corollary.

Corollary 3.3. For any integer $k \geq 1$,

$$DFV3-PTM(1, k + 1) - NFV3-PTM(o(n), k) \neq \phi.$$

4 Conclusion

This paper investigated fundamental properties of three-dimensional parallel Turing machines with bounded number of processors. We conclude the paper by giving several open problems.

(1) What is a relationship between the accepting powers of $FV3-PTM$'s and $3-PTM$'s?

(2) What is a relationship between the accepting powers of deterministic and nondeterministic $FV3-PTM$'s?

(3) What is a hierarchy of the accepting powers of $FV3-PTM$'s, based on the hardware complexity depending on the side-length of input tapes?

References

- [1] K. Okinaka, K. Inoue, A. Ito, and Y. Wang, "A note on hardware-bounded parallel Turing machines", *Proc. of the 2nd International Conference on Information*, Beijing, China, pp. 90-100, 2002.
- [2] A. L. Rosenberg, "On multihead finite automata", *IBM J. Res. and Dev.*, Vol. 10, pp. 388-394, 1996.
- [3] M. Sakamoto, K. Inoue, and I. Takanami, "Three-dimensionally fully space constructible functions", *IECE Transactions on Information and Systems*, E77-D(6), pp. 723-725, 1994.
- [4] S. Sakurayama, K. Inoue, I. Takanami, H. Taniguchi, and H. Matsuno, "A note on multi-head on-line Turing machines", *Technical Report of the Yamaguchi University*, Vol.3, No.2, pp.183-192, 1983.
- [5] J. Wiedermann, "Parallel Turing machines", *Technical Report RUU-CS-84-11*, Dep. of Computer Science, University of Utrecht, the Netherlands, 1984.
- [6] A. C. Yao and R. L. Rivest, "k+1 heads are better than k", *J. ACM*, Vol.25, No.2, pp.337-340, 1978.

Remarks on Recognizability of Topological Components by Three-Dimensional Automata

Yuusuke NAGAMIZU¹, Makoto SAKAMOTO¹, Takao ITO¹, Kouichi IIHOSHI¹, Naoko TOMOZOE¹,
Hiroshi FURUTANI¹, Michio KONO¹, Satoshi IKEDA¹, Tatsuhiro TAMAKI², and Katsushi INOUE³

¹Dept. of Computer Science and Systems Engineering, University of Miyazaki, Miyazaki 889-2192, JAPAN

²Dept. of Business Administration, Ube National College of Technology, Ube 755-8555, JAPAN

³Dept. of Computer Science and Systems Engineering, Yamaguchi University, Ube 755-8611, JAPAN

Abstract

It is conjectured that the three-dimensional pattern processing has its own difficulties not arising in two-dimensional case. One of these difficulties occurs in recognizing topological properties of three-dimensional patterns because the three-dimensional neighborhood is more complicated than two-dimensional case. Generally speaking, a property or relationship is topological only if it is preserved when an arbitrary 'rubber-sheet' distortion is applied to the pictures. For example, adjacency and connectedness are topological; area, elongatedness, convexity, straightness, etc. are not. In recent years, there have been many interesting papers on digital topological properties. For example, an interlocking component was defined as a new topological property in three-dimensional digital pictures, and it was proved that no one marker automaton can recognize interlocking components in a three-dimensional digital picture. In this paper, we deal with recognizability of topological components by three-dimensional Turing machines, and investigate some properties.

KeyWords : digital geometry, interlocking component, one marker automaton, three-dimensional automaton, Turing machine, topological component

1 Introduction

Digital geometry has played an important role in computer image analysis and recognition[3]. In particular, there is a well-developed theory of *topological* properties such as *connectedness* and *holes* for two-dimensional arrays[4]. On the other hand, three-dimensional information processing has also become of increasing interest with the rapid growth of computed tomography, robotics, and so on. Thus it has become desirable to study the geometrical properties such as *interlocking components* and *cavities* for three-dimensional arrays[2,5]. In[2], interlocking components was proposed as a new topological property

of three-dimensional digital pictures : Let S_1 and S_2 be two subsets of the same three-dimensional digital picture. S_1 and S_2 are said to be interlocked when they satisfy the following conditions:

- (1) S_1 and S_2 are *toruses*,
- (2) S_1 goes through a *hole* of S_2 ,
- (3) S_2 goes through a *hole* of S_1 .

The interlocking of S_1 and S_2 is illustrated in Fig.1. This relation may be considered as a chainlike connectivity.

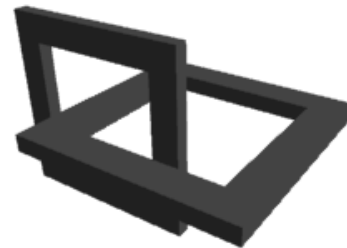


Fig. 1: Interlocking components.

It is proved that no one marker automaton can recognize interlocking components in a three-dimensional digital picture in [2]. In this paper, we investigate recognizability of topological properties such as interlocking components by three-dimensional Turing machines.

2 Preliminaries

Definition 2.1. Let Σ be a finite set of symbols. A *three-dimensional tape* over Σ is a three-dimensional rectangular array of elements of Σ . The set of all three-dimensional tapes over Σ is denoted by $\Sigma^{(3)}$. Given

a tape $x \in \Sigma^{(3)}$, for each $j(1 \leq j \leq 3)$, we let $l_j(x)$ be the length of x along the j^{th} axis. When $1 \leq i_j \leq l_j(x)$ for each $j(1 \leq j \leq 3)$, let $x(i_1, i_2, i_3)$ denote the symbol in x with coordinates (i_1, i_2, i_3) , as shown in Fig. 2. Furthermore, we define

$$x[(i_1, i_2, i_3), (i'_1, i'_2, i'_3)],$$

when $1 \leq i_j \leq i'_j \leq l_j(x)$ for each integer $j(1 \leq j \leq 3)$, as the three-dimensional tape y satisfying the following :

- (i) for each $j(1 \leq j \leq 3)$, $l_j(y) = i'_j - i_j + 1$;
- (ii) for each r_1, r_2, r_3 ($1 \leq r_1 \leq l_1(y)$, $1 \leq r_2 \leq l_2(y)$, $1 \leq r_3 \leq l_3(y)$), $y(r_1, r_2, r_3) = x(r_1 + i_1 - 1, r_2 + i_2 - 1, r_3 + i_3 - 1)$.

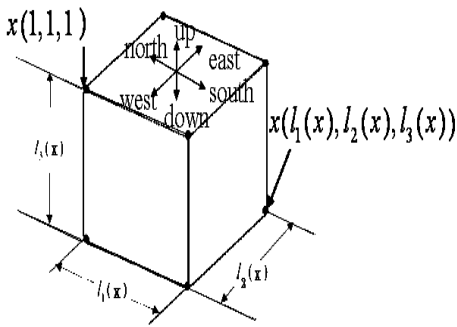


Fig. 2: Three-dimensional input tape.

Definition 2.2. A three-dimensional nondeterministic one-marker automaton $3-NM_1$ is defined by the six-tuple

$$M = (Q, q_0, F, \Sigma, \{+, -\}, \delta),$$

where

- (1) Q is a finite set of states;
- (2) $q_0 \in Q$ is the initial state;
- (3) $F \subseteq Q$ is the set of accepting states;
- (4) Σ is a finite input alphabet ($\# \notin \Sigma$ is the boundary symbol);
- (5) $\{+, -\}$ is the pair of signs of presence and absence of the marker; and
- (6) $\delta: (Q \times \{+, -\}) \times ((\Sigma \cup \{\#\}) \times \{+, -\}) \rightarrow 2^{(Q \times \{+, -\}) \times ((\Sigma \cup \{\#\}) \times \{+, -\}) \times \{\text{east, west, south, north, up, down, no move}\}}$ is the next-move function, satisfying the following: For any $q, q' \in Q$, any $a, a' \in \Sigma$, any $u, u', v, v' \in \{+, -\}$, and any $d \in \{\text{east, west, south, north, up, down, no}$

move}, if $((q', u'), (a', v'), d) \in \delta$
 $((q, u), (a, v))$ then $a = a'$, and
 $(u, v, u', v') \in \{(+, -, +, -), (+, -, -, +), (-, +, -, +), (-, +, +, -), (-, -, -, -)\}$.

We call a pair (q, u) in $Q \times \{+, -\}$ an extended state, representing the situation that M holds or does not hold the marker in the finite control according to the sign $u = +$ or $u = -$, respectively. A pair (a, v) in $\Sigma \times \{+, -\}$ represents an input tape cell on which the marker exists or does not exist according to the sign $v = +$ or $v = -$, respectively.

Therefore, the restrictions on δ above imply the following conditions. (A) When holding the marker, M can put it down or keep on holding. (B) When not holding the marker, and (i) if the marker exists on the current cell, M can pick it up or leave it there, or (ii) if the marker does not exist on the current cell, M cannot create a new marker any more.

Definition 2.3. Let Σ be the input alphabet of $3-NM_1 M$. An extended input tape \tilde{x} of M is any three-dimensional tape over $\Sigma \times \{+, -\}$ such that

- (i) for each $j(1 \leq j \leq 3)$, $l_j(\tilde{x}) = l_j(x)$,
- (ii) for each $i_1(1 \leq i_1 \leq l_1(\tilde{x}))$, $i_2(1 \leq i_2 \leq l_2(\tilde{x}))$, and $i_3(1 \leq i_3 \leq l_3(\tilde{x}))$, $\tilde{x}(i_1, i_2, i_3) = x(i_1, i_2, i_3, u)$ for some $u \in \{+, -\}$.

Definition 2.4. A configuration of $3-NM_1 M = (Q, q_0, F, \Sigma, \delta)$ is an element of

$$((\Sigma \cup \{\#\}) \times \{+, -\})^{(3)} \times (Q \times \{+, -\}) \times N^3,$$

where N denotes the set of all nonnegative integers. The first component of a configuration $c = (\tilde{x}, (q, u), (i_1, i_2, i_3))$ represents the extended input tape of M . The second component (q, u) of c represents the extended state. The third component (i_1, i_2, i_3) of c represents the input head position. If q is the state associated with configuration c , then c is said to be an accepting configuration if q is an accepting state. The initial configuration of M on input x is

$$I_M(x) = (x^-, (q_0, +), (1, 1, 1)),$$

where x^- is the special extended input tape of M such that $x^-(i_1, i_2, i_3) = (x(i_1, i_2, i_3), -)$ for each i_1, i_2, i_3 ($1 \leq i_1 \leq l_1(\tilde{x}), 1 \leq i_2 \leq l_2(\tilde{x}), 1 \leq i_3 \leq l_3(\tilde{x})$). If M moves determinately, we call M a three-dimensional deterministic one-marker automaton $3-DM_1$.

Definition 2.5. A five-way three-dimensional Turing machine is defined by the six-tuple

$$M = (Q, q_0, F, \Sigma, \Gamma, \delta),$$

where

- (1) Q is a finite set of *states*;
- (2) $q_0 \in Q$ is the *initial state*;
- (3) $F \subseteq Q$ is the set of *accepting states*;
- (4) Σ is a finite *input alphabet* ($\# \notin \Sigma$ is the *boundary symbol*);
- (5) Γ is a finite *storage-tape alphabet* ($B \in \Gamma$ is the *blank symbol*); and
- (6) $\delta \subseteq (Q \times (\Sigma \cup \{\#\}) \times \Gamma) \times (Q \times (\Gamma - \{B\}) \times \{\text{east, west, south, north, down, no move}\} \times \{\text{right, left, no move}\})$.

If M moves determinately (nondeterminately), we call M a *five-way three-dimensional deterministic (nondeterministic) Turing machine FV3-DTM (FV3-NTM)*.

Let $L: \mathbf{N} \rightarrow \mathbf{R}$ be a function. A five-way three-dimensional Turing machine M is said to be $L(m)$ *space bounded* if for all $m \geq 1$ and for each x with $l_1(x) = l_2(x) = l_3(x) = m$, if x is accepted by M , then there is an *accepting computation path* of M on x in which M uses no more than $L(m)$ cells of the storage tape. We denote an $L(m)$ space-bounded FV3-DTM (FV3-NTM) by FV3-DTM($L(m)$) (FV3-NTM($L(m)$)).

Definition 2.6. Let $T(M)$ be the set of three-dimensional tapes accepted by a machine M , and let $\mathcal{L}[3-DM_1] = \{T | T(M) \text{ for some } 3-DM_1 M\}$. $\mathcal{L}[3-NM_1]$, etc. are defined in the same way as $\mathcal{L}[3-DM_1]$.

We can easily derive the following theorem by using ordinary technique[6].

Theorem 2.1. For any function $L(m) \geq \log m^2$, $\mathcal{L}[FV3-NTM(L(m))] \subseteq U_{c>0} \mathcal{L}[FV3-DTM(2^{cL(m)})]$.

3 Simulation of three-dimensional one-marker automata by three-dimensional Turing machines

In this section, we first investigate the sufficient spaces (i.e., upper bounds) for five-way three-dimensional Turing machines to simulate three-dimensional one-marker automata[6].

Theorem 3.1. $\mathcal{L}[3-DM_1] \subseteq \mathcal{L}[FV3-NTM(m^2 \log m^2)]$.

Proof : Suppose that a 3- DM_1 $M = (Q, q_0, F, \Sigma, \delta)$ is given. We partition the extended states $Q \times \{+, -\}$ into disjoint subsets $Q^+ = Q \times \{+\}$ and $Q^- = Q \times \{-\}$ which correspond to the extended states when M is

holding and not holding the marker in the finite control, respectively. We assume that M has a unique accepting state q_a , i.e., $|F| = 1$. In order to make our proof clear, we also assume that M begins to move with its input head on the southmost and eastmost bottom boundary symbols $\#$'s of input tape, i.e., position $(l + 1, m + 1, n + 1)$ and, when M accepts an input, it enters the accepting state at the same position $(l + 1, m + 1, n + 1)$ with the marker held in the finite control.

Suppose that an input tape x with $l_1(x) = l$, $l_2(x) = m$, and $l_3(x) = n$ is given to M . For M and x , define three types of functions $f_h^{\uparrow-}$, $f_h^{\uparrow+}$ and $f_h^{\downarrow-}$.

$f_h^{\uparrow-}(q^-, i, j) = (q'^-, i', j')$: Suppose that we make M start from the configuration $(x^-, q^-, (i, j, h - 1))$, i.e., no marker existing either on the input x or in the finite control of M . After that, if M reaches the h^{th} plane of x in some time, the configuration corresponding to the first arrival is $(x^-, q'^-, (i', j', h))$,

$f_h^{\uparrow+}(q^+, i, j) = (q'^+, i', j')$: Suppose that we make M start from the configuration $(x^-, q^+, (i, j, h - 1))$, i.e., holding the marker in the finite control of M . After that, if M reaches the h^{th} plane of x with its marker held in the finite control in some time (so, when M puts down the marker on the way, it must return to this position again and pick up the marker), the configuration corresponding to the first arrival is $(x^-, q'^+, (i', j', h))$,

$f_h^{\downarrow-}(q^-, i, j) = (q'^-, i', j')$: Suppose that we make M start from the configuration $(x^-, q^-, (i, j, h + 1))$, i.e., no marker existing either on the input tape or in the finite control of M . After that, if M reaches the h^{th} plane of x in some time, the configuration corresponding to the first arrival is $(x^-, q^-, (i', j', h))$,

l : M never reaches the h^{th} plane of x .

Then, we can show that there exists an FV3-NTM($m^2 \log(m^2)$) M' such that $T(M') = T(M)$. Roughly speaking, while scanning from the top plane down to the bottom plane of the input, M' guesses $f_h^{\downarrow-}$, constructs $f_{h+1}^{\uparrow-}$ and $f_{h+1}^{\uparrow+}$, checks $f_{h-1}^{\downarrow-}$, and finally at the bottom plane of the input, M' decides by using $f_{t+1}^{\uparrow-}$ and $f_{t+1}^{\uparrow+}$ whether or not M accepts x . In order to record these mappings for each h , $O(m^2)$ blocks of $O(\log m^2)$ size suffice, so in total, $O(m^2 \log m^2)$ cells of the working tape suffice. It will be obvious that $T(M) = T(M')$. \square

From Theorems 2.1 and 3.1, we get the following.

Corollary 3.1. $\mathcal{L}[3-DM_1] \subseteq \mathcal{L}[FV3-DTM(2^{O(m^2 \log m^2)})]$.

We next show that m^4 space is sufficient for FV3-NTM's to simulate 3- NM_1 's. The basic idea of the proof are the same as those of Theorem 3.1.

Theorem 3.2. $\mathcal{L}[3-NM_1] \subseteq \mathcal{L}[FV3-NTM(m^4)]$.

From Theorems 2.1 and 3.1, we get the following.

Corollary 3.2. $\mathcal{L}[3-NM_1] \subseteq \mathcal{L}[FV3-DTM(2^{O(m^4)})]$.

Next, we show that the algorithms described in the previous section are optimal in some sense.

Definition 3.1. Let x be in $\Sigma^{(3)}$ (Σ is a finite set of symbols) and $l_1(x)=l_2(x)=m$. For each r ($1 \leq r \leq Q[l_3(x)/m^2]$) (where $Q[l_3(x)/m^2]$ denotes the quotient when $l_3(x)$ is divided by m^2),

$$x[(1, 1, (r - 1)m^2 + 1), (m, m, rm^2)]$$

is called the r^{th} (m, m) -block of x . We say that the tape x has exactly $c(m, m)$ -blocks if $l_3(x) = cm^2$, where c is a positive integer.

Definition 3.2. Let $(m_1, m_1), (m_2, m_2), \dots$ be a sequence of points (i.e., pairs of three natural numbers), and let $\{(m_i, m_i)\}$ denote this sequence. We call a sequence $\{(m_i, m_i)\}$ the *regular sequence of points* if $(m_i, m_i) \neq (m_j, m_j)$ for $i \neq j$.

Lemma 3.1. Let $\{x \in \{0, 1\}^{(3)} \mid \exists m \geq 1 [l_1(x)=l_2(x)=l_3(x)=m \ \& \ l_2(x)=m \ \& \ (each \ plane \ of \ x \ contains \ exactly \ one \ '1') \ \& \ \exists d \geq 2 [(x \ has \ exactly \ d \ (m, m)\text{-blocks, \ i.e., \ } l_3(x) = dm^2) \ \& \ (the \ last \ (m, m)\text{-block is equal to some other } (m, m)\text{-block}]]]\}$. Then,

- (1) $T_1 \in \mathcal{L}[3-DM_1]$, but
- (2) $T_1 \notin \mathcal{L}[FV3-DTM(2^{L(m)})]$ (so, $T_1 \notin \mathcal{L}[FV3-NTM(L(m))]$) for any function $L(m)$ such that

$$\lim_{i \rightarrow \infty} [L(m_i)/(m_i^2 \log(m_i^2))] = 0$$

for some regular sequence of points $\{(m_i, m_i)\}$.

Proof : (1) We construct a 3- DM_1 M accepting T_1 as follows. Given an input x with $l_1(x)=l_2(x)=l_3(x)=m$, M first checks, by sweeping plane by plane, that each plane of x contains exactly one '1,' and M then checks, by making a zigzag of 45°-direction from top plane to bottom plane, that x has exactly d (m, m) -blocks for some integer $d \geq 2$. After that, M tests by utilizing its own marker whether the last (m, m) -block is identical to some other (m, m) -block: In order to check whether the p^{th} plane of the h^{th} (m) -block is identical to the p^{th} plane of the last (m) -block ($1 \leq p \leq m^2, 1 \leq h \leq d$), M first puts the marker on the position $(i, j, m^2(h-1)+p)$. After that, M vertically moves down until encounters the bottom boundary, after which it moves up (m^2-p) plane by making a zigzag of 45°-direction. At this time, M arrives at the p^{th} plane of the last (m, m) -block. M then finds the '1' position on the plane and

moves up vertically from this position. In this course, each time M meets a '1' position, it checks whether or not there is a marker on the plane (containing the '1' position). In this way, M enters an accepting state just when it finds out some (m, m) -block, each of whose planes is identical to the corresponding plane of the last (l, m) -block. It will be obvious that $T(M)=T_1$.

(2) Suppose to the contrary that there exists an $FV3-DTM(2^{L(m)})$ M accepting T_1 , where $L(m)$ is a function such that

$$\lim_{i \rightarrow \infty} [L(m_i)/(m_i^2 \log(m_i^2))] = 0$$

for some regular sequence of points $\{(m_i, m_i)\}$. Then, by using the well-known technique [6], we can get the desired result. \square

From Lemma 3.1., we can conclude as follows.

Theorem 3.3. To simulate 3- DM_1 's, (1) $FV3-NTM$'s require $\Omega(m^2 \log(m^2))$ space and (2) $FV3-DTM$'s require $2^{\Omega(m^2 \log(m^2))}$ space.

Next, we can get the following lemma by using the same technique as in the proof of Lemma 3.1.

Lemma 3.2. Let $T_2 = \{x \in \{0, 1\}^{(3)} \mid \exists m \geq 1 [l_1(x)=l_2(x)=l_3(x)=m \ \& \ \exists d \geq 2 [(x \ has \ exactly \ d \ (m, m)\text{-blocks, \ i.e., \ } l_4(x)=dm^2) \ \& \ (the \ last \ (m, m)\text{-block is different from any other } (m, m)\text{-block}]]]\}$. Then,

- (1) $T_2 \in \mathcal{L}[3-NM_1]$, but
- (2) $T_2 \notin \mathcal{L}[FV3-DTM(2^{L(m)})]$ (so, $T_2 \notin \mathcal{L}[FV3-NTM(L(m))]$) for any function L such that $\lim_{i \rightarrow \infty} [L(m_i)/(m_i^4)] = 0$ for some regular sequence of points $\{(m_i, m_i)\}$.

From Lemma 3.2., we can conclude as follows.

Theorem 3.4. To simulate 3- NM_1 's,

- (1) $FV3-NTM$'s require $\Omega(m^4)$ space, and
- (2) $FV3-DTM$'s require $2^{\Omega(m^4)}$ space.

4 Recognizability of interlocking components in three-dimensional images

In this paper, we show that interlocking components are not recognized by any space-bounded three-dimensional Turing machines.

First of all, we consider a three-dimensional input tape T_3 that is 7 units in thickness. So, for some m , $T_3 = \{(i_1, i_2, i_3) \mid 1 \leq i_1, i_2 \leq m+2, 1 \leq i_3 \leq 7\}$.

Fig.3(a) represents T_3 . Now we define two different $5 \times 5 \times 5$ patterns as shown in Fig.3(b)(c). Then we consider an arbitrary n -by- n matrix of those $5 \times 5 \times 5$ patterns (see Fig.3).

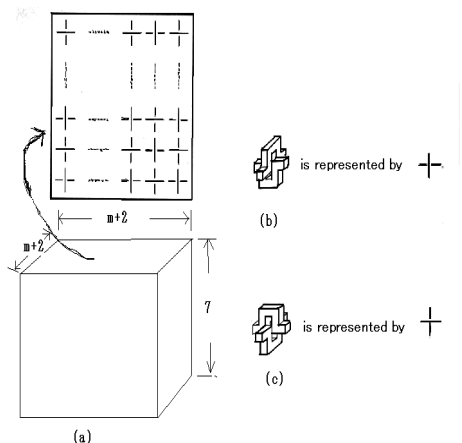


Fig. 3: Three-dimensional input tape including interlocking components $T_3[2]$.

Then, we can get the following lemma from Lemma 2.1 in [2].

Lemma 4.1. *3-DM, cannot recognize interlocking components of an arbitrary given digital picture.*

From Theorem 3.3 and Lemma 4.1, we can get the following.

Theorem 4.1. *Interlocking components are not accepted by any FV3-DTM ($L(m)$)(FV3-NTM($L(m)$)) for any function $L(m)$ such that $\lim_{m \rightarrow \infty} [L(m)/2m^2 \log m^2] = 0$ ($\lim_{m \rightarrow \infty} [L(m)/m^2 \log m^2] = 0$).*

Next, we can get the following lemma by using a technique similar to that in the proof of Lemma 2.1 in [2].

Lemma 4.2. *3-ND₁ cannot recognize interlocking components of an arbitrary given digital picture.*

From Theorem 3.4 and Lemma 4.2, we can get the following.

Theorem 4.2. *Interlocking components are not accepted by any FV3-DTM($L(m)$) (FV3-NTM($L(m)$)) for any function $L(m)$ such that $\lim_{m \rightarrow \infty} [L(m)/2m^4] = 0$ ($\lim_{m \rightarrow \infty} [L(m)/m^4] = 0$).*

5 Conclusion

In this paper, we investigated recognizability of topological components by three-dimensional automata, and showed that interlocking components are not recognized by any space-bounded three-dimensional deterministic or nondeterministic Turing machines. By the way, what is the situation for a two or three marker automata, or for alternation (see [1])? This question seems very interesting. We will deal with the problem in further papers.

References

- [1] A.K. Chandra, D.C. Kozen, and L.J. Stockmeyer, Alternation, *J. of ACM*, 28(1):114-133(1981).
- [2] A.Nakamura and K.Aizawa, Detection of interlocking components in three-dimensional digital pictures, *Information Sciences* 40:143-153(1986).
- [3] A.Rosenfeld and K.C. Kak, *Digital Picture Processing*, Academic Press, New York(1976).
- [4] A.Rosenfeld, *Picture Languages*, Academic Press, New York(1979).
- [5] A.Rosenfeld, Three-dimensional digital topology, *Information and Control* 50:119-127(1981).
- [6] M.Sakamoto, Three-dimensional alternating Turing machines, *Ph. D. Thesis, Yamaguchi University* (1999).

Leaf-Size Hierarchy of Four-Dimensional Alternating Turing Machines

Kouichi IIHOSHI¹, Makoto SAKAMOTO¹, Takao ITO¹, Naoko TOMOZOE¹, Yuusuke NAGAMIZU¹, Hiroshi FURUTANI¹, Michio KONO¹, Satoshi IKEDA¹, Tatsuhiro TAMAKI², and Katsushi INOUE³,

¹Dept. of Computer Science and Systems Engineering, Miyazaki University, Miyazaki 889-2192, JAPAN

²Dept. of Business Administration, Ube National College of Technology, Ube 755-8555, JAPAN

³Dept. of Computer Science and Systems Engineering, Yamaguchi University, Ube 755-8611, JAPAN

Abstract

The recent advances in computer animation, motion image processing and so on prompted us to analyze computational complexity of multi-dimensional information processing to explicate the properties of four-dimensional automata, i.e., three-dimensional automata with the time axis. From this point of view, we first introduced four-dimensional alternating Turing machines 4-ATM's, and investigated leaf-size bounded computation for 4-ATM's in [4,6]. In this paper, we continue the investigations about 4-ATM's, and mainly investigate leaf-size bounded computation of 4-ATM's. Basically, the 'leaf-size' is the minimum number of leaves of some accepting computation trees of alternating Turing machines. Leaf-size, in a sense, reflects the minimum number of processors that run in parallel in accepting a given input.

KeyWords : alternation, configuration, four-dimensional input tape, leaf-size, space bound, Turing machine.

1 Introduction and Preliminaries

In 1967, the problem of computational complexity was also arisen in the two-dimensional information processing. Blum et al. first proposed two-dimensional automata, and investigated their pattern recognition abilities [1]. Since then, many researchers in this field have been investigating a lot of properties about automata on two- or three-dimensional tapes. In 1976, Chandra et al. introduced the concept of 'alternation' as a theoretical model of parallel computation [2]. After that, Inoue et al. introduced two-dimensional alternating Turing machines as a generalization of two-dimensional nondeterministic Turing machines and as a mechanism to model parallel computation [5]. Moreover, Sakamoto et al. presented three-dimensional alternating Turing machines in [7,9].

On the other hand, recently, due to the advances in many application areas such as computer animation, motion image processing, and so forth, it has become increasingly apparent that the study of four-dimensional pattern processing, i.e., three-dimensional automata with the time axis should be of crucial importance. Thus, we think that it is very useful for analyzing computation of four-dimensional pattern processing to explicate the properties of four-dimensional automata. From this viewpoint, we introduced some four-dimensional automata [6, 10].

In this paper, we continue the investigations about four-dimensional alternating Turing machines [4, 6], and mainly investigate leaf-size hierarchy of four-dimensional alternating Turing machines which each sidelength of each input tape is equivalent. Leaf-size bounded computation was introduced as a simple, natural new complexity measure for alternating Turing machines [5]. Basically, the 'leaf-size' (or 'branching') is the minimum number of leaves of some accepting computation trees of processors that run in parallel in accepting a given input.

Let Σ be a finite set of symbols. A *four-dimensional input tape* over Σ is a four-dimensional rectangular array of elements of Σ . The set of all the four-dimensional input tapes over Σ is denoted by $\Sigma^{(4)}$. Given an input tape $x \in \Sigma^{(4)}$, for each $j(1 \leq j \leq 4)$, we let $l_j(x)$ be the length of x along the j th axis. The set of all $x \in \Sigma^{(4)}$ with $l_1(x) = m_1, l_2(x) = m_2, l_3(x) = m_3$, and $l_4(x) = m_4$ is denoted by $\Sigma^{(m_1, m_2, m_3, m_4)}$. If $1 \leq i_j \leq l_j(x)$ for each $j(1 \leq j \leq 4)$, let $x(i_1, i_2, i_3, i_4)$ denote the symbol in x with coordinates (i_1, i_2, i_3, i_4) . Furthermore, we define $x[(i_1, i_2, i_3, i_4), (i'_1, i'_2, i'_3, i'_4)]$, when $1 \leq i_j \leq i'_j \leq l_j(x)$ for each integer $j(1 \leq j \leq 4)$, as the four-dimensional input tape y satisfying the following:

- (i) for each $j(1 \leq j \leq 4)$, $l_j(y) = i'_j - i_j + 1$;
- (ii) for each r_1, r_2, r_3, r_4 ($1 \leq r_1 \leq l_1(y), 1 \leq r_2 \leq l_2(y), 1 \leq r_3 \leq l_3(y), 1 \leq r_4 \leq l_4(y)$), $y(r_1, r_2, r_3, r_4) = x(r_1 + i_1 - 1, r_2 + i_2 - 1, r_3 + i_3 - 1, r_4 + i_4 - 1)$.

As usual, a four-dimensional input tape x over Σ is surrounded by the boundary symbols $\#$'s ($\# \notin \Sigma$). Furthermore, four-dimensional tape is the sequence of three-dimensional rectangular arrays along the time axis. By $Cube_x(i)$ ($i \geq 1$), we denote the i th three-dimensional rectangular array along the time axis in $x \in \Sigma^{(4)}$ which each sidelength is equivalent.

Let Σ_1, Σ_2 be finite set of symbols. The *projection* is a mapping $\tilde{\tau} : \Sigma_1^{(4)} \rightarrow \Sigma_2^{(4)}$ which is obtained by extending a mapping $\tau : \Sigma_1 \rightarrow \Sigma_2$ as follows: $\tilde{\tau}(x) = x'$ if and only if (i) $l_i(x) = l_i(x')$ for each i ($1 \leq i \leq 4$), and (ii) $\tau(x(i_1, i_2, i_3, i_4)) = x'(i_1, i_2, i_3, i_4)$ for each (i_1, i_2, i_3, i_4) ($1 \leq i_1 \leq l_1(x), 1 \leq i_2 \leq l_2(x), 1 \leq i_3 \leq l_3(x), 1 \leq i_4 \leq l_4(x)$). If $T \subseteq \Sigma_1^{(4)}$, we let $\tilde{\tau}(T) = \{\tilde{\tau}(x) \mid x \in T\}$.

We now recall the definition of a *four-dimensional alternating Turing machine (4-ATM)*, which can be considered as an alternating version of a four-dimensional Turing machine (4-TM) [6].

4-ATM M is defined by the 7-tuple

$$M = (Q, q_0, U, F, \Sigma, \Gamma, \delta), \text{ where}$$

- (1) Q is a finite set of *states*;
- (2) $q_0 \in Q$ is the *initial state*;
- (3) $U \subseteq Q$ is the set of *universal states*;
- (4) $F \subseteq Q$ is the set of *accepting states*;
- (5) Σ is a finite input alphabet ($\# \notin \Sigma$ is the *boundary symbol*);
- (6) Γ is a finite *storage-tape alphabet* ($B \in \Gamma$ is the *blank symbol*), and
- (7) $\delta \subseteq (Q \times (\Sigma \cup \{\#\}) \times \Gamma) \times (Q \times (\Gamma - \{B\}) \times \{\text{east, west, south, north, up, down, future, past, no move}\} \times \{\text{right, left, no move}\})$ is the *next-move relation*.

A state q in $Q - U$ is said to be *existential*. As shown in Fig. 1, the machine M has a read-only four-dimensional input tape with boundary symbols $\#$'s and one semi-infinite storage tape, initially blank. Of course, M has a finite control, an input head, and a storage-tape head. A *position* is assigned to each cell of the read-only input tape and to each cell of the storage tape, as shown in Fig. 1. The *step* of M is similar to that of a two- or three-dimensional Turing machine [3-5, 7], except that the input head of M can move in eight directions. We say that M *accepts* the tape x if it eventually enters an accepting state. Note that the machine cannot write the blank symbol. If the input head falls off the input tape, or if the storage head falls

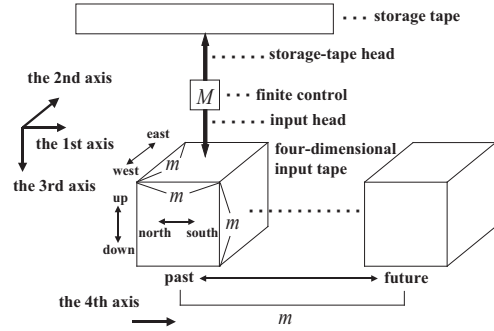


Fig. 1: Four-dimensional alternating Turing machine.

off the storage tape (by moving left), then the machine M can make no further move.

Let $L(m) : \mathbf{N} \rightarrow \mathbf{R}$ be a function with one variable m , where \mathbf{N} is the set of all positive integers and \mathbf{R} is the set of all nonnegative real numbers. With each 4-ATM M we associate a space complexity function $SPACE$ that takes configurations to natural numbers. That is, for each configuration $c = (x, (i_1, i_2, i_3, i_4), (q, \alpha, j))$, let $SPACE(c) = |\alpha|$. M is said to be $L(m)$ *space-bounded* if for each $m \geq 1$ and for each x with $l_1(x) = l_2(x) = l_3(x) = l_4(x) = m$, if x is accepted by M , then there is an accepting computation tree of M on input x such that for each node v of the tree, $SPACE(L(v)) \leq \lceil L(m) \rceil^1$. We denote an $L(m)$ space-bounded 4-ATM by 4-ATM ($L(m)$).

A 4-ATM(0) is called a *four-dimensional alternating finite automaton*, which can be considered as an alternating version of a four-dimensional finite automaton (4-FA), and is denoted by 4-AFA.

In order to distinguish among determinism, non-determinism, alternation with only universal states, and alternation, we denote a deterministic 4-TM [nondeterministic 4-TM, 4-ATM with only universal states, deterministic 4-TM($L(m)$), nondeterministic 4-TM($L(m)$), 4-ATM($L(m)$) with only universal states, deterministic 4-FA, nondeterministic 4-FA, 4-AFA with only universal states] by 4-DTM [4-NTM, 4-UTM, 4-DTM($L(m)$), 4-NTM($L(m)$), 4-UTM($L(m)$), 4-DFA, 4-NFA].

Let M be an automaton on a three-dimensional tape. We denote by $T(M)$ the set of all three-dimensional tapes accepted by M . As usual, for each $X \in \{D, N, U, A\}$, we denote, for example, by $\mathcal{L}[3-XTM]$ the class of sets of all the four-dimensional tapes accepted by 4-XTM's. That is, $\mathcal{L}[4-XTM] = \{T \mid T = T(M) \text{ for some } 4-XTM \ M\}$. $\mathcal{L}[4-XTM$

¹ $\lceil r \rceil$ means the smallest integer greater than or equal to r .

$(L(m))$], and $\mathcal{L}[4-XFA]$ also have analogous meanings.

Let $L(m): \mathbf{N} \rightarrow \mathbf{R}$ be a function. For each tree t , let $LEAF(t)$ denote the leaf-size of t (i.e., the number of leaves of t). We say that a 4-ATM M is $Z(m)$ leaf-size bounded if for all x with $l_1(x)=l_2(x)=l_3(x)=l_4(x)=m$ and for each computation tree t of M on x , $LEAF(t) \leq \lceil Z(m) \rceil$.

By 4-ATM($L(m), Z(m)$), we denote a $Z(m)$ leaf-size bounded 4-ATM($L(m)$). Especially, a 4-ATM($0, Z(m)$) is denoted by 4-AFA($Z(m)$). Define $\mathcal{L}[4-ATM(L(m), Z(m))] = \{T \mid T = T(m) \text{ for some } 4-ATM(L(m), Z(m)) M\}$. We use 4-AFA(k) (4-UFA(k), 4-DFA) to denote a 4-ATM($0, k$) (4-UTM($0, k$), 4-DTM(0)).

2 Unbounded Leaf-Size Hierarchy

A function $L(m) : \mathbf{N} \rightarrow \mathbf{R}$ is called *four-dimensionally space constructible* if there is a *strongly* 4-ATM($L(m)$) M such that for each $m \geq 1$, there exists some input tape x with $l_1(x) = l_2(x) = l_3(x) = l_4(x) = m$ on which M halts after its storage head has marked off exactly $\lceil L(m) \rceil^2$ cells of the storage tape. (In this case, we say that M constructs the function L .)

We first show a hierarchy of complexity classes based on leaf-size bounded computations.

The main theorem is

Theorem 2.1. *Let $k \geq 1$ be a positive integer. Let $L : \mathbf{N} \rightarrow \mathbf{N}$ and $L' : \mathbf{N} \rightarrow \mathbf{N}$ be any functions such that*

- (1) *L is a four-dimensional space-constructible function such that $L(m)^{k+1} \leq m$ ($m \geq 1$),*
- (2) $\lim_{m \rightarrow \infty} L(m)L'(m)^k / \log m = 0$, and
- (3) $\lim_{m \rightarrow \infty} L'(m) / L(m) = 0$.

Then there is a set in $\mathcal{L}[4-ATM(L(m), L(m)^k)]$, but not in $\mathcal{L}[4-ATM(L(m), L'(m)^k)]$.

Proof: Let M be a four-dimensional deterministic Turing machine which constructs the function L . Let $T_k[L, M]$ be the following set, which depends on k , L and M :

$$T_k[L, M] = \{x \in (\Sigma \times \{0, 1\})^{(4)} \mid \exists m \geq 2 [l_1(x) = l_2(x) = l_3(x) = l_4(x) = m \& \exists r (r \leq L(m) \text{ [(when the tape } \tilde{h}_1(x) \text{ is presented to } M, \text{ its read-write head marks off } r \text{ cells of the storage tape and then halts)} \& \exists i (1 \leq i \leq m-1) [\tilde{h}_2(x[(1, 1, m, 1), r^{k+1}, r^{k+1}, m, 1])] = [\tilde{h}_2(x[(1, 1, i, 1), (r^{k+1}, r^{k+1}, i, 1)]])]]\},$$

where Σ is the input alphabet of M , and $\tilde{h}_1(\tilde{h}_2)$ is the *projection* which is obtained by extending the mapping $h_1 : \Sigma \times \{0, 1\} \rightarrow \Sigma$ ($h_2 : \Sigma \times \{0, 1\} \rightarrow \{0, 1\}$) such that for any $c = (a, b) \in \Sigma \times \{0, 1\}$, $h_1(c) = a$ ($h_2(c) = b$).

We first show that $T_k[L, M] \in \mathcal{L}[4-ATM(L(m), L(m)^k)]$. Suppose that an input x with $l_1(x) = l_2(x) = l_3(x) = l_4(x) = m$ ($m \geq 2$) is presented to M_1 . M_1 directly simulates the action of M on \tilde{h}_1 . If M does not halt, then M_1 also does not halt, and will not accept x . If M_1 finds out that M halts (in this case, note that M_1 , has marked off at most cells of the storage tape because M constructs the function L), then M_1 existentially chooses some i ($1 \leq i \leq m-1$) and moves its input tape head on $x(1, 1, i, 1)$. After that, M_1 universally tries to check that, for each $1 \leq j \leq r^k$, where r is the length of the non-blank part of the storage tape just after M_1 has found out that M halts,

$$\begin{aligned} & \tilde{h}_2(x[(j-1)r+1, (j-1)r+1, i, 1), (jr, jr, i, 1)]) \\ & = \tilde{h}_2(x[((j-1)r+1, (j-1)r+1, m, 1), (jr, jr, m, 1)]). \end{aligned}$$

That is, on $x((j-1)r+1, (j-1)r+1, i, 1)$ ($1 \leq j \leq r^k$), M_1 enters a universal state to choose one of two further actions. One action is to pick up and store the segment $\tilde{h}_2(x[(j-1)r+1, (j-1)r+1, i, 1), (jr, jr, i, 1)])$ on some track of the storage tape, to compare the segment stored above with the segment $\tilde{h}_2(x[((j-1)r+1, (j-1)r+1, m, 1), (jr, jr, m, 1)])$, and to enter an accepting state only if both segments are identical. The other action is to continue moving to $x(jr+1, jr+1, i, 1)$ (in order to pick up the next segment $\tilde{h}_2(x[jr+1, jr+1, i, 1), ((j+1)r, (j+1)r, i, 1)])$ and compare it with the corresponding segment $\tilde{h}_2(x[(jr+1, jr+1, m, 1), ((j+1)r, (j+1)r, m, 1)])$.

Note that the number of pairs of segments which should be compared with each other in the future can be easily seen by using r cells of the storage tape. It will be obvious that the input x is in $T_k[L, M]$ if and only if there is an accepting computation three of M_1 on x with at most $L(m)^k$ leaves. Thus $T_k[L, M] \in \mathcal{L}[4-ATM(L(m), L(m)^k)]$.

On the other hand, we can next show that $T_k[L, M] \notin \mathcal{L}[4-ATM(L(m), L'(m)^k)]$ by using the well-known counting argument [3,7]. This completes the proof of the theorem. \square

Corollary 2.1. *Let $k \geq 1$ be a positive integer. Let L*

² $\lceil r \rceil$ means the greatest integer smaller than or equal to r .

: $\mathbf{N} \rightarrow \mathbf{N}$ and $L' : \mathbf{N} \rightarrow \mathbf{N}$ be any functions satisfying the condition that $L'(m) \leq L(m) (m \geq 1)$ and satisfying conditions (1), (2) and (3) described in Theorem 2.1. Then,

$$\mathcal{L}[4-ATM(L(m), L'(m)^k)] \subsetneq \mathcal{L}[4-ATM(L(m), L(m)^k)].$$

For any r in \mathbf{N} , $\log^{(r)} m$ be the function defined as follows :

$$\log^{(1)} m = \begin{cases} 0 & (m = 0) \\ \log m & (m \geq 1), \end{cases}$$

$$\log^{(r+1)} m = \begin{cases} \log^{(1)}(\log^{(r)} m). \end{cases}$$

As shown in Theorem 2.1 of [8], the function $\log^{(r)} m (r \geq 1)$ is three-dimensionally space-constructible, and thus four-dimensionally space-constructible. It is easy to see that for each $r \geq 1$, $\log^{(r+1)} m \leq \log^{(r)} m (m \geq 1)$ and $\lim_{m \rightarrow \infty} \log^{(r+1)} m / \log^{(r)} m = 0$. Further, for each $r \geq 2$ and each $k \geq 1$, $\lim_{m \rightarrow \infty} \log^{(r)} m (\log^{(r+1)} m)^k / \log m = 0$. From these facts, we have the following.

Corollary 2.2. For any $r \geq 2$ and any $k \geq 1$,
 $\mathcal{L}[4-ATM(\log^{(r)} m, (\log^{(r+1)} m)^k)] \subsetneq$
 $\mathcal{L}[4-ATM(\log^{(r)} m, (\log^{(r)} m)^k)].$

3 Constant Leaf-Size Hierarchy

We next investigate a constant leaf-size hierarchy : Are $k + 1$ leaves better than k ? We first show that in the case of an alternating Turing machine with only universal states, no hierarchy exists for any space bound.

Theorem 3.1. For any $k \in \mathbf{N}$ and any function $L(m)$,

$$\mathcal{L}[4-UTM(L(m), k)] = \mathcal{L}[4-DTM(L(m))].$$

Proof: Given a k leaf-size bounded 4-UTM M and an input tape x , a 4-DTM M' performs a *depth-first-search* on the computation tree of M on x without any extra cells of the working tape : Normal tree-search method needs one stack for backtracking, Instead, M' adopts only the forward tracking from the root to each leaf and uses finite internal memories in the finite control. Note that since M has constant leaves, the branching structure of universal configurations of M on x is also constant. After each traversal of a path and finding out its leaf is labeled with an accepting configuration M' adds the newly obtained information about the tree structure into a memory cell of the finite control. Then M begins to walk from the root to the next leaf, whose route can be specified

by referring the memories of the finite control. When the whole travel have been done and if M is surely k leaf-size bounded, M' enters an accepting state. Note that M' accepts exactly $T(M)$ and that M' is L space-bounded if and only if M is L space-bounded. \square

Corollary 3.1. For any $k \in \mathbf{N}$,

$$\mathcal{L}[4-UFA(k)] = \mathcal{L}[4-DFA].$$

In contrast to universal machines, we can show that there exists an infinite hierarchy of $o(\log m)$ space-bounded four-dimensional alternating Turing machines based on leaf-size by using the block of input tape and the counting argument [3,7].

Theorem 3.2. For each $k \in \mathbf{N}$, if $L(m) = o(\log m)$, then

$$\mathcal{L}[4-ATM(L(m), k)] \subsetneq \mathcal{L}[4-ATM(L(m), k+1)].$$

Corollary 3.2. For each $k \in \mathbf{N}$,

$$\mathcal{L}[4-AFA(k)] \subsetneq \mathcal{L}[4-AFA(k+1)].$$

References

- [1] M. Blum et al., *IEEE Symposium on Switching and Automata Theory* :155-160(1967).
- [2] A. K. Chandra et al., *J. ACM* 28(1):114-133 (1981).
- [3] J. E. Hopcroft et al., *Introduction to Automata Theory, Languages, and Computation*, Addison-Wesley, Reading, Mass. (1979).
- [4] K. Iihoshi et al., *Proc. 11th AROB*(2006).
- [5] K. Inoue et al., *Theoret. Comput. Sci.* 27:61-83 (1983).
- [6] H. Okabe et al., *Proc. 7th Words Multiconf. on SCI* :241-246 (2003).
- [7] M. Sakamoto et al., *Inform. Sci.* 72:225-249 (1993).
- [8] M. Sakamoto, et al., *Trans. IEICE Jpn.* E77-D(6):723-725(1994).
- [9] M. Sakamoto, *Ph.D. Thesis* (1999).
- [10] M. Sakamoto et al., *WSEAS Trans. on Computers*, Issue 5, Vol. 3 :1651-1656 (2004).

A Relationship between the Accepting Powers of Alternating Finite Automata and Nondeterministic On-Line Tessellation Acceptors on Four-Dimensional Input Tapes

Naoko TOMOZOE¹, Makoto SAKAMOTO¹, Kouichi IHOSHI¹, Yuusuke NAGAMIZU¹,
Takao ITO¹, Hiroshi FURUTANI¹, Michio KONO¹,
Satoshi IKEDA¹, Tatsuhiko TAMAKI², and Katsushi INOUE³

¹Dept. of Computer Science and Systems Engineering, University of Miyazaki, Miyazaki 889-2192, JAPAN

²Dept. of Business Administration, Ube National College of Technology, Ube 755-8555, JAPAN

³Dept. of Computer Science and Systems Engineering, Yamaguchi University, Ube 755-8611, JAPAN

Abstract

Recently, due to the advances in dynamic image processing, computer animation, and so forth, it has become increasingly apparent that the study of four-dimensional pattern processing should be very important. Thus, we think that the research of four-dimensional automata as the computational model of four-dimensional information processing has been significant. During the past about five years, automata on a four-dimensional tape have been proposed and several properties of such automata have been obtained. One model is the four-dimensional alternating finite automaton (4-AFA) which is an alternating version of a four-dimensional finite automaton, and another is the four-dimensional nondeterministic on-line tessellation acceptor (4-NOTA) which is a natural extension of the three-dimensional nondeterministic on-line tessellation acceptor to four dimensions. In this paper, we mainly investigate a relationship between the accepting powers of 4-AFA's and 4-NOTA's.

Key Words : alternation, finite automaton, four-dimensional input tape, nondeterminism, on-line tessellation acceptor

1 Introduction and Preliminaries

The question of whether processing four-dimensional digital patterns is much difficult than two- or three-dimensional ones is of great interest from

the theoretical and practical standpoints. In recent years, due to the advances in many application areas such as dynamic image processing, computer animation, and so on, the study of four-dimensional pattern processing has been of crucial importance. Thus, we think that the research of four-dimensional automata as the computational model of four-dimensional pattern processing has been meaningful. This paper mainly deals with *four-dimensional alternating finite automaton* (4-AFA) and *four-dimensional nondeterministic on-line tessellation acceptor* (4-NOTA), and investigate some results concerning a relationship between the accepting powers of 4-AFA's and 4-NOTA's [1,4].

Let Σ be a finite set of symbols. A *four-dimensional tape* over Σ is a four-dimensional rectangular array of elements of Σ . The set of all four-dimensional tape over Σ is denoted by $\Sigma^{(4)}$. Given a tape $x \in \Sigma^{(4)}$, for each $j(1 \leq j \leq 4)$, we let $l_j(x)$ be the length of x along the j th axis. When $1 \leq i_j \leq l_j(x)$ for $j(1 \leq j \leq 4)$, let $x(i_1, i_2, i_3, i_4)$ denote the symbol in x with coordinates (i_1, i_2, i_3, i_4) . Furthermore, we define $x[(i_1, i_2, i_3, i_4), (i'_1, i'_2, i'_3, i'_4)]$, when $1 \leq i_j \leq i'_j \leq l_j(x)$ for each integer $j(1 \leq j \leq 4)$, as the four-dimensional tape y satisfying the following:

- (i) for each $j(1 \leq j \leq 4)$, $l_j(y) = i'_j - i_j + 1$;
- (ii) for each $r_1, r_2, r_3, r_4 (1 \leq r_1 \leq l_1(y), 1 \leq r_2 \leq l_2(y), 1 \leq r_3 \leq l_3(y), 1 \leq r_4 \leq l_4(y))$, $y(r_1, r_2, r_3, r_4) = x(r_1 + i_1 - 1,$

$r_2+i_2-1, r_3+i_3-1, r_4+i_4-1$). We let the input tapes, through this paper, be restricted to ones which each sidelength is equivalent in order to increase the theoretical interest, as shown in Fig.1.

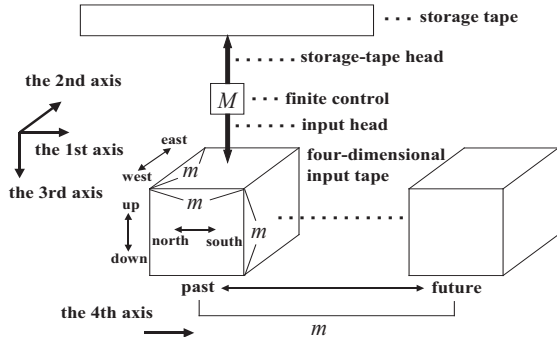


Fig. 1: Four-dimensional input tape.

A 4-AFA M is a four-dimensional finite automaton whose state set is partitioned into *universal* and *existential* states. The machine M has a read-only four-dimensional tape. A *step* of M consists of reading one symbol from the input tape, moving the input head in specified direction $d \in \{\text{east, west, south, north, up, down, future, past, no more}\}$, and entering a new state, in accordance with the next-move relation. A *seven-way four-dimensional alternating finite automaton* (SV4-AFA) is a 4-AFA whose input head can move in only seven directions — east, west, south, north, up, down, or future.

A 4-NOTA M is an infinite mesh-connected four-dimensional array of cells. Each cell of the four-dimensional array consists of a nondeterministic finite-state machine. The nondeterministic finite-state machines are all identical. M decides whether a four-dimensional tape is accepted or not by on-line fashions. For more details of the definitions of 4-AFA and 4-NOTA, see [4] and [1], respectively.

Let $T(M)$ be the set of four-dimensional tapes accepted by a machine M , and let $\mathcal{L}[4\text{-AFA}] = \{T \mid T = T(M) \text{ for some 4-AFA}\}$. $\mathcal{L}[\text{SV4-AFA}]$ and $\mathcal{L}[4\text{-NOTA}]$ are defined in the same way as $\mathcal{L}[4\text{-AFA}]$. Further, for a set $T(M)$ of four-dimensional tapes accepted by a machine M , the complementation of $T(M)$ is denoted by $\bar{T}(M)$.

2 Results

We first investigate a relationship between the accepting powers of 4-AFA's and 4-NOTA's.

Lemma 2.1. $\mathcal{L}[4\text{-AFA}] \not\subseteq \mathcal{L}[4\text{-NOTA}]$.

Proof : We consider the four-dimensional tape embedding of directed bipartite graphs with equal number of vertices on both sides [2,3]. Let $\Sigma = \{v_i, e, w, s, n, u, d, f, p, +, x, 0\}$ be a finite set of symbols used for the embedding. We use the following embedding rule. The symbol v_i represents the i th vertex for each i ($1 \leq i \leq 2n$), symbol $+$ means an intersection of two edges (i.e., where they join or split), symbol x is for a cross-over of two-edges, symbol 0 represents a blank space, and symbol $e, w, s, n, u, d, f,$ and p are the symbols needed to form eastward, westward, southward, northward, upward, downward, future, and past edges, respectively. Let \underline{P} be a four-dimensional tape embedding of a directed bipartite graph with $k=2m(m+1)-m$ vertices on both sides. The size of \underline{P} will be $(4m+3) \times (4m+3) \times (4m+3) \times (4m+3)$ (including the boundary symbols). The $(2m+2)$ th plane of some two cubes of \underline{P} defines $2k$ vertices of a bipartite graph, where the westmost k vertices on the $(2m+2)$ th plane of one cube form one group and eastmost k vertices on the $(2m+2)$ th plane of the other cube form the other group. The $2k$ v_i 's are placed such that there are blanks separating the first m vertices of one cube from the second m vertices of the other cube on each odd-numbered row, and there is a blank between consecutive v_i 's in both the eastmost and westmost groups. An example of such embedding is given in Fig.2. Consider language $L_1 = \{P \mid P \in \Sigma^{(4)} \text{ and } \underline{P} \text{ is a four-dimensional tape embedding of some acyclic directed bipartite graph with equal number of vertices on both sides}\}$. We can show that L_1 can be accepted by a 4-AFA but not by any 4-NOTA.

Lemma 2.2. For every 4-AFA A , $\bar{L}(A)$ is accepted by a 4-NOTA.

Proof : Let A be a 4-AFA. Define the complement 4-AFA of A to be \bar{A} . That is, \bar{A} is obtained by swapping the universal and existential states, and the

accepting and nonaccepting states of A . Note that in general, $\bar{L}(A) \neq L(\bar{A})$, since A may reject an input by entering an infinite loop. We construct a 3-NOTA M to accept $\bar{L}(A)$. Let x be an input pattern. Given x , M tries to guess and verify the existence of a (possibly infinite) computation tree of \bar{A} on x whose leaves are all labeled with accepting configurations. Let π denote the computation tree of \bar{A} on x that M will guess. Let $R(i_1, i_2, i_3, i_4)$ denote the set of all states of \bar{A} when its input head is at the (i_1, i_2, i_3, i_4) cell, $1 \leq i_1 \leq l_1(x)$, $1 \leq i_2 \leq l_2(x)$, $1 \leq i_3 \leq l_3(x)$, $1 \leq i_4 \leq l_4(x)$, in the guessed computation tree π . For each $q \in R(i_1, i_2, i_3, i_4)$, call $(x, (i_1, i_2, i_3, i_4), q)$ a configuration (of \bar{A}) represented by q . Generally, the (i_1, i_2, i_3, i_4) cell of M operates as follows. It receives the sets $R(i_{1-1}, i_2, i_3, i_4)$ and $R(i_1, i_2, i_3, i_4)$ from the (i_{1-1}, i_2, i_3, i_4) cell, the sets $R(i_1, i_{2-1}, i_3, i_4)$ and $R(i_1, i_2, i_3, i_4)$ from the (i_1, i_{2-1}, i_3, i_4) cell, the sets $R(i_1, i_2, i_{3-1}, i_4)$ and $R(i_1, i_2, i_3, i_4)$ from the (i_1, i_2, i_{3-1}, i_4) cell, and the sets $R(i_1, i_2, i_3, i_{4-1})$ and $R(i_1, i_2, i_3, i_4)$ from the (i_1, i_2, i_3, i_{4-1}) cell, and verifies that $R(i_1, i_2, i_3, i_4)$ is consistent with the neighboring sets $R(i_{1-1}, i_2, i_3, i_4)$, $R(i_1, i_{2-1}, i_3, i_4)$, $R(i_1, i_2, i_{3-1}, i_4)$, $R(i_1, i_2, i_3, i_{4-1})$, $R(i_{1+1}, i_2, i_3, i_4)$, $R(i_1, i_2+1, i_3, i_4)$, $R(i_1, i_2, i_3+1, i_4)$, $R(i_1, i_2, i_3, i_4+1)$. That is, the following conditions must hold : (a) none of the members of $R(i_1, i_2, i_3, i_4)$ represents a terminating nonaccepting configuration; (b) if $q \in R(i_1, i_2, i_3, i_4)$ and q is universal, then all immediate successors of the configuration $(x, (i_1, i_2, i_3, i_4), q)$ are represented by the states contained in $R(i_{1-1}, i_2, i_3, i_4) \cup R(i_1, i_{2-1}, i_3, i_4) \cup R(i_1, i_2, i_{3-1}, i_4) \cup R(i_1, i_2, i_3, i_{4-1}) \cup R(i_{1+1}, i_2, i_3, i_4) \cup R(i_1, i_2+1, i_3, i_4) \cup R(i_1, i_2, i_3+1, i_4) \cup R(i_1, i_2, i_3, i_4+1) \cup R(i_1, i_2, i_3, i_4)$; and (c) if $q \in R(i_1, i_2, i_3, i_4)$ and q is existential, then at least one of the immediate successors of the configuration $(x, (i_1, i_2, i_3, i_4), q)$ is represented by the states contained in $R(i_{1-1}, i_2, i_3, i_4) \cup R(i_1, i_{2-1}, i_3, i_4) \cup R(i_1, i_2, i_{3-1}, i_4) \cup R(i_1, i_2, i_3, i_{4-1}) \cup R(i_{1+1}, i_2, i_3, i_4) \cup R(i_1, i_2+1, i_3, i_4) \cup R(i_1, i_2, i_3+1, i_4) \cup R(i_1, i_2, i_3, i_4+1) \cup R(i_1, i_2, i_3, i_4)$. Also, the (i_1, i_2, i_3, i_4) cell passes the sets $R(i_1, i_2, i_3, i_4)$ and $R(i_{1+1}, i_2, i_3, i_4)$ to the (i_{1+1}, i_2, i_3, i_4) cell, the sets $R(i_1, i_2, i_3, i_4)$ and $R(i_1, i_2+1, i_3, i_4)$ to the (i_1, i_2+1, i_3, i_4) cell, and so on. It addition,

the $(1,1,1,1)$ cell makes sure that $R(1,1,1,1)$ contains q_0 .

The 4-NOTA M constructed above verifies that for every configuration in the guessed tree π , either it is a terminating accepting configuration or it is nonterminating and all of its immediate successor configurations exist. It is easy to see that, if x is rejected by A , then there exists a (possibly infinite) computation tree of \bar{A} on x whose leaves are all labeled with accepting configurations, and vice versa. Hence, M accepts $\bar{L}(A)$.

Lemma 2.3. $\mathcal{L}[4\text{-NOTA}] \not\subseteq \mathcal{L}[3\text{-AFA}]$.

Proof : Suppose that $\mathcal{L}[4\text{-NOTA}] \subseteq \mathcal{L}[4\text{-AFA}]$.

Let T_1 be the same language that we considered in the proof of Lemma 2.1. From Lemma 2.2 and hypothesis, \bar{L}_1 is accepted by a 4-AFA. By Lemma 2.2, L_1 is accepted by a 4-NOTA. But L_1 is not accepted by any 4-NOTA, as shown in the proof of Lemma 2.1. This is a contradiction. Hence, $\mathcal{L}[4\text{-NOTA}] \not\subseteq \mathcal{L}[3\text{-AFA}]$.

From Lemmas 2.1 and 2.3, we have the following result.

Theorem 2.1. $\mathcal{L}[4\text{-AFA}]$ and $\mathcal{L}[4\text{-NOTA}]$ are incomparable.

Next, we investigate a relationship between the accepting powers of SV4-AFA's and 4-NOTA's.

Lemma 2.4. $\mathcal{L}[\text{SV4-AFA}]$ is closed under complementation.

Proof : Let A be an SV4-AFA and \bar{A} be the complement of A as in the proof of Lemma 2.2. By using the same idea as in the proof of Theorem 4.4 in [3], we can construct an SV4-AFA A' from \bar{A} such that $L(A') = \bar{L}(A)$.

Theorem 2.2. $\mathcal{L}[\text{FV4-AFA}] \subsetneq \mathcal{L}[4\text{-NOTA}]$.

Proof : From Lemma 2.4, $\mathcal{L}[\text{SV4-AFA}]$ is closed under complementation. The inclusion follows from Lemma 2.2. That it is proper follows since $\mathcal{L}[\text{SV4-AFA}] \subseteq \mathcal{L}[4\text{-AFA}]$ and $\mathcal{L}[4\text{-AFA}]$ is incomparable with $\mathcal{L}[4\text{-NOTA}]$.

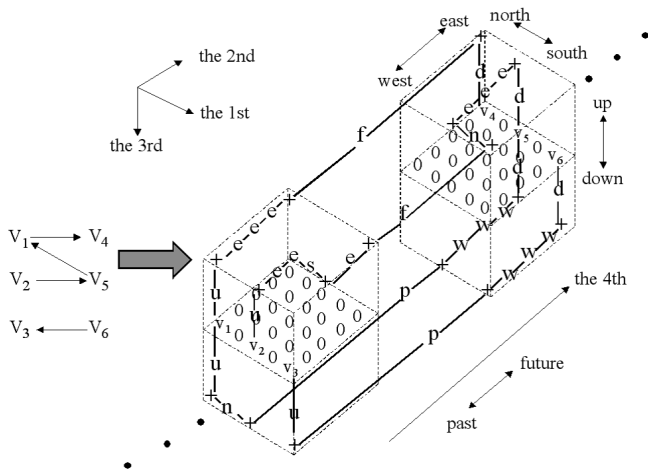


Fig. 2: An example of embedding ($m=1$).

3 Conclusion

This paper mainly investigated a relationship between the accepting powers of alternating finite automata and nondeterministic on-line tessellation acceptors on four-dimensional input tapes. It is interesting to investigate closure properties about their four-dimensional automata. We will treat this problem in further papers.

References

[1] K. Inoue and A. Nakamura, An n-dimensional on-line tessellation acceptor (in Japanese), *The Transaction of the IECE* J59-D(4):229-236, 1976.

[2] K. Inoue, I. Sakuramoto, M. Sakamoto, and I. Takanami, Two topics concerning two-dimensional automata operating in parallel, *International J. of Pattern Recognition and Artificial Intelligence* 6(2&3):211-225,1992.

[3] T. Jiang, O. H. Ibarra, and H. Wang, Some results concerning 2-D on-line tessellation acceptors and 2-D alternating finite automata, *Theoretical Computer Science* 125 : 243-257, 1994.

[4] H. Okabe, S. Taniguchi, T. Makino, S. Nogami, Y. Nakama, M. Sakamoto, and K. Inoue, Computation for motion image processing by 4-dimensional alternating Turing machines, *Proceedings of the 7th World Multiconference on Systemics, Cybernetics and Informatics*, Orland, USA, 2003.

Guaranteed cost control of discrete time system with performance index including cross term

†Nobuya TAKAHASHI, ‡Kenji HIRANUMA, †Michio KONO, †Osamo SATO

† Faculty of Engineering, University of Miyazaki
‡ Department of Electronic and Mechanical Engineering,
Tokyo University of Mercantile Marine

1 Introduction

Guaranteed cost control problem is the design method of the robust control system [1]. This method guarantees the robust stability of disturbed control system by using existing of the upper bound of quadratic performance index. Kono extended this method to the case with cross term in performance index and show the condition for robust stability [2]. In this paper, we extend this problem to the discrete time system. As the result of formulation, stochastic discrete Riccati equation is obtained. We show and prove the condition of the closed loop system to be stable. Finally, through showing the numerical example, we validate out method.

2 Derivation of discrete time stochastic Riccati equation

In this section, we derive the stochastic discrete Riccati equation with performance index including cross term of input vector and state vector. Wonham proposed this equation which is obtained as the result of stochastic control problem [3]. In this literature, the stochastic discrete Riccati equation is formed as the discrete Riccati equation with additional structured term. In this section, we extend this problem to the performance index with cross term with state vector and input vector. We abbreviate stochastic discrete

Riccati equation as SDARE.

Let us consider the discrete time linear control system with uncertainty in state matrix,

$$x(k+1) = A(\xi)x(k) + Bu(k) \quad (1)$$

$A(\xi)$ is defined as

$$A(\xi) = A_0 + \sum_{i=1}^p \xi_i A_i \quad (2)$$

where A_0 is nominal structure of the state matrix, A_i is structure of the uncertainty, and ξ_i is size of the uncertainty. Performance index is defined as

$$\begin{aligned} J &= \sum_{k=0}^{\infty} \{x(k)^T Q x(k) + u(k)^T R u(k) + 2x(k)^T S u(k)\} \\ &= \sum_{k=0}^{\infty} l(x, u) \end{aligned} \quad (3)$$

where $Q \geq 0, R > 0$ and $S \geq 0$ are weighting matrices for state vector, input vector and cross term of state and input vector, respectively. These matrices take appropriate dimension size. Lyapunov function $V(\cdot)$ is

$$V(x(k)) = x(k)^T P(k)x(k) \quad (4)$$

From the principle of optimality, we have

$$\begin{aligned} H(V, x, u, \xi) &= l(x, u) + V(x(k+1), k+1) - V(x(k), k) \\ &= x^T C^T C x + u^T R u + 2x^T S u - x^T P(k)x \\ &\quad + (A(\xi)x + Bu)^T P(k+1)(A(\xi)x + Bu) \end{aligned}$$

$$\begin{aligned}
 &+x^T A(\xi)^T P(k+1)A(\xi)x + u^T B^T P(k+1)Bu \\
 &+2x^T A(\xi)^T P(k+1)Bu - x^T P(k)x \leq 0 \quad (5)
 \end{aligned}$$

In the LQR problem of discrete time system, by using solution $P(k)$ of the SDARE, the optimal input vector $u(k)$ is defined as follows,

$$u(k) = -(B^T P(k+1)B+R)^{-1}(A_0^T P(k+1)B+S)^T x(k) \quad (6)$$

Then, let $(B^T P B + R)^{-1}(A_0^T P B + S)^T = \Omega(P)$ and substitute into equation (5), we have

$$\begin{aligned}
 &= x^T C^T C x + x^T \Omega(P(k+1))^T R \Omega(P(k+1))x \\
 &\quad - x^T S \Omega(P(k+1))x - x^T \Omega(P(k+1))^T S^T x \\
 &\quad + x^T A(\xi)^T P(k+1)A(\xi)x \\
 &\quad + x^T \Omega(P(k+1))^T B^T P(k+1)B \Omega(P(k+1))x \\
 &\quad - x^T A(\xi)^T P(k+1)B \Omega(P(k+1))x \\
 &\quad - x^T \Omega(P(k+1))^T B^T P(k+1)A(\xi)x - x^T P(k)x \\
 &\leq 0
 \end{aligned}$$

Now, let us substitute structured uncertainty $A(\xi) = A_0 + \Delta A$, then

$$\begin{aligned}
 &= x^T C^T C x + x^T \Omega(P(k+1))^T R \Omega(P(k+1))x \\
 &\quad - x^T S \Omega(P(k+1))x - x^T \Omega(P(k+1))^T S^T x \\
 &\quad + x^T A_0^T P(k+1)A_0 x + x^T \Delta A^T P(k+1)\Delta A x \\
 &\quad + x^T A_0^T P(k+1)\Delta A x + x^T \Delta A^T P(k+1)A_0 x \\
 &\quad + x^T \Omega(P(k+1))^T B^T P(k+1)B \Omega(P(k+1))x \\
 &\quad - x^T A_0^T P(k+1)B \Omega(P(k+1))x \\
 &\quad - x^T \Omega(P(k+1))^T B^T P(k+1)A_0 x \\
 &\quad - x^T \Delta A^T P(k+1)B \Omega(P(k+1))x \\
 &\quad - x^T \Omega(P(k+1))^T B^T P(k+1)\Delta A x - x^T P(k)x \\
 &= x^T \{C^T C + A_0^T P(k+1)A_0 + \Omega(P(k+1))^T B^T \\
 &\quad \cdot P(k+1)B \Omega(P(k+1)) - A_0^T P(k+1)B \\
 &\quad \cdot \Omega(P(k+1)) - \Omega(P(k+1))^T B^T P(k+1)A_0 \\
 &\quad + \Omega(P(k+1))^T R \Omega(P(k+1)) - S \Omega(P(k+1)) \\
 &\quad - \Omega(P(k+1))^T S^T - P(k) + \Delta A^T P(k+1)\Delta A
 \end{aligned}$$

$$\begin{aligned}
 &-\Delta A^T P(k+1)B \Omega(P(k+1)) \\
 &-\Omega(P(k+1))^T B^T P(k+1)\Delta A \} x \leq 0 \quad (7)
 \end{aligned}$$

From the positive semi-definitively of $H(\cdot)$, we obtain following inequality

$$\begin{aligned}
 T(x, k, P) &= T_0(P(k+1)) + T_1(P(k+1)) \\
 &\quad + C^T C - P(k) \leq 0 \quad (8)
 \end{aligned}$$

Now, $T_0(\cdot)$ and $T_1(\cdot)$ are

$$\begin{aligned}
 &T_0(P(k+1)) \\
 &= A_0^T P(k+1)A_0 - (A_0^T P(k+1)B + S)(B^T \\
 &\quad \cdot P(k+1)B + R)^{-1}(A_0^T P(k+1)B + S)^T \quad (9) \\
 &T_1(P(k+1)) \\
 &= \Delta A^T P(k+1)\Delta A + \Delta A^T P(k+1)A_0 \\
 &\quad + A_0^T P(k+1)\Delta A - \Delta A^T P(k+1)B \Omega(P(k+1)) \\
 &\quad - \Omega(P(k+1))^T B^T P(k+1)\Delta A \quad (10)
 \end{aligned}$$

where, let U_1 is the upper bound matrix of $T_1(\cdot)$, form inequality condition (8), we have following difference equation.

$$T_0(P(k+1)) + C^T C + U_1 - P(k) = 0 \quad (11)$$

Suppose that there exists stationary solution of equation (11)

$$P = T_0(P) + C^T C + U_1 \quad (12)$$

Therefore, we obtain the SDARE with performance index including cross term as follows

$$\begin{aligned}
 P &= A_0^T P A_0 - (A_0^T P B + S)(B^T P B + R)^{-1} \\
 &\quad \cdot (A_0^T P B + S)^T + C^T C + U_1 \quad (13)
 \end{aligned}$$

In equation (13), if we omit the upper bound matrix, it coincide with the SDARE of nominal system.

3 Robust stability

In this section, under the assumption that there exists a solution P of SDARE, we prove stability of

$$\begin{aligned}
 &= A_0^T P A_0 + A_0^T P \Delta A + \Delta A^T P A_0 + \Delta A^T P \Delta A \\
 &\quad - A_0^T P B \Omega(P) - \Delta A^T P B \Omega(P) \\
 &\quad - \Omega(P)^T B^T P A_0 - \Omega(P)^T B^T P \Delta A \\
 &\quad + \Omega(P)^T B^T P B \Omega(P) - P \\
 &= A_0^T P A_0 - A_0^T P B \Omega(P) - \Omega(P)^T B^T P A_0 \\
 &\quad + \Omega(P)^T B^T P B \Omega(P) - P + T_1(P) \quad (19)
 \end{aligned}$$

Theorem 1 In the system (1), optimal input u^* which minimized the performance index (3) is obtained

$$\begin{aligned}
 u^*(k) &= -(B^T P B + R)^{-1} (A_0^T P B + S) x(k) \\
 &= -\Omega(P) x(k) \quad (14)
 \end{aligned}$$

Then the closed-loop system $A_c(\cdot)$ is

$$x(k+1) = A_c(A(\xi), B, P) x(k) \quad (15)$$

where

$$A_c(A(\xi), B, \Omega(P)) = A(\xi) - B\Omega(P)$$

Now, we suppose following assumption

Assumption 1 Let

$$\begin{aligned}
 A_c^T P B \Omega(P) + \Omega(P)^T B^T P A_c \\
 - \Omega(P)^T R \Omega(P) + C^T C = D^T D, \quad (16)
 \end{aligned}$$

then $D^T D$ is positive semi-definite.

Next, we derive theorem for asymptotical stability of closed-loop system.

Theorem 2 The closed-loop system (15) with optimal feedback control input (14) is asymptotic stability, if there exists positive semi-definite solution P of SDARE (13) and assumption 1 is satisfied.

(proof of Theorem 2) In discrete time system, from stability condition in the sense of Lyapunov, we have

$$A_c^T P A_c - P \leq 0 \quad (17)$$

Substitute A_c into inequality (17), left-hand side of the inequality becomes

$$\begin{aligned}
 &= (A(\xi) - B\Omega(P))^T P (A(\xi) - B\Omega(P)) - P \\
 &= A(\xi)^T P A(\xi) - A(\xi)^T P B \Omega(P) - \Omega(P)^T B^T P A(\xi) \\
 &\quad + \Omega(P)^T B^T P B \Omega(P) - P \quad (18)
 \end{aligned}$$

Where, we substitute P of equation (13) into (19), we have

$$\begin{aligned}
 &= A_0^T P A_0 - A_0^T P B \Omega(P) - \Omega(P)^T B^T P A_0 \\
 &\quad + \Omega(P)^T B^T P B \Omega(P) - P + T_1(P) \\
 &= A_0^T P A_0 - A_0^T P B \Omega(P) - \Omega(P)^T B^T P A_0 \\
 &\quad + \Omega(P)^T B^T P B \Omega(P) + T_1(P) \\
 &\quad - \{A_0^T P A_0 - \Omega(P)^T (B^T P B + R) \Omega(P) \\
 &\quad + C^T C + U_1\} \\
 &= -A_0^T P B \Omega(P) + \Omega(P)^T B^T P B \Omega(P) \\
 &\quad - \Omega(P)^T B^T P A_0 + \Omega(P)^T B^T P B \Omega(P) \\
 &\quad + \Omega(P)^T R \Omega(P) - C^T C - (U_1 - T_1(P)) \\
 &= -(A_0 - B\Omega(P))^T P B \Omega(P) - \Omega(P)^T B^T P \\
 &\quad \cdot (A_0 - B\Omega(P)) + \Omega(P)^T R \Omega(P) - C^T C \\
 &\quad - (U_1 - T_1(P)) \\
 &= -\{A_c^T P B \Omega(P) + \Omega(P)^T B^T P A_c - \Omega(P)^T R \Omega(P) \\
 &\quad + C^T C\} - (U_1 - T_1(P)) \leq 0 \quad (20)
 \end{aligned}$$

From equation (20), we obtain the stabilizable condition

$$\begin{aligned}
 A_c^T P B \Omega(P) + \Omega(P)^T B^T P A_c \\
 - \Omega(P)^T R \Omega(P) + C^T C \geq 0 \quad (21)
 \end{aligned}$$

Q. E. D.

4 Eigenvalue upper bound

From equation (10), uncertainty is described as

$$\begin{aligned}
 T_1(P) &= \Delta^T A P \Delta A + \Delta A^T P (A_0 - B\Omega(P)) \\
 &\quad + (A_0 - B\Omega(P))^T P \Delta A \quad (22)
 \end{aligned}$$

equation (2), substitute uncertainty of system matrix $\Delta A = \sum_{i=1}^p \xi_i A_i$ and we obtain

$$\begin{aligned}
 &= \sum_{i=1}^p \xi_i \zeta_j D_{ij} + \sum_{i=1}^p [A_i^T P(A_0 - B\Omega(P)) \\
 &\quad + (A_0 - B\Omega(P))^T P A_i] \quad (23)
 \end{aligned}$$

where

$$D_{ij} = A_i^T P A_j + A_j^T P A_i$$

Because $A_i^T P(A_0 - B\Omega(P)) + (A_0 - B\Omega(P))^T P A_i$ and D_{ij} are symmetric matrices, then there exist orthogonal matrices Y_i and Z_{ij} which satisfy

$$\begin{aligned}
 &Y_i^T [A_i^T P(A_0 - B\Omega(P)) \\
 &\quad + (A_0 - B\Omega(P))^T P A_i] Y_i = \Lambda_i \quad (24)
 \end{aligned}$$

$$Z_{ij}^T D_{ij} Z_{ij} = \Gamma_{ij} \quad (25)$$

where Λ_i and Γ_{ij} are diagonal matrices. By using Y_i, D_{ij}, Λ_i and Γ_{ij} , the upper bound matrix of $T(P)$ is expressed as

$$U_E = \sum_{i=1}^p Y_i^T \|\Lambda_i\| Y_i + \frac{1}{2} \sum_{i=1}^p \sum_{j=1}^p Z_{ij}^T \|\Gamma_{ij}\| Z_{ij} \quad (26)$$

where U_E is called eigenvalue upper bound matrix. In the next section, we show the numerical example.

5 Numerical example

We consider following system parameter,

$$\begin{aligned}
 A_0 &= \begin{bmatrix} 0 & 1 \\ 1.5 & 0 \end{bmatrix}, \quad A_1 = \begin{bmatrix} 0 & 0 \\ 0.5 & 0 \end{bmatrix}, \\
 B &= \begin{bmatrix} 0 \\ 1 \end{bmatrix}, \quad Q = \begin{bmatrix} 1 & 0 \\ 0 & 1 \end{bmatrix}, \\
 S &= \begin{bmatrix} 1 \\ 0 \end{bmatrix}, \quad R = 1
 \end{aligned}$$

Using these parametr, we solve the SDARE with eigenvalue upper bound and obtain stationary solution P . Poles of the nominal closed-loop system is obtained as

$$(0.40825 \quad , \quad -0.40825)$$

$$(0.81650 \quad , \quad -0.81650)$$

This result shows that the perturbed system remains in stable, then we had confirm robust stability for disturbance of our proposed method.

6 Conclusion

In this paper, we consider the guaranteed cost control problem for the performance index including cross term of discrete time system. We show the structure of uncertainty and discuss about stationary condition. We apply eigenvalue upper bound matrix to this problem and show the numerical example. From this result, we confirm the robust stability of the closed-loop system for the system matrix disturbance. Future study is to consider about linear upper bound. It is pointed out that there exists relationship between linear upper bound matrix and LMI solution of the structured uncertain system.

References

- [1] S. S. Chang and T. K. C. Peng, "Adaptive guaranteed cost control of systems with uncertain parameters", *IEEE Transactions on AC*, vol. 17, no. 4, pp. 474-483, 1972.
- [2] M. Kono, N. Takahashi, O. Sato and A. Sato, "Generalization of guaranteed cost control - Extension to the case with cross terms", *Proceedings of the SICE Annual Conference 2002 in Osaka*, pp. 542-545, August 5-7, 2002. Osaka, Japan.
- [3] W. M. Wonham, "On a matrix Riccati equation of stochastic control", *SIAM Journal of Control*, vol. 6, no. 4, pp. 681-697, 1968.

An LMI approach to observer-based guaranteed cost control

Masaaki Miyachi and Mitsuaki Ishitobi
Department of Mechanical
Systems Engineering
Kumamoto University
Kumamoto 860-8555

Nobuya Takahashi and Michio Kono
Department of Computer Science
and Systems Engineering
University of Miyazaki
Miyazaki 889-2192

Abstract

In this paper, we present the design of observer-based guaranteed cost controller for a class of uncertain linear systems, in which full state cannot be measured. The perturbations are assumed to be described by structural uncertainties. Linear matrix inequality (LMI) approach is used to design the observer-based controller. The controller and observer gains are given from LMI optimization and feasibility problems, respectively. A numerical example shows the potential of the proposed method.

1 Introduction

During the last decades, considerable attention has been directed to the problem of robust stability analysis and robust stabilization of systems with parameter uncertainties. Recently, in addition to the simple stabilization, there has been much effort to design a controller which not only achieves the stability of the uncertain system but also guarantees an adequate level of performance. One approach to this problem is the guaranteed cost control method originally introduced by Chang and Peng [1]. Although the controller is usually constructed by using state variables, it may not be possible to measure all the states of the system in many cases [2,3]. Therefore, the problem of designing an observer-based guaranteed cost controller has received some attention in recent years. However, the algorithm presented by Lien cannot be implemented by the LMI control toolbox of MATLAB because it contains the equality condition [4]. Mahmoud *et al.* deal with the case where both the controller gain and the observer gain have prespecified forms, and they don't discuss the reduction of the performance index [5]. This paper deals with the design method which doesn't restrict the type of the observer gain and further achieves the reduction of the performance index. This method can be implemented by the LMI control

toolbox of MATLAB.

2 Problem statement

Consider a continuous-time uncertain system of the form

$$\dot{\mathbf{x}}(t) = (A_0 + \Delta A(t))\mathbf{x}(t) + B_0\mathbf{u}(t) \quad (1)$$

$$\mathbf{y}(t) = (C_0 + \Delta C(t))\mathbf{x}(t) \quad (2)$$

where $\mathbf{x}(t) \in \mathbb{R}^n$ is the state vector, $\mathbf{u}(t) \in \mathbb{R}^m$ is the control input vector, $\mathbf{y}(t) \in \mathbb{R}^p$ is the measured output, A_0, B_0, C_0 are known constant real-valued matrices of appropriate dimensions, $\Delta A(t), \Delta C(t)$ denote real-valued matrix functions representing parameter uncertainties. It is assumed that the system uncertainties have the form

$$\Delta A(t) = D_1 F_1(t) E_1$$

$$\Delta C(t) = D_2 F_2(t) E_2$$

with

$$F_i^T(t) F_i(t) \leq I$$

and where D_1, D_2, E_1, E_2 are known constant real-valued matrices of appropriate dimensions and $F_1(t)$ and $F_2(t)$ are unknown real time-varying matrices

The problem considered here is to design an observer-based controller of the form

$$\dot{\hat{\mathbf{x}}}(t) = A_0 \hat{\mathbf{x}}(t) + B_0 \mathbf{u}(t) + K_o(\mathbf{y}(t) - \hat{\mathbf{y}}(t)) \quad (3)$$

$$\hat{\mathbf{y}}(t) = C_0 \hat{\mathbf{x}}(t) \quad (4)$$

$$\mathbf{u}(t) = K_c \hat{\mathbf{x}}(t) \quad (5)$$

which gives an upper bound on the following quadratic performance index associated with the uncertain system (1) and (2)

$$J = \int_0^\infty (\mathbf{x}^T(t) Q \mathbf{x}(t) + \mathbf{u}^T(t) R \mathbf{u}(t)) dt \quad (6)$$

where Q and R are given positive-definite symmetric matrices.

3 Main results

In this section, a sufficient condition is established for the existence of an observer-based guaranteed cost controller for the uncertain system (1) and (2). Here, it is assumed that

$$K_c = -R^{-1}B_0^T P \quad (7)$$

Theorem 1. The feedback control law (3)-(5) with (7) is an observer-based guaranteed cost controller if there exist a matrix $K_o \in \mathbb{R}^{m \times n}$, a symmetric positive-definite matrix $P \in \mathbb{R}^{n \times n}$, such that the following matrix inequality holds

$$\Omega < 0 \quad (8)$$

where

$$\Omega = \begin{bmatrix} \Sigma_1 & (\Delta A - K_o \Delta C)^T P \\ P(\Delta A - K_o \Delta C) & \Sigma_2 \end{bmatrix}$$

$$\Sigma_1 = P(A_0 + \Delta A) + (A_0 + \Delta A)^T P + Q - PB_0 R^{-1} B_0^T P$$

$$\Sigma_2 = P(A_0 - K_o C_0) + (A_0 - K_o C_0)^T P + PB_0 R^{-1} B_0^T P$$

Moreover, the performance index is evaluated as

$$J < \phi^T(0)P\phi(0) + \psi^T(0)P\psi(0) \quad (9)$$

Proof. The input (3)-(5) with (7) yields the closed-loop system

$$\dot{\mathbf{x}}(t) = (A_0 + \Delta A(t) - B_0 R^{-1} B_0^T P)\mathbf{x}(t) + B_0 R^{-1} B_0^T P \mathbf{e}(t) \quad (10)$$

$$\dot{\mathbf{e}}(t) = (A_0 - K_o C_0)\mathbf{e}(t) + (\Delta A(t) - K_o \Delta C(t))\mathbf{x}(t) \quad (11)$$

where $\mathbf{e}(t) = \mathbf{x}(t) - \hat{\mathbf{x}}(t)$ is the estimated error of the system. Define a candidate of Lyapunov function as

$$V(\mathbf{x}, \mathbf{e}) = \mathbf{x}^T(t)P\mathbf{x}(t) + \mathbf{e}^T(t)P\mathbf{e}(t) \quad (12)$$

then, the time derivative of (12) along to (10) and (11) is calculated as

$$\begin{aligned} \dot{V}(\mathbf{x}, \mathbf{e}) &= 2\mathbf{x}^T(t)P\dot{\mathbf{x}}(t) + 2\mathbf{e}^T(t)P\dot{\mathbf{e}}(t) \\ &= 2\mathbf{x}^T(t)P\{(A_0 + \Delta A(t) - B_0 R^{-1} B_0^T P)\mathbf{x}(t) \\ &\quad + B_0 R^{-1} B_0^T P \mathbf{e}(t)\} \\ &\quad + 2\mathbf{e}^T(t)P\{(A_0 - K_o C_0)\mathbf{e}(t) \\ &\quad + (\Delta A(t) - K_o \Delta C(t))\mathbf{x}(t)\} \\ &= \mathbf{z}^T(t)\Omega\mathbf{z}(t) \\ &\quad - (\mathbf{x}^T(t)Q\mathbf{x}(t) + \mathbf{u}^T(t)R\mathbf{u}(t)) \end{aligned} \quad (13)$$

where

$$\mathbf{z}(t) = \begin{bmatrix} \mathbf{x}(t) \\ \mathbf{e}(t) \end{bmatrix} \quad (14)$$

Applying (8) to (13) gives

$$\dot{V}(\mathbf{x}, \mathbf{e}) < -(\mathbf{x}^T(t)Q\mathbf{x}(t) + \mathbf{u}^T(t)R\mathbf{u}(t)) < 0 \quad (15)$$

for any $\mathbf{x}(t) \neq \mathbf{0}$. Thus, the closed-loop system is asymptotically stable.

Further, integrating (15) from 0 to T leads to

$$\begin{aligned} &\mathbf{x}^T(T)P\mathbf{x}(T) - \mathbf{x}^T(0)P\mathbf{x}(0) \\ &+ \mathbf{e}^T(T)P\mathbf{e}(T) - \mathbf{e}^T(0)P\mathbf{e}(0) \\ &< -(\mathbf{x}^T(t)Q\mathbf{x}(t) + \mathbf{u}^T(t)R\mathbf{u}(t)) < 0 \end{aligned} \quad (16)$$

Here, the asymptotic stability of the closed-loop system implies that

$$\mathbf{x}^T(T)P\mathbf{x}(T) \rightarrow 0, \quad \mathbf{e}^T(T)P\mathbf{e}(T) \rightarrow 0 \quad (17)$$

as T tends to the infinity. Hence, it is obtained that

$$\begin{aligned} J &= \int_0^\infty (\mathbf{x}^T(\tau)Q\mathbf{x}(\tau) + \mathbf{u}^T(\tau)R\mathbf{u}(\tau))d\tau \\ &< \mathbf{x}^T(0)P\mathbf{x}(0) + \mathbf{x}^T(0)P\mathbf{x}(0) \\ &= \phi^T(0)P\phi(0) + \psi^T(0)P\psi(0) \end{aligned} \quad (18)$$

As a result, the proof is complete. \square

Next, on the basis of Theorem 1, we prove another sufficient condition without uncertain parameters. Before stating Theorem 2, a necessary lemma will be introduced.

Lemma 1 [5]. Let D and E be matrices of appropriate dimensions, and F be a matrix function satisfying $F^T F \leq I$. Then for any positive scalar α , the following inequality holds

$$DFE + E^T F^T D^T \leq \alpha DD^T + \alpha^{-1} E^T E \quad (19)$$

Theorem 2. If there exist scalars $\gamma > 0$, $\delta > 0$, $\epsilon > 0$, a matrix K_o , a symmetric positive-definite matrix P such that the following matrix inequality

$$\begin{bmatrix} \Sigma_3 & 0 \\ 0 & \Sigma_4 \end{bmatrix} < 0 \quad (20)$$

where

$$\begin{aligned} \Sigma_3 &= PA_0 + A_0^T P - PB_0 R^{-1} B_0^T P + Q \\ &\quad + \gamma PD_1 D_1^T P + \frac{1}{\gamma} E_1^T E_1 + \frac{1}{\epsilon} E_1^T E_1 + \frac{1}{\delta} E_2^T E_2 \\ \Sigma_4 &= P(A_0 - K_o C_0) + (A_0 - K_o C_0)^T P \\ &\quad + PB_0 R^{-1} B_0^T P + \epsilon PD_1 D_1^T P \\ &\quad + \delta PK_o D_2 D_2^T K_o^T P \end{aligned}$$

is satisfied, then the memoryless state feedback control law (5) is an observer-based guaranteed cost controller and

$$J^* = \phi^T(0)P\phi(0) + \psi^T(0)P\psi(0) \quad (21)$$

is a guaranteed cost for the uncertain system (1) and (2).

Proof. By applying Lemma 1, it follows for any $\gamma > 0$, $\delta > 0$, $\epsilon > 0$ that

$$\begin{aligned} 2\mathbf{x}^T(t)P\Delta A\mathbf{x}(t) &= 2\mathbf{x}^T(t)PD_1F_1E_1\mathbf{x}(t) \\ &\leq \gamma\mathbf{x}^T(t)PD_1D_1^TP\mathbf{x}(t) + \frac{1}{\gamma}\mathbf{x}^T(t)E_1^TE_1\mathbf{x}(t) \end{aligned} \quad (22)$$

$$\begin{aligned} 2\mathbf{e}^T(t)P\Delta A\mathbf{x}(t) &= 2\mathbf{e}^T(t)PD_1F_1E_1\mathbf{x}(t) \\ &\leq \epsilon\mathbf{e}^T(t)PD_1D_1^TP\mathbf{e}(t) + \frac{1}{\epsilon}\mathbf{x}^T(t)E_1^TE_1\mathbf{x}(t) \end{aligned} \quad (23)$$

$$\begin{aligned} -2\mathbf{e}^T(t)PK_o\Delta C\mathbf{x}(t) &= -2\mathbf{e}^T(t)PK_oD_2F_2E_2\mathbf{x}(t) \\ &\leq \delta\mathbf{e}^T(t)PK_oD_2D_2^TK_o^T\mathbf{e}(t) \\ &\quad + \frac{1}{\delta}\mathbf{x}^T(t)E_2^TE_2\mathbf{x}(t) \end{aligned} \quad (24)$$

Substituting (22), (23), (24) into (8) yields the desired result. \square

Theorem 3. For a given pair of $\delta > 0$, $\epsilon > 0$, if the following LMI optimization problem; $\min\{\text{tr}(P)\}$

$$\begin{bmatrix} \Sigma_5 & XE_1^T & XE_2^T & XE_2^T & X \\ E_1X & -\gamma I & 0 & 0 & 0 \\ E_1X & 0 & -\epsilon I & 0 & 0 \\ E_2X & 0 & 0 & -\delta I & 0 \\ X & 0 & 0 & 0 & -Q^{-1} \end{bmatrix} < 0 \quad (25)$$

where

$$\Sigma_5 = A_0X + XA_0^T - B_0R^{-1}B_0^T + \gamma D_1D_1^T$$

has a solution of scalar $\gamma > 0$, and symmetric positive-definite matrix X , and if

$$\begin{bmatrix} \Sigma_6 & PK_oD_2 & PB_0 & PD_1 \\ D_2^TK_o^TP & -\frac{1}{\delta}I & 0 & 0 \\ B_0^TP & 0 & -R & 0 \\ D_1^TP & 0 & 0 & -\frac{1}{\epsilon}I \end{bmatrix} < 0 \quad (26)$$

where

$$\Sigma_6 = PA_0 + A_0^TP - PK_oC_0 - C_0^TK_o^TP$$

has a solution of matrix K_o , then the control law

$$\mathbf{u}(t) = -R^{-1}B_0^TX^{-1}\hat{\mathbf{x}}(t) \quad (27)$$

is a suboptimal guaranteed cost controller which gives the optimal value of the guaranteed cost (21) for the given parameters $\delta > 0$, $\epsilon > 0$.

Proof. Pre- and post-multiplying Σ_3 by P^{-1} on both sides, and denoting $X = P^{-1}$ lead to the equivalent inequality

$$\begin{aligned} A_0X + XA_0^T - B_0R^{-1}B_0^T + \gamma D_1D_1^T + \frac{1}{\gamma}XE_1^TE_1X \\ + \frac{1}{\epsilon}XE_2^TE_2X + \frac{1}{\delta}XE_2^TE_2X + XQX < 0 \end{aligned} \quad (28)$$

It follows from Schur Complement that (28) is equivalent to (25).

Next, using Schur Complement for Σ_4 , we obtain

$$\begin{bmatrix} \Sigma_6 & PK_oD_2 & PB_0 & PD_1 \\ D_2^TK_o^TP & -\frac{1}{\delta}I & 0 & 0 \\ B_0^TP & 0 & -R & 0 \\ D_1^TP & 0 & 0 & -\frac{1}{\epsilon}I \end{bmatrix} < 0 \quad (29)$$

$$\Sigma_6 = PA_0 + A_0^TP - PK_oC_0 - C_0^TK_o^TP$$

For given scalars $\delta > 0$, $\epsilon > 0$, if there exist γ , X in (25) which is a solution of optimal LMI problem; $\min\{\text{tr}(P)\}$, and if there exists a matrix K_o which satisfies (26) using $P = X^{-1}$, the guaranteed cost under δ , ϵ is suboptimal. \square

Remark 1. The suboptimal guaranteed cost controller (27) for over all parameters δ , ϵ can be determined by a search such as the optimization problem in Theorem 3 has a solution.

4 An illustrative example

Consider the uncertain time-delay system described by the state equation

$$\dot{\mathbf{x}}(t) = (A_0 + \Delta A(t))\mathbf{x}(t) + B_0\mathbf{u}(t) \quad (30)$$

$$\mathbf{y}(t) = (C_0 + \Delta C(t))\mathbf{x}(t) \quad (31)$$

and full state observer for nominal part of the system

$$\dot{\hat{\mathbf{x}}}(t) = A_0\hat{\mathbf{x}}(t) + B_0\mathbf{u}(t) + K_o(\mathbf{y}(t) - \hat{\mathbf{y}}(t)) \quad (32)$$

$$\hat{\mathbf{y}}(t) = C_0\hat{\mathbf{x}}(t) \quad (33)$$

and the performance index (6), where

$$A_0 = \begin{bmatrix} 0 & 1 \\ -1 & 1 \end{bmatrix}, \quad B_0 = \begin{bmatrix} 0.2 \\ 3 \end{bmatrix},$$

$$C_0 = [1 \quad 2], \quad D_1 = \begin{bmatrix} 0.1 & 0.1 \\ 0 & 0 \end{bmatrix},$$

$$D_2 = [0.3 \quad 0.1], \quad E_1 = E_2 = \begin{bmatrix} 1 & 0 \\ 0 & 1 \end{bmatrix}$$

and $\delta = 4.3$, $\epsilon = 8.8$

The suboptimal observer-based guaranteed cost controller can be determined by solving (25) and (26). We obtain

$$P = \begin{bmatrix} 2.5925 & 0.2558 \\ 0.2558 & 0.5849 \end{bmatrix}, \quad K_o = \begin{bmatrix} 0.1142 \\ 7.9563 \end{bmatrix},$$

$$K_c = -R^{-1}B_0^T P = \begin{bmatrix} -1.2858 & -1.8057 \end{bmatrix},$$

$$\gamma = 4.3974, \quad J^* = 6.3547$$

The simulation results are shown in Figs. 1-4.

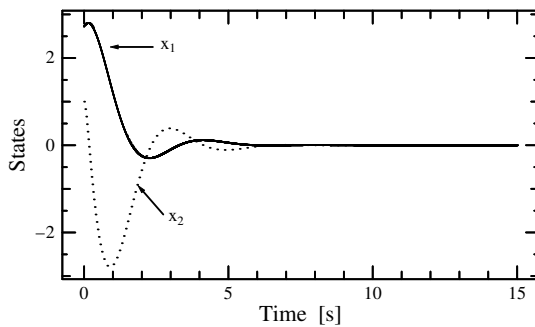


Fig.1 Trajectories of states.

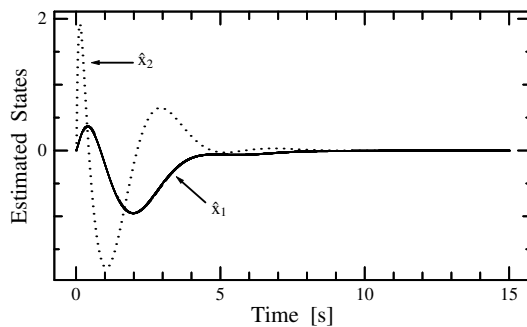


Fig.2 Trajectories of estimated states.

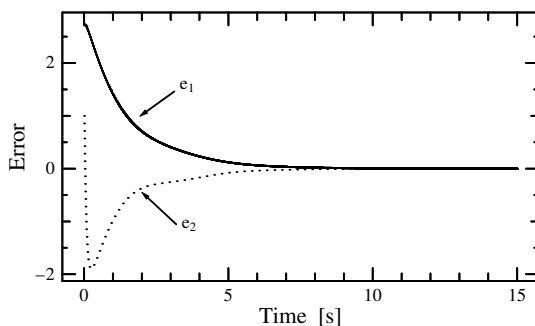


Fig.3 Trajectories of errors.

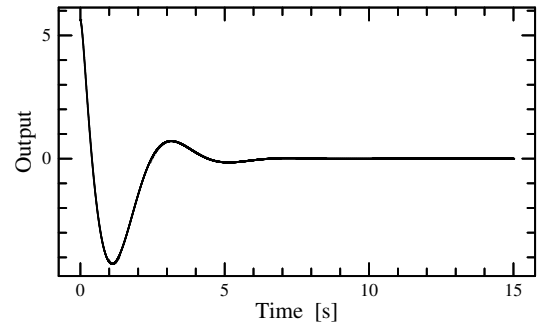


Fig.4 Trajectory of output.

5 Summary

This paper discusses an LMI approach to observer-based guaranteed cost control problem. A sufficient condition for the existence of memoryless state feedback guaranteed cost controllers is derived on the basis of the LMI approach. A numerical example shows the potential of the proposed method.

References

- [1] S. S. L. Chang and T. K. C. Peng: Adaptive guaranteed cost control of systems with uncertain parameters," *IEEE Transactions on Automatic Control*, **AC-17**, (4), pp. 474-483, 1972
- [2] C. H. Lien: Robust observer-based control of systems with state perturbations via LMI approach," *IEEE Transactions on Automatic Control*, **AC-49**, (8), pp.1365-1370, 2004
- [3] S. Won, and J. H. Park: Design of observer-based controller for perturbed time-delay systems," *JSME International Journal C*, **42**, (1), pp.129-132, 1999
- [4] C. H. Lien: Guaranteed cost observer-based controls for a class of uncertain neutral time-delay systems," *Journal of Optimization Theory and Applications*, **126**, (1), pp.137-156, 2005
- [5] M. S. Mahmoud, and M. Zribi: Guaranteed cost observer-based control of uncertain time-lag systems," *Computers and Electrical Engineering*, **29**, pp.193-212, 2003

Isomorphic Structure of Graphs with the Maximum Number of Trees

Hideshi Ido^{*}, Yosuke Ohama^{*1}, and Sigeru Omatu^{**}

^{*} Electrical Engineering and Computer Science, ^{*1} Advanced Engineering Course,
 Niihama National College of Technology,
 7-1 Yagumo, Niihama, Ehime 792-8580, Japan
 ido@ele.niihama-nct.ac.jp

^{**} Computer and Systems Sciences, Graduate School of Engineering,
 Osaka Prefecture University, Sakai, Osaka 599-8531, Japan
 omatu@sig.cs.osakafu-u.ac.jp

Abstract

Two graphs G_A and G_B with the same number of nodes n and the same number of branches b are said to be isomorphic if these graphs have the same adjacency relations between nodes. We have got many graphs with the same maximum number of trees in the process of continuous branch additions. These graphs have same numbers of nodes n , branches b and trees t . We certified those graphs are isomorphic by a computer algorithm. This algorithm is based on permutations of nodes with the same degree in a sequence of node degrees. Examples of isomorphic graphs are presented in the process of adding branches one by one. If two graphs with same numbers of nodes n and branches b are isomorphic, these graphs have same numbers of trees. The further problem will be to prove the reverse condition.

Keywords: Isomorphic graph, Maximum number of trees, Continuous branch addition

1 Introduction

The number of trees of a graph would be an index to estimate the reliability of probabilistic communication networks with either high or low link probabilities when those probabilities are independent and equal [1].

Some analytical methods have been reported to calculate the number of trees of graphs obtained from the complete graph by deleting several types of subgraphs [2],[3]. Other ones are to maximize the number of trees when some branches or subgraphs are deleted from the complete graph [4],[5]. Another one is to get the expressions of trees of a graph which is obtained by connecting graphs of special structures [6].

These analytical methods are based on obtaining the expressions derived from a node determinant of the target graphs with some special structures. But simple expressions haven't been known for graphs without any structural conditions so far.

On the other hand, using numerical method, we constructed graphs with the maximum number of trees by adding a new branch continuously to the original graph[7].

In this paper, we have noticed that two or more graphs with the same maximum number of trees appeared many

times in the process of branch additions. All of those graphs are made sure to be isomorphic for some examples which are started branch additions from a tree of series branches with nodes $n=7$ and a star-shaped tree of $n=8$.

In the following sections, we will show two algorithms for graph construction and isomorphism. Results of estimation by connectivity are also presented to examine strength of these graphs.

2 Preliminary results [7]

First, we introduce some graph theoretical terms. A graph denoted by $G = (V, E)$ is composed with a node set V and a branch set E . Each branch denoted by (i, j) connects a pair of nodes i and j . A graph is said to be simple if it has no parallel branches, no self-loops and no directed branches. In this paper, we treat only simple graphs as shown in Fig.1 (a). A tree is a subgraph which connects all nodes of a graph G and includes no closed circuits, as shown in Fig.1 (b).

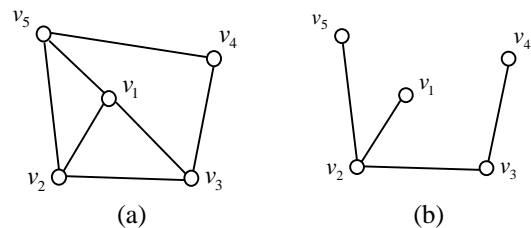


Fig.1. (a) Simple graph, (b) Tree

The complete graph of n nodes has one branch (i, j) between every node pair i, j , and includes $\frac{1}{2}n(n-1)$ branches. The matrix $A = (a_{ij})$ can be constructed from a graph G with n nodes, where for $1 \leq i, j \leq n-1$, each diagonal element a_{ii} is the number of branches incident to node i , and each non-diagonal element a_{ij} is -1 if there is a branch (i, j) between two nodes i and j , otherwise 0. Then the number of trees T of the graph G is represented by the determinant $|A|$. Since the value of T is always an integer for any graph, the determinant T must be calculated by using double precision floating

point number for matrix A . Usual Gaussian elimination is available for this purpose.

Algorithm: Max-trees

Step1. Find the set \bar{P} of position (i, j) where there isn't an branch (i, j) in the given original graph $G(V, E)$. Now, set $G_0 = G(V, E)$ and $k = 0$.

Step2. Calculate the number of trees T^* of each graph obtained by adding a branch (i, j) to the graph G_k , for each position $(i, j) \in \bar{P}$, respectively.

Step3. Find the branch (i, j) that gives the maximum number of trees among T^* 's in *Step2*. Replace $G_{k+1} = G_k + \text{branch}(i, j)$, $\bar{P} = \bar{P} - \text{position}(i, j)$, and $k = k+1$.

Step4. If the set \bar{P} is empty, then terminate. Otherwise go to *Step2*.

3 Isomorphic structure of graphs

3.1 Isomorphic graphs

When the algorithm starts from a series-branch tree graph of Fig.2(a), we obtain the sequence of branches represented by numbers near dotted lines as shown in Figs.3.

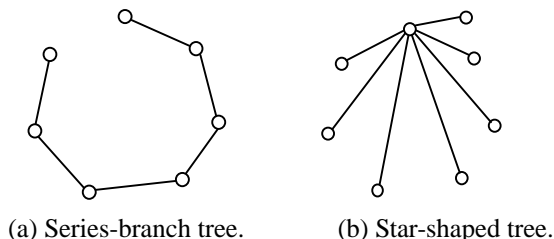


Fig.2. Initial graphs.

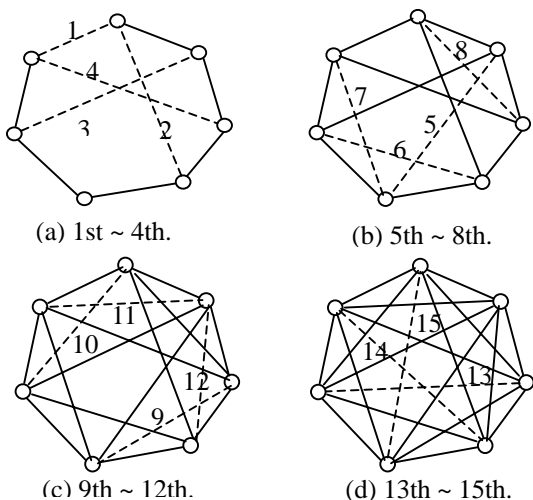


Fig.3. Branch sequence for Series-branch tree of $n=7$.

In the process to obtain this branch sequence, there are many isomorphic graphs with the same maximum number of trees as shown in Table 1.

Table 1. Isomorphic graphs with the same maximum number of trees of Fig.3.

Added branch	Total branches b	Max. number of trees	Isomorphic graphs*
0	6	1	1
1	7	7	1
2	8	19	7
3	9	51	2
4	10	117	1
5	11	231	4
6	12	408	2
7	13	720	1
8	14	1200	1
9	15	1840	4
10	16	2800	1
11	17	4200	3
12	18	6125	2
13	19	8575	3
14	20	12005	2
15	21	16807	1

* Number of isomorphic graphs including itself

For example, on added branch 5 of the Table 1, there are 4 graphs with 11 branches and 231 trees as shown in Fig.4. In this figure, each of 4 branches represented by dotted lines A, B, C, and D is the candidate to be added next.

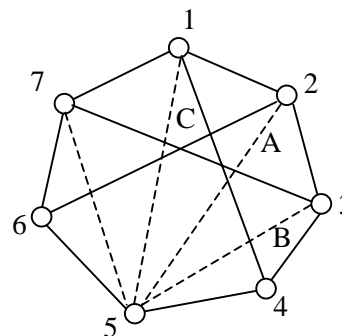


Fig.4. Four candidate branches

According to the criterion to select one branch that gives the maximum number of trees, any one among 4 branches can be selected. But its selection may cause different results in the later process of branch additions. Now, we denote graphs including branch A, including branch B, including branch C, and including branch D as G_A , G_B , G_C , and G_D , respectively in Fig.4.

G_A and G_C are isomorphic because of symmetric structure. Also G_B and G_D are isomorphic. To investigate

isomorphism between G_A and G_B , we have constructed the next algorithm.

3.2 Algorithm for Isomorphic Structure

A node degree $d(v)$ of a node v of a graph G is a number of branches incident to node v in G . A degree sequence S of a graph G is a sequence of node degrees of all nodes of a graph G . We assume that S is arranged in a decreasing order and separated into subsequences S_1, S_2, \dots, S_m , where S_i includes the same degrees. In general, two graphs G_A and G_B must have the same degree sequences S_A and S_B to be isomorphic. Then we assume that degree sequences S_A and S_B corresponding to graphs G_A and G_B are composed with the same subsequences $S_A = S_B = (S_1, S_2, \dots, S_m)$. The number of nodes for subsequence S_k is denoted by $|S_k|$.

Outline of the algorithm to determine isomorphism between G_A and G_B is as follows.

Algorithm Isomorphic

Step1. Set $k=1$ (Subsequence k is noticed).

Step2. Generate next permutation of $|S_k|$ nodes corresponding to S_k of S_B .
If permutation exhausted, G_A is not isomorphic to G_B (terminate the algorithm).

Step3. Examine adjacency relations of graphs G_A and permuted G_B within the range of $S_1 \sim S_k$.
If this examination has succeeded and $k < m$, then set $k = k+1$ and go to *Step2*.
If this examination has succeeded and $k = m$, then G_A is isomorphic to G_B (terminate the algorithm).

Step4. Otherwise, set $k = k-1$ and return to *Step2*.

For programming of this algorithm, the generation of permutation in *Step2* is skipped for subsequence S_k with $|S_k|=1$.

Using this algorithm, all graphs with the maximum number of trees in Table 1 have been found out to be isomorphic. Of course, cases of symmetric structures are omitted. For another initial graph of star-shaped tree shown in Fig.2(b) with nodes $n=8$, the number of isomorphic graphs are shown in Table 2.

Isomorphic graphs have appeared many times in the process of continuous branch additions. The rate of a number of cases that give two or more isomorphic graphs is $9/14=64\%$ in Table 1, and $15/20=75\%$ in Table 2.

3.2 Estimation of Graphs with the Maximum Number of trees by Connectivity

The number of trees of a graph G has the relation with the reliability of communication networks with the same branch probability p .

As another criterion to estimate communication networks, we introduce the connectivity of corresponding graph.

Table 2. Isomorphic graphs with the same maximum number of trees started from Fig.2(b).

Added branch	Total branches b	Max. number of trees	Isomorphic graphs*
0	7	1	1
1	8	3	21
2	9	9	10
3	10	27	3
4	11	72	6
5	12	168	4
6	13	377	4
7	14	841	1
8	15	1537	7
9	16	2800	2
10	17	4928	1
11	18	8056	4
12	19	12440	2
13	20	19200	1
14	21	28800	1
15	22	40800	4
16	23	57600	1
17	24	80640	3
18	25	110592	2
19	26	147456	3
20	27	196608	2
21	28	262144	1

* Number of isomorphic graphs including itself

A local connectivity $k(i,j)$ between distinct two nodes i and j of a graph $G=(V,E)$ is the minimum number of nodes removed to separate G . Then the connectivity of

Table 3. Connectivity $k(G)$ of the graph G appeared in Table 1.

Branches b	Ideal k	Real $k(G)$
6	1	1
7	2	2
8	2	2
9	2	2
10	2	2
11	3	3
12	3	3
13	3	3
14	4	3*
15	4	4
16	4	4
17	4	4
18	5	5
19	5	5
20	5	5
21	6	6

Table 4. Connectivity $k(G)$ of graphs started from series branch tree of nodes $n=8$.

Branches b	Ideal k	Real $k(G)$
7	1	1
8	2	2
9	2	2
10	2	2
11	2	2
12	3	3
13	3	3
14	3	3
15	3	3
16	4	4
17	4	4
18	4	4
19	4	4
20	5	4*
21	5	4*
22	5	5
23	5	5
24	6	6
25	6	6
26	6	6
27	6	6
28	7	7

graph G denoted by $k(G)$ is the minimum value of local connectivity $k(i,j)$. Connectivity $k(G)$ represents the strength of the network against damages of nodes and branches.

Table 3 shows a comparison between ideal connectivity k and real $k(G)$ for the graphs in Fig. 2. Ideal connectivity k is given by $\lceil 2b/n \rceil$, where $\lceil \]$ denotes Gaussian notation[1]. Table 4 shows for graphs started from series branch trees with $n=8$.

From Tables 3 and 4, graphs with the maximum number of trees constructed by algorithm *Max-trees* give good results in most cases except for cases marked with *.

Graphs shown in Tables 3 and 4 started from series branch trees tend to balance node degrees into two consecutive integers.

5. Conclusion

We demonstrated that graphs with maximum number of trees constructed by simple algorithm *Max-trees* have isomorphic structures in many cases as more than 60%. Graphs with the maximum number of trees are needed to be the models of reliable networks.

Connectivity $k(G)$ of a graph G is adapted as another criterion to estimate the strength of networks against damages of nodes and branches. Except for few cases graphs with maximum number of trees give good performance.

We used computer algorithm to examine isomorphism for graphs with the same number of nodes n , branches b , and trees. If the same numbers of trees means isomorphic of graphs, it is very easy to examine isomorphism. This is the future problem.

References

- [1] Leggett J.D., Bedrosian S.D., "Synthesis of Reliable Networks", IEEE Trans. Circuit Theory, Vol. CT-16, No. 8, pp.384-385, 1969.
- [2] Kasai T., Kusaka H., Yoneda S. and Taki I., "Total Number of Trees in Four Kinds of Incomplete Graphs Derived from a Complete Graph (in Japanese)", Jour. Inst. Elect. Comm. Engrs. Japan. Vol.49, No.1, pp.69-77, 1966.
- [3] Ishikawa H., Ido H., and Sasaki T., "Number of Trees in a Certain Incomplete Graph (in Japanese)", Trans. IEICE, Vol.57-A, No.5, pp.423-424, 1974.
- [4] Shier D.R., "Maximizing the Number of Spanning Trees in a Graph With n Nodes and m Branches", Jour. Res. of Nat. Bur. of Stds.-B. Math. Sci., Vol.78B, No.4, pp.193-196, 1974.
- [5] Ido H., Ishikawa H., and Sasaki T., "Number of Trees in a Specified Incomplete Graph and its Min-Max Problem (in Japanese)", Trans. IEICE, Vol.58-A, No.1, pp.81-82, 1975.
- [6] Hatakeyama M., Sato K., "Construction Method for a Connection Graph of Cycles from a General Graph (in Japanese)", Proc. IEICE Gen Conf. A-1-6, 2003.
- [7] Ido H., Ohama Y., and Takahashi T., "Graph Construction with the Maximum Number of Trees by Continuous Edge Addition", Artificial Life and Robotics, Vol.10, No.2, pp.185-188, 2006.

Relations between Network Reliability and Number of Trees of Graph

Hideshi Ido* and Sigeru Omatu**

*Electrical Engineering and Computer Science,
Niihama National College of Technology,
7-1 Yagumo, Niihama, Ehime 792-8580, Japan
ido@ele.niihama-nct.ac.jp

** Computer and Systems Sciences, Graduate School of Engineering,
Osaka Prefecture University, Sakai, Osaka 599-8531, Japan
omatu@sig.cs.osakafu-u.ac.jp

Abstract

Network reliability is the probability that all stations of the network are connected by only unfailling links under independent link failures. The communication network can be represented by an undirected graph G , where communication stations and links are corresponding to nodes and branches of its graph, respectively. Therefore, network reliability can be defined as the probability that there exists at least one tree in the corresponding graph. We assume that each branch connects its two end nodes with the same independent probability p and disconnects with probability $q=1-p$. In case of $p=1$ or $p=0$, it is known that the most reliable network has the maximum number of trees within graphs of n nodes and b branches.

In this paper, we present a network reliability $Pr(G)$ and a number of trees $t(G)$ of graph G by using the generation algorithm of exclusive events which include trees. Then given two graphs G_A and G_B with same numbers of nodes n , branches b , and different number of trees $t(G_A) < t(G_B)$, we demonstrate network reliabilities $Pr(G_A) < Pr(G_B)$ with respect to probabilities $p(0 < p < 1)$ in case of smaller graphs with $n=4, b=4$ and $n=5, b=7$.

Keywords: Network reliability, Number of trees,
Exclusive events

1 Introduction

If we focus on relations of connection between stations by links, the communication network can be represented by an undirected graph G , where communication stations and links are corresponding to nodes and branches of its graph, respectively. A graph denoted by $G=(V, E)$ is composed with a node set V and an edge set E . For simplicity, graph G is assumed a simple graph which is an undirected graph with no self-loops and no multiple branches.

Network reliability is defined as the probability that all stations of the network are connected by only unfailling links under independent link failures. Then the network reliability $Pr(G)$ of a graph G is a probability that there exists at least one tree composed with only normal branches.[1],[2] Namely, if we can obtain all trees of graph G as T_1, T_2, \dots, T_k , then $Pr(G)$ would be

represented by expression (1) below.

$$Pr(G) = Pr(T_1 \cup T_2 \cup \dots \cup T_k) \quad (1)$$

It is not an efficient method to expand expression (1) to calculate $Pr(G)$ for a large graph G with relatively many trees $k=t(G)$. To avoid these tedious operations, the procedure was proposed that generates exclusive events including trees and cuts of graph at the same time.[1] This procedure can also calculate probability $Pr(G)$ within an arbitrary error. Now, assuming each branch connects its two end nodes with independent, equal probability p and disconnects with probability $q=1-p$, it is known that the most reliable network has the maximum number of trees in case of $p=1$ or $p=0$. [2]

We first present a procedure to estimate the number of trees $t(G)$ and the network reliability $Pr(G)$ of graph G by using the generation algorithm of exclusive events including trees of graph G .

Next, given two graphs G_A and G_B with same numbers of nodes n , branches b , and different number of trees $t(G_A) < t(G_B)$, we demonstrate network reliabilities $Pr(G_A) < Pr(G_B)$ with respect to probabilities $p(0 < p < 1)$ in case of smaller graphs with $n=4, b=4$ and $n=5, b=7$.

2 Preliminary

First, we introduce some graph theoretical notations. A graph denoted by G is composed with a node set and a branch set. In graph G , we denote an event of existing branch e by e , and an event of not existing branch e by \bar{e} . Union and product of events are denoted by $+$ and \cdot , respectively. Then two events τ_i and τ_j ($i \neq j$) that include at least one tree of G are said to be exclusive events if $\tau_i \cdot \tau_j = \emptyset$ (empty event). Union event $T_x[G]$ of exclusive tree events including all trees of G can be generated by next expression (2) with respect to a multiple branch $\{e_1, e_2, \dots, e_k\}$ of $k(k-1)$ branches.[1]

$$T_x[G] = (e_1 + e_2 + \dots + e_k) \cdot T_x[G(e_1 + e_2 + \dots + e_k)] \\ \oplus (\bar{e}_1 \cdot \bar{e}_2 \cdot \dots \cdot \bar{e}_k) \cdot T_x[G(\bar{e}_1 \cdot \bar{e}_2 \cdot \dots \cdot \bar{e}_k)] \quad (2)$$

where, $G(e_1 + e_2 + \dots + e_k)$ and $G(\bar{e}_1 \cdot \bar{e}_2 \cdot \dots \cdot \bar{e}_k)$ are graphs derived from G by short circuiting and open circuiting all branches of multiple branch $\{e_1, e_2, \dots, e_k\}$, respectively. \oplus denotes direct sum of exclusive events. As the result of repeating (2), we have obtained next expression (3).

$$\left. \begin{aligned} T_X[G] &= \tau_1 \oplus \tau_2 \oplus \dots \oplus \tau_{t_X} \\ \tau_i &= \prod_{j=1}^{n-1} (e_{ij1} + e_{ij2} + \dots + e_{ijk}) \\ &\cdot \prod_{\ell=1}^s (\bar{e}_{i\ell 1} \cdot \bar{e}_{i\ell 2} \cdot \dots \cdot \bar{e}_{i\ell m}) ; i = 1, 2, \dots, t_X \end{aligned} \right\} (3)$$

where, n denotes the number of nodes, s is the number of multiple branches short circuited in j -th order and open circuited in ℓ -th order respectively, and t_X is the number of exclusive tree event. Since simultaneous occurrence probability $Pr(\tau_i \cdot \tau_j \cdot \dots \cdot \tau_k) = 0$

($i \neq j \neq \dots \neq k$) with respect to these τ_i 's, network reliability $Pr(G)$ result in (4).

$$\left. \begin{aligned} R(G) &= Pr(T_X[G]) = Pr\left(\bigcup_{i=1}^{t_X} \tau_i\right) = \sum_{i=1}^{t_X} Pr(\tau_i) \\ Pr(\tau_i) &= \prod_{j=1}^{n-1} \left(1 - \prod_{h=1}^k (1 - p_{ijh})\right) \cdot \prod_{\ell=1}^s \left(\prod_{h=1}^m (1 - p_{i\ell h})\right) \end{aligned} \right\} (4)$$

3 Number of trees and network reliability

Figure 1 shows two graphs G_1 and G_2 with same numbers of nodes $n = 4$ and branches $b = 4$.

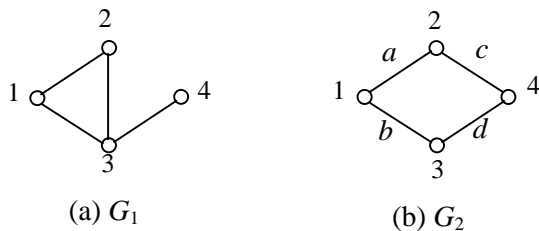


Fig.1. Graphs $n=4, b=5$.

Figure 2 represents the process of generating exclusive tree events τ_i using (2) with respect to (multiple) branch incident to a node in the order of 1,2,... of graph G_1 in Fig.1(a), where each branch is discriminated by symbols a, b, c and d . As shown in Fig.2, graph G_1 has $t_X = 2$ exclusive tree events τ_1 and τ_2 , where τ_1 and τ_2 include two and one trees, respectively. Then the total number of trees $t(G_1) = 3$. Now if all of four branches of G_1 operate normally by the same probability $p(q=1-p)$, the network reliability $R(G_1)$ of corresponding graph G_1 can be calculated into

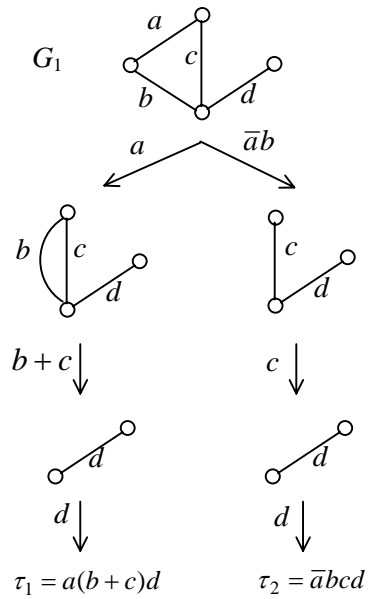


Fig.2 Generation of exclusive tree events.

expression (5) using (3) and (4).

$$\begin{aligned} R(G_1) &= Pr(T_X[G_1]) = Pr\left(\bigcup_{i=1}^{t_X} \tau_i\right) \\ &= p^2(1-q^2) + p^3q \end{aligned} (5)$$

For graph G_2 in Fig.1(b), next three exclusive tree events were derived in similar way.

$$\begin{aligned} \tau_1 &= ab(c+d) \\ \tau_2 &= a\bar{b}dc \\ \tau_3 &= \bar{a}bdc \end{aligned}$$

As a result of these exclusive events, the number of trees is $t(G_2) = 4$. For equal branch probability p ($q=1-p$), network reliability was obtained as (6).

$$R(G_2) = p^2(1-q^2) + 2p^3q (6)$$

Figure 3 shows two graphs G_3 and G_4 with $n=5, b=7$.

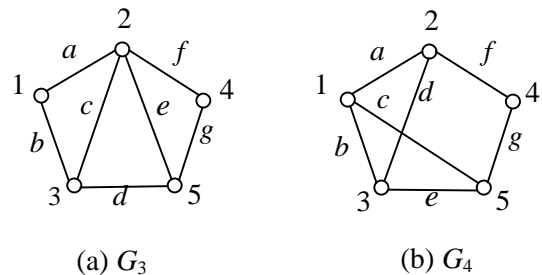


Fig.3. Graphs with $n=5, b=7$.

In the similar way as graph G_1 , there are 8 exclusive tree events that each includes 1~8 trees of G_3 . There are 10 exclusive tree events that each includes 1~6 trees of G_4 . Then the number of trees is $t(G_3)=21$ and $t(G_4)=24$. For equal branch probability p ($q=1-p$), network reliability was obtained as (7) and (8).

$$R(G_3) = 2p^4q^3 + 4p^3(1-q^2)q^2 + p(1-q^2)^3 + p^3(1-q^3)q \quad (7)$$

$$R(G_4) = 3p^4q^3 + 4p^3(1-q^2)q^2 + p^2(1-q^2)(1-q^3) + p^2(1-q^2)^2q + p^3(1-q^3)q \quad (8)$$

Comparing (5),(6) with (7),(8), it is observed that increase of nodes and branches makes reliability expressions rapidly complicated.

In case of $p=1$ or $p=0$, the necessary condition that the network is most reliable becomes the graph to have the maximum number of trees. If the network with the maximum number of trees is unique, the above necessary condition becomes also sufficient condition.[2]

We compare the network reliability $R(G)$ with respect to branch probability $p=0.1 \sim 0.9$ for graphs of same numbers of nodes n and branches b used in Figs. 1 and 3.

The result is shown in table 1.

Table 1. Network reliability and the number of trees.

nodes n , branches b	$n=4, b=4$		$n=5, b=7$	
	G_1	G_2	G_3	G_4
graph	G_1	G_2	G_3	G_4
trees $t(G)$	3	4	21	24
Network relia. $R(G)$ branch prob. p	$R(G_1)$	$R(G_2)$	$R(G_3)$	$R(G_4)$
0.9	0.8748	0.9639	0.90345	0.98415
0.8	0.7168	0.8704	0.79299	0.91750
0.7	0.5488	0.7399	0.65283	0.78753
0.6	0.3888	0.5904	0.48833	0.60653
0.5	0.25	0.4375	0.32031	0.40625
0.4	0.1408	0.2944	0.17490	0.22528
0.3	0.0648	0.1719	0.07234	0.09428
0.2	0.0208	0.0784	0.01834	0.02413
0.1	0.0028	0.0199	0.00145	0.00192

Table 1 shows that graphs G_2 and G_4 which have larger number of trees give higher reliability compared with graphs G_1 and G_3 .

4. Conclusion

Analytical expressions for network reliability are

presented using exclusive tree events for smaller number of nodes and branches. The number of trees would play an important role for network reliability. Since the number of trees becomes huge for large graph, it is tedious to obtain analytical expressions of reliability. Then numerical computation, for example the number of trees become useful.[3]

References

- [1] Ido H., "A Note on Calculation of System Reliability (in Japanese)", Trans. IEICE, Vol.61-A, No.1, pp.72-74, 1978.
- [2] Leggett J.D., Bedrosian S.D., "Synthesis of Reliable Networks", IEEE Trans. Circuit Theory, Vol. CT-16, No.8, pp.384-385, 1969.
- [3] Ido H., Ohama Y., and Takahashi T., "Graph Construction with the Maximum Number of Trees by Continuous Edge Addition", Artificial Life and Robotics, Vol.10, No.2, pp.185-188, 2006.

Appendix

Exclusive tree events for graph G_3

$$\tau_1 = a(b+c)(d+e)(f+g)$$

$$\tau_2 = a(b+c)\bar{d}\bar{e}fg$$

$$\tau_3 = \bar{a}\bar{b}\bar{c}ed(f+g)$$

$$\tau_4 = \bar{a}\bar{b}\bar{c}\bar{e}fdg$$

$$\tau_5 = \bar{a}\bar{b}cf(d+e+g)$$

$$\tau_6 = \bar{a}\bar{b}cf(e+d)g$$

$$\tau_7 = \bar{a}\bar{b}\bar{c}fd(e+g)$$

$$\tau_8 = \bar{a}\bar{b}\bar{c}\bar{f}edg$$

Exclusive tree events for graph G_4

$$\tau_1 = a(b+d)f(c+e+g)$$

$$\tau_2 = a(b+d)\bar{f}(e+c)g$$

$$\tau_3 = \bar{a}\bar{b}\bar{d}f(c+g)e$$

$$\tau_4 = \bar{a}\bar{b}\bar{d}fceg$$

$$\tau_5 = \bar{a}\bar{b}df(c+e+g)$$

$$\tau_6 = \bar{a}\bar{b}df(c+e)g$$

$$\tau_7 = \bar{a}\bar{b}\bar{d}f(c+e)g$$

$$\tau_8 = \bar{a}\bar{b}\bar{c}de(f+g)$$

$$\tau_9 = \bar{a}\bar{b}\bar{c}d\bar{e}fg$$

$$\tau_{10} = \bar{a}\bar{b}\bar{c}d\bar{f}ge$$

Acoustic Signals Separation of Mechanical Devices Using the ICA with Band-Pass Filters

Sigeru Omatu

Computer Science and Intelligent Systems, Graduate School of Engineering
Osaka Prefecture University, Sakai, 599-8531, Osaka, Japan
Tel: +81-722-254-9278, Fax: +81-722-257-1788, E-mail: omatu@cs.osakafu-u.ac.jp

Abstract

In this paper, a method of separating the acoustic signals of motors and gears of mechanical devices by using the independent component analysis (ICA) with band-pass filters is proposed. The frequency distribution of a recorded acoustic signal of the operating mechanical device can be divided into three fields, the low-frequency field, which corresponds to the frequency characteristics of the gear, the medium-frequency field, which is mixed with the frequency characteristics of the gear and the motor, and the high-frequency field, which corresponds to the frequency characteristics of the motor. Since only the medium-frequency components are the mixture of acoustic signals of gears and motors, the ICA with band-pass filters is expected to separate the acoustic signals of motors and gears more accurately than the conventional ICA. The simulation and experimental results show that the proposed method can separate the acoustic signals of motors and gears of mechanical devices successfully.

Keywords:

ICA, Signal processing, Neural Networks

Introduction

In the quality evaluation of mechanical devices, it is important to separate the acoustic signals of motors and gears in order to identify the causes of failures. The ICA method, which is developed to solve the cocktail-party problem, can separate two independent acoustic signals from their mixtures by using the information measure of statistically independent properties [1]-[3]. However, many applications in practice denote that the ICA does not perform well in separation by using the observed acoustic signals directly [4]-[5]. In order to separate the independent acoustic signals correctly, additional data processing is necessary before applying the ICA.

By applying the fast fourier transform (FFT) to a recorded acoustic signal of the operating mechanical device, we observe that its frequency distribution can be divided into three fields, the low-frequency field, which corresponds to the frequency characteristics of the gear, the medium-frequency field, which is mixed with the frequency characteristics of the gear and the motor, and the high-frequency field, which corresponds to the frequency characteristics of the motor. Since the frequencies of a

motor may be harmonics of the fundamental frequencies of a gear, which causes the independence assumption of the sources to fail and affects the separation accuracy. Therefore, the mixed acoustic signals with less frequency components are expected to be separated more accurately. In this paper, the ICA with band-pass filters is used to separate the acoustic signals of gears and motors. We first record the acoustic signals of the operating mechanical devices. By applying the band-pass filters, the respective components of low-frequency, medium-frequency and high-frequency can be obtained. Then the medium-frequency components are given to the ICA. After separation, the acoustic signals of gears and motors are recovered by adding the low-frequency and high-frequency components to the separated results, respectively. In this paper, the mixtures of two independent signals are also designed to simulate the separation process of acoustic signals of a gear and a motor. Both the simulation results and the experimental results show that the better separation results can be obtained by using the mixed medium-frequency field than using the whole frequency field.

Simulation Results

Suppose there are two independent signals s_1 and s_2 , their frequency characteristics are illustrated in Figures 1 and 2, respectively where f_1 , f_2 and f_4 are constant and f_3 is variable.

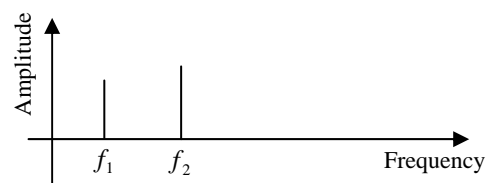


Figure 1 - Frequency characteristic of s_1

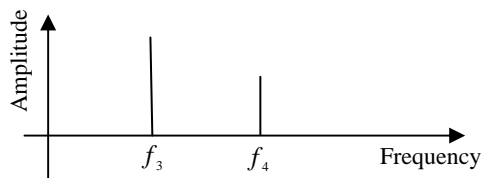


Figure 2 - Frequency characteristic of s_2 .

If we use two microphones to record the acoustic signals, we have two observed signals $x_1(t) = a_{11}s_1 + a_{12}s_2$, $x_2(t) = a_{21}s_1 + a_{22}s_2$. We use the ICA to separate the two independent signals s_1 and s_2 from the observed signals.

Table I shows the separation results where “Y” denotes that the independent signals s_1 and s_2 can be separated correctly and “N” denotes that they cannot be separated correctly. From Table I, it can be seen that sometimes we fail in separating the acoustic signals s_1 and s_2 by using the observed signals x_1 and x_2 directly.

Table I - Separation results of observed signals (unit: Hz)

f_3	30	40	50	60	70	80	90	100	110
Y/N	Y	Y	Y	N	Y	Y	Y	N	Y
f_3	120	130	150	160	170	180	190	200	210
Y/N	N	Y	Y	Y	Y	N	Y	Y	Y
f_3	220	230	$f_1 = 20, f_2 = 140, f_4 = 240$						
Y/N	Y	Y							

However, after filtering the frequency components f_1 and f_4 with a band-pass filter, the frequency components f_2 and f_3 can be separated successfully by using the ICA. Thus, the original acoustic signals s_1 and s_2 can be obtained by adding the frequency components f_1 and f_4 to the separation results of the ICA, respectively. As an example, Figures 3 and 4 show the frequency characteristics of separated signals s_1' and s_2' by using the ICA with band-pass filters, respectively where $f_3 = 100$ Hz. From these figures, it can be seen that the two acoustic signals of s_1 and s_2 are separated correctly.

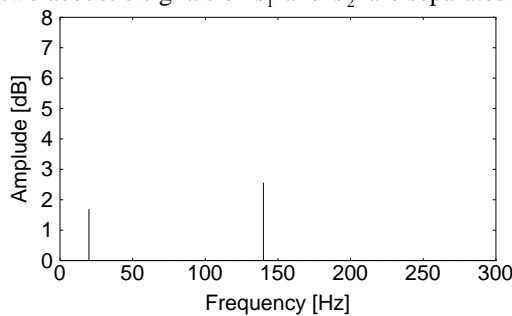


Figure 3 - Frequency characteristic of separated signal s_1' with band-pass filters

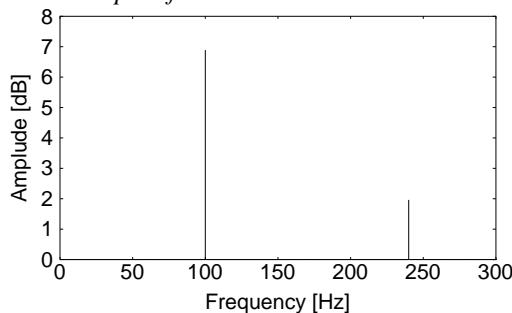


Figure 4 - Frequency characteristic of separated signal s_2' with band-pass filters.

Similarly, other unsuccessful separation experiments of Table I are redone by using the ICA with band-pass filters. The simulation results show that all the signals are separated successfully. And the separation experiments of mixed acoustic signals with multi-frequencies also show that the ICA with band-pass filters performs better than the conventional ICA in acoustic signals separation.

Experimental Results

According to the above simulation results, we separate the acoustic signals of motors and gears of mechanical devices by using the ICA with band-pass filters. The acoustic signals recording system is shown in Figure 5. Two microphones, which are held in different locations, are used to record the acoustic signals of operating mechanical devices. By applying the band-pass filters, we obtain the respective components of low-frequency, medium-frequency and high-frequency. Since only the medium-frequency components are the mixture of acoustic signals of gears and motors, we input the medium-frequency components to the ICA. Then the acoustic signals of gears and motors can be recovered by adding the low-frequency and high-frequency components to the separation results of the ICA, respectively.

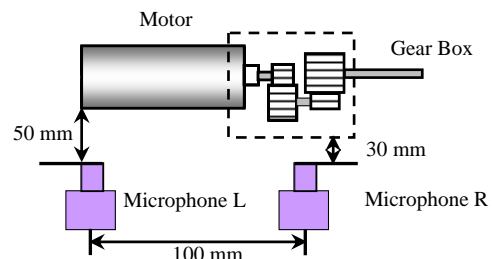


Figure 5 - The acoustic signals recording system

An example of acoustic signals recorded by microphones L and R are shown in Figures 6 and 7, respectively where the sampling rate is 8,000. Their frequency characteristics are shown in Figures 8 and 9.

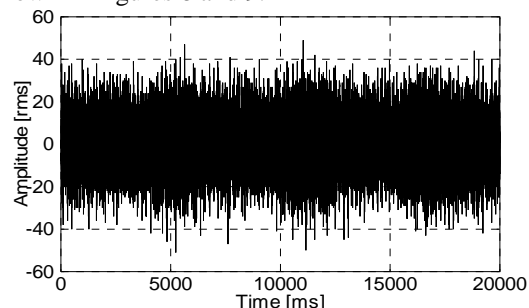


Figure 6 - Acoustic signal recorded by the left microphone

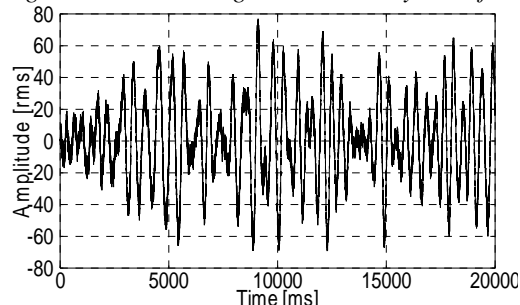


Figure 7 - Acoustic signal recorded by the right microphone

Since the rotational speed of the motor is 3600 rpm and the rotor has 12 poles, the fundamental frequency of the motor is about 360 Hz. Similarly, since the gear ratio is 30:1, the fundamental frequency of the gear is about 12 Hz. Thus, it can be considered that the medium-frequency is the range

of 300 to 2,000 Hz and the relevant band-pass filters are designed.

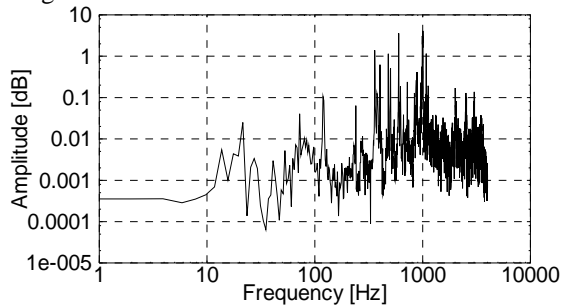


Figure 8 - Spectrum of acoustic signal of left microphone

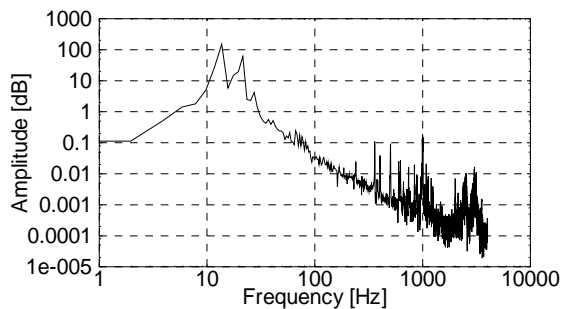


Figure 9 - Spectrum of acoustic signal of right microphone

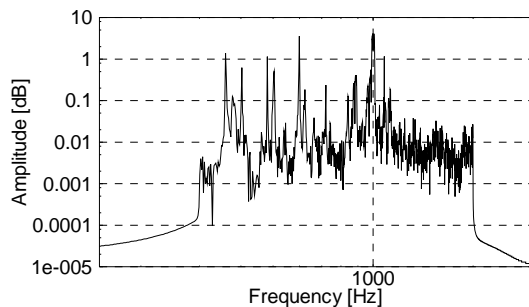


Figure 10 - Spectrum of Figure 8 with a band-pass filter

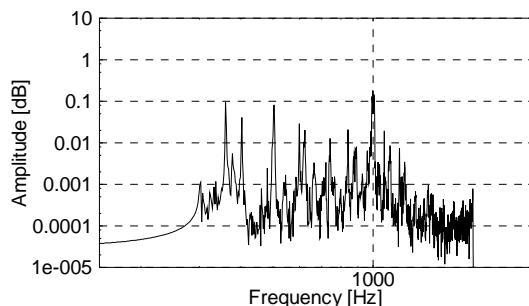


Figure 11 - Spectrum of Figure 9 with a band-pass filter

In Figures 10 and 11, the medium-frequency fields of acoustic signals of left and right microphones with the band-pass filter are given respectively. The filtered signals are used as the input of the ICA. The spectra of the separated acoustic signals are shown in Figures 12 and 13. Since a peak of amplitude nearby 1,000 Hz, which is about 3 times of the fundamental frequency of the motor, can be observed in Figure 12, it is regarded that Figures 12 and 13 show the medium-frequency fields of acoustic signals of the motor and the gear, respectively.

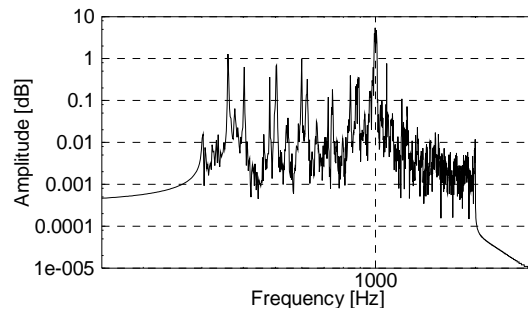


Figure 12 - Spectrum of the separated acoustic signal by using the ICA with a band-pass filter (motor)

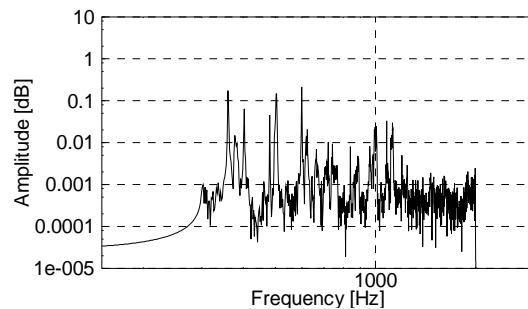


Figure 13 - Spectrum of the separated acoustic signal by using the ICA with a band filter-pass (gear)

To verify the effectiveness of our proposed method, we also give the separation results by applying the recorded acoustic signals of mechanical devices to the ICA directly. The frequency characteristics of the separated acoustic signal are shown in Figures 14 (a) and 15 (a), and the medium-frequency characteristics are shown in Figures 14 (b) and 15 (b). Comparing with Figures 8 and 9, it can be concluded that Figures 14 and 15 show the frequency characteristics of the motor and the gear, respectively.

From the above figures, it can be seen that the ICA with band-pass filters performs better than the conventional ICA in acoustic signals separation. The spectrum of Figure 14 (b) is similar with the one of Figure 15 (b), especially the peaks of amplitudes appeared in both figures, which are located in the multiple of fundamental frequency of the motor, denote that the separation results of acoustic signals of the motor and the gear are not good.

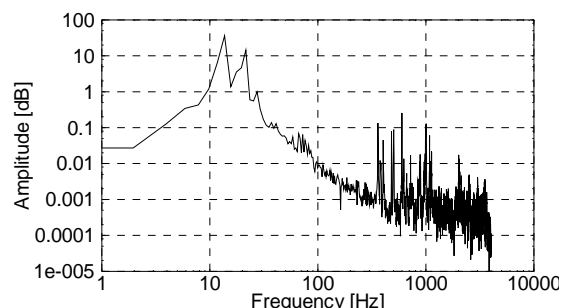


Figure 14 (a) - Frequency characteristics of the separated acoustic signal by using the ICA (motor)

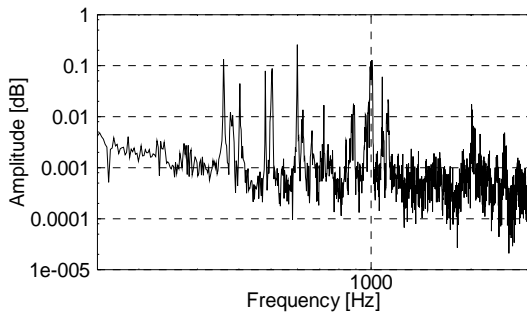


Figure 14 (b) - Medium-frequency characteristics of the separated acoustic signal by using the ICA (motor).

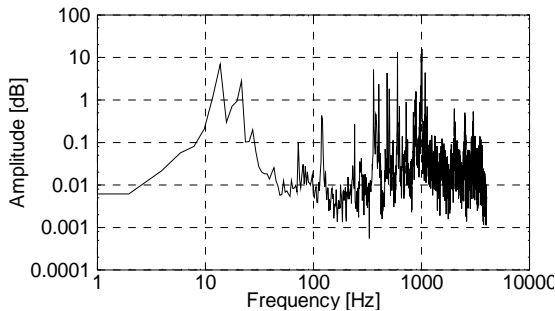


Figure 15 (a) - Frequency characteristics of the separated acoustic signal by using the ICA (gear)

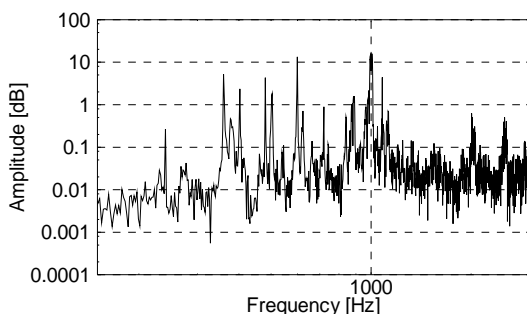


Figure 15 (b) - Medium-frequency characteristics of the separated acoustic signal by using the ICA (gear)

The acoustic signals of the gear and the motor are recovered by adding the low-frequency and high-frequency components to the separation results of Figures 12 and 13, respectively. The spectra of recovered acoustic signals of the gear and the motor are shown in Figures 16 and 17 where the amplitudes of medium-frequency are adjusted according to the amplitudes of low-frequency and high-frequency, respectively. Comparing with the above figures, it can be concluded that the separation results are reasonable. The separated acoustic signals of the gear and the motor are also checked by a technician, the sounds of the motor and the gear denote that the acoustic signals of the gear and the motor are separated successfully by using the ICA with band-pass filters.

Conclusions

In this paper, a method of separating the acoustic signals of gears and motors of mechanical devices by using the ICA with band-pass filter is proposed. The simulation results denote that the mixed acoustic signals with less frequency

components can achieve better separation performance by using the ICA. Therefore, for those independent signals which are mixed only in medium-frequency field, the ICA with band-pass filters can separate the independent original signals more accurately than the conventional ICA. Using the proposed method, we have solved the acoustic signals separation problem of gears and motors of mechanical devices successfully.

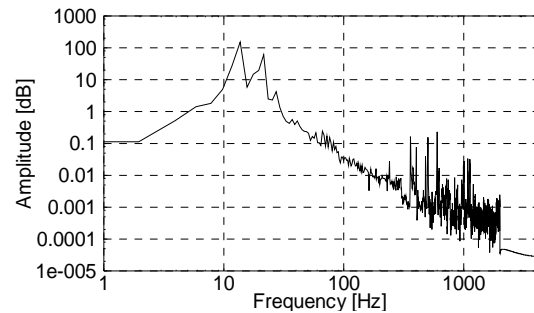


Figure 16 - Spectrum of recovered acoustic signal of the gear

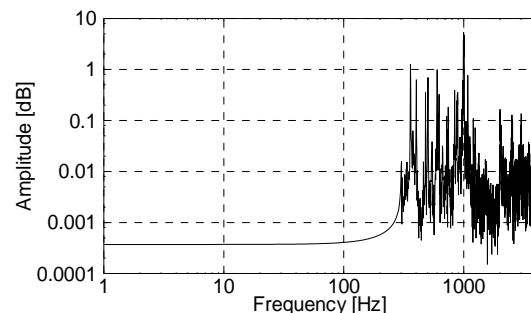


Figure 17 - Spectrum of recovered acoustic signal of the motor

References

- [1] Hyvarinen A, Karhunen J, and Oja E (2001), *Independent Component Analysis*, Wiley Publisher, New York
- [2] Bingham E, and Hyvarinen A(2002), A Fast Fixed-Point Algorithm for Independent Component Analysis of Complex Valued Signals, *International Journal of Neural Systems*, Vol. 10, No. 1, pp. 1-8
- [3] Hochreiter S, and Schmidhuber J(1999), LOCOCODE Performs Nonlinear ICA without Knowing the Number of Sources, *Proceedings of the First International Workshop on ICA and Signal Separation*, Aussois, France, pp. 149-154
- [4] Lee TW(1998), *Independent Component Analysis: Theory and Applications*, Kluwer Academic Publishers, Boston
- [5] Cichocki A, and Amari S (2002), *Adaptive Blind Signal and Image Processing: Learning Algorithms and Applications*, Wiley Publisher, New York

Reliability of Bank Note Classifier by Neural Networks

Sigeru Omatu

*Computer Science and Intelligent Systems, Graduate School of Engineering
Osaka Prefecture University, Sakai, 599-8531, Osaka, Japan
Tel: +81-722-254-9278, Fax: +81-722-257-1788, E-mail: omatu@cs.osakafu-u.ac.jp*

Abstract

This paper addresses the reliability of neuro-classifiers for bank note recognition. A local principal component analysis (PCA) method is applied to remove non-linear dependencies among variables and extract the main principal features of data. At first the data space is partitioned into regions by using a self-organizing map (SOM) model and then the PCA is performed in each region. A learning vector quantization (LVQ) network is employed as the main classifier of the system. By defining a new algorithm for rating the reliability and using a set of test data, we estimate the reliability of the system. The experimental results taken from 1,200 samples of US dollar bills show that the reliability is increased up to 100% when the number of regions as well as the number of codebook vectors in the LVQ classifier are taken properly.

Keywords:

Bank Note Classifier, Neural Networks, Reliability

Introduction

The recognition of bank note recently has been concerned effectively by using of neural networks, and it is shown that neuro-classifiers are robust for recognition of defective, taint, and worn out bank note. Takeda et al. [1] have used a random mask for preprocessing the data and then a multi-layer neural network as the classifier for recognition of bank note. Teranishi et al. [2] have applied a method based on acoustic cepstrum patterns for extracting the features of bill and then a competitive neural network as the classifier. Tanaka [3] has employed a probabilistic principal component analysis (PCA) for extracting the main characteristics of bill data.

Due to high risk of misclassification in such systems, the reliability of recognition becomes of a high importance. Basically the classifier must be fully robust for frayed or dirty bills of different models, and also has insensitivity to shift rotation and different directions of inserting bill. In fact, even if the classification rate is 100% over the data space, still it is necessary to make sure about the reliability of classification over all variety of real data.

We have already proposed in our pervious study [4] a method which uses the PCA algorithm for extracting the features of bill image data and utilizes a learning vector quantization (LVQ) network as the main classifier, where the reliability is evaluated thorough a new defined algorithm using Gaussian mixture densities for distribution of data. We have found out that in case of large variability

in input data or any non-linear correlation between the data, some additional discrimination process is needed to keep the reliability high enough.

As the main limitation of PCA is its global linearity, that is, it only defines a linear projection of data and does not model non-linear relationship among variables, some developments of non-linear principal component analysis (NLPCA) have been presented to address this limitation [5]. However, both PCA and NLPCA algorithms try to model the entire data by the same global features. As an alternative, the complexity of the data can be modeled by using a mixture of the local linear PCA. The local PCA algorithm clusters the input data into regions and performs PCA on the data that falls within each region.

In this paper, we apply a local PCA method where a SOM model is used as for clustering the data into homogenous regions. Our approach is similar to Kerschen [6] in the sense of local PCA application but differs in the clustering method as he has used vector quantization (VQ) for clustering phase.

The current system is intended for classifying different kinds of bank note, however, we examined only US dollar bills. The experimental results show a growth in reliability by 0.2% after using feature extracted by the local PCA model comparing to the method based on the conventional PCA, and a growth by 2.3% comparing to classification without the PCA.

Bill Data Preprocessing

The original image of bill money comes as a 10x170 array of data taken through three main advance sensors and two auxiliary ones. Each sensor uses two different waves lengths for generating two channels of data. At first by using a linear function we generate a new channel of data based on two channels of each sensor. Thus totally 15 channels are obtained among them we select 6 main channels which represent the main characteristic of data. A simple compression algorithm is used to reduce the size of data from 170 pixels in each channel to 30. Then a linear transformation is applied for normalization as follow:

$$z_i = \frac{x_i - \bar{x}}{S_x} G + C$$

where x_i is the pixel value in each channel, \bar{x} is the mean value of pixels, S_x is standard deviation, and $G=512$ and $C=128$ are the coefficients of gain and offset, respectively whose values are taken experimentally. Thus, a matrix of 6x30 size is provided for using in feature extraction step.

Data Compression

CA is one of the most popular methods for preprocessing, compression and feature extraction of data and it is discussed in most documents on multivariate analysis. The most common derivation of the PCA is in terms of a standardized linear projection which maximizes the variance in the projected space. As explained in the introduction, the PCA only removes linear correlation among the data and is only sensitive to second order statistics, i.e., it is assumed that the distribution of data is Gaussian. In case of non-linear relations among the variables, we need to consider higher order statistics to eliminate the dependencies which are not removed by the PCA. Here, we apply a local PCA model where the data is clustered into regions by using a SOM model at first and then the PCA is performed on the data of each region. The procedure is explained in the following.

A Pre-Clustering

SOM is shown to have desirable properties compared to classical clustering methods. It provides a natural measure for the distance of a vector from a cluster which is adaptive from the local statistics of the data [7]. The SOM forms a map corresponding to the data distribution so that regions of the map can be interpreted as clusters in the data space. The main key point is defining a set of codebook vectors \mathbf{m}_i , $i=1,2,\dots,m$ which represent units of the map. Then as for a given input \mathbf{x} , it is mapped to a unit associated to \mathbf{m}_c such that:

$$\|\mathbf{x} - \mathbf{m}_c\| = \min_i \{\|\mathbf{x} - \mathbf{m}_i\|\}$$

\mathbf{m}_i codebook vectors are updated through a training process iteratively as:

$$\mathbf{m}_i(t+1) = \mathbf{m}_i(t) + h_{ci}(t) [\mathbf{x}(t) - \mathbf{m}_i(t)]$$

where t indicates the iteration and h_{ci} is a neighborhood function taken as:

$$h_{ci} = \alpha(t) \cdot \exp(-d_{ci}^2 / 2r^2(t)).$$

Here, α and r are learning rate and neighborhood radius, respectively both decrease monotonically as a linear function of time. d_{ci} is the distance between \mathbf{m}_c and \mathbf{m}_i . We consider a 6x5 map size for clustering the preprocessed data and mapping the data of 24 classes onto 30 partitions. The initial radius for neighborhood is taken 10 and initial learning rate is taken 0.2.

B PCA Modeling

If \mathbf{x}_i is supposed to be an n -dimensional vector of a data set with $i=1,\dots,N$, then the goal of the PCA is to find r dimensional axes \mathbf{p}_i onto which the retained variance under projection is maximal. These axes are given by the eigenvectors associated with r largest eigenvalues of the covariance matrix of data as:

$$\Sigma \Phi = \Lambda \Phi$$

where $\Phi = [\mathbf{p}_1, \mathbf{p}_2, \dots, \mathbf{p}_r]$ is the eigenvectors matrix, Λ is the eigenvalue matrix as $\text{diag}\{\lambda_1, \lambda_2, \dots, \lambda_p\}$ with $\lambda_1 > \lambda_2 > \dots > \lambda_p$, and Σ is the covariance matrix which is defined as:

$$\Sigma = E[(\mathbf{x} - \boldsymbol{\mu})(\mathbf{x} - \boldsymbol{\mu})^T]$$

where $\boldsymbol{\mu} = E[\mathbf{x}]$ is the mean vector of data.

Then the transformed data vector \mathbf{y}_i is determined as:

$$\mathbf{y}_i = f(\mathbf{x}_i) = \Phi^T (\mathbf{x}_i - \boldsymbol{\mu})$$

which is a reduced r -dimensional representation of data vector \mathbf{x}_i .

But here considering the q local regions which have been already provided by SOM, we apply a sort of functions $f_i(\cdot)$ with $i=1,\dots,q$ instead of a single encoding function. As we consider the local regions small enough according to number of different classes, we expect an adequate representation of data within each region by using this local PCA algorithm. The procedure is taken place as follow:

For each cluster of data corresponding to each region of the SOM with the mean vector value of $\boldsymbol{\mu}_j$, the covariance matrix is estimated as:

$$\Sigma_j = \frac{1}{N_j} \sum_{\mathbf{x} \in S_j} (\mathbf{x} - \boldsymbol{\mu}_j)(\mathbf{x} - \boldsymbol{\mu}_j)^T$$

where N_j is the number of vectors lied in the cluster S_j . Then by determining the eigenvectors ($\mathbf{p}_{j1}, \dots, \mathbf{p}_{jr}$) of each matrix Σ_j , the function f_j and thereby the transformed vector \mathbf{y}_i can be obtained for each region as follow:

$$\mathbf{y}_i = f_j(\mathbf{x}_i) = [\mathbf{p}_{j1}, \dots, \mathbf{p}_{jr}]^T (\mathbf{x}_i - \boldsymbol{\mu}_j) \quad \mathbf{x}_i \in S_j$$

As explained in the following, in this paper the data dimension n is 180 and the r dimension is taken as 30. The number of regions q is taken as 30 according to SOM partitions as described in the following A.

Accordingly through application of the PCA over all partitions a new 30 dimensional data set is produced which contains the main features of 180 dimensional data.

Classification

Kohonen's LVQ is a supervised learning algorithm associated with the competitive network [7] which basically consists of an input layer and an output layer, and an array of weight vectors \mathbf{w}_i where w_{ij} denotes a connection weight between the j th node in the input layer and i th node in the output layer (Figure 1). Given a training data set X , each labeled with a class identifier, and a set M of codebooks vectors, the LVQ network adaptively modifies these codebooks so that they represent the class probability distribution in the training data set. This modification of codebooks consists of applying a "punishment" when a codebook is near a sample of a different class and "reward" when it is near a sample of its own class.

Since the LVQ network is beneficial in classification of data with large number of inputs and explanation of the misclassification, it is applied as the main classifier of present system. As we consider 6 kinds of US bills including 1, 5, 10, 20, 50, and 100 dollars and for each bill there exists 4 direction of inserting (Figure 2), totally 24 (i.e. 6x4) output categories are considered for the classifier. The system is trained by taking trial number of codebook vectors for each class looking for the best classification rate and maximum reliability. A total number of 120 codebook vectors (averagely 5 vectors per class) is experimentally found to be the best. The number of iterations for each training epoch is taken 10,000 while a linear function as $\alpha(t) = \alpha(0)(1.0 - t/T)$ is supposed for learning where T

is the number of iterations.. Therefore, the LVQ classifier has a number of 30 neurons (the number of extracted features) in the input layer and a number of 120 neurons in the output.

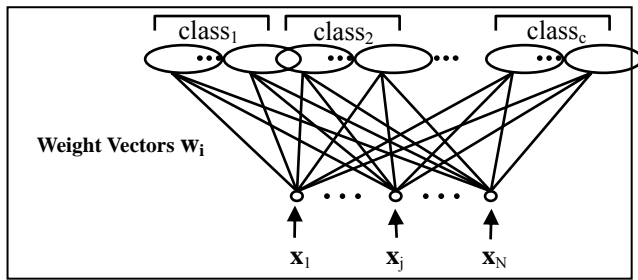


Figure 1 - A Schema of LVQ Network Structure

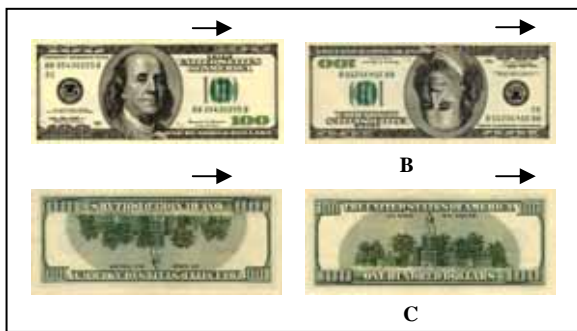


Figure 2 - Four Different Directions for Inserting a Bill

Reliability Evaluation

We propose a simple but effective algorithm for evaluating the classification reliability. After the LVQ classifier is trained and the codebook vectors are determined, the test data set is used to estimate the parameters of probability density function (pdf) supposing a Gaussian distribution around each codebook vector as:

$$p_i(\xi) = \sigma_i^{-1} (2\pi)^{-d/2} \exp\left(-(\xi - \mu_i)^2 / 2\sigma_i^2\right)$$

where ξ is the distance between data vector and codebook vector (i.e. $\|\mathbf{x}_i - \mathbf{m}_i\|$), μ_i and σ_i are the mean and variance in pdf of codebook vector i respectively, and d is the dimensionality of the feature vectors (here, 30). Assuming the Gaussian probability density function, the interval $[\mu_i - 4.5\sigma_i, \mu_i + 4.5\sigma_i]$ can be considered as an area that covers almost 100% of probabilities ($100 - 5.122 \times 10^{-5}$). For a given class of codebook vectors if the densities have no overlap within this interval with densities of other classes, the reliability for this class is supposed to be 100%, but in case that this interval is overlapped with other classes, the reliability can be calculated as:

$$RM = \sum_i^L \alpha_i \int_{\mu_i - 4.5\sigma_i}^{\theta} p_i(\xi) d\xi$$

where L is the number of codebooks within each class, α_i is a normalizing coefficient, ($\sum \alpha_i = 1, \alpha_i > 0$), and θ is the cross point of each pdf with the interval boundary of nearest density from another class (Figure 3).

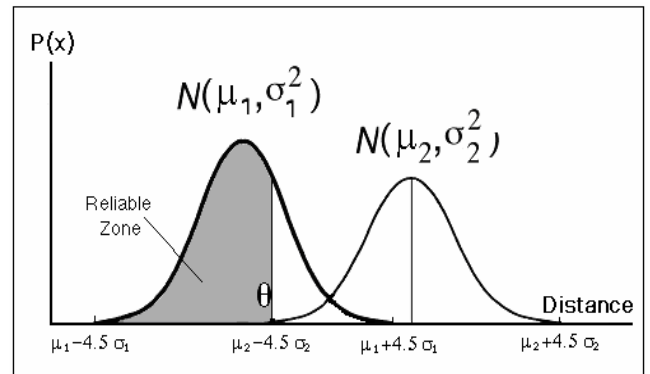


Figure 3 - The Overlap between Codebook Densities of Two Near Classes

Thus, the total reliability rate of the system finally can be determined by averaging these class reliability values.

Experimental Results and Discussion

A set of 2,400 sample data from 6 kinds of US dollar bills including 1, 5, 10, 20, 50, and 100 dollar and four directions for each bill (i.e. 100 samples for each direction), is used for learning the LVQ classifier. Also a number of 1,200 samples containing both normal data and slightly shifted data (to right and left) is taken for evaluating the system (that is 50 samples for each direction). The bills we used were of various levels of fatigue and made in different years. However, globally they can be considered as normal bills not frayed ones. The order of inputting data is quite random either in learning and testing phase. As for learning the LVQ classifier we have tried different number of codebook vectors from 3 to 10 per class looking for the best results.

On the other hand, concerning to local PCA application, we have tried different number of regions from 24 to 48 as the output of SOM to study its influence on the classification and reliability. The result of classification rate and reliability is shown in Table 1. The reliability is evaluated through the algorithm we have defined in the following. As it can be seen in Table 1 by increasing the number of codebook vectors in classifier as well as the number of regions in local PCA process, the reliability can be increased significantly. We have found that by taking a number of 120 codebook vectors in the LVQ classifier and 30 regions for the local PCA the reliability of system can be extended up to 100%.

Figure 4 indicates the relation between number of regions and reliability of system, clearly. As can be observed increasing the number of regions makes a significant increment in reliability value firstly but after some extend, the reliability is not influenced anymore by larger number of

regions and if the number of regions increases so much, it makes an inverse affect on the reliability.

Table 1 –The Classification Results and Reliability Test Data (The Number of PCA Components in all Cases Is 30)

No. of Codebooks	No. of Regions	Recog. Rate (%)	Reli. Rate (%)
60	1 (Standard PCA)	100	82.1
	12	100	90.1
	24	100	90.4
	30	100	94.6
	48	100	94.7
80	1	100	96.6
	12	100	97.5
	24	100	98.3
	30	100	98.4
	48	100	98.4
120	1	100	99.8
	12	100	99.98
	24	100	99.99
	30	100	100
	48	100	100
200	1	100	99.99
	12	100	99.99
	24	100	100
	30	100	100
	48	100	100

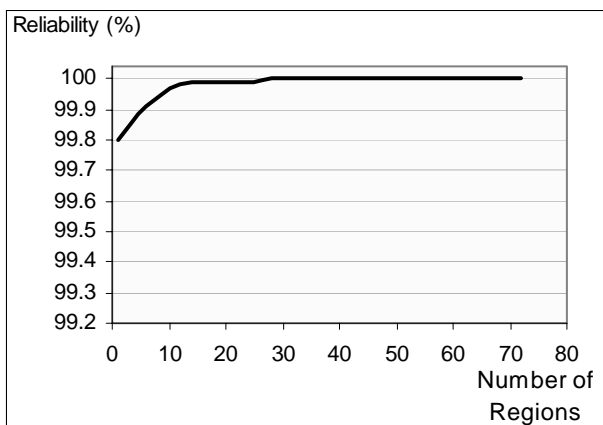


Figure 4 - The Relation between the System Reliability and Number of Regions in Local PCA

As we have used a test data set which contains shifting data, i.e., the data of bills with slightly shift to right or left at the inserting time, the high classification rate of system shows that the system is robust enough on shifting and sliding.

Conclusions

In this paper we have presented a local PCA approach for feature extraction of data in classification of bank note. The aim is to model the complexity of data and correlation between variables by using a simple linear model. The method first exploits a SOM model to cluster the data space into disjoints regions. Then a standard PCA model is applied in each region. The experimental results taken from 1,200 US dollar bills show that by taking a proper number of regions and also an optimized number of codebook vectors for LVQ classifier, the reliability of system can be increased up to 100%. Comparing to the conventional PCA method which was our pervious approach, the present method shows a significant growth in reliability rate. However, we have applied only US dollars for training and testing the system, it can be easily generalized for other kinds of bank note and considered as a multi-currency classifier with wide variety of data.

References

- [1] Takeda F and Omatu S (1993), Bank Note Recognition System Using Neural Network with Random Masks, Proceeding of the World Congress on Neural Networks, Portland, USA, Vol. 1, pp. 241-244
- [2] Teranishi M, Omatu S and Kosaka T (2000), Neuro-classifier of Currency Fatigue Level Based on Acoustic Cepstrum Patterns, Journal of Advanced Computational Intelligence, Vol. 4, No. 1, pp. 18-23
- [3] Tanaka M (1999), Modeling of Mixtures of Principal Component Analysis Model with Genetic Algorithm, Proc. 31st Int'l Symposium on Stochastic Systems Theory and Its Applications, Yokohama, Japan, pp. 157-162
- [4] Ahmadi A and Omatu S (2003), A High Reliability Method for Classification of Paper Currency Based on Neural Networks, Proceeding of The Eighth International Symposium on Artificial Life and Robotics (AROB 8th '03), Oita, Japan, Vol. 2, pp. 601-604
- [5] Kramer MA (1991), Non-linear Principal Components analysis Using Auto-associative Neural Networks," A.I.Ch.E Journal, Vol. 37, pp. 233-243
- [6] Kerschen G. and Golinval JC (2002), Non-linear Generalization of Principal Components Analysis: From A Global to Local Approach, Journal of Sound and Vibration , Vol. 254, No. 5, pp. 867-876
- [7] Haykin S (1999), Neural Networks, New Jersey: Prentice Hall

A New Concept of Flexible Organization for Distributed Robotized Systems

Peter Sapaty Anatoly Morozov

Institute of Mathematical Machines and Systems, National Academy of Sciences
Glushkova Ave 42, 03187 Kiev Ukraine
Tel: +380-44-5265023, Fax: +380-44-5266457
sapaty@immsp.kiev.ua

Robert Finkelstein

Robotic Technology Inc., 11424 Palatine Drive, Potomac Maryland 20854
Tel: 301-983-4194 Voice, Fax: 301-983-3921
RobertFinkelstein@compuserve.com

Masanori Sugisaka

Department of Electrical and Electronic Engineering, Oita University
700 Oaza Dannoharu 870-1192 Japan,
Tel: 097-554-7831, Fax: 097-554-7841
msugi@cc.oita-u.ac.jp

Dale Lambert

Fusion for Situation Awareness Initiative, Defence Science and Technology Organisation
PO Box 1500 Edinburgh South Australia 5111
Tel: (+61) 8 8259 7175, Fax: (+61) 8 8259 5589
Dale.Lambert@dsto.defence.gov.au

Abstract

The presented concept for management of distributed dynamic systems is based on installing in all system components of a universal intelligent module interpreting special high-level language, in which any centralized or distributed control can be expressed. The mission scenario in the language, starting from any interpreter, is collectively executed by their network. The interpreters perform appropriate operations in nodes, while passing other parts of the scenario, together with intermediate data, to other interpreters in a coordinated manner. This process covers the system at runtime and sets up distributed command and control infrastructures providing the overall integrity and goal orientation. The approach allows us to manage robotized systems in unpredictable and hostile environments, with possible failures of components. The language description and programming examples in it are provided.

Keywords: crisis management, cooperative engagement capability, ubiquitous command and control, distributed systems, high level language, mission scenario, interpretation network, robotized systems.

1 Introduction

In managing large systems, whether civil or military, we usually think of them as of something already existing, with proper expertise in parts (nodes) and relations between them. We also assume that there exists a sort of command and control infrastructure, usually hierarchical, covering all its

parts, through which any external orders to these systems are received and both internal and outside impacts realized. This infrastructure should also support the overall system stability and integrity and guide its internal behavior in accordance with the existing rules and local and global goals pursued.

But in complex environments, the system organization may be indiscriminately damaged at any moment of time, with skills vanished in nodes, relations broken, and infrastructures destroyed. To put the system back into life, we may need to restore its parts, as well as the whole, at runtime [1].

Moreover, quite different philosophies, supported by new technologies, to the organization of dynamic emergent systems may be needed. First of all, the power and universality of the traditional command and control (or C2) may be questioned, as this already takes place in the area of crisis and disaster response [2,3].

The C2 approach is based on the idea that the right way to manage disasters is through centralized control and hierarchies. But actual community crisis response networks, as indicated by reaction on the recent well known disasters, looked nothing like the military-like C2 hierarchies [2]. They consisted of loosely-coupled collections of individuals, groups, and organizations that continually changed, having permeable boundaries.

Rather than being organized according to the principles of command and control, disaster response activities were undertaken through a complex and varied set of organizational arrangements characterized by a high degree of emergence and improvisation. New

networks formed that blended the activities of existing organization with those of emergent groups, which dealt with local problems as they emerged, using the existing resources in novel ways. The decentralized multiorganizational responses appeared to be a major strength, rather than weakness, and a source of resilience. Centralization and hierarchy only slowed down and hampered response efforts.

In this paper, we propose to automate the process of runtime composition of dynamic distributed systems from dissimilar, possibly casual, elements and creation of any infrastructures covering them -- by shifting the overall system organization to a higher, semantic level with orientation on both manned and unmanned systems dedicated to operate in emergency situations.

First, we briefly describe the two well-known organizational approaches to distributed dynamic systems, namely, Cooperative Engagement Capability (CEC) and Ubiquitous Command and Control (UC2) [6-8]. We then reveal a technology, based on a higher-level control language, which can effectively support both CEC and UC2, as well as any other, especially crisis management, systems. Related programming examples will be presented too.

The previous applications of the technology presented include intelligent network management, distributed interactive simulation, distributed knowledge bases, group behavior, and support of robotized infrastructures [4, 5].

2 Basic Trends in Organization of Distributed Systems

We outline here the CEC and UC2 approaches, originally with military orientation, but with obvious significance to any systems with limited local resources but oriented on global problems. The first one provides global awareness to the distributed system in any its local node, and the second one allows us restructure the system's command and control at runtime, without loss of global functionality and goal orientation. CEC and UC2 actually complement each other, rather than compete, with UC2, however, being potentially a broader approach, covering the CEC capabilities as well.

2.1 Cooperative Engagement Capability

The Cooperative Engagement Capability [6] brings a new power to distributed systems, not by adding new sensor and impact components, but by distributing data from them in a significantly different manner. CEC fuses high quality tracking data from participating sensors and distributes it to all other participants in a filtered and combined state, using identical algorithms to create a single, common picture. CEC has a robust communications system with considerable improvement to bandwidth and countermeasures, as well as the advantages offered by the global positioning system. CEC's main components and functions are as follows.

The Data Distribution System provides line-of-sight (LOS) communication with other units. The Cooperative Engagement Processor provides processing of data received from other units and incorporates it with own platform data

to form a single composite data, forming the same picture on each unit. The Data Distribution Function provides real time data transfer in LOS and over-the-horizon. The Command/Display Support Function performs doctrine management and distribution, also group operations in defending against threats. The Sensor Cooperation Function provides increased detection and track performance by using composite track data from active sensors. The Engage Decision Function provides the capability for decisions to be made by an automated process based on doctrine entered by the Net Control Unit. The Engagement Execution Function supports the control process for impact of designated targets and responds to command directions and decisions.

2.2 Ubiquitous Command and Control

A Ubiquitous Command and Control system [7, 8] is a system of assets, all of which possess a similar C2 capability. UC2 systems represent devolution of decision making power from C2 centers to platforms which are designed to provide alternative functionality. Under this philosophy, command and control becomes an additional function performed in any manned or unmanned units, and ubiquitous C2 systems are so named because they advocate a C2 capability on every platform. Automation is the primary mechanism for acquiring a similar C2 capability in any unit, and some decision making can be fully automated. Other aspects will perform better with human interaction, with the choice between the two being mediated empirically.

The automated and human decision making are fully integrated, and this includes the option of allowing the machine to override or substitute the human. UC2 systems primarily endorse a distributed and decentralized management structure. It also introduces a command fusion problem, as each decision maker may fuse requests for its resources from multiple sources. In the information age, C2 centers may often become the prime targets for surgical impacts. In defending against the latter, one approach is to build duplicate C2 centers. Supporting this, UC2 also enables C2 functionality to reconfigure as necessary, offering greater sustainability, as well as quality of system performance, with graceful, rather than instantaneous, degradation.

3 Flexible Distributed Management Model

The distributed computation and control model and technology, previously known as WAVE [4] and WAVE-WP (or World Processing) [5], is based on a higher-level language describing parallel distributed solutions in computer networks as a single seamless spatial process rather than traditional collection and interaction of parts (agents). Communicating copies of the language interpreter (as universal control modules U in Fig. 1) should be installed in important system resources (like internet hosts, mobile robots, or mobile phones), which may be emergent. Parallel spatial scenarios written in the language can start from any

interpreter, covering the network at runtime, cooperating or competing with each other in the distributed space.

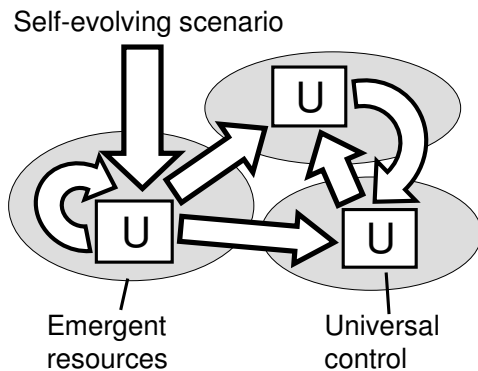


Figure 1. The universal control network.

The spreading scenarios can create dynamic knowledge infrastructures arbitrarily distributed between computers (robots). Subsequently or simultaneously navigated by same or other scenarios, these infrastructures can effectively support distributed databases, command and control, global situation awareness, parallel inference, and autonomous decisions. It is possible to operate in this seamless virtual world fully ignoring its physical distribution, whereas virtual networks can migrate (partially or as a whole) in physical networks while being processed. The distributed virtual world can optimize and guide movement and operations in the physical world, say, by robotic groups (armies).

The system mission in the language sets what the system should do in a distributed space rather than how to do this, which resources to use, or how C2 should be organized. The main burden on actual composition of the system, its internal organization, and runtime recovery is shifted to efficient distributed implementation of the scenario language. This allows us to continuously support the development of missions and global goal orientation regardless of the state of system resources, keeping the system operable if at least a single node remains functional. Any top down, bottom up and combined solutions are available within this spatial programming paradigm. The approach often provides hundreds of times application code reduction and simplification, allowing us to concentrate on efficient global solutions rather than implementation details.

4 Distributed Scenario Language

Let us symbolically call it within the current application context as Distributed Scenario Language (or DSL), whereas the earlier versions carried names WAVE [4], WAVE-WP [5], and WPL [9]. The DSL syntax in the most general form can be represented as follows:

```
wave → rule ( { move , } )
move → constant | variable | wave
variable → nodal | frontal | environmental
```

The program, or *wave*, is represented as one or more constructs called *moves*, which are separated by a comma and embraced altogether by another construct called *rule* (in

the functional style, using parentheses). The name “wave” reflects the general space navigation ideology of the approach, where the program code can cooperatively cover the distributed system in parallel wavelike steps. And similarly, “move” highlights the potential mobility of all language constructs.

Rules serve as various supervisory, regulatory, coordinating, integrating, navigating, and data processing functions, operations or constraints over moves, which, for example, may be:

- elementary arithmetic, string or logic operations on data returned by moves;
- hops in physical, virtual or combined spaces parameterized by moves;
- hierarchical fusion and return of (remote) data provided by moves;
- parallel and distributed control over the development of moves as programs, covering control flow of usual languages too;
- special contexts of navigation in space, for example, causing creation of different infrastructures by the evolving and spreading moves.
- sense of values expressed by moves, for their proper use by other rules.

Moves can represent values directly, as a *constant* or *variable*, or can recursively be arbitrary waves themselves. Variables can be classified as *nodal*, or stationary, associated with space positions and shared by different waves; *frontal*, moving in space with the program control; and *environmental*, accessing the navigated environment in the points reached. If control splits by parallel moves, each move receives independent copies of all frontal variables. Constants may reflect information or physical matter, the latter to be processed if proper physical equipment is available.

Wave is applied in a certain position of the distributed world, providing data processing and space navigation and transformation, eventually terminating in the same or in other positions (which may be multiple and remote). It provides final result that unites local results in the positions (or nodes) reached, and also produces a resultant control state. These two can be subsequently used for further data processing and decision making on higher program levels.

If moves are set to advance in space one after the other (defined by a proper rule), each new move is applied in parallel in all the nodes reached by the previous move, with the rest of the program also moving to the new locations (virtually or if needed, physically). Different or same moves (by other rules) can also apply independently from the same node, reaching new nodes asynchronously and in parallel.

The syntax shown above can represent any program in DSL, but if convenient, other notations can be used, like the infix one. For example, the program

```
advance (move1, move2, move3)
```

ordering three moves develop sequentially, each move

from the positions in space reached by the previous move, can be represented as:

```
move1. move2. move3
```

with the period indicating advancement in space. Similarly,

```
parallel (move1, move2, move3)
```

can be written as:

```
move1; move2; move3
```

with the semicolon setting independent and parallel development. As another example,

```
assign (R, multiply (sum (a, b, c), d))
```

can be substituted by:

```
R = (a + b + c) * d
```

For improving readability, spaces can be inserted in arbitrary places of the programs; they (as well as carriage returns) will be automatically removed (except when reside in strings in quotes) during the program interpretation. Also, it is often useful to show programs using indentations, with placing related opening and closing parentheses exactly one over the other.

More details about different constructs and their meanings can be obtained from the previous versions of the language [4, 5].

5 Parallel Language Interpretation

The peculiarities of the syntax and semantics of DSL allow us to provide its effective, fully distributed and parallel, interpretation without central resources. During this process, the spatial unwrapping and replication of the recursive program formula takes place, rather than its traditional reduction.

A DSL program covers and matches the physical or virtual world in parallel, establishing full control over the distributed space. Each operation is performed in the reached nodes on local data there (environmental, and in nodal variables), on what has been brought to these nodes in frontal variables with the program control, and on the obtained and returned results (possibly, remote) by subordinate waves.

The intermediate and final results of the work of DSL programs may be scattered throughout the whole navigated space; they may be grouped and returned into a certain point (or points) if this is needed. Different evolving parallel and distributed waves can cooperate or compete in the common, open, distributed space.

The DSL interpreter consists of a number of specialized modules working in parallel (like *parser*, *data processor*, *control processor*, and *communication processor*). These are handling and sharing specific data structures supporting persistent virtual worlds and temporary hierarchical control mechanisms, like *wave queue*, *incoming and outgoing queues*, local part of the *distributed knowledge network*, *track forest*, *nodal, environmental and frontal variables*, etc. [4, 5].

The interpreter may have its own physical body (say, in

the form of mobile or humanoid robot), or can be mounted on humans (e.g. in mobile phones). The whole network of the interpreters can be mobile and open, changing the number of nodes and communication structure between them, as robots or humans can move at runtime. The DSL operations may trigger a combination of data processing and physical movement in space, with exchange of information and physical matter between the interpreters both electronically and in a direct contact.

6 Dynamic Creation of Distributed Infrastructures

We will consider here simplified programs in DSL, which are creating different infrastructure topologies over the distributed, and possibly scattered, system nodes. The main feature of all these programs is that they can do the job in a fully distributed manner, by covering and flooding the dynamic and open system in parallel and cooperative mode, without any central resources.

These programs, as well as those in subsequent sections, have a quite different semantics than usual ones, as each their construct may work in other locations in space (and in other computers), not in the same as the previous ones. Despite this, all the programs constantly preserve full integrity and controllability as the whole, similar to traditional single-machine programs operating in the same memory. This possibility is effectively achieved by a powerful implicit distributed track system and also internal "command and control" infrastructures underlying the distributed DSL interpretation, see for previous versions at [4, 5].

6.1 Star

Starting in any node, the following program forms oriented links with name *star* to all other nodes that can be reached directly or indirectly (i.e. via other nodes) from the current node (as in Fig. 2).

```
Create links (+ 'star', other nodes)
```

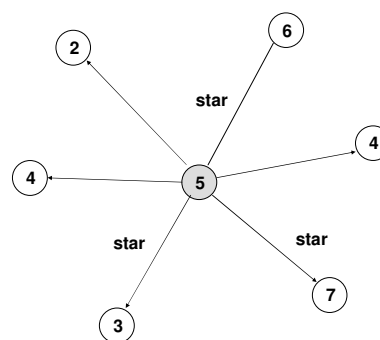


Figure 2. A star infrastructure.

6.2 Full Graph

Starting in any node too, the program below first hops to all directly or indirectly reachable nodes, including itself, and then from all the nodes reached forms a non-oriented link named *full* to all other nodes,

reached directly or indirectly too (see Fig. 3).

```
Hop (all nodes).
Create links (
  'full', other nodes (inferior)
)
```

To avoid duplicate links, the formation of a link between any two nodes takes place only in one way, allowing the superior node (or inferior, as another solution) to create the link (by comparing certain node's values, e.g. addresses).

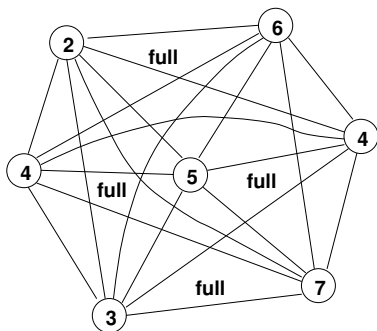


Figure 3. The full graph infrastructure.

6.3 Hierarchy

Starting from any node, the following program, in a repeated advancement in the distributed space, creates oriented links named `hierarchy` from the current nodes to new nodes reached. A new iteration (together with the whole program code) starts in parallel from all nodes reached by the previous iteration.

```
Repeat (
  Create links (
    + 'hierarchy', first come,
    range (20)
  )
)
```

To have the resultant network structured as a tree (with its root in the node the program started), the program allows entering nodes only once, on the first arrival into them. It also tries to establish the next level of hierarchy within certain vicinity (`range`) from the current nodes, to make this hierarchy optimized territorially.

This program, however, may not cover the whole system if the distance between nodes may exceed the range given. In this case, we may decide either to increase the range or select the descendent nodes of the hierarchy among any other nodes that can be reached, at any distance, also allowing us to have only a certain number of subordinate nodes for each node, as follows (see Fig. 4):

```
Repeat (
  Create links (
    + 'hierarchy', first come,
    other nodes, quantity (2)
  )
)
```

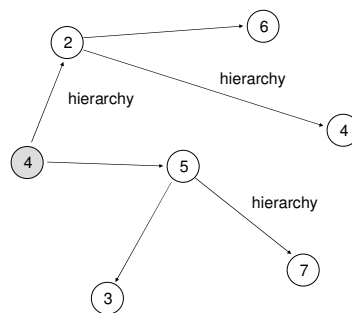


Figure 4. A hierarchical infrastructure.

We can also offer a combined solution where, first, subordinate nodes are tried to be chosen within the range given, and second, if this is not possible, among any nodes reached (directly or indirectly). We may also set up the maximum number of subordinate nodes allowed as the precondition for the both options, with the resultant program being as follows:

```
Repeat (
  Create links (
    + 'hierarchy', first come,
    Or (range (20), other nodes),
    quantity (2)
  )
)
```

Another solution, easily programmable too, may be where the range is floating, gradually increasing unless the needed number of subordinate nodes is found.

6.4 Line

Any other distributed topologies can be created in a similar way. For example, a line connecting all nodes can be just produced by the previous program by allowing only a single new node at each step (let it uses now non-oriented link `line`), as follows (see Fig. 5):

```
Repeat (
  Create links (
    'line', first come,
    Or (range (20), other nodes),
    quantity (1)
  )
)
```

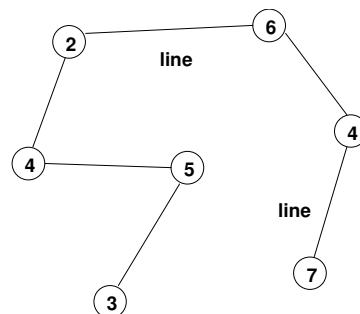


Figure 5. A line infrastructure.

6.5 Ring

With minimal extension, the previous program can create a ring, by connecting the last node of the line with its first node (also changing link names to `ring` and making them oriented), as follows, where the starting node address is always accessible by the special variable `START` (see Fig. 6):

```
Repeat (
  Create links (
    + 'ring', first come,
    Or (range (20), other nodes),
    Quantity (1)
  )
).
Create link (+ 'ring', START)
```

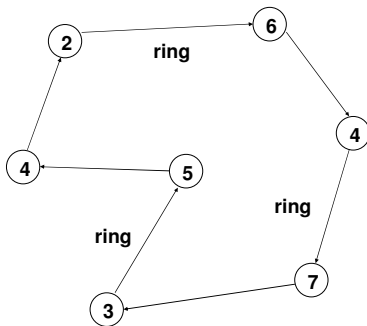


Figure 6. A ring infrastructure.

All these programs can work in a fully distributed way, without any central control, as already mentioned. All the infrastructures above can be built (and can exist) simultaneously between the same nodes, and any changes to them can be easily done at runtime, without interrupting local or global processes which may take place over them.

7 Hierarchical Command and Control

Using the infrastructures built above, we can organize any centralized or distributed system management and control in DSL. Let us show how traditional command and control can work via the hierarchical infrastructure, starting from its root node and using oriented links `hierarchy`. The following program applies recursive command and control procedure (enclosed in braces) in each reached node of the hierarchy, after being delivered there in frontal variable `C2`, as its content.

```
Frontal (C2, Command, Control, Level).
Assign (C2,
  {Increment (Level).
   Detail and apply (Command, Level);
   Detail and apply (Control, Level);
   (Hop (+ 'hierarchy'). Apply (C2))
  }
).
Assign (Command, command_scenario).
Assign (Control, control_scenario).
Apply (C2)
```

This procedure `C2`, in its turn, applies in parallel (which is indicated by semicolons, see Section 4) the command and

control scenarios given from the beginning in frontal variables `Command` and `Control` (these scenarios may be of human, robotic, or mixed orientation). `C2` also simultaneously passes them and itself for a recursive activation and execution in all directly subordinate nodes of the hierarchy, which will be acting in the same way, and so on. At each level of hierarchy (incremented downwards), the original command and control scenarios are detailed for their execution with taking into account peculiarities of this level, as shown in Fig. 7.

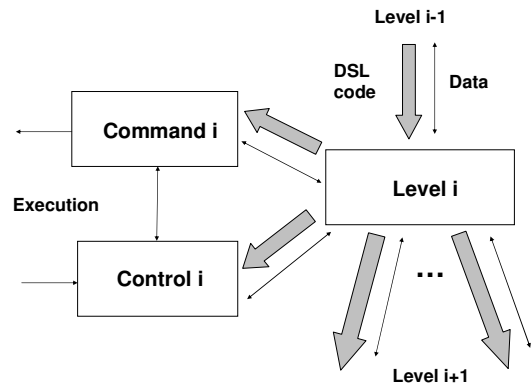


Figure 7. The C2 interpretation in nodes.

The scenarios delivered to, and activated in, nodes can be written in DSL in such a way that could be capable of accessing and sharing data and operations in any nodes of the whole hierarchy, not only in the current one, therefore the organization in Fig. 7 can potentially be much more advanced and flexible than the strictly hierarchical command and control. The program above reflects only a possible organizational skeleton, or framework, that can be set up in DSL.

This program works on the already existing hierarchical infrastructure, where it starts from the root and then covers with activity the whole infrastructure at runtime, beginning to work during, rather than after, being deployed. We can modify this program to be capable of creating the very infrastructure it operates on, during its coverage, not before. We can also form a temporary hierarchy without explicit links (based on internal, invisible interpretation infrastructures) and for the current mission only, with its automatic self-removal after the mission is completed. This latter case can be represented by the following modified program.

```
Frontal (C2, Command, Control, Level).
Assign (C2,
  {Increment (Level).
   Detail and apply (Command, level);
   Detail and apply (Control, Level);
   (Hop (first come, range (20)).
    Apply (C2))
  }
).
Assign (Command, command_scenario).
Assign (Control, control_scenario).
Apply (C2)
```

This program absorbs mechanisms of the hierarchy-creation programs discussed earlier, with their spatial

repetition effectively expressed now by spatial recursion.

8 Collection and Distribution of Targets

8.1 Using Hierarchical Infrastructure

We can write a spatial program in DSL which self-spreads from the root node to all other nodes of the hierarchical infrastructure, picks up data on all objects (targets) seen in all nodes passed and reached, and merges and fuses all this data while echoing upwards the hierarchy. The data fusion may include removal of duplicate records, as the same targets can be seen from different nodes simultaneously.

Having collected in the root node all targets detected by a distributed system, we can replicate and spread their refined list back to all nodes of the hierarchy by the parallel self-descending process again, allowing each node to select individually targets of interest from their list and impact those it can. All these operations can be performed on the hierarchical infrastructure by the following simple program, which globally loops in the root node, while repeating the detection-collection-fusion, followed by distribution-selection-impact indefinitely (as shown in Fig. 8).

```

Loop (
  Assign (frontal (Seen),
    Fuse (
      Repeat (
        Free (detect (targets));
        Hop (+ 'hierarchy')
      )
    )
  ).
  Repeat (
    Free (select and impact (Seen));
    Hop (+ 'hierarchy')
  )
)

```

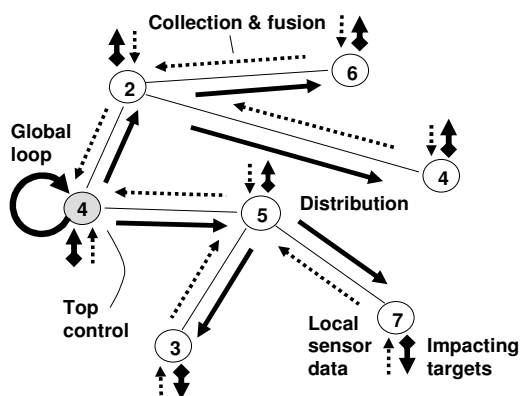


Figure 8. Hierarchical collection and distribution of targets.

8.2 Using Any Infrastructure

Many other efficient solutions of collection and distribution of targets detected by a distributed system can be proposed in DSL. One of them, the most universal and simple, is a fully distributed one, with using any available infrastructure (including the ones we have built before like

star, tree, line, ring or their combinations). The idea is in the following.

Each node, fusing what it directly sees with what it gets from other nodes, regularly exchanges all information it accumulates with direct infrastructure neighbors only, updating the records in them if the targets brought are fresher or new. With all nodes doing this in an infinite local loop, the information about all targets seen by all nodes of the distributed system will be eventually reaching all its nodes (of course, if the system is connected in principle), thus guaranteeing global awareness in each node. The following simple program implements this distributed algorithm, additionally setting certain time delay between the iterations in each node (see also Fig. 9).

```

Nodal (Seen).
Hop (all nodes).
Loop (
  Wait (60).
  Fuse and assign (
    Seen, detect (targets)
  ).
  Select and impact (Seen);
  Fuse and assign (
    (Hop (all links). Seen), Seen
  )
)

```

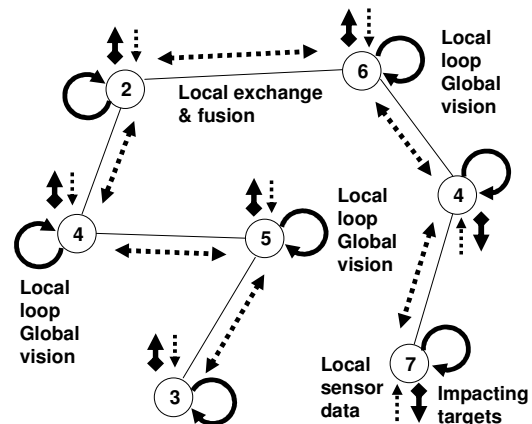


Figure 9. Fully distributed global vision.

This fully distributed algorithm can work well also without any infrastructures built in advance, by merely regularly accessing from all nodes any other nodes in their vicinity (say, within available or given radio or laser range, and not necessarily same neighbors each time, as nodes can move), by substituting the line with the hop by the following one:

```

(Hop (range (100)). Seen), Seen

```

These were only the simplest programming examples of dynamic, on the fly, creation of distributed infrastructures and using them for emergent command and control and global vision and targeting. More complex ones can be effectively written too, without any limitations on centralization or, vice versa, distribution of activities (and any their combinations) in distributed systems, with program code optimally staying in nodes or moving between them, cooperatively covering the whole system or its parts with activities needed. And all

this (re)organization can be implemented at runtime, on the active and operating system, which is especially important in crisis situations, where improvisation and flexibility of dealing with emergent resources are the qualities of primary values.

9 Conclusions

A new approach to organization of distributed dynamic systems has been presented which, as was shown, can effectively support and implement basic trends of organization of distributed systems with limited local resources but capable of solving complex global problems. Among these trends are the well known Cooperative Engagement Capability and Ubiquitous Command and Control. Using our approach, the CEC and UC2 systems will also be able to function under indiscriminate damages of their components and infrastructures, while preserving functionality and goal orientation.

The approach presented is based on a special language describing mission scenarios on a semantic level while delegating usual programming routines to automatic interpretation. Communicating interpreters of the language can be installed in internet hosts, mobile robots and cellular phones, integrating any manned and unmanned resources under a unified control. Being both high level and fully formal, the approach may open a real way to a massive use of mobile robotics in advanced crisis relief missions, where job division and subordination between humans and robots may be emergent. Its advantages for robotized crisis management applications may include the following:

- It drastically simplifies the overall control of multi-robot systems, making it comparable to the control of a single robot, regardless of the number of robotic platforms used, which can vary at runtime.
- Does not need any central resources as its global control can start from any available manned or unmanned unit and cover the system at runtime.
- Allows robotized systems to be designed and implemented from the topmost, linguistic, level with considerable reduction of the time and funds needed in comparison with usual bottom up integration.

The previous, or WAVE, version of the technology has been written in C under Unix, and is being used in different countries, especially for intelligent network management, with recent results in Ireland [10, 11] and Canada [12]. The WAVE system is available on the Internet, and can be downloaded, say, from [13]. The current version of the language is in patenting and reimplementation process; it can be installed on any platform within a short time. The universal wave chip, as hardware language interpreter for distributed crisis management systems, is being planned too.

References

- [1] P. Sapaty, M. Sugisaka, R. Finkelstein, J. Delgado-Frias, N. Mirenkov, "Advanced IT Support of Crisis Relief Missions", Journal of Emergency Management, Vol.4, No.4, ISSN 1543-5865, July/August 2006, USA,

pp.29-36 (www.emergencyjournal.com).

- [2] K. Tierney, "Disaster Beliefs and Institutional Interests: Recycling Disaster Myths in the Aftermath of 9-11", Terrorism and Disaster: New Threats, New Ideas, Research in Social Problems and Public Policy, Volume 11, 33—51, 2003 Published by Elsevier Ltd., JSSN: 0196-11 52.
- [3] K. Tierney, C. Bevc, and E. Kulikovski, "Metaphors Matter: Disaster Myths, Media Frames, and Their Consequences in Hurricane Katrina", The Annals of the American Academy, AAPSS, 604, March 2006, pp. 57-81.
- [4] P. S. Sapaty, Mobile Processing in Distributed and Open Environments, John Wiley & Sons, ISBN: 0471195723, New York, February 1999, 436 p. (www.amazon.com).
- [5] P. S. Sapaty, Ruling Distributed Dynamic Worlds, John Wiley & Sons, New York, May 2005, 256p, ISBN 0-471-65575-9 (www.amazon.com).
- [6] The Cooperative Engagement Capability, John Hopkins APL Technical Digest, Vol. 16, No. 4, 1995.
<http://www.jhuapl.edu/techdigest/td1604/APLteam.pdf>.
- [7] Lambert, D.A. (1999a), "Ubiquitous Command and Control", Proceedings of the 1999 Information, Decision and Control Conference, Adelaide, Australia, pp. 35-40, IEEE.
http://www.eleceng.adelaide.edu.au/ieee/idc99/papers/lambert_dale_2.pdf.
- [8] Lambert, D.A, and Scholz, J.B. (2005), "A Dialectic for Network Centric Warfare", Proceedings of the International Command and Control Research and Technology Symposium (ICCRTS).
<http://www.dodccrp.org/events/2005/10th/CD/papers/016.pdf>.
- [9] P. Sapaty, "Crisis Management with Distributed Processing Technology", International Transactions on Systems Science and Applications, vol. 1, no. 1, 2006, UK, pp. 81-92, ISSN 1751-1461 (<http://www.xiaglow-institute.org.uk/itssa/itssa.htm>).
- [10] S. Dragos and M. Collier, "Macro-routing: a new hierarchical routing protocol", Proc. 47th annual IEEE Global Telecommunications Conference, Texas, USA.
- [11] Sanda-Maria Dragos, "Scalable QoS Routing in MPLS Networks Using Mobile Code", PhD Dissertation, School of Electronic Engineering, Dublin City University, July 2006, 235p.
- [12] Gonzalez-Valenzuela, S. and Leung, V.C.M, "QoS-Routing for MPLS Networks Employing Mobile Agents". IEEE Network Magazine, Special Issue, May-June 2002.
- [13] Wave system public domain in Canada: <http://www.ece.ubc.ca/~sergiog/wavefiles/>.

Skill-Based Manipulation and Error Recovery in Maintenance Tasks

Akira Nakamura and Kosei Kitagaki

Intelligent Systems Research Institute
National Institute of Advanced Industrial Science and Technology (AIST)
Central 2, 1-1-1 Umezono, Tsukuba, Ibaraki, 305-8568 Japan
a-nakamura@aist.go.jp, k.kitagaki@aist.go.jp

Abstract

Dexterous manipulation is an important function for working robots. Manipulator tasks such as assembly and disassembly can generally be divided into several motion primitives. We call these "skills" and explain how most manipulator tasks can be composed of skill sequences. We are currently planning to construct a maintenance robot for household electrical appliances. Skill techniques are effective when a robot needs to achieve high-accuracy results. However, since failure also occurs easily, it is important to implement error recovery technology. Various errors are classified and a new type of error recovery processing is presented in this paper.

Key words: manipulation skill, planning, modeling, visual sensing, error recovery

1. Introduction

To be useful in several fields, manipulation robots need to achieve various tasks using special techniques. We analyzed human motions in such tasks as assembly and disassembly and found that movements consisted of several significant motion primitives. We call these "skills" and have demonstrated that most tasks of a manipulator can be composed of sequences of skills [1]–[6]. We demonstrated that robots can perform various human tasks by using this concept of skills. Skill level control is positioned in the hierarchy of manipulator control between task level control and servo level control. Programmers can describe a task program easily as a sequence of these skills without taking into account servo level control. Skills in which the contact states vary during assembly and disassembly tasks are particularly significant. We considered three important fundamental skills for these tasks: "move-to-touch," "rotate-to-level" and "rotate-to-insert."

We have researched maintenance robots working in various plants, such as a nuclear power plant, and considered the skill technique used by such robots. As a target for future research, we will consider manipulation

robots used for the maintenance of such items as household electrical appliances, furniture and stationery. At present, we are working to produce a prototype of a maintenance robot for system components and personal computers (Fig. 1). Recent recycling and environmental problems will increase the need for robots that perform repair and inspection. The robots open and close the equipment enclosures and replace parts (Fig. 2). It is thus necessary for these robots to be able to perform tasks requiring high accuracy, such as loosening a screw using a screwdriver.

Manipulation tasks with skills are performed by the sequences of visual sensing, geometric modeling, planning and execution. In actual manipulation, however, errors often occur for various reasons and the processes are interrupted. Failure causes can be divided into several kinds of errors such as execution errors, planning errors, modeling errors and sensing errors. Various approaches for error recovery have been studied [7]–[10]. However, few realistic methods for error recovery have been proposed for various errors that might occur when performing maintenance tasks. We have grouped the errors into several classes according to potential causes. If an error occurs, the parameters of planning, modeling or sensing are corrected by specifying the class and then the task process is performed again. We propose a method of error recovery that uses the concept of error classification. This method allows the flow of system processes,

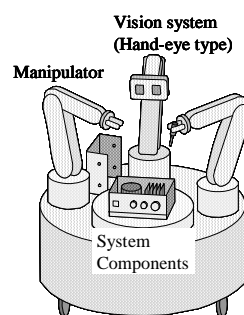


Fig. 1 Maintenance robot for system components

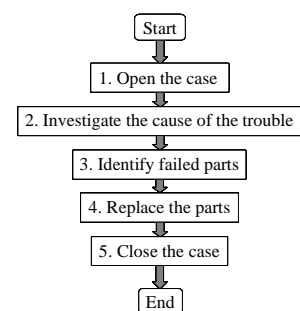


Fig. 2 Maintenance procedure

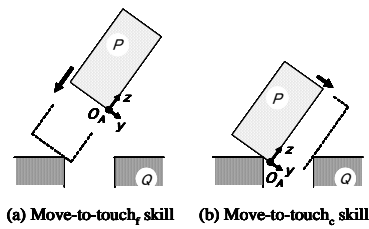


Fig. 3 Move-to-touch skills

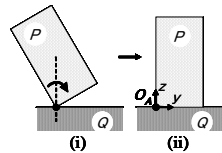


Fig. 4 Rotate-to-level skill

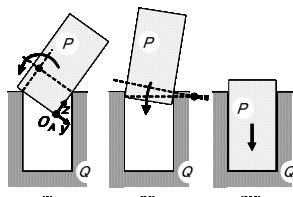


Fig. 5 Rotate-to-insert skill

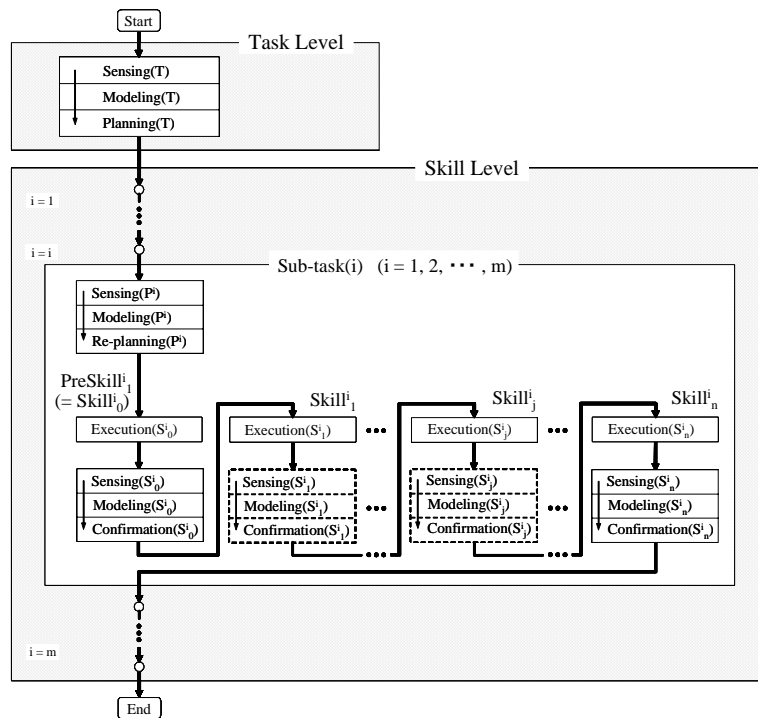


Fig. 6 Process flow

including error recovery, to be derived easily and systematically. In this paper, we explain the concept of manipulation skills and skill-based processes for maintenance, and we propose systematic classification of errors and recovery from such errors.

The next section explains manipulation skills and the composition of skill sequences. The processes of visual sensing, geometric modeling, planning and execution are then explained for task and skill levels in section 3. A maintenance robot must first of all open the case of a household appliance by loosening screws. Additional skills used in the loosening task are explained in section 4. The classification of errors and error recovery to improve the success of task achievement are shown in sections 5 and 6, respectively.

2. Manipulation Skills

This section explains our concept of skills. See References [1]–[3] for more details.

In assembly and disassembly tasks, the skills in which contact states vary are particularly significant. In References [4], [6], we considered three skills, "move-to-touch," "rotate-to-level" and "rotate-to-insert," all of which play an important part in such tasks.

(1) Move-to-touch Skill: The move-to-touch skill is defined as the transition of a grasped object P in a constant direction that continues until contact with another object Q occurs (Fig. 3).

(2) Rotate-to-level Skill: This skill is defined as the rotation around either a contact point or a contact edge to

align the face of the grasped object P with the face of another object Q (Fig. 4).

(3) Rotate-to-insert Skill: This skill is the motion of rotating the object P obliquely into the hole in another object Q to insert it accurately (Fig. 5).

A specific task is composed of sequences of skill primitives such as these move-to-touch, rotate-to-level and rotate-to-insert skills. The skill sequences can be decided by several methods. We have already presented a method using variations of the number of contact points in skill primitives [4].

3. Process of Sensing, Modeling, Planning and Execution

The procedures for sensing, modeling, planning and execution are shown in Fig. 6. In this scheme, the planning of the task level is first performed, and then the executions of the skill level are performed according to the sequences derived from the task planning. See References [5] for more details. In the following descriptions, we assume that an error does not occur in each component.

(Step 1) Task Level

At the task level, the skill sequence composing a given task is decided. First, visual sensing of the working environment of the robot is performed using a vision system and modeling is done. Next, planning follows, and skill command sequences and the initial position and orientation of an object to be grasped and manipulated are derived.

(Step 2) Skill Level

At the skill level, each *Sub-task*(i) ($i=1, \dots, m$) is performed successively and each skill $Skill_j^i$ ($j=1, \dots, n$) in *Sub-task*(i) ($i=1, \dots, m$) is executed successively. Before this sequence in each *Sub-task*(i) ($i=1, \dots, m$) is performed, the transition of the grasped object P to the initial state is completed. We represent the transition as $PreSkill_j^i$ ($= Skill_0^i$) ($i=1, \dots, m$).

4. Task of Loosening a Screw

We considered three fundamental skills in section 2. However, we will also consider several skills used in the task of loosening a screw. Let us consider loosening a Phillips screw using a Phillips screwdriver.

(4) Rotate-to-bite Skill: This skill is a rotation around the axis of the screwdriver to fit the tip of the screwdriver into the flutes of the screw head (Fig. 7). This skill is performed with pushing force.

(5) Rotate-to-loosen Skill: This skill is defined as an initial rotation to loosen the fixed screw (Fig. 8). This is performed by matching the axes of rotation of a part and a tool.

(6) Rotate-to-extract Skill: This skill is defined as the rotation of the screw to pull the screw out. The skill continues after the rotate-to-loosen skill.

We will consider the task of loosening a screw using a screwdriver [5]. We assume that the task of loosening a screw using a screwdriver is composed of the following skills (Fig. 9); $Skill_1$: Move-to-touch skill, $Skill_2$: Rotate-to-bite skill, $Skill_3$: Rotate-to-(loosen / extract) skill (without interruption).

5. Classification of Errors

In the processing flow described in section 3, the possibility of errors was ignored since it was assumed that all the components were operating under ideal conditions. However, errors could actually occur for various reasons. Whether an error has occurred or not is judged at $Confirmation(S_j^i)$ in each skill of the procedure flow. In the task of opening the outside case of an electrical appliance for maintenance, errors are classified as follows.

(1) Execution error

This is an error caused in the manipulator mechanism such as a backlash of a manipulator gear. There are many possible failures for a manipulator with bad accuracy, and this includes failures occurring stochastically.

(2) Planning error

This is an error caused by inaccurate parameter values in planning. For instance, when a control uncertainty cone is used for the fine motion planning of the manipulator, an error occurs due to an incorrect angle at the top of the

cone.

(3) Modeling error

This is an error caused by a difference in the real object and geometric model in the computer software being used, such as CAD modeling software. This might be caused by, for example, a difference in the size, a polygonal approximation and an expression of rounding and chamfering of an edge.

(4) Sensing error

This is an error occurring during visual sensing. For example, possible causes might be occlusion, imperfect calibration or undesirable lighting conditions.

6. Error Recovery

A process flow that takes error recovery into account is shown in Fig. 10. At the step of $Confirmation(S_j^i)$ in each skill primitive, whether the result is correct or a failure is judged by an automatic process or by an operator. Error recovery is performed using the following error classification.

(1) Class 1: The sub-task(i) is executed again without correcting the parameter when it is judged to be an execution error.

(2) Class 2: The sub-task(i) is executed again with change of planning parameter when it is judged to be a planning error.

(3) Class 3: The sub-task(i) is executed again with change of modeling parameter when it is judged to be a modeling error.

(4) Class 4: The sub-task(i) is executed again with change of sensing parameter when it is judged to be a sensing error.

(5) Class 5: The process being executed is interrupted when it is judged to be required by several changes, and the process returns to the start of the task.

7. Conclusions

It is necessary to increase the reliability of maintenance robots that work on household appliances since most of the tasks have to be performed in high-precision environments. Therefore, error recovery is important. We have demonstrated a new processing flow for recovery from errors of various causes in skill-based manipulation tasks. We have expressed the procedure for error recovery systematically by taking into account the classification of errors.

In the future, we will further study optimum adjustment methods for error recovery parameters and a fully automatic confirmation method of skill achievement. We will attempt to apply our method to real maintenance robots.

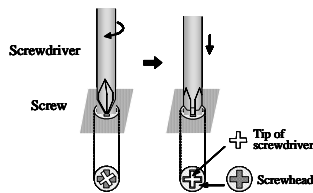


Fig. 7 Rotate-to-bite skill

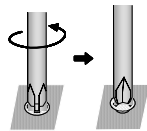


Fig. 8 Rotate-to-loosen skill

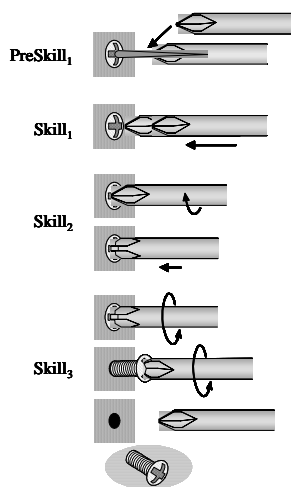


Fig. 9 Skill sequence of loosening with a Phillips screwdriver

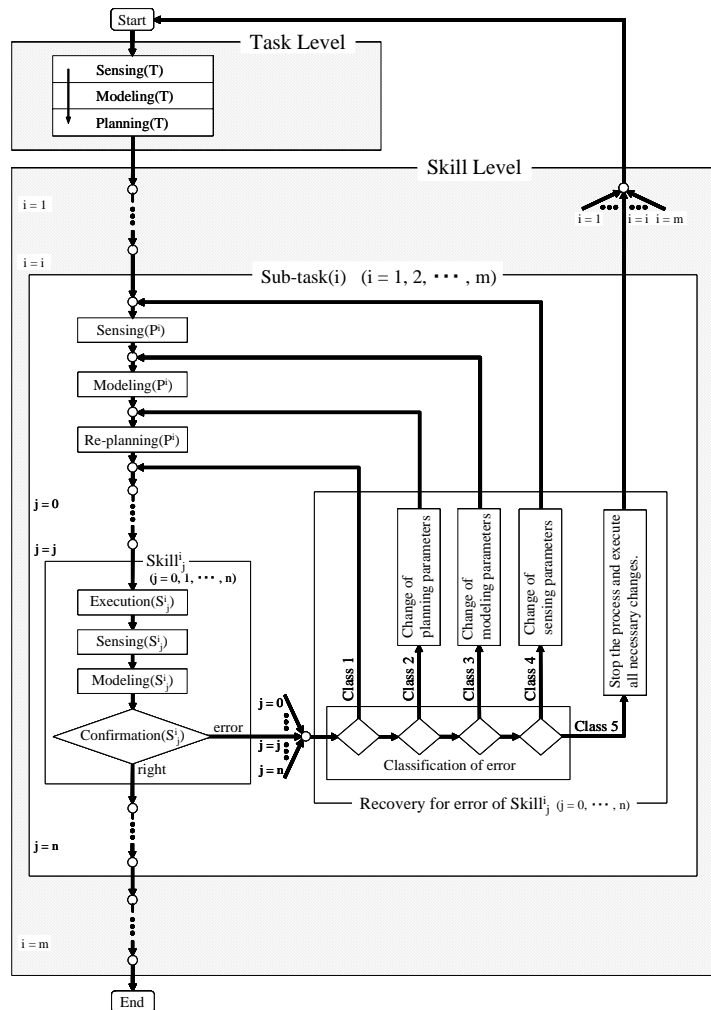


Fig. 10 Process flow with error recovery

Acknowledgment

A part of this study was financially supported by the Budget for Nuclear Research of the Ministry of Education, Culture, Sports, Science and technology, based on the screening and counseling by the Atomic Energy Commission.

References

- [1] Hasegawa T, Suehiro T, Ogasawara T, Matsui T, Kitagaki K, Takase K (1990), An integrated tele-robotics system with a geometric environment model and manipulation skills. In: Gotoh T, Kato I, Paul RP (eds) Proceedings of the IEEE International Workshop on Intelligent Robots and Systems (IROS '90), Tsuchiura, Japan, July 3-6, 1990, pp.335-341
- [2] Suehiro T, Takase K (1990), Skill based manipulation system (in Japanese). J Robotics Soc Jpn 8:551-562
- [3] Hasegawa T, Suehiro T, Takase K (1992), A model-based manipulation system with skill-based execution. IEEE Trans Robotics Autom 8(5):535-544
- [4] Nakamura A, Ogasawara T, Suehiro T, Tsukune H (1996), Skill-based backprojection for fine motion planning. In: Asada M, Arai T, Kak A, Sandini G (eds) Proceedings of the

IEEE/RSJ International Conference on Intelligent Robots and Systems (IROS '96), Osaka, Japan, Nov 4-8, 1996, pp.526-533

- [5] Nakamura A, Ogasawara T, Kitagaki K, Suehiro T (2001), Using robust and simplified geometric models in skill-based manipulation. In: Tarn T J, Burdick J, Papanikolopoulos N (eds) Proceedings of the IEEE/RSJ International Conference on Intelligent Robots and Systems (IROS 2001), Hawaii, USA, Oct 29-Nov 3, 2001, pp.138-145
- [6] Nakamura A, Ogasawara T, Suehiro T, Tsukune H (1998), Fine motion strategy in three-dimensional space using skill-based backprojection. Artificial Life and Robotics 2(3):134-137
- [7] Donald BR (1989), Error detection and recovery in robotics. Springer-Verlag, Berlin Heidelberg New York, pp.1-256
- [8] Evans EZ, Lee CSG (1994), Automatic generation of error recovery knowledge through learned reactivity. In: Gruver WA, Stephanou HE (eds) Proceedings of the IEEE International Conference on Robotics and Automation (IRCA '94), California, USA, May 8-13, 1994, pp.2915-2920
- [9] Xue G, Fukuda T, Asama H (1995), Error recovery in the assembly of a self-organizing manipulator by using active visual and force sensing. Autonomous Robots 1(2):179-186
- [10] Moon CW, Lee BH (2001), A model-based error recovery scheme for a multi-robot system. Robotica 19(4): 371-380

Information Display System using Active Projector in Intelligent Space -Integration of distributed devices based on RT-Middleware

Yoshihisa TOSHIMA

Dept. of Electrical Engineering
The University of Tokyo
4-6-1 Komaba, Meguro-ku, Tokyo
153-8505 JAPAN
toshima@hlab.iis.u-tokyo.ac.jp

Noriaki ANDO

Intelligent Systems Research Institute
Advanced Industrial Science and Technology
Tsukuba Central 2, 1-1-1 Umezono,
Tsukuba, Ibaraki 305-8568 JAPAN
n-ando@aist.go.jp

Hideki HASHIMOTO

Institute of Industrial Science
The University of Tokyo
4-6-1 Komaba, Meguro-ku, Tokyo
153-8505 JAPAN
hashimoto@iis.u-tokyo.ac.jp

Abstract

This paper presents information display system using active projector in Intelligent Space. Intelligent Space has distributed sensors for observing and actuators for acting in the space, in order to provide various services to human. Proposed Information display support in Intelligent Space has realized providing interactive information based on the human movement using active projector, which is installed in this space.

To make the environment space or several applications easily to be applicable with our active projector system, RT-Middleware is used (AIST, Japan) due to its features in flexibility and expansion of the system in the future.

First, Information display system using active projector in Intelligent Space and its implementation configuration are introduced. Next, the solutions of issues on active projection are described. Finally, the system design of Intelligent Space based on RT-Middleware is discussed.

Key Words: Intelligent Space, RT Middleware, Active P rojector, Information display

1 Introduction

This paper presents information display system using active projector in Intelligent Space. Intelligent Space is an environmental system realized by cooperation of Robot technology (RT) elements such as robots, sensors or actuators inside a space (room, corridor or street) and has distributed sensors for observing and actuators for acting in the space, in order to provide various services to human [1]. The purpose of proposed information display system is to provide informative support and has realized providing interactive information based on the human movement using active projector, which is installed in this space.

The concept of information display system in Intelligent Space is shown in Fig. 1. On observation of Intelligent Space, the space can obtain human movement as user information, and the space can obtain object information (embedded information in the space) such as the position of bookshelf, the direction of emergency exit or their contents as spatial or environmental information. By using those information,

active projector provides interactive informative services based on human movement.

Active projector is located on pan-tilt stand, which is able to project toward any position. Also it is network based and micro-controller embedded [2].

By utilizing the interactive information, many applications can be realized, for example, walking path guidance, the sign or mark illustration in the public space or private space in daily life.

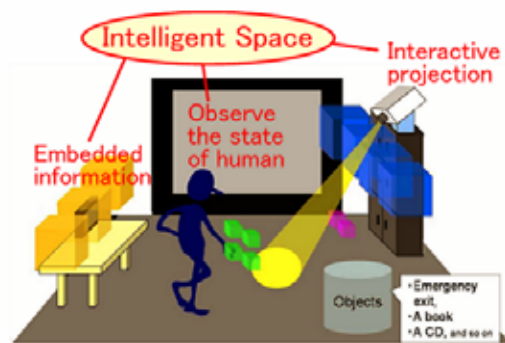


Fig. 1 Information Display System in Intelligent Space.

2 Information display system based on RT-Middleware

2.1 RT-Middleware based system

In the case of the environmental system such as Intelligent Space, the system tends to be large-scale and complex and it is one of the essential problems. Intelligent Space desires more flexible and more expandable system to correspond the change of the environment or scenario because we assume various spaces as Intelligent Space. So the system requires easy integration and cooperation with RT devices and simple addition, modification or deletion of devices and functions. RT-Middleware supports new framework to make composite components for RT-Component [3]. In the other words, RT-Component becomes robot technology module which has common input/output channels. Therefore, by making and preparing RT-Components for sensors, actuators or applications, and connecting those RT-Components, we can integrate flexible system.

RT-Component-Lite[4] is a Component for small devices as micro controller and active projector, we developed, is embedded RT-Component-Lite for expansion of application into daily life.

2.2 Configuration of hardware

The configuration of information display system is shown in Fig. 2. In this system, ultrasound 3D location system ZPS (Furukawa Co.) is used for human positioning. ZPS consists of ultrasound receivers and transmitters. A lot of receivers are installed on ceiling and two transmitters (tags) are held on user's neck and hand. User information is given as position and direction of user by calculation vector of its two tags.

This user information is sent to active projector through RT-Middleware installed in PC. OpenRTM-aist (AIST, Japan) is used as RT-Middleware. Finally, active projector realizes projection according to applications.

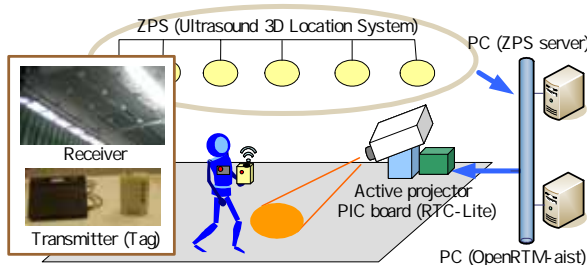


Fig. 2 Configuration of information display system.

2.3 System architecture using RT-Components

The system architecture based on RT-Middleware is shown in Fig. 3. The system is built up with the combination of RT-Component and consists of three component parts. Sensing Components obtain user information. ZPSOut2 Component receives two tags position data from ZPS server. HumanState Component calculates position and direction of the user by two tags position and sends user information to Application Components.

Next, Application Components decides reference for active projector and calculates image filename and characteristics of an image (projection target, image size, image direction) according to the application. By preparing Application Components and switching the connection of Components, various applications could be realized.

Finally, Device Components control the projected image generation and the pan-tilt drive according to the request. Image Projection Component outputs projected image according to image source, image size and direction. MovePConverter Component converts pan-tilt angle from reference target position by this coordinate transformation equation. RTUnitCtrl Component is connected with RT Component-Lite through the control panel so that we could control active

projector.

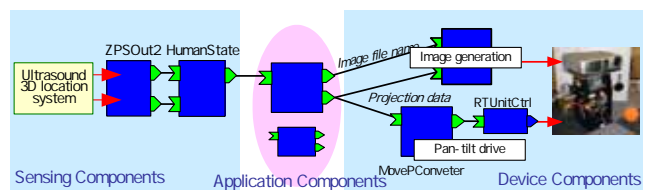


Fig. 3 System architecture based on RT-Middleware.

3 Solutions of Issues by using Active Projector

3.1 Occlusion Avoidance

When projection light is obstructed by human or objects, projection occlusion prevents providing correct information. Therefore to avoid occlusion problem, the system modifies projected position. In this system, occlusion avoidance method is built up as one RT-Component and is connected between Application Components and Device Components. The developed Component receives projection data and user information and sends modified projection data by occlusion avoidance method (see Fig. 3).

Proposed occlusion avoidance method is divided into two steps: detection and avoidance.

1) Occlusion detection

Occlusion occurs when human enter into the area where human himself obstruct the projection. Therefore, by creating occlusion area and human model and judging the overlap between those each other, occlusion can be detected. In Fig. 4, geometrical image of active projection is shown. The below figure is overhead view of upper figure and the figure is transformed into 2D. Occlusion area is projection light and the shape is corn. But when the projection is projected over human's body, occlusion does not occur. In the other word, occlusion occurs in the area under the human's height. Hence, Human model can be assumed as a circle and by estimation the margin, occlusion area can be assumed as a sector on 2D. Finally, we judge the overlap between those 2D models.

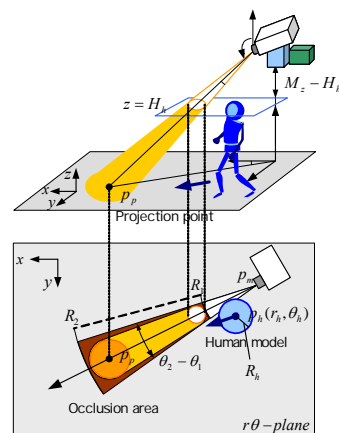


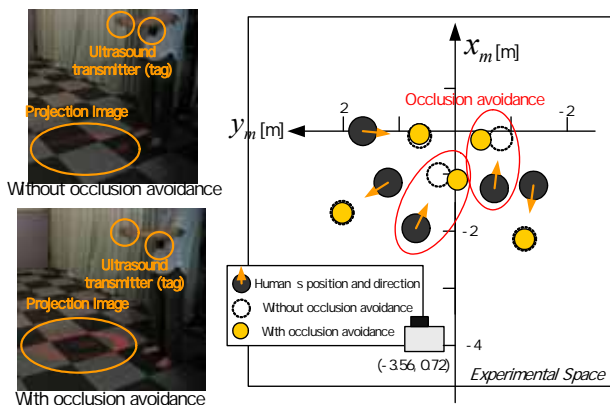
Fig. 4 Transformation of geometrical human model and occlusion area from 3D to 2D.

2) Occlusion avoidance

To modify (move) projected position toward easily viewable position, avoidance method results from the direction of projected position in the view of human position. In the situation that projection target is on the left side of human model, modified position moves to the left which is closer than to the right direction to avoid occlusion. On the contrary, when projection target is on the right side of human model, it moves to the right for the same reason. If limited rotation angle is reached, the radius direction to projection position is kept away to avoid occlusion.

Over more, not only human but also other objects such as chair and table could cause occlusion problem, our proposed method can treat those objects as the human model and perform the occlusion avoidance algorithm.

The result is shown in Fig. 5. The information display system performs projection toward the front of user. As Fig. 5(a) shows, in projection without occlusion avoidance, image is obstructed by user. On the other hand, in projection with occlusion avoidance correct image projection is realized. Fig. 5(b) is the results of several situation in experimental space. When occlusion occurs (two cases), projection position is modified. We can verify successfully activation of occlusion avoidance.



(a) Comparison (b) Several situation in experimental space. Fig. 5 Occlusion avoidance.

3.2 Compensation of projection image

In the case of active projection, the shape of projected image is not same as that of the source image because projection is not always orthogonal to the projected surface and the distance to projected surface from projector is not constant. The change of projection target causes image distortion and varies the image size. Therefore, projected image requires compensation of distortion, size and rotation to provide uniform image to user. In the system based on RT-Middleware, this compensation is performed in Image Projection Component (see Fig. 3). Compensation method is described respectively as the follows.

1) Image size

Projector light radiates out so that projected ima

ge size depends on distance to projected surface. By calculation the relation of those factors, it is able to pre-compensate projected image size to request size \$W\$. resize ratio \$\alpha\$ is given by Eq. 1. Where \$t(d)\$ is a image size on projection direction \$d\$.

$$\alpha(d) = W / t(d) \tag{1}$$

2) Rotation

Projection image (source image) is rotated according to the request from Application Component. For example, it enables the arrow toward any position or projection in response to human direction. So we (user) don't want to see the sign or the mark upside down.

3) Distortion

Distortion is caused by the angle-relation between projector and projected surface. Geometrical definition is shown in Fig. 6. As this figure shown, active projector projects toward \$O_p\$. where plane Q is projected surface and plane R is orthogonal to projection direction through \$O_p\$. \$r_1\$ to \$r_4\$ are assumed as corner of source image or non distortion image. And \$q_1\$ to \$q_4\$ are corresponding points with \$r_1\$ to \$r_4\$. A relation between a point \$p_R\$ on plane Q and a point \$p_R\$ on plane R is shown in Eq. 2 as perspective conversion. This conversion matrix \$H_{QR}\$ is a \$3 \times 3\$ matrix and the degree of freedom is 8. Therefore, if more than four sets of corresponding points of \$p_R\$ and \$p_R\$ are given, we can find \$H_{QR}\$ and represent image distortion. The corresponding points can be found by the intersection of plane Q with the line through \$r_i\$ from projection origin (lens). Finally, inverse matrix of \$H_{QR}\$ represents compensation of distortion image and we can get pre-compensated output image.

$$\begin{pmatrix} p_Q \\ 1 \end{pmatrix} \cong H_{QR} \begin{pmatrix} p_R \\ 1 \end{pmatrix} \tag{2}$$

Proposed method uses normal vector of plane Q for finding the corresponding points. Plane Q shows projected surface so that it is possible to compensate projection toward any surface by setting normal vector according to the space.

Comparison of projection image with and without compensation is shown in Fig. 7. The system performs the projection of double-rectangle. As shown in this figure, the projection without compensation causes inexpectant projection image depending on projection

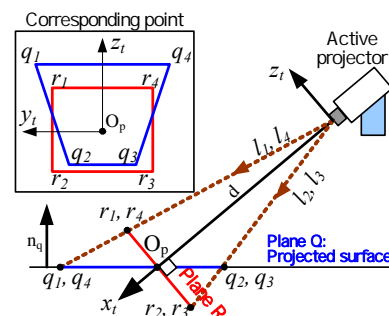


Fig. 6 Geometrical definition of image distortion

target. On the other hand, the projection with compensation provides correct information (considered size, direction and distortion of projection image) compared with the one without compensation.

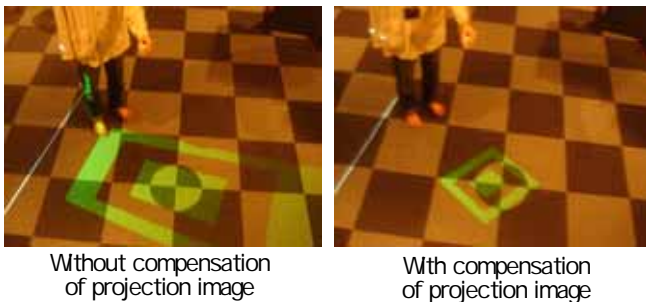


Fig. 7 Compensation of projection image with and without compensation.

4 Integration of distributed devices based on RT-Middleware

RT-Middleware is a kind of software platform based on distributed object middleware. As described in section 2, it is suitable for environmental system such as Intelligent Space. Intelligent Space is considered to have RT elements in a space to utilize RT-Middleware for the integration of its system. And Intelligent Space is expected to become useful and easy to integrate for system development. By using RT-Middleware as platform, Intelligent Space is intensive stage of RT (Robot Technology).

Proposed system based on RT-Middleware is considered as integration with various distributed devices as Intelligent Space system. The system design of information display system (Intelligent Space) based on RT-Middleware is shown in Fig. 8. Environmental system including Intelligent Space will be integrated with various sensors or actuators and has difficulty to implement as whole system. As shown in Fig. 9, the system based on RT-Middleware enables the system to be flexible, which is not depends on the hardware device. For example, various sensors can be treated as position or posture sensors according to their features. Over more, by converting various actuators or devices to the components, it is possible to send the command to control and interact with those actuators. As an example, we developed a RT-Component for mobile robot. This mobile robot is implemented in Hashimoto lab.(The Univ. of Tokyo, Japan) [5]. Because only the interface part is created as the component, the robot's required subsystems such as feedback control, mapper are not needed to be modified. Therefore, Application Components sends target position as command to robot. By demonstration using active projector and mobile robot (however the sensor that used to recognize the user's position is not integrated into the system yet), when an active projector provides a message "Calling robot ..." toward a user, the robot can come to a user as shown on Fig. 9.

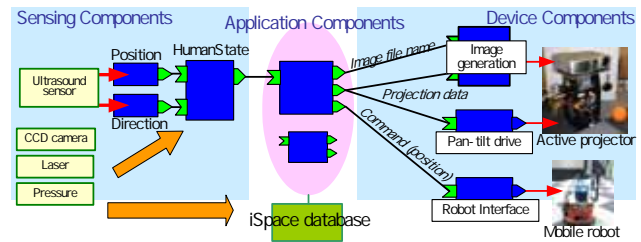


Fig. 8 System design based on RT-Middleware.

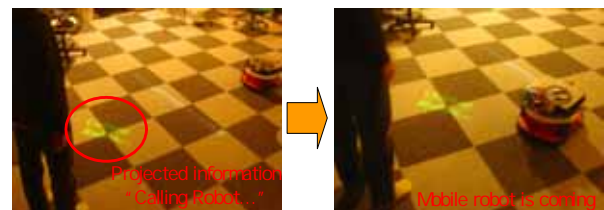


Fig. 9 Demonstration using active projector and mobile robot.

5 Conclusion

This paper presents information display system using active projector in Intelligent Space. Active projector provides interactive informative services for user. To realize this purpose, as two solutions of issues on active projection occlusion avoidance and compensation of projection image are described. We plan to develop smooth working according to human movement and demonstrate the effectiveness on informative services.

Proposed system is based on RT-Middleware. With the feature of RT-Middleware, we will integrate information display system with other devices such as vision sensors or robot, and as a first step, the cooperation of active projector and mobile robot had been performed as described in this paper. In the future, we plan to design and implement the Intelligent Space system by using RT-Middleware.

References

- [1] J. H. Lee and H. Hashimoto, "Intelligent Space – concept and contents", *Advanced Robotics*, Vol.16, No.3, pp.265-280, 2002.
- [2] Y. Toshima, Q. Wang, N. Ando, T. Suzuki and H. Hashimoto, "Network based Display System for Intelligent Space", *ROBOMECH2006*, 2P1-E19, 2006 (in Japanese).
- [3] N Ando, T Suehiro, K Kitagaki, T Kotoku and W.-K. Yoon, "RT-Middleware: Distributed Component Middleware for RT (Robot Technology)", *IROS2005*, pp.3555-3560, 2005.
- [4] T. Suzuki, N. Ando, M. Inagaki, K. Ohara, K. Ohba and K. TanieY, "A Development if RT Component-Lite for Multiple Embedded Devices", *ROBOMECH2006*, 1P1-C35, 2006 (in Japanese).
- [5] D. Brscic, T. Sasaki and H. Hashimoto, "Implementation of Mobile Robot Control in Intelligent Space", *SICE-ICCAS2006*, A1011, 2006.

Elementary Developmental Process of Intentional Agency: Artificial Construction of Gaze Alternation in Communicative Eye Gaze by Infants

Takeshi Konno

School of Knowledge Science,
Japan Advanced Institute of Science and Technology
1–1, Asahidai, Nomi, Ishikawa, 923–1292 Japan
t-konno@jaist.ac.jp

Takashi Hashimoto

School of Knowledge Science,
Japan Advanced Institute of Science and Technology
1–1, Asahidai, Nomi, Ishikawa, 923–1292 Japan
hash@jaist.ac.jp

Abstract

It has been pointed out that gaze alternation by infants, which is a basis for social communication, is related to the process of the development of intentional agency. Intentional agency is defined as an act with a desired goal and a means. It has been pointed out that infants understand others' intentions based on intentional agency. In our recent work, we constructed a computational model which acquired gaze alternation behavior with elementary intentional agency. In this paper, through the analysis of the behavior and the internal states of the constructed model, we confirm that two mechanisms, discrimination and accumulation, play an important role in developing elementary intentional agency. The former discriminates between a caregiver and objects that are producing stimuli. The latter associates the caregiver with the objects by accumulating relationships between sensory states. We also argue that a nested structure, in which gaze alternation composed of a goal and a means is utilized as a means to achieve another goal, is an important feature in the development of intentional agency.

Index Terms — **Gaze Alternation, Communicative Eye Gaze, Understanding Others' Intention, Intentional Agency, Constructive Approach.**

1 Introduction

We study the gaze alternation behavior in communicative eye gaze by infants through the construction of a computational model. Gaze alternation is behavior by infants alternately gazing at a caregiver and particular objects. Tomasello [1] points out that gaze alternation, which is a basis of social communication, is related to the developmental process of intentional agency. Intentional agency is defined as an act composed of a desired goal and a means. It has been pointed out that the infants understand the intentions of others based on intentional agency. From this viewpoint, gaze alternation is not merely behavior returning an infant's gaze point to a caregiver after looking at particular objects, but intentional behavior of gazing at a caregiver based on an infant's desire. This intentional behavior can be developed into more a commu-

nicative use of eye gaze – i.e., social referencing and the utilization of gaze alternation.

In our recent work, we constructed a computational model [2] in which acquiring the visual orientation of gazing at a caregiver or at objects in the center of the visual field became a means by reinforcement learning and in which acquiring the gaze alternation between a caregiver and objects became a goal through memorizing sensory states. However we have not yet clearly shown the mechanisms by which intentional agency is acquired. In this paper, in order to study the elementary developmental process of intentional agency, we investigate the mechanisms in the constructed model. we analyze the behavior and internal states of this model, by which goals are separated from actions in intentional agency.

2 Model

The agent model of an infant (the infant agent, hereafter) has the functions of visual orientation and gaze alternation. In this section, after explaining the agent's visual field, we describe the functions.

2.1 Visual Field of Infant Agent

The infant agent's visual field is a square area that is 0.2m on each side on a flat surface. The sensory state of the infant agent is defined by three kinds of information from the visual field and its motion (Fig.1): (a) the feature of a visual stimulus, which is one of 13 stimuli composed of the caregiver's eye directions (a total of 10) and the type of objects (3 shapes), (b) the position of the visual stimulus consisting of the direction and the gaze, and (c) the proprioception of the muscle states that are related to the orientation of the gaze point. We suppose that the muscle states are integrated to represent the direction of the gaze point.

2.2 Visual Orientation

The visual orientation is the ability to gaze at the caregiver and the objects in the center of the visual field and consists of three modules: the selector, the

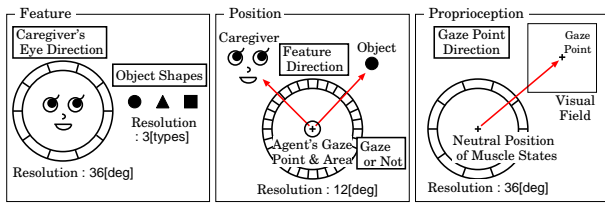


Figure 1: State information about the feature, position, and proprioception in the visual field. In the position, a state of gaze is determined by whether or not the stimulus comes within the gaze area. The gaze area is created by small circle from the gaze point.

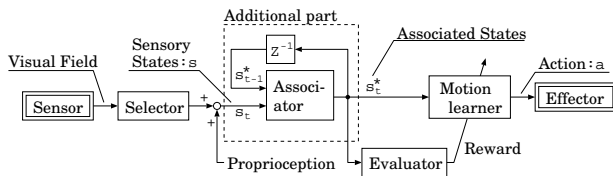


Figure 2: System block diagram of gaze alternation.

evaluator, and the motion learner, shown in Fig.2 without the additional part (which is surrounded with a dashed line). The selector picks up the most distant stimulus from the gaze point in the visual field, an object or a caregiver; then it outputs information about the feature and the position of the selected stimulus. A sensory state, s , is constructed by merging three kinds of sensory information: the feature, position, and proprioception. The sensory state is related to an action to move the gaze point¹ by reinforcement learning algorithm which is known as a standard temporal difference learning with tabular SARSA [3]. In this algorithm, the action is determined according to a probability with an action-value function. The motion learner reinforces the action which allows the gaze point to approach a target².

2.3 Gaze Alternation

The gaze alternation system is equipped with an associator in addition to the visual orientation system (Fig.2). The associator stores relationships between three sensory states: the present sensory states, s_t ; previous associated states, s_{t-1}^* ; and future sensory states, s_{t+1} in a frequency distribution. The frequency distribution is updated according to the sensory states.

$$F(s_t, s_{t-1}^*, S) = F(s_t, s_{t-1}^*, S) + 1, \quad (1)$$

where S is conditioned by

$$S = \begin{cases} s_t & \text{if } \text{cond.}A, \\ s_{t-1}^* & \text{if } \text{cond.}B, \\ s_{t+1} & \text{if } \text{cond.}C. \end{cases} \quad (2)$$

¹The moving direction of the gaze point has 30 divisions.

²For more details, see paper [2].

Table 1: Storing condition in the frequency distribution.

cond.		C(s_{t-1}^*)						
		ϕ		CGV		OBJ		
		0	1	0	1	0	1	
C(s_t)	ϕ	0	A	A	B	B	B	B
		1	A	A	B	B	B	B
	CGV	0	A	A	A	A	B	A
		1	A	A	A	C	B	A
	OBJ	0	A	A	B	A	A	A
		1	A	A	B	A	A	C

The condition, $\text{cond.}A, B, C$, is defined by Table.1, where $C(s)$ judges the feature, the caregiver (CGV), the object (OBJ) or non-existence (ϕ), and $G(s)$ determines whether the sensory state is a gaze (1) or not (0). The output of the associator, s_t^* , is determined according to a probability:

$$p(s|s_t, s_{t-1}^*) = \frac{F(s_t, s_{t-1}^*, s)}{\sum_{s'=1}^{N_c} F(s_t, s_{t-1}^*, s')}, \quad (3)$$

where N_c is the total number of the sensory states.

3 Experiments and Results

3.1 Experimental Setups

At first, we display the caregiver and the objects in the agent's visual field in its visual orientation system. By reinforcement learning, the agent develops a probability distribution of the action-value function, shown in Fig.3. The agent acquires the ability of visual orientation because the probability distribution of the moving gaze point develops to match the direction of the caregiver and the objects.

Second, in a training phase, we display the caregiver and the objects alternately in the agent's visual field

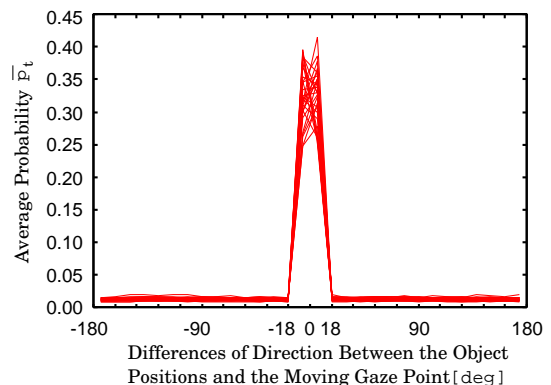


Figure 3: The average probability of the moving gaze points in the positions of the caregiver and the objects.

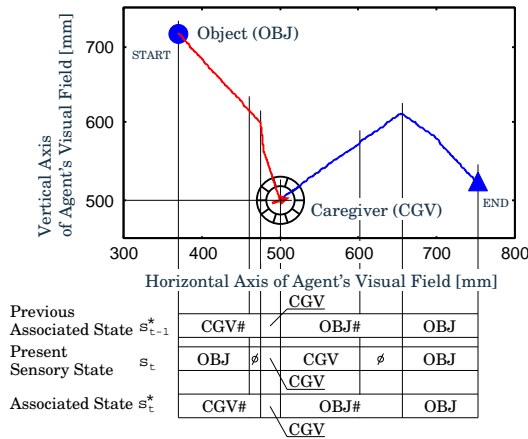


Figure 4: For the process of gaze alternation between a caregiver and objects which are placed outside the visual field, the corresponding internal states of the associator are indicated. The mark ‘#’ means the state does not coincide with the present sensory state.

in the gaze alternation system (Fig.2). In this training phase, the objects are placed in the direction the caregiver looks. After adequate training, we display the objects outside the visual field. As a result, the agent can acquire a gaze alternation behavior outside the visual field.

3.2 The Process of Gaze Alternation

The trajectory of the agent’s gaze point with the corresponding internal states of the associator in the gaze alternation behavior is exemplified by Fig.4. In the behavior toward the caregiver from the circular object which is placed on the left side of Fig.4, when the present sensory state, s_t , is an object (OBJ) or non-existence (ϕ), the associated state, s_t^* , is the previous sensory state, s_{t-1}^* which indicates the caregiver (CGV). If the present sensory state is the caregiver – specifically, if the caregiver appears in the visual field – the associated state coincides with the present sensory state, and the agent adjusts the direction to move its gaze point. When the agent gazes at the caregiver, the associated state becomes the future sensory state, s_{t+1} , and designates a new object (OBJ), which does not appear in the visual field. The new object is associated with the caregiver, based on the frequency distribution [Eq.(3)].

In behavior to look at a new object, which is the triangular object placed on the right side of Fig.4, while the present sensory state is the caregiver (CGV) or non-existence (ϕ), the associated state is the same as the previous associated state, indicating the object (OBJ) to be seen. At the point where the object comes into the visual field – that is, when the present sensory state turns into the object – the associated state indicates the object. The agent can modify the

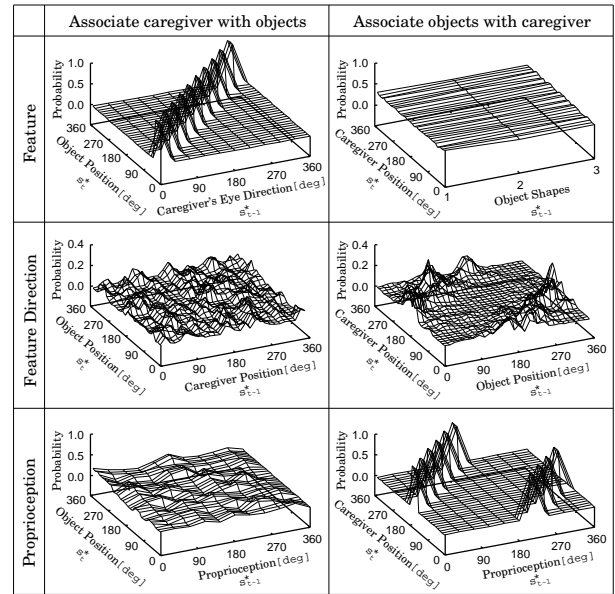


Figure 5: Association probability between the previous associated states, s_{t-1}^* , and the associated state, s_t^* .

trajectory of the moving gaze point even if the previous direction has been considerably different from that of the object to be seen. Through the transition of internal states of the associator, the agent realizes the gaze alternation behavior outside the visual field.

When the present sensory state and the previous associated state are different features, the associator keeps the previous associated state because the agent accumulates the sensory states in the frequency distribution according to *cond.B* in Eq.(2), which is based on discrimination about the category (that is, the caregiver, the object, or non-existence) using function $C(s)$ in Table.1. If the present sensory state and the previous associated state become the same feature, the associator changes to the present sensory state because the frequency distribution has accumulated according to *cond.A* in Eq.(2). When the agent gazes at the caregiver or the objects, the associator associates the caregiver with the objects using the frequency distribution that is accumulating the sensory states according to *cond.C* in Eq.(2).

3.3 Association Probability Distribution

In the association of the caregiver (CGV) with the object (OBJ), the agent uses the probability distribution shown in the left column of Fig.5. In the top left of Fig.5, the association probability distribution between the caregiver’s eye directions and object positions is shown. Using this distribution, the agent can detect the unique object position from the caregiver’s eye direction since one-to-one correspondence between these two pieces of information is formed in this distribution. The distributions of the other sensory in-

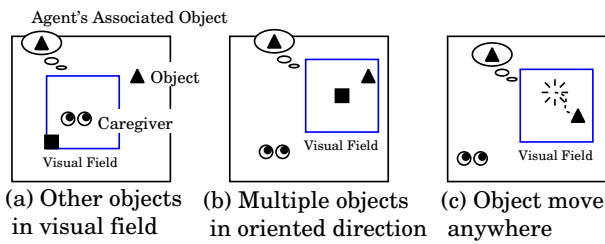


Figure 6: Showing the intentional agency.

formation, the caregiver position and proprioception, do not form such a one-to-one structure and, thus, are unable to be used to detect the object position.

On the other hand, when the agent associates the object with the caregiver, the agent can determine the direction of the caregiver using the state of the proprioception since only the frequency distribution between the proprioception and the caregiver position possesses the one-to-one correspondence structure, as shown in the right column of Fig.5. In sum, we find that the infant agent makes use of the caregiver's eye direction to gaze at the objects and uses the proprioception to return its gaze to the caregiver.

4 Discussion

4.1 Development of Intentional Agency

We confirmed that the constructed agent model can acquire gaze alternation behavior outside the visual field. In the behavior of gaze alternation depicted in Fig.4, three functional properties in the internal states of the associator are identified: **1.** The agent can keep the associated object when different objects appear in its visual field. Therefore the agent can properly gaze at the object that is indicated by the caregiver shown in Fig.6 (a). **2.** For the same reason, if two or more objects are placed in the caregiver's eye direction, as in Fig.6 (b), the agent can gaze at the associated object. **3.** Once the associated object appears in the visual field, the agent can adapt the moving direction of its gaze point to the direction of the associated object. Therefore, even though the object may move anywhere, the agent can follow the object, as shown in Fig.6 (c).

In these functional properties, the associated states play the role of the goal at which the agent wants to gaze, and the agent through its visual orientation ability selects the action of gazing at the caregiver and the objects as a means of achieving the goal. The three functional properties of gaze alternation suggest that the agent acquires elementary intentional agency.

4.2 The Nested Structure of Intentional Agency

It is known that infants tell their desire to others to get an object by utilizing gaze alternation, and of-

ten others hand over the object to the infants. Accordingly, gaze alternation is thought of as a means of achieving the desired goal of getting the object. In this behavior, we can discover a nested structure in which the behavior composed of a goal and a means is utilized as a means to achieve another goal. This behavior consists of a goal to get the object and a means of alternatively gazing at the caregiver and at the object. Furthermore, the means consists of the goal of gazing something which the infants want to see and the means of moving their gaze point.

The constructed model of gaze alternation has been composed of the goals of gazing at the caregiver or the objects and the means of achieving those goals. When we develop the agent model to perform utilizing gaze alternation based on the present model, the nested structure must be observed.

5 Conclusion

In this paper, in order to study the elementary developmental process of intentional agency, we investigate how the infant agent of our constructed model acquires intentional agency that involves separating goals from actions. Through the analysis of the gaze alternation behavior and the internal states, we confirm that two mechanisms – discrimination and accumulation – play an important role in acquiring intentional agency. The former discriminates within the category – that is, between the caregiver, the object, and non-existence – in the visual stimuli and determines whether or not the agent gazes at the stimulus. The latter accumulates the relationships between the continual sensory states in a frequency distribution. Through these two mechanisms, the agent acquires the goals – that is, objects or a caregiver – at which the agent wants to gaze and that are to be realized by the means of moving its gaze point with its visual orientation. Through discussion of the developmental process of intentional agency, we suggest that a nested structure, in which the gaze alternation composed of a goal and a means is utilized as a means to achieve another goal, is an important feature in the developmental process of intentional agency.

References

- [1] Tomasello, M., "Joint attention as social cognition," In Moore, C. & Dunham, P.J. (Eds.), *Joint Attention: Its Origins and Role in Development*, Lawrence Erlbaum, pp.103-130, (1995).
- [2] Konno, T. and Hashimoto, T., "Developmental Construction of Intentional Agency in Communicative Eye Gaze," *Proceedings of the International Conference on Development and Learning, ICDL '06, Indiana Univ., Bloomington, USA, May 31 - June 3, (2006)*.
- [3] Sutton, R.S. and Barto, A.G., *Reinforcement Learning*, A Bradford Book, MIT Press, Cambridge, MA, (1998).

The Research of Data Mining for Quantitative Association Rules and Algorithm for Numerical Attribute

Du Junping
School of Computer Science
Beijing University of Posts and
Telecommunications, Beijing, 100876

Wang Rui jie
School of Information Engineering
University of Science and
Technology, Beijing, 100083

Abstract

In this paper we proposed the concept and types of the quantitative association rules. We proposed the data mining for the quantitative association rules in detail. We also researched the concept for discretization of numerical attribute, and the strategy of discretization result. We established the better algorithm for discretization of numerical attribute.

1 Introduction

Association rules reflect dependency and association of one event and others. Data association in database is representation of things' relation in real world. As a sort of structured data organization's format, database makes use of possibility of adhered data model to describe association of data (e.g. primary key and foreign key). At the same time, association among data is very complicate, which not only means association adhered in data model mentioned above, but also means a majority of hidden association. The aim of Data mining for Association rules is finding hidden association information. Association can be divided into simple association, time series association, causal

association, quantitative association and etc.

These associations are not always forecasted, but gained by analyzing data association in database. As a result, it provides business decision making with new value.

Data mining for association rules is the most common method for finding association knowledge, of which Apriori and its amelioration. For finding significant association rules, two threshold vales are needed to be given: minimum support and minimum confidence. Mined association rules must satisfy minimum support stated by users, and it denotes minimum association degree that a group of associated items need to satisfy. Mined association rules need to satisfy minimum confidence stated by users, and it reflects minimum reliability of one association rule. In this sense, the aim of data mining system is mining association rules which satisfy minimum support and minimum confidence from source database. Research and application for association rules are the most active and embedded branches of data mining. Many theories and algorithm of data miming for association rules are raised.

Discretization of Numerical Attribute is the key issue of data miming for association rules, and actually it partitions attribute field into intervals. Partition methods play a significant role in quality of data mining for the quantitative association rules. Min-confidence: if numbers of

Supported by Beijing Natural Science Foundation of China (4042012), Key Project of Beijing Educational Committee (KZ200510011009) and Project of National Science Foundation of China (60442003).

interval are exiguous, the number of group which support interval will increase, and the support degree of strong item set of inclusion interval will go up. At the same time, if support of strong item set's subset remains the same, the rule confidence of right end inclusion subset will decline. If confidence threshold value cannot be reached, information will be lost.

Min-support: if numbers of interval partitioned are overabundant, support of interval will decline, and entire strong item set will not be created effectively.

2 Quantitative Association Rules

A. Concept of Quantitative Association Rules

Quantitative association rules are association rules including classify attribute (Boolean attribute can be deemed to special classify attribute) and quantitative attribute. Generally, quantitative association rules are multidimensional association rules issues, in which the key issue is discretization of Numerical Attribute to satisfy a certain data mining criterion. Quantitative association rules also need to satisfy $X \cap Y = \emptyset$ and constraint condition of support and confidence. In a general way, Quantitative association rules issues are different from Boolean association rules in knowledge representation, Boolean association rules seeks for frequent item sets, moreover, quantitative association rules seeks for frequent predication set. Some characters of Quantitative association rules are listed as below.

Subset of frequent item set to a certainty is frequent. This character is consistent with Boolean association rules.

Suppose X^{\wedge} is generalization of X , X is specialization of X^{\wedge} , if X^{\wedge} is frequent, then X is frequent, and $\text{support}(X^{\wedge}) > \text{support}(X)$,

It is impossible that two items in frequent item set have same attribute. These characters are easily understood from analogy in previous

Boolean association rules (its demonstration is ignored); whereas the time that $k+1$ item set are created by frequent k item set reduces greatly. When $k+1$ item set are created by frequent, algorithm only needs to calculate different attributes, and it is impossible that the disjoint intervals with same attribute are frequent.

B. Categories of quantitative association rules

Numerous intervals are created after Discretization of Numerical Attribute, and then these intervals are mapped to Boolean attribute directly and mined by Boolean association rules. It is a common method for data mining for the quantitative association rules, and it is characterized by complicated format of rules. In fact, users are usually interested in rules of a certain format, i.e. Reference[3] of data mining for the quantitative association rules is mostly based upon a certain rules model. So we can classify the quantitative association rules mining to 3 types according to the rules formation.

(1) Rules of mining similar to "numerical value attribute \cap classification attribute \Rightarrow numerical value attribute \cap classification attribute", e.g. $\text{sex}=\text{female} \cap \text{age} \in [20,30] \Rightarrow \text{wage} \in [\$5, \$10]$. This sort of rules is complicate, and they are normal quantitative association rules.

(2) Rules of mining similar to "numerical value attribute \cap classification \Rightarrow classification attribute", e.g. $\text{opppocation}=\text{bussiniessman} \cap \text{age} \in [35,50] \Rightarrow \text{goa board}=\text{Yes}$. This sort of rules' left end generally denotes one subset of database. Any attributes in database, and any value combination can be used as left end of rules, the right end denotes one predefined category, and it is quite similar to classification rules. The typical classification methods are decision tree、genetic algorithms、neural network、Bayesian classification and etc. The efficiency of resolving classification problems by association rules is very high, especially to large data set, classical classification algorithm is difficult to gain mining result.

(3) Rules of mining similar to “classification attribute=> numerical value attribute \cap classification attribute”, e.g. sex=females =>salary \in [\$1000,\$2000]. It is opposite to the second sort of rules, yet to some problems, we will not expatiate anymore here.

C. Common steps of quantitative association rules

Mining quantitative association rules by Boolean association rules algorithm and its theory, such as support, confidence, frequent item set and other concepts are most effective approach of resolving quantitative association problems.

One typical method is ameliorating Aprior algorithm to adapt to data mining for quantitative association rules, and mainly divided into five steps that shown as Fig. 1.

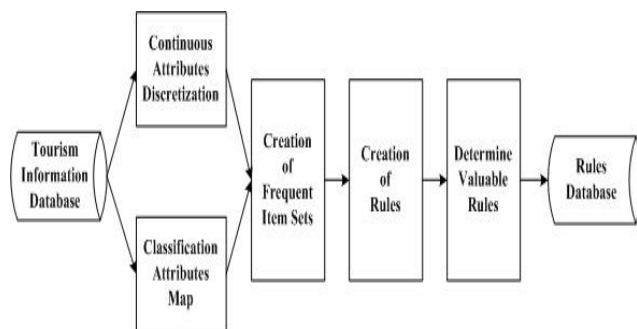


Fig.1 Common steps of quantitative association rules

(1) Pointed to each numerical value attribute, Reference [4] of proper discretization algorithm is selected and the number of intervals is determined. The difficulty of this step is selecting proper discretization algorithm. At first, discretization algorithm has not unified criterion, we should select one or several sort of algorithm according to distribution characters of data. For instance, this text will discuss that equi-depth partitioning method is not ideal for highly skewed data discretization, but it works well on partition of equally distributed data. In the next place, numbers of intervals partitioned, i.e. granularity of partition, too many or too little

will lead to information lost.

(2) The value is mapped to continuous integers to classification attribute. To those numerical value attributes which need not partitioning intervals, such as some numerical value attributes with little value, and the value can be mapped to continuous integers when they are sorted by size. If numerical value attributes are discretized to intervals, intervals will be mapped to continuous integers according to discretized order of intervals. The operation to these continuous integral value is equal to operation to data set will be mined, and these continuous integers are transparent to algorithm. All classification attributes and continuous attributes are mapped to Boolean attribute, and all of such attributes compose item sets.

(3) Creation of frequent item sets. This step is the same to the steps of frequent item set created by Aprior algorithm. Aprior amelioration algorithm is also applicable here. Based on Character 3, new item sets will not be created from adjacent sections, in this way they can be merged by definite merging criterion.

(4) Application for frequent set creation association rules. If both ABCD and AB are frequent sets, the rule AB=>CD is true or not needs to be determined by result of calculating $conf = \frac{supp(ABCD)}{supp(AB)}$ exceeds minimum confidence or not.

(5) The valuable association rules are determined as output. For helping users to mine valuable rules and decline redundancy of rules, the association rules based on interest measure has been established in Boolean data mining for association rules, and extensively applied in data mining for the quantitative association rules.

3 Concept and strategy for discretization

Algorithm for discretization of numerical attribute will face the same problems during resolving classification problems, however, problems of data mining for association rules is different from classification. From the machine

learning point of view, data mining for association rules is unsupervised learning category, but data mining for classification model is supervised category. In other words, discretization algorithm that suits classification does not necessarily suit data mining for association rules; hence it is necessary to research new discretization methods combined with characters of data mining for association rules. Combined with characters of data mining for association rules, methods for numerical value discretization mainly are equi-width partition, equi-depth partition and distance-based partition.

A. Equi-depth Partition Method

During numerical value discretization, equi-depth partition is the most common discretization method, commonly adequate for data set with low association among attributes. For the data set with tight association, application of equi-depth partition is difficult to mine ideal result. Equi-depth partition method tends to partition adjacent value with commonness and high support into different intervals. When data distribution reach peak value near to a certain point, the mechanical method like equi-depth partition cannot reflect characters of data itself, hence it does not work well on highly skewed data discretization. For example, during tourist data mining, all kinds of discretization methods suit for processing scenic spot attribute and other data with low association, such as tourists' age、 numbers of scenic spots.

R is one relation, A is one attribute of it, T is one tuple, C is one condition of R, T(A) denotes A attribute value for tuple T.

$B_i = [X_i, Y_i]$ of which $i=1, 2, \dots, m, X_i \leq Y_i \leq Y_{i+1}$;

If A is one numerical value attribute, and its interval is $[X_l, Y_m]$. Interval of A is partitioned into a series of disjoint fields, viz.

$B_i = [X_i, Y_i]$ of which $i=1, 2, \dots, m, X_i \leq Y_i \leq Y_{i+1}$;

B_i is entitled "one bucket of A", and number

of tuples in $T \in R$ and $T(A) \in B_i$ is entitled "size of bucket", noted as u_i . if size of tow buckets are same, and they are entitled "equi-depth bung".

Algorithm shows as below:

Input: numerical attribute A, number of bucket n

Output: discretized interval

- (1) Numerical attribute in order;
- (2) Scan database, Stat the database item number N;
- (3) Get the depth of bucket $h=N/n$;
- (4) Scan A in order one by one. According to Definition 2, get number i and i+h in sequence, the make the output of discretized interval $[l_i, v_{i+h}]$.

B. Equi-width Partition Method

The equi-width partition method is the simplest discretization method which is used to distributing equably data. Because this algorithm need only one time to scan the database, it has a high efficiency. The equi-width partition method simply partition from mathematics' point. It doesn't consider the characteristic of the data distributing. As this method is more directly and adapt to prophase dispose of data attribute, it always unites the clustering method and get good discretization result. For example, in the tourism data mining, it used to discretize tourists' age and income, etc.

Algorithm shows as below:

Input: numerical attribute A, number of bucket n

Output: discretized interval

- (1) Scan database, Get the $\max(A)$ and $\min(A)$;
- (2) Try the width w of interval, $w = (\max(A) - \min(A)) / n$;
- (3) Make the output $(l_i = \min(A) + (i - 1) * w, v_i = \min(A) + i * w)$ of discretized interval $[l_1, v_1], [l_2, v_2], \dots, [l_n, v_n]$.

C. Classification Partition Method

Both of equi-width partition and equi-depth partition methods are considering neither the

data distribution, nor the experts' proposal to the attribute discretization. They only partition the data attribute according to the geometry and mathematics. The classification partition method can take attribute discretization according to data distribution feature based on the field experts' proposal. To solve the quantitative association rules problem, we can use the classification partition method to partition each attribute item to proper category which the equi-depth partition method can not solve. This can show data distribution status. The aim of classification is to partition similar data to same category.

For example, in the tourism information data mining technology, field expert hold up the classification model. The process of quantitative data discretization is partitioning one group data to different class according to the classification model. The result of classification should make the data distance in same types much shorter and in different types much longer.

The process of data classification partition is: Firstly field expert take the characteristic value $A[1...k]$ of the partitioned k intervals, then scan every data in sequence, classify data to the category which is nearest to data number, update characteristic value of this category.

Algorithm shows as below:

Input: Numerical attribute A , Interval characteristic value $A[1...k]$

Output: Discretized k intervals

do

(1) Read one data, Calculate the distance between it and every characteristic value;

(2) Partition data to category which is nearest to data number;

(3) update characteristic value to average value of its interval;

until all data partitions finished.

5 Conclusion

In this paper we proposed the algorithm for discretization of numerical attribute in quantitative association rules mining. Through

the analysis of the above 3 discretization algorithms, we defined divergent density as evaluation criterion of discretization effect.

Definition: If discrete category $[a,b],c$ is the number belong to the discrete category, then $p=c/|b-a|\times 100\%$ is the density of this discrete category. We call the density average value of all discrete category which is

$$\varpi = \left(\sum_{i=1}^n \rho_i \right) \frac{1}{n}$$

as discrete density. If this

discrete density is larger, the effect of partition is better.

By this method, we calculate the discrete densities of above 3 discretization algorithms: The discrete density of equi-width partition is 10%. The discrete density of equi-depth partition is 40.84%. The discrete density of classification partition is 100%. To this data group, the effect of classification partition is the best. But because the cost of classification partition algorithm is much higher, we should take different discretization methods according to data feature.

References

- [1] R. A. Grawal, T. Imielinski, and A. Swami. Mining association rules between sets of items in large data bases, SIGMOD'93, Washington, 1993: 207-216.
- [2] Jong Soo Park, Ming-Syan Chen, and Philip S. Yu, An effective hash based algorithm for mining association rules, KDD-94.
- [3] Hilderman Robert, Hamilton Howard. Knowledge Discovery and Interestingness Measures: A Survey. Technical Report CS 99 - 04, University of Regina, Saskatchewan, Canada, 1999.
- [4] Zhang Chaohui, Chen Yucang, Zhang Qian, An Algorithm for Mining Quantitative Association Rules, Journal of Software, Beijing, China, 1998(11): 801-805.
- [5] Liu Tongming, etc. The Data Mining Technology and Applications, National Defence Industry Press, Beijing, China, 2001

TV Program Recommender Using User's Preference

Jungmin Kim, Seongpyo Cheon, Byung-Wook Jung, Jinyoung Kim, and Sungshin Kim

School of Electrical and Computer Engineering, Pusan National University, Busan, Korea
Pusan National University 30 Changjeon-dong, Keumjeong-ku, Busan 609-735, Korea
E-mail: kjm16@naver.com, buzz74@pusan.ac.kr, wooroogi@pusan.ac.kr king_ioi@pusan.ac.kr, and sskim@pusan.ac.kr

Abstract – Due to the expansion of TV channels in the digital era, the number of TV programs selected by users has had an explosive increase. This expansion makes hard to find preferred TV programs. Because of this, it is necessary to automatically customized recommendation system for TV programs. In this paper, we propose a novel recommendation system to overcome this problem. The proposed recommendation system has two main algorithms that consist of personalized recommendation algorithm and a general recommendation algorithm. The personalized recommendation algorithm is constructed from individual user-information (e.g. channel, title, time, etc) and the other is constructed from personal information (e.g. age, gender, occupation, etc). However if we don't have sufficient user-information regarding the preferences of TV programs then the recommendation has a high failure rate. To overcome this difficulty, we propose the use of a general recommendation algorithm in this paper. In this paper, we address the problems and solutions by describing the proposed algorithms and experiments.

Keywords: TV recommendation, preference, anytime, personalized, general

1. Introduction

TV is the requisite mass media on this society, because it allows us to experience many things that we never experienced before second hand, and it is an entertainment program to relieve our tension when we get tired. Because the were not as many channels in previous broadcasts as the TV programs Included in cable TV and sky wave TV, we could learn our favorite channel number. However, TV offers a variety TV programs and custom broadcasting services to users as the expansion of TV channels in the digital era is resulting in a soaring number of TV programs available to users. In this environment, the broadcast service that answers the demands of users focuses on user and Research on TV program recommendation has been vigorously conducted for 10 years [1, 2].

Based on three months of data from May 1, 2006 to July 31, 2006 received from AGB Nielsen Media Research, we utilized the users' preference analysis for the recommendation of TV programs. We used the first dimensional analysis method among various statistical analysis tools. Data was analyzed using individual

viewing TV information, and it is utilized not only in the personalized recommendation method, which recommends in the order of title, genre, and channel information that the user mainly watched on the corresponding weekday and time, but also in the general recommendation method, which uses is used general information such as gender, age, occupation, etc. TV program recommendation algorithms could satisfy the user's preference well through the personalized recommendation algorithm, but when there is not enough viewing information for the corresponding user, the possibility of failure is also increased. Therefore, when the viewing information of a user is not sufficient, we recommended TV programs using the general recommendation method.

The rest of this paper is organized as follows: Section 2 reviews related work in the field. An overview of the software system architecture is given in section 3. Section 4 presents the implementing and simulation result. Finally, section 5 summarizes the paper.

2. Related Work

The recommendation method uses general recommendation and information abstraction method using Data-mining. The general Recommendation method is divided into the Content-based Recommendation (CBR) method and the Collaborative Recommendation (CR) method [3-6].

The content-based Recommendation requires the user to ask questions to the retrieval system and the system shows results to the questions as in Fig. 1 [4, 5].

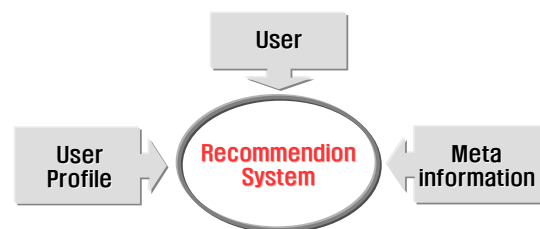


Fig. 1 Content-based Recommendation.

The collaborative Recommendation collects people whose inclinations are similar to the group and recommends programs with assumption that other people also are interested in TV programs that people enjoy within the related group. Such a general recommendation method has problems with the quality of recommendation. The quality drops greatly when we have little user's information data and when there are few

people whose inclinations are similar. We propose a recommendation engine that has a content-based recommendation method and a collaborative recommendation method that mutually supplement each other in order to solve this problem [5, 6].

Data-mining and information abstraction methods bring rules and information using this data; this abstraction process is shown in Fig. 2.

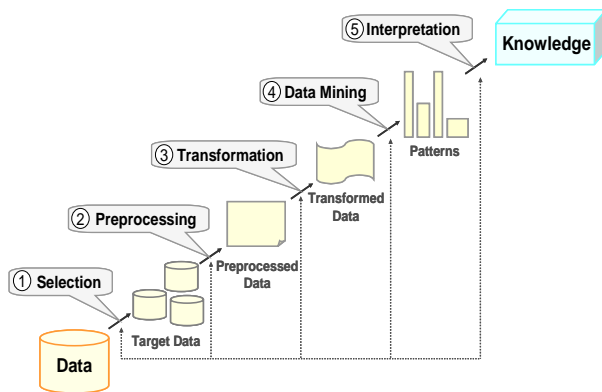


Fig. 2 Data-mining architecture.

Figure 2 shows a typical process in which information is abstracted from data. There are very much technological methods to Data-mining, and there are Data-mining loadmaps that arrange data systematically and bring rules or information effectively from data in Data-mining. A Data-mining loadmap is shown in Fig. 3.

In this paper, we could increase the reliability of the recommendation and optimize the recommendation system by analyzing data from various subjects and domains using a Data-mining loadmap.

3. System Architecture

The proposed software architecture is based on CBR (Content -based Recommendation) and CR (Collaborative Recommendation). The system architecture consists of a User Interface, which receives user information from interactive TV and a TV Program Search Engine, which receives TV program information on the air, from the Recommendation Engine, and from the Database. The system architecture is shown in Fig. 4. Each Recommendation Engine and Database is described in Section 3.a, and Section 3.b.

A. Data Analysis

Table 1 Summary of the AGB Nielsen Media Research' data

Section	Remark
The number of participant	550 family - 3,953 persons (man : 2003, woman : 1950)
The number of TV program	98,350 (it gather all channel from May, 2006 to July, 2006)
Information of TV viewing	It gather channels and start/end times of individual TV viewing
Genre	94 (overlapping mark is able to do)

Based on three months data from May 1, 2006 to July 31, 2006 received from AGB Nixon Media Research, we utilized users' preference analysis for the recommendation of TV programs. And Table 1 shows a summary of the related data.

The user's Information consists of nine items: gender, age, dwelling form, dwelling area, income, scholarship, etc. This is shown in Fig. 5.

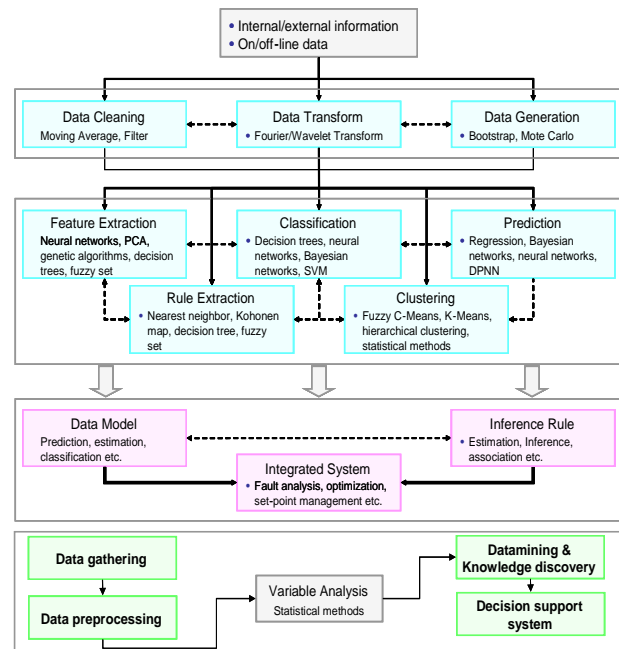


Fig. 3 Data-Mining loadmap.

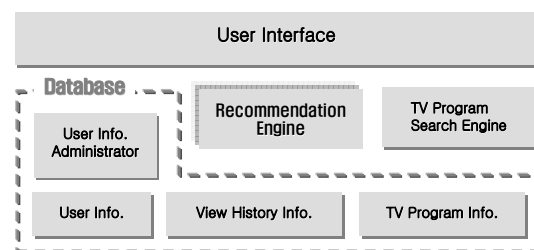


Fig. 4 System architecture.

Genre data from sky-wave TV is separated into three architectures according to each TV program schedule. However, the whole work to standardize the code is insufficient. In the case of cable and satellite broadcasting, doesn't offer to separate information according to each program schedule. In order to solve this problem, we integrate a combination of 94 items according to genre to 13 representative genres and used these on sky-wave and cable TV.

We made a database to analyze the AGB Nielsen Media Research's data. Correlation to each entity is shown in Fig. 6.

We used the first dimensional analysis method among various statistic analysis tools for data analysis. Because the user' information has 9 items, in the case of to extend dimension gradually, the number of case is overfull.

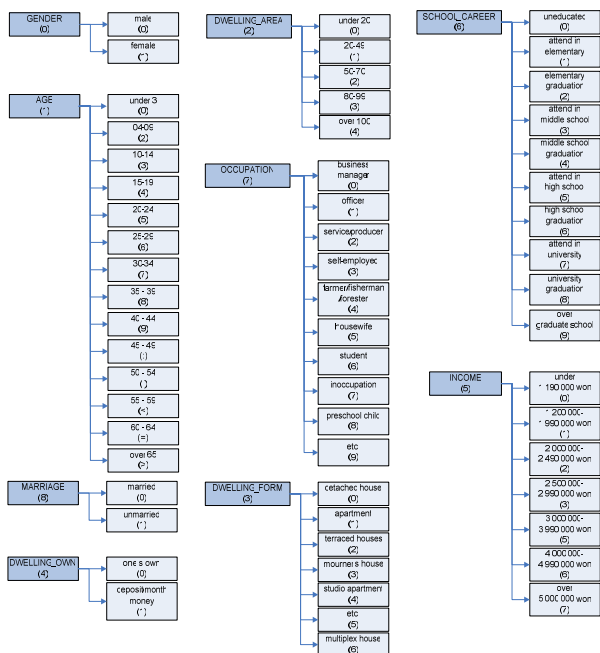


Fig. 5 Code arrangement information connected to information from viewing TV.

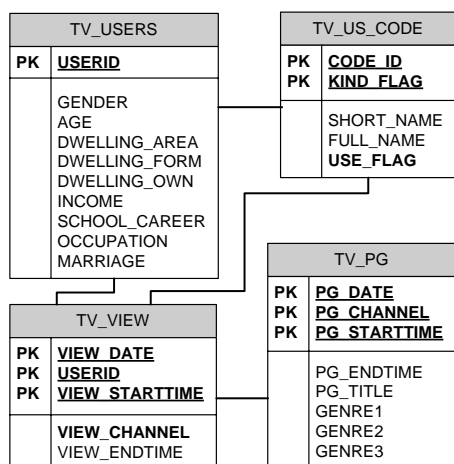


Fig. 6 Entity relation of the AGB Nielsen Media Research' data from viewing TV.

In order to solve this problem, after one dimension analysis, we separated user information items into groups where binary classification is possible and other groups where binary classification is impossible. The results of the one dimension analysis are shown in Fig. 7. Gender, dwelling form, and matrimony can be classified using binary classification according to the results of the one dimension analysis. However, The binary classification method can classify when integrate code according to dwelling form by “Is it apartment?” or “is not it apartment?”. And dwelling area is excepted because there are so many '20 - 49' overwhelmingly.

Age, income, scholarship and occupation reflect personalized inclinations of the user's profile. This paper chooses item in order to reflect individual inclination using binary classification.

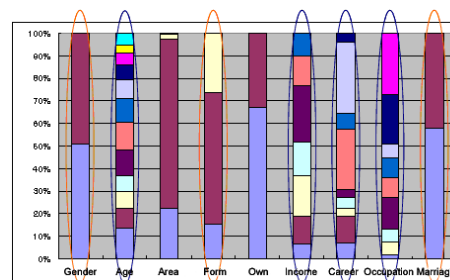


Fig. 7 1D analysis result of viewing TV.

B. Recommendation Engine

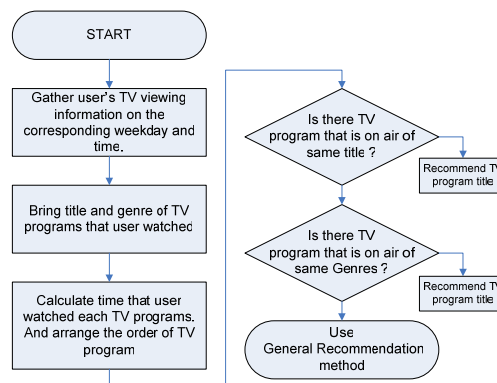


Fig. 8 General Recommendation method.

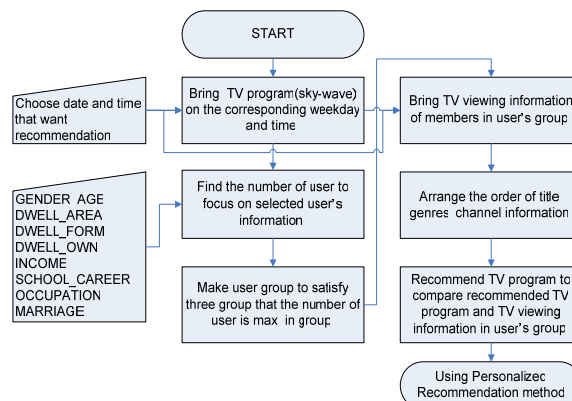


Fig. 9 Personalized Recommendation method.

The recommendation engine consists of CR (Collaborative Recommendation), and CBR (Content-based Recommendation), and supplementation each lacking part. CR (Collaborative Recommendation) and CBR (Content-based Recommendation) are called the general recommendation method and the personalized recommendation method here. The recommendation engine solves the problem of insufficient user' viewing information or can not believe the result. Actually, when we used the personalized recommendation method, we could get a satisfying recommendation result. However, the probability of failure was high when we had little data of user's TV viewing information. In this case, we could recommend TV programs using the general recommendation method, but because the general recommendation method also has a high probability of failure when user's inclination is unique, we

supplemented the methods with each other

The TV program recommendation method must recommend a program to the user based on TV program time and TV program schedules. In this paper, the general recommendation classifies binary classification items and other items, and utilizes them. We divided the group through a combination of binary classification items. And then we created a new subgroup using items that reflect individual inclination according to the group in which it was divided. The general recommendation algorithm is shown in Fig. 8.

The personalized recommendation method of TV programs was analyzed using individual viewing TV information and recommended using the order of TV program title, genre, and channel information that the user mainly watched on the corresponding weekday and time. The personalized recommendation algorithm is shown in Fig.9.

4. Implementation and result

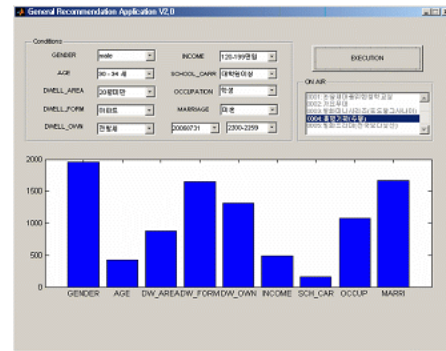
We used MATLAB R2006A GUI in order to embody whole program on Windows 2003 server. We use only use data of sky-wave based on three months data from May 1, 2006 to July 31, 2006 received from AGB Nixon Media Research. And we made a database to interlock DBMS (DataBase Management System) and ODBC (Open DataBase Connectivity) using data of sky-wave. The general TV Program recommendation application described the histogram of a group to similar to user in order to analyze the user's TV viewing information according to the day of the week when the user chooses the date and time that they want a recommendation. In the case of the personalized recommendation application, because the personalized recommendation application analyzes the user's TV viewing information more than the user's general information and recommends using the order of the title, genre, and channel information, we experimented after adding the user's TV viewing information screen. The screen of the general recommendation application and the personalized recommendation application are shown in Fig. 10.

We could get satiable results that compare the results of the General Recommendation and the results of the Personalized Recommendation in order to search the recommendation results.

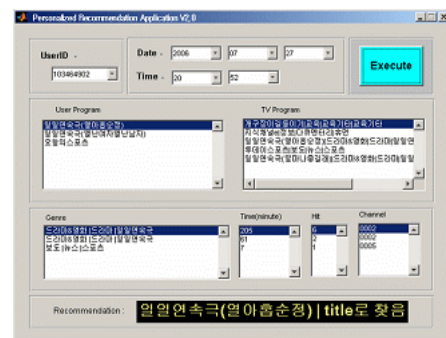
5. Conclusion

We made a database applying the fundamental pretreatment process to resource data. In addition, we arranged each data code in this paper and grasped attribute of data using statistical analysis techniques. The general recommendation method and personalized recommendation method mutuality complement the proposed method, and we had satisfactory results from the experiment.

We are going to improve the integration domain of the recommendation algorithm through continuous research.



a. General Recommendation Application



b. Personalized Recommendation Application

Fig. 10 Application (Korean language).

ACKNOWLEDGEMENTS

This work was supported by the Second-stage of the Brain Korea 21 project in 2006.

References

- [1] T. Isobe, M. Fujiwara and H.kaneta, "Development and features of a TV navigation system," IEEE Trans. on Consumer Electronics, vol. 50, no. 1. pp. 393-399, Nov. 2003.
- [2] J. Xu, L. Zhang, H. Lu and Y. Li, "The development and prospect of personalized TV program," Proceedings of the IEEE 4th International Symposium on Multimedia Software Engineering (MSE OZ), California, USA, 2002.
- [3] Metadata, Specification Series of the TV-Anytime forum, Document SP003v1.1, August17. 2001.
- [4] Peter W. Foltz and Susan T. Dumais, Personalized Information Delivery: An Analysis of Information Filtering Methods, CACM 35(12) pp.51-60, 1992.
- [5] Marko Balabnovic and Yova Shoham, Fab: Content-Based, Collaborative Recommendation, CACM 40(3) pp.66-72, 1997.
- [6] Resnick, P., Iacovou, N., Sushak, M., Bergstrom, P., and Riedl, J. GroupLens: An open architecture for collaborative filtering of netnews. Proceedings of the 1994 Computer Supported Collaborative Work Conference. 1994.

A Multi-labeled Classification based on Error-correcting Output Coding

Tetsuya Yamashita

Takashi Takenouchi

Shin Ishii

Graduate School of Information Science, Nara Institute of Science and Technology
8916-5 Takayama, Ikoma, Nara 630-0192, Japan
{tetsuya-y, ttakashi, ishii}@is.naist.jp

Abstract

We propose a new framework to deal with multi-labeled classification problems based on error-correcting output coding (ECOC). In multi-labeled classification problems, it is required to assign multiple classes to a single input. In this study, we show naive multi-label approach can be improved based on probabilistic modeling of misclassification process in the ECOC method. We examine performance of the proposed method with synthetic datasets and show that the proposed method accurately predicts multiple labels of a new input, relatively to the existing method.

1 Introduction

In a multi-labeled classification problem, a single input is assigned to multiple classes or categories. A typical example of multi-labeled problems is the text categorization problem on the World Wide Web, where each text may belong to some of multiple categories. For such a problem, there are two conventional approaches. One is the binary classification approach in which each text is classified into multiple classes by integrating individual results from binary classifiers. The other approach simultaneously deals with multiple classes by considering multinomial models; Ueda and Saito [5] proposed Parametric Mixture Model (PMM) in which the multinomial distribution is extended to represent the dependence of multiple classes. In this study, we take the former approach.

In the context of multiclass classification problems, the error-correcting output coding (ECOC) method was formerly proposed by Dietterich and Bakiri [2]. This method decomposes the original multi-class classification problem into multiple binary classification problems whose each output is $\{+1, -1\}$. In the framework of ECOC, a k class problem is decomposed into l binary classification problems and each class label is represented by a code word which is a row vector of

a code matrix $W \in \{+1, -1\}^{k \times l}$. An example code matrix in a four-class problem would be

$$W = \begin{pmatrix} 1 & -1 & -1 & -1 \\ -1 & 1 & -1 & -1 \\ -1 & -1 & 1 & -1 \\ -1 & -1 & -1 & 1 \\ 1 & 1 & -1 & -1 \\ 1 & -1 & 1 & -1 \\ 1 & -1 & -1 & 1 \end{pmatrix}.$$

Then, each binary classifier is trained using binary labels associated with the corresponding column vector of W . We can predict the class label of a new input using the outputs of binary classifiers, where the simplest method is the Hamming decoding. For outputs of binary classifiers, the closest code word in W with respect to the Hamming distance is used as the predicted class label of the input. Allwein et al. [1] proposed a more flexible framework that allows W to include 0 which signifies "do not care" classes in the corresponding binary classifier. Moreover, the Hamming distance was extended to general loss functions.

In this study, we apply the framework of ECOC to multi-labeled problems by formulating a probabilistic model that represents the relationship between a code word and a set of outputs from classifiers. We in particular develop the method based on the information transmission theory. The model regards a misclassification of each binary classifier as a bit inversion in the code word due to a noisy channel. An addition of parity bits which leads to redundant representation of multiple labels and adaptive identification of the noisy channel based on the probabilistic model enables an accurate prediction of multiple labels.

In section 2, basic setting and a probabilistic model of the noisy channel are formulated. In section 3, we examine the performance of the proposed method, in comparison to the simple multi-labeled classification method, using synthetic datasets.

2 Method

In this section, we describe the probabilistic model of the bit inversion, which represents the misclassification error, in the multi-label classification, and its decoding method.

2.1 Notation

Let \mathbf{x} be an input vector and $\mathbf{y} \in \{1, -1\}^b$ be a vector of labels associated with b categories. Typically, \mathbf{x} is an element of the *Bag-of-Words* [3]. We assume that a dataset $\{\mathbf{x}^i, \mathbf{y}^i\}_{i=1}^N$ is given. Let $y_j (1 \leq j \leq b)$ be a component of \mathbf{y} , defined by

$$y_j = \begin{cases} 1 & \mathbf{x} \text{ belongs to class } j \\ -1 & \text{otherwise.} \end{cases} \quad (1)$$

We consider parity bits $\mathbf{z} \in \{1, -1\}^c$ associated with \mathbf{y} , whose j -th component is denoted as z_j . Note that the parity $\mathbf{z} = \mathbf{z}(\mathbf{y}) : \{1, -1\}^b \rightarrow \{1, -1\}^c$ is designed in *a priori* manner.

Using the dataset and the corresponding set of parity bits, $\{\mathbf{z}^1, \dots, \mathbf{z}^N\}$, we can train $(b+c)$ binary classifiers. We denote outputs of binary classifiers associated with the code word \mathbf{y} as $\tilde{\mathbf{y}}$, and those augmented by the parity bits \mathbf{z} as $\tilde{\mathbf{z}}$, both of which are assumed to be disturbed by a noisy transmission channel.

2.2 Probabilistic model and decoding method

The probabilistic model of $(\tilde{\mathbf{y}}, \tilde{\mathbf{z}})$ given \mathbf{y} is defined as

$$\begin{aligned} p(\tilde{\mathbf{y}}, \tilde{\mathbf{z}}|\mathbf{y}) &= p(\tilde{\mathbf{y}}|\mathbf{y})p(\tilde{\mathbf{z}}|\mathbf{y}) \\ &= \exp(\tilde{\mathbf{y}}^t \mathbf{y} - b\varphi(\cdot)) \exp(\tilde{\mathbf{z}}^t \mathbf{z} - c\varphi(\cdot)) \\ &= \exp(\tilde{\mathbf{y}}^t \mathbf{y} + \tilde{\mathbf{z}}^t \mathbf{z} - (b+c)\varphi(\cdot)), \end{aligned} \quad (2)$$

where t denotes a transpose, $\varphi(\cdot) = \ln(e^{\cdot} + e^{-\cdot})$ is a normalization constant, and \cdot is a positive constant that represents the noise level of the noisy channel. We assume that the label prior $p(\mathbf{y})$ is the uniform distribution, then $p(\mathbf{y}|\tilde{\mathbf{y}}, \tilde{\mathbf{z}})$ is calculated as follows.

$$\begin{aligned} p(\mathbf{y}|\tilde{\mathbf{y}}, \tilde{\mathbf{z}}) &= \frac{p(\tilde{\mathbf{y}}, \tilde{\mathbf{z}}|\mathbf{y})P(\mathbf{y})}{\sum_{\mathbf{y}} p(\tilde{\mathbf{y}}, \tilde{\mathbf{z}}|\mathbf{y})P(\mathbf{y})} \\ &\propto (\tilde{\mathbf{y}}^t \mathbf{y} + \tilde{\mathbf{z}}^t \mathbf{z}). \end{aligned} \quad (3)$$

This is equivalent to the Hamming distance between $(\tilde{\mathbf{y}}^t, \tilde{\mathbf{z}}^t)$ and (\mathbf{y}, \mathbf{z}) , then an estimate $\hat{\mathbf{y}}$ of the original label \mathbf{y} can be decoded as

$$\hat{\mathbf{y}} = \operatorname{argmax}_{\mathbf{y}} p(\mathbf{y}|\tilde{\mathbf{y}}, \tilde{\mathbf{z}}). \quad (4)$$

This decoding method is equivalent to the Hamming decoding with parity bits and reduces to the naive multi-labeled decoding method when the parity bits \mathbf{z} are omitted.

2.3 Estimation of confidence

In model (2), \cdot was set at a positive constant, implying all classifiers are assumed to have the same reliability (confidence). This assumption is not natural, however, because performances of classifiers are different from each other according to the difficulty in corresponding classification problems or the underlying geometrical structure of dataset. Takenouchi and Ishii [4] introduced the confidence of classifiers into multi-class classification problems. Following this existing study, we introduce the confidence for each classifier, and then the probabilistic model is extended as

$$\begin{aligned} p(\tilde{\mathbf{y}}, \tilde{\mathbf{z}}|\mathbf{y}; \boldsymbol{\beta}, \boldsymbol{\gamma}) &= p(\tilde{\mathbf{y}}|\mathbf{y}; \boldsymbol{\beta})p(\tilde{\mathbf{z}}|\mathbf{y}; \boldsymbol{\gamma}) \\ &= \exp\left(\sum_{j=1}^b (\tilde{y}_j y_j - \varphi(\tilde{y}_j))\right) \\ &\quad \times \exp\left(\sum_{k=1}^c (\tilde{z}_k z_k - \varphi(\tilde{z}_k))\right) \end{aligned} \quad (5)$$

where $\boldsymbol{\beta} = (\beta_1, \dots, \beta_b)$ and $\boldsymbol{\gamma} = (\gamma_1, \dots, \gamma_c)$ are parameter vectors representing the confidence of each dimension of the noisy channel. Parameters $\boldsymbol{\beta}, \boldsymbol{\gamma}$ can be estimated as to maximize the log-likelihood:

$$L(\boldsymbol{\beta}, \boldsymbol{\gamma}) = \sum_{i=1}^N \log p(\tilde{\mathbf{y}}^i, \tilde{\mathbf{z}}^i|\mathbf{y}^i; \boldsymbol{\beta}, \boldsymbol{\gamma}). \quad (6)$$

Stationary conditions of equation (6) become

$$\begin{aligned} \frac{\partial L}{\partial \beta_j} &= \sum_{i=1}^N (\tilde{y}_j^i y_j^i - \frac{\exp(\beta_j) - \exp(-\beta_j)}{\exp(\beta_j) + \exp(-\beta_j)}) \\ &= 0, \end{aligned} \quad (7)$$

$$\begin{aligned} \frac{\partial L}{\partial \gamma_k} &= \sum_{i=1}^N (\tilde{z}_k^i z_k^i - \frac{\exp(\gamma_k) - \exp(-\gamma_k)}{\exp(\gamma_k) + \exp(-\gamma_k)}) \\ &= 0. \end{aligned} \quad (8)$$

Those equations can be analytically solved as

$$\hat{\beta}_j = \frac{1}{2} \ln \frac{1 - C_{y_j}}{C_{y_j}}, \quad \hat{\gamma}_k = \frac{1}{2} \ln \frac{1 - C_{z_k}}{C_{z_k}}, \quad (9)$$

where $C_{y_j} = \frac{1}{N} \sum_{i=1}^N \frac{1 - (\tilde{y}_j^i y_j^i)}{2}$ is the error rate of the classifier associated with the code \mathbf{y}_j and $C_z =$

$\frac{1}{N} \sum_{i=1}^N \frac{1 - (\tilde{z}_k^i z_k^i)}{2}$ is that with the parity bits z_k . After identifying the characteristics of the noisy channel, the label $\hat{\mathbf{y}}$ can be decoded as a maximum *a posteriori* (MAP) estimate:

$$\hat{\mathbf{y}} = \operatorname{argmax}_{\mathbf{y}} p(\mathbf{y} | \tilde{\mathbf{y}}, \tilde{\mathbf{z}}; \hat{\boldsymbol{\beta}}, \hat{\boldsymbol{\gamma}}). \quad (10)$$

Note that the posterior probability in equation (10) is rewritten as

$$\begin{aligned} p(\mathbf{y} | \tilde{\mathbf{y}}, \tilde{\mathbf{z}}; \hat{\boldsymbol{\beta}}, \hat{\boldsymbol{\gamma}}) &= \frac{p(\tilde{\mathbf{y}}, \tilde{\mathbf{z}} | \mathbf{y}; \hat{\boldsymbol{\beta}}, \hat{\boldsymbol{\gamma}}) p(\mathbf{y})}{\sum_{\mathbf{y}} p(\tilde{\mathbf{y}}, \tilde{\mathbf{z}} | \mathbf{y}; \hat{\boldsymbol{\beta}}, \hat{\boldsymbol{\gamma}}) p(\mathbf{y})} \\ &\propto \sum_{j=1}^b \tilde{y}_j y_j + \sum_{k=1}^c \tilde{z}_k z_k \quad (11) \end{aligned}$$

Namely, this decoding is a weighted version of the Hamming decoding, but the weight is estimated by the maximum likelihood estimation from multi-labeled classification results of the training data. This approach is natural, because our decoding is based on the weighted Hamming distance and its weight is determined based on the classification performance of each binary classifier for the training dataset.

2.4 Difficulty of decoding process

In the previous subsection, we applied the MAP decoding (10) in which the number of candidates to be searched becomes exponential, 2^b . If the number b of categories is large, this decoding process becomes hard. To avoid this problem, one practically good way is to restrict the multiplicity being small such as

$$\{\mathbf{y} | \sum_{i=1}^b \frac{y_i + 1}{2} \leq 3\}.$$

This restriction seems plausible, in practical for example, in the text categorization problem, because major part of texts are likely assigned each to a few classes. Using this assumption, the number of code candidates to be searched is reduced to ${}_a C_3$, which makes the MAP decoding feasible.

3 Experiment result

In this section, we examine the performance of the proposed method by comparing with the naive classification based method, using synthetic datasets. The parity bits were randomly generated and the MAP decoding was employed in the proposed method. For binary classifiers, we employed the simplest linear discriminant analysis. A typical example of dataset consisting of 90 input data with 3 categories, is shown in Figure 1.

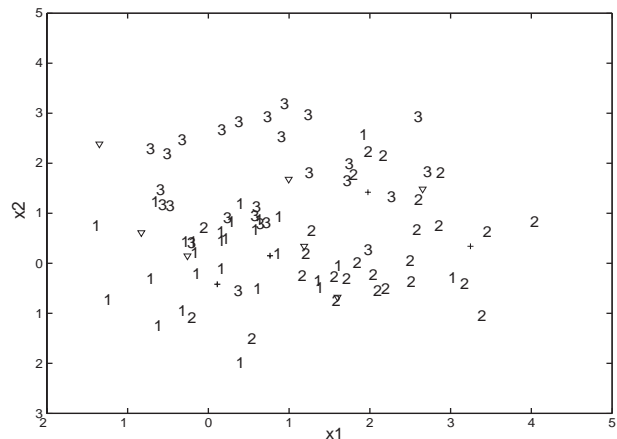


Figure 1: An example dataset. Each numerical character indicates the class to which an input vector is assigned. A symbol ∇ indicates an input assigned to two categories and $+$ means that the corresponding input does not belong to any category.

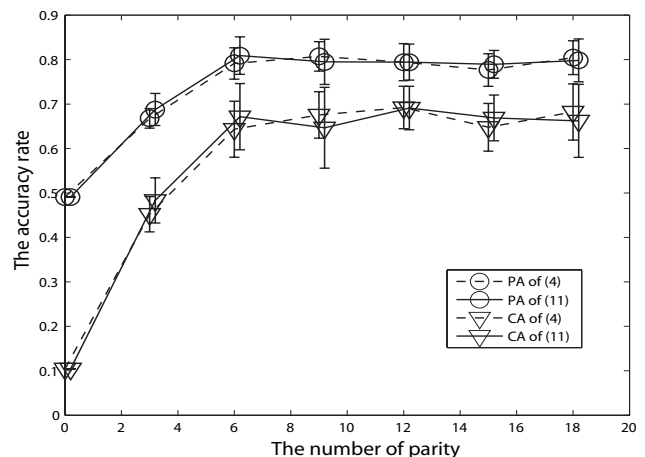


Figure 2: PA and CA of the two decoding methods, the Hamming decoding with parity bits (equation(4)) and the weighted Hamming decoding with parity bits (equation(11)), against the length of parity bits.

For performance evaluation, we used two kinds of quantities: complete accuracy rate (CA) and partial accuracy rate (PA). CA is the rate of events in which the vector (three-dimensional, in this case) of decoded label completely coincides with that of the original label, and PA is the rate with which the element of the decoded label is consistent with that of the original label.

Figure 2 shows averaged CA and PA of the proposed method for 10 trials. The error bar is the standard deviation in the 10 trials. In this figure, we compared the Hamming decoding with parity bits (equation(4)) and the weighted Hamming decoding with parity bits (equation(11)). For comparison, we also applied a naive multi-labeled classification method, that is, a set of individual binary classifiers assign the label for the corresponding category. CA and PA of the naive method were 0.1111 and 0.5056, respectively. From the comparison, we can see (1) the proposed methods outperformed the naive method; and, (2) when the parity length was $c \geq 6$, the performance by our methods was consistently good.

4 Conclusion

We proposed a novel method for multi-labeled classification problems based on the framework of ECOC. This regard the classification errors of classifiers as the noise of the channel. Using the parity associated with the label, we can improve the classification accuracy in comparison to the naive classification based method. As a future work, we plan to apply the proposed method for real datasets. For this application, the decoding method discussed in subsection 2.4 will be improved. However, the design of parity bits on in our future work.

References

- [1] E. L. Allwein, R. E. Schapire, Y. Singer. "Reducing Multiclass: A unifying Approach for Margin Classifiers," *Journal of Machine Learning Research*, **1**, 113-141, 2001.
- [2] T. G. Dietterich, G. Bakiri. "Solving multi-class learning problems via error-correcting output codes," *Journal of Artificial Intelligence Research*, **2**, 263-286, 1995.
- [3] S. T. Dumais, J. Platt, D. Heckerman, M. Sahami. "Inductive learning algorithms and representations for text categorization," *ACM-CIKM'98*, 1998.
- [4] T. Takenouchi, S. Ishii. "Multiclass classification by an extension of ECOC decoding," *2006 Workshop on Information-Based Induction Sciences*, 2006 (in Japanese).
- [5] N. Ueda, K. Saito. "Parametric Mixture Models for Multi-Labeled Text," *Advances in Neural Information Processing Systems 15*, 721-728, 2002.

A control method of an electric vehicle

Masanori Sugisaka¹, Hiroaki Tanaka¹ and Masayoshi Hara¹

¹ Department of Electrical and Electronic Engineering, Oita University, Oita, Japan
 (+81 -975-54-7831, E-mail: msugi@cc.oita-u.ac.jp, mhara@cc.oita-u.ac.jp)

Abstract: The research of the electric vehicle in our laboratory is developed in two fields. One is the control of the speed (operation of the accelerator and the brake), the other is the controls of the steering wheel. We controlled the speed by using turning on and turning off control at the early stage. We could get a moderate result in this experiment. And we controlled the speed by the another control method that also had generality being possible to correspond to road situation. As a result, we could do the appropriate control of accelerator. Needing the control of the accelerator and the brake is combined with the control of steering wheel is running at a constant speed. This becomes a necessary, indispensable technology in doing the driving support and actually running on the road.

Keywords: operation of the accelerator and the brake, control method

1. INTRODUCTION

If the automatic driving technology based on “Active Safety” develops, the number of accidents by a human factor decreases. The control of the steering wheel by the image data processing using CCD camera was possible recent work. But control of an accelerator and a brake is not automatic. So in this system, combining the operation of the accelerator and the brake is a problem. Needing the control of the accelerator and the brake is combined with the control of steering wheel is running at a constant speed. Therefore, we research the speed control as a basic research to combine the control of the accelerator and the brake with the steering control by the visual system. We controlled the speed by using turning on and turning off control at the early stage of the research. We could get a moderate result in this experiment. But we controlled the speed by the PID control that also had generality being possible to correspond to more road situation.

2. ELECTRIC VEHICLE

We show this vehicle in Fig.1 and configurations of this vehicle in Table 1.



Fig. 1 An electric vehicle

Table 1 A configuration of an electric vehicle

Length	2,395(mm)
Wide	1,010(mm)
Height	1,490(mm)
Weight	470(kg)
Max speed	45(km/h)
Motor	DC brassieres motor
Max power	5.2(kw)

3. CHARACTERISTIC OF ACCELERATOR AND BRAKE

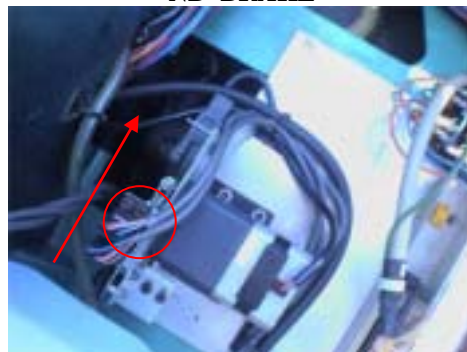


Fig.2 Motor of accelerator

The accelerator of the electric vehicle does a usual accelerator operation by rotating the motor. In another word, the accelerator wire is pulled by depressing the accelerator when the driver person, and it leads to the drive of the DC motor.

Another wire is pulled by rotating, and the DC motor is driven the stepping motor the act of pulling the accelerator wire. Moreover, the brake ties to the stepping motor the brake pedal with the wire. They greatly depend on the parameter, the number of movement pulses, and the passing speed used to control the stepping motor, and control the amount of depressing of the accelerator brake and the depressed speed by changing these parameters.

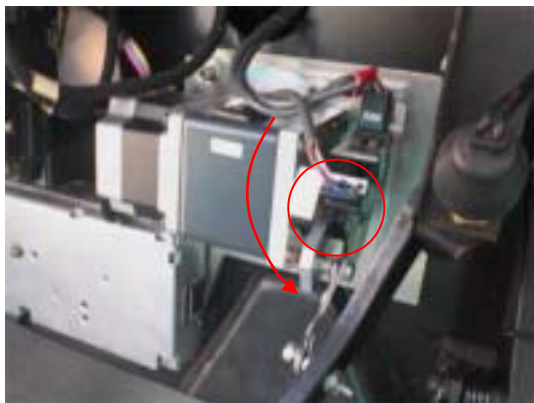


Fig.3 Motor of brake

Here, the moving speed is a parameter in the amount of depressing of the accelerator and the brake in the number of output pulses corresponding to each depressed speed. It is based on the specification of the stepping motor of the amount of the rotation in the number of pulses in this and the specification of the rotational speed at the pulse frequency.

4. Control method

We get speed characteristic of this vehicle from experiments and below equation.

Speed characteristic with load

$$y(k) = \frac{1.46}{751.2} (R(k) - R(k-1)) (m/s)$$

$$= \frac{1.46 \cdot 3.6}{751.2} (R(k) - R(k-1)) (km/h)$$

(1)

here: sampling time 1(sec)

The difference of the encoder value is taken in this computational method, and the speed is calculated by the change.

We do experiments use this equation. And control method is using simple PID control. At first, we do a constant moving speed experiments. It is for the characteristic of this vehicle moving speed. It runs in the straight line by using a general road as the experiment method. It is set that the measurement time is assumed to be 60(sec), and the stop operation is done after it runs of 40(sec). The accelerator and the brake operation between those are due to the program, and the experimenter (driver) does the steering wheel operation.

The expression from which the number of movement pulses is:

$$u(k) = 33.657 \left\{ e(k) + 1 \cdot \sum_{j=k-1}^k e(j) + 1 \cdot (e(k) - e(k-1)) \right\} \quad (2)$$

$$e(k) = r(k) - y(k)$$

(3)

$u(k)$: number of moving pulse

$e(k)$: difference

$y(k)$: speed value

One of the experiment result is presents Fig. 4. It is understood that the shifting value at the speed that is the problem in the current result is considerably improved from the experiment result. Moreover, it becomes a repetition of a detailed error margin about other shifting value parts, and the more error has disappeared. It became the result of understanding number of the accelerator increased in shape corresponding to this about number of the accelerator in the inclination of going up. However, there is an insufficient part as a control of the speed.

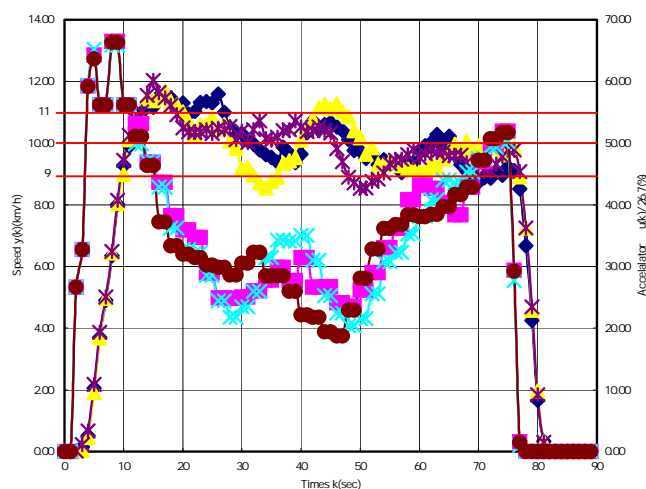


Fig.4 Speed chara. using PID control

5. CONCLUSION

In this research, first of all, the base of the speed control was done. Next, the speed by PID was controlled. Various parameters in the PID control were decided from the experiment. However, the characteristic was led by using the speed characteristic of not a real load but no-load-condition that the speed settled to some degree. The adjustment of each parameter has properly adjusted a necessary part repeating the experiment. One of the results was shown. However, it is thought that the problem by the delay of the processing speed occurs in both the steering control, the accelerator, and the brake control by increasing the speed.

It is necessary to examine the combination with the steering control as a problem in the future with the improvement at the parameter and the sampling time.

The Influence for Human Boredom in Interaction by Mutual Prediction

M. Shimamoto, T. Shiose, H. Kawakami and O. Katai
Dept. of Systems Science
Graduate School of Informatics, Kyoto Univ.
Kyoto, Japan, 606-8501

Abstract

In the research fields of Human-Robot interaction (HRI) and Human-Agent interaction (HAI), human boredom of robots or agents is a significant problem that needs solving. Clarifying the human characteristic of boredom may be conducive to designing agents and on HRI framework. In this study, we focus on mutual prediction, which is a distinct property of animal-animal interaction, including humans, and we aim to clarify how mutual prediction affects human-agent interaction. In this paper, we explain our experimental setup for investigating influence of mutual prediction on human boredom in human-agent interaction and of subjective cognition of opponents. In these experiments, we set two axes to represent experimental conditions, one is subjective cognition of an opponent, which means subjects believe the opponent is human or a computer, the other is the presence or absence of the opponent's prediction.

1 Introduction

Since the emergence of robots designed to communicate with humans, research in HRI (Human-Robot Interaction) and HAI (Human-Agent Interaction) has gathered momentum [1, 2]. In this research field, human boredom of robots or agents is one of the main problems preventing sustained human-robot or human-agent interaction.

In this study, we aim to clarify one aspect of the human property of boredom with human-agent interaction. We focus especially on mutual prediction, which is a distinct property of interaction between intentional entities such as humans and animals that have the abilities of prediction, adaptation and so on. We aim to clarify how mutual prediction affects human boredom with human-agent (computer) interaction.

2 Research Background

2.1 Psychological Saturation and Boredom in Interaction

In the field of psychology, boredom is called "psychological saturation", and it has been researched from the early twentieth century. Psychological saturation is a psychological state in which someone can't stay with a certain uniform action any more and stops it, even when he/she is told to continue performing that uniform action. Psychological saturation was manifested experimentally by Karsten [3].

However, when we consider HRI or HAI, there is another aspect of human boredom that can't be treated as psychological saturation. Psychology saturation is a psychological state specific to a certain uniform action, whereas in HRI or HAI, if a robot has a abilities of prediction and adaptation, there is a nested structure of prediction and adaptation between humans and robots (agents) due to interaction between humans and robots (agents). That means humans naturally predict and adapt to objects, but objects also predict and adapt to humans. The phenomenon above is called mutual prediction or mutual adaptation [2, 4].

In this study, we examine how mutual prediction affects human boredom, which can't be treated as psychological saturation.

2.2 Mutual Prediction

We behave based on our prediction of others' behavior in daily life. Naturally others also behave based on their prediction of our behavior. In the case of such interaction that establishes mutual prediction of each other's behavior, there is infinite regress caused by nested structures. Consequently, there is no optimal solution in such interaction.

Luhmann focused on mutual prediction in interaction, and considered how laws and regulations are constituted by mutual prediction [5]. He separated prediction into two types: "cognitive prediction" and "pre-

scriptive prediction". Cognitive prediction is that humans reform and accommodate their prediction when actual results are different from the predicted one. On the other hands, prescriptive prediction is that humans do not reform their prediction even when actual results are different. Once prediction is formed, prescriptive prediction can be applied to a certain uniform action or physical objects because these do not change drastically. On the contrary, we need to apply cognitive prediction to objects that possess the abilities of prediction and adaption such as humans, animals, or agents because there is a nested structure of prediction and adaptation.

Iizuka and Ikegami proposed a computational model of mutual prediction in interaction [4]. They used a simulated mobile robot with a recurrent neural network, and two agents performed turn-taking behavior. And they reported that there are two phases of turn-taking behavior: one is a stable phase because each agent can predict the other and there are certain trajectory patterns, the other is unstable phase because prediction of each agent collapses and there are chaotic trajectories. The above phenomenon occur because of mutual prediction, which composes nested structure.

As described above, there is a different aspect in HRI or HAI from interaction between humans and physical objects. We suppose that the ambivalent directional properties described above affect human boredom in HRI or HAI.

2.3 The Difference from Subjective Cognition on Opponents

The study by Reeves and Nass is pioneering research in the field of human-computer interaction[6]. They reported that people unconsciously treat computers and television as the same as humans.

On the contrary, Gallagher et al. reported that the activated region of the human brain is different when subjects believe an opponent is human from when they believe an opponent is a computer [7]. In their rock-scissors-paper game experiments, subjects were taught that an opponent is either human or a computer, even though the opponent is always a computer whose behavior was programmed randomly in both conditions. Although winning percentages of subjects are the same in both conditions, the activated region of the human brain actually differed according to the conditions. Takahashi et al. also reported that subjects' behavior differs due to subjective cognition of an opponent [8]. When subjects were taught that an opponent was human, their behavior became more explorative than

that of the condition in which they were taught that the opponent was a computer. Their experimental results indicate that when people believe an opponent is a computer, people behave more exploitatively which means they use "prescriptive prediction" rather than "cognitive prediction".

As the above reports outline, human behavior differs between when people believe an opponent is human and when it is a computer. This difference may arise from people's belief or perceived notion that a computer must be routine and that it must be ruled by constant rules and designs.

Based on the above perspective, we aim to clarify the following two points in this study.

- First, we aim to clarify the differences among subjects' boredom from subjective cognition to an opponent.
- Does mutual prediction affect human boredom in a little more complex situations than the rock-scissors-paper game?

In the next section we explain the experimental setup for a method to these two points.

3 Experimental Setting

In this study, we conduct experiments using a simple card game. In this game, a subject and an opponent put down a card from the three each is holding (numbered 1 to 3) at the same moment, and the one who puts down the higher card wins. Players can not put down a card before he/she put down once in one set, and the player who wins two of three games wins a set. For example, if a subject put down cards 3→1→2 in series and an opponent put down cards 2→3→1, the subject wins two games and, therefore, wins that set (Fig:1). Subjects repeat this card game a few dozen times.

This card game is essentially no different from the rock-scissors-paper game, but it may be a little more tactical rather than the rock-scissors-paper game because the card to be put down is restricted by the sequence in which cards are put down. There are 36 possible patterns by which a player and an opponent can put down cards sequentially in a set. The probabilities of the subject's winning and losing are both 1/6, and the remaining 2/3 are for a draw. If the subject wins a set, he/she gets +100 points, if the result is a draw, 0 points, and if he/she loses, -100 points. Subjects play this card game using a display and a

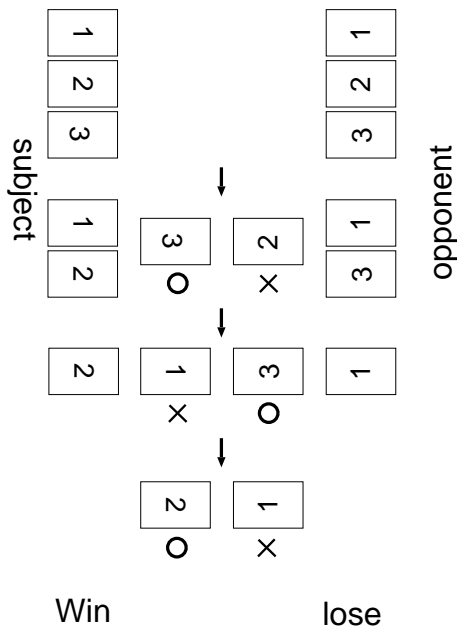


Figure 1: transition of a set

keyboard, and they cannot see the opponent's display and keyboard directly.

3.1 Experiment 1

In this experiment, we examine whether the difference in subjects' boredom arises from subjective cognition of an opponent. We set following two conditions:

- subjects believe the opponent is human;
- subjects believe the opponent is a computer;

To make subjects believe the opponent is human, we allocate an experimental assistant, and have the experimental assistant pretend to play the card game. We set up the assistant's display and keyboard so as to be invisible to the subjects (Fig:2).

The order of putting down the cards in series is decided randomly by a program in both conditions. It is natural that subjects become bored with the game itself, therefore, order of the experimental conditions becomes equal to about two conditions so as to counteract the effect of the sequence. After finishing each condition, we ask the subjects to answer questionnaires about the trial.

To analyze patterns of subjects' behavior and the questionnaire results, we examine whether subjective

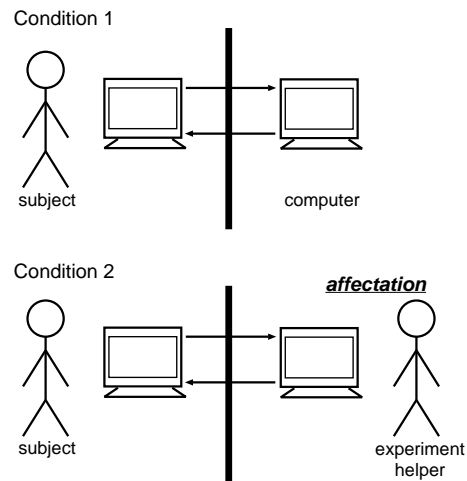


Figure 2: experimental conditions

cognition of an opponent affects subjects' boredom. That is to say, we investigate whether subjects believe the trial is boring because they think the opponent is a computer.

3.2 Experiment 2

In this study, we focus on mutual prediction in interaction, and aim to clarify how mutual prediction affects human boredom. In experiment 2, we build a mechanism that can predict subjects' behavior from their behavioral history. We then investigate how the mechanism affects subjects' boredom and subjective cognition of an opponent. We set following two conditions.

- How cards are put down decided at random
- How cards are put down is decided by the mechanism that may predict subjects' behavior

In both conditions, we do not tell subjects whether the opponent is human or a computer. As in experiment 1, the order of experimental conditions become equal to about two conditions so as to counteract the effect of sequences, and we ask subjects to answer questionnaires about the trial.

We set the predictive mechanism that the probability of how to put down cards changes based on the sequence in which subjects put down their cards. We describe the process of subject putting down cards as a_{s1}, a_{s2}, a_{s3} in a trial, and that of a computer as a_{c1}, a_{c2}, a_{c3} . Furthermore we define a situation as $s = \{a_{s1}, a_{s2}, a_{s3}, a_{c1}, a_{c2}, a_{c3}\}$. The first card to be

put down of a computer in a trial is decided as follows.

$$P_1(d|s) = \frac{\text{Count}(d|s)}{\sum_a \text{Count}(a|s)} \quad (1)$$

After a trial, we add +1 to $\text{Count}(a = A|s = S)$, where A is the first instance of subjects putting down card in that trial, and S is the situation of the previous trial.

The second card to be put down of a computer is simply decided by the first instance of both the subject and the computer. just as with the first instance, we add +1 to the count after a trial, and the probabilities change.

$$P_2(d|a_{s1}, a_{c1}) = \frac{\text{Count}(d|a_{s1}, a_{c1})}{\sum_a \text{Count}(a|a_{s1}, a_{c1})} \quad (2)$$

In this experiment, subjects must judge whether opponent is either human or a computer, and we investigate how establishing a certain degree of mutual prediction affects subjective cognition of an opponent, and whether if subjective cognition has a relationship with human boredom in interaction.

4 Summary

In this study, we aimed to clarify one aspect of the human property of boredom. Especially, we focused on mutual prediction, that is a distinct property of humans and animals. We discussed how HRI and HAI are different from interaction between humans and physical objects from the viewpoint of mutual prediction and mutual adaptation, and we explained experimental settings for investigating a the influence of mutual prediction on human boredom. The experimental results will be reported on the day of our presentation.

We plan to measure not only responses in subjects' questionnaires but also their biological information in the near future, and we would like to deal with human boredom quantitatively to some extent. We intend to use electrocardiograms and skin conductance, which are used to measure stress and excitation, to achieve this.

References

- [1] C. Breazeal, "Social Interactions in HRI: The Robot View," in *IEEE SMC Transactions*, Part C., 2004.
- [2] S. Yamada and T. Yamaguchi, "Mutual Adaptation to Mind Mapping in Human-Agent Interaction," *IEEE International Workshop on Robot-Human Interaction (ROMAN-2002)*, pp. 105-110, 2002.
- [3] A. Karsten, "Psychology Satuartion," *Psychological Research*, Vol. 10, pp. 612-628, 1928.
- [4] H. Iizuka and T. Ikegami, "Adaptability and Diversity in Simulated Turn-taking Behaviour", *Journal of Arti cial Life*, Vol.10, No.4, pp.361-378, 2004.
- [5] N. Luhmann, "Rechtssoziologie", *Rowohlt Taschenbuch Verlag*, 1972. (translated into Japanese)
- [6] B. Reeves and C. Nass, "The Media Equation: How People Treat Computers , Television and New Media Like Real People and Places," *University of Chicago Press*, 1996.
- [7] H. Gallagher, A. Jack, A. Roepstroff and C. Frith, "Imaging the Intentional Stance in a Competitive Game," *NeuroImage*, Vol. 16, No. 3a, pp. 814-821, 2002.
- [8] H. Takahashi and T. Omori, "Intentional Stance Regulates Behavioral Balance of Exploration and Exploitation in a Competitive Game," *2nd Annual Computational Cognitive Neuroscience Conference*, 2006.

A property of associative memory models with replacing units

Akira Date
Faculty of Engineering
University of Miyazaki
Miyazaki 889-2192
date@cs.miyazaki-u.ac.jp

Koji Kurata
Faculty of Engineering
University of the Ryukyus
Okinawa 903-0213
kurata@mibai.tec.u-ryukyu.ac.jp

Abstract

This paper describes a property of associative memory networks in which a number of units are replaced when the networks learn. In our network, every time the network learns a new item or pattern, a number of neurons die and the same number of neurons are born. It is shown that the memory capacity of the network depends on the number of replaced units, and that the memory capacity is maximized when the number of replaced units is optimal. The optimal number of replaced units is small and seems to be independent of the network size. Although our model was not motivated by higher nervous function, the results suggest that small number of newly born neurons might be optimal in some sense for the distributed memory system.

Keywords: associative memory, collective memories, catastrophic interference, new neuron

1 Introduction

The purpose of this paper is to describe a property of associative memory networks in which a number of units are replaced when the networks learn a new item. The neural network models of associative memory have been studied extensively since 1960's [1, 2, 3, 4, 5]. Most familiar learning for association among memories is the Hebb rule or a *correlation*-based learning in which each connection weight between two neurons are modified according to the correlation between the activities of the neurons. The learning is *local*, and easy to implement in the circuits. There exists a memory capacity for the network. The addition of new memories beyond the capacity overloads the system and makes all memory states irretrievable (catastrophic forgetting) unless there is a provision for forgetting old memories.

If the dynamics of weight connections of the network have decay [3, 4] or saturation[1], the catastrophic forgetting does not occur and the network can keep recent memories. Here we describes the alternative network which share

the same properties; avoidance of catastrophic forgetting, keeping recent memories. In our network, every time the network learns, neurons die and are born. The number of replaced units was varied in the experiment to maximize the memory capacity. We found that the optimal number of replaced units was small and independent of the network size. Although our model was not motivated by higher nervous function, the results might suggest that small number of newly born neurons is enough and optimal for a temporal memory system such as the hippocampus.

2 Associative Memory

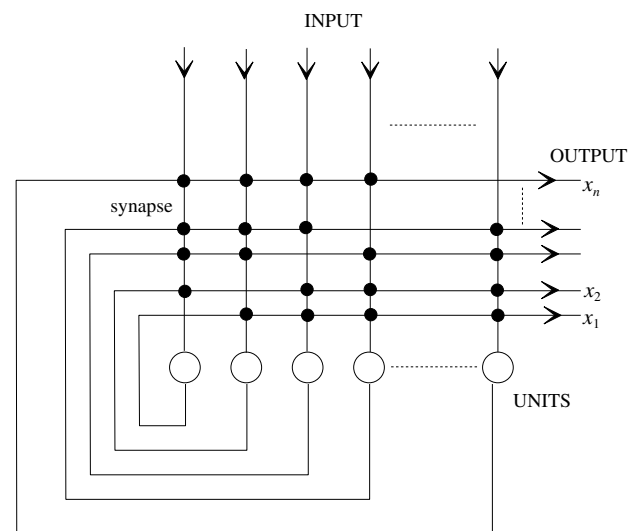


Figure 1: A network of associative memory

2.1 Network dynamics

In our network of associative memory (Fig.1, [1]), each unit, j , has two states, and is described by a variable

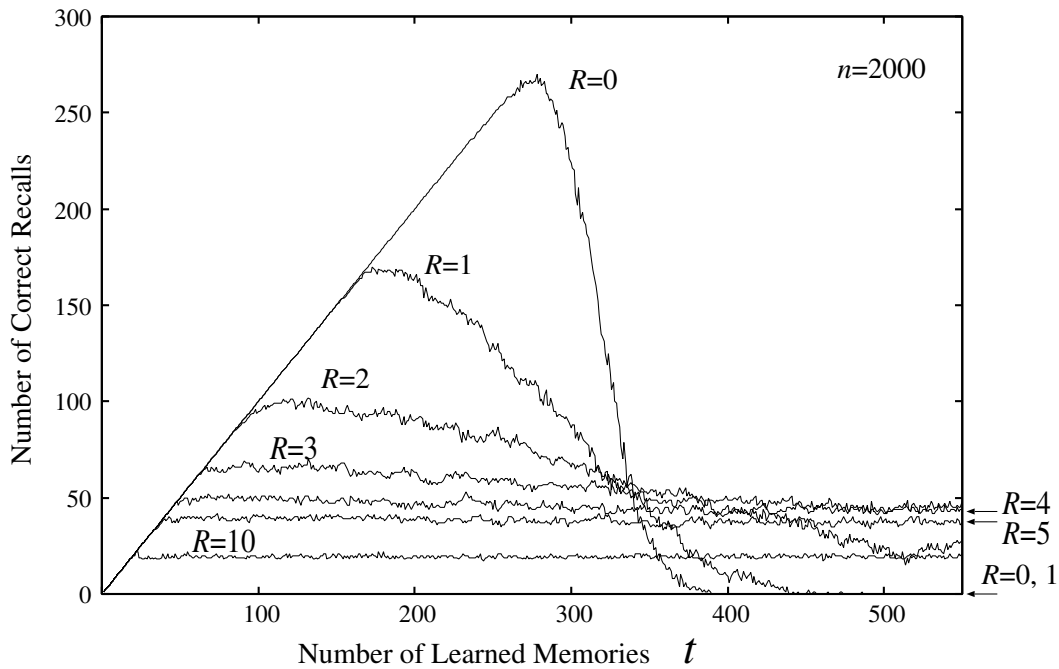


Figure 2: Number of memories correctly recalled as a function of number of learned ones.

$x_j = \pm 1$. The instantaneous state of the system of n units can be thought of as an n -dimensional vector having components x_i . The units are inter-connected by a network of synapses, with a synaptic strength w_{ij} from unit j to unit i . The instantaneous input to unit i is

$$u_i = \sum_{j=1}^n w_{ij} x_j \quad (1)$$

where x_j is the present state (± 1) of unit j . The state of the system changes in time; Each unit i readjust its state, setting $x_i = \pm 1$ according to whether u_i , the input to i at that moment is greater or less than zero. The units act asynchronously in a random order. This algorithm defines the time evolution of the state of the system. For any symmetric connection matrix $\{w_{ij}\}$; $w_{ij} = w_{ji}$, there are stable states of the network of units; Starting from any arbitrary initial state, the system reaches a stable state and ceases to evolve [1].

2.2 Content addressable memory

The Hebb rule has served as the starting point for the study of information storage in simplified models. Suppose we wish to store the set of states $\mathbf{x}^\mu, \mu = 1, 2, \dots, m$. To learn a new memory \mathbf{x}^1 , increment w_{ij} by

$$\Delta w_{ij} = x_i^1 x_j^1. \quad (2)$$

This learning process is local; the increment for connection w_{ij} does not depend on the global structure of the state or past memories, but only on x_i^1 and x_j^1 . It is fast and does not need to learn each memory repeatedly.

This network now functions as an associative memory. If started from an initial state which resembles somewhat state \mathbf{x}^1 and which resembles other $\mathbf{x}^\mu (\mu \neq 1)$ very little, the state will evolve to the state \mathbf{x}^1 . The state \mathbf{x}^1 is evocable memory, and the system correctly reconstructs an entire memory from any initial partial information, as long as the partial information was sufficient to identify a single memory. Detailed properties of the collective operation of this network have been studied extensively [1, 2, 3, 4, 5].

2.3 Catastrophic forgetting or interference

Computer modeling of memory storage according to equation (2) was carried out for $n = 2000$. 550 random memory states ($\mathbf{x}^1, \dots, \mathbf{x}^{550}$) were chosen in each of which half of units were in the active firing state on the average. The network learned one by one by updating w_{ij} incrementally, i.e., new memories were continually added to w_{ij} . There is a memory capacity for this network [1, 2, 5]; About $280 (= 0.14n)$ states can be simultaneously memorized without error in recall. The addition of new memories beyond the capacity overloads the system and makes all memory states irretrievable (catastrophic forgetting) unless

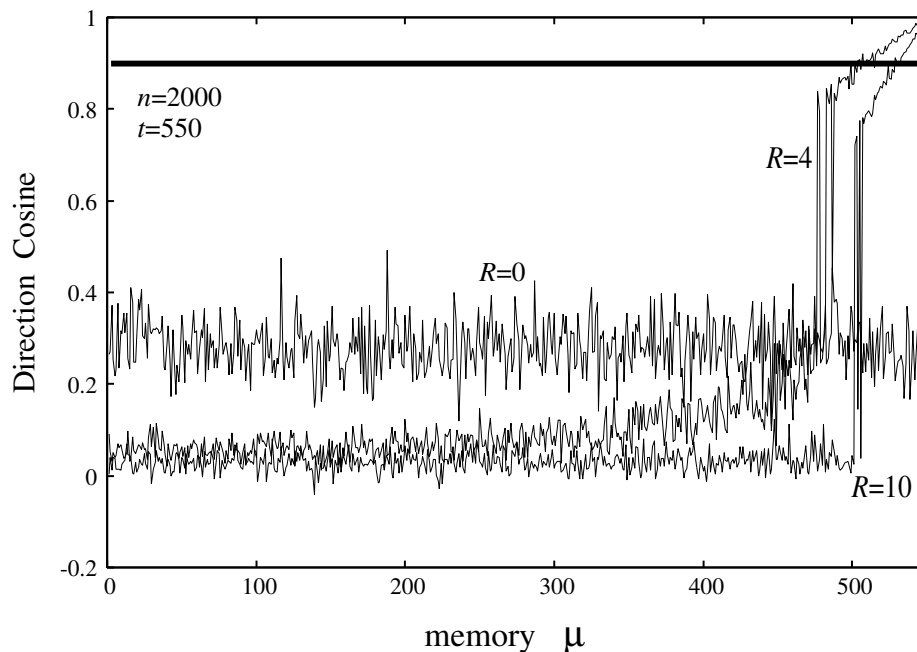


Figure 3: Closeness between each learned state x^μ and the recalled state for each memory, $x^\mu, \mu = 1, \dots, 550$.

there is a provision for forgetting old memories.

The network learned 550 memories one by one in which a memory x^t was learned at time t . We tested at each time t , whether network can recall each learned memory without error. Each learned state $x^\mu, \mu = 1, \dots, t$ was given as a starting state to the network. The network quickly reached a stable state x . We compared x^μ to x thus obtained. The proximity of the two states was measured by retrieval overlap

$$a = \frac{1}{n} \sum_{i=1}^n x_i^\mu x_i.$$

We counted the number of successfully recalled memories in which the proximity was larger than 0.9. A curve of $R = 0$ in Fig. 1 illustrates how many states there were remembered without error in recall at time t ; The network was able to remember all of memorized patterns for $t < 280$, where it was able to learn, But at $t = 280$, forgetting started, and any memories could not be remembered correctly after $t = 380$, i.e., the network could not recall even the most recent memory.

3 Results

For simplicity, we assume the following throughout the present experiment: Every time the network learns a new memory, a number of neurons, say R neurons, die and the

same number of neurons are born; we assumed that the total number of neurons does not change in time. It corresponds to reset connection weights $w_{ij} = w_{ji} = 0, j = 1, \dots, n$ for replaced neurons i . Units were replaced from the oldest one, i.e., they were replaced always in the same order. Simulation were carried out on a computer for $n = 2000$ with varying R , number of replacing units. Results are shown in Fig.1. Larger was the number of replacing units R , earlier the start of forgetting. For $R = 1$, forgetting started at around $t = 180$ and for $R = 3$ it started at around $t = 60$. Our interest was the properties of the network whose structure had already been stable ($t > 500$). The network for $R = 0, 1$ could not recall any memory at $t > 420$. For large $R \geq 2$, the network could recall a number of memories; 44 memories were recalled successfully for $R = 4$.

To see which 44 memories out of 550 were kept successfully, we tested the network at $t = 550$; each learned memory x^μ was given as a initial state, and the closeness of stable state of the network and memories was measured. Results are shown in Fig.2. As we expected, only the newest memories were recalled correctly. Results of the networks for $R = 4$ and $R = 10$ show that the number of memory successfully retained (a network capacity) was dependent on R , the number of replacing units. It turned out that there was a optimal replacing number near $R = 3$ for $n = 2000$. Computer simulation was carried out for $n = 5000$ with

varying R , we found that the optimal replacing number was the same as before, near $R = 3$. The number of success recalls depends on R , and the network for $R \approx 3$ was the optimal to maximize the number, which seems to be independent to the network size.

4 Discussion

To our surprise, the optimal $R \approx 3$ seemed to be independent to the size of the network. The proof of this conjecture might be possible under the following assumption: The present network is equivalent to the network in which weight connections have decay [3, 4] or saturation [1]. The networks share the same properties: avoidance of catastrophic forgetting, keeping recent memories.

The CA3 area of hippocampus is involved in associative memory recall [6, 7], and often modeled by a fully connected network in which each memory is represented by the activity of distributed and sparsely coded pattern. The models proposed so far for explanations of neurogenesis in hippocampus were layered networks which was designed based on known anatomical knowledge [8, 9, 10, 11, 12] in which hypothetical functions were assigned such as making sparse representation, enlarging a dimension of input signal, assigning distinct codes to similar inputs. In our simple system, replacing only a small number of units prevent from the catastrophic forgetting, maximizing a memory capacity. Memories in the hippocampus seems to move into the cortex within 6 weeks. The role of the hippocampus memory systems seems to retain recent limited number of memories. Our example also might answer from a mathematical viewpoint the question of why most newly born neurons die before they mature, and substantial number of replaced neurons observed is so small. It seems that the properties revealed in the present paper does not change by a slight modification of the model. (e.g., sparsely coded memory, the order of turnover)

Acknowledgments

This works was partly supported by Grant-in-Aid (16700232) from the Japanese Ministry of Education, Culture, Sports, Science and Technology (MEXT).

References

[1] J. J. Hopfield, "Neural networks and physical systems with emergent collective computational abilities," *Proceedings of the National Academy of Science USA*, vol. 79, pp. 2554–2558, 1982.

- [2] D. J. Amit, H. Gutfreund, and H. Sompolinsky, "Storing infinite numbers of pattern in a spin-glass model of neural networks," *Physical Review Letters*, vol. 55, pp. 1530–1533, 1985.
- [3] J. P. Nadal, G. Toulouse, J. P. Changeux, and S. Dehaene, "Network of formal neurons and memory palimpsests," *Europhysics Letters*, vol. 1, pp. 535–542, 1986.
- [4] M. Mézard, J. P. Nadal, and G. Toulouse, "Solvable models of working memories," *Journal of Physique*, vol. 47, pp. 1457–1462, 1986.
- [5] S. Amari and K. Maginu, "Statistical neurodynamics of associative memory," *Neural Networks*, vol. 1, pp. 63–73, 1988.
- [6] B. L. McNaughton and R. G. M. Morris, "Hippocampal synaptic enhancement and information storage within a distributed system," *Trends in Neurosciences*, vol. 10, pp. 408–415, 1987.
- [7] K. Nakazawa, M. C. Quirk, R. A. Chitwood, M. Watanabe, M. F. Yeckel, L. D. Sun, A. Kato, C. A. Carr, D. Johnston, M. A. Wilson, and S. Tonegawa, "Requirement for hippocampal CA3 NMDA receptors in associative memory recall," *Science*, vol. 297, pp. 211–218, 2002.
- [8] D. Marr, "Simple memory: a theory for archicortex," *Philosophical transactions of the Royal Society of London B*, vol. 262, pp. 23–81, 1971.
- [9] D. Willshaw, "An assessment of marr's theory of the hippocampus as a temporary memory store," *Philosophical transactions of the Royal Society of London B*, vol. 329, pp. 205–215, 1990.
- [10] S. Becker, "A computational principle for hippocampal learning and neurogenesis," *Hippocampus*, vol. 15, pp. 722–738, 2005.
- [11] M. O. M. Guillermo A. Cecchi, "Computational models of adult neurogenesis," *Physica A*, vol. 356, pp. 43–47, 2005.
- [12] L. Wiskott, M. Rasch, and G. Kempermann, "A functional hypothesis for adult hippocampal neurogenesis: Avoidance of catastrophic interference in the dentate gyrus," *Hippocampus*, vol. 16, pp. 329–343, 2006.

Force Control of 6-DOF Pneumatic Joystick

Takashi MORIKI*, Yoshito TANAKA**, Yutaka TANAKA***, Isao YOKOMICHI**,
Yasunobu HITAKA**, Junko ISHII**, Chikamune Wada*

*Department of Graduate School of Life Science and Systems Engineering,
Kyushu Institute of Technology, Japan

**Department of Control and Information Systems Engineering,
Kitakyushu National College of Technology, Japan

***Department of Mechanical Engineering, Hosei University, Japan
E-mail : stanaka@kct.ac.jp

Abstract

In this study we develop a new type joystick with force control. A developed joystick consists of a six-degree-of-freedom (6DOF) Stewart platform type⁽¹⁾ of joystick using pneumatic actuated parallel link mechanism. The thrust force of the cylinder is controlled by the PWM of the solenoid valve that uses PIC. When the thrust force of the cylinder is controlled, the control characteristic of the cylinder is improved by the effect of the accumulator so that it might make amends for the influence on the compressibility of air exerted on the characteristic of the thrust force of the cylinder. It is confirmed that the thrust force of the cylinder can be applied to the pneumatic joystick, and the z-axial force control is possible in the experiment.

1 Introduction

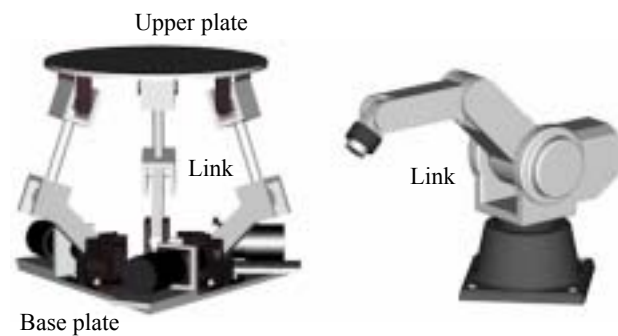
The necessity of the rehabilitation work support the technology expected for the social life independence of senior citizen nowadays. The function to support the multi degree of freedom movement of the rehabilitation equipment is necessary corresponding to the patient with various symptoms^{(2),(3)}. Then, we paid attention to a parallel mechanism with high rigidity that has a flexible motor function and performs high-speed and highly accurate six degree of freedom movement. We developed the force control system of 6-DOF Pneumatic Joystick and implemented it to the prototype model^{(3),(4)}. Force control system makes up a compact composition that consists of the small air pressure cylinder and the solenoid valve, and achieves the control of the thrust force of the cylinder by the PWM control of the solenoid valve.

This system was applied to the test pneumatic joystick, and the result of controlling force will be reported.

2 Force control of 6-DOF joystick

2.1 Parallel mechanism

Parallel and serial mechanisms are illustrated in Fig.1⁽⁵⁾. As shown in Fig.1 (a), parallel mechanism typically consists of a moving platform that is connected to a fixed base by several limbs⁽²⁾. Typically, the number of limbs is equal to the number of degrees of freedom such that every limb is controlled by one actuator and all the actuators can be mounted at or near the fixed base. Two plates (upper and base plates) are connected through six articulated links in which a linear actuator can change the link length. The links are jointed by universal joints. The length of links controls the position and orientation of the upper plate with respect to the base plate. The individual errors in the active links are not cumulative. The external forces applied to the upper plate are distributed among all parallel links and actuators. The parallel mechanism has usually the basic advantages of high positioning accuracy, high rigidity, high operational speed and very high load capacity compared to serial mechanisms as shown in



(a) Parallel mechanism (b) Serial mechanism

Fig.1 Parallel and serial mechanisms

Fig.1 (b). The disadvantage of the parallel mechanism is to have a small volume of its working range relative to the dimensions of the links⁽⁴⁾.

2.2 System configuration

Fig.2 shows the force control system configuration of the pneumatic joystick that consists of a parallel mechanism. An arbitrary signal is given from PC, and the on-off values of solenoid valve are controlled by the PWM control with PIC. Then, the thrust force of six cylinders that compose the joystick is changed. The force control of the joystick is achieved by controlling the thrust force of each cylinder.

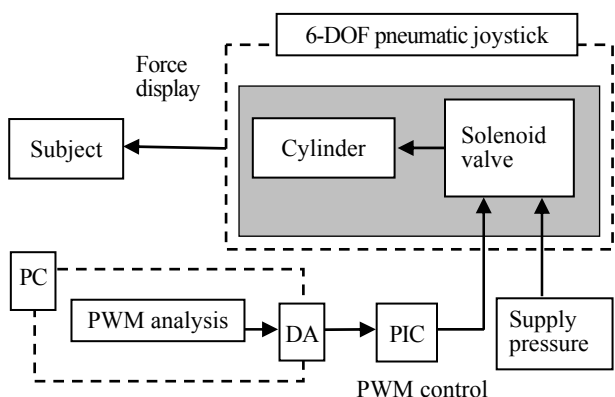


Fig.2 System configuration

Fig.3 (a) shows design model by three-dimensional CAD. Fig.3 (b) shows the pneumatic joystick test structure. The joystick consists of platform, pneumatic cylinder, solenoid valve, and fixed base.

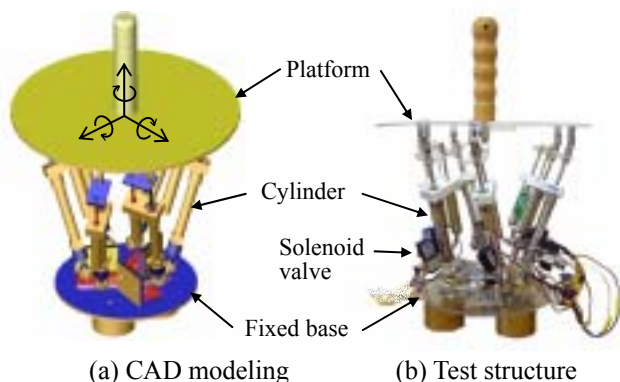


Fig.3 Pneumatic joystick system

Working range is calculated from this joystick by the reverse-movement study analysis in consideration of the geometrical restraint condition by the amount of expansion and contraction of the cylinder. Table 1 shows the working range of six degree of freedom.

Table 1 Working range

Translation (mm)	x	- 30.7 ~ 41.9
	y	- 32.6 ~ 32.6
	z	- 16.6 ~ 16.3
Rotation (degree)		- 9.1 ~ 9.1
		- 8.9 ~ 9.2
		- 41.8 ~ 41.8

2.3 PWM control that uses PIC

PIC is a kind of the microcomputer that the microchip technology company developed. It controls connected part of the computer and peripherals, and 35 instruction words are used.

PIC16F877 is used to provide the PWM output function and the AD output function.

The PWM control is a method to change the turning on time to the pulse wave at a constant cycle, and the modulation rate is the ratio of the on time in a constant cycle.

2.4 Control of thrust force of cylinder

The PWM control of the solenoid valve is used to control the thrust force of the pneumatic cylinder. Fig.4 (a) and (b) show respectively turn on and off of three-way solenoid valve⁽⁴⁾.

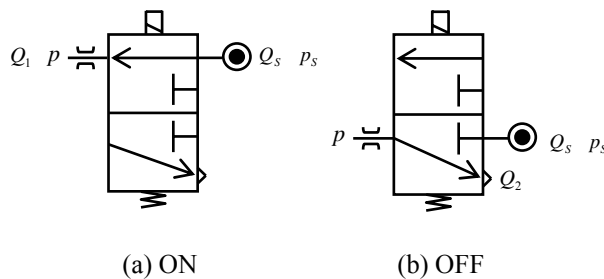


Fig.4 Three-way solenoid valve

Moreover, the driving circuit of pneumatic cylinder is shown in Fig.5. The decided with PC is converted in DA, the solenoid valve is controlled by PWM control based on by PIC, and the thrust force of the cylinder is controlled⁽⁴⁾.

The relation between the average control pressure at this time and the modulation rate of PWM becomes expression (1). Here, P_s is supply pressure.

Thrust force F of the cylinder is given from expression (1) by expression (2).

$$P = P_s \frac{\tau^2}{\tau^2 + (1 - \tau)^2} \quad \dots(1)$$

$$F = \eta A p_s \frac{\tau^2}{\tau^2 + (1 - \tau)^2} \dots (2)$$

Here, A is an area of the pushing side of the cylinder, is a load factor.

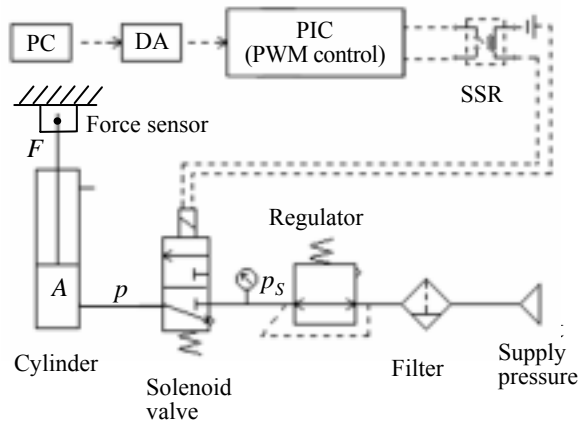


Fig.5 Driving circuit of pneumatic cylinder

3 Experimental result

3.1 Characteristics of pneumatic cylinder

We experimented with a single cylinder. The load cell is set up between a fixed wall and the cylinder to measure the thrust force of the cylinder as shown in Fig.6. The supply pressure is adjusted to 0.15MPa. In three conditions (2, 15, and 27mm) with different amount of the cylinder expansion and contraction (min 0, max 30mm), the thrust force of the cylinder for the change in the modulation rate is measured. The measurements and predictions by expression (2) are shown in Fig. 7 (a). When the amount of the cylinder expansion and contraction is small, difference of the characteristic of the thrust force by prediction and experiments exists.

Then, the different capacity of the accumulator of three conditions (314, 942, and 1570mm³) is set between the solenoid valve and the cylinder, and the results of the thrust force of the cylinder in each case are shown in Fig.7 (b). Here, the supply pressure is adjusted and

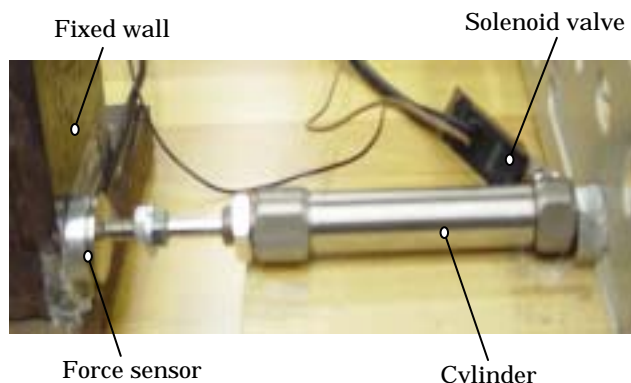
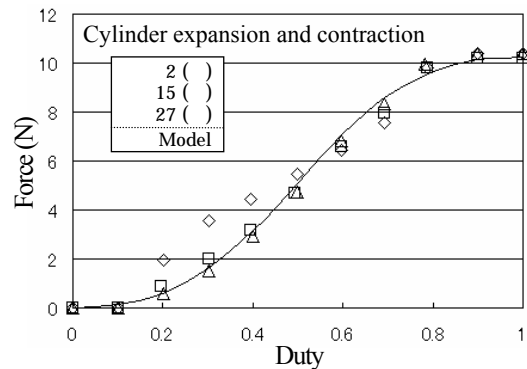


Fig.6 Experiments with a single cylinder

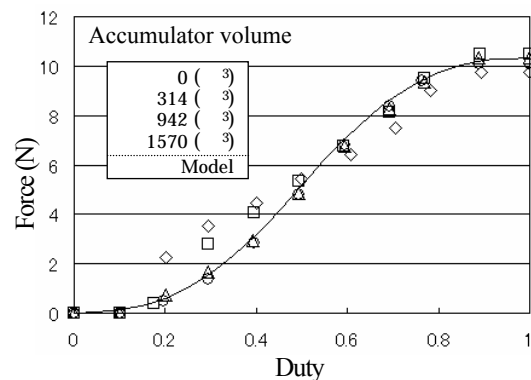
0.15MPa and the amount of the cylinder expansion and contraction are adjusted to be 2mm.

The experiment value has been improved by greatly taking the capacity of the accumulator.

From the result, when the amount of the cylinder expansion and contraction is small, that is, when the volume between the solenoid valve and the cylinder is small, the compressibility of air influences the pressure characteristic. And it is understood that the force characteristic is depend on the capacity of the accumulator.



(a) Without accumulator



(b) With accumulator

Fig.7 Cylinder force

3.2 Characteristics of pneumatic joystick

The thrust force of the pneumatic cylinder is controlled, and it supplies the force control of the pneumatic joystick shown in Fig.1. The force sensor (0 ~ 100N) consists of the strain gauge, and the force in z-direction is measured. The same modulation rate is given for six cylinders, and the force of z-axis is measured. Fig.8 shows results of experiment, when the posture is adjusted to be neutral position (cylinder expansion and contraction 15mm) and the supply pressure is 0.15Mpa.

The calculated value is summation of each thrust force of 6 cylinders in vertical direction obtained from expression (2).

The prediction agrees well with the measurements, and the z-axis force control is possible. A force of approxi-

mate 53N is generated when the supply pressure is 0.15Mpa, and it has been understood that enough forces experienced by man is generated.

[5] <http://www.ms.t.kanazawa-u.ac.jp/design/contents/research/parallelmechnizm/hpm.html>

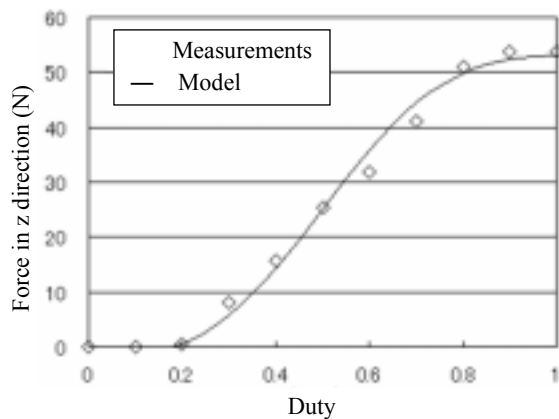


Fig.8 Force control of joystick

4 Summary

The pneumatic joystick has been developed, and the six-degree of freedom force control was achieved.

The conclusion is shown below.

- (1) The thrust force of the cylinder is generated by the PWM control of the solenoid valve. And the control characteristic of the thrust force of the cylinder was confirmed by the change in the amount of the cylinder expansion and contraction
- (2) The compressibility of air can be compensated with accumulator, and the control characteristic of the thrust force of the cylinder has been improved.
- (3) The pneumatic 6-DOF parallel mechanism type joystick was developed. The z-axis force control was evaluated by the experiment, and the force control by the PWM control is possible.

References

- [1] Stewart, D., A Platform with 6 degrees of freedom, Proc. Inst. Mech. Eng., Vol.180, Part I, No.15, pp.371-386, 1965-66.
- [2] Lung-Wen Tsai, Robot Analysis, John Wiley & Sons, Inc. 1999, pp116
- [3] Takaiwa, M., Noritsugu, T., Development of Human-Robot Haptic Interface Using Pneumatic Parallel Manipulator, Proc. 4th JHPS Int. Symp. on Fluid Power, pp.181-186, 1999.
- [4] Tanaka, Y., Nakajima, T., Sawada, T., Desktop Type of Force Display Using Pneumatic Parallel Mechanism, Proceedings of the Fourth International Symposium on Fluid Power Transmission and Control (ISFP'2003, Paper for Plenary Session), April 2003, pp.267-271.

Force Analysis of the 6DOF Parallel Manipulators

Yasunobu HITAKA*, Yoshito TANAKA*, Junko ISHII*

*Department of Control and Information Systems Engineering,
 Kitakyushu National College of Technology, Japan
 E-mail:hitaka@kct.ac.jp

Abstract

The 6DOF (degrees of freedom) Parallel Manipulators have some advantages that are high power, high rigidity, high precision for positioning and compact mechanism compared with conventional serial link manipulators. For these Parallel Manipulators, it can be expected to work in the new fields such that the medical operation, high-precision processing technology and so on. For this expectation, it is necessary to control the action reaction pair of forces which act between the Parallel Manipulator and the operated object. In this paper, we analyze the dynamics of the 6DOF Parallel Manipulator and present numerical simulation results.

1 Introduction

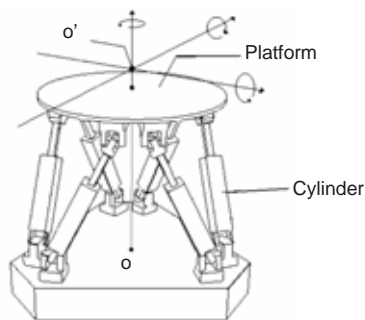


Figure 1: Parallel manipulator

Figure 1 is a type of the parallel manipulators that is called "Stewart Platform"[1]. It consists of a top plate, a bottom plate, and 6 hydraulic cylinders attached to the top and bottom plates. The top plate is called "platform", and the bottom plate is "base". The platform can be achieved six degree of freedom

motion by six cylinders stretching. The character of this manipulator is that the workspace is narrow compared with conventional serial link manipulators. However, Stewart Platform have many redeeming features that are high power, high rigidity, positioning accuracy and compact mechanism. Then, it can be expected to work in the fields which require the operation with high power and high accurate positioning such that the operative treatment, high-precision processing in factory and so on. For these purpose, the force control of this manipulator is necessary but the force analysis for Stewart Platform type of manipulator has never been examined. Thus, we analyze the dynamics of this manipulator.

This paper is consist of 6 sections. This section is introduction. Next section, kinematics of the parallel manipulator is discussed. In 3rd section, we consider the forces which act on the platform. And then, in section 4, we will analyze the dynamics of parallel manipulator. Section 5, we show the numerical simulation results and summary is in section 6.

2 Kinematics of the parallel manipulator [2]

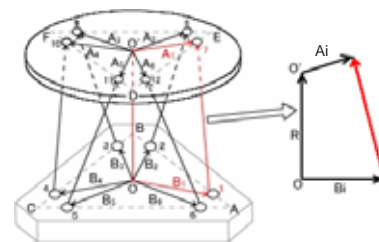


Figure 2: Vector diagram of the parallel manipulator

Figure 2 is a relationship diagram for the vectors of the parallel manipulator. This manipulator has two

reference frame. The one is the motion frame and the other is the base fixed frame. The motion frame is located at the centroid o' of the platform, while the base fixed frame has its origin at the centroid o of the base of the manipulator. The attitude of the platform is specified by the orientation of the motion frame and the position of the centroid o' is located with respect to the base fixed frame.

The right part of Figure 2 focuses the vectors related to the i -th cylinder ($i=1, \dots, 6$). The position of the centroid o' is represented by vector $\mathbf{R} = (x, y, z)^T$ with respect to the base fixed frame. The vector \mathbf{A}_i denotes the attachment point of the cylinder on the platform and the vector \mathbf{B}_i denotes attachment point on the base of the manipulator with respect to the base fixed frame. Then, the cylinder length vector \mathbf{l}_i can be calculated by

$$\mathbf{l}_i = \mathbf{A}_{im} \mathbf{T} + \mathbf{R} - \mathbf{B}_i, \quad (1)$$

where \mathbf{A}_{im} describes the attachment point of the cylinder on the platform relative to the motion frame and \mathbf{T} is the oriental matrix of the platform which can be represented by

$$\mathbf{T} = \begin{bmatrix} 1 & 0 & 0 \\ 0 & \cos \phi & \sin \phi \\ 0 & -\sin \phi & \cos \phi \end{bmatrix} \\ \times \begin{bmatrix} \cos \theta & 0 & -\sin \theta \\ 0 & 1 & 0 \\ \sin \theta & 0 & \cos \theta \end{bmatrix} \begin{bmatrix} \cos \psi & \sin \psi & 0 \\ -\sin \psi & \cos \psi & 0 \\ 0 & 0 & 1 \end{bmatrix}. \quad (2)$$

with roll-pitch-yaw angles as ϕ , θ and ψ .

3 The forces act on the platform

Figure 3 is the force analytical model of the parallel manipulator. As shown this diagram, the platform are acted three types of force: the cylinder force \mathbf{F}_i ($i = 1, \dots, 6$), an external force \mathbf{L} and gravity force \mathbf{M} . We consider these force vectors having coordinates $(F_{ix}, F_{iy}, F_{iz}, i = 1, \dots, 6)$, (L_x, L_y, L_z) and $(0, 0, -mg)$ with respect to the base fixed frame, respectively. Where m is the mass of the platform and g is the gravity acceleration.

If the motion frame and base fixed frame are expressed by $(\mathbf{i}, \mathbf{j}, \mathbf{k})^T$ and $(\mathbf{e}_1, \mathbf{e}_2, \mathbf{e}_3)^T$, respectively, the relations among two frames can be described as $(\mathbf{i}, \mathbf{j}, \mathbf{k})^T = \mathbf{T}(\mathbf{e}_1, \mathbf{e}_2, \mathbf{e}_3)^T$ or $(\mathbf{e}_1, \mathbf{e}_2, \mathbf{e}_3)^T = \mathbf{T}^T(\mathbf{i}, \mathbf{j}, \mathbf{k})^T$. Where $\mathbf{T}^T = \mathbf{T}^{-1}$ is given because the oriental matrix \mathbf{T} is the orthogonal transformation

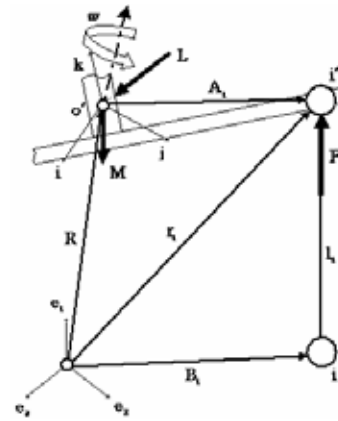


Figure 3: Analytical model of parallel manipulator

matrix. Then, for the cylinder force \mathbf{F}_i , the following relationships

$$\begin{aligned} (F_{ix}, F_{iy}, F_{iz}) &= (F_{i1}, F_{i2}, F_{i3}) \mathbf{T} \\ (F_{i1}, F_{i2}, F_{i3}) &= (F_{ix}, F_{iy}, F_{iz}) \mathbf{T}^T \end{aligned} \quad (3)$$

can be obtained, where (F_{i1}, F_{i2}, F_{i3}) is a coordinate of the vector \mathbf{F}_i with respect to the motion frame.

Furthermore, when the coordinate of i -th cylinder vector \mathbf{l}_i is represented by (l_{ix}, l_{iy}, l_{iz}) with respect to the base fixed frame, we obtain a relation

$$(F_{ix}, F_{iy}, F_{iz}) = \frac{\mathbf{F}_i}{\sqrt{l_{ix}^2 + l_{iy}^2 + l_{iz}^2}} (l_{ix}, l_{iy}, l_{iz}). \quad (4)$$

By the equation (3) and (4), the coordinate (F_{i1}, F_{i2}, F_{i3}) can be written by

$$(F_{i1}, F_{i2}, F_{i3}) = \frac{\mathbf{F}_i}{\sqrt{l_{ix}^2 + l_{iy}^2 + l_{iz}^2}} (l_{ix}, l_{iy}, l_{iz}) \mathbf{T}^T. \quad (5)$$

4 Analysis for the platform dynamics

In order to analyze the platform dynamics, the motion of the platform is considered to be divided into two parts. The one is the translational motion and the other is the rotational motion. First, the translational motion of the platform is discussed.

4.1 Analysis for the translational motion

The equation for the translational motion of the centroid o' of the platform is represented

$$m \frac{d^2 \mathbf{R}}{dt^2} = \sum_{i=1}^6 \mathbf{F}_i + \mathbf{L} + \mathbf{M} \quad (6)$$

with respect to the fixed frame. By using the equation (4) which represents the components of the cylinder force vector relative to the base fixed frame, following three dynamical equations can be obtained.

$$\begin{aligned} m \frac{d^2 x}{dt^2} &= \sum_{i=1}^6 \frac{l_{ix}}{\sqrt{l_{ix}^2 + l_{iy}^2 + l_{iz}^2}} \mathbf{F}_i + L_x \\ m \frac{d^2 y}{dt^2} &= \sum_{i=1}^6 \frac{l_{iy}}{\sqrt{l_{ix}^2 + l_{iy}^2 + l_{iz}^2}} \mathbf{F}_i + L_y \\ m \frac{d^2 z}{dt^2} &= \sum_{i=1}^6 \frac{l_{iz}}{\sqrt{l_{ix}^2 + l_{iy}^2 + l_{iz}^2}} \mathbf{F}_i + L_z - mg \end{aligned} \quad (7)$$

4.2 Analysis for the rotational motion

Next, let us consider about the rotational motion of the platform. The equation for this motion is given

$$\frac{d\mathbf{H}}{dt} + \boldsymbol{\omega} \times \mathbf{H} = \sum_{i=1}^6 \mathbf{A}_{im} \times \mathbf{F} \quad (8)$$

with respect to the motion frame. $\boldsymbol{\omega}$ denotes the angular velocity vector for the platform and \mathbf{H} is an angular momentum vector. The $\boldsymbol{\omega}$ is

$$\begin{aligned} \boldsymbol{\omega} &= \omega_1 \mathbf{i} + \omega_2 \mathbf{j} + \omega_3 \mathbf{k} \\ &= \omega_1 \mathbf{i} + \omega_2 \mathbf{j} + \omega_3 \mathbf{k} \end{aligned} \quad (9)$$

with respect to the motion frame. Where, $\omega_1, \omega_2, \omega_3$ in (9) can be described with Euler angles ϕ, θ, ψ and these derivatives $\dot{\phi}, \dot{\theta}, \dot{\psi}$ as

$$\begin{aligned} \omega_1 &= \dot{\phi} - \dot{\psi} \sin \theta \\ \omega_2 &= \dot{\theta} \cos \phi + \dot{\psi} \cos \theta \sin \phi \\ \omega_3 &= -\dot{\theta} \sin \phi + \dot{\psi} \cos \theta \cos \phi \end{aligned} \quad (10)$$

The vector \mathbf{H} can be derived by

$$\mathbf{H} = \begin{bmatrix} H_1 \\ H_2 \\ H_3 \end{bmatrix} = \begin{bmatrix} I_{11} & I_{12} & I_{13} \\ I_{21} & I_{22} & I_{23} \\ I_{31} & I_{32} & I_{33} \end{bmatrix} \begin{bmatrix} \omega_1 \\ \omega_2 \\ \omega_3 \end{bmatrix}, \quad (11)$$

where $I_{ij} (i, j = 1, 2, 3)$ denotes the moment of inertia of the platform. Note that we considered the rotating frame of $\boldsymbol{\omega}$ as the motion frame which is fixed the platform and the square matrix for the inertia in eq (9) is diagonalizable and we obtain following equation

$$\mathbf{H} = \begin{bmatrix} H_1 \\ H_2 \\ H_3 \end{bmatrix} = \begin{bmatrix} I_{11} & 0 & 0 \\ 0 & I_{22} & 0 \\ 0 & 0 & I_{33} \end{bmatrix} \begin{bmatrix} \omega_1 \\ \omega_2 \\ \omega_3 \end{bmatrix}. \quad (12)$$

Therefore, the equation (8) can be rewritten as

$$\begin{aligned} \begin{bmatrix} \frac{dH_1}{dt} & \frac{dH_2}{dt} & \frac{dH_3}{dt} \end{bmatrix} \begin{bmatrix} \mathbf{i} \\ \mathbf{j} \\ \mathbf{k} \end{bmatrix} + \begin{bmatrix} \mathbf{i} & \mathbf{j} & \mathbf{k} \\ \omega_1 & \omega_2 & \omega_3 \\ H_1 & H_2 & H_3 \end{bmatrix} \\ = \sum_{i=1}^6 \begin{bmatrix} \mathbf{i} & \mathbf{j} & \mathbf{k} \\ a_{i1} & a_{i2} & a_{i3} \\ F_{i1} & F_{i2} & F_{i3} \end{bmatrix}. \end{aligned} \quad (13)$$

a_{i1}, a_{i2} and a_{i3} are the components of the vector \mathbf{A}_{im} which denotes attachment point of the cylinder on the platform relative to the motion frame. The elements for Equation (13) can be described as

$$\begin{aligned} I_1 \frac{d\omega_1}{dt} + (I_3 - I_2) \omega_2 \omega_3 &= \sum_{i=1}^6 (a_{i2} F_{i3} - a_{i3} F_{i2}) \\ I_2 \frac{d\omega_2}{dt} + (I_1 - I_3) \omega_3 \omega_1 &= \sum_{i=1}^6 (a_{i3} F_{i1} - a_{i1} F_{i3}) \\ I_3 \frac{d\omega_3}{dt} + (I_2 - I_1) \omega_1 \omega_2 &= \sum_{i=1}^6 (a_{i1} F_{i2} - a_{i2} F_{i1}). \end{aligned} \quad (14)$$

For above equations, let us rewrite F_{i1}, F_{i2} and F_{i3} to the cylinder force \mathbf{F}_i with the relations in equation (5), the following equations

$$\begin{aligned} I_1 \frac{d\omega_1}{dt} + (I_3 - I_2) \omega_2 \omega_3 &= \sum_{i=1}^6 \frac{a_{i2}(l_{ix} T_{31} + l_{iy} T_{32} + l_{iz} T_{33})}{\sqrt{l_{ix}^2 + l_{iy}^2 + l_{iz}^2}} \mathbf{F}_i \\ &\quad - \sum_{i=1}^6 \frac{a_{i3}(l_{ix} T_{21} + l_{iy} T_{22} + l_{iz} T_{23})}{\sqrt{l_{ix}^2 + l_{iy}^2 + l_{iz}^2}} \mathbf{F}_i \\ I_2 \frac{d\omega_2}{dt} + (I_1 - I_3) \omega_3 \omega_1 &= \sum_{i=1}^6 \frac{a_{i3}(l_{ix} T_{11} + l_{iy} T_{12} + l_{iz} T_{13})}{\sqrt{l_{ix}^2 + l_{iy}^2 + l_{iz}^2}} \mathbf{F}_i \\ &\quad - \sum_{i=1}^6 \frac{a_{i1}(l_{ix} T_{31} + l_{iy} T_{32} + l_{iz} T_{33})}{\sqrt{l_{ix}^2 + l_{iy}^2 + l_{iz}^2}} \mathbf{F}_i \\ I_3 \frac{d\omega_3}{dt} + (I_2 - I_1) \omega_1 \omega_2 &= \sum_{i=1}^6 \frac{a_{i1}(l_{ix} T_{21} + l_{iy} T_{22} + l_{iz} T_{23})}{\sqrt{l_{ix}^2 + l_{iy}^2 + l_{iz}^2}} \mathbf{F}_i \\ &\quad - \sum_{i=1}^6 \frac{a_{i3}(l_{ix} T_{11} + l_{iy} T_{12} + l_{iz} T_{13})}{\sqrt{l_{ix}^2 + l_{iy}^2 + l_{iz}^2}} \mathbf{F}_i \end{aligned} \quad (15)$$

can be obtained. $T_{ij}(i, j = 1, 2, 3)$ in equation (15) is the element of the oriental matrix \mathbf{T} .

Therefore, the dynamics of the 6DOF parallel manipulator can be described by six differential equations in equation (7) and (15).

5 Simulation

In this section, we provide the numerical simulation based on our analysis. Figure 4 shows the result for the surge motion (x direction) of the platform. Where, "cyl.1" denotes the 1st cylinder of the parallel manipulator. In Figure 4, the top diagram denotes the amount of the cylinder stretch and the bottom denotes the cylinder force amount for six cylinders. The lateral axis of both diagrams indicate the distance for the centroid o' of the platform. Figure 5 is the result for the yaw motion of the platform.

The trajectories for these motions are designed by using trigonometric function. The amplitude of the motion trajectory is 90mm and the frequency is 0.5Hz.

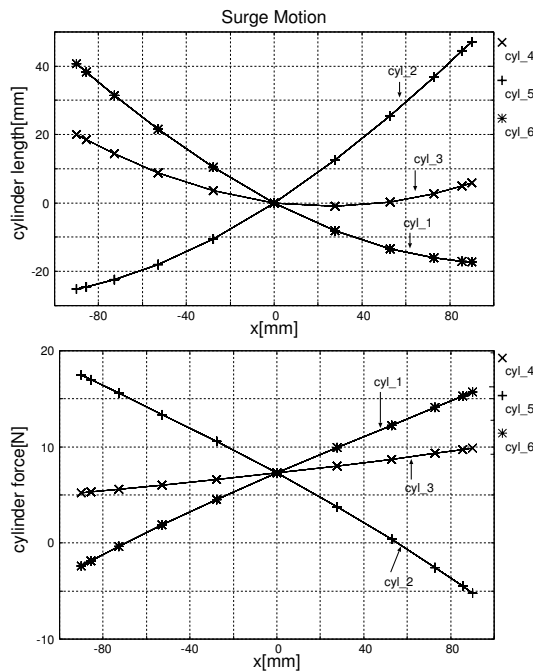


Figure 4: Results for surge motion

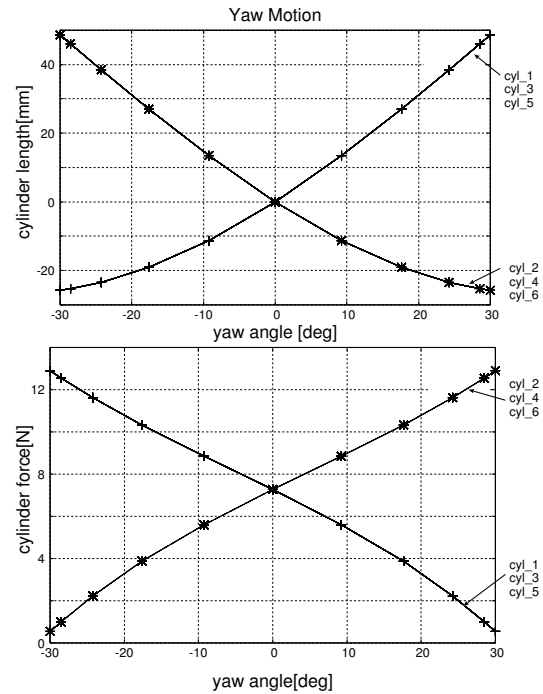


Figure 5: Results for yaw motion

6 Summary

In this paper, we analyzed the dynamics of the 6DOF parallel manipulator and showed the numerical simulation results.

In our future work, we'll confirm our analysis to compare with our simulation results and the experimental results for the actual parallel manipulator. And moreover, we'll utilize our analytical result to the force control for the parallel manipulator in order that the parallel manipulators can be useful in many fields such that the medical operation, high-precision processing technology and so on.

References

- [1] Stewart.D, A Platform with 6 degrees of freedom, Proc. Inst Mech. Eng, Vol.180, Part I, No15, pp.371-386, 1965-66.
- [2] K.H.Hunt, Structural Kinematics of In-Parallel-Actuated Robot-Arms, ASME, J.Mechanisms, Transmissions and Automation in Design, 105, (1983-12),705.

Braille Block Recognition for an Autonomous Wheelchair

Masayoshi Tabuse

Dept. of Environmental Information
Kyoto Prefectural University
Kyoto, 606-8522, Japan

Yuki Takehara

NTT Data Sanyo System Corp.
Osaka, 570-8686, Japan

Abstract

By using a Braille block on a sidewalk, a senior citizen and a handicapped person may run safely getting on an autonomous wheelchair. A Braille block is a sign to guide a visually handicapped person and its standard color is yellow, but the colors other than a standard color are often used. In addition, misrecognition of Braille block by a color is often happen under various light conditions. Therefore, we examine the recognition method of Braille blocks using two dimension discrete cosine transform (DCT). We find that the average recognition rates of guide blocks and of warning blocks are 77% and 68%, respectively.

Keywords: Braille Block Recognition, DCT, Autonomous Wheelchair

1 Introduction

According to a report on disability children and persons [1], there are about 300,000 visually handicapped persons in Japan. Visually handicapped persons of the first class, who cannot walk using their sight, are about 100,000. 80 percent or more of them lose their sight midway through their life. About 30,000 persons can walk alone with a white cane and the other persons cannot walk without a help or doesn't walk at all.

Aging society is proceeding and persons who lose their sight increase, so walking support systems are more important in the future. One of walking support systems is an autonomous mobile robot [2,3]. It must have a function that it can run in various environments. Therefore, there are various researches of an autonomous mobile robot, which runs out of doors recognizing typical objects in a complex environmental condition.

In this research, we propose a recognition method of a Braille block set up on a sidewalk for a visually handicapped person by discrete cosine transform.

2 Braille Block

A Braille block is a sign to guide visually handicapped persons and set up on a sidewalk. A Braille block in our work is shown in Fig. 1, 2. There are two kinds of Braille blocks. One is a warning block where small round convex parts line up like the lattice and another is a guide block where rectangular convex parts line up in parallel. A standard color of a Braille block is yellow so that a weak-sighted person can recognize it easily by the contrast with surroundings. However, blocks of another color are often used in consideration of the correspondence with a surrounding spectacle. A Braille block is used in the world and its size and shape are various types. So in this research we consider a Braille

block designed in Japan.

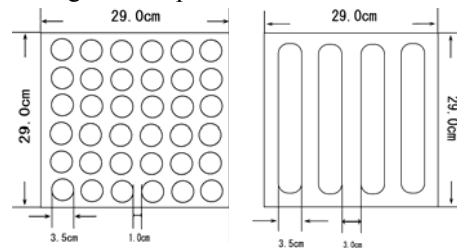


Fig.1 A warning block Fig.2 A guide block

3 Detection and Recognition of a Braille Block

Since a warning block consists of small round convex parts lining up like the lattice and a guide block consists of rectangular convex parts lining up in parallel, we consider a Braille block a constant periodic pattern. Therefore, we propose a method of using two dimensional discrete cosine transform that resolves light and shade information in the image to the frequency element to detect and recognize a Braille block.

3.1 Two Dimensional Discrete Cosine Transformation

Discrete cosine transform (DCT) is orthogonal transformation that uses the cosine function for the transformation base, and the image data is transformed into the frequency element. Two dimensional DCT and inverse DCT of an $M \times N$ pixels image $f(x,y)$ are given by

$$DCT : F(u, v) = \alpha(u)\alpha(v) \sum_{x=0}^{M-1} \sum_{y=0}^{N-1} f(x, y) \cos\left(\frac{(2x+1)u\pi}{2M}\right) \cos\left(\frac{(2y+1)v\pi}{2N}\right)$$

IDCT :

$$f(x, y) = \sum_{u=0}^{M-1} \sum_{v=0}^{N-1} \alpha(u)\alpha(v) F(u, v) \cos\left(\frac{(2x+1)u\pi}{2M}\right) \cos\left(\frac{(2y+1)v\pi}{2N}\right)$$

where

$$\alpha(u) = \begin{cases} \sqrt{\frac{1}{M}} & u = 0 \\ \sqrt{\frac{2}{M}} & u = 1, 2, \dots, M-1 \end{cases}, \alpha(v) = \begin{cases} \sqrt{\frac{1}{N}} & v = 0 \\ \sqrt{\frac{2}{N}} & v = 1, 2, \dots, N-1 \end{cases}$$

and $f(x,y)$ is an image and $F(u,v)$ is a frequency element (DCT coefficient).

In this research 640×480 pixels image is divided into the block of 12 pieces, called the unit block, that consists of 160×160 pixels. We perform two dimensional DCT to each unit block and obtain a frequency element that indicates the feature of a Braille block.

3.2 Feature Mask

As a preprocessing of Braille block recognition, a feature mask of the warning block and the guide block is constructed by DCT coefficient. First we prepare three images of warning blocks and guide blocks, respectively,

as training images and perform DCT to them to determine the frequency elements that show the feature of a Braille block. In each image there are 12 unit blocks, so that we have 36 unit blocks for the warning block and the guide block, respectively.

Next we select DCT coefficients, which are high rank 10% of absolute values of DCT coefficients except for the direct current element included in all the unit blocks. Then we calculate the average and the standard deviation of their DCT coefficients and determine *average - standard deviation* as a threshold, which judges whether a unit block is a Braille block.

In addition, there is a characteristic distribution of large absolute value of DCT coefficients of the warning block and the guide block respectively. Figure 3 and 4 are the distributions of large absolute value of DCT coefficients of the high rank 3% for a Braille block. Therefore, the remarkable frequency domains are 40×40 except the low frequency area of 10×10 , which show the periodicity of the light and shade image of the warning block and the guide block.

Moreover the distribution of DCT coefficients of the high rank 10% is also different depending on the inclination angle of a Braille block. For instance, distributions for various inclination angle are shown in Fig. 5 in the guide block. The feature mask of the warning block and the guide block is constructed according to the inclination angle of each block. The feature mask used in our experiment is shown in Table 1 and 2.

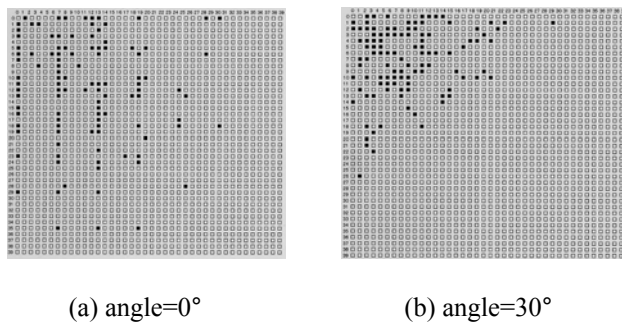


Fig.3 Distributions of DCT coefficients for warning blocks

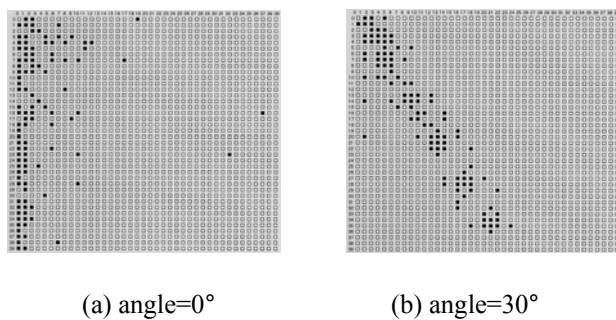
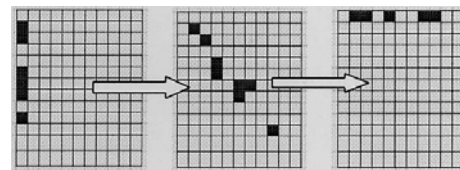
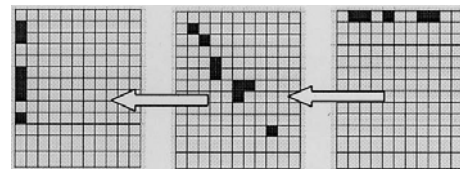


Fig.4 Distributions of DCT coefficients for guide blocks



(a) angle = 0 ° ~ 90 °



(b) angle = 90 ° ~ 180 °

Fig.5 Changes of distributions of DCT coefficients for angles of guide blocks

3.3 Perspective Transformation

The video camera that takes a picture of Braille blocks is set up in the electric wheelchair at constant height and the angle. Therefore, we convert images of Braille blocks into images taken at a vertical angle using perspective transformation shown in Fig. 6. When the height of the video camera from the ground is represented by H , and the angle with a horizontal plane is represented by θ , the perspective transformation equations are given by

$$\begin{cases} x' = \frac{Hx \cos^2 \theta}{H - y \sin \theta \cos \theta} \\ y' = \frac{Hy \cos^3 \theta}{H - y \sin \theta \cos \theta} \end{cases}$$

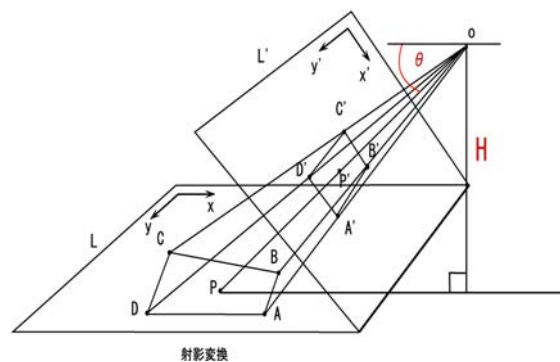


Fig.6 Perspective transformation

4 Detection of a Braille Block

4.1 Detection of a Braille Block in Each Unit Block

The image taken with the video camera is transformed by perspective transformation, DCT

coefficients corresponding to the feature mask are taken out at each unit block, and they are compared with the threshold. If the ratio of absolute value of DCT coefficients larger than the threshold is 50% or more, we classify the unit block as a Braille block, and if the ratio is less than 50%, we classify the unit block as another image. In Fig. 7, we shows a Braille block classification chart, in which the unit block classified as a Braille block is described by [O] and the unit block is described by [X] if it is not a Braille block.

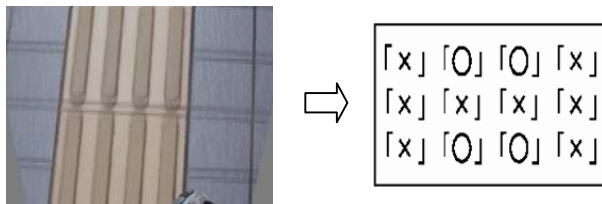


Fig.7 Perspective transformation image and Braille block classification chart

4.2 Braille Block Area

Next we determine a Braille block area in the classification chart. If there are unit block classified as a Braille block ([O]) in surroundings of a unit block classified as other ([X]), the unit block is classified as a Braille block ([X] --> [O]) as shown in Fig. 8.

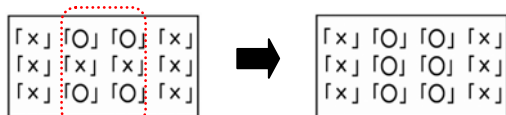


Fig.8 Extraction of Braille block area

5 Recognition of a Braille Block

If the unit block is denoted by [X] both in the warning block classification chart and in the guide block classification chart, its unit block is recognized as a part which is not a Braille block. If the unit block is denoted by [O] only in the guide block classification chart, its unit block is recognized as a guide block. If the unit block is denoted by [O] both in the warning block classification chart and in the guide block classification chart, its unit block is recognized as a warning or guide block according to classification of neighborhood unit blocks.

6 Experiment and Results

6.1 Experimental Conditions

Experimental conditions are as follows.

Video camera : SONY DCR-TRV20

Height of camera : 58cm

Downward angle of camera : 40°

Electric wheelchair : SUZUKI MC2000 (Fig. 9)

Velocity of electric wheelchair : 1.0km/h

Experimental location: Kyoto Prefectural University



Fig.9 Electric wheelchair

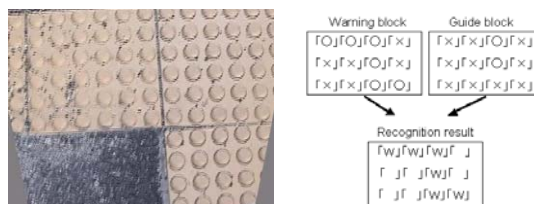
6.2 Experiment

We run the electric wheelchair along Braille blocks in Kyoto Prefectural University. Images taken with the video camera are converted into vertical angle images using perspective transformation. Then we examine the recognition rate of Braille blocks.

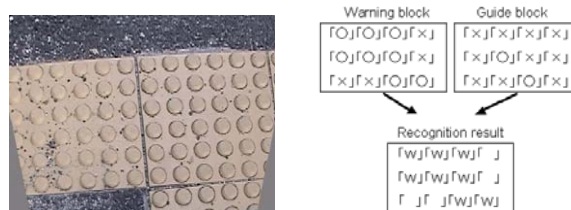
6.3 Results

We investigate recognition of 10 warning block images and 20 guide block images captured with the video camera. For 10 warning block images, the experiment results are shown in Fig. 10, where [W], [G] and [] denote a warning block, a guide block and other, respectively. For 20 guide block images, the experiment results are shown in Fig. 11.

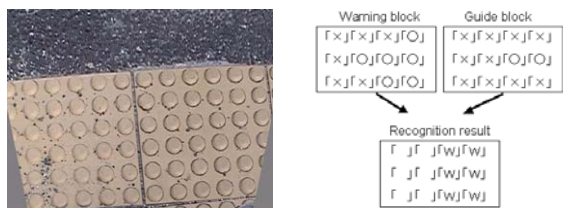
The recognition rates of 10 warning block images and 20 guide block images shown in Table 1 and 2, respectively. We find that the average recognition rate of the warning block and the guide block are 68% and 77%, respectively, and the average recognition rate in the part that was not the Braille block is 64%.



(a) First image

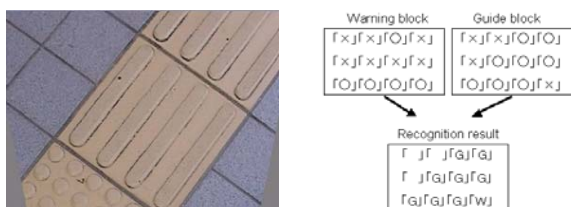


(b) 5th image



(c)10th image

Fig.10 Recognition of warning blocks



(a)First image



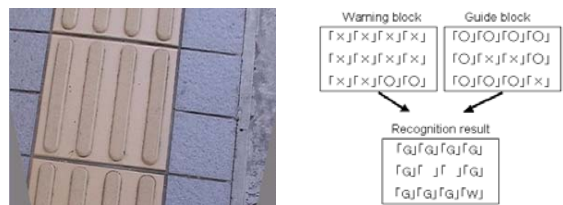
(b)5th image



(c)10th image



(d)15th image



(e)20th image

Fig.11 Recognition of guide blocks

7 Conclusion

In this paper, we propose a recognition method of a Braille block using specific frequency elements of the warning block and the guide block obtained by discrete cosine transform. In the experimental results recognition rate of the warning block and the guide block were 68% and 77% on the average, respectively. These results are not sufficient because we use only one condition that judge whether each unit block is a Braille block.

In the future, we consider a method of recognizing a Braille block by processing time series images to raise the recognition rate. Moreover, we consider a method that can distinguish a Braille block from other objects, which have a similar periodic pattern.

Table 1 Recognition rates of warning blocks

image	# of unit blocks in a warning block	# of unit block recognized a warning block	recognition rate	# of unit blocks in other	# of unit block recognized other	recognition rate
1	10	6	0.60	2	2	1.00
2	12	9	0.75	0	0	—
3	12	5	0.42	0	0	—
4	12	11	0.92	0	0	—
5	12	8	0.67	0	0	—
6	12	8	0.67	0	0	—
7	11	5	0.45	1	0	0.00
8	10	9	0.90	2	1	0.50
9	10	6	0.60	2	2	1.00
10	10	8	0.80	2	2	1.00
ave			0.68			0.78

Table 2 Recognition rates of warning blocks

image	# of unit blocks in a guide block	# of unit block recognized a guide block	recognition rate	# of unit blocks in other	# of unit blocks recognized other	recognition rate
1	10	8	0.80	2	1	0.50
2	10	6	0.60	2	0	0.00
3	10	6	0.60	2	2	1.00
4	11	9	0.82	1	1	1.00
5	10	7	0.70	2	2	1.00
6	9	7	0.78	3	3	1.00
7	10	8	0.80	2	2	1.00
8	10	10	1.00	2	2	1.00
9	10	10	1.00	2	2	1.00
10	9	7	0.78	3	0	0.00
11	10	8	0.80	2	2	1.00
12	10	7	0.70	2	0	0.00
13	9	6	0.67	3	3	1.00
14	9	4	0.44	3	2	0.67
15	9	6	0.67	3	1	0.33
16	9	6	0.67	3	1	0.33
17	10	8	0.80	2	1	0.50
18	10	9	0.90	2	1	0.50
19	9	9	1.00	3	3	1.00
20	9	7	0.78	3	0	0.00
ave			0.77			0.62

References

- [1] "Report on disability children and persons", The Ministry of Health, Labour and Welfare statistics database system, 2001.
- [2] T.Yoshida, A.Ohya, S.Yuta, "Braille Block Detection for Autonomous Mobile Robot Navigation", IROS2000, pp.633-638, 2000.
- [3] Y.Shi, S.Kotani, H.Mori, "A Route Understanding Support System of the Robotic Travel Aid", IEICE Transactions, J86-D-I, pp.269-279, 2003.

Throwing Motion of Manipulator with Passive Revolute Joint

Asaji SATO
Dept. of Mechanical Engineering,
Miyakonojo National college of Technology,
Miyakonojo, 885-8567, Japan

Osamu SATO, Nobuya TAKAHASHI, Michio KONO
Dep. of Computer Science and Systems Engineering,
Faculty of Engineering, University of Miyazaki,
Miyazaki, 889-2192, Japan

Abstract

In this paper, equations of motion of a manipulator, whose mechanism has a passive revolute joint, are derived in consideration of characteristics of driving source. Considering the final condition about displacement and velocity, trajectories of velocity for saving energy are calculated by iterative dynamic programming. And, the dynamic characteristics of manipulator controlled based on the trajectory for saving energy are analyzed theoretically.

Keywords: Manipulator, Trajectory, Dynamic Programming, DC Motor, Minimum Energy, Throwing Motion

1 Introduction

For the purpose of enlarging the work space, it is necessary for studying the optimal control of the manipulator in throwing motion. In a previous report [1], a casting manipulator is introduced, and the merit of this type is its large work space compared with its simple mechanism. But, the consideration of energy consumption of driving source is not enough. Also, the throwing motion of 2-DOF robot was studied to reduce the target error[2]. But, the consideration about trajectory of saving energy is not enough.

In previous report by the authors[3], trajectories for saving energy of manipulator, whose mechanism has two active joints, were easily calculated by iterative dynamic programming.

In rescue and agricultural field, it is considered that hand of tray type with passive joint is available for throwing the object which is various shape. In this paper, equations of motion of a manipulator, whose mechanism has a passive revolute joint, are derived in consideration of characteristics of the DC servomotors, and a performance criterion for saving energy is defined in consideration of energy consumption of driving source. When the manipulator is operated in a vertical plane, the system is highly non-linear due to gravity and an analytical solution can not be found. Then, a numerical approach is necessary. Considering the final condition about displacement and velocity, trajectories of velocity for saving energy are calculated by iterative dynamic programming. Initial searching region, which is surrounded by two sine-wave translated in parallel, is shifted to minimize the energy consumption of the motor. The dynamic characteristics of manipulator controlled based on above mentioned trajectory are analyzed theoretically.

2 Modeling of manipulator with passive joint

The dynamic equations of the manipulator with two degrees of freedom as shown in Figure 1 which is able to move in a vertical plane are as follows.

$$\begin{bmatrix} a_{11} & a_{12} \\ a_{21} & a_{22} \end{bmatrix} \begin{bmatrix} \ddot{\theta}_1 \\ \ddot{\theta}_2 \end{bmatrix} = \begin{bmatrix} a_{13} \\ a_{23} \end{bmatrix} \quad (1)$$

where

τ_1, τ_2 ; torque which acts on link 1 and 2,

θ_1, θ_2 ; angular displacement of link,

$$a_{11} = I_{G1} + m_1 l_{g1}^2 + m_2 l_1^2 + m_2 l_1 l_{g2} \cos \theta_2$$

$$a_{12} = m_2 l_1 l_{g2} \cos \theta_2$$

$$a_{13} = \tau_1 - \tau_2 + m_2 l_1 l_{g2} (\dot{\theta}_1 + \dot{\theta}_2)^2 \sin \theta_2 - (m_1 l_{g1} + m_2 l_1) g \cos \theta_1$$

$$a_{21} = I_{G2} + m_2 l_{g2}^2 + m_2 l_{g2} l_1 \cos \theta_2$$

$$a_{22} = I_{G2} + m_2 l_{g2}^2$$

$$a_{23} = \tau_2 - m_2 l_{g2} l_1 \dot{\theta}_1^2 \sin \theta_2 - m_2 g l_{g2} \cos(\theta_1 + \theta_2)$$

Joint 2 is passive revolute joint, and $\tau_2 = 0$.

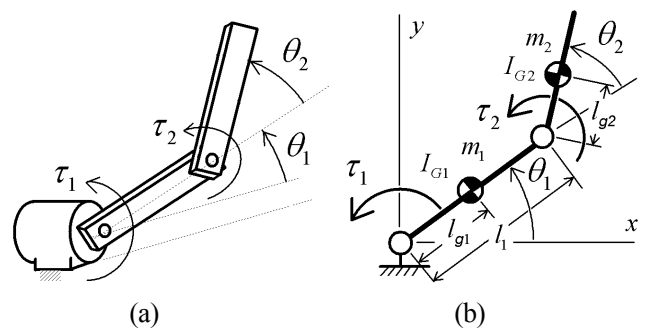


Fig. 1 Mechanism of manipulator

Table 1 Parameters of the manipulator

Parameter	Value	Parameter	Value
l_1, l_2 (m)	0.1	m_1, m_2 (kg)	0.1
l_{g1}, l_{g2} (m)	0.05	A_1 (Nm)	0.04
I_{G1}, I_{G2} (kgm ²)	8.33×10^{-5}	T_1 (sec)	0.52

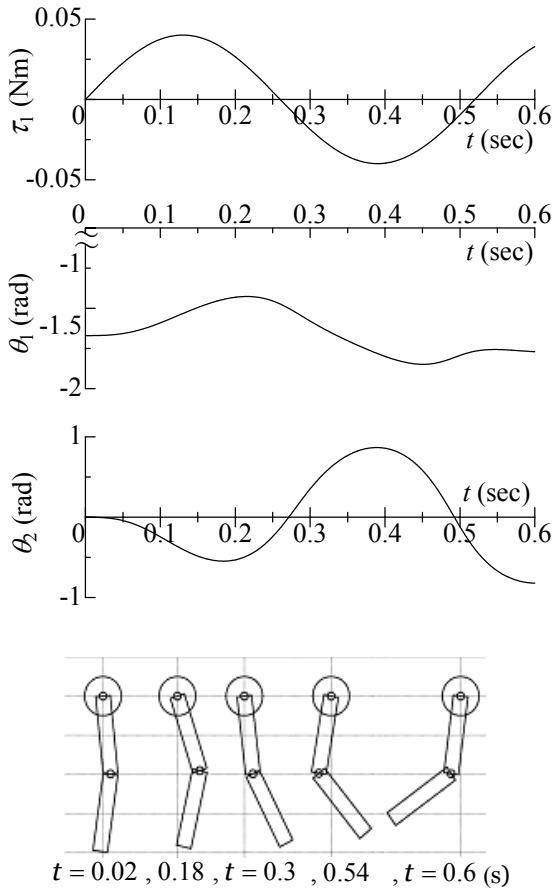


Fig. 2 Response of manipulator with a passive joint

We shall take the parameters of the system as shown in Table 1. The simulations of the system are done as follows. The period of pendulum movement of link 2 is approximated as

$$T_1 = 2\pi \sqrt{\frac{I_{G2} + m_2 l_{g2}^2}{m_2 g l_{g2}}} \quad (2)$$

Then, output torques of the motor 1 and 2 are

$$\tau_1 = A_1 \sin\left(\frac{2\pi}{T_1} t\right), \quad \tau_2 = 0 \quad (3)$$

A response of the manipulator from initial position ($\theta_{1i} = -\pi/2, \theta_{2i} = 0$) is shown in Figure 2. Amplitude of pendulum movement caused by inertia force increases as the response time increases.

3 Throwing motion of manipulator

The applied voltage of the servomotor is

$$e_1 = b_1 \dot{\theta}_1 + b_2 \ddot{\theta}_1 + b_3 \tau_1 + b_3 \tau_1 \text{sign}(\dot{\theta}_1) \quad (4)$$

where

$$\tau_1 = (I_{G1} + m_1 l_{g1}^2 + m_L l_1^2) \ddot{\theta}_1 + (m_1 l_{g1} + m_L l_1) g \cos \theta_1 \quad (5)$$

$$b_1 = k_v + (R_a / k_t) D_m, \quad b_2 = (R_a / k_t) I_m, \quad b_3 = R_a / k_t,$$

i_a : electric current of the armature ,

R_a : resistance of armature ,

I_m : moment of inertia of armature,

D_m : coefficient of viscous damping.

Then, the electric current is $i_a = (e - k_v \dot{\theta}) / R_a$. (6)

And, the consumed energy is $E = \int (e \cdot i_a) dt$. (7)

The velocity of object for throwing is expressed as

$$v = \frac{x_f - l_1 \cos \theta_{1f}}{\cos \phi} \sqrt{\frac{g}{2|x_f - l_1 \cos \theta_{1f}| \tan \phi - 2(y_f - l_1 \sin \theta_{1f})}}$$

where

(x_f, y_f) ; position of arrival

$(\theta_{1f}, \theta_{2f})$; angle of link 1 and 2 at release time .

Figure 3 shows a flow chart for iterative dynamic programming method. In frame (A), the trajectory for saving energy is searched by dynamic programming [4]. In frame (B), the searching region is shifted to minimize the consumed energy, and width of the region is changed smaller. Figure 4 shows the trajectory for searching, and the initial trajectory for searching is expressed as

$$\Theta_1(t) = \frac{v}{2l_1 t_f} t^2 + \theta_{1i} + \frac{t_f}{2} \left(\frac{\theta_{1f} - \theta_{1i}}{t_f} - \frac{v}{2l_1} \right) \left[1 - \cos\left(\frac{\pi}{t_f} t\right) \right]$$

This proposed trajectory is used as a center line of initial searching region of the iterative dynamic programming, and the region is shifted along the axis of coordinate to minimize the consumed energy of the motor.

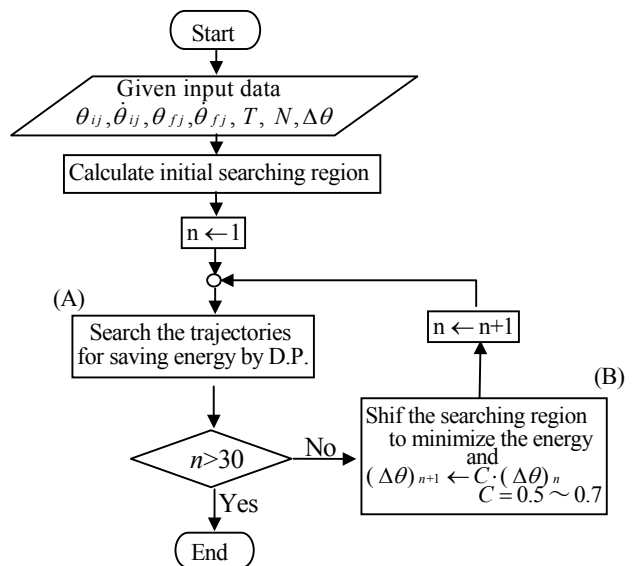


Fig. 3 Flow chart for simulation

Table 2 Parameters of the manipulator for throwing

Parameter	Value	Parameter	Value
l_1 (m)	0.080	k_{r1}, k_{r2} (Nm/A)	0.046
l_2 (m)	0.035	k_{v1}, k_{v2} (Vs/rad)	0.046
l_{g1} (m)	0.044	R_{a1}, R_{a2} (Ω)	3.5
l_{g2} (m)	0.031	D_{m2}, D_{m2} (Nms/rad)	7.9×10^{-5}
I_{G1} (kgm ²)	1.07×10^{-5}	τ_{f1}, τ_{f1} (Nm)	0.0013
I_{G2} (kgm ²)	0.36×10^{-5}	m_1 (kg)	0.020
I_{m1}, I_{m2} (kgm ²)	8.5×10^{-6}	m_2 (kg)	0.004
		m_L (kg)	0.005

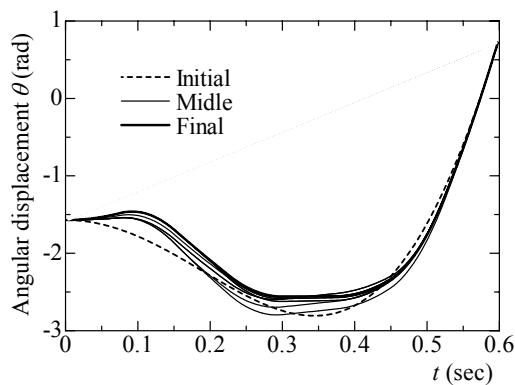


Fig. 4 Trajectory for searching

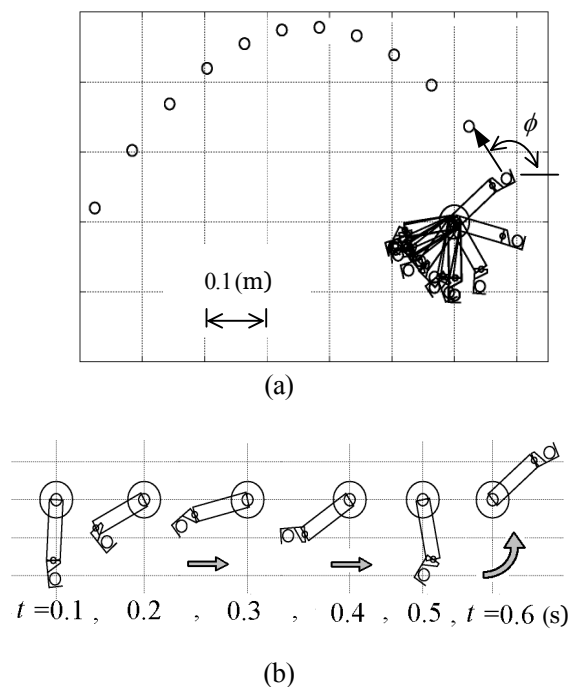


Fig. 5 Throwing motion of manipulator

We shall take the parameters of the system as shown in Table 2.

A response of the manipulator from initial position ($\theta_{1i} = -\pi/2, \theta_{2i} = 0$) to the position of release ($\theta_{1f} = \pi/4, \theta_{2f} = -\pi/10$) is shown in Fig.5, under the condition that distance from origin to the point of arrival is $x = -0.6$ [m], release angle is $\phi = 3\pi/4$, and the working time is $T = 0.6$. In Figure 5, it is shown that the locus of every sampling time (0.04 [s]) is like a pendulum movement, and circles are locus of object under the condition that link 1 and 2 are stopped at the time of release (0.6 [s]). They show the motion of object caused by kinetic energy at the time of release.

Figure 6 shows the response of angular displacement and angular velocity in throwing motion of Fig. 5. The angular velocity of links are $\dot{\theta}_1 = 28$ [rad/s], $\dot{\theta}_2 = -18$ [rad/s] at the time of release (0.6 [s]). And, velocity of object,

$$v = \sqrt{(l_1 \cdot \dot{\theta}_1)^2 + \{l_o \cdot (\dot{\theta}_1 + \dot{\theta}_2)\}^2 + 2l_1 \cdot l_o \cdot \dot{\theta}_1 (\dot{\theta}_1 + \dot{\theta}_2) \cos(\theta_2)}$$

$$\cong 2.5 \text{ [m/s]}$$

($l_o = 0.027$ [m]; length between joint and center of object) is enough for throwing motion. The kinetic energy of object is 0.016[J], and on the other hand consumed energy of the motor is 0.79[J]. From these analysis, it is considered that the manipulator with a passive joint is available for throwing the object.

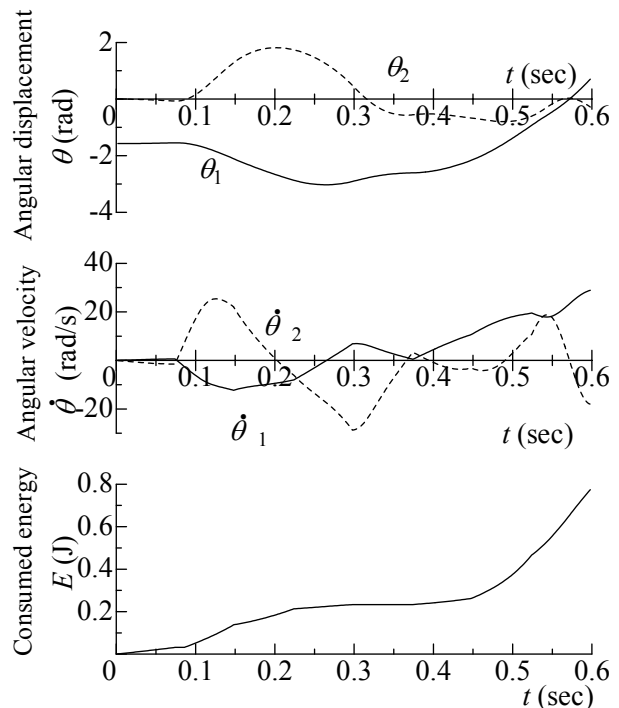


Fig. 6 Response of the manipulator with a passive joint

4 Experimental results

In this section, the results of fundamental experiment are shown to examine the effectiveness of modeling for the simulations.

Figure 7 shows an experimental apparatus, which is used in previous report by the authors [3]. A tray for holding the object is connected to link 2 by a passive revolute joint. It is able to use Equation (1) for calculating the motion of link 2 and the tray, under the condition that motion of link 1 (θ_1) is the same as link 2 (θ_2). And, the parameters of system are shown in Table 3. The motors 1 and 2 (rated 24 V, 60 W) are on the frame. Figure 8 shows a mechanism of manipulator.

Figure 9 shows the locus of every sampling time (0.05 [s]), under the condition that initial position is ($\theta_{1i} = -\pi/4$, $\theta_{2i} = -\pi/2$), the finale position is ($\theta_{1f} = \pi/4$, $\theta_{2f} = 0$), and the working time is $T=0.4$ [s].

Figure 10 shows the experimental response under the condition that sampling time of the control is 0.002 [s], the feedback gain for angular displacement is 50 [V/rad], and the feedback gain for angular velocity is 0.5 [Vs/rad]. In Figure 10, the response of angular displacement θ_2 and θ_3 are measured by rotary encoder, and angular velocity $\dot{\theta}_3$ is calculated by angular displacement. Theoretical results (broken line) agree with experimental results (solid line).

From these results, it is confirmed that modeling for the simulations is effective.

5 Conclusions

The results obtained in this paper are summarized as follows.

- (1) It is considered that manipulator with passive revolute joint is available for throwing motion.
- (2) From experimental results, it is considered that modeling for simulation is effective.

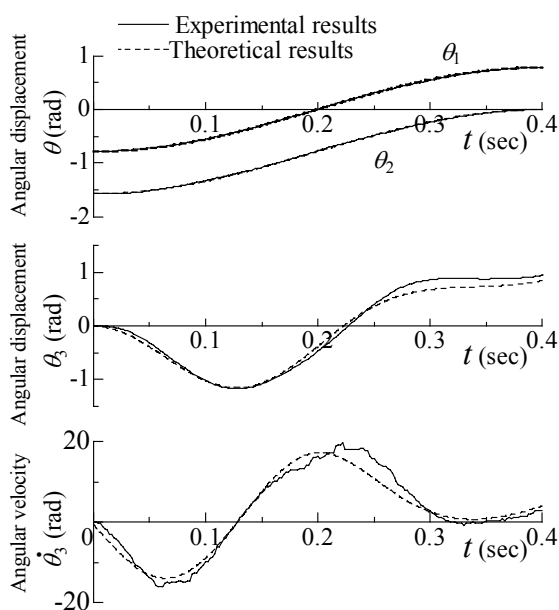


Fig. 10 Experimental results

References

1. H.Arisumi, K.Yokoi, T.Kotoku et al, "Casting Manipulation (Experiments of Swing and Gripper Throwing Control)," *International Journal of JSME*, Vol.45, No. 1C, pp.267-274, 2002.
2. N.Kato, and T.Nakamura, " Throwing Control for 2-DOF Robot (in Japanese) ," *JSME*, Vol. 63, No. 614C, pp.3571-3576, 1997.
3. A.Sato, O.Sato, N.Takahashi et al, " Trajectory for Saving Energy of Direct-Drive Manipulator in Throwing Motion," *Proc. of 11th Conference on Artificial Life and Robotics*, pp.783-786, 2006.
4. O.Sato, H.Shimajima, and H.Yoinara, " Minimum-energy Control of a Manipulator with Two-degree of Freedom," *Bulletin of JSME*, Vol.29, No.248, pp.573-579, 1985.

Table 3 Parameters of experimental apparatus

Parameter	Value	Parameter	Value
l_1 (m)	0.080	I_{G1} (kgm^2)	1.73×10^{-5}
l_2 (m)	0.115	I_{G2} (kgm^2)	8.42×10^{-5}
l_{g1} (m)	0.044	I_{G3} (kgm^2)	9.43×10^{-6}
l_{g2} (m)	0.078	m_1 (kg)	0.0202
l_{g3} (m)	0.030	m_2 (kg)	0.0468
D_3 (Nms/rad)	7.35×10^{-6}	m_3 (kg)	0.0218

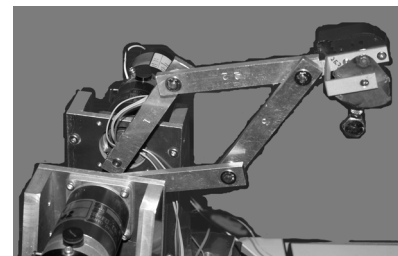


Fig. 7 Experimental apparatus

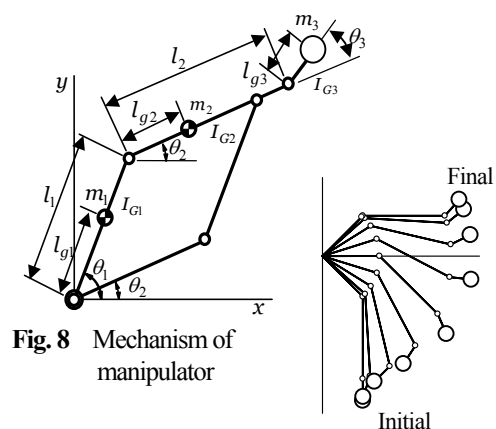


Fig. 8 Mechanism of manipulator

Fig. 9 Locus of manipulator

A Study on Real Time Intelligent Control of a Three-Fingers Hand System

Xuan-Thu Le, Se-Bong Oh, Woo-song Lee, Won-II Kim, and Sung-Hyun Han

Division of Mechanical and Automation Eng., Kyungnam Univ., Masan, 631-701, Korea
E-mail: shhan@kyungnam.ac.kr Tel: +82-55-249-2624 Fax: +82-55-249-2617

Abstract:

We present an experimental performance for the validation of a robotic hand gripper for space applications. In particular this researches focus on the compatibility of the gripper with the Fara robot arm, developed by Esp. Co., Ltd. This hand gripper is the wide working space compared with its physical dimensions and the capability to deal with free-flying objects in no-gravity conditions. This capability is achieved by using force/torque sensor and by properly controlling and coordinating the gripper and the carrying arm. After a brief illustration on the main features of the gripper, the experimental activity is presented and the results achieved are discussed.

1. INTRODUCTION

The development of robotic hand gripper to execute automatic operations in space is foreseen to grow and cover a relevant part of the activities. With this respect, as already demonstrated in the industrial environment, a bottleneck is constituted by the end effector, that often is a very simple device with poor sensoriality and limited operational capabilities. Besides the numerous prototypes of articulated robotic hands, developed in more than 30 years of research, mainly in academic environment, see e.g. [1],[2] among many others, limited effort has been devoted to seek and evaluate alternative solutions, maybe simpler from the mechanical point of view than a multi-fingered hand, but with sufficient dexterity to perform in any case non trivial operations on a wide range of objects.

Therefore, referring specifically to the case of space applications, a scenario could be considered in which operations have to be performed in a no-gravity environment, where objects cannot be constrained and are therefore free to float in space. At the moment, this gripper is installed on a six degree of freedom arm, see Fig. 1. In order to emulate the capabilities of the FARA arm and to develop suitable coordinating strategies taking into account the kinematics capabilities of the whole arm/gripper system, [4]-[8].

2. HAND GRIPPER SYSTEM DESIGN AND ANALYSIS

The gripper has been designed considering its installation on the FARA arm proposed. This system



Fig. 1: The hand gripper installed on FARA manipulator

aims to substitute the astronauts in periodical operations with a semi autonomous robotic device. The end-effector for the robot manipulator needs therefore compactness, simplicity and reduced weight as well as capability of operation even on irregular floating objects.

Besides the three D.O.F gripper, main objective of this research, the overall robotic system consists of the following main components: a 6 D.O.F arm with an "open control", a standard force/torque sensor at the wrist and a vision system. These components are schematically shown in Fig. 2.

The gripper has three one D.O.F fingers whose

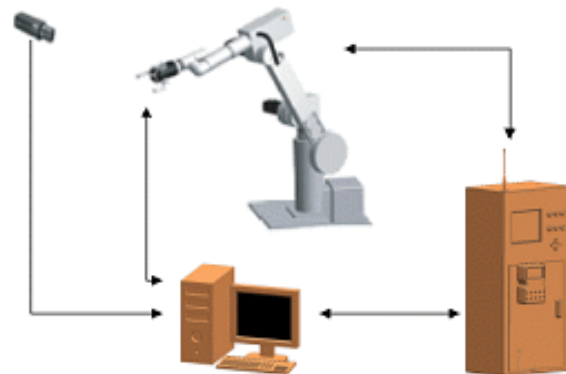


Fig. 2: The overall system.

distal phalange can move on a linear trajectory. These fingers are disposed radically, in a symmetric configuration as shown in Fig. 3. This kinematics configuration has several interesting features, as described in details in [4]-[6], including the capability of firmly grasping objects with irregular shapes and

with a rather wide range of dimensions.

In this manner, it is possible to control the motion of each finger, its distance from the object and the forces applied on it during the grasp.

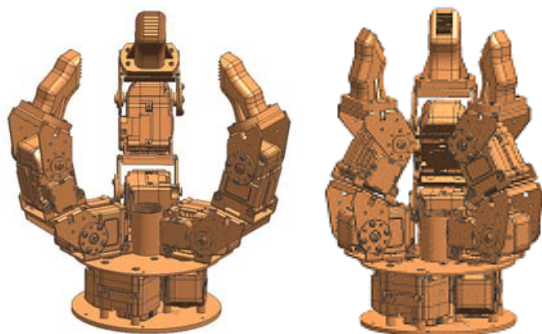


Fig. 3: The gripper in different configurations.

3. INTERLLIGENT CONTROL OF ROBOTIC HAND

The real time control of the gripper is based, at the moment, on standard HW/SW components. The control is performed with a DSP (TMS320C31) board connected to the motor drives and to an input board for the sensors. This board has been purposely designed because of the relatively high number of signals to be acquired in real-time. Currently, the DSP is hosted on a PC. From the software point of view, besides a real-time kernel on the DSP board, an interface between the DSP and the PC has been developed, allowing to use both real-time software and high-level environments for user interface.

At the moment, the servo control level has been implemented considering a simple logic switching between three classes of controllers: a position control (based on the position sensor), a proximity control (based on the proximity sensor) and the force control, based on the force/torque sensor.

The set points and the controlled variables of the servo loops are considered according to two main modalities: position control or proximity control. In the first case, the absolute position of the fingertip is controlled by planning the desired motion with a fourth-order polynomial function and assigning the desired motion time. The controlled variable is the position x (the radial distance from the center of symmetry of the gripper) of the fingertip obtained by means of the forward kinematics¹ from the joint position measured by the Hall effect sensor.

In the second case, the controlled variable is the distance of the finger with respect to the approached object. This modality is activated when the finger is sufficiently close to the object. The controlled variable is now the distance from the object, as measured by the

proximity sensor. This information can be used both to start the grasp of the object (if all the fingers are at the same distance from it) or to maintain constant the distance between the finger and the object.

The force control is based on the same PI structure of the position and proximity controllers, and at the moment can be classified as a simple compliance control obtained by specifying the compliance parameter K , see Fig. 4.

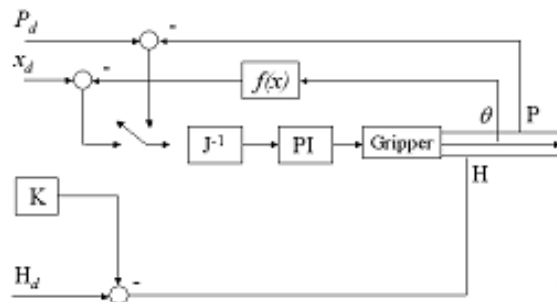


Fig. 4: Position/force control scheme.

Obviously, a proper switching logic between the above three control modalities must be adopted in the different phases of the execution of the tasks in order to ensure a smooth behavior of the gripper.

The prototype of the gripper has been installed on a 6 D.O.F anthropomorphic robot, a FARA with an open-control architecture, a PC connected to the standard robot controller C and equipped with a force/torque sensor on the wrist. The open control architecture allows in particular synchronizing the tasks of both the gripper and the arm for micro-motion during task execution.

The real time OS chosen for this application is Linux[10] running in our case on a Pentium IV PC. This PC may carry out the robot position control, based on the feedback provided by the position sensors, the wrist force/torque sensor and by the vision system. At the same time, the operating system allows the communication between the robot control task (executed as real-time procedure in the Linux environment) and the corresponding routines on the DSP board for the gripper control. It is possible to control the robot under Linux in two main modalities. In the first, the servo loops for each actuator are performed, the standard robot controller. In this modality, a new position set point is generated by the PC every 10 msec. In the second case, the PC performs directly the control of each actuator, with a sampling period of 1 msec.

4. EXPERIMENT AND RESULTS.

Examples of these experimental results are shown in Fig. 6-Fig. 8. Set-up is shown in Fig. 5.

A number of laboratory experiments have been

performed both on single finger modules and sensorial/actuation subsystems in order to test the



Fig. 5: Experiments set-up

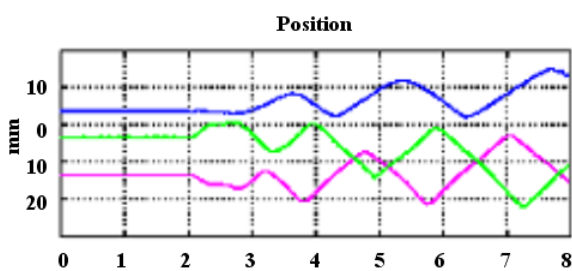


Fig. 6: Tracking a moving objects by exploration with the proximity sensors and computation of the normal directions.

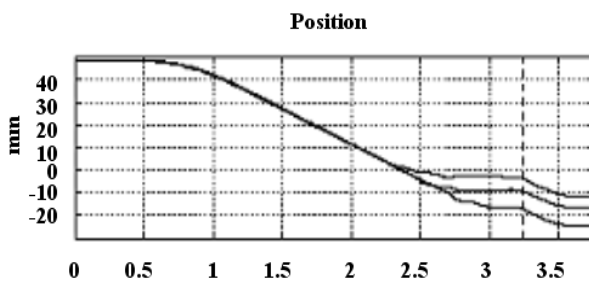


Fig. 7: Grasp of a floating object

efficiency of each finger structure and of the control system. The validation has also included verification of the procedures for the object approach, based on the use of both the distance and the position sensor information, and the use of the force/torque sensors.

Concerning the approach and contact phases, it must be observed that the possibility of independently moving the fingers has noticeably increased the capability of grasping moving objects. As a matter of fact, the object may be tracked with a coordinated movement of both the arm and the fingers. Once the motion is tracked, the grasp may be firmly applied without losing contact.

Finally, an experiment involving force control is shown in Fig. 9.

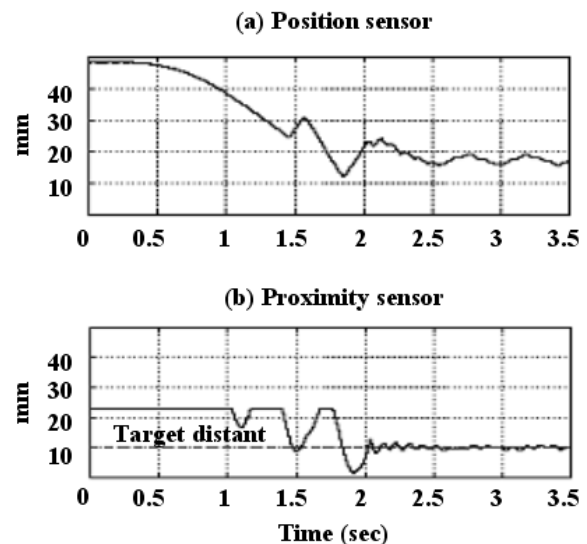


Fig. 8: Measurements of the position (a) and proximity (b) sensor.

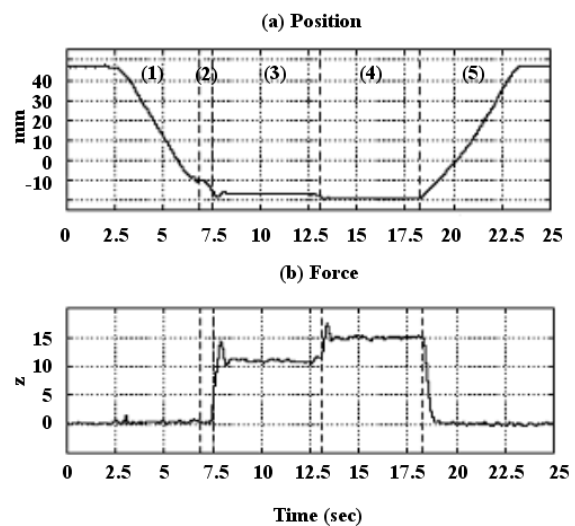


Fig. 9: Motion of the finger (a) during an approach and a grasp and force applied on the object (b).

5. CONCLUSION

We presented a new technique to control of a three-fingered with 12 degrees of freedom robotic gripper for real application.

It presents a very large workspace with respect to its body size, and is capable of operation both on small and on large objects; its sensory equipment seems to be sufficiently rich and more than adequate for the expected tasks. Future improvements will concern the refinement of the current version of the gripper and the conclusion of the verification phase, in particular with respect to the force control and to the possibility of applying simple manipulation procedures on the grasped objects.

REFERENCES

- [1] A. Rusconi, R. Mugnuolo, F. Bracciaferri, A. Olivieri, F. Didot, "EUROPA (External Use of Robotics for Payloads Automation)", *ASTRA 2000, ESTEC, Noordwijk, NL*, 5-7 dic.2000.
- [2] C. Melchiorri, "Slip Detection and Control Using Tactile and Force Sensors", *IEEE Trans. on Mechatronics, special Issue on Advanced Sensors for Robotics*, Vol. 5, No. 3, Sept. 2000, pp. 235-243.
- [3] L. Biagiotti, C. Melchiorri, G. Vassura, "Experimental activity on grasping objects in free floating conditions", *ASTRA'2000, ESTEC, Noordwijk, NL*, 5-7 dic. 2000.
- [4] C. Melchiorri, G. Vassura, "Design of a Three-Finger Gripper for Intra-Vehicular Robotic Manipulation", *1st IFAC Workshop on Space Robotics, SPRO98, Montreal, CA*, Oct. 19-22, 1998.
- [5] <http://www.aero.polimi.it/projects/rtai/>
- [6] G. Vassura, C. Melchiorri, "Three Finger Grasping for Intra Vehicular Space Experiments", *WAC'2000, Maui, Hawaii*, June 11-16 2000.
- [7] C. Melchiorri, G. Vassura, "Implementation of Whole Hand Manipulation Capability in the U.B. Hand System Design", *J. of Advanced Robotics, Special Issues on "Enveloping Grasp and Whole-Hand Manipulation"*, pp. 547-560, Vol. 9, No. 5, 1995.
- [8] T. Oomichi et al. Development of working multifinger hand manipulator *Proc. IEEE Int. Workshop on Intelligent Robots and Systems*, 873-880, 1990.
- [9] M. Ishikawa et al. A CMOS vision chip with SIMD processing element array for 1ms image processing. *Dig. Tech. Papers of IEEE Int. Solid-State Circuits Conf.*, pages 206- 207, 1999.
- [10] R.A. Grupen et al. A survey of general-purpose manipulation. *Int. J. Robot. Res.*, 8(1): 38-62, 1989.
- [11] L. Biagiotti, C. Melchiorri, and, G. Vassura, Position/Force Control of a Arm/Gripper System for Space Manipulation. *Proc. of the 2003 IEEE/RSJ Intl. Conference on Intelligent Robots and Systems*, October 2003.
- [12] J. Butterfass et al. DLR-hand II: Next generation of a dexterous robot hand. *Proc. IEEE Int. Conf Robot. and Automat.*, pages 109- 114, 2001.

A Study on Design of Multifingered Robot Hand with 15 D.O.F and Applications

Xuan-Thu Le, Se-Bong Oh, Haeng Bong Shin, Yoon Kyu Kim, and Sung-Hyun Han

Division of Mechanical and Automation Eng., Kyungnam Univ., Masan, 631-701, Korea.
E-mail: shhan@kyungnam.ac.kr Tel: +82-55-249-2624 Fax: +82-55-249-2617

Abstract

The focus of this paper is to design a flexible three fingered hand system with 15 D.O.F for dynamic manipulation with an intelligent controller, and to build a useful database for dynamic manipulation based on the experimental results. The weight of the hand module is only 0.6 kg, but flexible motion and powerful grasping are possible. To achieve such a dynamic motion in a robotic hand, we have developed a flexible fingered hand with a control system incorporating image recognition system in which we deal with the problems of not only accuracy and range of motion but also the flexibility of hand.

1. INTRODUCTION

Recently several hands have been developed in which actuators are placed directly in each finger link. Several human-like robotic hands have been developed with this approach [1], [2]. These robotic hands have many degrees of freedoms to achieve the dexterous grasp of a human hand, but power and speed are not enough to achieve dynamic manipulation. General Hand is lightweight and powerful, but the number of degrees of freedom is not enough to achieve precise motion.

In order to develop a dexterous and skillful artificial hand, such as a human hand, various types of multifingered hands have been researched. Such hands were designed with attention to range of motion and accuracy, and less attention to speed of motion [3]-[5].

Examples of this dynamic change are "pushing", "hitting", "throwing", "catching", etc. A human takes advantage of such dynamic motion for manipulation. This is one of the reasons that a human manipulation is more dexterous and flexible than a robotic hand.

There has been considerable theoretical work on a multifingered hand addressed to: grasp stability, force analysis, and dynamic control [6]. But in most of this research static or quasi-static movement was assumed, and there has been little work on dynamic manipulation.

Various types of robotic hands have been developed [7], [8]. In most hands a wire driven mechanism is used with control through high-power actuators that are placed outside of the main body of the hand [8]-[12]. But the mechanism is complicated and the total system is big and heavy.

On the other hand, in dynamic manipulation, transitions in the contact condition often occur when the fingers let a target go, or the fingers touch a target. It is difficult to observe a target only using force and tactile sense; vision plays an important role in this case. To observe a moving object in realtime, a flexible vision system in which the sampling rate is more than 1.2 kHz is effective. Several types of vision chips have been developed [13], [14], and this technique was applied to a sensory motor fusion system, and to produce high speed grasping.

In this paper we describe a newly developed intelligent flexible hand system and its application to a catching task. The hand has 10 joints and 3 fingers. A newly developed small harmonic drive gear and a high power mini actuator are fitted in each finger link, and a strain gauge sensor is in each joint.

2. FLEXIBLE HAND SYSTEM DESIGN

The mechanism of a flexible hand gripper requires the mass of the hand should be as low as possible. It is highly desirable that the hand weigh less than 1kg. Furthermore the low mass of the finger mechanism is desirable not only to achieve flexible motion but also for stable control.

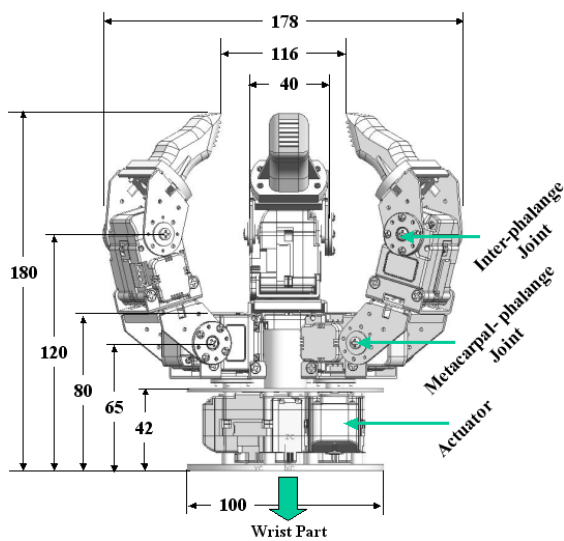
Our philosophy about dynamic manipulation is maximization of the power and minimization of the mechanism. In particular three factors are important: (1) light weight, (2) high speed and high acceleration, (3) accuracy.

Fig. 1 shows the mechanical design of the hand, and Fig. 2 shows a scene of the Gripper control. It has three fingers, and we call the fingers "left finger", "index finger" and "right finger" looking from the left side. We call the joints of each finger, inter-phalange joint, metacarpal-phalange joint, trapezoid-metacarpal joint, corresponding to human anatomy.

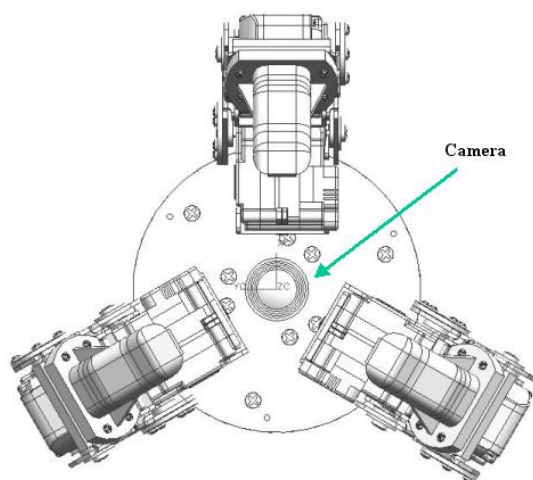
To achieve the light mechanism, we reduced the number of joints and fingers as much as possible. We used three fingers, which is the minimum number to achieve a stable grasp.

The index finger has 3 degrees of freedom, and the other fingers have 3 D.O.F, so that the hand has 15 D.O.F total. In general a hand needs 9 D.O.F to move a target to any position and orientation. But in our hand 1

D.O.F of the index finger is omitted, and the wrist joint of the manipulator takes its place.



(a) Front view



(b) Top view

Fig. 1: Kinematics design

The fingers are arranged so as to grasp both circular and prismatic objects. Both left and right thumbs play the role of the “thumb” of a human hand. Each thumb has only 3 D.O.F, which is less than the 5 D.O.F of a human thumb, but various types of grasping can be achieved because the joint can move in a wide range.

In order to achieve “lightning” high acceleration, we have developed a new actuator that allows a large current flow for a short time.

The design is based on the new concept that maximum output should be improved rather than rate output. As a result this actuator can generate maximum power only for a short period of time, but the power output is high, to prevent the actuator from overheating,

the amount of current is controlled by software in realtime.



Fig. 2: Scene of the hand gripper control

The finger has strain gauges at the inter-phalange and metacarpal-phalange joints for force control. In addition a 6-axis force/torque sensor and a tactile sensor will be mounted on each fingertip.

The flexible motion imposes a heavy load on the finger mechanism. For this reason a simple mechanism should be used for reduction gear, transmission, etc. In most traditional hand systems a wire-driven mechanism is used. But this is not suitable for a lightweight mechanism, because it is large and complicated.

In our hand a newly developed small harmonic drive gear and a high-power mini actuator are fitted in each finger link. A harmonic drive gear has desirable properties for control such as no backlash and a high reduction rate.

As the transmission mechanism between actuator and joint, we adopt a bevel gear. This is because the axis of the actuator should be orthogonal to the axis of the joint, and a bevel gear is simple and strong enough to achieve flexible rotation. Normally a bevel gear has a large amount of backlash. To reduce backlash the bevel gear was processed precisely, and derris coated on the surface.

We added dual vision to the hand system, as shown in Fig. 3. Vision is with a massive parallel vision system called column-parallel high-speed vision system [14]. It has 128×128 photo detectors with an all pixel parallel

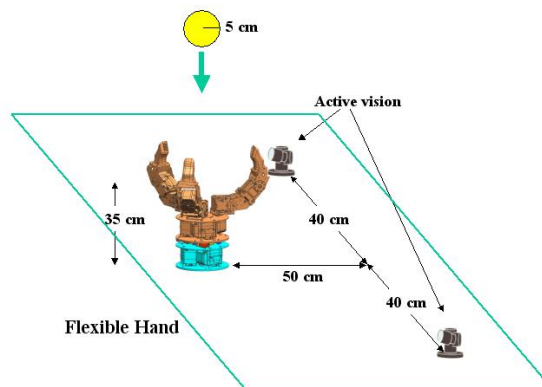
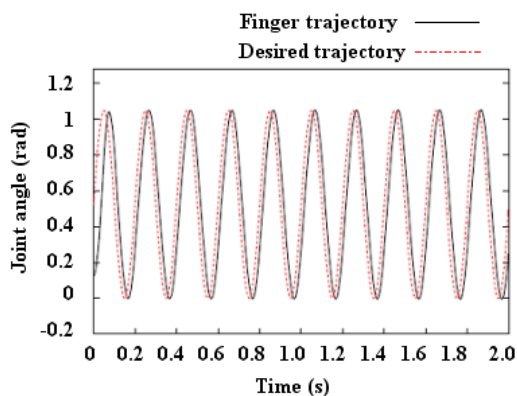


Fig. 3: Visual feedback control system

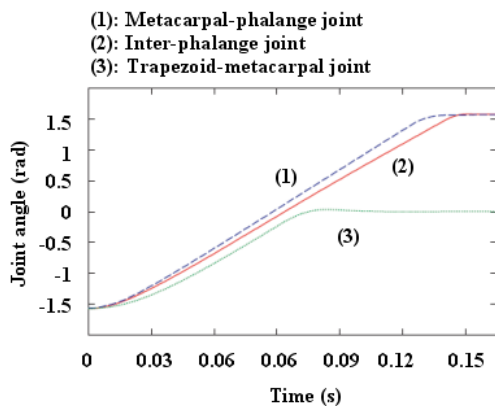
processing array based on vision chip architecture and an exclusive summation circuit for calculating moment values. Because the visual processing is executed in parallel in the processing array, flexible visual processing (moment detection, segmentation, etc.) is achieved within 1ms.

Early image processing is performed in order to achieve segmentation of the image, extraction of the target area, and computation of the image moments. From these data, the position of the target is computed.

Each vision sensor is mounted on an active vision, as shown in Fig. 4. Because the joint angle sensor has high resolution, high resolution of 3D position sensing



(a) Sine wave



(b) Step

Fig. 4: Result of Performance

is achieved by fusing image information with joint angle information. The information acquired by the vision system is sent to the hand actuator at the rate of 1.2 kHz, which is the same rate as the joint angle sensor and the joint torque sensor.

3. PERFORMANCE TEST

The main advantage of a multi fingered hand is that it can grasp various objects by changing its shape. Several classifications of grasping have been proposed. In this proposal various grasps are classified into three large categories: a power grasp that passively resists arbitrary external forces exerted on the object, a precise grasp to manipulate the object, and an intermediate grasping which some fingers are used for a power grasp and the other fingers are used for a precise grasp.

We achieved these typical grasp types in our developed hand. Fig. 5 shows the results. It is not



Fig. 5: Grasping examinations

always necessary that all types of grasping be achieved, but it is most useful to achieve dexterous manipulation.

Catching is one of the most important tasks for dynamic manipulation. In this section catching is shown using our flexible hand with a visual feedback controller.

To simplify the problem, suppose that the target and the hand are on a 2 dimensional plane, the target is a sphere, and two fingers catch the target. From various experimental trials, we have decided on the catching strategy shown in Fig. 6.

The fingertips impact the target, and the target is moved to a stable grasp position. Finally two fingers catch the target, and the impact from both sides' stops the falling motion of the target.

To simplify the problem we assume that the inter-phalange joint is always controlled at 90deg. In Fig.7, $q_0 \in \mathbb{Q}^2$ is the target position, $q_i \in \mathbb{Q}^2$ is the i-th tip position, $e_{i1} \in \mathbb{Q}^2$ and $e_{i2} \in \mathbb{Q}^2$ are the unit vectors fixed on the finger link, $Q \in \mathbb{Q}$ is a target radius, and $\theta_i \in \mathbb{Q}$

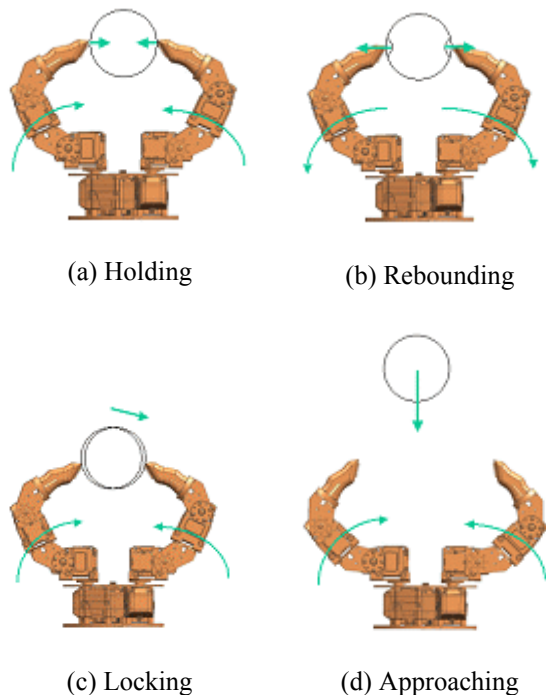


Fig. 6. Catching strategy

represents the angle of the metacarpal-phalange joint of the i -th finger.

With two fingertips the optimal grasp points are both sides of the sphere: $q_0 \pm Qe_x$, where e_x is the x -axis unit vector. In order to bring the tip close to the point in the approaching phase, we define the following virtual constraints:

$$[(-1)^i Q_0 e_x + q_0 - q_i] e_{i1}^T = 0, \quad (i = 1, 2). \quad (1)$$

This means that the fingertips are always directed to the

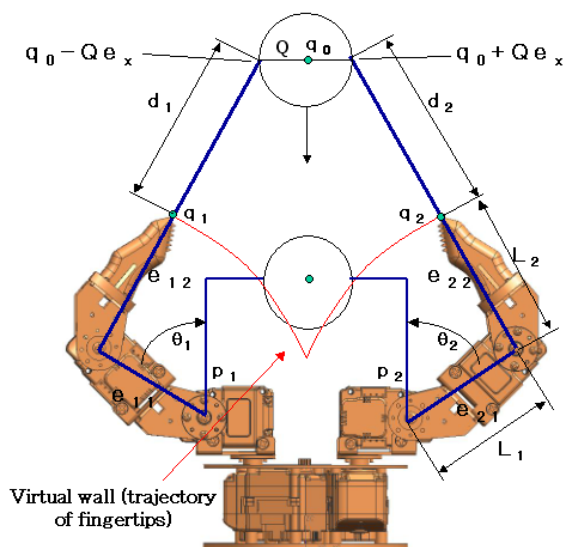


Fig. 7. Catching algorithm

optimal grasp points, and it is regarded as the process to make a “virtual wall” along the trajectories of both fingertips. If the speed of fingertip is fast enough to track the target, the target falls along the virtual wall. For this reason, the locking and holding phases are also achieved.

Because e_{i1} , e_{i2} , and q_i are a function of the joint angle θ_i , Eqn. (1) is rewritten as

$$f_i(\theta_i, q_0) = 0, \quad (i = 1, 2), \quad (2)$$

where f_i represents a nonlinear function. The desired trajectory of metacarpal-phalange joint $q_{di} \in \mathbb{Q}$ is given as the solution of Eqn.2. It is written as

$$\theta_{d_i} = g_i(q_0), \quad (i = 1, 2), \quad (3)$$

where g_i is the implicit function of f_i .

As a result, the control method is written as

$$\tau_i = K_p [g_i(q_0) - \theta_i] - K_d \dot{\theta}_i, \quad (i = 1, 2). \quad (4)$$

where τ_i is the command torque of the metacarpal-phalangeal joint, and K_p and K_d are appropriate scalars. Because the finger mechanism is light and the output of the actuator is high power, the inertia of the link almost can be ignored, and the PD feedback control achieves good performance.

In the rebounding phase, it is desirable that the movement of the fingertips caused by the rebound is small enough. To solve this problem, the gain K_p is increased temporary in the moment both fingertips touch the target.

We used a rubber ball with radius of 5cm as a target, and we dropped it from about 1.2m in height. The speed of the falling ball is about 5.9m/s just before it hits the ground.

The catching task for the ball is:

- Approaching (0÷40ms)
- Locking (40÷50ms)
- Rebounding (50÷60ms)
- Holding (60ms÷).

Fig. 8 shows the changes in the target position q_0 , and Fig. 9 shows the changes in the distance d_1 and d_2 .

The success rate was more than 95% and tolerance of position error of the target was about ± 1.5 cm from the center of the palm.

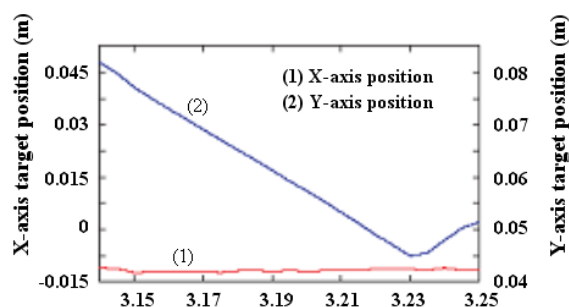


Fig. 8. Time response: target position

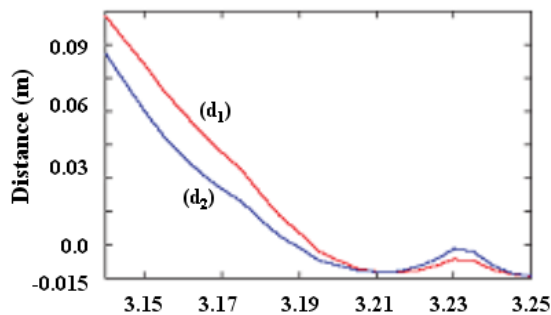


Fig. 9. Time response: distance

Several types of failure modes were observed. The direction of a bounced ball depends on the coefficient of friction and restitution. It is difficult to know the accurate values of these parameters, but the errors in their measurement may be ignored if the speed of the fingertip is fast enough.

4. CONCLUSION

We have described a lightweight flexible hand with 15 D.O.F, and the associated visual feedback control. We are now developing a flexible manipulation system, which consists of a dual flexible multi-fingered hand-arm system, and a dual active vision system. In the future this new hand-arm system will be used for tasks.

The need for a robotic hand that works in the real world is growing. And such a system should be able to adapt to changes in environment. We think that the concept of a flexible hand system with realtime control implementation will become an important issue in robotic research.

REFERENCES

[1] H. Kawasaki et al. Dexterous anthropomorphic robot hand with distributed tactile sensor: Gifu hand II. *IEEE/ASME Trans. Mechatronics*, 7(3): 296-303, 2002.

[2] S.C. Jacobsen et al. Design of the Utah/MIT dexterous hand. *Proc. IEEE Int. Conf. Robotics and Automation*, pages 1520-1528, 1986.

[3] A.A. Rizzi and D.E. Koditschek. Further progress in robot juggling: The spatial two-juggle. *Proc. IEEE Int. Conf. Robot. and Automat.*, 3:919-924, 1993.

[4] W.T. Townsend. The BarrettHand grasper - programmably flexible part handling and assembly. *Industrial Robot*, 27(3): 181-188, 2000.

[5] M. R. Cutkosky. On grasp choice, grasp models, and the design of hand for manufacturing tasks. *Proc. IEEE Int. Conf. Robot. and Automat.*, 5(3): 269-279, 1989.

[6] M.T. Mason and K.M. Lynch. Dynamic manipulation. *Proc. Int. Conf. Intelligent Robots and Systems*, pages 152-159, 1993.

[7] A. Namik and M. Ishikawa. Robotic catching using a direct mapping from visual information to motor command. *Proc. IEEE Int. Conf. Robot. and Automat.*, 2003.

[8] J.K. Salisbury and J.J. Craig. Articulated hands (force control and kinematics issues). *Int. J. Robotics Research*, 1(1): 4-20, 1982.

[9] A. Namiki et al. 1ms sensory-motor fusion system. *IEEE/ASME Trans. Mechatron.*, 5(3): 244-252, 2000.

[10] T. Oomichi et al. Development of working multifinger hand manipulator *Proc. IEEE Int. Workshop on Intelligent Robots and Systems*, 873-880, 1990.

[11] M. Ishikawa et al. A CMOS vision chip with SIMD processing element array for 1ms image processing. *Dig. Tech. Papers of IEEE Int. Solid-State Circuits Conf.*, pages 206-207, 1999.

[12] Akio Namiki, Yoshiro Imai, and Makoto Kaneko, Development of a High-speed Multifingered Robot Hand System and Its Application to catching, *Proc. of the 2003 IEEE/RSJ Intl. Conference on Intelligent Robots and Systems*, Las Vegas, Nevada, October 2003.

[13] J. Butterfass et al. DLR-hand II: Next generation of a dexterous robot hand. *Proc. IEEE Int. Conf. Robot. and Automat.*, pages 109-114, 2001.

[14] K.B. Shimoga. Robot grasp synthesis algorithms: A survey. *Int. J. Robot. Res.*, 15(3): 230-266, 1996.

Accuracy Improvement of a 5-axis Hybrid Machine Tool

Jun-Woo Kim*, Hye-Yoon Kim, and Han-Sung Kim

School of Mechanical Engineering and Automation,
Kyungnam University,
449 Wolyoung Dong, Masan, Kyungnam, 631-701, Korea (hkim@kyungnam.ac.kr)

Abstract

In this paper, a novel 5-axis hybrid-kinematic machine tool is introduced and the research results on accuracy improvement of the prototype machine tool are presented. The 5-axis hybrid machine tool is made up of a 3-DOF parallel manipulator and a 2-DOF serial one connected in series. The machine tool maintains high ratio of stiffness to mass due to the parallel structure and high orientation capability due to the serial-type wrist. In order to acquire high accuracy, the methodology of measuring the output shafts by additional sensors instead of using encoder outputs at the motor shafts is proposed. In the kinematic view point, the hybrid manipulator reduces to a serial one, if the passive joints in the $U-P$ serial chain at the center of the parallel manipulator are directly measured by additional sensors. Using the method of successive screw displacements, the kinematic error model is derived. Since a ball-bar is less expensive than a full position measurement device and sufficiently accurate for calibration, the kinematic calibration method of using a ball-bar is presented. The effectiveness of the calibration method has been verified through the simulations. Finally, the calibration experiment shows that the position accuracy of the prototype machine tool has been improved from 153 to 86 [μm].

1 Introduction

A Conventional 5-axis machine tool provides high accuracy and large workspace. However, due to the serial-kinematic structure, it generally requires very massive structure to maintain high stiffness. In order to increase the ratio of stiffness to mass, the 3-DOF parallel-kinematic manipulator is employed as an arm and for high orientational capability, the 2-DOF serial-kinematic manipulator is used as a wrist. Hence, the proposed machine tool has a 5-DOF hybrid-kinematic structure as shown in Fig. 1. This machine tool will be applied for both machining and assembling tasks of automobiles' cylinder blocks. Specifically, the parallel manipulator has three $U-P-S$ legs at the side and one $U-P$ leg at the center, where the prismatic joints in the $U-P-S$ chains are controlled by linear actuators and the prismatic joint in the $U-P$ chain is passive.

In design and control of a machine tool, to obtain high accuracy is one of the most important tasks to be

accomplished. In order to guarantee high accuracy, the methodology of measuring the output shafts by additional sensors instead of using encoder outputs at the motor shafts is proposed. For the parallel manipulator, we additionally install two angular encoders and one linear encoder at the $U-P$ chain and two angular encoders at the output shafts of the serial manipulator as shown in Fig. 1. Therefore, we can calculate the position and orientation of the tool tip by the outputs of the five sensors connected in series. Hence, we can consider the hybrid manipulator as a serial manipulator, i.e., the $U-P-R-R$ chain. In modeling kinematic errors, we used the method of successive screw displacements [1] instead of the Denavit-Hartenberg notations because the former is more general and straightforward [2].

Since a ball-bar is less expensive than a full position measurement device and sufficiently accurate for calibration, the kinematic calibration on the proposed machine tool will be performed by using a ball-bar. For a length measurement, i.e., using a ball-bar, the kinematic calibration is reduced to a nonlinear least square method of minimizing the calculated and measured lengths of a ball-bar. The effectiveness of the kinematic calibration method with a ball-bar is verified through the simulations. Through calibration experiment, the accuracy has been improved from 153 to 86 [μm].

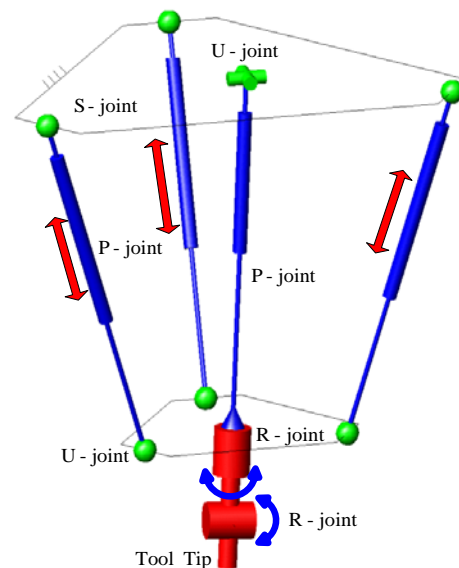


Fig. 1 Structure of the hybrid-kinematic machine tool.

2 Position Analysis

The forward kinematics of the machine tool can be obtained by considering the central leg, i.e., *U-P-R-R* serial chain in the middle if the *U-P* passive joints are measured. At a reference position, the kinematic parameters may be listed in Table 1, where s_i and s_{0i} denote the direction and location of the i^{th} joint axis with respect to the fixed coordinate system $A(x, y, z)$ when the machine tool is at the reference position.

Substituting the coordinates of the joint axes into the equation of the general spatial displacement, known as *Rodrigues's formula*, the screw transformation matrices:

$$\begin{aligned}
 A_1 &= \begin{bmatrix} 1 & 0 & 0 & 0 \\ 0 & c\theta_1 & -s\theta_1 & 0 \\ 0 & s\theta_1 & c\theta_1 & 0 \\ 0 & 0 & 0 & 1 \end{bmatrix}, A_2 = \begin{bmatrix} c\theta_2 & 0 & s\theta_2 & 0 \\ 0 & 1 & 0 & 0 \\ -s\theta_2 & 0 & c\theta_2 & 0 \\ 0 & 0 & 0 & 1 \end{bmatrix}, \\
 A_3 &= \begin{bmatrix} 1 & 0 & 0 & 0 \\ 0 & 1 & 0 & 0 \\ 0 & 0 & 1 & t_3 \\ 0 & 0 & 0 & 1 \end{bmatrix}, A_4 = \begin{bmatrix} c\theta_4 & -s\theta_4 & 0 & 0 \\ s\theta_4 & c\theta_4 & 0 & 0 \\ 0 & 0 & 1 & 0 \\ 0 & 0 & 0 & 1 \end{bmatrix}, \\
 A_5 &= \begin{bmatrix} c\theta_5 & 0 & s\theta_5 & -(L_0 + L_1)s\theta_5 \\ 0 & 1 & 0 & 0 \\ -s\theta_5 & 0 & c\theta_5 & (L_0 + L_1)(1 - c\theta_5) \\ 0 & 0 & 0 & 1 \end{bmatrix}, \quad (1)
 \end{aligned}$$

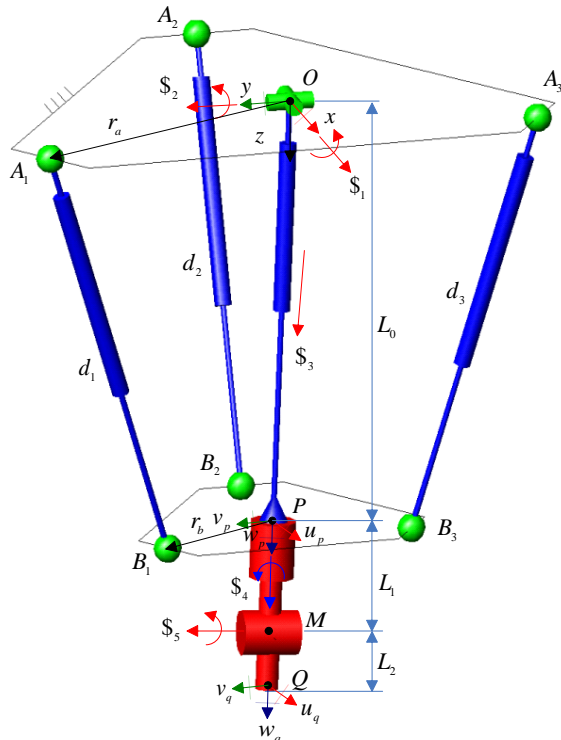


Fig. 2 Kinematic parameters of the machine tool.

Table 1 Screw axis locations and reference position.

Joint	s_i	s_{0i}
1	(1,0,0)	(0,0,0)
2	(0,1,0)	(0,0,0)
3	(0,0,1)	(0,0,0)
4	(0,0,1)	(0,0,0)
5	(0,1,0)	(0,0, $L_0 + L_1$)

where $c\theta_i = \cos \theta_i$, $s\theta_i = \sin \theta_i$ and t_3 denotes the linear displacement of the prismatic joint in the middle of the machine tool.

The target position of the tool tip Q can be given by

$$\begin{bmatrix} R_q & q \\ 0_{1 \times 3} & 1 \end{bmatrix} = A_1(\theta_1)A_2(\theta_2)A_3(t_3)A_4(\theta_4)A_5(\theta_5) \begin{bmatrix} I_{3 \times 3} & q_0 \\ 0_{1 \times 3} & 1 \end{bmatrix} \quad (2)$$

where $q_0 = [0, 0, L_0 + L_1 + L_2]^T$ denotes the tool tip Q when the machine tool is at the reference position. At the reference position, the orientation of the moving frame coincides with that of the fixed frame.

For the inverse kinematics of the *U-P-R-R* serial chain, only 5 of the 12 parameters associated with the end-effector position vector and rotation matrix can be specified at will. This is because the manipulator has only 5 degrees of freedom. In this work, the position vector (q) and the approach vector (w_q) are specified and the other two unit vectors, u_q and v_q , are to be determined after the joint angles are found. The point M can be obtained by

$$m = q - L_2 w_q \quad (3)$$

We observe that the position of the point M depends only on the first three joint variables, θ_1 , θ_2 , and t_3 . From the geometry, the direction vector and the travel distance of the prismatic joint is determined by

$$s_3 = m / \|m\| \text{ and } t_3 = \|m\| - (L_0 + L_1) \quad (4)$$

Furthermore, the other two angles can be easily obtained in the following.

$$s_3 = R_1 R_2 R_3 w_{q0} \text{ where } w_{q0} = [0, 0, 1]^T \quad (5)$$

This equation reduces to

$$\begin{bmatrix} s_{3x} \\ s_{3y} \\ s_{3z} \end{bmatrix} = \begin{bmatrix} s\theta_2 \\ -s\theta_1 c\theta_2 \\ c\theta_1 c\theta_2 \end{bmatrix} \quad (6)$$

Then,

$$\theta_2 = \sin^{-1}(s_{3x}), \text{ and } \theta_1 = \text{Atan2}[-s_{3y}/c\theta_2, s_{3z}/c\theta_2] \quad (7)$$

From Eq. (2), we obtain

$$w_q = R_1 R_2 R_3 R_4 R_5 w_{q0}. \quad (8)$$

Since θ_1 , θ_2 , and t_3 are already known, the above equation can be reduced to

$${}^3w_q = R_4 R_5 w_{q0} \quad (9)$$

where ${}^3w_q = R_3^T R_2^T R_1^T w_q$. So, we can obtain the following relation.

$$\begin{bmatrix} {}^3w_{qx} \\ {}^3w_{qy} \\ {}^3w_{qz} \end{bmatrix} = \begin{bmatrix} c\theta_4 s\theta_5 \\ s\theta_4 s\theta_5 \\ c\theta_5 \end{bmatrix} \quad (10)$$

Then,

$$\theta_5 = \cos^{-1}({}^3w_{qz}), \text{ and } \theta_4 = \text{Atan2}[{}^3w_{qy}/s\theta_5, {}^3w_{qx}/s\theta_5] \quad (11)$$

It is noted that two solution sets are possible in the working range, i.e., $\theta_5 = \theta_5^+$ or $-\theta_5^+$.

The inverse kinematics of the 3-DOF parallel manipulator is simply determined by

$$d_i = \|R_p b_i + p - a_i\| \text{ for } i=1,2,3 \quad (12)$$

where

$$\begin{bmatrix} R_p & p \\ 0_{1 \times 3} & 1 \end{bmatrix} = A_1(\theta_1)A_2(\theta_2)A_3(t_3) \begin{bmatrix} I_{3 \times 3} & p_0 \\ 0_{1 \times 3} & 1 \end{bmatrix}, \quad p_0 = [0,0,L_0]^T,$$

$$a_1 = r_a \begin{bmatrix} 1/2 \\ \sqrt{3}/2 \\ 0 \end{bmatrix}, \quad a_2 = r_a \begin{bmatrix} -1 \\ 0 \\ 0 \end{bmatrix}, \quad a_3 = r_a \begin{bmatrix} 1/2 \\ -\sqrt{3}/2 \\ 0 \end{bmatrix}, \text{ and}$$

$$b_1 = r_b \begin{bmatrix} 1/2 \\ \sqrt{3}/2 \\ 0 \end{bmatrix}, \quad b_2 = r_b \begin{bmatrix} -1 \\ 0 \\ 0 \end{bmatrix}, \quad b_3 = r_b \begin{bmatrix} 1/2 \\ -\sqrt{3}/2 \\ 0 \end{bmatrix}.$$

3 Error Model

When there some kinematic errors exist in the $U-P-R-R$ serial chain, the kinematic parameters for an actual model can be summarized in Table 2. For a revolute joint, four kinematic errors (two for the direction of joint axis and two for location error) can be considered, however, for a prismatic joint, only two kinematic errors for the joint

direction exist. The total kinematic errors associated with directions and locations of joint axes are 18 and there are 5 joint offsets ($\delta\theta_1, \delta\theta_2, \delta t_3, \delta\theta_4, \delta\theta_5$). Therefore, 23 kinematic errors should be estimated by the following kinematic calibration.

Once the kinematic errors in the serial chain is determined, the relation between the $U-P$ chain and three $S-P-U$ chains needs to be investigated. The kinematic errors in the $S-P-U$ chains are summarized as follow:

Joint location errors: δa_i and δb_i for $i=1,2,3$

Length offset errors: δd_i for $i=1,2,3$

The kinematic errors will be determined by using Eq. (12).

Table 2 Kinematic parameters for an actual model.

Joint	s_i	s_{0i}
1	$(\sqrt{1-u_{1y}^2-u_{1z}^2}, u_{1y}, u_{1z})$	$(0, \delta y_1, \delta z_1)$
2	$(u_{2x}, \sqrt{1-u_{2x}^2-u_{2z}^2}, u_{2z})$	$(\delta x_2, 0, \delta z_2)$
3	$(u_{3x}, u_{3y}, \sqrt{1-u_{3x}^2-u_{3y}^2})$	$(0,0,0)$
4	$(u_{4x}, u_{4y}, \sqrt{1-u_{4x}^2-u_{4y}^2})$	$(\delta x_4, \delta y_4, 0)$
5	$(u_{5x}, \sqrt{1-u_{5x}^2-u_{5z}^2}, u_{5z})$	$(\delta x_5, 0, L_0 + L_1 + \delta z_5)$

4 Kinematic Calibration

In this work, the kinematic calibration method will be performed by using a length measurement, i.e., ball-bar [3-7]. In the following derivation, the superscripts, "c" and "m" are used to denote the calculated and measured values, respectively, and the subscript, "j" is employed to indicate the measurement number. As illustrated in Fig. 3, the calibration methods using length measurement is to find the set of kinematic parameters satisfying the following equation:

$$\|q^c(\theta_j^m + \delta\theta, \beta) - c\| = l_j^m \quad (13)$$

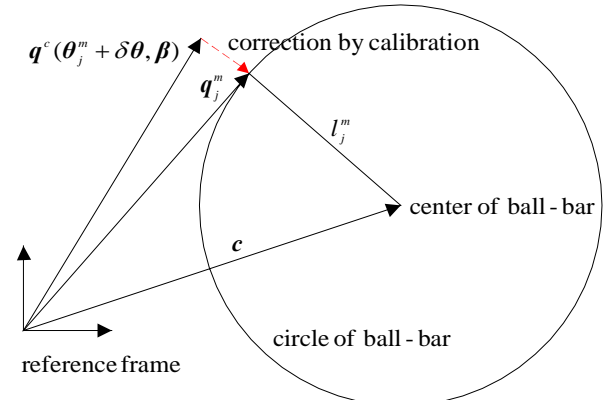


Fig. 3 Outline of the calibration methods using a ball-bar.

where $q(\cdot)$ denotes the forward kinematics function of the $U-P-R-R$ serial chain, θ_j^m and $\delta\theta$ denote the measured joint angle and the joint offset vectors, β is the kinematic error vector in Table 2 to be updated, and $c = \bar{c} + \delta c$ and l_j^m denote the position vector of the fixed center of a ball-bar and the measured length of a ball-bar, respectively.

The purpose of this work is to develop and to verify the effectiveness of a kinematic calibration method suitable for the prototype of a 5-axis hybrid machine tool being developed as shown in Fig. 4. The main kinematic parameters of the machine tool are listed in Table 3.

Prior to a real calibration experiment in near future, we assume a virtual prototype with realistic kinematic errors. The error bound is determined from the information on machining and assembling tolerances and its direction is generated by the random function in Matlab. We also assume that the prototype machine will be calibrated by a ball-bar, specifically, the QC10 ball-bar of Renishaw with the accuracy, $\pm 0.5[\mu\text{m}]$. For the collection of measurement data, one center of the ball-bar is fixed at $\bar{c} = [0, 0, 1500]^T [\text{mm}]$ expressed in the reference frame. The $n = 32$ measurement points are selected on the hemisphere surfaces with 150 mm radius. The n sets of encoder values from the three linear actuators and the $U-P-R-R$ serial chain and the corresponding n ball-bar lengths are measured at the same time, which are actually calculated from the virtual prototype for numerical simulations. Using Eq. (13) and "lsqnonlin" function of Matlab, the kinematic parameters and the position error of the ball center are updated so as to minimize the error between the calculated and measured lengths of the ball-bar.



Fig. 4. Prototype of a 5-axis hybrid machine tool.

Table 3 Parameters for a prototype machine tool.

Parameters	Unit [mm]
Radius of the fixed plate (r_a)	600
Radius of the moving plate (r_b)	250
Reference height (L_0)	840
Distance between A and C (L_1)	291
Tool length (L_2)	340
Initial length of an actuator (d_{i0})	910
Linear actuator stroke (Δd_i)	800

We assume that the maximum error bounds for angle and length are $\pm 25[\text{arcsec}]$ and $\pm 25[\mu\text{m}]$, respectively. The assumed kinematic errors for a virtual prototype are written in parentheses of Table 4. The estimated kinematic parameters by the suggested calibration method are also in Table 4. It is noted that estimated values are close to the assumed ones and at least the signs are identical. It is also noted that estimated values does not necessarily following the assumed ones.

In order to show the effectiveness of the suggested calibration method, the well-known circular test on the XY plane with the radius of 150 mm is presented in Fig. 5. From the kinematic calibration and error compensation, the maximum absolute kinematic error has been reduced from $214.5[\mu\text{m}]$ to $48.2[\mu\text{m}]$.

Table 4 Assumed and estimated kinematic errors.

i	s_i	Estimated (Assumed)	s_{0i}	Estimated (Assumed)	$\delta\theta_i$	Estimated (Assumed)
1	u_{1y}	14.6132 (22.5065)	δy_1	-22.1156 (-16.1867)	$\delta\theta_1$	3.6879 (5.7716)
	u_{1z}	-4.7791 (-13.4431)	δz_1	-12.6657 (-4.7147)		
2	u_{2x}	13.2356 (5.3421)	δx_2	37.9109 (21.7735)	$\delta\theta_2$	9.8016 (14.5969)
	u_{2z}	-1.0796 (-0.7009)	δz_2	12.9004 (20.8452)		
3	u_{3x}	15.6955 (19.5649)			δt_3	7.7064 (15.6583)
	u_{3y}	13.4825 (13.1048)				
4	u_{4x}	-6.1924 (-2.1766)	δx_4	12.5541 (-4.4865)	$\delta\theta_4$	-1.3791 (21.0906)
	u_{4y}	-22.605 (-24.0748)	δy_4	6.9893 (19.6825)		
5	u_{5x}	1.3792 (16.0704)	δx_5	-29.9936 (-22.1054)	$\delta\theta_5$	1.5168 (11.9104)
	u_{5z}	-3.5677 (-2.7648)	δz_5	-7.3568 (-7.3566)		
	δc_x	-46.8734 (-15.5173)	δc_y	11.9864 (-15.3284)	δc_z	-7.9520 (9.1112)

[Unit: [arc sec] for angle and [μm] for length]

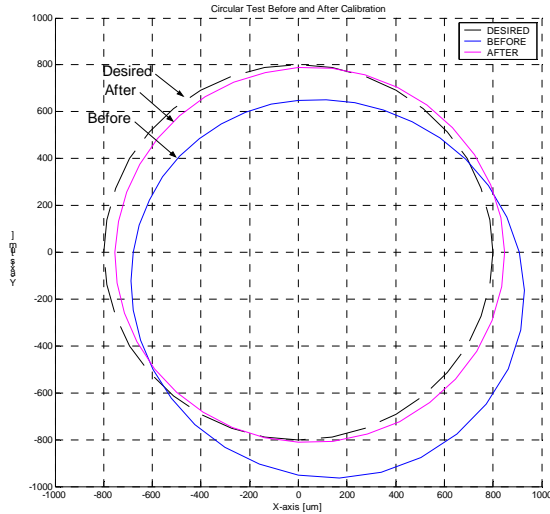


Fig. 5. Circular test before and after calibration.

Using the proposed algorithm and verified calibration procedure through simulation, calibration experiment has been performed on the prototype machine tool as shown in Fig. 6. In the experiment, The Renishaw QC10 ball-bar with $\pm 0.5[\mu\text{m}]$ is used. The $n=32$ points on the hemisphere surface with radius 150 mm are collected for updating kinematic parameters. We first calibrated some major errors, for example, the offset lengths of linear actuators. Then, the well-known circular test was performed (refer to Fig. 7(a)). The circular test result after calibration experiment is shown in Fig. 7(b). From the two tests, it is verified that position accuracy of the prototype machine tool has been improved from 153 to 86 $[\mu\text{m}]$.



Fig. 6. Calibration experiment using a ball-bar.

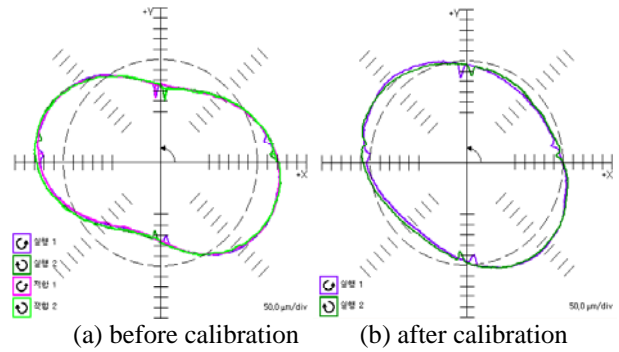


Fig. 7. Circular tests with radius 150 mm.

5 Conclusion

In this paper, a new hybrid-kinematic structure for both machining and assembling is proposed. By attaching additional sensors to passive joints in the central leg, the hybrid structure can be considered as a pure serial manipulator. Using the successive screw displacements, the kinematics analysis is performed and a kinematic error model is developed for the 5-DOF serial chain. The 5-DOF serial chain is calibrated by using a length measurement, i.e., ball-bar. Once all the kinematic parameters in the serial chain are determined, the kinematic parameters associated with the parallel-kinematic manipulator will be estimated. In order to verify the effectiveness of this suggested method, the simulation results of the kinematic calibration for a virtual prototype have been presented. We further performed the calibration experiment on the prototype machine tool. From the kinematic calibration and error compensation, the maximum kinematic error has been reduced from 153 to 86 $[\mu\text{m}]$.

REFERENCES

- [1] L. W. Tsai, *Robot Analysis: the mechanics of serial and parallel manipulators*, Wiley, 1999.
- [2] B. W. Mooring, et al, *Fundamentals of Manipulator Calibration*, Wiley, 1991.
- [3] H. S. Kim, "Kinematic Calibration of a Cartesian Parallel Manipulator," *International Journal of Control, Automation, and Systems*, Vol. 3, No. 3, pp. 1-8, 2005.
- [4] A. J. Patel and K. F. Ehmann, "Calibration of a Hexapod Machine Tool using a Redundant Leg," *International Journal of Machine Tools & Manufacture*, Vol. 40, pp. 489-512, 2000.
- [5] Y. Takeda, G. Shen, and H. Funabashi, 2004, "A DBB-based Kinematic Calibration Method for In-Parallel Actuated Mechanisms Using Fourier Series," *Journal of Mechanical Design*, Vol. 126, No. 5, pp. 856-865
- [6] B. Siciliano, 1999, "The Tricept Robot: Inverse Kinematics, Manipulability Analysis and Closed-loop Direct Kinematics Algorithm," *Robotica*, Vol. 17, pp. 437-445.
- [7] L. Beyer and J. Wulfsberg, 2004, "Practical Robot Calibration with ROSY," *Robotica*, Vol. 22, pp. 505-512.

The Design of Automatic Grease Lubricator Type of the Cylindrical Cam Piston Pump

Wooseok Choi, Jinseok Yang, Hyun Soo Koo, Duck Hyun Wang, Se-Han Lee

Mechanical Engineering and Automation

Kyungnam University 449 Wolyoungdong, Masan City, Gyungnam, 631-701, South Korea

wooseok@gmail.com

leesehan@kyungnam.ac.kr

Abstract

A new piston mechanism is proposed for an automatic grease lubricator, which is able to supply equipment with grease automatically for smooth motion. The mechanism adopts a cylindrical cam system, which is able to convert rotational motion to translational motion, and is composed without any check valve for preventing back flow even though existing lubricator has two check valves. Since the mechanism has a feature of all in one, which combines piston and valves. The automatic grease lubricator includes a micro controller system, which makes feeding pressure, period, and amount of grease in accuracy.

Key Words: Grease lubricator, Cylindrical cam, Piston pump, Microcontroller, Check Valve.

1. Introduction

As the industrial technologies are developed, automation is widely spreading for product efficiency and unmanned production system. Automatic grease lubricator is equipment that provides adequate amount of fresh grease constantly to the shaft and the bearings of machines. It minimizes the friction heat and reduces the friction loss of machines. For proper operating of machinery, accurate feeding period and amount of grease is most important thing. To obtain these performances, it is required of high accuracy for feeding grease mechanism.

There are many kinds of grease lubricators such as a gas generating, a spring pre-pressurized, a pressurizing piston type for creating pressure. In case of gas generating type, chemical reaction is used for creating pressure. The gas type is subject to be affected by

environmental temperature. When the chemical reaction starts, it is hard to respond to unexpected situations [1].

The pressurizing piston type requires very complicated structure with check valves while it shows very good feeding performances.

In this research, we proposed a simple new mechanism for easy control. It adopts cylindrical cam piston pump and is almost similar to the pressurizing piston type lubricator. The mechanism proposed here is simple form and requires no check valves that make the mechanism complicated.

2. Design of cylindrical cam-driving mechanism of piston pump system

The piston mechanism proposed here is creating pressure for feeding grease by using special feature formed around the piston without check valve, which conventional lubricator uses for preventing back flow of grease. In order to activate the special feature formed around the piston, there needs to rotate the piston.

In order to realize rotational and reciprocal motion of the piston simultaneously, a cylindrical cam mechanism is adopted. The piston mechanism proposed here is shown in Fig. 1. It is required the bulky images of cylindrical cam for development purpose.

Fig. 1 shows an essential feature of the mechanism proposed here. As the driving motor is rotating, the piston is moving reciprocally and rotating simultaneously by guide pin and cylindrical cam formed around the piston. [2]

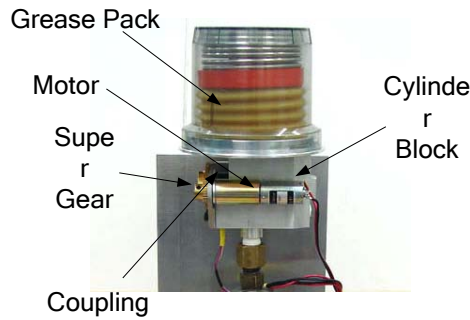


Fig. 1: Cylindrical cam mechanism prototype

The motion of the cylindrical cam is that as it rotates the piston is moving reciprocally and rotating with interaction between cylindrical cam slot and guide pin. One revolution of the motor is able to produce one cycle of reciprocal motion. The reciprocal motion of the piston is responsible for creating pressure and the rotating motion of that is responsible for closing-opening of valves. Fig. 2 and Fig. 3 show graphically view of the procedure of multi motions of the piston, respectively.

2.1 Motion of cylindrical cam and piston

Fig. 2(a) and Fig. 3(a) show initial stage of the piston motion. In this case, the piston moves close the inlet hole and outlet hole for flowing grease simultaneously. When the piston is only rotating with cam rotation the piston itself is about to open the inlet hole while the outlet hole is still closed. In succession the piston is rotating and retreating, the volume of the cylinder is increasing (becoming low pressure) and the grease is sucked. Fig. 2(b) and Fig. 3(b) show the piston reaching at 90 degrees position.

Fig. 2(c) and Fig. 3(c) show the piston reaching at 180 degrees position which is stroke of 5.5mm. At that time, the cylinder is full of grease, the inlet and outlet hole are closed simultaneously. As the piston is rotating successively, the cylinder volume is about to be decreased becoming pressurized and grease is outing. Fig. 2(d) and Fig. 3(d) show piston is outing grease and opening outlet hole while the inlet is still closed. The mechanism proposed here is feeding grease with repeating the procedure described above.

As the piston proposed here is rotating, the piston itself is closing and opening inlet and outlet hole

reciprocally, while a conventional lubricator is closing and opening the holes with check valves. It is noticeable that there is position of closing the two holes while there is no position of opening the two holes.

This feature is very important. Though any unpredictable stop motion of the piston occurs, i.e. the piston stops at any position, there is no chance to open inlet and outlet hole simultaneously. It means that it never happens to flow grease by itself at any situations.

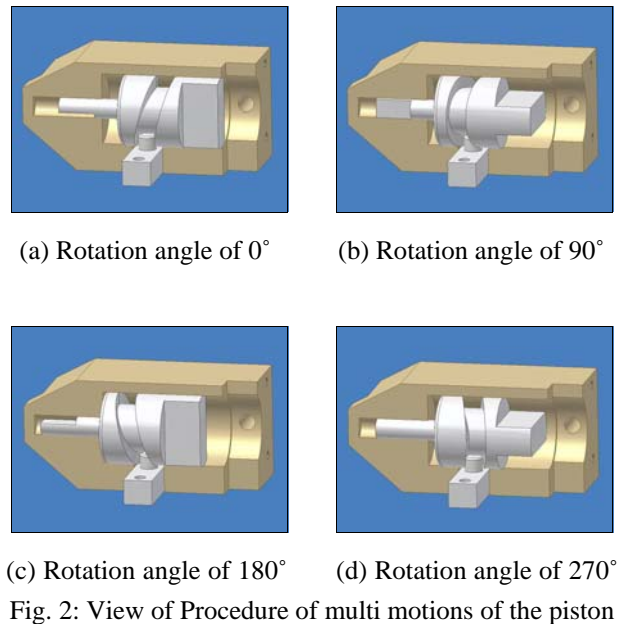


Fig. 2: View of Procedure of multi motions of the piston

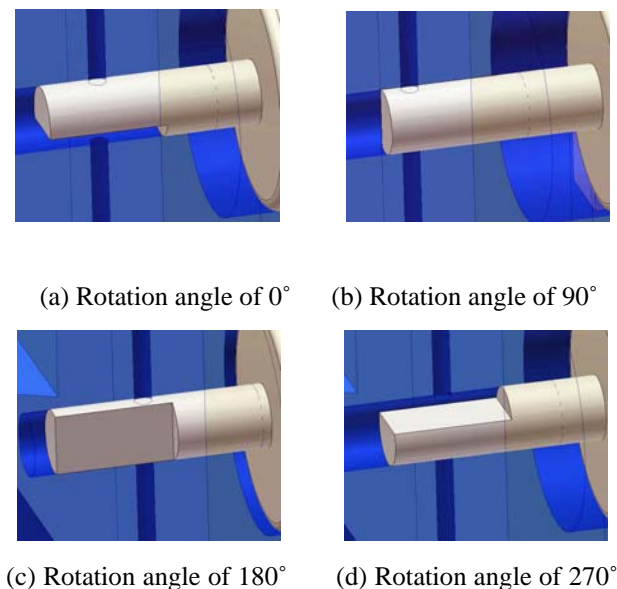


Fig. 3: Front view of the procedure of multi motions of the piston

2.2 Design value of the grease

A required amount of grease for one stroke is about 0.125cc (0.125cc/rev.) Diameter and stroke of the piston are governed by feeding pressure and motor output torque. The government equation is following. As the piston is moving reciprocally, the created pressure is variable according to the cam feature. For practical sense, average pressure is reasonable. In order to calculate the average pressure, an energy conservation equation is needed. The input energy by rotational motion is equal to the output energy by reciprocal motion as following

$$dF = \pi \tau \quad (1)$$

where d denotes piston stroke, F does piston thrust, τ denotes motor torque.

In order to calculate an important variable, pressure p , the both sides of (1) are divided by sectional area A .

$$\frac{dF}{A} = \frac{\pi \tau}{A} \rightarrow p = \frac{F}{A} = \frac{\pi}{V} \tau \quad (2)$$

where $V = Ad$ denotes the volume of the cylinder.

Equation (2) says that feeding pressure is dependent on motor output torque and displacement which is volume per revolution. Details of the piston diameter and stroke are determined by manufacturing conditions. There exists a minimum dimension to form cam and valve feature around piston.

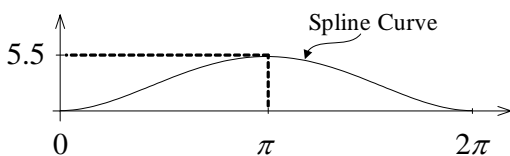


Fig. 4: Displacement of cam

Fig. 4 shows a cylindrical cam trajectory candidate that stands for piston stroke versus motor rotation. The cylindrical cam trajectory is generally formed by spline curve. It is noticeable that the cylindrical cam trajectory is adjusted not to occur only rotational motion without reciprocal motion at stage of opening or closing the holes, since the grease fluid is incompressible. At the first and end stage of the piston stroke, the following

condition should be met.

$$\frac{\Delta d}{\Delta \theta} = 0 \quad (3)$$

where Δd denotes infinitesimal stroke of the piston, $\Delta \theta$ does infinitesimal angle of the piston rotation. A candidate of the piston dimensions is listed in Table 1.

Table 1. Dimensions for Piston

Require Flux (cc)	Piston Diameter (mm)	Require Displacement (mm)
0.125	5.40	5.4580

Important dimensions of the piston, diameter and stroke are determined based on manufacturing. The reason is that difficulty of manufacturing is not free from productivity. A diameter and stroke of the piston should be more than 5mm and 5.5mm, respectively. Dimensions listed in Table 1 are nearly met the above conditions.

A high performance automatic grease lubricator should be able not only to out proper pressure but also to supply destinations regularly with proper amount of grease. These conditions for an automatic grease lubricator are able to be met by implementing micro controller and its peripherals.

In this research, there is introduced an 8-bit micro controller, AT89C2051 [3](manufactured by Atmel) and peripherals, LB1630[4] for driving motor and SG2BC[5] for detecting motor ration state.

In order to program software for the micro controller, we use C-language, which is very familiar for user to use. In order to control the motor precisely, the main part of the software consists of an internal timer and interrupts. Fig. 5 shows a flow chart of the software.

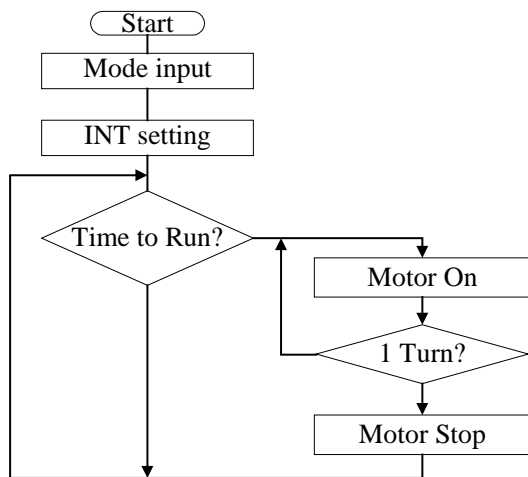


Fig. 5: Flow chart of the software

In order to verify the mechanism proposed here, a micro controller board is constructed. Fig 6 shows the test board

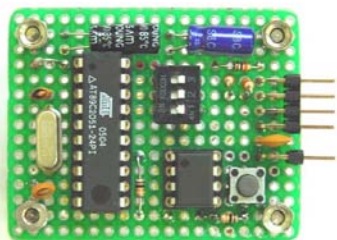


Fig. 6: Micro controller for the mechanism test

3. Experimental result

A lubrication mechanism test was conducted, Fig. 7 shows the photo of the experimental set-up (left) and essential parts of the piston system (right). [6][7]



Fig. 7: Experimental set-up and its exploded parts

First, for identifying only transmission load (reduction gear train, etc.), no-load current of the driving motor was measured and it was 95mA. At the maximum nominal

torque (2770g-cm) produced by the reduction motor, the corresponding pressure is obtained as following by using eq. (2)

$$p = \frac{\pi}{V} \tau = \frac{\pi \times 2.77 \times 9.8 \times 10^{-2}}{2.29 \times 10^{-5} \times 5.5 \times 10^{-3}} \quad (4)$$

$$= 6.2 \times 10^6 \text{ (N/m}^2\text{)} = 62.0 \text{ (kgf/cm}^2\text{)}$$

The maximum nominal torque is performed at a nominal current of 300mA. On the other hand, the manometer as shown in Fig. 8 actually shows pressure of about 5MPa (=50kgf/cm²). Fig. 9 shows produced pressure with respect to applied motor input current. The discrepancy (about 22.5%) is supposed to be caused by mechanical friction force between the prototype cylindrical cam and guide pin.



Fig. 8: Pressure value of 50kgf/cm² measured by manometer

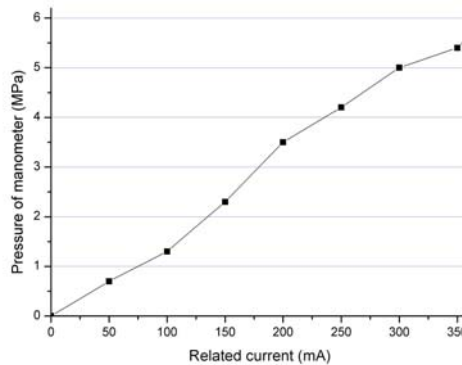


Fig. 9: Diagram of comparative theoretical and experimental Data

We can be detecting the defect on the first experimental test, which is frictional wear in the piston. Fig 10 shows wear of piston feature.



Fig. 10: Frictional wears of piston

This is important defect while the driven cylindrical cam piston mechanism. We settle the defect after changing the material of piston.

4. Conclusion

An automatic grease lubricator using cylindrical cam mechanism of piston pump was developed. The mechanism proposed here is simple as it eliminates a check valve, which is able to prevent back flow. Eliminating a check valve is helpful for cheaper product. Additionally, Cylindrical Cam Mechanism performs high force at instantaneous stop range where Coulomb friction force may be maximized.

As closing and opening the valve is synchronized to the rotation of the piston automatically, a micro controller needs to control only the driving motor and has no burden to control the flow valves.

The discrepancy between theoretical and actual pressure is supposed to be caused by mechanical friction force between the prototype cylindrical cam and guide pin. And also find the defect about the same material problem which is occurred frictional wear between the piston and cylinder.

Acknowledgment

This research was supported by the New University for Regional Innovation program of the Ministry of Education & Human Resources Development (NURI MECHANO21)

References

- [1] P. I. Cherednichenko, Lubricator Design as A factor in the Yarn Quality, pp. 68-69
- [2] Robert L. Norton, Design of Machinery, New York, 2004, Chap. 8, pp. 378-384.
- [3] AT89C2051 datasheet from <http://www.atmel.com>
- [4] LB1630 datasheet from <http://www.sanyo.co.jp>
- [5] SG2BC datasheet from <http://kodenshi.co.jp>
- [6] Teale. J. L., Lebeck, A. O., "An Evaluation of the Average Flow Model for Surface Roughness Effects in Lubrication Technology", 1980, Vol. 102. July, pp. 360-367.
- [7] D. H. Wang, K. Y. Lee and S. H. Lee, "The Development of Automatic Grease Lubricator Driven by Gear Mechanism with Controlled Operation Time", J. of KSPE, 2006, Vol. 23, No. 2, pp. 199-206.

Non-contact 3-D surface profiler using optical fiber

Yong Kwan Kwon**, Seo Heon Kim**, Eun Chang Heo**, and Byoung Chang Kim*

*School of Mechanical and Automation Engineering, Kyungnam University (bckim@kyungnam.ac.kr)

** School of Mechanical and Automation Engineering, Graduate school, Kyungnam University
449 Wolyoung Dong, Masan, Kyungnam, 631-701, Korea

Abstract

We present a non-contact 3-D surface profiler specially devised for the measurement of silicon wafer or CSP (Chip Scale Package) of which surface profile is difficult to be measured with conventional interferometers. The profiler comprises multiple light sources made of single-mode optical fiber. It turns out to be well suited for the warpage inspection of microelectronics components.

1. Introduction

Recently new profile measurement techniques are needed in the industry because of various product developments. Especially microelectronics components such as chip package and silicon wafer are difficult to be measured with conventional non-contact profiler. Which is based on the following two points of view. Their profile should be fabricated with within a few micrometer accuracy, but their surfaces have a characteristic of light scattering.

Until now, the existing typical metrology to overcome these problems has two methods. At first, Kwon and Wyant have measured rough surfaces by using CO₂ laser of 10.6 μ m wavelength.[1] The second, Petriccione and Ume have just applied typical Shadow Moire method to measure rough surface.[2] Because of using extended wavelength; this two metrology could not obtain very high accuracy.

Therefore, we present a non-contact 3-D surface profiler using optical fiber system that has been specially devised for the inspection of microelectronics components such as unpolished backsides of silicon wafers and plastic molds of integrated-circuit chip packages.

2. Principle of the proposed method

Figure 1 shows the overall optical configuration for the measurement method proposed in this investigation. The system is constituted with six light sources and a CCD camera of two-dimensional photo-detectors array. The light sources are deployed along the circumference of a circle, while the camera is located about at the center of the circle facing the object surface during measurement.

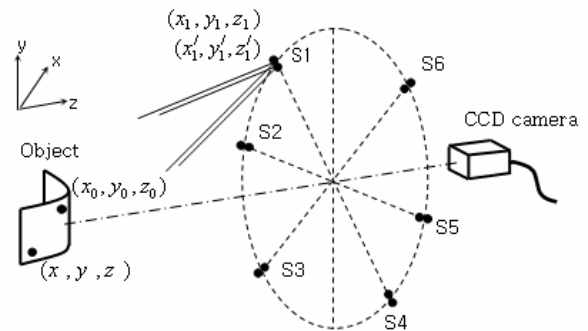


Figure 1. Geometrical arrangement of the 3-D profiler configured for the profile measurement of microelectronics surfaces. S1 to S6 are the light sources, each of which projects a unique fringe pattern generated by the interference of two spherical wavefronts diffracted from a pair of single-mode optical fibers. The light sources are activated one by one in sequence, while resulting fringe patterns are observed using a CCD camera of two-dimensional photo-detector array.

Each light source is an independent one made of a pair of single-mode optical fibers that are connected to a He-Ne laser via a 2X1 coupler as shown in Figure 2. The fibers are polished in their ends and housed in a single ceramic ferrule side by side with a predetermined lateral offset. Each single mode fiber works as a light source emitting an almost perfect spherical wave front. Two spherical wave fronts emanate from the two fibers constituting a light source interfere with each other and subsequently generate a unique fringe pattern over the target surface to be tested. A He-Ne source provides coherent light to the two fibers through a 2X1 optical fiber coupler, while one of the fibers is elongated using a piezoelectric PZT tube to produce phase shifting.

Two spherical wave fronts emanate by diffraction at the ends of the fibers, which then interfere with each other and generate a unique fringe pattern on the object surfaces to be profiled. The PZT tube extends the length of a fiber to induce phase shifting in the resulting fringe pattern.

The camera captures fringe patterns while switching on and off all the diffraction sources one by one in sequence

to obtain multiple fringe images projected from different geometrical angles as shown in Figure 3.

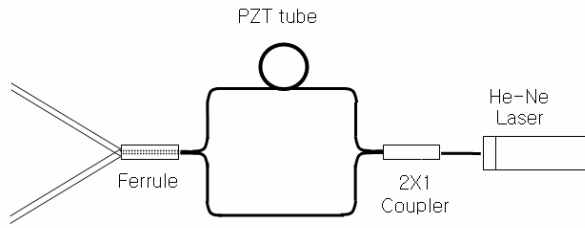


Figure.2 Optical configuration of a two-point diffraction source made of a pair of single-mode optical fibers coupled to a single coherent source

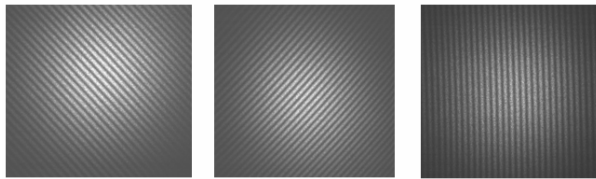


Figure.3 Fringe images captured by CCD camera which are projected on the non-polished backside of silicon wafer from three different geometrical angles.

For analysis, two conjugate spherical wave fronts from a single diffraction source is designated as u_1 and u'_1 , whose complex amplitudes are expressed in the xyz-coordinate system as

$$u_1(x, y, z) = \frac{A_1}{r_1(x, y, z)} \exp[-j(kr_1(x, y, z) + \phi_1)] \quad (1)$$

where $r_1(x, y, z) = \sqrt{(x-x_1)^2 + (y-y_1)^2 + (z-z_1)^2}$ and

$$u'_1(x, y, z) = \frac{A_2}{r'_1(x, y, z)} \exp[-j(kr'_1(x, y, z) + \phi'_1)] \quad (2)$$

where $r'_1(x, y, z) = \sqrt{(x-x'_1)^2 + (y-y'_1)^2 + (z-z'_1)^2}$.

Note that ϕ_1 and ϕ'_1 are the initial phases of u_1 and u'_1 which are measured at their origins located at (x_1, y_1, z_1) and (x'_1, y'_1, z'_1) , respectively. Then, the intensity of the fringe pattern generated on the object surface by the interference between u_1 and u'_1 is worked out as

$$I(x, y, z) = |u_1(x, y, z) + u'_1(x, y, z)|^2 = a(x, y, z) + b(x, y, z) \cos[\Phi(x, y, z)] \quad (3)$$

$$\text{where } a(x, y, z) = \frac{A_1^2}{r_1^2} + \frac{A_2^2}{r_1'^2}, b(x, y, z) = 2 \frac{A_1 A_2}{r_1 r_1'},$$

$$\Phi(x, y, z) = k(r_1 - r_1') + \Delta\phi, \text{ and } \Delta\phi = \phi_1 - \phi'_1.$$

There are three fringe variables; $a(x, y, z)$ is the background intensity, $b(x, y, z)$ is the amplitude of intensity variation, and $\Phi(x, y, z)$ is the absolute phase. Among them, the absolute phase $\Phi(x, y, z)$ relates to the xyz-coordinates of the surface profile to be measured with a most uncomplicated relationship, i.e., by the difference of the distances to the two diffraction sources plus the difference of the initial phases. Adopting well-established phase-shifting technique allows for the principal value of $\Phi(x, y, z)$ to be accurately determined within the range of $-\pi$ to π [3], for which one of the fibers in each diffraction source is elongated using a piezoelectric PZT extender.

Therefore, at least three measurements of $\Phi(x, y, z)$ are required to determine the coordinates (x, y, z) , each of which should be performed with a different diffraction source.

3. Experimental results

A series of tests has been performed against actual rough surfaces whose profiles cannot be measured using conventional Fizeau or Twyman-Green interferometers due to their too high surface height irregularities. [4]

Figure 4 shows a measurement result, which was obtained from the backside profile of a silicon wafer in the middle of integrated-circuit fabrication process.

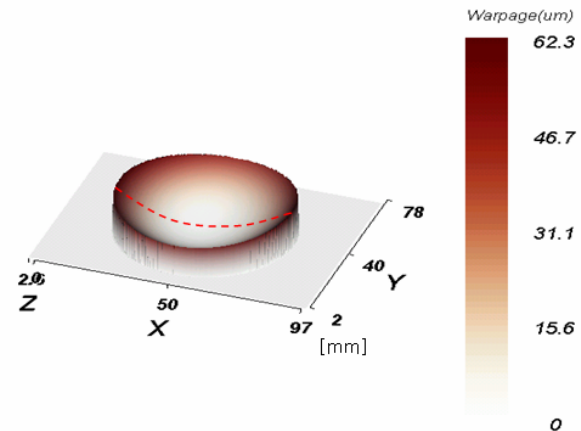


Figure.4 A measurement result of the non-polished backside profile of a silicon wafer for warpage inspection; an exemplary three-dimensional profile measured and reconstructed by the proposed 3-D surface profiler.

Another measurement example is presented in Figure 5, which has been performed for the warpage inspection of chip scale package (CSPs) that are tape-mounted on ball grid arrays (BGAs). The measured result indicates that the global surface is distorted by high temperature environment during curing process.

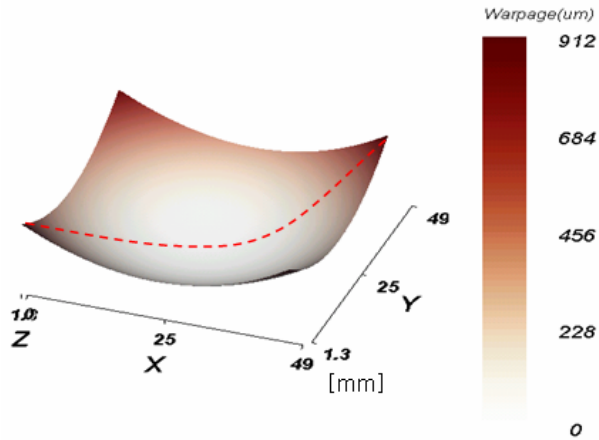


Figure.5 Inspection of IC package warpage; an exemplary three-dimensional profile measured and reconstructed by the proposed 3-D surface profiler.

4. Conclusions

A new 3-D surface profiler has been proposed to measure the warpage of electronics with light scattering surfaces. This method uses multiple sets of light sources made of two single-mode optical fibers emitting spherical wave fronts to generate unique fringe patterns on the target surface. The experimental results turn out to be well suited for the warpage inspection of microelectronics components.

References

- [1] O. Kwon, J. Wyant, C. Hayslett, "Rough surface interferometry at 10.6 μ m", Appl. Opt. vol.19, pp.1862, 1980.
- [2] G.J. Petriccione, I.C. Ume, "Warpage studies of HDI test vehicles during various thermal profiling", IEEE Transactions on advanced packaging, 22(3), 624(1999)
- [3] I.B. Kong, S.W. Kim, "General algorithm of phase-shifting interferometry by iterative least-square fitting," Opt. Eng. Vol.34, pp.183, (1995)
- [4] B.C.Kim, S.W. Kim, "Absolute interferometer for three-dimensional profile measurement of rough surfaces," Opt. Lett, vol.28, pp.1, (2003)

Fault Tolerant Control of Magnetic Actuators

Uhn Joo Na

Dept. of Mechanical Design, Graduate School,
Kyungnam University,
Masan, Gyeongnam, 631-701, Korea

Dong Dae Lee

Dept. of Mechanical Design, Graduate School,
Kyungnam University,
Masan, Gyeongnam, 631-701, Korea

Jin Seok Won

School of Mechanical and Automation Eng.,
Kyungnam University,
Masan, Gyeongnam, 631-701, Korea

Cheol Woong Ju

School of Mechanical and Automation Eng.,
Kyungnam University,
Masan, Gyeongnam, 631-701, Korea

Abstract

This paper develops the theory for a fault-tolerant, permanent magnet biased, homopolar magnetic bearing. If some of the coils or power amplifiers suddenly fail, the remaining coil currents change via a novel distribution matrix such that the same magnetic forces are maintained before and after failure. Lagrange multiplier optimization with equality constraints is utilized to calculate the optimal distribution matrix that maximizes the load capacity of the failed bearing. The overall load capacity of the bearing actuator is reduced as coils fail.

1 Introduction

A magnetic bearing system is a mechatronics device consisting of a magnetic force actuator (an active magnetic bearing, or AMB), motion sensors, power amplifiers, and a feedback controller (DSP), that suspends the spinning rotor magnetically without physical contact, and suppresses vibrations. Magnetic bearings find greater use in high speed, high performance applications since they have many advantages over conventional fluid film or rolling element bearings, such as lower friction losses, lubrication free, temperature extremes, no wear, quiet, high speed operations, actively adjustable stiffness and damping, and dynamic force isolation. Though magnetic bearings find more applications in industry, reliability requirements limit magnetic bearings from being used in highly critical applications. Failure of components such as coils or power amplifiers in magnetic bearings may result in a failure of the entire system.

Fault tolerant control provides continued operation of magnetic bearing actuators even if its power amplifiers or coils suddenly fail. Much research has been devoted to fault-tolerant heteropolar magnetic bearings. Maslen and Meeker [1] introduced a fault-tolerant 8-pole heteropolar magnetic bearing actuator with independently controlled currents and

experimentally verified it in [2]. Flux coupling in a heteropolar magnetic bearing allows the remaining coils to produce force resultants identical to the unfailed bearing, if the remaining coil currents are properly redistributed. Na and Palazzolo [3, 4] also investigated the optimized realization of fault-tolerant magnetic bearing actuators and experimentally showed it on a flexible rotor such that rotor displacements after failure can be maintained close to the displacements before failure for up to all combinations of 4 coils failed and certain combinations of 5 coils failed out of 8 coils. Na and Palazzolo [5] introduced a fault-tolerant control scheme utilizing the grouping of currents to reduce the required number of controller outputs and to remove decoupling chokes.

The present work describes the theory and following numerical analysis for the novel fault-tolerant homopolar magnetic bearing. Energy efficient homopolar magnetic bearings with fault tolerant capability may find great use in some applications such as flywheel energy storage systems and momentum wheels.

2 Bearing Model

The schematic drawing of an 8-active pole, permanent magnet biased homopolar magnetic bearing is shown in Fig. 1.

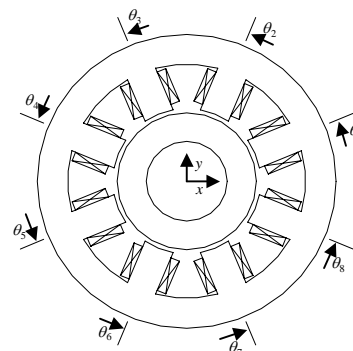


Figure 1. Schematic of an 8-Active Pole, Permanent Magnet Biased Magnetic Bearing

Assuming that eddy current effects and material path reluctances are neglected, Maxwell's equations are reduced to the equivalent magnetic circuit for the homopolar magnetic bearing. The feedback control voltages v_{cx} and v_{cy} , determined with any type of control law and measured rotor motions, are distributed to each pole via \tilde{T} in normal operation, and create effective stiffness and damping of the bearing to suspend the rotor around the bearing center position. With the uniform current distribution with \tilde{T} as well as the symmetric bearing geometries, magnetic forces are (x, y) decoupled and vary linearly with respect to control currents and rotor displacements around the bearing center position. If symmetry is lost due to a coil failure, magnetic forces are no longer decoupled and linear with respect to control currents and rotor displacements, and even it may be difficult to maintain stable control. Reassigning the remaining currents with a redefined current distribution scheme may remedy this by providing the same decoupled magnetic forces as those before failure. Magnetic forces developed in the active pole plane are described as;

$$f_x = v^T M_x v \quad (1)$$

$$f_y = v^T M_y v \quad (2)$$

3 Bias Linearization

The magnetic forces in Eqs. (1) and (2) can be linearized about the bearing center position and the zero control voltages by using Taylor series expansion. The linearized magnetic forces are;

$$\begin{bmatrix} F_x \\ F_y \end{bmatrix} = - \begin{bmatrix} k_{pxx} & k_{pxy} \\ k_{pyx} & k_{pyy} \end{bmatrix} \begin{bmatrix} x \\ y \end{bmatrix} + \begin{bmatrix} k_{vxx} & k_{vxy} \\ k_{vyx} & k_{vyy} \end{bmatrix} \begin{bmatrix} v_{cx} \\ v_{cy} \end{bmatrix} \quad (3)$$

The position stiffnesses are defined as;

$$k_{p\varphi\omega} = -H^T \frac{\partial Q_{\varphi b}}{\partial \omega} \Big|_{\substack{\varphi=0 \\ \omega=0}} H \quad (4)$$

where

$$Q_{\varphi b} = -G_b \frac{\partial D}{\partial \varphi} G_b$$

The parameters φ and ω represent either x or y . The position stiffnesses of the homopolar bearing remain unchanged with a coil failure since the position stiffnesses are only influenced by the bias flux driven with permanent magnets. The voltage stiffnesses are defined as;

$$k_{v\varphi\omega} = 2H^T Q_{b\varphi} \Big|_{\substack{\varphi=0 \\ \omega=0}} \hat{T}_\omega \quad (5)$$

where

$$Q_{b\varphi} = -G_b \frac{\partial D}{\partial \varphi} G_c$$

Employing an optimal current distribution matrix T may decouple the linearized forces of the failed bearing,

and even maintain the same decoupled magnetic forces as those of an unfailed magnetic bearing. Maslen and Meeker [1] introduced a linearization method which effectively decouple the control forces for a failed bearing by choosing a proper distribution matrix. Though not identified in [1], the direct voltage stiffness k_v is used to yield the same linearized control forces as those of the unfailed bearing. The necessary conditions to yield the same decoupled magnetic control forces are;

$$M_x = k_v \begin{bmatrix} 0 & 1/2 & 0 \\ 1/2 & 0 & 0 \\ 0 & 0 & 0 \end{bmatrix}, M_y = k_v \begin{bmatrix} 0 & 0 & 1/2 \\ 0 & 0 & 0 \\ 1/2 & 0 & 0 \end{bmatrix} \quad (6)$$

If the distribution matrix \hat{T} is determined such that Eq. (20) should be met, the magnetic forces at bearing center position in Eqs. (12) and (13) lead to;

$$f_x = k_v v_{cx}, f_y = k_v v_{cy} \quad (7)$$

Equations (6) can be written in 18 scalar forms, and then boils down to 10 algebraic equations if redundant terms are eliminated. The equality constraints to yield the same control forces before and after failure are;

$$\begin{aligned} h_1(\hat{T}) &= \hat{T}_x^T Q_{x0} \hat{T}_x = 0 \\ h_2(\hat{T}) &= \hat{T}_y^T Q_{x0} \hat{T}_y = 0 \\ h_3(\hat{T}) &= H^T Q_{bx0} \hat{T}_y = 0 \\ h_4(\hat{T}) &= \hat{T}_x^T Q_{x0} \hat{T}_y = 0 \\ h_5(\hat{T}) &= H^T Q_{bx0} \hat{T}_x = k_v / 2 \\ h_6(\hat{T}) &= \hat{T}_x^T Q_{y0} \hat{T}_x = 0 \\ h_7(\hat{T}) &= \hat{T}_y^T Q_{y0} \hat{T}_y = 0 \\ h_8(\hat{T}) &= H^T Q_{by0} \hat{T}_x = 0 \\ h_9(\hat{T}) &= \hat{T}_x^T Q_{y0} \hat{T}_y = 0 \\ h_{10}(\hat{T}) &= H^T Q_{by0} \hat{T}_y = k_v / 2 \end{aligned} \quad (8)$$

4 Optimal Distribution

Some examples of distribution matrices are calculated for the 8-pole homopolar magnetic bearing with the nominal air gap g_0 (0.508 mm), pole face area a_0 (602 mm²), number of coil turns n (50 turns). It is assumed that permanent magnets are selected to produce bias flux density of 0.6 Tesla in the air gaps of the active pole plane. The design of the permanent magnets for a homopolar magnetic bearing is beyond the scope of this paper. The direct voltage stiffness k_v is then calculated as 106.651 N/volt. A distribution matrix for an 8-pole homopolar bearing with the 7th-8th coils failed operation is calculated as;

$$T_{78} = \begin{bmatrix} 1.9337 & -0.5171 \\ -0.7557 & 2.1604 \\ -0.2844 & 0.3313 \\ -0.3109 & 0.2836 \\ -2.1707 & 0.7506 \\ 0.5313 & -1.9159 \\ 0 & 0 \\ 0 & 0 \end{bmatrix} \quad (9)$$

A distribution matrix with the 6th-7th-8th coils failed operation is calculated as;

$$T_{678} = \begin{bmatrix} 1.5852 & 0.5941 \\ -0.9194 & 1.4034 \\ -0.5185 & 1.2468 \\ -0.3469 & 1.6607 \\ -2.2336 & -0.0018 \\ 0 & 0 \\ 0 & 0 \\ 0 & 0 \end{bmatrix} \quad (10)$$

A distribution matrix with the 5th-6th-7th-8th coils failed operation is calculated as;

$$T_{5678} = \begin{bmatrix} 1.8351 & 0.8207 \\ 0.2480 & 1.6421 \\ -0.2480 & 1.6422 \\ -1.8351 & 0.8206 \\ 0 & 0 \\ 0 & 0 \\ 0 & 0 \\ 0 & 0 \end{bmatrix} \quad (11)$$

Similarly, the distribution matrices can be calculated for a failed homopolar bearing up to all combinations of 5 coils failed out of 8 coils. In the previous fault tolerant scheme with heteropolar magnetic bearings [3, 4], distribution matrix solutions do not exist for a certain combination of 5 failed coils (for example, no solution exists for 5 adjacent coils failed heteropolar bearings).

The following system dynamics simulation illustrates the transient response of a rotor supported by magnetic bearings during a coil failure event. An unbalance force of $m\epsilon\Omega^2$ with m (2.0 grams), ϵ (0.01 m) and Ω (spinning speed) are applied at the two bearing locations. The distribution matrix of \tilde{T} is switched to T_{5678} and T_{45678} when 4 adjacent coils failed at 0.02 seconds and then 5 adjacent coils failed at 0.04 seconds. The rotor speed is held constant at 20,000 RPM. Figures 2 shows transient response of the current inputs to the outboard bearing from the normal unfailed operation through the 5-6-7-8th coils and 4-5-6-7-8th coils of the outboard bearing failed at 0.02 seconds and 0.04 seconds, respectively. This indicates that very much the same rotordynamic responses are maintained throughout the series of failure events, while currents and fluxes in the homopolar magnetic bearing change significantly.

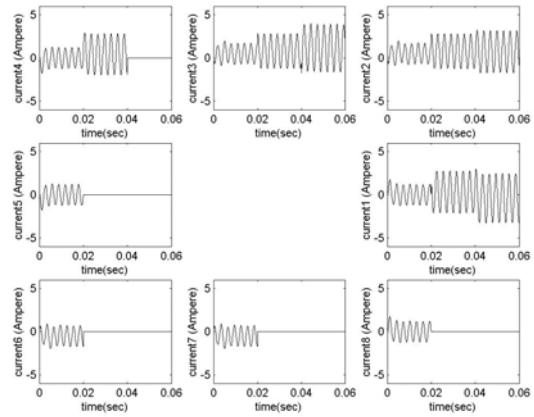


Figure 2. Current Plot for a Series of Failures

5 Conclusion

A fault tolerant control scheme is developed for an energy efficient homopolar magnetic bearing. The homopolar bearing actuator using the fault tolerant control algorithm can preserve the same linearized magnetic forces by redistributing the remaining currents even if some components such as coils or power amplifiers suddenly fail. The distribution matrix T of control voltages is determined by using the Lagrange Multiplier optimization with equality constraints for a failed bearing in a manner that the load capacity should be maximized. Simulations show that very much the same vibrations (orbits or displacements) are maintained throughout failure events while currents and fluxes change significantly with different distribution scheme. Only control currents as well as control fluxes are redistributed for the failed bearing while bias flux driven by permanent magnets remains constant. Less strict constraints of only 10 equations are required for the fault tolerant homopolar bearing to produce the same magnetic forces, while 12 constraint equations are required for the fault tolerant heteropolar bearing in [3]. This released conditions may give some benefits to the realization of fault tolerant homopolar bearings. The solution space of distribution matrices is extended for the homopolar bearing. The distribution matrices can be calculated for a failed homopolar bearing up to all combinations of 5 coils failed out of 8 coils. In the previous fault tolerant scheme with heteropolar magnetic bearings, no solutions exist for certain combinations of 5 failed coils. The load capacities of the failed homopolar magnetic bearings are greatly increased compared to those of heteropolar magnetic bearings.

Fault tolerance of the magnetic bearing actuator is achieved at the expense of additional hardware requirements and reduction of overall bearing load capacity. Therefore, the fault tolerant magnetic bearing should be designed enough to support loads even in case of a severe failure (5 coils failed out of 8 coils).

Otherwise, disturbances from unbalance, runouts, and sideloads should be maintained at low level to prevent saturation.

Acknowledgements

This research was supported by the New University for Regional Innovation program of the Ministry of Education & Human Resources Development (NURI MECHANO 21).

References

- [1] E. H. Maslen and D. C. Meeker, Fault Tolerance of Magnetic Bearings by Generalized Bias Current Linearization. *IEEE Transactions on Magnetics* 31 (1995) 2304 – 2314.
- [2] E. H. Maslen, C. K. Sortore, G. T. Gillies, R. D. Williams, S. J. Fedigan, and R. J. Aimone, A Fault Tolerant Magnetic Bearings. *ASME Journal of Engineering for Gas Turbines and Power* 121 (1999) 504-508.
- [3] U. J. Na and A. B. Palazzolo, Optimized Realization of Fault-Tolerant Heteropolar Magnetic Bearings for Active Vibration Control. *ASME Journal of Vibration and Acoustics* 122 (2000) 209-221.
- [4] U. J., Na, A. B., Palazzolo, and A., Provenza, Test and Theory Correlation Study for a Flexible Rotor on Fault-Tolerant Magnetic Bearings. *ASME Journal of Vibration and Acoustics* 124 (2002) 359-366.
- [5] U.J. Na and A. B. Palazzolo, The Fault-Tolerant Control of Magnetic Bearings With Reduced Controller Outputs. *ASME Journal of Dynamic Systems, Measurement, and Control* 123 (2001) 219-224.

Automated wildlife monitoring using self-configuring sensor networks deployed in natural habitats

Vlad M. Trifa^{1,3*} Lewis Girod² Travis Collier³ Daniel T. Blumstein³ Charles E. Taylor³

¹ATR CNS Humanoid Robotics ²Comp. Science and AI Lab. ³Department of Ecology and
Evolutionary Biology
Comput. Neuroscience Lab[†] Massachusetts Inst. of Tech. University of California
Kyoto, 619-0288 Japan Cambridge, MA, 02139 USA Los Angeles, CA, 90095 USA

Abstract

To understand the complex interactions among animals within an ecosystem, biologists need to be able to track their location and social interactions. There are a variety of factors that make this difficult. We propose using adaptive, embedded networked sensing technologies to develop an efficient means for wildlife monitoring. This paper surveys our research; we demonstrate how a self-organizing system can efficiently conduct real-time acoustic source detection and localization using distributed embedded devices.

1 Introduction

It is now well-recognized that artificial life systems can make useful contributions to a wide variety of problems in biology [8]. Typically, these contributions have come from the study of complex adaptive systems, simpler versions of natural life. Such abstractions permit isolation and control of features of interest [3]. In this paper we describe a novel application of adaptive systems for biology: looking at natural systems with the purpose of describing their structure and behavior.

The presence of human observers in the field is both time consuming and disruptive to the habitat under observation. An automated system would be desired. However, deployment of unattended recording stations is also fraught with difficulty. Among the current limitations are limited recording capacity and energy, and limited ability to be able to adapt to rapidly changing environments.

*Email: vlad.trifa@ieee.org

[†]The work presented here was mainly carried out at UCLA.

We illustrate that sensor network technology can be used as an efficient and powerful data collection system that can be easily used by biologists with little programming experience. Beyond simply recording of raw data, these tools have the potential to perform autonomous wildlife monitoring by being programmed to detect and react in a proper way to pre-specified conditions, with almost no human intervention. In addition, they form a network that enables remote management of the system, system health assessment, re-tasking, real-time triggering of additional sensing modalities, and visualization of real-time data from the field.

The distributed structure of these systems allows us to deploy them to cover wide territories and to capture data from different modalities in response to events in real time, e.g., capturing image data only when animals are active. Distributed signal processing algorithms are also a promising approach to data reduction. Spatial filtering techniques based on beamforming using a distributed collection of small arrays, can often identify a target species in situations where many species and individuals are present. Also, we will illustrate how self-organizing and adaptive methods can be used to develop robust and efficient methods to detect and localize acoustic sources.

2 Tools and methods

This section describes the embedded platform we used for our experiments, and then we will briefly describe different contexts where adaptive methods have been employed.

2.1 CENS nodes

For our experiments we have developed a network of Acoustic Embedded Networked Sensing Boxes (Acoustic ENSBox) as a prototype for wildlife monitoring system [5, 6, 7]. Each system is a small embedded computer running Linux, self-contained in a waterproof case, with an external four microphone array and 802.11b wireless communication (Figure 1). In com-



Figure 1: *Left:* Acoustic ENSBOX, the embedded device we used for our experiments. *Right:* close-up of the microphone array.

parison to other wireless sensor systems such as the Crossbow Mote, the Acoustic ENSBox has the computational, storage, and network resources to process audio data in real time and to implement distributed algorithms, including high precision 3D location and orientation self-calibration.

This combination of high processing power and communication with a small form factor makes the ENSBox platform particularly well-suited to explore novel solutions for animal vocalization analysis and accurate acoustic source localization through collaboration of multiple arrays.

2.2 Self-configuration

Collections of arrays enable localization by combining bearing estimates and time-difference of arrivals. However, none of this potential can be realized without the ability to rapidly deploy the sensor arrays and to determine their precise location *and* orientation. There are many positioning techniques, including those based on GPS, magnetic compass, sensor

correlation, and time-of-flight measurements of radio and acoustic signals, however many of these alternatives are not a good fit for these applications. For example, GPS reception is often poor in locations of interest such as forests and canyons, and even with good reception GPS requires differential corrections to meet the stringent precision requirements for these applications.

The Acoustic ENSBox self-localization is based on measuring time-of-flight and direction of arrival of acoustic signals. This solution has many advantages, including high precision and high resilience to noise. Initially, each node emits a chirp in turn, while all other nodes estimate the range R based on time of flight and bearing θ using local time differences of arrival. Then, a centralized algorithm combines the (R, θ) estimates for every node, and a non-linear least squares algorithm is used to compute the relative map (X, Y, Z, Θ) of the network. Finally, the relative map is fit to surveyed locations to obtain a map in absolute coordinates. This capability eliminates the need to survey all the array locations, a process that often takes hours to complete and that is generally extremely challenging to accomplish accurately.

2.3 Adaptive detection

We have developed a detection module that can detect animal vocalizations from background noise, by continuous adaptation to the current noise level. A generic statistically optimum approach to solve this problem is based on the *constant false alarm rate (CFAR)* method that identifies high energy segments in continuous streams of audio data. The algorithm first estimates the statistical distribution of the amount of energy in specific frequency bands contained in the ambient noise on n consecutive samples (we assume that noise follows a normal distribution $N(\mu, \sigma^2)$ in frequency space). Afterwards, the energy present in the same bands is monitored, and a threshold function detects when the energy changes significantly from a statistical point of view, that is when the energy of the current segment exceeds the threshold defined $\mu + \beta \cdot \sigma$, where β is a threshold parameter (usually $\beta = 3$). However, noise in real environments usually varies significantly over time, in which case it is necessary to update the noise distribution as it varies. For this purpose, *exponentially weighted moving average (EWMA)* can be used to update iteratively the mean μ and variance σ of the noise power as follows:

$$\mu_{t+1} = \alpha \mu_{new} + (1 - \alpha) \mu_t$$

$$\sigma_{t+1} = \alpha \sigma_{new} + (1 - \alpha) \sigma_t$$

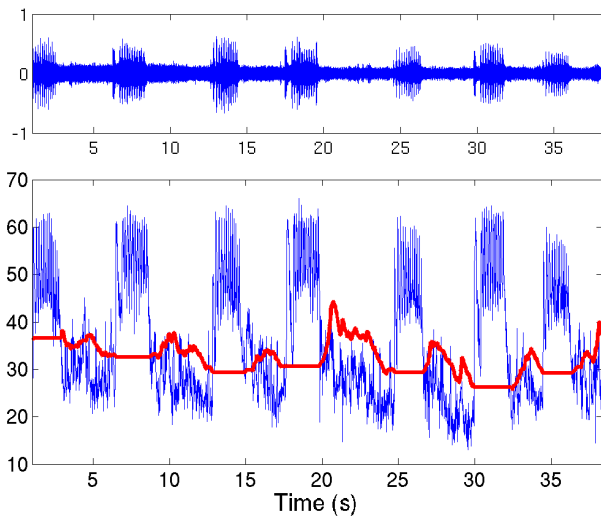


Figure 2: Adaptive detection algorithm. *Top:* Amplitude of the signal of a field recording. *Bottom:* Evolution of the energy in the signal is represented as the thin line. The thick line represents the detection threshold. When a song is detected, one can see that the threshold is not changed to avoid influencing the statistical estimation of background noise.

Where $\alpha \in [0, 1]$ is the changing rate. A low value for α should be used, as we want to avoid including spurious short sounds as part of the background noise model and updating the noise distribution based on insignificant events. Figure 2 illustrates the detection process of seven bird songs recorded in the rain-forest at Monte Azules Biosphere Natural Reservation in Mexico.

Using a modified and streamlined version of this algorithm, described in [4], we have also detected yellow bellied marmot (*Marmota flaviventris*) alarm calls in real-time on a network of ENSBoxes in the field. The marmot detector computes a 32-point FFT over each window of samples and computes the magnitude of the complex sum of the frequency bins corresponding to the bands used by marmot calls (3-6 KHz). This energy value is then passed into a CFAR detector, with a hysteresis detection to ensure that the complete call is acquired. We found that we could improve efficiency without losing detections by applying the FFT only to 1 out of every 4 32-point windows.

2.4 Collaborative localization

Kung Yao and students have developed a localization algorithm that can track multiple sources in real-time [1]. They developed an approximate maximum-

likelihood (AML) method for the localization of wide-band acoustic sources. The ML estimation method is known to be an optimum estimation procedure. The term approximate refers to the condition that the data length is finite and consequent edge effects yield a slight sub-optimality from the ML method. The AML algorithm has been used to perform localization of single and multiple acoustic source(s), even when they overlap in time and frequency, in the near/far-fields as well as in open-field and in reverberant scenarios. For each possible angle of arrival, the signals recorded by each microphone are recombined using a model of the array and the coherence of the resulting signal is obtained for each angle.

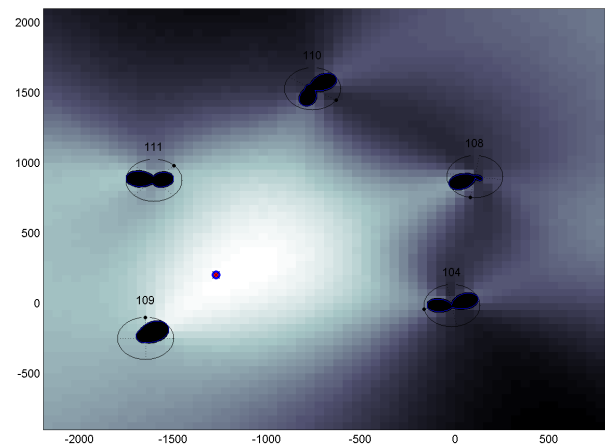


Figure 3: Results of the collaborative localization algorithm, presented as a 2D pseudo-likelihood map. Black lobes represent the likelihood for source AOA. Individual estimates of the angle of arrival (AOA) for each node are combined using their location as estimated by the self-calibration process.

In our implementation, every node that detects a vocalization will also compute a likelihood describing the likely bearing to the source. These likelihoods are collected at a central point and combined together into a 2D pseudo-likelihood map, according to the positions and orientations computed in the self-calibration step. This map is formed by projecting each likelihood metric outwards from each node to form the joint approximate likelihood of a source at every point in the 2D space. Beyond source localization, this information can also enable further signal enhancement through beam-forming, in which signals captured from different sensors are combined together to amplify the target signal and attenuate noise.

3 Results and discussion

The automated self-localization system illustrates many of the same requirements as our target applications, by being a distributed sensing application itself. This feature of the Acoustic ENSBox solves the problem of fastidious deployment by automatically determining array orientations to within 1 degree, and array positions to within 9cm in a 40x70m wooded area. This process can be run periodically, so that calibration of the system is maintained even when the location of the sensors is changed.

We originally implemented an offline version of the detection algorithm to automatically isolate tropical bird songs from hours of recordings on a standard desktop computer. Using the streamlined implementation, we have been able to reduce half an hour of raw recording to only 13 seconds of audio, capturing all of the marmot calls as well as a few false positives from other sources. The CFAR method is known to be statistically optimum in the sense that, for a fixed CFAR, the probability of event detection is maximized, with the assumption that the nominal background noise is a quasi-stationary stochastic process.

The collaborative localization algorithm has been used to localize marmot alarm calls in a field test at the Rocky Mountain Biological Laboratory (RMBL), in Colorado. The results of one of the localization tests are shown in Figure 3. The RMBL tests demonstrated that these algorithms could reliably locate marmots by their calls to within 1.5 meters, when compared with ground truth based on human observations, given that collaboration reduces the ambiguity of the local estimations computed by each node.

This paper described how adaptive methods can be used to develop a robust and self-organized monitoring systems. We have been able to detect animal vocalizations in very noisy environments using an adaptive threshold mechanism. This approach can be useful in several contexts where detection of acoustic activity is required; for example, human-robot interaction with humanoid robots [2]. Also, we explained how several acoustic sources can be localized using an efficient direction of arrival estimation method, and how collaboration between sensors can improve the results.

Acknowledgements

This research was supported by the National Science Foundation under Award Number 0410438 and 0120778. The authors would like to thank Alex

Kirschel and Yoosook Lee for their contribution to this paper.

References

- [1] C.E. Chen, A. Ali, H. Wang, S. Asgari, H. Park, R.E. Hudson, K. Yao, and Charles E. Taylor. Design and testing of robust acoustic arrays for localization and beamforming. In *IEEE IPSN*, 2006.
- [2] Gordon Cheng, Akihiko Nagakubo, and Yasuo Kuniyoshi. Continuous humanoid interaction: An integrated perspective - gaining adaptivity, redundancy, flexibility - in one. *Robotics and Autonomous Systems*, 37:161-183, 2001.
- [3] Travis C. Collier and Charles E. Taylor. Self-organization in sensor networks. *Journal of Parallel and Distributed Computing*, 64(7):866-873, 2004.
- [4] L. Girod, K. Jamieson, Y. Mei, R. Newton, S. Rost, A. Thiagarajan, H. Balakrishnan, and S. Madden. Wavescope: A signal-oriented data stream management system. In *Third Biennial Conference on Innovative Data Systems Research (CIDR07)*. (To appear), January 2007.
- [5] Lewis Girod. *A Self-Calibrating System of Distributed Acoustic Arrays*. PhD thesis, University of California Los Angeles, 2005.
- [6] Lewis D. Girod, Martin Lukac, Vlad Trifa, and Deborah Estrin. The design and implementation of a self-calibrating distributed acoustic sensing platform. In *The 4th ACM Conference on Embedded Networked Sensor Systems (SENSYS 06)*, 2006.
- [7] Vlad Trifa. A framework for bird songs detection, recognition and localization using acoustic sensor networks. Master's thesis, École Polytechnique Fédérale de Lausanne, 2006.
- [8] H. Wang, C.E. Chen, A. Ali, S. Asgari, R.E. Hudson, K. Yao, D. Estrin, and C.E. Taylor. Acoustic sensor networks for acoustic woodpecker localization. In *SPIE conference on Advanced Signal Processing Algorithms, Architectures and Implementations*, 2005.

Analysis of Circuit Breakers Using Artificial Stock Market

Shigeto Kobayashi

School of Knowledge Science,
Japan Advanced Institute of Science and Technology
1–1, Asahidai, Nomi, Ishikawa, 923–1292 Japan
s-kobaya@jaist.ac.jp

Takashi Hashimoto

School of Knowledge Science,
Japan Advanced Institute of Science and Technology
1–1, Asahidai, Nomi, Ishikawa, 923–1292 Japan
hash@jaist.ac.jp

Abstract

In various stock markets, there is a system called “circuit breakers” that interrupts dealing of stocks for a certain period when stock price changes greatly. In this paper, we consider the influence of the circuit breakers on a stock market using an agent-based artificial market simulator called “U-Mart”, by controlling the period of interruption and the criterion to invoke the circuit breakers. From experiments, we found the following: circuit breakers play an important role in the control of price fluctuations and the stabilization of the settlement system, while the circuit breakers reduce the stock trading volume. We also suggest that the period of interruption is important parameter in an institutional design of the circuit breakers, since the stock trading volume and the volatility are sensitive to the period.

1 Introduction

Financial markets are vulnerable to “bubbles” and excess volatility. In such a case, sharp stock price fluctuations may significantly affect, not only financial markets, but entire socioeconomy. Most systems in a financial market contribute to the stability of a market by eliminating uncertainty from the market fluctuations and from trading. In addition, rapid price fluctuations may cause the fall of liquidity in the market, and may disturb price discovery. Circuit breaker is one of the market systems founded in order to reduce the stock price volatility risk. In this paper, we define the circuit breakers as a temporary stoppage of trading.

Introduction of circuit breakers was advocated in the report of the Brady Committee[1] that investigated “Black Monday”. According to the Brady Report, the main purpose of introducing this system is to directly reduce excessive stock price volatility and to mitigate market disruptions. There have been some arguments about the pros and cons of the system since

its introduction after Black Monday. However, an extremely large-scale change of a stock price that invokes the circuit breakers is so rare that empirical research on the system has not been possible, and the efficiency of the system has not been confirmed.

It is very difficult to design market systems that contribute to the stability of the market, as a large-scale economic experiment cannot be performed in a real stock market. Therefore, by using a simulation technique, we examined whether the circuit breakers reduce volatility and contribute to the stability of a market.

2 Circuit breakers implemented in “U-Mart”

We incorporated the circuit breakers into the artificial market simulator “U-Mart”¹. In the U-Mart system, stock index futures are traded, and prices are calculated independently of the actual prices. The U-Mart system adopts the pricing method called “itayose” in which orders are accumulated for a certain period. A price is decided so as to achieve the maximum contracted volume for the accumulated orders. We introduced interruptions of trading stock into the U-Mart system by halting itayose for certain periods. For the conditions of interruption, we referred to the system of the Osaka Securities Exchange (OSE) dealing with Nikkei 225 futures. We halt the trading of stock, when the stock price advances (or declines) in excess of a certain range from the standard price, and at the same time, differs in excess of a certain range from the fair value. The conditions are defined by

$$|P_c - P_s| > R_p, \quad (1)$$

$$|P_c - P_t| > R_m \quad (2)$$

where, P_c is the current stock price, P_s is the standard price that is the last day’s closing price, P_t is the

¹For further details, the reader should refer to [2].

theoretical price², R_p is the price range determined based on P_s , and R_m is the mispricing range determined based on P_s . When the market prices simultaneously satisfy the two conditions of Eqs.(1) and (2), trading is halted.

3 Outline of simulation

We considered how the operation of the circuit breakers affects a market using our modified U-Mart system. As a main parameter, we controlled the period of interruption (the times of itayose to halt), $T_s = 0$ (no circuit breakers), 1, 2, 3 and 4. We fixed the price range at $R_p = 700$ yen.

The configuration of the machine agents is indicated in Table 1. The standard agent set adopts the simple technical analysis. The contest agent set is a participant in the U-Mart machine agent contest. A random agent has the strategy of placing an order at random around a latest spot price or a futures price³. The ratio of two types of random agents, "SpotRandomAgent (SRA)" and "FuturesRandomAgent (FRA)", is set to 1:1. A total of 200 machine agents is prepared.

Table 1: The configuration of the machine agents

Agent Set	Strategy	Ratio
standard agent set	8	3
contest agent set	8	2
random agent set	2	variable

In this simulation, in order to observe the differences in market behaviors among different configurations of agents, we conducted experiments by changing the ratio of random agents to other agents. Ueki et al.[3] have pointed out that random agents may play an important role such as market maker who gives liquidity to the market. Hence, we set the ratios (A_r) of the random agents to the total of number of agents at $A_r = 0\%, 5\%, 10\%, 20\%, 40\%$, and 60% , respectively.

We adopted the daily Nikkei Index that showed a downward trend (2000/4/17-2000/10/10) as the spot price series given to the U-Mart system. The other settings are as follows.

²theoretical price = latest stock price + theoretical basis
 theoretical basis = last day's closing spot price * {(short-term interest rate - dividend yield) * T / 365}
 T: number of days (period)

³The agents buy or sell randomly. The SRA sets the limited price on order around the latest spot price. The FRA sets the limited price on order around the latest futures price.

- Trading days (period): 15
- Sessions (itayose) per day⁴: 8
- Short-term interest rate: 3-month CD rate
- Dividend yield: Expected yield of the Nikkei Index

4 Simulation with changing periods of interruption

We analyzed the liquidity in the market, which reflects how many orders can be executed without causing stock price change in a market[4]. A high liquidity denotes that a lot of orders are executable in a matter of minutes. In order to realize smooth price discovery after interruption in dealing the stock, it is necessary to ensure the liquidity in a market. Even if the steep fall in stock prices is avoided and the fluctuation in stock prices is reduced by interruption of dealing, the liquidity declines, and this may discourage investing activity if stock trading volume decreases greatly. Thus, we mainly observed the volume of trading and the historical volatility. All experimental results are the averages of 100 trials, and "steps" of the horizontal axis in the figures shows times of itayose.

4.1 Total trading volume

Total trading volume is the total of the stocks traded in 15 days. The changes of the total trading volume are shown in Fig. 1. It turns out that the total trading volume falls when the period of interruption increases, irrespective of the ratio of random agents. This is considered to be the result of simply having lost the opportunity to trade due to the circuit breakers. In changes of the total trading volume according to the ratio of random agents, there is a tendency for the total trading volume to increase as the ratio becomes larger. We surmise that this is because the supply and demand balance is maintained when the SRAs continue to place orders at random around the spot prices, even if the supply and demand is skewed by a large price fluctuation.

4.2 Historical volatility

Proponents of circuit breakers often claim that halting dealings reduces fluctuation of the stock price. Let

⁴Halting itayose for 4 times means that the market is closed for half a day in this simulation.

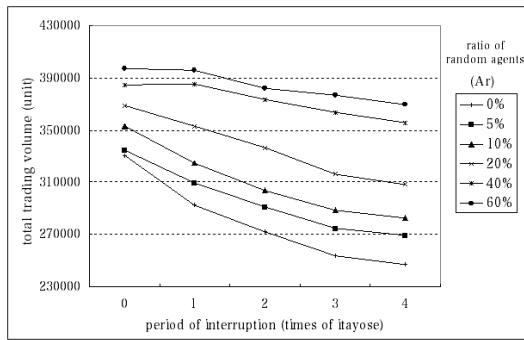


Figure 1: The changes of the total trading volume related to the periods of interruption for various ratios of random agents

us examine whether this is actually the case. In general, volatility is used to measure the fluctuation of the price in a market. The following formulas define historical volatility (v_x) in this paper:

$$v_x = \sqrt{\frac{1}{N-1} \sum_{i=1}^N (x_i - m_x)^2}, \quad (3)$$

$$x_i = \log S_i - \log S'_i \quad (i = 1, \dots, N), \quad (4)$$

$$m_x = \frac{1}{N} \sum_{i=1}^N x_i, \quad (5)$$

where S_i is the present stock price, S'_i is the latest stock price, and N is the sample size in a trading period. Equation(4), x_i , calculates the logarithmic rate of change of stock price and Eq.(5), m_x , calculates a sample mean of x_i .

The changes of historical volatility related to the periods of interruption are shown in Fig. 2. The historical volatility decreases as the period of interruption increases, especially for a small ratio of random agents. Due to the interruption of dealing, the stock price recovers to a proper price without falling to the bottom. But this effect is weakened when the ratio of random agents is higher. In such a case, the price fluctuation is extremely low, since the random agents give sufficient liquidity for a market, as we described in the preceding section. Even when the ratio of random agents is small and the fluctuation is relatively large, unless the period of interruption is long enough, historical volatility does not decrease. Thus, in order to suppress a short-term fluctuation, the length of interruption of trading should be flexibly decided.

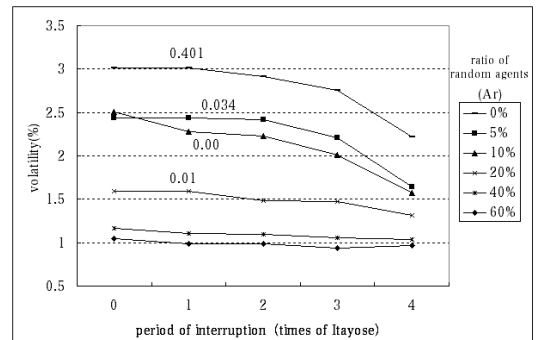


Figure 2: The changes of historical volatility related to the periods of interruption for various ratios of random agents: Only numbered lines show the significant probability according to the Kruskal-Wallis test among the historical volatility of the periods of interruption, $T_s = 1, 2, \text{ and } 3$.

4.3 Bankruptcy

The circuit breakers give decision-making time to individual investors, so that those who cannot always monitor a market can catch up with change of a market, and they are protected against a drastic loss[4]. The increase of bankrupt may destroy a settlement system of a futures market based on netting. We consider many agents going bankrupt by dealings as a factor to destabilize a settlement system, and investigated how the circuit breakers affect bankruptcy.

As shown in Fig. 3, we found that the number of bankrupt agents decreases greatly after introduction of the circuit breakers, regardless of the ratio of random agents. We confirmed that the difference in the number of bankrupt agents is significant using the Mann-Whitney U test, under the criterion of $P < 0.05$. The circuit breakers may prevent agents with heavy losses from going bankrupt.

5 Simulation with price fluctuations in the spot price series

In this section, we investigated the influence of the circuit breakers on a market under larger price fluctuation. In this experiment, the spot price series of the Nikkei Index is increased range of fluctuation. The amounts of fluctuation are 1%, 3%, and 5%.

In this section, random agents were set to 20%. In this experiment, the tendency for the total trading volume to decrease, as in the former simulations, was ob-

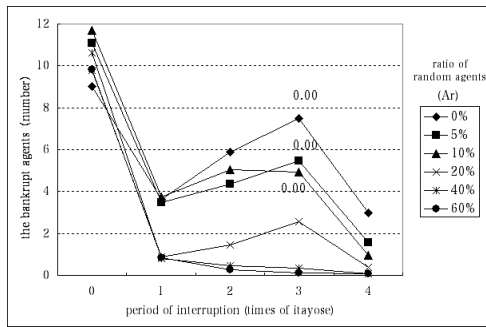


Figure 3: The changes of the number of bankrupt agents related to the periods of interruption for various ratios of random agents: Only numbered lines show the significant probability according to the Mann-Whitney U test between the number of the bankrupt agents of the period of interruption, $T_s = 0$ and 3.

served whenever the period of interruption increased. Concerning total trading volume, it turns out that the circuit breakers have only the effect of decreasing volume, even if price fluctuation is large.

The changes of the historical volatility of the futures price are shown in Fig. 4. In the case where the expansion rate is 5%, though the interruption period is one period ($T_s = 1$), there is a big effect to control volatility. The significant difference of the historical volatility between no circuit breakers ($T_s = 0$) and circuit breakers with one period ($T_s = 1$) was proved by Mann-Whitney U test. Since fluctuation is artificially added to the spot price, the price fluctuation in 1 time of itayose becomes larger than in the former simulations. Therefore, it is thought that the circuit breakers are critically effective against price fluctuation control. However, when the range of price fluctuation is small, the range of decline of volatility is small. In $T_s = 4$, reduction in volatility has taken place sharply for all rates of change.

From these results, in order to reduce excessive volatility, it is better to invoke a circuit breaker for a short period, in the case that a big price fluctuation happens intermittently. If more fluctuation control is required, the period of interruption should be lengthened, but we must be prepared to decrease the total trading volume.

6 Summary and conclusion

From experimental results, we found the following: The circuit breakers work to suppress the fluctuations

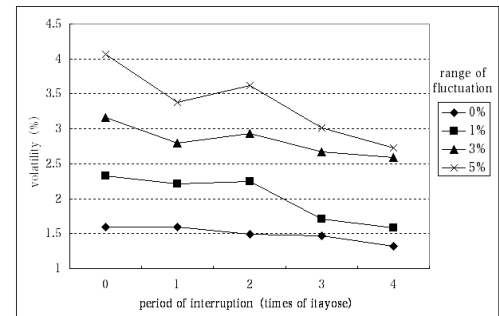


Figure 4: The changes of the historical volatility of the futures price with fluctuation of the spot price series

of stock prices, but decrease the total trading volume. The longer trading is interrupted, the more effectively the volatility of the stock market is decreased. When the degree of fluctuation is large, the decrease is conspicuous. Since the operation of the circuit breakers lowers the number of bankrupt agents sharply, it is suggested that introducing the circuit breakers prevents the bankruptcy of the agents. Therefore, it is thought that the circuit breakers contribute also to stabilization of the settlement system of a market.

It is concluded that the circuit breakers play an important role for the control of price fluctuations and the stabilization of the settlement system, while the circuit breakers reduce the stock trading volume. We also suggest that the period of interruption is an important parameter in institutional design of the circuit breakers, since the stock trading volume and the volatility are sensitive to the period.

References

- [1] Brady Commission Presidential Task Force, *Report of the Presidential Task Force on Market Mechanisms*, 1988.
- [2] T. Terano et al, "U-Mart: an artificial market to bridge the studies on economics and multi-agent systems," *Proceedings of Fourth Pacific Rim International Workshop on Multi-agents*, pp. 371-385, 2001.
- [3] J. Ueki et al, "Simulation Study Using U-Mart (in Japanese)," *Papers of the Annual Conference of The JAFEE*, Vol. 6, pp. 323-329, 2002.
- [4] K. Omura et al, *Microstructure in the Stock Market* (in Japanese), Nihon Keizai Shimbun, Inc, 1998.

Interactive musical editing system to support human errors and offer personal preferences for an automatic piano

Method of searching for similar phrases with DP matching and inferring performance expression

Yuta HIKISAKA

*Graduate School of Computer Science
and System Engineering
Kyushu Institute of Technology
680-4, Iizuka City, Fukuoka, Japan, 820-8502
hiki@mmcs.mse.kyutech.ac.jp*

Eiji HAYASHI

*Department of Mechanical Information
Science and Technology
Kyushu Institute of Technology
680-4, Iizuka City, Fukuoka, Japan, 820-8502
haya@mse.kyutech.ac.jp*

Abstract

We have developed a system that allows a piano to perform automatically. In order to play music in the manner of a live pianist, we must add expression to the piano's performance. In the case of piano music, there are often 1000 or more notes in the score of even a short piece of music, and the editor must spend a huge amount of time to accurately simulate the emotionally expressive performance of a highly skilled pianist. Therefore, we have developed an interactive musical editing system to edit music more efficiently utilizing a database.

We have analyzed MIDI data regarding the performances of highly skilled pianists in order to observe the stylistic tendencies of their performances. As a result, it was found that phrases having similar patterns in the same composition were performed in similar styles.

Therefore, we developed a system that searches for similar phrases throughout the musical score and infers the style of their performance. Here, we propose a method using DP (Dynamic Programming) matching as a way to search for similar phrases and a method for inferring performance expression.

Key words: *automatic piano, knowledge database, computer music, DP matching*

1. Introduction

We have developed a performance system for an automatic piano. In this system, 90 actuators are installed in the 88 keys and 2 pedals of a grand piano. Those actuators operate key strokes and pedaling to be executed on the piano. (See Figure 1)

Reproducing music with the piano is similar in some ways to reproducing music on the computer. Essentially, variations in tempo, dynamics, and so on are needed to arrange the respective tones in the desired way. However, in the case of piano music, there are 1000 or more notes in a score of even a short piece of music, and

the editor must spend an enormous amount of time working with the arrangement in order to simulate the expressions of an actual performance.

Therefore, in this research, we have developed an interactive musical editing system to edit music more efficiently^[1].

We have analyzed MIDI data regarding the performances of highly skilled pianists in order to observe the stylistic tendencies of their performances. As a result, it was found that phrases having similar patterns in the same composition were performed in similar styles. Moreover, it was found that the pattern of notes in the score sometimes influences the music's expression.

In this research we developed a system that searches for similar phrases throughout a musical score and infers the style of the performance. We propose a method using DP matching as a way to search for similar phrases. This system converts notes into character strings. As well, it runs DP matching using character strings and calculates the degree of disagreement between these strings. We use these calculations as an index to determine whether the strings resemble each other. Moreover, we designed a method for inferring the performance expression of similar phrases found by DP matching.

In this paper, we describe the results of searching for similar phrases using DP matching and inferring performance expression.



Figure 1: View of the automatic piano

2. Musical Editing Support System

2.1 System Architecture

The structure of the system is shown in Figure 2. The user edits performance information via the user's interface on the computer display (We discuss this performance information in the next paragraph). Also, the user can access a database of musical grammar, the user's preferences, and so on. As a result, editorial work is reduced and efficient editing becomes possible.

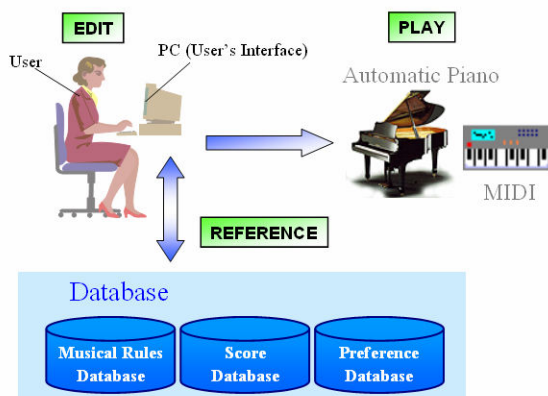


Figure 2: Structure of the editing system

2.2 Format of Performance Information

The automatic piano that we have developed uses a music data structure that is similar to MIDI. We defined performance information, dividing it into two categories, the notes and the pedals.

The note information consists of six parameters involved in producing a tone: "Key (note)", "Velo (velocity)", "Gate", "Step", "Bar", and "Time". "Velo" is dynamics, given by the value of 1~127. "Gate" is the duration of the note in milliseconds. "Step" is the interval of time until the next note, and it also exhibits tempo. "Bar" is the vertical line placed on the staff to divide the music into measures.

The pedal information consists of four parameters: "Key (indicating the kind of pedal, "Damper" or "Shifting")", "Velo (the pedaling quantity)", "Time (the duration of applying the pedal)", and "Bar".

2.3 Automatic Translation with Database

Our system can automatically apply a rough performance expression using a Musical Rules Database and Score Database. (See Figure 3)

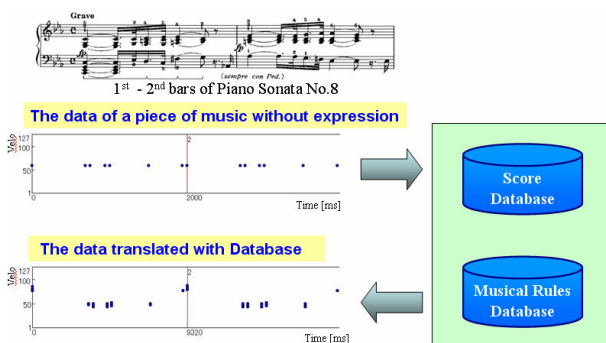


Figure 3: Automatic translation with database

2.3.1 Musical Rules Database

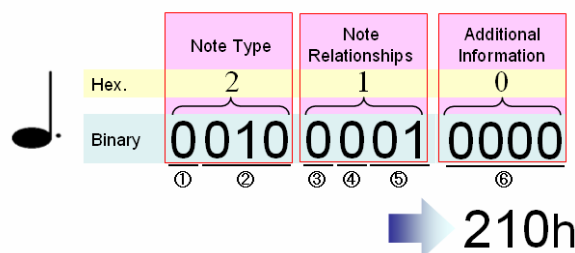
This database has the architecture of musical grammar necessary to interpret symbols in musical notation. This database consists of five tables containing "Dynamics marks", "Articulation marks", "Symbol of Changing Dynamics or Changing Tempo (Symbol that affects the speed of a note or the increase or decrease of the volume)", "Time signature", and "Tempo marks".

This database enables a general performance expression to be applied to music automatically.

2.3.2 Score Database

This database has symbols including notes, time signature, rests and so on in standard musical notation. Symbols were pulled together in the order of bars, and bar symbols are arranged in a time series.

This database consists of three tables, the "Element table" (showing the position of the notes and the composition of the chords), the "Symbol table" (showing the position of the music symbol) and the "Similarity Table" (showing the position of the repetition of the phrase).



- ① Note or Rest (0: Note, 1: Rest)
- ② Note Value (000: whole note, 001: half note ...etc)
- ③ Tie (If the note has a tie then this number is 1.)
- ④ Ornament (If the note has an ornament then this number is 1.)
- ⑤ The number of dots (Exceptionally, if it is "11" then the note is triplet.)
- ⑥ Additional Information (The number of triplets. (Triplets: 0011) The type of an ornament. (Trill: 0101) etc...

Figure 4: Note Value

The element table contains the field "Note Value". The data in this field indicates the type of note, e.g., a quarter note, a triplet, and so on. "Note Value" is expressed by three hexadecimal numbers. The "Note Value" numbers are shown in Figure 4.

3. Searching for Similar Phrases

As a result of the analysis, it was found that phrases of the same pattern existing in the same tune are performed in a similar expression^[2].

This time, we used DP matching to search for similar phrases.

3.1 DP matching

DP matching^[3] is a technique used well in the field of speech recognition, bioinformatics and so on. It has a feature that can calculate similarity between two words that are different in a number of characters from each other.

In Figure 5, the route of minimum cost in each point is taken and the route with the lowest cost is assumed to be an optimal path finally. The cost at that time is defined as the distance between patterns. In this system, this distance is handled as a threshold to judge whether the phrases are similar to each other.

□ Moving cost

- Up or to the right: +1
- To the upper right: 0

□ In each point ...

- If the character do not correspond: +5

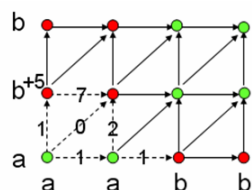


Figure 5: Method of calculating the distance

3.2 Searching with DP matching

In this passage, we describe a method of searching with DP matching. We had to convert a musical score into character strings (Note Pattern) before searching for similar phrases. This process is explained below.

3.2.1 Note Pattern

Our system converts a score into a Note Pattern using Note Value (See Passage 2.3) to perform DP matching. Of the three columns of Note Value, we used the two columns from the left. The system replaces the second column with letters of the alphabet (from G)

because a letter should not be the same as the first column with the second column since it expresses one note with two columns. An example of a Note Pattern conversion is shown in Figure 6.

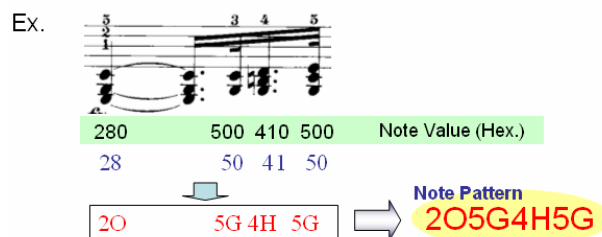


Figure 6: Example of Note Pattern

3.2.2 The Method of Searching

The flow of the similar phrase search is shown in Figure 7.

Essentially two rounds of search processing are performed. The first processing round narrows down the point that may be the point of resemblance in all search ranges. A pattern of the same number as the search phrase is pulled out and the distance between two patterns is calculated using DP matching. If they are in complete accord (distance = 0) then the phrase is stored in the Similar Table. If the distance is lower than the threshold then the phrase is stored in the Temporary Table. In the second round of processing, DP matching is performed again using the phrases in Temporary Table while increasing the number of characters. In other words, the system looks for the most similar phrases in the surrounding phrase. The threshold of this system has been decided by trial and error.

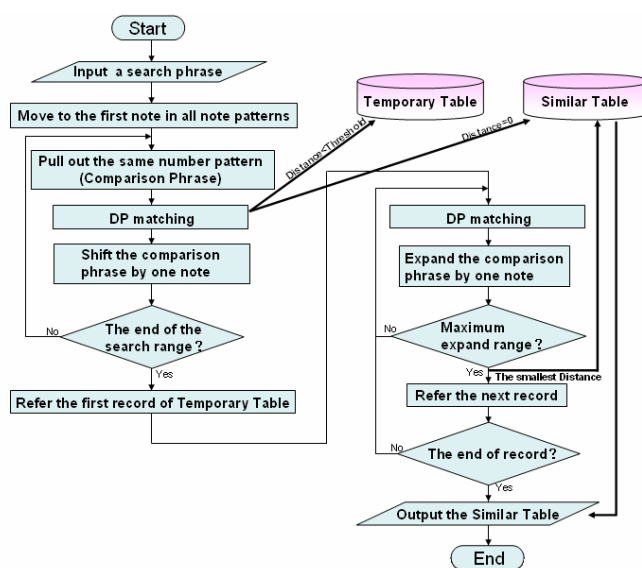


Figure 7: The flow of the similar phrase search (Search range and expand range are set beforehand.)

3.2.3 Searching Result

An actual search was performed using the search method explained in paragraph 3.2. Part of the result of the search using this system is shown in Figure 8. The horizontal axis of each graph is time (in milliseconds), and the vertical axis is velocity (1 to 127). This graph was made based on performance data by Gerhard Oppitz.

The arrangement of each note also looks like the searched phrase. Especially, it is understood that the performance expression was also very similar in the graph of (a) whose distance is 0. The graph of (b) does not completely correspond. But based on the change in Velo, it seems similar.

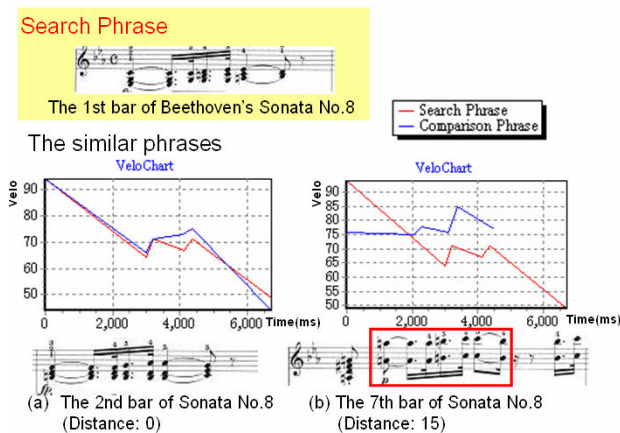


Figure 8: The result of the searching

4. Inferring Phrase Expression System

The similar phrases searched for by the method of the description in Chapter 3 are inferred using the expression of the performance of the search phrase.

4.1 Method of inferring phrase expression

The correspondence of the note patterns is revealed when the distance is minimized in DP matching. Next, the ratio of Velo to the previous sound is calculated in each sound of the searching phrase. Velo of the associated phrase is inferred using a ratio. Thus, the Velo of a similar phrase is inferred. The value of Time uses the value decided by Automatic translation (See Passage2.3).

4.2 Inference Result

The result of the inference using this inference system is shown in Figure 9. The phrase of the seventh bar of Beethoven's Sonata No. 8 was inferred from the first bar, which Gerhard Oppitz performed.

Thus, the inferred phrase was similar to the expression of the performance of the search phrase.

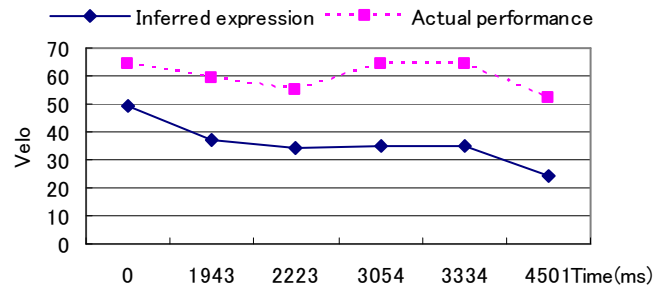


Figure 9: Inferred performance expression

5. Conclusion

We designed a method of searching for similar phrases and inferring the performance expression using DP matching and constructed these as one system.

In the similar phrase search, the system was able to search for similar phrases using DP matching in a short time, and it was even possible to search for phrases whose resemblance might not be immediately apparent.

In the inference of the performance expression, a performance expression was able to be inferred using the best associating by the DP matching from the search.

The performance expression of some similar phrases that exist in the tune can be inferred at the same time using this system. It is regarded that the work efficiency increases by this automatic editing in contrast to editing the piece by hand from the beginning, without sacrificing quality.

In this study, a general performance expression was used for musical symbols such as Crescendo. But, it is thought that it will be possible to infer the user's intentions for such symbols as well in the future.

Reference

- [1] Takamatsu Y, Hayashi E, et al, "Study on the Performance Information Edit Support System for an Automatic Piano (*in Japanese*)", Technical Report of Information Processing Society of Japan, MUS-52, pp.111-118, 2003.
- [2] Hikisaka Y, Hayashi E, et al, "Interactive musical editing system for supporting human error and offering personal preferences for an automatic piano -A system of inferring phrase expression-", Proc. of the 11th International Symposium on Artificial Life and Robotics, pp 296-299, 2006.
- [3] Nakagawa S, "Speech recognition based on probabilistic model (*in Japanese*)", IEICE, pp18-28, 1988.

Self-reproduction on 1-bit communication cellular automata

Ryoh Takebayashi, Koutarou Tachibana and Hiroshi Umeo

Univ. of Osaka Electro-Communication, Graduate School of Engineering,
Faculty of Information Science and Technology, Department of Informatics,
Neyagawa-shi, Hatsu-cho, 18-8, 572-8530, Osaka, Japan

Abstract

Many researchers have constructed a self-reproduction model on cellular automata so far. C. G. Langton constructed a simple model on the 2-D cellular automata, and it is a *dynamic-loop* [4]. We consider embedding the Langton's model in 1-bit communication cellular automata. The 1-bit communication cellular automata are restricted communication-capacity to 1-bit. The Langton's model has 8 internal states and generally it is impossible to represent 8 by 1-bit. Thus it occurs time-loss in communication of information. In this paper, we will embed Langton's model in 1-bit communication cellular automata without time-loss. However the embedding model has a large number of internal states, so we construct the second model. In the second model, by excluding some properties of Langton's model, we reduced internal states.

1 Introduction

Studies for life phenomena have been made for many years. Especially, structures of many lives have been made clear by progress of technology from middle of 20th century. However, evolution process of life phenomena and process that cells constitute a large scale structure according to genes are not clear.

Some of researches, which are actively done in artificial life, are about self-reproduction of life. Especially, a lot of self-reproduction models on 2-D cellular automata have been suggested by many researchers [2-4, 6, 7, 9, 10]. A self-reproduction model constructed by C. G. Langton on 2-D cellular automata is very simple. It has a *dynamic-loop* structure. In this paper, we will embed the simple model in communication-restricted cellular automata.

2 Self-reproduction loop

At first, self-reproduction model was suggested by John von Neumann. Neumann considered a machine that has information for self-reproduction, and replicates itself, and then he get an idea. It is that a universal machine is able to do such behavior. Moreover,

for simplification of problem, Neumann used the 2-D cellular automata and he constructed an universal machine that has 29 internal states on 2-D cellular automata [6].

The 2-D cellular automata are a parallel processing model where finite automata are placed as plane. We call each automaton cell. Each cell has a set of internal states Q and a transition function δ such that $Q^4 \rightarrow Q$. In the 2-D cellular automata, inputs of transition function are states of neighbors (north, west, east, south and itself). Thus, transition function δ on 2-D cellular automata is defined as the following.

$$\begin{aligned} \delta(q_n, q_w, q, q_e, q_s) &= q' \\ (q_n, q_w, q, q_e, q_s, q' \in Q) \end{aligned} \quad (1)$$

Codd designated that Neumann's model can behave in 8 internal states [3], and Serisawa designated that Neumann's model can behave in 3 states (Neumann neighbors) or 2 states (Moore neighbors) [9, 10].

On the other hand, Langton considered a more simple model, because cells in nature don't seem to be *universal machine*. So Langton constructed such self-reproduction model on 2-D cellular automata. Langton's model uses 8-states per cell [4]. We call Langton's self-reproduction model on 2-D cellular automata *Langton-Loop* by the shape. Figure 1 shows transition of *Langton-Loop*, where t means time. *Langton-loop* exists in cellular space filled by state "0" cells. The state "0" is called quiescent state.

Langton-Loop is surrounded by cell wall states. We call a part which is surrounded cell wall inner-loop. *Langton-Loop* reproduces a pattern by state transitions in inner-loop. Here, we consider separating *Langton-Loop* into *loop-part* and *arm-part*, to assist understanding transition of *Langton-Loop* (Fig. 2). By the signals from *loop-part*, *Langton-Loop* extends *arm-part* and builds left hand corners 3 times at the time which is decided beforehand.

A signal to *arm-part* consists of five state "7" and two state "4". *Loop-part* send out these states to the

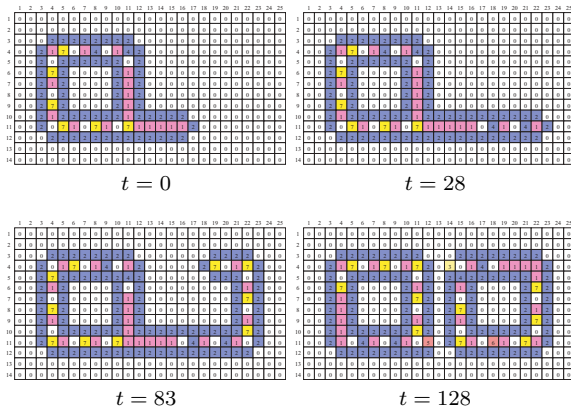


Figure 1: Langton-Loop

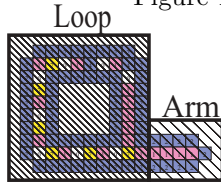


Figure 2: Loop-part and arm-part

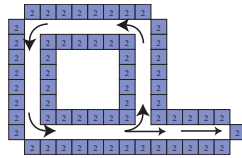


Figure 3: Direction of signals

end of *arm-part* (Fig. 3). When state "7" reaches the end of *arm-part*, *arm-part* can extend length of one cell.

By state "4" reaches the end of *arm-part* two times, *arm-part* turns. The first state "4" changes a direction of *arm-part*'s extension to left hand by using temporary state "3". Then, when second state "4" reaches a cell which assumes state "3", the state "3" cell changes state to state "1". So *arm-part* can change direction of extension.

By iteration of this action, *loop-part* is constructed. For that purpose, *loop-part* must continue sending the signal which consists state "7" and state "4" to *arm-part*. This action is done by sending state "7" and state "4" to *arm-part*, and feed back into *loop-part* at once (Fig. 3).

3 Self-reproduction loop on 1-bit communication cellular automata

3.1 2-D 1-bit communication cellular automata

The 1-bit communication cellular automata were suggested by Mazoyer [5] and Umeo [8]. The 2-D 1-bit communication cellular automata are 2-D cellular automata that are restricted communication-capacity to 1-bit. Figure 4 shows structure of 2-D 1-bit communication cellular automata. Each cell of 2-D 1-bit communication cellular automata has a set of inner-states

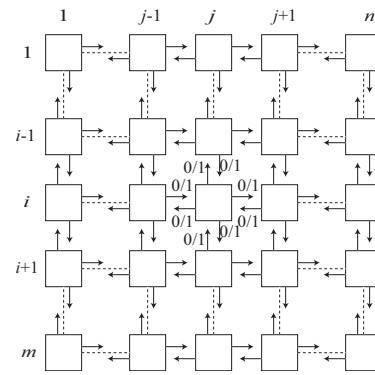


Figure 4: 2-D 1-bit communication cellular automata

Q and transition function δ , as well as 2-D cellular automata. Transition function δ in 2-D 1-bit communication cellular automata is defined to the following, by the property.

$$\delta(b_n, b_w, q, b_e, b_s) = (b'_n, b'_w, q', b'_e, b'_s) \quad (2)$$

Where $q, q' \in Q$ and $b_n, b_w, b_e, b_s, b'_n, b'_w, b'_e, b'_s \in \{0, 1\}$. In 1-bit communication cellular automata, an information from a north, south, east, west cell is always 0 or 1.

3.2 Self-reproduction model M_α

In this paper, we suggest two self-reproduction models. We call first model M_α and second model M_β . At first, we will explain about M_α

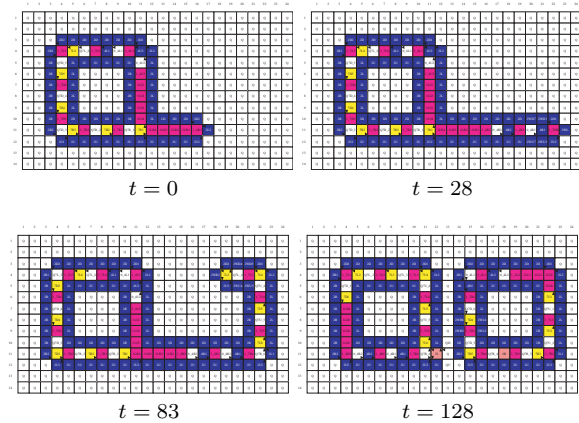


Figure 5: Self-reproduction model M_α

We constitute M_α by embedding Langton's model to 1-bit communication cellular automata. M_α has 263 internal states. Figure 5 shows model M_α . 1-bit signal is represented by small triangles in the figure. If a small triangle exist, it means sending 1 signal and a small triangle don't exist it means sending 0 signal.

M_α also has *arm-part* and *loop-part* and performs as *Langton-Loop*. All cells except reproducing pattern are filled by quiescent state.

When an algorithm is executed on 1-bit communication cellular automata, there are problems proper to 1-bit communication cellular automata. One of problem is number of transition rules an state. Since a cell on 1-bit communication cellular automata changes the state by its state and 1-bit signals from neighbors, the cell may refers a same transition rule, even if neighbor's state is different. We solve the problem as following.

M_α extends *arm-part* by cycling signals in *loop-part*, as well as *Langton-Loop*. For above problems, each cell has to recognize its own part, a junction of *loop-part* and *arm-part*, the corner of *arm-part*, the termination of *arm-part*, or others.

At first, we explain about a termination of *arm-part*. The cell at termination of *arm-part* recognizes its part by receiving 1-bit signals by forward and left, right cells against the direction of signal. The cell at termination of *arm-part* extends *arm-part* by "7-0" signal (Fig. 6) and makes corner by "4-0" signal.

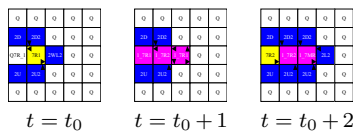


Figure 6: Extension by "7-0" signal

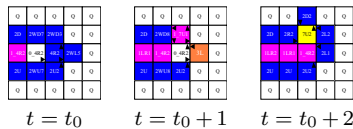


Figure 7: Making corner by "4-0" signal

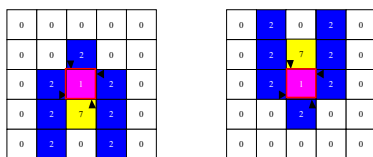


Figure 8: No information of the direction

However, a bad effect occurs by above problem. Although at both two cases in Fig. 8, the cell which assumes state "1" recognizes that its position is termination of *arm-part*, the cell doesn't recognize the direction of extension. Because, the cell doesn't have information of the direction. So, we add information of the direction to each state. For example, state "2" is transformed into "2U", "2D", "2R", "2L" (each state means north, south, east, west). By this transforma-

tion, each cell recognizes the direction of signals from an internal state.

The cell at the corner of *loop-part* recognizes that it is the corner of *loop-part* by receiving 1-bit signal from the cell on the forward and right toward the direction of signals. So the cell can change the direction of signals to the left toward (Fig. 9).

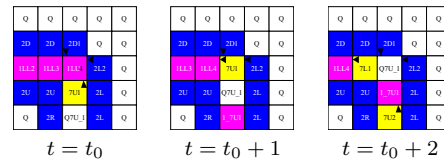


Figure 9: Recognition of corner

A cell at junction of *loop-part* and *arm-part* recognizes that itself by receiving 1-bit signal from the cell on the right toward the direction of signals. So, the cell can send signals to *loop-part* and *arm-part* (Fig. 10). M_α can self-reproduce by these actions without time-loss.

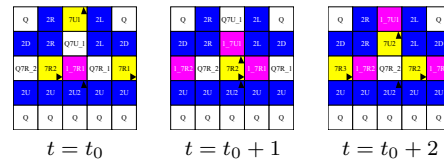


Figure 10: A junction of *loop-part* and *arm-part*

3.3 Self-reproduction loop M_β

The second model M_β has 77 internal states. Figure 11 shows action of M_β . M_β also has *loop-part* and *arm-part*, cells surrounding pattern assume quiescent state. The algorithm of reproduction is also same; by sending signal from *loop-part*, *arm-part* is extended and make a corner. However, as Fig. 11 shows, there are some different points.

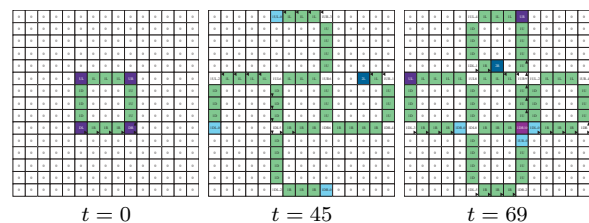


Figure 11: Self-reproduction model M_β

M_β is different from *Langton-Loop* in three points. The first point is that M_β doesn't have cell wall state which is state "2" in *Langton-Loop*. The second point is that M_β reproduces to four direction (north, south,

west, east) at the almost same time. The third point is that signals which cycles in *loop-part* for reproduction are a sequence of 1-bit signal.

The initial pattern of M_β is square and the length of a side is more than two cells and arbitrary. Reproduced loops have same size as well as initial pattern. Initial pattern must have 1-bit signals which can be propagated anti-clockwise and have length of a side.

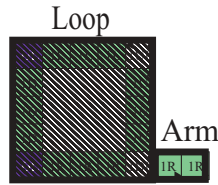


Figure 12: *Loop-part* and *arm-part*(M_β)

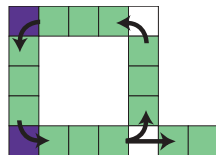


Figure 13: Direction of signal

In this model, *arm-part* extends length of one cell by a 1-bit signal (Fig. 14). While 1-bit signal continuously send to the end of *arm-part*, *arm-part* extends. But, when 1-bit signal interrupts, the end of *arm-part* assumes a state which can build a left hand corner. As a result, when another signals arrive to the end of *arm-part*, *arm-part* extends to left hand (Fig. 15).

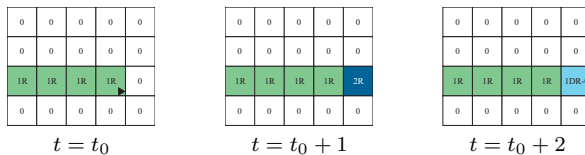


Figure 14: Extension of *arm-part*(M_β)

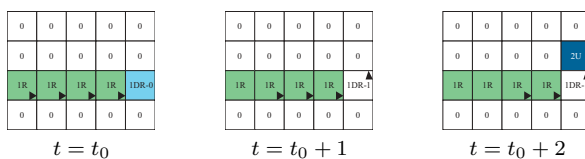


Figure 15: Changing direction of the line(M_β)

On the other hand, each corner cell of *loop-part* sends two signals, when each corner cell gets input signal. These two signals which are duplicated at junction of *loop-part* and *arm-part* are respectively propagated to *loop-part* and *arm-part* as well as *Langton-Loop* (Fig. 13). Thus, corner cells of *loop-part* have function that controls signals sent *arm-part*. Continuous 1-bit signals which are sent to *arm-part* are sent 5 times, to build new *loop-part*. Signals from once to fourth times have a function which extends *arm-part* and builds new *loop-part*. Signal of the fifth times

has a function that gives ability of self-reproduction to new *loop-part*. Therefore, signals of the fifth times will have been propagated in new *loop-part*. Thus, when signals of the fifth times have inputted to new *loop-part*, self-reproduction that includes an ability of self-reproduction is finished. A corner cell that have sent signals 5 times assumes a state that does not send signal to *arm-part*.

4 Conclusion

In this paper, we have constructed two models which behaves on 1-bit communication cellular automata as well as *Langton-Loop*. The model has 263 internal states. And by excluding some property of *Langton-Loop*, we get a model that has 77 internal states. These models designate that the relation of communication capacity and internal states has a trade-off, we want to analyze strictly as well.

References

- [1] T. Arita: Artificial life, Science Press, 2000.
- [2] J. Byl: Self-reproduction in small cellular automata, *Physica*, 34D, pp. 295-299, 1989.
- [3] E. F. Codd: Cellular automata, Academic Press, 1968.
- [4] C. G. Langton: Self-reproduction in cellular automata, *Physica*, 10D, pp. 135-144, 1984.
- [5] J. Mazoyer: A minimal time solution to the firing squad synchronization problem with only one bit of information exchanged, Ecole Normale Supérieure Lyon, *Technical report*, No. 89-03, pp. 51, April, 1989.
- [6] John von Neumann: Theory of self-reproducing automata, University of Illinois Press, 1966.
- [7] J. A. Reggia, S. L. Armentrout, H. H. Chou, Y. Peng: Simple systems that exhibit self-directed replication, *Science*, vol. 259, pp. 1282-1287, 1993.
- [8] H. Umeo: "A design of cellular algorithms for 1-bit intercell communications and related cellular algorithms, *Proc. of MCU'98*, vol. 1, pp. 210-227, 1998.
- [9] T. Serizawa: Universal cellular automata with minimal states and neighbors(1), *Technical report of IEICE*, AL 77-26, pp. 1-10, 1977.
- [10] T. Serizawa: Universal cellular automata with minimal states and neighbors(2), *Technical report of IEICE*, AL 77-26, pp. 11-18, 1977.

On the Abundance of Energy Sources and Evolution of Collective Swarm in Auto-Constructive Artificial Life

A.R. Adzni

Center for Artificial Intelligent,
School of Engineering and
Information Technology,
Universiti Malaysia Sabah,
Locked Bag 2073, 88999 Kota
Kinabalu, Sabah,
Malaysia.
adzni@yahoo.com

Jason Teo

Center for Artificial Intelligent,
School of Engineering and
Information Technology,
Universiti Malaysia Sabah,
Locked Bag 2073,
88999 Kota Kinabalu, Sabah,
Malaysia.
jtwteo@ums.edu.my

Azali Saudi

Center for Artificial Intelligent,
School of Engineering and
Information Technology,
Universiti Malaysia Sabah,
Locked Bag 2073,
88999 Kota Kinabalu, Sabah,
Malaysia.
azali@ums.edu.my

Abstract

We demonstrated a collective swarm of flying agents simulated in Breve auto-constructive artificial life, where their behavior is governed by its own simple set of programs expressed in Push programming language. Agents are programmed to seek the food sources to re-grow their energy as a main goal to survive for the next generation, thus collective agents may be capable of reproducing their own children. In this paper, the main concepts we are trying to get across concern on how reproductive competence may be affected by the quantity of food energy moves through an environment. We performed 50 runs test per parameter setting and will eliminate at 6000 generations each run. From the result, we found that the more increasingly the quantity of food energy are injected would encourage the more increase in the percentage of reproductive competence achieved within 50 runs. The reproductive competence means the point in which generation agents are able to reproduce their own children for the next generation without any new agent been injected.

Keywords–Swarm Behavior, Collective Intelligence, Artificial Life, Auto-construction, Genetic Programming, Parametric Analyses

Introduction

Artificial life refers to creating and simulating the living system to model life form, which can be implemented in computer. Artificial life also is defined as “life made by human”. The main purpose of Alife is to create synthetic life in an artificial component and compare it with the natural life, as we know it [1]. Alife has a great potential

to explore especially in context of self-reproducing system.

Nowadays, a number of self-reproducing systems have been explored. In 1940, Cellular Automata (CA) environment was invented by John Von Neuman who created a set of rules describing how in one specific state of the system a particular configuration of cells is to be transformed or converted to another state of the system. One of the most well known CA rules, namely the “game of life”, was conceived by Conway in the late 1960s.

From this drawback, many researchers come out with their own system to model life form through computer simulation. An example of open-ended selection was Tierra, which was a simulation of evolving self-replicating programs with a mortality queue to ensure they had to try and copy or maintain themselves [2]. Similar to Avida and cosmos, where Avida was inspired by Tierra system that; relies on external mutating mechanism [3]. These systems must be seeded initially with the simple human coded self-replicating program. This is in contrast with Breve auto-constructive evolution, which relies on the Push program to support self-reproductive “PushPop” program in which the higher performance individuals are able to reproduce their own children [4].

By applying Breve application provides us a powerful framework [5], we presented a set of collective agents in 3D simulation. Over the years, one of the main difficulties that a user faces is on how to decide an appropriate set of parameter values, as user has to specify a number of parameter when applying a Genetic Evolution Algorithm.

Thus, evolved dynamic parameter values of food energy, which is defined as feeder in Breve simulation. The aim of this work is to investigate how the energy sources in environment would have an affect the reproductive competence in auto-constructive artificial life.

Methodology Approach

Breve environments

The swarm intelligence of flying agents was presented in 3D simulation using the piece of software called Breve environment. This system provides a framework for artificial life that can create realistic object in 3D simulation and includes a simple programmable language such as “Push” language for use in evolutionary computation [5].

The behavior of each agent in simulation environment was governed by one complete code program expressed in Push programming language. Push program has a simple syntax and can process multiple data types that allow Push to support the automatic evolution such as “auto constructive evolution. Thus, the genetic operator and other evolutionary system evolve themselves.

Auto-constructive evolution is a framework for evolutionary computation system [6], an evolving population of programs expressed in the Push programming language. This system is responsible for producing a new program through the mutation process for the next generation and evolves within the individuals as the system run.

Experiment setup

Characteristic of feeder

The environment in this simulation will be supplied with the needs of organisms such as energy sources are defined as feeder. Feeder is simulated in white sphere and contains energy that needed by agents as food to increase their energy and also for longevity. As shown in Figure 1.0 (a), the movements of feeders were in limited areas and horizontally either axis-x or axis-z the movement on the axis-y (dot line arrow) and were not included to avoid the difficulties of seeking for food.

The agent with polygon shape in simulation as shown in Figure 1.0 (b), was programmed to fly and close the food energy with the aim to re-grow energy.

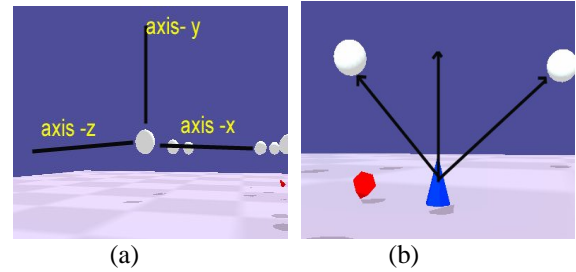


Figure 1.0: (a) The direction of feeder moving to axis-x and axis-z.
 (b) The direction of agents moving to the nearest food sources.

Parameters that were altered

Dynamic parameter refers to the number of feeders injected into Breve simulation. As shown in table 1.0, five different numbers are evolved before and after the point of default value. By applying this parameter value, we would like to investigate how this different number of food would have an effect on the reproductive competence in auto-constructive artificial life.

Parameter Values	Ranges
10	↑ ↓
12	
14	
16	
18	
20	Default Value
22	↑ ↓
24	
26	
28	
30	

Table 1.0: Parameter values are altered

Before running the algorithm, for each parameter values we performed 50 runs with 50 different seeds and will be eliminated at 6000 generations.

Reproductive competence

Each agent represented a complete Push program that will be evaluated. Agents were programmed to seek for food in order to increase their energy. Unsuccessful agent will quickly die thus the number of agents will decrease.

If the number of agents falls below user-defined threshold of 10 individual, the system will automatically inject new agents into the system in order to maintain the

minimum population size. If this phenomenon occurs to the next generation, then the swarm in that particular point of generation will not be considered to be reproductively competent. Alternatively, if this phenomenon does not occur, agents may be capable to reproducing their own children, in which case the collective swarm will be considered to be reproductive competent.

Measuring reproductive competence

We measured the point in times where reproductive competence is achieved within 5500 generations completely without any new agent injected into simulation as shown in table 1.2:

Components	Feeder	
Dynamic Parameter setting	10(x 50 runs)	
Generations	Agents generated by:	
	System	Agents
1	1	0
2	0	0
3	.	1
4	.	.
5	.	.
.	0	.
.	1	1
.	1	0
456 ←	0	1
.	0	0
2356	0	0
.	0	1
3564	0	1
6000	0	0
Average	$(456 + \dots + y) / N$	
Percentage	$(N/50) * 100$	

N = The number of runs which the reproductive Competence achieved.

Table 1.2: The way to measure the reproductive competence

Result and discussion

Table.1.3, displays a set of reported data on the mean and standard deviation of reproductive competence achieved within 5500 generations in 50 runs of test. As statistics, average refers to the measurement of the central tendency of the data set of reproductive competence and in relation to the mean we also measured the standard deviation of how spread out are the data values away from the mean.

According to this table, the smallest value of mean shows the reproductive competence achieved earlier where agents are able to reproduce to make their own population for the future generation without any new agent randomly being injected. This can be seen at parameter 12 with average of 2 rather than 303.00 at parameter 10.

Parameter	Mean	Standard Deviation
10	303.00	0.00
12	2.00	0.00
14	300.00	164.01
16	181.38	140.10
18	165.54	166.76
20	180.91	178.24
22	130.14	154.31
24	151.14	149.14
26	189.12	194.86
28	190.40	198.42
30	186.17	195.38

Table 1.3: Average of reproductive competence within 5500 generations

From our analysis, this may due to the cause of the distribution of food energy located near the group that could have been caught by agents. As we can see the behavior of agents in Figure 1.2(a), even if a group of agents compete with each other but the same species (same color) among them will share energy to their friends. Thus, unsuccessful agents with less energy will get additional energy from their group's friend that would give it a chance to find food energy nearby Figure 1.2(b). However, if a group of agents were different species that is different color as shown in Figure 1.2(c), because of their rest energy that could not catch a nearby feeder.

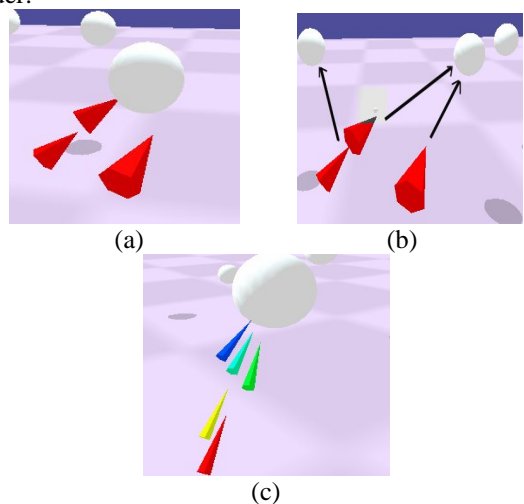


Figure 1.2: Behavior of collective agents:

Figure 1.3, showing the percentage of reproductive competence achieved within 50 runs. As we can see, the percentage of reproductive competence achieved at axis-y increased slowly against dynamic parameter values of feeder but suddenly showed a large difference at parameter 20 of 20% from parameter 18. This may due

to the quantity of food more than agents that cause less competence among agents. Similarly even a 2% decrease at parameter 22 instead of at parameter 20 after 44% runs, we also found that the mean of reproductive competence shows the better result of 130.14 rather than at parameters 26 and 28.

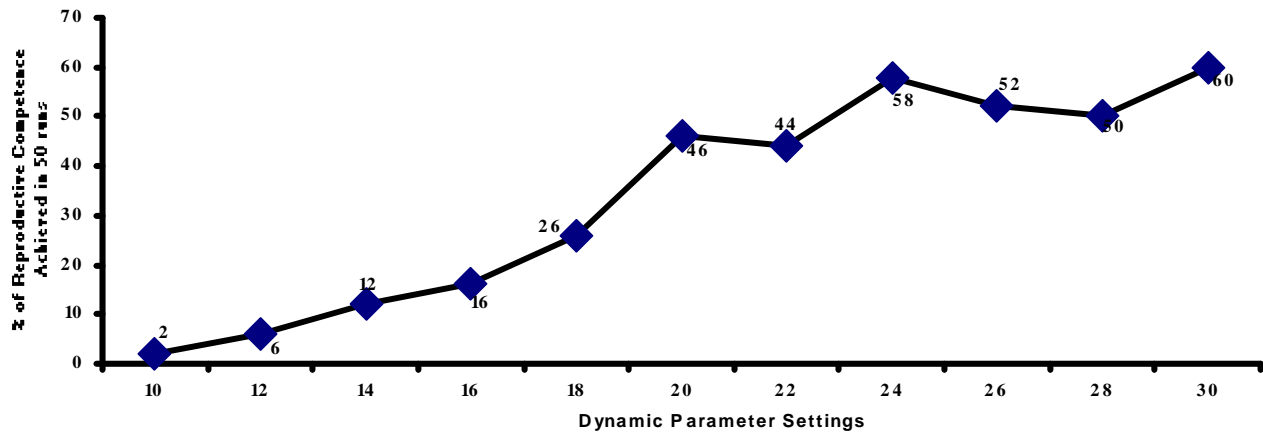


Figure 1.3: Percentage of reproductive competence achieved within 50 runs

Conclusion

The elements that appear in this work are focused on the main aspect on how reproductive competence may be affected by the quantity of food energy moves through an environment. The most specific approach is on the population of energy sources analysis, which estimates the energy budget of a particular population. The analysis is done by determining the amount of energy in the form of organic matter that is consumed, assimilated and excreted by individual organisms. The second approach is the study on the capability of each individual organism to survive, how fit are these individuals in competing with each other. In summary, the dynamics of energy in environment, each of which has its own inherent strengths and weaknesses. There are many other factors that would also affect the growth of population in environment. This would be interesting to explore for the future work.

Acknowledgments

Many thanks to PTPTP (Pelan Tindakan Pembangunan Teknologi Perindustrian) for Postgraduate scholarship, University Malaysia Sabah for this research. I would like to thank to Mr. David Low for his help in grammatical, Mr. Saidin and Riz Faizal for helping in Lab facilities.

References

[1] C.Adami, Introduction to life. Springer-Verlag. New York 1998.

[2] T.S. Ray, An Approach to the Synthesis of Life, in C. G.Langton Taylor, J. D Farmer & Rasmussen, eds, Artificial Life II Vol. X of Series: Sante Fe Institute Studies in the Sciences of Complexity, Addison-Wesley Publishing Company Inc.,Redwood City, California, 1992 pp. 371-408.

[3] T.J Taylor and J.Hallam, Studying Evolution with Self-Replicating Computer Program. Fourth European Conference on Artificial Life, University of Edinburgh. In P. Husband and I. Harvey, editor.MIT Press/ Bradford Books, 1997, pp. 550-559.

[4] L. Spector and A Robinson, Genetic Programming and Autoconstructive Evolution with the Push Programming Language. In Genetic Programming and Evolvable Machines. Cognitive science, Hampshire College, Amshert, MA 01002. Vol.3, NO.1, 2001. pp.7-40

[5] J.Klein, BREVE: A 3D Environment for the simulation of Decentralized Systems and Artificial Life, Proc. Eighth Intl. Conf. on Artificial Life. The MIT Press, Cambridge, MA (2002), 2003, pp. 329-334.

[6] L. Spector. Autoconstructive evolution Push, PushGP and PushPop. Proceeding of the Genetic and Evolutionary Computation Conferenc, GECCO-2001, san Francisco, CA:Morgan Kaufmann Publishers, pp.137-146.

Interactive musical editing system to support human errors and offer personal preferences for an automatic piano

- Information system regarding a musical sign -

Yuichi Chigoi

*Graduate School of Computer Science
and System Engineering
Kyushu Institute of Technology
680-4, Iizuka City, Fukuoka, Japan, 820-8502
chigoi@mmcs.mse.kyutech.ac.jp*

Eiji Hayashi

*Department of Mechanical Information
Science and Technology
Kyushu Institute of Technology
680-4, Iizuka City, Fukuoka, Japan, 820-8502
haya@mse.kyutech.ac.jp*

Abstract

We have developed an automatic piano that can accurately control the motion of both the keys and the pedal based on performance data that a user has inputted for a particular piece of music. However, this system cannot sight read a new piece of music, as in the simulation of a human being's expressive performance. Therefore, we developed a program that can memorize and use knowledge databases and user preferences concerning the interpretation of a piece of music.

We analyzed performance data of performances of highly skilled pianists in order to observe performance tendencies, and found that phrases of similar patterns existing in the same composition were performed with similar expression by the same pianist. Moreover, it was found that the pattern of notes in the score sometimes influence how the expression emerges.

Therefore, we developed a system for inferring phrase expression from the patterns of the notes. We evaluated the system by comparing performance information inferred from the databases with the pianist's actual performance.

Key words: *automatic piano, knowledge database, music interface, user's preference, computer music, inference system*

1. Introduction

We developed a performance system for an automatic piano. In this system, 90 actuators are installed in the 88 keys and 2 pedals of a grand piano. Those actuators operate key strokes and pedaling to be executed on the piano. (See Figure 1)

Reproducing music with the piano is similar in some ways to reproducing music on the computer. Essentially, variations in tempo, dynamics, and so on are needed to arrange the respective tones in the desired way. However, in the case of piano music, there are 1000 or more notes in a score of even a short piece of music, and the editor must spent enormous amounts of time working with the

arrangement in order to simulate the expressions of an actual performance.

Even for a skilled computer user, it becomes prohibitively burdensome to reproduce a score and add expression simultaneously using the automatic piano and a computer music system. The reason is because the musical data cannot be rewritten all at once. By contrast, highly skilled pianists can sight-read an unfamiliar piece of music, even if the performance is not completely in accord with a specific musical interpretation. The computer system cannot sight-read a new piece of music, and cannot simulate a human pianist's expressive performance.

Therefore, in this research, we have developed an interactive musical editing system to edit music more efficiently^{[1]-[4]}.

We devised a method for inferring a performance from information on the score and a particular user's editing characteristics for similar phrases. We evaluated the system by comparing performance information inferred from individualized databases with the pianist's actual performance.

In this paper, we describe the method of inference based on analytical results, and its result in an actual simulated performance.



Figure1. View of the automatic piano

2. Musical Editing Support System

2.1 System Architecture

The structure of the system is shown in Figure 2. The user edits music via the user's interface on the computer display. The user can also access a database that has musical grammar, the user's preferences, and so on. As a result, editorial work is reduced and efficient editing becomes possible.

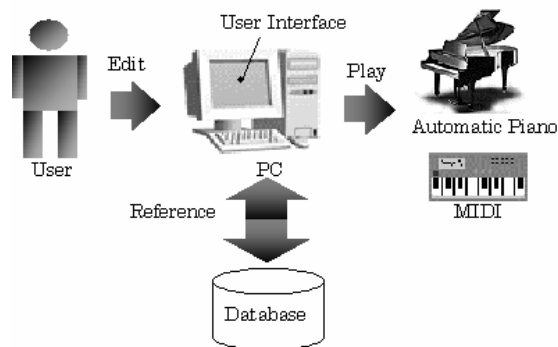


Figure 2.1 Structure of the editing system

2.2 Format of Performance Information

The parameters of performance information are shown in Tables 1 and 2.

The automatic piano that we have developed uses a music data structure that is similar to MIDI. We defined performance information, dividing it into two categories, the notes and the pedals.

The note information is comprised of the six parameters involved in producing a tone: "Key (note)", "Velo (velocity)", "Gate", "Step", "Bar", and "Time". "Velo" is the dynamics, given by the value of 1~127. "Gate" is the duration of the note in milliseconds. "Step" is the interval of time until the next note, and it also exhibits tempo. "Bar" is the vertical line placed on the staff to divide the music into measures.

The pedal information is comprised of four parameters: "Key (indicating the kind of pedal, "Damper" or "Shifting")", "Velo (the pedaling quantity)", "Time (the duration for which the pedal is applied)", and "Bar".

Table 1. The parameters of note information

Parameter	Key	Velo	Gate	Step	Time	Bar
Unit	-	-	m sec	m sec	m sec	-
Reference	21~108	1~127	-	-	-	-

Table 2. The parameters of pedal information

Parameter	Key	Velo	Time	Bar
Unit	-	-	m sec	-
Reference	Damper or Shift	0~127	-	-

2.3 Editing Support Process with Database

The procedure for editing by the system is shown in Figure 3.

Temporary music data (TMD) is the data of a piece of music without expression. Because expression has not been added, the necessary editing of the TMD is extensive.

Therefore, if the user chooses, the TMD is automatically translated by the system into original music data (OMD), similar in structure to TMD; after that, the user can start to edit it. The automatic translation program uses a Score Database, Musical Rules Database, and Preference Database, the details of which are described later in the paper. The user adds editing to the OMD and makes slight adjustments. When editing, the system watches over the data the user enters and music knowledge is provided. Concurrently, phrases in the music are discovered. When a phrase with the same pattern as one already edited occurs in the music, it is automatically translated. After editing, the system extracts the expressions and preferences that are peculiar to the user from the OMD. These expressions are stored in the Preference Database, which is then used when editing other music, resulting in improved editorial efficiency.

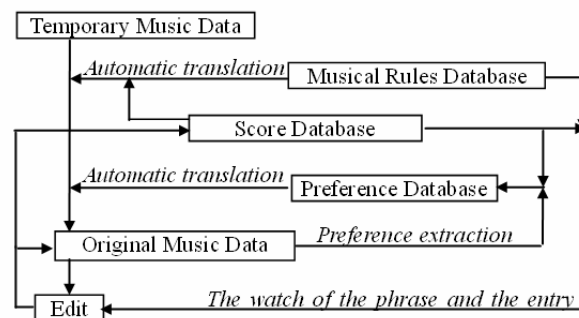


Figure 2.2. Structure of the editing system

2.4 Details of the Databases

2.4.1 Score Database

This database has symbols including notes, time signature rests, and other standard musical notations. Symbols were pulled together in order of bars, and bar symbols are arranged in time series.

This database is composed of three tables, the

“Element table” (showing the position of the note and composition of the chord), the “Symbol table” (showing the position of the music symbol), and the “Same table” (showing the position of the repetition of the phrase).

2.4.2 Musical Rules Database

This database contains the architecture of musical grammar necessary to interpret symbols in musical notation. This database is composed of five tables containing “Dynamics marks”, “Articulation marks”, “Symbol of Changing Dynamics or Changing Tempo (symbol that affects the speed of a note or the increase or decrease of the volume)”, “Time signature”, and “Tempo marks”.

Analyzing a music symbol according to its usage allows efficient information processing by the system.

2.4.3 Preference Database

This database contains the expressions of the user’s characteristic performance. The expressions show the relationship between tempo and dynamics.

The “Edit” selection in the user’s interface gives the user access to the parameters for expression. A user can edit his or her parameters, and the respective databases will automatically change at least one of their parameters.

3. Construction of the Preference Database

We analyzed a tendency to editing (a characteristic of a performance) based on a performance of a pianist and built a Preference Database. Among a lot of existing music symbols, we focused on the musical notation indicating Staccato.

We used the Pathétique sonata by Beethoven as the object music for our analysis.

We used “Gate (length of a sound),” “Step (an interval of a sound)” and “Gate ratio (the ratio of gate for step)” for the performance information that we analyzed.

3.1 Analytical Results

3.1.1 About a Sforzando

We analyzed a sound-added Sforzando sign and sounds that were not added.

Figure 3.1 shows the score of bars 11 to 14 of Beethoven’s sonata Pathétique. This phrase appears in the score of bars 19 to 22 and 121 to 124. There are no Sforzando signs in the score of bars 121 to 124. In addition, there is repeat sign at the top of the score.

Therefore, this phrase is played six times total. We analyzed these data. The general Gate ratio is 0.7 to 0.8.



Figure 3.1 The score of bars 11 to 14 of Beethoven’s sonata Pathétique

Table 3.1 Analytical Result[s]

Bar number	Gate ratio
11-14 (1st)	0.130
11-14 (2nd)	0.125
19-22 (1st)	0.144
19-22 (2nd)	0.148
121-124 (1st)	0.881
121-124 (2nd)	0.905

Table 3.1 shows the analytical result. It also shows that the Gate ratio tends to become small by addition of the Sforzando sign. In addition, the Gate ratio thereby becomes approximately constant.

3.1.2 About a Staccato

Figure 3.2 shows the score of bars 35 to 36 of Beethoven’s sonata Pathétique. This phrase appears in the score of bars 39 to 40 and 43 to 44. In addition, there is a repeat sign at the top of the score. Therefore, this phrase is played six times total. We analyzed these data.



Figure 3.2 The score of bars 35 to 36 of Beethoven’s sonata Pathétique

Table 3.2 Analysis of Result

Bar number	Gate ratio
35-36 (1st)	0.356
35-36 (2nd)	0.277
39-40 (1st)	0.350
39-40 (2nd)	0.388
43-44 (1st)	0.419
43-44 (2nd)	0.394

Table 3.2 shows the analytical result. It shows that the Gate ratio tends to become small by addition of the Staccato sign. In addition, the Gate ratio thereby

becomes approximately constant

Furthermore, we analyzed the case of a half-note. The result showed that a half-note has a smaller Gate ratio than a quarter-note.

We also analyzed the case of a Staccato that did not continue. As a result, the Gate ratio tends to become big.

3.1.3 Summary of An Analytical Result

We understood that the Gate ratio changed by the presence of musical signs from these analysis results. When the Sforzando sign is added, the Gate ratio tends to become small. The case of a Staccato sign being added is special. When a staccato continues in a phrase, the Gate ratio tends to become approximately constant. However, when the Staccato sign does not continue, the Gate ratio tends to become big

3.2 Making of GateratioData

We understood that the Gate ratio changed by the presence of musical signs from these analysis results. Therefore, we used GateratioData in the Preference Database to automatically convert user's editing characteristics. GateratioData consists of the Gate ratio, role (right or left hand), a kind of note, and a kind of musical sign.

4. Automatic conversion by musical sign

We converted the note with a Staccato sign (Figure 4.1) automatically by using Gateratio Data in the Preference Database. Figure 4.2-(a) shows TMD. Figure 4.2-(b) shows OMD that was converted to TMD automatically by using the Musical Database and Score Database. Therefore, Figure 4.2-(c) shows the OMD that was converted to Figure 4.2-(b) automatically by using Gateratio Data. The process from (a) to (b) is converted musical process. The process from (b) to (c) is converted in consideration of the user's editing character.

Therefore, we are able to offer playing-information that took in user's editing character to user, and we efficiency of work rose.



Figure 4.1 The score of bars 3 of Beethoven's sonata Pathétique

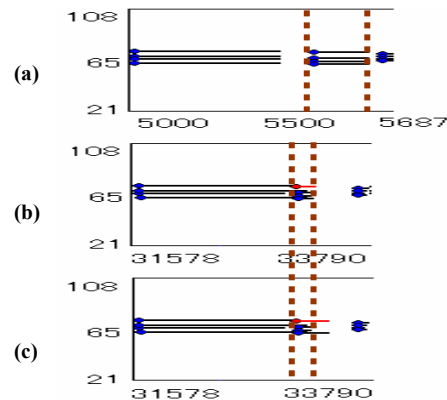


Figure 4.2 Automatic Changing Result

5. Summary

On an interactive musical editing system to support human errors and offer personal preferences for an automatic piano, we focused on [he user's editing character by the addition of a musical sign, and worked to store the Gate ratio in the Preference Database.

We were able to develop an automatic conversion processing function that based on Step. This function can offer playing information that took in user's editing character to user.

In the future, we plan to analyze other musical signs besides Staccato and Sforzando, improve the Preference Database, and develop a system that is able to convert plural musical signs.

References

- [1] Hayashi, E. et al, "Behavior of piano-action in a grand piano.I", Journal of acoustical Society of America, Vol.105, pp.3534-3544, 1999.
- [2] Hayashi, E et al, "Interactive musical editing system for supporting human errors and offering personal preferences for an automatic piano", Proc. of the 7th International Symposium on Artificial Life and Robotics, Vol.2, pp 513-516, 2002.
- [3] Takamatsu, Y., Hayashi, E., et al, "Study on the Performance Information Edit Support System for an Automatic Piano", Technical Report of Information Processing Society of Japan, MUS-52, pp.111-118, 2003. (in Japanese)
- [4] Takamatsu, Y., Hayashi, E., et al, "Interactive musical editing system for supporting human error and offering personal preferences for an automatic piano -Preference database for crescendo and decrescendo-", Proc. of the 10th International Symposium on Artificial Life and Robotics, pp 309-312, 2005.

Cognitive Modeling of Artificial Fish Learning and Memory

Dongmei Ai¹ Xiaojuan Ban² Shujun Zhang³ Wenli Wang⁴

1) School of Applied Science, University of Science and Technology Beijing, China
aidongmei@sina.com

2) School of Information Engineering, University of Science and Technology Beijing, China

3) Remote Sensing Institute, Ocean University of China, China

4) Shandong Agriculture Mechanism Administration, China

Abstract

Artificial fish is a kind of artificial animal living in three-dimensional virtual environment, and a computer animation created by using the method of artificial life. In nature, behaviors of fish are not only driven by its instinct. They also try to adapt to new environment by their learning and memory, and then to turn what they have learned and their memory into the experience knowledge. The more abundant the experience knowledge of fish is, the stronger ability the individual has in adapting to the environment. To enrich the natural life characteristic of the artificial fish, the relation cognitive modeling of learning and memory of artificial fish is established in this paper, based on the ecological theory and their learning and memory mechanism of fish in nature. This is to control the behavior of the artificial fish, so that they will play a more independent and intelligent role.

1、 Introduction

By taking advantage of animal forms, habits and behaviors, X. Tu [1] has successfully created artificial fish, called "Xiaoyuan Fish", which realized the common basic characteristics of artificial animals through computer animation: bio-mechanics, movement, sense and behavior. Every artificial fish is a self-animating autonomous agent. "Xiaoyuan's Fish" starts a new way for computer animation---artificial life method;

Grzeszczuk[2] and Terzopoulos[3] developed a learning technology, which can automatically synthesize the vivid movement based on physical animal modeling. This technology is especially suitable for the movement synthesizing of the animals with highly soft body, such as fish, dolphin and snake. It can automatically learn effective methods in movement control and abstract proper parameter format out of them. They also development dolphin modeling in visual environment, which can perform kinds of "ocean acrobatics";

John Funge[4] put forward the idea of controlling the behaviors of animals in the game through cognitive modeling and expressing the uncertainty in cognition by adopting method based on interval mathematics and situation calculus, which has realized the animation character and behavior with cognitive ability; Learning and memory are two cognitive processes

At present, the study in the cognitive method of learning and memory of artificial fish is still not systematic and more effective methods are called for.

The study in the animal cognition involves a wide range, and the research mainly starts from psychology, ethology

and biology with different emphasis and methods. Manning, an ethologist, thinks that the behavior of an animal "includes all those processes by which the animal senses the external world and the internal state of its body and responds to changes which it perceives." And cognition just studies how to respond. Shettleworth[5] put forward some important opinions about animal cognition and studied the cognitive process of animal communication, predator learning, attention modeling, space cognition, social learning, etc.

Learning and memory are two cognitive processes closely related to each other, important means to realize cognition and basic intelligent characteristics of human and animals. Learning is the neural process when human and animal acquire environmental knowledge while memory is the process of storing and reading the acquired knowledge, which is the necessary condition for learning. The importance of learning and memory lies in that they can guarantee that human and animal can adapt to the changing environment and seek existence and production. How could the brain learn and memorize, i.e., how to acquire and store information, has become one of the most heated scientific topics at present. Biologists have pointed out that ocean creatures such as dolphin and fish have very strong learning and memory ability. They seem to be simple and common, but in fact they are extraordinarily acute and flexible in some aspects. Therefore, the study of cognitive modeling of artificial fish based on learning and memory and the realization of the advanced cognitive functions of animation characters of artificial fish is a charming and challenging topic.

2. System structure of artificial fish

In the real-time dynamic complex virtual ocean environment, every artificial fish is an autonomous Agent with independent perception, decision and behavior. The ocean world composed of multiple artificial fish is a multi-Agent system, in which there exist the interaction among artificial fish and the interaction between artificial fish and environments. Firstly, we provide the cognition-based architecture for artificial fish Agent.

It adopts the features of hybrid Agent to construct the whole structure model of cognition-based artificial fish. (as shown in Figure 1). Artificial fish includes three sub-systems: perception, cognition and behavior. These

sub-systems are connected by information flows and control flows. Among them, the content in the dashed box is the perception system. The sensors in the perception system can pass the perceived external environment information to the cognition system for processing, and then the behavior decision will control the behavior system to let the actuator generate detailed actions, which take effects on the external environment.

Sometimes, when artificial fish perceives some information, they will be driven by instinct directly, without the stimulation of cognition processing response action, e.g., collision avoidance. During making decision, intuition actions have the highest priority, and should be handled as interrupts in the program.

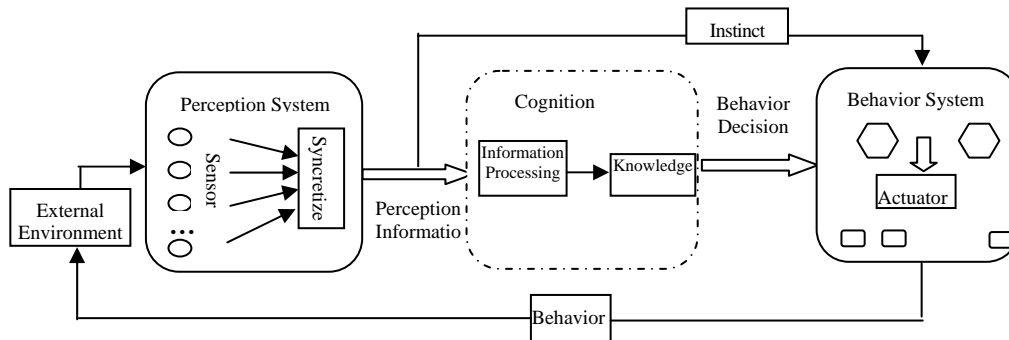


Figure 1: Collectivity Structure Modeling of Artificial Fish

The structures and functionalities of three sub-systems of artificial fish are as follows:

1. Perception system: information acquisition system, including a set of sensors and information aggregation module. The artificial fish has various kinds of sensors, e.g., visual sensor, audial sensor, olfactory sensor. At the same time, different sensors can get different environment information. We need to synthesize such information to facilitate the later information processing and behavior decision. Perception is the prerequisite of cognition and behavior planning.

2. Cognition system: information processing system, which takes the output of perception system as the input. For perceived information, the agent utilizes stored experiences and continuous learning to perform induction, deduction and decision to transform the information into the knowledge of its own. The agent then makes the behavior decision, which is transferred to the behavior system for execution.

3. Behavior system: execution system for behavior planning, which directly takes effects on the environment. It includes a set of behavior programs and a set of actuators. The behavior programs are the high-level actions, and the actuators execute the detailed actions. Every behavior program can be divided into a series of low-level actions, which are executed by actuators.

3. Relation between learning and memory of artificial fish

Animals acquire skills and knowledge from other animals, and fishes are no exception. There is now strong experimental evidence that many species of fish exhibit social learning and traditional behaviors[6].

Social learning refers to any incidence in which individuals acquire new behavior or information about

their environment via observation of, or interaction with, other animals or their products[7].

Social learning is sometimes assumed to be more common in, of a more sophisticated form in, or even restricted to, 'intelligent' or 'large-brained' taxa. However, research over the last 50 years has demonstrated that social learning is common amongst fish, birds and mammals, and should now be regarded as a regular feature of vertebrate life [7][8].

In the study of memorizing ability of animals, many ichthyologists have, through experiments, shown that many species of fish have the ability to seek food by using visual space information, i.e., they have a certain capacity of working memory and reference memory. Thus they can adopt food-clue association and guide their behaviors in seeking food with the help of memorized information. Couzin[9], etc. put forward self-organizing modeling of three-dimensional group lineup to study the spatial dynamic characteristics of animal groups, such as fish and bird, to show that the minor change in individual interaction may result in transference of group behavior mode and that similar animal groups have group memory. Ransom Winder[10] etc. studied the issue of group memory. The experiment of improving self-organizing behavior by giving distributed limited memory to each individual in groups and achieving the goal in the environmental with obstacles showed that those with memorizing ability can achieve goals more rapidly than those without memorizing ability.

According the characteristics of fish in learning and memory, we design the relation modeling of artificial fish learning and memory. In its environment, artificial fish processes the perception information: after it has received information through audial sensor, visual sensor, tactual sensor, olfactory sensor, etc., it will compare the information with the past experience knowledge. If it is

similar to the past experience, it can solve problems by using existing experience knowledge; if it is new information, it will take advantage of social learning process, receive useful solutions, change it into

knowledge and store it in the memory, which will become the experience knowledge in the brain of fish.

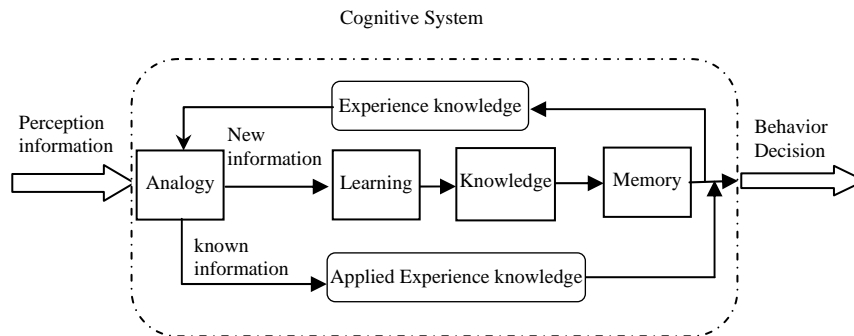


Figure 2: Relation modeling of artificial fish learning and memory

4. Learning cognitive modeling of artificial fish

Documented cases of social learning in fish are now commonplace. there are evidence show that social learning plays a role in fish : antipredator behavior; migration and orientation; foraging; mate choice. In these processes, young and inexperienced individuals

often learn from others' behavior and acquire proper responses or abstract these responses. Then they can make correct responses and the response speed is becoming faster and faster. According to the fish situation, we put forward the cognitive modeling of artificial fish learning by using a reinforcement learning algorithm based on BP neural network. as shown in Figure 3 .

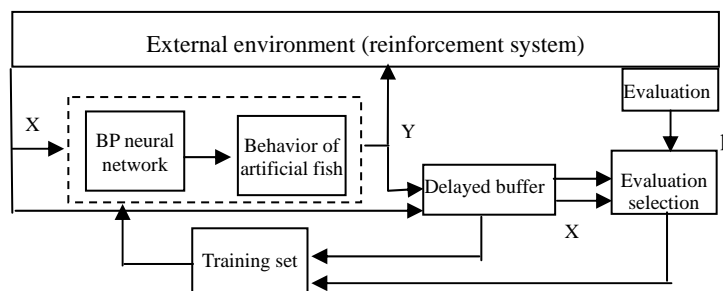


Figure 3: Learning modeling of artificial fish

BP Neural Network[11]: system input (status) X, output Y.;

Evaluation: Based on the output Y, the environment generates the evaluation signal p;

Delayed buffer: Due to the delay of evaluation during reinforcement learning, so delay np steps to synchronize Y ,X and evaluation.

When training cases reach certain number, training set is putted in network learning . the rule of producing training set is " better than average".

System put evaluation to neural network for adjusting weight by delay.

The input and output of traditional BP neural network are produced by increment. The knowledge that studied ago is forgotten. But reinforcement learning based on neural network may make function mapping to input according to ancient experiment knowledge by improving traditional BP.

Artificial fish acquires useful experience knowledge through the rewarding and punishing mechanism of

environment and cultivates good behavior control ability through behavior system. There are two possible results of artificial fish behavior: 1.satisfactory effect; 2. dissatisfactory effect. If it is satisfactory, the process of solving problems is the process of reinforcement learning. If it is dissatisfactory, it will change and update the existing experience knowledge by adjusting the solution according to the environment.

5. Conclusion

This paper takes artificial fish as the research topic. According to the ecology principles of fish in the nature and the features of fish learning and memory, we build the architecture of artificial fish and propose the learning and cognitive model of artificial fish. As the social learning of fish is a gradual learning process, which is the result of long-term interactions with the environment and is also the learning in the environment, we propose reinforcement learning based on BP network to enable

artificial fish to perform learning during the interaction with environments. These models enrich the original cognitive model of artificial fish, and let it with more features of natural beings.

References

- [1].X.Tu, D.Terzopoulos, Artificial Fishes: Physics, Locomotion, Perception and Behavior, Proceedings of SIGGRAPH 94, 1994, pp.24-29
- [2].Radek Grzeszczuk, Demetri Terzopoulos, Automated Learning of Muscle-Actuated Locomotion Through Control Abstraction, (1995), 63-70
- [3].Demetri Terzopoulos, Tamer Rabie, Radek Grzeszczuk, Perception and Learning in Artificial Animals, Artificial Life V: Proc. Fifth Inter. Conf. on the Synthesis and Simulation of Living Systems, Nara, Japan, May, (1996)
- [4].J.Funge. AI for Games and Animation: A Cognitive modeling approach. U.S.A : A K Peters, Ltd. Massachusetts, 1999.
- [5] Shettleworth, S.J. Animal cognition and animal behaviour. *Animal Behaviour* 61, 2001, pp.277-286.
- [6].Culum Brown and Kevin N Laland, Social learning in fishes: a review. *fish and fisheries*. 4(3) , 2003, pp.280-295
- [7]. Heyes, C.M. and Galef, B.G. Social learning in animals: the Roots of Culture. Academic Press, London, 1996.
- [8] Lefebvre,L.and Palameta, B. Mechanisms, ecology and population diffusion of socially-learned, food-finding behavior in feral pigeons. In: *Social Learning* (eds Zentall T.R. and B.G. Galef Jr) Erlbaum, Hillsdale, NJ, (1988),. 141-164.
- [9]Iain D.Couzin, Jens Krause, Richard James, etc, Collective Memory and Spatial Sorting in Animal Groups, *Journal of Theoretical Biology*, (2002), 218:1-11
- [10] Ransom Winder, James A.Reggia, Using Distributed Partial Memories to Improve Self-Organizing Collective Movements, *IEEE Transactions on Systems, Man and Cybernetics-part B: Cybernetics*, 34 (4) ,(2004),1697-1706
- [11]. Xin lu,Yang gao, Research on a reinforcement learning algorithm based on neural network. *Journal ofcomputer research and development*. 39(8), 2002,pp 981-985.

Design of robotic behavior that imitates animal consciousness

Naoki Goto

Graduate School of Computer Science
and System Engineering
Kyushu Institute of Technology
680-4, Iizuka City, Fukuoka, Japan, 820-8502
naoki@imcs.mse.kyutech.ac.jp

Eiji Hayashi

Department of Mechanical Information
Science and Technology
Kyushu Institute of Technology
680-4, Iizuka City, Fukuoka, Japan, 820-8502
haya@mse.kyutech.ac.jp

Abstract

A six degrees of freedom serial hand is designed to move toward an object in an unseen environment. A consciousness-based architecture (CBA) we developed, i.e., a hierarchical human development model showing the relationship between consciousness and behavior, is used to imitate a human groping action. As it moves toward the target, the robot collects information which allows the robot to avoid obstacles. CBA organizes such information in order to determine a path for retracing its motion to the origin without contacting the obstacles it previously avoided. Experimental results show that CBA successfully enables the hand to reach its goal while avoiding obstacles.

Key words: CBA, Learning, Reflection, Hierarchical Structure.

1 Introduction

Recently, robots other than industrial robots (such as home robots, personal robots, medical robots, and amusement robots) have seen active development. Further development of these robots requires improvement of both their intellectual capabilities and manual skills as well as further increases in user compatibility. Up to now, these areas constituted problematic issues in regard to the robot's use by robots other than industrial robot. User compatibility in this case entails ease of use, no fatiguing control, robot "friendliness" (i.e., sympathetic use), and human-like capricious behavior. Endowing the robot with "consciousness" of the kind identified in humans and animals is a part of these requirements.

In our laboratory we have studied an animal's adjustment to its environment in an attempt to emulate its behavior. We constructed a hierarchic structure model to which consciousness and behavior were hierarchically related. This model is based on the mechanistic

expression model of animal consciousness and behavior advocated by the Vietnamese philosopher Tran Duc Thao^[1].

In regard to this, we have developed a software architecture we call Consciousness-based Architecture (CBA). CBA introduces an evaluation function for behavior selection, and controls the robot's behavior.

In the present study, we developed a robotic arm that has six degrees of freedom, with the aim of providing the robot the ability to autonomously adjust to a target position. The robotic arm that we use has a hand consisting of three fingers in which a small monocular CCD camera is installed. The landmark object is detected in the image acquired by the CCD camera, enabling it to perform holding and carrying tasks. An experiment was conducted in a work space in which were arranged two cylindrical obstacles. The robotic arm attempted to eventually reach the landmark object while evading these obstacles.

When a person attempts to grasp an object in a box whose internal structure is unknown, he gropes with his hand in the box. In the present study, this groping action is performed by the robotic arm by means of CBA. Holding and carrying tasks, such as approaching a target position, avoiding obstacles, and detouring around obstacles, are performed autonomously.

In this paper, a robot's autonomous behavior in relation to a target position is achieved by using CBA. It is shown experimentally that the robotic arm can trace an optimal return route by studying the route to the target position. These results verify the utility of CBA.

2 System structure

Figure 2-1 shows an overview of robotic arm used by this experimental test. Figure 2-2 shows a schematic view of the robotic arm's degree of freedom. Figure 2-3 shows a diagram of the experimental system's configuration. The robotic arm manufactured by Kihara Iron Works is 450 millimeters long and has 6 degree of

freedom. The robotic hand part of robotic arm has 3 fingers and 1 degree of freedom. Additionally, there is a small CCD camera (MTV-54K0N[]) in the robotic hand.

We applied a Dynamixel DX-117 manufactured by ROBOTIS CO., LTD. as an actuator in each joint of robotic arm. The DX-117 contains a motor, decelerator, and an angular sensor in a single unit. This actuator can perform position control by providing the robotic arm with a target angle while limiting its torque and speed, and so on. The actuator uses an RS485 transmission method. Hand wiring can be simplified by connecting each actuator used as a joint of the robotic arm in the form of a daisy chain.

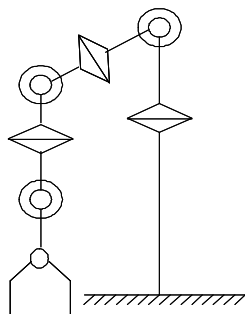


Fig. 2-1 Overview of robotic arm Fig. 2-2 Arrangement chart of degree of freedom

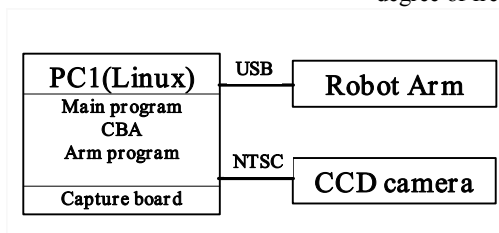


Fig. 2-3 System structure of the robotic arm

3 Autonomous behavior

3.1 The learning control system of the robotic arm

Figure 3-1 shows the experimental environment consisting of a robotic arm, the target object, and two circular cylinders as obstacles. In this figure, consciousness architecture was applied in regard to the space between the robotic arm in the default position (state S) and the target position (state G).

In the first trial, the robotic arm approaches its destination from state S (Approach). If the robotic arm comes in contact with an obstacle, it approaches again (Avoid• Detour) to state G by rotating each joint accordingly. After that, the consciousness architecture considers the return route based on conventional

information, allowing the robotic arm to return to the default position (state S) without contacting another object.

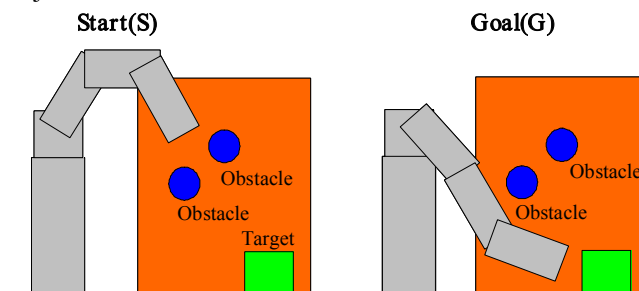


Fig. 3-1 Schematic diagram of experimental environment

3.2 Consciousness architecture (CBA)

Figure 3-1 shows a diagram of the hierarchical structure model called CBA (Consciousness-based Architecture) that relates consciousness to behavior hierarchically. In this model, the consciousness field and the behavior field are built separately. In a dynamic environment, the robotic arm determines the most appropriate consciousness level in relation to this environment and selects an action corresponding to its awareness of its environment and then performs the action. This model is able to advance to an upper level of consciousness and act accordingly when an earlier action was discouraged by some factor in the external environment.

Additionally, upper-level consciousness can choose to perform lower-level actions. The mechanism of this model is that it selects most comfortable behavior in the low-level behaviors at pleasure, so the robot aims for goals.

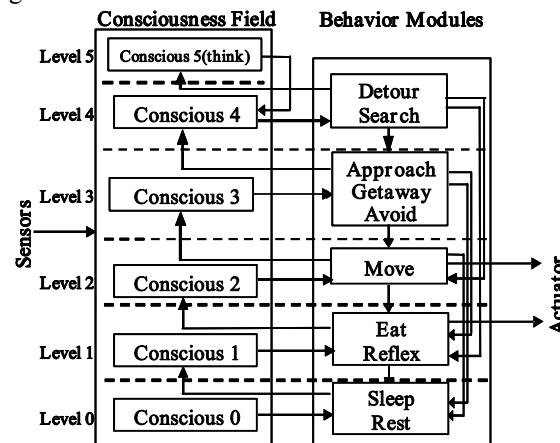


Fig. 3-2 Consciousness-based Architecture (CBA)

3.3 Evaluation function

The following are evaluation functions to select the

behavior in CBA in order to imitate human groping action.

$$C_i(t) = \sum_{j=1}^2 |\beta_{ij}(t)| + \sum_{j=1}^2 |\zeta_{ij}(t)| \quad (i = 0 \dots p) \quad (3-3-1)$$

$$I_i(t) = \sum_{j=1}^2 \beta_{ij}(t) + \sum_{j=1}^2 \zeta_{ij}(t) \quad (3-3-2)$$

In eq.(3-3-1), $C_i(t)$ is an evaluation function for determining the robot's consciousness level, $\beta_{ij}(t)$ is degree of perception of an external object, and $\zeta_{ij}(t)$ is the expected value necessary for the robot to perceive an external object. The variables are normalized within ± 1 . If the robot is in a positive state and "feels good," they are positive values, and if robot is in a negative state or "feels uncomfortable," they are negative values.

First, $C_i(t)$ of each level was calculated and the level that the robot is most aware of is determined as the robot's actual level of consciousness. Next, each $I_i(t)$ of each behavior in the level for determining the robot's behavior is calculated, and the largest $I_i(t)$ value or a behavior that makes robot most comfortable is selected as the robot's behavior, as expressed in eq.(3-3-2). Thus the robot's autonomous behavior is realized.

3.4 Autonomous behavior

A geometric model of the robotic arm was constructed and experiments were performed regarding autonomous detour and shuttle movements. Figure 3-4-1 shows the experimental environment. Two cylindrically shaped obstacles are placed between the default position and the target position. In the experiment, the robotic arm is not given information regarding the target position and the obstacle's positions.

When robotic arm arrives at the target position, the default position becomes a renewed target position. It is intended that the robotic arm follow the optimal return route without contacting the obstacles during its return movement.

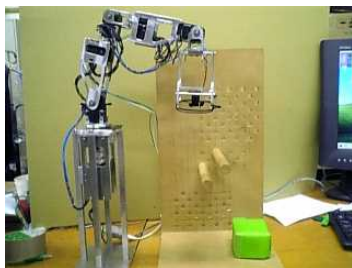


Fig. 3-4-1 Experimental environment

Figure 3-4-2 shows an experimental result. Figure 3-4-2 shows the movement of the robot's consciousness level during the arm's approach and return. First, the consciousness level becomes level-2 and the robotic arm

selects the behavior of "move" and goes straight to the target object if the CCD camera in the robot hand locates the target object. At T1, the robotic arm senses obstacles when it comes into contact with them. The consciousness level moves to level-4 and the robotic arm selects the behavior of "detour" and discourages its previous movement. The robotic arm then performs a "detour" action, and when the robotic arm considers that it has finished detouring the obstacle, it memorizes its position as a sub-goal and again selects the "move" action of level-2 (T2). When the robotic arm reaches the target position by repeating "move", "approach", and "detour" (T3, T4), the robotic arm stops (T5). In the approach route, the robotic arm contacted the obstacles twice. However, it could return to its default position without contacting obstacles by running through the sub-goals (T7).

As the robotic arm reaches its default position, its sense of safety increases little by little. It selects the behavior of "rest" of level-0, and ceases its action.

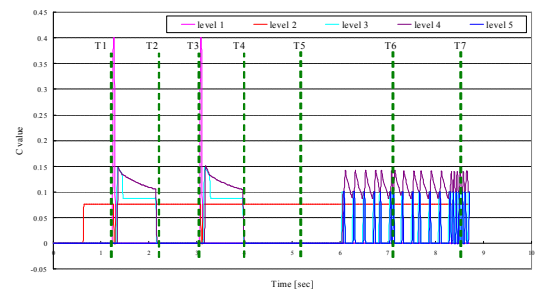


Fig. 3-4-2 Temporal data of C value at autonomous behavior

4 Model correlating between mind and body

4.1 Development of correlative model between mind and body

We developed a correlative model between the mind and body. This model integrates "cognition," "consciousness," "behavior," and "circulatory physiology." CBA is used as a function of "cognition," "consciousness," and "behavior." A model of circulatory physiology that integrates a model in which the human circulatory system is integrated called "HUMAN", and a model of the heart beat, "Beat by Beat", is used as function of "circulatory physiology." This model can calculate stressors and the degree of stress and can simulate stress response, tiredness, and changes in hormone level during exercise^[2] (Fig.4-1).

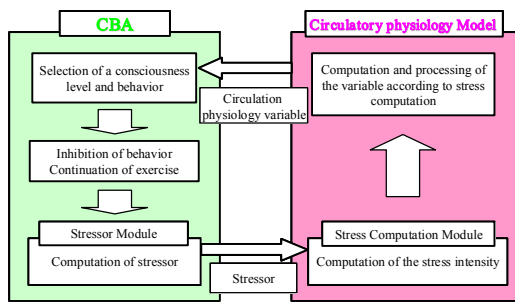


Fig. 4-1 Bilaterally linking the two models of CBA and circulatory physiology

4.2 Method of simulation

An artificial animal was given an exercise stress test by exercising it at an intensity of 88% for 15 minutes. Changes in neurotransmitters and blood lactate and hormone levels were compared to real data.

4.3 Experimental results

Figure 4-3-1 shows the simulation results and those from a human experiment regarding noradrenaline in the blood^[3]. Figure 4-3-2 shows the results regarding blood lactate. The graph shows that noradrenaline in the blood and blood lactate influence the artificial animal's condition regarding tiredness and flush.

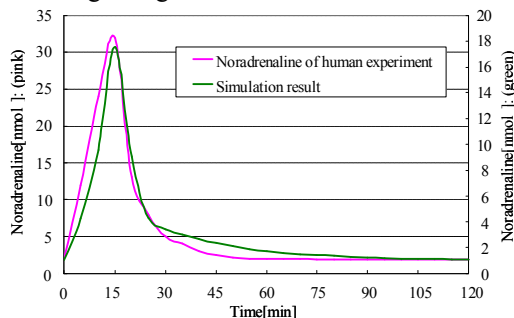


Fig. 4-3-1 Simulation result of noradrenaline by exercise stress

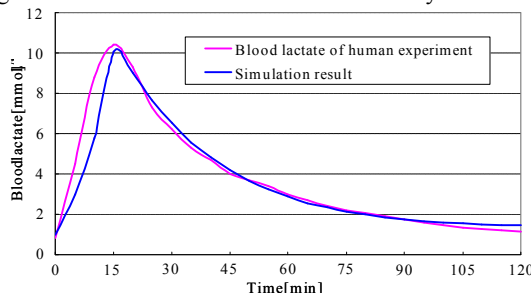


Fig. 4-3-2 Simulation result of blood lactate by exercise stress

5 Conclusion

In this paper, consciousness architecture (CBA) was applied as a control algorithm for the autonomous behavior of a robotic arm. Experiments were conducted in which a robotic arm reached for a target position in an unknown environment by imitating human groping

action. The robotic arm established sub-goals in determining an approach route and used these sub-goals in returning to its default position without contacting obstacles.

We integrated models of CBA and circulatory physiology and imposed exercise stress on the model". We estimated an artificial animal's stress and found that the simulation result were similar to those obtained in a human experiment. In a future study, we will load the integrated models of CBA and circulatory physiology into the robotic arm and evaluate the robotic arm's behavior.

6 Acknowledgements

The authors would like to acknowledge the advice and assistance of the late Prof. Tadashi Kitamura of Kyushu Institute of Technology and pray for the repose of his soul.

References

- [1] Tran Duc Thao, "Phenomenology and Dialectical Materialism", Godo-shuppan CO., LTD. 1989.
- [2] Kitamura T. et al, "Development of Correlative Model between Mind and Body(2nd report)" ROBOMECH04 in Nagoya CD-ROM. 2A1-H-49.
- [3] Marliss, Errol B., and Stuart H. Kreisman, et al, "Gender differences in glucoregulatory responses to intense exercise." J. Appl. Physiol. 88: 457-466, 2000.

Design and Implementation of a User Friendly JAVA based GUI Software for Manoeuvring Mobile Robot

T.C. Manjunath

Research Scholar (doing Ph.D), IEEE / SPIE / IOP Student Member, ISOI / SSI / ISTE Life Member,
Interdisciplinary Programme in Systems and Control Engineering, 101 B, ACRE Building,
Indian Institute of Technology Bombay, Powai, Mumbai-400076, Maharashtra, India.
Email : tcmanju@sc.iitb.ac.in tcmanjunath@rediffmail.com ; Web : <http://www.sc.iitb.ac.in/~tcmanju>
Phone : +91 22 25764884 ; FAX : +91 22 25720057

Abstract

The main objective of this work is to develop a user friendly GUI developed in JAVA language for manoeuvring a mobile robot named 'OCTAGON' with algorithms for obstacle avoidance in its path of motion. A user-friendly module is designed and successfully implemented for the operation of the entire system to do some specific operations. OCTAGON employs a sophisticated application - controlling interface created in JAVA, as it is a fantastic programming language for any application software development.

The software module application facilitates the user interaction with OCTAGON and has many in built features such as the security and authentication. When the java code is executed, the default GUI screen appears as shown in the Fig. 2 and all the motors status is displayed. For activating a particular motion, we can navigate to its page by selected the left hand menu. The software is designed for maximum robot control & working efficiency. It is so designed such that the user can have complete control over each movable part of the robot.

Also, the user can easily maneuver the robot & make it traverse a path towards the object to be picked. He or she can then manipulate the different limbs of the robotic arm so that the gripper comes closer to the object & eventually picks it up. Throughout this process the software interface guides the user through the usage of various parts of the robot & provides him with responses from the robot. Given the time on hand, the ease of programming and power of JAVA, it was an ideal choice for use in designing our application interface to the octagon.

The software is designed for maximum robot control & working efficiency. It is so designed that the user can have complete control over each movable part of the robot. Also the user can easily maneuver the robot & make it traverse in a path towards the object to be picked. He/she can then manipulate the different limbs of the robotic arm so that the gripper comes closer to the object & eventually picks it up. Throughout this process, the software interface guides the user through the usage of various parts of the robot & provides him with responses from the robot.

1. Introduction

Imagine a day in your life when you wake up in the morning and find a machine walking up to you and saying "GOOD MORNING SIR ! Have a cup of tea". How would you respond to such a situation ? With so much progress made in the filed of science, engineering and technology, this dream is absolutely realizable in the automation age. Keeping in pace with the current technology, we have designed and fabricated a mobile robot named OCTAGON as shown in Fig. 1, which is basically a moveable mobile trolley on which the articulated robotic manipulator arm is mounted to perform Pick aNd Place (PNP) operations [1].

These operations are defined by the program typed in by the user using a user friendly language specifically developed for this robot in JAVA. In this paper, we concentrate only on the software design for controlling and maneuvering the octagon. The design and fabrication was presented in the previous conference of AROB-2006. This work was taken up as a research project work by the post-graduate students of VJTI under the guidance of the author from IIT. The paper is organized as follows. First, a introduction to the designed robot is given. This is followed by the software design, control algorithms and the conclusions [2].



Fig. 1 The designed OCTAGON

2. Software Design

OCTAGON system employs a sophisticated application controlling interface created in JAVA as it is a fantastic programming language for any application software development. The developed software module for controlling the robot is shown in Fig. 5. The software module application facilitates the user interaction with OCTAGON and has many in built features [8]. The software is designed for maximum robot control & working efficiency. It is so designed that the user can have complete control over each movable part of the robot. Also the user can easily maneuver the robot & make it traverse a path towards the object to be picked [3]. He can then manipulate the different limbs of the robotic arm so that the gripper comes closer to the object & eventually picks it up. Throughout this process, the software interface guides the user through the usage of various parts of the robot & provides him with responses from it.

The features of the developed software for the robot are as follows :

- Start up screen for the software application.
- Features a complete HELP file, which can be invoked from the menu provided.
- Has a menu, which enables the user to select different options.
- Simple yet powerful interface.
- Cut - copy - paste instruction function.
- Facility to save current program.
- Facility to save current program with a different name.
- Insert function.
- Minimization of typing.
- Editing of program is possible by use of up / down buttons.
- Manual control of each motor
- Fine positioning of the base, rack, elbow and roll.
- Facility to rotate the motors clockwise and counter clockwise
- Automatic RESET function to bring the robot to the reset/home position on startup.
- Dynamic reset function to allow the user to bring the robot to the reset position at any instant.
- Auto Teach facility.

Software for octagon manoeuvring : OCTAGON has the following additional features, viz., REAL TIME MANUAL MODE CONTROL, REAL TIME RUN MODE CONTROL, PROGRAMMING INTERFACE, FACILITY TO LOOP OPERATIONS, ACCURATE POSITIONING, PARALLEL PORT INTERFACE & CONTROL, INTELLIGENT PATH DECISION MAKING. The screens used in the application are a default screen, which combines all the features of the PROGRAMMING MODE, MANUAL MODE, RUN MODE and the GRAPHICAL MODE [4].

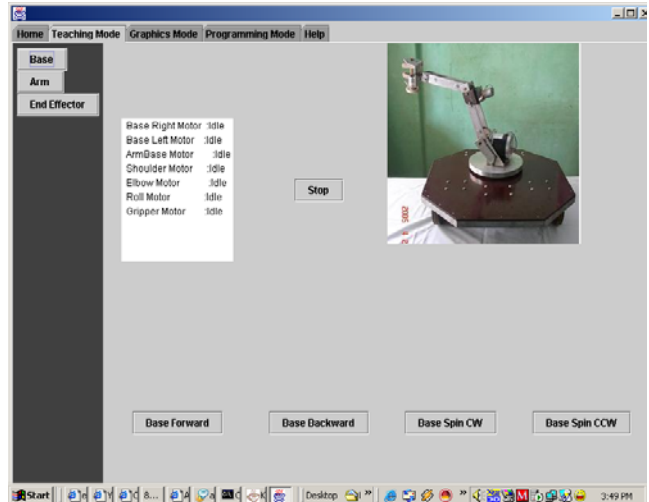


Fig. 2 General Graphical User Interface (GUI) for the robot control via JAVA environment

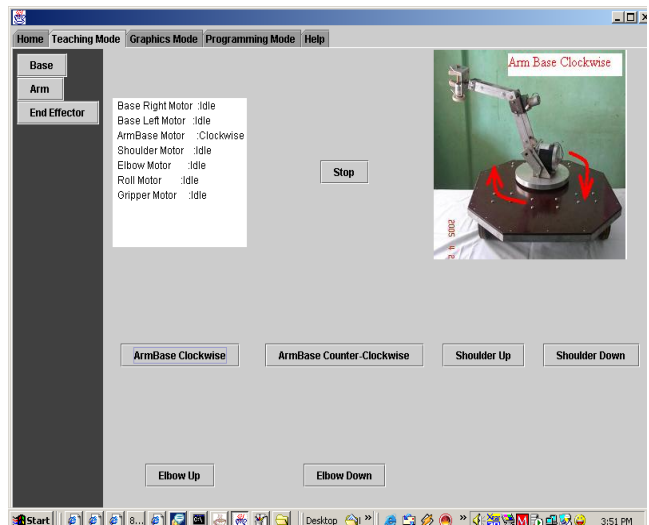


Fig. 3 GUI showing the arm base motor in operation

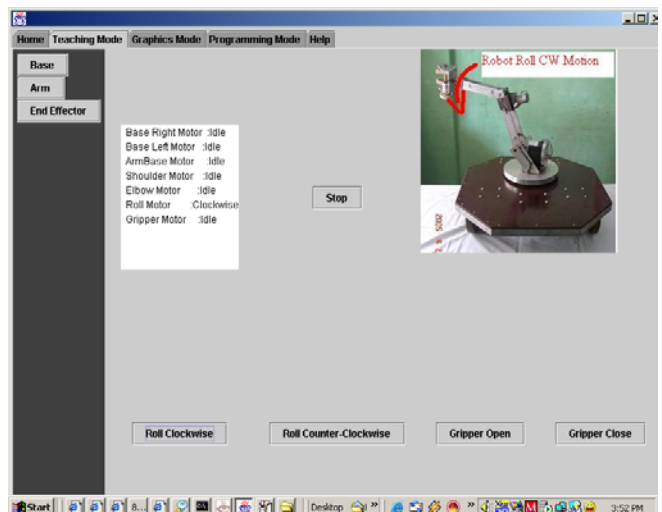


Fig. 4 GUI showing the roll motor in operation

When the java code is executed, the default GUI screen appears as shown in the Fig. 2 is displayed showing all the motors status. For activating a particular motion, we can navigate to its page by selected the left hand menu. The flow chart for the java code is shown below in Fig. 5.

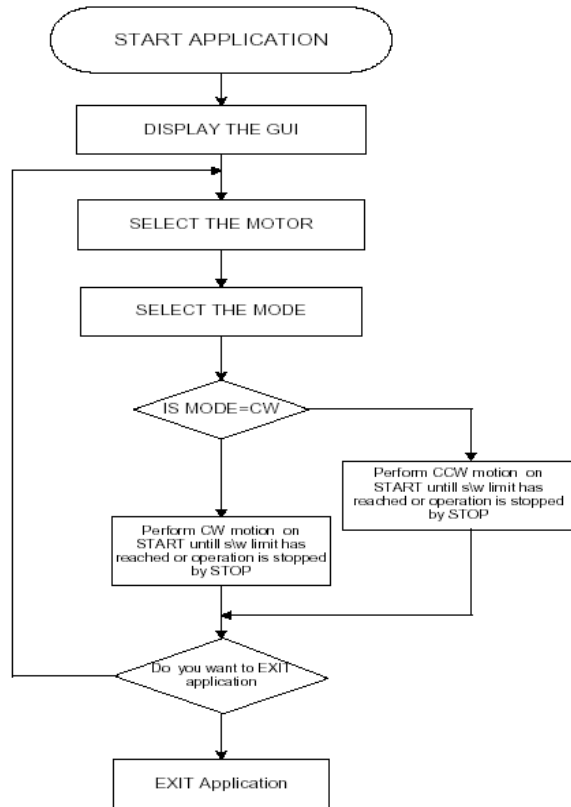


Fig. 5 Flow chart module of software module

3. Description about the GUI

The graphical user interface has check-boxes which are discussed in details as follows.

MOTOR SELECTION LIST BOX :

The screen features a listbox, where the user selects the desired motor. The user selects the motor by double-clicking on the motor name in the list box.

MOTOR SELECTED TEXT BOX :

The selected motor is then highlighted and displayed in the motor selected textbox.

DIRECTION OPTION BUTTONS :

The clockwise option button is enabled by default. The user can change the direction of rotation prior to pressing the start button. The user is required to click on the option button for selection of the direction.

START BUTTON :

The START button, when clicked, enables rotation of the desired motor. On clicking the start button, all the remaining components on the screen except the stop button are disabled as a precautionary measure [5].

STOP BUTTON :

The STOP button, when clicked, disables rotation of the desired motor by sending byte '0' to the port. On clicking the stop button, all the components disabled by the start button are re-enabled.

STATUS SIGNALS and MESSAGES :

The status signals and messages are an indication, to the user, of the motor selected, the direction of rotation and the byte sent to the port.

RESET BUTTON :

The screen features a reset button that is coded to respond to the click event. On clicking the button the software brings the robot to the HOME position or reset position. The reset is an important function, which is used in conjunction with the auto teach facility provided in the manual mode screen since it is mandatory that any teaching process be preceded by a reset, so that all calculations made by the robot software are with respect to the reset position of the robot [6].

Mobile (8 motions)	Arm (10 motions)
Forward	Arm base clockwise
Backward	Arm base anticlockwise
Forward Left	Arm shoulder up
Forward Right	Arm shoulder down
Backward Left	Arm elbow up
Backward Right	Arm elbow down
Spin Clockwise	Arm roll clockwise
Spin Anti-clockwise	Arm roll counter-clockwise
	Arm gripper open
	Arm gripper close

Table 1 : Table to show 18 motions of OCTAGON

AUTO TEACH FACILITY :

The manual mode provides the user with an auto teach facility, in which the program calculates the time delays and the associated angles, corresponding to the sequence of manually activated motors in an operation.

4. JAVA Programming Platform

JAVA is a simple, object-oriented, network-savvy, interpreted, robust, secure, architecture neutral, portable, high-performance, multithreaded, dynamic language, which provides you with a complete set of tools to simplify rapid application development. We wanted to use a system that could be programmed easily without a lot of esoteric training and which leveraged today's standard practice. We could have used C, or object-oriented programming language C++. But, Java omits many rarely used, poorly understood, confusing features of C++ that in our experience bring more grief than benefit. These omitted features primarily consist of operator overloading multiple inheritance, and extensive automatic coercions [7].

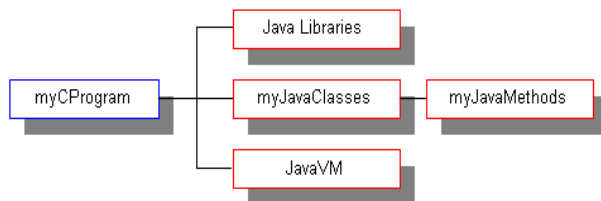


Fig. 6 Java Structure

Octagon uses JNI Technology to access parallel port using advanced JAVA. JAVA is Object-Oriented which a buzzword in industry is. Object-oriented design is very powerful because it facilitates the clean definition of interfaces and makes it possible to provide reusable “software ics”. Simply stated, object-oriented design is a technique that focuses design on the data (=objects) and on the interfaces to it. To make an analogy with carpentry, an “object-oriented” carpenter would be mostly concerned with the chair he was building, and secondarily with the tools used to make it; a “non-object-oriented” carpenter would think primarily of his tools. Object-oriented design is also the mechanism for defining how modules “plug and play”. Java has an extensive library of routines for coping easily with TCP/IP protocols like HTTP and FTP. This makes creating network connections much easier than in C or C++. Java applications can open and access objects across the net via URLs with the same ease that programmers are used to when accessing a local file system.

Java is intended for writing programs that must be reliable in a variety of ways. Java puts a lot of emphasis on

early checking for possible problems, later dynamic (runtime) checking, and eliminating situations that are error prone. One of the advantages of a strongly typed language (like C++) is that it allows extensive compile-time checking so bugs can be found early. Unfortunately, C++ inherits a number of loopholes in compile-time checking from C, which is relatively lax (particularly method/procedure declarations). In Java, we require declarations and do not support C-style implicit declarations. The linker understands the type system and repeats many of the type checks done by the compiler to guard against version mismatch problems. The Java Native Interface (JNI) is the native programming interface for Java that is part of the JDK. By writing programs using the JNI, you ensure that your code is completely portable across all platforms.

5. Conclusions

A user friendly graphical user interface in JAVA programming language was developed and the octagon was controlled in various modes such as the manual mode, teach mode, programming mode, automatic mode. A number of pick and place operations were successfully performed by the developed robot by using the above mentioned 4 types of modes.

References

- [1]. Robert, J.S. (1992), Fundamentals of Robotics : Analysis and Control, *PHI*, New Delhi.
- [2]. Klafter, Thomas and Negin (1990), Robotic Engineering *PHI*, New Delhi.
- [3]. Fu , Gonzalez and Lee (1995), Robotics : Control , Sensing , Vision and Intelligence, *McGraw Hill*, Singapore.
- [4]. Ranky, P. G., C. Y. Ho (1998), Robot Modeling, Control & Applications”, *IFS Publishers, Springer*, UK.
- [5]. T.C.Manjunath (2005), Fundamentals of Robotics, *Nandu Publishers, 4th Revised Edition*, Mumbai.
- [6]. T.C.Manjunath (2005), Fast Track To Robotics, *Nandu Publishers, 2nd Edition*, Mumbai.
- [7]. Ranky, P. G., C. Y. Ho (1999), Robot Modeling, Control & Applications, *IFS Publishers, Springer*, UK.
- [8]. Groover, Weiss, Nagel and Odrey (2000), Industrial Robotics, *McGraw Hill*, Singapore.

The Effect of Occasional Rational Decision on the Cooperative Relationship between Groups

Tetsushi Ohdaira^{†1}, Hirotada Ohashi[†]

[†]Department of Quantum Engineering and Systems Sciences,
Graduate School of Engineering, University of Tokyo,
2-11-16 Yayoi, Bunkyo-ku, Tokyo, 113-0032 Japan
Tel / Fax: +81-3-5841-6991

¹ohdaira@crimson.q.t.u-tokyo.ac.jp.

Abstract

Prisoner's Dilemma Game is one of the most common game theory treating a conflict of interest. In this research, we set a new model for simulating a conflict of interest between groups. It has mainly two features. First, the game player is not affected by the previous move of the opponent because it makes more difficult to build and keep cooperative relationship. Second, the structure of strategy takes a form of sequential array so that it can evolve through the interaction with the other. Using this model, we show the rapid collapse of cooperative relationship induced by only a few times of rational decision.

Keywords: Social Simulation, Conflict of Interest, Decision Making Problem, Evolutionary Game Theory, Prisoner's Dilemma Game.

1 Introduction

Prisoner's Dilemma Game (PDG) and its repeated form, Iterated Prisoner's Dilemma Game (IPDG) are very popular and often used for modeling a conflict of interest between nations, companies, animals, human beings and so on.

An eminent work of IPDG is the Robert Axelrod's tournament which was held twice about 20 years ago [1]. In the study, he found the toughness of Tit-for-Tat (TFT) strategy and the factor for the development of mutual cooperation.

In the study of PDG, there are two important topics. First, what a method is effective for the

emergence of cooperation. Second, if you observe a cooperative relationship, how stable it is. These topics have been discussed for a long period, but they're still inconclusive.

This research is like common one-to-one IPDG, but our model does not have any memory in a strategy of agent and includes a method of updating strategy with an evolutionary computation. We offer the model as a new candidate to deal with the matter about a conflict of interest between groups. The main purposes of this research are summarized below.

- Creating a new PDG model with an evolutionary strategy update mechanism.
- Proposing irrational decision as a new element essential for cooperation.
- Demonstrating that only a few rational decisions seriously unravel favorable relationship.

2 The Model

2.1 Prisoner's Dilemma Game (PDG)

We intend to devise a model for discussing a conflict of interest between two groups and an effect of irrational decision by each group. To attain this goal, we introduced a novel structure about the strategy.

The following is a well-known PDG scenario. 1. There are two Players and they can choose their strategies (Defection or Cooperation). 2. They are separated each other, so that each of them can not know the strategy of the opponent. 3. After choosing strategies, they get their payoff according to the payoff matrix (Table1).

The strategy of Defection is the undefeated one in PDG. However, if PDG is repeated many times, defection is no longer the optimum. There is no 'unbeaten' strategy in the repeated PDG, which is called Iterated Prisoner's Dilemma Game (IPDG). The effectiveness of strategy depends on the strategy of the opponent.

As noted before, the remarkable work of IPDG is the Robert Axelrod's contest with computer simulation. From the result, he picked up the important points for cooperation as follows [1,2]: 1. Player needs to remember the previous strategy of the opponent (Memory). 2. Player must give profit each other, that is, they have to take the same action as the past move of the opponent (Reciprocity).

Table 1: Prisoner's Dilemma Game Payoff Matrix

	Player B		
		Defection	Cooperation
Player A			
	Defection	(P: 1, P: 1)	(T: 5, S: 0)
	Cooperation	(S: 0, T: 5)	(R: 3, R: 3)

Every capital bold alphabet means:
T - Temptation to defect,
R - Reward for mutual cooperation,
P - Punishment,
S - Sucker's payoff.
 In Prisoner's Dilemma Game,
 The condition $T > R > P > S$ is necessary,
 and about Iterated Prisoner's Dilemma Game,
 additional condition $2R > T + S$ should be satisfied.
 This payoff matrix meets both conditions.

2.2 Sequential PDG

In this research, we investigate a conflict of interest between two groups using the idea of PDG. Our goal is not searching the prevailing strategy. We intended to reveal the dynamics between groups through the interaction. To achieve this purpose, a new scenario is devised for simulation, that is, there is no fixation of strategy and strategy itself evolves based on the decision of each group. We name this advanced PDG as "Sequential PDG". The main features are listed below.

- There are two different groups which have eight agents respectively.
- Agents of each group have an ID (from no.1 to 8) and one strategy.
- The strategy regulates the behavior of the agent in each round of PDG. Therefore agents

can not change its move during Sequential PDG.

- Every strategy of agents (that will be simply noted as strategy) is a sequential array whose length is 30 characters as mathematical expression (1) convenient for the evolutionary process (described later). Each character represents a strategy of one round (D: Defection, C: Cooperation).
- Every agent plays Sequential PDG using their strategy against the opponent of identical ID belonging to the other group.

$$S_{g-u}(u) = \{ \alpha_{g-u}^n(u) \mid \alpha_{g-u}(u) \in \{D, C\}, 1 \leq u \leq 8, n = 30 \} \quad (1)$$

D or C means the component vector, it is expressed as (0, 1) or (1, 0). The former represents that the selection at one round is defection, the latter means the agent chooses cooperation.

The payoff of each agent in the group at the generation g is numerically expressed in this way (2). If we focus the group i whose opponent group has the ID j , the agent u in the group i get its payoff $P_i^g(u)$ respectively. A denotes the payoff matrix, and α_i^k and α_j^k means the element of strategy (1).

$$A = \begin{pmatrix} 3 & 0 \\ 5 & 1 \end{pmatrix}$$

$$P_i^g(u) = \sum_k \alpha_i^k(u) A \alpha_j^k(u)^T \quad (1 \leq k \leq 30) \quad (2)$$

After the all agents experienced Sequential PDG, the decision of each group will be made separately. "Decision" in this case is to select the representative strategy of the group. In this process, every strategy will be updated as the following way.

1. The strategies of the group are graded according to its score (ranking).
2. One strategy in the group is selected according to the irrational decision (noted below) and becomes the representative strategy. This strategy is chosen "by the group" (not by the agents).
3. Two parts of the representative strategy is copied to the same position of the other 7 strategies in turn. The length of fraction randomly changes from 1 to 15 in every copying process.
4. After finishing above, each character of created new strategies is reversed according to the probability (1/1000).

Above steps are executed independently in both groups. Representative strategy itself does not

change except the mutation (Step 4). This mechanism of selecting representative and updating strategy is named as the "evolutionary process". Through the process, every strategy is updated and ready for the following match. Above procedure, that is, Sequential PDG between groups and the following evolutionary process is defined as one generation, and to investigate fluctuation in long period, one game simulation lasts until generation reaches to 5,000. All results described later are the average of 30 times simulation.

2.3 Introducing Irrational Decision

In the context of PDG, it is usually thought that cooperative relationship would not develop if there were no additional elements. The supplement often mentioned before is the "Tag" [3, 4, 5] or the "Spatial Structure" [6, 7, 8, 9]. The former is the way to distinguish agents by giving each of them identification. An agent can check the tag of another agent and know whether he is cooperative or not. The latter is introduced to define neighborhood connection around agents. In the condition, agents interact only with those who are

directly connected.

In this research, as a new candidate to generate cooperative relationship, we introduce the "Irrationality" that means 'irrational decision of the group (that will be abbreviated as irrational decision)'. The reason why we propose this is derived from the fact that above previous methods can not express altruistic behavior of human society.

In the irrational decision, the greatest score strategy in the group is not selected as representative. Therefore the representative strategy will be one of the strategies except the highest. It is selected randomly from the strategy of score grade 2 to 8 in the group (Irrational selection). The strategy with the lowest score may be chosen as representative, but this event does not occur in every evolutionary process. The selection of the lowest strategy may be regarded as human mistake in decision making.

3 Results

To tell the truth, in a one sense it could be predictable before executing simulation that unconditionally irrational decision has an effect on emergence and maintenance of mutual cooperation. If you want to keep a good (cooperative) relationship to the other, you should not be prepossessed with the temptation of recent future [1,2]. Fully irrational decision faithfully follows this rule by sacrificing payoff of the group.

Therefore, we probed the traits of this cooperative relationship by introducing

probabilistic rational decision. When every group sometimes makes rational decision, how is the cooperative relationship affected? Next we give the answer for this question.

The influence of occasional rationality is exhibited in Figure 1a and 1b. From the result you can see how the rate of rationality affects mutual cooperation. Note that the rate of rationality means the probability how rationally the decision of each group is made in every evolutionary process (generation). Therefore if the rate of rationality is 0.3, it indicates that the rational decision will be made with that probability (and also the possibility of the irrational decision should be 0.7). This probability is independent between two groups.

As shown in the result, increase of rationality accelerates the growth of mutual defection and induces the decline of mutual cooperation. However, the acuteness for the rate of rationality is different between mutual defection and cooperation. The frequency of mutual cooperation decreases more rapidly than the linear line does, whereas the growth of mutual defection is comparatively slow.

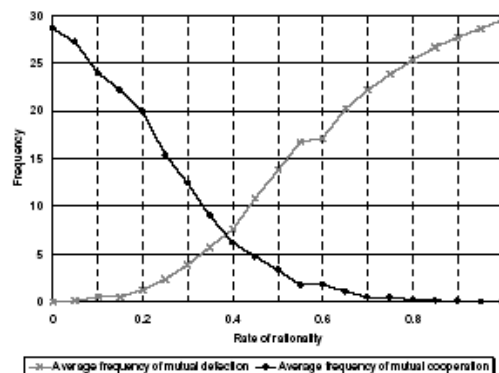


Figure 1a: Effect of rationality on average frequency of mutual defection and cooperation in last generation. The rate of rationality designates that how often the rational decision is made in every group during the simulation.

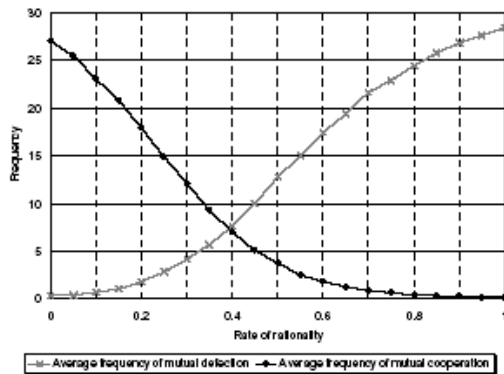


Figure 1b: Effect of rationality on average frequency of mutual defection and cooperation about all generation.

4 Conclusion

We have introduced a new model for researching a conflict of interest within two groups. The character of the model is summarized in three points: First, strategy has no memory. Second, the structure of strategy is the sequential array of fixed length. Third, through the evolutionary process, it is consistently overwritten by representative strategy. In the works of IPDG, which partly resembles Sequential PDG, strategy is often defined as a reaction for a previous move of opponent. From that point of view, someone may

criticize our work because the strategy of our model has no reactive action explicitly. However, if you know well about the study of PDG and IPDG, you can recognize it is not the rare case that agent doesn't use its remembrance (such as [6, 10] or the case of no iteration and memory is [4]). Sequential PDG is like not so much standard IPDG as one shot PDG because agents have no chance to adjust their strategies if once Sequential PDG starts between them. However, due to the length of the strategy, there are quite many various patterns of strategy (2^{30}) in comparison with PDG (only 2 patterns). That mechanism supports the operation like genetic algorithm in evolutionary process. In addition, because the elimination of memory makes it more difficult to build cooperative relationship with each other, it is quite significant that cooperative relationship emerges within that condition. That's the reason we designed Sequential PDG as noted before.

The effect of occasional rationality (Figure 1a, 1b) offers a suggestive idea that mutual cooperation is strongly influenced by a little rational behavior. If you want to maintain cooperative relationship with the other, you should not desire to get more payoffs. Only a few times of

defection will cause the serious collapse of cooperation.

This research is still at a preliminary stage and so has many ways of extension. We have already started to apply the model to the spatial game, using networks of various topologies. Some interesting properties have been obtained from this further research. It will be shown in the near future.

References

- [1] Axelrod R (1984), *The Evolution of Cooperation*. Basic Books, New York.
- [2] Maynard Smith J (1982), *Evolution and the Theory of Games*. Cambridge University Press, Cambridge.
- [3] Riolo R L (1997), The effects and evolution of tag-mediated selection of partners in populations playing the iterated prisoner's dilemma. *Proc. of the 7th Int. Conf. on Genetic Algorithms (ICGA97)*, San Francisco: Morgan Kaufmann, pp.378-385.
- [4] Hales D (2001), Tags produce cooperation in the prisoner's dilemma. *Simulating Society V workshop: "The frontiers of social science simulation"*, Kazimierz Dolny, Poland.
- [5] Riolo R L, Cohen M D C, Axelrod R (2001), Evolution of cooperation without reciprocity. *Nature* 414, pp.441-443.
- [6] Nowak M A, May R M (1992), Evolutionary games and spatial chaos. *Nature* 359, pp.826-829.
- [7] Cao Z, Hwa R C (1999), Phase transition in evolutionary games. *Int. Jour. of Mod. Phys. A* 14, pp.1551-1560.
- [8] Ahmed E, Hegazi A S, Elgazzar A S (2002), On spatial asymmetric games. *Advances in Complex Systems* 5, pp.433-443.
- [9] Kim B J et al. (2002), Dynamic instabilities induced by asymmetric influence: prisoner's dilemma game on small-world networks. *Phys. Rev. E* 66, 021907.
- [10] Fort H (2003), Cooperation with random interaction and without memory or "tags". *Jour. of Art. Societies and Social Simulation* 6, <http://jasss.soc.surrey.ac.uk/6/2/4.html>.

Intelligent Motor Control Using Advanced Bacterial Foraging Combined With Immune Algorithm

Dong Hwa Kim*, Jae Hoon Cho*, Yong Dal Kim**

*Dept. of Instrumentation and Control Eng., Hanbat National University,

**Dept. of Electrical Eng., Hanbat National University

16-1 San Duckmyong-Dong Yuseong-Gu, Daejeon City, Korea, 305-719.

E-mail: kimdh@hanbat.ac.kr, Homepage: aialab.net

Tel: +82-42-821-1170, Fax: +82-821-1164

Abstract

This paper suggests advanced bacterial foraging strategy using membership function of fuzzy logic and clonal selection of immune system. Bacteria foraging based optimal solution is defined by the positions of each member in the population of the S bacteria at the j th chemotactic step, k th reproduction step, and l th elimination-dispersal event. Therefore, chemotactic step is important to have an optimal solution in system. Up to now, a foraging strategy uses fixed chemotactic step. This paper introduces clonal selection of immune algorithm and fuzzy logic into bacterial foraging to enhance running speed and patch of optimal condition (e.g., group of objective with conditions). This approach provides us with novel hybrid model based on foraging behavior and clonal selection for a higher running time and optimal solution.

1. introduction

In the last decade, evolutionary computation based approaches have received increased attention from the engineers dealing with problems which could not be solved using conventional problem solving techniques. Natural selection are more likely to apply reproductive success to have an optimal solution. Since a foraging animal takes actions to maximize the energy obtained per unit time spent foraging, in the face of constraints presented by its own physiology such as, sensing and cognitive capabilities and environment. Evolution can provide optimization within these constraints and essentially apply to engineering field by what is sometimes referring to as an optimal foraging policy. That is, optimization models can provide for social foraging where groups of parameters communicate to cooperatively forage in engineering. This paper provides a brief literature overview of the area of bacterial foraging as it forms the biological foundation for this paper. Then, this paper also focuses on dealing with an enhanced optimal solution using a hybrid approach consisting of BF (Bacterial Foraging), and CL (Clonal Selection) and fuzzy logic. Finally, we focus on evidence for the proposed hybrid system for indirect vector control of induction motor.

2. Hybrid Optimization Based on Bacteria Foraging and Clonal Selection

Equation represents the positions of each member in the population of the N bacteria at the j th chemotactic step, k th reproduction step, and l th elimination-dispersal event. Let $P(i, j, k, l)$ denote the cost at the location of the i th bacterium $\phi^i(j, k, l) \in R^n$, and

$$\phi^i(j+1, k, l) = \phi^i(j, k, l) + C(i)\varphi(j), \quad (1)$$

so that $C(i) > 0$ is the size of the step taken in the random direction specified by the tumble. If at $\phi^i(j+1, k, l)$ the cost $J(i, j+1, k, l)$ is better (lower) than at $\phi^i(j, k, l)$, then another chemotactic step of size $C(i)$ in this same direction will be taken and repeated up to a maximum number of steps N_s . N_s is the length of the lifetime of the bacteria measured by the number of chemotactic steps. Functions $P_c^i(\phi)$, $i=1, 2, \dots, S$, to model the cell-to-cell signaling via an attractant and a repellent is represented by

$$P_c(\phi) = \sum_{i=1}^N P_{cc}^i = \sum_{i=1}^N \left[-L_{attract} \exp\left(-\delta_{attract} \sum_{j=1}^n (\phi_j - \phi_j^i)^2\right) \right] + \sum_{i=1}^N \left[-K_{repellant} \exp\left(-\delta_{repellant} \sum_{j=1}^n (\phi_j - \phi_j^i)^2\right) \right], \quad (2)$$

where $\phi = [\phi_1, \dots, \phi_p]^T$ is a point on the optimization domain, $L_{attract}$ is the depth of the attractant released by the cell and $\delta_{attract}$ is a measure of the width of the attractant signal. $K_{repellant} = L_{attract}$ is the height of the repellent effect magnitude, and $\delta_{attract}$ is a measure of the width of the repellent.

3. Intelligent Vector Control Using Advanced Bacteria Foraging Based on Fuzzy Logic and Immune Algorithm

3.1 Vector Control System of Induction Motor

As the vector controlled induction machine is assumed to be current fed from an ideal current controlled PWM inverter, operation with constant, rated flux command would be discussed. As the indirect vector controller is the scheme composed of the appropriate decoupling circuit for each of the three orientation possibilities such as

stator, air-gap, and rotor flux oriented control, it incorporates only PI speed controller. Decoupling circuits neglect iron loss, magnetic saturation and resistance variations

and have the well-known form, representation of the induction machine, in terms of space vectors.

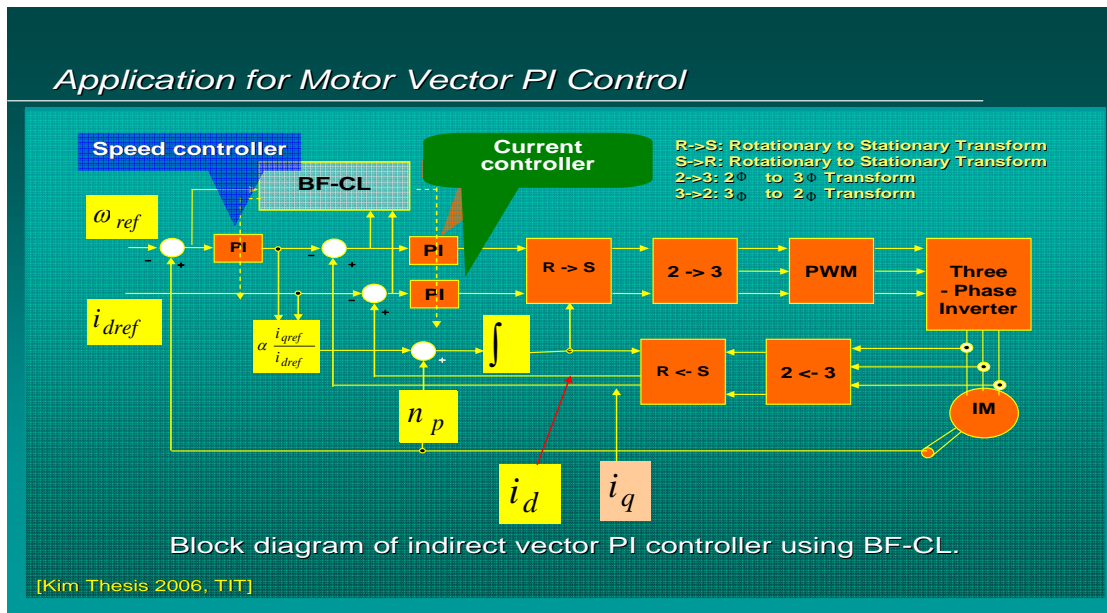


Fig. 1. Block diagram of indirect vector PI controller using advanced BF (bacterial foraging) based on fuzzy logic and clonal selection.

That is, the indirect vector control system neglects the core loss. The electrical torque in an induction machine can be expressed as:

$$T_e = \frac{3}{2} \frac{P}{2} \frac{L_m}{L_r} \lambda_{dr}^e i_{qs}^e, \quad (3)$$

where, rotor flux instantaneous speed ω_e ,

$$\lambda_r^e = \lambda_{dr}^e + j \lambda_{qr}^e = \lambda_{dr}^e, \quad \lambda_{qr}^e = 0, \quad i_{qs}^e = -\frac{L_r}{L_m} i_{qr}^e.$$

The slip equations for an induction motor in an arbitrary synchronously rotating reference frame are given by:

$$\omega_e - \omega_r = \omega_{sl} = -\frac{R_r i_{qr}^e}{\lambda_{dr}^e} = \frac{R_r}{\lambda_{dr}^e} \frac{L_m}{L_r} i_{qs}^e = \left[\left(1 + p \frac{L_r}{R_r} \right) \frac{1}{i_{ds}^e} \right] \frac{R_r}{L_r} i_{qs}^e. \quad (4)$$

where, i_{qs}^e is torque current, i_{ds}^e is flux current. When i_{ds}^e and i_{qs}^e is decided by ω_{sl} , rotor flux position θ_e is given by:

$$\theta_e = \int_0^t \omega_e d\tau = \int_0^t (\omega_r + \omega_{sl}) d\tau \quad (5)$$

In indirect vector control, stator current and slip angle ω_{sl} through θ_e is controlled, then $\lambda_{qr}^e = 0$ become [2].

3.2 BF-CL based Optimization Tuning of PI Controller for Induction Motor

This paper describes the method in the form of an algorithm to search optimal value of parameters [11-13].

[step 1] Initialize parameters $n, N, N_C, N_S, N_{re}, N_{ed}, P_{ed}, C(i)$ ($i=1,2,\dots,N$), ϕ^i , Where, n : Dimension of the search space, N : The number of bacteria in the population, N_C : chemotactic steps, N_{re} : The number of reproduction steps, N_{ed} : the number of elimination-dispersal events, P_{ed} : elimination-dispersal with probability, $C(i)$: the size of the step taken in the random direction specified by the tumble.

[step 2] Elimination-dispersal loop: $l=l+1$

[step 3] Reproduction loop: $k=k+1$

[step 4] Chemotaxis loop: $j=j+1$.

[step 5] Compute objection function and store best individuals in memory cell of clonal selection loop.

[substep a] Differentiate clone from memory cell

[substep b] Compute objective function for clonal bacteria done cross over and store in memory cell by best value order.

[step 6] Decide search direction of bacteria foraging action after objective function in memory cell and objective function of [step 5].

[step 7] If $j < N_C$, go to step 5. In this case, if chemotaxis loop and objective function are satisfied by user, stop calculation, otherwise go to [step 5] computing chemotaxis loop until the life of the bacteria is over.

Table 1. Parameter ranges for Learning of bacteria foraging.

Parameters	Value
N : The No. of BF group	100
N_c : The No. of chemotaxis loop	300
N_{re} : The No. of reproduction steps	2
N_{ed} : The number of elimination-dispersal events	5
P_{ed} : elimination-dispersal with probability	0.5
T : The No. of clones	5
T_m : Probability of crossover of clone	0.25
A_m^* : Gain margin of plant	2.5
ϕ_m^* : Phase margin of plant	45

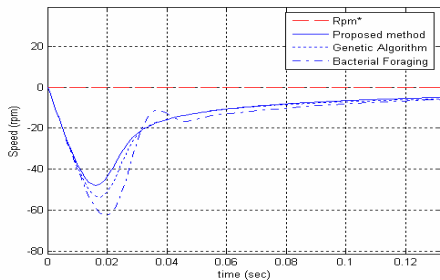


Fig. 3. Speed tracking of indirect vector PI controller (time : 0~0.13 sec).

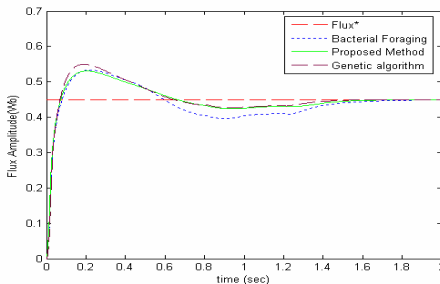


Fig. 4. Flux amplitude tracking of indirect vector PI controller.

[step 8] If $k < N_{re}$, go to [step 4]. In this case, we have not reached the number of specified reproduction steps, so we start the next generation in the chemotactic loop.

[step 9] If $l < N_{ed}$, go to [step 3]. In this case elimination-dispersal: For $i=1,2,\dots,N$, with probability P_{ed} , eliminate and disperse each bacterium, and this results in

keeps the number of bacteria in the population constant. To do this, if you eliminate a bacterium, simply disperse one to a random location on the optimization domain.

In bacterial foraging strategy, because the number of elimination-dispersal events and, for each elimination-dispersal event, each bacterium in the population is subjected to elimination-dispersal (death, then random placement of a new bacterium at a random location on the optimization domain) with probability, bacterium swim straight alternatively running at 10–20 [microsec] and tumbling. When the flagella rotate clockwise and counterclockwise, they operate as propellers and hence an E. Coli may run or tumble and search avoid unfavorable environments. The objective is simply to capture the gross characteristics of chemotactic hillclimbing and swarming for optimal solution.

Fig. 2 represents computation procedure of optimal solution based on BF-CL learning and Table 1 illustrates parameter ranges for learning of bacteria foraging. Fig. 3 shows speed tracking of indirect vector PI controller (time: 0~0.13 sec) and Fig. 4 means flux amplitude tracking of indirect vector PI controller. Fig. 5 is search process for optimal parameters of PI controller using BF-CL suggested in this paper. Table 2 represents comparison of PI parameters by each method (BF, GA, Proposed algorithm).

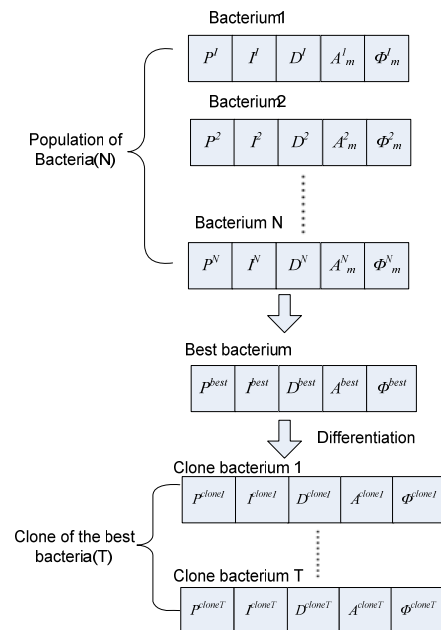


Fig. 2. Computation procedure of optimal solution based on BF-CL learning.

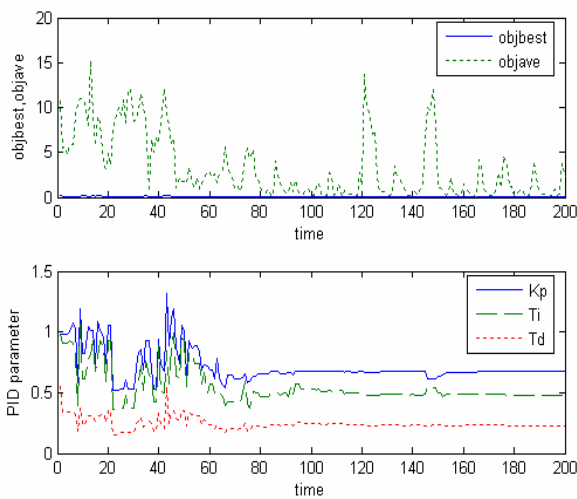


Fig. 5. Search process for optimal parameters BF-CL.

4. Conclusion

Recent many approaches of evolutionary of intelligence algorithms for the evaluation of improved learning algorithm and control engineering have been studying. The general problem of evolutionary algorithm based engineering system design has been tackled in various ways because of learning time and local or suboptimal solution. GA has also been used to optimize nonlinear system strategies but it might be local optimized. This paper suggests the advanced hybrid system consisting of BF (Bacterial foraging Algorithm) and CL (Clonal Selection) for PID controller tuning of induction motor control system. Ref [13] depicts characteristic to variation of step size when generations from 1 to 50 and from 270 to 300, respectively. From Ref [13], the bigger step size, the convergence is faster. Ref [13] are also showing relationship between objective function and the number of generations in different chemotactic steps. When the chemotactic step is smaller, the objective function has a faster convergence with a small generator. In Ref [13] is showing characteristics between objective function and generators for different life times N_s of bacteria in the hybrid system, GA-BF. In BF system, chemotactic step, total number of chemotactic reaction of bacteria, step size, basic unit for movement of bacteria N_s , the number of critical reaction S , the number of bacteria G , generations μ , mutation C_r , and crossover is very important for learning condition.

Therefore, this paper extends variable step size against environmental condition using fuzzy logic and clonal selection to illustrate characteristics. This approach proposed in this has the potential to be useful in practical optimization problems (e.g., engineering design, online distributed optimization in distributed computing and cooperative control) as models of social foraging are also distributed nongradient optimization methods. It can also may be used a wide variety of fruitful research directions and ways to improve the models (e.g., modeling more dynamics of cell motion).

Table 2. PI parameters for each method.

Method	Speed control		Current control	
	Kp	Ti	Td	Td
Bacterial Foraging	0.98	0.55	4.54	82.72
Genetic Algorithm	0.93	0.76	6.56	114.21
Proposed Algorithm	0.99	0.64	5.32	85.62

Moreover, other species of bacteria or biological based computing approach could be studied but it remains to be seen how practically useful the optimization algorithms are for engineering optimization problems, because they depend on the theoretical properties of the algorithm, theoretical and empirical comparisons to other methods, and extensive evaluation on many benchmark problems and real-world problems.

References

- [1] Chung-Liang Lin, Huai-Wen Su, "Intelligent control theory in guidance and control system design: an Overview," Proc. Natul. Sci., Counc. ROC(A), vol. 24, no. 1, pp. 15-30, 2000.
- [2] P. J. Fleming and R. C. Purshouse, "Evolutionary algorithms in control system engineering: A survey," Control Eng. Practice, vol. 10, pp. 1223-1241, 2002.
- [3] G. J. Gray, D. J. Murray-Smith, Y. Li, K. C. Sharman, and T. Weinbrenner, "Nonlinear model structure identification using genetic programming," Contr. Eng. Practice, no. 6, pp. 1341-1352, 1998.
- [4] K. Kristinnson and G. A. Dumont, "System identification and control using genetic algorithms," IEEE Trans. System, Man, Cybern., vol. 22, pp. 1033-1046, Sept.-Oct. 1992.
- [5] R. A. Krohling and J. P. Rey, "Design of optimal disturbance rejection PID controllers using genetic algorithms," IEEE Trans. Evol. Comput., vol. 5, pp. 78-82, Feb. 2001.
- [6] Zwe-Lee Gaing, "A Particle Swarm Optimization Approach for Optimum Design of PID Controller in AVR System", IEEE Trans. Energy Con. Vol. 19, pp. 384-391, No. 2, June, 2004.
- [7] STEPHENS, D. W., and KREBS, J. R., "Foraging Theory, Princeton University Press, Princeton, New Jersey, 1986.
- [8] ALCOCK, J., Animal Behavior, "An Evolutionary Approach, Sinauer Associates," Sunderland, Massachusetts, 1998.
- [9] Dong Hwa Kim, "Robust PID controller tuning using multiobjective optimization based on clonal selection of immune algorithm," Proc. Int. Conf. Knowledge-based intelligent information and engineering systems. Springer-Verlag. pp. 50-56, 2004.
- [10] Dong Hwa Kim, "Genetic Algorithm Combined with Particle Swarm Optimization/Bacterial Foraging and Its Application to PID Controller Tuning," TIT (Tokyo Institute of Technology Thesis, April, 2006.

Unmanned Navigation of Container Transporter Using U-SAT(Ultrasonic Satellite System)

Kil Soo Lee, Su Yong Kim,
Taek Young Shin
Department of Mechanical and
Intelligent Systems Engineering
Pusan National University
Busan, 609-735, KOREA

Jung Min Lee
Automation System R&D Team
SAMSUNG ELECTRONICS CO.,LTD,
416, Maetan-3Dong, Yeongtong-Gu,
Suwon-City, Gyeonggi-Do, 443-742
KOREA

Man Hyung Lee
School of Mechanical
Engineering, Pusan
National University,
Busan, 609-735, KOREA

Abstract

The positioning of vehicle is an important part of control problem. Dead Reckoning is widely used for positioning of vehicle. However this method has problems because it accumulates estimation errors. In this paper, we propose a new method to increase the accuracy of estimated position using the U-SAT(Ultrasonic Satellite system). It is shown that we will be able to estimate the position of vehicle precisely, in which errors are not accumulated. And unmanned navigation experiment of the container transporter, which is one of the part of the development for the harbor automation project, was performed in the case that container transporter moves to the desired trajectory using U-SAT. Unmanned navigation of container transporter by using U-SAT is verified by experiments.

1 Introduction

The process of finding vehicle in environment is a major concern in vehicle navigation. To measure the position of a vehicle, a variety of studies are going on and vehicle positioning has been done in two basic methods. They are not only absolute and relative positioning but also a combination of them.

The dead-reckoning method has been widely used as one of the methods of relative positioning. Dead-reckoning method uses the encoded information which gains the wheels to determine the position of the vehicle. But because of wheel slippage, mechanical tolerance and surface roughness, this method has its unbounded accumulation of errors. So the real position is hardly maintained as it moves longer distance [1].

On the other hand, absolute positioning is accomplished by using a CCD camera, infrared light, global positioning system (GPS), and ultrasonic sensor. Vision system by CCD camera requires complicated signal processing to analyze images. In addition, it is expensive and highly depends on camera calibration and image sensitivity [2]. Positioning by using infrared light is easy and inexpensive. However, this method leads to

problems such as low performance and limitations in terms of its application in an outdoor environment. The GPS can give accurate information to identify locations. By a differential GPS, the accuracy of positioning is also improved. However, this type of sensor usually provides measurements at 1-10 Hz. This sampling rate may not be sufficient if the dynamics of a positioning object changes relatively fast. Besides, it does not operate well in the place where no GPS satellite signal is available or where there are less than four visible satellites [3]. In addition, pseudo-satellites for indoor or outdoor places have been researched. Ultrasonic ranging systems, which are similar to the basic concept of GPS, have advantages such as low costs and a high update rate a disadvantage is its low accuracy which is caused by air turbulence, humidity, temperature dependence, transmitter misalignment and transmitter bandwidth [4]. In contrast to the conventional GPS, it is possible to build up cell structures in widely ramified buildings.

In the measurement of the distance using direct ultrasonic waves, the method with high precision is proposed [5]. Absolute positioning system using ultrasonic sensors based on this method is represented as U-SAT (Ultrasonic Satellites). So in order to evaluate the performance of U-SAT, it is compared with RTK-DGPS that is more accurate than any other absolute positioning system. The possibility of using U-SAT as pseudolites in the place where GPS is not available is discussed. And unmanned navigation experiment of the container transporter, which is one of the part of the development for the harbor automation project, was performed in the case that container transporter moves to the desired trajectory using U-SAT. Unmanned navigation of container transporter by using U-SAT is verified by experiments.

2 Concept of U-SAT

The measurement of the distance using the ultrasonic waves is calculated with sound velocity and the delivering time. TOF (Time of Flight) is defined as the time difference between transmitter and receiver. It is shown in Fig.1. The distance is

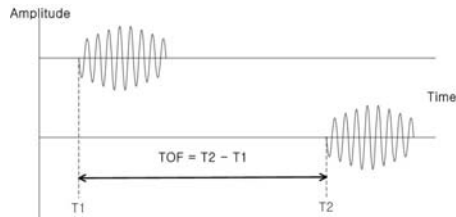


Fig.1 Definition of TOF

determined in Equation (2) and sound velocity is represented as a function of temperature.

$$TOF = T2 - T1 \quad (1)$$

$$d = c \times TOF + d_0 \quad (2)$$

$$c = 331.5 + 0.60714T \quad (3)$$

Where, d is distance and c is sound velocity in the air temperature of T .

This shows the detection accuracy of about 2mm by the ultrasonic frequency detection method [5]. And the distance between separated transmitter and receiver is calculated by direct ultrasonic waves. U-SAT is based on this method. Ultrasonic transmitters function as ultrasonic satellites and locate on the fixed places whose coordinates are known. So ultrasonic receivers receive ultrasonic waves transferred from ultrasonic satellites and the distance between ultrasonic receivers and ultrasonic satellites is calculated. The basic idea of U-SAT is similar to that of GPS. Although ultrasonic receivers exist in the ultrasonic satellites, the position of ultrasonic receiver is calculated respectively. Therefore multiple mobile robots can be used.

In Fig.2, U-SAT consists of four ultrasonic satellites. In order to calculate the distance using ultrasonic waves, the time when ultrasonic satellite radiates ultrasonic waves must be measured. U-SAT does not inform the transmission time. So transmission time is known by using RF signal. U-SAT calculates the distance by measuring the time when the ultrasonic waves is received. It is supposed that there is no time delay during receiving RF signal. In Fig.2, U-SAT transmitter (1) transfers synchronized RF signals to other U-SAT transmitters and U-SAT receiver at the period of 83ms. They receive synchronized RF signals and find when ultrasonic waves are radiated. In accordance with this period, ultrasonic satellites radiate ultrasonic waves by turns and U-SAT receiver calculates the distance by using Equation (2). Synchronized RF signals are transferred with the period of 83ms in order to avoid the interference of ultrasonic waves and the influence of the reflection of them and this period can be flexibly regulated according to the environment.

Fig.3 shows the timing diagram for ultrasonic receiver to be synchronized by RF signal. After U-SAT receiver receives ultrasonic waves which radiated ultrasonic satellites respectively, each distance d_1 , d_2 , d_3 , and d_4 between ultrasonic radiated ultrasonic satellites respectively, each distance d_1 , d_2 , d_3 , and d_4 between ultrasonic

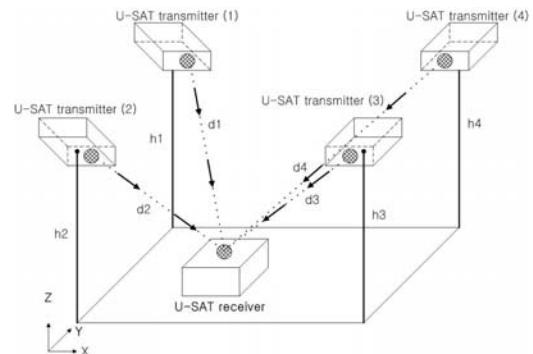


Fig.2 System description

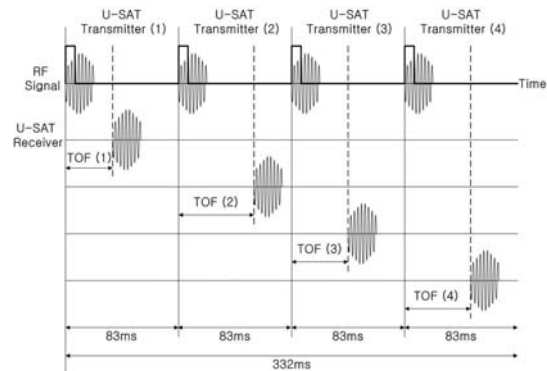


Fig.3 Timing diagram

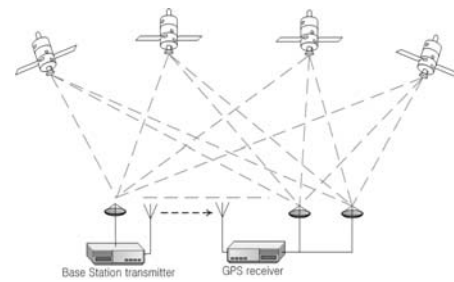


Fig.4 RTK-DGPS

waves and its satellites are calculated. The coordinate of the ultrasonic receiver can be obtained by L.M.S (Least Mean Square method). The sampling time of GPS is 1Hz while that of U-SAT is 3Hz shown in Fig.3. Since U-SAT is more flexible and faster than GPS, it can frequently acquire the position information.

3 RTK-DGPS

GPS is a space-based positioning, navigation, and timing system developed by U.S. Department of Defense (DoD). GPS receiver receives GPS signals from more than four GPS satellites and calculates its position real time. But it doesn't function well in the place where GPS satellite signal doesn't reach or visible satellites are less than four.

In order to increase the accuracy of the position error, DGPS is most frequently studied around the world. Usually, code differential positioning can satisfy positioning accuracy of meter level, while carrier phase differential positioning can achieve positioning accuracy of centimeter level for the

real-time positioning in three dimensions. RTK realizes real-time positioning by the carrier-phase differencing algorithm in moving. As shown in Fig.4, its principle is that, the reference station transmits the collected raw carrier-phase and pseudorange measurements to the rover station, thus the rover station can calculate the coordinate by differencing algorithm. The accuracy of RTK-DGPS used in this experiment is 1.6 cm.

4 System Configuration

A system configuration is shown in Fig.5 in order to analyze the performance of U-SAT using DGPS. Four U-SAT transmitters are located on the four points of the rectangular in 1m height whose length and width are 5m and 3m respectively. And they are the ultrasonic receiver, GPS receiver, and the turntable which is used to evaluate the position information of U-SAT and GPS. The turntable rotates constant speed in proportion to the voltage and the length of the arms installed at the turntable is 1m. GPS and the ultra-sonic receiver are connected with the turntable by the arms on both sides. The performance of U-SAT using DGPS is analyzed. So the accuracy of U-SAT has been estimated comparing with GPS.

5 Experimental Results

In this experiment, the position information of GPS and U-SAT is respectively measured using the consisted experimental system. Since two positions information are represented in different coordinate system, centers of the circle created by each position information are accorded using transformation.

First the GPS and U-SAT receiver is fixed and the static position is measured during a few minutes. Shown in Fig.6, the errors of U-SAT are wider range than those of GPS. However the position information of GPS and U-SAT does not obtain the accumulative errors. Second in case the turntable rotates the constant speed the position information of U-SAT is compared with that of GPS. The experiment has been implemented at constant speed of 0.1 m/s, 0.2 m/s, 0.3 m/s, and 0.4 m/s. The circles of the position information using GPS and U-SAT are U-SAT does not obtain the accumulative errors. Second in case the turntable rotates the constant speed the position information of U-SAT is compared with that of GPS. The experiment has been implemented at constant speed of 0.1 m/s, 0.2 m/s, 0.3 m/s, and 0.4 m/s. The circles of the position information using GPS and U-SAT are shown in Fig.7.

In Fig.7, The errors of GPS are not influenced by the speed but those of U-SAT are increased as the speed is increased. Since the four U-SAT transmitters radiate ultrasonic waves by turns, the receiver can determine the position after U-SAT receiver finishes receiving the signals from all four

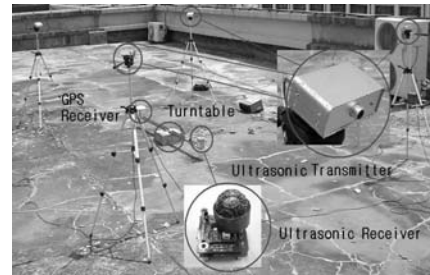


Fig.5 Experiment configuration

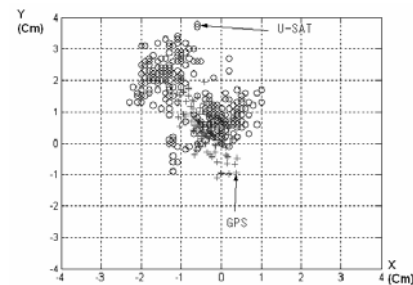


Fig.6 Experimental results of the static position (GPS: +, U-SAT: o)

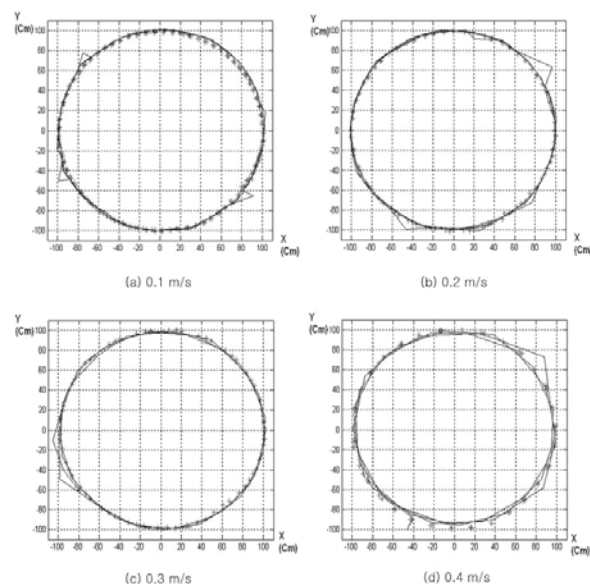


Fig.7 Experimental results of the dynamic position (GPS: +, U-SAT: line)

transmitters. Therefore the errors of U-SAT are influenced by the speed. It causes many problems at the high speed. To solve this problem, the sampling time of the system should be change or more U-SAT transmitters have to be used for faster reception. At the above experiment, the performance of GPS is better than that of U-SAT. However, U-SAT shows a good performance concerning price and has an improvement possibility through more researches. In case that several U-SAT receivers exist, the position of U-SAT receiver can be calculated respectively. Therefore U-SAT is very suitable for pseudolite system in the place where GPS is not available. Although U-SAT is affected by the condition of the outdoor environment, it is more stable at the indoor environment.

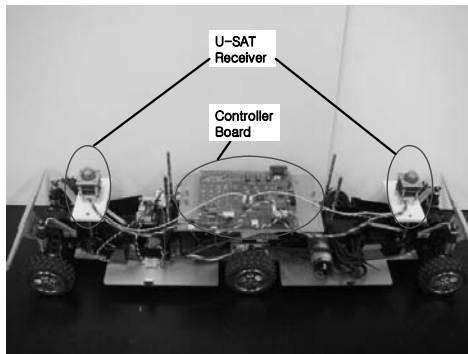


Fig.8 Configuration of the container transporter

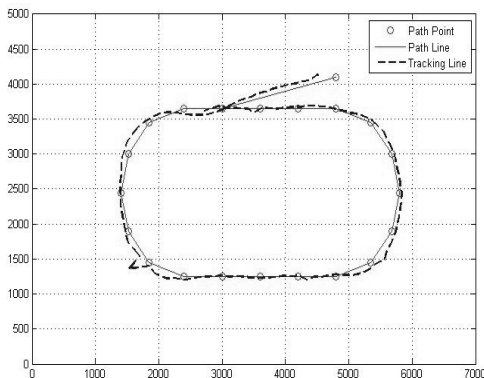


Fig.9 Unmanned navigation of the container transporter

6 Unmanned navigation of the container transporter

Fig.8 depicts the configuration of the container transporter. Two ultrasonic receivers are mounted on the container transporter so that they can obtain the position information and orientation. The localization information is sent to PC via bluetooth. And PC executes its trajectory tracking control. So the container transporter moves along the reference path in a counterclockwise direction. As seen in Fig.9, the reference path is situated on the twenty target points on a track [6].

Experiment was conducted in order to verify that the container transporter can move accurately along the reference path using U-SAT. lateral controller is designed as PID controller. Fig.9 shows the experimental result. A maximum translational velocity of 0.3m/s was used for this experiment, resulting in a maximum error of 5cm for this run. Experimental result shows that the container transporter is navigated precisely along the reference path. And the accumulative error can be eliminated for this method using U-SAT. The experimental result shows good performance and is acceptable.

7 Conclusion

In this paper, the performance of U-SAT has

been evaluated using RTK-DGPS that is more accurate than any other absolute positioning system. Though the performance of RTK-DGPS is better than that of U-SAT, the result of U-SAT is also acceptable. In case of the vehicle which moves slowly or stops, the position information guarantees very stable performance. In Addition, U-SAT can be used as a proper system in the place where GPS is not available, such as indoor area. Finally Experiments were performed in the case that the container transporter moves to the target point using U-SAT. The container transporter can move accurately along the reference path using U-SAT. As a result of experiment, unmanned navigation of the container transporter using U-SAT shows good performance and is suitable. There exist many problems mentioned above to solve such influences of speed and environmental conditions. Many researches are being implemented to improve the accuracy of U-SAT.

Acknowledgment

This work was supported by the Brain Korea 21 Project.

References

- [1] Jae Hwan Kim and Poong Hyun Seong, "Experiments on orientation recovery and steering of autonomous mobile robot using encoded magnetic compass disc," *IEEE Transactions on, Instrumentation and Measurement*, Vol. 45, Feb, 1996, pp. 271~274.
- [2] Kai-Tai Song and Wen-Hui Tang, "Environment perception for a mobile robot using double ultrasonic sensors and a CCD camera," *IEEE Transactions on, Industrial Electronics*, Vol. 43, June, 1996, 5293219, pp. 372~379.
- [3] Alan G. Evans, Everett R. Swift, James P. Cunningham, Robert W. Hill, Geoffrey Blewitt, Thomas P. Yunck, Stephen M. Lichten, Ron Hatch, Stephen Malys, and John Bossler, "The Global Positioning System Geodesy Odyssey," *Navigation : Journal of The Institute of Navigation*, Vol. 49, No. 1, Spring, 2002, pp. 7~33.
- [4] S. Y. Yi and J. H. Jin, "Self-localization of a mobile robot using global ultrasonic sensor system," *Journal of Control, Automation, and Systems Engineering*, Vol. 9, No.2, Feb, 2003, pp. 145~151.
- [5] D. H. Lee, H. T. An, K. R. Baek, and M. H. Lee, "A study on resolution Enhancement in the detection of ultrasonic signal," *The KSAE Annual Fall Conference, Branch of Busan-Ulsan-Gyeongnam*, 2003, pp. 95~102.
- [6] Y. H. Lee, S. I. Kim, M. W. Suh, H. S. Son and S. H. Kim, "Linearized Dynamic Analysis of a Four-Wheel Steering Vehicle," *The Korean Society of Automotive Engineers*, Vol. 2, No. 5, 1994, pp. 101-109.

Spreader Pose Control Using Dual-electric Compasses

SoonShin Han
Dep. of EE.
Pusan National University.
Busan, Republic of Korea.
Ranger112@pusan.ac.kr

HeeSeok Jeong
Dep. of EE.
Pusan National University.
Busan, Republic of Korea.
heeseok@pusan.ac.kr

JangMyung Lee
Dep. of EE.
Pusan National University.
Busan, Republic of Korea.
jmlee@pusan.ac.kr

Abstract

A spreader pose control system using dual-electric compasses has been implemented by measuring the skew angle of the spreader with dual-electric compasses. In the conventional spreader pose measurement, CCD cameras, laser sensors or tilt sensors are mostly used. However those sensors are not only sensitive to the weather and disturbances but also expensive to build the system. To overcome the shortcomings, an inexpensive and efficient system to control the spreader pose has been implemented using the dual-magnetic compasses. Since the spreader iron-structures are noise sources to the magnetic compass, it is not considered to use the magnetic compass to measure the orientation of the spreader. An algorithm to eliminate the interferences of metal structures to the dual compasses has been developed in this paper. The 10:1 reduction model of a spreader control system is implemented and the control performance is demonstrated to show the effectiveness of the dual-magnetic compasses proposed in this research.

Keyword: Magnetic compass, Dual compass, Electronic compass, Spreader, Skew angle

1. Introduction

Many of hub-ports are trying to develop a fully automated loading/unloading system to escape from the heavy human work loads. Main technologies for the successful management of the automated port are the automated loading/unloading using cranes and the automated navigation of carrying vehicles.

Especially the loading/unloading time is a crucial factor for the ship staying at a port. The two types of containers, 20 ft and 40 ft, are handled by the specialized equipment. Main equipments are a container crane and a yard crane. The container crane speed is one of the most important in determining the container processing capability of a port. The yard crane is carrying the containers to stock and to load on the carrying vehicle. Both of these two cranes have the same structures of a horizontal-motion trolley and a vertical-motion spreader, and carry the containers to a desired location.

To load or unload the containers precisely, the pose control of the spreader is essential with the precise measurement of the skew and sway angles. The precise

pose measurement reduces the monitoring operator's care about the unmanned crane in the automated port[1]. For the spreader pose measurement, CCD cameras, lasers, and tilt sensors mainly have been utilized in the most operating automated ports[2-4]. However, there are some limitations in using the conventional sensors for the measurement of spreader pose. The CCD cameras require the image processing procedures which take a lot of time, and the images are very sensitive to weather conditions. The laser sensors are very expensive and have the dead angle in measuring skew angles.

In this paper, the spreader orientation is measured and controlled by using the dual electric compasses which are robust against the iron structures. In general, the compass is very sensitive to the iron structures, and it cannot be used near at the iron structure. Using the dual electric compasses, the sensitiveness to the iron structures has been eliminated and also the disturbances from the neighboring objects have been filtered out[5,6] to achieve the skew angle control. Section 2 introduces the conventional usage of the electric compass. In section 3, the principle of the dual-electric compasses proposed in this paper have been described. Section 4 analyzes the experimental results, and section 5 concludes this paper and indicates future works on this topic.

2. Single Compass Compensation

There are three basic compensations required for the compass: zero-offset, output sensitivity variation, and non-orthogonal error. The error compensation techniques are explained for the general single compass.

2.1 Zero-offset

The output offset of the compass comes from the device itself and from the amplifier. The offset depends on the sensor tolerance and temperature, and the offset value is obtained as

$$V_{offset} = (V_{x,y \max} - V_{x,y \min}) / 2 \quad (1)$$

where V_{offset} is zero when there is neither disturbance nor device-offset.

Using the offset value, the output is corrected as

$$V_{x,y \text{ corrected}} = V_{x,y \text{ output}} - V_{offset} \quad (2)$$

2.2 Output sensitivity variation

The two sensors for x- and y-axis may have different sensitivity to magnetism and amplification factors. The errors can be compensated by using scale factors. That is, when the scale factor for x-axis is represented as, $S_{V_x} = 1$, then the scale factor for y-axis, S_{V_y} can be represented as

$$S_{V_y} = \frac{V_{y \max} - V_{y \min}}{V_{x \max} - V_{x \min}} \quad (3)$$

Using the scale factor for y-axis, S_{V_y} , the outputs along x- and y-axis are matched to represent the azimuth angle correctly.

2.3 Non-orthogonal error

In the manufacturing process of the sensor, the non-orthogonal error of up to 2° exists. The error can be represented as

$$V_y = V_{\max} \cdot \sin(\alpha + \beta) \quad (4a)$$

$$V_x = V_{\max} \cdot \cos \alpha \quad (4b)$$

From Eq's. (4a) and (4b), α and β can be obtained. Therefore the corrected y-axis output can be obtained as

$$V_{y \text{ corrected}} = \frac{V_y}{\cos \beta} - V_x \cdot \tan \beta \quad (5)$$

3. Dual Compass Compensation

The compass is very sensitive to the interferences from magnetic materials. To resolve this shortcoming, in this approach, dual compasses arranged in 180° phase difference have been utilized as shown in Fig. 1.

3.1 Output phase error

The interference from the metal-structures to the two sensors in 180° phase difference can be modeled and compared with the earth magnetism in Fig. 1.

The spread magnetism represents the magnetism of the iron structures which are magnetized by the earth magnetism. The interference results in the addition to one sensor and the subtraction to the other 180° phase difference sensor with the earth magnetism. If there exists only the pure earth magnetism, the addition of the two x- and y-axis outputs of the two compasses is zero.

However by the effects of the interference, the summation is not zero in the metal-structures normally. This compensation algorithm for this interference has been developed in this paper and will be described in detail in the following subsection.

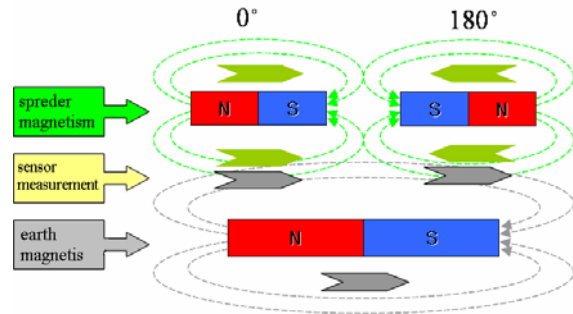


Fig. 1. Relation between earth magnetism and the interference.

3.2 Output amplitude compensation

The outputs of the dual compasses are recorded on the metal-structure to be used while the structure is rotated by 360° , the results are represented as two circles in Fig. 2. To remove out the interference effects, the two circles are properly shifted to the center and to match the radii of the circles to the same.

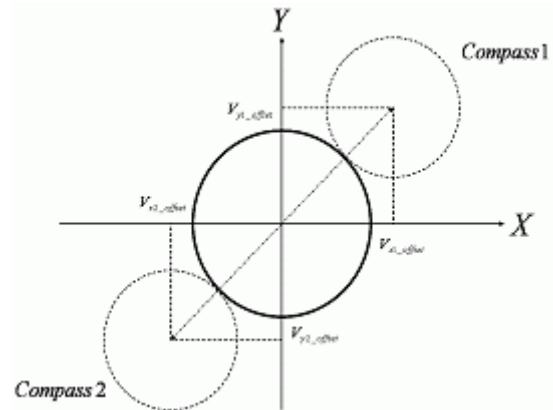


Fig. 2. Change of magnetized circles with metal-structures.

Through this compensation process, the interference from the metal-structure is pre-specified and the results can be utilized for the real-time interference compensation.

The normalization process for the two compass outputs starts with the measured offset value as follows:

$$V_{1r} = \left| V_{1\max} - V_{1\text{offset}} \right| \quad (6a)$$

$$V_{2r} = \left| V_{2\max} - V_{2\text{offset}} \right| \quad (6b)$$

where $V_{1\max}$ and $V_{2\max}$ are the maximum values obtained from Fig. 2, $V_{1\text{offset}} = \sqrt{V_{1x,\text{offset}}^2 + V_{1y,\text{offset}}^2}$ and $V_{2\text{offset}} = \sqrt{V_{2x,\text{offset}}^2 + V_{2y,\text{offset}}^2}$. Now the scale factor for the sensor 2 can be defined, assuming $V_{1sf} = 1$ as follows:

$$V_{2.sf} = \frac{V_{1r}}{V_{2r}}. \quad (7)$$

Therefore the normalized x-directional output can be obtained as

$$V_{x1.corrected} = V_{x1} - V_{x1.offset} \quad (8a)$$

$$V_{x2.corrected} = (V_{x2} - V_{x2.offset}) \cdot V_{2.sf}. \quad (8b)$$

Note that the y-directional output can be also obtained by replacing x as y in equations (8a) and (8b).

Through the process, the magnetized circle can be moved to the origin of the measuring coordinates.

3.3 Disturbance compensation

The interference from the neighboring structures cannot be filtered out on the real time with only a single compass. In this approach, using the dual compasses, the interference is eliminated.

To implement a stable skew angle measuring system using the dual compasses, here the rejection of dynamic disturbances using the dual-compasses has been proposed. By the Eq. (8), the two magnetized circles are normalized, and the two circles may have exactly same outputs when there is no disturbance. When there exists disturbing magnetism, the rotation of θ does not result in the same variations in both compasses. Instead, the compasses have the azimuth angles of ρ and σ which do not have 180° phase difference but have ε error.

The x and y directional error components can be obtained from the outputs of the dual compasses, respectively, as

$$error_x = \frac{V_{x1} + V_{x2}}{2} \quad (9a)$$

$$error_y = \frac{V_{y1} + V_{y2}}{2} \quad (9b)$$

where V_{x1}, V_{x2}, V_{y1} and V_{y2} are x and y directional outputs of sensors 1 and 2, respectively. The magnetized circle can be described by the radius and phase as follows:

$$R = \sqrt{V_x^2 + V_y^2} \quad (10a)$$

$$\theta = \tan^{-1} \frac{V_y}{V_x}. \quad (10b)$$

Since the radius is not constant by the disturbance, the shape of the magnetized circles becomes ellipsoid with this disturbance.

4. Experiments and Results

In this section, the constitution of the experimental equipment has been illustrated, which measures and controls the skew angle of the 10:1 reduction model spreader. The dual compasses are utilized for the angle measurements and the control results show that the

control accuracy with the dual compasses is high enough to be used for the spreader pose control within the flipper error tolerance.

4.1 Experimental environment

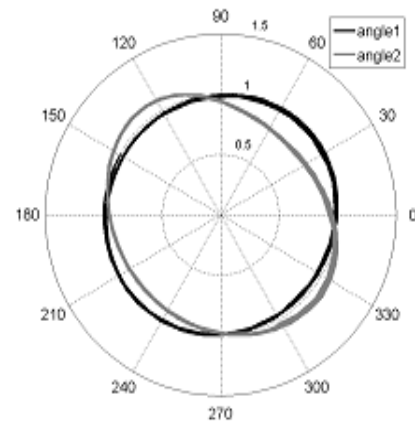
Since there were some difficulties in feeding the control cables on the center of the model spreader, the compasses are installed at each end of the spreader symmetrically. By the experiment 1, the compasses become ready to be used by compensating all the offsets. In the experiment 2, the structural inference is added by putting the two compasses on the metal-frame.

For the calibration process, a motor is installed at the bottom of the spread and its angle is controlled according to the encoder value.

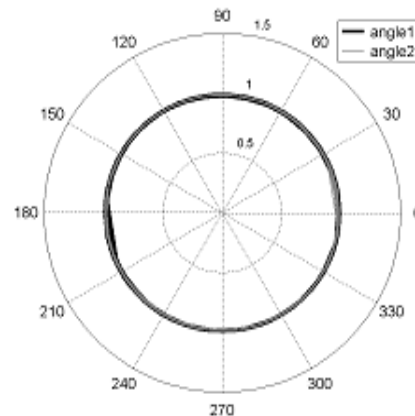
4.2 Error compensation

By the first experiment, the magnetized circles before and after compensation have been drawn in Fig. 3(a) and Fig. 3(b), respectively.

The magnetic field intensity has been increased at a compass while for the other has been decreased. Also the interference is not constant so that the magnetized circles become ellipsoids as expected.



(a). Before interference compensation.



(b). After interference compensation

Fig. 3. Dual compass output.

4.3 Skew angle measurement

The spreaders of the crane operating in the harbors can be rotated about $\pm 15^\circ$ during the loading and unloading operations. And the allowable angle error for both of 20 ft and 40 ft containers are 1° for the normal loading/unloading operations. Therefore for the fully automated crane, the skew angle error should be kept within 1° by the control system.

Using the single compass, the skew angle of the spreader which is rotated $\pm 15^\circ$ has been measured and recorded in Fig. 4.

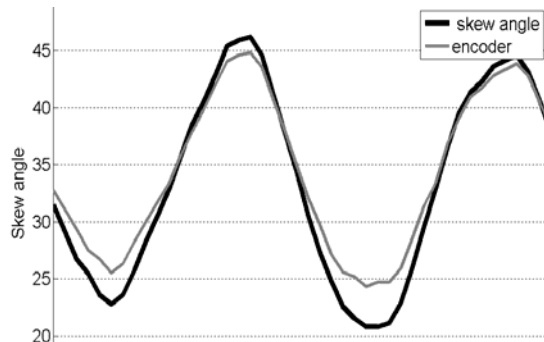


Fig. 4. Experiments of measuring of skew angle.

Notice that for the error measurement, the high precision encoder data have been used as the reference values. As it is illustrated in Fig. 4, the skew angle measurement by the single compass has the maximum 4° error which is out of the allowable angle error for the flipper. There is no effective scheme to reduce this error so far.

When the dual compasses have been used for the skew angle measurements, there was nearly recognizable error in Fig. 5. With the dual compasses, the maximum measurement error for the skew angle is less than 0.5° . Therefore it is precise enough to be utilized to control the pose of the spreader as a skew angle sensor.

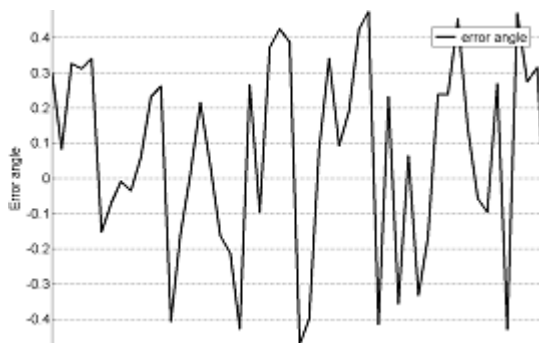


Fig. 5. Experiment of skew angle.

5. Conclusions

The spreader pose control system has been implemented by using the dual-electric compasses which are robust against both the structural interference and

dynamic disturbances. The skew angle control is the most difficult problem in the control of the spreader for the loading/unloading operations since there is not any suitable sensor for the measurement of the skew angle. With the development of the dual-electric compasses, the automated crane can be robust against the weather conditions and be a precise and economical system. In the compensation processes, there were magnetic hysteresis which can be modeled and eliminated to improve the accuracy as a future research.

Acknowledgment

This work was supported by the Regional Research Centers Program (Research Center for Logistics Information Technology), granted by the Korean Ministry of Education & Human Resources Development.

References

- [1] Kanji Obata, Koji Uchida, Takashi Chikura, Hirofumi Yoshikawa and Tadaaki Monzen, "Automated Transfer Crane," *Mitsubishi Heavy Industries Technical Review*, Vol. 40, no. 2, pp. 1 ~ 5, Jan. 2003.
- [2] John R. Holmquist, "Laser Guided Loading System," *IEEE Trans. Industry Applications*, Vol. 38, no. 3, pp. 752~757, May, 2002.
- [3] Kyung-Moon Lee, Yang-Hwan Kim, Jae-Mu Yun and Jang-Myung Lee, "Magnetic-interference-free dual-electric compass," *Sensors and Actuators*, A120, pp. 441~450, Jan. 2005.
- [4] J. Ko, W. Kang, Y. H. Kim and Jang-Myung Lee, "Robust Electric Compass to Dynamic Magnetic Field Interference," *Journal of Control, Automation, and Systems Engineering*, Vol.11, no. 1, pp. 27~33, Jan. 2005.
- [5] Lenz, J.E, "A review of magnetic sensors," *Proceedings of the IEEE*, Vol. 78, Issue 6, pp. 973~989, Jun. 1990.
- [6] Rac. R, Schott. C and Huber. S, "Electronic compass sensor," *Sensors, Proceedings of IEEE*, Vol. 3, pp. 1446 ~ 1449, Oct. 2004.

P2P Sensor Data Mining System for School Temperature Measurement System

Ayahiko Niimi
Masaaki Wada

Hiroshi Shimada
Kei Ito

Rika Goto
Osamu Konishi

Department of Media Architecture
Future University-Hakodate

116-2 Kamedanakano-cho, Hakodate-shi, Hokkaido 041-8655, JAPAN

Abstract

In this paper, we propose the technique of the sensor data mining by the P2P (Peer-to-Peer) network. The mechanism that it is possible to share on the P2P network is considered by receiving information from the sensor by the P2P application. Searching request for sensor unit and mining the sensor data does on the P2P application. We consider that the proposed technique is applied to the school environment measurement system. In its system, sensor units are arranged on campus, user can measure room's temperature and humidity. The temperature sensor and the humidity sensor are implemented in a microcomputer board that can connect to the Internet, and we define the microcomputer board as a sensor unit. We construct the P2P sensor network on which a PC accesses the sensor unit and P2P application on its PC uploads on the P2P network. The P2P network becomes possible disclosing sensor information after more advanced processing is given by thinking as P2P application not the sensor unit but on the sensor unit and PC.

Keyword:

Sensor Data Mining System, P2P, JXTA, School Temperature Measurement System

1 Introduction

Recently, we can obtain various data easily by a high performance of computer and the Internet. Data mining that extracted significant knowledge from a large amount of data become popular. The technique for applying data mining to text information such as Web page is developed recently though the data stored in databases was targeted in normal data mining. In the Internet, various time series data can be obtained. For instance, the image data of the weather satellite and the data of various sensors can be obtained. The

feature of these data is continuous data in the time series. The techniques which applied data mining from databases are used for time series data, but some techniques were improved for time series data.

The digital measurements of the temperature and humidity, etc. become possible, and connecting the system that acquired the measured data on the network becomes possible. However, there are many measurement systems which are rich systems that are used sensors on PC or which are cheap microcomputer systems that need to construct a special network for the sensor network. We propose the sensor network system using the microcomputer board that can connect to the Internet. This proposed system can acquire information from the sensor of the microcomputer group arranged on the network, and can view collected information on Web browser.

In KES2006 [1], it was shown to be able to construct easily the microcomputer's sensor network which was combined microcomputer modules (Micro Cube) and the database server and the Web application server. The system that measured the room temperature in school campus was constructed, it has run for four months, and the effectiveness is verified.

In this paper, we propose the technique of the sensor data mining by the P2P (Peer-to-Peer) network. The mechanism that it is possible to share on the P2P network is considered by receiving information from the sensor by the P2P application. Searching request for sensor unit and mining the sensor data does on the P2P application. The advantage of P2P system is scalability of the number of sensors. It becomes to be able to correspond to the change in the number of sensors easily by constructing the sensor network on the P2P network.

Chapter 2 describes the sensor module using Micro Cube. Chapter 3 describes the composition of the sensor network as server-client system. We describe the installation of Micro Cube, the server and the client and the technique of collecting and viewing

data. Chapter 4 describes the P2P sensor data mining system. In chapter 5, we describe construction of our proposed system, and discuss about the problem when constructing sensor network. Section 6 describes conclusion and enhancing in a future.

2 Sensor Module

In this section, we describe proposed sensor module.

2.1 Outline of Micro Cube

The Micro Cube is a board computer and is composed of several stackable boards [2, 3]. Fig. 1 is a photo showing one of the combinations of stacked Micro Cube. It has a CPU board with a RENESAS H8 CPU and a TCP/IP Protocol stack. Stackable boards can vary as follows: Ethernet LAN board, compact flash board, PCMCIA board, serial board (RS232C and RS422) and so on. Since the different combinations of stackable boards make a seamless connection with the sensors, users can structure an ad hoc sensor network very easily. To get sensor information through the Internet, HTTP is also employed so that user can get data via a standard Web browser.

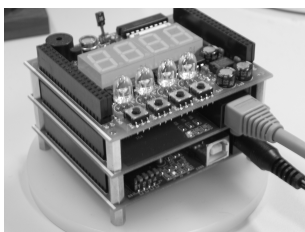


Figure 1: Photo of a Stacked Micro Cube

2.2 Instrumentation of the present system

The Micro Cube used in the system to get the information of room condition is composed of the H8/3069 CPU board, LAN board, and special sensor board. The special sensor board is utilized the board used of the programming practice class in Future University-Hakodate. (The sensor board is shown in Fig. 1) Future University-Hakodate has the programming practice class with the microcomputer and assembler language as “Media Architecture Practice II”. The special board for Micro Cube was designed for its practice class. The push switch, the thermally sensitive

resistor (temperature sensor), and CdS sensor (optical sensor) were attached on this board as an input. Moreover, four digits seven-segments LED and four two-color LED were attached as an output. Because an accurate temperature measurement using the thermally sensitive resistor is difficult, a digital sensor is added in this board for our experiment. Humidity can be also measured in this digital sensor. Only the temperature data is acquired this experiment though some sensors are attached on the board. The exchange and the addition of the sensor can be easily done by exchanging the sensor boards.

To confirm the measurement data easily, the measured temperature was displayed in seven-segments LED. Moreover, data can be got by HTTP though the network. When only one sensor module runs, the user can display a present temperature when the user accesses it using Web browser.

3 Network Configuration

The sensor network was constructed by using the microcomputer that explained in Chapter 2. Fig. 2 shows the composition of the constructed sensor network system. First of all, we constructed proposed sensor network system as server-client system.

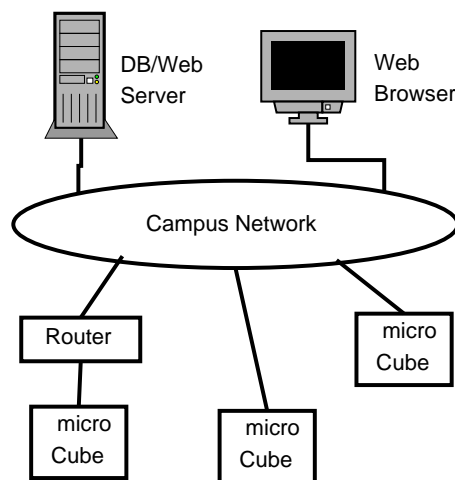


Figure 2: Network Configuration

The used software is shown below (see table 1). The data store part is implemented by Perl, and the data display part is implemented by JSP.

The following steps shows the steps of the collection of data and the display stored data.

1. Data storage

Table 1: Software used in the web database server

System	Software
OS	Red Hat Linux release 9
HTTP	Apache 2.0.40
Database	PostgreSQL 7.3.2
Software codes	Tomcat 5.0.28 and Perl 5.8.0

- (a) The Perl script accesses to URL of Micro Cube.
- (b) Micro Cube returns the measurement result by HTML format.
- (c) HTML is parsed, and necessary data is preserved in the database.

2. Data browse

- (a) URL of the server is opened from a Web browser.
- (b) JSP accesses the database.
- (c) Necessary data is acquired from the database.
- (d) The result is processed to the graph and displayed it on a browser.

The micro cube arranged in school is connected with campus network (LAN). The data of each sensor module is acquired with the server set up on the campus network at regular intervals, and stores in the database. In this experiment, data is acquired from the sensor module every ten minutes. The acquired data is processed with the Web application server set up on the same server, and can be displayed from Web browser of PC on the campus network.

At first, Micro Cube connected to campus network by arranging it in the router because the router had not been exceeded in LAN of the micro cube. Afterwards, connecting Micro Cube to the campus network even if we modified the program, and the router is not set up became possible so that the router was exceeded.

4 P2P Data Mining System

In this paper, we propose the technique of the sensor data mining by the P2P (Peer-to-Peer) network. The mechanism that it is possible to share on the P2P network is considered by receiving information from the sensor by the P2P application. Searching request

for sensor unit and mining the sensor data does on the P2P application. The advantage of P2P system is scalability of the number of sensors. It becomes to be able to correspond to the change in the number of sensors easily by constructing the sensor network on the P2P network.

We consider that the proposed technique is applied to the school environment measurement system. In its system, sensor units are arranged on campus, user can measure room's temperature and humidity. The temperature sensor and the humidity sensor are implemented in a microcomputer board that can connect to the Internet, and we define the microcomputer board as a sensor unit. We construct the P2P sensor network on which a PC accesses the sensor unit and P2P application on its PC uploads on the P2P network. The P2P network becomes possible disclosing sensor information after more advanced processing is given by thinking as P2P application not the sensor unit but on the sensor unit and PC. Moreover, even if one-sensor unit-one peer is not allocated, it is also possible to arrange peer that integrates some sensor units on the network. We construct P2P sensor data mining system used Micro Cube as sensor units and JXTA as P2P platform.

The sensor data constructs the system that can flexibly correspond also to the different kind sensor data by using the XML form. The advantage of the proposal approach is that it is easy to correspond to the change in the number of data sources. The change of the system is not to hard even when the composition of the sensor changes. Moreover, the data acquisition system from the sensor in the remote place can be easily constructed by constructing the system on the Internet.

5 Experimental Results

The system that explained in Chapter 3 was actually constructed. The system is constructed in December, 2005, and it is running at November, 2006. Because a lot of modules were able to be reused, the time that had constructed to development was about one week.

Some data display examples are shown as follows. (See Fig. 3) The displayed data can be switched to all or a part of room. The displayed range can be switched to a day, a week, a month, or all. Fig. 3 shows all data in one chart, and Fig.

At first, Micro Cube connected to campus network by arranging it in the router because the router had

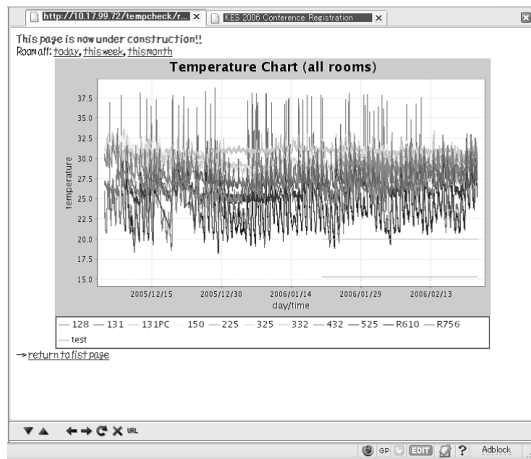


Figure 3: All Data in One Chart

not been exceeded in LAN of the micro cube. However, data might not be able to be acquired normally when some router's passing. Then, connecting Micro Cube to the campus network even if we modified the program, and the router is not set up became possible so that the router was exceeded.

It took time to divide the problem when data was not able to be acquired normally because Micro Cube connected to the campus network. Then, the problem was considered in cooperation with SE that resided in school. For the exceeding router problem, we constructed some environment, such as the dummy server with the PC-UNIX server, passing the router setting, bypassing the router setting, and it undertook the resolution of a problem while capturing the packet that flowed in the network.

Because data began to collect, temperature data is scheduled to be analyzed in the future.

6 Conclusion

We proposed the technique of the sensor data mining by the P2P for the sensor network system using the microcomputer board that can connect to the Internet. This proposed system can acquire information from the sensor of the microcomputer group arranged on the network, and can view collected information on Web browser. It was shown to be able to construct easily the microcomputer's sensor network which is combined microcomputer modules (Micro Cube) and the database server and the Web application server. The system that measured the room temperature in school campus was constructed, it has run for about

one year, and the effectiveness was verified. We also proposed P2P sensor data mining system. Because data began to collect, temperature data is scheduled to be analyzed in the future. In the analysis of data, it is thought that it is possible to refer to a technique of the multiagent base [4, 5] and an analytical technique of the analysis of the fixed point observation data [6]. We discussed P2P sensor data mining system with microcomputers and JXTA.

The system that expands acquired more different type of sensor information will be constructed, and then, obtained data is scheduled to be analyzed in the future. In addition, we want to attach the IR I/O module on the microcomputer board, and to do the research for the ubiquitous computing of the indoor environment controlling.

References

- [1] Ayahiko Niimi, Masaaki Wada, Kei Ito, Osamu Konishi (2006), Construction of School Temperature Measurement System with Sensor Network. KES'2006, Proceedings, Part III, Lecture Notes in Artificial Intelligence 4253, Springer: pp.813–819.
- [2] Wada. M., Hatanaka, K., Kimura, N., Amagai, K. (2004), Applying an Information Technology in Fishing Industry I. Acquisition of a Three Dimensional Topography. Journal of Japan Institute of Navigation, vol. 112, pp.189–198 (in Japanese)
- [3] Hatanaka, K., Wada, M., Kotaki, M. (2005), Instrumentation for the Measurement of Shallow Seabed Topography by a Fishing Echo Sounder. Oceans 2005 MTS/IEEE Conference Proceedings, Ocean Instrumentation I, pp.1–6
- [4] Niimi, A., Konishi, O. (2003), Data Mining for Distributed Databases with Multiagents. KES'2003, Proceedings, Part II, Lecture Notes in Artificial Intelligence 2774, Springer, pp.1412–1418
- [5] Niimi, A., Konishi, O. (2004), Extension of Multiagent Data Mining for Distributed Databases. KES'2004, Proceedings, Part III, Lecture Notes in Artificial Intelligence 3215, Springer, pp.780–787
- [6] Toda, M., Osanai, A., Niimi, A., Akita, J., Kimura, K., Konishi, O. (2005), Information Access Method to Meteorological Data for Educational Application. ED-MEDIA2005, Proceedings, pp.4404–4408

A probabilistic modeling of MOSAIC learning

Satoshi Osaga, Jun-ichiro Hirayama, Takashi Takenouchi and Shin Ishii
Graduate School of Information Science
Nara Institute of Science and Technology
Takayama 8916-5, Ikoma, Nara, 630-0192, Japan
{satosh-o, junich-h, ttakashi, ishii}@is.naist.jp

Abstract

Humans can generate accurate and appropriate motor commands in various and even uncertain environments. MOSAIC (MODular Selection And Identification for Control) was originally proposed to describe such human ability, but it includes some complex and heuristic procedures. In this article, we present an alternative and probabilistic model of MOSAIC (p-MOSAIC) as a mixture of normal distributions, and an online EM-based learning method for its predictors and controllers. A theoretical consideration shows that the learning rule of p-MOSAIC corresponds to that of MOSAIC except for some points mostly related to the learning of controllers. The results of experiments using synthetic datasets demonstrate some practical advantages of p-MOSAIC. One is that the learning rule of p-MOSAIC stabilizes the estimation of “responsibility.” Another is that p-MOSAIC realizes accurate control and robust parameter learning in comparison to the original MOSAIC, especially in noisy environments, due to the direct incorporation of the noise into the model.

1 Introduction

Humans have the remarkable ability to generate accurate and appropriate motor commands in various and even uncertain environments. Studies of human motor controls have shown that dis-adaptation and re-adaptation to a learned environment are more rapid than adaptation to a novel environment [5], implying that the human motor control could be performed by a modular structure consisting of multiple controllers each adapting to a specific environment.

MOSAIC [1] was originally proposed to model the motor control system with such a modular structure. In MOSAIC, each controller is coupled with a corresponding predictor, and a motor command is determined by a weighted mean of outputs of multiple controllers, where the weight for each controller (responsibility) is estimated based on the prediction error of the corresponding predictor. However, MOSAIC includes

some complex and heuristic procedures that make it difficult to understand the model.

In this study, we re-formulate MOSAIC as a probabilistic model in order to construct an easily understandable framework. Parameters of predictors and controllers are estimated by the online EM algorithm [4], which maximizes the log-likelihood of the model, given the history of control results. We also show results of computer simulations in which behaviors of responsibility and controller learning of p-MOSAIC are compared with those of MOSAIC.

2 MOSAIC

We consider a situation where the dynamics of the motor system is given by a discrete-time system:

$$\tilde{x}_{t+1} = \Phi(\tilde{x}_t, u_t),$$

where \tilde{x}_t and u_t are the system state and the applied motor command, respectively, at time t . The task of the motor control is to make the system state \tilde{x}_t to keep on a given trajectory x_t .

To perform the control task, we assume M pairs of a controller and a predictor. The aim of the controller is to generate an appropriate motor command u_t which produces the desired state x_{t+1} . We assume that an output of the i -th controller is represented as

$$\psi_{i,t} = \psi(\tilde{x}_t, x_{t+1}; v_i),$$

where v_i is the parameter of the i -th controller. The objective of the predictor is to accurately predict the system state at the next time step, and an output of the i -th predictor is given by

$$\phi_{i,t} = \phi(\tilde{x}_{t-1}, u_{t-1}; w_i),$$

where w_i is the variable parameter of the i -th predictor. Because there are M pairs of a controller and a predictor, the responsibility for each controller (and predictor) should be defined. The responsibility signal

$\lambda_{i t}$ for the i -th pair is defined by

$$\lambda_{i t} = \frac{\exp(-|\tilde{x}_t - \phi_{i t}|^2/\sigma^2)\hat{\lambda}_{i t}}{\sum_{j=1}^M \exp(-|\tilde{x}_t - \phi_{j t}|^2/\sigma^2)\hat{\lambda}_{j t}}, \quad (1)$$

where σ is a constant and $\hat{\lambda}_{i t}$ is a rough prediction of the responsibility signal $\lambda_{i t}$ which is typically given as a constant (then ignored). The responsibility represents how well each predictor reproduces the target dynamics, then an overall motor command \tilde{u}_t at time t is given by a linear combination of outputs $\psi_{i t}$ of the M controllers as

$$\tilde{u}_t = \sum_{i=1}^M \lambda_{i t} \psi_{i t} + u_t^{\text{fb}}. \quad (2)$$

Here, u_t^{fb} is a feedback motor command, which is assumed to be produced by a PID or PAD controller, based on the difference between x_t and \tilde{x}_t .

MOSAIC is trained by updating the parameters of controllers and predictors. A learning rule is given by

$$\Delta v_i = \kappa \lambda_{i t} \frac{\partial \psi_{i t}}{\partial v_i} (u_t - \psi_{i t}) \quad (3)$$

$$\Delta w_i = \kappa \lambda_{i t} \frac{\partial \phi_{i t}}{\partial w_i} (\tilde{x}_t - \phi_{i t}), \quad (4)$$

where Δv_i and Δw_i are the updates of parameters v_i, w_i in a single learning step, κ is the learning rate, and u_t is the desired motor command. Although it is assumed that the desired motor command u_t is available in Eq. (3), this assumption is not practical. Thus, the controller learning (3) is approximately performed using the feedback-error learning [3] as

$$\Delta v_i \approx \kappa \lambda_{i t} \frac{\partial \psi_{i t}}{\partial v_i} u_t^{\text{fb}}. \quad (5)$$

3 p-MOSAIC

With a set of M predictors, $\tilde{x}_t = \phi(\tilde{x}_{t-1}, \tilde{u}_{t-1}; w_i) + \varepsilon_i$, where ε_i is the noise of the i -th predictor, the state prediction by integrating those predictions is given probabilistically as a mixture of normal distributions:

$$p(x_t | \tilde{x}_{t-1}, \tilde{u}_{t-1}; \boldsymbol{\lambda}, \mathbf{w}, \mathbf{v}) = \sum_{i=1}^M \lambda_i N(x_t | \phi(\tilde{x}_{t-1}, \tilde{u}_{t-1}; w_i), \sigma_i^2),$$

where x_t is a random variable for the predicted state at time t , $\boldsymbol{\lambda} = (\lambda_1, \dots, \lambda_M)$ is the mixing rate vector such that $\lambda_i \geq 0$ and $\sum_{i=1}^M \lambda_i = 1$, $\mathbf{w} = (w_1, \dots, w_M)$ is the set of predictors' parameters, and $\mathbf{v} = (v_1, \dots, v_M)$ is

the set of controllers' parameters. The motor command \tilde{u}_{T-1} is deterministically given by Eq. (2). In our particular experiments in Section 4, we use a linear predictor:

$$\phi(x_{t-1}, u_{t-1}; w_i) = w_i x_{t-1} + w_i u_{t-1}. \quad (6)$$

For a desired trajectory $x_{1:T} = (x_1, \dots, x_T)$ and an actual trajectory $\tilde{x}_{0:T} = (\tilde{x}_0, \dots, \tilde{x}_T)$, the probability of a state sequence $x_{1:T} = (x_1, \dots, x_T)$ of random variables is represented as

$$p(x_{1:T} | \tilde{x}_{0:T}, x_{1:T}; \boldsymbol{\lambda}, \mathbf{w}, \mathbf{v}) = \prod_{t=1}^T p(x_t | \tilde{x}_{t-1}, x_t; \boldsymbol{\lambda}, \mathbf{w}, \mathbf{v}),$$

where the random variables are assumed to be independent of each other. Given $x_{1:T}$ and $\tilde{x}_{1:T}$, the parameters of the predictors and the controllers are determined by the maximum likelihood estimation. In the following two subsections, we describe learning rules of the predictors and the controllers.

3.1 Learning rule of predictors

Parameters $\boldsymbol{\lambda}$ and \mathbf{w} of the predictors are primarily estimated so as to maximize the log-likelihood:

$$\sum_{t=1}^T \log p(x_t = \tilde{x}_t | \tilde{x}_{t-1}, x_t; \boldsymbol{\lambda}, \mathbf{w}, \mathbf{v}),$$

by means of the online EM algorithm, in which the controller parameters \mathbf{v} are fixed. By introducing a hidden variable c_t that indexes predictor-controller pairs, the online free energy for any distribution of the hidden variable, $q_p(c_t)$, is defined as

$$F_T[\{q_p(c_t)\}, \boldsymbol{\lambda}, \mathbf{w}] = \sum_{t=1}^T \Gamma_T(t) \left\langle \log \frac{q_p(c_t)}{p(\tilde{x}_t, c_t | \tilde{x}_{t-1}, x_t, \boldsymbol{\lambda}, \mathbf{w})} \right\rangle_{q_p(c_t)},$$

where $p(\tilde{x}_t, c_t | \tilde{x}_{t-1}, x_t, \boldsymbol{\lambda}, \mathbf{w}) = N(\tilde{x}_t | \phi_{c_t t}, \sigma_{c_t}^2) \lambda_{c_t}$. $\langle \cdot \rangle_{q_p(c_t)}$ is the expectation with respect to the distribution $q_p(c_t)$, and $\Gamma_T(t)$ is given by

$$\Gamma_T(t) = \frac{1}{\prod_{s=t+1}^T s} \quad (t = T),$$

$$\frac{1}{\prod_{s=t+1}^T s} \quad (0 \leq t < T),$$

where s ($0 \leq s < 1$) is called the forgetting factor. The online free energy is minimized by the online EM algorithm, in which the following two steps are implemented once after seeing x_T and \tilde{x}_{T-1} at a time step T :

E-step

$$q_p(c_T) \propto p(\tilde{x}_T, c_T | \tilde{x}_{T-1}, x_T, \boldsymbol{\lambda}, \mathbf{w}) \propto N(\tilde{x}_T | \phi_{c_T T}^{(T)}, 1/\sigma_{c_T}^2) \lambda_{c_T}^{(T)},$$

where the superscript $T-1$ means the time step, $T-1$.

M-step

$$\lambda_i^{(T)} = (1 - \tau) \lambda_i^{(T-1)} + \tau q_p(c_T = i) \quad (7)$$

$$\begin{aligned} \Delta w_i^{(T)} = & (1 - \tau) \Delta w_i^{(T-1)} \\ & + \tau \kappa_i q_p(c_T = i) (\tilde{x}_T - \phi_{iT}) \frac{\partial \phi_{iT}}{\partial w_i}, \end{aligned} \quad (8)$$

where τ is given by

$$\tau = 1/N_T, \quad N_T = \tau N_{T-1} + 1 \quad (N_0 = 0).$$

The above learning rules of p-MOSAIC involve a smoothing effect on the sufficient statistics in the M-step, because of the online free energy. On the other hand, they become similar to the learning rules of MOSAIC in a special setting of $\tau = 0$ ($t = 1, \dots, T$), which corresponds to discarding the smoothing effect. Even in this special setting, however, the learning rule of p-MOSAIC contains an additional term associated with the inverse variance κ_i of each predictor (Eq. (8)), which represents the noise level of the predictor.

3.2 Learning method of controllers

The controller parameters \mathbf{v} are primarily estimated so as to maximize the log-likelihood:

$$\sum_{t=1}^T \log p(x_t = x_t | \tilde{x}_{t-1}, x_t; \boldsymbol{\lambda}, \mathbf{w}, \mathbf{v}),$$

while the predictor parameters, $\boldsymbol{\lambda}$ and \mathbf{w} , are fixed. According to the online EM algorithm, instead of the log-likelihood, the online free energy:

$$\begin{aligned} & F_T[\{q_c(c_t)\}, \mathbf{v}] \\ = & \sum_{t=1}^T \Gamma_T(t) \left\langle \log \frac{q_c(c_t)}{p(x_t = x_t, c_t | \tilde{x}_{t-1}, x_t, \mathbf{v})} \right\rangle_{q_c(c_t)} \end{aligned}$$

for any distribution of the hidden variable, $q_c(c_t)$, is minimized, where $p(x_t = x_t, c_t | \tilde{x}_{t-1}, x_t, \mathbf{v}) = N(x_t | \phi_{c_t t}, \kappa_{c_t}^{-1}) \lambda_{c_t}$. $\langle \cdot \rangle_{q_c(c_t)}$ is the expectation with respect to the distribution $q_c(c_t)$. As an incremental minimization of the online free energy, the following two steps are implemented once, given the desired state x_T and the previous state \tilde{x}_{T-1} :

E-step

$$\begin{aligned} q_c(c_T) & \propto p(x_T = x_T, c_T | \tilde{x}_{T-1}, x_T, \mathbf{v}) \\ & \propto N(x_T | \phi_{c_T T}, 1/\kappa_{c_T}) \lambda_{c_T}^{(T-1)}. \end{aligned}$$

M-step

$$\begin{aligned} \Delta v_i^{(T)} = & (1 - \tau) \Delta v_i^{(T-1)} \\ & + \tau \kappa_i \lambda_i \frac{\partial \psi_{iT-1}}{\partial v_i} \sum_{j=1}^M j q(c_T = j) w_{ju}(x_T - \phi_{jT}). \end{aligned} \quad (9)$$

Here, w_{ju} is the predictor parameter defined in Eq. (6). Even if the forgetting factor τ is constant at zero, the M-step equation reduces to

$$\Delta v_i^{(T)} = \kappa_i \lambda_i \frac{\partial \psi_{iT-1}}{\partial v_i} \sum_{j=1}^M j q(c_T = j) w_{ju}(x_T - \phi_{jT}),$$

which is obviously different from Eq. (3), the learning rule of controllers in MOSAIC. The controller learning in MOSAIC is defined as a gradient-based feedback-error learning, which tries to minimize the time-lag difference between the previous actual state \tilde{x}_{t-1} and the previous desired state x_{t-1} . In p-MOSAIC, the controller learning tries to minimize the difference between the current predicted state \hat{x}_t and the current desired state x_t . Moreover, the learning rule of p-MOSAIC includes the inverse variance κ_j (Eq. (9)). These two points arise from the difference in the learning criteria between MOSAIC and p-MOSAIC.

4 Simulation studies

To compare p-MOSAIC with MOSAIC, we simulated the control of a spring-mass-damper system. The desired trajectory of the object (mass position) followed a mixture of sine waves for 12 seconds. To show the adaptability of the motor control system, environment (mass of the object M , damping B and spring constant K) switches every 4 sec between the following three settings:

$$(M, B, K) = \begin{cases} 1.0, 2.0, 8.0 & (0 \text{--} 4\text{sec}) \\ 5.0, 7.0, 4.0 & (4 \text{--} 8\text{sec}) \\ 8.0, 3.0, 1.0 & (8 \text{--} 12\text{sec}). \end{cases}$$

In both MOSAIC and p-MOSAIC, we prepared three predictor-controller pairs. Observation and control were performed at 1,000 Hz, and a single trial was continued for 12 seconds. The predictors (6) were input by the motor command, the state (position and velocity) of the object at the present time, and output the predicted acceleration of the object at the next time. The controllers were input by the state at the present time and the desired acceleration at the next time, and output a motor command at the present time. In this simulation, we used a PAD controller to produce the feedback motor command. Note that

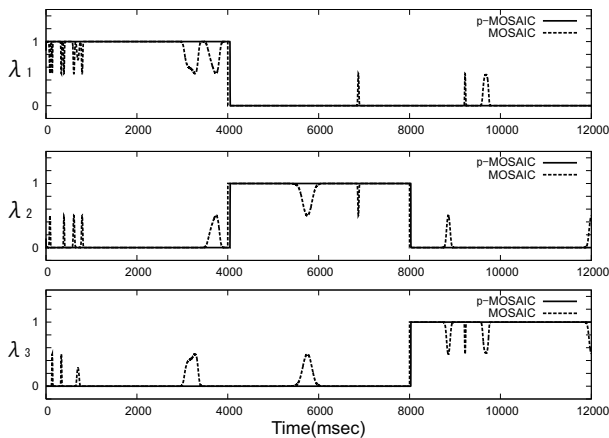


Figure 1: The responsibility along time

our task for the spring-mass-damper system is almost the same as in the previous work [2]. A regularization term is introduced to the estimation of responsibility in MOSAIC and p-MOSAIC in order to suppress any overfitting to the noisy environment.

4.1 Responsibility

We first examined how the responsibility behaves. Prior to the experiment, three predictor-controller pairs were completely adapted to their own environments. Since there is no learning factor, we can compare solely the estimation of the responsibility between Eq. (7) with the forgetting factor being zero (for comparison), and Eq. (1). Figure 1 shows the result. Although p-MOSAIC achieved a complete switching of controllers in response to changes of environments, MOSAIC sometimes failed.

4.2 Controller learning

We compared the controller learning, Eq. (9) of p-MOSAIC, and Eq. (5) of MOSAIC, assuming the predictors were completely trained to adapt to their own environments. To compare controller learning only, we used Eq. (7) in both MOSAIC and p-MOSAIC to estimate responsibility, and the forgetting factor was fixed at zero. We examined the controller learning in particular when the actual state \tilde{x}_t is disturbed by a noise.

Figure 2 shows the results for a small noise and a relatively large one. When the noise level was low (upper panel), p-MOSAIC achieved more accurate control than MOSAIC. When the noise level was relatively high (lower panel), on the other hand, the learning by MOSAIC proceeded faster, but it was substantially unstable; hence, the performance improved due to p-MOSAIC after about 1,000 trials. In the early learning phase, the controller learning of p-MOSAIC proceeded

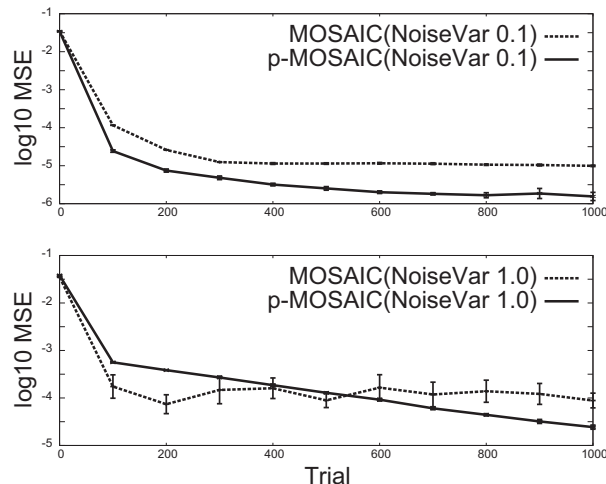


Figure 2: Logarithm of the mean square error between the actual and the desired trajectory vs. number of trials

slowly due to the control of the inverse variance σ_i . Because the environmental noise was large, the adaptive control of the inverse variance made the learning slow but stable, suggesting adaptive adjustment of learning speed in p-MOSAIC.

5 Summary

In this study, we proposed p-MOSAIC, a probabilistic model of MOSAIC, and derived learning rules according to the online EM algorithm. P-MOSAIC achieved an appropriate estimation of responsibility in the predictor, and accurate control and robust learning when the controllers learned.

References

- [1] D.M. Wolpert and M. Kawato. (1998). *Neural Networks*, **11**, 1317-1329.
- [2] M. Haruno, D.M. Wolpert, M. Kawato. (2001). *Neural Computation*, **13**, 2201-2220.
- [3] M. Kawato. (1990). Feedback-error-learning neural network for supervised learning. In R. Eckmiller (Ed.), *Advanced neural computers* (pp. 365-372). Amsterdam: North-Holland.
- [4] M. Sato and S. Ishii. (2000). *Neural Computation*, **12**(2), 407-432.
- [5] R.B. Welch, B. Bridgeman, S. Anand and K.E. Browman. (1993). *Perception and Psychophysics*, **54**(2), 195-204.

Iterative Learning Control for Linear Time-Variant Continuous Systems Based on Two-Dimensional System Theory *

Deyuan Meng and Yingmin Jia

The Seventh Research Division
Beihang University (BUAA)
Beijing 100083, P.R.China
dymeng23@126.com, ymjia@buaa.edu.cn

Abstract

In this paper, an iterative learning control (ILC) scheme is presented for linear time-variant continuous multi-variable systems based on two-dimensional (2-D) system theory. Three ILC schemes are discussed, and the corresponding convergence and effectiveness are proved where only the structure of 2-D system model, the property of λ -norm, and the Bellman-Gronwall inequality are employed. Two numerical simulation examples are included to validate the effectiveness of the proposed ILC procedures.

1. Introduction and Problem Formulation

Iterative learning control (ILC) was firstly introduced in 1984 by Arimoto et al. [1], and it has generated considerable research interest over the past years. The objective of ILC is to determine a control input iteratively, resulting in the plant's ability to track the given reference signal or the output trajectory over a fixed time interval. Hence, the most widely used ILC scheme is the PID-type scheme because this enables the conventional PID-like system for processing the tracking error [1]-[4]. However in [5], Geng et al. pointed that all PID-type ILC schemes inevitably suffer from a tight restriction. Moreover, the understanding of the structure and parameters of the unknown systems cannot be directly increased through the PID-type learning scheme because it is difficult to generalize the obtained results from a particular task to other similar tasks [6].

In fact, one of the main difficulties that ILC suffers is to establish a suitable mathematical model to clearly describe the dynamics of the control system and the behavior of the learning process [5]-[7]. Two-dimensional

(2-D) model provides an excellent mathematical platform due to its two independent dynamic process [7]-[8], and hence 2-D system theory is introduced to ILC schemes.

In this paper, we discuss ILC problem for the following linear time-variant continuous system:

$$\begin{aligned}\dot{x}(t) &= A(t)x(t) + B(t)u(t) \\ y(t) &= C(t)x(t)\end{aligned}\quad (1)$$

where $x(t) \in R^n$, $u(t) \in R^m$, $y(t) \in R^p$ are the state vector, the input vector, the output vector, respectively, and $A(t), B(t), C(t)$ are real time-variant matrices of appropriate dimensions that can be estimated. The boundary condition is $x(0) = x_0$.

Then, the ILC problem we are dealing with is stated as follows. Given system (1) with boundary condition $x(0) = x_0$, iteratively find an appropriate control input $\{u(t), 0 \leq t \leq T\}$ such that the system output follows the reference trajectory $y_d(t) \in R^p, 0 < t \leq T$, i.e.,

$$\sup_{0 < t \leq T} \|y(t) - y_d(t)\| < \varepsilon$$

where $\varepsilon > 0$ is a required tolerance, and $y_d(0) = C(0)x_0$. Since the system matrices are not fully known, we are required to derive an ILC technique. In this paper, 2-D system theory is used to solve the above-mentioned problem. Main difficulty we solve is to establish a suitable 2-D system model to describe the dynamics of the control system and the behavior of the learning process, and a 2-D continuous-discrete Roesser's model is successfully derived by using the derivative of output tracking error instead of direct output tracking error.

2. ILC Schemes for Linear Time-Variant Continuous Systems

Suppose that k denotes the learning iteration, then a general ILC scheme is given as $u(t, k+1) = u(t, k) +$

*Supported by the National Science Foundation of China (60374001), and the Ministry of Education of China (20030006003).

$\Delta u(t, k)$. Sequentially system (1) can be modeled as the following 2-D time-variant form

$$\begin{aligned} \frac{\partial x(t, k)}{\partial t} &= A(t)x(t, k) + B(t)u(t, k) \\ y(t, k) &= C(t)x(t, k) \end{aligned} \quad (2)$$

The boundary conditions for system (2) are given as $x(0, k) = x_0$ for $k = 0, 1, 2, \dots$, and $u(t, 0) = u_0(t)$ for $t \in [0, T]$. If $y_d(t)$ and $C(t)$ are differentiable for $t \in [0, T]$, denote

$$\begin{aligned} e(t, k) &= y_d(t) - y(t, k) \\ \xi(t, k) &= \frac{\partial e(t, k)}{\partial t} \\ \eta(t, k) &= x(t, k+1) - x(t, k) \end{aligned} \quad (3)$$

Thus, we can obtain

$$\begin{aligned} \frac{\partial \eta(t, k)}{\partial t} &= \frac{\partial (x(t, k+1) - x(t, k))}{\partial t} \\ &= A(t)\eta(t, k) + B(t)\Delta u(t, k) \end{aligned} \quad (4)$$

$$\begin{aligned} \xi(t, k+1) - \xi(t, k) &= \frac{\partial (e(t, k+1) - e(t, k))}{\partial t} \\ &= -\frac{\partial (y(t, k+1) - y(t, k))}{\partial t} \\ &= -[C(t)A(t) + \dot{C}(t)]\eta(t, k) \\ &\quad - C(t)B(t)\Delta u(t, k) \end{aligned} \quad (5)$$

Equations (4) and (5) can be written in compact form

$$\begin{aligned} \begin{bmatrix} \frac{\partial \eta(t, k)}{\partial t} \\ \xi(t, k+1) \end{bmatrix} &= \begin{bmatrix} A(t) & 0 \\ -C(t)A(t) - \dot{C}(t) & I \end{bmatrix} \begin{bmatrix} \eta(t, k) \\ \xi(t, k) \end{bmatrix} \\ &\quad + \begin{bmatrix} B(t) \\ -C(t)B(t) \end{bmatrix} \Delta u(t, k) \end{aligned} \quad (6)$$

Applying the following ILC scheme

$$\Delta u(t, k) = K(t)\xi(t, k) \quad (7)$$

we can derive a system with respect to the derivative of control error in accordance with the 2-D continuous-discrete Roesser's model

$$\begin{aligned} \begin{bmatrix} \frac{\partial \eta(t, k)}{\partial t} \\ \xi(t, k+1) \end{bmatrix} &= \begin{bmatrix} A(t) & B(t)K(t) \\ -C(t)A(t) - \dot{C}(t) & I - C(t)B(t)K(t) \end{bmatrix} \begin{bmatrix} \eta(t, k) \\ \xi(t, k) \end{bmatrix} \end{aligned} \quad (8)$$

The boundary conditions for (8) are $\eta(0, k) = 0$ for $k = 0, 1, 2, \dots$ and finite $\xi(t, 0)$ for $t \in [0, T]$. Also, suppose that there exists a positive number $L_{T_{10}}$ such that the following inequality holds:

$$\left\| \begin{bmatrix} A(t) & B(t)K(t) \\ 0 & 0 \end{bmatrix} \right\| \leq L_{T_{10}} \quad \text{for } t \in [0, T] \quad (9)$$

Thus, the following theorem can be proved by employing the structure of 2-D system model, the property of λ -norm, and the Bellman-Gronwall inequality.

Theorem 1. For a 2-D ILC model (2), suppose that both the desired output $y_d(t)$ and system matrix $C(t)$ are differentiable for $t \in [0, T]$. If

$$\sup_{0 \leq t \leq T} \left\| \begin{bmatrix} 0 & 0 \\ -C(t)A(t) - \dot{C}(t) & I - C(t)B(t)K(t) \end{bmatrix} \right\| < 1 \quad (10)$$

then the ILC scheme

$$u(t, k+1) = u(t, k) + K(t) \left[\frac{dy_d(t)}{dt} - \frac{\partial y(t, k)}{\partial t} \right] \quad (11)$$

can ensure that $\lim_{k \rightarrow \infty} e(t, k) = 0$ for $t \in [0, T]$.

According to Theorem 1, algorithm 1 is introduced.

Algorithm 1:

- 1). The system matrices $A(t), B(t), C(t)$, the reference output trajectory $y_d(t)$, the required form $\phi(t)$ of the whole resulting error matrix $I - C(t)B(t)K(t)$, and the trajectory tolerance $\varepsilon > 0$ are given for $t \in [0, T]$.
- 2). Let $k = 0$, $u_0(t) = 0$, $x(0) = x_0$, $K(t) = (C(t)B(t))^T [C(t)B(t)(C(t)B(t))^T]^{-1} (I - \phi(t))$.
- 3). According to system (2), calculate $y(t, k)$. If $\sup_{0 \leq t \leq T} \|y(t, k) - y_d(t)\| \geq \varepsilon$, then calculate $u(t, k+1)$ according to (11), else go to step 5).
- 4). $k = k + 1$, return to step 3).
- 5). End.

To improve the learning efficiency, a modification of learning scheme (7) is given as: $\Delta u(t, k) = -K_1(t)\eta(t, k) + K_2(t)\xi(t, k)$. Then, the system (8) can be formulated as

$$\begin{bmatrix} \frac{\partial \eta(t, k)}{\partial t} \\ \xi(t, k+1) \end{bmatrix} = \begin{bmatrix} A_{11}(t) & A_{12}(t) \\ A_{21}(t) & A_{22}(t) \end{bmatrix} \begin{bmatrix} \eta(t, k) \\ \xi(t, k) \end{bmatrix} \quad (12)$$

where submatrices are given as $A_{11}(t) = A(t) - B(t)K_1(t)$, $A_{12}(t) = B(t)K_2(t)$, $A_{21}(t) = -C(t)A(t) - \dot{C}(t) + C(t)B(t)K_1(t)$, $A_{22}(t) = I - C(t)B(t)K_2(t)$. If $C(t)B(t)$ has uniform full-row rank for $t \in [0, T]$, then we have

$$\begin{aligned} \hat{K}_1(t) &= (C(t)B(t))^+ [C(t)A(t) + \dot{C}(t)] \\ \hat{K}_2(t) &= (C(t)B(t))^+ \end{aligned}$$

so that $-C(t)A(t) - \dot{C}(t) + C(t)B(t)\hat{K}_1(t) = 0$ and $I - C(t)B(t)\hat{K}_2(t) = 0$, where $(\cdot)^+$ represents the Moore-Penrose inverse of matrix. Set $K_1(t) = \hat{K}_1(t)$, $K_2(t) = \hat{K}_2(t)$, and hence we have $\xi(t, 1) = 0$ no matter what $\xi(t, 0)$ is. Then, we can obtain $e(t, 1) = 0$ for $t \in [0, T]$ based on the initial condition $y_d(0) = C(0)x_0$.

Theorem 2. For a 2-D ILC model (2), if $C(t)B(t)$ has uniform full-row rank for $t \in [0, T]$, then there exists an

ILC scheme

$$u(t, k + 1) = u(t, k) - \hat{K}_1(t)[x(t, k + 1) - x(t, k)] + \hat{K}_2(t) \left[\frac{dy_d(t)}{dt} - \frac{\partial y(t, k)}{\partial t} \right] \tag{13}$$

that can drive the control error to zero for the whole reference output trajectory after only one learning trial.

Though Theorem 2 provides an effective ILC scheme (13), $x(t, k + 1)$ is not available, and hence further modification is needed. If system matrices of (1) are accurately known, then from equations (2) and (13), we can derive

$$\begin{aligned} \frac{\partial x(t, k+1)}{\partial t} = & [A(t) - B(t)\hat{K}_1(t)]x(t, k + 1) \\ & + B(t)[I - \hat{K}_2(t)C(t)B(t)]u(t, k) \\ & + B(t)\hat{K}_1(t)x(t, k) + B(t)\hat{K}_2(t) \times \\ & \left[\frac{dy_d(t)}{dt} - (C(t)A(t) + \dot{C}(t))x(t, k) \right] \end{aligned} \tag{14}$$

Therefore, we can apply control law

$$\begin{aligned} \hat{u}(t) = & [I - \hat{K}_2(t)C(t)B(t)]u(t) + \hat{K}_1(t)x(t) \\ & + \hat{K}_2(t) \left[\frac{dy_d(t)}{dt} - (C(t)A(t) + \dot{C}(t))x(t) \right] \end{aligned} \tag{15}$$

to the following system

$$\begin{aligned} \dot{\hat{x}}(t) = & [A(t) - B(t)\hat{K}_1(t)]\hat{x}(t) + B(t)\hat{u}(t) \\ y(t) = & C(t)\hat{x}(t) \end{aligned} \tag{16}$$

which is the state feedback form of system (1). Hence, the output of the closed-loop system is identical with the reference output, namely, $y(t) = y_d(t), t \in [0, T]$. This result can be directly verified by the response formula of system (16). Thus, the following theorem can be proved.

Theorem 3. For a 2-D ILC model (2), if the matrix $C(t)B(t)$ has uniform full-row rank for $t \in [0, T]$, then the following ILC scheme

$$u(t) \leftarrow \hat{u}(t) - \hat{K}_1(t)\hat{x}(t) \tag{17}$$

can drive the control error to zero for the whole reference output trajectory after only one learning iteration, where $\hat{x}(t)$ is the state vector of system (16).

Similarly, we give the second algorithm based on Theorem 3.

Algorithm 2:

- 1). For $t \in [0, T]$, the system matrices $A(t), B(t), C(t)$, the reference output trajectory $y_d(t)$, the initial input sequence $u(t)$, and the initial state vector of system $x(0) = x_0$ are given.
- 2). Calculate $\hat{K}_1(t), \hat{K}_2(t)$, and measure $x(t), y(t)$ from system (1).
- 3). Use (15) to calculate $\hat{u}(t)$, then apply $\hat{u}(t)$ to system (16) and measure $\hat{x}(t)$.
- 4). Apply control $\hat{u}(t) - \hat{K}_1(t)\hat{x}(t)$ to system (1).

3. Examples

Example 1: Consider the ILC problem for the following linear time-variant continuous system:

$$\begin{aligned} \dot{x}(t) = & \begin{bmatrix} -0.1\cos(t^{0.2}) & 3 \\ 0.02t & 10\sin(t) \end{bmatrix} x(t) \\ & + \begin{bmatrix} 0.027t + 1 \\ 0.12 \end{bmatrix} u(t) \\ y(t) = & [0.45 \quad -0.001t] x(t) \end{aligned} \tag{18}$$

where $x(0) = [0 \ 0]^T$, and the matrix $C(t)B(t)$ has uniform full-row rank for $t \in [0, 1]$. The desired output is given as $y_d(t) = 12t^2(1 - t)$. Using Algorithm 1, we set the initial input sequence of ILC as $u(t, 0) = 0$, and let $K(t) = 0.6(C(t)B(t))^T [C(t)B(t)(C(t)B(t))^T]^{-1}$. Additionally, the accuracy of tracking is evaluated by the following total square error of tracking:

$$S = \int_0^1 [y_d(\tau) - y(\tau)]^2 d\tau$$

Figure 1 shows the tracking error performance of the ILC system output at different time-steps and iterations, and Figure 2 performs the curves of the total square error of tracking in the process of Algorithm 1 being iteratively executed. From Figure 1-2, it can be concluded that the convergence rate of Algorithm 1 is high and the output is capable of tracking the desired trajectory accurately within few iterations.

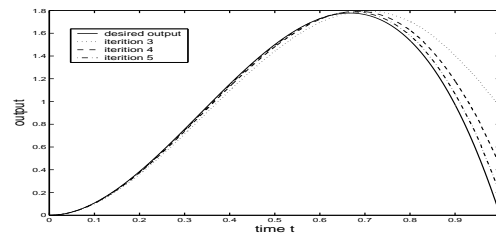


Figure 1: (Example 1) Tracking error performance of ILC system output using Algorithm 1.

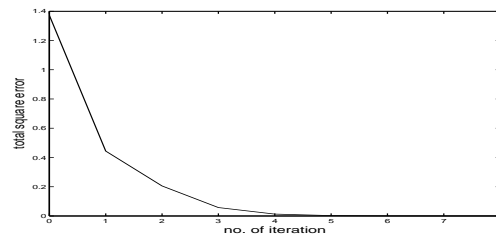


Figure 2: (Example 1) Total square error of different iterations using Algorithm 1.

Example 2: To demonstrate Algorithm 2, consider the following linear time-variant continuous system:

$$\begin{aligned} \dot{x}(t) &= \begin{bmatrix} 0.18 & 0 \\ 0.02t & -0.5 \end{bmatrix} x(t) + \begin{bmatrix} 0.1 \\ 0.01t + 2 \end{bmatrix} u(t) \\ y(t) &= \begin{bmatrix} -0.52 & 0 \end{bmatrix} x(t) \end{aligned} \quad (19)$$

where $x(0) = [00]^T$, and the matrix $C(t)B(t)$ has uniform full-row rank for $t \in [0, 1]$. The desired output is given as $y_d(t) = \sin(\pi t)$. Here, provided that the accurate information on the system parameters in system (19) is unavailable, and only its estimated system is given as

$$\begin{aligned} \dot{x}(t) &= \begin{bmatrix} 0.2 & 0 \\ 0.02t & -0.46 \end{bmatrix} x(t) + \begin{bmatrix} 0.13 \\ 0.015t + 2.1 \end{bmatrix} u(t) \\ y(t) &= \begin{bmatrix} -0.54 & -0.01 \end{bmatrix} x(t) \end{aligned} \quad (20)$$

Despite of this situation, Algorithm 2 is still effective. Figure 3 shows the tracking performance of the ILC system output at different time-steps and iterations. Also, Figure 4 describes the curves of total square error of tracking in the process of Algorithm 2 being iteratively executed. From Figure 3-4, it can be noticed that it takes few iterations for Algorithm 2 to drive the tracking error to a very low level for the whole desired output. Moreover, this simulation result demonstrates that Algorithm 2 is robust with respect to small perturbations of system parameters.

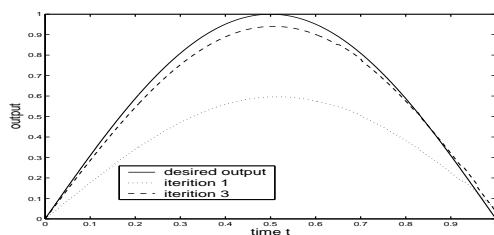


Figure 3: (Example 2) Tracking error performance of the system output using Algorithm 2.

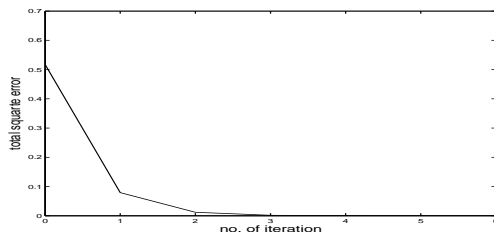


Figure 4: (Example 2) Total square error of different iterations using Algorithm 2.

4. Conclusions

Main difficulty of ILC is to establish a suitable mathematical model to describe the dynamics of the control system and the behavior of the learning process. This paper successfully established the 2-D continuous-discrete Roesser's model with respect to the derivative of the output tracking error. Then, three ILC schemes were given, and sufficient conditions for convergence of these three learning schemes were presented. Example 1-2 validated that these ILC procedures were effective and robust with respect to small perturbations of system parameters.

References

- [1] S. Arimoto, S. Kawamura, and F. Miyazaki, Bettering operation of robots by learning, *J.Robot Syst.*, vol. 1, 1984, pp. 123-140.
- [2] Kwang-Hyun Park, An average operator-based PD-type iterative learning control for variable initial state error, *IEEE Trans.Autom.Contr.*, vol. 50, no. 6, Jun., 2005, pp. 865-869.
- [3] Saner S. Saab, Optimal selection of the forgetting matrix into an iterative learning control algorithm, *IEEE Trans.Autom.Contr.*, vol. 50, no. 12, Dec., 2005, pp. 2039-2043.
- [4] Geng Ji, and Qi Luo, An open-closed-loop PID-type iterative learning control algorithm for uncertain time-delay systems, *Proceedings of the Fourth International Conference on Machine Learning and Cybernetics*, Guangzhou, 18-21, Aug., 2005, pp. 1154-1159.
- [5] Z. Geng, R. Carroll, and J. Xies, Two-dimensional model and algorithm analysis for a class of iterative learning control systems, *Int.J.Control*, vol. 52, 1990, pp. 833-862.
- [6] T. W. S. Chow, and Y. Fang, An iterative learning control method for continuous-time systems based on 2-D system theory, *IEEE Trans. Circuits Syst., I Fundam. Theory Appl.*, vol. 45, no. 4, Apr., 1998, pp. 683-689.
- [7] X.-D. Li, T. W. S. Chow, and J. K. L. Ho, 2-D system theory based iterative learning control for linear continuous systems with time delays, *IEEE Trans. Circuits Syst., I Regular Papers*, vol. 52, no. 7, Jul., 2005, pp. 1421-1430.
- [8] X.-D. Li, J. K. L. Ho and T. W. S. Chow, Iterative learning control for linear time-variant discrete systems based on 2-D system theory, *IEEE Proc.-Contr., Theory Appl.*, vol. 152, no. 1, Jan., 2005, pp. 13-18.
- [9] J. E. Kurek and M. B. Zaremba, Iterative learning control synthesis based on 2-D system theory, *IEEE Trans.Autom.Contr.*, vol. 38, no. 1, Jan., 1993, pp. 121-125.
- [10] T. Kaczorek, *Two-Dimensional Linear Systems*. New York: Springer-Verlag, 1985.

Solution Searching for Multi-variable Optimization Problems by GA with Momentum Offspring

Hiroshi KINJO, Sam DUONG CHAU, Moriyoshi MAESHIRO, Kunihiko NAKAZONO, and Tetsuhiko YAMAMOTO
Faculty of Engineering, University of the Ryukyus
Nishihara, Okinawa 903-0213, Japan

Abstract

Genetic Algorithm (GA) is known as one of the most powerful solution searching mechanism for non-linear and multi-variable optimization problems. Generally, GA takes a long time to find the solutions and sometimes it can not find the optimum solutions. In order to improve the search performance, we propose a fast algorithm of GA and a mutation method. The fast algorithm is usage of a momentum offspring (MOS). The MOS is an individual not the crossover but by the best individuals of current and past generations. The MOS is considered to have higher probability for desired solution and the effect of MOS is fast searching of the optimum solution. Furthermore, we proposed a constant range mutation (CRM) for the GA. The CRM is considered to have effect of avoiding the ineffective individual production. We apply the GA with MOS and CRM to optimization problems of two multi-variable functions and neural network training problem. Simulations show that proposed method has good performances.

Keywords: Genetic algorithm, fast algorithm, momentum offspring, constant range mutation, optimization problem, neural network training.

1 Introduction

Genetic algorithms (GAs), with many precious advantages, are now widely used in various fields, especially in solving optimization problems. Generally, GAs are also time-consuming in computing, however, and sometimes it can not produce the desired results. In order to improve the search performance, we propose a fast algorithm of GA and a mutation method, i.e. momentum offspring (MOS) and constant range mutation (CRM).

In section 2, we describe a new method, then, in section 3, we investigate the search performance of the method for multi-variable functions. Finally, we apply

the method for neural network training problem. We conclude this paper in section 5.

2 Fast GA

2.1 New Method of Recombination

Conventionally, GAs use the recombination, known as genetic operations or offspring production process, which typically involves crossover and mutation operators to yield offspring at each generation. The conventional recombination is shown in Figure 1 (a). To improve the performance of GA, we now propose a new recombination which includes constant range mutation (CRM) and momentum offspring (MOS) operators, as shown in Figure 1 (b). In this method, MOS and CRM are applied simultaneously but with different rates of R_{mo} and R_{mu} , respectively.

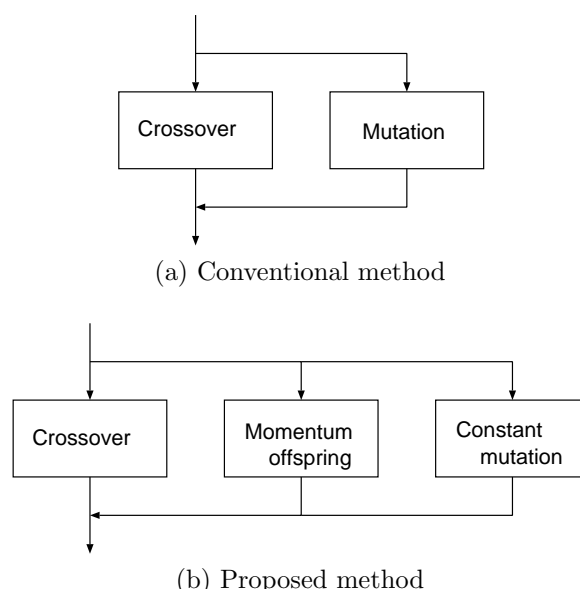


Fig. 1 Offspring production process

2.2 Momentum Offspring

For each generation, conventional GAs produce offspring by random process. In our proposed method, i.e. MOS, the next best individual will be determined based on the best individuals of the past and current generations. Namely, if the best individuals of the past generation ($g - 1$) and current generation (g) are x_{best}^{g-1} and x_{best}^g , respectively, then the best individual of next generation ($g + 1$) can be determined as:

$$x_m^{g+1} = cr \left(x_{best}^g - x_{best}^{g-1} \right) + x_{best}^g \quad (1)$$

where, c is a constant coefficient (we set $c = 1$ here) and r is a random coefficient in the range of $[0, 1]$. Figure 2 shows the idea of MOS method.

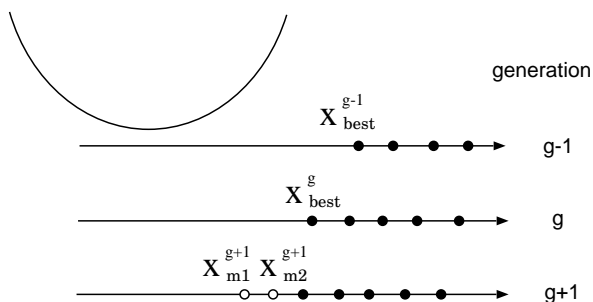


Fig. 2 Momentum offspring

2.3 Constant range mutation

Sometimes, GAs has problem when it just can produce the local optimum values. But GAs can also reduce this possibility by mutation operator. A simple way to achieve mutation would be to alter one or more genes. For reducing this problem more properly, we propose a new mutation operator that is constant range mutation (CRM). In this CRM, we will apply mutation by generating random real values in the range that widens from two parents x_{p1} and x_{p2} ($x_{p1} < x_{p2}$) a constant range of L . Namely, the applied range of mutation is $[x_{p1} - L, x_{p2} + L]$ as shown in Figure 3.

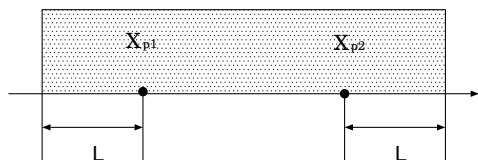


Fig. 3 Constant range mutation

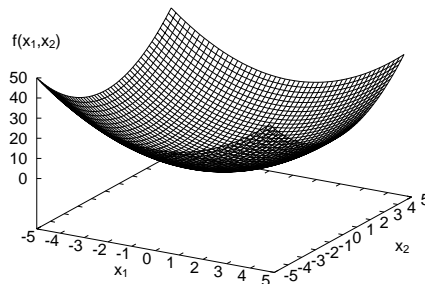
3 Optimization of multi-variable functions

We consider optimization problems of following two multi-variable functions, Sphere function and Rastrigin function,

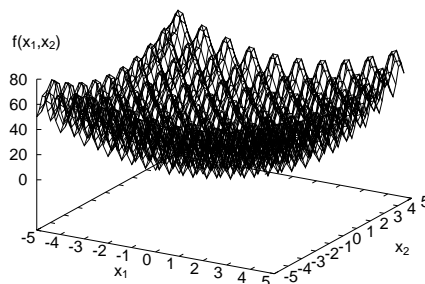
$$f(x) = \sum_{i=1}^n x_i^2 \quad (2)$$

$$f(x) = 10n + \sum_{i=1}^n (x_i^2 - 10 \cos(2\pi x_i)) \quad (3)$$

where, n is number of dimensions. In this research, we will investigate the search performances of GA with MOS and CRM for above functions with $n = 2$. The ranges of variables are $x_i \in [-5.0, 5.0]$. $x_i = 0$. Parameters for GA are as followings: number of population is 20, number of generation is 100 and the range parameter is $L = 1.0$. The search performance is evaluated by successful evolution rates obtained from the minimum values of the function in the GA. The simulation results are shown in Figure 5, for Sphere function, and Figure 6, for Rastrigin function. Generally, it can be observed that the search performances of our proposed GA increase with R_{mo} and R_{mu} and it has better performances than the conventional GA. For Rastrigin function, it is more difficult to find the optimum value because this function is more complicated and it has some local optimum values, the performance in this case is therefore lower than the performance obtained from Sphere function.



(a) Sphere function



(b) Rastrigin function

Fig. 4 Test functions

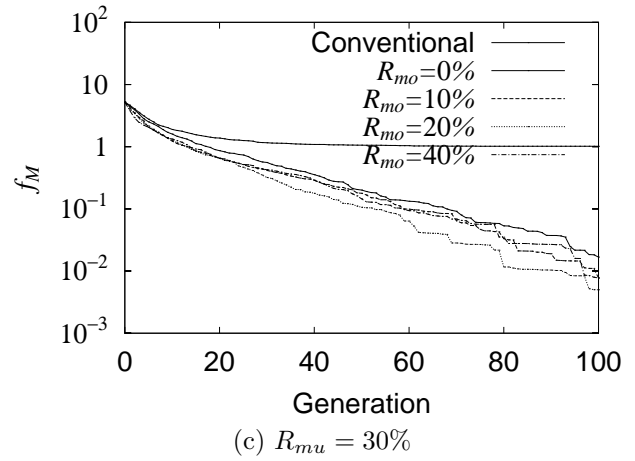
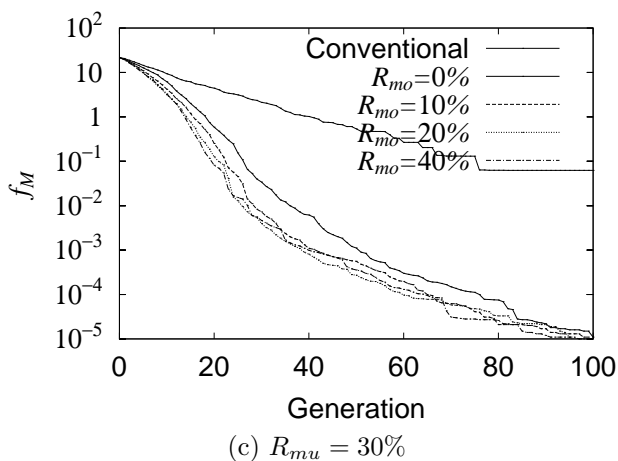
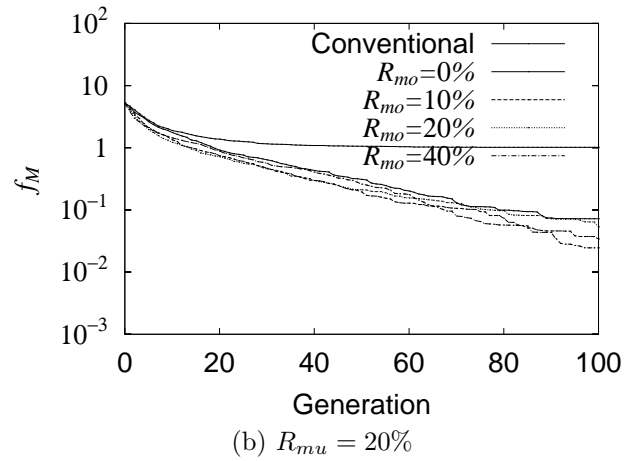
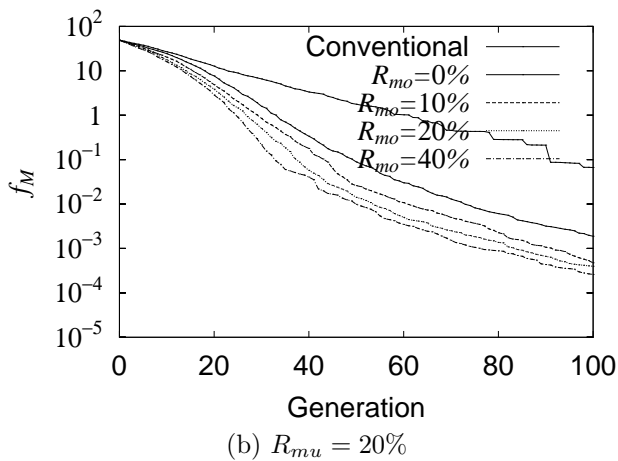
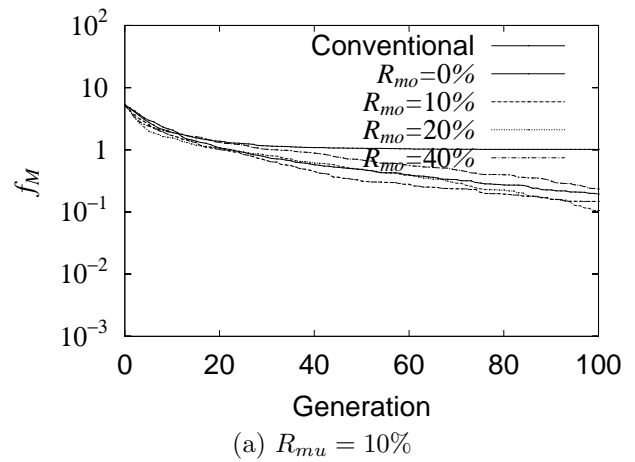
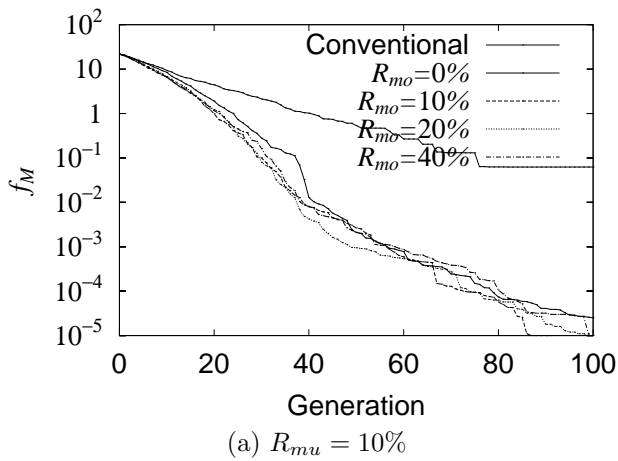


Fig. 5 Evolution results for Sphere function ($n = 2$)

Fig. 6 Evolution results for Rastrigin function ($n = 2$)

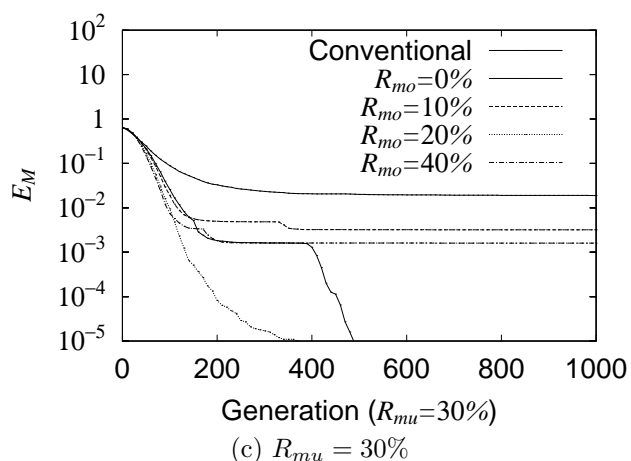
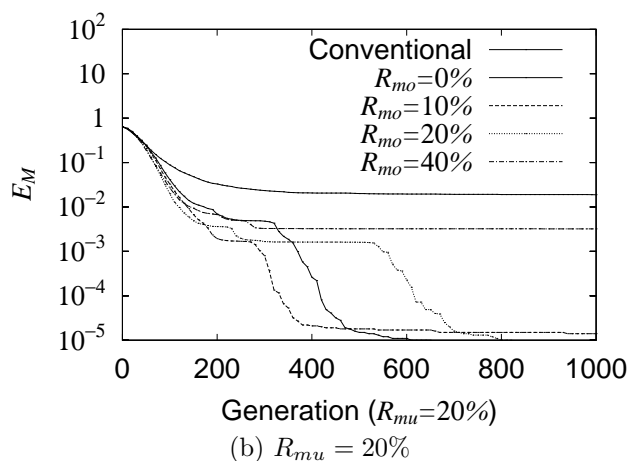
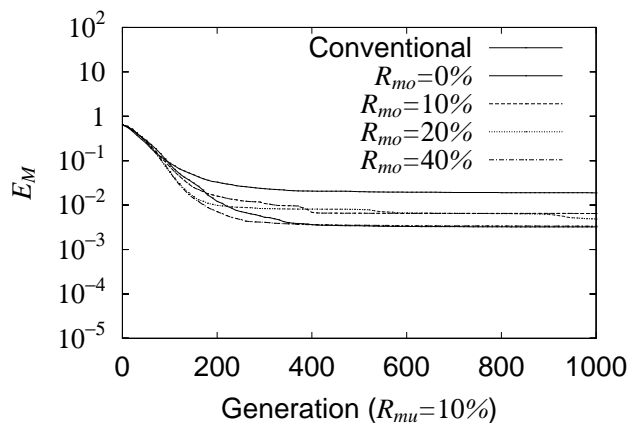


Fig. 7 Training results of NN

4 Neural network training

This section presents simulation results of neural network training problem; known as a nonlinear multi-variable optimization problem. In order to evaluate the performance of our proposed GA, we will use the well-known exclusive - or problem (XOR). Figure 7 shows the simulation results. It can be seen that the proposed method has better training performance than that of conventional method.

5 Summary

Improving GAs by design new recombination process may achieve advantages. In this research, we have presented a new method for improving the performance of GA by using a fast algorithm with momentum offspring (MOS) and constant range mutation (CRM). The simulations show that our proposed method has a good performance.

References

- [1] D. E. Goldberg, *Genetic Algorithms in Search, Optimization & Machine Learning*, Addison-Wesley, 1989.
- [2] L. Davis, *Hand Book of Genetic Algorithms*, Van Nostrand Reinhold, 1991.
- [3] M. Gen and R. Cheng, *Genetic Algorithm and Engineering Design*, Wiley-Interscience, 1997.
- [4] L. J. Eshelman and J. D. Schaffer, "Real-Coded Genetic Algorithms and Interval-Schemata" *Foundations of Genetic Algorithms 2*, Edited by L. Darrell Whitley, Morgan Kaufmann Publishers, 1993.
- [5] M. Maeshiro, H. Kinjo, K. Nakazono, and T. Yamamoto, *Fast Method of Genetic Algorithm Searching and Its Application to Neural Network Training*, Technical Reprint of the IEICE NC2006-22-37, pp. 81-84, 2006. (in Japanese)
- [6] H. Okamura, K. Kitasuka and T. Dohi, "Performance Evaluation of Genetic Algorithms Based on Markovian Analysis - Evaluation by Relaxation Time and Application to Real-Coded Genetic Algorithms," *Transactions of the ISCIE*, Vol. 16, No. 7, pp. 303-312, 2003. (in Japanese)

Improvement of Training Method for Dynamic Neural Network

Kunihiko Nakazono
University of the Ryukyus
Senbaru 1, Nishihara, Okinawa. 903-0213
nakazono@mibai.tec.u-ryukyu.ac.jp

Kouhei Ohnishi
Keio University
Hiyoshi 3-14-1, Yokohama. 222-8522
ohnishi@sd.keio.ac.jp

Hiroshi Kinjo
University of the Ryukyus
Senbaru 1, Nishihara, Okinawa. 903-0213
kinjo@tec.u-ryukyu.ac.jp

Tetsuhiko Yamamoto
University of the Ryukyus
Senbaru 1, Nishihara, Okinawa. 903-0213
yamamoto@tec.u-ryukyu.ac.jp

Abstract

In this research, we propose a dynamic neural network (DNN) with the characteristics of stiffness, viscosity, and inertia and a training algorithm based on the back-propagation (BP) method to include a momentum term. In a previous research, we proposed a training algorithm for the DNN based on the BP method or GA-based training method. However, in the previous method it was necessary to determine the values of the DNN parameters by trial and error. So, the modified BP method and GA-based training method were designed to train not only the connecting weights but also the property parameters of the DNN.

We develop the BP method to include a momentum term in order to increase the convergence of the training effect. Simulation results show that the DNN with characteristics of stiffness, viscosity, and inertia trained by the modified BP method to include the momentum term obtains good training performances for time series signals generated from periodic function. In this paper, we compare the DNN with a conventional training method in order to verify the effectiveness of the DNN.

1 Introduction

In recent years, recurrent neural networks and spiking neural networks have attracted more research interest than layered neural networks having simple structure [1, 2, 3, 4]. The recurrent neural network is a possible candidate for improving the system dynamics because it takes time delayed inputs into consideration and incorporates a feedback structure in the neuron unit. Research on spiking neural networks is also on-

going. Spiking neural networks treat spike trains and process the signals based on spike pulses. However, the network structure in recurrent neural networks and spiking neural networks is complex compared to that in layered neural networks with a training method.

Here, we propose a dynamic neural network (DNN) that realizes a dynamic property and has a network structure with the properties of stiffness, viscosity, and inertia without time delayed input elements. In a previous research, the DNN was constructed with a training algorithm that used error back-propagation (BP) method [5]. However, the BP method updated only the connecting weights for the DNN, and the property parameters for the DNN had to be decided by trial and error. Therefore, we designed a GA-based training method [6] to train both the connecting weights and the parameters of the DNN. But the GA-based training method took the executing time of computer program that evolved in GA simulation [7, 8]. We developed the modified BP method to train both the connecting weights and the parameters [9].

In the present paper, we design the BP method to include a momentum term in order to increase the convergence of the training effect. The effectiveness of the proposed DNN is verified by identifying time series signals [5, 7, 8, 9]. Simulation results show that the proposed DNN provides higher performance than the conventional method.

2 Structure of DNN

In this research, we propose a DNN using a neuron unit having the properties of stiffness, viscosity, and inertia without time delayed input elements. In the

neuron unit, we assume that the output from the neuron possesses the properties of stiffness, viscosity, and inertia, and that the output is propagated in the next neuron unit. The proposed DNN is composed of three hierarchy layers, and the proposed neuron adopts only in a hidden layer. The structure of the DNN is shown in Figure 1.

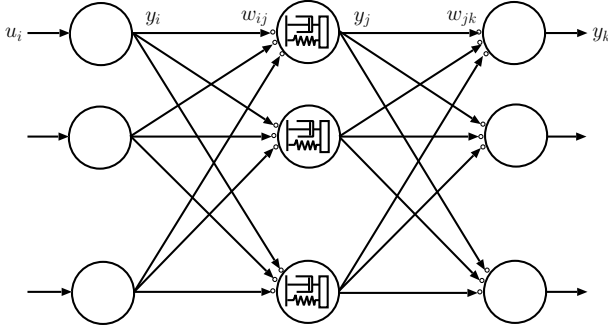


Fig. 1 Structure of DNN

The equations for the DNN are expressed as follows:

$$y_i = u_i, \quad (i = 1, 2, \dots, N_I) \quad (1)$$

$$y_j = K_j f_j(\text{net}_j) + D_j \dot{f}_j(\text{net}_j) + M_j \ddot{f}_j(\text{net}_j) \quad (2)$$

$$\text{net}_j = \sum_{i=1}^{N_I} w_{ij} y_i, \quad (j = 1, 2, \dots, N_J) \quad (3)$$

$$y_k = f_k(\text{net}_k) \quad (4)$$

$$\text{net}_k = \sum_{j=1}^{N_J} w_{jk} y_j, \quad (k = 1, 2, \dots, N_K) \quad (5)$$

where u_i is the input value to the DNN, and y_i , y_j , and y_k are the output values in the input, hidden, and output layers, respectively. The connecting weight from unit i in the input layer to unit j in the hidden layer is denoted by w_{ij} . Similarly, w_{jk} is a connecting weight from unit j in the hidden layer to unit k in the output layer. The total sum of the products of the connecting weight w_{ij} and w_{jk} and the output value is denoted by net_j and net_k , respectively. M_j , D_j , and K_j are the property parameters of inertia, viscosity, and stiffness, respectively, and N_I , N_J , and N_K are the number of neurons in the input, hidden, and output layers, respectively. The activation function $f_j(x)$ in the hidden layer uses a sigmoid function in range of $[-1, 1]$. Also the activation function $f_k(x)$ in the output layer is a linear function.

3 BP-based training method

First, we derive a minimizing sequence of the measurement of error function E :

$$E = \frac{1}{2} \sum_{k=1}^{N_K} e_k^2 = \frac{1}{2} \sum_{k=1}^{N_K} (d_k - y_k)^2 \quad (6)$$

where d_k is the desired signal. In order to minimize the measurement of the error function E of equation (6), both of the connecting weights and the property parameters of the DNN are modified.

The BP-based training method is shown in section 3. The connecting weights and the property parameters of the DNN are updated sequentially based on the steepest descent method.

$$\Delta w_{ij} = w_{ij}^{(\text{new})} - w_{ij}^{(\text{old})} = -\varepsilon \frac{\partial E}{\partial w_{ij}} \quad (7)$$

$$\Delta w_{jk} = w_{jk}^{(\text{new})} - w_{jk}^{(\text{old})} = -\varepsilon \frac{\partial E}{\partial w_{jk}} \quad (8)$$

$$\Delta K_j = K_j^{(\text{new})} - K_j^{(\text{old})} = -\varepsilon \frac{\partial E}{\partial K_j} \quad (9)$$

$$\Delta D_j = D_j^{(\text{new})} - D_j^{(\text{old})} = -\varepsilon \frac{\partial E}{\partial D_j} \quad (10)$$

$$\Delta M_j = M_j^{(\text{new})} - M_j^{(\text{old})} = -\varepsilon \frac{\partial E}{\partial M_j} \quad (11)$$

ε is the training rate ($\varepsilon > 0$).

$\partial E / \partial w_{jk}$ and $\partial E / \partial w_{ij}$ are described as follows.

$$\frac{\partial E}{\partial w_{jk}} = \frac{\partial E}{\partial \text{net}_k} \cdot \frac{\partial \text{net}_k}{\partial w_{jk}} = \frac{\partial E}{\partial \text{net}_k} \cdot y_j \quad (12)$$

$$\frac{\partial E}{\partial w_{ij}} = \frac{\partial E}{\partial \text{net}_j} \cdot \frac{\partial \text{net}_j}{\partial w_{ij}} = \frac{\partial E}{\partial \text{net}_j} \cdot y_i \quad (13)$$

In the upper expression, the derivations are defined as

$$\delta_k = \frac{\partial E}{\partial \text{net}_k} \quad (14)$$

$$\delta_j = \frac{\partial E}{\partial \text{net}_j} \quad (15)$$

and δ_k and δ_j are calculated, respectively. First, δ_k is expanded as

$$\begin{aligned} \delta_k &= \frac{\partial E}{\partial \text{net}_k} = \frac{\partial E}{\partial e_k} \cdot \frac{\partial e_k}{\partial y_k} \cdot \frac{\partial y_k}{\partial \text{net}_k} \\ &= -e_k f'_k(\text{net}_k) \end{aligned} \quad (16)$$

δ_k finally becomes equation (16).

When δ_j is calculated in the same way, it becomes Equation (17).

$$\begin{aligned} \delta_j &= \frac{\partial E}{\partial \text{net}_j} \\ &= \sum_{k=1}^{N_K} \left(\frac{\partial E}{\partial e_k} \cdot \frac{\partial e_k}{\partial y_k} \cdot \frac{\partial y_k}{\partial \text{net}_k} \right) \cdot \frac{\partial \text{net}_k}{\partial y_j} \cdot \frac{\partial y_j}{\partial \text{net}_j} \\ &= \sum_{k=1}^{N_K} \delta_k \cdot w_{jk} \cdot \frac{\partial y_j}{\partial \text{net}_j} \end{aligned} \quad (17)$$

$\partial y_j / \partial \text{net}_j$ is expressed as equations (18)–(21).

$$\begin{aligned} \frac{\partial y_j}{\partial \text{net}_j} &= K_j \frac{\partial f_j(\text{net}_j)}{\partial \text{net}_j} + D_j \frac{\partial \dot{f}_j(\text{net}_j)}{\partial \text{net}_j} + M_j \frac{\partial \ddot{f}_j(\text{net}_j)}{\partial \text{net}_j} \end{aligned} \quad (18)$$

$$\frac{\partial f_j(\text{net}_j)}{\partial \text{net}_j} = f'_j(\text{net}_j) \quad (19)$$

$$\frac{\partial \dot{f}_j(\text{net}_j)}{\partial \text{net}_j} = f''_j(\text{net}_j) \cdot \dot{\text{net}}_j \quad (20)$$

$$\frac{\partial \ddot{f}_j(\text{net}_j)}{\partial \text{net}_j} = f'''_j(\text{net}_j) \cdot \text{net}_j^2 + f''_j(\text{net}_j) \cdot \ddot{\text{net}}_j \quad (21)$$

Next, the derivation of $\partial E / \partial K_j$ is described as follows.

$$\begin{aligned} \frac{\partial E}{\partial K_j} &= \sum_{k=1}^{N_K} \frac{\partial E}{\partial \text{net}_k} \cdot \frac{\partial \text{net}_k}{\partial y_j} \cdot \frac{\partial y_j}{\partial K_j} \\ &= f_j(\text{net}_j) \cdot \sum_{k=1}^{N_K} w_{jk} \delta_k \\ &= f_j(\text{net}_j) \gamma_j \end{aligned} \quad (22)$$

where $\gamma_j = \sum_{k=1}^{N_K} w_{jk} \delta_k$.

When the property parameters D_j and M_j for the error function E are calculated in the same way, it becomes Equations (23) and (24).

$$\begin{aligned} \frac{\partial E}{\partial D_j} &= \sum_{k=1}^{N_K} \frac{\partial E}{\partial \text{net}_k} \cdot \frac{\partial \text{net}_k}{\partial y_j} \cdot \frac{\partial y_j}{\partial D_j} \\ &= \dot{f}_j(\text{net}_j) \gamma_j \end{aligned} \quad (23)$$

$$\begin{aligned} \frac{\partial E}{\partial M_j} &= \sum_{k=1}^{N_K} \frac{\partial E}{\partial \text{net}_k} \cdot \frac{\partial \text{net}_k}{\partial y_j} \cdot \frac{\partial y_j}{\partial M_j} \\ &= \ddot{f}_j(\text{net}_j) \gamma_j \end{aligned} \quad (24)$$

In order to increase the convergence of the training effect, we modify the equations (7)–(11) to include a momentum term. These equations are described as follows.

$$\Delta w_{ij}(t+1) = -\varepsilon \delta_j y_i + \eta \Delta w_{ij}(t) \quad (25)$$

$$\Delta w_{jk}(t+1) = -\varepsilon \delta_k y_j + \eta \Delta w_{jk}(t) \quad (26)$$

$$\Delta K_j(t+1) = -\varepsilon f_j(\text{net}_j) \gamma_j + \eta_k \Delta K_j(t) \quad (27)$$

$$\Delta D_j(t+1) = -\varepsilon \dot{f}_j(\text{net}_j) \gamma_j + \eta_d \Delta D_j(t) \quad (28)$$

$$\Delta M_j(t+1) = -\varepsilon \ddot{f}_j(\text{net}_j) \gamma_j + \eta_m \Delta M_j(t) \quad (29)$$

where t indexes the present time, and η , η_k , η_d , and η_m are small constant values.

In this way, the connecting weights and property parameters of the DNN are updated based on the concept of the modified BP algorithm to include the momentum term.

4 Numerical simulation

The effectiveness of the DNN proposed in the paper is verified by numerical simulation in order to identify a periodic function. The DNN is structured to have a single input and single output (SISO). The method by which a time series signal can be identified is shown in Figure 2. The desired signal, namely the training

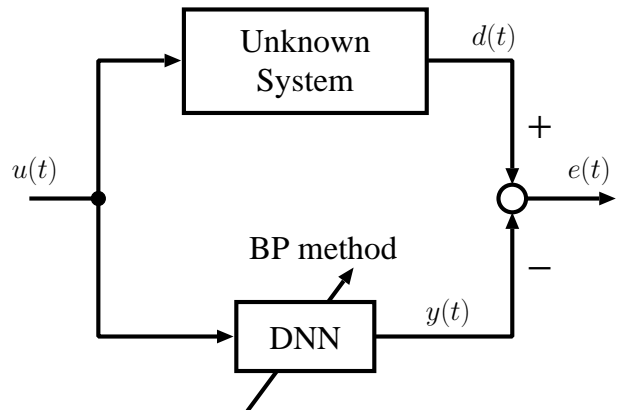


Fig. 2 Identification of signals

data $d(t)$, is the signal that has passed one sampling period prior to the input signal $u(t)$.

In order to facilitate analysis, simulation shows that the DNN identified the time series signal of the single sine periodic function with cycle T as

$$u(t) = \sin\left(\frac{2\pi t}{T}\right). \quad (30)$$

In numerical simulation, the number of neurons N_J in the hidden layer is 5 units, and the cycle T equals 16. The initial range of the connecting weights of the DNN is set to $[-0.3, 0.3]$ at random, and the initial range of the property parameters is set to 1.0. The training rate is set to $\varepsilon = 0.1$, and the momentum rates are set to $\eta = 0.0005$, $\eta_k = \eta_d = \eta_m = 0.0$, respectively.

The training involved 1,000 iterations. The result of the error function E is shown in Figure 3.

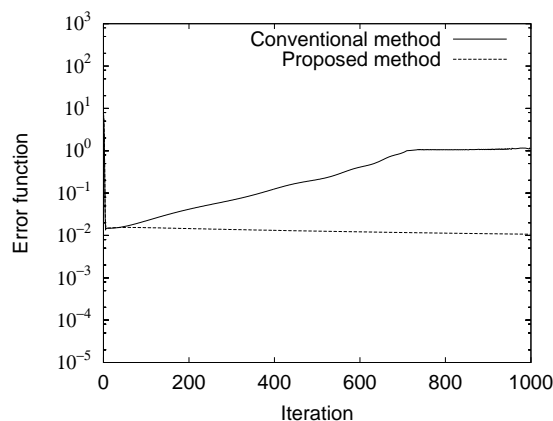


Fig. 3 Iteration result

The result of the simulation shows that the proposed DNN provides good performance compared with the conventional method without momentum term ($\eta = 0.0$, $\eta_k = \eta_d = \eta_m = 0.0$). The error function E decreases gradually and E almost converge about 0.01. The output of the DNN deviated negligibly from the desired signal.

5 Conclusion

In the present paper, the proposed DNN, showing the validity of dynamic neuron with properties of stiffness, viscosity, and inertia, was structured. The training algorithm adopt the modified BP method. We designed a modified BP method to include a momentum term in order to train both the connecting weights and the parameters of the DNN. Simulation results showed that the DNN trained by the BP method realized good training performance compared with the conventional method for time series signals generated from a periodic function.

References

- 1 D. E. Rumelhart, J. L. McClelland, and PDP Research Group (1989), Parallel distributed processing, MIT Press.
- 2 R. J. Williams and D. Zipser (1989), A Learning algorithm for continually running fully recurrent neural networks, *Neural Computation*, 1, No.2, pp.270-280.
- 3 H. Kinjo, K. Nakazono, and T. Yamamoto (1997), Pattern Recognition for time series signals using recurrent neural networks by genetic algorithms (in Japanese), *Trans. of ISCIE*, Vol. 10, No. 6, pp.304-314.
- 4 W. Mass and C. M. Bishop (1999), Pulsed neural networks, pp. 16-53, MIT Press.
- 5 K. Nakazono, K. Ohnishi, H. Kinjo, and T. Yamamoto (2003), Identification of periodic function using dynamical neural network, *AROB 8th '03*, Vol.2, pp. 633-636.
- 6 Edited by L. Davis (1991), *Handbook of genetic algorithms*, Van Nostrand Reinhold, New York.
- 7 K. Nakazono, K. Ohnishi, and H. Kinjo (2004), System identification using dynamical neural network with GA-based training, *AROB 9th '04*, Vol.1, pp. 75-78.
- 8 K. Nakazono, K. Ohnishi, and H. Kinjo (2005), Identification of time series signals using dynamical neural network with GA-based training, *AROB 10th '05*, CD-ROM, pp. 25-28.
- 9 K. Nakazono, K. Ohnishi, and H. Kinjo (2006), Identification using dynamical neural network with modified BP method, *AROB 11th '06*, CD-ROM, pp. 126-129.

A learning model of head-direction cells and grid cells by VQ layers connected via anti-Hebbian synapses

Naoki Oshiro, Koji Kurata and Tetsuhiko Yamamoto
Faculty of Engineering, University of the Ryukyus,
1 Senbaru, Nishihara, Okinawa. 903-0213
oshiro@mibai.tec.u-ryukyu.ac.jp

Abstract

In this paper, we proposed three layered self-organizing model to extract head direction and position of a moving object separately. The model consists of three layers, each of which is a self-organizing vector quantization (VQ) model. The second layer receives inhibitory input from the first, and the third layer receives inhibitory input from the first and the second. The first layer is to detect head direction and the second and the third are to detect position. The information representation in the second and the third layers is shown to be multi-ary expression and the units in the third layer develop receptive field with grid structure as was observed in entorhinal cortex of a rat.

1 Introduction

The self-organizing map (SOM) and the vector quantization (VQ) are very famous and widely used among many self-organizing models. They are useful for application and also important as a computational models of neural systems.

SOM algorithm was proposed by Kohonen[1] as a model of the cerebral cortex and its self-organization. It was successful at reproducing a functional map of the visual cortex[2, 3], and was applied to many kinds of data as a statistical tool of nonlinear auto-regression[1]. This map can extract major informations from multi-dimensional data[4].

The vector quantization (VQ) is an on-line learning algorithm to generate reference vectors for a set of input vectors[1, 5, 6, 7]. For a given input vector, the closest reference vector is chosen to approximate it. VQ algorithm can generate a set of reference vectors which minimizes mean square of approximation error. The algorithm can be interpreted as a self-organizing neural network model adopting competitive Hebbian

learning rule, i.e. a self-organizing map (SOM) lacking neighborhood learning. Thus, VQ and SOM are very similar models closely related to each other.

We studied a model consisting of two SOMs connected via anti-Hebbian connections, and showed that it can extract two different information components on the two SOMs each[8]. The model was applied to extract position and head direction from visual information. In this application, one of the two SOMs consists of two-dimensional array of cells so that it can represent two-dimensional positional information, and the other SOM consisting of one-dimensional array of cells is assigned for one-dimensional information of direction of the moving object. Simulation results showed that position-sensitive and direction-insensitive cells are formed on the two-dimensional SOM, and direction-sensitive and position-insensitive cells are formed on the one-dimensional SOM.

In recent study of cortical micro circuits, it was found that positional information are represented by 'grid cell' in the dorsocaudal medial entorhinal cortex (dMEC)[9]. Grid cells are a kind of position cells but their *receptive field* shows periodic grid structure in the area within which rats are allowed to walk around. A receptive field of a position cell is the set consisting of all positions at which the cell fires. It is striking that the receptive field of the grid cell in dMEC was not connected but distributed periodically in hexagonal lattice, for in most of the self-organizing models receptive fields of the cells tend to be connected. We, however, succeeded in reproducing grid-cell-like position cells by a self-organizing model consisting of two VQ layers connected by anti-Hebbian inhibitory synapses[10]. In the study we simplified the problem by using input carrying positional information only. Here, we propose a more natural model consisting of three VQ layers all of which are trained by 4D inputs carrying both of positional and directional information. Computer simulation showed that also in

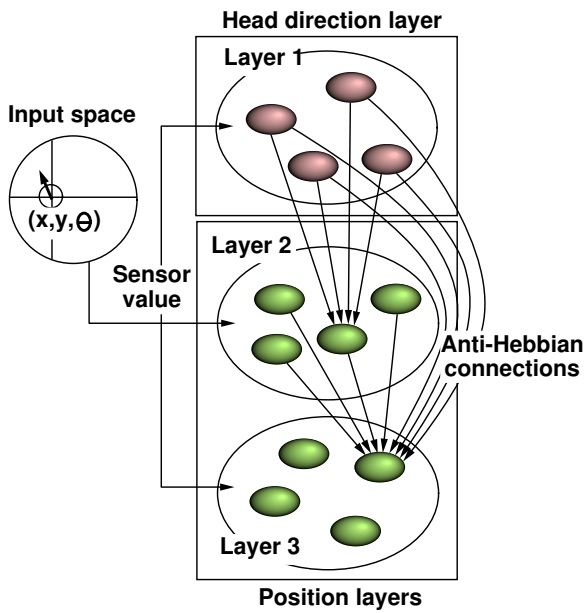


Figure 1: Structure of the proposed model. Three layers receive a same input at a time. Input vector contains two-dimensional positional information and one-dimensional directional information. Layer 1 is for directional information and Layers 2 and 3 are for positional information.

this model grid-cell-like position cells were generated in Layer 3.

2 Layer composition of connected VQs

Our model consists of three layers. Layer 1 is to detect head direction of the object and Layers 2 and 3 to detect position. Any unit in Layer 2 receives inhibitory input from all units in Layer 1 via anti-Hebbian synapses, and any unit in Layer 3 receives inhibitory input from all units in Layers 1 and 2 via anti-Hebbian synapses.

All the cells in the three layers receive a same input vector \mathbf{x} which is a function of position (x, y) and head direction θ of the object moving randomly in a room (Figure 1). Layer 1 receives no inputs from Layer 2 or 3, so it works just as an usual VQ model for the input data. On the other hand, the learning processes of Layers 2 and 3 are influenced by the cells of Layer 1 through the anti-Hebbian synapses.

The learning rule is described as follows. In this description, we refer to our algorithm as ‘VQ-AH’:

(VQ-AH1) Assign random values for reference vectors of all units in the three layers $\mathbf{m}_i^{(1)}, \mathbf{m}_j^{(2)}, \mathbf{m}_k^{(3)}$, where $i = 1, \dots, N^{(1)}$,

$j = 1, \dots, N^{(2)}$, $k = 1, \dots, N^{(3)}$, and superscript $(1), (2)$ and (3) stand for the Layers 1, 2 and 3, respectively. Initialize all inhibitory connections $s_{j,i}^{(2)(1)}, s_{k,i}^{(3)(1)}, s_{k,j}^{(3)(2)}$ to zero.

(VQ-AH2) Set the position (x, y) , ($x^2 + y^2 \leq 1$) and the head direction θ ($-\pi \leq \theta < \pi$) of the object randomly w.r.t the uniform distribution. Calculate input vector $\mathbf{x} = (x, y, \cos \theta, \sin \theta)$ to the VQ layers.

(VQ-AH3) Find the winner, $c^{(1)}$ in Layer 1 for the input \mathbf{x} :

$$c^{(1)} = \underset{i}{\operatorname{argmin}} \left\{ \left\| \mathbf{m}_i^{(1)} - \mathbf{x} \right\|^2 + \theta_i \right\} \quad (1)$$

where θ_i is the threshold or handicap of cell i in Layer 1. Then find the winner $c^{(2)}$ in Layer 2, considering the inhibitory input $s_{j,c^{(1)}}^{(2)(1)}$ from the winner in the superior layer:

$$c^{(2)} = \underset{j}{\operatorname{argmin}} \left\{ \left\| \mathbf{m}_j^{(2)} - \mathbf{x} \right\|^2 + s_{j,c^{(1)}}^{(2)(1)} \right\} \quad (2)$$

Finally, find the winner, $c^{(3)}$ in Layer 3 with inhibitory inputs $s_{k,c^{(1)}}^{(3)(1)}, s_{k,c^{(2)}}^{(3)(2)}$ from the other two layers

$$c^{(3)} = \underset{j}{\operatorname{argmin}} \left\{ \left\| \mathbf{m}_k^{(3)} - \mathbf{x} \right\|^2 + s_{k,c^{(1)}}^{(3)(1)} + s_{k,c^{(2)}}^{(3)(2)} \right\}. \quad (3)$$

(VQ-AH4) After finding three winners $c^{(1)}, c^{(2)}$ and $c^{(3)}$, we assign winners’ information to variable $y_i^{(1)}, y_j^{(2)}$ and $y_k^{(3)}$, respectively:

$$y_i^{(l)} = \begin{cases} 1, & i = c^{(l)}, \\ 0, & \text{otherwise,} \end{cases} \quad (l = 1, 2, 3) \quad (4)$$

(VQ-AH5) Update the reference vectors of the winners in the three layers.

$$\mathbf{m}_i^{(l)} := \mathbf{m}_i^{(l)} + y_i^{(l)} \alpha^{(l)} (\mathbf{x} - \mathbf{m}_i^{(l)}), \quad (l = 1, 2, 3) \quad (5)$$

where $\alpha^{(l)}$ is the learning parameter of the reference vectors.

(VQ-AH6) Update the threshold values of Layer 1

$$\theta_i := \theta_i + \gamma \left(y_i^{(1)} - \frac{1}{N^{(1)}} \right) \quad (6)$$

where γ is the learning parameter of the threshold, and update the inhibitory connections

$$\begin{aligned} s_{j,i}^{(2)(1)} &:= s_{j,i} + \beta^{(2)(1)} \left(y_i^{(1)} y_j^{(2)} - \frac{1}{N^{(1)} N^{(2)}} \right), \\ s_{k,i}^{(3)(1)} &:= s_{k,i} + \beta^{(3)(1)} \left(y_i^{(1)} y_k^{(3)} - \frac{1}{N^{(1)} N^{(3)}} \right), \\ s_{k,j}^{(3)(2)} &:= s_{k,j} + \beta^{(3)(2)} \left(y_j^{(2)} y_k^{(3)} - \frac{1}{N^{(2)} N^{(3)}} \right) \end{aligned} \quad (7)$$

where $\beta^{(2)(1)}$, $\beta^{(3)(1)}$, $\beta^{(3)(2)}$ are the learning parameters of the inhibitory connections.

(VQ-AH7) Return to (VQ-AH2) and repeat (VQ-AH2)–(VQ-AH6) many times.

As iterative learning proceeds, the learning parameters $\alpha^{(l)}$ ($l = 1, 2, 3$) and $\beta^{(2)(1)}$, $\beta^{(3)(1)}$, $\beta^{(3)(2)}$ are updated as follows:

$$\begin{cases} \alpha^{(l)} &:= \alpha_0^{(l)} (1 - t/t_{\max}), \quad (l = 1, 2, 3) \\ \beta^{(2)(1)} &:= \beta_0^{(2)(1)} (1 - t/t_{\max}), \\ \beta^{(3)(1)} &:= \beta_0^{(3)(1)} (1 - t/t_{\max}), \\ \beta^{(3)(2)} &:= \beta_0^{(3)(2)} (1 - t/t_{\max}). \end{cases} \quad (8)$$

where $\alpha_0^{(l)}$, $\beta_0^{(2)(1)}$, $\beta_0^{(3)(1)}$, $\beta_0^{(3)(2)}$ are initial values of $\alpha^{(l)}$ and correspondig β , and t , t_{\max} are iterative learning times and maximum of iterative learning times, respectively. This update leads stability of learning.

3 Input Data

We need additional learning rules to assign directional information to Layer 1 and positional information to Layers 2 and 3. We divide the whole input sequence into short periods. There are two kinds of periods coming up alternatively. One is a *position-fix* period and the other *direction-fix* period. A direction-fix period consists of some sequential inputs which share a fixed direction θ but have different positions (x, y) . A position-fix period consists of some sequential inputs which share a fixed position (x, y) but have different directions θ . For the first input of a direction-fix period the winner of Layer 1 is defined by (1), but for the rest of the inputs in the period the winner remains unchanged, while the winners of Layers 2 and 3 are defined for each inputs by (2) and (3), respectively. For the first input of a position-fix period the winners of Layers 2 and 3 are defined by (2), (3), but for the rest of the inputs in the period the winners remain unchanged, while the winner of Layer 1 is defined for

each inputs by (1). In this simulation the either kind of period consists of 15 inputs.

4 Simulation results

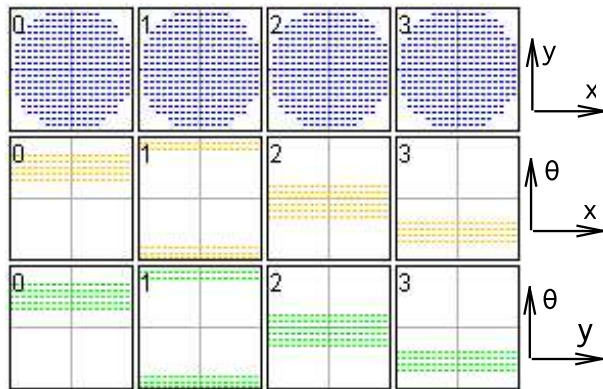
In the equilibrium of the learning process, the learning rule (6) assures that the distribution of the winner on Layer 1 should be uniform over the layer. Similarly, the learning rules (7) assure that the distribution of the two winners on two of the the three layers should be statistically pairwise-independent of each other or the joint probability of the two winners should be uniform. It should be noted this does not mean that the distributions of the three winners are independent.

Each of the three VQ layers consists of 4 units ($N^{(1)} = N^{(2)} = N^{(3)} = 4$). Learning parameters of this experiment are $\alpha^{(1)} = 0.01$, $\gamma = 0.01$; $\alpha^{(2)} = 0.0008$, $\beta^{(2)(1)} = 0.01$; $\alpha^{(3)} = 0.0005$, $\beta^{(3)(1)} = 0.05$, $\beta^{(3)(2)} = 0.005$. Also, $t_{\max} = 800,000$. Learning results are shown in Figure 2. For plots in this figure θ was calculated from Layer 3 and fourth components of the reference vector of each unit by $\theta = \arctan(m_{i3}, m_{i4})$. In Figure 2 (a), (b) and (c), each of the four columns corresponds to each unit. The figure 2 (a) shows that the units in Layer 1 are position insensitive and direction sensitive. The figure 2 (b) and (c) show that Layers 2 and 3 are position sensitive and direction insensitive. Each of the four positional receptive fields of the units in Layer 2 is connected. The whole disk area is divided into four receptive fields. In Layer 3, however, each of the receptive fields of the units consists of four disconnected sub-fields, each of which is contained in one of the four receptive fields of the units in Layer 2. The representation of the positional information in Layers 2 and 3 is similar to two-digit quaternary number system.

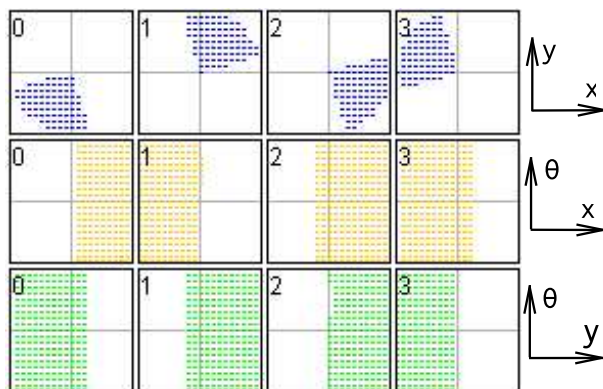
5 Conclusion

We showed that three VQ layers connected via anti-Hebbian synapses can extract directional and positional information separately, and the units in Layer 3 forms disconnected receptive fields, which is similar to what was observed in dMEC of rats by Hafting et al.[9]. Our model suggests that there should be some other position cells with larger and connected receptive fields in somewhere in rats' brain.

Unlike our preceding results [10] the sub-fields do not show clear hexagonal lattice pattern. This is because we used only four units for Layer 3. we assume



(a) Layer 1: The layer in head direction field



(b) Layer 2: The superior layer in position field



(c) Layer 3: The inferior in position field

Figure 2: Learning results: (a) Each row consisting of three small figures shows the property of each unit in Layer 1. The receptive field in 3D feature space (x, y, θ) is projected in three different ways. The units in Layer 1 show direction sensitivity only. (b) The units in Layer 2 show position sensitivity only. The positional receptive fields are connected. (c) The units in Layer 3 show position sensitivity only. The positional receptive fields are divided into four sub-fields.

that with more units in Layer 3 we can reproduce the hexagonal lattice pattern. The model should be tested with more realistic high-dimensional visual input.

References

- [1] Kohonen T (1994) Self-organizing maps., Springer, Berlin
- [2] Erwin E, Obermayer K, Schulten K (1995) Models of orientation and ocular dominance columns in the visual cortex: A critical comparison. *Neural Comput.*, 7: 425-468
- [3] Shouno H, Kurata K (2001) Formation of a direction map using Kohonen's self-organization map by projection learning. *Biol Cybern*, 85: 241-246
- [4] Kurata K, Oshiro N (2004) Separating visual information into position and direction by SOM. *Artificial Life and Robotics*, 8 (1): 5-8
- [5] Gersho A (1979) Asymptotically Optimal Block Quantization. *IEEE Trans. on Inform. Theory*, IT-25 (4): 373-380
- [6] Linde Y, Buzo A, Gray R (1980) An algorithm for vector quantizer design. *IEEE Trans. on Communications*, COM-28: 84-95
- [7] Gray R (1984) Vector quantization. *IEEE ASSP Magazine*: 4-29
- [8] Oshiro N, Kurata K (2005) Separating visual information into position and direction by two inhibitory-connected SOMs. *Artificial Life and Robotics*, 9 (2): 86-89
- [9] Hafting T, Fyhn M, Molden S, Moser M, Moser E (2005) Microstructure of a spatial map in the entorhinal cortex. *Nature*, 436: 801-806
- [10] Oshiro N, Kurata K, Yamamoto T (2006) A self-organizing model of place cells with periodically distributed receptive fields. *Proceedings of the International Symposium on Artificial Life and Robotics (AROB) 11, Beppu, Oita, Japan, Jan 23-25, 2006: OS10-4*

Color system for skin color extraction

Naruaki TOMA

Dept. of Information Engineering
Univ. of the Ryukyus
1 senbaru, Nishihara, Okinawa
903-0213, JAPAN

Emi TAMAKI

Dept. of Intelligent Interaction Tech.
Univ. of Tsukuba
1-1-1 Tennodai, Tsukuba-shi Ibaraki-ken
305-8577, JAPAN

Abstract

This paper describes a skin color extraction method, which comes with high-speed and -accuracy. There were many typical systems to achieve the requirements, however, they were useless due to tough limitations such as using two cameras to recognize correct coordinates, running only a specific background, wearing some gears, learning the users detailed information in advance, making personalized database and so on. In contrast, our approach which used YIQ color system with a background estimation method for skin color extraction, achieved well performance more than 30 fps with strong robustness on any-complicated and -illuminated environments.

1 Introduction

This research concerns an intuitively useable and high efficiency interface system, especially be focusing a system based on image processing techniques (vision-based interface).

Recently, vision based interfaces that they were introduced any sensor(s) to use user's behaviors as inputs into interface system, were studied [1, 2, 3, 4]. These type systems give friendly and efficiently interface for specialized situation. However, their systems don't use in general because of strict requirements, for example, they require two cameras to recognize correct coordinates, to set a specific background to recognize correct hand position, to wear some gears (e.g., marker tracking equipments), to learn the users detailed information (e.g., their color skin, finger form) and make personalized database.

This paper describes a skin color extraction method, which comes with high-speed and -accuracy, based on YIQ color system with a background estimation method to adjust the extraction parameters. We preliminarily evaluated the performances compared with other color systems (RGB, HSV and HQV [5]), and our method showed well performance (more than

30 fps) with strong robustness (more than 90% accuracy) on any-complicated and -illuminated environments.

2 Skin color extraction

2.1 Basic idea

Our supposed environment requires only one color movie camera, which must be able to acquire each image with high speed (more than 30 fps). Note that, we don't use any kinds of other sensors, don't care any backgrounds and illuminated environments, don't use any database (don't need to learn detailed information in advance).

Each captured images are processed through 1st stage: translating the color space from RGB space to the target space, then 2nd stage: calculating the thresholds to extract skin color. We use YIQ color system in 1st stage, and, if necessary, we use a background estimation method to adjust the thresholds automatically.

2.2 HSV and HQV

Some color systems were used for the extraction, and HSV and HQV were typical color systems. HSV based approach showed very low (fast) calculation costs and better extraction accuracy than RGB one. HQV (and also modified HQV) were proposed to improve the accuracy and it was achieved some studies (see [5]), but the calculation costs were too large to use for real-time processing like an interface system.

2.3 YIQ color system

YIQ is a color space, formerly used in the NTSC television standard. The YIQ color system is intended to take advantage of human color-response characteristics. The eye is more sensitive to changes in the orange-blue (I) range than in the purple-green range

(Q), therefore less bandwidth is required for Q than for I .

There are two stages to translate from RGB space into YIQ space, gamma correction is performed as equation 1, and then YIQ space was given by equation 2.

$$R' = \begin{cases} 4.5 \times R & R < 0.018 \\ 1.099 \times (R^{0.45}) - 0.099 & R \geq 0.018 \end{cases}$$

$$G' = \begin{cases} 4.5 \times G & G < 0.018 \\ 1.099 \times (G^{0.45}) - 0.099 & G \geq 0.018 \end{cases}$$

$$B' = \begin{cases} 4.5 \times B & B < 0.018 \\ 1.099 \times (B^{0.45}) - 0.099 & B \geq 0.018 \end{cases} \quad (1)$$

$$Y = 0.299 \times R' + 0.587 \times G' + 0.144 \times B'$$

$$I = 0.596 \times R' - 0.274 \times G' - 0.322 \times B'$$

$$Q = 0.211 \times R' - 0.522 \times G' + 0.311 \times B' \quad (2)$$

2.4 Filtering with thresholds

Thresholds on each color axis in the color space must be calculated in order to extract skin color. In other words, we assign a color zone on each axis to measure the pixel whether skin color or not.

2.5 Background estimation

When the background image or color is fixed like a blue screen, we can extract our desired objectives easily. But such extraction methods aren't functional in real world (complex background), because the methods require really tough settings on each unknown environments such as different illuminated ones or really complicated places in advance. In order to decrease user's preliminary settings, we use a background estimation method to adjust the thresholds for extraction automatically.

The background estimation calculates a distance on the color space between current image and a few frames previous image. In Exactly, all distances on each pixel are calculated by formula 3, where \vec{D} is 3-dimensional vectors on the color space, $\vec{M}(n)$ is movie image at the time n , and the i is a pixel position.

$$\vec{D} = |\vec{M}(n)i - \vec{M}(n-1)i| \quad (3)$$

If the \vec{D} has small values, the estimated background are calculated by formula 4, where \vec{P} is the estimated

background image and α is adding ratio of current image \vec{M} .

$$\vec{P}(n+1)i = \alpha \times \vec{M}(n)i + (1 - \alpha) \times \vec{P}(n)i \quad (4)$$

2.6 Adjusting thresholds

Our system decides a set of thresholds based on the estimated background image described above section. The thresholds are calculated by formula 5, where $M(R, G, B)$ is a set of average (mean) values, F is translation from RGB to other color system, $D(R, G, B)$ is a dispersion values and F is a constant value.

$$Threshold = F(M(R, G, B)) \pm \beta \times D(R, G, B) \quad (5)$$

3 Experiments

For evaluation of proposed method, we performed one preliminary experiment and four experiments with numerical evaluation, which are compared with traditional color skin extraction methods (based on RGB, HSV and HQV).

We performed some experiments on table 1, and our system was written in Processing language[6] and JMyron library[7] to process movie images.

Table 1: Hardwares.

Video camera	iSight1.0.3
OS	MacOSX 10.4.4
CPU	Dual 2GHz, PowerPC G5
Memory	4GB DDR SDRAM

3.1 Exp1: Background estimation

Left side of figure 1 shows an actual image, which has hidden background parts with fingers, and right side shows the estimated image. It is enough result to decide the set of thresholds, because we use the meanscore only calculated from the image (see also formula 3).

3.2 Exp2: Computational speed

Experiment 2 evaluated computational speeds to translate of RGB to each color system only, here, we



Figure 1: An estimated background result (left: actual image, right: estimated image).

don't care about the accuracy of skin color. In figure 2, *Base* denotes a computational time to get and to display a movie image with Processing. That shows a basic speed without any calculations.

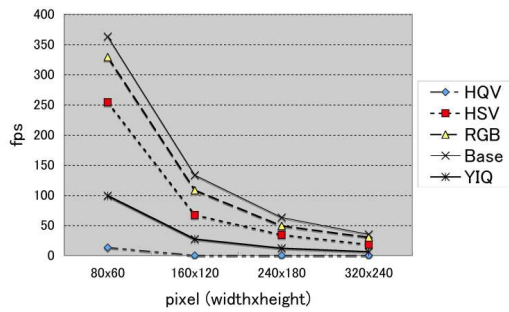


Figure 2: Computational speed for color translation from RGB into the target color space.

As the results, HSV was fastest except for RGB, and YIQ also was fast enough to achieve 30 fps with 160x120 (19,200 pixels) processing. HQV was too slow to use real time processing however it was evaluated as fine color system.

3.3 Exp3: Extraction accuracy 1

Experiment 3 evaluated the extraction accuracy on several backgrounds: *Black* background, *PC* background experimented on keyboard of note-pc, *Table* background experimented on the table with some objects, and *Complex* background experimented on really complicated situation. We measured three kinds of value. However, due to limitations of space, we showed one value 'total recognition-miss ratio' measured by 6, where N_{total} denotes the number of total

pixels in one frame, and \bar{N}_{total} denotes the number of total miss-counted pixels.

$$total_miss_ratio(\%) = \bar{N}_{total}/N_{total} \times 100 \quad (6)$$

Each recognition-miss ratios are shown in table 3.3, where *YIQ_I* denotes a result used *I* value only in YIQ color system. The thresholds on each color system were adjusted in order that recognition-miss ratios become lowest on *Black* background. Note that, the correct skin color pixels are decided by hand, so these results have a margin of error with a few percentages.

Table 2: Total-miss ratio on several backgrounds(%).

color	Black	PC	Table	Complex
RGB	1.69	23.55	56.62	50.41
HSV	2.22	40.08	63.18	67.19
HQV	6.88	6.78	55.42	52.83
YIQ	2.86	1.60	3.41	2.48
YIQ _I	5.12	3.61	5.00	2.88

According to these results, the accuracies of RGB and HSV were through 8 to 61 percentages on complicated one. The other, YIQ showed very robust performances, which the accuracies were keeping with through 92 to 96 percentages even though the experiment performed in complicated environments.

3.4 Exp4: Extraction accuracy 2

Experiment 4 evaluated the extraction accuracy on several illuminated environments: *Fluor* illuminated with fluorescent lamp, *Incan* illuminated with incandescent lamp, *Sun(in)* illuminated indoor with sunlight, and *Sun(out)* illuminated outdoor with sunlight. In this experiment, the background was fixed on *PC* environments.

Table 3: Total-miss ratio on several illuminated environments(%).

color	Fluor	Incan	Sun(in)	Sun(out)
RGB	52.99	78.74	62.82	8.22
HSV	54.68	74.43	67.74	29.08
HQV	32.88	90.17	56.37	65.35
YIQ	3.14	94.40	2.17	13.33
YIQ _I	3.15	94.75	2.03	13.33

The results (see table 3.4), showed all kinds of color system didn't have enough accuracy on incandescent lamp. One of the reasons, I axis of YIQ has similar characteristics as the light of incandescent lamp even though I axis is most important axis to extract skin color.

3.5 Exp5: Extraction accuracy 3

To resolve the previous problem (weak recognition rate on incandescent lamp), background estimation method described in section 2.5 was introduced. Here, we don't experiment with RGB, HSV and HQV because they don't have robustness against the difference of illumination.

Tables 3.5 showed the accuracies with background estimation, where *withoutBS* denotes the results without background estimation (same values on experiment 4), and *withBS* denotes with background estimation. Figure 3 showed a extracted result without BS in leftside and with BS in rightside, where black color in hand part shows skin-miss pixels, dark light grey around of hand shows background-miss pixels and dark grey mainly showed in hand part of right-side shows correct recognized pixels.

Table 4: Total-miss ratio with background estimation(%).

color	without BS	with BS
YIQ	94.40	2.40
YIQ_I	94.75	2.17



Figure 3: An extracted result (leftside with BS, right-side with BS).

The accuracy of YIQ with proposed threshold adjusting based on background estimation was pretty improved through 97 to 98 percentages. These results shows that our approach has highly robustness not only complicated backgrounds but also several illuminated environments.

4 Conclusion

In case of using only extraction based color system, the accuracy on all color systems were too low to use for practical. The accuracy of YIQ with proposed threshold adjusting based on background estimation was pretty improved through 97 to 98 percentages.

In summary, the proposed method showed well performance with strong robustness for skin color extraction on any-complicated and -illuminated environments. According to this summary, this method so as to apply widely applications because our method requires only one camera and without any personalized database.

References

- [1] Nozomu Matsui and Yoshikazu Yamamoto, "Virtual Keyboard with Single Video Camera (in japanese)", in Programming Symposium, 1999.
- [2] Nozomu Matsui and Yoshikazu Yamamoto, "Virtual Keyboard: Realization of Robust Real-Time Fingertip Detection from Video-Image (in japanese)", in JSSST SPA2000, 2000.
- [3] Yishiyuki Kojima, "Hand Interface for Wearable Mixed Reality - Clip Interface -", Master 's Thesis, Department of Information Processing, Graduate School of Information Science, Nara Institute of Science and Technology, NAIST-IS-MT0051037, February 8, 2002.
- [4] Takeshi Kurata, Takashi Okuma, Masakatsu Kourogi, and Katsuhiko Sakaue, "The Hand Mouse: GMM Hand Color Classification and Mean Shift Tracking", In Proc. Second International Workshop on Recognition, Analysis and Tracking of Faces and Gestures in Real-time Systems (RATFG-RTS 2001) in conjunction with ICCV 2001, pp.119-124.
- [5] Satoshi matsuhashi, Osamu Nakamura and Toshi Minami, "Human-Face Extraction Using Modified HSV Color System and Personal Identification Through Facial Image Based on Isodensity Maps", IEEE CCGEI 1995, Vol 2, No 2, pp.909-912.
- [6] Processing.org, <http://www.processing.org/>
- [7] Myron WebCamXtra, <http://webcamxtra.sourceforge.net/>

Cooperative Manipulation of a Floating Object by Some Space Robots

– Application of a Tracking Control Method Using Transpose of Generalized Jacobian Matrix –

Shinichi Sagara

Dept. of Control Engineering
 Kyushu Institute of Technology
 Tobata, Kitakyushu 804-8550, Japan
 sagara@cntl.kyutech.ac.jp

Yuichiro Taira

Dept. of Ocean Mechanical Engineering
 National Fisheries University
 Nagata-Honmachi, Shimonoseki 759-6595, Japan
 taira@fish-u.ac.jp

Abstract

For free floating space robots with manipulators, we have proposed a digital tracking control method using the transpose of the Generalized Jacobian Matrix (GJM). In future space missions, it is considered that many tasks will be achieved by cooperative motions of some space robots. In this paper, the tracking control method using the transpose of the GJM is applied to cooperative manipulations of a floating object by some space robots. Simulation results show the effectiveness of the control method.

1 Introduction

Many control methods of space robots with manipulators have been proposed [1]. Most of them use the inverse of the Generalized Jacobian Matrix (GJM) which is a coefficient matrix between the end-effector's velocity and the joint velocity of the manipulator. Therefore, if the robot system becomes in a singular configuration, the manipulator is out of control because the inverse of the GJM does not exist. We have proposed discrete time control methods using the transpose of the GJM [2,3]. Since the control methods belong to a class of constant value control such as PID control, we have proposed a digital tracking control method based on the reference [3].

In future space missions, it is considered that many tasks will be achieved by cooperative motions of some space robots. We have studied on control problems for realizing cooperative manipulations and reported that a system consisting of some space robots with manipulators and a floating object can be treated as a kind of distributed system [5,6]. Using the distributed system representation each robot constituting the distributed system can be designed the control system individually.

In this paper, the tracking control method using the

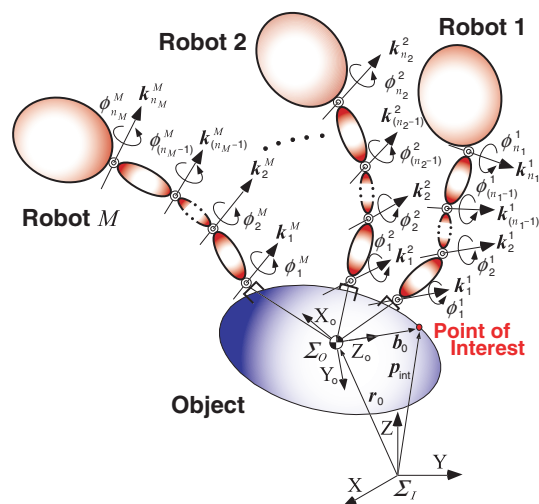


Fig. 1 Model of space robot system

transpose of the GJM is applied to cooperative manipulations of a floating object by some space robots. To validate the control method computer simulations are done. Simulation results show the effectiveness of the control method.

2 Modeling

2.1 Robot system model

In this paper, we consider a space robot system consisting of M robots with manipulators and a floating object shown in Fig. 1. The h -th robot ($h = 1, \dots, M$) is consisting of an uncontrolled base and n_h -DOF manipulator with revolute joints. Assumptions and symbols used in this paper are defined as follows:

[Assumptions]

- A1) All elements of the space robot are rigid.
- A2) The robot system is standing still at an initial state, i. e., the initial linear momentum and an-

- gular momentum of the space robots are zero.
A3) No external force acts on the robot system.
A4) Positions and attitude angles of robots and an object in inertial coordinate frame can be measured.

[Symbols]

- Σ_I : inertial coordinate frame
 Σ_{int} : point of interest coordinate frame
 Σ_T : target coordinate frame
 i^h : number of link or joint i of robot h
 \mathbf{p}_{int} : position vector of point of interest
 \mathbf{p}_T : position vector of origin of Σ_T
 \mathbf{r}_o : position vector of mass center of object
 \mathbf{v}_* : linear velocity vector of point of interest (* = int) or mass center of object (* = 0)
 $\boldsymbol{\omega}_*$: angular velocity vector of point of interest (* = int) or mass center of object (* = 0)
 \mathbf{p}_i^h : position vector of joint i^h
 \mathbf{r}_i^h : position vector of mass center of link i^h
 \mathbf{k}_i^h : unit vector indicating joint axis direction of joint i^h
 \mathbf{r}_g : position vector of mass center of system
 \mathbf{r}_g^h : position vector of mass center of robot h
 \mathbf{q} : joint angle vector
 ${}^I\mathbf{A}_*$: rotation matrix from Σ_* (* = int, T) to Σ_I
 ϕ_i^h : relative angle of joint i^h
 $\boldsymbol{\phi}^h$: joint angle vector of robot h
 m_o : mass of object
 m_i^h : mass of link i^h
 \mathbf{I}_o : inertia tensor of object
 \mathbf{I}_i^h : inertia tensor of link i^h
 \mathbf{E} : identity matrix

The tilde operator stands for a cross product such that $\tilde{\mathbf{r}}\mathbf{a} = \mathbf{r} \times \mathbf{a}$. All position and velocity vectors are defined with respect to the inertial reference frame.

2.2 Kinematic model

The robot system shown in Fig. 1 can be understood as one robot with M manipulators by regarding the object as a robot body, and M robot arms and robot bodies as M manipulators. The kinematic formulation of such space system has been derived by Yoshida et al. [7]. The relation obtained from its geometrical relationships, and the conservation laws of linear momentum and angular momentum under the above assumptions as follows:

$$\boldsymbol{\nu}_{\text{int}} = \begin{bmatrix} \dot{\mathbf{p}}_{\text{int}} \\ \boldsymbol{\omega}_{\text{int}} \end{bmatrix} = \mathbf{J}_s \begin{bmatrix} \mathbf{v}_o \\ \boldsymbol{\omega}_o \end{bmatrix}, \quad \mathbf{H}_s \begin{bmatrix} \mathbf{v}_o \\ \boldsymbol{\omega}_o \end{bmatrix} + \mathbf{H}_m \dot{\boldsymbol{\phi}} = \mathbf{0} \quad (1)$$

where

$$\mathbf{J}_s = \begin{bmatrix} \mathbf{E} & \tilde{\mathbf{r}}_o - \tilde{\mathbf{p}}_{\text{int}} \\ \mathbf{0} & \mathbf{E} \end{bmatrix}, \quad \mathbf{H}_s = \begin{bmatrix} w\mathbf{E} & w(\tilde{\mathbf{r}}_o - \tilde{\mathbf{r}}_g) \\ w\tilde{\mathbf{r}}_g & \mathbf{I}_w \end{bmatrix},$$

$$\mathbf{H}_m = \begin{bmatrix} \mathbf{J}_{T_w} \\ \mathbf{I}_\phi \end{bmatrix}, \quad \boldsymbol{\phi} = [(\phi^1)^T, (\phi^2)^T, \dots, (\phi^M)^T]^T,$$

$$\mathbf{I}_w = \sum_{h=1}^M \mathbf{I}_w^h + \mathbf{I}_o, \quad \mathbf{J}_{T_w} = \sum_{h=1}^M \mathbf{J}_{T_w}^h, \quad \mathbf{I}_\phi = \sum_{h=1}^M \mathbf{I}_\phi^h,$$

$$\mathbf{I}_w^h = \sum_{i=1}^{n_h} \{ \mathbf{I}_i^h - m_i^h \tilde{\mathbf{r}}_i^h (\tilde{\mathbf{r}}_i^h - \tilde{\mathbf{r}}_0^h) \}, \quad \mathbf{J}_{T_w}^h = \sum_{i=1}^{n_h} m_i^h \mathbf{J}_{T_i}^h,$$

$$\mathbf{I}_\phi^h = \sum_{i=1}^{n_h} (\mathbf{I}_i^h \mathbf{J}_{R_i}^h + m_i^h \tilde{\mathbf{r}}_i^h \mathbf{J}_{T_i}^h),$$

$$\mathbf{J}_{T_i}^h = [\mathbf{O}_a \quad \bar{\mathbf{J}}_{T_i}^h \quad \mathbf{O}_b], \quad \mathbf{J}_{R_i}^h = [\mathbf{O}_a \quad \bar{\mathbf{J}}_{R_i}^h \quad \mathbf{O}_b],$$

$$\bar{\mathbf{J}}_{T_i}^h = [\tilde{\mathbf{k}}_1^h (\mathbf{r}_i^h - \mathbf{p}_1^h), \dots, \tilde{\mathbf{k}}_i^h (\mathbf{r}_i^h - \mathbf{p}_i^h), \mathbf{0}, \dots, \mathbf{0}],$$

$$\bar{\mathbf{J}}_{R_i}^h = [\mathbf{k}_1^h, \dots, \mathbf{k}_i^h, \mathbf{0}, \dots, \mathbf{0}],$$

and $\mathbf{O}_a \in \mathbf{R}^{3 \times n_a}$ ($n_a = \sum_{i=1}^{h-1} n_i$) and $\mathbf{O}_b \in \mathbf{R}^{3 \times n_b}$ ($n_b = \sum_{i=h+1}^M n_i$) are zero matrices.

From Eq. (1), the relation between velocity $\boldsymbol{\nu}_{\text{int}}$ of the object and joint angular velocity $\dot{\boldsymbol{\phi}}$ of the manipulator can be derived as follows:

$$\boldsymbol{\nu}_{\text{int}} = \mathbf{J}^* \dot{\boldsymbol{\phi}} \quad (2)$$

where $\mathbf{J}^* = -\mathbf{J}_s(\mathbf{H}_s)^{-1}\mathbf{H}_m$ is a GJM of the system shown in Fig. 1.

2.3 System partition

For the system shown in Fig. 1 control systems can be easily constructed by using Eq. (2). However, if the number of robots is changed, Eq. (2) must be recalculated. Furthermore, if the number of robots becomes increased, a large amount of calculation for the system is necessary. To solve the problems described above, This total robot system is regarded as a distributed system.

By examining parameters and variables included in the matrix \mathbf{H}_s and vector $\mathbf{H}_m \dot{\boldsymbol{\phi}}$ in Eq. (1), the matrix and vector can be rewritten as follows:

$$\mathbf{H}_s = \mathbf{H}_s^0 + \sum_{h=1}^M \mathbf{H}_s^h, \quad \mathbf{H}_m \dot{\boldsymbol{\phi}} = \sum_{h=1}^M \mathbf{H}_m^h \dot{\boldsymbol{\phi}}^h \quad (3)$$

where

$$\mathbf{H}_s^0 = \begin{bmatrix} m_o \mathbf{E} & \mathbf{0} \\ m_o \tilde{\mathbf{r}}_o & \mathbf{I}_o \end{bmatrix}, \quad \mathbf{H}_s^h = \begin{bmatrix} m^h \mathbf{E} & m^h (\tilde{\mathbf{r}}_0^h - \tilde{\mathbf{r}}_g^h) \\ m^h \tilde{\mathbf{r}}_g^h & \mathbf{I}_w^h \end{bmatrix},$$

$$\mathbf{H}_m^h = \begin{bmatrix} \bar{\mathbf{J}}_{T_w}^h \\ \bar{\mathbf{I}}_\phi^h \end{bmatrix}, \quad m^h = \sum_{i=1}^{n_h} m_i^h,$$

$$\bar{\mathbf{J}}_{T_w}^h = \sum_{i=1}^{n_h} m_i^h \bar{\mathbf{J}}_{T_i}^h, \quad \bar{\mathbf{I}}_\phi^h = \sum_{i=1}^{n_h} (\mathbf{I}_i^h \bar{\mathbf{J}}_{R_i}^h + m_i^h \tilde{\mathbf{r}}_i^h \bar{\mathbf{J}}_{T_i}^h).$$

\mathbf{H}_s^h and \mathbf{H}_m^h are matrices including parameters the h -th robot only, and \mathbf{H}_s^0 is a matrix including parameters of the object only.

Eqs. (1) and (3) make the following relation:

$$\left(\mathbf{H}_s^0 + \sum_{h=1}^M \mathbf{H}_s^h \right) \mathbf{J}_s^{-1} \boldsymbol{\nu}_{\text{int}} + \sum_{h=1}^M \mathbf{H}_m^h \dot{\boldsymbol{\phi}}^h = \mathbf{0}. \quad (4)$$

It is clear that the following set of equations is one of solutions of Eq. (4), when a constant and diagonal matrix \mathbf{A}_h is introduced.

$$\bar{\mathbf{H}}_s^h \mathbf{J}_s^{-1} \boldsymbol{\nu}_{\text{int}} + \mathbf{H}_m^h \dot{\boldsymbol{\phi}}^h = \mathbf{0} \quad (h=1, \dots, M) \quad (5)$$

where

$$\bar{\mathbf{H}}_s^h = \mathbf{H}_s^h + \mathbf{A}_h \mathbf{H}_s^0, \quad \sum_{h=1}^M \mathbf{A}_h = \mathbf{E}.$$

Then, the following relation can be derived from Eq. (5).

$$\boldsymbol{\nu}_{\text{int}} = -\mathbf{J}_s (\bar{\mathbf{H}}_s^h)^{-1} \mathbf{H}_m^h \dot{\boldsymbol{\phi}}^h \quad (h=1, \dots, M). \quad (6)$$

Therefore, for each robot of the system the control system can be designed individually.

3 Digital Control

Eq. (6) can be rewritten:

$$\boldsymbol{\nu}_{\text{int}}(k) = \mathbf{J}_L^h \dot{\boldsymbol{\phi}}^h(k), \quad \boldsymbol{\omega}_{\text{int}}(k) = \mathbf{J}_A^h \dot{\boldsymbol{\phi}}^h(k) \quad (7)$$

where

$$\begin{bmatrix} \mathbf{J}_L^h \\ \mathbf{J}_A^h \end{bmatrix} = -\mathbf{J}_s (\bar{\mathbf{H}}_s^h)^{-1} \mathbf{H}_m^h.$$

For Eq. (7) the following digital tracking control law using the transpose of the GJM [4] is utilized:

$$\begin{aligned} \boldsymbol{\tau}_d^h(k) &= (\mathbf{J}_L^h)^T(k) \left[\hat{k}_p(k) e_{PI}(k) - \hat{\mathbf{K}}_{LV}(k) \boldsymbol{\nu}_{\text{int}}(k) \right] \\ &+ (\mathbf{J}_A^h)^T(k) \left[\hat{k}_o(k) e_{OI}(k) - \hat{\mathbf{K}}_{AV}(k) \boldsymbol{\omega}_{\text{int}}(k) \right] \end{aligned} \quad (8)$$

where $\boldsymbol{\tau}_d^h(k)$ is the joint torque input vector and

$$e_{PI}(k) = \mathbf{p}_T(k) - \mathbf{p}_{\text{int}}(k),$$

$$e_{OI}(k) = -\frac{1}{2} \mathbf{E}_X^T(k) \mathbf{E}_{OI}(k),$$

$$\mathbf{E}_{OI}(k) = \begin{bmatrix} \mathbf{n}_T(k) - \mathbf{n}_{\text{int}}(k) \\ \mathbf{s}_T(k) - \mathbf{s}_{\text{int}}(k) \\ \mathbf{a}_T(k) - \mathbf{a}_{\text{int}}(k) \end{bmatrix}, \quad \mathbf{E}_X(k) = \begin{bmatrix} \tilde{\mathbf{n}}_{\text{int}}(k) \\ \tilde{\mathbf{s}}_{\text{int}}(k) \\ \tilde{\mathbf{a}}_{\text{int}}(k) \end{bmatrix},$$

$$\hat{k}_p(k) = k_p \{1 + \alpha_L \nu_L(k)\}, \quad \hat{k}_o(k) = k_o \{1 + \alpha_A \nu_A(k)\},$$

$$\hat{\mathbf{K}}_{LV}(k) = \mathbf{K}_{LV} \{1 - \beta_L \nu_L(k)\},$$

$$\hat{\mathbf{K}}_{AV}(k) = \mathbf{K}_{AV} \{1 - \beta_A \nu_A(k)\},$$

$$\nu_L(k) = \frac{\|\boldsymbol{\nu}_{\text{int}_d}(k)\|}{v_{d_{\text{max}}}}, \quad \nu_A(k) = \frac{\|\boldsymbol{\omega}_{\text{int}_d}(k)\|}{\omega_{d_{\text{max}}}}.$$

Table 1 Physical parameters of robots and object

	Length m	Mass kg	Moment of inertia kg·m ²
Base	3.5	2000	3587.9
Link 2	2.5	50	26.2
Link 1	2.5	50	26.2
hand	0.5	5	0.23
Object	4.0	1200	2400.0

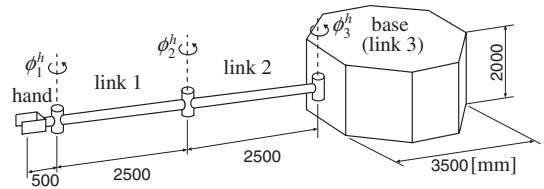


Fig. 2 Space robot

The vectors \mathbf{n}_* , \mathbf{s}_* and \mathbf{a}_* ($*$ = T , int) are unit vectors along the axes of Σ_* with respect to Σ_I , i. e., $\mathbf{A}_* = [\mathbf{n}_*(k) \ \mathbf{s}_*(k) \ \mathbf{a}_*(k)]$. $\boldsymbol{\nu}_{\text{int}_d}(k)$ and $\boldsymbol{\omega}_{\text{int}_d}(k)$ are the desired velocities of $\boldsymbol{\nu}_{\text{int}}(k)$ and $\boldsymbol{\omega}_{\text{int}}(k)$, $v_{d_{\text{max}}}$ and $\omega_{d_{\text{max}}}$ are the maximum values of the norm of $\boldsymbol{\nu}_{\text{int}_d}(k)$ and $\boldsymbol{\omega}_{\text{int}_d}(k)$, α_{\dagger} ($\alpha_{\dagger} \geq 0$) and β_{\dagger} ($0 \leq \beta_{\dagger} \leq 1$) ($\dagger = L, A$) are setting parameters. Furthermore, k_p and k_o are positive scalar gains for position and orientation, and \mathbf{K}_{LV} and \mathbf{K}_{AV} are symmetric and positive definite gain matrices for linear and angular velocities of the point of interest on the object.

To examine the performance of the tracking control law Eq. (8), simulations are performed by using three and same horizontal planar 3-DOF robots shown in Fig. 2 and an object.

Physical parameters of the robots and object are shown in Table 1. Simulations are carried out under the following condition. A point of interest on the object moves along a straight path from the initial position to the target position and the object angle is set up the initial value. The sampling period is $T = 0.01$ s and the coefficient matrices are $\mathbf{A}_1 = \mathbf{A}_2 = 0.33\mathbf{E}$ and $\mathbf{A}_3 = 0.34\mathbf{E}$. The feedback gains are $k_p = k_o = 2 \times 10^5$, $\mathbf{K}_{LV} = \text{diag}\{2 \times 10^4, 2 \times 10^4\}$ and $\mathbf{K}_{AV} = 2 \times 10^4$. The setting parameters are $\alpha_{\dagger} = 2$ and $\beta_{\dagger} = 0.2$ ($\dagger = L, A$).

Fig. 3 shows the motion of the robot system. From this figure, the object is successfully moved by three robots. Fig. 4 shows the time history of the simulation. This figure also shows the case of constant gains, i. e., $\alpha_{\dagger} = \beta_{\dagger} = 0$. From Fig. 4, it can be seen that good control performance can be achieved using the tracking control law.

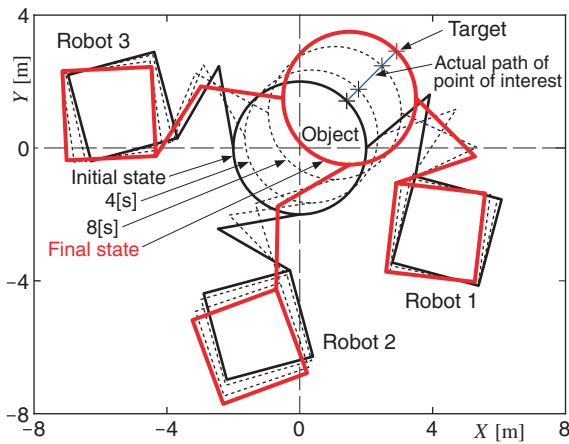


Fig. 3 Motion of the robot system

4 Conclusion

In this paper, we propose a tracking control method using the transpose of the GJM for handling a floating object cooperatively by some space robots. Simulation results show the effectiveness of the control method.

References

- [1] Y. Xu, T. Kanade (eds), *Space Robotics: Dynamics and Control*, Kluwer Academic Publishers, 1993.
- [2] Y. Taira, S. Sagara, R. Katoh, "Digital Control of a Space Robot Using the Transpose of the Generalized Jacobian Matrix," (in Japanese), *Trans. JSME Series C*, Vol. 67, No. 654, pp. 436 - 442, 2001.
- [3] Y. Taira, S. Sagara, R. Katoh, "Digital Control of a Space Robot Using the Transpose of the Generalized Jacobian Matrix (2nd Report, A Unified Approach for Torque and Velocity Type Control Laws)," (in Japanese), *Trans. JSME Series C*, Vol. 67, No. 663, pp. 3540 - 3547, 2001.
- [4] S. Sagara, Y. Taira, "Digital Tracking Control of Space Robots using Transpose of Generalized Jacobian Matrix", *Proc. AROB'06*, pp. 237 - 240, 2006.
- [5] R. Katoh, K. Nakatsuka, S. Sagara, J. Kobayashi, F. Ohkawa, "Manipulation of a Floating Object by Two Space Manipulators", *Proc. IECON'97*, pp. 1397 - 1402, 1997.
- [6] S. Sagara, M. Hideura, R. Katoh, T. Yamashita, J. Kobayashi, F. Ohkawa, "Adaptive RMRC for Cooperative Manipulation of a Floating Object by Two Free-Based Space Robots", *Proc. IROS'98*, pp. 1467 - 1472, 1998.

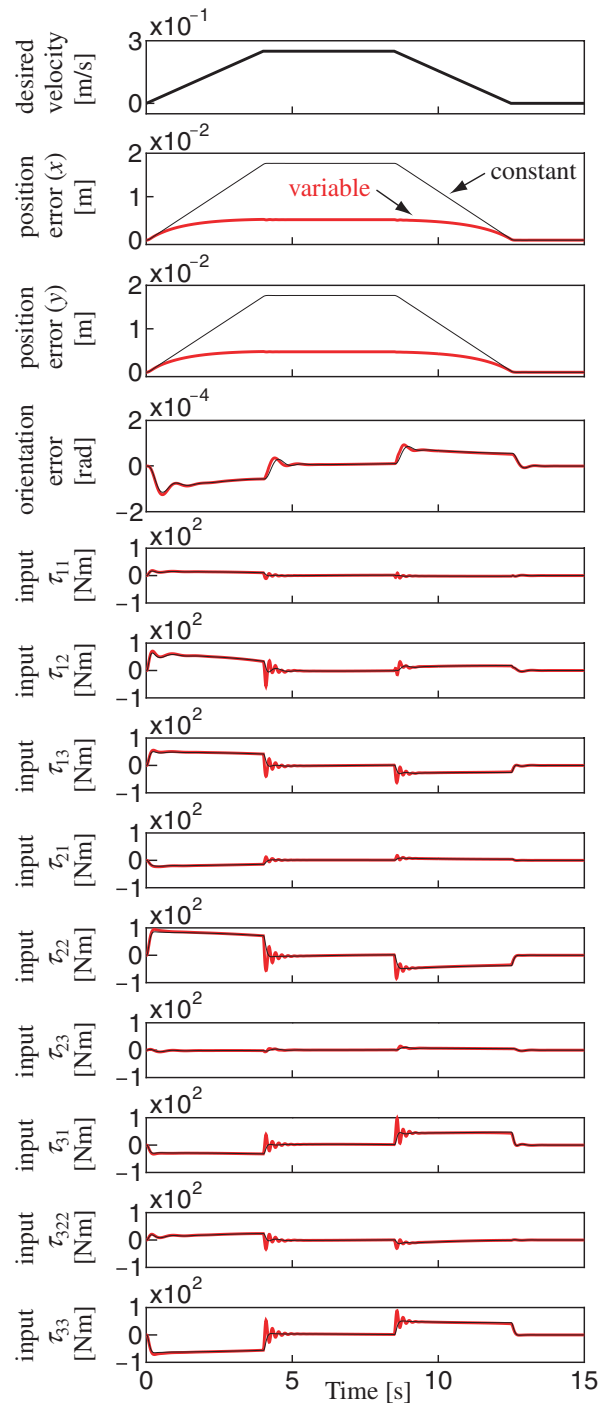


Fig. 4: Time history (variable: $\alpha_{\dagger} = 2$ and $\beta_{\dagger} = 0.2$, constant: $\alpha_{\dagger} = 0$ and $\beta_{\dagger} = 0$ ($\dagger = L, A$))

- [7] K. Yoshida, R. Kurezume, Y. Umetani, "Coordinated Control of Multiple Manipulators in Space Robots", *J. Robotics Society of Japan*, Vol. 9, No. 6, (in Japanese) pp. 718-726, 1991.

Improvement of the Algorithm for the Search of Periodic Gaits of a Passive Dynamic Walker

Xuemin Su
Department of Automation
Tsinghua University
BeiJing China, 100084
suxm06@mails.tsinghua.edu.cn

Mingguo Zhao
Department of Automation
Tsinghua University
BeiJing China, 100084
mgzhao@mail.tsinghua.edu.cn

Mengdi Wang
Department of Automation
Tsinghua University
BeiJing China, 100084
wang.mandy@hotmail.com

Abstract

Periodic gaits of passive dynamic walking are found by solving nonlinear dynamic equations, and the convergence speed of numerical solving of the equations is greatly affected by the choice of initial values. This paper investigates the iterative searching algorithm for periodic gaits by studying the simplest passive dynamic walking model. An improved algorithm for choosing the initial values is proposed based on the work of Garcia etc. The effectiveness of the proposed algorithm is demonstrated by numerical simulations.

1 Introduction

Why can human walk? One may focus on the control of nerve and muscle but relatively neglect other important factors. Passive dynamic walking proposed by McGeer [1] presented a novel idea.

Passive dynamic walker is a simple mechanism normally composed of some solid links connected by frictionless hinges. Without motors and controllers, it can walk down a small slope stably by gravity and have a human-like gait.

The key to analyze passive dynamic walking is to find periodic gaits, normally by numerically solving nonlinear differential equations with iterative method like Newton-Raphson method [2]. The iterative method first selects a set of initial values, then searches directly in the solution space whose dimension is relatively high for the fixed points of the equations. The choice of the initial values is quite important since it directly affects the convergence and the convergence speed of the iterative method, but how to choose the initial values is still a problem. Garcia et al. [3] had developed a method to solve this problem. They first got a low-order approximation to the equations, solved them for the analytical solutions which could be used as the initial values of the iterative method.

This method works well when the equations are simple but involves some complicated symbolic manipulation. This article proposes an improved algorithm which searches in the parameter space whose dimension is relatively low instead of the solution space. The effectiveness of the algorithm is demonstrated by numerical simulation and comparison with the original algorithm.

2 Model

The model used here is the simplest walking model proposed by Garcia et al. [3], which is shown in Figure 1.

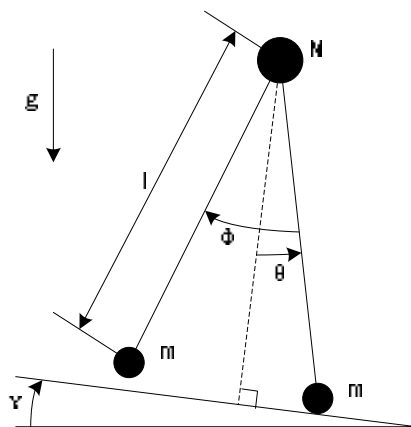


Figure 1: The simplest model of passive dynamic walking

Assumptions of the model are:

1 Mass: The only mass is at the hip and the feet, and the foot mass m is much smaller than the hip mass M , satisfying $\beta = \frac{m}{M} \rightarrow 0$.

2 Actuator: No actuators are used.

3 Collision: When the swing foot hits the ground, the collision is completely inelastic (no slip or bounce) and the double support phase is instantaneous (the stance foot leaves the ground when the swing foot hits the ground).

4 Ground: The swing foot may be below the ground level during the swing phase. To solve this problem, we allow the swing foot to move below the ground in numerical simulation and use a chessboard-like ground for real-world experiments.

According to Lagrange function, equations of the motion for the swing phase are

$$\begin{bmatrix} \bar{M} & \left(\frac{\partial g}{\partial q}\right)^T \\ \frac{\partial g}{\partial q} & 0 \end{bmatrix} \begin{bmatrix} \ddot{q} \\ \lambda \end{bmatrix} = \begin{bmatrix} \bar{f} \\ -\frac{\partial^2 g}{\partial q \partial q} \dot{q} \dot{q} \end{bmatrix} \quad (1)$$

and the relation of the velocities before and after the collision can be written as follows according to the angular momentum conservation

$$\begin{bmatrix} \bar{M} & \left(\frac{\partial g}{\partial q}\right)^T \\ \frac{\partial g}{\partial q} & 0 \end{bmatrix} \begin{bmatrix} \dot{q}^+ \\ \rho \end{bmatrix} = \begin{bmatrix} \bar{M} \dot{q}^- \\ 0 \end{bmatrix} \quad (2)$$

where $q = (u, v, \theta, \phi)^T$ is the configuration of the model, $x = F(q)$ the coordinates of the hip and the feet, $g(q) = 0$ the constraints of the ground, M the general mass matrix, f the force vector, λ, ρ the Lagrange multipliers, and $\bar{M} = \left(\frac{\partial F}{\partial q}\right)^T M \frac{\partial F}{\partial q}$, $\bar{f} = \left(\frac{\partial F}{\partial q}\right)^T \left[f - M \frac{\partial^2 F}{\partial q \partial q} \dot{q} \dot{q}\right]$.

We define the start of a stride as the moment the swing foot hits the ground and the stance foot leaves the ground, which is also the end of the last stride. The state at this moment is the initial state of the model, which is $v = (\theta, \dot{\theta}, \dot{\phi})^T$. A Stride Function $v_{k+1} = S(v_k)$ is a map from the state of the k^{th} stride to the state of the $(k+1)^{th}$ stride.

3 Search of the Fixed Points of the Equation

A periodic gait corresponds to a fixed point of the Stride Function, which is normally found by iterative method. If an initial value v satisfies the equation $v = S(v)$, it is a fixed point of the Stride Function S , otherwise the iterative method should modify the initial value by Δv to make the modified value satisfy $v + \Delta v = S(v + \Delta v)$. Since we can't explicitly write

the expression of $S(v + \Delta v)$, we use the first-order approximation

$$S(v + \Delta v) \approx S(v) + J\Delta v, \text{ where } J = \frac{\partial S}{\partial v} \quad (3)$$

then we get

$$\Delta v = (I - J)^{-1} (S(v) - v) \quad (4)$$

The iterative method can be described as

$$\begin{array}{l} \text{repeat} \\ \Delta v = (I - J)^{-1} (S(v) - v) \\ v = v + \Delta v \\ \text{until } |S(v) - v| < \varepsilon \end{array} \quad (5)$$

This is the Newton-Raphson method.

4 Improvement of the Search of the Fixed Points of the Equation

Since we use the first-order approximation to the Stride Function, the initial value v should be near the fixed point. In a stride, the swing foot first moves below the ground level, then moves above it, and then moves downwards and hits the ground. If the initial value is far from the fixed point, the swing foot may not be able to move above the ground level, and the collision may not occur. Since we can't get the state after heel-strike, $S(v)$ and Jacobian matrix J can't be obtained. In a word, the initial value should guarantee that at least one heel-strike can happen.

To solve this problem, we propose an improved method. We assume that if the parameters of the model change slightly, the fixed point will not change too much. Based on this assumption, a fixed point for one set of parameters can be used as the initial value for another set of parameters if these two sets of parameters are near together. On the other hand, an initial value not suitable for one set of parameters may be a good choice for another set of parameters. Based on the above observation, we propose an improved method as follows:

1. Given a slope angle γ , choose an initial value v ;
2. Search for the fixed point using Newton-Raphson method; if not found, jump to 3;
3. Keep the initial value v unchanged, let $\gamma = \gamma + \Delta\gamma$, and use Newton-Raphson method again; modify $\Delta\gamma$ until the fixed point is found. Let the found slope angle be γ^* and the fixed point v^* ;
4. Use v^* as the initial value, let $\gamma^* = \gamma^* + \Delta\gamma$, search for the fixed point. Modify the slope angle by

$\Delta\gamma$ at a time, and search for the fixed point using the fixed point with the slope angle unchanged as the initial value. Repeat until $\gamma^* = \gamma$.

The dimension of the parameter space is 1 while the dimension of the state space is 3. The improved method searches in the parameter space instead of the state space, making the search easier.

5 An Example of the Algorithm

To demonstrate the effectiveness of the algorithm, we first give a plot of the fixed points versus the slope angles, see Figure 2. The same result was shown by Garcia et al. [4] too.

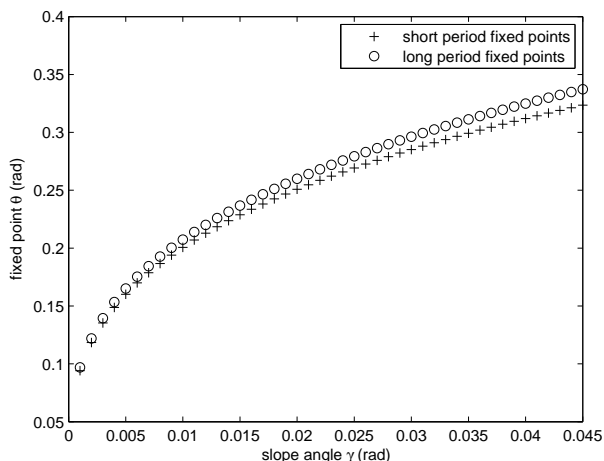


Figure 2: Fixed points of the stride function

We give an example here to demonstrate that the improved method can find the fixed point even when the initial value is not suitable.

1. Given a slope angle $\gamma = 0.016[rad]$, choose an initial value $v = (\theta, \dot{\theta}, \dot{\phi})^T = (0.1, -0.01, -0.002)^T$;

2. Search for the fixed point using Newton-Raphson method; we can't find the fixed point after 80 iterations;

3. Keep the initial value v unchanged, let $\gamma = \gamma - 0.001[rad]$, and use Newton-Raphson method again; we find the fixed point

$$v = \begin{bmatrix} \theta \\ \dot{\theta} \\ \dot{\phi} \end{bmatrix} = \begin{bmatrix} 0.2259204891316 \\ -0.22237603365099 \\ -0.022316588434412 \end{bmatrix}$$

when $\gamma = 0.013[rad]$;

4. Use the fixed point when $\gamma = 0.013[rad]$ as the initial value, search for the fixed point when $\gamma = 0.014[rad]$; Use the fixed point when $\gamma = 0.014[rad]$ as the initial value, search for the fixed point when $\gamma = 0.015[rad]$; finally we get the fixed point when $\gamma = 0.016[rad]$ using the fixed point when $\gamma = 0.015[rad]$ as the initial value

$$v = \begin{bmatrix} \theta \\ \dot{\theta} \\ \dot{\phi} \end{bmatrix} = \begin{bmatrix} 0.2259204891316 \\ -0.22237603365099 \\ -0.022316588434412 \end{bmatrix}$$

The procedure is shown in Table 1.

slope angle $\gamma (rad)$	initial value $\theta (rad)$	fixed point $\theta (rad)$
0.016	0.1	not found
0.015	0.1	not found
0.014	0.1	not found
0.013	0.1	0.2259204891316
0.014	0.2259204891316	0.23144913545946
0.015	0.23144913545946	0.23671218331329
0.016	0.23671218331329	0.24173855862323

Table 1: An Example of the Algorithm

6 Conclusion

This paper investigates the iterative searching algorithm for periodic gaits by studying the simplest passive dynamic walking model. An improved algorithm for choosing the initial values is proposed based on the work of Garcia etc. The effectiveness of the proposed algorithm is demonstrated by numerical simulations.

References

- [1] T. McGeer, "Passive dynamic walking," *Intern. J. Robot. Res.*, Vol. 9, pp. 62-82, 1990.
- [2] W. Martijn, "Essentials of dynamic walking; Analysis and design of two-legged robots," Doctor thesis, Delft University of Technology, Mechanical Engineering, 2004.
- [3] M. Garcia et al., "The simplest walking model: Stability, complexity, and scaling," *ASME J. Biomech. Eng.*, Vol. 120, pp. 281-288, 1998.

- [4] M. Garcia et al., "Speed, efficiency, and stability of small-slope 2d passive-dynamic bipedal walking," *In Proc., IEEE Int. Conf. on Robotics and Automation*, pp. 2351-2356, 1998.

Clothes Manipulation by Inchworm Robot Grippers

Khairul Salleh

Hiroaki Seki

Yoshitsugu Kamiya

Masatoshi Hikizu

Department of Mechanical Systems Engineering
Kanazawa University, Kakuma-machi, Kanazawa, Ishikawa 920-1192 JAPAN
E-mail: hseki@t.kanazawa-u.ac.jp

Abstract

Deformable objects manipulation by robot is very challenging. We focused on clothes manipulation as an example and applied edge tracing method in order to search for corners of particular clothes. Tracing in this paper context involves tracing the towel's edge, with the robot arm movement based on feedback from sensors. Development of special tools for deformable object manipulation is also considered to be important as well and must consider the properties of the deformable objects. We designed inchworm type grippers for the purpose of clothes manipulation. This paper proposes a unique tracing method for towel spreading using the inchworm grippers. Experimental results have demonstrated the effectiveness of both the proposed method and the grippers.

Keywords

Edge tracing, deformable object, robot gripper, inchworm, spreading of clothes, home service robot

1. Introduction

The world is full of deformable objects. Let's just look around us. Clothes, papers, cables, plastic bags; they are all deformable objects. Even in today's robotics, researches concerning deformable object manipulation are becoming more and more popular. The presence of these objects means that home service robots need to be dexterous in object handling [1]. In handling clothes, for example, the robot must first recognize the shape of clothes. Due to contact and gravity, clothes rarely show their original shape. In this case, edge tracing is important in object recognition [2]. We use it here to spread clothes, which is important in folding or hanging clothes out to dry. Much research has been done on deformable object manipulation [3,4,5,6,7,8] but very little on clothes manipulation. Even that on clothes manipulation is largely theoretical [9,10] rather than practical. We propose practical research on towel spreading as an example of clothes manipulation using sensor-based edge tracing.

Spreading clothes basically involves holding two corners of the clothes to spread or fold them [10]. The problem is finding the appropriate corners. Vision sensors help find corners [11], but corners are not necessarily visible or exposed to the camera, causing the robot to hold the clothes unsatisfactorily (Figure 1). Even when a camera detects a corner, the corner may not be appropriate. By using tracing manipulation to find the second corner, it is proven that the

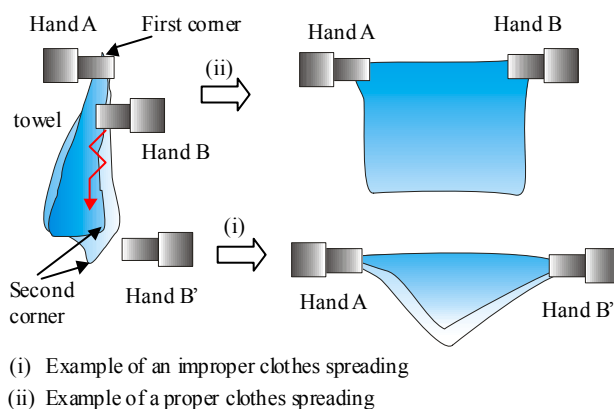


Figure 1 - Problems in clothes spreading

second corner found is that next to the initially found corner and not the one apposite it [12,13]. But there are also problems concerning tracing manipulation. One of the major problems is how to retrieve the fabric when it is in danger of slipping away from the gripper. The robot may be able to detect that the fabric is about to slip but it is hard to retrieve or prevent it. If the robot tries to regrasp the fabric, it would probably slip away. If the robot tries to retrieve the fabric without regrasping it, it would most probably drag the fabric along, flexing it instead of retrieving it. This is due to the fact that deformable objects are sensitive to contact forces. The robot can be programmed to retrace the fabric from the beginning but this will take time. The solution to this problem is to design a special tool that can trace the fabric and does not release it. This paper proposes tracing using inchworm type grippers as a solution.

2. Clothes Manipulation System

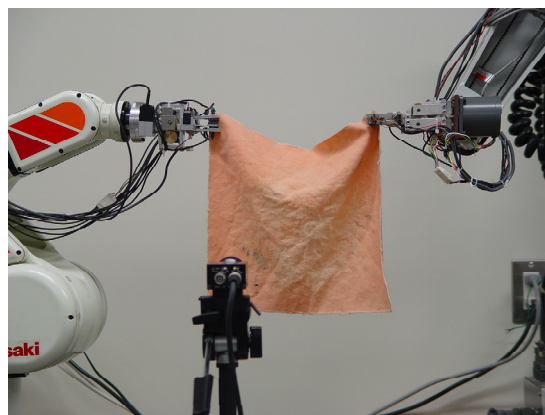


Figure 2 - Clothes spreading scene

Figure 2 shows a scene in towel spreading. In this research, we use two robot arms, Js2 (Kawasaki Heavy Industries) with 6 degrees of freedom (DOF) and RCH-40 (Yamaha) with 5 DOF. Both arms are equipped with grippers designed for clothes manipulation. A CCD camera that detects and confirms corners is located in front of the two robot arms. The images taken by the CCD camera are in 8-bit gray scale and 640x480 pixels in size. TRV-CPW5 image processing board (Fujitsu) speeds up image processing.

The robot grippers designed for fabric manipulation play important roles in clothes manipulation. Figure 3 shows the details of the inchworm grippers attached to the Js2's wrist. There are two pairs of gripper, one is a fixed gripper and the other one capable of sliding sideways using a Maxon motor with rotary encoder (18V, 3.0W, lift-torque 10.8mNm, max rpm 16000rpm) via 2 spur gears of the same diameter and a ball screw with a 1mm lead. The encoder's resolution is 100pulse/rotation. The maximum distance between the two pairs of grippers is 60mm. The grippers both have 3 pairs of infrared sensors to check whether or not the fabric is inside them. Infrared LED OP298B (Optek) and phototransistor TPS601A (Toshiba) is used. The grippers can also detect force being applied to the fabric via strain gauges attached to them. The thick part of the gripper just behind the thin part acts as a stopper to protect the thin part from breaking due to excessive force. The gap between the two fingers of a gripper (gripper gap) is controlled using an RC servomotor from Futaba.

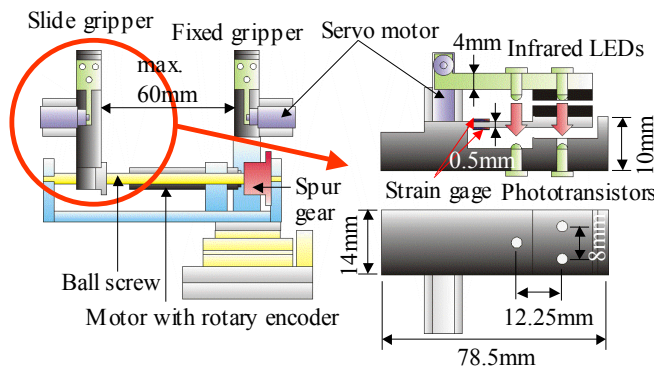


Figure 3 - Inchworm robot grippers

4. Finding a Corner using Edge Tracing Manipulation

Let's assume that the RCH-40 gripper is grasping the first corner. This can be achieved using the CCD camera [12]. After Js2 gripper is positioned at the edge of the towel just beneath the first corner, it will start tracing the edge of the towel by smartly using the feedbacks from the infrared sensors (Figure 4) with the fixed gripper positioned on top and the slide gripper below. This movement pattern is based on the feedbacks from Js2 gripper's infrared sensors and should enable Js2 to find a corner next to the one being held and not the one across it. Since the inchworm type robot grippers have two sets of grippers, at least one of the grippers can be made to grasp the towel while the other gripper traces the edge of the towel. The advantage of using the inchworm

grippers is that Js2 will be grasping the fabric all the time, reducing the probability for the towel to slip away during tracing besides no precise force control is required during tracing. This is because the two grippers of the inchworm type grippers are near to each other and in case the tracing gripper accidentally releases the towel, it can regrasp and retrace the towel from under the other gripper without the Js2 having to trace the towel back from the start.

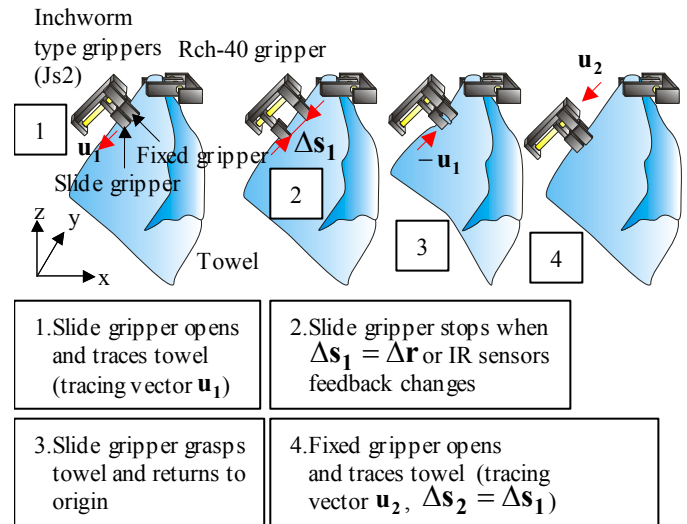


Figure 4 - Inchworm movement during tracing

The gripper movement during tracing is like the movement of an inchworm (Figure 5). The slide gripper will trace the towel until the slide gripper reaches the maximum sliding distance (maximum tracing distance Δr) during infrared feedback patterns A and B or until the infrared sensors feedback changes while the fixed gripper maintain its firm hold of the towel. During this process, Js2 will remain static. The actual tracing distance is Δs_1 . The relation between Δr and Δs_1 can be written as follows:

$$\Delta s_1 \leq \Delta r \quad (1)$$

The tracing vector for the sliding gripper \mathbf{u}_1 is perpendicular with the orientation of the inchworm type grippers on the xz-plane. The tracing vectors \mathbf{u}_1 can be written as follows:

$$\mathbf{u}_1 = (-\sin \theta, -\cos \theta), \quad |\mathbf{u}_1| = 1 \quad (2)$$

After either $\Delta s_1 = \Delta r$ or the infrared sensors feedback changes from pattern A to pattern B (Figure 4) or vice versa, the slide gripper will grasp the towel and then return to its origin. This means that during this process, both grippers are supposed to firmly hold the towel. The new tracing vector for the slide gripper during this process \mathbf{u}_{1new} can be written as follows:

$$\mathbf{u}_{1new} = -\mathbf{u}_1 = (\sin \theta, \cos \theta) \quad (3)$$

The sliding distance is $\Delta s_1'$ where:

$$\Delta s_1' = \Delta s_1 \quad (4)$$

After returning to its origin, the fixed gripper will open slightly and then the Js2 will move downwards. The fixed gripper will be tracing the towel's edge during this process

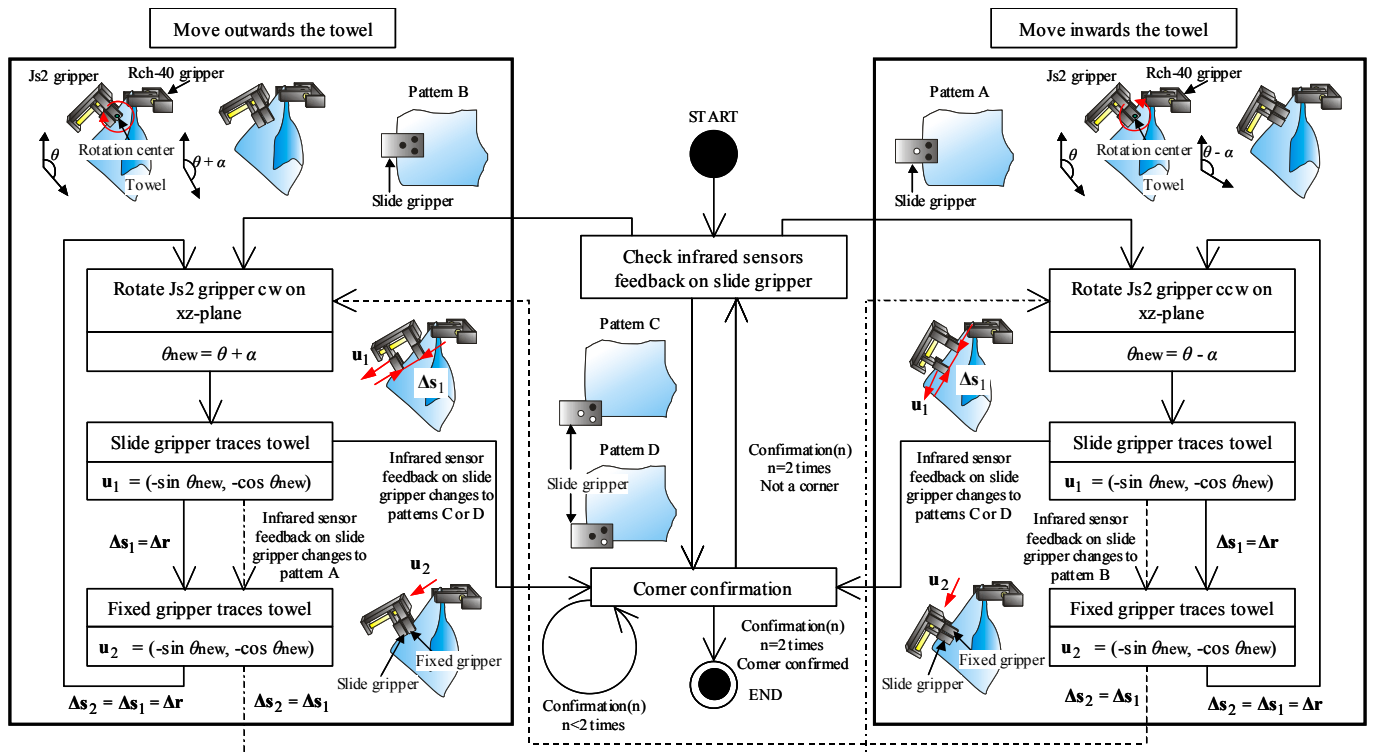


Figure 5 – Tracing algorithm using inchworm grippers

(tracing vector for the fixed gripper \mathbf{u}_2 and tracing distance Δs_2). \mathbf{u}_2 and Δs_2 can be written as follows:

$$\mathbf{u}_2 = \mathbf{u}_1 = (-\sin \theta, -\cos \theta), \quad |\mathbf{u}_2| = |\mathbf{u}_1| = 1 \quad (5)$$

$$\Delta s_2 = \Delta s_1 \quad (6)$$

Both grippers will then grasp the fabric firmly before Js2 changes the inchworm grippers' orientation θ based on the final infrared feedback pattern of the slide gripper when it first traced the towel. In case of pattern A, the robot will open the slide gripper slightly before Js2 rotates the inchworm grippers counter clockwise (rotating angle α) on the xz -plane so that the tracing direction will be facing deeper into the towel. In case of pattern B, the robot will open the fixed gripper slightly before Js2 rotates clockwise (rotating angle α) instead on the xz -plane so that the tracing direction will be facing away from the towel. The rotation center is the center of the fixed gripper's fingertip. The slide gripper will then again starts tracing the towel. The new tracing vector $\mathbf{u}_{1_{new}}$ can be written as follows:

$$\mathbf{u}_{1_{new}} = (-\sin(\theta - \alpha), -\cos(\theta - \alpha)), \quad (7)$$

$$\mathbf{u}_{1_{new}} = (-\sin(\theta + \alpha), -\cos(\theta + \alpha)), \quad (8)$$

where eq.(7) represents the new tracing vector for pattern A and eq.(8) represents the new tracing vector for pattern B.

Js2 will trace the edge of the towel until the infrared sensors feedback on the sliding gripper turns to patterns C or D, indicating that Js2 is holding a possible corner, and corner confirmation process will take place. This is done by changing the orientation of the Js2 gripper θ and checking it the feedback stays at pattern C, D or not. The corner

confirmation process is done two times. If the second corner is reached and confirmed, Js2 gripper will firmly grasp the corner and the towel is then spread.

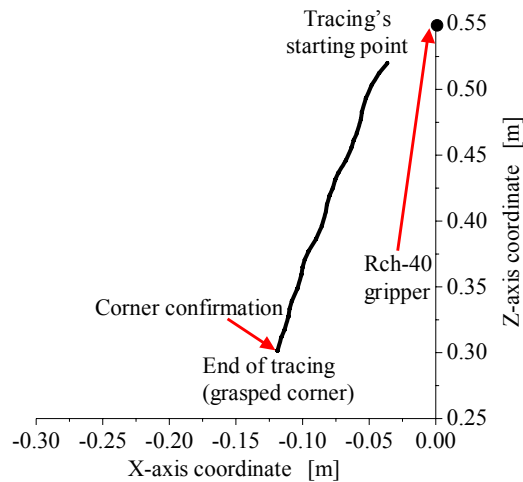
5. Experimental Results

Experiments were conducted 20 times to evaluate the proposed edge-tracing algorithm using a towel with the following properties: size 32cm x 32cm, thickness 2.28mm, mass per unit 0.037g/cm², coefficient of friction 0.615, and stretch rate 0.005cm/gf. All experiments were started with the Rch-40 gripper holding a corner of the towel. Δr and α are set at 5mm and 5deg respectively.

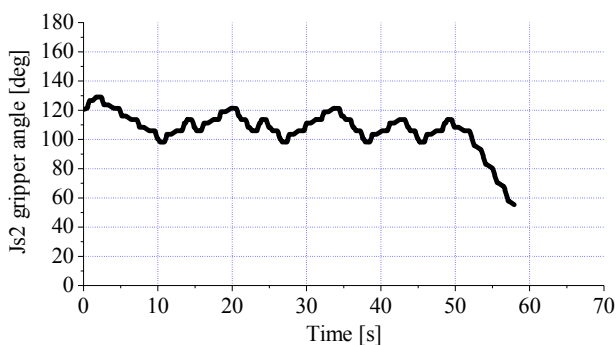
Figure 6 shows the data acquired during one of the tracing experiments. From Figure 6 (c), we can see that at the end of tracing, the infrared sensors feedback on the slide gripper turned to patterns C or D. This proves that the robot knows when it is approaching a corner. We can also see from Figure 6 (c) that corner confirmation process took place based on the number of times the feedback turned to patterns C or D at the end of tracing. Figure 6 (a) shows the trajectory for inchworm grippers. Figure 6 (b) shows the orientation of the inchworm grippers on the xz -plane. The percentage for Js2 finding a corner is 80%, proving that our proposed tracing manipulation method has been successful. The average time is approximately 58sec. Failures are mainly due to the Js2 gripper failing to trace along the edge of the towel. This happens when Js2 gripper does not hold the edge of the towel at the beginning of the tracing manipulation.

6. Conclusion

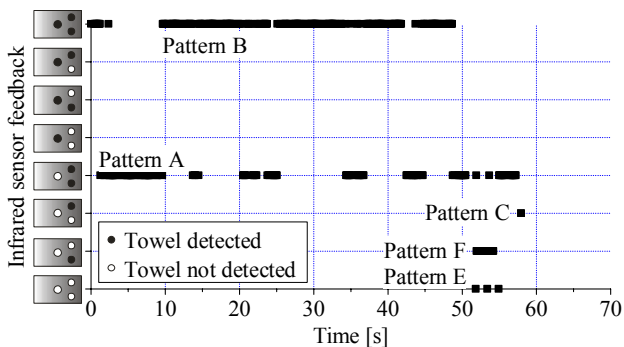
A method for finding a corner of a towel using a unique edge



(a) Js2 gripper trajectory



(b) Js2 gripper orientation θ on the xz-plane



(c) Infrared sensors feedback from slide gripper

Figure 6 - Experimental data obtained during edge tracing of towel by Js2 with inchworm type grippers

tracing method by inchworm grippers is presented. The gripper has enabled Js2 to trace the edge of the towel with more stability and also successfully even without the help of a vision sensor.

Projected plans include the improvement in both speed and reliability of the process. Collaboration with the existing vision sensor might solve this problem. Applying the current algorithm to other clothes such as shirts and skirts is also important to check the robustness of the method to other kinds of clothes as well.

References

- [1] Hirai, S. 1998. Deformable object manipulation. *Journal of the Robotics Society of Japan* 16(2): 136-139.
- [2] Arslan, A. and Turkoglu, I. 1999. An edge tracing method for object recognition. In *Proceedings of International Conference in Central Europe on Computer Graphics, Visualization and Interactive Digital Media, Vol 3. Citing Internet sources URL <http://wscg.zcu.cz/wscg99/papers/H53-final.pdf>*
- [3] Wakamatsu, H. and Wada, T. 1998. Modeling of string objects for their manipulation. *Journal of the Robotics Society of Japan* 16(2): 145-148.
- [4] Nakagaki, H. 1998. Insertion task of a flexible beam or a flexible wire. *Journal of the Robotics Society of Japan* 16(2): 159-162.
- [5] Abegg, F., Henrich, D., and Worn, H. 1999. Manipulating deformable linear objects –Vision-based recognition of contact state transitions-. In *Proceedings of the 9th International Conference on Advanced Robotics. Citing Internet sources URL http://www.ipr.ira.uka.de/de/Publikationen/detailed_publication.htm?id=976207040.*
- [6] Balkcom, D.J. and Mason, M.T. 2004. Introducing robotic origami folding. In *Proceedings of IEEE International Conference on Robotics and Automation, 3245-3250*.
- [7] Kraus Jr., W. and McCarragher, B.J. 1997. Case studies in the manipulation of flexible parts using a hybrid position/force approach. In *Proceedings of IEEE International Conference on Robotics and Automation, 367-372*.
- [8] Smith, P.W., Nandhakumar, N. and Tamadorai, A.K., 1996. Vision based manipulation of non rigid objects. In *Proceedings of IEEE International Conference Automat, Vol.4, 3191-3196*.
- [9] Desbrun, M., Schroder, P. and Barr, A. 1999. Interactive animation of structured deformable objects. In *Proceedings of the Graphics Interface Conference, 1-8*.
- [10] Hamajima, K. and Kakikura, M. 1998. Planning strategy for task of unfolding clothes. In *Proceedings of the 16th Annual Conference of the Robotics Society of Japan, 389-390*.
- [11] Ono, E., Kita, N. and Sakane, S. 1997. Unfolding a folded using information of outline with vision and touch sensor. *Journal of the Robotics Society of Japan* 15(2): 113-121.
- [12] Salleh, K., Seki, H., Kamiya, Y. and Hikizu, M. 2004. Spreading of clothes by robot arms using tracing method. In *Proceedings of the 5th International Conference on Machine Automation, 63-68*.
- [13] Salleh, K., Seki, H., Kamiya, Y. and Hikizu, M. 2006. Tracing manipulation by robot grippers equipped with gear tips. In *Proceedings of IEEE International Conference on Robotics, Automation & Mechatronics, 278-283*.

Development of an obstacle recognition system for autonomous robots in indoor environments

Hiroshi Mizoguchi

Eiji Hayashi

Department of Mechanical Information Science and Technology

Faculty of Computer Science and Systems Engineering , Kyushu Institute of Technology
680-4, Kawazu, Iizuka-City, Fukuoka Prefecture, Japan

Key Words: Robot, Recognition, Autonomous, Obstacle

Abstract

We are currently developing an autonomous robot that can work in human living environments and that can carry out users' basic instructions. When such a robot moves and works in a human living space, the robot should be able to recognize elements of its environment.

Thus, we are engaged in research aimed at the acquisition of a sense of distance from based on image information, utilizing sight information and not necessitating remodeling of the human living space.

We give our robot a "finite space map." This map contains information describing a floor plan including obstacles (desk and sofa, etc.), and the robot's position. The robot searches for a route based on the finite space map, and moves along that route. However, numerous obstacles that would disturb the movement of the robot can exist in a human living environment; in addition, these objects are often unknown to the robot. The robot thus needs a system to recognize unknown obstacles not provided by the finite space map beforehand.

Thus, we developed an obstacle recognition system that discovers detects obstacles, and detects determines the distance to the obstacle and obtains three-dimensional data describing the obstacle.

1. Introduction

Recently, the chances of seeing a working robot in our surroundings have increased. Robots with various functions have been developed based on recent technological advances. However, a robot capable of helping us autonomously has not yet appeared. Thus, our laboratory is developing an autonomous personal robot that can work in the home and the hospital while being easy to command.

In order to allow the robot to work autonomously, it is necessary to create a program for the robot that allows it a variety of actions.

We are advancing the development of a robot that acts autonomously by giving the robot functions that allow it to work and move easily in a room, and that allow easy communication with the person it is

intended to serve.

Our robot's only sensor is a CCD camera installed in the robot's head, which can rotate and tilt forward and backward. Our robot moves on two motorized wheels (front wheels) and two castor wheels (rear wheels). Moreover, the robot has two arms with which to perform simple work (e.g., grasping an object). The PC installed in the main body executes control of the device and runs an autonomous program. An installed wireless LAN provides the option of remote control for humans. Lead batteries supply the robot's electric power. [1] [2]

In order to detect obstacles, the system extracts the pixel groups whose shapes are much different from the main background pixels and interprets them as obstacles. The system can predict the distances to the obstacles and also the obstacle's height and width by using the extracted information and attached drive encoders.

In addition, the position and the size of the detected object are reflected in a finite space map, and the robot evades the obstacle by calculating an evasion route.

In this paper, we explain our robot's processing mechanism. In addition, we describe the details of the obstacle recognition system, and show the results of an experiment using this system.

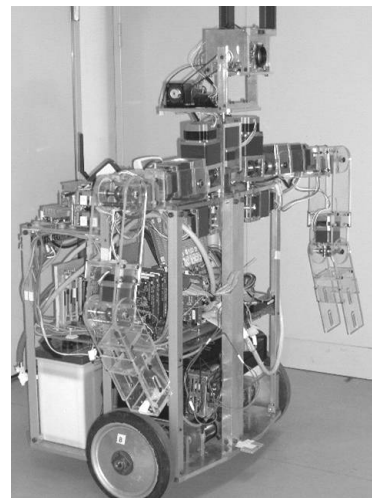


Fig. 1 Robot appearance

2. Self-drive control for robot

Our robot has an action determination program that enables it to act autonomously. The obstacle recognition system explained in this paper is part of this program. The robot has a system that enables it to communicate with humans and recognize moving objects. These action determination programs use the feedback values returned from the CCD camera and the motor encoders. In addition, these programs control the arm and the wheels and command the driving motors. [3]

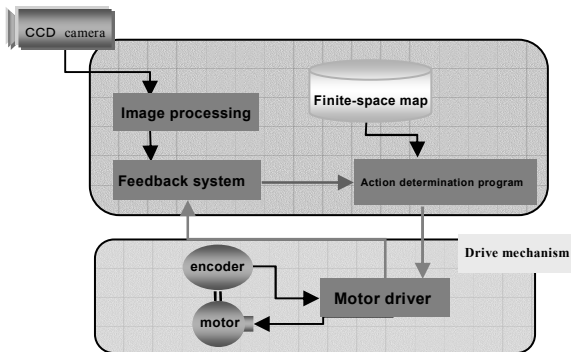


Fig.2 Self drive control for robot

3. Obstacle recognition system

3.1 Outline of the system

In order to ensure that the robot can drive safely in an indoor environment, the system must detect obstacles. Thus, data that can allow it to avoid obstacles is needed. We have developed a system of recognizing obstacles that uses only image data captured by a CCD camera. The purpose of this system is to enable the robot to detect obstacles and roughly recognize an obstacle's size and position. In addition, the position and the size of the detected object are reflected in the finite space map, and the robot evades the obstacle by calculating an evasion route.

3.2 Method of extracting obstacles

First of all, the system converts 24bit RGB image data into HSV data. HSV data shows the image elements of hue, saturation, and value. The processing of the image data could be simplified by using HSV. The system samples a group of image pixels in a rectangular region at the bottom center of an image. The system uses the group of image data inside this region as its sample image data and then uses the deflection calculated by the sample data. The system extracts the floor region in terms of the difference of all pixels in the image. Figure 3 shows an extracted obstacle.



Fig.3 Extract the obstacle

Labeling is used to make one set of each group of image pixels extracted from an image. This is processed from the extraction result of the floor region. The group of image pixels that leads to the detection of an obstacle is distinguished by this process. Figure 4 shows an example of labeling.

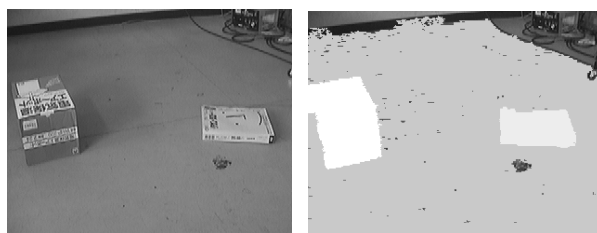


Fig.4 Example of labeling

Next, the system analyzes the object that has been determined to be an obstacle. We define the lower side of a group of image pixels as the distance to the object, and the system presumes the width of the obstacle based on the width of a group of image pixels. In addition, we defined the uppermost part of a group of image pixels as the height or a depth of the object. The robot runs on the floor side, and presumes determines the height of the obstacle based on the position of the change in the image pixel group, the camera position, and the angle between the two images.

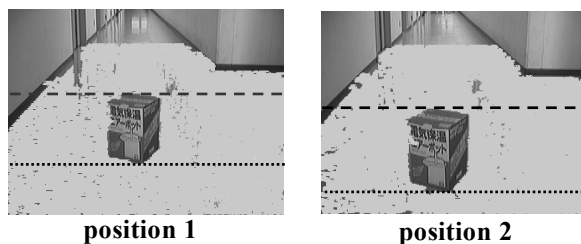


Fig.5 Estimation of an obstacle's data

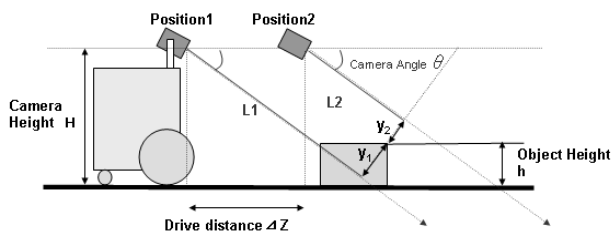


Fig.6 Object recognition from motion stereo

We process the calculation of We process the data of these obstacles in consideration of the focus and geometric calculation of the camera. Lastly, we show the flow of the obstacle estimation processing in Figure.7. [4]

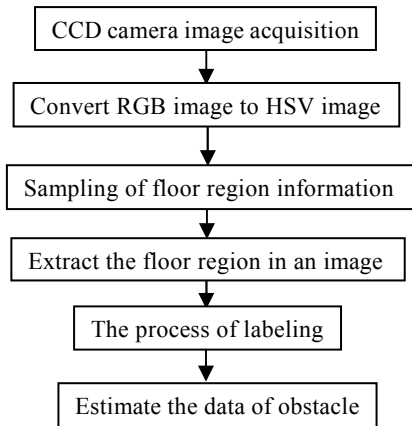


Fig.7 Flow of processing

3.3 Evaluation of the obstacle extraction process

We show the results of a test regarding the accuracy of the estimation of an object. When the system is actually used, processing will be repeated while the robot is moving. However, two images acquired to accurately measure the distance when the robot was in a fixed position were used to verify the accuracy of the data describing the obstacle (width, height, and depth). Table.1~3 shows an example of the verified obstacle data. Figure 8 shows the results in 3-D space.

Table.1 Calculation result of object data (box)

	Actual measurement	Calculation result
Distance to obstacle	100cm	98cm
Obstacle position(horizontal direction)	Right 1cm	Right 3cm
Height	31cm	34cm
width	21cm	30cm
depth	21cm	17cm

Table.2 Calculation result of object data (plate)

	Actual measurement	Calculation result
Distance to obstacle	130cm	128cm
Obstacle position(horizontal direction)	Left 69cm	Left 78cm
Height	0.5cm	0cm
width	50cm	63cm
depth	50cm	57cm

Table.3 Calculation result of object data (ball)

	Actual measurement	Calculation result
Distance to obstacle	96cm	93cm
Obstacle position(horizontal direction)	Right 29cm	Right 33cm
Height	22cm	18cm
width	22cm	27cm
depth	22cm	8cm

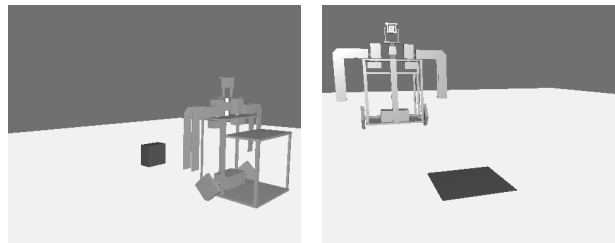


Fig.8 Estimation of obstacle displayed in 3-D

Based on these results, it was judged that the system collects obstacle data at a sufficient level of accuracy to evade an obstacle.

3.4 Method of evading obstacle

The robot evades an obstacle by using the results of obstacle estimation. When the obstacle is initially estimated, the system saves the camera image (the first image). As the robot advances in a regular fashion, the system obtains a second image that is used by the motion stereo process. The distance from the first image to the second image can be obtained according to the value of the encoder installed in the robot's drive wheel. Obstacle data is obtained by using these two images and the method of obstacle extraction.

When the height of an obstacle is detected (if the height of the obstacle is 0, the system determines that the robot need not evade the obstacle), the obstacle's data (width and depth) is written into the finite space map.

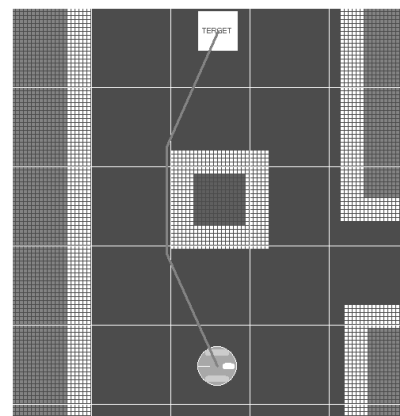


Fig.9 Finite space map

The finite space map is one of the knowledge databases that the robot has beforehand. This map contains information regarding the floor plan including obstacles (desk and sofa, etc.), and the robot's own position. The robot searches for a route based on the finite space map, and moves along that route.

In addition, the route for evading the obstacle is calculated by using the route searching system installed in the robot, and the robot then performs an evasive action. The route searching system calculates and controls the route of the robot by using the finite space map. Figure 10 shows the flow of the evasive action.

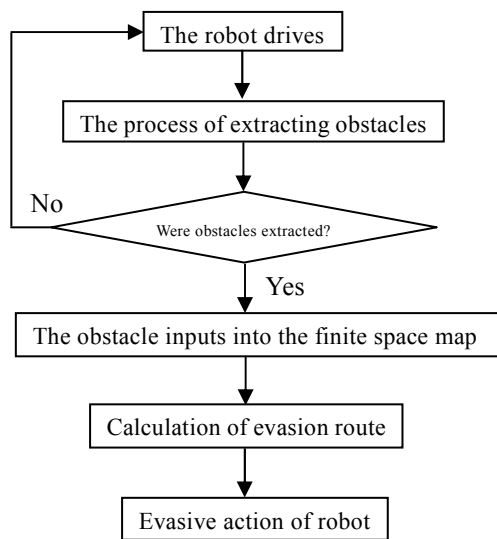


Fig.10 Flow of evasive action processing

4. Conclusion

We developed an obstacle recognition system that allows a robot to drive safely in an indoor environment. This system is able to roughly recognize a three-dimensional object. In addition, the obstacle could be successfully avoided by using data describing the recognized obstacle.

However, the current method for calculating the obstacle's height and depth cannot accurately calculate an obstacle having an intricate shape. Our next focus of study is to find a solution to this problem and to make the system more stable by improving its processing speed and efficiency.

References

- [1] Toru Azuma, Yoshihiro Takenaga, Eiji Hayashi, Development of a self-driven personal robot, Artificial Life and Robotics (AROB 8th '03), pp.1-3, Oita, Japan, 2003
- [2] Eiji Hayashi, Keisuke Ikeda, Development of a system for self-driving by an autonomous robot, proceeding of 10th international symposium on artificial life and robotics, Vol.10th, pp.4, Beppu, Oita, Japan, 2005
- [3] Takuma Umeno, Eiji Hayashi, Development of an autonomous personal robot "The visual processing system for autonomous driving", proceedings of the 10th international symposium on artificial life and robotics, Vol.10th, pp.44, Beppu, Oita, Japan, 2005
- [4] Takuma Umeno, Eiji Hayashi, Navigation system for an autonomous robot using an ocellus camera in indoor environment, proceedings of the 11th international symposium on artificial life and robotics, Vol.11th, pp.229, Beppu, Oita, Japan, 2006

Autonomous control of a robot arm based on contact with an object

Motoki Shimono

Graduate School of Computer Science
and System Engineering
Kyushu Institute of Technology
680-4, Iizuka City, Fukuoka, Japan, 820-8502
shimono@imcs.mse.kyutech.ac.jp

Eiji Hayashi

Department of Mechanical Information
Science and Technology
Kyushu Institute of Technology
680-4, Iizuka City, Fukuoka, Japan, 820-8502
haya@mse.kyutech.ac.jp

Abstract

In this paper, I focused on developing a robot arm with three degrees of freedom and an autonomous function. I modeled my research on the actions of animals, which adjust well to environmental change, and aimed for control of an autonomous robot that would imitate the action of an animal. Our laboratory developed a software architecture to control the action of the robot by introducing an evaluation function for action choice into the hierarchically structured model. This is the element that specifically connects the consciousness of the robot with its action, and I named it Consciousness-based Architecture (CBA). In this research, I ran an experiment on a search action for a robot arm executing a detour around obstacles and arriving at a target position. An experiment was performed to evaluate the effectiveness of CBA, and its results are discussed. I let the robot arm imitate the groping movement of a human being and allowed a search action to proceed. In the case of an outward trip, the robot arm recognized the positions of obstacles by touching them, and it avoided these obstacles by executing detours. As a result, the robot arm arrived at the target position while memorizing the course of detours around the obstacles that it recognized.

Key words: robot arm, evaluation function, Consciousness-based Architecture, autonomous function

1. Introduction

The Japanese robots industry developed for the field of manufacturing has played a key role in producing robots that can assemble cars and operate precision instruments.^[1] Hence, in this research, I focused on developing a robot arm with three degrees of freedom and an autonomous function. Fig.1-1 shows the system constitution of this research; Fig.1-2 presents a diagram showing the placement of the degrees of freedom of the robot arm.

This arm is not equipped with sensors to the outside world and cannot take in nearby environmental information before touching it. Therefore, I let the robot

arm imitate the groping movement of a human being and allowed a search action to proceed. This paper describes control of a joint angle by a computed torque method, the consciousness architecture incorporated in the robot arm that allows it to act on a search, and an experiment of a course search.

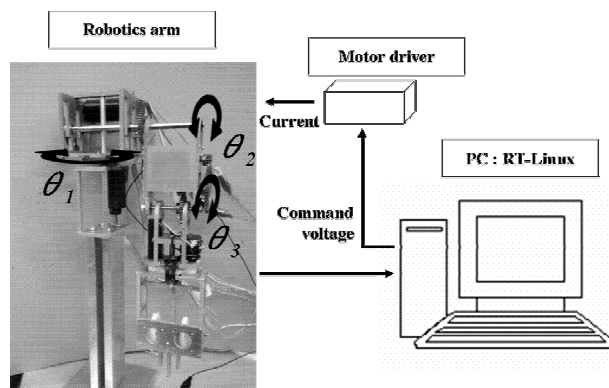


Fig. 1-1 Schematic diagram of the system structure for the robot arm

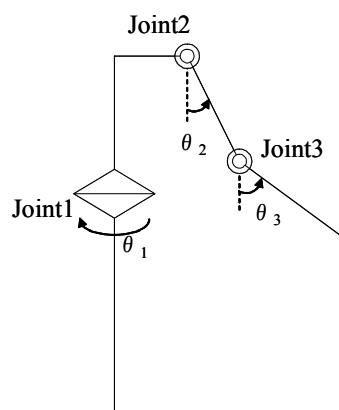


Fig. 1-2 Overview of the 3 DOF of the robot arm

2. Positioning of a robot arm by a computed torque method

A computed torque method is a control technique to make compensations by a reverse dynamics calculation that does not consider centrifugal force and Coriolis force to be agitation.^[2] Expression (2-1) below is an exercise equation for motors; expression (2-2) is an exercise equation for a robot arm by the Lagrange method; and expression (2-3) is a law of control.

$$J\ddot{\theta} + C\dot{\theta} = \tau \quad (2-1)$$

J : Rotor inertia [kgm^2]

C : Braking constant [kgm^2/sec]

τ : Torque [Nm]

$$\tau = M(\theta)v(t) + h(\theta, \dot{\theta}) + g(\theta) \quad (2-2)$$

$M(\theta)$: inertia matrix

$h(\theta, \dot{\theta})$: considering centrifugal force and coriolis force

$g(\theta)$: gravity

$$v(t) = \ddot{\theta}_r + K_p(\theta_r - \theta) + K_d(\dot{\theta}_r - \dot{\theta}) \quad (2-3)$$

θ_r : aim angle [deg rec]

Each feedback gain is derived with a pole assignment technique.^[3] Two poles constitute conjugate imaginary poles, and I assume $s = -\alpha \pm j\beta$. And when I assume $\alpha = \zeta\omega_n, \beta = \omega_n\sqrt{1-\zeta^2}$, each feedback gain is found according to expressions (2-4) and (2-5):

$$K_d = \frac{2J\omega_n - C}{M(\theta)} \quad (2-4)$$

$$K_p = \frac{J\omega_n^2}{M(\theta)} \quad (2-5)$$

In addition, each parameter is demanded through consideration of the response and the greatest electric current which a motor permits experimentally. I show a result for a shoulder joint in Fig.2-1. I assumed parameters which determined feedback gain $\alpha = 30, \zeta = 0.90$.

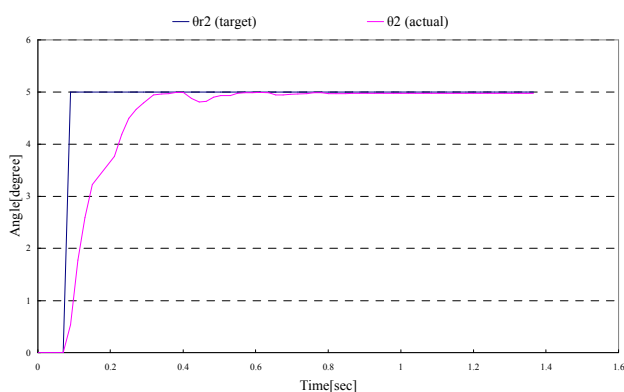


Fig. 2-1 Response of Joint2

3. An autonomous action

3-1 Consciousness-based Architecture (CBA)

Fig. 3 shows a summary of a search action in this research. I applied CBA to a robot arm at level 5 this time. The robot arm moves the shoulder (B) and elbow (C) from (S), which is in an appropriate initial state, and it leads to the aim state (G), while detouring around an obstacle.

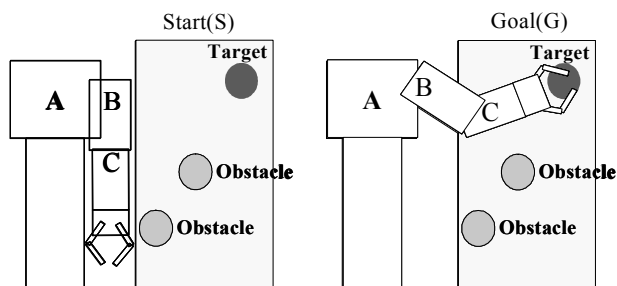


Fig. 3 Schematic diagram of the experimental environment

In addition to the robot arm shown here, our laboratory constructed a hierarchically structured model based on an expression mechanism model of consciousness and the action of an animal. Table 3-1 shows a consciousness module and a restraint object, aspects of an action module applied in this research.

Table 3-1 Details of consciousness, behavior, and deterrent at each level

Level	Consciousness	Behavior	Deterrent
5	Memory for an obstacle	think	A startup to an initial position
4	Memory for an obstacle	detour	A stop of link AB, bc by contact
	Confirmation of an assistant goal position	search	
3	Confirmation of fingers position	avoid	A stop of link AB, bc by contact
	Confirmation of an aim position		
	Confirmation of the obstacle position where a robot arm		
2	Confirmation of fingers position	move	A stop of link AB, bc by contact
	Confirmation of an aim position		
1	*****	reflex	A stop of link AB, bc by contact
0	*****	sleep	*****

In explanation of this hierarchical structure model, a consciousness level first emerges at 1 when a performed action is restrained. A robot arm then makes the best choice from actions on a lower level.

3-2 An evaluation function for behavior choice

Various elements participate in the ground rule of an animal. The thing which a function makes inside the state of an animal is "an evaluation function." In this experiment; an evaluation function assumes an outside environmental state to be a component. Expression (3-1)

defines the strength of consciousness C_i of level i in a time t ; expression (3-2) defines an evaluation function that chooses an action:

$$C_i(t) = \sum_{j=1}^{N_E} |\beta_{ij}(t)| \quad (i = 0 \dots p) \quad (3-1)$$

$$I_i(t) = \sum_{j=1}^{N_E} \beta_{ij}(t) \quad (3-2)$$

where N_E = the number of things outside perception, and β_{ij} = the degree of the physical outside perception.

4. An autonomy action experiment

I applied an action module and an autonomy action algorithm that I built into a robot arm. I then experimented with a diplomatic shuttle action using these. I tested the action in the environment shown in Fig. 3. In the test, I gave the robot arm only coordinate information about the aim position, none about obstacles. When the fingers arrived at the aim position, the robot arm changed its initial position to the new aim position and moved.

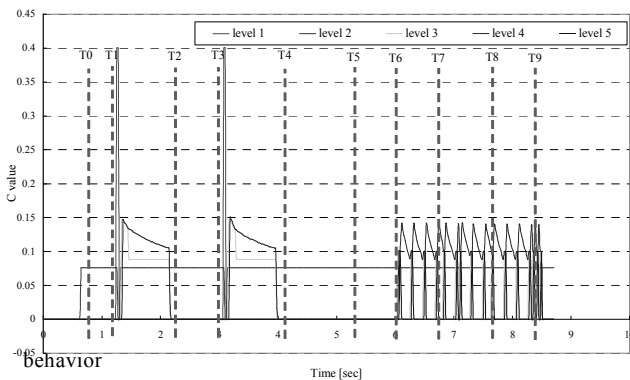


Fig.4-1 and 4-2I show the experimental result. Fig. 4-1 shows the consciousness evaluation function in CBA when the arm moved to a destination. The vertical axis shows the size of the evaluation function at each level, and the horizontal axle shows time. The figure indicates a series in consciousness from the beginning of movement to arrival at the aim position and an action. T_i ($i=0 \dots 9$) in an explanation helps to support Fig. 4-1

The consciousness level rises to 2 when the program of the robot arm is at T0. When the robot arm comes in contact with an obstacle at T1 and causes a reflection, the consciousness level falls to 1. When the consciousness of level 1 fades away afterwards, a restraint produces an action at level 2 with the memory of the obstacle remaining, and then the consciousness level stops at 2, 3, and 4 sequentially.

Because the consciousness level rises to 4, the robot arm chooses an action to detour around an obstacle. The robot arm judges the obstacle to be a detour in T2, and the consciousness level goes down to 2. Because the

consciousness level fell to 2, a robot arm reopens an action to go to an aim position. Just like in the sequence above, the robot arm chooses a reflection/detour action at T3 - T4 and moves towards an aim position. The robot arm judges that the finger reached the target position and stops at T5.

At T4, the robot arm begins a movement to return to its startup posture. In the return journey, the robot arm will trace the most suitable course. Therefore, the consciousness level rises to 5, and it refers to the assistant goal information memorized in the outward trip given it at level 4. Assistant goals given then are the fingers position when the robot arm judged that a detour action was completed at T2 and T4. The robot arm acts on a search in level 4 and starts movement towards a given assistant goal. At T6 and T7, the fingers of a robot arm arrive at an assistant goal. Therefore, the consciousness level rises to 5 and is given at level 4 the next assistant goal information. The robot arm judges that the finger reached the initial position and stops at T9.

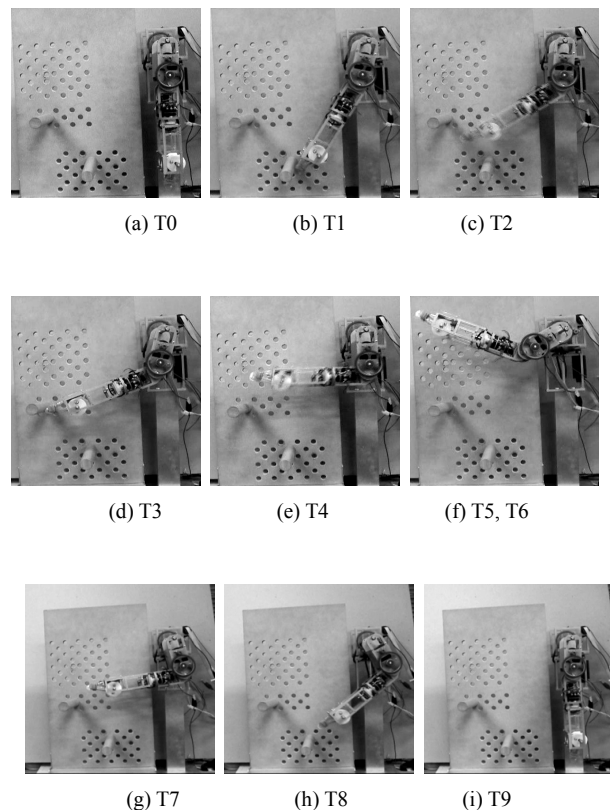


Fig. 4-2 Robot arm postures for each time

5. Conclusion

I report performing the positioning of a robot arm by a computed torque method and also an experiment

regarding a search action. I will aim at the realization of more practical feel movements in three dimensions in the future. However, a search action recognizes an obstacle only after it is restrained in an action bringing it into contact with the obstacle. Therefore, when an obstacle is soft, there is the danger that it might be damaged. This is a problem for the future.

6. Acknowledgment

The authors would like to acknowledge the advice and assistance of Professor Tadashi Kitamura of Kyushu Institute of Technology who died in 2006.

References

- [1] The Japan Machinery Federation, "Technical strategic working papers for robot society creation in the 21st century," 2001, pp.10.
- [2] Kobayashi, N., Masuda, R., "Real robot control," Corona Publishing Co., 1997, pp.127.
- [3] The Japan Society of Mechanical Engineers, "JSME text series, Control Engineering," 2002, pp.160.

Real-Time Target Detection Using Infrared Camera

M. Sugisaka^{1*}, Erma Rahayu Mohd. Faizal²

Department of Electrical Engineering, Oita University, Japan

(Tel: +81-097-554-7841; Email: ermarahayu81@yahoo.co.jp)

Abstract

Infrared (IR) cameras are often used in a vehicle based multi-sensor platform for landmine detection. Additional to thermal contrasts, an IR polarimetric sensor also measures surface properties and therefore has the potential of increased detection performance. This paper describes all the steps to reach detection performance. The first step is the acquisition of the polarimetric IR image data. The next step is the pre-processing to (re)construct polarimetric images. A subsequent segmentation step is made to identify objects. Features, like intensity, reflectivity and shape, of these objects are measured. For independent performance analyses, the data set is divided into a training and evaluation section. A classifier is trained on the training section and evaluated on the classification section.

Keywords: *Infrared camera; Infrared thermography; Data analysis; Image Processing, Thermography processing.*

1. Introduction

1.1 Computer Vision and Surveillance

Many current surveillance systems consist of cameras and monitors with human dependence to analyze and report possible problems. This type of

system is not hardware expensive system, however the human requirement to monitor 24 hours per day is expensive and source of inaccuracy. Some of the systems may include recording media to capture all the events for a later viewing. The problem with this is it turns the surveillance system into a forensic tool to solve a possible robbery or illegal action that has already happened nowadays.

Instead, a better solution is to have real-time continuous and automated surveillance systems to detect and alert a potential threat in progress. The need for automated surveillance is very important in medical, commercial, law enforcement and transportation.

The computational power required for a real-time video processing is large. The field of computer vision is taking advantage of the computational power available and monitors the applications into real-time automated surveillance for reasonable cost. As the fields of computer vision continues to grow, new technologies will make it possible for reliable and cost effective means of implementing better smart surveillance systems.

1.2 Purpose and Objectives

For this research, we have done several experiments to achieve a few objectives. The objectives are the system should be able to detect any movement object in real-time. As far as we concern, any movement detect by the camera could be in fast or slow motion. If the image taken while the object is moving fast, the image could be blur or hardly been seen.

Therefore the objectives, we are proposing a method to overcome such problem. Whenever we use such technique of the image processing, it is guaranteed that the image after going through image processing, the image produce will be in better result. In image processing we can't run from detecting edges. Therefore the proposed method will also has the ability to detect edges precisely to easily recognize the object taken whether in fast or slow moving object. Beside, it is also feature one of the important techniques in image processing, which is filtering. The filter use will be able to sharpen the image taken.

2. Image Processing

2.1 Edge Detection

In this research, the method proposed for edge detection is using the Canny Edge Detection Method. In this method, there are three issues that an edge detector must be address.

1. **Error rate** – The edge detector should respond only to edges, and should find all of them; no edges should be missed.
2. **Localization** – The distance between the edges

pixels as found by the edge detector and the actual edge should be as small as possible.

3. **Response** – The edge detector should not identify multiple edge pixels where only a single edge exists.

2.2 Filtering

To sharpen the blur image taken we propose a new method in filtering which used the capability of Gaussian equation to filter images. In one dimension, the response of the filter f to an edge G is given by a convolution integral:

$$H = \int_{-w}^w G(-x)f(x)dx$$

The Canny detector method attempts to find the filter f that maximizes the product SNR x localization subject to the multiple-response constraint, and while the result is too complex to be solve analytically, an efficient approximation turns out to be the first derivative of a Gaussian function. Recall that a Gaussian has the form:

$$G(x) = e^{-x^2/2\sigma^2}$$

The derivative with respect to x is therefore:

$$G'(x) = \left(-\frac{x}{\sigma^2}\right) e^{-\left(\frac{x^2}{2\sigma^2}\right)}$$

In two dimension, a Gaussian is given by:

$$G(x, y) = \sigma^2 e^{-\left(\frac{x^2+y^2}{2\sigma^2}\right)}$$

and G has derivatives in both the x and y directions. The approximation to Canny's optimal filter for edge detection is G' , and so by convolving the input image

with G' , the result obtain is an image E that has enhanced edges, even in the presence of noise, which has been incorporated in to the model of the edge image.

A convolution with two- dimensional Gaussian can be separated into two convolutions with one-dimensional Gaussian, and the differentiation can be done afterwards. Indeed, the differentiation can also be done by convolutions in one dimension, giving the two images: one is the x component of the convolution with G' and the other is the y component.

2.3 Difference Picture Technique

The most obvious method of detecting edges between the two frames is to directly compare the corresponding pixels of the two frames to determine whether they correspond to the same pixels value. In the simplest form, difference picture $DP_{jk}(x, y)$ between frames $F(x, y, j)$ and $F(x, y, k)$ is obtained by:

$$DP_{jk}(x, y) = |F(x, y, j) - F(x, y, k)|$$

where x, y are the spatial coordinates in the frame, j and k represent frame j and frame k taken at different time sequence. In our experiment, $DP_{jk}(x, y)$ output is displayed as indicator for motion study. After a differentiate checking using detection of edges and pixel luminance comparison, we managed to differentiate whether the output is moving object or noises.



Figure 2.1: Image taken in two frame of different time

However, we purposely did not remove the noises as necessary information is obtained, in order to save time computing. As long as we achieved the required goal, extra computing process should be eliminated to save time computing and moving detection in real time required immediate response. Illumination changes can possibly give an error results in detecting changes.



Figure 2.2: Image after going through edge detection

3. Conclusion

Infrared (IR) cameras are often used in a vehicle based multi-sensor platform for landmine detection. Additional to thermal contrast, an IR polarimetric sensor also measures surface properties and therefore has the potential of increased detection performance. This paper describes all the steps to reach detection performance. The first step is the acquisition of the polarimetric IR image data. The next step is the pre-processing to reconstruct polarimetric images. A subsequent segmentation step is made to identify objects. Features like intensity, reflectivity and shape, of these objects are

measured. For independent performances analyses, the data set is divided into a training and evaluation section. A classifier is trained on the training section and evaluated on the classification section.

Utilizing a desktop PC and a infrared thermal imaging camera, a real-time vision system was able to detect and collects targets within the field of view of the camera. Using fast image processing tools the system detects regions of heat and collects attributes about the objects. Using this information about each object overlay graphics are drawn on the image as rectangles around the object. The implementation of this project is in Visual C++ with all functions for image processing and real-time detection. Beside the method of Canny Edge Detector is proposed in this research. It implies the way to detect edges of the image more relevant and effective. The speed of the application allows real-time computation and functionality with the capability for integration with a larger surveillance system in the capacity of target detection with or without human interaction.

There are so many directions to take this to develop a new system for automated surveillance applications. This application of the thermal imaging camera could be integrated with other CCD camera. Once the infrared and system like this detects and marks potential region of heat, it could trigger the activation and position of these cameras to continue with the analysis. Such a system would integrate the different hardware technologies for a more complete automated computer vision based surveillance system.

References

- [1] "Introduction to the Special Section on Video Surveillance", Robert T. Collins, Alan J. Lipton, and Takeo Kanade, IEEE Transactions on Pattern Analysis and Machine Intelligence, Aug 2000
- [2] "Recent Advances in Computer Vision", M. Piccardi, The Industrial Physicist, Feb/Mar 2003
- [3] *Practical Computer Vision Using C*, J.R. Parker, John Wiley and Sons, 1994
- [4] J. Ruffner, K. Woodward, *Computer-based and web-based applications for night vision goggle training*, Proc. SPIE Vol. 4361, p. 148-158, Helmet- and Head-Mounted Displays VI, 2001.
- [5] B. Tingzhu, N. Li, *Digital simulation for low-light-level night vision imaging system*, Proc. SPIE Vol. 4222, p. 100-104, Process Control and Inspection for Industry, 2000.
- [6] J. Ruffner, K. Woodward, *Development of a night vision device driving training aid*, Proc. SPIE Vol. 3691, p. 184-194, Enhanced and Synthetic Vision 1999, 1999.

Digital Type Disturbance Compensation Control of a Floating Underwater Robot with 2 Link Manipulator

Takashi Yatoh Shinichi Sagara Masakazu Tamura

Department of Control Engineering, Kyushu Institute of Technology
 Tobata, Kitakyushu 804-8550, Japan
 E-mail: sagara@cntl.kyutech.ac.jp

Abstract

We have proposed continuous and discrete time resolved acceleration control methods for underwater vehicle-manipulator systems and the effectiveness of the control methods have been shown by experiments. In this paper, we propose a digital type disturbance compensation control method based on the RAC method considering singular configuration of manipulator. Experimental results show the effectiveness of the proposed method.

1 Introduction

Underwater Vehicle-Manipulator Systems (UVMSs) are expected to make important roles in ocean exploration. Many studies about dynamics and control of UVMS have been reported [1-3], however the experimental studies are only a few. We have proposed analog and digital Resolved Acceleration Control (RAC) methods for UVMS [4-7], and the effectiveness of the RAC methods are demonstrated by using a floating underwater robot with vertical planar 2-link manipulator. Furthermore, we have proposed a RAC method

considering singular configuration of manipulator [8].

In general, added mass, added moment of inertia and drag coefficient are used constant value that depends on the shape of the robots [9]. Our proposed methods described above can reduce the influence of hydrodynamic force by position and velocity feedbacks.

In this paper, to obtain higher control performance we propose a digital type disturbance compensation control method based on the RAC method considering singular configuration of manipulator. The influence of hydrodynamic force is treated as a disturbance, and the disturbance is compensated by using a disturbance observer. To verify the effectiveness of the RAC method with the disturbance observer, experiments using the 2-link underwater robot are performed. The experimental results show that the control method has a good control performance.

2 Modeling

The underwater robot model used in this paper is shown in Fig. 1. It has a robot base and a 2-DOF manipulator which can move in a vertical plane. Thrusters are mounted on the base to provide propulsion for position and attitude control of the base.

Symbols used in this paper are defined as follows:

- Σ_U : inertial coordinate frame
- Σ_i : link i coordinate frame ($i = 0, 1, 2$; link 0 means base)
- ${}^U R_i$: coordinate transformation matrix from Σ_i to Σ_U
- p_e : position vector of end-tip of manipulator with respect to Σ_U
- p_i : position vector of origin of Σ_i with respect to Σ_U
- v_i : linear velocity vector of Σ_i with respect to Σ_U
- ω_i : angular velocity vector of Σ_i with respect to Σ_U
- x_0 : position and attitude vector of Σ_0 with respect to $\Sigma_U (= [p_0^T, \phi_0]^T)$
- ϕ_i : relative angle of joint i

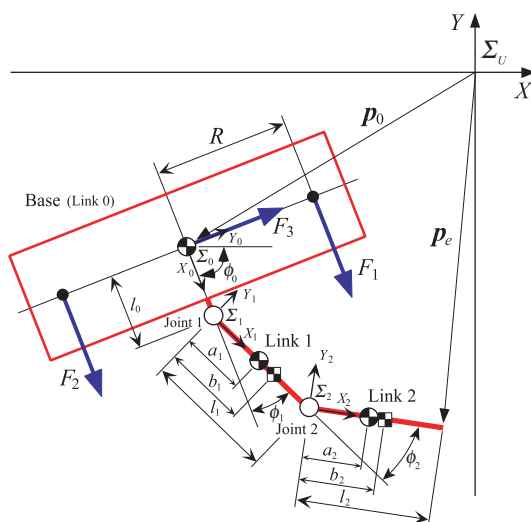


Fig. 1 2-link underwater robot model

- ϕ : relative joint angle vector ($= [\phi_1, \phi_2]^T$)
- l_i : length of link i
- \mathbf{a}_i : position vector from joint i to center of gravity of link i with respect to Σ_i
- \mathbf{b}_i : position vector from joint i to center of buoyancy of link i with respect to Σ_i
- F_j : thruster force ($j = 1, 2, 3$)
- R : length from origin of Σ_0 to thruster

From Fig. 1 kinematic and momentum equations can be obtained [4]:

$$\dot{\mathbf{p}}_e = \mathbf{A}\dot{\mathbf{x}}_0 + \mathbf{B}\dot{\phi}, \quad \mathbf{s} = \mathbf{C}\dot{\mathbf{x}}_0 + \mathbf{D}\dot{\phi} \quad (1)$$

where $\mathbf{A} \in R^{2 \times 3}$ and $\mathbf{B} \in R^{2 \times 2}$ are matrices consisting of attitude angle of base and joint angles. $\mathbf{C} \in R^{3 \times 3}$ and $\mathbf{D} \in R^{3 \times 2}$ are matrices including the added mass \mathbf{M}_{a_i} and the added inertia \mathbf{I}_{a_i} .

In the meanwhile, the drag force and moment of joint i can be generally represented as follows [10]:

$$\mathbf{f}_{d_i} = \frac{\rho}{2} C_{D_i} D_i \int_0^{l_i} \|\mathbf{w}_i\| \mathbf{w}_i d\hat{\mathbf{x}}_i \quad (2)$$

$$\mathbf{t}_{d_i} = \frac{\rho}{2} C_{D_i} D_i \int_0^{l_i} \hat{\mathbf{x}}_i \times \|\mathbf{w}_i\| \mathbf{w}_i d\hat{\mathbf{x}}_i \quad (3)$$

where $\mathbf{w}_i = \mathbf{v}_i + \boldsymbol{\omega}_i \times \hat{\mathbf{x}}_i$ and $\hat{\mathbf{x}}_i = [x_i, 0, 0]^T$, ρ is the fluid density, C_{D_i} is the drag coefficient, D_i is the width of link i . Furthermore, the gravitational and buoyant forces acting on link i are described as follows:

$$\mathbf{f}_{g_i} = (\mathbf{R}_i)^T (\rho V_i - m_i) \mathbf{g} \quad (4)$$

$$\mathbf{t}_{g_i} = (\mathbf{R}_i)^T (\mathbf{b}_i \times \rho V_i - \mathbf{a}_i \times m_i) \mathbf{g} \quad (5)$$

where V_i and m_i are the volume and mass of link i , and \mathbf{g} is the gravitational acceleration vector.

Considering the hydrodynamic forces and using Newton-Euler formulation, the following equation of motion can be obtained:

$$\mathbf{M}(\mathbf{q})\ddot{\mathbf{q}} + \mathbf{N}(\mathbf{q}, \dot{\mathbf{q}})\dot{\mathbf{q}} + \mathbf{f}_H = [f_x \ f_y \ \tau_0 \ \tau_1 \ \tau_2]^T \quad (6)$$

where $\mathbf{q} = [\mathbf{x}_0^T \ \phi^T]^T$ and $\mathbf{M}(\mathbf{q})$ is the inertia matrix consisting of the added mass and inertia, $\mathbf{N}(\mathbf{q}, \dot{\mathbf{q}})\dot{\mathbf{q}}$ is the vector of Coriolis and centrifugal forces, \mathbf{f}_H is the vector consisting of the drag and lift forces. f_x and f_y are input forces of the X and Y directions, τ_i ($i = 0, 1, 2$) is the joint torque.

With respect to the base input $\mathbf{u}_B = [f_x \ f_y \ \tau_0]^T$ and joint input $\mathbf{u}_M = [\tau_1 \ \tau_2]^T$, matrices and vectors of Eq. (6) can be represented by the following block matrices:

$$\mathbf{M} = \begin{bmatrix} \mathbf{M}_{BB} & \mathbf{M}_{BM} \\ \mathbf{M}_{MB} & \mathbf{M}_{MM} \end{bmatrix}, \quad \mathbf{N} = \begin{bmatrix} \mathbf{N}_{BB} & \mathbf{N}_{BM} \\ \mathbf{N}_{MB} & \mathbf{N}_{MM} \end{bmatrix},$$

$$\mathbf{f}_H = [\mathbf{f}_{HB}^T \ \mathbf{f}_{HM}^T]^T, \quad \mathbf{u} = [\mathbf{u}_B^T \ \mathbf{u}_M^T]^T$$

Then, for a disturbance compensation described in the next section the following equation with respect to the base input can be obtained:

$$\mathbf{M}_{BB}\ddot{\mathbf{x}}_0 + \mathbf{M}_{BM}\ddot{\phi} + \mathbf{N}_{BB}\dot{\mathbf{x}}_0 + \mathbf{N}_{BM}\dot{\phi} + \mathbf{f}_{HB} = \mathbf{u}_B \quad (7)$$

3 Control Method

3.1 Digital RAC [8]

Differentiating Eq. (1) with respect to time, the following equation can be obtained:

$$\mathbf{W}(t)\boldsymbol{\alpha}(t) = \boldsymbol{\beta}(t) + \mathbf{f}(t) - \dot{\mathbf{W}}(t)\mathbf{v}(t) \quad (8)$$

where

$$\mathbf{W} = \begin{bmatrix} \mathbf{C} + \mathbf{E} & \mathbf{D} \\ \mathbf{A} & \mathbf{B} \end{bmatrix}, \quad \boldsymbol{\alpha} = [\ddot{\mathbf{x}}_0^T \ \ddot{\phi}^T]^T,$$

$$\boldsymbol{\beta} = [\ddot{\mathbf{x}}_0^T \ \ddot{\mathbf{p}}_e^T]^T, \quad \mathbf{f} = [\dot{\mathbf{s}}^T \ \mathbf{0}^T]^T, \quad \mathbf{v} = [\dot{\mathbf{x}}_0^T \ \dot{\phi}^T]^T$$

$\dot{\mathbf{s}}$ is the external force including hydrodynamic force and thrust of the thruster which act on the base, and \mathbf{E} is the unit matrix.

Discretizing Eq. (8) by a sampling period T , and applying $\boldsymbol{\beta}(k)$ and $\dot{\mathbf{W}}(k)$ to the backward Euler approximation, we have

$$\mathbf{W}(k)\boldsymbol{\alpha}(k-1) = \frac{1}{T} [\boldsymbol{\nu}(k) - \boldsymbol{\nu}(k-1) + T\mathbf{f}(k) - \{\mathbf{W}(k) - \mathbf{W}(k-1)\}\mathbf{v}(k)] \quad (9)$$

where $\boldsymbol{\nu} = [\dot{\mathbf{x}}_0^T, \dot{\mathbf{p}}_e^T]$. Note that a computational time delay is introduced into Eq. (9).

For $\boldsymbol{\alpha}(k)$ and $\boldsymbol{\nu}(k)$ in Eq. (9), the desired acceleration $\boldsymbol{\alpha}_d(k)$ and velocity $\boldsymbol{\nu}_d(k)$ are defined as

$$\boldsymbol{\alpha}_d(k) = \frac{1}{T} \mathbf{W}^{-1}(k) [\boldsymbol{\nu}_d(k+1) - \boldsymbol{\nu}_d(k) + \boldsymbol{\Lambda} \mathbf{e}_\nu(k) + T\mathbf{f}(k)] \quad (10)$$

$$\boldsymbol{\nu}_d(k) = \frac{1}{T} \{\mathbf{p}_d(k) - \mathbf{p}_d(k-1) + \boldsymbol{\Gamma} \mathbf{e}_p(k-1)\} \quad (11)$$

where $\boldsymbol{\Lambda} = \text{diag}\{\lambda_i\}$ and $\boldsymbol{\Gamma} = \text{diag}\{\gamma_i\}$ ($i = 1, \dots, 5$) are the velocity and position feedback gain matrices, $\mathbf{e}_\nu(k) = \boldsymbol{\nu}_d(k) - \boldsymbol{\nu}(k)$ and $\mathbf{e}_p(k) = \mathbf{p}_d(k) - \mathbf{p}(k)$ are the velocity and position error vectors, $\mathbf{p}_d(k)$ is the desired value of $\mathbf{p}(k) = [\mathbf{x}_0^T(k), \mathbf{p}_e^T(k)]^T$. When λ_i and γ_i are selected to satisfy $0 < \lambda_i < 1$ and $0 < \gamma_i < 1$, $\mathbf{e}_p(k) \rightarrow \mathbf{0}$ ($k \rightarrow \infty$) is guaranteed.

In order to avoid the singular configuration of manipulator, the desired value of the base is modified by using the determinant of the Jacobian matrix $J(k) = \det \mathbf{J}(k)$ of manipulator. The desired linear acceleration of the base $\ddot{\mathbf{p}}_{0d} = [\ddot{\mathbf{p}}_{0xd}, \ddot{\mathbf{p}}_{0yd}]$ is defined as

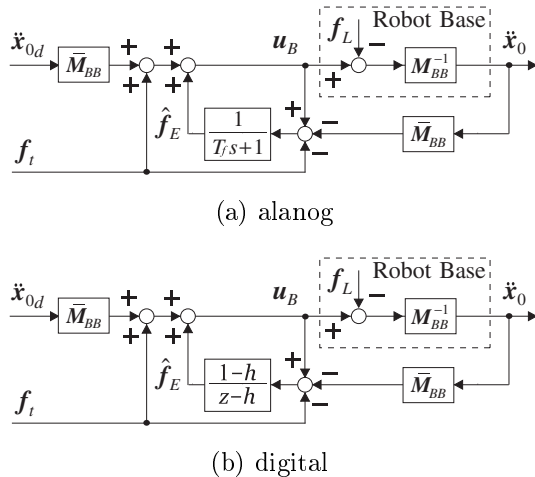


Fig. 2 Disturbance compensation

$$\ddot{\mathbf{p}}_{0_d} = \begin{cases} \dot{\mathbf{p}}_{e_d} & (k_1 \leq k < k_1 + n) \\ 0 & (\text{otherwise}) \\ -\dot{\mathbf{p}}_{e_d} & (k_2 \leq k < k_2 + n) \end{cases} \quad (12)$$

where $\dot{\mathbf{p}}_{e_d}$ is the desired linear velocity of the end-tip of the manipulator, and $k_1 T$ and $k_2 T$ are the time when $|J(k)|$ becomes less or greater than a threshold J_s , respectively, and nT is the acceleration time.

3.2 Disturbance compensation

In general, added mass and moment of inertia and drag coefficient are used constant value that depends on the shape of robots [9]. Our proposed methods described above can reduce the influence of hydrodynamic force by position and velocity feedbacks.

Here, to obtain higher control performance, the influence of hydrodynamic force with respect to the base is treated as a disturbance and a disturbance compensation method is introduced.

The nominal model of \mathbf{M}_{BB} in Eq. (7) is defined as $\bar{\mathbf{M}}_{BB}$. In $\bar{\mathbf{M}}_{BB}$ the added mass and moment of inertia and the drag coefficient are constant. Furthermore, the following force is similarly defined:

$$\mathbf{f}_t = \bar{\mathbf{M}}_{BM} \ddot{\phi}_d + \bar{\mathbf{N}}_{BB} \dot{\mathbf{x}} + \bar{\mathbf{N}}_{BM} \dot{\phi} + \bar{\mathbf{f}}_{HB} \quad (13)$$

where $\bar{\mathbf{M}}_{BM}$, $\bar{\mathbf{N}}_{BB}$, $\bar{\mathbf{N}}_{BM}$ and $\bar{\mathbf{f}}_{HB}$ are nominal.

When the modeling error with respect to the hydrodynamic force regards the disturbance \mathbf{f}_E , the following estimated value can be obtained:

$$\hat{\mathbf{f}}_E = F(s) (\mathbf{u}_B - \bar{\mathbf{M}}_{BB} \ddot{\mathbf{x}}_{0_d} - \mathbf{f}_t) \quad (14)$$

where $F(s) = 1/(T_f s + 1)$ and $\ddot{\mathbf{x}}_{0_d}$ is the desired value of $\ddot{\mathbf{x}}_0$, T_f is a time constant.

Using Eqs. (13) and (14) we have the following control input of the base:

Table 1 Physical parameters of underwater robot

	Base	Link 1	Link 2
Mass [kg]	26.04	4.25	1.23
Moment of inertia [kg m ²]	1.33	0.19	0.012
Link length (x axis) [m]	0.2	0.25	0.25
Link length (y axis) [m]	0.81	0.04	0.04
Link width [m]	0.42	0.12	0.12
Added mass(x) [kg]	72.7	1.31	0.1
Added mass(y) [kg]	6.28	3.57	2.83
Added moment of inertia [kg m ²]	1.05	0.11	0.06
Drag coefficient (x)	1.2	0	0
Drag coefficient (y)	1.2	1.2	1.2

$$\mathbf{u}_B = \bar{\mathbf{M}}_{BB} \ddot{\mathbf{x}}_{0_d} + \mathbf{f}_t + \hat{\mathbf{f}}_E \quad (15)$$

The configuration of the disturbance compensation is shown in Fig. 2(a). In Fig. 2(a) \mathbf{f}_L is the external force of the base excepting $\bar{\mathbf{M}}_{BB} \ddot{\mathbf{x}}_0$. Furthermore, for the digital control system, Fig. 2(a) is discretized to Fig. 2(b) [11]. In Fig. 2(b) $h = e^{-T_f/T}$.

4 Experiment

In this section, to verify the effectiveness of the proposed control method, experiments are done.

Physical parameters of the underwater robot are shown in Table 1. The details of the system and the thruster characteristics are shown in the reference [8].

The experiments are carried out under the following condition. The desired end-tip position is set up along a straight path from the initial position to the target. On the other hand, the basic desired position and attitude of the base is set up the initial values, and the threshold of the determinant of the Jacobian matrix is $J_s = 0.045$. The sampling period is $T=1/60$ [s], the time constant of the filter is $T_f = 10$ [s], and the feedback gains are $\mathbf{A} = \text{diag}\{0.3, 0.3, 0.2, 0.2, 0.2\}$ and $\mathbf{I} = \text{diag}\{0.3, 0.3, 0.2, 0.2, 0.2\}$. Furthermore, the initial relative joint angles are $\phi_0 = -\pi/2$ [rad], $\phi_1 = \pi/3$ [rad] and $\phi_2 = -5\pi/18$ [rad].

The motion of the robot with the disturbance compensation is shown in Fig. 3. From Fig. 3, it can be seen that the end-tip follows the desired trajectory. The time history of the results with and without the disturbance compensation are shown in Fig. 4 and 5. From these figures, we can see that the base position and attitude errors become small values using the disturbance compensation. Furthermore, reducing the base errors the end-tip position error is also reduced. Therefore, the control performance can be improved by using the proposed method.

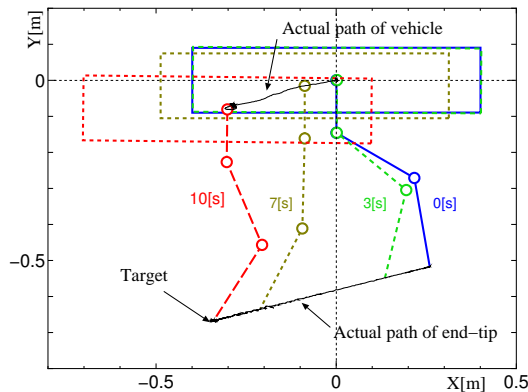


Fig. 3 Motion with disturbance compensation

5 Conclusion

In this paper, a digital RAC method for UVMS using disturbance compensation was proposed. The experimental results showed the effectiveness of the proposed method.

References

- [1] T. W. McLain *et al.*, “Experiments in the Coordinated Control of an Underwater Arm/Vehicle System”, *Autonomous Robots 3*, Kluwer Academic Publishers, pp. 213 – 232, 1996.
- [2] G. Antonelli *et al.*, “Tracking Control for Underwater Vehicle-Manipulator Systems with Velocity Estimation”, *IEEE J. Oceanic Eng.*, Vol. 25, No. 3, pp. 399 – 413, 2000.
- [3] N. Sarkar, T. K. Podder, “Coordinated Motion Planning and Control of Autonomous Underwater Vehicle-Manipulator Systems Subject to Drag Optimization”, *IEEE J. Oceanic Eng.*, Vol. 26, No. 2, pp. 228 – 239, 2001.
- [4] S. Yamada, S. Sagara, “Resolved Motion Rate Control of an Underwater Robot with Vertical Planar 2-Link Manipulator”, *Proc. AROB 7th*, pp. 230 – 233, 2002.
- [5] S. Sagara, “Digital Control of an Underwater Robot with Vertical Planar 2-Link Manipulator”, *Proc. AROB 8th*, pp. 524 – 527, 2003.
- [6] S. Sagara *et al.*, “Experiment of Digital RAC for an Underwater Robot with vertical Planar 2-Link Manipulator”, *Proc. AROB 9th*, pp. 337 – 340, 2004.
- [7] T. Yatoh *et al.*, “RAC for Underwater Vehicle-Manipulator Systems Using Dynamic Equation”, *Proc. AROB 11th*, pp. 233 – 236, 2006.
- [8] S. Sagara *et al.*, “Digital RAC for Underwater Vehicle-Manipulator Systems Considering Singular Configuration”, *J. AROB*, Vol. 10, No. 2, pp. 106 – 111, 2006.
- [9] T. I. Fossen, *Guidance and Control of Ocean Vehicles*, John Wiley & Sons, pp. 431–452, 1995.
- [10] B. Lévesque, M. J. Richard, “Dynamic Analysis of a Manipulator in a Fluid Environment”, *Int. J. Robot. Res.*, Vol. 13, No. 3, pp. 221 – 231, 1994.
- [11] I. Godler *et al.*, “Design Guidelines for Disturbance Observer’s Filter in Discrete Time”, *Proc. 7th Int. Workshop on Advanced Motion Control*, pp. 390 – 395, 2002.

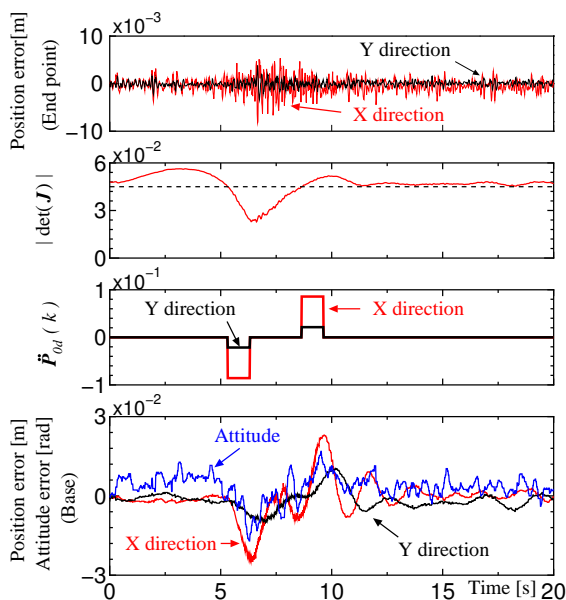


Fig. 4 Result with disturbance compensation

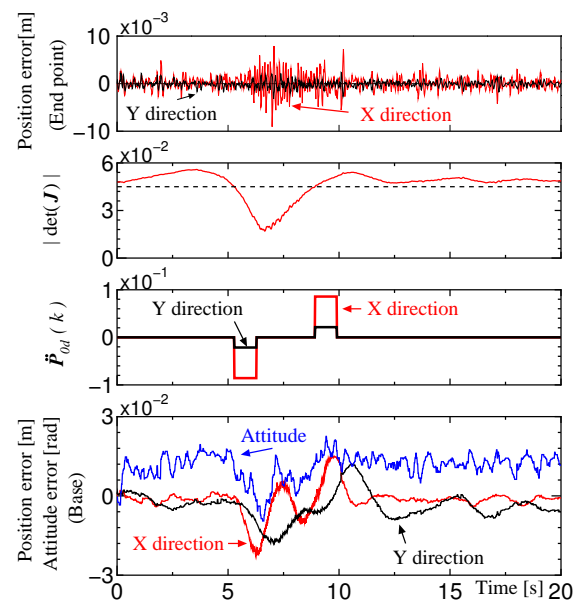


Fig. 5 Result without disturbance compensation

Simulating Crowd Motion with Shape Preference and Fuzzy Rules

Jen-Yao Chang

Computer Science Department
National Chengchi University
64, Sec. 2, Zhi-Na Rd., Taipei, Taiwan 116

Tsai-Yen Li

Computer Science Department
National Chengchi University
64, Sec. 2, Zhi-Na Rd., Taipei, Taiwan 116

Abstract

Crowd simulation is becoming indispensable in computer games and animations. Several approaches to this problem have succeeded in generating flocking behaviors with virtual forces but it remains difficult to manipulate the collective behaviors of a crowd to respect certain desired shape. In this paper, we propose a crowd simulation system that can generate a feasible path taking the crowd to the goal while maintaining a user-specified shape as much as possible. The system consists of two key components: a path planner that can search for a feasible path for a region of flexible shape and a local motion controller based on three classes of fuzzy rules for generating desired agent behaviors. We will demonstrate the implemented system with several examples to show the generated path and the corresponding crowd motions adhering to a desired shape.

Keyword: Motion planning, computer animation, multi-agent system, crowd simulation

1 Introduction

Group formation has many applications in the entertainment industry. For example, formation of a group in a battle game like the one shown Figure 1 could be a key factor in defeating an enemy. Different shapes formed by a group could provide different functions for distinct physical and visual effects. We often see animations showing a crowd of congregated animals through a shape of elephant, geometry, or a death's-head in traditional cartoons to exaggerate the visual effects and to convey special contextual meanings to the audience.

In traditional animation production, animators manually arrange the position of every animated object in each key-frame in order to show the final flocking behavior. This process is very tedious and time-consuming even with the helps of animation tools available today. In the literature of computer animation, some motion-planning techniques have been proposed to generate a path for a rectangle shape and then constrain motions of the agents in a group in this shape. However, the rigid shape greatly limits the applicability of this technique in a real animation production. In this paper, we propose a new crowd animation tool, in which a new motion planner is designed to take the requirement of flexible shape into account. Given the geometric description of environment, the planner is capable of generating a collision-free path for the deformable object while account-

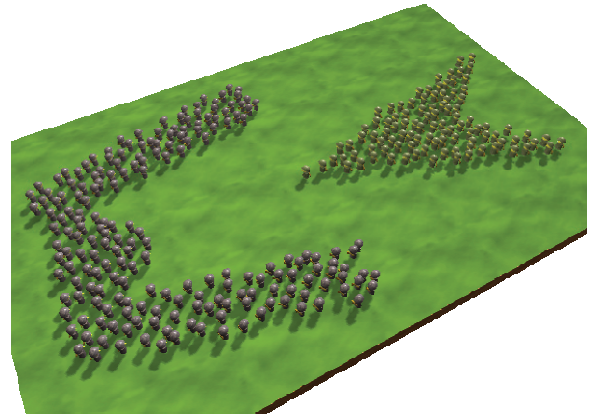


Figure 1. Snapshot of group formation in a battle game

ing for the preference of a user on the shape of the crowd. The final crowd motion is generated with the help of fuzzy rules in a agent-based simulation system to show the desired visual effect.

Next, we will first describe some research pertaining to our work and then show how to formulate this new planning problem and the algorithm for generating such a path automatically. Several experimental results showing how the shape of the crowd changes during a path will also be given at the end.

2 Related Work

Simulating emergent behaviors for virtual agents is a common topic in computer animation. Reynolds proposed a virtual force model (separation, cohesion, and alignment forces) for the simulation of flocking behaviors [1][2]. The main advantage of this approach is ease of use. However, it is also difficult to tune the weights of these forces directly in order to achieve a specific effect. Anderson used a simple force model in [3] to create a flocking behavior for a crowd with an expected appearance by continuously adjusting the position and velocity of the agents according to the estimated global shape. This method can generate a crowd motion respecting the given desired appearance but the time spent in adjusting the positions and velocities of the agents is also too large for on-line applications.

In the literature of Robotics, it has been a classical problem to generate a feasible path for a robot moving from its initial configuration to a goal configuration. One can find many approaches to this problem in Latombe's book [4]. However, most the traditional motion planner

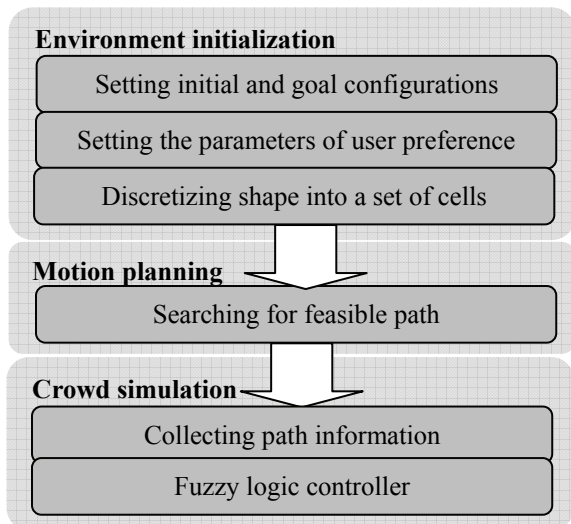


Figure 2. System architecture

considers the robot as a rigid body or chains of rigid bodies whose shape cannot be changed during the trajectory. In [5], Bayazit added some global information in the roadmap of the environment to facilitate more sophisticated flocking behaviors, and proposed three group behaviors exploiting global knowledge of the environment.

Kamphuis modeled a group of crowd with a deformable shape, and planned the global motion of the shape by Probabilistic Roadmap Method (PRM) [6]. He used a group potential field to control the local motion of entities in the shape. This method can solve the problem of controlling the appearance of a moving crowd, which cannot be solved by applying behavior rules only. However, the bottleneck of this method is that the crowd can only move along the path consisting of simple shapes and constrained by narrow passages.

Adaptive fuzzy logic controller (FLC) provides a good solution for autonomous robot to move in an uncertain environment. The main advantage of FLC is that it is highly adaptive and nimble in tackling the uncertainty of control system through linguistic presentation. Tunstel used the idea of FLC to design an autonomous robot having three types of basic behaviors as described in [7]: *goal-seek*, *route-follow*, and *localize*. Corresponding primitive actions were also designed for each behavior.

3 Problem Description

The architecture of the system proposed in this work, as shown in Figure 2, consists of two key components: a path planner to search for a feasible path for a flexible region and a local motion controller based on fuzzy logics. We assume that we are given a geometric description of the environment as well as the initial configuration and a goal position of the virtual crowd. We hope that that proposed motion planner can generate a feasible path for the region of flexible shape automatically. While

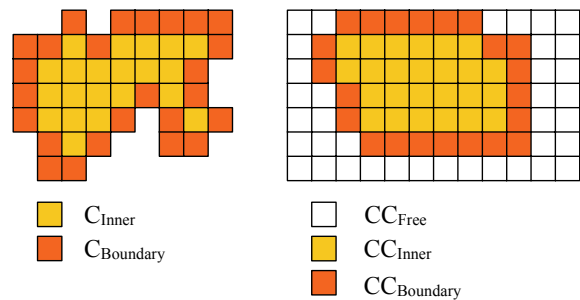


Figure 3. Example of shape configuration and configuration coverage map

accounting for the length of the path, the planner should generate a path that can allow the crowd to maintain some preferred shape as much as possible during the movement of the crowd along the path.

Our system first searches for a feasible path for the flexible region of a fixed volume. We use a set of cells called *shape configuration* to describe the region of the flexible shape. The system generates new shape configurations in the neighborhood of the current shape configuration in the process of motion planning until the goal configuration is reached. The path returned by the planner consists of a sequence of shape configurations in which the crowd will be put into simulation using fuzzy logic controllers to control the motions of the agents for desired flocking effects.

4 Path Planning for a Flexible Shape

4.1 Configuration and coverage map

We represent a region of flexible shape with a conserved volume by a fixed number of connected discrete cells in the workspace. The obstacles in the environment are also represented as forbidden cells in the workspace. A shape configuration, denoted by S , is collision-free if and only if all of the cells in S do not overlap with the obstacle cells.

In order to facilitate the measure of incremental movement of S , we distinguish two types of cells in S : *inner cells* and *boundary cells*. A boundary cell for a shape configuration, denoted by $C_{Boundary}$, is defined as the cell having at least a free cell in its neighbors. An inner cell for a shape configuration, denoted by C_{Inner} , is the cell inside the region of shape configuration but is not a boundary cell. Examples of these two types of cells are illustrated on the left of Figure 3. Note that these two types of cells are for a shape configuration. Since each cell consists of two degrees of freedom, the complexity of the overall configuration space, growing exponential in the overall degrees of freedom is rather large. However, the spatial and temporal relations of these cells are not without constraints. We assume that the region needs to move as a connected component and the speed of the movement for each cell is limited. In the planner, we ensure that the region moves continuously by allowing

Procedure: Generate_New_Shape_Configuration

Input. A configuration S .

Output. A new shape configuration S' .

1. Clone S' from S
2. **if** all cells in $C_{Boundary}(S')$ have no collision-free neighbors **then return nil**
3. Randomly choose C_f in $C_{Boundary}$ such that a neighbor of C_f must be collision-free
4. let v be the vector from C_f to the free neighbor
5. Add all $C_{Boundary}$ cells of S' into a list Q sorted according to the distance to C_f
6. **while** Q is not Empty
7. **begin**
8. poll the front element C_i from Q
9. **if** $C_i + v$ is free in workspace **then**
10. poll the rear element C_j from Q
11. remove C_j from S'
12. add $C_i + v$ into S'
12. **end**
13. **return** S'

Figure 4. Procedure for the generation of a new shape configuration

only one cell of difference in two consecutive configurations. Hence, we only need to consider the variation of $C_{Boundary}$ in generating a new shape configuration.

We use a data structure called *Configuration Coverage Map (CC-Map)* to record the trace of regions covered by the generated shape configurations. This coverage map contains three types of cells: CC_{Inner} , $CC_{Boundary}$, and CC_{Free} as shown on the right of Figure 3. CC_{Free} are the unvisited cells in the freespace. Similar to the definition of the region in shape configuration, CC_{Inner} are the set of inner cells in the covered region so far while $CC_{Boundary}$ is the set at the boundary. In order to ensure that the motion planner makes progress in each step of the search process, a new shape configuration is considered valid only if it can expand the coverage region by at least one cell. In other words, the difference of the region for a new shape configuration, S_{new} , and the existing coverage map must be at least one cell.

4.2 Generating a new shape configuration

The procedure used for generating a new valid shape configuration is shown in Figure 4. The procedure starts by duplicating the given shape configuration S to S' . Then the system checks if there exists at least one cell in $C_{Boundary}$ of S' that is collision-free. The system randomly chooses a seed cell C_f and a moving direction from the intersection of $CC_{Boundary}$ and $C_{Boundary}$ of S' . If the new neighboring cell along the chosen direction is collision-free, then we move other cells in $C_{Boundary}$ along the same direction by one cell if the new cells are collision-free. The way we move the whole region is by removing the cells at the other side of the boundary and put them in the new cells along the moving direction.

Since the number of cells is not changed, the volume of the region is also conserved.

4.3 Motion planning for flexible shape

In the planner, we use a Best-First Search (BFS) algorithm, commonly used in the motion planners for low dimensional search space, to search for a feasible path. In the algorithm, the planner keeps track of the explored valid configurations that can be further expanded, called OPEN, and selects the best configuration in it to explore further according to some criteria such as an objective function. In this work, we define the objective function as the weighted sum of the following two scores. One is the distance score computed according to the average distance between the cells of the current configuration and the goal position. The other is the shape score determined by the difference of the ideal shape and the current shape.

When a shape configuration is selected for exploration, all new configurations that can extend the region of CC-Map further are inserted into the OPEN list for future exploration. The system will continue to generate new shape configurations, update the CC-Map until the generated shape configuration covered the goal position (success) or the OPEN list becomes empty (failure). If the goal configuration (any configuration that can contain the goal position) is found, we can then backtrack the search tree to obtain the path for the flexible shape.

5 Fuzzy Rules for Crowd Simulation

According to our observation of the interaction between people in our real life, we model the behaviors of the agents in a crowd with a three-layer fuzzy logic: *type of model*, *behavior model*, and *primitive action*. Each type of models contains several behavior models, and each behavior model contains primitive actions. Three types of behaviors are defined in our system: *Intra-agent*, *reactive*, and *inter-agent*. The fuzzy behaviors use rules and linguistic variables to describe the relation between sensation and actions. Each primitive action is represented by a distinct control policy governed by fuzzy inference. We use a fuzzy knowledge base (FKB) to store the fuzzy rules and linguistic variables and use a fuzzy logic controller (FLC) to control the motions of the agents. In each control loop, the system fuzzifies the position and velocity of the agents and some environmental information for the processing of FKB. Then it defuzzifies the results to obtain the control parameters driving the motions of the agents.

6 Experimental result

We use the scene in Figure 5 to demonstrate how the selection of different weights on distance and shape affect the paths generated by the planner. Key snapshots,

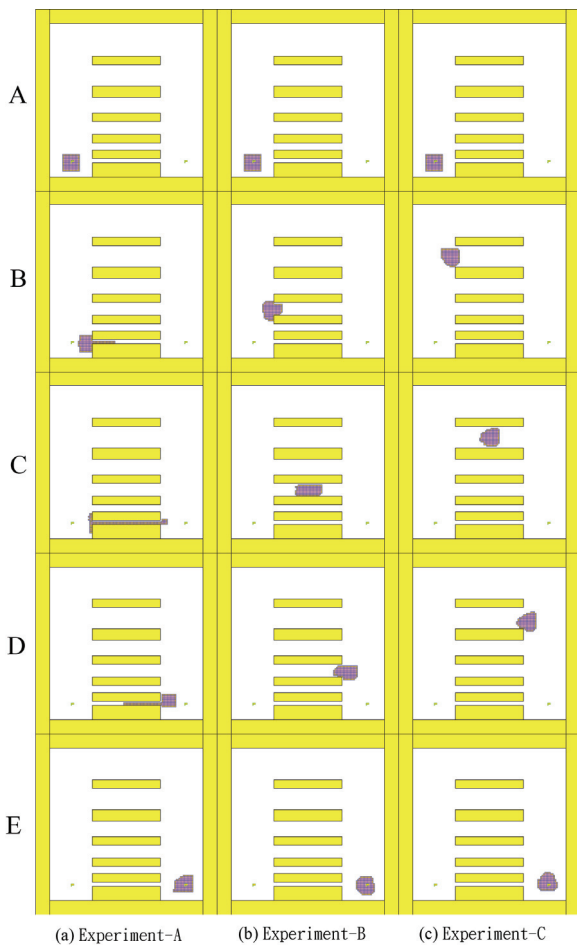


Figure 5. Key snapshots along the paths of a flexible object in various experiments

arranged from the top to the bottom, of these experiments are shown in Figure 5. The weights on the distance score and shape score are the only parameters that are different among these experiments. The weights (shape/distance) for experiments A, B, and C are (0%/100%), (25%/75%), and (75%,25%), respectively. Since distance is the only criteria used in searching for the path in experiment A, a shortest path passing through the narrowest passage was generated.

7 Conclusion

It is a time-consuming and challenging task to create the animation of a crowd motion that conforms to the environment and respects a specific shape. In this paper, we have designed a motion planner to address the problem of how to generate the path for a region with flexible shape and fixed volume. We use the concept of coverage map in workspace to ensure the completeness of the best-first search algorithm. The system allows a user to specify his/her preference on path length or ideal shape with weights on the corresponding evaluation scores. In addition to the application of crowd simulation, the configurations and paths generated by the motion planner

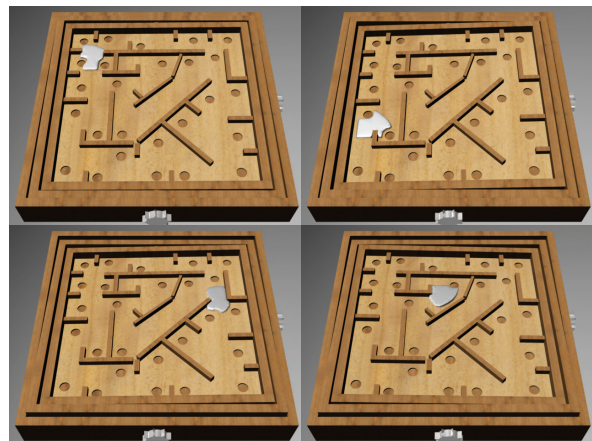


Figure 6. Applying the result generated by the planner to the simulation of liquid motion

can also be applied to liquid simulation as show in Figure 6. We have also designed a fuzzy-behavior model to facilitate the motion control of the agents inside the moving shape. More examples created with these fuzzy control rules will be reported in the future.

Acknowledgement

This research was funded in part by the National Science Council (NSC) of Taiwan under contract no. NSC 93-2213-E-004-001

References

- [1] Reynolds CW (1987), Flocks, Herds, and Schools: A Distributed Behavioral Model. *Computer Graphics: ACM SIGGRAPH*, pp.25-34
- [2] Reynolds CW (1999), Steering behaviors for autonomous characters. In *Proc. of 1999 Game Developers Conference*, pp.763-782
- [3] Anderson M, McDaniel E, Chenney S (2003), Constrained Animation of Flocks. In *Proc. of ACM Eurographics/SIGGRAPH Symp. on Computer Animation 2003*
- [4] Latombe JC (1991), *Robot Motion Planning*, Kluwer, Boston, MA
- [5] Bayazit OB, Lien JM, Amato NM (2002), Better Flocking Behaviors in Complex Environments Using Global Roadmaps. In *Proc. of the 2002 Artificial Life (ALIFE)*, pp.528-534
- [6] Kamphuis A and Overmars MH (2004), Finding Path for Coherent Groups using Clearance. In *ACM SIGGRAPH/Eurographics Symposium on Computer Animation*, pp.193-202
- [7] Tunstel E, Danny H, Lippincott T, Jamshidi M (1997), Autonomous Navigation using an Adaptive Hierarchy of Multiple Fuzzy-Behaviors. In *Proc. of Intl Symp on Computational Intelligence in Robotics and Automation*, pp. 276-281

Development of an autonomous driving personal robot “Development of arm’s mechanism and control program”

Makoto Tone

Eiji Hayashi

**Department of Mechanical Information Science and Technology
Faculty of Computer Science and Systems Engineering, Kyushu Institute of Technology
680-4, Kawazu, Iizuka-City, Fukuoka Prefecture, Japan**

Key Words: Personal robot, Autonomous driving, control

1. Introduction

Japan is facing a declining birthrate and a growing proportion of elderly people in its population. In such a society, the lack of a sufficient workforce is almost guaranteed. Specifically, the lack of caregivers to support the lives of senior citizens and handicapped persons will become a problem in the future. Therefore, efforts are underway to develop personal robots to provide independent life support for patients or perform light work in the home or office and thus to reduce caregivers' work.

This research was aimed at the development of a personal robot that acts with users in a human living environment to assist the work of humans. Specifically, I designed an arm mechanism that could perform light work such as taking a glass or newspaper or turning on a wall switch, and I created a control program for it.

2. Basic policy of the personal robot

Up to now, robots have primarily been developed to work in a factory or at the scene of a disaster. These robots can operate in a severe environment and can continuously perform simple work at high power and high speeds and with a high degree of accuracy. However, a skilled operator with special knowledge is necessary for their use. They are not easy for the average person to use.

Conversely, a personal robot is designed to live together with humans in a human living environment, and communications skills with humans are demanded. Moreover, because the situation in the surroundings of the robot is always changing, programming that is autonomous and flexible is demanded.

However, at present it is difficult to meet all of the various work instructions that may arise in various environments. Thus, in this research the range in which the robot acts was limited to the home, the office, and the hospital, and the type of work was limited to light work.

3.1 Hardware composition of the robot

Parts of the personal robot under development are the head that carries a CCD camera, the running drive part, the frame chassis, the arm part, and the hand. The camera on the head recognizes the external world. Because it can move in both horizontal and vertical directions, a wide-ranging search is possible both up and down and right and left. A personal computer, battery, ACDC inverter, and various drivers have been placed in the frame chassis.

The driving part is composed of the DC servo motor in the front of the robot, and the caster in the back of the robot. With the pulse, the DC servo motor can control the position of the robot. As for the arm part, five stepping motors are used and make possible an operation that brings the point part of the arm as close to the target object as possible. Hands have three fingers, and three servo motors are in the center finger and four servo motors are in the outside finger. The two outside fingers can move the position of the root and have achieved a flexible correspondence matched to the shape of an object.

3.2 Software composition of the robot

The processing system of the robot is divided chiefly into four parts. It is composed of a space recognition part that consists of the CCD camera, an operation decision part that consists of a limited space map and a movement pattern database, a driving control part that consists of a driver and amplifier, and a driving part that consists of various actuators for arm, hand, and movement mechanisms. With the space recognition part, the robot that receives instruction from a human sets information obtained from the CCD camera against a shape pattern DB. Moreover, the coordinates for the situation and the work object where the robot is being placed are now understood based on information in a limited space map. This information is given to the operation decision part, and the operation that should be executed is determined. For the movement, the best route to a destination is found from the limited space map. The operation that is decided upon is sent to the driving control part, and each actuator is driven. Realtime processing is done by repeating these

operations, and the instructions are executed.

4.1 Development of the arm part

I assumed that this mechanism would mainly aim the hand to grip an object. And on this basis I designed this. Figure 1 shows a schematic view of an arm.

A multi-jointed arm that was able to do complex work was adopted as the mechanism in the development of the arm part. The parameters for three postures and three positions are necessary to describe the position of an object in three-dimensional space. I designed the arm with five degrees of freedom in this research. The robot is moved up to a distance from which an object can be easily gripped and then grips the object. Such an operation involves only a small degree of freedom. Moreover, motors and gears are constructed in the arm. This method makes for a simpler mechanism than one with wires, and it can increase the accuracy of positional control. The arm does become heavy because of the weight of the motor, and therefore the weight that it can handle decreases. However, it is not a problem in this research to limit the content of work to light work.

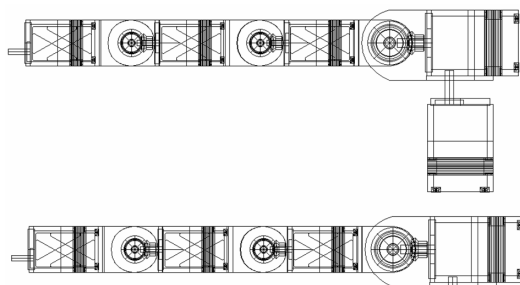


Fig.1 Schematic view of the arm

4.2 Development of the hand part

In this research, the work is limited to light work such as gripping an object or pushing a button. The work object could be something like a glass. The size of each hand part was designed based on the size of the human hand. The weight of the work object is assumed to be about 1kg. The outside two fingers can move the root position through a feature of this hand. Form 1 is the basic arrangement. When a spheroidal object is gripped, Form 2 is used because it is the steadiest one that can add power from three points. When the work object is gripped from the right and left, Form 3 is used. Figure 2 shows the schematic view of the arm. And in Figure 3 the hand was seen from the tip of a finger.

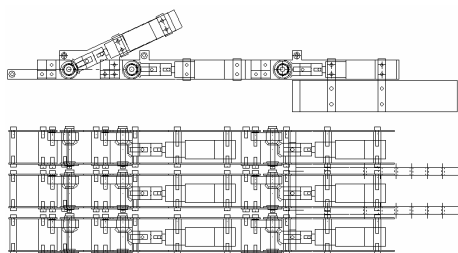


Fig.2 Schematic view of hand

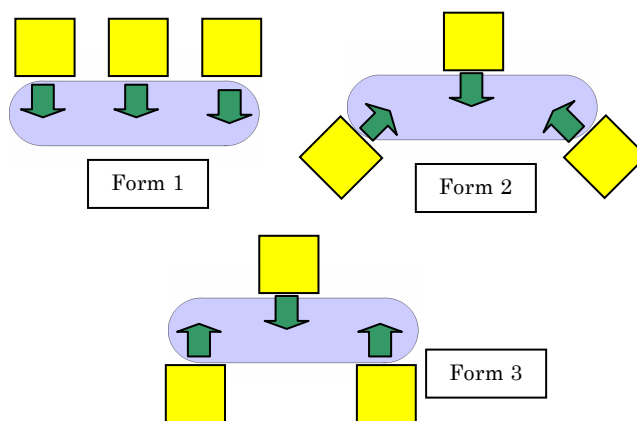


Fig.3 The hand that was seen from the tip of a finger.

5.1 About the control of the arm and hand

Operations that stop the hand in a target location and direction for a particular purpose are called positional control and posture control. By these operations a work object can be grasped and placed. It is necessary to calculate how many degrees each motor must be rotated to control a position. This calculation is called a reverse kinematics calculation.

Before this calculation, it is necessary to calculate the value of the hand's position and posture from the angle of each motor. This calculation is called a direct kinematics calculation. I created the control program based on this principle.

5.2 Coordinates calculation by a transformation matrix

First, I defined a relative position of a link and coordinate system like in Figure 4.

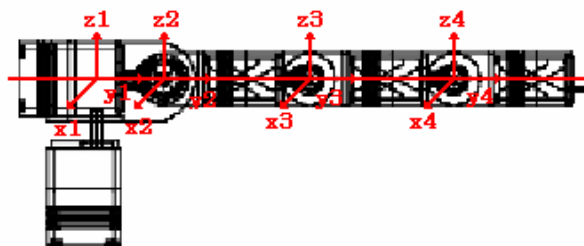


Fig.4 The relative position of the link and the definition of the coordinate system

These relative positions are shown by multiplying the following by the transformation matrix of 4x4.

$$T = \begin{bmatrix} A & a \\ 000 & 1 \end{bmatrix}$$

A is a procession which shows the rotation of the three-dimension procession coordinate system, and A is a three-dimension vector in which the movement is

shown. If the positional vector shown in certain three-dimension coordinate systems is r , by the transformation matrix T the new positional vector r' is

$$\begin{bmatrix} r' \\ 1 \end{bmatrix} = T \begin{bmatrix} r \\ 1 \end{bmatrix}$$

The driving corner of joint i is θ_i . The transformation matrix T_i when the distance between joint j and joint $j+1$ is assumed to be L_j . When O_1 is the reference point and O_1 is joint i is θ_i . The transformation matrix T_i when the distance between joint j and joint $j+1$ is assumed to be L_j . When O_1 is reference point and O_1 is $^T(0001)$, positional vector O_i of joint i is

$$O_i = T_1 \cdot T_2 \cdot T_3 \cdot \dots \cdot T_{i-1} \cdot O_1$$

As a result, the simultaneous equations to calculate coordinates of each joint can be derived. If the driving corner is determined, the coordinates of each joint can be calculated.

5.3 Calculation of the joint corner using reverse kinematics

The driving corner to drive the hand to the coordinates of the target can be derived when you solve the above-mentioned simultaneous equations about the driving corner θ . At this time, the driving corner can be calculated by imposing the conditions that the angle and the height of the hand be kept constant. The control program was made based on these assumptions.

5.4 Control program of the arm

The control program was made based on the above-mentioned theory. Figure 5 shows the execution screen of the control program.

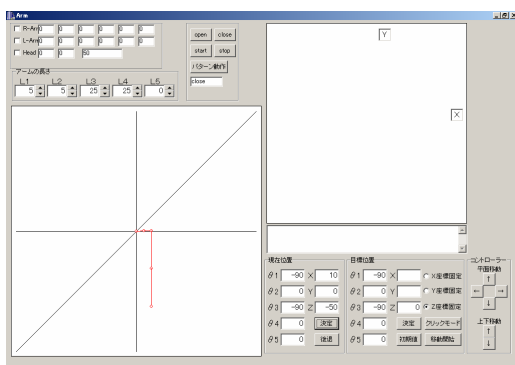


Fig.5 The execution screen of the control program

The left figure displays the present appearance of the arm and the parameter of the angle of each arm joint. The target and the minion's coordinates are displayed on the right side. First, the coordinates of minion's target are input. Next, the joint corner of the arm that fills the

coordinates of the target by using the reverse kinematics calculation is calculated. The condition of the drive that locks the direction of the wrist at this time can be added. Figure 6 and Figure 7 show the appearance of the driving experiment that uses an existing arm.

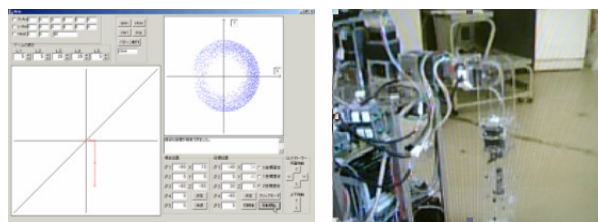
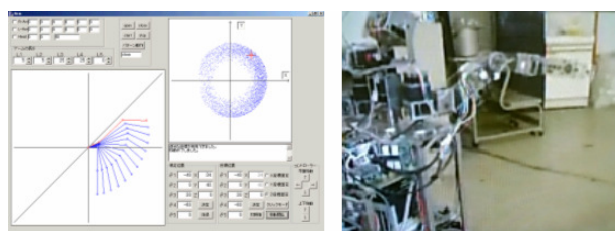


Fig6 Program before it drives and



the appearance of the arm
Fig.7 Program after it drives and
the appearance of the arm

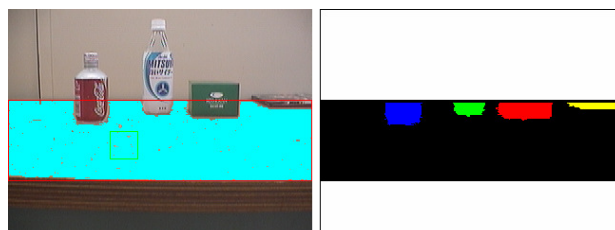
There is a difference in time from the start to the stop of each motor. However, the minion was almost able to be driven to coordinates of the target. As a result, there is no problem regarding its practical use.

6. Recognition of the work object

A plane that is of a similar color is extracted from one image obtained from the CCD camera, and the desk and the floor are recognized. A plane part on the desk and the floor is extracted using the HSV conversion. Next, the part not extracted is considered to be a part of the object, and it is extracted. Figure 8 shows the appearance of the object extraction.

Fig.8 The appearance of the object extraction

The relative coordinates of the work object and the rough size of the object can be calculated by the main body of the robot. These data is sent to the control program of the arm and using it, the robot can grip the work object. Figure 9 shows the size and the relative



coordinates of the work object on the output screen.

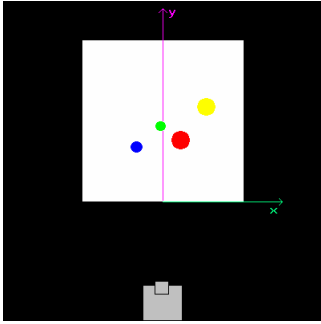


Fig.9 The screen for the output
of the parameters of the work object

7. Conclusions

In this research, the robot arm that met the demand required by a personal robot was designed. It is possible to create the various conditions that will drive the hand to a target position by the driving control program, and it is thought that the work object can be gripped by the hand.

References

- [1] Shinya Fujiwara, Eiji Hayashi, Development of an autonomous driving personal robot “Design of mechanism and control system”
- [2] Yoshitaka Hane, Eiji Hayashi, Development of an autonomous driving personal robot “Design of mechanism of hand”

Knowledge Evolution in a Dynamic Environment of RoboCup Simulation

T. Nakashima, H. Ishibuchi
Graduate School of Engineering
Osaka Prefecture University
1-1 Gakuencho, Sakai, Osaka 599-8531, Japan
{nakashi, hisaoi}@cs.osakafu-u.ac.jp

M. Nii
Department of Computer Engineering
University of Hyogo
2167 Shosha, Himeji, Hyogo 671-2201, Japan
nii@eng.u-hyogo.ac.jp

Abstract

In this paper we examine the performance of the evolutionary algorithm for a dynamic environment where the opponent team changes during the evolution of strategies. In the dynamic environment, the dash power of opponent players in ball intercept behavior is adjusted. We consider two adjustment modes of the dash power in our experiments. In one mode the dash power of the opponent players is gradually increased over generation of the evolutionary algorithm. The other mode monitors the performance of the evolved team strategies to increase or decrease the dash power of opponent players accordingly. We compare the evolution of team strategies between the two modes and discuss for the future extension to the current experimental settings. We also discuss the possibility of knowledge extraction from the obtained team strategies by the evolutionary algorithm.

1 Introduction

RoboCup soccer is a competition between soccer robots/agents. Its ultimate aim is to win against the human soccer champion team by the year 2050 [1]. Developing RoboCup teams typically involves solving the cooperation of multiple agents, the learning of adaptive behavior, and the problem of noisy data handling. Many approaches have been presented that try to tackle these problems, an example is the application of soft computing techniques.

In this paper we examine the performance of the evolutionary algorithm for a dynamic environment of RoboCup simulation where the opponent team changes during the evolution of strategies. In the dynamic environment, the dash power of opponent players in ball intercept behavior is adjusted. We consider

two adjustment modes of the dash power in our experiments. In one mode the dash power of the opponent players is gradually increased over generation of the evolutionary algorithm. The other mode monitors the performance of the evolved team strategies to increase or decrease the dash power of opponent players accordingly. We compare the evolution of team strategies between the two modes and discuss for the future extension to the current experimental settings. We also discuss the possibility of knowledge extraction from the obtained team strategies by the evolutionary algorithm.

2 Team Setup

We use the following action rules to determine player's action

$$R_j : \begin{array}{l} \text{If Agent is in Area } A_j \text{ and} \\ \text{the nearest opponent is } B_j \\ \text{then the action is } C_j, \quad j = 1, \dots, N, \end{array} \quad (1)$$

where R_j is the rule index, A_j is the antecedent integer value, B_j is the antecedent linguistic value, C_j is the consequent action, and N is the number of action rules. In this paper we evolve action rule sets to find a competitive soccer team strategy.

The antecedent integer value A_j , $j = 1, \dots, N$ refers to a subarea of the soccer field. We divide the soccer field into 48 subareas as in Fig. 1.

Each subarea is indicated by an integer value. The antecedent value A_j of the action rule R_j is hence an integer value in the interval $[1, 48]$. In this paper 12 actions are available for the consequent action C_j .

Note that each player has a set of action rules. Since there are 48 subareas in the soccer field and *near* and

1	7	13	19	25	31	37	43
2	8	14	20	26	32	38	44
3	9	15	21	27	33	39	45
4	10	16	22	28	34	40	46
5	11	17	23	29	35	41	47
6	12	18	24	30	36	42	48

Figure 1: Soccer field

not near are available for the second antecedent part in action rules (i.e., B_j), the number of action rules for a single player is $48 \times 2 = 96$. There are $96 \times 10 = 960$ action rules in total for a single team with ten field players. Action rules for a goal keeper are not considered in this paper.

If the ball cannot be kicked by a player, there are two kinds of actions. One is ball intercept where the player move toward the ball in order to be able to kick it. The other action is positioning where the agent keep its position that is determined from the ball position and its home position. The player determines which action to take based on the positional relation among all the objects including teammates, opponent players, and the ball.

3 Evolutionary Computation

3.1 Encoding

The action of the agents is specified by the action rules in (1) when they keep the ball. Considering that the soccer field is divided into 48 subareas (see Fig. 1) and the position of the nearest opponent agent (i.e., it is *near* the agent or *not near*) is taken into account in the antecedent part of the action rules, we can see that there are $48 \times 2 = 96$ action rules for each player. We apply our evolutionary method to ten soccer agents excluding the goal keeper. Thus, the total number of action rules for a single team is $96 \times 10 = 960$. We use an integer string of length 960 to represent a rule set of action rules for ten players. The task of our proposed evolutionary method is then to evolve the integer strings of length 960 to obtain team strategies with high performance.

On the other hand, the actions of the agent in the case where the nearest opponent agent is not near the agent are shown in the other 48 integers. The value of each integer ranges from an integer interval of [1, 12] as the number of possible actions for each rule is twelve.

3.2 Dynamically Changing Opponent

In our previous studies on the evolutionary computation for RoboCup soccer, the opponent team was fixed during the course of the evolutionary algorithm. Obtained strategies by the evolutionary algorithm are therefore able to successfully perform against the fixed opponent team. However, it is not necessarily said that the obtained strategies are successfully able to play the soccer game against different team strategies as successfully as against the fixed opponent team. In this paper we consider a dynamically changing environment in order to solve this problem.

In our implementation of the dynamically changing environment, dash power is used as a parameter of dynamically changing opponent strategies. The higher the dash power of opponent agents is, the harder it is for evolutionary teams to defeat the opponent team. In the beginning of the evolutionary algorithm the dash power of the opponent is zero and linearly increase as the number of generations increases.

3.3 Evolutionary Operation

We use one-point crossover, mutation, and ES-type selection as evolutionary operations in our evolutionary method. New integer strings are generated by crossover and mutation, and selection is used for generation update.

In the crossover operation, we first randomly select two integer strings. Then latter part of both strings is exchanged with each other from a randomly selected cut-point. Note that we do not consider any evaluation results when two integer strings for the crossover operation are selected from the current population. In the mutation operation, the value of each integer is replaced with a randomly specified integer value in the interval [1, 12] with a prespecified mutation probability. It is possible that the replaced value is the same as the one before the mutation operation. It should be noted that new integer strings generated by the crossover and the mutation operations do not have their match history. Thus the fitness evaluation of the new integer strings are made by using the game result of only a single game.

Generation update is performed by using ES-type selection in our method. We use a so-called $(\mu + \lambda)$ -ES [3] for our generation update scheme. By iterating the crossover and the mutation operations we produce the same number of new integer strings as that of current strings. Then the best half integer strings from the merged set of the current and the new strings are chosen as the next population. The selection is based

on the match results. Note that the current strings are also evaluated in this selection process. Thus, it is possible that a current integer string with the best performance at the previous generation update is not selected in the next generation update because the average goals of the integer string after the next performance evaluation may become lower if the result of the game at the next evaluation is poor.

To summarize, our proposed evolutionary method is written as follows:

[Procedure of the proposed evolutionary method]

- Step 1. Initialization. A prespecified number of integer strings of length 960 are generated by randomly assigning an integer value from the interval [1, 12] for each integer.
- Step 2. Generation of new integer strings. First randomly select two integer strings from the current population. Then the one-point crossover and the integer-change mutation operations are performed to generate new integer strings. This process is iterated until a prespecified number of new integer strings are generated.
- Step 3. Performance evaluation. The performance of both the current integer strings and the new integer strings generated by Step 2 is evaluated through the results of soccer games. Note that the performance of current integer strings is also evaluated every generation because the game results are not constant but different game by game.
- Step 4. Dynamic environmental change. The dash power of the opponent team is increased. The schedule of the change of the dash power is make so that at the first generation it is zero and becomes full (i.e., 100%) at the final generation.
- Step 5. Generation update. From the merged set of the current integer strings and new ones, select best integer strings according to the performance evaluation. In the performance evaluation goals for are used as the first criterion. If multiple individuals have the same goals for, then goals against are used as the second performance criterion. The selected integer strings form the next generation.
- Step 6. Termination of the procedure. If a prespecified termination condition is satisfied, stop the procedure. Otherwise go to Step 2.

4 Computer Simulations

The following parameter specifications were used for all the computer simulations in this paper:

- The number of integer strings in a population: 5,
- The probability of crossover: 1.0,
- The probability of mutation for each integer: 5/96,
- Generation update: 500.

The population size is specified as five. This is a small number comparing to commonly used parameter specifications. This is because it takes at least five minutes to complete a single soccer game. If the population size is specified large, it is difficult to perform the evolutionary method for a large number of generations. Currently we use a 16-node cluster system for the computational experiments in this paper. It still takes several days to perform a single run of the evolutionary process. The population size will be increased when more powerful computational environments are equipped.

We show the evolution of the soccer teams in Fig. 2. Total scores of goals for and goals against are plotted in Fig. 2. From this figure we can see that the offensive performance degrades as the evolution proceeds as the dash power of the opponent teams increases during the course of the evolution.

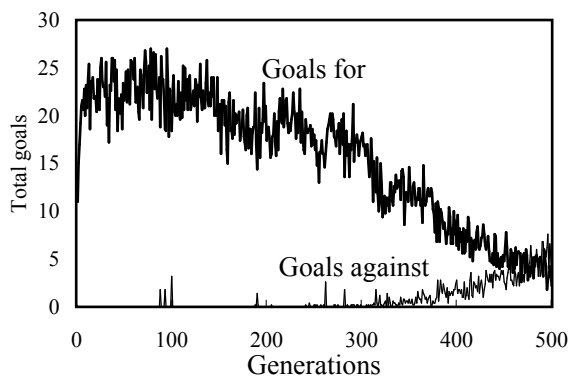


Figure 2: Performance of evolutionary teams.

Now we closely investigate obtained strategy by the evolutionary algorithm. Figure 3 shows the trajectory of the ball by an individual at the initial population. We can see from Fig. 3 that the ball is somewhat kicked randomly at different directions. This is because the initial individual was generated by randomly assigning an action to each action rule. Next we show in Fig. 4 the trajectory of the ball by an individual at the final population (i.e., at the 500-th generation). From

Fig. 4, we can see that the evolved team obtained offensive knowledge where the side forward drives the ball toward the opponent area from the side of the field and place the ball to the center when the ball is near the opponent goal. This strategy is intuitively understandable because human soccer teams normally take this strategy. It is shown that the evolutionary algorithm automatically obtained the human-like strategy from the initial population that was randomly generated.

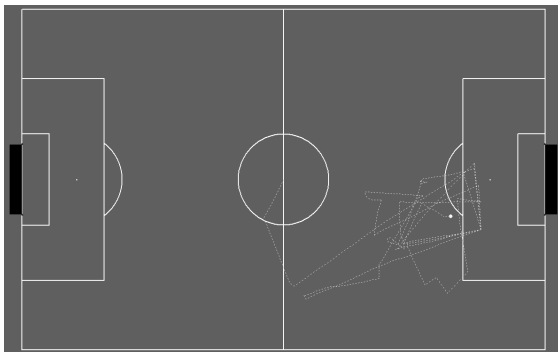


Figure 3: Ball trajectory at the first generation.

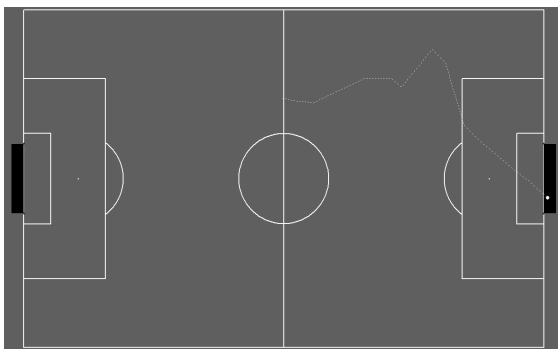


Figure 4: Ball trajectory at the final generation.

5 Conclusions

In this paper we proposed an evaluation method of soccer team strategies by using match history. The match history is used to calculate the average goals and the average goals against. Those teams with high average goals are evaluated as better than those with low average goals. The average goals against are used when the average goals are the same among more than one soccer team strategies. This method avoids the problem caused by uncertainty in the RoboCup soccer such as noise in object movement and the sensing information.

In the evolutionary process of this paper the action of soccer players that keep the ball is determined by a set of action rules. The antecedent part of the action rules includes the positions of the agent and its nearest opponent. The soccer field is divided into 48 subareas. The action of the agent is specified for each subareas. The candidate actions for the consequent part of the action rules form a set of 12 basic actions such as dribble and kick. The strategy of a soccer team is represented by an integer string of the consequent actions. In the evolutionary process, one-point crossover, replacement mutation, and ES-type generation update are used as evolutionary operators. The generation update is performed in a similar manner to the $(\mu + \lambda)$ -ES of evolution strategy. That is, the best integer strings are selected from a merged set of current integer strings and new integer strings that are generated from the current integer strings by the crossover and mutation operations. The performance of the soccer team strategies becomes better over generation. For example, the average goals at the end of the evolution process is larger than in the initial population. We also observed that the average goals against did not increase as the evolutionary computation progressed.

In a series of computer simulations, we examined the performance of our evaluation method. We showed that the evolutionary algorithm automatically obtained a human-like strategy from random strategies through the process of evolutionary trial-and error.

This paper focused on offensive strategy rather than defensive one. Developing a method for the defensive strategy is left for our future work.

Acknowledgment

This work was partially supported by Grant-in-Aid for Scientific Research on Priority Areas: KAKENHI (18049065) and KAKENHI (1770241).

References

- [1] RoboCup official page, <http://www.robocup.org/>.
- [2] T. Nakashima, M. Takatani, M. Udo, H. Ishibuchi, and M. Nii, "Performance Evaluation of an Evolutionary Method for RoboCup Soccer Strategies," *RoboCup 2005: Robot Soccer World Cup IX*, in press.
- [3] T. Bäck, *Evolutionary Algorithms in Theory and Practice*, Oxford University Press, New York, 1996.

Control of Autonomous Mobile Robot through Environment Recognition with Photoelectric Sensor

**Takahiro Kurita, Norihiro Abe,
Kazuaki Tanaka**
Kyushu Institute of Technology
680-4 Kawazu, Iizuka-shi,
Fukuoka, 820-8502, JAPAN
E-mail: kurita@sein.mse.kvutech.ac.jp

Shoujie He
Eastman Kodak Company
Plano, Texas, USA

Hirokazu Taki
Wakayama University
930 Sakaedani, Wakayama-shi, Wakayama,
680-8510, JAPAN

Abstract

With the advancement of computing technology, robot industry has grown substantially in the past few years. However, most of the current robots are still simply following through the pre-defined procedures and moving in a well-defined workspace. The control of an autonomous mobile robot remains challenging. A truly autonomous mobile robot will definitely benefit our life in many areas, including but not limited to nursing care services and office guide.

How to get to know the current location is the most difficult issue that an autonomous mobile robot has to deal with. Without knowing its current location, it is impossible for the mobile robot to move towards its destination. Let us think how we identify our location when we are put in an unfamiliar place. The most common things that we do will be to collect the geographical features and then match what we have collected with the information on a map. The method is considered applicable to an autonomous mobile robot as well. This paper discusses how to collect the geographical features with a photoelectric sensor and how to identify the current location by comparing the sensor information and the map information.

Key Words

Autonomous Mobile Robot, Environment Recognition, Photoelectric Sensor,

1 Introduction

Mobile robots in use are still moving within a well-defined static environment. This indicates that the research and development of autonomous robots still have a long way to go. Some day in the future, if a mobile robot could autonomously move in a dynamically changing environment, it would definitely have a lot of applications in many areas of our daily life.

At the current stage, however, our very first goal is to come up with a practical approach to the control of a mobile robot so that it will move autonomously towards its destination within a static environment. Our second goal is basically along the same line, which is to keep the mobile robot moving smoothly with no stops. Although

it sounds unavoidable to stop in order to avoid obstacles, sensor information integration and fast-speed route planning will be used so that stops are not needed anymore.

With the control program experimented in this study, a mobile robot could move autonomously to the destination specified by a person.

2 System Organization

2.1 Communication subsystem

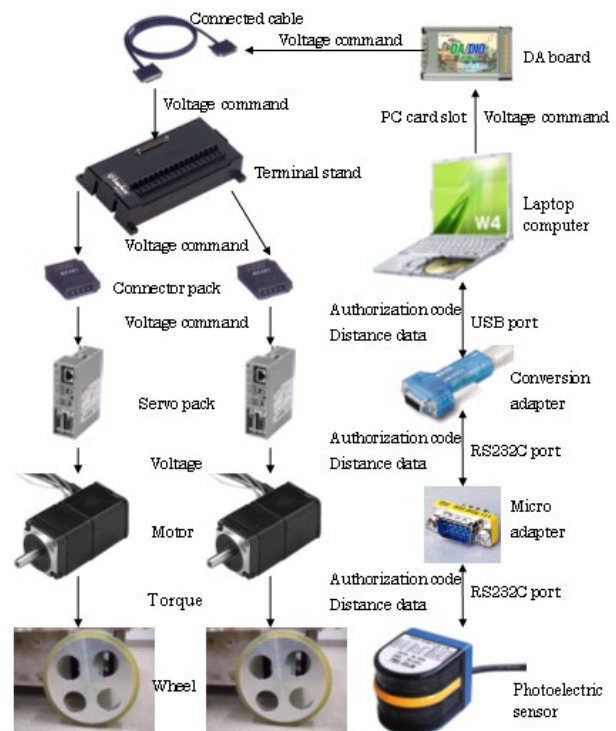


Fig.1. Communication configuration

A laptop computer is put on the mobile robot for the communication with a motor and a photoelectric sensor. At the beginning, the laptop computer sends an authentication code over to the photoelectric sensor. Once the code has been authenticated by the photoelectric sensor, will the laptop computer start receiving the distance data from the photoelectric sensor. The laptop computer recognizes the environment of its current location through the analysis of the distance data.

Based on the result of environment recognition, the laptop issues a voltage command to the servo pack through the DA board. The servo pack will apply a steady voltage to motors, which control the wheels for the movement.

2.2 Driving subsystem

The mobile robot in this study can move forward as well as backward, turn right as well as left, and can even change its facing directions through rotation without turning right or left. Changing the facing directions of a mobile robot could of course be achieved by turning right or left. But instead of turning, using the freedom of rotation could keep the photoelectric sensor staying at the same location and the same direction. This is because the photoelectric sensor is mounted between the front wheels, which are the driving wheels. The benefit is that the environment recognition results obtained before the rotation stay valid even after the rotation.

3 Control program

The environment recognition is accomplished by applying the minimum mean square algorithm to the distance data. As a result, a set of feature points are extracted. The feature points here are the uneven points on the walls. Figure 2 shows the flow chart of the program.

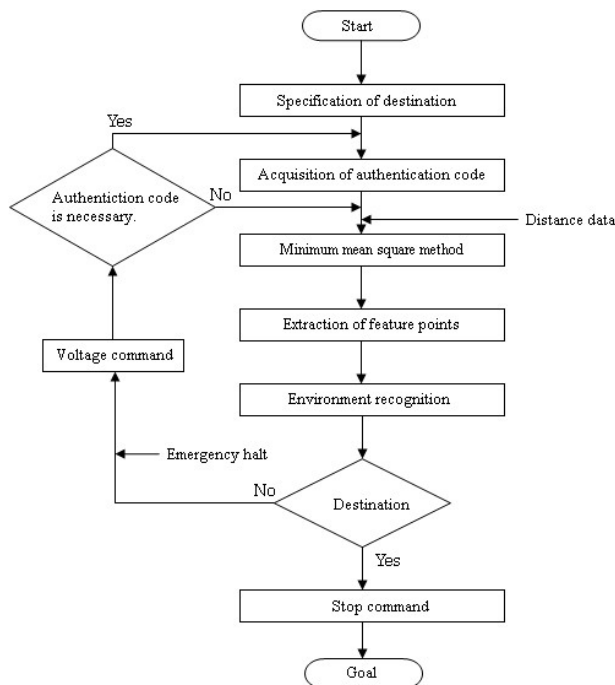


Fig.2. Flow chart of the program

3.1 Minimum mean square method

The photoelectric sensor generates 100 samples of

distance data every 1.8 degrees. If all the samples are directly used for the feature point extraction, an overwhelmingly large number of feature points will be extracted. This is because the existing variance among the samples leads to the extraction of uneven points from a flat wall. The minimum mean square algorithm is used for the approximation of straight lines so that no feature point is extracted from a flat wall.

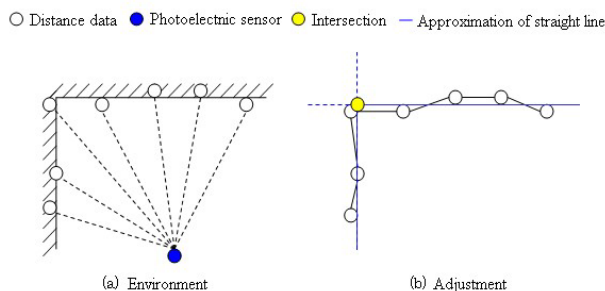


Fig.3. Minimum mean square method

3.2 Extraction of feature points

Environment recognition is solely based on the extraction of feature points, which makes the extraction of feature points extremely important. The feature points here are the uneven points on the walls. Let us see the triangle in Figure 4, where the vertexes, A , B , and C are the points that three approximated straight lines intersect. As soon as the length of all the three sides of the triangle a, b, c is calculated, could the angle θ at B be calculated with the formula (1).

$$\theta = \arccos\left(\frac{a^2 + b^2 - c^2}{2ab}\right) \quad (1)$$

If θ is smaller than a pre-determined threshold, point B will be extracted as a feature point.

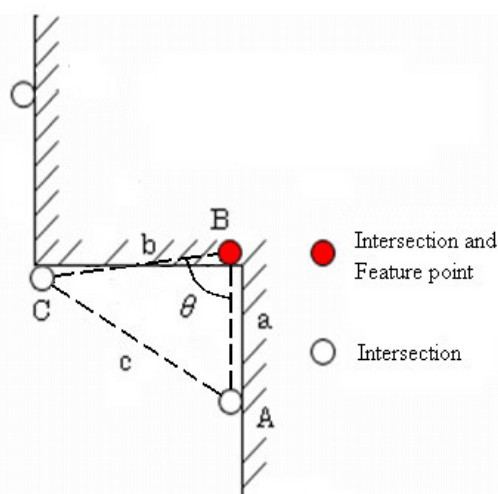


Fig.4. Extraction of feature points

Although the minimum mean square algorithm has already been applied, it is still possible to extract extra feature points. One solution to this problem is to dynamically reduce the threshold from 150 to 140

degrees in the process of selecting the feature points. Another criterion is to choose one when two or more feature points are nearby. Since the two criteria are applied to the feature points extracted, the removed extra feature points will not be re-selected.

3.3 Environment recognition

The length of the wall is used as a reference for the environment recognition. Since the feature points correspond to the joint points of different walls, the length of a wall could be measured by finding the distance between the feature points. The current location is identified by comparing the length of walls with the information given in a map.

3.4 Autonomous movement

When the robot moves, the control program compares the distance data sampled at 35 degrees on the right side with the distance data at 145 degrees on the left side. In order to minimize the potential collision, the robot is kept moving along the centerline of the road. To keep it on the centerline, the wheels with shorter distance data will be controlled to move forward while the wheels on the opposite side move backward. This adjustment keeps going until the robot moves to the point on the centerline. When the distance data sampled at 35 and 145 degrees are equal, wheels on both sides will be controlled to move forward. The data sampling and the control of wheel rotation are constantly happening during the entire movement until the robot arrives at the destination.

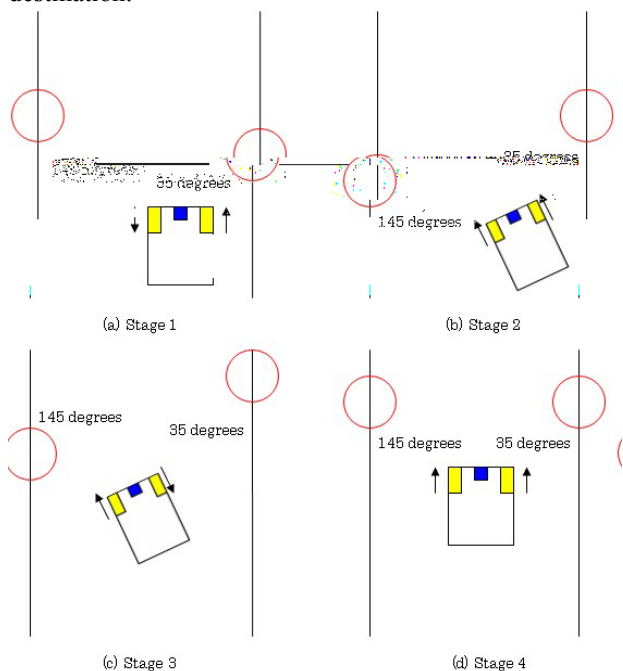


Fig.5. Move to the center

3.5 Obstacle avoidance

When the robot moves, the control program compares the distance data sampled at 35 degrees on the right side with those at 145 degrees on the left side this time. When there is an obstacle that doesn't exist in the given map on the road, the robot may collide with it. How to avoid collision against an obstacle is shown here.

To detect unknown obstacle, it examines distance data captured with the photoelectric sensor from 35 to 145 degrees. When an obstacle is found on the road, the distance between the obstacle and the right wall is compared with that between the obstacle and the left wall. Then the robot changes the moving direction toward the center of the wider space and successfully passes over the obstacle. After the robot recognizes that it has passed over the obstacle, it switches back the moving direction to the previous one.

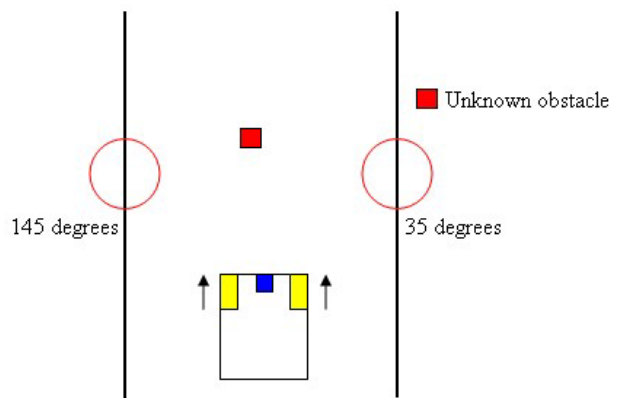


Fig.6. Evading obstacle

4 Experiment

The autonomous mobile robot has been experimented in a narrow indoor environment. Simply with the distance data collected by the photoelectric sensor, the mobile robot is moving autonomously.

4.1 Test cases

The following two experiments are conducted:

- Experiment 1: the centerline of the road is specified as the destination.
- Experiment 2: the destination is specified to be on the side of a road.

In Experiment 2, when the robot arrives at a point with the same y coordinates as the destination, it rotates by 90 degrees and then move forward to the specified destination. The moving speed of the robot is set to be $0.5\text{km} / h$.

4.2 Experimental result

4.2.1 Experiment 1

Figure 7 shows the console of our control program in execution. It indicates that the robot has arrived at the

specified destination. Point d is the destination. Point e is the current location and c is the wall that was identified through the environment recognition by point a and b . The error of the x coordinate was -45mm in the destination and the error of the y coordinate was -20mm . The total execution time was 21360msec .

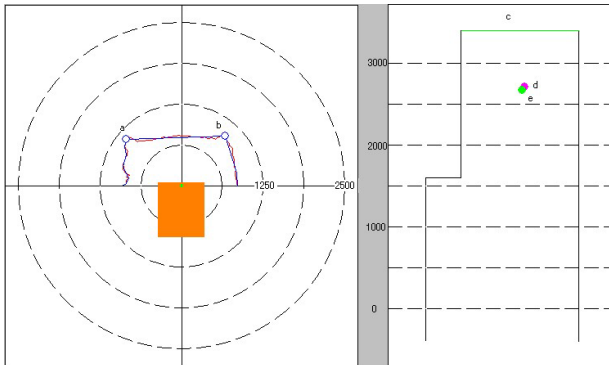


Fig.7. Result of experiment 1

4.2.2 Experiment 2

Figure 8 shows the console of our control program in execution. It indicates that the robot has arrived at the specified destination. Point e is the destination. Point f is the current location and d is the wall that was identified through the environment recognition by point b and c . The error of the x coordinate was $+10\text{mm}$ in the destination and the error of the y coordinate was -90mm . The total execution time was 15000msec .

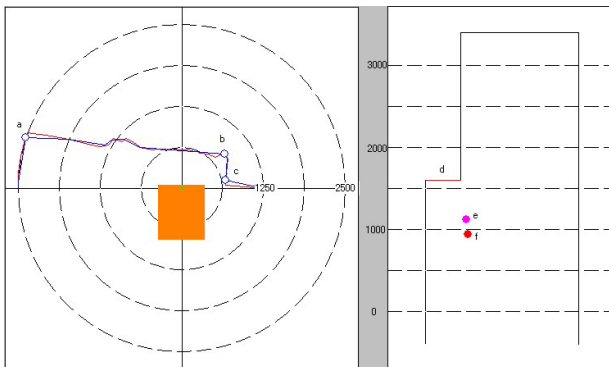


Fig.8. Result of experiment 2

4.3 Result analysis

The experimental results in Experiment 1 showed us that the error of each coordinates could be 50mm or less, which indicates that the destination set at centerline of a road could be easily reached with very high accuracy. The experimental results in Experiment 2, however, showed big errors. The reason is because the robot is controlled to move along the centerline of the road all the way to the point with the same y coordinate as the destination and then rotates by 90 degrees and move towards the destination. In the case that 90 degrees rotation is not accurate enough, the error occurred along the y axis will be increased

substantially. As a future solution, a counter board can be used to measure the cycle of wheels so that the rotation could be well controlled to be close to 90 degrees.

The control program in the experiments is to control the robot move along the centerline while doing the environment recognition. It stops the movement only when both the environment recognition is achieved as well as the destination is reached. In another words, in the case that the robot arrived at the destination with no environment recognition completed, the robot may keep going and pass the destination. One solution could be to keep track of the previous locations and match with the current location. This way, the speed of robot could be reduced as soon as it is identified that it getting close to the destination. With the reduced speed, the robot will have more distance data collected for the environment recognition. As a result, the robot will stops at the destination more frequently.

5 Conclusion

In this research the environment recognition was achieved by processing the distance data obtained through the photoelectric sensor. The control of an autonomous mobile robot through the environment recognition has been experimented. The goal of controlling the mobile robot so that it moves autonomously to the destination in a static environment was achieved. The second goal that the robot moves with no stops was achieved.

The approach in this study is going to be enhanced to deal with the issues that an autonomous mobile robot may encounter in a dynamically changing environment. A dynamically changing environment could be an environment with people walking around or some other moving objects. In a dynamically changing environment, the robot needs to predict the movement of other objects including people and try not to interfere with other moving objects.

Acknowledgment

We greatly appreciate the aid of Ministry of Internal Affairs and Communications (MIC) and the Grant-in-Aid for Scientific Research.

Reference document

- [1] Jean-Claude Latombe, "Robot Motion Planning", Kluwer Academic Publishers
- [2] Robin R. Murphy, "Introduction to Ai Robotics", MIT Press
- [3] Chrystopher L. Nehaniv, Kerstin Dautenhahn, "Imitation in Animals and Artifacts", MIT Press
- [4] John M. Holland, "Designing Mobile Autonomous Robots", Elsevier

An Interactive System for Creating a 3-D Graphical Road Map

Kouhei Tou
Department of Mechanical
and Control Engineering
Kyushu Institute of
Technology
Sensuicho 1-1, Tobata
Kitakyushu 804-8550
JAPAN

Tohoru Irie
Research & Development
Department
GEO Technical
Laboratory
Hakataekihigashi 3-1-26
Fukuoka 812-0013
JAPAN

Joo Kooi Tan
Department of Mechanical
and Control Engineering
Kyushu Institute of
Technology
Sensuicho 1-1, Tobata
Kitakyushu 804-8550
JAPAN

Seiji Ishikawa
Department of Mechanical
and Control Engineering
Kyushu Institute of
Technology
Sensuicho 1-1, Tobata
Kitakyushu 804-8550
JAPAN

Abstract

Recently, Information Technology has been introduced to social systems for various purposes. The map that was the paper medium has been changed into an electronic form and digital maps have become familiar in our life such as the map for car navigation. They are also introduced in the Internet and mobile phones. Now, the demand on a 3-D map has rapidly risen to the digital map users. This is because a 3-D map excels in the visibility and is intuitively understood when the location information is passed on to a user three-dimensionally in the digital map.

This paper proposes a novel technique for creating a 3-D road map. It includes proposal of a vehicle that collects ground-view information of a road environment and an interactive graphic system for producing a 3-D road map employing the collected information. The function of the proposed technique is to make a 3-D map electronically by fitting measured data to a given 2-D digital map. In order to evaluate the proposed technique, we performed experiments at Paris (France) and Fukuoka (Japan), and produced a highly realistic 3-D graphical map of the road environment. This confirms the availability of the proposed technique.

Keywords: 3-D maps, road maps, car navigation, GIS, ITS, image processing

1. Introduction

Recently, Information Technology (IT) has been introduced to social systems for various purposes. The map provided by the paper medium has changed its style to an electronic and digital form. It has been introduced to car navigation. The Internet and mobile phones also employ digital maps. In this way, the digital map has become much familiar in our life.

A 3-D road map is the present concern of major map-related companies, since it may be easily accepted to people because of its realistic and therefore

understandable nature, particularly in car navigation. Although lots of researches on creating 3-D road maps have been done so far using aerial or satellite photograph resources, methods of collecting geographic information without using such aerial view resources has a strong demand from map-related industries, since certain kinds of geographic information (roads in tunnels, roads hidden by street trees, building texture, etc.) are difficult or even impossible to collect their information using these resources. Particularly, in the field of car navigation, frequent map update is indispensable for providing a driver with most recent and exact geographic information having a driver's view.

In this circumstance, some studies have proposed methods of measuring 3-D shape of buildings and objects from a driver's view. There are established techniques such as the stereo vision [1] and the factorization [2] that use video images or still images measured by a camera. A method of using aerial photos [3] also exists as a passive technique. The literature [4] employs a laser range finder as a sensor. These techniques can recover actual 3-D shape, but they need much complicated post-processing to handle the obtained large amount of data and their noise reduction.

If these kinds of measurement information are arranged on the 2-D map with latitude and longitude information obtained from the Global Positioning System (GPS) receiver, it causes some difficulty in its accuracy because of the noise contaminated in the GPS signal.

In this paper, we propose a novel technique for creating 3-D graphical road maps that contain road environments. The technique includes a vehicle that collects road environmental information and an interactive graphic system for producing a 3-D road map from the information. The interactive system assumes the employment of a 2-D electronic map and aerial photographs as reference and creates a 3-D road map from the video images the vehicle provides. This procedure is done on the computer display by man-machine collaborative work. Visual operation of a user on the

display supported by some automated procedures by computer is much effective. This system will certainly open up a new application field in the development of man-machine systems.

The paper is organized as follows. Section 2 outlines a method of data collection. Section 3 outlines a mapping method of measured data to a 2-D map. Section 4 explains how to make a 3-D map from the measured data. Section 5 shows experimental results on the data collection and the produced 3-D maps of the streets in Fukuoka (Japan) and Paris (France) using the proposed method. Discussion and conclusions are given in Section 6.

2. Data Collection

It is assumed in the proposed technique that the information obtained from the real world contains horizontal surfaces and vertical surfaces. We obtain the information on road surfaces as horizontal surfaces and the information on the walls of buildings, sign boards, etc., as vertical surfaces. It is also assumed that a 2-D electronic road map is available. In the technique, the measurement position on the 2-D map is specified by using horizontal geographic information, and after that, 3-D information is mapped by using vertical geographic information. The outline of the entire procedure on the proposed system is described in three parts (See Fig. 1).

The principal data obtained by the proposed vehicle measurement system is as follows;

- A) Road image data for detecting the car position and collecting road surface information.
- B) Scene image data for collecting geographic objects information such as buildings, traffic signals, etc.
- C) Distance data for detecting the car position.

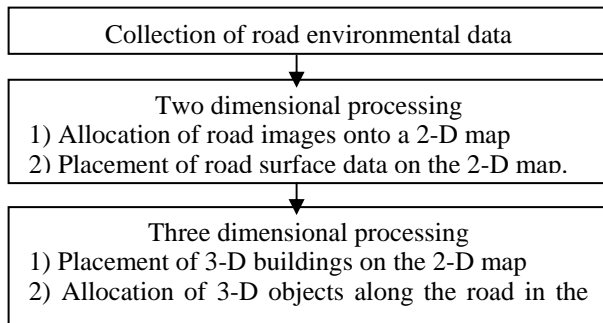


Fig. 1 Overview of the procedure.

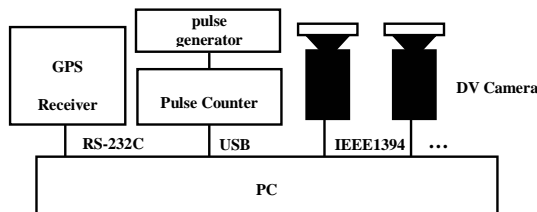


Fig. 2 Configuration of the devices employed in the measurement vehicle.

In this data collection, synchronization between the car position/time and the sensor data is important. Therefore, we propose the measurement system as shown in Fig. 2.

In Fig. 2, multiple digital video cameras are employed to obtain the data A and data B above. The images of the cameras are recorded on DV tapes, and time code is recorded on the personal computer to synchronize the pulse generator. The pulse generator that is connected to the computer through the pulse counter makes equidistance information (The pulse generator is set up at the rear wheel of the measurement vehicle). GPS is connected to the computer to obtain the rough position of the car. All the data obtained from these sensors (DV cameras, a GPS receiver, and the computer time) synchronize by the signal of the pulse generator. Herewith, the DV time code (i.e., DV images) and the GPS data (i.e., rough position of the car) are obtained at an equidistance interval.

3. Two-dimensional Processing

A method of producing initial state of the 3-D map from measurement data by two dimensional processing is described in this section.

3.1 Data improvement & allocation of road images onto a 2-D map

3.1.1 Geometrical conversion of road images

In order to obtain the road surface images from the original road images in the video taken by the camera in the vehicle, geometrical conversion is applied to the original image. Here, we assume that the road has a flat surface, and the gradient value (roll) of the car is vanishingly small.

In the first place, the point marks are arranged in front of the car in the form of the lattice and having equal intervals to obtain geometrical conversion parameters, and it is recorded with a DV camera (See Fig. 3). In the second place, coordinates of each quadrangle that consists of four point marks in the image are obtained and geometrical conversion parameter (pseudo affine transformation parameter) is calculated. The pseudo affine transformation is given as follows;

$$x' = ax + by + cx + d, \quad (1a)$$

$$y' = ex + fy + gy + h. \quad (1b)$$

The result of having applied Eq.(1) to the quadrangle image in Fig. 3(a) is given in (b). It is the image of the lattice observed from above and is called an ortho-image.

Referring to the time code, the original road image in the video is separated horizontally to make rectangle patches on the computer display, to each of which Eq.(1) is applied and the rectangle patch is transformed into an

ortho-image. The separation of the road is done by a user, whereas the transformation to the ortho-image is performed by computer. In this way, the ground-view road images obtained from the frontal camera in the vehicle measurement system is converted into corresponding ortho-images which are then placed on the 2-D road map.

3.1.2 Extraction of crossroads

In this technique, crossroads are considered to be a checkpoint on the 2-D map. Checkpoints are basic points of measurement data at the position on the 2-D map.

In this section, the technique is explained for extracting the candidate of the checkpoint by recognizing the crosswalk from the ortho-image.

Extraction of white line edges

To extract white line edges of a crosswalk, some image processing algorithms are combined. The following four processed images are examined whether or not there are frequent white areas on the images (See Fig. 4).

- 1) Emphasis of Contrast
- 2) Thresholding - Emphasis of Contrast
- 3) Emphasis of Contrast - Minimizing Average Error - Median Filter (5 times)
- 4) Thresholding - Emphasis of Contrast - Minimizing Average Error - Median Filter (5 times)

The Sobel filter in the horizontal direction is applied to the above four images and vertical edges are extracted in the images.

Recognition of crosswalk

A crosswalk is judged by the number of intersections of the horizontal straight line that passes the center of the image and the extracted vertical edge. It is recognized as a crosswalk if the number of the intersection is larger than a threshold on at least one of the above four preprocessed images.

3.1.3 Allocation of road images onto a 2-D map

Road surface images (See Fig. 5, for example) can be made, using Eq.(1), from the ground-view images obtained from the frontal downward camera equipped in the vehicle and distance data. A road interested is separated into successive rectangle patches as shown in Fig. 5. They are transformed ortho-images. The patches are roughly arranged onto the corresponding road on the 2-D map automatically according to the GPS information. Since the GPS information is not very exact, crossroads at the junctions along the road are detected by the technique stated in 3.1.2. These crossroads specify check points on the 2-D map. Two check points between the adjacent crossroads are combined on the 2-D map by computer by fitting a NURBS (Non-Uniformed Rational B-Spline) [5]

curve along the road. The road patches are then rearranged on the NURBS curve automatically to get their exact locations. This map is the initial state of the 3-D map produced and is called an initial 3-D map.

3.2 Placement of road surface data on the 2-D map

Road features are obtained from road surface images. We input stop lines, lane lines, traffic lights, crosswalks, etc., to the initial 3-D map by referring to the road surface images on the 2-D map and aerial photo.

4. Three-dimensional Processing

A method of producing a 3-D map employing the obtained video data and the initial 3-D map is described in this section. Here, the 3-D map does not contain exact 3-D shapes of real buildings, trees, or others, but it contains their pseudo shapes registered in the system.

4.1 Placement of 3-D buildings on the 2-D map

A 3-D object is displayed by 3-D volume data that is made from building 2-D frames of the object (See Fig. 6).

The wall texture obtained as vertical geographic information is put on the building.

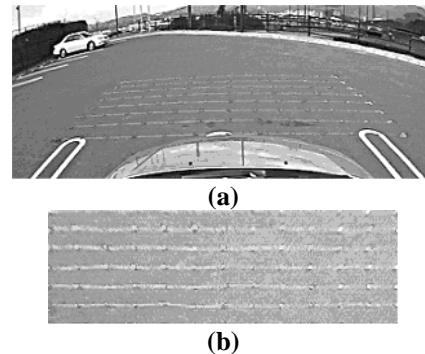


Fig. 3 Image of the lattice in front of a vehicle and its ortho-image.

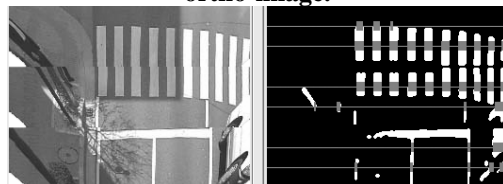


Fig. 4 Ortho-Image (left), and the extracted white area image (right)



Fig. 5 Road surface image segmented into rectangle parts.

4.2 Allocating traffic objects and plants along the road on the map

There are some typical objects along a road such as street-lights, trees, traffic signals, traffic signs, *etc.* The developed system stores their 3-D models in a database. Once they are observed along the road in the video image, their models are chosen by a user and placed at appropriate positions in the 3-D map.

5. Experimental Results

Experiments were performed to show the performance of the proposed technique.

5.1 Experimental environment

Five cameras were installed in the vehicle. Two of them (Cam 1, Cam 2) were used to measure the road surface data, and other two (Cam4, Cam5) were used to measure the wall of buildings, *etc.* The last one was used to measure the signs, signals, *etc.* Also, to obtain distance data, the magnetic pulse generator was set in the vehicle. Additionally, GPS and note PC were set. The road images were taken in Paris, France, and in Fukuoka, Japan, with these devices. We rented a vehicle in the locale, and all the devices were set up in the vehicle.

5.2 Results

Figure 7(a) shows a photo of a road environment in Paris and (b) is the created 3-D map. Satisfactory correspondence is obtained between the 3-D map and the actual road environment. It may provide enough information for driving this route.

Similar result was obtained with Fukuoka.

6. Discussion and Conclusions

In this research, we proposed a simple and useful method of producing a 3-D geographical map by mapping onto a given 2-D map the data measured in the street using video cameras and several sensors on the vehicle. In the experiment, it was confirmed that allocating the measurement road surface data that are difficult or even impossible to collect using the aerial or satellite photograph resources in the 2-D map was possible. Moreover, we were able to produce a highly realistic three-dimensional map with the acquired data. The work efficiency has been raised 30% than before with respect to the production time.

In the future, to raise the work efficiency of the post-processing of the measurement data, we plan to introduce image recognition techniques more in the procedure and a new measurement method, so that we can develop an easy and simple 3-D map production application.

References

- [1] M. Okutomi and T. Kanade, "A multiple-baseline stereo", *IEEE Trans. on Pattern Analysis and Machine Intelligence*, vol.15, no.4, 1993.
- [2] C. Tomasi and T. Kanade, "Shape and motion from image streams under orthography: A factorization method", *Int. J. Computer Vision*, vol.9, no.2, pp.137-154, 1992.
- [3] K. Azmi, S. Ono, M. Kagesawa, and K. Ikeuchi, "Automatic reconstruction of large-scale virtual environment for intelligent transportation systems simulation", *Proc. The 11th ITS World Conference*, October, 2004.
- [4] H. Zhao and R. Shibasaki, "Reconstructing a textured CAD model of an urban environment using vehicle-borne, laser range scanners and line cameras", *Machine Vision and Applications*, Vol. 14, No. 1, pp. 35-41, 2003.
- [5] T. Hayashi, K. Kato: *3D-CG Programming Using Open GL*, Corona Publishing, 2003. (in Japanese)

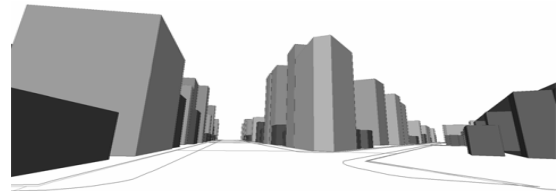


Fig. 6 Buildings on the 3-D map produced automatically



(a)



(b)

Fig. 7 Photo of a road in Paris and its 3-D Map

ITERATIVE DENOISING USING NON LINEAR FILTER IN WAVELET DOMAIN

M. Hariharan¹, Paulraj M P¹, Sazali Yaacob¹, M. Rizon¹, M. Sugisaka² and D. Hazry²

¹School of Mechatronics Engineering, Northern Malaysia University College of Engineering (KUKUM), Malaysia

²Department of Electrical and Electronic Engineering, Oita University, 700 Oaza Dannoharu, Oita 870-1192, Japan

Abstract

Digital images are prone to different noise during acquisition and transmission. Noise reduction is a traditional problem in image processing. This paper explores a novel neural network-based non-linear filter in wavelet transform domain for image denoising. In this method, using wavelet transformation a noisy image is decomposed into four subbands. A simple procedure is suggested to extract the training patterns from these four subbands. Using a layered neural network architecture denoising is performed. The denoised image is thereafter obtained through the inverse transform on the noise-removed wavelet coefficients. Simulation results demonstrate that this method is very efficient in removing the noise. Compared with other methods performed in wavelet domain, it requires no a priori knowledge about the noise and needs only one level of signal decomposition to obtain very good denoising results.

Keywords: Wavelet transform, Neural Network Filter, White Gaussian noise, Image denoising

1. INTRODUCTION

An image is degraded by noise due to various factors during its acquisition and transmission phases. Image denoising is aimed to remove or reduce the noise so that a

good-quality image can be obtained for various applications. This paper investigates the problem of image denoising when the image is corrupted by additive white Gaussian noise. Traditionally, linear processing methods such as wiener filter, mean and median filters are employed for this purpose. However, mean filters tend to blur the edges in the images and median filters are ineffective in dealing with non-impulse noise components. To preserve the edges, non-linear methods have become the mainstream approaches in the field of image denoising.

Wavelet transform provides excellent properties for image processing. Non-linear denoising methods performed in the wavelet transform domain have received wide research attention. One of the standard non linear methods is wavelet thresholding. In this method a threshold value is chosen for each subband of the image. The better result depends on the choice of the thresholding parameters. It is difficult to find the optimum threshold value. In wavelet thresholding, the local space-scale information is not considered adaptively. In order to overcome these drawbacks here a Neural network based Non linear method is developed for image denoising.

A layered neural network (LNN) is properly designed and trained to explore the learning capability of the neural network to learn the correlation among the noisy

wavelet coefficients, thus removing noise from them. The LNN filter method generates better results than the linear processing methods. Traditional wavelet thresholding methods which usually require three or more levels of wavelet decomposition and need the accurate estimate of the noise to obtain good denoising results. But this method needs only one level of wavelet decomposition and can adapt itself to the various noise environments by learning.

2.DENOISING IN IMAGES

Applied scientists and engineers who work with data obtained from the real world know that signals do not exist without noise. There are several fact that noise into an image depending on how image is created. For example:

- ❖ If the image is scanned from a photographic made on film, the film grain is source of noise. Noise can also be the result of damage to the film, or be introduced by the scanner itself.
- ❖ If the image is acquired directly in a digital format, the mechanism for gathering the data (such as a CCD detector) can introduce noise.
- ❖ Electronic transmission of image data can introduce noise.

There are different types of noises like gaussian noise, salt and pepper noise and speckle noise.

2.1.IMAGE DENOISING

Denoising is the process of removing/reducing noise from the noisy image and retaining the original image. The general additive noise reduction problem can be formulated as follows[1]:

$$y=x+v$$

where, y is the corrupted image.

x is the original uncorrupted image

v is the additive noise

The objective of noise reduction is to reduce the noise in y and to make the estimate \hat{x} from y which is as close to x as possible. Here it is assumed that the noise is Gaussian zero mean and variance σ^2 , i.e., $N(0, \sigma^2)$.

3.LAYERED NEURAL NETWORK FOR IMAGE DENOISING

An artificial neural network (ANN or NN for short) is an artificial intelligence closely modeled after a human brain[5]. Such a neural network is composed of computer-programming objects called nodes. These nodes closely correspond in both form and function to their organic counterparts, neurons. Individually, nodes are programmed to perform a simple mathematical function, or to process a small portion of data. A node has other components, called weights, which are an integral part of the neural network. Weights are variables applied to the data that each node outputs. By adjusting a weight on a node, the data output is changed, and the behavior of the neural network can be altered and controlled. By careful adjustment of weights, the network can learn. Networks learn their initial behavior by being exposed to training data. The network processes the data, and a controlling algorithm adjusts each weight to arrive at the correct or final answer(s) to the data. These algorithms or procedures are called learning algorithms.

Neural networks are often used for image denoising and compression. Their adaptability and learning capabilities make them excellent choices for removing noisy coefficients. Image processing using neural networks is a very broad field, but one of the common use for an NN is image denoising. This neural network based non linear filter removes the noise effectively than the standard filters. There are different types algorithms to train the network. Here we

used the Back propagation Neural Network for image denoising.

In image denoising, filtering is a common technique. In this paper, neural network is used as a non linear filter. Their adaptability and learning capabilities make them excellent choices for removing noisy coefficients.

The LNN filter is a three-layer neural network with inputs derived from an $N \times N$ neighborhood of the transformed image and appropriately selected neuron activation functions. As shown in Figure(1), the network takes Y_p and ΔY_k as the inputs, where Y_p is the wavelet transform coefficient under consideration, which is the center of a $N \times N$ processing window, and $\Delta Y_k = Y_k - Y_p$ is the difference value between Y_p and the coefficient Y_k ($k=0,1,2,\dots,N^2-1, k \neq p$) of the other points in the $N \times N$ window, Figure(2) shows an example of a processing window with a size of a 5×5 pixels. In this example, Y_{12} is the center of the window, and $\Delta Y_k = Y_k - Y_{12}$ ($k=0,1,\dots,24, k \neq 12$).

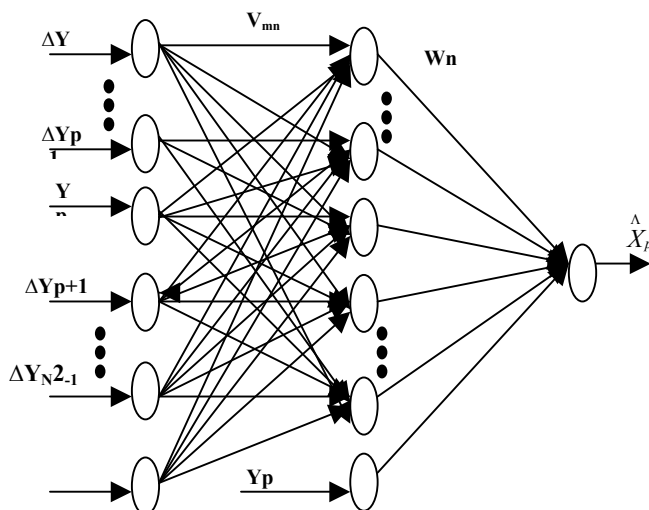


Figure.1 Structure of the neural network

In this figure v_{mn} is the weight of the connection between the m -th neuron in the

input layer and n -th neuron in the hidden layer and is initialized randomly between -1 to 1. w_n is the weight connecting the n -th neuron in the hidden layer to the neuron in the output layer and is initialized as randomly between -1 to 1.

Y_0	Y_1	Y_2	Y_3	Y_4
Y_5	Y_6	Y_7	Y_8	Y_9
Y_{10}	Y_{11}	Y_{12}	Y_{13}	Y_{14}
Y_{15}	Y_{16}	Y_{17}	Y_{18}	Y_{19}
Y_{20}	Y_{21}	Y_{22}	Y_{24}	Y_{25}

Fig.2 5×5 processing window

3.1 TRAINING THE LAYERED NEURAL NETWORK

In this paper, neural network is trained using back propagation algorithm. In this algorithm, first error is calculated between the noise free coefficients and the output of the neural network. Error is back propagated to output and hidden layer. According to the error weights are updated. This algorithm minimizes the output error by updating the weights based on the gradients of the output error. The proposed algorithm is as follows: The input 25 elements are normalized using the formula as given:

$$NV = \frac{2(y - y_{\min})}{y_{\max} - y_{\min}} - 1 \quad (1)$$

Where y_{\min} is minimum value among the 25 values. y_{\max} is the maximum value among the 25 values. NV is the normalized value between -1 to 1. The net input to the hidden layer is calculated as[7]:

$$net_{hn} = \sum_{m=0}^{N^2+1} i_m v_{mn} \quad (2)$$

The output of the hidden layer is calculated as:

$$z_n = f_h(\text{net}_{hn}) \quad (3)$$

where i_m is the m -th input of the input layer and takes its from set $(\Delta y_0, \Delta y_1, \dots, \Delta y_{24}, y_P, 1)$, and activation function of the hidden layer is selected as:

$$f_h(x) = \frac{2}{1 + e^{-\lambda x}} - 1 \quad \lambda > 0 \quad (4)$$

In this work, the λ value is taken as 1.

The net input to the output layer is calculated as[7]

$$\text{net}_o = \sum_{n=0}^{N^2+1} z_n w_n \quad (5)$$

The output of the output layer can be formulated as:

$$\hat{X}_p = f_o(\text{net}_o) \quad (6)$$

Where \hat{X}_p is the output of the neural network at pixel under consideration and the activation function of the neuron in the output layer is of the following form:

$$f_o(x) = \frac{2}{1 + e^{-\lambda x}} - 1 \quad \lambda > 0 \quad (7)$$

The value of the λ here is 1.

The update equations of the weights and function coefficients are as follows[7] :

$$\begin{aligned} v_{mn}^{k+1} &= v_{mn}^k - \alpha \frac{\partial E}{\partial v_{mn}} \\ &= v_{mn}^k - \alpha \frac{\partial E}{\partial o} \frac{\partial o}{\partial \text{net}_o} \frac{\partial \text{net}_o}{\partial z_n} \frac{\partial z_n}{\partial \text{net}_{hn}} \frac{\partial \text{net}_{hn}}{\partial v_{mn}^k} \\ &= v_{mn}^k + \alpha(d-o)f_o'(net_o)w_n f_h'(net_{hn})i_m \end{aligned} \quad (8)$$

$$w_n^{k+1} = w_n^k - \beta \frac{\partial E}{\partial w_n} = w_n^k + \beta(d-o)f_o'(net_o)z_n \quad (9)$$

In the above equations, $E = (d_i - o_i)^2 / 2$ is the square error, d_i is the Noise free coefficients, o_i is the output of the neural network, and α , β are the learning factors. Here α , β are initialized as 0.8 and 0.6. Weights are updated based on error accordingly. Finally neural network will give the noise removed coefficients. They are value between -1 to 1. It should be denormalized to obtain the original value. The equation for denormalization is as follows:

$$DNV = \frac{(NV+1.0)*(x_{\max} - x_{\min})}{2.0} + x_{\min} \quad (10)$$

Where DNV is the denormalized value. NV is the noise free coefficients from the neural network. The LNN filter explores the strong correlation between the pixel under consideration and its neighbors and utilizes the mapping function of the layered network to remove the white Gaussian noise.

3.2. PROCEDURAL STEPS INVOLVED IN LNN FILTER METHOD

The steps involved in this method are as follows[6] :

- Step 1: A noisy image is decomposed into four subbands using a wavelet transform. Here Daubechies wavelets family is applied.
- Step 2: For each subband, a layered neural network is properly designed.
- Step 3: Each of the LNNs is trained using one of the four subbands of the decomposed image. All the four LNN have same structure.
- Step 4: The inputs to the neural network are derived from an NxN neighborhood of the transformed image. Here we have taken 5x5 window. It consists of

25 elements. They are given as inputs to the neural network. Before applying to the network the inputs are normalized.

- Step5: Back propagation is used to train the network. The activation functions used are bipolar activation for both hidden and output layer. Weights are updated according to the error criterion. This algorithm minimizes the error by adjusting weights accordingly.
- Step 6: After the training process, the four LNNs are applied to the corresponding subband of the wavelet transformed noisy image.
- Step 7: The outputs of the networks are normalized noise-removed coefficients. Hence it is denormalized using original image to obtain original value of the noise removed wavelet coefficients.
- Step 8: The denoised image is obtained by performing an inverse wavelet transform on the noise free wavelet coefficients.

4. SIMULATION AND RESULTS

This algorithm is implemented using Matlab6.5. The LNN filter was implemented and the computer simulation results are presented. We used cameraman and parrots image of size 256 x 256 are used as the test image. Noises of different decibels are added and the denoised images are produced. The Daubechies wavelet family(db2) is used and one level 2D DWT of noisy image is taken.

The noisy images of above are used for training the neural network. PSNR(in dB) is used as performance measure for comparing the quality of denoising. The PSNR is calculated using the formula

$$PSNR = 10 * \log_{10} \frac{\sum_{i=1}^M \sum_{j=1}^N Original\ image^2}{\sum_{i=1}^M \sum_{j=1}^N (Original - noise)^2} \dots\dots(11)$$

Where NxN is the size of the image.

Table 1 - shows the PSNR values of the Noisy image of cameraman image and PSNR value obtained from proposed method and standard denoising methods. It shows that the PSNRs of the images are improved at all of the noise levels. The table also shows that the proposed method outperforms all of the standard methods.

The Figure 3 shows that output images obtained for cameraman image when noise level is 20 dB.

Figure 4 shows that output images obtained for parrots image when the noise level is 25 dB.

Simulations demonstrate that the proposed method can remove the noise efficiently, and improve the visual quality of the degraded image.

5. CONCLUSION AND FUTURE WORK

In this paper, a neural network based non linear filter in wavelet domain is constructed for the removal of noises in digital images. In this method LNN learn the correlation of the wavelet coefficients and generate the noise-removed values from their noisy versions. Simulation demonstrates that it can efficiently remove the noise, and improve the visual quality of the degraded image. The LNN filter method requires no priori knowledge about the noise and needs only one level of signal decomposition to obtain very good denoising result. In terms of PSNR, this method outperforms the standard denoising methods. This work can be extended by using

functional link neural network to reduce the computation complexity and time.

REFERENCES:

- [1]. Xiao-Ping Zhang, “Thresholding Neural Network for Adaptive noise Reduction”, IEEE, 2001.
- [2]. R.C. Gonzalez and R.E Woods, “Digital Image Processing” , Addison Wesley reading, MA, 1992.
- [3].Raghuveer M. Rao, and Ajit S. Bopardikar, “ Wavelet Transforms”, Pearson Education”, 2004.
- [4]. K.P. Soman and K.I Ramachandran, “Insight into Wavelets”, Prentice-hall India, 2004.
- [5] Dr. S.N. Sivanandam, and Dr. Paulraj, “Introduction to Neural networks” , Vikas Publications, 2003.
- [6].S. Zhang and E. Salari, “Image Denoising using a Neural Network based Nonlinear filter in Wavelet domain”, ICASSP 2005.
- [7]. S. Zhang and E. Salari, “A Neural Network based Nonlinear filter for Image Enhancement”, Wiley Periodicals, 2002.

ORIGINAL IMAGE NOISY IMAGE LNN FILTER METHOD



SOFT THRESHOLDING HARD THRESHOLDING WIENER FILTER



Figure 3. Output images obtained for cameraman image when the noisy level is 20 dB

ORIGINAL IMAGE NOISY IMAGE LNN FILTER METHOD



SOFT THRESHOLDING HARD THRESHOLDING WIENER FILTER



Figure 4 Output images obtained for parrot image when the noisy level is 25 dB

TABLE 1 PSNR VALUES OF THE NOISY IMAGE OF CAMERAMAN AND PARROTS BY THE LNN FILTER METHOD AND STANDARD METHODS

INPUT IMAGE AT VARIOUS NOISE LEVELS(dB)	NOISY IMAGE (PSNR)	NOISE REDUCED PSNR(dB)			
		LNN FILTER METHOD	SOFT THRESHOLDING	HARD THRESHOLDING	WIENER FILTER
Cameraman $\sigma = 10$	28.0358	49.2130	27.0826	28.2188	29.0423
$\sigma = 15$	24.5421	49.1069	25.6131	26.1911	28.1453
$\sigma = 20$	22.0035	49.0588	24.4724	24.7728	27.1147
$\sigma = 25$	20.1172	48.9956	23.4326	23.5968	26.2004
Parrots $\sigma = 10$	28.1397	49.9619	29.2103	30.2771	32.3015
$\sigma = 15$	24.6220	50.8412	27.2710	27.7628	30.7722
$\sigma = 20$	22.1618	50.7787	25.8742	26.1187	29.4985
$\sigma = 25$	20.1807	46.6144	24.5230	24.6293	28.2893

Computer Aided Diagnosis System for Pulmonary Nodules Using Hierarchical Feature Extraction

K. Takei
Grad. Sch. of Eng.
Tohoku Univ.
Sendai, Aoba
980-8579

N. Homma, T. Ishibashi
Faculty of Med.
Tohoku Univ.
Sendai, Seiryomachi
980-8575

M. Sakai
Grad. Sch. of Info. Sci.
Tohoku Univ.
Sendai, Kawauchi
980-8576

M. Yoshizawa
Info. Syn. Center
Tohoku Univ.
Sendai, Aoba
980-8579

K. Abe
Col. of Eng.
Nihon Univ.
Koriyama, Tamura
963-8642

Abstract

In this paper, we propose a new diagnosis method of pulmonary nodules in CT images to reduce false positive rate (FP) for a high true positive rate (TP) conditions. An essential core of the method is in its hierarchical feature extraction. In the 1st stage, novel orientation features of nodules in a small region of interest (ROI) are extracted in addition to several conventional features, while a more structural feature of a surrounding area of the ROI is extracted in the 2nd stage. Without the orientation features, when TP was 90%, FP was about 65% and 55% in the 1st and 2nd stage, respectively. On the other hand, using the orientation features, FP was about 15% and only 5% in the 1st and 2nd stages, respectively. These improvement of the discrimination rate clearly demonstrates the effectiveness of the proposed hierarchical method on the nodules diagnosis.

1 Introduction

With the increasing of the mortality rate for lung cancer, computed tomography (CT) has been used for detection of lung cancer at early stages [1]. However, using CT may exhaust for radiologists because CT generates a large number of images (over 30 per patient) and they must read all of them. Therefore, some computer-aided diagnosis (CAD) systems have been developed. Okumura et al. proposed a N-Quoit filter [2]. Lee et al. proposed a nodule detection system using a genetic algorithm [3]. However, although these CAD systems can automatically detect pulmonary nodules with a high true positive rate (TP), the false positive rate (FP) is also high. This is not appropriate for clinical use since such high FP may disturb radiologist's diagnosis process. To reduce FP, several methods have been proposed. Suzuki et al. proposed a massive training artificial neural network (MTANN) for reduction of FP [4]. Nakamura et al.

proposed a nodule recognition system using subspace method [5].

In this paper, we propose a new method to diagnose pulmonary nodules in CT images. Especially, compared to the methods mentioned above, we aim to further reduce FP for a high TP conditions by extracting novel orientation and structural features of the nodules in a hierarchical manner.

2 Discrimination algorithm

The proposed method for discrimination between shadows of nodules and non-nodules mainly consists of 2 stages. In the first stage, nodule candidates are differentiated from the non-nodule ones using novel orientation features of a small size image of region of interest (ROI). On the other hand, in the second stage, a structural feature of surrounding area of the ROI is used for further discriminating the final nodule candidates from the nodule ones in the first stage.

2.1 Discrimination using orientation features of shadows

Orientation information can be very important to recognize shapes of subjects, but as we know, there is no CAD system using effective orientation features of nodules. To extract the orientation features, we may use a gabor filter whose impulse response is defined by a harmonic function multiplied by a Gaussian function. Indeed, due to its orientation selectivity, the gabor filter has been applied to feature extraction problems for various image recognition systems, such as face recognition, fingerprint recognition and so on [6] [7].

2.1.1 Feature extraction

In the first stage, to extract features for nodules and non-nodules recognition, we firstly binarized the

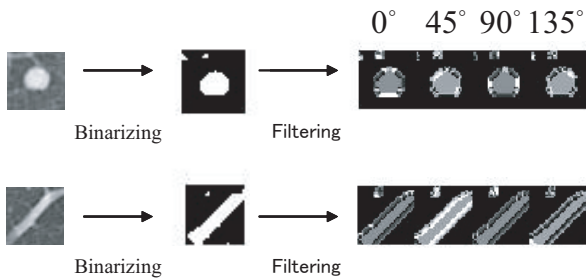


Figure 1: Examples of 4 orientation features.

images in ROI. Then, we extracted M_1 orientation features from the binarized image by using the gabor filter given as

$$g(x, y, \sigma, \lambda, \theta) = \exp \left[-\frac{x'^2 + 2y'^2}{2\sigma^2} - \cos \frac{2\pi x'}{\lambda} \right] \quad (1)$$

where θ is the angle of orientation, σ is the bandwidth, λ is the aspect ratio, and λ is the wave length. x' and y' are, respectively, given by

$$x' = x \cos \theta + y \sin \theta, \quad y' = -x \sin \theta + y \cos \theta \quad (2)$$

The orientation features are obtained from the convolution of the binarized image $I(x, y)$ of the original image $I(x, y)$ and $g(x, y, \sigma, \lambda, \theta)$ given as

$$O(x, y) = I(x, y) * g(x, y, \sigma, \lambda, \theta) \quad (3)$$

Figure 1 shows examples of filtered image of 4 orientations. For the original binarized and each orientation images, we calculated three features (mean, variance, and entropy of intensity). Consequently, by adding $3 \times M_1$ features to the 3 original features, we got total $3 \times (1 + M_1)$ features of the binarized image. Then we defined a feature vector X of $3 \times (1 + M_1)$ features, $X = [x_1, x_2, \dots, x_{3(1+M_1)}]^T$, of nodule or non-nodule image.

2.1.2 Clustering

Using C_1 dominant principal components of the feature vectors X of training data, we made nodule and non-nodule clusters of the binarized images by K -means method [8]. The K -means method algorithm is implemented as

1. Initialize vectors of cluster centroids μ_1, \dots, μ_k .
2. Classify each feature vector X to the cluster \hat{p} with the smallest distance

$$\hat{p} = \arg \min_{1 \leq j \leq k} D(X, \mu_j) \quad (4)$$

where $D(X, \mu_j)$ denotes the Euclidean distance of X and μ_j .

3. Based on the classification, update the cluster centroids as

$$\mu_j = \frac{1}{n_j} \sum_{i=1}^{n_j} X_i^{(j)} \quad (5)$$

where $n_j, j = 1, 2, \dots, k$, are the numbers of nodules or non-nodules in clusters j , and $X_i^{(j)}$ are the i th feature vectors in cluster j .

4. If any clusters centroid is changed, go to step 2., otherwise stop the algorithm.

In determination of the number of clusters k , we employed the cluster validity analysis [8]. The cluster separation measure $\rho(k)$ is defined as

$$\rho(k) = \frac{1}{k-1} \sum_{i=1}^{k-1} \max_{i < j \leq k} \frac{i+j}{ij} \quad (6)$$

where

$$j = \frac{1}{n_j} \sum_{i=1}^{n_j} D(X_i^{(j)}, \mu_j) \quad (7)$$

and

$$i_j = D(\mu_i, \mu_j) \quad (8)$$

j is the intra-cluster distance of cluster j , while i_j is the inter-cluster distance of clusters i and j . The optimal number of clusters \hat{k} is selected as

$$\hat{k} = \min_{1 \leq k \leq L} \rho(k) \quad (9)$$

In other words, the K -means algorithm is firstly tested for all candidates $k = 1, 2, \dots, L$, and after that k which gives the lowest value of $\rho(k)$ is chosen.

However, since $\rho(k)$ decreases as L increases, it is not appropriate to determine the number of clusters by the minimum value of $\rho(k)$ simply. Therefore, in this paper, we employed the local minimum [9]. In other words, we determined L when $\rho(L+1) - \rho(L)$ is maximum, and chose \hat{k} which gives minimum value of $\rho(k), k = 1, 2, \dots, L$.

2.1.3 Determination of candidate clusters

Using the dominant C_1 principal components, we made, respectively, P_1 and Q_1 clusters of nodule and non-nodule images by the method in Section 2.1.2.

Then, we calculated Euclidean distances between test image and all the clusters. Let us consider $(P_1 + Q_1)$ distances $d_{p_1}^{A1}$, $p_1 = 1, 2, \dots, P_1$, from P_1 nodule clusters and $d_{q_1}^{N1}$, $q_1 = 1, 2, \dots, Q_1$, from Q_1 non-nodule ones. The discrimination in this first stage was conducted by comparing the minimum distances $d_{p_1^*}^{A1}$, $p_1 \in p_1$, from the nearest nodule cluster to the distances $d_{q_1^*}^{N1}$, $q_1 \in q_1$, from the non-nodule one. That is, if the ratio $d_1 = d_{p_1^*}^{A1} / d_{q_1^*}^{N1}$ is less than a threshold τ_1 , then the test image can be a nodule candidate, otherwise a non-nodule one.

2.2 Discrimination using structural feature of shadows

In the second stage, we further discriminated the final nodule candidates from the nodule candidates in the first stage by using a structural feature of surrounding area of the ROI which includes nodule or non-nodule shadows. The reason why we pay attention to the surrounding feature is that there are differences between surrounding images of nodules and non-nodules as shown in Fig. 2. That is, even there is no big difference between nodule and non-nodule images in the small ROI, significant structural differences between surrounding areas of them can be found: The nodule tends to exist in isolation comparatively, while the non-nodule tends to exist with other shadows (vessel etc.).

To extract such structural feature, we used the fractal dimension of the surrounding area. The fractal dimension is a statistical quantity that gives an indication how completely a fractal appears to fill space. In fact, usefulness of the fractal dimension to quantify image structures has widely been reported in CAD systems [10][11]. The brief explanation of the algorithm in this second stage is as follow.

We binarized the surrounding images of shadows and calculated the three features of mean, variance and entropy by the same method as in the first stage. We also calculated the new feature of the fractal dimension using box counting algorithm [10][11]. For the original and M_2 orientation, i.e., $(1 + M_2)$ images, three and one new $(3 + 1 = 4)$ features are calculated. Consequently, we got total $4 \times (1 + M_2)$ features of the surrounding binarized image. Using dominant C_2 principal components of the $4 \times (1 + M_2)$ features of nodule and non-nodule training images, we made, respectively, P_2 nodule and Q_2 non-nodule clusters. Let us denote the minimum distance $d_{p_2}^{A2}$, $p_2 \in p_2 = 1, 2, \dots, P_2$, from the nearest nodule cluster and $d_{q_2}^{N2}$, $q_2 \in q_2 = 1, 2, \dots, Q_2$, from the nearest non-

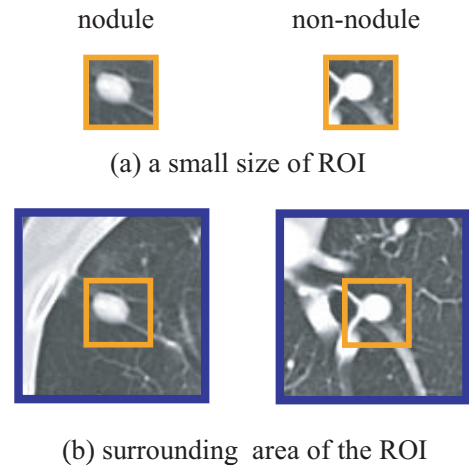


Figure 2: Examples of the surrounding images.

nodule cluster. If the ratio $d_2 = d_{p_2^*}^{A2} / d_{q_2^*}^{N2}$ is less than a threshold τ_2 , then the test image can be a nodule, otherwise a non-nodule.

3 Experimental results

We used 97 nodule data (59 training image and 38 test image) and 174 non-nodule data (104 training image and 70 test image) from the database [12]. Image's size was 33×33 and 99×99 pixels in the first and second stages, respectively. Gabor filter's parameters σ , λ , and θ were 1.5, 2.6 and 1, respectively. The numbers of clusters P_i and Q_i , $i \in \{1, 2\}$, orientations M_i , principal components C_i are shown in Table 1. The M_i was determined empirically, and the C_i was determined as the minimum value that satisfies the condition $\sum_{j=1}^{C_i} u_j > 0.95$, where u_j is the contribution ratio of principal component j .

Figure 3 shows the 4 receiver operating characteristic (ROC) curves by 4 different methods. Without 12

Table 1: Experimental conditions.

Number of	1st stage	2nd stage
Nodule clusters	$P_1=3$	$P_2=2$
Non-nodule clusters	$Q_1=15$	$Q_2=3$
Orientations	$M_1=4$	$M_2=4$
Principal componets	$C_1=5$	$C_2=4$

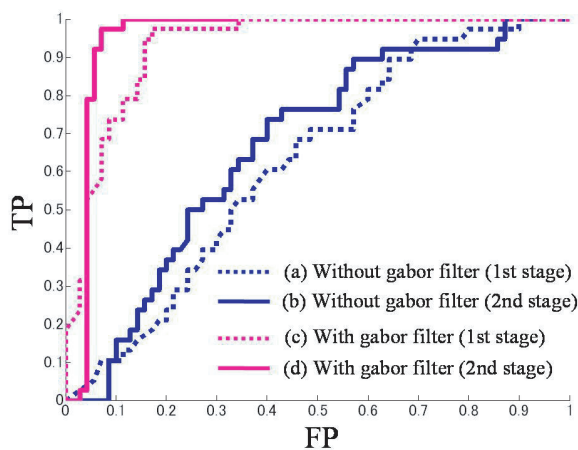


Figure 3: Comparison of ROC curves by using (a) conventional, (b) fractal, (c) orientation, and (d) orientation and fractal features.

features of 4 orientation outputs extracted by the gabor filter, FP was, respectively, about 65% and 55% in the first and second stages when TP was 90%. On the other hand, by using gabor filter, FP was about 15% (first stage) and 5% (second stage). The improvement of the discrimination rate, i.e. from 65% to 15% and from 55% to 5% in the first and second stages, respectively, clearly demonstrates effectiveness of the orientation and surrounding features on the pulmonary nodules diagnosis. In addition to this, FP was about 35% under the same condition by using a MTANN [4]. Although this rate can be improved if we could choose more suitable settings for the MTANN, we may claim that the discrimination rate of the proposed method is the same level or more than that of the MTANN.

4 Conclusion

We have proposed a new diagnosis method of pulmonary nodules in CT images. The results demonstrated that the proposed method can further reduce FP under a high TP condition compared to the conventional ones. This improvement has been achieved by extracting new orientation features of nodules in the small ROI using the gabor filter and by the hierarchical combination with the structural feature quantified by the fractal dimension of the larger area surrounding the ROI.

References

- [1] T. Iinuma et al., "Preliminary specification of X-ray CT for lung cancer screening (LSCT) and its evaluation on risk-cost-effectiveness," *Nippon Acta Radiologica*, Vol. 52, pp.182-190, 1992. (in Japanese)
- [2] T. Okumura et al., "Variable-N-Quoit filter applied for automatic detection of lung cancer by X-ray CT," *Proc. of Computer-Assisted Radiology*, pp.242-247, 1998. (in Japanese)
- [3] Y. Lee et al., "Nodule detection on chest helical CT scans by using a genetic algorithm," *Proc. of IASTED International Conference on Intelligent Information Systems*, pp.67-70, 1997.
- [4] K. Suzuki et al., "Massive training artificial neural network (MTANN) for reduction of false-positives in computerized detection of lung nodules in low-dose computed tomography," *Med.Phys*, Vol. 30 (7), pp.1602-1617, 2003.
- [5] Y. Nakamura et al., "Recognition of X-ray CT image using subspace method considering translation and rotation of pulmonary nodules," *TECHNICAL REPORT OF IEICE*, MI2004-102, pp.119-124, 2005. (in Japanese)
- [6] K. C. Chung et al., "Face recognition using principal component analysis of gabor filter responses," *Proceedings. International Workshop on 26-27 Sept*, pp.53-57, 1999.
- [7] C. J. Lee et al., "A Gabor filter-based approach to fingerprint recognition," *IEEE Workshop on 20-22 Oct*, Vol. 52, pp.371-378, 1999.
- [8] C. W. Ngo et al., "On clustering and retrieval of video shots through temporal slice analysis," *IEEE Trans. Mlt.*, Vol. 4, No.4 pp.446-458, 2002.
- [9] S. Hattori et al., "Video classification based on video description space," *TECHNICAL REPORT OF IEICE*, CS2003-150, pp. 55-60, 2003. (in Japanese)
- [10] S. Kido et al., "Fractal analysis of interstitial lung abnormalities in chest radiography," *Radiographics*, Vol. 15, pp. 1457-1464, 1995.
- [11] T. Ishida et al., "Trabecular Pattern Analysis using Fractal Dimension," *Japanese Journal of Applied Physics*, 32 Part1(4), pp. 1867-1871, 1993.
- [12] National Cancer Imaging Archive (NCIA), <https://imaging.nci.nih.gov/ncia/faces/baseDef.tiles>

Segmentation and tracking of cells in the image sequences

Tomasz Kubik[†]

Masanori Sugisaka^{*}

[†] Institute of Computer Engineering, Control and Robotics, Wrocław University of Technology,
Janiszewskiego 11/17, Wrocław 50-372, Poland

E-mail: Tomasz.Kubik@pwr.wroc.pl

^{*} Department of Electrical and Electronic Engineering, Oita University,
700 Dannoharu, Oita 870-1124, Japan

E-mail: msugi@cc.oita-u.ac.jp

Keywords: cells tracking, image processing

Abstract

In the paper the method of automated cells tracking in the sequence of images is presented. The method starts with a sequence of images processing by the use of an adaptive threshold operator. Then the cells are detected, labeled and parameterized by their size, position, orientation, bounding box, etc. Each pair of two consecutive images in the sequence is analyzed next in order to find corresponding (i.e. matching) cells. In that way all observed cells might be recognized and traced. The tracking, associated with cells parameters measurements, provides data in a form of time series. This data can be used for a particular cell activity observation, complex interaction modeling of multicellular organisms, etc. Such analysis can give detailed information about cells time-space dynamics. The method proposed is demonstrated on a set of biological data.

1 Introduction

In the biological research in vivo live confocal microscopy has enabled scientists to perform observation and store their results for further analysis, [1]. Usually the data is available in the form of sequences of images with time stamps assigned. Especially the GFP (*Green Fluorescent Protein*) images became the sources of valuable data. It comes from the fact that GFP intensity may reflect protein concentration and thus GFP intensity observation within a cell can serve as a method of its inspection. In the consequence the data provided can be used for cells activity observation, complex interaction modeling of multicellular organisms, cell growth and proliferation examination, gene expression modeling, etc. But to draw valid conclusions or build models with a great accuracy the amount and quality of collected data should

be significant enough. Because the amount of data to be analyzed is huge usually, there is a need for automated data processing. The problems of GFP fluorescence intensities measurements and cells tracking were concern in [2, 3].

In this paper we present the method of automated cells tracking in the sequence of images, which is based on image segmentation. The method proposed assumes that sampling rate of image taking is fast enough to assure that a new cell positions and old cell positions on two consecutive images are relatively closed. The methods consist of some computation steps, which are repeated for each image in the sequence analyzed. Thus, the computation starts with an image processing by the use of an adaptive threshold operator. Then the cell detection is done. The cells detected are labeled and parameterized by their size, position, orientation, centroid, bounding box, etc. (recognition of cell splits and merges events is not addressed here, for the details on this problem please refer to [4]). Two consecutive images in the sequence are analyzed then in order to find corresponding cells. The result of tracking can be used for many purposes. It can serve, for example, as a base for the changes in the cells color intensities detection. The averaged intensity within a cell can be interpreted as a relative protein concentration, while the number of a particular image corresponds to the time of observation. Other cell attributes (such as: position, size) can be used to observe the cell movement and growing dynamics. The method is demonstrated on a set of biological data which is a sequence of images with living cells colonies.

2 Cell tracking algorithm

The cell tracking problem can be formulated as follows: Given a sequence of images with species, de-

termine the positions of each cell at each time point (track cells through time). In the method proposed we assumed that the images are captured from a video stream with a preset sampling rate, and stored in a sequence for the further processing. Thus the idea of the algorithm proposed can be expressed as follows:

- segment each image in the sequence in order to find the areas covered by the cells (create a segmented image for each original image in the sequence);
- analyze the original images within areas corresponding to the areas found (analyze the interiors of the cells detected, and extract individual cell attributes such as: cell placement, shape, average of lightness, etc.);
- find the matching cells for every two consecutive images in the sequence and evaluate the dynamics of parameters changes and cells movements (identify the same cells on two consecutive images using cells attributes just extracted, and estimate dynamics of changes knowing the time slice's length between two image captures).

In a confocal microscopy the observations can be captured by different video capturing devices. It may happen, that a lighting conditions in the experimental setup are varying due to some reasons (voltage instabilities for example may produce different lighting intensities). More over, the distribution of the lighting can be non uniform (most often the distribution is radial as a result of the light source's characteristic). Thus before performing any observation some preliminary steps are needed. These steps can include a lighting distribution measuring in an experimental setup without species. The result of such steps can be used later to adjust the observed light intensities by removing a non uniform background. The influence of the varying lighting intensity can be canceled by the intensity tuning during image processing. The following subsection provides some clues on the way it can be done.

2.1 Adaptive threshold operator

The cell detection method discussed in the next section requires that the images provided are monochromatic with different colors for the background and the areas of interest. The simplest way to create such images is to apply the threshold operator on the re-quantized original images (images with a reduced number of colors). But the threshold value can not be kept on the same level for all images. If it would be

so, the varying lighting intensities would cause filtering out underexposed cells, or accepting overexposed background as an area of interests. The solution to this problem can be an application of an adaptive threshold operator.

The adaptive threshold operator uses the threshold level which is calculated on the base of the histogram of the re-quantized original image. It appeared (see Figure 2) that all histograms of the re-quantized images in the sequence analyzed were of the similar shape. The maximums of histograms were observed for the values which were standing in correspondence to the lighting intensities. Thus the threshold value in the adaptive threshold operator can be calculated as follows:

$$v_t = x_{MAX} + d \quad (1)$$

where v_t is the threshold value, x_{MAX} is the most often observed pixel intensity in the re-quantized original image, d is a parameter which assure the proper background elimination (in the experiments performed this value was set to 4).

2.2 Cell detection

The images obtained after adaptive threshold operator application contains areas of interest. These areas are groups of pixels but not objects yet. To find the objects the following algorithm is proposed:

let A, B, T, O be the colors of pixels belonging to, respectively, the area of interest, the background, the temporary area, and the area of an object.

1. trace an image starting from the upper left pixel in order to find a pixel whose color is A
2. beginning with the pixel found fill the area with a color T
3. extract parameters of the area filled in 2 (size, position, orientation, centroid, bounding box, etc.)
4. if the area filled in 2 is interesting (is a cell), fill it with a color O and memorize the parameters of it in a list, otherwise fill this area with a color B
5. repeat 2, 3, 4 until the lower right pixel is not reached

The fill procedure (step 2) tries to mark all connected points having the same color A with a color T , starting from a given pixel. This procedure returns the bounding box of the area filled. There are, of course, several more general algorithms for region filling, which are

working with non monochromatic images. In these algorithms some criterions are defined, which are used to classify the neighboring pixels as belonging to the region being filled or not. In our case we have an image obtained after adaptive threshold operator use, so the areas of interest are already filled. Now we want to know, what kind of the object is represented by each area, and what are the objects parameters. Thus our fill method is used mainly to find the bounding box of the area filled. Having bounding box we can simply extract objects parameters by looking at pixels in this box and at corresponding pixels in the original image (step 3).

There might be several objects parameters. One of the most important parameters of the object is the position of its geometric center. This parameter is used in the corresponding objects finding (see section 2.3). The coordinates of the object center expressed in the coordinate frame associated with a bounding box can be calculated from the formula:

$$x_c = \frac{M_{10}}{M_{00}}, \quad y_c = \frac{M_{01}}{M_{00}} \quad (2)$$

where: $M_{ji} = \sum_{x,y} \sigma(x_j, y_i) x_j \cdot y_i$ is a spacial moment; $\sigma(x_j, y_i)$ is an indicator function which returns 1 if a pixel at position (x_j, y_i) has color T , and 0 otherwise. The average intensity of the cell, avg , can be calculated from the formula:

$$avg = \sum_{x,y} \frac{I(x + dx, y + dy)}{M_{00}} \quad (3)$$

where dx, dy are the coordinates of the upper left corner of the bounding box expressed in the image coordinate frame. Several other parameters can be obtained in similar manner.

It is not known, weather objects detected are cells or uninteresting parts of the observed field. Once the objects parameters are extracted, the task of objects identification becomes a problem of classification with extracted parameters as features. Finding the correspondence between cells at different time points simplifies then to finding the correspondence between cells detected on the consecutive images.

2.3 Cell tracking

The problem of finding correspondences between image objects is well known in the computer image analysis field. It can be NP-complete, if an object in one image potentially match every object in another image. To limit the number of possible matches we propose to consider the distance between matching candidates. The assumption we have made about

the sampling rate allows as to define matching candidates as objects from two consecutive images which are most closely, and lying within a distance which does not exceed an assumed limit. Lets assume that the detection of cells ended successfully and the cell parameters have been collected. Thus to find the matching candidates for an object from one image it is enough to search for them in the second image within a circular area centered at the object center. The matching object should be the closest one (and most similar one, if we take into account extracted earlier objects parameters). If there is no matching objects it means, that cell "disappeared". The correspondence analysis can be summarized with some information about cells movements, appearance, etc.

3 Experiments

The experiments were performed on the sequence of captured images, which was processed off-line. Each captured image was, in fact, a frame of 672×512 pixel size, stored in 48 bit grayscale image format. The images were converted into 8 bit grayscale and then processed by the method described. In the Figure 1 the characteristics of the lighting conditions we met can be observed. It is clear, that the radial background intensity should be considered. The use of an

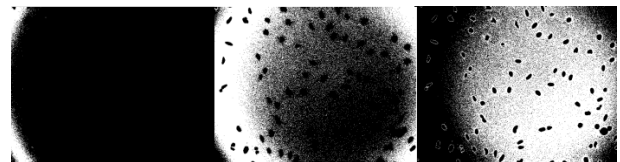


Figure 1: Three pictures representing the same image after filtering with gradual increased threshold.

adaptive threshold operator was connected with histogram's analysis. In the Figure 2 two histograms (in a logarithmic scale) are shown. In most cases the histograms were similar. Thus on the base of observations the value of d parameter (equation (2)) was set to 3. After thresholding the objects detection was done. For each object detected different parameters were extracted (this included object's area and position of its center). The objects detected with the area of 20 pixels were filtered out. The rest of the objects was classified as cells. The cells centers calculated are shown in the Figure 3b) as black dots within cells interior. The part a) of this figure represent the first, original image in the sequence analyzed. The part b) represents final

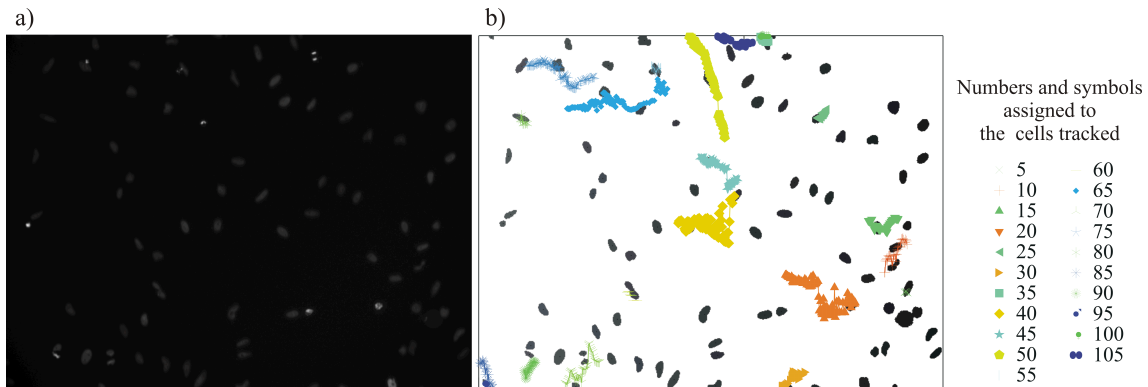


Figure 3: The first image in the sequence of 238 original images analyzed, a); and results of 21 cells tracking with cells detected for the first image in the background, b).

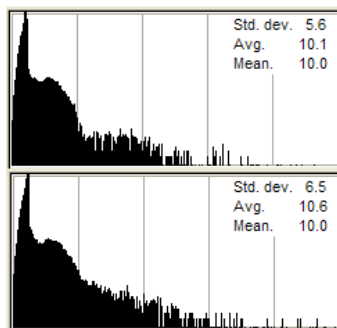


Figure 2: Histogram examples of images analyzed, drawn in the logarithmic scale.

results of cell tracking. For better visualization the tracks of 21 chosen cells are shown only.

4 Conclusions

In the paper a method of automated cells tracking was presented. The method was successfully applied to the sequence of GFP images of biological species. For the good method's performance method parameters tuning might be necessary.

The data used in the experiment performed were processed off-line, but processing on-line is also possible. The experiments showed, that adaptive thresholding shortens the time necessary for cells detection and their parametrization coming next (the thresholding depends on the image histogram shape). The cell tracking was implemented as a problem of cell matching on two consecutive images, while the sampling time provided the clue about time line. The cells param-

eters found were extensively used there (cells parameters are calculated on the base of cells detected in a thresholded image and image intensities inside corresponding areas of the original image).

The data collected during processing can be used for different purposes, for example for a particular cell activity observation, intercellular processes modeling, complex interaction modeling of multicellular organisms, etc.

Aknowledgement: We would like to thank Lukasz Miroslaw for his contribution to this work.

References

- [1] V. Gor, T. Bacarian, M. Elowitz, and E. Mjølness: Tracking Cell Signals in Fluorescent Images. In *Proceedings of the 2005 IEEE Computer Society Conference on Computer Vision and Pattern Recognition (CVPR05)*, (2005).
- [2] L. Vincent and P. Soille: Watersheds in digital spaces: an efficient algorithm based on immersion simulations. *Trans. Patt. Anal. Mach. Intell.*, 13(6), (1991).
- [3] H. Shen, G. Nelson, S. Kennedy, D. Nelson, J. Johnson, D. Spiller, M. R. White, and D. B. Kell: Automatic tracking of biological cells and compartments using particle filters and active contours. *Chemometrics and Intelligent Laboratory Systems*, 82(1-2):276-282, (2006).
- [4] J. Withers and K. A. Robbins: Tracking cell splits and merges. In *Proceedings of the IEEE Southwest Symposium on Image Analysis and Interpretation*, (1996).

Level Set Methods and Auto-Relation for Detection of Objects

Xin Wang^{1,2} Masanori Sugisaka² Jin Wang³

¹Department of Electrical and Information, Niihama National College of Technology, Japan

²Department of Electrical and Electronic Engineering, Oita University, Japan

³College of Textile & Garments, Hebei University of Science and Technology, China

Abstract

This paper presents a framework for detecting objects in images. The motive of this research can be found in onsite requirements. We focus on the practical need on distinguishing salt called purity from impurities, which are sand, soil, and other substance in the heaped salt on a conveyer belt. In this work, basing on image energy, we formulate the auto-relation function on image energy to construct a piloting set which includes possible elements to classify objects and the impurity object in order to lead the front propagation. We use level set method to detect the topologic changes for evolution curves and to catch the objects/impurity.

1. Introduction

Image vision technology has matured substantially in the last decade to be successfully applied to a variety of industrial tasks. Three methods, optical device-based, algorithm-based technology and special image device-based are the main in industrial applications. In the field of factory automation, successful applications of image technology are roughly divided into assembling and inspection. For example to decide a 2D positions as analogical robot sensor or 3D positions when measuring automobile's body, surface inspections, inspecting LSI pattern, and mask and printing board etc [1][2][3][4]. With the development of cheaper color cameras, more people have been more and more interested in digital image application or algorithm technologies [5][6][9]. There are many successful industrial applications in the past years, but the past works mostly depend on the constraints of possible pattern matching. Image technologies for applications, especially in industry, are strong case-dependence. Because we want to solve our problem by image technology instead of paying more cost to some special material inspection sensor device, it is our intelligent selection to develop the image algorithm.

The aim of this paper is to introduce level set methods based on the auto-relation techniques and provide a basic framework for applications. The key idea of Level set methods in image plane is implicit curve evolution in the planer image. We notice the fact that when purity and impurity are mixed in an images, their different textures and gray values are certainly bringing about gradients changes. These changes show

us a lot of clues for image classification and recognition. We induce the propagating interfaces by those high image energy parts to label the object from their background. The evolving surface of impurity is presented as the zero level function. To reduce the computation cost required by level set formulation scheme, a new approach exploited by image auto-relation is proposed. Making a piloting set is a process calculating image energy. It supports level set function a limited domain and speed up evolving front effectively.

The present approach is described as followings. The image pre-process is at the first. This will take us the advantages that the changes we are interested in will not be suppressed by some smoothing, which tends to suppress the effects of noise. We introduce the important auto-correlation method to pilot the interest point in an image. Such a fact has been noticed that the border between sand and soil certainly cause an obviously image energy changes i.e. gray value changes. We will illustrate either how the auto-correlation algorithm catches these changes or how its results give us a coarse pilot on the objectives we are interested in. We want to classify the coarse positions by some local windows, to inspect the detail changes and compare the results with our preset models, which are the features of their Gaussian distributions. Based on the similarities between the results and the models, we judge whether a class is accepted as an object soil or not [14] and these are our following works.

In this paper, we give the auto-relation model in next section. The pre-process and classification are also introduced in the section 2. Section 3 describes the principle of curve evolution based on level set methods. Some experimental results and discussions are at the last.

2. Auto-relation Model

2.1 Image pre-process

In general, any change of significance to us has effects over a pool of pixels. For many kinds of noise model, large image derivatives due to noise are an essentially local event. This means that smoothing a differentiated image tends to support the changes we are interested in and to suppress the effects of noise. In a pre-process, the smoothing filter can be chosen by taking a model of an edge and using some set of



Fig. 1: The soil grains image for test.

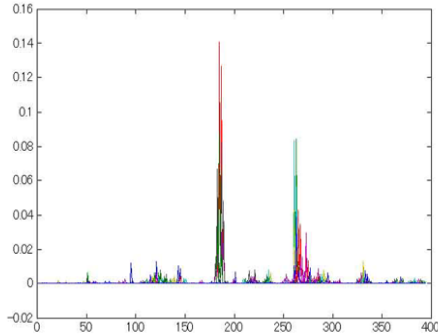


Fig. 2: The horizontal is the horizontal coordinate in Fig.1, the vertical is $\mathcal{M}(X)$ in Eq. (6).

criteria to choose a filter that gives the best response to that model. It is difficult to pose this problem as a two-dimensional problem because edges in 2D can be curved. Conventionally, the smoothing filter is chosen by formulating a one-dimensional problem and then using a rotationally symmetric version of the filter in 2D. In our case, we select a nonlinear rank-value median filter for image pre-process. We take all the gray values of the pixels which lie within the filter mask and sort them by ascending gray value. The rank-value filter only differs by the position in the list from which the gray value is picked out and written back to the center pixel, well known as median filter. Let $\mathcal{M}_1 = \{M_1(n, n)\}$ (n is odd) be those gray values around a pixel. To an array $\mathcal{M}_2 = \{M_2(k)\}$ ($k = 1, 2, \dots, S = n \times n$), this filter use the value $M_2(S/2)$ as it responses. This made us easily adjust the smoothing scales to different size of objects.

2.2 Auto-relation on image energy

Let $I(X)$ (also denoted as I) be the image function in an image frame. Given a shift $(\Delta x, \Delta y)$ and $X = (x, y)$, $X \in \mathcal{R}^2$. The auto-correlation function is defined as:

$$f(x, y) = \sum_w (I(x_k, y_k) - I(x_k + \Delta x, y_k + \Delta y))^2 \quad (1)$$

where (x_k, y_k) are the points in the working local widow w . Based on the Taylor expansion:

$$\begin{aligned} I(x_k + \Delta x, y_k + \Delta y) &= I(x_k, y_k) + I_x(x_k, y_k)\Delta x + I_y(x_k, y_k)\Delta y + \dots \\ &\approx I(x_k, y_k) + (I_x(x_k, y_k) \ I_y(x_k, y_k)) \begin{pmatrix} \Delta x \\ \Delta y \end{pmatrix} \end{aligned} \quad (2)$$

where $I_x = \partial I(X) / \partial x$, $I_y = \partial I(X) / \partial y$. Substituting the above approximation (2) into Eq.(1), we obtain:

$$\begin{aligned} f(x, y) &= \sum_w \left((I_x(x_k, y_k) \ I_y(x_k, y_k)) \begin{pmatrix} \Delta x \\ \Delta y \end{pmatrix} \right)^2 \\ &= \sum_w (\Delta x \ \Delta y) \begin{pmatrix} I_x^2 & I_x I_y \\ I_x I_y & I_y^2 \end{pmatrix} \begin{pmatrix} \Delta x \\ \Delta y \end{pmatrix} \\ &= (\Delta x \ \Delta y) \left[\sum_w \begin{pmatrix} I_x^2 & I_x I_y \\ I_x I_y & I_y^2 \end{pmatrix} \right] \begin{pmatrix} \Delta x \\ \Delta y \end{pmatrix} \\ &= (\Delta x \ \Delta y) [\Gamma(x, y)] \begin{pmatrix} \Delta x \\ \Delta y \end{pmatrix} \end{aligned} \quad (4)$$

To $I(X) = G * \mathcal{I}$, $*$ is the convolution operation, we change $\Gamma(x, y)$ as $\nabla I (\nabla I)^T$, build up a transform relation $\mathcal{H}(X)$ in a local window about X .

$$\begin{aligned} \mathcal{H}(X) &= \mathcal{T}(X) * \sum \{ \nabla I (\nabla I)^T \} \\ &= \mathcal{T}(X) * \sum \left\{ \begin{pmatrix} (G_x * \mathcal{I})^2 & (G_x * \mathcal{I})(G_y * \mathcal{I}) \\ (G_x * \mathcal{I})(G_y * \mathcal{I}) & (G_y * \mathcal{I})^2 \end{pmatrix} \right\} \end{aligned} \quad (5)$$

where G is a Gaussian with standard deviation one, $G_x = \partial G / \partial x$, $G_y = \partial G / \partial y$. $\mathcal{T}(X)$ is a weight mask to weight the derivatives over the window. In Eq. (5), there relations $\partial I / \partial x = \partial / \partial x * \mathcal{I}$, $\partial / \partial x * (G * \mathcal{I}) = (\partial / \partial x * G) * \mathcal{I} = \partial G / \partial x * \mathcal{I}$. This matrix captures the local structure. The eigenvectors of this matrix are the principal curvatures of the auto-correlation function. We consider a cost function $\mathcal{M}(X)$:

$$\mathcal{M}(X) = \mathcal{E}[\mathcal{H}(X)] + \mathcal{C}[\mathcal{H}(X)] \quad (6)$$

where $\mathcal{E}[*]$, $\mathcal{C}[*]$ are the determinant and trace of $\mathcal{H}(X)$ respectively. For example, $\mathcal{M}(X)$ is shown in Fig. 2.

2.3 Image classification

$\mathcal{M}(X)$ in Eq. (6) gives the distributions of image energy clearly. We classify those points by $\mathcal{M}(X)$ further. Assume the i_{th} point $P_i(X)$ be presented by a complex OP_i , the j_{th} point $P_j(X)$ by OP_j , to a constant ϵ_1 , if it is true that

$$|OP_i - OP_j| < \epsilon_1 \quad (7)$$

$P_i(\mathbf{X}(i))$ and $P_j(\mathbf{X}(j))$ are put into same set C^k , $C^k \subset C$. C is defined as the classification set.

$$C = \bigcup_{k=1}^s C^k \quad (8)$$

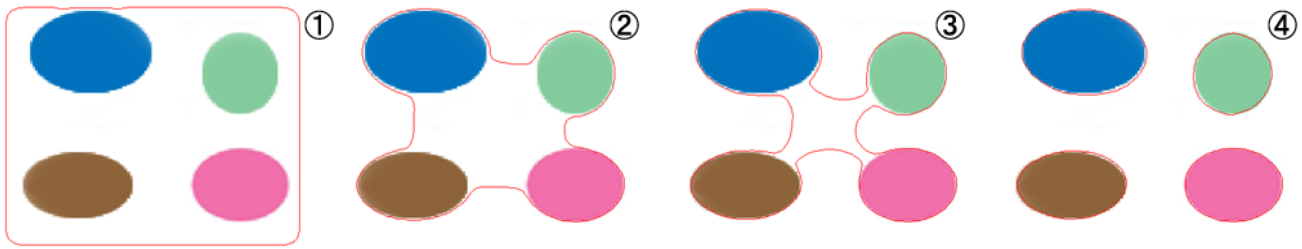


Fig. 3: 1: the initial curve; 2 and 3: the evaluating curve; 4: The entire objects are caught.

where s is a preset constant to decide the subsets in C . The elements in C^k are coarse results classified. Assume the center of gravity of the elements in C^k be $P_c(X)$, $M(X)$ will be recalculated by Eq. (5) and Eq. (6) with a smaller preset constant ϵ_t ($\epsilon_t < \epsilon_{t-1}$, $t \leq \text{constant}$) around $P_c(X)$ in a smaller local window several times. If the results under ϵ_t will be treated as the part of the soil, the calculations finish. The reason we did this is that it is hardly to get complete pixels about the object, for the reasons that the surface of any object reflects light in all direction, smaller ϵ_t can use more fine resolutions to analyze objectives.

3. Skeleton of Level Set Methods

Level set methods add dynamics to implicit surfaces. The key idea that started the level set fanfare was the Hamilton-Jacobi approach to numerical solutions of a time-dependent equation for a moving implicit surface. Given a moving closed hypersurface $\mathcal{G}(t)$, we wish to produce an Eulerian formulation for the motion of the hypersurface propagating along its normal direction with speed \mathcal{F} , where \mathcal{F} can be a function of various arguments, including the curvature, normal direction, etc. This propagating interface is embed as the zero level set of a higher dimensional function $\phi(\mathbf{x}, t)$ (also denoted as ϕ in this paper). Let $\phi(\mathbf{x}, t=0)$, where \mathbf{x} is a n -dimension space, be defined by

$$\phi(\mathbf{x}, t = 0) = D \quad (9)$$

where D is the signed distance from \mathbf{x} to $\mathcal{G}(t=0)$, and plus/minus sign is chosen if the point \mathbf{x} is outside/inside the initial hypersurface $\mathcal{G}(t=0)$. Thus, we have an initial function $\phi(\mathbf{x}, t=0)$ with the property that

$$\mathcal{G}(t = 0) = (x | \phi(\mathbf{x}, t = 0) = 0) \quad (10)$$

Our goal is to produce an equation for the evolving function $\phi(\mathbf{x}, t)$ which contains the embedded motion of \mathcal{G} as the level set $\phi = 0$. Let \mathbf{x} be the path of a point on the propagating front. That is, $\mathbf{x}(t=0)$ is a point on the initial front $\mathcal{G}(t=0)$, and $d\mathbf{x}/dt = \mathcal{F}(\mathbf{x})$ with the vector $d\mathbf{x}/dt$ normal to the front at \mathbf{x} . Since the evolving function $\phi(\mathbf{x}, t)$ is always zero on the propagating hypersurface, we must have the constraint

$$\phi(\mathbf{x}, t) = 0 \quad (11)$$

By the chain rule,

$$\phi_t + \nabla(\mathbf{x}, t)\mathbf{x}_t = 0 \quad (12)$$

We then have the evolution equation for $\phi(\mathbf{x}, t)$

$$\phi_t + \mathcal{F}|\nabla\phi| = 0 \quad (13)$$

with a given value of $\phi(\mathbf{x}, t=0)$. This is referred as Hamilton Jacobi "type" equation because, for certain forms of the speed function \mathcal{F} , we obtain standard Hamilton Jacobi equation. Because $\phi(\mathbf{x}, t)$ remains a function as it evolves, we may use a discrete grid in the domain of \mathbf{x} and substitute finite difference approximations for the spatial and temporal derivatives. We use a uniform mesh of spacing h , with grid nodes ij , and employing the standard notation that ϕ_{ij}^n is the approximation to the solution $\phi(ih, jh, n\delta t)$, where δt is the time step, we may write

$$\frac{\phi_{ij}^{n+1} - \phi_{ij}^n}{\delta t} + (\mathcal{F})(\nabla_{ij}\phi_{ij}^n) = 0 \quad (14)$$

Here, we have used forward differences in time, and let ϕ_{ij}^n be some appropriate finite differences in time, and let $\nabla_{ij}\phi_{ij}^n$ be some appropriate finite difference operator for the spatial derivative. To a given speed function \mathcal{F} , we update the front by the modified version of an Engquist-Osher scheme [11]. The front propagation is illustrated in Fig. 3.

4. Experiments and Discussions

We compute a practical images, which was taken on-site, by the proposed algorithm. In Fig. 4, using the original images on the left, we indicated the processes. Based on the result of Eq. (5) and Eq. (6), the positions of image energy are detected. We have gotten two positions or two significant $M(X)$. Locating the two positions, we give the closed initial front curve for evolution. This decrease the computation cost obviously. The results in Fig. 4 also show us that $M(X)$ bring us less image noise in the closed front curve and, this is very helpful for the recognition using the finished evolution results. Fig. 4-4 show that the contour of the objects are caught perfectly. This is one of successful applications by means of the advantage of the level set based active contour technique.

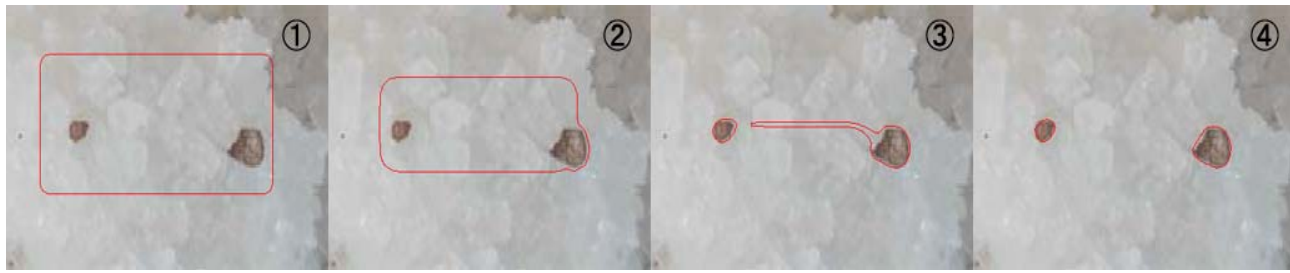


Fig. 4: 1: starting contour based on the image auto-relation; 2 and 3: the evaluating curve; 4: the objects are caught.

5. Conclusions

We proposed in this work a piloted level set methods. This approach uses traditional rank-value median filter as pre-processor, creates an image energy auto-relation function to lead an initial front propagation in order to perform classification and calculate features about their textures and so on for the purpose of recognition. When different kinds of objects/grains appear on the same image, most of them will bring about image energy changes presented by the form of gray gradients. The auto-relation function is excellent way to describe these features, especially in the case of objectives have the global dominant positions in an image, just like the case of the soil-in-salt. The finished front propagation can give more information for recognition. We can adjust the cost constants from coarse to fine in a widow around piloted positions dynamically. Then those features can be compared with their models made in advance. Not limited by this application, the developed technique will be also available when the environment is changed, with some modification. Though this approach faces the problem of computation cost, it still is a basic frame work.

In this algorithm, if the objects don't have an obvious energy features in a global detection, it will cause s in Eq.(8) increased, and hard to be classified. We suggest s should be maximum three, number constrain companies it, or it is an intelligent way to consider this problem from other bases.

Acknowledgements

This research was also done while Xin Wang was employed at Graduate School of Engineering, the University of Tokushima.

References

- [1] A. Kumar, A. Tannenbaum, and G. Balas, "Optical flow: a curve evolution approach," *IEEE Trans. Image Processing*, vol. 5, no. 5, pp. 598-610, 1996.
- [2] R. Green, D. Gray, and J. Powers, *Artificial Vision*, Academic Press, London, 1997.
- [3] G. Carneiro, and A. Jepson, "Phase-based local features," *Computer Vision - ECCV 2002, Part I*, pp. 283-296, 2002.
- [4] W. Yu, K. Daniilidis, and G. Sommer, "Approximate orientation steer ability based on angular Gaussians," *IEEE Trans. Image Processing*, vol. 10, no. 2, pp. 193-205, 2001.
- [5] D. A. Forsyth, J. Ponce, *Computer Vision*, Prentice Hill, USA, 2003.
- [6] W. Kropatsch, R. Klette, F. Solina, and R. Albrecht, *Theoretical foundations of computer vision*, Springer Wien, New York, 1996.
- [7] B. Jähne, *Image processing for scientific applications*, CRC Press, New York, 1997.
- [8] M. Brown, D. Terzopoulos, *Real time computer vision*, Cambridge University Press, 1994.
- [9] H. Zhang, S. Roth, it Camera aided robot calibration, CRC Press, Boca Raton, 1996.
- [10] L. Torresani, C. Bregler, "Space-time tracking," *Computer Vision - ECCV 2002, Part I*, pp. 801-812, 2002.
- [11] B. Engquist, S. Osher, "Stable and entropy satisfying approximations for transonic flow calculations," *Math. Comp.*, vol. 34, 45, 1980.
- [12] S. Osher, R. Fedkiw, *Level Set Methods and Dynamic Implicit Surface*, Springer, USA, 2003.
- [13] J. A. Sethian, *Level Set Methods and Fast Marching Methods*, Cambridge University Press, 2002.
- [14] X. Wang, M. Sugisaka, W. Xu, "Image Energy Pilot, FA Soil-Salt Recognition Approach," Proc. of the 4th Int. Conference on Advanced Mechatronics-Toward Evolutionary Fusion of IT and Mechatronics, CD-ROM. 2004.
- [15] X. Wang, M. Sugisaka, J. Wang, "Auto-Correlation Probabilistic Relaxation Matching Method," Proc. of the 11th Int. Symposium on Artificial Life and Robotics, Vol.2, CD-ROM, Jan. 2005.
- [16] X. Wang, M. Sugisaka, W. Xu, "Feature point based object tracking," *IEEJ Transactions on Electronics, Information and Systems*, Vol.124, No.8, pp. 1585-1591, 2004.

Motion trace in real-time processing

Eiji GOUBARU Masanori SUGISAKA

Department of Electrical and Electric Engineering, Oita University
700 Dannoharu Oita 870-1192 Japan.

E-mail: msugi@cc.oita-u.ac.jp

Abstract

Recent years, researches about visual tracking are extensively studied. If we can visual tracking, we can apply the skills of automotive control and so on. For example, if obstacle avoidance of moving object instead of obstacle avoidance of the static object becomes possible, the control becomes possible as for a more complex situation. Facial recognition was researched in my laboratory, however, this research is weak of change in light, so that my main research improve that and to motion trace through head control of mobile robot.

1 Introduction

Recent years, the introduction of robot was been considered in various fields. Various functions were been required and the robot use was expanded. One of the functions requires environmental recognition and avoidance of an obstacle. In order to develop such robot, this laboratory, for some time, has mainly respond to the field of welfare and nursing. A mobile recognition robot has been researched and developed [1][2][3].

Researches about visual tracking are extensively studied. In this research, the following are conditions.

- (1) Moving object is red circle marks.
- (2) Moving object is near the CCD camera.

We used our laboratory robot. Image import from CCD camera, we compute feature point and center point to track moving object, and implement motion control of the head.

2 Experiment System

The robot which is being used in this research was manufactured by incorporated company DENKEN in 2000. The figure is shown in Fig.1. It consists of 2 drive 2 caster (2DC2W) systems.

The mobile robot is equipped on the right and left with the driving wheel, auxiliary caster rings at the front and back, a driving wheel on either side rotates by DC motor. Equipped with the rotary encoder of resolution 80 (Pulse Per Resolution) beside the driving wheel, and counting the number of pulses, the right-and-left independence can be achieved and a wheel can be controlled.

The difference in the rotation speed of a right-and-left driving wheel performs a steering function. The CCD camera (EVI-G20: Sony) is carried by the height of about 130 [mm] at 55 degrees of perpendicular directions at the head. The picture obtained from the camera is taken in by the memory on an image-processing board (FDM-PCI3: FOTORON).



Fig. 1 View of The Mobile robot

3 Image Processing

3.1 Pixel Skipping

When the size of image is 300 by 300 [pixel], it is difficult to implement in real time processing, when the size of picture is small, moving object will be not detected.

In order to make realize real time processing, image processing time must be shortened. Therefore, by setting the area of pixel which to be removed and to be taken the image is processing again by re-sizing and showing only

the taken pixel area. In this research, re-sizing of image is 60 by 60. Fig. 2 shows that gray color is taken pixel area.

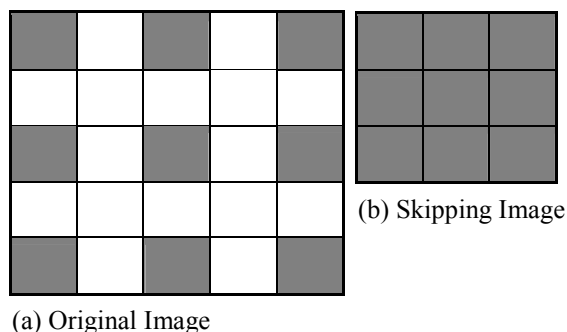


Fig. 2 Pixel Skipping

3.2 Conversion From RGB To HSI

The image is taken in from a CCD camera; it is a picture expressed with a total of 24 bits of 8 bits each of RGB. Then, in order to treat the feature from a picture independently as much as possible, the following equation performs HSI conversion of the hue, saturation and intensity. Each of R, G and B is standardized to take values between 0 and 1, with a maximum total intensity of 1. Following equations are Hue, Saturation and Intensity.

$$I = \max(R, G, B) \quad (1)$$

$$S = 255 \times \frac{I - \min(R, G, B)}{I} \quad (2)$$

$$H = \begin{cases} 60 \times \frac{G - B}{I - \min(R, G, B)} & (\max(R, G, B) = R) \\ 60 \times \frac{B - R}{I - \min(R, G, B)} + 120 & (\max(R, G, B) = G) \\ 60 \times \frac{R - G}{I - \min(R, G, B)} + 240 & (\max(R, G, B) = B) \end{cases} \quad (3)$$

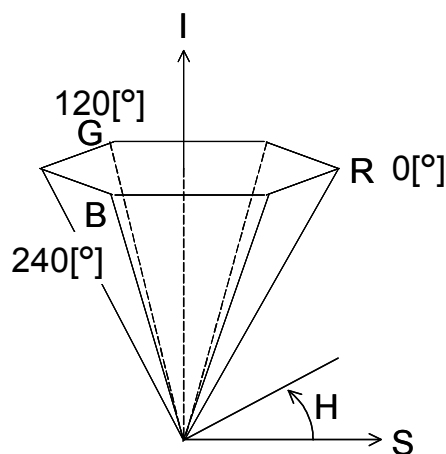
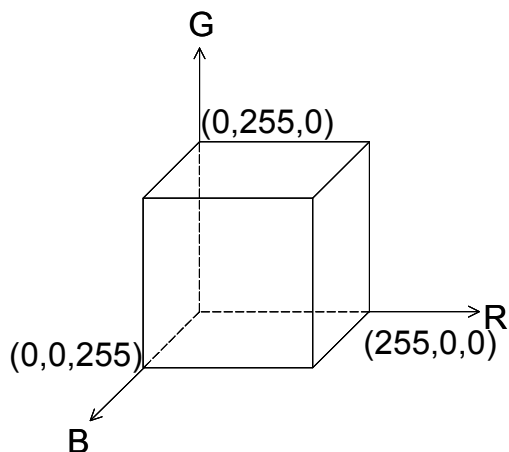
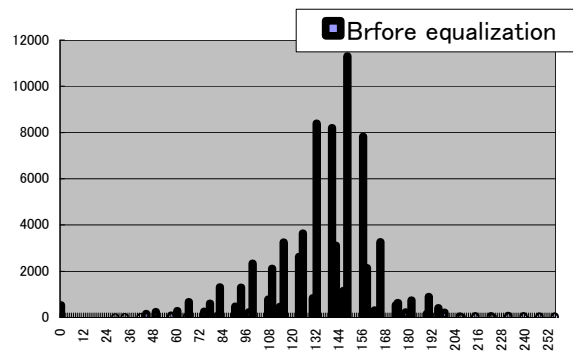


Fig. 3 Coordinates About RGB & HSI

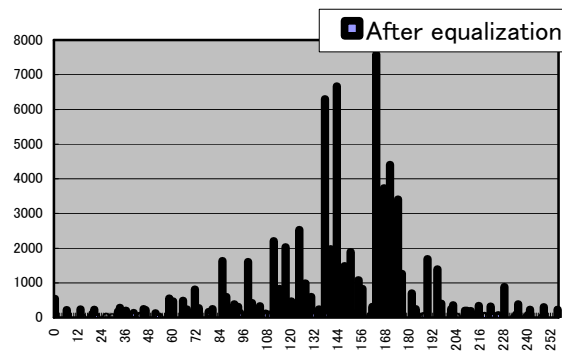
However, if HSI value is not threshold area, the camera will not recognize the object.

3.3 Equalization Processing

When the light is strong or weak, visual tracking can not be performed by using color information. Then, converse from RGB to HSI. We improve to be constant curve of cumulative frequency of I(intensity). Equalization processing is shown in Fig.4.



(a) Original Image

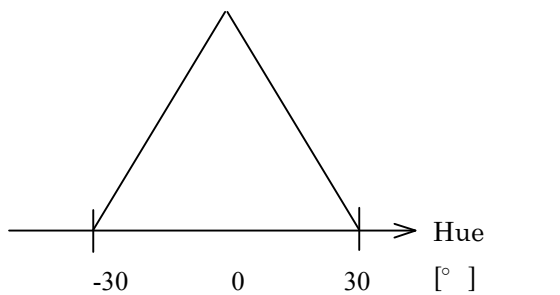


(b) Equalization

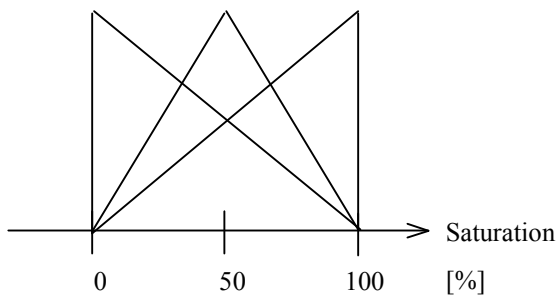
Fig. 4 Equalization Processing

3.4 Fuzzy Control

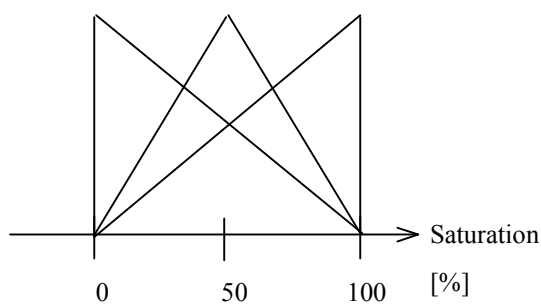
To perform the visual tracking, there is threshold processing. In many cases, human decided threshold. However, there are some problems. For example, difference object of same saturation, threshold cannot be detected. In this research, to prevent this problem, we perform fuzzy control of saturation. Input and output fuzzy set is shown in Fig. 5. Result is shown in Fig. 6. The green point is center of circle.



(a) Input Hue



(b) Input Saturation



(c) Output Saturation

Fig. 5 Fuzzy Set



(a) Original Image



(b) Human decided Threshold



(c) Fuzzy Control Of Threshold

Fig. 6 Fuzzy Control

3.5 Labeling Technique

The label represents number. The number, which represents value from 0 to 255, is boundary value. The processed image is labeled separate boundary value. Labeling-propagation processing by using raster scanning is shown in Fig. 7. Fig. 7 shows that the label represents by using alphabet value. As a result, characteristics of the moving object are calculated.

	A				1
	1				1
	1				1
	1				1
	1	1	1	1	1
		1	1	1	

(a) Labeling Start

	A				A
	A				A
	A				A
	A				A
	A	A	A	A	A
		B	B	B	

(b) Labeling End

Fig. 7 labeling-propagation processing by using raster scanning

4 Motion Detect Experiment

Motion detect experiment was actual conducted in the environment. Tracking moving object motion trace using red circle mark is carried out. After the red circle mark is detected, the head of the robot will move following the direction of the red circle mark movement. As the first step of processing is pixel skipping, second step is conversion from RGB to HSI, equalization and third step is labeling. The green point of the image (c) is shown in Fig. 8 is center of circle.



(a) Original Image



(b) Skipping Image



(c) Result Image

Fig. 8 Motion Detect Process

Since the image (c) is shown in Fig. 8, center of the circle is calculated. Therefore, head of the robot rotate to center of the circle. However, moving object is difficult to detect in strong light. When moving object and other object are similar saturation, other object is detected, too.

5 Conclusions

In this research, we are able to improve threshold in light. However, moving object is difficult to detect in strong light. When moving object and other object are similar saturation, other object is detected, too. Therefore, we would like to improve than this research in strong light and weak light, and we would like to consider about occlusion.

References

[1]Syuiti Otsu, Masanori Sugisaka “ Research on the environmental recognition in a mobile robot “, Oita University Graduate School Master Paper , 2003.

[2]Syohei Kuriyama, Masanori Sugisaka “ Development of the mobile robot run system using dead reckoning and vision information ”, Oita University Graduate School Master Paper , 2003.

[3]Toshio Maeyama , Masanori Sugisaka “ The obstacle avoidance run in the mobile robot using the CCD camera ”, Oita University Graduate School Master Paper , 2002.

[4]
<http://www.cse.unr.edu/~looney/cs674/ch6html.htm>
 Chapter 6. Processing Color Images.

On the Application of Lip Features in Classifying Human Emotions

M. Karthigayan¹, M. Rizon^{1,2}, S. Yaacob¹, R. Nagarajan¹, M. Sugisaka^{2,3}, M. Rozailan⁴ and D. Hazry²

¹School of Mechatronics Engineering, Kolej Universiti Kejuruteraan Utara Malaysia (KUKUM), Jejawi, Perlis, Malaysia

²Department of Electrical and Electronics Engineering, Oita University, 700 Oaza Dannoharu, Oita 870-1192, Japan

³Advance Research Institute for Science and Engineering, Waseda University, 2-2 Hibikino, Wakamatsu, Kitakyushu, Fukuoka 808-0135, Japan

⁴Terengganu Advanced Technical Institute, Kampus TATI, Jalan Panchor, Teluk Kalong, 24000 Kemaman, Terengganu, Malaysia
Email: karthigayan@ieee.org

Abstract

In this paper, lip features are applied to classify the human emotion using a set of irregular ellipse fitting equations using Genetic algorithm. As South East Asian (SEA), is considered in this study. All six universally accepted emotions are considered for classifications. Lip is usually considered as one of the features for recognizing the emotion. In this work, three feature extraction methods are proposed and their respective performances are compared for determining the feature of the lips. The method which is fastest in extracting lip features is adopted in this study. Observation of various emotions of the subject lead to unique characteristic of lips. GA is adopted to optimize such irregular ellipse characteristics of the lip features in each emotion. That is, the top portion of lip configuration is a part of one ellipse and the bottom of different ellipse. Two ellipse based fitness equations are proposed for the lip configuration and relevant parameters that define the emotion. This has given reasonably successful emotion classifications.

Keywords: Feature extraction, Irregular ellipse fitness function, Genetic algorithm, Face emotion recognition.

1. Introduction

In recent years, there has been a growing interest in improving all aspects of interaction between humans and computers especially in the area of human emotion recognition by observing facial expression. Ekman and Friesen developed the most comprehensive system for synthesizing facial expression based on what they call as action units [1]. In the early 1990's the engineering community started to use these results to construct automatic methods of recognizing emotion from facial expression in still or video images [2]. Human being possesses an ability of communication through facial emotions in day to day interactions with others. Some emotions attracted most of the interest in human computer interaction environments. Double structured neural network has been applied in the methods of face detection and emotional extraction. In this, two methods are proposed and carried out; they are lip detection neural network and skin distinction neural network [3]. Facial action coding is given to every facial points. For example, code 23 is given for lip funnel, code 4 for eye brow lower, code 10 for chin raise etc. The cods are grouped for a specific facial emotion. In order to determine the category of emotion, 15 facial points in a face-profile sequence has been recommended. The algorithm performs both automatic

segmentation of an input video images of facial expressions and recognition of 27 AUs occurring alone or in combinations in the input face-profile video. A recognition rate of 87% is reported [4]. The motion signatures produced are then classified using Support Vector Machines as either non-expressive or as one of the six basic emotions. The completed system is demonstrated in two simple but effective computing applications that respond in real-time to the facial expressions of the user, thereby providing the potential for improvements in the interaction between a computer user and technology [5]. The method uses edge counting and image correlation optical flow techniques to calculate the local motion vectors of facial feature [6]. Cauchy Naïve Bayes classifier is introduced in classifying the face emotion. The person dependent and Person-independent experiments shows that the Cauchy distribution assumption typically provides better results that the Gaussian distribution assumption [7]. The universally accepted categories of emotion, as applied in human computer interaction are: Sad, Anger, Joy, Fear, Disgust (or Dislike) and Surprise. In this paper, image preprocessing, filtering, edge detection methods that are suitable for feature extraction are presented and compared towards applying it to get lip features. A set of fitness function for the GA methods are also proposed as suitable for face emotion recognition. Such an approach of determining the emotions are highly suited for a personified face and cannot be common to all faces of all human being. A subject (South East Asian) as shown in Figure 1 has been used for emotion classification. The generalized process flow for the image processing, feature extraction and classifying the emotions is shown in Figure 2.

2. Face Image Processing

As the first step in image processing, the region of interest (ROI) has been selected in the acquired image. The ROI image is converted into grayscale image (0-256).



Figure 1. The Angry Emotion SEA

Before obtaining the filtered grayscale image, a histogram equalization method has been applied. Histogram equalization [8] improves contrast in the grayscale and the goal of histogram equalization is to obtain a uniform histogram. The histogram equalization method also helps the image to redistribute the intensity distributions as shown in Figure 3. New intensities will not be introduced into the image. Existing intensities values will be mapped to new values but the actual number of intensities in the resulting image will be equal or less than the original number of intensities. In the image sequence, the histogram equalized image is filtered using average and median filters in order to make the image smoother. Finally, Sobel edge detection method is applied to the filtered image. The cropped ROI lip region is shown in Figure 4.

Noises are added to the cropped ROI lip region. The salt and pepper noise are added to the image. This type of noise consists of random pixels being set to black or white. The application of the filter such as average filter and median filter to the noise added image is to remove the unwanted noise. This method creates a two-dimensional filter and returns with a correlation kernel. Median filtering [9] is that

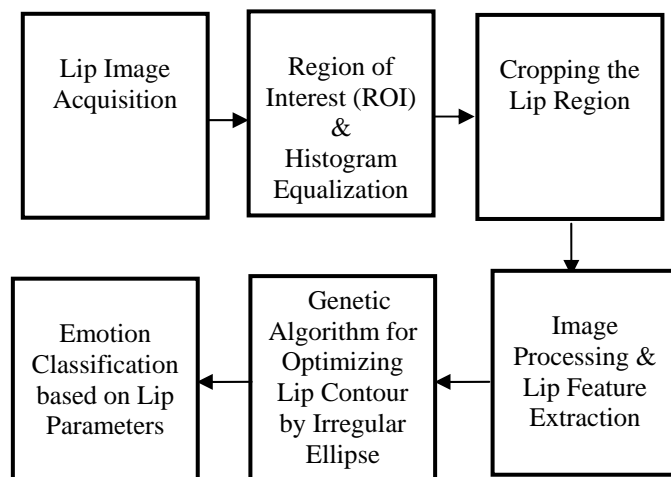


Figure 2. Process Flow of Image Processing



Figure 3. Histogram Equalization of Face ROI

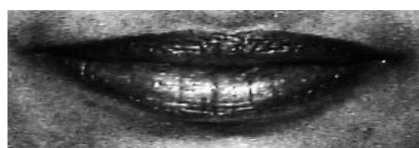


Figure 4. Cropped ROI Lip

each output pixel is set to an average of the pixel values in the neighborhood of the corresponding input pixel. However, with median filtering, the value of an output pixel is determined by the median of the neighborhood pixels, rather than the mean. The median is much less sensitive than the mean to extreme values (called outliers). Median filtering is therefore better in the ability to remove these outliers without reducing the sharpness of the image. The median filter with various matrix sizes such as 3*3, 4*4, 5*5, 6*6, 7*7 and 8*8 are applied. The 5*5 size matrix has been found to be suitable in removing unwanted noise in the image.

Threshold has been performed to the filtered image by selecting a suitable threshold value. Various edge detection methods such as Sobel, Prewitt, Canny, Roberts and Log have been applied to the image. A comparison has been made among the edge detection methods and it is found that the Sobel edge detection method [9] performed well compared to other four methods. The sobel edge detection region of lip region is shown in Figure 5



Figure 5. Sobel Edge Detected Lip Region

3. Feature Extraction

A feature extraction method is now to be applied to the edge detected image to extract features. Three feature extraction methods are considered and their capabilities are compared in order for adopting the one that is suitable for the proposed face emotion recognition problem. They are projection profile, contour profile and moments.

The performance of each of the above described feature extracting methods can be compared with respect to processing time using the edge detected image of the lips. The processing time includes the image reading, preprocessing, filtering, edge detection and feature extraction processes. Table 1 shows the processing time for obtaining the lip features of all three feature extraction methods. The projection profile is found to perform well in feature extraction with regards to the processing time and is adopted here. The projection profile has been also found to have performed well in earlier works [10,11].

Table 1. Processing Time for Lip Feature Extraction

Feature Extraction Method	Processing Time (Seconds)
Projection Profile	0.691 – 0.862
Moments	0.865 – 0.892
Contour Profile	23.07 – 33.31

4. Face Emotion Recognition using Genetic Algorithm

In the early 1970s, John Holland, one of the founders evolutionary computations, introduced the concept of genetic algorithm [12]. Genetic algorithm (GA), or GA is a heuristic method used to find approximate solutions to solve problems through application of the principles of evolutionary biology. GA adopts biologically-derived techniques such as inheritance, mutation, natural selection, and recombination (or crossover). GA is a particular class of evolutionary algorithms. A population containing a number of trial solutions each of which is evaluated (to yield fitness) and a new generation is created from the better of them. The process is continued through a number of generations with the aim that the population should evolve to contain an acceptable solution. GA is well known for optimization of nonlinear functions. It offers the best optimized value for any fitness or objective functions suitably selected for particular problems.

GA has been applied in various applications which include in image processing, control, design of aircraft, robot trajectory generation, air-injected hydro cyclone optimization, multiple fault diagnosis, a hybrid technique for engineering design optimization the traveling salesman, sequence scheduling and quality solutions where nonlinear optimization are required [13] Some aspects of vision system and image processing methodologies have been discussed towards approximating the face as a best ellipse using GA. In the feature extraction stage, the GA is applied to extract the facial features such as the eyes, nose and mouth, in a set of predefined sub regions. Some simulation has been carried out [9]. A method that extracts region of eyes out of facial image by genetic algorithm has been suggested recently [14].

The human lip shape is more of towards combination of two ellipse and we call this is as irregular ellipse. The word 'irregular' means that the ellipse has two different minor axes wherein a major axes remains the same. The preprocessed lip image is considered as a irregular ellipse. Lengths of minor axes of the lip feature for each emotion are computed. In Figure 6, the whitened area of edge detected lip image for a particular emotion of SEA is shown. The major axis "2a" (considered to be fixed) and two minor axes are "2b1" and "2b2" (to be computed). This is shown in Figure7. A general form of the regular ellipse is defined by

$$\frac{x^2}{a^2} + \frac{y^2}{b^2} = 1 \quad (1)$$



Figure 6 Image Processed Lip for SEA

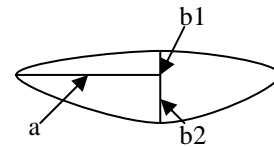


Figure 7 Irregular Ellipse with Minor and Major Axis

A fitness equation is suggested in this work in order to find the two minor axes so that the emotion changes can be recognized. A fitness function, to be discussed latter, for applying GA, is derived to optimally compute semi-minor axes, b1 and b2, for the top lip area and bottom lip area respectively; emotions can thus be related to the values of b1 and b2.

4.2 Fitness Function

A fitness function is a particular type of objective function that quantifies the optimality of a solution (that is, a chromosome) in a GA problem so that that particular chromosome may be ranked against all the other chromosomes. A fitness value reflecting the amount of overlapping between the regions covered by the overlaid boundaries is computed for each chromosome. A pair of individuals are selected with a probability proportional to their fitness and mated to reproduce their next generation. The process is repeatedly performed with the same number of individuals of the previous epoch. The fitness function equation, Equation (2) and Equation (3) with b1 and b2 are derived based on the general ellipse equation, Equation (1).

$$f(x) = \left(\sum_i^m \sum_j^n col(j) - 2\sqrt{X_1^2 \left(1 - \frac{row(i)^2}{a^2}\right)} \right)^2 \quad (2)$$

$if X_1 \geq 0$

$$\overline{f(x)} = \left(\sum_i^m \sum_j^n col(j) - 2\sqrt{X_2^2 \left(1 - \frac{row(i)^2}{a^2}\right)} \right)^2 \quad (3)$$

$if X_2 \leq 0$

In Equation (2) and Equation (3), X_1 and X_2 are variables which finally converged to optimized values as b1 and b2 respectively. White pixels of the preprocessed lip feature for each column are calculated. In Equation (2) and Equation (3), col(j) is sum of white pixels occupied by j^{th} column and row(i) is number of rows of white pixels in i^{th} row. Equation (2) and Equation (3) are fitness equations of top and bottom lip respectively.

4.3 Results and Discussion

In this study on a SEA subject, six emotions and one neutral have been considered. The lip features have been given as input to the genetic algorithm to find the optimized values. The selected values of GA parameters are indicated in the Table 2. The process of optimization has been carried out for 5 times for each emotion. This process of optimization is found to be giving favorable two minor axis value b1 and b2 for top and bottom areas of the lips. Table 3 indicates the manually measured values of b1 and b2 and the

corresponding optimized values of X1 and X2. The emotion based on minor axes of the lip feature can now be estimated for the subject. The experiment result shows that the two minor axis (b1 and b2) of the lip feature are different for each emotion there by distinctions are possible.

Table 2 Parameter Settings

Generation	250
Population size	20
Fitness scaling	Rank
Selection Function	Roulette
Mutation	Gaussian
Crossover	Scattered
Stall generation	50
Stall time	20

Table 3 Classification of Emotion (SEA)

Emotions	Manually Computed Value		Optimized Mean Value by GA	
	b1	b2	X1	X2
Neutral	44	56	49.9294	47.7074
Fear	38	57	40.8410	54.9664
Happy	31	178	22.5574	74.1890
Sad	44	16	45.5745	17.9480
Angry	19	61	12.6218	64.5633
Dislike	76	47	37.9206	41.9958
Surprise	60	75	52.1640	77.4762

5. Conclusion

In this paper, a set of suitable sequences in image processing and new fitness function for the GA application have been proposed for determining the top-lip and bottom-lip features. The face and lip are obtained under uneven lighting. In image processing task, the average and median filters are applied to smoothen the image. The Sobel edge detection is found to perform well for edge detection. The suggested sequence of image processing offers acceptable lip images compared to other methods suggested in this work. The lips are considered as an irregular ellipse. The GA is then applied to get the optimized values of the minor axes, b1 and b2, of the irregular ellipse by using a set of proposed fitness functions. These optimized values of minor axes indicate that the values b1 and b2 can be regarded as identifying the emotion. The new method has shown successful classifications emotion. The proposed method of emotion classification is a general approach to lips of any face. The parameters listed in Table 3 are for a personified face. Such a table look-up can be applied to a particular bed-ridden disabled dumb patient for identifying the patient's reaction.

References

- 1) Haibo Li, "Computer Recognition of Human Emotion", Proceedings of International Symposium on Intelligent Multimedia, Video and Speech Processing, Hong Kong, 2-4 May 2001, pp. 490-493.
- 2) Nicu Sebe, Michael S. Lew, Ira Cohen, Ashutosh Garg and Thomas S. Huang, "Emotion Recognition Using a Cauchy Naïve Bayes Classifier", Proc. of Sixteenth International Conference on Pattern Recognition, vol. 1, 11-15 August 2002, pp. 17-20.
- 3) Hironori Takimoto, Yasue Mitsukura, Minoru Fukumi and Norio Akamatsu, "Face Detection and Emotional Extraction System Using Double Structure Neural Network", Proc. of the International Joint Conference on Neural Networks, vol. 2, pp. 53-1257, 20-24 July 2003.
- 4) Maja Panti and Ioannis Patras, "Dynamics of Facial Expression: Recognition of Facial Actions and Their Temporal Segments from Face Profile Image Sequences, IEEE Transactions on Systems, Man, and Cybernetics—Part B: Cybernetics, Vol. 36, No. 2, pp. 433-449, April 2006
- 5) Keith Anderson and Peter W. McOwan, "A Real-Time Automated System for the Recognition of Human Facial Expressions", IEEE Transactions on Systems, Man, and Cybernetics—Part B: Cybernetics, Vol. 36, No. 1, pp. 96-105, February 2006.
- 6) Liyanage C De Silva and Suen Chun Hui, "Real-time Facial Feature Extraction and Emotion Recognition", Proceedings of Fourth Pacific RIM Conference on Multimedia, vol. 3, 15-18 Dec 2003, pp. 1310-1314.
- 7) Nicu Sebe, Michael S. Lew, Ira Cohen, Ashutosh Garg and Thomas S. Huang, "Emotion Recognition Using a Cauchy Bayes Classifier". Proceeding of 16th International Conference on pattern Recognition, vol. 1, 11-15 August 2002, pp. 17-20.
- 8) Rafael C Gonzalez and Richard E Woods, "Digital Image processing". Pearson Education, Inc, India, 2002.
- 9) Gary G. Yen and Nethrie Nithianandan, "Facial Feature Extraction Using Genetic Algorithm", Proceedings of Congress on Evolutionary computation, vol. 2, 12-17 May 2002, pp. 1895-1900.
- 10) M. Karthigayan, Mohammed Rizon, Sazali Yaacob and R. Nagarajan, "An Edge Detection and Feature Extraction Method Suitable for Face Emotion Detection under Uneven Lighting", The 2nd Regional Conference on Artificial Life and Robotics (AROB'06), July 14 - July 15, 2006, Hatyai, Thailand.
- 11) R. Nagarajan, Sazali Yaacob, Paulraj Pandiyan, M. Karthigayan, Marzuki Khalid and Shamsudin H Amin, "Real Time Marking Inspection Scheme for Semiconductor Industries", International Journal of Advance Manufacturing Technology (IJAMT), Springer Publisher, 2006. (Accepted for publication).
- 12) Michael Negnevitsky, "Artificial Intelligence", Addison Wesley, Pearson education Limited, England, 2002.
- 13) http://neo.lcc.uma.es/TutorialEA/semEC/cap03/cap_3.html, 1997.
- 14) Hideaki Tani, Kenji Terada, Shunichiro Oe and Junichi Yamaguchi, "Detecting of One's Eye from facial Image by Using Genetic Algorithm", The 27th Annual Conference of the IEEE Industrial Electronics Society, 2001, pp. 1937-1940.

Face localization for facial features extraction using symmetrical filter and linear Hough transform.

Hamzah Arof
Dep. of Electrical Engineering
University Malaya,
Malaysia

Fauzan Ahmad
Fac. of Engineering and Industrial Technology
IUCTT, Malaysia

Noraisyah M. Shah
Dep. of Electrical Engineering
University Malaya
Malaysia

Abstract

In this paper, face localization for facial feature extraction is presented. The method consist three steps: (1)facial features enhancement using symmetrical filter, then the morphological process is applied to examine the edge, peaks and valley fields. (2) Line construction using linear Hough transform and (3) localization of face region based on the constructed lines and the elimination of excess area outside of face boundary.

Key words: face localization, symmetrical filter, linear Hough transform.

1. Introduction

Face detection defined by [1] is the following: given an arbitrary input image, find the location and size of the human face in the image. There is no assumption made regarding the number of the faces in the image. In face localization it is normally assumed that the input image only contains one face in the foreground. Face segmentation as defined by [2] is described as a process as finding the location and actual shape of face(s) appearing in a given image. Face segmentation is more challenging because it not only locates the position of human face, but also segments the actual shape of complete human face [3]. In this paper, we will discuss our approach for face localization, which will start with coarse face region extraction. Our algorithm tries to localize the face with the complete facial features and if possible, it will segment the face to get the actual shape of complete human face. The localized or segmented face could be further processed for facial features extraction such as eyes, nose and mouth detection, which is a key requirement for face recognition. Among those facial features, eyes are the most salient feature due to its

interocular distance which is constant among people and not easily effected by moustache or beard.

1.1 Face region extraction and facial features enhancement

Our algorithm extracts the face region using a similar method to the one shown in [4].



Fig1. A head-shoulder image



Fig.2 The face region extracted from the image of Fig.1

Then the estimated face area is further cropped by removing the top region of the face image where hair lies. If hair is not found in the top region the image is left uncropped



Figure3 Cropped face region.

After that, a symmetrical filter is applied to the cropped face region to remove sharp edges and occluded dark patches while maintaining the salient features of the eyes

0	-2	-4	-2	0
-2	2	6	2	-2
-4	6	8	6	-4
-2	2	6	2	-2
0	-2	-4	-2	0

Figure 4 Symmetrical mask



Figure 5 The face region after we apply the symmetrical mask on figure 3.

1.2 EXTRACTION OF THE EDGE, VALLEY AND PEAK INFORMATION

Let $I(x,y)$ be the image obtained by cutting off the face region from the original intensity image given as input. We produce an edge image $E(x,y)$, a valley $V(x,y)$ and a peak image $P(x,y)$ in the following ways. $E(x,y)$ is given by applying the Sobel operator to $I(x,y)$. The valley $V(x,y)$ and peaks $P(x,y)$ images are obtained from mathematical morphology as follows. Let $G(x,y)$ denote the image obtained by applying a grayscale closing [6] to $I(x,y)$ and $H(x,y)$ be the image obtained by applying a grayscale opening [6] to $I(x,y)$. Then, the valley image $V(x,y)$ is given by $G(x,y)$ minus $I(x,y)$ and the peak image $P(x,y)$ is given by $I(x,y)$ minus $H(x,y)$. The mathematical morphology is followed by linking process based on the gradient of the edge field. This process is useful to combine isolated edge pixels in the filtered image while reducing the effect of white spots on irises. In figure 5, we could observe that there are broken edges and isolated pixels where the edges are not connected and they are visibly different from their surrounding neighbours. The best example to illustrate this condition is by observing the eye area. We notice that the eyeball is not totally full of black pixels and it contains dots of white pixels due to reflection. This effect can be

reduced by linking process and therefore better peak and valley images are obtainable.



Figure 6 The output after linking process

After the linking process, we obtain the final enhanced image by combining the linked image, the edge image, the peak and valley fields in the following way.

$$H(i, j) = L(i, j) + E(i, j) + I(i, j) - V(i, j)$$

Where $H(i, j)$ is the enhanced image, $L(i, j)$ the image after linking process, $I(i, j)$ the original image, $V(i, j)$ the valley image. The output of the enhanced image is shown in figure 7 below.



Figure 7 Enhanced image

Figure 8 compare the valley and peaks for the image before enhancement and after we apply the symmetrical filter, linking process and image enhancement.

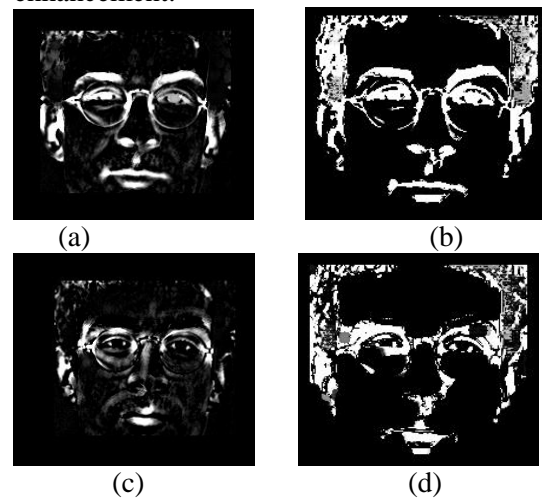


Figure 8 Comparison the valley image (a) before image enhancement (b) after image enhancement. Comparison of peaks image (c) before image enhancement (d) after image enhancement

1.3 Linear Hough transform

The edge field $E(x,y)$ obtained in the last section is reused in the linear Hough transformation. For every edge pixel, the line angle can be varied from 0° to 180° with an increment of 1° . The distance from the origin to the nearest point on the line is calculated. Both the angle and the discretized distance will become an index to the 2-D accumulator array where its frequency is accumulated. Then an accumulator array is used to store the frequency of various lines for every single edge pixel. After the accumulation process, a data reduction scheme is employed to reduce the size of the accumulator array and therefore avoid redundancy. The accumulator array is divided into 2×2 subarrays. For each 2×2 subarray only one major value is retained (out of four) while the remaining three values are set to zero. In our experiment θ is restricted until from 0° - 30° and 0° - 45° . By applying this approach, the size of array will not be a major drawback in the execution time of our program. Figure 9 show the edges and the line constructed using Linear Hough transform.

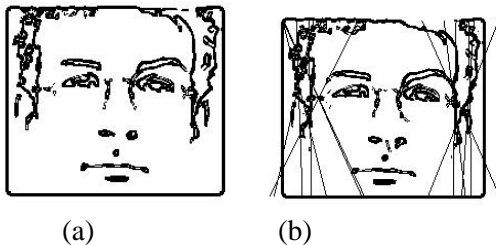


Figure 9 (a) Edges of the image (b) Lines constructed using Hough transform.

1.4 Using constructed line for face localization and segmentation

Finally, selected lines will be constructed around the face region based on the information from the accumulator array. The constructed lines will be used to localize face region by eliminating areas outside the face boundary. The examination of each line involves inspecting the minor area covered by the line and the intensity pixel distribution lying on the respective line. The line will divide the image into two areas, namely minor area and major area as shown in figure 10. We will examine the minor area to

check if the area is less than 30% of the total area.

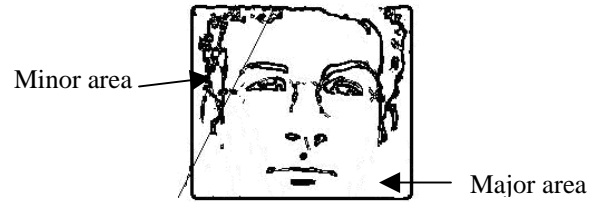


Figure 10 One of the line divided the image into minor area.

From our experiment, if the percentage of the minor area over the total area is higher than 30%, it will dissect part of the face region and therefore erroneous. For each line with area less than 30%, we will examine the pixel distribution lying on the respective line and if the black pixels are greater than 70% of the total pixels on the line, the pixel in the minor area will all be set to zero. The second threshold is used to indicate that the line should lie on the hair. The process stops when there is no more line to consider.

1.5 Experimental results

The efficiency of this method was tested on university of Bern face database which contains 300 frontal faces under controlled lighting conditions. The database is characterized by small changes in facial expression and immediate changes ($\pm 30^\circ$) in head pose, with two images for each of the poses right, left, up, down and straight. Using the 300 face image in the database, line constructed by varying the angles (θ) from 0° - 30° and from 0° - 45° are examined. For simplicity, let θ_1 to represents bounded angles of 0° - 30° and θ_2 for bounded angles of 0° - 45° . Table 1 shows the experimental result for θ_1 and θ_2 . For θ_1 , the maximum line investigated is 30° and for θ_2 the maximum line investigated is 45° .

Facial features	θ_1	θ_2
Eyes	100%	100%
All (eyes,mouth,nose)	85%	85%
Mouth eliminated	8%	8%
Mouth and nose eliminated	1.33%	1.33%
Eye corner eliminated	0.33%	0.66%

Table 1 Comparison of the facial features contains in the localizes face for θ_1 and θ_2

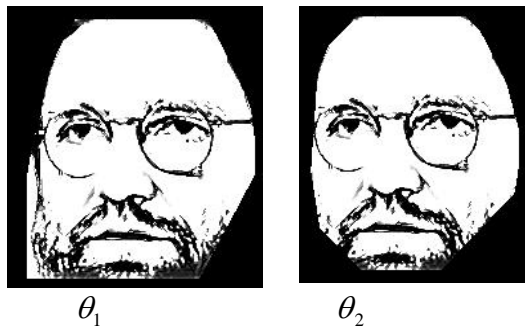


Figure 11 Differences localize face between θ_1 and θ_2

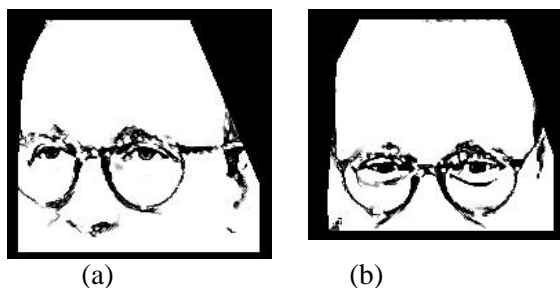


Figure 12 sample of the localize face with
 (a)Mouth eliminated (b)Mouth and nose
 eliminated



Figure 13 Sample of the eliminated eye corner
 for θ_2

Summary

In this paper, face localization for facial feature extraction is presented. The coarse region of the face is extracted, and then the facial features are enhanced using symmetrical filter. The morphological process is applied to produce the edge, peaks and valley fields. Lines are constructed in the face region using Linear Hough transform and the constructed lines are used to localize face region by eliminating areas

outside of the face boundary. For the two bounded angles, the face localization rate which contains all facial features are 85%, while the rate for images that contain both eyes is 100% and the future works will concentrate on eye detection or eye feature extraction.

References

- [1]M. Yan, D.J Kreigman ,N Ahuja (2002). Detecting faces in image: a survey. PAMI 24(1) 34-58.
- [2] F. Marques ,V.Vilaplana (2002). Face segmentation and tracking based on connected operator and partition projection. Pattern recognition 35,601-604.
- [3] Z. Liu,J. Yang, N.S Peng(2005). An efficient face segmentation algorithm based on binary partition tree. Signal processing: Image communication 20, 295-314.
- [4] T. Kawaguchi, M. Rizon (2003).Iris detection using intensity and edge information. Pattern Recognition 36, 549-562.
- [6] S.R Sternberg (1986).Grayscale morphology. Comput. Vision Graphics and Image Process, 35,333-335.

Imitation of Human Action Intelligence for the Environment of Desktop Teleoperation

Tao Shang

School of Information Science and
Engineering
Shenyang University of Technology
Shenyang, 110023, P.R.China
shangtao@sut.edu.cn

Shuoyu Wang

Department of Intelligent Mechanical System
Engineering
Kochi University of Technology
Kochi, 782-8502, Japan
wang@mech.kochi-tech.ac.jp

Abstract

It is well known that humans have high-level action intelligence. If such action intelligence could be represented in certain form, it could contribute to the path-planning problem of autonomous mobile robot. Therefore we shall address to transfer human action intelligence to mobile robot by means of imitation and acquire such action intelligence. Based on the effectiveness of previously proposed imitation method in simulation environment, we need to further verify the effectiveness of proposed imitation method and achieve the imitation of action intelligence on a real mobile robot. In this paper, the imitation of human action intelligence for the environment of desktop teleoperation, including experimental platform, research methods, and experimental procedures, was discussed. Firstly, imitation problem was clarified from the viewpoint of problem solving system, which provides guidance to the construction of imitation system. As an experimental platform, a desktop teleoperation system, including mobile robot and manipulation interface, was introduced. Through the developed teleoperation system, the intention representing human action intelligence can be easily transferred into mobile robot and meanwhile the corresponding action data can also be obtained for modeling. Then, based on the teleoperation system, the imitation procedure of human action intelligence was described. Finally, the effectiveness of proposed imitation method was illuminated by experiment.

1 Introduction

It is well known that humans have high-level action intelligence. If such action intelligence could be acquired in certain form, it can be applied to various fields such as the development of autonomous mobile robot, which can freely move even under complex environment. Naturally, if desired actions were appropriately achieved by imitating human action, such imitation methods would transfer human action intelligence into practical application and facilitate the acquisition of human action intelligence. So far, many imitation approaches have been popularly developed in the field of both robotics and artificial intelligence [1-3]. For our

research, we believe that human action can remain in form of direct data and human action intelligence is certainly hidden in the remaining data. Thus we address to extract action knowledge representing human action intelligence from human action data and then imitate human action by employing the extracted action knowledge. Based on the effectiveness of previously proposed imitation method in simulation environment [4], we need to further verify the effectiveness of proposed imitation method and achieve the imitation of action intelligence on a real mobile robot.

The construction of this paper is organized as follows: imitation problem is clarified from the viewpoint of problem solving system in section 2. The objective imitation system is verified to construct in term of reasoning method, knowledge acquisition and knowledge base. As an experimental platform, the teleoperation system is described in section 3. Then an imitation procedure is proposed to construct objective imitation system. Here, learning method and reasoning method emphasizing knowledge usage are considered to implement the imitation of action intelligence. To illustrate the characteristics of proposed method, the experiments are conducted in section 4. The paper finishes with a conclusion in section 5.

2 Problem solving system for imitation

As the basic definition of imitation, imitation is not to create an original act or instance, but to try to reproduce an existing one so that same or similar act or instance could happen in imitator. Consequently, it can be said that if an imitation system (virtual imitator) does same or similar act as human, such system can be thought to be as intelligent as human. According to the development of problem solving system [5], the imitation system of action intelligence can be constructed just as in figure 1 by means of acquiring action knowledge, memorizing action knowledge, and reproducing the action. Knowledge acquisition method can be adopted to acquire action knowledge; knowledge base can be constructed to memorize knowledge representing human action intelligence; based on the acquired and memorized knowledge, not only precise action, but also predictive action for environmental variation is needed to reproduce, so fuzzy reasoning method can be adopted to implement this function.

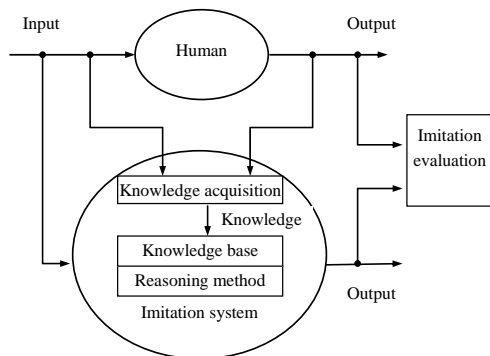


Figure 1. Construction of imitation system

3 Teleoperation system

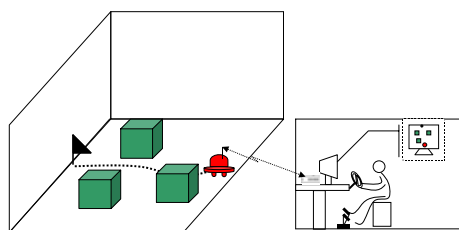


Figure 2. Teleoperation system

Just as in the figure 2, the developed teleoperation system connects the interaction between human and corresponding environmental space and provides a platform to fully employ human's obstacle avoidance ability. The platform mainly includes two parts: mobile robot equipped with digital camera and supersonic sensor, manipulation interface with the functions of both manual operation and autonomous operation.

Facing the visual environmental space of manipulation interface, an operator can control the speed and direction of a mobile robot by joystick. By judging the goal and surrounding obstacles, operator can try to avoid obstacle and arrive at the goal. As a result, operation is treated as successful operation, only if the robot controlled by operator arrives at a goal from a starting point with free collision during a specified time interval; otherwise, it is treated as failed one.

3.1 Mobile robot

The mobile robot is equipped with ball actuator so as to be able to move on any direction of 0~360 degree. Figure 3 is the appearance of the mobile robot, and table 1 shows the specification of the mobile robot. Figure 4 shows the Hardware construction of the mobile robot. DC motor and omni-wheels are evenly arranged every 90 degrees on the lower part of robot. The regular output of DC motor is 90W and its regular torque is 45kg.cm. Five supersonic sensors are evenly equipped on the upper part of robot to measure the distance between robot and surrounding object. Its maximum measure distance is 3000mm.



Figure 3. Photo of the mobile robot

Table 1 Specification of the mobile robot

Item	Detail
Height	600mm
Length/Width	800mm/800mm
Weight	about 50kg
Moving velocity	about 0.3m/sec

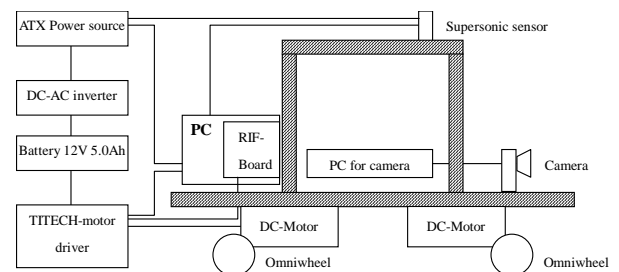


Figure 4. Hardware of the mobile robot

3.2 Manipulation interface

Manipulation interface was developed by means of Visual C++ 6.0 under the environment of windows XP. Figure 5 shows the software of manipulation interface. The left part of Figure 5 is the visual surrounding environment of mobile robot from camera (Creative technology Corp., WEBCAM NX Pro), while the right part of figure 5 are the experimental module such as teleoperation, learning and reasoning for imitation.

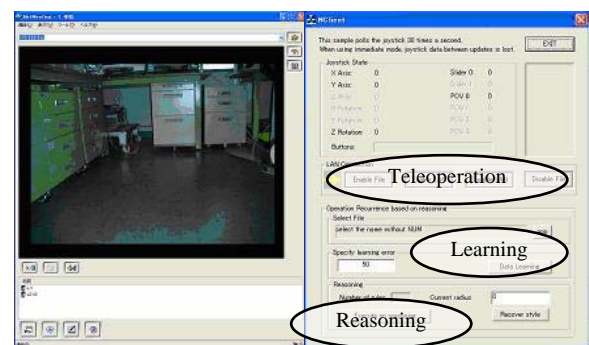


Figure 5. Manipulation interface

According to the structure of imitation system in section 2, these modules are necessary components for implementing imitation. Teleoperation module is used for manual operation

of mobile robot to obtain the action data of operators. Both learning module and reasoning module are for autonomous operation of mobile robot. Learning module is used to acquire action knowledge from data, while reasoning module is used to reproduce the action of human.

Concrete learning and reasoning algorithms have been described in the literature [4]. Based on the effectiveness of previously proposed imitation method in simulation environment, we need to further verify the effectiveness of proposed imitation method and achieve the imitation of action intelligence on a real mobile robot. Compared with most of methods focusing on how to acquire knowledge better such as the acquisition and adjustment of fuzzy rules and membership function [6-8], alternatively, we are taking it into account that it will be more meaningful to pay attention to the importance of knowledge usage for imitation performance, according to the theorem that the SAM (Standard Additive Model) architecture allows independent rules to function cooperatively and the credibility of knowledge source is equivalent [9]. Also, considering the fact that human selectively employ knowledge for reasoning, i.e., not all knowledge in one's brain is used for reasoning. Considering the quantifiable characteristics of the relationship between the fact and rule, we shall adopt the distance between fuzzy set as the criterion of knowledge selection to strengthen knowledge usage during reasoning process. Concretely, the concept of knowledge radius[11] is introduced for knowledge selection. Knowledge radius q is the number of rules with the nearest distance between fact and antecedent of a rule. Where, q is an integer, $[2, \dots, n]$, n is the number of rules.

The Distance-Type Fuzzy Reasoning method with knowledge radius is adopted to develop manipulation interface of teleoperation system. The fuzzy reasoning method is developed on the Distance-Type Fuzzy Reasoning (DTFR) method, which is a kind of fuzzy reasoning method considering the distance between fuzzy sets [10]. It features two main characteristics: asymptotic and decomposition characteristics (Modus Ponens is strictly satisfied). Thus the physical meaning of rules for reasoning is clear and reasoning tendency can be predicted appropriately.

Also, an improved learning algorithm for Distance-Type Fuzzy Reasoning is adopted for knowledge acquisition [4], because it is strongly related to the above reasoning method. Compared with conventional data learning methods for the generation of fuzzy rule such as GA or NN, this algorithm is very fast and simple with an arbitrarily specified error for learning, especially, it is suited for common numerical data learning. Meanwhile it also considers the statistical characteristics of teacher data to improve the selection of consequent for contradictive rule.

3.3 Imitation procedure

Based on the reasoning engine of the Distance-Type Fuzzy Reasoning method with knowledge radius, and the acquired knowledge by the learning algorithm for Distance-Type Fuzzy Reasoning, optimum knowledge radius is verified to implement the imitation of action intelligence. The imitation procedure consists of the following four steps:

Step1: Acquire the action data of human by means of teleoperation module of manipulation interface;

Step2: Acquire knowledge from the remaining action data by means of learning module of manipulation interface;

Step3: Calculate the evaluation value of knowledge radius and set the optimum value of knowledge radius;

Step4: Treat the reasoning performance of manipulation interface based on optimum knowledge radius as the imitation performance.

4 Experiments

4.1 Learning procedure

In order to describe variable environment for knowledge acquisition, the physical units between robot and objects, including goal and obstacle, are given by (1).

$$\text{if } S1 \ S2 \ S3 \ S4 \ S5 \quad \text{then } X \ Y \ Z \quad (1)$$

Where

$S1 \ S2 \ S3 \ S4 \ S5$: respectively denotes the distance between robot and the nearest point of an obstacle/goal, its value varies in;

$X \ Y \ Z$: denotes the control behavior in form of joystick's position, $X \in [-790, 627]$ $Y \in [-930, 215]$ $Z \in [-961, 96]$.

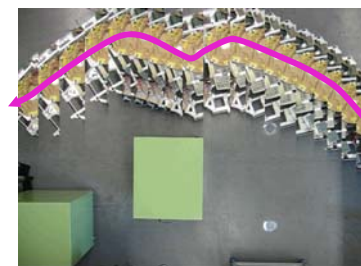


Figure 6. Operation path

As can be observed in figure 6, an operator conducted obstacle avoidance and successfully arrived at the goal point. Then by using the learning module of manipulation interface, action rules were generated. Concretely, table 2 lists the parameters for learning procedure.

Table 2. Learning parameters

Environment	Two Static obstacles o1(250,100) o2(20,90)
Number of data	435
Learning error	50
Learning time	1.8 Second
Number of rules	96

4.2 Search of effective knowledge radius

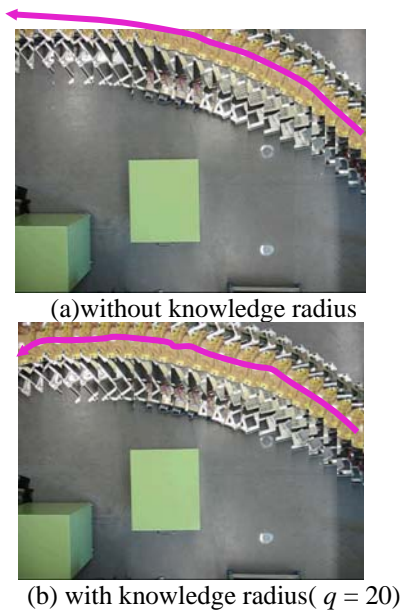


Figure 8. Reasoning results

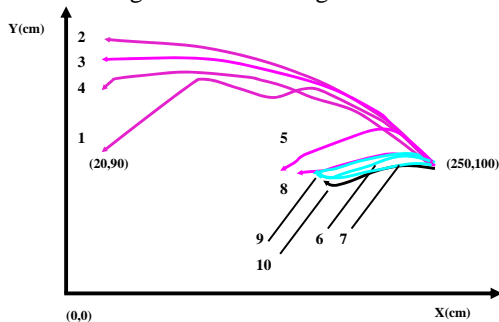


Figure 8. Control path and reasoning path

(1: control path 2: without knowledge radius 3: $q = 30$ 4: $q = 20$ 5: $q = 16$ 6: $q = 15$ 7: $q = 14$ 8: $q = 12$ 9: $q = 10$ 10: $q = 5$)

For convenient analysis of imitation performance, path area error S between human's control path and reasoning path is calculated as criterion. Considering the practical problem of robot, the search scope of q is limited in [5, 10, 12, 14, 15, 16, 20, 30]. Figure 7 and 8 show the imitation performance corresponding to different knowledge radiuses. We can verify that the only optimum knowledge radius q is 20 with the minimal path area error.

4.3 Validation

The above experiment demonstrated the good performance based on the acquired rules with optimal knowledge radius 20, which does not mean the only rules within knowledge radius are useful, but all the more illuminate the effectiveness of both knowledge radius and current rules. We can draw the same conclusion as simulation that all of rules are useful, and good performance can be achieved by focusing on local knowledge, i.e., the control path can be effectively imitated by emphasizing knowledge selection.

5 Conclusion

In this paper, we discussed the imitation performance of proposed imitation method based on a developed teleoperation system and proposed corresponding imitation procedure. Through this teleoperation system, the data representing human action intelligence can be acquired and further be used for imitation. The effectiveness of imitation can be verified by experiment. Furthermore, the identification of knowledge radius is still needed to discuss for the guideline to specific problem.

References

- [1] Stefan Schall: Is Imitation Learning The Route to Humanoid Robots?, Trends in Cognitive Science, Vol. 3, pp.233-242, 1999.
- [2] Dautenhahn, K. and Nehaniv, C.L.: Imitation in animals and artifacts, Cambridge, Massachusetts: the MIT press, 2002.
- [3] A. Billard and M. Mataric: Learning human arm movements by imitation: Evaluation of a biologically-inspired connectionist architecture, Robotics & Autonomous Systems 941, pp.1-16, 2001.
- [4] Tao Shang and Shuoyu Wang: Knowledge Acquisition and Evolution Methods for Human Driving Intelligence, International Journal of Innovative Computing, Information and Control, Vol.2, No.1, pp.221-236, 2006.
- [5] K. Forbus and J. de Kleer: Building Problem Solvers, MIT Press, 1993.
- [6] H. Ishibuchi and M. Nii: Generating Fuzzy Classification Rules from Trained Neural Networks, Journal of Japan Society for Fuzzy Theory and systems, Vol. 9, No.4, pp. 512-524, 1997.
- [7] K. Tachibana and T. Furuhashi: A Proposal of Fuzzy Modeling Method with Generation/Deletion of Membership Functions, Journal of Japan Society for Fuzzy Theory and systems, Vol. 11, No.6, pp. 1078-1088, 1999.
- [8] H. Inoue, L. Hng, K. Miyasaka, and M. Tsukamoto: An Acquisition Method of Fuzzy Classification Rules using Hyper-cone Membership Function by Gas, Proceedings of 19th Fuzzy system symposium, pp. 445-448, Sakai, 2003.
- [9] B. Kosko: Fuzzy Engineering, Prentice hall, New Jersey, 1997.
- [10] S.Y. Wang, T. Tsuchiya, and M. Mizumoto: Distance-Type Fuzzy Reasoning Method, Journal of Biomedical Fuzzy System Association, vol.1, no.1, pp.61-78, 1999.
- [11] S.Y. Wang: The Development of Human Reasoning Engine, 2002 IPA Project, 2002.

An Introduction of Multi-Step K-means Clustering Applied to Rice Microarray Data

[†]Daehoon Park, [†]Yountae Kim, ^{††}Ok-Kyung Ham, [†]Sungshin Kim, and ^{††}Choon-Hwan Lee

[†]School of Electrical and Computer Engineering, Pusan National University, Busan, Korea
Pusan National University 30 Changjeon-dong, Keumjeong-ku, Busan 609-735, Korea
E-mail: dhsmile@pusan.ac.kr, dream0561@pusan.ac.kr, sskim@pusan.ac.kr

^{††}School of Molecular Biology, Pusan National University, Busan, Korea
Pusan National University 30 Changjeon-dong, Keumjeong-ku, Busan 609-735, Korea
E-mail: 82dhrud@pusan.ac.kr, chlee@pusan.ac.kr

Abstract – Long gene sequences and their products have been studied by many methods. The use of DNA(Deoxyribonucleic acid) microarray technology has resulted in an enormous amount of data, which has been difficult to analyze using typical research methods. This paper proposes that mass data be analyzed using division clustering with the *K*-means clustering algorithm. To demonstrate the superiority of the proposed method, it was used to analyze the microarray data from rice DNA. The results were compared to those of the existing *K*-means method establishing that the proposed method is more useful in spite of the effective reduction of performance time.

Keywords: K-means clustering, Microarray, Rice

1. Introduction

Since the inception of biotechnology, large amounts of new genetic information have been amassed for organisms varying from bacteria to human beings. This information has provided many clues for solving biological problems. However, new technologies are urgently needed because most genetics engineering methods have limitations. One method that has been developed to overcome the problems of the existing methods is searching genetic material using a DNA chip. The DNA chip is divided into a cDNA chip and oligonucleotide chip depending on the size of the genetic material. A large amount of genetic information can be obtained by using this DNA chip analysis technique [1]. The development of an efficient clustering algorithm for DNA microarray data will contribute to research in several important fields such as functional genomics and genetic networks. Furthermore this information can be analyzed by various data mining methods, and these results can be evaluated by many methods. A literature review of former data mining methods reveals a data clustering algorithm using graph theory and an algorithm by Hartuy and Ben-Dor et al. [2] [3], and Tamayo et al. developed the Self-Organizing Maps (SOM) algorithm [4]. And Eisen et al. proposed and developed a method using hierarchical clustering [5].

The most typical method of analysis for microarray is clustering. Clustering analysis classifies a large amount of genetic information into several groups that have similar properties, so it is effective for analyzing data. The hard clustering method has been especially useful because it is intuitive and its ease of use.

In this paper division clustering using a two step structure *K*-means clustering method is proposed in order to treat process the thousands of pieces of microarray data effectively. The proposed method processes enormous amounts of microarray data faster because it classifies and clusters data twice. The reliability of these clusters has been evaluated by comparing these results with those of the earlier *K*-means clustering method.

2. Microarray

People usually think that enormous number of genes and their products of a living organism create the mystery of life. Most molecular biological methods are used to study one gene during one experiment. Consequently, the DNA microarray method has attracted wide-spread attention from biologists to monitor the whole genome on a single chip so that researchers can better monitor the results of the simultaneous interactions of the numerous genes [6]. The DNA microarray technique is comprised of the cDNA microarray and oligonucleotide microarray techniques.

Microarray data from an experiment on the manifestations of a gene can be classified using the data clustering method. Thus results can be used in many fields including the development of drugs and toxicological research. In this paper we used the microarray data from rice genes consisting of 17,000 units.

3. Clustering Algorithm

3.1 Several Clustering Algorithms

The clustering algorithm classifies a whole data set into several clusters that have similar characteristics. This algorithm has been used in a variety of fields such as pattern analysis and classification, grouping, decision making, machine-learning situations, and data mining [7]. This clustering algorithm has been developed by experts from various scientific fields such as statistics, computer

science and biology. Now the application of the clustering algorithm is more actively studied than the algorithm itself. The clustering algorithm is largely divided into a hierarchical clustering algorithm and a partitional clustering algorithm [7].

In the clustering algorithm, it is important to define the similarity of two clusters. Similarity was determined by Euclidian distance and measured using equation (1).

$$d(x_i, x_j) = \left\{ \sum_{k=1}^d (x_{i,k} - x_{j,k})^2 \right\}^{\frac{1}{2}} \quad (1)$$

3.2 K-means Clustering Algorithm

The K-means clustering algorithm used in this paper is the most frequently used of the partitional clustering algorithms. K-means clustering differs from hierarchical clustering in that the number of clusters, *k*, needs to be determined at the outset. The goal of the K-means clustering algorithm is to divide the objects into *k* clusters such that some metric relative to the centroids of the clusters is minimized. Two procedures are available to search for the optimum set of clusters. The first assigns each object to a cluster and the second sets initial positions for the cluster centroids. The K-means algorithm consists of the K-means method and K-medoid method. In this paper we used the average value as the center of the cluster.

4. Implementation of the Division System Using the Two-Step Structure K-means Algorithm

In this paper, we used Matlab 7.1 and GUI is shown in Figure 1. GUI is divided into three parts: input, clustering, and results. On the left-side of GUI, the results are shown in the graph window and character window. On the right-side of the GUI, the button that are used to operate the algorithm in the order they are needed.

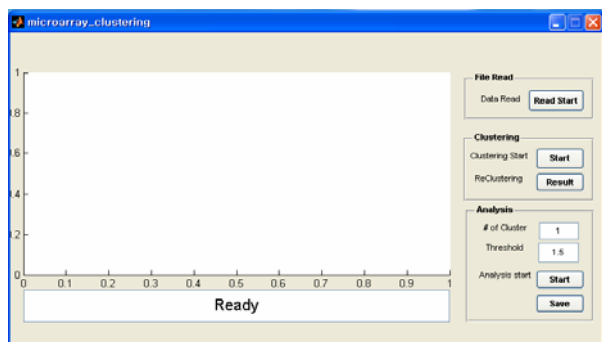


Fig. 1. GUI of the divided clustering system.

Figure 2 shows the flow chart of the program used in this paper, as can be seen, the rice gene microarray data has been normalized and clustered twice. The clustering step ends when the data has been clustered for the second time then the data from the center value of each cluster can be gathered, and the results saved.

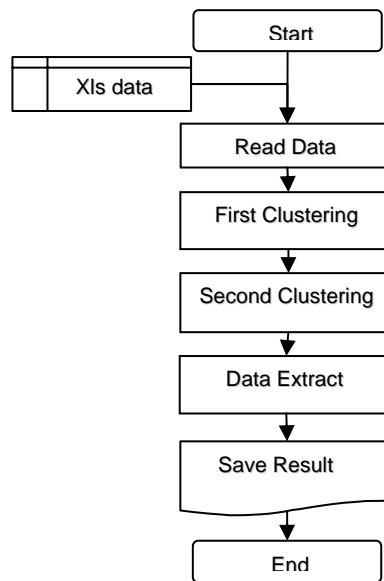


Fig. 2. Flow chart of the proposed algorithm.

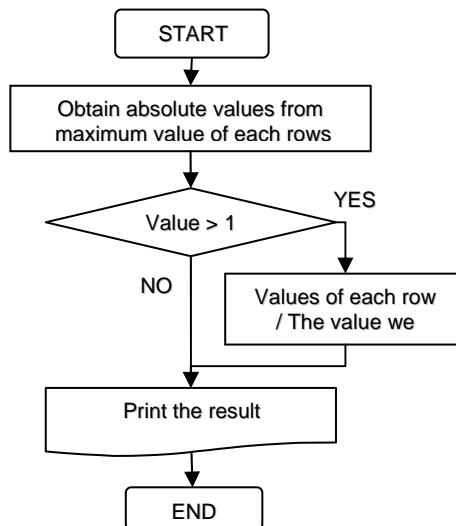


Fig. 3. Normalization flow chart of normalization.

4.1 Normalization

The microarray data used in this paper has a value between -1 and 1, but a few datum are out of this range. The clustering algorithm is based on the similarities between the data, so if the data is outside of the normal range, that value determines its total similarity. Therefore this data needs to be adjusted so that it is between -1 and 1. Consequently it is divided by the maximum or minimum value to normalization. Figure 3 shows the normalization flow chart.

4.2 Division Clustering Algorithm

The data consisted of 17,000 units, so it took too long to cluster the entire data set at one time. First, the 17,000 units were divided into 17 groups consisting of 1,000 units, and then each group was clustered. In this paper, *k* was set at 36. The clustering algorithm was performed a second time using the typical values of the first

clustering. Thus the data was processed twice, and 17,000 units of data were clustered.

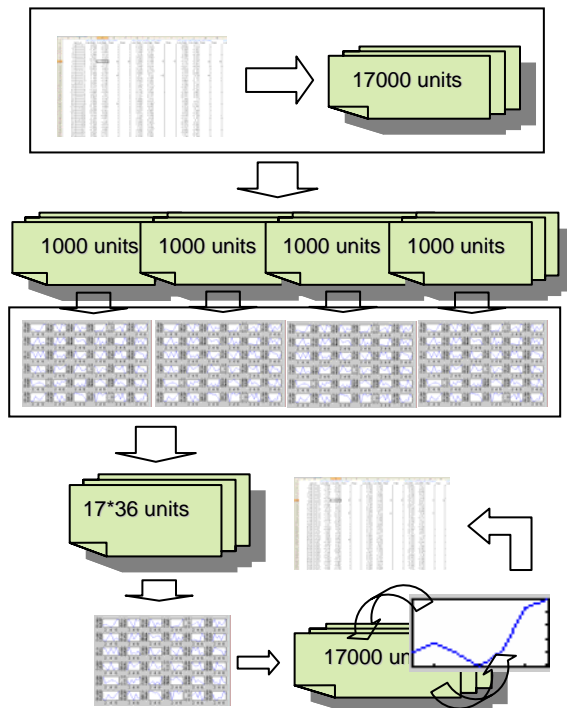


Fig. 4. Process of dividing the clustering.

4.3 Data Analysis and Saved Data

The results of the clustering determined the data that was saved. The graph file of typical values and the text file of the gene numbers were saved from the clustering results.

5. Simulation and Results

In this paper the clustering method for rice microarray data was analyzed and a new clustering method for a large amount of data like that in the rice microarray data was proposed. Figure 5 shows the results of the clustering of the proposed algorithm.

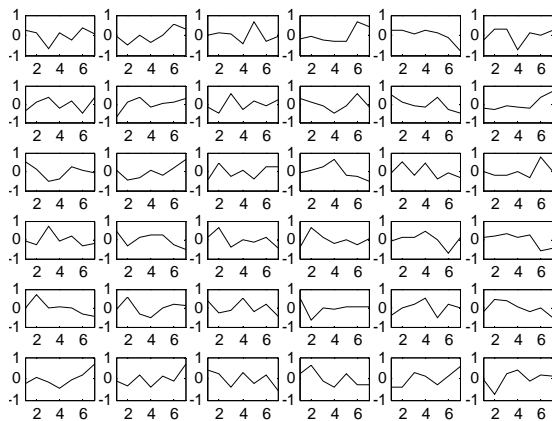


Fig. 5. The clustering results using the proposed method.

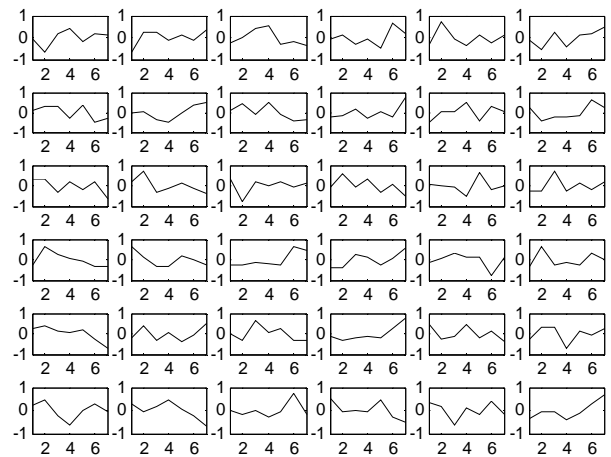


Fig. 6. The clustering results using the previous method.

Figure 6 shows the result of the previous method that clustered the entire data set of 17,000 units at one time. Table 1 compares the results of both method using two values. First, the time each method needed to cluster each data set was compared, and the shorter time is considered to be better. And second, the standard deviation between the typical values resulting from each algorithm was compared, and the larger standard deviation is an indication of a clever classification of the data. A computer with a 3GHz CPU and 512 MB RAM was used to run the algorithm. The previous method required 251 seconds to cluster the data and the proposed method, 47.76 seconds. Therefore, the proposed method sharply reduced the clustering time and is better than the previous method. The standard deviation of the previous method is 0.7702, and the standard deviation is proposed method, 0.7987. Consequently it can be concluded that the proposed method is better.

Table 1. Comparison of the performance of the previous method and proposed method.

clustering method	former method	proposed method
performance time (sec)	251	46.45
standard deviation	0.7702	0.7987

Figure 7 compares two typical values of the two methods when k is 36. As can be seen, the clustering results are similar. Figure 8 compares the methods when k is 16, and the result are also similar.

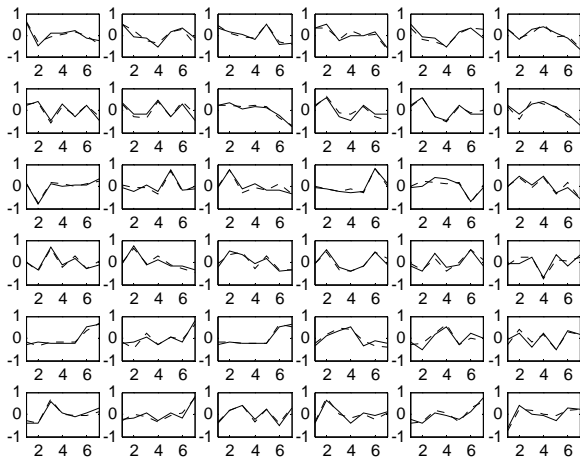


Fig. 7. Comparison of two typical values of the two methods using 17 groups, and a k of 36.

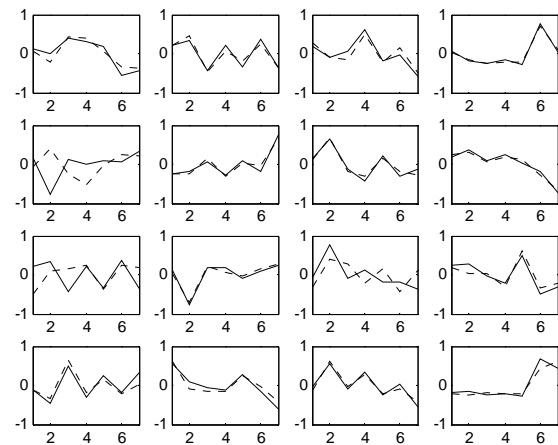


Fig. 8. Comparison of two typical values: two methods using 17 groups, and a k of 16.

6. Conclusion

Most of the study methods used previously have limits. For example, the hierarchical clustering methods cannot process mass data. The previous partitional clustering method can takes more time than proposed method to classify data. In this paper, clustering was divided into two steps using K -means clustering. This method allowed a large amount of data to be processed more quickly than the previous K -means method but with similar results. The speed of the proposed algorithm needs to be verified using other large data sets.

ACKNOWLEDGEMENT

This work was supported by the Second-stage of the Brain Korea 21 project in 2006.

References

[1] Hwang, Seung Yong: DNA chip technology. *Korea Information Science Society*, 18(8).(2000), 23- 28

(in Korean)

[2] Hartuv, E., Schumitt, A., Lange, J., Meier-Ewert, S., Legrach, H. and Shamir, R.: An Algorithm for Clustering cDNAs for Gene Expression Analysis. *Proceedings of the Third International Conference on Computational Molecular Biology (RECOMB 99)*, (1999), 188- 197

[3] Ben-Dor, A., Shamir, R., Yakhini, Z.: Clustering Gene Expression Patterns. *Journal of Computational Biology*, 6. (1999), 281- 297

[4] Tamayo, P., Slonim, D., Mesirov, J., Zhu, Q., Kitareewan, S., Dmitrovsky, E., Lander, E. S. and Golub, T. R.: Interpreting patterns of gene expression with self-organizing maps : Methods and application to Hematopoietic differentiation. *Proceedings of National Academy of Sciences of the USA* , 96. (1999), 2907- 2912

[5] Eisen, M. B., Spellman, P. T., Brown, P. O. and Botstein, D.: Cluster analysis and display of genome-wide expression patterns. *Proceedings of National Academy of Sciences of the USA* , 95. (1998), 14863- 14868

[6] <http://gene-chips.com>

[7] Jain, A. K., Murty, M. N. and Flynn, P.J.: Data clustering: A review. *ACM Computing Surveys*, 31(3). (1999), 264-323

A Cost-Based Fuzzy System for Pattern Classification with Class Importance

T. Nakashima, Y. Yokota, H. Ishibuchi

Graduate School of Engineering
Osaka Prefecture University
Gakuen-cho 1-1, Sakai, Osaka 599-8531, Japan
{nakashi, hisaoi}@cs.osakafu-u.ac.jp
yokota@ci.cs.osakafu-u.ac.jp

G. Schaefer

School of Engineering and Applied Science
Aston University
Birmingham B4 7ET, U.K.
g.schaefer@aston.ac.uk

Abstract

This paper proposes a cost-based fuzzy classification system for pattern classification problems with an order class importance. The task here is to minimize the misclassification of patterns from an important class. It is assumed in this paper that the classification importance is given for each class, not for each pattern. Another assumption in this paper is that only the order of importance is given for given classes without any numerical measures of importance. We show the performance of the proposed cost-based fuzzy classification system for a real-world pattern classification problem.

1 Introduction

Fuzzy rule-based systems have been mainly applied to control problems [1]-[3] while more recently they have also been applied to pattern classification problems. One advantage of fuzzy rule-based systems is its interpretability. There are many approaches to the automatic generation of fuzzy if-then rules from numerical data for pattern classification problems [4]-[11].

There are several cases where misclassification of a particular input pattern causes extra costs. For example, in the medical diagnosis of cancer diagnosing malignant tumors as benign and hence mistaking a cancer patient as healthy could be penalized more than interpreting benign tumors as malignant. In [12] a pattern classification problem is re-formulated as a cost minimization problem. The concept of a weight is introduced for each training pattern in order to handle this situation. The weight of an input pattern can be viewed as the cost of misclassification of the pattern. Fuzzy if-then rules were generated by considering the

weights as well as the compatibility of training patterns.

In many cases it is difficult to specify an exact value of the cost for misclassification. Contrary to this, the order of importance is easily available for a problem domain. For example, in the medical diagnosis of cancer it is reasonable to consider that the misclassification of malignant tumors as benign incurs higher cost than the other misclassification even if we do not know how high the cost is for both types of misclassification (i.e., misclassifying malignant tumors as benign and benign ones as malignant).

In this paper we propose a method for constructing a fuzzy classification system that considers the order of class importance. The assumption here is that a set of training patterns and the order of class importance is given a priori. We compare the performance of the proposed fuzzy classification systems and the conventional ones for a real-world pattern classification problem.

2 Classification Problem

Without loss of generality, we assume that given training patterns are distributed over an n -dimensional pattern space $[0, 1]^n$. We also assume that m training patterns $\mathbf{x}_p = (x_{p1}, x_{p2}, \dots, x_{pn})$, $p = 1, 2, \dots, m$, from C classes are given a priori.

In many real-world problems, the misclassification cost is different for different patterns. It is often the case that misclassification cost is different class by class. As an example let us consider the medical diagnosis of cancer where the task is to diagnose a tumor as benign (not cancerous) or malignant (cancerous). Although any misclassification should be avoided, more

attention should be put into the correct diagnosis of malignant than that of benign tumors because the misdiagnosis of the cancer patient as not having the disease leads to much higher costs than the other misclassification. In this paper, we handle this situation by specifying different misclassification costs for different classes and put more emphasis on minimizing the misclassification costs rather than minimizing the number of misclassified input patterns.

3 Fuzzy Rule-Based Classification

The proposed method is based on a fuzzy rule-based classification system that was proposed by Ishibuchi et al.[6]. A fuzzy rule-based classification system is composed of a set of fuzzy if-then rules. The antecedent part of a fuzzy if-then rule specifies a fuzzy subarea in the pattern space while the consequent part describes the class and the degree of certainty for the specified fuzzy subarea. A fuzzy if-then rule is automatically generated from numerical data that are given as a set of training patterns. This section explains the generation of fuzzy if-then rules from given training patterns.

The following type of fuzzy if-then rules is used in the fuzzy rule-based classification system for an n -dimensional C -class pattern classification problem:

$$\begin{aligned} \text{Rule } R_j: & \text{ If } x_1 \text{ is } A_{j1} \text{ and } \dots \text{ and } x_n \text{ is } A_{jn} \\ & \text{ then Class } C_j \text{ with } CF_j, \quad j = 1, 2, \dots, N, \end{aligned} \quad (1)$$

where R_j is the label of the j -th fuzzy if-then rule, A_{j1}, \dots, A_{jn} are antecedent fuzzy sets on the unit interval $[0, 1]$, C_j is a consequent class (i.e. one of the C given classes), CF_j is the grade of certainty of rule R_j , and N is the total number of fuzzy rules. We use triangular-type membership functions in Fig. 1 for antecedent fuzzy sets A_{j1}, \dots, A_{jn} . Figure 1 shows four fuzzy partitions. We denote the number of fuzzy sets in the unit interval as L . The total number of generated fuzzy if-then rules N depends on the dimensionality of a pattern classification problem n and the number of fuzzy partitions L . For a ten-dimensional pattern classification problem for instance, the total number of generated fuzzy if-then rules is $N = 2^{10} = 1024$ when the number of fuzzy sets for each attribute is specified as $L = 2$. While we use a homogeneous fuzzy partition as in Fig. 1, it is also possible to use a heterogeneous fuzzy partition that reflects the distribution of training patterns. In this paper only homogeneous fuzzy partition is used because of the interpretability of the fuzzy rule-based classification systems.

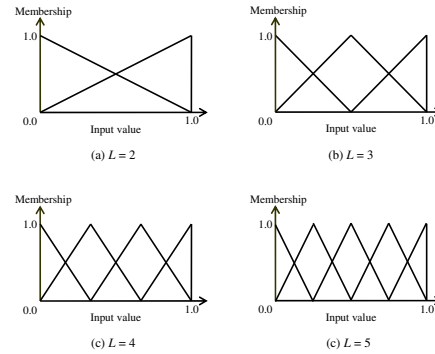


Figure 1: Triangular-type membership function used for antecedent fuzzy sets.

The generation procedure of fuzzy if-then rules consists of three steps: specification of the antecedent part, determination of the consequent class, and the calculation of the grade of certainty. Once the number of fuzzy sets L for each attribute is specified by an expert with the domain knowledge, the pattern space is divided into L^n fuzzy subareas where n is the dimensionality of a pattern classification problem at hand. Thus the specification of the antecedent part of a fuzzy if-then rule is already performed once a fuzzy subarea to generate a fuzzy if-then rule is fixed. The consequent part (i.e., the consequent class and the grade of certainty) is determined from the given training patterns [6]. In [15] it is shown that the use of the grade of certainty in fuzzy if-then rules allows us to generate comprehensible fuzzy rule-based classification systems with high classification performance. In the following we describe the remaining two steps in detail.

3.1 Determination of Consequent Class

The consequent class C_j for the fuzzy if-then rule R_j is determined from a set of the given training patterns \mathbf{x}_p , $p = 1, 2, \dots, m$. In [13] first the sum of the compatibility is calculated for each class. Then the class with the largest value is taken as the consequent class of the fuzzy if-then rule. The procedure of determining the consequent class in the conventional fuzzy rule-based classification systems is summarized as follows:

[Conventional determination of C_j]

Step 1: Calculate $\beta_{\text{Class } h}(j)$ for Class h as

$$\beta_{\text{Class } h}(j) = \sum_{\mathbf{x}_p \in \text{Class } h} \mu_j(\mathbf{x}_p), \quad (2)$$

where

$$\mu_j(\mathbf{x}_p) = \mu_{j1}(x_{p1}) \cdots \mu_{jn}(x_{pn}), \quad (3)$$

$\mu_{j1}(\cdot), \mu_{j2}(\cdot), \dots, \mu_j(\cdot)$ are the membership function of the fuzzy sets $A_{j1}, A_{j2}, \dots, A_{jn}$, respectively.

Step 2: Find Class \hat{h} that has the maximum value of $\beta_{\text{Class } h}(j)$:

$$\beta_{\text{Class } \hat{h}}(j) = \max_{1 \leq k \leq C} \{\beta_{\text{Class } k}(j)\}. \quad (4)$$

Since the above procedure does not consider misclassification costs nor class importance, we propose a cost-based determination method. In this approach the consequent class of a fuzzy if-then rule is determined from its compatible training patterns. Let us define the number of compatible training patterns for Class k with the fuzzy if-then rule R_j as n_j^k . A pattern $\mathbf{x} = (x_1, x_2, \dots, x_n)$ is compatible with the fuzzy if-then rule R_j if the following condition holds:

$$\mu_{j1}(x_1) \cdot \mu_{j2}(x_2) \cdots \mu_{jn}(x_n) > 0, \quad (5)$$

where $\mu_{j1}(\cdot), \mu_{j2}(\cdot), \dots, \mu_{jn}(\cdot)$ are the membership functions of antecedent fuzzy sets $A_{j1}, A_{j2}, \dots, A_{jn}$ of R_j . The consequent class of R_j is determined as the class with the maximum misclassification cost among the n_j^k training patterns. We use a multiplication operator to calculate the compatibility of an n -dimensional pattern with a fuzzy if-then rule in this paper.

The cost-based class determination procedure is performed as follows:

[Proposed determination of C_j]

Step 1: Calculate n_j^k for Class $k, k = 1, 2, \dots, C$.

Step 2: Find Class \hat{h} that is the most important (i.e., has the highest misclassification cost) among those classes with n_j^k as follows:

$$\text{Cost}_j^{\hat{h}} = \max_{\substack{1 \leq k \leq C \\ n_j^k > 0}} \text{Cost}_j^k. \quad (6)$$

3.2 Calculation of the Grade of Certainty

The procedure of calculating the grade of certainty in this paper is different from that in [13]. In [13] the grade of certainty CF_j of rule R_j is determined as follows:

$$CF_j = \frac{\beta_{\text{Class } \hat{h}}(j) - \bar{\beta}}{\sum_h \beta_{\text{Class } h}(j)}, \quad (7)$$

where

$$\bar{\beta} = \frac{\sum_{h \neq \hat{h}} \beta_{\text{Class } h}(j)}{C - 1}. \quad (8)$$

On the other hand, the proportion of $\beta_{\text{Class } \hat{h}}(j)$ over the sum of $\beta_{\text{Class } \hat{h}}(j), 1 \leq h \leq C$, is used in this paper. This is because the grade of certainty sometimes becomes an invalid value (e.g., negative) with the conventional determination.

3.3 Fuzzy Inference for Classification

Using the rule generation procedure outlined above we can generate N fuzzy if-then rules as in Equation (1). After both the consequent class C_j and the grade of certainty CF_j are determined for all N rules, a new pattern $\mathbf{x} = (x_1, \dots, x_n)$ is classified by the following procedure:

Step 1: Calculate $\alpha_{\text{Class } h}(\mathbf{x})$ for Class $h, j = 1, \dots, C$, as

$$\alpha_{\text{Class } h}(\mathbf{x}) = \max\{\mu_j(\mathbf{x}) \cdot CF_j | C_j = h\}. \quad (9)$$

Step 2: Find Class h' that has the maximum value of $\alpha_{\text{Class } h}(\mathbf{x})$:

$$\alpha_{\text{Class } h'}(\mathbf{x}) = \max_{1 \leq k \leq C} \{\alpha_{\text{Class } k}(\mathbf{x})\}. \quad (10)$$

If two or more classes take the maximal value, then the classification of \mathbf{x} is rejected (i.e. \mathbf{x} is left as an unclassifiable pattern), otherwise \mathbf{x} is assigned to Class h' .

4 Computational Experiments

In the computational experiments performed to evaluate our proposed classifier we use Appendix data set. The appendix represents a seven-dimensional two-class pattern classification problem. There are 106 patterns in the data set, 21 patterns from Class 1 and 85 from Class 2. We assume in the computational experiments in this paper that Class 1 is more important than Class 2.

We apply both the cost-based fuzzy classification system and the conventional to the three data sets. First we examine the performance of both fuzzy classification systems on the training data. That is, the performance is measured on the whole data set that is used to generate fuzzy classification systems. We specified the number of fuzzy partitions $L = 3$ for each axis. We show the experimental results in Fig. 2.

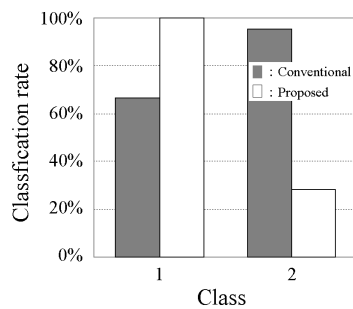


Figure 2: Results for training data.

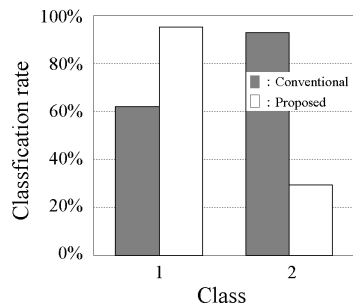


Figure 3: Results for test data.

5 Conclusions

In this paper we have proposed a cost-based fuzzy classification systems for pattern classification problems with an order of class importance. The task is to minimize the total misclassification cost. Experimental results demonstrated the effectiveness of the proposed method compared to a conventional fuzzy-rule classification system.

References

- [1] C. C. Lee. 1990, "Fuzzy Logic in Control Systems: Fuzzy Logic Controller Part I and Part II", *IEEE Trans. Syst., Man, Cyberetics*, Vol. 20:404-435.
- [2] C. T. Leondes. 1999, "Fuzzy theory Systems", *Techniques and Applications*. Academic Press, San Diego, Vol.1-4, 1999.
- [3] M. Sugeno. 1985, "An Introductory Survey of Fuzzy Control", *Information Science*, Vol. 30, No. 1/2:59-83.
- [4] K. Nozaki, H. Ishibuchi, H. Tanaka. 1996, "Adaptive fuzzy rule-based classification systems", *IEEE Trans. on Fuzzy Systems*, Vol. 4, No. 3:238-250.
- [5] G.J. Klir, B. Yuan. 1995, *Fuzzy Sets and Fuzzy Logic*, Prentice-Hall.
- [6] H. Ishibuchi, K. Nozaki, H. Tanaka. 1992, "Distributed representation of fuzzy rules and its application to pattern classification", *Fuzzy Sets and Systems*, Vol. 52, No. 1:21-32.
- [7] M. Grabisch. 1996, "The representation of importance and interaction of features by fuzzy measures", *Pattern Recognition Letters*, Vol. 17:567-575.
- [8] M. Grabisch, F. Dispot. 1992, "A comparison of some methods of fuzzy classification on real data", *Proc. of 2nd Int. Conf. on Fuzzy Logic and Neural Networks*, 659-662.
- [9] M. Grabisch, and J.-M. Nicolas. 1994, "Classification by fuzzy integral: performance and tests", *Fuzzy Sets and Systems*, Vol. 65, No. 2/3:255-271.
- [10] G.G. Yen, P. Meesad. 2001, "Constructing a fuzzy rule-based system using the ILFN network and genetic algorithm", *International Journal of Neural Systems*, Vol. 11, No. 5:427-443.
- [11] Y. Chen, J.Z. Wang. 2003, "Support Vector Learning for Fuzzy Rule-Based Classification Systems", *IEEE Transactions on Fuzzy Systems*, Vol. 11, No. 6:716-728.
- [12] T. Nakashima, Y. Yokota, H. Ishibuchi, A. Bargiela. 2005, "Constructing Fuzzy Classification Systems from Weighted Training Patterns," *Proc. of European Simulation Conference*, 2386-2391.
- [13] H. Ishibuchi, K. Nozaki, N. Yamamoto, H. Tanaka. 1995, "Selecting fuzzy if-then rules for classification problems using genetic algorithms", *IEEE Trans. on Fuzzy Systems*, Vol. 3, No. 3:260-270.
- [14] H. Ishibuchi, T. Nakashima. 1999b, "Improving the performance of fuzzy classifier systems for pattern classification problems with continuous attributes", *IEEE Trans. on Industrial Electronics*, Vol. 46, No. 6:1057- 1068.
- [15] H. Ishibuchi, T. Nakashima. 2001, "Effect of rule weights in fuzzy rule-based classification systems", *IEEE Trans. on Fuzzy Systems*, Vol. 9, No. 4:506-515.

A Verification of Normalization Results using Variable Clustering Methods in cDNA Microarray Data

[†]Gyeongdong Baek, [†]Yuntae Kim, ^{††}Ji-Young Kim, [†]Sungshin Kim, and ^{††}Choon-Hwan Lee

[†]School of Electrical and Computer Engineering, Pusan National University, Busan, Korea
Pusan National University 30 Changjeon-dong, Keumjeong-ku, Busan 609-735, Korea
E-mail: gdbaek@pusan.ac.kr, dream0561@pusan.ac.kr, sskim@pusan.ac.kr

^{††}School of Molecular Biology, Pusan National University, Busan, Korea
Pusan National University 30 Changjeon-dong, Keumjeong-ku, Busan 609-735, Korea
E-mail: dryoung82@pusan.ac.kr, chlee@pusan.ac.kr

Abstract – cDNA microarray analysis has enabled the measurement of thousands of gene expressions at the same time. The gene expression levels are monitored using log ratios between green and red fluorescent intensities. However, imbalances can be caused by different incorporations of dyes, amounts of mRNA, and scanning parameters and these biases result in incorrect conclusions. Normalization makes gene expression data more accurate by removing these systematic variations. Therefore, the study of normalization is important for clustering and also profitable by making groups that show similar expression patterns. We tried to certify the results of normalization by comparing the operation time of k -means and fuzzy c -means clustering methods. When it takes less time for k -means clustering and more time for fuzzy c -means clustering relatively, we can say the result of the normalization is good. In addition, we analyzed characteristics of standard normalization using two clustering methods. These two methods will be used as the verification methods of any normalization in cDNA microarray.

Keywords: fuzzy clustering, fuzzy c -means algorithm, k -means clustering, microarray, normalization

1. Introduction

The latest advancements in genetics has made many things possible [1]. They ascertain the facts how the gene expressed in body and what to do. cDNA microarray maps and sequences all the genes on a small chip. It looks over gene expression patterns. For example, a disease happens because of an interaction between genes and not simply because of one gene.

cDNA microarray is useful to observe the whole expression pattern in this case[2]. The cDNA microarray data needs normalization steps before classification steps are possible [3]. Because there are more noise than any experimentation. The difference the physical properties of two dyes accounts for that noise. This noise is the exact intensity of temperature or fluorescence, sometimes the green dye seems to have high fluorescence intensity. It doesn't have the

same dye intensity for this reason [4]. There are other problems which the efficiency of dye incorporation, data collection, the data scanning process, the difference between pin-groups and slide heterogeneity. All of these problems generate noise. The quality of data is poorer as the noise adds up. The noise differs in degree due to an experimenter's skill or chemical materials used. The purpose of normalization is to correct errors in the patterns among the kinds of noise. cDNA microarray normalization means the revision of fluorescence intensity and the comparison of gene expression level through experiments or slides. cDNA microarray normalization is divided into three divisions of selection methods. In the first method, let us suppose that a small ratio is expressed in all genes. This normalization applies to almost all of the genes. The second method, genes are normalized based on constant expression. This method applies to a subset of genes instead of all genes. In the third method, genes are either arranged by spiked control or the titration series of control sequence is used. This paper uses the first method in which all genes in the cDNA microarray are used.

This paper verifies the normalization results of the cDNA microarray data. It uses the eigen feature of k -means clustering and the fuzzy c -means clustering algorithm [5-8]. The eigen feature makes rules according to experiment data. It influences operation time of the termination tolerance. The notion of cDNA microarray analysis decreased the average operation time of k -means clustering and increased the time of fuzzy c -means clustering. The cause of the operation time is an appraised method of cluster position selection. Section 2 explains the difference and features of the two clustering algorithms. Section 3 explains the structure of the experiment data. Section 4 explains the noise reduction method and normalization to be used. Section 5 shows the result based on the proposal theory, and shows the proper objective. The last section presents conclusions and suggests future study.

2. The Clustering Characteristic Analysis

Clustering analysis uses general Euclidean distance between an independent entity. The calculated distance indicates similarity and non-similarity. For k -means

clustering, it makes using (1) and (2).

$$c_i^i = \frac{\sum_{j=1}^d u_{ij}^{(l-1)} m_j}{\sum_{j=1}^d u_{ij}^{(l-1)}} \quad 1 \leq i \leq c \quad (1)$$

$$u_{ij}^{(l)} = \begin{cases} 1 & \text{if } d(m_j, c_i^{(l)}) = \min_{1 \leq k \leq c} d(m_j, c_k^{(l)}) \\ 0 & \text{otherwise} \end{cases} \quad (2)$$

When it satisfies (3), it stops the operation.

$$\text{If } \|U^{(l)} - U^{(l-1)}\| \leq \delta \text{ then END} \quad (3)$$

This means the change of U , the cluster membership set, is confined to the limits of the termination tolerance. Fuzzy c-means clustering uses Euclidean distance to estimate similarity, too. It uses U , which is a real number $[0,1]$, but not $\{0,1\}$.

$$u_{ij}^{(l)} = \frac{1}{\sum_{k=1}^c (d_A^2(m_j, c_i^{(l)}) / d_A^2(m_j, c_k^{(l)}))^{1/(c-1)}} \quad (4)$$

The membership matrix changes can be explained by Figure 1.

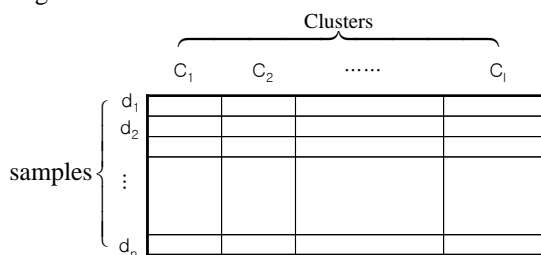


Fig. 1 Membership matrix.

Sample $D = \{d_i | i = 1, \dots, N\}$ belongs to each cluster with membership values. This means that each sample has an overlap, so it gives the problem careful consideration. For the last section, the normalization corrects fluorescent intensity imbalances and gene expression levels between slides. When it corrects two factors, the cDNA microarray data removes absolute fluorescence intensity and only the variation between samples remains. So it is difficult to divide clusters. We may be thought that it is more convergent than k -means clustering, because fuzzy c-means clustering fully considers cluster membership. However, fuzzy c-

means clustering time is shortened after normalization. This result can be explained by the cluster membership error effects decreased. If there are more samples, it becomes a remarkable large difference. Unlike fuzzy c-means clustering, k -means clustering takes longer and the variance becomes larger after normalization.

3. Experiment Data Structure Analysis

cDNA microarray data is generally represented in matrix form. The matrix expresses the genes in rows, and the cDNA chips or samples in columns. This paper uses the cDNA microarray data from 17,000 genes and 7 chips. The microarray data matrix form is as follows.

Table. 1 DNA microarray matrix

Gene	Chip 1	Chip 2	...	Chip 7
1	$x_{1,1}$	$x_{1,2}$...	$x_{1,7}$
2	$x_{2,1}$	$x_{2,2}$...	$x_{2,7}$
...
17,000	$x_{17000,1}$	$x_{17000,2}$...	$x_{17000,7}$
...

For example, $x_{1,1}$ is the expression value of sample 1 and gene 1, and $x_{3,2}$ is the expression value of sample 2 and gene 3. Each expression is a log-ratio value. The microarray software uses this matrix form in the majority of cases.

4. Noise Removal and Normalization

4.1 Noise Removal

When the flag which means reliability level is -50 or -100, it is cut out. In addition, when the sum of gene change rate doesn't rise above the threshold, it is also cut out. The threshold this paper used is 2. It was able to remove 300 genes.

$$\text{IF } |x_{i,1} + x_{i,2} + \dots + x_{i,n}| < 2$$

$$X(i,:) = []$$

END

4.2. 1 Generalization of Normalization

The normalization method is illustrated in figure 2.

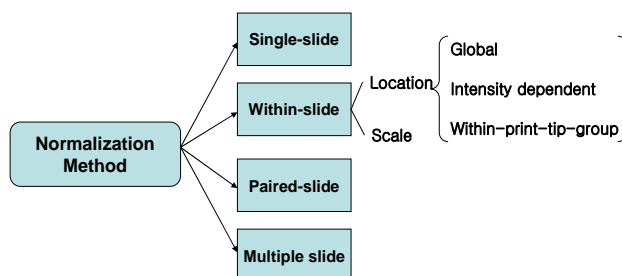


Fig. 2 Normalization Method.

Common normalization methods correct errors using means and variances of the slide by matching the red and green intensities. That is to say, the gene expression level corrects as many errors as α .

$$\log\left(\frac{R}{G}\right) - \alpha \quad \alpha = \text{Normalization method}$$

α can build up to several normalization. If a special α is made, there will be need to verify.

4.2.2 The Normalization Equation to be used

This paper uses the standardization method[3]. The sample is updated to calculate a mean and standard variation. (5) is the mean of each sample, (6) is the standard variation of sample.

$$\bar{x}_i = \frac{x_{i,1} + x_{i,2} + \dots + x_{i,n}}{n} \quad (5)$$

$$s_i = \sqrt{\frac{(x_{i,1} - \bar{x}_i)^2 + (x_{i,2} - \bar{x}_i)^2 + \dots + (x_{i,n} - \bar{x}_i)^2}{n-1}} \quad (6)$$

The value of each normalized is updated on the cDNA microarray data matrix.

$$\frac{x_{i,1} - \bar{x}_i}{s_i}, \frac{x_{i,2} - \bar{x}_i}{s_i}, \dots, \frac{x_{i,n} - \bar{x}_i}{s_i} \quad (7)$$

5. The Experimentation Result

The result of experimentation is drawn in box-plot, changing the sample size and the cluster number. A box-plot can reasonably show the feature affected by the first random centers.

5.1. The Result of *k*-means Clustering

If the normalization of the cDNA microarray goes well, a operation time of *k*-means clustering takes longer. The interquartile range of the box-plot has 50 percent of the observed data. When the value of the median is similar, the large rate of interquartile takes longer, as in figure 3 and figure 4. After the normalization, *k*-means clustering takes longer. That is to say, the rate of change is more emphatic than the absolute fluorescent intensity, because *k*-means clustering has a sensibility for uclidean distance. This feature of normalization also occurs in fuzzy c-means clustering

5.2.1 The Result of Fuzzy c-means Clustering

The features of *k*-means clustering are certainly observed in fuzzy c-means clustering. When the value of the median is similar, the rate of interquartile takes longer, as in figure 5 and figure 6. Figure 5 is ambiguous, but figure 6 shows that the operation does not take long, because fuzzy c-means clustering has a sensibility of cluster membership.

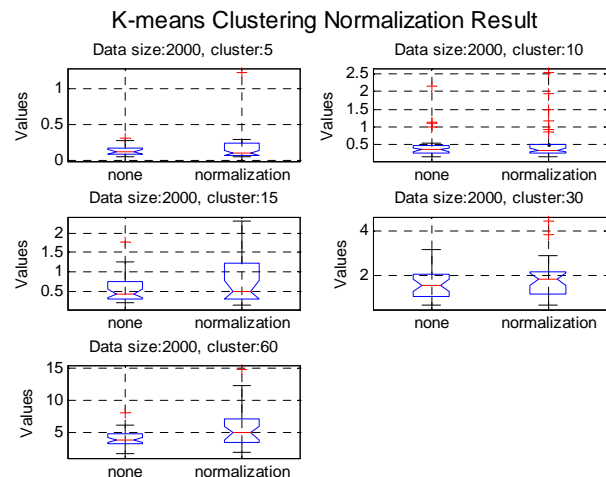


Fig. 3 The result of *k*-means clustering (size:2000).

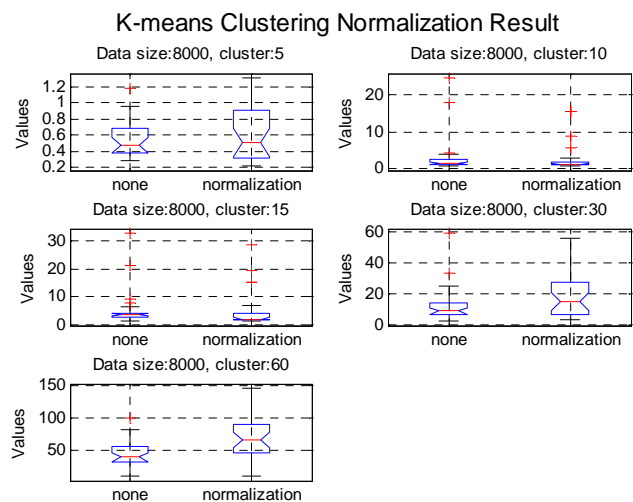


Fig. 4 The result of *k*-means clustering (size:8000).

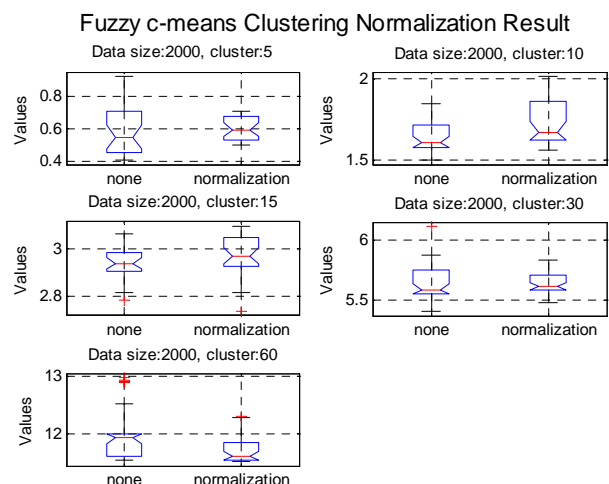


Fig. 5 The result of fuzzy c-means clustering (size:2000)

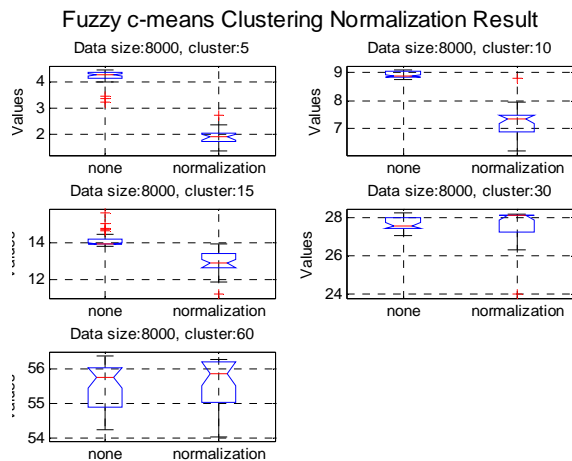


Fig. 6 The result of fuzzy c-means clustering (size:8000).

5.2.2 A High Spot

A high spot is found in figure 6. Figure 7 zooms cluster:30 and cluster:60 in figure 6. It is difficult to show the change of time before and after. Although the normalization emphasizes sample expression, it is difficult to classify to the number of clusters, so it can be assumed that the 8000 samples have 15~30 clusters. When the interquartile rate of fuzzy c-mean clustering keeps their distance, the cluster of gene expression is determined.

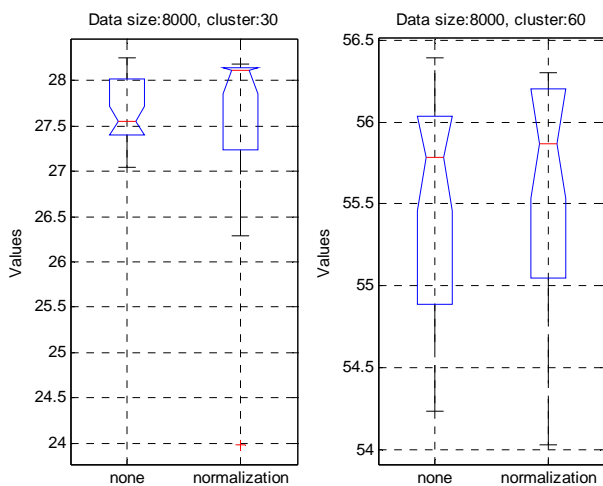


Fig. 7 Zoom in Fig. 6 (cluster:30 and 60).

6. Conclusion

This paper proposes an appraised method of normalization in the cDNA microarray. The proposed model uses the difference of cluster membership update method. However, in this model, it is difficult to determine optimized data-size and cluster number in the microarray. Therefore, in subsequent research, the cluster number of gene expression by the interquartile rate is expected to be determined.

ACKNOWLEDGEMENT

This work was supported by the Second-stage of the Brain Korea 21 project in 2006.

References

- [1] Brown PO, Botstein D. 1999. Exploring the new world of the genome with DNA microarrays. *Nat Genet* 1999 Jan;21(1 Suppl):33-7
- [2] D. Wishart, "Efficient hierarchical cluster analysis for data mining and knowledge discovery." *Computing Science and Statistics*. pp. 257-263, 1998.
- [3] William Shannon, Robert Culverhouse, Jill Duncan." Analyzing microarray data using cluster analysis",2003.
- [4] J. Derisi, V. Iyer and P. Brosh, "Exploring the metabolic and genetic control of gene expression on a genomic scale," *Science*, vol. 278, pp. 680-686, 1997.
- [5] Kjersti Aas, "Microarray Data Mining: A Survey", 2001.
- [6] E. Hartuv, A. Schumitt, J. Lange, S. Meier-Ewert, H. Legrach and R. Shamir, "An Algorithm for Clustering cDNAs for Gene Expression Analysis," *Proceedings of the Third International Conference on Computational Molecular Biology (RECOMB 99)*, pp.188- 197, 1999.
- [7] J. C. Bezdek, *Pattern recognition with fuzzy objective function algorithms*, Plenum Press, 1981.
- [8] F. Hoppner, F. Klawonn, R. Kruse and T. Runkler, *Fuzzy cluster analysis*, Wiley, 2000.

Improvement of Color Images Halftoning with Simulated Annealing

Ken-ichi Tanaka Ryouta Isoi

Meiji University
1-1-1, Higashimita, Tama, Kawasaki, Kanagawa, 214-8571, Japan
E-mail: {tanaken, ce66003}@isc.meiji.ac.jp

Keyword : halftoning, simulated annealing, color image, quantization, cost function

Abstract

In this paper, it introduced simulated annealing (SA) as a method of halftoning in the color image. 3 methods called Type1, Type2 and Type3 are research in the paper. Type1 is using the SA with resolving of color image into three primary colors ingredient of Red (R), Green (G) and Blue (B). Those applied the halftoning by SA respectively, and composed process result. In the Type2, a color regards as the 3 dimensions vector of R, G and B. Not only size of error vector but also angle error added to cost. In the Type3, the basis of above two results, it made not to consider the cost of angle error at Type2. The appropriation pixel becomes R=G at the process image when R=G of original image was formed. Similarly, in case of becoming R=B and B=G, it were assumed to a restriction.

In case of SA is adapted to the halftoning in color image. we could get result the superior image quality using Type3. Therefore, availability to the halftoning to the color image of SA became clear.

1.Introduction

Halftoning¹⁾⁻³⁾ has an important role in the hard copy of a printer and facsimile communication system. The digital halftoning of the gray scale images has dither method¹⁾, error diffusion method²⁾, application of the solution of combinatorial optimization proble^{3),6)} and various methods.

In case halftoning is thought as combinatorial optimization problem, ideal image to visual sensation is searched. It has been proposed that genetic algorithms (GA) on the process to the gray scale image. String size is not taken greatly, there is influence by the non-continuity in the boundary³⁾. For this reason, we introduce makes to hasten calculation speed substantially clear at using SA⁴⁾⁻⁶⁾. In this paper, it introduces Simulated Annealing (SA) at the halftoning in the color image. We can get result that halftoning of color image is good visual sensation and when input image became a gray scale image, gray scale image can be obtained in process image.

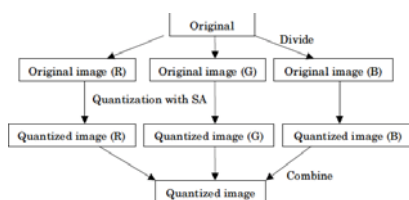


Fig. 1 Procedure of the halftoning with deviding the three primary colors

2. Extension to color image of halftoning used SA in gray scale image

It is mentioned procedure for halftoning of color image based on halftoning⁶⁾ for gray scale image as mentioned using SA. At the color image the case of Windows Bit Map, the three primary colors of R, G and B has density information of 0-255 respectively. These 3 plains would be piled with regarding R, G and B as three gray scale images. It stands for the flow of this process to Fig. 1, and states the process to the following. This method is called Type1.

- 1) The color image is resolved into 3 planes on three primary colors of R, G and B.
- 2) It uses Cost function that is the same as the case of the gray scale image and carries out SA on each planes.
- 3) Process image can be obtained by each solution.

Cost function used in the SA is assumed to stand by linear combination with cost E_m on present of gray level and cost E_c on contrast of edge, those showed by following equation.

$$E = \alpha_m E_m + \alpha_c E_c \quad (1)$$

Here, α_m and α_c are each weight. The relation is filled $\alpha_m + \alpha_c = 1$.

Cost E_m on present of gray level showed by following equation.

$$E_m = \sum_{(x,y) \in block} \frac{1}{N_p} |F(x,y) - q_F(x,y)| \quad (2)$$

Here, gray level density of original image regards $F(x,y)$ and gray level density of process image regards $Q(x,y)$ in coordinates (x,y) . Then $q_F(x,y)$ is gray level density of binary pattern in Gaussian filter convolute, N_p is pixel number in *block*. In case of changing color of a pixel, *block* in this equation is domain where effect cost function. It indicates the pixel and 24 neighborhood pixels here. Cost E_c about the contrast shown by following equation.

$$E_c = \sum_{(x,y) \in block} \frac{1}{N_p} |F'(x,y) - Q'(x,y)| \quad (3)$$

$$\begin{cases} F'(x,y) = F(x,y) - f_s(x,y) \\ Q'(x,y) = Q(x,y) - M/2 \end{cases} \quad (4)$$

Here, $f_s(x,y)$ is local average of $F(x,y)$ in 5×5 pixels. M is gray level number in original image.

The process image could be got by the method that is shown a Fig. 2.

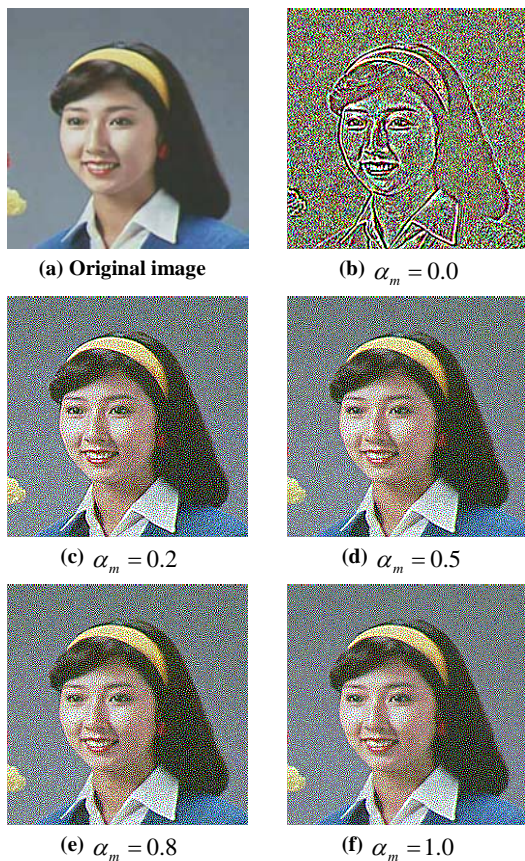


Fig. 2 Halftone Images using the Procedure Type1 (Original images is full color image)

These images are $256(H) \times 256(V)$ pixels, 24bit images. Therefore, α_m shows cost on weight about the gray level density, α_c shows cost on weight about the contrast, ($\alpha_c = 1 - \alpha_m$). In SA, initial temperature T_0 is equal to 100, decreasing coefficient α is equal to 0.995. The chapter is explained again about Compromise type of the initial temperature and the temperature fall coefficient. The gray scale image is well known³⁾⁶⁾ for getting the best result at $\alpha_m = 0.2$. Also at the result of Fig. 2(b)-(f), the outline is clear and also the reappearance of color is good when the color image is used in case of $\alpha_m = 0.2$. Therefore, halftoning in the color image also consider ratio of weight about gray level density α_m and weight about contrast α_c is the same.

The same process is applied to the gray scale image (It is RGB24bit but calculates brightness information, and $R=G=B$ is consisted). This is shown a Fig. 3. The color other than white and black is breaking out. The reason, it is because same solution can't get necessarily in R plane, G plane and B plane by multimodal of a solution in SA. And the result that convoluted them appeared the color other than white and black. Inherence the gray scale image is desirable that the color other than white and black is not to break out. Therefore, the color image could get good result. However, the gray scale image could get bad result.

3. Primary color process when it doesn't resolve into 3 primary colors ingredient

The color image is resolved into each ingredient of R, G, B, after did halftoning on SA, it was adapted to reset

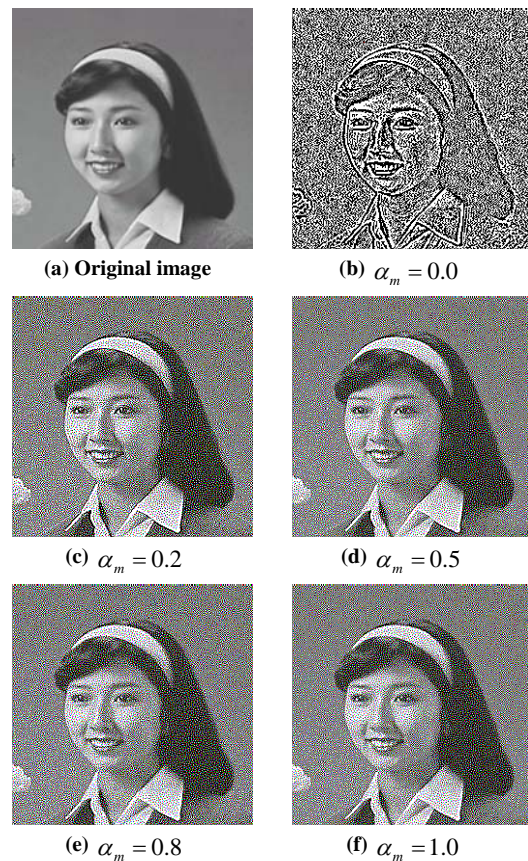


Fig. 3 Halftone Images using the Procedure Type1 (Original images is gray scale image)

method in previous chapter. Original image is case of full color image, it became comparatively good result. However, Original image is case of gray scale image, the result is necessary to improve that the color other than white and black break out. Because in this chapter uses method that it is not resolved into three primary colors of R, G, B. This method is called Type2.

3.1 Process procedure

Fig. 4 is shown flow diagram in the quantization of color images on SA⁶⁾. It is not resolved into 3 planes on R, G, B, it process same procedure that halftoning used SA in the gray scale image. The procedure is shown a following.

- 1) Random pattern of 8 colors is selected as initial process image.
- 2) The element in each pixel of color is changed. It changes color by using random number of 0 form 7.
- 3) Cost E_{ola} conducts before step 2 and cost E_{new} conducts after step 2 calculate. Change volume of cost function gets dE .

$$dE = E_{new} - E_{old} \quad (5)$$

- 4) The turning over can accept at probability p .

$$p = \begin{cases} 1 & (dE \leq 0) \\ \exp(-\frac{dE}{kT(n)}) & (dE > 0) \end{cases} \quad (6)$$

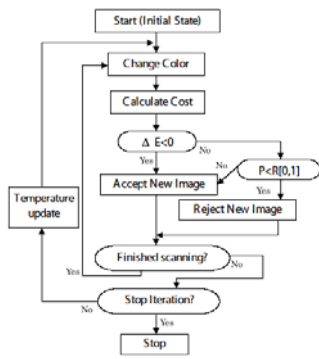


Fig. 4 Flow diagram

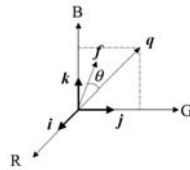


Fig. 5 Treatment of the vector for color

Here, $T(n)$ is temperature in the calculation, k is Boltzmann constant.

- 5) Trial of the above step2-4 does as order of raster operation against all pixels. After trial in all pixels finished, temperature $T(n)$ is let to fall, shown by following equation.

$$T(n) = \alpha T(n-1) \quad (7)$$

Here, α is constant how many 0 and over less than 1.

- 6) Step2-5 is repeated by change value of cost function becomes small.

3.2 Treating of cost function like the vector

The process method is shown in previous section needs to think about the cost function newly. Because it is not divided into the plane of 3 primary color. Treatment of the vector for color shows Fig. 5. Color vector c shows by following equation.

$$c = ri + gj + bk \quad (8)$$

Here, i, j, k are unit vector to each R, G, B direction. And r, g, b are shown size of vector to each R, G, B direction. Therefore, cost function E is considered as follow.

- 1) $F(x, y), f_s(x, y), Q(x, y), q_F(x, y)$ is replaced in a foregoing chapter with each $\bar{F}(x, y), \bar{f}_s(x, y), \bar{Q}(x, y), \bar{q}_F(x, y)$. And calculation of cost E that related to expression of gray level is shown follow equation.

$$E_m = \sum_{(x,y) \in block} \frac{1}{N_p} |\bar{F}(x, y) - \bar{q}_F(x, y)| \quad (9)$$

- 2) Similarly, cost E_c about the contrast shown by following equation.

$$E_c = \sum_{(x,y) \in block} \frac{1}{N_p} |\bar{F}'(x, y) - \bar{Q}'(x, y)| \quad (10)$$

$$\begin{cases} \bar{F}'(x, y) = \bar{F}(x, y) - \bar{f}_s(x, y) \\ \bar{Q}'(x, y) = \bar{Q}(x, y) - \bar{M}/2 \end{cases} \quad (11)$$

- 3) An angle error θ with color vector of original image and process image is considered because only using the above (1), (2) can be the result that is same as the one

obtained in a foregoing chapter. It considers that length of vector becomes 0 in seven colors of other either if color of process image is black ($R=G=B=0$), an angle error θ is taken 0 too.

- 4) Cost function is shown by following equation from above result.

$$E = (1.0 + \beta\theta)(\alpha_m E_m + \alpha_c E_c) \quad (12)$$

In this expression, there is a constant 1.0 to prevent that the cost become 0 used an angle error θ , β is an angle error.

- 5) Calculation of cost in equation (19) is used $\alpha_m = 0.2$ and $\alpha_c = 0.8$.

Process image using SA above procedure is shown by Fig. 6 and Fig. 7. Fig. 6 is process image using color image as original image. Here, It follows that it is similar to the Fig. 2(c) that is process image in a foregoing chapter in the case of $\beta = 0$. However, it is become color reappearance such as achromatic color when β value is much. This is considered a ratio of angle error θ grows big and error of gray level density of color of each is made light of one. The above, $\beta = 0$ is considered that color image is effective and introduction of an angle error is meaningless.

Fig. 7 is process image by use of gray scale image (It is RGB24bit, but $R = G = B$ is taken advantage of only intensity information) as original image. Here, in case of $\beta = 0$ follows that it is similar to Fig. 3(f) that it is process image a foregoing chapter. The reason is considered to make neighboring color vector average and it should become same color. However, there is not outbreak except for white color and black color when weight of an angle error θ is heavy. In this way the color except white and black does not appear in gray scale image when the angle error into the cost function introduced, but it become color reproduction such as achromatic color in the color image. Therefore, even this method is the method that is poor in versatility for color image and gray scale image.

4. Introduction of a limitation condition in choice of a color

Type1 is suitable to halftoning of color image, but it is a problem to occur that the color except white and black when gray scale image is extended. Type2 dose not occur that the color except white and black in gray scale image, it is a problem of color reproduction such as achromatic color in the color image. Among both of a trade-off is connected with each other. Therefore, it must be think about a method to satisfy the following conditions at the same time.

- 1) Color image should be natural color reproduction visually.
- 2) Gray scale image should appear the color that except white and black.

To satisfy this condition, the method use the versatility to gray scale image of Type2 with good point of Type1. Therefore, there is following method.

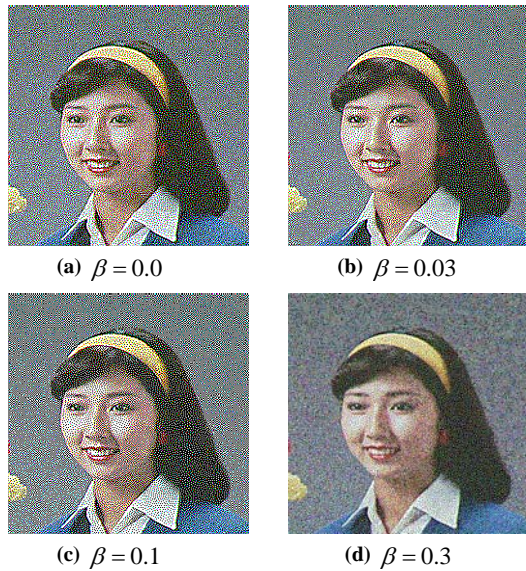


Fig. 6 Halftone Images using the Procedure Type2 (Original images is full color image)

1) Weight $\beta = 0$ for angle error θ as cost function is following equation in Type2.

$$E = \alpha_m E_m + \alpha_c E_c \quad (13)$$

Here, it is assumed $\alpha_m = 0.2$, $\alpha_c = 0.8$ from an argument to a foregoing chapter.

- 2) If there is a relationship of R=G in original image, the choice of color in process image should be restricted within the relationship of R=G.
- 3) If there is a relationship of G=B in original image, the choice of color in process image should be restricted within the relationship of G=B.
- 4) If there is a relationship of R=B in original image, the choice of color in process image should be restricted within the relationship of R=B.

The above method is called Type3. Process image obtained by this Type3 is shown as Fig. 8. This result is same as result of process image of Type1 with $\alpha_m = 0$ in color image. Only white and black appear in gray scale image and it is well result.

5. Conclusions

Type1 was the same as the knowledge in the gray scale image of SA, and when the weight of cost E_m on present of gray level, contrast E_c on contrast decides each 0.2, 0.8, the image understood to have become the expression were prominent subjectively by this method. In case of using this method, It is adapted to the gray scale image that consist of R=G=B. Then the color other than black and white is breaking out by multimodal of a solution, as a result, process image does not become the gray scale image. Type2 could prevent the occurrence of others color in gray scale image. However, it became the process image of little saturation in color image. Follow, Type3 made the basis of above two results. When it made not to consider the angle error at Type2, the same process image could get by color image. And in case of gray scale image, the color other than black and white doesn't appear by process image.

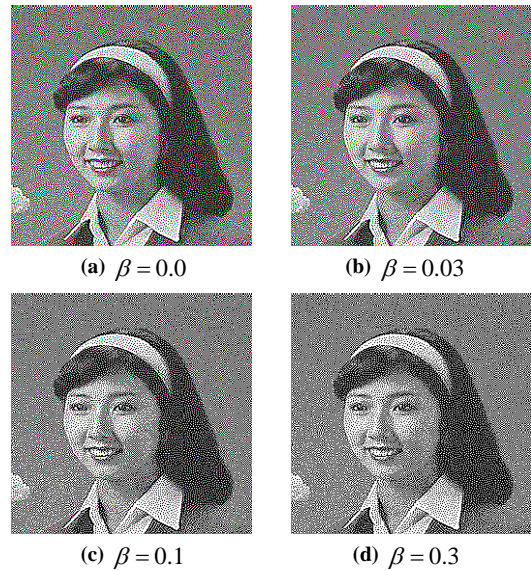


Fig. 7 Halftone Images using the Procedure Type1 (Original images is gray scale image)

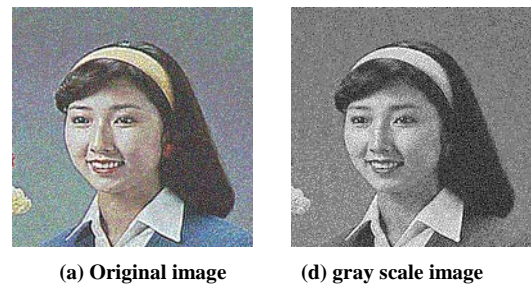


Fig. 8 Halftone Images using (Type3)

Therefore, in case of SA is adapted to the halftoning in color image, we could get result good as the visual sensation at using Type3. Therefore, availability to the halftoning to the color image of SA became clear. Method of SA is calculated 15 minutes degree at CPU is 2GHz of Pentium4, Memory capacity is 1.5GB and OS is WindowsXP. Mention as assignment, the cutting of calculation cost and the shortening of process time.

6. References

- [1] B.E. Bayer, "An optimum method for two-level rendition of continuous-tone pictures", Ineternl. Conf. On Comm., vol.50, pp.69-77 (1976).
- [2] R. W. Floyd and L. Steinberg, "An adaptive algorithm for spatial gray-scale," Proc. Soc. Inf. Disp., vol.17, pp.75-77 (1976).
- [3] N. Kobayashi and H. Saito, "Halftoning Technique Using Genetic Algorithm", Trans. IEICE., J78-D-II, pp.1450-1459 (1995).
- [4] S. Kirkpatrick, C. D. Gellatt and M. P. Vecchi, "Optimization of simulated annealing", Science, vol.220, pp.671-680 (1983).
- [5] H. Szu and R. Hartley, "Fast simulated annealing", Phys. Lett., vol.122, pp.157-162 (1987).
- [6] Ken-ichi Tanaka, "Improvement of Halftone Images Using SA", Journal of ITE., vol.54, no.3, pp.1104-1106 (2000).

Optimization of area traffic control parameter using a GA

Haruka Sasaki Manami Shinohar
Graduate School of Engineering
Utsunomiya Univ.
Utsunomiya-city,
321-8585 Japan

Kenji Shoji Toyama Fubito Juichi Miyamichi
Faculty of Engineering
Utsunomiya Univ.
Utsunomiya-city,
321-8585 Japan

Abstract

In this paper, we propose a method for optimizing common cycle length and offsets among signal control parameters in area traffic control of a grid street network using a genetic algorithm. The gene of each offset is expressed by three bits, and that of a common cycle length by six bits. Each individual (a candidate of solution) is evaluated based on the weighted sum of delay time and stop percentage using CORSIM simulator in TSIS traffic integration software. The results of simulation experiments for regular and irregular grid street networks show that the optimal solutions obtained by the proposed method are better than theoretical ones based on a linear model in traffic signal control.

1 Introduction

Increasing number of vehicles in use generates serious problems such as traffic accidents and congestion. It is deeply desired that automobile traffic safety and smooth traffic flow are realized by appropriate traffic light control. There are three types of traffic light control: independent control handling a single signal, coordinated control in which two or more signals on a arterial road work in association with each other, and area traffic control which is a two dimensional version of coordinated control. Especially, large effects can be expected in coordinated control and area traffic control if they are optimized.

The object of this study is to improve the performance in area traffic control. Among the parameters of area traffic control, common cycle length, splits, and offsets, we focus attention on the common cycle length and offsets. The decision of common cycle length and offsets is considered as a combinatorial problem. If the number of intersections increases, the number of combinations becomes huge, and it is difficult to find an optimal solution. Hisai and Sakai [1] proposed analytical method for optimizing the offsets

of signals on a grid street network. The time cost of the method is small but it is difficult to optimize them globally. Therefore, we have to solve the problem by some heuristic method. Abu-Levdeh and Benekohal [2] examined several genetic algorithms (GAs) applied to the optimization of traffic control parameters. GA is metaheuristics applied in versatile as a methodology for optimization, adaptation, and learning. Their target system in experiments was a signalized arterial road. In this paper, we propose a method for optimizing common cycle length and offsets among signal control parameters in area traffic control of a grid street network using a GA.

2 Area traffic control

Coordinated control is an approach to manipulating two or more signals on an arterial road in association with each other. Area traffic control (ATC) is a method by which a traffic signal group placed on a street network spreading two-dimensionally is controlled concentratedly. It can be considered as a two-dimensional version of coordinated control. Common cycle length and offsets are particular parameters of area traffic control. Common cycle length is a total time to complete one cycle in common with all signals. Offset is the delay from the start of the green phase of a reference signal to that of the signal concerned. According to the manual of JSTE [3], if round trip time T of a link in overall speed V is multiple integer of cycle length C , that is,

$$T = \frac{2D}{V} = nC, \quad (1)$$

vehicle delay time can be minimal. In the equation of (1), D is the link length. In the method adopted by present Japan, a region to be controlled by ATC is manually divided into several blocks based on the amount of traffic flow for every traffic situation con-

sidered. The control parameters are decided in every block and they are integrated. For a traffic situation, a set of control parameters corresponding with the situation is chosen from among the several sets of them obtained in advance and applied. However, because the frequent renewal of the several sets of them is difficult in this system, the system can not deal with unexpected traffic situations immediately. And, it is difficult to automate such work. So, we aim at optimizing ATC parameters of all signals in the region of interest by a heuristic method. In this study, we limit street networks to grid ones as the simplest case, and propose an optimization method of the control parameters.

3 Applying a GA to ATC

In this study, a combinatorial optimization problem of the set of control parameters, the common cycle length and offsets, is considered for a grid street network which consists of the streets of L rows and R columns and the intersections of $L \times R$. Each intersection points is called a 'signal' and each connecting street between two adjacent intersections is called a 'link'. Using the traffic micro simulator CORSIM, we simulate the street network with the sets of control parameters represented by viable solutions generated by a GA. Evaluating the results of the simulations, we use the output data of CORSIM; Vt (Vehicle Trips : the number of vehicles that have been discharged from the link), Tt (Total Time : total time on the link for all vehicles), Dt (Delay Time : the time that vehicles are delayed if they cannot travel at the free flow speed), Sp (StopPercentage : the ratio of the number of vehicles that have stopped at least once on the link to the total link trips) where the link means unidirectional one. We calculate a performance index (PI) as follow:

$$PI = \sum_{n=1}^N \left\{ \frac{Dt_n}{Tt_n} \times \frac{Vt_n}{Td} + K \times Sp_n \times \frac{Vt_n}{Td} \right\} \quad (2)$$

where K is the weight coefficient of Sp , Td is the simulation time, and N is the number of unidirectional links, $N = 2L(R - 1) + 2(L - 1)R$. The PI is the weighted sum of delay and stop. So, the smaller the PI the better the evaluation.

This optimization is carried out by a GA. GA is a metaheuristics applied in versatile as a methodology for optimization, adaptation and learning. The coding method of the GA is as follows. A chromosome for the GA consists of 30 bits as shown in Figure 1, where

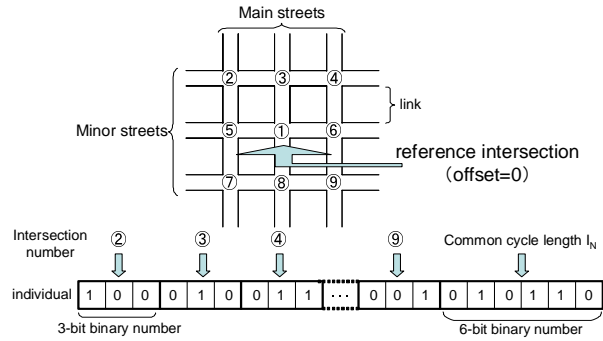


Figure 1: Coding method of cycle length and offsets

an offset is represented by a 3-bit binary number, and common cycle length is represented by a 6-bit binary number. Each intersection is numbered as shown in Figure 1. Actual offset values represented by 3-bit binary numbers I_k are taken as center values of equally divided 8 intervals between 0 and a common cycle length C , as shown in Figure 2. Actual common cycle length $C (MIN \leq C \leq MAX)$ represented by a 6-bit binary number I_N is ranging from 40 to 150 seconds, and obtained as

$$C = MIN + \frac{MAX - MIN}{2^6 - 1} I_N. \quad (3)$$

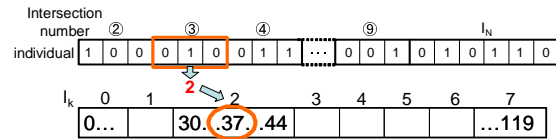


Figure 2: Calculating method of offsets

The fundamental algorithm of the GA is expressed in the following. First, M individuals (the initial population) are generated using uniform random numbers. All individuals of the current generation are evaluated by the fitness F defined by the inverse number of PI as

$$F = \frac{1}{PI}. \quad (4)$$

Secondly, the operations based on genetic rules are applied to them for the construction of the next generation. As the genetic rules, we adopt elitism, and apply crossover and mutation to the individuals selected by roulette. Elitism is a mechanism that protects the chromosomes of most-highly-fit population from the genetic operations. In experiments, the top of the individuals becomes elite. Crossover is the main mechanism of the GA which expects the more-highly-fit children than their parents. For crossover, $M/2$ pairs of parents with permitted duplication are chosen from

M individuals based on the roulette selection at the probability proportional to the F value. From $M/2$ pairs of parents, their copies are made as M children, and one-point crossover is applied for the children in the probability of 1.0, and the last child is exchanged for elite. The mutation inverts a randomly chosen bit among 30 bits in each chromosome according to the probability of 0.1. The set of offsets with most highly fitness at the last (T th) generation is made to be the best solution. Considering the calculation efficiency, the GA optimizes the offset of each intersection in the resolution of 3 bits. Then, we apply a coarse-to-fine approach to raise the resolution of the offset. In the first stage, the interval between 0 and C is coarsely divided into 8 segments, each offset is represented by the segment number 0 to 7 which corresponds to the 3-bit binary number, and the offset of all signals are optimized by the GA. In the second stage, for each offset the interval is diminished by one quarter, its center is set to the center of the segment obtained in first stage, and the same procedure as the first stage is carried out. After the third stage performed as same as the second one, each offset can be obtained at the accuracy of $1/4 \times 1/4 \times 1/8 = 0.78\%$ in the interval between 0 and C . Whereas, the common cycle length C is optimized in the first stage, and it is fixed in the second and third ones.

4 Results of simulation experiments

4.1 Regular grid network

First, we compare the solution of a linear model with that of the proposed method under the situation where the actual traffic condition is simplified. That is, the street network is made to be the regular grid one with 3 columns of main streets and 3 lines of minor ones and having 9 intersections and 24 unidirectional links (12 bidirectional links) of equal length $D = 1000$ [ft]. In the GA, the size of population is made to be 50 individuals and the number of generations to be 30. Traffic and signal conditions of the simulator CORSIM is set as follows.

- Free flow speed : 27[ml/h]
- traffic flow : (main street) 0.35[vehicles/s]
 (minor street) 0.20[vehicles/s]
- phase probability : 0.50
- right and left turn : no turn
- yellow time : 3[s]
- all red time : 2[s]

The reference signal of the grid network is made to be the center one and its offset to be 0. In the linear model, the offset of each signal connected to the reference one by the link is calculated by D/V , where V is the free flow speed. The offset of each of the rest of 4 signals are calculated by adding D/V for the vertical link to the offset of the signal connected by the link. And the common cycle length in the linear model is equal to the round trip time T of a link according to the equation (1).

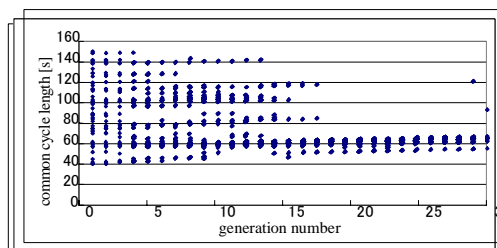


Figure 3: Distribution of the common cycle length as a function of generation in the first stage of the GA (regular grid network)

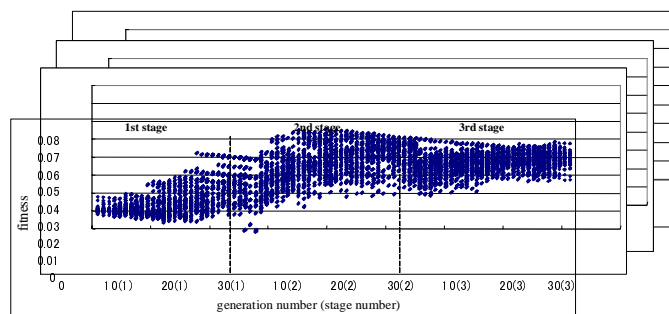


Figure 4: Distribution of the fitness value of each individual as a function of generation (regular grid network)

Table 1: The best solution of the GA and the linear model (regular grid network)

	cycle length	offsets of ① to ⑧								fitness	
GA	57[s]	0	2	31	1	28	28	1	31	1	0.0754
linear model	50[s]	0	0	25	0	25	25	0	25	0	0.0279

As experimental results, Figure 3 shows the distribution of the common cycle length as a function of generation in the first stage of the GA. Figure 4 shows the distribution of the fitness value of each individual as a function of generation. Table 1 shows the best solution of the GA and the linear model.

4.2 Irregular grid network

Next, we examine the linear model and the proposed method under more actual situation than the above. That is, the street network is made to be the irregular grid one with 3 columns of main roads and 3

lines of minor ones and having 9 intersections and 24 unidirectional links (12 bidirectional links) of unequal length as shown in Figure 5.

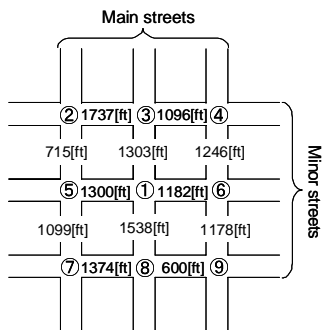


Figure 5: The setting of the link lengths

The parameters of the GA and the traffic and signal conditions of CORSIM are same as the above experiments. The reference signal and its offset are set as same as the above. In the linear model, the offset of each signal is also calculated as same manner as the above. And the common cycle length in the linear model is equal to the average of the round trip times of all links.

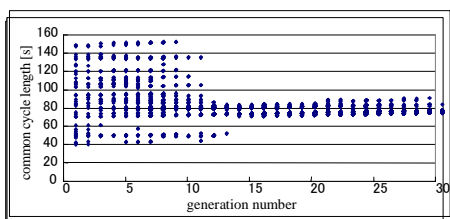


Figure 6: Distribution of the common cycle length as a function of generation in the first stage of the GA (irregular grid network)

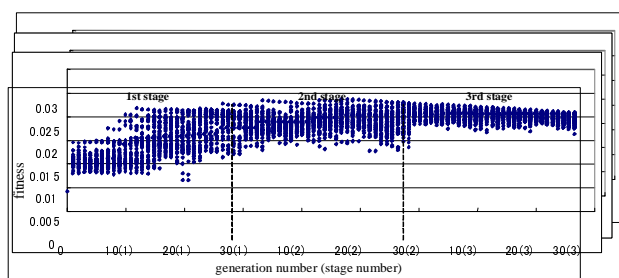


Figure 7: Distribution of the fitness value of each individual as a function of generation (irregular grid network)

As experimental results, Figure 6 shows the distribution of the common cycle length as a function of generation in the first stage of the GA. Figure 7 shows the distribution of the fitness value of each individual as a function of generation. Table 2 shows the best solution of the GA and the linear model.

Table 2: The best solution of the GA and the linear model (irregular grid network)

	cycle length	offsets of ① to ⑨	fitness
GA	70[s]	0 15 43 12 35 45 69 30 10	0.0279
linear model	61[s]	0 51 33 0 33 30 0 39 60	0.0196

5 Discussion

In Tables 1 and 2, the fitness values of the optimal parameters obtained by the GA are higher than those by the linear model on the regular and irregular grid street networks. Figures 3 and 6 show the convergence to constant values of the common cycle length in the course of generation. In Figures 4 and 7, we can see that the fitness values become high and converge, in the course of generation. And, the effect of the coarse to fine approach of the 3 stage GA can be seen. After all, on both of the regular and irregular grid street networks the availability of the proposed method is confirmed.

6 Conclusion

In this paper, we propose an optimization method for common cycle length and offsets among signal control parameters in area traffic control of a grid street network using a GA. As future work, we intend to investigate the goodness of the proposed method by comparing it with the other methods, and to apply other metaheuristics such as ant colony optimization in order to raise the efficiency of the proposed method.

References

- [1] Abu-Levdeh and Benekohal, "Convergence variability and population sizing in micro-genetic algorithms", *Computer-Aided Civil and Infrastructure engineering*, 14, pp. 321-34,1999.
- [2] Masakazu Odawara and Mamoru Hisai, "A Study on Common Cycle Length of Coordinated Signal System through Genetic Algorithm", *The Infrastructure Planning Committee*, vo.20(2), pp. 815-818,1997 (in Japanese).
- [3] Japan Society of Traffic Engineers et al., *Manual on Traffic Signal Control*, Japan Society of Traffic Engineers, 1994 (in Japanese).

Three dimensional medical image recognition of the lungs using artificial neural network

Takaomi Matsuki
School of Health Sciences
The University of Tokushima
3-18-15 Kuramoto-cho,
Tokushima 770-8509, Japan
takao_dq69@yahoo.co.jp

Tadashi Kondo
School of Health Sciences
The University of Tokushima
3-18-15 Kuramoto-cho,
Tokushima 770-8509 Japan

Junji Ueno
School of Health Sciences
The University of Tokushima
3-18-15 Kuramoto-cho,
Tokushima, 770-8509, Japan

Abstract

In this study, we propose a method of 3-dimensional medical image recognition of the lungs, pulmonary vessels and bronchial trees by using an artificial neural network. Two neural networks trained using the back propagation algorithm are applied to medical image recognition. First, the neural network recognizes the outline of the lungs and outputs the lung regions and 3-dimensional images of the lungs are displayed. Then, second neural network recognizes outline of the pulmonary vessels and bronchial trees and outputs the regions of them and 3-dimensional images are displayed accurately. These image processing proposed in this study can be easily applied to another medical image such as MRI image.

Keywords: Neural network, lungs, 3-dimensional image

1 Introduction

Neural network used in this study has a three layered neural network architecture that is constructed with the input layer, the hidden layer and the output layer. Weights of the neural network are estimated using the back propagation algorithm. Two neural networks are applied to 3-dimensional medical image recognition of the lungs, pulmonary vessels and bronchial trees. First, the neural network is organized in order to recognize the outline of the lungs and extract the lung regions. Then, the subtraction images of the lungs are extracted and are used to organize the second neural network. Second neural network is recognized and extracts the pulmonary vessels and bronchial trees regions. These image processing are carried out for all slices of multi detector row computed tomography (MDCT) images and 3-dimensional images of pulmonary vessels and bronchial trees are displayed with the volume rendering software.

2 Artificial neural network architecture

The neural network, which has 3-layered architecture with the input layer, the hidden layer and the output layer, is trained using back propagation algorithm. Architecture of the neural network is shown as follows:

(1) Input layer

$$u_i = x_i \quad (i=1, 2, \dots, p) \quad (1)$$

Here, x_j is input variables and p is the number of the input variables.

(2) Hidden layer

$$y_j = \sum_i^p w_i u_i - \theta, \quad (j = 1, 2, \dots, g) \quad (2)$$

$$u_j = \frac{1}{1 + \exp(-y_j)}, \quad (j = 1, 2, \dots, g) \quad (3)$$

Here, w_i ($i=1, 2, \dots, p$) is the weights between the input and the hidden layer and g is the number of neurons in the hidden layer.

(3) Output layer

$$y_k = \sum_j^g w_j u_j - \theta, \quad (k = 1, 2, \dots, r) \quad (4)$$

$$u_k = \frac{1}{1 + \exp(-y_k)}, \quad (k = 1, 2, \dots, r) \quad (5)$$

Here, w_i ($i=1, 2, \dots, g$) is the weights between the hidden and the output layer and r is the number of neurons in the output layer.

3 Application to medical image recognition of the lungs

The neural network trained using the back propagation algorithm was applied to the medical image recognition of the lungs. MDCT images of the lungs were used in this study.

3.1 Image recognition of the lung regions

An original image shown in Fig.1 was used for learning weights of the artificial neural network. The statistics of the image densities in the neighboring region, the $N \times N$ pixel regions, were used as the image features. Three parameters namely, mean, standard deviation and variance were used as the useful input variables [1]. The output value of the neural network was zero or one. When $N \times N$ pixel region was contained in the region of the lungs, the neural network set the pixel value at the center of the $N \times N$ pixel region to one and this pixel was shown as the white point. In this study, we set the value of N to 4. Figure 2 shows the output image of the neural

network after the post-processing. In the post-processing, small isolated regions were eliminated by the image processing such as the dilatation and the erosion. Then, outlines of lung regions were expanded by $N/2$ pixels and outline of the lungs were extracted. In order to check matching between original and output image of the neural network. The output image was overlapped on original image after the post-processing. Overlapped image is shown in Fig.3. Gray scale image (Fig.4) of the lungs was subtracted from the original image (Fig.1) using the output image (Fig.2) of the neural network. These image processing were carried out for all slices of MDCT images and 3- dimensional images of the lungs are displayed with volume rendering software as shown in Fig.5.

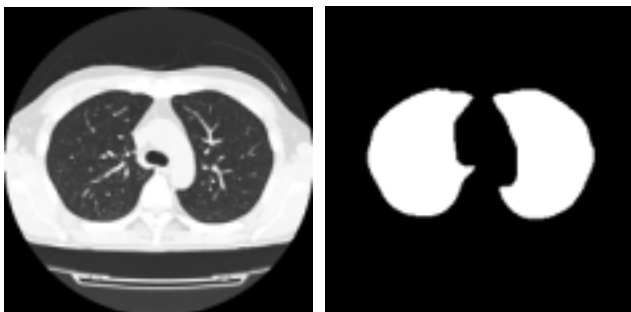


Fig.1 Original image

Fig.2 Output image(1)

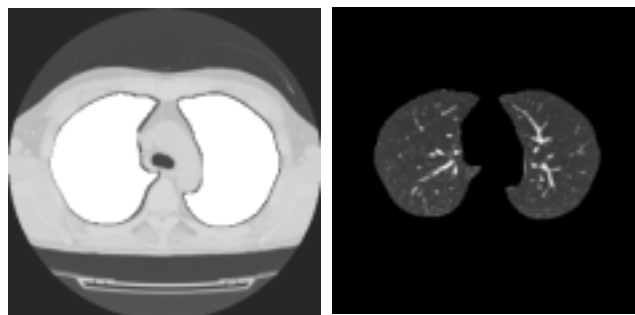


Fig. 3 Overlapped image

Fig.4 Subtraction image(1)



Fig.5 3-dimensional image of the lungs

3.2 Image recognition of the pulmonary vessel and bronchial tree regions

Gray scale image shown in Fig.4 was used as a new original image to organize second neural network. The organized neural network recognizes the outlines of

pulmonary vessels and bronchial trees and outputs the regions of them. Figure 6 shows the output image of second neural network. Then, the gray scale images (Fig.7) of the pulmonary vessels and bronchial trees are extracted from the new original image (Fig.4) using the output image (Fig.6) of the neural network. These image processing were carry out again to all slice images of the MDCT. Then, 3-dimensional images were displayed by the volume rendering software using these gray scale images of the pulmonary vessels and bronchial trees. By these procedures, the regions of pulmonary vessels and bronchial trees were recognized and extracted accurately by the neural network.

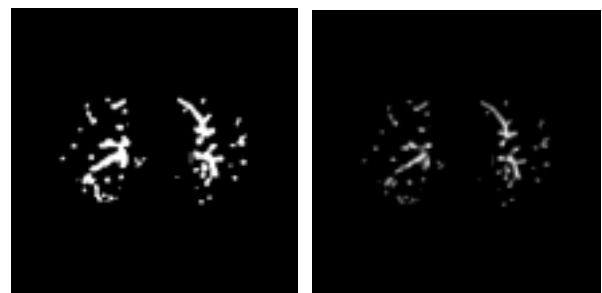


Fig.6 Output image(2)

Fig.7 Subtraction image(2)

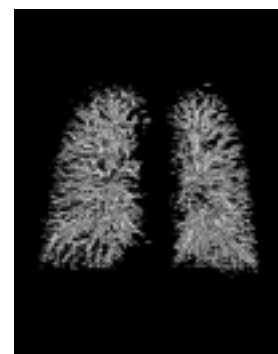


Fig.8 3-dimensional image of the pulmonary vessels and bronchial trees

4 Conclusion

In this study, the neural networks trained using the back propagation algorithm were applied to the 3-dimensional medical image recognition of the lungs, the pulmonary vessels and bronchial trees and 3-dimensional images were displayed accurately. These image recognition procedures using the artificial neural networks can be applied easily to another medical image such as the MRI.

References

- [1] T.Kondo, J.Ueno and K.kondo, "Revised GMDH-type neural networks using AIC or PSS criterion and their application to the medical image recognition", *Journal of advanced computational intelligence and intelligent informatics*, Vol.9, No.3, pp.257-267,2005.

Counter”, and “Sorter”. Figure 3 shows the block diagram of “Reconstruction-Unit”. It is necessary for

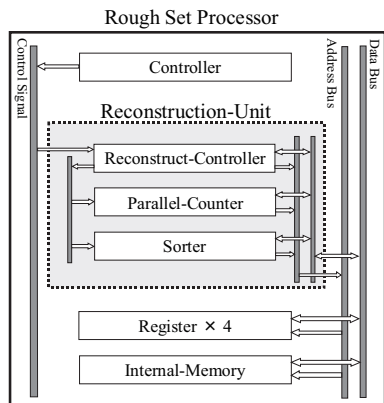


Figure 3: Block Diagram of “Reconstruction-Unit”

“Reconstruction-Unit” to repeat three steps to discover the important rules. The step 1 is the parallel count process to find the number of each variable in the logical function. The step 2 is the sort process to select the variable that has the largest counts. The step 3 is the delete process to delete the row that has the selected variable. The discovery of the most important rules is realized by repeating these three steps until all rows are deleted. Figure 4 shows the schematic of “Reconstruction-Unit”.

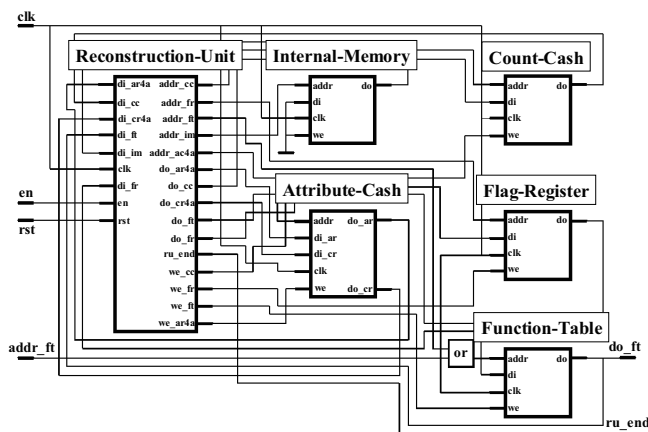


Figure 4: Schematic of “Reconstruction-Unit”

3 Experiments

The authors performed the design and the simulation using the logic synthesis tool (Xilinx ISE WebPACK 8.2i) and HDL simulator (Mentor Graphics ModelSim XE 6.1e). The experiment of the designed processor is performed on

Table 1: Gate Count for Design and Processing Time

unit name	gate count (gates)	time (μs)
Core-Selector (16 core-data)	9,400	82.5
Covering-Unit (16 core-data)	2,100	263.1
Reconstruction-Unit (4 rules)	36,200	4,152.7

the FPGA evaluation board (Xilinx Spartan-3E Starter Kit, 500 thousand gates). Table 1 shows the number of gates and the processing time of the proposed processor. Figure 5 shows the experiment of “Reconstruction-Unit” in the post-processing.

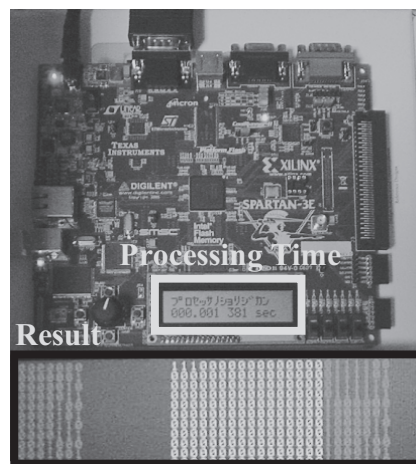


Figure 5: Experiment of “Reconstruction-Unit”

4 Conclusion

In this paper, the design and the experiment of rough set processor is described. The future works are the experiment with the actual database and the improvement of the processing speed.

This research is partially supported by Research Institute for Science and Technology of Tokyo Denki University under Grant Q03-04.

References

- [1] Pal S K and Skowron A (1999), Rough Fuzzy Hybridization - A New Trend in Decision - Making, Springer Verlag.
- [2] Kanasugi A (ed. by Inuguchi M et al.) (2002), Rough Set Theory and Granular Computing, Springer-Verlag, pp. 273-280.

An Outdoor Autonomously Moving Robot Using a Distributed Image Processing System

Hiroki GOTO, Norihiro ABE
Kyushu Institute of Technology
680-4 Kawazu, Iizuka, Fukuoka 820-8502, Japan
Email: goto@sein.mse.kyutech.ac.jp

Hirokazu TAKI
Wakayama University
930 Sakaedani, Wakayama-shi
Wakayama 680-8510, Japan

Shoujie He
Eastman Kodak Company,
Plano, Texas, USA

Abstract

This study aims at building an autonomous robot that is capable of comprehending complicated image processing algorithms rapidly and concurrently via a wireless communication network. The entire system includes a mobile robot, a network camera mounted on the mobile robot, a wireless LAN, and a distributed image processing system. Images captured by the network camera are first transmitted to one of the clustered computers through the wireless LAN. The computer receiving the images then distributes the images to the other computers in the cluster. The image processing results will be collected and reported back to the robot through the wireless LAN also by the same computer. With the clustered computers, multiple image-processing algorithms could be applied to a single image in a concurrent fashion. As an experiment, the mobile robot has been put on a street. In order for the mobile robot to move autonomously on the street, three targets including white lines on the road, static and moving obstacles, have been identified necessary for the distributed image processing system to detect. The experimental results indicate that the distributed image processing system successfully meet the needs for the autonomous movement of the mobile robot.

Keywords: Network, Distributed Image Processing, Autonomously Moving Robot

1 Introduction

This study aims at the research and development of an autonomously moving robot so that the quality of our daily living could be further improved. The potential applications include the automated car driving, ITS (Intelligent Transport System), environmental and safety issues, and social welfare improvements such as the replacement of the guide dogs.

The fundamental problem with an autonomously moving robot is the computational intensiveness. While moving autonomously, the robot needs to process all kinds of information such as the dynamically changing scene, sensor data, path finding, control of the movement, and so on. Recognition of the dynamically changing

scene requires running a lot of complicated image processing algorithms, which consumes a lot of resources in terms of memory and CPU usages. The computer carried by the robot is overwhelmed by data processing needs.

Over the past few years, network based communication technologies have made remarkable progress. Sharing the computational resources such as memory and CPU power and load balancing could easily be achieved through the network. This makes us think the possibility for the mobile robot to have its computational burden shared with others through the network, as well. With the computational burden shared, real-time processing of all the data could be possible and thus an autonomously moving robot could be expected.

Based on the above-mentioned idea, we mounted a network camera on the mobile robot so that the robot could have the image processing load shared by a couple of high performance computers through a wireless LAN. The feasibility has been verified and the experimental results will be reported in this article.

2 System Organization

As shown in Figure 1, the entire system could be divided into the following three subsystems.

- Mobile robot
- Network communication
- Data processing for the autonomous movement

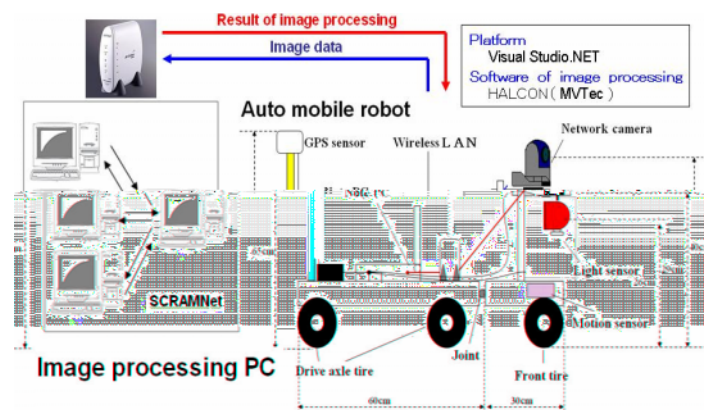


Figure 1: System organization of the autonomously moving robot.

2.1 Mobile Robot

The mobile robot used in this research is 90 cm long and 60 cm wide. A network camera is mounted on the front of the mobile robot. The network camera keeps transmitting images through the wireless LAN to a high-performance server machine. The network camera has its own IP address, with which the communication with the remote server machine will not consume any of the computational resources on the computer carried by the robot. Images are transmitted through an IEEE 802.11a wireless router that is mounted on the robot as well.

In addition to the network camera, the mobile robot is equipped with photoelectric sensor, GPS (Global Positioning System) sensor, and 3D motion sensor. The computer carried by the robot processes the data from all these sensors. The same computer will also control the servomotor of the robot. Since the remote high-performance computers have shared the heavy-load data-processing tasks such as image processing and path finding, the computer on the robot could have more computational resources for the overall control of the movement. Visual Studio.NET from Microsoft has been used for the software development. The image processing tasks are executed with HALCON, an image processing software package from MVTec, a German company.

2.2 Network Communication

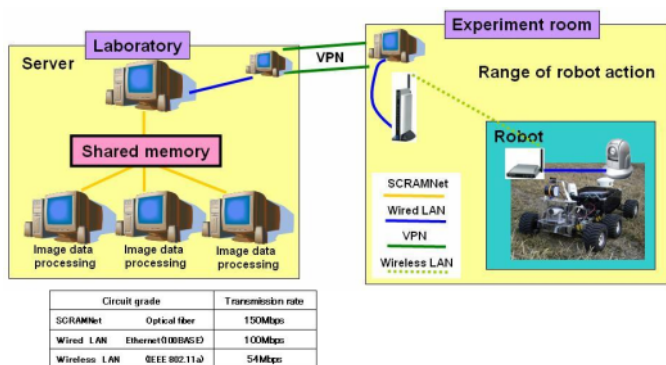


Fig. 2. Architecture of the network organization.

The needs for the network communication could be divided into two major areas. One is the area where the mobile robot is moving around. The other is the server machine and the other high performance computers. Considering the limited transmission performance of wireless LAN, the usage of wireless LAN is minimized by using the VPN (Virtual Private Network) so that the existing wired LAN could be used as much as possible. It could be a challenge to discover the existing wired LAN when the robot is put into operation in the real world. The benefit of using wireless LAN, however, includes the possibility of extending the area that the

mobile robot could move around by the relay of the wireless LAN.

The network communication on the server side, on the other hand, involves large amount of data processing. It requires high-speed and high throughput communication network. SCRAMNet, an optical network is used to reduce the communication delay.

With the above optimization of the network resources, real-time processing could be expected.

2.3 Distributed Image Processing

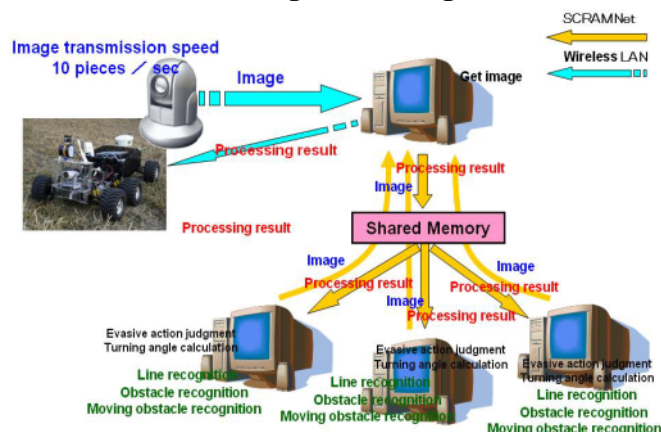


Fig. 3. Distributed Image Processing System

Figure 3 shows the organization of the distributed image processing subsystem. The server machine that is receiving images from the network camera will write the image data into the shared memory. The same server will read the results processed by the other computers and report the results back to the robot.

All the computers involved in the image processing basically share the shared memory. The synchronization is achieved through the SCRAMNet. The server machine is receiving images at the speed of 10 images per second. It will write the image data to the shared memory at the same speed. The other computers will read the image data from the shared memory and start processing. Since the robot is put on a street, at the very least three targets, white lines, static and moving obstacles, need to be detected through the image processing algorithms. Three high-performance computers accomplish the detection of the three targets independently and concurrently. The benefits of this system architecture include the scalability and the maintainability.

3 Image Processing

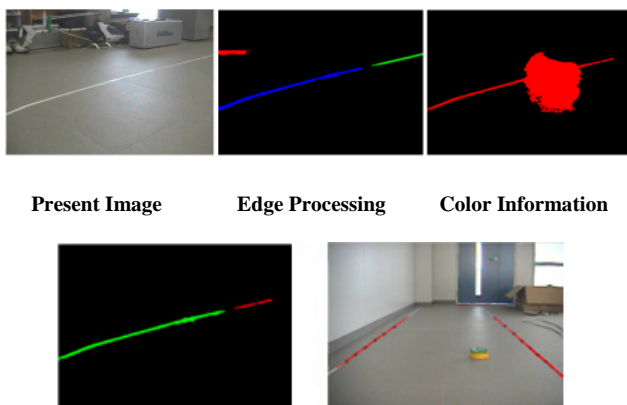
The following three image processing tasks are assigned to the distributed image processing system.

- White line recognition
- Static obstacle identification
- Moving obstacle identification

Based on the feature analysis of each of the target objects, a corresponding image processing algorithm has been developed. The outdoor scene is unstable due to the sunlight, shadow, and the vibration caused by the movement of the robot. This requires high robustness to the image processing algorithms.

3.1 White Line Recognition

Basically, two approaches have been taken toward the extraction of white lines. One is color-based. The other is edge element based. The white lines are finally identified by integrating the information from the two approaches. With the information integration, the lighting effects could be reduced to the minimum level. Furthermore, real-time straight line approximation algorithm is introduced to improve the robustness of white line recognition even if when the white lines are shaded by other objects. Figure 4 shows the entire process of extracting white lines.



White line extraction

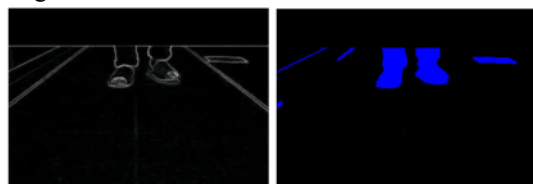


Approximate deriving

Fig. 4. Results of white line extraction

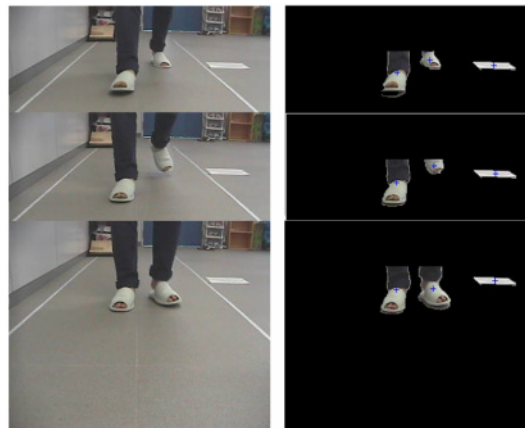
3.2 White Line Recognition

Figure 5 shows the entire process of extracting a moving obstacle.



Edge Processing

Making Up



The person's movement forecast

Fig. 5. Extraction of moving obstacles

Similar to the extraction of white lines, both color information and edge elements are used for the extraction of the static and moving obstacles. With a properly selected threshold, the boundary of obstacles could be extracted. If the area of the enclosed region is larger than a preset threshold, the enclosed region is considered as the existence of an obstacle. The coordinates of the center of the obstacle are persisted to the memory on the computer that is processing the image. As soon as the center of an obstacle extracted from the subsequent image is measured, the results will be compared to the previously persisted data. Whether the obstacle is a static one or a moving one is decided by the difference. The difference could also tell the moving direction and speed of a moving obstacle. The information regarding the moving obstacle is useful for the robot to decide the next movement.

4 Experiments

The experiments are focused on the distributed image processing subsystem and the overall network communication. The main purpose is to verify the response time from the distributed image processing system to the robot. The experimental results have successfully verify the feasibility of the robot system proposed in this study.

4.1 Methodology

1. Capture images with the network camera.
2. Transmit the images to the server machine through the wireless LAN.
3. Distribute the images to the computers dedicated to image processing through the shared memory.
4. Process the images with the algorithms described in Section 3.
5. Suggest the next movement of the robot based on the image processing results by turning on or off the flags in the shared memory.

6. Server machine will check the flags and decide whether and what to report back to the robot.
7. Measure the time from the transmission of image data to the server machine and the response from the server machine.
8. Measure the response time through steps 1 to 7. Also measure the time spent for processing an image by a single computer. Do the comparison between the two.

4.2 Experimental Results

TABLE I
 Experimental Result (Time of image processing)

	Possible image processing frequency (1 sec)	Necessary time for image data processing of one time
Necessary time only for image data processing	8.5 times	0.118 sec

TABLE
 EXPERIMENTAL RESULT (RESPONSE TIME)

	Reception of result for every 100 seconds frequency	Time necessary for reception once(reactive speed)
Robot reaction time	480 times	0.208 sec

In order to measure the response time, one image processing computer is used for the experiment. The experimental results in table 1 and 2 are all collected from the same computer. In the case that more than one computer are used for more image processing algorithms, the response time will increase. Considering the possible number of images transmitted per second, approximately 8 computers will be possibly used for the image processing. The response time will increase to 0.95 seconds at most. The time needed for processing one image will not exceed 0.2 second. The data in Tables 1 and 2, however, are collected from the indoor scene. To measure the outdoor scene, we have to extend the coverage of the wireless LAN, the response time will for sure increase.

5 Discussion

The experimental results indicate that the proposed system architecture for supporting autonomously moving robot provides fast enough image processing capability.

Assume that the robot is moving at the speed of 1 m per second. It will be considered necessary to do the image processing 10 times per second. The network camera mounted on the robot is capable of transmitting 10 images per second to the server machine. The response time measured from the experiments is 0.2 second. Therefore, doing image processing 5 times per second is possible. In order to further improve the

response time, we are investigating the possible of converting image format during the transmission. With the improvement, more complicated image processing algorithms requiring image processing 10 times per second could be achieved.

Furthermore, edge detection, shape features could be further improved so that the entire response time could be substantially shortened. However, in order to deal with the outdoor scene, a lot more different type of obstacles needs to be taken into account. Accordingly, the image processing algorithms need to be sophisticating enough to handle the complicated scene. Algorithms such as obstacle identification based on pattern matching, accurate distance measurement based on stereo matching, and the processing high-resolution images are being considered. With all the availability of all these algorithms, the truly autonomously moving robot could be expected.

6 Future Work

In the current distributed image processing system, one computer is dedicated to process an entire image. It is possible that the lack of responsiveness is due to the completion of a complicated image-processing algorithm. If it is possible to divide the image into 3 portions and have three computers to apply the same image processing algorithm only to one third of the image data. The entire processing time will be reduced by one third. It is also possible that the movement of the robot at the next moment has been decided already while finishing processing only one third of an image. In that case, the image processing algorithms should be applied to the subsequent incoming images. This divide-and-conquer approach is promising and still has a lot of uncertainties that need to be resolved in the near future.

Acknowledgements

We greatly appreciate the aid of Ministry of Internal Affairs and Communications (MIC) and the Grant-in-Aid for Scientific Research.

References

- [1].Kazushi Hirano,"Research on remote control systems for half autonomous movement robot in outdoor", Kyushu Institute of Technology Information Department of Engineering graduation thesis,2003
- [2]. J. Miura and Y. Shirai,"Vision and Motion Planning for a Mobile Robot under Uncertainty",Int. J. of Robotics Research, Vol. 16, No. 6, pp.806-825, 1997
- [3].T.TAOKA, M.MANABE, M.KANBAYASHI, Y.OHNISHI, M.FUKUI "An Efficient Lane Recognition Algorithm for Automobile Applications" Information Processing Society of Japan Research Report, Vol.2006, No.111, 2006-SLDM-126, pp.63-68

Lateral Control Design of an Autonomous Land Vehicle Using RTK-DGPS

Hyung Gyu Park, Jae Heon Ryu
and Seong Taek Hwang
Department of Mechanical and
Intelligent Systems Engineering
Pusan National University
Busan, 609-735, KOREA

Man Hyung Lee
School of Mechanical Engineering,
Pusan National University
Busan, 609-735, KOREA

Abstract

This paper describes the development of the H_∞ lateral control system for an autonomous ground vehicle in a limited area using the RTK-DGPS (Real Time Kinematic - Differential Global Positioning System). Before engaging in autonomous driving, map data are acquired by using the RTK-DGPS. The data are the reference trajectory for autonomous vehicles. The navigation system with the map data computes the reference yaw angle of the vehicle using its present position and next position. Also, the yaw angle of the vehicle is controlled by the H_∞ controller. A prototype of the autonomous vehicle by the navigation method is developed. In addition, the performance of the vehicle is evaluated by experiment. The experimental results show that the H_∞ controller and the RTK-DGPS based navigation system can sufficiently track the map at low speed. We expect that this navigation system can be made more accurate by augmenting other sensors.

1 Introduction

Research centered on ITS (Intelligent Transportation System) and PATH (Partners for Advanced Transit and Highways) has led to the development of the autonomous vehicle. Generally, it has been realized using MR sensors and vision sensors, among other technologies. Though the autonomous vehicle was created in part by using them, it is difficult to operate autonomous vehicles in all conditions [1]. For example, if we use MR sensors, we must mark magnet points on the road and stochastic error occur. With vision sensors, the problem is that they are sensitive to weather conditions or light [2]. Now, concerning about the navigation systems by using the absolute coordinate system has progressed [3]. So, we realized an autonomous vehicle using the absolute coordinate system with an RTK-DGPS (Real Time Kinematic-DGPS)

Generally, a differential GPS has been used for improving the accuracy of GPS. All the DGPS reference stations have transmitters to forward the error factors to DGPS receivers by radio or other methods, which gives

the information to the GPS receiver so it can use the data to correct its own measurements and calculations. This differential correction technique applies to GPS receivers performing code-phase navigation.

When a receiver navigates in carrier-phase mode, it is measuring a different GPS observable, namely the GPS carrier wave. In order to obtain high accuracy with carrier-phase measurements, it is necessary to compute the number of GPS wavelengths between the roving GPS receiver's antenna and the satellites using the information (i.e., carrier-phase measurements) from a base receiver. This technique yields accuracy to the cm-level in dynamic environments called RTK-DGPS. So, the method is used to make a digital road map and computes vectors for navigation.

In this paper, the H_∞ control by the feedback of the yaw angle error was used to design a robust lateral control against modeling uncertainty [4]. Furthermore, its property is compared that of the PID controller.

2 Lateral Control

2.1 Lateral Vehicle Model

This section considers a classic linearized bicycle model with two degrees of freedom for the lateral and yaw dynamics of a vehicle. We used the PATH car model (Fig. 1) in order to design controller. Because our main interest is with steering control, we ignored the roll, pitch, and vertical movement of the vehicle. And if we suppose that the vehicle runs on a flat road, we can regard the lateral slip angle and the yaw angle as small [5]. Also, if the speed of the vehicle is constant, the complex car

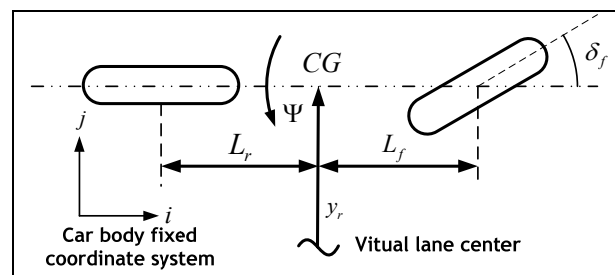


Fig. 1 Integration concept of operation

model equation can be simplified. The curvature of the road was not considered in this study for simplifying the model, since the effect of the curvature on vehicle control at the low speed and in the large curvature is less than that of other uncertainties and external disturbances.

The linearized dynamic equation can be simple, as follows:

$$\frac{d}{dt} \begin{bmatrix} y_r \\ \dot{y}_r \\ \Psi_r \\ \dot{\Psi}_r \end{bmatrix} = \begin{bmatrix} 0 & 1 & 0 & 0 \\ 0 & \frac{A_1}{V} & -A_1 & \frac{A_2}{V} \\ 0 & 0 & 0 & 1 \\ 0 & \frac{A_3}{V} & -A_3 & \frac{A_4}{V} \end{bmatrix} \begin{bmatrix} y_r \\ \dot{y}_r \\ \Psi_r \\ \dot{\Psi}_r \end{bmatrix} + \begin{bmatrix} 0 \\ B_1 \\ 0 \\ B_2 \end{bmatrix} \delta_f, \quad (1)$$

where $A_1, A_2, A_3, A_4, B_1,$ and B_2 are defined as

$$A_1 = -\frac{C_f + C_r}{m}, \quad A_2 = -\frac{(C_f L_f - C_r L_r)}{m},$$

$$A_3 = \frac{(-C_f L_f + C_r L_r)}{J}, \quad A_4 = -\frac{(C_f L_f^2 + C_r L_r^2)}{J},$$

$$B_1 = \frac{C_f}{m} \quad \text{and} \quad B_2 = \frac{C_f L_f}{J}.$$

The front wheel steering actuator is assumed to be dominated by the first order delay.

$$\theta_m = \frac{1}{T_m s + 1} u_f, \quad (2)$$

where, T_m is the time constant of the motor and u_f is the control input and θ_m is the motor (or steering wheel) angle.

The steering system from the motor (or steering wheel) angle θ_m to the wheel angle δ_f is modeled as a gear with the gear ratio of n . So, δ_f is given by

$$\delta_f = n \theta_m. \quad (3)$$

Combining the dynamics of the actuator and the vehicle dynamics, a 5th order state space model with

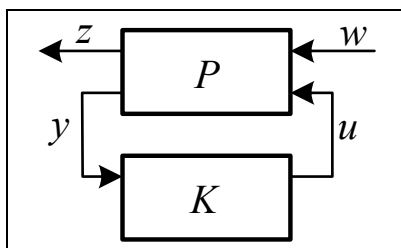


Fig. 2 The basic block diagram of H_∞ controller

states $X = [y_r \ \dot{y}_r \ \Psi_r \ \dot{\Psi}_r \ \theta_m]^T$ is obtained as follows:

$$\dot{X} = \begin{bmatrix} 0 & 1 & 0 & 0 & 0 \\ 0 & \frac{A_1}{V} & -A_1 & \frac{A_2}{V} & B_1 \cdot n \\ 0 & 0 & 0 & 1 & 0 \\ 0 & \frac{A_3}{V} & -A_3 & \frac{A_4}{V} & B_2 \cdot n \\ 0 & 0 & 0 & 0 & -\frac{1}{T_m} \end{bmatrix} X + \begin{bmatrix} 0 \\ 0 \\ 0 \\ 0 \\ \frac{1}{T_m} \end{bmatrix} u_f. \quad (4)$$

2.2 Lateral Control of an Autonomous Vehicle

Fig. 2 is general a block diagram of H_∞ control. The components of w are all the exogenous inputs to the system [6]. Typically, these consist of disturbances, sensor noise reference commands and fictitious signals that drive frequency weights and models of the uncertainty in the dynamics of the system. The components of z are all the variables we wish to control like the tracking errors and the actuator signals. The inputs generated by the controller are denoted u . The sensor measurements that are used by the feedback controller are denoted y .

The generalized plant P , which is assumed to be linear and time-invariant, contains all the information a designer would like to incorporate into the synthesis of the controller, K . System dynamics, models of the uncertainty in the system's dynamics, frequency weights to influence the controller synthesis, actuator dynamics, sensor dynamics, and implementation hardware dynamics are all included in P .

The relation of the variable z and the exogenous input is $z = T_{zw} w$. So, the H_∞ control is represented as

$$\|T_{zw}\|_\infty \leq \gamma. \quad (5)$$

The H_∞ control is represented as (6) with the method of Glevor and Doyle [7].

$$\left\| \begin{matrix} W_1 S \\ W_3 T \end{matrix} \right\|_\infty \leq \gamma. \quad (6)$$

Regarding the mixed-sensitivity problem, W_1 and W_3 are weighting functions for improving performance of the system. In addition, S and T are the sensitivity function and the loop transfer function of the system, respectively. Based on the time domain performance specifications, the corresponding requirements in a frequency domain in terms of the bandwidth ω_b and the peak sensitivity M_s can be determined. This assumes that the steady state error of the step response ε has to

satisfy $|W_1(0)| \geq 1/\varepsilon$. A possible choice of W_1 can be obtained by modifying the weighting function as follows:

$$W_1 = \frac{s/M_s + \omega_b}{s + \omega_b\varepsilon} \quad (7)$$

Additionally, the magnitude of $|KS|$ in the low-frequency range is essentially limited by the allowable cost of control effort and saturation limit of the actuators; hence, in general, the maximum gain M_r of KS can be fairly large, while the high-frequency gain is essentially limited by the controller bandwidth (ω_{bc}) and the sensor noise frequencies. A candidate weight W_3 would be

$$W_3 = \frac{s + \omega_{bc}/M_r}{\varepsilon_1 s + \omega_{bc}} \quad (8)$$

for a small $\varepsilon_1 > 0$.

Fig. 3 is the bode plot of each weighting function.

3 Navigation Algorithm

Fig. 4 shows the target points are determined using map data. When the unmanned vehicle navigates the road, it compares current position with map data. However, the navigation system cannot compare all data for searching target points. So, it calculates maximum moving distance r of the vehicle by using velocity of the vehicle until acquiring the next set of RTK-DGPS data. It compares the current position with maximum distance position M_{n+2} within the circle that has a radius r . It calculates the yaw reference $|\psi_{ref}|$ by the dot product of vectors. It uses the prior position P_{t-1} , the current position P_t and the target position M_{n+2} , which is shown in equation (9) as follows:

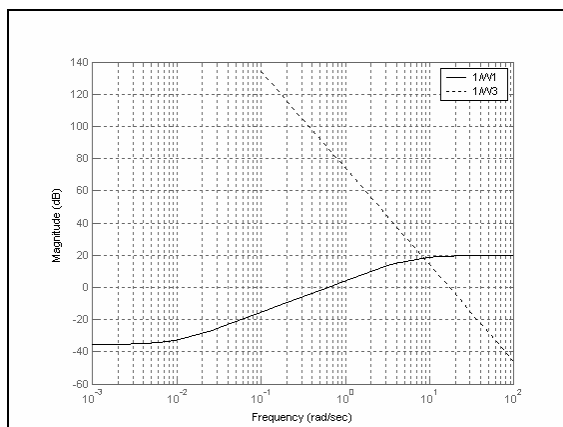


Fig. 3 Selected weighting functions

$$|\psi_{ref}| = \cos^{-1} \frac{\overline{P_{t-1}P_t} \cdot \overline{P_tM_{t+2}}}{|\overline{P_{t-1}P_t}| \cdot |\overline{P_tM_{t+2}}|} \quad (9)$$

Also, the sign of direction is solved by using the sign of the cross product of vectors. So, we can acquire ψ_{ref} as follows:

$$\psi_{ref} = \text{sign}(\overline{k(P_{t-1}P_x \times P_tM_{t+2_y} - P_{t-1}P_{t_y} \times P_tM_{t+2_x})}) \times |\psi_{ref}| \quad (10)$$

For determining the target point, r is calculated by using velocity V of the vehicle, sampling time (t) of the RTK-DGPS and α , the coefficient considered curvature of the road. α is used for determining the proper target point. If target points are calculated at 1 second intervals, the variation of yaw severely increases. So, angle data λ of the vectors are added to the path data by post-processing. The data are calculated using $n-1$ th, n th and $n+1$ th data in the path data. The coefficient α is acquired by using equation (11). It is optimized by simulation and experiments as follows:

$$\begin{cases} \lambda > 0.1 \text{ radian,} & \alpha = 1 \\ \lambda < 0.1 \text{ radian,} & \alpha = 180\lambda^2 - 37\lambda + 3. \end{cases} \quad (11)$$

4 Experiment

4.1 Experimental System

The experiment vehicle is SPORTAGE of KIA motors. The RTK-DGPS system is from the Z-family of Ashtech. The accuracy of the synchronized RTK mode is 0.5cm+1ppm. In addition, the maximum position output rate at the remote receiver is 1Hz. The communication between the base station and the remote station in the vehicle was accomplished by using a PDL (Positioning Data Link) system that uses an RF connection. Also, we used the digital compass of Robot electronics. Its absolute error is 3°, with a resolution of 0.1°. The navigation computer was PXI-1002 from National Instrument. Finally, the navigation software was coded

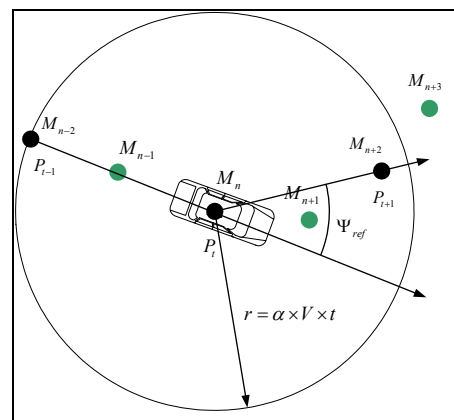


Fig. 4 Navigation concept

by using LabVIEW 6.1.

4.2 Experiment Results

The width of the test road was a minimum 3.6 m and the vehicle width was 1.735 m. Before the test, the path data were acquired by using the RTK-DGPS. Fig. 8 is the path data. The full lap of it was 160 m.

The velocity of the vehicle is about 2.778 m/s (about 10 km/h). Fig. 6 shows the test results when the parameter is similar to that used in designing the controller. In Fig. 7, the velocity and mass of the vehicle are changed in the test driving condition. This was done in order to compare performance of each controller considering modeling uncertainty. The performance of the H_∞ controller is more robust than a PID controller for a change of system parameters. Table 1 presents the maximum and mean of the errors of each experiment.

5 Conclusion

In this paper, the real vehicle was implemented to verify the performance of a proposed lateral control and

a simple navigation algorithm. To control the yaw of the vehicle, an H_∞ control algorithm was introduced. To cope with the sensor noise and the modeling uncertainty, a robust lateral controller was designed by the feedback of the yaw angle error of the vehicle.

The position and attitude of the vehicle was calculated by using the RTK-DGPS and a digital compass. The vehicle was steered by DC motors which were controlled by a real time module. The experimentation for the real scale vehicle showed that the proposed lateral controller improved the tracking performance.

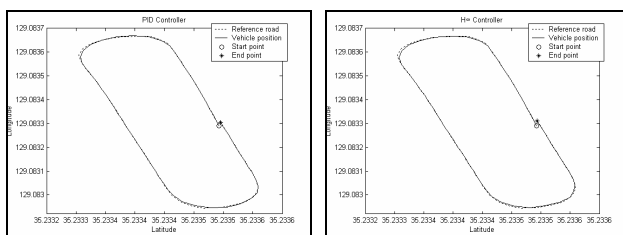
We also considered current related work concerned with improving the precision of dead reckoning by correction of the diameters of tires. In such cases, the vehicle navigates for a longer time by dead reckoning in an urban canyon environment. We expect such applications will be useful in the future to create a wheel chair system for blind.

Acknowledgment

This work was supported by the Brain Korea 21 Project.

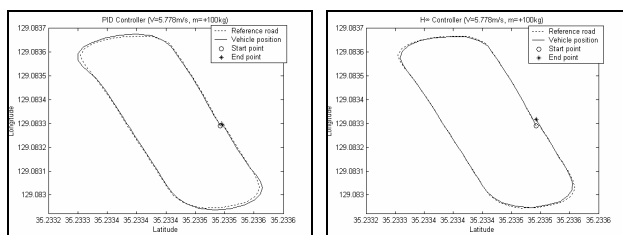
Reference

- [1] Huei, P., Wei-Bin, Z., Alan, A., Ye, L., Thomas, H., Peter, D., Masayoshi, T., and Steven, S, Experimental Automatic Lateral Control System for an Automobile, PATH Research Report, 1992.
- [2] Maurer, M., Behringer, R., Furst, S., Thomanek, F. and Dickmanns, E. D., "A Compact Vision System for Road Vehicle Guidance Pattern Recognition," in *Proceedings of the 13th International Conference*, Vol. 4, pp. 2243-2247, 1998.
- [3] Han Shue, Farrell, T., A., and Yunchun, Y., "Automatic Vehicle Steering Controls: DGPS/INS and Magnetic Markers," in *Proceedings of American Control Conference*, Vol. 1, pp. 60-65, 2003.
- [4] Shladover, S., "Automated Vehicle Control Developments in the PATH Program," *IEEE Transaction on vehicular technology*, Vol. 40, No. 1, pp. 114-130, 1991.
- [5] Huei, P., and Masayoshi, T., Lateral Control of Front-Wheel-Steering Rubber-Tire Vehicles, PATH Research Report, 1990.
- [6] Kemin, Z., Essential of Robust Control, The first edition, Prentice-Hall, New Jersey, 1998.
- [7] John, C., Keith, G, Pramod, P., and Bruce, A., "State-Space Solutions to Standard H_2 and H_∞ Control Problems," *IEEE Transactions on Automatic Control*, Vol. 34, No. 8, pp. 831-847, 1998.



(a) PID Controller (b) H_∞ Controller

Fig. 5 Trajectories for each controller



(a) PID Controller (b) H_∞ Controller

Fig. 6 Trajectories for each controller(+2m/s,+100kg)

Table 1. Results of driving test

Test result	Maximum error[m]	Mean error[m]
PID	0.447	0.276
H_∞	0.521	0.220
PID(+2m/s,+100kg)	0.914	0.483
H_∞ (+2m/s,+100kg)	0.732	0.310

Navigation system for a mobile robot using an omni-directional camera

Tatsuya Mochizuki

*Graduate School of Computer Science
and System Engineering
Kyushu Institute of Technology
680-4, Iizuka City, Fukuoka, Japan, 820-8502
hiki@mmcs.mse.kyutech.ac.jp*

Eiji Hayashi

*Department of Mechanical Information
Science and Technology
Kyushu Institute of Technology
680-4, Iizuka City, Fukuoka, Japan, 820-8502
haya@mse.kyutech.ac.jp*

Abstract

This study developed a self-localization system that uses landmarks and movement to pursue a moving object. Specifically, an omni-directional camera was adopted as a visual sensor and was installed on a robot.

The image from the omni-directional camera was processed to detect a landmark (an object), and the robot's distance from that landmark was then measured. These functions allowed the mobile robot to pursue a moving object. The measurement of distance based on the omni-directional image depends on the precise inclination of the camera. Consideration of this factor enabled the measurement of distance of relatively close objects with a high degree of precision.

In this study, the effectiveness of this system was investigated by various experiments evaluating the measurement of distance, the movement to pursuit a moving object, and self-localization. The robot demonstrated its ability to recognize a moving object and to measure its distance and its angle in relation to the object. Based on these abilities, the robot could successfully follow a moving object. The robot's ability to recognize its location was seen to be based on its ability to recognize certain landmarks, the functions of which are mentioned above.

1. Introduction

With the increase of the elderly population comes an increase in individuals who need attendant care. These increases will also bring about an increase in the burden of caregivers.

This study aimed to develop technology for a personal care robot that will reduce the burden of the caregiver. Specifically, an omni-directional camera was adopted as a visual sensor and was installed on a robot.

The image of the omni-directional camera was processed to detect a landmark (an object), and the robot's distance to that landmark was then measured.

Thus, a self-localization system that uses landmarks and

movement to pursue a moving object were developed.

2. Omni-directional camera

2.1 Background of an Omni-directional camera

Fig. 1 shows the omni-directional camera. It can shoot a circumference of 360 degrees. Fig. 2 is an image that was shot by the omni-directional camera.



Fig. 1 The omni-directional camera Fig. 2 Omni-directional image

2.2 Principle of the omni-directional camera

An omni-directional camera consists of a hyperboloidal mirror and an upward camera. It shoots the circumjacent environment that is reflected in the mirror. Thus, it acquires an omni-directional image (Fig. 3).

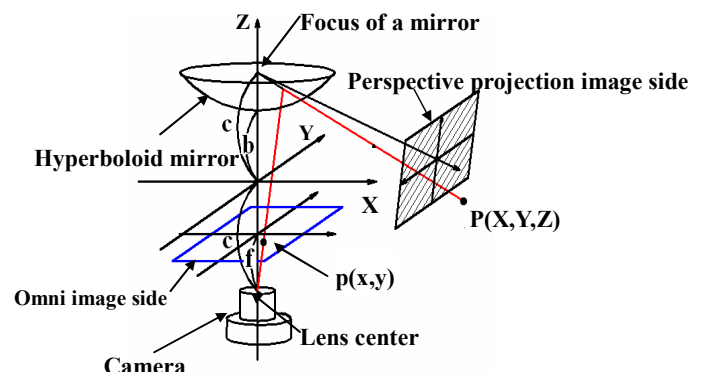


Fig. 3 Structure of visual system

The arbitrary point $P(X,Y,Z)$ in 3-dimensional space corresponds with point $p(x,y)$ on the omni-directional image.

The relation can be expressed by expression (1).

$$\begin{aligned}
 x &= X \times f \times \frac{(b^2 - c^2)}{(b^2 + c^2)Z - 2bc\sqrt{X^2 + Y^2 + Z^2}} \\
 y &= Y \times f \times \frac{(b^2 - c^2)}{(b^2 + c^2)Z - 2bc\sqrt{X^2 + Y^2 + Z^2}}
 \end{aligned}
 \tag{1}$$

3. Detecting a landmark

The image processing applied to the image from the omni-directional camera (Fig. 4) used color information.

When detecting a landmark by use of color information, an RGB color model has to discriminate a color based on three values (R, G, and B). This makes detection challenging. However, a HSV color model is able to discriminate a color by one value. Accordingly, the RGB color model was converted to a HSV color model, and thereby detected the landmark by HSV values.

When detecting a landmark using HSV values, some noise is present. In such cases, the image processing removes the noise. Also, it discriminates an object using labeling.

Fig. 4 shows an omni-directional image and Fig. 5 shows how it was processed by means of image processing.



Fig. 4 The picture before the image data processing



Fig. 5 The picture after the image data processing

4. Measuring the distance to the landmark

The distance between the omni-directional camera and a landmark was measured by means of the omni-directional image. This study derived relations between the distance on the omni-directional image and the real distance. And it directly calculated the distance from the image.

Concretely speaking, we experimentally derived relations between the distances on an omni-directional image and real distances. From this experiment result, we were able to derive relations between the distance of an image in the directions of 0, 45, 90, 135, 180, 225, 270, and 315 degrees and the real distance. But the system could not measure distances in between these directions because it only derived relations of 45

degree intervals. Therefore, it interpolated the distance using an interpolating spline, and was able to derive a relation expression that calculated real distances. Fig. 6 shows a graph of the relation expression.

The omni-directional camera was strapped into a tripod stand, and measured real distances. As a result, the value of the average error was 13[mm].

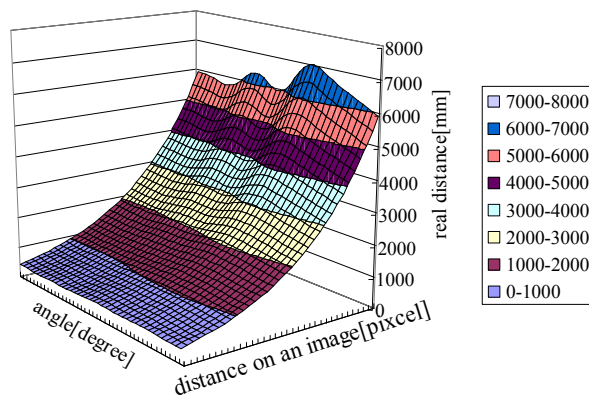


Fig. 6 The spline surface

5. Installing on a mobile robot

5.1 Mobile robot KITASAP2

In this study, we used a mobile robot that was fabricated in this laboratory. Fig. 7 shows a picture of the mobile robot. The robot we adopted has three wheels. The two front wheels have independent drives while the rear wheel is free.

The following devices were adopted in the mobile robot.

- PC
- H8 microcomputer
- Sensor
 - ① Omni-directional camera
 - ② Encoders

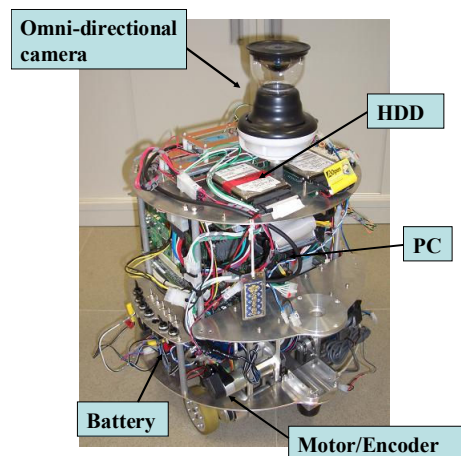


Fig. 7 The mobile robot

5.2 Compensation of slippage by an incline

The omni-directional camera was installed in the mobile robot, and it measured distance as before. While the error in the case described above was 13[mm], the error in this case was 53.52[mm].

It is thought that cause of this greater error was the slippage on the incline that occurred when we installed the camera. Therefore, we revised the slippage.

In Fig. 8, the dashed line indicates the direction in which the omni-directional camera inclines, and the continuous line is the horizontal.

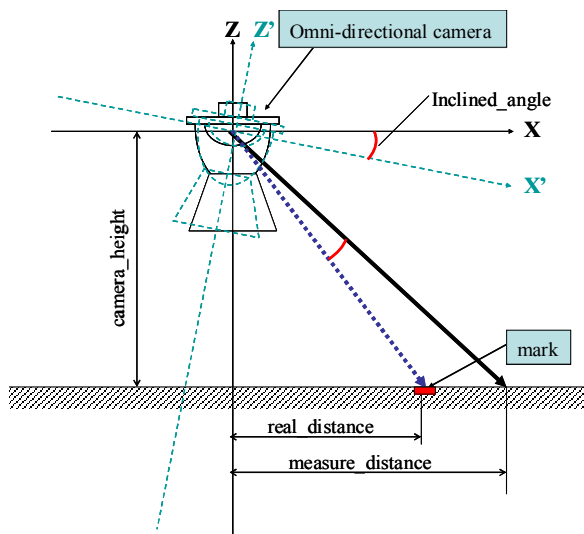


Fig. 8 Inclinations of the omni-directional camera

Assuming the height of the camera is given, we can express the incline (the angle between arrows) in the following expression.

$$\text{inclined_angle} = \tan^{-1}\left(\frac{\text{camera_height}}{\text{measure_distance}}\right) - \tan^{-1}\left(\frac{\text{camera_height}}{\text{real_distance}}\right) \quad (2)$$

We calculated the inclines of each direction from this expression (2), and revised the data using calculated inclines and expression (1).

The average error before revising was 53.32[mm], while that after revising was 9.72[mm]

6. Following a mobile object

Applying the above-described detection of a landmark and measurement of the distance to the landmark, we attempted to have the mobile robot follow a mobile object. Mobile robots calculate the movement course by measuring distance and angle information. Here, we explain the calculation method of the movement course of the robot. The mobile robot

calculates a circle such that the direction of the robot's progress is a tangent line and the circle passes through the position of the object (Fig. 9)

This circle is unique. Therefore, the mobile robot assumes this circle as its movement course. The radius of this circle can be calculated with expression (3). By performing these calculations and movements repeatedly, we succeeded in having the robot follow a mobile object.

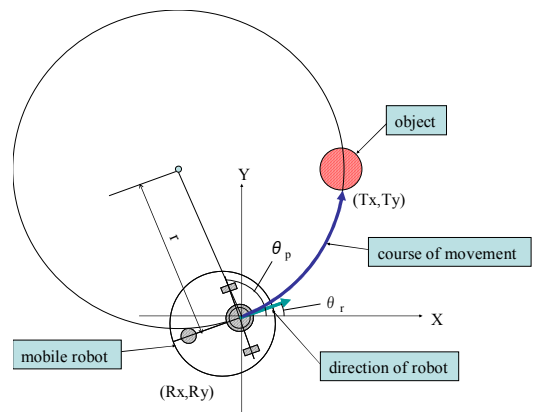


Fig. 9 Course of movement

$$r = \frac{(Tx - Rx)^2 + (Ty - Ry)^2}{2\{\cos\theta_p(Tx - Rx) + \sin\theta_p(Ty - Ry)\}} \quad (3)$$

7. Self-localization

We applied the above-described detection of a landmark and measurement of the distance to the landmark in creating a self-localization system. Here, I explain the method of self-localization. The mobile robot calculates circles using the distance to the landmark (Fig.10). The point where three circles cross becomes its self-position.

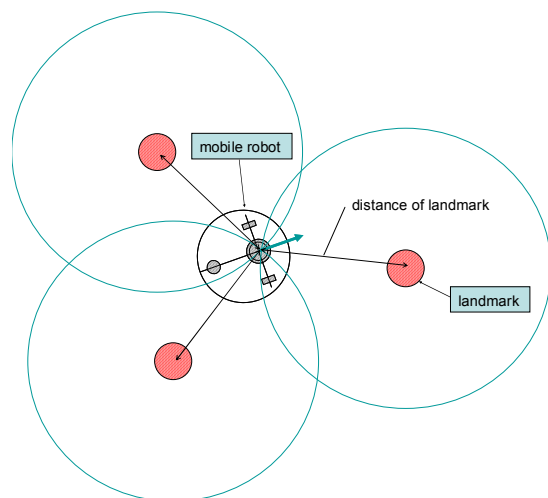


Fig.10 Self-localization

In addition, we tested self-localization in an environment such as that shown in Fig.11. We moved the robot from the A spot (-500,-500) to the B spot (500,-500) and moved it again afterwards to the A spot (-500,-500). During movement, we tested the robot's self-localization. The result is shown in Fig. 12.

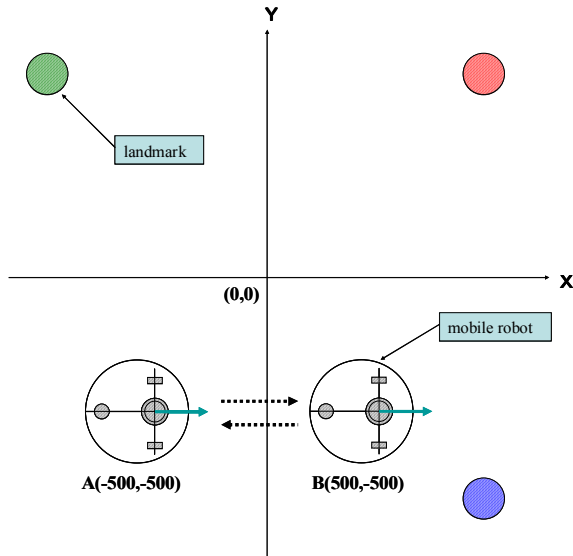


Fig. 11 Result of experiment

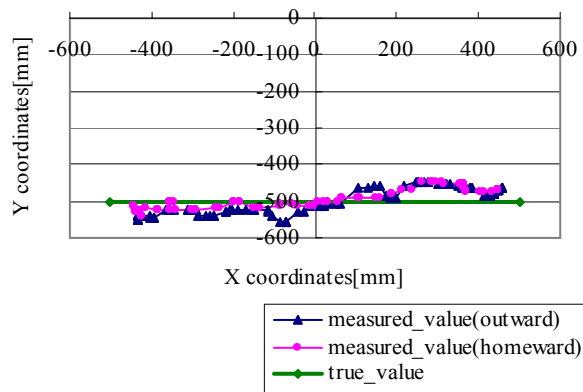


Fig. 12 Result of experiment

8. Conclusion

In this paper, as elements of a navigation system for a mobile robot using an omni-directional camera, we developed systems for following a mobile object and for self-localization using a landmark. The robot demonstrated its ability to recognize a moving object and to measure its distance and its angle in relation to the object. Based on these abilities, the robot could successfully follow a moving object. However, the precision decreased sharply when the distance of the landmark became remote.

Therefore in the future, we will aim at improving self-localization. Concretely, in considering the shape of landmarks, the robot will be able to detect its position more precisely.

8. Acknowledgment

The authors would like to acknowledge the advice and assistance of Professor Tadashi Kitamura of Kyushu Institute of Technology who died in 2006.

References

- [1] Kazumasa Yamazawa: "HyperOmni Vision: Visual Navigation with an Omnidirectional Image Sensor",
- [2] Akira Sakurai: Introduction to spline function

Adaptation of a distributed controller depending on morphology

Nathan Labhart and Shuhei Miyashita
Artificial Intelligence Laboratory
University of Zurich
Zurich, Switzerland
{labhart,miya}@ifi.unizh.ch

Abstract

In this paper we investigate the influence of an agent's morphology on its neural controller. Our model consists of a number of identical modules, each of which comprises of two half-wheels for movement and a Central Pattern Generator (CPG) as its own neural control. Based on a series of simulation experiments, we conclude that one single type of CPG can adapt well to different types of morphologies, and that there seems to be a suitable or optimal morphology depending on the environmental givens.

Keywords: Morphology, Central Pattern Generator, evolutionary algorithm

1 Introduction

It is a widely accepted fact that the neural controller of an agent has to match the complexity of its body as well as the complexity of its task environment ("Principle of Ecological Balance", [1]). Normally, controller and morphology evolve in parallel, mutually influencing each another, and taking into account the interaction with the environment. In this paper, we investigate the influence of an agent's morphology on the evolution of its neural control – inspired by the centipede, where locomotion is achieved by "synchronizing" a number of two-legged body segments.

In the present research, a series of simulation experiments are carried out with modular robots, where each module consists of a body and a Central Pattern Generator (CPG).

J. C. Bongard and R. Pfeifer tested hypotheses about the behavioral effect of specific morphological features by keeping the neural controller constant across different body sizes, masses, and morphologies [2]. The essential issues of how to develop a cellular robotic system were described by Y. Kawauchi et al. Their project "CEBOT" included optimization meth-

ods for the structure of both hardware and software [3]. S. Murata et al designed a modular robotic system in hardware, which could metamorphose into desired configurations, and showed results of changes in morphology [4]. In the "Conro" project by A. Castano, A. Behar, and P. M. Will, each module was self-contained (it included its own processor, power supply, communication system, sensors, and actuators). These modules were designed to work in groups as part of a large configuration [5]. A similar project is presented by M. W. Jørgensen et al with "ATRON", which consists of several fully self-contained robot modules [6]. Using nonlinear coupled oscillators for the CPG was described by A. Ijspeert and J.-M. Cabelguen. Their experiments on salamander movement show how configurations could combine global couplings from the segment oscillators in order to achieve "realistic" locomotion data [7].

2 Model

2.1 Single Module

In this first set of experiments, the agents are simulated in the physics engine ODE. In its base form, a module consists only of a motor, rigid joints to stick several modules together, one set of half-wheels, and a neural control mechanism (Fig. 1).

The half-wheels of one module are connected by a fixed axis (i.e. they always turn in parallel) and are constrained in movement from $-\frac{\pi}{2}$ to $+\frac{\pi}{2}$. This restriction is introduced to exploit the interaction with the environment: by taking into account the static and dynamic friction on the ground, the back-and-forth movement of the half-wheels causes the whole configuration to move.

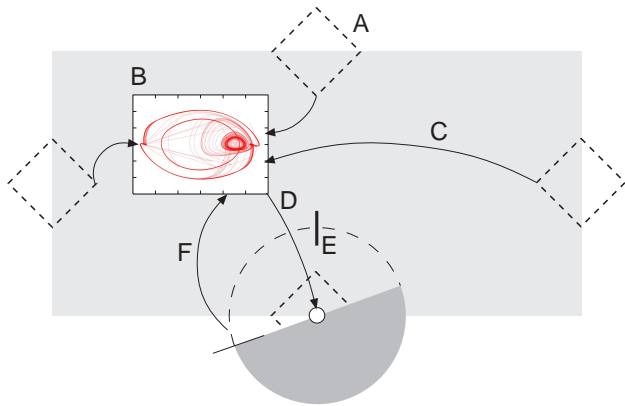


Figure 1: A single module. A: connector to neighbor module; B: CPG; C: input from neighbor module; D: forward/backward command; E: stopper (to restrict movement from $-\frac{\pi}{2}$ to $+\frac{\pi}{2}$); F: half-wheel angle input.

2.1.1 CPG

The CPGs are modeled as nonlinear oscillators in x, v space, taking the angles of the corresponding half-wheels as inputs and returning a “forward” or “backward” command depending on a threshold θ .

The controller inside every module is connected not only to its own half-wheels, but also to the immediately neighboring modules. Thus, every CPG has a limited knowledge about the state of its neighborhood, but not about the entire configuration:

$$\tau \dot{v}_i = -\frac{x_i^2 + v_i^2 - E_i}{E_i} v_i - x_i + \sum_j w_j s_j \quad (1)$$

$$\tau \dot{x}_i = v_i \quad (2)$$

where i is the number of the current module, j is the number of the neighbor module, w_j are the weights for the connection to the neighbors s , and τ and E_i are constants. This CPG is an oscillator with amplitude $\sqrt{E_i}$ and period $2\pi\tau$.

$$\begin{cases} x + v > \theta_{high} & \text{“backward”} \\ x + v < \theta_{low} & \text{“forward”} \end{cases} \quad (3)$$

2.2 Configurations

Like building blocks, these modules are attached to each other to form various morphologies. In order to understand the influence of morphology on the

controlling mechanism, we implement the same type of neural control in two different configurations and compare the CPGs as well as the traveled distances.

module mass	1.4kg	τ	0.2
module L×W×H	1×0.5×0.5m	θ_{low}	-0.3
half-wheel radius	0.2m	θ_{high}	0.3

Table 1: Simulation properties

This model is deliberately kept simple and easily extensible for future experiments. In addition, it allows a relatively straightforward way of implementing it in hardware in order to test the outcome of the simulation in the real world.

3 Simulation

We implement two configurations with 8 modules each, which differ only in the distribution of the four top modules, so that the center of gravity is shifted to one end of the robot (Fig. 2).

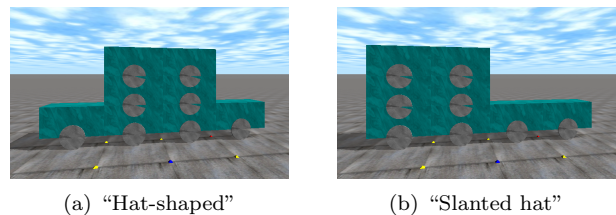


Figure 2: Two configurations simulated in ODE.

In order to understand the influence of morphology on the controlling mechanism, we let the two configurations evolve the E_i parameters of their CPGs over 1000 generations and then compare their performance. Minimal Generation Gap [8] evolution is applied to adapt this controller to the respective morphology (i.e. configuration of the modules). The fitness function is defined as the distance a configuration can cover within a limited time frame. In addition, we analyzed the trajectories of the CPG parameters from the first, the 500th, and the 1000th generation.

For each generation, the simulation runs for 2000 time steps. In every 50th step, the positions of the half-wheels are recorded, and the CPG values (x, v) are calculated for 1000 iterations (Δt steps), taking into account the half-wheel positions. The resulting CPG values define whether a “forward” or “backward”

command is issued to the corresponding half-wheel. Once the movement command has been executed, the configuration “slides” on the ground for a few (less than 50) timesteps, and the next CPG calculation cycle takes place.

4 Results and discussion

As can be seen from the distance plots (Fig. 3), the asymmetrical configuration clearly “makes use” of the shifted center of gravity with an average distance of 0.8387m, compared to 0.4482m in the symmetrical configuration. The different morphology is also reflected in the CPG trajectories (Fig. 4, 5).

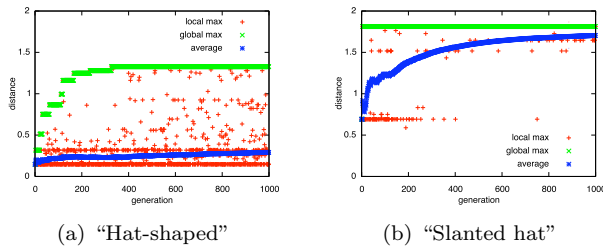


Figure 3: Performance (traveled distance) of both configurations.

The experiments show that a slight change in morphology results in different performances. The average distance covered by the asymmetrical configuration is about 6 times as large as that of the symmetrical one; furthermore, the symmetrical morphology takes much longer to evolve its CPG parameters into a set of values that performs well.

By comparing the CPG’s x , v trajectories of one morphology over time we find that the further the configuration moves, the more distinct the trajectories become (Fig. 4(b), 5(b)). In contrast to the symmetrical “hat-shaped” morphology, the CPG adapts to the asymmetrical morphology of the “slanted hat” configuration more quickly, and the CPG trajectories are more distinct.

A comparison of the two morphologies suggests that evolution apparently exploits the friction on the ground, taking into account the asymmetrical weight distribution of the “slanted hat” morphology where the weight on the left side is higher than on the right.

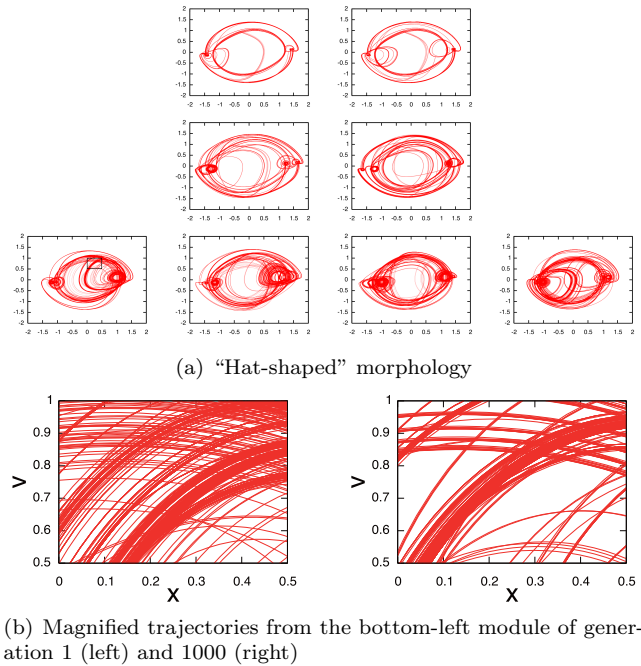


Figure 4: CPG trajectories of the symmetrical configuration.

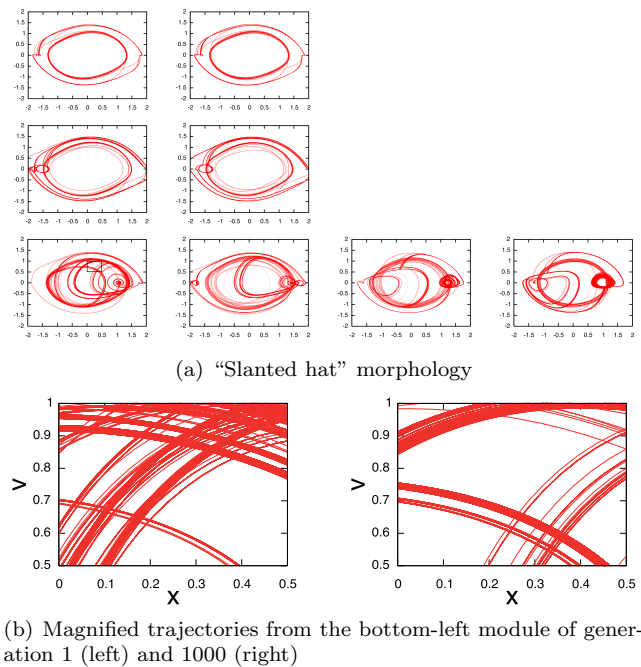


Figure 5: CPG trajectories of the asymmetrical configuration.

These results imply two things: On the one hand, one single CPG can adapt well to different types of

morphologies; on the other hand, there seem to be suitable or optimal morphologies depending on the environmental givens (in this case, friction).

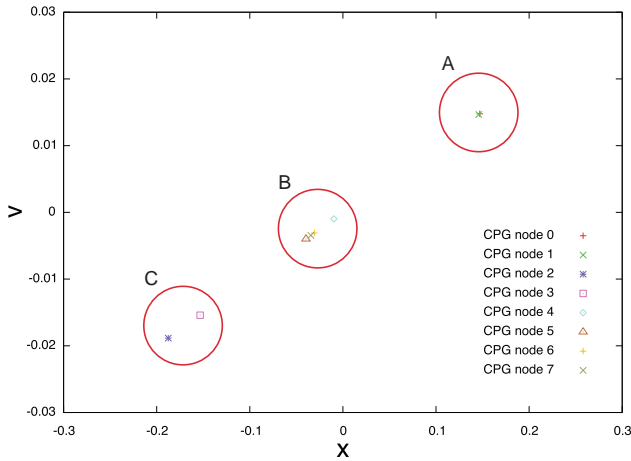


Figure 6: Mean values of all CPGs in the 1000th generation of the symmetrical configuration. The four modules which touch the ground are marked with A and C, the four upper modules are marked with B.

Furthermore, we observe in the symmetrical configuration that the four modules which touch the ground shift their CPG's center (mean value) away from the zero point in an asymmetric way (Fig. 6). This enables the "hat shaped" morphology to move at all, rather than staying at the same position (as could be expected from its symmetrical shape). The top four modules, where the half-wheels do not directly influence the movement of the configuration, keep their CPG centers very close to the zero point. The "slanted hat" morphology does not exhibit such a behavior, as it is already asymmetric by design.

Acknowledgments

This research is partially supported by the Swiss National Science Foundation, project #200021-105634/1 and project #200021-109864/1.

References

[1] Pfeifer R, Scheier C (1999), *Understanding Intelligence*. MIT Press, Cambridge, pp. 312-315

[2] Bongard JC, Pfeifer R (2002), A Method for Isolating Morphological Effects on Evolved Behaviour. In: Hallam B, Floreano D et al (ed), *Proceedings of the Seventh International Conference on the Simulation of Adaptive Behaviour (SAB2002)*, MIT Press, pp. 305-311

[3] Kawauchi Y, Inaba M, Fukuda T (1994), A Study on Cellular Robotic System (A Realization of a Robotic System Capable of Adaptation, Self-organization, and Self-evolution). *JRSJ* 12(1):116-132

[4] Murata S, Tomita K, Yoshida E et al (1999), Self-Reconfigurable Robot - Module Design and Simulation. *Proceedings of 6th International Conference on Intelligent Autonomous Systems (IAS-6)*, pp. 911-917

[5] Castano A, Behar A, Will PM (2002), The Conro Modules for Reconfigurable Robots. *IEEE/ASME Transactions on Mechatronics*, 7(4):403-409

[6] Jørgensen MW, Østergaard EH, Lund HH (2004), Modular ATRON: Modules for a self-reconfigurable robot. *Proceedings of 2004 IEEE/RSJ International Conference on Intelligent Robots and Systems*, pp. 2068-2073

[7] Ijspeert A, Cabelguen J-M (2003), Gait Transition from Swimming to Walking: Investigation of Salamander Locomotion Control Using Nonlinear Oscillators. In: Kimura H, Tsuchiya K, Ishiguro A et al (ed), *Adaptive Motion of Animals and Machines*. Springer, Tokyo, pp. 177-188

[8] Satoh H, Yamamura M, Kobayashi S (1996), Minimal Generation Gap Model for GAs Considering Both Exploration and Exploitation. *Proceedings of IIZUKA '96*, pp. 494-497

On-line Variational PCA for Adaptive Visual Tracking

Torazo Date* Takashi Bando* Tomohiro Shibata* Shin Ishii*

* Graduate School of Information Science
Nara Institute of Science and Technology (NAIST)
Takayama 8916-5, Ikoma, Nara 630-0192, Japan

Abstract

In the research area of visual tracking as well as recognition, there have been numerous attempts to use appearance-based object representation which does not require explicit knowledge or precise geometric representation of the object. In particular, the eigenspace representation has been widely used for visual tracking of a target, because of its rich representational power based on clear mathematical properties. There is, however, a big problem that the appearance of a target object may vary in time due to various factors such as changes in the lighting condition, and in location, pose, scale, and shape of the object. On-line algorithms that incrementally update eigenvectors (basis images) can be an answer to this problem. In this study, we propose an adaptive visual tracking method by combining an on-line variational Bayesian version of principal component analysis (PCA) and particle filtering. Computer simulations demonstrate our method enables robust visual tracking of a target whose appearance varies in noisy environments.

1 Introduction

In the research area of visual tracking as well as recognition, there have been numerous attempts to use appearance-based object representation which does not require explicit knowledge or precise geometric representation of the object. In particular, the eigenspace representation has been widely used (e.g., [6, 5]) because of its computational efficiency based on clear and established mathematical properties. There is, however, a serious problem that the conventional eigenspace method is not robust against changes in the appearance of a target, such as lighting condition, pose, scale, shape, and so on. This problem can be mediated if every appearance variation of the target object is prepared as basis images, but this is quite

impractical. An algorithm which updates eigenvectors (basis images) on-line can be an answer to this problem. Lim et al. (2004) proposed such a visual tracking algorithm [2] that employed a sequential algorithm based on singular value decomposition (SVD), called R-SVD method, and demonstrated robust face tracking of a person walking in cluttered backgrounds.

In this article, we propose an adaptive visual tracking method by combining an on-line variational Bayesian version of principal component analysis (PCA) and particle filtering [4]. Computer simulations demonstrate our method enables robust visual tracking of a target whose appearance varies in noisy environments.

2 Algorithm

2.1 Overview

Our visual tracking algorithm is basically combination of on-line variational PCA and particle filter. Particle Filter (PF) [7] is an approach to making Bayesian estimation of intractable posterior distributions from time-series observation signals disturbed by non-Gaussian noises. The effectiveness of PFs has been reported in various research area, such as real-time visual tracking in Computer Vision (e.g., [4]). Under an assumption that the target dynamics form temporal Markov chains and observations are independent, incremental Bayesian estimation of the hidden target state \mathbf{X}_t at time t is computed by

$$p(\mathbf{X}_t | \mathcal{I}_t) \propto p(\mathbf{I}_t | \mathbf{X}_t) \int p(\mathbf{X}_t | \mathbf{X}_{t-1}) p(\mathbf{X}_{t-1} | \mathcal{I}_{t-1}) d\mathbf{X}_{t-1} \quad (1)$$

where $\mathcal{I}_t = \{\mathbf{I}_1, \dots, \mathbf{I}_t\}$ is a set of observed images.

In this study, smoothness is assumed for target motions: $\mathbf{X}_t - \mathbf{X}_{t-1} = \mathbf{X}_{t-1} - \mathbf{X}_{t-2} + \mathbf{v}_t$, where \mathbf{v}_t denotes a process noise. In the next subsection, we describe the

likelihood term $p(\mathbf{I}_t|\mathbf{X}_t)$, based on on-line variational PCA.

2.2 On-line Variational PCA

Principal component analysis (PCA) is a well-established method of multivariate analysis to perform feature extraction from a data point or a set of data. A data space is reduced by a projection to a comparatively low-dimensional subspace, a feature space. In PCA, this projection is linear. PCA can be reformulated into a probabilistic model including latent variables, which is called Probabilistic Principal Component Analysis (PPCA).

Our proposed method is an on-line updating method whose generative model is given by PPCA, to construct the basis images. This method assumes observed data include noise, thereby robust basis images can be obtained in a real-world environment which includes various distracters or occlusion.

An observed image vector \mathbf{I}_t is given by

$$\begin{aligned} \mathbf{I}_t &= \boldsymbol{\mu} + W\mathbf{s}_t + \mathbf{n}_t \\ &= \tilde{W}\tilde{\mathbf{s}}_t + \mathbf{n}_t, \quad \mathbf{n}_t \sim \mathcal{N}_{Nd}(\mathbf{n}_t|\mathbf{0}, \Sigma_t), \end{aligned} \quad (2)$$

where $\boldsymbol{\mu} \in \mathcal{R}^{Nd}$ is the mean of observed images, $W \in \mathcal{R}^{Nd \times Nb}$ is the basis images (the eigen-images), $\tilde{W} = (W, \boldsymbol{\mu})$, $\mathbf{s}_t \in \mathcal{R}^{Nb}$ is basis score, $\tilde{\mathbf{s}} = (\mathbf{s}_t^T, 1)^T$, Nd is the number of pixels, and Nb is the number of bases. $\mathcal{N}_D(\mathbf{I}|\boldsymbol{\mu}, \Sigma)$ denotes a D -dimensional Gaussian distribution with the mean $\boldsymbol{\mu}$ and the variance Σ . Then, we obtain the following formulation:

$$p(\mathbf{I}_t|\tilde{W}, \mathbf{s}_t) = \mathcal{N}_{Nd}(\mathbf{I}_t|\tilde{W}\tilde{\mathbf{s}}_t, \Sigma_t). \quad (3)$$

We also assume the prior distribution of \mathbf{s}_t is given by

$$p(\mathbf{s}_t) = \mathcal{N}_{Nb}(\mathbf{s}_t|\mathbf{0}, E_{Nb}), \quad (4)$$

where E_{Nb} is a $Nb \times Nb$ unit matrix. Using the Bayes theorem, we have

$$p(\mathcal{I}_t, \mathcal{S}_t|\tilde{W}) = \prod_{s=1}^t p(\mathbf{s}_s)p(\mathbf{I}_s|\mathbf{s}_s, \tilde{W}). \quad (5)$$

For the prior distribution of the eigen-vectors, we assume natural conjugate:

$$p(\tilde{W}) = \prod_{d=1}^D \mathcal{N}_{Nb}(\mathbf{e}_d|\mathbf{e}_d, \Sigma), \quad (6)$$

where $\mathbf{e}_d = (w_d^{(1)}, \dots, w_d^{(Nb)})^T \in \mathcal{R}^{Nb}$, $\mathbf{e}_d = (1, \dots, 1) \in \mathcal{R}^{Nb}$, $\Sigma = \frac{1}{Nb} E_{Nb} \in \mathcal{R}^{Nb \times Nb}$,

$\tilde{N}b = Nb + 1$, and then $(\mathbf{1}, \dots, \mathbf{1})^T = \tilde{W}$. δ_{ij} is the Kronecker delta:

$$\delta_{ij} = \begin{cases} 1 & (i = j) \\ 0 & (i \neq j). \end{cases} \quad (7)$$

Then, the posterior distribution of the basis scores and the parameter (basis images) is given by

$$q(\tilde{W}, \mathcal{S}_t) = q(\mathcal{S}_t)q(\tilde{W}), \quad q(\mathcal{S}_t) = \prod_{s=1}^t q(\mathbf{s}_s), \quad (8)$$

where $\mathcal{S}_t = \{\mathbf{s}_1, \dots, \mathbf{s}_t\}$.

In the variational Bayes, the free energy is defined and maximized. The following is an on-line version of the free energy in which a forgetting factor is introduced in order to be insensitive to inaccurate past data, and to cope with sudden changes of a target appearance or changes in the environment.

In our on-line variational PCA, the forgetting factor $\lambda_s (0 \leq \lambda_s \leq 1)$ is introduced in order to forget (discount) gradually the influence of the past incorrect estimation. $\alpha_t = \sum_{s=1}^t \Lambda(\tau, t)$ is a normalization coefficient, $\Lambda(\tau, t) = \prod_{s=\tau}^t \lambda_s$, and then the on-line free energy is given by

$$\begin{aligned} \mathcal{F}_t[q] &= \sum_{s=1}^t \Lambda(\tau, t) \{ \log p(\mathcal{I}) \\ &\quad - KL(q(\tilde{W}, \mathcal{S}) || p(\mathcal{S}, \tilde{W}|\mathcal{I})) \}. \end{aligned} \quad (9)$$

The maximization of the free energy is equivalent to the minimization of the discounted KL divergence between $q(\mathcal{S}_t, \tilde{W})$ and $p(\mathcal{S}_t, \tilde{W}|\mathcal{I}_t)$.

On variational Bayes estimation, $q(\mathcal{S}_t)$ and $q(\tilde{W})$ that maximize the free energy are computed by repeating a VB-E step and a VB-M step. After convergence, we obtain approximated solutions of factor score matrix \mathcal{S} and eigen-vector matrix \tilde{W} . Then, eigen-vector matrix \tilde{W} can be used as basis images.

The tracking is achieved by particle filter governed by the observation model $p(\mathbf{I}_t|\mathbf{X}_t)$, which is the likelihood of \mathbf{X}_t given \mathbf{I}_t , and the dynamics model between two states $p(\mathbf{X}_t|\mathbf{X}_{t-1})$. The observation model is given by using the estimated basis \tilde{W} as

$$p(\mathbf{I}_t|\mathbf{X}_t) \propto \exp \left[-\frac{1}{2\sigma^2} \|\mathbf{I}_t(\mathbf{X}_t) - \tilde{W}\tilde{\mathbf{s}}_t\|^2 \right], \quad (10)$$

where $\mathbf{I}_t(\mathbf{X}_t)$ is an observed image at the target state (position) \mathbf{X}_t , and σ^2 denotes the measurement noise variance assumed to be a constant for simplify. In this study, the motion of the target object between

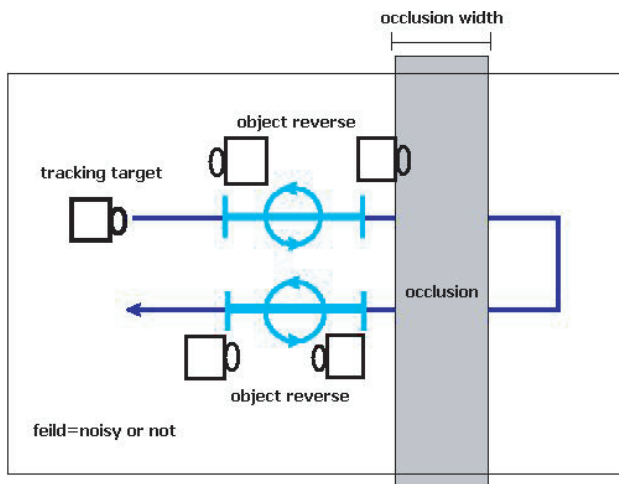


Figure 1: Simulation environment

two consecutive frames is assumed to be linear. The target state is defined as $\mathbf{X}_t = (x_t, y_t)$, where x_t and y_t denote the two-dimensional position on the image plane at time t .

3 Experiments

3.1 Setup

We conducted tracking experiments through computer simulations to examine the effectiveness of our proposed method, that is, adaptive basis image updates and robust visual tracking.

Figure 1 illustrates the simulation environment. A target, a coffee cup, moved from the left side of the image toward the right side with a velocity of 2 [pixels/frame], and turned back to the right side, as depicted by an arrow. During this course, the appearance of the target was reversed twice with specific intervals indicated by gray lines. There were four experimental conditions; normal condition, noise condition in which pixel-wise Gaussian noise was added, occlusion condition in which a stationary occluder depicted as a shade was added, and noise-occlusion condition in which both noise and the occluder were added (cf. Figure 2). In each condition, 10 times of simulations were conducted to estimate statistically the performance of our method.

200 particles were used. The image stream was 110 frames of 120×160 gray scale images. The image of the target coffee cup was of 20×20 pixels. The width of occlusion was 15 pixels. The pixel-wise Gaussian

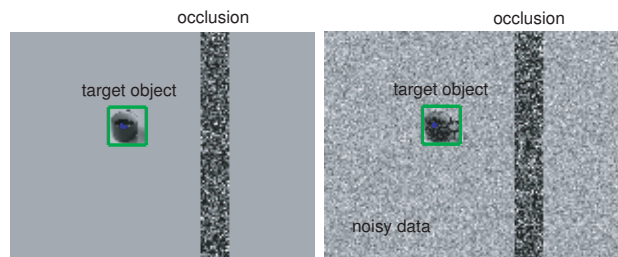


Figure 2: Sample images in simulation

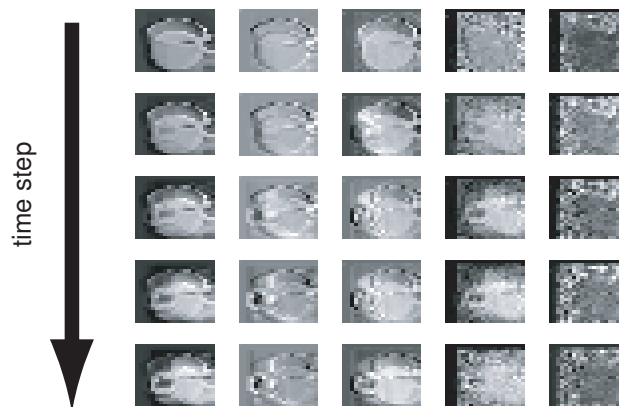


Figure 3: Time course of basis images when the target object was reversed (for the normal condition).

noise was zero-mean with variance 30^2 . The maximum number of basis images was set to 10.

3.2 Results

Figure 3 demonstrates how the basis images were updated. This figure shows the time course of five basis images of the tracked object every three frames just after the object was reversed. Each basis was quickly and successfully adapted to the reversed images, in which the handgrip of the cup was a salient feature in the appearance of the cup. This result suggests three or four bases would be enough to represent this specific target object.

Figure 4 presents an example time course of the on-line free energy. Shaded areas and unshaded areas correspond to the two different appearances of the coffee cup (see Figure 1). The free energy sharply dropped down just after the target appearance was reversed, followed by quick recoveries. Because the free energy strongly correlates with the reliability of the estimation of basis images, this result indicates our successful implementation of the on-line variational PPCA. The time course shown in Figure 4 was for the normal con-

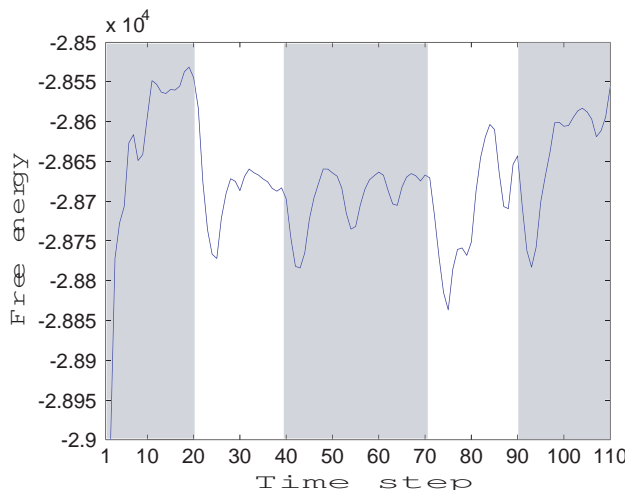


Figure 4: Example time course of on-line free energy

Table 1: Average tracking error over 10 trials

Task	error(MSE)
normal	4.29±2.68
noisy	4.42±2.63
occlusion	4.39±2.67
noisy and occlusion	4.52±2.62

dition, but we confirmed that profiles in other cases were almost consistent to this time course.

The tracking performance in the four conditions is summarized in Table 1. The tracking errors are similar. Increasing the number of particles from 200 should decrease the errors.

4 Conclusion and Future Work

In this study, we proposed an adaptive visual tracking method by combining the on-line variational Bayesian PCA and particle filtering. Simulation experiments demonstrated that the algorithm realized accurate and robust visual tracking of a target whose appearance was suddenly reversed, even in the case where Gaussian noise was artificially added and an occluder was placed in the pathway of the target.

There are many issues opened for future work. First of all, the performance comparison with existing methods like R-SVD [2] is necessary. Our preliminary experiments using the same simulation environment suggests that the tracking performance of R-SVD is as high as our method. Further exploration is required

for the performance comparison, and for making the difference salient.

One of the most interesting and useful extensions would be on-line control of the forgetting factor. Hirayama et al. proposed a method in which the forgetting factor was controlled by the free energy calculated based on their probabilistic model, and demonstrated the effective detection of abrupt changes in face images [1]. As shown in their study, probabilistic models different from the conventional PCA model can be considered to improve the tracking performance in real-world environments.

References

- [1] J. Hirayama and J. Yoshimoto and S. Ishii, "Bayesian representation learning in the cortex regulated by acetylcholine", *Neural Netw*, Vol.17(10), pp.1391-1400, 2004.
- [2] J. Lim and D. Ross and R.-S. Lin and M.-H. Yang, "Incremental Learning for Visual Tracking", *Advances in Neural Information Processing Systems*, 2004.
- [3] Z. Khan and T. Balch and F. Dellaert, "A Rao-Blackwellized Particle Filter for EigenTracking", *Proc Comput Vis Pattern Recogn*, Vol.2, pp.980-986, 2004.
- [4] M. Isard and A. Blake, "CONDENSATION-Conditional Density Propagation for Visual Tracking", *Int J Comput Vis*, Vol.29(1), pp.5-28, 1998.
- [5] M.J. Black and A.D. Jepson, "EigenTracking: Robust Matching and Tracking of Articulated Objects Using a View-Based Representation", *Int J Comput Vis*, Vol.26(1), pp.63-84, 1998.
- [6] H. Murase and S. Nayar, "Visual Learning and Recognition of 3-D Objects from Appearance", *Int J Comput Vis*, Vol.14, pp.5-24, 1995.
- [7] N.J. Gordon and D.J. Salmond and A.F.M Smith, "Novel approach to nonlinear non-Gaussian Bayesian state estimation", *IEEE Proc Radar Signal Processing*, Vol.140, pp.107-113, 1993.

The Development of an Indoor Positioning System Using Incident Angle Detection of Infrared Emitters

**Seong Taek Hwang
and Jea Heon Ryu**
Department of Mechanical and
Intelligent System Engineering
Pusan National University,
Busan, 609-735, KOREA

Chun Han Lee
Department of Electric Control
Volvo Construction
Equipment-KOREA, Ltd.,
Changwon, 641-430, KOREA

Man Hyung Lee
School of Mechanical
Engineering,
Pusan National University,
Busan, 609-735, KOREA

Abstract

In this paper, a new indoor positioning system based on incident angle measurement of infrared lights has been suggested. Though there have been various researches on indoor positioning methods using vision sensor or ultrasonic sensor, they have not only advantages, but also disadvantages. To minimize the disadvantages they have, this new method using incident angle of infrared light has been invented. In a new positioning system, there are three infrared emitters on fixed known positions. An incident angle sensor measures the angle differences between each two emitters. Measured angle differences determine a position. This method is available only inside the triangle which is composed of three emitters. Mathematical problems to determine the position with angle differences and position information of emitters has been solved. To solve the non-linear equations without prior position information, iterative linearization process has been used. Simulations and experiments have been implemented to show the performance of this new positioning system.

1 Introduction

Positioning is a major problem for mobile robots and autonomous vehicles. So, various positioning systems and algorithms have been researched to develop a navigation algorithm. GPS (Global Positioning System) is a precise absolute positioning system for the outdoors [1]. But, several indoor absolute positioning systems have been researched. The ultrasonic positioning system is very similar to GPS [2]. It measures distances from emitters to a measuring point. Then it solves the equations to determine its position. Since ultrasonic waves are much slower than electromagnetic waves, it is easier to count the spent time that diffused waves need to reach the measuring points than it does for GPS. However, waves radiated from other emitters interfere with each other. Thus, only one emitter can radiate ultrasonic waves at a time. Since all the

transmitters radiate their waves by turns, it takes more time to measure all the distances from different transmitters.

An absolute position measurement system based on incident angle detection of infrared light is proposed [3]. Infrared light sources are mounted on a robot as markers. Then an observation agent mounted on a ceiling detects incident angles of infrared light emitted from markers. Though much infrared light is also contained in sunlight, it is rejected using filters. Emitters and a receiver use the same carrier frequency. And all the other frequencies are filtered out while passing the bandwidth filter.

In this paper, an absolute position measurement system based on incident angle detection of infrared light is proposed. Three infrared light sources are mounted in fixed positions as emitters. And three infrared incident angle sensors measure the incident angles of the infrared light from each of the three emitters. Then anyone who tries to measure their position can estimate their absolute position without external assistance.

2 Mathematical Problems of the System

Consider three points. A(0,0) point is the origin, B($x_2, 0$) point is on the x-axis, and the C(x_1, y_1) point is a point on the upper part of the right-half plane. Assume that all the coordinates of the three points are given as shown in Fig. 1. The relative

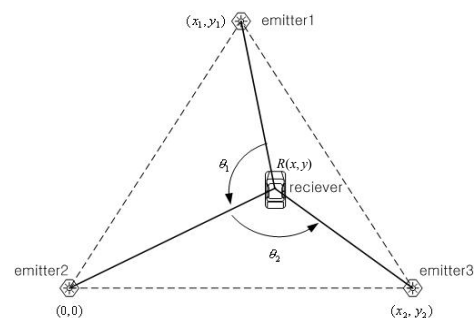


Fig. 1 Concept of new positioning system

position $R(x, y)$ to the origin can be determined.

First, we can obtain the following equations to determine the position with given angle differences, θ_1 and θ_2 . θ_1 is calculated by using an inner product of \overrightarrow{RA} and \overrightarrow{RC} . And also, θ_2 is solved by using it for \overrightarrow{RA} and \overrightarrow{RB} .

$$\frac{\overrightarrow{RA} \cdot \overrightarrow{RC}}{|\overrightarrow{RA}| \cdot |\overrightarrow{RC}|} = \cos \theta_1 \quad (1)$$

$$\frac{\overrightarrow{RA} \cdot \overrightarrow{RB}}{|\overrightarrow{RA}| \cdot |\overrightarrow{RB}|} = \cos \theta_2 \quad (2)$$

To solve the equations (1), (2) about θ_1 and θ_2 :

$$\theta_1 = \cos^{-1} \frac{x^2 - x_1x + y^2 - y_1y}{\sqrt{x^2 + y^2} \cdot \sqrt{(x_1 - x)^2 + (y_1 - y)^2}} \quad (3)$$

$$\theta_2 = \cos^{-1} \frac{x^2 - x_2x + y^2}{\sqrt{x^2 + y^2} \cdot \sqrt{(x_2 - x)^2 + y^2}} \quad (4)$$

Equations (3), (4) are linearized by using Fourier Transformation.

$$\delta \theta_1 = \left. \frac{\partial f_1}{\partial x} \right|_{\substack{x=x_0 \\ y=y_0}} \delta x + \left. \frac{\partial f_1}{\partial y} \right|_{\substack{x=x_0 \\ y=y_0}} \delta y + H.O.T.'s \quad (5)$$

$$\delta \theta_2 = \left. \frac{\partial f_2}{\partial x} \right|_{\substack{x=x_0 \\ y=y_0}} \delta x + \left. \frac{\partial f_2}{\partial y} \right|_{\substack{x=x_0 \\ y=y_0}} \delta y + H.O.T.'s \quad (6)$$

Where (x_0, y_0) is the point of linearization, $H.O.T.'s$ represents the higher-order terms in the expansion, and f_1 and f_2 are the functions as follows:

$$f_1 = \cos^{-1} \frac{x^2 - x_1x + y^2 - y_1y}{\sqrt{x^2 + y^2} \cdot \sqrt{(x_1 - x)^2 + (y_1 - y)^2}} \quad (7)$$

$$f_2 = \cos^{-1} \frac{x^2 - x_2x + y^2}{\sqrt{x^2 + y^2} \cdot \sqrt{(x_2 - x)^2 + y^2}} \quad (8)$$

Finally the equation (9) is obtained in representation of vectors as follows:

$$\underline{\theta} = \underline{\theta}_0 + P \delta \underline{r} + H.O.T.'s \quad (9)$$

where $\underline{\theta}_0$ is the initial value of $\underline{\theta}$,

$$\underline{\theta} = \begin{pmatrix} \theta_1 \\ \theta_2 \end{pmatrix}, \quad \delta \underline{r} = \begin{pmatrix} \delta x \\ \delta y \end{pmatrix},$$

and

$$P = \begin{pmatrix} \left. \frac{\partial f_1}{\partial x} \right|_{\substack{x=x_0 \\ y=y_0}} & \left. \frac{\partial f_1}{\partial y} \right|_{\substack{x=x_0 \\ y=y_0}} \\ \left. \frac{\partial f_2}{\partial x} \right|_{\substack{x=x_0 \\ y=y_0}} & \left. \frac{\partial f_2}{\partial y} \right|_{\substack{x=x_0 \\ y=y_0}} \end{pmatrix}$$

Assuming that the rows of P are linearly independent, equation (9) can be solved by inversion of the P matrix:

$$\delta \underline{r} = P^{-1} \delta \underline{\theta} \quad (10)$$

with error $P^{-1}(H.O.T.'s)$.

When measurements from more than 3 emitters are available, the least-squares solution is

$$\delta \underline{r} = (P^T P)^{-1} P^T \delta \underline{\theta} \quad (11)$$

With knowledge of the position error $\delta \underline{r}$, the actual position is determined as

$$\underline{r} = \underline{r}_0 + \delta \underline{r} \quad (12)$$

Assuming no prior position information, the iterative linearization process will be initialized at a fixed point in the triangle consisting of the given three points.

3 Simulations

In order to examine the performance of the positioning algorithm, Matlab 6.1 is used.

Consider the process shown in Fig. 3. The three points are $(0, 0)$, $(0, 2)$, and $(1, \sqrt{3})$ respectively so that they compose a regular triangle. The fixed initial point to determine the position without prior position information is $(1, 1\sqrt{3})$. So, that is the centroid of the given regular triangle shown in Fig. 2.

First, test the algorithm without the prior position information. To determine the exact position without it, iterative calculations are necessary. Using the iterative linearization process based on equation (12), position values are converged very fast, as shown in Fig. 2. The angle differences used in this simulation are 80 and 130 degrees. The position values are converged within 4 steps with very small errors.

Secondly, test the algorithm along the path, not a point. The test path is a horizontal straight line passing through the centroid in the range of $0.5 \leq x \leq 1.5$. In order to simulate the algorithm, angle differences θ_1 and θ_2 of the test path are

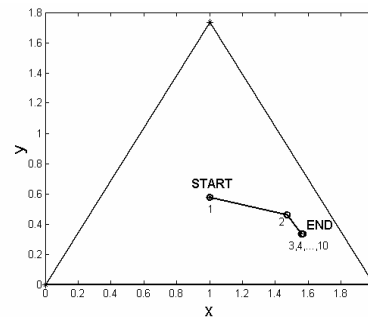


Fig. 2 The iterative linearization process

needed. Fig. 3 shows the result of the simulation
 Fig. 4 is the result of the curvature test.

4 Experimental and Result

To determine the incident angle, current passing through the sensor has to be measured. The incident angle sensor is composed of two photodiodes. And the incident angle is determined by two current values from each photodiodes as follows:

$$\text{ANGLE} = \frac{a-b}{a+b} \times 0.012[\text{deg}] \tag{13}$$

where a and b are output currents from the two photodiodes.

The picture of the incident angle sensor (HI-M600H3-2) and its characteristic is shown in Fig. 5. It detects tuned signals at 32kHz. In the range of $\pm 45[\text{deg}]$, the value of the incident angle from the sensor is absolutely linear.

Figure 6 shows the circuit to convert the current value to voltage value. The following relation is satisfied in the circuit:

$$V_0 = -I \times R \tag{14}$$

where V_0 is the output voltage, and I is current from photodiode.

To measure the incident angles of the infrared lights, it is very important to reject the interferences and to amplify the signal. Bandwidth filter rejects all the frequencies except the carrier frequency. Op-Amps amplify the signal to a suitable voltage level for an A/D converter.

Experiments have been implemented inside the regular triangle of 2.36m for each side length, since

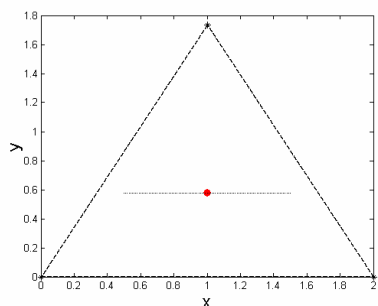


Fig. 3 Simulation result in a straight path

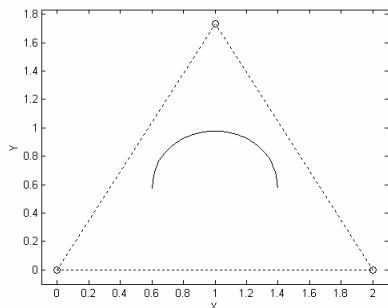


Fig. 4 Simulation result in a curve path

the intensity of the emitters and infrared LED has been limited and we have had difficulties in signal conditioning. Figure 7 is the system configuration for the test. The system consists of 3 emitters and 1 receiver. Each receiver has a slit. It forbids the surrounding signals to interfere. The receiver is rotated by using a 400 pulse stepping motor. Its angular rate is 360deg/sec. Therefore the proposed system can get position data with 1Hz resolution. If the angular rate of the motor and signal processing time is faster, we can get higher resolution data. Figure 8 shows the emitter and receiver systems.

For each test, 11 points and 9 points are selected on the straight and curved path and the mean data are calculated using data every 10sec.

As shown in Fig. 9, the experimental result is very similar to the simulation result in Fig. 3 except for the limitation of ranges. The ranges of x and y in the experiment has been limited is because of the emitting shape of the infrared LED. Most of all, the infrared LED is produced for remote

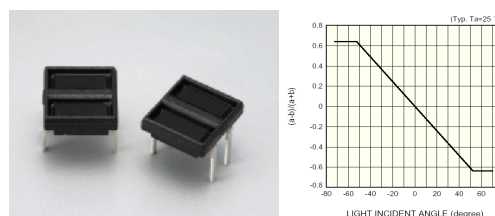


Fig. 5 Incident angle sensors

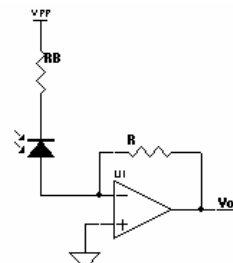


Fig. 6 Circuit to convert the currents to voltage

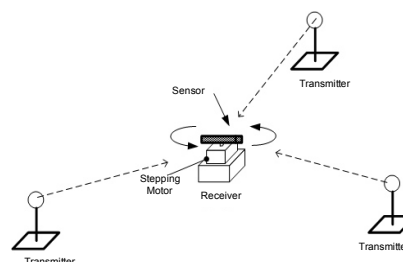


Fig. 7 System configuration for test

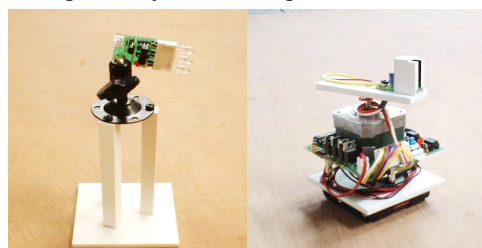


Fig. 8 Emitter and receiver

controllers or wireless communications. Therefore, the infrared light radiated from the LED is acutely focused on the center region.

Figure 10 shows the test result in a curved path.

5 Conclusions

In this paper, the new indoor positioning method using infrared lights has been suggested. Users are independent of the number of users provided in this positioning service. Since this method has no interactive process between emitters and receivers, the measuring time is less than any other positioning system. Mathematical problems necessary for the determination of the position have been derived. To solve these non-linear problems, an iterative linearization process has been used.

The algorithm to determine the position has been simulated and experimented. Results of the simulations were reasonable. Experiments have had many problems, such as the limitation of intensity of emitters and signal conditioning problems. Thus, the experiments have been implemented in a very bounded area, inside the regular triangle with 2.36m side length. However, the experimental result was acceptable.

This new positioning method can be applied to any indoor system that needs absolute position information. To apply this method to mobile robots or for industrial purposes, emitters should be improved to a more suitable form and signals from the sensors should be well-conditioned. More emitters can achieve more accurate positions using the Least Mean Square method.

Acknowledgment

This work was supported by the Brain Korea 21 Project.

References

- [1] Farrell, Jay and Barth, Matthew, *The Global Positioning System & Inertial Navigation*, McGraw-Hill, 1998.
- [2] Lee, Jung-Min et al., "Ultrasonic Satellite System for the Positioning of Mobile Robots," in *Proceedings of Industrial Electronics Society (IECON 2004)*, Vol. 1, pp. 448-453, 2004.
- [3] ARAI, Y., SEKIAI, M., "Absolute Position Measurement System for Mobile Robot based on Incident Angle Detection of Infrared Light," in *Proceedings of the 2003 IEEE/RSJ International Conference on Intelligent Robots and Systems (IROS2003)*, pp. 986-991, 2003.

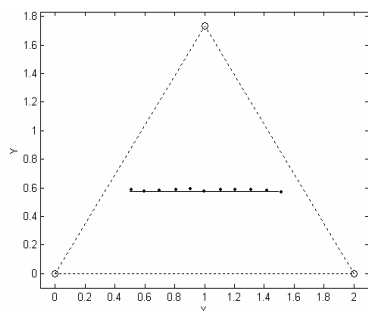


Fig. 9 Test results in a straight path

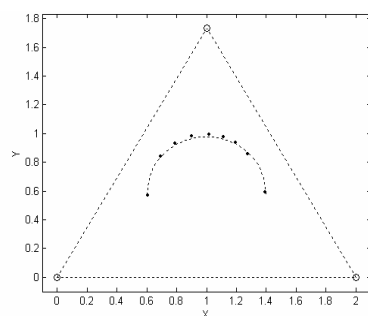


Fig. 10 Test results in a curved path

An Efficient Localization Algorithm in the RFID Sensor Space for Mobile Robot Localization

EunTae Lyu
Dept. of Electronics Eng.
Pusan Nat. Univ.
pbman02@pusan.ac.kr

HyungSoo Lim
Dept. of Electronics Eng.
Pusan Nat. Univ.
chojja_tpz @pusan.ac.kr

JangMyung Lee
Dept. of Electronics Eng.
Pusan Nat. Univ.
jmlee@pusan.ac.kr

Abstract

This paper proposes an efficient localization algorithm in the RFID sensor space for the precise localization of a mobile robot. The RFID sensor space consists of embedded sensors and a mobile robot. The embedded sensors, that is, tags are holding the absolute it is called as antenna usually, gets several tag data at the as position data and provide them to the robot which carries a reader and requests the absolute position for localization. The reader, me time within its readable range. It takes time to read all the tags and to process the data to estimate the position, which is a major factor to deteriorate the localization accuracy. In this paper, an efficient algorithm to estimate the position and orientation of the mobile robot as quickly as possible has been proposed. Along with the algorithm, a new allocation of the tags in the RFID sensor space is also proposed to improve the localization accuracy. The proposed algorithms are demonstrated and verified through the real experiments.

Keyword: RFID, Tag allocation, Localization, Mobile robot, Estimation error.

1. Introduction

An RFID (Radio Frequency IDentification) technology is a non-touching recognition system that transmits and processes the information on events and environments using a wireless frequency and small chips [1]. The RFID system can read the tags at high-speed and send data within various distances. Therefore, the application of the RFID technology has recently been increased and an RFID has been applied for the robot technology [2]. With the development of the personal robot and advanced ubiquitous network robots, it is essential for the robots to recognize their own location and environment and to keep high security in a common space with people. If an RFID technology is properly applied to the robot, the services for the users can be provided by the service robot at anytime at any place.

The passive RFID technology has been utilized for the researchers to recognize the position of the service robot [3]. The method is that RFID passive tags are arranged on the floor to provide the absolute position data, which are free

from the problems of conventional systems [4]. Note that dead reckoning sensors suffer from accumulating errors, laser and ultra-sonic sensor from line-of-sight errors, and CCD from the illumination. The absolute location of the robot can be obtained robustly, with the RFID tag and reader in sensor network space [5] where sensors are properly embedded several places to provide the absolute position information to the service robot. However some shortcomings are found in the localization systems using the RFID [6]. The antenna detects several tags within its detecting range and the numbers of detected tags are not constant at all times, which causes the position estimation error.

On account of this, the precise localization is not feasible using the RFID tags unless it is located many tags in a very short interval ignoring economics. Also, in the posture estimation of the mobile robot, two antennas are necessary to recognize the orientation of the robot since the orientation cannot be detected by using only one antenna.

In this paper, the problem of acquiring position information, including the orientation of the robot, is introduced in the robot localization using the RFID system. Also, the algorithms to reduce estimation error of the robot and to achieve more efficient localization are newly proposed.

2. Position Estimation of a Mobile Robot

In order to estimate the location of the robot using RFID system, RFID tags are arranged in a fixed pattern on the floor. Absolute coordinates of the location have been stored in each tag to provide the position data to the mobile robot. An RFID reader (antenna) has been installed to read the tag data on the bottom of the mobile robot. If the robot moves and stays on any tag, the RF field is formed by RFID reader antenna. All the tags within the circle of radius, r , which are under the effective area of RFID antenna, are activated.

When the localization process starts, the RFID reader gathers the position data of the tags under the effective area of antenna. The RFID reader repeatedly gathers the tag information sequentially when there are more than one tag in the RF field, since it can recognize only one tag signal at a time. In order to receive other tag data within the effective area of the RF reader, the tag data previously read are stored

to the PC. Then, the reader gathers the next tag information, and

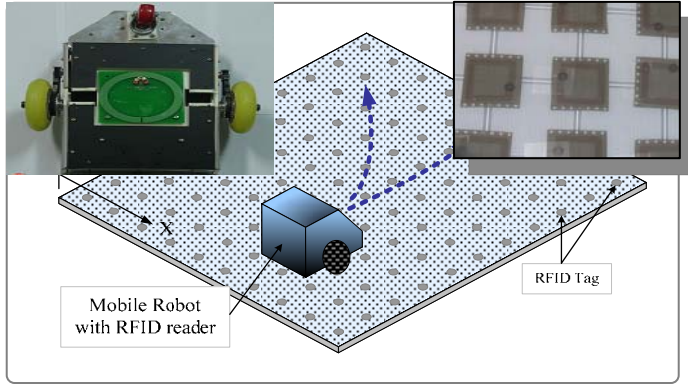


Fig. 1. Configuration of the Experimental System..

repeats this procedure until there is no unread tag left within the RF field. The configuration of the experimental system is shown in Fig. 1.

The orientation of the robot can be estimated using the multiple sets of the tag position data. The initial orientation can be estimated using the sets of position readings. And the traveling orientation can be estimated by the two sets of position data, the previous and current position data, assuming that the mobile robot is moving forward all the times.

3. Uncertainty of Position Estimation

In the passive RFID localization system, the utilization of tag information is dependent on the system characteristics. In other words, even though the RFID reader detects RFID tags within the recognition area, it cannot obtain a precise location value from the tags since there is no position information between tags. The distance between RFID reader and tag is also a variable to be considered in the localization process. Therefore the classical localization system based on the triangulation technique with three distance data has too big error to be used for the mobile robot navigation.

The estimation error is unavoidable when the robot location is estimated by the coordinates of tags within the recognition area of the reader. The estimation error is modeled in this research to minimize this estimation error. When the tags are arranged in a square pattern and the distance between them does not exceed the range of reader, the recognition area of the reader for the tags can be represented as a circle as shown in Fig. 2.

The position of the mobile robot (x_{est}, y_{est}) that carries a reader antenna on the bottom, can be obtained through the position data of the tags that are located within the recognition area of the reader as

$$x_{est} = \frac{\max\{x_1, \dots, x_N\} + \min\{x_1, \dots, x_N\}}{2} \quad (1)$$

$$y_{est} = \frac{\max\{y_1, \dots, y_N\} + \min\{y_1, \dots, y_N\}}{2} \quad (2)$$

where N represents the number of tags detected by the reader and $x_1, x_2, x_3, y_1, y_2, \dots$ represents the coordinates information of the tags.

The position of antenna --coordinates of the mobile robot-- is estimated by Eqs. (1) and (2) using the absolute coordinates in the tags. However, the real position of mobile robot has the estimation error because of the gap between the tags. Therefore the estimation error is proportional to the gap between the RFID tags. Figure 2 illustrates the relationship between the estimation error and the gap between the RFID tags where only X-dimensional tags are considered. Each tag from left to right has coordinates, $a_1, a_2, a_3, \dots, a_{n-1}, a_n$, and a_{n+1} , and the gap between the tags is d_{tag} .

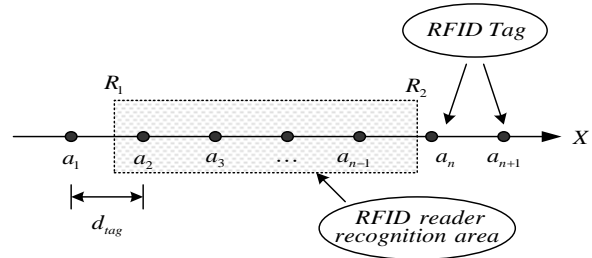


Fig. 2. Estimation error and the gap of tags.

The left boundary of the reader recognition area is denoted as R_1 and the right as R_2 . That is, the RFID reader can detect tags located between R_1 and R_2 . The estimated coordinates, R_{est_x} , and the real center position of the reader R_{real_x} , are represented as follows:

$$R_{est_x} = \frac{a_2 + a_{n-1}}{2} \quad (3)$$

$$R_{real_x} = \frac{R_1 + R_2}{2} \quad (4)$$

The estimation error, e_{est} , is defined as

$$e_{est_x} = \left| R_{est_x} - R_{real_x} \right| = \left| \frac{R_1 + R_2}{2} - \frac{a_2 + a_{n-1}}{2} \right| \quad (5)$$

where the ranges of R_1 and R_2 can be described as

$$\begin{cases} a_1 < R_1 < a_2 \\ -d_{tag} < R_1 - a_2 < 0 \end{cases} \quad (6-a)$$

$$\begin{cases} a_{n-1} < R_2 < a_n \\ 0 < R_2 - a_{n-1} < d_{tag} \end{cases} \quad (6-b)$$

From (5) and (6), now the range of estimation error can be represented as

$$e_{est_x} = \left| \frac{(R_1 - a_2) + (R_2 - a_{n-1})}{2} \right| \quad (7)$$

$$\leq \frac{1}{2} |d_{tag}|.$$

Equation (7) shows that the estimation error is proportional to the gap between the tags and the maximum value is half of the gap. Therefore, the maximum estimation error in the X-Y Cartesian coordinates is represented as

$$e_{est_max} = \sqrt{(1/4)d_{tag}^2 + (1/4)d_{tag}^2} \quad (8)$$

$$\cong 0.707d_{tag}.$$

4. Algorithm for Reduction and Compensation of the Error

For the localization process of the mobile robot in the RFID sensor space, two schemes are introduced to reduce the error in this paper.

When the gap between the tags is reduced, the accuracy of the estimation is improved as described in the previous section. But, this solution increases costs because it increases the number of tags. The optimal allocation of the RFID tags in the sensor space proposed in this paper aims at improving the accuracy of the position estimation without increasing the number of tags. Traditionally tags have been allocated in a square pattern (Fig. 3), but in this paper a triangular pattern (Fig. 4) is proposed to decrease the estimation error without increasing the number of tags.

Figure 5 illustrates the decrease of the estimation error in the triangular pattern space.

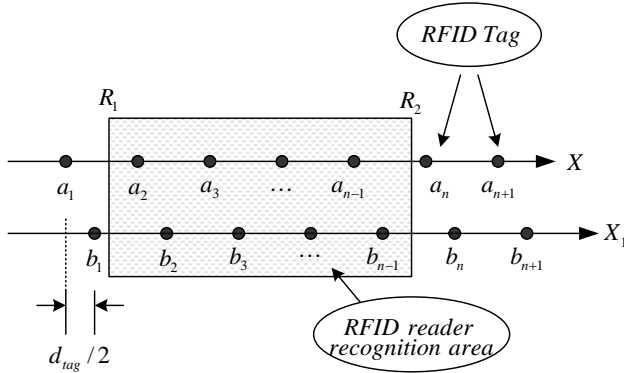


Fig. 3. Estimation error decrease in triangular pattern.

The coordinates of R_1 and R_2 are represented as follows:

$$\begin{cases} b_1 < R_1 < a_2 \\ -\frac{d_{tag}}{2} < R_1 - a_2 < 0 \end{cases} \quad (9-a)$$

$$\begin{cases} b_{n-1} < R_2 < a_n \\ 0 < R_2 - b_{n-1} < \frac{d_{tag}}{2} \end{cases} \quad (9-b)$$

When the RFID tags are arranged in the triangular pattern, the estimation error in x-direction can be decreased as follows:

$$e_{est_x} = |R_{est_x} - R_{real_x}| \quad (10)$$

$$= \left| \frac{R_1 + R_2}{2} - \frac{a_2 + b_{n-1}}{2} \right|$$

$$e_{est_x} = \left| \frac{(R_1 - a_2) + (R_2 - b_{n-1})}{2} \right| \quad (11)$$

$$\leq \frac{1}{4} |d_{tag}|.$$

Therefore, the maximum estimation error in X-Y Cartesian coordinates can be represented as

$$e_{est_max} = \sqrt{(1/2)d_{tag}^2 + (1/4)d_{tag}^2} \quad (12)$$

$$\cong 0.58d_{tag}.$$

5. Experiments and Results

For the localization of a mobile robot, it is assumed that the mobile robot moves along the designated path.

5.1 Experimental environment

The main frequency of the RFID is 13.56 MHz, The positions of the tags are pre-stored, and the tags are regularly allocated following a designed pattern. To show the superiority of the triangular pattern, the tags are allocated at every 0.05m in a row for both patterns. The size of the RFID reader antenna is 0.1m*0.1m and that of epoxy tags is 3cm*3cm. The mobile robot moves in the 1m*1m space along the designed path. The velocities of right and left wheels are sent in radio frequency from the main computer to the differential-driving mobile robot. The reader antenna is at the bottom of the robot, and is connected to the reader. The reader and main computer are linked through the RS-232 serial communication channel.

5.2 Experimental results

The first experiment aims at the comparison of robot localization accuracies in triangular and rectangular patterns of tag allocation. The mobile robot follows the path-1 and path-2 in Fig. 4 with the velocity of 0.25 m/s and the sampling time of 0.04 sec.

The estimation errors are illustrated in Fig. 5 for path-1. As it can be seen by comparing the errors, the estimation errors for the triangular pattern are a lot smaller than the square pattern. For the Path-2, the same results are obtained.

To express correct values, the average position error and orientation error is represented in Table 1. The fact that the triangular pattern of RFID tag allocation reduces the estimation error is described in section 4 by using the error model and it is demonstrated by the experiment.

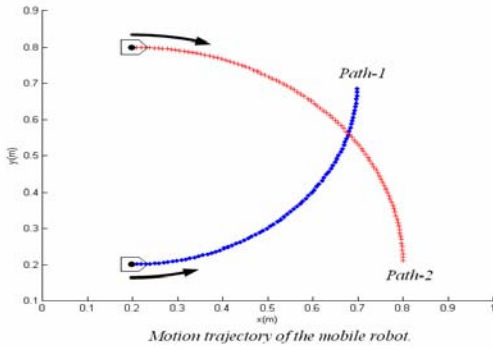
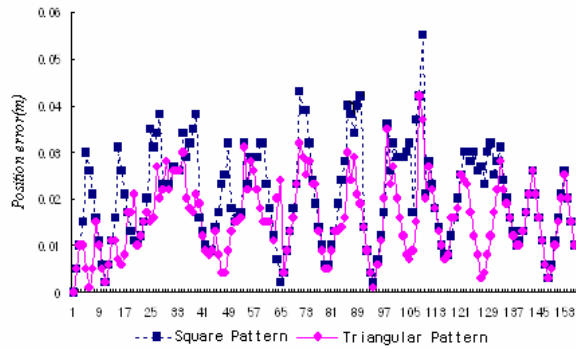
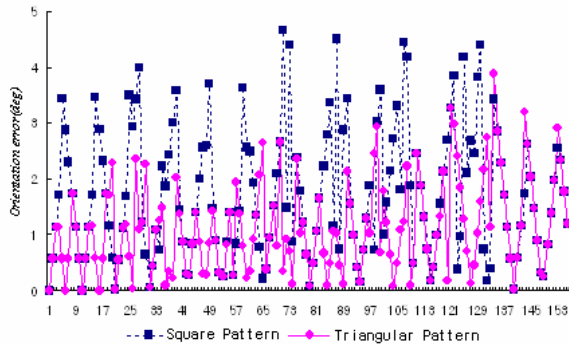


Fig. 4. Two different paths (Path-1 and Path-2).



(a) Position estimation error.



(b) Orientation estimation error.

Fig. 5. Estimation errors of Path-1.

Table 1. Average of the position and orientation error

	Path-1		Path-2	
	Position Error(m)	Orientation Error(deg)	Position Error(m)	Orientation Error(deg)
Square Pattern	0.02	1.72	0.02	1.42
Triangle Pattern	0.016	1.12	0.015	0.89

6. Conclusions

This paper proposes a new localization scheme in an RFID based sensor space, which is derived from the new ideas on the tag allocation and on the accurate and efficient estimations. This scheme overcomes the shortcomings of the conventional absolute position estimations and improves the localization efficiency and accuracy. The main ideas are demonstrated by the experiments of a mobile robot navigating over the RFID based sensor space. To illustrate the improved accuracy and efficiency of the position estimation scheme, the square and triangular tag patterns have been compared. The triangular pattern has shown better performance than the square pattern for position estimation of a mobile robot. When the robot moves in the RFID sensor space, the velocity and position of the robot are estimated and compensated to reduce the estimation error according to the localization scheme developed in this paper. Therefore, this scheme is very effective for the position estimation of any object in the sensor space and it could be a good tool to form a ubiquitous environment for a mobile robot.

Acknowledgment

This work was supported by the Regional Research Centers Program (Research Center for Logistics Information Technology), granted by the Korean Ministry of Education & Human Resources Development.

References

- [1] D. Hahnel, W. Burgard, D. Fox, K. Fishkin, and M. Philipose, "Mapping and localization with RFID technology," *Proc. IEEE Int. Conf. on Robotics and Automation*, vol. 1, pp. 1015-1020, 2004.
- [2] V. Kulyukin, C. Gharpure, J. Nicholson, and S. Pavithran, "RFID in robot-assisted indoor navigation for the visually impaired," *Proc. IEEE/RSJ Int. Conf. Intelligent Robots, Systems*, pp. 1979-1984, 2004.
- [3] Kentaro Yamano, Kanji Tanaka, Mitsuru Hirayama, Eiji Kondo, Yoshihiko Kimuro and Michito Matsumoto, "Self-localization of mobile robots with RFID system by using support vector machine," *Proc. IEEE/RSJ Int. Conf. on Intelligent Robots and Systems*, vol. 4, pp. 3756-3761, Sep. 28-Oct. 2, 2004.
- [4] K. Nagatani, Y. Iwai, and Y. Tanaka, "Sensor based navigation for car-like mobile robots using generalized Voronoi graph," *Proc. IEEE Int. Conf. on Robotics and Auto.*, vol. 3, pp. 3068-3073, 2002.
- [5] Joo-Ho Lee and Hideki Hashimoto, "Controlling Mobile Robots in Distributed Intelligent Sensor Network," *IEEE Transaction on Industrial Electronics*, Vol. 50, No. 5, pp. 890-902, Oct. 2003.
- [6] Heesung Chae and Kyuseo Han, "Combination of RFID and Vision for Mobile Robot Localization," *Proc. IEEE Int. Conf. on Intelligent Sensors, Sensor Networks and Inform. Processing*, pp. 75-80, 2005.

Development of an autonomous mobile robot:

Self-Localization and Mapping using Odometry and a Laser Range Sensor

Keisuke Niimoto

Graduate School of Computer Science
and System Engineering
Kyushu Institute of Technology
680-4, Iizuka City, Fukuoka, Japan, 820-8502
niimoto@imcs.mse.kyutech.ac.jp

Eiji Hayashi

Department of Mechanical Information
Science and Technology
Kyushu Institute of Technology
680-4, Iizuka City, Fukuoka, Japan, 820-8502
haya@mse.kyutech.ac.jp

Abstract

We are attempting to develop an autonomous mobile robot that has the ability to perform practical tasks in a human living environment by using information derived from sensors and a knowledge database. When a robot is made to adjust to a human environment, robots require systems that can recognize the external world and perform correct driving control. We have developed a self-localization method for an autonomous robot.

Odometeri offers a self-localization method that is of the greatest use, providing a method of calculating and determining the tracks of a robot. However, there is a limit to the accuracy of this self-localization because a cumulative error occurs regarding the self-position determined by Odometeri. To solve this problem, this paper describes the development of a self-localization method based on a fusion of Odometeri and LRS (Laser Range Sensor) data.

Key words: autonomous mobile robot, LRS (Laser Range Sensor), Odometeri, ICP (Iterative Closest Point) algorithm, Self localization, mapping.

1. Introduction

In our country now, the population is aging, and the number of people who receive nursing in hospitals and welfare facilities is increasing. At the same time, the proportion of the working population continues to decrease. Robots are expected to make a contribution in helping to solve the problem of the labor shortage this is creating. Indoor robots intended for use in a general life environment include, among others, cleaning robots, house-sitting robots, and guard robots. Indoor mobile robots that have movement functions like these robots are expected to evolve.

Environmental recognition is required so that the robot may coexist among humans. An autonomous mobile robot requires map information regarding its range of action. This includes a grasp of the position where the robot is located on the map. By recognizing

this environmental information, the robot can search for a route to its destination and can accurately reach the destination. Therefore, the robot's knowledge of its position on the map is one of the important environmental recognitions that is required.

Odometeri is the self-localization method that has been of the greatest use; it can calculate distances and determine the tracks of the robot. However, there is a limit to the accuracy of this self-localization because a cumulative error occurs regarding the calculated tracks by encoder data ^{[1][2]}. To solve this problem, we developed a self-localization method based on a fusion of Odometeri and LRS (Laser Range Sensor) data.

In our research up to last year, in which the data obtained from the LRS made a straight line, self-position was determined by matching the robot with an already-known obstacle. However, the inability to establish a correspondence to obstacles other than by a straight line (because in this technique the LRS data required a straight line) meant that the robustness was low. In addition, there was the problem that it was necessary to give information about the obstacle to the database before the position of the robot could be determined. Therefore, in our new system the LRS data does not require a straight line. The earlier problems were solved using an ICP algorithm to match LRS data with the database. Moreover, by using this method, the robot becomes able to construct a map without being supplied with a map beforehand. We mounted this system on the robot in an indoor environment and conducted an experiment involving self-localization and mapping.

2. System Architecture

In this research, we used a mobile robot, Kitasap2, developed in our laboratory. Figure 1 shows the externals of Kitasap2. It is composed of three wheels; the two front wheels are independent drives, and the rear wheel uses a ball. An encoder is installed on the front wheel, and a LRS is installed in front of the bottom of the robot. The robot is equipped with a computer that controls all devices; lithium-ion batteries supply the electric power.



Fig. 1 Mobile robot

3. Self-Localization and Mapping

3.1 ICP algorithm

The ICP algorithm is a technique of the optimization of overlapping point sets [3]. For each point of point sets, the nearest point is looked for and related mutually. The least square method concerning the distance is calculated based on them (expression 1). And points are updated using a homogeneous transformation (expression 2). It then optimizes matching by repeating these procedures. The ICP algorithm has the following advantages. It is strong in suppressing noise; it need not be given correspondence points; it can be matched even if two sets of points are off to some degree; it does not require location information; and it can deal with overlapping of complex shapes. In this research, by applying this algorithm to match the LRS data with map information, the position of the robot is presumed.

$$F(X_g, Y) = \frac{1}{N} \sum_{i=1}^N |X_{g_i}^{(m)} - Y_i|^2 \quad (1)$$

$$X_{g_i}^{(m+1)} = \text{Trans}^{(m)} + \text{Rot}^{(m)} \cdot X_i^{(m)} \quad (2)$$

N	: Number of points
X_{g_i}	: LRS Data in global coordinates system
Y_i	: The map data of database
X_i	: Scanning data of LRS
Trans	: Translation procession
Rot	: Rotation procession

3.2 Self-localization method

The procedure for self-localization is shown below (See Figure 2).

- The rotation angle of the tire is acquired from the encoder. Tracks of the robot are calculated, and the position of the robot is presumed.
- Acquired data from LRS is transformed into a global coordinate system based on the self-position presumed from encoder.
- The map information (database) and the LRS data that transformed into a global coordinate system are compared. The nearest points are related mutually.
- The related point data is substituted for the evaluation function of the ICP algorithm (expression 1).
- If the value of the evaluation function is less than the threshold, it is considered to match. The value of the transformation matrix at that time is the position of the robot. (End)
- If the value of the evaluation function is greater than the threshold, the transformation matrix is calculated.
- A geometric transformation is performed using the homogeneous transformation (expression 2). (Return to)

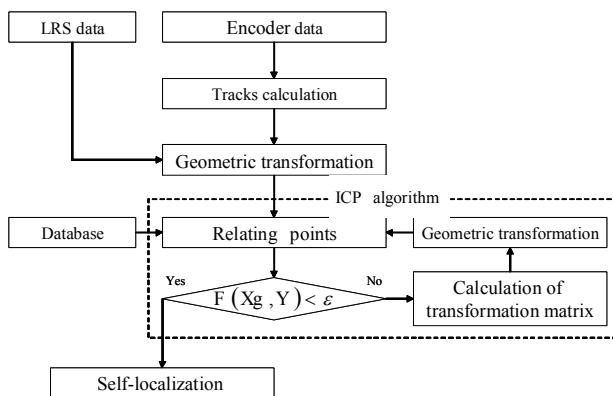


Fig. 2 Procedure for self-localization

3.3 Mapping method

The mapping procedure is shown below (See Figure 3).

- ~ . See the corresponding steps in the procedure of self-localization.
- . If the value of the evaluation function is less than the threshold, the transformation matrix at that time is the position of the robot. (Go to)
- . If the value of the evaluation function is greater than the threshold, the transformation matrix is calculated.
- . A geometric transformation is performed using the homogeneous transformation (expression 2). (Return to)
- . If the value of the evaluation function is less than the threshold and converges, the map is constructed, and the database is updated based on this map. (Return to)

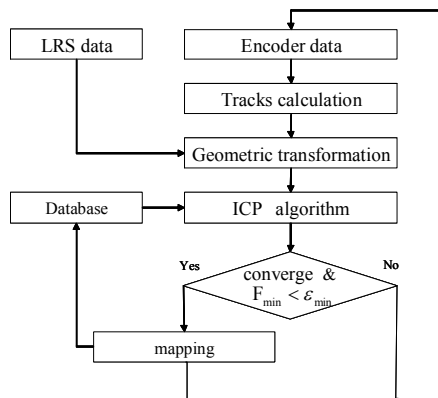


Fig. 3 Mapping procedure

4. Experiment

4.1 Experiment of self-localization

We performed experiments to verify the self-localization method proposed in this research. In experiment 1, the robot (Kitasap2) is arranged on in the environment of Figure 4, and robot presumes its self-position.

In experiment 2, to verify the robustness, the robot is lifted and is moved to position of Figure 4 compulsorily. Again, the robot presumes its self-position. The amount at this time of the movement is -1m to the direction of Y coordinates, and the robot orientation is rotated by 90 degrees.

We conducted each experiment 100 times. The error

margins of self-localization are shown in Figures 5 and 6, respectively. The average error, the maximum error, and the standard deviations of the results are shown in Tables 1 and 2.

From Figure 5 and Table 1, it can be confirmed that the error of X coordinates and the error of Y coordinates are within ±3.0cm. Moreover, we confirmed that the orientation of the robot was able to be presumed within an error of ±0.01rad. Therefore it is proven that accuracy of this self-localization method is high.

From Figure 6 and Table 2, in the case where the robot is compulsorily moved, it can be confirmed that the estimated position converges in the correct vicinity of coordinates. And, it can be confirmed that the accuracy of self-localization is high. Therefore, it is proven that robustness improves with the accuracy maintained.

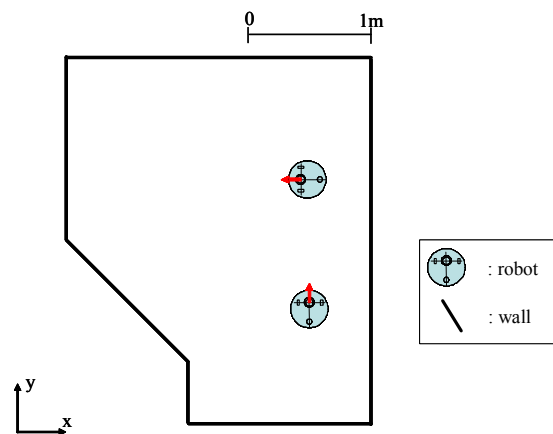


Fig. 4 Environment of the self-localization experiment

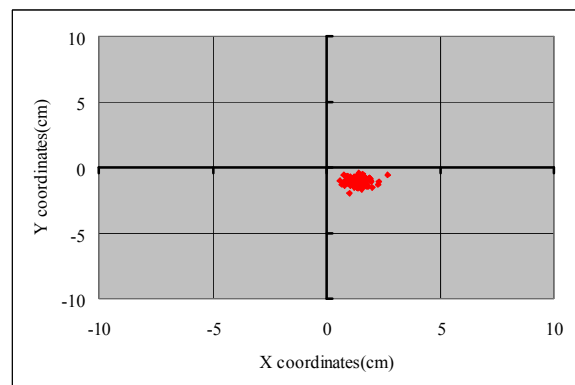


Fig. 5 Localization result of experiment 1

Table 1 Results of experiment 1

	X	Y
Average [cm]	1.4	-1.0
Maximum [cm]	2.7	-1.9
Standard deviation	0.4	0.3

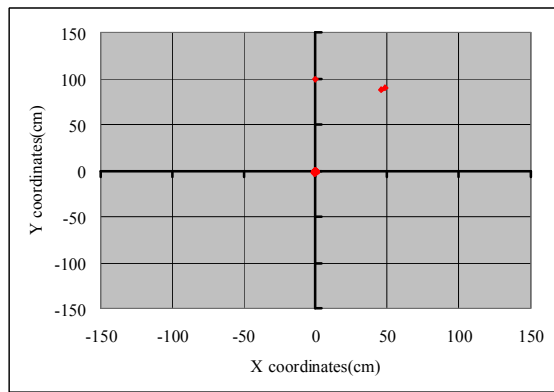


Fig. 5 Localization results of experiment 2

Table 2 Results of experiment 2

	X	Y
Average [cm]	0.1	-1.2
Maximum [cm]	0.7	-3.1
Standard deviation	0.3	0.4

4.2 Mapping experiment

We also performed an experiment to verify the mapping method proposed in this research. In this experiment, no map information is given to the robot beforehand, and the robot is arranged in an unknown environment (Figure 6). Figure 7 (a) is a map of the environment of Figure 6. The robot moves on the tracks shown by the arrow in Figure 7 (a), and constructs the map. The movement speed of the robot is about 20cm/sec. The map the robot generated is shown in Figure 7 (b).

From the experimental results, it can be confirmed that even if no map information is given to the robot beforehand, the robot is able to construct a map. However, the constructed map includes an error. And this experiment occasionally failed in mapping.



Fig. 6 Environment of the mapping experiment

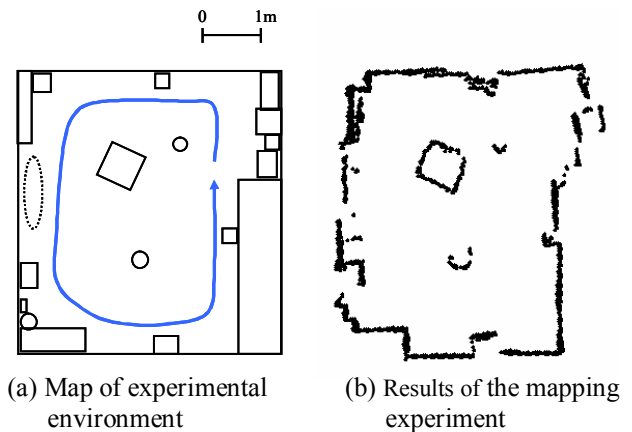


Fig. 7 Map of the mapping experiment and experimental results

5. Conclusion

Our research has developed a self-localization method based on a fusion of Odometer and LRS (Laser Range Sensor) data. To solve the problems in our research up to last year, we used the ICP algorithm to match the LRS data with the database.

By using this method, the robot has improved robustness, and becomes able to construct a map without being supplied with a map beforehand.

The next problem is to improve the accuracy and the success probability of the mapping.

Thanks

I'd like to acknowledge the advice and assistance of the late Prof. Tadashi Kitamura of Kyushu Institute of Technology and pray for the repose of his soul.

References

- [1] Masato Tashiro: "Interface development for cooperation work with a semi-autonomous mobile robot (2nd report)", Proc. of the 2004 JSME Conference on Robotics Mechatronics, 2P2-H-16(CD-ROM), 2004
- [2] Shinya Nakao: "Development of a control system based on imitative leaning animal behavior for semi-autonomous mobile robot: Search for a detour by using subgoals," Proc. of the 2004 JSME Conference on Robotics Mechatronics, 1P2-N-56(CD-ROM), 2005
- [3] P.J.Besl and N.D.Mckay: "A Method of Registration of 3-D Shapes", IEEE Trans. on PAMI, Vol.14, No.2, pp.239-256 (1992)

Linux-based Real Time Monitoring System of Mobile Robots

SeungHo Cho
Dept. of Electronics Eng.
Pusan Nat. Univ.
Sungho123@pusan.ac.kr

HyoSik Choi
Dept. of Electronics Eng.
Pusan Nat. Univ.
chs3040 @pusan.ac.kr

JangMyung Lee
Dept. of Electronics Eng.
Pusan Nat. Univ.
jmlee@pusan.ac.kr

Abstract

Real time monitoring is necessary for the dynamic obstacle avoidance and trajectory tracking of mobile robots. However there are several problems in implementing a real time operating system: 1. It is expensive to develop since a high license fee is required and 2. Standards for the real-time systems are not well-established yet. For an educational system under these difficulties, a Linux-based real time system is possible to receive the display data with the minimum time delay by the kernel compiling to fit to the user system. Notice that Windows OS is suffering from code bloating phenomena, which may result in a long operation time. An i-BOT is developed for a demonstration system to show the localization schemes using the RFID and ultrasonic sensors, named as iGS (indoor GPS). An RFID is designated to synchronize the transmitter and receiver of the ultrasonic signal, and the traveling time of the ultrasonic signal has been used to calculate the distance from the iGS to a mobile robot.

Keywords: real-time, Linux, localization, RFID

1. introduction

In the near future, various new services come to our daily lives through the ubiquitous computing and network environment. Especially for a mobile service robot, it is very important to estimate the position and to recognize human beings and obstacles at any instance. The localization and recognition techniques are very important to provide various services to human beings in various environments [1].

Since the mobile robot is able to move in the working area, it can be used for various tasks unless it causes collisions to the obstacles in the environment. On account of its mobility, the mobile robot can replace human beings for the hard and dangerous tasks. To execute the given tasks successfully, the mobile robot needs to identify its own position for a certain task including sensing the environment and controlling the motors. Unexpected disasters may happen through the malfunction of the mobile robot in synchronizing to the environment. Therefore the mobile robot is a real time system to move to the goal as well as to avoid obstacles concurrently,

Most of the robot control systems are being developed using Windows O/S. Windows has many advantages of easy developing environment, such as, supporting abundant device drivers and multitasking. However it cannot support hard real time capabilities since the Windows is not designed for the real-time system originally, which emphasizes the graphic display. Moreover it is difficult and takes a lot of time to develop the device drivers [2] in Windows O/S.

Basically a real time O/S is suitable to implement a real time control system. The commercial QNX and VxWorks have the hard real time capabilities. However, the price is too high to be used for education and research purposes. Their support of device drivers for custom designed controllers is so weak that the expendability is very low [3].

In this paper, for the autonomous navigation of the intelligent robot, i-BOT, a real time control software is developed and evaluated. To keep the hard real time capabilities, Linux with RTAI has been used.

In section 2, the development environments of real time Linux and Windows O/S are analyzed to show the differences. Section 3 illustrates the hardware platform of i-BOT and the constitution of iGS (indoor GPS), and section 4 describes the operating platform for the autonomous navigation and the position estimation algorithm of iGS, and the simulation and experimental results follow in section 5. The ideas and contributions of this paper are summarized in section 6.

2. Comparison of Real Time Linux and Windows

2.1 Stability of Linux control system

Linux is a next generation O/S which can replace the Windows O/S which has code bloat caused by the continuous addition of functions when they are required. That is, the unnecessary code increase (Actually Windows has about 35 to 40 million unnecessary lines.) degrades the operating performance in the real time control system. On the contrary, the real time Linux can be ported on the small memory such as a floppy disk since it can be reconfigured by the compiler to fit to the user system. On this reason, the Linux has been widely utilized for embedded systems.

2.2 Flexibility of development environment

There are several reasons that the Windows platform has been dominant so far. It provides a user friendly interface and various services, and the educational cost is very low. Now the Linux also has almost all the advantages of Windows by the continuous development. Figure 1 is a screen shot of Visual Studio which is the Windows development environment, and Fig. 2 is a screen shot of QT which is the Linux development environment. Since both of these two environments support C and C++ as a basic programming language, the developing environments are almost the same.

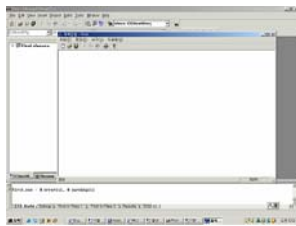


Fig. 1. Visual Studio Screen shot.

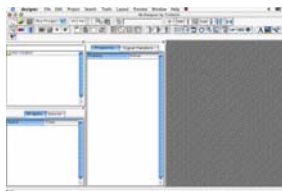


Fig 2. QT screen shot.

Linux also enables to form the tele-debugging environment by a terminal, which is very rare in Windows. Moreover the source codes of Linux are open to public. Therefore it is possible to modify the source codes according to developing objects and application environments promptly and easily. However the performance of the real time system in the Windows degrades on account of the additional codes for the various functions.

Therefore in this paper a mobile robot controller is developed based on a real time Linux, and the performance is compared to the Window based system. The modularity and real time performance of the Linux based system are emphasized to show the superiority of Linux to Windows.

3. i-BOT Platform and iGS

3.1 i-BOT Platform

The mobile robot used in this research, i-BOT, is made by Ninety Corp., which is shown in Fig. 3. For the power supply, 12 V rechargeable batteries are used. Two active wheels and one auxiliary wheel are driving the mobile robot. For the simplicity of driving mechanism,

two stepping motors are used. The mobile robot can be controlled wirelessly from a PC through Bluetooth.



Fig. 3. i-BOT system.

3.2 Structure of the iGS system

The proposed localization scheme can be applied for any of moving objects, such as, home robot, service robot, humanoid robot, *etc.* The indoor environment consists of columns, corners, and two dimensional flat walls which can include desks, tables, and computers depending on the size of the objects.

There are four beacons in the workspace of i-BOT. Each beacon is located at a specific corner with a specific coordinates and it transmits the ultrasonic signal when it is requested. Notice that most of cases, it is convenient to install the beacon at the corner of ceiling. On the mobile robot, there is a receiver which detects the arrival time of the ultrasonic signal from the beacon. The receiver has a RF transmitter in the same body, which sends out an ID for a specific beacon assigned to the ID to request the ultrasonic transmission. To identify the orientation of the mobile robot, there are two receivers on the robot. The beacon receives an RFID from the receiver, and checks whether the ID matches to itself or not. When the matching succeeds, it sends out the ultrasonic signal to the receiver on the mobile robot.

4. O/S platform for autonomous navigation

4.1 Real-Time System

To incorporate various functions to i-BOT, not only improvement of the mechanical structure but also design and implementation of real-time software structures are important [4]. The real-time software governs the efficient flow of resources and defines data-flows among the elements, for the real-time control system. The real-time position estimation and object recognition are necessary for higher level functions, such as, the autonomous navigation and recharge. For the precise estimation and recognition, the data which have different physical dimensions from various sensors need to be processed and fused efficiently. The autonomous mobile robot may confront with unwanted collisions to obstacles when one of these elements does not keep the time constraint.

For the autonomous navigation of i-BOT, many tasks, such as, motor control, sensing, position estimation commands, need to be processed in real time. Each task

has its own control period, priority, execution time, and computational complexity. Since the hard real-time properties are required in the control of motors using sensor data in these tasks, a real-time operating system which manages the resources efficiently is essential to implement the real-time control system.

The most important feature for the controller is real-time capability. Notice that the real time operating system is a higher level program to make the tasks being executed in real time. The operating system does not solely aim at the high speed operation. Within the allowed time slot, it provides the desired output utilizing the predictable system functions. Both of Windows and Linux are not possible to execute hard real time tasks, by themselves. Therefore, each operating system suggests real time kernels with the basic operating system to be used for the necessary real time system. For Windows, RTX is the most popularly used kernel. There are several on-going projects to make the Linux a real time operating system, such as, RTLinux and RTAI. The real time operating system supports the programs of multi-tasking structure with time tags, and also provides communication synchronization among tasks and scheduling mechanisms to implement the real time systems.

Linux is a performance-oriented O/S, which has the round-robin scheduler. That is, each task holds the token in a fixed period. Therefore the real time processing cannot be guaranteed. Even though a preemption function is added in the recent kernel version 2.6x, it is still not suitable for the hard-real time system, such as, a mobile robot system. There is a Linux based real-time operating system, RTLinux which is commercially available but applicable to very limited types of processors.

As a sort of interface program, RTAI is developed and it is free of charge. The RTAI provides most of the hard real-time properties, such as, task pre-emption and priority setup/inheritance. Therefore it is suitable for the real-time systems under Linux operation system.

Figure 4 shows the basic structure of RTAI. The Linux kernel is treated as a task. RTAI and Linux kernel can be interfaced to the hardware by HAL (Hardware Abstract Layer). HAL manages to execute the real time tasks preferentially, while it leaves Linux kernel and the processes working in the kernel as the lower priority tasks in RTAI [5].

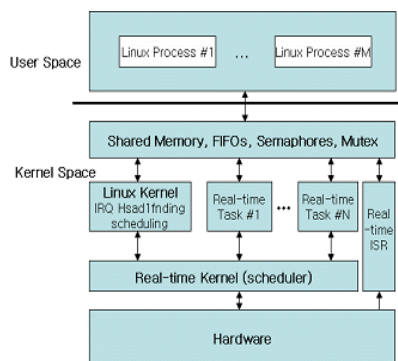


Fig. 4. Structure of RTAI.

4.2 Hierarchical control architecture

There are three levels in the architecture depending on the execution period and characteristics: 1. The highest level is the task goal which sets up the goal of the navigation, 2. The second level is the path planner which generates a path to the goal, and 3. The lowest level is the trajectory generator which specifies location and time pairs of the mobile robot on the path.

When the final goal for the autonomous navigation is determined, the highest level monitoring system plans the trajectory to the goal by selecting appropriate via and through points for the mobile robot to follow.

The path planner decides the existence of obstacles and changes the path to avoid the obstacles. For the obstacle detection, the ultrasonic transmitter sends out the signal every 100 msec, and the corresponding receiver computes the TOF (time of flight) of the ultrasonic signal and detects the obstacles within the dangerous range. After the collision avoidance, the current and goal positions are newly set in the monitoring system to execute the trajectory planning again.

In the lowest level, the stepping motors are controlled to follow the trajectory by the timer interrupt service routine in every control cycle, which provides a frequency output to control the motor.

The obstacle avoidance routine is activated when there are some static or dynamic obstacles in the path of the mobile robot, i-BOT, which senses and avoids the possible collisions using the ultrasonic sensors and the two stepping motors, respectively. When it is not possible to avoid the collision, the routine may send out STOP command to the motor controllers. After the successful avoidance, the current mobile robot follows the desired trajectory to the goal.

4.3 iGS position estimation algorithm

The localizer starts to count when it sends out an RFID signal assuming that the transmission time to a beacon is negligible. When a beacon receives its RFID, it sends out the ultrasonic signal immediately. The counting at the localizer continues until it receives the ultrasonic signal. After the distance computation using the counter value which corresponds to the TOF of the ultrasonic signal, the localizer sends out another RFID to the next beacon. When the distances to all the expected-nearby beacons are measured, the coordinates of the mobile robot is going to be calculated.

The TOF which can be calculated by the counter is basis for the computation of the distance between the ultrasonic transmitter (beacon) and receiver (localizer) as follows:.

$$v = 331.5 + 0.6 \times T \quad [\text{m/sec}] \quad (1)$$

$$s = n \times C - t_d \quad [\text{sec}] \quad (2)$$

$$r = v \cdot s \quad [\text{m}] \quad (3)$$

where T is the room temperature, C is the period of counter clock, n is the number of counter, t_d is the

time delay for ultrasonic signal detection, s is the total freight time of the ultrasonic signal, and r is the distance between the beacon and the mobile robot.

The synchronization between the beacon and the receiver on the mobile robot is very important in measuring the TOF of the ultrasonic signal without interferences. To select a beacon at a time, an RFID is transmitted to the beacon from the mobile robot. At the moment of the RFID receipt, the corresponding beacon transmits the ultrasonic signal to the receiver. Therefore there is an RF receiver with a specific ID and an ultrasonic transmitter at each beacon; there is an RF transmitter and an ultrasonic receiver on the mobile robot.

For the localization of the mobile robot using the triangulation technique, at least three beacons are necessary for a mobile robot in the 3D space..

5. Simulations and experiments

To implement and to analyze the performance of a mobile robot control system under Linux O/S, a test-bed is implemented using iGS and i-BOT as shown in Fig. 5. The height, length, and width of the iGS space are 3.0 m, 3.0 m, and 2.0 m, respectively. The speed of i-BOT is kept below 35cm/sec considering the localization accuracy and safety of the mobile robot.

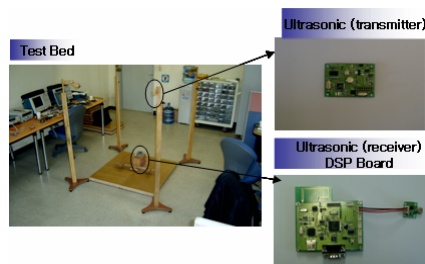
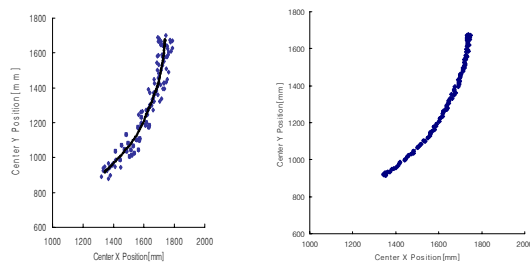


Fig. 5. Experiment environment.

Monitoring program manages the display of the position data measured by iGS and the counter values of the stepping motors sent through the Bluetooth, and it also sends out the motor control commands. In this paper, the monitoring program is implemented on a PC with the Linux using QT program, which gathers the data through Serial-COM and displays on the monitor.

To make the ultrasonic receiver free from reflected interference signals. An RFID is sent out every 20 ms for each beacon. The total data processing time of iGS to obtain the location coordinates is 90 ms.



(a) Trajectory estimation. (b) EKF results.
Fig. 6. Trajectory of a moving object.

Figure 6(a) shows experimental trajectories of the mobile robot: the black solid line represents the actual trajectory while the rectangular marks represent the estimated trajectory by the triangulation method. In the middle of the path, there are filled rectangular marks which represent the positions estimated by only two sensor data. Fig. 13 represents the trajectory obtained by the EKF (extended Kalman filter) using the data set from the triangulation method. By applying the extended Kalman filter, the error between the real and estimated trajectories has been reduced to 20 % as it is clearly recognized by comparing Fig. 6(a) and Fig. 6(b).

6. Conclusion

A flexible controller is designed to satisfy the various requirements of customers working on the Linux environment. RTAI has been utilized to form a real time control system based on Linux, since its source codes are open to public and it has higher flexibility than Windows to satisfy the controller specifications and environment. Through the various experiments, RTAI is proved to be efficient for modular and real-time programming. A monitoring system is specifically designed for the improvement of i-BOT control precision by taking advantage of this Linux-based real time O/S. It is concluded that the i-BOT working in the Linux environment developed in this research, is useful and flexible for education and researches.

Acknowledgements

This Work was supported in part by MIC&IITA through IT Leading R&D Support Project

REFERENCES

- [1] S. Singh, "Obstacle detection for high speed autonomous navigation," Proc. Of IEEE Int. Conf. on Robotics and Automation, pp. 2798-2805, 1991.
- [2] C. H. Lee and C. Mavroidis, "PC based control of and mechatronic systems under MS-windows NT workstation," IEEE/ASME Trans. on Mechatronics, vol.6, no. 3, pp. 311-321, 2001.
- [3] W. F. Lages and E. M. Hemerly, "Linux as a software platform for mobile robots," submitted to IEEE Transactions on Software Engineering, 2000.
- [4] I. S. Song and F. Karray, "Software architecture for realtime autonomous agents : a case study for digital train system," Proc. of IEEE International Symp. on Intelligent Control, pp. 403-408, 2002.
- [5] L. Dozio and P. Mantegazza, "Linux real time application interface (RTAI) in low cost high performance motion control," Motion Control 2003, a Conference of ANIPLA, Italy, March, 2003.
- [6] SeungBu Kim, Gi-Gun Nam and JangMyung Lee, "Indoor Localization Scheme of a Mobile Robot Using RFID" international robot Week, Deajeon, Korea, 2005.

Ontological Representation of Vision-based 3D Spatio-Temporal Context for Mobile Robot Applications

Gi Hyun Lim, Jongleul Chung,
Gwang Geun Ryu, Jong Bok Kim,
Sang Hyoung Lee, Sanghoon Lee,
and Il Hong Suh

Jung Hwa Choi and Young Tack Park

School of Computing
Soongsil University, Seoul, 156-743, Korea

College of Information and Communications
Hanyang University, Seoul, 133-791, Korea

Abstract

In this paper, we propose an ontology-base context model that consists of high level context as well as primitive spatial and temporal context. Moreover reasoning tools are used to find out not only simple contextual information such as object location, movement and distance but also hidden contextual information such as some objects disappeared by moving behind bigger objects. Also we use axiomatic rules for resolving uncertainties which might be caused by the mismatches of 3D SIFT key points. Some practical examples will be provided to show the validities of our proposed ontology-based context model.

1 Introduction

The intelligent robot needs high level perceptual tasks - context awareness[1][4][5][6], SLAM[10], object recognition. Especially contextual information is necessary for robot intelligence with which robots can recognize environments and plan their behaviors to complete missions while adapting to their environments. Such perceptual tasks are often required to be implemented by relatively inexpensive vision sensors of which visual data can be made very informative by employing many data processing algorithms. We note that vision-based context understanding system requires not only recognition of objects in the scene, but also contextual interpretation of the scene. Spatio-Temporal (ST) context is the basis for high level context understanding. However, visual data could be almost partial and occult in real environment. And such visual data processing knowledge have been specially designed for the domain-specific application. Thus, there can be hardly shared knowledge such as data

structure, data processing mechanisms and rules. Using ontological representation makes it easy for intelligent robot to share its knowledge and common concepts[3][4][5][7]. Therefore, ontological representation and reasoning tools will open possibility for robots to find hidden knowledge and/or to make that knowledge is growing and reusable.

In this paper, we propose an ontology-base context model that consists of high level context as well as primitive spatial and temporal context. Moreover reasoning tools are used to find not only simple contextual information such as object location, movement and distance but also hidden contextual information such as some objects disappeared by moving behind bigger objects. Also we use axiomatic rules for resolving uncertainties which might be caused by the mismatches of 3D SIFT key points. For example, objects cannot float in the air by themselves. Instance of our proposed ontological context model will be generated based on 3D SIFT features. Specifically, after recognition of objects using SIFT features[2], primitive spatial data including location of objects, distances between objects, movement of objects are created. When the primitive spatial data are generated, an approximated center of an object is selected as a representative point for fast and efficient data processing. The compensated primitive spatial data are then clustered to instantiate primitive ST contexts. Then, higher level ST contexts are also instantiated by classifying these primitive ST contexts according to ontological taxonomy of context model. The instance is stored with a time-tag . Instances are then used to extract some missing information and/or to resolve uncertain relations by inference tools. Some practical examples will be provided to show the validities of our proposed ontology-base context model.

In the following sections, robot-centered ontology

is described. Robot-centered ontology includes ontological model of perception, model, context and activity. Second, it will shown how context ontology instances are generated. Third, our ontology model will be tested on home service environment. Finally, a conclusion and consideration for future research are provided.

2 Robot-centered ontology

Robot-centered ontology is an ontological representation of robot knowledge that supports intelligent robot to perceive the environment, to model the state of the world, to plan the sequence of job, to perform the selected activity and to aware a given situation - context. Robot ontology is necessary for robot to share and reuse its knowledge, because robot perceives the environment and puts into action in a different way as human do[3]. It requires that ontological representation of robot knowledge should be suitable for its own sensors, behaviors as well as their coordination. Fig. 1 shows the architecture of ontology-based multi-layered robot knowledge framework (OMRKF), which includes 4 dimensions; KLevel, KLayer, OLayer and time and 4 levels of knowledge ($KLevel_i$); Perception(P_i), Model(M_i), Context(C_i) and activity(A_i). And those knowledge are represented by ontology.

2.1 4 Levels of Robot ontology

Robot perceives objects with its sensors, models world, plans some sequence of task, performs the task with behavior and perceive again, or robot behaves through its sensor values not with planning but with pre-programmed behaviors[11]. But, those sensor data are uncertain and partial information[10]. And service robot needs context-awareness[4], [5], [6], so that they can adapt themselves to changing situations. Context offers a few clues of the proper action selection mechanism for robot. According to the advance of context, it is necessary to develop formal context models to facilitate context representation, context sharing. Thus, OMRKF is composed of KBoards and rules, and KBoards is composed of 4 levels of knowledge perception, modeling, activity and context. each level and dimension are connected by association rules as in Fig. 1.

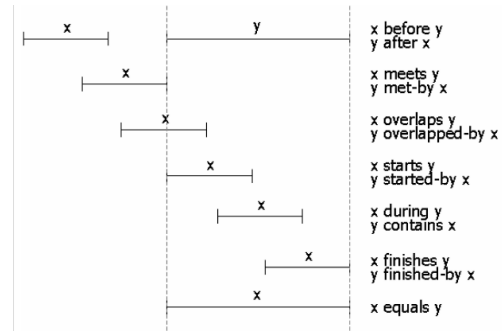


Figure 3: The Definition of Interval Relation by Allen

2.2 Context ontology

The context KLevel ($KLevel_4$) of OMRKF has 3 knowledge layers ($KLayer_{ij}$); spatial context (C_1 or $KLayer_{41}$), temporal context (C_2 or $KLayer_{42}$) and high level context (C_3 or $KLayer_{43}$) as shown in Fig.1. C_1 is generated by primitive spatial data and includes spatial concept such as on, in, near, far, left and right. C_2 is clustered with compensated primitive spatial contest and includes spatial concepts; object-fixed, move-near, temp-moving. And C_3 is more abstracted context in specific domain with rules such as dinner, appetizer, main dish and dessert. And, basic ontological elements of OMRKF is 3 ontology layer ($OLayer_{ijk}$) such as meta ontology layer ($OLayer_{ij1}$), ontology layer ($OLayer_{ij2}$) and ontology instance layer ($OLayer_{ij3}$). Fig. 2 shows an example of OMRKF.

2.3 Temporal ontology

Time information is absolute measure which is obtained regardless of location and movement[9]. For temporal ontology, we reference thirteen interval relations as shown in Fig. 3 to define relations among actions which were proposed by J. Allen to formalize time[8]. Temporal ontology makes it possible to obtain knowledge not defined in ontology by inferring relations among locations using interval relation.

3 Instantiation of Context ontology

In this paper, vision-based objects recognition is performed by SIFT features. After recognizing objects, some instance of spatial context ontology including location of objects, distances between objects, movement of objects are created. When the spatial

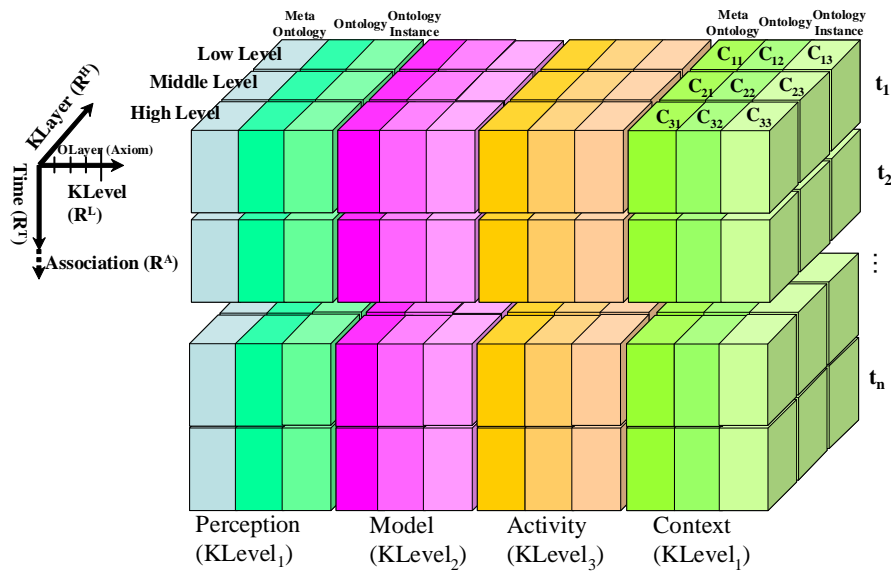


Figure 1: 4 Dimensional OMRKF

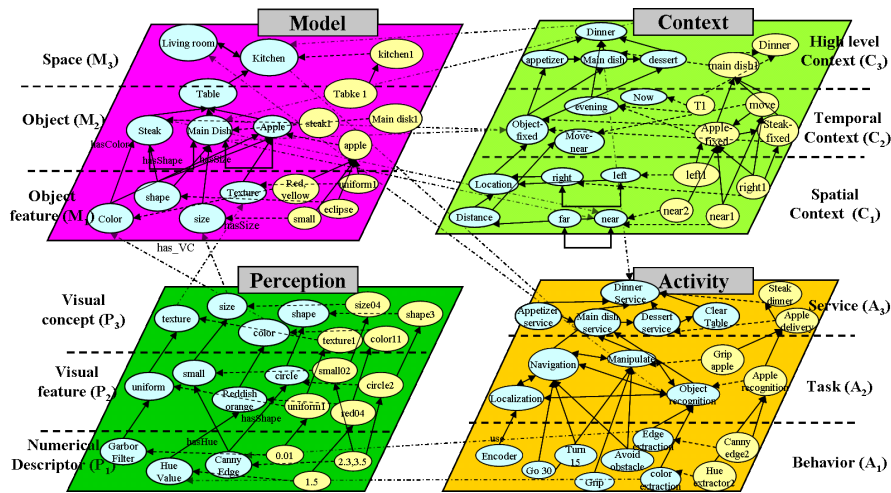


Figure 2: An Example of Robot-centered ontology Schema

contexts are instantiated ($OLayer_{413}$ or C_{13}), an approximated center of an object is selected as a representative point with axioms such as "Solid objects cannot penetrate other solid objects" and "Objects cannot float in the air by themselves". The compensated spatial context are then clustered to generate temporal context instances ($OLayer_{423}$ or C_{23}). Finally, we can get high context instances ($OLayer_{433}$ or C_{33}) by domain specific rules. And also we can get hidden ST contexts by inferencing pre-instantiated ST contexts.

3.1 Instantiation of Spatial Context Ontology ($OLayer_{413}$ or C_{13})

In order to recognize objects, we use a model-based approach. First of all, we use a 3D OFM (Object Feature Model) as the reference model which includes images of object, their corresponding SIFT keypoints, and representative point. By simply matching of 3D keypoints between OFM and input image, we can identify objects and obtain positions of objects with respect to robot. After identifying objects, primitive spatial data which describe geometric relations of recognized objects and are composed of location, distance, and movement data are generated. Also, the primitive spatial data are instantiated one of spatial context ontology ($OLayer_{413}$ or C_{13}).

Location Data: Location data for an object ob is defined as $R(ob) = (t, obj, R(ob))$, where t is a time when the location data is created, obj is the name of object ob , and $R(ob)$ is a position vector of object ob with respect to the robot coordinate.

Distance Data: Distance data for objects $ob1$ and $ob2$ is defined as $D(ob1, ob2) = (t, obj1, obj2, D(ob1, ob2))$, where t is a time when the distance data is created, $obj1$ and $obj2$ represent names of object $ob1$ and $ob2$, respectively. And, $D(ob1, ob2)$ is a position vector from object $ob1$ to object $ob2$ with respect to the robot coordinate.

Movement Data: Movement data for an object ob is defined as $M(ob) = (t, obj, M(ob))$, where t is a time when the movement data is created, and obj represents the name of object ob . $M(ob)$ is the vector of movement which can be simply obtained by the vector difference $R_t(ob)$ and $R_{(t-1)}(ob)$.

Table 1 shows definitions used in generation of primitive-ST data.

3.2 Instantiation of Temporal Context Ontology ($OLayer_{423}$ or C_{23})

Temporal context ontology is instantiated by inferencing spatial context ontology instance such as location,

Table 1: Definition for Primitive-ST Data

Definitions	Description
t_s	start time
t_e	end time
$t_d = (t_e - t_s)$	time interval of interest
t_{freq}	sampling time
t_i	time acquiring i-th data
$N_{max} = \frac{t_d}{t_{freq}}$	maximum number of available data
e_R	threshold of position error
e_D	tolerance of distance error
T	trustability

distance, and movement data.

Primitive location data of object $ob(pR(ob))$ shows that the object ob stays at the same location for a given period of time td . And $pR(ob)$ is defined as $pR(ob) = (id, t_s, t_e, obj, R(ob), T)$. The primitive location data can be generated as follows;

- For any time $t_i \in \{0 < t_s \leq t_i \leq t_e\}$
- 1: If $abs(R(ob) - R_{t_i}(ob)) \leq e_R$ then count = count + 1
 - 2: $T = \text{count} / N_{max}$
 - 3: Generate $pR(ob)$

Temporal context ontology are instantiated with one or more spatial context ontology instance about the same objects. Table 2 show the spatial context and temporal context ontology and their FOL[7] rules.

3.3 Reasoning of context ontology

We represent OMRKF with FOL. Moreover, OMRKF includes sub-symbolic data that are seldom utilized by conventional ontology system. The data generated from robot perception or activities are numerical data, which are partial and incomplete. The probabilistic approach has dominated the solution of that case [2]. However, those systems may be application-specific, which is difficult to reuse and requires verification of the procedures. OMRKF applies sub-symbolic data to ontology-based knowledge representation, so that OMRKF can deduce hidden knowledge that is generated by a partial observation or an observation error, and make it easy to reuse and verify. Moreover, OMRKF needs rules that associate each level of knowledge, these rules enable robot to query not only unidirectional reasoning but also bidirectional reasoning. Table 2 show rules for the generation of context represented by FOL.

4 Experimental result

The ST context generation experiment was performed for objects in a refrigerator. For sequentially changing context in the refrigerator as shown in Fig.4. Mobile robot

Table 2: Rules for spatial context and temporal context ontology

Layer	Context	Logical representation
C_1	SC_1	$\forall o_1, o_2, t$ $location(o_1, t) \wedge location(o_2, t) \wedge$ $positive((o_1.x - o_2.x), t) \Rightarrow left$
C_1	SC_3	$\forall o_1, o_2, t$ $location(o_1, t) \wedge location(o_2, t) \wedge$ $dis_err((o_1.x - o_2.x), t, e_D) \wedge$ $dis_err((o_1.y - o_2.y), t, e_D) \wedge$ $dis_err((o_1.z - o_2.z), t, e_D) \Rightarrow near$
C_1	SC_4	$\forall o_1, o_2, t$ $location(o_1, t) \wedge location(o_2, t) \wedge$ $positive((o_1.y - o_2.y), t) \wedge$ $near(o_1, o_2, t) \Rightarrow over$
C_1	SC_6	$\forall o_1, o_2, t$ $over(o_1, o_2, t) \wedge equal((o_1.y -$ $o_2.y), (o_1.height + o_2.height)) \wedge$ $dis_err((o_1.y - o_2.y), t, e_D) \Rightarrow on$
C_2	TC_1	$\forall o, t, t_1$ $location(o, t) \wedge location(o, t_1) \wedge$ $loc_err(o, t, t_1, e_D) \Rightarrow object - fixed$
C_2	TC_2	$\forall o_1, o_2, t, t_1$ $distance(o_1, o_2, t) \wedge$ $distance(o_1, o_2, t_1) \wedge$ $dis_err(o_1, o_2, t, t_1, e_D) \Rightarrow$ $fixed - distance$
C_2	TC_3	$\forall o_1, o_2, t, t_1$ $distance(o_1, o_2, t) \wedge$ $distance(o_1, o_2, t_1) \wedge$ $dis_near(o_1, o_2, t, t_1) \Rightarrow object - near$
C_2	TC_5	$\forall o_1, o_2, t, t_1$ $contain(o_1, o_2, t) \wedge contain(o_1, o_2, t_1) \Rightarrow$ $inside$
C_2	TC_7	$\forall o_1, o_2, t, t_1, dis_1, dis_2$ $distance(o_1, o_2, t) \wedge$ $distance(o_1, o_2, t_1) \wedge$ $positive(dis_1, dis_2) \Rightarrow move - near$

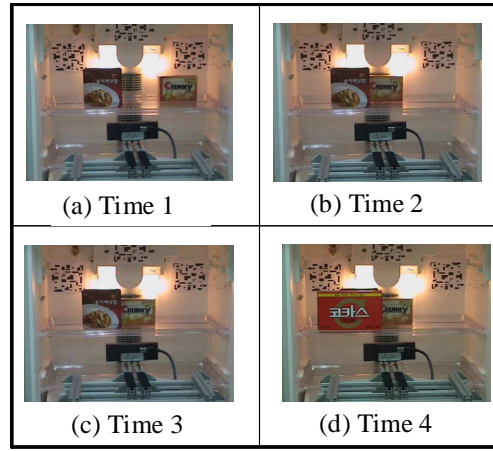


Figure 4: Sequentially Changing Contexts

may generate primitive spatial data and instantiate spatial context and temporal context ontology. At $t = t_1$, there are two objects (obj2 and obj3) apart from each other in a refrigerator(obj1). At $t = t_2$ and $t = t_3$, obj3 moves left and forward, respectively. Finally, a large object(obj4) appears in front of obj2 and occludes it.

Fig.5 shows the display of our context generation system. In the left upper corner, images captured by stereo camera attached on top of the mobile robot are displayed continuously. In the right upper corner, the location of objects, where the location is obtained by our proposed point-based approach and compensated by our proposed axiomatic rules, can be also observed. In the lower part of Fig.5, ST Context predicates generated at experiment are displayed. And ST Context Predicates for situations inside refrigerator are listed in Table 3. Note that the proposed system can extract the relationship between objects which are not directly visible by inferencing relationship among the instance of spatial context and temporal contexts created at previous times. In this experiment, although obj2 is occluded by obj4, contexts such as $front(obj4, obj2)$ and $front(obj2, obj3)$ were generated.

5 Conclusion

We proposed ontology-based context model for the household service robot, and the ontology is represented by FOL. This model allow robot to find contexts in spite of hidden and partial data. Moreover OMRKF enable robot to query through any directional reasoning between each layer as well as between each level of knowledge with small number of clues.

For a future work, we would like to extend our context model to include knowledge to handle uncertain and partial data. We also would like to represent our knowledge model as OWL/SWRL which is known to be decidable.

5.1 Acknowledgements

This work was performed by a grant of the Second Stage of BK21 Research Division for Advanced IT Education Program on Industrial Demand. and for the Intelligent Robotics Development Program, one of the 21st Century Frontier R&D Programs funded by Korea Ministry of Commerce, Industry and Energy.

References

- [1] J. Chung, H.W. Kim, S. Lee et al, "Vision-based 3D Spatio-Temporal Context Generation for Mobile Robot Applications," The 21st International Technical Conference on Circuits/Systems, Computers and Communications(ITC-CSCC2006), pp I-77 I80, 2006
- [2] D. Lowe, "Distinctive image features from scale-invariant keypoints," *International Journal of Computer Vision*, Vol.60, pp.91-110, 2004.
- [3] E. Bozsak, M. Ehrig, S. Handschuh et al, "KAON ? Towards a Large Scale Semantic Web," *Lecture notes in computer science*, No. 2455, 2002, pp. 304-313.
- [4] W. Hwang, J. Park, H. Suh et al. "Ontology-based Framework of Robot Context Modeling and Reasoning for Object Recognition," to appear in /em Lecture Notes in Computer Science, 2006.
- [5] X.H. Wang, D.Q Zhang, T. Gu and H.K. Pung, "Ontology Based Context Modeling and Reasoning using OWL," Proc. of the Second IEEE Annual Conference on Pervasive Computing and Communication Workshops (PERCOMW04), 2004.
- [6] K. Henriksen, J. Indulska, and A. Rakotonirainy, "Modeling Context Information in Pervasive Computing Systems," *Lecture notes in computer science*, 2002, no. 241, pp. 167-180.
- [7] I. Bratko, *Prolog programming for artificial intelligence*, 3rd ed. Pearson education, 2001, pp. 57.
- [8] J.F. Allen, and H.A. Kautz, *A model of naive temporal reasoning*, In Formal Theories of the Commonsense World. J. R. Hobbs and R. C. Moore, eds., Ablex., pp.251-268, 1985.
- [9] J.R. Hobbs, J. Pustejovsky, "Annotating and reasoning about time and events," In Proceedings of AAAI Spring Symposium on Logical Formalizations of Commonsense Reasoning, 2003.
- [10] S. Thrun, W. Burgard and D. Fox, *Probabilistic Robotics*, MIT Press 2005, ch. 1.
- [11] R.C Arkin, *Behavior-based Robotics*, MIT Press, 1998.

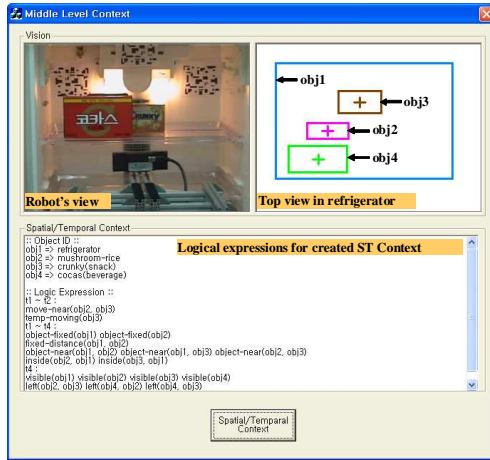


Figure 5: Shapshot of Experiments: Inside a Refrigerator

Table 3: ST Context Predicates generated at Experiment

Time	ST Context Predicates for situations inside refrigerator
$t_1 \sim t_2$	move-near(obj2, obj3), temp-moving(obj3)
$t_1 \sim t_4$	object-fixed(obj1), object-fixed(obj2), fixed-distance(obj1, obj2), object-near(obj1, obj2), object-near(obj1, obj3), object-near(obj2, obj3), inside(obj2, obj1), inside(obj3, obj1)
t_4	visible(obj1), visible(obj2), visible(obj3), visible(obj4), left(obj2, obj3), left(obj4, obj2), left(obj4, obj3), front(obj2, obj3), front(obj4, obj2), front(obj4, obj3), near(obj1), near(obj2), near(obj3), near(obj4)

Cortical current sources for processing visual target motion revealed by MEG and fMRI

D. Kawawaki T. Shibata Y. Fujiwara
Theoretical Life-Sciences Lab.
NAIST
8916-5, Takayama, Ikoma
Nara 630-0192, JAPAN

O. Yamashita M. Sato M. Kawato
Computational Neuroscience Lab.
ATR
2-2-2, Hikaridai, "Keihanna Science City"
(Seika, Soraku), Kyoto 619-0288, JAPAN

Abstract

Experiments of a magnetoencephalography (MEG) and an functional magnetic resonance imaging (fMRI) were conducted to reveal the cortical mechanisms related to covert pursuit to a moving visual target. Subject was asked to gaze a fixation point at the center of screen and to track covertly a horizontally moving target. The MEG was measured when the subjects were tracking the target covertly. Current sources of about 7,000 dipoles on the cortical surface were estimated from the MEG data by a hierarchical Bayesian method incorporating the fMRI data. We investigated whether the target velocity can be reconstructed from estimated current sources. One of the datasets was used for training of the weight parameter, and validation tests were conducted using other two datasets. The result showed that target velocities could be reconstructed from the current sources in the cortical areas, related to processing target motion in eye movements, such as primary visual cortex, lateral occipito-temporal cortex, parietal cortex, and pre-frontal cortex. This result suggested that these areas were responsible for tracking a moving target, in consistent with previous studies using noninvasive recording of brain function.

1 Introduction

The purpose of smooth pursuit eye movements is successively gazing on a smoothly moving object with the central fovea. It has been known that the main computational goal of smooth pursuit is to minimize the retinal slip, i.e. target velocity projected onto the retina. It has been known that eyes were able to pursue a sinusoidal target motion (its frequency up to around 1Hz) without delays in primates' smooth pursuit (e.g., in humans [1], in monkeys [2]), whereas there is a significant delay (60ms in monkeys [3], more than 70ms in humans [4]) in the control loop of smooth pursuit. Thus, the central nervous systems of primates predict the target motion for smooth pursuit eye movements [5].

There are many reports that reveal predictive mechanisms for smooth pursuit eye movements by noninvasive functional brain imaging methods, e.g. functional magnetic resonance imaging (fMRI) [6, 7, 8, 9]. But, Cortical activity patterns with millisecond-order temporal resolution related to predictive smooth pursuit eye movements cannot be obtained by fMRI in principle. In contrast, magnetoencephalogram (MEG) can record cortical activities with high temporal resolution. Georgopoulos et al. [10] reported that trajectories controlled by joystick were predicted from signals recorded by 248 MEG channels. The result suggested that MEG signals represented information related joystick trajectories. However, it was not clear which areas were important for predicting joystick trajectory because of small number of MEG channels.

In this study, we analyzed current sources on cerebral cortex with high spatiotemporal resolution, which was estimated by hierarchical Bayesian method [11] incorporating fMRI activities. We conducted an fMRI-based MEG experiment for investigating the neural mechanisms supporting predictive smooth pursuit eye movements and for dissociating neural signals related to prediction from response signals derived from visual inputs. In this experiment, we performed Covert pursuit task in which subject was asked to orient their attention to a target and to pursue the target motion in mind because the electrooculogram (EOG) component contaminates MEG signals when subject's eyes are moved actually. Note that there is agreement that Covert pursuit is based on common mechanisms with eye movements [12].

2 Methods

2.1 Subject

A healthy male human volunteer with normal vision participated in this study. The subject gave informed consent in writing and the study was approved by the Ethics and Safety Committee of Advanced Telecommunications

Research Institute International (ATR).

2.2 Stimuli and apparatus

MEG recorded for 4096ms at 1000Hz by 201-channel sensors of whole-head biomagnetic imaging system (Shimazu). A white target (with a diameter of 0.3deg and a luminance of 1.30cd/cm²) and a red fixation point (0.3deg and 1.68cd/cm²) were projected by DLA-G11 (Victor) at a 60Hz refresh rate. The screen (a background luminance of 1.30cd/cm²) was placed 100cm in front of the subject's eyes.

Target motion patterns were generated as output signals of a second order linear system with Gaussian noise were input. The second order linear system was defined in the Laplace domain as

$$H(s) = \frac{\omega^2}{s^2 + \omega^2}, \quad \omega = 2\pi \quad (1)$$

the pole of $H(s)$ was $s = 0 \pm \omega i$. Therefore the cycle of target motion patterns was about 1Hz ($2\pi/\omega$). These parameters were determined through trial and fault for that subject can perform smooth pursuit eye movements to the target. Three patterns were picked up randomly from the signals generated by the second order linear system with Gaussian noise input for our experiment.

2.3 Procedures

Subject sat in front of a projector screen. An MEG dewar was put on the subject's head. His head was held on a chin supporter. Two sessions of covert pursuit task were conducted. In each a session, each target motion pattern was presented at 30-trials respectively, and additional 30 exploratory trials were performed in random order. In each trial, the target was stationary at a center of screen for 100ms, and moved for 3996ms. Then, it was extinguished and subject was required their eyes blinked for about 2s.

2.4 Current source estimation

A baseline correction, drift removal, and invalid sensors/trials removal were applied to the recorded MEG data. Surviving MEG data were collected up with respect to each session and each target pattern, and were used for current source estimation.

The three-dimensional cerebral cortex model was made from the high-resolution MRI structure image by using Brain Voyager (Brain Innovation), and used for current source estimation and result presentation. The number of vertices on the brain surface model was 27513 points.

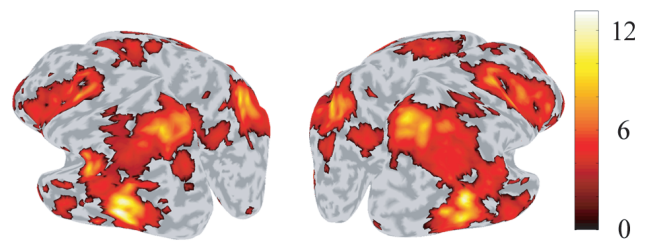


Figure 1: Result of statistical analysis of fMRI data. Color (contrasting density) bar represents magnitude of t-value.

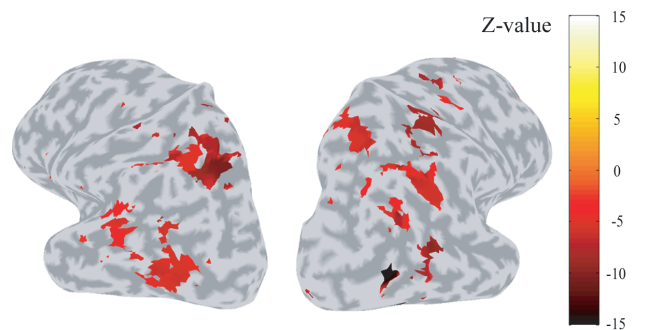


Figure 2: Colored area shows areas in which reconstruction error was significantly smaller than errors calculated from pseudo data.

Cortical areas in which current sources were assumed were decided by the statistical result of the fMRI experiment in which the same task as this MEG experiment was performed. In detail, current sources were assumed at each vertices perpendicular to cortical surface. The areas were significantly activated ($p < 0.001$, uncorrected) when subject pursued a moving target in mind with gazing a fixation point compared with when subject just gazed a fixation point. The fMRI data were analyzed by SPM5 (The Wellcome Department of Cognitive Neurology). This process limited the number of vertices on the surface of cerebral cortex to 7266 points. The statistical result of fMRI experiment was shown in figure-1.

The time courses of current sources were estimated by a hierarchical Bayesian method [11]. In order to apply this method, the leadfield was calculated by a sphere model, a Gaussian filter of 6mm FWHM was applied to spatial filtering, and the fMRI information (t-value) was used as a prior.

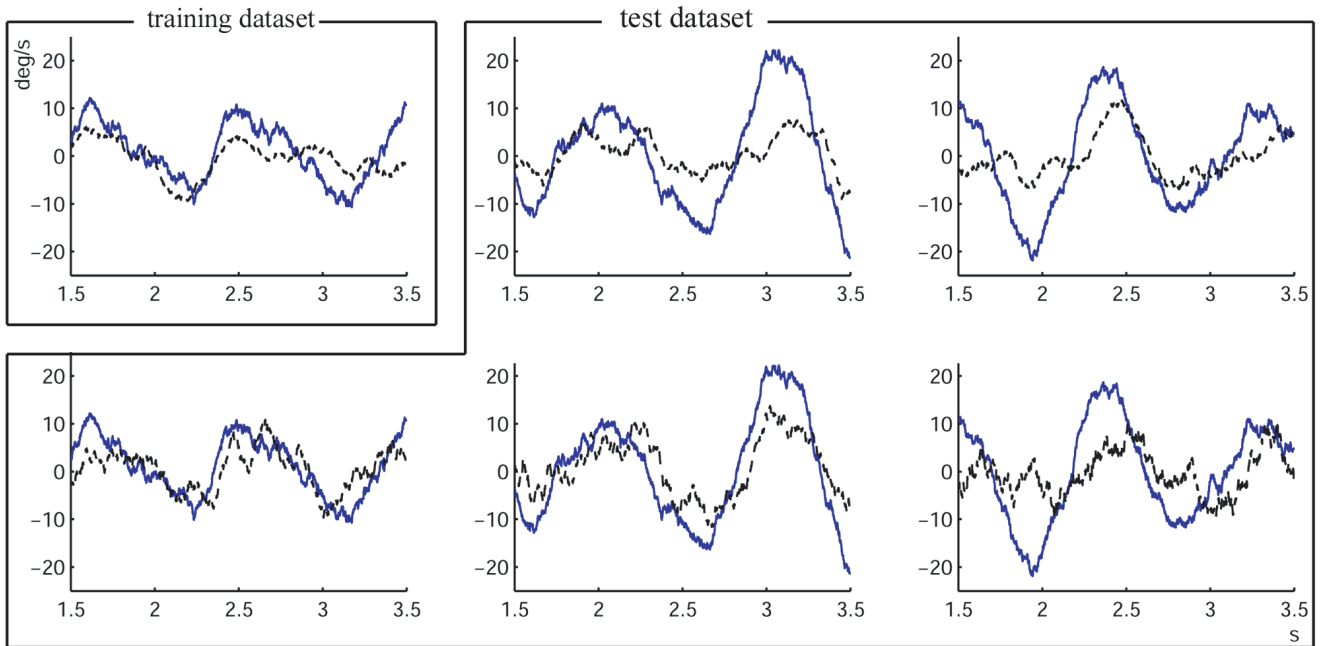


Figure 3: Results of reconstructing target velocities from current time course in right lateral occipito-temporal cortex. Solid and dashed lines denote actual and reconstructed target velocity, respectively. Weight parameters were trained with training dataset.

3 Results

We assumed that current time courses on each vertices x and target velocities y were explained by the following equation with parameter a_τ , ($\tau = 1, 2, \dots, 150$), and the parameter a_τ was estimated by using training dataset. The number of 150-parameters was determined through our trial and error process.

$$y_t = \sum_{\tau=1}^{150} a_\tau x_{t-\tau} + \epsilon_t \quad (2)$$

Target velocities were reconstructed from the current time course of test datasets by using the estimated parameters a_τ , and reconstruction error was calculated.

$$\hat{y}_t = \sum_{\tau=1}^{150} a_\tau x_{t-\tau} \quad (3)$$

$$e = \sqrt{\sum_t (\hat{y}_t - y_t)^2} \quad (4)$$

The error e was statistically evaluated by null hypothesis that the current sources could reconstruct any patterns of target velocity. First, fifty pseudo-datasets were prepared by the same way as presented target velocity patterns.

Here, the power spectrum of the pseudo target velocities was same as the original target velocities but the patterns were different from the original velocities. Next, Parameters of the pseudo datasets were estimated by the same way as the original datasets. Finally, the reconstruction tests were performed by using the estimated parameters, and reconstruction errors were calculated. We performed statistical test whether the original reconstruction error was statistically smaller than the pseudo reconstruction errors. Here, we assumed that distribution of the pseudo reconstruction errors follows normal distribution, and the original error was transformed into Z-score using the mean and standard deviation of the pseudo-errors. Figure-2 shows areas in which the original error was statistically small [$Z < 3.09$, $p < 0.001$, one-sided, uncorrected for multiple comparison].

Figure-2 shows that the reconstruction errors were significantly small in V1 of right hemisphere, lateral occipito-temporal and intra-parietal cortex of both hemispheres, right pre-central cortex, and left supra-marginal gyrus.

Figure-3 shows reconstructed target velocities from current time course in the right lateral occipito-temporal cortex. This result showed that target velocity was able to be reconstructed from the estimated current in test dataset by using weight parameters estimated in training dataset.

4 Discussions

In this research, we recorded MEG data during covert pursuit task and estimated current sources on cerebral cortex from the MEG data by hierarchical Bayesian method [11] incorporating fMRI data recorded during the same task. We also reconstructed the target velocities from current time course and to perform statistical test for the reconstruction error. The result showed that target velocities were able to be reconstructed from the current in V1 of right hemisphere, lateral occipito-temporal and intraparietal cortex of both hemispheres, right pre-central cortex, and left supra-marginal gyrus.

Previous studies related to Brain Machine Interface (BMI) reported that actions intended by subjects were able to be reconstructed and predicted by the biomedical signals that were brought out from electrodes embedded in the brain or from EEG/MEG channels. However, global cortical activations are hard to be captured by current electrophysiology. Also, signals driven by cortical neurons are mixed and recorded by EEG/MEG channels. In contrast, this study employing a hierarchical Bayesian method showed that the current signals contributing to reconstruction of the target velocities localized in the cortical areas related to processing of target motion in eye movements. This result suggested that these areas were responsible for tracking a moving target, in consistent with previous studies using noninvasive of brain function.

Acknowledgements

This research was supported in part by the National Institute of Information and Communications Technology (NICT-KARC).

References

- [1] G. Westheimer: “Eye movement responses to a horizontally moving visual stimulus”, *AMA Arch Ophthalmol*, **52**, 6, pp. 932–941 (1954).
- [2] K. Fukushima, T. Yamanobe, Y. Shinmei and J. Fukushima: “Predictive responses of periaruate pursuit neurons to visual target motion”, *Exp Brain Res*, **145**, 1, pp. 104–120 (2002).
- [3] M. M. Churchland and S. G. Lisberger: “Experimental and computational analysis of monkey smooth pursuit eye movements”, *J Neurophysiol*, **86**, 2, pp. 741–759 (2001).
- [4] K. Miura, K. Suehiro, M. Yamamoto, Y. Kodaka and K. Kawano: “Initiation of smooth pursuit in humans. dependence on target saliency”, *Exp Brain Res*, **141**, 2, pp. 242–249 (2001).
- [5] T. Shibata, H. Tabata, S. Schaal and M. Kawato: “A model of smooth pursuit in primates based on learning the target dynamics”, *Neural Netw*, **18**, 3, pp. 213–224 (2005).
- [6] R. Lencer, M. Nagel, A. Sprenger, S. Zapf, C. Erdmann, W. Heide and F. Binkofski: “Cortical mechanisms of smooth pursuit eye movements with target blanking. an fmri study”, *Eur J Neurosci*, **19**, 5, pp. 1430–1436 (2004).
- [7] J. J. Barton, T. Simpson, E. Kiriakopoulos, C. Stewart, A. Crawley, B. Guthrie, M. Wood and D. Mikulis: “Functional mri of lateral occipitotemporal cortex during pursuit and motion perception”, *Ann Neurol*, **40**, 3, pp. 387–398 (1996).
- [8] S. P. Dukelow, J. F. DeSouza, J. C. Culham, A. V. van den Berg, R. S. Menon and T. Vilis: “Distinguishing subregions of the human mt+ complex using visual fields and pursuit eye movements”, *J Neurophysiol*, **86**, 4, pp. 1991–2000 (2001).
- [9] D. Kawawaki, T. Shibata, N. Goda, K. Doya and M. Kawato: “Anterior and superior lateral occipitotemporal cortex responsible for target motion prediction during overt and covert visual pursuit”, *Neurosci Res*, **54**, 2, pp. 112–123 (2006).
- [10] A. P. Georgopoulos, F. J. P. Langheim, A. C. Leuthold and A. N. Merkle: “Magnetoencephalographic signals predict movement trajectory in space”, *Exp Brain Res*, **167**, 1, pp. 132–135 (2005).
- [11] M. A. Sato, T. Yoshioka, S. Kajihara, K. Toyama, N. Goda, K. Doya and M. Kawato: “Hierarchical bayesian estimation for meg inverse problem”, *Neuroimage*, **23**, 3, pp. 806–826 (2004).
- [12] M. Corbetta, E. Akbudak, T. E. Conturo, A. Z. Snyder, J. M. Ollinger, H. A. Drury, M. R. Linenweber, S. E. Petersen, M. E. Raichle, D. C. Van Essen and G. L. Shulman: “A common network of functional areas for attention and eye movements”, *Neuron*, **21**, 4, pp. 761–773 (1998).

Robust Tracking Control Based on Neural Network for Nonholonomic Mobile Robot

Yaonan WANG and Jinzhu PENG
College of Electrical and Information Engineering
Hunan University

Changsha Hunan, P.R. China, 410082
{wang_yaonan@hotmail.com and pengjinzhu1980@126.com}

Abstract

To deal with the unknown factors of nonholonomic mobile robot, such as model uncertainties and external disturbances, a robust tracking controller with bounded estimation based on neural network is proposed. A neural network is to approximate the uncertainties terms, the interconnection weights of the neural network can be tuned online. And the robust controller is designed to compensate for the external uncertainties and the approximation error. Moreover, an adaptive estimation algorithm is employed to estimate the bound of the approximation error. The stability of the proposed controller is proven by Lyapunov function. The proposed robust tracking controller based on neural network can overcome the uncertainties and the disturbances. The simulation results demonstrate that the proposed method has good robustness.

Keywords: Robust Control; Neural Network; Bounded Estimation; Mobile Robot; Nonholonomic Constraint

1 Introduction

The tracking control of nonholonomic mobile robot has been a topic of research during recent years. The characteristic of the nonholonomic system is that the constraints, which are imposed on the motion, are not integratable, i.e., the constraints cannot be written as time derivatives of some functions of the generalized co-ordinates. It is a typical nonholonomic mechanical system with high nonlinearity and its control is very difficult. It is also a typical nonlinear uncertain system with both the parametric uncertainty in the dynamic model of the robot including motor dynamics and disturbances from the external environment or unmodelled dynamics.

For the tracking control problem of the mobile robot, lots of control methods have been applied. J. M. Yang and J. H. Kim [1] proposed a robust tracking controller for nonholonomic wheeled mobile robots using sliding mode technique. Y. Kanayama et al. [2] developed smooth static time invariant state feedback for a velocity-controlled mobile robot with nonholonomic constraint. In [3-8], the backstepping technique was used to design the adaptive and robust controller for the nonholonomic system. M.S.

Kim et al. [9] applied a robust adaptive dynamic controller for a nonholonomic mobile robot with modeling uncertainty and disturbances. In recent years, intelligent systems, such as fuzzy logic [10] and neural network [5, 11-13], have been applied to approximate the models or to deal with the disturbances and dynamic uncertainties of dynamic systems [14, 15]. F. M. Raimondi, M. Melluso [10] developed a new theoretical control method based on the dynamic behavior of a wheeled vehicle, where a mechanism of fuzzy inference for designing a robust control system was present. In [5], a robust motion controller based neural network and backstepping technique is proposed for a two-DOF low-quality mobile robot. In [11-13], the neural network controllers in the proposed control structure were to deal with unmodeled bounded disturbances and unstructured unmodeled dynamics in the vehicle.

In this paper, we proposed a robust tracking controller based on neural network for a mobile robot with nonholonomic constraints. The proposed controller can guarantee robustness to parametric and dynamics uncertainties and also rejects any bounded, immeasurable disturbances entering the system. The stability is proved by the Lyapunov theory.

The rest of this paper is organized as follows. In Section II, a mobile robot with nonholonomic constraints is introduced. An robust controller based on neural network with bounded estimation for the mobile robot is designed in Section III, and the stability is proven using the Lyapunov method the velocity tracking error, the neural network weights error and the bounded estimation error are all bounded. Section IV gives some simulation results and conclusions are given in section V.

2 Dynamic Model of a Nonholonomic Mobile Robot

2.1 Preliminary definitions

A mobile robot is shown in Fig. 1, which contains two driven wheels mounted on the same axis and a castor. It is a typical example of a nonholonomic mechanical system.

An inertial Cartesian frame $\{O, X, Y\}$ linked to the

world and $\{C, X_C, Y_C\}$ linked to the mobile platform are used here. It is assumed that the centre of mass of the mobile robot is local in C . The pose of the mobile robot is completely specified by:

$$\mathbf{q} = [x, y, \theta]^T \quad (1)$$

The nonholonomic constraint states that the mobile robot satisfies the conditions of pure rolling and non-slipping, i.e., the mobile robot can only move in the direction normal to the axis of the driving wheels:

$$\dot{y} \cos \theta - \dot{x} \sin \theta - d \dot{\theta} = 0 \quad (2)$$

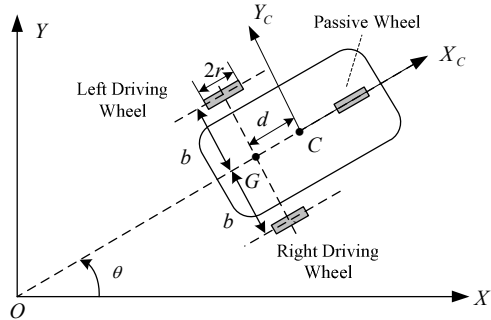


Fig. 1 A nonholonomic mobile robot

2.2 Dynamic model of a mobile robot

Consider a nonholonomic mobile robot system with n generalized coordinate \mathbf{q} and subject to m constrains can be described by [12]:

$$\mathbf{M}(\mathbf{q})\ddot{\mathbf{q}} + \mathbf{C}(\mathbf{q}, \dot{\mathbf{q}})\dot{\mathbf{q}} + \mathbf{F}(\mathbf{q}, \dot{\mathbf{q}}) + \boldsymbol{\tau}_d = \mathbf{B}(\mathbf{q})\boldsymbol{\tau} - \mathbf{A}^T(\mathbf{q})\boldsymbol{\lambda} \quad (3)$$

$$\mathbf{A}(\mathbf{q})\dot{\mathbf{q}} = \mathbf{0} \quad (4)$$

where $\mathbf{M}(\mathbf{q}) \in \mathcal{R}^{n \times n}$ is a symmetric, positive definite inertia matrix, $\mathbf{C}(\mathbf{q}, \dot{\mathbf{q}}) \in \mathcal{R}^{n \times n}$ is the centripetal and coriolis matrix, $\mathbf{F}(\mathbf{q}, \dot{\mathbf{q}}) \in \mathcal{R}^n$ denotes the surface friction and the gravitational vector, $\boldsymbol{\tau}_d \in \mathcal{R}^n$ denotes bounded unknown disturbances including unstructured unmodeled dynamics, $\mathbf{B}(\mathbf{q}) \in \mathcal{R}^{n \times r}$ is the input transformation matrix, $\boldsymbol{\tau} \in \mathcal{R}^r$ is the input vector, $\mathbf{A}^T(\mathbf{q}) \in \mathcal{R}^{m \times n}$ is the matrix associated with the constrains, $\boldsymbol{\lambda} \in \mathcal{R}^m$ is the vector of constrain forces.

Let $\mathbf{S}(\mathbf{q}) = [s_1(\mathbf{q}), \dots, s_{n-m}(\mathbf{q})]$ be a set of smooth and linearly independent vector fields in $N(A)$, the null space of $\mathbf{A}(\mathbf{q})$, i.e.,

$$\mathbf{S}^T(\mathbf{q})\mathbf{A}^T(\mathbf{q}) = \mathbf{0} \quad (5)$$

It is possible to find a velocity vector $\mathbf{v}(t) \in \mathcal{R}^{n-m}$,

such that

$$\dot{\mathbf{q}} = \mathbf{S}(\mathbf{q})\mathbf{v}(t) \quad (6)$$

Multiplying both sides by \mathbf{S}^T and using (5), we have

$$\mathbf{S}^T \mathbf{M} \mathbf{S} \dot{\mathbf{v}} + \mathbf{S}^T (\mathbf{M} \dot{\mathbf{S}} + \mathbf{C} \mathbf{S}) \mathbf{v} + \mathbf{S}^T \mathbf{F} + \mathbf{S}^T \boldsymbol{\tau}_d = \mathbf{S}^T \mathbf{B} \boldsymbol{\tau} \quad (7)$$

$$\bar{\mathbf{M}} \dot{\mathbf{v}} + \bar{\mathbf{C}} \mathbf{v} + \bar{\mathbf{F}} + \bar{\boldsymbol{\tau}}_d = \bar{\boldsymbol{\tau}} \quad (8)$$

Where $\mathbf{v} = [v, \omega]^T$, v is the velocity of mobile robot, ω is the angle velocity, $\bar{\mathbf{M}} = \mathbf{S}^T \mathbf{M} \mathbf{S}$, $\bar{\mathbf{C}} = \mathbf{S}^T (\mathbf{M} \dot{\mathbf{S}} + \mathbf{C} \mathbf{S})$, $\bar{\mathbf{F}} = \mathbf{S}^T \mathbf{F}$, $\bar{\boldsymbol{\tau}}_d = \mathbf{S}^T \boldsymbol{\tau}_d$, $\bar{\boldsymbol{\tau}} = \mathbf{S}^T \mathbf{B} \boldsymbol{\tau}$.

Property 1. $\bar{\mathbf{M}}$ is a symmetric positive definite matrix.

Property 2.

$$\bar{M}_{\min} \leq \|\bar{\mathbf{M}}(\mathbf{q})\| \leq \bar{M}_{\max}, \quad \|\bar{\mathbf{C}}(\mathbf{q}, \dot{\mathbf{q}})\| \leq \bar{C}_b \|\dot{\mathbf{q}}\| \quad (9)$$

where \bar{M}_{\min} , \bar{M}_{\max} , \bar{C}_b are some positive constants that assumed to be unknown. and $\|\cdot\|$ denotes Euclid norm.

Property 3. The matrix $(\dot{\bar{\mathbf{M}}}(\mathbf{q}) - 2\bar{\mathbf{C}}(\mathbf{q}, \dot{\mathbf{q}}))$ is skew-symmetric.

Assumption 1. The friction and gravity are bounded by $\|\bar{\mathbf{F}}(\mathbf{q}, \dot{\mathbf{q}})\| \leq \xi_0 + \xi_1 \|\dot{\mathbf{q}}\|$, where ξ_0 and ξ_1 are some positive constants.

Assumption 2. Disturbance is bounded by $\|\bar{\boldsymbol{\tau}}_d\| \leq \bar{\tau}_D$, where $\bar{\tau}_D$ is a positive constant.

For a two-wheeled mobile robot, the kinematic model can be given as [2]:

$$\begin{bmatrix} \dot{x} \\ \dot{y} \\ \dot{\theta} \end{bmatrix} = \begin{bmatrix} \cos \theta & -d \sin \theta \\ \sin \theta & d \cos \theta \\ 0 & 1 \end{bmatrix} \begin{bmatrix} v \\ \omega \end{bmatrix} \quad (10)$$

In order to simplify the problem formulation, it is assumed that $d = 0$. The alternative formulations can be readily deduced when $d \neq 0$ [5].

Suppose the mobile robot is required to follow a reference trajectory, with position and velocity are

$$\begin{cases} \mathbf{q}_r = [x_r, y_r, \theta_r]^T \\ \mathbf{v}_r = [v_r, \omega_r]^T \end{cases} \quad (11)$$

Then the tracking error expressed with respect to a frame fixed on the mobile robot are given as [2]

$$\mathbf{e}_q = \begin{bmatrix} e_1 \\ e_2 \\ e_3 \end{bmatrix} = \begin{bmatrix} \cos \theta & \sin \theta & 0 \\ -\sin \theta & \cos \theta & 0 \\ 0 & 0 & 1 \end{bmatrix} \begin{bmatrix} x_r - x \\ y_r - y \\ \theta_r - \theta \end{bmatrix} \quad (12)$$

The Lyapunov candidate is Chosen as

$$L_1 = \frac{1}{2}(e_1^2 + e_2^2) + \frac{(1 - \cos e_3)}{k_2} \quad (13)$$

Differentiating L_1 , then we obtain

$$\begin{aligned} \dot{L}_1 &= e_1 \dot{e}_1 + e_2 \dot{e}_2 + \sin e_3 \cdot \dot{e}_3 \\ &= e_1(-v + v_r \cos e_3) + \frac{\sin e_3}{k_2}(\omega_r - \omega + k_2 e_2 v_r) \end{aligned} \quad (14)$$

The velocity control law v_d achieves stable tracking of the mobile robot for the kinematic model (10) as:

$$v_d = \begin{bmatrix} k_1 e_1 + v_r \cos e_3 \\ \omega_r + k_2 e_2 v_r + k_3 \sin e_3 \end{bmatrix} \quad (15)$$

where $k_1 > 0, k_2 > 0, k_3 > 0$ are the controller gains.

Then, the equation (14) can be rewritten as

$$\dot{L}_1 = -k_1 e_1^2 - \frac{k_3}{k_2} \sin^2 e_3 \leq 0 \quad (16)$$

The velocity control law (15) may achieve theoretical stability with respect to a reference trajectory. In practice, however, the velocity v_d cannot be generated directly by the motors. Instead, the motor provide a control torque to the wheels, which will result in an actual velocity v . So it is necessary to design the torque for the robot system.

3 Robust Control Based on Neural Network with Bound Estimation

Dynamics of mobile robotic are highly nonlinear and may contain uncertain elements. Many efforts have been made in developing control schemes to achieve the precise tracking control of mobile robot [8]. In order to control the mobile robot effectively, a neural network-based robust controller with bound estimation is proposed in this paper. The structure for the tracking control system is presented in Fig. 2.

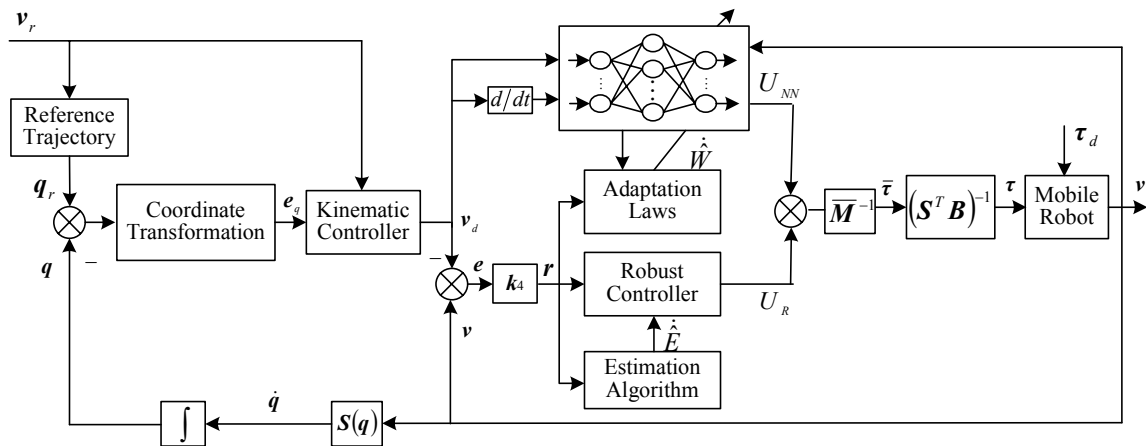


Fig. 2 The structure of the control system

First, we define the velocity tacking error as

$$e = v - v_d \quad (17)$$

Then, define a filtered tracking error as

$$r = k_4 e \quad (18)$$

where k_4 is a positive coefficient vector. The time derivative of the filtered tracking error can be written as

$$\dot{r} = -\bar{M}^{-1}(\bar{C}v + \bar{F} + \bar{\tau}_d) + \bar{M}^{-1}\bar{\tau} - \dot{v}_d \quad (19)$$

In general, the inertia matrix is known while uncertainties in the centripetal and coriolis matrix are sometimes difficult to compute. So, a new control vector is defined as $U = \bar{M}^{-1}\bar{\tau}$, and the unknown term of the equation (19), denoted by f , is an unknown smooth function, that is

$$f(x) = -\bar{M}^{-1}(\bar{C}v + \bar{F}) - \dot{v}_d \quad (20)$$

In this paper, we want to approximate this unknown function using a two-layer neural network, where the vector x can be defined as $x = [v^T \ v_d^T \ \dot{v}_d^T]^T$. Therefore, by the universal approximation theorem, there exist ideal vector W such that [11, 13]

$$f = W^T \sigma(V^T x) + \varepsilon \quad (21)$$

where the neural network approximation error ε is assumed to be bounded by $\|\varepsilon\| \leq \Delta$. $\sigma(\cdot)$ is a continuous sigmoid activation function. The first layer weights V are selected randomly and will not be tuned while the second layer weights W are tunable. The ideal

neural network weights in vectors W that are needed to best approximate the given function f are difficult to determine. All one needs to know for control purposes is that, for a specified value of E some ideal approximating neural network weights exist. Then, an estimate value of f can be given by

$$\hat{f} = \hat{W}^T \sigma(V^T x) \quad (22)$$

where \hat{W} is the estimated value of W .

Choose the tracking control law as

$$U = -\hat{W}^T \sigma(V^T x) - U_R \quad (23)$$

where U_R is robust controller.

Then, equation (19) can be rewritten as

$$\dot{r} = \tilde{W} \sigma(V^T x) - U_R + \varepsilon_d \quad (24)$$

where $\tilde{W} = W - \hat{W}$ is the estimation error, $\varepsilon_d = \varepsilon - \bar{M} \bar{\tau}_d$ is the uncertain term of the approximation error and the external disturbances.

According to (21) and Assumption 2, we can know that the uncertain term is bounded, that is,

$$\|\varepsilon_d\| \leq \|\varepsilon\| + \|\bar{M}\| \|\bar{\tau}_d\| \leq \Delta + \bar{M}_{\max} \bar{\tau}_D = E \quad (25)$$

Theorem: Given the system (8), choose the velocity control law (15) the tracking control law (23), and the adaptation law of the neural network as

$$\dot{\hat{W}} = -\dot{\tilde{W}} = \Gamma r \sigma(V^T x) \quad (26)$$

where $\Gamma > 0$ is the learning rate of the neural network.

The robust controller is designed as

$$U_R = -\hat{E} \operatorname{sgn}(r) \quad (27)$$

where \hat{E} is the estimated value of E , $\operatorname{sgn}(\cdot)$ is a standard sign function. And the bound estimation law is choose as

$$\dot{\hat{E}} = -\dot{\tilde{E}} = \eta r \operatorname{sgn}(r) \quad (28)$$

where $\tilde{E} = E - \hat{E}$ is the estimation error, η is a positive constant.

Then, the closed-loop system (8) and (23) is asymptotically stable, the filtered error r , the neural network weights error \tilde{W} and the bounded estimation error \tilde{E} are all bounded.

Proof: Choose Lyapunov function candidate as

$$L = L_1 + \frac{1}{2} r^2 + \frac{1}{2} \tilde{W}^T \Gamma^{-1} \tilde{W} + \frac{1}{2} \tilde{E}^T \eta^{-1} \tilde{E} \quad (29)$$

Differentiating yields

$$\dot{L} = \dot{L}_1 + r \dot{r} + \tilde{W}^T \Gamma^{-1} \dot{\tilde{W}} + \tilde{E}^T \eta^{-1} \dot{\tilde{E}} \quad (30)$$

Substituting (16), (24), and (25)-(28) into (30), we can obtain:

$$\begin{aligned} \dot{L} &= \dot{L}_1 + r \left(-\tilde{W}^T \sigma(V^T x) - U_R + \varepsilon_d \right) \\ &\quad + \tilde{W}^T \Gamma^{-1} \dot{\tilde{W}} - \tilde{E}^T r \operatorname{sgn}(r) \\ &= \dot{L}_1 + r \left(\varepsilon_d - \hat{E} \operatorname{sgn}(r) \right) - \tilde{E}^T r \operatorname{sgn}(r) \\ &\quad - \tilde{W}^T \left(r \sigma(V^T x) + \Gamma^{-1} \dot{\tilde{W}} \right) \\ &\leq r \varepsilon_d - \hat{E} r \operatorname{sgn}(r) - (E - \hat{E}) r \operatorname{sgn}(r) \\ &\leq -\alpha \|r\| (E - \|\varepsilon_d\|) = -\alpha \|r\| \leq 0 \end{aligned} \quad (31)$$

where $\alpha = E - \|\varepsilon_d\| > 0$ is a small positive constant.

Since $\dot{L} \leq 0$, it can be inferred that the filtered error r , the neural network weights error \tilde{W} and the bounded estimation error \tilde{E} are all bounded. Let function $\Xi(t) = -\dot{L} = \alpha \|r\|$, and integrate function $\Xi(t)$ with respect to time[14, 15]

$$\int_0^t \Xi(\tau) d\tau \leq L(r(0), \tilde{W}, \tilde{E}(0)) - L(r(t), \tilde{W}, \tilde{E}(t)) \quad (32)$$

Because $L(r(0), \tilde{W}, \tilde{E}(0))$ is bounded, and $L(r(t), \tilde{W}, \tilde{E}(t))$ is nonincreasing and bounded, the following result is obtained

$$\lim_{t \rightarrow \infty} \int_0^t \Xi(\tau) d\tau \leq 0 \quad (33)$$

In addition, $\dot{\Xi}(t)$ is bounded, by Barbalat's Lemma, it can be show that $\lim_{t \rightarrow \infty} \Xi(\tau) = 0$. That is, $r(t) \rightarrow 0$ as $t \rightarrow \infty$. As a result, the closed-loop system (8) and (23) is asymptotically stable.

4 Simulation Results

In order to verify the validity of the proposed controller, a nonholonomic mobile robot is used for illustration in this paper, as shown in Fig. 1. The dynamical equations of the mobile robot can be expressed in (1) where [12]

$$M(q) = \begin{bmatrix} m & 0 & md \sin \theta \\ 0 & m & -md \cos \theta \\ md \sin \theta & -md \cos \theta & I \end{bmatrix}$$

$$C(q, \dot{q}) = \begin{bmatrix} 0 & 0 & md \dot{\theta} \cos \theta \\ 0 & 0 & md \dot{\theta} \sin \theta \\ 0 & 0 & 0 \end{bmatrix},$$

$$B(q) = \frac{1}{r} \begin{bmatrix} \cos \theta & \sin \theta \\ \sin \theta & \cos \theta \\ b & -b \end{bmatrix}$$

$$\tau = \begin{bmatrix} \tau_r \\ \tau_l \end{bmatrix}, \quad A^T(q) = \begin{bmatrix} -\sin \theta \\ \cos \theta \\ -d \end{bmatrix},$$

$$\lambda = -m(\dot{x}_c \cos \theta + \dot{y}_c \sin \theta)\dot{\theta}$$

where $m = 10\text{kg}$, $I = 5\text{kg} \cdot \text{m}^2$, $b = 0.25\text{m}$, $r = 0.05\text{m}$, and $v_r = 0.5\text{m/s}$. The external disturbance $|\tau_{d_i}| \leq 3.0$ is a random noise with the magnitude bounded.

The initial values of neural network weights W are selected randomly in $[-1, 1]$, and the estimations are $\hat{E}(0) = [0, 0]^T$. The controller gains are $k_1 = 10$,

$k_2 = 5$, $k_3 = 4$, and $k_4 = \text{diag}\{10, 10\}$.

Defining a straight line, starting from

$$q_r(0) = [x_r(0) \quad y_r(0) \quad \theta_r(0)]^T = [0 \quad 1 \quad 45^\circ]^T$$

The mobile robot, however, is initially at

$$q(0) = [x(0) \quad y(0) \quad \theta(0)]^T = [1 \quad 0 \quad 0^\circ]^T$$

where $\theta(0) = 0^\circ$ indicates that the robot is heading toward positive direction of x .

Fig. 3 shows the simulation results for tracking a straight line using computed torque method. Since there are the uncertainties and disturbance, the mobile robot cannot track the trajectory and exhibit a steady state error.

Under the same conditions, Fig. 4 shows the results for tracking a straight line using the proposed method. As it can be seen from the figure, the mobile robot can reach the line quickly and continues to track it.

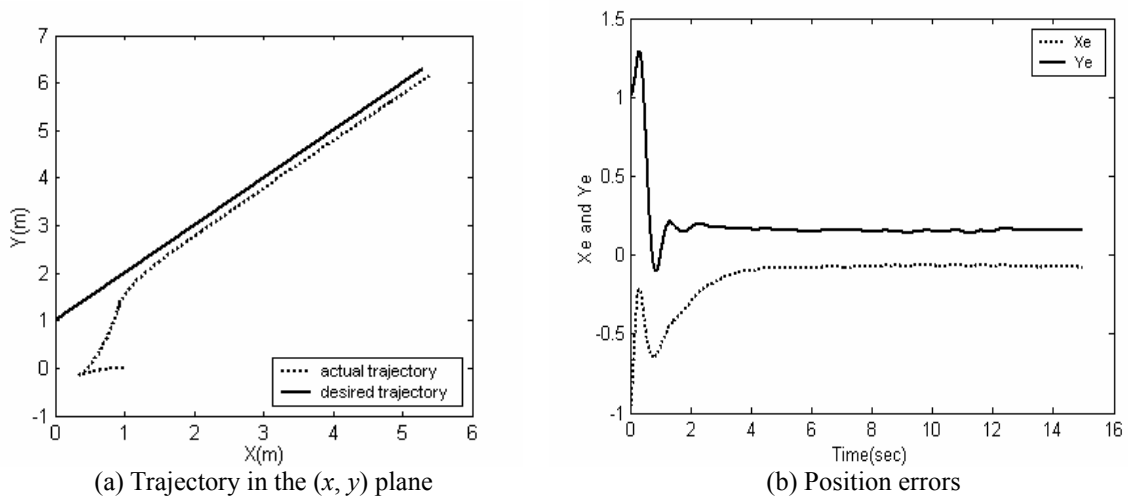
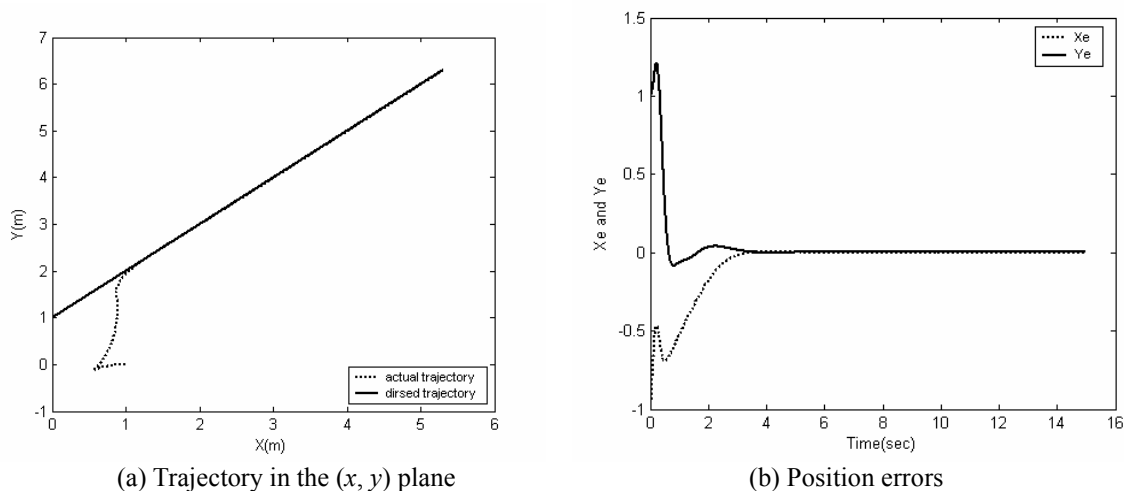
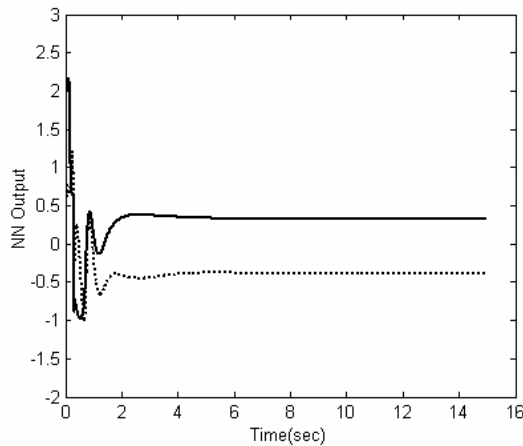
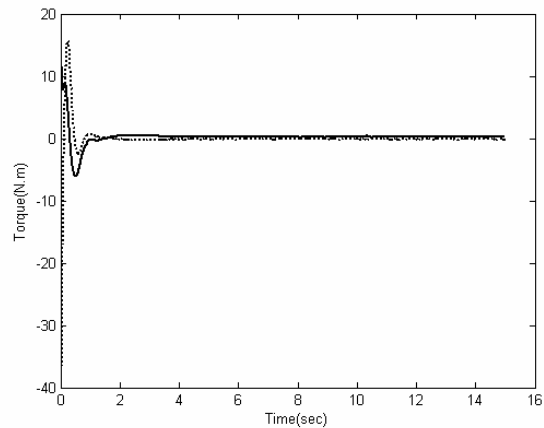


Fig. 3 Results by computed torque controller





(c) Neural network outputs



(d) Torques

Fig. 4 Results by the proposed method

5 Conclusions

Using the robust and neural network methods, a robust tracking controller with bounded estimation based on neural network is proposed for a nonholonomic mobile robot. This controller can guarantee robustness to parametric and dynamics uncertainties and also rejects any bounded, immeasurable disturbances entering the system. The stability is proven using the Lyapunov method. The velocity error, the neural network weights error and the bounded estimation error are all bounded. Finally, some simulation examples are utilized to illustrate the control performance.

Acknowledgements

The author would like to acknowledge the support of the National Natural Science Foundation of China, No. 60375001.

References

- [1] J. M. Yang and J. H. Kim. "Sliding Mode Control for Trajectory of Nonholonomic Wheeled Mobile Robots," *IEEE Trans. on Robotics and Automation*, Vol. 15, no. 3, pp. 578-587, 1999.
- [2] Y Kanayama, Y Kimura, F. Miyazaki, T. Noguchi. "A stable tracking control method for an autonomous mobile robot," *Proc. IEEE Int. Conf Robot. Automation*, pp. 384-389, 1990.
- [3] Z.P. Jiang, H. Nijmeijer. "Tracking control of mobile robots: a case study in backstepping," *Automatica*, Vol. 33, no. 7 pp. 1393-1399, 1997.
- [4] R. Fierro, F.L. Lewis. "Control of a nonholonomic mobile robot: backstepping kinematics into dynamics," *Journal of Robotic Systems*, Vol. 14, no. 3 pp. 149-163, 1997.
- [5] Q. Zhang, J. Shippen, B. Jones. "Robust backstepping and neural network control of a low-quality nonholonomic mobile robot," *Int. J. of machine Tools & manufacture*, Vol. 39 pp. 1117-1134, 1999.
- [6] T. C. Lee, K. T. Song C. H. Lee and C. C. Teng. "Tracking Control of Mobile Robots Using Saturation Feedback Controller," *Proc. of IEEE International Conf. on Robotics & Automation*, pp. 2639-2644, 1999.
- [7] M.S. Kim, J.H. Shin, S.G. Hong et al. "Designing a robust adaptive dynamic controller for nonholonomic mobile robots under modeling uncertainty and disturbances," *Mechatronics*, Vol. 13, pp. 507-519, 2003.
- [8] N. Sarker, X. Yun and V. Kumar. "Control of mechanical System with Rolling Constraints: Application to Dynamic Control of Mobile Robots," *Int. J. Robot. Res.*, Vol. 13, no. 1 pp. 55-69, 1994.
- [9] S. Yildirim. "Adaptive robust neural controller for robots," *Robotics and Autonomous Systems*, Vol. 46, pp. 175-184, 2004.
- [10] F. M. Raimondi and M. Melluso. "A new fuzzy robust dynamic controller for autonomous vehicles with nonholonomic constraints," *Robotics and Autonomous Systems*, Vol. 52, pp. 115-131, 2005.
- [11] S. Lin and A. A. Goldenberg. "Neural-Network Control of Mobile Manipulators," *IEEE Trans. on Neural Network*, Vol. 12, no. 5, pp. 1121-1133, 2001.
- [12] R. Fierro and F. L. Lewis. "Control of a Nonholonomic Mobile Robot Using Neural Networks," *IEEE Trans. on Neural Network*, vol. 9, no. 4, pp. 589-600, 1998.
- [13] C. Oh, M. S. Kim, J. Y. Lee et al. "Control of Mobile Robots using RBF Network," *Proc. IEEE/RSJ Conf. on Intelligent Robots and Systems*, pp. 3528-3533, 2003.
- [14] C. M. Lin and C. F. Hsu. "Neural-Network-Based Adaptive Control for Induction Servomotor Drive System," *IEEE Trans. on Industrial Electronics*, vol. 49, no. 1 pp. 115-123, 2002
- [15] R. J. Wai. "Tracking control based on neural network strategy for robot manipulator," *Neurocomputing*, vol. 51, pp. 425-445, 2003.

Parallel Software Architectures Analysis for Implementing P Systems

Luis Fernández
Natural Computing Group
Universidad Politécnica de Madrid
Madrid (Spain), Campus Sur. 28031

Fernando Arroyo
Natural Computing Group
Universidad Politécnica de Madrid
Madrid (Spain), Campus Sur. 28031

Iván García
Natural Computing Group
Universidad Politécnica de Madrid
Madrid (Spain), Campus Sur. 28031

Abraham Rodriguez
Natural Computing Group
Universidad Politécnica de Madrid
Madrid (Spain), Campus Sur. 28031

Abstract

This paper presents software processes architectures for implementing P systems on parallel hardware architectures. In order to analysis three different software architectures present in literature, two parameters are established: parallelisms degree and computational overload. This parameters will allow us to compare the three different studied software architectures. Finally, this analysis determines the candidate software architecture depending on available hardware architecture and the P system structure.

1 Introduction

P systems are a new computational model based on the membrane structure of living cells [1]. This model has become, during last years, a powerful framework for developing new ideas in theoretical computation. P systems with simple ingredients are Turing complete. In particular, P systems are a class of distributed, massively parallel and non-deterministic systems. "As there do not exist, up to now, implementations in laboratories (neither in vitro or in vivo nor in any electronic medium), it seems natural to look for software tools that can be used as assistants that are able to simulate computations of P systems" [2].

There are many simulators, but "the next generation of simulators may be oriented to solve (at least partially) the problems of storage of information and massive parallelism by using parallel language programming or by using multiprocessor computers" [2]. "Several authors have implemented the first ver-

sions of simulators based on parallel and distributed architectures, which is close to the membrane computing paradigm" [2]. From them, we emphasize the following ones: Ciobanu presents an implementation based on a computer cluster that "consists of 64 dual processor nodes. [...] The rules are implemented as threads" [3], this implies that a one to one relationship is established between processes and evolution rules, we refer his parallel software architecture as *evolution rules oriented*; Syropoulos presents a simulation that "is characterized as distributed in the sense that a number of objects -modeling membranes- execute code on different machines" [4], we will refer this as parallel software architecture as *membrane oriented*; finally, Tejedor presents in [5] a new parallel software architecture in which only exists one process per processor establishing a one to one relationship between processes and processors, we refer to it as *processor oriented*.

The aim of this work is to determine the appropriate parallel software architecture for a given P system and a hardware architecture. So, it pretends to determine the set of process and their relationships (parallel software architecture, *PSA*) that are appropriate to be executed over a set of connected processors (hardware architecture). In order to do it, it is necessary to establish the evaluation parameters for the analysis of parallel software architectures independently of software and hardware technologies.

This paper is structured as following: first, they are established the evaluation parameters for the analysis of a given parallel software architecture; the three following points evaluate the different parallel soft-

ware architectures in bibliography; next, it is presented a comparative of the three previous architectures through the established evolution parameters; finally, we present our conclusions.

2 Evaluation Parameters

Evaluation of parallel software architecture must be independent of particular hardware technology in which it is implemented on. This abstraction process is only dependent on the number of processors available on the hardware architecture; we will refer to this number as attribute P from now on. As first parameter for evaluating a parallel software architecture, we define the parallelism degree, PD_{PSA} as follows:

$$PD_{PSA} = \frac{P}{R} \cdot 100 \quad (1)$$

where R is the number of evolution rules. The range of values for PD_{PSA} belongs to $(0 - 100]$.

On the other hand, each process will be executed sequentially on its own processor. But, in case of there is less processors than processes, multiprogramming technique gets concurrency of several processes assigned to a same processor but it does not get real parallelism. However "while the general motivation for demand-driven concurrency is laudable, the implementations [...] may not produce optimal results. To understand why, we must consider the subtleties of process creation and scheduling" [6]. Consequently, in multiprogramming cases, it is required a computational overload of the operating system to manage processes. Process management costs, $\Delta_{PM}(N, P)$, is increased when the number of processes, N , increase keeping the same number of processors, P . Hence,

$$\Delta_{PM}(N_a, P) < \Delta_{PM}(N_b, P) \Leftrightarrow N_a < N_b \quad (2)$$

Moreover, concurrent and/or parallel processes interrelate between each other by two types of behaviour: cooperating and/or competing. These relationships require synchronization and communication interactions between processes. At the end, these interactions become conditional and barrier synchronizations and mutual exclusions when there are shared resources. These interactions fall into a new computational overload. In particular, costs of conditional synchronization, $\Delta_{CS}(N)$, and barrier synchronization, $\Delta_{BS}(N)$, are linear dependent on the number of processes while costs of mutual exclusion $\Delta_{ME}(N)$

do not depend on the number of processes. Therefore, we get following equations:

$$\Delta_{CS}(N_a) = k \cdot \Delta_{CS}(N_b) \text{ where } N_a = k \cdot N_b \quad (3)$$

$$\Delta_{BS}(N_a) = k \cdot \Delta_{BS}(N_b) \text{ where } N_a = k \cdot N_b \quad (4)$$

Then, our second evaluation parameter for the parallel software architecture is defined as computational overload, $\Delta_{PSA}(N, P)$, being N the number of processes and P the number of processors, this parameter is expressed by.

$$\Delta_{PSA}(N, P) = \Delta_{PM}(N, P) + \Delta_{CS}(N) + \Delta_{ME}(N) + \Delta_{BS}(N) \quad (5)$$

Let C be the sequential execution cost of a P system on a monoprocessor hardware architecture. Then it could be define the performance of a parallel software architecture with N processes on a hardware architecture with P processors by the following equation:

$$\frac{C + \Delta_{PSA}(N, P)}{P} \quad (6)$$

Next three sections are devoted to the analysis of evaluation parameters over the three parallel software architectures mentioned above.

3 PSA Evolution Rules Oriented

First architecture establish one process per evolution rule of the P system. Therefore, the number of processes is R and each one of them is responsible for applying one evolution rule over the multiset of its membrane. So, parallelism is given when each one of the R processes progresses over the membrane multiset.

This parallel software architecture reaches a parallelism degree equal to 100% when $P = R$. But when $P < R$, it does not exists a total parallelism because, necessary, it is made use of multiprogramming techniques. Thereby, its parallelism degree decays to $P/R \times 100$ %. Moreover, computational costs of the P system evolution is overloaded by multiprogramming of R processes over the P processors, that we will refer as $\Delta_{PM}(R, P)$. If $P \ll R$, this overload degrades the system because of $\Delta_{PM}(R, P) \rightarrow \infty$ as these architectures "do not bound concurrency are a risk in an environment that presents a heavy load. Concurrency can increase until operating system

becomes swamped with processes" [6].

On the other hand, algorithms for evolution rules application over a membrane multiset gathered in literature [2] always answer to the same scheme: "Since many rules are executing concurrently and they are sharing resources, a mutual exclusion algorithm is necessary to ensure integrity" [3]. So, "when more than one rule can be applied in the same conditions, the simulator randomly picks one among the candidates" [2]. Therefore, processes include pre-protocols and post-protocols for critical sections of their code that necessary must work under mutual exclusion. We will refer to this overloaded computational cost as $\Delta_{ME}(R)$.

At this point, it has to be highlighted one aspect of synchronization between processes that is determinant for the parallelism degree of this architecture: granularity of critical sections referred above. Thus, we have coarse-grained critical sections when majority of the process of evolution rule application over its multiset is located in a critical section and fined-grained critical sections otherwise.

For the case of coarse-grained critical sections, concurrent execution of subsets of processes of rules of a same membrane offers a sequential behavior. Therefore, repercussion of coarse-grain critical sections in processes implicates in a direct way that parallelism degree is reduced to a $M/R \times 100\%$, where M is the number of membranes.

Last, we would like to highlight the following synchronization between processes and the communication phases in the P system evolution:

- A barrier synchronization that ensures that every process ends its corresponding evolution rule application before that it begins the communication of current evolution transfer.
- A conditional synchronization that ensures that every process waits to apply its evolution rule until it ends the communication phase of the previous evolution step ends.

So, it has to be considered a new computational overload that ensures these synchronizations for the R processes, that we will refer $\Delta_{CS}(R)$ and $\Delta_{BS}(R)$ respectively.

Figure 1 summarizes the parallelism degrees presented in this point for parallel software architecture

evolution rule oriented. Thus, it brings in as determinant parameters: number of processors and critical section of process granularity. Moreover, on every case, it is attached the computational added costs to the evolution of the P system.

4 PSA Membranes Oriented

In this architecture it is established one process per membrane of the P system. Therefore, the number of processes is M and each one of these processes is responsible for applying sequentially every evolution rule of a membrane over the multiset of its region. So, parallelism is reached when each one of the M processes progresses over the multiset and the evolution rules of its membrane.

This architecture is bounded by a degree of parallelism equal to $M/R \times 100\%$ when $P = M$. But, when $P < M$, it is necessary to use multiprogramming techniques, in a similar way to the architecture presented above. In similar manner, its parallelism degree decay to $P/R \times 100\%$. Moreover, computational costs of the P system evolution are overloaded with the multiprogramming of M processes over the P processors, that we will refer as $\Delta_{PM}(M, P)$. In the case of $P \ll M$, this overload degrades the system due to $\Delta_{PM}(M, P) \rightarrow \infty$.

On the other hand, sequential algorithms for the application of evolution rules does not use concurrent access to shared information because only one process applies every evolution rule over the multiset sequentially.

Finally, synchronizations between processes and communication phases in the evolution of the P system are the same than in the previous architecture: barrier synchronization respect to the communication of the current evolution step and conditional synchronization respect to the communication of previous evolution step. So, it is also necessary to consider the computational overload that ensures these synchronizations for the M processes, that we will refer as $\Delta_{CS}(M)$ and $\Delta_{BS}(M)$ respectively.

Figure 1 summarizes the parallelism degrees presented in this point of membrane oriented parallel software architecture. So, it brings in just one parameter: the number of processors. Moreover, on every case, it is attached the computational added costs to the evolution of the P system.

<u>Granularity of critical section</u>	<u>Number of Processors</u>	PD_{PSA}	Δ_{PSA}	
Parallel Software Architecture Evolution Rules Oriented				
<u>Fine Grain</u>	$P = R$	100 %	$\Delta_{CS}(R) + \Delta_{ME}(R) + \Delta_{BS}(R)$	$\Delta_{PM}(R,P) \rightarrow 0$ (A)
	$P < R$	$P / R \times 100$ %	$\Delta_{CS}(R) + \Delta_{ME}(R) + \Delta_{BS}(R) + \Delta_{PM}(R,P)$	(B)
	$P \ll R$	0 %	∞	$\Delta_{PM}(R,P) \rightarrow \infty$ (C)
<u>Gross Grain</u>	$P = R$	$M / R \times 100$ %	$\Delta_{CS}(R) + \Delta_{ME}(R) + \Delta_{BS}(R)$	$\Delta_{PM}(R,P) \rightarrow 0$ (D)
	$P < R$	$\min(P,M) / R \times 100$ %	$\Delta_{CS}(R) + \Delta_{ME}(R) + \Delta_{BS}(R) + \Delta_{PM}(R,P)$	(E)
	$P \ll R$	0 %	∞	$\Delta_{PM}(R,P) \rightarrow \infty$ (F)
Parallel Software Architecture Membranes Oriented				
	$P = M$	$M / R \times 100$ %	$\Delta_{CS}(M) + \Delta_{BS}(M)$	$\Delta_{PM}(M,P) \rightarrow 0$ (G)
	$P < M$	$P / R \times 100$ %	$\Delta_{CS}(M) + \Delta_{BS}(M) + \Delta_{PM}(M,P)$	(H)
	$P \ll M$	0 %	∞	$\Delta_{PM}(M,P) \rightarrow \infty$ (I)
Parallel Software Architecture Processors Oriented				
		$P / R \times 100$ %	$\Delta_{CS}(P) + \Delta_{BS}(P)$	(J)

Figure 1: Parallel Software Architecture Analysis

5 PSA Processors Oriented

Last proposed architecture establishes a process per available processor in hardware architecture. Therefore, every one of these processors is responsible for applying sequentially every evolution rule over the multisets of a subset of membranes. These subsets of membranes assigned to processes define a wrapper over the set of membranes. Hence, parallelism is reached when each one of the P processors progresses over the multisets and the evolution rules of the membranes of each subset.

This architecture is bounded by a parallelism degree equal to $P/R \times 100$ %. On the other hand, it has to be highlighted that it does not exist computational overload for processes multiprogramming, because it exists a one to one ratio a priori established. "In fact, because a single-process implementation requires less switching between process contexts, it may be able to handle a slightly higher load than an implementation that uses multiple processes" [6]. In an analogous manner to the previous architecture, given the sequential character of the processes of evolution rules application, neither exist computational overload for the mutual exclusion.

Last, synchronizations between processes and communication phases are the same as previous architectures. So, it is also necessary to consider the computational overload that ensures these synchronizations for the P processes, that we will refer as $\Delta_{CS}(P)$ and $\Delta_{BS}(P)$ respectively.

Figure 1 summarizes the parallelisms degree presented in this point of processors oriented parallel software architecture. Moreover, on every case, it is attached the computational added costs to the evolution of the P system.

6 PSA Comparative

In this point, we show a comparative of the three parallel software architectures presented above. In order to this, it is presented a detailed study of parallel software architectures behavior respect to the different states that a P system evolution can be found. So, considering the relation of P with M and R as the determinant condition, following cases are contrasted: a) $R \leq P$; b) $M \leq P < R$; c) $P < M$. Subsequently, obtained general conclusions are presented:

- A. $R \leq P$. On evolution rules oriented architecture it is obtained the same computational overload in (A) and (D) of figure 1, but with a lesser parallelism degree with coarse-grained critical sections. This fact, lead us to avoid evolution rules oriented architecture with coarse-grained critical sections.

On the other hand, in membranes oriented and processors oriented architectures, it is obtained the same parallelism degree and computational overload in (G) and (H) of figure 1. This is due to, being $R \leq P$ and $M < R$, processors oriented

architecture makes responsible for a subset of an only one membrane to each process. Which is an analogous situation to the membrane oriented architecture.

From (3), (4) and (6) equations and (A) and (G) equations of figure 1, it is obtained the necessary condition (7) for assuring that processors oriented architecture with fined-grained critical section has better performance than membranes and processors oriented architectures.

$$C > \frac{M}{R - M} \cdot \Delta_{ME}(R) \quad (7)$$

In case (7) is not fulfilled, membranes and processors oriented architectures will give a better performance despite of their lesser parallelism degree.

- B. $M \leq P < R$. In this second case, we find same situations than the point above: the convenience of fined-grained critical sections over coarse-gross granularity in evolution rules oriented architecture. Equivalent results for membranes and processors oriented architectures have been obtained.

From (3), (4) and (6) equations and equations (B) and (G) from figure 1, it is obtained the new necessary condition (8) for assuring that processors oriented architecture with fined-grained critical sections has better performance than membranes and processors oriented architectures.

$$C > \frac{M}{P - M} \cdot (\Delta_{PM}(R, P) + \Delta_{ME}(R)) + \frac{R - P}{P - M} \cdot (\Delta_{CS}(M) + \Delta_{BS}(M)) \quad (8)$$

It occurs the same that in previous case, if (8) is not fulfilled, parallel software architectures membranes and processors oriented will give a better performance despite of their lesser parallelism degree.

- C. $P < M$. In this third case, it can be noticed that every parallel software architecture offers the same parallelism degree. But, considering that $P < M < R$ and so it is $\Delta_{CS}(P) < \Delta_{CS}(M) < \Delta_{CS}(R)$ and that $\Delta_{BS}(P) < \Delta_{BS}(M) < \Delta_{BS}(R)$, lesser computational overload is always obtained with processors

oriented architecture.

Moreover, in the most restrictive case in which $P \ll M < R$, computational overload of $\Delta_{PM}(M, P)$ and $\Delta_{PM}(R, P)$ degrade the system.

Detailed study permits us to conclude that:

- The parallel software architecture membranes oriented always has a worse behavior than processors oriented. In particular, it is observed that membrane oriented is a particular case of processors oriented architecture where the membranes subset assigned to each processor is always equal to one membrane. Therefore, flexibility of processors oriented architecture allows suiting to different conditions always balancing or improving to the other more restrictive architecture.
- In cases in which evolution rules oriented architecture is suitable, it always need parallel algorithms of rules application with fined-grained critical sections. Otherwise, it never raises as a parallel software architecture candidate.
- Most appropriate parallel software architecture for a given hardware architecture, it is not always the one with a better parallelism degree. For cases where $P > M$, it has to be fulfilled (7) or (8) conditions.
- Moreover, for these cases, for a given hardware architecture there will not be only one suitable parallel software architecture. It also depends on the number of evolution rules and membranes of the P system. Therefore, combination of a hardware architecture and a particular P system will determine the parallel software architecture suitable for its implementation.

It is important to remarks the goodness of parallelism opposite to totally sequential implementation. "In particular, one must consider the cost of concurrency as well as its benefits" [6]. So, in order to guarantee that parallelism offers better results, it must be ensured that computational overload costs is taken by a bigger number of processors and that it reduces the evolution time of the P system with respect to be taken by just one processor. Therefore, it must be fulfilled:

$$\frac{C + \Delta_{PSA}(n, P)}{P} < C \quad (9)$$

In particular, the processors oriented parallel software architecture must fulfill:

$$C > \frac{\Delta_{CS}(P) + \Delta_{BS}(P)}{P - 1} \quad (10)$$

While, the evolution rules oriented parallel software architecture must fulfill:

$$C > \frac{\Delta_{CS}(R) + \Delta_{ME}(R) + \Delta_{BS}(R) + \Delta_{PM}(R, P)}{R - 1} \quad (11)$$

7 Conclusions

In this work, we present mechanisms for evaluating parallel software architectures for the evolution of a P system over a given hardware architecture. We propose the parallelism degree and the computational overload for processes management and synchronization as evaluation parameters.

With these parameters and the appropriate set of equations based on them, we have analyzed evolution rules, membranes and processors parallel software architectures. Each one of these architectures proposes different number of processes depending and the P system. But, obtained results in this study shows that the best performance is not parallel software architecture independent, neither always offered by the higher parallelism degree.

In particular, we show that membranes oriented architecture never improves the other two studied parallel software architectures. Moreover, evolution rules oriented architecture requires the design of processes with fined-grained critical sections to offer better results than processors oriented one. Finally, we present here a set of equations establishing the conditions for determining the appropriate parallel software architecture, and the conditions for the parallelism to overcome a totally sequential implementation.

Analysis of these equations permits to conclude that the candidate parallel software architecture is dependent on the number of processors of the hardware architecture and on the P system structure.

References

[1] Gh. Păun, "Computing with Membranes", *Journal of Computer and System Sciences*, 61(2000).

- [2] G. Ciobanu, M. Pérez-Jiménez, Gh. Păun, "Applications of Membrane Computing". *Natural Computing Series*, Springer Verlag, (October, 2006).
- [3] G. Ciobanu, G. Wenyuan, "A P system running on a cluster of computers", *Proceedings of Membrane Computing. International Workshop*, Tarragona (Spain). *Lecture Notes in Computer Science*, vol 2933, Springer Verlag (2004), 123-150.
- [4] A. Syropoulos, E.G. Mamatas, P.C. Allilomes, K.T. Sotiriades, "A distributed simulation of P systems". *Preproceedings of the Workshop on Membrane Computing* (A.Alhazov, C.Martin-Vide and Gh.Paun, eds); Tarragona, vol July 17-22 (2003), 455-460.
- [5] J.A. Tejedor, G. Bravo, L. Fernández, F. Arroyo, "An Architecture for Attacking the Bottleneck Communication in P System". *AROB 12th. International Symposium on Artificial Life and Robotics*, Oita (january, 2006) (accepted).
- [6] D.E. Cormer, D.L. Stevens, "Internet networking with TCP/IP. Vol 3". *Prentice Hall, International Editions* (1993).

An Architecture for Attacking the Bottleneck Communication in P Systems

J. A. Tejedor
Natural Computing Group
Universidad Politécnica de Madrid
Madrid, Spain

L. Fernández
Natural Computing Group
Universidad Politécnica de Madrid
Madrid, Spain

F. Arroyo
Natural Computing Group
Universidad Politécnica de Madrid
Madrid, Spain

G. Bravo
Natural Computing Group
Universidad Politécnica de Madrid
Madrid, Spain

Abstract

The distributed implementation of P system on a cluster of processors has met with the bottleneck communications problem. When the number of membranes grows in the system, the network gets congested and the times to execute an evolution step degrades.

In this paper, we suggest a software architecture denominated “partially parallel evolution with partially parallel” communication where some membranes are located in each processor, proxys are used to communicate with membranes located in different processors and a policy of access control to the network communications is mandatory. With all this, we get a certain parallelism in the system and an acceptable functioning in the communications. In addition to this, it establishes a series of equations that allows us to determine in the architecture the optimum number of processors needed, the required time to execute an evolution step, the number of membranes to be located in each processor and the conditions to determine when it is best to use the distributed solution or the sequential one.

keywords: architecture, bottleneck, communication, P systems

1 Introduction

The transition P systems were presented by Gheorghe Păun in 1998 [1] who based his work on basic features of biological membranes. A membrane defines a region where a series of chemical elements (multisets)

may experience a series of chemical reactions (evolution rules) and produce other elements. Inside the region limited by a membrane may be, at the same time, other membranes creating a complex hierarchical structure that may be represented by a tree. The products generated by the chemical reactions may stay in the same region or travel to the container region or to the regions contained by a membrane. As a result of such reaction, a membrane may dissolve itself (its chemical elements transfer to the container membrane) or inhibit itself (the membrane becomes impermeable and does not allow any object to pass).

The membranes systems are dynamic as the chemical reactions produce elements that cross the frontiers of the membranes to travel to other regions in order to produce new reactions. This dynamic behaviour can be sequenced in a series of evolution steps between one and another configuration system that will be determined by the membrane structure and multisets present inside membranes. In the transition P systems formal model two phases are distinguished in each evolution step: rules application and communication. In the rules application phase inside each membrane its rules are applied to the multisets in parallel. Once the previously described phase has concluded, the communication phase begins and the generated multisets travel towards the target membranes. These systems perform a computation through transition between two consecutive configurations, transforming into computational device with the same capacities that Turing machines.

The power of this computation model lies in the fact that the process is massively parallel in the rules application phase as well as in the objects communication phase. The challenge for the researchers is

to get hardware or software implementations of P systems with a high parallelism degree.

A natural and intuitive implementation of P systems in electronic devices is carried out based on the following:

1. To locate in each processor a membrane where the evolution rules are applied parallelly on their multiset.
2. To carry out the communication between 2 membranes (2 processors) using 4 interfaces and 2 communications buses. The data travel in each direction (father-son or son-father) using a communication interface in the outgoing processor and another one in the incoming processor that are connected by a data bus.

The main problem of this implementation model is that it is unfeasible. Nowadays technologies do not allow for a processor to have as many communication interfaces as membranes are connected to it.

The aim of this work is to establish a communications architecture that will adapt to the special features of P systems. For this, it is structured in the following way: in the first place, the related works are enumerated analyzing the proposed architectures, next a communication architecture model is introduced stating its economical and computational cost as well as its viability, to continue with a more detailed analysis of the model, to end describing the conclusions obtained.

2 Related Works

The implementation of P system in digital hardware device is being carried out from the point of view of Hardware as well as Software. Most of the solutions have been focused, mainly, in the first phase of the P system evolution describing digital circuits or software architectures/designs that have allowed the application of the defined evolution rules inside the membranes. The phase of multisets membranes communication has not been contemplated or it has simply been performed by shared memory, except Syropoulos [2] and Ciobanu [3] that in their distributed implementations of P systems use Java Remote Method Invocation (RMI) and the Message Passing Interface (MPI) respectively, on a cluster of PC connected by Ethernet. These last authors do not

carry out a detailed analysis of the importance of the time used during communication phase in the total time of P system evolution, although Ciobanu affirms that "the response time of the program has been acceptable. There are however executions that could take a rather long time due to unexpected network congestion" [3].

A model of impementacion of P system simplifying and generalizing the ideas of the works of Syropoulos and Ciobanu would be the following one:

1. In each processor a membrane is located where its rules will be applied. A processor can be a digital circuit implemented by Field-Programmable Gate Arrays (FPGAs), a microcontroller or a microprocessor.
2. All processors are connected to a common bus through a communication interface governed by a protocol.

In this model, all the membranes apply its rules in parallel for later communicating among them. Due to the fact that the communication line is common to all of them, at a particular time there will only be a membrane or processor communicating. Then, the communication becomes sequentially. The problem is more complex as Ciobanu advices [3], because if no special measures are taken, there may be more than one processor trying to communicate at a particular time and collisions will produce that will delay the whole communication process.

Assuming that no collisions happen in the network and taking into consideration that the information transfer between 2 membranes is made in both directions (father-son/son-father), the total number of communications made up during a transition step is $2(M - 1)$. Therefore, the total time to perform the evolution step is:

$$T = T_{apl} + 2(M - 1)T_{com} \quad (1)$$

where M is the number of membranes of the P system, T_{apl} is the maximum time used by the slowest membrane in applying its rules in the whole system and T_{com} is the maximum value of all times of communication between 2 nodes. Meaning that the time T is linear dependent on the number of membranes that the P system has.

The system throughput (processors and communications) can be expressed in accordance with the following:

$$Th_{evo} = \frac{T_{apl}}{T_{apl} + 2(M - 1)T_{com}} \quad (2)$$

$$Th_{com} = \frac{2(M - 1)T_{com}}{T_{apl} + 2(M - 1)T_{com}} \quad (3)$$

So if the number of membranes grows, the processors throughput will approach zero, while the communications will practically be working 100% of the time.

Considering the system costs, this model is expensive because it needs as many processors and communication interfaces as membranes in the system:

$$C = MC_{pro} + MC_{com} \quad (4)$$

The analysis of this model makes us reach the following conclusions:

- The time used in a step of P system evolution is huge and it grows lineally with the number of membranes.
- The system cost is very high with the processors throughput practically nil.
- Considering that T_{apl} is normally smaller than T_{com} , it complies with:

$$MT_{apl} < T_{apl} + 2(M - 1)T_{com} \quad (5)$$

The time used in a step of P system evolution is worse than the one obtained using a single processor. Consequently, it is useless to choose this software architecture for the P systems implementation.

Therefore, it is necessary to carry out a study of the communications problem in a processors distributed architecture in order to determine the viability implementation of a P system.

3 Partially parallel evolution with partially parallel communication Model

The communication model that is being introduced in this section allows a certain parallelism degree in the rules application phase, as well as in a P system communication phase. In this way, the system cost decreases and the acceptable time used in a P system evolution step is obtained. In short, this new model is denominated “partially parallel evolution with partially parallel communication” and it is based on the following:

1. **Membranes Distribution:** In each processor, K membranes are located that will evolve, at worst, sequentially. The value of K is determined by the relation between the number of membranes M and processors P , where $K \geq 1$.

The benefit obtained is that the number of the external communications decreases. The total number of communications splits in two classes: a group of internal communications for pairs of membranes located in the same processor and another group of external communications to interchange information among pairs of membranes located in different processors. Therefore, the number of external communications against the previous model will always be smaller. Moreover, this is an important fact because the run time to carry out the internal communications will be negligible.

For example, the 22 external communications performed by an architecture with a membrane located in each processor (Figure 1) have been reduced to 10 in the architecture that has located 3 membranes in 4 processors (Figure 2).

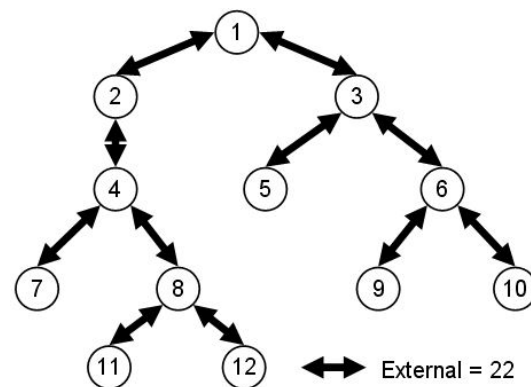


Figure 1: P system communications

2. **Proxy for processor:** When a membrane wants to communicate with another one located at a different processor, the first one uses a proxy (programs or device located in the processor that carries out an action in representation of another), instead of doing it directly. Therefore, the communications that use the common line (external communications to the processor) are carried out between proxys, not between membranes. This intermediate element located between the bus and the membranes concentrates the information in two stages:

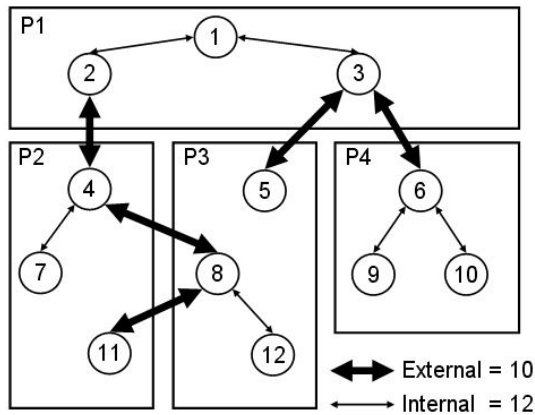


Figure 2: Communications with membranes distribution

- (a) N multisets of N membranes located in a processor that has a common father membrane in another processor, becoming integrated in a single multiset that is the one that will be sent.
- (b) The S communication packet of L length necessary to communicate between S pairs of membranes located in 2 different processors are reduced to one single packet of $S.L$ length.

The benefit of using proxys in the communication among membranes against direct communication is double:

- (a) Due to the first stage previously described, the amount of information sent is smaller. This is produced by the fact that the N packet necessary to communicate N membranes with the same father, are transformed into a single packet of the length of a single multiset.
- (b) Due to the second stage, the number of external communications is smaller although packets are bigger. But, considering that the communication protocols penalize the transmission of small packets because to the data encapsulated processes and to the time safety intervals between future transmission, it is better to send one packet of length equal $S.L$ than S packets of length equal L .

Figure 3 shows that if proxys are introduced in the processors, then the number of external communications are reduced to 8.

3. **Tree topology of processors:** In graph theory it is established that $P - 1$ connections is the minimum number required to interconnect a connected graph of P processors. This restriction imposes on the graph a tree topology. The ben-

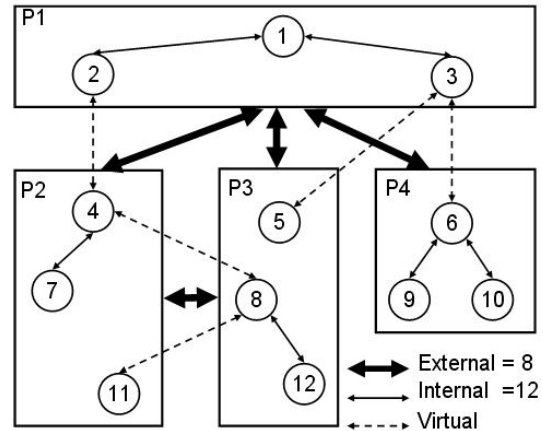


Figure 3: Communications with a proxy for processor

efit obtained with the tree topology of processor is that it minimizes the total number of external communications made as the proxys interchange information only with its direct predecessor and its direct successors, and therefore the total number of external communications in each evolution step is $2(P - 1)$.

Figure 4 shows that external communications are reduced to 6 when a tree topology of processors is used to connect them.

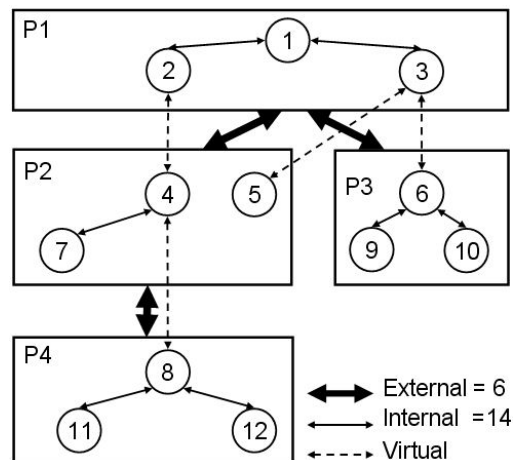


Figure 4: Communications using a tree topology

4. **Token passing in the communication:** No proxy can start a communication until it is invited to do it by means of token passing. This token travels through a depth first search sequence in the topology of processors tree. In this way, when a X proxy receives a communication from its father proxy acquires the token and then sends information to its first child proxy (C1) passing the token and keeps waiting. When C1 sends information in answer to X, the later acquires the token again and sends information to its second son proxy (C2) passing the token and keeps waiting, and so on until all father-childrens communications have been carried out. Finally, X proxy sends its answer to its father returning the token. The whole process starts with the root proxy of processors hierarchy.

This communication policy prevents that more than one proxy are trying to transmit information at the same time. Therefore, there are no collisions and no congestion in the line. Figure 5 shows the communication sequence of the four processors proposed in the sample.

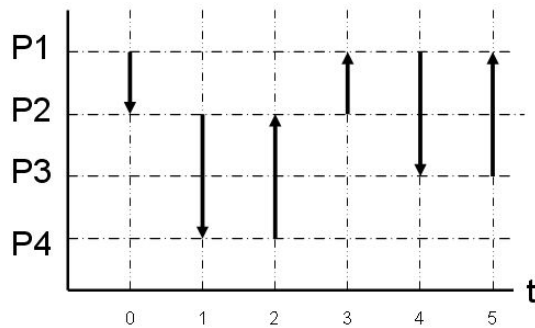


Figure 5: Communication sequence

4 Detailed analysis of the partially parallel evolution with partially parallel communication model

In this software architecture K membranes have been located in each processor. At the worst, the application of the rules in each one of these membranes will be made sequentially in each processor. Therefore, the run time to carry out the application of the rules of M membranes will be:

$$KT_{apl}$$

Due to the establishment of tree topology of processors, the number of external communications in each evolution step of the P system will be:

$$2(P - 1)$$

Therefore, the required time to perform a complete evolution step will be:

$$T = KT_{apl} + 2(P - 1)T_{com_pro} \quad (6)$$

Being T_{com_pro} the maximum time required to communicate 2 proxys using the common bus. T_{com_pro} value will depend on the topology of P system and also the distribution that has been made of M membranes in P processors. In the most favourable case, when a unique membrane located in a processor has to communicate with a unique membrane located in another processor, T_{com_pro} is similar to T_{com} . The worst case takes place when K membranes located in a processor send information to other K membranes located in a different processor. However, keeping in mind that the protocol penalizes the short packets (there is not much difference sending 10 or 10000bytes through TCP/IP according to the experimental data obtained), that the encapsulation processes take its time and that the information can be compressed before sending it, we can assume that T_{com_pro} is similar to the product of a constant by T_{com} , being this constant much smaller than K when K is big. Therefore,

$$T_{com_pro} = cT_{com} \text{ where } c \geq 1 \ll K \quad (7)$$

Once it is known the required time to perform an evolution step, we can determine the number of membranes that should be located in each processor in order to minimize the time:

$$K_{opt} = \left\lceil \sqrt{\frac{2cMT_{com}}{T_{apl}}} \right\rceil \text{ where } 1 \leq K_{opt} \leq M \quad (8)$$

This K_{opt} value allows to calculate the number of processors necessary to run the P system minimizing the necessary time to carry out an evolution step.

$$P_{opt} = \left\lceil \sqrt{\frac{M \cdot T_{apl}}{2cT_{com}}} \right\rceil \text{ where } 1 \leq P_{opt} \leq M \quad (9)$$

From the values K_{opt} and P_{opt} the minimum time required to perform an evolution step is:

$$T_{min} = 2\sqrt{2cMT_{apl}T_{com}} - 2cT_{com} \quad (10)$$

Therefore, the system evolution time is obtained by adding twice the square root of the result of multiplying the number of membranes M by T_{apl} and by T_{com} .

The processors and the communications throughput is calculated as follows:

$$Th_{pro} = \frac{\sqrt{2cMT_{apl}T_{com}}}{2\sqrt{2cMT_{apl}T_{com}} - 2cT_{com}} \quad (11)$$

$$Th_{com} = \frac{\sqrt{2cMT_{apl}T_{com}} - 2cT_{com}}{2\sqrt{2cMT_{apl}T_{com}} - 2cT_{com}} \quad (12)$$

If we disregard the $2cT_{com}$ term, the value got in both cases is 0.5, therefore, a more balanced system has been obtained (50% working the processors, 50% working the communications) than the one obtained with the other software architectures.

With regards to the cost of this architecture, we can assure that it is moderate against the other architectures proposed, as P processors are needed with P communication interfaces and the value of P is around the square root of the number of membranes M .

$$C = PC_{pro} + PC_{com} \quad (13)$$

About the main factors that influence in the time used in a step of P system evolution in this software architecture (T_{apl} and T_{com}) we really can influence only on the first one in order to improve this time. The software engineers can make that the K membranes of a processor apply faster the evolution rules, thus developing faster sequential or parallel algorithms. Nevertheless, it is difficult to get faster communicate among processors as it is necessary to invest many resources that are only within reach of the telecommunications industry. If it is possible to make that T_{apl} be N faster times the values of K_{opt} , T_{opt} and T_{min} will be:

$$K_{opt} = \left\lceil \sqrt{\frac{2cMNT_{com}}{T_{apl}}} \right\rceil \text{ where } 1 \leq K \leq M \quad (14)$$

$$P_{opt} = \left\lceil \sqrt{\frac{M \cdot T_{apl}}{2cNT_{com}}} \right\rceil \text{ where } 1 \leq P \leq M \quad (15)$$

$$T_{min} = 2\sqrt{\frac{2cMT_{apl}T_{com}}{N}} - 2cT_{com} \quad (16)$$

Therefore, the number of membranes that would be runned in a processor would be multiplied by \sqrt{N} , the number of required processors would be divided by the same factor and the time required to perform

an evolution step would improve approximately with the same factor \sqrt{N} .

Finally it is important to know, when a distributed architecture is better than a momoprocessor architecture to perform a computation. Therefore we will have to determine under which conditions the following is fulfilled:

$$2\sqrt{2cMT_{apl}T_{com}} - 2cT_{com} < MT_{apl} \quad (17)$$

Then, the several processors solution is better when:

$$M > \frac{2cT_{com}}{T_{apl}} \quad (18)$$

5 Conclusions

In this paper a communications architecture to implement P system has been introduced. This architecture is based on the location of several membranes in the same processors, the use of proxys for communicating processors placed in a tree topology and token passing in the communication. This solution avoids communication collisions, reduces the number and length of the external communications. All this, allows to obtain a better step evolution time than in other suggested architectures congested quickly by the network collisions when the number of membranes grows. Also, our architecture is highly scaleable with moderate costs.

References

- [1] Gh. Păun (2000), "Computing with membranes", Journal of Computer and System Sciences, 61, 1, 108-143
- [2] A. Syropoulos, E.G. Mamatas, P.C. Allilomes et al (2003), "A distributed simulation of P systems", A. Alhazov, C. Martin-Vide and Gh. Păun (Editors): Preproceedings of the Workshop on Membrane Computing; Tarragona, July 17-22, 455-460
- [3] G.Ciobanu, W.Guo (2004), "P Systems Running on a Cluster of Computers". Workshop on Membrane Computing (Gh. Păun, G. Rozenberg, A. Salomaa Eds.), LNCS 2933, Springer, 123-139.

Dynamics of an abstract chemical system with few molecular

Yasuhiro Suzuki

Department of Complex Systems Science
School of Information Science, Nagoya University
Furocho Chikusa Nagoya, 464-8603, JAPAN

Abstract

Under the mass action law of chemical reactions, the calculations of Abstract Rewriting System on Multisets can be regarded as linear maps. Therefore, in order to analyze the dynamical behaviors of the system, we use the method of analyzing linear dynamical systems. We consider the brusselator model and analyze its dynamical stability.

1 introduction

Abstract Rewriting System on Multisets (ARMS) is a class of P Systems[6]. Since in ARMS we can model a system intuitively, it has been applied in various fields, such as systems biology (modeling the signaling pathway of P53 protein in a cell[4], modeling inflammation response, etc.); bio-chemistry and the science of complexity (modeling and simulation of proto-cells which is composed of membranes, modeling proto-enzyme networks and their evolution, etc.).

ARMS is not only a model of computation based on computational algebra (rewriting systems) but also a hybrid model that connects between discrete systems and continuous systems; under the mass action law of chemistry, ARMS can be regarded as a discrete expression of the master equation[?][?], which describes chemical reactions[6]. Furthermore, if we assume the system size is large enough, we have a continuous approximation of the ARMS[6].

In this paper, we consider the ARMS under the mass action law, where calculations of ARMS can be regarded as sequences of linear maps and where, in order to analyze the system, we will use methods of linear dynamical systems[3].

2 Abstract Rewriting System on Multisets, ARMS

ARMS is a model of computation of chemical re-

actions, in which floating *molecules* can interact with each other according to given reaction rules. Technically, in ARMS a chemical solution is a finite multiset of elements denoted by symbols from a given alphabet, $A = \{a, b, \dots\}$; these elements correspond to *molecules*. Reaction rules that act on the molecules are specified in ARMS by reaction rules.

Let A be an *alphabet* (a finite set of abstract symbols). A *multiset* over a set of objects A is a mapping $M : A \mapsto \mathbf{N}$, where \mathbf{N} is the set of natural numbers, $\mathbf{N}, 0, 1, 2, \dots$. The number $M(a)$, for $a \in A$, is the *multiplicity* of object a in the multiset M . We denote by $A^\#$ the set of all multisets over A , including the empty multiset, \emptyset , defined by $\emptyset(a) = 0$ for all $a \in A$. A multiset $M : A \mapsto \mathbf{N}$, for $A = \{a_1, \dots, a_n\}$ is represented by the vector $w = (M(a_1) \ M(a_2) \ \dots \ M(a_n))$. The union of two multisets $M_1, M_2 : A \mapsto \mathbf{N}$ is addition of vectors w_1 and w_2 that represent the each multisets respectively. If $M_1(a) \leq M_2(a)$ for all $a \in A$, then we say that multiset M_1 is included in multiset M_2 and we write $M_1 \subseteq M_2$.

Since we consider population dynamics of molecules and a reaction rule denotes the population change in this paper, we define a *reaction rule* $u \rightarrow v, u, v \in A^\#$ is defined as a vector $r, r = -u + v$ (it cannot express catalytic reaction such as $A + C \rightarrow B + C$). In general, a reaction rule is defined as the pair of vectors, (u, v) (in general case see [?]).

A *reaction* is the addition of vectors $M \in A^\#$ and $r \in R$, and it can be defined only when $r \subseteq M$. We can define over $A^\#$ a relation: (\rightarrow) : for $M, M' \in A^\#, r \in R$ we write $M \rightarrow M'$ iff $M' = (M + r) \geq 0$.

m times of reactions from $S_0 \in A^\#$ corresponds to m times of vector addition, $S_m = S_0 + a_i r_i + a_j r_j + a_k r_k + \dots, (a_i, a_j, a_k, \dots \in \{1, 2, 3, \dots\}, a_i + a_j + a_k + \dots = m, r_i, r_j, r_k, \dots \in R) = S_0 + \sum_{i=1}^m r_j, m = 1, 2, 3, \dots, r_j \in R$.

Definition (cycle) The sequence of reactions such

that $S_{i+m} = S_i + \sum_{j=1}^m r_j$, $m \geq 2$ is called cycle and m is the period.

Definition (Rule Matrix) The rule matrix A is composed of the transpose of all rule vectors. For example, the rule matrix of the rule vectors of $\{(-1 \ 1), (1 \ -1)\}$ is

$$A = \begin{pmatrix} -1 & 1 \\ 1 & -1 \end{pmatrix} .$$

3 Theoretical Remark on ARMS

Remark

If the rules of R of an ARMS are linearly independent, there are no cycles in any sequence of reactions.

proof: If the rules of an ARMS r_1, r_2, \dots, r_n are linearly independent, there does not exist any sequence of reactions such that $S_{i+m} = S_i + \sum_{j=1}^m r_j$, $m \geq 2$. If such a sequence existed, it would require $a_i r_i + a_j r_j + a_k r_k + \dots = 0$, but since we assumed that the rule vectors are linearly independent, it is satisfied only when $a_i = a_j = a_k = \dots = 0$.

This remark also claims that if sub sets of rule vectors are not linearly independent, there can exist cycles in the sequence of reaction. ¹

It is noted that even if a set of reaction rules are linearly independent, there can exist cycles in its subspace. The rule vector

$$\begin{pmatrix} a \\ b \\ c \end{pmatrix} \equiv \begin{pmatrix} -3 \\ -1 \\ 1 \end{pmatrix}, \begin{pmatrix} 5 \\ 1 \\ -1 \end{pmatrix}, \quad (1)$$

are linearly independent, but since the subspace of b and c is not linearly independent, there can exist cyclic reaction sequences in the $b - c$ space so that the trajectory of reaction sequences will spiral in the $a - b - c$ space.

4 Analysis of the dynamics of Brusselator

The brusselator model is a mathematical model of an autocatalytic, oscillating chemical reaction, known

¹ $rank(R)$ illustrates the ARMS may have cycles or not in its sequences of reactions

as the Belousov Zhabotinsky reaction (BZ reaction)[2]. The brusselator model is given by:

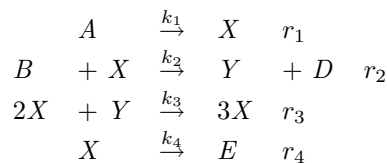


Figure 1: Brusselator

where A and B are input and are continuously supplied to or richly exist in the system. Since we are interested in the behavior of the number of X and Y , we will use the two-dimensional rule vector $\mathbf{x}=(x \ y)$ where:

$$\mathbf{r}_1 = (1, 0), \mathbf{r}_2 = (-1, 1), \mathbf{r}_3 = (1, -1), \mathbf{r}_4 = (-1, 0), \quad (2)$$

respectively. Although there are some of simulation based works on this model by using various models, basically they follow:

$$\begin{array}{l} x_{n+1} = 1 + \frac{ax_n^2 y_n}{C} - 1 + \frac{bx_n}{C} - 1 + \frac{x_n}{C} - 1 \\ y_{n+1} = 0 + \frac{ax_n^2 y_n}{C} - 1 + \frac{bx_n}{C} + 1 + \frac{x_n}{C} - 0 \end{array} .$$

where C is a constant for normalization and defined by $ax^x y_n + bx_n + x_n = C$. For simplicity, we assume that k_1 and k_4 are equal to 1, $k_2 = b$ and $k_3 = b$. The molecules A and B are assumed to be in large excess so that their concentrations do not change with time. Furthermore, in analyzing dynamics we ignore the constant C (we can ignore it without loss of generality).

Equilibria

Since $(1 \ 0) + (1 \ 1) + (-1 \ 1) + (-1 \ 0) = (0 \ 0)$ when $ax^2 y = bx = x = 1$, obviously these rule vectors are not linearly independent and there can exist cyclic reaction sequences. It is apparent that $ax^2 y = bx = x = 1$ is satisfied only when $(x, y) = (1, \frac{b}{a})$, so this is the only equilibrium of the system.

Stability

Since $X, Y \in A^\#$, by calculating partial difference we obtain the Jacobian of the system:

$$Jf(x, y) = \begin{pmatrix} -b\epsilon - \epsilon + 2axy\epsilon + aye^2 & ax^2 y \\ b\epsilon - 2ax\epsilon - ay\epsilon^2 & -ax^2 \epsilon \end{pmatrix}, \quad (3)$$

where ϵ is given as;

$$\epsilon = \frac{([X] + [Y]) +}{[X] + [Y]}, (0 < < [X] + [Y]) \quad (4)$$

where denotes the change of concentration of $x \in X$ or $y \in Y$. While is fixed, if $[X] + [Y]$ (system size) is getting larger (macroscopic), is getting smaller in relation to the system size, on the other hand, if $[X] + [Y]$ is getting smaller (mesoscopic), the is relatively getting larger ($\epsilon > 1$). It is noted that $\epsilon \in$ the set of quotient, \mathbf{Q} .

Evaluated at $(x, y) = (1, \frac{b}{a})$,

$$Jf(1, \frac{b}{a}) = \begin{pmatrix} -b\epsilon + b\epsilon^2 & a\epsilon \\ -b\epsilon - b\epsilon^2 & -a\epsilon \end{pmatrix}. \quad (5)$$

Thus the trace, τ and determinant, \det are

$$\tau = \text{Trace } Jf(1, \frac{b}{a}) = (b - a - 1 + b\epsilon)\epsilon, \quad (6)$$

$$\det = \text{Det } Df(a, \frac{b}{a}) = a\epsilon^2, \quad (7)$$

Since $a > 0, \epsilon > 0$, this implies that $(1, \frac{b}{a})$ is not a saddle point. If $b < \frac{1}{+1}(a + 1)$, then $\tau < 0$ and the equilibrium is an attractor, while if $b > \frac{1}{+1}(a + 1)$, it is a repeller. This shows that when a system is macroscopic, its stability is close to the model of differential equations, while when the system is mesoscopic, $\frac{1}{+1}(a + 1), \epsilon \gg$ is getting smaller and the unstable region is expanding. Thus, the behavior of a system on a mesoscopic scale is likely to be destabilized by fluctuations.

5 Conclusion

On the simulation of the brusselator model, especially, on a mesoscopic scale, Vladimir[7], using the Monte-Carlo simulation on two-dimensional lattice, reported that decreasing the system size down to mesoscopic may result in the periodic kinetic oscillations becoming aperiodic and disappearing. We have also found this behavior throughout simulations by using ARMS [5]. We believe that it is the descritization that makes the system unstable. However, its physical significance is still open to discussion.

Since under the mass action law ARMS can be regarded as a linear map, we attempted to use methods of analyzing linear dynamical systems in our investigation of the stability of the system. It is a challenge to apply this method to P Systems or the reaction map systems[1] will be the subject of our future study.

Acknowledgments

The authors are grateful to prof. Yuki Sugiyama, Ryosuke Ishiwata for discussions and Julia Wilson for discussion and English corrections. This research was supported by Grants-in-Aid for Scientific Research No. 14085205.

References

- [1] L.Bianco, F. Fontana, V. Manca, P systems with reaction maps. Int. J. Found. Comput. Sci. 17(1): 27-48 (2006)
- [2] G. Nicolis and I. Prigogine, *Exploring Complexity, An Introduction*. San Francisco: Freeman and Company (1989).
- [3] H.W. Hirsch, S Smale, *Differential equations, dynamical system and linear algebra*, Academic Press, (1974).
- [4] Y Suzuki and H. Tanaka, Modeling p53 Signaling Pathways by Using Multiset Processing, Applications of Membrane Computing Springer-Verlag, Berlin, (August 2005).
- [5] Y. Suzuki and H. Tanaka. 1997. Chemical oscillation on symbolic chemical systems and its behavioral pattern, In *Proceedings of the International Conference on Complex Systems*, Nashua, NH, 21-26 Sept (1997).
- [6] Y. Suzuki, Y.Fujiwara, J.Takabayashi and H.Tanaka, Artificial Life Applications of a Class of P Systems: Abstract Rewriting System on Multisets, Multiset Processing, LNCS2235, pp299-346, Springer Verlag Berlin Heidelberg (2001).
- [7] P. Vladimir, Disappearance of oscillations in the Brusselator on the mesoscopic scale, Phys. Chem. Chem. Phys., 3, 1432-1434, (2001).

Spiking Neural P Systems with Inhibitory Axons

Rudolf FREUND Marion OSWALD
Faculty of Informatics
Vienna University of Technology
Vienna, Austria
rudi@emcc.at marion@emcc.at

Abstract

We extend the original model of spiking neural P systems by adding inhibitory axons. We show how computational completeness can already be obtained with extended spiking neural P system with inhibitory axons, and we also exhibit that finite extended spiking neural P systems with inhibitory axons characterize the regular sets. As a specific application example, we show how logical gates can be modelled with a static simple variant of (extended) spiking neural P systems with inhibitory axons.

1 Introduction

Based on the biological background of neurons sending electrical impulses (also called *spikes*) along axons to other neurons, in the area of neural computation several new models have been introduced, e.g., see [4], [6], [7]. P systems (membrane systems) have been introduced as a formal model implementing the hierarchical structure of membranes in living organisms and the biological processes in and between cells (an introduction to this field can be found in [9], for the actual state of the art in this area see [12]). Just recently, combining the ideas of P systems and spiking neurons, this led to a new variant of tissue P systems (see [3]) called spiking neural P systems, e.g., see [5], [10]. An extended version of spiking neural P systems allowing to send different informations along the axons between two neurons was investigated in [1].

In spiking neural P systems (see [5]), the contents of a neuron consists of a number of so-called spikes. The rules assigned to a cell allow us to send information to other neurons in the form of electrical impulses – spikes – which are summed up at the target cell; the application of the rules depends on the contents of the neuron. As inspired from biology, the cell sending out spikes may be “closed” for a specific

time period corresponding to the refraction period of a neuron; during this refraction period, the neuron is closed for new input and cannot get excited (“fire”) for spiking again. In [1], an extended version of this original model of spiking neural P systems was introduced based on some other observations from biology: for example, the length of the axon may cause a time delay before a spike arrives at the target; moreover, the spikes coming along different axons may cause effects of different magnitude.

Another quite natural feature found in biology and also used in the area of neural computation is that of inhibitory neurons or connections between neurons. Hence, in this paper we consider spiking neural P systems with inhibitory axons, thus extending again the model of extended spiking neural P systems by considering inhibitory axons that allow for “closing” a neuron for one step by sending a spike along such an inhibitory axon to this neuron from another one.

The rest of the paper is organized as follows: In the next section, after giving some preliminary definitions, we introduce the model of extended spiking neural P system with inhibitory axons. In Section 3, we exhibit some theoretical results for this new model of extended spiking neural P system with inhibitory axons: finite spiking neural P systems with inhibitory axons (where the number of spikes that may be stored in each neuron can be bounded) characterize the regular sets in the same way as the well-known McCulloch-Pitt networks (e.g., see [8]); without any bounds on the number of spikes in the neurons we obtain computational completeness as already shown for the other models of spiking neural P systems. As a specific application, in Section 4 we show how spiking neural P systems with inhibitory axons can be used to specify/simulate logical gates. A short summary and an outlook to future research conclude the paper.

2 Definitions

For the basic elements of formal language theory needed in the following, we refer to any monograph in this area, e.g., to [2] and [11]. We just list a few notions and notations: V^* is the free monoid generated by the alphabet V under the operation of concatenation and the empty string, denoted by λ , as unit element; for any $w \in V^*$, $|w|$ denotes the number of symbols in w (the *length* of w). \mathbb{N}_+ denotes the set of positive integers (natural numbers), \mathbb{N} is the set of non-negative integers, i.e., $\mathbb{N} = \mathbb{N}_+ \cup \{0\}$. The interval of non-negative integers between k and m is denoted by $[k..m]$. For any $k \in \mathbb{N}$, $RE(\mathbb{N}^k)$ and $REG(\mathbb{N}^k)$ denote the sets of recursively enumerable and regular subsets of \mathbb{N}^k , respectively. $REG(\{a\})$ denotes the set of regular languages over the alphabet $\{a\}$ (observe that there is a one-to-one correspondence between the sets in $REG(\{a\})$ and the sets in $REG(\mathbb{N})$).

Extended spiking neural P systems with inhibitory axons

For the motivation and the biological background of spiking neural P systems we refer the reader to [5].

An *extended spiking neural P system with inhibitory axons* is a construct

$$\Pi = (m, S, R, F)$$

where

- m is the number of *cells* (or *neurons*); the neurons are uniquely identified by a number between 1 and m (obviously, we could instead use an alphabet with m symbols to identify the neurons);
- S describes the *initial configuration* by assigning an initial value (of spikes) to each neuron;
- R is a finite set of *rules* of the form $(i, E/a^k \rightarrow P, d)$ such that $i \in [1..m]$ (specifying that this rule is assigned to cell i), $E \subseteq REG(\{a\})$ is the *checking set* (the current number of spikes in the neuron has to be from E if this rule shall be executed), $k \in \mathbb{N}$ is the “number of spikes” (the energy) consumed by this rule, P is a (possibly empty) set of *productions* of the form (l, w) where $l \in [1..m]$ (thus specifying the target cell), and $w = \bar{a}$ (we also call \bar{a} *inhibitor*) or $w \in \{a\}^*$ is the *weight* of the energy sent along the axon from neuron i to neuron l , and d is the delay.

- $F \subseteq [1..m]$ specifies the set of neurons which store the output.

Starting from the initial configuration of the system that is given by S , a *transition* from one configuration to another one now works as follows: for each neuron i , we first check whether we find an applicable rule $(i, E/a^k \rightarrow P, d)$ (i.e., the number of spikes in neuron i coincides with the regular checking set E). If this is the case and the neuron is not blocked due to the delay of a previously applied rule, then the neuron “fires”, i.e., for every production (l, w) occurring in the set P the corresponding package (l, w) is sent from i to neuron l ; if $d > 0$, then the neuron is blocked for the next d steps, i.e., it cannot apply another rule and, moreover, all inputs arriving during the next $d - 1$ steps are ignored. Now for every neuron we have to consider the following two cases:

- If in any of the packages just having arrived in a neuron we find an inhibitor \bar{a} , then neuron l is blocked for one step, i.e., no rule can be applied in neuron l and no input from other cells is taken in this step.
- On the other hand, if in the packages just having arrived in a neuron we find no inhibitor, for the other packages (l, w) with $w \in \{a\}^*$, the weight w in such package is added to the corresponding number of spikes in neuron l (provided the neuron is not closed for input).

A *computation* is a sequence of configurations starting with the initial configuration given by S . The result of a halting computation (where no neuron is blocked, no rule can be applied anymore) then can be found in the output neurons specified by F .

Note that in the system defined above, we did not introduce any delay for the packages along the axons, as e.g. done in [1]. The original version of spiking neural P systems as defined in [5] corresponds with a very restricted variant of extended spiking neural P system with inhibitory axons where we do not use inhibitors and, moreover, the number of spikes sent from a neuron i to others is always fixed and (i) either no spikes are emitted, which corresponds to the case $P = \{ \}$ in the rule $(i, E/a^k \rightarrow P)$ – such a rule is called a *forgetting rule* –, or (ii) the rule is of the form $(i, E/a^k \rightarrow \{(l, a) \mid l \in M_i\})$ for some $M_i \subseteq [1..m]$ only depending on i – such a rule is called a *spiking rule*. On the other hand, this variant can easily be extended to *spiking neural P systems with inhibitory axons* by also allowing rules of the form

$$(i, E/a^k \rightarrow \{(l, a) \mid l \in M_i\} \cup \{(l, \bar{a}) \mid l \in N_i\})$$

for some $N_i \subseteq [1..m]$ only depending on i , with $M_i \cap N_i = \{ \}$.

If we only allow the rules to be of the form $(i, E/a^k \rightarrow P)$ with $E = \{a^l\}$ for some $l \geq 1$ and with all productions (l, w) being of the form $w = a^j$ for some $j \geq 0$ or $w = \bar{a}$, then such an extended spiking neural P system with inhibitory axons is called *finite*.

3 Theoretical Results

Extended spiking neural P systems without inhibitory axons were shown to be computationally complete [1] even if not using any delay in the neurons or axons, which also proves the computational power of the systems introduced in this paper. Hence, we obtain the following result:

Theorem 1. For every set L in $RE(\mathbb{N}^k)$, we can construct an extended spiking neural P systems with inhibitory axons Π generating L .

It remains a challenging research topic for future theoretical investigations whether inhibitory axons could be used to obtain computational completeness with various restrictions thereby trading inhibitory axons for some other features like forgetting rules.

Finite extended spiking neural P systems with inhibitory axons (where we only allow the rules to be of the form $(i, E/a^k \rightarrow P)$ with $E = \{a^l\}$ for some $l \geq 1$ and with all productions (l, w) being of the form $w = a^j$ for some $j \geq 0$ or $w = \bar{a}$) can only generate regular sets, because the number of spikes to be stored in each neuron can be bounded (following the construction given in [1] for extended spiking neural P systems), i.e., we obtain the following result:

Theorem 2. Finite extended spiking neural P systems (with inhibitory axons) characterize $REG(\mathbb{N}^k)$.

4 Simulating Logical Gates

In this section we restrict ourselves to *spiking neural P systems with inhibitory axons*, i.e., all the rules are of one of the following forms:

- $(i, E/a^k \rightarrow \{ \})$; such a rule is called a *forgetting rule*;
- $(i, E/a^k \rightarrow \{(l, a) \mid l \in M_i\} \cup \{(l, \bar{a}) \mid l \in N_i\})$ for some $M_i, N_i \subseteq [1..m]$, $M_i \cap N_i = \{ \}$, only depending on i ; such a rule is called a *spiking rule*.

The restriction to these kinds of rules allows us to represent such a *spiking neural P system with inhibitory axons* by a directed graph as follows:

- the neurons are represented by the nodes of the graph;
- the spiking rules and the forgetting rules are specified in the nodes;
- for each $j \in M_i$ we draw a directed edge from i to j and mark it as *excitatory* edge;
- for each $j \in N_i$ we draw a directed edge from i to j and mark it as *inhibitory* edge.

Using spiking neural P systems with inhibitory axons, we now can easily represent (simulate) logical gates. For example, the simulation of a NAND-gate by a spiking neural P systems with inhibitory axons can be seen in Figure 1; it corresponds to a system

$$(3, \{(1, a), (2, \lambda), (3, \lambda), R, \{3\}\})$$

with R containing the rules

$$(1, \{a^2\}/a \rightarrow \{(3, \bar{a})\}), (1, \{a\}/a \rightarrow \{ \}),$$

$$(2, \{a\}/a \rightarrow \{(2, a), (3, a)\}), \text{ and}$$

$$(3, \{a\}/a \rightarrow \{(out, a)\}) - out \text{ specifies that the signal coming from neuron 3 is the output of the system, but it can be taken as input signal for another NAND-system.}$$

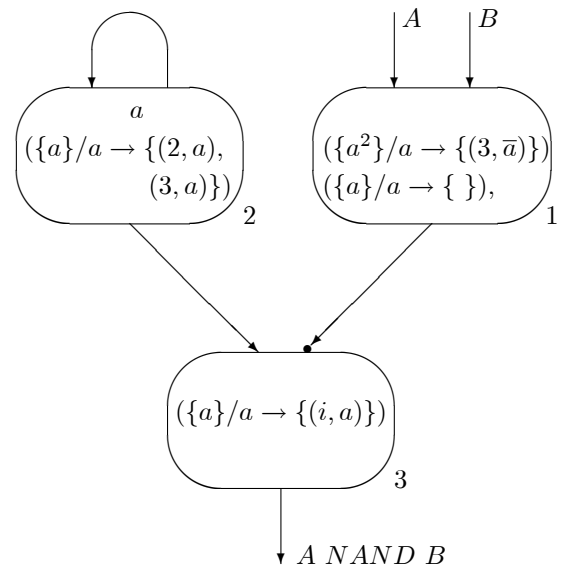


Figure 1: NAND-gate.

In each step, neuron 2 sends one spike to neuron 3. Neuron 1 has two input axons (marked by A and B).

If a spike arrives from only one of these axons, then the rule $(\{a\}/a \rightarrow \{ \})$ is executed, and the output neuron 3 spikes. Only if neuron 1 gets a spike from both its input axons, then the rule $(\{a^2\}/a \rightarrow \{(3, \bar{a})\})$ will be applied, which now inhibits neuron 3 from firing because the *inhibitory axon* (indicated by a dot at the end of the directed edge) from neuron 1 to neuron 3 is activated.

As a specific feature of the spiking neural P system with inhibitory axons described above, we can see that for every neuron j in this system, either M_j or N_j is empty.

As is well known, every boolean function can be represented by just using NAND-gates. Hence, combining such systems as described above, we can easily represent every boolean function by a corresponding spiking neural P system with inhibitory axons. In this case, the answer to an input arrives in $2k$ steps where k is the depth of the logical network of NAND-gates representing the given function. Moreover, in this case we do not consider halting computations, yet instead observe the spike train (the sequence of zeroes and ones in the output neuron) taking into account the delay of $2k$.

5 Conclusion

We have introduced the model of extended spiking neural P systems with inhibitory axons. Based on the theoretical results already proved in [1] and [5], we have exhibited that finite extended spiking neural P systems with inhibitory axons characterize the regular sets; on the other hand, already very restricted variants of extended spiking neural P systems with inhibitory axons allow us to obtain computational completeness, i.e., to characterize the recursively enumerable sets.

Spiking neural P systems with inhibitory axons can be used to specify logical gates, but they also promise to be interesting for specifying other models of computation; for example, in the future we shall also investigate the relation between extended spiking neural P systems with inhibitory axons and Petri nets.

Acknowledgements

The work of Marion Oswald is supported by FWF-project T225-N04.

References

- [1] A. Alhazov, R. Freund, M. Oswald, M. Slavkovik, Extended Spiking Neural P Systems Generating Strings and Vectors of Non-Negative Integers, in H. J. Hoogeboom, Gh. Paun, G. Rozenberg (Eds.), Pre-proceedings of the 7th Workshop on Membrane Computing WMC7, 88-101 (2006)
- [2] Dassow J, Păun Gh (1989) Regulated Rewriting in Formal Language Theory. Springer, Berlin
- [3] Martín-Vide C, Pazos J, Păun Gh, Rodríguez-Patón A (2002) A new class of symbolic abstract neural nets: Tissue P systems. In: Proceedings of COCOON 2002, Singapore, Lecture Notes in Computer Science 2387, Springer-Verlag, Berlin, 290-299
- [4] Gerstner W, Kistler W (2002) Spiking Neuron Models. Single Neurons, Populations, Plasticity. Cambridge Univ. Press
- [5] Ionescu M, Păun Gh, Yokomori T (2006) Spiking neural P systems. Fundamenta Informaticae 71, 2-3:279-308
- [6] Maass W (2002) Computing with spikes. Special Issue on Foundations of Information Processing of TELEMATIK 8, 1:32-36
- [7] Maass W, Bishop C (eds) (1999) Pulsed Neural Networks. MIT Press, Cambridge
- [8] Minsky M L (1967) Computation: Finite and Infinite Machines. Prentice Hall, Englewood Cliffs, New Jersey
- [9] Păun Gh (2002) Computing with Membranes: An Introduction. Springer, Berlin
- [10] Păun Gh, Pérez-Jiménez MJ, Rozenberg G (2006) Spike trains in spiking neural P systems, Intern J Found Computer Sci, to appear (also available at [12])
- [11] Rozenberg G, Salomaa A (eds) (1997) Handbook of Formal Languages (3 volumes). Springer, Berlin
- [12] The P Systems Web Page, <http://psystems.disco.unimib.it>

Genetic Algorithms for Buffer Size and Work Stations Capacity in Serial-Parallel Production Lines

Abu Qudeiri Jaber¹, Rizauddin Ramli² and Yamamoto Hidehiko³
Intelligent Manufacturing Systems Laboratory, Gifu University
1-1 Yanagido, Gifu Shi, 501-1193, Japan
{¹k3812203, ²k3812205}@edu.gifu-u.ac.jp, ³yam-h@gifu-u.ac.jp

Abstract

Recently, many production lines that have complicated structures such as parallel, reworks, feed-forward, etc. are widely used in high volume industries. Among them, the serial-parallel production line (S-PPL) is one of the more common production styles in many modern industries. One of the methods used for studying the S-PPL design is through genetic algorithms (GA). One of the important jobs to use GA is how to express a chromosome. In this paper, we attempt to find the nearest optimal design of an S-PPL that will maximize production efficiency by optimizing the following 3 decision variables: buffer size between each pair of work stations, machine numbers in each of the work stations; and, machine types. In order to do this we present a new GA-simulation based method to find the nearest optimal design for our proposed S-PPL. For efficient use of GA, our GA methodology is based on a technique that is called gene family arrangement method (GFAM) which arranges the genes inside individuals. An application example shows that after a number of operations based on the proposed simulator, the nearest optimal design of S-PPL can be found.

Keywords: Serial-parallel production line, buffer size, Genetic algorithms, Throughput evaluation.

1. Introduction

Production lines that have complicated structures such as parallel, reworks, feed-forward, etc. are widely used in high volume industries [1, 2]. Among them, the serial-parallel production line (S-PPL) [1, 3] is one of the more common production styles in many modern industries. S-PPL is mainly used to increase the capacity of one work station that has a lower speed than other work stations by reducing the variation of material flow speed through the overall production line. Furthermore, S-PPL also reduces the effect of machine failure during processing time. Despite many methodologies developed to study S-PPL, several researchers have described the optimization of production lines using various optimization methods, such as functional approximation and evaluation [4], knowledge-based methods [5], simulated annealing [6], heuristics algorithm [7], dynamic programming method [8], and other search methods. One of the methods used for studying the buffer size in production lines is genetic algorithms (GA) [9, 10].

Almost all researchers assumed that the machine numbers are fixed and only concentrate on finding the buffer size. In this paper, we attempt to find the nearest optimal design of an S-PPL that will maximize production efficiency by optimizing the following 3 decision variables: buffer size between each pair of work stations, machine numbers in each of the work stations; and, machine types. In order to do this we present a new GA-simulation based method to find the nearest optimal design for our proposed S-PPL. One of the important tasks in using GA is how to express a chromosome. For the efficient use of GA, our GA methodology is based on a technique that is called gene family arrangement method (GFAM) which arranges the genes inside individuals.

In evaluating the S-PPL, each work station that consists of multiple parallel machines is combined into one equivalent single machine that turns the S-PPL into a serial production line. Then, the serial production line includes equivalent machines which can be approximated by using a well known decomposition approach.

2. Problem Description

Consider a series-parallel production line with K work stations (S_1, S_2, \dots, S_K) and $K-1$ buffers. Each work station i ($i = 1, 2, \dots, K$) in the S-PPL can contain several multiple parallel machines as shown in Figure 1.

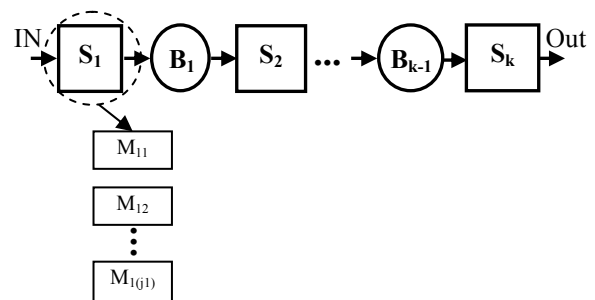


Figure1: S-PPL Model

Before formulating the problem, notations are introduced as follows.

- P the total production rate
- B $\{B_i\}$ buffer size between stations i and $i+1$
- S maximum capacity of buffer
- C $\{C_i\}$ number of parallel machines in work station i
- T $\{T_{ij}\}$ type of machine j that is located in

station i

M_{group}^a the available types of machines,

$$M_{group}^a = \{M_1^a, M_2^a, \dots, M_l^a\}.$$

The problem can be formulated mathematically as follows:

$$\text{Maximize } P(B, C, T) \quad (1)$$

$$\text{Subjected to } l \leq B \leq S \quad (2)$$

$$T_{ij} \in \{M_1^a, M_2^a, \dots, M_l^a\} \quad (3)$$

3. Throughput Evaluation of the S-PPL

In order to evaluate the S-PPL, the multiple parallel machines in each work station are combined into one equivalent single machine. In this way the S-PPL can be converted into a serial production line where each machine in the serial line is equivalent to one set of multiple parallel machines. Then, the serial production line includes equivalent machines which can be approximated by using a well known decomposition approach [11].

3.1. Replacing Each Work Station by an equivalent machine

Let us consider a work station i in the S-PPL model with machines $M_{ij}, j=1, \dots, j_l$ as shown in Figure 1. Assume that the uptime and the downtime of the aggregated machines M_{ij} are randomly variable and distributed exponentially with parameters P_i and R_i . Then, the parameters P_e and R_e for the equivalent machine can be calculated as follows.

$$P_e = S \frac{P_{11} R_{11} \sum_{i=2}^K (P_{i1} + R_{i1})}{\sum_{i=1}^K S_i R_{i1} \sum_{i=1, j \neq i}^K (P_{j1} + R_{j1})} \quad (4)$$

$$R_e = S \frac{P_{11} R_{11} \sum_{i=2}^K (P_{i1} + R_{i1})}{\sum_{i=1}^K S_i P_{i1} \sum_{i=1, j \neq i}^K (P_{j1} + R_{j1})} \quad (5)$$

Where $S = \sum_{i=1}^K S_i$

3.2. Serial Line Aggregation

Previously, no closed form expression for performance of a serial line with more than two (non-identical) machines has been available. Therefore, many approximation approaches have been used to evaluate the production line based on aggregation and decomposition. In this paper, we introduce the aggregation procedure proposed by Li [11], which modifies the machine downtime parameter to accommodate starving and blocking information. This

aggregation procedure is a good approximation and results in good accuracy. Consider a serial line with machines $(M_1^e, M_2^e, \dots, M_K^e)$ and buffer size B_l to B_{K-1} . The first two machines aggregate into a single machine M_2^f with downtime parameter r_2^f and the uptime parameter p_2^f is defined as follows.

$$r_2^f = r_2 [1 - Q(p_1, r_1, p_2, r_2, N_1)] \quad (6)$$

$$p_2^f = p_2 + r_2 Q(p_1, r_1, p_2, r_2, N_1) \quad (7)$$

Where $Q(p_1, r_1, p_2, r_2, N_1)$ is the probability that machine M_2^e is starved and is defined by [12] as follows:

$$Q(p_1, r_1, p_2, r_2, N) = \begin{cases} \frac{(1-e_1)(1-\Phi)}{1-\Phi e^{-\beta N} + r_2}, & \text{if } \frac{p_1}{r_1} \neq \frac{p_2}{r_2} \\ \frac{p_1(pp_1)(rr_1)}{(p_1+r_1)[(pp_1)(rr_1) + p_2r_1(pp_1+rr_1)N]}, & \text{if } \frac{p_1}{r_1} = \frac{p_2}{r_2} \end{cases} \quad (8)$$

$$e_i = \frac{r_i}{p_i + r_i}, i=1, 2, \quad \Phi = \frac{e_1(1-e_2)}{e_2(1-e_1)}, \quad pp_i = p_i + p_{i+1}$$

$$rr_i = r_i + r_{i+1} \text{ and } \beta = \frac{(p_1 + p_2 + r_1 + r_2)(p_1 r_2 - p_2 r_1)}{(p_1 + p_2)(r_1 + r_2)}.$$

Next, M_2^f is aggregated with M_3^e to result in M_3^f , and so on until all K machines are aggregated in a single one, M_n^f . This constitutes forward aggregation. Then, in backward aggregation, the last machine, M_K^e , is aggregated with M_{K-1}^e to result in M_{n-1}^b and so on until all machines are aggregated in a single machine, M_1^b . The procedure is repeated until convergence is satisfied. By following the aggregation procedure, the production rate can be approximated as,

$$PR(p_1, r_1, \dots, p_n, r_n, N_1, \dots, N_{n-1}) = \frac{r_n^f}{p_n^f + r_n^f} = \frac{r_1^b}{p_1^b + r_1^b} \quad (9)$$

4. Gene Family Arrangement Method

One of the important tasks in using GA is how to express a chromosome. As we described above, this research solves three different decision variables. To represent these variables, we propose GFAM as a new arrangement method which arranges the genes in each individual. Furthermore, GFAM adopts two groups of genes in each individual. The first group represents the buffer size and is located in the even positions of the individual ($G_2, G_4, \dots, G_{2k-2}, G_{2k}$), where k is the number of work stations. The second group represents the number of machines in each work station and it is located in the odd positions of the individual ($G_1, G_3, \dots, G_{2k-3}, G_{2k-1}$). Each of the items in the odd group includes a family of genes which represent the machine types in each work station; each family of genes is coded as follows.

$$G_i = \begin{bmatrix} G_{i1} \\ \vdots \\ G_{ij} \end{bmatrix} \quad \forall i = 1, 3 \dots 2k-3, 2k-1 \quad (10)$$

Where j is the number of parallel machines in work station i . The number of items in the odd and even groups is not limited, which means that any production line with any number of work stations that include any number of machines and any buffer size between each pair of work stations can be dealt with.

5. Genetic Algorithms for the Optimal Design of S-PPL

GA is a global optimization technique used for various optimization problems [9, 10]. In this paper, we present the determination of a near optimal design for an S-PPL. Since the developed GFAM is different from conventional individual expressions, the operational procedure for our GA is also different. The characteristics of the GA are described in sections 5-1 and 5-2.

5.1. Crossover

In this research, the encoding method to express each individual using GFAM is different from that obtained using conventional encoding methods. The crossover operations for our GA system operate by using two processes. The first crossover is similar to the conventional crossover method, i.e., the genes after the crossover point are swapped between two individuals. On the other hand, the second crossover method swaps the genes between two families for each of the individuals that results from the first process.

The crossover operations are generated by using the following steps:

- Step 1:** Randomly select two individuals from the current population.
- Step 2:** Randomly select a crossover point and swap the genes after that crossover point.
- Step 3:** Randomly select two items (families), $I1$ and $I2$ from the odd group in the first individual generated from step 2.
- Step 4:** Randomly select a family crossover point.
- Step 5:** Randomly select the number of genes after the family crossover point to be included in the crossover, N^f . $N^f < I1$ and $N^f < I2$.
- Step 6:** Replace the genes after the family crossover point one by one. If one of the two families reaches its last gene, continue the replacement from the first gene in the family.
- Step 7:** Repeat steps 3-7 for the second individual generated from step 2.

Figure 2 shows the crossover process graphically.

5.2. Mutation

The mutation of our GA system is different from the traditional mutation operator because the gene expression adopts GFAM. The mutation is carried out by using the following steps:

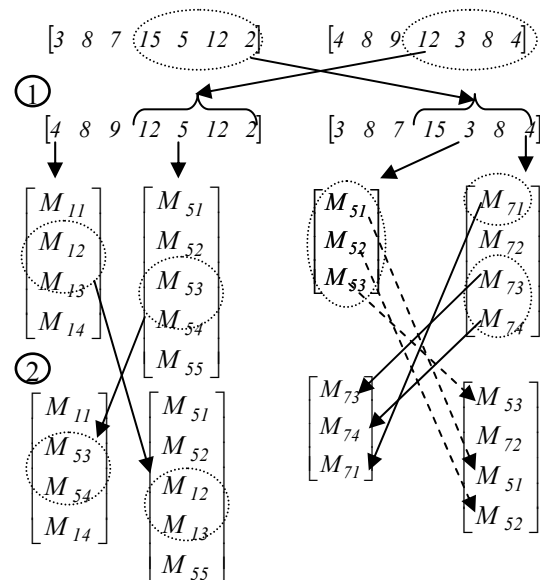


Figure 2: Crossover process

- Step 1:** Select one individual randomly from the current population.
- Step 2:** Randomly select one of the genes of a single gene type (first group).
- Step 3:** Change the value of the selected gene to a new value, which can also be selected randomly between $(1-S)$.
- Step 4:** Randomly select one gene family (Second group).
- Step 5:** Change the value of the selected gene to a new value, which can also be selected randomly between $(1-\text{the number of the selected family members})$.
- Step 6:** Randomly select one gene family, again.
- Step 7:** Randomly select one member of the selected gene family.
- Step 8:** Change the type of the selected family member to a new value, which can also be selected randomly.

5.3. Implementation of the GA

Before describing our implementation of the genetic algorithm, the following notations are defined.

Notations:

PS	Population size.
P_c	Crossover rate.
P_m	Mutation rate.
P_i	Selection probability of the individual i .
F_i	Fitness of individual i .
N	Number of individuals in the population.
D_i	Individual i in the population.

The implementation of GA is presented below.

- Step1 [Initialization]** Randomly generate an initial population.
- Step2 [Evaluation]** Evaluate the fitness for each individual in the population.
- Step3 [Selection]** Calculate the roulette selection probability P_i , $\forall i = 1, 2, \dots, N$ by using equation (11).

$$P_i \leftarrow \frac{F_j}{\sum_{k=1}^N F_k} \quad (11)$$

Step4 [Create new population] For $i \leq (P_c \times N)$, create $D_{i...i}$ using crossover operations. Set the other individuals using the roulette selection process.

Step5 [Carried out mutation] Apply mutation operations on $(P_m \times N)$ individuals.

Step6 [Keep fittest using elitist selection strategy] Randomly select one individual from the generated population. Replace the selected individual with the best individual in the current generation if it has not been selected through the roulette selection process.

Step7 [Loop]: Loop until fitness reaches its maximum value.

6. Numerical Experiments

6.1. Simulation model

The simulation model of our S-PPL was developed using C++. The uptimes and the downtimes of the machines were all assumed to be randomly variable and distributed exponentially. The model was run until the fitness (throughput) attained maximum value. In each generation the parallel machines, each work station is replaced by an equivalent machine. Then, the throughputs of the serial line of the equivalent machines are evaluated. GA operations improve the throughput until the fitness becomes constant.

6.2. Results

We applied our algorithm to an example of an S-PPL with 10 work stations. The maximum allowable number of machines to be connected in parallel is 5. The algorithm was tested by performing many trials. Figure 3 shows the (fitness) throughput versus the number of generations.

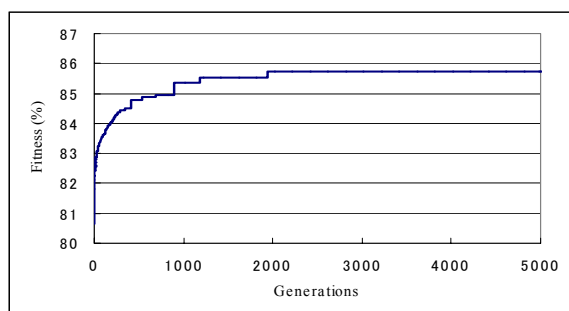


Figure 3: Best fitness curve

7. Conclusion

This study describes a new GA-simulation based method to find the nearest optimal design for a S-PPL. Instead of using buffer size as a single decision variable, this paper proposes an optimal design for the S-PPL by using three decision variables: buffer size between each pair of work stations, machine numbers inside the workstations, and machine types. The GA methodology

is based on a new technique of gene expression that is called gene family arrangement method (GFAM) which arranges the genes inside individuals. We used the new GA-simulation based method to determine some S-PPL designs. After a number of generations, the nearest optimal S-PPL could be determined. The results of this study can be used to improve S-PPL design, and production engineers can use these results when they design a new S-PPL.

References

- [1] Dallery, Y. and Gershwin, S. B., "Manufacturing Flow Line Systems: A Review of Models and Analytical Results", *Queueing Systems theory and Applications, Special Issue on Queueing Models of Manufacturing Systems*, Vol 12, No. (1-2), pp. 3-94, 1992.
- [2] Gershwin, S.B., "Manufacturing systems engineering", *Prentice-Hall*, 1993
- [3] Burman, M.H., "New Results in Flow Line Analysis", *Ph. D. Thesis, MIT, Cambridge MA*, 1995.
- [4] Enginarlar, E., Li, J., Meerkov, S. M. and Zhang, R. Q., "Buffer capacity for accommodating machine downtime in serial production lines", *International Journal of Production Research*, Vol. 40 No. 3, pp. 601-624, 2002.
- [5] Vouros, G. A., and Papadopoulos, H. T., "Buffer allocation in unreliable production lines using a knowledge based system", *Computers and Operations Research*, Vol. 25, No. 12, pp. 1055-1067, 1998.
- [6] Spinellis, D., Papadopoulos, C.T., and MacGregor, J., "Large production line optimization using simulated annealing", *International Journal of Production Research*, Vol. 38, No.3, pp. 509-541, 2000.
- [7] Papadopoulos, H.T. and Vidalis, M.I., "A heuristic algorithm for the buffer allocation in unreliable unbalanced production lines", *Computers & Industrial Engineering*, Vol. 41, No. 3, pp. 261-277, 2001.
- [8] Jafari, M. A. and Shanthikumar, J. G., "Determination of optimal buffer storage capacities and optimal allocation in multistage automatic transfer lines", *IIE Transactions*, Vol. 21, No.2, pp. 130-135, 1989.
- [9] Forrest, S., "Genetic Algorithms", *ACM Computing Surveys*, Vol. 28, No. 1, pp. 77-83, 1996.
- [10] Goldberg, D. E., "Genetic Algorithms: In Search of Optimization & Machine Learning", *Addison-Wesley*, 1989.
- [11] Jingshan Li, "Overlapping Decomposition: A System-Theoretic Method for Modeling and Analysis of Complex Production Systems", *Technical Report*, General Motors Research & Development Center, 2003.
- [12] Chiang S.Y., Kuo C.-T. and Meerkov S.M., "DT-Bottlenecks in Serial Production Line: Theory and Application", *IEEE Transactions on Robotics and Automation*, Vol. 16, pp. 567-580, 2000.

Implementation of a GA Driven Programming Training Support System

Eiji Nunohiro, Kenneth J. Mackin, Masanori Ohshiro, Kotaro Matsushita, Kazuko Yamasaki
Department of Information Systems, Tokyo University of Information Sciences
1200-2 Yatoh-cho, Wakaba-ku, Chiba 265-8501, Japan
{nunohiro, mackin, ohshiro, matsushita, yamasaki}@rsch.tuis.ac.jp

Abstract

Based on the analogy that the process for building a program is similar to configuring a puzzle, we propose a programming training method in which the user reconfigures program fragments or program puzzle pieces, and improves program structure and program flow comprehension skills. The proposed training system applies genetic algorithm (GA) to realize the problem creation feature which creates a program puzzle which best matches the user's level of comprehension. The GA process evaluates both the level of comprehension of the user and the estimated difficulty of the puzzle, to determine the target problem difficulty, i.e. the difficulty of the puzzle. With this GA feature, we developed a programming training support system which automatically creates appropriate programming training problems matching the user's comprehension level. In this paper, we first describe the features and functions of the developed puzzle style programming training support system. Next, we describe the results of implementing the developed system to a C language programming course at Tokyo University of Information Sciences. Finally, we apply statistical tests to the results of changes in the students programming skills, to show the validity of the proposed system.

key words: genetic algorithm, e-learning, programming education, T test.

1 introduction

Computer education, such as Information literacy and Programming training, has received much interest recently in a wide range of academic programs, including high schools and liberal arts undergraduate programs. In the case of early programming training, there are many topics that need to be studied together, i.e. programming language syntax, programming design methods for object oriented design, and problem

solving algorithms.

In this research we aim at creating a training support system which targets an introductory or beginner level programming user, and allows the user to develop and improve programming skills through a game-like learning process.

There has been previous research on automatic generation of programming exercises [1]. In this system proposed by Suganuma et. al., in order to modify the difficulty of the created exercise, various parameters must be modified by the administrator. On the other hand, our proposed system determines the difficulty of the exercise by evaluating the current level of the user from the user's training history, and automatically creates appropriate programming exercises matching the user's level of understanding. The programming training support system developed in this research is designed upon the similarity between the building process of a software program and a jig-saw puzzle. The proposed system trains the programming skill of the user by providing exercises in which the user must rearrange source code fragments, similar to a puzzle building task. By providing an interface to solve programming exercises much like puzzle solving, it allows users who are weak in programming to continue training through a game-like experience. In our proposed system, the difficulty of the problem is adjusted by modifying the granularity of the source code fragments, and the location of the breakpoints of the fragments or puzzle pieces. For this system, we developed an algorithm applying genetic algorithm (GA) to automatically generate exercises of appropriate difficulty that match the user's level of proficiency[2].

We used the proposed training system in a beginner level class for a C language programming course in Tokyo University of Information Sciences. We analyzed the changes in the students' programming skill in order to evaluate the validity and effectiveness of the proposed system.

2 Outline of Programming Training Support System

In order to improve programming skills, it is important to practice coding programs to fulfill a given problem specifications. But it is also important to learn to analyze a given program code to (a) understand the algorithm flow, (b) confirm that the source code correctly fulfills the requirements, and (c) suggest possible improvements in performance or maintenance. The proposed programming training support system provides a training method to improve (1) program flow analyzing skills, and (2) program structures comprehension skills. The proposed system trains these aspects by having the user reconstruct programs from program fragment pieces, much like building a puzzle by finding the right puzzle pieces. The proposed system evaluates the student's current level of progress from past training history, and automatically generates programming exercises which match the student's level of progress.

The programming exercise is automatically generated using the following 2 features.

- (a) The progress management feature calculates the student's current level of progress from the user's history of training with the system.
- (b) The puzzle creation feature generates the program puzzle exercise from a completed program source code. The puzzle creation feature can create different patterns of puzzle exercises from the same source code, so that the user can repeatedly try solving different exercises with the same correct answer. The different patterns of puzzle exercises generated are selected to be of the correct level of difficulty for the user's current level of progress. The level of difficulty of the generated puzzle is determined by the number fragments and location of break points. Genetic algorithm is applied in the algorithm to determine the number of fragments, and the location of the break points to divide the program into fragments.

Processing flow of programming training support system is described in the following.

- (1) System shows a problem to user according to the learning contents such as a syllabus of program practice or algorithm that user wishes.
- (2) User selects a problem to answer from the problem that system showed
- (3) System breaks up a program into puzzle pieces depending on user level by using genetic algorithm

to determine the location and number of separation for the program.

- (4) User reconstructs the program by selecting the correct program puzzle pieces in the correct order.
- (5) System estimates user's result, and accumulates as the user history.

The basic component of this system to achieve the above mentioned processing is shown in Fig.1.

- ① **exercise display section** indicates the problem which is proposed by system using the learning item and the user's proficiency.
- ② **puzzle generation section** breaks up a program into puzzle pieces depending on user progress level by using genetic algorithm.
- ③ **exercise selection section** selects a problem from the learning item that user wishes or user proficiency.
- ④ **program management section** manages the program used as a problem.
- ⑤ **progress display section** indicates user progress status from user proficiency.
- ⑥ **progress management section** manages user progress status.
- ⑦ **progress evaluation section** evaluates user progress from the user proficiency.
- ⑧ **result display section** indicates a result of user.
- ⑨ **answer evaluation section** estimates user's answer.

3 Programming problem creation

In this research, we created programming exercises targeted towards beginner learners. The exercise required the student to arrange program fragments or pieces in the correct order to complete the program described. In general, if the exercise given is much too difficult or too easy for the student, the exercise will not assist the learning process of the student, and may adversely affect the motivation to study the subject. Therefore, it is necessary to create program puzzle exercises of appropriate difficulty according to the level of comprehension of the student. To realize this, we considered the following method to create program puzzle exercises.

- 【step1】 Analyze the program source code by determining for each program statement, a) the control

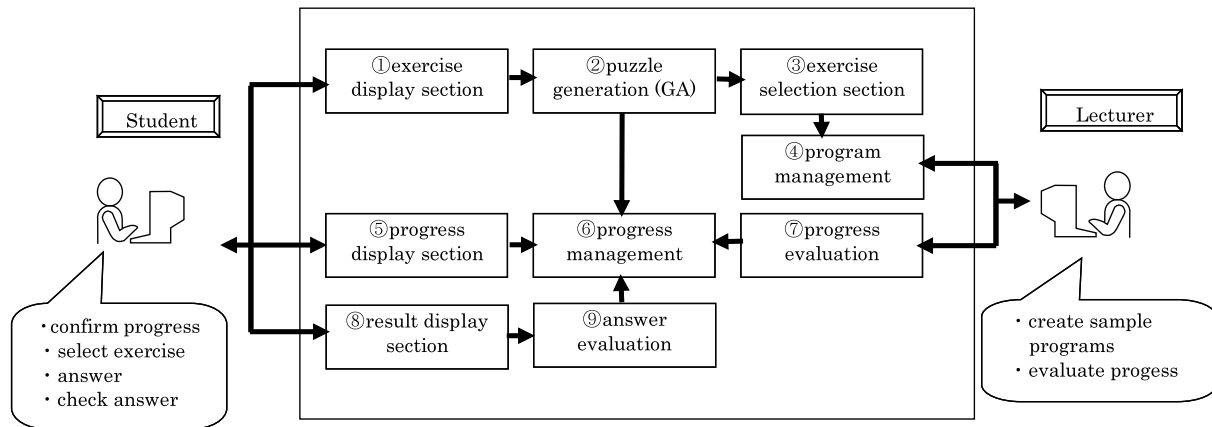


Figure 1: Configuration of programming training support system

structure depth (control information) and b) variable reference (reference information).

[step2] Calculate the difficulty level for each statement using the above control and reference information.

[step3] Apply genetic algorithm (GA) search to find the optimal combination of partition-points which best match the progress level of the user.

In the following sections, we describe the genetic algorithm search applied.

3.1 Puzzle fragment granularity

Possible granularity of program fragments or divisions are at identifier, expression, statements, or block levels. For this research we create program fragments between lines of code. Program fragment granularity at the expression level will be implemented in the future.

3.2 Source code analysis

Each line of code is analyzed for information to be used in determining the difficulty of the partition. For each line of code, the control depth, and variable reference is calculated to measure the complexity of the source code.

[step a] control information analysis

The "control depth" for each statement is calculated. The control depth is the depth of the nest of control statements, such as if, for, and while statements.

Program	Depth	Reference
1: public class EvenOrOdd {	0	0
2: public static void main(String[] args) {	1	1 (def:1, use:0)
3: int Evev = 0;	1	1 (def:1, use:0)
4: int Odd = 0;	1	1 (def:1, use:0)
5: for(int i=0 : i<=100 : i++){	1	4 (def:2, use:2)
6: if(i % 2 == 0) {	2	1 (def:0, use:1)
7: Even = Evev+1;	3	2 (def:0, use:1)
8: }else{	2	0
9: Odd = Odd+1;	3	2 (def:1, use:1)
10: }	2	0
11: }	1	0
12: System.out.println(" Number of Even : "+Evev);	1	1 (def:0, use:1)
13: System.out.println(" Number of Odd"+Odd);	1	1 (def:0, use:1)
14: }	0	0
15: }	0	0

Figure 2: Example of program

[step b] reference information analysis

The "variable reference" count for each statement is calculated. The following criteria are used to determine the variable reference for statement S:

- a variable is defined in statement S
- a variable is used in statement S

The variable reference count for a statement is the total number of times a variable is defined or used in the statement.

An example of source code analysis is shown in Fig. 2.

3.3 Relation between Program partition points and difficulty of puzzle

The program puzzle pieces are created by selecting partition points between two lines of code. The difficulty of the puzzle is dependent on the number of pieces and the location of the partition points. If a

partition occurs at a location with high control depth and high reference count, the puzzle can be assumed to have a high difficulty. From this assumption, we define the following function to evaluate the difficulty of the partition. Partition point difficulty k is the evaluated difficulty when a partition occurs after program code statement k . Partition point difficulty Ppd_k is defined as:

$$Ppd_k = control_depth * reference_count \quad (1)$$

The difficulty of the puzzle is also affected by the difficulty of the program algorithm used in the given program source code, but this degree difficulty is dependent on the prior knowledge of the individual user. For this research we let the user decide on the degree of difficulty for an algorithm.

3.4 Program partition by GA

The partition pattern (number of partitions and location of partitions) is selected using the user's progress level and puzzle difficulty. This puzzle difficulty is calculated using algorithm and language specification that is used in problem and partition difficulty which is total value of partition point difficulty for each partition point. We apply genetic algorithm (GA) to select the partition pattern.

3.5 Chromosome expression

The partition pattern expressed as a binary string is used as the chromosome in the genetic algorithm. The length of the chromosome is 1 less than the lines of code (statements) in the program. In the chromosome, the value 1 indicates a partition at that location (line), and 0 indicates no partition at that location. Fig. 3 illustrates the relationship between chromosome and partition points. In Fig. 3 an example of a 15 line program is shown, and the partition points are the locations where the chromosome value is 1, i.e. after lines 2,5,6,8,10.

3.6 Fitness evaluation

Fitness is evaluated using the user's level of progress, target problem difficulty, and difficulty of the created program puzzle. Below we describe the fitness evaluation method.

【puzzle difficulty】

Puzzle difficulty is decided by 3 factors.

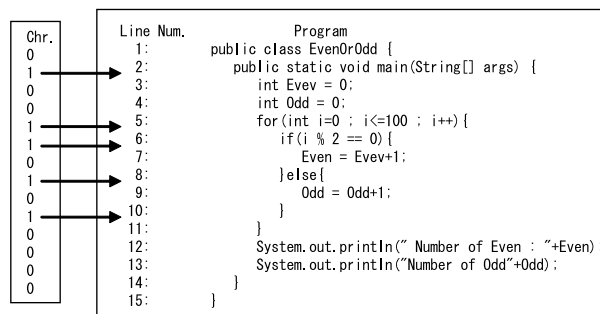


Figure 3: Example of program

- ① language specification which is being used by a program.
- ② algorithm which is used in a program.
- ③ partition difficulty for a program.

The above ① and ② are difficulty about a component of a program, and these are divided into 10 stages as following.

- * Level of language specification : $g(1 \leq g \leq 10)$
- * Level of algorithm : $a(1 \leq a \leq 10)$

The partition difficulty is the sum of the partition point difficulty value for the given program puzzle chromosome, calculated with the following equation.

$$partition\ difficulty(pd) = \sum_{k=1}^n (Ppd_k * Chr_k) \quad (2)$$

where: n is number of program, Ppd_k is the puzzle difficulty at position k , Chr_k is the value of the chromosome at position k .

Puzzle difficulty is calculated as follows using the above g , a and pd .

$$puzzle\ difficulty(d) = g * a * pd \quad (3)$$

【User's level of progress】

The user's level of progress is defined as the puzzle difficulty of the last cleared problem.

【fitness function】

The value of the degree of adaptation is to estimate whether degree of difficulty of a problem is suitable for the intelligibility of the learner, and it's calculated using the degree of fitness function.

The fitness function is defined as the following:

$$fitness = |p - d| \quad (4)$$

where : p is user's level of progress, d is the puzzle difficulty.

The chromosome with the fitness value closest to 0 is selected as the optimal program puzzle combination for the user.

4 Training Implementation and System Evaluation

4.1 Course procedure and evaluation method

The proposed system was implemented in a beginner level class for a C language programming course for 1st year students in the environmental information department curriculum at Tokyo University of Information Sciences. In the programming course, all students take a preliminary questionnaire in order to divide the course in 4 classes depending on past programming experience and knowledge. The four classes are higher level, standard level, and 2 beginner level classes. The beginner level students are divided into 2 classes which are beginner class A and beginner class B from the questionnaire taken at the beginning of the course. Fig. 4 shows the course and evaluation flow of the beginner classes. The number in the figure represents the number of 90 min lectures. The questionnaire includes short quizzes which evaluate aptitude in logical thinking, and students with higher scores were placed in the beginner class A, and students with lower scores were placed in the beginner class B. As a result, 31 students were placed in beginner A, and 24 students were placed in beginner class B. The proposed training system was applied only to the beginner class B after the first mid-term exam, and changes in the exam scores between the mid-term and end-of-term exams were compared and evaluated.

4.2 Course Content

Table 1 shows the lecture content for the beginner class. Basic programming language topics were explained through lecture, and students create simple programs applying the selected topic. The contents of the lecture were identical for both beginner class A and beginner class B, and the educational experience of the lecturers for both classes were roughly the same.

4.3 Evaluation Results

Table 2 shows the results of the mid-term exam, the end-of-term exam, and the statistical T test. From

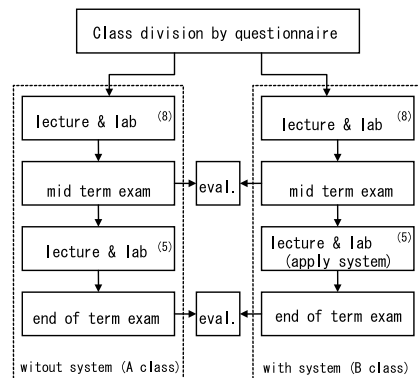


Figure 4: Course and Evaluation Flow

Table 1: Lecture content

lecture topic
- constants and variables
• I/O statements (printf, scanf)
• if statement (include nesting)
• for statement (include nesting)
• array (1 dimensional array)

the results of the mid-term exam, there was a large difference between the average scores of the 2 beginner classes, and at 5% significance level, a statistical significance was noted between beginner class A and beginner class B. From the results of the end-of-term exam, the difference in average scores between the 2 classes is much smaller, and a statistical significance was not found between beginner class A and beginner class B.

In order to collect the subjective views of the students towards the proposed system, an anonymous questionnaire (5 being the highest rating) was taken after the end-of-term exam. Table 3 shows the results

Table 2: Exam and T Test results

class		mid	end
without system beginner A	average	73.7	66.3
	standard deviation	20.3	19.6
with system beginner B	average	61.9	63.3
	standard deviation	23.0	20.3
t test of beginner A & beginner B	t value	2.02	0.56
	significance	*p<0.05	none

Table 3: Questionnaire results

question	results[%]				
	5	4	3	2	1
1. The system was effective in improving programming skill.	18.2	59.1	22.7	0.0	0.0
2. The system will be useful in future studies.	30.4	52.2	17.4	0.0	0.0

of the anonymous questionnaire.

The questionnaire also asked for free opinions regarding the system in general. For positive views, comments such as "It was fun to study using the system." and "It was easy to understand programming using the system" were received. On the other hand comments such as "The operability was poor" gave feedback on points to be considered in the future.

4.4 Discussion of Results

From the exam results in Table 2, it can be seen that the beginner class B which had much lower average scores at mid-term compared to beginner class A, had improved to similar scores by the end of term. From Table 3 showing the results of the questionnaire, 77.3% of the students marked 4 or higher to the question "The system was effective in improving programming skill". Also, 82.6% of the students marked 4 or higher to the question "The system will be useful in future studies". From the free opinion question, many positive comments such as "It was fun to study using the system" and "It was easy to understand programming using the system" were received. From these results, we conclude that the proposed training system had been effective in supporting programming education.

On the other hand, points to be considered in the future were raised through the questionnaire. There were comments on the poor operability of the system, and we feel that the man-machine interface and screen layout needs to be reconsidered for improvement.

5 Conclusion

For software programming classes and other lab based courses, there is an inherent problem of how

to address the needs of the beginner and slower learning students. Especially when the size of the class becomes larger, it becomes more difficult to supervise every student individually. The effectiveness of the training course can be improved by providing a self learning environment in which these students can study at their own paces.

In this research, we proposed a programming training support system which targeted beginner and slower learners. The system aims at improving programming skill through a game-like interface. We applied the proposed system in a C language course, and evaluated the educational effectiveness of the system. From the research results, we were able to show that this system was effective in supporting the learning of beginner and slower students. We feel that similar positive results can be expected in programming courses for students without strong mathematical background.

For future works, we plan to redesign the man-machine interface and screen layout to improve the operability of the system. We also plan to add features to enable algorithm training and object-oriented programming training, in order to expand the application area of the proposed training system.

References

- [1] AKIRA SUGANUMA, TSUNENORI MINE, TAKAYOSHI SHOUDA, Automatic Exercise Generating System That Dynamically Evaluates both Students' and Questions' Levels, IPSJ (Information Processing Society of Japan) Journal, pp.1810-1817, Vol.46 No.7 July 2005
- [2] Eiji Nunohiro, Kenneth J. Mackin, Masanori Ohshiro, Kazuko Yamasaki, Applying Genetic Algorithm to a Programming Training Support System, The eleventh International Symposium on Artificial Life and Robotics (AROB 11th '06) Program p75, Proceeding Index GS10-1, January 2006

Computer Simulation of an Augmented Automatic Choosing Control Designed by Hamiltonian and Absolute Anti-windup Measure

Toshinori Nawata

Department of Information and Computer Sciences,
Kumamoto National College of Technology,
Kumamoto, Japan. 861-1102

Hitoshi Takata

Department of Electrical and Electronics Engineering,
Faculty of Engineering, Kagoshima University,
Kagoshima, Japan. 890-0065

Abstract

In this paper we consider a nonlinear feedback control called augmented automatic choosing control (AACC) for nonlinear systems with constrained input. Constant terms which arise from sectionwise linearization of a given nonlinear system are treated as coefficients of a stable zero dynamics. Parameters included in the control are suboptimally selected by Hamiltonian and absolute anti-windup measure with the aid of the genetic algorithm.

1 Introduction

A genetic algorithm (GA) is one of evolutionary computing algorithms in engineering sciences[1]. The GA has been used to solve such complicated tasks as nonlinear global optimization problems. The purpose of this paper is to present a nonlinear feedback control called AACC (Augmented Automatic Choosing Control), which is designed by making good use of the GA.

Generally, it is easy to design the optimal control laws for linear systems, but it is not so for nonlinear systems, though they have been studied for many years[2]~[7]. One of most popular and practical nonlinear control laws is synthesized by applying a linearization method by Taylor expansion truncated at the first order and then the linear optimal control method. This is only effective in a small region around the steady state point or in almost linear systems. Controllers based on a change of coordinates in differential geometry are effective in wider region, but it is not easy to implement them to practical systems. Controllers based on Fuzzy linearization are more practical, but they usually need a lot of complicated divisions. In many physical problems of interest to the control engineer there are various constraints on the control vector. Recently many controls with constraints have been studied.

In this paper we present the AACC with constrained input using the GA for nonlinear systems and its design procedure is as follows. Assume that a system is given by a nonlinear differential equation.

Choose a separative variable, which makes up nonlinearity of the given system. The domain of the variable is divided into some subdomains. On each subdomain, the system equation is linearized by Taylor expansion around a suitable point so that a constant term is included in it. This constant term is treated as a coefficient of a stable zero dynamics. The given nonlinear system approximately makes up a set of augmented linear systems, to which the optimal linear control theory is applied to get the linear quadratic (LQ) controls. These LQ controls are smoothly united by sigmoid type automatic choosing functions to synthesize a single nonlinear feedback controller.

This controller is of a structure-specified type which has some parameters, such as the number of division of the domain, regions of the subdomains, points of Taylor expansion, and gradients of the automatic choosing function. These parameters must be selected optimally so as to be just the controller's fit. Since they lead to a nonlinear optimization problem, we are able to solve it by using the GA suboptimally. The suboptimal values of these parameters are obtained by minimizing a performance function. It is made of the Hamiltonian and an absolute anti-windup measure which is a time-derivative of quadratic function.

This approach is applied to a field excitation control problem of power system to demonstrate the splendor of the AACC. Simulation results show that the new controller enables us to improve performance remarkably well.

2 Augmented Automatic Choosing Control

Assume that a nonlinear system is given by

$$\dot{x} = f(x) + g(x)u, \quad x \in \mathbf{D} \quad (1)$$

subject to

$$u_{j,min} \leq u[j] \leq u_{j,max} \quad (j = 1, \dots, r) \quad (2)$$

where $\cdot = d/dt$, $x = [x[1], \dots, x[n]]^T$ is an n -dimensional state vector, $u = [u[1], \dots, u[r]]^T$ is an

r -dimensional control vector, $f(x) : \mathbf{D} \rightarrow R^n$ is a nonlinear vector-valued function with $f(0) = 0$ and is continuously differentiable, $g(x) : \mathbf{D} \rightarrow R^{n \times r}$ is a driving matrix with $g(0) \neq 0$ and is continuously differentiable, $\mathbf{D} \subset R^n$ is a domain, and T denotes transpose.

Considering the nonlinearity of the system (1), introduce a vector-valued function $C : \mathbf{D} \rightarrow R^L$ which defines the separative variables $\{C_j(x)\}$, where $C = [C_1 \cdots C_j \cdots C_L]^T$ is continuously differentiable. Let D be a domain of C^{-1} . For example, if $x[2]$ is the element which has the highest nonlinearity of (1), then

$$C(x) = x[2] \in D \subset R \quad (L = 1)$$

(see Section 4). The domain D is divided into some subdomains: $D = \cup_{i=0}^M D_i$, where $D_M = D - \cup_{i=0}^{M-1} D_i$ and $C^{-1}(D_0) \ni 0$. $D_i (0 \leq i \leq M)$ endowed with a lexicographic order is the Cartesian product $D_i = \prod_{j=1}^L [a_{ij}, b_{ij}]$, where $a_{ij} < b_{ij}$.

Introduce a stable zero dynamics :

$$\dot{x}[n+1] = -\sigma_i x[n+1] \quad (x[n+1](0) \simeq 1, 0 < \sigma_i < 1) \quad (3)$$

where the value of σ_i shall be selected so that $\sigma_i = -\dot{x}[n+1]/x[n+1] \leq -\dot{x}[k]/x[k]$ holds for all $k (k = 1, \dots, n)$. This tries to keep $x[n+1] \simeq 1$ for a good while when the system (1) is not on $C^{-1}(D_0)$.

Combine (1) with (3) to form an augmented system

$$\dot{\mathbf{X}} = \bar{f}(\mathbf{X}) + \bar{g}(\mathbf{X})u \quad (4)$$

where

$$\mathbf{X} = \begin{bmatrix} x \\ x[n+1] \end{bmatrix} \in \mathbf{D} \times R$$

$$\bar{f}(\mathbf{X}) = \begin{bmatrix} f(x) \\ -\sigma_i x[n+1] \end{bmatrix}, \quad \bar{g}(\mathbf{X}) = \begin{bmatrix} g(x) \\ 0 \end{bmatrix}.$$

Let a cost function be

$$J = \frac{1}{2} \int_0^\infty (\mathbf{X}^T \mathbf{Q} \mathbf{X} + u^T \mathbf{R} u) dt \quad (5)$$

where

$$\mathbf{Q} = \begin{bmatrix} Q & 0 \\ 0 & q \end{bmatrix}, \quad R \ni q > 0,$$

$Q = Q^T > 0$ and $\mathbf{R} = \mathbf{R}^T > 0$ which denote positive symmetric matrices. Values of \mathbf{Q} and \mathbf{R} are properly determined based on engineering experience.

On each D_i , the nonlinear system is linearized by the Taylor expansion truncated at the first order about a point $\hat{X}_i \in C^{-1}(D_i)$ and $\hat{X}_0 = 0$:

$$\begin{aligned} f(x) + g(x)u &\simeq A_i x + w_i + B_i u \\ &\simeq A_i x + w_i x[n+1] + B_i u \end{aligned} \quad (6)$$

where

$$\begin{aligned} A_i &= \partial f(x) / \partial x^T |_{x=\hat{X}_i}, \quad B_i = g(\hat{X}_i), \\ w_0 &= 0, \quad w_i = f(\hat{X}_i) - A_i \hat{X}_i. \end{aligned}$$

That is, an approximation of (4) is

$$\dot{\mathbf{X}} = \bar{A}_i \mathbf{X} + \bar{B}_i u \quad \text{on } C^{-1}(D_i) \times R \quad (7)$$

where

$$\bar{A}_i = \begin{bmatrix} A_i & w_i \\ 0 & -\sigma_i \end{bmatrix}, \quad \bar{B}_i = \begin{bmatrix} B_i \\ 0 \end{bmatrix}.$$

An application of the linear optimal control theory[3] to (5) and (7) yields

$$u_i(\mathbf{X}) = -\mathbf{R}^{-1} \bar{B}_i^T \mathbf{P}_i \mathbf{X} \quad (8)$$

where the $(n+1) \times (n+1)$ matrix \mathbf{P}_i satisfies the Riccati equation :

$$\mathbf{P}_i \bar{A}_i + \bar{A}_i^T \mathbf{P}_i + \mathbf{Q} - \mathbf{P}_i \bar{B}_i \mathbf{R}^{-1} \bar{B}_i^T \mathbf{P}_i = 0. \quad (9)$$

Introduce an automatic choosing function of sigmoid type:

$$I_i(x) = \prod_{j=1}^L \left\{ 1 - \frac{1}{1 + \exp(2N(C_j(x) - a_{ij}))} - \frac{1}{1 + \exp(-2N(C_j(x) - b_{ij}))} \right\} \quad (10)$$

where N is positive real value, $-\infty \leq a_{ij}$ and $b_{ij} \leq \infty$. $I_i(x)$ is analytic and almost unity on $C^{-1}(D_i)$, otherwise almost zero (see Figure 1).

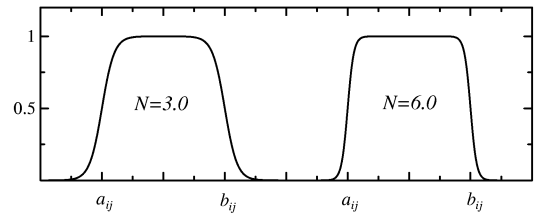


Figure 1: Automatic Choosing Function ($N=3.0, 6.0$)

Uniting $\{u_i(\mathbf{X})\}$ of (8) with $\{I_i(x)\}$ of (10) yields

$$\begin{aligned} \hat{u}(\mathbf{X}) &= [\hat{u}(\mathbf{X})[1], \dots, \hat{u}(\mathbf{X})[j], \dots, \hat{u}(\mathbf{X})[r]]^T \\ &= \sum_{i=0}^M u_i(\mathbf{X}) I_i(x). \end{aligned}$$

We finally have an augmented automatic choosing control which is satisfied with the constraint condition (2) by

$$u(\mathbf{X}) = [u(\mathbf{X})[1], \dots, u(\mathbf{X})[j], \dots, u(\mathbf{X})[r]]^T \quad (11)$$

where

$$u(\mathbf{X})[j] = \begin{cases} u_{j,max} & \text{if } \hat{u}(\mathbf{X})[j] \geq u_{j,max} \\ u_{j,min} & \text{if } \hat{u}(\mathbf{X})[j] \leq u_{j,min} \\ \hat{u}(\mathbf{X})[j] & \text{otherwise} \end{cases} \quad (1 \leq j \leq r).$$

3 Parameter Selection by GA

The Hamiltonian for Eqs.(4) and (5) is given by

$$H(\mathbf{X}, u, \lambda) = \frac{1}{2} (\mathbf{X}^T \mathbf{Q} \mathbf{X} + u^T \mathbf{R} u) + \lambda^T (\bar{f}(\mathbf{X}) + \bar{g}(\mathbf{X})u). \quad (12)$$

Assume that the adjoint vector $\lambda(\mathbf{X}) \in R^{n+1}$ is defined by

$$\lambda(\mathbf{X}) = [\lambda^I(\mathbf{X})^T, \lambda^{II}(\mathbf{X})^T]^T \quad (13)$$

where $\lambda^I(\mathbf{X}) = [\lambda[1], \dots, \lambda[r]]^T = -(G^T(x))^{-1} \mathbf{R} u(\mathbf{X})$, $\lambda^{II}(\mathbf{X}) = [\lambda[r+1], \dots, \lambda[n+1]]^T = [\mathbf{0}, E] \hat{\lambda}$,

$$\hat{\lambda} = \sum_{i=0}^M \{(\bar{B}_i - \bar{g}(\mathbf{X})) \bar{g}(\mathbf{X})^\dagger + E\}^T \mathbf{P}_i \mathbf{X} I_i(x) \in R^{n+1},$$

$\bar{g}(\mathbf{X})^\dagger \bar{g}(\mathbf{X}) = E$, E is an appropriate-dimensional unit matrix, and \dagger denotes pseudo inverse.

There are two necessary conditions of the optimality. One of them is $\partial H / \partial u = 0$ or $u = -\mathbf{R}^{-1} \bar{g}(\mathbf{X})^T \lambda = -\mathbf{R}^{-1} G^T(x) \lambda^I(\mathbf{X})$, which is satisfied with Eq.(11) from Eq.(13). By it, Eq.(12) becomes

$$H(\mathbf{X}, u, \lambda) = \frac{1}{2} \mathbf{X}^T \mathbf{Q} \mathbf{X} - \frac{1}{2} u^T \mathbf{R} u + \bar{f}^T(\mathbf{X}) \lambda. \quad (14)$$

The other one is $\dot{\lambda} = -\partial H / \partial \mathbf{X}$.

Moreover, as a measure of suppressness of output windup which might arise by constraint inputs, we consider a swiftly decreasing motion of the following quadratic function:

$$V(t) = \frac{1}{2} \|\mathbf{X}(t)\|^2 \tilde{P} = \frac{1}{2} \mathbf{X}^T(t) \tilde{P} \mathbf{X}(t)$$

where \tilde{P} is $(n+1) \times (n+1)$ matrix. That is, the measure about the movement of $V(t)$ is assumed to be described by the absolute mean of time-derivative of $V(t)$:

$$\begin{aligned} \frac{1}{2} \int |\dot{V}(t)| / \mathbf{X}^T \mathbf{X} d\mathbf{X} &= \int |\mathbf{X}^T(t) \tilde{P} \dot{\mathbf{X}}(t)| / \mathbf{X}^T \mathbf{X} d\mathbf{X} \\ &= \int |\mathbf{X}^T \tilde{P} (\bar{f}(\mathbf{X}) + \bar{g}(\mathbf{X})u)| / \mathbf{X}^T \mathbf{X} d\mathbf{X}. \end{aligned}$$

Therefore in this paper we define the performance

$$\begin{aligned} PI &= \omega_1 \int_{\mathbf{D}} |H(\mathbf{X}, u, \lambda)| / \mathbf{X}^T \mathbf{X} d\mathbf{X} \\ &+ \omega_2 \int_{\mathbf{D}} \left\| \dot{\lambda} + \partial H(\mathbf{X}, u, \lambda) / \partial \mathbf{X} \right\| / \mathbf{X}^T \mathbf{X} d\mathbf{X} \\ &+ \omega_3 \int_{\mathbf{D}} |\mathbf{X}^T \tilde{P} (\bar{f}(\mathbf{X}) + \bar{g}(\mathbf{X})u)| / \mathbf{X}^T \mathbf{X} d\mathbf{X}, \end{aligned} \quad (15)$$

where $\omega_i \geq 0 (i = 1, 2, 3)$ are weights. A set of parameters included in the control of Eq.(11) is $\bar{\Omega} = \{M, N, \hat{X}_i, a_{ij}, b_{ij}, \dots\}$ which is suboptimally selected by minimizing PI with the aid of GA[1] as follows.

<ALGORITHM>

step1:A-priori: Set values $\bar{\Omega}_{apriori}$ appropriately.

step2:Parameter: Choose a subset $\Omega \subset \bar{\Omega}$ to be improved and rewrite it by $\Omega = \{M, N, \hat{X}_i \dots\} = \{\alpha_k : k = 1, \dots, K\}$.

step3:Coding: Represent each α_k with a binary bit string of \tilde{L} bits and then arrange them into one string of $\tilde{L}K$ bits.

step4:Initialization: Randomly generate an initial population of \tilde{q} strings $\{\Omega_p : p = 1, \dots, \tilde{q}\}$.

step5:Decoding: Decode each element α_k of Ω_p by $\alpha_k = (\alpha_{k,max} - \alpha_{k,min}) A_k / (2^{\tilde{L}} - 1) + \alpha_{k,min}$ where $\alpha_{k,max}$:maximum, $\alpha_{k,min}$:minimum, and A_k :decimal value of α_k .

step6:Control: Design $u = u(\mathbf{X})_p$ ($p = 1, \dots, q$) for Ω_p by using Eq.(11).

step7:Adjoint: Make $\lambda = \lambda(\mathbf{X})_p$ ($p = 1, \dots, q$) for Ω_p by using Eq.(13).

step8:Fitness value calculation: Calculate PI_p by Eqs.(14) and (15), or fitness $F_p = -PI_p$.

Integration of PI_p is approximated by a finite sum.

step9:Reproduction: Reproduce each of individual strings with the probability of

$$F_p / \sum_{j=1}^q F_j.$$

step10:Crossover: Pick up two strings and exchange them at a crossing position by a crossover probability P_c .

step11:Mutation: Alter a bit of string (0 or 1) by a mutation probability P_m .

step12:Repetition: Repeat step5~step12 until prespecified G-th generation. If unsatisfied, go to step2.

As a result, we have a suboptimal control $u(\mathbf{X})$ for the string with the best performance over all the past generations.

4 Numerical Example

Consider a field excitation control problem of power system which is described[6][7] by

$$\tilde{M} \frac{d^2 \delta}{dt^2} + \tilde{D}(\delta) \frac{d\delta}{dt} + P_e(\delta) = P_{in}$$

$$P_e(\delta) = E_I^2 Y_{11} \cos \theta_{11} + E_I \tilde{V} Y_{12} \cos(\theta_{12} - \delta)$$

$$E_I + T'_{d0} \frac{dE'_q}{dt} = E_{fd}$$

$$E_I = E'_q + (X_d - X'_d) I_d(\delta)$$

$$I_d(\delta) = -E_I Y_{11} \sin \theta_{11} - \tilde{V} Y_{12} \sin(\theta_{12} - \delta)$$

$$\tilde{D}(\delta) = \tilde{V}^2 \left\{ \frac{T''_{d0}(X'_d - X''_d)}{(X'_d + X_e)^2} \sin^2 \delta + \frac{T''_{q0}(X_q - X''_q)}{(X_q + X_e)^2} \cos^2 \delta \right\},$$

where δ : phase angle, $\dot{\delta}$: rotor speed, \tilde{M} : inertia coefficient, $\tilde{D}(\delta)$: damping coefficient, P_{in} : mechanical input power, $P_e(\delta)$: generator output power, \tilde{V} : reference bus voltage, E_I : open circuit voltage, and E_{fd} : field excitation voltage. Put $x = [x[1], x[2], x[3]]^T = [E_I - \hat{E}_I, \delta - \hat{\delta}_0, \dot{\delta}]^T$ and $u = E_{fd} - \hat{E}_{fd}$, so that

$$\begin{bmatrix} \dot{x}[1] \\ \dot{x}[2] \\ \dot{x}[3] \end{bmatrix} = \begin{bmatrix} f_1(x) \\ f_2(x) \\ f_3(x) \end{bmatrix} + \begin{bmatrix} g_1(x) \\ 0 \\ 0 \end{bmatrix} u \quad (16)$$

where $f_1(x) = -\frac{1}{kT'_{d0}}(x[1] + \hat{E}_I) + \frac{(X_d - X'_d)\tilde{V}Y_{12}}{k}x[3] \cdot \cos(\theta_{12} - x[2] - \hat{\delta}_0)$, $f_2(x) = x[3]$, $f_3(x) = -\frac{\tilde{V}Y_{12}}{M} \cdot (x[1] + \hat{E}_I) \cos(\theta_{12} - x[2] - \hat{\delta}_0) - \frac{Y_{11} \cos \theta_{11}}{M}(x[1] + \hat{E}_I)^2 - \frac{\tilde{D}(x)}{M}x[3] + \frac{P_{in}}{M}$, $\tilde{D}(x) = \tilde{V}^2 \left\{ \frac{T''_{d0}(X'_d - X''_d)}{(X'_d + X_e)^2} \cdot \sin^2(x[2] + \hat{\delta}_0) + \frac{T''_{q0}(X_q - X''_q)}{(X_q + X_e)^2} \cos^2(x[2] + \hat{\delta}_0) \right\}$, $g_1(x) = \frac{1}{kT'_{d0}}$, $k = 1 + (X_d - X'_d)Y_{11} \sin \theta_{11}$.

Assume that the constrained input is subject to $u_{min} + \hat{E}_{fd} \leq E_{fd} \leq u_{max} + \hat{E}_{fd}$.

Parameters are $\tilde{M} = 0.016095[pu]$, $T'_{d0} = 5.09907[sec]$, $\tilde{V} = 1.0[pu]$, $P_{in} = 1.2[pu]$, $X_d = 0.875[pu]$, $X'_d = 0.422[pu]$, $Y_{11} = 1.04276[pu]$, $Y_{12} = 1.03084[pu]$, $\theta_{11} = -1.56495[pu]$, $\theta_{12} = 1.56189[pu]$, $X_e = 1.15[pu]$, $X''_d = 0.238[pu]$, $X_q = 0.6[pu]$, $X''_q = 0.3[pu]$, $T''_{d0} = 0.0299[pu]$, $T''_{q0} = 0.02616[pu]$.

Steady state values are $\hat{E}_I = 1.52243[pu]$, $\hat{\delta}_0 = 48.57^\circ$, $\dot{\hat{\delta}}_0 = 0.0[deg/sec]$, $\hat{E}_{fd} = 1.52243[pu]$. Set $\mathbf{X} = [x^T, x[4]]^T = [x[1], x[2], x[3], x[4]]^T$, $n = 3$, $\hat{X}_0 = \hat{\delta}_0 = 48.57^\circ$, $C(x) = x[2]$, $L = 1$, $\mathbf{Q} = \text{diag}(1, 1, 1, 1)$, $\mathbf{R} = 1$, $\omega_1 = \omega_2 = 1$, $\tilde{P} = \mathbf{I}$ and $x[4](0) = 1$, where \mathbf{I} is $(n + 1) \times (n + 1)$ unit matrix. Experiments are carried out for the new control(AACC) and the ordinary linear optimal control(LOC)[2][3].

Table 1: Performances \tilde{J}

Method	$x^T(0)$		
	[0, 0.6, 0]	[0, 1.0, 0]	[0, 1.6, -3]
LOC	2.587	×	×
AACC($\omega_3 = 0.5$)	2.101	2.740	2.937
AACC($\omega_3 = 1$)	2.099	2.738	2.929

× : very large value

1) AACC($\omega_3 = 0.5$):

The parameters are suboptimally selected along the algorithm of section 3. $\omega_3 = 0.5$, $u_{max} = -u_{min} = 0.5$, $\Omega = \{M, N, \hat{X}_i, a_{ij}, b_{ij}\}$, $\tilde{G} = 100$, $\tilde{q} = 100$, $\tilde{L} = 8$, $P_c = 0.8$, $P_m = 0.03$, $\mathbf{D} = [-1, 1] \times [-1, 1.5] \times [-5, 5] \times [0, 1.5]$. It results that $M = 1$, $N = 1.0$, $\hat{X}_1 = 95^\circ$ and $a_1 = b_0 = 49.0^\circ$.

2) AACC($\omega_3 = 1$):

The parameters are suboptimally selected by using a similar way of the AACC($\omega_3 = 0.5$). $\omega_3 = 1$. It results that $M = 1$, $N = 1.0$, $\hat{X}_1 = 95^\circ$ and $a_1 = b_0 = 49.7^\circ$.

Table1 shows performances by the AACC and the LOC. The cost function of Table1 is $\tilde{J} = \frac{1}{2} \int_0^{20} (\mathbf{X}^T \mathbf{Q} \mathbf{X} + u^T \mathbf{R} u) dt$. These results indicate that the AACC is better than the LOC.

5 Conclusions

We have studied an augmented automatic choosing control using zero dynamics for nonlinear systems with constrained input. This approach have been applied to a field excitation control problem of power system. Simulation results have shown that this controller using the GA can improve performance remarkably well.

References

- [1] D. E. Goldberg, "Genetic Algorithms in Search, Optimization, and Machine Learnings", Addison-Wesley Pub. Co. Inc., 1989.
- [2] Y. N. Yu, K. Vongsuriya and L. N. Wedman, "Application of an Optimal Control Theory to a Power System", *IEEE Trans. Power Apparatus and Systems*, 89-1, pp.55-62, 1970.
- [3] A. P. Sage and C. C. White III, "Optimum Systems Control (2nd edition)", *Prentice-Hall, Inc.*, 1977.
- [4] M. Vidyasagar, "Nonlinear Systems Analysis", *Prentice-Hall, Inc.*, 1978.
- [5] A. Isidori, "Nonlinear Control Systems : An Introduction (2nd edition)", *Springer-Verlag*, 1989.
- [6] Y. Takagi and T. Shigemasa, "An Application of State-Space Linearization to a Power System Stabilizer", *Proc. 29th CDC*, TA8-1, pp.1553-1558, 1990.
- [7] H. Takata, "An Automatic Choosing Control for Nonlinear Systems", *Proc. 35th CDC*, FA10-5, pp.3453-3458, 1996.

ESTIMATION OF SOURCE-FILTER MODEL VIA ACOUSTICAL FEATURE EXTRACTION BY GA-LIKE ALGORITHM

Mizuki Ihara, Shin-ichi Maeda and Shin Ishii

Graduate School of Information Science,
Nara Institute of Science and Technology
8916-5 Takayama Ikoma, 630-0192 JAPAN

Abstract

This study presents an estimation method for a source-filter model, which takes a temporal continuity of pitch and amplitude into account and is useful, for example, for instrument identification.

We assume pitch and amplitude as hidden variables that tend to change continuously in time while the resonant property is fixed in order to reduce inherent indeterminacy in the source-filter model. In the observation process of this dynamical system, which models the generation of sound spectra from the hidden variables of the dynamics, pitch and amplitude are highly nonlinear and non-Gaussian, i.e., a nonlinear dynamical system. Therefore, it is intractable to analytically estimate the hidden variables as well as the model parameters which define the resonant property. For this parameter estimation, we employed a GA (Genetic Algorithm)-like algorithm. After the parameter of each instrument was estimated from isolated notes, we verified the possibility of this system identification method by reconstructing the spectrum and by whether synthesized log-spectrum are close to the original log-spectrum.

Index Terms – State space methods, Nonlinear acoustics, Nonlinear dynamics, Acoustic filters

1 Introduction

The estimation of elements in sound such as pitch, amplitude and timbre has many applications, including audio encoding with a small number of parameters, sound synthesis, extraction of instrument properties and music transcription. In this study, we in particular focus on one of those applications, instrument identification.

As an example of existing studies of instrument identification, Eronen used instrument features to create an instrument classifier in a hierarchical structure and evaluated it on solo tones from 30 instruments,

achieving an identification rate for individual instruments of approximately 80 percent [1]. Brown presented a classifier with Gaussian mixture models, and obtained 75-85 percent accuracy in monophonic music instrument identification [2]. However, these studies could still not identify the instruments perfectly, especially for time-varying monophonic music.

For estimation of sound source or filter, Fant's source-filter model was sometimes used, which is originally used for modeling production processes of sound and speech [4]. In this model, it is assumed that the combination of a sound-source generation pattern and the filter that represents the resonant property of the target instrument produces observable power spectra. Simultaneous estimation of the time-varying sound-source pattern and the resonant property, however, suffers from the problem of indeterminacy; that is, observable spectra can be expressed in various ways. To determine the source-filter model, therefore, some kind of constraint is necessary.

Itakura and Saito attempted to solve this problem by identifying the filter part first. They modeled the short-term speech signal as a stationary Gaussian process and estimated the filter using maximum likelihood spectrum estimation [5]. The assumption of the stationary Gaussian process, however, ignores the effect of time-varying pitch and amplitude. Because of this assumption, the model does not include the continuity of pitch and amplitude, and then, it is not enough to express real sound-source characteristics or resonant properties.

In this study, we aim at simultaneous estimation of a sound-source and a filter with a less number of parameters. We propose an estimation method for the source-filter model that takes a temporal continuity into account by constructing a dynamical system model for the sound-source. In particular, dynamics of pitch and amplitude are considered. Additionally, we assume that the resonant property does not vary in time from the fact that the body of instrument itself

should be consistent in time.

2 The sound generative model

Using the source-filter model, unknown sound source generation G_t and resonant property (the filter part) H_t are both estimated from observable power spectra of sound s_t , whose generation process is described as

$$s_t = \phi(x_t) = G_t \odot H_t, \quad (1)$$

where s_t is a d -dimensional vector representing the spectrum amplitude of each digitized frequency, and the operation \odot means the Hadamard product (element-by-element product). The representation of source-filter model has an inherent indeterminacy that we cannot identify G_t or H_t without additional constraints. To solve this problem, therefore, we introduce the continuity in sound source G_t as a nonlinear dynamical system and assume the resonant property H_t does not vary in time, written as H in the followings.

2.1 Nonlinear dynamical system

The nonlinear dynamical system with Markov properties consists of the observation process and the state transition process:

$$s_t = \phi(x_t) \odot n_1, \quad (2)$$

$$x_t = \psi(x_{t-1}) + n_2, \quad (3)$$

where the function $\psi(\cdot)$ describes acoustical dynamics. In these equations, $x_t = \{a_t, f_t\}$ is a two-dimensional hidden vector representing internal acoustical dynamics, where a_t and f_t denote log-amplitude and pitch, respectively. We express these equations as probabilistic models, $p(s_t|x_t, \theta)$ and $p(x_t|x_{t-1}, \theta)$.

2.2 Observation process

When the sound is assumed to be stationary Gaussian as in Linear Predictive Coding (LPC), Gaussian noise in the time domain is closely represented as multiplicative Chi-square distribution with $\gamma = 3$ in the frequency domain [5], so we employ that for the noise distribution. Since observable spectra can be written as the multiplication of noise and estimated with G_t and H : $s_t = \hat{s}_t \odot n$ where $\hat{s}_t = G_t \odot H$, we obtain

$$\begin{aligned} & \log p(s_t|x_t, \theta) \\ &= \frac{1}{4\Gamma(1.5)\sigma_o\hat{s}_t(i)} \sum_{i=1}^N \left[\log \left(\frac{s_t(i)}{2\sigma_o\hat{s}_t(i)} \right) - \frac{s_t(i)}{\sigma_o\hat{s}_t(i)} \right] \\ &\simeq \frac{1}{4\Gamma(1.5)\sigma_o s_t(i)} \sum_{i=1}^N \left[\log \left(\frac{s_t(i)}{2\sigma_o\hat{s}_t(i)} \right) - \frac{s_t(i)}{\sigma_o\hat{s}_t(i)} \right]. \end{aligned} \quad (4)$$

Here, we define the time-fixed function of the resonant property as

$$\begin{aligned} H(\tilde{\omega}) &= 2^{1-p} \left\{ \sin^2 \frac{\tilde{\omega}}{2} \prod_{k=2,4,\dots,p} (\cos \tilde{\omega} - \cos b_k)^2 \right. \\ &\quad \left. + \cos^2 \frac{\tilde{\omega}}{2} \prod_{k=1,3,\dots,p-1} (\cos \tilde{\omega} - \cos b_k)^2 \right\}^{-2}, \end{aligned} \quad (5)$$

which follows the one of Line Spectrum Pair (LSP) in LPC [6]. In equation (5), $\tilde{\omega}$ represents normalized frequencies $\tilde{\omega} = \frac{\omega \mathbf{F} \mathbf{s}}{2\pi}$, where $\mathbf{F} \mathbf{s}$ is the sampling frequency, and b_k ($k = 1, \dots, p$) is the parameter of H . The sound-source is time-dependent and represented as the sum of Gaussians whose peaks are located at harmonic frequencies:

$$\begin{aligned} & G_t(\omega_i; a_t, f_t, K, \sigma_p, \tau) \\ &= \exp \left(a_t + A \exp \left(-\frac{\omega_i}{\tau} \right) \sum_k^K N(\omega_i | k f_t, \sigma_p^2) \right). \end{aligned} \quad (6)$$

Here, $-\frac{\omega_i}{\tau}$ indicates exponential decay in frequency, A is an adjusting parameter for power, and $N(x|\mu, \sigma)$ denotes the Gaussian distribution of x with mean μ and variance σ . K and σ_p are the number of Gaussians in the resonant property and the variance of each Gaussian, respectively.

2.3 State transition

In addition to the constraint of time-invariance in the resonant property H , the hidden variables for sound source $x_t = \{a_t, f_t\}$ are assumed to change either continuously or discontinuously in time [7]. Whether continuous or discontinuous is modeled by means of a two-component Gaussian mixture:

$$\begin{aligned} p(x_t|x_{t-1}, \theta) &= \bar{\eta} N(x_t; m_1, \sigma_1^2) + (1 - \bar{\eta}) N(x_t; m_2, \sigma_2^2) \\ &= \bar{\eta} \left(N(a_t; a_{t-1} + \log \rho, \sigma_{1a}^2) N(f_t; f_{t-1}, \sigma_{1f}^2) \right) \\ &\quad + (1 - \bar{\eta}) \left(N(a_t; m_{2a}, \sigma_{2a}^2) N(f_t; m_{2f}, \sigma_{2f}^2) \right), \end{aligned} \quad (7)$$

where ρ is an attenuation constant ranging from 0 to 1, m_1 and m_2 are mean vectors of a_t and f_t . Covariance matrices for continuous transition are $\sigma_1^2 = \{\sigma_{1a}^2, \sigma_{1f}^2\}$, and those for discontinuous transitions are $\sigma_2^2 = \{\sigma_{2a}^2, \sigma_{2f}^2\}$. The first term corresponds to the continuous transition where amplitude decreases exponentially and pitch does not change much. The second transition corresponds to the discontinuous one, approximated as a Gaussian process with a large variance σ_2 . Under these assumptions, the proportion of the state transition being either continuous or discontinuous is represented by $\bar{\eta}$ that takes a value from 0 to 1.

2.4 Joint distribution

For time-series of the observable variable s_t and the hidden variable x_t during $t = 1, \dots, T$, which are wholly expressed as $S_{1:T} = \{s_1, s_2, \dots, s_T\}$ and $X_{1:T} = \{x_1, x_2, \dots, x_T\}$, respectively, the joint distribution for $X_{1:T}$ and $S_{1:T}$ is given by

$$p(X_{1:T}, S_{1:T}) = p(s_1|x_1, \theta)p(x_1|\theta)\prod_{t=2}^T p(s_t|x_t, \theta)p(x_t|x_{t-1}, \theta), \quad (8)$$

where θ is the parameter vector that defines the functions of G_t and H . Likelihood $p(S_{1:T})$ can be calculated by integrating this joint distribution with respect to $X_{1:T}$.

3 Parameter estimation

When the model has hidden variables, the EM algorithm has often been used for the parameter estimation. It requires the posterior probability of hidden variables to be calculated, but this calculation is often intractable in many nonlinear dynamical systems, like our case. Therefore, instead of the EM algorithm, we used an equivalent but practically different methodology, a coordinate descent of free energy.

3.1 The EM algorithm and free energy

Free energy is defined for any trial distribution of the hidden variable, $q(X_{1:T})$, as

$$F(q(X_{1:T}), \theta) = -\log p(S_{1:T}|\theta) + KL[q(X_{1:T})||p(X_{1:T}|S_{1:T}, \theta)]. \quad (9)$$

where $KL[q||p] = \int q(x) \log \frac{q(x)}{p(x)} dx$ is the Kullback-Leibler divergence. Apparently, minimizing the free energy with respect to the trial distribution $q(X_{1:T})$ yields the negative log-likelihood $-\log p(S_{1:T}|\theta)$, and in that case, $q(X_{1:T})$ is equal to $p(X_{1:T}|S_{1:T}, \theta)$ because of the positivity of the Kullback-Leibler divergence. Therefore, the maximum likelihood (ML) estimation is achieved by the simultaneous minimization with respect to $q(X_{1:T})$ and θ :

$$\begin{aligned} \hat{\theta} &= \arg \max_{\theta} \log p(S_{1:T}|\theta) \\ &= \arg \min_{\theta} (\min_{q(X_{1:T})} (F(q(X_{1:T}), \theta))). \end{aligned} \quad (10)$$

In this optimization, we can employ alternate minimization of the free energy with respect to $q(X_{1:T})$ and θ , and it is known that the minimization of the free energy becomes identical to the ML estimation by the

EM algorithm when we employ strict alternate minimization of the free energy. Instead of the intractable calculation of posterior distribution, however, we relax the strict alternate minimization as to restrict the trial distribution $q(X_{1:T})$ being a single Gaussian distribution, and then use a GA-like algorithm for the parameter estimation.

3.2 GA-like algorithm approximation

For the estimation of optimal parameters, we used GA-like algorithm known as a simplex method [8]. This method looks for an optimal point by moving to a new vertex whose function value is equal to or better than that of the previous vertex. When there is no such vertex, the current vertex is the locally optimal solution.

4 Experimental evaluation

4.1 Sound database

To verify the performance of the proposed method as an instrument identification application, we used isolated notes from five kinds of instruments, taken from the University of Iowa Electronic Music Studios samples [9]. The dataset consists of samples of flute, horn, trumpet, viola and cello. For each instrument, we prepared fifteen training data which consists of three data from five different tones, and six test data which contain the different tones with training data.

4.2 A sound-source and a filter estimation

The performance of the proposed system was first examined by seeing if a sound-source and a filter can be well estimated. Fig. 1 shows the original log-spectrum and the log-spectrum synthesized by the identified system for cello. In the log-spectrum after learning parameters, the characteristic of pitch expressed as peaks with constant intervals and the gradually decaying amplitude were well reconstructed.

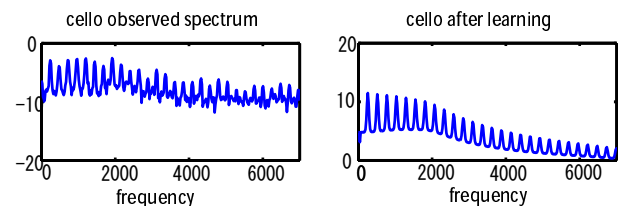


Figure 1: original log-spectrum and synthesized log-spectrum

4.3 Tracking of pitch and amplitude

We next evaluated whether the model can track the pitch and amplitude of the original cello sound. The result of pitch and amplitude tracking is shown in Fig. 2. In the left panel (frequency), since we used three

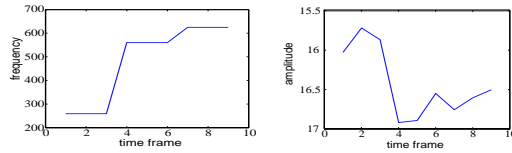


Figure 2: Pitch and amplitude tracking

data for each tone, frequency in each group of three are almost the same. That means the pitch tracking was successful.

4.4 Feature extraction

In addition, the classification performance was plotted with Local Fisher Discriminant Analysis (LFDA) [10]. From the results in Fig. 3 that each instrument tends to group, the system has the possibility to be used in instrument identification.

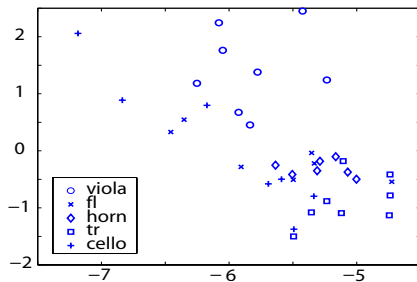


Figure 3: Instrument classification of isolated notes by learned characteristics of H

5 Conclusion and future work

We presented a system identification approach to the estimation of sound-source generation and resonant properties. To consider the time-varying phenomena, a nonlinear dynamical system was employed, while the filter representing the resonant property was fixed in time but estimated. A GA-like algorithm was used for identification of this complex model based on available data. This model well reconstructed the original sounds from the estimated sound source generation G_t and the resonant property filter H_t .

For the practical use of this model for instrument identification, we should evaluate this model with monophonic and polyphonic music to know the ability to identify instruments being played. Although the GA-like algorithm used for parameter estimation does not require explicit gradients of the objective function, it does not guarantee global minimization. In our future work, we also consider more strict free-energy minimization for the parameter estimation.

References

- [1] A. Eronen and A. Klapuri, "Musical instrument recognition using cepstral coefficients and temporal features," *ICASSP*, 2000.
- [2] J.C. Brown, O. Houix and S. McAdams, "Feature dependence in the automatic identification of musical woodwind instrument," *J. Acoust. Soc. Am.*, Vol.109(3), Mar. 2001.
- [3] L.J. Lee, H. Attias, L. Deng, and P. Fieguth, "A multimodal variational approach to learning and inference in switching state space models," *ICASSP*, 2004.
- [4] G. Fant, *Acoustical Theory of Speech Production*, The Hague, 1960.
- [5] F. Itakura, and S. Saito, "A statistical method for estimation of speech spectral density and formant frequencies (in Japanese)," *Trans. IECE Jpn.*, Vol.53A, pp.36-43, 1967.
- [6] N. Sugamura, and F. Itakura, "Speech Data Compression by LSP Speech Analysis-Synthesis Technique (in Japanese)," *Trans. IECE Jpn.*, Vol.64A(8), pp.599-606, 1981.
- [7] R.A. Irizarry, "Local Harmonic Estimation in Musical Sound Signals," *Journal of American Statistical Association*, Vol.96(454), 2001.
- [8] J.C. Lagarias, J.A. Reeds, M.H. Wright, and P.E. Wright, "Convergence Properties of the Nelder-Mead Simplex Method in Low Dimensions," *SIAM Journal of Optimization*, Vol.9(1), pp.112-147, 1998.
- [9] The University of Iowa *Electronic Music Studios: MIS*, <http://theremin.music.uiowa.edu/>
- [10] M. Sugiyama, *Dimensionality reduction of multimodal labeled data by local Fisher discriminant analysis*, Technical Report TR06-0008, Department of Computer Science, Tokyo Institute of Technology, Japan, 2006.

A Network Analysis of Simple Genetic Algorithms

Hiroyuki Funaya
Department of Systems Science
Kyoto University
Kyoto 606-8501 Japan

Kazushi Ikeda
Department of Systems Science
Kyoto University
Kyoto 606-8501 Japan

Abstract

In recent years, network analysis has revealed that some real networks have the properties of small-world and/or scale-free networks. In this study, a simple Genetic Algorithm (GA) is regarded as a network where each node and each edge respectively represent a population and the possibility of the transition between two nodes. The characteristic path length with the crossover operation, which is one of the most popular criterion in small-world networks, shows how effective the crossover operation is, compared to that with only the mutation operation.

1 Introduction

There have been several theoretical results on the properties of genetic algorithms (GAs), such as the schemata theorem [1,2] and the asymptotic theory [3-5]. However, GAs are not optimizers; They find a good but not optimal solution in a short time. Such a solution is termed a quasi-optimal solution. The above results do not seem to explain why GAs are good quasi-optimizers.

This study takes another approach to this problem: We regard a GA as a network, where a node is a possible set of individuals, and investigate the connectivity of the network from a network analytical point of view. Network analysis has recently attracted much attention as a new method to analyze complex phenomena in the world, where the following two properties have been found in many real networks [6-9]: One is referred to as a small-world network, which means that a network simultaneously has dense local connections and short pairwise distances. The other is a scale-free network, which means that the distribution of the orders of nodes in a network has a long tail obeying the power law.

We shed light on the former property. That is, we analytically derive the characteristic path length (CPL) ν , defined as the shortest path length (SPL)

between two nodes averaged over all possible pairs. Since it is expected that a GA with a smaller CPL takes a shorter time to find a solution, we see how the two basic genetic operations in GAs, crossover and mutation, affect the CPL.

2 Network of Genetic Algorithms

Although many variants of GAs have been proposed since the original GA was born [1,2], we analyze the simplest case as formulated below.

Each individual consists of a binary sequence of length L . That is, we have 2^L kinds of individuals. A set of individuals defines a population. We assume that each population has only two individuals at first and consider more general cases later. Then, the cardinality of the different populations becomes

$$N \equiv 2^{L-1}(2^L - 1). \quad (1)$$

When the generation proceeds, a population changes by one of the two basic genetic operations, one-point crossover or mutation. The former randomly chooses one crossover-point from $L - 1$ candidates and exchanges the bits rightward from the point, while the latter randomly chooses one of $2L$ loci (or gene-positions) in the two individuals and inverts its bit from 0 to 1 or vice versa. Note that we do not treat any fitness function because we are only considering the possibility of population-transition from one in a generation to another in the next generation.

We regard a population as a node of a GA network. Hence, the network has N nodes. Two nodes are linked by an edge if and only if one of the two nodes can change to the other in a one-point crossover or mutation operation (Fig. 1).

If a network consists of only the edges from mutation, it is a lattice of the $2L$ -dimensional hypercube because an individual is an L -bit sequence and a population consists of two individuals. Therefore, the path-length of any two distinct nodes is the same as the

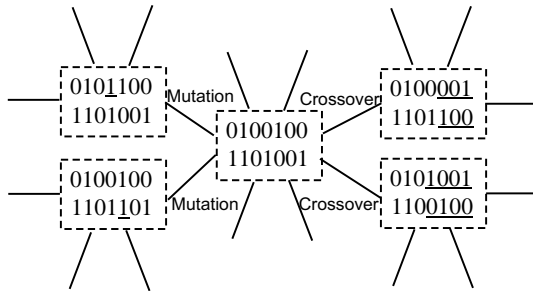


Figure 1: A part of the network of a genetic algorithm.

Manhattan distance, that is, L on average. This means that we need L generations to reach a quasi-optimal population from an initial one.

On the contrary, the edges from crossover are shortcuts in the network where plural bits can change at once. It is likely that these shortcuts enable GAs to find a quasi-optimal solution in a short time. The purpose of this study is to evaluate quantitatively how these shortcuts work to shorten the CPL and to clarify their effects in GAs.

3 Characteristic Path Length

In many cases of network analysis, the CPL is numerically calculated from the empirical data collected. However, the CPL of the GA network treated here can be derived analytically due to its simplicity, as shown below.

One of the main ideas for derivation is to classify L loci into four types according to how two populations can be matched by genetic operations:

Type 1 All four genes have the same alphabet.

Type 2 The two genes of a population are the same but the two genes of the other population are different.

Type 3 The two genes of each population are the same but the two populations have different alphabets.

Type 4 Each population has two different genes. That is, the genes at the locus are 0110, 1001, 0101 or 1010. The former two are termed Type 4-1 while the others Type 4-2.

Note that the crossover operation cannot change the type of a locus and the mutation operation works bitwise. Therefore, the loci belonging to Types 1, 2

A Gene in Population 1 g_1	0 1 0 1 0
A Gene in Population 2 g_2	1 0 0 0 1
$p = g_1 \text{ XOR } g_2$	1 1 0 1 1
$p_1 = \text{Shifted } p$	1 1 0 1 1
$q = p \text{ XOR } p_1$	0 1 1 0

Figure 2: How to calculate the SPL of two nodes consisting of the loci of Type 4.

and 3 respectively contribute zero, one and two for the SPL no matter where they are located. Hence, the SPL of two nodes is the sum of the above and the SPL of the two shorter nodes consisting of only the loci of Type 4. The latter for l -bit individuals can be calculated using the following procedure, as shown in Fig. 2:

1. Take l -bit XOR bitwise between an individual in a population and one in the other population and denote it by p .
2. Take $(l - 1)$ -bit XOR bitwise between p and 1-bit shifted p and denote it by q .
3. Count the number of 1s in q .

The other of the main ideas for derivation is to count the number of node-pairs with the SPL M , instead of evaluating the SPL of each node-pair directly. Let the numbers of Type 1, 2, 3 and 4 in L loci be denoted by l_1, l_2, l_3 and l_4 , and the numbers of links in M by m_1, m_2, m_3 and m_4 , respectively. Here,

$$L = l_1 + l_2 + l_3 + l_4, \quad (2)$$

$$M = m_1 + m_2 + m_3 + m_4, \quad (3)$$

$$m_1 = 0, \quad m_2 = l_2, \quad m_3 = 2l_3 \quad (4)$$

stand by definition.

In the case of $m_4 = 0$, the number of node-pairs satisfying (3) is written as

$$\frac{L! 2^{l_1} 8^{l_2} 2^{l_3}}{l_1! l_2! l_3!} \quad (5)$$

for fixed l_1, l_2 and l_3 . Since they must satisfy

$$l_2 + 2l_3 = 0 \quad (6)$$

$$l_1 + l_2 + l_3 = L \quad (7)$$

$$0 \leq l_3 \leq \lfloor L/2 \rfloor \quad (8)$$

from (2) to (4), the ratio of the number of node-pairs to the possible pairs for $m_4 = 0$ is

$$\frac{1}{2^{4L}} \sum_{M=1}^{2L} \sum_{l_3=0}^{\lfloor L/2 \rfloor} \frac{ML! 2^{L+2M-4l_3}}{(L-M+l_3)!(M-2l_3)!l_3!}, \quad (9)$$

which is denoted by $\tilde{\nu}_1$. Otherwise, for fixed l_1, l_2, l_3 and l_4 , the number of combinations of positions is equal to

$$\frac{L!}{l_1!l_2!l_3!l_4!} \quad (10)$$

and the number of combinations of places where crossover occurs is $l_4 - 1 C_{m_4}$. Taking into account the cardinality of Type 4 and the possibility that the left-most in the Type 4 loci belongs to Type 4-1 or Type 4-2, the total number of node-pairs is written as

$$\frac{L!2^{l_1}8^{l_2}2^{l_3}2^{l_4+1}l_4-1C_{m_4}}{l_1!l_2!l_3!l_4!}. \quad (11)$$

Summing up for all possible combinations of l_1, l_2, l_3, l_4 and m_4 under the conditions (2) to (4) and $m_4 \leq l_4 - 1$, the ratio of the number of node-pairs to the possible pairs is written as

$$\frac{1}{2^{4L}} \sum_{M=1}^{2L} \sum_{l_1, l_2, l_3, l_4, m_4} \frac{ML!2^{l_1}8^{l_2}2^{l_3}2^{l_4+1}l_4-1C_{m_4}}{l_1!l_2!l_3!l_4!}, \quad (12)$$

which is denoted by $\tilde{\nu}_2$. In total, the complete expression for the CPL is

$$\tilde{\nu} = \tilde{\nu}_1 + \tilde{\nu}_2. \quad (13)$$

For convenience, we show $\hat{\nu}$ for some L 's in Table 1. Since the CPL of the network consisting of only the edges from mutation is L , the ratio shows how the crossover operation shortens the CPL. We see that the CPL is rather large even when the edges from crossover are added.

L	$\hat{\nu}$	ratio
3	2.3359	0.7786
8	6.5501	0.8188
13	10.887	0.8375
18	15.253	0.8474
28	24.000	0.8571
48	41.500	0.8646
68	59.000	0.8676

Table 1: The CPL $\hat{\nu}$ for some L 's.

Note that the path length is calculated in Type 4 as if the individuals in a population are ordered. However, the CPL $\tilde{\nu}$ of the network where individuals in a population are ordered is expressed as

$$\tilde{\nu} = \frac{2N\nu + L}{\tilde{N}} \quad (14)$$

where ν is the true CPL and $\tilde{N} \equiv 2^{2L}$ [10, 11]. Hence, the difference is negligible when L is large.

4 Inductive Approach

As is expected, it is not easy to discuss more general cases such that a population consists of K individuals for $K > 2$ and the exact analysis is to be done yet. Instead, we give an upper bound of the CPL for a general $K > 2$, by taking an inductive approach.

In order to make our new method clear, we first discuss the method for the case of $K = 2$. Let a pair of populations of length l be expressed as a $4 \times l$ matrix denoted by Π_l , where the first and second rows correspond to one population and the third and fourth do the other. Some matrices represent a pair of populations any of whose shortest paths includes one or more crossover operations, which we term C matrices. The others are called M matrices. Let the cardinality of C matrices be denoted by $p_c(l)$ and that of M matrices by $p_m(l)$. Obviously, $p_c(l) + p_m(l) = 2^{4l}$. We denote the SPL of each of C matrices by $r_c(l, j)$, $j = 1, \dots, p_c(l)$, and the SPL of each of M matrices by $r_m(l, i)$, $i = 1, \dots, p_m(l)$. Then, $\tilde{\nu}$ is expressed as

$$\tilde{\nu} = \frac{q_c(l) + q_m(l)}{2^{4l}}, \quad (15)$$

where $q_c(l)$ and $q_m(l)$ are defined as

$$q_c(l) = \sum_{j=0}^{p_c(l)} r_c(l, j), \quad (16)$$

$$q_m(l) = \sum_{i=0}^{p_m(l)} r_m(l, i). \quad (17)$$

Let us consider the populations of length $l+1$. Any pair of them is expressed as one of the following 16 matrices,

$$\begin{pmatrix} 0 \\ 0 \\ \Pi_l 0 \\ 0 \end{pmatrix}, \begin{pmatrix} 0 \\ 0 \\ \Pi_l 0 \\ 1 \end{pmatrix}, \begin{pmatrix} 0 \\ 0 \\ \Pi_l 1 \\ 0 \end{pmatrix}, \dots, \begin{pmatrix} 1 \\ 1 \\ \Pi_l 1 \\ 1 \end{pmatrix}. \quad (18)$$

Using this property, we can derive the update equation as

$$p_c(l+1) = 16p_c(l) + 4p_m(l), \quad (19)$$

$$p_m(l+1) = 12p_m(l), \quad (20)$$

$$q_c(l+1) = 16q_c(l) + 4q_m(l) + 14p_c(l), \quad (21)$$

$$q_m(l+1) = 12q_m(l) + 12p_m(l), \quad (22)$$

where the initial condition is

$$p_c(1) = 4, \quad p_m(1) = 12, \quad (23)$$

$$q_c(1) = 0, \quad q_m(1) = 12. \quad (24)$$

See [10] for detail. This result completely agrees to the result by the combinatorial method, (13).

Although (13) is exact, it is difficult to see the characteristics of this formula. A rather rough analysis below gives a simple conclusion, that is, the crossover operation reduces the CPL to its 7/8 at most. See (18) again. In four of the sixteen matrices, the added column vector is classified to Type 4. This means that the crossover operation cannot contribute to decrease the CPL in the twelve of the matrices. Moreover, a Type-4 locus belongs to either Types 4-1 or 4-2. If the SPL of one of them is the same as Π_l , the other is necessarily larger. In total, only two of the sixteen matrices have shorter SPL. This means that the crossover operation reduces the CPL to its 7/8 at most. In fact, the ratio in (13) seems to approach 7/8.

This idea still holds in the case of $K > 2$, by considering choosing two individuals from a population and the corresponding two individuals from the other population in a pair.

5 Conclusions

We regarded a simple GA as a network and analytically derived its exact CPL for $K = 2$ and an upper bound for a general K . The result shows how the crossover operation works to shorten the CPL of a network consisting of only the edges from mutation. In short, even when the crossover operation is applied, the CPL is not so small, and the same order $O(L)$ as in the case when only the mutation operation is employed.

One of the reasons is averaging: Since the CPL is the SPL averaged over any pair of populations, it is almost ignored how the information is encoded into the genes. To overcome this problem, we need to introduce the selection pressures of the GA, which were neglected here. Our future work will investigate such matters.

Acknowledgements

This study is supported in part by a Grant-in-Aid for Scientific Research (15700130, 18300078) from the Japanese Government.

References

- [1] J. H. Holland, *Adaptation in Natural and Artificial Systems*. Univ. Michigan Press, 1975.
- [2] D. E. Goldberg, *Genetic Algorithms in Search, Optimization, and Machine Learning*. Addison-Wesley Pub., 1989.
- [3] J. Suzuki, "A markov chain analysis on simple genetic algorithms," *IEEE Trans. on Systems, Man and Cybernetics (TSMC)*, vol. 25, no. 4, pp. 655–659, 1995.
- [4] —, "A further result on the markov chain model of genetic algorithms and its application to a simulated annealing-like strategy," *IEEE Trans. SMC-B*, vol. 28, no. 1, pp. 95–102, 1998.
- [5] H. Mühlenbein and R. Höns, "The estimation of distributions and the minimum relative entropy principle," *Evolutionary Computation*, vol. 13, no. 1, pp. 1–27, 2005.
- [6] D. J. Watts and S. H. Strogatz, "Collective dynamics of 'small-world' networks," *Nature*, vol. 393, pp. 440–442, 1998.
- [7] A.-L. Barabasi and R. Albert, "Emergence of scaling in random networks," *Science*, vol. 286, pp. 509–512, 1999.
- [8] D. S. Callaway, M. E. J. Newmann, S. H. Strogatz, and D. J. Watts, "Network robustness and fragility: Percolation on random graphs," *Physical Review Letters*, vol. 85, pp. 5468–5471, 2000.
- [9] S. H. Strogatz, "Exploring complex networks," *Nature*, vol. 410, pp. 268–276, 2001.
- [10] H. Funaya, *An analysis of genetic algorithms using network science*, Bachelor's thesis, Kyoto University, 2006. In Japanese.
- [11] H. Funaya and K. Ikeda, "On properties of genetic operators from a network analytical viewpoint," *Proc. ICONIP*, Part III, pp. 746–753, 2006.

Function-discovery-system by the evolutionary strategy using the search-accumulation

Mitsutoshi SAITO and Seiichi SERIKAWA

Graduate School of Electric Engineering

Kyushu Institute of Technology

1-1 Sensui-cho, Tobata-ku, Kitakyushu-shi, Fukuoka, 804-8550, JAPAN

Abstract

Recently, the system using bug type of artificial life was proposed for discovering the function, and it was improved. It is one of the extended models of Genetic Algorithm (GA) and Genetic Programming (GP). However, the function is not found sometimes when the observation data is very complicated.

In this study, a new concept is introduced so that the function-search can be applicable to the complicated observation data. The function-search by S-System is executed two or more times as a basic idea. This is called "search-accumulation". To confirm the validity of search-accumulation, equal-loudness-level contours (ISO226) are used as the observation data. Since the contours are very complicated, it is very difficult to express the counters as a function. In reality, the function-search was tried by the conventional S-System, but the function does not agree well with the data. By the use of the strategy of search-accumulation, the function in agreement well with the contours is found successfully. Thus, the validity is conformed.

Keywords: search accumulation, genetic programming

1. Introduction

Recently, a variety of problem-solving systems that use genetic algorithm (GA) and genetic programming (GP) are proposed. The purpose of GA is mainly the optimization of the numerical value, while that of GP is the generation of the symbol. Koza proposed the function-discovery-system using GP [1]. It generates the approximate function that shows the relationship between input data and output data in observation data. In GP, the chromosome which represents a function is expressed by the tree structure. It is optimized by the crossover and mutation. However, there are problems that the schema is destroyed and the length of generated function becomes extremely long. To solve the problem,

the function-discovery-system that used the concept of an artificial life was proposed [2]. This is called "S-System", because it is the system that uses the concept of sexual and asexual reproduction. The improved model was also proposed [3]. However, both GP and S-System cannot discover the approximate function, when the observation data is complex.

In this study, a new concept is introduced to generate the approximate function corresponding with the complicated data. A basic idea is the execution of the function-search by S-System two or more times. This strategy is called "search-accumulation" in this study. As the result, the generated function agrees well with the complicated observation data.

2. The model for discovering function

2.1 Summary of S-System

The S-System is one of the evolutionary strategies, and the mail flow is the same as that of GA and GP. The chromosome and the fitness are designed according to the purpose of applied field. In general, the fitness is defined as an evaluation-function in which the quality of the chromosome is expressed. The main flow of evolutionary strategy is as follows.

(i) A lot of chromosomes are generated at random as the first stage. (ii) The chromosome is selected. The selected probability of the chromosome with high fitness is high than of the chromosome with low fitness. (iii) The crossover and the mutation are practiced between two selected chromosomes. As a result, a new chromosome is born. (iv) The procedures of (ii) and (iii) are repeated until the fitness exceeds a certain threshold value.

As the result, the chromosome changes and the value of fitness increases, according as the generation proceeds.

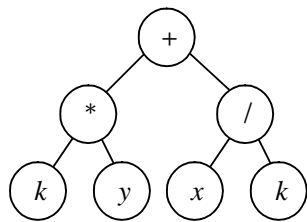


Fig.1 The example of chromosome for GP (tree structure of $k \cdot y + x/k$).

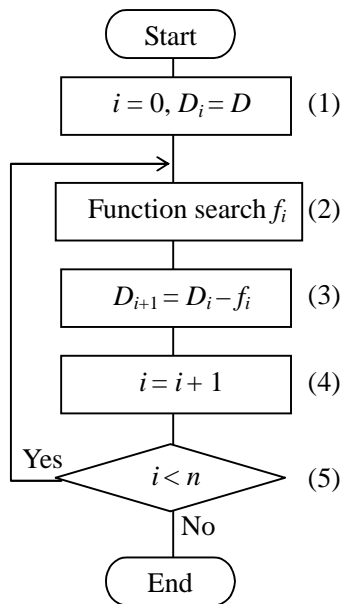


Fig. 2 The flowchart of function-discovery-system using search-accumulation.

The length of chromosome for GA is fixed, but that for GP changes. The purpose of GA is the optimum of the numerical value. On the other hand, that of GP is the generation of the symbols. The tree structure is regarded as the chromosome for GP as shown in Fig. 1. The S-System also represents the tree structure as the chromosome. The crossover of GP is different from that of S-System. For GP, it is practiced between the chromosomes with different tree structure. Therefore, the form of tree structure dramatically changes. For example, when the chromosome shows a function as shown in Fig.1, the form of function greatly changes by the crossover. Thus, the solution is changeable. On the other hand, the function form doesn't change by the crossover in S-System. The concepts of homogeneity and heterogeneity have been introduced into S-System. If two individuals have the same tree structure, they are called homogeneity. The individual with a different tree structure is called heterogeneity. The crossover is practiced between homogeneities. It is called “sexual reproduction”. The tree structure is not broken by the

sexual reproduction, but only the constant value included in the function changes. This is because the tree structure of homogeneity is equal. Therefore, the constant value is optimized as the generation proceeds. On the other hand, the individual without homogeneity generates its two copies. This is called “asexual reproduction”. By the strategy, the sexual reproduction can be practiced to the next generation, because two homogeneities are born by the asexual reproduction. In S-System, the change of tree structure occurs at the mutation. As the result, the optimization of the numerical value is practiced, the length of function doesn't become long compared with GP, and the solution is stabilized. For more details, refer to Ref [2].

2.2 Function-discovery by search-accumulation

In this study, a new concept is introduced so that the function-search can be applicable to the complicated observation data. The function-search by S-System is executed two or more times. This is called “search-accumulation”. Here, the observation data is assumed to be D , and its approximate function is assumed to be f . Figure 2 shows the flowchart of the function-discovery-system using search-accumulation. The details are described as follows.

- (1) The counter i is set to be 0, and observation data D is regarded as the initial data D_0 .
- (2) An approximate function that agrees with the observation data D_i is searched by S-System. The obtained function is assumed to be f_i .
- (3) The difference (i.e. $D_i - f_i$) between D_i and f_i is regarded as the new observation data D_{i+1} .
- (4) One is added to the value of the counter i .
- (5) The search finishes when the value of counter i reaches a threshold. Otherwise, jump to (2).

After the search, the approximate function f is obtained by the following equation.

$$f = \sum_{i=0}^n f_i \quad (1)$$

When $n = 0$ in Eq. (1), the equation corresponds to the function discovered by the conventional S-System. Thus, the proposed search-accumulation is regarded as the extended model of conventional S-System.

3. Experimental Result and investigation

To confirm the validity of the proposal method, equal-loudness-level contours (ISO226) [4] are used as an observation data. From the data, good approximate

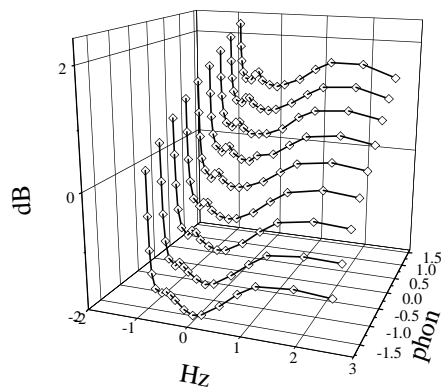


Fig.3 Equal-loudness-level contours about sound (ISO226) [4].

Table 1. The value of parameters for S-System.

Number of chromosomes	900
Maximum generation	4000
Generation gap	0.5
Number of homogeneities at next generation	20
Number of gates at next generation	200
Tournament size	2
Crossover rate	0.2
Limitation of the number of homogeneities	30
Maximum number of gates	300
Threshold for going back	0.01
Mutation rate of virus	0.3
Mutation rate of bugs	0.2
Mutation rate of constant	0.2
Maximum depth of tree	8
Threshold of fitness for ending program	1

function was not obtained by the conventional S-System.

Figure 3 shows the contours. The loudness level [dB] that man psychologically perceives changes by frequency [Hz] and the sound pressure level [phone]. In another word, the loudness [dB] is represented as a function f of the frequency [Hz] and the sound pressure level [phone]. In this study, the frequency [Hz] and the sound pressure level [phone] are regarded as the input data, and the loudness level [dB] is regarded as the output data. The approximate function $f(\text{Hz}, \text{phone})$ is obtained from those data. The search-parameter of S-System is shown in Table 1. The search is tried under

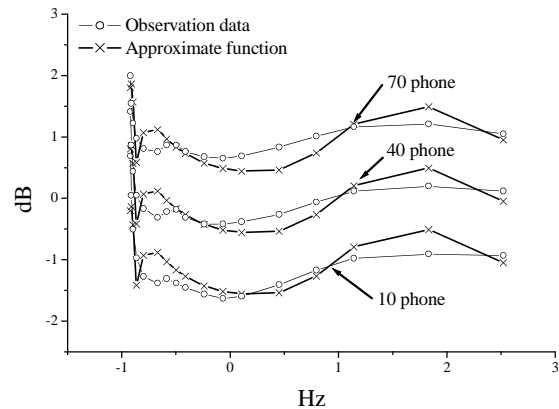


Fig.4 Example of approximate function by Condition I (fitness=0.781).

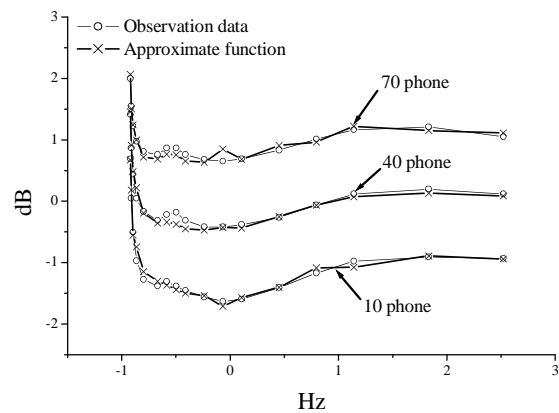


Fig.5 Example of approximate function by Condition II (fitness=0.918).

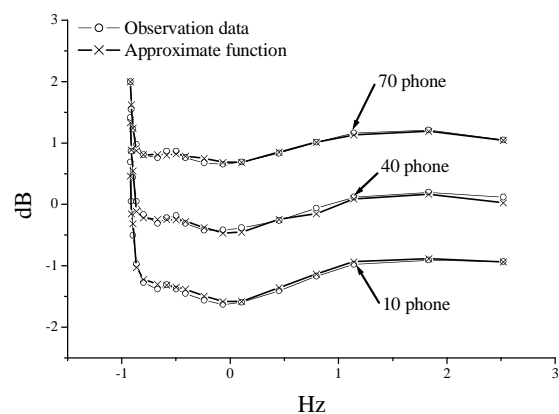


Fig.6 Example of approximate function by Condition III (fitness=0.927).

the following three conditions.

Condition I: Conventional method.

Condition II: Search-accumulation I.

Condition III: Search-accumulation II.

As for Condition II and Condition III, the method of the accumulation is different. In Condition II, after the

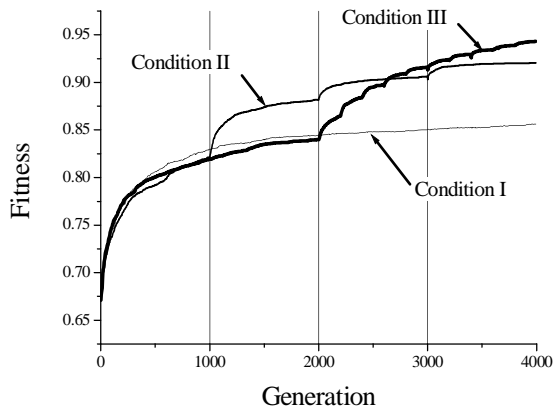


Fig. 7 Relationship between the generation and the fitness in Condition A, B, and C (average of 30 trials).

search of 1000th generation, the accumulation is practiced. It is repeated every 1000 generation. Total generation is 4000 ($=1000 \times 4$). In Condition III, the first search is practiced until the 2000th generation. After that, the accumulation is repeated every 200 generation. Total generation is 4000 ($=2000 + 200 \times 10$). The examples of the experimental result are shown in Fig. 4, 5, and 6. To avoid the confusion of drawing curves, only the results of 10, 40, and 70 phones are shown. As understood from these Figs, the waveform by Condition II and Condition III are corresponding with the observation data well compared with that of Condition I. Figure 7 shows the relationship between the generation and the fitness in Condition I, II, and III. There is little increase in fitness, when the generation exceeds 2000 for Condition I. As for Condition II and III, it is understood that the fitness has improved whenever the search-accumulation is repeated. Therefore, the validity of the proposal method is mentioned.

The fitness rapidly increases in Condition II after the 1000th generation. This is corresponding to the generation when the first search-accumulation started. On Condition III, the fitness rapidly increases after the 2000th generation is over. This is also corresponding to the generation when the first search-accumulation started. Thus, it is understood that fitness increases by the search-accumulation. The final fitness of Condition III is higher than that of condition II. The frequency of the search-accumulation of condition III is more than that of condition II. From the above-mentioned, even if the number of total generations is the same, it is understood that the search-ability is different if the accumulation-frequency is different.

4. Conclusions

The search-accumulation of the function-discovery by S-System has been proposed in this study. When this method is used, the function corresponding well with the complicated observation data is generated. To confirm the validity of the proposed method, equal-loudness-level contours (ISO226) are used as an observation data. In conventional method, the function in agreement with this data is not obtained. On the other hand, the function corresponding well with the observation data has been discovered by proposed method.

As the problem in the future, there is the reduction of the length of discovered function. In addition, the effectiveness should be verified by applying to more practical problems.

References

- [1] J. Koza, *Genetic Programming*, *Auto Discovery of Reusable Subprograms*, MIT Press, p.109, (1994).
- [2] S. Serikawa and T. Shimomura, "Proposal of a System of Function-Discovery Using a Bug Type of Artificial Life", *Trans. IEE*, Vol.118-C, 2, p.170, (1998).
- [3] S. Serikawa and T. Shimomura, "Improvement of the Search Ability of S-System (A Function-Discovery System)", *Trans. IEE*, Vol.120-C, 8, p.1281, (2000).
- [4] National Astronomical Observatory, *Chronological Scientific Tables 2006*, Maruzen Co., Ltd, p.424, (2005).

Development of Satellite Image Searching using Distributed Genetic Algorithm with Normalized Correlation

Kotaro Matsushita[1], Kei Katayama[2], Kenneth J. Mackin[1], Eiji Nunohiro[1]
[1]Tokyo University of Information Sciences
[2]Graduate School of Tokyo University of Information Sciences
1200-2 Yatoh-cho, Wakaba-ku, Chiba 265-8501, Japan
{matusita, mackin, nunohiro}@rsch.tuis.ac.jp, g05004kk@edu.tuis.ac.jp

Abstract

Tokyo University of Information Sciences maintains and distributes MODIS (Moderate Resolution Imaging Spectroradiometer) satellite data as part of the research output for Frontier project. An intelligent image search system is being developed as part of the project, in order to retrieve requested images such as matching images patterns or forest and field fires extraction. The intelligent image search system applies GA (Genetic Algorithm) in the search algorithm. When searching for a target image area within the MODIS image database, it is possible that the search algorithm cannot match the optimal location when the brightness of the search image data and MODIS data image are very different. In order to solve this problem, we applied normalized correction to the GA fitness function to improve the matching accuracy. Further, we implemented the image search as distributed genetic algorithm search over a PC cluster network, in order to increase the search speed within the satellite image database. We tested the proposed system and verified the effectiveness of distributed genetic algorithm for the distributed MODIS satellite database search process.

Keyword: Satellite image data, Image search system, Brightness, Distributed genetic algorithm, normalized correction

1 Introduction

Tokyo University of Information Sciences receives MODIS image data from NASA satellites Terra and Aqua, and distributes collected data to universities and research institutions. MODIS sensors are the key sensors aboard the Terra and Aqua satellites. Moderate resolution remote sensing allows the quantifying of land surface type and extent, which can be used

to monitor changes in land cover and land use for extended periods of time.

In order to effectively utilize the large scale satellite image database, an efficient search algorithm allowing quick retrieval of the required information from the large database is required. An intelligent image search system is being developed as part of the research output for the Frontier project, in order to retrieve requested images such as matching images patterns or forest and field fires extraction. The intelligent image search system applies GA in the search algorithm.

In our previous work, we have proposed applying GA to match partial images from MODIS image data [2]. But when searching for a target image area within the MODIS image database, it is possible that the search algorithm cannot match the optimal location when the brightness of the search image and MODIS data image are very different due to differences in time of day of the satellite image retrieval. In order to solve this problem, we applied normalized correction, which is effective in matching images with different relative brightness, to the GA fitness function to improve the matching accuracy. Further, we implemented the image search as distributed genetic algorithm search over a PC cluster network, in order to increase the search speed within the satellite image database.

We applied our proposed method in our MODIS data image matching system, and verified that the proposed method improved matching accuracy for images with different relative brightness.

2 Outline of Image Match Search Processing

We develop an image search system which retrieves matching images with similar features and characteristics to the search image, from the MODIS image database. When searching for a matching image area

within the MODIS image database, it is possible that the search algorithm cannot match the optimal location for the following reasons.

- (1) The MODIS image data for the correct location of the search may be masked by clouds, or changed from land surface alterations.
- (2) The range of brightness for the requested search image and compared MODIS image data may be different due to difference in data retrieval time of the satellite data.

For the solution to problem (1), we proposed using multiple time-series data for the same search space, and applying GA within the time-series data to search for the requested image. For the solution to problem (2), we propose applying normalized correction, which is effective in matching images with different relative brightness, to the GA fitness function to improve the matching accuracy. We describe the basic flow of the proposed search process below. Figure 1 shows the image match search system outline.

- (1) At the server, the requested search image, search area, and search time span is specified.
- (2) The server distributes the search image, search area, and search time span for each individual client machine.
- (3) The requested search image and MODIS search space image data are converted from color images to grayscale images by each client. Each client applies distributed genetic algorithm to search for the requested image pattern among the distributed search space. Brightness of the gray-scale images is adjusted by the distributed genetic algorithm.
- (4) Clients which finished the search relays the search result to other clients.
- (5) When the search location is determined, each client analyzes the image data for the same location, and evaluates the land cover change for the time span.

3 Image Search Process using Distributed Genetic Algorithm

Recently, GA has attracted much attention as an effective method for solving large scale complex problems [1]. GA searches for the optimum solution by applying genetic operations of 'mutation', 'crossover',

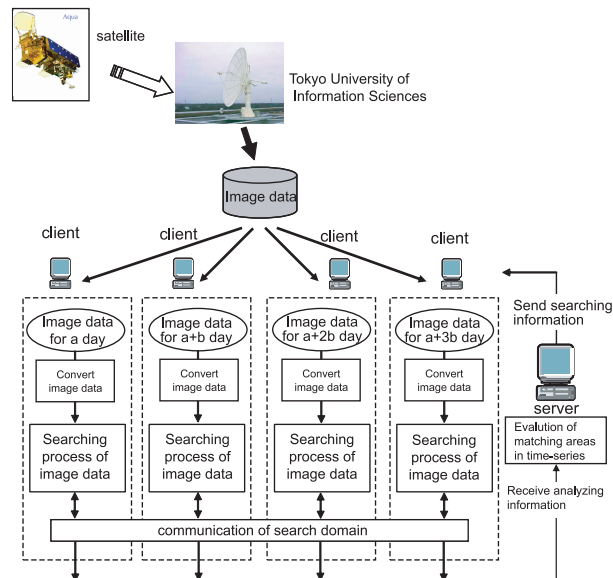


Figure 1: Outline of the image match search system

'evaluation' and 'selection' to the population. In the distributed GA model, the main population is divided into several subsets, and genetic operations are repeated among the distributed sub-population.

3.1 Distingued Genetic Algorithm

DGA (Distributed Genetic Algorithm) is a parallel model of GA. In DGA, the main population is divided into sub-populations. DGA is also called the 'island model' from to this feature.

The divided sub-population is distributed into several clusters for parallel processing, and each cluster executes the GA search on the sub-population received. At each predefined interval or number of generations, each cluster exchanges individual solutions or chromosomes. This is defined as a 'migration' operation.

For this research, time-series image data are distributed to PC clusters, and in each cluster the GA search is processed in parallel. The parallel search process is completed when any one of the clusters finds a strong match to the requested image pattern.

Figure 2 shows the outline of DGA model, executed that preprocessing brightness confronts.

3.2 Brightness Adjustment Method

MODIS data is the value of the strength of reflected wavelengths for specified bands. This means that the value of MODIS data (i.e. brightness) for

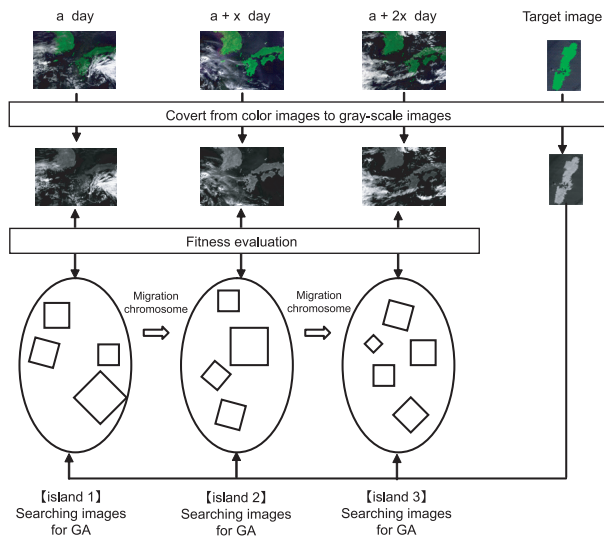


Figure 2: Outline of DGA model

the same location vary depending on the time of day. When searching for a matching image area within the MODIS image database, it is possible that the search algorithm cannot match the optimal location when the brightness of the search image and MODIS data image are very different.

MODIS data is the value of the strength of reflected wavelengths for specified bands. This means that the value of MODIS data (i.e. brightness) for the same location vary depending on the time of day. When searching for a matching image area within the MODIS image database, it is possible that the search algorithm cannot match the optimal location when the brightness of the search image and MODIS data image are very different. The pattern matching algorithm, such as GA, must be able to match similar location images with different brightness. In this research, we applied normalized correction, which is effective in matching images with different relative brightness, to the GA fitness function to improve the matching accuracy. Details of the fitness function is described in section 3.6. In order to shorten the computation time to acceptable limits for actual use, we first convert the RGB color image data for the search image to gray-scale images using the following equation [3].

$$p = 0.299 * R + 0.587 * G + 0.144 * B \quad (1)$$

where p is the image pixel of the gray-scale image, R,G,B are the respective red, green, and blue pixel data of the color image at the same pixel location.

x	y	rate	angle
---	---	------	-------

Figure 3: Contents of the chromosome

3.3 Chromosome Expression

The image matching problem is defined as an optimization problem of finding the highest matching rate image by modifying the 4 parameters: 1)x-axis location, 2)y-axis location for the center of the matching image, 3)the magnification rate, and 4)the rotation angle of the matching image. The GA chromosome is designed to encode the 4 parameters, and the fitness is defined as the matching rate of the compared image pixels. Figure 3 shows contents of the chromosome.

3.4 Selection, Crossover, Mutation Operations

In this paper, we evaluated the following genetic operation methods.

- (a) Selection Operation
The elite selection strategy was applied, in which the individuals with the highest fitness will be selected for the next generation.
- (b) Crossover Operation
For the selection operation, a single locus method is applied, in which a random locus or break point is selected and two parents chromosomes swap one side of the chromosome up to the break point. This creates two child chromosomes of the same length combining information of both parents.
- (c) Mutation Operation
For the mutation operation, 2 points in a single chromosome are selected at random, and the bit information between these 2 points are replaced in reverse order.

3.5 Distributed Genetic Algorithm Procedure

In this research, DGA is applied to the image match search system. The procedure for each client is the following.

- (1) Receive the search image, search area and search time span, and read the specified date and location MODIS data from the MODIS database.
- (2) Convert the color search image and color MODIS image data to gray-scale images.

- (3) Create initial population
Create an initial population of chromosomes with random parameters, with coordinates (x,y) for center of search region, magnification m, and rotation r.
- (4) Calculate the fitness of the chromosomes.
- (5) Evaluate the search completion condition.
- (6) If the search completion condition is met, notify the result to other clients.
- (7) If the completion condition is not met, continue with (8).
- (8) Selection
Select individuals based on fitness, and create m pairs randomly.
- (9) Crossover
Create new child chromosomes from the selected pairs as parents, applying the specified crossover operation strategy.
- (10) Mutation
Applying the specified mutation strategy, randomly modify a part of the selected chromosome.
- (11) Migration
At each specified number of generations, migrate selected chromosomes according to the specified migration strategy.
- (12) repeat from (3).

3.6 Fitness Evaluation

The fitness is evaluated by calculating the matching rate of the selected image pixel data that is specified by the search parameters encoded in the chromosome. The fitness function (C) is shown in equation (2), where the compared image size is $M(\text{pixel}) \cdot N(\text{pixel})$, the brightness value (color value) for the template (MODIS) image and compared search image at coordinates(x,y) are $T(x,y)$ and $I(x,y)$, respectively.

$$C = \frac{\sum_{x=1}^N \sum_{y=1}^M \{I(x,y) - \mu_I\} \cdot \{T(x,y) - \mu_T\}}{\sqrt{\sum_{x=1}^N \sum_{y=1}^M \{I(x,y) - \mu_I\}^2 \cdot \sum_{x=1}^N \sum_{y=1}^M \{T(x,y) - \mu_T\}^2}} \quad (2)$$

where

$$\mu_I = \frac{1}{NM} \sum_{x=1}^N \sum_{y=1}^M I(x,y) \quad (3)$$

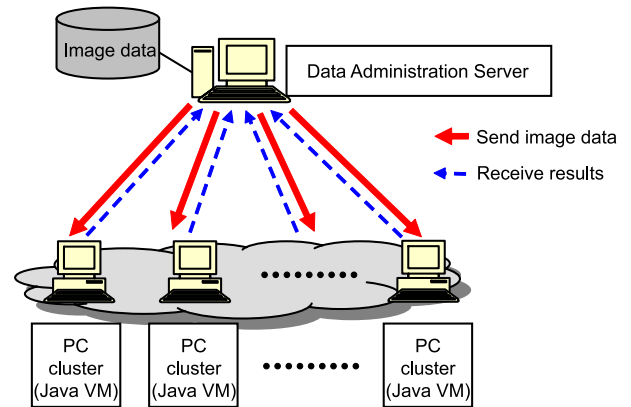


Figure 4: Outline of System Configuration

$$\mu_T = \frac{1}{NM} \sum_{x=1}^N \sum_{y=1}^M T(x,y) \quad (4)$$

The fitness function is evaluated, and when the fitness result exceeds a predefined value, the specified regions is selected as an optimal match of the search.

4 System Configuration

Figure 4 shows the image searching system configuration. The responsibilities of the data management server are 1)Managing the MODIS Image database, 2)Transmission of search information (MODIS satellite images and search space), 3)Configuration and transmission of DGA parameters. Each PC clustering client receives the search information and GA parameters from the server, and processes the image data search. Taking into account the ease of portability for a multiplatform cluster environment, the system was implemented using Java programming language. Java RMI (Remote Method Invocation) architecture was used to implement the network messaging and control features.

5 Expreiment Results

In this experiment, the effectiveness of the proposed brightness correction method in the image search system is evaluated. The system configuration of the experiment is shown in table 1. Table 2 shows the DGA parameters applied. Figure 5 shows the image of chromosome migration between islands (clients).

The mean retrieval times of 100 independent trials with different random initial populations were used

Table 1: Specification of PC Cluster system

Item	Contents
Number of PC	16
Specifications of PC	CPU: Intel Celeron D 310(2.13GHz) Memory: PC2700 DDRSDRAM 512MB

Table 2: DGA's parameter

Parameters		Contents
Basic GA	Population	200
Basic GA Parameters	Number of generations	2500
	Selection	Comparing fitness value of each generation
	Crossover type	1 point
	Crossover rate	0.5
	Mutation rate	0.05
	Maximum fitness value	0.6
	Strategy of selection	Elite
	Number of island	16
DGA Parameter	Interval of migrations	20
	Number of migrations	1 (population of maximum fitness value)
	Method of migrations	Neighbor (Migration to neighbor island)
	Strategy of migrations	The best chromosome is migration to the worst chromosome of neighbor island.

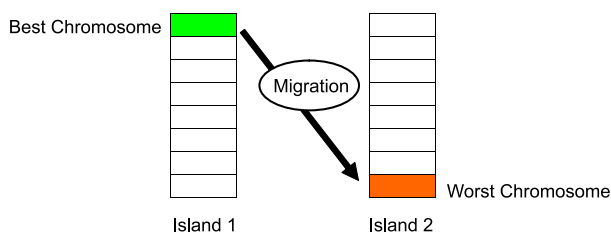


Figure 5: Example of migration between islands

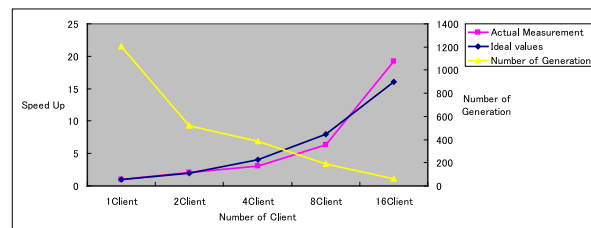


Figure 6: Evaluation results

to evaluate the performance of the proposed system. Figure 6 shows the results.

The measurement of each trial uses the elapsed time of when the performance measurement started searching and found the similarity image data. We were able to verify that by applying normalized correction, the matching accuracy for images with different relative brightness had improved compared to previous research[2]. Parallel efficiency is not enough in comparison with cluster number. However, the searching time of DGA decrease as increasing number of cluster and we confirmed the requested search image that have range of brightness is difference compared with MODIS image data can be searched.

6 Conclusion

We developed a distributed parallel processing system which searches for requested image patterns within a large-scale satellite image database. We applied normalized correction to the DGA fitness function used for the image search algorithm.

The tested results showed that the developed system with the proposed normalized correction method improved the matching accuracy for images with different relative brightness, compared to previous research. From this result we were able to verify that the proposed method was effective for matching images within templates of different relative brightness.

For future works, we plan to research algorithms to effectively search for complex formations and features, as well as investigate different methods to evaluate the time series change in land formations.

References

- [1] Akio YAMAMOTO, Hiroshi HASHIMOTO, Application of the Distributed Genetic Algorithm for IN-Core Fuel Optimization Problems under Parallel Computation Environment, Journal of NUCLEAR SCIENCE and TECHNOLOGY, Vol.39, No.12, P.1281-1288, December 2002.
- [2] Eiji Nunohiro, Kei Katayama, Kenneth J. Mackin, Masanori Ohshiro, Kazuko Yamasaki, Image Match Search System using Distributed Genetic Algorithm, SCIS&ISIS 2006, pp.1536-1541, September 2006.
- [3] Kunio Kashino, Takayuki Kurozumi, Hiroshi Murase, Quick AND/OR Search for Multimedia Signals Based on Histogram Features, The transactions of the institute of electronics, information and communication engineers D-II Vol.J83-D-II No.12 pp.2735-2744, December 2000.

Job-shop Scheduling Problems Based on Immune Ant Colony Optimization

Ming-lei SUI

Yong-li ZHANG

Engineering Institute of Engineering Corps
 PLA Univ. of Science and Technology
 Nanjing 210007, Jiang Su China

Engineering Institute of Engineering Corps
 PLA Univ. of Science and Technology
 Nanjing 210007, Jiang Su China

Email: good823@163.com; zyl19810723@yahoo.com.cn

Abstract

Mathematic model of Job-shop scheduling problem was established, and a kind of immune ant colony algorithm is introduced to dispose Job-shop scheduling problem. Through introducing the mechanism of immunity into the operations of genetic algorithm, the vaccines is obtained and updated in those operations. Then, the immune operation is used on the evolution of populations. And the problems on easy appeared precocity, low searching efficiency can be avoided when immune operation takes effect. The simulations show that the algorithm is feasible and efficient.

Keywords: job-shop scheduling; Ant colony algorithm; artificial immune algorithm

1 Introduction

The job shop scheduling problem (JSP) is a central NP-hard problem in Operations Research and Computer Science [1] that has been studied extensively from a variety of perspectives in the last thirty years. Genetic algorithm has been heavily employed in JSP [2]. Aiming to GA's inefficiency and pre-mature, this paper combines the ideals of the Ant colony algorithm and Immune algorithm together, and applies the proposed algorithm into JSP. The main ideal is to distill and inject the vaccines from and in the evolving colony, in order that the evolution will be more steady-going and quickly.

2 Description for the problem and its math model

Job-shop scheduling problem's math model is a typical integer programming model. To this problem, there are two subjects: machine subject, which is

processing order, another is time subject, which is the subject that process's time wasting.

$$\min \sum_{i=1}^n \max \{c_{ih}\} \tag{1}$$

$$s.t. c_{ik} - t_{ik} + M_0(1 - a_{ihk}) \geq c_{ih} \tag{2}$$

$$i, j = 1, 2, \dots, n; \quad h, k = 1, 2, \dots, m$$

$$c_{jk} - c_{ik} + M_0(1 - x_{ijk}) \geq t_{jk} \tag{3}$$

$$i, j = 1, 2, \dots, n; \quad h = 1, 2, \dots, m$$

$$c_{ik} \geq 0; \quad i, j = 1, 2, \dots, n; \quad h = 1, 2, \dots, m$$

Define a_{ihk} and x_{ijk} as follows:

$$a_{ihk} = \begin{cases} 1 & \text{machine } i, \text{ if machine } i \text{ before } k \\ 0 & \text{else} \end{cases} \tag{4}$$

$$x_{ijk} = \begin{cases} 1 & \text{workpiece } i \text{ before } j \text{ to reach machine } k \\ 0 & \text{else} \end{cases} \tag{5}$$

M_0 is a maximum, which is used as a punishment for the subjects.

3 Ant colony optimization and Immune algorithm

Ant algorithm was first proposed by Dorigo and colleagues [3, 4]. Its essential idea of ACA is that: the individual searching behavior which is directed by the different probabilities to the next node forms colony intelligent. It is *versatile* and *robust* in solving integer programming such as NP problem[5].

However, due to its inherent *defects* it needs more time to find the global optimal, its complexity can reflects that. It is likely to be trapped in local optimal and stop evolving, and can't exploit new search space. This phenomenon can be seen in many simulations.

Immune algorithm (IA) is a bionic algorithm as a

simulation of immune system, which combines the certain and random together and has the capacity to reconnaissance and exploit. It's a developmental random search algorithm. Immune algorithm is inspired of cell theory and net theory, and it realized the function of self-adjust and creation of different antibody. It's a new algorithm which is characteristic of searching in multi-peak value and the capacity of global searching [6]. Through the combination of ACA and IA, we can diversify the colony and the colony's evolution will not only be directed by the pheromone, but also by the immune system. We combined the random factor and certain factor together, so we can improve the search efficiency and quality, enrich the diversity and resist the pre-mature.

4 Job shop scheduling based on immune ACA

4.1 Initialize the antibodies

The antibodies are initialized as a series of random permutations of the integers from 1 to $m \times n$, which stand for the ants' routing order. We obtain the antibodies as Ref.7, after the steps as follows.

Step1: Create a random permutation of the integers from 1 to 9: such as [5 2 8 4 3 9 7 6 1].

Step2: array=array-1: [5 2 8 4 3 9 7 6 1]-1=[4 1 7 3 2 8 5 0].

Step3: divide matrix by m , and then add 1: $\text{int}([4 1 7 3 2 8 5 0]/3)+1=[2 1 3 2 1 3 3 2 1]$.

Then we obtain an antibody as Ref.7, where: 1 stands for job 1, and the same to 2, 3. The first 2 stands for stage 1 of job 2, the same to 1, 3.

4.2 Decoding scheme

The crucial of the procedure is to guarantee two steps:

- (1) The same stage can't be done on two different machines;
- (2) The same machine can't do two job at the same time.

In programming, two tags are set: job time tag (JobTime_Tag) and machine time tag (Mac_Time_Tag).

Every stage's start time is $\max(\text{MacTime_Tag}, \text{JobTime_Tag})$.

The steps to operate are as follows:

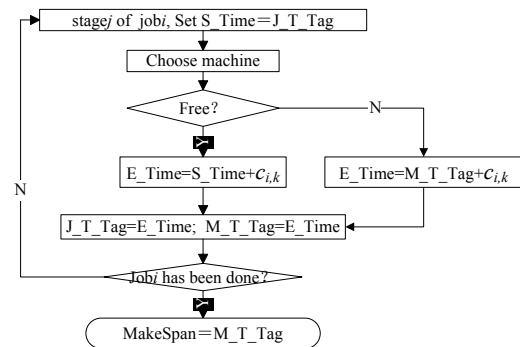


Fig. 1. sketch map for decoding

4.3 Steps for immune ACA

The procedure of the ACO algorithm manages the scheduling of three activities: ants' generation, actions and pheromone update. The steps of Immune Ant Colony Algorithm in this are follows:

1) Select list replace tabu list

The way in tabu list results in that it's hard to select next node. If some nodes have been selected, there will be some vacancies. It's more complex to handle the data, so change the tabu list to select list. The operations are explained as follows:

If the node has been selected, erase it from the select list, and the following nodes move forward. For example: if node.1 has been selected, change the list to: {2→3→4→5→6→7→8→0}, then the node.7: {2→3→4→5→6→8→0→0}, until the last: {5→0→0→0→0→0→0→0}.

2) Pick-up vaccines from memory storeroom

Memory storage is used for storing the best ant, the better ant and the poor ant. Vaccines are picked-up from the memory storage through the follow formulas at a certain probability.

The antibodies of higher thickness and lower appetency will be restrained, and the antibodies of lower thickness and higher appetency will be promoted. So the ant colony will be more diversiform. The i th antibody will be selected as [8]:

$$D(X_i) = \frac{1}{\sum_{j=1}^{N_0} |f(x_i) - f(x_j)|} \quad i=1,2,\dots,N_0 \quad (6)$$

$$p(x_i) = \frac{1}{D(X_i)} = \frac{\sum_{j=1}^{N_0} |f(x_i) - f(x_j)|}{\sum_{i=1}^{N_0} \frac{1}{D(x_i)} \sum_{j=1}^{N_0} |f(x_i) - f(x_j)|}, i=1,2,\dots,N_0 \quad (7)$$

3) Decide the next one to be processed

Take advantage of Roulette select scheme in GAs: select operation is based on the individual's adaptive value. The most well-known scheme is Roulette select scheme proposed by Holland [9].

$$p_{si} = f_i / \sum_{i=1}^N f_i \quad (8)$$

N is the number of nodes that are can be selected, $f_i = [\tau_{ij}(t)]^\alpha \cdot [\eta_{ij}]^\beta$. The steps are as follows: Compute the value according to f_i ; accumulate every element; the array divides the sum of every element.

4) Injection vaccine

Select a piece of information segment from the selected antibody at a certain probability, and inject the vaccine to the ant. Just as fig.2 shows:

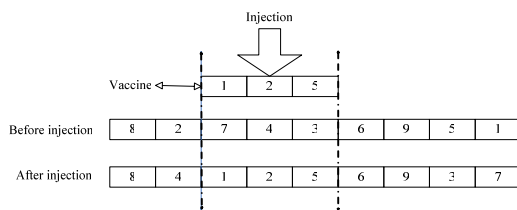


Fig. 2. sketch map for vaccinating

5) Introduce mutation, crossover

In order to avoid the pre-maturity of the ACA, mutation, crossover[10] are introduced into this way which can guarantee the diversity of solutions, exploit new search space, and then the phenomena trapped in the local optimal can be avoid to a certain extent.

Mutation is operated when the route has been done by an ant. Randomly select two nodes in its path, swap them, and then replace them to the rout.

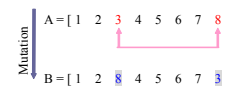


Fig. 3. Sketch map for mutation

After mutation, compute the new ants' f_i , select the better to save.

Crossover is operated after all the ants finished their routs. Randomly select two ants and operate as Fig.4 illustrates:

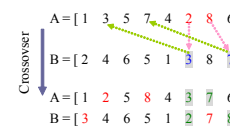


Fig. 4. Sketch map for crossover

After crossover, compute the new individuals' f_i , and the better individuals survive to the next repetition.

5 Instances simulation

Literature [12] gives the study conclusion on how to select α , β , ρ . In this paper, after some tries, the parameters are set as follow: $\alpha=1$, $\beta=5$, $\rho=0.6, Q=1000$, and set iterations=500.

5.1 Instance 1

This is a Job-shop scheduling problem select from Ref.13: LA01(10×5). All of the basic ACA and IACA obtain the optimum: 666, the comparisons between them are showed as follows:

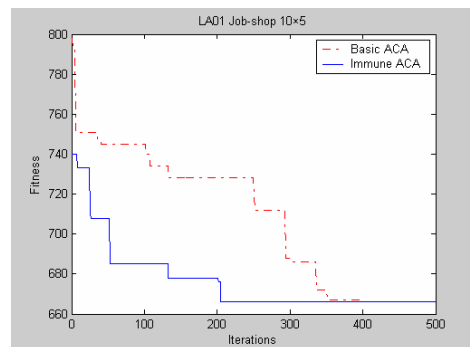


Fig. 5. Comparison in solving LA01

5.2 Instance 2

This is a Job-shop scheduling problem select from Ref.13: LA06(10×10). All of the basic ACA and IACA haven't obtained the optimum; basic ACA: 990, IACA: 945. The comparisons between them are showed as follows:

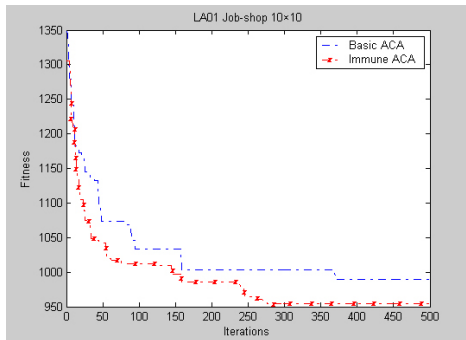


Fig. 6. Comparison in solving LA06

6 Conclusions

This paper applies ant colony algorithm to JSP, and then introduces immune algorithm to the ACA, and designed the selection and the injection criterions for vaccines. From the simulations we know that the search efficiency and quality are improved, and the diversity is enriched, the pre-mature is refrained.

References

- [1] Dimitris Bertsimas, Jay Sethuraman (2002), From fluid relaxations to practical algorithms for job shop scheduling: the makespan objective. *Math. Program., Ser. A* 92: 61-102
- [2] WANG Ling, ZHENG Da-zhong (2001), Advances in Job Shop Scheduling Based on Genetic Algorithm. *Control and Decision*, 11(16):641-646.
- [3] M Dorigo, V Maniezzo and A Colomi (1991). The Ant System: An Autocatalytic Optimizing Process[R]. Technical Report No.91-016 Revised, Politecnico di Milano, Italy.
- [4] Marco Dorigo (1996). The Ant System: Optimization by a colony of cooperating agents[J]. *IEEE Transactions on System, Man, and Cybernetics-part B*, 26(1): pp29-41.
- [5] A.Colomi, M.Dorigo, V.Maniezzo, M.Trubian (1994), Ant system for Job-Shop Scheduling, *Belgian Journal of Operations Research, Statistics and Computer Science*.
- [6] GE Hong (2002). Immune Algorithm: A Survey, *JOURNAL OF SOUTH CHINA NORMAL UNIVERSITY (NATURAL SCIENCE EDITION)*, 3:12-126
- [7] CHEN Xiong, LI Hai-gang, WU Qi-di (2002). Study on Job - shop Scheduling Problem Based on Genetic Algorithm. *JOURNAL OF TONG JI UNIVERSITY*, 30(1):88-91.
- [8] Lovbjerg M, Rasmussen T K, Krink T (2001), Hybrid particle swarm optimization with breeding and subpopulations[C]. In: Proc of third Genetic and Evolutionary computation conference, San Francisco, USA.
- [9] D. Goldberg and R. Lingle (1985), Alleles, loci and the traveling salesman problem, *The first International Conference on Genetic Algorithm*, pp. 154-159.
- [10] Bierwirth C, Mattfeld D C (1999). Production Scheduling and Rescheduling with Genetic Algorithms. *Evolutionary Computation*, 7(1):1-17
- [11] Zne-Jung Lee, Chou-Yuan Lee and Shun-Feng Su (2002), An immunity-based ant colony optimization algorithm for solving weapon-target assignment problem. *Applied Soft Computing*. (2) pp:39-47.
- [12] YE Zhi-wei, ZHENG Zhao-bao (2004), Configuration of Parameters α , β , ρ in Ant Algorithm. *Geomatics and Information Science of Wuhan University*. 07 pp:597-601. (In Chinese)
- [13] WANG Ling (2001), *Intelligence Optimal Algorithm & Application*. Beijing: Tsinghua press.

Features of action potential initiation in cortical neurons with multiple internal states

Miki Matsuo and Kazuyuki Aihara,
Aihara Complexity Modeling Project
ERATO, JST, The University of Tokyo
4-6-1, Meguro-ku, Komaba, Tokyo, 153-8505, Japan.
Institute of Industrial Science, The University of Tokyo
4-6-1 Komaba, Meguro-ku, Tokyo 153-8505, Japan.

Abstract

Analyzing the dynamics of action potential initiation in cortical neurons *in vitro*, some features of the initiation dynamics of cortical neuron action potentials are shown to be outside the range of behaviors described by the Hodgkin-Huxley formalism. We propose a new model which describes the dynamics of sodium channel, where we are based on the hypothesis that the gate subunits are interacting each other. This model can reproduce one of the features of action potential initiation in cortical neurons, variant onset potential.

1 Introduction

Hodgkin-Huxley formalism is a great guidepoint in physiology, because it showed that a mathematical study can contribute to understand the function of nerve for the first time. This formalism not only describe the electrical phenomena of nerve excitation well as data fitting but also describes nature of electrically excitable membrane. Hodgkin-Huxley formalism considers excitable membrane as a population of ionic channels, and provides us various insights about functional structures of ionic channels [1].

Hodgkin-Huxley formalism has several assumptions in the starting point of the consideration. Here we give three assumptions of those.

- The state of an ionic channel is determined by conformation of subunits called gates.
- A gate can be in either of two conformations which are uniquely determined by membrane potentials.
- Gates are independent of each other.

In terms of structure of channel, these assumptions means that channel is not fundamental element itself but is composed of more fundamental gate elements, the gate obeys to very simple rules, and the actions of the gates are affected by voltage sensor. Thus we see that these assumptions provide rigorous descriptions about structure of ionic channel. These descriptions have been verified by cloning or X-ray structure analysis [2, 3], but even now these are fundamental concepts in understanding ionic channel.

On the other hand, the phenomena which are not described by H-H formalism are also discussed. About twenty years ago, Matsumoto insisted that, in order to describe action potentials in squid axon, it is necessary to assume that the conformation changes of gates are not only determined by membrane potentials but also the time after onset [4]. Recently Naundorf *et al.* insisted that two characteristic features of action potential initiation in neurons in cat visual cortex *in vitro* and *in vivo*, rapid onset of action potential and variance of onset potential, cannot be described by H-H formalism [5]. As shown in Fig.(1), action potential initiation recorded from rat hippocampal CA3 pyramidal cell *in vitro* also shows variance of onset potential. Thus detailed analysis have revealed features that are impossible to be described by H-H formalism. How those features are made by ionic channel, and how should we change our recognition of ionic channel? In this paper, we especially note on one of the features, variant onset potential. We propose that this variance can be produced by gates which interacts each other, while gates are assumed to be independent in the H-H formalism. With this proposition, we will see that ionic channel is not a simple but a complicated object which is composed of mutually communicating several subunits.

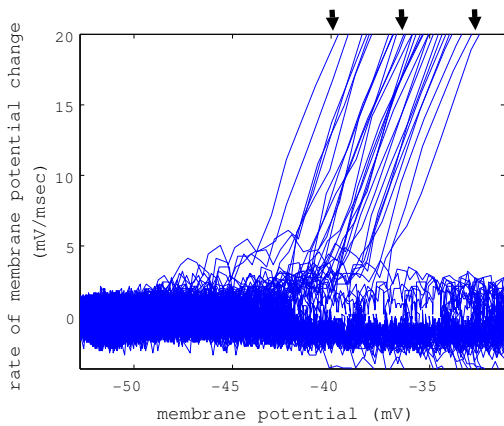


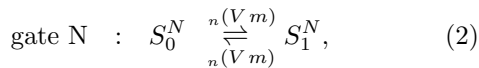
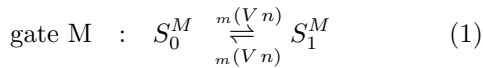
Figure 1: Phase plot (dV/dt versus V) of the action potential around the initial phase of the action potential in cortical neurons recorded *in vitro*. Arrows indicate three sample action potentials. The experimental data was provided by Hujisawa *et al.* [6].

2 Model

In order to understand the features of the action potential initiation, we consider a sodium channel composed of several gates that are not independent. (Here we call fundamental subunit which take two state "gate", even when it is not related to open-close of the channel.) This model is shown to be able to produce variation of onset potential.

The model is defined as following. We assume a sodium channel is composed of three types of gates, M, N, and H, and their gate variables are m, n , and h . Among these gates, M and H are activation and inhibition gates for each as given in the H-H formalism, and N is another gate that we introduce here. We assume that H gate does not work, that is $h = h_0(\text{const})$, in this paper.

Conformation changes of gates M and N are assumed to mutually catalyze as



where catalytic relation is included in state dependence of transition rate of gate state. The rate equations of these reactions are given by

$$\frac{dm}{dt} = m(V, n)(1 - m) - m(V, n)m \quad (3)$$

$$\frac{dn}{dt} = n(V, m)(1 - n) - n(V, m)n \quad (4)$$

Now we restrict the catalytic reaction to first order, so that the transition rates become

$$m(V, n) \simeq \frac{0}{m}(V) + \frac{1}{m}(V)(n - n_0), \quad (5)$$

$$n(V, m) \simeq \frac{0}{n}(V) + \frac{1}{n}(V)(m - m_0), \quad (6)$$

$$m(V, n) \simeq \frac{0}{m}(V), \quad n(V, m) \simeq \frac{0}{n}(V), \quad (7)$$

where m_0, n_0 are constants which imply gate states where catalytic function works well. Thus the rate equations are linearized as

$$\frac{dm}{dt} = \frac{0}{m}(V)(1 - m) - \frac{0}{m}(V)m + \frac{1}{m}(V)(n - n_0) \quad (8)$$

$$\frac{dn}{dt} = \frac{0}{n}(V)(1 - n) - \frac{0}{n}(V)n + \frac{1}{n}(V)(m - m_0) \quad (9)$$

The ionic current caused by the sodium channel is assumed to be affected gate M and N as

$$I_{Na} = \bar{g}_{Na} m h_0 (V - V_{Na}). \quad (10)$$

Eqs.(8)(9)(10) and the balance equation between membrane potential and ionic current are taken as our model of action potential. In our numerical simulations, we assume that the transition rates takes following sigmoid forms,

$$\frac{0}{m}(V) = \tau_{m0}^{-1} / (1 + \exp(-(V - V_{m0})/k_{m0})) \quad (11)$$

$$\frac{0}{n}(V) = \tau_{n0}^{-1} / (1 + \exp(-(V - V_{n0})/k_{n0})), \quad (12)$$

$$\frac{1}{n}(V) = \tau_{n0}^{-1} / (1 + \exp(-(V - V_{n0})/k_{n0})) \quad (13)$$

$$\frac{0}{n}(V) = \tau_{n0}^{-1} / (1 + \exp(-(V - V_{n0})/k_{n0})), \quad (14)$$

$$\frac{1}{m}(V) = \tau_{m1}^{-1} / (1 + \exp(-(V - V_{m1})/k_{m1})) \quad (15)$$

$$\frac{1}{n}(V) = \tau_{n1}^{-1} / (1 + \exp(-(V - V_{n1})/k_{n1})). \quad (16)$$

The concept of our model is illustrated in Fig.(2), but detailed explanation is given latter.

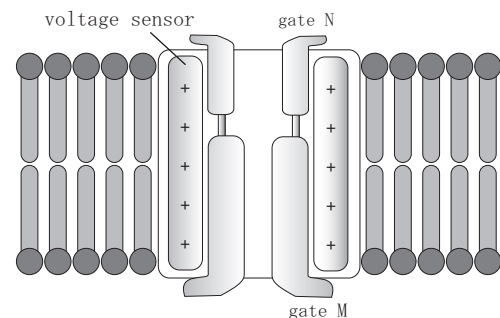


Figure 2: Illustration of the concept of the interacting gates model. Voltage sensor affects to the actions of gate M and gate N, while these gates interact each other.

3 Result

Now we investigate behavior of the model. In our simulation, values of the parameters are assigned referring parameters used in the H-H equations, except for the parameters used in Eqs. (11)~(16). We used parameter values as $\tau_{m0} = 0.1\text{ms}$, $V_{m0} = 35\text{mV}$, $k_{m0} = 6\text{mV}$, $\tau_{n0} = 60\text{ms}$, $V_{n0} = 80\text{mV}$, $k_{n0} = 4\text{mV}$, $\tau_{m1} = \tau_{n1} = 0.1\text{ms}$, $V_{m1} = V_{n1} = 30\text{mV}$, $k_{m1} = k_{n1} = 6\text{mV}$. Phase plot that graph the rate of change of the membrane potential dV/dt against the instantaneous membrane potential V is shown in Fig.(3). Although the onset is seen to be slow compared to experimental data, we can see the variance of onset potential. (Note that it is necessary to consider another mechanism in order to get a rapid onset [5].) This variance of onset potential is considered to be

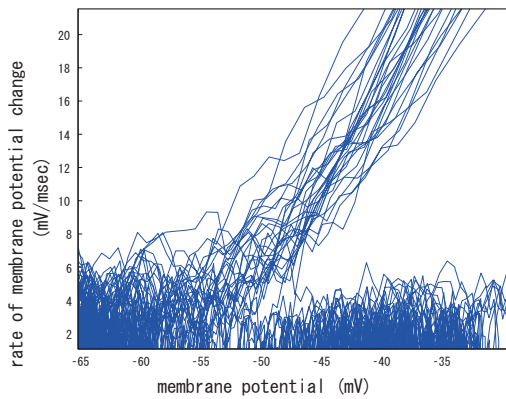


Figure 3: Phase plot calculated with the interacting gates model. Although the onset is seen to be slow compared to experimental data, the variant onset potential is seen.

made by internal dynamics of the state of the sodium channel. In Fig.(4), we show the orbit of the channel state (m, n) . As we see, the channel is closed ($m = 0$) and the value of n gradually decreases before action potential initiation, and excitation follows ($m > 0$) afterward. Here we note that excitation happens not at a constant value of n but at various values of n . And we can show with Eq.(8) that the onset value of potential depends on the value of n . Thus it can be said that the channel with interacting gates as shown in Fig.(4) can produce the onset potential variation.

Lastly we say about relation between dynamical feature supposed in the interacting gates model and structure of ionic channel. In the H-H formalism, the action of voltage sensor is transmitted to each selective

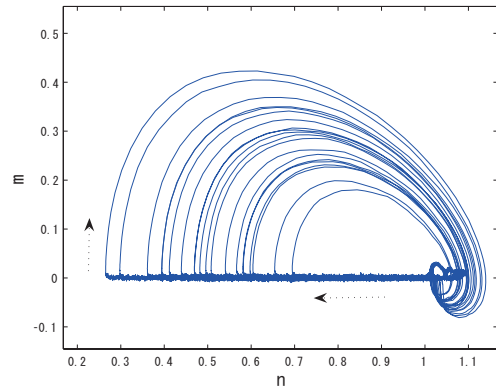


Figure 4: Orbit of the channel state (m, n) . Excitation of gate M is not happened at constant value of gate variable n , but excitations can be initiated at various values of n .

filter (gate), and each selective filter independently open or close. In interacting gates model, voltage sensor affects to not only selective filter but also hidden gate component, and this hidden gate component mutually interacts with the selective filter (Fig.(2)). This might be related to paddle hypothesis recently proposed by MacKinnon *et al.* [3]. In the conventional idea, the action of voltage sensor affects only to local structure around sensor, while paddle hypothesis consider that voltage sensor can change global form of the channel. The change of global structure can be interpreted as the case that the local subunits are strongly correlated. In our study, we have seen that fluctuation of action potential includes features which does not emerge in the case that channel is a simple compound of local units. This would also imply that analysis of fluctuation is useful to generally consider structure and function of channel.

4 Summary

In order to understand the features of the action potential initiation, we proposed a new model which describes dynamics of sodium channel, where we assumed the channel is composed of several gates that are not independent. One of the features of action potential initiation, fluctuating onset potential, were shown to be able to be reproduced by this new model. This implies that the ionic channels are not simple compound of local units but global and complex object whose subunits are strongly correlated. This would

mean that analysis of fluctuation is useful to generally consider structure and function of channels.

Acknowledgements

We thanks to S. Fujisawa to kindly provide us experimental data of action potential.

References

- [1] A. L. Hodgkin and A. F. Huxley, *J. Physiol. (Lond.)*, vol. 117, pp. 500-544, 1952.
- [2] M. Noda, H. Takahashi, T. Tanabe, M. Toyosato, S. Kikuyotani, Y. Furutani, T. Hirose, H. Takashima, S. Inayama, T. Miyata, S. Numa, *Nature* vol. 302, pp. 528 - 532 1983.
- [3] Y. Jiang, A. Lee, J. Chen, V. Ruta, M. Cadene, B. T. Chait and R. MacKinnon, *Nature*, vol. 423, pp. 33-41, 2003.
- [4] G. Matsumoto, *J. theor. Biol.*, vol. 107, pp. 649-666, 1984.
- [5] B. Naundorf, F. Wolf, and F. Volgushev, *Nature*, vol. 440, 1060-1063, 2006.
- [6] S. Fujisawa, N. Matsuki and Y. Ikegata, *em Cerebral Cortex*, vol. 16, pp. 639-654, 2006.

Signal Processing With Spikes

Michael Gutmann
Grad. School of Inf. Science and Technology
The University of Tokyo
gutmann@sat.t.u-tokyo.ac.jp

Kazuyuki Aihara
Institute of Industrial Science
The University of Tokyo,
& Aihara Complexity Modelling Project
ERATO, JST
aihara@sat.t.u-tokyo.ac.jp

Abstract

In the past, notable advances in the understanding of neural processing have been made when sensory systems were investigated from the viewpoint of adaptation to the statistical structure of its input space. Here, we point out that emphasis on the input structure has happened at cost of the biological plausibility of the corresponding neuron models which process the natural stimuli. Hence, we propose a spiking neuron model to process natural stimuli for which we derive here a learning rule to estimate its parameters.

1 Introduction

Science is about exploring structure and function of incompletely understood systems or phenomena. What concerns the system “brain” or the phenomena of “learning” or, say, “vision”, great advances have been made since the debates in the early 20th century whether individual neurons are the basic elements of the nervous system or not (keyword neuron doctrine). Since then, much emphasis has been on *structure*, i.e. on individual neurons or on how distinct classes of neurons are connected with each other. However, the *functional* aspect of these networks of neurons cannot be fully understood by its structure alone: How are the interconnected neurons marshaled to give rise to behavior? Why are the neurons as they are? Why are they connected they way they are?

2 Background

These kind of questions were mostly addressed from the second half of the 20th century onwards. The brain was considered as a information processing system, and principles of signal processing and information theory were used to understand the *function* of

some parts of the brain (redundancy reduction hypothesis) [2]. As information theory requires knowledge about the statistical structure of the information source, this approach triggered research into properties of the sensory environment, especially with respect to vision [4, 6, 14, 16], and its link to neural processing [1, 3, 5, 15, 17]. What regards vision, in addition to the principles of information theory, other principles were used to explain its function in the form of “The early visual system might be optimized for ...”, including energy expenditure [18], minimal wiring among neurons [8], or minimal number of active neurons [12]. The early visual system comprises the retina, thalamus and the primary visual cortex. But higher visual areas have also been investigated in this manner, making interesting predictions on yet undiscovered cell types [9, 10].

3 Research question

What regards the early visual system in the retina, multiple “principles of operation” for its function have thus been formulated. Which is the right one? We think that this question is ill posed since it is unlikely that the forces of evolution can be reduced to a single optimization scheme. But it is worth remembering that the above theories for the retina use the following assumptions which we might summarize as linear rate-coding assumption.

- Information is conveyed using a firing rate code.
- Retinal processing is described by a linear filter.
- The statistics of the natural scenes is described by the power spectrum.

Although these assumptions are of course well justified as a first approximation to reality, we feel it is

time to re-consider some of them. Motivation comes from the finding that the linear rate-coding assumption becomes a limiting factor for the deeper understanding of the retina – as explained above, actually different optimization schemes give the same results under that assumption – and for the link to experimental results. First, single spikes were found to be information carrier in the early visual system of for example the fly [13], second, significant redundancy was found between retinal ganglion cells (also for cells with non-overlapping receptive fields) [11]. Hence, in the following, we re-address the neural processing of the retina. Specifically, we make the modification that neurons are modeled as integrate and fire elements, so that the research question becomes

Which properties of the neural system “retina” can be explained with the function-hypothesis that neurons in the retina encode the input with spikes such that it can be linearly reconstructed from the spike times with a minimal reconstruction error.

4 Processing natural stimuli with spikes

Here, we present a learning rule for the minimization of the reconstruction error. The learned filters and their relation to the early visual system will be discussed elsewhere. Further, we limit ourselves to a single neuron. In Section 4.1, we present the model, in Section 4.2 we derive a learning rule for the minimization of the reconstruction error, and in Section 4.3, we discuss the obtained learning rule.

4.1 Model

A neuron is modeled with the *SMR₀*-model [7]

$$u(t) = \eta(t) + \int_0^t \kappa(t-s)I(s)ds, \quad (1)$$

where

$$\eta(t) = \sum_{f:t^f < t} \eta_0 \exp\left(-\frac{t-t^f}{\tau_r}\right) \quad (2)$$

$$I(s) = \int_0^s w(s-v)Y(v)dv. \quad (3)$$

The spike times $\{t^f; f = 1, 2, \dots\}$ are defined by the instant of time where u reaches the threshold θ . Each spike triggers the reset of u from θ to $\theta - \eta_0$, and the neuron enters a time of reduces excitability modeled

with an exponential kernel with refractory time constant τ_r . The neuron is driven by external input I , which is obtained through linear filtering of the natural stimulus Y with the encoding filter w . The kernel κ models the soma impulse response function with an exponential kernel with time constant τ_m .

From the obtained spike times $\{t^f\}$, we linearly reconstruct the stimulus Y via

$$\hat{Y}(t) = \sum_{f:t^f < t+T_d} \Phi(t-t^f), \quad (4)$$

with the decoding filter Φ and estimation time delay T_d .

Both the encoding filter w and the decoding filter Φ are unknown, and have to be found in order to minimize the average reconstruction error J

$$J = \left\langle \frac{1}{2} \int_0^{T_t} e(t)^2 dt \right\rangle \quad (5)$$

$$\text{where } e(t) = \hat{Y}(t) - Y(t), \quad (6)$$

and $\langle \rangle$ denotes the sample average over the database of natural stimuli Ω_Y .

4.2 Learning rule to minimize the reconstruction error

Above, we have silently assumed that we know the spike timings $\{t^f\}$ exactly. However, both in experiments as well as in computer simulations, spikes can only be tracked to a maximal temporal precision Δ . This implies that the integration in Eq. (1) has to be replaced by a summation, and all variables take values in bins of size $h \geq \Delta$. This means that only finitely many parameters $w[1], \dots, w[N]$ and $\Phi[-Nd], \dots, \Phi[Nt-1]$ with $N = Nd + Nt = (T_d + T_t)/h$ have to be learned.

For a steepest descent learning algorithm, direct calculation shows that the gradient for the encoding filter is given by

$$\frac{\partial J}{\partial w[n]h} = \left\langle \sum_{k=1}^{Nt} h e[k] \Psi_n[k] \right\rangle \quad (7)$$

$$\Psi_n[k] = \sum_{k^f \in T(n, k+Nd)} \Phi[k-k^f] c_n^f \quad (8)$$

$$c_n^f = \frac{1}{\alpha(u[k^f] - u[k^f-1])} \left(\bar{Y}[k^f-n] + \sum_{p^m \in T(n, k^f)} c_n^m \eta_0 \exp\left[-\frac{(k^f-1-p^m)h}{\tau_r}\right] \right), \quad (9)$$

where $n = 1, \dots, N$. The term $T(x, y)$ denotes the set of spike times k^f satisfying $x \leq k^f < y$, and the constant α is a real number slightly less than 1. \bar{Y} is the natural stimulus Y input after filtering with the soma response kernel κ .

Similarly, for $n = -Nd, \dots, Nt - 1$ the gradient for the decoding filter is given by

$$\frac{\partial J}{\partial \Phi[n]h} = \left\langle \sum_{k^f \in T_n} e[k^f + n] \right\rangle \quad (10)$$

$$\text{for } T_n = T(\max(1, 1 + n) - n, Nt - n). \quad (11)$$

4.3 Interpretation

We discuss the obtained formulae for the gradients for the decoding and encoding filters.

4.3.1 Decoding filter

From Eq. (4), we see that the reconstruction kernel $\Phi[n]$ bears a different interpretation for $n > 0$ and $n < 0$. That is why we obtain slightly different formulae for the gradient of the decoding filter Φ .

For $n = k - k^f < 0$, the spike k^f happens after the time step k for which we try to *reconstruct* Y . Thus, by $\Phi[n]$ we try to estimate the stimulus which precedes the spike at k^f by n units. Here, T_n becomes

$$T_n = T(1 + |n|, Nt + |n|), \quad (12)$$

so that for, say, $n = -Nd$, we consider spikes happening from $Nd + 1$ till the end $N = Nd + Nt$, and the gradient is given by the sum of errors which were made Nd time steps before the spike event.

For $n = k - k^f > 0$, however, the spike k^f happens before the stimulus $Y[k]$ which we try to approximate with $\Phi[n]$. Thus $\Phi[n]$ is used to *predict* from the spike time k^f the stimulus which happens n time units afterwards. Here, T_n becomes

$$T_n = T(1, Nt - n), \quad (13)$$

so that for, say, $n = 1$, we consider spikes happening from time step 1 till $Nt - 1$, and the gradient is given by sum of errors made one time step after the spike event.

4.3.2 Encoding filter

The gradient of the encoding filter w is given by the inner product between the reconstruction error e and the function Ψ_n . From the formulae, we see that this function is a superposition of shifted, weighted decoding

filters. The weighting coefficient c_n^f is determined by the input $\bar{Y}[k^f - n]$ and the prior coefficients $c_n^1 \dots c_n^{f-1}$ as well as the slope with which the membrane voltage u crosses the threshold θ . The influence of the prior coefficients decays exponentially with the distance between the spike times. Since η_0 is a constant less than zero, the influence of the prior coefficients is subtractive for spike times which are close together.

5 Summary

In the ongoing search for understanding of the early visual system great advances have been made through investigations in the statistical properties of natural stimuli. We pointed out that the corresponding neuron models, which process the natural stimuli, tend to be however too simple and might be a limiting factor for further advances. Here, we made the step to biologically more plausible models and considered processing of natural stimuli by means of spiking neurons. Requiring linear reconstructability of the input from the spike train, we derived a learning rule for both encoding and decoding filter, showing thus how parameters of a spiking neuron model can be learned from natural stimuli.

Acknowledgments

This study is partially supported by Grant-in-Aid No. 17022012 for Scientific Research on Priority Areas System study on higher-order brain functions from the Ministry of Education, Culture, Sports, Science and Technology of Japan. MG is further supported by MEXT grant No. 040680.

References

- [1] J.J. Atick and A.N. Redlich. Towards a theory of early visual processing. *Neural Computation*, 2:308–320, 1990.
- [2] H.B. Barlow. Possible principles underlying the transformations of sensory messages. In W. Rosenblith, editor, *Sensory Communication*, pages 217–234. MIT Press, 1961.
- [3] Yang Dan, Joseph J. Atick, and R. Clay Reid. Efficient coding of natural scenes in the lateral geniculate nucleus: Experimental test of a computational theory. *J. Neurosci.*, 16(10):3351–3362, May 1996.
- [4] Dawei Dong and Joseph Atick. Statistics of natural time-varying images. *Network: Computation in Neural Systems*, 6(3):345–358, August 1995.

- [5] Dawei Dong and Joseph Atick. Temporal decorrelation: a theory of lagged and nonlagged responses in the lateral geniculate nucleus. *Network: Computation in Neural Systems*, 6(2):159–178, May 1995.
- [6] Robert A. Frazor and Wilson S. Geisler. Local luminance and contrast in natural images. *Vision Research*, 46(10):1585–1598, May 2006.
- [7] W. Gerstner and W. K Kistler. *Spiking Neuron Models*. Cambridge University Press, 2002.
- [8] Daniel J. Graham, Damon M. Chandler, and David J. Field. Can the theory of "whitening" explain the center-surround properties of retinal ganglion cell receptive fields? *Vision Research*, 46(18):2901–2913, September 2006.
- [9] A. Hyvärinen, M. Gutmann, and P.O. Hoyer. Statistical model of natural stimuli predicts edge-like pooling of spatial frequency channels in V2. *BMC Neuroscience*, 6:12, 2005.
- [10] A. Hyvärinen, P. O. Hoyer, J. Hurri, and M. Gutmann. Statistical models of images and early vision. In *Proceedings of the Int. Symposium on Adaptive Knowledge Representation and Reasoning*, 2005.
- [11] Jason L. Puchalla, Elad Schneidman, Robert A. Harris, and Michael J. Berry. Redundancy in the population code of the retina. *Neuron*, 46(3):493–504, May 2005.
- [12] Martin Rehn and Friedrich T. Sommer. A network that uses few active neurones to code visual input predicts the diverse shapes of cortical receptive fields. *Journal of Computational Neuroscience*, Published online: 12 October:–, 2006.
- [13] F. Rieke, D. Warland, R. de R. van Steveninck, and W. Bialek. *Spikes: Exploring the neural code*. MIT Press, 1997.
- [14] Daniel Ruderman. The statistics of natural images. *Network: Computation in Neural Systems*, 5(4):517–548, November 1994.
- [15] Eero P Simoncelli and Bruno A Olshausen. Natural image statistics and neural representation. *Annual Review of Neuroscience*, 24(1):1193–1216, 2001.
- [16] A. Srivastava, A.B. Lee, E.P. Simoncelli, and S.-C. Zhu. On advances in statistical modeling of natural images. *Journal of Mathematical Imaging and Vision*, 18(1):17–33, January 2003.
- [17] J.H. van Hateren. A theory of maximizing sensory information. *Biol. Cybernetics*, 68:23–29, 1992.
- [18] Benjamin Vincent, Roland Baddeley, Tom Troscianko, and Iain Gilchrist. Is the early visual system optimised to be energy efficient? *Network: Computation in Neural Systems*, 16(2 - 3):175–190, June 2005.

A Mathematical Model of Planning in the Prefrontal Cortex

Makito Oku*

Kazuyuki Aihara^{†,‡,*}

*Department of Mathematical Informatics, Graduate School of Information Science and Technology, The University of Tokyo, 7-3-1 Hongo, Bunkyo-ku, Tokyo 113-8656, Japan

[†]Institute of Industrial Science, The University of Tokyo, 4-6-1 Komaba, Meguro-ku, Tokyo 153-8505, Japan

[‡]Aihara Complexity Modelling Project, ERATO, Japan Science and Technology Agency (JST), 3-23-5-201 Uehara, Shibuya-ku, Tokyo 151-0064, Japan

Abstract

The prefrontal cortex is involved in a lot of complex cognitive behaviours, such as problem solving, planning, reasoning, and decision making. However, the biological mechanisms of these computations are not clear. To understand the mechanisms, we theoretically consider the experimental result of path-planning task by Mushiake et al., using a mathematical model which we name the potential network model. The result of simulations shows that our model is able to take a correct path in most trials regardless of goal positions and block patterns. Our model also reproduces the characteristics of neurons' activities both in the prefrontal cortex and the primary motor cortex. This study indicates that although the potential network model is abstract, it can be useful for modelling higher brain functions.

1 Introduction

Planning is one of the most complex cognitive functions of human brain. It includes a lot of aspects, such as selection of future actions, anticipation of future events that will occur as a result of those actions, temporal maintenance of sequence of those events, evaluation of the sequence, generation of new strategy if needed, and memorisation of finally decided plan so that the planner will take actions according to the plan. Planning is also related to some major problems about brain, such as working memory,¹ cognitive control,² mental imagery,³ and reward systems.⁴

A lot of studies from neuropsychology and brain imaging show that planning is related to the prefrontal cortex (PFC).^{5,6} The PFC has thought to be involved in the executive control of behaviour, and planning is an important aspect of the executive control. Here the question arises: what role does the PFC take during planning of multistep behaviours?

To answer this question, we made a mathematical model of a path-planning task. The path-planning task was a task that required multiple stepwise movements of a cursor within a maze to reach a goal.⁷⁻⁹ Fig. 1 shows the maze used in the task. Players of this task started from the centre of the maze and tried to reach the goal avoiding obstacles. If the player of the task was monkey, it moved its arm to move around in the maze. If the player was human, the player pushed buttons. The rule which assigned muscular-movements to cursor-movements was replaced for every several trials. By recording of neuron spikes in monkeys' brains, it was shown that many PFC neurons selectively fired when specific cursor-movement was on specific step during both the preparatory period and movement execution.⁷

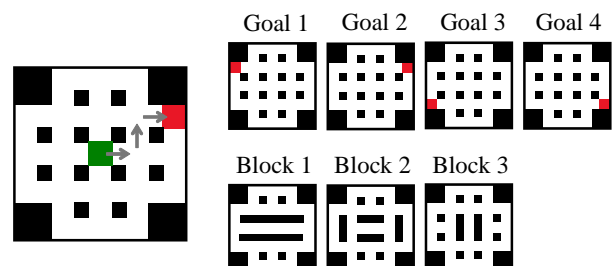


Fig. 1. Path-planning task

On the other hand, Bachmann et al.¹⁰ proposed a mathematically abstract model of neural network. They considered a firing pattern of Hopfield network as a point in high dimensional state space, and attractors as points in the space. This model had no spurious attractors. Furthermore, basins of attractors were well-defined. In this paper, we connected simplified neural assemblies similar to Bachmann's model, considered interactions among them, and named it the potential network model.

2 Potential network model

The potential network model is a network model where each node changes its state continuously according to its potential. The potential is influenced by connected nodes. Suppose a network consists of N nodes. Each node has a state $\mathbf{x}_i(t) \in \mathbf{R}^m (i = 1, \dots, N)$ and a potential $U_i (i = 1, \dots, N)$. The state of each node is changing on the potential.

$$\frac{d\mathbf{x}_i(t)}{dt} = -\alpha \nabla U_i(t) \quad (i = 1, \dots, N).$$

Each node has several fixed points $\mathbf{s}_i^1, \dots, \mathbf{s}_i^{L_i} \in \mathbf{R}^m (i = 1, \dots, N)$. These points are called attractors because they could be local minimum potentials. Fig. 2 shows an example. When node A's state is near enough to one of its attractors, then the node affects next node B's potential so that one of attractors in node B gets stable. For simplicity, each node's potential is formed by linear summation of all attractors of connected nodes.

$$U_j(t) = \sum_{i \in P_j} \sum_{k=1}^{L_i} f(\mathbf{x}_i, \mathbf{s}_i^k) U_{ij}^k \quad (j = 1, \dots, N).$$

Here U_{ij}^k is the potential from k -th attractor of i -th node to j -th node and P_j is a set of nodes connected to j -th node.

f is a closeness function. It is a function of distance between the state of the node and each attractor. In this paper, we use Gaussian function as the closeness function.

$$f(\mathbf{x}_i, \mathbf{s}_i^k) = \beta \exp\left(-\frac{\|\mathbf{x}_i - \mathbf{s}_i^k\|^2}{\sigma^2}\right).$$

3 Simulations of path-planning task

3.1 Setup of simulations

We constructed a potential network model for the path-planning task (Fig. 3). We assumed that cursor-movements for three steps were represented separately in the PFC. 1st, 2nd, and 3rd nodes were corresponding to the three steps and each of them had four attractors corresponding to four directions (up, down, left, and right). Goal and block information were represented in goal node and block node respectively. These two nodes biased the three nodes to select appropriate path. Step node made strong potential in the cursor node to inhibit action execution during preparatory

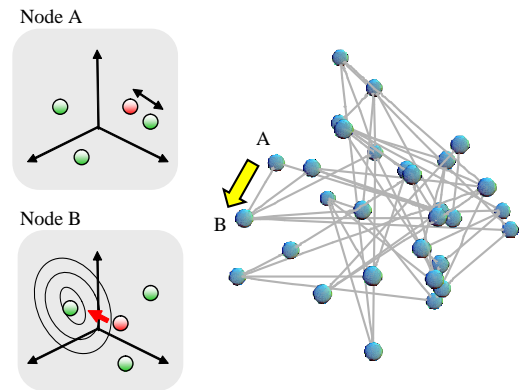


Fig. 2. Schematic diagram of the potential network model

period. When cue signals were displayed, this node also reactivated corresponding node to trigger action execution.

The forms of potentials were mixture of Gaussian functions. They biased an attractor or several attractors. There was a potential with its centre at the origin of the state space, which prevented the state from approaching any attractors.

In the original experiment, assignment rule between cursor-movements and arm-movements was changed for every several trials. Rule, arm, and motion nodes were expected to perform the translation from cursor-movements to arm-movements. In this paper, however, we did not add these three nodes.

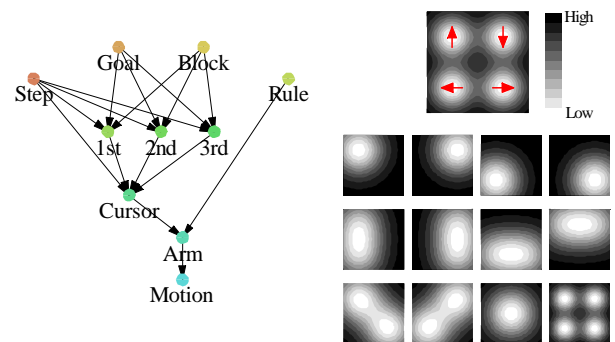


Fig. 3. Potential network model for path-planning and examples of potential patterns

3.2 Result of simulations

Fig. 4 shows an example of state transition of 1st, 2nd, 3rd, and cursor nodes in block 3 condition. Tem-

poral sequence of events during the task was the same to the original experiment. Two shadowed regions correspond to goal displaying period and block displaying period. Three black bars indicate movement executions for each step. During preparatory period, states of 1st, 2nd, and 3rd nodes were biased by goal node and block node to approach attractors corresponding to proper cursor movements. In contrast, state of cursor node was under strong inhibitive potential made by step node so that it stayed far from any attractors. After preparatory period, states of the three nodes fluctuated in the state space because of noise. So they left from attractors. When step node reactivated the three nodes, their states approached attractors again, which changed the state of cursor node.

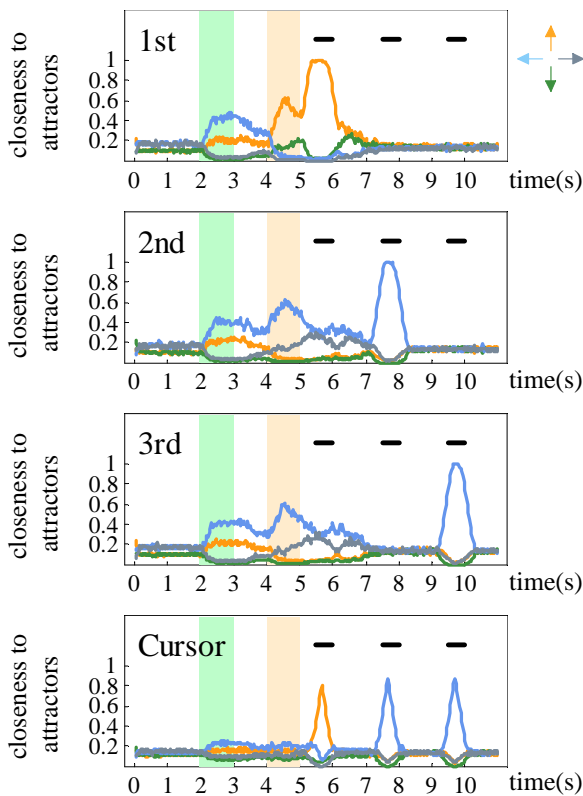


Fig. 4. An example of time series of state transition

Fig. 5 shows the probability of cursor-movement selection of each step. In most cases this model chose a correct path. Some errors were seen in the 3rd step in all conditions. The state of nodes seemed to fluctuate getting away from the basins of attractors. Another errors were seen in the 1st step of block 3 condition, which was failure to overwrite reflective response.

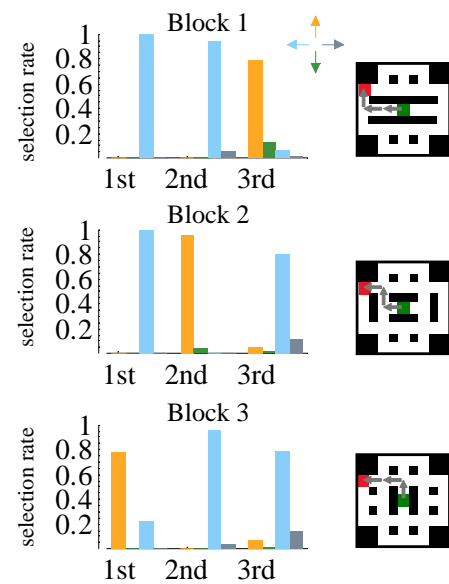


Fig. 5. Cursor-movement selection rate

4 Discussion

Medium of modelling of cognitive functions In general, there are two streams of modelling of human's complex cognitive behaviours: production system^{11,12} and connectionist model.¹³ In addition, there are some hybrid studies.^{14,15} The production system is good at highly complex problems. However, its biological basis is not clear. On the other hand, connectionist model has biological background and it has flexible performance. However, this approach has a risk to be redundant and to have complexity irrelevant to the essence of computation.

The potential network model we proposed here was intrinsically based on connectionist model. At the same time, it was easy to implement if-then rules in this model because each attractor's basin and effect were well-defined. Therefore, this model had advantages of both sides.

Role of prefrontal cortex There are many hypotheses about the role of the PFC.¹⁶⁻¹⁹ Among them, the *cognitive control hypothesis* is broadly accepted. This study was consistent with the hypothesis. In the framework of cognitive control hypothesis, the PFC sends bias signal to posterior cortex to overwrite reflective, innate, or prepotent responses.² In our model, goal and block node made potentials to the three nodes corresponding to each step, biasing appropriate action.

Other issues involved in planning Our model for the path-planning task concerned only limited aspects of planning. For example, the players of the path-planning task were well-trained, so they could accurately find correct path immediately. In fact, neuron spike data from monkeys' brains suggested that 1st, 2nd, and 3rd cursor-movement-selective neurons in the PFC started to fire simultaneously during the preparatory period.⁷ Accordingly, stepwise rehearsal of event sequence during the preparatory period was not performed in our model. In Addition, our model did not include evaluation system and learning mechanism, which is our future works.

5 Summary

To understand the mechanism of planning in the prefrontal cortex, We theoretically considered the experimental result of path-planning task by Mushiake et al., using the potential network model. The result of simulations showed that our model was able to take a correct path in most trials regardless of goal positions and block patterns. Our model also reproduced the characteristics of neurons' activities both in the PFC and the primary motor cortex. This study indicated that although our model was abstract and concerned only limited aspects of planning, it could be useful for modelling higher brain functions.

Acknowledgements

This study is partially supported by Grant-in-Aid No. 17022012 for Scientific Research on Priority Areas System study on higher-order brain functions from the Ministry of Education, Culture, Sports, Science and Technology of Japan.

References

- [1] Baddeley A (2003), Working memory: looking back and looking forward. *Nat. Rev. Neurosci.* 4(10):829–839
- [2] Miller EK (2000), The prefrontal cortex and cognitive control. *Nat. Rev. Neurosci.* 1(1):59–65
- [3] Kosslyn SM (2005), Mental images and the brain. *Cogn. Neuropsychol.* 22(3–4):333–347
- [4] Schultz W, Dayan P, Montague PR (1997), A neural substrate of prediction and reward. *Science* 275(5306):1593–1599
- [5] Unterrainer JM, Owen AM (2006), Planning and problem solving: from neuropsychology to functional neuroimaging. *J. Physiol. Paris* 99(4–6):308–317
- [6] Goel V, Grafman J (2000), Role of the right prefrontal cortex in ill-structured planning. *Cogn. Neuropsychol.* 17(5):415–436
- [7] Mushiake H, Saito N, Sakamoto K, et al. (2006), Activity in the lateral prefrontal cortex reflects multiple steps of future events in action plans. *Neuron* 50(4):631–641
- [8] Mushiake H, Saito N, Sakamoto K, et al. (2001), Visually based path-planning by Japanese monkeys. *Cogn. Brain Res.* 11(1):165–169
- [9] Mushiake H, Saito N, Furusawa Y, et al. (2002), Orderly activations of human cortical areas during path-planning task. *Neuroreport* 13(4):423–426
- [10] Bachmann CM, Cooper LN, Dembo A, et al. (1987), A relaxation model for memory with high storage density. *Proc. Natl. Acad. Sci. U.S.A.* 84(21):7529–7531
- [11] Anderson JR, Bothell D, Byrne MD, et al. (2004), An integrated theory of the mind. *Psychol. Rev.* 111(4):1036–1060
- [12] Kieras DE, Meyer DE (1997), An overview of the EPIC architecture for cognition and performance with application to human-computer interaction. *Human-Computer Interaction* 12(4):391–438
- [13] Dehaene S, Changeux JP (1997), A hierarchical neuronal network for planning behaviour. *Proc. Natl. Acad. Sci. U.S.A.* 94(24):13293–13298
- [14] Polk TA, Simen P, Lewis RL, et al. (2002), A computational approach to control in complex cognition. *Cogn. Brain Res.* 15(1):71–83
- [15] Newman SD, Carpenter PA, Varma S, et al. (2003), Frontal and parietal participation in problem solving in the Tower of London: fMRI and computational modeling of planning and high-level perception. *Neuropsychologia* 41(12):1668–1682
- [16] Wood JN, Grafman J (2003), Human prefrontal cortex: processing and representational perspectives. *Nat. Rev. Neurosci.* 4(2):139–147
- [17] Miller EK, Cohen JD (2001), An integrative theory of prefrontal cortex function. *Annu. Rev. Neurosci.* 24:167–202
- [18] Duncan J (2001), An adaptive coding model of neural function in prefrontal cortex. *Nat. Rev. Neurosci.* 2(1):820–829
- [19] Fuster JM (2001), The prefrontal cortex—an update: time is of the essence. *Neuron* 30(2):319–33

Pattern Recognition in Chaotic Neural Networks

Guoguang HE^{1,2,3,*}, Luonan CHEN^{1,2,4} and Kazuyuki AIHARA^{1,2}

¹Aihara Complexity Modelling Project, ERATO, JST, Komaba 4-6-1, Meguro-ku, Tokyo, 153-8505, Japan

²Institute of Industrial Science, The University of Tokyo, Komaba 4-6-1, Meguro-ku, Tokyo, 153-8505, Japan

³Department of Physics, College of Science, Zhejiang University, Hangzhou, 310027, P.R. China

⁴Osaka Sangyo University, Osaka 574-8530, Japan

*Corresponding author, e-mail: gghe@aihara.jst.go.jp

Abstract

A chaotic neural networks (CNNs) constructed with chaotic neurons have rich dynamics. The CNNs can generate chaotic associative memory dynamics and has been denoted to be a promising technique in information processing, such as pattern recognition or memory search. But the outputs of the CNNs wander around all stored patterns and can not be stabilized in one of its stored patterns or a periodic orbit. It is difficult to judge when to terminate the chaotic dynamics, which is imperative in information processing. In this paper, we discuss pattern recognition in a CNNs. We propose a chaos control method firstly for the CNNs. Then we employ the controlled CNNs to carry out pattern recognition tasks. The simulation results show that the outputs of the controlled CNNs are period, not a fixed point. The outputs are dependent on initial pattern. The controlled network has the ability of identifying two initial patterns with small difference. This is an advantage of CNNs comparing with Hopfield model.

Keywords: Chaotic neural networks; Controlled dynamics; Pattern recognition; Controlling chaos

1 Introduction

Pattern recognition is one of important fields of artificial intelligence. One focuses on how a system can observe the environment, distinguish patterns of interest from their background and make decisions about their classification or categorization in pattern recognition study. Many methods and techniques have been proposed for pattern recognition, for example, the template matching, syntactic or structural matching, statistical classification, and artificial neural networks (ANNs) approaches[1]. ANNs have the ability of learning complex nonlinear input-output relationships and therefore drawn more and more attentions in recent years. However, there is an essential difference between ANNs approaches and the brain in pattern recognition. Once an output pattern is identified, ANNs remains in the state until the arrival of next external input, but the brain does not “stick” to the state and can recall other associative memory patterns without additional external stimulus when a pattern is retrieved from a memory location. A conventional artificial neuron model is a simply threshold element transforming a weighted summation of inputs into the output through a nonlinear

output function with threshold. This model is oversimplified so that the actual characteristics of the biological neurons that have the ability to “jump” from one memory state to another in the absence of a stimulus cannot be represented in such neuron model. Biological neurons have chaotic behaviors which was observed in a single neuron by electrophysiological experiments[2], but chaotic behaviors are lack in the conventional artificial neurons. Therefore various neuron models and neural networks with chaotic dynamics have been proposed and investigated[3-6]. In this paper, we focus on a chaotic neural networks (CNNs)[3] composed of chaotic neurons which were proposed based on electrophysiological experiments in the squid giant axons. The chaotic neuron model and CNNs have been shown to have rich dynamics. Adachi et al.[7] have proved that the CNNs can generate chaotic associative memory dynamics in several parameter regions. Due to the chaotic associative memory dynamics, the CNNs is expected to be use in information processing, such as pattern recognition or memory search, etc. However, the outputs of the CNNs wander around all stored patterns and can not be stabilized in one of its stored patterns or a periodic orbit. It is difficult to judge when to terminate the chaotic dynamics, which is imperative in pattern recognition. The chaos control techniques for the CNNs were therefore proposed by Nakamura *et al.*[8], Kushibe *et al.* [9], He *et al.*[10] etc. In Ref. 8 and 9, the chaos in the CNNs was controlled by making the CNNs to a Hopfield model[11]. The output of the controlled networks is a fixed point. The pattern recognition or memory search therefore achieved. However, the control target is refereed by comparing the initial pattern with stored patterns in their works. In other words, the initial pattern mapped on a stored pattern had been assigned *a priori*, which limits the real application in pattern recognition. Besides, a fixed output of the controlled CNNs makes the CNNs lost advantages of chaotic dynamics. In Ref. 10, the control target also should been assigned. Tan and Ali[12] proposed a synchronization method to achieve pattern recognition in a neural network with chaos. However, the desired orbit also should been assigned *a priori* too.

In order to promote the CNNs to be used in information processing, such as pattern recognition, memory search, a chaos control method without assigning a control target, i.e. a self-adaptive chaos control method, is necessary. In this paper, we will propose a chaos control method which need not assign control target or desired orbit for the CNNs. Then we

will perform pattern recognition task by using the controlled CNNs.

The article is organized as follows. In section 2, the models of the CNNs are described briefly. A chaos control method for CNNs is proposed. In section 3, we apply the controlled CNNs to carry out the pattern recognition task. The discussion and conclusion are given in the final section.

2 Chaotic Neural Networks and Chaos Control Method

2.1 Chaotic Neural Networks model

A chaotic neural networks (CNNs) used for pattern recognition is constructed with chaotic neurons by considering the spatio-temporal summation of both external inputs and feedback inputs from other chaotic neurons[3]. The structure of the CNNs is shown in figure 1. When the external input term is temporally constant, it can be included in the threshold term. The dynamics of the i th chaotic neuron in the CNNs at time t can be described simply as follows:

$$x_i(t+1) = f(\eta_i(t+1) + \zeta_i(t+1)), \quad (1)$$

$$\eta_i(t+1) = k_f \eta_i(t) + \sum_{j=1}^N w_{ij} x_j(t), \quad (2)$$

$$\zeta_i(t+1) = k_r \zeta_i(t) - \alpha x_i(t) + a_i, \quad (3)$$

$$f(x) = \frac{1}{1 + \exp(-x/\varepsilon)}. \quad (4)$$

where the $x_i(t)$ is the output of the i th chaotic neuron at time step t , the $\eta_i(t)$ and $\zeta_i(t)$ are the internal state variables of feedback input from the constituent neurons in the network and refractoriness of the chaotic neuron at time t , respectively. N is the number of neurons in the network. k_f and k_r are the decay parameters of the feedback inputs and the refractoriness, respectively. The parameter a_i is the threshold of the i th neuron. The parameter α is the refractory scaling parameter of a neuron, and the output function of neuron $f(\cdot)$ is sigmoidal function with the steepness parameter ε described by equation (4). w_{ij} are synaptic weights to the i th constituent neuron from the j th constituent neuron. A neuron does not receive the synaptic connection from itself, i.e. $w_{ii} = 0$. The weights are defined according to the following symmetric auto-associative matrix of n binary patterns:

$$w_{ij} = \frac{1}{n} \sum_{p=1}^n (2x_i^p - 1)(2x_j^p - 1), \quad (5)$$

where x_i^p is the i th component of the p th binary pattern with a discrete value of 0 or 1. In this way, the binary patterns can be stored as basal memory patterns

in the network. n is the total number of stored memory patterns.

In the paper, four patterns shown in Fig. 2 are employed as stored memory patterns, or namely learning patterns. Each pattern is composed of 10 by 10 binary pixels. Correspondently the network is constructed with 100 neurons, that is $N = 100$. A neuron will be represented by a block "■" when its output, x_i , is equal to 1, which means the neuron is "excited", while a neuron is denoted by a dot "." when its output is equal to 0, which means the neuron is "resting".

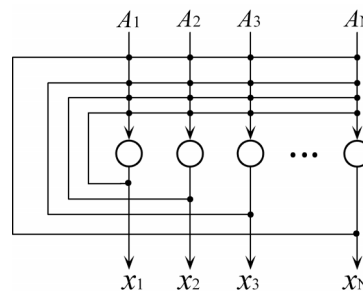


Figure 1 The structure of the CNNs

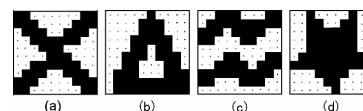


Figure 2 Four stored patterns

The dynamics of the chaotic neural networks is dependent on the network parameters. In our numerical simulations the network parameters are kept as follows: $k_f = 0.95$, $k_r = 0.20$, $\alpha = 10.0$, $a_i = 2.0$ ($i = 1, 2, \dots, 100$), and $\varepsilon = 0.015$. It has been shown that the CNNs with above parameters is chaotic[7, 10]. The outputs of the CNNs are wandering around all stored and their reversal patterns, namely associative memory dynamics [7].

2.2 Chaos control method

The chaos control technique was proposed firstly by Ott et al. in 1990(OGY method)[13]. Since the pioneer work of OGY, the chaos control methods have been greatly developed. Although most of these controlling methods have been mainly applied to chaotic system with small degree of freedoms, several methods have been adopted for a system with large degree of freedoms, such as CNNs [8-10]. Nakamura *et al.*[8], Kushibe *et al.*[9], He et al.[10], had proposed chaos control methods for the CNNs, but in their methods, the control target should be assigned. Their control methods can not be applied to real information processing. In order to make the CNNs to be used in pattern recognition with chaotic dynamics, we purpose a new scheme of controlling chaos for the CNNs by considering following aims: (I) the output of the controlled CNNs

can be stabilized to a periodic orbit or a fixed point; (II) the stable output of the controlled CNNs should be related with the stored patterns and initial state of the network. (III) the control target should not be assigned, i.e. the control method is a self-adaptive method. In our previous work[14], we have known that the chaotic dynamics in the CNNs is dependent on the refractory scaling parameter of the neurons. When the refractory scaling parameter is small, the dynamics of the CNNs is a fixed points or periodic. As the refractory scaling parameter increase, the output of the CNNs becomes chaotic. We therefore assume the chaos in CNNs can be controlled if the refractory scaling parameter of the neurons is changed by a control signal. This is the idea of our control method to be proposed here. Considering self-adaptive method, we take the delay feedback signal as the control signal. The controlled CNNs is described in following equations:

$$x_i(t+1) = f(\eta_i(t+1) + \zeta_i(t+1)), \quad (6)$$

$$\eta_i(t+1) = k_f \eta_i(t) + \sum_{j=1}^N w_{ij} x_j(t), \quad (7)$$

$$\zeta_i(t+1) = k_r \zeta_i(t) - \alpha \beta^{k_c u(t)} x_i(t) + a_i, \quad (8)$$

$$u(t) = \sum_i^N |x_i(t) - x_i(t-\tau)|. \quad (9)$$

where $u(t)$ is a control signal determined by the difference of the output of the chaotic neuron at different time, β is a control parameter, a positive value smaller than 1.0, k_c is a control strength. When the output of the chaotic neuron is chaos, the control signal $u(t)$ is not zero and $\alpha \beta^{k_c u(t)} < \alpha$. Thus the dynamics of the chaotic neuron will be changed.

3 Pattern Recognition

Now we investigate the pattern recognition in CNNs. After the CNNs learning the stored pattern shown in figure 2, the output sequence of the CNNs wanders around all stored pattern and their reversal patterns, as mentioned in introduction, namely associative memory dynamics[7]. We perform chaos control in CNNs according to proposed control method by equations (6) ~ (9). The parameters of the control method are taken as $\beta = 0.945$, $\tau = 3$ and $k_c = 0.6$. As pattern recognition tasks, we take stored patterns shown in figure 2 and noisy stored patterns, patterns with small noises to stored patterns, as the initial patterns, and investigate output sequences of the controlled CNNs. A initial pattern is injected in the CNNs by taking $x_i(0)$ as the initial pattern in the internal state η_i and ζ_i . The initial internal states are set as 0. We find the dynamics of the network is changed when the CNNs is controlled by equations(6) ~ (9). The output sequences of the controlled chaotic neural networks are periodic. The period and the output sequence are dependent on the initial states. Due to the

limited space, we only show the periodic output sequence slice of the controlled CNNs in figure 3. The left parts of the figure are the initial patterns, the right parts are the output sequence of one period of the controlled network.

From the figure, one can find no matter a initial pattern is a stored pattern (top four initial patterns) or its noisy pattern (bottom four initial patterns), the most part of patterns appearing in the output periodic sequence of the controlled CNNs are the stored pattern and its reversal pattern while other stored patterns and their reversal patterns are not appeared in the output sequence. That is, the controlled CNNs can identify the initial pattern from the stored patterns. The pattern recognition tasks are therefore achieved.

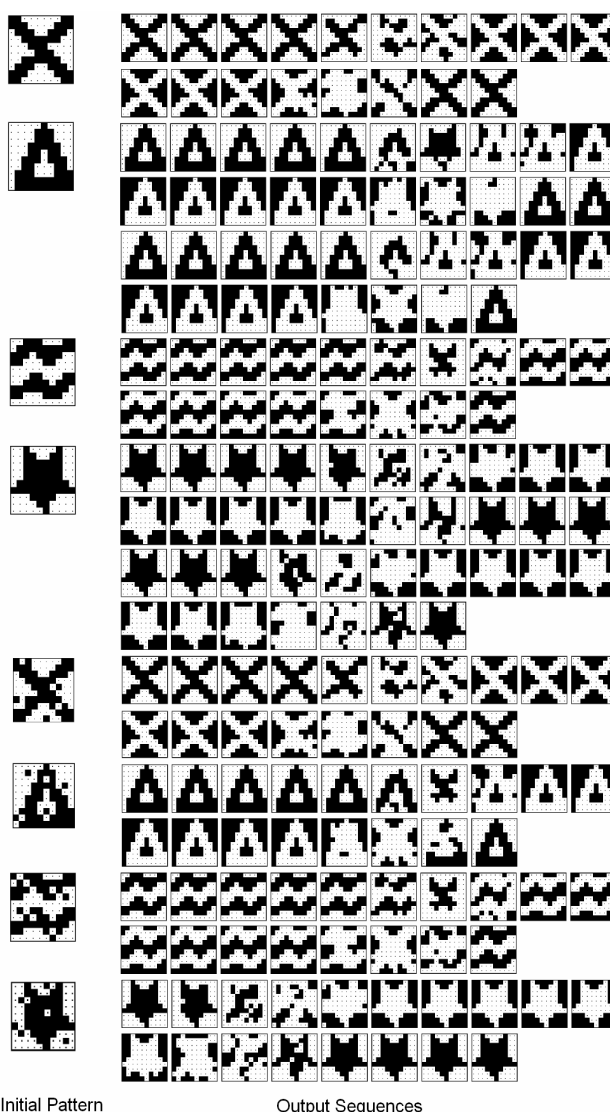


Figure 3 Initial patterns and their response output sequence slice of the controlled CNNs. The left parts of the figure are the initial patterns, the right parts are the output sequence of one period of the controlled network. The control parameters are taken as $\beta = 0.945$, $\tau = 3$ and $k_c = 0.6$.

4 Discussion and Conclusion

To promote the CNNs to be a technique of information processing, such as pattern recognition, memory search, a self-adaptive chaos control method for the CNNs was proposed based on the fact that the dynamics of the chaotic neural networks is dependent on the refractory scaling parameter. The controlled CNNs was employed to carry out pattern recognition tasks. The simulation results have shown that the chaotic dynamics disappear when the refractory scaling parameter is changed by a control signal which is determined by the difference of two outputs with time delay. The dynamics of the controlled CNNs is periodic. The output sequences of the controlled CNNs are dependent on the initial pattern. The pattern recognition tasks are therefore achieved.

We control the CNNs to be a periodic state, not a fixed point as in Ref. 8 and 9, which make the output sequences of the controlled CNNs sensitive to the initial state. From figure 3, we find the period and the output pattern sequences of the controlled CNNs are different when the initial pattern are a stored pattern (b) shown in Fig. 2 and its noisy stored pattern. The same situation exists when the initial patterns are a stored pattern (d) and its noisy stored pattern, which means the controlled CNNs is sensitive to the initial state. In fact, when control parameter β take as 0.95, the output sequences of the controlled CNNs with a stored pattern taken as an initial pattern are different from those with its noise pattern as the initial pattern even if the period is same. We do not show the results of $\beta = 0.95$ here because the period of the controlled CNNs is long and it is difficult to show the output sequences in a short space. The sensitiveness to the initial state in our controlled method means the controlled CNNs can distinguish initial patterns with small difference. This is the advantage of our controlled CNNs compared to previous control methods [8, 9], or the conventional auto-associative network, such as Hopfield network[11], where the output converge on a fixed point, no matter the initial pattern is a stored pattern or a noisy stored pattern.

It should be notice that a rejection mechanism is lack in the controlled CNNs. It means that an initial pattern may be attracted to a stored pattern though it shows low similarity with the stored pattern. Proposing an improved control method or an improved CNNs model, with which the CNNs not only recognize an initial pattern if it has high similarity with a stored pattern but also reject recognizing as any stored pattern if it has low similarity with a stored pattern, will be our future direction.

References

- [1] Jain AK, Duin RPW, Mao J, Statistical pattern recognition: A review, IEEE trans. Pattern Anal. Mach. Intell., vol. 22, pp. 4-37, 2000
- [2] Aihara K, Matsumoto G, Chaotic oscillations and bifurcations in squid giant axons, In Holden AV (Ed.), Chaos, Princeton: Princeton University Press, 1986, pp.257-269.
- [3] Aihara K, Takebe T, Toyoda M, Chaotic neural networks, Phys. Lett. A, vol. 144, pp. 333-340, March 1990.
- [4] Freeman WJ, Simulation of chaotic EEG patterns with a dynamic model of the olfactory system, Biological Cybernetics, vol. 56, pp. 139-150, 1987.
- [5] Tsuda I, Dynamic link of memory-chaotic memory map in nonequilibrium neural networks, Neural Networks, vol. 5, pp. 313-326, 1992
- [6] Nara S, Davis P, Learning feature constraints in a chaotic neural memory, Phys. Rev. E, vol. 55, pp. 826-830, Jan. 1997.
- [7] Adachi M, Aihara K, Associative dynamics in a chaotic neural network, Neural Networks, vol. 10, pp. 83-98, 1997.
- [8] Nakamura K, Nakagawa M, On the associative model with parameter controlled chaos neurons, J. Phys. Soci. Jpn. Vol. 62, pp. 2942-2955, 1993.
- [9] Kushibe M, Liu Y, Ohtsubo J, Associative memory with spatiotemporal chaos control, Phys. Rev. E53, 4502-4508, 1996.
- [10] He G, Cao Z, Zhu P, Ogura H, Controlling chaos in a chaotic neural network, Neural Networks, vol. 16, pp. 1195-1200, Oct. 2003.
- [11] Hopfield JJ, Neural Networks and Physical Systems with Emergent Collective Computation abilities, Proc. Natl. Acad. Sci. USA, vol. 79, pp.2554-2558, 1982.
- [12] Tan Z, Ali MK, Pattern recognition in a neural network with chaos, Phys. Rev. E58, pp. 3649-3652, 1998
- [13] Ott E, Grebogi C, Yorke JA, Controlling Chaos, Phys. Rev. Lett., vol. 64, pp. 1196-1199, March 1990.
- [14] He G, Kuroiwa J, Ogura H, Zhu P, Cao Z, Chen P, A type of delay feedback control of chaotic dynamics in a chaotic neural network, IEICE Trans. Fundamentals, vol. E87-A, pp. 1765-1771, July 2004.

Bistability of Synchronous and Desynchronous Dynamics in a Network with Gap Junctions

Yuichi Katori^{1,*}, Yoshito Hirata¹, Hideyuki Suzuki² and Kazuyuki Aihara^{1,2}

¹ Aihara Complexity Modelling Project,
ERATO, Japan Science and Technology Agency,
4-1-8 Honcho Kawaguchi, Saitama, Japan

² Institute of Industrial Science, Univ. of Tokyo,
4-6-1 Komaba, Meguro-ku, Tokyo 153-8505, Japan

*E-mail: katori@sat.t.u-tokyo.ac.jp

Abstract

Recent physiological studies show a transient synchrony which means an alteration behaviour between synchronous and desynchronous states. These experimental findings and related theoretical studies have suggested that the importance of this kind of dynamics as bases of cognitive functions. However, an origin of this characteristic dynamics is still unclear. Here, we report that the transient activity can be realized in the network consisted of conductance-based model neurons with a bistability of firing and non-firing states. Neurons in this network are coupled with gap junctions which is a direct electrical connection with neighbor neurons. The bistability of the neuron play a key role to produce the transient dynamics of synchronous and desynchronous states.

Key words: Gap junction, bistability, neural coding, neural dynamics, chaotic itinerancy, synchronization.

1 Introduction

Recent experiments have revealed the transient dynamics between synchronous and desynchronous states, e.g., spiking patterns observed in rat inferior olive neurons show the alteration of rhythmic synchronous states and desynchronous states [1], local field potential (LFP) data of an animal and electro encephalography (EEG) data of human [3] also exhibit the transient synchronous activity. Further, functions of this kind of dynamics have been investigated. The transient dynamics correlates with an attention and a perceptual binding, facilitates a synaptic plasticity, and coordinates a long-range interaction in the brain

[2, 3]. Theoretical study have suggested that neural codes switch dynamically along with the state transition [4]. Little is known, however, about how the transient activity emerges in the neural systems.

Moreover, experiments have revealed the massive number of gap junctions in various region of the brain. These gap junctions are specialized areas of the cell membranes connecting neighbor cells; they induce synchronous firing [5]. In addition to the synchronous activity, theoretical studies suggest that gap junctions induce chaotic activities including the chaotic itinerancy [6, 7]. The chaotic itinerancy is one of possible scenarios to realize the transient dynamics between synchronous and desynchronous states in the network with gap junctions.

The purpose of this paper is to present an alternative scenario to produces the transient dynamics in the gap junction-coupled neural system, base on a characterization of the bistability of neuron. The paper is organized as following. First, in the next section, we show the conductance-based model with the bistability and a characteristics of their behaviours. After that, we construct the network with this neuron by connecting with gap junctions. In the third section, we show the result of computer simulation.

2 Model

Here, we describe the model mentioned in above. First, single neuron model is described in following subsection. After that, we construct the network consisted of this neuron and gap junctions.

2.1 Conductance based model with bistability

We used a simple two-variable conductance-based model, which is more plausible than a one-variable neuron model like the integrate-and-fire model, and is extracting the essential neural dynamics. [6, 8].

This model consists of two variables which are a membrane potential V and a potassium channel activation n [8].

$$C \frac{dV}{dt} = I(t) - g_L(V - E_L) - g_{Na}(V - E_{Na}) - g_K(V - E_K), \quad (1)$$

$$\tau_n \frac{dn}{dt} = n_\infty(V) - n, \quad (2)$$

$$m_\infty(V) = \frac{1}{1 + \exp\left[\frac{V_1 - V}{V_2}\right]}, \quad (3)$$

$$n_\infty(V) = \frac{1}{1 + \exp\left[\frac{V_3 - V}{V_4}\right]}. \quad (4)$$

The neuron is driven by the external input $I(t)$, the leaky current, the sodium current, and the potassium current. We chose following parameters to realize the bistable structure. We set $C = 31\text{ms}$, $\tau_n = 31\text{ms}$, the membrane conductances $g_L = 1$, $g_{Na} = 4$, $g_K = 4$, and corresponding reversal potentials $E_L = -78\text{ mV}$, $E_{Na} = 60\text{ mV}$, $E_K = -90\text{ mV}$. We use steady-state activation curves $m_\infty(V)$, and $n_\infty(V)$ with the slope factor $V_2 = 7\text{mV}$, $V_4 = 5\text{mV}$ and parameters $V_1 = -30\text{ mV}$ and $V_3 = -45\text{ mV}$ satisfy $m_\infty(V_1) = n_\infty(V_3) = 0.5$.

Figure 1 shows the phase portrait to describes the geometric view of the model neuron. The model includes two attractors as shown in this figure. The first is a stable fixed point corresponding to the rest state. The other is a stable limit cycle with the action potential. The dashed curve in figure 1 indicates a unstable limit cycle. If the orbit starts inside of this region, the orbit converges to the stable fixed point. On the other hand, If the orbit starts outside of this region, the orbit makes the action potential and converges to the stable limit cycle. Figure 2 shows a time course of the membrane potential as a typical response of the neuron. This neuron takes two states of firing and non-firing even on same intensity inputs. These two states can be switched by fluctuating inputs (Fig 2 (b)).

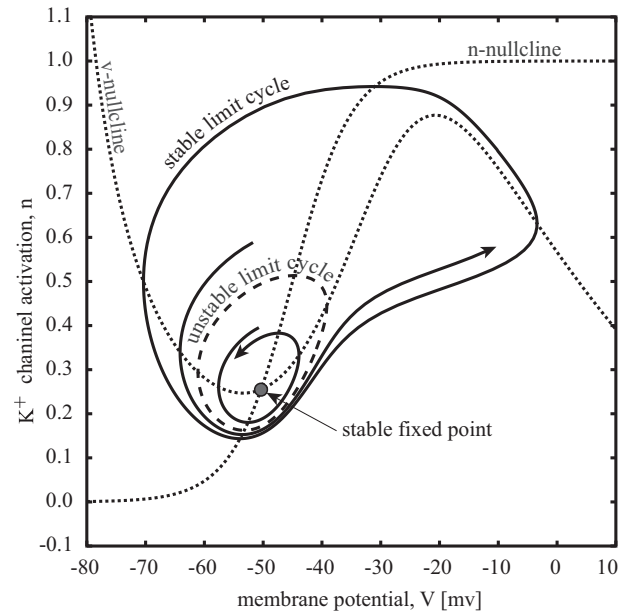


Figure 1: Phase portrait of the model neuron. Dotted curves indicate nullcline of V and n . The bold curve is the stable limit cycle. The point in the crossing of these nullclines is the stable fixed point. The dashed curve is unstable limit cycle. Curves with arrow indicate typical orbits of the model.

2.2 Network with gap junctions

The network with gap junctions and neurons specified in above is described as follows. We used two dimensional lattice network with 25 neurons as in figure 3.

$$C \frac{dV_i}{dt} = I_i(t) - g_L(V_i - E_L) - g_{Na}(V_i - E_{Na}) - g_K(V_i - E_K), \quad (5)$$

$$\tau_n \frac{dn_i}{dt} = n_\infty(V_i) - n_i, \quad (i = 1, \dots, 25), \quad (6)$$

$$m_\infty(V) = \frac{1}{1 + \exp\left[\frac{V_1 - V}{V_2}\right]}, \quad (7)$$

$$n_\infty(V) = \frac{1}{1 + \exp\left[\frac{V_3 - V}{V_4}\right]}, \quad (8)$$

The i in the subscript of V , n , and $I(t)$ indicates the index of neurons. We used 25 neurons in this network, therefore, the i takes an integer of from 1 to 25.

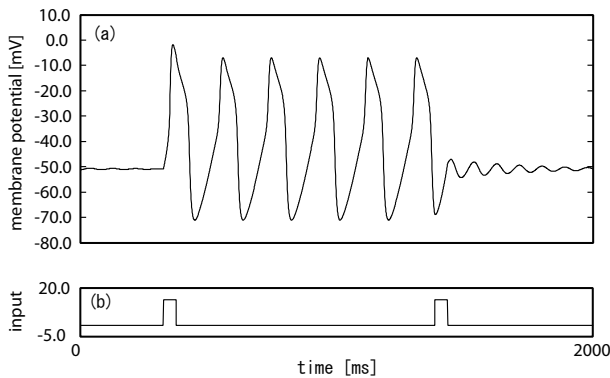


Figure 2: The typical response of the conductance-based model with bistable structure. The time course of the membrane potential (a) and the fluctuating input (b) are shown. The firing state as in the middle part of (a) and the rest states as in the both end of (a) are corresponding to the stable limit cycle and the stable fixed point in figure 1 respectively. These two states can be switched by the fluctuating input.

$I_i(t)$ is a current induced by external inputs and gap junctions, and is consisted of three terms:

$$I_i(t) = I_0 + i(t) + g_E \sum_j^{neighbors} (V_j(t) - V_i(t)). \quad (9)$$

The first term I_0 specify a constant input. The second term is a Gaussian noise $i(t)$ that is individually applied to each neuron with the strength D . The third is the current induced by the gap junction with the conductance g_E . Each neuron coupled with nearest neurons as in figure 3. We assumed the conductance g_E are uniform for all gap junction connections.

3 Simulation Results

Figure 4 shows the typical response of this model. We can observe the transient activity between synchronous and desynchronous states. In the synchronous states, we can also see the rhythmic firing with a period of about 180 ms. The period is corresponding to the period of the stable limit cycle of the neuron. In the desynchronous states, the firing frequency is low and that spike timing are almost irregular.

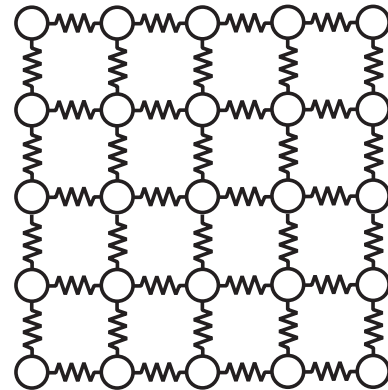


Figure 3: The structure of the network. The network is consisted of 25 neurons described in the body of this paper. Each neuron is connected with nearest neurons. The coupling strength of gap junction are uniform and specified by g_E .

The key mechanism of the alteration of these two states originate in the bistability of the conductance-based model as you see in the figure 1. The orbit of each neuron coupled with gap junctions attracts each other. Consequently, the orbits of these neurons tend to stay in one side of two attractors. In the synchronous states, the orbits stay on the stable limit cycle. In the desynchronous states, almost of these orbits trap each other near the stable fixed point. The fluctuating noise allows to escapes from this region and make the desynchronous spiking. If a certain amount of neurons fire in short time period, the state can change to the synchronous state.

4 Conclusion

In this paper, we have shown that the transient dynamics of synchronous and desynchronous states can be realized in the network consisted of bistable type neurons and gap junction connections.

The model examined here may play an important role for the information coding in the brain, and cognitive roles mentioned in the introduction.

References

- [1] E. J. Lang, I. Sugihara, and R. Llinas (1996), "GABAergic modulation of complex spike activity by the cerebellar nucleoolivary pathway in rat" *Journal of neurophysiology*, 76, 1, 225-275.

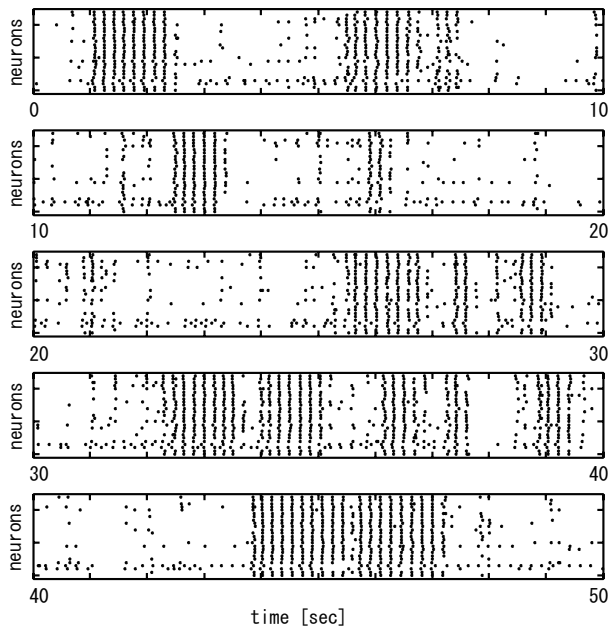


Figure 4: The typical response of 25 neurons in this model as a raster plot on the time from 0 to 50 s. Vertical axes of each plot show the index of neurons. Each dot in these plot indicate the timing of the spiking.

- [8] E. M. Izhikevich (2006), *Dynamical Systems in Neuroscience: The Geometry of Excitability And Bursting*, The MIT press.

- [2] G. Buzsaki and A. Draguhn (2004), "Neuronal Oscillations in Cortical Networks" *Science* 304,5679,1926-1929.
- [3] F. Varela, J. P. Lachaux, E. Rodriguez, and J. Martinerie (2001), "The Brainweb: Phase Synchronization and Large-Scale Integration" *Nature Reviews Neuroscience*,2,229-239.
- [4] Y. Katori, N. Masuda, and K. Aihara (2006), "Dynamic switching of neural codes in networks with gap junctions" *Neural Networks*,19,10,1463-1466.
- [5] M.Galarreta and S.Hestrin (1999), "A network of fast-spiking cells in the neocortex connected by electrical synapses" *Nature*,402,72-75.
- [6] I.Tsuda, H.Fujii, S.Tadokoro, et al (2004). "Chaotic itinerancy as a mechanism of irregular changes between synchronization and desynchronization in a neural network" *Journal of Integrative Neuroscience*,3,159-182.
- [7] H.Fujii and I.Tsuda (2004), "Neocortical gap junction-coupled interneuron systems may induce chaotic behavior itinerant among quasi-attractors exhibiting transient synchrony" *Neurocomputing*,58-60,151-157.

Digital Spiking Silicon Neuron: Concept and Behaviors in GJ-coupled Network

Takashi Kohno^{*†} and Kazuyuki Aihara^{*†}

^{*} Aihara Complexity Modelling Project, ERATO, JST, Shibuya-ku, Tokyo 151-0064

[†] Institute of Industrial Science, The University of Tokyo, Meguro-ku, Tokyo 153-8505

Abstract

Silicon neuron is electrical circuit that is analogous to biological neurons. Most spiking silicon neurons comprise analog circuit technology. We propose a new concept of spiking silicon neuron that is composed of only digital circuit technology. The system equations were designed by a mathematical-model-based design method that we proposed for analog silicon neurons in previous works. This allowed us to design a simple digital spiking silicon neuron (DSSN) model that produces rich dynamical behaviors comparable to biological neurons. We analyzed an elemental DSSN model to validate if it possesses fundamental characteristics of neurons, and its behaviors in gap junction (GJ)-coupled networks were studied in order to demonstrate its ability to exhibit rich dynamical behaviors.

1 Introduction

Silicon neuron study is an attempt to produce neuron analog utilizing electrical circuit technology. One of its objectives is to construct artificial silicon neural networks that process information similarly to neural systems in creatures. Although knowledge on the information processing principles in neural systems is inadequate, silicon neuron and neural networks are being studied actively. This is not only because of some realistic potential applications such as associative memory and brain-machine interfacing, but also because analysis by synthesis is one of the most effective tools for brain science. Many silicon neurons have been constructed using analog electrical circuit technology, because neural phenomena are produced by real-valued dynamics. Conventionally, in the analog silicon neuron design trade-off between the circuit size and richness of neuronal properties has been a disadvantage. In the previous works [1][2], we proposed a mathematical-model-based design policy that allows us to implement a compact silicon neuron that possesses rich neuronal dynamics.

For silicon neurons, digital circuit technology has not been applied as extensively as analog technol-

ogy. However, it has some appealing features such as insensitivity to the fluctuations in the environment and continuous improvement in the fabrication technology. Additionally, field programmable gate arrays (FPGAs) allow users to construct their own ICs. Currently, most digital silicon neurons and neural networks are dedicated processors for classical non-spiking neuron models and network models or simulators for spiking neuron models [3][4]. In this paper, we propose a new concept for digital silicon neuron design. By applying a mathematical-model-based design policy to digital circuits, we can design a digital spiking silicon neuron (DSSN) that possesses properties supported by theoretical models for biological neurons with compact circuitry. It is intended to be a constituent element for digital spiking neural networks that operate in real time, and has the potential to be an alternative to analog silicon neurons.

In the next section, we introduce the concept and design a model for an elemental DSSN model. In the third section, we report complex behaviors observed in a GJ-coupled network of the model to demonstrate that it has potential to exhibit rich dynamical behaviors comparable to analog silicon neurons. Finally, we will briefly refer to the implementation of our model.

2 Concept and Model of DSSN

The basic concept of DSSN is a dedicated system for solving differential equations of spiking neuron models. The hardware is an ordinary arithmetic circuit used for numerical integration. The keypoint lies in the designation of system equations. To implement a solver for a biological neuron model, massive hardware resources are required because most of the models are described using complex differential equations. We can avoid this problem by designing the system equations by a mathematical-model-based design method. Here, equations that have topological structures in their phase portrait similar to some theoretical models are designed first, and then, their parameters are tuned on the basis of bifurcation analysis.

The most fundamental property of biological neurons is the generation of action potentials. Neural excitability is another property, which classifies neurons according to the firing frequency at the onset of repetitive firing induced by a sustained stimulus that is increased gradually. Neurons with Class I excitability begin to fire repetitively with arbitrarily zero frequency, whereas those with Class II excitability begin with a non-zero frequency. Theoretical studies have elucidated the mathematical structure behind these properties by utilizing the phase portrait and bifurcation analyses [5][6]. These studies not only succeeded in explaining the mechanism of various properties of action potentials but also showed that saddle-node on invariant circle and Hopf bifurcations of a stable equilibrium corresponding to a resting state produce Class I and II excitabilities, respectively.

Based on the above mentioned information, we designed a model for elemental DSSN, whose equations are:

$$\frac{dv}{dt} = \frac{\phi}{\tau}(f(v) - n + I_0 + I_{stim}) \quad \text{and} \quad (1)$$

$$\frac{dn}{dt} = \frac{1}{\tau}(g(v) - n), \quad (2)$$

where

$$f(v) \equiv \begin{cases} a_n(v + b_n)^2 - c_n & \text{when } v < 0, \\ -a_p(v - b_p)^2 + c_p & \text{when } v \geq 0, \end{cases} \quad (3)$$

$$g(v) \equiv \begin{cases} k_n(v - p_n)^2 + q_n & \text{when } v < r, \\ k_p(v - p_p)^2 + q_p & \text{when } v \geq r. \end{cases} \quad \text{and} \quad (4)$$

Parameters a_x , b_x , c_x , k_x , p_x , q_x , and r determine the form of the nullclines, and ϕ and τ are time constant parameters (for $x = n$ and p). These equations were designed so that they could reproduce topological structures in the phase plane of the Morris-Lecar model [7]. It is one of the simplest models that show both Class I and II excitabilities depending on parameter sets. In our equations, multiplication operations between variables are significantly reduced because they consume large hardware resources (cubic curve is constructed by two quadratic curves). Note that multiplication between a parameter and a variable can be implemented by the shift operation if we select the parameter from $\{2^n | n \in \mathbf{Z}\}$.

We selected the parameter values so that our model reproduced the phase plane structure in the Morris-Lecar model in the Class I and II modes (see Appendix for values). In Fig. 1 (a), (b), and (c), the phase planes for Class I and II modes of our DSSN model are shown. These topological structures in the phase

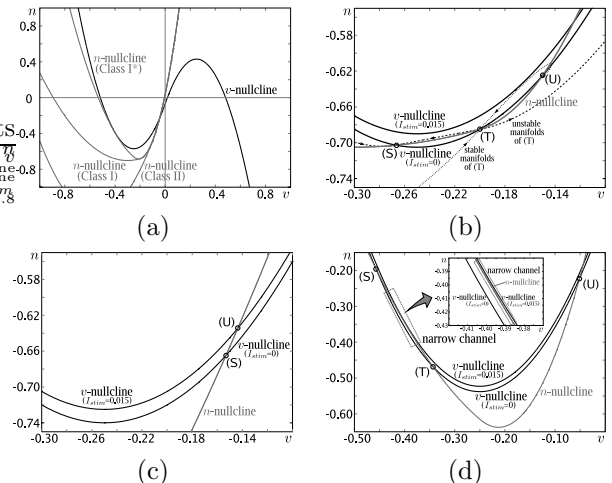


Figure 1: Phase planes for our DSSN model. (a) Nullclines for Class I, II, and I* modes. (b), (c), and (d) Closeup around critical structures for Class I, II, and I* modes, respectively. (S) is a stable equilibrium (resting state); (T), a saddle; and (U), an unstable equilibrium. Stimulus current (I_{stim}) shifts the v -nullcline up, resulting in repetitive oscillation. In the Class I* mode, v - and n -nullclines are very close to each other (narrow channel) around $v = -0.4$.

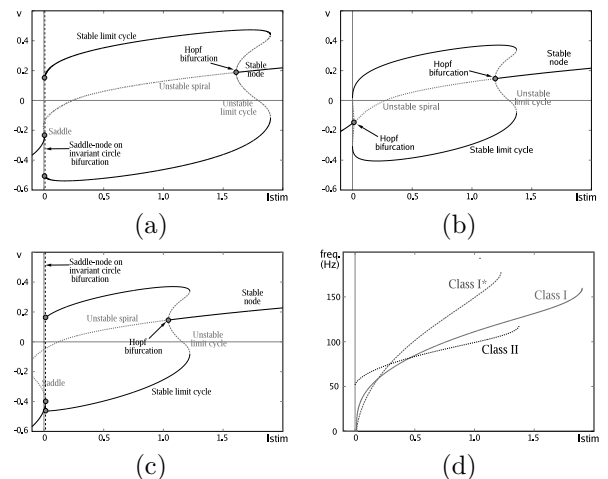


Figure 2: Bifurcations in our DSSN model. (a), (b), and (c) Bifurcation of variable v . Limit cycles are represented by the maximum and minimum values. (d) Bifurcation of frequency for limit cycles.

plane were proved to exhibit fundamental properties of action potentials by theoretical studies [5]. By selecting the descending limb of the n -nullcline, we can select the neural excitability classes. Fig. 2 (a), (b), and (d) show the results of the bifurcation analysis. They confirmed that our parameter sets produced the expected classes of excitability. Additionally, in the Class II mode, our DSSN model produced chaotic re-

sponses against repetitive pulse stimuli similar to those in biological neurons [8] and an analog silicon neuron [1]. This indicates the potential of our DSSN model to exhibit rich dynamical behavior.

3 GJ-coupled DSSN models

A gap junction (GJ) is a type of physical connection between neuronal cells, which is electrically equivalent to linear resistance. Various regions in the brain are known to contain numerous GJs, whose functions have attracted considerable interest from many researchers. In 2004, Fujii and Tsuda [9] found that some of Class I neuron models exhibited characteristic chaotic behaviors when interconnected via GJs. They classified these neuron models as Class I* and indicated that the following two conditions in phase plane structures supported this class. The first condition is the existence of a phase plane structure called narrow channel, which means that the nullclines for the membrane and ionic conductance variables remain close to each other in certain regions. The second one requires the unique crosspoint of the above two nullclines to be an unstable spiral equilibrium. These conditions are satisfied when a weak stimulus current is given to a neuron model with nullclines having specific shapes. In Fig. 1 (a) and (d), we show the phase planes for our DSSN model in the Class I* mode (see Appendix for the parameter set). A narrow channel is formed in the region shown by the dashed square, when $I_{stim} = 0.015$. Bifurcation analysis demonstrated that our DSSN model belonged to Class I in this mode (Fig. 2 (c) and (d)).

We calculated the maximum lyapunov exponent for the GJ-coupled network of DSSN models to demonstrate that our model with this parameter setting could operate as a Class I* neuron. This network is composed of a one-dimensional array of 20 DSSN models interconnected with two nearest neighbors via GJs (see Fig. 3). The current through GJ applied to the i -th DSSN model (I_{gj}^i) is given as follows:

$$I_{gj}^i = (v_{i+1} + v_{i-1} - 2v_i)/R_{gj}, \quad (5)$$

where i is the index number for DSSN model (from 1 to 20); v_i , v for the i -th DSSN model ($v_0 \equiv v_1$ and $v_{21} \equiv v_{20}$); and R_{gj} , the resistance of the GJ. These currents are added to I_{stim} for each neuron. In Fig. 4 (a), the maximum lyapunov exponents for the Class I, II, and I* modes are shown. It is large in the Class I* mode when R_{gj} is approximately between 2.5 and 20, whereas it is approximately zero, independent of R_{gj} in the Class I and II modes. In the Class I* mode,

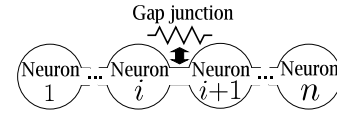


Figure 3: One dimensional GJ-coupled network.

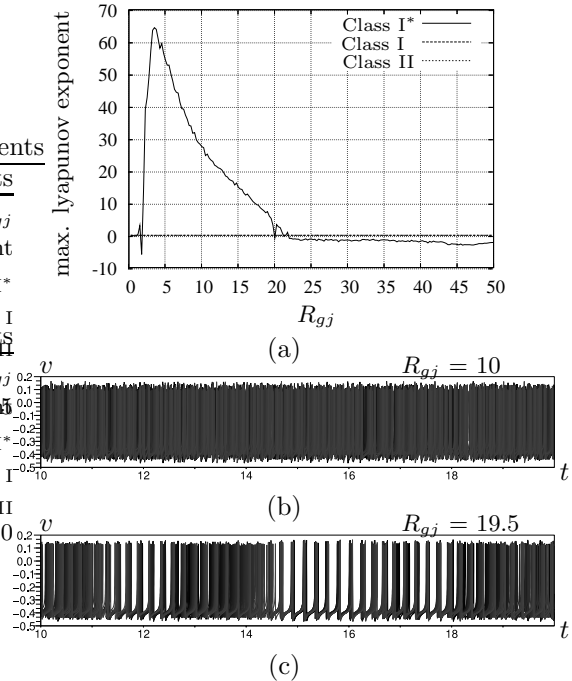


Figure 4: Behaviors of a GJ-coupled network of 20 DSSN models. (a) Maximum lyapunov exponents in Class I, II, and I* modes. Large values are obtained only in the Class I* mode. (b) and (c) Superimposed waveforms for v in the Class I* mode when R_{gj} is 10 and 19.5, respectively. Intermittently chaotic behavior is observed when R_{gj} in (c), when the maximum lyapunov exponent is relatively small.

the network is synchronous when R_{gj} is sufficiently small, becomes chaotic (Fig. 4 (b)) as R_{gj} increases, and then returns to the synchronous state when R_{gj} is sufficiently large. We observed intermittently chaotic behaviors for the R_{gj} values during the transition from the chaotic to synchronous states (Fig. 4 (c)). These behaviors are consistent with that of an analog silicon neuron model we designed in the previous work [10].

4 Concluding remark

In the previous sections, we proposed a DSSN model and indicated that it has potential to reproduce the fundamental characteristics of neurons. We also showed that our model could exhibit complex behav-

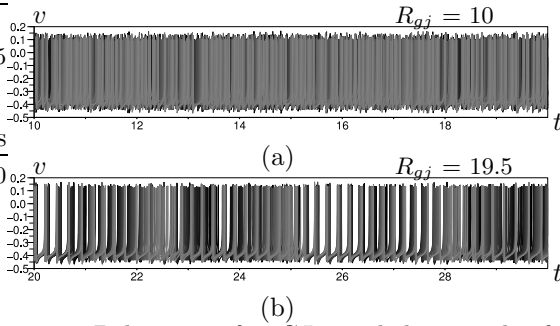


Figure 5: Behaviors of a GJ-coupled network of 20 DSSNs. (a) $R_{gj} = 10$. (b) $R_{gj} = 19.5$. Numerical integration was performed by Euler's method and precision was 28 bit fixed-point. Chaotic and intermittently chaotic behavior that are consistent with model simulation (Fig. 4 (b) and (c)) were observed.

ior with monotonic stimulus in GJ-coupled networks.

We are planning to implement our DSSN model in FPGA devices and are performing numerical simulations. Reasonable results are obtained when we select Euler's method and fixed-point expressions for numerical integration. For example, we observe complex behaviors in the Class II mode of the DSSN model when it is stimulated repetitively (not shown), and chaotic and intermittently chaotic behaviors in a GJ-coupled network of 20 DSSNs (Fig. 5) that is consistent with the accurate simulation of the model. These results are obtained with a time step of 1.0^{-5} for Euler's method and 28 bit fixed-point expression. Numerical precision is an important factor that affects the circuit size and operation speed. However, it is quite a difficult problem to give objective criteria for determining the required precision. This is because interconnected neurons and even a single neuron are complex systems and the assessment of their dynamical behavior is a complicated subject.

For the implementation of a digital spiking silicon neural network, a silicon synapse circuit is required. We will design this circuit in the near future by using a mathematical-model-based method referring to kinetic models for biological synapses.

Acknowledgements

This study is supported by Aihara Complexity Modelling Project, ERATO, JST, Japan.

References

[1] Takashi Kohno and Kazuyuki Aihara, "A MOSFET-based model of a Class 2 Nerve membrane," *IEEE*

Trans. Neural Networks, Vol. 16, No. 3, pp. 754-773, May 2005.

- [2] Takashi Kohno and Kazuyuki Aihara, "Mathematical-model-based design method of silicon burst neurons," *Submitted to Neurocomputing*.
- [3] Dan Hammerstrom, "Digital VLSI for Neural Networks," in *"The Handbook of Brain Theory and Neural Networks second ed."*, ed. M. A. Arbib, pp. 349-353, MIT Press, 2003.
- [4] "FPGA Implementations of Neural Networks", ed. A. R. Omondi and J. C. Rajapakse, Springer, 2006.
- [5] J. Rinzel and B. Ermentrout, "Analysis of Neural Excitability and Oscillations," in *"Methods in Neural Modeling"*, ed. C. Koch and I. Segev, pp. 251-291, MIT Press, 1998.
- [6] E. M. Izhikevich, "Neural Excitability, Spiking, and Bursting," *Int. J. Bifurcation and Chaos*, Vol. 10, pp. 1171-1266, 2000.
- [7] C. Morris and H. Lecar, "Voltage Oscillations in the Barnacle Giant Muscle Fiber," *Biophys. J.*, Vol. 35, pp. 193-213, Jul., 1981.
- [8] K. Aihara, G. Matsumoto, and Y. Ikegaya, "Periodic and non-periodic responses of an periodically forced Hodgkin-Huxley oscillator," *J. Theor. Biol.*, Vol. 109, p. 249-269, 1984
- [9] H. Fujii and I. Tsuda, "Itinerant dynamics of class I* neurons coupled by gap junctions.," *Computational Neuroscience: Cortical Dynamics Lecture Notes In Computer Science*, Vol. 3146, pp. 140-160.
- [10] T. Takemoto, T. Kohno, and K. Aihara, "Circuit Implementation and Dynamics of A Two-Dimensional MOSFET Neuron Model," *Int. J. Bifurcation and Chaos*, will appear in Feb. 2007.

Appendix

A Common parameters:

Par.	Value	Par.	Value	Par.	Value
a_n	8.0	b_n	0.25	c_n	0.5
a_p	8.0	b_p	0.25	c_p	0.5
k_p	16.0	p_p	-0.2125	q_p	-0.6875

B Class I parameters:

Par.	Value	Par.	Value	Par.	Value
k_n	2.0	p_n	-0.3	q_n	-0.705
ϕ	1.0	τ	0.003	r	-0.2
I_0	-0.205				

C Class II parameters:

Par.	Value	Par.	Value	Par.	Value
k_n	4.0	p_n	-0.55	q_n	-1.295
ϕ	0.6	τ	0.003	r	-0.1
I_0	-0.24				

D Class I* parameters:

Par.	Value	Par.	Value	Par.	Value
k_n	4.0	p_n	-0.1	q_n	-0.755
ϕ	0.6	τ	0.002	r	-0.25
I_0	-0.25				

Hexagon-Based Q-Learning for Object Search with Multiple Robots

Hyun-Chang Yang, Ho-Duck Kim, and Kwee-Bo Sim

School of Electrical and Electronics Engineering, Chung-Ang University
221, Heukseok-Dong, Dongjak-Gu, Seoul 156-756, Korea
e-mail : hoduck@wm.cau.ac.kr, kbsim@cau.ac.kr

Abstract

This paper presents the hexagon-based Q-learning for object search with multiple robots. We organized an experimental environment with five small mobile robots, obstacles, and an object. Then we sent the robots to a hallway, where some obstacles were lying about, to search for a hidden object. In experiment, we used three control algorithms: a random search, an area-based action making (ABAM) process to determine the next action of the robots, and hexagon-based Q-learning to enhance the area-based action making process.

Keywords : Hexagon-based Q-Learning, Multiple robots, Area-Based Action Making, Markovian

1. Introduction

Nowadays, robots are performing human's work in dangerous field, such as rescue jobs at fire-destroyed building or at gas contaminated sites; information retrieval from deep seas or from space; and weather analysis at extremely cold areas like Antarctica. Sometimes, multiple robots are especially needed to penetrate into hard-to-access areas, such as underground insect nests, to collect more reliable and solid data.

Multiple robot control has received much attention to offer a new way of controlling multiple agents more flexibly and robustly. Ogasawara used distributed autonomous robotic systems to control multiple robots that transport a large object[1]. In this paper, we propose an area-based action making (ABAM) process, which is the basis of hexagon-based Q-learning, to control multiple robots against collision and lead individual robot to search through its own trajectory.

Reinforcement learning allows an agent to actively decide an action policy based on explorations of its environment. During exploration of an uncertain state space with reward, an agent can learn what to do by continuous tracking of its state history and appropriately propagating rewards through the state space[2]. In our

research, we focused on Q-learning as a reinforcement learning technique. Because Q-learning is a simple way to solve Markovian action problems with incomplete information and on the basis of the action-value function Q that maps state-action pairs to expected returns [3]. In addition to this simplicity, Q-learning can adopt to the real world situation. For example, the state space can be matched with the physical space of the real world. An action also can be regarded as physical robot movement. In this paper, we propose the hexagon-based Q-learning to enhance the area-based action making process so that the learning process can better adapt to real world situations.

The organization of this paper is as follows. In chapter 2, the area-based action making process is introduced. In chapter 3, hexagon-based Q-learning adaptation is presented. In chapter 4, experimental results from the application of three different searching methods to find the object are presented. In chapter 5, conclusions are presented.

2. Area-Based Action Making Process

Area-based action making (ABAM) process is a process that determines the next action of a robot. The reason why this process is referred to ABAM is that a robot recognizes surrounding not by distances, from itself to obstacle, but by areas around itself. The key idea of the ABAM process is to reduce the uncertainty of its surrounding. It is similar with the behavior-based direction change, to control the robots [4]. The robots recognize the shape of its surrounding, then take an action (turn and move forward) to where the widest space will be guaranteed. Consequently, each robot can avoid an obstacle and collision with other robots. Figure 1 depicts the different actions taken by distance-based action making (DBAM) and by ABAM in the same situation [5]. Our small mobile robot has the six emitter-detector infrared sensor pairs, which are placed at an angle of 60 degrees with one another to cover 360 degrees. The advantage of ABAM is illustrated by the

following example. Figure 2 presents the result of each action making process by DBAM and ABAM. In both case, the robot is surrounded by 4-obstacles. By DBAM, the robot will be confused because it perceives that there is no obstacle in the southeast direction, and then it will try to keep tracking to the southeast. Finally, it will get stuck between two obstacles. This scenario is shown in the left picture in Fig. 2. By ABAM, however, the robot will calculate the areas of its surrounding, and then it will recognize that an action to the northeast will guarantee the widest space. Therefore, the robot will change its direction to the northeast. This scenario is presented in the right picture in Fig. 2.

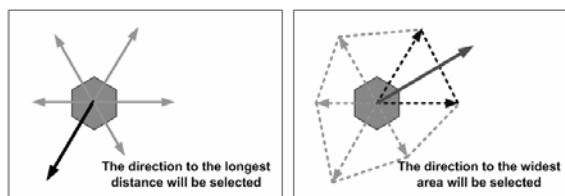


Fig. 1. The different actions will be taken by DBAM and by ABAM in the same situation

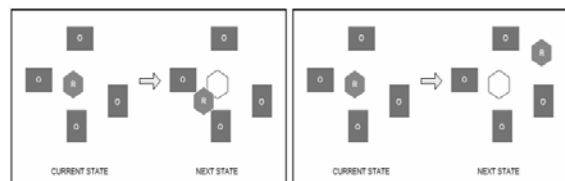


Fig. 2. An illustrative example of robot maneuvers by DBAM(left) and by ABAM(right)

In addition to the obstacle avoidance, ABAM also make the robots to search their own space [6]. This feature is advantageous when 2 or 3 robots meet at the same place. When they face each other, each robot will try to find more wide space. Consequently, the robot will change its direction to avoid the other robots and start to search in its own space again.

3. Hexagon-Based Q-Learning

Q-learning is a well-known algorithm for reinforcement learning. It leads the agent to acquire optimal control strategies from delayed rewards, even when the agent has no prior knowledge of the effects of its actions on the environment [7][8]. Figure 3 is an illustrative example to explain Q-learning algorithm more clearly. The 'R' stands for a robot or agent. The values upon the arrows are relevant \hat{Q} values with the state transition. For example, the value $\hat{Q}(s_1, a_{right}) = 72$, where a right refers to the action that moves R to its right [8].

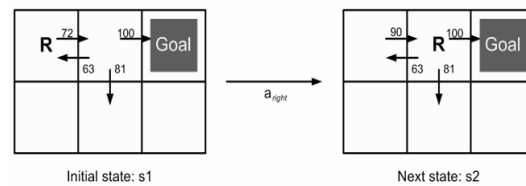


Fig. 3. An illustrative example of Q-learning

If the robot takes the action to the right, the value will be updated for this entry where $r = 0$, $\gamma = 0.9$ are predetermined values. The formula is presented below.

$$\begin{aligned} \hat{Q}(s, a) &\leftarrow r + \gamma \max_{a'} \hat{Q}(s', a') \\ &\leftarrow 0 + 0.9 \max\{63, 81, 100\} \\ &\leftarrow 90 \end{aligned} \quad (1)$$

The Q-learning for our robot system was adapted to enhance the ABAM process. The adaptation can be performed with a simple and easy modification, named hexagon-based Q-learning. Figure 4 is an illustrative example of hexagon-based Q-learning. In Fig. 4, intuitively, we know that the only thing that was changed is the shape of state space. We changed the shape of the space, from a square to a hexagon, so that the robot can recognize its surrounding by 6-areas. According to this adaptation, the robot takes an action to 6-direction and has 6-table entry \hat{Q} value. In the left of Fig. 4, the robot is in the initial state. Now, if the robot decides that +60 degree guarantee the widest space after calculation of its 6-areas of surrounding, the action of the robot would be a_{+60° . After the action is taken, if Area3 is the widest area, the value of $\hat{Q}(s_1, a_{+60^\circ})$ will be updated by the formula (2) in the Q-learning algorithm as

$$\begin{aligned} \hat{Q}(s_1, a_{init}) &\leftarrow r + \gamma \max_{a'} \hat{Q}(s_2, a_{+60}) \\ &\leftarrow 0 + \gamma \max\{Area1, Area2, \dots, Area6\} \\ &\leftarrow \gamma Area3 \end{aligned} \quad (2)$$

where 0 is the predetermined immediate reward. After the movement from the initial state to the 1st next state, immediate reward becomes the difference between the sum of total area before action is taken and the sum of total area after action is taken.

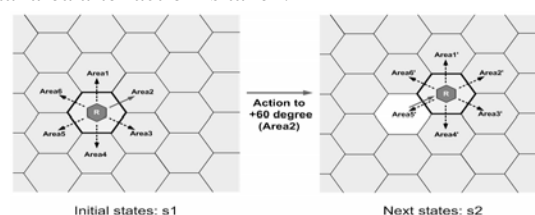


Fig. 4. Hexagon-Based Q-learning

Ultimately, the robot can determine its trajectory by learning this \hat{Q} value. In the real world experiment, however, battery consumption is a problem. If the robot has to perform infinite iterations to complete task, total system will fail. Therefore, a system must be set up to cancel the former action and move back to the earlier state, when the former action causes any bad reward or result. The hexagon-based Q-learning algorithm is presented in Table 1.

Table 1. Hexagon-based Q-learning algorithm

<p>For each s, a initialize the table entry $\hat{Q}(s, a)$ to zero</p> <p>Calculate each 6-areas at the current state s</p> <p>Do until task is completed.</p> <ul style="list-style-type: none"> • Take an action a to the widest area • Receive immediate reward r • Observe the new state s' <p>If $\hat{Q}(s', a)$ is greater or equal than $\hat{Q}(s, a)$</p> <ul style="list-style-type: none"> • Update the table entry for $\hat{Q}(s, a)$ • $s \leftarrow s'$ <p>If $\hat{Q}(s', a)$ is too less than $\hat{Q}(s, a)$</p> <ul style="list-style-type: none"> • Move back to the previous state • $s \leftarrow s$
--

4. Experiment Results

We performed experiments by using three different control methods: random search, ABAM, and enhanced ABAM by hexagon-based Q-learning. In the first part of this chapter, we introduce our self-made small mobile robot system. Then, we present experimental result with three different control methods.

4.1 Architecture of Small Mobile Robot

Our small mobile robot system consisted of four sub-parts and a main micro-controller part. The sub-parts were camera vision, sensor, motor, and Bluetooth communication module. Each sub-part had its own controller to perform its unique function more efficiently.

Figure 5 shows the appearance, anatomy, and functional block diagram of the robot. The main components of the robot are as follows. For the eye of the robot, Movcam II made by Kyosera is used. It is the CCD camera and its size is $30 \times 47 \times 29$ mm. The robot has six infrared sensors, emitter and detector pairs, to measure the distance around itself. The detector is ST-1kla, high sensitivity NPN silicon phototransistors. NMB PG25L-024 stepping motor is used as the driving part. Its characteristics are the following: drive voltage-12V, drive method 2-2 phase and 0.495° step angle.

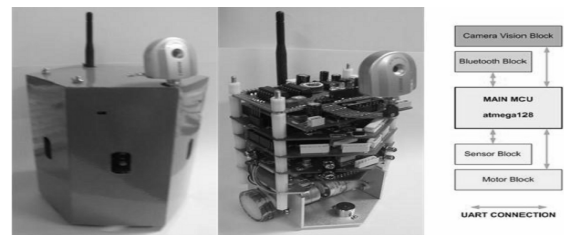


Fig. 5. Appearance (left), anatomy (center), and functional block diagram (right) of the robot

4.2 Experiments

The task of the robots is as follows: “Find the hidden object while tracking through an unknown hallway.” We set up the color of the object as green and that of 5-robots as orange. The object was a stationary robot having the same shape. It was located at a hidden place near the obstacle. The 5-robots, which try to search the object, recognize the object by the object’s color and shape. The 5-robots will decide whether they have finished the task by detecting the object after each action is taken. First, we used the random search control method to find the hidden object. The main controller generated a random number and decided the next action corresponding to this number. Random search is not so strong method to control the robot efficiently. Therefore, random did not perform well. Moreover, it is very time and power consuming in the real world situation. In Fig. 6, the white arrow points out the object (same in Fig. 7 and Fig. 8). During random search, even though the robots are within a close distance to the search object, some robots failed to find the object.



Fig. 6. 5-robots are searching the object using random search

Second, we applied ABAM to the robots. With the feature of ABAM, the robots sense their environment by 6-infrared sensors and calculate 6-area with these values. When the calculation is done, each robot tries to move to where the widest area will be guaranteed. In our 2nd experiment, after the robots started to move, each robot spread out into the environment. Consequently, the ABAM performed better than random search. Figure 7 shows that the two robots, which is located the right side of the object, succeeded to complete the task. These two robots are designated by black arrow in Fig. 7.



Fig. 7. 5-robots are searching the object using ABAM

Finally, we adopted the hexagon-based Q-learning to ABAM as a modified control method. This method allowed the robots to reduce the probability of wrong judgment and compensated wrong judgment by reinforcement learning. Each robot tried to search its own area as in the 2nd experiment, however, it canceled the decided action if the action caused negative (or bad) immediate reward value. The search with hexagon-based Q-learning is presented in Fig. 8. The results of our experiment are presented in Fig. 9. With random search, one robot found the object at the 2nd trial and 6th trial, although these detections can be considered as just coincidence. Therefore, we can say the random search has no remarkable meaning. With ABAM, the robots performed better than with random search, with the average performance above 1 during the all trial. Finally, with the adaptation of hexagon-based Q-learning to ABAM, the results were remarkable.



Fig. 8. 5-robots are searching the object using hexagon-based Q-learning

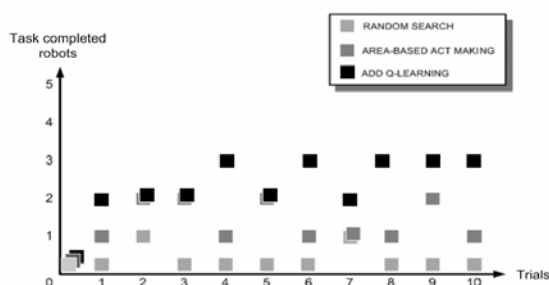


Fig. 9. Experimental result with 3 different control methods

5. Conclusion

In this paper, we presented the area-based action making process and hexagon-based Q-learning to search the object, hidden in unknown space, for 5 of our self-made small mobile robots. The experimental results from the application of the three different control methods in the

same environmental situations were presented. The area-based action making process and hexagon-based Q-learning can be a new way for robot to search an object in unknown space. This algorithm also makes the agents avoid obstacles during their search. In our research, first, we need to clarify the problem of accessing to the object.

This means that if multiple robots are to carry out a task such as object transporting or block stacking, the robots need to recognize the object then approach to it. Therefore, we need to develop the robust accessing algorithm. Naturally, some grippers need to be attached to both sides of the robot. Second, our robot systems should be improved so that the main part and the sub-parts adhere more strongly. In addition, stronger complex algorithms such as Bayesian learning or TD(λ) method should be adapted. Third, a self-organizing Bluetooth communication network should be built so that robots can communicate with each other robustly even if one or more robots are lost. Finally, the total system should be refined.

Acknowledgment:

This research was supported by the Development of Social Secure Robot using Group Technologies of Growth Dynamics Technology Development Project by Ministry of Commerce, Industry and Energy, Korea.

References

- [1] G. Ogasawara, T. Omata, T. Sato, "Multiple movers using distributed, decision-theoretic control," *Proc. of Japan-USA Symposium on Flexible Automation 1*, pp. 623-630, 1992.
- [2] D. Ballard, "An Introduction to Natural Computation," The MIT Press Cambridge, 1997.
- [3] J. Jang, C. Sun, E. Mizutani, "Neuro-Fuzzy and Soft Computing," *Prentice-Hall New Jersey*, 1997.
- [4] W. Ashley, T. Balch, "Value-based observation with robot teams (VBORT) for dynamic targets," *Proc. of Int. Conf. on Intelligent Robots and Systems*, 2003.
- [5] J. B. Park, B. H. Lee, and M. S. Kim, "Remote Control of a Mobile Robot Using Distance-Based Reflective Force," *Proc. of IEEE Int. Conf. on Robotics and Automation 3*, pp. 3415-3420, 2003.
- [6] P. Ögren, N. E. Leonard, "Obstacle Avoidance in Formation," *Proc. of IEEE Int. Conf. on Robotics and Automation 2*, pp. 2492-2497, 2003.
- [7] T. Mitchell, "Machine Learning," *McGraw-Hill Singapore*, 1997.
- [8] C. Clausen, H. Wechsler, "Quad-Q-Learning," *IEEE Trans. on Neural Network 11*, pp. 279-294, 2000.

Motion generation of pneumatic artificial muscle

S. ICHIKAWA, M. HARA, M. SUGISAKA

Department of Electrical and Electric Engineering, Oita University
700 Dannoharu Oita 870-1192 Japan.
E-mail: msugi@cc.oita-u.ac.jp

Abstract

Various commodities that support the senior citizen physically and psychologically appear by the coming of the aged society. A lot of supplementary equipment are installed directly in the user and used. As for such equipment, physical safety and a psychological sense of security are requested. Then, recently, artificial muscle is researched as a wearable actuator that a user can use in comfort. Therefore, we research the support equipment by using the pneumatic artificial muscle. The past research in our laboratory, we made an artificial muscular robot. And, we measured the characteristic of each artificial muscle.

In this research, we generate motion of pneumatic artificial muscular robot.

1. Introduction

Since the advent of aged society, various support instruments that support the senior physically and mentally is created. Many of them are equipped directly by the user.

As for support instruments, physical safety and a mental sense of security are requested. To secure physical safety and a mental sense of security, the following are needed.

- (1) Even if controlling becomes impossible, support instruments doesn't become a trouble.
- (2) Support instruments are small and light.
(The senior citizen can easily carry possession.)
- (3) Support instruments fits flexibly the human body.
- (4) No operation sound.

Recently, as a wearable actuator with which a user can equip in comfort, artificial muscles attract attention.

Therefore, we will research the support instrument by using the artificial muscle.

As the first step, in this research, we measure the characteristic of each artificial muscle, and, we make motion generation of artificial muscular robot.

2. Artificial muscle

There are various kinds of artificial muscles. Artificial muscle has following kind.

<Polymer actuator>

(Actuator that used polymeric material.)

<Shape-memory actuator>

(Actuator that used shape-memory material.)

<Electrostatic actuator>

(Actuator using electrostatic power.)

<Pneumatic actuator >

(Actuator that used air pressure.)

In this research, we used the Pneumatic actuator (McKibben artificial muscle) as a suitable actuator for the support instrument that the user equips, because the balance of the generative force and the contraction percentage is good, and, the viscoelasticity characteristic is similar to human's muscle.

The McKibben artificial muscle has structure that wrapped the rubber tube by a plastic fiber mesh. Fig.1 and Fig.2 show pattern diagrams of artificial muscle. When Pneumatic muscle was pressurized, it expands in the radius direction. Power to contract axially is generated. If the artificial muscles is set to 100, the maximum pressurization will be set to 70. The artificial muscle has the expansion and contraction rate of 30%.

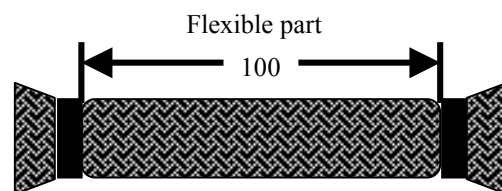


Fig.1 Pattern diagrams before artificial muscle is pressurized

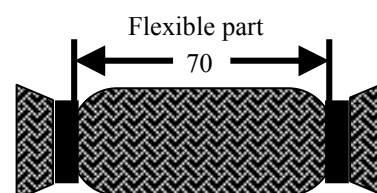


Fig.2 Pattern diagrams after artificial muscle is pressurized

3. Artificial muscular robot

Fig.3 shows pattern diagrams of artificial muscular robot. The frame of the robot is wooden, and it has the hip joint, the knee joint, and the ankle joint. The hip joint and the ankle joint are made from the spheroid joint. The knee joint is made from the hinge joint. Number of Fig.3 expresses arrangement of artificial muscles.

- 1: long peroneal muscle, short peroneal muscle (125mm)
- 2: anterior tibial muscle, posterior tibial muscle (125mm)
- 3: tibialis anterior (245mm)
- 4: musculus triceps surae (400mm)
- 5: musculus quadriceps femoris (330mm)
- 6: hamstrings (330mm)
- 7: gluteus maximus (305mm)
- 8: musculus iliopsoas (305mm)

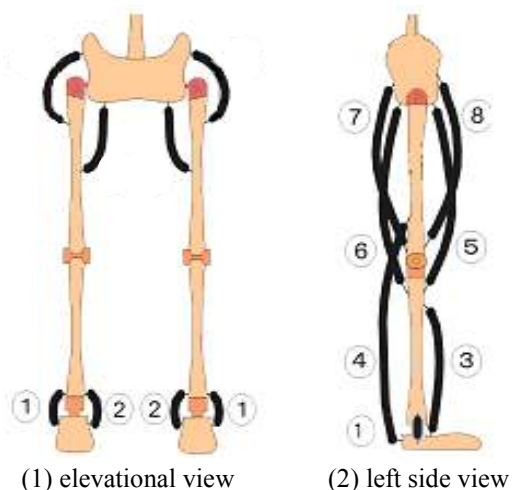


Fig.3 Pattern diagrams of artificial muscular robot

4. Experimental apparatus

The outline chart of the apparatus used by this research is shown in Fig.4.

The air tube of the artificial muscle and the air tube of air compressor are connected with the air pressure controller. The control signal from the computer is given to the air pressure controller, and the artificial muscle can be expanded and contracted.

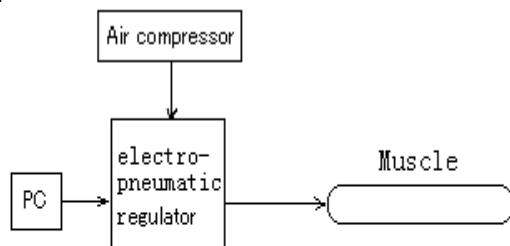


Fig.4 Experiment device outline chart

5. Expansion and contraction characteristic measurement

We used the artificial muscle of different four lengths (160,240,300,400mm) in this experiment. First of all, the load is not put on the artificial muscle. And, constant air pressure is injected. Next, the load is not put on two artificial muscles and constant air pressure is exhausted. The measurement result is shown in Fig.5-6.

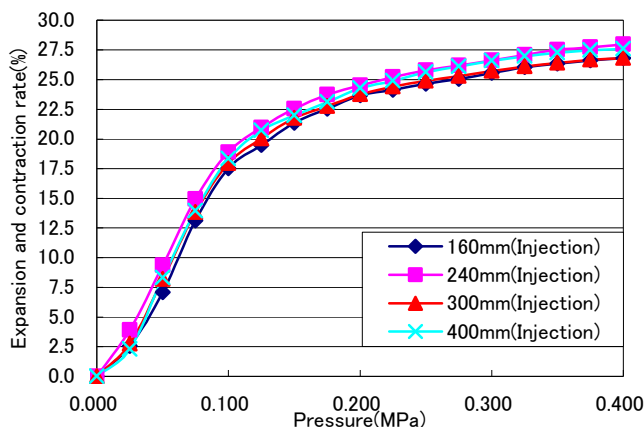


Fig.5 No load characteristic of each length (Injection)

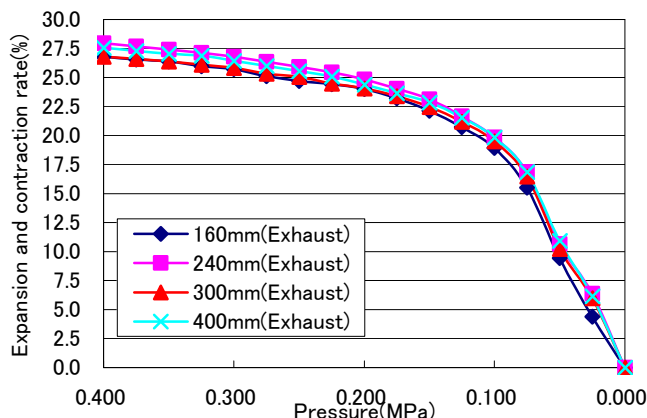


Fig.6 No load characteristic of each length (Exhaust)

These are collectively shown in Fig.7-10.

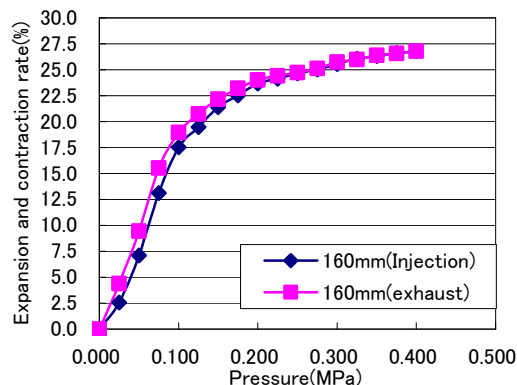


Fig.7 No load characteristic of 160mm in length (Injection-exhaust)

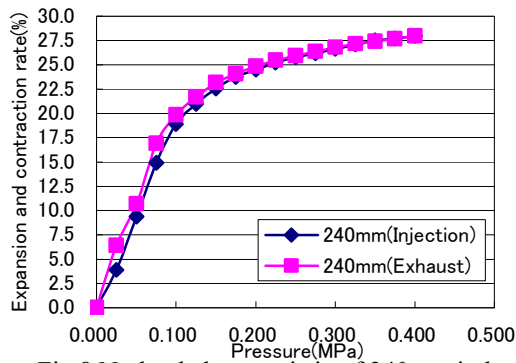


Fig.8 No load characteristic of 240mm in length
 (Injection-exhaust)

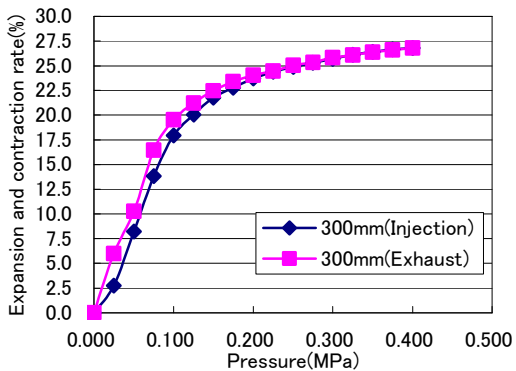


Fig.9 No load characteristic of 300mm in length
 (Injection-exhaust)

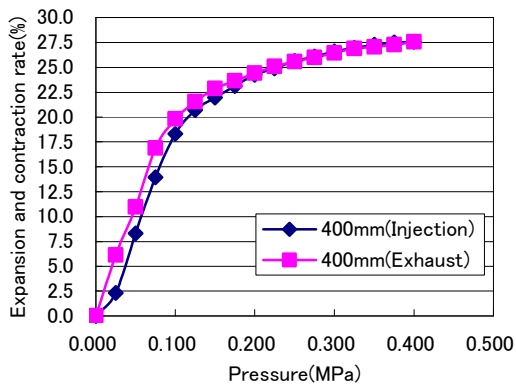


Fig.10 No load characteristic of 400mm in length
 (Injection-exhaust)

Injection and exhaust in the same length showed the characteristic with a different each curve (Fig.7-10). Cause of hysteresis was thought elastic deformation of rubber tube in the artificial muscle.

6. Load characteristics

Next, we add the loads of certain degree to the artificial muscles, and, we measure the characteristics of expansion and contraction. The measurement result is shown in Fig.11-14. (The measurement result in the artificial muscle of 300mm in length is shown in this paper.)

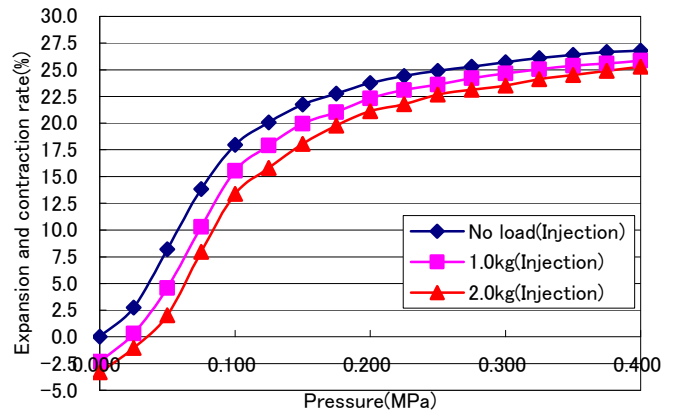


Fig.11 Load characteristic of 300mm in length
 (Injection)

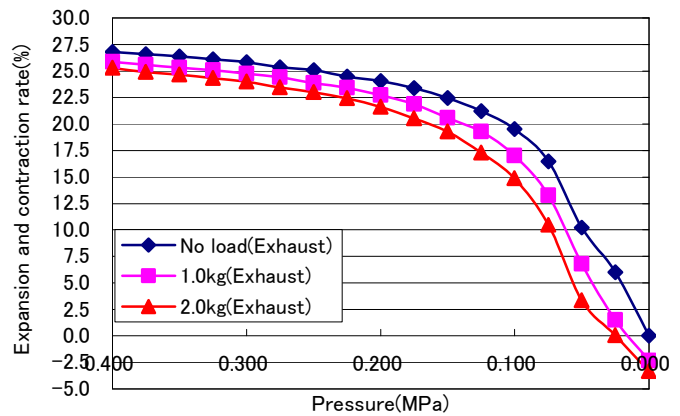


Fig.12 Load characteristic of 300mm in length (Exhaust)

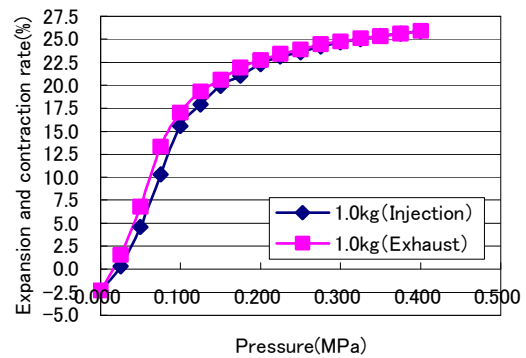


Fig.13 Load characteristic of 300mm in length
 [Load=1.0kg] (Injection-exhaust)

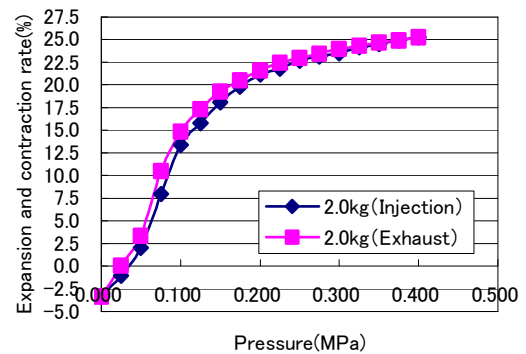


Fig.14 Load characteristic of 300mm in length
 [Load=2.0kg] (Injection-exhaust)

From the above, the expansion and contraction rate lowers when the load is put regardless of the length of the artificial muscle.

Next, when no-load, the error of injection and exhaust was 3.2% at the maximum. When we put the load of 1.0kg, the error of injection and exhaust was 3.0% at the maximum. When we put the load of 2.0kg, the error of injection and exhaust was 2.5% at the maximum. As a result, artificial muscles can perform a certain amount of hysteresis improvement by applying load.

Moreover, because the error of injection and exhaust is about 3% at the maximum, the expansion and contraction characteristic of using for motion generation of artificial muscles uses the average value of injection and exhaust.

7. Motion generation of bending and stretching

We generated the bending and stretching motion of the robot by using the above-mentioned measurement result. The home position of the robot is shown in Fig.15 (a),(c). The bending position of the robot is shown in Fig.15 (b).



(a) Home position of the robot (b) Bending position of the robot (c) Home position of the robot

Fig.15 Bending and stretching motion of the robot

8.CONCLUSION

In this research, we made Expansion and contraction characteristic measurement of artificial muscles, and the improvement of hysteresis. And, we performed an artificial muscular robot expansion-and-contraction operation generation using the result. However, because the load added to the artificial muscle changes while operating, we cannot accurately control the robot. In the future, we will improve the above issue. In addition, we will generate walk operation of an artificial muscular

robot.

REFERENCES

- [1] S.Douno,A.Saitou,R.Kuwata
“Knit Structure SMA Actuator for Wearable Artificial Muscle Systems”
- [2] Takashi TAKUMA(Osaka Univ.), Koh HOSODA, Minoru ASADA(Osaka Univ., Handai FRC)
“Stabilization of the biped walker with pneumatic muscle actuator”
- [3]<http://f-kawaraban.cside.com/find/kinoukaibou/muscles.htm>
- [4]<http://www.katto.comm.waseda.ac.jp/~katto/Class/GazoTokuron/code/thread.html>
- [5]<http://www.hlla.is.tsukuba.ac.jp/~yas/sie/pdsoft-2001/2002-01-17/>
- [6] <http://yokohama.cool.ne.jp/chokuto/urawaza/api/>

An Antibody-Based Computing: An Application to Stable Marriage Problem

Yoshiteru Ishida^{1, 2}

¹ Department of Knowledge-Based Information Engineering,
Toyohashi University of Technology,
Tempaku, Toyohashi, 441-8580 Japan

²Intelligent Sensing System Research Center
Toyohashi University of Technology,
Tempaku, Toyohashi, 441-8580 Japan

Abstract

Antibodies, among others, are important components of the immune system. This paper proposes using specific recognition capability exhibited by antibodies for computation, in particular, solving *stable marriage problem* which have been studied as combinatorial computational problems. Antibody-based computation is proposed by integrating the recognition capabilities of antibodies. The computation is carried out on an array form that is suitable not for only expressing stable marriage problems but for further integration to antibody microarrays.

1 Introduction

After Adelman pioneered DNA-based computing in his seminal work [1], many researches established that not only DNA but also other macro molecules could have computational capability comparable to DNA (e.g. [2]). Elowitz and Leibler even demonstrated that a genetic circuit may not be a dream [3,4]. Even synthetic multicellular systems have been recently studied [5], leading to synthetic biology. Possible drug production by engineering yeast [6] has given a great impact on the area. These new bio-engineering technologies have provided bioinformatics with not only new tools but systemic views.

On the other hand, post-genome era proved that sequence information of human genome alone is not sufficient, but higher knowledge of function must be revealed. Post-genome age naturally proceeds to study immune systems (as in [7]) focusing not only components such as antibodies and MHC but its systemic organization.

After the demonstration of DNA based computing by Adelman, protein based computing had been proposed by Hug and Schuler [2] and extended

by Balan and Krithivasan [8]. This paper, in a similar spirit of synthetic biology and system biology, tries to construct an information processing devices incorporating specific recognition capabilities of antibodies. Stable marriage problem [9, 10] is used as a benchmark problem for demonstrating an array format implementation of antibody-based computation.

2 Antibody-based Computing: An Introduction

One of the major components propelling the information processing of the immune system is the specific recognition of antigens. The immune system is capable of recognizing even artificially synthesized substances. Also, it can further classify substances into the self (those derived from the individual) and nonself. Among those bearing recognition capabilities, antibody is undoubtedly important. Further, antibodies have been studied in great detail not only in theoretical biology but in bio-engineering. Antibody-based computing directly focuses on the recognition capability and integrates it for problem solving including combinatorial problems.

2.1 Antibody-based computing and DNA-based computing

Similarly to the DNA-based computing, antibody-based computing utilizes complementary matching between macro molecules: antibodies. Since the computational capabilities that DNA-based computing could be inherited to antibody-based computing, we rather focus on the difference between them. Roughly said in the context of solving combinatorial problems, the difference may be clarified by the correspondence between a

complementary matching (as in *Marriage Theorem*) and a stable pairing based on preference (as in *Stable Marriage Problem*).

Affinity between antigens and antibodies can be measured and their intensities can be ordered (as formatted in an affinity matrix). That is, in contrast to **Matching**($DNA1, DNA2$)=1 (matched) 0 (not matched), **Affinity**($Antigen1, Antibody2$) could vary from 0 (no agglutination) to 1 (highest agglutination). This difference would suggest that antibody-based computing could potentially implement error tolerance that could not be implemented on the DNA-based computing. The difference would further suggest that the antibody-based computing may be extended to a problem solver, if adaptive mechanism of the immune system realized by antibodies and their maintenance is also involved.

3 Solving a Combinatorial Problem

3.1 Stable Marriage Problem

In a naive form, the problem assumes n men and n women with each member having preference lists to the members of opposite sex. A pair of a man M_i and a woman W_j is called a blocking pair if they are not pair in the current solution, but M_i prefers W_j to the current partner and W_j prefers M_i to the current partner as well. A matching between men and women with no such blocking pair is called *stable*.

Having stated the stable marriage problem, it would be natural to think of the algorithm for antibody-based computing. That is, the stable marriage problem (SMP) may be mapped to antigen-antibody reaction so that preference order of each person in SMP will be reflected in the affinity intensity between an antibody and an antigen. After antibodies and antigens are so arranged, the solution of SMP will emerge by observing concentration of the agglutination. It should be remarked that agglutination process could be any agglutination (not necessarily between antibodies and antigens) if their intensities are measurable and ordered.

3.2 Mapping a stable marriage problem to antibody-based computing

As stated above, mapping a combinatorial

problem to antibody-based computing can be done by composing antigens-antibodies compounds corresponding to a problem entity. Antibodies and antigens for a compound corresponding to a particular individual will be determined by considering her (his) preference list over men (women).

Landsteiner's ABO blood group system [11] may be most familiar and yet simple example. His blood type system is based on antigens (as agglutinogen) on red blood cells and antibodies (as agglutinin) in the blood serum. **Table 1** shows agglutinogen and agglutinin of each blood type. Affinity between antibody and antigen is shown in **Table 2**. **Table 3** indicates the well-known incompatible transfusion among the blood type A, B, AB, and O.

Table 1. Landsteiner's ABO Blood Group System

Blood Type	A	B	AB	O
Antigen (agglutinogen)	A	B	A, B	None
Antobody (agglutinin)	β	α	None	α, β

Table 2. Affinity Matrix. Circle indicates that the antibody-antigen reaction would occur if the antibodies in the column meet with antigens in the row.

Antigen	A	B
Antibody		
α (anti-A)	○	
β (anti-B)		○

Table 3. Agglutination when the blood type in the column is transfused with the blood type to the row. Circle indicates that the blood type of the column when transfused to that of the column would agglutinate.

Blood Type	A	B	AB	O
A		○		○
B	○			○
AB	○	○		⊙
O				

In this example, we map the relation the woman W_i (the man M_i) prefers the man M_j (the woman W_j) to other to the relation that if the blood of W_i (M_i) would be agglutinate when the blood of M_j (W_j) were transfused. That is, if the woman W_i prefers the man M_j most the blood type should be so assigned that the type for W_i comprises of antibody AbW_i and antigen AgW_i ; and that for M_j of antibody AbM_j and antigen AgM_j and the affinity $\mathbf{Aff}(AbW_i, AgM_j)$ are highest.

For the trivial case when the preference lists of men and women are as in **Table 4**, simple assignment would suffice: a man to type A and another man to type B; for the woman who like a man with type A to type B and for another woman type A (**Fig. 1**). It should be noted that assignment to A for two men and to B for two women would not work, since the assignment does not reflect the preference of men and women.

In a nontrivial preference list shown in **Table 5**, one assignment would be type O to M_1 and W_1 , type A to M_2 , and type B to W_2 (**Fig. 2**) For other two preference lists (with the graph topologically different from those shown Figs. 1 and 2), it is not possible to map the blood type with the above correspondence, and other compounds should be synthesized for realizing the preference lists.

These examples suggest a scheme for synthesizing antigen-antibody compounds that realize mapping from given preference lists to the compounds. If the woman W_i prefers the man M_j to other men, the compound corresponding to W_i contains antibody AbW_i and the compound corresponding to M_j contains antigen AgM_j that satisfies $\mathbf{Aff}(AbW_i, AgM_j)$ highest among other AgM_j ($j=1\dots n$).

If M_j is the second in the preference list of W_i , then $\mathbf{Aff}(AbW_i, AgM_j)$ must be second highest and so on. AgM_j must realize orders from women W_k other than W_i , hence the affinity $\mathbf{Aff}(AbW_k, AgM_j)$ must realize the order accordingly. (If AgM_j alone cannot realize the order, then new antigen realizing the order must be added to the corresponding compound. In fact, the above example also suggests that compounds can be composed of a set of antigens and a set of antibodies.) Constraints for selecting antibodies and antigens for a compound corresponding to a person can be summed up as follows:

- $\mathbf{Aff}(AbW_i, AgM_j) > \mathbf{Aff}(AbW_i, AgM_k)$ if the woman W_i prefers M_j to M_k in her preference list for all $W_i \in W$, and for all distinct pairs $M_j, M_k \in M$; and
- $\mathbf{Aff}(AbM_i, AgW_j) > \mathbf{Aff}(AbM_i, AgW_k)$ if the man M_i prefers W_j to W_k in his preference list for all $M_i \in M$, and for all distinct pairs $W_j, W_k \in W$.

Table 4. A trivial preference list for two by two stable marriage problem.

	M1	M2
W1	2	1
W2	2	1

	W1	W2
M1	2	1
M2	2	1

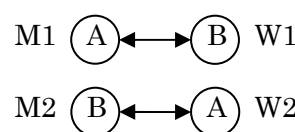


Fig. 1. A blood type assignment reflecting the preference

Table 5. A non-trivial preference list for two by two stable marriage problem.

	M1	M2
W1	1	2
W2	2	1

	W1	W2
M1	1	2
M2	2	1

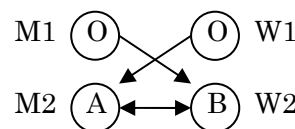


Fig. 2. A blood type assignment reflecting the preference

3.3 Solving a stable marriage problem with an array format

An illustrative example with Landsteiner's blood group suggests the following algorithm to solve SMP with an array format. In the array, row i and column j correspond to the compound for man i (i.e. AbM_i and AgM_i) and that for woman j (i.e. AbW_j and AgW_j). In other word, at the cross-point ij , two antigen-antibody reactions between AbM_i and AgW_j (reflecting man i 's preference) and between AbW_j and AgM_i (reflecting

woman j 's preference) will take place.

Under the assumption that the concentration observed at each cross-point is proportional to both $\mathbf{Aff}(AbM_i, AgW_j)$ and $\mathbf{Aff}(AbW_j, AgM_i)$, the array can find a stable matching by selecting one cross-point with highest concentration from each row and column. This matching is certainly stable one, for suppose otherwise there must be a blocking pair M_k and W_l such that $\mathbf{Aff}(AbM_k, AgW_l) > \mathbf{Aff}(AbM_k, AgW_{p(M_k)})$ and $\mathbf{Aff}(AbW_l, AgM_k) > \mathbf{Aff}(AbW_l, AgM_{p(W_l)})$ where $p(M_k)$ denotes a partner of M_k in the current matching. Then both concentration at the cross-point kl is higher than those of $kp(M_k)$ and those of $lp(W_l)$ reflecting the affinities.

Although obtaining a stable matching shows some computational power, it can be solved in $O(N^2)$ time where N is the size of men (and women). Gale and Sharpley have invented a well-known algorithm for giving stable matchings for man-oriented matching or woman-sided one [9]. By further assuming that the concentration observed at a cross-point can reflect the amount of antibodies imposed, the array is capable of obtaining any stable matching in the array from the man-oriented (man optimal and woman pessimal) matching to the woman-oriented (woman optimal and man pessimal) one. By equally increasing all the antibodies AbM_i ($i=1..n$) (or equivalently antigens AgW_j $j=1..n$), from a unit to α the matching would become close to the man-oriented one. Similarly, increase of AbW_i ($i=1..n$) will bias the matching towards the one of woman-oriented one. Since there are many variants of the stable marriage problem, which are NP-hard, devising the array for solving these problems is a challenging problem. Another challenge is to devise the array as a component of problem solver that can deal with not only a particular problem but with similar problems, as the immune system has done.

4 Conclusion

We have shown that antibodies, a macro molecule of the immune system, with a specific recognition capability can be used for computation as a macromolecule DNA is used for DNA computing. Focusing on a stable marriage problem, and extending ABO blood group system, it is shown that the antibody-based computation will be implemented on

an antibody microarray.

Acknowledgements

This work was supported in part by Grants-in-Aid for Scientific Research (B) 16300067, 2004. This work was partly supported also by the 21st Century COE Program "Intelligent Human Sensing" of the Ministry of Education, Culture, Sports, Science and Technology of Japan.

References

- [1] L.M. Adleman, "Molecular Computation of Solutions To Combinatorial Problems," *Science* 266 (11): 1021-1024 (2004)
- [2] H. Hug and R. Schuler, "Strategies for the development of a peptide computer," *Bioinformatics* 17(4): 364-368 (2001)
- [3] M.B. Elowitz, and S.A. Leibler, "Synthetic oscillatory network of transcriptional regulators," *Nature* 403, 335-338 (2000).
- [4] D. Sprinzak and M.B. Elowitz, "Reconstruction of genetic circuits," *Nature*, 438-24 November 2005
- [5] S. Basu et al., "A synthetic multicellular system for programmed pattern formation," *Nature*, Vol. 434, 1130-1134 (2005)
- [6] Dae-Kyun Ro et al., "Production of the antimalarial drug precursor artemisinic acid in engineered yeast," *Nature* 440, 940-943 (13 April 2006)
- [7] Z. Guo, L. Hood, et al., "Long-range Multi-locus Haplotype Phasing of the MHC" *the Proceedings of the National Academy of Sciences*, 103-18 (May 2, 2006)
- [8] M.S. Balan and K. Krithivasan, "Parallel Computation of Simple Arithmetic Using Peptide-Antibody Interactions," *Biosystems*, 76(1-3): 303-7, (Aug-Oct 2004)
- [9] D. Gale and L. Shapley, "College admissions and the stability of marriage," *American Mathematical Monthly*, 69:9-15, (1962)
- [10] R.W. Irving and P. Leather, and Dan Gusfield, "An efficient algorithm for the optimal stable marriage," *J. ACM*, 34(3):532-543, (1987)
- [11] K. Landsteiner, "Zur Kenntnis der antifermentativen, lytischen und agglutinierenden Wirkungen des Blutserums und der Lymphe," *Zentralblatt Bakteriologie*, 27:357-62 (1900)

Network Route Design of Public Transport System with Network Evolution

Takahiro Majima
Center for Logistics Research
National Maritime Research Institute
Email: majy@nmri.go.jp

Keiki Takadama
Faculty of Electro-Communications
University of Electro-Communications
Email: keiki@hc.uec.ac.jp

Daisuke Watanabe
Center for Logistics Research
National Maritime Research Institute
Email: watanabe@nmri.go.jp

Mitujiro Katuhara
Hokkaido Intellect Tank
Email: fwht4182@nifty.com

Abstract

Characteristics of network in the real world have attracted a number of scientists and engineers. Various findings are given from recent studies on the real world network, sometimes called complex network. The network evolution to produce complex network is also investigated actively and a number of models are proposed. Some model succeeded to produce public transport networks in the real world. We make active use of the network evolution for generating public transport network. In our model, the network of the bus lines evolves with a local evaluation value defined by the OD (Origin-Destination) demand multiplied with the required time including riding time and waiting time. Since the algorithm with network evolution is simple, our method is able to provide bus line network immediately. It is advantage to generate bus line network especially when a transport operation is required urgently under disaster circumstances.

Keywords: Complex Network, Network Evolution, Public Transportation, Route Generation, Local Optimization, Weighted Graph

1. Introduction

Characteristics of network in the real world have attracted a number of scientists and engineers. Various findings are given from recent studies on the real world network, sometimes called complex network. The complex networks, such as small world network [1] or scale free network [2], lie between two extremes, i.e., random network and regularly connected network like lattice. Many complex networks in real world have interesting characteristics found in both random and regular networks simultaneously.

The properties on the complex network are revealed mainly by early studies focused on the un-weighted relational network [3], in which there is no weight on links or vertices, such as distance or traffic amount. Meanwhile, studies investigating weighted network has

begun to appear in recent year. Some of the papers the weight denotes distance between vertices [4][5] or traffic amount [6].

Further more, the network evolution to produce complex network is also investigated actively after the proposal of BA (Barabási and Albert) model [2]. The model produces the scale free network and the rule of its network evolution is known as preferential attachment (Rich gets richer). A number of models regarding to the network evolution were proposed [7][8][9] and some of them utilize the distance in the Euclidean space as a measure determining which node should be connected from the new added node. In the case of transport network in the Euclidean space, Gastner proposed a model of network evolution using the distance among nodes scattering in the Euclidean space and thereby presented that it can produce the subway network in Boston with the set of given nodes (stations) [9].

Considering this background, the knowledge of complex network seems to provide us useful information to design and construct the public transport networks. Our final purpose is to find an algorithm providing effective and optimized public transportation system, such as waterbus or bus expected to reduce traffic congestions and increase redundancy of transport system under disaster circumstances. We make active use of the knowledge of the network evolution to apply them to the problem in public transportation.

The design of public transport system is composed of four components, Network Route Design, Setting Time Tables, Scheduling of Vehicles and Scheduling of Drivers [10]. Toward the goal, this paper is focused on the process of the Network Route Design mainly and proposes a model to generate network using the network evolution. The network route design is the process to design the bus lines defined as a sequential order of stations at which vehicles stop. The bus lines also forms network over the stations on physical infrastructure network such as roads or rivers. In our model, the network of the bus lines evolves with a local evaluation value defined by the OD (Origin-Destination) demand multiplied with the required time (traveling time and waiting time). Since the algorithm with network evolution

is simple, this model is able to provide bus line network immediately. It is advantage to generate bus line network especially when a transport operation is required urgently under disaster circumstances.

2. Model

In this paper, the nodes represent bus stops or stations and one set of links connecting nodes represents one bus line. Vehicles shuttle along with the set of links representing the bus line. The model with network evolution for bus line network is described below. It separates two processes. One process is to determine which node should be connected newly added node (i.e. network evolution). The other process describes how to determine the number of buses to be engaged into a designed bus line.

In this paper, the destination is limited to one bus stop for brevity. However this situation is well observed around stations of commuter trains. The passengers travel from their residential area to the railway station by bus. Although, there are many bus stops in the residential area, the number of destination, station of commuter train, is limited.

2.1 Network Evolution

Our model is inspired by Gastner[9]. One node (bus stop) is added to the network at each evolution step and connected one of the existing nodes with one link composing a part of a bus line route. Fig.1 shows the process of the growing bus line network. The newly added node (Node 3 in Fig.1), defined as *target node* in this paper, is selected in the order of the distance between the destination and the target node. Then, one of the already existing nodes, defined as *connection node* in this paper, is selected with an evaluation function described below and one link connects the target node to the connection node. After the connection between target node and connection node, the links are created along with the existing links from the connection node to the destination and this set of links comprises one bus line. Therefore, at the first step of evolution, the node nearest to the destination is selected as target node and the destination node itself becomes connection node. Thus, the network connected to the destination spread outward from the destination and it has tree topology (no loop).

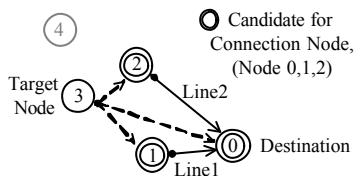


Fig.1 Schematic of Network Evolution

If selected connection node is terminal of the existing line, there are two types of connection as illustrated in Fig.2. One is *addition type*, the other is *subsumption type*. Number of bus lines is simply incremented by one for

addition type. For subsumption type, the line, which one terminal is connection node, subsumes the new bus line and target node. The evaluation function is applied at each growing step and it determines the connection node and connection type.

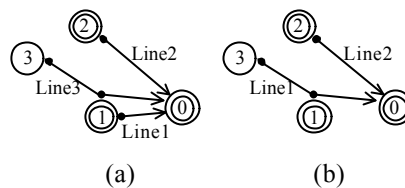


Fig.2 Two Types of Line Connection
(a) Addition Type (b) Subsumption Type

The evaluation function resembling in the following equation is applied frequently to the designed bus line network [11].

$$\min Z = Z_1 + Z_2 = \sum_i T_i D_i + w \sum_k B_k$$

Where, D_i is demand at bus stop i , T_i is required time for moving from bus stop i to destination composed of traveling time, Tm_i and waiting time, Tw_i , B_k is number of bus engaged into the bus line k , w is parameters controlling the balance of requirement between user and operator of vehicle. Users hope to reduce the first term, Z_1 and operators hope to reduce the second term, Z_2 . Usually, this evaluation function is applied to the whole bus line network. However, we apply it for the selection of the connection node and connection type. Thus, i and k mean the set of nodes already connecting to the network and already existing bus lines respectively.

The expected waiting time of a bus stop at where more than one bus lines stop can be calculated by the following equation [12].

$$Tw_i = t_i \left[\frac{1}{2} + \sum_{r=1}^{N-1} \frac{(-1)^r t_i^r}{(r+1)(r+2)} \sum_{j_1=2}^{N-r+1} \sum_{j_2=j_1+1}^{N-r+2} \dots \sum_{j_r=j_{r-1}+1}^N \frac{1}{t_{j_1} t_{j_2} \dots t_{j_r}} \right]$$

Where, N is the number of bus lines running through the node i , t_i is the smallest headway in the set of t_j representing headway of line j . Further more, the headway (frequency) is derived from the round trip time and bus number simply and the shortest path is found by Dijkstra's algorithm when considering the topology of the physical infrastructure network, such as road or rivers.

2.2 Determination of Vehicle Number

It should be satisfied that the transportation capacity is larger than the traffic amount. In the network evolution process, node is connected one by one and the bus line generated with addition type in Fig.2 is incremented by one at each evolution step. Thus, the number of vehicle assigned for a bus line can be calculated to satisfy the demand occurred at the target node and needless to consider the demand at nodes other than the target node.

Thus, the number of vehicle is calculated by the following equation simply.

$$B_k = \lceil Tr_k D_k / B_{capa} \rceil$$

Where, Tr is round trip time of target node k , and B_{capa} is capacity of one vehicle. We should consider another way for the case of subsumption type in Fig.2, because, the round trip time of existing line changes. There are several ways to determine the number of vehicles for subsumption type. In this paper, it is intended to determine the number of vehicle so that the headway of already existing line, which one terminal is the connection node, doesn't deteriorate. Thus, the following equation is employed.

$$B_k = \max \left(\lceil Tr_k D_k / B_{capa} \rceil, \lceil B_j Tr_k / Tr_j \rceil \right)$$

Where, subscript k and j represent target node and connection node respectively.

An example of network evolution is described in Fig.3. Although the number of nodes is only four, many possible network of bus line can be considered. It is easy to imagine that investigation for all patterns leads to combinatorial explosion when the number of nodes increases.

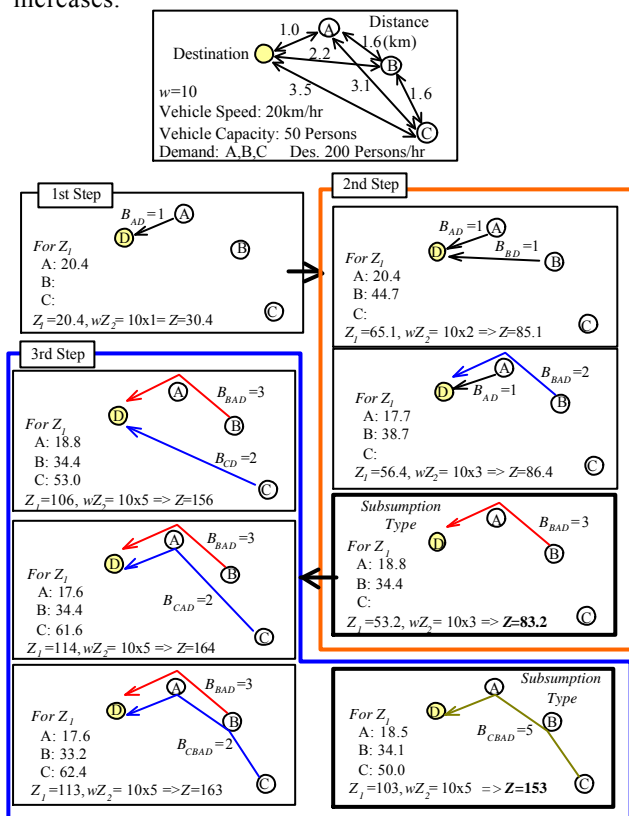


Fig.3 Example of process of network evolution

3. Application

In this section, the model described previous section is applied to two situations. One is simple physical

infrastructure network and the other is waterbus line in the three rivers running through Tokyo metropolitan.

3.1 Simple Network

The arrangement of nodes is illustrated in Fig.4(a). Twenty nodes are positioned on the circle with diameter of 5 km. The capacity of vehicle, B_{capa} and speed, B_s set to 50 persons and 20km/hr respectively. The demand of each node is 200persons/hr and the road network is assumed to have the topology of complete graph with straight line. Fig.4(b) and (c) show the bus line network generated by the model with $w=0$ and $w=25$ respectively.

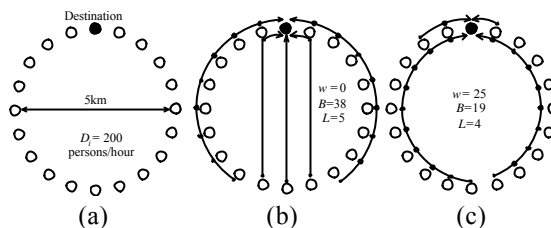


Fig.4 (a) Arrangement of nodes and problem to be solved. (b) Result of network evolution with $w=0$, (c) Result of network evolution with $w=25$, where L and B are total number of lines and vehicles respectively

As mentioned above, the model can analyze taking into account of the balance of requirement between user and operators with the control parameter, w . Fig.5 shows the relationship between total vehicle number and total required time, TD , normalized with riding time, Tm_{ideal} , calculated assuming that the all nodes are connected to the destination directly. The result varies by the controlling parameter, w . It is found the required time for traveling to the destination takes about 30% larger than that of the idealized bus line network for users. It is caused from the waiting time and the topology of not directly connected to the destination, even if w is set to 0 that is acceptable for users.

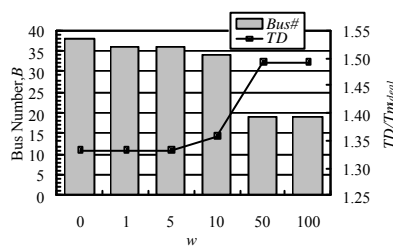


Fig.5 Relationship between bus number and total required time for the generated bus line

3.2 Application to waterbus line in the river system

The Tokyo metropolitan and around the region most populated area in Japan have been suffering from heavy traffic, congestions and commuter rushes on transport networks. Furthermore considering the fact that earthquakes occur frequently in Japan, road networks are collapsed when an earthquake causes massive destruction. The transport mode using rivers and ships that doesn't exist at this time is being expected to contribute to reducing traffic congestions or redundancy of logistics

system under disaster circumstances. Fig.6 shows physical infrastructure network composed of three rivers running through Tokyo. There are 24 possible waterbus stations in the river system.

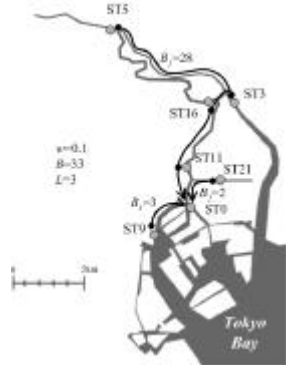


Fig.6 Rivers running through Tokyo, three solid lines connecting to ST0 represent generated waterbus lines.

For instance, making the Etchujima station represented by ST0 in Fig.6 to be destination, the model was applied. Table 1 shows the demand of six bus stops represented in Fig.6. The capacity of waterbus, B_{capa} and service speed, B_s set to 100 persons and 8 knot(15km/hr) respectively according to the ships operating for sight seeing around Tokyo bay area.

Table 1 Demand of Six Waterbus Stations (Destination: ST0)

Station No.	ST3	ST5	ST 9	ST11	ST16	ST21
Demand (Persons/hr)	34	3	358	607	119	287

Three waterbus lines generated with $w=0.1$ are drawn in Fig.6 by solid lines and Fig.7 shows relationship between the number of waterbus and normalized required time, as is shown in Fig.5. The generated bus lines network in Fig.6 seems rational and required time becomes about 30-40 larger than riding times of the network connected to destination directly.

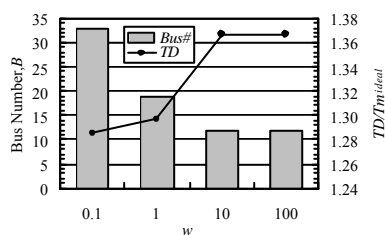


Fig.7 Relationship between waterbus number and total required time for the waterbus line

4. Discussion

Since our model generates bus line network with the evaluation function applied to the local network not to global network, it doesn't certify the completely optimized solution. However, the generated network and required time in this paper seem to be rational. Thus, advantage of our model is to produce the rational solution immediately. This advantage is considerably useful to engage a transport operation urgently such as disaster circumstance.

5. Conclusion

We proposed the model generating rational public transport network with network evolution. However, there are several subjects to be addressed for the practical use. For instance, the number of destination is limited to one station at this time. Furthermore, in the case of the waterbus, the congestion at bus stops should be considered, because the number of ships taking piers is limited.

Acknowledgement

This study is supported by the Ministry of Education, Culture, Sports, Science and Technology, Grand-in-Aid for Scientific Research (B), 17360424, 2005. We would also like to thank Kazue Honda for her support of programming.

References

- [1] D.J. Watts, S.H. Strogatz, Collective Dynamics of 'Small-World' Networks, Nature, Vol.393, 1998, pp.440-442
- [2] A.-L. Barabási, R. Albert, Emergence of Scaling in Random Networks, Science, Vol.286, 1999, pp.509-512,
- [3] S.H. Strogatz, Exploring Complex Networks, Nature, Vol.410, 2001, pp.268-276
- [4] V. Latora, M. Marchiori, Efficient Behavior of Small-World Networks, Phys. Rev. Lett. Vol.87, No.19, 2001
- [5] T. Majima, M. Katuhara, K. Takadama, Analysis on Transport Networks of Railway, Subway and Waterbus in Japan, WEIN06 (Workshop on Emergent Intelligence on Networked Agents) Proceedings, May 2006, Hakodate, pp.152-166
- [6] A. D. Montis, M. Barthélemy, A. Chessa, A. Vespignani, The Structure of Inter-Urban Traffic: A Weighted Network Analysis, arXiv:physics/0507106 v2, 2005
- [7] M. Barthélemy, A. Flammini, Optimal Traffic Networks, arXiv:physics/0601203v2, 2006
- [8] M. Kaiser, C.C. Hilgetag, Spatial Growth of Real-World Networks, Phys. Rev. E Vol.69, 036103, 2004
- [9] M.T. Gastner, M.E.J. Newman, Shape and Efficiency in Spatial Distribution Networks, arXiv:cond-mat/0409702, 2004
- [10] A. Ceder, Methods for Creating Bus Time Tables, Transportation Research, Vol.21A, No.1, 1986, pp.59-83
- [11] D. Dubois, G. Bel, M. Llibre, A set of Methods in Transportation Network Synthesis and Analysis, Journal of the Operational Research Society, Vol.30, No.9, 1979, pp.797-808
- [12] W. Lampkin, P.D. Saalmans, The Design of Routes, Service Frequencies and Schedules for a Municipal Bus Undertaking: A case study, Operation Research Quarterly, No.18, 1967, pp.375-397

Robot multiple tasks performance and neural complexity

Genci Capi¹ and Koco Bode²

¹Faculty of Information Engineering
Fukuoka Institute of Technology
3-30-1 Wajiro-Higashi, Higashi-ku, Fukuoka, 811-0195, Japan

²Faculty of Mechanical Engineering
Polytechnic University of Tirana
Sheshi Nene Tereza, Tirana, Albania

capi@fit.ac.jp

Abstract

This paper presents a new method for multiple tasks performance based on multiobjective evolutionary algorithm. In order to verify the effectiveness, the proposed method is applied to evolve neural controllers for the Cyber Rodent robot that has to switch properly between two different tasks. Furthermore, the tasks and neural complexity are analyzed by including the neural structure as a separate objective function. Results using Cyber Rodent robot show that multiobjective-based evolutionary method can be applied effectively for generating neural networks controlling the robot to perform multiple tasks, simultaneously.

KEY WORDS

Evolutionary robotics, neural controller, task complexity.

1. Introduction

Traditionally, the research on intelligent agents has mainly focused on evolution or learning of individual perceptual-motor and cognitive tasks. Nevertheless, intelligent agents operating in everyday life environments often are required to perform multiple tasks simultaneously or in rapid alternation, which is a challenge even for humans and primates.

Several approaches in the literature have been proposed to address robot multiple tasks performance problem. Up to now the standard methodology in machine learning has been to break large problems into small, independent subproblems, learn the subproblems separately, and then recombine the learned pieces [1]. In addition to learning, evolution of neural controllers is well known for providing a family of naturally-inspired algorithms which can successfully address a wide range of robot behavior learning problems ([2], [3]). In evolutionary robotics,

different constraints and objectives are handled as weighted components of the fitness function ([4], [5]), applying Single Objective Evolutionary Algorithm (SOEA).

This article presents a novel approach for robot multiple tasks performance based on Multiobjective Evolutionary Algorithm (MOEA) ([6]). Unlike previous methods, in the experiments presented here, each task is considered as a separate objective function. Nondominated Sorting Genetic Algorithm (NSGA) ([7]) is used to generate the Pareto set of neural networks.

In this method, we evolved one single neural controller for multiple tasks performance, considering relevant information of each task as sensory inputs. Therefore, as the number of tasks increases, the neural controllers become more complex. This makes the evolution process difficult. In addition, the hardware implementation of evolved neural controllers may result in poor performance due to the increased error in sensory data. In order to further investigate if the MOEA can also generate efficient neural controllers for multiple tasks performance; the structure of neural network is added as a separate objective function.

Simulation and experimental results show a good performance of the proposed method. The non-dominated optimal Pareto neural controllers have a good distribution and CR robot behavior varies from completing each of both considered tasks to flexibly switching between them. Therefore, as a specific contribution of proposed method is that in a single run of MOEA are generated agents with completely different behaviors, making it possible to select the appropriate neural controller based on our preferences. Moreover, efficient neural controllers with appropriate sensory inputs are selected through the course of evolution.

2. NSGA

A real number NSGA was employed to evolve the neural controller. In [8], the authors compared the NSGA with four others multiobjective evolutionary algorithms using two test problems. The NSGA performed better than the others did, showing that it can be successfully used to find multiple Pareto-optimal solutions. In NSGA, before selection is performed, the population is ranked on the basis of domination using Pareto ranking. All nondominated individuals are classified in one category with a dummy fitness value, which is proportional to the population size [7]. After this, the selection, crossover, and mutation usual operators are performed.

In the ranking procedure, the nondominated individuals in the current population are first identified. Then, these individuals are assumed to constitute the first nondominated front with a large dummy fitness value [7]. The same fitness value is assigned to all of them. In order to maintain diversity in the population, a sharing method is then applied. Afterwards, the individuals of the first front are ignored temporarily and the rest of population is processed in the same way to identify individuals for the second nondominated front. A dummy fitness value that is kept smaller than the minimum shared dummy fitness of the previous front is assigned to all individuals belonging to the new front. This process continues until the whole population is classified into nondominated fronts. Since the nondominated fronts are defined, the population is then reproduced according to the dummy fitness values. As the individuals in the first front have higher fitness value, they always get more copies than the rest of the population.

3. Multiobjective Evolution of Neural Controllers

3.1 Tasks and Environment

The CR robot has to learn to perform two different tasks: protecting another moving robot by following it closely; and keeping a high level of energy by capturing the battery packs distributed in the environment (Fig. 1). The entire environment is a rectangular of 4m x 3.5m surrounded by walls. There are 15 battery packs in green color distributed in the environment. The CR robot starts in the same initial position and orientation. The individual life time of each agent is 700 time steps, where each time step lasted 0.1s. During this time the red color protected robot follows a rectangular trajectory with a constant velocity of 0.1m/s.

3.2 Neural Architecture

We implemented a feed-forward neural controller with 11, 4 and 2 units in input, hidden and output layers, respectively. The inputs of neural controller are the angle

(A_{bat}), distance (D_{bat}) and color (C_{bat}) of the nearest battery pack, the angle (A_{rob}) and color (C_{rob}) of the protected robot, the sensor readings of five proximity sensors (PS_i) and the distance sensor (DS) in the front of CR robot. The five proximity sensors are angled as shown in Fig. 3. The egocentric angle to the protected robot or nearest battery pack varies from 0 to 1 where 0 corresponds to 45° to the right and 1 to 45° to the left. The value of these neurons becomes -1 when the protected robot becomes invisible or there is no battery pack in the visual field. The proximity sensors can measure up to 0.25m, while the distance sensor from 0.1m to 0.8m. The proximity and distance sensor reading varies from 0 to 1, where 0 means no obstacle and 1 touching the obstacle. Random noise, uniformly distributed in the range of +/- 5% of sensor readings, has been added to the angle of the nearest battery pack, angle of the moving robot, distance sensor and five proximity sensors. Because the distance to the nearest battery pack during the experiments is determined based on the number of pixels, the random noise in simulations is considered in the range of +/- 10%. Based on the characteristics of CR visual sensor, in simulations, the visual distance to the nearest battery pack is limited up to 1.2m.

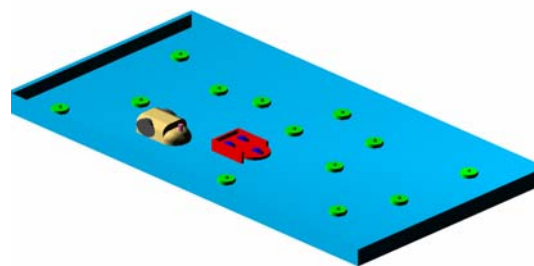


Fig. 1. Environment.

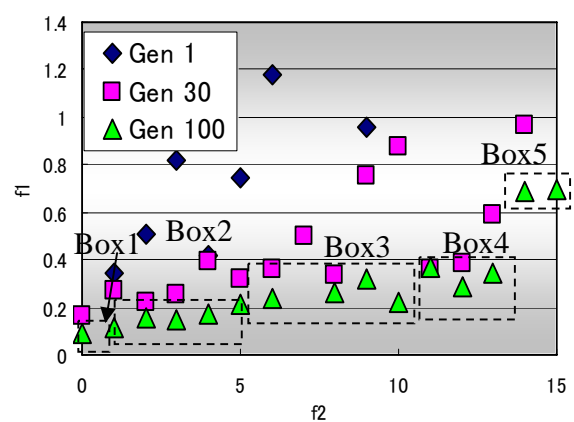


Fig. 2. Pareto optimal solutions of different generations.

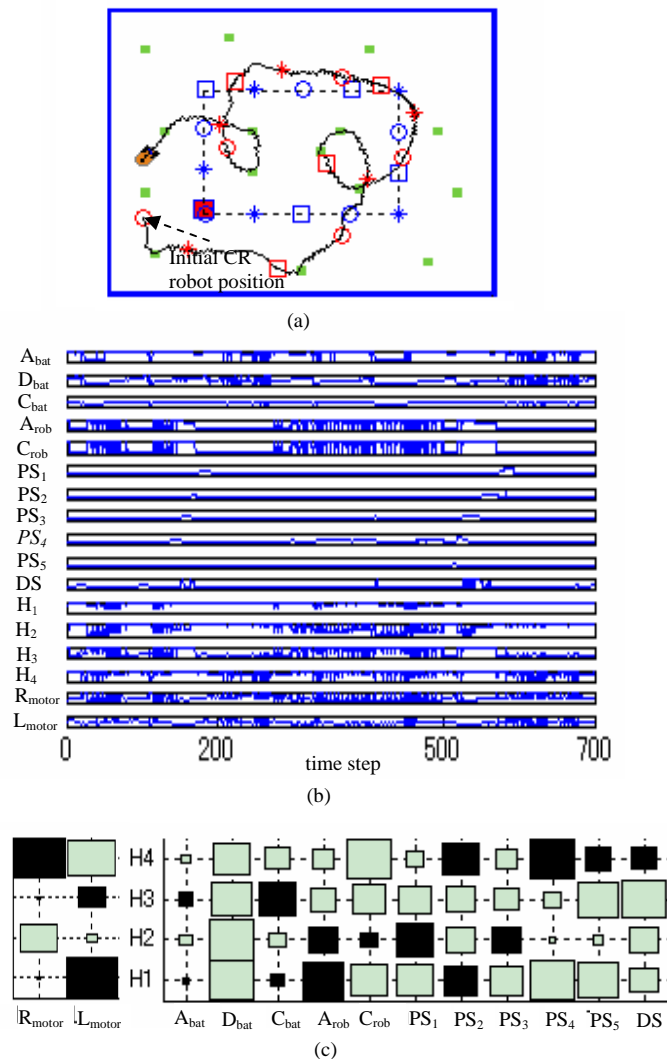


Fig. 3. CR multiple task performance (Box3). (a) CR trajectory. (b) Unit activation. (c) Hinton diagram of connection weights.

3.3 Evolution

For any evolutionary computation technique, a chromosome representation is needed to describe each individual in the population. The genome of every individual of the population encodes the weight connections of neural controller. The genome length is 52 and the connection weights ranged from -10 to 10. For the protecting task, the target distance d_t between the CR robot and the protected robot is considered 0.3m. In order to minimize the difference between the target and real distance d_r , the fitness, f_1 , is considered as follows:

$$f_1 = \sum_{i=1}^{\max_st} |d_t^i - d_r^i| \quad (1)$$

where \max_st is the maximum number of steps.

The fitness of battery capturing task, f_2 , is simply the number of battery packs captured during the individual lifetime. If an individual happens to hit the protected agent or the wall, the trial is terminated and a low fitness is attached. Therefore, such individuals will have a low probability to survive. The set of genetic parameters used are: $N_{ger}=100$, $N_{pop}=50$, $\sigma_{shared}=0.4$.

4. Results

In this section, we first discuss the best solutions obtained from the MOEA in terms of multiple task performance. All the simulations were performed in a Pentium 4 3.2GHz computer.

Fig. 2 shows the Pareto optimal front for generations 1, 30 and 100, averaged for five different runs of MOEA.

During the first 30 generations there is a great improvement on the quality and distribution of Pareto optimal solutions. From this figure, it can be deduced that MOEA is equally capable of finding the best solution for each objective when two conflicting objectives are considered, simultaneously.

The behavior of CR controlled by the neural controller of Box 3 solution is shown in Fig. 3(a). The CR robot, while follows the protected agent, captured eight of the battery packs distributed in the environment. Fig. 3(b) shows that all sensory units are activated during the CR motion. The proximity and distance sensors helped the CR robot not to hit the protected robot while it moves very close and perpendicular to the moving direction of the protected robot (around 150 steps and 575 steps). The Hinton diagram of Box 3 neural controller (Fig. 3(c)) shows the D_{bat} has strong weight connections with hidden units. This leads us to the conclusion that CR robot switches between two tasks based on the activation of D_{bat} unit.

4.1 Neural and Task Complexity

In the following, the results of applying MOEA to evolve efficient neural controllers are presented. In difference from previous approaches, where the fitness function of obstacle avoidance task and the structure of neural controller are included in a single fitness function, we considered the structure of the neural controller as a separate objective function. The complexity of evolved neural structure generated by MOEA could be also used as an index to measure empirically the task complexity.

In addition of 52 genes encoding the weight connections of the neural network, the genome encodes 15 binary genes (11 for sensory input neurons and 4 for the hidden neurons), which indicate if an input or hidden unit exists in the network or not.

The objective function f_3 is considered as follows:

$$f_3 = nr_i + nr_h \quad (2)$$

where nr_i, nr_h are the number of input and hidden units.

Fig. 4 shows that as the neural controller complexity increases, the solutions move to the upper-left corner, which means a better performance. Not surprisingly, the most complex neural networks control the CR robot to perform both tasks by switching between them based on the environment conditions. The neural network has seven units in the input and hidden layers and the CR robot captured fourteen battery packs while trying to keep a short distance from the protected robot. In addition, the number of units to complete only the protecting task is larger than that of battery capturing task, five and four units, respectively.

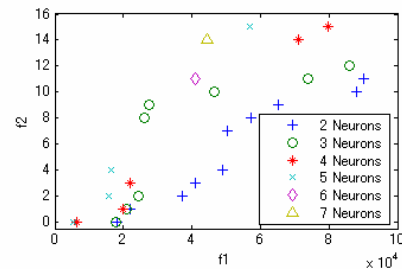


Fig. 4. Performance of neural controllers with different number of sensory and hidden units.

5. Conclusion

This paper has experimentally investigated the effectiveness of applying MOEA to address the robot multiple tasks performance problem. We considered two different tasks for the CR robot that has to protect another robot and capture the distributed battery packs. In particular, we demonstrated that in a single run of MOEA are generated robust neural controllers with completely different characteristics ranging from performing each of all considered tasks to simultaneously performing different tasks by flexibly switching between them. In addition, the MOEA generated efficient neural controllers with minimum number of sensory and hidden units for multiple tasks performance.

References:

- [1] A. Waibel, H. Sawai, and K. Shikano, "Modularity and scaling in large phonemic neural networks," IEEE Transactions on Acoustics, Speech and Signal Processing, vol. 37, no. 12, pp.1888-98, 1989.
- [2] S. Nolfi, "Evolving robots able to self-localize in the environment: The importance of viewing cognition as the result of processes occurring at different time scales," Connection Science, vol. 14, no. 3, pp. 231-244, 2002.
- [3] G. Capi, and K. Doya, "Evolution of neural architecture fitting environmental dynamics," Adaptive Behavior, vol. 13, no. 1, pp.53-66, 2005.
- [4] D. Floreano, and F. Mondada, "Evolution of homing navigation in a real mobile robot," IEEE Transactions on Systems, Man, and Cybernetics-Part B, vol. 26, pp. 396-407, 1996.
- [5] D. Cliff, and G. F. Miller, "Co-evolution of pursuit and evasion II: Simulation methods and results", From animals to animats 4, pp. 506-515, 1996.
- [6] K. Deb, *Multi-Objective Optimization using Evolutionary Algorithms*, John Wiley & Sons, Chichester, UK, 2001.
- [7] N. Srivinas, and K. Deb, "Multiobjective optimization using non-dominated sorting in genetic algorithms", Evolutionary Computation, vol. 2, no. 3, pp. 279-285, 1995.
- [8] A. H. F. Dias and J. A. de Vasconcelos, "Multiobjective genetic algorithms applied to solve optimization problems," IEEE Transactions on Magnetic, vol. 38, no. 2, pp. 1133-1136, 2002.

Motion control of biped robot by using simulation

K.KABATA, M.HARA, M.SUGISAKA

Department of Electrical and Electric Engineering, Oita University
700 Dannoharu Oita 870-1192 Japan.
E-mail: msugi@cc.oita-u.ac.jp

Abstract

Recent years, researches about biped robot are extensively studied at the enterprise and the university. The purpose is human assistance, but it aims entertainment now.

Modern society is created for human to live easily. Therefore, to assist human, we need robot that is suitable for life space.

The vertical projection area of biped robot on the floor side is small, therefore, biped robot can move crooked road and narrow road. So we think it is best system on life space that has many irregular ground.

In this paper, we calculate Center of Gravity and Zero Moment Point by simulation.

1. Introduction

Recent years, researches about biped robot are extensively studied at the enterprise and the university. The purpose is human assistance, but it aims entertainment now.

Modern society is created for human to live easily. Therefore, to assist human, we need robot that is suitable for life space.

In the past research, wheel type robot was a mainstream. As a reason, the major factor is easy and steady to control. But, the fault is not able to move at irregular ground.

The vertical projection area of biped robot on the floor side is small, therefore, biped robot can move crooked road and narrow road. So we think it is best system on life space that has many irregular ground. But, it is difficult to control.

In this paper, we made the biped robot with servomotor to generate walking motion by application software, and calculate Center of Gravity and Zero Moment Point by simulation.

2. Theory

2.1 ZMP (Zero Moment Point)

ZMP is a point to replace the floor reaction force of the normal element that joined on the backside of the foot.

Support polygon is shown in Fig.1. Left square shows the footprint of the left leg, and Right square shows the footprint of the right leg.

Operation that ZMP is not in support polygon cannot be achieved.

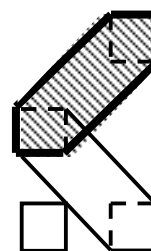


Fig.1 Support polygon

2.2 Rate of stance phase

Human's walking consists of state of one leg and state of both legs. State of one leg calls single stance phase, and state of both legs calls double stance phase.

Single stance phase is a period standing with one leg, and goes ahead. Double stance phase is a period standing with both legs, and switches axopodium.

Static walking cycle is always to keep balance. Dynamic walking cycle is presupposes to keep motion.

Human's walking cycle (static and dynamic) are shown in Table 1 and Table 2.

Table 1 Human's walking cycle (static)

Double stance phase	Single stance phase
40%	60%

Table 2 Human's walking cycle (dynamic)

Double stance phase	Single stance phase
20%	80%

3. Specific of biped robot and simulation

Specific of biped robot is shown in Table 3. Setting of simulation is shown in Table 4.

Table 3 Specific of biped robot

Actuator	Servomotor
Computer	Intel Pentium III 487MHz
Mother board	HSWB-01
Application software	HSWB-01C
Size	Height 449[mm]
	×
	Width 200[mm]
Degree of Freedom	×
	Length 120[mm]
Degree of Freedom	Hip joint 3×2
	Knee joint 1×2
	Ankle joint 2×2

Table 4 Setting of simulation

Language	Borland C++ Builder5
Length of thigh	0.145[m]
Length of shin	0.155[m]
Degree of Freedom	Hip joint 3×2
	Knee joint 1×2
	Ankle joint 2×2

We made Setting of simulation same as Specific of biped robot.

4. Experiment

4.1 Experiment of biped robot

We use HSWB-01C to control the biped robot. This application software is to control servomotor equipped in the biped robot.

First of all, we set home position to create motion of the biped robot. Next, we create the position of servomotor by the hour.

We can create various motions by the position of the servomotor. We set position by the trial and error.

In this paper, we use this method shown in Fig.2 to move biped robot.

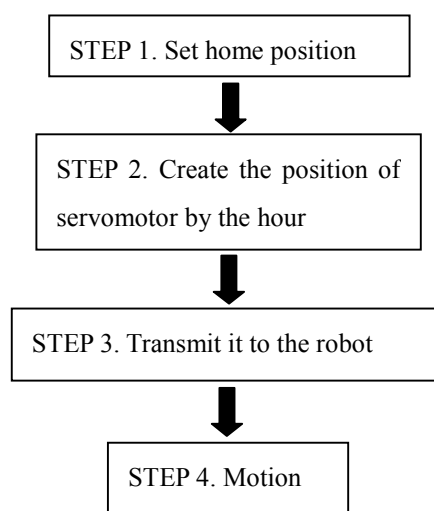


Fig.2 Method of motion creation

Figure of biped robot's joints are shown in Fig.3.

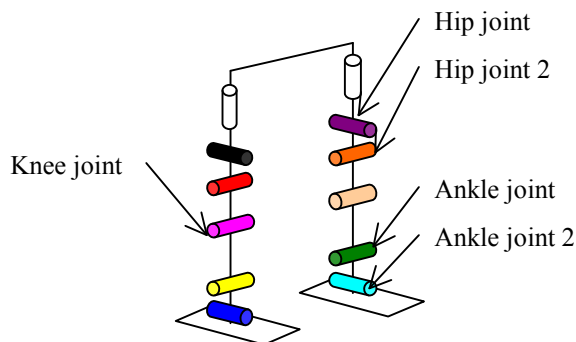
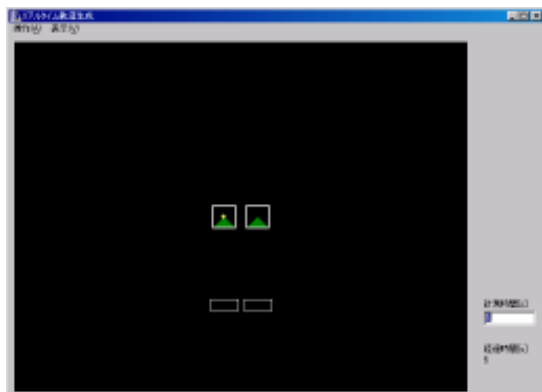


Fig.3 Figure of biped robot's joints

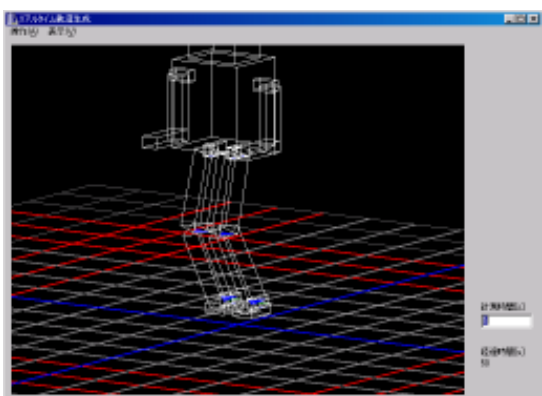
4.2 Experiment of simulation

Size and Degree of Freedom are done as well as biped robot, and perform the advancement operation for 5 seconds. We gain the result of ZMP and Center of Gravity, in that time.

Screen of simulation is shown in Fig.4.



(a) Top view



(b) 3D view

Fig.4 Screen of simulation

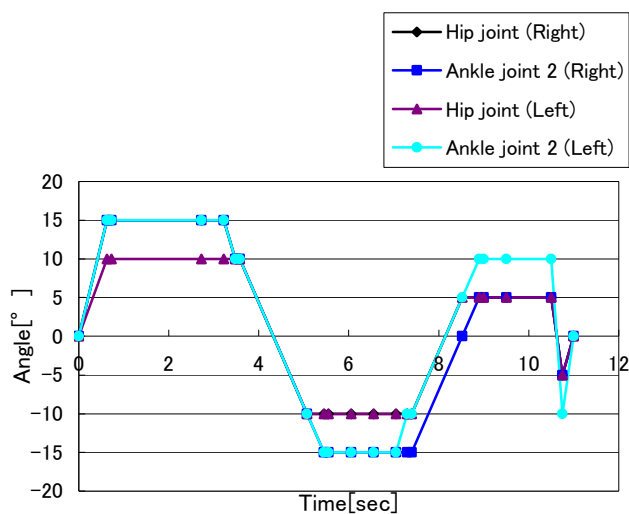
5. Result

5.1 Result of biped robot

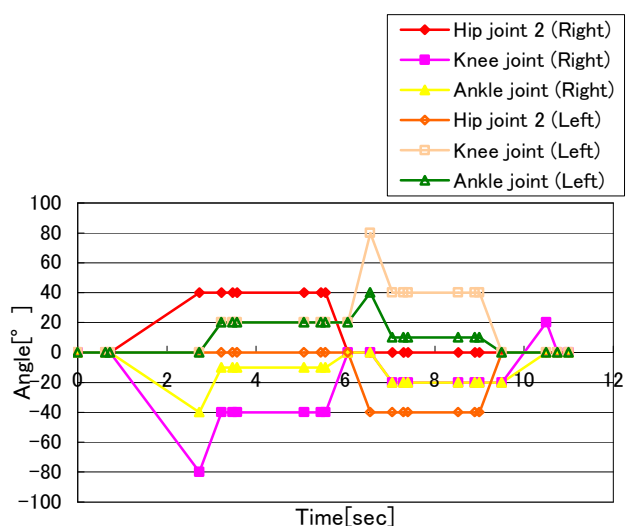
Angle change graph of Right-and-Left (Hip joint, Ankle joint 2) and Angle change graph of Backward-and-Forward (Hip joint 2, Knee joint, Ankle joint) are shown in Fig.5.

Position of servomotor (Fig.3) and the color of graph (Fig. 5) are corresponding.

Fig.5 (a) shows the change in Right-and-Left. Fig.5 (b) shows the change in Backward-and-Forward.



(a) Right-and-Left



(b) Backward-and-Forward

Fig.5 Angle change graph

Table 5 Robot's walking cycle result

Double stance phase	Single stance phase
41%	59%

The result of this experiment is similar to the ratio of double stance phase and single stance phase in human's static walking.

5.2 Result of simulation

Result of simulation is shown in Fig.6.

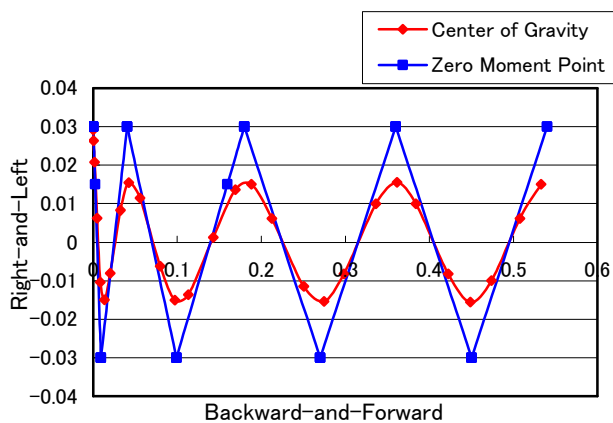


Fig.6 Result of simulation

6. Conclusions

In this paper, we researched about walking motion. We transmit instruction value to the biped robot, and generate walking motion by application software. And, we perform walking simulation.

Comparing with human walking motion and biped robot's walking motion, the ratio of this result is similar to the ratio of double stance phase and single stance phase in human's static walking.

It is necessary to research about Center of Gravity and Zero Moment Point more.

In the future, we complete motion of biped robot by using these results.

Reference

- [1] Nikkei mechanical · Nikkei design joint compilation, " Robolution " , Nikkei BP Co. , P.40~41, 2001
- [2] Ryuichi Nakamura, Hiroshi Saito, "Basic Kinematics", Ishiyaku publication Co.Ltd, P.334~342, 2002
- [3] T.Shinohara, "Real-time orbit generation of biped robot", 2001
- [4] <http://www.ops.dti.ne.jp/~manva/robot/zmp.htm>

A New Technique for Adjusting the Learning Rate of RPEM Algorithm Automatically

Xing-Ming Zhao^{1,2}, Yiu-ming Cheung³, Luonan Chen^{1,2,4}, Kazuyuki Aihara^{1,2}

1. Aihara Complexity Modelling Project, ERATO, JST, Japan

2. Institute of Industrial Science, The University of Tokyo, Japan

3. Department of Computer Science, Hong Kong Baptist University, Hong Kong, China

4. Department of Electrical Engineering and Electronics, Osaka Sangyo University, Japan

Abstract

Recently, a new Rival Penalized Expectation Maximization (RPEM) algorithm has been proposed for estimating the parameters of the normal mixture model, meanwhile determining the number of classes automatically. The RPEM is an adaptive algorithm utilizing a small constant learning rate. To speed up its convergence speed, this paper proposes a new method to dynamically adjust the learning rate of the RPEM algorithm on line. The numerical results have shown the promising results of the proposed algorithm.

1 Introduction

Mixture models have been widely used in data mining [1], image processing [2], gene expression analysis [3], and so forth. In the literature, the Expectation-Maximization (EM) algorithm [4] has been widely used to estimate the parameters of the normal mixture model, which, however, needs to pre-assign class number. Generally, the EM algorithm almost always leads to a poor result if the class number is not appropriately pre-assigned. Recently, a new Rival Penalized Expectation-Maximization (RPEM) algorithm was proposed by Cheung [2] [5]. The RPEM algorithm can determine the number of classes automatically by gradually fading out the redundant components from the mixture during the parameter learning process. In [2] [5], the RPEM utilizes a small constant learning rate to ensure the algorithm's convergence, which, however, needs more iteration steps. Indeed, we can dynamically adjust the learning rates to speed up the performance convergence of the RPEM. In this paper, we present a new method accordingly for such a task. Hereinafter, we denote the RPEM algorithm with dynamic adjustment of learning rate as RPEM-DLR algorithm.

2 The RPEM-DLR Algorithm

The mixture model assumes that each group of data is generated by an underlying probability distribution. Suppose the number of classes is k , and the number of samples is N . In the RPEM algorithm, the likelihood function for a mixture model can be defined in a weighted form, i.e.,

$$l(\Theta; \mathbf{x}) = \int \sum_{j=1}^k g(j|\mathbf{x}, \Theta) \ln p(\mathbf{x}|\Theta) dF(\mathbf{x}), \quad (1)$$

with

$$p(\mathbf{x}|\Theta) = \sum_{j=1}^k \alpha_j p(\mathbf{x}|\theta_j), \quad (2)$$

$$\sum_{j=1}^k \alpha_j = 1, \forall 1 \leq j \leq k, \alpha_j > 0, \quad (3)$$

and

$$\sum_{j=1}^k g(j|\mathbf{x}, \Theta) = 1, \quad (4)$$

where $\Theta = \{\alpha_j, \theta_j\}_{j=1}^k$ is the set of model parameters, $F(\mathbf{x})$ is the cumulative probability function of \mathbf{x} , $p(\mathbf{x}|\theta_j)$ is a multivariate probability density function (pdf) of \mathbf{x} , α_j is the proportion that \mathbf{x} comes from Class j , and g s are designable weights. The details can be found in [5].

The RPEM algorithm in normal mixture models can be summarized as follows:

- **Initialization:** Given a specific k ($k \geq k^*$, k^* is the true class number), we initialize Θ . Then, at each time step t , we implement the following two steps:

- **Step 1:** Fixing $\Theta^{(old)}$, calculate $h(j|\mathbf{x}_t, \Theta^{(old)})$, $g(j|\mathbf{x}_t, \Theta^{(old)})$ and $\alpha_j^{(old)}$, where

$$\alpha_j^{(old)} = \frac{\exp(\beta_j^{(old)})}{\sum_{i=1}^k \exp(\beta_i^{(old)})}. \quad (5)$$

- **Step 2:** Fixing $h(j|\mathbf{x}_t, \Theta^{(old)})$ s, update Θ

$$\beta_j^{(new)} = \beta_j^{(old)} + \eta_1 [g(j|\mathbf{x}_t, \Theta^{(old)}) - \alpha_j^{(old)}], \quad (6)$$

$$\mu_j^{(new)} = \mu_j^{(old)} + \eta_2 g(j|\mathbf{x}_t, \Theta^{(old)}) \Sigma_j^{-1(ol)} (\mathbf{x}_t - \mu_j^{(old)}), \quad (7)$$

$$\Sigma_j^{-1(new)} = [1 + \eta_2 g(j|\mathbf{x}_t, \Theta^{(old)})] \Sigma_j^{-1(ol)} - \eta_2 g(j|\mathbf{x}_t, \Theta^{(old)}) \mathbf{U}_{t,j},$$

where $\mathbf{U}_{t,j} = [\Sigma_j^{-1(ol)} (\mathbf{x}_t - \mu_j^{(old)}) (\mathbf{x}_t - \mu_j^{(old)})^T \Sigma_j^{-1(ol)}]$, η_1 and η_2 are small positive learning rates with $\eta_1 \ll \eta_2 \leq 1$. The procedure repeat until Θ converges.

In RPEM algorithm, it can be seen that the learning rate is generally a fixed small positive constant. Actually, the choice of the learning rate can affect the convergence performance of the RPEM. In general, there is a tradeoff between the residue deviation and rate of convergence [6]. When using a fixed learning rate, it should be small enough for the algorithm to converge. The smaller the learning rate, the smaller the residue deviation, but the slower the convergence speed. It is usually difficult to determine an optimal learning rate in advance because it is problem dependent.

According to the condition for the asymptotic convergence provided by a standard theorem [7] from stochastic approximation theory, the learning rate should satisfies:

$$\lim_{it \rightarrow \infty} \eta(it) = 0, \text{ and } \sum_{it=1}^{\infty} \eta(it) = \infty, \quad (8)$$

where it is the it -th epoch. Under the circumstances, we propose a new method here for adjusting the learning rate dynamically. The learning rate is defined as:

$$\eta(j, it) = \eta(j, it - 1) * \frac{1 - \alpha(j)}{1 + \alpha(j)},$$

$$1 \leq j \leq k, \text{ and } 1 \leq it < \infty,$$

where $\eta(j, it)$ is the learning rate for the j -th component in the it -th epoch, and α_j is the proportion that \mathbf{x} comes from Class j . The initial learning rate η_0 is set at a fixed small positive constant. Therefore, the learning rate will be adjusted dynamically according to α_j in each epoch.

3 Experimental Results and Discussions

In this section, two sets of data were used to investigate the performance of the RPEM-DLR algorithm. First, we generated 1,000 synthetic data points from a mixture of three bivariate Gaussian densities:

$$p1(\mathbf{x}|\Theta) = 0.3G[\mathbf{x} | \begin{pmatrix} 1 \\ 1 \end{pmatrix}, \begin{pmatrix} 0.10 & 0.05 \\ 0.05 & 0.20 \end{pmatrix}] \\ + 0.4G[\mathbf{x} | \begin{pmatrix} 1.0 \\ 5.0 \end{pmatrix}, \begin{pmatrix} 0.10 & 0.0 \\ 0.0 & 0.10 \end{pmatrix}] \\ + 0.3G[\mathbf{x} | \begin{pmatrix} 5.0 \\ 5.0 \end{pmatrix}, \begin{pmatrix} 0.10 & -0.05 \\ -0.05 & 0.10 \end{pmatrix}].$$

Suppose the number of seed points was set $k = 10$ and $k = 20$, respectively. We initialized each of Σ_j s to be an identity matrix, and all β_j s to be zero. The initial learning rate η_0 was set at 0.01. With the same initial parameters, the performance of the RPEM-DLR algorithm was compared to that of the RPEM algorithm. The results obtained by RPEM-DLR and RPEM are shown in Figure 1, where the points marked by '+' are the learned cluster centers via RPEM-DLR and EM, respectively. As shown in Figure 1, both the RPEM algorithm and RPEM-DLR can locate the cluster centers correctly by pushing away the redundant seed points when the pre-assigned class number is larger than the true mixture number, i.e., $k = 3$.

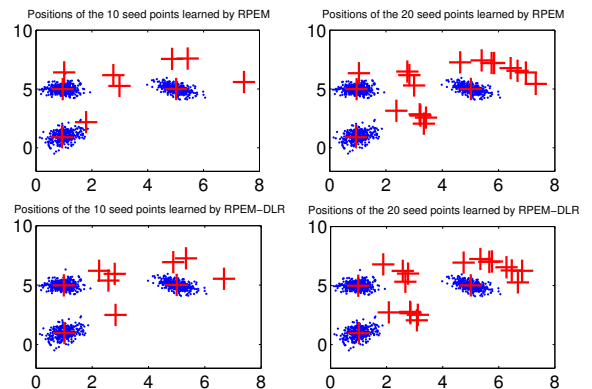


Figure 1: Convergent positions of the seed points learned via RPEM and RPEM-DLR for the data generated by $p1$.

Furthermore, we investigated the computation time taken by RPEM and RPEM-DLR algorithm during the learning procedure. The number of the seed points was set at 5, 10, 20 and 30, respectively. Table 1

Table 1: The comparison of computation time of RPEM and RPEM-DLR (seconds)

number of seed points	methods	
	RPEM	RPEM-DLR
5	101.5961	11.1861
10	239.0037	33.9889
20	402.2885	112.7221
30	1.0397e+003	225.6845

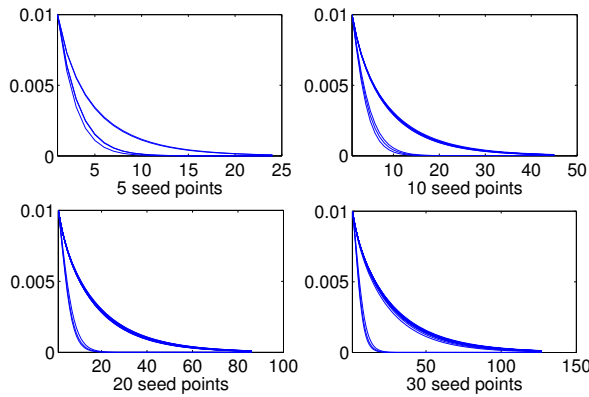


Figure 2: Learning curves of η_j s via RPEM-DLR for the data generated by p_1

shows the comparison of the computation time by RPEM and RPEM-DLR under the same conditions. As shown in Table 1, the computation time taken by RPEM-DLR is much less than that of the RPEM algorithm, i.e. our proposed RPEM-DLR algorithm largely reduces the calculation time. In a word, our proposed RPEM-DLR algorithm is really efficient, and speeds up the learning of the RPEM technique.

We further investigated the corresponding values of η_j s learned via RPEM-DLR when the number of seed points was set at 5, 10, 20 and 30, respectively. As shown in Figure 2, the values of η_j s corresponding to the extra seed points approached to zero slower than those of the true ones, which was reasonable because the learning rate was a monotonously dropping function of α_j s. It can be seen from Figure 2 that the learning rate was adjusted dynamically during the learning procedure, which speeded up the learning of the RPEM.

Upon the data clusters well-separated above, we further investigated the performance of the RPEM-DLR algorithm on the data clusters that were considerably overlapped. We generated 1,000 synthetic data points from a mixture of three bivariate Gaussian densities:

$$\begin{aligned}
 p_2(\mathbf{x}|\Theta) = & 0.3G[\mathbf{x} | \begin{pmatrix} 1 \\ 1 \end{pmatrix}, \begin{pmatrix} 0.15 & 0.05 \\ 0.05 & 0.20 \end{pmatrix}] \\
 & + 0.4G[\mathbf{x} | \begin{pmatrix} 1.0 \\ 2.5 \end{pmatrix}, \begin{pmatrix} 0.15 & 0.0 \\ 0.0 & 0.15 \end{pmatrix}] \\
 & + 0.3G[\mathbf{x} | \begin{pmatrix} 2.5 \\ 2.5 \end{pmatrix}, \begin{pmatrix} 0.15 & -0.1 \\ -0.1 & 0.15 \end{pmatrix}]
 \end{aligned}$$

The number of seed points was set at 10 and 20, respectively. We initialized each of Σ_j s to be an identity matrix, and all β_j s to be zero. The initial learning rate η_0 was set at 0.01. Again, The performance of the RPEM-DLR algorithm was compared to that of the RPEM algorithm. The results obtained by RPEM-DLR and RPEM are shown in Figure 3. It can be seen from Figure 3 that both the RPEM and RPEM-DLR algorithm can stabilize at the corresponding cluster centers when the number of seed points is larger than the true mixture number.

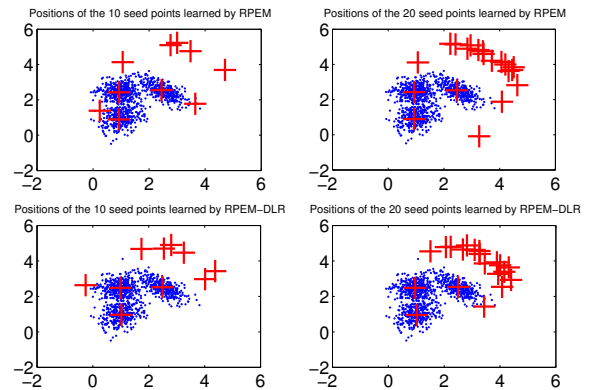


Figure 3: Convergent positions of the seed points learned via RPEM and RPEM-DLR for the data generated by p_2 .

The computation time taken by RPEM was compared to that of the RPEM-DLR algorithm during the learning procedure. The number of the seed points was set at 5, 10, 20 and 30, respectively. Table 2 shows the comparison of the computation time by RPEM and RPEM-DLR under the same conditions. As shown in Table 2, the computation time taken by RPEM-DLR is much less than that of the RPEM algorithm, which shows again that our proposed RPEM-DLR algorithm can adjust the learning rate dynamically and speed up the learning of RPEM.

Furthermore, Figure 4 shows the learning curves of η_j s when the number of seed points was set at 5, 10, 20

Table 2: The comparison of computation time of RPEM and RPEM-DLR (seconds)

number of seed points	methods	
	RPEM	RPEM-DLR
5	124.5791	9.3735
10	152.4893	25.9974
20	486.4795	111.0196
30	1.0870e+003	266.6434

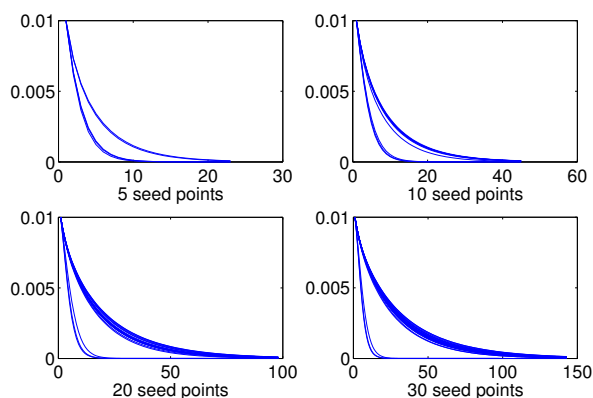


Figure 4: Learning curves of η_j s via RPEM-DLR for the data generated by p_2

and 30, respectively. As shown in Figure 4, the learning rates changed as we expected, and the RPEM-DLR technique can adjust the learning rate dynamically in the learning procedure. It can be concluded from the above experiments that the RPEM-DLR algorithm outperforms RPEM in terms of computation time, and adjusts its learning rate dynamically in the learning procedure.

4 Conclusions

This paper proposed a new method to dynamically adjust the learning rate of RPEM algorithm. Compared to the constant learning rate as used in the RPEM algorithm, our proposed method can efficiently speed up the performance convergence of RPEM algorithm. The numerical results have demonstrated its efficacy.

Acknowledgment

This work was partially supported by the Research Grant Council of Hong Kong SAR under Projects HKBU 2156/04E, HKBU 210306, and by Faculty Research Grant of Hong Kong Baptist University with the Project Code: FRG/05-06/II-42.

References

- [1] X. F. Zhang, C. M. Lam, and W. K. Cheung, "Mining Local Data Sources for Learning Global Cluster Models via Local Model Exchange," *The IEEE Intelligent Informatics Bulletin*, vol. 4, pp. 16–22, 2004.
- [2] Y. M. Cheung, "A rival penalized em algorithm towards maximizing weighted likelihood for density mixture clustering with automatic model selection," in *Proceedings of the 17th International Conference on Pattern Recognition (ICPR'04)*. United Kingdom: Cambridge, 2004, pp. 633–636.
- [3] X. F. Zhang, C. M. Lam, and W. K. Cheung, "Mining Local Data Sources for Learning Global Cluster Models via Local Model Exchange," *The IEEE Intelligent Informatics Bulletin*, vol. 4, pp. 16–22, 2004.
- [4] A. Dempster, N. Laird, and D. Rubin, "Maximum likelihood from incomplete data via the em algorithm," *J. Roy. Stat. Soc.*, vol. B39, pp. 1–38, 1977.
- [5] Y. M. Cheung, "Maximum weighted likelihood via rival penalized em for density mixture clustering with automatic model selection," *IEEE Transactions on Knowledge and Data Engineering*, vol. 17, no. 6, pp. 750–761, June 2005.
- [6] C. Chinrungrueng and C. H. Sequin, "Optimal adaptive k-means algorithm with dynamic adjustment of learning rate," *IEEE Transaction on Neural Networks*, vol. 6, no. 1, pp. 157–169, 1995.
- [7] A. Dvoretzky, "On stochastic approximation," in *Proc. 3rd Berkeley Sym. on Math. Stat. and Prob.*, J. Neyman, Ed.

Fitting a predictive model with a priori information: application in intermittent androgen suppression for prostate cancer

Yoshito Hirata^{1,2,*} and Kazuyuki Aihara^{1,2,3}

¹ Aihara Complexity Modelling Project, ERATO, JST,
45-18 Oyama, Shibuya-ku, Tokyo 151-0065, Japan

² Institute of Industrial Science, The University of Tokyo,
4-6-1 Komaba, Meguro-ku, Tokyo, 153-8505, Japan

³Department of Mathematical Informatics, The University of Tokyo,
7-3-1 Hongo, Bunkyo-ku, Tokyo 113-8656, Japan

* yoshito@sat.t.u-tokyo.ac.jp

Abstract

Although it is common to fit a phenomenological model with past observations only and predict the future, we sometimes have additional information on the system. For example, when we build a model for the intermittent androgen suppression (IAS), which is for prostate cancer, there are two pieces of a priori information. The first piece is that the value of prostate specific antigen (PSA), a maker of prostate cancer, does not get smaller than 0. The second piece is that the prostate cancer relapses and PSA starts increasing drastically if a patient keeps the medication for more than a certain period. Especially when we want to predict the relapse of prostate cancer, we encounter the difficulty because the second feature does not appear in past observations of PSA. In this talk, we introduce a cost function by which we reflect additional information to a predictive model. Our strategy is 1. write down constraints we want as inequalities and 2. include them into the cost function as penalties. Examples of IAS demonstrate that our model has the desired features and can predict the recurrence of prostate cancer.

Key words

prediction, mathematical model, a priori information, grey-box identification, prostate cancer, intermittent androgen suppression

1 Intermittent androgen suppression for prostate cancer

Prostate cancer is one of popular cancers in the world. One of the common treatments for prostate cancer is to suppress the androgen level [1]. By suppressing the androgen level, cancer cells die through apoptosis. In old days, medical doctors suppressed the androgen level by castration and/or estrogen injection. Nowadays, due to the improvement of antiandrogens, we can effectively suppress the androgen level without surgery [2].

Although the androgen suppression is effective at the beginning, prostate cancer relapses in some years time because the cancer cells will become able to grow without androgen [2]. A countermeasure for the relapse is intermittent androgen suppression [3, 4, 5]. By stopping the medication temporally, we can delay the independence of cancer cells from androgen. Since a good marker for prostate cancer, called prostate specific antigen (PSA), was proposed [6], we can monitor well the behaviour of prostate cancer and thus consider a better protocol for intermittent androgen suppression [5].

Recently, a mathematical model for prostate cancer has been proposed [7, 8]. It is based on linear equations. A mathematical model for intermittent androgen suppression was also proposed [9].

For deriving a better control strategy, we need to build a mathematical model of prostate cancer for each patient. But a trouble is that when fitting a model from patients' data, we cannot use the part of time series which shows the recurrence of prostate cancer. Since fitting a model only from observed data, we can

reproduce and predict phenomena which is similar to what we have observed. Thus a model obtained only from data typically cannot predict the recurrence of prostate cancer.

To overcome this difficulty, we use a priori knowledge about the cancer. We know that the cancer relapses within several years. Thus we enforce this condition on the mathematical model and fit its parameters.

2 Finding a predictive model

2.1 Grey box modelling

In practical applications, additional information has been used for finding a mathematical model of given system. For example, in statistics, we need the prior distribution for converting the relation of random variables in Bayes' rule and saying the probability of observation [10]. In the control community, methods for using additional information are called grey-box identification and additional information is reflected to a mathematical model by conditioning on parameters [11, 12, 13, 14] and/or choosing types of functions in the model [15, 16, 17, 18, 19]. They were used for obtaining stable models [11], better prediction [16, 18, 19] and better control [13], changing a problem to a well-posed one [12], and enhancing static response [14]. In the nonlinear dynamics community, work using additional information [20] started appearing, which used the information of fixed points for obtaining models that behave better locally around the fixed points.

2.2 Our approach

Our approach is slightly different from all the methods mentioned above because we condition on the behaviour directly. To tell our approach in detail, we need to describe our model. A model we consider looks the following: Let us consider three clone models. The volume of the i -th clone at month t is $x_i(t)$, where $i = 1, 2, 3$. Suppose that the sum of $x_i(t)$ corresponds to PSA. Let m show the medication condition. If $m = 1$, then the patient takes the medication. If $m = 0$, then the patient stops the medication. For

each case of m , we prepare a linear equation:

$$\begin{pmatrix} x_1(t+1) \\ x_2(t+1) \\ x_3(t+1) \end{pmatrix} = \begin{pmatrix} a_{11}^m & a_{12}^m & a_{23}^m \\ a_{21}^m & a_{22}^m & a_{33}^m \\ a_{32}^m & a_{33}^m & a_{33}^m \end{pmatrix} \begin{pmatrix} x_1(t) \\ x_2(t) \\ x_3(t) \end{pmatrix} + \begin{pmatrix} b_1^m \\ b_2^m \\ b_3^m \end{pmatrix}. \quad (1)$$

We have shown that a piecewise linear model is enough for describing the changes of PSA (not shown here). When fitting the model, we choose either the linear equations for $m = 1$ or those for $m = 0$ depending on patient's actual medication policy for the previous month.

Let us write down a priori knowledge. As for PSA, we know that

- PSA always takes a positive value, and
- If a patient keeps the medication for suppressing androgen, PSA increases again within several years.

The first condition can be written as

$$a_{i,j} \geq 0, \quad (2)$$

$$b_k \geq 0, \quad (3)$$

$$x_l(0) \geq 0, \quad (4)$$

where $i = 1, 2, 3, j = 1, 2, 3, k = 1, 2, 3$, and $l = 1, 2, 3$.

Let $\bar{x}_i(t)$ be the volume of the i -th clone at month t after applying the linear equations for the medication condition ($m = 1$). Then the second condition can be written, for example, as

$$\sum_i \bar{x}_i(60) \geq 10, \quad (5)$$

$$a_{3,3} \geq 1. \quad (6)$$

The second last inequality means that PSA becomes greater than 10 after continuing the medication for 5 years and the last inequality means that the third clone keeps increasing under the medication.

We include these conditions in a cost function. Namely, we solve the following optimisation program: Let $p(t)$ be PSA at month t , T , the number of observations, and C , some constant. Also denote by H the Heaviside function, i.e., if $x > 0$ then $H(x) = 1$ otherwise $H(x) = 0$. Then we use

$$\begin{aligned} \min_{a,b,x(0)} & \left[\frac{1}{T} \sum_{t=0}^{T-1} |p(t) - \sum_l x_l(t)| \right. \\ & + C \sum_{i,j,m} H(-a_{i,j}^m) + C \sum_{i,m} H(-b_i^m) \\ & \left. + C(1 + (1 - a_{3,3}^1))H(1 - a_{3,3}^1) \right]. \quad (7) \end{aligned}$$

In this paper, we used $C = 100$. We solve this minimisation problem using the differential evolution method [21, 22].

3 Examples

For testing the proposed problem, we generated test data using the model of Ideta *et al.* [9]. We generated 6 different datasets, 2 sets each for case (i), (ii), and (iii), in Ideta *et al.* [9]. In each case, a dataset is for bone metastasis case and the other for lymph node metastasis case. We used $r_1 = 15$ and $r_0 = 2$ for generating each dataset. For each dataset, we used the first 2 cycles for fitting the model and free ran the following cycles.

Firstly, we compared models which are obtained using different cost functions. When we did not use any constraints, the model did not reproduce the recurrence of prostate cancer (Fig. 1(a)). When we imposed the first condition, the non-negativity of PSA, still the model did not reproduce the relapse of prostate cancer (Fig. 1(b)). When we used both the first and the second conditions, we reproduced the relapse of prostate cancer (Fig. 1(c)). This time, the free-run was also qualitatively similar to the original dataset.

When we applied the proposed cost function to the other datasets, their free-runs looked similar to those of the original data (not shown here due to the limit of space).

4 Conclusion

In this paper, we fitted a mathematical model of intermittent androgen suppression for prostate cancer using a priori information that prostate cancer relapses if a patient continues the medication for suppressing androgen. The difficulty of the program is that we cannot use the relapsing part of data for finding the model. When we fitted the model only using observed data, the model did not reproduce the recurrence of prostate cancer. When we also imposed conditions for the non-negativity and the recurrence of prostate specific antigen during fitting the model, we found the model that reproduced the relapse of prostate cancer. We hope that the technique used here is also applicable to real data.

References

- [1] C. Huggins and C. V. Hodges, "Studies on prostatic cancer; effect of castration, of estrogen and of androgen injection on serum phosphatases in metastatic carcinoma of the prostate," *Cancer Res.* 1, 293 (1941).

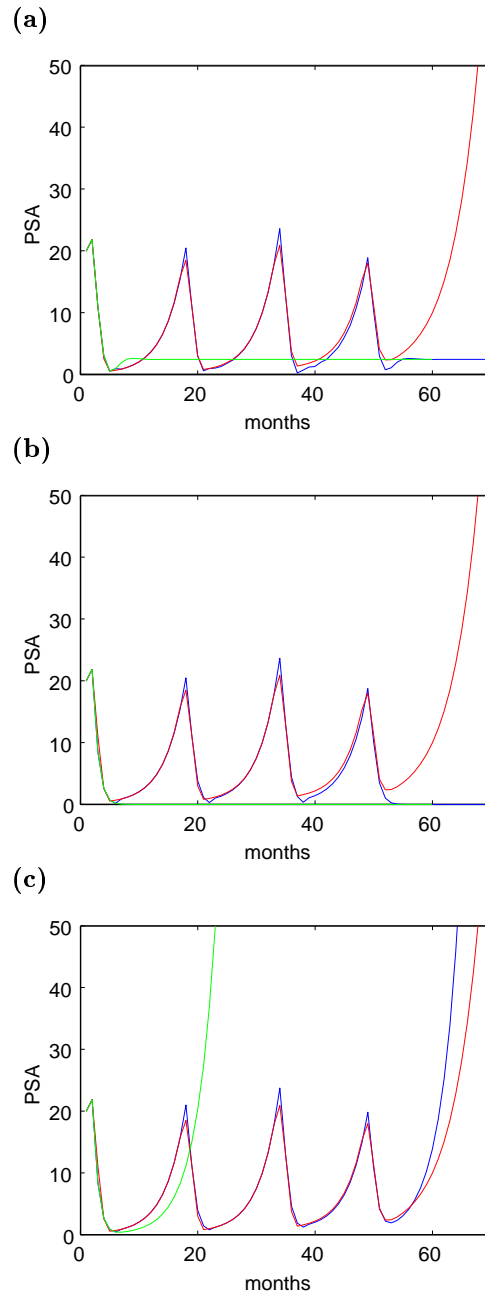


Figure 1: Predicting the relapse of prostate cancer. Fig. (a) is the case where we did not use any constraints for fitting the model. Fig. (b) is the case where we only use constraints for making PSA always positive. Fig. (c) is the case where we also use constraints that make PSA diverge. In each figure, the red line is the original data produced from Ideta model in case (ii), the blue line is our prediction, and the green line is the free run. We used the first 2 cycles for fitting the model. In the free run, we only used the model under the medication condition and tested whether the prostate cancer relapses or not. We used $r_1 = 15$ and $r_0 = 2$.

- [2] N. Bruchovsky, “Androgens and antiandrogens,” J. F. Holland *et al.* eds., *Cancer Medicine*, Lea & Febiger, Philadelphia, USA, 1993.
- [3] W. Vahlensieck *et al.*, “Comparison between continuous and intermittent administration of Estracyt in the treatment of carcinoma of the prostate,” *Urol. Res.* **13**, 209 (1985).
- [4] L. H. Klotz *et al.* “Intermittent endocrine therapy for advanced prostate cancer,” *Cancer* **58**, 2546 (1986).
- [5] N. Bruchovsky *et al.*, “Luteinizing hormone-releasing hormone agonists in prostate cancer: elimination of flare reaction by pretreatment with cyproterone acetate and low-dose diethylstilbestrol,” *Cancer* **72**, 1685 (1993).
- [6] J. E. Oesterling, “Prostate specific antigen: a critical assessment of the most useful tumor marker for adenocarcinoma of the prostate,” *J. Urol.* **145**, 907 (1991).
- [7] T. L. Jackson, “A mathematical model of prostate tumor growth and androgen-independent relapse,” *Discrete Cont. Dyn.-B* **4**, 187 (2004).
- [8] T. L. Jackson, “A mathematical investigation of the multiple pathways to recurrent prostate cancer: comparison with experimental data,” *Neoplasia* **6**, 697 (2004).
- [9] A. M. Ideta, G. Takana, T. Takeuchi, and K. Aihara, “A mathematical model of intermittent androgen suppression remedy for prostate cancer,” *Mathematical engineering technical reports*, METR 2006-32, (2006).
- [10] N. Gershenfeld, *The nature of mathematical modeling*, Cambridge University Press, Cambridge, UK, 1999.
- [11] H. J. A. F. Tulleken, “Grey-box modelling and identification using physical knowledge and Bayesian techniques,” *Automatica* **29**, 285 (1993).
- [12] T. A. Johansen, “Identification of non-linear systems using empirical data and prior knowledge: an optimization approach,” *Automatica* **32**, 337 (1996).
- [13] J. Abonyi, R. Babuška, H. B. Verbruggen, and F. Szeifert, “Incorporating prior knowledge in fuzzy model identification,” *Int. J. Syst. Sci.* **31**, 657 (2000).
- [14] E. G. Nepomuceno, R. H. C. Takahasi, L. A. Guirre, O. M. Neto, and E. M. A. M. Mendes, “Multiobjective nonlinear system identification: a case study with thyristor controlled series capacitor (TCSC),” *Int. J. Syst. Sci.* **35**, 537 (2004).
- [15] A. Alessandri and T. Parisini, “Nonlinear modeling of complex large-scale plants using neural networks and stochastic approximation,” *IEEE T. Syst. Man Cy. A* **27**, 750 (1997).
- [16] L. A. Aguirre, P. F. Donoso-Garcia, and R. Santos-Filho, “Use of a priori information in the identification of global nonlinear models: a case study using a buck converter,” *IEEE T. Circuits-I* **47**, 1081 (2000).
- [17] L. A. Guirre, M. V. Corrêa, and C. C. S. Cassini, “nonlinearities in NARX polynomial models: representation and estimation,” *IEE Proc.-Control Theory Appl.* **149**, 343 (2002).
- [18] M. V. Corrêa, L. A. Aguirre, and R. R. Saldanha, “Using steady-state prior knowledge to constrain parameter estimates in nonlinear system identification,” *IEEE T. Circuits-I* **49**, 1376 (2002).
- [19] L. A. Aguirre, M. F. S. Barroso, R. R. Saldanha, and E. E. A. M. Mendes, “Imposing steady-state performance on identified nonlinear polynomial models by means of constrained parameter estimation,” *IEE Proc.-Control Theory Appl.* **151**, 174 (2004).
- [20] D. M. Walker, “Parameter estimation using Kalman filters with constraints,” *Int. J. Bifur. Chaos* **16**, 1067 (2006).
- [21] R. Storn and K. Price, “Differential evolution—a simple and efficient heuristic for global optimization over continuous spaces,” *J. Global Optim.* **11**, 341 (1997).
- [22] K. V. Price, R. M. Storn, and J. A. Lampinen, *Differential evolution: a practical approach to global optimization*, Springer, Berlin, 2005.

Effect of facility closure in the SEIR epidemic model

Hiroshi Maeda¹

Yasushi Ohkusa²

Kazuyuki Aihara^{3,4}

¹Graduate School of Information Science and Technology, The University of Tokyo

²Infectious Disease Surveillance Center, National Institute of Infectious Diseases

³Institute of Industrial Science, The University of Tokyo

⁴Aihara Complexity Modelling Project, ERATO, JST

Abstract

Avian influenza H5N1 has caused large outbreaks in birds in Southeast Asia. This virus is highly virulent in humans who have been infected directly from birds. But, the virus has not achieved human-to-human transmission. If a new virus of bird flu capable of human-to-human transmission appears, this change could cause pandemic influenza. We propose the SEIR epidemic model of influenza transmission to assess the influence of facility closure as a containment strategy. Mathematical models are important tools in analyzing the spread and control of infectious diseases. If the fraction of infected individuals exceeds the set threshold, we execute the facility closure for the set period and there are assumed to be no transmission among a population. If the basic reproduction number R_0 was assumed to be 2.0, our model suggested that it was not necessarily the case that long period of facility closure reduced the prevalence. The final size of an epidemic depended on the number of infected individuals when the susceptible fraction was equal to $1/R_0$.

1 Introduction

The threat of pandemic influenza has increased for decades [1]. H5N1 highly pathogenic avian influenza is causing outbreaks among poultry in Southeast Asia. The transmission from birds to human and other mammalian species has been sporadic. The virus has not required the ability to be transmitted from human to human. But, if mutation of the virus occurs, the novel variant could be capable of sustaining human-to-human transmission. Besides, pandemic influenza can cause a public health crisis because many people are immunologically naive to the new virus. Although antiviral drugs offer protection against infection, production delays would limit availability in the first months

of pandemic [2].

Influenza prevention and containment strategies can be considered under the broad categories of antiviral, vaccine, and nonpharmaceutical measures. In this study, we focus on nonpharmaceutical measures, especially in the facility closure. For example, schools are known to be the primary context of influenza transmission [3]. However, no data or analyses exist for recommending illness thresholds or rates of change that lead to considering closing or reopening schools [4].

The purpose of this study is to clarify the impact of facility closure by changing the threshold or the duration of closure. Here we construct a simple epidemic model of influenza transmission with deterministic differential equations. Mathematical models and computer simulations are useful tools for building and testing theories, assessing quantitative conjectures, answering specific questions, and determining sensitivities to changes in parameter values [5]. The model formulation process clarifies assumptions, variables, and parameters. We can use mathematical models in comparing, planning, implementing, and evaluating various detection, prevention, and control programs.

2 Model and general theory

We use a mathematical model called the SEIR epidemic model, which is represented as follows:

$$\frac{dS}{dt} = -SI, \quad (1)$$

$$\frac{dE}{dt} = SI - \sigma E, \quad (2)$$

$$\frac{dI}{dt} = \sigma E - I, \quad (3)$$

$$\frac{dR}{dt} = I. \quad (4)$$

$S(t)$, $E(t)$, $I(t)$, and $R(t)$ are the number of susceptible, exposed, infective, and recovered individuals, respectively. This model is based on the Kermack-McKendrick model [6].

The susceptible class S contains individuals who have a risk of becoming infected. When there is a contact of a susceptible with an infective so that transmission occurs, the individual enters the exposed class E in the latent period. An exposed individual is infected but non-contagious. After the latent period, the individual enters the infective class I in the infection period. An infective individual is contagious, that is capable of transmitting the infection. After the infection period, the individual enters the recovered class R . A recovered individual is permanently immunity to further infection.

Movements out of the class E and I are governed by σE and I , respectively. It is shown that these terms correspond to exponentially distributed waiting times. For example, the transfer rate I corresponds to $P(t) = e^{-t}$ as the fraction that is still in the infective class t units after entering this class and to $1/t$ as the mean waiting time. We define the duration of latent period and infection period as $1/\sigma$ and $1/\gamma$.

The key value governing the time evolution of these equations is the basic reproduction number R_0 , which is defined as the mean number of secondary infections generated by a primary infection in a susceptible population [7]. R_0 for the SEIR model is given by

$$R_0 = \frac{N}{\sigma}, \tag{5}$$

where N is the total number of individuals so that $N = S(t) + E(t) + I(t) + R(t)$. If $R_0 < 1$, one infected individual will infect fewer than one susceptible individual before recovering. The infection will die out certainly. If $R_0 > 1$, one infected individual will infect more than one susceptible individual before recovering. There is some possibility of a major epidemic. Therefore, R_0 is considered as the threshold that determines whether an infection can persist in a population or not.

We propose the new epidemic model with facility closure. If the proportion of infective individuals exceeds the threshold of closure θ , we assume that facilities are closed for d days and that there is no transmission among the people. The dynamics with closure is represented as follows:

$$\frac{dS}{dt} = 0, \tag{6}$$

$$\frac{dE}{dt} = \sigma E, \tag{7}$$

$$\frac{dI}{dt} = \sigma E - I, \tag{8}$$

$$\frac{dR}{dt} = I. \tag{9}$$

If the proportion of infective individual is less than the threshold after the facility closure of d days, facilities reopen and the transmission occurs again. The dynamics with or without closure follows equations (1)-(4). Figure 1 shows the dynamics with or without closure schematically.

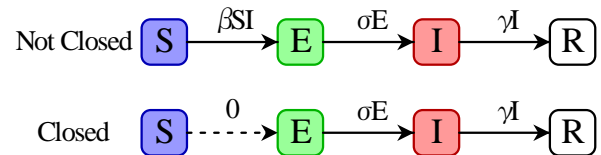


Figure 1: The dynamics of the SEIR epidemic model with or without closure

3 Results

We performed a numerical simulation to investigate the dynamics of our epidemic model. As an initial state, we set $\{S(0), E(0), I(0), R(0)\} = \{99, 1, 0, 0\}$. Since recent estimates of the basic reproduction number of the 1918 pandemic strain were in the range 2-3 [8], we assumed that $R_0 = 2.0$. We also assumed distributions of infectiousness consistent with previous studies [9], giving mean latent and infection periods of 1.9 days and 4.1 days, respectively. These assumed parameters are shown in Table 1. We estimated the value of σ , γ , and θ from equation (5) and Table 1.

Parameters	Description	Value
R_0	Basic reproduction number	2.0
$1/\sigma$	Mean latent period	1.9
$1/\gamma$	Mean infection period	4.1

Figure 2 shows the transition of the susceptible fraction, exposed fraction, infective fraction, and the sum of exposed and infective fraction without facility closure. The horizontal auxiliary line shows that the susceptible fraction is 0.5 and the vertical auxiliary one shows the day when it is 0.5. Both the susceptible fraction and infective fraction has the maximum on about 30th day. About 80% of a population is infected on the 180th day.

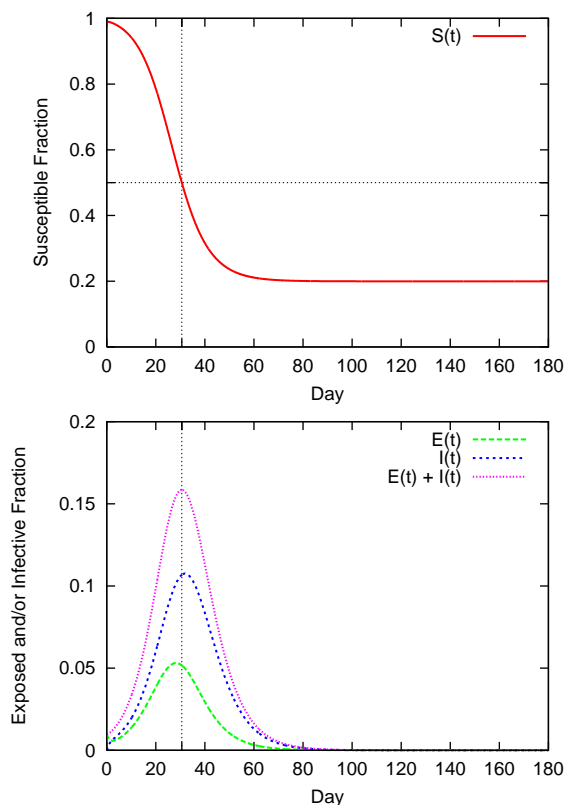


Figure 2: The transition of susceptible fraction, exposed fraction, infective fraction, and the sum of exposed and infective fraction without facility closure

Figure 3 shows the relation between the threshold of closure and the prevalence, which is the proportion of recovered individuals. We examined three parameters for the duration of closure d , i.e. three, five, and seven days. The prevalence doesn't reduce monotonically with reducing the threshold of closure regardless of the closed period. Many of the long term closure reduce the prevalence broadly if the threshold of closure is fixed. But, there is a little possibility that the long term closure produce somewhat high prevalence than short term one.

Figure 4 shows the transition of susceptible fraction and the sum of exposed and infective fraction with facility closure for five days. Thresholds of closure θ were assumed to be 0.06, 0.07, and 0.09. When the threshold is 0.06, the facility closure is implemented twice on the 20th and 40th day.

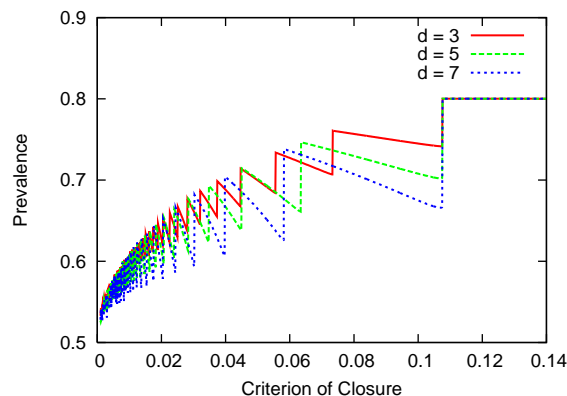


Figure 3: The relation between the threshold of closure and the prevalence

4 Discussion

Figure 2 represents that the number of exposed and infective individuals reaches a peak on the 30th day. After this time, the following formula is formed:

$$\frac{dE}{dt} + \frac{dI}{dt} < 0. \quad (10)$$

From equations (2), (3), and (5), we can obtain the following formula:

$$\frac{S}{N} < \frac{1}{R_0}. \quad (11)$$

This formula indicates that the number of exposed and infective individuals start to reduce when the susceptible fraction is less than $1/R_0$. This threshold of reduction is 0.5 because we assumed that $R_0 = 2.0$. This analytical solution gives good agreement with experimental results in Figure 2.

From equations (10) and (11), at least a half of a population is infected in this model. Therefore, the number of exposed and infected individuals when the susceptible fraction is equal to $1/R_0$ is important value to reduce the prevalence.

Figure 4 is an example of why zigzag lines are drawn in Figure 3. First, the transition of the sum of exposed and infective fraction achieves a peak twice when the threshold of closure θ is 0.09 or 0.07. If the threshold changes from 0.09 into 0.07, the sum of exposed and infective fraction in the first peak is reduced but in the second peak is increased. In the second peak, both susceptible fraction is the same by 0.5, and more prevalence is produced by more exposed and infective individuals with $\theta = 0.07$ than with $\theta = 0.09$. Second, if we reduce θ from 0.07 much further more, the

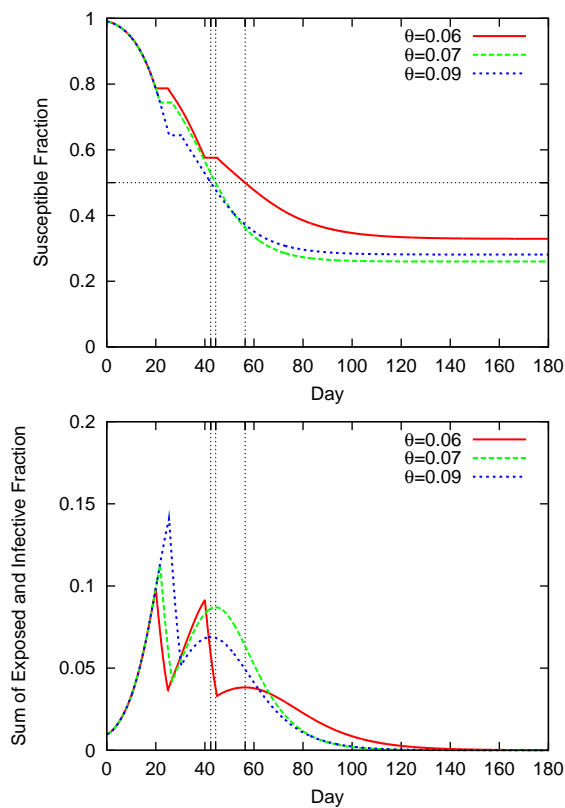


Figure 4: The transition of susceptible fraction and the sum of exposed and infective fraction with facility closure for five days

transition of the sum of exposed and infective fraction achieves a peak three times as $\theta = 0.06$ in Figure 4. The sum of exposed and infective fraction with $\theta = 0.06$ is less in the third peak when the susceptible fraction is equal to 0.5 than with $\theta = 0.07$. These two mechanism generate the zigzag line in Figure 3.

In this study, we reveal that the low prevalence is generated by the small number of exposed and infective individuals when the susceptible fraction is equal to $1/R_0$. However, since R_0 of a future newly emergent influenza strain is unknown, we can not change the number of exposed and infective individuals purposely. It seems to be the desirable measure to close facilities at the low threshold and for a long term if at all possible.

5 Conclusions

We propose the simple epidemic model based on the SEIR epidemic model to explore the effect of facility

closure. Long period closure has the high possibility to reduce the prevalence than short period closure. However, there are some situations it is better to close facilities for long period.

References

- [1] Anthony S. Fauci (2006) Pandemic influenza threat and preparedness. *Emerging Infectious Diseases* 12(1):73-77
- [2] Klaus Stöhr, Marja Esveld (2004) Will vaccines be available for the next influenza pandemic? *Nature* 306:2195-2196
- [3] Anthony Heymann, Gabriel Chodick, Brian Reichman, et al. (2004) Influence of school closure on the incidence of viral respiratory diseases among children and on health care utilization. *The Pediatric Infectious Diseases Journal* 23(7):675-677
- [4] World Health Organization Writing Group (2006) Nonpharmaceutical interventions for pandemic influenza, national and community measures. *Emerging Infectious Diseases* 12(1):88-94
- [5] Herbert W. Hethcote (2000) The mathematics of infectious diseases. *SIAM Review* 42(4):599-653
- [6] W. O. Kermack, A. G. McKendrick (1927) Contributions to the mathematical theory of epidemics-I. *Proceedings of the Royal Society* 115A:700-721
- [7] Roy M. Anderson, Robert M. May (1991) *Infectious diseases of humans: dynamics and control*. Oxford University Press, Oxford
- [8] Christina E. Mills, James M. Robines, Marc Lipsitch (2004) Transmissibility of 1918 pandemic influenza. *Nature* 432:904-906
- [9] Lila R. Elveback, John P. Fox, Eugene Ackerman, et al. (1976) An influenza simulation model for immunization studies. *American Journal of Epidemiology* 103(2):152-165

A Systematic Approach to Analysis of Robustness in Oscillatory Networks

Ruiqi Wang^{a,c}, Luonan Chen^{a,b,c}

^a Aihara Complexity Modelling
Project, ERATO, JST

^b Osaka Sangyo University

Kazuyuki Aihara^{a,c}

^c Institute of Industrial Science
The University of Tokyo

Abstract

Robustness as a system-level property is mainly determined by structural characteristics rather than fine-tuning parameter values. The relative contribution of network components or interactions to robustness remains little studied. By decomposing an overall network into smaller subnetworks and then analyzing effects of the interactions between them, relative importance of the network components for robustness property of oscillations can be derived. Moreover, the improvement of robustness against perturbations can be also made through modification of the structural characteristics or regulatory interactions of the network. Our analysis focuses on a molecular network that produces spontaneous oscillations in *Dictyostelium discoideum* cells.

1 introduction

Robustness is a property that allows a system maintains its functions despite external or internal perturbations and uncertainty [1]. It is a key to understanding cellular complexity and elucidating design principles. Owing to intimate links to cellular functions, robustness properties of many oscillatory networks through negative or interlocked feedback loops have been extensively investigated [2]. Investigation of robustness for general oscillators may focus on the persistence of regular oscillations, which does not prelude quantitative changes in period or amplitude to occur. While for circadian oscillators, it may focus on the period and amplitude sensitivities to evaluate their precise time-keeping ability with respect to noises or parameter variations. Most works mainly assess robustness as a system-level property. The relative contribution of network components or interactions to robustness remains little studied.

2 A linear analysis approach to robustness

We model a biochemical network as

$$\dot{x} = f(x, p), \quad (1)$$

where x is the state vector containing the concentration or activity of all components in the network and p are the parameters. Since our goal is to consider the relative importance of interactions for robustness, we decompose the overall network (1) into smaller subnetworks Γ_i consisting of single components modelled by

$$\dot{x}_i = f_i(x_i, u_i, p). \quad (2)$$

Each subnetwork Γ_i has components x_i as its only internal state and output, while all other components are treated as inputs u_i .

The linearization of system (1) around an equilibrium x_0 is given by

$$\Delta \dot{x}(t) = A \Delta x(t) \quad \text{with} \quad A = \left. \frac{\partial f(x(t), p)}{\partial x} \right|_{x_0}, \quad (3)$$

where $\Delta x(t) = x(t) - x_0$ denotes deviation of the concentrations or activities from the equilibrium x_0 . The decomposition of the linearized system (3) into one-component subnetworks Γ_i is as follows

$$\Delta \dot{x}(t) = \tilde{A} \Delta x(t) + (A - \tilde{A}) \Delta u, \quad (4)$$

where \tilde{A} is a diagonal matrix containing the diagonal entries of A . In this way, the linear biochemical network (3) can be seen as an open-loop interaction free network (4). In other words, we analyze the whole network by breaking the feedback loop at each step, viewing the effects of all other components on each x_i as input signals, and after analyzing the relative importance of each component on the robustness properties of the oscillations, we do re-close the loop by letting $\Delta u = \Delta x$.

The key to our approach is standard feedback control theory. Following Laplace transformation, the linear open-loop system (4) then transforms to an algebraic equation in s

$$\Delta x(s) = L(s)\Delta u(s), \quad (5)$$

where $L(s) = (sI - \tilde{A})^{-1}(A - \tilde{A})$. The element $L_{ij}(s)$ corresponds to the transform function from the component j to component i in the absence of any feedback effects, i.e. the ratio of the output x_i to the input x_j .

According to the generalized Nyquist criteria, for a stable open-loop network $L(s)$, a sufficient condition for instability under positive feedback is that one characteristic locus $\lambda_i(L(j\omega))$ crosses the real axis to the right of the point 1 at a single frequency $\omega = \omega_{\text{crit}}$. A perturbation applied to element $L_{ij}(j\omega_{\text{crit}})$ such that this $\lambda_i(L(j\omega))$ moves to the point 1 on the real axis corresponds to a stabilizing perturbation.

A perturbation that moves one characteristic locus $\lambda_i(L(j\omega))$ at $\omega = \omega_{\text{crit}}$ to the point on the real axis corresponds to making the return difference $I - L(j\omega)$ singular at the $\omega = \omega_{\text{crit}}$, that is,

$$\det(I - L_p(j\omega_{\text{crit}})) = 0, \quad (6)$$

where L_p is the perturbed open-loop system.

The required perturbation Δ_{ij} is given by

$$\Delta_{ij}(\omega_{\text{crit}}) = -\frac{1}{[\text{RGA}(I - L(j\omega_{\text{crit}}))]_{ij}}, \quad (7)$$

where $\text{RGA}(M) = M \times (M^{-1})^T$ and the \times symbol denotes element by element multiplication (Hadamard or Schur product). Thus, elements with relative small values of stabilizing perturbations $|\Delta_{ij}|$ correspond to pairwise interactions that have a large influence on stability and play an important role in destabilizing the equilibrium. In other words, elements with relative small values of stabilizing perturbations $|\Delta_{ij}|$ are sensitive to perturbations, while elements with relative large values of stabilizing perturbations are more robust to perturbations. If all stabilizing perturbations are large, the oscillations of the network will be more robust.

3 Results

Adenosine 3', 5'-cyclic monophosphate (cAMP) oscillations in *Dictyostelium discoideum* cells are necessary for chemotaxis and further development of *Dictyostelium* cells. The model, based on the network depicted in Fig.1, induces spontaneous oscillations in

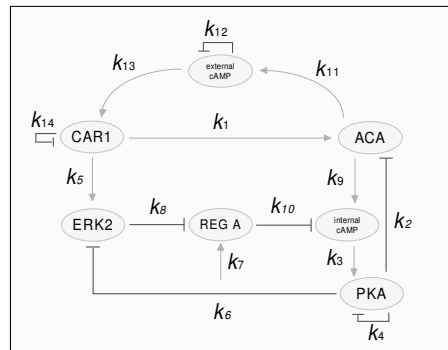


Figure 1: Molecular interactions generating cAMP oscillations in *Dictyostelium discoideum* cells. Components are connected by regulatory interactions that are direct or indirect. Arrows and bar heads indicate positive and negative regulation, respectively. Pulses of cAMP are produced when adenylate cyclase (ACA) is activated after the binding of extracellular cAMP to the surface receptor CAR1. When cAMP accumulates internally, it activates the protein kinase PKA. Ligand-bound CAR1 also activates the MAP kinase ERK2. ERK2 is then inactivated by PKA and no longer inhibits the cAMP phosphodiesterase REG A. A protein phosphatase activates REG A such that REG A can hydrolyse internal cAMP. When REG A hydrolyses the internal cAMP, PKA activity is inhibited by its regulatory subunit, and the activities of both ACA and ERK2 go up.

cAMP observed during the early development of *D. discoideum* [3]. The deterministic dynamics is governed by the following equations:

$$\begin{aligned} d[\text{ACA}]/dt &= k_1[\text{CAR1}] - k_2[\text{ACA}][\text{PKA}], \\ d[\text{PKA}]/dt &= k_3[\text{internal cAMP}] - k_4[\text{PKA}], \\ d[\text{ERK2}]/dt &= k_5[\text{CAR1}] - k_6[\text{PKA}][\text{ERK2}], \\ d[\text{REG A}]/dt &= k_7 - k_8[\text{ERK2}][\text{REG A}], \\ d[\text{internal cAMP}]/dt &= k_9[\text{ACA}] - k_{10}[\text{REG A}][\text{internal cAMP}], \\ d[\text{external cAMP}]/dt &= k_{11}[\text{ACA}] - k_{12}[\text{external cAMP}], \\ d[\text{CAR1}]/dt &= k_{13}[\text{external cAMP}] - k_{14}[\text{CAR1}], \end{aligned} \quad (8)$$

where k_i ($i = 1, \dots, 14$) are kinetic constants. The model is based on the common positive and negative control elements.

For the oscillatory network shown in Fig.1, from the linearization around the underlying equilibrium we obtain $\omega = \omega_{\text{crit}} = 0.8560$ rad/min, at which the critical characteristic locus $\lambda_{\text{crit}}(L(j\omega))$ crosses the real axis to

the right of the critical point (1, 0). The rank-ordered stabilizing perturbations are shown in Fig.2(a). Even the largest amplitude of stabilizing perturbations is small (< 0.035), and it shows the poor robustness properties of the model. Such result is also supported in [4].

Different from the parameter sensitivity analysis used in [2], by which the clues on the importance of individual regulatory processes on the oscillations and relative importance of individual regulatory processes can be directly derived by the linear analysis approach. The parameter sensitivity analysis needs a large amount of computing, as shown in [2], while the relative importance can be easily obtained by the linear analysis approach, as shown in Fig.2(a). For instance, the network shows a higher sensitivity toward perturbations affecting external cAMP. It has shown that constant high levels of external cAMP lead to attenuation, whereas a brief pulse of cAMP can advance or delay the phase such that interaction cells become entrained [3]. The regulation of PKA inhibiting ERK2 enhances the robustness properties, although its role in enhancing robustness is poor. The results show that different regulatory mechanisms are of different importance for the robustness of the network.

From the Lyapunov's indirect method, it follows that local stability of an equilibrium can be determined from the linearization of the system around the equilibrium. The system is locally unstable at the equilibrium if its Jacobian has some eigenvalues in the open right-half plane. Since oscillations can be traced to destabilization of an underlying equilibrium, linear stability analysis can be used to identify mechanisms causing the oscillations by analyzing the destabilizing mechanisms of the underlying equilibrium. Linear analysis, therefore, can also be used to determine the mechanistic basis of the robustness property due to the direct connection between robustness and functionality.

3.1 Improvement of robustness

The PKA holoenzyme is composed of two tightly bound regulatory subunits R and two catalytic subunits C. Different from the linear kinetics used in the original model [3], we use second-order kinetics as an approximation of the interactions of two molecules of internal cAMP on each of the two regulatory subunits. Thus, the rate of accumulation of the disassociated catalytic subunit is proportional to the square of the amount of internal cAMP. The catalytic subunits rebind with PKA independently, and hence their rate of removal is assumed to be proportional to the amount

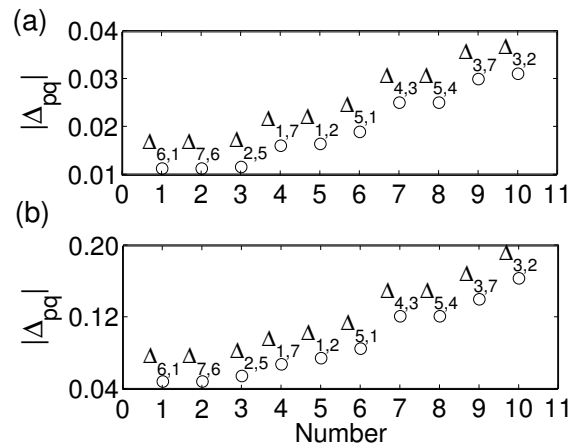


Figure 2: The magnitude of the relative perturbation $|\Delta_{pq}|$ required in element L_{pq} of the open-loop model, i.e. the effect of component q on component p in absence of feedback interactions, so stabilize the closed-loop system, where $x = [x_1, \dots, x_7]$ represents the concentrations of the seven proteins: $x_1=[ACA]$, $x_2=[PKA]$, $x_3=[ERK2]$, $x_4=[REG A]$, $x_5=[\text{internal cAMP}]$, $x_7=[\text{external cAMP}]$, and $x_7=[CAR1]$. (a) At the nominal parameter values. (b) At $k_2 = 1.5 \text{ Mol}^{-1}\text{min}^{-1}$ and $k_3 = 1.6 \text{ min}^{-1}$, all other parameters at their nominal values.

of catalytic subunit present. The modified form of the dynamics for PKA thus reads

$$d[\text{PKA}]/dt = k_3[\text{internal cAMP}]^2 - k_4[\text{PKA}]. \quad (9)$$

Note that the changes in the mathematical description capture the specific interactions between the internal cAMP and PKA. Equation (9) and other equations in Equations (8) except the second one define the structure of the modified model.

Still using the monotone control theory, we obtain that the modification of the structural characteristics does not change the number of equilibria. We still use the two sets of parameter values, because the modified model can produce similar oscillations at these values, and obtain $\omega_{\text{crit}} = 1.0545 \text{ rad/min}$ at the nominal parameter values. The perturbations required to stabilize the underlying equilibrium for the modified model at the same two sets of parameter values are shown in Fig.3. We can see that the relative perturbations required are largely increased due to the modification of the structural characteristics. A direct comparison of Fig.2 and Fig.3 indicates that the slight modification of the structural characteristics has a large impact on the robustness property. Even the smallest perturba-

tion required for the modified model is greater than the largest one for the original model.

For the original model, although the magnitude of the perturbations at the second set of parameter values is relatively larger than at the nominal ones, the order keeps unchanged. Although the order changes due to the parameter variations, the order of the most important pairwise interactions corresponding to $L_{2,5}$, $L_{6,1}$, $L_{7,6}$, $L_{5,1}$, and $L_{1,2}$, which involve the components ACA, PKA, REK2, internal cAMP, external cAMP, and CAR1, does not change despite the parameter variations. These components are instrumental to generate oscillations and relatively sensitive to perturbations. The large difference between the magnitude of the relative perturbations for the original and modified models further confirms that the structural characteristics is the major determining factor for robustness properties, although sometimes parameter variations can also have some contribution to them.

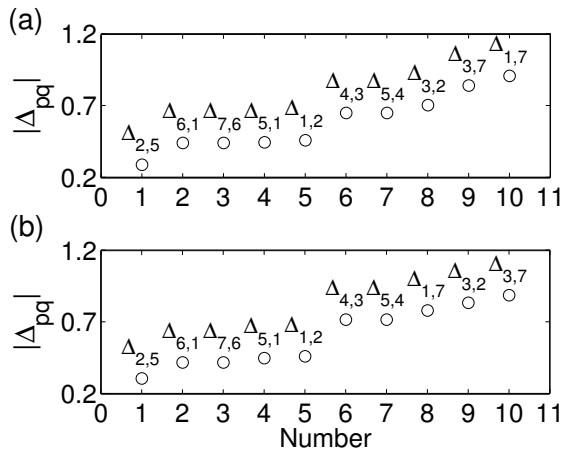


Figure 3: The magnitude of the relative perturbations $|\Delta_{pq}|$ required for the modified model. (a) At the nominal parameter values. (b) At $k_2 = 1.5 \text{ Mol}^{-1}\text{min}^{-1}$ and $k_3 = 1.6 \text{ min}^{-1}$, all other parameters at their nominal values.

The improvement of robustness properties by the modification of structural characteristics can be also supported by single parameter robustness analysis. The bifurcation points and degrees of robustness for the modified model are also shown in Table 1. We can see that all of them are largely increased due to the the modification of structural characteristics. it is clear that the single parameter intervals in which stable oscillations occur are largely increased.

Table 1: Comparisons of DOR for the two models

P	NV	original model			modified model		
		k_i^l	k_i^u	DOR	k_i^l	k_i^u	DOR
k_1	2.0	1.92	$k_{1,\max}$	0.04	0.64	28.22	0.68
k_2	0.9	0.72	1.60	0.20	0.08	20.18	0.91
k_3	2.5	$k_{3,\min}$	2.76	0.09	$k_{3,\min}$	38.96	0.94
k_4	1.5	$k_{4,\min}$	1.58	0.05	$k_{4,\min}$	4.64	0.68
k_5	0.6	0.54	$k_{5,\max}$	0.10	$k_{5,\min}$	$k_{5,\max}$	1.00
k_6	1.0	0.10	0.86	0.07	0.00	3.24	0.75
k_7	1.0	$k_{7,\min}$	1.10	0.09	$k_{7,\min}$	9.64	0.90
k_8	1.3	1.18	$k_{8,\max}$	0.09	0.34	$k_{8,\max}$	0.74
k_9	0.3	0.60	0.32	0.06	$k_{9,\min}$	1.18	0.75
k_{10}	0.8	0.00	0.88	0.09	$k_{10,\min}$	7.72	0.90
k_{11}	0.7	0.68	$k_{11,\max}$	0.03	$k_{11,\min}$	$k_{11,\max}$	1.00
k_{12}	4.9	2.64	5.18	0.05	1.52	13.38	0.63
k_{13}	23.0	22.22	$k_{13,\max}$	0.03	9.32	$k_{13,\max}$	0.59
k_{14}	4.5	2.58	4.78	0.06	1.46	12.42	0.64

Remarks. (1): $k_{i,\min} = 0$ and $k_{i,\max} = 90$, $i = 1, \dots, 14$. (2): Abbreviations: P, parameters; NV, nominal values. (3) $\text{DOR}_i = 1 - \max\{p_i^l/p_i, p_i/p_i^u\}$, stable limit cycles occur parameter range (p_i^l, p_i^u) .

4 Conclusion

A linear analysis approach was proposed to study the relative importance of components for robustness. A modification scheme which captures the specific interactions between the internal cAMP and PKA was developed to enhance robustness.

References

- [1] J. Stelling, U. Sauer, Z. Szallasi, F. J. Doyle III, J. Doyle, "Robustness of cellular functions," *Cell*, Vol. 118, pp. 675-685, 2004.
- [2] J. Stelling, E. D. Gilles, F. J. Doyle III, "Robustness properties of circadian clock architectures," *Proc. Natl. Acad. Sci.*, Vol. 101, pp. 13210-13215, 2004.
- [3] M. T. Laub, W. F. Loomis, "A molecular network that produces spontaneous oscillations in excitable cells of *Dictyostelium*," *Molecular Biology of the Cell*, Vol. 9, pp. 3521-3532, 1998.
- [4] L. Ma, P. A. Iglesias, "Quantifying robustness of biological network model," *BMC Bioinformatics*, Vol. 3, 38, pp. 1-13, 2002.

Phase Synchronization of Limit Cycle Oscillators in a Fluctuating Environment

Koh Hashimoto^{*1,*} and Kazuyuki Aihara^{*1,*2,*3}

^{*1} Aihara Complex Modelling Project, ERATO, JST
Room M203, Komaba Open Laboratory, The University of Tokyo,
4-6-1 Komaba, Meguro-ku, Tokyo 153-8505, JAPAN

^{*2} Institute of Industrial Science, The University of Tokyo
4-6-1 Komaba, Meguro-ku, Tokyo 153-8505, JAPAN

^{*3} Graduate School of Information Science and Technology, University of Tokyo
7-3-1 Hongo, Bunkyo-ku, Tokyo 113-8656, JAPAN

* koh@aihara.jst.go.jp

Abstract

We study the synchronization of limit cycle oscillators in a fluctuating environment. When environmental conditions fluctuate due to various kinds of noise, the dynamics of elements in the environment are inevitably perturbed and this may cause some synchronization between them. We analyze this phenomenon using models in which system parameters are subject to external noise and fluctuate within a certain range. Using the phase reduction method, we discuss the synchrony of limit cycle oscillators and show that the Lyapunov exponent is negative when amplitude of noise is sufficiently small, namely, synchronization of limit cycle oscillators in a fluctuating environment is stable.

1 introduction

Phase synchronization of limit cycle oscillators is a ubiquitous phenomenon, found in a variety of biological, chemical and physical fields, and has attracted much attention for several decades since Winfree's pioneering work [1] in 1960s. Populations of limit cycle oscillators that are subject to a strong periodic force may be entrained to oscillate at the same frequency as the periodic driving force. Alternatively, limit cycle oscillators interacting with each other directly or indirectly can synchronize precisely due to mutual interactions among oscillators. In either case, external or internal noise sources may disturb the phase synchronization of the oscillators because the main effect of noise on oscillation is phase diffusion. And therefore noise has long been considered to exert a negative influence on synchronization of limit cycle oscillators.

However noise can play also an active role in syn-

chronization of non-interacting oscillators. Challenging works by Teramae and Tanaka [2] and Goldobin and Pikovsky [3] have shown that oscillators under the influence of common weak additive noise can synchronize regardless of their intrinsic properties and the initial conditions. Since this noise-driven synchronization does not depend on the natural frequency of oscillators, it obviously differs from entrainment to an external periodic force. Using the phase reduction method, they proved in general that the maximal Lyapunov exponent of an orbit is always negative with little constraints when they are subject to weak Gaussian-white noise and this means the phase synchronization of the oscillators.

In their works, noise perturbs states of elements in the system directly and amplitude of fluctuations are identical for all elements. However, in some natural systems, the influence of noise on elements should be construed in a different way. In a variety of natural systems, environmental conditions such as temperature and pressure, which determine the dynamics of elements in the systems, are perturbed by various kinds of noise sources. In such systems, noise does not perturb system states directly but dynamics of systems. Under such an environment, dynamical elements, which exhibit oscillation, are perturbed indirectly by those kinds of noise sources and amplitude of fluctuations are depend on the states of elements. Thus we investigate behaviors of non-coupling limit cycle oscillators in a fluctuating environment and show another scenario to reach synchronization. In a mathematical model, we can treat this situation by adding noise on system parameters instead of system states. Using the phase reduction method which is applicable to an arbitrary oscillator [4, 5], we analytically calcu-

late the Lyapunov exponent of the synchronizing state and prove that the exponent is negative with some reasonable restrictions. With system parameters fluctuating within a structurally stable region under influence of external weak noise, phase synchronization of limit cycle oscillators can occur.

2 Model Description

Population of N identical nonlinear oscillators with fluctuating parameters is described as

$$\dot{\mathbf{x}}^{(i)} = \mathbf{F}(\boldsymbol{\mu}; \mathbf{x}^{(i)}) \quad (1)$$

$$\dot{\boldsymbol{\mu}} = \boldsymbol{\eta}(\boldsymbol{\mu}, t) = -\nabla U(\boldsymbol{\mu}) + \boldsymbol{\xi}(t) \quad (2)$$

where $i = 1, \dots, N$ and $\mathbf{x}^{(i)}$ is a state vector of the i -th element in this system. \mathbf{F} is common dynamics of the elements and $\boldsymbol{\mu}$ is a parameter vector of the function \mathbf{F} . $\boldsymbol{\mu}$ has its energy function U and is perturbed by noise $\boldsymbol{\xi}$. $\boldsymbol{\xi}$ is a vector of Gaussian white noise. The elements of the vector are normalized as $\langle \xi_k(t) \rangle = 0$ and $\langle \xi_k(s) \xi_l(t) \rangle = 2D_{kl} \delta(s - t)$, where $\mathbf{D} = (D_{kl})$ is a variance matrix of the noise components.

We assume that:

- (a) $\boldsymbol{\mu}$ is bounded within a bounded domain by the energy function U with probability 1,
- (b) \mathbf{F} has no bifurcation in the domain,
- (c) \mathbf{F} has a limit cycle attractor $C(\boldsymbol{\mu})$ in the domain,
- (d) \mathbf{F} is continuously differentiable by $\boldsymbol{\mu}$ and \mathbf{x} ,
- (e) D_{kl} is sufficiently small.

For these assumptions, we can assume that an attractor of \mathbf{F} is always a limit cycle, which varies continuously with changing of the parameter vector $\boldsymbol{\mu}$, and that a state of an element is always sufficiently close to the limit cycle $C(\boldsymbol{\mu})$.

3 Reduction To Phase Dynamics

Just as in the previous works, we use the phase reduction method to analyze this system. However, in this system, the limit cycle, on which the elements are, varies constantly according to fluctuations of the parameters. And this makes it difficult to define a phase for an element. Thus, we should make some preparations for phase reduction.

At first, with constant parameter vector $\boldsymbol{\mu}$, we can define a phase for a point on $C(\boldsymbol{\mu})$ following standard procedure [4, 5]. In this article, we normalize phase by the period of the limit cycle $C(\boldsymbol{\mu})$ so that its range is [0,1], where 0 and 1 represents the same

phase. We represent a phase θ for a point $\mathbf{x} \in C(\boldsymbol{\mu})$ with constant parameter vector $\boldsymbol{\mu}$ by $\theta = \Theta(\mathbf{x})$ and its reverse function by $\mathbf{x} = \mathbf{X}(\theta)$. If the parameter vector $\boldsymbol{\mu}$ is constant, phase dynamics are simply written as $\dot{\theta}^{(i)} = \omega(\boldsymbol{\mu})$. Note that the zero phase point $\mathbf{X}(0) (= \mathbf{X}(1))$ can be chosen arbitrarily.

Secondly, a phase for a point in neighborhood of $C(\boldsymbol{\mu})$ can be defined using an isochrone of a point on $C(\boldsymbol{\mu})$, i.e., identify a point $\mathbf{x}' \notin C(\boldsymbol{\mu})$ to a point $\mathbf{x} \in C(\boldsymbol{\mu})$ in a way that the orbits from the two points asymptotically coincide with the parameter vector fixed to $\boldsymbol{\mu}$ (see Fig.1), we represent this map from a point $\mathbf{x}' \notin C(\boldsymbol{\mu})$ to a point $\mathbf{x} \in C(\boldsymbol{\mu})$ by $\mathbf{x} = \Phi_{\Delta}(\mathbf{x}')$, and let the phase of \mathbf{x}' be the phase of $\mathbf{x} = \mathbf{X}(\theta)$ with constant parameter $\boldsymbol{\mu}$.

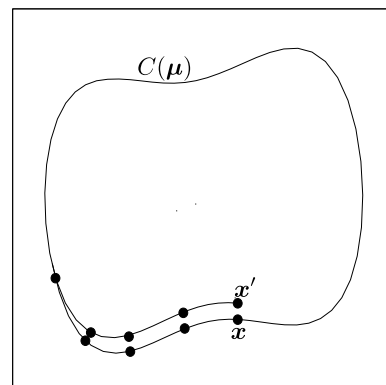


Figure 1: When the parameter vector is fixed to $\boldsymbol{\mu}$, a phase of a point \mathbf{x}' in a neighborhood of $C(\boldsymbol{\mu})$ can be defined by identifying its phase to a phase of a point \mathbf{x} which satisfies that the orbit from \mathbf{x} asymptotically coincide with the one from \mathbf{x}' .

When the parameter vector varies from $\boldsymbol{\mu}$ to $\boldsymbol{\mu} + \Delta\boldsymbol{\mu}$ at time t , a phase of an element varies according to changing of the attractor $C(\boldsymbol{\mu}) \rightarrow C(\boldsymbol{\mu} + \Delta\boldsymbol{\mu})$. A map from a phase with $\boldsymbol{\mu}$ to a phase with $\boldsymbol{\mu} + \Delta\boldsymbol{\mu}$ that describes phase slipping caused by varying the parameters at time t can be defined as

$$\theta' = \Phi_{\Delta}(\theta) = \Theta_{\boldsymbol{\mu} + \Delta\boldsymbol{\mu}}(\mathbf{X}_{\boldsymbol{\mu} + \Delta\boldsymbol{\mu}}(\theta)). \quad (3)$$

Fig.2 is an example of Φ_{Δ} . Note that, because the zero phase point can be chosen arbitrarily as mentioned above, we can always align the phase for $\boldsymbol{\mu} + \Delta\boldsymbol{\mu}$ to satisfy $\Phi_{\Delta}(0) = 0$ ($\Phi_{\Delta}(1) = 1$) as we see in Fig.2. With this alignment, a value $\Delta s = \Phi_{\Delta}(\theta) - \theta$ means a phase shift caused by changing of the parameter vector $\boldsymbol{\mu} \rightarrow \boldsymbol{\mu} + \Delta\boldsymbol{\mu}$.

Imagine that the variation of the parameter vector $\boldsymbol{\mu} \rightarrow \boldsymbol{\mu} + \Delta\boldsymbol{\mu}$ is occurred continuously during Δt

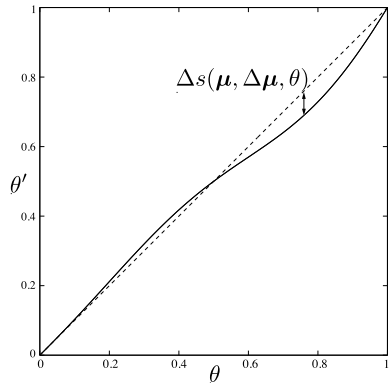


Figure 2: If the parameter vector varies from μ to $\mu + \Delta\mu$ at time t , a phase of each point is redefined by Eq.(3). Origin of phase for $\mu + \Delta\mu$ is aligned so that $\Phi_{\Delta}(0) = 0$ ($\Phi_{\Delta}(1) = 1$) is satisfied. $\Delta s = \theta' - \theta$ means a phase shift caused by changing of the parameters.

without moving an element x by F in order to extract only the effect of phase shift from dynamics. Now we should define a phase shift function not for μ and $\Delta\mu$ but for μ and $\dot{\mu}$. And this is derived by taking a limit of Δt to 0 as

$$\phi(\mu, \dot{\mu}, \theta) = \lim_{\Delta t \rightarrow 0} \frac{\Delta s(\mu, \Delta\mu, \theta)}{\Delta t}. \quad (4)$$

Using Eq.(4), we can reduce Eq.(1) as following:

$$\dot{\theta} = \omega(\mu) + \phi(\mu, \dot{\mu}, \theta) = \omega(\mu) + \phi(\mu, \eta, \theta) \quad (5)$$

where $\omega(\mu)$ is a rotating velocity term determined by μ and F , and $\phi(\mu, \eta, \theta)$ is a phase shift term determined by $\mu, \dot{\mu}$ and F . In fact, this reduction is valid only when $\omega(\mu)$ is sufficiently larger than $\phi(\mu, \eta, \theta)$ and the assumption (e) that we have in the previous section ensures this.

4 Phase Synchronization Induced By Fluctuating Environment

Suppose that the two phases have an infinitesimally small difference $\Delta\theta = \theta_2 - \theta_1$ where θ_i obeys Eq.(5). Then the Lyapunov exponent is defined as the long time average of $\frac{d}{dt} \log \Delta\theta$. By replacing the long time average with the ensemble average with respect to ξ , we can represent the Lyapunov exponent as

$$\lambda = \left\langle \frac{d}{dt} \log \Delta\theta \right\rangle.$$

With following additional assumptions:

- (f) ϕ is second-times continuously differentiable by θ ,
 - (g) ϕ is continuously differentiable by μ and η ,
- we can obtain the following formula:

$$\lambda = - \int_0^1 d\theta \int dP(\mu) \sum_{kl} D_{kl} \frac{\partial \phi'(\mu, \mathbf{0}, \theta)}{\partial \mu_k} \frac{\partial \phi'(\mu, \mathbf{0}, \theta)}{\partial \theta_l} \quad (6)$$

where ϕ' means $\phi' = \frac{\partial \phi}{\partial \theta}$ and $P(\mu)$ is a steady distribution function of μ .

We have the last assumption here:

- (i) $\phi(\mu, \eta, \theta) \neq 0$ for almost every (μ, η, θ) .

This assumption means that fluctuation of parameters almost always causes phase shift. Since this assumption ensures $\frac{\partial \phi(\mu, \eta, \theta)}{\partial \mu_k} \neq 0$ for almost every (μ, η, θ) and the variance matrix D_{kl} is always positive definite, λ is negative. This means that the phase synchronization induced by perturbation of system parameters is stable in an arbitrary oscillator system with the assumptions we have.

5 Simulation

In this section, we demonstrate that phase synchronization of limit cycle oscillators can occur when noise strength is sufficiently small by numerical simulation using van der Pol oscillator and measure the Lyapunov exponents numerically.

Dynamics of van der Pol oscillator is described as

$$\ddot{x} = (1 - x^2)\dot{x} - x - bx^3$$

where a and b are system parameters. Within a certain region of (a, b) , this system has a structurally stable limit cycle attractor. This differential equation can be rewritten in following form.

$$\begin{aligned} \dot{x}_1 &= x_2 \\ \dot{x}_2 &= (1 - x_1^2)x_2 - x_1 - bx_1^3 \end{aligned} \quad (7)$$

In order to implement a fluctuating environment, we regard all coefficients in the terms in these differential equations as parameters (μ_k) and attach some additional terms $(\mu_1, \mu_3x_2^2, \mu_8x_1^2)$ as follows:

$$\begin{aligned} \dot{x}_1 &= \mu_1 + \mu_2x_2 + \mu_3x_2^2 \\ \dot{x}_2 &= \mu_4(\mu_5 - \mu_6x_1^2)x_2 - \mu_7x_1 - \mu_8x_1^2 - \mu_9x_1^3 \end{aligned}$$

And we adopt a ‘‘U-shape’’ function $U(\mu) = \sum_k U_k(\mu)$ with

$$U_k(\mu) = \begin{cases} 0 & (|\mu_k(t) - \mu_k(0)| < 0.05) \\ 2.5(\mu_k(t) - \mu_k(0))^4 & (\text{otherwise}) \end{cases}$$

for the energy function of μ . Initially, the parameters are set as: $\mu_1 = \mu_3 = \mu_8 = 0, \mu_2 = \mu_5 = \mu_6 = \mu_7 = 1, \mu_4 = \dots, \mu_9 = b$ so that dynamics at the initial time is equivalent to the original equations Eq.(7). The simulation results are shown in Fig.3. At the initial time, the elements in the system are not synchronized at all. However, after long transient, they reach synchronization almost completely.

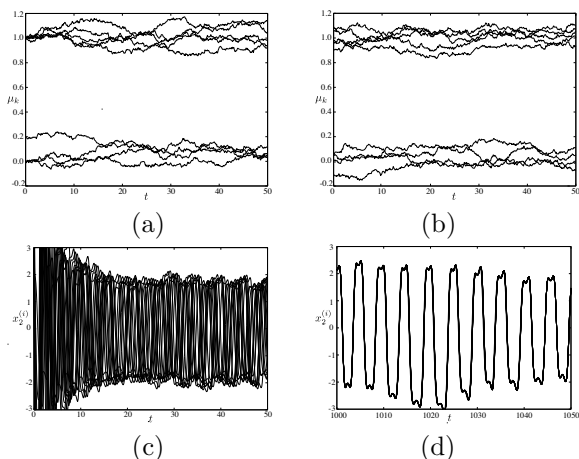


Figure 3: (a) and (b) show temporal evolution of parameters μ_1, \dots, μ_9 for $[0, 50]$ and $[1000, 1050]$ respectively. They fluctuate all along the time by noise although bounded by U . Temporal evolution of x_2 of 16 orbits which start from points randomly chosen is plotted in (c) and (d). The variance matrix of the noise is set as $D_{kk} = 0.01, D_{kl} = 0(k \neq l)$. The parameters and b are $\dots = 0.2$ and $b = 1$.

Fig.4 shows the Lyapunov exponents that are numerically calculated for various noise strengths. When noise strength is smaller than a certain value, λ decreases linearly with the increase of the noise strength as indicated by Eq.(6). Meanwhile, when noise strength is strong, λ increases with the increase of the noise strength and too strong noise eventually destabilize the synchronization of oscillators and the Lyapunov exponent is no longer negative.

6 Summary

We analyzed phase synchronization induced by perturbation of system parameters by reducing the dynamics to phase dynamics. And we proved that when noise that perturb parameters are sufficiently weak and perturbation of parameters almost always causes phase shift, the Lyapunov exponent becomes negative.

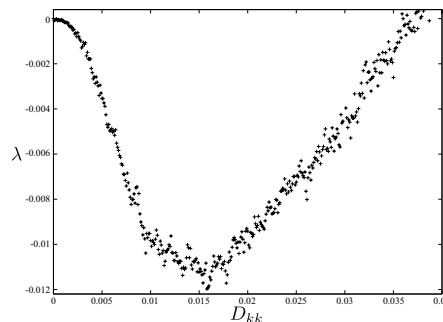


Figure 4: The horizontal axis is D_{kk} ($D_{kl} = 0$) and the vertical axis is the Lyapunov exponent λ . Each point is obtained by taking an average of 25 trials.

This result is achieved regardless of details of dynamics and initial distributions of elements.

In this article, we only treated the case in which parameters fluctuate continuously under influence of noise. Nagai and Nakao [6] discussed phase synchronization induced by a fluctuating input which jumps between two values at random moments and proved that when intervals of the jumps are sufficiently large and phase shift map is monotonic, the Lyapunov exponent of the system becomes negative. Using their ideas, our model is also applicable to the case in which parameters are perturbed discontinuously by noise. Studies for this case will be reported in the future.

References

- [1] A. T. Winfree, "Biological Rhythms and the Behavior of Populations of Coupled Oscillators", *J. Theor. Biol.*, Vol. 16 pp. 15-42, 1967.
- [2] J. Teramae, D. Tanaka, "Robustness of the Noise-Induced Phase Synchronization in a General Class of Limit Cycle Oscillators", *Phys. Rev. Lett.*, Vol. 93, pp. 204103, 2004.
- [3] D. S. Goldobin, A. S. Pikovsky, "Synchronization of self-sustained oscillators by common white noise", *Physica A*, Vol. 351, pp. 126-132, 2005.
- [4] Y. Kuramoto, *Chemical Oscillation, Waves, and Turbulence*, Springer-Verlag, Tokyo, 1984.
- [5] A. T. Winfree, *The Geometry of Biological Time*, Springer-Verlag, New York, 2001.
- [6] K. Nagai, H. Nakao, "Synchrony of neural oscillators induced by random telegraphic currents", *Phys. Rev. E*, Vol. 71, pp. 036217, 2005.

Mathematical Modeling of Frogs' Calling Behaviors and its Possible Application to Artificial Life and Robotics

Ikkyu Aihara¹, Hiroyuki Kitahata², Kenichi Yoshikawa², and Kazuyuki Aihara^{3,4}

¹Department of Applied Analysis and Complex Dynamical Systems,
Graduate School of Informatics, Kyoto University, Kyoto 606-8501, Japan

²Department of Physics, Graduate School of Science,
Kyoto University, Kyoto 606-8502, Japan

³Institute of Industrial Science, The University of Tokyo, Tokyo,

⁴ERATO Aihara Complexity Modelling Project, JST

Abstract

This paper theoretically describes calling behaviors of Japanese tree frogs *Hyla japonica* with a simple model of phase oscillators. Experimental analysis showed that while isolated single frogs called nearly periodically, a pair of interacting frogs called alternately. We model these phenomena as a system of coupled phase oscillators, where each isolated oscillator behaves periodically as a model of the calling of a single frog and two coupled oscillators shows anti-phase synchronization, reflecting the alternately calling behavior of two interacting frogs. Then, we extend the model to a system of three oscillators corresponding to three interacting frogs and analyse the dynamics. We also discuss a biological meaning of the calling behaviors and its possible application to Artificial Life and Robotics.

1 Introduction

Nonlinear dynamics like synchronization has been both experimentally and theoretically analyzed in many biological systems [1–7] with respect to possible functions. In this paper, we consider calling behaviors of frogs from the viewpoint of nonlinear dynamics. There have been some experimental studies on synchronization of calls of frogs. Loftus-Hills studied the synchronization in calling behaviors of frogs *Pseudacris streckeri* [8], where tape-recorded calls were used to evoke response of frogs. Lemon and Struger studied acoustic entrainment to randomly generated calls in frogs *Hyla crucifer* [9]. Here, we theoretically study spontaneous calling behaviors [10, 11] of Japanese tree frogs *Hyla japonica* shown in Fig. 1 and discuss a possible application to artificial life and robotics.



Figure 1: Japanese tree frog *Hyla japonica*.

2 Experimental Results

Male Japanese tree frogs *Hyla japonica* which were collected from breeding assemblages in paddy fields in Kyoto, Japan were used for the experiment. Spontaneous mating calls were recorded and analyzed.

Figure 2 shows an example of the waveforms of the calls recorded from (a) a single frog calling alone and (b) two interacting frogs calling together. While a single frog called nearly periodically as shown in Fig. 2(a), two frogs called alternately as shown in Fig. 2(b). The detail of the experiment was reported elsewhere [10, 11].

3 Mathematical Modeling of Frogs' calling behaviors

3.1 Phase oscillator model

We model the calling behaviors of frogs as phase oscillators. The calling of a single frog is regarded

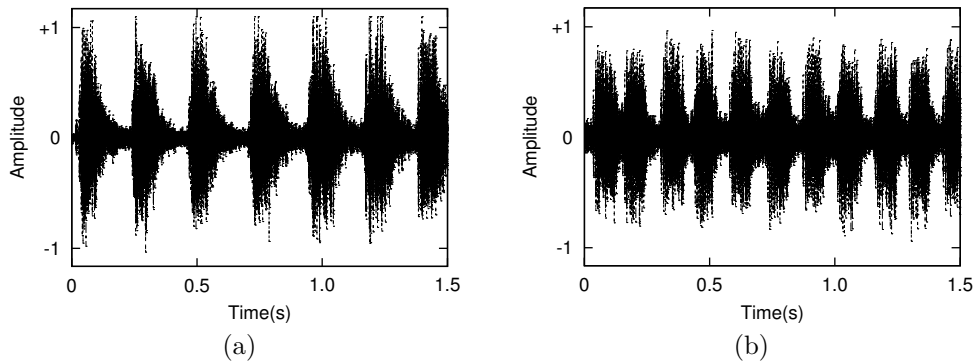


Figure 2: The waveforms of the calls of (a) a single frog and (b) two interacting frogs. A single frog called nearly periodically, and a pair of frogs called alternately.

as a periodic phase oscillator, and the calling of two interacting frogs as two coupled phase oscillators.

First, we consider the situation that each frog calls alone. The calling behavior of respective frogs is described as a phase oscillator with the phase variable θ with $\theta \in \mathbb{S}^1 = (\mathbb{R} \text{ mod } 2\pi) = [-\pi, \pi] / \{-\pi \equiv \pi\}$ [6] as follows:

$$\frac{d\theta}{dt} = \omega, \quad (1)$$

where ω is an intrinsic natural frequency. It is assumed that $\theta = 0$ correspond to each call. This model represents the property that single frog calls periodically.

Then, we model the situation that two frogs call together through interaction. The system is described as two coupled phase oscillators with two phase variables θ_A and θ_B as follows (see also [10, 11]):

$$\frac{d\theta_A}{dt} = \omega + g_{AB}(\theta_B - \theta_A), \quad (2)$$

$$\frac{d\theta_B}{dt} = \omega + g_{BA}(\theta_A - \theta_B), \quad (3)$$

where ω is the intrinsic frequency that is assumed to be the same between two frogs, and g_{AB} and g_{BA} are 2π -periodic functions that represent the mutual interaction. To examine whether two oscillators synchronize, we analyze the dynamics of the phase difference $\phi \equiv \theta_A - \theta_B$ with $\phi \in \mathbb{S}^1$. Subtracting Eq.(3) from Eq. (2), we obtain the following equation on ϕ :

$$\frac{d\phi}{dt} = g_{AB}(-\phi) - g_{BA}(\phi). \quad (4)$$

Here, we assume g_{AB} and g_{BA} to be a sinusoidal function for the sake of simplicity, according to the

former studies [2, 3], then, Eq.(4) is calculated as follows:

$$\frac{d\phi}{dt} = 2K \sin \phi, \quad (5)$$

where K is a positive coupling coefficient as schematically shown in Fig. 3(a). The stable equilibrium point ϕ^* which satisfies $\left. \frac{d\phi}{dt} \right|_{\phi=\phi^*} = 0$ and $\left. \left(\frac{d}{d\phi} \left(\frac{d\phi}{dt} \right) \right) \right|_{\phi=\phi^*} < 0$ is given by $\phi^* = \pi$. This stable equilibrium point reproduces the experimental result qualitatively, namely these two oscillators synchronize in anti-phase.

3.2 Extension to a system of three frogs

Next, we extend this model to a system of three coupled oscillators as follows:

$$\frac{d\theta_A}{dt} = \omega - K_1 \sin(\theta_B - \theta_A) - K_3 \sin(\theta_C - \theta_A), \quad (6)$$

$$\frac{d\theta_B}{dt} = \omega - K_1 \sin(\theta_A - \theta_B) - K_2 \sin(\theta_C - \theta_B), \quad (7)$$

$$\frac{d\theta_C}{dt} = \omega - K_3 \sin(\theta_A - \theta_C) - K_2 \sin(\theta_B - \theta_C), \quad (8)$$

where K_i 's ($i = 1, 2, 3$) are symmetrical coupling coefficients between two frogs as schematically shown in Fig. 3(b). Here, for the simplicity, we assume that $\omega = 1.0$ and $K_1 = K_3 = 1.0$. In order to examine dynamical properties in this system, we define the phase differences $\phi_1 \equiv \theta_A - \theta_B$ and $\phi_2 \equiv \theta_B - \theta_C$. Then, we change the value of K_2 from 0 to 1.0 as the bifurcation parameter and numerically examine the stable equilibrium points ϕ_1^* and ϕ_2^* .

The bifurcation diagram is shown in Fig. 4. In the region $0 < K_2 < 0.5$, oscillators A and B synchronize in anti-phase and oscillators B and C synchronize

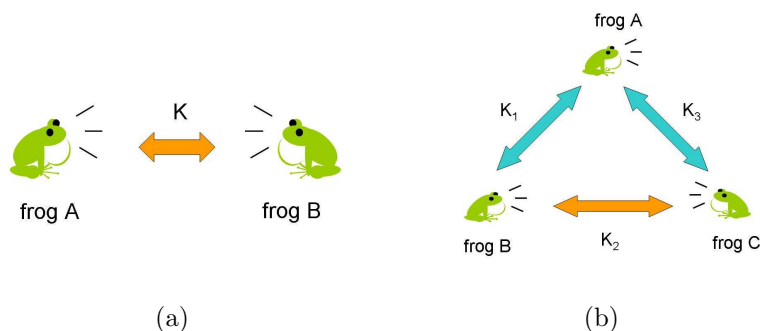


Figure 3: Schematic diagrams in modeling of a system of (a) two frogs and (b) three frogs.

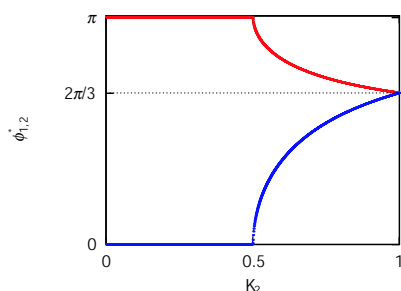


Figure 4: The bifurcation diagram in the system of three coupled oscillators, where the red line represents the phase difference $\phi_{1,2}^*$, and the blue line ϕ_2^* .

in-phase. With increasing the value of K_2 in the region $0.5 < K_2 < 1.0$, on the other hand, the property of synchronization in this system gradually changes, and finally three oscillators synchronize in tri-phase at $K_2 = 1.0$.

4 A Possible Application to Artificial Life and Robotics

We discuss a biological meaning of the calling behaviors and a possible application to artificial life and robotics. Generally speaking, it is said that the main purpose of calling by male frogs is to attract females and tell their own positions to other males [12].

If one male frog mates with one female in a one-to-one manner, it is important for two males to make females distinguish them each other. In fact, many kinds of frogs are known to mate in such a one-to-one manner [13], including the mating in Japanese tree frogs [14]. Thus, it is probable that two male Japanese tree frogs call alternately to be distinguished by a fe-

male. On the other hand, male Japanese tree frogs are known to inhabit with a low density in breeding assemblages [12]. Then, we suppose that the anti-phase synchronization of two male frogs can play a role of telling their own positions to other males, resulting in sparse distribution. In that meaning, anti-phase synchronization would be applicable for multiple artificial agents and robots to prevent collisions each other in some real or abstract spaces.

In the actual system of male frogs, coupling coefficients would depend on the distance between male frogs, because they interact by calling and hearing. It was numerically confirmed by varying the coupling coefficient K_2 that the system of three coupled oscillators shows more complicated properties than that of two frogs does similarly to coupled chemical oscillators [15]. Therefore, the calling behaviors in a system of many frogs should be much more complicated. For the purpose of understanding such a system, it is important to extend the model to a system of many oscillators. A simple extension of our model to a larger system composed of N frogs is given as follows:

$$\frac{d\theta_i}{dt} = \omega_i - \frac{1}{N-1} \sum_{j=1}^N K_{ij} \sin(\theta_j - \theta_i), \quad (9)$$

where for the i th frog ($i = 1, 2, \dots, N$), θ_i is the phase variable, ω_i is an intrinsic natural frequency, and K_{ij} represents interaction with the j th frog. It is an important future problem to analyze such a system of many frogs both experimentally and theoretically.

Moreover, such a study would provide useful mechanisms of controlling distributed systems composed of many artificial agents and robots. For example, in-phase synchronization and anti-phase one may represent cooperation and competition between agents and robots. Moreover, frogs that call in phase together can be interpreted as a cooperative cluster, which may

produce emergence of a kind of communication.

5 Conclusion

We have theoretically modeled the calling behaviors of Japanese tree frogs *Hyla japonica* as a system of coupled phase oscillators where two coupled phase oscillators synchronize in anti-phase like the real calling behaviors of two frogs. Biologically speaking, the anti-phase synchronization would be important for a frog to tell his own position to the other frog. In this meaning, anti-phase synchronization would be applicable to prevent collisions of multiple agents and robots. Then, we have extended the model to a system of three coupled oscillators and confirmed that such a system shows more complicated properties than that of two oscillators does. For the purpose of application to a system of many agents and robots, it would be an important future problem to analyze a system of many frogs both experimentally and theoretically. It is also our future problem to modify our models more realistic, for example, by considering phase shift parameters and distribution of intrinsic frequencies of frogs.

Acknowledgements

This study was partially supported by a Grant-in-aid for the Scientific Research (No.18GS0421) on “Construction of functional de novo cell” and the 21st Century COE Program of “Center of Excellence for Research and Education on Complex Functional Mechanical Systems” at Kyoto University from the Ministry of Education, Culture, Sports, Science and Technology of Japan. We would like to thank K. Tsumoto, K. Sogo, Y. Kuramoto, I. Tsuda, H. Daido, H. Kori, and A. Nagano for their stimulating discussions and valuable comments.

References

- [1] A.T. Winfree, “Biological Rhythms and the Behavior of Population of Coupled Oscillators,” *J. Theoret. Biol.*, **16**, 15 (1967).
- [2] Y. Kuramoto, “Chemical Oscillations, Waves, and Turbulence,” *Springer-Verlag*, Berlin (1984).
- [3] S.H. Strogatz, “Nonlinear and Chaos,” *Perseus Publishing*, Cambridge, (1994).
- [4] A. Pikovsky, M. Rosenblum, and J. Kurth, “Synchronization: A Universal Concept in Nonlinear Sciences,” *Cambridge University Press*, Cambridge (2001).
- [5] G.B. Ermentrout and J. Rinzel, “Beyond a Pacemaker’s Entrainment Limit: Phase Walkthrough,” *Am. J. Physiol.*, **246**, 102 (1984).
- [6] F.C. Hoppensteadt and E.M. Izhikevich, “Weakly Connected Neural Networks,” *Springer-Verlag*, N.Y., 73 (1997).
- [7] R.E. Mirollo and S.H. Strogatz, “Synchronization of Pulse-Coupled Biological Oscillators,” *Siam J. Appl. Math.*, **50**(6), 1645 (1990).
- [8] J.J. Loftus-Hills, “Analysis of an Acoustic Pacemaker in Strecker’s Chorus Frog, *Pseudacris streckeri* (Anura:Hyliidae),” *J. Comp. Physiol.*, **90**, 75 (1974).
- [9] R.E. Lemon and J. Struger, “Acoustic Entrainment to Randomly Generated Calls by the Frog, *Hyla crucifer*,” *J. Acoust. Soc. Am.*, **67**(6), 2090 (1980).
- [10] I. Aihara, H. Kitahata, S. Horai, K. Aihara, and K. Yoshikawa, “Synchronization Experimentally Observed in Calling Behaviors of Japanese Rain Frogs (*Hyla-japonica*),” *Proc. of 2006 Inter. Symp. on Nonlinear Theory and its Applications*, 767 (2006).
- [11] I. Aihara, S. Horai, H. Kitahata, K. Yoshikawa, and K. Aihara, “Dynamical Calling Behaviors Experimentally Observed in Japanese Tree Frogs (*Hyla japonica*),” submitted to *IEICE. Trans. on Fundamentals*.
- [12] M. Matsui, “Natural History of the Amphibia,” *University of Tokyo Press*, Tokyo (1996) in Japanese.
- [13] H. Iwasawa and M. Kuramoto, “Systematic Zoology,” *Nakayama-Shoten.*, **9**, 364 (1996) in Japanese.
- [14] T. Matsubashi and F. Okuyama, “Frogs and Toads of Japan +Salamander,” *Yama-Kei Publishers*, 53 (2002) in Japanese.
- [15] M. Yoshimoto, K. Yoshikawa and Y. Mori, “Coupling among Three Chemical Oscillators: Synchronization, Phase-Death and Frustration,” *Phys. Rev. E*, **47**, 864 (1993).

Local cause of coherence in Boolean networks

Chikoo Oosawa^{1,*}, Kazuhiro Takemoto², Shogo Matsumoto³, Michael A. Savageau⁴

¹Department of Bioscience and Bioinformatics, Kyushu Institute of Technology
Iizuka, Fukuoka, 820-8502, Japan

²Bioinformatics Center, Institute for Chemical Research, Kyoto University,
Gokasho, Uji, Kyoto, 611-0011, Japan

³Graduate School of Computer Science and Systems Engineering,
Kyushu Institute of Technology, Iizuka, Fukuoka, 820-8502, Japan

⁴Department of Biomedical Engineering, College of Engineering,
University of California, Davis, 95616, U.S.A.

Nov. 15 2006

Abstract

We have performed numerical study on random Boolean networks with power-law rank outdegree distributions to find local structural cause for emergence of high or low degree of coherence in binary state variables of the entire networks. The degree of randomness and coherence of the binary sequence, are measured by entropy and mutual information, depend on local structure that consists of a node with highly connected, called hub, and its upstream nodes, and types of Boolean functions for the nodes. With the larger number of output connections from a hub, the effects of Boolean function on the hub are more prominent. The local structures that give larger entropy tends to give rise to larger mutual information. On the basis of both numerical results and structural condition we derived time-independent transmission characteristic function of state variables for local structures. We show good relations between the numerical and the analytical results, reveals that dynamical properties from the whole networks can be inferred from the differences in the local structures.

keywords : Boolean networks; power-law; coherence; mutual information; entropy; transcriptional regulatory networks

1 Introduction

Biological system is consist of complex adaptive systems, for example neural and transcriptional regulatory system whose structure often can be abstracted to graph or network. In general the systems perform their functions correctly when certain appropriate communications among nodes are established because such systems need to add, delete own nodes or change a strength of connectivity to optimally adapt to exogenous inputs. Transcriptional regulatory network is one of the complex adaptive systems where the node mainly corresponds to transcriptional unit, and responds to environmental changes to survive and proliferate. The Boolean network[1] is one of the discrete dynamical models for the transcriptional regulatory network and exhibits binary sequences of state variables that represents expression pattern of transcriptional regulatory network. Since the state variables in Boolean network are sensitive to inputs from other nodes via directed edges, and affect on other nodes vice versa, a quality of communication is characterized as a size of mutual information. The mutual information indicates degree of coherence, synchronization, amount of information content in state variables or potential for computational capability of the network[2].

In this study, we show local structural cause for emergence of coherence in Boolean network. Since we embed power-law rank output connectivity distributions in Boolean networks whose input connectivity $K_{in}=2$, the model networks have some hubs that integrate many output connections. Because the hubs synchronously transmit their state to downstream nodes,

*Corresponding author: chikoo@bio.kyutech.ac.jp

† Also at :Bioalgorithm Project, Faculty of Computer Science and Systems Engineering, Kyushu Institute of Technology

the downstream nodes are affected by single or multiple hubs simultaneously. The structural condition seems to automatically provide global coherence in state variables, however the structural aspects give only possible influence from hubs, in fact we need to consider a type of Boolean function at hubs and their upstream nodes. We show both effect of Boolean functions and the number of output connections on size of entropy and mutual information. In addition some results can be explained by transmission characteristic functions that can be derived from numerical results and local structures.

Please notice that Table 2-3, Fig. 4-6 can be found in Sec.6, Appendix.

2 Model

Dynamics of the Boolean networks [1, 5] is determined by the

$$X_i(t + 1) = B_i[\mathbf{X}(t)] \quad (i = 1, 2, \dots, N), \quad (1)$$

where $\mathbf{X}(t)$ is the binary state, either 0 or 1, of node i at time t , $B_i(\cdot)$ is Boolean functions [See Table 1] used to simultaneously update the state of node i , and $\mathbf{X}(t)$ is a binary vector that gives the states of the N nodes in the network. After assigning initial states $\mathbf{X}(0)$ to the nodes, the successive states of the nodes are update by input states and its Boolean function. The dynamical behavior of these networks is represented by the time series of binary states. The time course follows a transient phase from an initial state until a periodic pattern, called an attractor, is eventually established.

Table 1: 4 of 16 Boolean functions with indegree $K_{in}=2$. In this paper we used only 1,2,4, and 8 are used because of feasibility and biological meaning of the functions[3, 4].

Inputs		Output			
0	0	0	0	0	1
0	1	0	0	1	0
1	0	0	1	0	0
1	1	1	0	0	0
Decimal	index	1	2	4	8

3 Numerical condition

We constructed 10^4 Boolean networks in each power-law rank distribution [See Fig. 1] with fixed network size. 2×10^3 initial states are applied to each network. Four different Boolean functions [See Table 1] are used in almost equalprobability [See Table 2]. Please note that all generated networks use the same amount of resources since the size of network is fixed, 256 nodes and 512 directed edges.

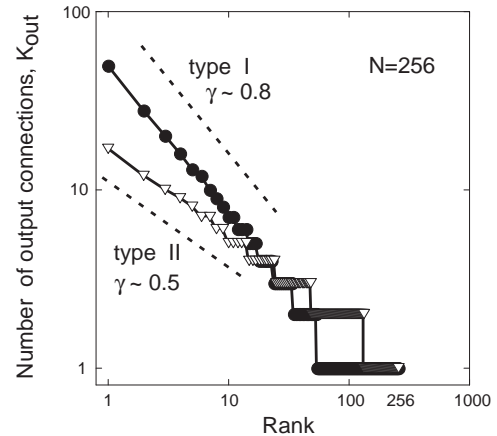


Figure 1: Power-law rank connectivity distributions in the model. Power exponent, for type I and II is about 0.8 and 0.5, respectively, where $K_{out}(rank) \sim rank^{-\gamma}$. We performed only single network size that is 256 in the paper.

We have measured entropy(randomness) and mutual information(coherence) of state variables to characterize the dynamics of Boolean networks[2, 5] [See Fig. 2].

4 Results

4.1 Numerical results

In total we obtained 70622 and 177098 attractors from type I and type II distribution, respectively. Size of entropy and mutual information are measured from the attractors. Together with the network structural condition we show the dependence of distribution's rank on entropy and mutual information in Fig. 3.

The dependence of Boolean function on entropy and mutual information are prominent in higher ranked-hubs on both style of output distributions. The Boolean functions that give larger entropy tends to

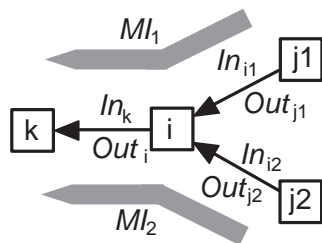


Figure 2: Flow of state variables from upstreams to downstream. Since input connectivity for all nodes equals to $2(=K_{in})$, there are two pathways for mutual information in each node. Input sequence In_{i1} for the node i is the same as the output sequence of an upstream node Out_{j1} and that the output sequence of Out_i for the node i is the same as the input sequence of a downstream node In_k . When node i has multiple output connections, they have the same binary sequence because state variables in networks is subject to Eq. (1).

give rise to larger mutual information. These results suggest that the collective(global) coherence in state variables of networks may be due to style of upstream(local) conditions, including connections among upstream nodes and assignment of Boolean functions.

4.2 Transmission characteristic function

In order to elucidate dependence of rank on randomness and coherence we first focus on local structure around hubs as shown in Fig. 4. Because each node has two inputs by definition, outputs from hubs are subject to 4 inputs and 3 Boolean functions. From numerical results we obtain statistical properties to determine the relationships between 4 inputs. Fig. 5 shows two statistical properties, 1) Range of input probability is almost limited from 0.0 to 0.5. 2) Degree of correlations between inputs are very low in the range of input probability.

The two statistical properties allow us to take a following analytical approach. We define the output property as a function of input probability, called transmission characteristic function [See fig. 6]. For the simplicity we assume that 4 inputs($p_1 \sim p_4$ in Fig. 4) receive binary sequence with the same probability[6]. The transmission characteristic functions can be described as at most 4th order polynomial and obtained with combination of Boolean functions[Table 3] on the local structure[Fig. 4].

When we ignore the specificity of Boolean functions in upstream nodes in a local structure, we can get av-

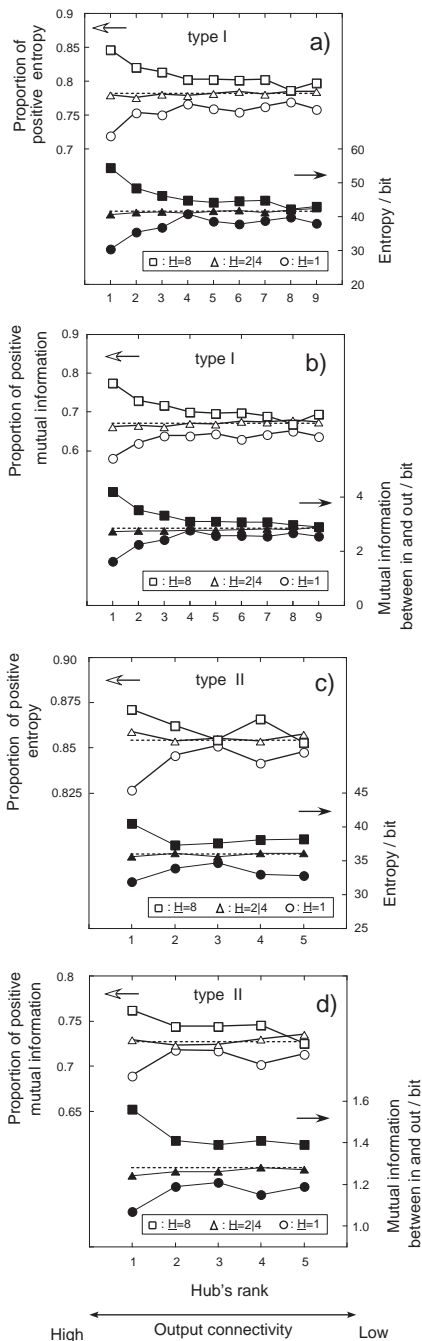


Figure 3: Dependence of proportion of positive entropy a) and c) and mutual information b) and d) on type I and II distribution in Fig. 1. Three different symbols denote different styles of Boolean function on hubs, square:type 8, triangle:type 2 or 4, and circle:type 1 [Table 1]. The vertical bar "|" in the legend denotes one of the either Boolean function on both side of the bar. \underline{H} denotes hub's Boolean function. Dashed horizontal lines indicate the proportions from all realizations [See Table 2].

verage transmission characteristic function, means that considering only hub's Boolean function, also be obtained from weighted average of the individual transmission characteristic functions. The average transmission characteristic function can be written in :

$$P_{out}^{(1)}(p) = \frac{1}{16} < P_{out}^{(2|4)}(p) = \frac{3}{16} < P_{out}^{(8)}(p) = \frac{9}{16} , \quad (2)$$

where an asterisk "*" denotes one of any Boolean functions in Table 1. The triple asterisks in the braces represent that the average transmission characteristic function from over all 18 [See Table 3 and Fig. 6] Boolean function combinations. The order of their entropies is described as:

$$H P_{out}^{(1)}(p) < H P_{out}^{(2|4)}(p) < H P_{out}^{(8)}(p) . \quad (3)$$

The same order of entropy size is already shown in Fig. 3 a) and c). In particular the tendency can be seen in higher-ranked hubs in both style I and II, demonstrating that transmission characteristic functions are useful tool to infer network dynamics.

5 Summary and Discussion

After making comparison average transmission characteristic functions and numerical results we found that good relations between them, suggesting that local structure at hubs effects on global dynamical properties in networks. These results may as well provide a blueprint of design principle for an artificial gene regulatory network and help to elucidate the role of hubs in dynamical system.

In recent years many large-scale complex networks such as social, metabolic and neural networks have been paid great attention from many fields. It has been revealed that the biological networks contain prominent local structures, called motif, subgraph or clique that consist of small number of nodes and edges [7, 8]. In the article we demonstrate just one of local structures in simplified dynamical model for transcriptional regulatory networks. In fact size of biological complex adaptive systems varies in very long time due to many various events. Since clique models[9, 10] seem to promising approach for explaining growing

complex networks , an exchange of information among a local structures may contribute to the mechanism for maintenance and growing of complex networks.

Acknowledgements

This work was partially supported by Grant-in-Aid No.18740237 from MEXT(JAPAN) and US Department of Defence Grant N00014-97-1-0364 from the Office of Naval Research.

References

- [1] Kauffman SA (1992), *The Origins of Order*, Oxford University Press, New York.
- [2] Langton CG (1990), Computation at the edge of chaos: phase transition and emergent computation. *Physica D*, 42:pp.12-37.
- [3] Raeymakers L (2002), Dynamics of Boolean Networks Controlled by Biologically Meaningful Functions. *J. Theor. Biol.*, 218:pp.331-341.
- [4] Setty Y, Mayo AE, Surette MG, Alon U (2003), Detailed map of a cis-regulatory input function. *Proc. Natl. Acad. Sci.*, 100:pp.7702-7707.
- [5] Oosawa C, Savageau MA (2002), Effects of alternative connectivity on behavior of randomly constructed Boolean networks. *Physica D*, 170:pp.143-161.
- [6] Oosawa C, Takemoto K (2005), Transmission characteristics of 3-node Boolean subnetworks with random binary sequence inputs. *Technical Report of IEICE*, NLP2005-73, NC2005-65(2005-11):pp.13-18.
- [7] Milo R, Shen-Orr S, Itzkovitz D, Kashtan N, Chklovskii D, Alon U (2002), Network Motifs: Simple Building Blocks of Complex Networks, *Science*, 298: pp.824-827.
- [8] Balázsi G, Barabási A-L, Oltvai ZN (2005), Topological units of environmental signal processing in the transcriptional regulatory network of *Escherichia coli*. *Proc. Natl. Acad. Sci.*, 102:pp.7841-7846.
- [9] Takemoto K, Oosawa C (2005), Evolving networks by merging cliques. *Physical Review E*, 72:046116-1~6.

- [10] Takemoto K, Oosawa C, Modeling for evolving biological networks with scale-free connectivity, hierarchical modularity, and disassortativity. *Mathematical Biosciences*, to be appeared.

6 Appendix

Table 2: The numbers of realizations out of 10^4 networks are indicated. Different 4 Boolean functions [See Table 1] at hubs are used equalprobably. "H" in the table denotes hubs Boolean function [See Fig.4].

Hub's rank	H=1	H=2	H=4	H=8
1	2496	2508	2540	2456
2	2564	2517	2459	2460
3	2463	2452	2564	2521
4	2575	2471	2518	2436
5	2454	2556	2529	2461
6	2516	2467	2476	2541
7	2525	2609	2486	2380
8	2502	2494	2491	2513
9	2529	2519	2445	2507

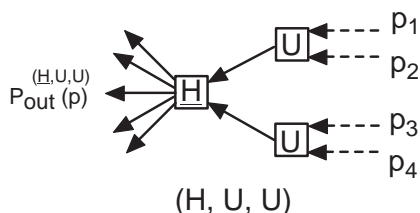


Figure 4: Typical local structure around hub: Squares and directed edges (arrows) correspond to nodes and connections that are pathways of binary sequence, respectively. Dashed arrows indicate inputs from upstreams. H and U in the squares correspond to Boolean function on hub and its upstream nodes. Each node has one of Boolean functions, 1,2,4, and 8 as shown in Table 1. A set of three characters in a brace at the bottom of each figure denotes a set of Boolean function combination on nodes in the local structure. $P_{out}^{(H, U, U)}(p)$ represents transmission characteristic function of input probability p [See Fig.6] and the combination of Boolean functions [See Table 3].

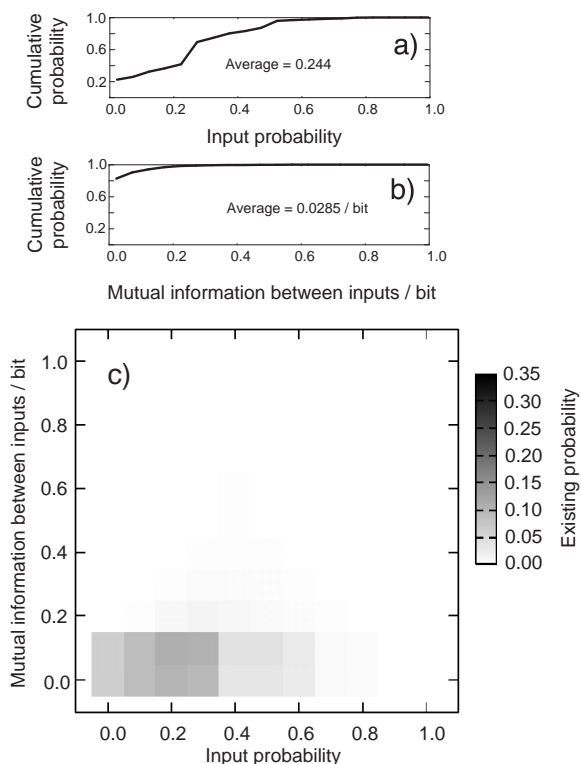


Figure 5: Statistical properties of inputs to local structure in Fig.4: a) Cumulative distribution of input probability ($p_1 \sim p_4$). b) Cumulative mutual information between 4 inputs. c) Correlation between input probability a) and mutual information b). These distribution are obtained from 1st-ranked hubs on the basis of 70622 attractors from 10^4 networks with style I distribution and 2×10^7 initial states.

Table 3: The combination number of Boolean functions on the local structure shown in Fig. 4. $64(= 4^3)$ combinations can be reduced into 18 because of symmetry in local structure [See Fig.4] and in-out relations in Boolean functions [See Table1]. There are two major columns and each major column consist 2 subcolumns. The left subcolumns contain all possible combinations of Boolean functions in the case that hub has one of Boolean funtions. The right subcolumns indicate integrated combinations. The combinations with dagger can be consolidated into the combinations with prime. A set of numbers at both ends of arrow at the bottom line in each major column denotes the original and reduced number of combinations. When Boolean function of 8 is located in hub, the similar procedure as shown in left major column can be taken.

(1,U,U)		(2,U,U) or (4,U,U)	
(1,1,1)	(1,1,1)	(2,1,1) [†]	(4,1,1) [†]
(1,1,2) [†]	(1,1,2 4)′	(2,1,2)	(4,1,2)
(1,1,4) [†]	(1,1,8)	(2,1,4)	(4,1,4)
(1,1,8)	(1,2 4,2 4)	(2,1,8)	(4,1,8)
(1,2,1) [†]	(1,2 4,8)	(2,2,1)	(4,2,1)
(1,2,2)	(1,8,8)	(2,2,2)	(4,2,2)
(1,2,4)		(2,2,4)	(4,2,4)
(1,2,8)		(2,2,8)	(4,2,8)
(1,4,1) [†]		(2,4,1)	(4,4,1)
(1,4,2)		(2,4,2)	(4,4,2)
(1,4,4)		(2,4,4)	(4,4,4)
(1,4,8)		(2,4,8)	(4,4,8)
(1,8,1)		(2,8,1)	(4,8,1)
(1,8,2)		(2,8,2)	(4,8,2)
(1,8,4)		(2,8,4)	(4,8,4)
(1,8,8)		(2,8,8)	(4,8,8)
$16 \implies 6$		$32 \implies 6$	

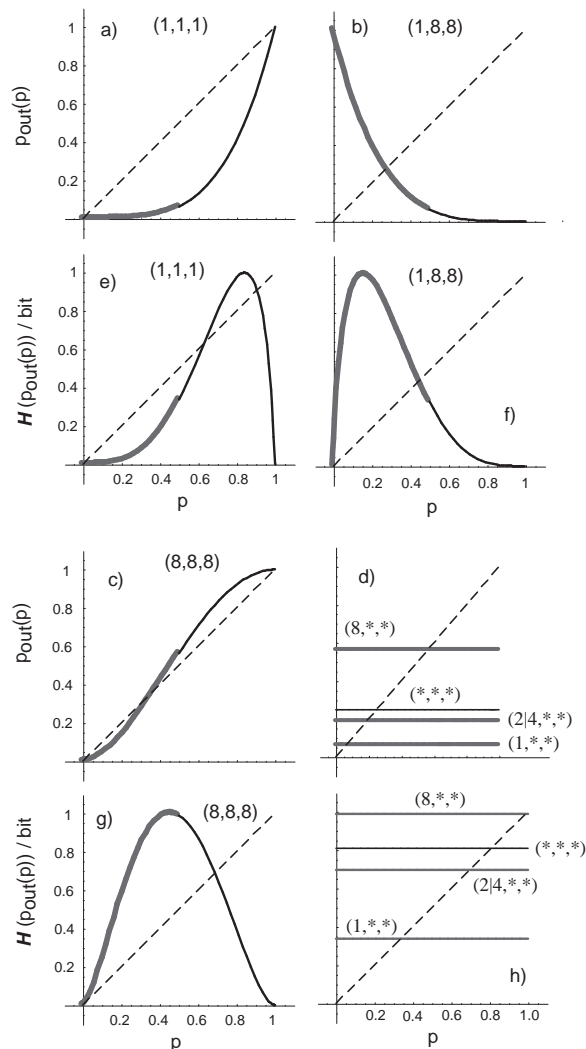


Figure 6: Example of transmission characteristic functions a)–d) and their output entropy e)–h). Each set of 3 characters in a brace shows a Boolean function combinations [See Table 1 and Fig.4]. A vertical bar "′" denotes one of the either Boolean function on both sides of the bar. An asterisk "*" denotes one of any Boolean functions in Table 1. The triple asterisks, (*,*,*) means that all 18 possible combinations. a) Transmission characteristic function for (1,1,1), $P_{out}^{(1\ 1\ 1)}(p) = p^4$. Other transmission characteristic functions are also described as at most 4th order polynomial. c) Entropy of the transmission characteristic function in a). d) Average transmission characteristic functions as indicated in braces. h) Entropy of the transmission characteristic function in d). As a guide for a)–d), thick region of these curves correspond to $p \in [0, 0.5]$. Dashed lines show $P_{out}(p) = p$ or $H(P_{out}(p)) = p$ relationship for e)–h).

Continuous Modeling of Biomolecular Systems Based on Process Calculus

Yang Pu, Xiaoju Dong
BASICS Lab

Department of Computer Science and Engineering
Shanghai Jiaotong University, Shanghai 200240, China

Abstract

Process calculus is a kind of models for concurrent systems. Recent researches in Systems Biology have applied process calculus as the computational model to capture the dynamic behaviors of biomolecular systems. In this paper, we integrate a continuous framework with stochastic π -calculus to model the biomolecular systems. To verify the correctness of this approach, a modified stochastic Pi machine (SPiM) which was previously developed to simulate the systems described by stochastic π -calculus is proposed. From the consistency of the data obtained from the simulation of biomolecular system and the experimental data, it shows that the continuous framework introduced into Stochastic π -calculus is effective in simulating biomolecular systems.

1 introduction

Concurrency theory [1], especially the process calculus [2], has been used as a suitable tool to study Systems Biology [3, 4]. The main characters of biomolecular systems are interaction and the concurrence. The systems modeled by process calculus is the same as biomolecular systems to some extent. The main idea of using process calculus is to model molecular processes as interaction/communicating systems. That is to see biological components as concurrent processes and their interaction as process communication or process movement.

Using stochastic π -calculus [5] to formal model biological systems was first introduced by C.Priami [6]. The stochastic π -calculus enables its application to a wide variety of biomolecular systems in which quantitative aspects are key. In stochastic π -calculus, *kinetic constant* in biological reactions are abstracted as channels with base rates, and the actual reaction rate is calculated as an actual channel rate from the base rate and the number of processes offering communications. The selection of a time step and actual communication is based on these actual rates and follows Gillespie algorithm. Using the Gillespie algorithm [7], we can obtain the probability distribution for rules and times.

The simulation of biomolecular processes which modeled by stochastic π -calculus is executed based on the Gillespie algorithm that calculates explicitly which reaction occurs next and how long it takes. But there are two problems in this simulation method. First, as we know, the biomolecular system is a concurrent system, all the reactions react independently. They are not sequential but parallel. But by using Gillespie algorithm, all the reactions occur one by one. It cannot describe the real biological system. Second, the most important benefit of process calculus is used to exhibit the concurrence of systems. By using Gillespie algorithm in the simulation, we cannot see the benefit of process calculus. Gillespie algorithm cannot simulate the systems described by process calculus accurately.

To address the above problems, we integrate continuous framework to simulate the biomolecular systems. This is inspired by the fact that, in vivo, biomolecular reactions evolve in a continuous way following a rate that depends on the concentration of the reactants. Therefore, we should deal with a non-integer number of processes in process calculus. Furthermore, we need to develop approximations in order to simulate the continuous reactions. Here we suppose time step $t_{i+1} - t_i$ is small enough to assume that the reaction rate and the concentrations of reactants remain constant. To address the concurrent problem, we use *Law of Mass Action* which states that the rate of a reaction is proportional to the product of the concentration of the reactants. And in every time step, the communications between processes are applied in parallel way according to the rate. In order to validate the efficiency of this continuous framework, we modified the stochastic Pi machine (SPiM) [8] to integrate the continuous framework, so called continuous SPiM. The original SPiM is a system used to simulate stochastic π -calculus based on Gillespie Algorithm. From the consistency of the data obtained from the simulation of Circadian Clock [9] by the continuous SPiM and the experimental data, it shows that the integration of this continuous framework with stochastic π -calculus is effective in modeling biomolecular systems.

The paper is organized as follows. The stochastic π -calculus used in this paper is introduced in the next section.

In section 3 the continuous simulation is described. We apply our approach to model Circadian Clock in Section 4. Finally, conclusions are given in section 5.

2 The Stochastic π -Calculus

In a biomolecular system, the molecules are abstracted as computational processes and the network of interacting molecules are abstracted as a mobile concurrent system in stochastic π -calculus. A complicated chemical process can always be decomposed into a set of many elementary bimolecular reactions, such as $(A + B \rightarrow \dots)$ or unimolecular reactions, such as $(A \rightarrow \dots)$. Two unimolecular reactions can be regarded as one bimolecular reactions, such as $(A + A \rightarrow \dots)$. Trimolecular reactions such as $(A + B + C \rightarrow \dots)$ are very rare. Therefore, the biochemical reactions between reactants can be abstracted as a communication between two channels with the same name. This kind of systems is composed by a community of co-existing computational process that communicate with each other and that change their interconnection structure at execution time. The stochastic π -calculus used in this paper is introduced in [8]. Here, we briefly introduce the syntax and the reduction of the stochastic π -calculus.

Definition 2.1 *The syntax of stochastic π -calculus is as follows*

$$\begin{aligned} P, Q &::= \nu x P && \text{Restriction} \\ &| P|Q && \text{Parallel} \\ \Sigma &&& \text{Summation} \\ \pi.P &&& \text{Replication} \end{aligned}$$

where:

$$\begin{aligned} \Sigma &::= 0 && \text{Null} \\ &| \pi.P + \Sigma && \text{Action} \\ \pi &::= x\langle n \rangle && \text{Output} \\ &| x(m) && \text{Input, } x \neq m \end{aligned}$$

Definition 2.2 *The reduction of stochastic π -calculus is as follows, each channel x is associated with a corresponding reaction rate given by $rate(x)$:*

$$\begin{aligned} Q \equiv P \xrightarrow{r} P' \equiv Q' &\Rightarrow Q \xrightarrow{r} Q' \\ P \xrightarrow{r} P' &\Rightarrow \nu x P \xrightarrow{r} \nu x P' \\ P \xrightarrow{r} P' &\Rightarrow P|Q \xrightarrow{r} P'|Q \\ x\langle n \rangle.P + \Sigma | x(m).Q + \Sigma' &\xrightarrow{rate(x)} P|Q_{\{n/m\}} \end{aligned}$$

According to Definition 2.1, the basic component is a summation Σ , which is a choice between zero or more output $x\langle n \rangle$ or input $x(m)$ actions that the component can perform. $P|Q$ is parallel composition, and a given component P can contain a restricted reaction channel $\nu x P$. Replication $! \pi.P$ represents multiple copies of a given component $\pi.P$. π is either output or input actions. Two components in a biological system can react by performing complementary input and output actions on a common reaction channel. As show in Definition 2.2, summation containing an output $x\langle n \rangle.P$ can react with a parallel summation containing an input $x(m).Q$. The reaction occur with $rate(x)$, after which the name n is bound to m in process Q and processes P and $Q_{\{n/m\}}$ execute in parallel.

3 Continuous Simulation

A configuration of the biomolecular system described by stochastic π -calculus is a matrix of $\mathcal{M}_{n \times 2}(R^+)$ where $m_{i,1}$ represents the concentrations of interacting molecules which is described by input channel $x_i(m)$, while $m_{i,2}$ represents the concentrations of output channel $x_i\langle n \rangle$. The elements in the matrix are real numbers. An instantaneous configuration $E(t) = (m_{i,j}(t))_{1 \leq i \leq n, j=1,2}$ with each instant $t \in R^+$.

To model the reactions we use the *Law of Mass Action* which states that the rate of a reaction is proportional to the product of the concentrations of the reactants. That is, if we have a reaction of the form $A + B \rightarrow \dots$, then the rate of this reaction is $r = k \times |A| \times |B|$, for unimolecular reactions, such as $(A \rightarrow \dots)$, the rate is $r = \frac{1}{4} \times k \times |A|^2$, where k is called *kinetic constant*. In the stochastic π -calculus, we are using the rate of channel to represents *kinetic constant*, and the concentrations of the reactants can be obtained from the configuration $\mathcal{M}_{n \times 2}(R^+)$. In order to simulate evolution of biomolecular systems in computer, we need to develop approximations. Here for simplicity we use the rectangle rule; that is, we suppose $t_{l+1} - t_l = p$ is small enough to assume that the rate and the configuration remain constant. With this assumption we can approximate the effect of a communication during an interval of time of length p by $p \times r$. The implementation of continuous simulation based on stochastic π -calculus executes five steps as follows:

1. Initialize the configuration of the biomolecular system described by stochastic π -calculus
2. Initialize the absolute simulation time $t = 0$
3. Select out the communications which can be applied.
4. According to the rates of the communications, configuration and the small enough time interval p , calculate

the quantities of reactants and productions changed in each communication, and update the configuration.

- Set the time $t = t + p$, and go to step 3.

4 Simulation of Circadian Clock

Circadian Clock phenomena are found in a large variety of organisms from cyanobacteria to mammals, and have probably evolved more than once. Recent works [9] suggest that the biomolecular mechanism of clocks shares common features over a wide range of organisms. The interaction consists of two interleaved feedback loops. In the positive loop, the activator element enhances its own expression. In the negative loop, the activator element enhances the expression of the negative element, which in turn sequesters the activator, as shown in Figure 1. The biological process involves two genes, an activator, A , and a repressor R , they are transcribed into mRNA and subsequently translated into protein. The activator A binds to the A and R promoters, and increases their basal transcription rates. Thus, A acts as the positive element in the system, whereas R acts as the negative element by sequestering the activator. This simple model is not intended to abstract any particular biomolecular system, but to capture the basic design principles shared by many systems, and believed to produce its basic functionality.

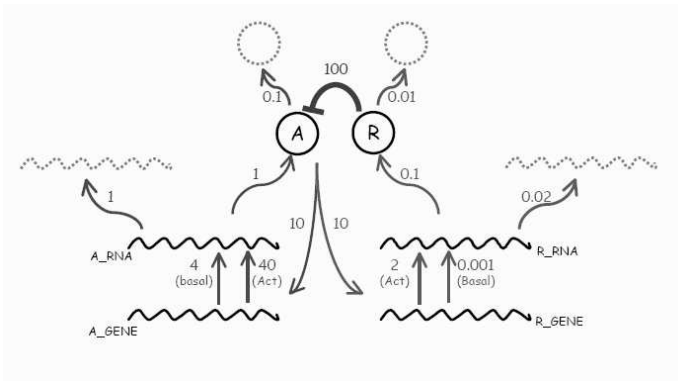


Figure 1: The network for a core Circadian Clock

We start by building a stochastic π -calculus abstraction of the Circadian Clock process. The reactions in the process are abstracted as communications on channels, and reaction rates as channel rates.

A-related process

```

DNA_A ::= tA().(DNA_A|RNA_A)|pA(u).DNA_A2(u)
DNA_A2(u) ::= tA'().(RNA_A|DNA_A2(u))|u().DNA_A
RNA_A ::= trA().(RNA_A|A)|drA()
A ::= pA(uA).uA().A|pR(uR).uR().A
      |vnu(bind(u).A_Bound(u))|dA()
A_Bound(u) ::= dA().ReleaseR|u().A
ReleaseR ::= u()
    
```

R-related process

```

DNA_R ::= tR().(DNA_R|RNA_R)|pR(u).DNA_R2(u)
DNA_R2(u) ::= tR'().(RNA_R|DNA_R2(u))|u().DNA_R
RNA_R ::= trR().(RNA_R|R)|drR()
R ::= bind(u).R_Bound(u)|dR()
R_Bound(u) ::= dR().ReleaseA|u().R
ReleaseA ::= u()
    
```

In order to simulate our model abstracted by stochastic π -calculus we chosen the following basal channel rate: $rate(tA) = 4$, $rate(tR) = 0.001$, $rate(trA) = 1$, $rate(trR) = 0.1$, $rate(drA) = 1$, $rate(drR) = 0.02$, $rate(bind) = 100$, $rate(pA) = 10$, $rate(pR) = 10$, $rate(tA') = 40$, $rate(tR') = 2$, $rate(dA) = 0.1$, $rate(dR) = 0.01$. And we take the stochastic π -calculus abstraction of Circadian Clock as the input of continuous SPiM. The numbers of channels and processes obtained from continuous SPiM were plotted as a function of time and illustrate the oscillatory behavior.

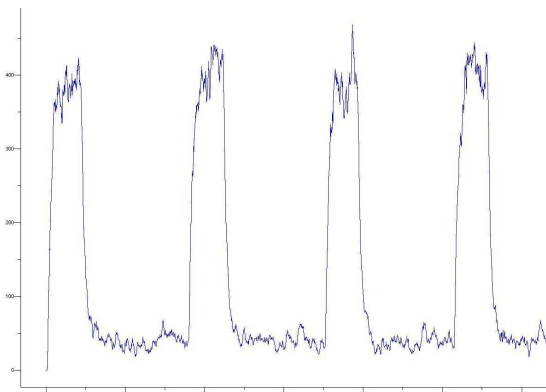


Figure2: The oscillatory behavior of $A_Protein$

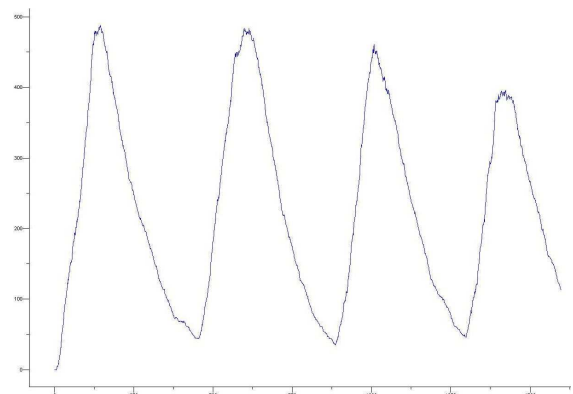


Figure3: The oscillatory behavior of $R_Protein$

From Figure2, we can see the oscillatory behavior of A protein, and Figure3 exhibits us the oscillatory behavior of R protein. At first, the *kinetic constant* of A promoter's transcription is larger than R promoter's. With the accumulation of A proteins, it will activate A and R promoters, increase their transcription rates. It will result in more A and R proteins, meanwhile, because $R - A$ binding has the largest *kinetic constant*, more R proteins will bind to A proteins to repress the binding between A protein and A , R promoters, and decrease the number of A proteins. Small number of A proteins may lead to low transcription rates of A and R promoters because there will be few activated A and R promoters. The small *kinetic constant* of R promoters then leads to oscillations, which can be described as successive transitions between induced and repressed states.

As shown in Figure2 and Figure3, the results of the model yield the required oscillatory behaviors. In this we have reproduced the known result of [9], providing support for the correctness of the continuous abstraction framework based on stochastic π -calculus.

5 Conclusion

In this paper we integrate a continuous framework with the stochastic π -calculus. The numbers of channels and processes in the stochastic π -calculus are regarded as the real number to show continuous quantities of the substances. The communications in the stochastic π -calculus occurred in a parallel way in each time unit. This approach has been used to formal model the Circadian Clock. In order to validate our approach, we modified the Stochastic Pi Machine (SPiM) to approximate the continuous simulation of biomolecular systems. From the continuous simulation of Circadian Clock, it can show us that the continuous framework of stochastic π -calculus is a reliable approach for simulating quantitative aspect of biomolecular systems.

Acknowledgements

This work is supported by The National Distinguished Young Scientist Fund of NNSFC (60225012), BDCC (03DZ14025), The National Nature Science Foundation of China (60473006), MSRA, and The BoShiDian Research Fund (20010248033).

References

[1] Milner R., Communication and Concurrency. *New York: Prentice Hall*, 1989.

- [2] Milner R., Parrow J., Walker D., A Calculus of Mobile Processes. *Information and Computation*, 1992, 100(1): 1-40(Part I), 41-77 (Part II).
- [3] Ciobanu G., Ciobotariu V., Tanasa B., A pi-Calculus Model of the Na Pump. *Genome Informatics*, 2002, 13: 469-471.
- [4] A. Regev, W. Silverman, and E. Shapiro. Representation and simulation of biochemical processes using the pi-calculus process algebra. *In Pacific Symposium on Biocomputing*, volume 6, pages 459-470, Singapore, 2001. World Scientific Press.
- [5] C.Priami, Stochastic π -Calculus, *The Computer Journal*, 38:578-589, 1995.
- [6] Priami C., Regev A., Shapiro E., Silverman W., Application of a Stochastic Name-passing Calculus to Representation and Simulation of Molecular Processes. *Information Processing Letters*, 2001, 80(1): 25-31.
- [7] D.T.Gillespie. Exact stochastic simulation of coupled chemical reactions. *Journal of Physical Chemistry*, 81(25):2340-2361, 1977.
- [8] Andrew Phillips and Luca Cardelli. A correct abstract machine for the stochastic pi-calculus. *In Bioconcur04. ENTCS*, August 2004.
- [9] N.Barkai, Leibler S. Circadian clocks limited by noise. *Nature*, 403(6767):267-268, 2000.

Modeling Chaos Neural Networks for Classification of EEG Signals

T. Q. D. Khoa, *IEEE member*
Department of Electrical Engineering
Nagaoka University of Technology
Nagaoka, Niigata 940-2188, JAPAN
khoa@ieee.org

M. Nakagawa, *IEICE member*
Department of Electrical Engineering
Nagaoka University of Technology
Nagaoka, Niigata 940-2188, JAPAN
masanaka@vos.nagaokaut.ac.jp

Abstract

This work proposes essential improvements based on Chaos theory to enhance adaptive ability of Feed-forward Neural Network (FFNN). A novel structure of a single neuron is proposed with a feedback connection and a periodic active function. The proposal model obtained the best results on least mean square error as well as dramatic decrease of training time. Results are also illustrated and compared through XOR problem, 7-point problem and application for classification of EEG data.

Keywords: Chaos Neural Networks, backpropagation, electroencephalogram (EEG)

1 Introduction

Artificial Intelligent (A.I) Computation always reaches higher ability to be adaptive with changes of realistic environments. Neural Networks is one of the most interesting areas of A.I. of which the well-known characteristic is the learning ability. However the training of networks is being argued to improve it. Freeman (1991) decided that chaos may be the chief property that makes the brain different from an artificial-intelligence machine. K. Aihara [2] said that a usual neuron model is a simple threshold element transforming a weighted summation of the inputs into the output through a non-linear. However from the viewpoint of neurophysiology, there is a firm criticism that real neurons are far more complicated than simple threshold elements.

One of the problems associated with the backpropagation algorithm is its parameterization. Beforehand, the value of a number of parameters needs to be specified. It has been found that very small variations in these values can make the difference between good, average or bad performance. This also implies that one can never be sure to have found the optimal solution.

Furthermore, the backpropagation algorithm can converge in a local minimum or oscillate between two (or more) different solutions shown in Fig. 1.

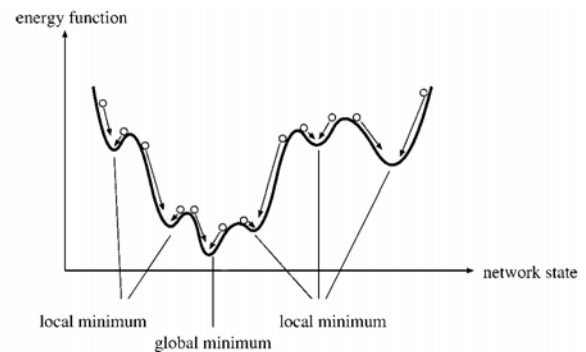


Fig. 1. Error surface of FFNN.

The rule for weight-modifications shows some similar structures with a well known chaotic equation, so a possible explanation for the hyper-sensitive and sometimes problematic behavior of the backpropagation algorithm may be found in chaos theory shown by K. Bertels and *et. al* in[5].

This work follows the approach considering neural networks as a Chaos dynamic system which has been proposed by K. Aihara [2], and M. Nakagawa [1]. Many of applications were examined in [1] such a chaotic memory retrieval model, image processing, telecommunication signal synchronous.

EEG signals classification have been carried out with many different methodologies as Autocorrelation in [7], Neural Networks in [8], Fuzzy logic in [9]. This work proposes a novel neural network with some improvements based on Chaos theory to speed up the learning time and to escape the local optimum. The present learning model is properly characterized in terms of periodic chaos

neuron to involve a chaotic dynamics as well as external or autonomous control of the periodicity. The obtained results are examined by XOR problem, 7-point problem and application for classification of Electroencephalogram (EEG) signals. In addition illustrations are compared to some conventional neural networks.

2 Electroencephalogram (EEG)

Electroencephalogram (EEG) signals provide one possible means of human-computer interaction, which requires very little in terms of physical abilities. By training the computer to recognize and classify EEG signals, users could manipulate the machine by merely thinking about what they want it to do within a limited set of choices.

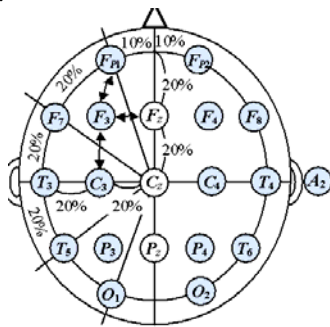


Fig. 2. EEG data acquisition.

The reliable operation of brain-computer interfaces (BCIs) based on spontaneous electroencephalogram (EEG) signals requires accurate classification of multi-channel EEG. The design of EEG representations and classifiers for BCI are open research questions whose difficulty stems from the need to extract complex spatial and temporal patterns from noisy multidimensional time series obtained from EEG measurements.

3 Models

3.1 The conventional Neuron

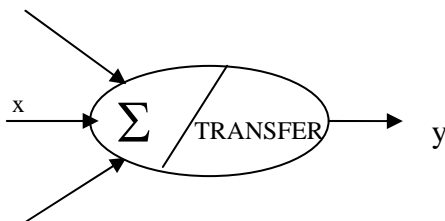


Fig. 3. Conventional NN model.

The standard FFNN is usually 3 layers following: Input layer: $X = \{x_1, x_2, \dots, x_N\}$, hidden layer and output layer. All neurons are connected by weights and their output s value are calculated through net value and transfer function.

Net value:

$$net = \sum_{i=1}^N w_{ij} \cdot x_i + \theta \quad (1)$$

Transfer function is usually used a saturation function such sigmoid function.

3.2 A Periodic Chaos Neural Network Model

This work mentions a novel FFNN with periodic active functions and a feedback factor, k , from the output to the inputs of a neuron. It is shown that a neuron with an ability of dynamic memory feedback is better the conventional model with such a monotonous mapping as a sigmoid function. The utility of periodic chaos is used to escape from local minimum values and speed up the learning time. In addition the global minimum value could be reached efficiently since chaos region in bifurcation diagram.

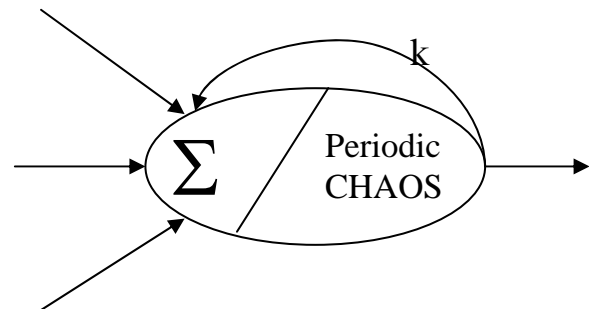


Fig. 4. Chaos Neural Network Model.

Modified net value:

$$net(t+1) = k \cdot net(t) + (\sum w \cdot x + \theta) \quad (2)$$

Periodic chaos transfer function:

$$Y(t) = \sin\left(\frac{net(t)}{\tau(t)}\right) \quad (3)$$

Where:

$$\tau(t+1) = \tau(t) + k \cdot e \cdot \tau(t) \cdot (1 - \tau(t)) \quad (4)$$

The use of chaos functional help networks independent on the initial conditions and can not trap in the saturation of transfer function. In addition, this speeds up the training time of network and can avoid the local minimum.

4 Results

The proposed model is compared to the conventional model within the same conditionals such as number of neurons, number of layers, initial values of weights, 10^{-3} in tolerance square error, and upper limit of learning epochs as 10^4 times.

4.1 XOR problem

Conventional Model: with 2 hidden neurons, logsig transfer function, learning rate=0.8. The conventional model result is Epochs =10.000, Tolerated error = 0.0619 shown in Fig. 5.

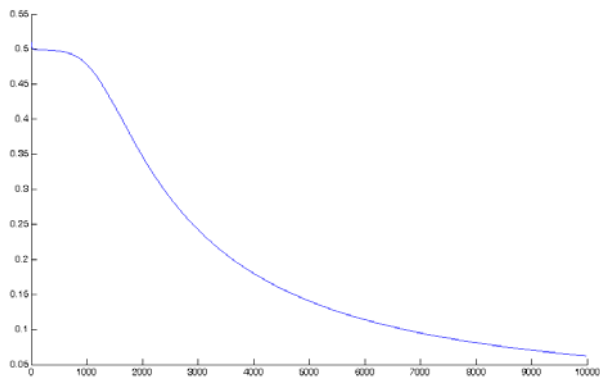


Fig. 5. Tolerance square error of conventional FFNN.

Result of Chaos Neural Networks Model is shown in Fig. 6. with Epochs=48, Tolerated error = 0.001

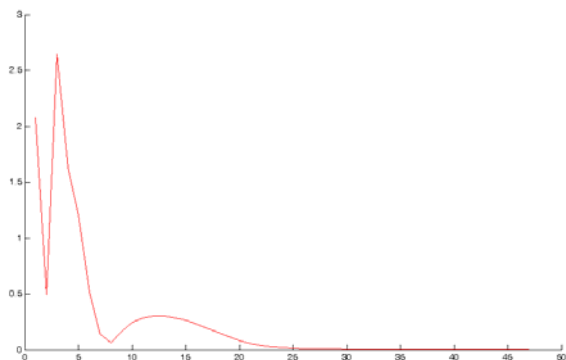


Fig. 6. Tolerance square error of Chaos Neural Networks.

4.2 7-point problem

This problem has 7 patterns with 2 inputs and 1 output. $X_1=[0\ 0\ 1\ 1\ 0.5\ 0.25\ 0.75]$, $X_2=[0\ 1\ 0\ 1\ 0.5\ 0.75\ 0.25]$, and $Y=[0\ 1\ 1\ 0\ 1\ 0\ 0]$. Conventional Model: 7 hidden neurons, logsig transfer function, learning rate=0.8. The conventional model result is Epochs =10.000, Tolerated error = 0.3884 shown in Fig. 7.

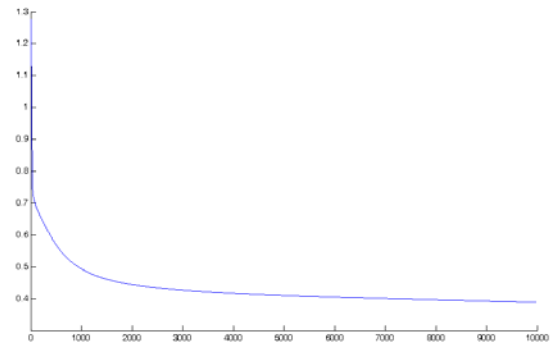


Fig. 7. Tolerance square error of conventional FFNN.

Result of Chaos Neural Networks Model is shown in Fig. 8. with Epochs=22, Tolerated error = 0.001

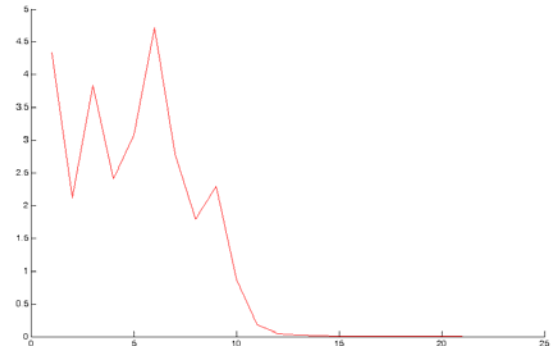


Fig. 8. Tolerance square error of Chaos Neural Networks.

4.3 Classification of 2 EEG types

Two types of EEG data used to examine are foot moving and left-hand moving. These data are obtained from 16 channels and they are equivalent to 16 inputs of Neural Models. Result of Chaos Neural Network classifies EEG data into 2 groups with Tolerance error=0.1. The output errors are shown in Fig. 11.

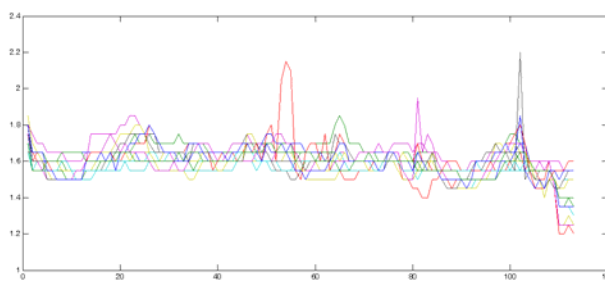


Fig. 9. EEG data of foot moving.

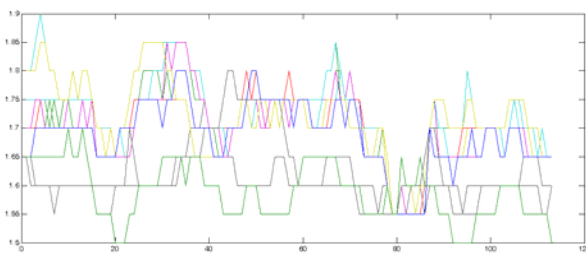


Fig. 10. EEG data of left-hand moving.

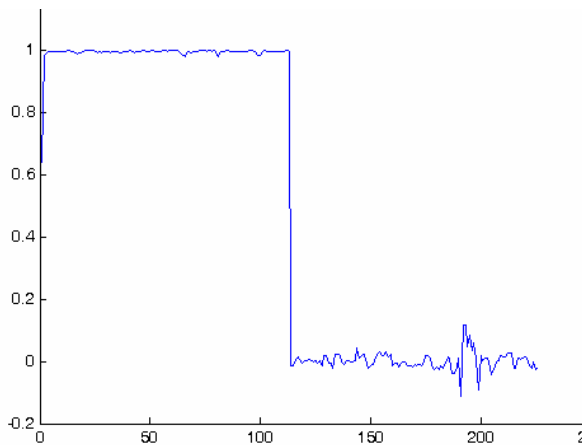


Fig. 11. Output error of classification 2types EEG data.

This results is just limited in 2 types of EEG signals, however the proposed neural network model is clearly adaptive with the kinds of EEG data. With more than 2 signals, the binary output will be extended with more than 1 neuron.

5 Conclusion

From conventional neural networks with the back-propagation learning algorithm, this work proposes some improvements based Chaos theory such as modifying net value with a feedback factor and changing the transfer function to avoid the saturation of outputs. However, all intelligent computing algorithms need to examine adaptive characteristic through realistic applications.

Therefore, other applications of the proposals will be investigated in future works.

Acknowledgements

This study was supported by The 21st Century COE (Center of Excellence) Program "Global Renaissance by Green Energy Revolution" from Ministry of Education, Culture, Sports, Science and Technology of Japan.

References

- [1] Masahiro Nakagawa, Chaos and Fractals in Engineering, World Science, 1999
- [2] K. Aihara, T. Takabe and M. Toyoda, "Chaotic Neural Networks", Physics Letters A, 1990, Vol 144, No.6,7, p333-339
- [3] Behera, L.; Kumar, S.; Patnaik, A.; "On Adaptive Learning Rate That Guarantees Convergence in Feedforward Networks", IEEE Transactions on Neural Networks, Volume 17, Issue 5, Sept. 2006 Page(s):1116 - 1125
- [4] Yu, X.; Onder Efe, M.; Kaynak, O. "A backpropagation learning framework for feedforward neural networks", The 2001 IEEE International Symposium on Circuits and Systems. ISCAS 2001. Volume 3, 6-9 May 2001 Page(s):700 - 702 vol. 2
- [5] K. Bertels¹, L. Neuberg¹, S. Vassiliadis and D.G. Pechanek, "On Chaos and Neural Networks: The Backpropagation Paradigm" © 2001 Kluwer Academic Publishers. Printed in the Netherlands. Artificial Intelligence Review 15: 165-187, 2001.
- [6] John Kolen and Jordan Pollack, "Back Propagation is sensitive to Initial conditions", Laboratory for Artificial Intelligence Research, the Ohio State University, USA.
- [7] Maiorescu, V.A.; Serban, M.; Lazar, A.M.; "Classification of EEG signals represented by AR models for cognitive tasks - a neural network based method" International Symposium on Signals, Circuits and Systems, 2003. SCS 2003. Volume 2, 10-11 July 2003 Page(s):441 - 444 vol.2
- [8] Fukuda, O.; Tsuji, T.; Kaneko, M.; "Pattern classification of time-series EEG signals using neural networks", IEEE International Workshop on Robot and Human Communication 5th, 1996., 11-14 Nov. 1996 Page(s):217 - 222
- [9] Gath, I.; Geva, A.B.; "Unsupervised optimal fuzzy clustering", IEEE Transactions on Pattern Analysis and Machine Intelligence, Volume 11, Issue 7, July 1989 Page(s):773 - 780

Truong Quang Dang Khoa was born in the South of Vietnam in 1979. He graduated from the Hochiminh University of Technology in 2002, and received the Master Degree in 2004. Now he is working as a research assistant in Nagaoka University of Technology under the support of COE program. His research interests are Artificial Intelligent Computation, Chaos, Fractals and Power System Analysis. He is a member of IEEE.

Masahiro Nakagawa was born in Kyoto, Japan in 1958. He received Ph. degree in the Department of Applied Physics from Nagoya University in 1988. He has been a faculty member of engineering at the Nagaoka University of Technology since 1982, and became a Professor in 2001. He is a member of the Japanese Neural Network Society, the Physical Society of Japan, Japanese Society of Applied Physics.

Fundamental Research on Polymer Material as Artificial Muscle

Takayuki Hanamoto, Yasuhiro Neba, Yutaka Fujihara, Junichi Hayashida

Matsue National College of Technology

Abstract

Presently, breakthrough industrial technology and scientific technology produce various instruments of downscale and weight saving. But the metal parts are widely used for magnetic motors. It is difficult to lighten the weight and to miniaturize the motor. Therefore, we need small, light actuators that can be built into motor. We focus attention on the polymer material artificial muscle that responds to electrical stimulation with a significant shape or size change.

In this research, the artificial muscle was produced by using the conductive grease and the polymer material. We used several kinds of polymer material films in our experiments to compare the performance of them. The displacement when the voltage is applied to electrode was measured. At last the result and conclusion are given.

Keyword: EAP, Artificial muscle, Acrylic form elastomer, Urethane gel

1. Introduction

The needs of miniaturization and weight saving of the machine are being increased more due to the development of the technology in recent years (For example, the small actuator for the miniature camera is mounted in the portable telephone). As we know, the biped robot which imitates a person's movement appears. But, it still seems that the movement of the robot is awkward. The reason is that person's muscle moves in a straight line, but the motion of the robot is by the rotation movement of servomotor, and this motion is thought as the main reason.

From these reasons, we paid attention to the soft actuator

which is usually regarded as the artificial muscle. In this paper, we describe the results of the basic experiment and application about the dielectric elastomer EAP (Electro Active Polymer).

2. Dielectric elastomer EAP artificial muscle^{[1][2][5][6]}

Dielectric elastomer EAP artificial muscle has the similar structure to the condenser that a dielectric is put with in the soft electrode as the Fig.1. A dielectric is film-shaped and very thin. The high voltage of about 4000V is impressed on that film. The big electric field occurs between the electrodes and electrodes attract each other. A dielectric film produces elastic deformation and expands in the horizontal direction by using elastomer of the acrylic form and the urethane gel.

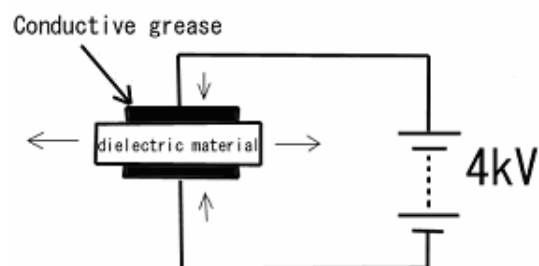


Fig.1 Structure of experiment

The displacement of compression between electrodes is very small. Therefore the dielectric elastomer EAP can be used as the actuator by applying the expanding force.

3. Fundamental experiment ^{[1][2][3][5][6]}

The stress that occurs between the electrodes is expressed by the equation (1).

$$P = \epsilon_0 \epsilon_r E^2 \quad (1)$$

,where P : stress, ϵ_0 : permittivity in vacuum, ϵ_r : relative permittivity, E : electric field strength.

By the experiment, we confirm that the relationship between the displacement and the electric field strength corresponds to the equation(1). And we also examine that which materials are suitable for the soft actuator

The urethane gel and the acrylic form elastomer are used for the experiments. Each sample is fixed on the frame of an acrylic, which is shown in Fig.2. Fig.3 shows the structure of Fig.2. The reason to fix the film is to prevent the film from slackening. And it is also to prevent the electric discharge which happens easily for the experiment by high voltage.

Conductive grease was used for the electrode. And the diameter of the electrode is 15mm. The voltage of 4000V was applied to the electrode. The displacement was measured by the displacement measure instrument which uses the image processing .

And also the characteristics of the multi-layer of acrylic form elastomer are examined. Fig.4 shows the structure of multi-layer experiment. Since acrylic form elastomer is easy to be tested, it is selected to be used as the sample.

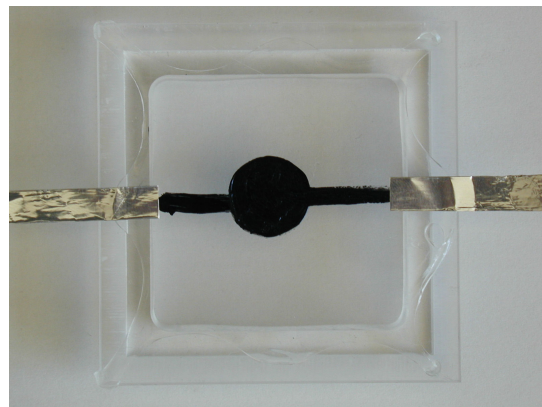


Fig.2. Photograph of experimental sample

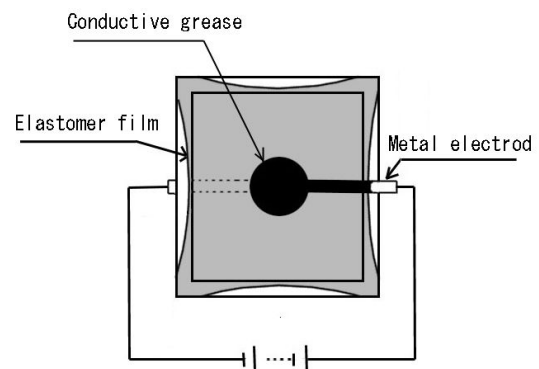


Fig.3. Structure of experimental sample

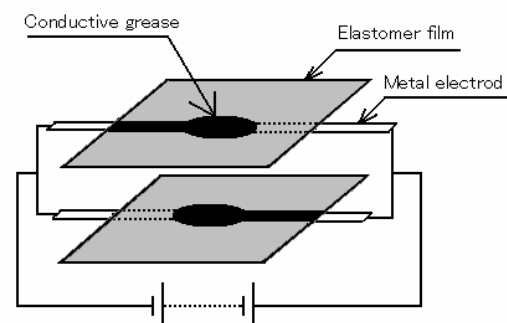


Fig.4. Structure of multi-layer experimental sample

4. Experimental result and consideration

4.1 Comparison urethane gel between acrylic form

Fig.5 shows the result of the comparative experiment between urethane gel between acrylic form. It shows that the displacement describe a parabola according to the increasing of the electric filed strength. The relationship between them coincides with the equation (1).

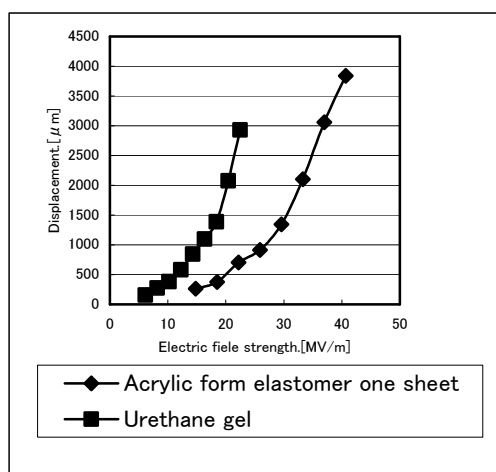


Fig.5 Relationship between electric field strength and displacement (One sheet)

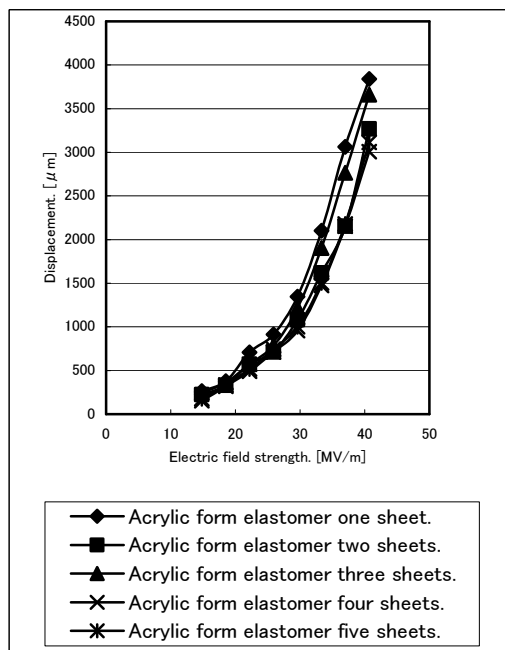


Fig6. Relationship between electric field strength and displacement (multi-layer)

From Fig.5, it is clarified that even a small voltage can affect the displacement of urethane gel when compared with acrylic form. And the maximum displacement of urethane gel can be obtained by the 20 MV/m of electric field strength, that is half of the voltage for the same displacement of acrylic form. But the response rate of urethane gel is slower than that of acrylic form.

4.2 Effect of the multi-layer of acrylic form

Next, for confirming the effect of the multi-layered acrylic form, the acrylic forms of from one layer to five layers are tested and the results of the multi-layer of acrylic form are shown in Fig.6. Each multi-layer of acrylic forms results in the similar curve.

High voltage is necessary to change dielectric elastomer EAP, and the thinner the film of EAP becomes, the lower the voltage to apply is. However, the thinner the film becomes, the more the strength of the film reduces.

On the other hand, the multi-layer of acrylic form can increase the strength by the same voltage of the single layer. Furthermore, it has the possibility that the compression displacement in the vertical direction to the electrodes can be used for the application of the multi-layer EAP.

The compression displacement in the vertical direction will be large when we increase the number of the multi-layer and the multi-layer EAP will be able to apply as an actuator.

5. An application example as an actuator

We propose an actuator for the pump to circulate the air as an application example. The main parts of the actuator can consist of the dielectric elastomer EAP and the spring. Therefore the actuator can be miniaturized and lightened the weight. The structure of the proposed application example is shown in the Fig.7.

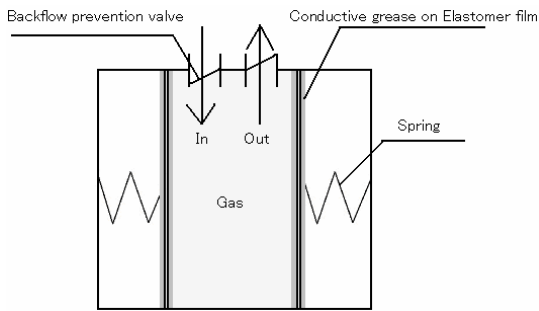


Fig.7 Structure of application example as actuator

At the initial condition, the springs press down the elastomer film to the central axis. And a film stretches by increasing a high voltage and at the same time the springs extend to the direction of the central axis. When the applied voltage becomes low, the spring regains the initial position. By repeating this cycle, the gas inside the pump is circulated. This simple mechanism can break down the problem which is the weak point of present pulse pattern pump that is difficult to miniaturize. And it also may be able to be applied to the artificial heart if the fluid circulate is strengthened by using the strong spring. However, because the high voltage power supply is used, it is necessary to take care about the electrical discharge.

6. Conclusions

In this paper, we described the soft actuator that is called dielectric elastomer EAP artificial muscle in the introduction. The fundamental experiment of artificial muscle was done, and the application of artificial muscle was proposed. The various other applications are suggested by a lot of researchers^{[3][4]}. Therefore, the artificial muscle is improved every day.

If the artificial muscle which respond instantly to the very weak electric stimulus from the human body can be developed, a big revolution will be brought to the artificial limb technology.

Big evolution was also made for the biped walking robot in recent years by easily imitating a person's movement. But, the vibration that occurs by the rotation movement of motors causes a big trouble when controlling many motors of the biped robot.

The soft actuator which can make a straight line-like movement by only given voltage without vibration attract the attention of the researchers of robotics. Because it is possible to be used to the various fields as mentioned above, a soft actuator can be thought as the new technology for the research and application of various filed.

References

- [1]Yoshihito Nagata(2004), The front of development of a soft actuator.,N·T·S(in Japanese)
- [2]Haruo sugi(2003) Muscle is mystery, p.p16-64, KODANSHA(in Japanese)
- [3]Scott Stanford, Neville Bonwit, Ron Pelrine, Roy Kornbluh, Oibing Pey, Seiki Chiba, (2004) Electroactive Polymer Artificial Muscle (EPAM) for Biomimetic Robotics, Second conference on artificial muscle, National Institute of Advanced Industrial Science and Technology
- [4]Yoseph Bar-Cohen(2004) Electroactive Polymer [EAP] Actuators as Artificial muscles, p.p529-581, SPIE.
- [5]J.Hayashida, F.Dai, Y.Fujihara, (2006) Fundamental Study of Dielectric Elastomer as Artificial Muscle, Proceedings of the Eleventh International Symposium on Artificial Life and Robotics 2006(AROB 11th 06), CDversion, p.p611-614
- [6]Y.Fujihara, J.Hayashida, F.Dai, (2006) Dielectric Elastomer Actuators as Artificial Muscles, Proceedings of the Eighth International Conference on Industrial Management, Qingdao(China), p.p891-894

Fundamental Research on Face Recognition by Genetic Algorithm

Fengzhi Dai¹, Touru Adachi¹, Yutaka Fujihara¹, Huailin Zhao²

¹ Department of Control Engineering,
Matsue National College of Technology, Japan
daifz (fujihara)@matsue-ct.jp

² College of Physics Science & Technology,
Zhengzhou University, China
zhao_huailin@yahoo.com

Abstract

Object recognition is playing an increasingly important role in modern intelligent control. Traditionally, special object can be recognized by the template matching method, but the recognition speed has always been a problem. In this paper, the genetic algorithm (GA) - based face recognition method is proposed. The chromosomes generated by GA contain the information of the facial model, by which can we recognize it in an image. The purpose of the paper is to propose a practical method of face recognition. Finally, the experimental results, and a comparison with the traditional template matching method, and some other considerations, are also given.

Key Words: Face recognition, Genetic algorithm, Template matching

1. Introduction

We know that the higher the degree of intelligence in a control system, the more important the image recognition technology. For an intelligent control system (autonomous mobile vehicle, robot, etc), it is necessary to acquire information about the external world automatically by sensors, in order to recognize its position and the surrounding situation. A camera is one of the most important sensors for computer vision. That is to say, the system endeavors to find out what is in an image (the environment) taken by the camera: traffic signs, obstacles or guidelines, etc.

The reliability and time-response of object recognition have a major influence on the performance and usability of the whole object recognition system [1]. The template matching method is a practicable and reasonable way used to the object detection [2]. This paper gives an improvement in the general template matching method.

Since GA has been considered to be a robust and global searching method (although it is sometimes said that GA cannot be used for finding the global optimization) [3], it is used as the recognizer. In this paper, the chromosomes generated by GA contain information about the image data, and the genetic and evolution operations are used to obtain the best match to the template. Searching for the best match is the goal of the paper.

In this paper, section 2 gives the encoding method of the GA and the experimental settings that is used. In section 3, the experiment and the analysis are addressed. Some conclusions are given in section 4.

2. Theory and experimental settings

For an image recognition system, the interested part that has special features has to be detected and recognized from the original image. The whole procedure is shown in Figure 1.

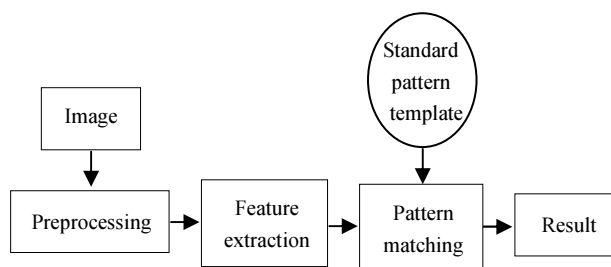


Figure 1 Object recognition system

One of the oldest techniques of pattern recognition is matching filtering [4], which allows the computation of a measure of the similarity between the original image $f(x, y)$ and a template $h(x, y)$. Define the mean-squared distance

$$d_{fs}^2 = \iint \{f(x, y) - h(x, y)\}^2 dx dy \quad (1)$$

$R_{fh} = \iint f(x, y)h(x, y)dxdy$, if the image and template are normalized by

$$\iint f^2(x, y)dxdy = \iint h^2(x, y)dxdy \quad (2)$$

and then

$$\begin{aligned} d_{fh}^2 &= \iint \{f(x, y) - h(x, y)\}^2 dxdy \\ &= \iint \{f^2(x, y) - 2f(x, y)h(x, y) + h^2(x, y)\}dxdy \\ &= 2\iint f^2(x, y)dxdy - 2R_{fh} \end{aligned} \quad (3)$$

For the right hand side of eqn.(3), the first term is constant, and thus R_{fh} can measure the least-squared similarity between the image and template [5]. If R_{fh} has a large value (which means that d_{fh}^2 is small enough), then the image is judged to match the template. If R_{fh} is less than a preselected threshold, the recognition process will either reject the match or create a new pattern, which means that the similarity between the object in the image and the template is not satisfied.

2.1 Genetic encoding

As introduced above, the chromosomes generated by the GA contain information about the image data, so the first step is to encode the image data into a binary string. The parameters of the center of a face (x, y) in the original image, the rate of scale to satisfy eqn.(2), and the rotating angle θ are encoded into the elements of a gene [6]. Some important parameters of the GA used here are given in Table 1, and the search field and region are given in Table 2.

As shown in Table 2, one chromosome contains 4 bytes: the coordinate (x, y) in the original image, the *rate* of scale and the rotation angle θ .

2.2 Experimental setting

The experiment is done by first loading the original and the template images. The GA is used to find whether or not there is the object of the template in the original image. If the answer is YES, then in the original image the result gives the coordinates of the center of the object, the scale, and the rotating angle

from the template [7].

For comparison, the general template matching method is also presented [8]. The executive time shows the effectiveness of the GA-based recognition method.

Figures 2 and 3 are the template and original images for the experiment. The values are the width \times height in pixels of the image.

Table 1 Some GA parameters

Source	The original and template images
Fields	$x, y, rate, \theta$
Generations	Max = 300 (the stopping criterion)
Population Size	200
Reproduction (selection)	P_r of the best individuals will be selected to survive. The remainder ($1-P_r$) will be treated by the genetic operators (crossover and mutation)
Crossover	Offspring are produced from parents by exchanging their genes at the crossover point, the ratio is P_c
Mutation	Produce spontaneous random changes in various chromosomes. General random changes occur at the rate of P_m

Table 2 Settings for the experiment

Parameters	Length	Region
x	8 bits	(0, max_x)
y	8 bits	(0, max_y)
<i>rate</i>	8 bits	(1.0, 3.0)
θ	8 bits	(-35°, 35°)
P_r	0.6	
P_c	0.2	
P_m	0.2	



32 \times 32

Figure 2 Template for matching
(size: $temp_x \times temp_y$)



320×240

Figure 3 The original image (size: max_x, max_y)

3. Experiment and comparison

The genetic operations and GA parameters are presented in Table 1 and Table 2. The fitness is defined as

$$fitness = 1.0 - \frac{\sum_{j=0}^{temp_y} \sum_{i=0}^{temp_x} |f(x, y, rate, \theta) - temp(i, j)|}{(temp_x) \times (temp_y) \times 255} \quad (4)$$

In eqn.(4), $temp(i, j)$ is the gray level of the coordinate (i, j) in the template image, the width and height of which are $temp_x$ and $temp_y$. $f(x, y, rate, \theta)$ gives the gray level in the original image, the coordinate of which is calculated by translation from (x, y) , and by changing the scale and the rotation angle θ from the template [6, 7]. Since the images are 256 gray-level images, in eqn.(4), division by 255 ensures that the resulting fitness is between 0 and 1.



Figure 4 Result of the GA-based recognition

The maximum number of generation is limited to 300, and the threshold of the matching rate is set to 0.9. Thus if within 300 generations the matching rate can reach 0.9, then it is said that the template is found in the original image (the template matched the original image by the threshold). The result of the GA-based face recognition is given in Figure 4 and Table 3. The result shows that it reaches the matching rate 0.944 at the 112th generation.

Table 3 Results of searching by GA

Fitness	0.944
Generation	112
Time [sec]	5
(x, y)	(112, 107)
Rate	1.02
Angle [deg]	2.24

For the purpose of comparing the effect of the GA-based algorithm, the result of the general matching method [8] is also presented. From Figure 5, we see that although both the original image (the top-left image in Figure 5) and the template (the top-right image) are simplified by binarization, the matching time is 3 min 18s. The recognized result is the bottom-left image in Figure 5.

Reference: <http://homepage3.nifty.com/ishidate/vcpp.htm>
Face recognition by Template matching

(1) : Original image(320 * 240)

(2) : Template image(32 * 32)

Threshold of binarization = 120.
Threshold of matching = 800

Table1 : Result of recognition

Start: 18:27:02 Monday, November 13, 2006
Stop: 18:30:20 Monday, November 13, 2006
Time: 00:03:18 and 0 days↑↑

Found the template
Matching rate = 0.817383

(3) : Binarized image and the result

Figure 5 Result for the general matching method

4. Conclusions

In this paper, the GA-based image recognition method is tested, and a comparison with the general

matching method is presented.

The GA starts with an initial set of random solutions called the population. Each individual in the population is called chromosome, and represents a solution to the problem. By stochastic search techniques based on the mechanism of nature selection and natural genetics, genetic operations (crossover and mutation) and evolution operation (selecting or rejecting) are used to search the best solution [9].

In this paper, the chromosomes generated by the GA contain information about the image, and we use the genetic operators to obtain the best match between the original image and the template. The parameters are the coordinate (x, y) of the center of the object in the original image, the rate of scale, and the rotation angle θ .

In fact, translation, scale and rotation are three main invariant moments in the field of pattern recognition. However, for face recognition, the facial features are difficult to extract, and are calculated by the general pattern recognition theory and method [10]. Even these three main invariant moments will not be invariant because the facial expression is changed in different images.

Thus the recognition only gives the best matching result within an upper predetermined threshold. The result in the paper shows that the recognition is satisfied.

By using GA-based recognition method, the settings of the search field (in this paper, $(x, y, rate, \theta)$ is selected), the determination of the genetic operations, and the selection and the optimization of the fitness function all have a strong effect on the level of recognition of the resultant image.

Based on the results of experiments described here, further work will emphasize (i) optimizing the fields of chromosomes, and (ii) improving the fitness function by adding some terms to it [7]. This work is important and necessary in order to improve the GA-based face recognition system.

References

[1] M. Sugisaka, X. Fan (2002), Development of a face recognition system for the liferobot, Proc. of

the 7th Int. Symp. on Artificial Life and Robotics, vol. 2, 538-541

- [2] K. R. Castleman (1998), Digital image processing, Original edition published by Prentice Hall, Inc., a Simon & Schuster Company, Press of Tsinghua University
- [3] H. Iba (1994), Foundation of genetic algorithm – solution of mystic GA, Omu Press (in Japanese)
- [4] K. Deguchi, I. Takahashi (1999), Image-based simultaneous control of robot and target object motion by direct-image-interpretation, Proc. the 1999 IEEE/RSJ International Conf. of Intelligent Robot and System, vol. 1, 375-380
- [5] B. Jaehne (1995), Digital image processing - concepts, algorithms, and scientific applications, The Third Edition, Springer-Verlag
- [6] T. Agui, T. Nagao (2000), Introduction to image processing using programming language C, Shoko-do press (in Japanese)
- [7] F. Dai, T. Kodani, Y. Fujihara (2006), Research on Face Recognition System by Genetic Algorithm, Proc. of the 11th Int. Symp. on Artificial Life and Robotics, CD version, 63-66
- [8] Ishibashi's Studying Room of C++ (in Japanese). <http://homepage3.nifty.com/ishidate/vcpp.htm>
- [9] M. Gen, R. Cheng (1997), Genetic algorithms and engineering design, A wiley-Interscience Publication
- [10] H. Takimoto, Tasue Mitsukura, M. Fukumi, N. Akamatsu (2002), A design of face detection system based on the feature extraction method, Proc. of 12th Symp. on Fuzzy, Artificial Intelligence, Neural Networks and Computational Intelligence, 409-410

The Characteristics of Mckibben Muscle Based on The Pneumatic Experiment System

Huailin Zhao^{*,**} (zhao_huailin@yahoo.com) Masanori Sugisaka^{**} Fengzhi Dai^{***}

^{*}College of Physics Science and Technology, Zhengzhou University, China

^{**}Department of Electrical and Electronic Engineering, Oita University, Japan

^{***}Department of Control Engineering, Matsue National College of Technology, Japan

Abstract: In the pneumatic experiment system in which Mckibben muscles are applied, the electropneumatic regulator provides gas pressure to Mckibben muscles. The structure of the electropneumatic regulator is analyzed, and that the electropneumatic regulator can stabilize its output gas pressure is pointed out. The stiffness expression of Mckibben Muscles is formulated from both its force model and the characteristic of the electropneumatic regulator. The process of gas pressure transmission with the whole pneumatic experiment system is investigated. The model of the gas pressure transmission based on the integrated pneumatic experiment system is established. The experiment is done to prove its validity. The result shows, that the inner pressure of Mckibben muscle doesn't vary when its length is changed by outer force, and there are bath a pure time delay and a raise course of gas pressure when Mckibben muscles are input by pressed air. The pure time delay comes from the turning on of the valve of the electropneumatic regulator, and the raise course corresponds with the filling process of the inner gas pressure of Mckibben muscle.

Keywords: Mckibben muscle; pneumatic experiment system; electropneumatic regulator; stiffness; gas pressure transmission

1. Introduction

Mckibben pneumatic artificial muscle (it will be called as Mckibben muscle later) is a kind of motion engine which is stimulated and can contract. It constructs with two layers-the inner layer rubber tube and the outer layer fiber wave. When the inner layer closed tube is input by pressed gas, the outer layer wave expands and shortens its two ends and then outputs pulling force^[1-3]. Therefore, the electro-pneumatic regulator is necessary, which is capable of providing the required gas pressure. In this case, the whole pneumatic experiment system includes

not only Mckibben muscles but also the electro-pneumatic regulator. But the former literatures usually didn't mention the electro-pneumatic regulator. Here the writer thinks that the integrated pneumatic system should include both Mckibben muscles and the electro-pneumatic regulator which will effect the characteristics of Mckibben muscles. This paper is just to investigate the characteristics of Mckibben muscles based on the integrated pneumatic experiment system.

2. Pneumatic experiment system

Fig.1 is an ordinary pneumatic experiment system. The computer-controlled electro-pneumatic regulator can output determined gas pressure. Mckibben muscle input by the pressed gas contracts and output pull force and then works on the load. The gas source is usually from a compressor. Obviously the experiment should mainly include both the electro-pneumatic regulator and Mckibben muscles.

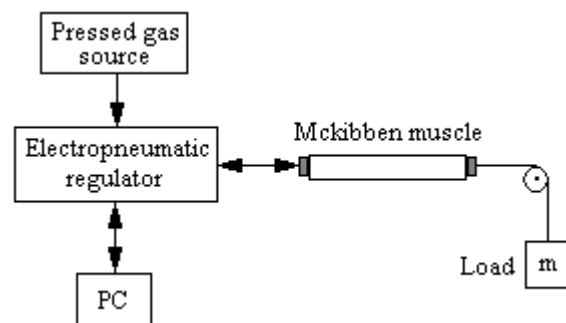


Fig.1 Pneumatic experiment system

Firstly let's discuss the electro-pneumatic regulator. It is a computer-controlled system which can output determined gas pressure. Its input is the electric current or electric voltage which's quantity can be controlled by the computer, and the output gas pressure is proportional to the current or the voltage within definite field. It has

multiple output channels for the practical need. Every output channel can output a gas pressure proportional to the input. Fig.2 is just the principle block diagram related one channel. Thereinto, the control circuit can control all the channels. From Fig.2, every channel consists of the control circuit, two electromagnetism proportion valves, and one pressure sensor. The pressure sensor measures the output gas pressure and feedback it to the control circuit. Accordingly, a closed feedback loop is made up. It is not difficult to understand that the closed loop can automatically regulate and restrain the out gas pressure when it changes because of the later links. This is why the electro-pneumatic regulator can output stable gas pressure. The compressor provides the pressed gas input to the electro-pneumatic regulator. The magnitude of the gas pressure should be larger than the maximal output gas pressure.

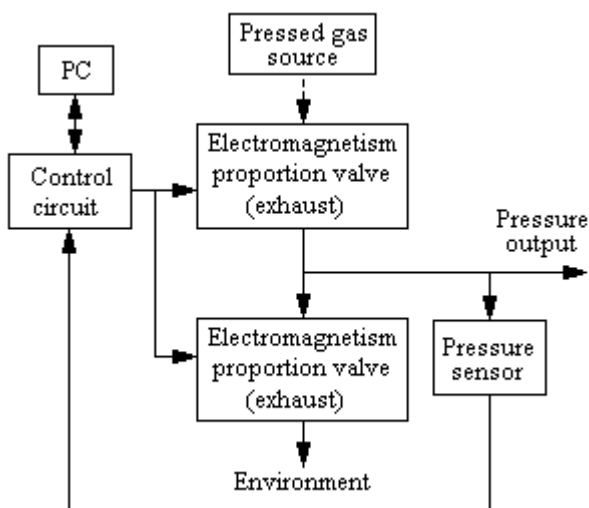


Fig.2 Principle figure of the electropneumatic regulator

3. The stiffness of Mckibben muscle

There have been many papers discussed the characteristics of Mckibben muscle itself, especially its force characteristic^[4-6]. But few paper mentioned its stiffness. Mckibben muscle changes its shape when acting, a little like the spring. To the spring, its stiffness is constant within definite field. To Mckibben muscle, how about its stiffness? Now let's discuss this problem.

The basic concept of the stiffness is the needed force making a shape change in unit length. It is just the differential of force to length in actual calculation. Based

on the concept, the stiffness of Mckibben muscle is the differential of its output force to its length. To Mckibben muscle, there has been clear conclusions about the force characteristic especially its static force characteristic. Different literatures gave the same ideal force output expressions. Some of them gave revisory ones for idiographic products of Mckibben muscles^[7-8]. In this paper the ideal force output characteristic will be used to discuss the stiffness.

The force characteristic expression is

$$F = Pb^2(3L^2/b^2 - 1)/(4\pi n^2) \quad (1)$$

Thereinto, F is the force output, P is the input gas pressure, and L is the current length of Mckibben muscle. Both b and n are structure parameters and they keep constant. Formula (1) expresses that the force output of Mckibben muscle is proportional to gas pressure, and is nonlinear to the length.

Based on both the stiffness and its force characteristic of Mckibben muscle, the stiffness k is

$$\begin{aligned} k &= dF/dL \\ &= d[Pb^2(3L^2/b^2 - 1)/(4\pi n^2)]/dL \\ &= Pb^2(3L^2/b^2 - 1)/(4\pi n^2)dP/dL + 3PL/(2\pi n^2) \end{aligned}$$

There are two items in the above formula. Generally, dP/dL in the first item is very difficult to calculate, because the inner pressure has to change with its volume varying to enclosed gas. To Mckibben muscle, if the related valve is shut up after some pressed gas is input, its inner gas becomes enclosed, and its length change must make its inner volume change, consequently its inner pressure P will change. Based on the above analysis to the electro-pneumatic regulator, the inner pressure actually as the controlled object, together with the related channel of the electro-pneumatic regulator, constitute a enclosed loop control system. In practice, the inner pressed gas can exchange its mass with the regulator. It is not an enclosed gas. The sensor in the channel of the regulator will send feedback signal about the change immediately to the control circuit when the

inner pressure varies because of some outer factors. Then the control circuit will make the related electromagnetism proportion valve act. Then definite gas will be input to or output from Mckibben muscle, so as to stabilize the inner pressure. Some experiments have clearly proved that. The inner pressure changes instantly and recover to the former immediately when the length of Mckibben muscle is enforced to change after determined gas pressure is input. Therefore it can get

$$dP/dL=0$$

So, the stiffness of Mckibben muscle is

$$k=3PL/(2\pi n^2) \quad (2)$$

Based on the formula (2), there is conclusion that the stiffness of Mckibben muscle is not constant. It is proportional to gas pressure, and is proportional to the length too. Larger the pressure, larger the stiffness. The stiffness at the beginning of contraction is larger than the one after contraction under the condition of the constant inner pressure. This is quite different from the spring with constant stiffness. Just like he spring, there is a length field within which the expression (2) is correct. Because there is a length field in the force expression (1), and the length field is just the normal operation field of Mckibben muscle.

Formula (2) express that the stiffness of Mckibben muscle has finite volumes within its normal operation field. In another word, the force needed to change its length is not very large. Just because there is so called "compliance" which means that the shape is easy to be changed by the outer force, the robot actuated by Mckibben muscles is related safe to human when contact with it^[9-10].

4. The model of gas pressure transmission in Mckibben muscle

Mckibben muscle is stimulated. In another word, it contracts after gas pressure is input and then output force. So the gas pressure is greatly related with the output force. Formula (1) has proved that the output force is proportional to the input gas pressure. Therefore, the

transmission of the gas pressure will greatly effect the forming of the contraction force of Mckibben muscle. To a factual pneumatic experiment system, the opening of the gas valve of the electropneumatic regulator has definite time delay, and different valves have different delays. To the familiar valve products, the time delay is usually less than 50ms. For simple calculation, it can be considered as a pure delay less than 50ms. The actual delay in the used electropneumatic regulator is about 30ms. In addition, the diameter of Mckibben muscle is usually much larger than the one of the gas transmission tube. So the gas pressure inputting to Mckibben muscle can't be stepped. It should have a very complicated rise course. For simple dealing with, the course is considered as one-order inertia link. Its rise time will be much larger than the delay of the electropneumatic regulator. Probably it can be a few hundred milliseconds^[7,11] and the ideographic quantity is related with the inner volume of Mckibben muscle. Based on the above analysis, the opening of the gas valve considered as the pure delay, and the gas pressure transmission from the output port of the gas valve to the inerior of Mckibben muscle as one-order inertia course, the input pressure P can be expressed as

$$P(t) = P_0 (1 - e^{-(t-T_d)/T_c}) u(t-T_d) \quad (3)$$

Thereinto, P_0 is the static volume, T_d is the time delay of gas valve, and T_c is the time constant of the one-order inertia course.

A experiment is conducted to validate the above conclusion. Because of that it is different to directly measure the inner pressure of Mckibben muscle, a measurement of its pull force is done to validate the formula (3) indirectly. Fig.3 shows the comparison between the pull force model and the experiment data in which the used Mckibben muscle has a nominal length 300mm and nominal diameter 20mm, under the condition of that P_0 equals to 0.5MPa and L keeps 300mm. Besides, the time delay of the electropneumatic regulator is 30ms and the time constant of the one-order inertia course is 260ms. From the formula (1), The pull force F and the gas pressure P will change in the same way if L keeps constant. From fig.3, the raise course of

the gas pressure is consistent with the experiment on whole. Then it infers that the gas pressure transmission model expressed by formula (3) is basically close to the factual system. This model will greatly consult the design of the control algorithm of Mckibben muscle.

From fig.3, the opening time delay of the electropneumatic is much less than the gas pressure filling time to mckibben muscle. Scanning he whole gas pressure transmission, according to the pull force model, the gas pressure gets to 90% of the stable volume at about 600ms.

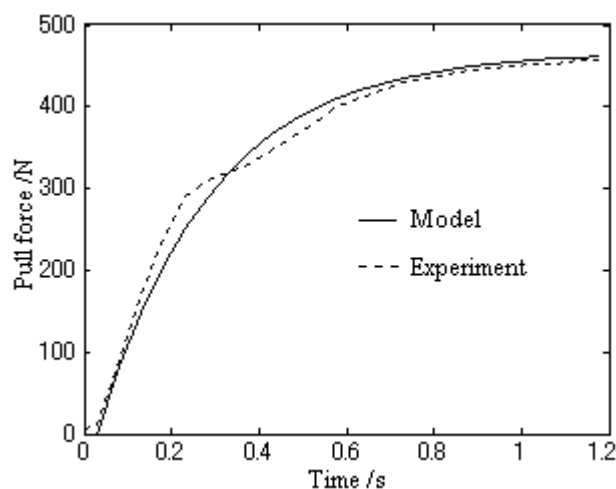


Fig.3 Comparison between the model and the experiment

5. Conclusion

In factual applications of Mckibben muscles, to a typical pneumatic experiment system, usually the electropneumatic regulator is used to control the gas pressure. Based on the whole system, the stiffness of Mckibben muscle is proportional to both its gas pressure and its length. Enforcing to change its length, its inner gas pressure doesn't change. When gas pressure input, there is a time delay of several hundred milliseconds because of both the delay of the gas valve of the electropneumatic regulator and the filling course of the inner gas pressure of Mckibben muscle. And the filling course is much larger than the delay of the gas valve.

Reference

[1] Frank D, Dirk L. Pneumatic Artificial Muscles:

actuators for robotics and automationp. *European Journal of Mechanical and Environmental Engineering*, 2002, 47(1): 10

- [2] Richard Q. Design, analysis, and control of a low power joint for walking robots by phasic activation of Mckibben muscles, *IEEE Transactions on Robots and Automation*, 1998,15(4): 599
- [3] John I. Artificial pneumatic muscle. *Poptronics*, 2000(11): 49
- [4] Chou C P. Study of human motion control with a physiology based robotic arm and spinal level neural controller. Washington University, 1996
- [5] Huailin Zhao, M.Sugisaka, Datai Yu, Modeling of pneumatic artificial muscle actuator, *Proceedings of the 10th international symposium on artificial life and robotics*, Feb.2005, Japan
- [6] Glenn K. Klute, Blake Hannaford. Accounting for Elastic Energy Storage in McKibben Artificial Muscle Actuators, *ASME Journal of Dynamic Systems, Measurement, and Control*, 2000,122(2): 386~388.
- [7] Bertrand T, Pierre L. Modeling and control of Mckibben artificial muscle robot actuators, *IEEE Control System Magazine*, 2000,20(2): 15
- [8] Manuello Bertetto, M.Ruggiu. Characterization and modeling of air muscles, *Mechanics Research Communications*, 2004(31): 185~194.
- [9] Kazuhiko K, R.Alan P, D.Mitchell W, et al. ISAC: Foundations in Human-Humanoid Interaction, *IEEE Intelligent Systems*, 2000(4): 38
- [10] Gabrielle J M, Tuijthof H, Just L H. Design, actuation and control of an anthropomorphic robot arm, *Mechanism and Machine Theory*, 2000, 35(7): 945
- [11] A.I.T Kunihiko, ITO.Kazuhiko KUNIEDA, Takasi KNODO, Yukihide HARADA, The bilinear model of muscle-skeletomotor system and the impedance characteristics of rubber artificial muscle[A], the fifth Japan robot conference, 1987

Effect of Using Partial Solutions in Creating New Candidate Solutions with EDA and ACO Schemes

Shigeyoshi Tsutsui
Department of Management Information
Hannan University
Matsubara, Osaka 580-8502 Japan

Abstract

In previous studies, we have proposed an algorithm named the edge histogram based sampling algorithm (EHBSA) with EDA scheme for permutation domains. In EHBSA, new solutions are obtained by combining partial solutions which exist in the current population, and partial solutions newly generated according to an edge histogram model of the current population. In this paper, we show using partial solutions can maintain the diversity of the population, resulting in a successful search. We also show that using partial solutions in ACO can greatly enhance its performance.

1 Introduction

Genetic Algorithms (GAs) are widely used as robust black-box optimization techniques applicable across a broad range of real-world problems. GAs should work well for problems that can be decomposed into sub-problems of bounded difficulty [1]. However, fixed, problem-independent variation operators are often incapable of effective exploitation of the selected population of high-quality solutions [1, 2]. One of the most promising research directions is to look at the generation of new candidate solutions as a learning problem, and use a probabilistic model of selected solutions to generate the new ones [3, 4]. The algorithms based on learning and sampling a probabilistic model of promising solutions to generate new candidate solutions are called estimation of distribution algorithms (EDAs) [5] or probabilistic model-building genetic algorithms (PMBGAs) [3].

Most work on EDAs focuses on optimization problems where candidate solutions are represented by fixed-length vectors of discrete or continuous variables. However, for many combinatorial problems permutations provide a much more natural representation for candidate solutions. Despite the great success of EDAs in the domain of fixed-length discrete and continuous

vectors, only few studies can be found on EDAs for permutation problems [6, 7].

In previous studies [8, 9], we have introduced a promising approach to learning and sampling probabilistic models for permutation problems using edge histogram models. This algorithm is called the edge histogram based sampling algorithm (EHBSA). In EHBSA, new solutions are created by combining partial solutions which exist in the current population, and partial solutions newly generated based on the edge histogram model of the current population. The EHBSA worked well on several benchmark instances of the traveling salesman problem (TSP). Nonetheless, the methods proposed are not limited to TSP, like most other TSP solvers and specialized variation operators. As a result, this approach provides a promising direction for solutions of other problems that can be formulated within the domain of fixed-length permutations; flow shop scheduling is an example of such a problem as described in [9].

In this paper, we focus our attention on the effects of using partial solutions in EHBSA. The basic sampling algorithms in EHBSAs are very similar to the sampling algorithms that are used in ant colony optimization (ACO) [10, 11] and thus this method can be applied to ACO [12]. We also discuss these results.

In the remainder of this paper, Section 2 gives a general scheme for using partial solutions in EDAs. In Section 3, we discuss the effect of using partial solutions in EHBSA and show how using partial solutions can maintain the diversity of the population, resulting in a successful search. The effectiveness of using partial solution in ACO is discussed in Section 4. Finally, Section 5 concludes this paper.

2 Using Partial Solutions in EDAs

Figure 1 shows a typical scheme of EDAs. EDAs evolve a population of candidate solutions to the

partial solution must be determined. Let us represent the number of nodes that are constructed based on *EHM* by l_s . Then, l_c , the number of nodes of the partial solution, which $c[]$ borrows from the template, is $l_c = L - l_s$. Here, let us introduce a control parameter which can define $E(l_s)$ (the average of l_s) by $E(l_s) = L \cdot \gamma$. To determine the sampling portion in a string, we used the n cut-point approach in previous study [8]. However with the approach, $E(l_s)$ is $L/2, L/3, \dots$ for $n=2, 3$, and so on, and, corresponds to $1/n$, i.e., can take only the values of 0.5, 0.333, and 0.25, corresponding to $n=2, 3, 4$ and so on. In the current research, we extend this elementary method to a more flexible technique which allows for taking values in the range $[0.0, 1.0]$. The probability density functions for l_s in this research are:

$$f_s(l) = \frac{1}{L} \left(1 - \frac{l}{n} \right)^{\frac{1}{n}-1}, \text{ for } 0 < \gamma < 0.5. \quad (1)$$

$$f_s(l) = \frac{l}{L(1-\gamma)} \left(\frac{l}{1-\gamma} \right)^{\frac{2}{1-\gamma}-1}, \text{ for } 0 < \gamma < 0.5. \quad (2)$$

Using partial solutions in EHBSA is summarized in Figure 4. For a given γ value, l_s is generated according to Eqs. 1 or 2, and c_{top} , the first position of partial solution for $c[]$ to borrow from the template, is sampled randomly. Then, the partial solution of length $l_c = L - l_s$, and which starts from c_{top} is copied to $c[]$ from the template. Then the remaining sequence of nodes of length l_s in $c[]$ is sampled according to EHM probabilistically.

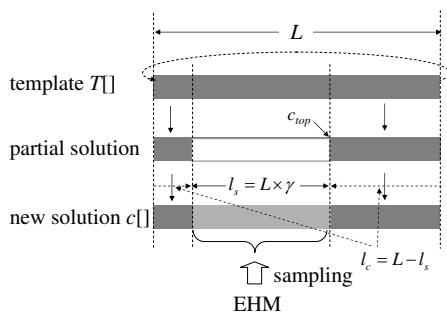


Figure 4: Using partial solutions in EHBSA

3.3 Results

In this section, we show the results using the scheme described in Section 3.2 on TSP instances of gr48 and pr76. The γ values were tested from 0.1 to 1 with step size 0.1. Here note that $\gamma = 1$ corresponds to the case

where no partial solutions are used. The following control parameter values were used: population size $N = L - 2$ (L is the number of cities), maximum number of tour constructions $E_{max} = L - 20,000$. Results are summarized in Table 1 where $\#OPT$ indicates the number of runs which found the best-known solution, MNE indicates the mean number of tour constructions to find the best-known solution in those runs where it did find the solution, and $Error$ indicates the average excess value from the best-known solution over 25 independent runs.

From these results, we can see that good results of $\#OPT$, MNE , and $Error$ are found with γ values in $[0.3, 0.4]$ for both gr48 and pr96. In the case in which we do not use partial solutions ($\gamma = 1$), the second worst results were obtained on both instances, i.e., $\#OPT = 0$ for both instances, and a $Error = 1.159\%$ for gr48 and $Error = 9.747\%$ for pr76, respectively.

Table 1: Results of EHBSA on gr48 and pr76

γ	gr48			pr76		
	$\#OPT$	MNE	$Error$	$\#OPT$	MNE	$Error$
0.1	0	-	1.753%	0	-	14.895%
0.2	25	185458.3	0.000%	10	1276794.0	0.175%
0.3	25	115680.5	0.000%	24	735272.6	0.005%
0.4	24	113575.6	0.022%	23	595011.3	0.010%
0.5	23	135540.6	0.029%	21	622464.3	0.045%
0.6	16	182385.0	0.099%	17	687602.9	0.092%
0.7	4	256192.0	0.278%	13	960202.4	0.115%
0.8	0	-	0.682%	2	1400801.5	1.076%
0.9	0	-	0.912%	0	-	5.336%
1	0	-	1.159%	0	-	9.747%

Figure 5 shows the change of the diversity of the population. Here, the diversity was measured by the standard deviation (STD) of tour length of individuals in the population and was averaged over 25 runs. From this figure, we can see that for $\gamma = 0.1$ the change of the STD is very slow. This is because only 10% of new edges are sampled in generating a new string on average. Thus, the population did not converge in the defined maximum number of tour constructions E_{max} . With γ values of 0.3, and 0.4, each STD gradually becomes smaller as the number of tour constructions increases, resulting in successful searches. However, in the case in which we do not use partial solutions ($\gamma = 1$), the population loses diversity rapidly, resulting in a failed search. Thus, we can see the effectiveness of using partial solutions with appropriate γ values.

4 Using Partial Solutions in ACO

As a bio-inspired computational paradigm, ACO has been applied with great success to a large number

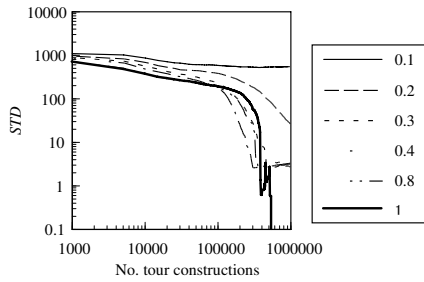


Figure 5: Change of population diversity on gr48

of hard problems in permutation domains [11]. The first ACO algorithm was called the Ant System (AS), and was applied to the TSP. Since then, many variant ACO algorithms have been proposed as extensions of AS [11]. On a TSP, AS works as follows: Let m be the total number of ants. Initially, each ant is put on a randomly chosen city $k(k=1, \dots, n)$. Let $\tau_{ij}(t)$ be the trail density on edge (i, j) at iteration t . Each of m ants at iteration t makes a tour by choosing a sequence of cities. When all ants complete their tours, the trail density of each edge on their tours is updated. We can note here that the $\tau_{ij}(t)$ corresponds to $EHM^t = (e_{ij}^t)$ of EHBSA and thus ACO has a tight relation with EDAs.

In this section, we present the results of a new ACO which uses partial solutions in generating new solutions. Please see [12] for more detail. The algorithm is called the *cAS* (cunning AS). In traditional ACO algorithms, each ant generates a solution probabilistically or pseudo-probabilistically based on the current pheromone trail $\tau_{ij}(t)$. In *cAS*, an agent called *cunning ant* (*c-ant*) is introduced. The *c-ant* differs from traditional ants in the manner of solution construction. It constructs a solution by borrowing a part of existing solutions. The remainder of the solution is constructed based on $\tau_{ij}(t)$ probabilistically as usual. An agent which has a solution borrowed by a *c-ant* is called a *donor ant* (*d-ant*). Using *c-ant* in this way, we can prevent premature stagnation the of search, because only a partial solutions are newly generated, and this can prevent over exploitation caused by strong positive feedback to $\tau_{ij}(t)$ as discussed in Section 2.

Figure 6 illustrate the convergence process by the change of *Error* on kroA100 TSP instance for values of 0.1, 0.3, 0.5, 0.7, and 0.9. Early stagnations of search can be observed with values of 0.7 and 0.9. With values of 0.3 and 0.5, stagnations of search occur much later in the search. With a value of 0.1, no stagnation can be observed. But the convergence

process is very slow. Thus we can see that using appropriate small values of can prevent over exploitation.

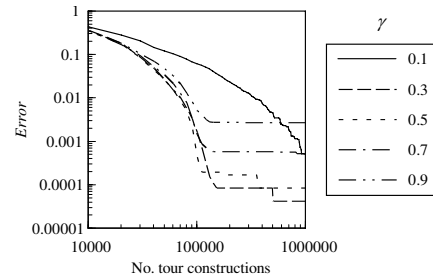


Figure 6: Convergence process on kroA100

Here we show *cAS* with a local search on TSP. One of the best performing local searches for TSP is the well-known Lin-Kernighan algorithm (LK) [13]. We used a Chained LK which applies the basic LK repeatedly. For value, $\gamma=0.4$ was used.

Table 2: Results of *cAS* with LK on TSP. T_{avg} is average time in second to find optimal in successful runs. The machine we used had two Opteron 280 (2.4GHz) processors with Java code.

TSP	<i>cAS</i>						MMAS			Chained LK			T_{max}
	<i>cAS</i> ($\gamma=0.4$)			<i>non-cAS</i> ($\gamma=1$)			#OPT	Error (%)	T_{avg}	#OPT	Error (%)	T_{avg}	
	#OPT	Error (%)	T_{avg}	#OPT	Error (%)	T_{avg}							
pr2392	25	0.00	104.9	24	0.00	137.2	12	0.00	211.3	4	0.17	122.4	240
fl3795	25	0.00	435.1	15	0.00	615.9	17	0.00	770.7	0	0.57	-	1400
rl5934	25	0.00	1336.1	1	0.00	1854.6	10	0.00	2533.6	0	0.27	-	3300

To confirm the effectiveness of combining *cAS* with LK, we also tested the following three algorithms: *non-cAS* with LK (i.e., $\gamma=1$; no partial solutions are used), MMAS with LK, and Chained LK alone. The results are shown in Table 2. We can see all algorithms of *cAS*, *non-cAS*, and MMAS showed very small values of *Error* by combining LK and thus the advantage of combining these algorithms with LK is very clear. However, when we focus our attention on the results of #OPT, all algorithms except for *cAS* could not attain #OPT = 25. In contrast to this, *cAS* could attain #OPT = 25 within the allowed run time T_{max} showing the smallest T_{avg} (average time in seconds to find optimal in successful runs) among algorithms tested. Thus, we can see that using partial solutions is useful when the approach is combined with local search. Figure 7 shows the variations of T_{avg} and #OPT for various values.

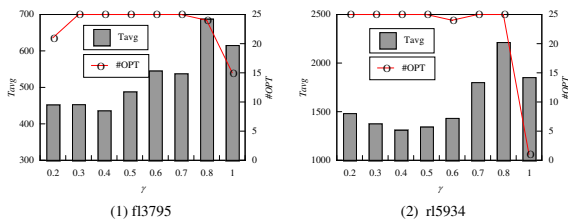


Figure 7: Results of cAS for variable γ values with LK on (1) fl3795 and (2) rl5934

5 Summary

In previous studies, we have proposed an algorithm referred to as the edge histogram based sampling algorithm (EHBSA) with EDA scheme for permutation domains. In EHBSA, new solutions are obtained by combining partial solutions which exist in the current population, and partial solutions newly generated according to an edge histogram model of the current population. In this paper, we showed that using partial solutions can maintain diversity of a population resulting in a successful search. We have also shown that using partial solutions in ACO can greatly enhance its performance. Thus, we can expect that a scheme using partial solutions in generating new solutions can be used in a wide range of EDAs. Applying this scheme to EDAs in other domains, such as real coding and binary coding remains for future work.

Acknowledgements

This research is partially supported by the Ministry of Education, Culture, Sports, Science and Technology of Japan under Grant-in-Aid for Scientific Research number 16500143.

References

- [1] D. E. Goldberg, *The design of innovation: Lessons from and for competent genetic algorithms* Vol. of Genetic and Evolutionary Computation, Kluwer, Boston, MA, 2002.
- [2] M. Pelikan, *Bayesian optimization algorithm: From single level to hierarchy*, Doctoral dissertation, University of Illinois at Urbana-Champaign, Urbana, IL, 2002. (Also IlliGAL Report No. 2002023).
- [3] M. Pelikan, D. E. Goldberg, and F. Lobo, "A survey of optimization by building and using probabilistic models," *Computational Optimization and Applications*, Vol. 20, No. 1, pp. 5-20, 2002.
- [4] P. Larrañaga and J. A. Lozano, *Estimation of distribution algorithms: A new tool for evolutionary computation*, Kluwer, Boston, MA, 2002.
- [5] H. Mühlenbein and G. Paa, "From recombination of genes to the estimation of distributions I. binary parameters," *Proc. of the 4th Parallel Problem Solving From Nature (PPSN IV)*, pp. 178-187, 1996.
- [6] P. A. N. Bosman and D. Thierens, "Permutation optimization by iterated estimation of random keys marginal product factorizations," *em Parallel Problem Solving From Nature (PPSN VII)*, pp. 331-340, 2002.
- [7] V. Robles, P. D. Miguel, and P. Larrañaga, "Solving the traveling salesman problem with edas," *Estimation of Distribution Algorithms*, pp. 211-229, 2002.
- [8] S. Tsutsui, "Probabilistic model-building genetic algorithms in permutation representation domain using edge histogram," *Proc. of the 7th Int. Conf. on Parallel Problem Solving from Nature (PPSN VII)*, pp. 224-233, 2002.
- [9] S. Tsutsui and M. Miki, "Solving flow shop scheduling problems with probabilistic model-building genetic algorithms using edge histograms," *Proc. of the 4th Asia-Pacific Conference on Simulated Evolution And Learning (SEAL02)*, 2002.
- [10] M. Dorigo and L. M. Gambardella, "Ant colony system: A cooperative learning approach to the traveling salesman problem," *IEEE Trans. on Evolutionary Computation*, Vol.1, No. 1, pp. 53-66, 1997.
- [11] M. Dorigo and T. Stützle, T., *Ant Colony Optimization*, MIT press, Massachusetts, 2004.
- [12] S. Tsutsui, "cAS: Ant colony optimization with cunning ant," *Proc. of the 9th Int. Conf. on Parallel Problem Solving from Nature (PPSN IX)*, pp. 162-171, 2006.
- [13] S. Lin, and B. W. Kernighan, "An effective heuristic algorithm for the traveling salesman problem," *Operations Research*, Vol. 21, pp. 498-516, 1973.

Stochastic Analysis of Schema Distribution in OneMax Problem

Hiroshi FURUTANI
Faculty of Engineering
University of Miyazaki
Miyazaki City, 889-2192

Susumu KATAYAMA
Faculty of Engineering
University of Miyazaki
Miyazaki City, 889-2192

Makoto SAKAMOTO
Faculty of Engineering
University of Miyazaki
Miyazaki City, 889-2192

Abstract

We have studied effects of stochastic fluctuation in the process of GA evolution of OneMax problem. We applied the Wright-Fisher model and the diffusion model for the analysis of GA with mutation and crossover. By using the diffusion model, we derived the stationary distribution of the first order schema frequency. In the comparison of numerical experiments and the theoretical calculations, we found that crossover is a very important factor determining the work of stochastic fluctuation.

1 Introduction

It is a difficult problem to determine the population size N in the application of GAs. Too small N may cause a poor performance in finding optimal solution(s), while too large N costs unnecessary computational power. The study of population sizing requires a stochastic treatment, which is in general a difficult task for the mathematical analysis.

In genetics, there are theories of Markov processes and diffusion equations. Population genetics uses the Wright-Fisher model of Markov processes [1], and diffusion models [2]. In the field of GAs, researchers apply Markov theory and its diffusion approximation. Nix and Vose proposed a stochastic model of GA evolution within the framework of Markov processes[3]. There are also analyses which use diffusion theories[4, 5].

Theoretical analyses in Genetics usually focus on one locus, and study the changes in frequencies of alleles within the locus. On the other hand, GA researchers treat multi-locus systems. This causes problems of dimensionality in Markov and diffusion approaches. To make the analysis tractable, Asoh and Mühlenbein restricted their study within the first order schemata[4]. In this study, we also used a mathematical framework of the first order schema theory,

and investigated their evolution by using the Wright-Fisher model and diffusion equations. We analyzed the evolution of GA with mutation and crossover in OneMax problem.

2 Mathematical Model

A population is consisted of N individuals, and we fix N throughout the evolution process. We represent individuals by binary strings of length ℓ , and there are $n = 2^\ell$ genotypes. We identify integers and binary strings by

$$i \equiv \langle i(\ell), \dots, i(1) \rangle,$$

where $i(k) \in \{0, 1\}$ is the k th component of the binary string.

Denoting a genotype $\langle i(\ell), \dots, i(1) \rangle$ by i , we represent the number of individuals with genotype i at generation t by $N_i(t)$. We also use the relative frequency $x_i(t)$ for describing the evolution

$$x_i(t) = N_i(t)/N.$$

The process of fitness proportionate selection is given by

$$x_i(t+1) = f_i x_i(t) / \bar{f}(t), \quad (1)$$

where $\bar{f}(t)$ is the average fitness of the population

$$\bar{f}(t) = \sum_{i=0}^{n-1} f_i x_i(t). \quad (2)$$

3 Deterministic Model

We derive here the evolution equation for the first order schema within the framework of the deterministic theory.

3.1 Linkage Equilibrium

Linkage means the correlation between the different loci in a population, and if there is some correlation we call this linkage disequilibrium [6]. In GA applications, we usually generate an initial population by producing 0 and 1 randomly and independently at each bit position. The initial population of this type is obviously in linkage equilibrium. However, as the GA calculation proceeds, the population frequently goes into linkage disequilibrium state. The causes of this change are the functional form of the fitness and genetic drift in the selection process [6]. It should be noted that crossover and mutation have the effect of recovering linkage equilibrium, and if crossover works sufficiently, the population is in linkage equilibrium throughout the evolution process.

The distribution of a population in linkage equilibrium is given by using relative frequencies

$$x_i(t) = \prod_{k=1}^{\ell} h_{i(k)}(t), \quad (3)$$

where $h_{i(k)}(t)$ is a frequency of the first order schema at position k , and $i = \langle i(\ell), \dots, i(1) \rangle$. We also use the notation of $h_0^{(k)}$ and $h_1^{(k)}$ for the first order schema frequencies of bit 0 and bit 1, respectively.

3.2 OneMax Function

In this study, we use the OneMax fitness function f_i

$$f_i = \sum_{k=1}^{\ell} i(k). \quad (4)$$

Since the string of all ones $\langle 1, 1, \dots, 1 \rangle$ is the optimum solution for this landscape, bit 1 is the favorable allele at all positions.

In the deterministic schema theory, the evolution of the first order schema in linkage equilibrium is given by [8]. The relative frequency of the first order schema at position k is determined by

$$h_1^{(k)}(t+1) = ah_1^{(k)}(t) + b, \quad (5)$$

where constants a and b are

$$a = (1 - \frac{1}{\ell})(1 - 2\mu), \quad b = \frac{1}{\ell}(1 - 2\mu) + \mu.$$

The solution is given in terms of a ,

$$b_0 = 1 - \frac{\mu}{2\mu + (1 - 2\mu)/\ell},$$

and the initial value $h_1(0)$

$$h_1(t) = a^t \{h_1(0) - b_0\} + b_0. \quad (6)$$

4 Markov Model

The stochastic model like Markov model explicitly treats the number of schemata. We consider the frequencies of two alleles at some locus. Two alleles are denoted by A and a, and the number of individuals having allele A and a are N_0 and N_1 , respectively. Since $N = N_0 + N_1$ is constant, we consider N_1 in this analysis.

We first consider the case in which both alleles have the same fitness. The probability $Q(j|i)$ that $N_1 = i$ at generation t becomes $N_1 = j$ at generation $t + 1$ is given by the binomial distribution

$$Q(j|i) = \binom{N}{j} \left(\frac{i}{N}\right)^j \left(1 - \frac{i}{N}\right)^{N-j}. \quad (7)$$

The probability $q_i(t)$ of $N_1 = i$ at generation t obeys the evolution equation

$$q_j(t+1) = \sum_{i=0}^N Q(j|i) q_i(t). \quad (8)$$

This equation is represented by using $(N + 1)$ -dimensional vector $\mathbf{q}(t)$

$$\mathbf{q}(t) = (q_0(t), \dots, q_N(t))^T,$$

where T is transversion, and the matrix $Q = [Q(j|i)]$

$$\mathbf{q}(t+1) = Q \mathbf{q}(t), \quad (9)$$

This model is called as the Wright-Fisher model[1].

We can express the evolution process analytically if we obtain the eigenvalues and eigenvectors of Q . We know the eigenvalues of the matrix [1]

$$1, \quad 1, \quad 1 - \frac{1}{N}, \quad \dots, \quad \prod_{i=1}^{N-1} \left(1 - \frac{i}{N}\right),$$

Unfortunately, we do not have the analytical expression of all eigenvectors. We only have two eigenvectors corresponding to the eigenvalue 1

$$\mathbf{q}_A = (1, 0, \dots, 0)^T, \quad \mathbf{q}_a = (0, 0, \dots, 1)^T,$$

These eigenvectors represent two absorbing states in Markov process. All processes converge to one of these absorbing states. The eigenvector \mathbf{q}_A stands for the extinction state where there is no favorable allele in the population, and \mathbf{q}_a for the fixation state of the favorable allele.

Next, we consider the case where two first order schemata have different fitness values. We use allele

A and a to denote binary values 0 and 1, respectively, and their fitness values are

$$f_A = 1, \quad f_a = 1 + s, \quad (s \geq 0).$$

The transition matrix $Q(j|i)$ is given by

$$Q(j|i) = \binom{N}{j} u(s)^j \{1 - u(s)\}^{N-j}, \quad (10)$$

$$u(s) = \frac{(1+s)i}{N+si}.$$

This matrix also has a maximum eigenvalue 1 with multiplicity 2, and their corresponding eigenvectors are

$$\mathbf{q}_A = (1, 0, \dots, 0)^T, \quad \mathbf{q}_a = (0, 0, \dots, 1)^T.$$

It is also true that \mathbf{q}_A and \mathbf{q}_a are absorbing states.

Finally, we derive the transition matrix on the OneMax fitness. Replacing

$$h_1(t) \rightarrow i/N$$

in the evolution equation of the first order schema (5), we have the transition matrix

$$Q(j|i) = \binom{N}{j} u(y)^j \{1 - u(y)\}^{N-j}, \quad (11)$$

$$u(y) = ay + b = a\frac{i}{N} + b,$$

where $y = i/N$. This transition matrix has eigenvalues ν_0, \dots, ν_N

$$\nu_0 = 1, \quad \nu_1 = a, \dots, \nu_k = \prod_{i=0}^{k-1} a(1 - i/N), \dots \quad (12)$$

These eigenvalues are independent of b , and the second largest eigenvalue $\nu_1 = a$ does not depend on N .

5 Diffusion Model

Though it is believed that Markov model can reproduce many evolution processes in biology, its mathematical analysis is very difficult. Therefore, the approximation of Markov model by the diffusion equation is used in genetics[1]. In the following, we derive the diffusion equation for OneMax problem.

We define

$$\Delta y(t) = y(t+1) - y(t),$$

Noting that i , therefore $y(t)$, is fixed, we calculate its expectation value

$$E\{\Delta y(t)\} = \sum_{j=0}^N \frac{j}{N} \cdot q_j(t+1) - y(t),$$

and variance

$$V\{\Delta y(t)\} = \frac{1}{N^2} \sum_{j=0}^N j^2 \cdot q_j(t+1) - E\{\Delta y(t)\}^2.$$

Using

$$\sum_{j=0}^N \frac{j}{N} \cdot q_j(t+1) = \sum_{j=0}^N \frac{j}{N} \binom{N}{j} u(y)^j \{1 - u(y)\}^{N-j},$$

we have

$$E\{\Delta y(t)\} = u(y) - y = (a-1)y + b. \quad (13)$$

In the same way, we have

$$V\{\Delta y(t)\} = u(y)\{1 - u(y)\}/N. \quad (14)$$

From equations (13) and (14), we define two functions of y

$$M(y) = (a-1)y + b, \quad V(y) = u(y)\{1 - u(y)\}/N.$$

The diffusion approximation of Markov process in OneMax problem is given in terms of $M(y)$ and $V(y)$

$$\frac{\partial \phi(y, t)}{\partial t} = \frac{1}{2} \frac{\partial^2}{\partial y^2} \{V(y)\phi(y, t)\} - \frac{\partial}{\partial y} \{M(y)\phi(y, t)\}. \quad (15)$$

This equation is called Kolmogorov forward equation, and $\phi(y, t)$ stands for the probability density function of the relative frequency y and time t .

We derive the solution of Kolmogorov forward equation (15). At $t \rightarrow \infty$, we try to obtain the stationary solution $\psi(y)$. Since $\partial \phi(y, t)/\partial t = 0$, $\psi(y)$ satisfies

$$\frac{d^2}{dy^2} \{V(y)\psi(y)\} - 2 \frac{d}{dy} \{M(y)\psi(y)\} = 0.$$

By integrating the differential equation, we have

$$\psi(y) = C (ay + b)^{2c_1-1} (1 - ay - b)^{2c_2-1} \quad (16)$$

where C is a normalization constant, and c_1 and c_2 are

$$c_1 = Nb/a^2, \quad c_2 = N(1 - a - b)/a^2.$$

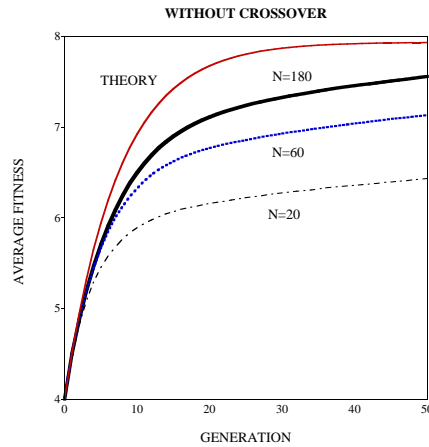
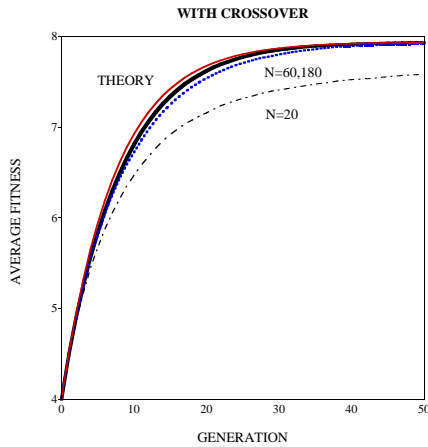


Figure 1: N dependence of $\bar{f}(t)$, with crossover. Figure 2: N dependence of $\bar{f}(t)$, without crossover.

6 Numerical Experiment

In this section, we compare results of the theoretical analysis with numerical experiments. We use the fitness proportionate selection and uniform crossover. The length of string is $\ell = 8$. We performed 1000 runs for each parameter set, and averaged over them.

Figure 1 shows the average fitness $\bar{f}(t)$ with the use of three population sizes, $N = 20, 60, 180$. We used the crossover rate $\chi = 1$ and mutation rate $\mu = 0.001$. The solid line with the label THEORY is obtained by the deterministic evolution equation (5) and $\bar{f}(t) = \ell h_1(t)$. Figure 2 shows the same results of GA calculations without crossover.

In the calculations with crossover, we observe small N dependence except for $N = 20$, and these results almost coincide with the deterministic theory. This fact can be explained by the fact that the population is in linkage equilibrium due to the action of crossover. In linkage equilibrium, Wright-Fisher model can describe the distribution of alleles in good approximation, in which the second largest eigenvalue does not have N dependence. Since the population size is small in the case of $N = 20$, there is large effect of genetic drift that makes the population in linkage disequilibrium.

On the contrary, we observe large differences in the results of different N in Fig.2. Especially, if N is small, the performance of the calculation is very poor. The strong N dependence suggests large effects of genetic drift in calculations without crossover.

Figure 3 explains the result of $N = 20$ with crossover. In 1000 repeated calculations, the numbers of fixations and extinctions of the favorable first order schema are shown as functions of generation. From

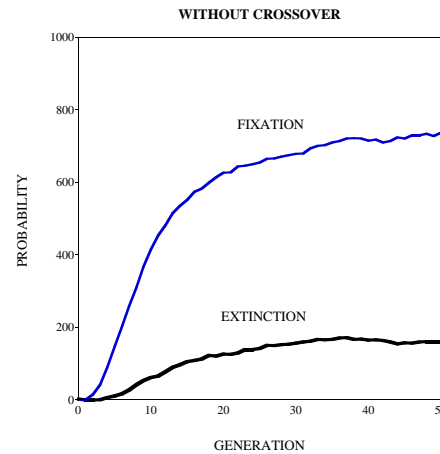


Figure 3: Fixation and extinction probabilities of the favorable first order schema. Without crossover. $N = 20$, $\ell = 8$, $\mu = 0.001$.

this figure, we see that about 15% of favorable schema disappear from the population.

Linkage equilibrium due to crossover does not mean small N dependence. Figures 4 and 5 show distributions of the favorable first order schema at the stationary states ($t = 100$) with $\mu = 0.02$ and $\chi = 1$. The abscissa represents the relative frequency of bit one. The solid lines are the results of numerical calculations and dotted lines are those of diffusion approximation (16). The large difference between two distributions comes from the difference in N .

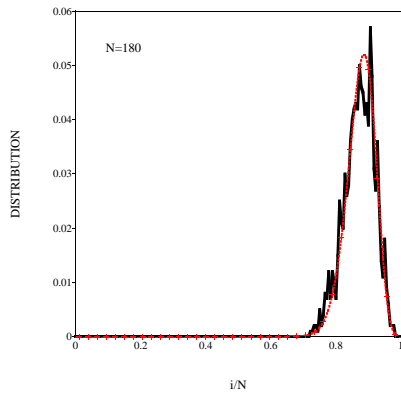


Figure 4: Distribution of the favorable first order schema, $\mu = 0.02$.

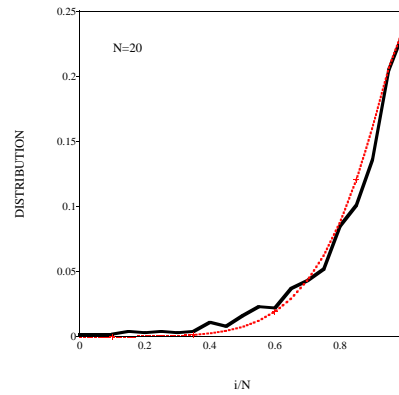


Figure 5: Distribution of the favorable first order schema, $\mu = 0.02$.

7 Summary

This study treats the schema evolution in OneMax by the use of the Wright-Fisher model and diffusion equations. If we can define favorable and unfavorable genes in one locus model, the fixation and extinction states are absorbing states in usual Markov processes, and this brings the N -dependence in GA calculations, for example, on the multiplicative landscape. While in the case of OneMax problem, the extinction state acts as a reflecting wall, and the probability of extinction state is zero. The reason is that the probability of the genotype $\langle 0, 0, \dots, 0 \rangle$ is zero. The assumption of linkage equilibrium means the probability of h_0 is also zero. Therefore the state $N_1 = 0$ cannot work as an absorbing wall. This partly explains the weak N -dependence in OneMax problem.

References

- [1] Ewens, W.J.: Mathematical Population Genetics. I. Theoretical Introduction, Second Edition. Springer-Verlag, New York (2004)
- [2] Crow, J. F., Kimura M.: An Introduction to Population Genetics Theory. Harper and Row, New York (1970)
- [3] Nix, A. E., Vose, M. D.: Modelling Genetic Algorithm with Markov Chains. Annals of Mathematical and Artificial Intelligence. **5** (1992) 79–88
- [4] Asoh, H., Mühlenbein, H.: On the Mean Convergence Time of Evolutionary Algorithms without

Selection and Mutation. Parallel Problem Solving from Nature, Lecture Notes in Computer Science, **866**, Springer-Verlag, New York, (1994) 88-97

- [5] Suzuki, H., Iwasa, Y.: Crossover Accelerates Evolution in GAs with a Babel-like Fitness Landscape: Mathematical Analyses. Evolutionary Computation, **7** (1999) 275-310; Errata: **8** (2000) 121-122
- [6] Maynard Smith, J.: Evolutionary Genetics. 2nd edition, (Oxford University Press, Oxford, 1998).
- [7] Furutani, H.: Schema Analysis of Genetic Algorithms on Multiplicative Landscape. in Recent Advances in Simulated Evolution and Learning, (World Scientific, Singapore, 2004) Chapter **6**
- [8] Furutani, H.: Schema Analysis of OneMax Problem –Evolution Equation for First Order Schemata–. in Foundations of Genetic Algorithms 7, (Morgan Kaufmann, San Francisco, 2003) 9–26
- [9] Whittaker, E.T. and Watson, G.N.: A Course of Modern Analysis, 4th Edition, (Cambridge University Press, Cambridge, 1927) 281–296

Identification of Exon-intron Boundaries by Integration of Base-oriented Genetic Programming and Statistical Heuristics

Kunihito YAMAMORI
Univ. Miyazaki
Miyazaki 889-2192

Yuji FUJITA
Mitsubishi Space Software
Ibaraki 305-0032

Masaru AIKAWA
Univ. Miyazaki
Miyazaki 889-2192

Ikuo YOSHIHARA
Univ. Miyazaki
Miyazaki 889-2192

Abstract

Genetic Programming (GP) is one of the promising methods to detect exon-intron boundaries from DNA sequences. In conventional method, two- or four-bit binary codes represent four bases, and each bit of codes are used as input to the identification model. These bit-oriented GP is simple, but it is difficult to know which bases are key to identify the boundary. Here we develop a novel base-oriented GP which can directly use bases as inputs. Moreover, we integrate the model generated by base-oriented GP with heuristics that is defined as bias of appearance frequencies on particular loci around "GT" and "AG" extracted from about 8,000,000 DNA sequences. Simulation results show that our method can improve the accuracy about 10% on the "AG" boundary identification.

1 Introduction

A gene in DNA consists two parts; one is exon and the other is intron. Exon encodes information how to synthesize proteins. Intron exists between exons, and function of intron is not clear still yet. Now it is a very important subject to automatically extract exon regions and intron regions from DNA to diagnose some kinds of diseases or to create new medicine. However, it is very difficult to analyze gene data because it is too many and still increasing day after day.

To automatically extract exons and introns from DNA sequences by computers, Some methods have been investigated until now. Kamimai[1] had proposed multi-modal neural network and succeeded to improve accuracy of identification. Ohta[2] had developed a combination of GA (Genetic Algorithm) and GMDH (Group Method of Data Handling), and showed good performance of identification. In these method all bases in a region including focusing bases are encoded to two- or four-bits binary codes, and each bit is used as inputs to the identification model. These binary encoding lead indistinctness which bases are the keys to identify boundaries.

Our aim is to develop a method that can directly use

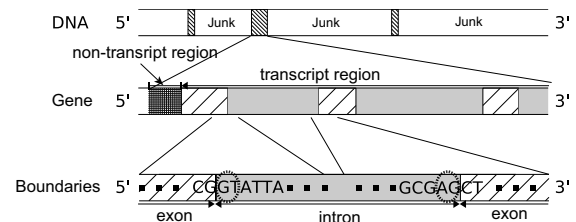


Figure 1: DNA and gene.

the bases as inputs to the model, and it also achieves accurate exon extraction from DNA sequences. So we modify Genetic Programming (GP) to be able to handle the base characters directly. And we combine the GP and statistical heuristics extracted from 8 million DNA sequences.

2 DNA sequences and heuristics

2.1 Decision of input region

Figure 1 illustrates that most 5'-end and 3'-end of introns has the bases "GT" and "AG"[3]. Since the sequences "GT" and "AG" also appear in exons and introns, it is impossible to identify boundaries by this rule. On the other hand some bases often appear in specific locus around the boundary. We utilize this bias of appearance to identify boundaries between exons and introns.

Human DNA sequences was obtained from NCBI¹ database, then ± 200 bases around "GT" or "AG" are extracted. The number of extracted sequences is as follows;

- Sequences with "GT"
 - Boundary data: 26,046
 - Non-boundary data: 7,610,718
- Sequences with "AG"
 - Boundary data: 22,633
 - Non-boundary data: 8,481,368

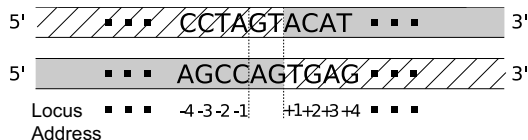


Figure 2: Addressing for loci.

Here $P(b, X)$ denotes the appearance probability of the base 'X' at the locus b , and the address of locus b is defined as shown in Figure 2. The $P(b, X)$ only from sequences including boundary is described as $P_B(b, X)$, and that without boundary is also described as $P_N(b, X)$. Then the difference $P_d(b, X)$ between $P_B(b, X)$ and $P_N(b, X)$ is calculated as Equation (1).

$$P_d(b, X) = P_B(b, X) - P_N(b, X), \quad (1)$$

here $b = \{-200, -199, \dots, +200\}$ and $X \in \{A, G, C, T\}$.

From the bias of $P_d(b, X)$, we decide to use 20 bases to identify "GT" boundary (10 bases for 5'-side and 3'-side), and 37 bases to identify "AG" boundary (30 bases for 5'-side, 7 bases for 3'-side)[4].

Fujita[4] also said that the appearance frequencies of specific bases at some loci are different between boundaries and non-boundaries. So we define heuristics as the combination of the base and the locus with high bias in appearance frequency. These combination of specific loci and bases is integrated with GP by the following two method.

2.2 Majority method

In this way $P_d(b, X)$ is used as heuristics and combined through the majority operator into the model generated by GP. Following steps shows how to combine the model and the heuristics.

Step.1 Calculation of $P_d(b, X)$.

Step.2 Four combinations of b and X with the highest $|P_d(b, X)|$ are selected as heuristics.

Step.3 Four sub-trees consisting of a terminal node and a comparing node explained in Section 3 are constructed. The comparing node has $Eq(X, I)$ if the bias of appearance frequency at the locus b is positive. Otherwise it has $\overline{Eq(X, I)}$.

Step.4 Four sub-trees and an individual generated by GP is combined through the tree-fifth majority node $M(3/5)$.

All individuals combine with the same heuristics, and the fitness is evaluated by the output of the final $M(3/5)$. The same sub-trees as the heuristics never appear in individuals.

¹National Center for Biotechnology Information

2.3 Embedding method

In this method a couple of bases are used as heuristics. These heuristics are called as 2-tuple heuristics. The 2-tuple heuristics are found from the ± 200 bases around the focusing "GT" and "AG", then 30 2-tuple heuristics will be combined with the model by the following steps.

Step.1 The appearance frequency $P_B^2(b_1, b_2, X_1, X_2)$ and $P_N^2(b_1, b_2, X_1, X_2)$ are calculated from boundary data and non-boundary data, respectively. Here b_1 and b_2 is address of locus, and X_1 and X_2 denote bases.

Step.2 Calculation of $P_d^2(b_1, b_2, X_1, X_2) = |P_B^2(b_1, b_2, X_1, X_2) - P_N^2(b_1, b_2, X_1, X_2)|$.

Step.3 30 combinations of (b_1, X_1) and (b_2, X_2) with the largest $P_d^2(b_1, b_2, X_1, X_2)$ are selected as the 2-tuple heuristics.

Step.4 Two sub-trees are constructed; a terminal node b_1 and a comparing node $Eq(b_1, X_1)$, and a terminal node b_2 and a comparing node $Eq(b_2, X_2)$.

Step.5 The comparing node with "AND" operator integrates two sub-trees if $P_d^2(b_1, b_2, X_1, X_2) > 0$. Otherwise they are integrated by a node with "NAND" operator.

These 2-tuple heuristics are inserted into individuals at the following processes.

Insertion into initial individuals: 30 individuals are randomly selected and a part of individual is exchanged to a 2-tuple heuristics at the generation of initial population.

Insertion at mutation process: A part of individual is exchanged to 2-tuple heuristics at the mutation process.

3 Genetic operations

3.1 Operators

In this research we directly use the base characters themselves as inputs to GP. Figure 3 shows an example of individual to identify boundaries generated by GP. Fig.3 shows that terminal nodes keep the address of locus, and a non-terminal node is either a logic operator or a comparing operator. A node with a logic operator calls as a logic node, and a node with a comparing operator also calls a comparing node. Equation (2) says that the comparing operator

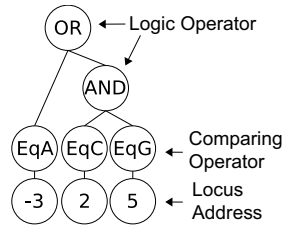


Figure 3: An example of individual.

Table 1: Logic operators in the model.

#s of arguments	logic operator
1	NOT
2	AND OR XOR NAND NOR XNOR
3	M(2/3) Two-third majority NM(2/3) Negative of M(2/3)

returns 1 if the input I from the terminal node is as same as the target base character X .

$$Eq(X, I) = \begin{cases} 1 & X = I, \\ 0 & X \neq I, X, I \in \{A, G, C, T\} \end{cases} \quad (2)$$

Table 1 shows available logic operators in logic nodes. Since an output of a terminal node is a character and inputs to a logic operator have to be boolean, a comparing node is coupled with a terminal node. These nodes are arranged as a tree for a boundary identification model.

3.2 Genetic operations

To make models, GP performs the following genetic operations.

Initialization: It randomly generates terminal nodes, logic nodes and comparing nodes, then arranges them as individuals.

Crossover: It randomly selects two individuals then exchange a part of individual (sub-tree) each other. So two children are generated by this operation. This operation does not allow some kinds of sub-tree exchanging because a terminal node must combine with a comparing node. The combinations of exchangeable nodes are completed in Table 2. In Table 2, L. node, C. node and I. node denote a logic node, a comparing node and an input node, respectively.

Fitness evaluation: Equation (3) defines the fitness.

$$fitness = \sum_{k=1}^T Z_k, \quad (3)$$

$$Z_k = \begin{cases} 1, & Y'_k = Y_k, \\ 0, & Y'_k \neq Y_k, \end{cases}$$

Table 2: Available combination at crossover operation.

	L. node	C. node	I. node
L. node	OK	OK	NG
C. node	OK	OK	NG
I. node	NG	NG	OK

where Y_k is 1 when the identification result by model says true (boundary) and Y'_k is also 1 when the k -th sequence is actually boundary. So $\sum_{k=1}^T Z_k$ means the sum of the correctly identified sequences.

Mutation: This operation randomly exchange the operator in a node to the other one with the same number of arguments if the selected node is a logic node. If a terminal node is selected, the other locus is employed. When a comparing node is selected, the other comparing operation take place of original one.

Selection: roulette strategy and elite preserving are employed.

4 Experiments and discussions

4.1 Parameters

We make eleven data sets from the sequences mentioned in Section 2, then a data set is used for model generation, and the others are used for model evaluation. No duplication exists among the data sets. The parameters of GP for simulations are as follows;

- Numbers of individuals: 100
- Maximum nodes in a model: 200
- Crossover ratio: 100%
- Mutation ratio: 1%
- Maximum generations: 4,000

The number of simulations are 10 on each data set for model evaluation.

4.2 Measures for evaluation

Sensitivity S_n and *Specificity* S_p defined by Equation (4) and Equation (5) evaluate accuracy.

$$S_n = \frac{N_c}{B} \times 100 \quad (\%), \quad (4)$$

$$S_p = \frac{N_c}{N_c + N_m} \times 100 \quad (\%), \quad (5)$$

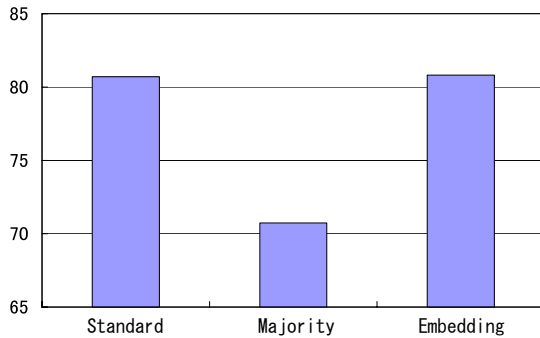


Figure 4: S_n by each method on "AG" boundaries.



Figure 5: S_p by each method on "AG" boundaries.

where B denotes the number of boundary data, N_c and N_m denote the number of correctly identified boundaries and miss identified non-boundaries, respectively.

4.3 Results and discussions

Figure 4 and Figure 5 show the average S_n and S_p for verification sequences. Here we only show the result on "AG" boundaries because relatively poor results was reported in previous works[2]. In Fig.4 and Fig.5, "Standard" means the result by GP without heuristics.

In Figure 4, S_n by majority method falls about 10% than that of standard GP, it means the model combined with the majority operator often ignore the boundaries. It is because the answer from the model generated by GP and answers from the heuristics sometimes compete and cancel each other. Figure 5 illustrates that the GP with 2-tuple heuristics improves S_p about 10% than that by standard GP. It means that the embedding method can detect more boundaries than those by the other methods, and less non-boundaries are detected as boundaries.

Experimental results show that embedding method with 2-tuple heuristics improves accuracy of boundary identification with keeping boundary detection.

5 Conclusions

Automatic extraction of exon regions from DNA sequences is very difficult because the sequences have too much variety, and the number of sequences is also too huge. In particular, the identification of "AG" boundaries was not accurate by previous works because features to identify "AG" boundaries dispersedly exist in sequences.

In this research we develop a novel method to identify boundaries. At first, we decide the appropriate region for boundary identification from the bias of appearance frequencies on bases at each locus. The analysis reveals that ± 10 bases are enough for "GT" boundaries, and 37 bases for "AG" boundaries. Then we think out a novel base-oriented identification model for GP that can directly handle the character of bases. Finally we compare the two method to integrate the model by GP and statistical heuristics. The embedding method achieved about 10% accuracy improvement to detect "AG" boundaries.

To achieve more accurate identification, the model considering solid structure of protein will be remaining as future works. Furthermore faster processing is also needed.

Acknowledgments

A part of this research is supported by Grant-in-Aid for Scientific Research #17700239.

References

- [1] Y. Kamimai, I. Yoshihara, K. Yamamori and M. Yasunaga, "Methods to Extract Exon Regions from DNA Sequence – Development of Multi-modal Neural Network –", *Fuzzy, Artificial Intelligence, Neural Networks and Computational Intelligence (FAN'02)*, pp. 385–390 (2002).
- [2] T. Ohta, I. Yoshihara, K. Yamamori and M. Yasunaga, "GP-based Method for Identifying Exon Region in DNA Sequences", *Proc. 4th Asia-pacific Conference on Simulated Evolution and Learning (SEAL'02)*, pp. cr1333(CD-ROM) (2002).
- [3] M. B.Shapiro and P. Senapathy, "RNA splice junctions of different classes of eularyotes: sequence statistics and functional implications in gene expressions", *Neucleic Acids Research*, Vol. 15, pp. 7155–7175 (1987).
- [4] Y. Fujita, K. Yamamori, I. Yoshihara and M. Aikawa, "Generation of Character-base Model by Genetic Programming to Identify Exon-Intron Boundaries", *Tech.Report IEICE (CAS2005-75)*, Vol. 105, No. 503, pp. 1–6 (2006) (In Japanese).

Variable-Length-Segmental-Transmission-Line and its Design Guidelines

KOIZUMI N. HAYASHI K. YASUNAGA M.
Univ. of Miyazaki, Univ. of Tsukuba, Univ. of Tsukuba,
Miyazaki, 889-2192 Japan Ibaraki, 305-8583 Japan Ibaraki, 305-8583 Japan

YAMAMORI K. YOSHIHARA I.
Univ. of Miyazaki, Univ. of Miyazaki,
Miyazaki, 889-2192 Japan Miyazaki, 889-2192 Japan

Abstract

Waveform distortion is a serious problem in higher-frequency signals on printed circuit boards (PCB). To overcome this problem, we have already proposed segmental transmission line (STL) method. That method divides transmission lines into several segments with different line width. Each line width is adjusted to make the reflection noises cancel out each other for minimizing the signal distortion.

In this research, we analyze the waveform reshaping mechanism of STL. Next, we apply STL to a DIMM (Dual In-line Memory Module) clock-line for high-speed computers. As a result, we obtained helpful STL design guidelines and we showed effective example of STL.

1 introduction

While VLSIs (e.g. Pentium CPU) perform in GHz clock-speed nowadays, signals propagating on motherboards in PCs are still in hundreds of MHz frequency-range. This great difference between two operation speeds is one of serious bottlenecks for high speed processing. In addition, higher signal integrity on the PCB is required to overcome this problem.

On a PCB, many ICs and other electronics components are connected with transmission lines. These connections cause characteristic-impedance mismatches in the transmission lines, and they bring reflection noises that distort signal waveforms considerably. Reflection noises increase as signal frequency increases, hence the higher speed electronics systems will be affected more terribly by the noises.

In order to overcome this problem, we propose the *segmental transmission line* (STL) formerly. STL is the method in which a transmission line is divided into multiple segments of different line-widths. We make

impedance mismatches intentionally so as to generate reflection waves. Each line width is adjusted to make the reflection noises cancel out one another to minimize the signal distortion.

We have shown the following three approaches:

- Single objective, fixed-length segment [1]:
Widths in fixed length segments are adjusted to reshape a waveform in a single point.
- Single objective, variable-length segment:
Both widths and lengths in segments are adjusted to reshape a waveform in a single point.
- Multi objective, variable-length segment [2]:
Both widths and lengths in segments are adjusted to reshape a waveform in a two points in a line.

In this research, we analyze the waveform reshaping mechanism of STL and the purpose is to obtain helpful design guidelines. Next, we show effective examples of DIMM clock-line using STL.

2 Segmental Transmission Line

2.1 Fixed-length STL

Fig.1-(a) shows a structure of the fixed-length STL. A transmission line is divided into 10 same-length segments of individual line widths W_1 to W_{10} , in this case. An R_{on} and a pulse source in the figure represent a source VLSI, and R_D and R_T are a dumping and termination resistances, respectively. Electronics components such as memory modules or VLSI chips connected to the transmission line are represented as capacitances C_i s that cause waveform distortion.

- In the transmission line, because of the characteristic-impedance mismatch between two segments a reflection noise occurs at the segment interface.

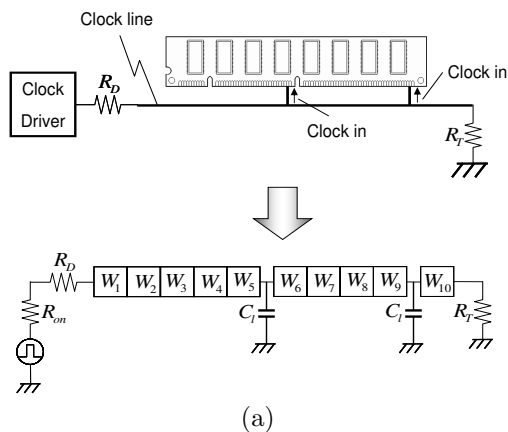


Figure 1: The structure of STL

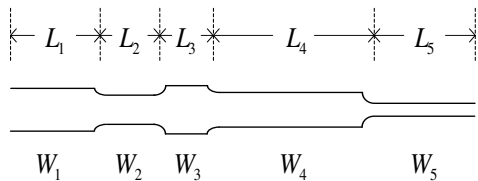


Figure 2: An example of variable-length STL

- Reflection noises are superimposed with the distorted signal at signal output point where an electronics component is connected.
- In the STL, multiple characteristic-impedances in the segments are adjusted together so that the their reflection noises superimposed at the output reshape the distorted signal.
- In the fixed-length STL, each segment is designed to give the designed characteristic-impedance by changing its line width as shown in Fig.1-(b).

Yasunaga et al. have designed transmission lines for two memory modules in PCs by using the fixed-STL. They used 10 to 20 segments in the designed under 99 width-candidates to reshape waveforms.

2.2 Variable-length STL

Next, we propose the variable-length STL to reduce the parameter set. In the variable-length STL, we use

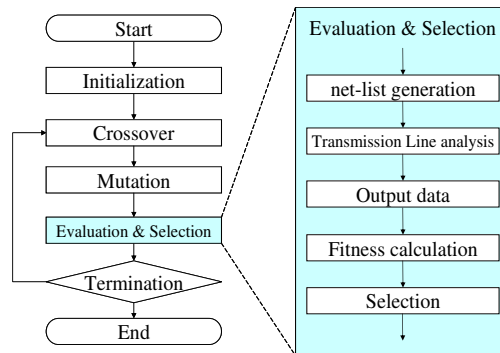


Figure 3: Parameter decision flow using GA

variable length segments (see Fig.2) instead of fixed ones with a reduced parameter set of line widths. Although the number of parameters increases due to the variable-length, we can decrease the line-width range drastically instead and reduce the parameter set as a whole. Given m segments and n line width, the total search space enlarges to n^m . Additionally given the length of segment by real number value, it is impossible to search the optimized parameter-set by analytical technique. Thus, we use GA (Genetic Algorithm) to decide parameters in the variable-length STL.

3 Optimization using GA

3.1 STL design flow

Fig.3 shows the design flow for the STL. This generation alternation model is combined with MGG (Minimal Generation Gap) [3] and POSS (Pareto Optimal Selection Strategy). POSS is just same idea as elitist strategy at single-objective optimization.

We use SPICE for fitness calculation in the GA. SPICE [4] is the analog circuit simulator which is most widely used.

3.2 Genetic Coding

We use two chromosomes separately to one transmission-line (see Fig.4):

- One chromosome is composed of pairs of widths of adjoining segments or resistors. (We call the chromosome is *width-chromosome*)
- The other chromosome is composed of site of the segment boundaries. (We call the chromosome is *length-chromosome*)

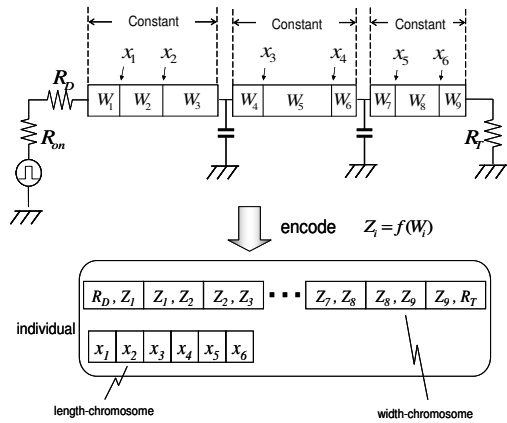


Figure 4: Composition of an individual with chromosomes

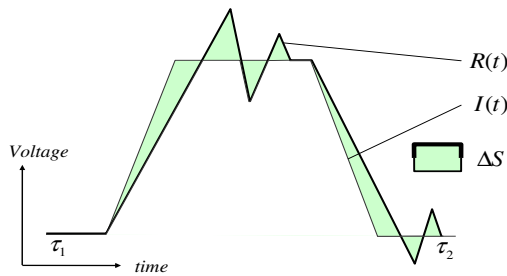


Figure 5: Fitness defined by the difference between observed waveform and ideal waveform

3.3 Genetic Operation

Crossover:

One point crossover is used for the width-chromosome. On the other hand, BLX is used for the length-chromosome. BLX is typically crossover of real-coded GA.

Fitness evaluation:

We define fitness function as follows. S is the difference area between the observed waveform on the designed transmission line and the ideal waveform, as shown in Fig.5. As S decreases getting close to the ideal waveform, fitness value increases.

$$S = \int_1^2 |I(t) - R(t)| dt \quad (1)$$

$$fitness = \frac{1}{S + \varepsilon} \quad (2)$$

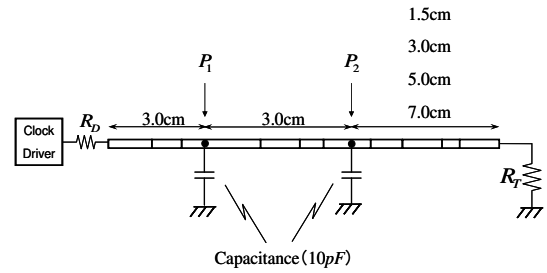


Figure 6: Model of clock line with a memory module

$I(t)$: Ideal waveform
 $R(t)$: Observed waveform
 ε : Small constant

4 Experiments

4.1 Design target

We designed an actual clock line with a memory module (DIMM: Dual In-line Memory Module) on a typical PCB in a personal computer by using our proposed method. The phase of the reflection depends on the length of the segment because the reflection is generated by the boundaries of the segments. Thus, we examine a correlate of line length and waveform distortion.

Fig.6 shows experimental target. Because the length between modules is given, we experiment changing with length of $P_2 - R_T$ like a Fig.6.

4.2 Conditions

Experimental conditions are as follows:

- Propagating signals
 - Signal amplitude 3.3V
 - Switching time 20ps
 - Signal cycle time 2ns
- GA Parameters
 - Population size 100
 - BLX- α 0.366
 - Crossover/generation 10
 - End condition over 1000 generations
- Variable length STL parameters
 - Impedances 20, 30, 100, 120 Ω
 - R_D & R_T 20 120 Ω
 - Number of segments
 - $R_D - P_1$ 3
 - $P_1 - P_2$ 3
 - $P_2 - R_T$ 3

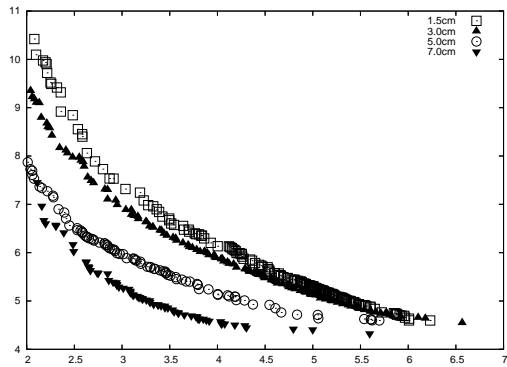


Figure 7: Pareto solutions

4.3 Results

Fig.7 shows Pareto group of each length at final generation. The horizontal axis shows area-difference at P_1 and the vertical axis shows area-difference at P_2 . As a result, the longer distance between P_2 and R_T is, the smaller area-difference is.

Fig.8 shows observed waveform at P_1 on normal transmission line. The normal transmission line is all-same-width (76Ω) transmission line. Fig.9 shows waveform in one of paretos of 7.0cm which was designed by our method. In those figures, the dashed lines show the ideal waveform without distortion. In Fig.8, the waveform is distorted like sin curve. On the other hand, the waveform in STL are reshaped like ideal waveform.

5 Conclusion

In this paper, we showed variable length STL with changing with transmission line length. We applied the variable length STL to a DIMM clock line and succeeded in reshaping waveform.

We will speed up the GA calculation and apply the variable length STL to other high-speed clock line in more practical-scale circuits on PCBs in the future works.

Acknowledgements

This work was supported in part by grant of the Japan Science and Technology Agency.

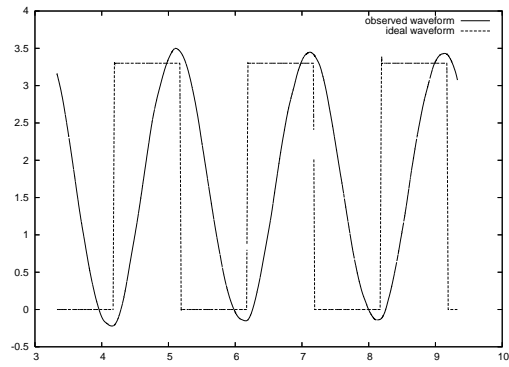


Figure 8: Waveform about normal transmission line

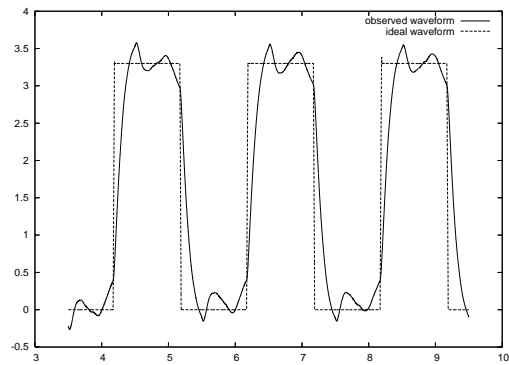


Figure 9: Waveform about STL

References

- [1] M. Yasunaga, I. Yoshihara and Jung H.Kimm, "The design of segmental-transmission-line for high-speed digital signals using genetic algorithms" *proc. of CEC2003*, pp. 1748-1755.
- [2] N. Koizumi, I. Yoshihara, K. Yamamori, M. Yasunaga, "Enhancement of the Variable-Length-Transmission-Line design method for multi-point optimization" *proc. of CEC2006*, CD-ROM.
- [3] H. Sato, I. Ono, S. Kobayoshi, "A New Generation Alternation Model of Genetic Algorithms and its Assessment" *Trans. of JSAI*, Vol.12, No.5, pp.734-744, 1997. (In Japanese)
- [4] <http://bwrc.eecs.berkeley.edu/Classes/IcBook/SPICE>

A Reconfigurable-VLSI-based Double-lens Tracking-camera

**Moritoshi Yasunaga,
Noriyuki Aibe,
Yoshiki Yamaguchi**

Graduate School of Systems
and Information Engineering,
University of Tsukuba,
Ten-no-dai 1-1-1, Tsukuba,
Ibaraki, 305-8573 Japan.
yasunaga@cs.tsukuba.ac.jp
susu@susutawari.org
yoshiki@cs.tsukuba.ac.jp

Yorihisa Yamamoto

Yamamoto System Design Inc.,
3481 Oozone, Tsukuba
Ibaraki, 300-3253, Japan
yorihisa@edonagasaki.ne.jp

Takaaki Awano

Bethel Inc.,
Aragane 3-11, Ishioka,
Ibaraki, 315-0021, Japan
t-awano@bethel.co.jp

Ikuo Yoshihara

Faculty of Engineering,
University of Miyazaki,
1-1 Gakuen Kibanadai Nishi,
Miyazaki, Miyazaki,
889-2192, Japan
yoshiha@cs.miyazaki-u.ac.jp

Abstract

Watching and tracking an object as seeing a wide whole view is one of advantages in the eye-system. We propose and develop a tracking camera system that mimics the eyes using double-lens modules. In the system, a wide whole view is captured through the wide-lens module while the target in it is tracked and magnified through the telescope-lens module. Electronic circuits for the tracking control are implemented onto the reconfigurable VLSI, or FPGA in order to embed the parallelism in the tracking algorithm into the hardware. An FPGA-based prototype developed successfully performs high speed tracking along with the video-rate.

1. Introduction

We human beings can watch and track an object without losing wide whole view. Thanks to this simple concurrent function, but with complex mechanism, of the eye we can recognize the target correctly under huge amount of information rushes into the brain via the eyes. Our goal in this paper is to propose and develop a novel tracking-camera composed of double-lens modules for wide and telescope views concurrently, which is the same function as the human eye has.

Initially, we designed a camera with a single lens-module system that resembled the eye in appearance. It has been, however, turned out that a fine-resolution sensor-device with high-speed random access capability is indispensable for the single lens-module system and its cost is much more expensive than for the consumer product.

On the basis of the initial examination mentioned above, in this paper, we propose a camera system consists of two lens-modules: one module is to capture wide views while the other one is to track and magnify the target with its pan-tilt mechanism. This camera system has been designed and developed based on the Bio-inspired camera [1] and the PNN (Probabilistic Neural Network) pattern recognition system [2] that was developed by us using FPGAs (Field Programmable Gate Array). On these days, the FPGA, in which we can reconfigure its logic circuits anytime in contrast to the VLSI processor or DSP, is getting well known and is widely used for rapid-prototyping-design in hardware developments. Novel architectures for the new tracking camera have been efficiently and easily implemented onto the previous systems and we could achieve a high-speed tracking process to keep up with the video-frame rate of 33ms through the reconfigurability of the FPGA.

2. Overview of the Tracking Camera System

Figures 1 and 2 show a photograph and a design for the double-lens tracking-camera prototype, respectively (an electrical-circuit board mounting an FPGA to control the camera is not included in it). Whole views are captured through the wide-view lens module (the small-lens module in the figure) in the beginning, and the captured images are processed in an FPGA. In the FPGA, the target position is detected immediately and it is fed back to the other lens-module for the telescope view with the pan-tilt mechanism (the large-lens module in the figure). The double-lens tracking camera does not closely



Fig. 1 Photograph of the Double-lens tracking-camera.

resemble the eye in appearance, but it gives us the same function as the eye has inexpensively.

Furthermore, we also newly developed a magnet-based pan-tilt drive in place of the traditional motor-based drive, which enables the lens-module to move faster than the traditional one by three times or more. The motor-based drive consists not only of the magnetic parts but also of the other mechanical parts that impede the camera from high-speed rotation and small size, while the troublesome mechanical parts are removed in the magnet-based pan-tilt drive.

With the newly developed magnet-based drive (see Fig. 2), the lens-module is directly driven to move in the pan-tilt directions. The lens-module has four magnets in the right-angled direction each other. An electromagnet is placed opposite to the four magnets and driving forces to move the lens module are generated and controlled by the amplitude and the directions of the current applied to the electromagnet. We could achieve high-speed pan-tilt movement of about 3-time faster and reduce its size to less than 1/2 of the conventional pan-tilt camera by the direct-drive mechanism.

Figure 3 shows a photograph of the electrical-circuit board to control the camera at the tracking-speed-rate of 33ms/frame. A novel tracking-algorithm, in which the image-template for the tracking process is updated according to the captured target-image in every frame rate of 33 ms interval (details are described later), is implemented into the FPGA. The camera shown in Fig. 1 controlled by the board demonstrates high-speed performance enough for the fish-tracking application in which the target fish is detected among a group of fish and is tracked with its magnified picture in an aquarium (details are described later).

The tracking algorithm described in the next section can be also implemented onto the general-purpose processors or DSPs. The software-based processing, however, does not fit to

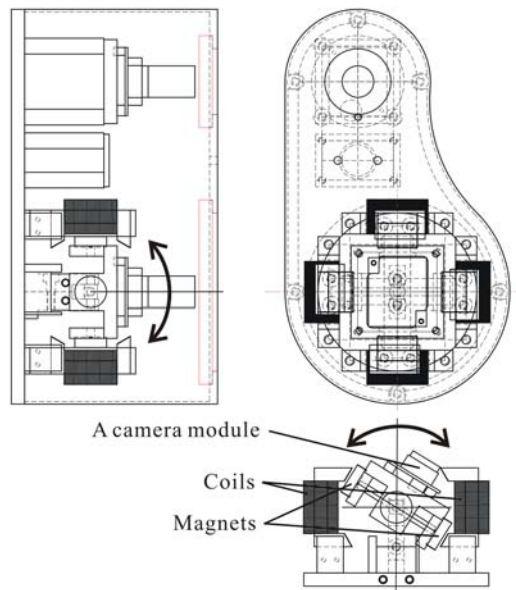


Fig. 2 Design for the Double-lens tracking-camera.

the sequence of the tracking processes because the intrinsic parallelism in the processes cannot be embedded into the programs. On the contrary, we can implement the parallelism as it is onto the FPGA, so that the tracking-procedure can be executed at the video-frame rate or more. Furthermore, by using FPGA, some parameters in the algorithm can be embedded into the logic circuits directly and they can be changed to meet each application. This hardware tuning improves the system performance well to meet desired conditions depending on each application.

3.Tracking Architecture for the Double-lens Camera

Figure 4 shows the block diagram according with the signal flow from the wide-lens camera module to the telescope lens camera module.

A whole view including the target is captured with the wide-lens module. During the A/D

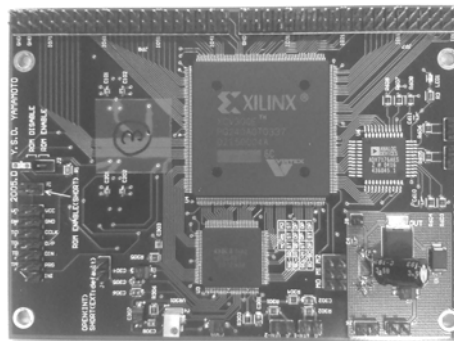


Fig. 3 Photograph of the FPGA-board.

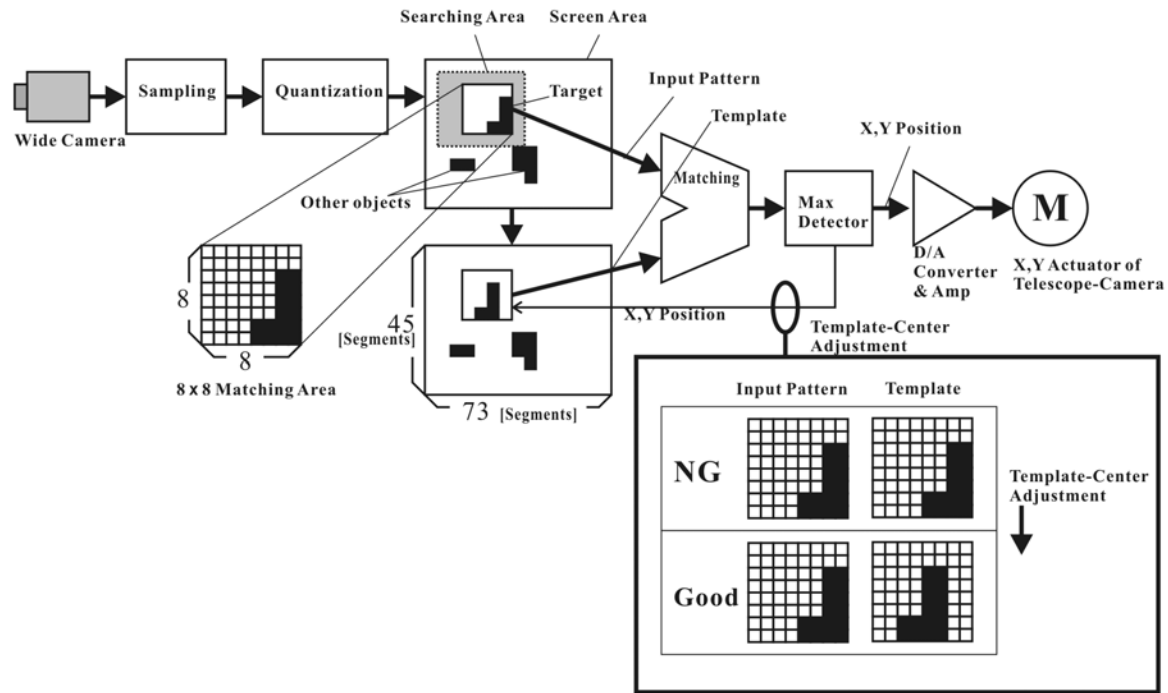


Fig. 4 Block-diagram of the tracking-process.

conversion process, the image is preprocessed before the target detection. The entire image is sampled digitally and its image size is reduced to 45 x 73 pixels. Each pixel is also digitalized or, quantized to 8-bit. The size reduction-rate and the quantization-rate are not fixed to 45 x 73 and 8-bit (we use binary quantization in the application in this paper). Those values can be changed and implemented, that is, reconfigured easily onto the FPGA directly.

In the ordinary algorithms for the target detection, the pre-sampled target-image-templates are scanned through the whole image and the object matched to the target is searched in it. In the ordinary approach, however, it is getting difficult to track the object correctly as its moving-speed increases. In our system, the target-image-template is updated during the tracking, contrastively to the fixed set of the pre-sampled target-image-templates. The target image that was tracked in one previous frame t_{n-1} is used as the template for the present frame of t_n . According to this updating procedure, the template is updated in real-time, or on-line manner. The target image in the present frame t_n is almost the same as in the previous one in the frame t_{n-1} , so that the template-image can correctly matches the target even under its high-speed motion because of the very short interval between frames. Under the real-time updating procedure, the target thus can be precisely tracked in the tracking.

The real-time updating mentioned above works well principally if the updating interval is much shorter than the target motion. The video-frame-rate

of 33ms, however, is not so short to the target that moves fast close to the camera, and it sometimes happens that the center of the target gradually moves from that of the template and the tracking fails finally.

In order to overcome this problem, we propose the following center-feedback algorithm and implement it in the system:

- 1) The weighed center of the template is calculated.
- 2) The difference, or distance between the weighed center and template center is calculated.
- 3) The template the center of which is adjusted is re-captured according to the difference calculated in 2).

The position of the target is searched in every frame using the template under the center-feedback algorithm. The most matched area to the template is detected and its position is output through the comparator and the max-detector. The detected position is converted to analog signal finally and is input to the pan-tilt drive of the telescope camera.

The real-time updating in the template has been reported in the other system already [3]. In [3], however, real-time updating was applied to the convolution images. We have overcome the problem of the real-time updating applied to the original images.

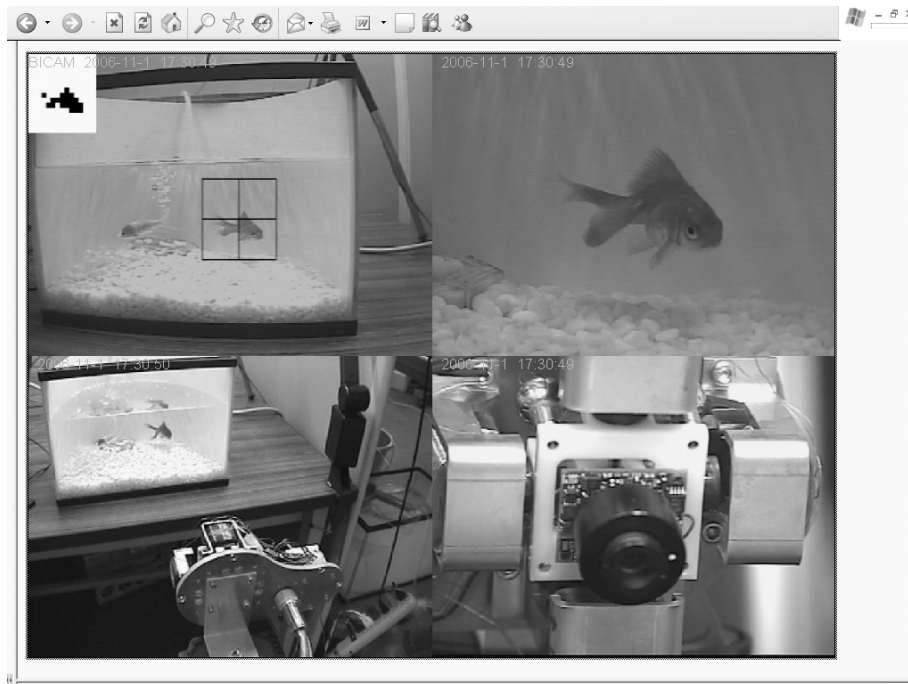


Fig. 5 A screen-shot of the fish-tracking.

4. Application to the Fish Tracking

We apply the system to the fish-tracking in which a target fish is detected among multiple fish in an aquarium under the wide-lens view and the target is tracked being magnified through the telescope-lens module. We also developed the network interface to connect the camera system with the Internet to broadcast the live images widely.

Figure 5 shows a screen-shot of the broadcasted image via the Internet. The upper-right picture shows the magnified image of the target fish tracked with the pan-tilt telescope lens module while the upper-left picture shows the wide-lens view of the entire aquarium. The target fish in the entire aquarium image is magnified by 3-time, so that its face and fins can be clearly observed. The lower-left and lower-right images are taken with another camera for the demonstration purpose. The lower-left picture shows the entire demonstration system in which the camera is set in front of the aquarium (the shield of the camera is removed). The lower-right picture shows the telescope-lens module tracking the target.

In the application, the target fish could be tracked successfully even under the multiple fish circumstances. And observers could watch the target fish clearly seeing the entire aquarium. We are now planning to apply this double-lens tracking-camera to the real surveillance applications.

5. Conclusions

A tracking-camera mimicking the eye was proposed and developed. The camera consists of double-lens modules: one for the wide-view and the other for the telescope view of the tracked target. The center-feedback algorithm was proposed and it was implemented onto a FPGA to track objects at high-speed motion. A magnet-based pan-tilt drive was also developed for high-speed tracking. A prototype of the camera was developed and it showed desired performances in a fish-tracking application.

Acknowledgements

The research and development in this paper is supported in part by the MEXT 2006 Cooperation of Innovative Technology and Advance Research in Evolutional Area and the 2006 grant of Japan Society for Promotion Science (No. 16360197).

References

- [1] N. Aibe, et al., "Performance Evaluation System for Probabilistic Neural Network Hardware," Proc. International Symposium on Artificial Life and Robotics (AROB 8th '03), pp.471-474, January 2003.
- [2] K. Hayashi, et al., "A Bio-inspired Tracking-camera System", International Symposium on Artificial Life and Robotics (AROB 11th '06), pp.755-758, Japan, 2006.
- [3] S. C. Wong, M. Jasiunas, and D. Kearney, "TOWARD A RECONFIGURABLE TRACKING SYSTEM," Proc. 2005 International Conference on Field Programmable Logic and Applications (FPL), pp. 456-462, August 2005.

Fault Detection by Evolution Strategies Based Particle Filters

K. Uosaki*

Dept. of Management and Information Sci.
Fukui University of Technology
Fukui 910-8505

T. Hatanaka

Dept. of Information and Physical Sci.
Osaka University
Osaka 565-0871

Abstract

Fault detection in dynamic systems has attracted considerable attention in designing systems with safety and reliability. Though a large number of methods have been proposed for solving the fault detection problem, it is hardly apply to nonlinear stochastic state space models. A novel filter called the Evolution Strategies based particle filter (ESP) proposed by recognizing the similarities and the difference of the processes between the particle filters and Evolution Strategies is applied here to fault detection of nonlinear stochastic state space models. Results of numerical simulation studies exemplify the applicability of this approach.

1 Introduction

The problem of fault detection in dynamic systems has attracted considerable attention in designing systems with safety and reliability. In the past two decades, a large number of methods have been proposed for solving the fault detection problem [1], [2], [3]. Among these, the model-based approaches using the quantitative analytical model of the system to be monitored are by nature the most powerful ones. For all model-based approaches, the decision of a fault is based on the innovations based on the state estimate obtained from the observed input-output data and a mathematical model of the system. Though the fault detection method can be easily constructed in linear/Gaussian state space models where the well-known Kalman filters [4], [5] can employ to evaluate the state estimate, the idea is generally difficult to apply to nonlinear systems with non-Gaussian noises. In this paper, a new fault detection method is proposed for nonlinear/non-Gaussian state space models using the idea of the backward sequential probability ratio test (BSPRT) [6] and the evolution strategies based particle filter (ESP).

*Supported in part by FUT Research Promotion Fund.

2 Fault detection

Consider here the following set of nonlinear state space models indexed by $m = 0, 1$.

$$x_{t+1} = f^{(m)}(x_t, u_t) + v_t \quad (1)$$

$$y_t = g^{(m)}(x_t) + w_t \quad m = 0, 1 \quad (2)$$

where x_t, u_t, y_t are the state variable, input and observation, respectively, $f^{(m)}(\cdot)$ and $g^{(m)}(\cdot)$ are known possibly nonlinear functions, and v_t and w_t are independently identically distributed (i.i.d.) system noise and observation noise sequences, respectively. The system works normally and its behavior is governed by the given normal mode model described as in (1) and (2) indexed by $m = 0$, and then the model may change to the given fault mode model indexed by $m = 1$ at unknown time $t = \tau$. The problem here is to develop a detection procedure to find a model change as quickly as possible.

3 Evolution Strategies Based Particle Filters

Recent massive increase of the computational power leads to much attentions to particle filters, a simulation-based filter based on Bayesian sequential analysis, and a lot of particle filters have been developed. Recognizing that the importance sampling and resampling processes in Sampling importance resampling (SIR) particle filter [7] are corresponding to mutation and selection processes in Evolution Strategies (ES) [8], which is one of Evolutionary Computation approaches [9], we can develop a novel particle filter called Evolution strategies based particle filter (ESP) as in [10].

Resampling process in SIR filter is introduced to avoid the degeneracy phenomenon in Sequential importance sampling (SIS) particle filter [11], [12], where all but one of the normalized importance weights are very close to zero after a few iterations and a large computational effort is wasted to updating trajectories whose contribution to the final estimate is almost zero. It selects offspring with probability proportional to the importance weight $w_t^{(i)}$, and this corresponds to selection process in ES with the importance

weight as fitness function. On the other hand, the importance sampling process in SIR filter samples $x_{t|t}^{(i)}$ according to the importance density $q(x_t|x_{t-1|t-1}^{(i)}, y_{1:t})$, and this corresponds to mutation process in ES from the viewpoint of generating offspring $x_{t|t}^{(i)}$ from the extrapolated parents $f(x_{t-1|t-1}^{(i)})$ with perturbation by v_t . The main difference is resampling in SIR is carried out probabilistically and the weights are set as $1/n$, while the selection in ES is deterministic and the fitness function is never reset. Hence, by replacing the resampling process in SIR by the deterministic selection process in ES, we can derive a new particle filter called Evolution strategies based particle filter comma (ESP(,)) and Evolution strategies based particle filter plus (ESP(+)) [10]. As shown in [10], the ESP filters behave more stable than SIR both in squared estimation errors and processing time by their deterministic selection process, we will develop fault detection methods using the ESP.

4 Fault Detection by Evolution Strategies Based Particle Filters

Then the fault detection problem to be considered here can be reduced to perform a hypothesis testing for the hypotheses:

- H_0 (Normal mode) : System models are indexed by $m = 0$
- H_1 (Fault mode) : System models are indexed by $m = 1$

Wald's sequential probability ratio test (SPRT) [13] is a common testing procedure, where the logarithm of likelihood ratio function (LLR) $\lambda_t = \log p(y_{1:t}|H_1)/p(y_{1:t}|H_0)$ is evaluated and compared with two threshold values $B^* < 0 < A^*$ until it exceeds these thresholds. It is known that the fault detection system based on the above mentioned Wald's SPRT formulation minimizes, on the average, the time to reach a decision for specified error probabilities if the system is either in the normal mode or the fault mode from the beginning of the test. However, the characteristics of the fault process differs from it; the system is initially operated in normal mode and then transition occurs to the fault mode at time instant τ during observations. To fit this situation, the idea of the backward SPRT (BSPRT) [6] is introduced.

Rewriting the hypotheses representing normal and fault modes in fault detection process as

- H_0 (Normal mode) :
 System models at time $t - k + 1$ are indexed by $m = 0$
- H_1 (Fault mode) :
 System models at time $t - k + 1$ are indexed by $m = 1$,
 $t > \tau, k = 1, \dots, t - \tau + 1$

we can introduce a backward LLR (BLLR), where LLR is computed in reverse (*backward*) from the current observation to the past observations:

$$\lambda_{t,k}^B = \log \frac{p(y_t, y_{t-1}, \dots, y_{t-k+1}|H_1)}{p(y_t, y_{t-1}, \dots, y_{t-k+1}|H_0)} \quad (3)$$

We can express the BLLR approximately with the conventional LLR as

$$\lambda_{t,k}^B = \lambda_t - \lambda_{t-k}, \quad k = 1, 2, \dots, n \quad (4)$$

with $\lambda_0 = 0$ by assuming $p(y_{1:t}) = p(y_{1:k})p(y_{k+1:t}|y_{1:k}) \approx p(y_{1:k})p(y_{k+1:t})$ ($y_{1:k}$ and $y_{k+1:t}$ are independent), and the decision rule for acceptance of the hypothesis that the system is in the fault mode can be restated as

$$\lambda_{t,k}^B = \lambda_t - \lambda_{t-k} > K \text{ for some } k = 1, 2, \dots, t \quad (5)$$

or,

$$\lambda_t - \min_{1 \leq k \leq t} \lambda_k > K \quad (6)$$

Introducing the statistics called the maximum BLLR,

$$S_t = \max[0, S_{t-1} + \ell_t], \quad t = 1, 2, \dots \quad (7)$$

$$S_0 = 0$$

with

$$\ell_t = \log \frac{p(y_t|y_{1:t-1}, H_1)}{p(y_t|y_{1:t-1}, H_0)} \quad t = 1, 2, \dots \quad (8)$$

where $p(y_t|y_{1:t-1}, H_m)$ is the one step output prediction density of y_t under the hypothesis H_m , ($m = 0, 1$), then the decision rule based on the BLLR can be expressed as

"If $S_t > K$, where K is a suitable constant, one terminates observation with acceptance of the hypothesis that the system is in the fault mode. Otherwise, one continue observations as the system is likely not in the fault mode."

To compute ℓ_t in the statistics (7), we can use the grid approximation

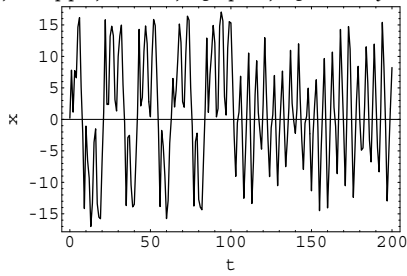
$$p(x_t|y_{1:t}, H_m) \approx \sum_{i=1}^n w_{t|t}^{(i,m)} \delta(x_t - x_{t|t}^{(i,m)}), \quad (m = 0, 1) \quad (9)$$

where the second superscript m is corresponding to the models. Then the pdf $p(x_t|y_{1:t-1}, H_m)$ ($m = 0, 1$) can be approximated as

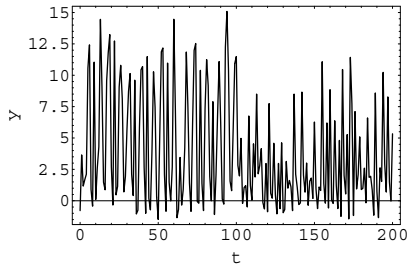
$$p(x_t|y_{1:t-1}, H_m) \approx \sum_{i=1}^n w_{t-1|t-1}^{(i,m)} p_v(x_t - f^{(m)}(x_{t-1|t-1}^{(i,m)}))$$

On the other hand, we can approximate the pdf $p(y_t|y_{1:t-1}, H_m)$ in (8) by

$$p(y_t|y_{1:t-1}, H_m) \approx \frac{1}{n} \sum_{i=1}^n p_w(y_t - g^{(m)}(x_{t|t-1}^{(i,m)}))$$



(a) State



(b) Observation

Figure 1: Sample behavior of state and observation processes

where $x_{t|t-1}^{(i,m)}$, ($i = 1, \dots, n$) are samples from the pdf $p(x_{t-1} | y_{1:t-1}, H_m)$. Thus, we can conduct the fault detection by evaluating the BLLR S_t with the pdf estimates obtained by two ESP filters under the system model H_m , ($m = 0, 1$) and compare S_t with suitable threshold K .

5 Numerical Examples

To exemplify the applicability of the proposed ESP filters, we carried out a numerical simulation. We consider the following nonlinear state space model with known parameters.

$$\begin{aligned} x_t &= \frac{x_{t-1}}{2} + \frac{a^{(m)} x_{t-1}}{1 + x_{t-1}^2} + 8 \cos(1.2t) + v_t \\ &= f^{(m)}(x_{t-1}) + v_t, \quad (m = 0, 1) \\ y_t &= \frac{x_t^2}{20} + w_t = g^{(m)}(x_t) + w_t \end{aligned} \quad (10)$$

with $a^{(0)} = 25$ for normal mode and $a^{(1)} = 12.5$ for fault mode, and v_t and w_t are i.i.d. zero-mean Gaussian random variates with variance 10 and 1, respectively. We assume that the fault occurs at $t = \tau = 101$. A sample behavior of the true state and corresponding observation processes is shown in Fig.1. Here the Gaussian distribution with mean $f(x_{t-1|t-1}^{(i)})$ and variance 10 is chosen as the importance

density $q(x_t | x_{t-1|t-1}^{(i)}, y_{1:t})$.

Sample behaviors of state estimates by ESP(.) with $n = 10$, $r = 2$ based on the model H_m , ($m = 0, 1$), and BLLR S_t and λ_t are given in Fig. 2 with corresponding results by EKF as well for comparison.

The test statistics BLLR S_t takes positive value and is growing up rapidly after the change point τ both in ESP and EKF, we can detect the model change when the BLLR exceeds the suitable threshold K . Moreover, it should be noted that, as shown in Fig. 2, the state estimate by EKF shows poor behavior and hence the behavior of test statistics sometimes provides poor detection result. Eventually, the rate of false alarm¹ and miss alarm² are higher by the detection procedure using EKF than by the procedure using ESP as shown in Table 1 that summarizes 10 simulation results of fault detection with the threshold $K = 25$. These

Table 1: Fault detection result

	False alarm rate	Miss alarm rate
Fault detection by ESP	1/20	0/20
Fault detection by EKF	5/20	1/20

results illustrate the applicability of the proposed approach for fault detection of nonlinear stochastic state space models. By introducing the other choice of evolution processes such as crossover and suitable choice of evolution parameters it is expected the improvement of the performance, and their better choice will be pursued.

6 Conclusions

Fault detection in dynamic systems has attracted considerable attention in designing systems with safety and reliability. Though a large number of methods have been proposed for solving the fault detection problem, it is hardly apply to nonlinear stochastic state space models. A novel filter called the Evolution Strategies based particle filter (ESP) proposed by recognizing the similarities and the difference of the processes between the particle filters and Evolution Strategies is applied here to fault detection of nonlinear stochastic state space models. Numerical simulation studies have been conducted to exemplify the applicability of this approach.

¹The test statistics exceeds the threshold, i.e., the decision that system model has changed is made even when the system model does not change.

²The test statistics never exceeds the threshold, i.e., decision that the system model does not change is made even when model changes.

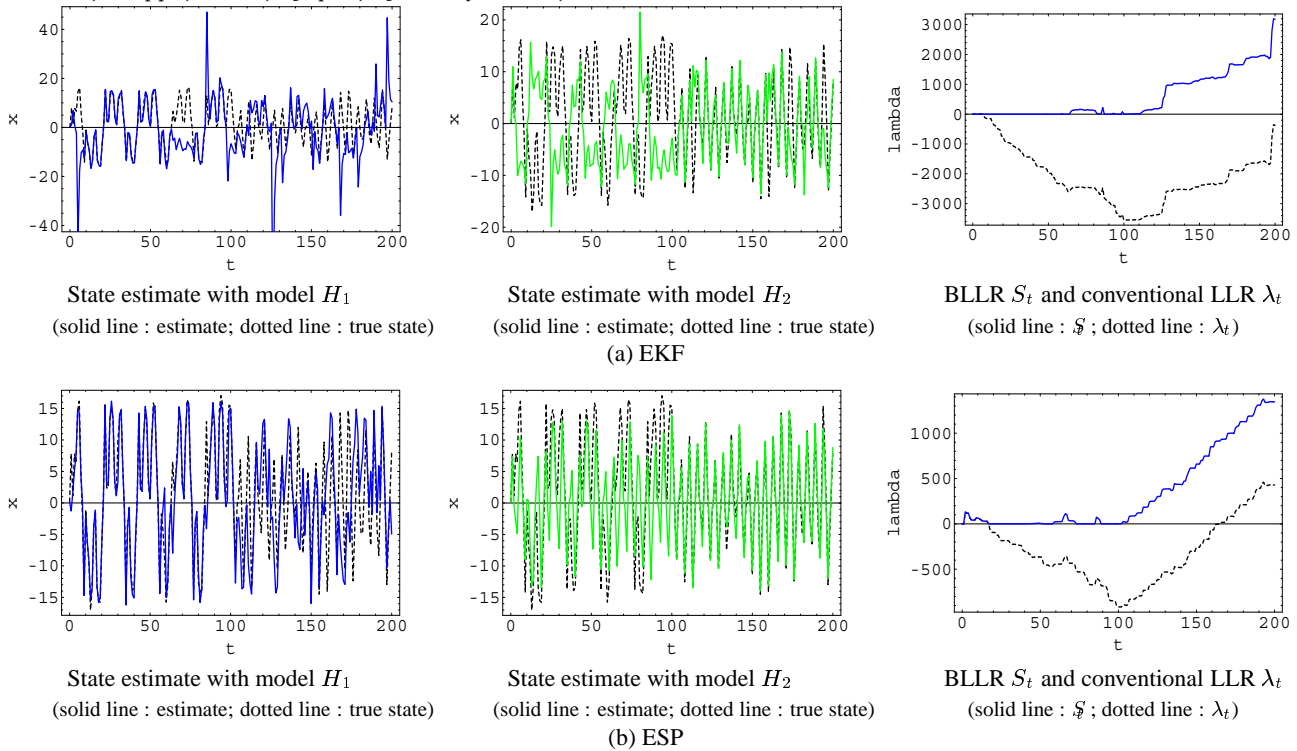


Figure 2: Sample behaviors of state estimates and test statistics by ESP and EKF

References

- [1] M. Basseville, "Statistical approaches to industrial monitoring problems — Fault detection and isolation," *Proc. 11th IFAC System Identification*, pp. 413–432, 1997.
- [2] P. M. Frank, "Fault diagnosis in dynamic systems using analytical knowledge based redundancy — A survey and new results," *Automatica*, vol. 26, pp. 459–474, 1990.
- [3] A. S. Willsky, "A survey of design methods for failure detection in dynamic systems," *Automatica*, vol. 12, pp. 601–611, 1976.
- [4] R. Kalman and R. Bucy, "New results in linear filtering and prediction theory," *J. of Basic Engineering, Trans. ASME Series D*, vol. 83, pp. 95–108, 1961.
- [5] B. D. O. Anderson and J. B. Moore, *Optimal Filtering*, Englewood Cliffs: Prentice-Hall, 1979.
- [6] K. Uosaki, "Failure detection using backward SPRT," *Proc. 7th IFAC Symp. System Identification and Parameter Estimation*, pp. 1619–1624, 1985.
- [7] D. B. Rubin, "Using the SIR algorithm to simulate posterior distribution," in *Bayesian Statistics*, Edited by J.M. Bernardo, M.H. DeGroot, D.V. Lindley and A.F.M. Smith, vol. 3, pp. 395–402, London: Oxford University Press, 1988.
- [8] H.-P. Schwefel, *Evolution and Optimum Seeking*, New York: J. Wiley, 1995.
- [9] T. Bäck, *Evolutionary Computation*, London: Oxford University Press, 1996.
- [10] K. Uosaki and T. Hatanaka, "Nonlinear state estimation by evolution strategies based particle filters," *Proc. 16th IFAC World Congress on Automatic Control*, 2005.
- [11] A. Doucet, N. de Freitas and N. Gordon (Eds.), *Sequential Monte Carlo Methods in Practice*, Berlin: Springer-Verlag, 2001.
- [12] S. Arulampalam, S. Maskell, N. Gordon and T. Clapp, "A tutorial on particle filters for on-line nonlinear/non-Gaussian Bayesian tracking," *IEEE Trans. on Signal Processing*, vol. SP-50, no.2, pp. 174–188, 2002.
- [13] A. Wald, *Sequential Analysis*, New York: J. Wiley, 1947.

A synergetic particle swarm optimization algorithm-DHPSO

Jinchao.Guo

skyzzuli@126.com

Department of control science & engineering
huazhong University of science & technology
Wuhan, HuBei,430074

Guangzhao.Cui

cgzh2008@163.com

Key lab of informationed apparatus
Zhengzhou university of Light industry
Zhengzhou, HeNan. 450002

Abstract

To improve the design-quality of robotics, more and more artificial intelligence and evolutionary algorithm were introduced into the design procedure, such as routing-programming, data-fusion, vision-processing, and so on. These new methods prompt the development of robotics greatly. An improved Particle Swarm Optimization (PSO) method, Dual-hierarchy Particle Swarm Optimization algorithm (DHPSO) was proposed in this paper. Compared with the regular particle swarm optimizer (RPSO), DHPSO adopts dual hierarchy structure. In the bottom layer, several particle groups try to find out current optimal solutions in the multi dimension searching space respectively. In the top layer, one group particles chase the global optima. The proposed method is tested on three benchmark functions. All simulation results show the proposed method is better than the regular PSO in speed and precision performance.

Keywords: Robotics, PSO, DHPSO, Hierarchy structure

1 introduction

Nowadays swarm algorithms and other intelligent algorithms are used widely in many fields. We have used Particle Swarm Optimization (PSO) algorithm in route programming of robot design successfully and made some improvement of this algorithm on its structure. More will be discussed about Particle Swarm Optimization algorithm below. Just like a wealth of heuristic algorithms such as genetic, evolution, and simulated annealing. Particle Swarm Optimization algorithm is a new entrant to the family of evolutionary algorithms originally introduced by Kennedy and Eberhart in 1995[1][2]. As parameters in PSO algorithm is fewer contrast to other evolution algorithm, moreover PSO algorithm is easy to realize and has a good performance in searching for the optima in real value searching space. Researchers and experts pay a great deal of attention to it in the last decades. Though PSO has so many merits,

it's easy to be trapped in local optima, and other drawbacks such as premature, low precision, and non-convergence. In order to overcome these demerits of PSO algorithm, many researchers make lots of contributions, and give out many modified algorithms based on the regular PSO. Junjun Li and Xinhua Wang propose a refined PSO algorithm based on simulated annealing[6]; Qianli Zhang, Xing Li and Quang-AHN TRAN introduce mutation operator to the regular PSO algorithm[7]; Chnming Yang and Dan Simon made Each particle learn from its previous worst position and its group's previous worst position, and give out a novel method to program PSO algorithm[8]; Jang-Ho Seo, Chang-Hwan Im, Chang-Geum Heo and Jae-Kwang use N groups of particle swarm to do the optimization, and get a new algorithm MGPSO[9]. Most of these algorithms put emphasis on parameter selection or combination with other evolution algorithms to get new derivations. This is difficult to solve the innate flaw of PSO algorithm-Local minima trapping, furthermore, enhance the complexity. Under these premises, we proposed dual hierarchy PSO algorithm, it holds the concepts of the regular PSO and tries to keep balance between "exploration" and "exploitation" between different hierarchies. Compared with the regular PSO algorithm, DHPSO improved searching speed and enhanced the global optima searching ability. The paper is organized as follows. In Section II, we introduce the concept of regular PSO and the method used in the study DHPSO, Section III outlines the experimental setup, parameter settings, and benchmark functions used. The experimental results are presented in Section IV. Finally, Section V contains a discussion of the experimental results.

2 The regular PSO and Proposed algorithm

2.1 The regular PSO

PSO algorithm was developed by Kenney and Eberhart to model birds flocking and fish schooling for food, in which particles representing the candidate solutions to

the problem in a multidimensional search space. Every particle has a position vector \vec{x} encoding a candidate solution to the problem and a velocity vector \vec{v} . Moreover, each particle contains a small memory that stores its own best position seen so far p_{id} and a global best position p_{gd} obtained through communication with its neighbor particles. The position and velocity vector of each particle are updated every iteration, and this is done respectively according to equation 1 and 2 as below, where ω is known as the inertia weight as described in [3][4]. The parameters c_1 and c_2 are set to constant values, which are normally given as 2, and rand is randomly generated value between 0 and 1. $i \in (1, 2 \dots N)$ and $N \in (1, 2 \dots D)$. N and D denote particle number and searching space dimension respectively. Inertia weight ω is adjusted with interaction according to equation 3.

$$v_{i+1,d} = \omega \cdot v_{id} + c_1 \cdot \text{rand} (p_{id} - x_{id}) + c_2 \cdot \text{rand} (p_{gd} - x_{id}) \quad (1)$$

$$x_{i+1,d} = x_{id} + v_{i+1,d} \quad (2)$$

$$\omega = \omega_{max} - \frac{\omega_{max} - \omega_{min}}{\text{Gen}_{max}} \cdot i \quad (3)$$

2.2 Proposed algorithm

Some researchers give out the concepts of "swarm fitness covariance" and "degree of convergence" and try to make criteria on which to investigate the convergence of algorithm. All these make contribution to meliorate regular PSO in a way, However, these methods can't improve PSO algorithm in essence, because they just try to enhance the global optimization searching rate by repeat of program running in a sense. Some existing methods adopt operators of genetic algorithm or evolutionary strategy, such as crossover, mutation, and sharing. These methods can modify regular PSO algorithm in some ways, but improve complexity considerably at the same time. All these make modified PSO algorithm not easy to realize. If groups are used for DHPSO, the computational cost increases only in the order of $O(N)$ compared with one-group PSO because each group follows the basic concepts of conventional PSO algorithm, whereas roughly $O(N^2)$ increments is required for GA crossover computations if a larger number of populations is used in GA. In DHPSO algorithm, The velocity of the bottom layer updating adopts equation 1 to guarantee a good local "exploration" performance, and in the top one, velocity updates according to equation 4—the local updating formula, to gain a better convergence speed.

$$v_{i+1} = \omega \cdot v_i + c_2 \cdot \text{rand} (p_{gd} - x_{id}) \quad (4)$$

3 Preparation of experiment and benchmark function

c_1 and c_2 are set to 2, the total population N of each algorithm will be set to equal, in experiment it is 1000. More seeds will be required when problem is complex. and ω_{max} and ω_{min} are set to 0.9 and 0.4, vector \vec{x} belongs to a scope of $[-50 \ 50]$ so that the search process will not last too long, vector \vec{v} is set to be $[-20 \ 20]$. For DHPSO, At different hierarchy the particle number in each group can be different, but the total number N —sum of particle number of different hierarchy should be the same with that of regular PSO algorithm, just to keep same complexity. In experiment, we set two groups in the bottom layer of DHPSO, and each group has 150 particles, so the top layer number is 700 obviously. The dimension number D is set to 2 and 10 respectively. Comparison functions adopted here are three benchmark functions used by many researchers. They are the Griewank, Rastrigrin and Rosebrock functions. The definitions of these functions are presented below:

$$f_1(x) = \frac{1}{4000} \cdot \sum_{i=1}^n x_i^2 - \prod_{i=1}^n \cos\left(\frac{x_i}{\sqrt{i}}\right) + 1 \quad (5)$$

$$f_2(x) = \sum_{i=1}^n (x_i^2 - 10 \cos 2\pi x_i + 10) \quad (6)$$

$$f_3(x) = \sum_{i=1}^n \left(100 (x_{i+1} - x_i^2)^2 + (x_i - 1)^2\right) \quad (7)$$

4 Simulation result comparison

Each test repeats 10 times and each iteration runs 100 generations. We list out the different minima of the benchmark functions that we got using RPSO and DHPSO method. The preliminary conditions are specified in the table list.

Fig.1 to Fig.6 show the convergence result of DHPSO and RPSO. The benchmark function used and the particular conditions of each figure are specified in the figure caption.

Table 1: the mean optimization result of RPSO and DHPSO with $D=2$ and $N=1000$

function	RPSO	DHPSO
f_1	0.0000	0
f_2	0.0000	0
f_3	0.0000	0

Table 2: The mean optimization result of RPSO and DH-PSO with D =10 and N=1000

funcion	RPSO	DHPSO
f_1	0.1076	0.1038
f_2	22.2080	18.6500
f_3	0.0000	0.0000

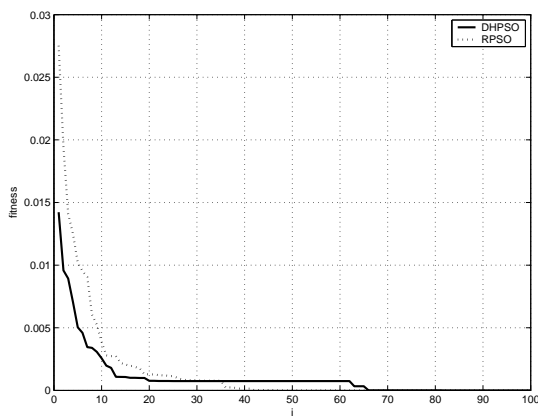


Fig. 1: Griewank, N=1000, D=2

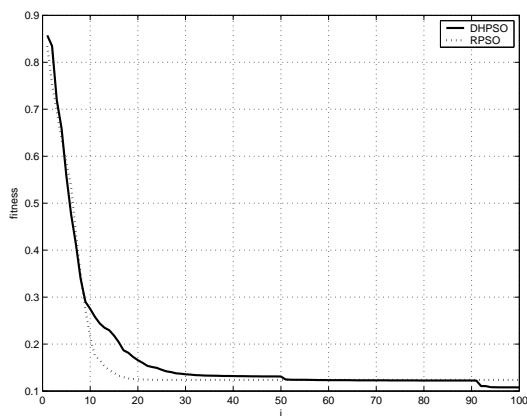


Fig. 2: Griewank, N=1000, D=10

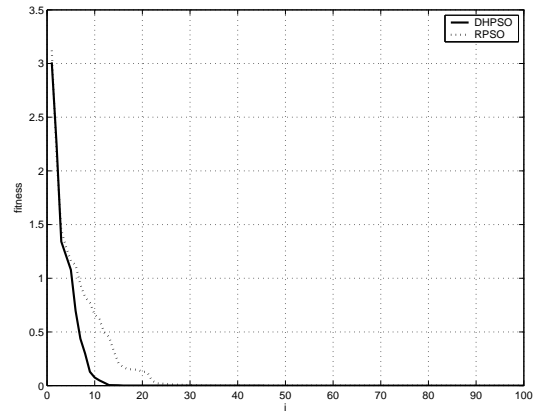


Fig. 3: Rastrigrin, N=1000, D=2

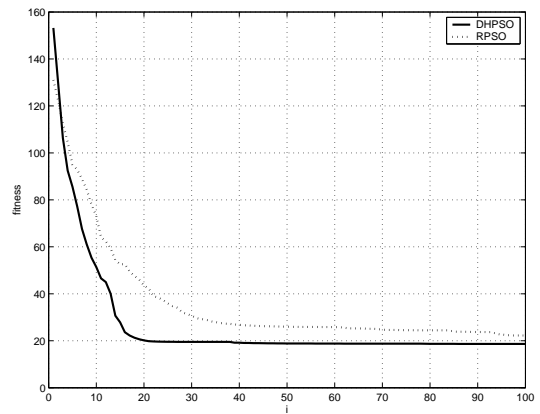


Fig. 4: Rastrigrin, N=1000, D=10

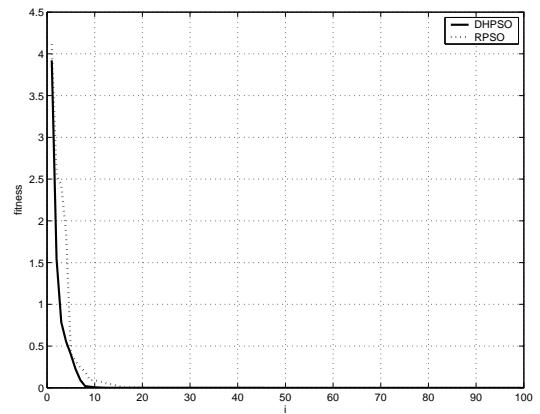


Fig. 5: Rosebrock, N=1000, D=2

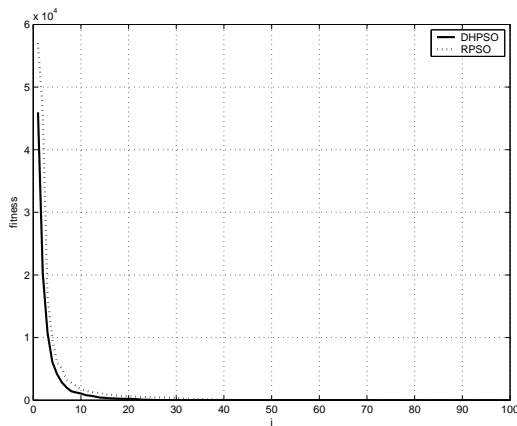


Fig. 6: Rosebrock, N=1000, D=10

Because vector \vec{x} and vector \vec{v} are generated randomly, the initial value may be different for the two algorithms in the beginning. However, the two algorithms still can be compared, for they have the same variation iteration and same complexity degree. From Fig.1 to Fig.6 above, we can get that DHPSO method has a good precision than RPSO method, and as well as the convergence speed.

5 Conclusion

From the simulation results, we can see DHPSO has a better performance than the RPSO algorithm, but these experiments are executed under a particular cases and narrow settings, so the conclusion is not comprehensive and definite. For further research, more work can be put into the following aspects:

1. The relationship between inertia weight and convergence of algorithm.
2. How to improve global searching ability of algorithm.
3. Seeking the theory support of PSO algorithm.
4. Combining other heuristic algorithm and applying PSO to more engineer use.

References

- [1] R. C. Eberhart and J. Kennedy, "A New Optimizer Using Particles Swarm Theory," in Proc. Sixth International Symposium on Micro Machine and Human Science, Nagoya, Japan, 1995, pp. 39-43.
- [2] R. C. Eberhart and J. Kennedy, "Particles Swarm Optimization," in Proc. IEEE International Conference on Neural Network, Perth, Australia, 1995.

- [3] Shi, Y.H., Eberhart, R.C., (1998). A modified particle swarm optimizer. Proceedings of the IEEE International Conference on Evolutionary Computation., Anchorage, Alaska, May 4-9, 1998.
- [4] Shi, Y.H, Eberhart, R.C., (1999). Empirical study of particle swarm optimization, 1999 Congress on Evolutionary Computation, Washington DC, USA, July 6-9, 1999.
- [5] S.L.HO, Shiyong Yang, Guangzheng Ni and H.C.Wang, "A particle swarm optimization method with enhanced global search ability for design optimizations of electromagnetic devices," IEEE, Tran. Magn, Vol.42, No.4, 2006
- [6] Junjun Li and Xihuai Wang, "A modified particle swarm optimization algorithm," in Proc. IEEE world congress on intelligent control and Automation, Hangzhou, China., 2004 ,pp.354-356.
- [7] Qianli Zhang, Xing Li and Guang-AHN.TRAN, "A modified particle swarm optimization algorithm," in Proc, IEEE International conference on Machine learning and cybernetics, Guangzhou, China, 2005,pp.2993-2995.
- [8] Chuming Yang and Dan Simon, "A new particle swarm optimization technique," in Proc. IEEE, International conference on systems engineering, August, 2005, pp.164-169.
- [9] Jang-Ho Seo, Chang-Hwan Im, Chang-Geum Heo and Jae-Kwang Kim, "multimodal function optimization based on particle swarm optimization," IEEE, Trans. Magn, vol. 42, No. 4, April 2006, pp. 1095 - 1098.

Inevitability of bio-molecules

Ken NAITOH

Waseda University, 3-4-1, Ookubo, Tokyo 169-8555 Japan
Email: k-naito@waseda.jp

Key Words: Origin, Inevitability, Asymmetry, Bases, Amino acids

Abstract

Inevitability of the bio-molecules which are related to nitrogenous-bases, amino-acids, DNA, RNA, and heavier molecules is clarified by using the molecular fluid-dynamics, i.e. the cyto-fluid dynamic theory. We try to solve the problem of why living beings use only five types of nitrogenous bases and twenty types of amino-acids. It should be stressed that the keyword is the mysterious number, the n -th root of n , which lies between 1.0 and the golden ratio. The present report may give the milestone for understanding the origin of life.

1. Introduction

There are some approaches in order to know the principle for designing life system.

Researchers on the origin of life have synthesized artificially amino-acids and nucleic-acids. [1] However, the chain reaction of the fundamental molecules is still in fog.

Chirality [2] is thought to be an important concept for understanding self-organizing process of life. However, this concept can not clarify all of the dynamical processes underlying life.

By using informatics and structure mechanics, Aristid Lindenmayer [3], D'Arcy Wentworth Thompson [4], and Donald E. Ingber [5] have showed the inevitability of large structures such as tree, shell, and cell. However, the inevitability of biological monomers and polymers has not been revealed so well, although the number of fundamental blocks is limited to only five bases and twenty types of amino acids.

Parameter or index is necessary to clarify the inevitability. DNA is composed by four bases of Adenine (A), Guanine(G), Cytosine(C), and Thymine(T). Frequency of usage of Guanine and Cytosine among these four bases (GC rate) is used world-widely as the important index property for controlling bio-chemical reaction processes. The hydrogen bond connection between Guanine and Cytosine is stronger than that between Adenine and Thymine. This index is related to the instability of molecules while increasing temperatures. Thus, the GC rate is important for optimizing the replication quality in the Polymerase chain reaction

(PCR). [6]

On the other hand, we can classify four bases such as A, T, G, and C into two groups, purine and pyrimidine. Purines, i.e., A and G, have relatively large size, while pyrimidines, i.e., C and T, are small. The present index, the size ratio of purine and pyrimidine (YU rate) is related to the molecular size, i.e., weight. However, the YU rate is not employed for analyzing biological processes so well.

2. Analysis based on YU rate

2.1 Size of bases [7, 8, 9, 10, 11]

Asymmetric size ratios of purines and pyrimidines are around 1.50 in their hydrogen bonds within DNA and RNA, although the size ratio of 1.0, for hydrogen bond connections of identical sizes of bases, is often observed in RNA (Figs. 1, 2, and 3). Size ratios of 1.0 and approximately 1.5 can be described by the mysterious number of the n -th root of n (Fig. 3). This key number proposed here for solving inevitability of the symbiosis is unrelated to chirality.

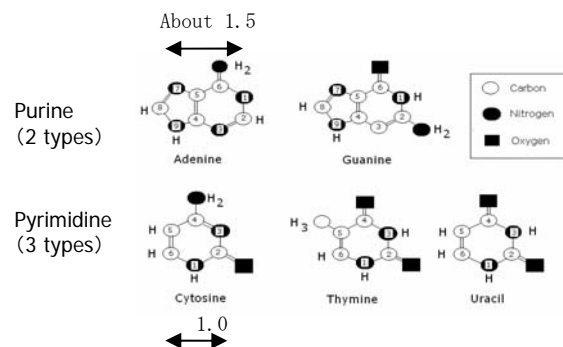


Fig. 1 Five types of nitrogenous bases for DNA and RNA.

Here, we will consider two nitrogenous bases, a purine and a pyrimidine, connected by hydrogen bonds in a large quantity of water. Owing to the influence of the nitrogenous bases, water molecules around the bases have different densities and arrays in comparison with those far away. (It is well-known that weight of hydrated water molecules per a base-pair inside DNA is of the order of that of the bases-pair.) Thus, we divide the water into two regions. A base and water molecules surrounding the base are defined as a continuum particle, parcel. Then, we

assume that the parcel size is proportional to the size of base. Further, we assume that the parcel acts as a flexible continuum particle.

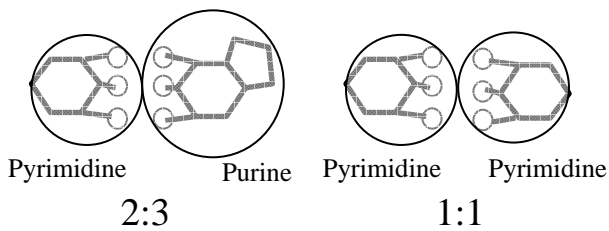


Fig. 2 Hydrogen-bonded bases.

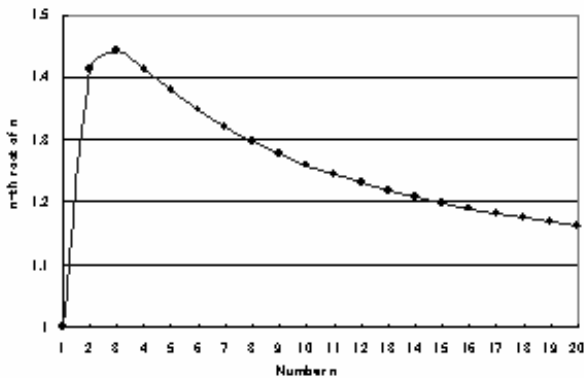


Fig. 3 Mysterious number, the n-th root of n, which appears in the size ratio of purines and pyrimidines.

Based on these assumptions, we derived the deterministic momentum equation describing particle deformation. The momentum equation shows that life prefers the size ratio of hydrogen-bonded nitrogenous bases taking the n-th root of n, which has the values of 1.0, 1.41, and 1.44 for n=1, 2 and 3, respectively (Fig. 3).

2.2 Two purines and three pyrimidines [9, 10, 11]

Asymmetric size ratio of purines and pyrimidines of around 1.50 results in different molecular weights. Molecular weight differences lead to “two” types of purines and “three” types of pyrimidines, because the larger purines produce fewer types. Mass balance leads to a frequency ratio of 1.5, i.e., two purines and three pyrimidines (Fig. 1).

2.3 Frequency ratios of purine and pyrimidine differ between tRNA and rRNA [11, 12, 13]

Let us examine hundreds of transfer RNA (tRNA). Averaged frequency ratio of purines and pyrimidines in tRNAs is about 1.10. The asymmetry can be confirmed, but the value is less than 1.50.

What is the frequency ratio of purines and pyrimidines in ribosomal RNA (rRNA)? The databases on rRNA show a value of around 1.30, which is relatively larger than that for tRNA.

This value less than 1.50 comes from three reasons. One is that the precise molecular weight is about 1.4 for

the G-C pair and 1.2 for the A-U pair. Second reason is related to the fact that base pairs are joined to sugars and phosphoric acids by covalent bonds. Total molecular weight, including those of the nitrogenous base, sugar, and phosphoric acids, decides the frequency ratio of purines and pyrimidines in RNA (Fig. 4).

Third reason is that, because the frequency ratio of purines and pyrimidines in the stems of tRNA is 1.0, RNAs having longer stems bring the mean value closer to 1.0. Ribosomal RNA shows frequency ratio of around 1.30, which is larger than that of tRNA, because rRNA has a shorter stem than tRNA. (An extremely long stem-length results in DNA without leaves.)

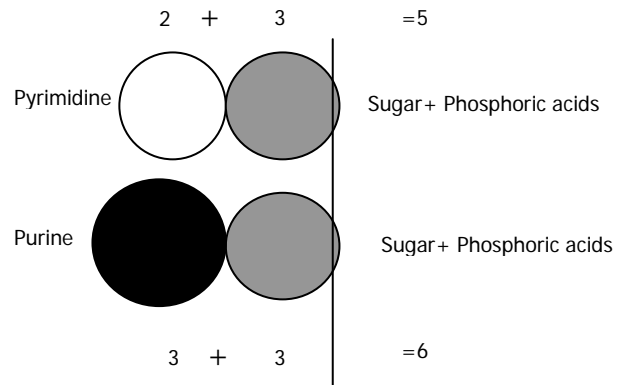


Fig. 4 Schematic diagram of nitrogenous bases connected by covalent bonds illustrating that sugars and phosphoric acids reduce the frequency ratio.

3. Clover structure [11, 12, 13]

The next question is why RNA has a complex clover structure. This stems from the third reason mentioned above. Density asymmetry of purines and pyrimidines results in a leaf structure.

We examined the stochastic computer model simplified based on molecular dynamics. [11, 12, 13] First, we prepared seventy-six individual nitrogenous bases (purines and pyrimidines) in an initial pool. These bases were connected randomly by hydrogen bonds. If we employ a lot of pools, an enormous variety of sequence arrays can be generated. Computational experiment revealed that, when the frequency ratio of purines and pyrimidines in the initial pool was between 1.0 and 1.5, clover structures were produced with a relatively high probability.

The reason why a frequency ratio between 1.0 and 1.5 promotes clover structures is simple. An extremely large frequency ratio, say, far above 1.5, can not produce the stem in tRNA, because the presence of only one type of base cannot form the pairing of purine and pyrimidine.

More complex structures such as ribosomal RNA (rRNA) can also be explained by the above-mentioned dynamical mechanism, which brings fractal structure.

4. Inevitability of non-coding RNA

Recently, the research group in RIKEN [16] has reported

that there are lots of non-coding RNA in introns and junk, although functions of the non-coding RNA are in fog. Here, we will show a hypothesis related to inevitability of this non-coding RNA. Stochastic computer model in Section 3 generates small amount of clover structures. Sequences having clover structures close to tRNA are about 1.0 % in all of the possible sequences, which generated randomly. What are the substantial sequences of unstable structures of 99 %? These sequences of unstable structures may correspond to those generated in ancient pre-biotic processes. Then, these sequences of unstable structures may become the non-coding RNA.

Stochastic model [11, 12, 13] may tell us that we know only 1 % of molecules existing inside living cell.

5. Inevitability of five bases

Density ratio of purine and pyrimidine in tRNA having smaller leaves is around 1.10, while that in rRNA having larger leaves is about 1.30. Why will two different sizes of leaves exist? Mass conservation can not clarify the inevitability of two different sizes of leaves. Energy conservation is necessary for explaining this point.

In many cases, GC pairs are richer in tRNA than in rRNA. Amount of GC pairs is related to the difference of stem length. Actually, tRNA, which has relatively small leaves and long stems, has richer G-C pairs than rRNA. Hydrogen bond connection in G-C pair is stronger than that in A-U. Stronger hydrogen bond will stabilize longer stems.

Two types of base-pairs, G-C and A-U, are necessary to produce two types of RNAs, i.e., tRNA and rRNA.

Inevitability of four bases among five can be understood by the present discussion.

6. Twenty types of amino acids

Triplet inside the leaf of tRNA, anti-codon, permits sixty-four patterns at the maximum, because A, U, G, and C are possible for each locus among the three ones. Then, because the third locus inside anti-codon has relatively weak connection with codon, the minimum number of patterns of triplet is sixteen. This implies that the number of amino acids are between sixteen and sixty-four. As the result, the weak connection at third locus permits twenty types of amino acids, a little more than sixteen.

It should be emphasized that clarification of leaf size shown in the above sections leads us to the outline of inevitability of twenty amino acids.

7. Hydrophobic and hydrophilic amino acids

As is well-known, three nitrogenous bases correspond to one type of amino acid. Array of these three nitrogenous bases is codon. The database shows that the frequency ratio of purines and pyrimidines in codons is also about 1.30. [11, 12, 13] The frequency ratio of purines and pyrimidines for the center locus of anti-codon is also asymmetric. (See Fig. 5.)

Most of hydrophobic and hydrophilic amino acids

correspond to whether the center locus in the anti-codon is a purine or a pyrimidine. [11, 12, 13]

Asymmetric frequency ratio of purine and pyrimidine in codons may lead to the frequency asymmetry of hydrophilic and hydrophobic amino-acids. Thus, the frequency ratio of purine and pyrimidine (YU rate) is also important for optimizing proteins and enzymes.

Hydrophilic <ul style="list-style-type: none"> • Asp: 110 • Glu: 111 • Lys: 111 • Arg: X1X • His: 010 • Gly: 11X • Ser: 110 • Thr: 10X • Cys: 010 • Tyr: 010 • Asn: 110 • Gln: 011 	Hydrophobic <ul style="list-style-type: none"> • Ala: 10X • Val: 10X • Le: 00X • Ile: 10X • Pro: 00X • Phe: 000 • Trp: 011 • Met: 101
---	--

X: 0 or 1

Fig. 5 Twenty types of amino-acids and anti-codon.

8. Structure of proteins

As the center locus inside codon mainly decides whether the amino acid corresponding is hydrophilic or hydrophobic, both of hydrophilic and hydrophobic amino acids exist in proteins. Symbiosis of hydrophilic and hydrophobic molecules brings the complex shapes of proteins, because hydrophobic parts are often folded inside proteins.

9. Causal chain of bio-molecules

Several types of molecules such as nitrogenous bases, amino-acids, RNA, DNA, and proteins are related to each other, through the principle of the n-th root of n and the conservation laws.

Although the inevitability of size ratio of purine and pyrimidine is explained by momentum conservation in the former section, mass conservation law explains that many sizes and frequencies of bio-molecules are inevitable in the causal chain of molecules. Will the explanations shown with mass conservation law be correct? This question is related to whether cell or earth is considered. If the system is earth, mass conservation law will be dominant, because there are less materials coming from the space, although energy comes from outside of the earth, the sun. Here, we think the earth as control volume, not cell. This relates to the food-chain.

Unbalance of purine and pyrimidine in living beings will lead to instability of life without doubt, because the pool of only purine can not generate clover structures such as tRNA and rRNA.

10. Origin

In foregoing sections, we examined the inevitability of several lengths of biological molecules, from base to protein. However, we do not explain how the molecular

length increases during 4600 million years.

Let us see the DNA length of representative species plotted against time. (See Fig. 6.)

The Earth might be born about 4600 million years ago and first life might emerge 3600 million years ago. T. Oshima thought that the first primitive cell had DNA of the order of 1.0×10^5 base pairs. [15] (The first cell can be generated with the DNA length of 1.0×10^5 base pairs, about 300 types of enzymes. Each enzyme can be coded with 300 base pairs of DNA.) Then, about 3600 million years after the first cell bring human beings of 3.0×10^9 bp.

Let us examine further on this. First, we assume that the DNA length increase with the rate of ten times per 1000 million years. As the DNA length was 1.0×10^5 base pairs 3600 million year ago, about 10^9 base pairs, the order of human being, can be possible now, because about 4000 million years pass from the first cell. This increasing rate of DNA length implies that DNA should have the order of 10^4 base pairs 4600 million years ago. (See Fig. 6.)

The problem is whether the synthesis of DNA with 10^4 base pairs could be possible or not, 4600 million years ago. The possibility is shown by Yanagawa et al. [1] that polymer macromolecules such as protein or cell membrane can be produced by synthesizing amino acids under high pressure and high density of metal during a few weeks. The other data which supports 10^4 bp of DNA 4600 million years ago is that too many cycles of PCR during hours produces longer DNA sequences. [23]

Discussion shown above does not give the clear answer to the question of whether life was born on the earth or not. DNA length plotted against time should be analyzed further.

11. Conclusion

Inevitability of the bio-molecules such as nitrogenous-bases, amino-acids, DNA, RNA, and heavier molecules is clarified, although there is also eventuality around the inevitable molecules.

References

- [1] Yanagawa, H. (1991), Seimeiwa Ikani Tsukuraretaka, TBS Britaniaca.
- [2] Kuroda, R. (1992) Seimei Sekai no Hitaishousei, Chuukou Shinsho.
- [3] Prusinkiewics P. And Lindenmayer A. (1990) The algorithmic beauty of plants, Springer-Verlag.
- [4] Thomson, D. (1961) On Growth and Form, Cambridge University Press.
- [5] Ingber, D.E. (1998) The Architecture of Life. 52. Scientific American.
- [6] Mullis K.B. et al (1994) PCR, BIRKHAUSER.
- [7] Naitoh, K. (1999). Cyto-fluid Dynamic Theory for Atomization Processes, *Oil&Gas Science and Technology*, Vol. 54, No.2 205-210.
- [8] Naitoh, K. (2000). Mesoscopic Kinetic Theory for Fluid Phenomena and Biochemical Reaction Processes. *J. of Advanced Science*, 12-3, 223 (2000).

- [9] Naitoh, K. (2001). Cyto-fluid Dynamic Theory, *Japan Journal of Industrial and Applied Mathematics*, Vol.18, No.1.
- [10] Naitoh, K. (2000). Cyto-fluid Dynamic Theory of the Origin of Base, Information, and Function. *Proc. of 6th Int. symp. on Artificial life and Robotics 6th*.
- [11] Naitoh, K. (2002). Cyto-fluid Dynamic Theory of the Origin of Base, Information, and Function. *Artificial Life and Robotics*, 6-1 & 2, 82.
- [12] Naitoh, K. (2005) Self-organising mechanism of biosystems, *Artificial life and robotics*, 9, 96-98.
- [13] Naitoh, K. (2005) Seimei no Kihon Bunshi wo Tsuranuku Patan (Patterns underlying bio-molecules), *NIKKEI SCIENCE*, 58-65.
- [14] Naitoh, K. (2006) Gene Engine and machine Engine, Springer Japan.
- [15] Oshima, T. (1995) Seimeiwa Nessoikara Hajimatta, Tokyo Kagaku Doujin.
- [16] RIKEN Genome Exploration Research Group and Genome Science Group. (2005) Antisense Transcription in the Mammalian Transcriptome, *SCIENCE*, 309.
- [17] Lowe, T.M., Eddy, S.R., (1997). *Nucleic Acids Res.*, 25, 955. (available at <http://rna.wustl.edu/tRNAdb/>.)
- [18] Benson, D.A., Boguski, M.S., Lipman, D.J., and Ostell, J., Ouellette, B. F. F., (1998). *Nucl. Acids Res.*, 26, 1.
- [19] Benson, D. A., Karsch-Mizrachi, I., Lipman, D. J., Ostell, J., Wheeler, D. L., (2003). *Nucleic Acids Res.*, 31, 23.
- [20] Nakamura, Y., Gojobori, T., Ikemura, T., (2000). *Nucl. Acids Res.*, 28, 292. (available at <http://www.kazusa.or.jp/codon/>.)
- [21] DNA Data Bank of Japan, <http://www.ddbj.nig.ac.jp/>.
- [22] JCM On-line catalogue, Japan Collection of Microorganisms, RIKEN (The Institute of Physical and Chemical Research), <http://www.jcm.riken.go.jp/>
- [23] Naitoh, K. (2005) DNA computing based on actual biological sequences and accurate reaction control, *Proc. of Sixth Int. Nobeyama Workshop on the new century of computational fluid dynamics*, 2003, 60-66.

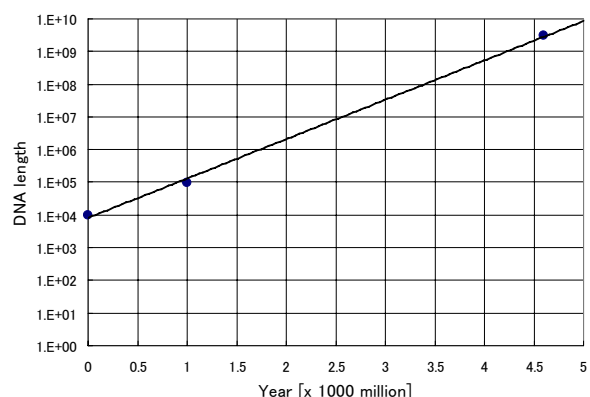


Fig. 6 DNA length plotted against year.

Calculation of 3-D nonnegative outer product expansion by the power method and its application to digital signal processing

Chiharu OKUMA*, Jun MURAKAMI* and Naoki YAMAMOTO**

Dept. of Information and Computer Sciences*,
Dept. of Information and Communication Engineering**,
Kumamoto National College of Technology,
2659-2, Suya, Koshi, Kumamoto pref., 861-1102, JAPAN E-mail:chiharu@cs.knct.ac.jp

Abstract

The power method is known as a convenient way to calculate eigenvectors of a matrix. We used this method for calculating 3-D outer product expansion previously. In this paper, we try calculating 3-D nonnegative outer product expansion by using the power method. In order to perform this calculation, we add nonnegative constraint conditions to the repetition process of the power method. Our method shows a significant reduction of computation time than the nonlinear optimization method.

key words:

3-D Outer Product Expansion, Power Method, 3-D array, Nonnegative Outer Product Expansion.

1. Introduction

In the field of image processing and digital signal processing, multi-dimensional digital filters are usually used. In order to design a multi-dimensional digital filter, multi-dimensional design specification is generally reduced to a set of 1-dimensional (1-D) specification array. Then the desired multi-dimensional filter can be obtained by designing a set of 1-D digital filters and combining them each other [1].

3-dimensional (3-D) outer product expansion [2] is usually used to decompose 3-D data arrays into products of 1-D vectors. This expansion is an extension of the singular value decomposition (SVD) of a matrix to a 3-D array. To simplify the structure of resultant 3-D digital filter, the number of terms of the expansion is desired to be reduced as much as possible. Therefore, such terms have to give least square approximation to the original 3-D array under some constraint conditions. In practice, although a large amount of computation time is required to calculate that expansion, the nonlinear optimization method is exploited ordinarily. We previously proposed the method, which uses the power method, for the purpose of calculating that 3-D outer product expansion and showed the efficiency of our method in comparison with the nonlinear optimization method [3]. The power

method is known as a basic numerical technique to

calculate eigenvalues of a matrix [4]. Since the 1-D vector obtained by 3-D outer product expansion represents magnitude response in the practical digital filter design problem, every elements of the vector should be physically nonnegative. We call this expansion 3-D nonnegative outer product expansion. Though the nonlinear optimization method can be used to calculate this expansion likewise as the case of ordinary 3-D outer product expansion, the computation time is the weakness of this method similarly as above.

In this paper, we try calculating 3-D nonnegative outer product expansion by using the power method. In order to perform this calculation, we add nonnegative constraint conditions to the repetition process of the power method.

2. Definition of 3-D Outer Product Expansion

A $L \times M \times N$ 3-D array A_3 can be decomposed by the 3-D outer product expansion as

$$A_3 = \sum_{i=1}^r \sigma_i (\mathbf{u}_i \otimes \mathbf{v}_i \otimes \mathbf{w}_i), \quad (1)$$

$$\sigma_1 \geq \sigma_2 \geq \dots \geq \sigma_r,$$

where the expansion vectors \mathbf{u}_i , \mathbf{v}_i , \mathbf{w}_i correspond to the singular vectors of the SVD of a matrix, the expansion coefficients σ_i and the number of expansion terms r correspond to the singular values and the rank of a matrix similarly, and \otimes denotes the outer product operation. The expansion vectors are normalized as

$$\|\mathbf{u}_i\| = \sqrt{\sum_{j=1}^L \mathbf{u}_i(j)^2} = 1,$$

$$\|\mathbf{v}_i\| = \sqrt{\sum_{j=1}^M \mathbf{v}_i(j)^2} = 1, \quad (2)$$

$$\|\mathbf{w}_i\| = \sqrt{\sum_{j=1}^N \mathbf{w}_i(j)^2} = 1,$$

where $\mathbf{u}_i(j)$, $\mathbf{v}_i(j)$, $\mathbf{w}_i(j)$ show the j -th element of the vector \mathbf{u}_i , \mathbf{v}_i , \mathbf{w}_i respectively.

3. Calculation Algorithm for 3-D Outer Product Expansion by the Power Method

The algorithm for calculating 3-D outer product expansion by the power method is described as follows [3].

Step 1. Choose the initial vectors $\mathbf{u}_n^{(p)}$, $\mathbf{v}_n^{(p)}$, $\mathbf{w}_n^{(p)}$ arbitrarily, where these vectors must be normalized, and the subscript p and n are set to zero and one respectively at the beginning of this repetitious procedure.

Step 2. The residual 3-D array \mathbf{B}_3 is obtained by subtracting sum of products of the expansion vectors \mathbf{u}_i , \mathbf{v}_i , \mathbf{w}_i , which has been calculated by this time, from original 3-D array \mathbf{A}_3 as follows:

$$\mathbf{B}_3 = \mathbf{A}_3 - \sum_{i=1}^{n-1} \sigma_i (\mathbf{u}_i \otimes \mathbf{v}_i \otimes \mathbf{w}_i). \quad (3)$$

Step 3. Calculate the $L \times M$ matrix \mathbf{F} by multiplying \mathbf{B}_3 by vector $\mathbf{w}_n^{(p)}$ as

$$\mathbf{F} = \mathbf{B}_3 \cdot \mathbf{w}_n^{(p)}. \quad (4)$$

The (i, j) element of the matrix \mathbf{F} can be represented as

$$\mathbf{F}(i, j) = \sum_k \mathbf{B}_3(i, j, k) \mathbf{w}_n^{(p)}(k). \quad (5)$$

Next, apply the power method to the matrix \mathbf{F} as follows:

$$\begin{aligned} \mathbf{u}_n^{(p+1)} &= \mathbf{F} \mathbf{v}_n^{(p)}, \\ \mathbf{v}_n^{(p+1)} &= \mathbf{F}^T \mathbf{u}_n^{(p+1)}. \end{aligned} \quad (6)$$

Like wise the $M \times N$ matrix \mathbf{G} and the $N \times L$ matrix \mathbf{H} are obtained by

$$\begin{aligned} \mathbf{G} &= \mathbf{B}_3 \cdot \mathbf{v}_n^{(p+1)}, \\ \mathbf{w}_n^{(p+1)} &= \mathbf{G} \mathbf{u}_n^{(p+1)}, \\ \mathbf{u}_n^{(p+1)} &= \mathbf{G}^T \mathbf{w}_n^{(p+1)}, \\ \mathbf{H} &= \mathbf{B}_3 \cdot \mathbf{u}_n^{(p+1)}, \\ \mathbf{v}_n^{(p+1)} &= \mathbf{H} \mathbf{w}_n^{(p+1)}, \\ \mathbf{w}_n^{(p+1)} &= \mathbf{H}^T \mathbf{v}_n^{(p+1)}, \end{aligned} \quad (7)$$

where the obtained vectors $\mathbf{u}_n^{(p+1)}$, $\mathbf{v}_n^{(p+1)}$, $\mathbf{w}_n^{(p+1)}$ must be normalized.

Repeat Step 3 until the following are satisfied for sufficiently small value ε :

$$\begin{cases} \|\mathbf{u}_n^{(p+1)} - \mathbf{u}_n^{(p)}\| < \varepsilon, \\ \|\mathbf{v}_n^{(p+1)} - \mathbf{v}_n^{(p)}\| < \varepsilon, \\ \|\mathbf{w}_n^{(p+1)} - \mathbf{w}_n^{(p)}\| < \varepsilon. \end{cases} \quad (8)$$

Step 4. The n -th expansion vectors $\mathbf{u}_n^{(p+1)}$, $\mathbf{v}_n^{(p+1)}$, $\mathbf{w}_n^{(p+1)}$ are obtained from Step 3. Here, rename these vectors as \mathbf{u}_n , \mathbf{v}_n , \mathbf{w}_n .

The n -th coefficient σ_n is obtained from inner product operation as as

$$\sigma_n = \mathbf{B}_3(\mathbf{u}_n \otimes \mathbf{v}_n \otimes \mathbf{w}_n). \quad (9)$$

Step 5. After increase n and set p to zero, repeat this procedure from Step 1.

4. Calculation of 3-D Nonnegative Outer Product Expansion by the Power Method

The method which we described in Section 3 can be applied to calculation of a 3-D nonnegative outer product expansion by adding nonnegative constraint conditions to the repetition process of the power method. Actually, the following steps are inserted into Step 3.

Step A1. The repetition vector $\mathbf{u}_n^{(p+1)}$ in equation (6) is divided into the vector of $\mathbf{u}_n^{(p+1)+}$ and $\mathbf{u}_n^{(p+1)-}$, where the former is composed of positive number or zero and the latter is composed of negative number or zero as

$$\begin{aligned} \mathbf{u}_n^{(p+1)} &= \mathbf{u}_n^{(p+1)+} - \mathbf{u}_n^{(p+1)-}, \\ \mathbf{u}_n^{(p+1)+} &= \max(\mathbf{u}_n^{(p+1)}, 0), \\ \mathbf{u}_n^{(p+1)-} &= -\min(\mathbf{u}_n^{(p+1)}, 0). \end{aligned} \quad (11)$$

Step A2. Calculate the norm of $\mathbf{u}_n^{(p+1)+}$ and $\mathbf{u}_n^{(p+1)-}$. Choose the nonnegative vector $\mathbf{u}_n^{(p+1)}$ from these vectors by following way.

$$\mathbf{u}_n^{(p+1)} = \begin{cases} \mathbf{u}_n^{(p+1)+} & \left(\|\mathbf{u}_n^{(p+1)+}\| \geq \|\mathbf{u}_n^{(p+1)-}\| \right) \\ -\mathbf{u}_n^{(p+1)-} & \left(\|\mathbf{u}_n^{(p+1)+}\| < \|\mathbf{u}_n^{(p+1)-}\| \right). \end{cases} \quad (12)$$

The vector $\mathbf{v}_n^{(p+1)}$ and $\mathbf{w}_n^{(p+1)}$ are also chosen as follows:

$$\mathbf{v}_n^{(p+1)} = \begin{cases} \mathbf{v}_n^{(p+1)+} & \left(\|\mathbf{v}_n^{(p+1)+}\| \geq \|\mathbf{v}_n^{(p+1)-}\| \right) \\ -\mathbf{v}_n^{(p+1)-} & \left(\|\mathbf{v}_n^{(p+1)+}\| < \|\mathbf{v}_n^{(p+1)-}\| \right), \end{cases} \quad (13)$$

$$\mathbf{w}_n^{(p+1)} = \begin{cases} \mathbf{w}_n^{(p+1)+} & \left(\|\mathbf{w}_n^{(p+1)+}\| \geq \|\mathbf{w}_n^{(p+1)-}\| \right) \\ -\mathbf{w}_n^{(p+1)-} & \left(\|\mathbf{w}_n^{(p+1)+}\| < \|\mathbf{w}_n^{(p+1)-}\| \right). \end{cases} \quad (14)$$

5. Calculation of 3-D Orthogonal Outer Product Expansion

Since the resultant expansion terms of 3-D outer product expansion do not satisfy orthogonality, the 3-D orthogonal outer product expansion [3] is defined by

$$\mathbf{A}_3 = \sum_{i,j,k} \sigma_{ijk} (\mathbf{u}_i \otimes \mathbf{v}_j \otimes \mathbf{w}_k), \quad (15)$$

where σ_{ijk} are the expansion coefficients. This expansion can be calculated by introducing the Gram-Schmidt orthogonalization process [5] into the Step 3 of the algorithm described in Section 3 as following procedure.

Step B1. Along with the Gram-Schmidt process,

calculate the vectors $\mathbf{u}'_n^{(p+1)}$, $\mathbf{v}'_n^{(p+1)}$, $\mathbf{w}'_n^{(p+1)}$ by subtracting the previously obtained quantities from vectors $\mathbf{u}_n^{(p+1)}$, $\mathbf{v}_n^{(p+1)}$, $\mathbf{w}_n^{(p+1)}$ respectively as

$$\mathbf{u}'_n^{(p+1)} = \mathbf{u}_n^{(p+1)} - \left(\mathbf{u}_1^T \mathbf{u}_n^{(p+1)} \right) \mathbf{u}_1 - \left(\mathbf{u}_2^T \mathbf{u}_n^{(p+1)} \right) \mathbf{u}_2 - \dots - \left(\mathbf{u}_{n-1}^T \mathbf{u}_n^{(p+1)} \right) \mathbf{u}_{n-1}, \quad (16)$$

$\mathbf{v}'_n^{(p+1)} = \mathbf{v}_n^{(p+1)} - \left(\mathbf{v}_1^T \mathbf{v}_n^{(p+1)} \right) \mathbf{v}_1 - \left(\mathbf{v}_2^T \mathbf{v}_n^{(p+1)} \right) \mathbf{v}_2 - \dots - \left(\mathbf{v}_{n-1}^T \mathbf{v}_n^{(p+1)} \right) \mathbf{v}_{n-1}, \quad (17)$

$\mathbf{w}'_n^{(p+1)} = \mathbf{w}_n^{(p+1)} - \left(\mathbf{w}_1^T \mathbf{w}_n^{(p+1)} \right) \mathbf{w}_1 - \left(\mathbf{w}_2^T \mathbf{w}_n^{(p+1)} \right) \mathbf{w}_2 - \dots - \left(\mathbf{w}_{n-1}^T \mathbf{w}_n^{(p+1)} \right) \mathbf{w}_{n-1}. \quad (18)$

Normalize the vectors in above equations to obtain $\mathbf{u}_n^{(p+1)}$, $\mathbf{v}_n^{(p+1)}$, $\mathbf{w}_n^{(p+1)}$.

Step B2. By the procedure in Section 3 and the Step B1 in this section, vectors $\mathbf{u}_1, \mathbf{u}_2, \dots, \mathbf{u}_m$ of the equation (15) are obtained in order, where $m = \min(L, M, N)$. In case that $L > m$, the remaining $L - m$ vectors terms can be calculated by using Gram-Schmidt orthogonalization process as

$$\mathbf{u}'_n = \mathbf{u}_n - \left(\mathbf{u}_1^T \mathbf{u}_n \right) \mathbf{u}_1 - \left(\mathbf{u}_2^T \mathbf{u}_n \right) \mathbf{u}_2 - \dots - \left(\mathbf{u}_{n-1}^T \mathbf{u}_n \right) \mathbf{u}_{n-1}, \quad (19)$$

$n = m + 1, \dots, L$

where \mathbf{u}_n are the initial vectors and the vectors \mathbf{u}'_n are to be renamed as \mathbf{u}_n after they are normalized. Likewise vectors $\mathbf{v}_{m+1}, \dots, \mathbf{v}_M$ and $\mathbf{w}_{m+1}, \dots, \mathbf{w}_N$ are calculated.

Step B3. For every combination of p , q and r , calculate the expansion coefficients σ_{pqr} as

$$\sigma_{pqr} = \mathbf{A}_3 \left(\mathbf{u}_p \otimes \mathbf{v}_q \otimes \mathbf{w}_r \right), \quad (20)$$

$(p = 1, 2, \dots, L, \quad q = 1, 2, \dots, M, \quad r = 1, 2, \dots, N)$.

To improve in calculation time of these steps, a part of the Step B1 is modified. The modification is described below.

After the calculation of the expansion vectors $\mathbf{u}_1, \mathbf{u}_2, \dots, \mathbf{u}_{m-1}$, the remaining vector \mathbf{u}_m can be calculated by

$$\mathbf{u}'_m = \mathbf{u}_m - \left(\mathbf{u}_1^T \mathbf{u}_m \right) \mathbf{u}_1 - \left(\mathbf{u}_2^T \mathbf{u}_m \right) \mathbf{u}_2 - \dots - \left(\mathbf{u}_{m-1}^T \mathbf{u}_m \right) \mathbf{u}_{m-1}, \quad (21)$$

where \mathbf{u}_m is the initial vector. The vector \mathbf{u}'_m is normalized immediately, then the vector renamed as \mathbf{u}_m . This slight modification leads to an improvement in calculation time.

6. Experimental Results

©ISAROB 2007 following magnitude specification

$\mathbf{h}_d(x_i, y_j, z_k)$ of a 3-D digital filter design problem [2] is used to consider the validity of calculation algorithm described above.

$$\mathbf{h}_d(x_i, y_j, z_k) = \begin{cases} 1, & (0 \leq r \leq 0.4) \\ (0.6 - r), & (0.4 \leq r \leq 0.6) \\ 0, & (r \geq 0.6), \end{cases} \quad (22)$$

where

$$\left. \begin{aligned} r &= \frac{1}{\pi} \sqrt{x_i^2 + y_j^2 + z_k^2}, \\ x_i &= \frac{i\pi}{L'-1}, (0 \leq i \leq L'-1), \\ y_j &= \frac{j\pi}{M'-1}, (0 \leq j \leq M'-1), \\ z_k &= \frac{k\pi}{N'-1}, (0 \leq k \leq N'-1). \end{aligned} \right\} \quad (23)$$

The 3-D array \mathbf{A}_3 is constituted by

$$\mathbf{A}_3(i, j, k) = \mathbf{h}_d(x_i, y_j, z_k). \quad (24)$$

Since the magnitude specification $\mathbf{h}_d(x_i, y_j, z_k)$ is zero when $r \geq 0.6$, the size of the 3-D array is reduced to $L \times M \times N$, where $L = L' \times 0.6$, $M = M' \times 0.6$, $N = N' \times 0.6$.

[3-D Outer Product Expansion]

Table 1 shows that the calculated expansion coefficients by the power method give good approximation to those by the nonlinear optimization method.

Table 1. Resultant coefficients of 3-D outer product expansion by the nonlinear optimization method and the power method.

($L'=M'=N'=20$)

σ_i	Nonlinear Optimization Method	Power Method	Relative Error[%]
1	2.275862E+01	2.275862E+01	0
2	4.283573E+00	4.283573E+00	0
3	3.025678E+00	3.025678E+00	0
4	1.400982E+00	1.400982E+00	0
5	1.129514E+00	1.129514E+00	0
6	6.526013E-01	6.526013E-01	0
7	3.698252E-01	3.698252E-01	0
8	3.454422E-01	3.454422E-01	0
9	3.403220E-01	3.403220E-01	0
10	2.840046E-01	2.840046E-01	0
11	2.598434E-01	2.598434E-01	0
12	2.108770E-01	2.108770E-01	0
13	2.008905E-01	2.008905E-01	0
14	1.767691E-01	1.767691E-01	0
15	1.535205E-01	1.535205E-01	0
16	1.494289E-01	1.494289E-01	0
17	1.064934E-01	1.064934E-01	0
18	1.006265E-01	1.006265E-01	0
19	1.002772E-01	1.002772E-01	0
20	9.568394E-02	9.568395E-02	-6.27E-06

[3-D Nonnegative Outer Product Expansion]

Figure 1 illustrates the convergence property of the power method described in Section 4. The relative error of the method, which calculates 3-D nonnegative outer product expansion, is about 10% at $n=10$, while the error less than 10% at $n=3$ in case of 3-D outer product expansion.

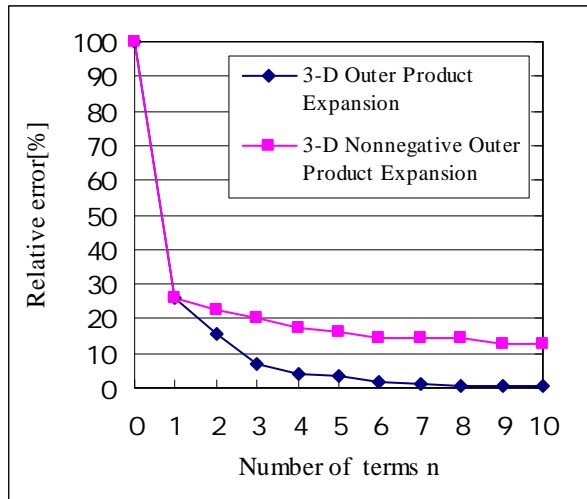


Figure 1. Convergence property of the power method.

[3-D Orthogonal Outer Product Expansion]

Figure 2 shows the calculation time of modified method in Section 5 compared with the usual method. In this experiments, the 3-D array is constructed by random integer in the range of [1,1000]. From the figure, the calculation time can be reduced slightly by using the proposed method.

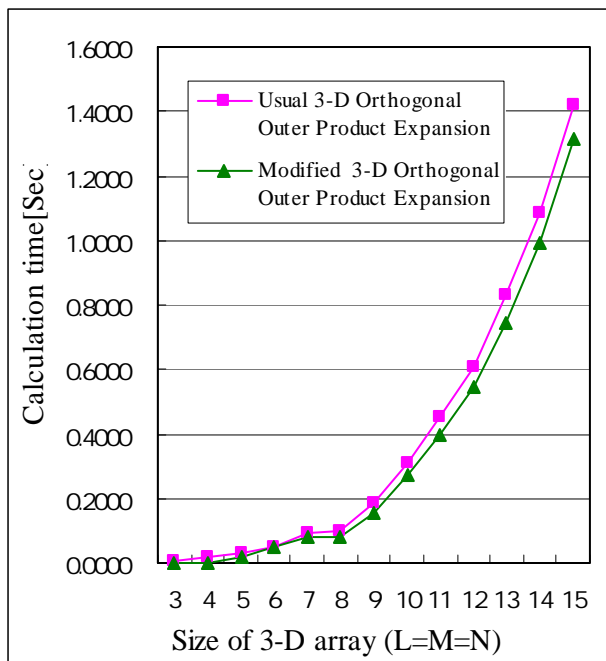


Figure 2 Calculation time of 3-D orthogonal outer product expansion.

7. Conclusions

In this paper, we showed the calculation results of the 3-D outer product expansion, 3-D nonnegative outer product expansion, and 3-D orthogonal outer product expansion in the following development environment.

System: FreeBSD 3.4-RELEASE

Development language:

C (GNU C compiler v2.7)

Accuracy:

floating point of double precision type

The results lead to the following conclusions:

- (1) Using the previously proposed method to calculate the 3-D outer product expansion and the 3-D nonnegative outer product expansion, we obtained the expansion coefficients and vectors precisely.
- (2) By modifying the usual method for calculation of the 3-D orthogonal outer product expansion, the calculation time could be reduced slightly in comparison with the previously proposed method.

References

[1]Deng, T. B. and Kawamata, M., "Design of Two-Dimensional Recursive Digital Filters Based on the Iterative Singular Value Decomposition", Trans. IEICE, Vol.E73, No.6, pp.882-892,1990.
 [2]Ohki, M. and Kawamata, M., "Design of Three-Dimensional Digital Filters Based on the Outer Product Expansion", IEEE Trans. Circuits Syst., Vol.CAS-37, No.9, pp.1164-1167, 1990.
 [3]Murakami, J., Yamamoto, N. and Tadokoro, Y., "High-Speed Computation of 3D Tensor Product Expansion by the Power Method", Electronics and Communications in Japan, Part 3, Vol.85, pp.63-72,2002.
 [4]Wilkinson, J. H., "The Algebraic Eigenvalue Problem", Oxford University Press, 1965.
 [5]Press, W. H., Flannery, B. P., Teukolsky, S. A. and Vetterling, W. T., "Numerical Recipes in C", Cambridge University Press, 1988.

Adaptive Knowledge Base for Japanese-to-Braille translation

Satoshi Ono Takashi Yamasaki Shigeru Nakayama
Department of Information and Computer Science,
Faculty of Engineering, Kagoshima University
1-21-40 Korimoto, Kagoshima, 890-0065 Japan
{ono, sc101056, shignaka}@ics.kagoshima-u.ac.jp

Abstract

This paper proposes a method for generating adaptive knowledge base involving two knowledge representations – rule and case. Combining rules and cases makes it possible to solve problems accurately and quickly, and to acquire new cases from problem-solving results. The proposed method does not require manually adjustment of the thresholds and provides highly qualified solutions. This paper also proposes a Japanese-to-Braille translation system which uses the adaptive knowledge base as mentioned above. Experimental results have showed that the case acquisition can reduce errors, and that the threshold adjustment significantly reduces segmentation errors.

keywords: knowledge base, rule-based reasoning, case-based reasoning, threshold adjustment, Japanese-to-Braille translation

1 Introduction

Rules and cases are valuable knowledge representations that mutually supplement drawbacks of each. While rules embody understanding that has been codified over the years by experts, cases contain the knowledge of a domain in a relatively unprocessed form. Rules are appropriate for representing general domain knowledge and cases are appropriate for representing the exceptions of that knowledge[1, 2, 3]. By combining rules and cases, it is possible to solve problems accurately and quickly, and to acquire new cases from problem-solving results[4, 5].

In previous methods using both rules and cases[4, 5, 6, 7], rule-based reasoning (RBR)[8] is performed first, and then case-based reasoning (CBR)[1, 2, 3] is performed. RBR solves a problem tentatively, but also chooses an exceptional case set. Retrieving the chosen cases, instead of all cases, reduces the processing time of case application, consequently a drawback of CBR. In the previous methods, only a common threshold

of similarity is used to judge which exceptional cases should be applied. Although the threshold is manually adjusted, such adjusting is difficult because the appropriate threshold differs with each exceptional case.

In this paper, we propose an adaptive knowledge base (AKB), which is composed of a rule base, an indexed case base and a method for adjusting cases' thresholds. The proposed method eliminates the manual adjustment of the threshold and provides higher qualified solutions than the existing methods with the same knowledge base. In AKB, each case has a threshold in order to reuse exceptional cases that the existing methods cannot reuse because of the unified threshold. The thresholds are automatically adjusted after case acquisition. Providing a threshold for each case makes it easier to automatically adjust thresholds. Moreover, adjusting the threshold for each case increases the opportunity of reuse and decreases the risk of incorrect use.

This paper also proposes a Japanese-to-Braille translation system AJ2B which uses AKB as mentioned above. Japanese-to-Braille translation is a task involving two procedures – sentence segmentation and kanji-to-kana conversion. Accurate automatic translation is difficult due to the ambiguous, complicated rules peculiar to Japanese-to-Braille translation and Japanese language itself. A Japanese sentence is a string of characters concatenated without blanks, so spaces must be inserted between words to get a proper interpretation. Kanji must be converted to kana, because Braille characters expressing Japanese correspond only to kana.

Experimental results shows that the case acquisition can reduce errors, that the threshold adjustment significantly reduces segmentation errors, and that the proposed system reaches almost the same translation quality as the most popular software on the market called “Extra Ver.4.0.”

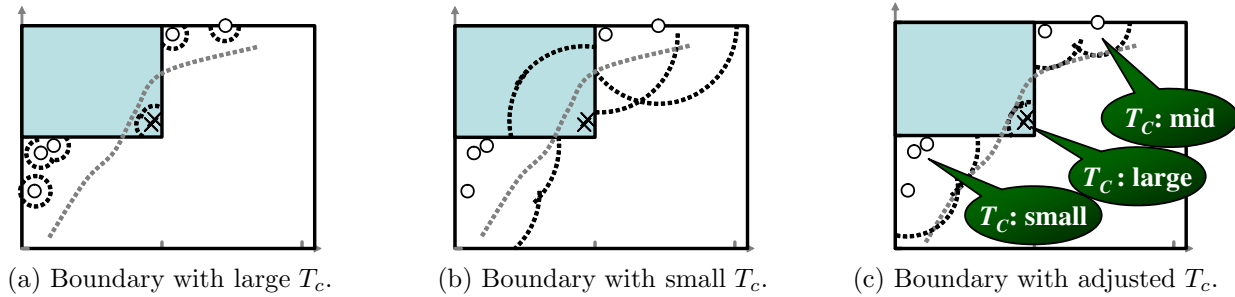


Figure 1: Boundaries depending on T_C .

2 Proposed adaptive knowledge base

2.1 Overview

In an attribute space, rules are represented as hyperrectangles and cases are represented as points whose coverage areas become Voronoi diagram. Although RBR quickly solves problems by applying a few rules, irregular or exceptional problems are difficult for RBR to solve. CBR can accurately solve these problems by applying many cases. Unfortunately, processing time increases proportionally to the number of cases used.

AKB utilizes rules to represent general knowledge, and cases to represent exceptional knowledge. This causes the knowledge base to maintain only negative cases, which have different operators from rules that they belong to. Positive cases, which have the same operator as rules that they belong to, are used only for learning process, not for solving problems. Consequently, the proposed knowledge base solves problems more accurately than RBR and more quickly than CBR because of less amount of knowledge than CBR.

2.2 Problem solving process

The fundamental idea of combining rules and cases is to apply the rules to a target problem to produce a draft solution; but if the target problem is judged to be compellingly similar to a known exceptional case of the rules, then the exceptional case is applied rather than the rules [4, 5, 6, 7]. The idea above is therefore realized through the following procedure:

Step 1: Use the rules to select an operator to apply.

Step 2: Search for exceptional cases that would contradict this choice of operator, stopping if and when a compelling case is found.

Step 3: If a compelling case was found, apply the operator it suggests, else proceed to apply the operator suggested by the rules.

2.3 Threshold adjustment

In the existing method using both rules and cases, the case coverage areas become hypersphere whose radiuses are decided by the unified threshold T_C in the attribute space. Large T_C prevents incorrect case application, but it also decreases the chances to reuse cases correctly are also decreased. In contrast, small T_C makes case coverage areas large and increases the changes to apply cases, but it increases the possibility of inadequate case application.

The AKB involves a threshold adjustment method for the hybridization of rules and cases. First, in the proposed knowledge base, each exceptional case has a threshold for deciding whether the case should be applied. This enables control of influence sphere at every exceptional case. Second, each threshold are adjusted automatically at a learning stage, while the existing method requires a developer to adjust the unified threshold manually. The AKB, therefore, reuses cases which are not reused efficiently in the existing method and prevents reusing cases which are reused incorrectly in the existing method.

The thresholds are adjusted one by one by the following procedure:

Step 1: Initialize a threshold T_{C_x} of an exceptional case C_x by $1.0 - \delta_T$.

Step 2: If $T_{C_x} \leq T_{C_x}^{(L)}$, terminate.

Step 3: For all learning data P_L in the root rule of C_x :

Step 3a: Apply C_x if $Sim(P, C_x) > T_{C_x}$.

Step 3b: If no error occurs, $T_{C_x} \leftarrow T_{C_x} - \Delta_T$ and go to Step 2.

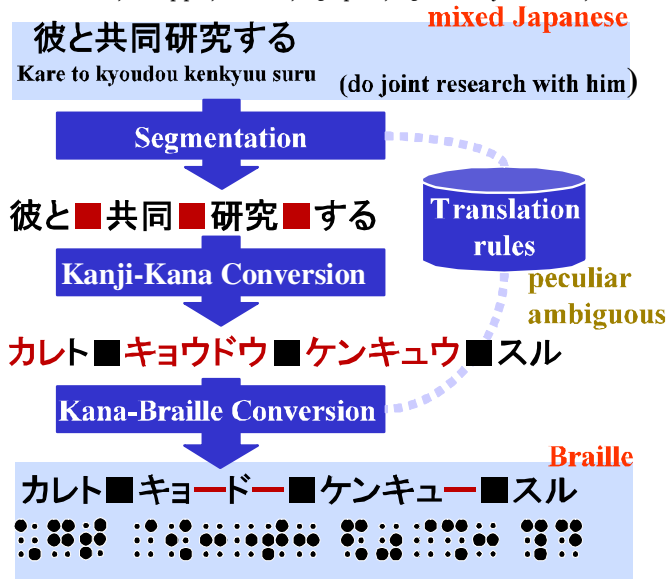


Figure 2: Japanese-to-Braille translation process.

Step 3c: If errors occur, $T_{C_x} \leftarrow T_{C_x} + \Delta_T$ and terminate.

3 Application to Japanese-to-Braille translation

The task for translating Japanese into Braille is defined as translation of mixed Japanese into Braille, and is done in two steps – sentence segmentation and kanji-to-kana conversion. A Japanese sentence is a string of characters concatenated without blanks, so spaces must be inserted between words to get a proper interpretation. Kanji must be converted to kana, because Braille characters expressing Japanese correspond only to kana.

The many translation rules that must be obeyed, are themselves ambiguous and full of exceptions[7, 9]. In sentence segmentation, for example, rules require that semantic and phonetic information be considered. In kanji-to-kana conversion, rules for distinguishing ordinary vowels are unclear, i.e., ‘ア’, ‘イ’, ‘ウ’, ‘エ’, and ‘オ’, and the symbol ‘ー’, denoting a long vowel, are used in writing, whereas a long vowel in regular Japanese is only used to express words of foreign origin or imitation sounds. It is thus very difficult to represent rules so that they are followed automatically by a computer.

Cases and rules segment sentences and revise strings in a draft. A rule consists of an operator (example: insert a space), conditions for applying the

operator, and a priority score to resolve rule conflicts. A condition is stated by checking the value of an attribute. Attributes are obtained by morphological analysis, e.g., parts of speech, character type, a mora, and reading which is a pronunciation written in kana. All of those attributes are defined as symbolic attributes.

A case consists of an operator, a set of attributes of morphemes to which the operator of this case makes revision, and an identification number of a root rule, i.e., the rule for which the case is an exception. We define an object to which an operator of a rule or a case makes revision, i.e., a string or an interval between characters, as a spot.

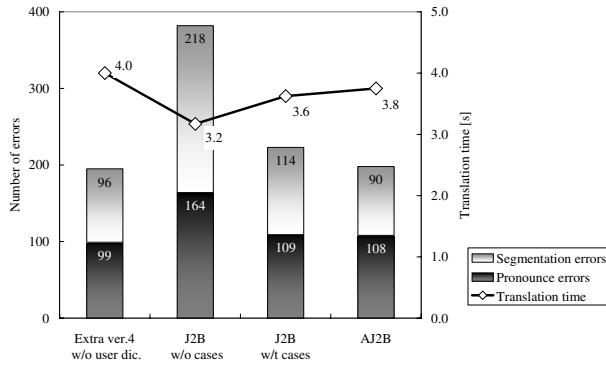
4 Experimental results

We compared AJ2B and the most popular Japanese-to-Braille translation software on the market — Extra Ver.4.0. A document “The Copyright Act” is used for evaluation. In the document, all sentences are divided into two groups — even sentences for training and odd ones for evaluation. The opposite experiments in which odd sentences are used for training and even sentences for evaluation are also performed. J2B[6, 7] is also tested for evaluating the effectiveness of threshold adjustment and case acquisition.

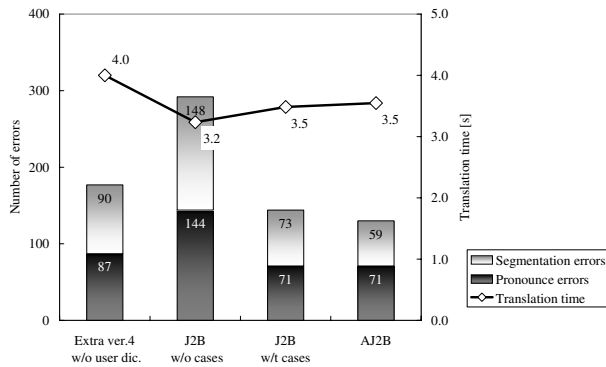
J2B and AJ2B utilizes a Japanese morphological analyzer called ChaSen with modified dictionary which does not involve extra foreign compound words. AJ2B parameters are decided as follows: $T_{C_R}^L = 0.9$, $T_{C_S}^L = 0.9$, $\Delta_T = 0.01$.

Figure 3 shows the number of errors and translation time of the proposed method and Extra in each experiment. Errors are categorized into pronounce and segmentation errors.

As shown Figure 3), case acquisition in J2B is significantly effective in decreasing errors. This is because “The Copyright Act” is a document that defines laws and that involves a lot of the same wording and quite similar wording. The important point to note is that the case acquisition in J2B can eliminate almost half of segmentation errors. This indicates that the flexibility of cases is effective in representing exceptional segmentation knowledge of Japanese-to-Braille translation. In addition, the threshold adjustment can also reduce segmentation errors to almost 80% of J2B with cases. This indicates that the threshold adjustment can expand the flexibility of each case. In contrast, the threshold adjustment has no effectiveness on pronounce errors because cases for revising the pronounce



(a) The Copyright Act: Even sentences are used for learning and odd sentences are used for test.



(b) The Copyright Act: Odd sentences are used for learning and even sentences are used for test.

Figure 3: Experimental results

errors should be applied only to the same or quite similar wordings.

A glance at the graphs in Figure 3 also reveals that the threshold adjustment does not affect the translation time, although translation time increased by using cases.

5 Conclusions

In this paper, we proposed an adaptive knowledge base composed of rules and cases. The proposed knowledge base acquires exceptional cases from existing Braille documents and adjusts their threshold for judging whether the case should be applied or not. Experiments in Japanese-to-Braille translation problem showed that acquiring cases and adjusting their thresholds reduce errors.

Acknowledgements

This research was partially supported by the Ministry of Education, Science, Sports and Culture, Grant-in-Aid for Young Scientist (B), No.16700412, 2004-2006.

References

- [1] C. K. Riesbeck and R. C. Schank (1989), Inside Case-Based Reasoning. Hillsdale, New Jersey: Lawrence Erlbaum
- [2] R. C. Schank, and A. Kassand, and C. K. Riesbeck (1994), Inside Case-Based Explanation. Hillsdale, New Jersey: Lawrence Erlbaum
- [3] B. Bartsch-Spörl, M. Lenz, and A. Hubner (1999), Case-based reasoning - survey and future directions, Proceedings XPS-99, Springer Verlag, LNAI
- [4] A. R. Golding and P. S. Rosenbloom (1991), Improving rule-based systems through case-based reasoning, in In Proceedings of the Ninth National Conference on Artificial Intelligence, pp. 22-27
- [5] — (1996), Improving accuracy by combining rule-based and case-based reasoning, Artificial Intelligence, vol. 87, pp. 215-254
- [6] S. Ono, Y. Hamada, Y. Takagi, et al.(2000), Interactive japanese-to-braille translation using case-based knowledge on the web, in Proceedings of the Sixth Pacific Rim International Conference on Artificial Intelligence, pp. 638-646
- [7] S. Ono, Y. Takagi, Y. Hamada, et al.(2003), Japanese-to-braille translation and error correction support using case-based knowledge, (in Japanese) Human Interface, vol. 5, no. 4, pp. 491-498
- [8] F. Hayes-Roth, D. Waterman, and D. Lenat (1983), Building Expert Systems. Addison-Wesley Publishing Co., Reading
- [9] E. Suzuki, S. Ono, T. Hiraoka, et al. (1997) Interactive japanese sentence segmentation system for translating japanese into braille, in Proceedings of the Natural Language Processing Pacific Rim Symposium, vol. 1, 1997, pp. 621-624

Language Evolution and the Baldwin Effect

Yusuke WATANABE Reiji SUZUKI Takaya ARITA

Graduate School of Information Science, Nagoya University

Furo-cho, Chikusa-ku, Nagoya 464-8601, Japan

E-mail: watanabe@alife.cs.is.nagoya-u.ac.jp, reiji@is.nagoya-u.ac.jp, arita@nagoya-u.jp

Abstract

Recently, a new constructive approach characterized by the use of computational models for simulating the evolution of language has emerged. This paper investigates the interaction between the two adaptation processes in different time scales, evolution and learning of language, by using a computational model. Simulation results show that the fitness increases rapidly and remains at a high level, while the phenotypic plasticity increases together with the fitness but then decreases and gradually converges to a medium value. This is regarded as the two-step transition of the so-called Baldwin effect. We investigate the evolutionary dynamics governing the effect.

Keywords: language evolution, Baldwin effect, genetic algorithm, recurrent neural network, artificial life.

1 Introduction

Humans are the only species that has evolved sophisticated language. For hundreds of years, many researchers have investigated why and how it could be possible. Recently, a new constructive approach characterized by the use of computational models for simulating the evolution of language has emerged. Language is an emergent system that has been created and maintained through language faculty evolution in a long time scale and cultural change in a short time scale, and thus these models treat either biological evolution or cultural evolution of language. The most obvious purpose of language is to communicate information. If we use natural selection to explain the evolution of language faculty, an individual carrying a "beneficial" grammatical mutation must have a higher fitness. However, how could the mutation be beneficial, if all the other less-evolved individuals in the population could not have understood her [1]. Therefore, it is a very plausible idea that learning combined with evolution played a crucial role in the evolution of language. We focus on the interaction between these two adaptation processes driving the evolution of language in different time scales by using a computational model based on the constructive approach.

The Baldwin effect, which is the focus of this paper, explains the interaction between evolution and learning in general by paying attention to balances between benefit and cost of learning through the two steps [2]. In the first step, life time learning gives individual agents chances to change their phenotypes. If the learned traits are useful for agents and make their fitness increase, they

will spread in the next population. The learning behavior acts as a benefit in this step. In the second step, if the environment is sufficiently stable, the evolutionary path finds innate traits that can replace learned traits (genetic assimilation), because of the cost of learning. Through these steps, learning can accelerate the genetic acquisition of learned traits without the Lamarckian mechanism, which has been clearly demonstrated with a variety of models [3]. When analyzing the interaction between evolution and learning, one of the most important aspects is the cost of learning, because the second step of the Baldwin effect can not occur, if learning is ideal, in other words, there is no cost at all arising from the learning process.

We adopt a speaker-hearer model proposed by Batali [4], in which each agent used a simple recurrent neural network and structured utterance, in other words, partially compositional communication could be obtained by learning from each other. We use the model in a combined framework of cultural learning and genetic evolution. Adopted cultural learning is an extended version of Iterated Learning proposed by Kirby and Hurford [5], which is based on vertical (oblique) communication from adults to children and horizontal communication between adults. Evolution of the weights in the neural network is achieved by a genetic algorithm. In order to examine whether and how the Baldwin effect might occur, we use a mechanism for the evolution of the plasticity (learnability) of each weight in the neural network as we did in [6].

2 Model

A conceptual overview of the model is shown in Figure 1. There are two types of communication: vertical (oblique) communication which is unidirectional transmission from adults to children and horizontal communication which is bidirectional transmission between adults (Figure 2). In the first stage, each child agent learns to interpret the characters produced by a biological parent and randomly-selected cultural parents in each communicative episode. In the second stage, a communicative episode is repeated between a pair of grown-up agents of their generation in which each agent alternates between learning to interpret sequences of the characters produced by other agents and producing sequences of characters. Then, the next generation is produced based on the fitness of agents based on their communicative accuracy in the first and second stages. In the third stage, each

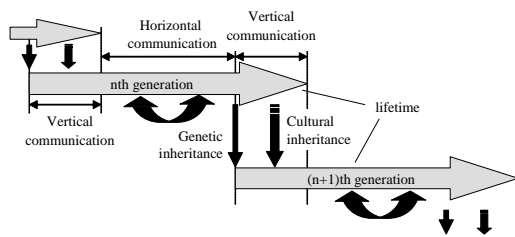


Figure 1: Overview of our model.

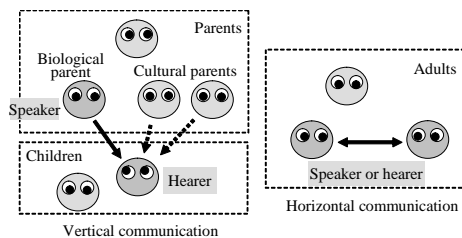


Figure 2: Two types of communication.

agent as a parent just produces sequences of characters for their biological and cultural children as their parents do for them in the first stage.

There are two forms of linguistic representation in this model: 1) I-language: Internal language as patterns of connection weights in the neural network, 2) E-language: External language as sequences of uttered characters. Linguistic information in I-language can be inherited from a generation to the next generation via the following two ways: 1) genetic inheritance: initial connection weights of the agents are transmitted to their children through evolutionary operations (Lamarckian inheritance is not adopted), 2) cultural inheritance: E-language is produced from I-language through use and is transmitted to the I-language of the next generation through learning (vertical communication).

Each agent uses a simple recurrent neural network (Elman network) consisting of three layers of neurons (4 character input units each of which corresponds to each of 4 character (a, b, c, or d) and 30 context input units, 30 hidden units and 10 output units). A communicative episode is illustrated in Figure 3. Agents produce sequences of characters to encode structural patterns (vectors) each of which stores 10 real values between 0 and 1. The values in the patterns are partitioned into two groups: the left four of the values are taken as encoding a subject and the right six of the values are taken as encoding a predicate. There are 5 patterns each for the subjects and predicates, and therefore 25 different patterns.

In the beginning of each communicative episode, a subject and a predicate are randomly selected. In order to choose which character to send at each point in a sequence, the speaker agent determines which of the four characters would bring its own output pattern closest to the structural pattern being conveyed. She stops sending if all the speaker's output units are correct for the structural pattern. If the sequence of characters which the

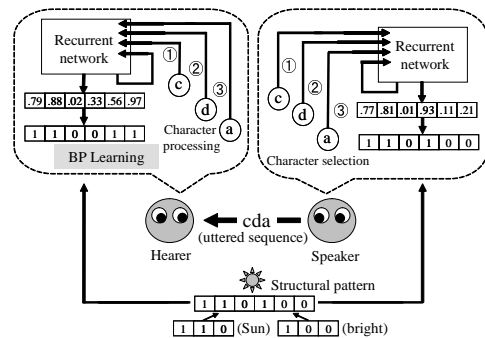


Figure 3: A communicative episode.

agent produces does not reach a limit length of ten characters, the agent succeeds in producing the sequence of characters. The hearer agent then processes the sequence of characters sent by the speaker, and produces an output pattern. The back-propagation algorithm is conducted to modify the weights of the network using the difference between the speaker's and the hearer's structural patterns. The network is trained until it converges.

Biological evolution is achieved by a genetic algorithm as follows. Each agent has a pair of chromosomes containing the same number of genes initially assigned to random values. Each gene in the chromosome GW encodes the initial connection weight in the neural network, and each gene in the chromosome GP represents whether the corresponding connection weight in the neural network is plastic ("1") or not ("0"). If a gene of GP is 0, the corresponding connection weight is invariable in the lifetime. GW consists of a real value within the range [-1.0; 1.0]. Agents obtain a reward when they correctly interpret a sequence of characters or when they successfully produce a sequence of characters in a communicative episode regardless of the hearer's success. Total rewards when the second stage is completed are used as their fitness values. A new population is generated by the tournament selection, and then a mutation is applied with a prespecified probability. A mutation in GW changes the current value into a randomly generated value within the range [-1.0; 1.0] and a mutation in GP flips the current binary value.

3 Experiments

We conducted an experiment for 140 generations. The following parameters were used: N (number of agents) = 100, N_p (number of parents) = 5, r (reward) = 1, m (mutation probability) = 0.01, s (tournament size) = 2, L_v (number of learning iterations for vertical communication) = 990000, L_h (number of learning iterations for horizontal communication) = 1485000. The initial population was generated on condition that initial values in GW were taken at random within the range [-1.0; 1.0] and the proportion of "1" in GP for each agent was uniformly distributed within the range [0.05; 0.95] at intervals of 0.05.

Figure 4 shows the transitions of the fitness that is the

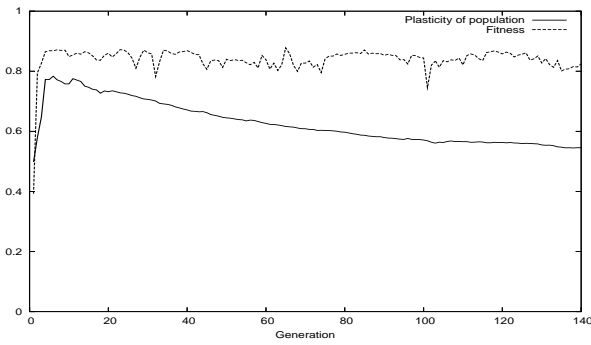


Figure 4: Fitness and plasticity of population.

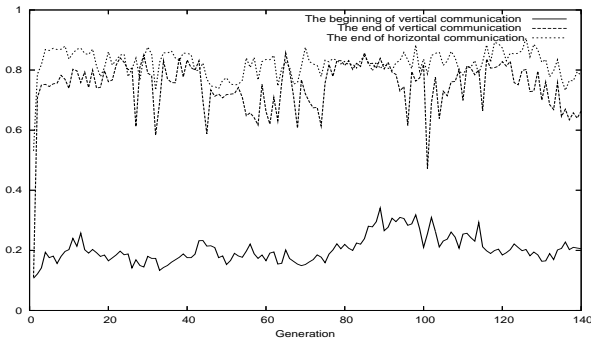


Figure 5: Linguistic coherence among the same generation.

average reward of a agent per communicative episode and the “plasticity of population” which is the ratio of “1” in all GPs of the population. We see that the fitness increased rapidly during the first several generations and kept high afterward, which means the agents have developed an accurate communication system through evolution and learning. Plasticity increased together with the fitness, but then decreased and gradually converged to some medium value (genetic assimilation). This is a typical two-step evolution caused by the Baldwin effect, a key concept clarifying the interaction between evolution and learning.

Figure 5 shows the transitions of the coherence at the beginning or end of each stage. Coherence is the average

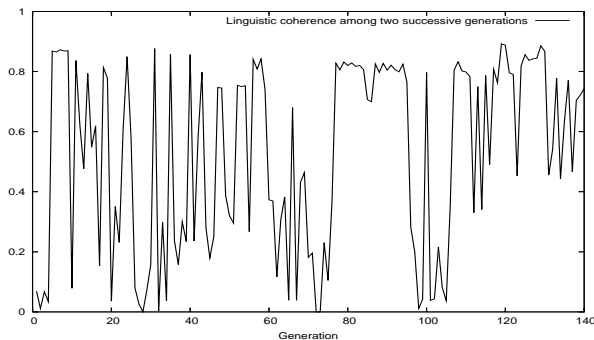


Figure 6: Linguistic coherence among two successive generations.

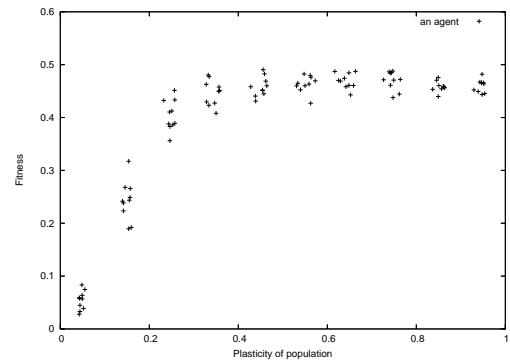


Figure 7: Correlation diagram of fitness and plasticity of population.

ratio of agents uttering the majority sequence for every possible structural pattern. The coherence both after the first and second stages increased rapidly and remained at a high level around 0.85. Also, the coherence before the first stage (innate coherence) moved from 0.1 to 0.2 in the first step. The difference in coherence between before the second stage and the third stage is supposed to mean the diversity amplified by the selected cultural parents in the first stage. Figure 6 shows that the coherence among two successive generations tends to increase while it shows a chaotic oscillation.

Table 1: A part of the characters shared most in the 140th generation. In most of the sequences, we observed that subjects correspond to suffixes (bold font) and predicates correspond to prefixes (underline).

subjects and predicates	1000	1011	0101
011100	<u>bb</u> d	<u>bb</u> c	<u>bd</u>
101001	<u>aa</u>	<u>ac</u>	<u>ad</u>
100011	<u>ca</u>	<u>cc</u>	<u>cd</u>

Table 1 shows a part of the sequences used by a majority of the population in the 140th generation. The agents in the 140th last generation tended to share a little shorter sequences than previous generations. Also, syntactic regularities in the order of token sequence tended to be observed more clearly.

Here, we investigate the evolutionary dynamics which governs the Baldwin effect. The agents in the first generation varies greatly both in the amount of the plastic phenotypes and the connection weights of the network. Agents with more plastic connections could communicate with others successfully in this situation and therefore could occupy the population within several generations. Figure 7 shows the correlation between plasticity and fitness in the 1st generation. This also supports the scenario that the plasticity drives the evolution in this step.

In the second step, plasticity gradually decreased to about 0.55 around the 140th generation while keeping the fitness high. This shows a dramatic change between the both steps in the necessity of the plasticity caused by the change in genetic organization. We conducted several additional experiments in order to clarify the factors

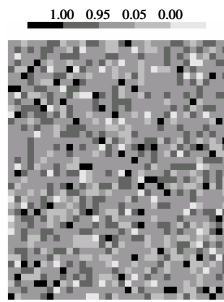


Figure 8: The distribution of the proportion of the plastic connection weights in each locus.

driving the evolution in the second step. As a result, the following factors drastically decreased the selection pressure for the evolution of plasticity compared with the evolution of the connection weights, and thus it gradually decreased to 0.55 by a random drift in the second step.

The first factor is the decrease in the necessity of learning caused by a linguistic shift towards easier language. The variation in the initial connection weights decreased rapidly in the first stage, which made the learning in the second stage easier because the language that should be learned and shared among agents became nearer to the innate language of each agent. The fact that the variation in the plasticity in the population decreased rapidly in the first stage also decreases the selection pressure for plasticity. We see that the coherence was about 0.1 in the first generation while it was 0.2 in the generations of the second step, which supports this explanation.

There is another language-specific factor. Figure 8 shows the distribution of the proportion of the plastic connection weights in each locus. It is shown that the architecture of the network (the location of the plastic connection weights) evolved to be identical. Also, there is a possibility that regularization and compactification in the uttered sequences played a role to become easier for agents to acquire. The fact that the coherence among two successive generations tended to keep high afterward is supposed to show this possibility. These factors are specific to language evolution and seem parallel with the idea by Deacon that language evolves to be adaptive to human cognitive capacity [7].

The second factor is implicit cost associated with learning. In our experiments, there is no explicit learning cost in learning such as fitness tax which is proportional to the learning period. Also, the length of each communicative episode seems enough for learning to converge, which is supported by the result of the experiment (not shown) in which the length of the episode was doubled. However, the interactions among weights or genetic epistasis based on abundant plasticity could cause the bad effect in the back-propagation learning, leading to the decrease in the reward. In this sense, phenotypic plasticity evolves under such selection pressure [6]. This type of cost becomes larger, as the necessity of learning decreases through the phase of evolution. Note that epistasis could have an opposite function to repress genetic assimilation

by making the relationship between genotype and phenotype less correlated [8].

Another aspect of implicit cost, which is purely specific to linguistic evolution, is related with the variation in parents. In the first stage, each child learns sequences uttered from the biological and randomly selected cultural parents. Overlearning to the parents with new local dialect owing to mutation could cause a decrease in rewards both in vertical communication and succeeding horizontal communication.

4 Conclusion

This paper investigates the interaction between evolution and learning of language by using a computational model which we believe to be a minimal model to capture the essence of it. We have found that the factors specific to language evolution or linguistic behavior might have a crucial role in shaping its evolutionary pathways. Specifically, it has been shown that the second step in the Baldwin effect (genetic assimilation) could be driven by the random drift caused indirectly by the adaptive shift in language or overlearning to a variety of parents. It should be noted that genetic assimilation in this evolutionary scenario does not necessarily need unchanged linguistic environment.

References

- [1] Geschwind, N.: Some Comments on the Neurology of Language in *Biological Studies of Mental Processes* (ed. D. Caplan), MIT P, 1980.
- [2] Turney, P., Whitley, D. and Anderson, R. W.: Evolution, Learning, and Instinct: 100 Years of the Baldwin Effect, *Evolutionary Computation*, 4(3), 4-8, 1996.
- [3] Hinton, G. E. and Nowlan, S. J.: How Learning Can Guide Evolution, *Complex Systems*, 1, 495-502, 1987.
- [4] Batali, J.: Computational Simulations of the Emergence of Grammar in *Approach to the Evolution of Language*, 405-426, Cambridge UP, 1998.
- [5] Kirby, S. and Hurford, J. R.: The Emergence of Linguistic Structure: An Overview of the Iterated Learning Model in *Simulating the Evolution of Language* (ed. A. Cangelosi and D. Parisi), Springer Verlag, 2002.
- [6] Suzuki, R. and Arita, T.: The Baldwin Effect Revisited: Three Steps Characterized by the Quantitative Evolution of Phenotypic Plasticity, *Proc. of 7th Eur. Conf. on Artificial Life*, 395-404, 2003.
- [7] Deacon, T. W.: *The Symbolic Species: The Co-evolution of Language and the Brain*, Norton, 1997.
- [8] Yamauchi, H.: The Difficulty of the Baldwinian Account of Linguistic Innateness, *Proc. of the 6th Eur. Conf. on Advances in Artificial Life*, 391-400, 2001.

A distributed algorithm of group robots applied to maze searching

T. Onitsuka O. Araki
Institute of Pure and Applied Physics
Tokyo University of Science
Tokyo, Japan

T. Tamura
Personal Computer & Network Company
TOSHIBA Corporation
Tokyo, Japan

Abstract

In this study, we proposed a simple algorithm of group robots, which assumes to work independently works on each of the robots. The algorithm uses local distance information without specific centralized control. Usually they move around randomly and individually. Whether the distance between the robots increases beyond a constant value or decreases below another constant switches their behavior into shrink mode or expansion (random search), respectively. In the shrink mode, a robot which is farthest from the others is selected as a leader, and the others go straight toward the leader until the distance decreases below the value. Applying this algorithm to maze searching on computer simulations, we observe interesting properties as follows: (1) The parameter values which switch shrink and expansion modes affect the performance of solving the maze problem, suggesting the important relation between the values and the structural scale of the maze. (2) Proceeding and exploring behaviors with dividing and merging subgroups are self-organized. This leads to better performance an average compared with the results by a set of robots composed of a random searching robot.

1 Introduction

Recently, robotic technologies have been developed such as humanoid robots who can walk using two legs, micromachines with electromagnetic oscillation, and so on. Generally, to make them more intelligent, more complicated algorithms and control systems are needed. However, even an insect can show complicated and intelligent behaviors, which suggests that a group composed of simple and distributed agents may have those functions. In this study, we focus on the algorithm of each simple component, which shows intelligent behaviors as a system. In other words, intelligent behaviors emerge, even though each robot follows the same and simple algorithm. Thus, there is no specific

leader who controls the group.

Research approaches inspired by emergent intelligent behaviors of swarms is called Swarm Intelligence (SI)[1][2][3]. SI systems are typically made up of a population of simple agents interacting locally with one another and with their environment. Although there is normally no centralized control structure dictating how individual agents should behave, local interactions between such agents often lead to the emergence of global behavior. Representative examples of SI systems are Ant Colony Optimization (ACO)[4] and Particle Swarm Optimization (PSO)[5][6]. In a swarm of insects or a school of fish, when one finds a desirable path, the rest of the members will follow it in PSO. Assuming an evaluation function over the search space, the vector of velocity of each agent is repeatedly modified depending on the agent's position with global minimum and on the local information. As this calculation proceeds, every agent tends to move toward the position where the objective function has an optimized value. While every agent follows a simple and the same algorithm, the group quickly reaches to optimized position as a group. Our study assumes the situation in which the objective function is not clear. We focus on clustered and searching behaviors such as swarm intelligence without using the objective function over the field.

The purpose of this study is to propose a simple algorithm in each agent distributed when the objective function cannot be used. Each agent can utilize limited local information and communicate each other. The key of the algorithm is the alternative modes of expansion and shrink. Each robot always measures the distance from each other, and notices a leader of the group when the distance increase beyond a constant. Every robot except the leader follows the leader until the distance decreases below another constant value (shrink mode). Then, each robot goes random direction again (expansion mode). While the simulation robots are searching in the maze, we can observe not only the performance of how soon they reach the

goal but also emergent behaviors of robustness and adaptability of the system. Our algorithm does not assume centralized control structure. Thus, the system will not stop, even if some of them are lost or broken. And our algorithm is so simple that we can implement it on the hardware robots easily. The most important feature of our algorithm is random searching and a clustered behavior like swarms or a school of fish at the same time. In this study, we did computer simulations in a maze using software robots to show the properties of the algorithm. The parameter values which decide mode switching are shown to be crucial to the performance of the maze searching. Depending on the values, the system was able to reach a goal earlier than random searching.

2 Algorithm

As a first step of our study, we constructed an agent model such as a swarm as simple as possible, whose algorithm is shown as follows (Fig.1): First, each robot moves around randomly without a leader (“expansion mode” (Fig.1-(1))). Each one assumes to go straight in one direction until it reaches a wall, then it reflects to another direction. The reflection angle is randomly selected in order to avoid infinite bouncing in a dead end. When a robot whose distance from the other robots exceeded a constant value of a parameter ($d1$), the robot becomes a leader (Fig.1-(2)). At this time, at least two robots or more become leader’s candidates. The position where the previous “expansion” mode starts in each robot is memorized, and the distances between the position and the current position are compared. Then the robot whose value is largest is selected as a leader. If the distance is also the same, it is randomly selected. This is because we think one which was advanced larger from the previous expansion should be a leader. Once the leader decided, the other robots go straight toward the leader (“shrink mode” (Fig.1-(3))). Only the leader keeps going before as it does, while the other robots changes each direction toward the position of the leader and keep following it at an equal speed until the longest distance between any two robots decreases below another constant parameter ($d2$). Then, the leader is dismissed and the group’s movement returns back to the first free searching (Fig.1-(4)). The velocity of all motions is assumed to be constant except when the direction is changed, when the mode has changed, and while one is following a leader. These procedures are repeated and the leader is selected every time the distance exceeds $d1$. This algorithm expects that some robots far

from the rest may find a new way, which will promote exploration as a group.

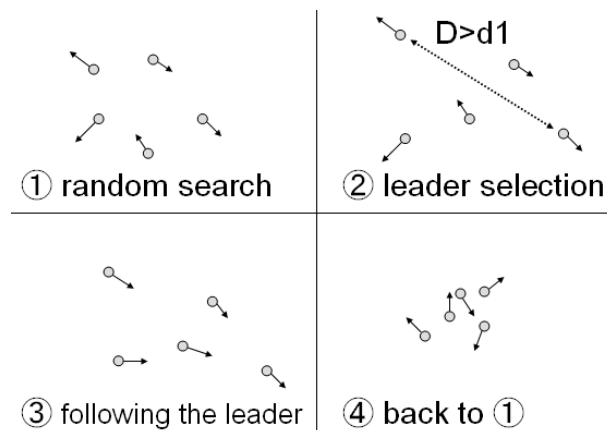


Figure 1: Schematic behaviors of the algorithm

Although an obstacle or walls in the maze may also split the group into some subgroups during searching, there is no problem because the leader is selected in each subgroup. As a result, two or more groups might coexist and continue searching, which will lead to an efficient search. When the leader is decided, the robots those follow the leader are limited in the range that the distance from the leader is less than the value of the third parameter ($d3$). This limitation is needed so that the effect of the robot whose position is too far away on the selection of a next leader becomes weaker. This may partially avoid back-and-forth motion of each group.

3 Computer simulations

3.1 Method

To examine properties of the above-mentioned algorithm, we did computer simulations using software robots in a simple maze. We observed behaviors of robots ($N=20$) in the maze (Fig.2), which start at the position in the corner and search around until they find the goal in another corner. In addition, we measured the time (number of procedural steps) spent by all of the robots from the start to the goal. The result is averaged over 100 trials with different random seeds for each combination of parameter values. When a robot reaches the goal, it assumes to stay there without becoming a leader.

The size and the width of walls of the maze is shown as follows: map size = 500x500 dot, and wall width =

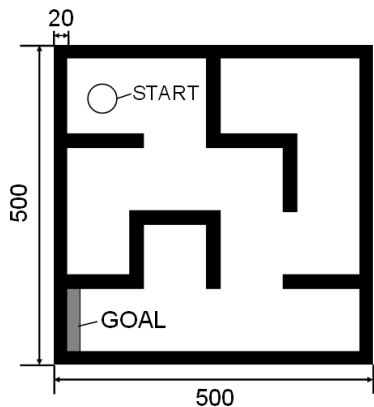


Figure 2: map

20 dot. Parameter values are as follows unless otherwise indicated: $d1 = 60 - 140$ (10 interval), $d2 = 50$, $d3 = d1 + 25$, Number of robots = 20, and Speed of robots = 6 dot/step.

3.2 Time to the goal

Figure 3 shows the average number of steps until all robots reach the goal as the value of $d1$ changes from 60 to 140 with fixed value of $d2$ and $d3$. The result suggests that there exists an optimal value around 110 for $d1$ (When $d1=110$, the mean value indicates 4299 steps). When $d2$ changes with fixed $d1$ and $d3$, the average steps are shown in Fig. 4 ($d1=100, d3=150$). The effect of $d2$ on the attainment is not so clear as $d1$.

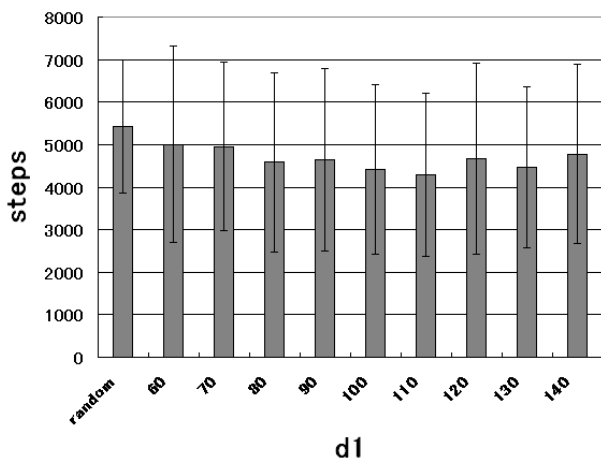


Figure 3: Average steps to the goal ($d2 = 50$, $d3 = d1 + 25$)

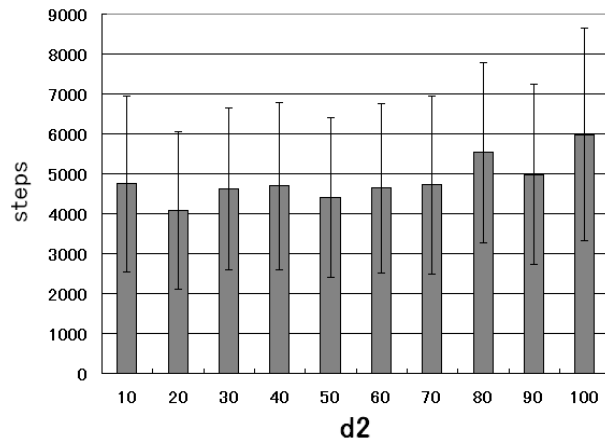


Figure 4: Average steps to the goal ($d1 = 100$, $d3 = 150$)

For comparison, we tried another set of simulations using a swarm of robots, which do not follow our algorithm but follow just individual random searching. They do not expand or shrink together. Each robot goes straight, reflects at the wall to a random direction, and stops when it reaches the goal. In this case, it takes 5425 steps on the average for all of them to reach the goal. Thus our algorithm shows better performance an average.

These results show that the value of the parameters, especially $d1$, affects the performance of solving the maze problem, which suggests the relationship between the values and the scale of the maze. When $d1$ is smaller than the width of a dead end, it will be difficult to escape from there. To escape there and explore other fields, $d1$ should be as large as the size. When $d1$ is much larger than the size of the maze, a leader is not be selected and emergent behaviors are random like a Brownian motion. Thus, matching of the parameter values are needed for the scales of the maze (width of the roads, for example) to improve the performance. Adaptation or dynamical fitting of the parameter values are one of our future problems.

3.3 Decentralized search

We observed interesting behaviors during the maze simulations. Two of them are shown in these subsections.

One mass of robots at first divides a few times at the walls as the time proceeds. Then each group explores here and there independently (Fig 5). This is one of the most interesting features of SI, decentralized search.

Acquired information during searching about position or evaluation, which is not communicated in current version, would be useful to make the behavior more intelligent.

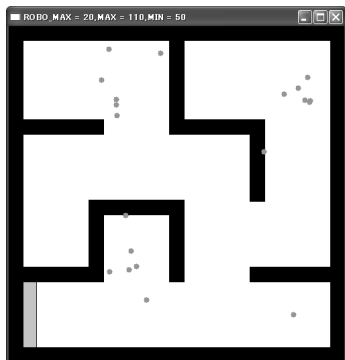


Figure 5: Decentralized search

3.4 Self-organized adaptation

Self-organized adaptational behaviors to circumstances are also observed. On the straight way they pass through there together, each explores independently in a closed way, and they return backward together. This is due to the shrink and expansion mechanism, which regularly corresponds to the searching behavior in the maze.

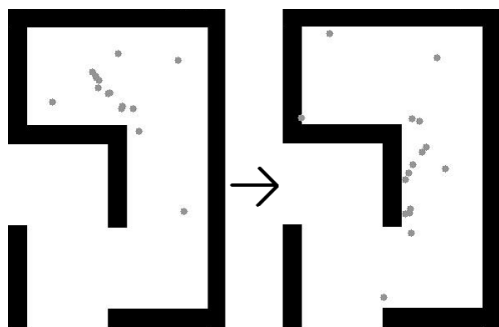


Figure 6: Escape from blind alley

Decision policy of choosing a remote leader promotes getting out from closed fields. Another important parameter $d2$ tends to limit the closest distance between the robots. While following the leader, each distance rarely decreases less than $d2$ because the speed of the leader and the others are the same. When the leader encounters a wall, which may be in a deadlock, the robot will be dismissed from the leader with the distance condition satisfied.

The behaviors such as proceeding and exploring in the maze emerge in spite of the simple algorithm using only local information i.e. distance from each other. This behavior can be regarded as emergent SI. Application to another problem, making the algorithm more general and distributed, and hardware implementation are also our future works.

4 Conclusion

In this study, we proposed a simple algorithm of group robots, which independently works on each of the robots. The algorithm uses local distance information without specific centralized control. Applying this algorithm to maze searching on computer simulations, we observe interesting properties as follows:

- (1) The values of the parameters, especially $d1$, affect the performance of solving the maze problem, suggesting the important relation between the values and the structural scale of the maze.
- (2) Proceeding and exploring behaviors with dividing and merging subgroups are self-organized. This may lead to better performance compared with the results by a set of robots composed of a random searching robot.

References

- [1] E. Bonabeau & M. Dorigo & G. Theraulaz, *Swarm Intelligence: From Natural to Artificial Systems*, Oxford Univ Press, 1999.
- [2] J. F. Kennedy & R. Eberhart & Y. Shi, *Swarm Intelligence*, Morgan Kaufmann Pub., 2001.
- [3] A. P. Engelbrecht, *Fundamentals of Computational Swarm Intelligence*, John Wiley & Sons, 2006.
- [4] M. Dorigo & T. Stutzle, *Ant Colony Optimization*, MIT Press, 2004.
- [5] J. Kennedy & R. Eberhart, "Particle swarm optimization," *Proc. of the IEEE Int. Conf. on Neural Networks*, Piscataway, NJ, pp. 1942-1948, 1995.
- [6] M. Clerc & J. Kennedy, "The Particle Swarm-Explosion, Stability, and Convergence in a Multidimensional Complex Space," *IEEE Transactions on Evolutionary Computation*, Vol. 6, pp. 58-73, 2002.

Interaction of agents in financial markets and informational method to quantify it

Aki-Hiro Sato

Department of Applied Mathematics and Physics
Graduate School of Informatics
Kyoto University, Kyoto, JAPAN 606-8501

Abstract

In this article the informational method to quantify behavioral similarities of the market participants is proposed regarding the financial market as a many-body system. An agent-based model of a financial market in which N market participants deal with M financial commodities is considered. In order to measure the agents' interaction the spectral distance defined by the Kullback-Leibler divergence between two normalized spectra of behavioral frequencies is introduced. The validity of the method is evaluated by using the behavioral frequencies obtained from the agent-based model. It is concluded that the perception and decision parameters of agents who treat two commodities tend to be similar when those behavioral frequencies are similar.

1 introduction

A concept of complex systems [1] is expected to provide new insights for the intelligence since the knowledge and wisdom which are composed of the intelligence are widely distributed into the whole human-beings. Recently economically motivated problems seem to become considerable issues in the literature of the artificial intelligence. When one regards economical processes as phenomena which occur in the many-body systems one realize that enormous amount of agents who interact with one another on the field form a complicated dynamical network and that they emerge through such agents' dynamical network [2]. Therefore one recognizes that the agent-based modeling is a promising methodology in order to deepen an understanding of such economical processes at a microscopic level.

In recent years processing performance of computers and storage capacity almost allow us to gather together large amount of data of economical processes [3] and to directly simulate economical processes for the order of population of the human-beings. Specif-

ically there exist some studies on a method to simulate large size systems and an application of simulation techniques to social/economical phenomena. Moreover an large amount of data about economical processes are available due to spreading of information and communication technology. When we treat with a phenomenon having large degree of freedom or large amount of data it is important to find a rule to reduce the information. When one numerically simulates such agent-based models one faces to the problem for inferring the whole parameters of agents from observable quantities of the objective. And one immediately senses that the number of parameters which one has to infer in order to make the agent-based simulation are explosive. Generally speaking it is hard to infer the whole parameters of a multi-dimensional nonlinear dynamical system from the less observable quantities than the number of parameters. Two kinds of possibilities to cope with this matter are addressed:

- (1) to employ the GA algorithm for the agent model, and to infer the whole parameters asymptotically.
- (2) to compare the behaviors of agents, to quantify relative differences among agents, and to infer distributions of parameters.

In this article according to the second possibility the method to quantify behavioral similarities among interacting agents is considered [4]. An agent-based model of the financial market is formalized [5] and usefulness of the proposed method is evaluated through the agent-based simulation.

The remainder of this article is organized as follows. In Section 2 the agent-based model of the financial market where N market participants exchange M financial commodities is formalized. In Section 3 the informational method to quantify the behavioral similarity of market participants is considered. As the result of applying the proposal method to the behavioral frequency it is confirmed that the behavioral frequencies have a tendency to be similar when both perception

and action parameters of the market participants are similar. Section 4 is devoted into concluding remarks.

2 Model

A model of the financial market where N market participants deal with M financial commodities is considered (see Figure 1). Each market participant perceives information from environment and makes a decision of his/her investment attitude based on the information and make an action. The actions for the market participants to be permitted are buying, selling and waiting.

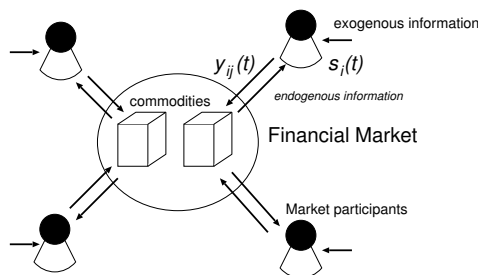


Figure 1: A conceptual illustration of the agent-based model of the financial market where N market participants exchange M financial commodities.

For simplicity the i -th market participant perceives information $x_i(t)$, which is evaluated as a scalar value. This information builds a momentum in which each market participant decides his/her investment attitude. The market participant interprets the information and determines his/her attitude on the basis of the interpretation. Since the possibility of interpretation is very high and dependent on time and market participants uncertainty for the i -th agent to interpret the information $x_i(t)$ at time t is assumed to be modeled by random variables $\epsilon_i(t)$. And the interpretation $x_i(t) + \epsilon_i(t)$ drives feeling to determine his/her investment attitude. Furthermore the feeling about the feeling valid the feeling and drives his/her actions. In order to model the feeling about the feeling we introduce a multiplicative factor $a_{ij}(t)$ which represents the feeling about the feeling of the i -th market participant for the j -th financial commodity. If $a_{ij}(t)$ is positive then the feeling about the feeling supports the feeling. If $a_{ij}(t)$ is negative then the feeling about the feeling refutes the feeling. The absolute value of $a_{ij}(t)$ represents intensity of the feeling about the feeling. Since the determination depends on both the feeling and the feeling about the feeling the investment at-

titude is assumed to be determined from the value $\Phi_{ij}(t) = a_{ij}(t)(x_i(t) + \epsilon_i(t))$. If it is large then the market participant tends to make a buying decision. Contrarily if it is small then he/she tends to make a selling decision. For simplicity it is assumed that a trading volume can be ignored.

The action is determined on the basis of his/her feeling about the feeling. Since the decision and action have strong nonlinearity the action is determined with Granovetter type threshold dynamics [6]. In order to separate three actions at least two thresholds are needed. Defining the threshold for the i -th market participant to determine buying the j -th financial commodity as $\theta_{ij}^B(t)$ and selling it as $\theta_{ij}^S(t)$ ($\theta_{ij}^B(t) > \theta_{ij}^S(t)$), three investment attitudes (buying: 1, selling: -1, and waiting: 0) are determined by

$$y_{ij}(t) = \begin{cases} 1 & (\Phi_{ij}(t) > \theta_{ij}^B(t)) \\ 0 & (\theta_{ij}^B(t) < \Phi_{ij}(t) < \theta_{ij}^S(t)) \\ -1 & (\Phi_{ij}(t) < \theta_{ij}^S(t)) \end{cases} \quad (1)$$

Furthermore it is assumed that the information is described as the endogenous factor, moving average of log return over T , plus the exogenous factor, $s_i(t)$:

$$x_i(t) = \sum_{k=1}^M C_{ik}(|\theta_{ik}^S(t)|, |\theta_{ik}^B(t)|) \frac{1}{T} \sum_{\tau=1}^T R_j(t - \tau \Delta t) + s_i(t), \quad (2)$$

where $C_{ij}(|\theta_{ij}^S(t)|, |\theta_{ij}^B(t)|)$ represents focal points of the i -th market participant for the j -th financial commodity. It seems reasonable to assume that $C_{ij}(x, y)$ is a monotonically decreasing function of x and y .

The excess demand for the j -th financial commodity, $N^{-1} \sum_{i=1}^N y_{ij}(t)$, drives the market price of the j -th financial commodity [7]. To guarantee positive market prices, we choose a log return,

$$R_j(t) = \log S_j(t + \Delta t) - \log S_j(t), \quad (3)$$

and define the log returns as the excess demand,

$$R_j(t) = \gamma N^{-1} \sum_{i=1}^N y_{ij}(t), \quad (4)$$

where γ is a positive constant to show a response of the return to the excess demand. Furthermore the total behavioral frequency to submit their quote request of the j -th financial commodity is defined as

$$A_j(t) = \frac{1}{\Delta t} \sum_{i=1}^N |y_{ij}(t)|. \quad (5)$$

In order to simulate the agent model we assume $C_{ij}(x, y) = CA_j(k)/(x^2 + y^2)$ ($C > 0$), and $a_{ij}(t) = a(t) + w_{ij}(t)$, where $a(t)$ and $w_{ij}(t)$ is sampled from the Gaussian distribution. $a(t)$ is assume to be a more slowly varying random variable than $w_{ij}(t)$. As shown in Figure 2 market price changes $R_j(t)$ show fat-tailed fluctuations. The probability density function of price changes is leptokurtic and have fat-tails.

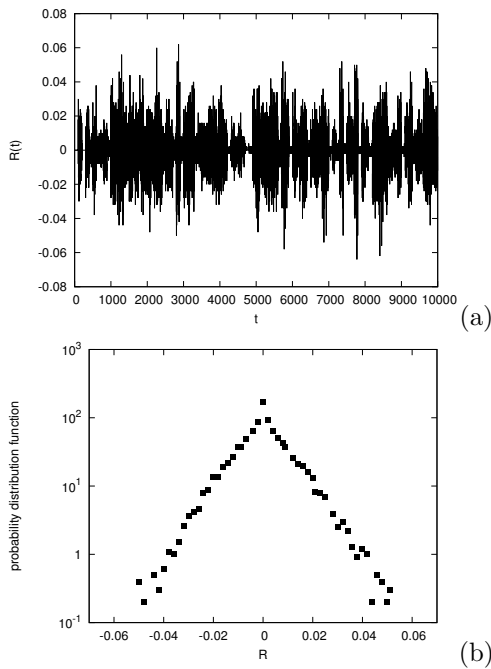


Figure 2: Time series of market price changes (a) and a probability density functions for them (b) for $N = 500$, $M = 10$, $T = 50$, $\Lambda = 0.23$, $\sigma = 0.1$, $a = 0.1$, $\sigma_a = 2.0$, $C = 100$.

3 Method

Market participants operate terminal computers and submit their quotation when they want to buy or sell several amount of financial commodities. Since their intention (internal states of the market participants) drives their behavior, observing their behaviors seems to be equivalent to inferring their internal states. Hence comparing their behavior may lead to comparing their perception and decision parameters.

In order to measure similarity of the agents' parameters from their behavior it is necessary to specify a representative quantity. One of candidates for specifying such a representative quantity is the behavioral frequency. If the behavioral frequencies of agents are

similar then one may think that perception and decision parameters of these agents have a tendency to be similar. In order to quantify the similarity of two behavioral frequencies the informational method with an asymmetric spectral distance defined by the Kullback-Leibler divergence between two normalized spectra of behavioral frequencies is employed. The reason employing this method is because the spectral distance can measure similarity of the underlying dynamics as well as that of time series.

The idea to measure the similarity of the behavioral frequencies $A_i(t)$ of the i -th financial commodity is to evaluate the power normalized spectra. By using the discrete Fourier transform of $A_i(t)$,

$$\tilde{A}_i(n) = \sum_{t=0}^{N-1} x_i(t) \exp(-2\pi i n t / N) \quad (0 \leq n \leq N-1), \tag{6}$$

the power spectrum is estimated by

$$P_i(n) = \tilde{A}_i(n) \tilde{A}_i^*(n) \tag{7}$$

where $*$ represents the complex conjugate. Because the Kullback-Leibler divergence (KL) is a functional of two normalized functions [8, 9] one needs to normalize the power spectrum in order to apply it to power spectra,

$$p_i(n) = \frac{P_i(n)}{\sum_{n=1}^{N-1} P_i(n)}. \tag{8}$$

The similarity of two spectra is defined by

$$K_{ij} = \sum_{n=1}^{N-1} p_i(n) \log \frac{p_i(n)}{p_j(n)}. \tag{9}$$

which is a non-negative $K_{ij} \geq 0$, and asymmetric $K_{ij} \neq K_{ji}$. $K_{ij} = 0$ if and only if $p_i(n) = p_j(n)$. What the direct current component is ignored is equivalent to eliminating the mean value of the behavioral frequency.

In general an asymmetric matrix can be described as $K_{ij} = J_{ij} + I_{ij}$ by using the transformation $J_{ij} = (K_{ij} + K_{ji})/2$ and $I_{ij} = (K_{ij} - K_{ji})/2$. Specifically J_{ij} is called a symmetric Kullback-Leibler divergence (SKL). The SKL possesses a symmetric and non-negative properties: $J_{ij} = J_{ji}$ and $J_{ij} \geq 0$ if and only if $p_i(n) = p_j(n)$. Of course an alternative symmetrical divergence, for example, Jensen-Shannon divergence [9], is also applicable for measuring the difference between power spectra.

Under the assumption that their whole actions are observable one can calculate the spectral distance of the sum of actions for the i th commodity and the

j th commodity. If the spectral distance is small then the agents who treat the i th commodity and the j th commodity seem to have similar focusing points and strategies. Namely we may estimate the rate of the market participants who have the same focusing points and the same strategies through the behaviors of agents.

This method to quantify the behavioral similarities of the market participants is demonstrated by using the agent-based model of financial market. From the numerical simulation of the agent-model of the financial market in which 10 financial commodities are dealt relationships between the similarities of the agents' parameters and the behavioral similarities are calculated. Figure 3 shows the SKL matrix as a fully connected network in which the thin/thick lines between two nodes (financial commodities) exhibit similar/dissimilar behavior between these financial commodities. It is found that the total behavioral frequencies of two financial commodities fluctuate similarly if the agents' parameters are similar.

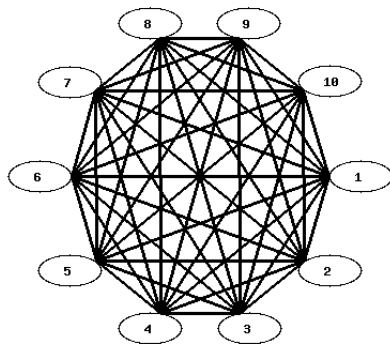


Figure 3: The SKL matrix among 10 financial commodities calculated from the behavioral frequencies obtained from the agent-based model for $N = 500$, $M = 10$, $T = 50$, $\Lambda = 0.23$, $\sigma = 0.1$, $a = 0.1$, $\sigma_a = 2.0$, $C = 100$ is shown as a fully connected network in which the thin/thick lines exhibit similar/dissimilar nodes (financial commodities).

4 Summary

The agent-based model where N market participants exchange M financial commodities was formalized. In order to measure the similarity of two total behavioral frequencies the spectral distance matrix de-

finied by the Kullback-Leibler divergence between two normalized power spectra of the behavioral frequency was calculated. It is concluded that the parameters of the agents who treat two commodities tend to be similar when the behavioral frequencies for two commodities are similar.

Acknowledgements

This study was partially supported by a Grant-in-Aid for Scientific Research (# 17760067) from the Ministry of Education, Culture, Sports, Science and Technology.

References

- [1] H. Haken, "Information and self-organization: a macroscopic approach to complex systems", Springer-Verlag, Berlin (1988).
- [2] M. Aoki, "New Approaches to Macroeconomic Modeling: Evolutionary Stochastic Dynamics, Multiple Equilibria, and Externalities as Field Effect", Cambridge University Press, New York (1996).
- [3] M.M. Dacorogna, R. Gençay, U. Müller, R.B. Olsen, and O.V. Pictet, "An introduction to high-frequency finance", Academic Press, San Diego (2000).
- [4] A.-H. Sato, "Quantifying similarity between markets with application to high-frequency financial data", the Physical Society of Japan, **75**, 084005 (2006).
- [5] A.-H. Sato, "Frequency analysis of tick quotes on foreign currency markets and the double-threshold agent model", *Physica A*, **369**, pp. 753-764 (2006).
- [6] M. Granovetter, "Threshold models of collective behavior", *The American Journal of Sociology*, Vol. 83, pp. 1420-1443 (1978).
- [7] J.L. CcCauley, "Dynamics of Markets", Cambridge University Press, Cambridge (2004).
- [8] R. Veldhuis, and E. Klabbers, "On the computation of the Kullback-Leibler measure for spectral distance", *IEEE transactions on speech and audio processing*, Vol. 11, pp. 100-103 (2003).
- [9] J. Lin, "Divergence measure based on the Shannon entropy", *IEEE Transaction on information theory*, Vol. 37, pp. 145-150 (1991).

Trend Predictions of Tick-wise Stock Prices by Means of Technical Indices Selected by Genetic Algorithm

Seiji Tokuoka and Mieko Tanaka-Yamawaki

Department of Information and Knowledge Engineering, Tottori University, Tottori 680-8550
Japan

Abstract

We propose a systematic method for predicting the trend of the price time series at several ticks ahead of the current price by means of genetic algorithm, used to optimize the combination of the frequently used technical indices such as various moving averages, deviation index from the moving averages, and so on. We show that the proposed method gives good predictions on the directions of motion with the rate as high as 80% for multiple stocks of NYSE selected from four different .business types. We also show that the performance improves if we combine two or three indices, compared to the case of using a single index. However, the performance seems going down as we increase the number of the indices from the optimum value.

1. Introduction

Forecasts of financial time series is a fascinating game to most of us. This game became more attractive than ever with the recent progress of Internet. Tick-wise price motions are by themselves thrilling news for day-traders. Many of them use the price charts as well as other information to help their decisions. Still no comprehensive enough way is known to compile those elements of knowledge into a systematic procedure. In this paper, we attempt to establish such a systematic procedure to make us win the game by using evolutionary computations to identify a combination of useful technical indices applied on the real-world tick data. Since the tick-wise prices have strong trends and features [1], unlike the daily close values of stock prices known to be the random walk, we expect such predictions quite possible. Indeed we have observed a long-term stability of the tick-wise price fluctuations in terms of the direction of move of the next tick [2]. For example, the conditional probability of the up motion after the down motion is almost like a universal constant for several years [3].

$$P(\text{up}|\text{down}) = 1 - P(\text{down}|\text{down}) = 0.7 \quad (1)$$

Guided by this fact, we have attempted to predict

the immediate future price by means of evolutionary computations [4].

However, it is hard to use the information of the next tick in a practical situation. It would be more useful to know the trend of the price time series a few minutes, or few hours ahead of us, to win the forecast game, for example. We therefore talk about predicting, say, the price level at 10-tick ahead by using several technical indices.

2. Tick data of stock prices

We have selected 8 stocks from NYSE, by choosing two from each of the four different groups of business, including retail stores, computer business, oil, automobile. We use bid-prices of those stocks for a year of 1993 (January 1 to December 31). We show the symbols, business types, total ticks in the year of 1993, and the average interval between ticks in Table 1.

Table 1 : Tick-wise stock prices in 1993

symbol	business	ticks	interval (s/tick)
BBY	retail	54821	109
SMRT	retail	12525	473
APC	oil	23685	253
BP	oil	73562	83
CA	computer	65051	92
IBM	computer	455233	14
F	automobile	194561	32
GM	automobile	277241	23

3. Elements of Technical Analysis

There are two kinds of approaches for financial forecasts: technical analyses and fundamental analyses. In the technical analyses, investors use the price motions such as chart patterns to predict the future price, while in the fundamental analyses they use global information on the company such as financial statements and health, its management and competitive advantages, and its competitors and markets

comprehensively, to judge the essential value of the stock under consideration.

In this paper, we use the technical analyses to predict the intra-day price motions. Although there are numbers of indices found in the literatures, we select the ones that are supposed to be effective for the intra-day analysis. For example, candlesticks are not included in our analysis. We focus on the following three types of indices:

- (1) Price trends (MA, EMA, MAD, SMA-LMA)
- (2) Price oscillations (MACD, RCI, RSI, MO, PHL)
- (3) Volume oriented indices

The investors use their favorite combinations of those indices. Our purpose is to study the way of choosing the most suitable combination of the indices for each stock and their conditions by employing the evolutionary computation, and establish the automatic prediction generator on the trend of the price movement at several ticks ahead.

4. Our Method

4.1 Quantization of indices

Each index is quantized into a number of finite states. For example, the moving average (MA) can take two different states in comparison to the price, $PRICE > MA$ or $PRICE < MA$. On the other hand, the rate correlation index (RCI) ranges between -100 and 100, which are quantized into five states of interval 40, such as [-100, -60], [-60, -20], [-20, 20], [20, 60], and [60, 100]. Table 2 shows the number of states we have chosen for each index.

Table 2 : Number of state for each index

Label	Index	# of States
0	MO1(Momentum)	3
1	MO2(Two-step-Momentum)	9
2	MA1(Moving Average)	2
3	MA2(LongMA+ShortMA)	6
4	RSI(Relative Strength Index)	6
5	MACD(MA Converg/Diverg)	2
6	MAD(MA Deviation rate)	4
7	RCI(Rank Correlation Index)	5
8	PHL(Psychological Line)	6
9	EMA(Exponential MA)	6

4.2 Combination of indices determined by GA

The total number of the possible combinations of 10 indices is 1023. By using the genetic algorithm, we attempt to search for the best combination for each stock under various conditions.

4.2.1 Gene representation

A chromosome is a set of indices determined by means of genetic algorithm. The best indices are supposed to be chosen after learning is completed.

Example1)

3	5	8	9
---	---	---	---

Example2)

1	2	3	5	6	8	9
---	---	---	---	---	---	---

Fig. 1: Two examples of gene coding

4.2.2 Genetic evolution based on adaptability

We have used the following parameters in the process of learning in genetic algorithm: Population=100, Number of generations repeated= 500, Crossover rate= 0.9, Mutation rate= 0.01. We use the elite preservation selection as well as the roulette selection.

4.2.3 Resulting combination of indices

The optimum combinations of indices obtained by applying the above method on the eight stocks are shown in Table 3.

Table 3: Best combination of indices for eight stocks

Symbol	Combination of indices
APC	MO1,MA1,MACD,RCI
BBY	MO2,RSI
BP	MO2,MA2,MAD
CA	MO1,MA2
F	MO2,MA1,MA2
GM	MO2,MAD,PHL
IBM	MO2,RSI,MAD
SMRT	MO2,MA2,MACD

4.3 Pattern classifications

Once the indices are selected, the prediction strategies are determined for all the possible states of the set of multiple indices by using data. For the choice of MO1, MA, and RCI, there exist 30(=3×2×5) combination of the states as shown in Fig.2.

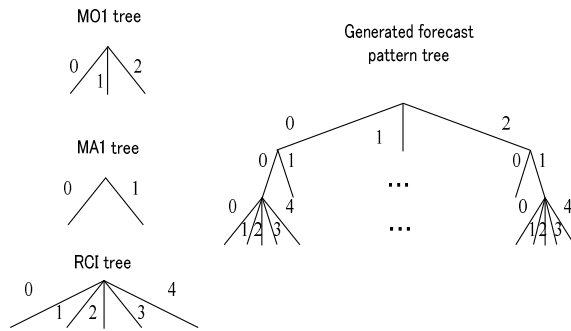


Fig. 2: A pattern represented in the tree structure

4.4 Method of Learning

The prediction strategy is identified as the majority of the direction of motion at X-ticks after the pattern of each combination of states appears. For example, the prediction strategy of X-ticks after the state (MO=0, MA=0, RCI=0) appears is learned to be “DOWN”, since there are more DOWN events than UP events after this pattern in the learning data as illustrated in Table 4.

Table 4: Strategy table

(MO1,MA,RCI)	UP	DOWN	Strategy
0,0,0	55	120	DOWN
0,0,1	23	6	UP
0,0,2	123	100	UP
⋮	⋮	⋮	⋮
2,1,3	23	123	DOWN
2,1,4	8	4	UP

5. Testing new data

5.1.1 Setting

We test those prediction strategies on new data. The last half of the data set is served for this purpose. The prediction referred here is the UP/DOWN motion of the price at 10 ticks ahead compared to the current price.

5.1.2 Index used for the test

We examine the following three cases.

1. One for each index (total 9)
2. Combination of indices obtained in Section 3.4
3. Combination of all the indices

Table 5: Parameter used for each index

Index	Period	
MO1	1	
MO2	1	
MA1	10	
MA2	short	5
	long	15
RSI	10	
MACD	short	5
	long	15
	signal	5
MAD	10	
RCI	10	
PHL	25	
EMA	short	5
	long	15

6. Result

Figure 3 shows the result of IBM and SMRT. The combination of indices selected by GA is the highest, though index 2, index 6, and index 9 are almost at the same level. This fact tells us that the combination of indices improves the result.

Indices related to moving averages, for example, MA, EMA, and MAD are proved effective for prediction. While MACD and RSI are not good alone, they improve the prediction rate if combined with other indices such as moving averages.

The combination of all the ten indices also performed well on the busy stocks of dense quot rates, although the result is poor for slow stocks like APC, BBY, and SMRT, which implies that the combination of all the indices requires heavy sized data for learning.

Figure 4 shows the prediction rate according to the number of indices. The best rate is shown for every size of the combined indices. For the case of APC, the combination of 3 indices performs best, and the rate decreases as the larger number of indices are combined. For GM, the rate of correct prediction increases as the number of indices increases up to 5, then starts decreasing after that.

The prediction rate improves when two or more indices are used. However, the combination of too many indices lowers the hitting rate.

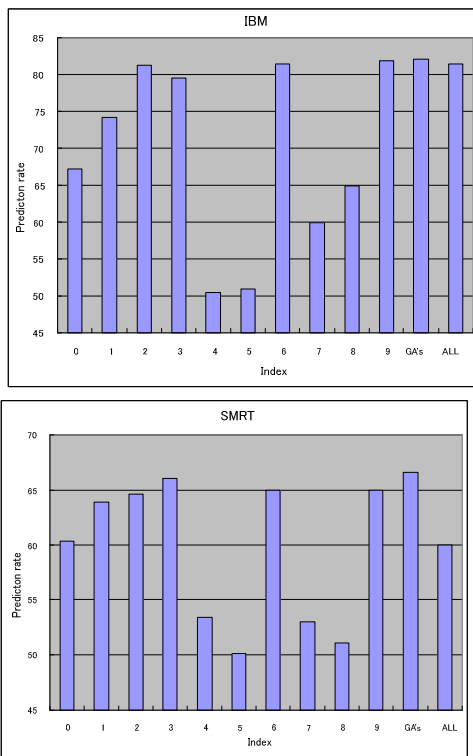


Fig.3: Prediction rate for IBM (above) and SMRT (below) according to each index

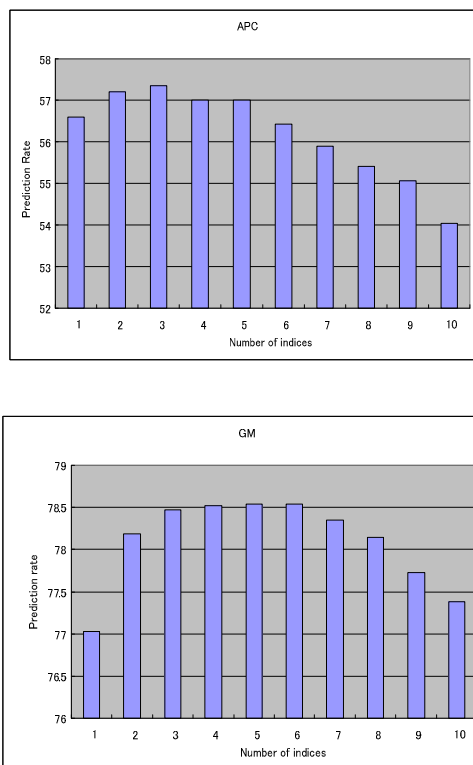


Figure 4: Comparison of prediction rate according to number of indices for APC(above) and GA (below).

Table 6 : Prediction rate according to stock symbols

Brand	Coming true rate (%)	
	1 st	average
APC	57.35	55.23
BBY	58.79	57.34
BP	65.36	63.44
CA	63.03	61.77
F	68.7	67.75
GM	78.54	77.37
IBM	82.25	81.38
SMRT	67.15	64.02

7. Conclusion

In this paper, we have extracted prediction strategies from the tick data of eight stocks of NYSE, by using the optimum combinations of technical indices chosen for each stock symbol based on genetic algorithm. As a result, we have obtained correct prediction rate as high as 81% for frequently exchanged stocks like IBM, or GM. The average prediction rate of eight stocks ended up to be about 65%.

We suppose that the reason of such a high rate of correct prediction lies in the characteristics of the tick-wise motion of stock prices. Especially, the strong correlation between the prices within the order of a few minutes (i.e., order of 10 ticks) resulted in the good performance of our method.

We have seen in this study that the moving averages are powerful tools for predicting the price range of the immediate future in the intraday time series of stock prices. We have also seen that the combination of multiple technical indices improves the prediction power compared to the case of using single index.

References

[1] Takayasu H(Ed.) (2001), Empirical Science of Financial Fluctuations, Springer
 [2] Tanaka-Yamawaki M (2003), Stability of Markovian Structure Observed in High Frequency Foreign Exchange Data, Ann. Inst. Statist. Math, Vol. 55, pp.437-446
 [3] Tanaka-Yamawaki M, Komaki S (2003), Characteristic Features of High Frequency Financial Time Series, Proc. AROB8th, pp.74-77
 [4] Tanaka-Yamawaki M, Motoyama T (2004), Predicting the Tick-wise Price Fluctuations by Means of Evolutionary Computation, Proc. IEEE-CEC, pp.955-958

Effective Indices to Characterize Short Sequences of Human Random Generations

Masashi Mishima and Mieko Tanaka-Yamawaki

Department of Information and Knowledge Engineering, Tottori University, Tottori
680-8550 Japan

Abstract

The brain impediment such as dementia is a serious problem today. It would be very useful if software for private diagnosis were available. In this paper, we show the effectiveness of the human random generation test (HRG) for such software and propose a set of four indices to be used for classifying the HRG data.

Human generated random numbers have strong characteristics compared to the computer-generated random numbers [1,2], and it is known to be correlated to the individual characters of subjects [3-6]. However, the analysis using the correlation dimension or HMM [4-6] requires a long data sequence thus not suitable for diagnoses.

We therefore focus on short sequences of HRG and search for effective indices to detect the sign of brain disability hidden in the HRG data. We study data taken from subjects of different age groups and successfully differentiated data from the different age groups.

1. Introduction

The human random generation test (HRG) is a handy way to measure the brain condition. It checks the flexibility of thinking in a simple manner without using any apparatus. Earlier it was used in the field of clinical psychology to test the degree of advanced stage of schizophrenia [1]. Around 1970 in Japan, a number of researchers in the field of developmental psychology conducted a statistical study of HRG by collecting data from subjects of various developing stages, including the elementary school pupils, high school students and grownup adults [2]. Later we employed computer-based analysis to detect subtle difference in the data taken from normal adults [3], by using the correlation dimension as well as the technique of HMM [4-6]. However, those methods implicitly assume large-sized data thus not suitable for practical need of diagnosis.

The longer the gathered number becomes, the more the subject's load increases.

Here we report our recent study on short HRG of length 50. Our purpose is to examine whether the short human random numbers can be used for early detecting of the brain impediment such as dementia, and identify effective indices to diagnose the symptom.

We examine various indices found in the literature [7] and select effective ones. We also propose a new index, RP, to classify the features of the short data sequences effectively. By using a set of four efficient indices, we have successfully classified data to the proper age groups. Assuming that the dementia is an extreme case of the shortage of memory capacity due to aging, we propose this method for diagnosis of the early symptom of brain deterioration. We further present our result in terms of self-organized map (SOM) [8,9].

2. Method of Data Acquisition

Our method of data acquisition is as follows. The subjects are asked to generate 50 numbers orally by randomly choosing one letter from {0, ..., 9}. Data are orally generated by the subjects and are immediately recorded by the researchers into computers. The oral test is more suitable than the writing test for detecting the level of concentration of the subjects who tries to generate the numbers evenly by memorizing the sequence in the past. During the test, the subjects are directed to close their eyes or to see the ceiling in order to avoid external disturbance. We do not specify the speed of generations in order not to give extra pressure to the subjects.

We have taken 50 data sets from each subject of age 20s (male and female) and 10 data sets from each subject of age 30s, 40s, and 50s (male and female). In

addition, we have obtained data of three patients of schizophrenia.

3. Human random numbers

3.1 Basic Properties

We assume that the degree of complexity of the human-generated random numbers reflect the capacity of the brain. If the subjects attempt to generate every figure of 0 to 9 as well as every arrays of figures evenly, they would employ the maximum brain capacity in order to memorize as many figures as possible they have generated so far. As the subjects get tired, the concentration level would go lower Thus we use the deviation from the randomness as the symptom of the deterioration. We attempt to quantify the memory capacity by using human random numbers. We introduce the used indices as follows. In this chapter, normal person's value is average of the 20s subject's data.

3.2 Entropy (H)

The Shannon-entropy H is the first index to examine the degree of randomness. H measures the average information obtained from a sequence of letters, and it measures how random the letters are in a sequence of letters. It can be quantified as in Eq.(1) by using the probability p_i of appearance of the i-th figure.

$$H = -\sum_i p_i \log p_i \quad (1)$$

H takes its maximum value when every letter appears with the same probability. Dividing this quantity by its maximum value H_{\max} , we use the relative entropy for convenience. In this definition, H ranges from 0 to 1. We assume that the higher value of H means the more active memory capacity of the brain of the subject, in order to use the letters evenly.

It would be necessary to consider the evenness of the arrays of letters, because, e.g., a sequence such as "0123456789" cannot be considered as random, although the nine letters appear evenly. We need to maximize entropies of arrays of various lengths in order to measure the randomness. However, those entropies of arrays are not suitable to measures the randomness of the sequences shorter than 100, because it is too short to have all the patterns of arrays within the capacity of

100 letters. For this reason, we consider only H defined in Eq. (1)

3.3 Coupon Score (CS)

The coupon score (CS) [3] is defined as the length of sequence before all the letters (0 to 9) appear. The CS is approximately 30 on the average for machine generated random numbers. However, the average of normal person is 17, which means that human strongly wish to use every letter compared to computer programs. The CS occasionally takes very large values for those who have very strong preference in choosing specific numbers.

3.4 Turning Point Index (TPI)

The turning point index (TPI) [3] measures how frequently the switch from ascending pattern to descending pattern, and vice versa, occurs in the data sequence. The turning point (TP) is defined as the letter after which the pattern changes. For example, "135426" has two turning points, 5 and 2. The turning point index (TPI) is defined as the ratio of TP and its expected value, where m ($=50$) denotes a maximum data size.

$$TPI = 100 \times \frac{TP_{\text{observed}}}{TP_{\text{expected}}} \quad TP_{\text{expected}} = \frac{2}{3}(m-2) \quad (2)$$

The TPI is highly vulnerable to the human brain condition. When the subjects is active, it tends to be larger than one, while for inactive subjects or patients in advanced stage of mental disease it tends to be smaller than one.

3.5 Adjacency (ADJ)

A remarkable feature of human generated random numbers is the lack of repeats of the same figures successively. Guided by this fact, we utilize the adjacency (ADJ) in order to characterize the data. Focusing on the difference between two adjacent figures, we classify the data by the absolute values of the differences (d) between adjacent figures into four types, $d=0$, $d=1$, $d=2$, $d>2$. All the data indicate that the rate of $d=0$ is extremely lower in human generated data compared to computer generated random numbers. Also the rate of $d=1$ is a good measure of mental condition. For example, the data taken from the schizophrenia patients are characterized by an excess

amount of $d=1$ compared to the data from normal subjects.

3.6 Null Score Quotient (NSQ)

The null score quotient (NSQ) [3] measures the degree of deviation from the even generation of pairs (array of length 2). It is defined as

$$NSQ = 100 \times \frac{NS}{a^2 - 1} \quad (3)$$

where NS denotes the numbers of pairs not appearing in the sequence and a denotes the size of letters used. In the case of using decimal figures $\{0, \dots, 9\}$, $a=10$.

This is a useful index for long sequences of HRG, since the differences between subjects/conditions in HRG reflect nicely in this index. However, NSQ is not suitable for the data of length 50, which is too short to contain all the patterns of pairs for $a=10$.

3.7 Repeat Pattern (RP)

We propose a new index to be used in place of NSQ for the case of short HRG. Since the subjects of HRG try to generate the next letter based on their memory of the last generated letter, NSQ is a good measure for the memory capacity of the subjects. However, the problem is that the value of NSQ ranges from 51.5 to 100 for the case of data sequence of length 50. We need a better index for short data.

Consider the case when the generated data is "1358763" so far, and 5 is about to come out next, one would make an effort to avoid 5, by considering the previously generated 35. Human would pay all the effort to improve the randomness (complexity, in fact). Guided by this thought, we define a new index as the frequency of repeated pairs, by Eq.(4).

$$RP = 1 - \frac{NRS}{m - (n - 1)} \quad (4)$$

where NRS denotes the number of unrepeated pairs, m denotes the length of the sequence ($m=50$), and n denotes the length of array ($n=2$ for pair). The more the repeated pairs, the larger the value of RP, indicate the deterioration of the memory capacity of the subject. We have also studied the case of $n=3$. The result was not very different from the case of $n=2$ (pair). Thus we stick to the case $n=2$ and consider only the case of

unrepeated pairs.

Note that RP ranges from 0 to 100, irrelevant to the size of the data sequence, unlike NSQ.

4. Study on the different age groups

We apply those indices introduced in the previous chapter on various data including schizophrenic patients, normal subjects in different age groups (20s, 30s, 40s, 50s and over), and computer-generated random numbers.

Figure 1 shows the mean values of indices, RP, NSQ, TPI, ADJ, CS, H, for 20 subjects, in the order of ascending age groups. The subject number from 1 to 10 belong to the age group of 20s, the number from 11 to 13 belongs to the age group of 30s, and the number from 14 and 15 belongs to the age group of 40s, and the number from 16 to 20 belongs to the age group of 50s and over. We do not distinguish the actual ages within an age group.

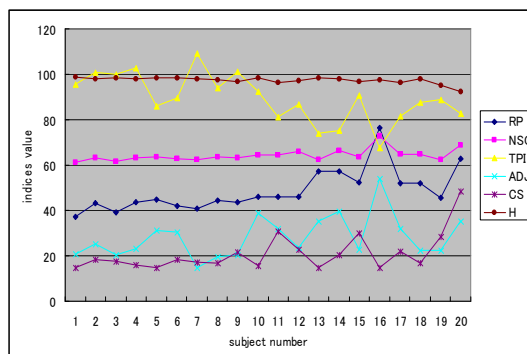


Fig. 1. Values indices vs. individual subjects

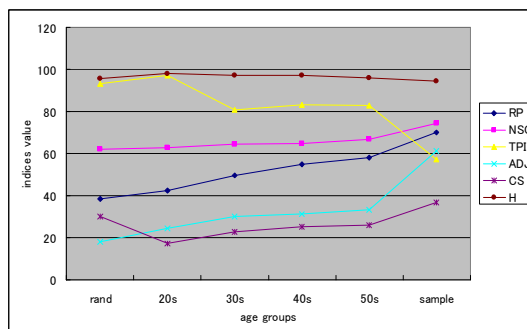


Fig. 2. The value of indices vs. age groups

Fig.2 shows the mean values of the same indices as in Fig.1 calculated for each different age group. In both figures, the entropy H show the relative value to its maximum, and are expressed in terms of percentage.

In both figures, the values of indices show strong correlation to the age groups. This fact suggests the possibility of using HRG for dementia diagnosis. It also indicates the effectiveness of the indices used in our work.

5. SOM for multi-dimensional data

The indices used so far are mutually dependent. We compute the Pearson product-moment correlation coefficient between indices and show the result in Table.1.

Table1. correlation coefficients

	RP	NSQ	TPI	ADJ	CS	H
RP		0.97	-0.25	0.34	0.13	-0.3
NSQ			-0.29	0.39	0.15	-0.33
TPI				-0.6	-0.07	0.1
ADJ					0.02	0.04
CS						-0.66

According to the result shown in Table.1, there is a strong positive correlation between NSQ and RP and the information from those two indices are overlapping. We prefer RP to NSQ because the range is larger in RP for short data of length 50 thus more suitable to observe the difference.

A negative correlation exists between H and CS. We prefer H to CS based on the following observation. The value of CS can easily become large if the subject forgets to say one letter no matter how random the other parts of the data are. It is rather hard to distinguish between a completely regular sequence but missing one letter, and a highly complex sequence but missing only one letter.

Thus, we are left with four indices, RP, TPI, ADJ and H. However, they are still mutually dependent. One good way of presenting multi-dimensional data is given by the self-organizing map (SOM), which works well for the case of mutually dependent multiple variables. The result is shown in Fig.3, where A, B, C denote the age group of 20s, 30s+40s, and 50s+up, respectively. All the indices are normalized to be in the range of [0, 1]. The parameters of SOM are chosen as follows. The Map size is 15×10, learning coefficient α is 0.5, the initial radius is 9, and 10000 cycles of learning.

Fig. 3 shows the data are properly classified by

means of those four indices. A denoting the young group of age 20s aggregate to the left, while C denoting the older group of age 50 and higher aggregate to the right, and B denoting the middle age group are located in between.

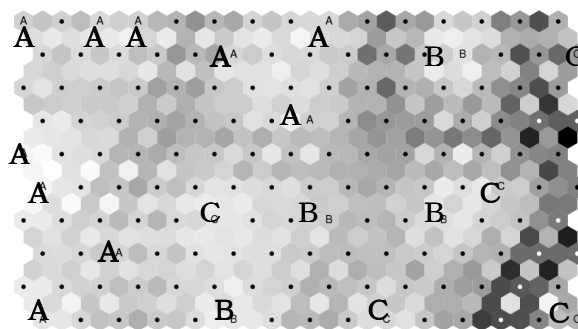


Fig. 3. RP, TPI, ADJ and H for data from three age groups, A(20s),B(30s,40s),C(50+) represented by SOM

6. Conclusion

We have examined indices applicable for short HRG in order to diagnose dementia, and selected a set of four effective indices including RP, which we have proposed in this paper. We have also presented the result by SOM. We have successfully classified the data of different age groups, conditions, etc. according to their characteristics by using the indices of our choice.

References

- [1] Early works are critically reviewed in: Wagenaar WA, (1972), Psychological Bulletin 77, pp.65-72.
- [2] Ransuu Test Kenkyuukai (Society of Human Random Generation Tests) (1973) Shizen 1973-8. pp.49-57
- [3] Iba Y, Tanaka-Yamawaki M (1996), Proc. 4th Int. Conf. Soft Computing IIZUKA'96, pp.467-472.
- [4] Tanaka-Yamawaki M, Masuda H, Kawagoe M (1998), Proc.3rd AROB, pp. 610-613
- [5] Tanaka-Yamawaki M (1998), Proc. ICONIP'98, pp.215-218;
- [6] Tanaka-Yamawaki M (1999), Human Generated Random Numbers and a Model of the Human Brain Functions; Proc.1999 IEEE SMC, pp. 223-228
- [7] Towse JN, Nell D (1998) Analyzing human random generation behavior, Behavior Research Methods, Instruments, & Computers,30(A), pp.583-59
- [8] Kohonen T (1995), Self-Organization maps (in Japanese)
- [9] SOM_PACK <http://www.cis.hut.fi/research/som-research/>

Intelligent Management of Distributed Dynamic Sensor Networks

Peter Sapaty

Institute of Mathematical Machines and Systems, National Academy of Sciences
Glushkova Ave 42, 03187 Kiev Ukraine
Tel: +380-44-5265023, Fax: +380-44-5266457, sapaty@immsp.kiev.ua

Masanori Sugisaka

Department of Electrical and Electronic Engineering, Oita University
700 Oaza Dannoharu 870-1192 Japan
Tel: 097-554-7831, Fax: 097-554-7841, msugi@cc.oita-u.ac.jp

Jose Delgado-Frias

School of Electrical Engineering & Computer Science,
Washington State University, Pullman, WA 99164-2752, USA
Tel: (509)335-1156, Fax: (509)335-3818, jdelgado@eecs.wsu.edu

Joaquim Filipe

Departamento Sistemas e Informática,
Escola Superior de Tecnologia de Setúbal, 2910-761 Setúbal, Portugal
+351 265 790 040, +351 265 721 869 (fax), j.filipe@est.ips.pt

Nikolay Mirenkov

University of Aizu, Aizu-Wakamatsu, Fukushima-ken 965-8580, Japan
+81-242-37-2500, +81-242-37-2528 (fax), nikmir@u-aizu.ac.jp

Abstract

A universal solution for management of dynamic sensor networks will be presented, covering both networking and application layers. A network of intelligent modules, overlaying the sensor network, collectively interprets mission scenarios in a special high-level language, which can start from any nodes and cover the network at runtime. The spreading scenarios are extremely compact, which may be useful for energy saving communications. The code will be exhibited for distributed collection and fusion of sensor data, also for tracking mobile targets by scattered and communicating sensors.

Keywords: sensor networks, intelligent management, distributed scenario language, distributed interpreter, tracking objects, hierarchical data fusion.

1 Introduction

Sensor networks are a sensing, computing and communication infrastructure that allows us to instrument, observe, and respond to phenomena in the natural environment, and in our physical and cyber infrastructure [1, 2]. The sensors themselves can range from small passive microsensors to larger scale, controllable platforms. Their computation and communication infrastructure will be radically different from that found in today's Internet-based systems, reflecting the device- and application-driven nature of these systems.

Of particular interest are wireless sensor networks (WSN) [3,4], consisting of spatially distributed autonomous devices using sensors to cooperatively monitor physical or

environmental conditions, such as temperature, sound, vibration, pressure, motion or pollutants, at different locations. WSN, however, have many additional problems in comparison to the wired ones. The individual devices in WSN are inherently resource constrained—they have limited processing speed, storage capacity, and communication bandwidth. These devices have substantial processing capability in the aggregate, but not individually, so we must combine their many vantage points on the physical phenomena within the network itself.

In addition to one or more sensors, each node in a sensor network is typically equipped with a radio transceiver or other wireless communications device, a small microcontroller, and an energy source, usually a battery. The size a single sensor node can vary from shoebox-sized nodes down to devices the size of grain of dust.

Typical applications of WSNs include monitoring, tracking, and controlling. Some of the specific applications are habitat monitoring, object tracking, nuclear reactor controlling, fire detection, traffic monitoring, etc. In a typical application, a WSN is scattered in a region where it is meant to collect data through its sensor nodes. They could be deployed in wilderness areas, where they would remain for many years (monitoring some environmental variable) without the need to recharge/replace their power supplies. They could form a perimeter about a property and monitor the progression of intruders (passing information from one node to the next). At present, there are many uses for WSNs throughout the world.

In a wired network like the Internet, each router

connects to a specific set of other routers, forming a routing graph. In WSNs, each node has a radio that provides a set of communication links to nearby nodes. By exchanging information, nodes can discover their neighbors and perform a distributed algorithm to determine how to route data according to the application's needs. Although physical placement primarily determines connectivity, variables such as obstructions, interference, environmental factors, antenna orientation, and mobility make determining connectivity a priori difficult. Instead, the network discovers and adapts to whatever connectivity is present.

Fig. 1 shows what we will mean as a sensor network for the rest of this paper. It will hypothetically consist of (many) usual sensors with local communication capabilities, and (a limited number of) those that can additionally transmit collected information outside the area (say, via satellite channels). Individual sensors can be on a move, some may be destroyed while others added at runtime (say, dropped from the air) to join the existing ones in solving cooperatively distributed problems.

The aim of this paper is to show how any imaginable distributed problems can be solved by dynamic self-organized sensor networks, if to increase their intelligence with a novel distributed processing and control ideology and technology effectively operating in computer networks.

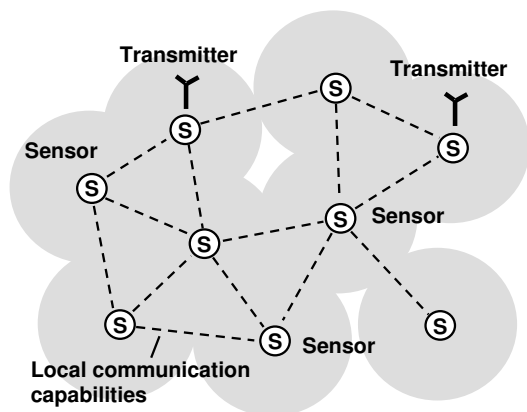


Figure 1. Distributed sensors and their emergent network.

2 The Distributed Management Model

The distributed information technology we are using here is based on a special Distributed Scenario Language (DSL) describing parallel solutions in computer networks as a seamless spatial process rather than traditional collection and interaction of parts (agents).

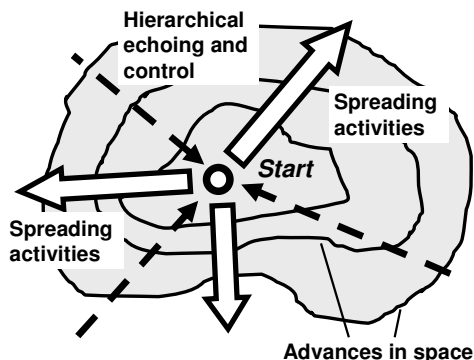


Figure 2. Runtime coverage of space.

Parallel scenarios can start from any interpreter of the language, and then spread and cover the distributed space at runtime, as shown in Fig. 2. The overall management of the evolving scenarios is accomplished via the distributed track system providing hierarchical command and control for the execution of scenarios, with a variety of special echo messages. We will mention here only key features of DSL, as the language details can be found elsewhere in the current proceedings [5] and from its previous versions described in [6-8].

A DSL program, or *wave*, is represented as one or more constructs called *moves* (separated by a comma), embraced by a *rule*, as follows:

$$wave \rightarrow rule (\{ move , \})$$

Rules may serve as various supervisory, regulatory, coordinating, integrating, navigating, and data processing functions, operations or constraints over moves. A move can be a *constant* or *variable*, or (recursively) an arbitrary wave itself:

$$move \rightarrow constant \mid variable \mid wave$$

Variables classify as *nodal*, associated with space positions and shared by different waves, *frontal*, moving in space with program control, and *environmental*, accessing the environment navigated. Constants may reflect both information and physical matter.

Wave, being applied in a certain position of the distributed world, can perform certain actions in a distributed space, terminating in the same or in other positions. It provides final result that unites local results in the positions (nodes) reached, and also produces resultant control state. The (distributed) result and the state can be subsequently used for further data processing and decision making on higher program levels. Parallel waves can start from different nodes in parallel, possibly intersecting in the common distributed space when evolving in it independently.

If moves are ordered to advance in space one after the other (which is defined by a proper rule), each new move is applied in parallel in all the nodes reached by the previous move. Different moves (by other rules) can also apply independently from the same node, reaching new nodes in parallel.

The functional style syntax shown above can express any program in DSL, but if useful, other notations can be used, like infix one. For example, an advancement in space can use period as operator (separator) between successive steps, whereas parallel actions starting from same node can be separated by semicolon. For improving readability, spaces can be inserted in any places of the programs--they will be automatically removed before execution (except when embraced by quotes).

The interpreter may have its own physical body (say, in the form of mobile or humanoid robot), or can be mounted on humans (mobile phones). A network of the interpreters can be mobile and open, changing its volume and structure, as robots or humans can move at runtime. We will be assuming for the rest of this paper that every sensor has the DSL interpreter installed, which may have a software implementation or can be a special hardware chip.

In the following sections we will show and explain the DSL code for a number of important problems to be

solved by advanced sensor networks, which confirms the efficiency of the proposed distributed computational and control model.

3 Collecting Events throughout the Region

Starting from all transmitter nodes, the following program regularly (with interval of 60 sec.) covers stepwise, through local communications between sensors, the whole sensor network with a spanning forest, lifting information about observable events in each node reached. Through this forest, by the internal interpretation infrastructure, the lifted data in nodes is moved and fused upwards the spanning trees, with final results collected in transmitter nodes and sent in parallel outside the system using rule Transmit (See Fig.3).

```
Hop (all transmitters).
Loop (
  Sleep (20).
  IDENTITY = TIME.
  Transmit (
    Fuse (
      Repeat (
        Free (observe (events));
        Hop (directly reachable, first come)
      )
    )
  )
)
```

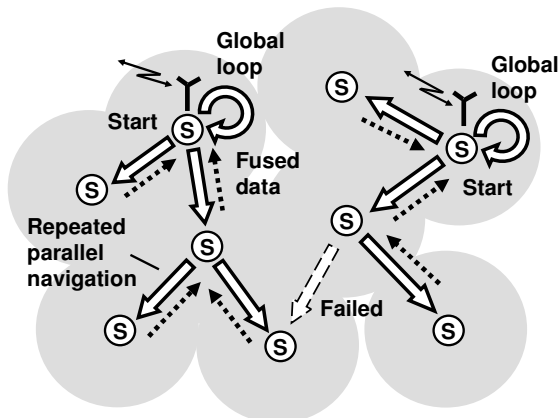


Figure 3. Parallel navigation and data collection.

Globally looping in each transmitter node (rule Loop), the program repeatedly navigates (rule Repeat) the sensor set (possibly, in competition with navigation started from other transmitters), activating local space observation facilities in parallel with the further navigation. The resultant forest-like coverage is guaranteed by allowing sensor nodes to be visited only once, on the first arrival in them. The hierarchical fusion rule Fuse, collecting the scattered results, also removes record duplicates, as the same event can be detected by different sensors, leaving only most credible in the final result.

To distinguish each new global navigation process from the previous one, it always spreads with a new identity for which, for example, current system time may be used (using environmental variables IDENTITY and TIME of the language).

4 Regular Creation of Hierarchical Infrastructures

In the previous program, we created the whole spanning forest for each global data collection loop, which may be costly. To optimize this process, we may first create a persistent forest infrastructure, remembering which nodes were linked to which, and then use it for a frequent regular collection and fusion of the scattered data.

As the sensor neighborhood network may change over time, we can make this persistent infrastructure changeable too, updating it with some time interval (much larger, however, than the data collection one), after removing the previous infrastructure version. This can be done by the following program, which regularly creates top-down oriented links named infra starting from the transmitter nodes (as shown in Fig. 4).

```
Hop (all transmitters).
Loop (
  Sleep (120).
  IDENTITY = TIME.
  Repeat (
    Hop (directly reachable, first come).
    Remove links (all).
    Stay (create link (-infra, BACK))
  )
)
```

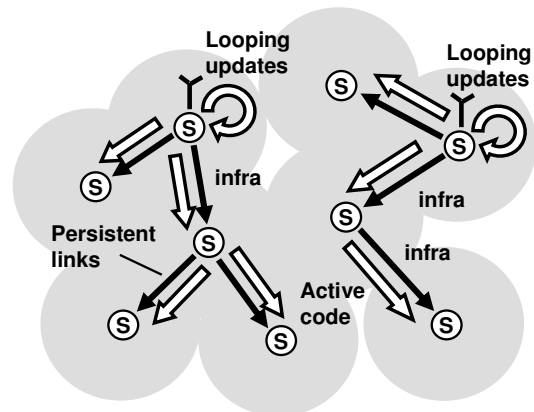


Figure 4. Runtime creation of hierarchical infrastructure.

This infrastructure creation program provides competitive asynchronous spatial processes, so each time, even if the sensors did not change their positions, the resultant infrastructure may differ, as shown in Fig. 5.

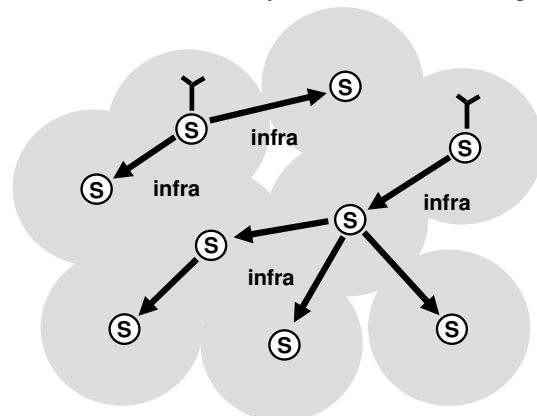


Figure 5. Another possible infrastructure.

Having created the persistent infrastructure, we can use it frequently by the event collection program which can be simplified and updated now as follows:

```
Hop (all transmitters).
Loop (
  Sleep (20).
  Transmit (
    Fuse (
      Repeat (
        Free (observe (events));
        Hop (+infra)
      )
    )
  )
)
```

The global infrastructure creation program (looping slowly) and the event collection and fusion one (looping fast) can operate simultaneously, with the first one guiding the latter on the data collection routes, which may change over time.

5 Routing Local Events to Transmitters

We have considered above the collection of distributed events in the top-down and bottom-up mode, always with the initiative stemming from root nodes of the hierarchy, the latter serving as parallel and distributed tree-structured computer.

In this section, we will show quite an opposite, fully distributed solution, where each sensor node, being an initiator itself, is regularly observing the vicinity for the case an event of interest might occur. Having discovered an event, each node independently from others launches a spatial cyclic self-routing process, via the infrastructure links built before, which eventually comes to the transmitter node, bringing with it the event information. The data brought to transmitters should be fused with the already existing there. The corresponding program will be as follows.

```
Hop (all nodes).
Frontal (Transfer). Nodal (Result).
Loop unconditional (
  Sleep (5).
  Nonempty(Transfer = observe (events)).
  Repeat (hop (-infra)).
  Fuse and assign (Result, Transfer)
)
```

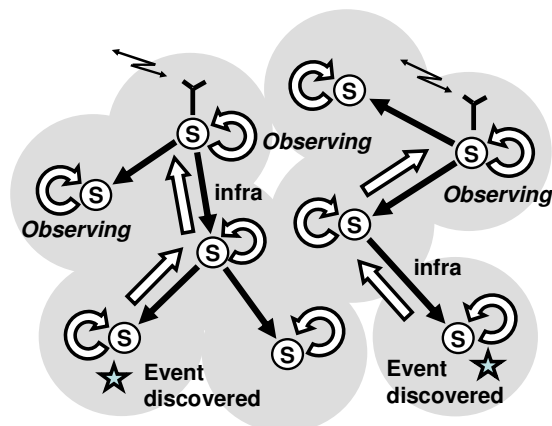


Figure 6. Routing scattered events to transmitters.

The transmitter nodes, accumulating and fusing local events, arriving from sensor nodes independently, can send them outside the system. Different strategies can be used here. For example, one could be waiting until there are enough event records collected in the transmitter before sending them, and the other one waiting for some threshold time and only then sending what was accumulated (if any at all). The following program combines these two cases within one solution, where arriving data from sensors is accumulated in nodal variable Result.

```
Hop (all transmitters).
Loop unconditional (
  Or (
    Quantity (nodal ((Result)) >= 100,
      (sleep 60. Result != nil)
    ).
  Transmit and clear (Result).
)
```

This program in every transmitter can work in parallel with the previous program collecting events and looping in every sensor (in transmitters as well, as they are assumed to be sensors too), and also with the earlier program, starting in transmitters, for the regular infrastructure updates.

6 Tracking Mobile Objects

Let us consider some basics of using DSL for tracking mobile (ground or aerial) objects moving through a region controlled by scattered but communicating sensors. Each sensor can handle only limited part of space, so to keep the whole observation continuous, the object seen should be handed over between the neighboring sensors during its movement, along with the data accumulated during its tracking and analysis.

The space-navigating power of the model discussed here can catch each object and accompany it individually, while moving between the interpreters in different sensors, just accompanying the movement in physical space by an active mobile intelligence spreading in a computer network [6]. This allows us to have an extremely compact and integral solution unattainable by other approaches based on communicating agents. The following program, starting in all sensors, catches an object it sees, and follows it wherever it should go if not seen at this point any more (more correctly: if its visibility becomes lower than the given threshold).

```
Hop (all nodes).
Frontal (Threshold) = 0.1.
Frontal (Object) = search (aerial).
Visibility (Object) > Threshold.
Repeat (
  Loop (
    visibility (Object) > Threshold
  ).
  Maximum destination (
    Hop (all directly reachable).
    Visibility (Object) > Threshold
  )
)
```

The program investigates the object's visibility in all

neighboring sensors in parallel, and moves control along with the program code and accumulated data (the latter not shown in this simplified program) to the neighboring sensor seeing it best -- again, if its visibility exceeds the threshold given (see Fig. 7).

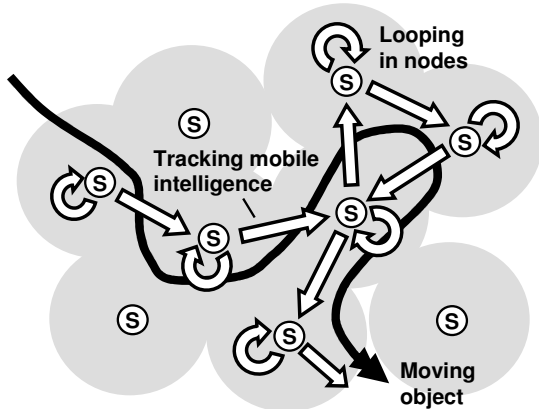


Figure 7. Active tracking of a mobile object.

This was only a skeleton program in DSL, showing the space tracing techniques for controlling single physical objects. It can be extended to follow collectively behaving groups of physical objects as a whole (say, flocks of animals, mobile robots, or troops). The spreading individual object-tracing intelligences can cooperate in the distributed sensor space, and can be optimized jointly for the pursuit of global mission goals.

7 Averaging Parameters from a Region

Let us consider how it can be possible to assess the generalized situation in a distributed region given, say, by a set of its border coordinates, in a fully distributed way, where sensors located in the region can communicate with direct neighbors only. Assume, for example, that the parameter of interest is maximum pollution level throughout the whole region (it may also be temperature, pressure, radiation level, etc.) together with coordinates of the location showing this maximum.

The following program, starting in all sensors located in the region, regularly measures the pollution level in its vicinity, updates local maximum, and by communication with direct neighbors attempts to increase maximum there too, if this is possible. Eventually, after some expected time of such local communication activity, all sensors will have the same maximum value registered in them, which will be the one of whole region too (see the overall organization in Fig. 8).

```
Nodal (Level, Max, Region).
Frontal (Transfer).
Region = region definition.
Hop (all nodes, Region).
Loop unconditional (
  Or parallel (
    Loop unconditional (
      Sleep (5).
      Level = measure (pollution).
      Stay (Level > Max. Max = Level).
      Transfer = Max.
      Hop (directly reachable, Region).
      Transfer > Max. Max = Transfer
```

```
),
  Sleep (120)
).
Level == Max.
Transfer = Max & WHERE.
Repeat (hop (- infra)).
Transmit (Transfer)
)
```

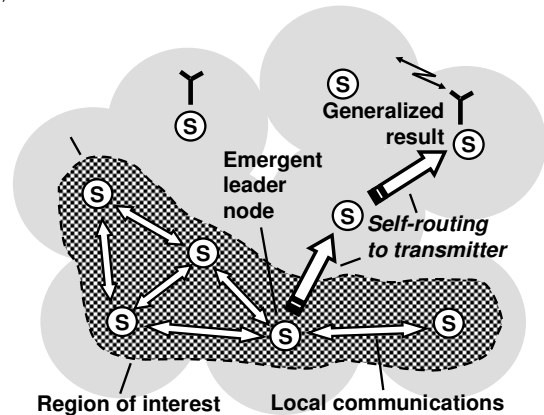


Figure 8. Distributed averaging with active routing.

As there may be many sensors located in the region of interest, we will need forwarding only a single copy of this resultant maximum value to a transmitter for an output. This can be achieved by delegating this only to the sensor whose measured local value is equal to the accumulated maximum in it, which will correspond to the overall region's maximum after some time. Having understood that it is the leader (after a proper time delay), such a sensor organizes repeated movement to the nearest transmitter via the earlier created infrastructure, carrying the resultant maximum value in frontal variable *Transfer*, outputting it outside the system in the transmitter reached, as shown in Fig. 8.

Similar organization may be introduced for finding averaged values, or even for assembling the global picture of the whole region with any details collected by individual sensors (the latter may be costly, however, with more practical solution shown in the next section).

8 Assembling Full Picture of a Region

To collect details from some region via local sensors and merge them into the whole picture could, in principle, be possible via local single-level exchanges only, as in the previous section, but the amount of communications and data transfer, as well as the time needed, may be unacceptably high. We were finding only a single value (maximum) via frequent internode communications, with minimal length exchanges. But for obtaining the detailed global picture of the region or some distributed phenomenon, we may have to gradually grow this picture in every sensor node (or in many of them) simultaneously, with high communication intensity between nodes. Also, there may be difficult to determine the completeness of this picture staying in local sensors only.

It is clear that much higher integrity and process structuring, especially with the use of hierarchies, may be required in order to see the whole distributed picture

via dispersed sensors with limited capabilities in nodes and emergent communications. Different higher-level approaches can be proposed in DSL for solving such classes of problems.

We will show only a skeleton here of how to make spanning tree coverage of the distributed phenomenon, and then hierarchically collect, merge, and fuse partial results from sensors into the global picture. The latter to be forwarded to the nearest transmitter via the previously created infrastructure using links *infra*, as shown in Fig. 9.

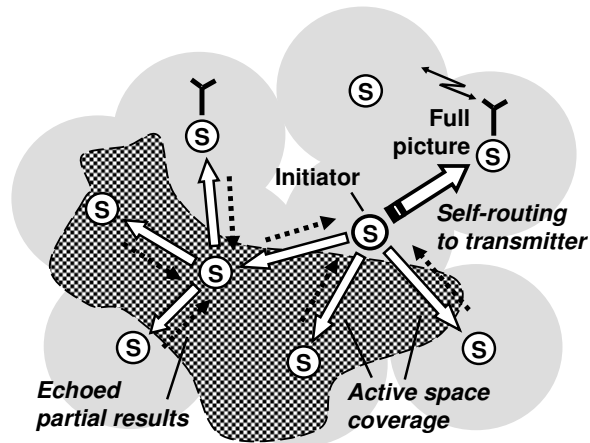


Figure 9. Space coverage with global picture fusion.

```
Hop (
  random, all nodes,
  detected (phenomenon)
).
Loop (
  Frontal (Full) = fuse (
    Repeat (
      Free (collect (phenomenon));
      Hop (
        directly reachable, first come,
        detected (phenomenon)
      )
    )
  ).
  Repeat (hop (-infra)).
  Transmit (Full)
)
```

In more complex situations, which can be effectively programmed in DSL too, we may have a number of simultaneously existing phenomena, which can intersect in a distributed space; we may also face combined phenomena integrating features of different ones. The phenomena (like flocks of birds, manned or unmanned groups or armies, spreading fire or flooding) covering certain regions may change in size and shape, they may also move as a whole having internal organization, etc.

In the previous versions of this language [6, 7], a variety of complex topological problems in computer networks had been investigated and successfully programmed in a fully distributed and parallel manner, which included connectivity, matching with graph patterns, weak and strong components like articulation points and cliques, also diameter and radius, optimum routing tables, and the like, as well as self-recovery after indiscriminate damages (see [6] especially).

9 Conclusions

We have presented a universal and flexible approach of how to convert distributed sensor networks with limited resources in nodes and casual communications into a *universal spatial machine* capable of not only collecting and forwarding data but also solving complex computational and logical problems as well as making autonomous decisions in distributed environments.

The approach is based on quite a different type of a high-level language allowing us to represent system solutions in the form of *integral seamless spatial processes* navigating and covering distributed worlds at runtime. This makes parallel and distributed application programs extremely short, which may be especially useful for the energy saving communications between sensors.

The code compactness and simplicity are achieved because most of traditional synchronization and data or agent exchanges (which are also on a high level, with minimum code sent) are shifted to efficient automatic implementation, allowing us concentrate on *global strategies and solutions* instead.

References

- [1] D. Culler, D. Estrin, and M. Srivastava, "Overview of Sensor Networks", Computer, August 2004, pp.41-49. Published by the IEEE Computer Society.
- [2] C-Y Chong, and S. P. Kumar, "Sensor Networks: Evolution, Opportunities, and Challenges", Proc. of the IEEE, Vol. 91, No. 8, August 2003, pp.1247-1256.
- [3] Wireless sensor network--Wikipedia, the free encyclopedia, www.wikipedia.org.
- [4] F. Zhao and L. Guibas, Wireless Sensor Networks: An Information Processing Approach (The Morgan Kaufmann Series in Networking), Morgan Kaufmann, 2004, 376p.
- [5] P. Sapaty, A. Morozov, R. Finkelstein, M. Sugisaka, D. Lambert, "A New Concept of Flexible Organization for Distributed Robotized Systems", Proc. Twelfth International Symposium on Artificial Life and Robotics (AROB 12th'07), Beppu, Japan, Jan 25-27, 2007. 8p.
- [6] P. S. Sapaty, Mobile Processing in Distributed and Open Environments, John Wiley & Sons, ISBN: 0471195723, New York, February 1999, 436p. (www.amazon.com).
- [7] P. S. Sapaty, Ruling Distributed Dynamic Worlds, John Wiley & Sons, New York, May 2005, 256p, ISBN 0-471-65575-9 (www.amazon.com).
- [8] P. Sapaty, M. Sugisaka, R. Finkelstein, J. Delgado-Frias, N. Mirenkov, "Advanced IT Support of Crisis Relief Missions", Journal of Emergency Management, Vol.4, No.4, ISSN 1543-5865, July/August 2006, pp.29-36 (www.emergencyjournal.com).

Brain Enhancement Attempt Based on Visual Recognition

Yinlai Jiang

Department of Intelligent Mechanical Systems
Kochi University of Technology
Kami, Kochi 782-8502, Japan
096404j@gs.kochi-tech.ac.jp

Shuoyu Wang

Department of Intelligent Mechanical Systems
Kochi University of Technology
Kami, Kochi 782-8502, Japan
wang.shuoyu@kochi-tech.ac.jp

Abstract

Cortical plasticity makes it possible to enhance the health and ability of the human brain through proper training task. In the present study, a visual interpolation task was proposed and two experiments were designed to evaluate it. In experiment 1, six subjects were asked to identify English letters, whose black pixels were partially erased to an erasure ratio by three kinds of erasure rectangle, displayed for short time periods. Its results shows the correct rate's descending trend with the increase of erasure ratio, the enlargement of erasure rectangle or the reduction of display time. In experiment 2, five subjects were asked to recognize the letters which were erased and displayed with the same parameters during three weeks, three times per week. The improvement in the correct rates approved the effectiveness of the task to brain enhancement.

Keywords: letter recognition, visual interpolation, cortical plasticity, brain enhancement.

1. Introduction

Brain, which interferes with nearly all the function of human body, is considered as the most complex and important part of the human body. It is desirable to develop and enhance the brain function so as to improve the human ability for life. Furthermore, it is reported that with the progress of aging, the incidence of brain disease such as senile dementia increase which reduces the quality of life in aged society [1]. Therefore, improvement of brain ability, maintenance of brain health and prevention of brain disease are becoming more and more necessary.

The human brain memorizes, reasons and concludes on the basis of the information from senses of vision, hearing, touch, smell and taste. Of all the senses, vision provides the most information which is about 83% [2]. In order to process and respond to visual information, most parts of the cerebral cortex such as visual cortex, parietal association area and frontal association area are engaged [3]. Therefore, it is possible to measure the brain's visual

information process ability and check the health of brain parts associated with vision through proper visual stimuli. Moreover, it is also possible to activate the vision associated parts by presenting proper stimuli to the eyes in order to improve the health and ability of these parts. [4~7] .

In this study, a method to enhance brain function through the human visual interpolation ability is proposed and validated. Visual interpolation ability is the ability that humans can recognize an object based on object parts. In order to study the human visual interpolation ability, an erased letter recognition task, in which an algorithm was designed to create incomplete letters, was presented. And on the basis of the task two experiments were designed to validate the effectiveness of the method.

2. Letter recognition task

A Hewlett-Packard Compaq nx9000 notebook computer was used for letter recognition task. LCD resolution was 1024×768 pixels, and color was 32 bits. Letters were extracted from the Microsoft Paint program installed in Windows 2000 environment. The font was MSP Gothic, and font size was 72. Letter color was black and the background was white. Letters were presented in the middle of 26 bitmap images of 128-pixels length and width. A program was developed to partially erase the letter images, display them, and record subjects' answers. The program interface and a representative letter image are shown in Fig.1.

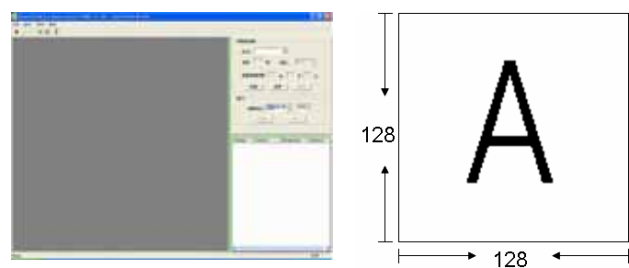


Fig.1 Program interface and letter image

The program used rectangles to partially erase the letters. Firstly, rectangle length, width, position over the

letters, and gradient were randomly determined. Then black letter pixels covered by the rectangles were then erased. This procedure was continued until the ratio of the number of erased pixels to the number of the black pixels in the original image reached a predefined ratio.

2.1 Experiment 1

In experiment 1 erasure was categorized into three levels according to rectangle size: In the first level, the rectangle size was 1 pixel × 1 pixel. In the second level the rectangle length was 4 ~ 8 pixels and width was 2 ~ 4 pixels. In the third level the rectangle length was 8 ~ 16 pixels and width was 4 ~ 8 pixels. Taking R as example, these three levels of erasure are shown in Fig.2 in which L denotes the length, and W denotes the width of the rectangle. As can be observed, the higher the ratio, the more difficult the erased letter is to recognize. On the other hand, the bigger the rectangle, the wider the blocks of left black pixels are while the farther the remaining parts of the letter become.

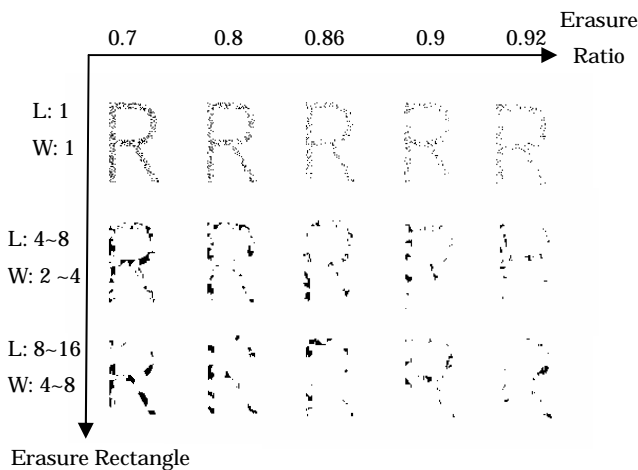


Fig.2 Erased letters in experiment 1 (R).

Six students at Kochi University of Technology served as volunteer subjects. Subject age was 20-30 years. Vision was normal or corrected to normal. In the experiment, firstly, a letter is chosen. Secondly, it was erased and displayed in the center of the screen for a short period. And then a dialog was presented for the subject to select an answer and next letter will be erased and displayed. If the subject was not sure whether the letter was correctly identified, he or she was instructed to skip to the next letter. Experiments were completed in 3 days, one erasure level per day. Five levels of erasure ratios (0.7, 0.8, 0.86, 0.9 or 0.92) were set at each erasure level, and the display duration was set to 300 ms, 200 ms and 100 ms at each erasure ratio. Thus the experiment was divided into 45 sections according to three parameters: rectangle size,

erasure ratio and display duration. In each section, 26 letters were selected and recognized at a random order.

2.2 Experiment 2

In experiment 2, the rectangle length was set to 1 ~ 16 pixels and width was set to 1 ~ 8 pixels. Erasure ratios were the same to those of experiment. Display duration was set to 200ms. Erased letters used in experiment 2 was illustrated in Fig. 3. The procedure was the same to that of experiment 1.

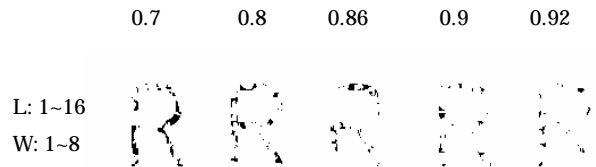


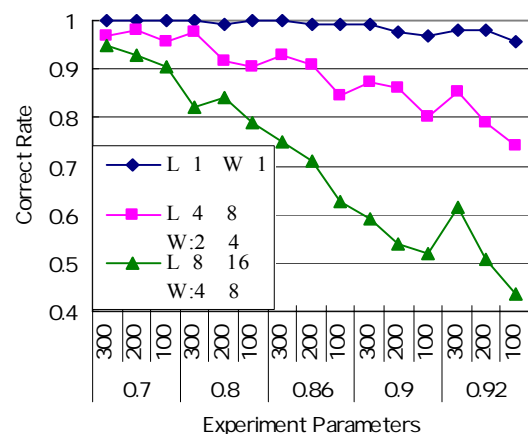
Fig.3 Erased letters in experiment 2 (R)

Five students at Kochi University of Technology served as volunteer subjects. Subject age was 20-30 years. Vision was normal or corrected to normal. Experiment 2 was finished in three weeks in order to examine changes of the subject's correct rates. In each week, the subjects can choose 3 days between Tuesday and Thursday optionally.

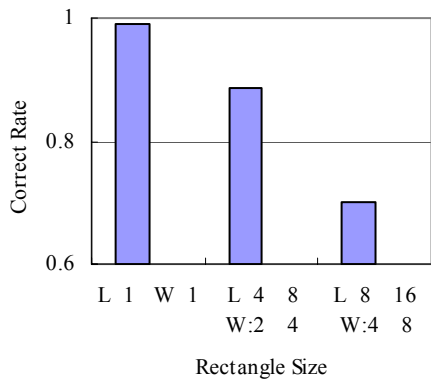
3. Results

3.1 Experiment 1

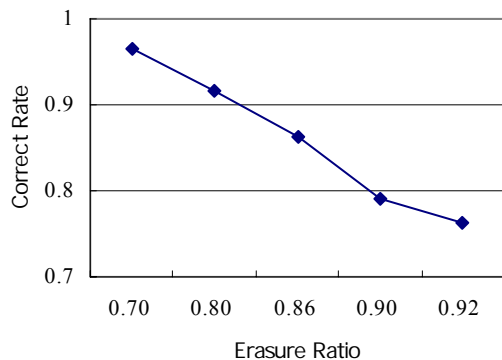
The results of Experiment 1 are shown in Fig.4. Six subjects' average correct rates of each section are plotted as a function of the experimental parameters in Fig.4a. And the average correct rates of different rectangle sizes, erasure ratios and display durations are plotted in Fig.4b, Fig.4c and Fig.4d respectively. In Fig.4b, the correct rate decreased with the increase of rectangle size. In Fig.4c the correct rate almost linearly decreased as the erasure ratio increased. The correct rate also decreased with the reducing of display duration as is shown in Fig.4d.



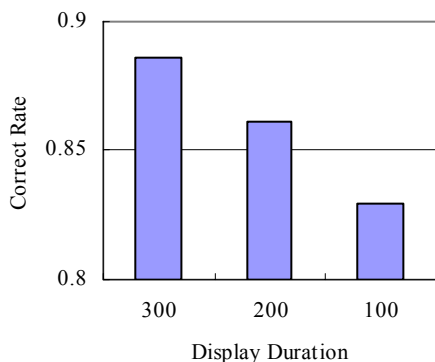
(a) Correct rates of different experiment



(b) Correct rates of different erasure levels



(c) Correct rates of different erasure ratios



(d) Correct rates of different display durations

Fig.4 Results of experiment 1

3.2 Experiment 2

Five subjects' average correct rates of each day in the 1st, 2nd, and 3rd weeks are listed in Table.1, Table.2, and Table.3 respectively. The total average correct rates of the 1st, 2nd, and 3rd weeks were 0.73, 0.79, 0.81 respectively. The increment of correct rate during each week gradually decreased. And that the ninth day's correct rate was lower than that of the eighth day. Compared with correct rate of the third day in the previous week, the correct rate of the first day in the current week decreased. The change in the correct rate shows that the correct rate increased during

every week while it decreased after 3 or 4 days break.

Table.1 1st week

	0.7	0.8	0.86	0.9	0.92	Avg
1	0.83	0.75	0.67	0.57	0.53	0.67
2	0.87	0.87	0.73	0.67	0.55	0.74
3	0.94	0.85	0.79	0.68	0.67	0.79

Table.2 2nd week

	0.7	0.8	0.86	0.9	0.92	Avg
1	0.96	0.89	0.79	0.62	0.55	0.76
2	0.95	0.88	0.85	0.68	0.61	0.79
3	0.95	0.88	0.85	0.73	0.65	0.81

Table.3 3rd week

	0.7	0.8	0.86	0.9	0.92	Avg
1	0.91	0.88	0.78	0.75	0.61	0.78
2	0.97	0.89	0.85	0.78	0.7	0.83
3	0.97	0.9	0.85	0.68	0.62	0.80

4. Discussion

In the present study, the human visual interpolation ability and the training of the ability was studied through a visual interpolation task using erased letter.

Humans recognize and remember objects according to their features, which are usually correlated [8, 9]. When being erased, a letter's features are reduced as well as the correlations between the features. When recognizing an erased letter, the features of the image are sampled from the remnant black pixels and compared with the memorized features, and a decision is made based on similarity [10]. Therefore, as the erasure ratio increases, more features are erased (Fig.2), leading to a decrease in correct identification rate (Fig.4a, Fig.4c). On the other hand, when the rectangle size was 1 pixel \times 1 pixel, the remnant black pixels symmetrically distributed in the erased letter images (Fig.2), it is easy for the human visual system to process the information, such as edge detection and shape recognition, so that nearly all the features can be sampled, which resulted in high correct rates close to 1. As the rectangle size increases, the distribution of remnant black pixels becomes asymmetrical in bigger blocks, which makes it difficult to sample the features from the remnant black pixels [11]. At the same time, features that

can not be sampled also increases. So the correct rate decreased in the experiment (Fig.4a, Fig.4b). The bigger the rectangle, the farther the parts of the erased letter become, which reduced the correlations between the remaining features (Fig 2). And the smaller the rectangle, the more easily edge and shape detection can be accomplished, which may also contribute to the increase of correct identification rate [12]. It is suggested that although the visual category of the stimulus shortly after visual processing has begun (e.g., 75 - 80 ms), decision making does not complete until 150 ms after stimulus is presented [13]. It takes time to transmit and process visual information in the brain. Therefore, when the display duration was prolonged, the features that can be sampled during the duration increased and the correct rate also improved (Fig.4a, Fig.4d).

Cortical plasticity endows the brain with the ability to adapt to stimulus it receives. And it makes it possible to enhance the brain ability through proper training. The changes in brain activity that occur as humans learn new perceptual skill through perceptual learning has been reported by several studies [14]. In this study, enhancement of the subjects' recognition ability was indicated by increase of correct rate in experiment 2. The results also suggested that the training should be done successively in order to keep the correct rate at a high level because the average correct rate declined after 3 or 4 days break in the experiment.

5. Summary

In this study, a brain enhancement method through the human visual interpolation ability was proposed. We analyzed the human visual interpolation ability using an erased letter recognition task. The results showed that as features and correlations between features in letter images were destroyed by erasing and as the display duration was shortened, the correct rate decreased. And we examined the changes in correct rate during a three-week task. The results indicated the possibility to improve human cognition ability through the human visual interpolation ability.

It has been reported that perceptual skill learning has been associated with increased activity in the inferior temporal and fusiform gyri as skill is acquired and activity of the caudate nucleus during skill learning [14]. In future work, we plan to measure and image the hemoglobin levels dynamically in the brain during the visual interpolation task in order to find out the regions that engage in the human visual interpolation.

References

- [1]. Hatakenaka K, Ikegami S, Arimatsu Y (1988), Brain aging--considering the life and death of neuron (in Japanese). Kyoritsu Shuppan, Tokyo.
- [2]. Treichler, D. G. (1967). Are you missing the boat in training aids?. Film and Audio-Visual Communication, 1: 14- 16.
- [3]. Fukuda J, Sato H (2002), Brain and vision — what and how to see?(in Japanese). Kyoritsu Shuppan, Tokyo.
- [4]. Karni A and Sagi D (1991), Where practice makes perfect in texture discrimination: evidence for primary visual cortex plasticity. Proceedings of the National Academy of Sciences, 88, pp. 4966 – 4970.
- [5]. Poldrack. RA, Desmond JE, Glover GH and Gabrieli JDE (1998), The neural basis of visual skill learning: an fMRI study of mirror reading. Cerebral Cortex, 8, pp. 1047- 3211.
- [6]. Liu Z (1999), Perceptual learning in motion discrimination that generalizes across motion directions. Proceedings of the National Academy of Sciences, 96(24): 14085- 14087.
- [7]. Gilbert CD (1998), Adult Cortical Dynamics. Physiol. Rev, 78(2): 467- 485.
- [8]. Bjork EL, Bjork RA (1998), Memory. Academic Press.
- [9]. Singer, HW, Gray CM (1995), Visual feature integration and the temporal correlation hypothesis, Annual Review of Neuroscience, 18, pp. 555- 586.
- [10]. Townsend JT, Ashby FG (1982), Experimental test of contemporary mathematical models of visual letter recognition. Journal of experimental psychology: Human perception and performance, 8(6): 834- 864.
- [11]. Pelli DG, Farell B, Moore DC (2003), The remarkable inefficiency of word recognition, nature. 423(12): 752- 756.
- [12]. Murray SO, Kersten D, Olshausen BA, PSchrater, and Woods DL (2002), Shape perception reduces activity in human primary visual cortex. Proceedings of the National Academy of Sciences, 99(23): 15164- 15169.
- [13]. Rufin V, Thorpe SJ (2001), The time course of visual processing: from early perception to decision-making. Journal of Cognitive Neuroscience, 13(4): 454- 461.
- [14]. Poldrack RA (2002), Neural systems for perceptual skill learning. Behavioral and cognitive neuroscience reviews, 1(1):76- 83.

Designing Brain Machine Interfaces for Rehabilitation: A Study

Hema C.R. Sazali Yaacob Abd. Hamid Adom R. Nagarajan Paulraj M.P. M. Rizon
School of Mechatronic Engineering
Northern Malaysia University College of Engineering,
02600 Jejawi, Arau, Perlis, MALAYSIA
E-mail: hema@kukum.edu.my

Abstract

Brain Machines Interfaces provide a digital channel for communication in the absence of the biological channels. Brain machine interfaces are considered as potential devices to rehabilitate patients with motor nerve disorders namely those who have lost their motor functions as well as communication functions. In this paper a study is conducted to understand the functions of the motor cortex region of the brain and its role in the designing of brain machine interfaces for rehabilitation. A survey on the current brain interfaces is also presented.

Keywords

Brain Machine Interfaces, Rehabilitation Robotics, EEG

1. Introduction

Locked-in syndrome is now becoming a popular term. Patients with this disease lose total control over their motor functions and communication channels. The patients are however aware of their surroundings due to a still active brain. Modern life support and medication help these patients to live longer lives prolonging their personal and social dependencies on the society. Current research on brain signals has shown the feasibility of using brain signals to directly control devices like computers. An extended approach is to use this signal to control devices like prosthetic arms and wheel chairs. This paper aims at highlighting some of the disease which disrupt the biological communication channels and the possibilities of brain signals to control external devices through a digital link.

Many disorders can disrupt the neuromuscular channels used by the brain to communicate with and control its external environment. Amyotrophic lateral sclerosis (ALS), brainstem stroke, brain or spinal cord injury, cerebral palsy, muscular dystrophies, multiple sclerosis, and numerous other diseases impair the neural pathways that control muscles or impair the muscles themselves. They affect nearly two million people in the United States alone, and far more around the world. Those most severely affected may lose all voluntary muscle control, including eye movements and respiration, and may be completely locked in to their bodies, unable to communicate in any way. In the absence of methods for repairing the damage done by these disorders, there are 3 options for restoring function.

The first is to increase the capabilities of remaining pathways. Muscles that remain under voluntary control can substitute for paralyzed muscles. People largely paralyzed by massive brainstem lesions can often use eye movements to answer questions, give simple commands, or even operate a word-processing program; and severely dysarthric patients can use hand movements to produce synthetic speech[1]. The second option is to restore function by detouring around breaks in the neural pathways that control muscles. In patients with spinal cord injury, Electromyography (EMG) activity from muscles above the level of the lesion can control direct electrical stimulation of paralyzed muscles, and thereby restore useful movement. The final option for restoring function to those with motor impairments is to provide the brain with a new, non-muscular communication and control channel, a direct brain-computer interface (BCI) for conveying messages and commands to the external world. At present, only EEG and related methods, which have relatively short time constants, can function in most environments, and require relatively simple and inexpensive equipment, offer the possibility of a new non-muscular communication and control channel, a practical BCI. EEG based communication attracted little serious scientific attention until recently, for at least 3 reasons. First, while the EEG reflects brain activity, so that a person's intent could in theory be detected in it, the resolution and reliability of the information detectable in the spontaneous EEG is limited by the vast number of electrically active neuronal elements, the complex electrical and spatial geometry of the brain and head, and the disconcerting trial-to-trial variability of brain function. The possibility of recognizing a single message or command amidst this complexity, distortion, and variability appeared to be extremely remote. Second, EEG-based communication requires the capacity to analyze the EEG in real-time, and until recently the requisite technology either did not exist or was extremely expensive. Third, there was in the past little interest in the limited communication capacity that a first generation EEG-based BCI was likely to offer. Recent scientific, technological, and societal events have changed this situation.

2. Motor Functions and the Brain

The anatomical region of the brain known as primary motor cortex is the focal region for muscle contractions. Stimulations in this region elicited highly localized muscle contractions at various locations in the

body. This mapping is represented somatotopically on the motor cortex, where the surface area devoted to controlling the movements of each body part varies in direct proportion to the precision of the movements that can be made by that part

The motor cortex is divided into the premotor area (or premotor cortex) and the supplementary motor area. The premotor cortex is believed to help regulate posture by dictating an optimal position to the motor cortex for any given movement. The supplementary motor area, for its part, seems to influence the planning and initiation of movements on the basis of past experience. The mere anticipation of a movement triggers neural transmissions in the supplementary motor area. Besides the frontal cortex, the posterior parietal cortex clearly plays a role in voluntary movements, by assessing the context in which they are being made. The parietal cortex receives somatosensory, proprioceptive, and visual inputs and then uses them to determine such things as the positions of the body and the target in space. It thereby produces internal models of the movement to be made, prior to the involvement of the premotor and motor cortices. The parietal lobes are themselves closely interconnected with the prefrontal areas, and together these two regions represent the highest level of integration in the motor control hierarchy. It is here that the decisions are made about what action to take. In brain imaging, when subjects are asked to move their thumbs, activity is observed in the posterior parietal and somatosensory areas [2].

3. Electroencephalography

EEG is a technique that reads scalp electrical activity generated by brain structures. The EEG is measured directly from the cortical surface. When brain cells or neurons are activated, the local current flows are produced. EEG measures mostly the currents that flow during synaptic excitations of the dendrites of many pyramidal neurons in the cerebral cortex. Only large populations of active neurons can generate electrical activity recordable on the head surface; weak electrical signals detected by the scalp electrodes are to be massively amplified. The cortex is a dominant part of the central nervous system. The highest influence of EEG comes from electric activity of cerebral cortex due to its surface position [3].

3.1 EEG Research History

The existence of electrical currents in the brain was discovered in 1875 by an English Physician Richard Caton. In 1924 Hans Berger a German neurologist amplified these electrical signals using ordinary radio equipment and coined the term *electroencephalogram* to describe brain electric potentials in humans. In 1934 Adrain and Mathews published a paper verifying the concept of 'human brain waves' [or EEG] and identified regular oscillations around 10 to 12 Hz which they termed as alpha rhythm. Brain waves have been categorized into four basic groups: beta (>13 Hz); alpha

(8-13 Hz); theta (4-8Hz); delta (0.5 -4 Hz) [3]. Until early 1990s, most of the researches on EEG were focused on analyzing brain related disease and sleep patterns. The early 1990s witnessed a rapidly growing body of research involving detection of human brain responses and putting these techniques to appropriate uses to help disabled people. Most of the research during this period involved surgically implanting electrodes to acquire the signals. With the introduction of external electrodes during the turn of the century [2000] EEG has initiated the development of BCI to control the cursor of computers. Currently this research has been directed towards producing BMI which can control a prosthetic arm or a wheelchair [1].

3.2 International 10-20 System

To perform consistent testing of EEG recordings a system called the International 10-20 electrode placement system was developed [4]. This system created a method of labeling electrode locations to be used worldwide. The EEG electrodes are placed on the scalp at 10 and 20 percent of a measured distance. Figure 1 shows the international 10-20 Electrode placement positions [4].

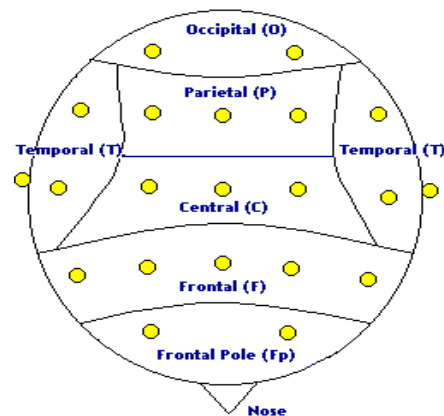


Figure 1 International 10-20 Electrode Placement System

4. Brain Machine Interface: Techniques

BMI can be broadly classified into two types, Sensory and Motor. Sensory BMI are designed to replace a damaged organ such as retinal prosthesis to help the blind and cochlear implants for the deaf. The Motor BMI, on the other hand, seeks to translate electrical brain activity that represents intent to move into useful commands to external devices. Sensory BMI requires very accurate placement of a few tiny electrodes that stimulate the appropriate site in the brain, and the device's job is to simulate the role of the appropriate sensory organ as accurately as possible. In motor BMI, the electrodes are placed "anywhere" in the appropriate cortex area and their number is much higher. The

decoding problem for motor BMI is much harder, since there is little knowledge of how the motor cortex encodes information, and also due to only a small fraction of the cells is being probed [1]. There are two basic types of motor BMI: non-invasive and invasive. Research on non-invasive BMI started in the 1980s by measuring brain electrical activity over the scalp.

Brain computer interfaces [BCI] have been developed to move computer cursors. Through training, subjects can learn to control their brain activity in a predetermined fashion that is classified by a pattern recognition algorithm, and converted into one of several discrete commands usually cursor actions (up/down, left/right) on a computer display. The computer presents a set of possibilities to the users, and they choose one of them through these cursor actions, until a task is completed. This approach, requiring only signal amplification and classification is known as a brain computer interface. BCI classification algorithms combine machine learning techniques with biomedical domain knowledge [1].

Five main techniques are adopted in designing brain computer interface [5].

a. P300 Detection

The P300 component is a positive going evoked response potential (ERP) in the EEG with a latency of about 300ms following the onset of a rarely occurring stimulus the subject has been instructed to detect. Detecting the P300 response reliably requires averaging the EEG response over many presentations of the stimuli.

b. EEG mu-rhythm Conditioning

Subjects' mu-rhythm [Appears at 9-11 Hz this activity appears to be associated with motor cortex [6]. Amplitudes are detected while training them to move a computer cursor up and down on the screen. Results also implied that frequency bands other than mu and beta ranges may contain useful information.

c. Visual Evoked Potential Detection

Electrodes are placed over the visual cortex to detect changes in evoke potentials when the subject concentrates on a particular block out of the 64 blocks on a computer screen.

d. EEG Pattern Mapping

In this technique the EEG patterns are detected and classified for a particular action. Readiness potentials or EEG patterns are studied during experiments such as moving joystick in four directions.

e. Detecting lateral hemisphere differences

Induced lateral differences in relative brain hemisphere activation are studied during experiments where subjects hear arguments through left, right or both headphones.

4.1 Need for Brain Machine Interfaces

EEG signals are being studied to rehabilitate people

with motor disorders. About 10 million people all over the world suffer from neurodegenerative diseases such as cerebral palsy or amyotrophic lateral sclerosis [locked-in people], stroke and paralysis [7]. These diseases impair their ability to control their muscles and are unable to grasp objects, work with appliances or communicate in any way except through their brains. In Malaysia the increase of stroke and paralytic patients is of major concern, modern life support technology allows these individuals even those who are locked-in, to live long lives, so that the personal, social and economic burdens of their disabilities are prolonged and severe.

There is a growing concern in the community today to help these disabled people and improve their living conditions. The Malaysian government has implemented many social welfare schemes such as rehabilitation and independent living policies to improve the conditions of these patients through rehabilitation service and by provision of assistive and rehabilitative devices.

4.2 Motor Disabilities and Restoring Options

Many disorders can disrupt the neuromuscular channels through which the brain communicates with and controls its external environment. Amyotrophic lateral sclerosis, brain stem stroke, brain or spinal cord injury, cerebral palsy, muscular dystrophies, multiple sclerosis and numerous other diseases impair the neural pathway that controls the muscles themselves. Peripheral nerve disorders like Guillain-Barré Strohl Syndrome, Chronic Inflammatory Demyelinating Polyneuropathy, Polyneuropathies, Diabetic Neuropathies, Mononeuropathies - including carpal tunnel syndrome and ulnar neuropathies Peripheral Nerve Injuries, Amyotrophic Lateral Sclerosis (ALS), Radiculopathies, Small Fiber Neuropathies, and Occupational Neuropathies also effect the communication channels and these patients can be provided rehabilitation through BMI.

Restoring these motor functions can be done depending on the severity of the impairment. In case of partial impairments, restoration can be done by increasing capabilities of remaining pathways, such as substituting muscles under control for paralyzed muscles, namely eye movements in the case of brainstem impairment and hand movements in the case of severely dysarthric patients. One other option is by rerouting around the neural breakaways that control muscles, for example using EMG signals from areas above the level of nervous break to restore useful movements. When the above two options are not possible the only solution to restore motor function is to provide a non muscular control channel directly from the brain to devices such as wheelchairs. Patients with diseases like locked-in syndrome and partial paralysis are not able to produce any type of movement. Independent to this the sensory and cognitive functions of the brain are not or partially affected. These patients are very much aware of their environment but are not able to communicate through

speech or eye movements. Though many physiological signals such as EMG, fMRI, MEG and PET are available, research has proved that only EEG signals and related methods which have short time constants, can function in most environments and require relatively simple and inexpensive equipment that offer the possibility of a new non-muscular channel for a practical BMI [9].

The development of BMI to control wheel chairs is still under proof of concept stage. The next section analyses some of the research efforts and studies towards developing a BMI for motor movement and subsequent control of a powered wheel chair.

4.3 Brain Machine Interfaces and Rehabilitation

EEG based BCI/BMI has been under study since the early nineties. BCI only provide interface between brain and computer, so far BCI have been developed to control computer cursors on the other hand BMI are more focused towards developing interfaces between brain and devices like prosthetic arms, wheelchairs etc.. BMI are used to replace impaired motor nerves and to provide an alternative communication channel to control devices like a wheelchair. Research studies have been conducted to study the EEG signals evoked by motor movements and recognition of these signals towards developing interfaces. Most research studies on EEG are currently focused on developing algorithms for classification of EEG signals related to movement. A review of the literature shows that three methods have been adopted in extracting the EEG feature data, namely Autoregression, Independent Component Analysis and Neural Networks. This section reviews some of these research studies.

A DSLVQ classifier for feature selection of EEG signals was proposed by Pregoner et al [10]. Two different types of experiments are used to show that DSLVQ is an appropriate feature selector for a BCI. The first experiment employs DSLVQ to select the most distinct electrode positions from a large number of possible positions. The second experiment uses DSLVQ to analyze the importance of 1-Hz bands of EEG power spectra for the prediction of three different types of movement. The conclusions of this study show that the most important electrode position and frequency bands are not identical for all subjects.

Guger and et al [10] use Common Spatial Pattern (CSP) filters to analyze real-time EEG signals. Experiments involved three subjects. Twenty seven EEG electrodes overlaying the whole primary and sensory motor cortex are used. The method proposed uses covariance to design common spatial patterns and is based on simultaneous diagonalization of two covariance matrices. The decomposition of the EEG leads to new time series which is optimal for discrimination of two populations. The patterns are designed such that signals resulting from filtering with CSP have maximum variance for left trials and minimum variance for right trials and vice versa. The research demonstrates that CSP can be used to analyse EEG signals in real time in order to give feedback to subjects as classification accuracy

improved with few days of trials.

Pfurtscheller and et al [11,12] have studied the separability of left and right motor imagery using autoregressive parameters. Four subjects were used in the experimental process and EEG, EMG and EOG signals are recorded from electrodes overlapping sensory motor area. Subject specific frequency components are selected using the DSLVQ classifier. Due to the laterality of the EEG patterns, the side [left or right] of the imagined movement can be determined with an online error between 10 to 31.8 %. The online classification of subject specific frequency bands were analyzed by a neural network. An overall improvement of classification was achieved using the off-line adaptive autoregressive model [ARR]. However the ARR method is found to be sensitive to artifacts, therefore artifacts must be controlled.

Haselsteiner and Pfurtscheller [13] have compared two different neural network topologies to classify a single trial EEG data from a BCI. The classifiers are the MLP and the FIR MLP. The static weight of the standard MLP is replaced with finite impulse response filters in the FIR MLP. The study shows that FIR MLPs performed better than standard MLP with lesser error rates.

Mahalanobis distance-based classifiers are analyzed by Babiloni et al [14], to classify the diagonal and full covariance matrix features of the EEG signals. EEG data are recorded from four electrodes placed in the C3, P3, C4 and Imagined hand movement recognition using Low Resolution Surface Laplacian and Linear P4 position of International 10-20 system. These classifiers were able to detect imagination of hand movements with a classification accuracy of 98%.

Another imagined hand movement recognition using Low Resolution Surface Laplacian and Linear Classifier is proposed by Concotti et al [15] which use nine electrodes; the classifiers have an accuracy of 90%.

Neural network based classifiers of EEG features have been investigated by some researchers [16, 17,18]. Back propagation neural classifiers have also been used to analyze the EEG signals related to mental tasks.

Research on BMI is being extended to the next stage of translating them to control signals to operate devices.

Conclusions

BMI is still at the proof-of-concept stage, currently this work is undertaken by bio and neuroscience researchers. The contributions from computer engineers, psychologists and mathematician are essential to take this to the next stage. The developments of more accurate data models that carry more spatio-temporal information from the spikes in the motor cortex are required. The signals are non-gaussian and non-stationary, so they are very difficult to model well with present algorithms [1].

So far, control BMI has focused on cursor movements, applying this concept to a mechanical hand or a device such as a wheelchair will prove to be more

challenging. Although the theoretical and technical problems are difficult, BMI research is at a very exciting phase, thanks to the tight integration of research in computer science, engineering, and neuroscience. There is optimism about impacting the daily lives of paraplegics in the same way that sensory BMIs benefited hearing impaired patients [1].

The non-invasive BMI has potential applicability beyond the restoration of lost movement and rehabilitation in paraplegics and would enable normal individuals to have direct brain control of external devices in their daily lives. Therefore, the impact of BMI on our society promises to surpass that of any earlier digital technology.

References

- [1] JOSE PRINCIPE,(2005). Brain Machine Interfaces: Mind over Matter.
http://www.ece.ufl.edu/publications/Archives/inthe_news/2005/brainmachine.html
- [2] The Brain from top to Bottom
http://www.thebrain.mcgill.ca/flash/a/a_06/a_06_cr/a_06_cr_mou/a_06_cr_mou.html
- [3] MICHAL TEPLAN.(2002). Fundamentals of EEG Measurement. Measurement Science Review, Volume 2, Section 2.
- [4] D.G. DOMENICK. (1998). International 10-20 Electrode Placement System for Sleep.
<http://members.aol.com/adaual/1020sys.html>
- [5] RICHARD H.C. SEABROOK . (1994). The Brain Computer Interfaces : techniques for Controlling Machine.
<http://www.cs.man.ac.uk/aig/staff/toby/research/bci/richard.seabrook.brain.computer.interface>
- [6] BEN & HUGH,(2004) EEG Biocontrol Technology and Applications' ,
<http://www.biocontrol.com/eeg.html>
- [7] NATIONAL INSTITUTE OF BIOMEDICAL IMAGING AND BIOENGINEERING, (2004) Catch a Brain Wave, online article,
<http://www.nibib.nih.gov/eAdvances/102104.htm>
- [8] CNI Neuromuscular & Peripheral Nerve Disorders Center website article
<http://www.thecni.org/neuromuscular/>
- [9] JONATHAN R WOLPAW, NILES BIRBAUMER, DENNIS J MCFARLAND, GERT PFURTSCHELLER, THERESA M. VAUGHAN. (2002). Brain-computer interfaces for communication and control. Elsevier Clinical Neurophysiology Transactions. 113(2002), 767-791.
- [10] M. PREGENZER AND G. PFURTSCHELLER . (1995) . Distinction Sensitive Learning Vector Quantization (DSLVQ) – Application as a Classifier based Feature Selection Method for a Brain Computer Interface. In the Proceedings of the Fourth International Conference on Artificial Neural Networks, 433 -436.
- [11] GERT PFURTSCHELLER, CHRISTA NEUPER, ALOIS SCHLOGL AND KLAUS LUGGER. (1998). Separability of EEG Signals Recorded During Right and Left Motor Imagery Using Adaptive Autoregressive Parameters. IEEE Transactions on Rehabilitation Engineering Vol.6 No. 3. 316-325.
- [12] C.GUGER, H.RAMOSER AND G. PFURTSCHELLER. (2000). Real-Time EEG Analysis with Subject-Specific Spatial Patterns for a Brain-Computer Interface (BCI). IEEE Transactions on Rehabilitation Engineering, Vol 8, No.4. 447 – 456.
- [13] ERNST HASELSTEINER AND GERT PFURTSCHELLER. (2000). Using Time Dependent Neural Networks for EEG Classification. IEEE Transactions on Rehabilitation Engineering Vol.8.No.4. 457-463.
- [14] FABIO BABILONI, LUIGI BIANCHI, FRANCESCO SEMERARO, JOSE del R MILLAN, JOSEP MOURINO, ANGELA CATTINI, SERENELLA SALINARI, MARIA GRAZIA MARCIANI AND FEBO CINCOTTI, (2001) 'Mahalanobis Distance-Based Classifiers are able to Recognize EEG Patterns by using Few EEG Electrodes., Proceedings of the 23rd Annual EMBS International Conference ,Istanbul Turkey.
- [15] FEBO CONCOTTI, LUGI BIANCHI, JOSE DEL R MILAN, JOSEPH MOURINO, SERNELLA SALINARI, MARIA GRAZIA MARCIANI AND FABIO BABILONI, (2001), Brain Computer Interface : the use of Low Resolution Surface Laplacian and Linear Classifiers for the Recognition of imagined Hand Movements, Proceedings of 23rd Annual EMBS International Conference , Turkey , pp 655-658.
- [16] TORSTEN FELZER AND BERND FREISLEBEN (2003), Analyzing EEG Signals Using the Probability Estimating Guarded Neural Classifier, IEEE Transactions on Neural Systems and Rehabilitation Engineering Vol. 11, No.4 2003. pp 361-371.
- [17] DAMIEN COYLE, GIRESH PRASAD AND THOMAS M MC.GINNITY (2004) , Extracting Features for a Brain Computer Interface by Self –Organizing Fuzzy neural Network based Time Series Prediction, 26th Annual International Conference of IEEE EMBS , USA , pp 4371- 4374.
- [18] C.W. ANDESON, S.V DEVULAPALLI AND E.A.STOLZ,(1994) EEG as a means of Communication: Preliminary experiments in EEG analysis using Neural Networks, Proc. 1st Annual ACM Conference on Assisitive Technologies ,pp 141-147.

Soft-Hard Memory for Cognitive Systems

Liang Xiong
Dept. of Automation
Tsinghua Univ.
Beijing, China. 100084

Nanyuan Zhao
Dept. of Automation
Tsinghua Univ.
Beijing, China. 100084

Changshui Zhang
Dept. of Automation
Tsinghua Univ.
Beijing, China. 100084

Abstract

We propose a novel memory infrastructure, called Soft-Hard Memory (SHM), and its corresponding learning scheme for cognitive learning systems. SHM is designed according to cognitive principles and based on the Soft-Hard Structure Theory. In SHM, memory is divided into soft-structure and hard-structure, which enables bootstrap and adaptive learning processes. It is intuitive, high-performance and easy to implement. Experiments in our robot project demonstrate its effectiveness.

Keywords: *Soft-Hard Structure, Memory, Learning, Cognitive System, Robot*

1 Introduction

People have been pursuing the object of "intelligent machine" for a very long time. Among all the intelligent features, learning is one of the most desirable. The most distinct feature of a learning system is that it can continuously learn from the environment, including its own performance and status, to improve itself. This feature is essential for life.

In recent years, machine learning (ML), a broad subfield of artificial intelligence, has developed rapidly. ML is concerned with techniques that enable computers to learn automatically. Researchers are making great efforts in developing such methods. Now, machine learning is receiving more and more attentions. And in the field of robot and computer vision, ML approaches are also widely applied. For example, Kazuhiko^[1] uses Isomap^[2], which is a non-linear dimensionality reduction (NLDR) technique in machine learning to discover low dimensional manifold, to learn the spatial-temporal structure of motion sequences in their robot system. In computer vision and graphics, clustering techniques have become a mainstream approach for graph-cut and image segmentation tasks^[3].

Although machine learning has achieved a lot in developing practical intelligent methods to solve specific problems, its current learning paradigms are not suitable for human-like learning. Typical machine learning algorithms are based on strong hypotheses or models. What the machine learns is in fact parameters, while the underlying models can seldom change. Consequently, the data storage structure (memory) is also hierarchical. This framework is clearly not eligible for adaptive learning tasks. It is very hard to make right hypotheses. Even if the hypotheses are proper now, it may become unsuitable when the environment has changed. Another question is that, where did the models come from? There is little predefined knowledge, if any, in a human baby's brain, but he/she can still learn and grow to be an intelligent being. In fact, there have long been arguments that mainstream AI researches has deviated from the nature of intelligence. Specifically, in the field of ML, adaptiveness and the ability of bootstrap are the two missing features in most algorithms. By contrast, we call a learning method with these two properties cognitive learning.

Memory is thought to be the core of a cognitive system, and learning relies heavily on it. Before we can develop an evolving learning machine, a competent memory structure has to be built. Extensive investigations have been taken on human memory, but its actual mechanism is still unclear. Here we only focus on a satisfying engineering realization. In cognition and psychology, human memory is divided into short-term memory, working memory and long-term memory. Existing memory structures for cognitive systems are mainly based on this notion. For instance, Kazuhiko^[1] uses the same memory configuration as described above, and has each part constructed specifically.

In this article, we design a memory infrastructure, called Soft-Hard Memory (SHM, pronounced as *shim*), to facilitate cognitive learning processes. In SHM, memory is divided into soft memory and its counterpart, hard memory. Basically, this memory scheme

is also similar to the natural classification of human memory. However, it is designed from the perspective of evolution. Through the interaction between these two parts, the system can hopefully realize bootstrap and adaptiveness.

The rest of this article is organized as follows: In section 2 we analyze the human learning process and indicate necessary features of a cognitive learning system. Section 3 introduces the theory of Soft-Hard Structure and describes the Soft-Hard Memory in detail. In section 4, we introduce some preliminary experiments of this memory structure in our cognitive robot project. Conclusion is in section 5.

2 Cognitive Learning

For any intelligent beings, either natural or artificial, adaptive learning is crucial to survive in changing environment. Current algorithms usually simplify the problems to estimation of parameters. However, unalterable models are obviously not suitable for adaptive learning, which is not just a process of accumulating and enhancing, it also involves the creation, reconstruction and oblivion of knowledge.

Moreover, human learning is a bootstrap process. That means we can learn infinite knowledge based on very few priors. From a micro-perspective, an infant can learn and grow to be an expert with little initial knowledge. And from a macro point of view, the accumulating of human knowledge is a phenomenal example. Neural science shows that this ability is mainly due to the structure of neural networks in human brains. From an engineering view, there must be some “grow point” in the system, where new models and concepts can be generated.

Adaptiveness and bootstrap ability are the two most important features for cognitive learning. Clearly these two features are not feasible on a hierarchical memory structure since the number of layers is necessarily infinite. There must be some kind of feedback mechanism. Soft-Hard Structure [4] in generalized evolution theory provides such a solution.

3 Soft-Hard Memory

3.1 Soft-Hard Structure Theory

Creation of knowledge is the most difficult task in learning. Ashby [5] proposed Ultra Stable System as the simplest model for creative machines. In this system, status of the machine keeps changing randomly

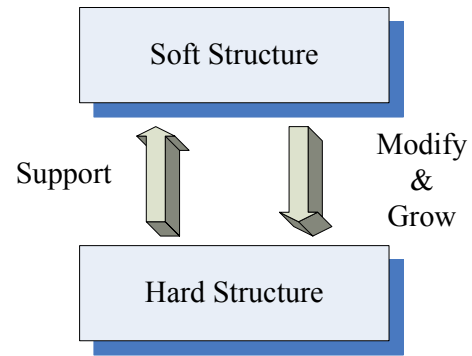


Figure 1: Soft-Hard Structure

until the evaluation module finds a good result. Thus a creation is realized. Yet, this system is not feasible for complex tasks since it is computationally impossible for a large amount of variables.

In order to avoid the difficulty of computing, the system should not run in a totally random manner. To solve this problem, we can learn from evolution, which is the most spectacular process of creation in nature. Aberrance and selection is the core of Darwin’s evolution theory. Zhao [4] proposed that soft-hard structure (SHS) is also a key for evolution to success.

According to SHS theory, an evolutionary system can be divided into two parts: soft structure and hard structure. Soft structure is the active part where creations and reconstructions occur. Hard structure is the static part which supports soft structure and subsistence of the system (Figure 1). The key idea of SHS is: soft structure provided the possibility of creation (by randomness and evaluation), while hard structure can maintain creations and keep evolution in a certain direction.

3.2 Learning Scheme

Cognitive learning is a process of evolution. The machine has to adjust itself according to the change of environment constantly. From this view point, soft-hard structure theory can shed light on the problem of bootstrap and adaptive learning.

Given some basic evaluation criterion, such as the chance to feed and the time to complete a task, the bootstrap process can be done by “soft learning”. When having to finish a task without any prior knowledge, a clear choice is to try randomly. Once a good result is found, this experience is recorded, “hard learned (modeled)” into hard structure. After enough accumulation of trials, the machine will have enough experience to do more complex jobs. And further knowledge

can be derived based on these experiences.

Adaptive learning can also be achieved by interactions between soft and hard structures. As a prior, the system has to be able to detect the inconsistency between new experiences and prior models, or the contradiction between existing models. Usually, the system uses existing knowledge (models) to go through ordinary jobs. When new contradicting experiences are gained, soft structure will decide how to deal with them: modify models, or build a new one. And when the inconsistency between models in the hard structure grows to a certain level, those models will be extracted back to the soft structure for further operation. Thus the system's knowledge can be updated as needed.

3.3 Soft-Hard Memory Infrastructure

In order to facilitate the learning scheme proposed above, we designed a soft-hard memory (SHM) infrastructure. In SHM, memory is divided into two parts. Soft memory (SM) provides an active data storage for the soft learners. It primarily stores direct, concrete materials that is perceived or generated by the system. Information in soft memory will be forgotten soon. Hard memory (HM) is a static and persistent database for the system. Information in hard memory is more important and highly condensed, such as basic value functions, learned models and concepts. These information is the core of hard structure and will not change unless obsolete.

Interactions between SM and HM are realized through proper learning algorithms. In principle, the soft learner uses functions and models from HM to examine the information in SM. When experiences are recognized as new knowledge, the hard learner will build new models. When inconsistency in HM is detected (e.g. when results from models contradicts with each other), those inconsistent parts will be extracted back to SM, either to be modified, fused or discarded.

Actual forms of SM and HM are not specified here. People can, and should, design particular storage scheme with regard to requirements. For example, SES^[1] can be used for SM, and a ordinary relational database is already competent for simple learning tasks.

The configuration of SHM is quite similar to traditional short-term/long-term memory. Their functions do overlap a lot. However, SHM is designed from the perspective of evolution, while most other architectures are from the point of psychology or information processing.

Soft-hard memory possesses many merits besides its bootstrap and adapt abilities. First of all, SHM is intuitive and compatible with common cognitive knowledge. It is similar to the classification of memory in psychology, and the working process is very clear. Secondly, this structure is flexible and can be readily extended. Actually there is no limitation on the number or the form of concepts, and all information stored can be changed as necessary. Thirdly, the conflict of vast information and processing speed can be well balanced under this structure. SM can work as a buffer of information. Data in it can be processed when the system is not busy, so the load of the machine will not fluctuate dramatically. Finally, it can be easily implemented as a parallel running system. This framework enables physical separation of memory system and other modules (such as reasoning). So the speed and scalability is guaranteed.

4 Application

4.1 Cognitive Robot Project Overview

In the cognitive robot project, we are planning to build a intelligent robot system to accomplish the following tasks:

Identify people: The robot will first identify the person appears in the camera as stranger or an acquaintance. Face images are used for recognition.

Learn acquaintance: If the robot sees a stranger for many times, it will turn him/her to an acquaintance.

Move to the target site: When a task is confirmed, the robot have to choose a route and move to the site. Possible obstacles must be avoided efficiently.

Fetch an object from the person: The robot will use its robot arm to fetch a specified object from the person's hand. Optimum motion sequence should be adopted.

During the process, this robot will use past experiences to solve current problems. This involves intensive learning. Furthermore, all these tasks have to be finished in a real-time situation. To do this, we will use the learning scheme in section 3.2 and SHM as its primary data storage.

4.2 Learning of acquaintance

In this task, the robot has to learn to know people. At first, all the people are strangers. As the robot sees

a person for certain times, it will classify him/her as an acquaintance. This is a basic cognitive behavior.

The identification of people is accomplished by face recognition. We use Bayesian Face Models [6] (BFM) for this task. In BFM, face images are used as training samples (prototype). When a new face is perceived, the system will calculate the probabilities that this new face is the same as each prototype. If no probability is high enough, it is rejected as belongs to no one. There are two key components in BFM: prototypes and the probability model, which are both stored in HM.

This module runs as follows: all perceived faces are initially stored in SM, and then soft learner will identify them using prototypes and probability model from HM. If a face is rejected, hard learner will turn it into a new prototype in HM. By continuously adding prototypes, the robot's knowledge about people keeps growing. We call this process "absorbing".

When the prototype set in HM changes, the probability model, which is calculated from prototypes, should be updated too. However, since the updating process is very time consuming, we can not do this on every change. Instead, when the system is idle, a monitoring thread will extract prototypes from HM to SM. Then a new model is learned and stored back to HM. Besides, because BFM is not perfect, there must be some redundancy or even mistakes in the prototype set. The system will refine it as necessary. We call these activities "reflection", which is in fact processes that reconstruct the knowledge. By using "absorbing" and "reflection", this system can learn acquaintances adaptively.

4.3 Learning of action

In order to fetch objects from peoples hand effectively, optimized motion sequence of the robot arm has to be learned. Compared with learning of people, this is a more complex job, and we are still improving it.

At the beginning, the robot will try randomly (basic heuristic guide may be incorporated for efficiency). Current environment and all the action/result pairs are stored in SM. Then the data are used to learn a model that can make decisions according to current environment configuration. On the low level, motion sequences to finish a basic action will be learned; on the high level, the robot has to make general decisions according to environment. In general, this is still an absorb/reflect process. Now, actual learning method for motion sequences is under consideration.

5 Conclusion

Based on soft-hard structure theory, we propose a cognitive learning scheme and its corresponding memory structure. They are designed from a evolutionary view point. Using them we can hopefully realize a cognitive learning machine, which is a machine with bootstrap ability and can learn adaptively. However, this proposal is still a conceptual guideline for the design of practical systems. Details have to be specified and implemented according to actual requirements. In our project, this guideline can be well suited into concept and action learning tasks.

Soft-Hard structure theory is a powerful foundation for developing evolutionary machines. In the future, more functional parts of the robot project will be designed based on it.

Acknowledgments

This study is carried out as a part of "R&D Promotion scheme funding international joint research" promoted by NICT (National Institute of Information and Communications Technology) of Japan.

References

- [1] Kazuhiko Kawamura, "Cognitive Approach to a Human Adaptive Robot Development", *Robot and Human Interactive Communication, 2005. ROMAN 2005. IEEE International Workshop on*, pp.629-634.
- [2] J. B. Tenenbaum, V. de Silva, and J. C. Langford. "A global geometric framework for nonlinear dimensionality reduction", *Science*, 290(5500):2319-2323, 2000.
- [3] Jianbo Shi, Malik, J. "Normalized cuts and image segmentation", *Pattern Analysis and Machine Intelligence, IEEE Transactions on*, Volume: 22, Issue: 8, pp.888 - 905, Aug. 2000
- [4] Nanyuan Zhao, *Cognitive Science and Generalized Evolution*, Beijing, China, Tsinghua Press, 1994.
- [5] W. R. Ashby. *Design for a Brain*. Chapman Hall Ltd, 1960.
- [6] B. Moghaddam, C. Nastar, A. Pentland. "A Bayesian Similarity Measure for Direct Image Matching", *Proc. of International Conference on Pattern Recognition (ICPR'96)*, vol.6, pp. 350-358.

Artificial Realization of Decision Making for Sleep Stage of EEG Contaminated with Artifacts: Conditional Probability of Knowledge-Base of Expert Visual Inspection

Bei Wang^{1,2}, Xingyu Wang², Junzhong Zou², Fusae Kawana³, Masatoshi Nakamura¹

¹Department of Advanced Systems Control Engineering,
Saga University,
Honjomachi, Saga 840-8502 (Japan)
wangbei@cntl.ee.saga-u.ac.jp

²Department of Automation, East China University of Science and
Technology, Meilong Road, Shanghai 200237 (China)

³Department of Clinical Physiology, Toranomon Hospital,
Tokyo 105-8470 (Japan)

Abstract

An artificial realization of decision making for sleep stages of EEG (electroencephalograph) contaminated with artifacts was developed in order to construct a reliable sleep stage recognition system for clinics. The methodology was based on the conditional probability of knowledge-base of expert visual inspection. Expert visual inspection was the manual scoring result of sleep stages by a qualified EEGer (F.K.). Knowledge-base was constructed in terms of probability density functions of characteristic parameters with each sleep stage, according to the expert visual inspection. Artificial realization of decision making for sleep stage was based on the value of conditional probability. Totally, the overnight sleep EEG recordings of four subjects were analyzed. The results showed a close agreement with the expert visual inspection by EEGer.

Key words: sleep EEG, artifacts, decision making for sleep stage, conditional probability, knowledge-base of expert visual inspection

1. Introduction

In human sleep, there are several types of sleep stages. Sleep stage determination has clinical importance for the inspection of sleep related disorders. As one's overnight sleep EEG is long-term recording, it is inevitably contaminated by variance artifacts under usual recording conditions in most hospitals and sleep laboratories (P. Anderer et al [1], D. P. Brunner et al [2]).

In many other studies, waveform detection technique (first applied by Smith et al. [3]) could be found for the computerized sleep stage scoring. When sleep EEG was recorded under the usual recording condition,

it had limitation to detect the characteristic waveforms from artifacts.

In this study, we investigated on the artificial realization of decision making for sleep stages of EEG contaminated with artifacts in order to construct a reliable sleep stage recognition system for clinics. The methodology was in the field of statistics by using conditional probability of knowledge-base of expert visual inspection, based on our previous study (M. Nakamura and T. Sugi [4]). Expert visual inspection was the manual scoring result of sleep stages by a qualified EEGer (F.K.). Knowledge base was constructed in terms of probability density functions of characteristic parameters, according to the expert visual inspection. The EEGer made visual inspection of sleep stages and artifact contamination for one's overnight sleep recordings. The artificial realization of decision making for sleep stage or artifact was based on the value of conditional probability.

2. Method

2.1 Subjects and Data Acquisition

The overnight sleep of four subjects after the treatment of Continuous Positive Airway Pressure were recorded in the Department of Clinical Physiology, Toranomon Hospital, Japan. Sleep EEGs were recorded at four sites C3/A2, C4/A1, O1/A2 and O2/A1, according to the International 10-20 System (H. H. Jasper [5]). EOGs (electrooculogram) were derived near the eyes, LOC/A1 and ROC/A1. Chin-EMG (electromyogram) was obtained from muscle areas on and beneath chin. Sleep EEGs and EOGs were recorded under a sampling rate of 100 Hz, Chin-EMG under a sampling rate of 200Hz.

Table 1: Classification of sleep stages and artifact contaminated stage A.

Stages	Characteristics
Awake	
with eyes opened	predominant rhythmic alpha activity (8-13Hz) in EEG
with eyes closed	eye blinks in EOG
REM	relatively low-voltage, mixed-frequency activity in EEG, episodic REM in EOG and low-amplitude EMG
NREM	
Stage 1	relatively low-voltage, mixed-frequency activity in EEG, without rapid eye movement in EOG
Stage 2	relatively low-voltage, mixed-frequency activity with sleep spindles (12-14Hz) and K complexes in EEG
Stage 3	moderate amounts of high-amplitude, slow-wave activity (0.5-2Hz) in EEG
Stage 4	large amounts of high-amplitude, slow-wave activity (0.5-2Hz) in EEG
Stage A	with artifact contamination, accompanied with body movement or tonic activity in EEG

2.2 Expert Visual Inspection

A qualified EEGer (F.K.), who is one of the co-author, made visual inspection on the sleep EEG recordings of four subjects. Their overnight sleep recordings were separated into consecutive 30-second segments, which is called epoch. Each epoch was assigned with a single stage or artifact contamination by the EEGer based on the well-known Rechtschaffen and Kales criteria [6] and her clinical experience.

Table 1 showed the expert visual inspection of sleep stages and the corresponding characteristics. In Rechtschaffen and Kales criteria, sleep is consisted of stage awake, rapid eye movement (REM) and non-REM (NREM) sleep which is further divided into stage 1, stage 2, stage 3 and stage 4. The EEGer inspected the sleep stages based on the corresponding characteristics of a certain frequency bands as in Table 1. In addition, stage awake was separated into open and close eyes awake. Because alpha activity is predominant when subjects closed eyes and was relaxed, significantly attenuates when subjects opened eyes or became tension. The EEGer also inspected the artifacts accompanied with tonic activity in sleep EEG. Stage A was defined as an extra stage of artifacts besides the other sleep stages.

2.3 Knowledge-base

Knowledge-base is in terms of probability density functions of characteristic parameters corresponding to each stage. Based on the manual scoring result of expert visual inspection, the epochs of ones overnight sleep recording can be classified into different stages. For each stage, a set of characteristic parameters (Table 2) are calculated to make the probability density functions in Cauchy distribution.

Based on the definition of Cauchy distribution, the probability density function of parameter y in stage ζ can be mathematically expressed by Eq. 1,

$$f(y|\zeta) = \frac{b}{\pi((y-a)^2 + b^2)} \quad (1)$$

where a is the location parameter and b is the scale parameter. The values of a and b are determined by applying least square method on the histograms.

Table 2: Parameter Definition

EEG	Duration of alpha activity (α : 8-13Hz) in O1/A2 or O2/A1 Duration of slow wave activity ($s1$: 0.5-2Hz) in C3/A2 or C4/A1 Amplitude of mixed frequency activity ($s2$: 2-7Hz) in C3/A2 or C4/A1 Amplitude of high frequency activity (h : 25-50Hz) in C3/A2 or C4/A1
EOG	Amount of eye movement (LOC: 2-10Hz) in LOC/A1 Amount of eye movement (ROC: 2-10Hz) in ROC/A1 Amount of eye movement (L-R: 2-10Hz) in LOC/ROC
chin-EMG	Amount of tonic activity (chin-EMG: 50-100Hz) in chin-EMG

2.4 Artificial Realization of Decision Making

Sleep stage determination can be considered as decision making problem. Artificial realization of decision making is proposed to solve the multiple decision making problem (M. Nakamura and T. Sugi [4]). It is carried out based on the value of conditional probability,

$$P_{k|k}(\zeta^i) = \frac{f(y_k | \zeta^i) P_{k|k-1}(\zeta^i)}{\sum_{j=1}^n f(y_k | \zeta^j) P_{k|k-1}(\zeta^j)}, \quad (2)$$

where $P_{k|k-1}(\zeta^i)$ is the predicted probability of previous segment. The decision of sleep stage or artifact contamination is made by choosing the stage which has the maximum value of conditional probability, as

$$\zeta^* : \max(P_{k|k}(\zeta^i)). \quad (3)$$

Then predicted probability is calculated by

$$P_{k+1|k}(\zeta^i) = \sum_{j=1}^n t_{ij} P_{k|k}(\zeta^j), \quad (4)$$

where t_{ij} corresponds to the transitional probability between every two stages.

3. Result

3.1 Knowledge-base of probability density functions

The overnight sleep recordings of two subjects were utilized to obtain knowledge-base. The probability density functions of each characteristic parameter and stage were shown in Figure 1. In Fig.1, black dots were the location parameter of Cauchy distribution and white dots the scale parameter. Stage awake with eyes closed

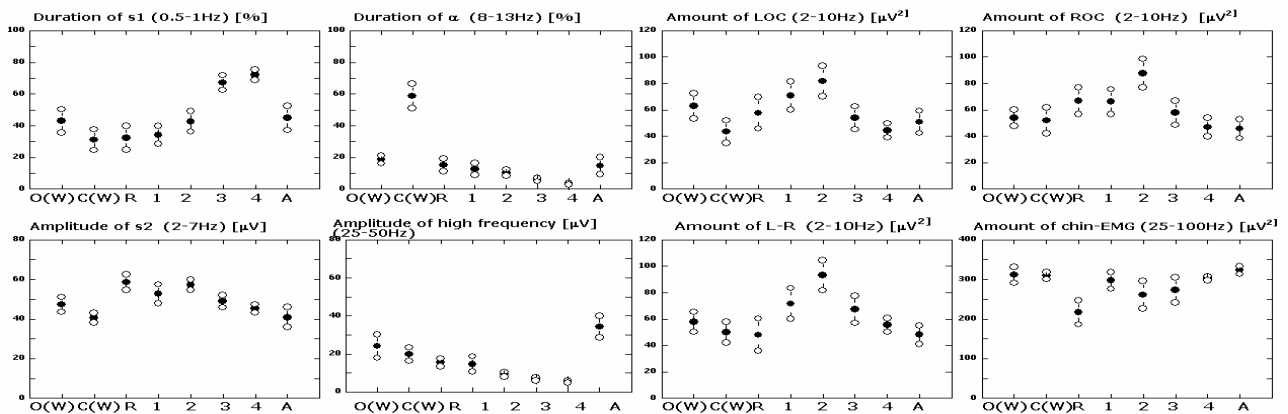


Figure 1: Probability density functions of characteristic parameters corresponding to each stage.

had the largest location value in the distribution of the duration of alpha activity (8-13Hz). In the amplitude of high frequency (25-50Hz), stage A of artifact contamination had the largest location value, discriminated from other sleep stages. Stage REM was separated from other stages with lowest location value in the amount of chin-EMG (25-100Hz). Stage 3 and 4 shared the largest location value in the duration of s1 (0.5-2Hz), which corresponding to the slow wave activity.

3.2 Decision Making of Sleep Stages

Another two subjects were analyzed as test data. The calculation processing of conditional probability and predicted probability was illustrated in Fig.2 with time series of an epoch. The later part of this epoch was contaminated by artifacts and detected by the artificial decision making method. The stage determination for this epoch was stage awake because half of sleep EEG was contaminated by tonic artifacts. The stage scoring result of expert visual inspection was also stage awake.

The evaluation of sleep stage determination for two test subjects were given in Table 3. Stage 1 and 2 were combined as light sleep of NREM, stage 3 and 4 were deep sleep of NREM. The number in Table 3 showed the agreement between artificial decision making of sleep stages and expert visual inspection for each subject respectively. Average accuracy was also evaluated in Table 3.

Table 3: Evaluation of sleep stage determination

	Subject A	Subject B	Average
Awake	92.8%	84.4%	88.6%
REM	63.8%	72.3%	68.1%
Stage 1/2	82.6%	82.2%	82.4%
Stage 3/4	94.6%	98.0%	96.3%

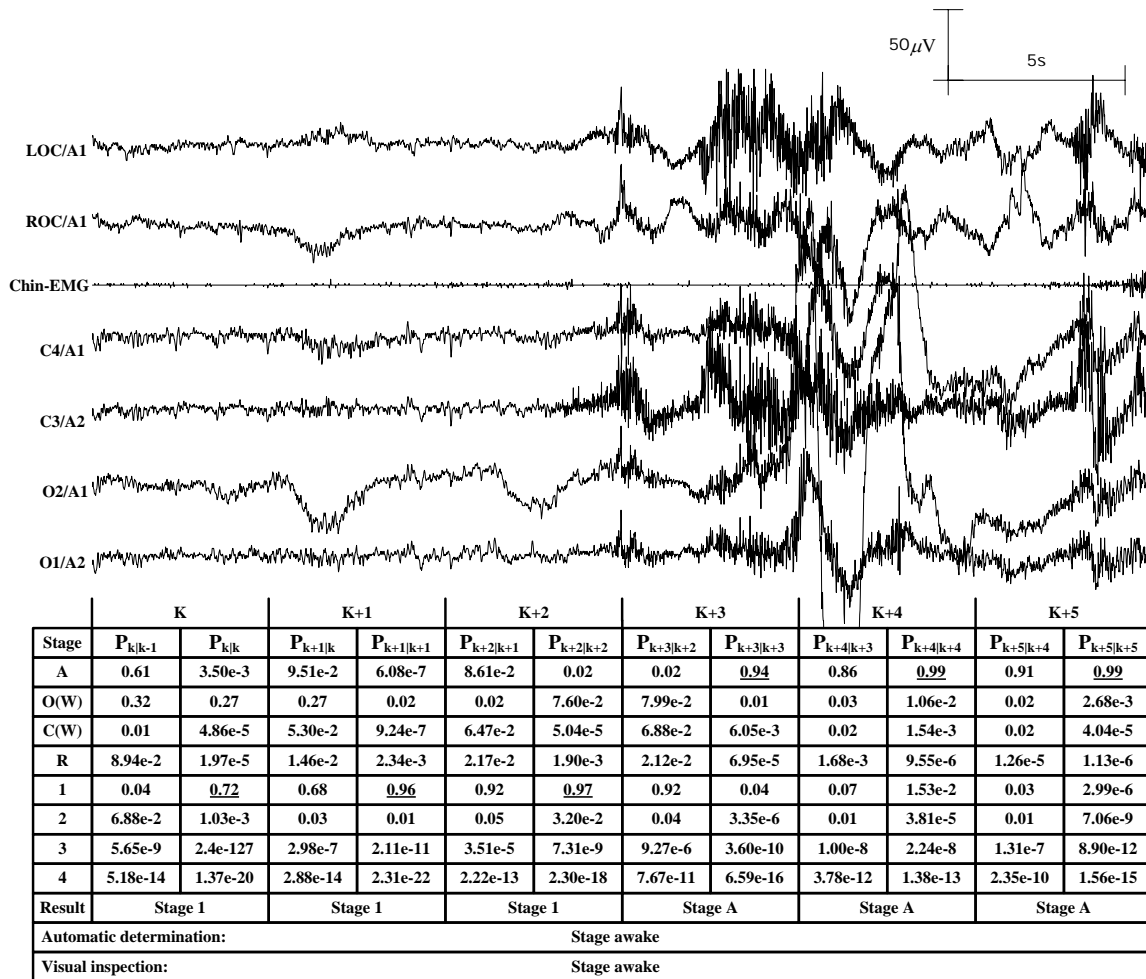


Figure 2: Artificial realization of decision making for sleep stage of EEG contaminated with artifact.

4. Conclusion

In this study, method of conditional probability of knowledge-base of expert visual inspection was utilized for sleep stage determination. The results showed a close agreement with expert visual inspection by EEGer. Artifact contamination can also be detected in sleep EEG. Compare with other sleep stages, REM was in low accuracy and need to be improved. With the knowledge-base of expert visual inspection, the proposed artificial realization system of decision making for sleep stage has strong performance in the clinical practice.

References

[1] P. Anderer, S. Roberts, et al, "Artifact Processing in Computerized Analysis of Sleep EEG - A Review", *Neuropsychobiology*, Vol.40, pp.150-157, 1999
 [2] D. P. Brunner, R. C. Vasko, et al, "Muscle artifacts in the sleep EEG: automated detection and effect on

all-night EEG power spectra", *Sleep Research*, Vol.5, pp. 155-164, 1996
 [3] J. R. Smith, I. Karakan and M. Yang, "Automated Analysis of the Human Sleep EEG, Waking and Sleeping", *Electroenceph. clin. Neurophysiol.*, Vol.2, pp. 75-82, 1978
 [4] M. Nakamura and T. Sugi., "Multi-Valued Decision Making for Transitional stochastic Event: Determination of Sleep Stages through EEG Record", *Transactions on Control, Automation and Systems Engineering*, Vol. 4, pp.239-243, 2002
 [5] H. H. Jasper, "Ten-twenty electrode system of the International Federation", *Electroenceph. clin. Neurophysiol.*, Vol.10, pp. 371-375, 1958
 [6] A. Rechtschaffen and A. Kales, A Manual of Standardized Terminology, Techniques and Scoring System for Sleep Stages of Human Subject, California Brain Information Service, USA, 1986

A Study on Quantum-Inspired Evolutionary Algorithm based on Pair Swap

Takahiro Imabeppu Shigeru Nakayama Satoshi Ono
Department of Information and Computer Science
Faculty of Engineering, Kagoshima University
Kagoshima-shi, 890-0065 Japan
{sc102005, shignaka, ono}@ics.kagoshima-u.ac.jp

Abstract

Quantum-Inspired Evolutionary Algorithm (QEA) is proposed as one of approximate algorithms to solve combinatorial optimization. QEA is evolutionary computation that uses quantum bits and superposition states in quantum computing. Although conventional QEA is a coarse-grained parallel algorithm, it involves many parameters that must be adjusted manually. This paper proposes a new method of Pair Swap which exchanges each best solution information between two individuals. Experimental result shows that the proposed method is a simpler algorithm and can find high quality solution in binary Knapsack Problem.

Keywords

evolutionary computation, quantum computing, quantum bit, pair swap, knapsack problem

1 Introduction

Quantum computer[1, 2] is a computation model using quantum mechanical principles such as superposition state, interference effect, and entanglement state. Recently, stochastic combinatorial search algorithms combined with evolutionary algorithm have been recently proposed by incorporating quantum mechanical principles or quantum bits[3, 4, 5, 6].

Han et al.[5, 6] have proposed Quantum-inspired Evolutionary Algorithm (QEA) in which each gene is represented by a quantum bit. QEA can do single-point search and automatically shift from global search to local search like Simulated Annealing (SA)[7]. QEA can also perform multi-point search like Classical Genetic Algorithm (CGA) in order to solve large-scale optimization problems.

In QEA, there are more than one subpopulations (groups) like Island GA (IGA)[8, 9], and inter- and intra-group migration procedures are performed. Evolution in each group enables coarse-grained paralleliza-

tion and prevents premature convergence, and the migration procedures can control search diversification and intensification. However, the adjustment of a number of parameters is required for the number of group and migration intervals for each problem.

Therefore, we propose Quantum-inspired Evolutionary Algorithm based on Pair-Swap method (QEAPS). We have showed that the performance of QEAPS is better than that of QEA in 0-1 Knapsack Problem(KP)[10]. In this paper, we keen on evaluating the performance of QEAPS against that of QEA in 0-1 KP, and we show that the effectiveness of QEAPS. To be concrete, the search performance and the robustness of QEAPS are verified by performance comparison of constraint handling methods (when the sum total of the item exceeds the capacity of the knapsack in 0-1KP).

2 Quantum-Inspired Evolutionary Algorithm based On Pair Swap

2.1 Quantum Bit Representation of Gene

QEA and QEAPS uses a quantum bit (qubit) as a gene, while, in conventional genetic algorithm (CGA), a gene is usually a definite value of binary, integer, real number, or character. The individual i in the generation t is composed of the chromosome represented as a tensor product of the qubits, $q_i = q_{i1} \otimes q_{i2} \otimes \dots \otimes q_{im}$ and the best solution information that is binary string discovered in search process (Personal Best) $b_i = [b_{i1}, b_{i2}, \dots, b_{im}]$. Here, m is the number of genes or qubits included in an chromosome. The qubit q_{ij} ($j = 1, \dots, m$) has stochastic superposition state (vector sum) of the two vectors $|0\rangle$ and $|1\rangle$ with each complex probability amplitude.

$$q_{ij} = \alpha_{ij} |0\rangle + \beta_{ij} |1\rangle = \begin{pmatrix} \alpha_{ij} \\ \beta_{ij} \end{pmatrix}, \quad (1)$$

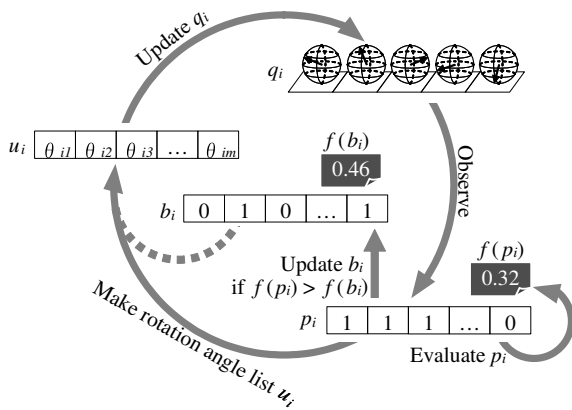


Figure 1: Evaluation of an individual.

Table 1: Lookup table of the rotation angle θ_{ik}

p_{ik}	b_{ik}	$f(p_i) \geq f(b_i)$	θ_{ik}			
			$\alpha_{ik}\beta_{ik} > 0$	$\alpha_{ik}\beta_{ik} < 0$	$\alpha_{ik} = 0$	$\beta_{ik} = 0$
0	1	false	θ_C	$-\theta_C$	—	$\pm\theta_C$
1	0	false	$-\theta_C$	θ_C	$\pm\theta_C$	—
		Otherwise	0	0	0	0

$|i_j|^2$ is the probability that the state of $|0\rangle$ is observed, and $|i_j|^2$ is the probability that the state of $|1\rangle$ is observed. The binary string p_i is obtained by observing q_i . The fitness value $f(p_i)$ of the individual i can be calculated from p_i like CGA.

2.2 Procedures in QEA and QEAPS

The algorithm of QEAPS that we propose is shown in Figure 2. We first describe the common process of QEA and QEAPS (white part of Figure 2), and then we describe the different process of QEA and QEAPS (black part of Figure 2).

To begin with, the initialization is carried out by setting i_k and i_k to $1/\sqrt{2}$ in order to equally observe the states of $|0\rangle$ and $|1\rangle$ in the individual $i(= 1)$. Next, the evolution of an individual with qubits and the exchange of the best solution information in the individual are repeated according to the following procedure, until a given termination condition is satisfied.

The procedure of the individual update is shown Figure 1 and as follows. First of all, p_i is obtained by observing q_i . And, the fitness $f(p_i)$ is calculated from p_i , and the fitness of the individual is decided.

Then, the rotation angle list $u_i = [\theta_{i1}, \theta_{i2}, \dots, \theta_{im}]$ is made from each value of p_{ij} and b_{ij} and the magnitude correlation of $f(p_i)$ and $f(b_i)$. This list is used to increase and decrease the observation probability of $|1\rangle$ and $|0\rangle$. How to decide the rotation angle $\theta_{ik}(k = 1, \dots, m)$ is shown in Table 1[5, 6]. Unitary

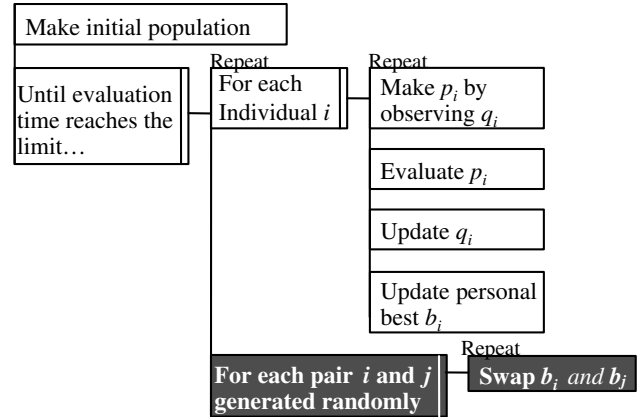


Figure 2: The algorithm of proposed QEAPS.

transformation can be used to change the ratio of the probability amplitudes i_k and i_k of the superposition state.

$$\begin{matrix} i_k \\ i_k \end{matrix} = \begin{matrix} \cos(\theta_{ik}) & \sin(\theta_{ik}) \\ \sin(\theta_{ik}) & \cos(\theta_{ik}) \end{matrix} \begin{matrix} i_k \\ i_k \end{matrix} \quad (2)$$

q_i is upgrade following the rotation angle list u_i and the rotation matrix.

If $f(p_i) > f(b_i)$, then the best solution of the new individual is replaced by the currently observed binary information.

2.3 Migration Method of QEA

Migration strategy of QEA involves local migration and global migration. The local migration is the process of distributing the best solution information of an individual with the highest fitness in each group, to all other individuals in each group, and repeated in every generations. The global migration is the process of distributing the best solution information of an individual with the highest fitness in all groups, to all other individuals in all groups, and repeated in every fixed generations. QEA shows the centralization of the search, but must determine two parameters of the number of groups and the timing of global migration by considering problem characteristics and scale, convergence speed in a group, rotation angle as QEA fundamental parameter[5, 6].

2.4 Pair Swap Method of QEAPS

QEAPS utilizes pair swap operation instead of global and local migration of QEA. To begin with, two individuals are randomly selected as a pair from all individuals in the whole group. Then, $n/2$ pairs are

generated by selecting two individuals from n (even number) individuals with no overlaps in the group. Only each best solution information is exchanged in each pair with out carrying out any operation on the qubits in the individual.

3 Computational Experiments

3.1 Experiment Preparation

The 0-1 KP is used for the evaluation experiments in order to prove the effectiveness of the proposed QEAPS. The KP in the paper [9] is used as a benchmark problem. The number of items N is 100(the first 100 items are used in the benchmark problem). The weight limit in the KP is set to be 50% of the total weight of all items. Parameters such as the population and the number g of groups in QEA are followed by the previous researches[6], respectively. Parameters used in QEAPS are followed by QEA as shown in Table 2.

When the evaluation times, the number of fitness calculation time, reach the preset value, the search stops. We perform the same experiments 30 times using each technique for each problem.

3.2 Constraint Handling Methods

We compare the performances of QEAPS and that QEA in the following three methods to handle constraint violation.

1. **Fitness = 0 (Zero)**

If the condition is not satisfied, then $f = 0$.

2. **Penalty Function (Penalty)**

The penalty function shown by the equation 3 is used.

$$f(p_i) = \sum_{j=1}^n a_j p_{ij} - \alpha \max \left\{ 0, \sum_{j=1}^n w_j p_{ij} - C \right\}, \quad (3)$$

where, p_{ij} is the value of the j -th gene in the chromosome of the i -th individual, a_j is the profit of item j , w_j is the weight of item j , and C is the capacity of the knapsack, and $\alpha = \max_{j=1}^n \{a_j/w_j\}$.

3. **Random Repair (Repair)**

Random Repair [5] that consists of the following procedures in applied. Step 2 is applied even when weight limits are satisfied.

Table 2: Parameter configurations.

Parameter names	Values used	
	QEA	QEAPS
Number of individuals	10, 20, 30, ..., 100	
Number of subpopulations (groups) (g)	5	-
Number of individuals in a subpopulation	2, 4, ..., 20	-
Rotation angle (θ_C)	0.01π	0.01π
Number of observations	1	1
Interval of global migration	100	-

Step 1: One item is randomly selected and removed until the knapsack capacity is filled.

Step 2: One item selected randomly is put in the knapsack until capacity are exceeded. When capacity are exceeded, the item put at the end is removed.

3.3 Experimental Result

Regarding evaluation criteria, we focus on the optimal solution discovery rate per trial number $Opt[\%]$, the mean fitness m_f . The upper limit of evaluation times is set to $N = 10^3$ as a termination condition of the search.

As a function of the individual total numbers, Opt , m_f are shown in Figure 3 and 4. First, when paying attention to Opt , The performance of QEAPS is better than that of QEA in the same number of individuals in all constraint handling methods. In Opt of QEA, Repair is the highest, and Zero and Penalty are lower. The difference is seen for all number of individuals between the methods. On the other hand, such difference is not so seen at QEAPS. Moreover, Opt is almost 100% in any method when more than 40 individuals are used.

The result of m_f in Figure 3 and 4 also indicate that QEAPS has higher-performance than QEA. In m_f of QEA, there is obvious difference between that of Repair and these of Zero and Penalty. In QEAPS, the highly qualified solutions are obtained in all constraint handling methods. It should be noted that m_f of Repair, Penalty and Zero of QEAPS is higher than that of Repair in QEA.

In QEAPS, the difference between Repair, Zero, and Penalty is quite small. Even though Zero and Penalty are simple and not specialized in the knapsack problem, they can search for optimal solutions, consequently QEAPS is more robust against constraint

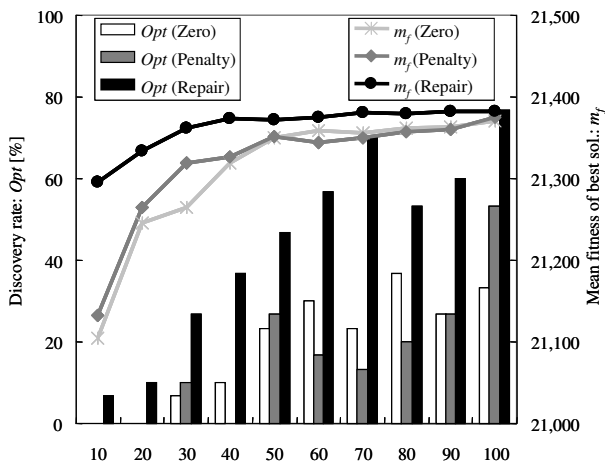


Figure 3: Discovery rate and evaluation time (QEA)

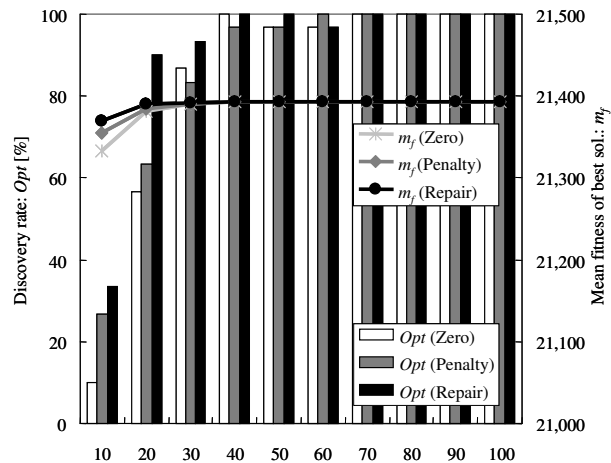


Figure 4: Discovery rate and evaluation time (QEAPS)

methods.

4 Conclusion

In this paper, we focused on evaluating the performance and robustness of QEAPS to improve QEA. We compared the performance between the constraint handling method in 0-1 KP. Experimental result show that QEAPS is able to discover the optimal solution at the higher probability compared with QEA, and that the solutions found by QEAPS are of even quality, and that QEAPS is robust against constrain handling methods.

We plan to verify the search performance in a larger-scale problem, improve the algorithm, examine application to other combination optimization problems, and clarify the characteristic of the problem to which QEAPS is effective.

References

- [1] M. A. Nielsen and I. L. Chuang. *Quantum Computation and Quantum Information*. Cambridge Univ. press, New York, 2000.
- [2] S. Nakayama, "Consideration on the square root gates of quantum logic gates (in Japanese)," *Trans. the Japan Society for Computational Engineering and Science*, 7:77–82, 2005.
- [3] A. Narayanan and M. Moore, "Quantum-inspired genetic algorithms," In *Proc. IEEE Int'l Conf. on Evolutionary Computation*, pages 61–66, 1996.
- [4] S. Nakayama, I. Iimura, and T. Ito, "Consideration on quantum interference crossover method in immune algorithm (in Japanese)," *IEICE Trans. Information and Systems, PT.1 (Japanese edition)*, J-88-D-I(12):1795–1799, 2005.
- [5] K.-H. Han and J.-H. Kim, "Quantum-inspired evolutionary algorithm for a class of combinatorial optimization," *IEEE Trans. Evolutionary Computation*, 6(6):580–593, 2002.
- [6] K.-H. Han and J.-H. Kim, "On setting the parameters of qea for practical applications: Some guidelines based on empirical evidence," In *Genetic and evolutionary computation GECCO 2003*, pages 427–428, 2003.
- [7] S. Kirkpatrick, C. D. Gelatt, and M. P. Vecchi, "Optimization by simulated annealing" *Science*, vol.220, no.4598, pp.45-54, 1983
- [8] T. C. Belding, "The distributed genetic algorithm revisited," In *Proc. the Sixth Int'l Conf. on Genetic Algorithms*, pages 114–121, 1995.
- [9] I. Iimura, S. Ikehata, and S. Nakayama, "Consideration on noah's ark strategy in parallel genetic algorithm with object-shared space (in Japanese)," *J. Japan Society of Information and Knowledge*, 13(2):1–7, 2003.
- [10] S. Nakayama, T. Imabeppu, S. Ono, and I. Iimura, "Consideration on Pair Swap Strategy in Quantum-Inspired Evolutionary Algorithm (in Japanese)," *IEICE Trans. Information and Systems, PT.1 (Japanese edition)*, J89-D-I(9):2134–2139, 2006.

Epidemic Models and a Self-Repairing Network with a Simple Lattice

Yuta Aoki¹ and Yoshiteru Ishida^{1,2}

¹ Department of Knowledge-Based Information Engineering,
Toyohashi University of Technology,
Tempaku, Toyohashi, 441-8580 Japan

²Intelligent Sensing System Research Center
Toyohashi University of Technology,
Tempaku, Toyohashi, 441-8580 Japan

Abstract

We proposed a self-repairing network where nodes are capable of repairing neighboring nodes by mutually copying. A critical point where faulty nodes can be eliminated has been investigated. This paper further studies dynamics of eradicating faulty nodes by comparing the self-repairing network with mathematical epidemic models such as SIS models. It is shown that the self-repairing network, which is a probabilistic cellular automaton, can be regarded as an epidemic model in some restricted situations.

1. Introduction

Information networks are complex systems with multiple and interacting processes work in parallel on various network structure. Self-recovery of such networks have been studied with a focus on the network structure [1] as well as interacting processes [2]. We have been studying on a self-repairing network with a focus on state propagation and regulation keeping the network model simple enough for analysis [3, 4]. In the model, the two state propagations have been involved: the abnormal state propagation by unsuccessful repair as well as the normal state propagation by successful repair.

Epidemic models have been studied for a long time, and nonlinear properties of the models have investigated in great detail. The models include not only those described by differential equations [5] but by probabilistic cellular automata [6] or even including moving agents [7]. On the other hand, phase transitions have been studied on models extended from an Ising model in the field of statistical physics but involving probabilistic cellular automata [8].

Our model has been already related with a model in statistical physics [3]. This paper specifically focuses on the relation between the self-repairing network and an epidemic model called SIS model.

2. A Self-Repairing Network Model

2.1. A model by a probabilistic CA [3]

The self-repairing network is a network whose nodes can be normal (0) and abnormal (1); and are capable of repairing the neighbor nodes by copying its content. Each node repairs the neighbor nodes with a probability P_r . The repair will be successful with a probability P_{rn} when it is done by a normal node, but with a probability P_{ra} when done by an abnormal node. Further, all the repair must be successful for the target node to be normal when repairing is done by multiple nodes (**Fig. 1**).

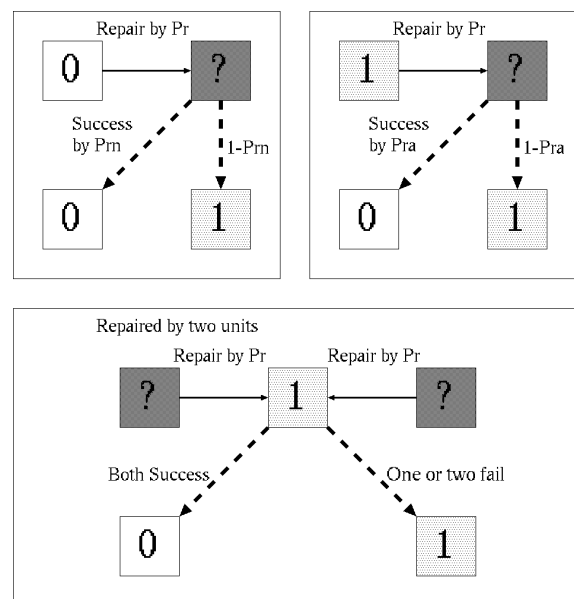


Fig. 1. Repair success rate when repairing is done by normal node (above, left) and by abnormal node (above right); all the repairs by neighbor nodes must be successful for the target node to be normal (below). Solid arcs indicate repairing and dotted arcs indicate state change.

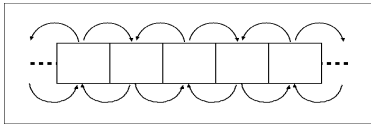


Fig. 2. 1-dimensional structure with two adjacent neighbor nodes

When repairing is done by copying, the marked difference from conventional repairing is that the repairing rather could have contaminated other nodes rather than cleaning: the *double edged sword* in repairing. Thus, it is important to investigate on conditions under which the network may be cleaned. To clarify the conditions, we used a probabilistic cellular automaton [3, 4] which turned out to be Domany-Kinzel model [8] is some particular cases.

In a 1-dimensional structure with two adjacent neighbor nodes (**Fig. 2**), the probabilities for each rule of state change are listed in **Table 1**.

Table 1. Transition probabilities of the one dimensional probabilistic cellular automaton [4]

State change	Transition Probability
000→1	$P_r(1 - P_{rn})(P_r P_{rn} - P_r + 2)$
001→1	$P_r^2(1 - P_{rn} P_{ra}) + P_r(1 - P_r)((1 - P_{rn}) + (1 - P_{ra}))$
101→1	$P_r(1 - P_{ra})(2 - P_r(1 - P_{ra}))$
010→1	$1 - P_r P_{rn}(2(1 - P_r) + P_r P_{rn})$
011→1	$1 - P_r((P_{rn} + P_{ra})(1 - P_r) + P_r P_{ra} P_{rn})$
111→1	$1 - P_r P_{ra}(P_r P_{ra} + 2(1 - P_r))$

2.2 Steady state analysis with mean field approximation [4]

Let y denote a fraction of abnormal nodes, and let the probability of being abnormal (1) be approximated by y at any nodes. Then the dynamics of y can be described by the equation (1) where a , b , and c are constants determined by the three parameters of the self-repairing network.

$$\frac{dy}{dt} = ay^2 + by + c, \quad (1)$$

$$\begin{aligned} a &= -P_r^2(P_{rn} - P_{ra})^2, \\ b &= -2P_r(1 - P_{rn})(P_r(P_{rn} - P_{ra}) + 1) + P_r(P_r - 2P_{ra}), \\ c &= P_r(1 - P_{rn})(2 - P_r(1 - P_{rn})) \end{aligned}$$

When $P_{rn} > P_{ra}$ hence $a < 0$, the steady state y_∞ can be calculated as follows.

$$y_\infty = \frac{1}{2a}(-b - \sqrt{b^2 - 4ac})$$

In order for abnormal nodes eradicated, c must be 0 i.e. $P_{rn} = 1$, for suppose otherwise normal nodes could have spread abnormal states. When $c = 0$, the following condition (2) must be satisfied for abnormal states eradication, since the time derivative $\frac{dy}{dt}$ must be negative in the equation (1).

$$\frac{P_{ra}}{P_r} \geq \frac{1}{2} \quad (2)$$

2.3 Simulation Results

Although the mean field approximation above suggested parameter conditions for abnormal node extinction, it must be verified by computer simulation for the self-repairing model by a probabilistic cellular automaton. To investigate the dynamics of normal node population when P_{rn} varies, a computer simulation is conducted with parameters listed in **Table 2**. **Fig. 4** plots the time evolution of normal nodes when P_{rn} varies as well as numerical calculation of the mean field approximation.

Table 2. Simulation Parameters

Parameters	Value
Time steps for each trial	1500
Number of trials	10
Number of nodes	400
Initial number of normal nodes	200
P_r	1.0
P_{rn}	0.6, 0.9, 1.0
P_{ra}	0~1(0.02)

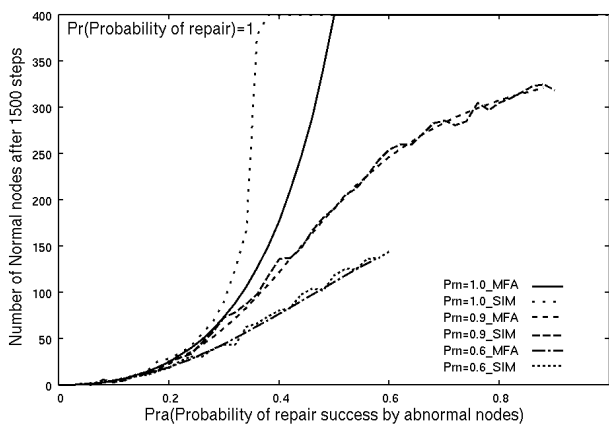


Fig. 4. Time evolution of the number of normal nodes when P_m varies (legends)

3. Self-Repairing Network and SIS Model

3.1 An SIS model

Epidemic models assume the states such as S (susceptible), I (infected), and R (recovered). Combining such states allowed, epidemic models varies from SI, SIS, and SIR. Among them, in an SIS model assumes that susceptible nodes will fall into the infected state with an infection rate β when the neighbor nodes are infected. The infected nodes will be recovered with a recovery rate γ and become susceptible state again. The SIS model can describe, for example, a sexually transmitted diseases; venereal disease gonorrhea [5].

Susceptible (S) and infected (I) state respectively correspond to normal (0) and abnormal (1) state in the self-repairing network. Fig. 5 shows the state transition between S(0) and I(1).

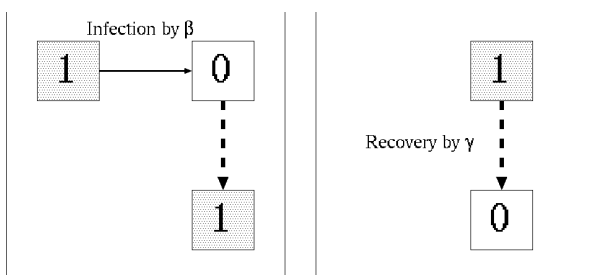


Fig. 5. State Transition in an SIS Model. Solid arcs indicate repairing and dotted arcs indicate state change. Solid arcs indicate repairing and dotted arcs indicate state change.

3.2 Parameter correspondence between an SIS model and a self-repairing network

In a random graph with a mean degree $\langle k \rangle$, the dynamics of the fraction of infected (abnormal) nodes y can be described as follows.

$$\frac{dy}{dt} = \beta \langle k \rangle (1-y)y - \gamma y$$

$$= -\beta \langle k \rangle y^2 + (\beta \langle k \rangle - \gamma)y$$

Thus, when $P_m=1$ and hence $c=0$ in the equation (1), parameters a, b of a self-repairing network will be related to the parameters of the above SIS model as follows.

$$a = -\beta \langle k \rangle$$

$$b = \beta \langle k \rangle - \gamma$$

Since we consider one-dimensional cellular automaton for the self-repairing network, $\langle k \rangle$ could be evaluated as 2, and hence;

$$\beta = \frac{P_r^2 (1 - P_{ra})^2}{2} \quad (3)$$

$$\gamma = P_r P_{ra} (P_r P_{ra} + 2(1 - P_r)) \quad (4)$$

3.3 Simulation Results

To examine the correspondence between the SIS Model and the self-repairing network, simulations are conducted with parameters listed in Table 3. Fig. 6 plots the number of normal nodes varying the repair success rate P_{ra} when repaired by abnormal nodes. The SIS model and the self-repairing network mostly matches, however, both models do not match with the numerical solution obtained from the mean field approximation (1), particularly when P_{ra} is greater than 0.3.

Table 3. Simulation Parameters

Parameters	Value
Time steps for each trial	500
Number of trials	10
Number of nodes	400
Initial number of normal nodes	200
P_r	1.0
P_{rn}	1.0
P_{ra}	0~1(0.02)
β	$\frac{P_r^2(1-P_{ra})^2}{2}$
γ	$P_r P_{ra} (P_r P_{ra} + 2(1 - P_r))$

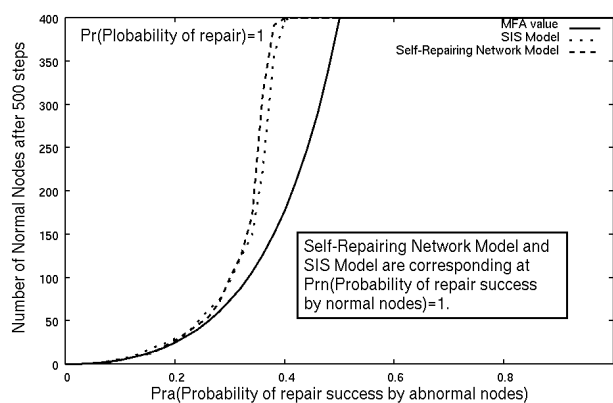


Fig. 6. Relation between SIS Model and Self-Repairing Model.

4. Conclusion

The self-repairing network involves repairing by mutual copying in a network. Hence, it models not only abnormal state propagation (unsuccessful repair) but normal state propagation (successful repair). Thus, it differs from the epidemic models which models only abnormal state propagation (infection), and recovery is modeled as an independent event (not as propagation). This paper shows, in spite of the difference, self-repairing network can be reduced to an SIS model under certain conditions.

Acknowledgements

This work was supported in part by Grants-in-Aid for Scientific Research (B) 16300067, 2004. This work was partly supported also by the 21st Century COE Program “Intelligent Human Sensing” of the Ministry of Education, Culture, Sports, Science and Technology of Japan.

References

- [1] Dezso, Z. and Barabasi, A.-L.: Halting viruses in scale-free networks, *Phys. Rev. E* 65, 055103, (2002)
- [2] Brown, A. and Patterson, D.: Embracing Failure: A Case for Recovery-Oriented Computing (ROC), *High Performance Transaction Systems Workshop (TTPS '01)* (2001)
- [3] Ishida, Y.: A Critical Phenomenon in a Self-Repair Network by Mutual Copying, *Lecture Notes in Artificial Intelligence (LNAI 3682)*, (2005), pp.86-92
- [4] Ishida, Y.: Complex Systems Paradigms for Integrating Intelligent Systems, in *Computational Intelligence Handbook*, Berlin & Heidelberg, Springer, to appear 2007.
- [5] Lajmanovich, A. and Yorke, J.A.: A deterministic model for gonorrhea in a nonhomogeneous population, *Mathematical Biosciences*, vol.28, (1976) pp.221-236
- [6] Rhodes, C.J. and Anderson, R.M.: Dynamics in a Lattice Epidemic Model, *Phys. Rev. Lett. A*, 210 (1996) pp. 183-188
- [7] Boccara, N. and Cheong, K.: Critical behaviour of a probabilistic automata network SIS model for the spread of an infectious disease in a population of moving individuals, *J. of Physics A: Math. Gen.* 26 (1993) pp. 3707-3717
- [8] Domany, E. and Kinzel, W.: Equivalence of cellular automata to Ising models and directed percolation, *Phys. Rev. Lett.* 53 (1984) pp. 311

The Novel Feature Selection Algorithm for Emotion Recognition

Ho-Duck Kim^{*}, Young-Im Cho^{**}, and Kwee-Bo Sim^{*}

^{*} School of Electrical and Electronics Engineering, Chung-Ang University
221, Heukseok-Dong, Dongjak-Gu, Seoul 156-756, Korea
e-mail : kbsim@cau.ac.kr

^{**} Department of Computer Science, The University of Suwon
San2-2, Wauri, Bongdam-eup, Hwaseong, Gyeonggi-do, 445-743, Korea
e-mail : ycho@suwon.ac.kr

Abstract

This paper presents an original feature selection method for Emotion Recognition which includes many original elements. Feature selection has some merit regarding pattern recognition performance. Thus, we developed a method called an 'Interactive Feature Selection' and the results (selected features) of the IFS were applied to an emotion recognition system (ERS), which was also implemented in this research. Our innovative feature selection method was based on a Reinforcement Learning Algorithm and since it required responses from human users, it was denoted an 'Interactive Feature Selection (IFS)'. By performing the IFS, we were able to obtain three top features and apply them to the ERS. Comparing those results from a random selection and Sequential Forward Selection (SFS) and Genetic Algorithm Feature Selection (GAFS), we verified that the top three features were better than the randomly selected feature set.

Keywords: Reinforcement Learning, Feature selection, Emotion Recognition, SFS, GAFS, IFS

1. Introduction

Emotion recognition research has been typically attempted using four kinds of medium. They are speech, image, physiological signal, and gesture. EEG, ECG, and SC sensors are used to obtain a physiological signal but the signal from those sensors may be obstructed by electrical signals from fluorescent lamps or electric home appliances. This problem is the one obstacle in emotion recognition using a physiological signal. For an image, this means facial expression recognition and the main problem in this case is usually lighting conditions, which often change, or personal accessories like glasses which affect recognition performance. A problem of

gesture recognition is similar to that of image recognition and the bigger problem is that it may not include much information regarding emotion. Apart from above the problems which these three media present, speech signal can send much more information regarding emotion. For example, talking over the telephone, one can recognize emotions and this shows the validity of speech signal for emotion recognition. The commonly used feature set for emotion recognition from speech consists of pitch, energy, formant, and speech rate. Some researchers select all four of the feature sets, others select only one, and the features are generally extracted statistically from the four feature sets. In [1], 17 features were extracted from pitch, energy, speech rate and so on with sex also being classified. In addition, In [2], 11, 40, and 13 features were extracted. The fact that feature set selection is not fixed suggests that features may or may not be relevant to emotion recognition. This problem will plague researchers in this field until exceptional results are obtained. For this case, there is a GA based selection method, Floating search method and so on which can somewhat reduce difficulties for researchers [3]. In [1], a Forward Selection (FS) method was used. In [4], a Sequential Forward Selection algorithm was also used and the best feature subset was selected out of 39 candidate feature sets. These feature selection methods provided a good solution for "The curse of dimensionality" and contributed to the performance of pattern recognitions. In addition, feature selection methods included supervised and unsupervised cases. Generally, a supervised case is employed more often than an unsupervised case. This is due to unsupervised feature selection methods having a high probability of incorrect results for corresponding patterns regarding perceived speech [5]. We propose a method using reinforcement learning taking advantage of both the supervised and unsupervised method, which can alleviate the shortcomings of both methods. Researches

of the reinforcement learning have been proceeded using many methods, i.e. Dynamic programming, Monte Carlo method, TD method, Q learning etc. proposed by Sutton and Barto. Since there is such a variety of methods and the main elements such as “state”, “action” and “reward” may be freely defined and implemented by a developer, this method is thought to be a very important one for machine learning techniques[7]. In this study, we propose a method which selects feature sets by calculating rewards received when an action is performed in a state. In particular, this method does not only calculate the frequency of emotion transit but also the sum of the rewards for the evaluation of a feature selection. Therefore, this method has the advantage that the more frequently it contacts a user, the better its performance becomes.

The outline of the paper is as follows, In Section 2, it explains the emotion recognition method and Section 3 explains the proposed algorithm. The Section 4 shows a simulation and result of using the proposed algorithm. The Section 5 concludes and shows future works.

2. Emotion Recognition Method

This paper addresses emotion recognition by extracting features of speech. The emotion recognition with speech is largely divided into cases using acoustic information and language or discourse information. The former is a method that uses some feature sets such as pitch, formant, speech rate, timbre, etc. and the latter uses the meaning of a word. That is, whether the word is positive or negative to whether it represents a happy or sad state. The process of emotion recognition consists of collecting emotional speech, the acoustic analysis, implementing DB, feature set extraction and such features are trained and classified with emotions using a pattern classification method.

We used an artificial neural network for pattern classification, which commonly performs well and is robust to a signal with noise. It has been the most popular method to use in the pattern recognition field.

This method commonly uses a Back Propagation Algorithm for tuning network parameters. In this study, we fixed the setting to ANN as follows, The number of Input Units and Hidden Units and Output Units and Learning rate and Tolerance and Sigmoid function are 3~5 and 11 and 2 and 0.003 and 0.25 and $1/(1 + e^{-3x})$, respectively.

3. The Interactive Feature Selection Algorithm

Typically, researchers in the emotion recognition use various feature sets. Some researchers looked into the relation between acoustic analysis and emotion and used the feature sets based on that relation. However, because this method is subjective, it may easily lead to local minima. For this reason, recent studies consider a feature selection method for finding small superior features (4~10) out of as many as 30 to 90 features. Most researchers do not use all features because they cannot confirm whether they are valid or not and noises with every features may deteriorate. Therefore, feature selection methods are popular in the pattern classification field [5]. In the former, a feature subset is selected independently of the learning method that will use it. In the latter, a feature subset is selected using an evaluation function based on the same learning algorithm that will consider this subset of features.

Although wrapper approaches have been shown to perform better, they can be rather time-consuming and it is sometimes infeasible to use them [5]. For this reason, the proposed algorithm tries to combine the characteristics of both the wrapper and filtering.

3.1 Reinforcement Learning Algorithm.

Reinforcement learning consists of an agent and environment and is a learning method that leads the agent to perform a target action for a user. The process of learning is as follows, given an environment, an agent firstly performs an action and the agent receives a reward for the action from the environment. At that time, each time step is denoted as t , an environment state which the agent may be include is denoted as $s_t \in S$ (S is a set of possible environments) and an action is denoted as $a_t \in A(s_t)$ ($A(s_t)$ is a set of possible actions in a state). A reward for an action is denoted as r_t and when an episode has been completed, the r_t is expressed as the following equation.

$$R_t = \sum_{k=0}^T \gamma^k r_t + k + 1 \quad (1)$$

Where γ is a discount coefficient in the above equation and does not make the sum of rewards an infinity in the case of being defined as $t = \infty$. In addition, if the discount coefficient is zero, it means that only the current reward value is admitted. That is, we can give the weight to a future value differently according to the discount coefficient. Finally, reinforcement learning is a method that determines a policy to maximize the eq. 1.

3.2 Sequential Forward Selection Algorithm

Sequential Forward Selection (SFS) is the simplest greedy search algorithm. In this paper, we will briefly explain this algorithm. Fig. 1(a) shows the algorithm. Starting from the empty set, sequentially add the feature x^+ that results in the highest objective function $J(Y_k + x^+)$ when combined with the feature Y_k that has already been selected.

3.3 Genetic Algorithm Feature Selection Algorithm

The Genetic Algorithm is popular method for finding an optimized solution. This algorithm has also good performance to the problems like nonlinear problems, which are hard to be solved by using the classic optimization techniques.

The problem we are treating is also a nonlinear problem, and thus we think this problem may be solved by Genetic Algorithm (Fig. 1(b)). So, we tried to search good feature set using the Simple Genetic Algorithm.

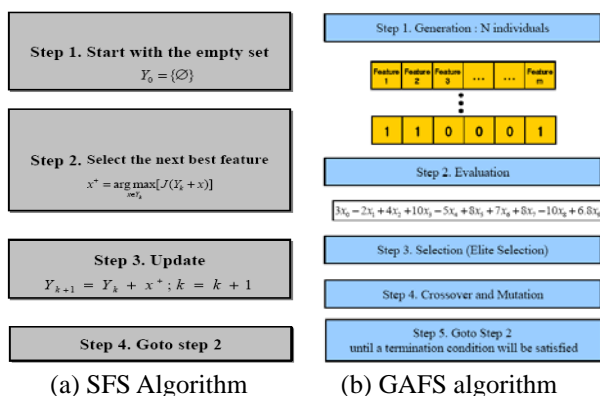


Fig. 1. SFS and GAFS algorithm

3.4 Interactive Feature Selection Algorithm

The Interactive Feature Selection (IFS) algorithm we are proposing is an algorithm based on reinforcement learning. Specially, popular algorithms such as SFS, SBS and so on, are deductive algorithms but our proposed algorithm is inductive. Also, these feature selection algorithms are based on the rationale of correlation and information-theoretic measures. Correlation is based on the rationale that good feature subsets contain features highly correlated with a class, yet are uncorrelated with each other. The IFS is also based on the correlation concept. Moreover, the feature selection algorithms consist of a search strategy and an evaluation by objective function but the conventional methods are incompetent in the search strategy part.

Fig. 2 shows an IFS process. We assume that an

emotion recognition system that includes this algorithm will be applied to a home robot or appliance. Due to this characteristic, this algorithm is a user adaptive system that can efficiently solve a problem and the more a user is in contact with this system, the better it will perform.

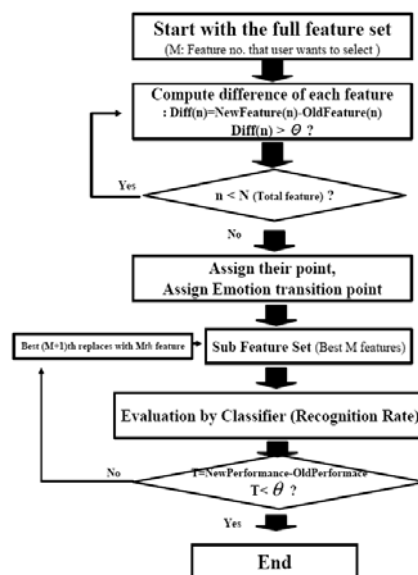


Fig. 2. IFS Algorithm

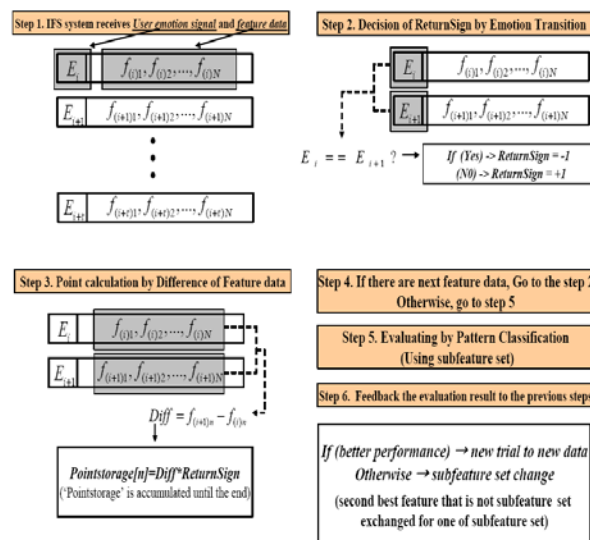


Fig. 3. IFS example

Fig. 3 shows an example of the IFS algorithm and is based on the fig. 2. First, this algorithm starts with a full feature set and when a new feature set and an emotion identifier is inputted, it assigns a +1 or -1 to the “return sign”(if an old emotion ID equals a new emotion ID then +1, Otherwise -1). Thereafter, the product of “return sign” and the difference of each feature is stored in an array “Point storage”. This iteration is repeated for one episode (user can arbitrarily define an episode). After the episode, the feature set that was selected first

is applied to an objective function (Pattern Classification System) and the evaluation result is stored. If the next evaluation result is worse than the previous, the worst feature of the selected feature set will be replaced with the best feature among those that were not selected (step 6 in fig. 3).

4. Experimental Results

We applied 11 original features to the IFS simulator; Pitch features (max, min, mean, median, crossing rate, increasing rate), Loudness; Intensity (max, min, mean), Sect. No and Speech rate. This program was made only for an IFS and the results from this program were applied to the Emotion Recognition System using ANN. That is, the feature set applied to ERS was the features previously outputted by IFS and then the emotion recognition experiment was performed. Classification was attempted using four methods.

We can see that the IFS system searched for better results and improved gradually. In the algorithm, because the searching work was performed again when the new evaluation result was worse than the previous one, there was some range in the steady state.

Fig. 4 is comparison graph of four methods (IFS, SFS, GAFS and random selection) with the changed feature no. As expected, random selection performed poorly but IFS and SFS and GAFS similarly performed better. In the IFS and SFS and GAFS case, the results show a subtle distinction but the IFS with features 1, 2 and 3 was better. However, with features 4 and 5, SFS showed better results.

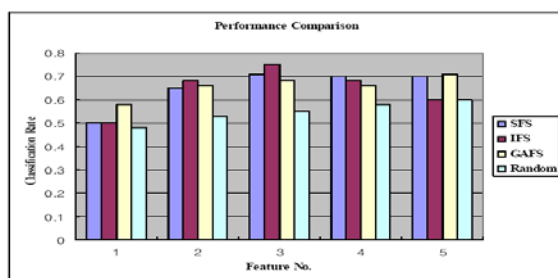


Fig. 4. Emotion Classification Rate Comparison

5. Conclusions

This paper presents a solution to feature selection when there is an emotion recognition problem. The solution called the IFS performed as well as an SFS. In particular, it is reinforcement based learning and

supplements the role of search strategy in the feature selection process. Using the IFS simulator, we found some of the best features and used them in the emotion recognition experiment and results were compared to those of SFS and Random selection. Performance was slightly better than SFS. However, IFS has some disadvantages. If the amount of training data is too small, selection results may be not good. SFS does not require much training data. It is also sufficient that training data be only one set. If an objective function is clear, SFS will be adequate. However, in the case of emotion recognition, SFS may not perform as well as it had. In this case, the correlation-based method like the IFS will be better.

Acknowledgment:

This research was supported by Seoul R&BD Program (No. : 106876) from Seoul city of Korea.

References

- [1] C. M. Lee and S. S. Narayanan "Toward detecting emotions in spoken dialogs," *IEEE Transactions on Speech and Audio Processing*, vol.13, pp. 293-303, 2005.
- [2] J. Wagner, J. H. Kim, and E. Andre, "From Physiological Signals to Emotions: Implementing and Comparing Selected Methods for Feature Extraction and Classification," *Proceedings of ICME*, pp. 940-943, 2005.
- [3] P. Pudil and J. Novovicova, "Novel Methods for Subset Selection with Respect to Problem knowledge," *IEEE Intelligent Systems*, March, pp. 66-74, 1998.
- [4] Y. L. Lin and W. Gang, "Speech Emotion Recognition based on HMM and SVM," *Proceedings of Machine Learning and Cybernetics*, Vol.8, pp. 4898-4901, 2005.
- [5] E. F. Combarro, E. Montanes, I. Diaz, J. Ranilla, and R. Mones, "Introducing a Family of Linear Measures for Feature Selection in Text Categorization," *IEEE transactions on Knowledge and Data Engineering*, Vol.17, No.9, pp. 1223-1232, 2005.
- [6] G. H. John, R. Kohavi, and K. Pflieger, "Irrelevant Features and the Subset Selection Problem," *Proceedings of Machine Learning*, pp. 121-129, 1998.
- [7] R. S. Sutton and A. G. Barto, "Reinforcement Learning," *An Introduction, A Bradford book*, London, 1998.
- [8] C. H. Park and K. B. Sim "The Implementation of the Emotion Recognition from Speech and Facial Expression System," *Lecture Notes in Computer Science(LNCS)*, vol. 3611, pp. 85-88, 2005.

A trial to improve the intelligibility of spontaneous concatenative speech synthesis

Kei Fujii

Department of Information and Computer Sciences
Kumamoto National College of Technology
2659-2, Suya, Kohshi-city, Kumamoto 861-1115
Email: fujii@cs.knct.ac.jp

ABSTRACT

Realization of spontaneous speech synthesis is a one of recently focused research purposes. In previous research, authors reported about a trial to apply concatenative speech synthesis to spontaneous speech, especially, some evaluations of unit selection performance in concatenative speech synthesis. From these results, we obtained the limit of the conventional method. In this paper, TD-PSOLA is introduced to obtain the synthetic speech improving about spectral and prosodic discontinuity which causes degradation of intelligibility. As the result, intelligibility score of synthetic speech has been improved by 4%.

Keywords: Spontaneous speech synthesis, Concatenative speech synthesis, Unit selection, Intelligibility, TD-PSOLA

1 INTRODUCTION

Techniques about spontaneous speech processing are a one of recently focused research areas, and are expected to apply to machines that used for our life such as robots. Corpora of Japanese spontaneous speech have constructed in Japan these days [1][2]. The realization of spontaneous speech synthesis is the one of these purposes. Akagawa et al have investigated about the possibility to realize HMM-based spontaneous speech synthesis [3]. As same purpose, authors have tried to apply concatenative speech synthesis to spontaneous speech, and have obtained 77.4% of sentence intelligibility (94.2% in case of natural speech) from the evaluation experiment about spontaneous synthetic speech by concatenative speech synthesis with about 100-minutes speech corpus [4]. Discontinuity between adjacent speech wave segments is a one of the reasons of this degradation about intelligibility. In this paper, author introduces TD-PSOLA as post processing of concatenative speech synthesis for intelligibility improvement.

1.1 Concatenative speech synthesis

Concatenative speech synthesis is the method that makes speech sound well-keeping naturalness and voice quality of a speaker by introducing large speech corpus [5]. Speech corpus for this method accumulates various speech wave segments of a speaker and their features.

Processing flow of this method for reading speech synthesis is shown in **Fig. 1**. The target feature generation part makes a series of appropriate target prosodic features from parsed input text information. According to these target feature series, the unit selection part chooses the most preferable wave segment series from the corpus. Output synthetic speech is made by connecting these wave segments, thus, is recycling of a speaker's natural voices.

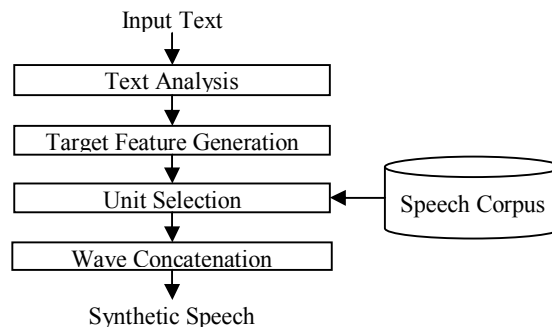


Fig.1: Processing flow of concatenative Text-to-Speech synthesis

In unit selection, quality degradation of a synthetic speech is expressed as two kinds of costs shown in **Fig.2**.

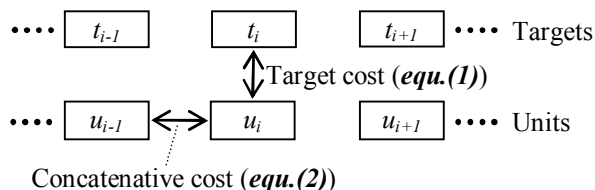


Fig.2: Cost calculation in unit selection

The target cost which expresses the quality degradation caused by the difference between i -th candidate unit u_i and i -th target t_i is defined as the norm of vector of sub-costs as follows

$$C_{tgt}(u_i, t_i) = \sqrt{\sum_{j=1}^{N_{tgt}} (SC_{tgt}(j, u_i, t_i))^2}, \quad (1)$$

where N_{tgt} is the number of sub-costs ($N_{tgt} = 3$ in this paper: difference of F_0 , difference of duration and

difference of power). SC_{tgt} means the j -th sub-cost function that is calculated according to the weighted distance between a feature of candidate unit and a feature of target.

The concatenative cost that expresses the difference between two candidate units which are stuck mutually is defined as

$$C_{con}(u_i, u_{i-1}) = \sqrt{\sum_{j=1}^{N_{con}} (SC_{con}(j, u_i, u_{i-1}))^2}, \quad (2)$$

where N_{con} is the number of sub-costs ($N_{con} = 3$ in this paper: F_0 , power and MFCC). SC_{con} is the j -th sub-cost function that is calculated as the weighted distance about prosodic features (F_0 and power) and phonetic features (MFCC) on the boundary.

These costs are integrated by follows

$$C(u_i, u_{i-1}, t_i) = \sqrt{C_{tgt}(u_i, t_i)^2 + C_{con}(u_i, u_{i-1})^2}. \quad (3)$$

When a target series are given as $(t_1 \dots t_M)$, the series of u which have the minimum value of the sum of *equ. (3)* are the most preferable. This series of u is searched through the corpus by using Viterbi algorithm.

Authors applied concatenative speech synthesis to spontaneous speech in the previous research, and obtained 77.4% of sentence intelligibility (94.2% in case of natural speech). One of the reasons of this degradation is the discontinuity of adjacent speech wave segments. In this paper, TD-PSOLA (described later) is introduced as post processing to connect each segment smoothly. *Fig. 3* shows the processing flow for performance evaluation in this paper. The target features are extracted from input natural speech (it is assumed that they are ideal features obtained by perfect target feature generation in *Fig. 1*). Prosody of each selected wave segment is modified by TD-PSOLA to the same as target prosody.

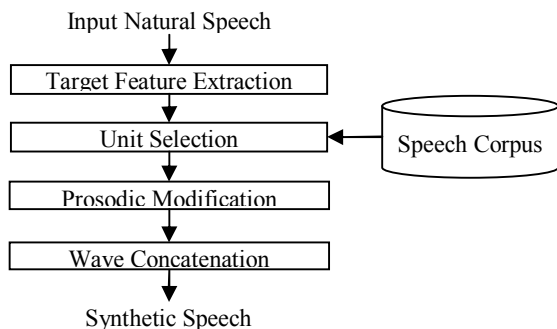


Fig.3: Processing flow of synthetic speech generation for performance evaluation of unit selection and post processing

1.2 TD-PSOLA

Time Domain Pitch Synchronous Overlap Add (TD-PSOLA) is a one of the techniques that modifies speech

prosody [6]. Prosodic modification by TD-PSOLA is done according to the following procedures:

1. Each glottal closure position is marked on source speech waveform (giving the pitch mark to source speech waveform).
2. Each pitch waveform is cut out from source speech waveform with the window function corresponding pitch interval. The window function used in this paper is the hanning window whose length of the left side and the right side of the window are set to the same as the preceding and the following pitch mark intervals.
3. Each pitch waveform is placed to the nearest target pitch mark position.
4. Target speech waveform is obtained by adding each pitch waveform.

Fig. 4 and *Fig. 5* depict the procedure which modifies F_0 of speech. If F_0 is lowered, the target pitch mark interval is wider than the source pitch mark interval, hence some pitch waves are deleted (*Fig. 4*). Oppositely, if F_0 is raised, the target pitch mark interval is narrower than the source pitch mark interval, and some pitch waves are used two or more times (*Fig. 5*).

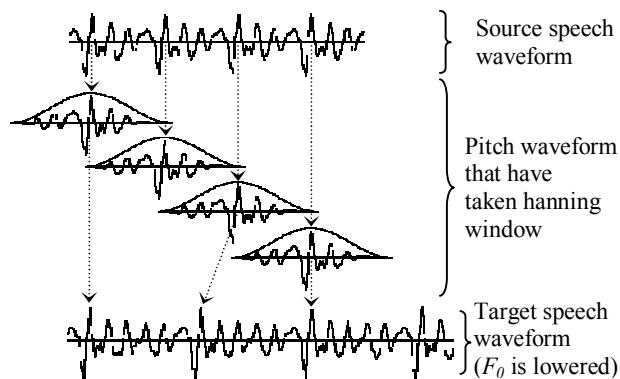


Fig.4: Pitch modification (F₀ is lowered)

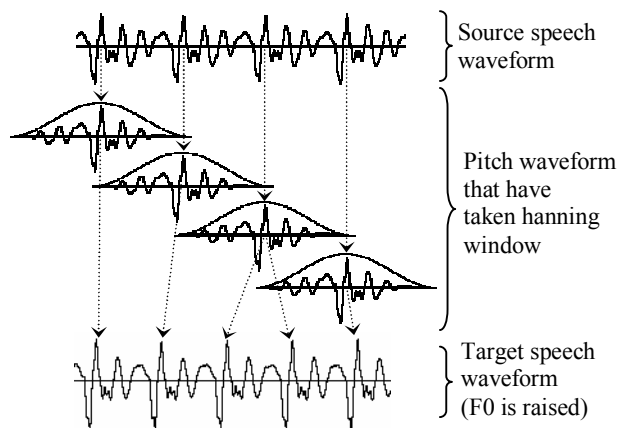


Fig.5: Pitch modification (F₀ is raised)

TD-PSOLA is simple processing and can modify speech prosody directly in time domain. If source pitch interval and target pitch interval are same, source

waveform can be kept exactly. By introducing TD-PSOLA as post processing of unit selection, prosody of each selected wave segment can be corrected to the target prosody. This also means that the prosodic sub-costs become comparatively not important if TD-PSOLA is used. Thus, it is expected that the spectral discontinuity between adjacent speech wave segments also can be decreased by increasing the weight of sub-costs about spectral continuity, or by decreasing the weight of sub-costs about prosodic features.

2 CORPUS SPECIFICATION

This section is described about the spontaneous speech corpus which we constructed to use for concatenative spontaneous speech synthesis.

2.1 Recording conditions

We employed two female professional narrators to collect their conversation. To record each conversation voice without mixing of the other's voice, the soundproof chamber and recording equipments settings are used (depicted in **Fig. 6**). The chamber has divided into two sub-rooms by soundproof wall with window. Each narrator put on the headphone and the lavalier microphone while spontaneous speech recording. Their voices were recorded by the digital recorder separately and sent to the other's headphone through the mixer. The recording equipments are shown in **Table 1**.

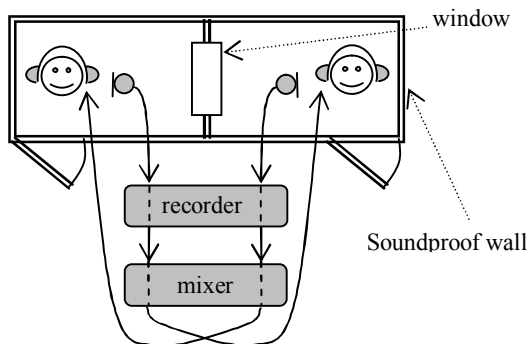


Fig.6: Soundproof chamber for conversation recording

Table 1: Recording equipments and conditions

Microphones	SONY ECM-77B
Recorder	marantz PMD670
Mixer	MACKIE 1202-VLZ Pro
Sampling frequency	48 kHz
Quantizing bit	16 bit

We recorded for three days and collected the spontaneous speech wave of about 140 minutes. From these data set, in this time, one speaker's voice was picked up and made into the corpus of about 100 minutes (including pause time) describing in the following subsection.

2.2 Corpus construction

The procedure that the recorded data is made into the corpus is the following.

2.2.1 Speech wave division

The recorded data was divided by sentences (it is difficult to define the sentence. One segment placed between silences is considered to be the sentence in this paper.).

As the result of this operation, 3004 speech files were obtained.

2.2.2 Utterance text dictation

The pronunciation of utterance of each speech wave file is dictated to text file with "hiragana (Japanese syllabary)". Conversation speech contains not only accurate pronunciation but also imprecise articulation, laugh, filler, disfluency and so on. Although these phenomena have an important role for composing natural communication, it is difficult to control them by a computer. A method having the possibility to solve this problem is to introduce some label set (e.g. speech act labels) [7] and develop a new unit selection technique which uses them. However in this paper, these label set were not used and all of utterances were described with "hiragana" phonologically as much as possible to examine the performance of the conventional speech unit selection.

2.2.3 Phoneme segmentation

Each speech wave is furthermore divided into phoneme segments. This operation was done by the Julian-segmentation-kit included in the Julius: an open-source continuous speech recognition software based on Hidden Markov Model [8]. Speech wave file, phoneme utterance text and acoustic model are necessary for this kit performing. Speech file must be down-sampled to 16 kHz. Phoneme utterance text is made from above-mentioned "hiragana" utterance text by the Perl script. Finally, the acoustic model for female speakers is used.

2.2.4 Feature extraction

Unit selection of concatenative speech synthesis needs some features (F_0 , Power and MFCC) to estimate the distortion degree between speech wave units. F_0 and power are extracted by the free software snack sound toolkit [9]. This toolkit has two methods of F_0 extraction. We selected the one that is equal to the `get_f0` command included in the toolkit ESPS/waves+ by Entropic Inc. Speech waves were pre-emphasized ($\alpha = 0.97$) for power extraction. MFCC is extracted by the tool (called `wav2mfcc`) provided by the Julius.

3 EVALUATION

To examine the quality of spontaneous synthetic speech, author has a subjective evaluation experiment. Ten sentences were prepared at random. Four subjects listened synthetic speech with a headphone in an office (not in a soundproof chamber), and told what they said. Two types of answers were requested to subjects: (a) the answer when they listened to a synthetic speech one times and (b) the answer when they listened to it again several times (the number of listening times are unrestricted). Sentence intelligibility is calculated as follows:

$$SI = \frac{100}{N_s} \sum_{i=1}^{N_s} \frac{CP_i}{P_i} [\%], \quad (4)$$

where N_s , P_i and CP_i are the number of subjects ($N_s = 4$ in this paper), the number of phonemes of synthetic sentences for i -th subject, and the number of correct phonemes included in the answer sentences of i -th subject respectively.

The result is shown in **Table 2**. The result of synthetic speech by only the unit selection (post processing has not used) and the result of natural speech are also shown for comparison. Although the result of synthetic speech with using TD-PSOLA is lower than the result of natural speech, it is higher than the conventional. That is, TD-PSOLA improved the intelligibility of the conventional synthetic speech (+4% for type (a) and +5.8% for type (b)).

Table 2: Sentence intelligibility (number of listening times are (a) once and (b) unrestricted)

Kind of speech	Sentence intelligibility [%]	
	(a)	(b)
Unit selection	62.9	77.4
Unit selection + TD-PSOLA	66.9	83.2
Natural speech	92.6	94.2

On the other hand, deteriorated synthetic speech by the proposal method was observed. It is thought that big modification to the prosody is a one of causes of the quality degradation. There are future works as follows: (a) employment of the sub-cost function corresponding to degree of prosodic modification, (b) comparison with other speech waveform modification method.

4 CONCLUSION

In this paper, TD-PSOLA is introduced as post processing of spontaneous concatenative speech synthesis to obtain the synthetic speech decreasing spectral and prosodic discontinuity which causes degradation of intelligibility. From the subjective evaluation experiment, intelligibility of synthetic speech has been improved +4% when once listening and +5.8% when listening time is

unrestricted. As future work, (a) employment of the sub-cost function considering about degradation caused by prosodic modification, (b) comparison with other speech waveform modification method.

Acknowledgements

The author is grateful to the Applied Linguistics Laboratory in Nara Institute of Science and Technology for the conversation recording cooperation.

References

- [1] The CREST/ESP Project, <http://feast.his.atr.jp/>
- [2] K. Maekawa, "Corpus of Spontaneous Japanese: Its Design and Evaluation," Proceeding of ISCA & IEEE Workshop on Spontaneous Speech Processing and Recognition (SSPR 2003), 2003.
- [3] T. Akagawa, K. Iwano and S. Furui, "Toward realization of HMM-based spontaneous speech synthesis," (in Japanese) Technical Report of the Institute of Electronics, Information and Communication Engineers (SP2005-16), pp.25-30, 2005.
- [4] K. Fujii, R. Ueda, H. Kashioka and N. Campbell, "A trial to apply concatenative speech synthesis to spontaneous speech," Proceeding of International Technical Conference on Circuits/Systems, Computers and Communications, Vol.2, pp.653-656, 2006.
- [5] N. Campbell and A. W. Black, "Prosody and the selection of source units for concatenative synthesis," in Progress in Speech Synthesis, Springer Verlag, Inc., New York, 1995, ch. 22.
- [6] E. Moulines and F. Charpentier, "Pitch-synchronous Waveform Processing Techniques for Text-to-speech Synthesis Using Diphones," Speech Communication, No.9, pp.453-467, 1990.
- [7] N. Campbell, "What Type of Inputs Will We Need for Expressive Speech Synthesis?," Proceeding of IEEE 2002 Workshop on Speech Synthesis, 2002.
- [8] <http://julius.sourceforge.jp/>
- [9] <http://www.speech.kth.se/snack/>

Feature Based Estimation for Mapping Robot Environments using Fuzzy Kalman Filter

Chandima Dedduwa Pathirana
Dept. of Advanced Systems Control Eng.
Graduate School of Science and Eng.
Saga University
1-Honjomachi, Saga 840-8502, Japan

Keigo Watanabe, Kiyotaka Izumi
Dept. of Advanced Systems Control Eng.
Graduate School of Science and Eng.
Saga University
1-Honjomachi, Saga 840-8502, Japan

Abstract

This paper introduces a fuzzy Kalman filter based approach for mapping robot environments. Takagi-Sugeno fuzzy models for nonlinear system are adopted to represent the vehicle and landmarks state equations. The complete system of the vehicle and landmarks model is decomposed into several linear models. Using the Kalman filter theory, each local model is filtered to find the local estimates. The linear combination of these local estimates gives the global estimate for the complete system. This estimator is simulated using Matlab for the vehicle-landmark system and results prove that the new approach can accurately map the environment.

1 Introduction

Simultaneous localization and map building (SLAM) has been a long term study in the autonomous vehicle research community. The ability to place an autonomous vehicle at an unknown location in an unknown environment and then have building a map, using only relative observations of the environment and moreover to use this map simultaneously to navigate would indeed make such a robot "autonomous." Thus the main advantage of SLAM is that it eliminates the need for artificial infrastructure or *a priori* topological knowledge of the environment. A solution to the SLAM problem would be inestimable value in a range of application where absolute position or precise map information is unobtainable, including amongst others, autonomous planetary exploration, subsea autonomous vehicles, autonomous airborne vehicles, and autonomous all-terrain vehicles in tasks such as a mining and construction.

The solution to the SLAM problem is the estimation of vehicle and landmarks states. How accurately these states are estimated depends on the estimator.

Estimation of an unknown variable distorted by noise can be challenged by probabilistic approaches to give a reasonable estimation. In SLAM problem, Kalman filtering of the state estimates is widely used due to its popularity as it directly provides both a recursive solution to the navigation problem and a means of computing consistent estimates for the uncertainty in the vehicle and landmark locations on the basis of statistical models for vehicle motion and relative landmark locations. Extended Kalman filter (EKF) has been identified as a very good state estimator for the SLAM problem because it gives very accurate solution to the SLAM. A good EKF algorithm for the SLAM problem has been demonstrated by Dissanayake *et al.* [1].

In the history of nonlinear control systems, fuzzy logic control has played a major role in controlling nonlinear systems. Fuzzy logic has been a promising control tool for the nonlinear systems. Fuzzy state estimation is a topic that has received very little attention. Fuzzy Kalman filtering [2] is a recently proposed method to extend Kalman filter to the case where the linear system parameters are fuzzy variables withing intervals. As a solution to fuzzy state estimation, Takagi-Sugeno (T-S) fuzzy model based on observation for nonlinear systems has been illustrated in [3]. As the first step of finding full fuzzy Kalman filter algorithm for the SLAM problem, we here introduce feature based mapping of the robot environment using the fuzzy Kalman filter algorithm presented in [3]. Simulation results show that the new approach to mapping with fuzzy logic gives accurate state estimation with less computational complexity compared to the EKF approach.

Section 2 presents the T-S fuzzy model for nonlinear system and the state estimation. Section 3 presents the state estimator for each local system in T-S model. Section 4 illustrates feature based mapping for vehicle-landmarks system and offers some simulation results and Section 5 mentions some concluding remarks.

2 Kalman Filtering for Nonlinear Systems Presented by Takagi-Sugeno Fuzzy Model

Nonlinear systems can be approximated as locally linear systems in much the same way that nonlinear functions can be approximated as piecewise linear functions. Nonlinear systems can be represented by fuzzy linear models of the following form

if $z_1[k]$ is F_{i1} and...and $z_g[k]$ is F_{ig} then

$$\begin{aligned} \mathbf{x}[k+1] &= A_i\mathbf{x}[k] + B_i\mathbf{u}[k] + G_i\mathbf{w}[k] \\ \mathbf{y}[k] &= C_i\mathbf{x}[k] + \mathbf{v}[k] \quad (i = 1, \dots, L) \end{aligned} \quad (1)$$

This is referred to as a Takagi-Sugeno fuzzy model. The z_j are premise variables, k is the time index, F_{ij} are fuzzy sets, $\mathbf{x}[k] \in R^n$ is the state vector, $\mathbf{u}[k] \in R^m$ is the deterministic input, $\mathbf{w}[k]$ is the process noise, $\mathbf{y}[k] \in R^r$ is the measured output, and $\mathbf{v}[k]$ is the measurement noise. The dynamic behavior of the $\mathbf{x}_i[k]$ and $\mathbf{y}_i[k]$ signals is presented as follows:

$$\mathbf{x}_i[k+1] = A_i\mathbf{x}_i[k] + h_i(z[k])B_i\mathbf{u}[k] + h_i(z[k])G_i\mathbf{w}[k]$$

$$\mathbf{y}_i[k] = C_i\mathbf{x}_i[k] + h_i(z[k])\mathbf{v}[k] \quad (i = 1, \dots, L) \quad (2)$$

Complete proof of Eq. (2) can be found in [3]. Suppose we are given an n -dimensional linear discrete time system of the form:

$$\begin{aligned} \mathbf{x}[k+1] &= A\mathbf{x}[k] + h[k]B\mathbf{u}[k] + h[k]G\mathbf{w}[k] \\ \mathbf{y}[k] &= C\mathbf{x}[k] + h[k]\mathbf{v}[k] \end{aligned} \quad (3)$$

where the scalar $h[k] \in [0, 1]$, the process noise $\mathbf{w}[k]$ is white with PSD S_w , the measurement noise $\mathbf{v}[k]$ is white with PSD S_v , and the process noise and measurement noise are uncorrelated. Although the A , B and C matrices are constant, the system is time-varying because of the time-varying scalar $h[k]$. If the premise variables are functions of the state or control, then the system is also nonlinear because $h[k]$ is a function of the state or control. The state \mathbf{x} of the system can be estimated by the Kalman filter, which can be derived by assuming a recursive estimator of the form:

$$\begin{aligned} \hat{\mathbf{x}}^+[k] &= M[k]\hat{\mathbf{x}}[k] + K[k]\mathbf{y}[k] \\ \hat{\mathbf{x}}[k+1] &= A\hat{\mathbf{x}}^+[k] + h[k]B\mathbf{u}[k] \end{aligned} \quad (4)$$

$M[k]$ and $K[k]$ are related by $M[k] = I - K[k]C$. If $h[k]$ is independent of \mathbf{x} , it can be shown that the covariance is propagated as follows:

$$P^+[k] = (I - K[k]C)P[k](I - K[k]C)^T$$

$$+h^2[k]K[k]S_vK^T[k] \quad (5)$$

We can find the optimal value of $K[k]$ by taking the partial derivative of the trace of $P^+[k]$ with respect to $K[k]$ and setting it equal to zero, which gives:

$$(K[k]C - I)P[k]C^T + h^2[k]K[k]S_v = 0 \quad (6)$$

3 A State Estimator for the T-S Fuzzy Model

The steady state Kalman filter presented in the preceding section can be used to estimate the states of each of the L dynamic systems given in Eq. (2). This will give us L local steady state estimated as follows:

$$P_i[k+1] = A_i(P_i[k] - K_i[k]C_iP_i[k])A_i^T + G_iS_wG_i^T$$

$$K_i[k] = P_i[k]C_i^T(C_iP_i[k]C_i^T + S_v)^{-1}$$

$$\hat{\mathbf{x}}_i^+[k] = (I - K_i[k]C_i)\hat{\mathbf{x}}_i[k] + K_i[k]\mathbf{y}_i[k]$$

$$\hat{\mathbf{x}}_i[k+1] = A_i\hat{\mathbf{x}}_i^+[k] + h_i[k]B_i\mathbf{u}[k] \quad (i = 1, \dots, L) \quad (7)$$

Note that S_w and S_v in the above equations can be replaced with $(1/3)S_w$ and $(1/3)S_v$ respectively for $E(h^2[k]) = 1/3$. Since we know that $\mathbf{x}[k] = \sum_{i=1}^L \mathbf{x}_i[k]$, we can combine the local state estimates in Eq. (7) to estimate the state of the T-S fuzzy model (Eq. (1)) as:

$$\hat{\mathbf{x}}[k] = \sum_{i=1}^L \hat{\mathbf{x}}_i[k] \quad (8)$$

4 Illustration of Feature Based Mapping using Fuzzy Kalman Filter

In the following, the vehicle state is defined by $\mathbf{x}_v = [x, y]^T$ where x and y are the coordinates of the center of the rear axle of the vehicle with respect to some global coordinate frame. The landmarks are modeled as point landmarks and represented by a cartesian pair $\mathbf{x}_f = [x_i, y_i]^T, i = 1, \dots, N$. Both vehicle and landmark states are registered in the same frame of reference.

1) *The Process Model*: Figure 1 shows a schematic diagram of the vehicle in the process of observing a landmark. The following kinematic equations can be used to predict the vehicle state from the orientation of the vehicle ϕ and velocity input V :

$$\begin{aligned} \dot{x} &= V\cos(\phi) \\ \dot{y} &= V\sin(\phi) \end{aligned} \quad (9)$$

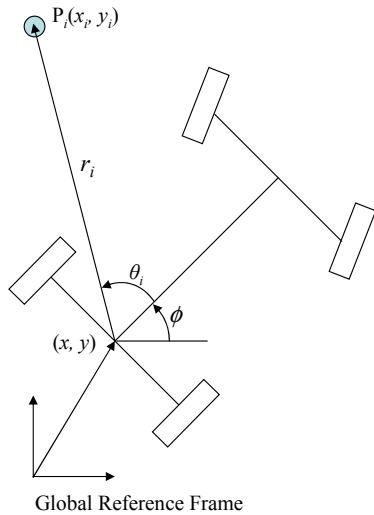


Figure 1: Vehicle and observation kinematics

Eq. (9) can be used to obtain a discrete-time vehicle process model in the form

$$\begin{aligned} x(k+1) &= x(k) + \Delta TV(k)\cos(\phi(k)) + \mathbf{w}[k] \\ y(k+1) &= y(k) + \Delta TV(k)\sin(\phi(k)) \end{aligned} \quad (10)$$

The landmarks in the environment are assumed to be stationary point targets. The landmark process model is thus

$$\begin{aligned} x_i(k+1) &= x_i(k) \\ y_i(k+1) &= y_i(k) \end{aligned} \quad (11)$$

for all landmarks $i = 1, \dots, N$. Eq. (10) together with Eq. (11) defines the state transition matrix for the vehicle-landmarks system.

2) *The Observation Model:* In general, the range $r_i(k)$ and the bearing $\theta_i(k)$ to a landmark i are recorded by the range and bearing sensors. In this illustration, it is assumed that sensor data are processed to give the horizontal $x_{vf}(k)$ and vertical $y_{vf}(k)$ distances between the vehicle position and a landmark position in the same reference frame as the observations. The range measurements and bearing measurements are taken from the center of rear vehicle axis where the vehicle position (x, y) is taken. Referring to Fig. 1 and the above description, the observation model for a specific landmark can be formulated as

$$\begin{aligned} x_{vf}(k) &= x_i(k) - x(k) + v_x(k) \\ y_{vf}(k) &= y_i(k) - y(k) + v_y(k) \end{aligned} \quad (12)$$

where v_x and v_y are the noise sequences associated with the x_{vf} and y_{vf} respectively and assumed to be

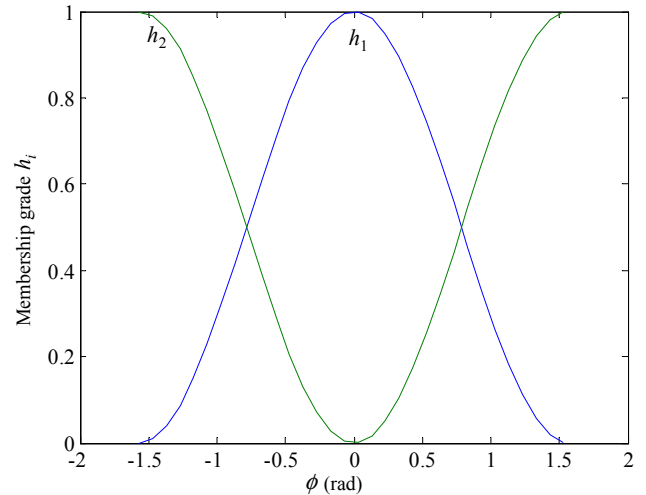


Figure 2: Vehicle-landmarks membership functions

equal.

3) *Estimation Process:* Fuzzy Kalman filter described in Sections 3 and 4 is employed to generate the estimates for the fuzzy dynamic models given in Eq. (2).

4.1 Simulation Results

In this section, we are going to show the simulation results for the feature based mapping for the system composite of Eqs. (10), (11) and (12) while assuming the initial estimate and covariance to start estimation process. The process model given by Eqs. (10) and (11), and the observation model given by Eq. (12) can be used to formulate the dynamic system as follows:

$$\begin{aligned} \mathbf{x}[k+1] &= \mathbf{x}[k] + \begin{bmatrix} \Delta T \cos(\phi(k)) \\ \Delta T \sin(\phi(k)) \\ 0 \\ 0 \end{bmatrix} V(k) + \mathbf{w}[k] \\ \mathbf{y}[k] &= \begin{bmatrix} -1 & 0 & 1 & 0 \\ 0 & -1 & 0 & 1 \end{bmatrix} \mathbf{x}[k] + \mathbf{v}[k] \end{aligned} \quad (13)$$

where ΔT is the sample time. $\mathbf{w}[k]$ and $\mathbf{v}[k]$ are the process and observation noise respectively. Now consider the following two subsystems.

The first system is as follows:

$$\begin{aligned} \mathbf{x}_1[k+1] &= \mathbf{x}_1[k] + h_1 \begin{bmatrix} \frac{\Delta T}{\cos(\phi(k))} \\ 0 \\ 0 \\ 0 \end{bmatrix} V(k) + h_1 \mathbf{w}[k] \\ \mathbf{y}_1[k] &= \begin{bmatrix} -1 & 0 & 1 & 0 \\ 0 & 0 & 0 & 0 \end{bmatrix} \mathbf{x}_1[k] + h_1 \mathbf{v}[k] \end{aligned} \quad (14)$$

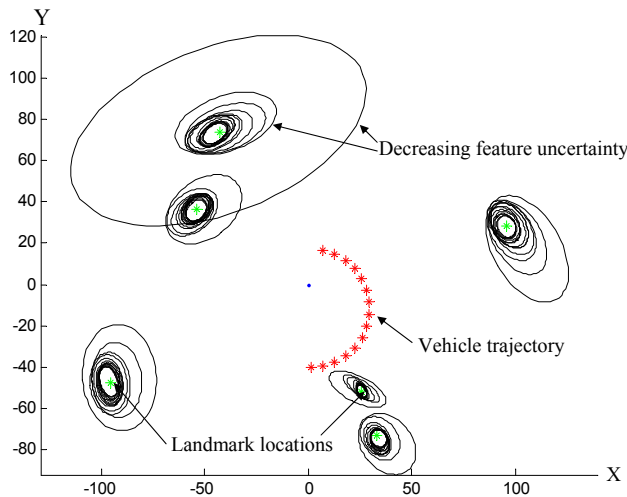


Figure 3: Evolution of map over time

where $h_1 = \cos^2(\phi(k))$ is the membership function for the first subsystem. The second subsystem system is given as:

$$\mathbf{x}_2[k+1] = \mathbf{x}_2[k] + h_2 \begin{bmatrix} 0 \\ \frac{\Delta T}{\sin(\phi(k))} \\ 0 \\ 0 \end{bmatrix} V(k) + h_2 \mathbf{w}[k]$$

$$\mathbf{y}_2[k] = \begin{bmatrix} 0 & 0 & 0 & 0 \\ 0 & -1 & 0 & 1 \end{bmatrix} \mathbf{x}_2[k] + h_2 \mathbf{v}[k] \quad (15)$$

where $h_2 = \sin^2(\phi(k))$ is the membership function for the second subsystem. Membership grade functions are shown in Fig. 2. It can be seen that $h_1 + h_2 = 1$ and the combination of these two subsystems results in the dynamic system model shown in Eq. (13). The two local state vectors of each subsystem are in the form of the two local state vectors given by Eq. (2) and are estimated according to the Eq. (7) and are combined according to the Eq. (8) to obtain the global state estimate. The system and Kalman filter equations were simulated using Matlab. An environment with 6 arbitrarily placed landmarks was simulated with a given vehicle trajectory. Landmark location states were updated using Kalman filter equations for 600 times. Simulation results are depicted in Figs. 3 and 4. Figure 3 shows the evolution of the map over the time. It can be seen that error ellipses are getting converged to the actual landmark locations as the map of the landmark locations is being built when the vehicle navigates through the environment. Figure 4 shows that the errors in each landmark state decrease over time and reach the minimum value 0. The above mentioned results indicate that the newly presented method for

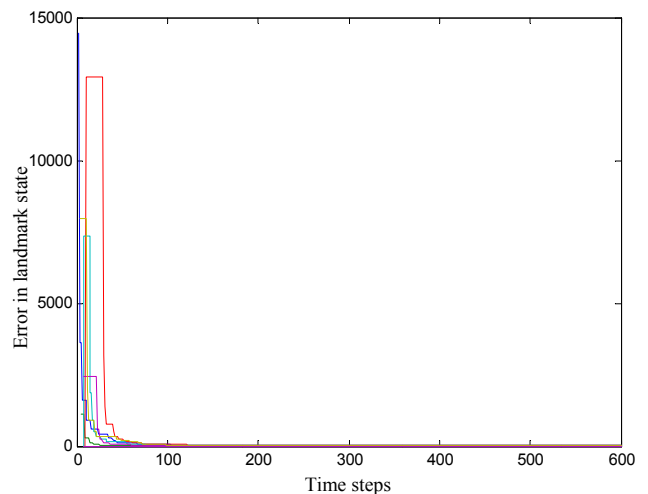


Figure 4: Landmark state estimation errors

map building performs well and provides state estimates that converge to zero.

5 Conclusion

We have proposed a new approach to state estimation based on Takagi-Sugeno nonlinear fuzzy model. Kalman filter state estimator was modified to give a fuzzy Kalman filter. Kalman filter state estimator equations were designed for each of the local systems of the T-S model and local filters were combined to obtain the global estimator. We showed that the proposed estimator minimizes the expected value of the estimation error and converges to zero over time. Simulation results have been presented for a nonlinear vehicle-landmark system, showing the effectiveness of this scheme of state estimation.

References

- [1] M. W. M. G. Dissanayake, P. Newman, S. Clark, H. F. D. Whyte and M. Csorba, "A solution to the simultaneous localization and map building (SLAM) problem," *IEEE Trans. on Robotics and Automation*, vol. 17, no. 3, pp. 229-241, June 2001.
- [2] G. Chen, Q. Xie and L. S. Shieh, "Fuzzy Kalman filtering," *Journal of Information Sciences*, no. 109, pp. 197-209, 1998.
- [3] D. Simon, "Kalman filtering for fuzzy discrete time dynamic systems," *Applied Soft Computing*, vol. 3, pp. 191-207, 2003.

Kansei with Behavioral Patterns for Human-Robot Interaction in Ubiquitous Environments

Janaka Chaminda Balasuriya*, Kouhei Kamohara*, Chandrajith Ashuboda Marasinghe**,
Keigo Watanabe*, and Kiyotaka Izumi*

*Department of Advanced Systems Control Engineering
Saga University, 1-Honjomachi, Saga 840-8502, Japan

**Software Engineering Lab, Department of Computer Software
University of Aizu, Aizu-Wakamatsu, Fukushima, Japan

*jcbala@lycos.com, k.kouhey.8-5017@docomo.ne.jp,
{watanabe,izumi}@me.saga-u.ac.jp, **ashu@u-aizu.ac.jp

Abstract

Humans have two distinct features with compared to any other living being; unique physical nature and emotions / feelings. Anybody who studies on humans or trying to construct human like machines should consider these two vital facts. When robots are interacting with humans and other objects, they certainly have a safe distance between them and the object. But how can this distance be optimized when interacting with humans? Will there be any advantages over achieving this? Will it help to improve the condition of robots? Can it be a mere constant distance? How will the humans react? In order to 'humanize' robots, they (robots) should also have certain understating of such emotions that we, humans have. In this research project, authors are trying to 'teach' one such human understanding, commonly known as 'personal space' to autonomous mobile robots.

1 Introduction

As Simmons et al. [1] describe, recent research in mobile robot navigation has utilized autonomous mobile robots in service fields. To operate them in an environment with people, it requires more than just localization and navigation. The robots should recognize and act according to human social behavior to share the resources without conflict [2].

The comfort level of the humans for which the robot is working will be very important if the robot is to do its job effectively. But very little work has been performed in trying to understand how people would interact with a robot, how to make them comfortable, ways for robots to indicate their feelings, etc. to analyze the

aesthetic qualities of the robots behavior patterns [2].

1.1 Distance from the robot to the vicinity

Usually there is a 'space gap' between the robot to the near by. As Stentz [3] and many others had mentioned, this was just a constant of space. This mechanism was quite acceptable for the systems such as transporting, surveillance and monitoring, etc. In other words, such kind of safe distance was good for non-human interacting purposes. Can the same be applied for human interaction? Although it will give some results, it will not enhance or optimize the real requirement in need, i.e. to build up harmonious relationship with humans.

1.2 Nakauchi model

When Nakauchi and Simmons [2] studied about personal space and applied it to moving robots, it was some improvement over the 'blind' safe distant. In their mechanism, Nakauchi and Simmons had experimented using human subjects for 'correct distance' or 'personal space' in order to have pleasant feeling towards the two interacting parties.

1.3 Walters experiments

Another set of experiments were conducted by Walters et al. [4] to find the personal space zones, initial distances between robot and humans, etc. They also tried to compare human-robot interpersonal distances with that of the human-human interpersonal distances as described by Hall [5]. According to Hall, the generally recognized personal space zones between humans

Table 1: Personal space zones.

Zone	Range (m)	Interaction
Intimate	0 – 0.15	Loved ones
Close	0.15 – 0.45	Close friends
Personal	0.45 – 1.20	Friends
Social	1.2 – 3.60	Strangers
Public	3.60 +	Public

are well known and are summarized (for Northern Europeans) in Table 1.

2 Variation of Personal Space

Although it is possible to find a personal space for a specific instance of environment, it is highly volatile depending on the two interaction parties and not definitely a constant. As Walters et al. [4] suggested, different robot social models, perhaps with very different initial personalities, may be more acceptable to different users. For example, adjustments of social distances according to a user’s personality trait will be a promising direction.

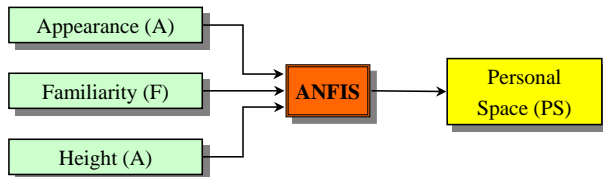


Figure 1: APS ANFIS block diagram.

The personal space at any given instance varies depending on cultural norms and on the task being performed. Appearance, familiarity, gender, age, height of the bodies, etc. were considered to be important. Height, appearance and familiarity were considered (as the initial stage for simplicity) to generate an active personal space (APS) determination system and the block diagram is shown in Figure 1.

3 ANFIS for Personal Space Determination

Adaptive Neural Fuzzy Inference System or simply ANFIS can be used as a basis for constructing a set of

fuzzy if-then rules with appropriate membership functions to generate the desired input-output combination. It is especially useful when needed to apply a fuzzy inference to already collected input-output data pairs for model building, model following, etc. where there are no predetermined model structures based on characteristics of variables in the system.

3.1 Gathering data

Considering the procedure as Nakauchi and Simmons [2] or the Walters et al. [4] to obtain a sense of personal space for robot / human interaction, a similar experimental condition was constructed. Here a robot (or a model) is kept at the end of a scaled line in a room and a human is asked to move closer to it.

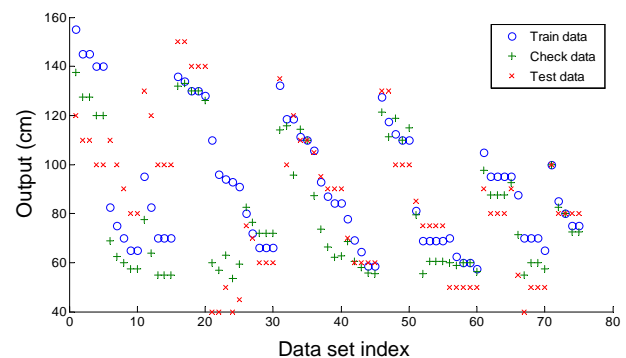


Figure 2: Input data sets (for training, checking and testing) to the APS ANFIS.

3.2 Experimental procedure

As the experiment proceeds, one human subject is instructed to move towards the robots as if he needs to talk with it. The human subject is asked to be along the scaled line and look at the robot face and move closer to it until he feels safe enough to make conversation with it. In the mean time the robotic model was positioned so as to make its face towards the human subject. During the whole time of the experiment, the robot did not do anything and the human subject did all the active tasks of walking, thinking, etc. The distance between the two parties was obtained by using a camera or by direct human observer (who reached the two parties once they got stabilized). The human subject had no previous experience with the robot and the authors wanted the human subjects to be curious as well as cautioned about the robot that they are going to meet. In other wards human subjects had no

idea what kind of robotic system that they are going to face with or any capabilities that it possesses until they meet the robot.

The robots and the robotic models used in these experiments are 'KooruKun' (PA10 robotic manipulator), 'BoxChyan' (robotic model), and 'BasinKun' (previously known as 'CHRCarry Hospital Robot' re-used with several modifications). The first one was a stationary robot with 200 cm in height and 20 cm average diameter, next was a movable robot model with 100 cm height, 50 cm diameter and around 3 Kg, and the last is also a movable robot with 170 cm height, generalized circular diameter of 60 cm and weight of about 25 Kg. The data gathered are grouped for training, checking and testing for the ANFIS and are shown in Figure 2.

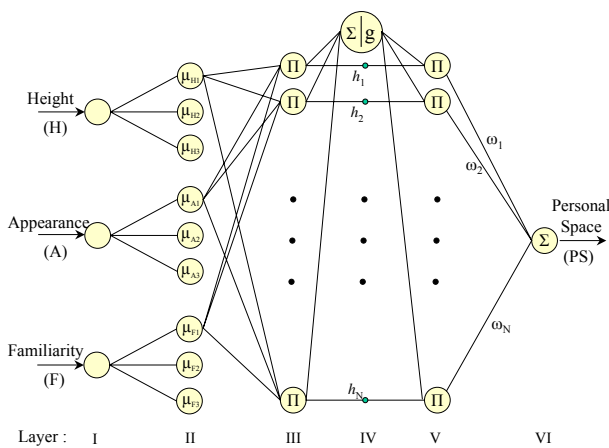


Figure 3: APS ANFIS architecture.

4 ANFIS Architecture

The architecture of the APS determination network is illustrated in Figure 3. Layer (I) to Layer (III) represent the antecedent part of the fuzzy neural network, whereas Layer (V) and Layer (VI) represent the consequence part. As shown in Figure 3, the domain of discourse of height (H) is described by fuzzy variable H with p number of linguistic values ($p = 3$), the domain of discourse of appearance (A) is described by fuzzy variable A with q number of linguistic values ($q = 3$), and the domain of discourse of familiarity (F) is described by fuzzy variable F with r number of linguistic values ($r = 3$). Hence each input variable is unique in the sense of domain of discourse. It is assumed that

each node of the same layer has a similar function, as described below. Here we denote the output of the i th node in layer (X) as $O_{(X),i}$.

Layer (I): Layer (I) consists of three types of nodes; height (H), appearance (A) and familiarity (F). The current value of height (H), i.e. the crisp input to the height node is H_i , appearance node is A_j and familiarity node is F_k . No computation is carried out at this layer.

Layer (II): This layer acts as the fuzzification layer of the fuzzy neural network. At this layer, the output of a node connected to the current value of input variable acquires the fuzzy membership value of the universe of discourse. Every node i , where $i = 1, \dots, p$ (or q or r), in this layer is an adaptive node with a node function

$$O_{II,i} = \mu_{X_i}(x) \quad (1)$$

where x is the input to node i , and X_i is the linguistic label (big, medium, small, etc.) associated with this node function. In other words, $O_{II,i}$ is the membership function of X_i and it specifies the degree to which the given x satisfied the quantifier X_i . Hence the output from the 2nd layer will be:

$$O_{II,p} = \mu_{H_i}(H_i) \quad (2)$$

$$O_{II,q} = \mu_{A_q}(A_j) \quad (3)$$

$$O_{II,r} = \mu_{F_r}(F_k) \quad (4)$$

for height, appearance and familiarity respectively.

Layer (III): In this layer, the nodes labeled as Π compute the T-norm of the antecedent part. Thus the rule evaluates the conditions of the inputs and they are continued to the layer (V) for normalization. The output of any node t , where $t = 1, \dots, N$, where $N = p * q * r$, in this layer is described by the following equation:

$$O_{III,t} = h_t = \mu_{H_i}(H_i) * \mu_{A_q}(A_j) * \mu_{F_r}(F_k) \quad (5)$$

where h_t represents the firing strength of the t th rule and there are N such rules as total.

Layer (IV): The first node of layer (IV) at fuzzy neural network, which has symbols Σ and g , generates the output through the following function:

$$g(x) = \frac{1}{x} \quad (6)$$

with a linear summed input. Then the output of the first node of layer IV is given by

$$O_{IV,1} = \frac{1}{\sum_{t=1}^N h_t} \quad (7)$$

Other nodes just carry forward the outputs of previous nodes to the next layer.

Layer (V): This layer normalizes the fired rule values. Each node labeled as Π in this layer multiplies the value carried forward by previous node with the output of the first node at Layer (IV). Then the output of any m th node of this layer can be given by the following equation:

$$O_{V,m} = \frac{h_m}{\sum_{t=1}^N h_t} \quad (8)$$

Layer (VI): Layer (VI) is the defuzzification layer of the fuzzy neural network. The node labeled as Σ in this layer calculates the overall output as the summation of all incoming signals. Then the personal distance value for certain input variables is given by:

$$O_{VI} = \text{Personal_Distance} = \frac{\sum_{m=1}^N w_m h_m}{\sum_{n=1}^N h_n} \quad (9)$$

where w_m denotes a constant value in the consequence part of the m th rule. The overall output is the weighted mean of w_m with respect to the weight h_m .

The connection weights are trained by applying the hybrid algorithm. The error tolerance was set to zero.

The error is calculated by comparing the output of the expert knowledge with that of fuzzy neural network for the same input data, x . The adaptation of the m th weight, w_m , at the l th time step is given by the following equation:

$$w_m(l+1) = w_m(l) + \gamma [y_d - y_a] \frac{h_m}{\sum_{n=1}^N h_n} \quad (10)$$

where γ represents a small positive learning rate, and y_d and y_a represent the desired output and actual output respectively for the personal space value selected for the training.

The trained ANFIS with check data is shown in Figure 4.

5 Summary

In this research project, a determination system of an active personal space has been analyzed. This can

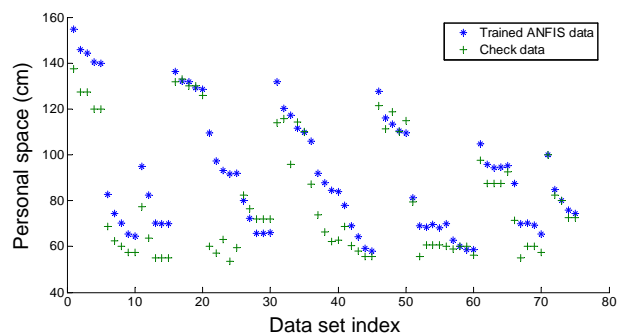


Figure 4: Trained FIS with check data.

be considered as the first step for constructing an active personal space system for any robot in any environment. But for a target as such, many experiments in vast environmental situations should have to be involved. It is a must to obtain similar data with the so-called humanoids to make this experiment complete. This system gave encouraging results in an off-line mode with limited facilities. Authors are planning to make the current system more realistic and get the functioning in a real time mode, and are continuously working on it.

References

- [1] R. Simmons, R. Goodwin, K. Z. Haigh, S. Koenig, and J. O'Sullivan, "A layered architecture for office delivery robots," in *Proc. of Autonomous Agents*, 1997, pp. 245-252.
- [2] Y. Nakauchi and R. Simmons, "A social behavioral robot that stands in line," *Autonomous Robots*, vol. 12, 2002, pp. 313-324.
- [3] A. Stentz, "Map-based strategies for robot navigation in unknown environments," in *Proc. of AAAI*, 1996, pp. 110-116.
- [4] M. L. Walters, K. Dautenhahn, K. L. Koay, et al. "Close encounters: spatial distances between people and a robot of mechanistic appearance," in *Proc. of 5th IEEE RAS Int. Conf. on Humanoid Robots*, Dec. 2005, pp. 450-455.
- [5] E.T. Hall, *The Hidden Dimension: Man's Use of Space in Public and Private*, The Bodley Head Ltd, London, UK. 1966.

Improvement of Group Performance of Job Distributed Mobile Robots by Emotionally Biased Control System

Sajal Chandra Banik, Keigo Watanabe and Kiyotaka Izumi
Department of Advanced Systems Control Engineering
Graduate School of Science and Engineering
Saga University, 1-Honjomachi, Saga 840-8502, Japan
baniksajal@yahoo.com, {watanabe, izumi}@me.saga-u.ac.jp

Abstract

This paper deals with the implementation of emotions in mobile robots performing a specified task in a group to develop intelligent behavior and easier form of communication. The overall group performance depends on the individual performance, group communication and synchronization of cooperation. With the emotional capability, each robot can distinguish the changed environment, can understand colleague robot's state, enables adaptation and reacts with changed world. The adaptive behavior of a robot is derived from the dominating emotion in an intelligent manner. In our control architecture, emotion plays a role to select the control precedence among the alternatives like behavior modes, cooperation plans and goals. Emotional interaction is happened among the robots and a robot is biased by the emotional state of the colleague robot in performing task. Here emotional control is used for better understanding to read the colleague's internal state, for faster communication and better performance eliminating dead time.

Keywords: Emotion, Multi-agent system, Markov modeling theory, Colleague robot, Distributed job, Emotional embodied intelligence.

1 Introduction

Emotions have important role in intelligence, decision making process, learning, social interaction, perception, memory, creativity and more [1]. At present emotional robotics is not an oxymoron, moreover researchers are working to incorporate emotional embodied intelligence in robotics. Damasio [2] suggested that emotions can provide a selection mechanism for eliminating bad alternatives and then decision making process is simplified. For a human team, a lot of emphasis is given on the emotional state of the members

of a team and on the understanding each others' emotions and thus keeping all motivated to the general goals [3], [4]. Emotions act like a value system, allowing each individual to take a decision rapidly through the perception of situation and then act quickly. By understanding the colleague's emotional state, others can understand the situation that they are in and also can be motivated to do the task. For example, if one is in happy state, others can find out the reason of happiness, then he is motivated to follow the happy colleague in doing job. On the other hand, if one is in fear state, then others can get alert and understand the situation and thus plan to escape the situation by collaborating with the feared colleague or by compensating for his action. In [5], Nair et al. showed that in mixed agent teams (agent-human teams) as well as in pure agent teams, the introduction of emotions could help in bringing the same advantages that emotions bring to human teams.

In this paper, we describe a method to increase the group performance of a team of robots with the implementation of emotionally biased control system by taking the advantages from emotional understanding, communication and synchronization. Here, the choice of behavior depends on the current emotional state of each robot as well as emotional state of colleague robot. The emotions can be considered mainly as a particular type of information that is exchanged among the robots. Section 2 describes the related works where some researchers have applied emotions to control robots and multiagent system. Section 3 clearly describes the purpose of the research work, the system where emotion is applying to control the robot team and the control strategy. Description of simulation software and its application to simulate emotional based behavior is given in Section 4. Finally, Section 5 concludes with advantages of the emotionally biased control method as well as discusses the limitations with some open issues.

2 Related work

The idea of artificial emotion is increasingly used in designing autonomous robotics agents, by making robots to experience emotionally with the changed environment or to make interaction with other agents [6], [7]. In our research work, the topics are related to cooperation between job distributed robot teams, computational architecture for modeling emotions, use of emotion for control and avoiding stagnation.

Mataric et al. [8] and Parker's [9] research works have relation with distributed coordination of robots, but have significant differences in backgrounds and approaches, and also have different architecture with different implementation. In [8], control architecture is based on subsumption architecture and cooperation emerged from the structure of behavior. Later, Schneider-Fontan and Mataric included an emotional model for using in communication for the minimization of interference [10]. In [11], Murphy et al. developed a multiagent control approach for interdependent tasks which imbues the agents with emotions and allows a satisfactory behavior to emerge. In this approach, a formal multilevel hierarchy of emotions is used where emotions modify active behaviors at the sensory-motor level and also change the set of active behaviors at the schematic level. It mainly focuses on interdependent tasks, not purely cooperative and one robot cannot perform the other one's task. Our work in this article is different in task mode (job is distributed to each robot, but each one is capable to do other one's job if necessary) and emotion is generated based on Markov modeling theory [12].

3 Approach

This section describes distributed job among the agents, control architecture and emotional model that has been applied for dominating emotion generator.

3.1 Distributed job

For the simplicity, we have considered two robots working in a group. One robot cleans the center part of a floor by pushing laid objects to the wall side and another (colleague robot) picks up the objects from the wall side simultaneously. But in case of any inability of the robot (due to over work-load with respect to time limit or if battery operated and power shortage occurred or any other causes), colleague can also help in cleaning floor and thus continuing the work process

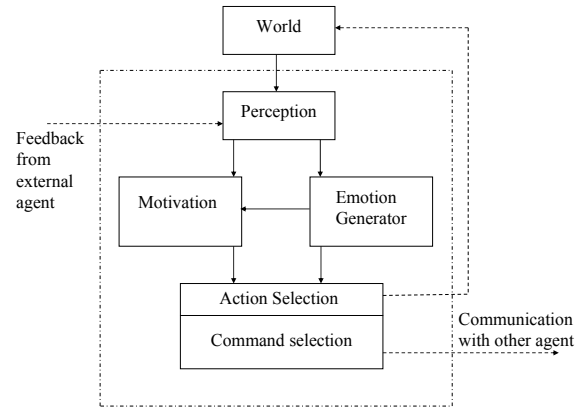


Figure 1: Architectural view of the control mechanism and communication

targeting to finish the assigned task in time maintaining a constant level of performance.

3.2 Control and communication strategy

The architecture is based on four basic subsystems: perception, motivation, emotion generator and action-command selection subsystems as shown in Fig. 1. The world (or environment) is perceived by the perception subsystem through some parameters. The motivation subsystem selects the present need (or goal) to be satisfied through the subsequent analysis of the perceived parameters and emotion. The behavior of the motivation subsystem can be expressed by the following equation:

$$f(p_1, p_2, \dots, p_n, e) = \text{Modification_input}$$

where p_1, p_2, \dots, p_n are the perceived parameters rendered by the perception subsystem and e is the generated emotional state of the agent. The selection subsystem selects two things at a time: one is the action to be performed by itself which is best suited with the present need and the other is a communication command to express its emotional state and situation to the external agent (colleague). In response to the command, colleague robot sends a feedback to its perception subsystem. Behaviors of each robot are adapted according to two emotional signals: global one, generating for all robots and local one, generating specifically for itself [18].

3.3 Emotional model

With the emotionally biased control system, we want to exploit the roles that emotion plays in biological systems which enhance adaptation in dynamic,

uncertain and cooperative environment. The emotional model consists of four basic emotions [13]: joy, anger, fear and sad. The eliciting conditions and functional responses of each emotion are summarized in Table 1. An application of Markov modeling theory for our purposes is described by Markovian emotion model as shown in Fig. 2. Although this model is justified by previous work in psychology of modeling human emotion [12], [14], [15], we have applied it for pure agents emotion due to its memoryless property as behaviors and commands are highly dependent on emotional present state than the history of arriving the state.

In the Markovian emotion model, the nodes represent the emotional states and the arcs/arrows indicate the probability of getting out of states to the directed state. The arc/arrow values are set to initial values (e.g. q_1, q_2, \dots, q_{16}) which give the initial state transition matrix of Markov model. These values can be modified later on with the influence of emotion inducing factors: α, β, γ and δ for joy, anger, fear and sad respectively. For example, the probability of state transition (arc/arrow values) from joy to other states can be expressed by following equations:

$$P_{anger \text{ joy}} = q_2 + (\alpha)q_2$$

$$P_{fear \text{ joy}} = q_3 + (\beta)q_3$$

$$P_{sad \text{ joy}} = q_4 + (\gamma)q_4$$

$$P_{joy \text{ joy}} = 1 - (P_{anger \text{ joy}} + P_{fear \text{ joy}} + P_{sad \text{ joy}})$$

where q_2, q_3, q_4 are the initial arrow values for $P_{anger \text{ joy}}, P_{fear \text{ joy}}$ and $P_{sad \text{ joy}}$ respectively. These new values are used to get the updated state transition matrix. In [12], [16], more details of the model and computational procedures are given.

4 Simulation Results

The simulation is performed using *KiKS* which is a Matlab based Khepera simulator and can simulate in a very realistic way [17]. For simulation purpose two robots are considered: the *Cleaner* and the *Collector*. The *Cleaner* robot is able to push the balls (as laid objects on the floor) to wall side and the *Collector* has the wall following character to collect the balls from wall side shown in Fig. 3. But it is also able to help in cleaning floor and vice versa, if necessary. The emotional state of each robot is a function of its present working condition, work load and *colleague's* emotional state. The emotion eliciting conditions and effects on colleague are created according to Table 1.

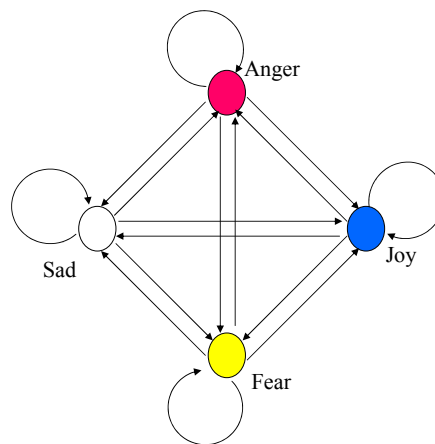


Figure 2: Markovian emotion model

Table 1: Emotion eliciting status and effects on colleague

Emotion	Eliciting status	Effects on colleague
Joy	Success in achieving goal.	Motivated to work.
Anger	Goal either fails or is about to fail due to colleague.	Commanded to increase performance.
Fear	Believes a goal is likely to fail.	To be care about other.
Sad	Unable to do usual job or goal fails.	Evoked to help or alternative.

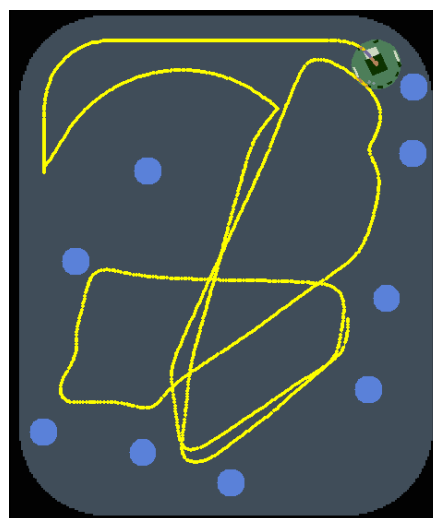


Figure 3: Floor cleaning and collecting behavior of a robot

5 Conclusion

The aim of this work has been to explore emotions as one of the possible methods to control multi-robot systems. This illustrated the way to achieve desired cooperation among the job distributed robots using emotions. Although emotion generation is very complex, here a Markovian emotion model is applied emphasizing the present state, which seems to work well. With the emotional causes, the collector robot can dynamically adjust its speed which leads to better collecting process in a synchronized way. On the other hand, the cleaner robot is also able to modify its behavior as well as environment by its internal emotions which lead it to actions.

To bring the same advantages for pure agent team that emotions bring in human teams, it needs more exploration of emotion generation and implementation. The behavior is also a function of emotional intensity, which is ignored for simplicity of the emotional model. Also a burning question arises about the co-occurrence of emotions and their filtration process. These drawbacks are the pending issues for future work.

References

- [1] R. W. Picard, *Affective Computing*, First MIT Press paperback edition, 2000.
- [2] A. R. Damasio, *Descartes' Error: Emotion, Reason, and the Human Brain*, New York: G.P. Putnam, 1994.
- [3] J. Katzenbach and D. K. Smith, *The Wisdom of Teams*, Harper Business, 1994.
- [4] J. Jennings, *The Teamwork: United in Victory*, Silver Burdett Press, Englewood Cliffs, NJ, 1990.
- [5] R. Nair, M. Tambe, and S. Marsella, "The role of emotions in multiagent teamwork: a preliminary investigation," in *Jean-Marc Fellous and Michael Arbib(Eds.), Who Needs Emotions: The Brain Meets the Robot*, Oxford University Press, 2005.
- [6] C. Breazeal and B. Scassellati, "Infant-like social interactions between a robot and a human caretaker," *Adaptive Behavior*, vol. 8, no. 1, pp. 47–72, 2000.
- [7] J. D. Velásquez, "A computational framework for emotion-based control," in *Workshop on Grounding Emotion in Adaptive System, Conference on Simulation of Adaptive Behavior*, 1998.
- [8] M. J. Mataric, M. Nilson, and Simsarian, "Cooperative multi-robot box-pushing," in *Proc. of IROS*, Pittsburgh, PA, pp. 556–561, 1995.
- [9] L. Parker, "Alliance: An architecture for fault tolerant multi-robot cooperation," *IEEE Trans. on Robotics and Automation*, vol. 14, pp. 220–240, 1998.
- [10] M. Schneider-Fontan and M. Mataric, "Territorial multi-robot task division," *IEEE Trans. on Robotics and Automation*, vol. 14, pp. 815–822, 1998.
- [11] R. R. Murphy, C. L. Lisetti, R. Tardif, L. Irish and A. Gage, "Emotion-based control of cooperating heterogeneous mobile robots," *IEEE Trans. on Robotics and Automation*, vol. 18, no. 5, pp. 744–757, 2002.
- [12] C. Arun, "A computational architecture to model human emotions," in *Proc. of International Conference on Intelligent Information System*, pp. 86–89, 1997.
- [13] K. Oatley, *Best Laid Schemes: The Psychology of Emotions*, Cambridge University Press, 1992.
- [14] J. Bates, "The role of emotion in believable Agents," *Communication of the ACM*, vol. 31, no. 7, pp. 122–125, 1994.
- [15] A. Margulies, "Empathy, virtuality, and the birth of complex emotional states: Do we find or do we create feelings in the other," in *S. L. Albon, D. Brown, E. J. Khantzian, and J. E. Mack(Eds.), Human Feelings: Explorations in Affect Development and Meaning*, The Analytic Press, 1993.
- [16] K. S. Trivedi, *Probability and Statistics with Reliability, Queuing, and Computer Science Application*, Prentice-Hall, 1982.
- [17] S. Theodor, *KiKS is a Khepera Simulator*, 2001.
- [18] R. Daneshvar, C. Lucas, "Improving reinforcement learning algorithm using emotions in multi-agent system," *Lecture Notes in Artificial Intelligence*, no. 2792, pp. 361–362, 2003.

Feed Rate Control Using Fuzzy Reasoning for NC Machine Tools

F. Nagata, K. Kuribayashi
Tokyo University of Science, Yamaguchi
Sanyo-Onoda, Japan

Y. Kusumoto K. Watanabe
Fukuoka Ind. tech. Center Saga University
Ohkawa, Japan Saga, Japan

Abstract

In this paper, a 3D design and machining system based on an NC machine tool with a rotary unit is introduced to effectively produce attractive paint rollers. A post-processor is first proposed to transform a base tool path called cutter location data (CL data) to NC data, mapping the y -directional pick feed to the rotational angle of the rotary unit. The 3D machining system with the post-processor allows us to easily transcribe a relief design on a flat model surface to on a cylindrical model surface. The post-processor has another function that systematically adjusts the feed rate according to the curvature of each design to prevent the machined surface from being chipped. The post-processor generates suitable feed rate codes by using a simple fuzzy reasoning method while checking edges in relief designs. Experimental results show that wooden paint rollers with attractive relief designs can be successfully machined without any chipping.

1 Introduction

In home making industry, handy paint rollers with a simple pattern are generally used to transcribe its design to a wall just after painting. Interior planners and decorators want to use more attractive paint rollers, however, the types of the patterns are limited to several common ones. In order to efficiently provide user-oriented roller designs, a new 3D design and machining system should be considered for limited production of a wide variety of paint rollers. Up to now, although advanced 3D machining systems have been developed in various manufacturing industries [1-3], roller models with a relief design don't seem to be successfully machined at the present stage.

In this paper, a 3D design and machining system based on an NC machine tool with a rotary unit is introduced to effectively produce attractive paint rollers. The paint rollers used in general have little or no attractive design, and their designs are also limited to flat or several simple patterns. This paper addresses how to easily make attractive paint rollers with high yield rate. The most important point is that proper

NC data are straightforwardly generated for the control of the rotary unit. To meet the need, a post-processor is proposed for the NC machine tool with a rotary unit. The proposed post-processor transforms a base tool path called cutter location data (CL data) to NC data, mapping the y -directional pick feed to the rotational angle of the rotary unit. The 3D machining system with the post-processor allows us to easily transcribe a relief design on a flat model surface to on a cylindrical model surface. The post-processor has another function that systematically adjusts the feed rate according to the curvature of each design to prevent the machined surface from being chipped and to shorten the cycle time for machining. The feed rate means the tangential velocity. The post-processor generates suitable feed rate codes by using a simple fuzzy reasoning method while checking edges in relief designs. Experimental results show that wooden paint rollers with attractive relief designs can be successfully carved without any chipping.

2 Post-Processor for NC Machine Tool with a Rotary Unit

In this section, an NC machine tool with a rotary unit and its post-processor are introduced to efficiently machine cylindrical models. The machined models can be used as elaborately designed paint rollers. The paint roller is very useful and convenient to directly transcribe a relief design to a wall just after painting. However, the paint rollers used in general have little or no attractive designs and also their designs are limited to flat or simple patterns. Unfortunately, even the 5-axis NC machine tools are not good at carving a relief design on a cylindrical model. To solve this problem, a post-processor is proposed for the NC machine tool with a rotary unit. The post-processor allows the NC machine tool to produce elaborately designed paint rollers. An attractive 3D design drawn on a flat model surface can be easily transcribed to a cylindrical model surface.

First of all, we introduce an NC machine tool MDX-650A provided by Roland D.G. as shown in

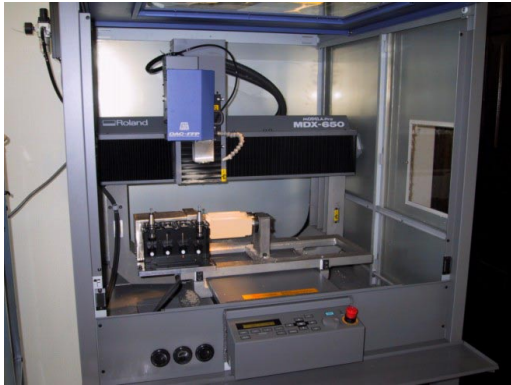


Figure 1: NC machine tool with a rotary unit.

Fig. 1. The NC machine tool equips with an auto tool changer ZAT-650 and a rotary unit ZCL-650A. The mechanical resolution of the rotary unit is about 0.0027 degrees. The NC machine tool has four degrees of freedom, i.e., three translations and one rotation. In order to provide many kinds of paint rollers with wide variety and low volume manufacturing, such a machining system that can directly carve a relief design on a cylindrical workpiece must be realized.

Next, we discuss the problem concerning the 3D machining of cylindrical shape with a relief design. When the modeling of a roller is conducted by using a 3D CAD, a base cylindrical shape is modeled in advance. Then a favorite relief design is drawn on the cylindrical model. However, the modeling of relief design on the cylindrical shape is so difficult and complicated task even if using any 3D CAD. Furthermore, its 3D machining is also more difficult even if using the 5 axis NC machine tool, in which NC data generated from the CAM are composed of x -, y -, z -, b - and c -directional components.

This paper addresses how to easily make a paint roller with an attractive relief design. The most important point is that proper NC data for the NC machine tool with a rotary unit can be generated straightforwardly. To meet the need, a post-processor is proposed to successfully transcribe the design on a flat model to on a cylindrical model. The post processor allows us to directly carve a relief design on a cylindrical workpiece. We here describe the feature of the post-processor. A desired relief design is first modeled on a flat base model. CL data are secondly generated with a zigzag path as shown in Fig. 2. In this case, the coordinate system should be set so that the pick feed direction is parallel to the table slide direction of the NC machine tool, i.e., y -direction. The proposed post-processor transforms the CL data into NC data, mapping the y -directional position to the rota-

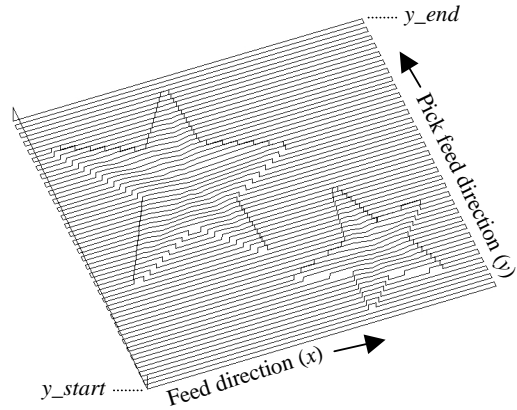


Figure 2: Example of zigzag path on a flat model.

tional angle of the rotary unit. As can be seen from the components of the NC data, when the rotary unit is active, the table slide motion in y -direction is inactive. The post-processor first checks all steps in CL data, and extracts the minimum value y_{min} and the maximum value y_{max} in y -direction. The angle $a(i)$ for the rotary unit is obtained from

$$a(i) = \frac{360 \times \{y(i) - y_{min}\}}{y_{length}} \quad (1)$$

where y_{length} is the length in y -direction and is easily obtained by $y_{max} - y_{min}$. The CL data in the i -th step $[x(i) \ y(i) \ z(i)]^T$ is transformed into the NC data composed of $[x(i) \ a(i) \ z(i)]^T$ by using Eq. (1). The length in y -direction is translated into the circumference of the roller model. It is expected that the relief design shown in Fig. 2 is desirably sculptured on the surface of a cylindrical workpiece. The proposed system provides a function that easily transcribes an attractive design from on a flat model to on a cylindrical workpiece fixed to the rotary unit.

3 Feed Rate Control Using Fuzzy Reasoning

It is known that an F-code such as F3000.0 (i.e., 3000 mm/min) is generally used to set the tool's feed rate to an NC machine tool. The feed rate is one of the most important parameters to smoothly control NC machine tools and to reduce the total machining time. Although the feed rate should be set as fast as possible, if the cutter path has a large curvature or small edge then undesirable vibrations and material chipping would occur. This means that the machining accuracy tends to go down and we can't obtain the precise shape as the model designed by a 3D CAD. Especially, when a wooden paint roller with a relief design is machined, the problem of edge chipping can't be avoided. The feed rate should be suitably down so

Table 1: Consequent constants of fuzzy reasoning for $d(i)$ and $\Delta d(i)$.

c_1^A	c_2^A	c_3^A	c_4^A	c_5^A	c_6^A
$F_{\min} + 0.1F_{base}$	$F_{\min} + 0.2F_{base}$	$F_{\min} + 0.4F_{base}$	$F_{\min} + 0.6F_{base}$	$F_{\min} + 0.8F_{base}$	$F_{\min} + F_{base}$
c_1^B	c_2^B	c_3^B	c_4^B	c_5^B	c_6^B
$-0.5F_{\min}$	$-0.2F_{\min}$	$-0.1F_{\min}$	$0.1F_{\min}$	$0.2F_{\min}$	$0.5F_{\min}$

that the model surface can't be damaged by the edge chipping. However, conventional post-processors don't possess the function to systematically adjust the feed rate so as to suppress the undesirable edge chipping.

The proposed post-processor has a function that automatically adjusts the feed rate according to the curvature of each model not only to shorten the total time for machining but also to keep out the edge chipping. Generally, the main-processor of CAM calculates the cutter path $\mathbf{p}(i) = [x(i) \ y(i) \ z(i)]^T$ with a linear approximation so that the workpiece can be machined within a tolerance to a designed model. Therefore, the larger the curvature is, the higher its point density is. Accordingly, considering the curvature results in acquiring the distance $d(i) = \|\mathbf{p}(i+1) - \mathbf{p}(i)\|$ between two adjacent steps of the CL data and its increment $\Delta d(i) = d(i+1) - d(i)$.

In this section, we propose a fuzzy feed rate generator that generates suitable feed rate codes according to $d(i)$ and $\Delta d(i)$. The fuzzy feed rate generator consists of two simple fuzzy reasoning parts whose consequent parts are constant. When the current position $\mathbf{X}(k) = [X(k) \ Y(k) \ Z(k)]^T$ of the end-mill at the discrete time k is $\mathbf{X}(k) \in [\mathbf{p}(i), \mathbf{p}(i+1)]$, the fuzzy rules are described by

- Rule 1 IF $d(i)$ is \tilde{A}_1 THEN $F(i) = c_1^A$
- Rule 2 IF $d(i)$ is \tilde{A}_2 THEN $F(i) = c_2^A$
- ...
- Rule L IF $d(i)$ is \tilde{A}_L THEN $F(i) = c_L^A$

and

- Rule 1 IF $\Delta d(i)$ is \tilde{B}_1 THEN $\Delta F(i) = c_1^B$
- Rule 2 IF $\Delta d(i)$ is \tilde{B}_2 THEN $\Delta F(i) = c_2^B$
- ...
- Rule L IF $\Delta d(i)$ is \tilde{B}_L THEN $\Delta F(i) = c_L^B$

where $\tilde{A}_j (j = 1, \dots, L)$ and \tilde{B}_j are the j -th antecedent fuzzy sets for two fuzzy inputs $d(i)$ and $\Delta d(i)$; c_j^A and c_j^B are respectively the consequent constants at the j -th rule for the feed rate $F(i)$ and its compensation $\Delta F(i)$; L is the fuzzy rule number. The confidence of each antecedent part at the i -th rule is obtained by

$$\omega_j^A = \mu_{A_j}\{d(i)\} \quad (2)$$

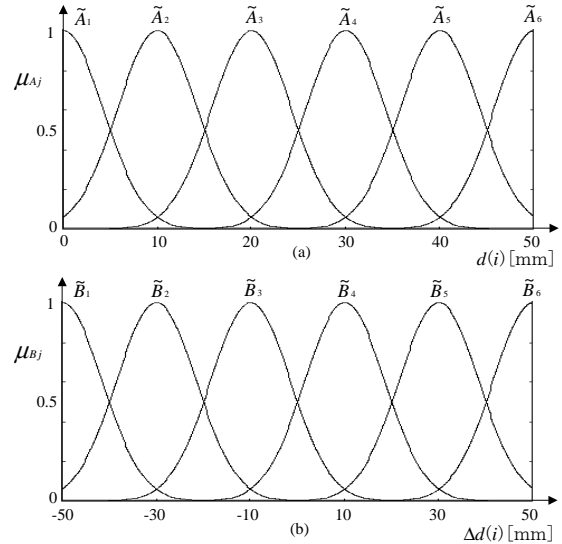


Figure 3: Antecedent membership functions.

$$\omega_j^B = \mu_{B_j}\{\Delta d(i)\} \quad (3)$$

where $\mu_X(\bullet)$ denotes the confidence of a fuzzy set labeled by X . Therefore, the fuzzy reasoning results for the feed rate and its compensation are respectively calculated by

$$F(i) = \frac{\sum_{j=1}^L \omega_j^A c_j^A}{\sum_{k=1}^L \omega_k^A} \quad (4)$$

$$\Delta F(i) = \frac{\sum_{j=1}^L \omega_j^B c_j^B}{\sum_{k=1}^L \omega_k^B} \quad (5)$$

The resultant fuzzy feed rate $\tilde{F}(i)$ is realized in the form

$$\tilde{F}(i) = F(i) + \Delta F(i) \quad (6)$$

Note that the fuzzy set used is the following Gaussian membership function

$$\mu_X(x) = \exp\{\log(0.5)(x - p)^2 q^2\} \quad (7)$$

where p is the center of membership function and q is the reciprocal value of standard deviation. Figures 3 (a) and (b) show the antecedent membership functions



Figure 4: Carving scene of a paint roller.

designed for $d(i)$ and $\Delta d(i)$, respectively. The reciprocal values of the standard deviations are 0.2 and 0.1, respectively. The corresponding constant values in consequent parts are tabulated in Table 1, in which F_{\max} and F_{\min} are the maximum and minimum values for the feed rate estimated in advance; F_{base} denotes $F_{\max} - F_{\min}$. These fuzzy rules are tuned based on the experience of a skilled operator. Note that the fuzzy reasoning part yields not only larger values than F_{\max} but also smaller values than F_{\min} with the combination of $d(i)$ and $\Delta d(i)$.

4 Experiments

Experiments using the proposed post-processor were conducted through actual machining of cylindrical workpieces. Figure 4 shows the carving scene of a paint roller without undesirable chipping. Figure 5 shows one of the results, where the feed rate codes are generated from the fuzzy feed rate generator described in previous section. It is observed from the result that the feed rate $\tilde{F}(i)$ is suitably varied according to the curvature of the surface. Note that the periodically appeared feed rate 600 mm/min is forcibly given every pick feed motion, where the rotary unit is rotated with a small angle, e.g., 0.56 degrees. The quantity of the small angle depends on the ratio of $y_{\perp length}$ to the pick feed as shown in Fig. 2. In the case of Fig. 5, the total machining time was reduced about 20% compared with the case of using a constant feed rate 600 mm/min. As can be seen, the proposed fuzzy feed rate generator provides a more intuitive and finely tunable feed rate function for post-processor.

5 Conclusions

In this paper, a post-processor using a fuzzy feed rate generator has been proposed for an NC machine tool with a rotary unit. The post-processor allowed

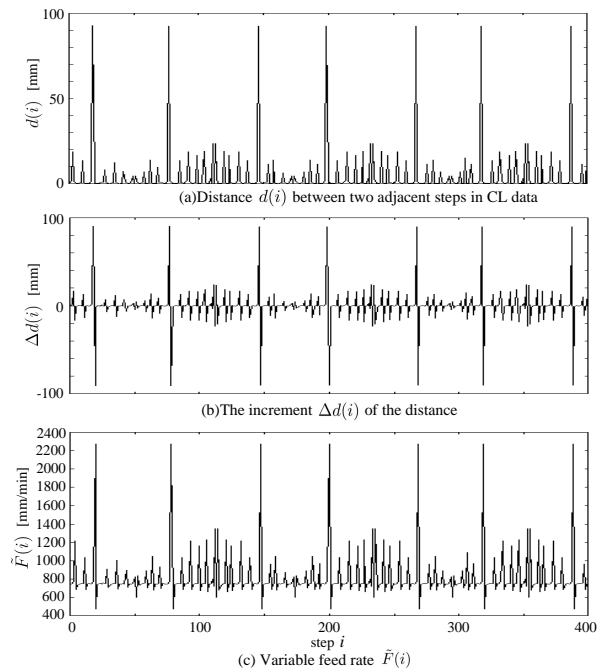


Figure 5: An example of the variable feed rate.

us to easily transcribe a relief design from on a flat model to on a cylindrical workpiece. The fuzzy feed rate generator also generated suitable feed rate codes according to the curvature of the relief design, so that the total machining time could be drastically reduced without any chipping on the carved surface. Experimental results showed that attractively designed relief paint rollers could be successfully carved by using the proposed 3D machining system.

References

- [1] Y. Takeuchi, K. Wada *et al.*, "Study on post-processor for 5-axis control machining centers – In case of spindle-tilting type and table/spindle-tilting type–," *Journal of the Japan Society for Precision Engineering*, Vol. 60, No. 1, pp. 75–79, 1994 (in Japanese).
- [2] X. J. Xu, C. Bradley *et al.*, "Tool-path generation for five-axis machining of free-form surfaces based on accessibility analysis," *International Journal of Production Research*, Vol. 40, No. 14, pp. 3253–3274, 2002.
- [3] S. L. Chen, T. H. Chang *et al.*, "Post-processor development of a hybrid TRR-XY parallel kinematic machine tool," *The International Journal of Advanced Manufacturing Technology*, Vol. 20, No. 4, pp. 259–269, 2002.

Control of Three-Link Underactuated Manipulators Using a Switching Method of Fuzzy Energy Regions

Keisuke Ichida, Kiyotaka Izumi, Keigo Watanabe, and Nobuhiro Uchida
Department of Advanced Systems Control Engineering,
Graduate School of Science and Engineering, Saga University,
1-Honjomachi, Saga 840-8502, Japan
E-mail: 05633001@edu.cc.saga-u.ac.jp; {izumi, watanabe}@me.saga-u.ac.jp

Abstract

In general, manipulators used for industry and academic laboratory have actuators to drive each joint. On the other hand, underactuated manipulators handled by our research have some passive or free joints without actuators and brakes. We recently developed a switching method of fuzzy energy regions to control such manipulators. In such a method, it needs to design parameters related to energy regions and gains of some partly stable controllers based on the computed torque method. The switching method is here applied for a three-link underactuated manipulator. We optimize such design parameters related to fuzzy energy regions by a genetic algorithm. The effectiveness of the present method is illustrated with some simulations.

1 Introduction

Underactuated manipulators have some passive or free joints in general, where the number of inputs is less than the degree of freedom. These passive or free joints cannot generate dynamic torques at all. To control underactuated manipulators, a number of researches have been studied[1]. These systems have complex structural properties, and they have to control a number of generalized coordinates by few inputs. However, reducing the number of actuators brings some advantages such as lightweighting, compactification and cost reduction. The present authors have already proposed a switching control method, in which some partly stable controllers were designed by computed torque method and the related switching laws in fuzzy reasoning or genetic algorithm (GA)[2] were obtained to select one controller among them. However, such a method does not necessarily give a robust result against the change of parameters, such as initial configurations of the manipulator. We discussed the application of a logic based switching method, which has

Table 1: Definition of input torques, generalized coordinates and physical parameters

Symbols	Physical meaning
τ_1, τ_2	Input torque [Nm]
$\theta_1, \theta_2, \theta_3$	Link angle [rad]
m_1, m_2, m_3	Mass of link [kg]
l_1, l_2, l_3	Link length [m]
l_{g1}, l_{g2}, l_{g3}	Distance between joint and center of gravity [m]
I_1, I_2, I_3	Moment of inertia [kgm ²]
μ_1, μ_2, μ_3	Viscous coefficient [Ns/m ²]

been proposed by Hespanha et al.[3], to systems like underactuated manipulators with drift term. We also recently developed a fuzzy energy region based switching method[4]. Note however that in such a method, it needs to design parameters related to energy regions and gains of some partly stable controllers based on the computed torque method. The present paper is concerned with a three-link underactuated manipulator by applying the similar switching method. We here optimize design parameters related to fuzzy energy regions by a GA. The effectiveness of the present method is illustrated with some simulations.

2 Underactuated Manipulator

Figure 1 shows a three-link underactuated manipulator where the first and second joints are active and the third joint is passive. In Table 1, τ_1 and τ_2 denote the torques applied to each joint; θ_1 , θ_2 and θ_3 denote the angle of each link; and other physical parameters are shown in it. The dynamical model of the underactuated manipulator is given as follows:

$$M(\theta) \ddot{\theta} + h(\theta, \dot{\theta}) = \tau \quad (1)$$

where

$$M(\cdot) = \begin{bmatrix} M_{11}(\cdot) & M_{12}(\cdot) & M_{13}(\cdot) \\ M_{12}(\cdot) & M_{22}(\cdot) & M_{23}(\cdot) \\ M_{13}(\cdot) & M_{23}(\cdot) & M_{33}(\cdot) \end{bmatrix}$$

$$\begin{aligned} M_{11}(\cdot) &= (m_1 l_{g1}^2 + I_1 + m_2 l_1^2 + m_3 l_1^2) \\ &+ (m_2 l_{g2}^2 + I_2 + m_3 l_2^2) + (m_3 l_{g3}^2 + I_3) \\ &+ 2l_1(m_2 l_{g2} + m_3 l_2) \cos \theta_2 \\ &+ 2m_3 l_1 l_{g3} \cos(\theta_2 + \theta_3) \\ &+ 2m_3 l_2 l_{g3} \cos \theta_3 \end{aligned}$$

$$\begin{aligned} M_{12}(\cdot) &= (m_2 l_{g2}^2 + I_2 + m_3 l_2^2) + (m_3 l_{g3}^2 + I_3) \\ &+ l_1(m_2 l_{g2} + m_3 l_2) \cos \theta_2 \\ &+ m_3 l_1 l_{g3} \cos(\theta_2 + \theta_3) \\ &+ 2m_3 l_2 l_{g3} \cos \theta_3 \end{aligned}$$

$$\begin{aligned} M_{13}(\cdot) &= (m_3 l_{g3}^2 + I_3) + m_3 l_1 l_{g3} \cos(\theta_2 + \theta_3) \\ &+ m_3 l_2 l_{g3} \cos \theta_3 \end{aligned}$$

$$\begin{aligned} M_{22}(\cdot) &= (m_2 l_{g2}^2 + I_2 + m_3 l_2^2) + (m_3 l_{g3}^2 + I_3) \\ &+ 2m_3 l_2 l_{g3} \cos \theta_3 \end{aligned}$$

$$M_{23}(\cdot) = (m_3 l_{g3}^2 + I_3) + m_3 l_2 l_{g3} \cos \theta_3$$

$$M_{33}(\cdot) = m_3 l_{g3}^2 + I_3$$

$$\mathbf{h}(\cdot, \dot{\cdot}) = [h_1(\cdot, \dot{\cdot}) \ h_2(\cdot, \dot{\cdot}) \ h_3(\cdot, \dot{\cdot})]^T$$

$$\begin{aligned} h_1(\cdot, \dot{\cdot}) &= l_1(m_2 l_{g2} + m_3 l_2)(2\dot{\theta}_1 \dot{\theta}_2 + \dot{\theta}_2^2) \sin \theta_2 \\ &+ m_3 l_1 l_{g3}(2\dot{\theta}_1 + \dot{\theta}_2 + \dot{\theta}_3)(\dot{\theta}_2 + \dot{\theta}_3) \\ &+ \dot{\theta}_3^2 \sin \theta_3 + \mu_1 \dot{\theta}_1 \\ &\sin(\theta_2 + \theta_3) \quad m_3 l_2 l_{g3}(2\dot{\theta}_1 \dot{\theta}_3 + 2\dot{\theta}_2 \dot{\theta}_3 \\ &+ \dot{\theta}_3^2) \sin \theta_3 + \mu_2 \dot{\theta}_2 \end{aligned}$$

$$\begin{aligned} h_2(\cdot, \dot{\cdot}) &= l_1(m_2 l_{g2} + m_3 l_2) \dot{\theta}_1^2 \sin \theta_2 + m_3 l_1 l_{g3} \dot{\theta}_1^2 \\ &\sin(\theta_2 + \theta_3) \quad m_3 l_2 l_{g3}(2\dot{\theta}_1 \dot{\theta}_3 + 2\dot{\theta}_2 \dot{\theta}_3 \\ &+ \dot{\theta}_3^2) \sin \theta_3 + \mu_2 \dot{\theta}_2 \end{aligned}$$

$$\begin{aligned} h_3(\cdot, \dot{\cdot}) &= m_3 l_1 l_{g3} \dot{\theta}_1^2 \sin(\theta_2 + \theta_3) + m_3 l_2 l_{g3}(\dot{\theta}_1 \\ &+ \dot{\theta}_2)^2 \sin \theta_3 + \mu_3 \dot{\theta}_3 \end{aligned}$$

3 Definition of Energy

Energy is defined by using generalized coordinates. The desired joint angle of each link is θ_{di} and the error of joint angle is denoted by

$$e_i \triangleq \theta_{di} - \theta_i. \quad (2)$$

Then, the energy of each link is defined by

$$E_i \triangleq e_i^2 + \dot{e}_i^2. \quad (3)$$

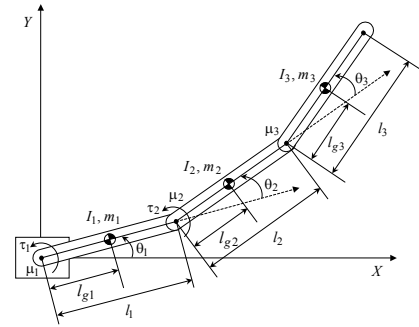


Figure 1: Model of three-link underactuated manipulator

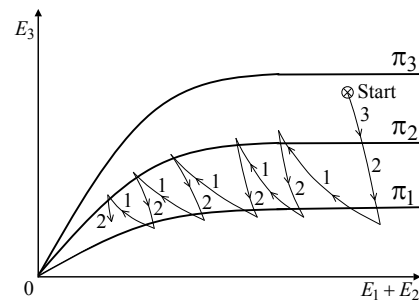


Figure 2: Ideal energy response

4 Fuzzy Energy Region Based Switching

We design controller 1 (C_1), controller 2 (C_2) and controller 3 (C_3) for a three link manipulator. They are used as partial stabilizing controllers to stabilize each link. We can define an energy region related to each controller. Assuming that we use the same fuzzy energy region method as used for two-link manipulator[4], we can express the energy plain in this paper as ideal responses of energy illustrated in Figure 2.

If an exponential function is used, the design parameters of boundary curve to divide energy region are denoted by the amplitude and the time constant. Control responses of manipulators depend on these parameters. Such parameters need to be set in an ideal way. But it is difficult to set at once, so that the boundary curve is denoted by fuzzy expression in this research. If a boundary curve has any fuzziness denoted by the present fuzzy reasoning, then there appears an advantage of present method in setting the design parameters roughly. We first consider a straight line approximation shown in Figure 3. After obtain-

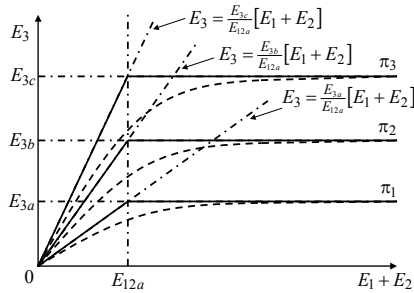


Figure 3: Region approximations for a logical switching

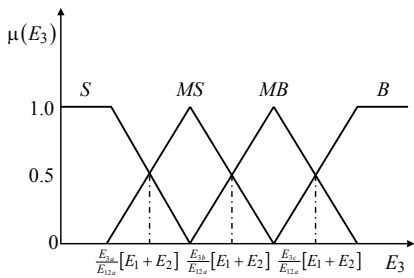


Figure 4: Membership functions for $E_1 + E_2 < E_{12a}$

ing such an approximation, fuzzy sets for E_3 can be defined for $E_1 + E_2 < E_{12a}$ and $E_1 + E_2 > E_{12a}$ cases respectively, as shown in Figure 4 and Figure 5, where E_{12a} , E_{3a} , E_{3b} , and E_{3c} are the design parameters of fuzzy sets. In order to realize ideal energy responses, fuzzy rules are given as follows:

- Rule 1: If $E_3 = S$ then $s_1 = 1$
- Rule 2: If $E_3 = MS$ and $I_{t-1} = 1$ then $s_2 = 1$
- Rule 3: If $E_3 = MS$ and $I_{t-1} = 2$ then $s_3 = 2$
- Rule 4: If $E_3 = MS$ and $I_{t-1} = 3$ then $s_4 = 2$
- Rule 5: If $E_3 = MB$ and $I_{t-1} = 1$ then $s_5 = 2$
- Rule 6: If $E_3 = MB$ and $I_{t-1} = 2$ then $s_6 = 2$
- Rule 7: If $E_3 = MB$ and $I_{t-1} = 3$ then $s_7 = 3$
- Rule 8: If $E_3 = B$ then $s_8 = 3$

Here, a parameter I_{t-1} which means the index of controller for one-step delay, is introduced, because one-step delayed controller must be retained in the overlapped energy region according to the ideal energy response. s_i is the index of controller that must be used in the fuzzy rule i . The corresponding control system is shown in Figure 6.

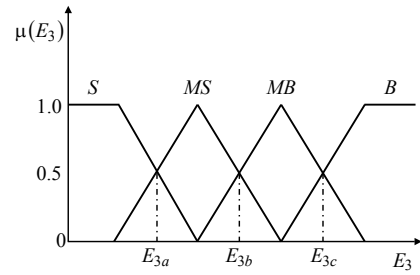


Figure 5: Membership functions for $E_1 + E_2 > E_{12a}$

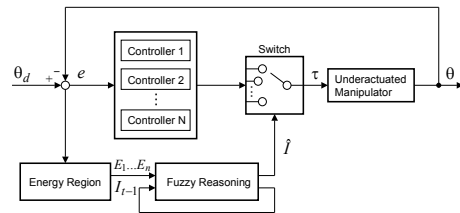


Figure 6: Block diagram of the proposed control system

5 Optimization by GA

We discuss about the design parameters of fuzzy rules using GA. These parameters related to the energy regions are E_{12a} , E_{3a} , E_{3b} , and E_{3c} . Each parameter is assumed to be encoded by 32 [bit]. A cost function is defined by using the error energy of time responses for different two initial state vectors:

$$\begin{aligned} {}^1\mathbf{x}(0) &= [{}^1T(0) \quad {}^1T(0)]^T \\ &= [\pi/4 \quad \pi/4 \quad \pi/4 \quad 0 \quad 0 \quad 0]^T \\ {}^2\mathbf{x}(0) &= [{}^2T(0) \quad {}^2T(0)]^T \\ &= [\pi/6 \quad \pi/6 \quad \pi/6 \quad 0 \quad 0 \quad 0]^T \end{aligned}$$

Then, the sampling interval is 0.01 [s], the simulation time is 30 [s], and the desired state vector is to be converged to zero.

The size of a population is 100 and the maximum number of generations is 500. Simulation condition used here are shown in Table 2.

The cost function is given by

$$f_c = \sum_{i=1}^2 f_i \quad (4)$$

$$f_i = \begin{cases} \sum_{j=2501}^{3000} \sum_{k=1}^3 E_k(j) & \text{if } E_1(j) + E_2(j) < 40 \text{ and } E_3(j) < 40 \\ 120(3000 - j_d) & \text{otherwise} \end{cases}$$

Central Pattern Generators Based on Matsuoka Oscillators for the Locomotion of Biped Robots

Guang Lei Liu , Maki.K.Habib , Keigo Watanabe , Kiyotaka Izumi
Department of Advanced Systems Control Engineering,
Graduate School of Science and Engineering, Saga University,
1 Honjomachi, Saga 840-8502, Japan

E-mail: liuguanglei@hotmail.com, {habib, watanabe, izumi}@me.saga-u.ac.jp

Abstract

Biologically inspired control approaches based on central pattern generators (CPGs) with neural oscillators have been drawing much attention to generate rhythmic motion for biped robots that resemble human-like locomotion. This paper describes the design of a neural oscillator based gait rhythm generator using a network of Matsuoka oscillators to generate a walk pattern for biped robots. This includes proper consideration of oscillator's parameters, such as a time constant adaptation rate, coupling factors for mutual inhibitory connections, etc., to obtain a stable and desirable response from the network. The paper examines the characteristics of a CPG network with six oscillators and the effect of assigning symmetrical and asymmetrical coupling coefficients among oscillators within the network structure under different possibilities of inhibitions and excitations. The kinematics and dynamic of a five-link biped robot has been modeled and its joints are actuated through simulation by the torques output from the neural rhythm generator to generate the trajectories for hip, knee, and ankle joints. The parameters of the neural oscillators are tuned to achieve flexible trajectories. The CPG based control strategy are implemented and tested through simulation.

1 Introduction

Recent studies on the biped locomotion enabled humanoid robots to navigate real environments [1]. ZMP (Zero Moment Point) based control approaches are used to describe the stability and control of biped robot systems by following a targeted trajectory [2]. These approaches have focused on the ability of executing planned movements at any instance by ensuring surface contact between the sole and the ground. In

general, the developed ZMP based control algorithms for bipedal locomotion have been shown to be effective to achieve bipedal locomotion in legged robots with flat feet. However, they require precise modeling and precise joint actuation with high control gains. From the biological point of view, locomotion of human and animals do not require such precision, and it is quite different from that of current biped robots. There are evidences showing the existence of various oscillatory or rhythmic pattern generation activities within the neural circuitry in almost every animal, and most of them are produced without receiving any particular extrinsic oscillatory stimulus [3]. The fundamental mechanisms of animals, rhythmic biological movement, such as locomotive motion of quadrupeds, flapping of bird wings, swimming of fish, crabs, etc. are typical examples of oscillatory activities that have been studied both in biological science and in engineering.

Neurobiological studies revealed that rhythmic motor patterns are controlled by neural oscillators referred to as CPGs which generate oscillatory signals [4]. It has been also suggested that sensory feedback plays an important role in stabilizing rhythmic movements by coordinating the physical system and the CPGs [5]. In contrast to off-line trajectory planning, biologically inspired control approaches based on CPGs with neural oscillators have been drawing much attention to generate rhythmic motion for biped robots that featured with self-adaptive properties to cope with change in their environment [6-8]. The neural oscillator proposed by Matsuoka [3] is widely used to model the firing rate of two mutually inhibiting neurons described in a set of differential equations. This model is used in robotic applications to achieve designated tasks involving rhythmic motion which requires interactions between the system and the environment. However, it is very difficult to determine the CPG parameter values for various robots and environments,

since there is no design principle to determine the parameter values.

This paper describes the design of an oscillator-based gait rhythm generator using a network of Matsuoka oscillators to generate a walk pattern for biped robots. This includes proper consideration of oscillator's parameters such as a time constant, coupling factors for mutual inhibitory connection, etc., to obtain a stable and desirable response from the CPG network. The paper examines the characteristics of CPG network with six oscillators and the effect of assigning symmetrical and asymmetrical coupling coefficients among oscillators within the network structure under different possibilities of inhibitions and excitations.

2 The CPGs and Neural Oscillator Model

Almost all species developed completely different form of locomotion perfectly suited to its morphology and environment to ensure its survival. To achieve locomotion, the neural system generates rhythmic signals that are sent to the musculo-skeletal system in order to produce torques on the different joints of the animal. There are some evidences showing that the locomotion patterns in human are generated at the spinal level, and as such, it has been considered that humans use a system that is comparable to a CPG for their locomotion. CPGs are neural networks that can produce rhythmic motor patterned outputs without rhythmic sensory or central input.

Bipedal locomotion seems to be more complicated than the mentioned process as the balance is much important and critical with only two legs, while it makes the control extremely crucial. CPG based approach is directly inspired from biological considerations and can be represented by different mathematical models such as oscillators, artificial neurons, vector fields, etc. Each CPG usually represents one degree of freedom (DOF). Oscillator based CPGs use the concept of limit cycles which are very convenient in the case of locomotion as they can return to their stable state after a small perturbation and they are almost not influenced by a change in the initial conditions. Different models could be used to represent the interaction between the CPG and the reflex system that represents the type of the feedback mechanism from internal sensory information and the interaction with robot environment. In order to represent the CPG and generate the required signals several nonlinear oscillators that are

coupled together have been developed, such as, Hopf, Rayleigh, Van del Pol, Matsuoka, etc. oscillators.

Due to its simplicity and effectiveness, Matsuoka oscillator is widely used in many researches on robotics and CPGs [3, 9]. It is based on the mutual inhibition of two artificial neurons that generate a periodic signal as output. The model of each neuron has represented by two equations with two state variables as below,

$$\tau_{ri} \frac{du_i}{dt} = u_i + \sum_{j=1}^n w_{ij}y_j + w_{s_i}s_0 - bf_i + feed_i \quad (1)$$

$$\tau_{ai} \frac{df_i}{dt} = f_i + y_i \quad (2)$$

$$y_i(u_i) = \max\{0, u_i\} \quad (3)$$

The first state variable is u_i that corresponds to the membrane potential of the neuron body, and the second state variable is f_i that represents the degree of fatigue or adaptation (self-inhibition) in the neuron, while y_i is the output of the neuron. The subscripts i, j denotes the neuron number, τ_{ri} , is the time constants that specifies the rise time when given step input. The frequency of the output is roughly proportional to $1/\tau_{ri}$. In addition, τ_{ai} , is the time constant that specifies the time lag of the adaptation effect. w_{ij} , denotes inhibitory synaptic connection weight from the j th neuron to the i th neuron; $w_{ij} = 0$ for $i \neq j$, and $w_{ij} = 0$ for $i = j$. $\sum(w_{ij}y_j)$, represents the total input from the neurons inside a neural network. s_0 is a driving input and w_{s_0} denotes a connection weight of the driving input, and $feed_i$, is an input feedback sensor signal to the neuron and represents the internal sensory information and interaction between the robot and its environment ($feed_i$ has been added to the neuron model of Matsuoka to represent the feedback sensory information [8]), and it is used mainly with a closed-loop CPG model.

Figure 1(a) shows the general Matsuoka neuron model described by equations 1, 2 and 3. Matsuoka oscillator consists of two neurons that are linked reciprocally while inhibit and excite each other alternatively to produce an oscillation as output. Such activity is used to account for the alternating activities of flexor and extensor muscle at each joint during walking. The self-inhibition is governed by the bf_i connections while the mutual inhibition is done through the $w_{ij}y_j$ and $w_{ji}y_i$ connections. The output torque will equal to $\tau_r = y_j - y_i$. Figure 1(b) shows two coupled neurons of the Matsuoka oscillator.

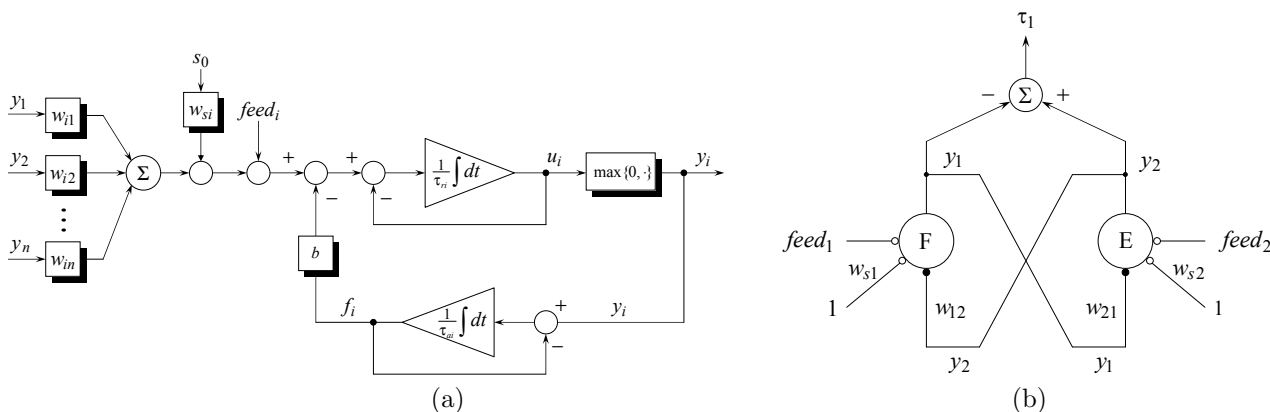


Figure 1: (a) General Matsuoka neuron model; (b) One oscillator consisting of an extensor and a flexor

3 Biped Robot and Neural Gait Rhythm Generator

3.1 The general control strategy for gait generation

Figure 2 introduces the adopted general control strategy for the bipedal robot aiming to generate flexible rhythmic walking gait, and it includes three parts. The first part consists of two major elements. The first element represents the high level activity coordinator that can set and activate the relevant neural rhythmic motion based on external and internal sensory information. The second element within the first part represents the network of coupled neural oscillators aiming to generate synchronized rhythmic signals. The locomotor movement results from torques generated by the neural rhythm generator and acting at each joint of the robot. The second part of the control strategy includes the model of the musculo-skeletal system along with the mathematical formulation of the dynamic equations of motion using Newton-Euler method. The last part represents the feedback signals that aim to establish a closed-loop to enable real time adaptation for the walking gait.

3.2 The bipedal musculo-skeletal model

Figure 3 shows the simple model for simulating a bipedal musculo-skeletal system that has been considered in this paper. It has five joints and two identical legs each with three DOFs corresponding to hip, knee and ankle joints. Each leg is composed of a thigh (links 2 and 3), and a shank (links 4 and 5). In the dynamic model of the bipedal musculo-skeletal system, the links are considered to be of uniform rectangular shape with

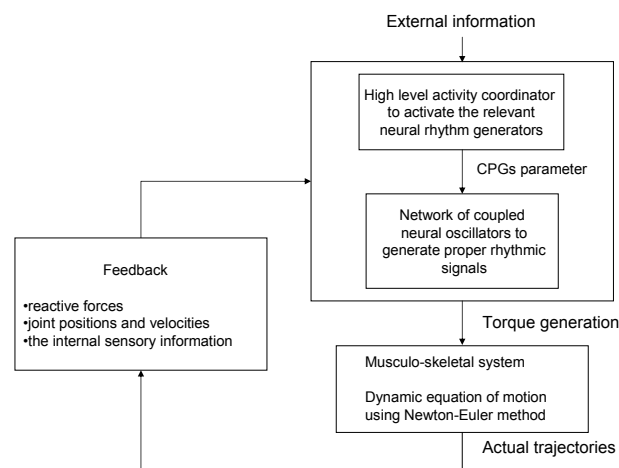


Figure 2: The general control strategy for the bipedal robot

mass at its center. A point mass is used to represent the remaining part of the body and it is described by link 1 at the hip. Both legs are integrated at link 1 while assuring suitable detachment. The joints are numbered as Joints 1, 2, 3, 4, 5 from the side of the body, where Joint 1 is the hip joint, Joints 2 and 3 are knee joints, and Joints 4 and 5 are ankle joints.

Due to their low inertia, a point foot has been considered into the dynamics during the support phase, and contact with the ground has been represented by two dimensional spring and damper. Vertical and horizontal ground reaction forces are modeled and calculated each time the ankle first makes contact with the ground respectively. A slippage model is established by using a condition that manages the relation between both reactive forces and the static friction coefficient of the ground. In addition, the described model

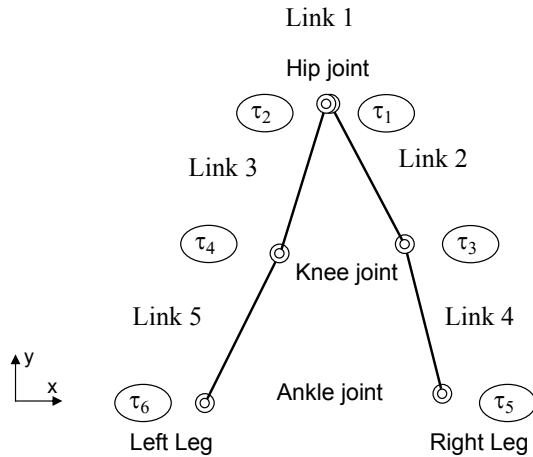


Figure 3: Five link model for a biped locomotion

is bounded to move within the sagittal plane, and the torques acting at the joints to realize the walking gait are assumed to be generated by the neural gait rhythm generator.

3.3 The mathematical motion formulation of the model

By using the Newton-Euler dynamic formulation, the general form of equations of motion for the bipedal musculo-skeletal are derived as below [8],

$$\ddot{\mathbf{x}} = P(\mathbf{x})F + Q(\mathbf{x}, \dot{\mathbf{x}}, T_r(\mathbf{y}), F_g(\mathbf{x}, \dot{\mathbf{x}})) \quad (4)$$

where \mathbf{x} is a (14 1) vector of the inertial positions of 5 links and the initial angles of 4 links; P is a (14 8) matrix; F is a (8 1) vector of constraint forces; Q is a (14 1) vector; T_r is a (6 1) vector of torques; F_g is a (4 1) vector of forces on the ankle which depends on the state of the terrain; and \mathbf{y} is a (12 1) vector of the output of the neural rhythm generator.

From the model, the equations of the kinematic constraints are formulated, and hence the acceleration can be obtained by differentiating these equations twice with respect to time. The yielded equations can be written in the following compact form,

$$C(\mathbf{x})\ddot{\mathbf{x}} = D(\mathbf{x}, \dot{\mathbf{x}}) \quad (5)$$

The constraint forces can be obtained by substituting equation (4) into equation (5), and to get the required accelerations without the use of the constraint forces, the yielded equation of forces is substituted into equation (4). Hence, the compact form of the acceleration equations that represents the motion of the bipedal

musculo-skeletal is,

$$\begin{aligned} \ddot{\mathbf{x}} = & P(\mathbf{x})[C(\mathbf{x})P(\mathbf{x})]^{-1}[D(\mathbf{x}, \dot{\mathbf{x}}) \\ & C(\mathbf{x})Q(\mathbf{x}, \dot{\mathbf{x}}, T_r(\mathbf{y}), F_g(\mathbf{x}, \dot{\mathbf{x}}))] \\ & + Q(\mathbf{x}, \dot{\mathbf{x}}, T_r(\mathbf{y}), F_g(\mathbf{x}, \dot{\mathbf{x}})) \end{aligned} \quad (6)$$

To solve the motion equations, the \mathbf{y} values are provided as an output from the neural rhythm generator that is proportional to the torque. In addition, the feedback signal from the bipedal robot to the neural rhythm generator is represented by the joint positions and velocity of different moving parts of the body, and the contact forces with the environment.

3.4 The model for the neural rhythm generator

The neural oscillators are the main elements that compose the model of the neural rhythm generator. The simplest model of the neural oscillator consists of two mutually inhibited neurons with the self adaptation in each of them. Each neural oscillator has four state variables. Two variables represent the inner state of each neuron (u_i and u_j), and the other two state variables represent the degree of adaptation for each neuron (f_i and f_j), respectively. Six of the neural oscillators have been used to model the neural rhythm generator for the bipedal robot. Two oscillators have been used at the left and right side of the hip and one oscillator has been used at each of the knee and ankle joints. Figure 4 illustrates the arrangement of the neural oscillators in relation to the adopted bipedal musculo-skeletal system. The odd number oscillator represents flexor (F) and the even number oscillator represents the extensor (E), while τ_1 to τ_6 represent the output torques from the oscillators. The configured neural oscillators have inhibitory connections. The two neurons of each oscillator generate torques in opposite direction, i.e., the direction of contraction of flexor and extensor muscle. The algebraic sum of the torques at each neural oscillator is proportional to the torque at the relevant joint during bipedal walk. The inhibitory connection between the hip oscillators produces alternate excitations to give the alternation between the movements of the two legs.

The parameters for each neural oscillator and the interconnection between the oscillators are tuned experimentally to achieve the generation of a consistent pattern that assembles human biped motion. The feedback signal from the bipedal robot to the neural rhythm generator is represented by the joint positions and velocity of different moving parts of the body, and the contact forces with the environment. In case of a

physical biped robot, the feedback sensory information are sensed through different internal and external sensors.

4 Simulation and Results

In order to produce a suitable relative phase at the joints of each side of the bipedal, the interconnection between the neural oscillators at each side of the bipedal has been chosen in the way that the flexor and extensor of the hip oscillators can inhibit the extensor neurons of the knee and ankle oscillators as illustrated in Figure 4 and we can call this model as one-rank model. The simulation result of the walking gait for bipedal robot is shown in Figure 5. Based on this model, both of the knees' oscillators have been chosen to inhibit the ankles' flexor neurons as shown in Figure 6 and we can call this model as two-rank model. The simulation result of this case is shown in Figure 7. The total time is 2 seconds and the ground is level.

5 Conclusions

This paper has presented a CPG based control approach composed of a network of coupled neural oscillators to generate proper rhythmic motion for bipedal robot. This approach avoids the need to have a perfect knowledge of the robot's dynamics as compared to the trajectory based methods. In addition, it is a more general and adaptive to design controllers for bided robots. Moreover, reflexes that are produced by the robot's feedback sensors are used to manage external effects within the robot environment and balance control. However, currently there is no systematic design principle that can determine the parameter values for the oscillators and assigning efficient coupling between oscillators. Hence, the next step of this work will focus on adapting the parameters of each neural oscillator with the possibility of reconfiguring the coupling mechanism between oscillators in real time through learning paradigm.

References

- [1] Hirai, K., Hirise, M., Haikawa, Y., and Takenaka, T., The development of Honda humanoid robot, in *Proc. of the International Conference on Robotics and Automation (ICRAf98)*, vol. 2, pp. 1321–1326. 1998.
- [2] Vukobratovic, M., Borovac, B., Surla, D., and Stokic, D., *Biped Locomotion: Dynamics, Stability, Control and Application*, Springer, 1990.
- [3] Matsuoka, K., Sustained oscillations generated by mutually inhibiting neurons with adaptation, *J. of Biological Cybernetics*, vol. 52, pp. 367–376, 1985.
- [4] Grillner, S., Wallen, P., and Brodin, L., Neuronal network generating locomotor behavior in lamprey — circuitry, transmitters, membrane properties, and simulation, *Annual Review of Neuroscience*, vol. 14, pp. 169–199, 1991.
- [5] Nakamura, Y., Sato, M., and Ishii, S., Reinforcement learning for biped robot, in *Proc. of the 2nd International Symposium on Adaptive Motion of Animals and Machines (AMAM2003)*, ThP-II-5, Kyoto, March 4–8, 2003.
- [6] Nakanishi, J., Morimoto, J., Endo, G., Cheng, G., Schaal, S., and Kawato, K., Learning from demonstration and adaptation of biped locomotion, *Robotics and Autonomous Systems*, vol. 47, pp. 79–91, 2004.
- [7] Williamson, M. M., Robot arm control exploiting natural dynamics, *Ph.D. Thesis*, MIT, Cambridge, Massachusetts, June 1999.
- [8] Taga, G., Yamaguchi, Y., and Shimizu, H., Self-organized control of bipedal locomotion by neural oscillators in unpredictable environment, *Biological Cybernetics*, vol. 65, pp. 147–159, 1991.
- [9] Matsuoka, K., Mechanisms of frequency and pattern control in the neural rhythm generators, *Biological Cybernetics*, vol. 56, pp. 345–353, 1987.

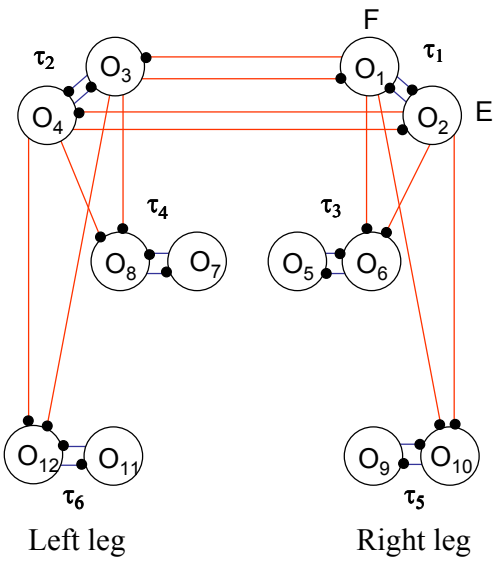


Figure 4: One-rank CPG network of biped model

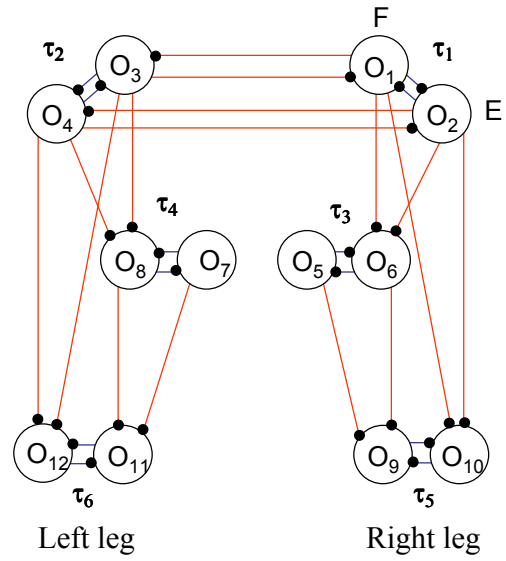


Figure 6: Two-rank CPG network for a biped locomotion

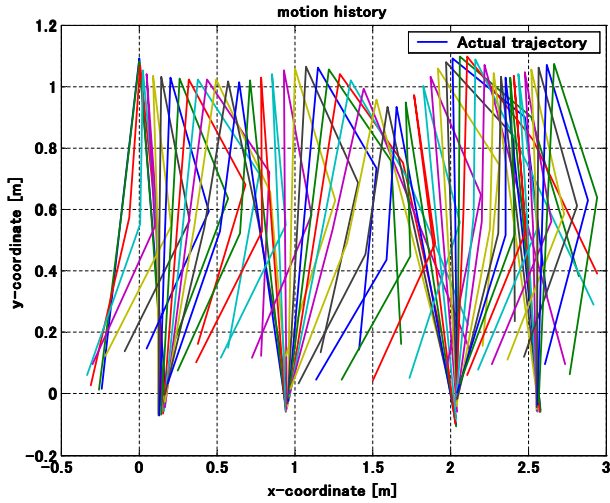


Figure 5: The simulated walking gait of bipedal using one-rank model in Fig. 4

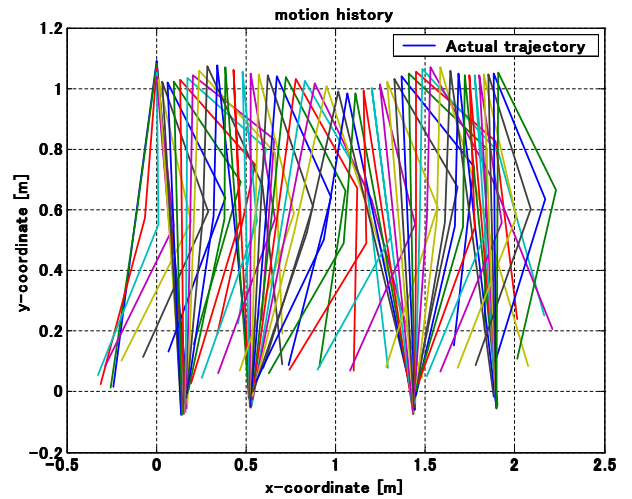


Figure 7: The simulated walking gait of bipedal using two-rank model in Fig. 6

Networks on Earth from the climate data

Kazuko Yamasaki
Masanori Ohshiro
Eiji Nunohiro

Kenneth J. Mackin
Kotaro Matusita

Abstract

We extract scale free networks from air temperature records covering whole earth of NCEP-NCAR reanalysis data. To do this, we use the phase synchronization which analyzes nonlinear nonstationary phase of the time series of the temperature at some locations on the earth and calculate the phase differences with time delay between every pare of them Networks shows scale free nature which is thought to contribute to the stability of the climate. These studies will help environmental conservation of our earth.

1 Introduction

Nowadays a lot of attention is paid to various networks in the world , especially which show scale free nature. But only a few studies have been done about climate networks on the earth. [4],[5] The earth is investigated in various methods like whole earth simulator. Empirical Orthogonal Function (EOF) decomposition is popular method to extract Elnino, Southern Oscillation etc. But networks may give us other kinds of understandings about climate on the earth. To extract meaningful networks from climate data of the earth, we use phase synchronization which describes synchronization of time dependent phase of nonlinear oscillations instead of linear method like cross-correlation. We use temperature of the atmosphere covering the whole surface of the earth. We draw networks by connecting two locations which synchronizes each other. We show some seasonal networks and study their scale free nature.

1.1 Data

The global National Centers for Environmental Prediction - National Center for Atmospheric Research(NCEP-NCAR) provides reanalysis dataset of various climate data in every 100-hPa atmospheric pressure levels and every grid with a resolution of 2° latitude \times 2° longitude. We choose 47 locations from the grids

so that density of the locations is almost equal on the earth and use 400-hPa, 500-hPa and 600-hPa and study the daily temperature data from 1979 to 2005.

1.2 Phase synchronization

Recently phase synchronization is applied to a lot of complex dynamical systems which shows nonlinear nature and traditional cross-correlation technique may not work well, for example chaotic system , brain activity[1], the binocular fixation eye movements [3] and temperature and precipitation in different regions etc [2]. In this method, we use nonlinear phase which is defined by a Hilbert transform and the generalized phase-difference is $\varphi_{n,m}(t) = n\phi_1(t) - m\phi_2(t)$ between two oscillators. After taking mod (π), if the generalized phase-difference is constant, we can say two oscillators are synchronized and shifted by the constant in phase. But generally has time dependence, so we have to see the histogram of $\varphi_{n,m}$ to judge whether two oscillators are systematically shifted or not. Then we use the Shannon entropy. If the entropy equals 0, they are shifted constantly and if the entropy is large, each cycle of two oscillators are independent so they are not synchronized. Here we have time series $x_j(t)$ of the temperature at the j th location on the earth.

- We construct the complex signals

$$z_j(t) = x_j(t) + iy_j(t) = A_j e^{i\phi_j(t)}$$

by Hilbert transform of $x_j(t)$. Now we have the nonlinear phase $\phi_j(t)$ at the j th location.

- We define the generalized phase-difference $\varphi_{n,m,i,j}(t)$ for various m and n values and every pare of the locations i and j .

$$\varphi_{n,m,i,j}(t) = (n\phi_i(t) - m\phi_j(t)) \bmod 2\pi$$

- We create a histogram of $\varphi_{n,m,i,j}$ with M bins of size $2\pi/M$ and we get the frequency distribution p_k of each bin k , that show how the phase-difference of the pare of two locations occurs.

- To quantify the systematic occurrence of the phase-difference, we use the Shannon entropy S and define an index $\rho_{n,m,i,j}$.

$$\rho_{n,m,i,j} = \frac{S_{\max} - S}{S_{\max}}, \quad S = - \sum_{k=1}^M p_k \ln p_k$$

By definition, the maximum entropy and the range of the index are $S_{\max} = \ln M$ and $0 \leq \rho_{n,m,i,j} \leq 1$. $\rho_{n,m,i,j} = 1$ means complete phase synchronization, in this case the distribution of the frequencies p_k shows sharp peak at a value of k .

- Next we shift the time $t \rightarrow t + \tau$ in one of the two time series $x_i(t)$, $x_j(t)$ and calculate the phase-difference $\rho_{n,m,i,j}(\tau)$ between one time series with shift τ and the other time series without shift. Finally we have max value of the index $\rho_{n,m,i,j}(\tau)$ among deferent values of τ .

The phase synchronization method is beyond the cross-correlation method in the two points. It analyzes the nonlinear relationship and considers the time delay directly. But for now we do not distinguish the negative and the positive correlation in the phase synchronization.

1.3 Climate Networks

We extract climate networks as follows. Here we consider only $n = 1$ and $m = 1$ phase-difference $\rho_{1,1,i,j}$. We standardize the max value of the index $\rho_{1,1,i,j}$ by dividing the average value of them among deferent values of time delays τ .

$$\rho_{\max,i,j} = \max(\rho_{1,1,i,j}(\tau)) / \text{mean}(\rho_{1,1,i,j}(\tau))$$

So every i th- j th location pare has the set values of $(\rho_{\max,i,j}, \tau_{\max,i,j})$. To decide the links of the networks, we use the thresholds $(\tilde{\rho}, \tilde{\tau})$ in both values of $(\rho_{\max,i,j}, \tau_{\max,i,j})$ and define the network matrix $N_{i,j}$

$$N_{i,j} = \begin{cases} 1 & \text{if } (\rho_{\max,i,j} > \tilde{\rho}) \wedge (\tau_{\max,i,j} < \tilde{\tau}) \\ 0 & \text{other wise} \end{cases}$$

To test the consistency of the networks, we check the common links of data in the consecutive pressure levels data and in the consecutive 6 years terms in 25 years data. Changing the thresholds $(\tilde{\rho}, \tilde{\tau})$, we calculate the correlation of two network matrixes in the two consecutive data Fig.1 shows the correlation of the two networks and the fraction of existing common links. We see the correlation of the two networks and

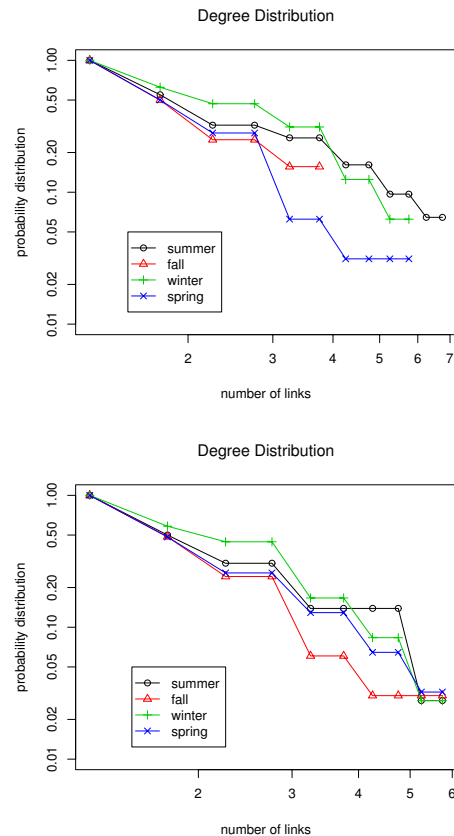


Figure 3: Degree distribution about outgoing links (left) and incoming links (right)

the fraction of existing common links are trade-off. When we need high consistency of the network and a lot of existing common links, this is multi-objective optimization problem. So we pay attention to Pareto-optimal frontier. We see $\tilde{\tau} \sim 10$ days calculations stay near the Pareto-optimal frontier and when we changes another threshold $\tilde{\rho}$, it almost reaches peak at $\tilde{\rho} \sim 4$. So we choose the two threshold $(\tilde{\tau}, \tilde{\rho}) = (10, 4)$. Now we can draw directed networks with the direction of time delays. Fig.2 show the networks in each seasons. We study the distribution of number of links and it shows scale free like Fig.3.

References

[1] P. Tass, M.G. Rosenblum, J. Weule, J. Kurths, A. Pikovsky, J. Volkmann, A. Schmitzler, H.-J. Freund, Phys. Rev. Lett. 81 (3291) (1998).

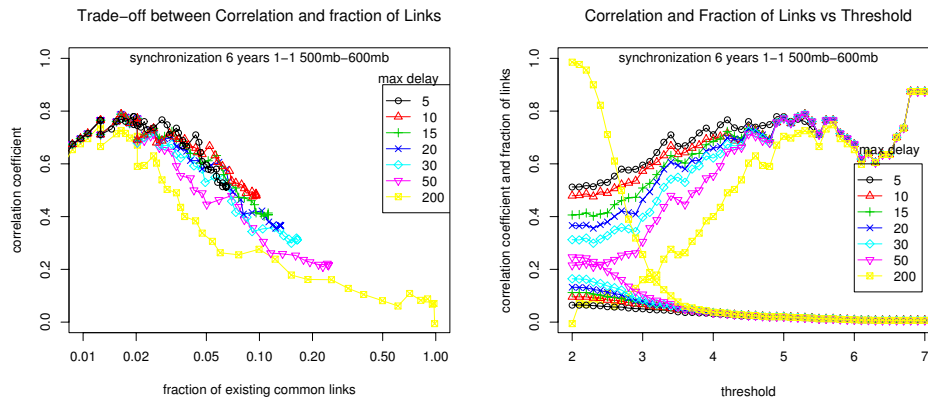


Figure 1: To test the consistency of the networks, we investigate the common links of data in the consecutive pressure levels data and in the consecutive 6 years terms in 25 years data. Changing the thresholds ($\tilde{\rho}, \tilde{\tau}$), we calculate the correlation of two network matrixes in the two consecutive data Fig.1 shows the correlation of the two networks and the fraction of existing common links.

[2] D. Rybsky, S. Havlin, A. Bunde, *Physica A* 320 (2003) 601.

[3] S. Moshel, J. Liang, A. Caspi, R. Engbert, R. Kliegl, S. Havlin, A.Z. Zivotofsky, *Ann. NY Acad. Sci.* 1039 (2005) 484.

[4] A.A. Tsonis, P.J. Roebber The architecture of the climate network *Physica A* 333 (2004) 497 - 504

[5] A.A. Tsonis, K.L. Swanson, and P. J. Roebber What do networks have to do with climate? :American meteorological society (2006) pp.585-595

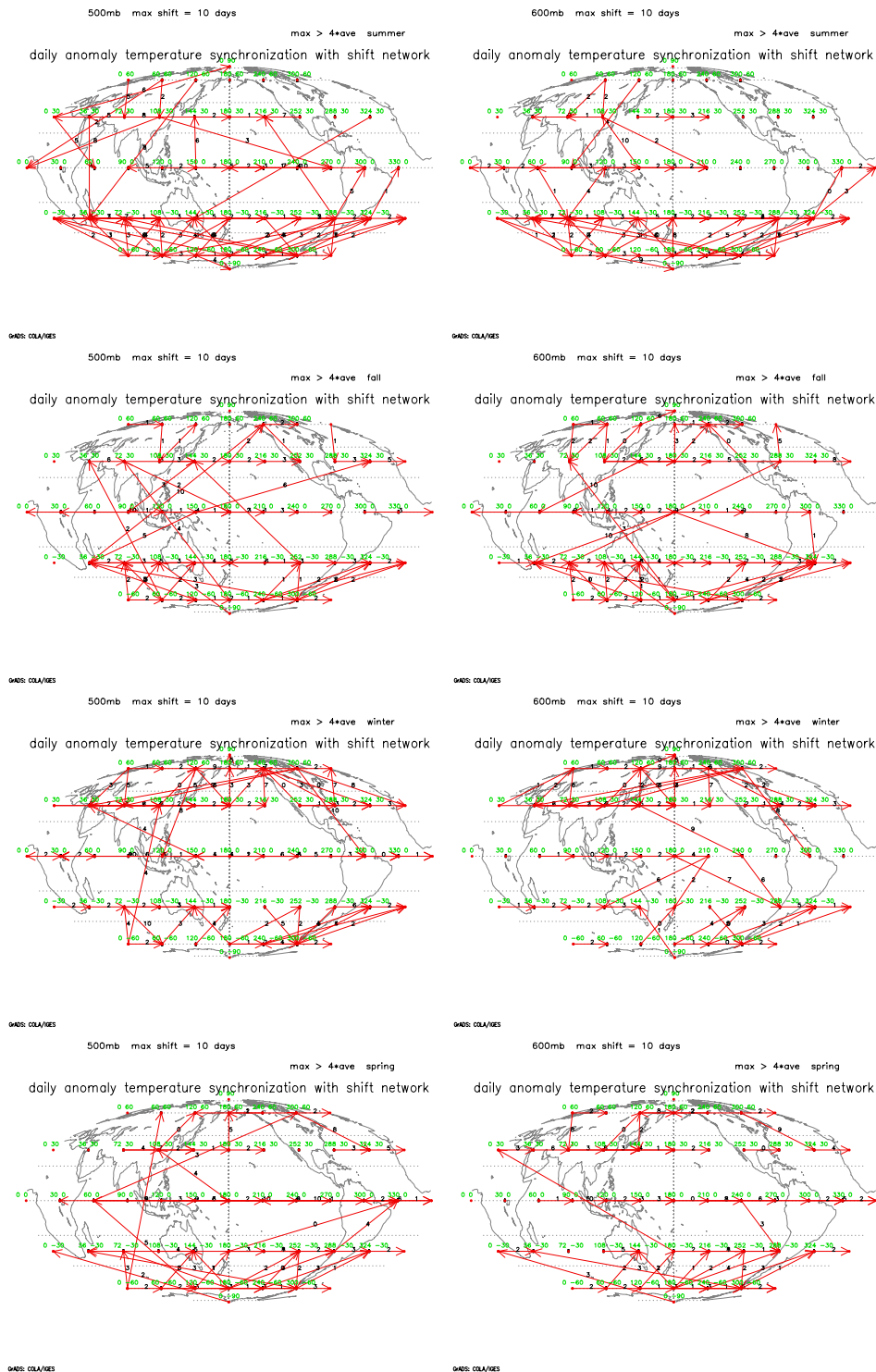


Figure 2: Seasonal networks by temperature of pressure level 500-hPa (left) and 600-hPa (right) with threshold $(\tilde{\tau}, \tilde{\rho}) = (10, 4)$

An Approach to the Learning Curves of an Incremental SVM

Takemasa Yamasaki
Department of Systems Science
Kyoto University
Kyoto 606-8501 Japan

Kazushi Ikeda
Department of Systems Science
Kyoto University
Kyoto 606-8501 Japan

Abstract

Support vector machines (SVMs) are known to result in a quadratic programming problem, that requires a large computational complexity. To overcome this problem, the authors proposed two incremental SVMs from the geometrical point of view in the previous study, both have a linear complexity with respect to the number of examples on average. One method was shown to produce the same solution as an SVM in batch mode, but the other, which stores the set of support vectors, was known to have a larger generalization error. In this study, we derive the learning curves of the latter method, assuming that the probability the set of support vectors is updated is proportional to the current margin and so is the decrease of the margin in the update, too. In the derivation, we employ the disc approximation which is to be justified yet, but the result agrees well with computer simulations.

1 Introduction

A support vector machine (SVM) nonlinearly maps given input vectors to feature vectors in a high-dimensional space and linearly separates the feature vectors with an optimal hyperplane in terms of margin [1, 2]. It has an advantage that there are no local minima in the error surface since finding the optimal hyperplane results in a convex quadratic programming problem (QP) with linear constraints. However, a QP requires a high computational complexity and even good QP solvers, such as interior-point methods, can solve problems of a limited size.

In order to cope with this limitation, we proposed two incremental methods in the previous study, based on another property of SVMs, that is, sparseness [3]. One can produce the same solution as that of the SVM in a batch mode, however, its implement is not easy. The other is simple and has a less complexity but its performance is a little worse. A rough geometrical analysis showed that the degradation of performance

is limited; its generalization error has the same order as that of the SVM in a batch mode [3]. In this paper, we derive the learning curves more quantitatively based on the disc approximation. Although the disc approximation is to be justified yet, the theoretical learning curves agree well with those of computer simulations.

2 Effective Examples and Support Vectors

An SVM maps an input vector \mathbf{x} to a vector $\mathbf{f} = \mathbf{f}(\mathbf{x})$ called a feature vector in the feature space. In this study, however, we employ the so-called linear kernel and assume that the feature vector is normalized. That is, $\|\mathbf{f}\| = \|\mathbf{f}(\mathbf{x})\| = \|\mathbf{x}\| = 1$ for any \mathbf{x} . In addition, we only consider SVMs with homogeneous separating hyperplanes, $\mathbf{w}^T \mathbf{f} = 0$, instead of inhomogeneous separating hyperplanes in the original SVMs, $\mathbf{w}^T \mathbf{f} + b = 0$, where T denotes the transposition. Note that a problem with inhomogeneous hyperplanes is easily transformed to one with homogeneous hyperplanes using the so-called lifting up, $\tilde{\mathbf{w}}' := (\mathbf{w}', b)$ and $\tilde{\mathbf{f}}' := (\mathbf{f}', 1)$, where $:=$ means definition, though they differ a little since the latter also penalizes the bias b [4].

An SVM is given N examples and the i th example is a pair of an input vector \mathbf{f}_i in the M -dimensional unit hypersphere S^M and the corresponding label $y_i \in \{\pm 1\}$ satisfying $y_i = \text{sgn}(\mathbf{w}^{*T} \mathbf{f}_i)$, where \mathbf{w}^* is the true weight vector to be estimated. Since the separating hyperplane is homogeneous, an example (\mathbf{f}_i, y_i) is completely equivalent to $(y_i \mathbf{f}_i, 1)$ and hence we can consider that any example has a positive label. In short, input vectors \mathbf{f} are chosen $S_+^M = \{\mathbf{f} | \mathbf{f}^T \mathbf{w}^* > 0\}$, which we call the input space.

We assume that $\mathbf{w} \in S^M$ without loss of generality where S^M is called the weight space. When an example (\mathbf{f}_i, y_i) is given, the true vector \mathbf{w}^* must be in the hypersemisphere $\{\mathbf{w} | y_i \mathbf{w}^T \mathbf{f}_i > 0\}$. This means

that an example is represented as a point in the input space and a hyperplane in the weight space (Fig. 1). On the other hand, a weight vector is represented as a hyperplane in the input space and a point in the weight space.

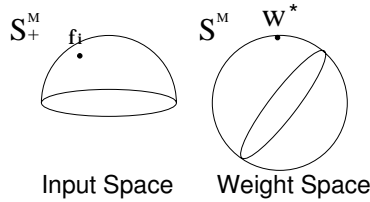


Figure 1: Duality of the Input space and the weight space.

When N examples are given, w^* has to be in an area

$$A_N = \{w | y_i w^T f_i > 0, i = 1, \dots, N\}, \quad (1)$$

which we call the admissible region [5] (Fig. 2). The admissible region A_N is a polyhedron in S^M . If the admissible region changes when an example is removed, the example is called effective. Note that the set of effective examples makes the same admissible region as all the examples. So, some algorithms for estimating w , including SVMs, utilize only effective examples.

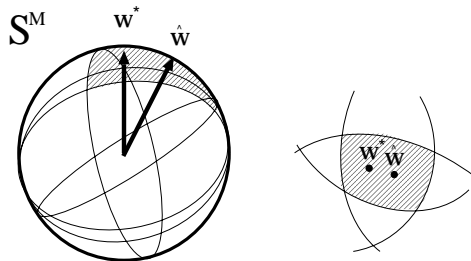


Figure 2: Admissible region in the weight space

Under the assumption that the feature vectors are normalized, an SVM solution has a clear geometrical picture. Finding a hyperplane that maximizes the margin results in a quadratic programming problem,

$$\min_{w, \xi} \frac{1}{2} \|w\|^2 \quad \text{s.t. } w' f_i \geq 1. \quad (2)$$

It is known that the SVM solution \hat{w} necessarily has the form

$$\hat{w} = \sum_{i=1}^N \alpha_i f_i \quad (3)$$

where α_i are the Lagrangian multipliers. When $\alpha_i \neq 0$, f_i is called a support vector. In other words, \hat{w} consists of only support vectors. From the Karush-Kuhn-Tucker optimality conditions, support vectors f_i satisfy $\hat{w}^T f_i = 1$ and the others do not. This means that the SVM solution \hat{w} is equidistant from support vectors [6]. Since $\|\hat{w}\|$ is not necessarily unity, we consider the meaning of the above in the weight space S^M . It is easily shown that \hat{w} in S^M (that is, $\hat{w}/\|\hat{w}\|$) is still equidistant from support vectors in the angular distance of S^M and the SVM solution \hat{w} is the center of maximum inscribed sphere in the admissible region A_N (Fig. 3) [7].

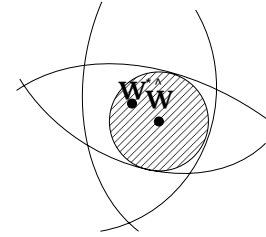


Figure 3: The optimal weight \hat{w} is the center of maximum inscribed sphere in the admissible region.

3 Incremental SVMs

The discussion above claims that a learning machine can get the same information from only the set of effective examples. Thus, the incremental algorithm below referred to as Method 1, gives the same answer as the SVM in batch mode:

1. The machine has the effective set of n given examples.
2. Unless the $(n + 1)$ st example is effective, neglect it.
3. Otherwise, the effective set is remade, adding the $(n + 1)$ st example.

This algorithm has a low computational complexity in average, but it is not easy to know whether an example is effective or not [3].

Two cope with the problem, we proposed to store support vectors instead of effective examples, since any support vector is effective by definition. Although there may be some loss in information, an example is easily determined whether it is a new support vector

or not: the example is a support vector if and only if its distance from the current separating hyperplane is less than the current margin. Hence, the algorithm referred to as Method 2 is written as below:

1. The machine has the set of support vectors of n given examples.
2. If the $(n + 1)$ st example is more distant from the separating hyperplane than the current margin, neglect it.
3. Otherwise, the set of support vectors is updated by an SVM solver with the support vectors and the $(n + 1)$ st example.

Method 2 neglects a new example which is effective but not a support vector. Since such a vector may become a support vector in the future, Method 2 has a lower performance than the conventional SVM or Method 1. How much is the degradation in Method 2? We give an answer to this problem in the next section.

4 Learning Curves of Method 2

We assume hereafter that examples are chosen from S_+^M uniformly and independently as well as a test input, as is done in [5]. The learning curves will be derived, as was in [3], based on the following two assumptions:

- The probability that the set of support vectors is updated is proportional to M_n .
- The decrease of the margin is also proportional to M_n .

The above assumptions lead to the following update equation

$$M_{n+1} = [1 - aM_n]M_n + aM_n[\lambda M_n] \quad (4)$$

$$= M_n - a[1 - \lambda]M_n^2, \quad (5)$$

by simple calculation that leads to

$$M_N = \frac{c_{ss}}{N} \quad c_{ss} = \frac{1}{a(1 - \lambda)}. \quad (6)$$

We here introduce a new approximation, which we term the disc approximation, and evaluate the values of a and λ in (5). In short, the disc approximation regards the admissible region a disc.

The probability aM_n that the set of support vectors is updated is approximately expressed as the ratio of the radius of the admissible region to that of

the hemisphere. In asymptotics of $N \rightarrow \infty$, the admissible region shrinks and can be regarded as a disc in a plane, however, the hemisphere cannot, since it is curved. Therefore, we evaluate an approximate of the radius of a hemisphere from its volume, using the fact that the volume is proportional to the radius power to M . As a result, the probability aM_n is evaluated as

$$aM_n = \left(\frac{\int_{S^{M-1}} \int_0^{M_n} \sin^{M-1} r dr d\omega}{\int_{S^{M-1}} \int_0^{\pi/2} \sin^{M-1} r dr d\omega} \right)^{1/M} \quad (7)$$

$$\approx \frac{M_n}{(MI_M)^{1/M}}. \quad (8)$$

where

$$I_M = \int_0^{\pi/2} \sin^{M-1} r dr d\omega = \frac{\sqrt{\pi}\Gamma[M/2]}{2\Gamma[(M+1)/2]}. \quad (9)$$

The decrease of the margin is also evaluated based on the volume of the admissible region. When the admissible region is a disc and the new example intersecting the region is distributed uniformly thereon, the decrease of the volume can be calculated as below, using the disc approximation and the radius-evaluation based on the volume, as before.

Suppose that the new example divides the admissible region A_n with radius M_n into two regions, A_{n+1}^L and A_{n+1}^R , at $x = \theta \in (-M_n, M_n)$ (see Fig. 4). Then, the radius of the maximum inscribed sphere in A_{n+1}^L is $M_n + \theta$ and that in A_{n+1}^R is $M_n - \theta$. Based on the disc approximation, their volumes are written as

$$|A_{n+1}^L| = |D^M|(M_n + \theta)^M, \quad (10)$$

$$|A_{n+1}^R| = |D^M|(M_n - \theta)^M, \quad (11)$$

$$|A_n| = |D^M|M_n^M, \quad (12)$$

where $|D^M|$ is the volume of the unit M -dimensional disc. Taking into account that the probability of the true parameter being located in A_{n+1}^L is given as $|A_{n+1}^L|/|A_n|$, the average ratio of the volume of the updated admissible region to the original is written as

$$\mathbb{E} \left[\frac{|A_{n+1}|}{|A_n|} \right] = \frac{1}{2M_n} \int_{-M_n}^{M_n} \left(\frac{|A_{n+1}^L|}{|A_n|} \right)^2 + \left(\frac{|A_{n+1}^R|}{|A_n|} \right)^2 d\theta \quad (13)$$

$$= \frac{2}{2M+1}. \quad (14)$$

Then λ is

$$= \left(\frac{2}{2M+1} \right)^{1/M}. \quad (15)$$

In total, c_{ss} is expressed as

$$c_{ss} = \frac{(MI_M)^{1/M}}{1 - \left(\frac{2}{2M+1}\right)^{1/M}} \quad (16)$$

from (6), (7) and (15).

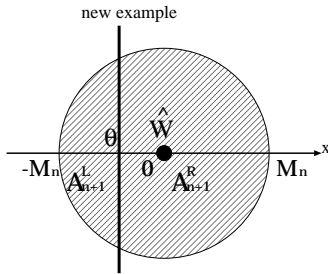


Figure 4: The new example divides the admissible region into two regions at $x = \theta \in (-M_n, M_n)$

5 Computer Simulations

In order to confirm the validity of (16), some computer simulations were carried out. $N = 5000$ examples are chosen from S_+^M uniformly and independently and Method 2 learns the examples gradually.

Fig. 5 shows the average margins versus the number of examples, where the solid lines represent the theoretical results and dashed lines the experimental results for $M = 4$ and $M = 20$. It is clearly shown that the experimental curves in both figures approach the theoretical ones.

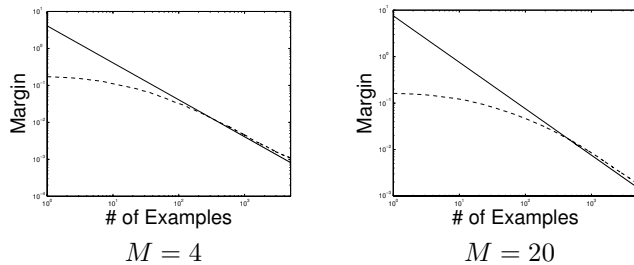


Figure 5: Learning curves of Method 2.

6 Conclusions

In this paper, we analyzed Method 2 more strictly under the assumption that both the probability of the

set of support vectors being updated and the decrease of the margin are proportional to the current margin than [3]. The disc approximation, we introduced here, makes it possible to evaluate their coefficients. The theoretical learning curves derived here agreed well the experimental results given by computer simulations.

Acknowledgements

This study is supported in part by a Grant-in-Aid for Scientific Research (15700130, 18300078) from the Japanese Government.

References

- [1] V. N. Vapnik, *The Nature of Statistical Learning Theory*. New York, NY: Springer-Verlag, 1995.
- [2] B. Schölkopf, C. Burges, and A. J. Smola, *Advances in Kernel Methods: Support Vector Learning*. Cambridge, UK: Cambridge Univ. Press, 1998.
- [3] K. Ikeda and T. Yamasaki, "Incremental support vector machines and their geometrical analyses," *Neurocomputing*, in press.
- [4] K. Ikeda, "Geometrical Properties of Lifting-Up in the Nu Support Vector Machines," *IEICE Trans. Information and Systems*, vol. E89-A, pp. 847–852, 2006.
- [5] K. Ikeda and S.-I. Amari, "Geometry of admissible parameter region in neural learning," *IEICE Trans. Fundamentals*, vol. E79-A, pp. 938–943, 1996.
- [6] R. Herbrich, *Learning Kernel Classifiers: Theory and Algorithms*. Cambridge, MA: MIT Press, 2002.
- [7] K. Ikeda and N. Murata, "Geometrical properties of nu support vector machines with different norms," *Neural Computation*, vol. 17, no. 11, pp. 2508–2529, 2005.

An Experimental Study on Geometric Support Vector Machines

Yoshihiko Nomura Takemasa Yamasaki Kazushi Ikeda
Department of Systems Science
Kyoto University
Kyoto 606-8501 Japan

Abstract

The Nu support vector machine is geometrically characterized as the problem of finding the shortest segment between two reduced convex hulls, each of which is made from the set of given examples belonging to one class. This paper discusses what happens if each reduced convex hull is replaced with the set of its vertices, which may lead to a smaller complexity. Our experimental study shows this substitution makes the performance much worse, which means that the SVM solution is not a vertex in many cases.

1 Introduction

A support vector machine (SVM) is a classifier that nonlinearly maps given input vectors to feature vectors in a high-dimensional space, and that linearly separates the feature vectors with an optimal hyperplane in terms of margin [1-4]. Although an SVM has good properties such that there are no local minima in its error surface and it has a high generalization ability, it requires a high computational complexity since the problem is equivalent to a quadratic programming (QP) with variables of the same number as given examples.

To reduce the complexity, Mavroforakis and Theodoridis [5] proposed an SVM implement based on geometric properties of the nu-SVM, a variant of SVMs proposed in [6] and analyzed in [7-10]. An important property of the nu-SVM utilized in [5] as well as the others is the fact that the SVM solution is strongly related to the reduced convex hull (RCH) of given examples in the feature space [11]. In the case of homogeneous separating hyperplane being employed, especially, the problem of SVM with soft margins is equivalent to finding the point nearest the origin in the RCH.

The nearest point may be located on a surface or an edge of the RCH. The point is sometimes a vertex of the RCH. As shown in [5], any vertex of the RCH

is a weighted sum of given examples where the weight takes one of the fixed three values. [5] utilized this property and reduced the complexity of the nu-SVM.

Suppose that we substitute the nearest vertex for the nearest point in the RCH. Although this operation obviously degrades the performance, it may reduce the complexity drastically at an expense of a slightly lower performance. The purpose of this study is to elucidate the trade-off experimentally.

Note that we treat only the linear kernel, that is, the input and feature spaces are identical, through this paper for simplicity.

2 Geometry of the Nu Support Vector Machines

The nu support vector machines (ν -SVMs) are a variation of SVMs where the margin is not set to unity but a variable β which is maximized as much as possible, differently from the original SVMs [6]. That is, given N input vectors $\mathbf{f}^{(n)}$ and the corresponding outputs $y^{(n)}$, the ν -SVM is formulated as

$$\begin{aligned} \min_{\mathbf{w}, b, \xi_n, \beta} & \left[\frac{1}{2} \|\mathbf{w}\|^2 + C \sum_{n=1}^N \xi_n - \beta \right] \\ \text{s.t. } & y^{(n)}(\mathbf{w}'\mathbf{f}^{(n)} + b) \geq \beta - \xi_n, \quad \xi_n \geq 0, \end{aligned} \quad (1)$$

where ξ_n are slack variables for the soft margin technique.

If we define $\tilde{\mathbf{w}} = (\mathbf{w}; b) \in \tilde{F}$ and $\tilde{\mathbf{f}} = (\mathbf{f}; 1) \in \tilde{F}$ where h is a positive constant and \tilde{F} is the augmented input space $F \times R$, the separating hyperplane $\mathbf{w}'\mathbf{f} + b = 0$ is expressed as a simple inner product $\tilde{\mathbf{w}}'\tilde{\mathbf{f}} = 0$, that is, the hyperplane is homogeneous. This operation is called lifting-up. The ν -SVM with homogeneous hyperplanes seems equivalent to but differs from the original ν -SVM (1), since the former also penalizes the offset in the cost function due to

$$\|\tilde{\mathbf{w}}\|^2 = \|\mathbf{w}\|^2 + b^2. \quad (2)$$

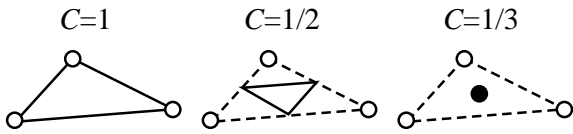


Figure 1: The reduced convex hull of examples. When C is the reciprocal to the size of the example set, it reduces to the centroid of the examples.

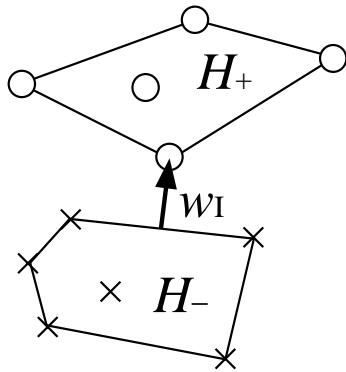


Figure 2: A geometrical view of the solution of a ν -SVM.

See [10] for the details on the effect of lifting-up. The Wolfe dual problem of (1) is derived as

$$\begin{aligned} \min_{\alpha_n} \frac{1}{2} \|\mathbf{w}\|^2 \quad \text{s.t.} \quad \mathbf{w} &= \sum_{n=1}^N \alpha_n y^{(n)} \mathbf{f}^{(n)}, \\ 0 \leq \alpha_n \leq C, \quad \sum_{n=1}^N \alpha_n &= 1, \quad \sum_{n=1}^N y^{(n)} \alpha_n = 0, \end{aligned} \quad (3)$$

where α_n are the Lagrange multipliers. Let $\tilde{\alpha}_n = 2\alpha_n$ and $\tilde{C} = 2C$. Then, (3) is written as

$$\begin{aligned} \min_{\tilde{\alpha}_n} \frac{1}{2} \|\mathbf{w}\|^2 \\ \text{s.t.} \quad \mathbf{w} &= \frac{1}{2} \sum_{y^{(n)}=1} \tilde{\alpha}_n \mathbf{f}^{(n)} - \frac{1}{2} \sum_{y^{(n)}=-1} \tilde{\alpha}_n \mathbf{f}^{(n)}, \quad (4) \\ 0 \leq \tilde{\alpha}_n \leq \tilde{C}, \quad \sum_{y^{(n)}=1} \tilde{\alpha}_n &= \sum_{y^{(n)}=-1} \tilde{\alpha}_n = 1. \end{aligned} \quad (5)$$

Here, (5) means that the first term of (4) is a vector in the convex hull of the examples with $y^{(n)} = 1$ and the second with $y^{(n)} = -1$ since the sum of $\tilde{\alpha}_n \geq 0$ is unity. And the restriction of the weight $\tilde{\alpha}$ between 0 and \tilde{C} reduces the convex hull to the so-called reduced convex hull (Fig. 1). Since the distance between such vectors is minimized in (4), the ν -SVM solution has

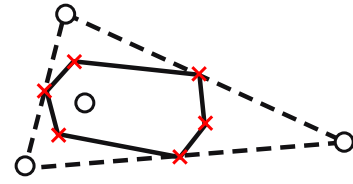


Figure 3: A reduced convex hull is the convex hull of centroids.

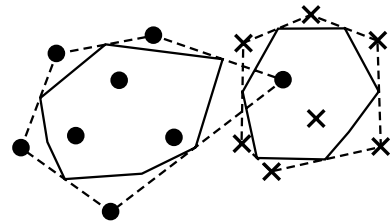


Figure 4: Soft-margin technique makes the examples linearly separable.

the direction vector \mathbf{w}_1 parallel to the segment connecting the two reduced convex hulls H_+ and H_- and having the minimum length (Fig. 2), while the bias of the solution is a little different from the center of the segment [10-12]. This clear geometrical picture is a reason why the ν -SVM is preferred to the original SVM in theoretical studies.

3 Discrete Support Vector Machines

Suppose $C = 1/M$ where M is an integer, since the generalization is straightforward. Then, the reduced convex hull of an example set is equivalent to the convex hull of the set which consists of the centroids of M distinct examples (Fig. 3). This fact clearly shows that the soft-margin technique, introducing C less than unity, is to change the distribution of the input vectors, that is, to make it milder by averaging and linearly separable (Fig. 4) [7]. Since the reduced convex hull shrinks to the centroid of all examples as $C \rightarrow 1/N$, any problem becomes separable then, except some special cases.

Suppose that we substitute the nearest vertex for the nearest point in the RCH. Although this operation obviously degrades the performance, it may reduce the complexity drastically at an expense of a slightly lower performance, since $\tilde{\alpha}_n$ takes either of the fixed values, 0 or $C = 1/M$. We term this method the discrete SVM in this paper.

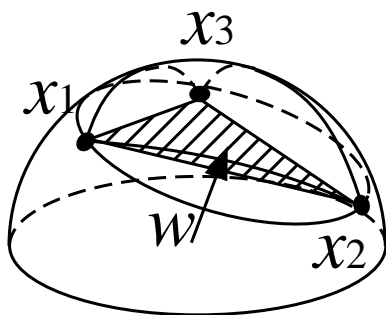


Figure 5: A geometrical view of the ν -SVM solution.

The discrete SVM produces a different hyperplane from the ν -SVM, except for special cases, e.g., when the input vectors distribute on the 1-dimensional hypersphere and the soft-margin parameter C is a half. From the geometrical viewpoint, they have different pictures: In homogeneous hyperplanes' case, the ν -SVM solution is the center of the minimum circumscribed circle including all the examples [8, 13] while the nearest vertex is the centroid of M examples (Fig. 5). We experimentally elucidate their difference in the next section.

4 Computer Simulations

We carried out some computer simulations to compare the discrete SVM with the ν -SVM. The discrete SVM is given N examples, where the input vector $\mathbf{x}^{(n)} \in R^K$ of the n th example $(\mathbf{x}^{(n)}, y^{(n)})$ obeys the normal distribution, $N((10y^{(n)}, \mathbf{0}_{K-1})', I_K)$, and $y^{(n)} = 1$ for $0 < n \leq N/2$ and $y^{(n)} = -1$ for $N/2 < n \leq N$.

It is known that the ν -SVM has the average generalization error of order $1/N$ [14, 15]. Hence, we evaluate the average generalization error of the discrete SVM in our experiments, which is given from the angle between the weight vector of the discrete SVM and the true one. The results are shown in Fig. 6, where K is 2 or 3 and N is 100 to 1000. As far as we see in the results, the average generalization errors did not decrease even when the number of examples, N , increases. This phenomenon is very strange.

5 Conclusions

We proposed the discrete SVM, which substitutes the nearest vertex for the nearest point in the RCH,

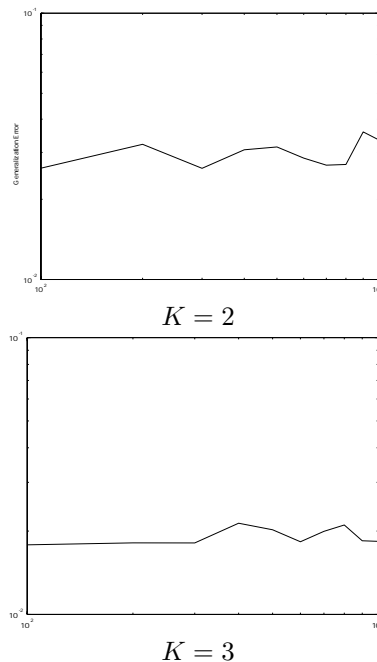


Figure 6: Generalization errors versus the number of examples.

to reduce the computational complexity. However, our experimental study of evaluating its performance showed that this algorithm is far from practical at this moment. We will elucidate the reason why the discrete SVM has such a strange learning curve and propose an improved algorithm in the near future.

Acknowledgments

This study is supported in part by a Grant-in-Aid for Scientific Research (15700130, 18300078) from the Japanese Government.

References

- [1] V. N. Vapnik, *The Nature of Statistical Learning Theory*. Springer-Verlag, 1995.
- [2] B. Schölkopf, et al., *Advances in Kernel Methods: Support Vector Learning*. Cambridge Univ. Press, 1998.
- [3] N. Cristianini and J. Shawe-Taylor, *An Introduction to Support Vector Machines*. Cambridge Univ. Press, 2000.

- [4] A. J. Smola, et al. eds., *Advances in Large Margin Classifiers*. MIT Press, 2000.
- [5] M. E. Mavroforakis and S. Theodoridis, “A geometric approach to support vector machine (SVM) classification,” *IEEE Trans. NN*, vol. 3, pp. 671–682, 2006.
- [6] B. Schölkopf, et al., “New support vector algorithms,” *Neu. Comp.*, vol. 12, no. 5, pp. 1207–1245, 2000.
- [7] K. Ikeda and T. Aoishi, “An asymptotic statistical analysis of support vector machines with soft margins,” *Neu. Netw.*, vol. 18, no. 3, pp. 251–259, 2005.
- [8] K. Ikeda and N. Murata, “Geometrical properties of nu support vector machines with different norms,” *Neu. Comp.*, vol. 17, no. 11, pp. 2508–2529, 2005.
- [9] K. Ikeda, “Effects of kernel function on nu support vector machines in extreme cases,” *IEEE Trans. NN*, vol. 17, no. 1, pp. 1–9, 2006.
- [10] —, “Geometrical properties of lifting-up in the nu support vector machines,” *IEICE Trans. Inf. and Sys.*, vol. E89-D, no. 2, pp. 847–852, 2006.
- [11] K. P. Bennett and E. J. Bredensteiner, “Duality and geometry in SVM classifiers,” *Proc. ICML*, pp. 57–64, 2000.
- [12] D. Crisp and C. Burges, “A geometric interpretation of nu-SVM classifiers,” *NIPS*, vol. 12, pp. 244–250, 2000.
- [13] R. Herbrich, *Learning Kernel Classifiers: Theory and Algorithms*. MIT Press, 2002.
- [14] K. Ikeda, “An asymptotic statistical theory of polynomial kernel methods,” *Neu. Comp.*, vol. 16, no. 8, pp. 1705–1719, 2004.
- [15] K. Ikeda and T. Yamasaki, “Incremental support vector machines and their geometrical analyses,” *Neurocomp.*, in press.

Towards integrated multimedia understanding for intuitive human-system interaction

Masao Yokota

Fukuoka Institute of Technology

yokota@fit.ac.jp

Abstract

The Mental Image Directed Semantic Theory (MIDST) has proposed an omnisensory mental image model and its description language L_{md} intended to facilitate intuitive human-system interaction such that happens between non-expert people and GISs (Geographic Information Systems). This paper presents a systematic method for formulating and computing natural concepts (i.e., mental images) of physical reality in L_{md} and its application to spatial language understanding in view of cross-media operation on text and picture.

1. Introduction

In the field of ontology, special attention has been paid to spatial language covering geography because its constituent concepts stand in highly complex relationships to underlying physical reality, accompanied with fundamental issues in terms of human cognition (for example, ambiguity, vagueness, temporality, identity, ...) appearing in varied subtle expressions [1]. Most of the traditional approaches to spatial language understanding have focused on computing purely objective geometric relations (i.e., topological, directional and metric relations) conceptualized as spatial prepositions or so, considering properties and functions of the objects involved [e.g., 2]. Such verb-centered expressions as S1 and S2, however, are assumed to reflect not much the purely objective geometrical relations but very much certain dynamism at human perception of the objects involved because they can refer to the same scene in the external world. This is also the case for S3 and S4 and we often encounter such intuitive spatial expressions in our daily life.

- (S1) The path sinks to the brook.
- (S2) The path rises from the brook.
- (S3) The roads meet there.
- (S4) The roads separate there.

Anyway, this fact may lead to a certain barrier preventing non-expert or ordinary people and computer systems from comprehensible communication in natural language in such a way as shown in Fig.1. Therefore, their semantic descriptions should be grounded in human perceptual representations, possibly, cognitively inspired and coping with all kinds of spatial expressions including such verb-centered ones as S1-S4 as well as preposition-centered ones. The Mental Image Directed Semantic

Theory (MIDST) [3] has proposed a dynamic model of human perception yielding omnisensory image of the world and classified natural event concepts (i.e., event concepts in natural language) into two types of categories, 'Temporal Events' and 'Spatial Events'. These are defined as temporal and spatial changes (or constancies) in certain attributes of physical objects, respectively, with S1-S4 included in the latter. Both the types of events are uniformly analyzable as *temporally* parameterized loci in attribute spaces and describable in a formal language L_{md} .

This paper presents a brief sketch of L_{md} and a systematic method to formulate and compute natural concepts of physical reality comprising spatial language semantics in order to facilitate intuitive human-system interaction, that is, interaction between non-expert people and computer systems such as GISs (Geographical Information Systems). This work is intended to model a more intuitive ontology of space and time by generalizing our concerned findings [e.g., 3-5] and to apply it to intuitive cross-media operation on text and picture.



Fig.1. Miscommunication due to different perceptual groundings.

2. Mental Image Description Language L_{md}

2.1 Omnisensory Image Model

The MIDST treats word meanings in association with mental images, not limited to visual but omnisensory, modeled as "Loci in Attribute Spaces". An attribute space corresponds with a certain measuring instrument just like a barometer, thermometer or so and the loci represent the movements of its indicator. Such a locus is to be articulated by "Atomic Locus" with an *absolute* time-interval $[t_i, t_f]$ ($t_i < t_f$) as depicted in Fig.2 (left) and formulated as (1).

$$L(x,y,p,q,a,g,k) \quad (1)$$

This formula is called ‘Atomic Locus Formula’ whose first two arguments are often referred to as ‘Event Causer (EC)’ and ‘Attribute Carrier (AC)’, respectively. A logical combination of atomic locus formulas defined as a well-formed formula (i.e., wff) in predicate logic is called simply ‘Locus Formula’.

The intuitive interpretation of (1) is given as follows. *“Matter ‘x’ causes Attribute ‘a’ of Matter ‘y’ to keep (p=q) or change (p ≠ q) its values temporally (g=G_t) or spatially (g=G_s) over a time-interval, where the values ‘p’ and ‘q’ are relative to the standard ‘k’.”*

When $g=G_t$ and $g=G_s$, the locus indicates monotonic change or constancy of the attribute in time domain and that in space domain, respectively. The former is called ‘temporal event’ and the latter, ‘spatial event’. For example, the motion of the ‘bus’ represented by S5 is a temporal event and the ranging or extension of the ‘road’ by S6 is a spatial event whose meanings or concepts are formulated as (2) and (3), respectively, where ‘A₁₂’ denotes ‘Physical Location’. These two formulas are different only at the term ‘Event Type (i.e., g)’.

- (S5) The bus runs from Tokyo to Osaka.
- (2) $(\exists x,y,k)L(x,y,Tokyo,Osaka,A_{12},G_t,k) \wedge bus(y)$
- (S6) The road runs from Tokyo to Osaka.
- (3) $(\exists x,y,k)L(x,y,Tokyo,Osaka,A_{12},G_s,k) \wedge road(y)$

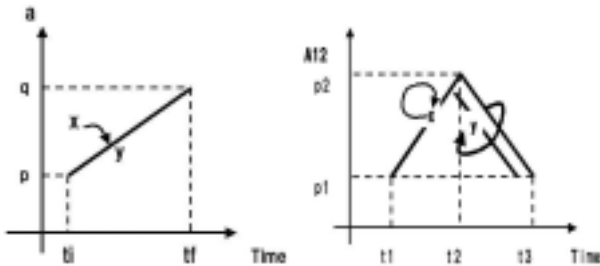


Fig.2. Atomic Locus (left) and Locus of ‘fetch’ (right).

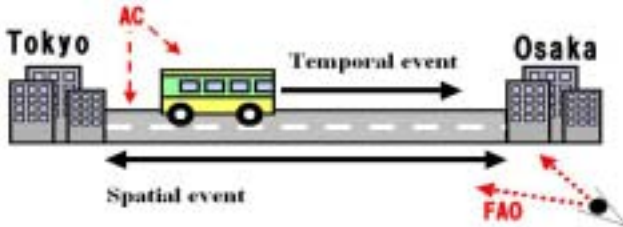


Fig.3. FAO movements and Event types.

The author has hypothesized that the difference between temporal and spatial event concepts can be attributed to the relationship between the Attribute Carrier (AC) and the Focus of the Attention of the Observer (FAO) [4]. To be brief, it is assumed that the FAO is fixed on the whole AC in a temporal event but *runs* about on the AC in a spatial event. According to this assumption, as shown in Fig.3, the *bus* and the FAO move together in the case of S5 while the FAO solely moves along the *road* in the case of S6.

2.2 Tempo-logical connectives

The definition of a tempo-logical connective K_i is given by **D1**, where τ_i , χ and K refer to one of *purely* temporal relations indexed by an integer ‘ i ’, a locus, and an ordinary binary logical connective such as the conjunction ‘ \wedge ’, respectively. The definition of each τ_i is provided with Table 1 implying the trivial theorem **T1**, where the durations of χ_1 and χ_2 are $[t_{11}, t_{12}]$ and $[t_{21}, t_{22}]$, respectively. This table shows the complete list of temporal relations between two intervals, where 13 types of relations are discriminated by the suffix ‘ i ’ ($-6 \leq i \leq 6$). This is in accordance with Allen’s notation [6] which, to be strict, is for ‘temporal conjunctions ($=\wedge_i$)’ but not for pure ‘temporal relations ($=\tau_i$)’.

D1. $\chi_1 K_i \chi_2 \leftrightarrow (\chi_1 K \chi_2) \wedge \tau_i(\chi_1, \chi_2)$

T1. $\tau_{-i}(\chi_2, \chi_1) \equiv \tau_i(\chi_1, \chi_2) (\forall i \in \{0, \pm 1, \pm 2, \pm 3, \pm 4, \pm 5, \pm 6\})$

The temporal connectives used most frequently are the temporal conjunctions ‘SAND (\wedge_0)’ and ‘CAND (\wedge_1)’, standing for ‘Simultaneous AND’ and ‘Consecutive AND’, conventionally denoted by ‘ Π ’ and ‘ \bullet ’, respectively. Employing these connectives, for example, the English verb concept ‘fetch’ can be defined as (4) and depicted as Fig.2 (right). Furthermore, the underlined part of (4) stands for the concept of ‘carry’ and this relation can be formulated as (5) employing the temporal implication ‘ \supset_4 ’, reading that an event ‘fetch(x,y)’ is necessarily *finished by* an event ‘carry(x,y)’. This kind of formula is not an axiom but a theorem deducible from the definitions of event concepts in the formal system.

$(\lambda x,y)fetch(x,y) \leftrightarrow (\lambda x,y)(\exists p_1,p_2,k)L(x,x,p_1,p_2,A_{12},G_t,k) \bullet$
 $((L(x,x,p_2,p_1,A_{12},G_t,k)) \Pi L(x,y,p_2,p_1,A_{12},G_t,k))$
 $\wedge x \neq y \wedge p_1 \neq p_2$ (4)

$fetch(x,y) \supset_4 carry(x,y)$ (5)

Table 1. List of temporal relations

Definition of τ_i	Allen’s notation
$t_{11}=t_{21}$	$\tau_0(\chi_1, \chi_2)$ equals(χ_1, χ_2)
$\wedge t_{12}=t_{22}$	$\tau_0(\chi_2, \chi_1)$ equals(χ_2, χ_1)
$t_{12}=t_{21}$	$\tau_1(\chi_1, \chi_2)$ meets(χ_1, χ_2)
	$\tau_{-1}(\chi_2, \chi_1)$ met-by(χ_2, χ_1)
$t_{11}=t_{21}$	$\tau_2(\chi_1, \chi_2)$ starts(χ_1, χ_2)
$\wedge t_{12} < t_{22}$	$\tau_{-2}(\chi_2, \chi_1)$ started-by(χ_2, χ_1)
$t_{11} > t_{21}$	$\tau_3(\chi_1, \chi_2)$ during(χ_1, χ_2)
$\wedge t_{12} < t_{22}$	$\tau_{-3}(\chi_2, \chi_1)$ contains(χ_2, χ_1)
$t_{11} > t_{21}$	$\tau_4(\chi_1, \chi_2)$ finishes(χ_1, χ_2)
$\wedge t_{12} = t_{22}$	$\tau_{-4}(\chi_2, \chi_1)$ finished-by(χ_2, χ_1)
$t_{12} < t_{21}$	$\tau_5(\chi_1, \chi_2)$ before(χ_1, χ_2)
	$\tau_{-5}(\chi_2, \chi_1)$ after(χ_2, χ_1)
$t_{11} < t_{21} \wedge t_{21} < t_{12}$	$\tau_6(\chi_1, \chi_2)$ overlaps(χ_1, χ_2)
$\wedge t_{12} < t_{22}$	$\tau_{-6}(\chi_2, \chi_1)$ overlapped-by(χ_2, χ_1)

2.3 Empty event

An ‘Empty Event (EE)’, denoted by ‘ ε ’, stands for nothing but for *absolute* time elapsing and is explicitly

defined as **D2** with the attribute 'Time Point (A_{34})' and the Standard of absolute time ' T_a '. Usually people can know only a certain *relative* time point by a clock that is seldom exact and that is to be denoted by another Standard in the L_{ma} . Hereafter, Δ denotes the total set of absolute time intervals. According to this scheme, the suppressed absolute time-interval $[t_a, t_b]$ of a locus χ can be indicated as (6).

$$\begin{aligned} \mathbf{D2.} \quad & \varepsilon([t_i, t_j]) \leftrightarrow (\exists x, y, g) L(x, y, t_i, t_j, A_{34}, g, T_a), \\ & \text{where } [t_i, t_j] \in \Delta (= \{[t_1, t_2] \mid t_1 < t_2 (t_1, t_2 \in \mathbf{R})\}). \square \\ & \chi \Pi \varepsilon([t_a, t_b]) \end{aligned} \quad (6)$$

3. Semantic description of physical reality

3.1 Event concepts

The semantic description of an event is compared to a movie film recorded through a floating camera because it is necessarily grounded in FAO's movement over the event. Therefore, as already pointed out, S1 and S2 can refer to the same scene in spite of their appearances, where what 'sinks' or 'rises' is FAO and whose conceptual descriptions are given as (7) and (8), respectively, where the special symbol ' $_$ ' is defined by (9), standing for an anonymous variable bound by an existential quantifier, and ' A_{13} ', ' \uparrow ' and ' \downarrow ' refer to the attribute 'Direction', and its values 'upward' and 'downward', respectively. Such a fact is generalized as '*Postulate of Reversibility of a Spatial Event* (PRS)' that can be one of the principal inference rules belonging to people's intuitive knowledge about geography. This postulation is also valid for such a pair of S7 and S8 as interpreted approximately into (10) and (11), respectively. These pairs of conceptual descriptions are called *equivalent in the PRS*, and the paired sentences are treated as *paraphrases* each other.

$$\begin{aligned} & (\exists y, p, z) L(_y, p, z, A_{12}, G_{s, _}) \Pi L(_y, \downarrow, \downarrow, A_{13}, G_{s, _}) \\ & \wedge \text{path}(y) \wedge \text{brook}(z) \wedge p \neq z \end{aligned} \quad (7)$$

$$\begin{aligned} & (\exists y, p, z) L(_y, z, p, A_{12}, G_{s, _}) \Pi L(_y, \uparrow, \uparrow, A_{13}, G_{s, _}) \wedge \text{path}(y) \\ & \wedge \text{brook}(z) \wedge p \neq z \end{aligned} \quad (8)$$

$$L(\dots, _ , \dots) \leftrightarrow (\exists \omega) L(\dots, \omega, \dots) \quad (9)$$

(S7) Route A and Route B meet at the city.

$$\begin{aligned} & (\exists p, y, q) L(_ \text{Route}_A, p, y, A_{12}, G_{s, _}) \Pi \\ & L(_ \text{Route}_B, q, y, A_{12}, G_{s, _}) \wedge \text{city}(y) \wedge p \neq q \end{aligned} \quad (10)$$

(S8) Route A and Route B separate at the city.

$$\begin{aligned} & (\exists p, y, q) L(_ \text{Route}_A, y, p, A_{12}, G_{s, _}) \Pi \\ & L(_ \text{Route}_B, y, q, A_{12}, G_{s, _}) \wedge \text{city}(y) \wedge p \neq q \end{aligned} \quad (11)$$

For another example of spatial event, Fig.4 (up) concerns the perception of the formation of multiple objects, where FAO runs along an imaginary object so called 'Imaginary Space Region (ISR)'. This spatial event can be verbalized as S9 using the preposition 'between' and formulated as (12), corresponding also to such concepts as 'row', 'line-up', etc.

(S9) \square is between Δ and \circ .

$$\begin{aligned} & (\exists y, p) (L(_y, \Delta, \square, A_{12}, G_{s, _}) \bullet L(_y, \square, \circ, A_{12}, G_{s, _})) \Pi \\ & L(_y, p, p, A_{13}, G_{s, _}) \wedge \text{ISR}(y) \end{aligned} \quad (12)$$

For more complicated examples, consider S10 and S11. The underlined parts are deemed to refer to some events neglected in time and in space, respectively. These events correspond with skipping of FAOs and are called 'Temporal Empty Event' and 'Spatial Empty Event', denoted by ' ε_t ' and ' ε_s ' as Empty Events with $g=G_t$ and $g=G_s$ at (6), respectively. Their concepts are described as (13) and (14), where ' A_{15} ' and ' A_{17} ' represent the attribute 'Trajectory' and 'Mileage', respectively. From the viewpoint of cross-media reference, the formula (14) can refer to such a spatial event depicted as the still picture in Fig.4 (down) while (13) is to be interpreted into a motion picture.

(S10) The *bus* runs 10km straight east from A to B, and *after a while*, at C it meets the street with the sidewalk.

$$\begin{aligned} & (\exists x, y, z, p, q) (L(_x, A, B, A_{12}, G_{t, _}) \Pi \\ & L(_x, 0, 10\text{km}, A_{17}, G_{s, _}) \Pi L(_x, \text{Point}, \text{Line}, A_{15}, G_{t, _}) \Pi \\ & L(_x, \text{East}, \text{East}, A_{13}, G_{t, _}) \bullet \varepsilon_t \bullet (L(_x, p, C, A_{12}, G_{t, _}) \\ & \Pi L(_y, q, C, A_{12}, G_{s, _}) \Pi L(_z, y, y, A_{12}, G_{s, _})) \\ & \wedge \text{bus}(x) \wedge \text{street}(y) \wedge \text{sidewalk}(z) \wedge p \neq q \end{aligned} \quad (13)$$

(S11) The *road* runs 10km straight east from A to B, and *after a while*, at C it meets the street with the sidewalk.

$$\begin{aligned} & (\exists x, y, z, p, q) (L(_x, A, B, A_{12}, G_{s, _}) \Pi \\ & L(_x, 0, 10\text{km}, A_{17}, G_{s, _}) \Pi L(_x, \text{Point}, \text{Line}, A_{15}, G_{s, _}) \Pi \\ & L(_x, \text{East}, \text{East}, A_{13}, G_{s, _}) \bullet \varepsilon_s \bullet (L(_x, p, C, A_{12}, G_{s, _}) \\ & \Pi L(_y, q, C, A_{12}, G_{s, _}) \Pi L(_z, y, y, A_{12}, G_{s, _})) \\ & \wedge \text{road}(x) \wedge \text{street}(y) \wedge \text{sidewalk}(z) \wedge p \neq q \end{aligned} \quad (14)$$

There are a considerable number of postulates of space and time to facilitate intuitive interaction between humans and IMAGES-M [4], and the PRS (Postulate of Reversibility of a Spatial Event) is one of the most important. This postulate can be formulated as (15) using ' \equiv_0 ', where χ and χ^R is a locus formula and its 'reversal' for a certain spatial event, respectively. The recursive operations to transform χ into χ^R are defined by (16)-(18), where the reversed values p^R and q^R depend on the properties of p and q . For example, (14) is transformed into (19) to be verbalized as S12, where $p^R = p$ and $q^R = q$ for A_{12} ; $p^R = -p$ and $q^R = -q$ for A_{13} .

$$\chi^R \equiv_0 \chi \quad (15)$$

$$(\chi_1 \bullet \chi_2)^R \leftrightarrow \chi_2^R \bullet \chi_1^R \quad (16)$$

$$(\chi_1 \Pi \chi_2)^R \leftrightarrow \chi_1^R \Pi \chi_2^R \quad (17)$$

$$(L(x, y, p, q, a, G_{s, k}))^R \leftrightarrow L(x, y, q^R, p^R, a, G_{s, k}) \quad (18)$$

$$\begin{aligned} & (\exists x, y, z, p, q) (L(_x, C, p, A_{12}, G_{s, _}) \Pi \\ & L(_y, C, q, A_{12}, G_{s, _}) \Pi L(_z, y, y, A_{12}, G_{s, _})) \bullet \varepsilon_s \bullet \\ & (L(_x, B, A, A_{12}, G_{s, _}) \Pi L(_x, 0, 10\text{km}, A_{17}, G_{s, _}) \Pi \\ & L(_x, \text{Point}, \text{Line}, A_{15}, G_{s, _}) \Pi L(_x, \text{West}, \text{West}, A_{13}, G_{s, _})) \\ & \wedge \text{road}(x) \wedge \text{street}(y) \wedge \text{sidewalk}(z) \wedge p \neq q \end{aligned} \quad (19)$$

(S12) The road separates at C from the street with the sidewalk and, after a while, runs 10km straight west from B to A.

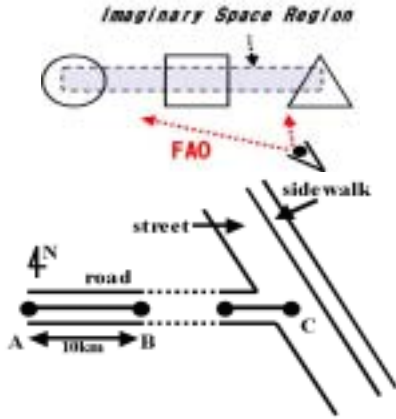


Fig.4. Complicated spatial events: 'row' (left) and 'example of road map' (right).

3.2 Object concepts

A physical object can be semantically defined as a combination of its properties and its relations with others. For example, the semantic descriptions of 'rain', 'wind' and 'air' can be given as (20)-(22), reading 'Rain is water attracted from the sky by the earth, makes an object wetter, is pushed an umbrella to by a human,...,' 'Wind is air, affects the direction of rain,...,' and 'Air has no shape, no taste, no vitality, ...,' respectively. The special symbols '*' and '/' are defined as (23) and (24) representing 'always' and 'no value', respectively.

$$\begin{aligned}
 &(\lambda x)\text{rain}(x) \leftrightarrow (\lambda x)(\exists x_1, x_2, \dots) L(_ , x, x_1, x_1, A_{41}, G_{t, _}) \\
 &\prod L(\text{Earth}, x, \text{Sky}, \text{Earth}, A_{12}, G_{t, _}) \prod L(x, x_2, p, q, A_{25}, G_{t, _}) \\
 &\prod L(x_3, x_4, x, x, A_{19}, G_{t, x_3}) \wedge \text{water}(x_1) \\
 &\wedge \text{object}(x_2) \wedge \text{human}(x_3) \wedge \text{umbrella}(x_4) \wedge (p < q) \dots \quad (20)
 \end{aligned}$$

$$\begin{aligned}
 &(\lambda x)\text{wind}(x) \leftrightarrow (\lambda x)(\exists x_1, x_2, \dots) L(_ , x, x_1, x_1, A_{41}, G_{t, _}) \\
 &\wedge \text{air}(x_1) \wedge (L(x, x_2, p, q, A_{13}, G_{t, _}) \wedge \text{rain}(x_2)) \dots \quad (21)
 \end{aligned}$$

$$\begin{aligned}
 &(\lambda x)\text{air}(x) \leftrightarrow (\lambda x)(\dots \wedge L^*(_ , x, /, /, A_{11}, G_{t, _}) \wedge \dots \wedge \\
 &L^*(_ , x, /, /, A_{29}, G_{t, _}) \wedge \dots \wedge L^*(_ , x, /, /, A_{39}, G_{t, _}) \wedge \dots) \quad (22)
 \end{aligned}$$

$$X^* \leftrightarrow (\forall [p, q]) X \Pi \varepsilon [p, q] \quad (23)$$

$$L(\dots, /, \dots) \leftrightarrow \sim (\exists p) L(\dots, \omega, \dots) \quad (24)$$

4. Discussions and conclusions

The cross-media operations between texts in several languages and pictorial patterns like maps were successfully implemented on our intelligent system IMAGES-M. Figures 5 and 6 show examples of Q-A on a map and text-to-action translation by IMAGES-M, respectively, where several kinds of intuitive postulates such as PRS were effectively utilized. In this research area, it is most conventional that conceptual contents conveyed by information media such as language and picture are represented in computable forms independent of each other and translated via 'transfer' processes which are often specific to task domains [e.g., 7-9]. That is, at my best knowledge, there is no other system that can perform cross-media operation in such a seamless way as mine.

Our future work will include establishment of learning facilities for automatic acquisition of word concepts from sensory data and human-robot communication by natural language under real environments.



H: What is between the buildings A and B?
S: The railway D.
H: Where do the street A and the road B meet?
S: At the crossing C.
H: Where do the street A and the road B separate?
S: At the crossing C.

Fig.5. Q-A on a map between a human (H) and IMAGES-M (S).



Fig.6. Text-to-Action translation by IMAGES-M: 'Sit down AND wave your left hand' was interpreted as 'Sit down BEFORE waving your left hand.'

References

- [1] Geo-ontology Concepts and Issues. Report of a workshop on Geo-ontology (Compiled and edited by Jenny Harding), Ilkley UK, Sept. 2002.
- [2] Coventry, K. R., Prat-Sala, M., Richards, L. V.: "The interplay between geometry and function in the comprehension of 'over', 'under', 'above' and 'below'," Journal of Memory and Language, 4, 376-398, 2001.
- [3] Yokota, M.: "An Approach to Integrated Spatial Language Understanding Based on Mental Image Directed Semantic Theory," Proc. of 5th Workshop on Language and Space, Bremen, Germany, Oct., 2005.
- [4] Yokota, M.: "A psychological experiment on human understanding process of natural language," Trans. of IEICE Japan, J71D-10, pp.2120-2127, 1988.
- [5] Yokota, M. & Capi, G.: "Cross-media Operations between Text and Picture Based on Mental Image Directed Semantic theory," WSEAS Trans. on INFORMATION SCIENCE and APPLICATIONS, Issue 10, 2, pp.1541-1550, Oct. 2005.
- [6] Allen, J.F.: "Towards a general theory of action and time," Artificial Intelligence, 23-2, pp.123-154, 1984.
- [7] Adorni, G., Manzo, M. Di, Giunchiglia, F.: "Natural Language Driven Image Generation," Proc. of COLING 84, pp. 495-500, 1984.
- [8] Shariff, A.R., Egenhofer, M., Mark, D.: "Natural-Language Spatial Relations Between Linear and Areal Objects: The Topology and Metric of English-language Terms," International Journal of Geographical Information Science, 12-3, pp.215-246, 1998.
- [9] Coradeschi, S., Saffiotti, A.: "An Introduction to the Anchoring Problem," Robotics and Autonomous Systems 43, pp.85-96, 2003.

Designing a Multi-modal Language for Directing Multipurpose Home Robots

Tetsushi Oka
Fukuoka Institute of Technology
oka@fit.ac.jp.

Masao Yokota
Fukuoka Institute of Technology
yokota@fit.ac.jp

Abstract

This paper discusses an approach to realising multipurpose home robots a wide spectrum of people can direct by speech, physical contact and gesture. A good spoken language interface allows ordinary people to direct robots without training in advance. However, many problems of Natural Language Understanding must be addressed if a wide range of utterances are to be understood immediately. Therefore, we design a practical multi-modal direction language combining a simple spoken language with nonverbal information. The spoken language has a simplified grammar and limited words, so that the robot should understand commands without complex computation or a large knowledge base. Nonverbal information makes commands more specific and eliminates ambiguity.

1 Introduction

Since the end of last century, more and more robots are coming into homes and offices to help ordinary people. As the birthrates in advanced countries are dropping, a robot that helps and cares elder or disabled people at home will be soon in demand in many societies. Such a robot is expected to understand what the user wants it to do as soon as a command is given. This raises an important issue of human-robot communication. For people who need helps, even computer GUIs, or remote controls of TVs are not ideal interfaces. Some people may give up using the robot before learning which commands all the buttons, sliders and levers are linked with. In addition, if the robots are to execute many kinds of commands, the user must learn long sequences of operations.

A spoken language interface, on the other hand, can be a good interface as it is not necessary to learn a new language if robots understand spoken commands in our language. However, there are still many difficult problems to tackle to realize a natural language interface by speech. For example, a spoken language interface based on a linguistically motivated grammar,

compositional semantics of logical forms and generic inference engines for natural language understanding has been applied to directing a mobile robot, asking it questions and giving it information by speech[1]. This system requires considerable computational power to check the consistency of semantic interpretations of user utterances in real time.

Recently, many robot systems implementing automatic speech recognition have been developed[2]. Many of them create word lattices from speech signals and interpret what the user means by means of keyword spotting, creating semantic representations of user utterances. In most systems, heuristic rules to construct semantic representations are built by the designer so that it should not take much time for semantic analysis. However, it is not clear to users what kind of an utterance the robot understands or misunderstands. Moreover, it is difficult to identify the meaning by this method alone if a variety of commands are given to the robot in many different situations. Therefore, this approach does not suit for multipurpose robots which help ordinary people at home.

Another way to reduce the computational cost of semantic analysis is to employ a simple command language. The most straightforward way is to design a command language which robots can directly execute, but the language would be difficult for humans to learn. Therefore, we design a command language based on a natural language by reducing the number and types of grammar rules, and the size of the lexicon. Obviously, a command language does not need to cover declarative and interrogative utterances. We presume that it is possible to build a practical and cost-effective spoken language interface by selecting words and phrases and constructing rules carefully. Besides spoken commands, gestures and physical contact provide a good means of intuitive direction. Nonverbal modalities of communication complement verbal communication and eliminate ambiguity. Thus, we design a multi-modal language combining a spoken language with nonverbal directions.

2 Target of the language

2.1 Multipurpose Home Robots

Home robots including pet robots like Sony AIBO (<http://www.aibo.com/>) and healing robots, PARO (<http://www.paro.jp/>) for instance, are already in the market and helping ordinary people at homes in some ways. Another example is a practical small robot available for cleaning our rooms (<http://www.irobot.com>). Although it is still difficult to build a robot which replaces a housekeeper or care worker, one can predict that home robots will evolve in the coming decades and be capable of doing many kinds of tasks given by us. They will be connected to home computer networks and collect useful information for us. They will move about in the home, bring something to us and move heavy objects. They will help us doing physical tasks, have a chat with us, control the air conditioner, TV and lights, and so forth. In short, we predict multipurpose home robots will find a place to help us.

In a way, a home robot can be thought of as a physical interface device with a home computer network or an intelligent house which follows the user and provides a means of interaction with the computers. At the same time, the robot is given physical tasks and helps the user. Most importantly, the robot has sensors and actuators and can change its location. This makes the way it interacts with a human utterly different from other interface devices.

2.2 Directing Mobile Robots

We believe that no matter how intelligent the robots may be, in some cases we have to direct them step by step telling them to stand up, turn back, go forward, look left, raise the right arm, grasp an object and so on, especially when the robots are physically helping them. Thus, the first step would be designing a multi-modal language which enables us to make robots turn, move forward/backward, look up/down and stop at will, saying "Turn left!", touching the robot, waving to it and so on.

It looks straightforward to realize a simple spoken language for this purpose, but things get a little complicated when we want to specify parameters of actions such as distance, angle and speed. On the one hand, "Turn right slowly!" does not include detailed information about the angle and speed, but on the other hand, "Turn 43 degrees clockwise within a second!" is not what we normally say. We could say "stop there", "faster", "a little bit more" after "go forward slowly" or "turn left a bit" many times until the robot

reaches a desirable position. Nonverbal signals such as gestures can allow the user to give the robot detailed information in a more natural manner. Thus, a multi-modal language combining a simple spoken command language with gestures and physical contact opens up possibilities to direct robots in natural ways.

The spoken language can be defined by a set of simple grammar rules and a relatively small lexicon. Besides, one can realize a wider coverage of commands to home robots using the same grammar rules and adding words or phrases to the lexicon: "Turn on the TV!", "Go to the kitchen", "(Make the room) warmer!", "Clean up the room", "Check my mailbox!", "Show me the weather forecast!", "Lift the box" and so on. Since in most of the environments of home robots, one can assume that e.g. there is only one TV in the room the user is in, little reasoning will be necessary to understand the commands if we properly design the language.

2.3 Directing Articulated Robots

Articulated robots with arms, hands and legs can perform many kinds of physical tasks. When using such robots, we will often want to tell the robot move its hands, arms or legs: "Stand up!", "Sit down!", "Walk a little!", "Raise the right arm higher!", "Stand on the left foot!", "Wave the arms slowly!", etc. These directions specify either a primitive action using the arms and legs or movements of individual limbs, so little confusion occurs in order to generate motor commands to the actuators, although a robust balance control system is indispensable.

As a humanoid has many degrees of freedom, the diversity of its motions is much larger than that of a wheeled mobile robot. Thus, we need a wider coverage in our multi-modal language. None the less, it is possible to adapt the language for this purpose by enhancing the lexicon without adding grammar rules.

If we could easily direct humanoids' various motions in a multi-modal language, it would be possible to make them help us in physical tasks and teach them how to move their limbs.

3 Spoken Language for Intuitive Direction of Home Robots

3.1 Grammar and Lexicon

Now, we discuss in more detail what kind of a spoken language is suitable for directing home robots.

What we have principally in mind is a grammar consisting of a small number of rules without recursions. For our purpose, we can select words necessary for directing robots. We presume that this is the class we should employ for a wide coverage of commands to multipurpose home robots. The grammar restricts the number of acceptable commands, but compositional semantics makes it possible to interpret a large number of spoken commands and convert them into robot actions. However, even a grammar in this simple class generates unnecessary utterances, so there are utterances which are grammatical but do not make sense. Only utterances which are grammatical and make sense should be converted into robot actions and the other grammatical input must be recognised as invalid at the stage in which their semantic representations are constructed. Thus, the robots need react to spoken commands in three, at least, different ways.

There are many ways to define a language of this class to cover verbal directions. Designing our language, we do not adhere to linguistic grammars and lexical categories of natural languages. For our purpose, it is more important to consider to what extent we should restrict directions to minimise the cost of computation and how easy for humans the language is to learn. Here are some examples of grammar rules:

$S \rightarrow ACTION\ PARAM$
 $ACTION \rightarrow turn$
 $PARAM \rightarrow DIRECTION\ SPEED$
 $DIRECTION \rightarrow ANGLE\ left$
 $ACTION \rightarrow OPERATION\ OBJECT$
 $OPERATION \rightarrow turn\ off$
 $OBJECT \rightarrow the\ TV$

Note that without recursions separate rules are necessary to allow the users to specify different combinations of parameters.

$PARAM \rightarrow DIRECTION\ DURATION$

3.2 Semantic Analysis and Robot Actions

Once the syntax of our language for verbal directions is defined, we need to give a meaning to each utterance. For example, if "Move!" is grammatical, we need to decide whether it is acceptable as a command or not and what actions it should be linked with depending on nonverbal input. Although generally

speaking the meaning of a command can vary depending on the context, we should avoid allowing such an ambiguous command. Instead, we should be able to choose one action, if an acceptable combination of an utterance and nonverbal input is given.

If the user says "Turn right!", the robot must change its orientation though it is not clear how much and how fast without nonverbal input. Perhaps the robot should turn, say, 45 degrees clockwise at a moderate speed. To execute an action, it needs all the parameters of it. For our purpose, the language interface should send action representations to the robot control system whenever the user commands the robot. A simple example of action representations passed to the robot system should look like the following:

```
action(name(turn),dir(45.0),speed(50.0),time(now))
```

Semantic analysis is necessary to construct action representations from verbal and nonverbal input. Methods of compositional semantics can systematically construct semantic and action representations from speech input. We believe that it is important to have a good framework for semantic analysis of multi-modal directions. Mapping utterances into actions in an ad hoc manner is not desirable for building a language for diverse directions. The Mental Image Directed Semantic Theory (MIDST) gives a framework for semantic processing in multi-modal interactions between a human and an articulated robot[3], and thus will give one for our purpose.

3.3 Disambiguation

As mentioned above, ambiguity in spoken commands should be avoided as much as possible. First, we can eliminate context dependent directions such as "Go *there!*" and "Approach *it!*". Secondly, we choose default values of action parameters. For example, we could link "Turn!" and an action to turn 360 degrees slowly, or "Pick *it!* up!" and an action to grasp anything near the robot and hold it. Thirdly, an utterance can be interpreted in more than one way because of multi-sense words or syntactically ambiguous expressions. Although most of such utterances are ruled out if the language is simple, we must consider this problem at both of the stages of designing the grammar and lexicon and mapping utterances into actions.

4 Nonverbal Direction

Home robots will have many different sensors for perceiving their circumstances and controlling their

bodies. Those sensors, especially tactile, proximity, and vision sensors, are useful as user interface devices. In our multi-modal language, nonverbal input through sensors plays an important role for disambiguation, filling slots of action representations. Pointing gestures disambiguate directions like “Go *over there!*” and “Touch *that wall!*”. Tapping a part of the robot implies the direction, speed and duration of the action: saying “Turn!” and tapping the robots left arm three times can be interpreted as “Turn 90 degrees to the left quickly!”.

5 Robot Systems for Usability Studies

For usability studies, we build robot systems one can direct in our multi-modal language and conduct experiments involving people who are not familiar with computers and robots.

The robot systems consist of a multi-modal language interface and robot control system. The language interface receives sound signals and other sensory input. It comprises components for speech recognition, gesture recognition, analysis of tactile and proximity sensor readings, and syntactic and semantic analysis. It sends the robot control system action representations which describe an action directed by the user in real time .

We are currently implementing robot systems with a multi-modal command interface. Our first prototype was built on a Sony AIBO (ERS-210) using the *Master Studio SDK*. The robot recognises about 50 Japanese words, simple hand gestures moving a pink ball and tactile messages on its tactile and infrared sensors. Its action repertoire includes standard action of the SDK, standing up, walking etc., and our original actions created using *Action Composer*, a part of the SDK. Although it can only react to single-word commands, it is possible to realise an intuitive interface to direct the robot. The major limitations are due to the small sets of spoken commands and nonverbal directions.

Our next setup, Lemon (Fig.1), is based on a new Sony AIBO (ERS-7M3), the *Open-R SDK* (<http://openr.aibo.com/>) which enables us to build the on-board control system in C++ and *MEdit* to create robot motions to add new actions. For speech recognition, we use *Julian* (<http://julius.sourceforge.jp/en/julius.html>), a grammar based recognition engine and its development kit which allows us to develop context free grammars¹ for speech input and test them on our PCs. We develop a

¹The engine actually parses only regular languages.

spoken language based on Japanese using Julian and study its usability on our robot system.

Another target is a humanoid robot one can direct using our multi-modal language. We are developing small humanoids for various objectives. The newest at the moment is Syokabe (Fig.1), which has 27 DOFs including effective yawing rotations at the body and legs. Running Julian on our PCs, we can use the same spoken language interface for Lemon and our humanoids.

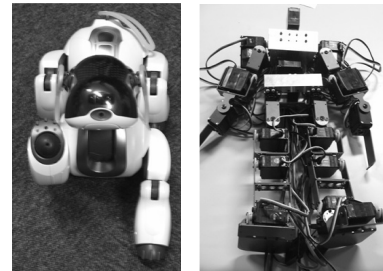


Figure 1: Lemon (left) and Syokabe

6 Summary

This paper proposed to design a practical multi-modal language to direct multipurpose home robots. We discussed basic features of the language, action representations, and command interface. The language is based on a natural language and has a smaller set of grammar rules to cover directions of home robots. We have implemented some prototypes and components of robot systems and are conducting usability studies using four legged robots and humanoids.

References

- [1] J. Bos and T. Oka “A spoken language interface with a mobile robot” *Journal of Artificial Life and Robotics*, Vol. 11, 2007.
- [2] R. Prasad, H. Saruwatari and K. Shikano, “Robots that can hear, understand and talk” *Advanced Robotics*, Vol. 18, pp. 533-564, 2004.
- [3] M.Yokota and G.Capi, “Integrated multimedia understanding based on Mental Image Directed Semantic Theory” *Proc. 11th International Symposium on Artificial Life and Robotics*, OS6-1, 2006.

Tele-Immersive Collaborative Virtual Environment for Intuitive Interpretation

Nobuyuki KUKIMOTO
Detpt. of Infomatics
Tohwa University
1-1-1 Chikushigaoka Minami-ku
Fukuoka,815-8510,Japan

Yasuo EBARA
Academic Center
for Computing and Media Studies
Kyoto University
Yoshida-Honmachi, Sakyo-ku
Kyoto,606-8501, Japan

Koji KOYAMADA
Center for the Promotion of
Excellence in Higher Education
Kyoto University
Yoshida-Nihonmatsucho, Sakyo-ku,
Kyoto,606-8501, Japan

Abstract

The purpose of tele-immersive collaboration is to enable people in separate locations to work together effectively by the Virtual Reality (VR) technology facilitating the human intuitive insight and interpretation. Consequently, it is important to cogitate with figures and characters as well as voice communication in Collaborative Virtual Environment (CVE). In this paper, we constructed tele-immersive CVE with annotation capability and free-hand drawing of characters and figures into Immersive Projection Technology (IPT) environment. In addition, participants from remote sites connected over a Wide Area Network (WAN) were enabled to interact with each other by sharing annotations via a PDA application. Moreover, we developed applications for scientific visualization and, for intellectual work based on KJ Method inside a tele-immersive CVE. From these results, we are able to maintain essential information for thinking by making annotation on IPT environment, and have proved the system can support intuitive understanding in remote collaborative work.

1 Introduction

Complexity and multiplicity of large-scale data sets generated from High Performance Computing (HPC) systems have been increasing at a proportional rate to their computational power and network bandwidth.

Collaboration between multi-field researchers using visualization techniques become important in order to inspect these large-scale data sets efficiently, and it can support human insight and interpretation.

In order to work smoothly with participants at remote sites via WAN, Computer Supported Cooperative Work (CSCW) tools, such as E-mail, WWW browser or a TV Conference system, have been used as general tools. However, CSCW tools are limited in 3D expression of data sets possessing depth information because 2D displays or projectors are generally used.

We consider that effective remote collaboration using 3D contents requires a tele-immersive CVE [1, 2] which enables high presence and reality. Collaboration in CVE is important to support problem solving and intellectual discovery by intuitive observation of 3D contents from various view-points in a shared environment.

In this paper, we describe a tele-immersive CVE which supports intuitive interpretation by making annotations within IPT environment. In addition, we describe our applications for scientific visualization and intellectual work in the CVE based on KJ Method.

2 SECI process and Collaboration

Knowledge is differentiated between “tacit” and “explicit” knowledge. Tacit knowledge, unable to be expressed verbally, is an individual’s knowledge or ex-

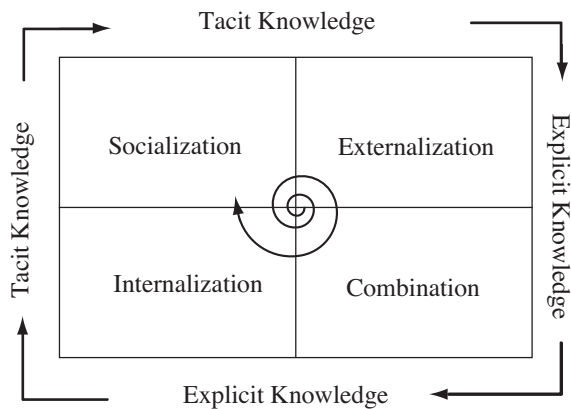


Figure 1: Knowledge Translation.

perience accumulated personally. In order to share tacit knowledge with others, it needs to be converted to a sharable explicit knowledge such as text or figures. On the other hand, the knowledge creation is a continuous process by dynamic interaction between these different kinds of knowledge.

This process is called “SECI process” [3] which has 4 modes (Figure1). Socialization is to share a common space through a communication between participants. Externalization is to translate from tacit knowledge to explicit knowledge. The explicit knowledge is shared by other participants. Combination is the integration of these into new more complex and systematic sets of explicit knowledge. Internalization is to absorb this explicit knowledge as tacit knowledge in practical use. These four modes configure the spiral model in the process for knowledge creation.

We consider that collaborative works in CVE have similarity to the SECI process. Socialization process is same as the construction of shared virtual environment. Communication between participants in CVE is similar to externalization and combination. Internalization looks like a simulation of work, and self-schooling in stand-alone mode is equivalent to the work in a VR environment. Externalization process in particular requires various expression methods in order to transmit their ideas and experiences. In addition, combination process requires the externalized explicit knowledge to be converted to own knowledge.

Therefore, it is important to cogitate with figures and characters as well as voice communication, because remote collaborative works in CVE has a tendency to use abbreviation or corresponding expressions. In order to support intuitive knowledge creation, we have constructed a tele-immersive CVE with

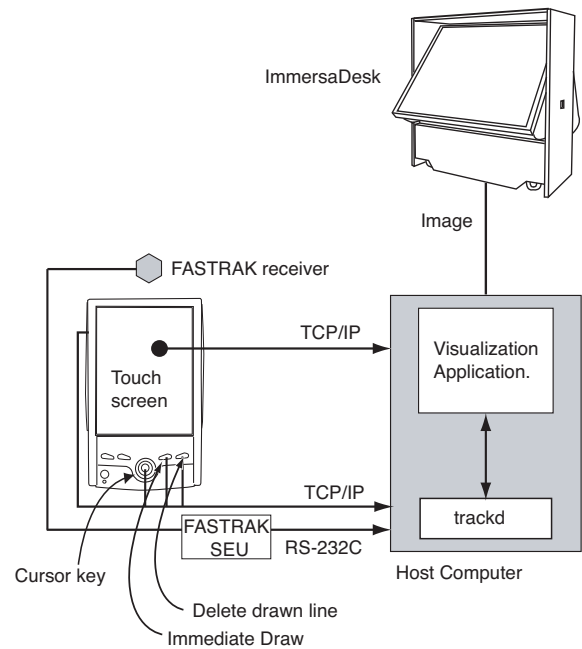


Figure 2: System configuration of our IPT environment.

annotation capability into IPT environment that consist of 3D contents. In this environment, we are able to change the visualization parameter and to make annotations by using PDA. We enabled collaborative to be an understanding of visualization data with annotations which shared with co-researchers of remote places.

3 System Configuration

3.1 Scientific Visualization in IPT Environment

VR technology is one of the useful visualization tools for intellectual discovery. We implemented a PDA-based application for IPT such as CAVE or ImmersaDesk. It can control parameters and make annotations for scientific visualization without moving between the IPT and host computer[4].

Figure 2 shows our system configuration. The host computer generates visualization images and displays them on the ImmersaDesk display. We used the Visualization Tool Kit (VTK) and CAVE Library for visualization. We established a private WAN by connecting several remote sites over the Japan Gigabit Network II (JGN II). Participants in each site can in-

interact by making annotations via a PDA application within IPT. Avatars represents other participants who access from remote places. Coordinate data of each participant's head and PDA in the IPT environment is transmitted between participants and each participant is represented as an avatar with motion.

3.2 Communication in Tele-immersive CVE

Collaborative works between remote places uses a lot of conversation[5]because participants in the IPT environment have difficulty using input interface such as keyboards or mice. Therefore,voice communication is indispensable in achieving smooth communication in CVE. We developed voice communication tools which enable adjustment of volume and PAN level corresponding to speaker's position in IPT environment.

In addition, we implemented two free-hand writing methods to use in CVE since it has a high tendency to use clipped words and anaphoric expressions. One method is the drawing of annotations directly in IPT environment by using a PDA like a virtual pen enabling to move it freely while pressing a PDA's button. This method is suitable for drawing 3D figures or large images. The other method is the use of PDA's touch screen to transfer a drawn annotation into the IPT. This is appropriate for drawing characters or texts. These drawing data are then sent to the IPT environments to be shared by all participants.

4 Application in Tele-immersive CVE

4.1 Scientific Visualization of Fluid Flow

We have implemented an environment for scientific visualization in tele-immersive CVE. Scientific visualization in IPT environment is suitable for intuitive interpretation of complex fluid data. Figure 3 shows an overview of fluid visualization.

Each participant can change visualization parameters and can make annotations in CVE by using a PDA application. Visualization parameter data and vertex position of annotations are sent to each participant's IPT environment in real-time.

4.2 Visualization of Bedrock Destroying Phenomenon

Traditional earthquake researchers have used three orthographic views, however the use of 3D visualization technology has been considered effective for the

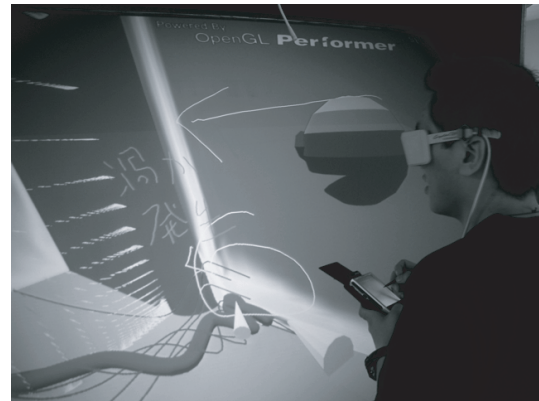


Figure 3: Overview of fluid visualization with participant's avatar.



Figure 4: Immersive bedrock destroying phenomenon visualization and annotations.

analysis of destruction phenomenon. Taking this into consideration, we attempted to use 3D visualization technique to the destruction phenomenon of earthquake in an IPT environment.

Figure 4 shows an example of earthquake data displaying. In this visualization, earthquake sources are represented by spheres and the intensities by colors. The earthquake source location becomes easy to understand by interactively configuring the dense spheres in the IPT environment. In addition, researchers have been facilitated to understand the construction of fault planes via intuitive observation by the virtual walk through to the underground structure.



Figure 5: Overview of KJ Method application in IPT.

4.3 Intellectual Works by KJ Method in IPT Environment

KJ Method is one of the well known techniques for knowledge creation. It makes groups for relationship between each other and the various information are described as cards or "Post-it". In addition, new ideas created by using the KJ Method are described as writing to cards. Since the task of making cards using the KJ Method is generally hard for the users, several software have been released to support this task in a Personal Computer (PC). However, users becomes interfered when the numbers of cards increase, because there is a limitation of working area on traditional PCs.

We implemented an application for using KJ Method within an IPT environment in order to serve as a CVE for knowledge creation. Figure 5 shows the overview of this KJ Method application in IPT. In this environment, various image files, such as graph, picture or 3D visualization image, are used as the cards in KJ Method. IPT environments have no limitation regarding working area and are able to add more axis of grouping. Image and additional annotation data in IPT environment are loaded from database system, and are saved in database after the work. Therefore, users are allowed to access the database from a WWW browser and are enabled to carry out the continuation of the work in another environment.

5 Conclusion

In this paper, we presented a tele-immersive CVE which we have developed with free-hand annotation

capability via PDA in IPT environment which consists of 3D visual contents.

Considering the use of annotations such as streamline drawing or marking the noteworthy point, we could conclude that collaboration with annotations inside the CVE supports better communication between participants. From these results, we are able to maintain essential information for thinking by making annotation such as characters or figures on IPT environment and have proved the system can support intuitive understanding in remote collaborative work.

In the future, we believe that the task of making 3D annotations in CVE will be effective for enriching communication tools during the collaborative investigation, and will be a more useful tools for human intellectual works.

Acknowledgements

This work was executed as a part of the research and development of Tele-immersive conference systems sponsored by National Institute of Information and Communications Technology (NICT). Special thanks goes to Dr. Jorji Nonaka at Kyoto University for his useful advices.

References

- [1] Leigh, J., Johnson, A., Vasilakis, C., DeFanti, T. "Multi-perspective Collaborative Design in Persistent Networked Virtual Environments," In Proc. of IEEE Virtual Reality Annual International Symposium '96, pp.253-260. (1996).
- [2] Ki, B., Klasky, S., "Collaborative scientific data visualization" *Concurrency: Practice and Experience*, Vol.9, No.11, pp1249-1259, (1997).
- [3] Nonaka, I., Takeuchi, H., *The Knowledge-Creating Company: How Japanese Companies Create the Dynamics of Innovation*, Oxford Univ Pr. (1995).
- [4] Kukimoto, N., Furusho, Y., Nonaka, J., Koyamada, K., Kanazawa, M., "PDA-based Visualization Control and Annotation Interface for Virtual Environment," In Proc. VIIP 2003, The 3rd IASTED International Conference on Visualization, Imaging, and Image Processing, pp.975-980, (2003).
- [5] Ruddle, R. A., Savage, J. C., Jones, D. M. "Verbal Communication During Cooperative Object Manipulation" In Proc. of ACM Collaborative Virtual Environments (CVE'02), pp.120-127, (2002).

A Next Generation Video Streaming System for Intuitive Remote Interaction

Kaoru Sugita Nobuhiro Nakamura Shinichi Baba Masao Yokota

Fukuoka Institute of Technology

sugita@fit.ac.jp, {mgm05008, mgm05011}@ws.ipc.fit.ac.jp, yokoya@fit.ac.jp

Abstract

In this paper, we propose a live video streaming system based on virtual reality technologies for intuitive interaction among people remotely located. This system is one kind of sever-client system and can provide remote users with virtual 3D audiovisual fields in real time via a very high-speed network. The server captures audio and video data from its clients, compiles them into one 3D audiovisual scene at a virtual conference and broadcasts it over the clients. At the present stage, our system captures 2 videos and creates one 3D video at a time. Our system can play 3D audiovisual contents on Windows XP systems as well as on CAVE systems.

1. Introduction

In recent years, live video streaming systems and TV conference systems are very popular [1, 2, 3]. We have also developed a WWW conference system in order to provide WWW browsers with a live video communication facility [4] and evaluated its performance [5, 6]. However, these systems are only to display flat pictures and thereby the users hardly feel talking face-to-face with the other participants at the same place.

On the other hand, there have been proposed several 3D model reconstruction methods [7, 8]. These are applicable to videos as well as to photographs and can be implemented on virtual reality systems such as CAVE system [9] and, as a further extension, can provide the remote users with face-to-face realities.

This paper proposes a VR live video streaming system in order to facilitate intuitive interactions among remote users and shows its implementation and evaluation based on the experimental results.

2. VR live video streaming system

Our VR live video streaming system can provide the remote users with such a communication facility as shown in Fig.1 where 3D audiovisual fields are available on Windows XP systems as well as on CAVE systems. The participants can allocate their images arbitrarily in the

video. The sound field, so called, Virtual Sound Field (VSF) is created so as to match the arrangement of the images. Therefore, each participant can communicate with the other users as if they were actually talking face-to-face at the same place.

Our proposed system is one kind of sever-client system as shown in Fig.2 and can provide remote users with virtual 3D audiovisual fields in real time via a very high-speed network. The server captures audio and video data from its clients, compiles them into one 3D audiovisual scene at a virtual conference and broadcasts it over the clients.

The server consists of 5 components as follows:

- (S1) User Interface - Provide windows to display 2D videos and to set up video capture parameters
- (S2) Video Capturer - Take in 2D video and audio data for 3D contents
- (S3) 3D Video Creator - Extract frames, detect parallaxes and create polygons with textures
- (S4) 3D Video Stream Controller - Broadcast polygons and textures controlling their numbers, frame sizes and rates
- (S5) Sound Stream Controller - Broadcast sounds controlling the sampling rates

Each client consists of 7 components as follows:

- (C1) User Interface - Provides windows to display 3D videos and to set up 3D video parameters
- (C2) 3D Video Allocator - Arrange 3D videos in the virtual world
- (C3) 3D Video Controller - Play 3D video with sounds synchronized
- (C4) 3D Video Stream Controller - Receive polygons and textures controlling their numbers, frame sizes and rates
- (C5) Virtual Sound Field Creator - Play sounds reflecting the arrangement of the 3D videos
- (C6) Sound Controller - Play sounds with 3D videos synchronized
- (C7) Sound Stream Controller - Receive sounds controlling the sampling rates

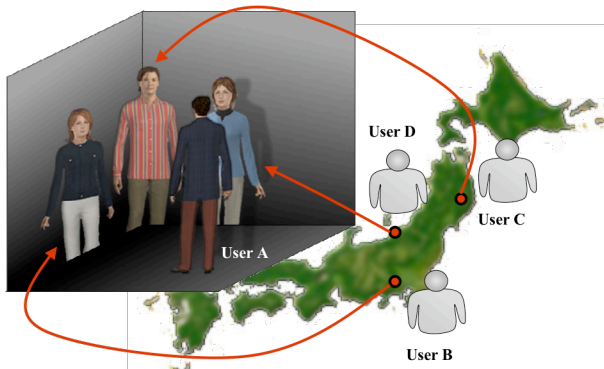


Fig.1. VR live video streaming system.

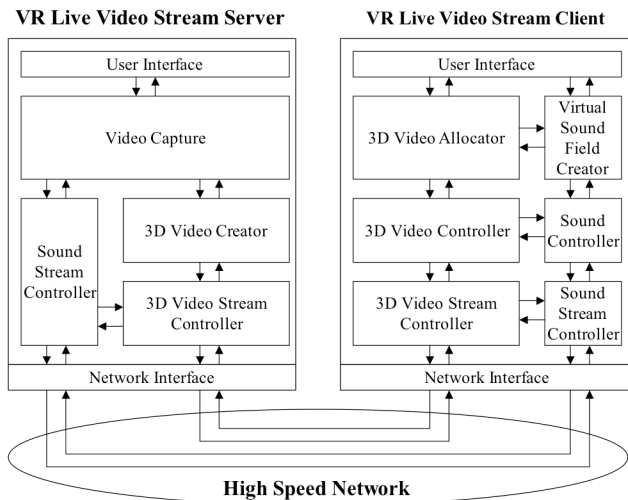


Fig.2. System architecture.

3. 3D video creation method

Figure 3 shows spatial relations of an object and its 2D video frames. As known well, the object's position (O) can be computed from the points ($P1$ and $P2$) projected on the two different frames according to (1)-(3), where $O(x_0, y_0, z_0)$, $P1(x_1, y_1, z_1)$, and $P2(x_2, y_2, z_2)$, respectively.

$$x_0 = (D/2d)(x_1 + x_2) \quad (1)$$

$$y_0 = (D/d)y_1 = (D/d)y_2 \quad (2)$$

$$z_0 = (D/d)f \quad (3)$$

A 3D model is composed of polygons each of which consists of vertexes with 3D coordinates. Such a model can be reconstructed by corresponding the 3D coordinates specifying the object's surface with the 2D coordinates in the video frames. A 3D video supplies a time-sequenced set of polygons and texture images. The details of 3D model creation are shown in Fig.4.

In order for modeling in real time, we have developed a new method to control the number of polygons for parallax detection. In this method, the parallax between the frames is calculated efficiently using one set of

candidate pairs of corresponding pixels so called 'Template for Candidate Projection Area (TCPA)' as shown in Fig.5. Usually such a candidate pair cannot be determined uniquely due to the ambiguous z coordinate of the object while it is prepared in advance by (4)-(7). Therefore, the pair minimizing the difference between TCPAs is selected as the most certain one.

$$x_1 = f \left(\frac{2x_0 + D}{2z_0} \right) \quad (4)$$

$$y_1 = f \left(\frac{y_0}{z_0} \right) \quad (5)$$

$$x_2 = f \left(\frac{2x_0 - D}{2z_0} \right) \quad (6)$$

$$y_2 = f \left(\frac{y_0}{z_0} \right) \quad (7)$$

4. Virtual sound field

The virtual 3D sound field is intended to play sound reflecting the relation between the 3D video display point and the viewpoint in the virtual world. As shown in Fig.6, the sound source and the sound receivers are located according to the 3D video. In order to realize the vertical stereo effect, each receiver is divided logically into 2 sub-receivers and each speaker plays the same sound twice reflecting the difference in distance and in vertical angle between the sub-receivers. The volume and delay time at the receiver is given by (8) and (9).

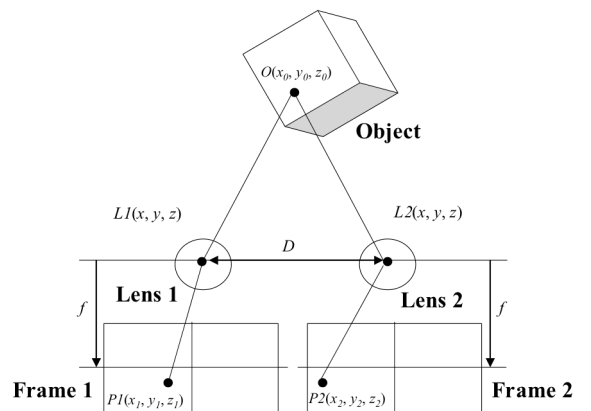


Fig.3. Spatial relations of object and frames.

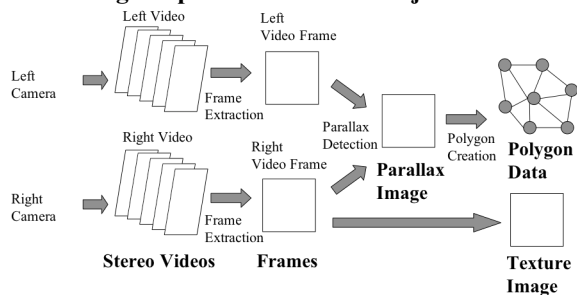


Fig.4. 3D model creation.

$$V_r = f_v(V_{ss}, L_{svx}) \quad (8)$$

$$D_r = \frac{f_d(L_{svx})}{c} \quad (9)$$

where

L_{svx} : the distance between the sound source and the sound receiver,

V_{ss} : the volume at the source,

V_r : the volume at the receiver,

$f_v(V_{ss}, x)$: the volume at the distance x from the source,

D_r : the delay time at the receiver,

c : the speed of sound, and

$f_d(x)$: the delay time at the distance x .

5. Implementation

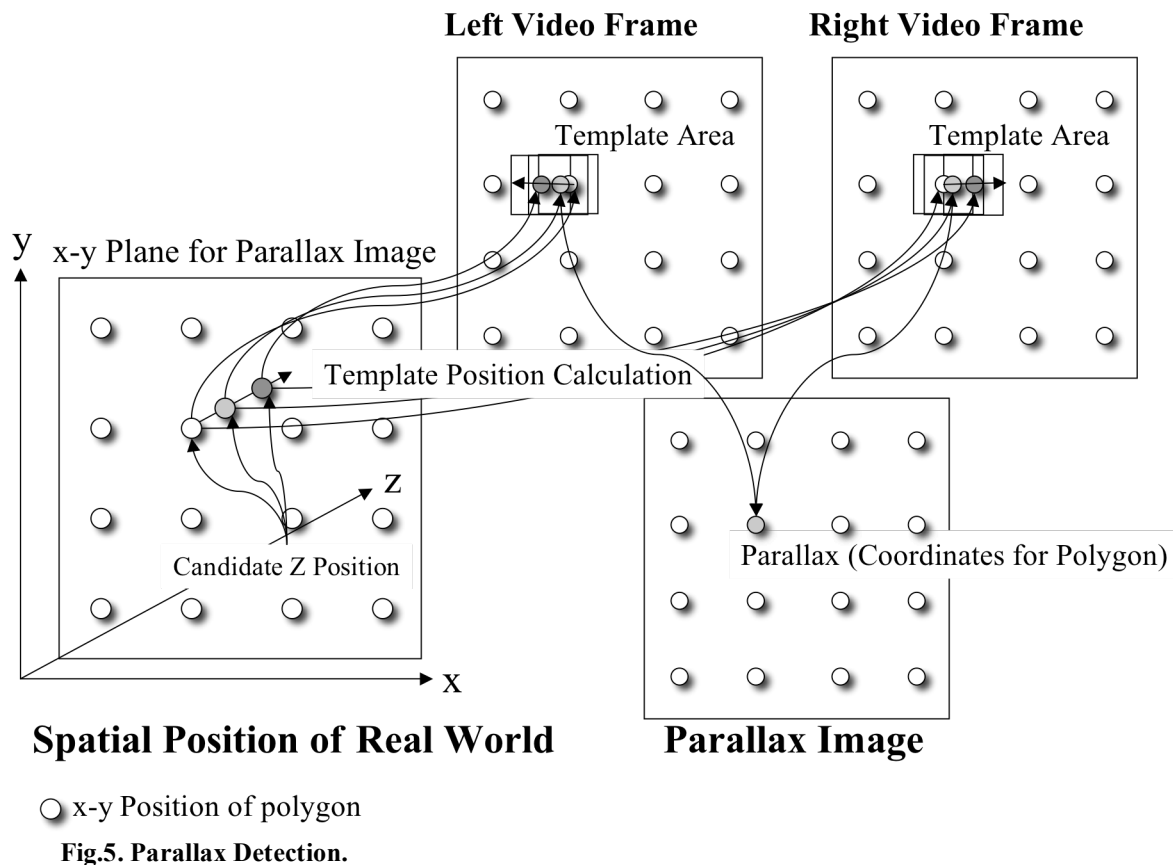
The server was implemented on Windows XP system while each client was implemented on either Windows XP system or CAVE system, employing the C Language, Intel Open Computer Vision Library (Open CV) [10], WinSock2, Open GL, GLUT and CAVE Library. The CAVE library was used to draw/display 3D videos and to support the head tracking on CAVE system only. The others were utilized for both the systems in the

conventional ways except that the Open CV was for capturing videos and extracting video frames.

Figure 7 shows the videos from the left camera (a) and the right camera (b) and the 3D video (c) composed on the server. Logicool Qcam for Notebooks Pros were employed as web cameras put at a space 25cm long enough for us to recognize easily the parallax between Fig.8 (a) and (b). Figure 8-c was viewed at a client on Windows XP System, where the user could control the viewpoint and view angle through the keyboard.

6. Conclusion

The VR live video streaming system and its implementation were described. At the present stage, our system captures 2 videos and creates one 3D video at a time. Our system can play 3D audiovisual contents on Windows XP systems as well as on CAVE systems while the existing live video streaming systems and TV conference system are only to display the flat pictures. Currently, we are evaluating our system in its precision and performance and also implementing the sound modules. In the future, we will introduce some highly precise certainty calculation method.



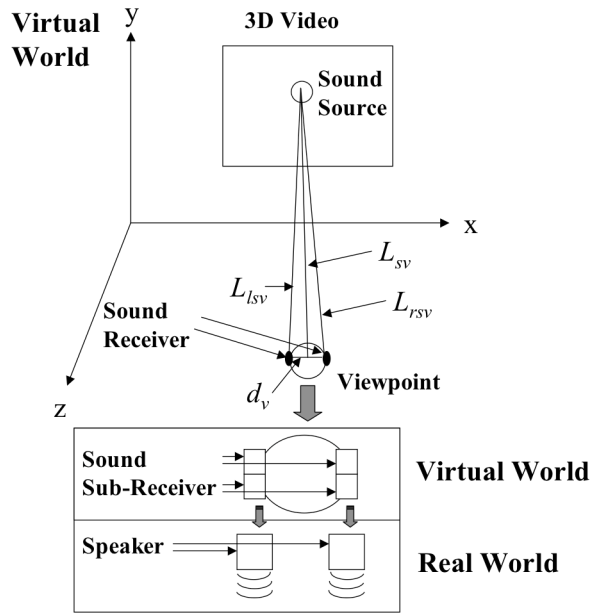


Fig.6. Virtual Sound Field.



Fig.7. Implemented System.

References

[1] D.Nishantha, Y.Hayashida and T.Hayashi: "Application Level Rate Adaptive Motion-JPEG Transmission for Medical Collaboration Systems", Proc. of the 6th International Workshop on

Multimedia Network Systems and Applications (MNSA-2004), pp. 64-69, 2004.

- [2] Y.Maita, K.Hashimoto, Y.Shibata: "A New TV Conference System with Flexible Middleware for Omni-directional Camera", Proc. of the 7th International Workshop on Network-Based Information System (NBIS-2004), pp. 84-88, 2004.
- [3] Y. Kato, D. Jiang and K. Hakoziaki: "A Proposal of a Streaming Video System in Best-Effort Networks Using Adaptive QoS Control Rules", Proc. of the 18th International Conference on Advanced Information Networking and Applications (AINA-2004), Vol.2, pp. 54-57, 2004.
- [4] Kaoru Sugita, Noriki Uchida, Akihiro Miyakawa, Leonard Barolli: "Implementation of WWW Conference System for Supporting Remote Mental Health Care Education", Proc of the Seventh International Workshop on Multimedia Network Systems and Applications (MNSA2005), pp.686-692, June.2005.
- [5] Kaoru Sugita, Noriki Uchida, Akihiro Miyakawa, Giuseppe De Marco, Leonard Barolli: "Performance Evaluation of WWW Conference System for Supporting Remote Mental Health Care Education", Proc. of the 11th International Conference on Parallel and Distributed Systems (ICPADS-2005), Vol.1, pp.271-277, July.2005.
- [6] S.Baba, K.Sugita, N.Uchida, G. De Marco, L.Barolli and A.Durrusi: "Performance Evaluation of WWW-based Conference System ", Proc. of the 8th International Workshop on Network-Based Information System (NBIS2005), pp.50-56, Aug.2005.
- [7] Yin Li, et al.: "Stereo Reconstruction from Multiperspective Panoramas ", IEEE Transactions on Pattern Analysis and Machine Intelligence, Vol. 26, No. 1, pp.45-62, 2004.
- [8] James Davis, et al.: "Spacetime Stereo: A Unifying Framework for Depth from Triangulation ", IEEE Transactions on Pattern Analysis and Machine Intelligence, Vol. 27, No. 2, pp. 296-302, 2005.
- [9] Cruz-Neira, C., Sandin, D.J., and DeFanti, T.A.: "Surround-Screen Projection-Based Virtual Reality: The Design and Implementation of the CAVE. ", Proc of SIGGRAPH '93 Computer Graphics Conference, pp. 135-142, August 1993.
- [10] Intel Open Source Computer Vision Library, <http://www.intel.com/technology/computing/opencv/index.htm>

Face Recognition Across Illumination

Saleh Aly
Department of Intelligent Systems
Kyushu University
744, Motoooka, Nishi-ku, Fukuoka, 819-0395
aly@limu.is.kyushu-u.ac.jp

Naoyuki Tsuruta
Department of Electronics Engineering
and Computer Science, Fukuoka University
8-19-1, Nanakuma, Jonan, Fukuoka 814-0180
tsuruta@tl.fukuoka-u.ac.jp.co.jp

Alaa Sagheer
Department of Intelligent Systems
Kyushu University
744, Motoooka, Nishi-ku, Fukuoka, 819-0395
alaa@limu.is.kyushu-u.ac.jp

Rin-Ichiro Taniguchi
Department of Intelligent Systems
Kyushu University
744, Motoooka, Nishi-ku, Fukuoka, 819-0395
rin@limu.is.kyushu-u.ac.jp

Abstract

Illumination variation in face images is one of the most difficult problems in face recognition system. The performance of self-organizing map-based face recognition system is highly degraded when the illumination of test images differ from training images. Illumination normalization is a way to solve this problem. Both global and local image enhancement methods are studied in this paper. Local histogram equalization method is highly improving the recognition accuracy of the CMU-PIE face database.

Keywords—Face recognition, illumination, SOM

1 Introduction

Important practical applications of automatic face recognition have made it a very popular research area in the last three decades [1]. Human-machine interface is considered as one of these applications. For example, the interaction between robots and human requires a fast and accurate identification of the person identity. In spite of the expanding research in the field of face recognition, many problems are still unsolved.

Recently, more researchers focus on robust face recognition which is invariant to pose, expression, illumination variations. Illumination variation is still a challenging problem in face recognition research area especially for appearance-based methods [2]. The same person can appear much differently under varying lighting conditions. Varieties of approaches have been proposed to solve the problem, and they can be classified into three categories: preprocessing and normalization [3, 4], invariant feature extraction [5], and face modeling [6].

Self-organizing map (SOM) [7] is a famous unsupervised neural network. In this work, SOM is used for feature extraction and dimensionality reduction. Two different shapes of SOM maps including sheet, and cylinder shapes are used to learn face manifold. However, the performance of SOM is highly degraded when the lighting condition of the test images differs from that of training images. Therefore,

it is proposed to improve its accuracy using illumination normalization techniques.

To improve the performance of SOM, several illumination normalization techniques are investigated. According to the processing strategy, these methods can be categorized into two classes. Global methods in which the whole image is processed at once. On the other hand, region-based methods process small regions from the image separately. In this work, two well-known image enhancement methods are used. Gamma intensity correction (GIC) which normalize the overall image intensity to a given intensity level and histogram equalization (HE) which reassigns the intensity values of pixels in the input image such that the output image contains a uniform distribution of intensities. Both unnormalized and normalized face images are projected on the 2-dimensional space spanned by the two greatest eigenvectors using principal component analysis (PCA); the structure of the projected manifold under different lighting directions is analyzed, moreover, the separability among different classes is explored.

The remainder of the paper is organized as follows: In section 2, the learning algorithm of self-organizing map neural network is discussed. Section 3 mainly describes global and local illumination normalization methods. Face database, experimental results, and conclusions are given in the following three sections.

2 Self-organizing Map

Consider the set of training images $\chi = \{x_i, 1 < i < M\}$, each image belong to N -dimensional space. SOM is usually represented as a neural network sheet or map whose units, usually called nodes or neurons, become tuned to different input vectors x_i . A weight vector w_j , sometimes called reference or codebook, is associated with each neuron j and the map weight vectors are given by $W = \{w_j, 1 < j < N\}$; such that $N < M$. In each training step, the following two steps are repeated for each input sample x_i .

1. Find the best matching neuron c using a similarity measure between the input and all

the map's neurons. This step name is *winner-take-all (WTA)*, where c is the desired *winner* and should satisfy:

$$\|x_i - w_c\| = \min_j(\|x_i - w_j\|) \quad (1)$$

- Update the weight vector of the winner c and also all its topological neighborhood in the map towards the prevailing input according to the rule:

$$w_j(t+1) = w_j(t) + h_{cj}(t)[x_i(t) - w_j(t)] \quad (2)$$

$$h_{cj}(t) = \alpha(t) \cdot \exp\left(-\frac{\|r_c - r_j\|}{2\sigma^2(t)}\right) \quad (3)$$

where $h_{cj}(t)$ is the neighborhood kernel function around the *winner* c at time t , $\alpha(t)$ is the learning rate and is decreased gradually toward zero and $\sigma^2(t)$ is a factor used to control the width of the neighborhood kernel.

The SOM codebook has the following characteristics:

- The probability Distribution Function (PDF) of the codebook is a good approximation for the PDF of the training data.
- The topographic order of the training data is preserved in the codebook, even if the dimensionality of the SOM is smaller than that of training data.

The second characteristic means that similar facial features are mapped to nearby positions in the feature map. This ordering takes place automatically without external supervision based on only the internal relations in the structure of the input patterns and the coordination of the neuron activities through the lateral connections among the neurons.

3 Normalization Methods

Illumination variation of face patterns is extremely complex due to varying texture reflectance properties, face shape, and type and distance of lighting sources. Hence, in such a general setup, it is difficult to learn. However, most of the variations can be described by dominant principal components, this motivates the illumination subspace analysis using PCA.

The original and the normalized image faces are projected on the 2-dimensional space spanned by the two greatest eigenvectors using principal component analysis (PCA). Figure 1 shows the distribution of Yale B database face images [6] for two subjects under 64 lighting conditions. It is clear that the manifold of these subjects is highly overlapped. Thus, the discrimination between different subjects will be a very hard task.

3.1 Histogram Equalization (HE)

Histogram equalization is most widely used method

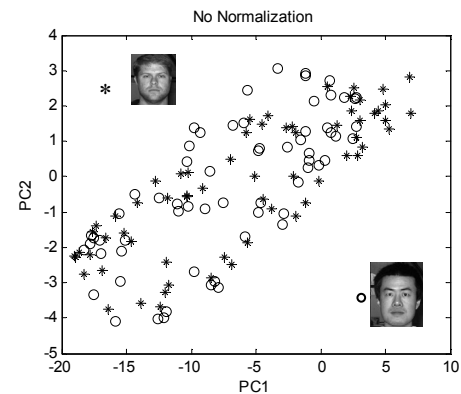


Figure 1: Unnormalized face images distributions under 64 illumination conditions along the first two principle components.

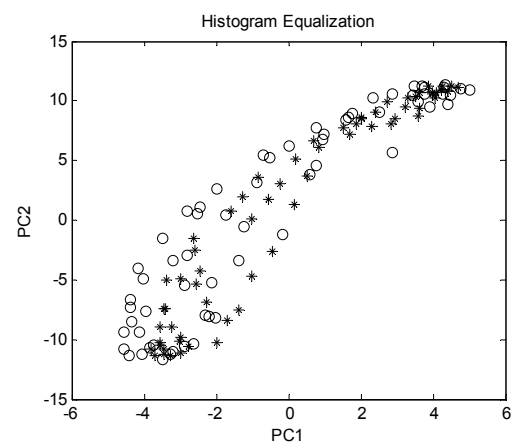


Figure 2: Normalized Face images distributions using histogram equalization method.

to enhance biased contrast image that some pixels are concentrated on a narrow range of the pixel intensity. The result is obtained using cumulative density function of the image as a transfer function. The result of this process is that the histogram becomes approximately constant for all gray values. As shown in Figure (2), the face distribution after applying HE algorithm is highly regularized.

3.2 Gamma Intensity Correction (GIC)

Gamma correction is a technique commonly used in the field of computer graphics. It concerns how to display an image accurately on a computer screen. Images that are not properly corrected can look dark. Gamma correction can control the overall brightness of an image by changing the Gamma parameter. The gamma transform of an image is a pixel transform in which the output and input are related by exponentiation

$$f(I(x, y)) = I(x, y)^\gamma \quad (4)$$

Depending on the value of γ the output image is darker or brighter. In GIC, the image is gamma

transformed as to best match a canonically illuminated image $I_C(x, y)$. Predefine a canonical face image, I_C , which should be lighted under some normal lighting condition To find the value of γ the following equation must be solved

$$\gamma = \arg \min_{\gamma} \sum_{x,y} [I(x,y)^\gamma - I_C(x,y)]^2 \quad (5)$$

This is a nonlinear optimization problem, and it can be solved using Golden section search algorithm.

As shown in Figure (3), face distribution using GIC normalization algorithm still overlapped and face data still have bad separation.

3.3 Region-based HE and GIC

It is obvious that both HE and GIC are global transforms over the whole image area. Therefore, they fail when side lighting exists. To solve this problem, region-based method is proposed to process the face images based on different local regions. That is, performing HE or GIC in some predefined face regions in order to alleviate the highlight, shading and shadow effect caused by the unequal illumination. As we know, face image is symmetrical around the vertical axis and contains different parts around the horizontal axis; therefore, it is proposed to partition it into four regions. As shown in figures (4, 5), region based normalization methods increase the separation between different subjects, thus the recognition accuracy will be improved.

4 Face Database

CMU-PIE face database [8] is available for studying pose, illumination, and expression problems in face recognition. There are 68 individuals under 43 different lighting and 3 different facial expressions for 13 poses. Since this work mainly deals with the illumination problem, frontal images under varying lighting conditions are selected, these which includes the images under 21 different directional flashes. Example images of one person in frontal pose are shown in Figure (6). The images are divided into four subsets according to the angle that the light source direction makes with the camera axis— Subset 1 (f06~f09, f11, f12, f20), Subset 2 (f05, f10, f13, f14, f19, f21), Subset 3 (f04, f15, f18, f22), and Subset 4 (f02, f03, f16, f17).

5 Experimental Results

In this experiment, subset 1 is used as the training set (gallery images) and other subsets are used for testing (probe images), all images are rescaled to the size of 48x48 in order to accelerate the computation time. All cropped images in the database are photometrically normalized using histogram equalization, gamma

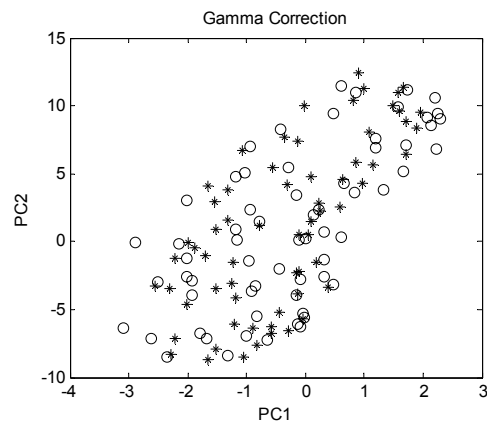


Figure 3: Normalized Face images distributions using Gamma Intensity Correction method.

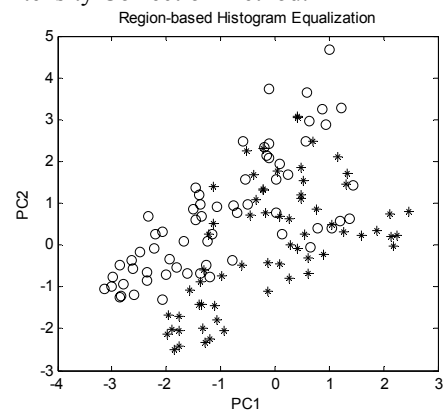


Figure 4: Normalized Face images distributions using Region-based histogram equalization method

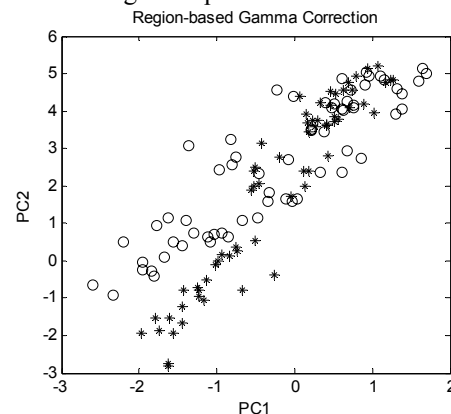


Figure 5: Normalized Face images distributions using Region-based Gamma Correction.

correction, and region-based methods.

Figure (7) shows the canonical face image used to calculate the γ coefficient of the GIC method. This image is the mean image of the training set enhanced with histogram equalization. In the region-based methods, the face images divided into four regions, and these regions are normalizing with the same algorithm of global HE or GIC.

Figure (8) shows results of applying different normalization methods for one subject in the CMU-PIE

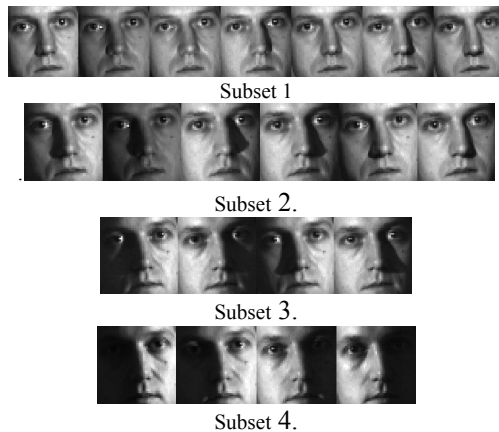


Figure 6: sample images of an individual divided into four subsets.



Figure 7: (a) Canonical face image (b) Facial four regions.

face database. Region-based normalization methods increase the contrast of the image rather than global normalization methods. It is clear that the quality of the image is improved and feature parts such as eyes, nose and mouth are made more clearly.

The local normalization method has the disadvantage that the output is not necessarily realistic. However, in the problem at hand, the objective is not to have a realistic image but to obtain a representation of the face that is invariant to illumination, while keeping the information necessary to allow a discriminative recognition of the subjects. With this idea in mind, it makes sense to use local illumination normalization methods for this type of application.

The normalized gallery images are used to train two different shapes of SOM, sheet and cylindrical. Each gallery image is represented by the index of the winner neuron; in this experiment 2-dimensional map is used for training. The winner of the normalized probe image is considered as the feature vector of the face image, this vector is compared with all gallery feature vectors. Nearest neighbor classifier based on the Euclidean distance is employed for classification. Figure (9) shows the recognition accuracy of applying all normalization methods to process all images before training and testing. The recognition accuracy for each subset and the accuracy for all subsets are calculated. It is clear that RHE improve the accuracy of recognition.

By studying the performance of two different shapes of SOM. Cylinder map shape gives good results than the sheet map shape, because of the circular shape of the face manifold in the image space.

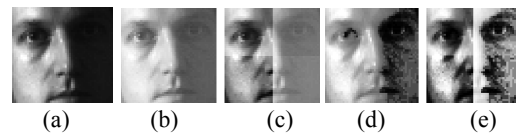


Figure 8: the processed images after applying different illumination normalization methods for one image in the CMU-PIE face database. (a) Unnormalized (b) GIC (c) RGIC (d) HE (e) RHE

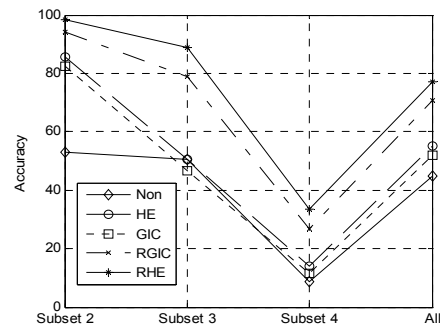


Figure 9: Recognition rate comparisons of different illumination normalization methods on CMU-PIE Face Database using cylinder SOM map.

6 Conclusion

The experimental results on CMU-PIE face database reveal a number of interesting points,

1. SOM performance highly degrades when the test sample lighting condition is different from the training samples condition.
2. Region-based illumination normalization outperforms the global normalization methods.
3. The cylinder shape of SOM is better than the sheet shape because face manifold of the training images tend to be circular.

References

- [1] W. Y. Zhao, R. Chellappa, A. Rosenfeld, and P. J. Phillips. "Face recognition: A literature survey", UMD Technical Report CAR-TR-948, 2000.
- [2] S. Z. Li, A. K. Jon, "Handbook of Face Recognition", Springer, 2005.
- [3] Bo Du; Shiguang Shan; Laiyun Qing; Wen Gao, "Empirical comparisons of several preprocessing methods for illumination insensitive face recognition", IEEE International conference on Acoustic, speech, and signal processing, vol.2,pii/981-ii/984, 2005.
- [4] W. Chen, M. J. Er, and S. Wu, "Illumination Compensation and Normalization for Robust Face Recognition Using Discrete Cosine Transform in Logarithm domain", IEEE Trans. On Systems, Man, and Cybernetics-part B: Cybernetics, vol. 36, No. 2, April 2006.
- [5] P.N. Belhumeur, J. Hespanha and D.J. Kriegman, "Eigenfaces vs. Fisherfaces: Recognition Using Class Specific Linear Projection," IEEE PAMI, Vol. 19, pp. 711-720, 1997.
- [6] A. Georghiades, D. Kriegman, and P. Belhumeur. "From few to many: Generative models for recognition under variable pose and illumination" IEEE Trans. on Pattern Analysis and Machine Intelligence, 40:643--660, 2001.
- [7] T. Kohonen, "Self-Organizing Maps", Springer, 1997.
- [8] Sim, T.; Baker, S.; Bsat, M. "The CMU pose, illumination, and expression database", IEEE Trans. Pattern Anal. Mach. Intell., vol.25, no. 12, pp. 1615-1618, 2003

Construction of super-micro sense of force feedback and visual for an elastic body

Takamasa Sonoda

*Graduate School of Computer Science
And System Engineering
Kyushu Institute of Technology
680-4, Iizuka City, Fukuoka, Japan, 820-8502
sonoda@imcs.mse.kyutech.ac.jp*

Eiji Hayashi

*Department of Mechanical Information
Science and Technology
Kyushu Institute of Technology
680-4, Iizuka City, Fukuoka, Japan, 820-8502
haya@mse.kyutech.ac.jp*

Abstract

This research aims to develop a combined sense system that uses the sense of force feedback and the visual by the shape of microscopic features of a micro sample. The visual and the sense of force feedback were expanded in an effort to improve the efficiency of the skill to operate the micro sample by creating conditions similar to actually feeling samples that are large enough to actually grip by finger. In this basic research, we use a haptic device that presents the expanded reaction force generated from virtual object of a micro sample.

Based on a feedback force presentation experiment using a reaction force, a feedback force transmission simulation model of actual force transmission was constructed. In this experiment, two control approaches were used such as position control and hybrid control. We discussed our experimental results considering the system's advantages and problems.

Key words: *Force feedback, Haptic interface, Simulation*

1. Introduction

Currently, bioindustry, the medical field, and the field of semiconductor production expect to see advancements in the efficiency of micro-technology. Recently, a current study focused on post-genomics, the field that investigates the use of the enormous amount of information analyzed. The field of semiconductor research also has incorporated nanoscale productive processes since 2004. It is difficult to manipulate micro-technology directly, however, because of its dependence on sight and the need for a considerable mastery of skills.

As a method for solving this problem, the reaction force of a minute sample improves the efficiency of functions such as identification and operation by utilizing the feedback force to the worker.

This study describes the development of a compound system that utilizes sight with a microscope and a force feedback manipulator.

This fundamental research utilizes a haptic device to show the amplified feedback force from a virtual minute sample. We also describe an interface that displays a graphic in a microscope and commands the x-y stage on the microscope.

2. System Structure

2.1 Summary of Structure

The structure of the system is shown in Figure 1. This system consists of a metallographic microscope, an automatic x-y stage on the microscope, a feedback stage controller to control the x-y stage, a haptic device for transmitting force feedback (Fig. 2), a minute power sensor (Fig. 3), and the PC with which I control and operate them.

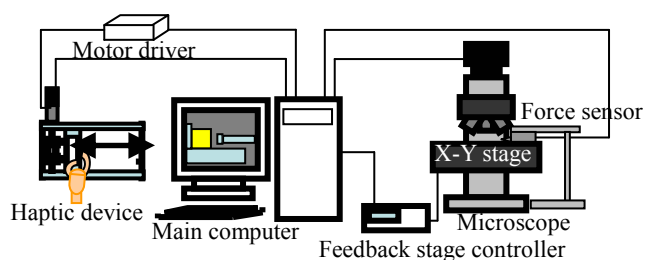


Fig. 1. Schematic diagram of system structure



Fig. 2. Haptic device



Fig. 3. Micro force sensor

2.2 Microscope Image Interface

In this paper, we constructed the microscope image interface shown in Figure 2. The functions of this interface are:

- to display the graphic shown from a microscope through a digital camera
- to move the x-y stage by pushing a button on the interface
- to measure the reaction force between a sample and sensor by a micro force sensor
- to display the virtual object through simulation and check any deformation of it.

Therefore, we are able to check for deformation in each minute sample using microscope images and the computer simulation.

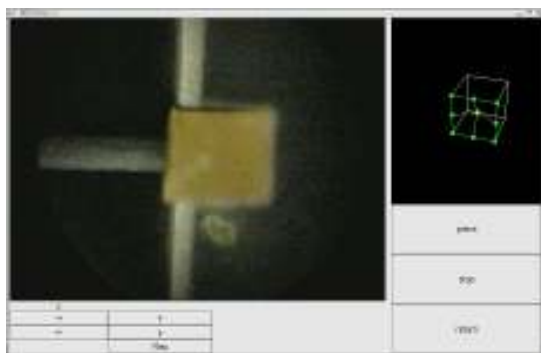


Fig. 4. Image of interface

3. Construction of virtual elastic body

Fig. 5 shows the construction of the virtual elastic body used in this study. It includes nine mass points and the spring-damper elements. The horizontal element and vertical element are constructed from a parallel model made with a spring and damper. The virtual elastic body contains fixed mass points, except the center mass point which acts as a condition of constraint.

We give the sample displacement and measure the reaction force to identify the elastic coefficient and viscous modulus on the simulation. We measure the elastic coefficient on the basis of the relation between the reaction force and the displacement, and the viscous modulus on the basis of the relation between time and displacement.

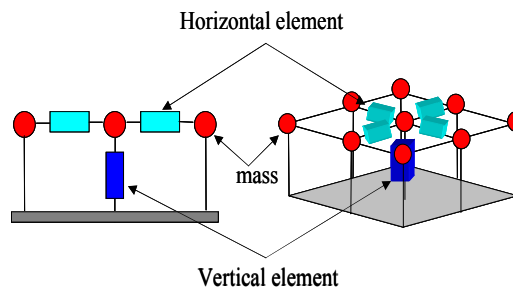


Fig. 5. Schematic diagram of dynamic model

4. Feedback Force Presentation Experiment

In this Chapter, we used the haptic device described in Chapter 2. We attempted to evaluate whether a worker can grasp an amplified micro reaction force form virtual object with the haptic device.

The experimental method of force feedback transmission involves hybrid control with a master-slave method. A worker touches the virtual object described in the previous chapter in PC. Then, the generated torque is amplified and transmitted by the haptic device.

These experimental results are shown in Fig. 6, Fig. 7, and Fig. 8. Fig. 6 and Fig. 7 use the same time line. In Fig. 6, the horizontal axis represents time in (seconds) and the vertical axis represents the angle (in degrees) of the master and slave. In Fig. 7, the horizontal axis represents time and the vertical axis represents the torque (milli newton meters) supplied by the reaction force in the slave and the torque transmitted to the master. In Fig.8, the horizontal axis is time (in seconds), the vertical axis is the torque (milli newton meters) supplied by the reaction force in the slave and the torque amplified ten times in the master.

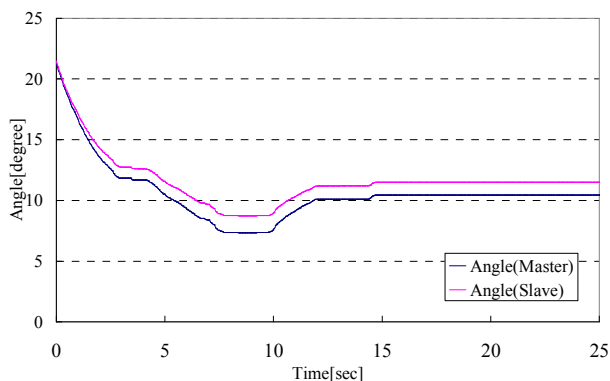


Fig. 6. Experimental result of hybrid control (Angle)

Acknowledgement

The authors would like to acknowledge the advice and assistance of Professor Tadashi Kitamura of Kyushu Institute of Technology.

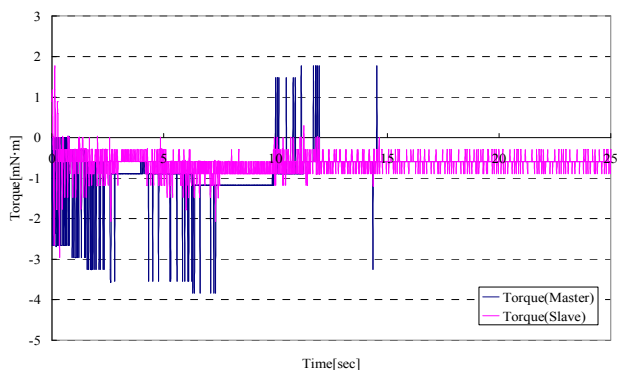


Fig. 7. Experimental result of hybrid control (Torque)

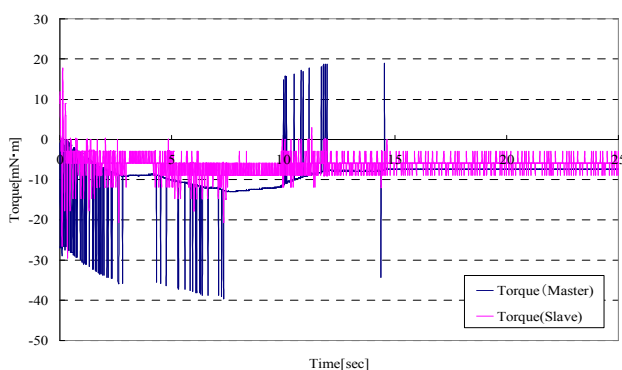


Fig. 8. Experimental result of hybrid control (Torque is amplified 10 times.)

We can confirm that the torque of the master was extended to 10[mN / m] according to Fig. 8. In addition, we can feel the elasticity to a slight degree by touching a virtual object with a haptic device that we actually built. However, we can not feel the softness when we touch a sample with haptic device. Considering the causes that can not feel the softness, it is likely that the mechanism of the haptic device is not pertinent, and the reaction force of a visual object is too small to induce with a haptic device.

5. Conclusion

In this paper, we evaluated whether force feedback is amplified by touching a virtual object with a haptic device in a PC. We can amplify the reaction force but we can not present a large enough reaction force for a worker to feel its elasticity.

In the future, I plan to build a system to show a minute reaction force extended precisely. Future research will focus on a system that will detect and express reaction forces more precisely. The system will be tested using a smaller sample. Therefore, I will build a manipulator and develop a system around it.

A System Allowing Concurrent Design and Implementation of Both Virtual and Real Robots

Toshiaki OOMORI, Norihiro ABE
Kyushu Institute of Technology
680-4 Kawazu, Iizuka, Fukuoka 820-8502, Japan
Email: oomori@sein.mse.kyutech.ac.jp

Hirokazu TAKI
Wakayama University
930 Sakaedani, Wakayama-shi
Wakayama 680-8510, Japan

Shoujie He
Eastman Kodak Company,
Plano, Texas, USA

Abstract

By the development of the VR technology in recent years, virtual debugging that uses a virtual environment to debug the robot is paid to attention. However, at the present stage the reliability of virtual debugging is low, and it is difficult to create and operate virtual robots without exclusive knowledge. Then, in this research, we use a virtual space according to rigid body dynamics, and aim the systems that we can create and operate virtual robots without exclusive knowledge.

Keywords: VR, Virtual Robots, Virtual Space

1 Introduction

In late years, more large-scale and complex embedded software is required. This makes it difficult to develop high-quality embedded software in a short term, and the delay of development is caused because developers cannot debug software until a real machine is completed. Consequently, a virtual machine should be built concurrently with a real one. Then this concurrent development allows developers to write and debug using a virtual robot the software to be installed into the corresponding real one. This makes it possible for developers to further examine the real machine in detail by downloading the software developed with the virtual one to the real one.

And as robots developed so far are supposed to act in safe environment, developers do not try to make them work in dangerous environment for fear that they may be broken owing to a tumble on a convex-concave road or falling from a high position.

In such cases, virtual robots will help them analyze the cause of accident, and improve fragile components of robots or incomplete control program leading robots to destruction.

In this research, reproducing the motor and the sensor, etc. in a virtual space according to a

physical law, we aim at building the virtual robot that can operate as if it were the real machine. In addition, we want the system to assist a naive user in both designing a virtual robot and debugging the software.

2 Construct of Virtual Space

A virtual machine designed based on the traditional static does not contribute to develop the corresponding real one, as it does not work well in real environment comparison with the fact that the virtual one works well in virtual environment because of the lack of dynamics including inertia. A real time solid body physics engine VORTEX (developed by CMLabs Simulations, Inc.) introducing dynamics into virtual environment is exploited to solve the above problem.

VORTEX provides following two restrictions:

Joint, which joins two elementary parts to construct an articulated body.

Contacts, which restricts movement of two geometrical models within tolerance.

As a sample of VORTEX, the robot arm is shown in Figure 1. This simulation faithfully reproduces the gravity, friction, and the torque of the motor, etc. in real time. Using VORTEX, we can execute the simulation of complicated models with a lot of physical parameters in real time.



Figure 1: Robot arm simulation by VORTEX

3 Development of Virtual Robot

VORTEX has many features but some of them are unnecessary for constructing a virtual robot. Then we took out only function necessary for the robot, and redefined them as the C++ class for facilitating to construct a virtual robot. As a result, we can change the specification of virtual robots, and shorten the debugging time. Using this class, we made a four-legged virtual robot and a two-legged one shown in Figure 2 and Figure 3, respectively.



Figure 2: Four-legged robot



Figure 3: Two-legged Robot

To model a servomotor of virtual robot, a hinge joint of VORTEX is used and controlled. The hinge joint restrains the two parts to rotate around one axis as shown in Figure 4.

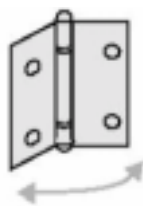


Figure 4: Hinge-joint image

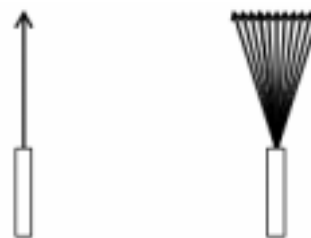
Moreover, we built in the walking program in both robots. It is difficult to have a two-legged robot walk stably though it is easy to have a four-legged robot walk. But, to make a four-legged robot pass the centerline of a corridor, a virtual gradient sensor is needed. Virtual sensors introduced into the system will be shown below.

4 Virtual Sensor

The robot needs a variety of kinds of sensors for both detecting its pose and localizing itself. Then, a virtual distance sensor and a virtual gradient sensor were invented. We configured the function of these two virtual sensors as C++ classes to make it easily for a developer to exploit them. This system allows a developer to implement the movement algorithm of the robot easily.

4.1 Virtual Distance Sensor

We made a sensor with high directivity like the laser distance sensor. And by combining the sensors together, a low directional sensor is obtained. Figure 4 shows these two sensors.



High directivity Low directivity
Figure 4: Distance sensor

4.2 Virtual Gradient Sensor

The mechanism of this sensor is very easy. Non-graphical two objects are set up in the model to be measured its gradient, and the grade is calculated from coordinates of the two objects.

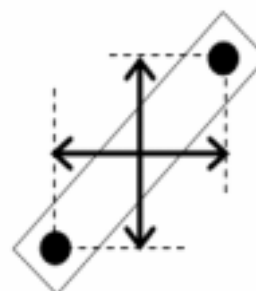


Figure 5: Gradient sensor

5 Installation of Virtual Sensor to Virtual Robot

Because a developer can make the sensors of various specifications expeditiously, the virtual

sensor class makes it brief to devise the movement algorithm of the robot by the trial and error.

Figure 6 shows a four-legged virtual robot in which four distance sensors are installed. This robot measures the distance to the wall with the sensor, and it is possible to walk without knocking against the wall. A developer can easily adjust the number and the time base range etc. of the sensor, and this leads the developer to the best operational condition. For instance, when we install two sensors on the forefoot of the robot, as it collides against the wall, it was not able to walk well. It was, however, possible to walk well when 4 sensors were installed on all feet of the robot. Thus, the developer can judge appropriate allocation of the sensors using a virtual robot instead of a real one.

Figure 7 shows a two-legged virtual robot equipped with a gradient sensor at the center of its body. So as not to fall, this robot corrects the angle of the joint by detecting the inclination of the body. It is very useful for making a real robot to make such a correction algorithm in a virtual one. The reason is clear considering the case where the algorithm is developed from the scratch using a real machine. The virtual debug allows a developer to operate both a real and virtual robot at ease, as the result the real machine debugging will complete briefly. The risk a real machine falls will decrease, and its breakdown also decrease as a result. On the other hand, it is difficult to expect the same result when a real machine is debugged from the scratch.



Figure 6: Four-legged robot with distance sensor



Figure 7: Two-legged robot with gradient sensor

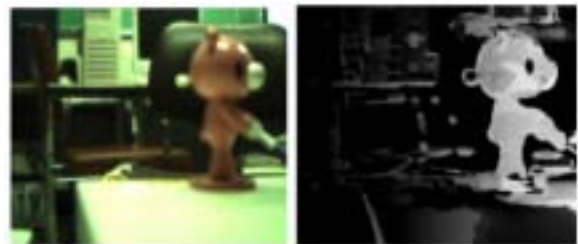
6 Stereo Vision System

It is difficult for robots to detect complex external world only by the distance sensor, then stereovision system is often built into it recently. This system calculates the distance to the object by the image data processing with two cameras.

At first, the parallax is calculated by extracting corresponding parts (called stereo matching) from two images captured with two cameras. Next, the distance to the object is obtained by using the acquired parallax and the distance between two cameras. For example, Figure 8 shows result of a stereo matching.

For simulating the stereo matching in virtual space, the aspects (two frame buffer of GL) captured with two cameras corresponding to the robot's eyes must be converted into the bit map images. Next a stereo matching algorithm is applied to them. This procedure is shown in Figure 9.

C++ class for implementing the stereovision system is so that the user might easily make eyes of virtual robots.



Left camera Image Depth image
Figure 8: Stereo matching example

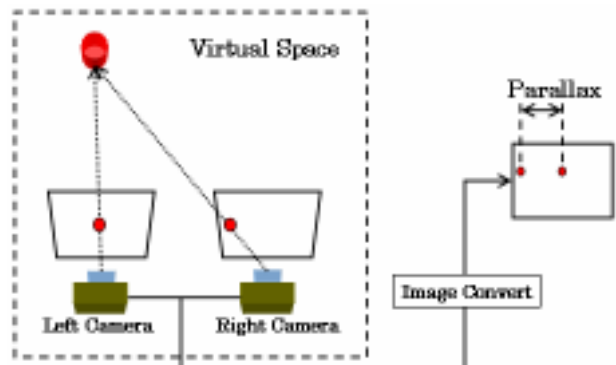


Figure 9: Procedure of stereo vision system

7 Combine virtual robot and stereo vision

We expect a virtual robot equipped with the stereo vision to following behavior.

A four-legged virtual robot will successfully avoid obstacles with the stereo vision system and reach the destination. The distance measurement using both stereo vision and virtual distance sensor will help the robot make an elaborate plan.

We want a two-legged virtual robot go up and down the stairs of which height and size are unknown. Many robots which can go up and down the stairs are given in advance such parameters. On the other hand, when our robot finds the stairs, it measures the height with the stereo vision. If there is enough space on the stair and the height is less than the tolerance, it will go up on the stair. At the moment, the robot will measure only the vicinity of its feet for conducting measurement of high-speed and high-accuracy.

8 Conclusions and Future Work

This research has aimed at making a virtual robot with the reality. Building virtual sensor and servomotor, etc. into VORTEX, we can make virtual robot with high reproducibility. And, by creating a variety of C++ classes, developers can make and change a virtual robot easily. In the future, various sensors and actuators should be provided to virtual machines and this will help us develop complex virtual robots that we cannot construct up to now. We would like to show how concurrent robots development would be able to solve various problems including development of a complex robot like a humanoid.

Acknowledgements

We greatly appreciate the aid of Ministry of Internal Affairs and Communications (MIC) and the Grant-in-Aid for Scientific Research.

References

- [1]Yi PAN, Norihiro ABE, Kazuaki TANAKA : The virtual debugging system for embedded software development, ICAT2002, pp.119-p124, 2002
- [2]Yi PAN, Norihiro ABE, Kazuaki TANAKA : The Virtual Debugging System for Embedded Software Development, SCI2003,pp78-84 , 2003
- [3]Yi PAN, Norihiro ABE, Kazuaki TANAKA : The Virtual Debugging System for Embedded Software Development, VRAI2003, 2003
- [4]Yi PAN, Norihiro ABE, Kazuaki TANAKA, Hirokazu TAKI : The Virtual Debugging System for Developing Embedded Software using Virtual machinery,

EUC2004

- [5]Toshiaki Oomori, Norihiro Abe, Kazuaki Tanaka, Hiroaki Taki, Shoujie He "Concurrent Development of Virtual Robots and Real Robots Based on Physical Law", 15th International Symposium on Measurement and Control in Robotics (ISMCR2005)

Real-time Interactive Dialog System between Human and Virtual Agent

Shunji UCHINO, Norihiro ABE
 Kyushu Institute of Technology
 680-4 Kawazu, Iizuka, Fukuoka 820-8502, Japan
 Email: s_uchino@sein.mse.kyutech.ac.jp

Hirokazu TAKI
 Wakayama University
 930 Sakaedani, Wakayama-shi
 Wakayama 680-8510, Japan

Shoujie He
 Eastman Kodak Company,
 Plano, Texas, USA

Abstract

In this research, a dialog environment between human and virtual agent has been constructed. With the actual VR technologies, special devices have to be used for the interaction with a virtual environment. This makes it extremely difficult for general users to manipulate an object in the virtual environment. In our daily life, when an object is out of our reach, we usually ask someone with direct access to the object to manipulate it on our behalf. If there is such a helper who has direct access to objects in a virtual space, we may do the similar thing. The question, however, is how to communicate with the helper, namely, the virtual agent. This paper presents a solution to the question. The basic idea is to utilize speech and gesture recognition systems and to integrate the verbal and non-verbal information. Experimental results have proved the effectiveness of the approach in terms of facilitating man-machine interaction and communication. The environment constructed in this research allows a user to communicate by talking and showing gestures to a personified agent in virtual environment. A user can use his/her finger to point at a virtual object and ask the agent to manipulate the virtual object.

Keywords: Virtual Agent, real time, voice and gesture recognition, interaction.

1 Introduction

Recently, toward a ubiquitous network society, products are developed that have some excellent functions based on Information Technologies. In future, it is expected that these products will be much more complex to provide multifunction. Nevertheless, main interface of computer such as mouse and keyboard will remain unchanged and it will make it difficult for elderly person to operate it. Further it will become a cause of digital divides. Also, it will be difficult even for experts in operating computer as instrument developers to use it when they grow older. So, developing new interface is expected which helps everyone to operate a computer easily. In this paper, a dialog environment between human and computer is proposed which unifies the

verbal information using the voice and the non-verbal information using a gesture, and verified the validity of the system. It permits a user and a virtual human rendered in display to communicate each other using pointing action and utterance. The configuration of this system is shown in Figure 1.

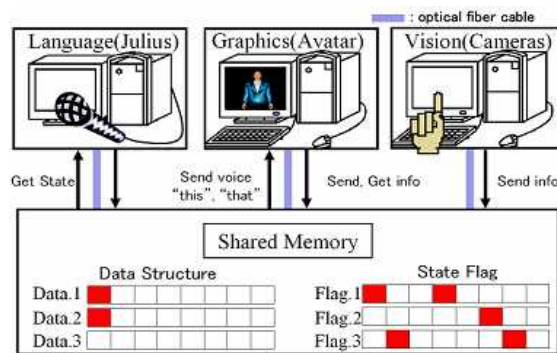


Figure 1: Concurrent processing among 3 PCs.

This system is divided into three parts: The language processing part which recognizes user's voice picked from mike. In the vision part, user's action is recognized based on image information obtained from cameras. The display part shows a virtual human and makes him speak and act responding to requirement from a user. This system realizes actual dialog environment using both utterance and gesture by connecting these three parts with a high speed network called Scram Net+ which makes the time needed to send information among computers less than one millisecond.

2 Space for conversation

We have developed a system in which an avatar responds to a user as a salesman in a virtual fountain pen store. The user tells him the pen he wants to buy using utterance and a pointing action. The typical user's utterance with pointing action is like, "Please give this to me". The system recognizes the appropriate pen based on the verbal and non-verbal information. If the pen that the user wants cannot be located with the pointing action, the avatar must uniquely determine the pen with some questions. However, if he asks question many times, the user feels much annoyed. So some devices are necessary to reduce questions. We have already reported the

method using a decision tree to have the avatar ask good question leading to unique identification of the pen.

3 Interaction from user to system

Pointing action is required to synchronize with utterance such as ‘What is this?’ In this system, the spoken language processing and the gesture recognition are conducted concurrently to identify an object of pointing action. There is a possibility that the avatar may misunderstand user’s instruction because pointing action involves ambiguity and thus pick up a wrong pen. In the case, the user has to immediately interrupt the action of the avatar and rectify wrong behavior.

3.1 Spoken language processing

Voice is analyzed with Julius for Windows version v3.3p4_jl2-1. It is possible to recognize a given utterances at about 1.1-1.3 times of the utterance time. The starting and ending time of each demonstrative pronoun appearing in utterance detected with Julius are used to judge the temporal relation between utterance of a demonstrative pronoun and pointing action. This function successfully finds temporal relation even if utterance includes several demonstrative pronouns, and several pointing actions are given.

The user does the pointing action toward the screen. The system extracts user's finger with a vertical stereo vision system excelling in detecting of a sidewise vector, and acquires the direction and coordinates of the user’s fingertip and knuckle.

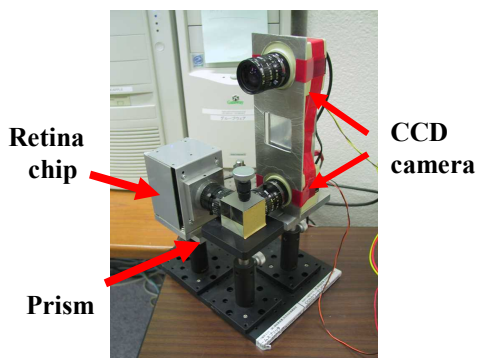


Figure 2: Combination of CCD and retina chip camera.

For the real-time processing, the system using only CCD color cameras is unsuitable. To reduce the cost of image processing, retina chip camera is used to narrow the image region to that including just a forefinger. The retina chip camera realizes a super-parallel image processing (“Moving object detection” and “Edge highlighting”...) with analog circuits embedded in each pixel. As shown in Figure 2, a ray passing through a prism is divided into two rays each of which is input to CCD and retina chip camera respectively. As the motion

of a hand stops to make the object of pointing action clear, the still image of the hand is captured with a retina chip camera using images deference function. Images of two CCD cameras corresponding to the above retina chip image are examined to measure the direction and coordinates of the user’s fingertip and knuckle.

3.2 Extraction of Skin Area

3.2.1 HSV Conversion

Generally color information data obtained from camera is RGB. It is difficult to extract a target object with peculiar colors from the environment illuminated with strong light. HSV color system helps an image processing system extract the target from such environment. Here, H of HSV, S and V means Hue, Saturation and Value of Brightness, respectively. The RGB color system is converted into the HSV color system. To extract skin-colored area, it is necessary to set threshold values in terms of HSV value. Each of threshold values for extracting skin-colored area are shown below.

$$\begin{aligned} \text{Hue:} & \quad 0 < H < 40 \quad [\text{Range: } 0 < H < 360] \\ \text{Saturation:} & \quad 0 < S < 140 \quad [\text{Range: } 0 < S < 255] \\ \text{Value of Brightness:} & \quad 0 < I < 255 \quad [\text{Range: } 0 < I < 255] \end{aligned} \quad (1)$$

3.2.2 Labeling processing to remove noises

Even if an effectual color values is given to extract skin-colored area, areas not corresponding to a hand are always extracted. The labeling process is useful to exclude all regions but the hand. This method is as follows.

- 1). Sequentially applying the label to each skin-colored region.
- 2). Extracting region of which area is the maximum value among them.
- 3). Making the image binary to remove noise except for the region with the maximum area.

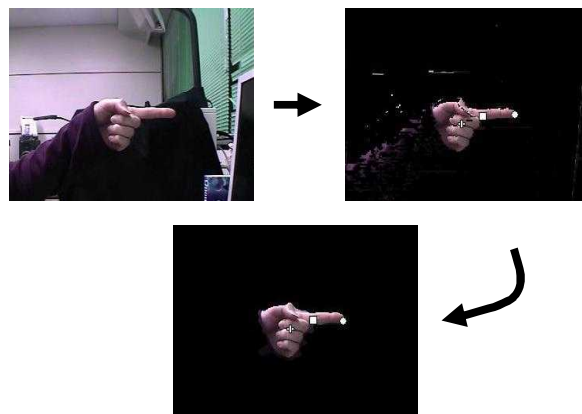


Figure 4: Extraction of skin colored area

3.3 Agreement of voice and action

The object in virtual space that the user specifies using pointing action can be determined based on the information through the spoken language processing. Even if a pronoun cannot be detected, when the pointing action is successfully found from the corresponding time span, it is possible to find the pronoun using the verbal-nonverbal relation described above and vice versa.

4 Result of conversation

Consider the case a user talks with an avatar in virtual space including 30 fountain pens in a showcase. Every fountain pen includes 6 attributes such as Size, Length, Color, Weight, Cost, and Product buy. It is possible to construct a decision tree and use the tree to decide which pen a user wants to buy. But the method does not allow the user to specify freely his favorite attributes but forces him to answer whether he likes or dislikes a peculiar attribute which the decision tree algorithm selects.

Instead, our system permits him to select his favorite pen by pointing action with the utterance such as "Would you show me this pen?" or "Would you take this and that pen here?" The first utterance must include just one pronoun and one favorite pen must be specified with pointing action. On the contrary, the second one include two pointing action but the discrimination of them is easy although it is not easy to find two pens if two pointing action specifies neighboring regions.

In both cases, the avatar has to find a set of candidate pens. For the first case, he can select two ways to determine what a user wants to buy. The first way is to ask if the user likes the one pointed or not with pointing one of candidates. This method is adequate if the number of the candidates is a few, otherwise the avatar may have to enumerate all of them. The second one is to make a decision tree from the set of candidates and then to ask the user which values his favorite pen has in terms of the attribute designated on the current node tracing the tree downward from the root. In this case, the number of inquiries to be asked will be smallest.

Here, the third one is proposed. Let us see an example. The flow of the conversation is shown in Figure 5. It is to use interrupt mechanism. Consider the following dialog in which a user specifies his favorite pen by pointing action (1). At this time, as 6 pens are selected as a candidate because of the ambiguity of pointing action, he asks the color to qualify a favorite pen. As a result, two red pens are left. Though he cannot decide which one is specified, instead of asking additional question he is unintentionally or instinctively going to grasp one of hem (2). Instantaneously, the user

interrupts his action to inform him of negation. This makes him understand what the user wants. For confirming his favorite pen, he grasps the pen (3).

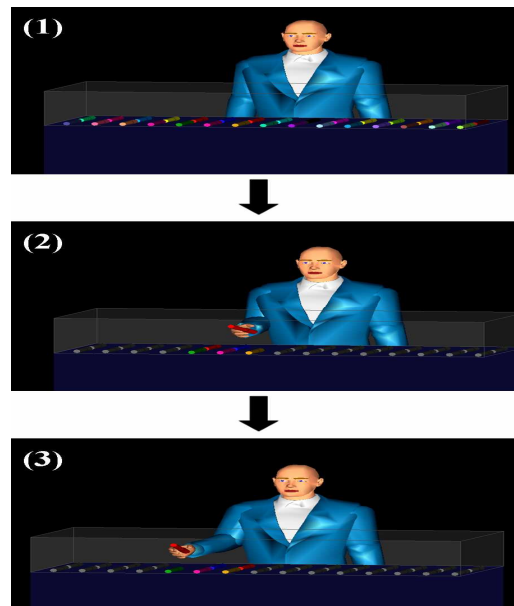


Figure 5: Flow of the conversation.

- Avatar: Which pen do you want to buy?
- User: Please show me this one. (Pointing a red pen) (1)
- Avatar: Which color do you like?
- User: Please give the red one. (The avatar is going to reaching his hand to one of two red pens.) (2)
- User: No, it is wrong.
- Avatar: Is this one? (Grasping another red pen) (3)
- User: Yes.
- Avatar: Thank you for purchasing this pen.

As a result, a user can feel actually as if he were talking to a real man. Thus, by constructing a natural conversation system with an avatar, it is possible for many users to use it as an easy interface instead of the mouse and the keyboard.

5 Dialog system with socket communication

In the existing system, SCRAMNet+ was used to connect the PCs, which is costly. For this reason, we developed a system that enables the communication between a user and a virtual agent through the socket communication, instead of the SCRAMNet+. This makes it possible that the regular PCs are used to achieve the same effects.

We use UDP communication protocol for the synchronization among the three PCs. In order to improve reliability, memory of each PC is always updated to the fresh data whenever the system writes data into memory.

5.1 Multicast

UDP can simultaneously transmit data to multiple destinations with the multicast option.

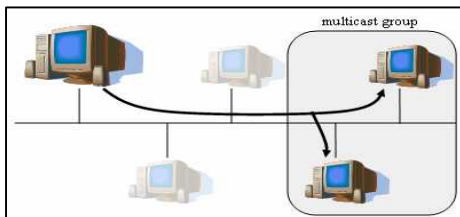


Figure 6: Multicast

The way of the multicast works is that the data is transmitted to the PCs that participate in the multicast group (Figure 6).

Compared to TCP that transmits data to each PC sequentially, UDP had better performance in terms of the time needed for the data transmission.

5.2 Reliability of data

UDP is a high-speed communication, but it is lack of reliability. The following approach has been taken to improve the reliability.

5.2.1 Distinction of Information

We made a two-way transmission port from each PC. If we use one single port, information collides and the data loss will occur at the time that data is transmitted from Avatar, Voice, and Vision unit (Figure 7).

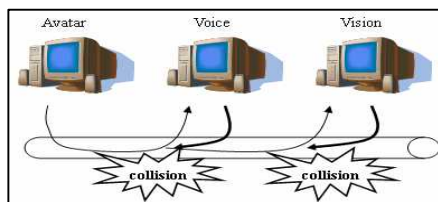


Figure 7: Collision of data

To avoid the collision, we prepared three ports, exclusively for Avatar, exclusively for Voice recognition system, and exclusively for Vision system (Figure 8). This way prevents the data collision from happening.

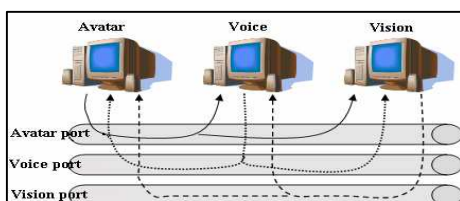


Figure 8: Each port

6 Conclusion

In this dialog environment, we introduced a virtual agent named avatar. So, we constructed the dialog environment in the real time between the user and the computer with the voice and gesture recognitions. Therefore, we developed the system that enables everyone to operate the computer easily. And, we completed a system that enables the communication through the socket communication, instead of the SCRAMNet which is costly. This result was able to be executed by equal ability with SCRAMNet. This made it possible that the regular PCs are used to achieve the same effects. However, in a current system, the human user cannot freely manipulate the virtual object. Therefore, we should construct the communication channel between the virtual space and the real world so that the virtual object could be manipulated. The manipulation includes translocation, rotation, and expansion and contraction of the object. This is an issue in the future.

Acknowledgements

We greatly appreciate the aid of Ministry of Internal Affairs and Communications (MIC) and the Grant-in-Aid for Scientific Research.

References

- [1] Ministry of Economy, Trade and Industry, "Society (e-Life strategy society) basic strategy report concerning strategy of making to market of information appliances - e-Life initiative -", 2003.
- [2] N. Abe, and Tsuji, "A consulting system which detects and undoes erroneous operations by novices", Proc. of SPIE, pp.352-358, 1986.
- [3] N. Abe, T. Amano, K. Tanaka, J.Y.Zheng, S. He, and Taki, "A Training System for Detecting Novice's Erroneous Operation in Repairing Virtual Ma-chines", ICAT, pp.224-229, 1997.
- [4] N. Abe, J.Y.Zheng, K. Tanaka, and Taki, "A training System using Virtual Machines for Teaching Assembling/Disassembling Operations to Novices", Inter-national Conference on System, Man and Cybernetics, pp.2096-2101, 1996.
- [5] K. Tanaka, T. Ozaki, N. Abe, H. Taki, "Verbal/Nonverbal communication between Man and Avatar in Virtual Mechanical Assembly Training System", Proc. VARI, pp.202-207, 2002.
- [6] T. Ozaki, "Verbal and Non-Verbal Communication Using Virtual Reality", Kyusyu Institute of Technology, Master Thesis, 2001.
- [7] T. Yagi, "Silicon visual area", Japanese Neural Network Society, Vol.8, No.2, pp.65-69, 2001

Design of the Tactile Sensor Element Using Microbending Optical Fiber Sensors

Jin-Seok Heo
Dept. of Mechanical Engineering
Korea Advanced Institute of
Science and Technology,
Daejeon, Korea 305-701
dandyheo3070@kaist.ac.kr

Cheol-Hee Han
Dept. of Mechanical Engineering
Korea Advanced Institute of
Science and Technology,
Daejeon, Korea 305-701
rapha012@kaist.ac.kr

Jung-Ju Lee
Dept. of Mechanical Engineering
Korea Advanced Institute of
Science and Technology,
Daejeon, Korea 305-701
leejungju@mail.kaist.ac.kr

Abstract

This paper describes the taxel for the flexible tactile sensor using the microbending optical fiber sensor. This sensor utilizes the microbending of the optical fiber which drives the light loss from the optical fiber. And the structure of this taxel with the optical fiber embedded in the silicone rubber is very simple: once the external force is loaded on the contact mesa of this taxel, the optical fiber experiences the microbending which makes the light loss, and then, the intensity of the transmitted light is decreased. Therefore, detecting this intensity change of the transmitted light, the external uniaxial force can be calculated. Compared with the other optical fiber sensor system, this sensor system can be easily evaluated using simple optical measuring system. Moreover, as the sense of touch of this taxel is similar to that of the human skin, it can be applied the intelligent robot system to the artificial skin.

1. Introduction

Sensory information of human skin for feeling some materials and determining many of their physical properties is provided by sensors in the skin. This tactile information is a kind of sense of touch that is one of the five senses including the sense of sight, hearing, smell and taste. Nowadays, many researchers try to apply the five senses to the intelligent robot system. Especially, many kinds of the tactile sensor combined small force sensors are introduced for intelligent robots, teleoperational manipulators and haptic interfaces. These tactile sensors which are able to detect the contact force, the vibration, the texture and the temperature can be recognized as the next generation information collection system.

Some tactile sensors using the MEMS(Micro Electric-Mechanical System) technology have been introduced[1-4]. Although these sensors have a good spatial resolution, they remain some problems to apply the practical system: they are not enough flexible to attach the curved surface and the more elements of sensor connect, the more wires they need. Therefore, in this paper, we will show the flexible uniaxial force sensor can be used the flexible optical fiber tactile sensor that can be easily applied to the curved surface minimizing the wiring.

2. The Structure of the Taxel

2.1 The Basic Principle of the Taxel

In general case, there is little light loss when the optical fiber is bended with a large radius of curvature. However, as shown in Fig.1, the conspicuous light loss is happened at the microbending of the optical fiber with the small radius of curvature. Although this microbending light loss is not effective to the optical communication, this can be utilized as the optical fiber sensor.

To be concrete, using this microbending loss, the environment change can be detected. This kind of sensor is called the microbending optical fiber sensor which is a sort of the intensity based optical fiber sensor. As this intensity based optical fiber sensor uses the light intensity change at the light detector, the optical measurement system of this type of sensor is composed of a simple light source and a light detector which cost too little.

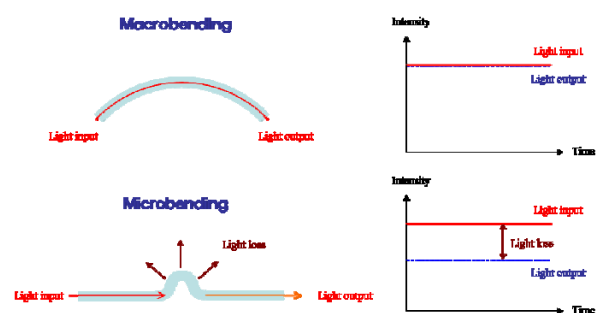


Fig.1 Microbending effect of the optical fiber.

2.2 The Structure of Taxel and the Tactile Sensor

In general case of small force sensor, the periodic zigzag transducer which can be easily microbended by the applied force is mostly used. But, this zigzag type transducer can be occupied large area considering the size of the optical fiber. Therefore, the minimizing the

size of the transducer must be needed. In this study, we propose the cross fiber structure which is embedded in the silicone rubber such as Fig. 2. Once the contact force is applied to the contact mesa, the upper optical fiber and the lower optical fiber are microbended simultaneously by the change of the inner stress of the silicone rubber. Using this phenomena, we can extend the tactile sensor with the fabric structure of the optical fibers embedded in the silicone rubber like Fig. 3.

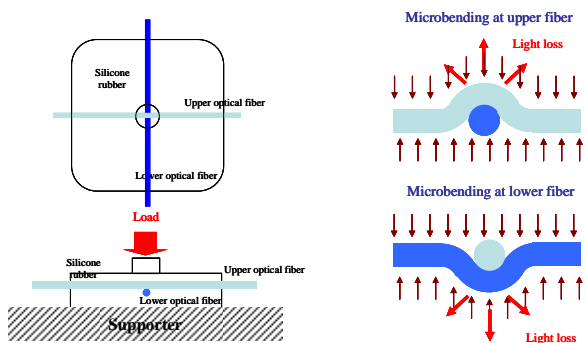


Fig. 2 Structure of the taxel using the microbending effect of the optical fibers.

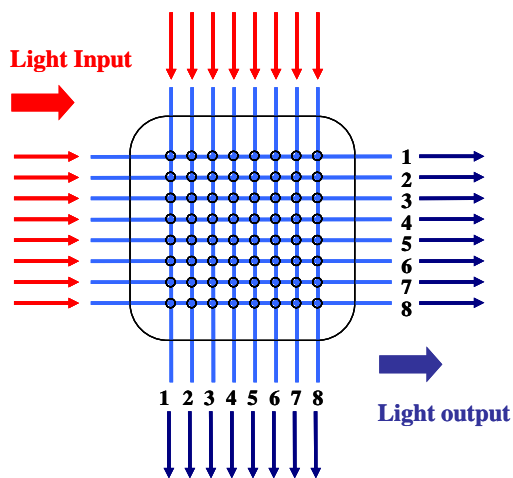


Fig. 3 Structure of the tactile sensor using the microbending effect of the optical fibers.

If the some area is contacted by some material, the contacted mesas make the microbending of the optical fibers in the silicone rubber which decreases the output of the light intensity of optical fiber. The numbers of the optical fiber contains the position of the contact area, and the light intensity informs the change of the contact force. Therefore, using this structure, the distributed contact force can be measured.

3. Fabrication of the Taxel

First of all, the dimension of this flexible force sensor must be decided. As this sensor will be applied to the tactile sensor system, the thinner we fabricate this sensor, the better we can apply it for the artificial skin. In this study, we decide the depth of this sensor to be 2mm by trial and error. 2mm depth can fix the optical fiber without the exposure of the optical fiber from the silicone rubber. The fabricate process is very simple as shown in Fig. 4. At first, a molding frame which can make the shape of the taxel must be prepared. And the optical fiber is aligned under the contact mesa position. Next, liquid silicone rubber is poured to the molding frame to the depth of the taxel. After cured the silicone rubber, the flexible taxel can be made removing the molding frame.

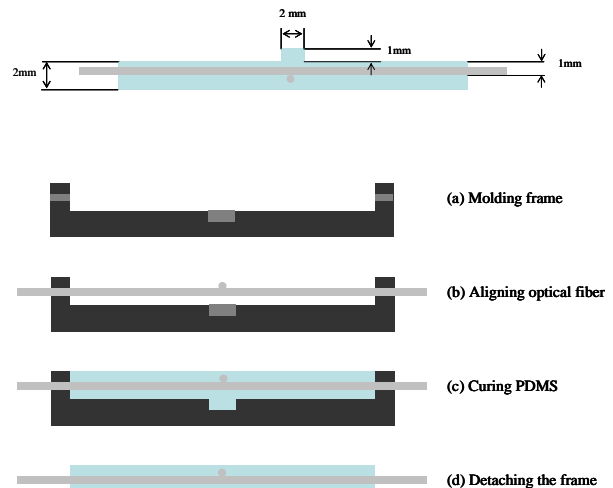


Fig. 3 Dimension of the taxel and its fabrication.



Fig. 4 Fabricated prototype taxel.

The fabricated prototype taxel is shown in Fig. 4. The prototype taxel is so flexible for the silicone rubber transducer that it can apply for the artificial skin for the intelligent robot system.

4. Evaluation of the taxel

The fabricated prototype taxel is calibrated by the verified experimental equipments composed of a uniaxial loadcell and a fatigue test system for small load as show in Fig. 5.

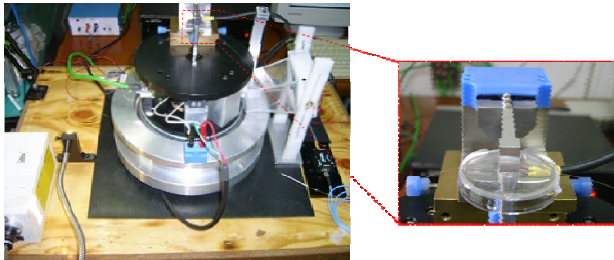


Fig. 5 Experimental setup for the evaluation of the taxel.

as shown in Fig. 6. A power LED(Light emitted diode) is used as the light source of this sensor, and a CCD(charge coupled device) plays a role of the light detector of this sensor system. Using the CCD as the light intensity detector, the intensity changes of each optical fiber can be measured when we apply this taxel for the tactile sensor. This means that a CCD makes it possible to minimize the optical measurement system. And we use the gray scale value from the output signal of CCD to evaluate the light intensity of the optical fiber.

The output signal of this prototype taxel is shown in Fig. 7. The light intensity of this taxel is decreased for its microbending loss as the contact load is increased. The sensitivity of this sensor is -20 gray scale value / N and the resolution of this prototype sensor is $0.05N$. The calibration process is very simple. By multiplying the sensitivity to the light intensity change, we can calculate the applied contact force as shown in Fig. 8.

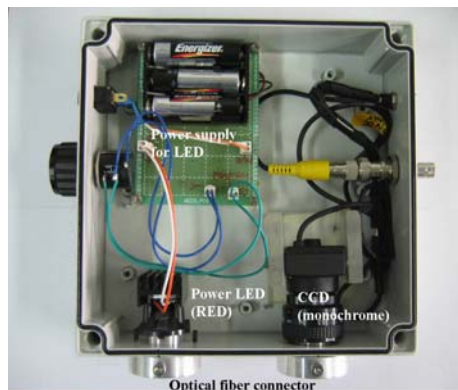


Fig. 6 Optical system of this tactile sensor system.

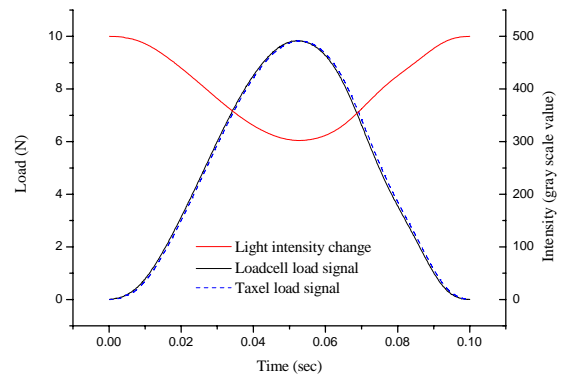


Fig. 8 Calibration of this prototype taxel.

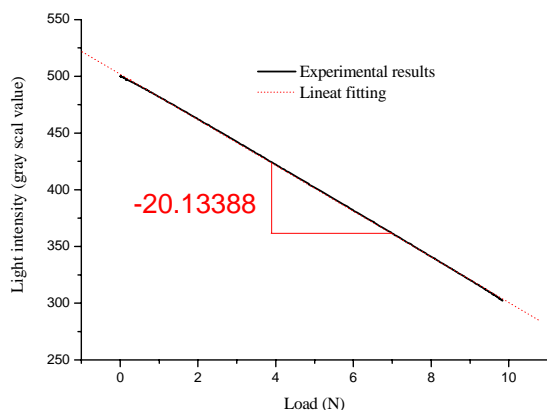


Fig. 7 Experimental verification of the prototype taxel.

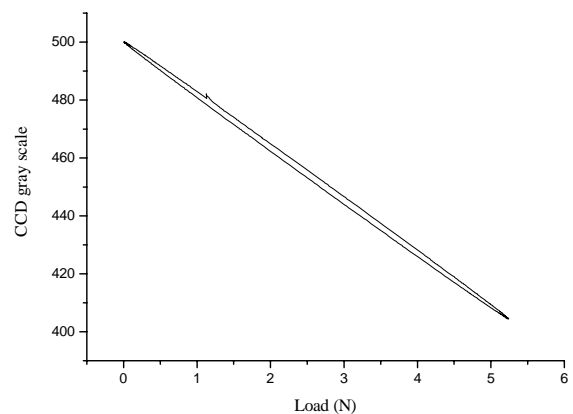


Fig. 9 Hysteresis of the prototype taxel.

As mentioned above, the optical system is very simple

And the hysteresis error of this sensor is about 6.3%

such as Fig. 9. This hysteresis error results in the characteristic of the silicone rubber which is the material of its transducer. And the error of repeatability is about 2%.

Next, we verified the maximum capacity of this prototype sensor. As shown in Fig. 10, the linearity between the light intensity change and the applied load is broken after 17N is applied. This non-linearity can be estimated as the abrupt stress change of the silicone rubber by the insertion of the contact mesa in Fig. 11. Therefore, the maximum capacity of this sensor is 17N which the linear response of the light intensity guarantees.

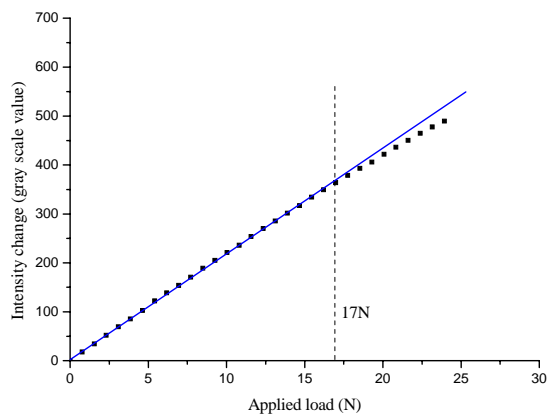


Fig. 10 Non-linear change of the light intensity by the applied contact load.

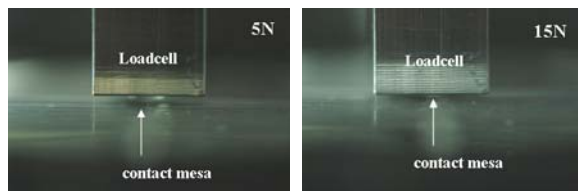


Fig. 11 Insertion of the contact mesa after 15N

5. Conclusion

In this paper, the force sensor using microbending light loss for the tactile sensor is newly designed and experimentally verified. The structure of this sensor with the crossed optical fiber embedded in the silicone rubber and the optical system which is composed of a simple power LED and CCD chip are very simple. The linear light intensity change by the applied load is verified by the experimental results. And this prototype sensor has a good performance: the resolution of this sensor is 0.05N for its maximum capacitance 17N. However, a little

hysteresis error exists for the material of its transducer, silicone rubber. This prototype sensor is sufficient for its application of the artificial skin which includes the tactile sensor.

Acknowledgement

This research (paper) was performed for the Intelligent Robotics Development Program, one of the 21st Century Frontier R&D Programs funded by the Ministry of Commerce, Industry and Energy of Korea.

Reference

- [1] T. Mei, W. J. Li, Y. Ge, Y. Chen, L. Ni and M. H. Chan, "An integrated MEMS three dimensional tactile sensor with large force range", *Sensors and Actuators (A)*, Vol. 80, pp155-162, 2000
- [2] M. J. Yoon, K. H. Yu, G. Y. Jeong, S. C. Lee and T. G. Kwon, "Development of a Distributed Flexible Tactile Sensor System", *J. of KSPE*, Vol. 19, No. 1, pp. 212~218, 2002
- [3] N. Futai, N. Futai, K. Matsumoto and I. Shimoyama, "A flexible micromachined planar spiral inductor for use as an artificial tactile mechanoreceptor", *Sensors and Actuators (A)*, vol. 111, pp293~303, 2004
- [4] U. Paschen, M. Leineweber, J. Amelung, M. Schmidt and G. Zimmer, "A novel tactile sensor system for heavy-load applications based on an integrated capacitive pressure sensor", *Sensors and Actuators (A)*, vol. 68, pp294~298, 1998

A Localization of Mobile Robot based on Ultra-sonic Sensor using Dynamic Obstacles

Byoung-Suk Choi

Dep. of EE and CS

Korea Advanced Institute of Science and Technology,

Daejeon, Republic of Korea 305-701

bs_choi@kaist.ac.kr

Ju-Jang Lee

Dep. of EE and CS

Korea Advanced Institute of Science and Technology,

Daejeon, Republic of Korea 305-701

jjlee@ee.kaist.ac.kr

Abstract

Localization is most important and necessary technology for mobile robot to work well. The robots need to recognize their position and pose in known environment as well as unknown environment. In the future, the robots will be human-friendly robots that are able to coexist with humans in dynamic space. The localization includes several restrictions which arise from dynamic obstacles-people, moving chair, and so on. It is desirable for a mobile robot to estimate his position using dynamic obstacles. In this paper, we propose the method for the localization of the mobile robot using a moving object. Throughout the computer simulation experiments, its performance is verified.

Keywords Mobile robot; Moving object; localization; position estimation;

1 Introduction

Localization of the mobile robot is one of the most important issues for successful autonomous navigation; therefore, a great number of localization methods have been proposed and developed so far[1][2].

The difficult problem that has a substantial impact on the localization of the mobile robot is the environment. The environments can be static or dynamics[3]. Static environments are environments where the only variable quantity state is the robot's pose. Put differently, only the robot moves in static environment. All other objects in the environments remain at the same location forever. Static environments have some nice mathematical properties that make them amenable to efficient probabilistic estimation. Dynamics environments possess objects other than the robot whose location or configuration changes over time. Specially, the changes persist over time. Examples of more persistent changes are people, and moving object such as furniture, chairs, and so forth. A good example of dynamic environments is shown in figure 1. Because of various uncertainties and limitation of sensor information for dynamic changes, localization in the dynamics environments is obviously more difficult than localization in the static ones. Therefore, there are two general methods for estimation of location under each environment. Under static environment, the localization of the mobile robot is based on landmark method using the wall, corner and

door recognition. This method requires feature extraction of static obstacle or landmark. However, unfortunately, most real environments are dynamics with state changes occurring at a range of different speeds. Thus, for most real-world application, it is desirable that mobile robots are capable of exploring or moving within a dynamics environments[4].

This paper considers the situation where a mobile robot is moving an unstructured environment, there is only moving object. In this paper, we present a method for solving previous problem using ultrasonic sensor, which is able to measure the distance between the moving object and the mobile robot. The movements of object can be detected by sonar sensor, and then the position of the moving object is estimated. Using the distance data, the robot's position can be estimated.

This paper is organized as follows. Section 2 shows a kinematics modeling and position estimation of the mobile robot. In Section 3, the method that detects the moving object using ultrasonic sensor is described, the position correction technique with Kalman-filter is shown. In Section 4, the experiments environment and computer simulation results are shown to prove the validity of the proposed method. Finally, in Section 5, conclusion and further research topic are presented.



Fig. 1. The mobile robot in dynamic environments.

2 Robot Modeling

2.1 Kinematics modeling of a mobile robot

The modeling of a mobile robot is shown in fig. 2, where

x_R : the y-component of the mobile robot position;

y_R : the x-component of the mobile robot position;

θ_R : the orientation of the mobile robot;

v_L : the velocity of left wheel;

v_R : the velocity of right wheel;

v_1 : the linear velocity of the mobile robot;

v_2 : the angular velocity of the mobile robot;
 l : the width of the mobile robot.

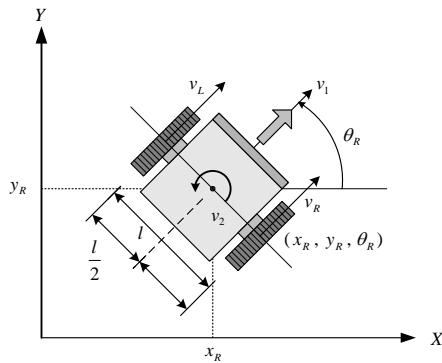


Fig. 2. Kinematics model of a mobile robot.

A mobile robot with differential driving mechanism has two wheels on the same axis, and each wheel is controlled by an independent motor. On the two dimensional $X - Y$ cartesian coordinates, position and orientation of the mobile robot is described by state vector as follow:

$$P_{robot} = [x_R \quad y_R \quad \theta_R]^T \quad (1)$$

The linear and angular velocities of the mobile robot can be described as follows:

$$v_1 = \frac{v_R + v_L}{2}, \quad (2)$$

$$v_2 = \frac{2(v_R - v_L)}{l}. \quad (3)$$

Now the kinematics model of the mobile robot can be represented as [5]

$$\dot{P}_{robot} = \begin{bmatrix} \cos \theta_R & 0 \\ \sin \theta_R & 0 \\ 0 & 1 \end{bmatrix} \begin{bmatrix} v_1 \\ v_2 \end{bmatrix} \quad (4)$$

Kinematics analysis aims at the proper velocity assignment to each wheel to drive the mobile robot to a desired position and orientation.

2.2 Position propagation

In previous session, we studied that the states of the mobile robot with differential driving mechanism are changing according to the two wheel velocities.

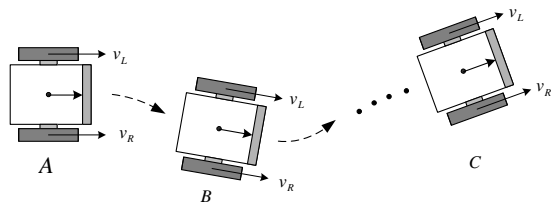


Fig. 3. Position propagation of the mobile robot.

In Fig. 3, when the mobile robot is moving from A where the robot is located on $P_{robot}^k = [x_R \quad y_R \quad \theta_R]_k^T$ at time = k to C where the position is on $P_{robot}^{k+n} = [x_R \quad y_R \quad \theta_R]_{k+n}^T$ at time = $k + n$. The state

transition of the mobile robot can be described in terms of currents state and inputs as follows[]:

$$x_R^{k+1} = x_R^k + T \frac{v_R + v_L}{2} \cos \theta_R^k, \quad (5-a)$$

$$y_R^{k+1} = y_R^k + T \frac{v_R + v_L}{2} \sin \theta_R^k, \quad (5-b)$$

$$\theta_R^{k+1} = \theta_R^k + T \frac{v_R - v_L}{l}. \quad (5-c)$$

where T is the sampling period.

Note when the position of the mobile robot is estimated, state estimation error is included, and represented as follow:

$$\hat{P}_{robot}^{k+1} = f(P_{robot}^k, u(k)) + v(k), \quad (6)$$

where $u(k)$ is the current input, $v(k)$ denotes estimation error as a noise term. The estimation error is unexpected components, when position is calculated[6]. The error can be corrected by applying Kalman filtering technique in Section 3.

3 The Localization by Ultrasonic Sensor

3.1 Detecting moving object using sonar sensor

In this section, we describe the procedure of detecting a moving object through a distance obtained by ultrasonic sensor. When the object is moving, it can be detected by sonar sensor, and then distance information between the object and the robot is available to robot. The position of the mobile robot is updated. Fig. 4. show the coordinates of the moving object and the mobile robot with 12 ultrasonic sensors.

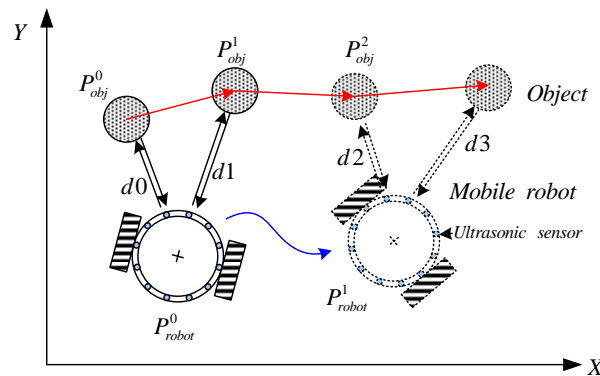


Fig. 4. The outline of motion of object and robot.

As shown fig. 4. the initial position of the object and mobile robot is precisely given as P_{obj}^0, P_{robot}^0 , respectively. Also, the distance d between the object and the mobile robot is denoted.

There are three steps in procedure of detecting the moving object.

Initially, the mobile robot and the object is kept stationary. When the object is moving, distance information at time k and $k+1$, respectively, generate the distance differences. When distance differences exceed the specified threshold value, thus, resulting in the detection of motion of the object.

Secondary, in case that a distance information is obtained by neighboring sensor due to movement of the object, the displacement and angular data with respect to measuring time, T_M of the object can be calculated as shown in fig. 5. And then, the current state of the moving object is estimated thought initial state and obtained information.

Finally, the mobile robot moves along a free path after estimation of the moving object is finished. The inverse method is used to estimate the position of the mobile robot. When the object is kept stationary and the mobile robot moves, the displacement and velocity with respect to the measuring time, T_M of the mobile robot can be obtained. The state vector of the mobile robot is estimated.

To obtained the sequential position estimation, we can use proposed step recursively. The outputs of step are chosen as the estimated state vector of the moving object and mobile robot.

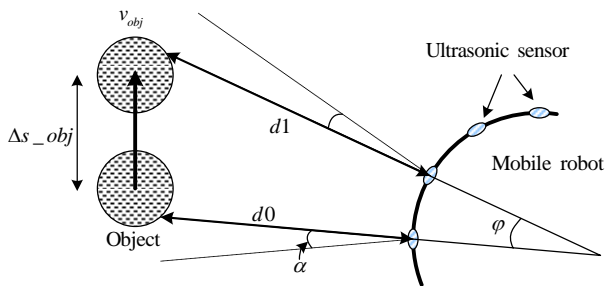


Fig. 5. The motion of object.

3.2 Correction using Kalman filter

The estimated position of the moving object includes some unexpected estimation error. This leads to failure in localization of the mobile robot. An Kalman filter[7] can be one of the good method to tackle this problem. To apply the state estimation of a moving object to the Kalman filter, eq.(7) and (8) of the state transition matrix are required. The Kalman filter minimizes the estimation error by modifying the state transition model based on the error between the estimated vectors and the measured vectors, with an appropriate filter gain. The state vector which consists of a position on the x-y plane, the direction, linear and angular velocity can be estimated using the measured vectors representing the position of the moving object[8].

$$x^k = \Phi^k x^{k-1} + w^{k-1} \quad (7)$$

$$z^k = H^k x^k + v^{k-1} \quad (8)$$

The Kalman filter is a recursive algorithm to determine \hat{x}^k , the optimal estimation value of state vector, x^k in a linear dynamic system. Kalman filtering is divided into the three steps of prediction, measurement, and correction.

In the prediction step, the next state vector $x_{(-)}^{k+1}$ and the covariance matrix of the estimated error $P_{(-)}^{k+1}$ are predicted. The symbol (-) means that the values don't correct through measurement. The covariance matrix of

the estimated error is just like eq.(9).

$$P_{(-)}^{k+1} = E[(x^k - \hat{x}^k)(x^k - \hat{x}^k)^T] \quad (9)$$

The projected estimates of the covariance matrix of the estimated error and the state vector in the prediction step are represented as

$$\hat{x}_{(+)}^{k+1} = \Phi^k \hat{x}_{(+)}^k + w^k \quad (10)$$

$$P_{(-)}^{k+1} = P_{(+)}^k + Q^k \quad (11)$$

where Φ^k is the state transition matrix of $\hat{x}_{(-)}^{k+1}$, w^k is the model noise of the system, where Q^k is the covariance matrix of w^k .

The measurement step is represented as

$$z^k = H^k \hat{x}^k + v^k \quad (12)$$

where z^k is the measurement vector, H^k represents the relationship between the measurement and the state vector, and v^k is the measurement error.

In the final correction step, the state vector and the estimate error are corrected to a new value based on the measurement value of the measurement step. The formula is represented as

$$K^k = P_{(-)}^k (H^k)^T [H^k P_{(-)}^k (H^k)^T + R^k]^{-1} \quad (13)$$

$$\hat{x}_{(+)}^k = \hat{x}_{(-)}^k + K^k [z^k - H^k \hat{x}_{(-)}^k] \quad (14)$$

$$P_{(-)}^k = [I - K^k H^k] P_{(-)}^k \quad (15)$$

where R^k is the covariance matrix of the measurement noise, and K^k represents the Kalman gain. The optimal filter gain K^k minimizes the estimate errors by the covariance matrix of the estimate error $P_{(-)}^k$, the measurement matrix

H^k , and the covariance matrix of measurement noise R^k in eq.(20). Next time, the estimate of the state vector $\hat{x}_{(+)}^k$ from the measurement z^k is expressed as eq.(21).

The Kalman gain functions as the weighting between the measurement and the estimate value when the state vector x^k is corrected. In the end, as in eq.(22), the covariance matrix of the estimated error is corrected.

4 Simulation Experiments

4.1 Experimental environment

The proposed approach is implemented on computer simulation program. The experimental parameters 1 for computer simulation are listed in Table.

Let assume some conditions for finding the position of moving object and localization of the mobile robot.

- 1) The maximum velocity of the mobile robot is faster than that of moving object.
- 2) There is no interference between other ultrasonic sensors
- 3) The initial position of the robot and object is given.
- 4) The path of the robot and object is piecewise continuously differential.

Table 1. Simulation parameter

Parameter list	Value
Size(diameter) of Robot	0.5 m
Size(diameter) of object	0.15 m
Number of ultrasonic sensor	12
Maximum detecting range of ultrasonic sensor	3 (m)
Directivity of ultrasonic sensor	10 (deg)

4.2 Experimental results and discussions

The initial position of the moving object and the mobile robot was set as (0.5, 3, 0°) and (1, 2, 10°), respectively. Fig. 6. shows the path of the moving object and the mobile robot.

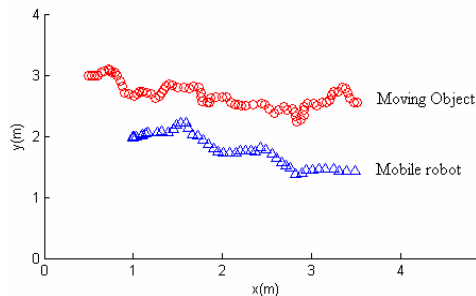


Fig. 6. The path of the moving object and robot.

The estimated state vector of the mobile robot by only dead-reckoning method with uncertainty is shown in fig. 7. And in fig. 8, reduced error with proposed algorithm is shown.

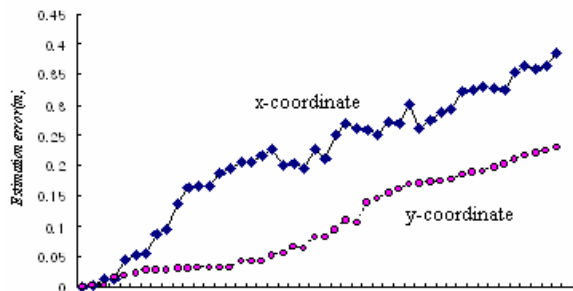


Fig. 7. Position estimation error of the mobile robot using only dead-reckoning method.

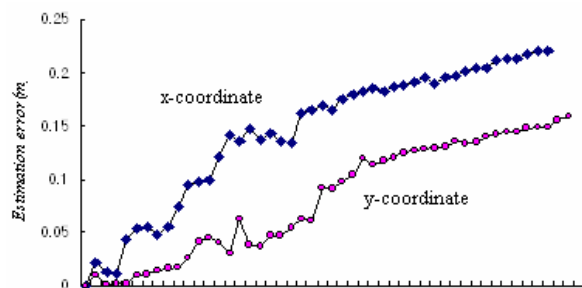


Fig. 8. Position estimation error of the mobile robot using moving object

5 Conclusions

In this paper, an state estimation method for a mobile robot with ultrasonic sensor was proposed using the moving object. The estimated errors is reduced using Kalman filter. It was demonstrated that localization of the mobile robot on computer simulation.

The localization is one of the fundamental functions for intelligent mobile robot. The mobile robot has to handle various dynamic uncertainties for localization robustly. In further research, proposed method will be verified throughout the real experiments with a robot system. And the effective localization of the mobile robot will be needed to improve the estimation accuracy.

References

- [1] Anastasios I. Mourikis, and Stergios I. Roumeliotis, "Performance Analysis of Multirobot Cooperative Localization," *IEEE Tras. Robotics*, vol. 22, no. 4, pp. 666-681, Aug. 2006.
- [2] Dongheui Lee, and Woojin Chung, "Discrete-Status-Based Localization for Indoor Service Robots," *IEEE trans. Industrial Electronics*, vol. 53, no. 5, pp. 1737-1746, Oct. 2006.
- [3] Probabilistic Robotics, Sebastian Thrun, Wolfram Burgard, and Dieter Fox, *the MIT Press*, 2005. pp.191-199.
- [4] Zhihua Qu, Jing Wang, and Clinton E. Plaisted, "A New Analytical Solution to Mobile Robot Trajectory Generation in the Presence of Moving Obstacles," *IEEE Trans. Robotics*, vol. 20, no. 6, pp. 978-993, Dec. 2004.
- [5] Hiromas Takahashi, Hiroaki Nishi, and Kouhei Ohnishi, "Autonomous Decentralized Control for Formation of Multiple Mobile Robots Considering Ability of Robot," *IEEE Trans. Industrial Electronics*, vol. 51, no. 6, pp. 1272-1279, Dec. 2004.
- [6] Cheol-Ho Hwang, Sang-Hun Lee, Jae-Pyung Ko, and Jang-Myung Lee, "Optimal path planning for the capturing of a moving object," in *Proc. Int. Conf. of Control, Autonomous and Systems (ICCAS)*, Gyeongju, Korea, Oct. 22-25, 2003.
- [7] G. Dudek and M. Jenkin, *Computational Principles of Mobile Robotics*, Cambridge university press, 2000, pp. 75-79.
- [8] Jang Myung Lee, K. Son, M. C. Lee, J.W. Choi, S. H. Han, Man Hyung Lee, "Localization of a Mobile Robot using the Image of a Moving Object," *IEEE Tras. Industrial Electronics*, vol. 50, no. 3, pp. 612-619, Jun. 2003.

On the periodic sequence of a discrete sliding mode control system for a single-link robot arm

Sung-Han Son* and Kang-Bak Park**

* Department of Guidance and Control, Agency for Defense Development, Korea
 (Tel : +82-42-484-9049; E-mail: shson@add.re.kr)

** Department of Control and Instrumentation Engineering, Korea University, Korea
 (Tel : +82-41-866-8140; E-mail: kbpark@korea.ac.kr)

Abstract: A novel sufficient condition for a sampled-data system with constant-gain discrete sliding mode controller (SMC) to be globally uniformly ultimately bounded (GUUB) is proposed. It is shown that the stability of the overall system can be known by checking out the one parameter. Simulation results for a single-link robot arm are presented to verify the feasibility of the proposed method.

Keywords: Sampled-Data System, Discrete Sliding Mode Control, GUUB.

1. INTRODUCTION

Almost all of studies of sliding mode control (SMC) have been proposed in the continuous-time domain[1-2]. In the actual system, however, controller is implemented in the discrete time domain since they use micro-processors and/or digital computers. Recently, discrete-time sliding mode control (DSMC) has been studied extensively to address various controllers using specific principles [3-6]. However, the research of discretizing a continuous-time SMC for digital implementation has not been fully explored. Furthermore, it is also well known that a control system designed in the continuous-time domain may become unstable after sampling.

Recently chaotic behaviors were found in discretizing continuous SMC systems by X. Yu [7-8]. Yu and G. Chen proposed the sufficient conditions for discretized system to be GUUB [9]. But these sufficient conditions can be only applied to limited sampling period and specialized cases.

In this paper, therefore, a novel sufficient condition for discrete sliding mode controller (SMC) to be globally uniformly ultimately bounded (GUUB) is proposed. It is shown that the stability of the overall system can be known by checking out the magnitude of one parameter which is an element of the discretized system matrix. The ultimate bounds of the system state variables are also derived. Simulation results for a single-link robot arm are presented to show the effectiveness of the proposed method.

2. SYSTEM DESCRIPTION

Consider a second-order system of the following form

$$\dot{x} = Ax + bu = \begin{bmatrix} 0 & 1 \\ -a_1 & -a_2 \end{bmatrix} x + \begin{bmatrix} 0 \\ 1 \end{bmatrix} u, \quad (1)$$

where $x \in R^2$ is the state vector, $u \in R^1$ is the

system input, and a_1, a_2 are elements of a system matrix. Let the sliding surface be $\sigma = c^T x = [c_1 \ 1]x$, where $c_1 > 0$ is assumed to be designed such that the sliding dynamics, $\sigma = 0$, are asymptotically stable. From $\dot{\sigma} = 0$, we can easily obtain the equivalent control law as

$$\dot{\sigma} = c^T \dot{x} = c^T Ax + c^T bu = 0 \Rightarrow u_{eq} = -(c^T b)^{-1} c^T Ax.$$

From the sliding mode existence condition, $\sigma \dot{\sigma} = 0$, we have the following equivalent control based SMC:

$$u = u_{eq} + u_s = -(c^T b)^{-1} c^T Ax - \alpha (c^T b)^{-1} \text{sgn}(\sigma(x)), \quad (2)$$

where $\alpha > 0$ is a control gain, and $\text{sgn}(\cdot)$ is a signum function. It's assumed that $c^T b$ is nonsingular.

To discretize the overall system, we convert the continuous-time system (1) under the zero-order hold (ZOH) to the discrete-time system

$$x(k+1) = e^{Ah} x(k) + \int_0^h e^{A\tau} d\tau bu(k), \quad (3)$$

where

$$u(k) = u_{eq}(k) + u_s(k) = -c^T Ax(k) - \alpha \cdot \text{sgn}(\sigma(x(k))), \quad (4)$$

h is a sampling period, and the index k indicates the k -th sample.

As the system state $x(k)$ evolves, the switching function $\text{sgn}(\sigma(x(k)))$ forms a sequence of binary values of -1 and $+1$. For simplicity, we denote $\text{sgn}(\sigma(x(k)))$ as $s_k \in \{-1, 1\}$.

Then the discretized system can be described by

$$x(k+1) = \Phi x(k) + \alpha \Gamma s_k = \begin{bmatrix} 1 & v(h) \\ 0 & d(h) \end{bmatrix} x(k) + \alpha \begin{bmatrix} \gamma_1(h) \\ \gamma_2(h) \end{bmatrix} s_k, \quad (5)$$

where $\Phi = e^{Ah} - \int_0^h e^{A\tau} d\tau bc^T A$, $\Gamma = \int_0^h e^{A\tau} d\tau b$.

Equation (5) can be rearranged as

$$x_1(k+1) = x_1(k) + vx_2(k) - \gamma_1 \alpha s_k, \quad (6)$$

$$x_2(k+1) = dx_2(k) - \gamma_2 \alpha s_k. \quad (7)$$

3. STABILITY CONDITION OF DISCRETE SLIDING MODE CONTROLLER

Generally, the asymptotic stability can be guaranteed if the sliding mode controller with a constant gain is implemented in the continuous-time domain. For the discrete-time system, however, the ultimate boundedness can be ensured. In the following theorem, we derive conditions for the stability of the closed-loop system with discrete SMC (4).

Theorem 1: For the discretized systems (6)~(7) with the discrete SMC (4), the overall system is globally uniformly ultimately bounded (GUUB) if

$$|d(h)| < 1. \quad (8)$$

and

$$\frac{v(h)\gamma_2(h)}{1-d(h)} + \gamma_1(h) > 0. \quad (9)$$

Furthermore, ultimately bound of the system state variables are given by

$$\lim_{k \rightarrow \infty} |x_1(k)| \leq |\gamma_1 \alpha| + \frac{(c_1^{-1} - v) |\gamma_2 \alpha|}{1 - |d|}, \quad (10)$$

$$\lim_{k \rightarrow \infty} |x_2(k)| \leq \frac{|\gamma_2 \alpha|}{1 - |d|}. \quad (11)$$

Proof: From (7), It is clear that (8) has to be satisfied because the pole of the system (7) should be located inside the unit circle. It is obvious that the ultimate bound of x_2 can be obtained as (11). When the state x_2 reaches its ultimate bound, we say x_2 is on the equilibrium line, (6) can be rewritten as

$$x_1(k+1) = x_1(k) - \frac{v\gamma_2 \alpha s_k}{1-d} - \gamma_1 \alpha s_k. \quad (12)$$

In order to the state x_1 converges to the sliding surface, the last two terms of (12) should satisfy the following inequality:

$$-\frac{v\gamma_2 \alpha s_k}{1-d} - \gamma_1 \alpha s_k \Rightarrow \frac{v\gamma_2}{1-d} + \gamma_1 > 0. \quad (13)$$

The ultimate bound of the state x_1 can be derived by considering the switching points – intersection of the sliding surface and the equilibrium lines. Since the points are on the sliding surface and equilibrium line, x_2 should have a value of its ultimate bound, and x_1 has to satisfy

$$x_1(k) = -c_1^{-1} x_2(k). \quad (14)$$

Substituting (14) into (6) gives

$$x_1(k+1) = \frac{(c_1^{-1} - v) |\gamma_2 \alpha| s_k}{1 - |d|} - \gamma_1 \alpha s_k. \quad (15)$$

From (15), therefore, the ultimate bound of x_1 can be obtained as (10). ■

Theorem 1 needs two conditions, (8) and (9), to check the stability of the discretized system. Actually, the condition (9) contains four variables, v , d , γ_1 , γ_2 , whereas the condition (8) is composed of only one variable d . In the following theorem, we show that it is sufficient to check the condition (8) to guarantee the stability of the overall system.

Theorem 2: For the closed-loop system (5), if the inequality (8) holds, then the inequality (9) is also satisfied. That is, $|d| < 1$ implies $\frac{v\gamma_2}{1-d} + \gamma_1 > 0$.

Proof: Due to the page limitation, the proof is omitted. ■

Remark 1: From Theorem 1 and 2, the stability of the overall system can be obtained by checking up the magnitude of d .

Remark 2: In the conventional digital system, the stability of the closed-loop system depends on the sampling period, and is given by one inequality. For the constant-gain sliding mode controller for the sampled-data system, however, the stable region of the sampling period may be composed of several supports. For example, for a single-link robot arm, the stable region for the sampling period h is given as a shaded region as in Figure 1.

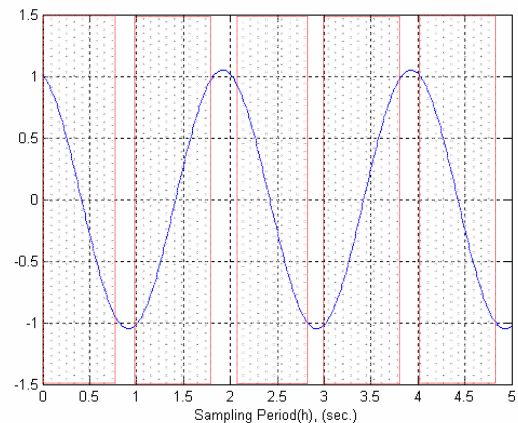


Fig. 1 Stable sampling period. ($|d(h)| < 1$).

4. SIMULATION STUDIES

Consider the model of a pendulum without damping. A second-order system of the pendulum can be represented as

$$\ddot{\theta} = -\frac{g}{l} \sin \theta + \frac{1}{m} u. \quad (55)$$

where g is the acceleration of gravity, $l=1m$ and $m=1kg$ are the length and mass of pendulum. Assume that θ is small enough that $\sin \theta \approx \theta$.

Figures 2~5 are results when $h=0.1$ second. From Figure 1, it's clear that the system is stable for the sampling period. Figure 2 shows the phase portrait. It's very similar to that of continuous-time system. In addition, it is shown that, in the steady state, the system states are bounded by the region given in Theorem 1:

$$|x_1(\infty)| \leq 0.61, |x_2(\infty)| \leq 0.67.$$

It is also can be seen in Figures 3~4.

Figures 6~9 are results when $h=1.5$ second. From Figure 1, it's obvious that the system is stable for the sampling period. For this sampling period, in the steady state, the profile of the state variables show a kind of limit cycle; periodic solution (Fig. 6), and their bounds given in Theorem 1 are as follows:

$$|x_1(\infty)| \leq 0.86, |x_2(\infty)| \leq 0.46$$

Figures 7~8 show that the state variables show the period-12 profiles.

Figures 10~12 are results when $h=0.9$ second. From Figure 1, it's easy to know that the system is unstable for the sampling period although the sampling period is shorter than the another stable one, $h=1.5$. The unstable profile can be seen in Figures 10~11.

5. CONCLUSION

In this paper, a condition to be GUUB for the sampled-data system with discrete SMC has been presented. The proposed scheme gives a simple way to check up the stability of the closed-loop system for a given sampling period.

REFERENCES

- [1] V. I. Utkin (1977), Variable Structure Systems with Sliding Modes, IEEE Trans. on Automat. Contr., vol. AC-22, no. 2, pp.212-222.
- [2] K. Furuta and Y. Pan (2000), Variable structure control with sliding sector, Automatica, vol. 36, pp.211-228
- [3] S. Z. Sarpturk, Y. Istefanopulos, and O. Kaynak (1987), On the stability of discrete-time skidding mode control system," IEEE Trans. on Automat. Contr., vol. 32, no. 10, pp. 930-932.
- [4] K. Furuta (1990), Sliding mode control of a discrete system, System & Control Letters, vol 14, pp. 145-152.
- [5] P. Myszkorowski (1990), Robust controller for the linear discrete-time system, Proc. 30th IEEE Conf. on Decision and Control, England, pp. 2972-2973
- [6] W. Gao, Y. Wang, and A. Homaifa (1995), Discrete-time variable structure control systems,

IEEE Trans. Ind. Electron., vol 42, no.2, pp. 117-122

- [7] X. Yu and S. Yu (2000), Discrete sliding mode control design with invariant sliding sectors, ASME Journal of Dynamic Systems, Measurement and Control, vol. 122, no. 4, pp. 776-782.
- [8] X. Yu (2001), Discretizing Sliding Mode Control: From Chattering to Unstable Motion, Proc. 40th IEEE Conf. on Decision and Control, USA, pp. 914-918
- [9] X. Yu and G. Chen(2003), Discretization Behaviors of Equivalent Control Based Sliding-Mode Control Systems, IEEE Trans. on Automat. Contr., vol. 48, no. 9, pp.1641-1646

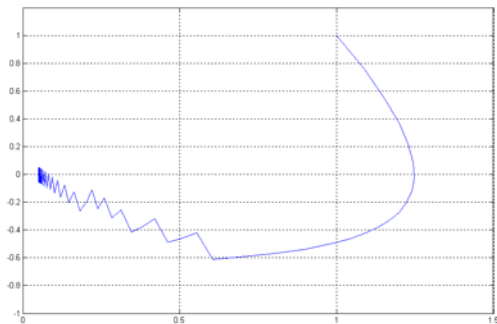


Fig. 2 Phase portrait when $h=0.1$

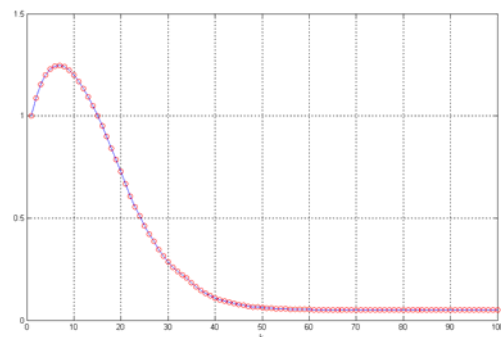


Fig. 3 State variable x_1 when $h=0.1$

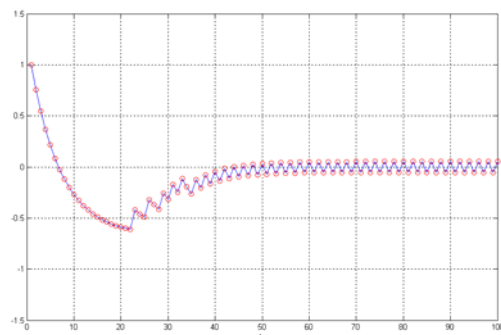


Fig. 4 State variable x_2 when $h=0.1$

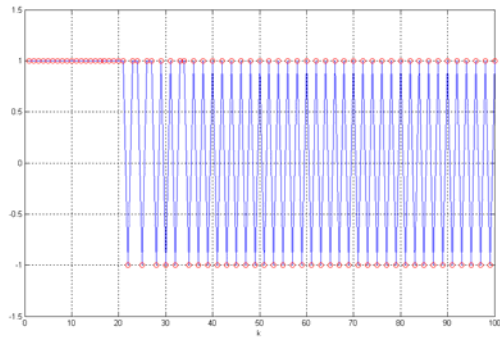


Fig. 5 Switching variable s when $h=0.1$

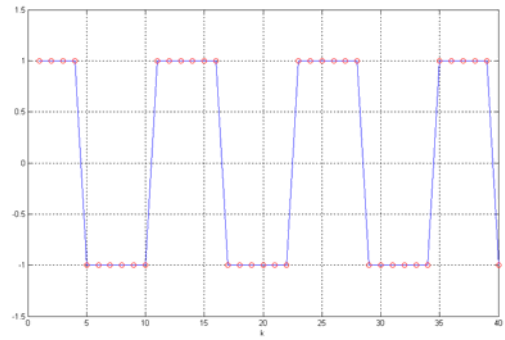


Fig. 9 Switching variable s when $h=1.5$

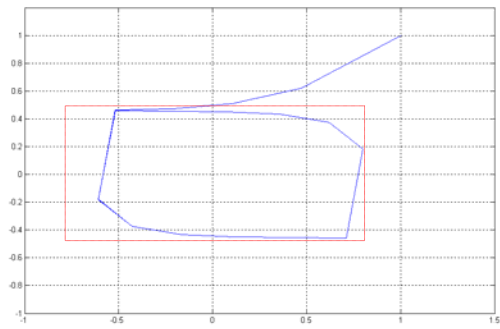


Fig. 6 Phase portrait when $h=1.5$

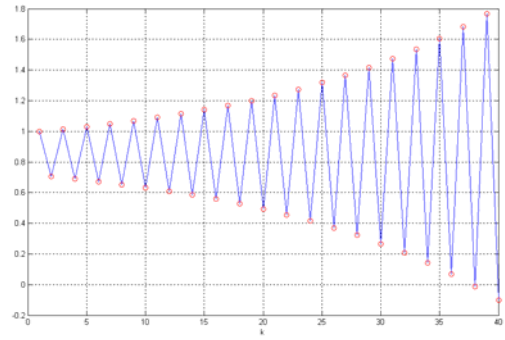


Fig. 10 State variable x_1 when $h=0.9$

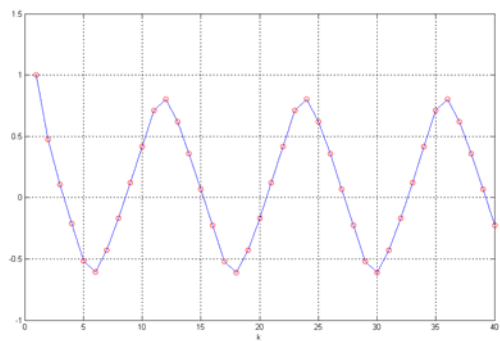


Fig. 7 State variable x_1 when $h=1.5$

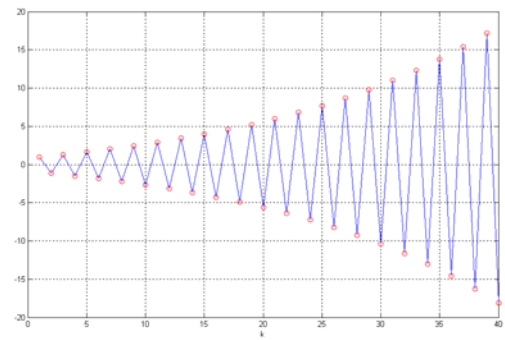


Fig. 11 State variable x_2 when $h=0.9$

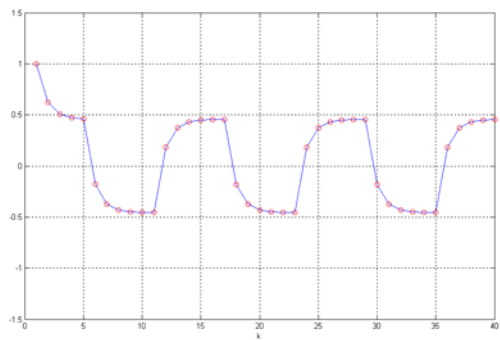


Fig. 8 State variable x_2 when $h=1.5$

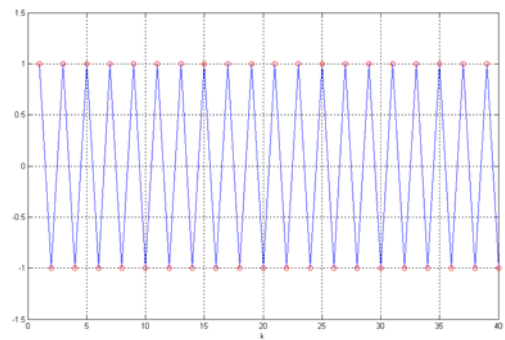


Fig. 12 Switching variable s when $h=0.9$

Stable Adaptive Neural Control for a Nonlinear Robot System in the Presence of Actuator Failures and Uncertainties

Jin-Ho Shin^{*1}, Kap-Ho Seo⁺, Min-Soeng Kim⁺, Ju-Jang Lee⁺, Won-Ho Kim^{*2},
Moon-Noh Lee^{*3}

^{*1,2}Department of Mechatronics Engineering, Dong-eui University,
^{*1,2}995 Eomgwangno, Busanjin-gu, Busan 614-714, Korea
^{*1}E-mail: jhshin7@deu.ac.kr

⁺Department of Electrical Engineering and Computer Science, Korea Advanced Institute of Science and
Technology, ⁺373-1 Guseong-dong, Yuseong-gu, Daejeon 305-701, Korea

^{*3}Department of Computer Engineering, Dong-eui University,
^{*3}995 Eomgwangno, Busanjin-gu, Busan 614-714, Korea

Abstract

The bounded nonlinear time-varying actuator torque coefficients as well as uncertainties may deteriorate the performance of a robot. This work presents a design methodology of a stable adaptive neural controller to overcome the performance degradation for an uncertain nonlinear robot system with actuator failures. The proposed control scheme is based on the Lyapunov stability approach for adaptive control using a GFN (Gaussian function network) to approximate a nonlinear dynamic terms. The proposed controller can improve performance degradation and achieve task completion despite actuator failures and uncertainties. Simulation results are shown to verify the validity and robustness of the proposed control scheme.

Keywords: Stable adaptive neural control, Robot system, GFN, Actuator failure, Uncertainty.

1 Introduction

Hardware or software failures at actuators as well as uncertainties such as parameter variations and disturbances cause performance degradation of robots.

Fault detection and fault tolerance for robots were dealt with and discussed in [1-4]. The adaptive, robust, and neural control issues for robot systems with uncertainties were discussed in [5-10].

Both actuator failures and uncertainties, which are two factors of performance degradation in a robot system, need to be considered at the same time in the control system design. In most of the previous works, control methods overcoming these two factors at the same time were not yet actively discussed.

In this paper, a stable adaptive neural control scheme for a nonlinear robot system in the presence of actuator failures and uncertainties is developed with guaranteeing the stability, based on adaptive control technique and a GFN. The validity of the proposed scheme is verified through simulation.

2 Robot System

The dynamic model of an n-link robot system with actuator failures and uncertainties can be described as

$$M(q)\ddot{q} + F(q, \dot{q}) = u + d(t) = K_a u_c + d(t) \quad (1)$$

where $q \in \mathcal{R}^n$ is the position vector of joint coordinates, $M(q)$ is the symmetric positive definite inertial matrix, $F(q, \dot{q}) = C(q, \dot{q})\dot{q} + F_f(\dot{q}) + G(q)$, $C(q, \dot{q})\dot{q}$ represents the centrifugal and Coriolis torques, $F_f(\dot{q}) = F_v\dot{q} + F_d(\dot{q}) + F_s(\dot{q})$ is the vector of friction forces/torques including the viscous, coulomb and static friction forces/torques, respectively, and $G(q)$ is gravitational torques, u is the actual joint torque vector, u_c is the commanded torque vector or controller output vector, and $d(t)$ is an external disturbance vector bounded as $\|d(t)\| \leq \theta_d$ where θ_d is an unknown positive constant. An unknown matrix $K_a \in \mathcal{R}^{n \times n}$ representing the current joint failure's situation is a bounded nonlinear time-varying diagonal matrix consisting of actuator torque coefficients, in other words, $K_a(t) = \text{diag}(K_{a1}(t), K_{a2}(t), \dots, K_{an}(t))$, and $\|K_a\| \leq \bar{k}_a$ with an unknown positive constant \bar{k}_a .

The block diagram of the robot control system with actuator failures is shown in Fig. 1.

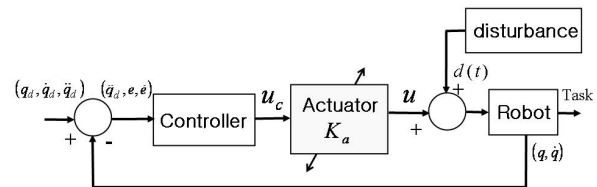


Fig. 1. The robot control system with actuator failures.

The boundary property for each dynamic term of the above dynamic equation (1) is shown as follows.

Property 1: There exist positive constants m_{\min} , m_{\max} , f_g , f_f , and f_c such that $m_{\min} \leq \|M(q)\| \leq m_{\max}$, and $\|F(q, \dot{q})\| \leq f_g + f_f \|\dot{q}\| + f_c \|\dot{q}\|^2$ [11].

As an ideal case, K_a is an $n \times n$ identity matrix

and then $u = u_c$, and it means no actuator failures.

On the contrary, in real robot systems, the commanded torques u_c may not be precisely delivered to the actual torques u due to the hardware or software actuator failures at some joints.

The actuator failures may deteriorate the robot performance. If fault tolerance is not considered in the control system, the more time passes the more degraded the system performance is, ultimately the desired task performance may not be achieved.

In this paper, it is considered that the actuator torque coefficient matrix K_a is not accurately an identity matrix and thus experiences the actuator failures, but it is assumed that K_a does not have any zero diagonal elements. This kind of failure is called as the partial actuator failure.

3 Stable Adaptive Neural Control

The joint position error and the augmented error are denoted by $e = q - q_d$ and $s = \dot{e} + \Lambda e$, respectively, where q_d is a desired position vector and $\Lambda \in \mathbb{R}^{n \times n}$ is a positive definite constant diagonal matrix.

The dynamic equation for the augmented error s is obtained as follows.

$$M(q)\dot{s} = -F(q, \dot{q}) - M(q)\ddot{q}_d + M(q)\Lambda\dot{e} + K_a u_c + d(t). \quad (2)$$

Now, u_c is defined as $u_c = \hat{K}_a^{-1} v_c$, where \hat{K}_a represents a guessed nominal model for K_a .

Substituting the commanded torque for Eq. (2) and writing it again, it is as follows,

$$M(q)\dot{s} = v_c + \bar{\eta} + \bar{\phi}, \quad (3)$$

where $\bar{\eta} = (K_a \hat{K}_a^{-1} - I_n) v_c + d(t)$, $\bar{\phi}(q, \dot{q}, \ddot{q}_d) = -F(q, \dot{q}) - M(q)\ddot{q}_d + M(q)\Lambda\dot{e}$, and I_n is an $n \times n$ identity matrix.

Assumption 1: There exists an unknown constant $c_0 \geq 0$ such that $\|K_a \hat{K}_a^{-1} - I_n\| \leq c_0 < 1$.

Let us consider the following Lyapunov function candidate to develop a GFN approximating a nonlinear function.

$$V_1 = s^T M(q) s / 2. \quad (4)$$

Differentiating Eq. (4) along the solution of the dynamic equation (3),

$$\dot{V}_1 = s^T (v_c + \phi + \bar{\eta}) = s^T (v_c + \eta), \quad (5)$$

where the lumped uncertainty η is $\eta = \phi + \bar{\eta}$, and

$$\begin{aligned} \phi(q, \dot{q}, q_d, \dot{q}_d, \ddot{q}_d) &= \bar{\phi}(q, \dot{q}, \dot{q}_d, \ddot{q}_d) + \dot{M}(q, \dot{q})s / 2 \\ &= (\phi_1 \ \phi_2 \ \dots \ \phi_n)^T \in \mathbb{R}^n. \end{aligned} \quad (6)$$

The unknown nonlinear function ϕ can be expressed by the following GFN.

$$\phi = L(x)w + b + e_a(t, x), \quad (7)$$

where $x \in \mathbb{R}^m$, ($m = 5n$) is the input variable vector such as $q, \dot{q}, q_d, \dot{q}_d$ and \ddot{q}_d , getting into the network, and $L(x) \in \mathbb{R}^{n \times nr}$ is the matrix that has the r Gaussian functions. $w \in \mathbb{R}^{nr}$ and $b \in \mathbb{R}^n$ are the desired unknown constant weight and desired unknown constant bias to very approximate the GFN (7) to the nonlinear function ϕ (6), together with $L(x) \in \mathbb{R}^{n \times nr}$. $e_a(t, x) \in \mathbb{R}^n$ is the approximation error.

The above GFN is illustrated in Fig. 2. $L(x)$ in Eq. (7) is shown as follows.

$$L(x) = \begin{bmatrix} N_1 & N_2 & \dots & N_r & 0 & 0 & \dots & 0 \\ 0 & 0 & \dots & 0 & N_1 & N_2 & \dots & N_r \\ \vdots & \vdots \\ 0 & 0 & \dots & 0 & 0 & 0 & \dots & 0 \\ \dots & \dots & \dots & 0 & 0 & \dots & 0 \\ \dots & \dots & \dots & 0 & 0 & \dots & 0 \\ \vdots & \vdots & \vdots & \vdots & \vdots & \vdots & \vdots \\ \dots & \dots & \dots & N_1 & N_2 & \dots & N_r \end{bmatrix}, \quad (8)$$

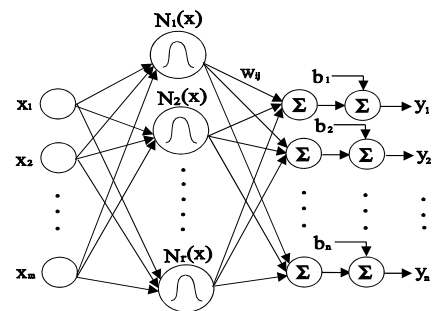


Fig. 2. The structure of the used GFN.

Assumption 2: There exist an unknown positive constant vector θ_e and a known positive function $\psi_e(t, x)$ such that $\|e_a(t, x)\| \leq \rho_e(t, x) = \theta_e^T \psi_e(t, x)$.

From the structure of the nonlinear function ϕ (6) and the GFN (7), it can be easily shown that the above assumption is very reasonable. We can find that the norm of ϕ (6) is bounded by a positive function from Property 1. In Eq. (7), the norm of the GFN is also bounded by a positive constant. Therefore, from Property 1, Eqs. (6) and (7), a positive function $\psi_e(t, x)$ can be obtained as follows.

$$\psi_e(t, x) = \left(1 \ \|\dot{q}\| \ \|\dot{q}\|^2 \ \|\ddot{q}_d\| \ \|e\| \ (\|\dot{q}\| \|s\|)\right)^T \in \mathbb{R}^6. \quad (9)$$

Theorem 1: Under Assumptions 1 and 2, if the following control law and adaptation law are applied to the robot system (1), then the joint position and velocity errors are globally uniformly ultimately bounded.

Control law:

$$u_c = \hat{K}_a^{-1} v_c = \hat{K}_a^{-1} \left(-K_c s - L\hat{w} - \hat{b} - \hat{\rho} \frac{s}{\|s\| + \varepsilon} \right), \quad (10)$$

$$\hat{\rho} = \hat{\theta}^T \psi, \quad \psi = \left(\|s\| \ \|\hat{w}\| \ \|\hat{b}\| \ \psi_e^T \right)^T \in \mathbb{R}^{10}, \quad (11)$$

$$\psi_a = \begin{pmatrix} \psi_e^T & 1 \end{pmatrix}^T \in \mathfrak{R}^7, \quad (12)$$

$$\psi_e = \begin{pmatrix} 1 & \|\dot{q}\| & \|\dot{q}\|^2 & \|\ddot{q}_d\| & \|\dot{\epsilon}\| & (\|\dot{q}\|\|s\|) \end{pmatrix}^T \in \mathfrak{R}^6, \quad (13)$$

where \widehat{K}_a is a guessed nominal actuator torque coefficient matrix as mentioned above and it is usually initially defined as an identity matrix. The gain $K_c \in \mathfrak{R}^{n \times n}$ is a positive definite constant diagonal matrix, \widehat{w} is an estimation weight vector of w and \widehat{b} is an estimation bias vector of b , ϵ is a small positive constant, and $\widehat{\theta} \in \mathfrak{R}^{10}$ is an estimate for a parameter vector $\theta \in \mathfrak{R}^{10}$.

Adaptation law:

$$\dot{\widehat{w}} = \Gamma_w L^T s, \quad \dot{\widehat{b}} = \Gamma_b s, \quad \dot{\widehat{\theta}} = \Gamma_\theta \left(\frac{\psi \|s\|^2}{\|s\| + \epsilon} - \sigma \widehat{\theta} \right) \in \mathfrak{R}^{10}, \quad (14)$$

where $\Gamma_w \in \mathfrak{R}^{nr \times nr}$, $\Gamma_b \in \mathfrak{R}^{n \times n}$ and $\Gamma_\theta \in \mathfrak{R}^{10 \times 10}$ are positive definite constant diagonal matrices, and $\sigma > 0$ is a small constant.

Proof: Let us define an overall Lyapunov function candidate using (4).

$$V = V_1 + V_a = z^T P z / 2 \leq \lambda_{\max}(P) \|z\|^2 / 2, \quad (15)$$

where $z = \begin{pmatrix} s^T & \widehat{\theta}^T & \widehat{w}^T & \widehat{b}^T \end{pmatrix}^T$, $V_a = (1 - \bar{\theta}_3) \widehat{\theta}^T \Gamma_\theta^{-1} \widehat{\theta} / 2 + \widehat{w}^T \Gamma_w^{-1} \widehat{w} / 2 + \widehat{b}^T \Gamma_b^{-1} \widehat{b} / 2$, $0 \leq \bar{\theta}_3 = c_0 < 1$, $\widehat{\theta} = \widehat{\theta} - \theta$, $\widehat{w} = \widehat{w} - w$, and $\widehat{b} = \widehat{b} - b$.

Taking the time derivative of V along the solution of the system and substituting the robot dynamics for the augmented error s (3), the upper-bound on the norm of lumped uncertainty based on Assumption 1 and Assumption 2, and the control laws (10)~(13) and the adaptation laws (14), the following result is made through some manipulations.

$$\begin{aligned} \dot{V} &\leq -s^T K_c s - (1 - \bar{\theta}_3) \sigma \widehat{\theta}^T \widehat{\theta} + \bar{h}(\rho, \widehat{\rho}, \|s\|) \\ &\leq -\lambda_{\min}(Q) \|z\|^2 / 2 + h(\rho, \widehat{\rho}, \|s\|) \end{aligned} \quad (16)$$

where $\widehat{\rho} = \widehat{\theta}^T \psi$, $\widehat{\theta} \in \mathfrak{R}^{10}$, $\psi = \begin{pmatrix} \|s\| & \|\widehat{w}\| & \|\widehat{b}\| & \psi_a^T \end{pmatrix}^T \in \mathfrak{R}^{10}$,

$$\psi_a = \begin{pmatrix} \psi_e^T & 1 \end{pmatrix}^T \in \mathfrak{R}^7, \quad \psi_e = \begin{pmatrix} 1 & \|\dot{q}\| & \|\dot{q}\|^2 & \|\ddot{q}_d\| & \|\dot{\epsilon}\| & (\|\dot{q}\|\|s\|) \end{pmatrix}^T,$$

$$\bar{h}(\rho, \widehat{\rho}, \|s\|) = \begin{pmatrix} \|s\| \epsilon \\ \|s\| + \epsilon \end{pmatrix} \left[\bar{\rho} \bar{\theta}_3 + \rho (1 - \bar{\theta}_3) \right], \quad Q = \begin{pmatrix} 2K_c & 0 \\ 0 & (1 - \bar{\theta}_3) \sigma I_{10} \end{pmatrix},$$

and $\lambda_{\min}(\cdot)$ represents the minimum eigenvalue of its argument, and $h(\rho, \widehat{\rho}, \|s\|) = (1 - \bar{\theta}_3) \sigma \widehat{\theta}^T \widehat{\theta} / 2 + \bar{h}(\rho, \widehat{\rho}, \|s\|)$.

From Eq. (15), Eq. (16) is expressed as

$$\dot{V} \leq -\mu V + h(\rho, \widehat{\rho}, \|s\|), \quad (17)$$

where $\mu = \lambda_{\min}(Q) / \lambda_{\max}(P)$, Q and P are positive definite matrices, and $\lambda_{\max}(\cdot)$ represents the maximum eigenvalue of its argument.

From the boundedness of the Lyapunov function (15), the augmented error $s(t)$, the parameter errors $\widehat{\theta}(t)$, $\widehat{w}(t)$ and $\widehat{b}(t)$ are bounded as follows.

$$\begin{aligned} \|s(t)\| &\leq [2V / \lambda_{\min}(M)]^{1/2}, \quad \|\widehat{\theta}(t)\| \leq [2V / (1 - \bar{\theta}_3) \lambda_{\min}(\Gamma_\theta^{-1})]^{1/2}, \\ \|\widehat{w}(t)\| &\leq [2V / \lambda_{\min}(\Gamma_w^{-1})]^{1/2}, \quad \|\widehat{b}(t)\| \leq [2V / \lambda_{\min}(\Gamma_b^{-1})]^{1/2}. \end{aligned}$$

Consequently, since the augmented error $s(t)$ and the parameter errors $\widehat{\theta}(t)$, $\widehat{w}(t)$ and $\widehat{b}(t)$ are globally uniformly ultimately bounded (GUUB), the stable dynamics $s = \dot{e} + \Lambda e$ guarantees that the position and velocity errors e and \dot{e} are also globally uniformly ultimately bounded, respectively. ■

Remark 1: In the controller (10), it is reasonable that the guessed nominal actuator torque coefficient matrix \widehat{K}_a is usually initially defined as an identity matrix, because it is hard to expect any kind of actuator failures initially in a robot system and a user can consider the initial actuator states as the normal state.

4 Simulation Study

The proposed controller is applied to a three-link robot moving on a horizontal plane shown in Fig. 3. The robotic parameters such as length (L_i), mass (m_i), moment of inertia (I_i), and center position of mass (L_{ci}) are $L_i = 0.5(m)$, $m_i = 1(kg)$, $I_i = 0.02083(kgm^2)$ and $L_{ci} = 0.25(m)$, $i = 1, 2, 3$, respectively. The viscous, coulomb and static friction coefficients at each joint are assigned to be $0.05(Nm \text{ sec} / \text{rad})$, $0.01(Nm)$ and $0.02(Nm)$, respectively.

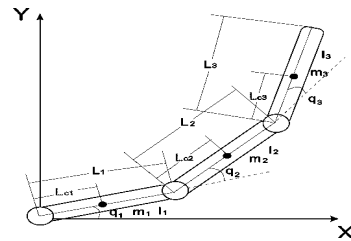


Fig. 3. A three-link planar robot.

The values of the nominal dynamic parameters used in the controllers are set to 50% of the values of the actual dynamic parameters. The nominal values of each friction coefficient are set to zero values. The external disturbance is the random noise of which norm is bounded by $\|d(t)\| \leq \sqrt{3} / 2$.

The control objective is the joint position control from the initial joint positions $q_1(0) = 0(\text{rad})$, $q_2(0) = 0(\text{rad})$, and $q_3(0) = 0(\text{rad})$ to the final desired joint positions $q_{1d} = 5\pi / 6(\text{rad})$, $q_{2d} = \pi / 2(\text{rad})$, and $q_{3d} = -2\pi / 3(\text{rad})$. The initial joint velocities $\dot{q}(0)$ and the desired joint velocities \dot{q}_d and accelerations \ddot{q}_d of all joints are zeros.

In the Gaussian functions, the 15 basis functions are used. The center positions are randomly initialized and updated by a k-means clustering method. Weights and

biases are initialized with very small random numbers and updated by the adaptation laws of the proposed control scheme. The widths are determined as $wid_k = d_{max} / \sqrt{2 \cdot N_{cen}}$, where d_{max} is the maximum distance between the chosen centers and N_{cen} is the number of centers.

The simulation scenario is given as follows. Total execution time is 10 (sec). Initially, no actuator failures are assumed. From the initial time to 3 (sec), the robot has the normal states without failures. The actuator failures at all joints occur at 3 (sec) and continue from 3 (sec) to 10 (sec). The actuator torque coefficients are shown in Fig. 4.

The guessed nominal actuator torque coefficient matrix \hat{K}_a is defined as an identity matrix.

In this simulation, the proposed adaptive neural control scheme and PD control method are compared, and Fig. 5 and Fig. 6 show the simulation results for each control method.

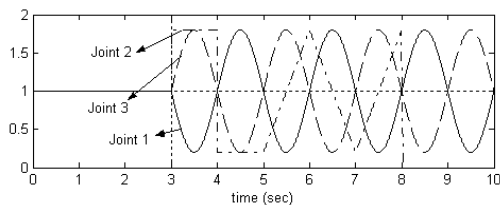


Fig. 4. Actual actuator torque coefficients (K_a).

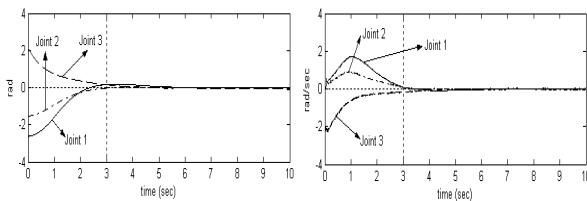


Fig. 5-(a). Joint position errors (e).

Fig. 5-(b). Joint velocity errors (\dot{e}).

Fig. 5. Control results using the proposed controller.

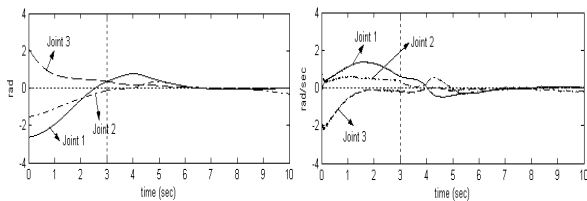


Fig. 6-(a). Joint position errors (e).

Fig. 6-(b). Joint velocity errors (\dot{e}).

Fig. 6. Control results using the PD controller.

As shown in Figs. 5-(a) and 5-(b), it is found that the position and velocity errors decrease to very small neighborhoods of zero even though the actuator failures occur under the uncertainties. From Figs. 6-(a) and 6-(b), it is shown that the position and velocity errors do not satisfactorily converge to very small neighborhoods of zeros due to actuator failures and uncertainties.

5 Conclusions

This work has presented a stable adaptive neural control scheme for a robot system with performance degradation due to actuator failures and uncertainties. The proposed controller can improve the performance in the presence of actuator failures and uncertainties, and it achieves task completion.

It has been observed that the proposed control scheme is valid and robust under the actuator failures and uncertainties through simulation study.

This work is applicable to an uncertain remote robot system of which independent actuators are partially failed. In other words, for an uncertain robot with partially failed actuators in remote sites, the actuator failures are compensated and the task can be completed by the proposed controller, without human intervention.

References

- [1] English J.D. and Maciejewski A.A. (1998), Fault Tolerance for Kinematically Redundant Manipulators: Anticipating Free-Swinging Joint Failures. *IEEE Trans. on Robotics and Automation*. 14(4):566-575.
- [2] Visinsky M. L., Cavallaro J.R. and Walker I.D. (1995), A Dynamic Fault Tolerance Framework for Remote Robots. *IEEE Trans. on Robotics and Automation*. 11(4):477-490.
- [3] Groom K.N., Maciejewski A.A. and Balakrishnan V. (1999), Real-Time Failure-Tolerant Control of Kinematically Redundant Manipulators. *IEEE Trans. on Robotics and Automation*. 15(6):1109-1116.
- [4] Dixon W.E., Walker I.D., Dawson D.M. and Hartranft J.P. (2000), Fault Detection for Robot Manipulators with Parametric Uncertainty: A Prediction-Error-Based Approach. *IEEE Trans. on Robotics and Automation*. 16(6):689-699.
- [5] Dawson D.M., Qu Z. and Lewis F. L. (1992), Hybrid Adaptive-Robust Control for a Robot Manipulator. *Int. J. of Adaptive Control and Signal Processing*. 6:537-545.
- [6] Yoo D.S. and Chung M. J. (1992), A Variable Structure Control with Simple Adaptation Laws for Upper Bounds on the Norm of the Uncertainties. *IEEE Trans. on Robotics and Automation*. 37(6):860-864.
- [7] Fu L.C. (1992), Robust Adaptive Decentralized Control of Robot Manipulators. *IEEE Trans. on Automatic Control*. 37(1):106-110.
- [8] Sanner R.M. and Slotine J.-J.E. (1992), Gaussian Networks for Direct Adaptive Control. *IEEE Trans. on Neural Networks*. 3:837-863.
- [9] Sanner R. M. and Slotine J.-J.E. (1991), Stable Adaptive Control and Recursive Identification Using Radial Gaussian Networks. *Proc. IEEE 30th Conf. on Decision and Control*, Brighton, England, 1991, pp. 2116-2123.
- [10] Mizerek R.T. (1994), Gaussian Neural Network for Direct Adaptive Control of Robotic Systems. *Proc. IEEE 33rd Conf. on Decision and Control*. Lake Buena Vista, FL, USA, 1994, pp. 3504-3505.
- [11] Lewis F.L., Abdallah C.T. and Dawson D.M. *Control of Robot Manipulators*. Macmillan Publishing Company, 1993.

Intelligent Automatic Community Grouping System by Multiagents

Young Im Cho

Dept. of Computer Science, The University of Suwon,
San 2-2, Wau-ri, Bongdam-eup, Hwaseong-si, Gyeonggi-do, 445-743, KOREA
ycho@suwon.ac.kr

Abstract

We developed an intelligent ubiquitous web based e-learning system based on multi agents. The proposed system, Intelligent Ubiquitous Web based e-learning Multi Agent System, is used the new distributed multi agent framework and neural network for e-learning grouping. The proposed system implements user's individual satisfaction network from analyzing the satisfaction degree among learners in groups on web environment. The satisfaction network is personalized by providing weights to the learners' satisfaction degree on e-learning grouping. So, it constructs the learners' satisfaction network model about the e-learning grouping. Based on this network model, the proposed system can decide if the group is remained or reorganized or break down for next time, and the system learn about the above states.

Keywords: multiagents, e-learning, community

1. Introduction

The dropout rate in e-learning is higher than that in traditional face-to-face learning due to its low degree of continuity. In order to lower this dropout rate, many researches have been done to heighten the degree of learners' satisfaction and to provide them with motivation [1,2,3,4,5].

The agent system, which began to appear in the 1990s, is a system that is automatically managed and self-operative. It is a very intelligent concept that can manage the information of each learner in the e-learning system, and recommend and search information that fits the inclination of each individual [6,7]. By applying the concept of the agent to the e-learning system, we can develop the next generation's technology which will contribute to the increase of the degree of satisfaction of learners, as well as the degree of learning achievement, by analyzing the inclination of each individual learner and reflecting its result in each group.

In this paper, as we recognize the importance of a learning community and intend to form a

learning community which is strong and at the same time, the most feasible, we will develop an intelligent web based e-learning multi agent system through the questionnaire called the inclination test with the method of intelligence based agent which will reflect the inclination and characteristic of an individual learner.

This paper is consisted of the followings. Chapter 2 will explain the proposed system's overview, module specification and the algorithm of the proposed system. Chapter 3 will evaluate the proposed system. And finally a conclusion is in chapter 4.

2. The Proposed System

2.1 System Structure

On the basis of the above researches, firstly we present a list of homogeneity and heterogeneous items for inclination testing for the effectiveness of online e-learning community.

As for a questionnaire, 10 items are included which are considered to be adequate for grouping, according to the characteristics of each category.

Information from individual learners through security and certification procedure as seen in Figure 1 is inputted to the system, Intelligent Ubiquitous Web based e-Learning Multi Agent System (IMAS), to be proposed in this paper, and IMAS creates each user's profile from the information. Based on it, learning community grouping suitable to each individual is automatically executed by using Self Organizing Feature Map (SOM) learning algorithm via multi agents.

In IMAS, the grouping and the learning is automatically performed on real time by multi agents, regardless of the number of learners. A new framework has been proposed to generate multi agents, and it is a feature that efficient multi agents can be executed by proposing a new negotiation mode between multi agents.

Overall structure is composed of the user information (user, learner), user profile in which user's tendency is saved, e-learning database,

which processes digitalized learning information and distributed multi agent framework (DIMAF), which generates multi agents, as well as multi agents that are comprised of grouping agent deciding a learner's group form DIMAF, user profile update agent who continuously updates learner's information continuously and learning evaluation agent who automatically informs learning evaluation as seen in Figure 1.

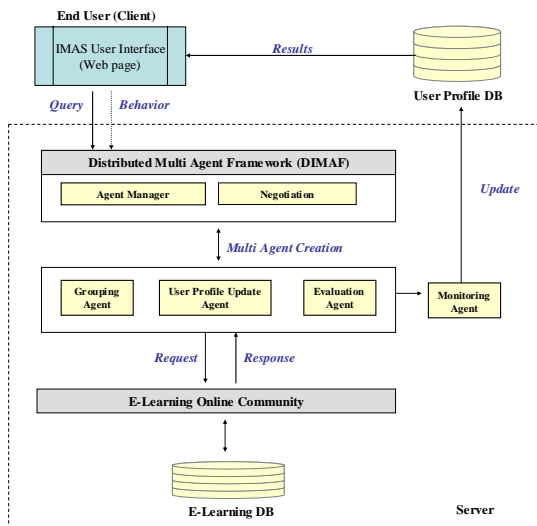


Figure 1. IMAS system configuration

2.2 Main Functions

2.2.1 User Profile Learning

One of multi agents in IMAS, Grouping agent is generated by learner's drawing a distribution map related to items using Kohonen's SOM learning algorithm, based on inputted information for homogeneity and heterogeneity. When homogeneous and heterogeneous items are inputted respectively, input vector is generated in order pairs, each. Then, learning grouping is automatically executed with the weight provided by drawing up a categorization map on real time through SOM network [8].

The explanation of user profile drawing method regarding each number is as follows. ① Input vector is generated with regard to learner's input value for 1st (homogeneous) and 2nd (heterogeneous) categorization criteria. ② A distribution map is drawn up by providing weight to detailed homogeneous and heterogeneous items via SOM network.

2.2.2 Multi Agent Framework

When an agent is generated, DIMAF consists of the negotiation algorithm between the agent

name server (ANS) providing agent ID, an agent manager controlling and monitoring generation, execution and movement of agent and multi agents.

The negotiation algorithm is greatly required for suitable grouping from grouping list by searching learned user profile with user input item inputted at an early stage in the grouping agent. In the grouping list, the user (ID), group number (G), satisfaction degree (SD) and team information (TI) are recorded. TI is recorded as a value among maintenance (M), don't care (D) and break (B). Maintenance (M) is the case where satisfaction degree of previous group members is very high, which means the value is required to be maintained constantly, not desiring to break. Don't care (D) is the value meaning that it may be changed, according to learners' responses in the normal position. Break (B) means the group to be regrouped, after breaking existing group, since satisfaction degree of the previous group members is very low.

The detailed negotiation process by negotiation algorithm proposed in this paper is as follows:

Step 1: Grouping agent searches concerned individual (ID), group number (G), satisfaction degree (SD) and team information (TI) from grouping list by inspecting user profile from the homogeneous items categorized primarily. If a concerned ID's TI value is M, the concerned grouping is maintained without executing 2nd step and you need to move to step 4. If TI value is D or B, you need to move to step 2 and continue.

Step 2: From the table saved in the temporary storage, grouping agent (GA) calculates G and SD which performed grouping by SOM learning algorithm by using user input homogeneous item. If TI value was B, you need to move to step 4, beyond step 3.

Step 3: When the grouping result value performed by GA in step 2 and the G value of grouping list are different, concerned grouping should be maintained in the user ID with priority in the result of grouping list in the user profile. However, concerned user should judge by showing the group member list to concerned user (ID).

Step 4: Show grouping information and member list to each learner.

Four multi agents are generated basically in the IMAS system. Grouping agent (GA) is the agent that generates user profile using 1st categorization criteria (homogeneous) and 2nd categorization criteria (heterogeneous). GA is in

charge of grouping. User profile update agent (UA) is the agent that saves user history and helps grouping performance, while consulting GA.

Evaluation agent (EA) evaluates learning satisfaction degree of user and grouping members and decides whether to maintain, don't care or break this group, according to satisfaction degree value.

Monitoring agent (MA) is the agent to identify state of a learner (user) by monitoring the number of grouping, number per group and satisfaction degree per group graphically through monitoring of learners' learning status.

In IMAS, grouping forms group via grouping agent. The grouping agent indicates homogeneous and heterogeneous distribution from homogeneous and heterogeneous items selected by a user through the use of SOM algorithm. Automatic grouping is made by learner's input with this distribution.

Among homogeneous items as you seen in section 2, a user selects detailed items (i.e. major subject is Korean) regarding each item. In the IMAS, 6 input nodes and random $10 \times 10 (=100)$ output nodes are provided for a learner to learn using learning algorithm of the SOM network regarding each detailed input value of the user-input homogeneous value. Here, the reason why 100 output nodes are provided is because maximum number of cases in which homogeneity can be generated is limited to 100.

With regard to input value, values were randomly generated in order of major subject, favorite sports, etc, giving priority to each item by valuing homogeneous values numerically. For example, ID: yicho1234, major subject: Korean, teaching experience: 1-5 years, favorite sport: swimming, hobby: movie, favorite food: Chinese food, favorite color: yellow were selected, they are expressed in the following data structure order by with priorities in order.

Among four heterogeneous items inputted by a user, nodes with regard to four detailed input values selected by the user and random $6 \times 6 (=36)$ output nodes are provided, and the user learned in the SOM network. Here, the reason why 36 nodes were provided is because maximum number of cases where heterogeneity can be generated was limited to 36. With regard to input values, they have been generated randomly with a priority in order of area and gender based on the priority of each item by valuation of heterogeneous values. The input values regarding four detailed items were generated randomly by valuing

heterogeneous values numerically. Like homogeneity, each detailed item selected with regard to four items was valued numerically and then learned.

For example, if ID: yicho1234, area: Seoul/Kyeonggi-do, gender: female, computer using hours: 1-2 hours, online training experience: yes were selected, the data structure of input node of the concerned ID is as follows. Here, users can learn through 10,000 inputs in the input nodes. Like homogeneity, output group distribution is formed in relation to input node. The distribution formed like this forms heterogeneous categorization map as seen in Figure 2(right). In the figure, $N=10,000$, and $a \sim d$ are the number of heterogeneous items and m is the group number in the heterogeneous categorization map. In this case, the number of group was 16. A user with ID 1 was categorized into heterogeneous group 4 in this instance.

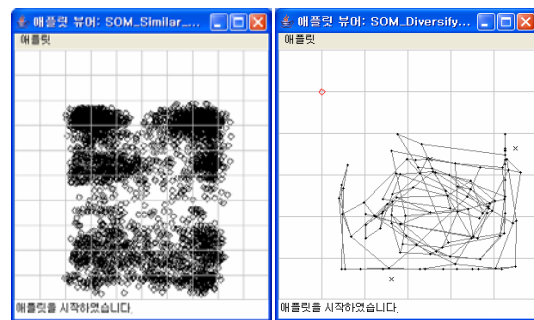


Figure 2. The process of group formation (left: Homogeneous, right: Heterogeneous)

Group is generated through input of learners with the distribution generated by homogeneous and heterogeneous SOM learning. The number of total group is decided by the number of people in a group, which is performed by manager's input. The input items of a learner are made by selecting 10 input items (homogeneous, heterogeneous). In order to meet homogeneity and heterogeneity with homogeneous and heterogeneous distributions learned through 10 input vectors, final learner's group meeting homogeneity and heterogeneity is generated by providing weight to each vector. The size of learning group (size of community) can be designated by manager randomly.

Finally, the homogeneous categorization map M generates the final group G for learning by randomly taking among groups excluding m to which concerned learner ID belongs in Figure 4.

3. Performance Evaluation

In this paper, a pilot test was conducted to evaluate actual users of the IMAS system. As a result, the evaluation of user satisfaction degree per group is seen in Figure 3. If the scale indicates 1 in satisfaction degree, it means very satisfactory, if the scale is 5, then it means very unsatisfactory. The scale from 1 to 5 with regard to 5 categories was expressed as value. Here, satisfactory means that members of a group or learning desire show a very positive result.

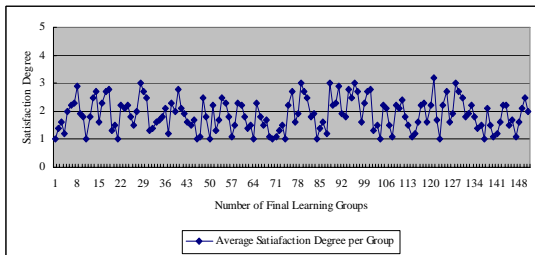


Figure 3. The satisfaction degree per group

As a result of surveying users' group satisfaction degree regarding 151 groups, we can see the average was distributed around scale value 2 of satisfaction degree. Accordingly, when automatic grouping was performed by agent, learners were generally satisfied. When they desired to maintain their group according to the value 2, around 51 groups of total 151 groups (34%) showed in favor of maintenance, while 61% showed don't care and less than 5% showed break.

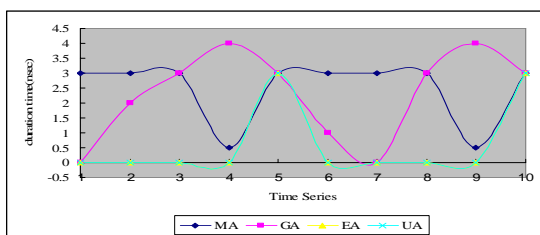


Figure 4. The average duration time and cycle in IMAS

The agent's duration (or activation) time by DIMAF framework on time slice in IMAS is drawn in Figure 6. In Figure 6, after GA is activated, UA is activated. But MA is activated all the way except the activation time of GA. EA is activated after GA's activation. This cycle is repeated in IMAS e-learning system. Owing to DIMAF, IMAS can activate intelligently among many users in ubiquitous environment.

4. Conclusions

To do development of e-learning community system, we have made an inclination test questionnaire for the formation of effective and efficient online learning community. And then, we have implemented and realized an automatic grouping system with information of learners that appear through the questionnaire and by using an intelligent agent.

The results of our experiment with 1,000 people in reality by means of developing the grouping system have shown that 151 groups are automatically formed.

In the future, it is necessary to improve services concerning the communication between users by supplementing the grouping system and to continue research on which multi agent system can be achieved effectively in automatic grouping.

References

- [1] M. J. Rosenberg, E-learning: Strategies for Delivering Knowledge in the Digital Age, McGraw Hill, New York, pp.28-29, 2001.
- [2] A. P. Rovai, "Building sense of community at a distance". International Review of Research in Open and Distance Learning, vol.3, no.1, 2002.
- [3] B. Winson, and M. Ryder, Dynamic learning communities: An alternative to designed instructional system. 2001.
- [4] B. Winson, and M. Ryder, Distributed learning communities: An alternative to designed instructional system. derived from <http://cudenver.edu/~bwilson>, 1998.
- [5] D.P. Fulford, and S. Zhang, "Perceptions of interaction: The critical predictor in distance education" The American Journal of Distance Education. vol.7, no 3, pp.181-198, 1993.
- [6] Stuart Russel, Peter Norvig, Artificial Intelligence: A Modern Approach, Prentice Hall International Editions, 1995.
- [7] John R. Graham, Keith S. Decker, Towards Distributed, Environment Centered Agent Framework. Appearing in Intelligent Agents IV, Agent Theories, Architectures, and Languages Springer-Verlag, Nicholas Jennings, Yves Lesperance, Editors, 2000.
- [8] Kohonen, [Self-Organizing Maps](#), Springer Series in Information Sciences, vol.30, 1995; [Third, extended edition, 2001](#).

PID Controller Design Using Double Helix Structured DNA Algorithms with Recovery Function

Jeong-Jung Kim and Ju-Jang Lee
Electrical Engineering and Computer Science
Korea Advanced Institute of Science and Technology(KAIST)
373-1, Guseong-dong, Yuseong-gu, Daejeon, 305-701, Korea
justi@odyssey.kaist.ac.kr, jjlee@ee.kaist.ac.kr

Abstract

PID controller has been widely used in industrial fields. Since PID parameters have a great influence on the stability and the performance of the control system, many approaches have been proposed to determine them. In this paper, we propose double helix structured DNA algorithms to design the type of PID controller and optimize PID parameters. The double helix structured DNA algorithms employ DNA encoding method based on a base-64 notational system to represent PID parameters, defines various mutation methods, and has a recovery function to preserve a DNA strand that has good fitness value. Computer simulation shows that we can get satisfactory results with the proposed method.

Keywords : DNA Algorithms, PID Controller.

1 Introduction

It is a well known fact that proportional integral derivative (PID) controller has been widely used in industrial fields, because, despite their simplicity, it can assure an adequate and satisfactory performance for a wide range of processes. Since PID parameters have a great influence on the stability and the performance of the control system, many approaches have been proposed to determine them.

One of the approaches that can obtain global optimization solution is GAs. Although this approaches can get optimal PID parameters, they have some disadvantages. As GAs' size of the chromosomes and populations increase, their computation time also increase, and a chromosome that has a good fitness value can be lost by a mutation.

The DNA(deoxyribonucleic acid) is a nucleic acid that contains the genetic instructions for the biological development of a cellular form of life. That is,

DNA is a blueprint of living things, because DNA makes RNA that makes proteins. If we implement DNA into a computer, we can mimic the process that occurred in organic life and can overcome the limitations of the traditional GAs. Some studies have been conducted to design controller inspired from the DNA. Yongsheng Ding et al.[1] designed the generalized membership-type Takagi-Sugeno fuzzy control system using DNA algorithms, Chu-Liang Lin et al.[2] suggested self-organizing PID control design based on DNA computing method and Huang Yourui et al.[3] proposed optimization for parameter of PID based on DNA Genetic Algorithm.

In this paper, we present a new method to design type of PID controller and optimize PID parameters by using a double helix structured DNA algorithms. More specifically, we use DNA encoding method based on a base-64 notational system to represent PID parameters, define various mutation methods, and suggest a recovery function to preserve a good DNA strand that has good fitness value. This paper is organized as follows. In Section 2, biological basis and implementation are given. Simulation results are shown in Section 3, and the conclusion is made in Section 4.

2 Biological Basis and Implementation

The nucleic acid DNA(deoxyribonucleic acid) serves as the genetic material in all living organisms and makes RNA that makes proteins. Base on the biological information about the DNA in [4], we implement DNA in a computer to design type of PID controller and optimize PID parameters.

2.1 DNA Encoding Method

The DNA molecule exists in cells as a long, coiled ladder like structure described as a double helix. Each

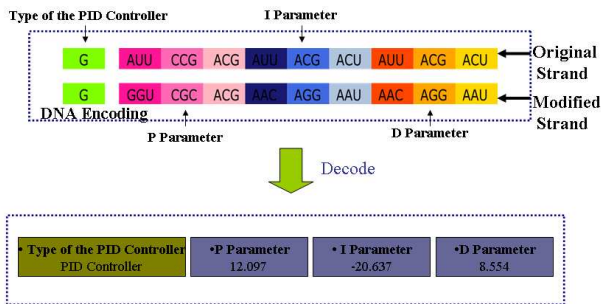


Figure 1: The encoding of stands corresponding to the type of the PID controller and PID parameters

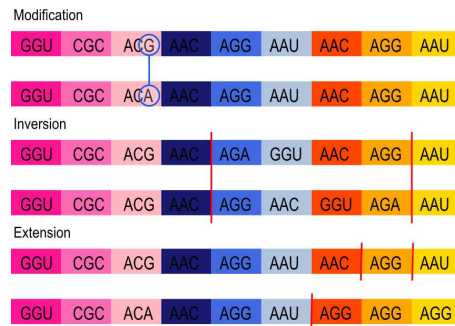


Figure 2: Description of each mutation

strand of the helix consists of a linear polymer made up of genetic building blocks called nucleotides, of which there are four types. Nucleotides vary, depending upon which of four nitrogenous base is part of the molecule - A(adenine), G(guanine), T(thymine), or C(cytosine). A triplet code of nucleotide bases specifies the codon, which in turn contains a specific anticodon on transfer RNA(tRNA) and assists subsequent transmission of genetic information in the formation of a specific amino acid. A chromosome consists of combinations of the above four bases and can represent different genes.

A single strand of DNA can be likened to a string consisting of a combination of for different symbols, A, G, C, T. Mathematically, this means we have a four-letter alphabet to encode information, which is more than enough, considering that an electronic computer needs only two digits, 0 and 1, for the same purpose. In the Fig.1, the first part of the DNA strand is the type of PID controller, and the second part is PID parameters. The type of PID controller is determined by only a nucleotide, while each PID Parameter is determined by three codons that use a base-64 notational system. Because each parameter is composed with three codons, a maximum decimal value is 262144(64x64x64). The length of DNA strand and maximum value are can be modified to meet a specification.

The double helix structured DNA is used to preserve good DNA strand. Each DNA strand is a template for synthesizing a new strand which is nearly identical to the previous strand. When one of strand is modified by a mutation operation, the modified strand is evaluated. If the modified strand is better than the original strand, the original strand is changed to modified strand. Otherwise, the modified strand is recovered from the original strand.

Further description about usage of double helix

structured DNA is shown in section 2.5.

2.2 Genetic Operators

Two genetic operators, DNA mutation operations and a PCR operation, are developed to modify our DNA.

Errors that occur in the synthesis are called mutations. Mutations are the results of the cells' attempts to repair chemical imperfections in this process, where a base is accidentally skipped, inserted, or incorrectly copied, or the chain is trimmed, or added to. Only three mutations, 'Modification', 'Inversion', 'Extension', are used to mutate DNA. One of the mutation methods is selected randomly. Description of each mutation is shown Fig.2. The Modification mutation is a point mutation that changes in one base of the DNA sequence. A randomly selected point is changed among A, G, T, C. In inversion mutation, a section determined by a randomly selected start point and an end point is inverted. After inversion, the order of the strand in the inversion region is reserved. An extension, last mutation method, is a kind of infection that influences adjacent codons.

2.3 DNA Shuffling

The polymerase chain reaction(PCR) is a rapid method of DNA cloning that has extended power of recombinant DNA research and eliminated the need for host cells in DNA cloning. PCR generates many copies of a specific DNA sequence through a series of a vitro reaction and can amplify target DNA sequences present in infinitesimally small quantities in a population of other DNA molecules. The PCR is implemented in a computer to shuffle DNA. A process of PCR is shown Fig.3. It is a process of the exchange of genetic information. All individuals are shuffled with best DNA by saving previous best individual.

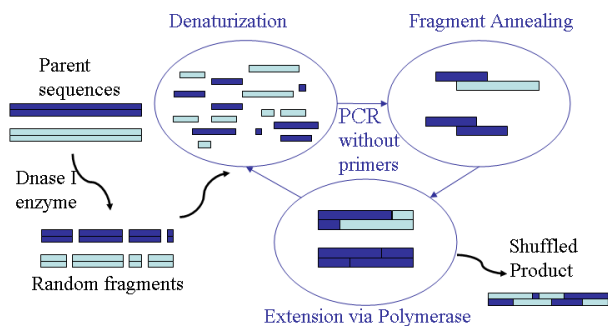


Figure 3: A process of PCR

2.4 Fitness Function

After decoding the type of PID controller and PID parameters that was encoded in a DNA strand, the PID controller design can be evaluated. A fitness function that minimizes rise time 15 steps, overshoot 5 percent, and settling time 50 steps is set. The fitness function is defined as (1) to evaluate decoded parameters. C_1 , C_2 and C_3 are determined by their priority.

$$f_{fit} = C_1 \times RTGap + C_2 \times OSGap + C_3 \times STGap \quad (1)$$

RTGap represents gap between real rise time and 15steps, OSGap represents gap between real Overshoot and 5 percent and STGap represents gap between real Settling Time and 50 steps.

2.5 Overall Process

An overall process of the double helix structured DNA algorithms is shown in Fig.4. The process first initialize each individual, and do mutation, DNA shuffling, evaluation, and recovery or change until maximum generation. An individual is the same as DNA, and has two strands. When one of strand is modified by a mutation operation, the modified strand is evaluated. If the modified strand is better than the original strand, the original strand is changed to modified strand. Otherwise, the modified strand is recovered from the original strand. This process is possible because the double helix structured DNA was used.

3 Simulation

To verify the PID controller design method that is designed in section 2, a motor model (2) is used to simulate.

$$G(z) = \frac{0.02937z^2 + 0.0153205z + 4.64302 \times 10^{-5}}{z^3 - 1.03869z^2 + 0.0386917z - 8.99251 \times 10^{-8}} \quad (2)$$

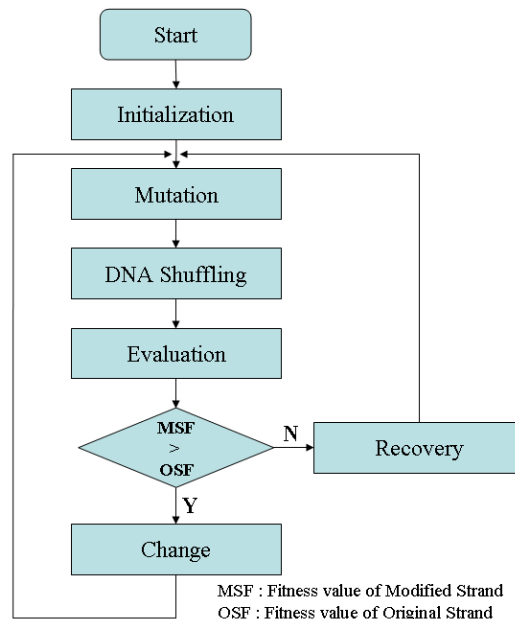


Figure 4: Overall process of the double helix structured DNA algorithms

Table 1: Simulation parameters

Parameter	Value
Maximum number of shuffling	10
Mutation rate for PID parameters	0.1
Mutation rate for type of PID controller	0.005
Number of individual	500
Maximum generation	1000

The fitness function that rise time has high priority, overshoot has medium priority and settling time has lower priority is set. And maximum fitness value is set to 10000.

The maximum number of shuffling for each process is 10, mutation rate of PID parameters is 0.1, mutation rate of PID controller type is 0.005. Furthermore the number of individual is set to 500, and Maximum is 1000. The specified parameter value that we use is given in Table1. Convergence behavior of the fitness function is shown in Fig.5. Initial fitness value is 10000, but it converges into 124 at the 1000 generation.

Some unit step response of the each PID controller designs are shown in Fig.6, and the PID parameters and specifications of PID controller are given in Table2.

Computer simulations show that after convergence

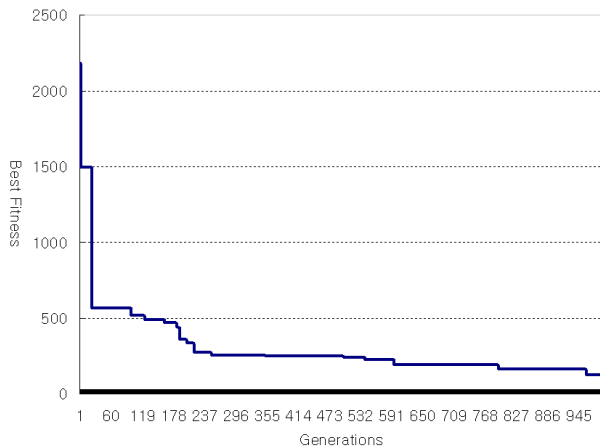


Figure 5: Convergence of the fitness function

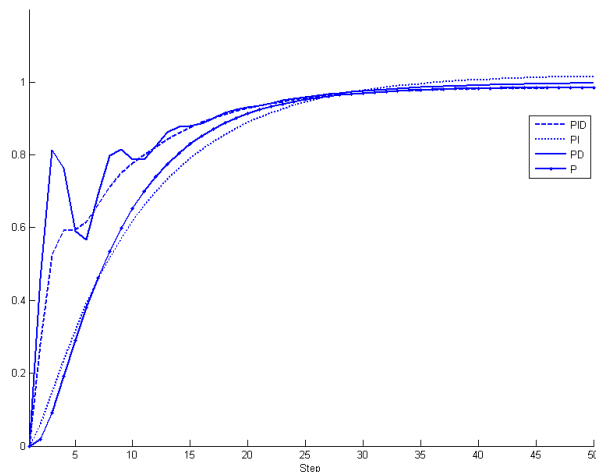


Figure 6: Unit step response of the each PID controller design

Table 2: Some the PID parameters and specifications of PID controllers

	PID	PI	PD	P
Kp	3.0337	1.9688	3.2827	2.1724
Ki	-0.0059	0.00391		
Kd	6.5205		12.3657	
Rise Time	15	18	15	15
Overshoot	0.000	1.945	0.000	0.000
Settling Time	36	29	30	35

of the double helix structured DNA algorithms, we can always find a group of parameter values for the type of PID controller and PID parameters that obtain satisfactory control performance.

4 Conclusions

This article uses the double helix structured DNA algorithms to design the type of PID controller and optimize PID parameters. The double helix structured DNA algorithms use DNA encoding method based on a base-64 notational system to represent PID parameters, define various mutation methods, and suggest a recovery function to preserve a DNA strand that has good fitness value.

The proposed method is well demonstrated and verified by simulations.

The Double helix structured DNA algorithms can be used for not only to design PID controller but also to design other controllers.

References

- [1] Chun-Liang Lin, Horn-Yong Jan and Thong-Hsing Huang, "Self-organizing PID control design based on DNA computing method," *Proc. IEEE International Conference on Control Applications*, 2-4 September 2004, pp. 568-573.
- [2] Yongsheng Ding and Lihong Ren, "DNA genetic algorithm for design of the generalized membership-type Takagi-Sugeno fuzzy control system," *Proc. IEEE International Conference on Systems, Man, and Cybernetics*, 8-11 October 2000, pp. 3862-3867.
- [3] Huang Yourui, Chen Xiuqiao and Hu Yihua, "Optimization for parameter of PID based on DNA genetic algorithm," *Proc. IEEE International Conference on Neural Networks and Brain*, 13-15 October 2005, pp. 859 - 861.
- [4] William S. Klug and Michael R. Cummings, "Essential of genetics fifth edition," *Pearson Prentice Hall*, 2005.

Authors' Index

[A]			Cheung	Y.	597
Abe	N.	376,442,809,813	Chigoji	Y.	276
Abe	K.	390	Cho	C-W.	33
Adachi	T.	639	Cho	J.H.	296
Adzni	A. R.	272	Cho	S.	474
Ahmad	F.	410	Cho	Y.I.	740
Ai	D.	280	Choi	B-S.	821
Aibe	N.	665	Choi	J.H.	474
Aihara	I.	617,613	Choi	W.	244
Aihara	K.	549,553,557,561, 565,569,601,605, 609,613,617,597	Chunh	J.	478
Aikawa	M.	657	Collier	T.	256
Aly	S.	802	Cui	G.	673
Ando	N.	183	[D]		
Aoki	Y.	736	Dai	F.	639,643
Araki	O.	693	Date	A.	210
Arita	T.	689	Date	T.	458
Arof	H.	410	Delgado-Frias	J.	709
Arroyo	F.	494,500	Dong	X.	627
Awano	T.	665	Doya	K.	106
			Du	J.	191
[B]			[E]		
Baba	S.	798	Eaton	M.	88
Balasuriya	J.C.	752	Ebara	Y.	794
Ban	X.	280	El-Sousy	F.F.M	37
Bando	T.	458	[F]		
Bank	S.C.	756	Faizal	E.R.M.	356
Beak	G.	426	Fernandez	L.	494,500
Blumstein	D.	256	Filipe	J.	709
Bode	K.	589	Finkelstein	R.	171
Bravo	G.	500	Freund	R.	509
[C]			Fubio	T.	430
Capi	G.	589	Fujihara	Y.	635,639
Chang	J-Y.	364	Fujii	K.	744
Chang	Y.Z.	60	Fujita	Y.	657
Chang	W-C.	33	Fujiwara	Y.	484
Chau	S.D.	320	Funaya	H.	531
Chen	L.	561597,609	Furutani	H.	131,135,140,144,652
Cheon	S.	196			

[G]			Hitaka	Y.	214,218
Garcia	I.	494	Homma	N.	390
Girod	L.	256	Hung	G.T.	60
Gobaru	E.	402	Hwang	S.T.	446,462
Goto	H.	442			
Goto	N.	284	[I]		
Goto	R.	308	Ichida	K.	764
Guo	J.	673	Ichikawa	S.	577
Gutmann	M.	553	Ido	H.	156.160
			Ihara	M.	527
[H]			Iihoshi	K.	131,135,140,144
Habib	M.K.	768	Ikeda	K.	96,531,778,782
Ham	O-K.	418	Ikeda	S.	131,135,140,144
Hamid	A.	719	Imabeppu	T.	732
Han	C-H.	817	Inoue	K.	131,135,140,144
Han	M.	46	Irie	T.	380
Han	S.	304	Ishibashi	T.	390
Han	S-H.	230,234	Ishibuchi	H.	372,422
Hanamoto	T.	635	Ishida	Y.	581,736
Hariharan	H.	384	Ishii	J.	214,218
Hayashida	J.	635	Ishii	S.	84,197,527,312,458
Hane	Y.	72	Ishikawa	S.	76,380
Hara	M.	204,577,593	Ishitobi	M.	152
Hashimoto	H.	183	Isoi	R.	430
Hashimoto	K.	613	Ito	K.	308
Hashimoto	T.	187,260	Ito	T.	131,135,140,144
Hatanaka	T.	669	Izumi	K.	748,752,756,764,768
Hayashi	E.	51,72,80,264,276, 284,348,352,368, 450,470,806	[J]		
Hayashi	K.	661	Jaber	A.Q.	513
Hazry	D.	384,406	Jeong	H.	304
He	G.	561	Jia	Y.	316
He	S.	376,442,813	Jiang	Y.	715
Hema	C.R.	719	Jie	W.R.	191
Henta	H.	80	Ju	C.W.	252
Heo	E.C.	249	Jung	B-W	196
Heo	J-S.	817	[K]		
Hikisaka	Y.	264	Kabata	K.	593
Hikizu	M.	344	Kanasugi	A.	440
Hiranuma	K.	148	Kang	S.H.	64
Hirata	Y.	565,601	Kamiya	Y.	344
Hirayama	J.	312	Kamohara	K.	752

Karthigayan	M.	406	Konno	T.	187
Katayama	K.	539	Kono	M.	131,135,140,144,148,152,226
Katayama	S.	652	Koo	H.S.	244
Katori	Y.	565	Koyamada	K.	794
Katuhara	M.	585	Kubik	T.	394
Kawakami	H.	206	Kukimoto	N.	794
kawamura	H.	56,68,92	Kurata	K.	210,328
Kawana	F.	728	Kuribayashi	K.	760
Kawato	M.	484	Kurita	T.	376
Kawawaki	D.	484	Kusumoto	Y.	760
Katai	O.	206	Kwon	Y.K.	249
Khoa	T.Q.D.	631			
Kim	B.C.	249	[L]		
Kim	H-D.	573,740	Labhart	N.	454
Kim	H-S.	239	Lambert	D.	171
Kim	H-Y.	239	Le	X-T.	230,234
Kim	J.B.	478	Lee	C-H.	418,426,462
Kim	Jungmin	196	Lee	D.D.	252
Kim	Jinyong	196	Lee	J.	304
Kim	J.J.	837	Lee	J.J.	817,821,829,837
Kim	J-W.	239	Lee	J.M.	300,466,474
Kim	J-Y.	426	Lee	K.S.	300
Kim	C.S.	64	Lee	M.H.	60,300,446,462
Kim	D.H.	296	Lee	M-N.	829
Kim	M-S.	829	Lee	S.	478
Kim	S.	196,418,426	Lee	S.H.	478
Kim	S.H.	249	Lee	S-H.	244
Kim	S.Y.	300	Lee	S.T.	60
Kim	W-H.	829	Lee	W-S.	230
Kim	W-I.	230	Li	T-Y.	364
Kim	Y.	418,426	Lim	G.H.	478
Kim	Y.D.	296	Lim	H.	466
Kim	Y.K.	234	Liu	GL.	768
Kinjo	H.	320,324	Lund	H.H	6
Kitagaki	K.	179			
Kitahata	H.	617	[M]		
Kobayashi	S.	260	Mackin	K.J.	104,116,517,539,774
Kohno	T.	569	Maeda	H.	605
Koizumi	N.	661	Maeda	S.	527
Kondo	E.	46	Maeshiro	M.	320
Kondo	T.	100	Majima	T.	585
Kondo	T.	123,438	Makino	K.	84
Konishi	O.	308	Manjunath	T.C.	288

Marasinghe	C.A.	752	Nunohiro	E.	517,539,774
Matsuki	T.	438			
Matsumoto	M.	440	[O]		
Matsumoto	S.	621	Offesen	M.	6
Matsuo	M.	549	Oh	S-B.	230,234
Matsushita	K.	517,539	Ohama	Y.	156
Matusita	K.	774	Ohashi	H.	292
Meng	D.	316	Ohdaira	T.	292
Minagawa	Y.	56,68	Ohkusa	Y.	605
Mirenkov	N.	709	Ohnishi	K.	324
Mishima	M.	705	Ohshiro	M.	517,774
Miyachi	M.	152	Ohtake	H.	110
Miyamichi	J.	430	Ohuchi	A.	56,68,92
Miyashita	S.	454	Oka	T.	790
Mizoguchi	H.	348	Okada	N.	46
Mochizuki	T.	450	Oku	M.	557
Moriki	T.	214	Okuma	C.	681
Morozoy	A.	171	Omatu	S.	156,160,163,167
Murakami	J.	681	Onitsuka	T.	693
			Ono	S.	685,732
[N]			Oomori	T.	809
Na	U.J.	252	Oosawa	C.	621
Nagamizu	Y.	131,135,140,144	Osaga	S.	312
Nagata	F.	760	Oshiro	N.	328
Naitoh	K.	677	Oswald	M.	509
Nakagawa	M.	631			
Nakamura	A.	179	[P]		
Nagarajan	R.	406,719	Park	D.	418
Nakayama	S.	685,732	Park	K-B.	825
Nakazono	K.	320,324	Park	H.G.	446
Nakamura	M.	119,728	Park	Y.T.	478
Nakamura	N.	798	Pagliarini	L.	13
Nakamura	Y.	84	Pathiranage	C.D.	748
Nakashima	T.	372,422	Paulraj	M.P.	384, 719
Narita	K.	96	Peng	J.	488
Nawata	T.	523	Pillai	B.	22
Neba	Y.	635	Pu	Y.	627
Ngo	T.D.	42			
Nii	M.	372	[R]		
Niimi	A.	308	Ramli	R.	513
Niimoto	K.	470	Raposo	H.	42
Nishioka	R.	92	Rizon	M.	406,384,719
Nomura	Y.	782	Rodriguez	A.	494

Rozailan	M.	406	Sugisaka	M.	1,171,204,356,384,
Ryu	G.G.	478			394,398,402,406,577,
Ryu	J.H.	446,462			593,643,709
			Sugita	K.	798
[S]			Suh	I.H.	478
Saito	M.	535	Sui	M-L.	545
Sakamoto	M.	131,135,140,144,652	Suziki	H.	565
Sakai	M.	390	Suzuki	R.	689
Sagara	S.	336,360	Suzuki	Y.	506
Sasaki	H.	430			
Salleh	K.	344	[T]		
Sapaty	P.	171,709	Tabuse	M.	222
Sato	A.	226,697	Tachibana	K.	268
Sato	M.	484	Taira	Y.	336
Sato	T.	106	Takadama	K.	585
Sato	O.	148,226	Takata	H.	523
Saudi	A.	272	Takaya	T.	56,68,92
Savageau	M.A.	621	Takahashi	N.	148,152,226
Sazali	Y.	719	Takebayashi	R.	268
Seki	H.	344	Takehara	Y.	222
Seo	K-H.	829	Takei	K.	390
Schaefer	G.	422	Takemoto	K.	621
Schioler	H.	42	Takenouchi	T.	197,312
Shah	N.M.	410	Taki	H.	376,442,813
Shang	T.	414	Takiguchi	N.	110
Serikawa	S.	535	Tamaki	T.	131,135,140,144
Shibasaki	H.	119	Tamaki	E.	332
Shibata	T.	84,484,458	Tamura	M.	360
Shimada	H.	308	Tamura	T.	693
Shimamoto	M.	206	Tan	J.K.	76,380
Shimono	M.	352	Tanaka	H.	204
Shin	J-H.	829	Tanaka	K.	376,430,809
Shin	H.B.	234	Tanaka	Yoshito	214,218
Shin	T.Y.	300	Tanaka	Yutaka	214
Shinohara	M.	430	Tanaka-Y	M.	701,705
Shiose	T.	206	Tang	L.	1
Shoji	K.	430	Taniguchi	R.	802
Sim	K-B.	573,740	Taylor	C.	256
Soh	Z.	110	Tejedor	J.A.	500
Son	S-H.	825	Teo	J.	272
Sonoda	T.	806	Tokuoka	S.	701
Su	X.	340	Toma	N.	332
Sugi	T.	119	Tomozoe	N.	131,135,140,144

Tone	M.	368	Yamaguchi	T.	116
Toshima	Y.	183	Yamaguchi	Y.	665
Tou	K.	380	Yamamori	K.	657,661
Trifa	V.	256	Yamamoto	M.	56,68,92
Tsugimura	K.	76	Yamamoto	Y.	681
Tsuji	T.	110	Yamamoto	H.	513
Tsumura	H.	18	Yamamoto	T.	320,324,328
Tsuruta	N.	802	Yamamoto	Y.	665
Tsusui	S.	647	Yamasaki	K.	517,774
			Yamasaki	T.	685,778,782
[U]			Yamashita	T.	197
Uchibe	E.	106	Yamashita	O.	484
Uchida	N.	764	Yang	H-C.	573
Uchino	S.	813	Yang	J.	244
Uehara	R.	46	Yasunaga	M.	661
Ueno	J.	100,123,438	Yasunaga	M.	665
Uewaki	T.	51	Yatoh	T.	360
Umeo	H.	268	Yokomichi	I.	214
Uosaki	K.	669	Yokota	M.	786,790,798
			Yokota	Y.	422
[W]			Yoshihara	I.	657,661,665
Wada	C.	214	Yoshikawa	K.	617
Wada	M.	308	Yoshizawa	M.	390
Wang	B.	728			
Wang	D.H.	244	[Z]		
Wang	M.	340	Zhang	C.	724
Wang	R.	609	Zhang	S.	280
Wang	S.	414,715	Zhang	T.	119
Wang	W.	280	Zhang	Y.G.	1
Wang	X.	398,728	Zhang	Y-I.	545
Wang	Y.	488	Zhao	H.	639,643
Watanabe	D.	585	Zhao	M.	340
Watanabe	K.	748,752,756,760, 764,768	Zhao	N.	724
Watanabe	Y.	689	Zhao	X.	597
Won	J.S.	252			
[X]					
Xiong	L.	724			
[Y]					
Yaacob	S.	384,406			
Yamada	T.	127			